

Xianmin Zhang
Nianfeng Wang
Yanjiang Huang
Editors

Mechanism and Machine Science

Proceedings of ASIAN MMS 2016 &
CCMMS 2016

Lecture Notes in Electrical Engineering

Volume 408

Board of Series editors

Leopoldo Angrisani, Napoli, Italy
Marco Arteaga, Coyoacán, México
Samarjit Chakraborty, München, Germany
Jiming Chen, Hangzhou, P.R. China
Tan Kay Chen, Singapore, Singapore
Rüdiger Dillmann, Karlsruhe, Germany
Haibin Duan, Beijing, China
Gianluigi Ferrari, Parma, Italy
Manuel Ferre, Madrid, Spain
Sandra Hirche, München, Germany
Faryar Jabbari, Irvine, USA
Janusz Kacprzyk, Warsaw, Poland
Alaa Khamis, New Cairo City, Egypt
Torsten Kroeger, Stanford, USA
Tan Cher Ming, Singapore, Singapore
Wolfgang Minker, Ulm, Germany
Pradeep Misra, Dayton, USA
Sebastian Möller, Berlin, Germany
Subhas Mukhopadhyay, Palmerston, New Zealand
Cun-Zheng Ning, Tempe, USA
Toyoaki Nishida, Sakyo-ku, Japan
Bijaya Ketan Panigrahi, New Delhi, India
Federica Pascucci, Roma, Italy
Tariq Samad, Minneapolis, USA
Gan Woon Seng, Nanyang Avenue, Singapore
Germano Veiga, Porto, Portugal
Haitao Wu, Beijing, China
Junjie James Zhang, Charlotte, USA

About this Series

“Lecture Notes in Electrical Engineering (LNEE)” is a book series which reports the latest research and developments in Electrical Engineering, namely:

- Communication, Networks, and Information Theory
- Computer Engineering
- Signal, Image, Speech and Information Processing
- Circuits and Systems
- Bioengineering

LNEE publishes authored monographs and contributed volumes which present cutting edge research information as well as new perspectives on classical fields, while maintaining Springer’s high standards of academic excellence. Also considered for publication are lecture materials, proceedings, and other related materials of exceptionally high quality and interest. The subject matter should be original and timely, reporting the latest research and developments in all areas of electrical engineering.

The audience for the books in LNEE consists of advanced level students, researchers, and industry professionals working at the forefront of their fields. Much like Springer’s other Lecture Notes series, LNEE will be distributed through Springer’s print and electronic publishing channels.

More information about this series at <http://www.springer.com/series/7818>

Xianmin Zhang · Nianfeng Wang
Yanjiang Huang
Editors

Mechanism and Machine Science

Proceedings of ASIAN MMS 2016 &
CCMMS 2016

 Springer

Editors

Xianmin Zhang
South China University of Technology
Guangzhou
China

Yanjiang Huang
South China University of Technology
Guangzhou
China

Nianfeng Wang
South China University of Technology
Guangzhou
China

ISSN 1876-1100 ISSN 1876-1119 (electronic)
Lecture Notes in Electrical Engineering
ISBN 978-981-10-2874-8 ISBN 978-981-10-2875-5 (eBook)
DOI 10.1007/978-981-10-2875-5

Library of Congress Control Number: 2016953857

© Springer Nature Singapore Pte Ltd. 2017

This work is subject to copyright. All rights are reserved by the Publisher, whether the whole or part of the material is concerned, specifically the rights of translation, reprinting, reuse of illustrations, recitation, broadcasting, reproduction on microfilms or in any other physical way, and transmission or information storage and retrieval, electronic adaptation, computer software, or by similar or dissimilar methodology now known or hereafter developed.

The use of general descriptive names, registered names, trademarks, service marks, etc. in this publication does not imply, even in the absence of a specific statement, that such names are exempt from the relevant protective laws and regulations and therefore free for general use.

The publisher, the authors and the editors are safe to assume that the advice and information in this book are believed to be true and accurate at the date of publication. Neither the publisher nor the authors or the editors give a warranty, express or implied, with respect to the material contained herein or for any errors or omissions that may have been made.

Printed on acid-free paper

This Springer imprint is published by Springer Nature
The registered company is Springer Nature Singapore Pte Ltd.
The registered company address is: 152 Beach Road, #22-06/08 Gateway East, Singapore 189721, Singapore

Contents

Part I Robotics and Mechatronics

Path Planning for Underwater Gliders with Motion Constraints	3
Zhiliang Wu, Mengyuan Zhao, Yanhui Wang, Yuhong Liu, Hongwei Zhang, Shuxin Wang and Ermai Qi	
A Novel Method for the Motion Planning of Hyper-redundant Manipulators Based on Monte Carlo	11
Jingdong Zhao, Liangliang Zhao and Yan Wang	
Gait and Trajectory Rolling Planning for Hexapod Robot in Complex Environment	23
Guiyang Xin, Hua Deng, Guoliang Zhong and Hengsheng Wang	
Real-Time Trajectory Plan for Six-Legged Robots to Open Doors Based on Tactile Feedback	35
Zhijun Chen and Feng Gao	
Optimized Body Position Adjustment of a Six-Legged Robot Walking on Inclined Plane	45
Yuan Tian and Feng Gao	
Evaluation of Spring Stiffness for Stable Grasp in Underactuated Fingers	57
Zhongyi Chu, Jian Hu and Shan Lu	
Kinematic Analysis of a Novel Hybrid Hand	75
Edison Tamilmanni and Sandipan Bandyopadhyay	
Research of the Relation Between Configuration and Skin-Friction Coefficient of an Underactuated Hand Based on the Maximum Grasping Space	89
Shangling Qiao, Hongwei Guo, Rongqiang Liu and Zongquan Deng	

Bionic Structure Design of a Flapping Wing Robot	101
Wenjuan Zhou, Huichao Deng and Xilun Ding	
LIPSA Hand: A Novel Underactuated Hand with Linearly Parallel and Self-adaptive Grasp	111
Yang Yang, Wenzeng Zhang, Xiangrong Xu, Handong Hu and Jian Hu	
COSA-FBA Hand: An Underactuated Hand with Five-gear Mechanisms and Built-in Actuators	121
Sijiao Ruan, Wenzeng Zhang, Tianyi Zhang and Shuang Song	
Topological Characteristics Analysis for a Family of Novel SCARA Parallel Mechanisms	131
Qingfei Zeng, Huiping Shen, Hengcun Qiang and TingLi Yang	
Friction Compensation in Trajectory Tracking Control for a Parallel Hip Joint Simulator	143
Xianlei Shan, Gang Cheng and Xihui Chen	
Sensitivity Analysis and Comparison of Parallel Schönflies-Motion Robots with a Single Platform	155
Guanglei Wu and Shaoping Bai	
Perception-Based Gait Planning for a Hexapod Robot Walking on Typical Structured Terrain	169
Xun Chai, Feng Gao and Yilin Xu	
Type Synthesis of <i>N</i>-Parallelogram-Based Surgical Arm with Remote Actuated Configuration	183
Fan Zhang, Xue Zhang, Lubin Hang, Cunyue Lu and Tomonari Furukawa	
Kinematics Analysis and Simulation of a Robot with Lower Extremity Exoskeleton	195
Maoyu Zhang, Yueri Cai and Shusheng Bi	
Equilibrium Conformation of Concentric-Tube Robots Under Loads Based on the Minimum Energy Principle	209
Long Huang, Changyan He, Yang Yang and Chenhan Guang	
Double-Parameter Regression Design of Drive Trains for Lightweight Robotic Arms	223
Haibin Yin, Cheng Kong, Mingchang He and Shansheng Huang	
Kinematics Analysis and Simulation of Two-Robot Coordination in Welding	237
Nianfeng Wang, Feiyue Zhang and Xianmin Zhang	
Development of Industrial Robot Teach Pendant Based on WinCE	249
Nianfeng Wang, Feiyue Zhang and Xianmin Zhang	

On the Output Motion of PMSM Driving a Planar Underactuated 2R Manipulator 261
 Jin Xie, Shicong Zhang and Zhaohui Liu

Fixed-Wing UAV Path Planning in a Dynamic Environment via Dynamic RRT Algorithm 271
 Liang Lu, Chengxing Zong, Xinyu Lei, Bozhi Chen and Ping Zhao

Design and Modeling of an Omni-Directional Vector Thrust Hexarotor 283
 MA Zhen-qiang, Dong Wen-han, Xie Wu-jie and Shao Peng-jie

Energy Consumption of Trotting Gait for a Quadruped Robot 295
 Xianbao Chen, Feng Gao, Chenkun Qi and Lin Wei

Spatial Rolling Contact Pair Generating the Specified Relative Motion Between Links 307
 Naoto Kimura and Nobuyuki Iwatsuki

Experiment Study of Positioning Accuracy for a SCARA Robot 317
 Yilong Tong, Yanjiang Huang, Lixin Yang, Changsheng Li and Xianmin Zhang

Part II Mechanism Design

The Automatic Generation for Type Synthesis of Serial Mechanisms Based on POC Method 327
 Chiyu Sun, Huiping Shen, Xiaorong Zhu, Anxin Liu, Lubin Hang and Tingli Yang

Dimensional Synthesis of a 2-PRS-PRRU Parallel Manipulator 341
 Lingmin Xu, Qiaohong Chen, Junhua Tong and Qinchuan Li

Synthesis of Two Primary Types of Walking Robot Legs 357
 Da Xi and Feng Gao

POC Analysis of Parallel Mechanisms Based on Conformal Geometric Algebra Description Method 367
 Chengwei Shen and Lubin Hang

Type Synthesis of the Hybrid Rotary Platform Mechanism with Three Degrees of Freedom 379
 Yundou Xu, Liangliang Chen, Wennan Yan, Bei Wang and Yongsheng Zhao

Conceptual Design and Analysis of a 6-Axis Double Delta Robot Towards High Acceleration 389
 Guanglei Wu

Design and Analysis of a Precise Adjustment Mechanism for Lithography Objective Lens Based on Slit Diaphragm Flexure.	403
Shize Dong, Kang Guo, Xianling Li, Huanan Chen and Mingyang Ni	
A Rolling Triangular-Bipyramid Robot Covering Bennett Linkage	415
Ran Liu and Yan-an Yao	
Mechanical Design and Dynamics Simulation of Locust-Inspired Straight Line Four-Bar Jumping Mechanism	429
Xiaojuan Mo, Wenjie Ge, Shaocong Wang and Donglai Zhao	
A Novel Ventricular Assist Miniscule Maglev Nutation Pump: Structure Design, 3D Modelling and Simulation.	443
Fengxiang Lin, Ligang Yao, Rongye Zheng, Wenjian Li and Changsheng Fang	
A Novel Mechanism for Winding Foaming Resin on Embedment Used in Aerospace.	455
Wuxiang Zhang, Keqing Zhang and Xilun Ding	
Mechanism Design and Analysis for a Lightweight Manipulator Based on Topology Optimization Methods	467
Hongchuan Zhang, Yanjiang Huang, Zhuowen Mo and Xianmin Zhang	
Synthesis of Branch Type Lower Limb Assistive Device	479
Yue Sun and Dar-Zen Chen	
On Passive Limbs in the Design of Parallel Mechanisms	493
Xu Wang, Weizhong Guo and Feng Gao	
The Application of Stewart Parallel Mechanism in Auricular Prosthesis Forming	505
Ruiqin Guo, Haiyan Gu and Qizhe Xu	
Modeling and Optimal Control of Rescue Quadruped Robot with High Payload	521
Nan Hu, Shaoyuan Li, Dan Huang and Feng Gao	
A Contrastive Study on the Force Analysis of the Active and Passive Overconstrained Parallel Mechanisms	537
Yundou Xu, Wenlan Liu, Jinwei Guo, Yongsheng Zhao, Jiantao Yao and Bo Han	
Parallel Manipulator of a Class RoboMech	547
Zhumadil Baigunchekov, Maksat Kalimoldayev, Sayat Ibrayev, Myrzabai Izmambetov, Talgat Baigunchekov, Batyr Naurushev and Nadira Aisa	

Unified Description of DOF of Crank Group Mechanism Based Screw Theory 559
 Yansong Liu, Jujiang Cao and Sheng Ren

An Introduction to the Reconstruction Model of Antikythera Mechanism 567
 Jian-Liang Lin and Hong-Sen Yan

Mobility Analysis of Generalized Mechanisms via Screw Algebra 581
 Tuanjie Li, Hanqing Deng and Lei Zhang

Research on the Mechanism of Alternating Temperatures on Space Bearing Preload 597
 Fengping Ning, Jiantao Yao, Ruiqin Li and Yongsheng Zhao

Development of a Continuously Statically Balanced Tablet Computer Stand 609
 Hsu-Kai Tsai, You-Shen Chen and Chin-Hsing Kuo

Part III Compliant Mechanism

The Local Optimum in Topology Optimization of Compliant Mechanisms 621
 Qi Chen and Xianmin Zhang

Minimizing the Difference Between Two Output Performances to Avoid de Facto Hinges in Topology-Optimized Compliant Mechanisms 633
 Benliang Zhu, Xianmin Zhang, Sergej Fatikow and Jinglun Liang

Topology Optimization of Compliant Mechanism Based on Minimum Manufacturing Constraints 645
 Zhang Yonghong, Sang Yang, Ge Wenjie and Xu Lei

A Boundary Reconstruction Algorithm Used in Compliant Mechanism Topology Optimization Design 657
 Nianfeng Wang, Hao Guo, Chaoyu Cui, Xianmin Zhang and Kai Hu

Topology Optimization of Thermally Actuated Compliant Mechanisms Using Node Design Variables 667
 Jinqing Zhan, Liangming Long and Zhichao Huang

Design of Bistable Pinned-Pinned Arches with Torsion Springs by Determining Critical Points 677
 Safvan Palathingal and G.K. Ananthasuresh

Optimal Design of a Novel Compliant Orthogonal Displacement Amplification Mechanism Considering Static and Dynamic Properties 689
 Weilin Chen and Xianmin Zhang

A Novel Bridge-Type Compliant Mechanism with Metastructures for Broadband Vibration Suppression	701
Xiaomeng Jiang, Zhong Chen, Wenqiang Cao and Xianmin Zhang	
Design of Micro-positioning Stage with Large Stroke Based on Novel Compliant Parallel Mechanism	709
Qinghua Lu and Youcai Zhang	
Design of a 3DOF Precision Positioning Stage Based on Corrugated Flexible Units	723
Nianfeng Wang, Zhiyuan Zhang, Xianmin Zhang and Luming Cui	
Part IV Reconfigurable Mechanism	
A Deployable Robot Based on the Bricard Linkage	737
Hao Shang, Dawei Wei, Rongjie Kang and Yan Chen	
Configuration Design and Kinematics Research of Scissor Unit Deployable Mechanism	749
Jianfeng Li, Sanmin Wang, Changjian Zhi and Yuantao Sun	
The Design and Simulation of a New Time-Controlled Spring Driven Hinge for Deployable Structures	761
Qi'an Peng, Sanmin Wang and Changjian Zhi	
The Configuration Design and Kinematic Analysis of the Deployable Mechanism Based on Bennett Linkage	773
Changjian Zhi, Sanmin Wang, Jianfeng Li and Qi'an Peng	
Design and Analysis of the Scissors Double-Ring Truss Deployable Antenna Mechanism	787
Bo Han, Yundou Xu, Jiantao Yao, Wenlan Liu, Xiangbin Li and Yongsheng Zhao	
Deployable Mechanism Design for Span Morphing Wing Aircraft	801
Binbin Gao, Rongjie Kang and Yan Chen	
Part V Kinematics	
Kinematics and Singularity of a 4-DOF Parallel Mechanism with Passive Spherical Joints	817
Binbin Peng, Wenchen Zhen, Xiangqian Wang, Kaituo He and Song FU	
Static Performance Analysis of an Exechon-like Parallel Kinematic Machine	831
Tengfei Tang, Jun Zhang and Marco Ceccarelli	
Motion Analysis of a 2-DoF Planar Mechanism	845
Ziming Chen, Xuedan Wei, Xiaomeng Liu, Dongliang Cheng and Peng Huang	

DOF and Kinematic Analysis of a Deployable Truss Antenna Assembled by Tetrahedral Elements 855
 Wenlan Liu, Yundou Xu, Yongsheng Zhao, Jiantao Yao, Bo Han and Liangliang Chen

Displacement Analysis of a 6R Serial Robot Mechanism Using Conformal Geometric Algebra 869
 Xiguang Huang and Dishuo Zhao

The Kinematics of a 3-DOF Mechanism for Wave Energy Converter 879
 Weixing Chen and Feng Gao

Isomorphism Identification of Planar Multiple Joint Kinematic Chains by Circuit Analysis Method 889
 Yanhuo Zou, Peng He, Dawei Xu and Jun Li

Automatic Synthesis of Planar Simple Joint Kinematic Chains by Single Kinematic Chain Adding Method 901
 Yanhuo Zou, Peng He, Dawei Xu and Jun Li

A Novel Geometric Modeling and Solution Method for Forward Displacement Analysis of 6-3 Stewart Platforms 911
 Ying Zhang, Qizheng Liao, Shimin Wei, Feng Wei and Duanling Li

Structural Conditions of Two Types of 3-DOF Parallel Mechanisms with Zero-Torsion Characteristics 925
 Jiexin Zou and Jingjun Yu

Kinematics and Stiffness Characteristics of 3-PRP Planar Parallel Mechanism 937
 Yuting Du, Ruiqin Li and Qianwen Dong

Topology Optimization of 3-DOF Peristaltic Structure Based on Vector Continuous Mapping Matrix 951
 Zhu Dachang and Feng Yanping

Vision-Aided Online Kinematic Calibration of a Planar 3RRR Manipulator 963
 Hai Li, Xianmin Zhang, Lei Zeng and Heng Wu

Workspace Analysis and Application of the PRRRP Decoupled Parallel Mechanism 973
 Shuwei Qu and Ruiqin Li

The Workspace Analysis and Simulation of a Novel Dexterous Hand FZU-I 987
 Fanlei Chen, Ligang Yao, Chen Peng, Changsheng Fang and Wenjian Li

Real-Time Solutions to the Forward Kinematics of a 2RSS + RRR Parallel Mechanism	995
Hongdong Zhang, Yuru Zhang and Dangxiao Wang	
A Step Identification Method for Kinematic Calibration of a 6-DOF Serial Robot.	1009
Huaiyan Tang, Zhenya He, Yexin Ma and Xianmin Zhang	
Part VI Dynamics of Machinery	
Dynamic Characteristics of Planetary Transmission with Thin-Walled Ring Gear on Elastic Supports under Different Working Conditions	1023
Jianying Li and Qingchun Hu	
Stiffness Modeling of Parallel Manipulator with Articulated Traveling Plate	1043
Tao Sun, Hao Wu, Binbin Lian, Panfeng Wang and Yimin Song	
The Vibration Control of Stick-Slip Actuated Precision Positioning Structure	1057
Yunzhi Zhang, Xianmin Zhang and Qinghua Lu	
Dynamics Analysis of a Modular Reconfigurable Parallel Robot	1069
Qisheng Zhang, Ruiqin Li and Jingjing Liang	
Inversion Study of Current Parameters Based on Attitude Data of Subsurface Buoy System	1083
Z.Y. Chang, Y.M. Fang and Z.Q. Zheng	
Dynamic Modeling of Spherical 5R Parallel Mechanism for Spherical Plain Bearing Running-in Equipment.	1097
Yilei Zheng, Weidong Guo and Yan Xie	
Dynamic Modeling and Analysis of Sucker Rod Pumping System in a Directional Well	1115
Dong-yu Wang and Hong-zhao Liu	
Dynamics Modeling, Control System Design and Simulation of Manipulator Based on Lagrange Equation.	1129
Da-quan Li, Hua-jie Hong and Xian-liang Jiang	
The Dynamic Characteristics Analysis of the Vertical Milling-Turning Machining Center	1143
Jialin Li, Yidu Zhang, Qiong Wu and Hanjun Gao	
Dynamic Modeling and Simulation of Q-Baller—A Spherical Wheeled Robot	1153
Jiamin Wang and Yuyi Lin	

Stiffness Analysis and Measurement Method for a 3-DOF Cable-Driven Joint Module 1167
 Kaisheng Yang and Guilin Yang

Part VII Joint Clearance

Elastodynamics of a Rigid-Flexible 3-RRR Mechanism with Joint Clearances 1185
 Xuchong Zhang and Xianmin Zhang

Accuracy Analysis of a 3-DOF Mechanism with Joint Clearances Under Different Working Modes 1199
 Xuchong Zhang and Xianmin Zhang

Dynamic Response and Stability Analysis of a Parallel Mechanism with Clearance in Revolute Joint 1211
 Yulei Hou, Guoning Jing, Yi Wang, Daxing Zeng and Xuesong Qiu

Chaos Suppression for Joint Clearances Based on Trajectory Planning of Robotic Mechanisms 1225
 Wanghui Bu, Chenguang Yang, Duyu Chen, Hangyu Zhou, Jia Hu and Yinfan Hou

Effects of Body Flexibility on Dynamics of Mechanism with Clearance Joint 1239
 Zheng Feng Bai, Xin Shi and Ping Ping Wang

The Dynamics Modeling of Serial Robot with Joint Clearance Based on the Massless Link Method 1249
 Chanyuan Chen, Lixin Yang, Yanjiang Huang, Haopeng Zhou, Jinying Zhang and Xianmin Zhang

Part VIII Gear and Transmissions

A Precise FE Model of a Spur Gear Set Considering Eccentric Error for Quasi-static Analysis 1263
 Huimin Dong, Chu Zhang, Xiwei Wang and Delun Wang

Velocity Ratio Variation Device Without Interruption and Control System for Automatic Ratio Change 1275
 Masaharu Komori and Yukihiro Kimura

An Elastic Transmission Model of Spur Gears for TE Analysis 1287
 Huimin Dong, Zhipeng Li and Delun Wang

Configuration Synthesis of Compound Gear Trains Based on State-Space Approach 1299
 Jun Qiu, Huimin Dong, Yali Ma, Shangkun Xu and Delun Wang

Identification and Modification of Closed Defect of the Location Function for *N*-Lobed Noncircular Gears 1315
 Xin Zhang and Shouwen Fan

Part IX MISC: Sensor, Actuator, Linkage, and Cam

Design of a Maximally Regular Acceleration Sensor Based on Generalized Gough-Stewart Platforms 1343
 Zhizhong Tong, Hongzhou Jiang, Hui Zhang and Jingfeng He

A Multi-objective Design Optimization of a Centrifugal Cooling Fan on a TEFC Motor 1355
 Qi Lu, Fei Zhen, Martin Kefer and Maria Nylander

Research on Slope Climbing Capacity of a Close Chain Five-Bow-Shaped-Bar Linkage 1365
 Lian-qing Yu, Yuan-yuan Mei, Yu-jin Wang and Chang-lin Wu

Multi-objective Optimization Design of Automated Side Loader of Arm Actuator 1377
 Binlin Yi and Jiangnan Liu

Optimal Design of Parallel Mechanism for Automobile Electro-Coating Conveyor 1395
 Suhua Yao, Guoqin Gao and Zhiming Fang

Design and Simulation of a Dual-Piezo-Driven Actuator Utilizing the Bridge-Type Mechanism 1405
 Junyang Wei, Xianmin Zhang and Sergej Fatikow

A Novel Method of Fault-Location in Long Power Cable 1419
 Jianwei Mi, Ximing Men, Xiaoli Fang and Libin Fan

The Study Status of the Key Techniques About the Toroidal Drive 1431
 Yanhua Zhang, Jujiang Cao and Beibei Liu

Motion Control of Pneumatic Muscle Actuator Using Fast Switching Valve 1439
 Shenglong Xie, Jiangping Mei, Haitao Liu and Panfeng Wang

Research on SEM’s Astigmatism Detection Based on Image Processing 1453
 Yihua Lu, Xianmin Zhang and Zhenya He

A New Position and Attitude Measurement Method for Planar Parallel Mechanism 1461
 Zhicong Jian, Xianmin Zhang and Zhenya He

Research on Robot Calibration Based on Laser Tracker 1475
 Yabo HuangFu, Lubin Hang, Wushan Cheng, Liang Yu, Chengwei Shen,
 Jun Wang, Wei Qin and Yan Wang

**Calculation and Analysis on Crest Thickness of Edge Tooth
 of Height-Modified TA Worm** 1489
 Chongfei Huai, Yaping Zhao and Yimin Zhang

**Architecture of a Hydraulic Hybrid Vehicle with Pressure
 Cross-Feedback Control** 1503
 Zhuoqun Chen, Chaoyu Yu, Wei Wu, Chongbo Jing, Shihua Yuan
 and Chongfeng Di

**The Vibration Modal Analysis of the Ball Screw About
 Precision Machine Tools** 1517
 Nian- Cong Liu, Jin Xie and Hao- Ran Zeng

**The Kinematic Invariants in Testing Error Motion
 of Machine Tool Linear Axes** 1525
 Yu Wu, Delun Wang, Zhi Wang, Huimin Dong and Shudong Yu

**Research on the Principle of Six Degree-of-Freedom
 Laser Tracker Metrology** 1541
 Liang Yu, Lubin Hang, Wushan Cheng, Yabo Huangfu, Wentao Li
 and Guobin Yang

**Kinematic Synthesis of Planar Cam Mechanism with Translating
 Roller Follower by Kinematic Analysis of Binary Link Chain** 1557
 W.W. Zhu and Z.H. Lan

Part I
Robotics and Mechatronics

Path Planning for Underwater Gliders with Motion Constraints

Zhiliang Wu, Mengyuan Zhao, Yanhui Wang, Yuhong Liu, Hongwei Zhang, Shuxin Wang and Ermai Qi

Abstract The underwater glider technology is a promising ocean observing technique. This paper presents path planning for underwater gliders as they travel in the water. The objective is that the underwater glider arrives at the destined depth while avoiding the obstacles in the way. Artificial potential field approach is used in the path planning algorithm, which is featured by adding motion constraints of the underwater glider into path generation.

Keywords Underwater glider · Path planning · Artificial potential field · Motion constraint

Z. Wu (✉) · M. Zhao · Y. Wang · Y. Liu · H. Zhang · S. Wang
School of Mechanical Engineering, Tianjin University, Tianjin 300072, China
e-mail: zhlwu@tju.edu.cn

M. Zhao
e-mail: zmy15@tju.edu.cn

Y. Wang
e-mail: yanhuiwang@tju.edu.cn

Y. Liu
e-mail: yuhong_liu@tju.edu.cn

H. Zhang
e-mail: zhanghongwei@tju.edu.cn

S. Wang
e-mail: shuxinw@tju.edu.cn

E. Qi
National Ocean Technology Center, 219 Jieyuanxi Rd, Nankai District,
Tianjin 300112, China
e-mail: qiermai@163.com

1 Introduction

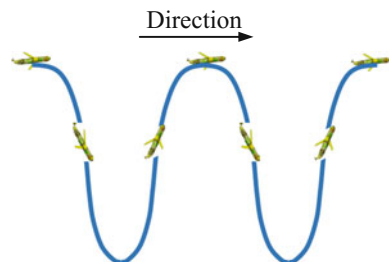
Underwater gliders are one type of autonomous underwater vehicles and have been increasingly used in oceanographic observations. Their outstanding advantage of long endurance make them competitive to conventional autonomous underwater vehicles (AUVs). They have been used to obtain long-term oceanographic parameters for scientific research purpose in both shallow waters and deep oceans. Unlike AUVs, underwater gliders use a pair of wings to glide downward and upward in the water, following a sawtooth path, and communicate with the shore station when surfacing. Figure 1 shows the typical trajectory of underwater gliders.

Underwater gliders usually take paths that are prescribed beforehand. Following the preset paths, underwater gliders should be able to safely measure the specific parameters with a certain sampling resolution. A safe measurement is defined as no collision with obstacles during observation. The obstacles that underwater gliders need to be avoided include those on the water surface, such as ships or boats and islands, as well as those that are in the water, such as the sea floor and underwater valleys. Interference between the objects at the water surface and the surfacing locations or collision with obstacles in the water may cause fatal damage and even loss of the underwater glider [1]. Hence, path planning for underwater gliders have attracted people's attention.

Most work focused on development of path planning algorithms for underwater gliders aims to generate either a collision-free path or an energy efficient path at the ocean surface, assuming that the obstacles are known ahead of planning [2–8]. However, underwater gliders may also encounter underwater obstacles. Under such circumstances, the underwater path taken by the underwater glider needs to be adjusted according to its motion constraints, such as the gliding angle and the turning radius. The overall path at the water surface may also need to be re-planned accordingly.

Artificial potential field (APF) approach was proposed by Khatib [9] to avoid obstacles. It is well known for simplicity and efficiency in finding an optimal solution. Many efforts have been contributed to improvement of APF approach [10–14]. This approach has been widely used for ground vehicles, aircrafts, and underwater vehicles. Compared with mobile robots travelling over rigid terrain, aircrafts and underwater gliders can move more freely in an open 3D space if no

Fig. 1 Typical underwater glider trajectory



constraints are posted. But for an underwater glider that has to follow a path with a certain glide slope, it will have to select a collision-free path on a spiral surface. It is also required to be steered according to the minimum turning radius requirement, which is similar to the ground vehicles. This paper presents path planning for underwater gliders when obstacles are detected in the water. Artificial potential field (APF) approach is used in the path planning strategy and the motion of the underwater glider is constrained in path generation.

The rest of this paper is arranged as follows: Sect. 2 states the path planning algorithm using APF approach; Sect. 3 presents the numerical simulation result of glider path planning; and Sect. 4 concludes this paper.

2 Underwater Glider Path Planning

In an oceanic observation, the underwater glider is supposed to autonomously find a safe path from the start point to the goal. It should arrive the destined depth and simultaneously measure the oceanographic parameters with a certain resolution along the path. A complete path planning for the underwater glider therefore refers to generation of a no-collision path for both surfacing locations and underwater movement.

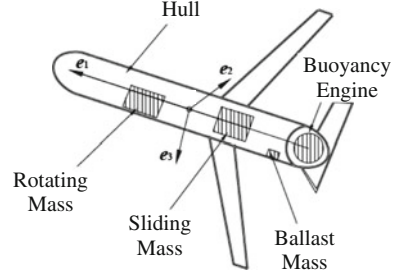
As the underwater glider moves in the water, it dives or goes up with specific motion parameters. It has to avoid obstacles detected by the sensors on board and approaches the destined depth and the specified waypoints for surfacing as closely as possible. When an obstacle is present and interferences with the underwater glider's current path in the water, a detour is needed and the underwater glider may have to change its current direction to avoid collision with the obstacle.

This section describes the artificial potential fields that are applied to represent the relations between the underwater glider and the goal, as well as the underwater glider and the obstacle. The underwater glider's motion constraints are also explained in this section.

2.1 *Underwater Glider Modeling*

The underwater glider is analogous to the gliders in the air, but it descends and ascends in the water by changing buoyancy to negative or positive states. The net buoyancy is controlled by an internal buoyancy engine, as shown in Fig. 2. The underwater glider moves the sliding and rotating masses to control its pitch and roll, while uses the rudder to control yaw and heading.

Fig. 2 Schematic diagram of a conventional underwater glider [15]



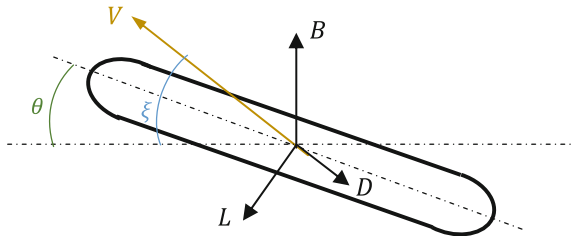
2.2 Underwater Glider Motion Constraints

As the underwater glider travels up and down in the water, its motion is subjected to certain constraints. Usually, the underwater glider is flown at a certain gliding angle in one observation according to the scientific research requirement [16]. The gliding angle is closely related to the pitch angle, which puts an orientation constraint for the underwater glider, as shown in Fig. 3. Another motion constraint that cannot be ignored in path planning is the turning radius, especially in shallow waters where the underwater glider may have to inflect frequently. The underwater glider is steered by shifting the rotating mass and rolls to turn. A minimum turning radius is therefore determined by the structure and physical properties of the underwater glider. For a specific operation, the constraints on the gliding angle ξ and the turning radius R can be expressed as:

$$\begin{cases} \xi = \xi_0 \\ R \geq R_{min}. \end{cases} \quad (1)$$

where ξ_0 denotes the desired gliding angle required by the operation and R_{min} denotes the minimum turning radius respectively.

Fig. 3 Schematic diagram of force balance and angle relationship (side view). B is the net buoyance, D is the drag, L is the lift, V is underwater glider velocity, θ is the pitch angle, and ξ is the glide angle



2.3 Artificial Potential Fields

Motion of the underwater glider during operation consists of a series of behaviors that are either approaching the goal or avoiding the obstacles. In our algorithm, the underwater glider's movement toward the goal is modeled as being driven by an attractive potential field created by the goal, while the obstacles are assumed to exert repulsive forces on the underwater vehicle, pushing it away from its original path to avoid potential collision [17, 18]. The attractive potential field exerted by the goal is expressed as:

$$U_{att} = \begin{cases} \frac{1}{2}k_a R_d^2, & R_d > D_d \\ 0, & 0 < R_d \leq D_d. \end{cases} \quad (2)$$

where U_{att} represents the potential function for the attractive potential field, k_a is a positive scalar control gain, R_d is the distance between the underwater glider and the goal, and D_d is the influence distance of the goal. The attractive force acted on the underwater glider can be obtained as the minus gradient of the attractive potential field, as indicated in Eq. (3).

$$\mathbf{F}_{att} = -\nabla U_{att} = \begin{cases} -k_a R_d \nabla R_d, & R_d > D_d \\ 0, & 0 < R_d \leq D_d. \end{cases} \quad (3)$$

The repulsive potential field generated by the obstacle is given as:

$$U_{rep} = \begin{cases} \frac{1}{2}k_r \left(\frac{1}{R_o} - \frac{1}{D_o}\right)^2, & 0 < R_o \leq D_o \\ 0, & R_o > D_o. \end{cases} \quad (4)$$

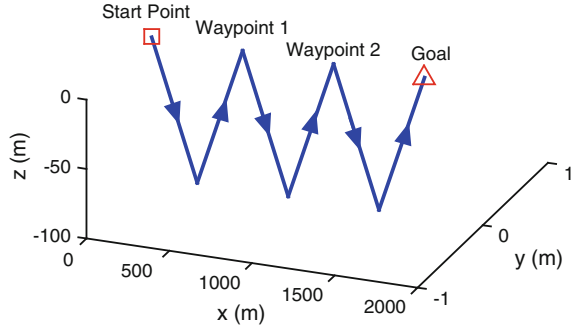
where U_{rep} represents the potential function for the repulsive potential field created by the obstacle, k_r is a positive scalar control gain, R_o is the distance between the underwater glider and the obstacle, and D_o is the influence distance of the obstacle. The repulsive force acted on the underwater glider is then:

$$\mathbf{F}_{rep} = -\nabla U_{rep} = \begin{cases} k_r (1/R_o - 1/D_o) / R_o^2 \nabla R_o, & 0 < R_o \leq D_o \\ 0, & R_o > D_o \end{cases} \quad (5)$$

3 Numerical Simulation

In this section, numerical simulation is conducted on path planning for an underwater glider with motion constraints. The prototype used in the simulation is PETREL [19], the underwater glider developed in our laboratory. In the simulation,

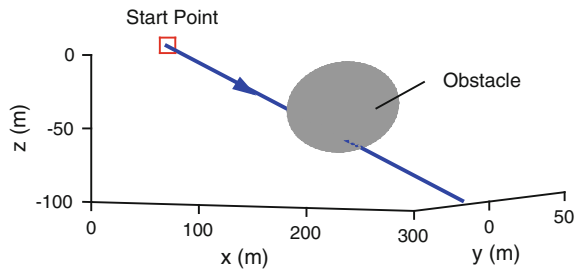
Fig. 4 The original path with specified waypoints. $z = 0$ denotes the water surface. $z = -100$ denotes the destined depth of 100 m



the underwater glider is modeled as a point mass with a minimum turning radius of 10 m. Assume that the underwater glider undergoes an oceanographic observation which requires an operating depth of 100 m underwater and a glide angle of 20° . The underwater glider starts the operation at $(0, 0, 0)$ and a series of profiles are expected. The original path with the waypoints is illustrated in Fig. 4.

Suppose the underwater glider encounters a spherical obstacle during its first dive, as shown in Fig. 5. The original path would no longer be feasible. The underwater glider will have to change its current direction and take a new path to avoid collision with the obstacle. Figure 6 shows the new path generated by the proposed path planning algorithm. The underwater glider turns first to avoid the obstacle with the minimum turning radius. As it glides away from the obstacle, the underwater glider starts to move toward the operating depth when it is beyond the influence distance of the obstacle. During the diving process, the underwater glider keeps the glide angle constant. Therefore, the generated path practical and effective for oceanographic observation. Another collision-free path that is generated without the motion constraints of the underwater glider is also indicated in Fig. 6 for comparison. It is apparent that although this path is safe, the underwater glider may not be able to follow due to the constraints on orientation and turning radius.

Fig. 5 Obstacle interference during the first dive. $z = 0$ denotes the water surface. $z = -100$ denotes the destined depth of 100 m



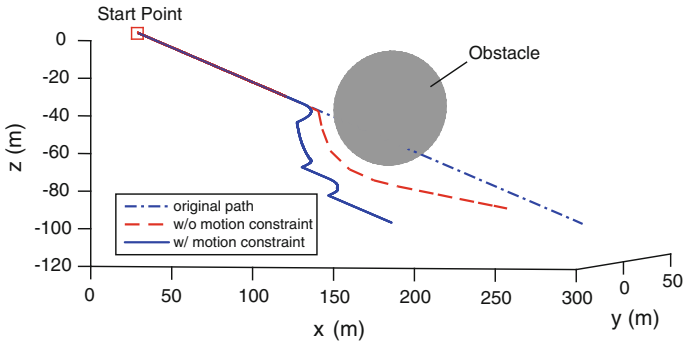


Fig. 6 Path generated with underwater glider motion constraints. $z = 0$ denotes the water surface. $z = -100$ denotes the destined depth of 100 m

4 Conclusions

Underwater gliders have been increasingly used for long-term oceanographic observation as one kind of promising autonomous underwater vehicles. This paper presents path planning for underwater gliders under the circumstances that obstacles are detected as the underwater glider travels through the water. Artificial potential fields approach is applied to represent the impacts of the goal and the obstacles on the underwater glider. The motion constraints of the underwater glider are also taken into account in path generation. A practical and effective collision-free path has been obtained.

Acknowledgments The authors thank the reviewers for their constructive comments. We also gratefully acknowledge the support from the National Natural Science Foundation of China (Grant No. 51205277, 51475319) and State Oceanic Administration of China (Grant No. cxsf2014-33).

References

1. Merckelbach L (2013) On the probability of underwater glider loss due to collision with a ship. *J Mar Sci Technol* 18:75–86
2. Witt J, Dunbabin M (2008) Go with the flow: optimal AUV path planning in coastal environments. In: 2008 Australian conference on robotics and automation, 2008
3. Zhang M, Inanc T, Ober-Blobaum S, Marsden JE (2008) Optimal trajectory generation for a glider in time-varying 2D ocean flows B-spline model. In: 2008 IEEE international conference on robotics and automation. IEEE Press, New Jersey, pp. 1083–1088
4. Rao D, Williams SB (2009) Large-scale path planning for underwater gliders in ocean currents. In: 2009 Australasian conference on robotics and automation
5. Thompson DR, Chien S, Chao Y, Li P, Cahill B, Levin J, Schofield O, Balasuriya A, Petillo S, Arrott M, Meisinger M (2010) Spatiotemporal path planning in strong, dynamic, uncertain currents. In: 2010 IEEE international conference on robotics and automation. IEEE Press, New Jersey, pp. 4778–4783

6. Isern-Gonzalez J, Hernandez-Sosa D, Fernandez-Perdomo E, Cabrera-Gamez J, Dominguez-Brito AC, Prieto-Maranon V (2011) Path planning for underwater gliders using iterative optimization. In: 2011 IEEE international conference on robotics and automation. IEEE Press, New Jersey, pp. 1538–1543
7. Lolla T, Lermusiaux PFJ, Uechermann MP, Haley PJ Jr (2014) Time-optimal path planning in dynamic flows using level set equations: theory and schemes. *Ocean Dyn* 64:1373–1397
8. Eichhorn M (2015) Optimal routing strategies for autonomous underwater vehicles in time-varying environment. *Robot Auton Syst* 67:33–43
9. Khatib O (1986) Real-time obstacle avoidance for manipulators and mobile robots. *Int J Robot Res* 5:90–99
10. Chanclo B, Luciani A (1996) Global and local path planning in natural environment by physical modeling. In: *Intelligent robots and systems '96*, pp. 1118–1125
11. Plumer E (1992) Neural network structure for navigation using potential fields. In: *International joint conference on neural networks'92*, pp. 327–332
12. Akishita S, Hisanobu T, Kawamura S (1993) Fast path planning available for moving obstacle avoidance by use of laplace potential. In: *1993 IEEE intelligent robots and systems*, pp. 673–678
13. Makita Y, Hagiwara M, Nakagawa M (1994) A simple path planning system using fuzzy rules and a potential field. In: *1994 IEEE world congress on computational intelligence*, pp. 994–999
14. Wu K, Chen C, Lee J (1996) Genetic-based adaptive fuzzy controller for robot path planning. In: *1996 IEEE international conference on fuzzy systems*, pp. 1687–1692
15. Wang Y, Zhang H, Wang S (2009) Trajectory control strategies for the underwater glider. In: *2009 IEEE international conference on measuring technology and mechatronics automation*. IEEE Press, New Jersey, pp. 918–921
16. Jenkins SA, Humphreys DE, Sherman J, Osse J, Jones C, Leonard N, Graver J, Bachmayer R, Clem T, Carroll P, Davis P, Berry J, Worley P, Wasyl J (2003) Underwater glider system study. Technical report, Scripps Institution of Oceanography
17. Yang Y, Wang S, Wu Z (2010) Multi-AUV coordination in the underwater environment with obstacles. In: *IEEE Oceans 2010*. IEEE Press, New Jersey, pp. 1–6
18. Yang Y, Wang S, Wu Z, Wang Y (2011) Motion planning for multi-HUG formation in an environment with obstacles. *Ocean Eng* 38:2262–2269
19. Wang S, Liu F, Shao S, Wang Y, Niu W, Wu Z (2014) Dynamic modeling of hybrid underwater glider based on the theory of differential geometry and sea trials. *J Mech Eng* 50:19–27 (in Chinese)

A Novel Method for the Motion Planning of Hyper-redundant Manipulators Based on Monte Carlo

Jingdong Zhao, Liangliang Zhao and Yan Wang

Abstract The motion planning of hyper-redundant manipulator has been viewed as the most challenging for computing the inverse kinematics due to its enormous work space and a large or infinite degree of freedom. In this paper, we introduce a new approach to solve the inverse kinematics problem that uses the Monte Carlo method to search manipulator configurations. We simulate thousands of random manipulator positions without any lookahead search. For the purpose of solving the problem of expending a great deal of time, an improvement search method was applied that combines Monte Carlo simulation with establish cubes in the reachable workspace of a hyper-redundant manipulator. Using this method, the simulation experiment expends approximate half of time than Monte Carlo method, and has the less positional errors.

Keywords Hyper-redundant manipulators · Motion planning · Monte Carlo · Random searching

1 Introduction

To our knowledge, hyper-redundant manipulators have been implemented in the highly constrained environments, which have a large number of degree of freedoms (DOFs) and greater robustness. The world-first snake-like manipulator Active Cord Mechanism was invented by Hirose and his team in 1972 [1]. Due to much more DOFs than ordinary manipulators, motion planning of a hyper-redundant manipulator is still a great challenge. The primal problem is the algorithm expend a great deal of time in the motion planning, and the delayed effects of the control system

J. Zhao · L. Zhao (✉) · Y. Wang
State Key Laboratory of Robotics and System, Harbin Institute of Technology,
Harbin 150001, China
e-mail: zhaoliangliang0619@126.com

© Springer Nature Singapore Pte Ltd. 2017
X. Zhang et al. (eds.), *Mechanism and Machine Science*,
Lecture Notes in Electrical Engineering 408,
DOI 10.1007/978-981-10-2875-5_2

become large. In order to solve this problem, we introduce an effective and intelligent algorithm in this paper for the motion planning to decrease the time delay of the manipulator control system.

Several algorithms have been developed for motion planning of hyper-redundant manipulators. H. Ananthanarayanan introduced a multi-pass sequential localized search algorithm to solve the problem of path planning of hyper-redundant manipulators for the shortest path in the presence of obstacles. The proposed method is guaranteed to find a locally optimal path, and applicable to higher DOF control space with realistic computation time [2]. N. Shvalb and his team presented an algorithm that differs from a probabilistic road map (PRM) algorithm in the motion between a pair of anchoring points, which takes place on the boundary of the obstacle subspace. The algorithm was exemplified on a redundant robot with 8 degrees of freedom and compare running results with those of the PRM [3]. Byung-Rok So employed a motion planning algorithm for redundant manipulator standing on the ground, with a geometric constraint equation is derived from the ZMP equation. The algorithm is verified by simulating and experimenting several motions though a planar 3-DOF manipulator model [4].

Monte Carlo methods are a search algorithm that have their roots in statistical physics, they have been used to obtain approximations to the difficult problem [5]. Based on the characteristics of generality of random sampling, and finding optimal decisions, Monte Carlo method is applied in a wide kinds of fields including games research.

Google DeepMind team introduce a new approach to computer Go that uses Monte Carlo tree search programs simulate thousands of random games of self-play. They also introduce a new algorithm that combines Monte Carlo simulation with value and policy networks. Using this search algorithm, the AlphaGo program defeated the human European Go champion by 5 games to 0 [6]. B. Sarkar propose a new method for the computation of importance weights in Monte Carlo localization on maps represented with line segments. The comparative study clearly establish that the proposed method is more accurate, robust and efficient than the other methods [7]. A. Peidr o presents the Monte-Carlo calculation of the work-space of a biped redundant robot. In his work, the solution to forward kinematics has been used together with a Monte-Carlo method to compute the reachable and constant-orientation workspaces of the robot [8].

This paper presents a method for the motion planning of a hyper-redundant manipulator by combination of the Monte Carlo method. The Sect. 2 illustrates the structure of the hyper-redundant manipulator, establishes the forward kinematic model, and uses Monte Carlo method to simulation the workspace of a manipulator. In Sect. 3, Monte Carlo method is used to generate the value of each joint angle of hyper-redundant manipulator. We write a program to random search configurations of a manipulator, and report on the results obtained from simulation experiment with different number of cloud points. In Sects. 4 and 5, for the purpose of solving the problem of expending a great deal of time, we propose an improved Monte Carlo method, and present the six different types of simulation experiment results, which implemented on a 14 DOFs manipulator.

2 Description of Hyper-redundant Manipulator

Hyper-redundant manipulator generally constitutes of a number of the same or similar links. In this paper, we regard the hyper-redundant manipulator as a collection of rigid bodies, which consists of 14 links include 7 pitch joints and 7 roll joints. The DOFs of the manipulator are 14. The 3-D view of simulated manipulator platform is shown in Fig. 1.

2.1 Kinematic of Hyper-redundant Manipulator

Due to the kinematic model of hyper-redundant manipulator should not be affected by the shape or arrangement of the links change, in this work, we simply it into a linkage mechanism. The kinematic model of the manipulator has 14 DOFs joints with each joint has $\pm \pi/2$ range of motion. The method that is implemented here for modelling forward kinematic of the manipulator is D-H method [9]. The D-H coordinate system of a simulated manipulator platform is shown in Fig. 2. The D-H parameters are listed in Table 1.

Where A_i is the link corner of hyper-redundant manipulator, a_i is the length of vertical line from the joint shaft i to $i + 1$, d_i is the link offset from link i to $i + 1$, θ_i is the angle of rotation of link i .

According to these D-H parameters of the manipulator, it is possible to establish the transformation matrix between coordinate frames i and $i + 1$. The matrix can be given as:

$${}^{i-1}T = \text{Rot}(x, \alpha_{i-1})\text{Trans}(\alpha_{i-1}, 0, 0)\text{Rot}(z, \theta_i)\text{Trans}(0, 0, d_i) \quad (1)$$

where $\text{Rot}()$ is the rotation coordinate transformations, $\text{Trans}()$ is the translation coordinate transformations. Base on the Eq. (1) and the D-H parameters in Table 1, we can get the transformation matrix of ${}^{i-1}T$ as shown in the Eqs. (2) and (3).

Fig. 1 The simulated manipulator platform

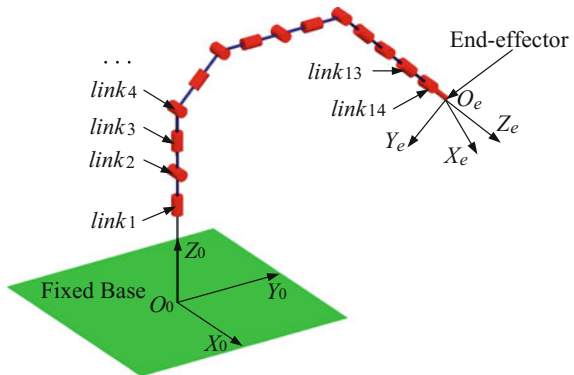


Fig. 2 The D-H coordinate system of a simulated manipulator platform

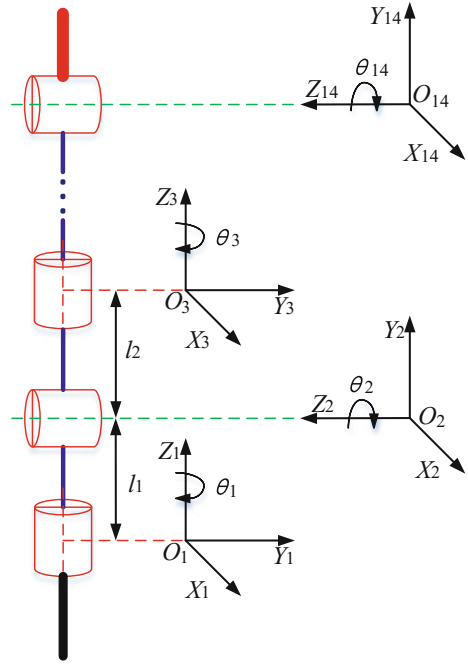


Table 1 D-H parameters of manipulator

Module number	D-H parameter			
	α_i	a_i	d_i	θ_i
1	0	0	0	θ_1
2	$\pi/2$	0	l_1	θ_2
3	$-\pi/2$	0	l_2	θ_3
4	$\pi/2$	0	l_3	θ_4
...	...			
13	$-\pi/2$	0	l_{13}	θ_{13}
14	$\pi/2$	0	l_{14}	θ_{14}

$${}^0_1T = \begin{bmatrix} \cos \theta_1 & -\sin \theta_1 & 0 & 0 \\ \sin \theta_1 & \cos \theta_1 & 0 & 0 \\ 0 & 0 & 1 & 0 \\ 0 & 0 & 0 & 1 \end{bmatrix}, \quad i = 1 \quad (2)$$

$${}^{i-1}_i T = \begin{bmatrix} \cos \theta_i & -\sin \theta_i & 0 & 0 \\ 0 & 0 & -\sin \alpha_{i-1} & -l_i \sin \alpha_{i-1} \\ \sin \theta_i \sin \alpha_{i-1} & \cos \theta_i \sin \alpha_{i-1} & 0 & 0 \\ 0 & 0 & 0 & 1 \end{bmatrix}, \quad (3)$$

$$i = 2, 3, \dots, 14$$

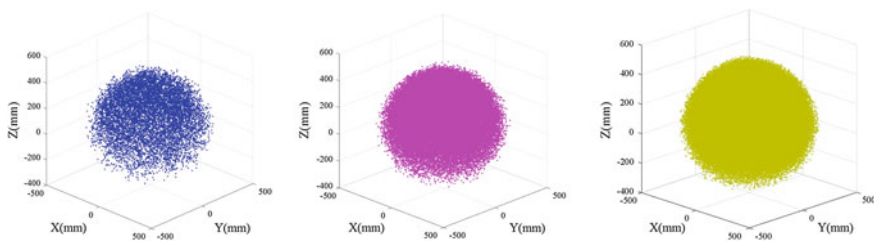


Fig. 3 The point cloud of reachable workspace

2.2 Manipulator Workspace Determination

The workspace of a hyper-redundant manipulator is the most important parameters when motion planning, it can be represented as the set of configurations that will be attaining by the end effector [10]. Due to a large or infinite degree of kinematic redundancy, the analytic method is much more complicated than ordinary manipulators. In this paper, we introduce the Monte Carlo method to simulation the workspace of a manipulator, and every link of the manipulator is checked for collision with other links simultaneously. Based on the kinematic model of the manipulator, the position of end effort can be parametrized in the general form:

$$\begin{bmatrix} x_t \\ y_t \\ z_t \\ 1 \end{bmatrix} = {}^0_{14}T \cdot L_{14} = {}^0_1T {}^1_2T {}^2_3T {}^3_4T \cdots {}^{12}_{13}T {}^{13}_{14}T \cdot L_{14}. \quad (4)$$

We shall exemplify our algorithm on a manipulator with the movement range of all pitch joints are -90° to $+90^\circ$, the roll joints are -90° to $+90^\circ$, and $l_1 = l_2 = \cdots = l_{14} = 40$ mm. The point cloud of reachable workspace is shown in Fig. 3, and the number of points are: $N_1 = 10,000$, $N_2 = 50,000$, $N_3 = 200,000$.

Figure 3 shows that increasing N increases the volume of the reachable workspace, and the shape of it is virtually unaffected. We also checked that the point evenly distributed throughout the sphere workspace, this is the physical characteristic of the hyper-redundant manipulator.

3 Monte Carlo Method to Search Random Configurations

In this work, Monte Carlo method uses random simulations to generate the value of each joint angle of hyper-redundant manipulator. As more simulation experiments are executed, the number of manipulator configurations grows larger and the end effector position values become more accurate. The algorithm used to select configurations during random search is also improve by selecting positional error with

lower values [11]. Asymptotically, this algorithm converges the configurations at a target point, and the positional errors converge to the optimal value.

3.1 Algorithmic Procedure of Monte Carlo

According to the introduction of the Monte Carlo method above, we can write a program to random search the configurations of a manipulator. A general overview of the Monte Carlo method is depicted in Algorithm 1.

Algorithm 1: The Random Searching Configurations

```

1:  algorithm RandomSearching ( $\theta_i, T$ )
2:    data inputs   $T, n, \Delta_1, \Delta_2$ 
3:    for  $i=1$  to  $n$  do
4:      ↓  $\theta_i \leftarrow$  random search each link angle
5:    end for
6:    for  $m=1$  to  $T$  do
7:      ↓
8:      for  $i=1$  to  $n$  do
9:        ↓  $error[i, T] \leftarrow$  calculate positional error
10:       end for
11:       for  $i=1$  to  $k$  do
12:         ↓ if  $error[i] < error_0$  then
13:           ↓  $\theta_i \leftarrow \theta_i + \Delta_1 \times random$ 
14:         else
15:           ↓  $\theta_i \leftarrow \theta_i + \Delta_2 \times random$ 
16:         end if
17:       end for
18:       if  $error[i, T+1] < error[i, T]$  then
19:         ↓ return  $\theta_i$ 
20:       end if
21:       for  $i=1$  to  $n$  do
22:         ↓  $[x_i, y_i, z_i] \leftarrow$  CalculatePos ( $\theta_1, \theta_2, \dots, \theta_n$ )
23:       end for
24:    end for
25:  end algorithm

```

In the algorithm 1, n is the number of random searching configurations, T represents the number of iterations of each configuration, $error$ represents the distance between the end effector point and the target point, and $random$ is the standard uniform distribution number on the open interval $(0,1)$. θ_i and $error$ can be given in Eqs. 5 and 6.

$$\theta_i = \frac{\pi}{2} + \pi \times random \quad (5)$$

$$error = \sqrt{(x - x_t)^2 + (y - y_t)^2 + (z - z_t)^2} \quad (6)$$

3.2 Simulation Experiment

The Monte Carlo method is implemented on a 14DOF manipulator which introduced in the Sect. 2. We report on the results obtained from six groups of the simulation experiment with different parameters of n . It is illustrated in Figs. 4 and 5. And its parameters of n have the following values: $n_1 = 500$, $n_2 = 1000$, $n_3 = 1500$, $n_4 = 2000$, $n_5 = 2500$, $n_6 = 3000$.

In the first stage of the Monte Carlo method, randomly generated the configurations into the reachable workspace of manipulator. For example, the first picture of Fig. 4 shows the reachable workspace is filled with 500 different configurations.

In the second step, the iterative process of each configuration is repeated T times and the return configurations are collected in a set. As shown in the Fig. 5, through the use of this method, we can get the configurations which satisfying a distance tolerance between the end effector and the target point.

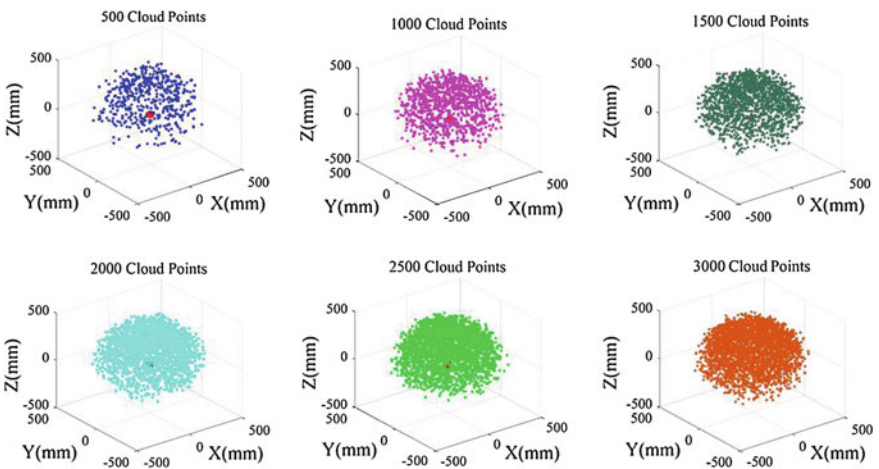


Fig. 4 The point cloud of random searching configurations

4 Improvement on Monte Carlo Method

According to the Sect. 3, the Monte Carlo method was presented and used for motion planning of the hyper-redundant with the generality of random configurations. The simulate experiments show that the presented method has many advantages, include the efficiency of motion planning of the manipulator is increased, and the positions of end effort are carried out with military precision. Simulation results demonstrate the feasibility and effectiveness of this method. Of course, there still exist many problems that need to be solved. The primal problem is the method expend a great deal of time in random selecting configurations. For the purpose of solving the problem, we divide the reachable workspace of s manipulator into a number of cubes, as shown in Fig. 6.

As shown in Fig. 6, we established a cube ABCDEFGH in the coordinate $O_0Y_0Z_0$. The end effector point of manipulator represents the center of the cube, and also it is the target point as mention in the Sect. 3. a represents the side length of the cube. In this work, the approach of equally dividing the reachable workspace of a manipulator into a number of cubes was used to extract configurations which satisfying the errors between the end effector to the target point. It is applied extract configurations by configurations from the point cloud which converge the random searching configurations at a target point as shown in Fig. 5.

We implement the identical Monte Carlo method on a 14DOF manipulator which be mentioned in the Sect. 3, with the extract configurations take the place of random searching configurations in the algorithm 1, and the target point coordinate inside of the cube. The simulation experimental result is illustrated in Fig. 7, the number of random searching configurations $n_1 = 500$, the end effector point of manipulator $(x_{r1}, y_{r1}, z_{r1}) = (200 \text{ mm}, 200 \text{ mm}, 200 \text{ mm})$, and the side length of the cube $a = 20 \text{ mm}$.

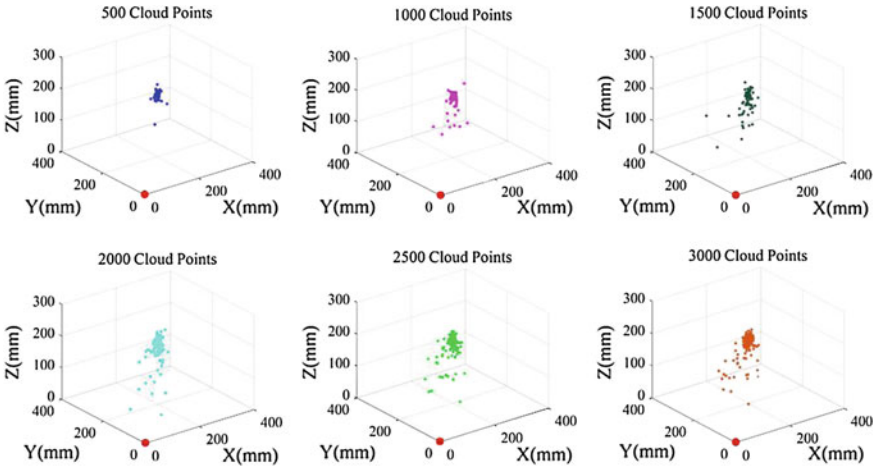
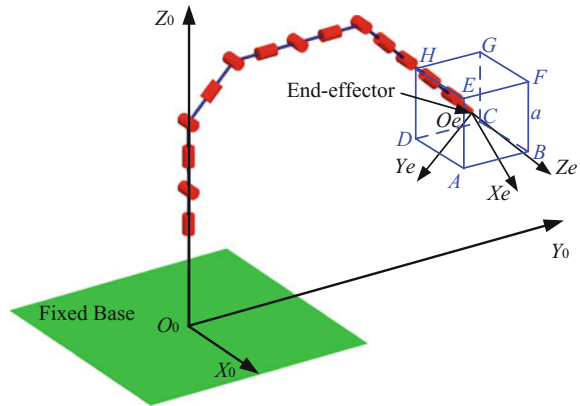


Fig. 5 The point cloud of converge the configurations at a target point

Fig. 6 Representation of the cube in workspace



On the basis of the process of simulation experiment which shown in the Sect. 3, in the first stage of the algorithm, the extract configurations fill in the reachable workspace of manipulator, and in the second step, the iterative process of each configuration is repeated T times and the return configurations are collected in a set. As shown in the Fig. 7, through the use of this method, the point cloud of the configurations moves from the center of the cube to the target point $B = (x_{t2}, y_{t2}, z_{t2}) = (190 \text{ mm}, 190 \text{ mm}, 190 \text{ mm})$.

5 Experimental Results

To evaluate improved Monte Carlo method, we compare six different types of the simulation experiments with different parameters of n , which identical to the simulation experiment in the Sect. 3.2. The experimental results are shown in Fig. 8. To efficiently combine the improved Monte Carlo method with simulation experiments, the method was executed in MATLAB R2015b on a PC with 3.60 GHz quad core Intel processor with 8 GB RAM running Windows 7. All of these simulation experiments are based on Monte Carlo algorithms.

According to Figs. 8, the improved Monte Carlo method make the point cloud of the configurations moves from the center of the cube to the target point. We also checked that increasing n increases the volume of the point cloud, and the general motion trend of point cloud virtually unaffected.

We also get the error change curve as shown in Fig. 9, and the computation time of the simulation experiments as shown in Fig. 10. The error change curve and the computation time of the experiment 1 are come from the simulation experiment in the Sect. 3.2. As depicted in Figs. 9 and 10, the Monte Carlo method and the improved Monte Carlo method were run for 6 different simulation experiments respectively. It is evidenced that the number of the parameters of n greatly influences the errors of generate configurations. And it also can be seen that the

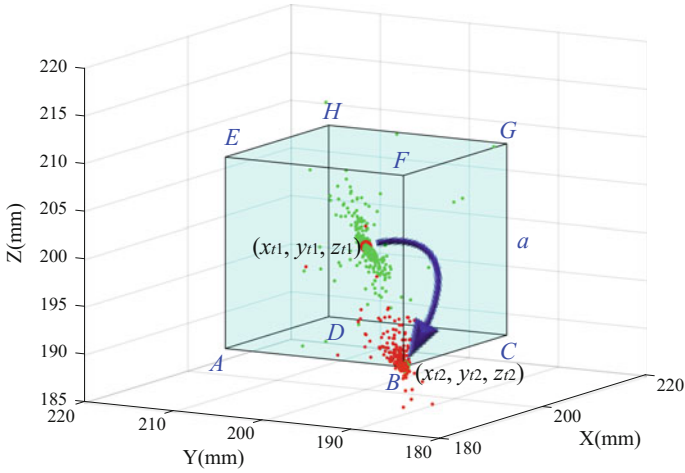


Fig. 7 The simulation experimental result

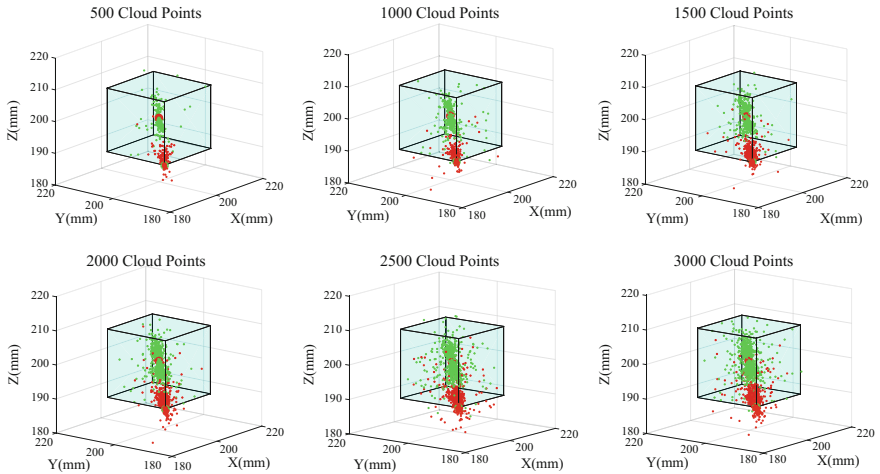


Fig. 8 The simulation experiment result

computation time is directly proportional to the number of random searching configurations n .

The results suggest that the improved Monte Carlo method was applied in the experiment 2 expends approximate half of time than Monte Carlo method, which was applied in the experiment 1 (see Fig. 10), and has the less positional errors (see Fig. 9). It demonstrated the feasibility and effectiveness of the improved Monte Carlo method.

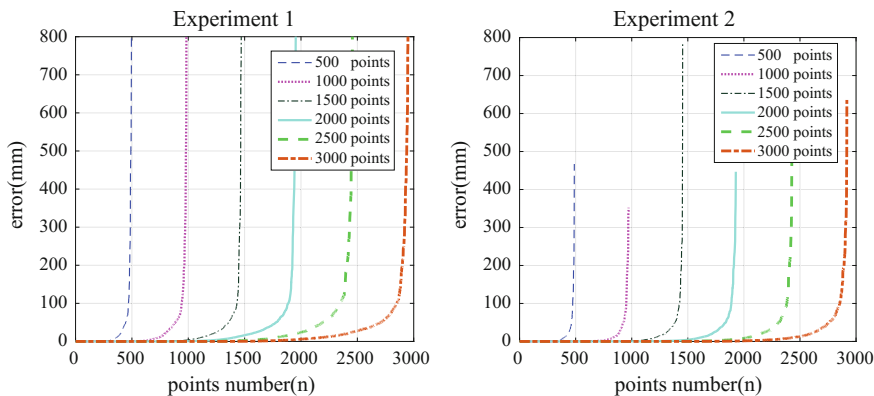
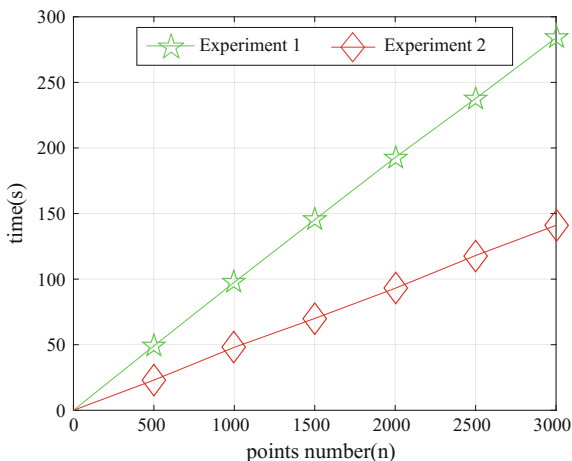


Fig. 9 The error of the simulation experiment

Fig. 10 The expend time of the simulation experiment



6 Conclusion

Due to much more DOFs, motion planning of a hyper-redundant manipulator is a great challenge when it takes place in real-time. In this paper, we introduce and analyze the improved Monte Carlo method to deal with the motion planning of hyper-redundant manipulator. In the Sect. 3, we randomly generated the value of each joint angle of hyper-redundant manipulator, and converges the configurations at a target point take advantage of the values of positional error. We presented six types of the simulation experiments on a 14 DOFs manipulator based on different parameters of the number of cloud points. Then, we proposed an improved Monte Carlo method by dividing the reachable workspace of s manipulator into a number

of cubes, and present the six different types of simulation experiment results, which implemented. All the experiment results demonstrated the feasibility and effectiveness of the improved Monte Carlo method.

References

1. Hirose S (1993) Biologically inspired robots-snake-like locomotors and manipulators. Oxford University Press, Oxford
2. Ananthanarayanan H, Ordonez R (2016) Adaptation of fast converging optimal techniques to path planning of hyper-redundant manipulators. *IEEE Trans Rob*
3. Shvalb N, Moshe BB, Medina O (2013) A real-time motion planning algorithm for a hyper-redundant set of mechanisms. *Robotica* 31:1327–1335
4. So B-R, Ryu H, Yi B-J (2015) ZMP-based motion planning algorithm for kinematically redundant manipulator standing on the ground. *Intel Serv Robot* 8:35–44
5. Browne CB, Powley E, Whitehouse D (2012) A survey of Monte Carlo tree search methods. *IEEE Trans Comput Intell AI Games* 4:1–43
6. Silver D, Huang A, Maddison CJ (2016) Mastering the game of Go with deep neural networks and tree search. *Nature* 529:484–489
7. Sarkar B, Saha S, Pal PK (2015) A novel method for computation of importance weights in Monte Carlo localization on line segment-based maps. *Robot Auton Syst Part A* 74:51–65
8. Peidr o A, Gil A, Mar n JM (2016) Monte-Carlo workspace calculation of a serial-parallel biped robot. In: *Robot 2015: second Iberian robotics conference: advances in robotics, vol 2*, pp. 157–169. Springer International Publishing
9. Denavit J, Hartenberg RS (1955) A kinematic notation for lower-pair mechanics based on matrices. *J Appl Mech* 22:215–221
10. Bayram A,  g ren MK (2012) The position control of a spatial binary hyper redundant manipulator through its inverse kinematics. *Proc Inst Mech Eng [C], J Mech Eng Sci*
11. Silver D, Sutton RS, M ller M (2012) Temporal-difference search in computer Go. *Mach Learn* 87:183–219

Gait and Trajectory Rolling Planning for Hexapod Robot in Complex Environment

Guiyang Xin, Hua Deng, Guoliang Zhong and Hengsheng Wang

Abstract Hexapod robots have stronger adaptability to dynamic unknown environment than wheeled or trucked ones due to their flexibility. In this paper, a control strategy based on rolling gait and trajectory planning that enables a hexapod robot to walk in dynamic environment is proposed. The core content of the control strategy is to constantly change the gait and trajectory according to the dynamic environment and predicted stability margin of robot. Kalman filter is employed to compute predicted zero moment point (ZMP) monitoring the stability of robot in order to keep balance with adjusting gait and trajectory. A hierarchical control architecture consisting of high-level gait planner, low-level trajectory planner, joint servo controller and compliance controller is presented. The control strategy is applied to a hexapod robot engaging to disaster rescue. Experiment results show the efficiency of our control strategy over challenging terrain.

Keywords Rolling planning · Hexapod robot · Stability control · Kalman filter

G. Xin (✉) · H. Deng · G. Zhong · H. Wang
School of Mechanical and Electrical Engineering, Central South University,
Changsha 410083, Hunan, China
e-mail: gyxin12@csu.edu.cn

H. Deng
e-mail: hdeng@csu.edu.cn

G. Zhong
e-mail: zhong001985@csu.edu.cn

H. Wang
e-mail: whsheng@csu.edu.cn

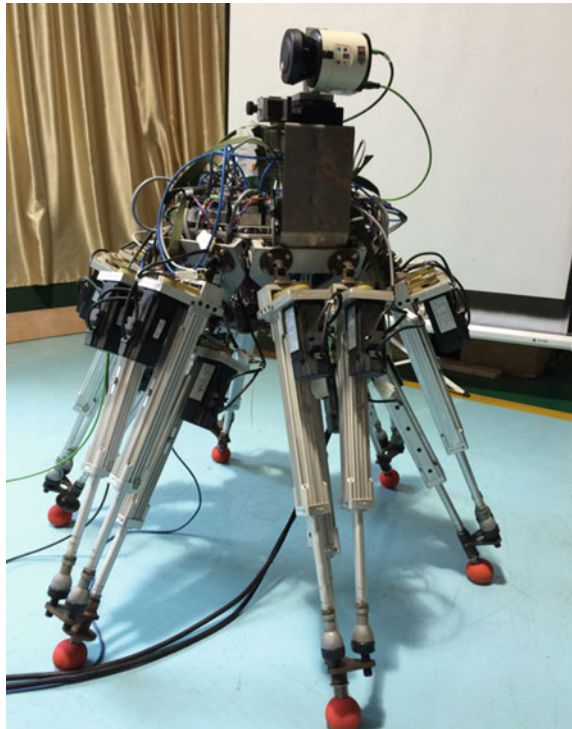
G. Xin · H. Deng · G. Zhong · H. Wang
State Key Laboratory of High-Performance Complex Manufacturing,
Central South University, Changsha 410083, Hunan, China

1 Introduction

Hexapod robots have attracted the attention of researchers because of their superior adaptability to complex environments than their wheeled counterparts. The leg mechanisms of most existing hexapod robot prototypes are 3-DOF serial mechanism including 3 links and 3 revolute joints, which is based on bionics principle. However, in the past works [1–3], we proposed a novel hexapod robot called as PH-Robot, as shown in Fig. 1, with parallel leg mechanism so as to bring the advantage of parallel mechanisms to legged robots.

In order to implement rolling planning of gait according to different missions and environmental conditions, different types of gait should be generated. Many studies have focused on the gait generation. As far as we know, it's hard for hexapod robots to execute dynamic gaits, such as trot or gallop which belongs to mammal gaits. The static gaits including tripod, quadruped, one-by-one types of gait as in [4] and other free gait in [5, 6] are widely used in hexapod robots. Wang et al. [7] discussed three different gaits, i.e., insect-wave gait, mammal-kick gait and mixed gait. They still belong to static gaits. Asif et al. [8] proposed a method that is to increase the number of supporting legs according to the roughness of terrain in order to increase stability. Other researchers [9–12] focused on the analysis of fault tolerant gait as

Fig. 1 Prototype of PH-robot



one or more legs are prevented from supporting and swing. In this paper, we will give some typical gaits, which establish the gait base for rolling gait planning, according to different tasks and environments.

In order to keep statically stable walking, stability control are another crucial elements except gait planning. Actually, hexapod robots are easier to obtain static stable walking compared with quadruped and humanoid robots because of the larger number of legs. Therefore, in most cases, we do not need to plan the center of gravity (COG) trajectory because the COG always stays in the support polygon naturally. However, there are many external disturbances, such as unknown-uneven terrain and impact force from flying objects or human's hit. Therefore, we need a closed-loop controller to keep balance when suffering disturbance. Asif et al. [13] proposed a control framework constituting a modified hybrid force-position controller to deal with the environmental disturbances. More research results on this issue are implemented on quadruped robots [14–16], but a common dynamic model of inverted pendulum is applied due to the heavy body relative to their legs. By contrast, hexapod robot's legs make more contribution to the entire mass of robot than the body. Therefore, their method is not suitable for hexapod robots. This paper proposes a new control method combining rolling planning and state observer based on Kalman filter.

After gait planning, we need a trajectory generator in order to plan the motion of body and swing legs. On this issue, we must address the coupled kinematics of legs and body. In fact, we have derived the inverse and forward kinematics in our earlier work [1]. We will present a new expression of kinematics that leads to convenience for dynamic modeling. Moreover, the curve of trajectory function should be determined according to some rules like avoiding impact between feet and the ground. To avoid impact, the initial and final velocity and acceleration of the trajectory are chosen to be zero. Wang et al. [17] used the combination function of sine and cosine functions to satisfy the abovementioned condition. We have successfully applied a similar function called as cycloid curve to accomplish tripod gait in [1, 3]. Rebula et al. [18] proposed a combined curve consisting of two linear segments and a parabolic segment. Kalakrishnan et al. [14] applied a series of quintic spline segments (fifth order polynomials) as the trajectories of COG and the end of swing legs. Kolter et al. [15] used a very simple trajectory like a box as the foot trajectory. We will also employ fifth order polynomials which can provide convenience for rolling trajectory planning.

The rest of this paper is laid out as follows. In Sect. 2, we give a brief overview of the PH-Robot's hardware. The proposed stability control architecture is analyzed in Sect. 3. Gait and trajectory planning is presented in Sect. 4. In Sect. 5, we present some experimental results. Finally, conclusions are presented in Sect. 6.

2 PH-Robot

PH-Robot is very different with most popular hexapods due to its parallel leg mechanism as shown in Fig. 1. The purpose of using parallel mechanism is to improve payload capability, which has been analyzed in [2]. The robot stands approximately 820 cm in initial state (The height of robot depends on the length of

linear actuators) with a total mass of about 130 kg. There are 18 actuated degrees of freedom excluding the one freedom of LIDAR. Each active joint is a prismatic joint corresponding to a linear actuator driven by servo motor with absolute encoder. An inertial measurement unit (IMU) mounted on the body can provide accurate 3-axis angle, angular rate and 3-axis acceleration data. Motion state will be estimated by the combination of IMU and encoders. There is a 6-axis force/torque sensor mounted on each foot to measure the contact force with ground. Data offered by all of the above sensors is processed by an embedded controller CX2030 produced by Beckhoff. CX2030 can accomplish all the computation within 2 ms that is the servo cycle.

A Sick LMS111 planar LIDAR is mounted on a spindle that can rotate in order to realize 3D scanning. Since the 3D point cloud has very huge data, we use a super laptop to process the data from LIDAR instead of using CX2030. CX2030 can require what we needs from that laptop via Ethernet communication.

3 Stability Control Architecture

The control architecture as shown in Fig. 2 can be separated into three levels. The highest level is the gait planning level which reserves a gait base to be used by robot according to different tasks, environments and stability state. The middle level

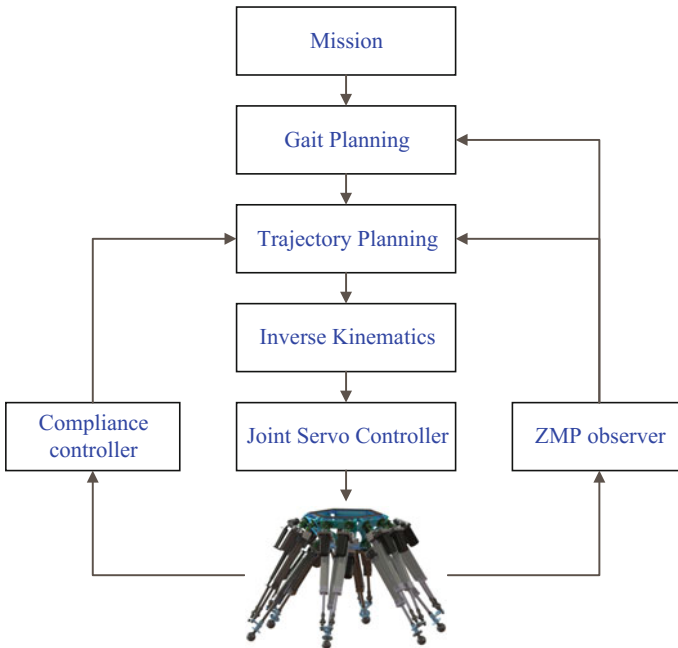
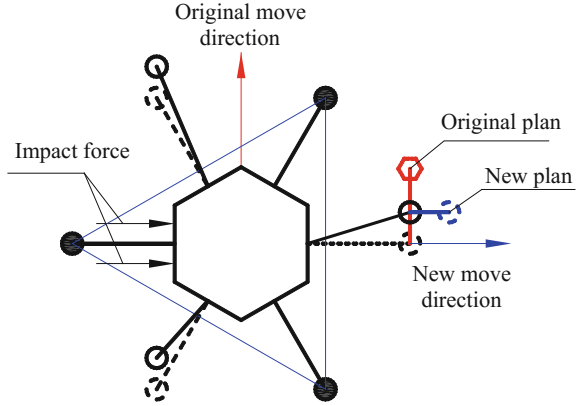


Fig. 2 Stability control architecture

Fig. 3 Stability control through trajectory rolling planning



consists of trajectory planner and inverse kinematics solver so as to achieve the upcoming footsteps. The low level is the joint servo control level which tries to ensure the planned motion executed with accuracy and robustness to disturbance. Besides these levels, there are a state observer based on Kalman filter and a compliance controller for stability state feedback and trajectory modification.

As we know, there are five procedures when using Kalman filter to estimate the optimal state of signal with noise. One procedure is to use the state corresponding to last sample to predict the state of next sample as follows,

$$\mathbf{X}(k|k-1) = \mathbf{A}\mathbf{X}(k-1|k-1) \quad (1)$$

Although $\mathbf{X}(k|k-1)$ is not the final estimated value, we can use it to predict stability state of robot, because we want to make adjustment of gait or trajectory before the robot lose stability and tip over. From this perspective, it is significant to introduce Kalman filter into stability controller. When the observer predicts the robot will tip over, the strategy to keep balance is to increase the number of supporting feet through changing original trajectory and gait plan. Figure 3 shows an example of stability control through trajectory rolling planning. In this case, the robot is impacted by external force when walking following the original trajectory. In order to avoid tip over, the new trajectory should be planned and implemented. The move direction should also be changed in order to get rid of the impact force.

Another element of our control architecture is the compliance controller with the purpose of avoiding impact with ground. Contacting with ground before finishing the planned trajectory is inevitable. If we suddenly shut down the motor with high rotating speed when detecting contacting force with ground by 6-axis force/torque sensor, it will damage the robot's components. Therefore, compliance control is applied on our robot. The control law of compliance control is

$$\Delta \mathbf{X}(s) = \frac{\Delta \mathbf{F}(s)}{\mathbf{M}_d s^2 + \mathbf{B}_d s + \mathbf{K}_d} \quad (2)$$

According to that control law, it is to control contacting force through changing the expected trajectory in Cartesian frame. From this perspective, the compliance control is also a rolling trajectory planning strategy.

4 Gait and Trajectory Planning

4.1 Gait Planning

As mentioned earlier, many types of gaits have been proposed by researchers. We can classify them according to the type of support polygon or the number of supporting and swing legs as “3 + 3” alternating tripod, “4 + 2” quadruped, and “5 + 1” one-by-one gait. Tripod gait is considered as the fastest movement gait as its duty factor β , which is defined as the fraction of cycle time in which a leg is in the supporting phase [19], is 1/2. By contrast, the duty factor β of quadruped and one-by-one gait is 2/3 and 5/6 respectively. However, we think sometimes duty factor β cannot be used as a criterion for walking speed. As shown in Fig. 4, when the same movement distance of robot body is adopted for tripod gait and quadruped gait, the movement speeds of the two types of gait are identical. But it should be noted that if the body movement distance is the maximum, quadruped gait cannot be realized because of the workspace limitation of leg 2 and 5. Therefore, if taking the limitation of legs’ stride and motors’ speed into consideration, tripod gait will be the fastest gait definitely.

Another important aspect worthy to analyze is the stability margin of different gaits. Static stability margin is defined as the minimum distance from the projection on the ground of gravity center of robot to each edge of the support polygon [20], and the edge corresponding to the minimum distance is called as tipping over trended edge. According to that definition, it seems that the stability margins of the three gaits are identical. However, the number of tipping over trended edge for tripod gait is 3, whereas that is 2 and 1 for quadruped gait and one-by-one gait respectively. Therefore, we would like to employ one-by-one gait to traverse highly uneven terrain, which is a strategy to control stability.

As for hexapod robots, it should be noted that we don’t have to plan the COG trajectory in order to keep stable walking, because all of these gaits have large static stability margin. That’s very different from humanoid robots that have to walk in quasi-dynamic gaits because of their small support polygon. This characteristic of hexapod robot will bring large convenience for trajectory planning and inverse kinematics, because it’s very difficult to compute joint trajectory according to COG trajectory, whereas it’s easy to compute joint motion according to the body’s motion using inverse kinematics. Therefore, although our trajectory planners includes COG trajectory planner, that is only used for several extreme cases.

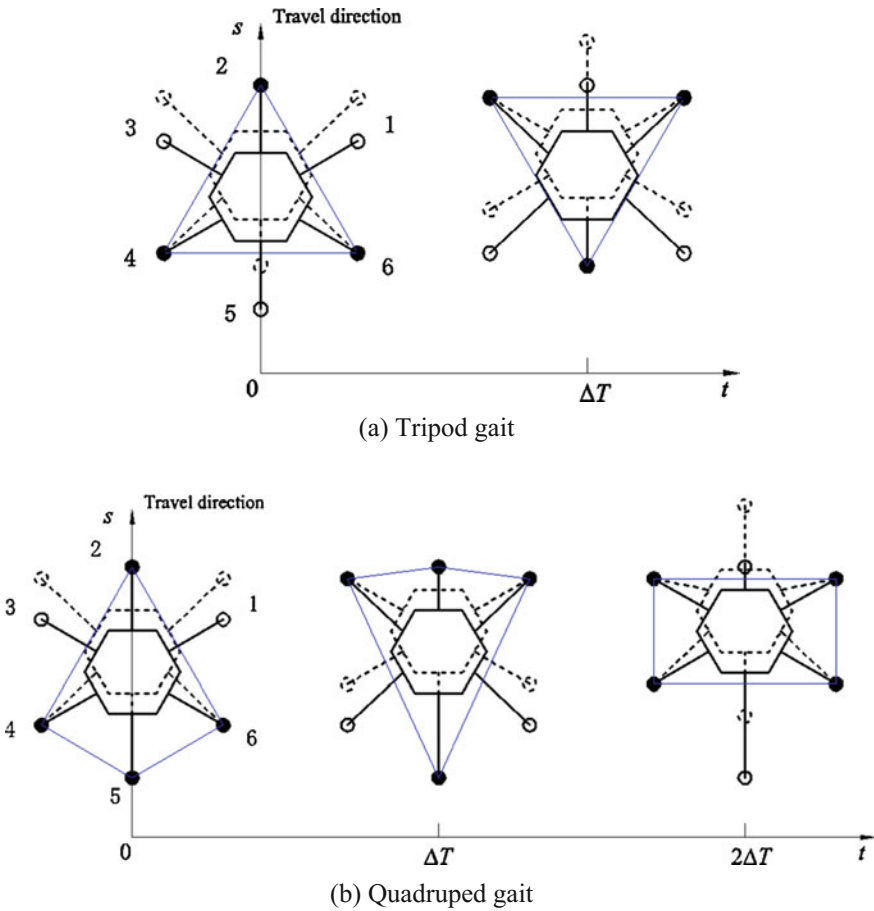


Fig. 4 Two typical gaits

Usually, we only plan the trajectories of body and swing legs when using these three normal gaits. Actually, the trajectories of COG and body are considered approximately identical in lots of literature [21–23] aimed at the locomotion of humanoid robots, because the mass of humanoid robot’s legs can be ignored compared with the mass of body. That cannot be applied on our robot, because the legs of our robot are very heavy on the contrary. Besides those three normal gaits, we can use mixed gait to deal with more complicated cases.

4.2 Trajectory Planning

In this section we will address the issue of choosing functions, motion range, and time interval for trajectories of COG, body, and swing feet. Firstly, note that hexapod

robot cannot keep a constant speed to walk because of the alternation of supporting phase and swing phase. The motions of swing legs' feet are forward with respect to robot body, whereas the motions of supporting legs' feet are back with respect to robot body, and therefore the motion speed of feet should be zero with respect to body in order to change movement direction when alternating phases. That means the initial and end velocities of trajectories of COG, body and swing feet should be zero. In order to obtain a smooth motion for actuators, the initial and end accelerations of the planned trajectory are chosen to be zero as well. These are the boundary conditions for trajectory planning.

In our previous publications [1, 3], we adopted cycloid function that satisfies the boundary conditions abovementioned. However, that function cannot be used for segmented function. Therefore, we choose a more flexible function that is fifth order polynomial as the trajectory function for the convenience of rolling planning. We can derive the formulation of that function according to the boundary conditions as follows,

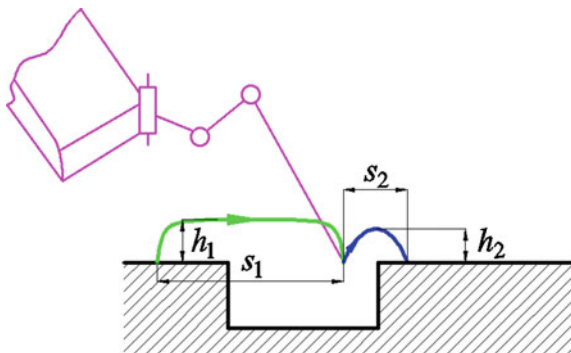
$$q(t) = q_0 + \frac{10(q_{\Delta t} - q_0)}{\Delta t^3} t^3 + \frac{-15(q_{\Delta t} - q_0)}{\Delta t^4} t^4 + \frac{6(q_{\Delta t} - q_0)}{\Delta t^5} t^5 \quad t \in [0 \quad \Delta t] \quad (3)$$

where q_0 denotes the start value, $q_{\Delta t}$ denotes the end value, Δt means the time interval. The motions of 3-axis of a 3D trajectory in Cartesian coordinate system are defined by Eq. (3) respectively. As for foot trajectory, the height and stride constrained by the reachable workspace are determined by $q_{\Delta t} - q_0$. Moreover, Eq. (3) is also constrained by motor's maximum speed and torque.

Some researchers [24–26] try to find efficient optimization method to solve this problem for real-time application. But we think it's not necessary to optimize the trajectory when walking. In fact, we can find some optimal trajectories offline under those constraints to be used as basic trajectories for rolling planning online. Compared with the velocity and torque limitation, we think the reachable workspace is the crucial constraint for online trajectory planning, because servo motors have overload ability while mechanisms never cannot reach outside reachable workspace. Therefore, it's necessary to ensure the end point of a trajectory satisfying the workspace constraint, and the time interval can be modified slightly according to the offline optimized trajectory.

Here is an example to explain this trajectory planning method as shown in Fig. 5. A legged robot follows an offline optimized trajectory, the green curve, within time interval t_1 . After finishing that trajectory, there is no contact force with ground because of the sag on the ground, and the robot therefore needs to plan a sequential trajectory, the blue curve, to contact ground. The stride, height and time interval of the new trajectory can be directly set as half of those of the offline optimized trajectory in order to avoid time-consuming optimization. As for our robot, default values of stride, height and interval time are set as 200 mm, 60 mm and 2 s respectively. Those values are not the limiting values in order to give more room to adjust for online rolling planning.

Fig. 5 Rolling planning for foot trajectory



As mentioned, after determining the trajectories of body and swing legs, the joint motion can be solved by inverse kinematics. These joint motions will be sent to joint servo controller and be tracked accurately.

5 Experiments with the PH-Robot

We applied the proposed control architecture on our robot. Figure 6 shows the sequence of snapshots of the PH-Robot crossing rough terrain with several bricks. In this experiment, the robot is walking in tripod gait. When the robot stepped on a brick, the original planned trajectory has not been tracked to the end, and the compliance controller therefore is executed to stop the foot sticking the brick while the other two swing legs continue to track the rest of the original trajectories. Meanwhile, the ZMP observer did not predict the robot will lose stability due to the brick. Consequently, it did not call the rolling planning strategy to keep balance. That experiment shows the advantage of hexapod robot in term of inherent stability compared with humanoid robot, and it also demonstrates the practicability on travelling rough terrain.

6 Conclusion

In this paper, we present our six-legged robot, the PH-Robot. Its high-powered hardware guarantees the execution of control commands. The stability control is based on a hierarchical control architecture composed of three levels. The application of this control strategy on PH-Robot enables the robot to traverse high uneven terrains. The predicted ZMP give the controller more time to adjust gait or trajectory in order to avoid tipping over. Gait and trajectory rolling planning is the core component for balance recovery and terrain adaptability.

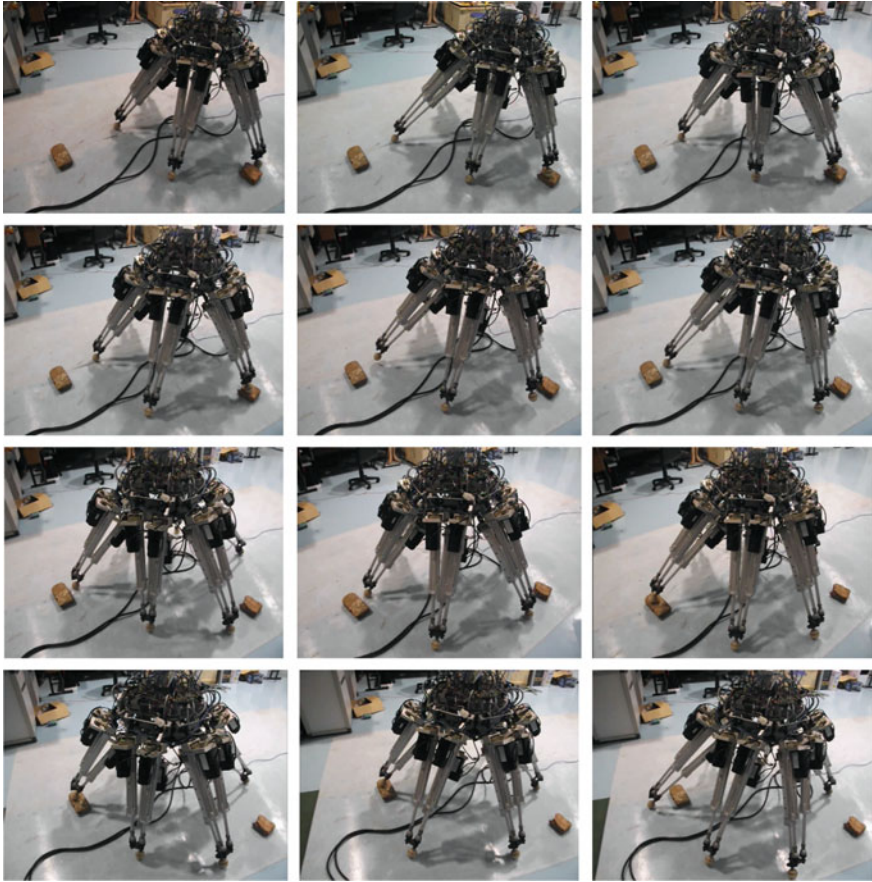


Fig. 6 Sequence of snapshots of the PH-robot crossing rough terrain using the proposed controller

Acknowledgments This study was supported by a grant from National Basic Research Program (973) of China (Grant No. 2013CB035504).

References

1. Xin G, Deng H, Zhong G, Wang H (2015) Hierarchical kinematic modelling and optimal design of a novel hexapod robot with integrated limb mechanism. *Int J Adv Robot Syst* 12:123. doi:[10.5772/59989](https://doi.org/10.5772/59989)
2. Xin G, Deng H, Zhong G, Wang H (2015) Dynamic analysis of a hexapod robot with parallel leg mechanisms for high payloads. In: 2015 10th Asian control conference (ASCC). IEEE, pp 1–6

3. Zhong G, Deng H, Xin G, Wang H (2016) Dynamic hybrid control of a hexapod walking robot: experimental verification. *IEEE T Ind Electron* 63(8):5001–5011
4. Lee BH, Lee IK (2001) The implementation of the gaits and body structure for hexapod robot. In: *IEEE international symposium on industrial electronics (ISIE 2001)*. IEEE, pp 1959–1964
5. Porta JM, Celaya E (2004) Reactive free-gait generation to follow arbitrary trajectories with a hexapod robot. *Robot Auton Syst* 47:187–201
6. Erden MS, Leblebicioglu K (2008) Free gait generation with reinforcement learning for a six-legged robot. *Robot Auton Syst* 56:199–212
7. Wang Z, Ding X, Rovetta A, Giusti A (2011) Mobility analysis of the typical gait of a radial symmetrical six-legged robot. *Mechatronics* 21(7):1133–1146
8. Asif U, Iqbal J (2012) On the improvement of multi-legged locomotion over difficult terrains using a balance stabilization method. *Int J Adv Robot Syst* 9:1
9. Yang J-M, Kim J-H (1998) Optimal fault tolerant gait sequence of the hexapod robot with overlapping reachable areas and crab walking. *IEEE Trans Syst Man Cybern Part A* 29(2):224–235
10. Yang J-M, Kim J-H (2000) A fault tolerant gait for a hexapod robot over uneven terrain. *IEEE Trans Syst Man Cybern Part B*. 30(1):172–180
11. Chu SK-K, Pang GK-H (2002) Comparison between different model of hexapod robot in fault-tolerant gait. *IEEE Trans Syst Man Cybern Part A* 32(6):752–756
12. Asif U (2012) Improving the navigability of a hexapod robot using a fault-tolerant adaptive gait. *Int J Adv Robot Syst* 9:33
13. Asif U, Iqbal J (2011) Motion planning using an impact-based hybrid control for trajectory generation in adaptive walking. *Int J Adv Robot Syst* 8(4):212–224
14. Kalakrishnan M, Buchli J, Pastor P, Mistry M, Schaal S (2010) Fast, robust quadruped locomotion over challenging terrain. In: *2010 IEEE international conference on robotics and automation (ICRA)*. IEEE, pp 2665–2670
15. Koller JZ, Rodgers MP, Ng AY (2008) A control architecture for quadruped locomotion over rough terrain. In: *2008 IEEE international conference on robotics and automation (ICRA)*. IEEE, pp 811–818
16. Garcia E, de Santos PG (2006) On the improvement of walking performance in natural environments by a compliant adaptive gait. *IEEE Trans Robot* 22(6):1240–1253
17. Wang Z, Ding X, Rovetta A (2009) Analysis of typical locomotion of a symmetric hexapod robot. *Robotica* 28:893–907
18. Rebula JR, Neuhaus PD, Bonnlander BV et al (2007) a controller for the littledog quadruped walking on rough terrain. In: *2007 IEEE international conference on robotics and automation*. IEEE, pp 1467–1473
19. Song SM, Choi BS (1990) The optimally stable ranges of 2n-legged wave gaits. *IEEE Trans Syst Man, Cybern Syst part b Cybern* 20(4):888–902
20. Long S, Xin G, Deng H, Zhong G (2015) An improved force-angle stability margin for radial symmetrical hexapod robot subject to dynamic effects. *Int J Adv Robot Syst* 12:59
21. Kajita S, Kanehiro F, Kaneko K et al (2003) Biped walking pattern generation by using preview control of zero-moment point. In: *2003 IEEE international conference on robotics and automation (ICRA'03)*. IEEE, pp 1620–1626
22. Liu J, Veloso M (2008) Online ZMP sampling search for biped walking planning. In: *2008 IEEE/RSJ international conference on intelligent robots and systems*. IEEE, pp 185–190
23. Erbatur K, Kurt O (2009) Natural ZMP trajectories for biped robot reference generation. *IEEE T Ind Electron* 56(3):835–845
24. Lampariello R, Nguyen-Tuong D, Castellini C, Hirzinger G, Peters J (2011) Trajectory planning for optimal robot catching in real-time. In: *2011 IEEE international conference on robotics and automation (ICRA)*. IEEE, pp 3719–3726
25. Macfarlane S, Croft EA (2003) Jerk-bounded manipulator trajectory planning: design for real-time applications. *IEEE Trans Robot Autom* 19(1):42–52
26. Gasparetto A, Zanotto V (2008) A technique for time-jerk optimal planning of robot trajectories. *Robot Comput-Integr Manuf* 24:415–426

Real-Time Trajectory Plan for Six-Legged Robots to Open Doors Based on Tactile Feedback

Zhijun Chen and Feng Gao

Abstract Opening doors is a basic and significant task for robots in applications of home service, security guard and disaster rescue. Previous researches basically use a multi-DOF manipulator mounted to a tracked, wheeled or biped robot platform to manipulate, use 3D vision system to recognize and roughly locate the door handle, and apply force sensors to precisely locate the handle and open the door. This paper proposes a method to plan the door-opening trajectory for six-legged robots, based on only the tactile feedback. Specially, by making a good use of the six DOFs and the enough workspace of the body, the robot uses a 0-DOF tool to operate. By touching the door and the handle at different positions and different directions, the robot can detect the positional relationship with the door and accordingly plan the trajectory to open the door in real-time.

Keywords Door-opening · Trajectory plan · Tactile feedback · Six-legged robots

1 Introduction

Applications of modern robots have been widely extended to various cases, such as home service, security guard and disaster rescue. In these cases, a robot must be able to autonomously accomplish some manipulation tasks in unknown and strong interface environments. Opening doors is a basic and significant one, which has already been intensively studied for more than two decades [1]. Related studies

Z. Chen · F. Gao (✉)
State Key Laboratory of Mechanical System and Vibration, Shanghai Jiao
Tong University, Shanghai 200240, China
e-mail: fengg@sjtu.edu.cn; gaofengsjtu@gmail.com

Z. Chen
e-mail: ppq67hwuxe@sjtu.edu.cn

mainly focus on two issues: how to recognize and locate the door and the handle in real-time precisely in unknown and strong interface environments, and how to optimize the process of opening doors properly to avoid large contact force because of the positioning error and the imprecise modeling of the environment.

Related works basically use vision systems to recognize and locate the door handle roughly, and apply force sensors to feedback real-time motion data for locating and controlling precisely [2–7]. Most of them are only applicable to locate specific types of door handles, and a few of them have also done some work to recognize various door handles of totally unknown geometry [8, 9]. However, harsh environments such as dim light, fire ground with smoke and nuclear accident site with radiation, can easily and quickly cause vision system to be invalid, which is not concerned by any above-mentioned examples. This paper focuses on such situations, and proposes a method which involves no vision system and uses only the tactile system to feedback the position data, thus fulfilling real-time trajectory plan.

In order to avoid the large contact force with the door when the manipulator moves along the trajectory, various strategies such as trajectory optimization [10, 11], mechanism optimization [12, 13], control method optimization [14–16]. However, the primary cause of the large contact force is that the motion of the manipulator cannot follow the position of the handle exactly because of the positional error, while a firm grasp compels the manipulator to follow. So in this paper, we apply a loose grasp to the handle, which can effectively release the large contact force and realize opening the door fluently.

Moreover, multi-DOF manipulator is indispensable for the existing door-opening method to generate the trajectory, because the wheeled, tracked, biped robot base have no enough DOFs or workspaces to operate. While in this paper, the body of the six-parallel legged robot has six DOFs and enough workspace to turn the handle and push the door open. By making a good use of the DOFs of the body and properly planning the trajectory of the body and the legs, a simpler 0-DOF tool mounted to the body can fulfill the door-opening task.

This paper is organized as follows: in Sect. 2 we introduce our six-parallel-parallel-legged robot system and the coordinate system definition; in Sect. 3 we present the trajectory plan of opening a door; in Sect. 4 we provide the experiment results and discuss about them; in Sect. 5 we conclude the paper.

2 System Overview

The platform we study on is a six-parallel-parallel-legged walking robot [17] as shown in Fig. 1. The robot is a 6-DOF parallel mobile platform with six legs, and each leg of the robot is a 3-DOF parallel mechanism with three chains: 1 UP chain and 2 UPS chains, thus called six-parallel-parallel-legged robot. The prismatic joint

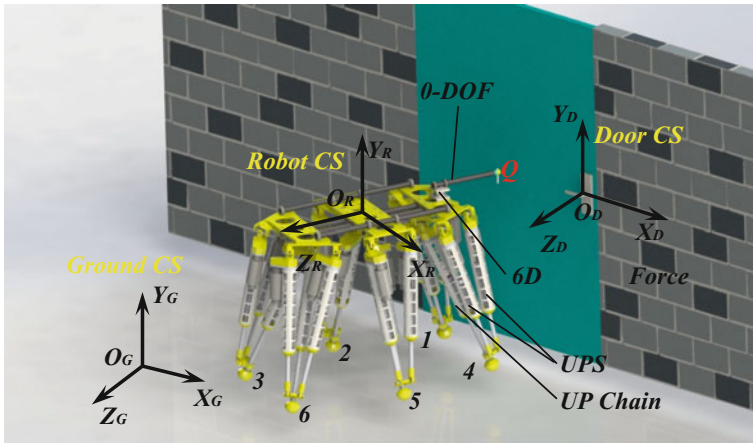


Fig. 1 Definition of coordinate systems

of each chain is the active input joint driven by a servo motor through a belt pulley. The onboard control system is integrated in a cabinet upside the robot body. At the head of the robot body, a 0-DOF tool with a 6D force sensor is mounted. The tool is composed of a horizontal rod and a vertical rod. The 6D force sensor we used is the ATI Mini58 IP68 F/T Sensor.

In order to well express the relative location between the door, the robot and the ground, it is essential to establish five main coordinate systems. The first one is the Robot Coordinate System (RCS), which locates at the center of the body plane with Z_R pointing to right astern of the body and Y_R normal to the body plane. The second one is the Ground Coordinate System (GCS), which superposes the RCS at anywhere the user sets. Then, the RCS moves together with the robot body and the GCS keeps still. Here the GCS is set to superpose the RCS as the door opening task starts. The third one is the Door Coordinate System (DCS), which locates at the intersection of the handle axis and the door plane, with Z_D normal to the door plane and Y_D along the door axis.

3 Door-Opening Approach and Trajectory Plan

The approach of opening a door is shown in Fig. 2. The task of opening a door starts when the robot is already guided to an uncertain position in front of the door. Some information about the door is already known: the direction of the handle, the range of the handle height but not the exactly value, the minimum width of the

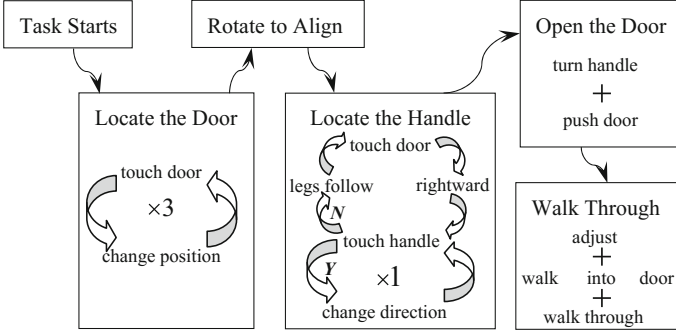


Fig. 2 Approach of opening doors

door. The task can be decomposed into five basic subtasks, which will be described in detail in this section.

The trajectory is generated by a force control model:

$$\begin{cases} M\ddot{S}_k = F_k - C\dot{S}_{k-1} \\ \dot{S}_k = \dot{S}_{k-1} + \ddot{S}_k\Delta t \\ S_k = S_{k-1} + \dot{S}_k\Delta t \end{cases} \quad (1)$$

where $S_k(x_k, y_k, z_k)^T$ and $S_{k-1}(x_{k-1}, y_{k-1}, z_{k-1})^T$ denote the coordinates of the body center O_R along the trajectory at time k and $k - 1$, $F_k(F_{xk}, F_{yk}, F_{zk})^T$ denotes the force integrated with the virtual force applied and the real force feedback from the sensor at time k , M and C denote the virtual mass and damp matrix. The M and C are kept constant, and generate different trajectories by applying different F_k .

3.1 Locate the Door Plane

The first subtask is to locate the door plane (O-A-B-C), in which the robot identifies the rotational relationship with the door by touching three non-colinear points on the door as shown in Fig. 3.

Three non-colinear points define a plane. According to this basic principle, the robot firstly moves its body forward ($-Z_R$) until the end of the tool touches the first point A on the door (O-A). Then, the robot moves its body both backward and leftward, and forward again to touch the second point B (A-B). Finally, the robot moves its body both backward and upward, and forward to touch the third point C (B-C).

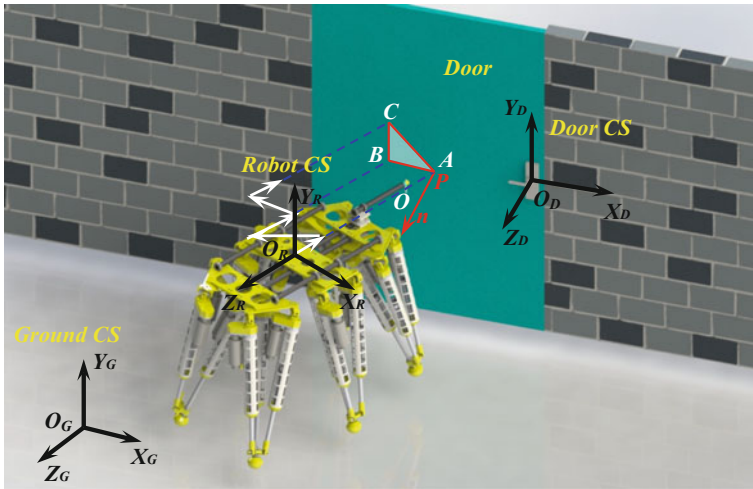


Fig. 3 Process of locating the door plane (O-A-B-C)

3.2 Rotate to Align

The second subtask is to align with the door (C-O-D), in which the robot rotates around Y_R -axis and X_R -axis to align the tool to be normal to the door plane and keeps the tool not to collide with the door plane during the process of detecting the handle.

As shown in Fig. 4, the robot firstly moves the tool from C back to the starting point O by using position control, the coordinates of O and C can be derived by the

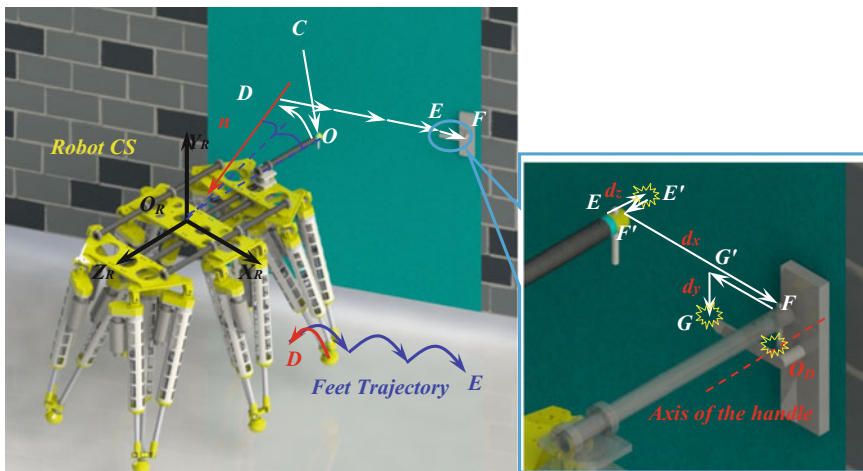


Fig. 4 Process of alignment (C-O-D) and process of locating the handle (D-E-F-G). The right figure shows the detail from E to G

forward kinematics at O and C. Then the robot rotates the body from O to D, and the rotating angles can be derived from the coordinates of A, B, C.

3.3 Locate the Handle

The third subtask is to locate the handle (D-E-F-G), in which the robot identifies translational relationship with the handle by three times of touching in three orthogonal directions.

As shown in Fig. 4, in case that the robot is far from the handle, the robot needs to move forward to touch the door and rightward to touch the handle cyclically, thus approaching the handle until touching. In every cycle except the last one, the robot successively moves its body forward ($-Z_R$) until touching the door plane, backward for a short constant distance to avoid rubbing with the door plane, rightward for a constant distance decided by the workspace of the tool, and moves its legs to follow the body, thus finishing the process of D-E.

In the last cycle (E-F-G in Fig. 4), after touching the handle, the robot moves its body leftward to a proper position, and downward until touching the handle.

3.4 Open the Door

The fourth subtask is to open the door (G-H-I), in which the robot firstly moves along a circular line in door plane to turn the handle (Fig. 5 left), and then moves forward for a proper distance to push the door open (Fig. 5 right).

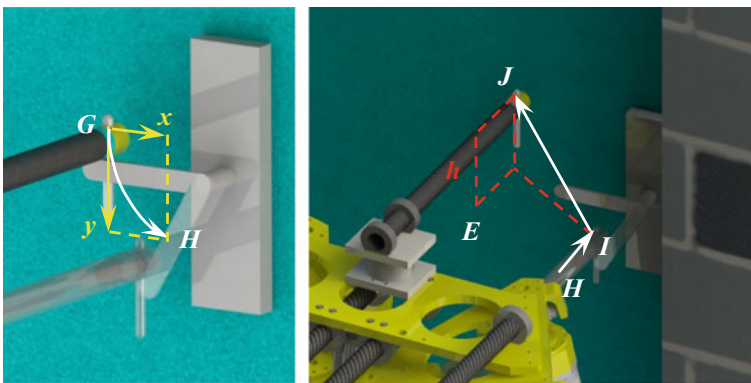
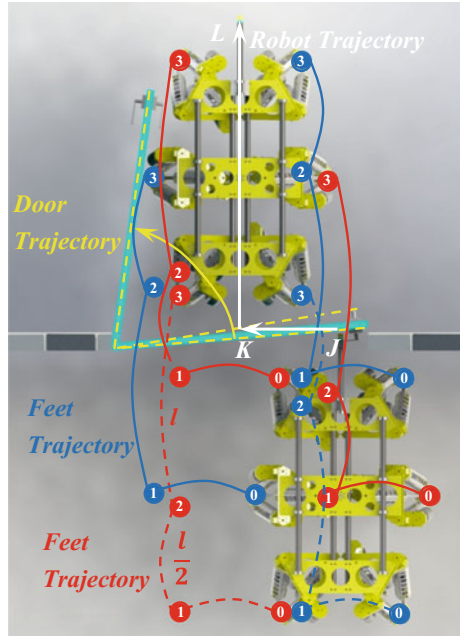


Fig. 5 Turn the handle (G-H in left), push the door (H-I in right), and adjustment before walking left (I-J in right)

Fig. 6 Process of walking through the doorframe (J-K-L)



3.5 Walk Through

The fifth subtask is to walk through the door (I-J-K-L), in which the robot adjusts its body to a proper pose (Fig. 5), walks leftward into the door range, and then walks forward to get through (Fig. 6).

During the adjustment, the tool translates parallel to the wall plane from I to J to release the handle and prepare for the left walking. The tool at point J is in the same vertical plane as at point E, and higher than E for h to avoid colliding with the handle.

During the leftward walking, the robot keeps the end effector Q in the range of the door frame to prevent the door from closing automatically. Considering the high load capacity, the robot can deal with doors with large rebounding forces.

4 Experiments and Results

In order to verify the proposed system and approach, experiments are carried out on the robot. The door is 2025 mm high and 1130 mm wide, with a door closer to provide rebound tendency. The robot autonomously plans its motion totally based on the force feedbacks from the tactile system in real-time. Figure 7 shows the process of opening the door in the experiment. Figure 8 shows the feedback force and the relevant position of the robot body.

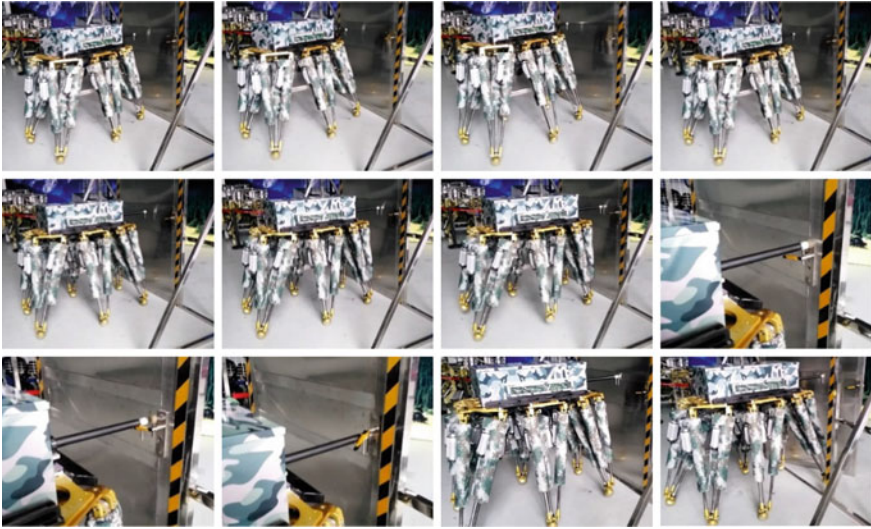


Fig. 7 Process of the experiment

The robot starts the task at O . Then the robot moves forward, and adjusts its position to prepare for next touch immediately after the tactile system detects a force pulse along Z_R which indicates the robot touches the door. After the third touch at C , the robot moves back to the starting position O , and rotates to D to keep the tool normal to the door plane.

Then, the robot tries to move rightward to touch the handle and makes different decisions based on different force feedbacks. If the tactile system feeds no force pulse back, the robot moves its legs to follow the body. If the tactile system feeds a force pulse back along X_R , the robot knows it has touched the handle at F , thus starts to adjust its position to detect the handle along Y_R . After feeling a force pulse indicating the touch along Y_R , the robot starts to turn the handle. Once the force feedback from the handle exceeds the threshold indicating the handle reaches the end H , the robot pushes the door open.

Finally, the robot walks leftward into the door range according to the calculated position of the handle and then walks through.

5 Conclusions

This paper presents a novel system for a six-parallel-parallel-legged robot to autonomously open doors. The six-parallel-parallel-legged robot enjoys six-legged robots' advantages in adaptability, mobility and stability and parallel robots' advantages in accuracy, rigidity and load capacity. Therefore it is suitable for executing tasks in unknown and strong interface environments, including opening

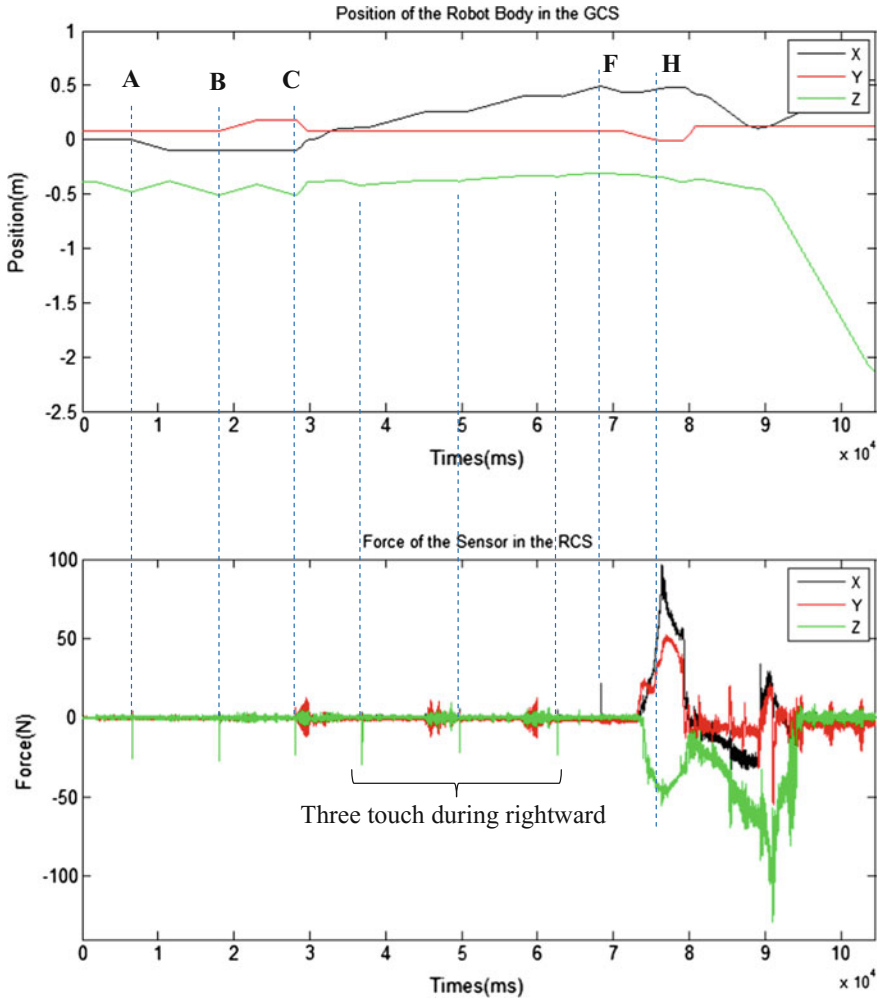


Fig. 8 Position and force

doors even with a rebound tendency. And the six DOFs and enough workspace of its body make it possible to use a 0-DOF tool mounted to the body to manipulate.

The robot calculates the positions of its body and legs in real-time by applying the forward kinematics, and detects the positions of the door and the handle by applying tactile system. Based on the good acknowledgement of the positional relationship between the robot and the door, the robot autonomously plans its motion to realize opening the door.

Acknowledgments This study is supported by the National Basic Research Program of China (973 Program) (No.2013CB035501).

References

1. Nagatani K, Yuta S (1994) Designing a behavior to open a door and to pass through a door-way using a mobile robot equipped with a manipulator. In: Proceedings of the IEEE/RSJ/GI international conference on intelligent robots and systems, 12–16 Sep 1994
2. Jain A, Kemp CC (2009) Behavior-based door opening with equilibrium point control. In: Proceedings of the RSS workshop on mobile manipulation in human environments
3. Chung W, Rhee C, Shim Y et al (2009) Door-opening control of a service robot using the multifingered robot hand. *IEEE Trans Ind Electron* 56(10):3975
4. Winiarski T, Banachowicz K, Seredyński D (2014) Multi-sensory feedback control in door approaching and opening. In: Intelligent systems'2014, advances in intelligent systems and computing 323
5. Prats M, Sanz PJ, del Pobil AP (2010) Reliable non-prehensile door opening through the combination of vision, tactile and force feedback. *Auton Robot* 29:201–218
6. Lee J, Ajoudani A, Hoffman EM et al (2014) Upper-body impedance control with variable stiffness for a door opening task. In 14th IEEE-RAS international conference on humanoid robots (humanoids), 18–20 Nov 2014
7. Ruhr T, Sturm J, Pangercic D et al (2012) A generalized framework for opening doors and drawers in kitchen environments. In: IEEE international conference on robotics and automation, 14–18 May 2012
8. Klingbeil E, Saxena A, Ng AY (2010) Learning to open new doors. In: IEEE/RSJ international conference on intelligent robots and systems, 18–22 Oct 2010
9. Ignakov D, Okounova G, Liu G (2012) Localization of a door handle of unknown geometry using a single camera for door-opening with a mobile manipulator. *Auton Robot* 33:415–426
10. Zucker M, Jun Y, Killen B et al (2013) Continuous trajectory optimization for autonomous humanoid door opening. In: IEEE international conference on technologies for practical robot applications, 22–23 Apr 2013
11. González-Fierroa M, Hernández-Garcíaa D, Nanayakkara T (2015) Behavior sequencing based on demonstrations: a case of a humanoid opening a door while walking. *Adv Robot* 29(5):315–329
12. Ahmad S, Zhang H, Liu G (2013) Multiple working mode control of door-opening with a mobile modular and reconfigurable robot. *IEEE/ASME Trans Mechatron* 18(3):833
13. Craft J, Wilson J, Huang WH (2011) Aladdin: a semi-autonomous door opening system for EOD-class robots. In: Proceedings of SPIE unmanned systems technology XIII, vol 8045, pp 804509-1
14. Ott C, Bauml B, Borst C et al (2005) Employing cartesian impedance control for the opening of a door: a case study in mobile manipulation. In: IEEE/RSJ international conference on intelligent robots and systems workshop on mobile manipulators: basic techniques, new trends & applications
15. Winiarski T, Banachowicz K (2013) Opening a door with a redundant impedance controlled robot. In: Proceedings of the 9th international workshop on robot motion and control, 3–5 July 2013
16. Karayiannidis Y, Smith C, Ogren P et al (2012) Adaptive force/velocity control for opening unknown doors. In: 10th IFAC symposium on robot control, 5–7 Sep 2012
17. Pan Y, Gao F (2013) A new six-parallel-legged walking robot for drilling holes on the fuselage. *Proc IMechE Part C: J Mech Eng Sci* 0(0):1–12

Optimized Body Position Adjustment of a Six-Legged Robot Walking on Inclined Plane

Yuan Tian and Feng Gao

Abstract In this paper, an optimized body position planner is proposed for a six-legged robot walking on inclined plane. First of all, the parametric features of an inclined plane is introduced with the relationship of the plane and the robot motion investigated. After that, an optimization-based approach is employed to generate appropriate body position adjustment corresponding to various plane parameters. Both kinematic reachability of robot legs and static stability of robot body are taken into consideration during the optimization process. Under these two constraints, the optimization objective is formulated to realize the maximum mobility indicated by the maximum step parameters. Computations are carried out demonstrating the relationship among different degrees of plane inclination, robot body displacement and robot maximum mobility.

Keywords Six-legged robot · Walking on inclined plane · Convex optimization

1 Introduction

Legged robots are advanced mobile robots that can traverse over a large range of tough terrains. Autonomous legged robot should be able to adjust their motions adaptively to overcome terrain variations. Such planning strategy should be good at building models of terrains and effectively propose respective motions to realize feasible and stable locomotion without much computational overhead. In this paper, the motion planning on a special type of tough terrain, the inclined plane, is investigated on our six-legged robot.

Y. Tian · F. Gao (✉)
State Key Laboratory of Mechanical System and Vibration, Shanghai Jiao
Tong University, 800 Dongchuan Road, Minhang, Shanghai 200240, China
e-mail: gaofengsjtu@gmail.com

Y. Tian
e-mail: tianyuan_123abc@sjtu.edu.cn

1.1 Problem Statement

For a legged robot that walks on an inclined plane or a slope, the key planning purpose is to let the robot stably move on the plane with feasible motions of mechanical joints. However, according to our experience, deadlock frequently occurs due to kinematic workspace limitations of the robot when the robot steps are as aggressive as those on flat plane. Other cases include falling over of the robot due to careless regulation of the robot COG (center of gravity). These are two main aspects when a legged robot fails to walk on an inclined plane. From the opposite perspective, some terrains are indeed too inclined that the robot could hardly step on. In this regard, to explore the maximum mobility of the robot on a given inclined plane is helpful and instructive.

Some insights could be gained after the above discussion of the problem. Yet, to solve the motion planning problem of a robot walking on a 3D spatial inclined terrain, efforts should be made in terms of robot mechanism design, gait planning, body pose regulation, etc. In this paper, we focus our study on the body pose regulation using a six-legged robot, taking both robot kinematics and stability limitations into account. We formulate the problem into a universal optimization problem and eventually obtain the optimal robot stance configuration on any given plane.

1.2 State of the Art

The problem of locomotion optimization for legged robot walking on inclined terrains has been addressed by Hong et al. [1] on humanoid robots applying a modifiable walking pattern generation method. Also, for humanoid robots, Kim et al. [2] presented an online control algorithm through which the robot could adapt to the floor conditions. Maneuvering on slopes of multi-legged robots are also discussed in [3] and [4] for hexapod and quadruped robot. More detailed stability evaluation was given in [5] and [6], in which different criteria of stability were compared and also the effect of the robot dynamics was proposed. Most of the above researches focused on the gait generation and the stability and of the legged robot. On the other hand, for more generous locomotion on rough terrain, leg kinematics played an important role and was investigated. Belter and Skrzypczyński [7] introduced an effective online posture optimization of a hexapod which could avoid deadlocks in most cases and enhance the robot mobility. In our study, we would like to consider the robot stability as well as the leg kinematics in one optimization scheme. Before that, we will firstly introduce our six-legged robot.

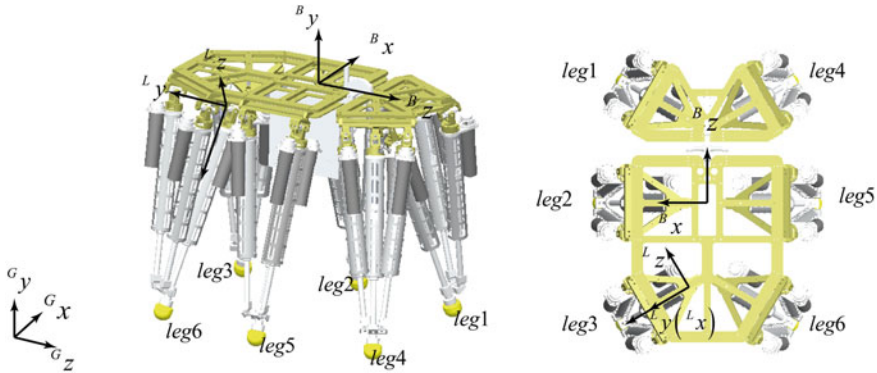


Fig. 1 Different (ground, body, leg) coordinate systems and sequence of legs

1.3 Robot Overview

The six-legged robot we employ has six legs symmetrically distributed (Fig. 1). All legs are in their standard stance positions. The ground reference coordinate system, body coordinate system and leg coordinate system are illustrated respectively. The default advancing direction of the robot is along its z axis. For the robot gait, we employed the most frequently used gait of the six-legged robot, the tripod gait. Two pairs of legs are numbered as (1, 3, 5) and (2, 6, 4), defined in an anti-clockwise order.

In terms of the control system, we utilize a Linux OS with a cross-compiled Xenomai real-time core. Onboard sensory system includes a Kinect 3D stereo vision system, six degree-of-freedom force/torque sensors mounted on each of the foot tips and an inertial measurement unit. Legs are actuated by eighteen 400 W motors. The command exchange in the actuation layer is through ethercat communication, with a frequency of 1 kHz.

2 Planning Strategy

In this paper, we propose to establish the explicit connection of the robot optimized pose and features of the inclined terrain. In this way, when the robot encounters any given terrains, the robot would be able to make fast response with a precomputed set of optimized control inputs as body translational offsets.

Unlike on other kinds of terrains with non-negligible obstacles, the difficulty of walking on inclined terrains mainly lies in the regulation of body pose, not the leg trajectories. Leg continuous motion could be generated applying simple trajectories such as the ellipsoid trajectory, rectangular trajectory, or their variations, etc.

What we would like to do is to generate a series of standard robot configuration primitives. More precisely, these are stance configuration primitives, with default position distributions of legs. Body poses of these configurations can cover a good range of robot motion on the given inclined terrain. In real world locomotion, we would then refer to these stored primitives and instruct for planning purpose. At the same time, feasible motions are restored into the table of primitives as a memorizing process to enrich the reference functionality.

In this paper, the primary mission is to generate the most general set of robot poses, depending on the different terrain parameters. The first term to accomplish is to model the inclined terrain feature.

2.1 Inclined Plane and Body Orientation

An ideal inclined plane in the 3D space could be mathematically expressed as a plane equation with respect to the given coordinate system.

$$Ax + By + Cz + D = 0 \quad (1)$$

in which the normal vector of the plane is given as $(A, B, C)_{terr}$.

Theoretically, when the robot is in its stance phase, the six foot tips locate on the same inclined plane. However, this is the case when the plane is a perfect surface. In real world applications, terrain feature always involves irregularities such as small convexity or concavity on the ground, tiny variations of elevation, etc. Therefore, we compute the plane with the actual stance foot tip positions. The obtained plane is computed by minimizing the least squares of the distance between stance foot tips and the plane.

$$J = \min \sum_{i=1}^6 \|Ax_i + By_i + Cz_i + D\|^2 \quad (2)$$

A ground coordinate system is set on the absolute flat terrain as the reference coordinate system. To express the inclined plane, we set another coordinate system attached to itself, in which the y axis coincides with the normal vector of the plane, with its vertical component pointing upward (Fig. 2). Therefore,

$$\mathbf{y}_{terr}^G = \text{sign}(B) \frac{(A \ B \ C)^T}{\sqrt{A^2 + B^2 + C^2}} \quad (3)$$

After that, we would like to set the z axis of the plane as the advancing direction of the robot along the plane. That is to say, if we express a transformation between the plane and the reference frame with the yaw-pitch-roll Euler angles, the plane would have the same yaw angle α as the robot w.r.t. the reference coordinate

system. It is the navigation angle of the robot, which is obtained from the navigation system or human instructions as the known variable. We can compute this coordinate system by the following steps.

Firstly, an auxiliary x axis is given, which is the pitch rotation axis during the Euler angle transformation after the yaw rotation,

$${}^G_{\text{terr}}\mathbf{x}_{\text{aux}} = \text{roty}({}^G\alpha_b) \cdot \begin{pmatrix} 1 \\ 0 \\ 0 \end{pmatrix} = \begin{pmatrix} \cos {}^G\alpha_b \\ 0 \\ -\sin {}^G\alpha_b \end{pmatrix} \quad (4)$$

Then, the advancing direction, namely z axis,

$${}^G_{\text{terr}}\mathbf{z} = \frac{{}^G_{\text{terr}}\mathbf{x}_{\text{aux}} \times {}^G_{\text{terr}}\mathbf{y}}{\|{}^G_{\text{terr}}\mathbf{x}_{\text{aux}} \times {}^G_{\text{terr}}\mathbf{y}\|} \quad (5)$$

Lastly, x axis and the overall rotation matrix.

$${}^G_{\text{terr}}\mathbf{x} = {}^G_{\text{terr}}\mathbf{y} \times {}^G_{\text{terr}}\mathbf{z} \quad (6)$$

$${}^G_{\text{terr}}\mathbf{R} = ({}^G_{\text{terr}}\mathbf{x}, {}^G_{\text{terr}}\mathbf{y}, {}^G_{\text{terr}}\mathbf{z}) \quad (7)$$

The rotation matrix could be also expressed by yaw-pitch-roll (213) Euler angles,

$${}^G_{\text{terr}}\mathbf{R} = \text{roty}({}^G\alpha_{\text{terr}}) \cdot \text{rotx}({}^G\beta_{\text{terr}}) \cdot \text{rotz}({}^G\gamma_{\text{terr}}) \quad (8)$$

where ${}^G\alpha_{\text{terr}}$ is the same as the robot yaw angle ${}^G\alpha_b$ and that leads to two determinant variables, the pitch ${}^G\beta_{\text{terr}}$ and roll ${}^G\gamma_{\text{terr}}$ angle of the plane. These two variables describe the fore-and-aft inclination and the lateral inclination when the robot is moving along a certain given direction.

As for the body orientation regulation, we choose to fix the body orientation with that of the inclined plane as a coarse optimization measure. Such handling of the body orientation is reasonable because first of all, the robot body is redundant with regard to the six stance legs and we prefer to coarsely adjust the body orientation and focus the precise optimization on body displacement. In this way, the problem variable space would have a lower dimension, which is efficient to solve. In addition, body orientation in parallel with the plane leaves each leg a considerably good kinematic margin. More importantly, as will be explained in the following chapters, the involvement of body orientation would violate the convexity of the overall optimization problem. We therefore fix it to strictly guarantee a feasible solution of the body displacement. The final body transformation matrix w.r.t. the reference frame is,

$${}^G_{\text{B}}\mathbf{T} = \begin{pmatrix} {}^G_{\text{terr}}\mathbf{R} & {}^G\mathbf{p}_b \\ \mathbf{0}_{(1 \times 3)} & 1 \end{pmatrix} \quad (9)$$

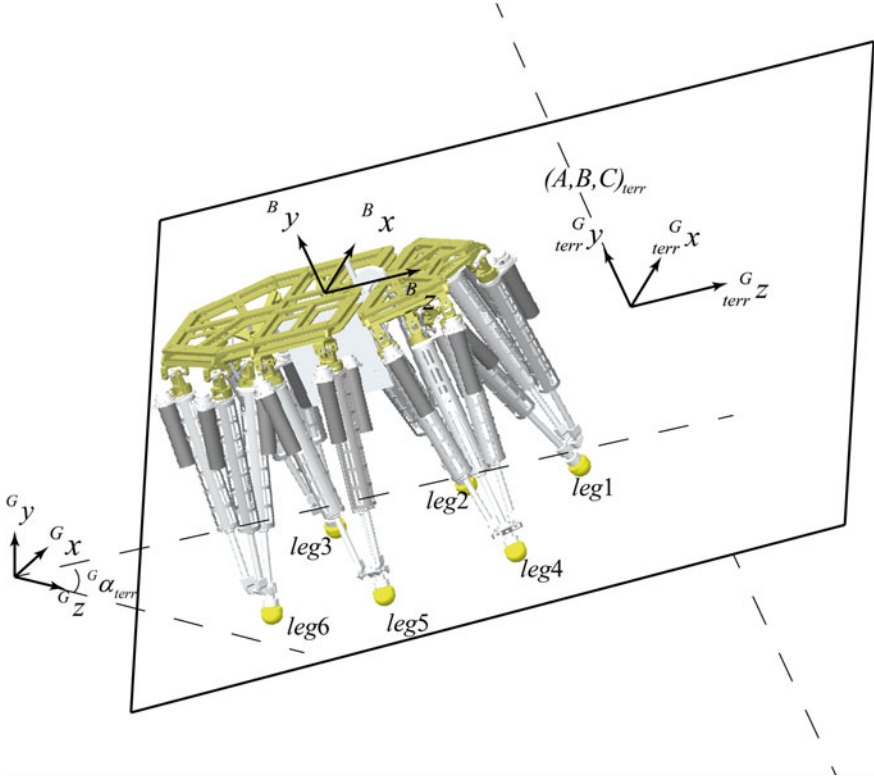


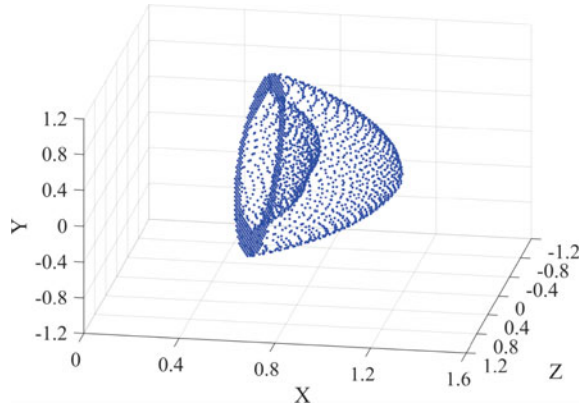
Fig. 2 The six-legged robot on inclined plane. Yaw angle of the robot is given by ${}^G\alpha_{terr}$. The plane normal vector is marked as $(A, B, C)_{terr}$

where the rotation matrix is obtained from the stance leg positions and only the robot position Gp_b serves as the undetermined variable, T being a linear transformation. The linearity of T is of great importance to relate variables in the body and the ground reference frames through an affine transformation, which guards the convexity of the optimization overall problem.

2.2 Leg Workspace Approximation

For each leg, there are three sub-chains of prismatic actuation to achieve three degrees of freedom for leg translation in space. Each prismatic actuation has upper and lower bounds of travel limits due to the mechanical constraint of the leading screw. Because of these bounds, the workspace of each leg is a non-convex

Fig. 3 Leg workspace boundary point cloud with respect to the leg coordinate system



3D space (Fig. 3). As a main aspect of the planning strategy, the kinematic margin of the leg is hard to evaluate in such irregular workspace. Out of this consideration, we propose an approximation of the workspace applying a convex subset of the workspace, formed by the intersection of a convex cone and the half space split by a spatial plane (Fig. 4). The convex subset only sacrifices some narrow workspace which is hardly reached in walking tasks. Moreover, the convex subset facilitates the formulation of the overall optimization problem.

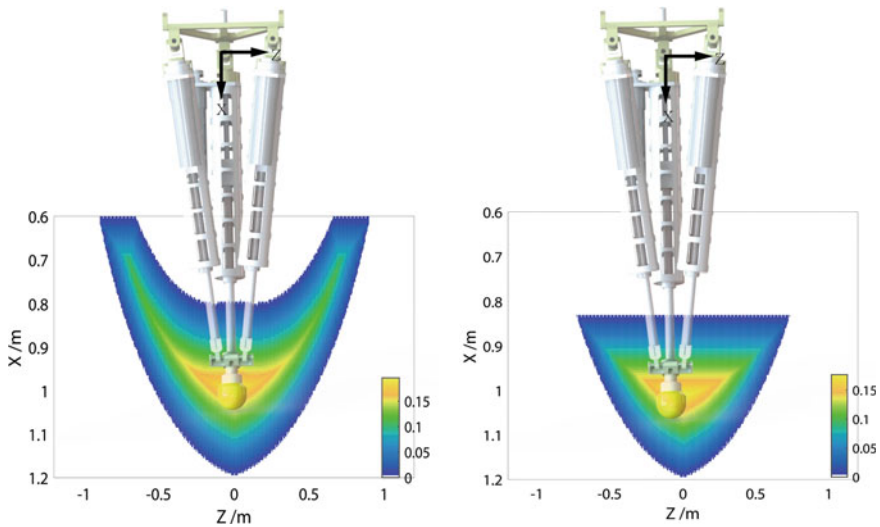


Fig. 4 Leg workspace and convex subspace viewed in the x-z plane

2.3 Convex Optimization Problem Formulation

The convex optimization formulation was adapted by various researches [8, 9] in robot trajectory and path planning. Generally, when any problem is formulated into a strict convex optimization problem, it could be resolved with efficient off-the-shelf algorithms. Algorithm implementation with software such as Mosek [10] often facilitates the computation process while only requires for the proper definition of problem variables, constraints and objective.

In our planning problem, with the plane parameters pitch and roll given, legs constraint in respective convex workspaces and body orientation fixed in parallel with the plane, the computation of optimized body position could be handled through the formulation of a general convex optimization problem. All leg and body variables are linearly related because transformations between different coordinate systems are already guaranteed as linear.

Apart from the body position, we assign another set of variables to express the possible reachable areas of the swing legs (Table 1).

The above three variables defines a box space w.r.t. the standard swing leg position. The vertices of the box are:

$$\begin{aligned} & (X_{\text{step}}/2, H_{\text{step}}, Z_{\text{step}}/2), (X_{\text{step}}/2, 0, Z_{\text{step}}/2), \\ & (-X_{\text{step}}/2, H_{\text{step}}, Z_{\text{step}}/2), (-X_{\text{step}}/2, 0, Z_{\text{step}}/2), \\ & (X_{\text{step}}/2, H_{\text{step}}, -Z_{\text{step}}/2), (X_{\text{step}}/2, 0, -Z_{\text{step}}/2), \\ & (-X_{\text{step}}/2, H_{\text{step}}, -Z_{\text{step}}/2), (-X_{\text{step}}/2, 0, -Z_{\text{step}}/2). \end{aligned}$$

These coordinates indicate synchronous motions corresponding to the swing leg w.r.t. the body coordinate system. That is to say, they are possible step motions of swing legs from the standard stance configuration along the inclined plane. In the formulation of the problem, we seek for the optimized body position satisfying that the box space of the swing leg is reachable with the least dimension of 0.2 m*0.2 m*0.08 m. The convexity of the box guarantees that all positions in the box are feasible as long as all eight motions of the vertices are feasible.

Constants

- (a) Robot mechanical dimensions.
- (b) Inclined terrain parameters (pitch and roll).
- (c) Lower bounds of dimensional parameters of the swing leg box workspace.

Table 1 Parameters of the reachable areas of swing legs with respect to the body frame

Parameter	Lower bound	Upper bound
Z_{step}	0.2 m (Z_{min})	+Inf
X_{step}	0.2 m (X_{min})	+Inf
H_{step}	0.08 m (H_{min})	+Inf

Variables

- (a) Body position (X_b, Y_b, Z_b).
- (b) Dimensional parameters of the swing leg box workspace ($X_{step}, H_{step}, Z_{step}$).

Convex/Affine Constraints

- (a) All legs in the standard stance configuration are bounded in the respective convex workspace.
- (b) All legs in the eight extreme configurations are bounded in the respective convex workspace.
- (c) The robot center of gravity lies inside the support polygon (triangle) formed by the support legs with a good stability margin, for all aforementioned configurations.

Objective

$$\max \frac{Z_{step} - Z_{min}}{Z_{max} - Z_{min}} \quad (10)$$

There could be various objective definitions of a convex optimization problem. However, in our study, we would like to reflect the relationship between the maximum mobility of the robot and the inclined terrain feature. Therefore we describe the mobility of the robot by the value of the motion Z_{step} which is along the advancement direction z axis and try to maximize the mobility. Z_{max} is the maximum step with zero inclination of the plane.

So far, the formulation of the general convex optimization problem is finished. A simple index is proposed to express robot mobility. In the next section, some computation results will be given.

3 Results and Discussion

It is illustrated in Fig. 5 that the robot mobility indeed varies according to the variation of inclination of the plane. The stability margin is given as 0.15 m. For our robot, because of the symmetric structure, the symmetric inclination results in identical body mobility. Also, it could be observed that, when the plane pitch and roll angles are small, the mobility would not alter violently. This indicates that small inclination does not influence much on the robot stability and motion performance.

In addition, body position adjustment with respect to the standard origin is given corresponding to the different terrain features (Table 2). Symmetric features are also observed.

In fact, the reachable workspace box could be modified according to the different motion preferences. In that way, body position adjustment could be more task dependent.

Fig. 5 Mobility index variation in terms of the terrain pitch and roll angles. *Red spots* represents infeasible inclinations of the terrain for the robot to walk (Color figure online)

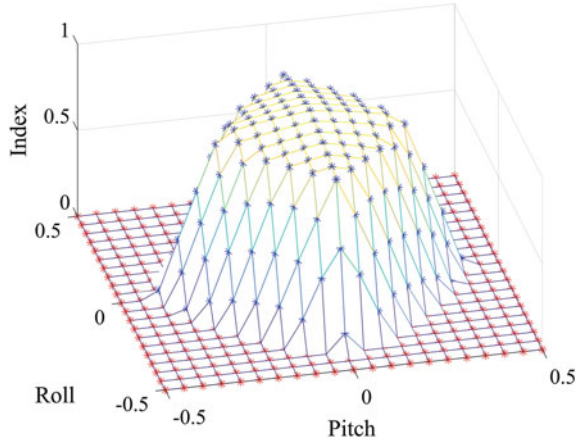


Table 2 Body position adjustment with respect to the standard original coordinate system

Pitch (rad)	Roll (rad)	Body position adjustment (m)
0	0	(0, 0.092, 0)
0.2	0	(0, 0.048, -0.186)
0.2	0.1	(0.097, 0.049, -0.179)
0.2	-0.1	(-0.097, 0.049, -0.179)
-0.1	0.2	(0.189, 0.070, 0.098)
0.1	0.2	(0.189, 0.070, -0.098)

To be conclusive, the proposed optimization based method did work effectively. The planner compromised both the robot stability and leg kinematics to gain a series of feasible configuration primitives on inclined planes. The planning method as well as the obtained results will offer more instructive help to the planning strategy in real world test. Future study includes real world terrain mapping and body pose estimation with the help of sensory systems. More dynamic motion planning and trajectory smoothing will also play an important role in future study.

Acknowledgments This study was partially supported by the National Basic Research Program of China (973 Program) (No. 2013CB035501).

References

1. Hong Y-D, Lee B-J, Kim J-H (2011) Command state-based modifiable walking pattern generation on an inclined plane in pitch and roll directions for humanoid robots. *IEEE/ASME Trans Mechatron* 16:783–789
2. Kim J-Y, Park I-W, Oh J-H (2007) Walking control algorithm of biped humanoid robot on uneven and inclined floor. *J Intell Rob Syst* 48:457–484

3. Bartsch S, Birnschein T, Cordes F, Küshn D, Kampmann P, Hilljegerdes J et al. (2010) Spaceclimber: development of a six-legged climbing robot for space exploration. In: Robotics (ISR), 2010 41st international symposium on and 2010 6th German conference on robotics (ROBOTIK), 2010, pp 1–8
4. Tsukagoshi H, Hirose S, Yoneda K (1996) Maneuvering operations of a quadruped walking robot on a slope. *Adv Robot* 11:359–375
5. Nagy PV, Desa S, Whittaker WL (1994) Energy-based stability measures for reliable locomotion of statically stable walkers: theory and application. *Int J Robot Res* 13:272–287
6. Hirose S, Tsukagoshi H, Yoneda K (2001) Normalized energy stability margin and its contour of walking vehicles on rough terrain. In: IEEE international conference on robotics and automation ICRA, pp 181–186
7. Belter D, Skrzypczyński P (2012) Posture optimization strategy for a statically stable robot traversing rough terrain. In: 2012 IEEE/RSJ international conference on intelligent robots and systems (IROS), 2012, pp 2204–2209
8. Deits R, Tedrake R (2014) Footstep planning on uneven terrain with mixed-integer convex optimization. In: 2014 14th IEEE-RAS international conference on humanoid robots (humanoids), pp 279–286
9. Kolter JZ, Ng AY (2009) Task-space trajectories via cubic spline optimization. In IEEE international conference on robotics and automation, 2009, ICRA'09, pp 1675–1682
10. Aps M. The MOSEK optimization software (2014). Available: <https://mosek.com/>

Evaluation of Spring Stiffness for Stable Grasp in Underactuated Fingers

Zhongyi Chu, Jian Hu and Shan Lu

Abstract The underactuated hand that combined the active actuators with passive springs has the function of maintaining a stable grasp and achieving high adaptable grasp of irregularly shaped objects by their mechanical behavior. The spring has an influence with the size of stable grasp region. If the spring becomes compliant, the adaptability of the hand will increase while the stable grasp region will decrease. On the other hand, if the spring becomes too stiff, although the system's stabilization will become better for some specific objects, the general performance of the hand will decrease. The objective of this paper is to present a metric to use the spring as a design parameter to affect the tradeoff between the ability to conform to the object and grasp stability. Firstly, both an underactuated finger and stable region would be reviewed based on the statics analysis. Secondly, the transition between various grasp types would be reviewed based on some parameters which used to design an underactuated hand. Finally, the proper spring correspond to a larger stable grasp region can be confirmed based on their relationship in a numerical way.

Keywords Underactuated fingers · Spring stiffness · Stable grasp · Grasp-state plane

Z. Chu (✉) · J. Hu
School of Instrument Science and Opto-electronics,
Beihang University, Beijing 100191, China
e-mail: chuzy@buaa.edu.cn

S. Lu
Shanghai Key Laboratory of Aerospace Intelligent Control Technology,
Shanghai Institute of Spaceflight Control Technology, Shanghai, China
e-mail: buaals@sohu.com

1 Introduction

On-orbit services using mechanical arm, such as assembling the space station, repairing or retrieving the satellite, refuelling the spacecraft are essential for extravehicular activities. As a critical part of the mechanical arm system, the behavior of the end effector could decide on-orbit services level to some extent. In the past few years, various types of end effectors have been studied. A special emphasis has been placed on underactuated robotic hands, in which the number of actuators is less than the degrees of freedom (DOF) and generally uses passive elements in their unactuated joints [1]. In an underactuated finger, the action of an active motor on the phalanges is transmitted through suitable mechanical instruments, e.g. tendon-actuated mechanisms and linkage-based mechanisms, etc. [2]. Pioneer designs such as the MARS hand and the SARAH hand [3] have the ability to conform to various unknown objects of large size. The MARS hand was the first underactuated hand which is built to study grasping strategies. Each of the three fingers is mounted on top of an actuation module, which can be independently controlled in order to obtain different grasp types. In order to further reduce the number of actuators and hence decrease the complexity of the controller required, the SARAH hands have been built based on the coupling between different fingers [3]. The SDM hand [4] has the same application with the SARAH hand, while Odhner focused on designing an underactuated finger to pick up small objects from a flat surface [5]. As for an underactuated hand, its compliance is not strictly necessary to conform to various objects; moreover, the null space inherent in underactuation also plays an important role. Numerous examples in the literature show that underactuated hands are relatively cheap, lightweight and easy to control compared with fully actuated hands [6–8], and can grasp various objects in diverse tasks as the fingers adapt themselves to the shape of the objects by their mechanical behaviour [9]. This means that the underactuated hand could constitute an affordable yet effective category of end effectors which is suitable for picking up and placing operations with different objects in unstructured environments.

Due to the underactuated character, many different types of passive elements were considered [3] to resolve the non-uniqueness question involved with the null space grasp [10], when the finger is not in contact with an object. Therefore, the problem of grasp stability is the crux of designing an underactuated hand. Generally, form-closure was used to characterize the robustness of a grasp. Krut focused on it and extended this property by adding a one-way movement mechanism to implement static constraint between phalanges and the object [11]. However, this method is based on the assumption that contact points between the finger and the object are fixed in space. When a grasp is exerted by an underactuated hand, it is impossible to control the position of each phalanx independently. Although underactuated fingers have a distinct advantage of grasping various objects, there are only a few available tools to solve the grasp stability problem numerically, and the design of underactuated fingers mostly results from an intuitive mode. Among a wide range of underactuated hands in research, adaptability

and stabilization are usually considered to evaluate the effect of grasping, and improving the level of stabilization is especially important for on-orbit services.

To achieve a stable grasp, Kragten, Herder and Gosselin did systematic work. With underactuated fingers able to conform to the object in a stable and multipoint way, they presented a visualized method which called grasp-state plane to attain the stable and ejection regions. Combining this method with the isotropy of a grasp, they proposed a rule to design the underactuated finger [3]. To solve the grasp stability problem numerically and produce analytical expressions, Kragten and Herder presented a method in [9]. They focused on bifurcations between grasps of different topology to determine the dimensions of the geometric and actuation design parameters of an underactuated hand so that it could grasp the objects in desired range, since individual joint angles cannot be set by the actuators in underactuated hands, the contact point can move. In addition, the effect of the number of contact points and even contact forces on the stable grasp was pointed out in [12]. For enveloping, the greater number of these contact points and forces with uniformity distribution, the better the grasp capability is. Ciocarlie presented a quasi-static equilibrium formulation to produce the underactuated hand for a wide range of grasping tasks [13] and to predict the stability of a given grasp [14]. Giannaccini presented a low-cost, soft cable-driven gripper and showed how its compliance can be passively varied to ensure an adaptive yet stable grasp [15]. However, the spring was often neglected in the process of mathematical modelling, or although it has been used in design of the hand but the particulars of the spring, such as its stiffness, were not critical. Under this situation, the spring was usually regarded as a “weak spring”, which only used to constrain the finger kinematically and ensure the shape-adaptation of the finger to the object grasped, while true spring can make the various grasp types transitioning from one to another with varying the contact forces.

For the underactuated fingers, the appropriate application of the spring makes it possible for one input torque to drive a finger that has more than one DOF [11, 16]. The balance between the contact forces, the motor actuation torque and the spring passive torque contributes to various grasp type makes great effect on the stable grasp. If the stiffness of springs is designed too small, underactuated fingers can adapt the shape of objects easily but have less stabilization; If the stiffness of springs is designed too hard, the grasp becomes more stable but could not adjust itself to a widely range of irregularly shaped object. That is to say, an opening ejection or a closing ejection can occur when stiffness is greater or smaller beyond a limitation, and it will lead to a fail mission [9]. To overcome this lack of interrelated knowledge, the objective of this paper is to propose a metric that is useful in the design of underactuated fingers of the type driven by links. The innovation of the work here is to explore the possibility of using the spring as a design parameter to affect the tradeoff between the ability to conform to the object and grasp stability. Firstly, an underactuated finger and the stable region are reviewed through statics analysis. As a 5-bar link with only one input torque is indeterminate, a spring which is in a different location from that of the SARAH hand is used to resolve the indeterminacy so that distal phalanges can move relative to one another in the parallel manner with less

energy consumption. Then, the paper takes the result of Kragten and Herder on grasp stability and bifurcations in the grasp type to obtain the spring stiffness's delimiter between regimes. Finally, the relationship between spring stiffness and stable region can be visualized in order to obtain the proper spring.

The paper is organized as follows. In Sect. 2, the statics analysis of the underactuated fingers and the stable region in the grasp-state plane are reviewed. In Sect. 3, the range of spring stiffness is figured out to be regarded as a delimiter between regimes, which is built on the basis of previous analysis. Then, the relationship between spring stiffness and stable region is confirmed in Sect. 4. Furthermore, the way on how to evaluate the effect of spring stiffness can be obtained. Finally, conclusions are given in Sect. 5.

2 Statics Analysis of the Underactuated Fingers

To determine the configurations where the finger can realize a stable grasp, this section reviews the statics analysis of the underactuated fingers. Without loss of generality, the model of the underactuated hand with two fingers can be shown in Fig. 1a, and it has a symmetrical design. Each finger consists of two phalanges L_1 and L_2 , and the actuation mechanism of each figure consists of four links a , b , c , and d , wherein link c and phalange L_2 are coupled together with an invariant angle ψ , link a and phalange b are coupled together with an angle γ , and d is a fixed link. The motor actuation torque T_a is applied to link a , which transmits the actuation torque to the phalanges. A spring passive torque T_k in O_4 is used to keep the finger from incoherent motions.

The statics will provide a relationship between the input actuator torques and the forces exerted on the object. The contact force can be expressed as [3]

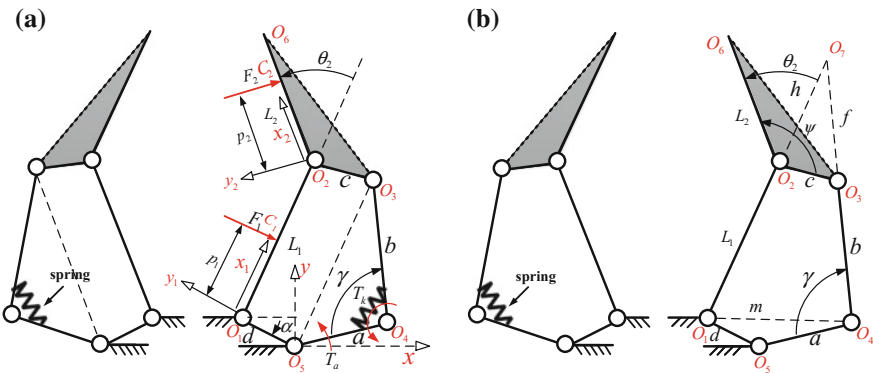


Fig. 1 Model (A) of the two-finger

$$\mathbf{f} = \mathbf{J}^{-T} \mathbf{T}^{-T} \mathbf{t} \quad (1)$$

where $\mathbf{f} = \begin{bmatrix} F_1 \\ F_2 \end{bmatrix}$ is the output vector expression of the contact force, $\mathbf{t} = \begin{bmatrix} T_a \\ T_k \end{bmatrix}$ is the input vector expression of the active actuator and the passive spring. Matrix \mathbf{J} is the Jacobian matrix of grasp, while matrix \mathbf{T} depends on the transmission mechanism used to propagate the actuation torque to the phalanges [3], which relates joint velocity vector to the time derivatives of the phalanx joint coordinates. Thus, one can obtain

$$\mathbf{J} = \begin{bmatrix} p_1 & 0 \\ p_2 + L_1 \cos \theta_2 & p_2 \end{bmatrix} \quad \text{and} \quad \mathbf{T} = \begin{bmatrix} 1 & S \\ 0 & 1 \end{bmatrix} \quad (2)$$

where the friction is neglected, variables p_1 ($0 < p_1 < L_1$) and p_2 ($0 < p_2 < L_2$) characterize the locations of the contact points defined in Fig. 1. One has $S = -h/(h + L_1)$. For the underactuated finger, the sign h is the distance between O_2 and the intersection of lines (O_1O_2) and (O_3O_4), which is a complex function of θ_2 and β . It is expressed as

$$h = c(\cos(\theta_2 - \psi) - \sin(\theta_2 - \psi) \cot \beta) \quad (3)$$

where θ_2 is the rotation of the distal phalanx with respect to the proximal phalanx, and β describes the opening of lines O_1O_2 and O_3O_4 , i.e.,

$$\cot \beta = \frac{Q}{P} \quad (4a)$$

where Q and P are expressed respectively as

$$Q = c \sin(\theta_2 - \psi) \sqrt{4a^2b^2 - N^2} + M(L_1 + c \cos(\theta_2 - \psi)) \quad (4b)$$

$$P = -(L_1 + c \cos(\theta_2 - \psi)) \sqrt{4a^2b^2 - N^2} + Mc \sin(\theta_2 - \psi) \quad (4c)$$

where M and N are expressed respectively as

$$M = -L_1(L_1 + 2c \cos(\theta_2 - \psi)) + a^2 - b^2 - c^2 \quad (4d)$$

$$N = L_1(L_1 + 2c \cos(\theta_2 - \psi)) - a^2 - b^2 + c^2 \quad (4e)$$

Hence, one obtains the analytical expressions

$$\mathbf{f} = \begin{bmatrix} -\frac{L_1(-p_2 + h \cos \theta_2)}{p_1 p_2 (h + L_1)} T_a - \frac{p_2 + L_1 \cos \theta_2}{p_1 p_2} T_k \\ \frac{h}{p_2 (h + L_1)} T_a + \frac{1}{p_2} T_k \end{bmatrix} \quad (5)$$

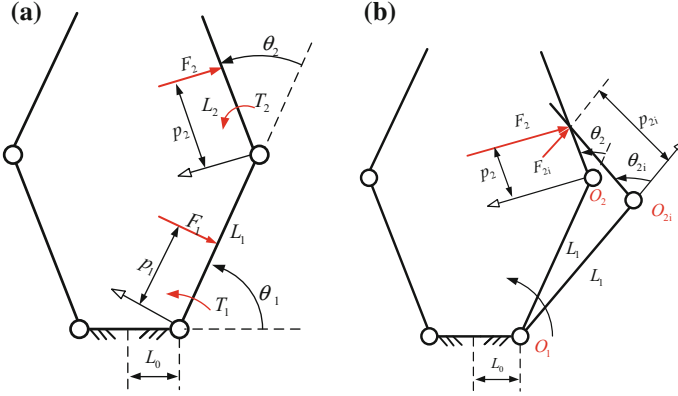


Fig. 2 Model (B) of the two-finger

where T_k is related to the spring stiffness K and expressed as

$$T_k = K\gamma T_a \quad (6)$$

For the sake of further analysis, internal torques should be expressed, which can be considered as a series of links redistribute the actuation torque to the joint space (Fig. 2a). The parameter of the length of the proximal phalanx L_1 , distal phalanx L_2 , and the palm width L_0 are called as the geometrical parameters in this kind of statics analysis model. The other design parameters related to the actuation mechanism of the fingers are called as the actuation parameters. The actuation mechanism of each figure distributes the input torque of the active actuator T_a and the passive spring T_k to the phalanges, which can be characterized by T_1 (acting on the proximal phalanx) and T_2 (acting on the distal phalanx). The following ratio is defined:

$$R = \frac{T_2}{T_1} \quad (7)$$

this ratio is not necessarily constant, but it depends on the actual rotation of the joints.

To simplify the calculations, friction is neglected, and the object initial location is enforced at the line of symmetry about the palm, so only the right finger is considered. For grasp equilibrium, the net wrench must be zero. However, we consider the situation with force balance only in this paper, the phalanges bring a compressive contact force to the object which is characterized by the radius r_{obj} . The magnitude of the contact forces depends on the position of the contact points and the rotation angle of the distal phalanx [9]:

$$\mathbf{f} = \begin{bmatrix} \frac{T_1}{p_1} (1 - R \frac{(p_2 + L_1 \cos \theta_2)}{p_2}) \\ \frac{T_1 R}{p_2} \end{bmatrix} \tag{8}$$

T_1 and T_2 are the equivalent effects of T_k and T_a combining and dispersing to each joint of the phalanges. Therefore, making corresponding items between Eqs. (5) and (8) equal with each other, one can get

$$\begin{aligned} T_1 &= T_a \\ T_2 &= \frac{h}{h + L_1} T_a + T_k \end{aligned} \tag{9}$$

As mentioned above, combining (7) and (9) and substituting (6) yields the spring stiffness

$$K = \frac{R - \frac{h}{h + L_1}}{\gamma} \tag{10}$$

Notice that the spring is useful for holding the finger with an expected motion. Four different patterns of grasping are illustrated in Fig. 3 including power (3-point, 4-point, 5-point) and pinch (2-point) grasp when R is changed [9]. That is to say, the existence of grasp equilibrium is determined by the spring stiffness. For a planar underactuated hand with fingers composed of two phalanges, it can smoothly adapt to contact forces to different objects in the grasping process, and there will be a stability area where the objects are attracted toward to the stable grasp equilibrium. Usually, 3-point grasp is a more universal type than anything else in this situation [3]. On one hand, pinch grasp type has difficulty in achieving stability [17]. Due to the potential energy of the system, the equilibrium point is not local minimum. On the other hand, although a 5-point grasp is an ideal situation of grasping because this state has a strong ability to prevent the grasped object from an unbalanced force distribution, it does not always occur for the final configuration because the closing

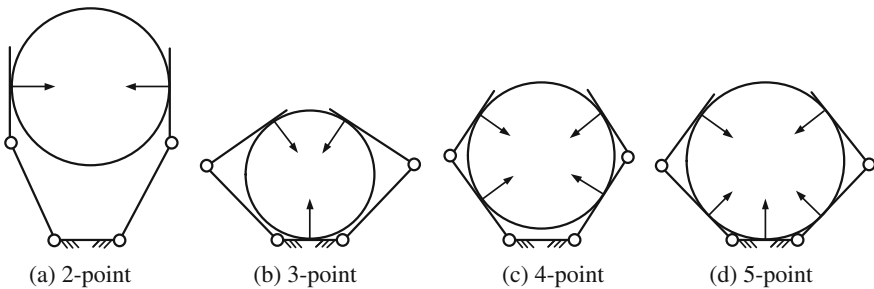


Fig. 3 Different patterns of grasping

process may force the finger to lose contact with the proximal phalanx. The situation of 4-point grasp is similar with 5-point grasp. At this moment, contact will still remain with the distal phalanx by sliding against the object. This sliding process will continue until a stable configuration with a zero proximal phalanx force is achieved, until a stable situation with joint limits are met (the shape adaptation is less effective), or until the last phalanx curl away and loose contact with the object (ejection). Thus, if the system is stable, it is common to emerge a slide by the distal phalanx of the finger in contact with the object, namely a 3-point grasp type, and an equilibrium position can be attained in the distal phalanx but just for one and unique particular position of contact p_2 , which corresponds to the solution of the (5) ($f_1(p_2) = 0$), i.e.

$$p_2 = e = \frac{T_k h + T_k L_1 + T_a h}{-T_k h - T_k L_1 + T_a L_1} L_1 \cos \theta_2 \quad (11)$$

where e is the location of p_2 at grasp equilibrium, which means the distance between a contact point on a distal phalange and its joint. Thereby, the equilibrium curve is defined.

In addition, as seen from the distal phalanx, the contact location will be introduced to analyze whether a sliding motion bring a stable position or not. It can be easily shown by considering the triangle constituted by O_1 , O_2 , and the contact point (illustrated in Fig. 2b), and if this contact exists and fixed in space, one has

$$p_2^2 - p_{2i}^2 + 2L_1(p_2 \cos \theta_2 - p_{2i} \cos \theta_{2i}) = 0 \quad (12)$$

where p_{2i} and θ_{2i} define an arbitrary initial configuration. This equation expresses that the distance between the base point of the finger and the contact location is constant for any pair (p_{2i}, θ_{2i}) . The contact curves can be tracked in the (p_2, θ_2) plane, which was regarded as the grasp-state plane [3], examples with certain parameters will be illustrated in Sect. 4.

From (12), the finger now has one degree of freedom while it is in contact with the object. This motion can be precisely described and referred to as a self-adaptive changing motion. Indeed, the contact trajectory is a curve in the contact plane (p_2, θ_2) , and if the contact trajectory crosses an equilibrium curve, the grasp is finally stable, otherwise the contact with the object will be lost, namely one obtains the ejection phenomenon due to the kinematic evolution.

In conclusion, depending on the contact trajectory (11) and the equilibrium curve (12), different final stability region can be obtained by defining different parameters of the mechanism including geometric parameters and spring stiffness and so on.

3 Bifurcations Between Grasps of Different Topology

From the statics analysis above, one can attain the function of spring stiffness K and express the stable region for a two-finger underactuated hand. Due to the performance of the stabilization affected by spring stiffness, the relationship between spring stiffness and stable region needs to be confirmed. Beyond that, the spring stiffness's delimiter between regimes should be figured out to make sure the spring is appropriate for the underactuated finger, and it can be obtained through the following steps.

3.1 The Range of Object Sizes Under Various Grasp Types

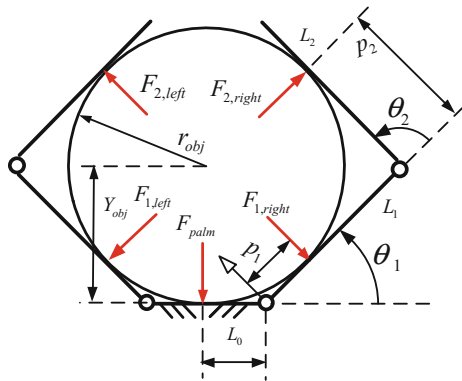
When the underactuated finger makes contact with an object, various mechanism characteristic parameters lead to various object sizes and contact points. As mentioned above, one can regard 3-point grasp as a special 5-point grasp wherein the force between proximal phalanx and object is zero since a 5-point grasp may be transformed into 3-point grasp through a form of sliding. As illustrated in Fig. 4, two constraint equations that describe contact between phalanges of the right finger and the object are as follows [9]:

$$\begin{pmatrix} L_0 + p_1 \cos \theta_1 \\ p_1 \sin \theta_1 \end{pmatrix} = \begin{pmatrix} r_{obj} \sin \theta_1 \\ Y_{obj} - r_{obj} \cos \theta_1 \end{pmatrix} \tag{13}$$

$$\begin{pmatrix} L_0 + L_1 \cos \theta_1 + p_2 \cos(\theta_1 + \theta_2) \\ L_1 \sin \theta_1 + p_2 \sin(\theta_1 + \theta_2) \end{pmatrix} = \begin{pmatrix} r_{obj} \sin(\theta_1 + \theta_2) \\ Y_{obj} - r_{obj} \cos(\theta_1 + \theta_2) \end{pmatrix} \tag{14}$$

where Y_{obj} is the distance between the center of the object and the palm ($Y_{obj} = r_{obj}$), θ_1 is the rotation of the proximal joint with respect to the palm, and

Fig. 4 Schematic representation of an underactuated hand



other signs were defined in Sect. 2. The vector equations of the left finger are similar but mirrored with respect to the vertical axis.

With the 3-point grasp type, only the constraint equation of the distal phalanx (14) has to be satisfied. Such grasp type can only exist if:

$$L_1 \leq L_0 + L_2 \quad (15)$$

The largest object that can be grasped in this type is obtained by substituting $Y_{\text{obj}} = r_{\text{obj}}$ and $\theta_1 + \theta_2 = \pi/2$ into (14) (because when the fingers are splaying to the greatest degree in a 3-point grasp type, it is in a critical state of the 2-point grasp type, and the requirement about $\theta_1 + \theta_2 = \pi/2$ is workable at this situation). Solving it for r_{obj} and θ_1 yields:

$$r_{\text{obj}} \leq \begin{cases} L_0 + L_1 & \text{if } L_1 \leq L_2 - L_0 \\ \frac{1}{2}(L_2 + L_0 + \sqrt{2L_1^2 - (L_2 - L_0)^2}) & \text{if } L_2 - L_0 < L_1 \leq L_0 + L_2 \end{cases} \quad (16)$$

Therefore, based on the geometric parameters of the finger's link, as well as the contact points between the object and the phalanges, one can attain the maximum object size that can be grasped. Then, to achieve static equilibrium of the system with a 3-point grasp, the rate of the finger's actuation torques should be analyzed as it is not determined yet.

Through (6), the existence of grasp equilibrium and the number of contact points is determined by R . If R increases, the magnitude of F_2 will also increase whereas F_1 will decrease. The object will thus be pushed against the palm. If R further increases, F_1 will become zero, the phalanx will lose contact, and the contact point on the distal phalanx will move towards the tip of the finger. In addition to the situation of stability, two different kinds of ejection have been identified, namely opening- and closing-ejection [11].

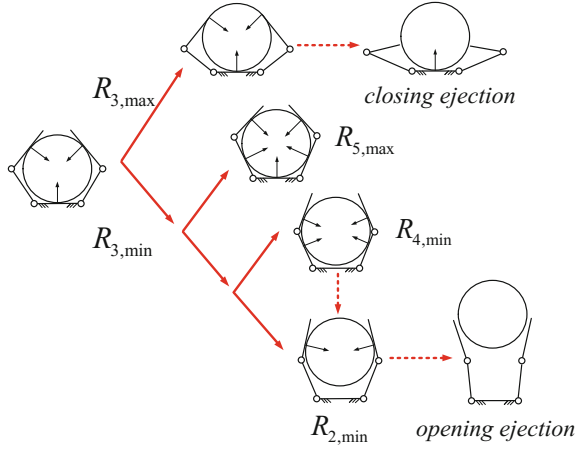
3.2 The Transition of Various Grasp Types

This process can be seen in Fig. 5. As for the 3-point grasp type, only the distal phalanges compress the object against the palm, and the proximal contact force must be zero, which can be obtained from (8):

$$1 - R\left(\frac{p_2 + L_1 \cos \theta_2}{p_2}\right) = 0 \quad (17)$$

This means that the loop closure vector equation of the distal phalanges must be satisfied with $Y_{\text{obj}} = r_{\text{obj}}$, while a compressive contact force between the palm and objects applies.

Fig. 5 Bifurcations between various grasp types



On one hand, when R reaches the upper limit $R_{3,max}$ (the maximal R with a 3-point grasp type), with constraint conditions of $L_1 > L_2 - L_0$ and $L_1 > L_0$, the contact point is located on the tip of the distal phalanges where $p_2 = L_2$ or with constraint conditions of $L_1 \leq L_2 - L_0$, the upper limit is determined by the boundary condition that $\theta_1 \geq 0$. Substitute $p_2 = L_2$ and $\theta_1 = 0$ into (14) and (17), respectively, and one can obtain the following analytical equations:

$$R_{3,max} \leq \begin{cases} \frac{(L_0 + L_1)(r_{obj}^2 + (L_0 + L_1)^2)}{r_{obj}^2(L_0 + L_1) + L_0L_1^2 + L_0^3 + 2L_0^2L_1} & \text{if } L_1 \leq L_2 - L_0 \\ \frac{2L_2(L_2^2 + r_{obj}^2)}{2r_{obj}^2L_2 + r_{obj}C - L_2(L_1^2 - L_2^2 - L_0^2)} & \text{if } L_1 > L_2 - L_0 \text{ and } L_1 \geq L_0 \end{cases} \quad (18)$$

where

$$C = \sqrt{-(L_0^2 - L_1^2 - L_2^2)^2 + 4L_1^2(L_2^2 + r_{obj}^2)} \quad (19)$$

On the other hand, when R reaches the lower limit $R_{3,min}$ (the minimal R with a 3-point grasp type), the proximal phalanges start to touch the object or the contact force between the palm and object becomes zero. It depends on the object size whose contact point is lost. As illustrated in Fig. 4, the first situation is actually the transition to a 5-point grasp type (i.e. $R_{3,min} = R_{5,max}$); the second situation is the transition to a 2-point grasp type or opening ejection. To obtain an analytical expression of $R_{3,min}$ for the second scenario, substitute $Y_{obj} = r_{obj}$ into (17) and (14), respectively, with a requirement of $0 < \theta_1 < \pi$, and one can obtain the following analytical equations:

$$R_{3,\max} \leq \begin{cases} R_{5,\max} = \frac{(L_0 - L_1)(r_{obj}^2 + (L_0 - L_1)^2)}{r_{obj}^2(L_0 - 2L_1) + L_0(L_0 - L_1)^2} & \text{if } r_{obj} > r_{obj,5} \\ \frac{r_{obj} - \sqrt{L_1^2 - (L_0 - r_{obj})^2}}{r_{obj}} & \text{if } r_{obj} \leq r_{obj,5} \end{cases} \quad (20)$$

where $r_{obj,5}$ is attained by substituting $\theta_1 + \theta_2 = \pi/2$ into (14):

$$r_{obj,5} \leq \frac{1}{2} \left(L_1 - \sqrt{L_1^2 - 4L_0^2 + 4L_0L_1} \right) \quad (21)$$

The previous analysis on R can be seen as a function of the geometric parameters and the maximum object size. It is worth noting that $R_{3,\max}$ equals $R_{3,\min}$ if the mechanism geometric parameters are fixed by calculating (18) and (20), and the next step is to figure out the spring stiffness's delimiter between regimes. For the underactuated finger, point O_7 is the intersection of lines O_1O_2 and O_3O_4 . One has respectively defined links O_3O_7 , and O_1O_4 as f , and m , respectively (illustrated in Fig. 1):

$$f = \frac{c \sin(\psi - \theta_2)}{\sin \beta} \quad (22)$$

$$m = \sqrt{(L_1 + g)^2 + (b + f)^2 - 2(L_1 + g)(b + f) \cos \beta} \quad (23)$$

According to the triangle $O_1O_4O_7$, the angle γ can be shown as

$$\gamma = \arcsin\left(\frac{(h + L_1) \sin \beta}{m}\right) + \arccos\frac{a^2 + m^2 - d^2}{2am} \quad (24)$$

Note that the term γ , as well as h , are the functions of θ_2 . Hence, as shown in (10), when R is regarded as constant and the range of θ_2 is confirmed, the spring stiffness K is related to the angle γ . That is to say, R and θ_2 decide the extent of the envelope grasping, which means the contact points' number and locations. If the designer confirms the size of an object and the extent of the envelope grasping, the range of spring stiffness K can be obtained.

4 Relationship Between Spring Stiffness and Stable Region Based on Grasp-State Plane

This section will focus on a graphical method with associated metric on the relationship between spring stiffness and the size of the stable region. According to (11), examples for two sets of geometric parameters with different spring stiffness presented in Table 1 and are shown in Fig. 6, where e/L_2 means the relative

Table 1 Geometric parameters

Set	L_1	L_2	Ψ	A	B	c
1	1	2/3	90°	1	1	1/3
2	1	2/3	90°	2/3	1	1/3

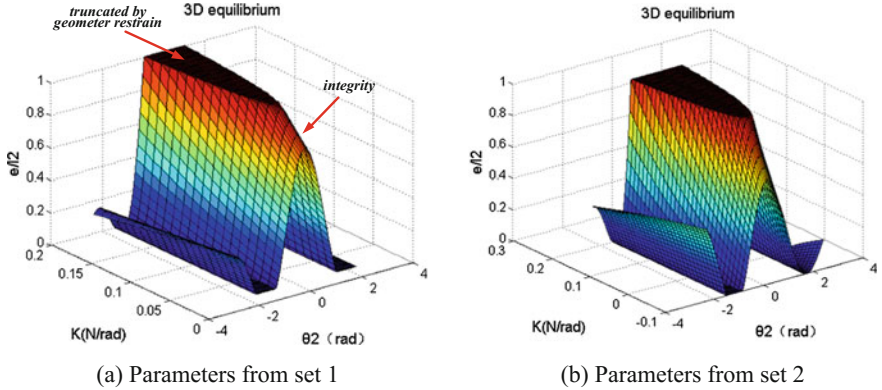


Fig. 6 The relationship between spring stiffness and equilibrium curves

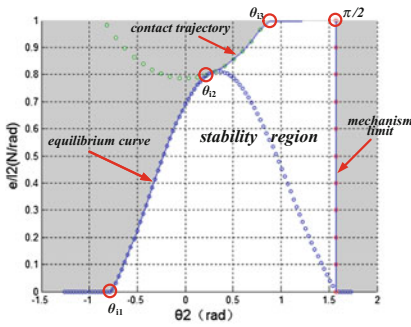
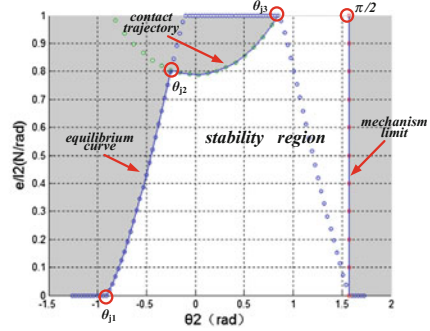
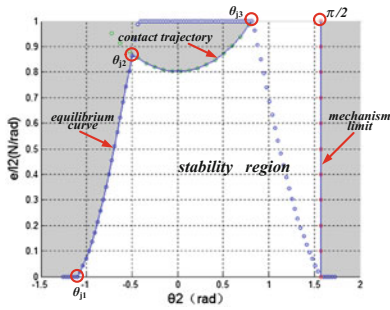
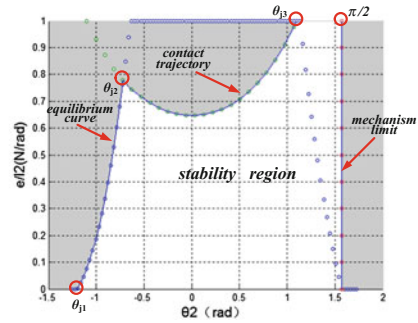
position of contact point on the distal phalange, and it is the phalange’s physical condition for successfully grasping an object.

Note that Fig. 6 includes two different types of equilibrium curves: the one truncated by geometer restrain (L_2) and the integrity one, which lead to two types of stability regions.

One type of stability regions, as shown in Fig. 7a, can be attained under the following steps. Firstly, the point of intersection (θ_{i2}) between equilibrium curve (11) and contact trajectory (12) whose slopes are equal should be found. Then, these two kinds of curves together with geometer restrain ($0 < p_2 < L_2$) and mechanism limit ($\theta_2 = \pi/2$), which is discretionary, would form a closed curve. S_i is the area of the stability region, which corresponds to the white area, and can be calculated as follows:

$$S_i = \int_{\theta_{i1}}^{\theta_{i2}} f(\theta_2)d\theta_2 + \int_{\theta_{i2}}^{\theta_{i3}} g(\theta_2)d\theta_2 + \int_{\theta_{i3}}^{\frac{\pi}{2}} \frac{e}{L_2}d\theta_2 \quad (25)$$

where θ_{ik} ($k = 1, 2, 3$) represent the changes of the angle θ_2 , and θ_{i1} is the point between equilibrium curve and geometer restrain that is located at $p_2 = 0$; θ_{i2} is intersection point as above; θ_{i3} is the point between the contact trajectory and geometer restrain that is located at $p_2 = L_2$. In addition, $g(\theta_2)$ is the segment of contact trajectory (12) between θ_{i2} and θ_{i3} in the grasp-plane, which is defined as follows

(a) Parameters from set 1($K=0.02$)(b) Parameters from set 1($K=0.10$)(c) Parameters from set 2($K=0.02$)(d) parameters from set 2($K=0.10$)**Fig. 7** Stability regions with different parameters

$$g(\theta_2) = \frac{p_2}{L_2} = \frac{\sqrt{p_i^2 + 2p_i L_1 \cos \theta_{2i} + L_1^2 \cos^2 \theta_2} - L_1 \cos \theta_2}{L_2} \quad (26)$$

where $f(\theta_2)$ is the segment of equilibrium curve (11) between θ_{12} and θ_{13} in the grasp-plane, which is defined as follows

$$f(\theta_2) = \frac{e}{L_2} = \frac{\frac{T_k h + T_k L_1 + T_a h}{-T_k h - T_k L_1 + T_a L_1} L_1 \cos \theta_2}{L_2} \quad (27)$$

Another type of stability regions, as shown in Fig. 7b, can be attained under the following steps. Firstly, the point of intersection (θ_{j2}) between equilibrium curve (11) and geometer restrain ($p_2 = L_2$) should be found. Then, the point will be used for choosing the contact trajectory (12). Finally, these two kinds of curves together with geometer restrain ($0 < p_2 < L_2$) and mechanism limit ($\theta_2 = \pi/2$) would form a closed curve. S_j is the area of the stability region, which can be calculated as follows:

$$S_j = \int_{\theta_{j1}}^{\theta_{j2}} f(\theta_2) d\theta_2 + \int_{\theta_2}^{\theta_3} g(\theta_2) d\theta_2 + \int_{\theta_3}^{\frac{\pi}{2}} \frac{e}{L_2} d\theta_2 \quad (28)$$

where $g(\theta_2)$, $f(\theta_2)$, and θ_{jk} ($k = 1, 2, 3$) were defined the same as previous.

Therefore, according to (25) and (28), the contrast of Fig. 7a, b is shown that same geometric parameters with different spring stiffness will deduce different stability region; besides, if the geometric parameters are dissimilar, the stability region is also inequitable although the finger has the same spring stiffness (Fig. 7a, c). In other words, as shown in Fig. 7, the equilibrium curves are the intersecting surfaces of Fig. 6, and the stability regions are the visualization of (25) and (28) to express the relation between the spring stiffness and the stable region.

Corresponding to different spring stiffness, various stability regions as shown in Fig. 7 can be calculated by (25) or (28). Thus, one can obtain a curve about the relationship between spring stiffness and stability regions as shown in Fig. 8. If the spring stiffness is too soft, the grasp would become less stabilized, and the stability region (soft interval) would become small as well. If the spring is too stiff, the finger would be similar to a fully actuated one, even the performance of stabilization would get better for some objects with specified size, and it would not be suitable for the majority. As a result, the performance of adaptability would degenerate and the stability region (stiff interval) will also become small. Thus, the spring shall be designed with a moderate stiffness. In a practical application, it is a guideline to choose the appropriate K , which can affect the tradeoff between the ability to conform to the object and grasp stability.

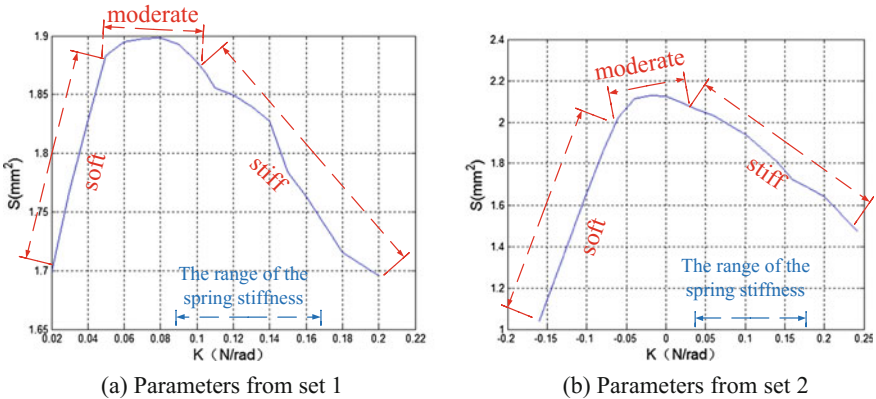


Fig. 8 Two sets of relationship between spring stiffness and stability regions

5 Conclusions

This paper presents a guideline to achieve appropriate spring stiffness for under-actuated fingers that can grasp various objects. Based on statics analysis, this method can quantify and visualize the relationship between the spring stiffness and stable region according to grasp-state plane together with the spring stiffness's delimiter between regimes. Then, the grasp stabilization with respect to spring stiffness could be evaluated in a quantitative way by analytical equations and graphs, meanwhile objects are enveloped adaptability to some extent.

Acknowledgments This work was jointly supported by the National Science Foundation of China (Grant Nos. 51375034, 61327809) and Shanghai Aerospace Science and Technology Foundation (2015-075).

References

1. Prattichizzo D, Malvezzi M, Gabiccini M, Bicchi A (2012) On the manipulability ellipsoids of underactuated robotic hands with compliance. *Robot Auton Syst* 60:33–346
2. Wu LC, Carbone G, Ceccarelli M (2009) Designing an underactuated mechanism for a 1 active DOF finger operation. *Mech Mach Theory* 44:336–348
3. Birglen L, Laliberté T, Gosselin C (2008) Underactuated robotic hands. Springer, Berlin
4. Dollar AM, Howe RD (2010) The highly adaptive SDM hand: design and performance evaluation. *Int J Robot Res* 29:585–597
5. Odhner LU, Ma RR, Dollar AM (2013) Open-loop precision grasping with underactuated hands inspired by a human manipulation strategy. *IEEE Trans Autom Sci Eng* 10:625–633
6. Borràs J, Dollar AM (2014) Analyzing dexterous hands using a parallel robots framework. *Auton Robot* 36:169–180
7. Mason MT, Rodriguez A, Srinivasa SS, Vazquez AS (2011) Autonomous manipulation with a general-purpose simple hand. *Int J Robot Res* 31:688–703
8. Odhner LU, Jentoft L, Claffee MR, Corson N, Tenzer Y, Ma R, Buehler M, Kohout R, Howe RD, Dollar AM (2014) A compliant, underactuated hand for robust manipulation. *Int J Robot Res* 33:736–752
9. Kragten GA, van der Helm FCT, Herder JL (2011) A planar geometric design approach for a large grasp range in underactuated hands. *Mech Sci* 46:1121–1136
10. Platt R, Fagg AH, Grupen RA (2010) Null-space grasp control: theory and experiments. *IEEE Trans Rob* 26:282–295
11. Krut S, Begoc V, Dombre E, Pierrot F (2010) Extension of the form-closure property to underactuated hands. *IEEE Trans Rob* 26:853–866
12. Jung GP, Koh JS, Cho KJ (2013) Underactuated adaptive gripper using flexural buckling. *IEEE Trans Rob* 29:1396–1407
13. Ciocarlie M, Allen P (2009) A design and analysis tool for underactuated compliant hands. In *Proceedings of IEEE/RSJ international conference on intelligent robots and systems*, Oct 2009, pp. 5234–5239
14. Ciocarlie M, Allen P (2011) A constrained optimization framework for compliant underactuated grasping. *Mech Sci* 2:17–26
15. Giannaccini ME, Georgilas I, Horsfield I, Peiris BHPM, Lenz A, Pipe AG, Dogramadzi S (2014) A variable compliance, soft gripper. *Auton Robot* 36:93–107

16. Odhner L, Dollar A (2011) Dexterous manipulation with underactuated elastic hands. In: Proceedings of IEEE international conference on robotics and automation, Karlsruhe, Germany, May 2011, pp. 5254–5260
17. Kragten GA, Baril M, Gosselin C, Herder JL (2011) Stable precision grasps by underactuated grippers. *IEEE Trans Rob* 27:1056–1066

Kinematic Analysis of a Novel Hybrid Hand

Edison Tamilmani and Sandipan Bandyopadhyay

Abstract This paper introduces a four-degrees-of-freedom robotic hand with a novel architecture, and presents its kinematic analysis. The hand is modelled as a hybrid manipulator, having three loops. The forward kinematic problem is relatively easier, and is readily solved to obtain all the 8 possible solutions in closed form. The inverse kinematic problem is more involved, and it is solved by decomposing the problem into three smaller subproblems, leading to a total of 48 solutions. The formulations are illustrated by numerical examples.

Keywords Robotic hand · Hybrid manipulator · Kinematic analysis

1 Introduction

This paper presents a new design of a robotic hand, and its kinematic analysis. The proposed hand is in the form of a hybrid manipulator, which has three different loops in architecture, and a total of four degrees-of-freedom.

In general, there is a trend to make robotic hands anthropomorphic, i.e., base these on the serial architecture. There are many serial hands in existence, such as [1, 2]. These hands have unhindered motions over relatively large workspaces. However, they suffer from the generic drawback of serial manipulators, i.e., they require large joint actuator efforts to manipulate relatively small payloads. This makes the serial robotic arms rather unsuitable not just for manipulation of heavy loads, but also for mounting on smaller mobile/autonomous platforms.

E. Tamilmani · S. Bandyopadhyay (✉)
Robotics Laboratory, Department of Engineering Design,
Indian Institute of Technology Madras, Madras 600036, TN, India
e-mail: sandipan@iitm.ac.in

E. Tamilmani
e-mail: edisonphnx@gmail.com

In comparison, the parallel manipulators can handle relatively heavier payloads. All the actuators are placed on the fixed base frame in a parallel manipulator. Hence unlike in the serial manipulators, there are no actuators mounted on the intermediate joints, and consequently there is no spurious loading of most of the actuators for carrying others. This advantage, however, comes at the cost of relatively smaller workspaces in parallel manipulators.

One remedy to this problem has been sought by using two serial hands together, effectively forming a single loop *hybrid* manipulator [3–6]. Further, individual hands can be also be designed as hybrid manipulators, as in [7, 8], so as to achieve a reasonable compromise between payload capacity, and workspace size. A hybrid robot is used for robot-assisted minimally invasive surgery in [9].

The hand architecture proposed in this paper has a combination of closed kinematic loops, allowing it to limit the serial aspect of the robot to only two stages. Thus only two of the four actuators are carried by the moving links. This makes the hand non-anthropomorphic, but gives it the advantage of being actuated primarily in parallel. As such, it is expected to afford smaller actuators than a standard serial counterpart having the same reach and payload. These advantages are the key motivations behind the proposed design.

The rest of the paper is organised as follows: in Sect. 2, the kinematic analysis of the hybrid hand is presented in detail. Section 3 presents the results of the forward and inverse kinematic analysis with the help of a numerical example. Finally, Sect. 4 concludes the paper.

2 Kinematic Analysis of the Proposed Hand

In this section, the geometry of the hybrid hand is presented, followed by its kinematic analysis.

2.1 Geometry of the Hand

The proposed conceptual design of the four degrees-of-freedom hybrid hand is shown in Fig. 1. The “hand” starts from a fixed *shoulder* (marked by the points \mathbf{o}_0 , \mathbf{o}_1 and \mathbf{o}_3 , and ends at the *wrist point*, \mathbf{p}_{11} . It should be noticed that the palm, fingers or any gripper is not a part of this design, but may be added on, as required. The red coloured links are *active*, i.e., actuated directly by motors. As mentioned before, there are three kinematic loops in the hand, namely, the RSSR loop, $\mathbf{o}_0\mathbf{p}_1\mathbf{p}_2\mathbf{o}_1\mathbf{o}_0$, which is confined to a plane, as the two rotary joint axes are considered to be parallel; the loop $\mathbf{o}_3\mathbf{p}_5\mathbf{p}_4\mathbf{p}_3\mathbf{o}_3$, which is equivalent to another RSSR loop, but spatial in nature; and the loop $\mathbf{p}_6\mathbf{p}_8\mathbf{p}_{10}\mathbf{p}_9\mathbf{p}_7\mathbf{p}_6$, which essentially forms a planar 5-R/five-bar chain. To perform the kinematic analysis of the hybrid hand, four coordinate

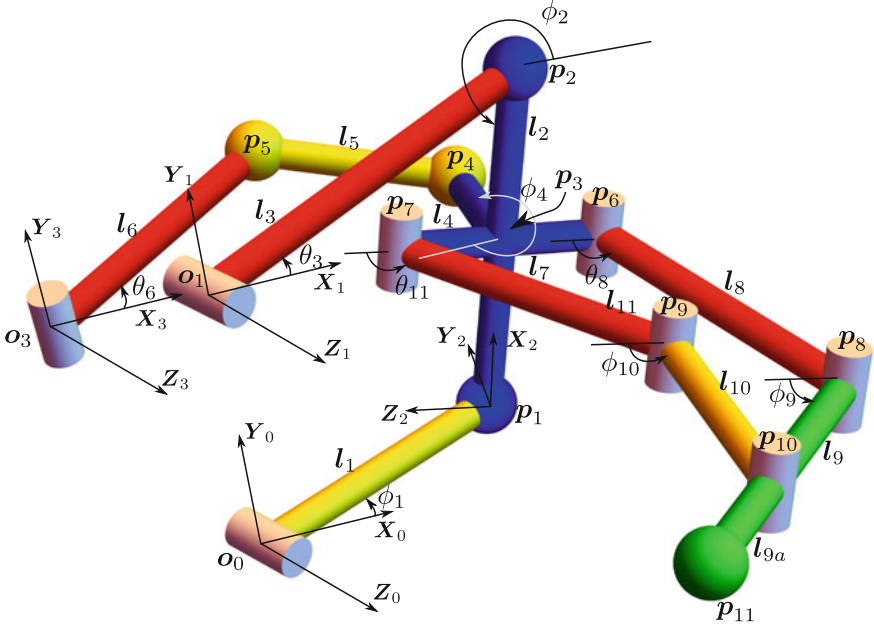


Fig. 1 A schematic of the proposed four-degrees-of-freedom hybrid hand

systems are introduced. The global coordinate system is attached to the point o_0 and its Z_0 -axis is along the joint axis of the last rotary joint of the first $\underline{\text{RSSR}}$ loop, located at o_0 . The first and third coordinate systems are attached to the points o_1 and o_3 , respectively, and their Y and Z -axes are parallel to the Y_0 and Z_0 -axes of the global coordinate system, respectively. The second coordinate system is attached to the point p_1 and its X_2 -axis is along the link 2 (i.e., p_1p_2) and the link 4 (i.e., p_3p_4) is considered to be in the X_2Y_2 plane.

The following *rotation matrices* are defined further, where ${}^i\mathbf{R}$ denotes the orientation of the coordinate system $\{i\}$ w.r.t. the coordinate system $\{j\}$:

$${}^1_0\mathbf{R} = \mathbf{R}_X(\alpha_1)\mathbf{R}_Y(\alpha_2)\mathbf{R}_Z(\alpha_3), \quad (1)$$

$${}^2_0\mathbf{R} = \mathbf{R}_Z(\phi_2 - \pi)\mathbf{R}_X(\phi_4), \quad (2)$$

$${}^3_0\mathbf{R} = \mathbf{R}_X(\beta_1)\mathbf{R}_Y(\beta_2)\mathbf{R}_Z(\beta_3). \quad (3)$$

The variables α_1, α_2 and α_3 are the *XYZ Euler angles* for the coordinate system $\{1\}$, and the variables β_1, β_2 and β_3 are the *XYZ Euler angles* for the coordinate system $\{3\}$; $\mathbf{R}_X(\cdot)$ indicates a CCW rotation about the positive X -axis, and so on.

2.2 Mobility Analysis

Mobility of any spatial mechanism is given by the standard formula:

$$F = 6(n - 1) - 5j_1 - 4j_2 - 3j_3 - 2j_4 - j_5, \quad (4)$$

where, n is the number of links and j_i is the number of i -degrees-of-freedom joints. The mobility of the proposed hand, when computed using Eq. (4), is *two*, as in this case, the non-zero constants are: $n = 10$, and $j_1 = 8$, $j_3 = 4$. However, this result is *anomalous*, due to the existence of some purely planar sub-chains in the mechanism. The anomaly can be resolved by the use of a more generic formula:

$$F = \dim(\mathcal{C}) - n_c, \quad (5)$$

where, $\dim(\mathcal{C})$ denotes the dimension of the *configuration space* of the manipulator (denoted by \mathcal{C}), and n_c is the number of *independent holonomic* constraints. For this manipulator the *configuration space* is given by (see Fig. 1):

$$\mathcal{C} = [\phi_1, \phi_2, \theta_3, \phi_4, \theta_6, \theta_8, \phi_9, \phi_{10}, \theta_{11}]^T, \quad (6)$$

and there are 5 independent holonomic constraints (given in Eqs. 11–15). Hence $F = \dim(\mathcal{C}) - n_c = 9 - 5 = 4$, as expected from physical considerations.

2.3 Forward Kinematics

The forward kinematic problem involves finding the configurations of the hand, given the rigid geometric parameters, and the actuator inputs. More precisely, the known variables are: $\theta_3, \theta_6, \theta_8, \theta_{11}$, and the unknown variables to be computed are: $\phi_1, \phi_2, \phi_4, \phi_9, \phi_{10}$.

To proceed with the analysis, it is necessary to define the key point positions first. The origin of the coordinate systems $\{0\}$, $\{1\}$ and $\{3\}$ are given by, respectively, ${}^0\mathbf{o}_0 = [o_{0x}, o_{0y}, 0]^T$, ${}^0\mathbf{o}_1 = [o_{1x}, o_{1y}, 0]^T$, ${}^0\mathbf{o}_3 = [o_{3x}, o_{3y}, o_{3z}]^T$. The end points of link 2 are given by:

$${}^0\mathbf{p}_1 = {}^0\mathbf{o}_0 + \mathbf{R}_Z(\phi_1)[l_1, 0, 0]^T, \quad (7)$$

$${}^0\mathbf{p}_2 = {}^0\mathbf{o}_1 + {}^1_0\mathbf{R}\mathbf{R}_Z(\theta_3)[l_3, 0, 0]^T. \quad (8)$$

The intermediate point ${}^0\mathbf{p}_3$ is given by: ${}^0\mathbf{p}_3 = {}^0\mathbf{p}_1 + {}^1_0\mathbf{R}[rl_2, 0, 0]^T$, where r is the distance between ${}^0\mathbf{p}_1$ and ${}^0\mathbf{p}_3$, expressed as fraction of l_2 . The end points of the link 5 (i.e., ${}^4\mathbf{p}_5$) can be written as:

$${}^0\mathbf{p}_4 = {}^0\mathbf{p}_3 + {}^2_0\mathbf{R}[0, l_4, 0]^T, \quad (9)$$

$${}^0\mathbf{p}_5 = {}^0\mathbf{o}_3 + {}^3_0\mathbf{R}\mathbf{R}_Y(\theta_6)[l_6, 0, 0]^T. \quad (10)$$

2.3.1 Formulation of the Loop-Closure Equations

The *loop-closure* equations of the RSSR loop, $\mathbf{o}_0\mathbf{p}_1\mathbf{p}_2\mathbf{o}_1\mathbf{o}_0$, are written as $\boldsymbol{\eta}_1 = [\eta_{1x}, \eta_{1y}]^T = [0, 0]^T$, where,

$$\eta_{1x} = o_{1x} + l_3 \cos \theta_3 + l_2 \cos \phi_2 - l_1 \cos \phi_1 - o_{0x}, \quad (11)$$

$$\eta_{1y} = o_{1y} + l_3 \sin \theta_3 + l_2 \sin \phi_2 - l_1 \sin \phi_1 - o_{0y}, \quad (12)$$

are the functions of passive variables ϕ_1 and ϕ_2 . For closing the loop $\mathbf{o}_3\mathbf{p}_5\mathbf{p}_4\mathbf{p}_3\mathbf{o}_3$, the rigidity of link 5 is considered:

$$({}^0\mathbf{p}_5 - {}^0\mathbf{p}_4) \cdot ({}^0\mathbf{p}_5 - {}^0\mathbf{p}_4) - l_5^2 = 0. \quad (13)$$

The loop closure equations of five-bar loop $\mathbf{p}_6\mathbf{p}_8\mathbf{p}_{10}\mathbf{p}_9\mathbf{p}_7\mathbf{p}_6$ are:

$$\eta_{2x} = l_8 \cos \theta_8 - l_{10} \cos \phi_{10} + l_9 \cos \phi_9 - l_{11} \cos \theta_{11} - l_7, \quad (14)$$

$$\eta_{2y} = l_8 \sin \theta_8 - l_{10} \sin \phi_{10} + l_9 \sin \phi_9 - l_{11} \sin \theta_{11}. \quad (15)$$

2.3.2 Solutions of the Loop-Closure Equations

The solution process of the loop-closure equations is fairly straightforward, and hence only a brief description of the steps is given below.

Firstly, Eqs. (11, 12) are solved for a pair of solutions in (ϕ_1, ϕ_2) , as these equations are *linear* in the sines and cosines of these angles. The sole remaining unknown in Eq. (13) is ϕ_4 , which is found next, leading once again to two solutions. Finally, Eqs. (14, 15) are solved for the remaining unknowns, ϕ_9, ϕ_{10} , in the same manner as in the case of ϕ_1, ϕ_2 , yielding a pair of solutions. Thus, there are a total of $2 \times 2 \times 2$ solutions to the forward kinematics problem. Once all the passive variables are solved for, the point ${}^0\mathbf{p}_{10}$ can be located as:

$$\begin{aligned} {}^0\mathbf{p}_{10} = & {}^0\mathbf{p}_3 + {}^2_0\mathbf{R}\mathbf{R}_X(\psi)[0, -l_7/2, 0]^T + {}^2_0\mathbf{R}\mathbf{R}_X(\psi + \theta_8)[0, l_8, 0]^T \\ & + {}^2_0\mathbf{R}\mathbf{R}_X(\psi + \phi_9)[0, l_9, 0]^T, \end{aligned} \quad (16)$$

where, ψ is the angle between link 4 and link 7 (i.e., $\mathbf{p}_6\mathbf{p}_7$) (which are the parts of the coupler link 2). The tip of the hand is given by:

$${}^0\mathbf{p}_{11} = {}^0\mathbf{p}_{10} + {}^2_0\mathbf{R}\mathbf{R}_X(\psi + \phi_9)[0, l_{9a}, 0]^T. \quad (17)$$

The solutions are illustrated numerically in Sect. 3.1.

2.4 Inverse Kinematics

As the hand has only four degrees-of-freedom, its task-space is a 4-dimensional subspace of $\mathbb{SE}(3)$, and as such, the parametrisation of the task-space is subject to choice, i.e., any four of the six position and orientation variables could be specified independently, in general. From a practical perspective, the position of the tip of the hand (i.e., the potential mount point of a gripper/wrist), and one of the orientation parameters of the last link, namely, the angle made by the link 9, (i.e., $\mathbf{p}_8\mathbf{p}_{11}$) with the plane X_0Y_0 , is chosen as the four task-space/output parameters. The said orientation parameter, γ , is given by,

$$\gamma = \pi - \text{atan2}(p_{11z} - p_{8z}, p_{11x} - p_{8x}), \quad (18)$$

where $\text{atan2}(\sin(\cdot), \cos(\cdot))$ denotes the *four-quadrant arc-tangent* function. Therefore, in the inverse kinematic problem, the known inputs are: $p_{11x}, p_{11y}, p_{11z}, \gamma$, and the unknowns to be solved for are: $\phi_1, \phi_2, \theta_3, \phi_4, \theta_6, \theta_8, \phi_9, \phi_{10}, \theta_{11}$. This is achieved by solving in a sequence three subproblems involving the different closed loops. Those subproblems are explained in detail in the following.

2.4.1 Subproblem of the Four-Bar Mechanism

This subproblem involves finding *all* the configurations of a planar four-bar mechanism, such that the join of a point \mathbf{p}_c on its coupler and a given point \mathbf{p} in the plane of the four-bar is *perpendicular* to the coupler, i.e., $\overline{\mathbf{p}\mathbf{p}_c} \perp \overline{\mathbf{p}_1\mathbf{p}_2}$, as shown in Fig. 2. As before, the analysis starts with the location of the key points. The end points of the coupler, \mathbf{p}_1 and \mathbf{p}_2 , can be written as, respectively:

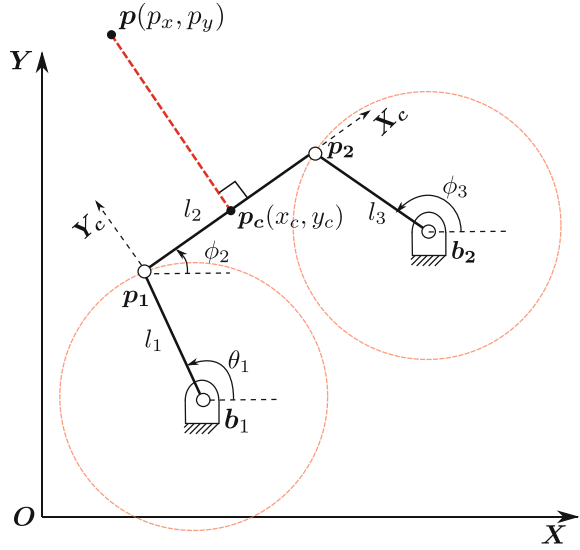
$$\mathbf{p}_1 = [b_{1x}, b_{1y}]^T + l_1[\cos \theta_1, \sin \theta_1]^T, \quad (19)$$

$$\mathbf{p}_2 = [b_{2x}, b_{2y}]^T + l_3[\cos \theta_3, \sin \theta_3]^T, \quad (20)$$

where $\mathbf{b}_1 = [b_{1x}, b_{1y}]^T$ and $\mathbf{b}_2 = [b_{2x}, b_{2y}]^T$ locate the fixed pivots, respectively. The point of interest on the coupler, \mathbf{p}_c , is given by:

$$\mathbf{p}_c = \mathbf{p}_1 + r(\mathbf{p}_2 - \mathbf{p}_1), \quad (21)$$

Fig. 2 Inverse kinematic subproblem of a four-bar mechanism



where r has been defined in Sect. 2.3. In terms of these points, the desired configurations can be defined by the equation $\eta_1 = 0$, where:

$$\begin{aligned}
 \eta_1 &= (\mathbf{p}_1 - \mathbf{p}_2) \cdot (\mathbf{p} - \mathbf{p}_c), \\
 &= l_1^2 + (b_{1x} - b_{2x})(b_{1x} - p_x) + (b_{1y} - b_{2y})(b_{1y} - p_y) - ((b_{1x} - b_{2x})^2 \\
 &\quad + (b_{1y} - b_{2y})^2 + l_1^2 + l_3^2)r - l_1(b_{2x} + p_x + 2b_{1x}(r - 1) - 2b_{2x}r) \cos \theta_1 \\
 &\quad - l_1(b_{2y} + p_y + 2b_{1y}(r - 1) - 2b_{2y}r) \sin \theta_1 \\
 &\quad + (p_x - 2b_{2x}r + (2r - 1)(b_{1x} + l_1 \cos \theta_1))l_3 \cos \phi_3 \\
 &\quad + (p_y - 2b_{2y}r + (2r - 1)(b_{1y} + l_1 \sin \theta_1))l_3 \sin \phi_3.
 \end{aligned} \quad (22)$$

In addition, the points $\mathbf{p}_1, \mathbf{p}_2$ define the end-points of the coupler link, and hence must satisfy the link length constraint $\eta_2 = 0$, where:

$$\begin{aligned}
 \eta_2 &= (\mathbf{p}_1 - \mathbf{p}_2) \cdot (\mathbf{p}_1 - \mathbf{p}_2) - l_2^2, \\
 &= b_{1x}^2 + b_{1y}^2 - 2b_{1x}b_{2x} + b_{2x}^2 - 2b_{1y}b_{2y} + b_{2y}^2 + l_1^2 - l_2^2 + l_3^2 \\
 &\quad + (2b_{1x}l_1 - 2b_{2x}l_1) \cos \theta_1 + (2b_{1y}l_1 - 2b_{2y}l_1) \sin \theta_1 - 2(b_{1x}l_3 - b_{2x}l_3 \\
 &\quad + l_1l_3 \cos \theta_1) \cos \phi_3 - 2(b_{1y}l_3 - b_{2y}l_3 + l_1l_3 \sin \theta_1) \sin \phi_3.
 \end{aligned} \quad (23)$$

Thus the two scalar equations, Eqs. (22) and (23), are of the form:

$$\begin{aligned}
 \eta_1(\sin \theta_1, \cos \theta_1, \sin \phi_3, \cos \phi_3) &= 0, \\
 \eta_2(\sin \theta_1, \cos \theta_1, \sin \phi_3, \cos \phi_3) &= 0.
 \end{aligned}$$

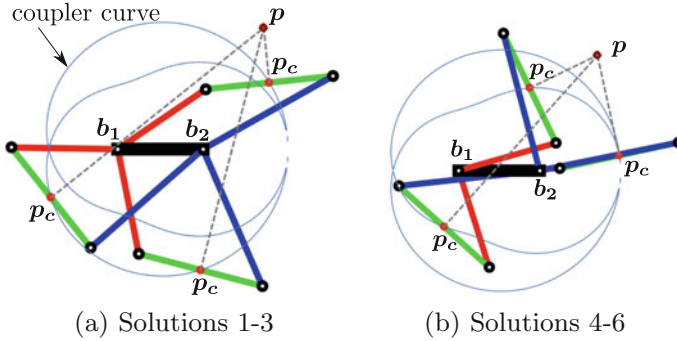


Fig. 3 Six real solutions of the subproblem

These are *linear* in the cosines and sines of the joint variable ϕ_3 . To solve these equations, first $\sin \phi_3, \cos \phi_3$ are computed in the closed form as functions of θ_1 , and then ϕ_3 is eliminated from these equations to obtain a single equation in θ_1 :

$$f_1(\theta_1) = \sin^2 \phi_3 + \cos^2 \phi_3 - 1 = 0. \quad (24)$$

Once Eq. (24) is converted to a polynomial in $t_1 = \tan(\theta_1/2)$, it becomes a *sextic* polynomial, indicating that this subproblem can have 6 solutions, at the most. Figure 3 shows a case where all the six solutions are real.

One needs to make the following correspondences, to appreciate the relevance of this subproblem in the context of the inverse kinematics of the hybrid hand (refer to Fig. 2, Fig. 1 for points on the LHS and RHS, respectively): $\mathbf{b}_1 \equiv \mathbf{o}_0, \mathbf{b}_2 \equiv \mathbf{o}_1, \mathbf{p}_1 \equiv \mathbf{p}_1, \mathbf{p}_2 \equiv \mathbf{p}_2, \mathbf{p}_c \equiv \mathbf{p}_3, \mathbf{p} \equiv [p_{11x}, p_{11y}]^T$ (i.e., the projection of the point \mathbf{p}_{11} onto the plane of the four-bar chain, $\mathbf{o}_0\mathbf{p}_1\mathbf{p}_2\mathbf{o}_1$).

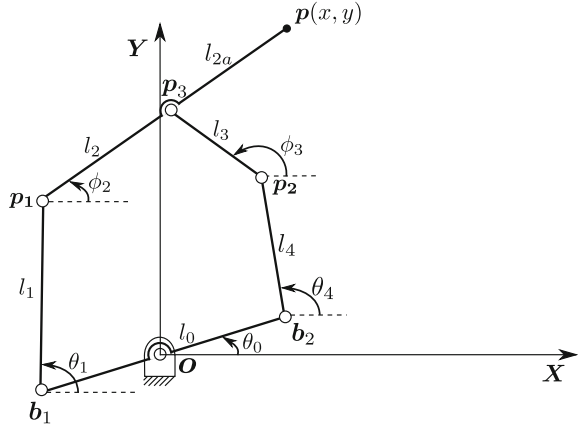
2.4.2 Subproblem of the Five-Bar Mechanism

A special variant of the five-bar mechanism is shown in Fig. 4, whose base orientation θ_0 is controllable by means of a third actuator positioned at \mathbf{o} , (in addition to those located at \mathbf{b}_1 and \mathbf{b}_2 . Accordingly, there are three independent outputs, the position and the orientation of the output link, namely, x, y and ϕ_2 , respectively. The problem is to find the joint variables $\theta_0, \theta_1, \theta_4$ and ϕ_3 for the given position, $\mathbf{p}(x, y)$, and orientation, ϕ_2 , of the end-effector. The position of the points \mathbf{p}_1 and \mathbf{p}_3 can be written as (see Fig. 4):

$$\mathbf{p}_1 = \mathbf{p} + (l_2 + l_{2a})[\cos(\phi_2 + \pi), \sin(\phi_2 + \pi)]^T, \quad (25)$$

$$\mathbf{p}_3 = \mathbf{p} + l_{2a}[\cos(\phi_2 + \pi), \sin(\phi_2 + \pi)]^T. \quad (26)$$

Fig. 4 Inverse kinematic subproblem of the five-bar mechanism



The point p_1 can also be located w.r.t. o as:

$$p_1 = o + \frac{l_0}{2} [\cos(\theta_0 + \pi), \sin(\theta_0 + \pi)]^T + l_1 [\cos \theta_1, \sin \theta_1]^T. \quad (27)$$

Equating the two expressions for p_1 , one obtains two scalar equations, which are linear in the cosines and sines of the joint variables θ_0 and θ_1 . As mentioned before, such equations can be solved to produce a pair of closed-form solutions for θ_0, θ_1 . Further, using either of the two solutions of θ_0 , one can locate the point b_2 as:

$$b_2 = o + \frac{l_0}{2} [\cos \theta_0, \sin \theta_0]^T. \quad (28)$$

Hence, p_3 can be written as:

$$p_3 = b_2 + l_4 [\cos \theta_4, \sin \theta_4]^T + l_3 [\cos \phi_3, \sin \phi_3]^T. \quad (29)$$

As above, the loop may be closed by equating the two expressions of p_3 , and from the resulting equations, a pair of solutions can be obtained for the remaining two unknowns, namely, ϕ_3, θ_4 . Thus, this subproblem leads to a total of 2×2 solutions.

This subproblem is used to find the solutions of inverse kinematics of the four degrees-of-freedom hybrid hand in such a way that the last five-bar loop, $p_6 p_8 p_{10} p_9 p_7 p_6$, can be solved for the joint variables $\theta_8, \phi_4, \theta_{11}$ and ϕ_{10} , by using the co-ordinates of the point p_{11} and the orientation parameter γ as inputs. The position of the points p_8 and p_{10} are computed by using this orientation parameter γ and the solution of the joint variable ϕ_2 (by using the previous subproblem). The relation between the two points p_8, p_{11} and the angle ϕ_2 is given by:

$$\phi_2 = \text{atan2}(p_{11y} - p_{8y}, p_{11x} - p_{8x}) - \frac{3\pi}{2}. \quad (30)$$

Another coordinate system $\{4\}$ is introduced to represent the points $\mathbf{p}_3, \mathbf{p}_8, \mathbf{p}_{10}$ and \mathbf{p}_{11} in the plane of five-bar chain. The origin of the coordinate system $\{4\}$ is the point \mathbf{p}_3 , its \mathbf{Z}_3 axis is parallel to the \mathbf{Z}_0 axis of the global coordinate system and its \mathbf{X}_3 axis is along the link 2. In the plane of five-bar chain, the position of the points $\mathbf{p}_3, \mathbf{p}_8, \mathbf{p}_{10}$ and \mathbf{p}_{11} (analogous to the points $\mathbf{o}, \mathbf{p}_1, \mathbf{p}_3$ and \mathbf{p} in the subproblem, respectively) can be written as,

$$[o_x, o_y, o_z]^T = \mathbf{R}_Z^T(\phi_2 - \pi)\mathbf{p}_3, \quad (31)$$

$$[p_{1x}, p_{1y}, p_{1z}]^T = \mathbf{R}_Z^T(\phi_2 - \pi)\mathbf{p}_8, \quad (32)$$

$$[p_{3x}, p_{3y}, p_{3z}]^T = \mathbf{R}_Z^T(\phi_2 - \pi)\mathbf{p}_{10}, \quad (33)$$

$$[p_x, p_y, p_z]^T = \mathbf{R}_Z^T(\phi_2 - \pi)\mathbf{p}_{11}, \quad (34)$$

where, the last two components of these vectors are considered to be in the plane of the five-bar mechanism. As p_y and p_z are the functions which are *linear* in $\cos(\theta_8 + \phi_4), \sin(\theta_8 + \phi_4), \cos \phi_4$ and $\sin \phi_4$, Eqs. (31, 34) are used to solve for the two joint variables, θ_8 and ϕ_4 . The other limb of the five-bar mechanism can be solved by using the obtained solutions of θ_8 and ϕ_4 to get the solutions of the joint variables θ_{11} and ϕ_{10} , thus the four branches of the five-bar loop of the hybrid hand are obtained.

The following correspondences place this subproblem in the context of the inverse kinematics of the hybrid hand (Fig. 4 and Fig. 1 show the points on the LHS and RHS, respectively): $\mathbf{o} \equiv \mathbf{p}_3, \mathbf{b}_1 \equiv \mathbf{p}_6, \mathbf{b}_2 \equiv \mathbf{p}_7, \mathbf{p}_1 \equiv \mathbf{p}_8, \mathbf{p}_2 \equiv \mathbf{p}_9, \mathbf{p}_3 \equiv \mathbf{p}_{10}, \mathbf{p} \equiv [p_y, p_z]^T$ (i.e., the projection of the point \mathbf{p}_{11} onto the plane of the five-bar chain, $\mathbf{p}_6\mathbf{p}_8\mathbf{p}_{10}\mathbf{p}_9\mathbf{p}_7\mathbf{p}_6$).

2.4.3 The Subproblem of RSSR Loop

This subproblem is identical to the analysis of a planar four-bar mechanism, and in this case it is used to find the joint variable θ_6 , from Eq. (13). As other joint variables of this equation are known from the previous steps, the two possible solutions can be computed easily. The details are hence skipped.

Finally, it can be seen that as a result of compounding the three subproblems, the total number of possible solutions to the inverse kinematics problem is $6 \times 4 \times 2 = 48$. The derivations presented above are verified in the following section numerically.

3 Numerical Examples

This section presents numerical examples illustrating the formulations described above. The results are verified by checking the inverse kinematic solutions against the forward kinematic inputs.

The constant architecture parameters given in Table 1 are used in all the calculations. All the lengths are expressed in meters, and the angles in radians.

3.1 Results of Forward Kinematics

The active joint variables used in the forward kinematics example are: $\theta_3 = 0.1$, $\theta_6 = 0.1$, $\theta_8 = 2.0$, $\theta_{11} = 2.4$. The eight branches of solutions are real for these inputs, and these solutions are presented in Table 2. Due to constraint of space, only the branches 1 and 2 are shown in Fig. 5.

Table 1 Numerical values of the architecture parameters

Parameter	Symbol	Value
Link lengths of first <u>RSSR</u> loop	(l_1, l_2, l_3)	(0.6, 0.7, 0.8)
Link lengths of second <u>RSSR</u> loop	(l_4, l_5, l_6)	(0.3, 0.4, 0.6)
Link lengths of five-bar loop	$(l_7, l_8, l_9, l_{9a}, l_{10}, l_{11})$	(0.4, 0.7, 0.5, 0.3, 0.5, 0.6)
Other design parameters	(r, ψ)	(0.5, $\pi/2$)
Euler angles relating {1} to {0}	$(\alpha_1, \alpha_2, \alpha_3)$	(0, 0, 0)
Euler angles relating {3} to {0}	$(\beta_1, \beta_2, \beta_3)$	(0, 0, 0)
Origin of {1}	${}^0\mathbf{o}_1$	(0, 0.6, 0)
Origin of {3}	${}^0\mathbf{o}_3$	(0, 0.3, -0.5)

Table 2 Numerical results for the forward kinematic analysis

Branch	Co-ordinates of the point p_{11}			Orientation parameter γ
	p_{11x}	p_{11y}	p_{11z}	
1	0.0013	0.5471	0.7621	6.1856
2	1.4000	0.1391	0.3495	3.7603
3	1.2970	0.1691	0.8152	1.3535
4	1.1232	0.2198	-0.6788	5.1633
5	0.3340	1.5358	0.4799	5.0086
6	0.5242	0.0447	0.5496	4.3246
7	0.3901	1.0959	0.9157	1.0608
8	0.5505	-0.1616	0.1049	4.6155

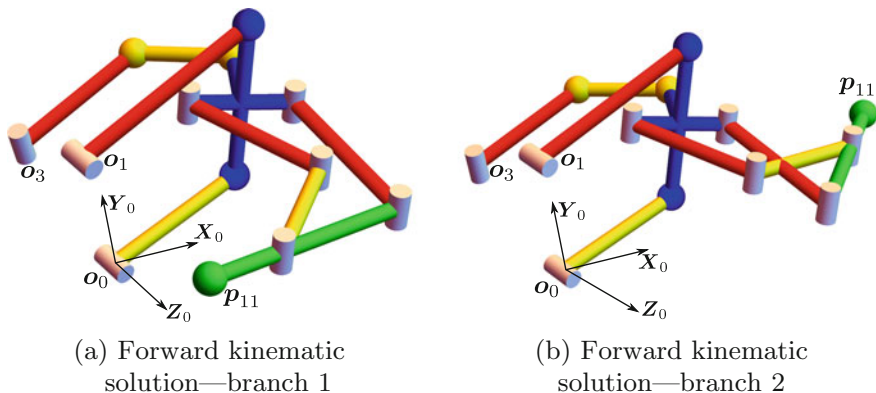


Fig. 5 Forward kinematic solutions—branches 1 and 2

3.2 Results of Inverse Kinematics

The inverse kinematic procedure is demonstrated using the numerical data corresponding to the first branch of the forward kinematics, shown in bold fonts in Table 2. For these data, 12 of the 48 solutions turn out to be real. These solutions are presented in Table 3. It may be noted that the first branch (detailed in bold fonts in the first row of Table 3) of the inverse kinematic solutions correspond to the inputs to the forward kinematic problem, thus validating the correctness of the results. It can also be seen that the inverse kinematic configuration corresponding to the first branch of the solution, shown in Fig. 6a, is identical to the configuration shown in Fig. 5a, depicting the result of forward kinematics.

Table 3 Numerical results for the inverse kinematic analysis

Branch	θ_3	θ_6	θ_8	θ_{11}
1	0.1000	0.1000	2.0000	2.4000
2	0.1000	-0.6642	2.0000	2.4000
3	0.1000	-0.6642	2.0000	1.2972
4	0.1000	0.1000	2.0000	1.2972
5	-1.6261	-1.4541	1.8037	3.1592
6	-1.6261	-0.4059	1.8037	3.1592
7	-1.6261	-1.4541	1.8037	2.4020
8	-1.6261	-0.4059	1.8037	2.4020
9	-1.6261	-1.5545	-1.8037	5.2709
10	-1.6261	-1.0014	-1.8037	5.2709
11	-1.6261	-1.5545	-1.8037	3.9596
12	-1.6261	-1.0014	-1.8037	3.9596

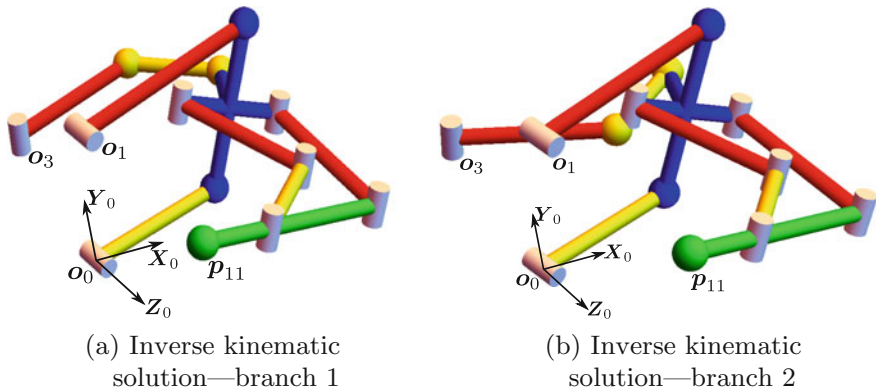


Fig. 6 Inverse kinematic solutions—branches 1 and 2

4 Conclusions

This paper introduces a novel design of a four-degrees-of-freedom robotic hand, and also presents the forward and inverse kinematic analysis of the same. It is shown that the forward kinematic problem is rather trivial, with 8 solutions, which can be computed analytically in the closed-form. The inverse kinematic problem is more interesting, having a total of 48 solutions. Further, the inverse kinematic problem can be decomposed into three subproblems, which allow for a systematic solution of the problem, as well as an intuitive geometric visualisation of the solutions. The mathematical formulations are illustrated via numerical examples. The validity of the solutions is established by retrieving the forward kinematic results in inverse kinematics.

References

1. Sawyer: Rethink Robotics unveils new robot. <http://www.rethinkrobotics.com/news-item/rethink-robotics-unveils-newest-smart-collaborative-robot>. Online; Accessed 28 July 2016
2. Oceaneering, Atlas hybrid manipulator. <http://www.oceaneering.com/rovs/rov-technology/atlas-hybrid-manipulator>. Online; Accessed 28 July 2016
3. ABB, ABB has developed a collaborative, dual arm robot that includes flexible hands. <http://new.abb.com/products/robotics/yumi>. Online; Accessed 28 July 2016
4. Ju Z, Yang C, Ma H (2014) Kinematics modeling and experimental verification of baxter robot. In: 33rd Chinese control conference (CCC), 2014. IEEE, pp. 8518–8523
5. Garage W (2009) Overview of the PR2 robot. <http://www.willowgarage.com/pages/pr2/overview>. Online; Accessed 28 July 2016
6. Tunstel EW Jr, Wolfe KC, Kutzer MDM, Johannes MS, Brown CY, Katyal KD, Para MP, Zeher MJ (2013) Recent enhancements to mobile bimanual robotic teleoperation with insight toward improving operator control. Johns Hopkins APL Tech Digest 32:584–594

7. Zeng Q, Fang Y, Ehmann KF (2011) Design of a novel 4-DOF kinematotropic hybrid parallel manipulator. *J Mech Des* 133(12):121006
8. Liu H, Huang T, Mei J, Zhao X, Chetwynd DG, Li M, Hu SJ (2007) Kinematic design of a 5-DOF hybrid robot with large workspace/Limb–Stroke ratio. *J Mech Des* 129(5):530–537
9. Pîsla D, Gherman B, Vaida C, Suciú M, Plitea N (2013) An active hybrid parallel robot for minimally invasive surgery. *Robot Comput Integr Manuf* 29(4):203–221

Research of the Relation Between Configuration and Skin-Friction Coefficient of an Underactuated Hand Based on the Maximum Grasping Space

Shangling Qiao, Hongwei Guo, Rongqiang Liu and Zongquan Deng

Abstract In order to complete the grasping mission in space, a novel underactuated robotic hand which belongs to not only the tendon-pulley transmission but also the double-stage mechanisms, is proposed. The hand which has three joints is controlled by a single motor during the grasping process. Based on grasping model, the relation equation which reveals the relation among the driving force, the equivalent torques on joints, and the grasping forces is established by using vector mechanics and the principle of virtual work. Under the condition that the maximal grasping space is an envelope circle with the radius of 1250 mm, all the stable grasping configurations and the relation between the shortest lengths of finger and the skin-friction coefficient is analyzed.

Keywords Stable grasp · Underactuated · Robotic hand · Tendon-pulley transmission

1 Introduction

According to NASA studies [1], more than twenty thousand aircrafts have been launched to the space debris. On one hand, a huge numbers of working aircrafts need maintenance on-orbit. On the other hand, thousands of disabled aircrafts and

S. Qiao (✉) · H. Guo · R. Liu · Z. Deng
State Key Laboratory of Robotics and System,
Harbin Institute of Technology, Harbin 150001, China
e-mail: qiaosl_hit@163.com

H. Guo
e-mail: guohw@hit.edu.cn

R. Liu
e-mail: liurq@hit.edu.cn

Z. Deng
e-mail: dengzq@hit.edu.cn

space debris need be cleaned up on-orbit. With the increase of human space activities and deep space exploration missions, the on-orbit capture mechanism is playing an increasingly important role in space.

Typical operational targets on orbit are cooperative in the sense that they allow friendly communication for synchronization manipulation, as well as dedicated grappling fixtures and artificial markers to support docking [2]. The capture process of cooperative spacecraft is almost static or quasi-static in low earth orbits. Nowadays, the robotic hands with full driven have been widely applied to the tasks in space, such as grasping, handling and assembling. The Shuttle Remote Manipulator System (SRMS) [3] is a part of the Space Transportation System (STS) designed by the National Research Council of Canada, which comprises a 15 m long, six-degree-of-freedom, anthropomorphic manipulator arm. The SRMS, designed mainly for the deployed and retrieval of payloads from and to the orbiter cargo bay, is one of the earliest space capture robotic mechanisms [4, 5]. Another typical application is the FRENDS plan [6], designed by Defense Advanced Research Projects Agency (DARPA), which owns the ability to grab the space target, and on-orbit servicing, contains three 7-DOF manipulator and visual system [7, 8]. Both of them be applied to catch the cooperative targets. Furthermore, the structures of those full driven robotic hands are relatively complex, heavy, and having more motors. However, the space debris are generally non-cooperative targets with uncertain patterns and grappling fixtures. Space debris are often out of control and their movement characteristics might not be known beforehand, so they cannot be captured in a stable environment [9]. To solve the shortcomings of the full-actuated robotic hands, much efforts have been made to develop the underactuated robotic hands.

Recently, much attention has been given to the novel space robotics where the number of control inputs is less than that of degrees of freedom (DOF). Such space robotics are known as underactuated space robotics. Compared with general full-actuated robotic hands, the underactuated robotic hands have some competitive advantages which the full drive hands don't have, such as light weight, less number of motors, etc. SARAH, developed by MD ROBOTICS in Canada, is the most international representative underactuated robotic hand. The hand, driven by two motors, has three fingers and 10-DOF, through mechanical limits and the torsional spring to control the movement of unpowered joints in [10] and [11]. Many new types of robot hands on the foundation of SARAH are carried out, such as [12]. Besides, although many manipulators have the characteristics of underactuated mechanisms, some shortcomings of complex structures, non-expandable and many drive motors still be there in [13] and [14]. Thus, a class of mechanical manipulators which overcome those shortcomings have been worked out, such as the [15] and [16], driven by cable. But those hands have bad expandability, bad self-adaptability and can't be applied on grasping on-orbit.

In this paper, a novel underactuated robotic hand is proposed, which overcomes those shortcomings and owns the advantages of simple structure, good self-adaptability, etc. This paper is organized as follows. Design principle and detailed structure of the finger are introduced in Sect. 2. Section 3 gives the

establishment of grasping model and the analysis of grasping force. Configuration analysis of hand based on maximal grasping space is introduced in Sect. 4. Finally, Sect. 5 concludes this paper.

2 Design Principle of the Finger

As shown in Fig. 1, a novel robotic hand is designed by using the cables and bars. Four bars and two cables wound through a certain way are used to construct a cable-bar unit, which is a basic assembled unit to the underactuated robotic hand. The four bars are assembled and installed in the order of end to end to construct the parallel quadrilateral mechanism. One cable is used to control the parallel quadrilateral mechanism moving in clockwise direction. The other cable is used to control the parallel quadrilateral mechanism moving in anti-clockwise direction. By controlling the tensile force exerted on the cables, the direction of motion of the cable-bar unit can be controlled.

As shown in Fig. 2, it is a sample grasping of the finger which is assembled by 5 cable-bar units. And the grasping space is the circular envelope of the cylinder. The significance is that the novel underactuated hand driven by cables can grasp objects and the hands owns excellent extendibility and modularity.

Once the roller 1 moves in clockwise direction and applies a tensile force on the cable 1, the finger will start closing, shown in Fig. 3. The winding way of cable 2 (the pink line) is similar to cable 1. Once the roller 2 moves in anti-clockwise direction and applies a tensile force on the cable 2, the finger will start opening. If the roller 1 works, then roller 2 does not work (just follows the steps of roller 1). Similarly, if the roller 2 works, then roller 1 does not work. At the same time, only one roller moves in active and the other one moves in passive. It means that the finger which owns more than 1-DOF is actuated by a single motor at any time. Thus, the hand belongs to a class of highly underactuated mechanisms.

There exist a lot of forms of movements such as all the cable-bar units moving simultaneously or moving in the defined sequence. With each joint friction damping configured, can not only realize cable-bar units moving at the same time, but also realize units moving in the defined sequence. Which is the prominent advantage of the hand. With the moving of roller 1 in a certain speed, the cable 1 wound in the finger becomes shorter and shorter and the finger bends inside. With the bending of

Fig. 1 The theoretical model of a finger

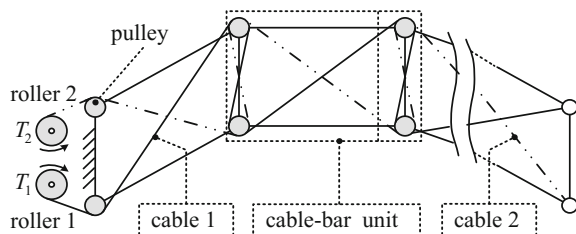


Fig. 2 The sample grasping

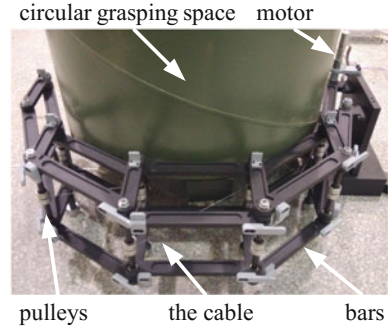
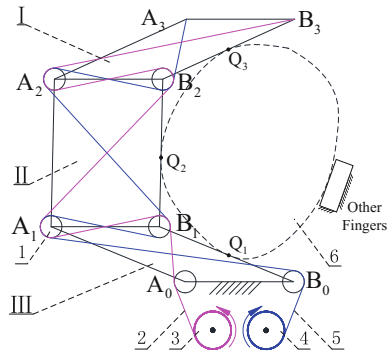


Fig. 3 The grasping model of one finger. Notes: *I* the distal segment; *II* the middle segment; *III* the original segment; *1* the pulley; *2* the cable *2*; *3* the roller *2*; *4* the roller *1*; *5* the cable *1*; *6* the grasped object



the finger, the segments will contact with the grasped object at $Q_1, Q_2,$ and Q_3 (maybe random combination of Q_1, Q_2 and Q_3). When no segment can continue to move, the grasping mission is completed. Because of the reaction force from the grasped object, the finger keep on a state of dynamic balance.

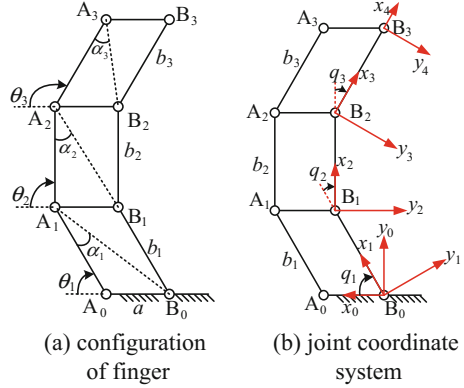
In this paper, the underactuated hand, assembled by 3 units, is taken as the research object. Based on the same maximum grasping space, the grasping model of the hand on a completely stable grasping state is established. We analysis the configuration and grasping characteristics of the 3-DOF hand.

3 Grasping Model and Grasping Force Analysis

3.1 General Grasping Model

As shown in Fig. 4, the general kinematic model of finger is built. The parallelogram cable-bar units are important components of the finger. To simplify the analysis and calculation of statics and facilitate analysis of the relation between the driven tensions cables pulling force and catch grasping force, some rules of

Fig. 4 Kinematic model of finger



simplification in statics analysis and calculation as following. The double-stage linkage units are regarded as the ideal truss units. Ignore the radius of the pulley, and the cable tension directly effect on the respective joints.

We can obtain the relation between θ_i and q_i ,

$$\begin{pmatrix} q_1 \\ q_2 \\ q_3 \end{pmatrix} = \begin{pmatrix} 1 & 0 & 0 \\ -1 & 1 & 0 \\ 0 & -1 & 1 \end{pmatrix} \cdot \begin{pmatrix} \theta_1 \\ \theta_2 \\ \theta_3 \end{pmatrix} \tag{1}$$

Although the finger belongs to tendon-pulley transmission mechanism, it can be equivalent to the full joint driven mechanism. As shown in Fig. 5, the equivalent model of finger in grasping stage is built. The model is used for analyzing the relation between the grasping force and the cable driving force when the grasping mission finished. The meaning of the parameters in the models is shown in Table 1.

Fig. 5 The equivalent model in grasping stage

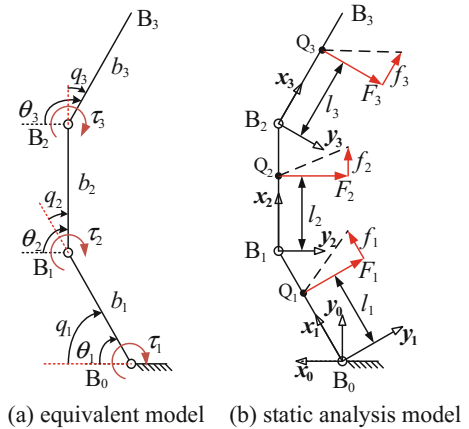


Table 1 Symbol definition

Symbol	Description	Position
a	The width of the finger	Figure 4
b_i	The length of each segment	Figure 4
R	The max radius of the grasping space	Figure 7
α_i	The angle between A_iA_{i-1} and A_iB_{i-1}	Figure 4
θ_i	The angle between $A_{i-1}B_{i-1}$ and $A_{i-1}A_i$	Figure 4
q_i	The joint coordinates	Figure 5
l_i	The distance from B_{i-1} to F_i	Figure 5
T_i	The tension cable forces	Figure 1
F_i	The grasping force in normal direction	Figure 4
f_i	The grasping force in tangential direction	Figure 4

3.2 Analysis of Equivalent Joint Driving Torques

As mentioned earlier, the tendon-pulley transmission mechanism can be equivalent to the full joint driven. In order to obtain the relation between the cable force and the equivalent joint driving torques, resultant moments of cable forces in a finger which own one cable-bar unit is built, shown in Fig. 6.

According to the virtual work principle, we have,

$$dW_T = dW_{M_e} \tag{2}$$

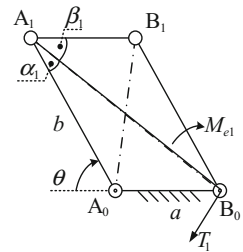
$$dW_T = T \cdot dL \tag{3}$$

$$dW_{M_e} = M_e \cdot d\theta \tag{4}$$

Where, $dL_{B_0A_1} \approx -\frac{ab \sin \theta}{\sqrt{a^2 + b^2 + 2ab \cos \theta}} d\theta$. Thus, we have,

$$M_{e1} = \frac{T_1 ab \sin \theta}{\sqrt{a^2 + b^2 + 2ab \cos \theta}} = T_1 b \sin \alpha_1 \tag{5}$$

Fig. 6 Resultant moment of cable driving force



In the finger, composed by one cable-bar unit, the equivalent joint driving force is equal to the resultant moment of cable force. As shown in Fig. 5a, we can obtain,

$$\begin{pmatrix} \tau_1 \\ \tau_2 \\ \tau_3 \end{pmatrix} = \begin{pmatrix} 1 & 1 & 1 \\ 0 & 1 & 1 \\ 0 & 0 & 1 \end{pmatrix} \cdot \begin{pmatrix} M_{e1} \\ M_{e2} \\ M_{e3} \end{pmatrix} = \begin{pmatrix} 1 & 1 & 1 \\ 0 & 1 & 1 \\ 0 & 0 & 1 \end{pmatrix} \cdot \begin{pmatrix} T_1 b_1 \sin \alpha_1 \\ T_1 b_2 \sin \alpha_2 \\ T_1 b_3 \sin \alpha_3 \end{pmatrix} \quad (6)$$

3.3 Analysis of Grasping Force

According to the virtual work principle, we have,

$$\boldsymbol{\tau}^T \cdot d\mathbf{q} = {}^0\hat{\mathbf{F}}^T \cdot d^0\mathbf{Q} \quad (7)$$

Let $\mathbf{J} = \frac{d^0\mathbf{Q}}{d\mathbf{q}}$, we have,

$$\boldsymbol{\tau} = \mathbf{J}^T \cdot {}^0\hat{\mathbf{F}} \quad (8)$$

Where, $\boldsymbol{\tau} = (\tau_1, \tau_2, \tau_3)^T$, ${}^0\hat{\mathbf{F}} = ({}^0\hat{\mathbf{F}}_1, {}^0\hat{\mathbf{F}}_2, {}^0\hat{\mathbf{F}}_3)^T$, $\mathbf{q} = (q_1, q_2, q_3)^T$, ${}^0\mathbf{Q} = ({}^0\mathbf{Q}_1, {}^0\mathbf{Q}_2, {}^0\mathbf{Q}_3)^T$, ${}^0\mathbf{Q}_i = (Q_{ix}, Q_{iy}, Q_{iz})^T$, and $\mathbf{J} = (\mathbf{J}_1, \mathbf{J}_2, \mathbf{J}_3)^T$.

According to Fig. 4b, we have,

$$\begin{aligned} \mathbf{J}_1 &= \begin{pmatrix} -l_1 S_{-q_1} & 0 & 0 \\ l_1 C_{-q_1} & 0 & 0 \\ 0 & 0 & 0 \end{pmatrix}, \\ \mathbf{J}_2 &= \begin{pmatrix} -l_2 S_{-q_{1,2}} - b_1 S_{-q_1} & -l_2 S_{-q_{1,2}} & 0 \\ l_2 C_{-q_{1,2}} + b_1 C_{-q_1} & -l_2 S_{-q_{1,2}} & 0 \\ 0 & 0 & 0 \end{pmatrix}, \\ \mathbf{J}_3 &= \begin{pmatrix} -l_3 S_{-q_{1,2,3}} - b_2 S_{-q_{1,2}} - b_1 S_{-q_1} & -l_3 S_{-q_{1,2,3}} - b_2 S_{-q_{1,2}} & -l_3 S_{-q_{1,2,3}} \\ l_3 C_{-q_{1,2,3}} + b_2 C_{-q_{1,2}} + b_1 C_{-q_1} & l_3 C_{-q_{1,2,3}} + b_2 C_{-q_{1,2}} & l_3 C_{-q_{1,2,3}} \\ 0 & 0 & 0 \end{pmatrix} \end{aligned}$$

Notes: $C_{-q_i} = \cos(q_i)$, $S_{-q_i} = \sin(q_i)$, $C_{-q_{i,j}} = \cos(q_i + q_j)$, $S_{-q_{i,j}} = \sin(q_i + q_j)$.

Due to ${}^i\hat{\mathbf{F}}_i = (f_i, F_i, 0)^T$, ${}^i\mathbf{F}_i = (0, F_i, 0)^T$, ${}^i\mathbf{f}_i = (f_i, 0, 0)^T$, $F_i = \mu f_i$, we obtain,

$$\boldsymbol{\tau} = \mathbf{J}^T \cdot \mathbf{R} \cdot \hat{\mathbf{F}} = \mathbf{J}^T \cdot \mathbf{R} \cdot \boldsymbol{\mu} \cdot \mathbf{F}_{nor} \quad (9)$$

Let $J^* = J^T \cdot R \cdot \mu$, we have,

$$\tau = J^* \cdot F^* \quad (10)$$

Where, $R = \text{dig}({}^0R_1, {}^0R_2, {}^0R_3)$, $\mu = \text{dig}(\mu_1, \mu_2, \mu_3)$, $\mu_i = (\mu_i, 1, 0)^T$,
 $F^* = F_{nor} = (F_1, F_2, F_3)^T$, and

$$J^* = \begin{pmatrix} l_1 & l_2 + b_1 C_{-q_2} + \mu_2 b_1 S_{-q_2} & l_3 + b_2 C_{-q_3} + b_1 C_{-q_{2,3}} + \mu_3 (b_2 S_{-q_3} + b_1 S_{-q_{2,3}}) \\ 0 & l_2 & l_3 + b_2 C_{-q_3} + \mu_3 b_2 S_{-q_3} \\ 0 & 0 & l_3 \end{pmatrix}$$

Obviously, the relation between the cable force and the grasping forces can be computed.

$$F^* = J^{*-1} \cdot \tau \quad (11)$$

4 Configuration Analysis Based on Maximal Grasping Space

As shown in Fig. 7, a certainly kind of position and shape of the finger under the maximum grasping space. Figure 7a shows the configuration of the finger and Fig. 7b shows the grasping forces on each knuckle. However, under the condition of the maximal grasping, the grasped target body has a tendency to be squeezed out. Thus, the grasped object is forced the friction forces in the tangential direction pointing to the negative direction of y axis.

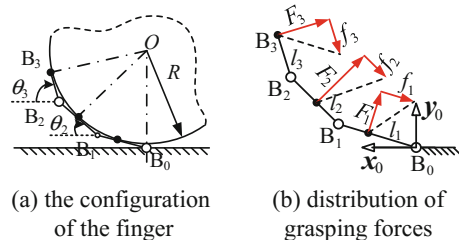
According to Fig. 7a, based on the geometric relationships between the configuration of the finger and the grasped enveloping circle, we have,

$$\begin{cases} l_1 = R \tan q_1 \\ l_2 = R \tan \frac{q_2}{2} \\ l_3 = R \tan \frac{q_3}{2} \end{cases} \quad (12)$$

Thus, the lengths of knuckles can be deduced,

$$\begin{cases} b_1 = l_1 + l_2 = R(\tan q_1 + \tan \frac{q_2}{2}) \\ b_2 = l_2 + l_3 = R(\tan \frac{q_2}{2} + \tan \frac{q_3}{2}) \\ b_3 = l_3 = R \tan \frac{q_3}{2} \end{cases} \quad (13)$$

Fig. 7 Configuration of a 3-knuckle finger under the maximal grasping space



As shown in Fig. 7b, f_1 , f_2 and f_3 are the tangential component forces of the grasping forces, meeting the requirements $f_1 = \mu_1 F_1$, $f_2 = \mu_2 F_2$ and $f_3 = \mu_3 F_3$. Because the definition of completely stable grasping is that whole of the knuckles contact the grasped object. According to Eq. (10), we have,

$$\begin{pmatrix} l_1 & b_1 C_{-q_2} + \mu_2 b_1 S_{-q_2} & b_1 C_{-q_{2,3}} + \mu_3 b_1 S_{-q_{2,3}} \\ 0 & l_2 & b_2 C_{-q_3} + \mu_3 b_2 S_{-q_3} \\ 0 & 0 & l_3 \end{pmatrix} \begin{pmatrix} F_1 \\ F_2 \\ F_3 \end{pmatrix} = T_1 \begin{pmatrix} b_1 S_{-\alpha_1} \\ b_2 S_{-\alpha_2} \\ b_3 S_{-\alpha_3} \end{pmatrix} \quad (14)$$

When the finger is in relative steady grasping state, sum of the component of grasping forces in y -axis direction can be described as,

$$\begin{aligned} F_y &= F_3(C_{-\theta_3} - \mu_3 S_{-\theta_3}) + F_2(C_{-\theta_2} - \mu_2 S_{-\theta_2}) + F_1(C_{-\theta_1} - \mu_1 S_{-\theta_1}) \\ &= F_3(C_{-q_{1,2,3}} - \mu_3 S_{-q_{1,2,3}}) + F_2(C_{-q_{1,2}} - \mu_2 S_{-q_{1,2}}) + F_1(C_{-q_1} - \mu_1 S_{-q_1}) \end{aligned} \quad (15)$$

The maximum grasping space is an envelope circle of $R_{\max} = 1250$ mm. According to the definition of completely stable grasping, the condition of steady grasping state can be described as $F_y \leq 0$.

Setting the width of the finger is $a_0 = 320.00$ mm. Through the numerical analysis by using MATLAB, the shortest length of finger, the corresponding length of each knuckle and the configuration of the finger can be obtained. Furthermore, considering the skin-friction coefficient on the surface of every knuckle, the influence of the skin-friction coefficient on the shortest length of finger is analyzed. By calculation, the values of these parameters are shown in Table 2.

The relation between the shortest lengths of finger and the skin-friction coefficient is shown in Fig. 8. Along with the rising of the skin-friction coefficient on the surface of every knuckle, the shortest length of the underactuated finger becomes shorter. According to Fig. 8b, although there are some fluctuations in length of every knuckle, the overall trend of lengths is shorter. In addition, based on the same friction coefficient, the characteristics of the lengths of every knuckle can be concluded as a whole is that the root knuckle refers to the shortest, the end knuckle refers to the second, and the middle knuckle is the longest.

The relation between the normal grasping forces on knuckles and the friction coefficient is shown in Fig. 9. The nor-grasping force on the end knuckle F_3 is

Table 2 Parameters list of cable-bar units

Parameters	a	R	T_1	μ	θ_1	θ_2	θ_3
Values (mm)	320.00 mm	1250 mm	1 N	0.05–2.00	$(0, \pi)$	$[\theta_1, \pi)$	$[\theta_2, \pi)$

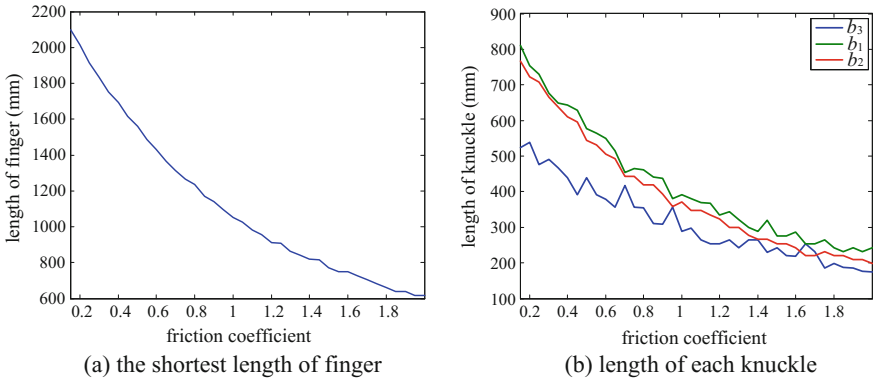
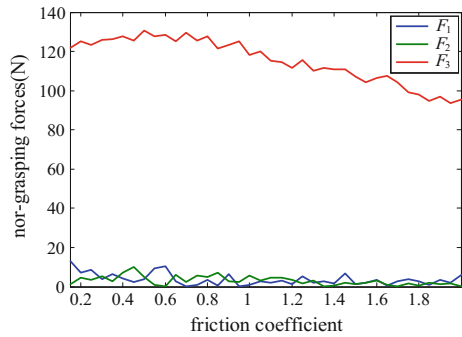


Fig. 8 The relation between the shortest lengths of finger and the skin-friction coefficient

Fig. 9 The relation between normal grasping forces and the skin-friction coefficient



keeping the biggest than the rest, and its values are larger than 100 N. Due to the 1 N driving force, thus the nor-grasping force on the end knuckle is at least 100 times than the driving force. Comparing with F_3 , the nor-grasping forces F_1 and F_2 are almost 1–15 times than the driving force, and the two forces are far less than F_3 .

Normally, the friction coefficient on the skin surface of human finger is 0.5. Because of the humanoid robotic hand, the skin-friction coefficient of the finger is set as $\mu_1 = \mu_2 = \mu_3 = 0.5$. Then, based on grasping the maximum size envelope circle of $R_{\max} = 1250$ mm, all the grasping configurations and the corresponding distributions of the grasping forces can be obtained, shown in Fig. 10a. Especially, the grasping configuration and the corresponding distribution of the grasping forces are shown in Fig. 10b. Which is corresponding to the shortest length of the finger among all grasping configurations as the skin-friction coefficient is 0.5.

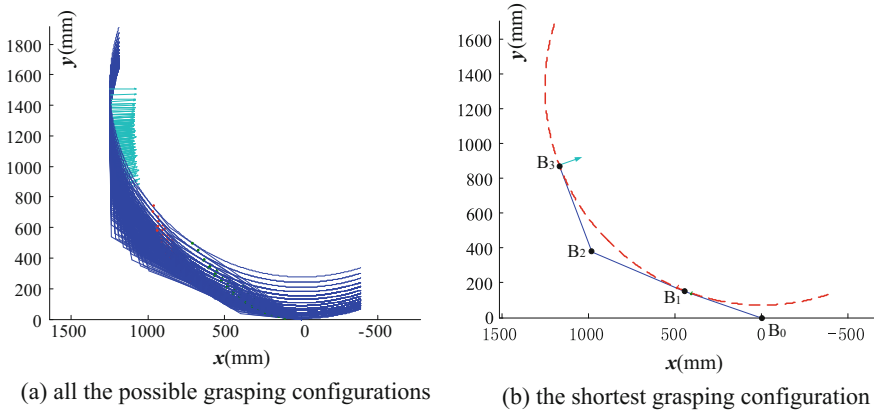


Fig. 10 Grasping configurations and corresponding distributions of grasping forces ($\mu = 0.5$)

5 Conclusion

In this paper, general grasping model of a novel underactuated finger is established. According to the model, the equivalent joint driving torques are analyzed, which are equivalent to the tendon-pulley transmission. Based on the equivalent grasping model, the relation equation is established by using vector mechanics and the principle of virtual work, which reveals the relation among the driving force, the equivalent torques on joints, and the grasping forces. Through numerical analysis, the relation between the shortest lengths of finger and the skin-friction coefficient is analyzed. Along with the rising of the skin-friction coefficient on the surface of every knuckle, the shortest length of the underactuated finger becomes shorter. And the length of every knuckle becomes shorter on overall trend. In addition, all grasping configurations, the shortest grasping configuration and the corresponding distributions of grasping forces are drawn as the skin-friction coefficient is 0.5.

Future work includes the design of a robotic hand consisted of two or more than two underactuated finger and the analysis of dynamics for controlling the robotic finger. Also, the grasping characteristics of a real robotic hand will be analyzed.

Acknowledgments Funding for this work is provided by the National Natural Science Foundation of China (Project NO. 51275107).

References

1. NASA (2013) U.S. launch vehicle components land in Africa. NASA Orbital Debris Quart News 17:1–2
2. Zimpfer D, Kachmar P, Tuohy S (2005) Autonomous rendezvous, capture and in-space assembly: past, present and future. In: 1st space exploration conference, vol 1. Continuing the Voyage of Discovery, Orlando, Florida, USA, pp 234–245

3. Nguyen PK, Ravindran R, Carr R, Gossain DM, Doetsch KH (1982) Structural flexibility of the shuttle remote manipulator system mechanical arm. In: Proceedings of the guidance and control conference, pp 246–256
4. Weydandt J, Richarz HP, Wartenberg H, Kerstein L (1987) The evolution of a serviceable EURECA. *Acta Astronaut* 15:1035–1049
5. Oda M, Nishida M, Nishida S (1996) Development of an EVA end-effector, grapple fixtures and tools for the satellite mounted robot system. In: Proceedings of the 1996 IEEE/RSJ international conference on intelligent robots and systems' 96, IROS 96, vol 3. IEEE Press, pp 1536–1543
6. Hunter DG (1991) The space station freedom special purpose dexterous manipulator (SPDM). In: Proceedings of the tele systems conference, 1991, vol 1, NTC'91, National. IEEE Press, pp 371–376
7. Piedboeuf JC, De Carufel J, Aghili F, Dupuis E (1999) Task verification facility for the Canadian special purpose dextrous manipulator. In: Proceedings 1999 IEEE international conference on robotics and automation, 1999 vol 2. IEEE Press, pp 1077–1083
8. Mukherji R, Ray DA, Stieber M, Lymer J (2001) Special purpose dexterous manipulator (SPDM) advanced control features and development test results. In: Proceedings of the international symposium on artificial intelligence robotics and automation in space (i-SAIRAS), pp 18–22
9. Xu W, Liang B, Li C, Xu Y (2010) Autonomous rendezvous and robotic capturing of non-cooperative target in space. *Robotica* 28:705–718
10. Laliberté T, Gosselin CM (1998) Simulation and design of underactuated mechanical hands. *Mech Mach Theory* 33:39–57
11. Gosselin CM, Laliberté T (1998) Underactuated mechanical finger with return actuation. U.S. Patent No. 5762390. U.S. Patent and Trademark Office, Washington, DC
12. Gosselin C, Laliberté T (2010) Underactuated versatile gripper for the cleaning of nuclear sites. In: 2010 1st international conference on applied robotics for the power industry (CARPI). IEEE Press, pp 1–6
13. Odhner LU, Dollar AM (2015) Stable, open-loop precision manipulation with underactuated hands. *Int J Robot Res* 34:1347–1360
14. Odhner LU, Jentoft LP, Claffee MR, Corson N, Tenzer Y, Ma RR, Dollar AM (2014) A compliant, underactuated hand for robust manipulation. *Int J Robot Res* 33:736–752
15. Jin J, Zhang W, Sun Z, Chen Q (2012) LISA hand: indirect self-adaptive robotic hand for robust grasping and simplicity. In: 2012 IEEE international conference on robotics and biomimetics (ROBIO). IEEE Press, pp 2393–2398
16. Aukes DM, Heyneman B, Ulmen J, Stuart H, Cutkosky MR, Kim S, Edsinger A (2014) Design and testing of a selectively compliant underactuated hand. *Int J Robot Res* 33:721–735

Bionic Structure Design of a Flapping Wing Robot

Wenjuan Zhou, Huichao Deng and Xilun Ding

Abstract As a new field of research, the flapping wing micro air vehicle has a widely application in civil and defense. This paper analyzes the specific state of the flapping wing in flight, and determines the variation range of the flapping angle and the angle of attack. Then we design a simple double crank and double rocker mechanism, in addition we propose a passive rotation mechanism to meet the requirement of micro flapping wing mechanism. Compared to previous flapping wing structures, the mechanism is technically more simple and practical, which is benefit to minimize the flapping wing micro air vehicle. We design the specific structure of Micro Air Vehicle (MAV) and calculate the dimension of the mechanism. Finally, we use the Solidworks to model it and prove the feasibility and accuracy of this flapping wing structure.

Keywords Flapping wing · Micro air vehicle · Flapping angle · Angle of attack

1 Introduction

With the rapid development of aerodynamics and MENS technology, Micro Air Vehicle has been paid a widely attention by lots of researches due to its small volume, portable, flexible flight and excellent concealment. So it has become a promising new air vehicle in the civil and defense fields' application. Compare with fixed-wing and rotary-wing aircraft, the flapping wing aircraft do not have propeller or jet devices, thus it can take off quickly, accelerating, hovering in situ or small grand [1–6].

At present, many research institutions have started to study the flapping—wing Micro Air Vehicle (FMAV). Georgia Institute of Technology and the University of Cambridge using reciprocating chemical muscle jointly developed FMAV

W. Zhou · H. Deng (✉) · X. Ding
Robotics Institute, Beijing University of Aeronautics and Astronautics,
Beijing 100191, China
e-mail: denghuichao@buaa.edu.cn

—“Entomopter” [7]. University of California, using PZT piezoelectric actuators and double rocker four-bar linkage independently developed mechanical fly —“MFI” [8]. California Institute of Technology and AeroVironment use a micro-motor driven single crank and double rocker mechanism jointly developed the world’s first palm-sized electric ornithopter—“MicroBat” [9]. Harbin Institute of Technology designs a FMAV using the elliptic cylindrical cam drive mechanism and the wing twisting machine mechanism, which reduces negative lift effect on the wing of up-flapping and improves the flight capacity.

This paper based on the bionics research, analyzes the rotation and flapping state of flying insects in flight. We determine the angle of rotation and flapping which insect wings can be achieved. According to the results of the bionics research, we compare and analyze the advantages and disadvantages of all kinds of flapping wing mechanisms. Then, we design the suitable mechanism to meet the requirement of micro flapping wing mechanism. Finally, we design the specific mechanism, and calculate the dimension of each part.

2 The Study of Flapping Wing Aircraft’s Flight

According to the structure of different wings, flying insects can be classified into two categories: Hard-winged insects and Soft-winged insects. Common hard-winged insects include Cicadas, flies, and so on. Such insects have good maneuvering characteristics, and have small deformation amplitude of wings during flight. This type of wings generally has two degrees of freedom: the flapping action which set itself as the axis and the rotational action around the wingspan direction. Common soft-winged insects include butterflies, moth and so on. Such insect wings have a large deformation in flight, and accompanied with the body pitching. These kind of insect wings generally have only one degree of freedom, that mean it is only have the flapping action which set its body as the axis, so the body pitch and wings deformation make up the lack of another freedom. Because of the insect wings with two degrees of freedom have a good maneuvering characteristics, this paper mainly studies the flapping action and rotational action of the hard-winged insects [10].

Based on C.P. Elington’s theory that is insects flap their wings in a sinusoidal way, we can get the flapping equation and rotational equations of insect wing when during flight. The flapping process: at the beginning of flapping, wings go through a phase of acceleration; the angular velocities of wings are accelerated from zero to a certain value, and then the wings flap in a constant velocity. After a while, the angular velocities of wings start to decelerate. The wings angular velocity will reduce to zero until the end of down-flapping stage, and then the wings begin the up-flapping stage. The rotation procedure is same as the flapping procedure and these two procedures happen at the same time. When the insect wings start the down stroke, the angle of attack has turned most angles in the previous cycle, and the velocity of the angle of attack will continue reverse in the manner of simple harmonic motion. After a period, it will achieve the magnitude of the torsion, and

the angle of attack will keep still. Then it will continue reverse in the manner of simple harmonic motion. When it completes the majority of rotation, the process ends. The insect wing flapping equation:

$$\omega(t) = \begin{cases} \omega_m \sin(t\pi/\Delta t) & t \in [0, 0.5\Delta t] \\ \omega_m & t \in [0.5\Delta t, 0.5T - 0.5\Delta t] \\ \omega_m \sin[(0.5T - t)\pi/\Delta t] & t \in [0.5T - 0.5\Delta t, 0.5T + 0.5\Delta t] \\ -\omega_m & t \in [0.5T + 0.5\Delta t, T - 0.5\Delta t] \\ \omega_m \sin[(t - T)\pi/\Delta t] & t \in [T - 0.5\Delta t, T] \end{cases} \quad (2.1)$$

Where ω is the angular velocity of the flapping wings; ω_m is the maximum speed in the process; T is a flapping cycle; Δt is the minimum time interval in the wings' motion.

The rotation equation:

$$\omega'(t) = \begin{cases} \bar{\omega} + \bar{\omega} \cos((t + 0.5\Delta t)2\pi/\Delta t) & t \in [0, 0.5\Delta t - dt] \\ 0 & t \in [0.5\Delta t - dt, 0.5T - 0.5\Delta t - dt] \\ \bar{\omega} - \bar{\omega} \cos((t - 0.5T + 0.5\Delta t)2\pi/\Delta t) & t \in [0.5T - 0.5\Delta t - dt, 0.5T + 0.5\Delta t - dt] \\ 0 & t \in [0.5T + 0.5\Delta t - dt, T - 0.5\Delta t - dt] \\ -\bar{\omega} + \bar{\omega} \cos((t - (T - 0.5\Delta t))2\pi/\Delta t) & t \in [T - 0.5\Delta t - dt, T] \end{cases} \quad (2.2)$$

Where ω' is the angular velocity of the angle of attack; $\bar{\omega}$ is the average rotation angular velocity; dt is the advanced time in the advanced mode; T is a flapping cycle; Δt is the minimum time interval in the wings' motion.

According to the flapping equation and rotation equation above, we can simulate a motion change graph of the insect wing, and then compare it to the graph [11, 12] of fly's wings measured by sun mao' group, you will find these motion variation rules are nearly the same. After the analysis above, we can conclude that the magnitude of the angle of the flapping wing and the angle of attack is approximately: -30° to 50° and 30° to 150° . Therefore, design purpose of flapping wing angles are the two magnitude of the angle of the flapping wing and the angle of attack above, and we need to design a flapping wing mechanism to achieve that goal.

3 The Overall Design and Modeling of the Flapping Wing Mechanism

3.1 The Structural Analysis and Dimension Calculation of the Flapping Wing Mechanism

According to the determined magnitude of the flapping angle and the rotation angle, we need to design a flapping wing mechanism for flapping-wing Micro Air Vehicle, to achieve the desired flapping angle and the rotational angle. There are many

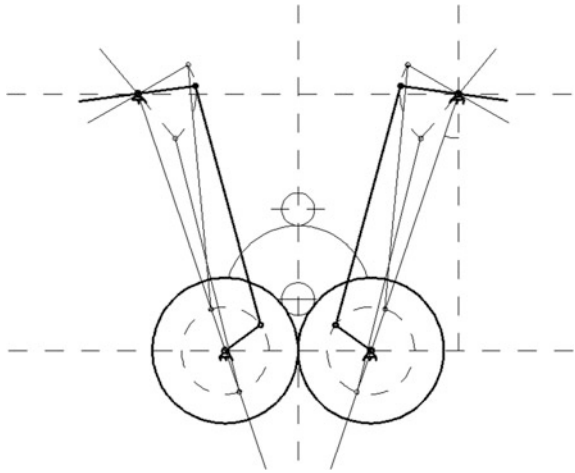
different kinds of mechanism about the flapping-wing Micro Air Vehicle currently, such as the single crank and double-rocker mechanism, double-crank and double-rocker mechanism, slider-crank mechanism, the cam spring mechanism, space rocker mechanism, single crank as well as double crank rocker mechanism, etc. The flapping frequency required by flapping-wing Micro Air Vehicle that is very high, which means that flapping-wing mechanism needs high frequency of rotation and movement. However, the slider-crank mechanism and the cam spring mechanism have a large friction and low efficiency, and they cannot have a good flapping action. The advantage of spatial crank-rocker mechanism is simple and completely symmetrical in structure as well as its resulting motion. However, it requires an elaborately devised mini-spherical hinge, with high processing costs. The single crank and double-rocker mechanism has simple structure, high efficiency, lightweight, and it is easy to miniaturization. Unfortunately, the flapping actions of the two sides' wings are not completely symmetrical, and there is a phase difference between them, which will cause tilting and even falling. The crank-shaft based crank-rocker mechanism is the improved version of the single-crank and double-rocker organization. Its flapping action is completely symmetrical, but its rocker is asymmetric and its structure is more complex. The double-crank and double-rocker mechanism's structure and movement are completely symmetrical, but the two driven motors executing on such structure will not only produce phase difference but also increase the weight of the entire ornithopter. The specific information is shown in Table 1.

Based on the aforementioned analysis, we decide to adopt a simple double crank and double-rocker mechanism, and we use a motor to drive two cranks synchronously via a gear train, eliminating the burden of the two motors. Figure 1 is a double crank and double-rocker flapping wing mechanism. The motor drives the following two gears to rotate through a reducer, and a position of gear is connected to the link, and the rotation of the gear drives the link to move, which leads to the

Table 1 Comparison for advantages and disadvantages of the mechanisms

Mechanism	Advantage	Disadvantage
Single crank and double-rocker mechanism	Simple, high efficiency, light weight, easy miniaturization	Flapping action is not completely symmetrical, there is a phase difference
Double crank and double rocker mechanism	Structure and movement are completely symmetrical	Two motors are out of phase, and increases the weight of the bodies
Slider-crank mechanism	The structure is simple and easy to implement	Slide has big friction, efficiency is not high
The cam spring mechanism	The structure is simple and compact	Point, line contact, easy to wear, difficult to manufacture
Double crank and double rocker mechanism + passive rotation mechanism	The structure is simple and compact, completely symmetrical, easy small	

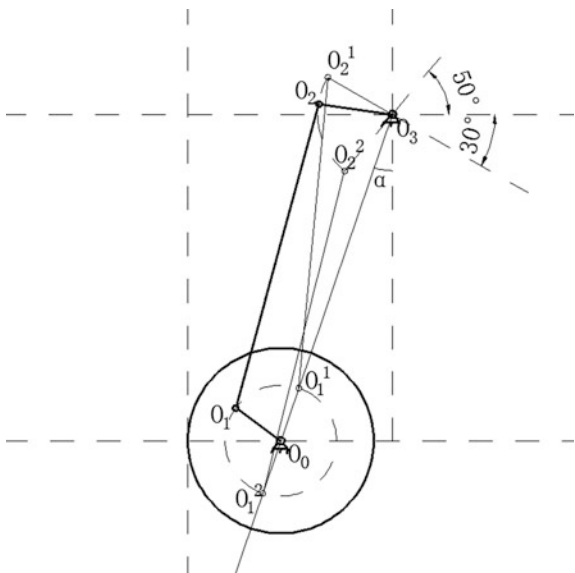
Fig. 1 Double crank and double-rocker mechanism



rocker’s swing, the rocker’s swing angle represents wing’s flapping angle range. Considering the two wings’ flapping angle range acquired is within -30° to 50° , We need to calculate the length of every link in order to meet the requirements.

Figure 2 is crank-rocker mechanism. As shown in Fig. 2, the basic principle of the flapping wing mechanism is a crank rocker mechanism denoting by $O_0O_1O_2O_3$. The overall size of the mechanism cannot be too large due to the design requirements, Therefore, we predetermine the length of O_0O_1 , O_0O_3 as 3, 21 mm, and the value of the angle α set in Fig. 2 is 20° , the link’s angle range is -50° to 30° .

Fig. 2 Crank-rocker mechanism



When the mechanism approaches to the limit position $O_0O_1^1O_2^1O_3$, it forms a triangle $O_1^1O_2^1O_3$, and $\angle O_2^1O_3O_1^1 = \alpha_1 = 100^\circ$. When the mechanism approaches to the limit position $O_0O_1^2O_2^2O_3$, it forms the triangle $O_1^2O_2^2O_3$, and $\angle O_2^2O_3O_1^2 = \alpha_1 = 100^\circ$. Then according to the law of cosines, we can compute the length of O_1O_2, O_2O_3 :

$$\cos \alpha_1 = \frac{(O_0O_3 - O_0O_1)^2 + O_2O_3^2 - O_1O_2^2}{2 \times (O_0O_3 - O_0O_1) \times O_2O_3} \quad (3.1)$$

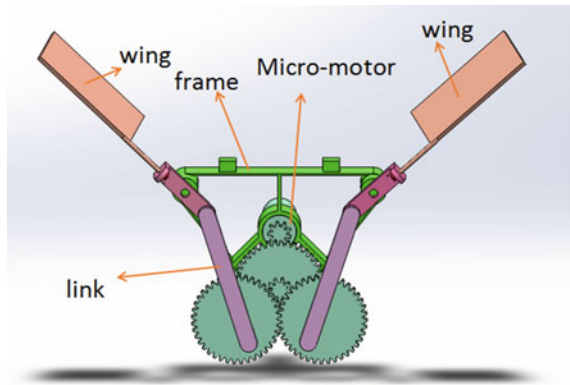
$$\cos \alpha_2 = \frac{(O_0O_3 + O_0O_1)^2 + O_2O_3^2 - O_1O_2^2}{2 \times (O_0O_3 + O_0O_1) \times O_2O_3} \quad (3.2)$$

Substituting the above formulas, yielding: $O_2O_3 = 4.9 \text{ mm}$, $O_1O_2 = 19.5 \text{ mm}$. Therefore we get all the dimensions of the crank rocker mechanism and it can reach the requirement of the flapping angle range.

3.2 Model and Simulation of the Flapping Wing Mechanism

After the analysis of the above mechanism, we determined all the size of each part of the flapping mechanism. Then we will use the solidworks software to model it and design the basic structure of our Micro Air Vehicle, which is shown in Fig. 3. Since the focus of this 3D model is flapping actuator of the flapping wing aircraft, we simplify other parts such as the wing. As shown in the picture, the micro-motor fixed on the frame, and the motor shaft drive the link to move by a reducer, and the rocker fixed on the frame connect to the link and the wing, and it converts the movement of the link into the wing's flapping motion.

Fig. 3 FMAV's simulation models



We use the Solidworks to execute kinematics simulation. The corresponding results shows that this mechanism can achieve the assigned flapping angle range, which demonstrates the feasibility and accuracy of this mechanism.

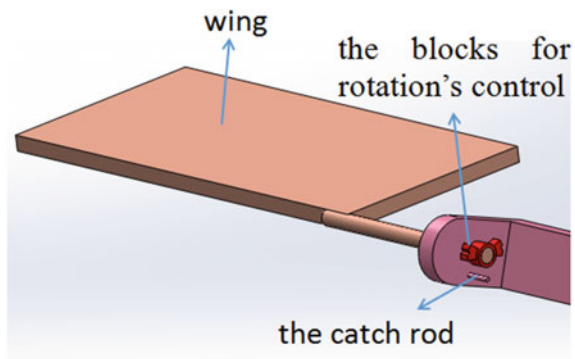
4 The Design and Analysis of Passive Rotation Mechanism

4.1 The Structural Design and Modeling of the Passive Rotation Mechanism

We design the wing's flapping motion of the flapping aircraft above, and it has meet the design angle requirement of -30° to 50° . Then we will continue to realize the wings' rotation around the wingspan direction in the process of flapping, and we should achieve the amplitude range of the angle of attack: 30° to 150° . In order to make the wing rotate freely, we design a simple passive rotation mechanism [13] in the connecting portion between the wing and the link, which makes the flapping wing robot can rotate according to the change of airflow during the flight and accommodate the airflow to improve the flying ability.

Figure 4 is a three-dimensional model of passive rotation mechanism. The wing along with the blocks for rotation's control connect with the link, between the wing and the link use the clearance fit, and they connected through the sleeve in the middle, so the wing can rotate freely around the link; there are tapered shaft interference fit between the wing shaft and the block for rotation's control, and the block for rotation's control can rotate following the rotation of wing shaft. When the wings are rotated to a certain angle, the block for rotation's control will be stuck, and thereby it controls the wing to stop. This passive rotation mechanism is simple and can control the rotation range of the angle of attack effectively. Meanwhile, this mechanism allows the wing to rotate freely in an air stream, and it will be more fitting to the real flight.

Fig. 4 Three-dimensional model of passive rotation mechanism



4.2 The Dimension Analysis of Passive Rotation Mechanism

After the basic mechanism design, the particular structure of the passive rotation mechanism should be analyzed. Figure 5 is the front view of the passive rotation mechanism, and we can see the workspace that the rotation control block can achieve. As shown in Fig. 5, position 1 represents the wing angle of attack at 30° , and position 2 represents the wing angle of attack at 150° . The wing can only rotate between position 1 and position 2, and it cannot exceed the range of rotation. The catch rod is located at position 1, and the angle between the stopper A and B on the rotation control block is 150° . Therefore, when the stopper is rotated from the position 1 to the position 2, the stopper B will be blocked by the catch rod, then it will prevent the further rotation of the wing, thereby it will restrict the angle of attack within the range of 30° to 150° .

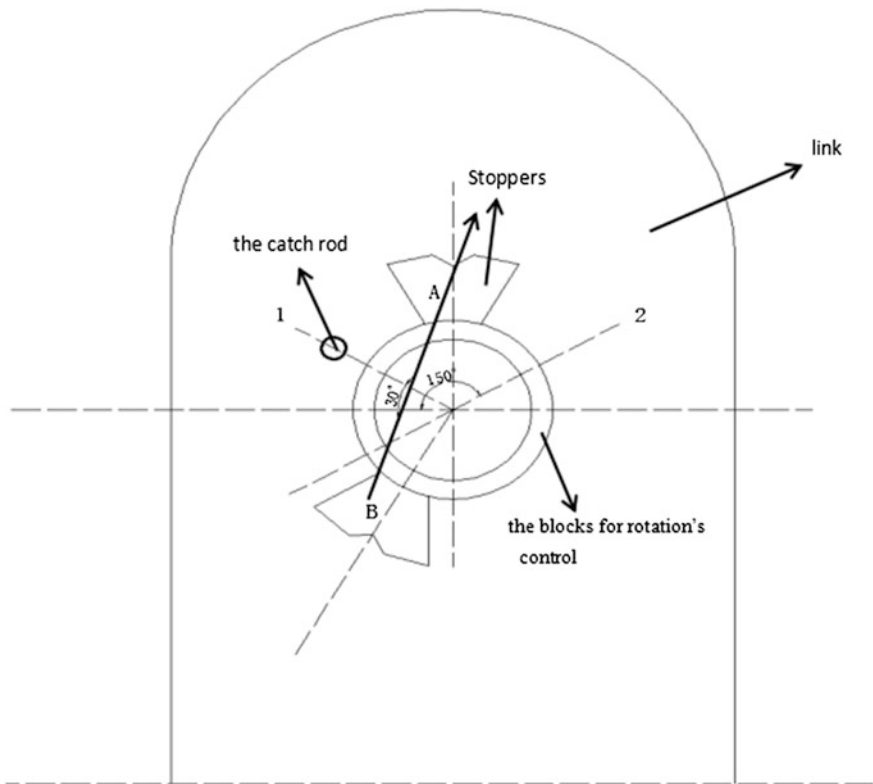


Fig. 5 The front view of the passived rotation mechanism

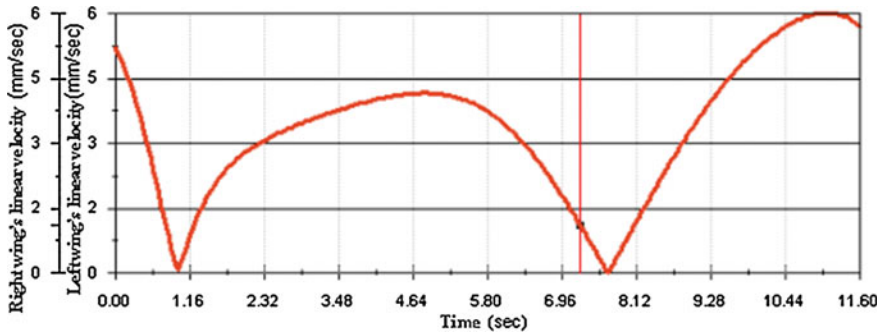


Fig. 6 Amplitude curve of the wing beat velocity

5 Motion Analysis of Mechanism

Motion analysis the above mechanisms and compare the amplitude of the curve at both ends of the wing beat velocity, and then we can obtain the velocity curve of the wings. As shown in Fig. 6, we can see that the right and left wing's movement are completely symmetrical. Thus, we can adjust the wing's beat frequency by adjusting the motor speed.

6 Conclusion

This paper designed a new double crank and double rocker mechanism and passive rotation mechanism. The mechanism is simple and compact, easy to realize the miniaturization. We modeled these mechanisms and calculate the mechanisms' dimensions, which proved the feasibility and the accuracy of the flapping wing mechanism, thus providing a practical workable structure model for the further study of FMAV.

Acknowledgments The authors gratefully acknowledge the support of the National Natural Science Foundation of China (Project No.51605012).

References

1. Hailin H, Bing L (2014) Geometric design of a bio-inspired flapping wing mechanism based on bennett-derived 6R deployable mechanisms. In: ASME 2014 international design engineering technical conferences and computers and information in engineering conference, American Society of Mechanical Engineers
2. Phan HV, Truong QT, Au TKL et al (2016) Optimal flapping wing for maximum vertical aerodynamic force in hover: twisted or flat? J Bioinspiration Biomimetics 11:10–14

3. Hou Y, Fang ZD, Liu L et al (2005) Dynamic analysis and engineering design of biomimetic flapping-wing micro air vehicles. *J Acta Aeronautica Et Astronautica Sinica* 25:102–104
4. Zhu HB, Xie J, Chen Y (2011) Analysis of the lift and Lift coefficients occurred by the flapping motion of a bionic wing using fluent. *J Mach Des Manuf* 15:41–45
5. Keennon M, Klingebiel K, Won H et al (2012) Development of the nano hummingbird: a tailless flapping wing micro air vehicle. *AIAA Aerospace sciences meeting*, Reston
6. Gerdes JW, Gupta SK, Wilkerson SA (2012) A review of bird-inspired flapping wing miniature air vehicle designs. *J J Mech Robot* 4:21–25
7. Jin XY, Yan JP (2007) Status and prospects of driving mode about the wing for the bionics flapping aircraft. *J Manufact Autom* 5:17–20
8. Xiao Y (2001) Study on present situation and development of micro air vehicles. *J J Astronautics* 8:78–79
9. Wood RJ (2008) The first takeoff of a biologically inspired at-scale robotic insect. *J IEEE Trans Rob* 24:341–347
10. Yan XY (2008) A research to simplified aerodynamic modal of insect-like MAV. *Electrical Engineering of Zhejiang University, Zhejiang University, Hangzhou*
11. Sun M, Wu J (2002) Biomimetic aerodynamics of micro-air vehicles-aerodynamic force and power requirements in forward flight of insect. *Acta Aeronautica et Astronautica Sinica* 23:385–393
12. Sun M, Xiong Y (2001) Biomimetic mechanics of micro air vehicles-dynamic flight stability of a hovering honeybee. *National Youth Seminar Fluid Mechanics*
13. Hu Z, Deng X (2002) Design and performance of insect inspired high frequency flapping wing robots. *J Stainless Steel* 8:20–23

LIPSA Hand: A Novel Underactuated Hand with Linearly Parallel and Self-adaptive Grasp

Yang Yang, Wenzeng Zhang, Xiangrong Xu, Handong Hu
and Jian Hu

Abstract This paper proposes a novel robotic hand which contains linearly parallel and self-adaptive grasping modes, called LIPSA hand. The LIPSA hand is composed of a common basement, two fingers, two motors and the transmission mechanism. The LIPSA hand contains three modes: linearly parallel (LIP) gripping mode, self-adaptive (SA) grasping mode and the LIP-SA hybrid grasp mode. One finger linearly parallel grip the object and the other finger self-adaptive grasp the object on the same time. It is the object's position, size, shape and weight that the mode which the LIPSA hand chooses depends on. The LIPSA hand is wide range in grasp, light in weight, small in size and low in cost. The Analysis results show that the LIPSA hand is valid and can be used in the various environment.

Keywords Robot hand · Underactuation · Linearly parallel gripping · Self-adaptive grasping · Hybrid grasping

1 Introduction

The robot technology is one of the most important tendencies of the improvement of the technology. It is the robot hand (end effector) that the robot mainly depended on to replace the human's work [1]. Nowadays, there are many kinds of the robot hand have been created, such as multi-finger hand, particular hand and soft hand. The multi-finger hand has several fingers and each finger has several joints and phalanxes which can rotate or linearly move. The multi-finger hand is mainly divided into two kinds: dexterous hand and actuated hand.

Y. Yang · W. Zhang (✉)

Department of Mechanical Engineering, Tsinghua University,
Beijing 100084, China
e-mail: wenzeng@tsinghua.edu.cn

Y. Yang · X. Xu · H. Hu · J. Hu

School of Mechanical Engineering, Anhui University of Technology,
Ma'anshan 243002, China

1.1 *Dexterous Hand*

The dexterous robot hand is made by several dexterous fingers which have more than one joints and the motor. The number of the motors is same as the number of the degree of the freedom (DOF) of the hand. One motor could control one joint rotate for an angel and the cooperation among the different joint can make the dexterous hand realize numerous of movement. So, the dexterous hand can imitate the human's hand better to make complex actions and the different grasping mode. The dexterous hand is one of the most important trends of the robot development.

There are many sensors set on the dexterous hand to probe the object, such as the distance sensor probes the distance between the object and the hand, pressure sensor probes the force put on the hand. During the process of the grasp experiment, one sensor must get a signal and transmit the information to the controller. Then, the controller will drive the motor running to make the signal transforms to real movement. At the same time, all the sensor must work to probe the object to get a most convenient method to grasp the object before the grasping. It is the real-time sensing, complicated controller requirement and expensive cost in production and maintenance that hinder the development of the dexterous hand.

There are many famous dexterous hands have been produced for nearly 40 years researched. The Okada Hand [2], DLR-I Hand and DLR-II Hand [3], Utah-MIT hand [4], Shadow hand [5], DLR-HIT hand [6], Robonaut hand [7] and Gifu hand [8] play an important role in the robot history.

1.2 *Underactuated Hand*

The structure of the underactuated hand is that the number of the motor is less than the number of the degrees of the freedom of the hand. The pure mechanism which the underactuated hand relies on can achieve grasping self-adaptively. The underactuated hand could adapt object's shape, size and the position by rotating deferent joint to pinch or envelop the object. There is no need adding a real-time controller to drive the finger making some actions. One joint can continue rotating by the pure mechanical transmission while others joint stops. The underactuated hand is lighter in weight, smaller in size and lower in cost than the traditional dexterous hand.

Such under-actuated hand has been produced, for example, SARAH hand [9] made by the Laval university in Canada at 1970s which was using five links to achieve PASA mode. After that, the Laval University has made some improvement [10–13] at the basic of it. There is also some other famous robot hand such as TUAT/Karlsruhe Humanoid hand [14], TH-3B hand [15]. Many kinds of underactuated hands have been developed such as multi-finger underactuated hand [16], passive adaptive underactuated hand [17], underactuated prosthetic hands [18], and coupled self-adaptive hand [19].

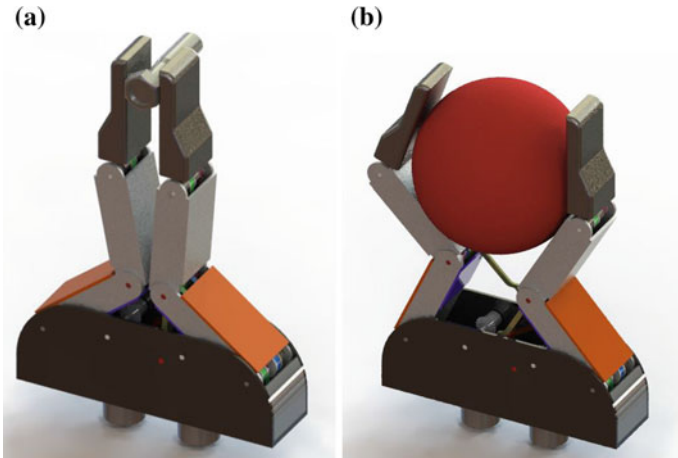


Fig. 1 The LIP mode and the SA mode

2 The Grasping Modes

Supposed that there is coin put on the table, it is so tiny that one cannot hold it by our hand, but one can use our finger to pinching it. At the same time, if there is an apple on the table, our fingers do not have enough power to pinch it, so one will hold the an apple by enveloping our different phalanxes of fingers. There are two main kinds of grasping modes in reality, (1) parallel pinching and (2) self-adaptive enveloping.

Parallel pinching means using the distal phalanx to clamp the object by two parallel phalanxes of two fingers to contact the object grasped. It is mainly aimed to grip objects of small sizes or big object with opposite surfaces. Enveloping grasp means using two or more phalanxes enveloping around the object by the multiple points contacting to realize more stable grasping.

One can find that the first phalanx of the traditional PASA hand is rotating around its joint and the distal phalanx is moving as an arc, the distal phalanx cannot move as a linearly. If there is a tiny object on the table, the distal phalanx can only linearly parallel (LIP mode) pinches the object without any bending (Fig. 1).

3 The Concept and Design of the LIPSA Hand

3.1 The Structures of the LIPSA Hand

The design of the LIPSA hand mainly consists of a common basement, two fingers, two motors and two transmission machine. Each finger is composed of the distal phalanx, proximal phalanx, corbelled phalanx, distal joint, proximal joint, eight

pulleys, four belts, two links, four rotated joints, two springs, a mechanical limit and a limited block. The transmission machine is composed of the driving pulley, driven pulley, belt, driving gear and the driven gear.

The first joint is set on the base, the first pulley and the driven pulley are fixed with the first joint, the mechanical limit is fixed with the first pulley, the eighth pulley is set on the first joint. The corbelled phalanx is set on the first joint. The proximal joint is set on the corbelled phalanx. The first phalanx is set on the proximal joint. The second pulley, third pulley, sixth pulley and the seventh pulley are also set on the proximal joint. The second pulley and the third pulley are fixed with each other, the sixth pulley and the seventh pulley are also fixed with each other. The fourth pulley, the fifth pulley and the second pulley are fixed on the distal joint. the second phalanx is fixed with the distal joint. One end of the first link is set on the second joint, the other end of it is set on the third joint. One end of the second link is set on the third joint, the other end of it is set on the distal joint, and the middle point is set on the proximal joint. The spring is connected with the mechanical limit and limit block (Fig. 2).

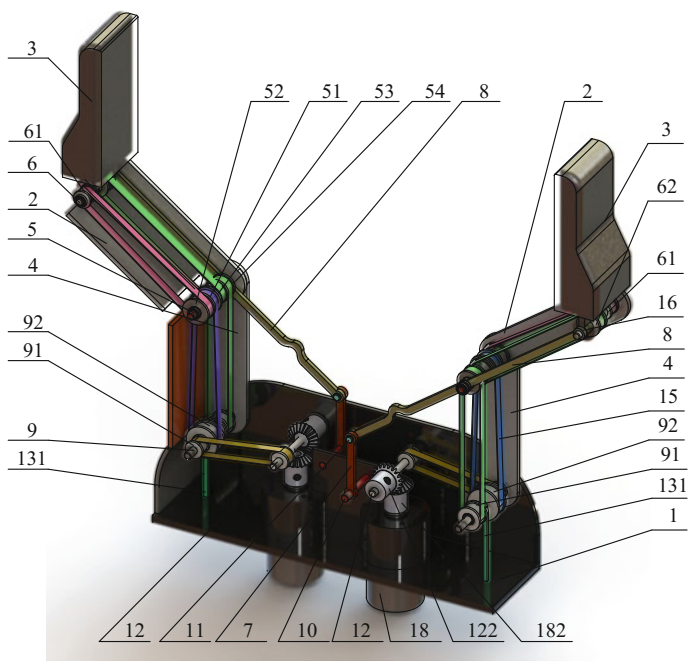


Fig. 2 Structure of LIPSA hand. 1 base, 2 1st phalanx, 3 2nd phalanx, 4 corbelled phalanx, 5 proximal joint, 6 distal joint, 7 1st link, 8 2nd link, 9–12 first joint to forth joint, 122 driven gear, 131 limit block, 15 belt, 18 motor, 182 driving gear, the rest parts are the pulleys

3.2 The Principle of the LIPSA Hand

The center point of the first joint is regarded as A, the center point of the second joint is regarded as B, the center point of the third joint is regarded as C, the center point of the proximal joint is regarded as D, the center point of the distal joint is regarded as E, it is showed in Fig. 3.

Here are some relations between these links:

$$AB = 2BC, CD = DE = AD = 2.5BC. \tag{1}$$

As it is seen in Fig. 3, when the link AD is rotating, the link BC will be driven to rotate, and the point E will move as a line sometime, the process of the movement as a line is what one want. The length of the proximal phalanx is same as the length of the corbelled phalanx. The radius of the fifth pulley, sixth pulley, seventh pulley and the eighth pulley are same. The radius of the first pulley is larger than the second pulley, the radius of the third pulley is larger than the fourth pulley.

At the beginning of the movement, the spring is connected with the mechanical limit and limit block to prevent those two limitations separated apart. Once the motor is rotating, it will transmit its power to the first pulley making the pulley rotating. But the eighth pulley is limited by the mechanical limit, the eighth pulley cannot rotate around the first joint, as well as the fifth pulley, sixth pulley and the seventh pulley. The fourth pulley cannot rotate either because it is fixed on the distal joint. The first phalanx is connected with the second link. So the corbelled phalanx will rotate toward the object, and the second phalanx still keeps the original form. Two second phalanxes are always parallel until the second phalanx touches the object. It is the process of the LIP grasping mode.

Once the first phalanx touches the object before the second phalanx, the corbelled phalanx stops rotating. But the first pulley still running. The first pulley

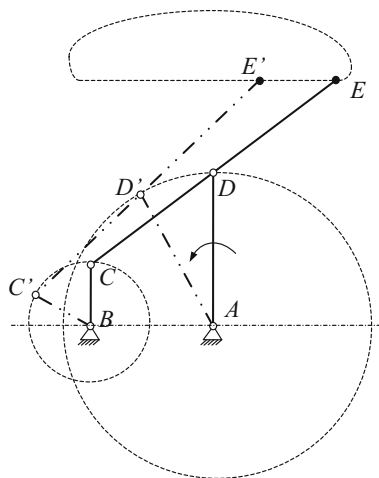


Fig. 3 The principle of the four links

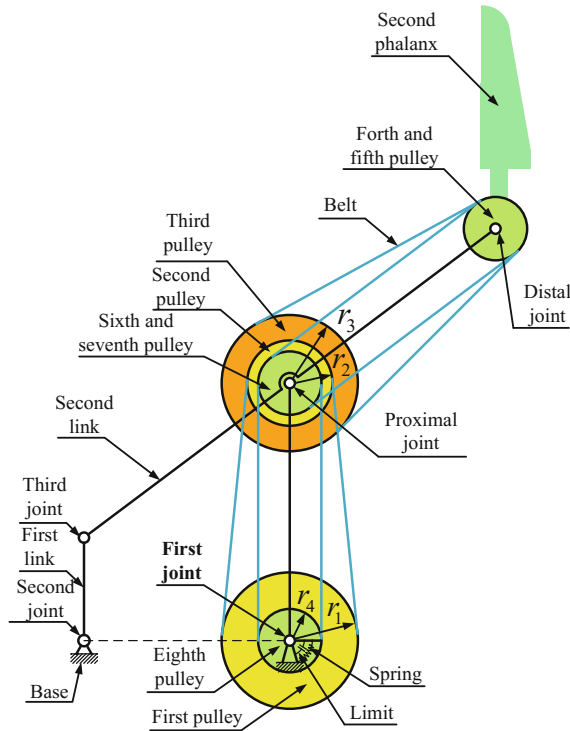


Fig. 4 The schematic diagram of mechanism

would continue forcing the second pulley, at the transmission of the belt, the fourth pulley will rotate around the distal joint as well as the second phalanx. At the end, the eighth pulley will be driven. The spring will be stretched because of the separation of the mechanical limit and the limit block. Such movement will not finish until the second phalanx touches the object. The schematic diagram of LIPSA hand is showed in Fig. 4.

4 The Analysis of the LIPSA Hand

As it is show in Figs. 4 and 5, the principle of LIPSA hand can be replace by some line and circle.

The length of the line BC is a ;

The radius of the first pulley is r_1 , the radius of the second pulley is r_2 , the radius of the third pulley is r_3 , the fourth pulley and the fifth pulley is r_4 ;

The rotation speed of the motor is w ;

The rotation speed of the link AD is w_1 ;

The rotation angel of the link AD is β ;

The movement speed of the point E (the distal phalanx) is v_E .

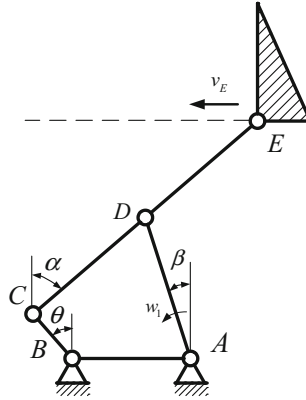


Fig. 5 The kinematic diagram of mechanism

So when the motor running time is t , one can get the relation between the first pulley and the second pulley:

$$R_1 = r_2/r_1 \tag{2}$$

So the rotation angel β is

$$wt = \beta(1 - R_1) \tag{3}$$

When the motor drives the corbelled phalanx rotating, the extreme position of the corbelled phalanx is that the first link has rotated for 180° . Through the relation among the four links, one can get the biggest β is: $\beta = \arctan(4/3) \approx 53.17^\circ$

For the quadrilateral ABCD, there is a relation:

$$\vec{AB} + \vec{BC} + \vec{CD} + \vec{DA} = \vec{0} \tag{4}$$

Supposed that the point B is the origin point, the angel between the link CD and the y-coordinate is α , the angel of the rotation of the link BC is θ ,then one can get:

$$\begin{cases} a \sin \theta + 2a = 2.5a \sin \alpha + 2.5a \sin \beta \\ a \cos \theta + 2.5a \cos \alpha = 2.5a \cos \beta \end{cases} \tag{5}$$

In every time, the coordinate of the point E is:

$$\begin{cases} x_E = 5l \sin \alpha - l \sin \theta \\ y_E = 5l \cos \alpha + l \cos \theta \end{cases} \tag{6}$$

Through those equations, the position of the second phalanx can be defined.

From Eq. 3, there is an equation:

$$w_1 = \frac{w}{1 - R} \quad (7)$$

Taking derivation of Eq. 5, one can get:

$$2.5w_1 \begin{bmatrix} \cos \beta \\ -\sin \beta \end{bmatrix} = \begin{bmatrix} \cos \theta & -2.5 \cos \alpha \\ -\sin \theta & -2.5 \sin \alpha \end{bmatrix} \begin{bmatrix} w_2 \\ w_3 \end{bmatrix} \quad (8)$$

The angular velocity of the link BC is w_2 , the angular velocity of the link CD is w_3 , then taking derivation of Eq. 6,

$$\begin{bmatrix} v_{Ex} \\ v_{Ey} \end{bmatrix} = \begin{bmatrix} -a \cos \theta & 5a \cos \alpha \\ -a \sin \theta & -5a \sin \alpha \end{bmatrix} \begin{bmatrix} w_2 \\ w_3 \end{bmatrix} \quad (9)$$

Through those equations, the speed of the second phalanx can be defined. But it is obvious that sometimes $v_{Ey} = 0$, that is what this machine want.

5 Conclusion

This paper proposes a novel robotic hand which contains linearly parallel gripping and self-adaptive grasping modes, called LIPSA hand. The LIPSA hand is composed of a common basement, two fingers, two motors and the transmission machine. The LIPSA hand contains three modes: linearly parallel (LIP) grasping mode which can grip thin objects such as coins putting on the plane, self-adaptive (SA) grasping mode which can envelop large objects depending on the shape of the objects such as a bottle, and the LIP-SA hybrid grasp mode. One finger linearly parallel grip the object and the other finger self-adaptive grasp the object on the same time. It is the object's position, size, shape and weight that the mode which the LIPSA hand chooses depends on. The LIPSA hand is wide range in grasp, light in weight, small in size and low in cost. The Analysis results show that the LIPSA hand is valid and can be used in the various environment.

Acknowledgments The research was supported by National Nature Science Foundation of China (No.51575302).

References

1. Zhang L, Yang Q, Xu F et al (2004) The current situation of the research of the robot dexterous hands with multi-finger and its actuation system. *Trans CSAE* 20(3):271–275
2. Okada T (1982) Computer control of multijointed finger system for precise object-handing. *IEEE Trans Syst Man Cybern* 12(3):289–299

3. Lovchik CS, Difer MA (1999) The robonaut hand: a dexterous robotic hand for space. *IEEE International Conference on Robotics and Automation*. Detroit, Michigan, pp 907–912
4. Jacobsen SC, Iversen EK, Knutti DF et al (1986) Design of the Utah/MIT dexterous hand. *Proceedings of IEEE International Conference on Robotics and Automation*, pp 1520–1532
5. Tuffield P, Elias H (2003) The shadow robot mimics human actions. *Ind Robot: Int J* 30(1):56–60
6. Liu H, Meusel P, Seitz N et al (2007) The modular multisensory DLR-HIT-Hand. *Mech Mach Theory* 42:612–625
7. Ambrose RO, Aldridge H, Askew RS et al (2000) Robonaut: NASA's space humanoid. *IEEE Intell Syst* 15(4):57–63
8. Kawasaki H, Shimomura H, Shimizu Y (2001) Educational-industrial development of an anthropomorphic robot hand "Gifu hand". *Complex Adv Robot* 15(3):357–363
9. Thierry L, Gosselin CM (1998) Simulation of underactuated mechanical hands. *Mech Mach Theory* 33(1):39–57
10. Birglen L, Gosselin CM (2001) Optimally unstable underactuated gripper: synthesis and applications. *IDETC/CIE ASME International Design Engineering Technical Conferences and Computers and Information in Engineering Conference*, vol 14(2). Philadelphia, USA, pp 1–9
11. Laliberte T, Birglen L, Gosselin C (2002) Under-actuation robotic grasping hands. *Mach Intell Robot Control* 4(3):1–11
12. Birglen L, Gosselin CM (2004) Kinetostatic analysis of underactuated fingers. *IEEE Trans Robot Autom* 20(2):211–221
13. Birglen L, Gosselin CM (2006) Geometric design of three-phalanx underactuated fingers. *ASME J Mech Des* 128(2):356–364
14. Fukaya N, Toyama S, Asfour T et al (2000) Design of the TUAT/Karlsruhe humanoid hand. *IEEE/RSJ Int Conf Intell Robot Syst (IROS)* 3(1):1754–1759
15. Zhang W, Che D, Liu H et al (2009) Super underactuated multi-fingered mechanical hand with modular self-adaptive gear-rack mechanism. *Ind Robot: Int J* 36(3):255–262
16. Zhang W, Tian L, Liu K (2007) Study on multi-finger under-actuated mechanism for TH-2 robotic hand. *IASTED International Conference on Robotics and Applications*, pp 420–424
17. Zhang W, Chen Q, Sun Z et al (2003) Under-actuated passive adaptive grasp humanoid robot hand with control of grasping force, *IEEE International Conference on Robotics and Automation (ICRA)*, pp. 696–701
18. Massa B, Roccella S, Carrozza MC et al (2002) Design and development of an underactuated prosthetic hand, *IEEE International Conference on Robotics and Automation (ICRA)*, pp. 3374–3379
19. Li G, Liu H, Zhang W (2012) Development of multi-fingered robotic hand with coupled and directly self-adaptive grasp. *Int J Humanoid Rob* 9(4):1–18

COSA-FBA Hand: An Underactuated Hand with Five-gear Mechanisms and Built-in Actuators

Siqiao Ruan, Wenzeng Zhang, Tianyi Zhang and Shuang Song

Abstract This paper proposes a novel underactuated hand, COSA-FBA hand, which performs coupled and self-adaptive grasping. The COSA-FBA hand consists of 5 fingers and 14 degrees of freedom. The COSA-FBA finger consists of an actuator embedded into its proximal phalange, a five-gear mechanism and a spring, which allows it to finish multiple grasping postures such as enveloping and pinching, depending on the shape, size, and dimension of the object. The COSA-FBA hand has advantages of concise structure, low cost, high efficiency and space-saving of the palm. The coupled and self-adaptive hand has a wide arrange of applications.

Keywords Robot hand · Underactuated finger · Coupled and self-adaptive grasp

1 Introduction

Robot hands have already played a critical role in industrial production and high-risk operation. However, there are still many human workers and operators working on the assembly line who are exposed to some life-threatening situations. In order to completely revolutionize and automate these industries, a versatile grasping tools becomes necessary. For the purpose of inventing a robot hand that is agile, easy to control, and capable of multi-tasking, humanoid hands become a direction that researchers try to approach, since human hands is capable of finishing many grasping mode and posture which can grasp the object effectively.

To imitate human hand, dexterous hands were designed and developed. Dexterous hand is the robot hand that every joint requires a motor to actuate.

S. Ruan · W. Zhang (✉) · S. Song
Department of Mechanical Engineering, Tsinghua University, Beijing 100084, China
e-mail: wenzeng@tsinghua.edu.cn

T. Zhang
Department of Mechanical Engineering, University of Hong Kong, Hong Kong, China

The Utah/MIT Dexterous Hand [1], Stanford/JPL Hand [2], BH Hand, DLR/HIT Hand and Robonaut hand [1] are good examples of dexterous hand.

Dexterous hand is capable of achieving multiple grasping modes like pinching, gripping, and catching. Also, through controlling each joint, the hand can adapt to the shape and size of different objects. However, the dexterous hand has many serious flaws. On one hand, the great number of DOA makes the whole hand cumbersome and expensive in cost. On the other hand, it is hard to control so many actuators spontaneously.

Due to the flaw of dexterous hands, underactuated robot hand has become a new concentration of many researchers [3]. An underactuated robot hand is defined as the robot hand that possesses less DOA (Degrees of Actuation) than DOF (Degrees of Freedom) [4]. The underactuated robot hand solves some flaws of Dexterous hand. It is cheaper, simpler in structure, and easier to control due to the fact that it has less actuators [5].

However, the traditional underactuated hands [6] usually have simplex grasping modes such as coupled, self-adaptive and parallel grasping modes. In order to diversify the grasping mode. Hybrid grasping mode underactuated hand is being proposed [7, 8]. Hybrid grasping mode combines the flexibility of dexterous hands and the stability and simplicity of traditional underactuated hands, which brings underactuated hand to a higher level.

This paper introduces a coupled and self-adaptive underactuated finger with a novel built-in actuator five-gear mechanism. Different from the existing hybrid underactuated hand, COSA-FBA hand uses two gears that sleeved on the transitional axis and connected to each other with a spring to accomplish the function of decoupling which effectively switch the grasping mode from coupling to self-adaptive, making the whole structure more compact.

The second part of this paper introduces the concept of the coupled and self-adaptive (COSA) underactuated hand, the third part analyzes the structure of the COSA-FBA finger, the fourth part analyzes the grasping-force distribution of the COSA-FBA hand, the fifth part presents the grasping experiment of the COSA-FBA finger, and the sixth part demonstrates the design of the humanoid COSA-FBA hand.

2 Concept of the Coupled and Self-adaptive (COSA) Grasp

Coupled grasping mode is the grasping mode that every joint rotates with a fixed rotating ratio. This grasping mode is similar to human grasping, and the whole grasping process is relatively stable. Nonetheless, its defect is that its grasping mode is fixed, that it cannot adapt to the shape of the object. Therefore, it has a poor performance of grasping different kinds of objects.

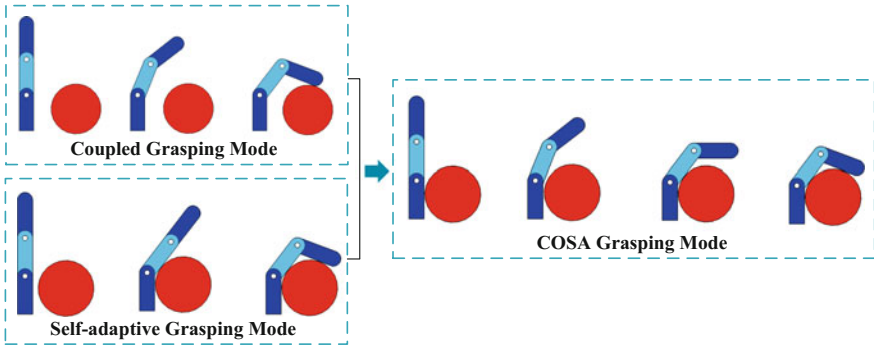


Fig. 1 Concept of coupled and self-adaptive (COSA) grasping mode

Self-adaptive grasping mode is the grasping mode that when it grasps an object, through one actuator, the first joint rotates, and the middle-phalange moves towards the object while the other joint keep static. When the middle-phalange contacts with the object, the second joint starts to rotate, and the terminal-phalange starts moving until it envelopes the object. Self-adaptive grasping mode is capable of adapt to different shapes of object. Its flaw is that its grasping posture is rigid and not personified, because when the finger does not contact with the object, the whole finger straightens. Also, when the middle-phalange squeezes the object, some objects with smooth surfaces may be pushed away, which may cause instability in the grasping process.

The COSA grasping mode combines the advantages of these two traditional grasping mode and neutralizes their disadvantages. As Fig. 1 shows, when coupled self-adaptive grasping mode is performed, the finger would first approach the object with coupled grasping mode. If the terminal-phalange makes contact with the object, the grasping process is done. If the middle-phalange contacts with the object, the next phalange would turn into self-adaptive mode and envelope the object. Coupled self-adaptive grasping mode is not only more similar to human grasping mode but also possesses the ability to adapt to the shape of object.

3 Design of the COSA-FBA Finger

3.1 Structure of the COSA-FBA Finger

As Fig. 2 shows, the structure of COSA-FBA finger is mainly composed of the base, the middle-phalange, the terminal-phalange, the actuator, the first joint-shaft, and the second joint-shaft. The first joint-shaft is fixed in the base. The second joint-shaft is sleeved on the middle-phalange. The terminal-phalange is fixed on the second axis.

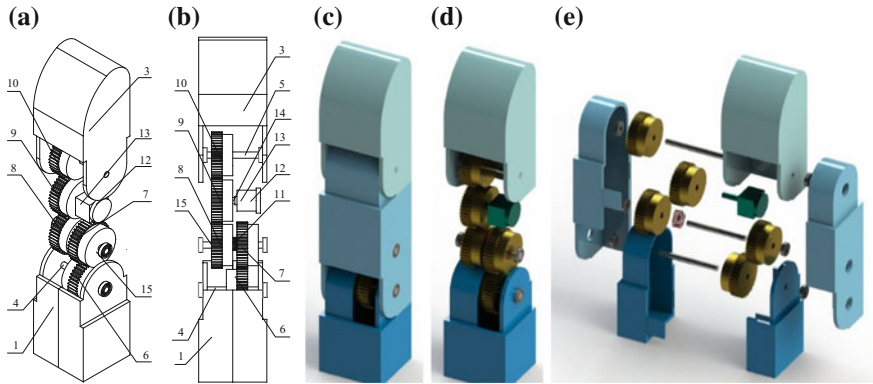


Fig. 2 The structure of COSA-FBA finger. 1 base; 2 middle-phalange; 3 terminal-phalange; 4 first axis; 5 second axis; 6 first gear; 7 second gear; 8 third gear; 9 active gear; 10 fourth gear; 11 spring; 12 motor; 13 reducer; 14 driving mechanism; 15 transitional axis

The first joint-shaft is parallel with the second joint-shaft. Furthermore, this device also contains a transitional axis, an active gear, a first gear, a second gear, a third gear, a fourth gear and a spring. The actuator is fixed on the middle-phalange. The active gear is fixed on the output axis of the actuator. The transitional axis is set in the middle-phalange. The middle-phalange is sleeved with the first joint-shaft. The first joint-shaft is parallel with the transitional axis. The active gear is meshed with the third gear. The third and the second gear are sleeved on the transitional axis. The spring is connected to the second gear and the third gear. The second gear is meshed with the first gear. The first gear is fixed on the first axis. The fourth gear is meshed with the active gear and fixed on the second axis. In this structure, a torsional spring is used as the spring. The gear ratio of the first gear and the second gear is 1. The gear ratio of the active gear and the third gear is “a”. The gear ratio of the active gear and the fourth gear is a. “a” is a positive rational number. An example of its specific structure and mechanism is shown in Fig. 2. In this example, “a” equals 1.

3.2 Grasping Process of COSA-FBA Finger

The grasping process is presented as Fig. 3 shows, the initial state of the finger is perpendicular with the palm, and both the first and the terminal-phalange straighten up as Fig. 3a has shown. When the grasping motion starts, the output axis of the actuator starts rotating. Through the reducer, the power is transmitted to the active gear, making it start to rotate. The active gear transmits the power to the third gear which sleeved on the transitional axis and the fourth gear which fixed on the second axis, making them start to rotate. The third gear pulls the second gear through the

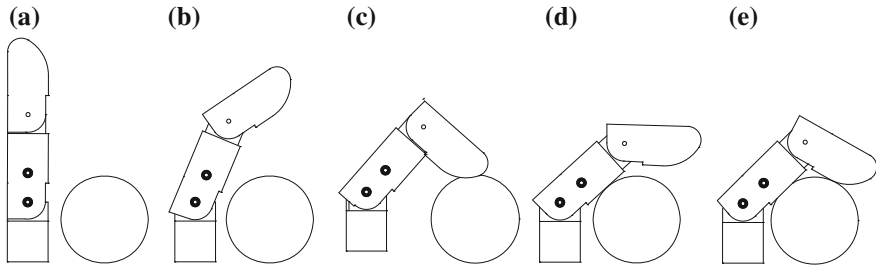


Fig. 3 The grasping process of COSA-FBA finger

twisting force of the spring. In the meantime, the second gear meshes with the first gear.

When the finger does not contact with the object as Fig. 3b has shown, the active gear drags the fourth gear which fixes on the second joint-shaft. Since the second joint-shaft is fixed on the terminal-phalange, the terminal-phalange starts rotating. Through transmission in the second and the third gear, the middle-phalange rotates around the first gear which fixes on the base. The angle that the middle-phalange rotates from its initial state and the angle between the terminal-phalange and the middle-phalange is the same. The coupling grasping process is performed.

If the terminal-phalange first makes contact with the object as Fig. 3c has shown, the fourth gear is unable to continue rotating which makes the motor stop moving. Therefore, the whole grasping process is ended. A coupling anthropathic pinching posture is performed.

If the middle-phalange first makes contact with the object as Fig. 3d has shown, the second gear is no longer able to rotate around the first gear. However, the third gear is able to keep rotating, and the spring starts to deform. The fourth gear is still able to rotate, making the terminal-phalange keep rotating until it contacts with the object. When the terminal-phalange contacts with the object, the motor stops moving. Therefore the whole grasping process is ended as Fig. 3e has shown. A self-adaptive grasping process is performed.

4 Grasping Force Distribution Analysis of COSA-FBA Finger

This part focus on the grasping force distribution of COSA-FBA finger. For the reason of simplification, the gravity force of the finger and objects and the friction between phalanges are neglected, and the contact forces are applied on points (Fig. 4).

When the finger fully envelopes an object, the grasping force and the total arm of the force is in an equilibrium state. Based on this characteristic, several moment equations can be reached as follows (η is the percentage of transmission loss).

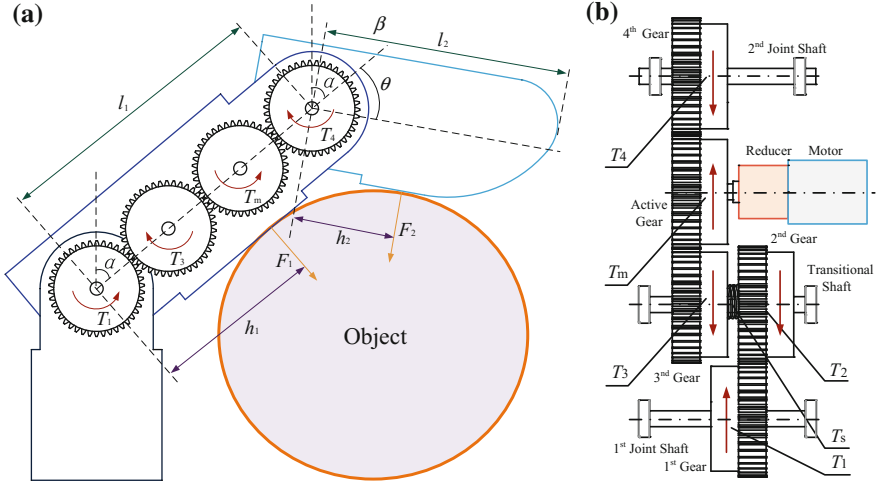


Fig. 4 Grasping-forces distribution analysis of the COSA-FBA finger. F_1 , F_2 —The grasping force to the object by middle-phalange and terminal-phalange, l_1 , l_2 —The length of middle-phalange and terminal-phalange, h_1 , h_2 —The arm of force F_1 and F_2 , α —The rotational angle of middle-phalange, θ —The rotational angle of terminal-phalange in self-adaptive process, β —The rotational angle of terminal-phalange, T_1 —Torque of the first gear, T_2 —Torque of the second gear, T_3 —Torque of the third gear, T_4 —Torque of the fourth gear, T_m —Torque of the motor to the active gear, T_s —Torque of the spring

First, relative to the first axis, the torque relationship can be drawn as follow:

$$T_4 = F_1 h_1 + F_2 (h_2 + l_1 \cos \alpha). \quad (1)$$

Second, according to the output axis of the motor, the torque relationship can be reached as follows:

$$\eta T_m = T_4 + T_3. \quad (2)$$

Third, relative to the transitional axis, the torque relationship can be drawn as follows:

$$T_2 = T_3, \eta T_m = T_4 + T_2. \quad (3)$$

At last, according to the first axis, the torque relationship can be reached as follows:

$$T_1 = \eta T_2, T_2 = T_1 / \eta. \quad (4)$$

$$\eta T_m = T_4 + T_1 / \eta. \quad (5)$$

Plug Eq. (1) into Eq. (5), the torque relationship can be drawn as follows:

$$\eta T_m = F_2 h_2 + [F_1 h_1 + F_2 (h_2 + l_1 \cos \alpha)] / \eta. \quad (6)$$

For the spring, according to Hooke law, the following equation can be get:

$$T_s = k\theta. \quad (7)$$

Because of $\eta T_s = T_4$, one can get:

$$\eta k\theta = T_4 = F_1 h_1 + F_2 (h_2 + l_1 \cos \alpha). \quad (8)$$

Plug Eq. (8) into Eq. (6), the equation of F_2 can be drawn as follows:

$$F_2 = (\eta T_m - k\theta) / h_2. \quad (9)$$

Plug Eq. (9) into Eq. (6), the equation of F_1 can be reached as follows:

$$F_1 = [k\theta(\eta + 1) - \eta T_m] / h - [l_1 \cos \alpha (\eta T_m - k\theta)] / h_1 h_2. \quad (10)$$

Using Eq. (9) and Eq. (10), the relationship between grasping force, rotational angle, and the arm of the force are analyzed and studied.

According to Fig. 5a, the grasping force of the first phalange reaches maximum when the arm of the force is minimized and θ reaches maximum (90°). The grasping force of the second phalange reaches maximum when the arm of the force is minimized and θ reaches minimized (0°). This is because the spring would consume a large amount of the torque of the motor, so the grasping force in the coupling process is bigger than the grasping force in the self-adaptive process.

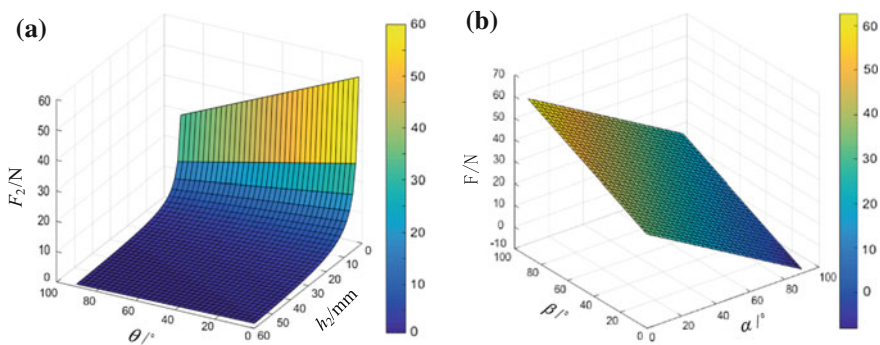


Fig. 5 Contact-force distribution by h_1 , h_2 , and θ , where **a** $T_m = 60$ N mm, $l_1 = 60$ mm, $k = 50$ N mm, $\alpha = 30^\circ$, $\eta = 95\%$, $h_2 = 30$ mm **b** $T_m = 60$ N mm, $l_1 = 60$ mm, $k = 5$ N mm, $\eta = 95\%$, $h_1 = 30$ mm, $h_2 = 30$ mm

According to Fig. 5b, when the rotational angle of the first phalange increases, the grasping force of the first phalange decreases. When the rotational angle of the second phalange increases, the grasping force of the first phalange increases, while the grasping force of the second phalange decreases. This is because the two transmission routes have distributed the torque of the motor. Overall, the COSA-FBA robot finger is capable of grasping object effectively and stably.

5 Grasping Experiment of COSA-FBA Finger

To evaluate the performances of the COSA-FBA finger, several grasping experiment is conducted. Depending on the size, dimension and shape of the object, the COSA-FBA finger can perform enveloping and pinching posture when it grasps the object as Fig. 6 has shown. When the object is located on the upper side of the finger, the COSA-FBA finger would perform coupled grasping mode and pinch the object. When the object is located on the lower side of the finger, the COSA-FBA finger would perform COSA grasping mode and envelop the object. It has been proved that the COSA-FBA finger is capable of grasping object effectively and stably.

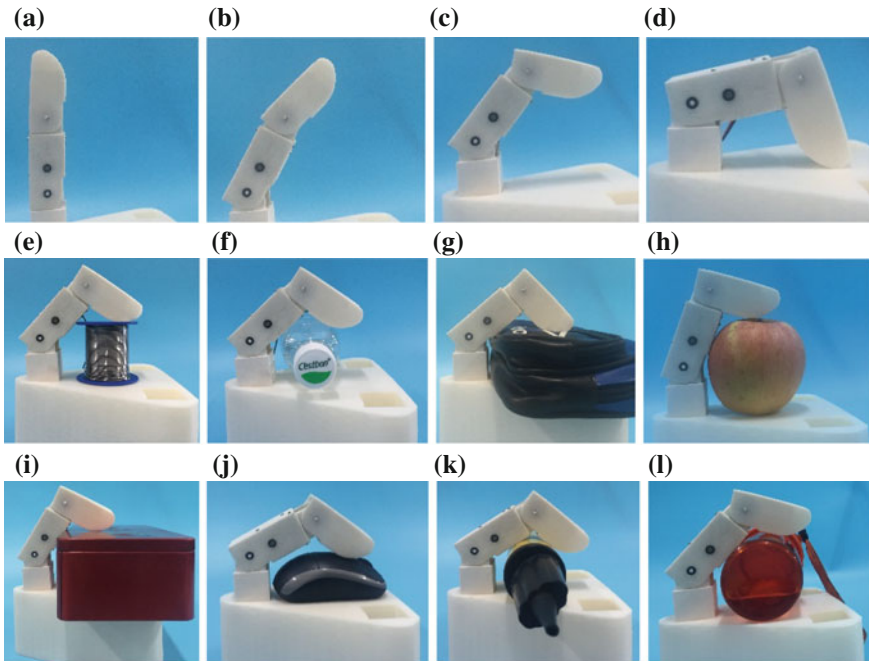


Fig. 6 Grasping experiments of COSA-FBA finger

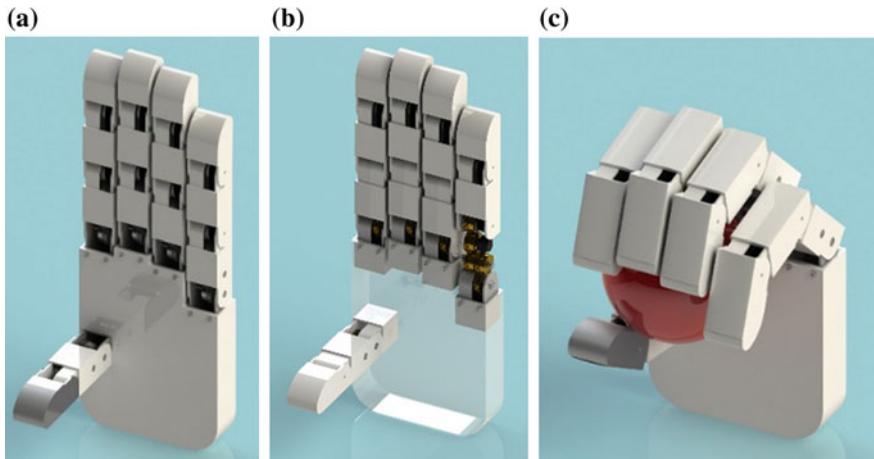


Fig. 7 COSA-FBA Humanoid Hand

6 Design of COSA-FBA Humanoid Hand

A humanoid robot hand is designed adopting the finger mechanism already described. The appearance of this humanoid hand is shown in Fig. 7. This robot hand consists of five COSA-FBA robot fingers. Each finger consists of three joints and three phalanges, except for the thumb which possess two joints and two phalanges. The second phalange can repeat the mechanism above or other coupling structure. This example uses an 8-shape pulley-belt mechanism to accomplish coupling.

7 Conclusions

This paper proposes a novel underactuated finger, COSA-FBA finger. The COSA-FBA finger has a built-in actuator, five-gear mechanism, which allow it to finish coupled and self-adaptive grasping. Its features of easy-control, anthropomorphic, adaptive, and low-cost allow it to be widely used.

Acknowledgments This research was supported by National Natural Science Foundation of China (No. 51575302).

References

1. Biagiotti L, Lotti F, Melchiorri C et al (2004) How far is the human hand? A review on anthropomorphic robotic end-effectors, Bologna

2. Loucks C, Johnson V, Boissiere P et al (1987) Modeling and control of the Stanford/JPL hand. 1987 IEEE international conference on robotics and automation (ICRA), pp 573–578
3. Kragten GA, Herder JL (2010) The ability of underactuated hands to grasp and hold objects. *Mech Mach Theory* 45(3):408–425
4. Laliberté T, Gosselin CM (1998) Simulation and design of underactuated mechanical hands. *Mech Mach Theory* 33(1):39–57
5. Kragten GA (2011) Underactuated hands: fundamentals, performance analysis and design. PhD thesis, Delft University of Technology
6. Zhang W, Che D, Liu H et al (2009) Super underactuated multi-fingered mechanical hand with modular self-adaptive gear-rack mechanism. *Ind Rob: Int J* 36(3):255–262
7. Che D, Zhang W (2011) A dexterous and self-adaptive humanoid robot hand: GCUA Hand. *Int J Humanoid Rob* 8(1):73–86
8. Li G, Liu H, Zhang W (2012) Development of multi-fingered robotic hand with coupled and directly self-adaptive grasp. *Int J Humanoid Rob* 9(4):1250034

Topological Characteristics Analysis for a Family of Novel SCARA Parallel Mechanisms

Qingfei Zeng, Huiping Shen, Hengcun Qiang and TingLi Yang

Abstract The 4-dof parallel mechanisms (PMs) which can achieve SCARA motion have broad industrial applications. However, studies on the 4-dof PMs are less than that of three-translation PMs or three-rotation PMs. At the same time, not enough attention has been paid to topological structures analysis which can give important basis on type selection and performance evaluation of PMs. According to the topological design theory and method for PMs based on position and orientation characteristic (POC) and the ordered single-open-chain (SOC), this paper gives a total topological structure analysis on seven typical SCARA PMs proposed by the authors. Five major topological features of PMs are revealed, which are POC set, the degree of the freedom (including the selection of drive pair), over-constraint degree, coupling degree and the input-output motion decoupling. This paper provides a theoretical basis for the kinematics analysis, design and applications for these new SCARA PMs.

Keywords Parallel mechanism · POC · Topological structure analysis · Coupling degree · Topological structure characteristics · Type synthesis

1 Introduction

The theory and method for topological structure design of parallel mechanisms (PMs) based on POC set and single-open-chain (SOC) unit are proposed and established by Chinese scholars [1, 2], which is different from other type synthesis theories such as the screw theory, the displacement subgroup theory and the theory based on linear transformation and evolutionary algorithm. This theory describes the motion with respect to axis of kinematic pair of moving platform that has no relationship with fixed coordinate system and the positions of mechanism, which

Q. Zeng · H. Shen (✉) · H. Qiang · T. Yang
Research Center for Advanced Mechanism Theory, Changzhou University,
213016 Changzhou, People's Republic of China
e-mail: shp65@126.com

ensure that this method is geometric and can obtain non-instantaneous mechanisms without over-constraint and common mechanisms with over-constraint. This method possesses definite physical meaning and is convenient for people to understand because only simple “ \cap ” and “ \cup ” symbolic linear calculations for POC set are needed. Many scholars have designed a large number of parallel mechanisms based on these existing type synthesis methods.

On the one hand, three kinds of typical output motions, including three-translation, three-rotation and SCARA motion (three translations and one rotation about the axis of a fixed direction of the movable platform), have very wide industrial applications. However, the development and application of new 4-DOF parallel robots with SCARA motion are relatively fewer than three-translation and three-rotation motion.

In 1999, ABB developed a SCARA robot [3] called FlexPicker. Based on three-translation parallel manipulator Delta [4] (Clavel, in 1985), a three-translation and one-rotation hybrid manipulator was obtained through a mid-branch chain (R-U-P-U-R) located between the moving platform and the static platform. As a matter of fact, this hybrid manipulator can be regarded as having two moving platform (i.e., three-translation Delta mechanism sub-platform and one-rotation platform amounted with manipulator effector). The manipulator has been widely used but its mid-branch is easy to be worn at high-speed. The working space of the manipulator was not large enough.

To overcome these disadvantages of the manipulator, Pierrot and other scientists invented the H4, I4, PAR4, and series of 4-dof (i.e., three translations and one rotation) SCARA manipulators [5–7]. They retained the complex branched chains with parallelogram structure R// (4S) or R//R- //R (4R) -//R (s - spherical joint, R-rotational joint) and the three-translational Delta mechanism possessed. Those 4-dof SCARA manipulators have advantages of high speed and good dynamic performance just like Delta mechanism, so they are also known as the family members of Delta robots.

The family of Delta parallel robots are constituted by two complex branches which are symmetrical distributed, and each complex branch has two identical parallelogram structure, the planes of parallelogram are perpendicular to each other, the terminal output link is sub-moving platform of three translational mechanism; Then, the two sides of the output platform (which is installed grasper operation at both ends of the third sub moving platform) uses rotate pair to connect to the two complex branches as the moving platform of three translational mechanism, Moreover, the relative motions (rotations or translations) among the three sub platform are amplified as an output rotation through the amplifying device (gear, gear-rack, belt, etc.). Therefore, the family of Delta parallel robot can be regarded as having three moving platforms.

In China, Huang [8] proposed a 4-URU type 3T1R(three translations and one rotation) parallel robot in 2000; Jin Qiong and Yang Tingli [9] proposed a class of

three-translation and one-rotation parallel robot with a single moving platform according to topological structure design theory of PMs based on SOC unit in 2001 [10]. Huang Tian invented high-speed three-translation and one-rotation Cross-IV handling robot based on the idea of H4, I4, Par4 and realized the industrialization in 2010 [11]; In 2012, Liu Xinjun developed the prototype [12] of X4 PM which is a three translations and one rotation mechanism with single moving platform for the first time in China. X4 PM can achieve large rotation though dimension optimization [13].

Compared to the three-translation Delta manipulator, the structure, kinematics, dynamics and control system of the 4-DOF H4, I4, Par4, Cross-IV, X4 and other series of SCARA type mechanisms (whether they have a single moving platform, a double moving platform, or a triple moving platform) are more complex and difficult, theoretic research and industrial applications are relatively slower, so it is high time to develop the new 4-DOF SCARA mechanisms.

Under the above background, according to design theory of PM based on position and orientation characteristics (POC) and orderly single opened chain (SOC), the author proposed 13 potential parallel mechanisms with three-translation and one rotation recently, among of which seven mechanisms has been applied for China's invention patent [14–17].

On the other hand, evaluation and optimization of topological performance for parallel mechanism has become one of the key issues in the study of PMs. The premise of that is analysis of mechanism topological characteristics, and the kinematics and dynamics performance of the mechanism can be obtained in the process of mechanism selection. So that kinematics and dynamics analysis and calculations can be simplified. Therefore, the complexity of mechanism design can be reduced and the design cycle can be shorten.

Accordingly, the author believes that topological structure analysis should be added before the type synthesis, kinematics and dynamics analysis of mechanism. Moreover, specific topological analysis includes POC, DOF, coupling degree calculation, I-O kinematic decoupling analysis, calculation of the constraint degree, so as to provide a clear direction for the optimization, the kinematics and dynamics solutions of mechanisms. But so far these topics are relatively less currently.

The topological structure analysis of famous commercialization PMs, such as Delta, Diamond, Tricept, the Trivariant and Exechon, Z3, H4, steward, or the other PMs with potential applications have been performed. Some valuable conclusions or rules have been obtained. This work could provide some inspiration for the design and application of the other new mechanisms [17].

In this paper, topological structure analysis of 7 3T1R parallel mechanisms with practical value proposed by authors recently is performed to reveal the POC sets, DOF, coupling degree and the other main topological structure characteristics of mechanisms. This study provides theoretical basis for its design and application.

2 Topological Characteristics of Parallel Mechanisms

In this paper, twelve topological structure characteristics of the PMs are analyzed, including position characteristics set (POC) and its dimension, the number of independent loops ν , independent displacement equation number, over-constraint degree N_{ov} , the type and the number F of degrees of freedom (DOF), and the basic kinematic chain (BKC) types and number, BKC, coupling degree κ , input–output kinematic decoupling (I-O decoupling), passive kinematic pair, number of inputs, redundancy and other indicators. Further, we discover that [17]:

- (1) POC set and its dimension reflect the basic function of the mechanism;
- (2) The number of independent displacement equations, redundancy, BKC coupling, I-O decoupling and driving pair selection indicate kinematics and dynamics performance of the mechanism;
- (3) DOF type and number, BKC coupling degree, redundancy, dimension of POC set and I-O decoupling manifest the control performance of the mechanism.
- (4) Over-constraint degree (N_{ov}) reflects the stiffness of the mechanism and the sensitivity of precision to the manufacturing error: the greater of the N_{ov} , the greater stiffness of the mechanism, and the higher sensitivity of the manufacturing error.

Due to limited space, only five important characteristics indicators including POC set, DOF, N_{ov} , coupling degree constraint number κ , I-O decoupling are described in the paper and the corresponding calculation formulas [1, 2] are shown in Table 1.

3 Topological Analysis of SCARA PMs

Authors recently obtained 13 potential SCARA type PMs with great application value [14–17], seven of them (I~VII) are analyzed below, and topological structure characteristics of them such as POC set of the mechanism, number of DOF, the

Table 1 The indexes of topological structure characteristics of the mechanism

Indexes	Equations and judgment criterias
POC set and the number	$M_S = \bigcup_{i=1}^m M_{J_i}; M_{pa} = \bigcup_{i=1}^{\nu+1} M_{b_i}$
DOF	$F = \sum_{i=1}^m f_i - \sum_{j=1}^{\nu} \dim \cdot \{(\bigcap_{j=1}^j M_{b_j}) \cup M_{b_{(j+1)}}\}$
Over-constraint degree	$N_{ov} = 6\nu + \xi$
BKC type	Criteria of BKC [1, 2]
Coupling degree	$\kappa = \frac{1}{2} \min \left\{ \sum_{j=1}^{\nu} \Delta_j \right\}$
I-O decoupling	Criteria of I-O decoupling [1, 2]

number of over-constraint N_{ov} , coupling degree κ , I-O decoupling are addressed accordingly. One typical novel SCARA type IPM is analyzed in detail and the analysis process is as follows. The analysis results of the remaining novel SCARA type PMs (II–VII) are also obtained and listed in Tables 3 and 4.

3.1 Type I 3T1R Mechanism

3.1.1 Description of Type I 3T1R Mechanism

Type I 3T1R mechanism is shown as Fig. 1, which is composed of the static platform 0, moving platform 1 and four identical chains. From static platform 0 to moving platform 1, the former three revolute pairs are parallel to each other, the latter two revolute pairs are parallel to each other, and the third revolute pair axis is perpendicular to the fourth revolute pair axis. The one end of each of four branch chains are connected to the moving platform 1 by revolute pair R_{15} , R_{25} , R_{35} and R_{45} , the four axis of which should be parallel to the normal of moving platform 1. The other end of each of four chains is connected to the static platform by the actuated pair of R_{11} , R_{21} , R_{31} and R_{41} . Further, $R_{11} \perp R_{21}$ and $R_{31} \perp R_{41}$ are must satisfied. Here notation “ \perp ” means the relation of perpendicular and “//” means the relation of parallel. The same is below.

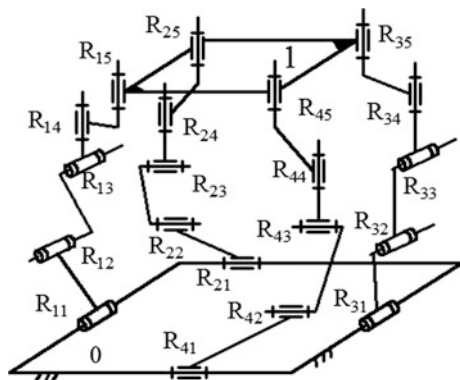
3.1.2 DOF, N_{ov} and POC of Type I 3T1R Mechanism

(1) Topological structure

$$SOC\{-R_{i1} \parallel R_{i2} \parallel R_{i3} \perp R_{i4} \parallel R_{i5}-\}, (i = 1 \sim 4)$$

(2) POC set of branch chains

Fig. 1 3T1R type I parallel mechanism



Agreement: any point O' on the moving platform 1 is chosen as the base point. The same is below.

$$M_{b_i} = \left[r^2(\|\diamond(R_{i3}, R_{i4})\|) \right], (i = 1 \sim 4)$$

(3) Determine ξ_{L_1} , the number of independent equations of first basic loop

(a) The first basic loop

$$\begin{aligned} \xi_{L_1} &= \dim \cdot \{M_{b_1} \cup M_{b_2}\} = \dim \cdot \left\{ \left[r^2(\|\diamond(R_{13}, R_{14})\|) \right] \cup \left[r^2(\|\diamond(R_{23}, R_{24})\|) \right] \right\} \\ &= \dim \cdot \left\{ \begin{bmatrix} t^3 \\ r^3 \end{bmatrix} \right\} = 6. \end{aligned}$$

(b) DOF and POC

$$F_{(1-2)} = \sum_{i=1}^m f_i - \sum_{j=1}^1 \xi_{L_j} = 10 - 6 = 4$$

$$M_{pa(1-2)} = \left[r^2(\|\diamond(R_{13}, R_{14})\|) \right] \cap \left[r^2(\|\diamond(R_{23}, R_{24})\|) \right] = \left[r^1(\|\diamond(R_{14})\|) \right]$$

(4) Determine ξ_{L_2} (number of independent equations of second basic loop)

(a) The second basic loop

$$\begin{aligned} \xi_{L_2} &= \dim \cdot \{M_{pa(1-2)} \cup M_{b_3}\} = \dim \cdot \left\{ \left[r^1(\|\diamond(R_{14})\|) \right] \cup \left[r^2(\|\diamond(R_{33}, R_{34})\|) \right] \right\} \\ &= \dim \cdot \left\{ \begin{bmatrix} t^3 \\ r^2(\|\diamond(R_{33}, R_{34})\|) \end{bmatrix} \right\} = 5 \end{aligned}$$

(b) DOF and POC

$$F_{(1-3)} = \sum_{i=1}^m f_i - \sum_{j=1}^2 \xi_{L_j} = 15 - 6 - 5 = 4$$

$$M_{pa(1-3)} = \left[r^1(\|\diamond(R_{14})\|) \right] \cap \left[r^2(\|\diamond(R_{33}, R_{34})\|) \right] = \left[r^1(\|\diamond(R_{14})\|) \right]$$

(5) Determine ξ_{L_3} (number of independent equations of third basic loop)

$$\begin{aligned}\xi_{L_3} &= \dim \cdot \{M_{pa(1-3)} \cup M_{b_4}\} = \dim \cdot \left\{ \left[\begin{array}{c} t^3 \\ r^1(\|R_{14}) \end{array} \right] \cup \left[\begin{array}{c} t^3 \\ r^2(\|\diamond(R_{33}, R_{34})) \end{array} \right] \right\} \\ &= \dim \cdot \left\{ \left[\begin{array}{c} t^3 \\ r^2(\|\diamond(R_{43}, R_{44})) \end{array} \right] \right\} = 5\end{aligned}$$

(6) Calculate DOF of the mechanism

$$F = \sum_{i=1}^m f_i - \sum_{j=1}^3 \xi_{L_j} = 20 - 6 - 5 - 5 = 4$$

(7) The over-constraint degree

$$N_{ov} = 6v + F - \sum_{i=1}^m f_i = 6 \times 3 + 4 - 20 = 2$$

(8) POC set of the moving platform

$$M_{pa} = M_{pa(1-3)} \cap M_{b_4} = \left[\begin{array}{c} t^3 \\ r^1(\|R_{14}) \end{array} \right] \cap \left[\begin{array}{c} t^3 \\ r^2(\|\diamond(R_{43}, R_{44})) \end{array} \right] = \left[\begin{array}{c} t^3 \\ r^1(\|R_{14}) \end{array} \right]$$

Therefore, according to the criteria of the driving pair selection [1, 2], the moving platform 1 will generate 3 translations and 1 rotation about the normal axis of the moving platform 1 when the revolute pairs R_{11} , R_{21} , R_{31} , R_{41} on the static platform 0 are assigned to the driving pair.

3.1.3 κ and I-O Decoupling Analysis of Type I 3T1R Mechanism

(1) Loop₁ and its constraint degree Δ_1

$$\text{loop}_1 \{-R_{11} \| R_{12} \| R_{13} \perp R_{14} \| R_{15} - R_{24} \| R_{25} \perp R_{21} \| R_{22} \| R_{23} -\}$$

$$\Delta_1 = \sum_{i=1}^{m_1} f_i - I_1 - \xi_{L_1} = 10 - 2 - 6 = 2$$

(2) Loop₂ and its constraint degree Δ_2

$$\text{loop}_2 \{-R_{31} \| R_{32} \| R_{33} \perp R_{34} \| R_{35} -\}$$

$$\Delta_2 = \sum_{i=1}^{m_2} f_i - I_2 - \xi_{L_2} = 5 - 1 - 5 = -1$$

Table 2 Topological characteristics of 3T1R type I mechanism

POC set	v	F	N_{BKC}	κ	N_{ov}	I-O	Manufacturability
$\begin{bmatrix} r^3 \\ r^1 \end{bmatrix}$	3	4	1	2	2	No	Complex

(3) Loop₃ and its constraint degree Δ_3

$$\text{loop}_3\{-R_{41} \| R_{42} \| R_{43} \perp R_{44} \| R_{45}-\}$$

$$\Delta_3 = \sum_{i=1}^{m_3} f_i - I_3 - \xi_{L_3} = 5 - 1 - 5 = -1$$

(4) BKC and coupling degree of the mechanism κ

$$\kappa = \frac{1}{2} \sum_{j=1}^v |\Delta_j| = \frac{1}{2} (|+2| + |-1| + |-1|) = 2$$

The mechanism contains only one BKC. The 4 driving pairs are located within one BKC, therefore, the mechanism has no I-O decoupling.

The topology characteristics of the mechanism are listed in Table 2

3.2 The Remaining Novel SCARA Type PMs

Similarly, the analysis results of the remaining eight novel SCARA type PMs (II~VII) shown as in Table 3, are obtained and listed in Table 4 as follows.

Note: The SCARA mechanism X₄ [12] has four complex identical branch chains while the type VII mechanism has only two complex branch chains. Therefore, type VII mechanism can be regarded as the improved type X₄. The advantage of this mechanism is that the structure is simpler, manufacturing and maintenance are easier compared with X₄.

So far, the topological structure characteristics analysis of seven 4-DOF 3T1R PMs (type I to VII) has been completed. This work lays the foundation for design and optimization of these mechanisms.

4 Conclusions

(1) According to design theory and methods of parallel mechanisms based on POC and SOC, author analyses the topology structures of a class of 7 potential SCARA PMs with better practical value proposed by authors, and reveal 5 most important

Table 3 Schematic diagram of the remaining novel SCARA type PMs (II–VII)

Type	Diagram	Type	Diagram
II		III	
IV		V	
VI-1		VI-2	
VI-3		VII	

topological characteristics such as the POC set, DOF (including selection of driving pair), N_{ov} , coupling degree k , I-O decoupling, etc. The coupling degree κ being 2 indicates that the position kinematics and dynamics calculation of these PMs are very complex. Therefore, structure coupling degree reducing of the seven SCARA PMs will be another coming important work for authors to do, which may lead to some promising 4-DOF 3T1R PMs with low coupling degree being 1.

(2) The topological structure characteristics analysis of mechanisms, that is, to analyze and reveal the PMs position orientation characteristics set (POC) and its

Table 4 Topological characteristics of the remaining novel SCARA type PMs (II–VII)

Type	POC set	v	F	N_{BKC}	κ	N_{ov}	I-O	Manufacturability
II	$\begin{bmatrix} r^3 \\ r^1 \end{bmatrix}$	3	4	1	2	2	NO	Complex
III						6		
IV						2		
V						2		
VI-1						0		
VI-2						2		
VI-3						0		
VII						2		

dimension, the number of independent loops v , the number of independent equations, constraint degree N_{ov} , degree of freedom (DOF) and the number of DOF (F), the type and number of basic kinematic chain (BKC), BKC coupling degree κ , I-O decoupling analysis, passive kinematic pairs, selection of driving pairs and redundancy. These indicators can provide important basis for type selection of PMs and its performance evaluation. These indicators can also provide a clear direction for the type selection, the kinematics and dynamics of the mechanisms, which greatly accelerates the design progress of the mechanism and reduce the time for lengthy kinematics and dynamics analysis. Therefore, topological structure characteristics analysis is one of the important parts of the parallel mechanism theoretic research and applications.

Acknowledgments This research is sponsored by the NSFC (Grant No. 51375062, 51475050), Jiangsu Key Development Project (No. BE2015043) and Jiangsu Scientific and Technology Transformation Fund Project (No. BA2015098).

Appendix

M_{pa}	the POC elements of the moving platform
M_{bi}	the POC elements of the i th chains
F	DOF of the mechanism
f_i	DOF of the i th kinematic pairs
m	the number of kinematic pairs
n	the number of links of the mechanism
v	the number of independent loops in the mechanism ($v = m - n + 1$)
ξ_{L_j}	the number of independent equations of j th basic loop
M_{bi}	the POC sets of the i th legs;

(continued)

(continued)

$\cap_{i=1}^j M_{b_i}$	POC sets of sub-parallel mechanism moving platform consisted with j th chain and the former chains;
I_j	the number of inputs in the j th SOC_j
κ	coupling degree of the mechanism
Δ_j	constraint degree of j th SOC_j
BKC	basic kinematic chain

References

1. Yang T (2004) Topology structure design of robot mechanisms. China Machine Press, Beijing
2. Yang T, Liu A, Luo Y et al (2012) Theory and application of robot mechanism topology. Science Press, Beijing
3. ABB. IRB 360 Flexpicker [EB/OL].[2015-05-06]. [http://www.new.abb.com/ products/robotics/industrials-robots/irb-360](http://www.new.abb.com/products/robotics/industrials-robots/irb-360)
4. Clavel R (1990) Device for the movement and positioning of an element in space. U.S. Patent No. 4,976,582
5. Pierrot F, Company O (1999) H4:A new family of 4-dof parallel robots. In: Proceedings of the IEEE/ASME international conference on advanced intelligent mechatronics, September 19–23, 1999, Atlanta. New York: IEEE, 1999, pp 508–513
6. Krut S, Company O, Benoit M, et al. I4 (2003)A new parallel mechanism for SCARA motions. In: Proceedings of the IEEE international conference on robotics and automation, September 14–19, 2003, Taiwan, China:IEEE, 2003, pp 1875–1880
7. Nabat V, Company O, Krut S et al (2005) Par4:Very high speed parallel robot for pick-and-place. In: Proceedings of the IEEE/RSJ international conference on intelligent robots and systems, August 2–6, 2005, Alberta. New York:IEEE, pp 1202–1207
8. Tieshi Z, Zhen H (2000) Theory and application of selecting actuating components of spatial parallel mechanisms. Chin J Mech Eng 36(10):81–85
9. Qiong J, Tingli Y, Anxin L et al (2001) Kinematics analysis of a parallel pneumatic and hydraulic linkage based on single-opened-chain. Chin J Mech Eng 12(9):1038–1043
10. Yang T, Jin Q, Luo Y et al (2003) Virtual axis machine tools and robots for a kind of parallel mechanism, China,200310106012.4, 2003
11. Huang T, Liu H, Li M (2005) The robot with five degree of freedom: China CN1709657, 2005
12. Liu X, Xie F, Wang L et al (2012) A four freedom of degree parallel mechanism with single moving platform which can achieve SCARA move. China, 201210435375.1, 2012
13. Xie, FG, Liu XJ (2015) Design and development of a high-speed and high-rotation robot. ASME J Mech Rob 2015
14. Shen H, Yang T, Shao G et al (2015) A parallel robot hand with three translations and one rotation. Patent application number: 201510640394.X, 2015.10.9
15. Shen H, Yang T, Li Y et al (2015) A parallel robot picker with three translations and one rotation. Patent application number: 201510648948.2, 2015.10.9

16. Shen H, Yang T, Zhu W et al (2015) A parallel robot platform with three translations and one rotation. Patent application number: 201510566840.9, 2015.9.8
17. Shen H, Yang T, Zhu X et al (2015) A parallel mechanism with three translations and one rotation. Patent application number: 201510564382.5, 2015.9.8

Friction Compensation in Trajectory Tracking Control for a Parallel Hip Joint Simulator

Xianlei Shan, Gang Cheng and Xihui Chen

Abstract To evaluate the friction and wear characteristics of hip joint prosthesis biomaterials, a hip joint simulator with a 3SPS + 1PS (P: prismatic joint, S: spherical joint) spatial parallel manipulator as the core module is proposed. To improve the control performance of the parallel hip joint simulator, a friction compensation control method is proposed. First, with the help of Lagrange's Equations, the dynamic model of the parallel hip joint simulator is established, and a Coulomb + viscous friction model is adopted to describe the friction of the hip joint and the thrust ball bearing. Second, identification experiments are conducted, and parameters of the friction model are estimated. Third, a friction compensation controller is obtained based on computed torque control method, and the friction is served as the feed-forward compensation. As can be observed from the experiment results, the tracking accuracy of the parallel hip joint simulator is improved with the friction compensation.

Keywords Parallel hip joint simulator · Coulomb + viscous friction · Friction compensation · Computed torque control

1 Introduction

Hip joint simulator is used to evaluate the friction and wear characteristics of hip joint prosthesis biomaterials. The machine is required the replication of the kinematic and dynamic characteristics of the natural human hip joint and also the

X. Shan · G. Cheng (✉) · X. Chen
School of Mechatronic Engineering, China University of Mining and Technology,
Xuzhou 221116, China
e-mail: chg@cumt.edu.cn

X. Shan
e-mail: shanxlei@cumt.edu.cn

X. Chen
e-mail: chenxh@cumt.edu.cn

realization of dynamic loading. Parallel manipulators generally possess several advantages, including high stiffness, strong bearing capacity and complex trajectory simulation. Hence, a parallel hip joint simulator with a 3SPS + 1PS spatial parallel manipulator as the core module is proposed [1].

Because of the complexity structure of parallel manipulator, the motion control is generally more difficult. At present, motion control for planar or spatial parallel manipulators are widely studied by many researchers [2, 3]. For parallel manipulators, control strategies, such as fuzzy control method [4], computed torque control method [5], adaptive control [6], robust learning control method [7], and so on, are always applied. With regard to the parallel hip joint simulator, because of the complex motion trajectory of the moving platform and the dynamic loading from the hydraulic cylinder (300–3000 N), the nonlinear dynamics is more complex. Friction is one of the main disturbances of the parallel hip joint, and it will affect the control performance, therefore, in the design process of the controller, the influence of friction should be considered.

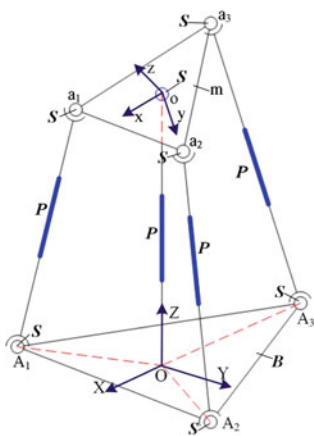
Modeling and identification of friction have attracted many scholars over the past few years, and to reduce the influence of friction on the control performance, friction compensation methods are always adopted. Shang [8] developed a friction compensation method based on a nonlinear friction for a planar parallel manipulator; Casalillaa [9] applied a simple friction model to the friction compensation for a 3-DOF parallel manipulator; Kim [10] studied the friction compensation for a 6-DOF parallel manipulator based on a robust nonlinear control method. With regard to the spatial parallel manipulators, the dynamics is more complex, which increasing the difficulty of parameter identification, especially for the parallel manipulators with dynamic loading, such as the parallel hip joint simulator. Therefore, a friction model that is simple enough and has good precision at the high speed at the same time is very important for friction compensation of the parallel hip joint simulator.

In the paper, to reduce the influence of friction on the control performance of the parallel hip joint simulator, a friction compensation method is developed. First, with considering of Coulomb + viscous friction of the hip joint and the thrust ball bearing, a dynamic model of the parallel hip joint simulator is established. Second, to estimate the friction parameters of the dynamic model, identification experiments are carried out. Third, based on computed torque control strategy and served the friction as the feed-forward compensation, a controller for the parallel hip joint simulator is designed. Lastly, friction compensation control experiments are conducted.

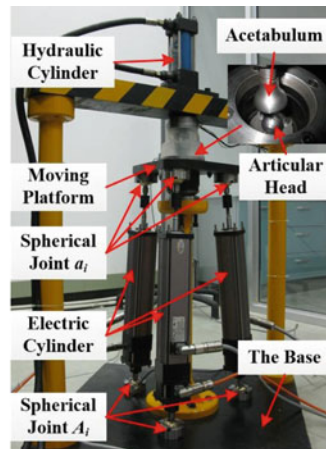
2 Dynamic Modeling and Identification of Friction Parameters

The topology structure and prototype of the 3SPS + 1PS parallel hip joint simulator are shown in Fig. 1. The parallel hip joint simulator is composed of a moving platform (m), a base platform (B) and peripheral supports. The moving platform and the base are connected by three identical surrounding SPS-type active branched-chains and one PS-type intermediate branched-chain. In Fig. 1 a, a_i and A_i ($i = 1, 2, 3$) are the fix points of the spherical joints (S) on the moving platform and the base platform, and o and O denote the centroids of the triangles $a_1a_2a_3$ and $A_1A_2A_3$, respectively.

The absolute coordinate system OXYZ is fixed on the base platform B at point O. The negative X-axis passes through point A_3 , and Z-axis is perpendicular to the base platform and pointing to the moving platform. The Y-axis can be determined by the other two axes following the Right-Hand-Rule. The relative coordinate system oxyz is attached to the moving platform at point o. The y-axis passes through point a_2 , and z-axis is perpendicular to the moving platform pointing upward. The x, y and z axes follow the Right-Hand-Rule. Three spherical joints are installed symmetrically about o on the moving platform. Each mount point is equidistant from o and the distance denoted as e . Another three spherical joints are installed on the base in the same way and the distances from the mount points to O is E . Each active branched-chain connects the moving platform and the base platform by spherical joints. The intermediate branched-chain is fixed on the base, and connects the moving platform by a thrust spherical plain bearing. Driving forces of the active branched-chains are supplied by three electric cylinders. The



(a) Topology structure.



(b) Prototype.

Fig. 1 3SPS + 1PS parallel hip joint simulator

intermediate branched-chain is used to install the artificial hip joint and balance the loading force from the hydraulic cylinder, and the height is fixed. The spatial locations of the moving platform are determined by the lengths of the active branched-chains.

2.1 Dynamic Modeling

Suppose that γ , β and α are the Euler angles of the moving platform, and $\mathbf{q} = (\gamma, \beta, \alpha)^T$. The position equation of branched-chain $A_i a_i$ ($i = 1, 2, 3$) can be obtained from Fig. 1a:

$$l_i \mathbf{e}_i = \mathbf{R} \cdot \mathbf{r}_{a_i} + \mathbf{P} - \mathbf{r}_{A_i}. \quad (1)$$

where l_i is the length of branched-chain $A_i a_i$, \mathbf{e}_i is the unit vector of $A_i a_i$, \mathbf{R} is the rotation matrix of $oxyz$ relative to $OXYZ$, \mathbf{r}_{a_i} and \mathbf{r}_{A_i} are the position vectors of spherical joints a_i and A_i in $oxyz$ and $OXYZ$, respectively, and \mathbf{P} is the centroid position vector of the moving platform in $OXYZ$, and $\mathbf{P} = [0, 0, Z]^T$.

Supposing that the angular velocity of the moving platform is $\boldsymbol{\omega}$, the velocity of the i th electric cylinder is \dot{l}_i ($i = 1, 2, 3$), and the velocity of point a_i is \mathbf{v}_{a_i} , and the following expressions can be obtained.

$$\dot{\mathbf{l}} = \mathbf{J}_1 \mathbf{v}_a, \mathbf{v}_a = \mathbf{J}_2 \boldsymbol{\omega}. \quad (2)$$

where $\dot{\mathbf{l}} = [\dot{l}_1, \dot{l}_2, \dot{l}_3]$, $\mathbf{v}_a = [v_{a1}, v_{a2}, v_{a3}]$, $\mathbf{J}_1 = \begin{bmatrix} \mathbf{e}_1^T & 0 & 0 \\ 0 & \mathbf{e}_2^T & 0 \\ 0 & 0 & \mathbf{e}_3^T \end{bmatrix}$,

$\mathbf{J}_2 = [-\tilde{r}_{a1}, -\tilde{r}_{a2}, -\tilde{r}_{a3}]^T$, and \tilde{r}_{a_i} is the antisymmetric matrix of \mathbf{r}_{a_i} .

With regard to the parallel hip joint, friction exist in the hip joint, the thrust ball bearing, the spherical joints and the electric cylinders, because of the loading force from the hydraulic cylinder is directly acting on the hip joint and the thrust ball bearing, therefore, only the friction of the hip joint and the thrust ball bearing are considered in the paper. The Coulomb + viscous friction model is adopted to describe the friction of the joints, and the friction torque can be expressed as follows:

$$\mathbf{M}_f = -[\mu_h F_N \frac{\boldsymbol{\omega}}{\|\boldsymbol{\omega}\|} + f_{vh} \boldsymbol{\omega}] r_h - [\mu_t (F_N + m \cdot g) \frac{\boldsymbol{\omega}}{\|\boldsymbol{\omega}\|} + f_{vt} \boldsymbol{\omega}] r_t. \quad (3)$$

where μ_h and μ_t are the friction coefficients of the hip joint and the thrust ball bearing, respectively; f_{vh} and f_{vt} are the viscous friction coefficients of the hip joint and the thrust ball bearing, respectively; F_N is the loading force from the hydraulic cylinder; m and g are the mass of the moving platform and the gravitational

acceleration, respectively; and r_h and r_t are the radii of the hip joint and the thrust ball bearing, respectively.

With the help of the Lagrange's Equations, the dynamic model of the parallel hip joint simulator can be established, as shown in Eq. (4).

$$\mathbf{M}(\mathbf{q})\ddot{\mathbf{q}} + \mathbf{C}(\mathbf{q}, \dot{\mathbf{q}})\dot{\mathbf{q}} + \mathbf{G}(\mathbf{q}) = \mathbf{J}(\mathbf{F} + \mathbf{J}^{-1}\mathbf{M}_f). \quad (4)$$

where $\mathbf{M}(\mathbf{q})$ is the inertia matrix, and $\mathbf{C}(\mathbf{q}, \dot{\mathbf{q}})$ is the coriolis and centrifugal force matrix, $\mathbf{G}(\mathbf{q})$ is the gravity item, \mathbf{J} is the Jacobi matrix of the parallel hip joint simulator, and $\mathbf{J} = \mathbf{J}_1\mathbf{J}_2$, and \mathbf{F} is the driving forces of the electric cylinders.

2.2 Identification of Friction Parameters

In Eq. (4), the structure parameters, the mass and inertia parameters of the parallel hip joint simulator can be obtained directly, therefore, the values of $\mathbf{M}(\mathbf{q})$, $\mathbf{C}(\mathbf{q}, \dot{\mathbf{q}})$, $\mathbf{G}(\mathbf{q})$ and \mathbf{J} can be calculated, and only the friction parameters are unknown. Supposing that $\mathbf{D} = \mathbf{J}^{-1}[\mathbf{M}(\mathbf{q})\ddot{\mathbf{q}} + \mathbf{C}(\mathbf{q}, \dot{\mathbf{q}})\dot{\mathbf{q}} + \mathbf{G}(\mathbf{q})]$, and the measured driving forces of the three electric cylinders are $\mathbf{f}_a = [f_{a1}, f_{a2}, f_{a3}]^T$. Therefore, Eq. (4) can be rewritten as follows:

$$\mathbf{D} - \mathbf{M}_f = \mathbf{f}_a. \quad (5)$$

To estimate the friction parameters in Eq. (5), an optimization function J_m can be defined, as follows:

$$\min J_m = \sum_{j=1}^n \sum_{k=1}^3 (f_{ak}^j - D_k^j + M_{fk}^j)^2. \quad (6)$$

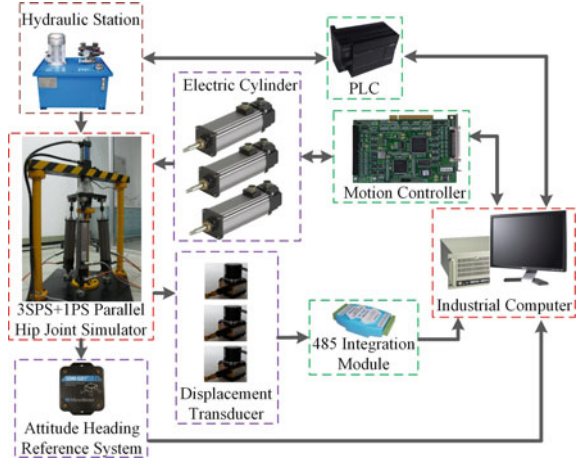
where n denote the number of the sample, for example, f_{ak}^j means the driving force of the k th electric cylinder at the j th sampling point; $\mathbf{D} = [D_1, D_2, D_3]^T$, and $\mathbf{M}_f = [M_{f1}, M_{f2}, M_{f3}]^T$.

In Eq. (6), the parameters μ_h , f_{vh} , μ_t and f_{vt} are selected as the optimization variables, and they are estimated by making the optimization function J_m minimum. The parameter optimization procedures are programmed with MATLAB, and an optimization function, which is named *fmincon*, is adopted.

2.3 Identification Experiment

With regard to the prototype of the parallel hip joint simulator, the product type of the electric cylinder is GSM 30 produced by Exlar, and the product type of the

Fig. 2 Control system diagram of the parallel hip joint simulator



servo driver is S300 produced by Kollmorgen. The control system of the parallel hip joint simulator is mainly composed of an industrial computer (IPC-610H), a motion controller (GTS-400), 3 displacement transducers (CESI-S1000P), and 1 attitude heading reference systems (3DM-GX1). The attitude heading reference system, which is fixed on the moving platform, is used to measure the spatial pose of the moving platform. The inverse kinematic model of the parallel hip joint simulator is solved by the software which is installed on the industrial computer. The industrial computer is applied to send control signal to the motion controller, and receive the information from the displacement transducer and the attitude heading reference system. The loading force from the hydraulic cylinder is controlled by a PLC (S7-200). The control system diagram of the parallel simulator is shown in Fig. 2.

The main parameters of the parallel hip joint simulator are shown in Table 1.

To estimate the friction parameters of the parallel hip joint simulator, a motion trajectory of the moving platform is selected, which is shown in Eq. (7), and the loading force from the hydraulic cylinder is 300 N.

$$\begin{cases} \alpha = 10t^2 \\ \beta = 10t^2 \\ \gamma = 20(1-t)^2 \end{cases} (0 \leq t \leq 1). \quad (7)$$

Identification results of the Coulomb + viscous friction model are shown in Table 2.

Table 1 Main parameters of the parallel hip joint simulator

Parameters/units	Values	Parameters/units	Values
Mass of the electric cylinder rod/kg	0.4	Gravitational acceleration/m/s ²	9.8
Mass of the electric cylinder body m_d /kg	3	Length of the electric cylinder rod/mm	300
Mass of the moving platform/kg	10	Length of the electric cylinder body/mm	400
Radius of the thrust ball bearing/mm	64	Radius of the hip joint/mm	15
Distance e /mm	144	Distance E /mm	200
Height of the intermediate branched-chain/mm	690	Mass of the spherical joint/kg	0.93
Inertia tensor of the moving platform/kg·mm ²	Diag(152140, 152270, 270970)	Inertia tensor of the spherical joint/kg·mm ²	Diag(107.5, 107.5, 107.5)
Inertia tensor of the electric cylinder rod/kg·mm ²	Diag(10843, 10842, 37.8)	Inertia tensor of the electric cylinder body/kg·mm ²	Diag(114370, 114460, 5664)

Table 2 Identification of the friction parameters

Parameters	Values	Parameters	Values
μ_h	0.124	μ_t	0.067
f_{vh}	9.35	f_{vt}	31.42

3 Controller Design and Trajectory Tracking Experiment

3.1 Controller Design

Computed torque, which is an application of feedback linearization of nonlinear systems, has gained popularity in modern systems theory. Computed torque control allows the design of considerably more precise, energy-efficient and compliant controls for parallel manipulators [11].

Based on Eq. (4), the control law of the computed torque control for the parallel hip joint simulator can be given as follows:

$$F = J^{-1} [M(q)(\ddot{q} + K_d \dot{e} + K_p e) + C(q, \dot{q})\dot{q} + G(q) - J^{-1} M_f]. \quad (8)$$

where $e = q - q_s$, q and q_s are the desired and real attitude angles of the moving platform; K_p and K_d are constant gain matrices.

Submitting Eq. (8) into Eq. (4), the error dynamics can be obtained, as follows:

$$M(q)(\ddot{e} + K_d \dot{e} + K_p e) = 0. \quad (9)$$

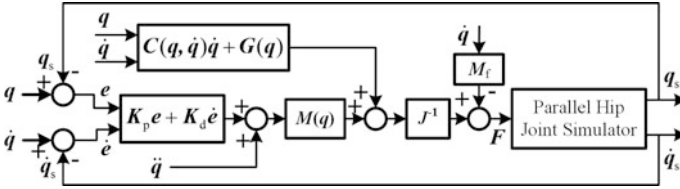


Fig. 3 Block diagram of the computed torque control

Since $M(q)$ is positive definite, therefore, the following express can be obtained:

$$\ddot{e} + K_d \dot{e} + K_p e = 0. \tag{10}$$

Because of K_p and K_d are positive definite, and the global asymptotic stability of equilibrium point is given by $(e, \dot{e}) = (0, 0)$.

The block diagram of the computed torque control for the parallel hip joint simulator can be presented in Fig. 3.

3.2 Trajectory Tracking Experiment

From ISO14242-1: 2002(E) [12], the operation frequency of the wear test machines for the hip joint prosthesis is $1 \text{ Hz} \pm 0.1 \text{ Hz}$ and the ranges of the AA (Abduction/Adduction), IER (Internal/External) and FE (Flexion/Extension) are $-4^\circ-7^\circ$, $-10^\circ-2^\circ$ and $-18^\circ-25^\circ$, respectively. In the paper, the X-axis, Y-axis and Z-axis are defined as the spin axes of AA, IER and FE, respectively, as shown in Fig. 4a. The loading force is shown in Fig. 4b.

In the trajectory tracking experiment, K_p and K_d are tuned and determined by the actual experiments. K_p and K_d are tuned as follows: $K_p = \text{diag}(15000, 7500,$

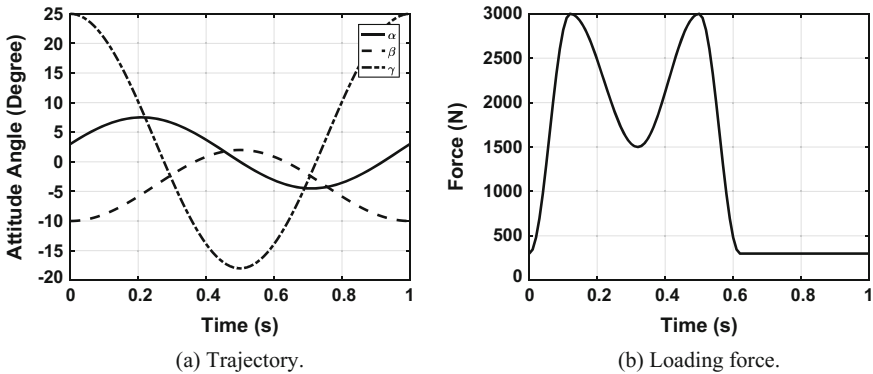


Fig. 4 Trajectory and loading force

20000), $\mathbf{K}_d = \text{diag}(150, 100, 150)$. In order to compare with the friction compensation control method, a controller, which is also based on the computed torque control method and without friction compensation, is designed.

Furthermore, root-square mean error of the trajectory tracking is used to evaluate the trajectory tracking performance of the moving platform [8].

$$RSME_w = \sqrt{\frac{1}{n} \sum_{j=1}^n [(\alpha_j - \alpha_{sj})^2 + (\beta_j - \beta_{sj})^2 + (\gamma_j - \gamma_{sj})^2]}. \quad (11)$$

where n is the number of sampling, and $(\gamma_j, \beta_j, \alpha_j)$ and $(\gamma_{sj}, \beta_{sj}, \alpha_{sj})$ are the desired and the real attitude angles of the moving platform at the j th sampling point.

The trajectory tracking errors of the moving platform are shown in Fig. 5.

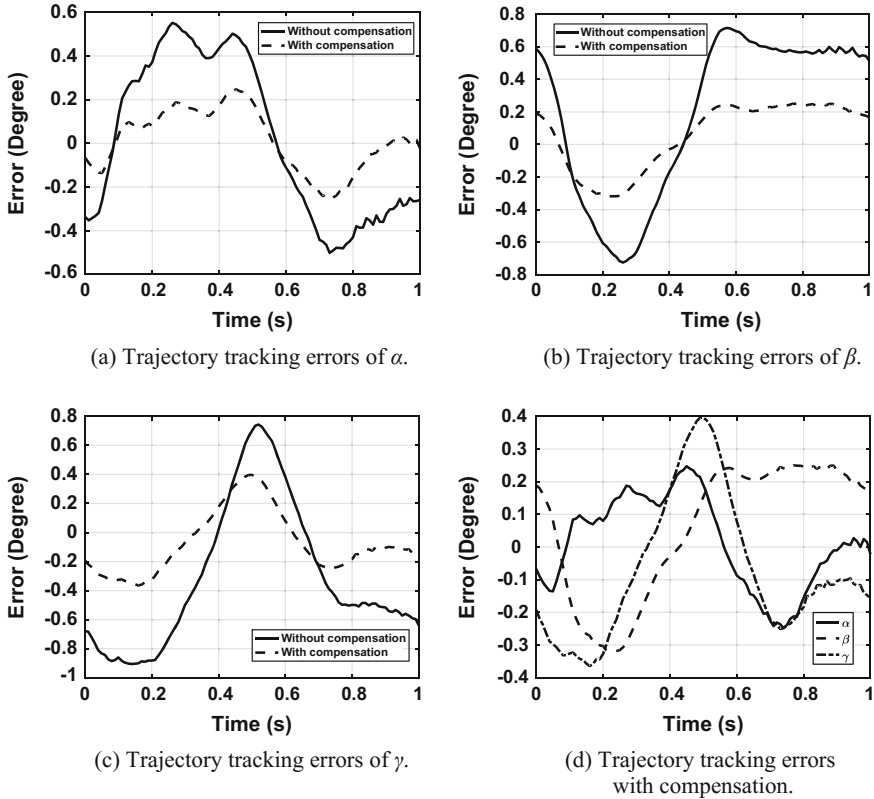


Fig. 5 trajectory tracking errors of the moving platform

As can be observed from Fig. 5, compared with the control method without friction compensation, the trajectory tracking accuracy of the moving platform is improved obviously. With the help of the friction compensation control method, the maximum errors of α , β and γ are decreased from 0.55° , 0.73° and 0.91° to 0.23° , 0.32° and 0.40° , respectively, and the RSMEs of the trajectory tracking errors are decreased from 0.87° to 0.34° . The results of the trajectory tracking experiments verify the effectiveness of the proposed friction compensation method.

4 Conclusions

In the paper, to improve the trajectory tracking accuracy of the parallel hip joint simulator, a friction compensation control method is proposed. Coulomb + viscous friction model is adopted to describe the friction of the hip joint and the thrust ball bearing, and then the dynamic model of the parallel hip joint simulator is established with the help of the Lagrange's Equations. To estimate the friction parameters, identification experiments are conducted, and the friction parameters are obtained through an optimization function. Subsequently, a friction compensation controller is designed based on the computed torque control method. At the last of the paper, trajectory tracking experiment is conducted. The experiment results show that the trajectory tracking accuracy of the moving platform is improved obviously, which verify the effectiveness of the proposed friction compensation control method.

Acknowledgments Financial support for this work provided by the National Natural Science Foundation of China (Grant No. 51275512), Natural Science Foundation of Jiangsu Province (Grant No. BK20141128), the Top-notch Academic Programs Project of Jiangsu Higher Education Institutions and the Priority Academic Program Development of Jiangsu Higher Education Institutions are gratefully acknowledged.

References

1. Cheng G, Shan XL (2012) Dynamics analysis of a parallel hip joint simulator with four degree of freedoms (3R1T). *Nonlinear Dynam* 70:2475–2486
2. Wu J, Wang JS, Wang LP, Li TM (2008) Dynamics and control of a planar 3-DOF parallel manipulator with actuation redundancy. *Mech Mach Theory* 44:835–849
3. Yang CF, Huang QT, Han JW (2012) computed force and velocity control for spatial multi-DOF electro-hydraulic parallel manipulator. *Mechatronics* 22:715–722
4. Linda O, Manic M (2011) Uncertainty-robust design of interval Type2 fuzzy logic controller for delta parallel robot. *IEEE T Ind Inform* 7:661–670
5. Dumlu A, Erenturk K (2014) Modeling and trajectory tracking control of 6-DOF RSS type parallel manipulator. *Robotica* 32:643–657
6. Wang XY, Pi YJ (2013) Trajectory tracking control of a hydraulic parallel robot manipulator with lumped disturbance observer. *Int J Robot Autom* 28:103–111

7. Cheung WF, Hung YS (2009) Robust learning control of a high precision planar parallel manipulator. *Mechatronics* 19:42–55
8. Shang WW, Cong S, Zhang YX (2008) Nonlinear friction compensation of a 2-DOF planar parallel manipulator. *Mechatronics* 18:340–346
9. Cazalilla J, Vallésa M, Matab V, Díaz-Rodríguezc M, Valeraa A (2014) Adaptive control of a 3-DOF parallel manipulator considering payload handling and relevant parameter models. *Robot Cim-Int Manuf* 30:468–477
10. Kim HS, Cho YM, Lee KL (2005) Robust nonlinear task space control for 6DOF parallel manipulator. *Automatica* 41:1591–1600
11. Kelly R, Davila VS, Loría A (2005) *Control of robot manipulators in joint space*. Springer, London
12. British Standards Institution: ISO 14242-1 (2002) *Implants for surgery-wear total hip-joint prostheses-part 1, loading and displacement parameters for wear testing machine and corresponding environmental conditions for test*. British Standards Institution, London

Sensitivity Analysis and Comparison of Parallel Schönflies-Motion Robots with a Single Platform

Guanglei Wu and Shaoping Bai

Abstract This paper deals with the sensitivity analysis of parallel Schönflies-motion robots. The influence of the kinematic parameters for the manipulator components, including the parallelogram, on the motion accuracy is studied. Sensitivity indices are defined to evaluate the influence of the geometric parameters to the manipulator end-effector. A comparative study is carried out for two robots to highlight their (dis)advantages.

Keywords Schönflies motion · Sensitivity · Variational method · Parallelogram

1 Introduction

Four-degree-of-freedom (4-DOF) parallel robots with Schönflies motion are intended for high-speed pick-and-place (PnP) operations serving light industries. Of the existing parallel Schönflies-motion robots [1–4], most of robots inherit the architecture from the Adept Quattro robot, which has a fully symmetrical base platform and four identical limbs as displayed in Fig. 1a. On the other hand, these robots' architecture determines a cylindrical workspace, whereas, the PnP trajectories are usually confined within a cuboid volume. To better utilize the shop-floor space, an asymmetrical robot [5, 6] as shown in Fig. 1b is developed, which admits a rectangular workspace suitable for PnP operations.

In designing parallel robots, a fundamental problem is that their performance heavily depends on their geometry. The variations in the geometric parameters of parallel robots can be either compensated or amplified, therefore, it is important to analyze the sensitivity of their end-effectors to variations in its geometric parameters.

G. Wu (✉)

School of Mechanical Engineering, Dalian University of Technology, Dalian, China
e-mail: gwu@dlut.edu.cn

G. Wu · S. Bai

Department of Mechanical and Manufacturing Engineering, Aalborg University,
9220 Aalborg, Denmark

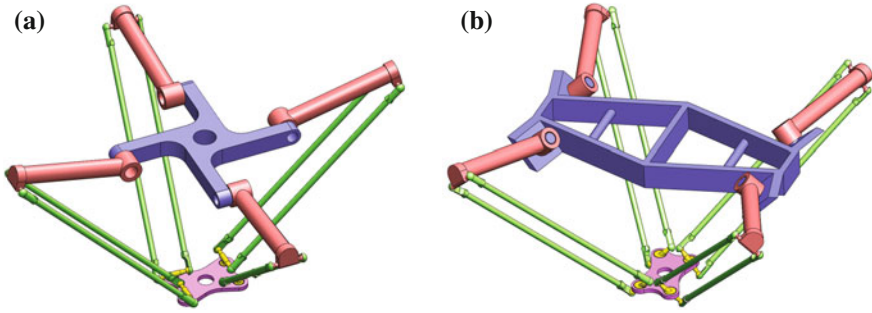


Fig. 1 The CAD models of 4-DOF **a** symmetrical and **b** asymmetrical robots

Up to date, a number of work concerning the effects of the manufacturing tolerances, geometric variations and joint clearances on the end-effector accuracy of different parallel manipulators have been reported [7–10]. Moreover, as the asymmetrical robot is based on the modified architecture of the Quattro robot, it is necessary to assess the robot performance beside the optimized workspace shape. Sensitivity analysis will be the focus in this work.

This paper deals with the sensitivity analysis of parallel Schönflies-motion robots to variations in their geometric parameters and actuated joints. The sensitivity coefficients of the end-effector pose to variations in the geometric parameters are derived by means of the variational method. Sensitivity indices are defined for the performance evaluation and comparison of two robot counterparts to highlight their (dis)advantages.

2 Geometric Model

The robot is composed of four identical $\underline{RR}\Pi RR^1$ -typed limbs which connect the base and the end-effector (EE). Different from the Quattro robot, the four motors of the asymmetrical robot are mounted at different orientations on the base frame, of which the actuating lines are not coplanar.

Figure 2 illustrates one limb of the asymmetrical robot. The global coordinate frame \mathcal{F}_b is built with the origin located at the geometric center of the base frame, of which the x -axis is parallel to segment A_2A_1 (A_3A_4). The moving coordinate frame \mathcal{F}_p is attached to the mobile platform and the origin is at the geometric center, where x -axis is parallel to segment C_2C_1 (C_3C_4). Here and after, vectors \mathbf{i} , \mathbf{j} and \mathbf{k} represent the unit vectors of x -, y - and z -axis, respectively. The orientation of

¹R and Π stand for revolute joint and parallelogram, respectively, and an underlined letter indicates an actuated joint.

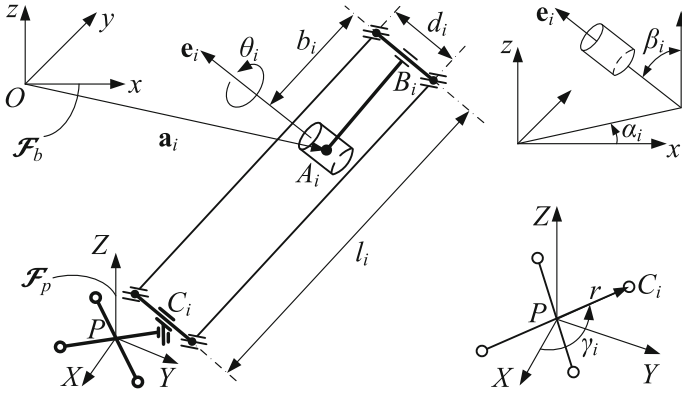


Fig. 2 Parameterizations of the i th kinematic leg of asymmetrical robot

the i th motor is described by its yaw angle α_i and pitch angle β_i , which means $\mathbf{e}_i = \mathbf{E}_i \mathbf{k}$, $\mathbf{E}_i = \mathbf{R}_z(\alpha_i) \mathbf{R}_y(\beta_i)$, and $-\alpha_{1(3)} = \alpha_{2(4)} = \alpha$, $-\beta_{1(4)} = \beta_{2(3)} = \beta$.

Under the coordinate systems in Fig. 2, the position vectors of point A_i in frame \mathcal{F}_b are denoted by

$$\mathbf{a}_1 = -\mathbf{a}_3 = [a_x \quad a_y \quad 0]^T; \quad \mathbf{a}_2 = -\mathbf{a}_4 = [-a_x \quad a_y \quad 0]^T \quad (1)$$

and the position vector of point B_i is derived as

$$\mathbf{b}_i = b \mathbf{h}_i + \mathbf{a}_i; \quad \mathbf{h}_i = \mathbf{R}_i \mathbf{i}, \quad i = 1, \dots, 4 \quad (2)$$

where $\mathbf{R}_i = \mathbf{E}_i \mathbf{R}_z(\theta_i)$, and θ_i is the angle of rotation of motor from a reference position.

Let the mobile platform pose be denoted by $\mathbf{x} = [\mathbf{p}^T \quad \phi]^T$, $\mathbf{p} = [x \quad y \quad z]^T$, the Cartesian coordinates of point C_i in frame \mathcal{F}_b are expressed as

$$\mathbf{c}_i = \mathbf{Q} \mathbf{c}'_i + \mathbf{p} \quad (3)$$

where $\mathbf{Q} = \mathbf{R}_z(\phi)$ is the EE rotation matrix and \mathbf{c}'_i is the position vector of C_i in the frame \mathcal{F}_p :

$$\mathbf{c}'_i = r [\cos \gamma_i \quad \sin \gamma_i \quad 0]^T; \quad \gamma_1 = -\gamma_4 = \gamma, \quad \gamma_{2(3)} = \pi \mp \gamma \quad (4)$$

3 Kinematic Sensitivity Analysis

We first develop a sensitivity model by means of variational method, which is applicable to the Delta robot and Quattro architecture based robots. Here, the i th limb of the robot can be split to depict the variations in the design parameters in a vectorial form. The closed-loop kinematic chains is described by $O-A_i-B_i-B_{ij}-C_{ij}-C_i-P$, $i = 1, \dots, 4, j = 1, 2$. Vectors \mathbf{o} , \mathbf{a}_i , \mathbf{b}_i , \mathbf{b}_{ij} , \mathbf{c}_{ij} , \mathbf{c}_i , \mathbf{p} , are the Cartesian coordinates of points O , A_i , B_i , B_{ij} , C_{ij} , C_i , P in the frame \mathcal{F}_b , respectively.

According to Fig. 3,

$$\mathbf{a}_i - \mathbf{o} = \mathbf{a}_{0i} + \delta\mathbf{a}_i \tag{5}$$

where \mathbf{a}_{0i} is the nominal position vector of A_i with respect to O in the frame \mathcal{F}_b and $\delta\mathbf{a}_i$ is the positioning error of A_i .

According to Fig. 4,

$$\mathbf{b}_i - \mathbf{a}_i = (b_i + \delta b_i)\mathbf{Q}_{A_i}\mathbf{i} \tag{6}$$

with [11]

$$\mathbf{Q}_{A_i} = (\mathbf{I} + [\delta\boldsymbol{\varphi}_i])\mathbf{E}_i(\mathbf{I} + [\delta\boldsymbol{\psi}_{A_i}])\mathbf{R}_z(\theta_i)(\mathbf{I} + \delta\theta_i[\mathbf{k}]) \tag{7}$$

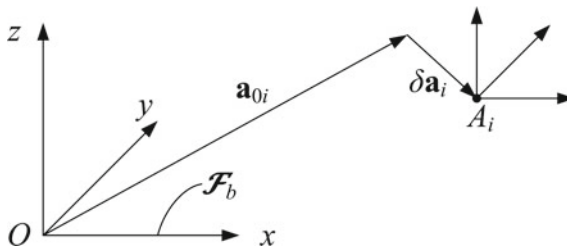


Fig. 3 Variations in $O-A_i$ chain

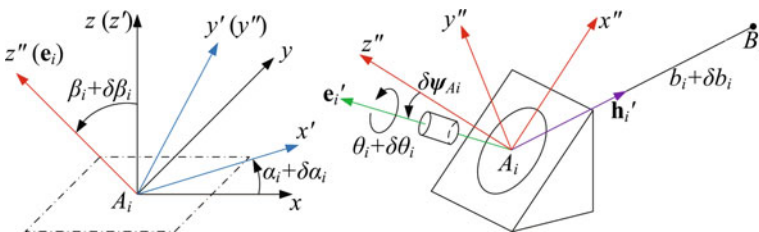


Fig. 4 Variations in A_i-B_i chain

where $[\cdot] = \text{CPM}(\cdot)$ denotes the cross-product matrix (CPM) and \mathbf{I} is the 3×3 identity matrix. Term δb_i is the variation in b_i , and $\delta \boldsymbol{\varphi}_i = [0 \quad \delta \beta_i \quad \delta \alpha_i]^T$, $\delta \alpha_i$ and $\delta \beta_i$ being the variations in α_i and β_i , respectively. Moreover, $\delta \theta_i$ is the error of input angle θ_i of the i th actuator and $\delta \boldsymbol{\psi}_{A_i} = [\delta \psi_{A_{ix}} \quad \delta \psi_{A_{iy}} \quad \delta \psi_{A_{iz}}]^T$ being the angular variation of manufacturing tolerance [11].

According to Fig. 5,

$$\mathbf{b}_{ij} - \mathbf{b}_i = \varepsilon(j)(d_i/2 + \delta d_{ij})(\mathbf{I} + [\delta \boldsymbol{\psi}_{B_{ij}}])\mathbf{Q}_{A_i}\mathbf{k}; \varepsilon(j) = \begin{cases} 1, & j = 1 \\ -1, & j = 2 \end{cases} \quad (8)$$

where $\delta \boldsymbol{\psi}_{B_{ij}} = [\delta \psi_{B_{ix}} \quad \delta \psi_{B_{iy}} \quad \delta \psi_{B_{iz}}]^T$ is the orientation error of link $B_i B_{ij}$ with respect to \mathbf{e}'_i , and δd_{ij} is the variation of d_i in the j th direction.

According to Fig. 6,

$$\mathbf{c}_{ij} - \mathbf{b}_i = l_i \mathbf{w}_i + \delta l_{ij} \mathbf{w}_i + l_i \delta \mathbf{w}_{ij} \quad (9)$$

where δl_{ij} is the variation in the length of link $B_{ij} C_{ij}$ along the direction \mathbf{w}_i , and $\delta \mathbf{w}_{ij}$ is the variation in this direction, orthogonal to \mathbf{w}_i .

Let assume all four axes of the four holes of the EE plate parallel to Z-axis. According to Fig. 7,

$$\mathbf{c}_{ij} - \mathbf{c}_i = (\mathbf{I} + \delta \phi_{C_i}[\mathbf{k}])\varepsilon(j)(d_i/2 + \delta c_{ij})(\mathbf{I} + [\delta \boldsymbol{\psi}_{C_i}])\mathbf{e}_i \quad (10)$$

Fig. 5 Variations in B_i – B_{ij}

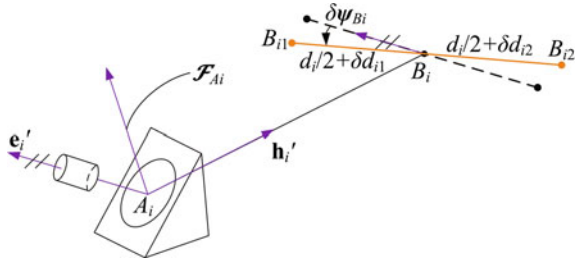


Fig. 6 Variations in B_{ij} – C_{ij} chain

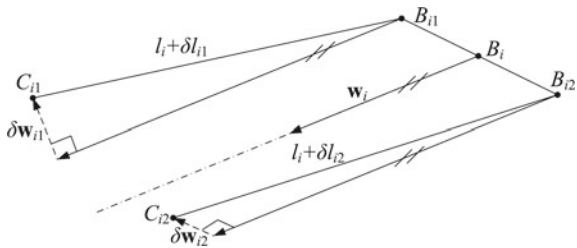
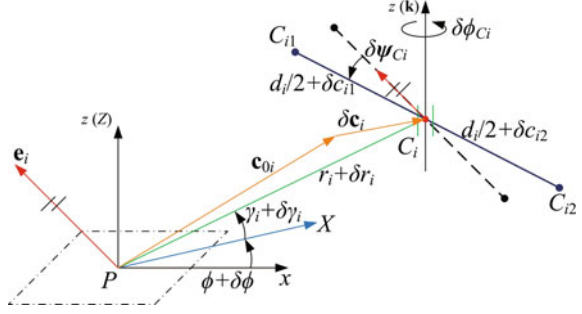


Fig. 7 Variations in C_{ij} – C_i – P chain



where $\delta\psi_{C_{ij}} = [\delta\psi_{C_{ix}} \quad \delta\psi_{C_{iy}} \quad \delta\psi_{C_{iz}}]^T$ is the orientation error of link C_iC_{ij} with respect to \mathbf{e}_i , and $\delta\phi_{C_i}$ is the angular displacement of the i th passive revolute joint on the end-effector. Moreover, from Fig. 7,

$$\mathbf{c}_i - \mathbf{p} = (r_i + \delta r_i) \mathbf{R}_z(\phi + \gamma_i) (\mathbf{I} + \delta\phi[\mathbf{k}] + \delta\gamma_i[\mathbf{k}]) \mathbf{i} \quad (11)$$

Equations (5), (6), (8)–(10) and (11) can be linearized by ignoring the high-order small terms. Afterwards, removing the nominal kinematic constraint equation $\mathbf{p}_0 = \mathbf{a}_0i + b_i\mathbf{h}_i + l_i\mathbf{w}_i - \mathbf{c}_0i$ leads to

$$\begin{aligned} \delta\mathbf{p} = \mathbf{p} - \mathbf{p}_0 &= \delta\theta_i b_i \mathbf{R} \mathbf{j} + \delta\mathbf{a}_i + \delta\alpha_i b_i [\mathbf{k}] \mathbf{R} \mathbf{i} + \delta b_i \mathbf{h}_i + \delta\beta_i b_i \cos\theta_i \mathbf{e}_i \\ &\quad - b_i \mathbf{E}_i [\mathbf{R}_z(\theta_i) \mathbf{i}] \delta\psi_{A_i} + \delta\beta_i \varepsilon(j) d_i / 2 \mathbf{E}_i \mathbf{i} - \varepsilon(j) d_i / 2 \mathbf{E}_i [\mathbf{k}] \delta\psi_{A_i} \\ &\quad + \varepsilon(j) \delta s_{ij} \mathbf{e}_i - \varepsilon(j) d_i / 2 [\mathbf{e}_i] \delta \mathbf{y}_{di} + \delta l_{ij} \mathbf{w}_i + l_{ij} \delta \mathbf{w}_{ij} \\ &\quad - \delta\phi_{C_i} \varepsilon(j) d / 2 [\mathbf{k}] \mathbf{e}_i - \mathbf{R}_z(\phi + \gamma_i) (\delta r_i \mathbf{i} + \delta\phi r_i \mathbf{j} + \delta\gamma_i r_i \mathbf{j}) \end{aligned} \quad (12)$$

where $\delta s_{ij} = \delta d_{ij} - \delta c_{ij}$ and $\delta\psi_{di} = \delta\psi_{B_i} - \delta\psi_{C_i}$ are the relative length and orientation errors of links $\overline{B_{ij}B_i}$ and $\overline{C_{ij}C_i}$ with respect to \mathbf{e}_i , respectively. By addition of Eq. (12) written for $j = 1$ and $j = 2$, the relationship between the pose errors and geometric/joint variations of the i th limb is expressed as

$$\begin{aligned} \delta\mathbf{p} &= \delta\theta_i b_i \mathbf{R} \mathbf{j} + \delta\mathbf{a}_i + \delta\alpha_i b_i [\mathbf{k}] \mathbf{R} \mathbf{i} + \delta b_i \mathbf{h}_i + \delta\beta_i b_i c\theta_i \mathbf{e}_i \\ &\quad - b_i \mathbf{E}_i [\mathbf{R}_z(\theta_i) \mathbf{i}] \delta\psi_{A_i} + \delta d_i \mathbf{e}_i + l_i / 2 (\delta \mathbf{w}_{i1} + \delta \mathbf{w}_{i2}) \\ &\quad + \delta l_i \mathbf{w}_i - \mathbf{R}_z(\phi + \gamma_i) (\delta r_i \mathbf{i} + \delta\phi r_i \mathbf{j} + \delta\gamma_i r_i \mathbf{j}) \end{aligned} \quad (13)$$

where $\delta l_i = (\delta l_{i1} + \delta l_{i2}) / 2$ is the mean of relative length error of links $\overline{B_{i1}C_{i1}}$ and $\overline{B_{i2}C_{i2}}$, $\delta d_i = (\delta s_{i1} - \delta s_{i2}) / 2$ is the mean of the relative length error of the connecting bars $\overline{B_{i1}B_{i2}}$ and $\overline{C_{i1}C_{i2}}$ in the parallelogram.

Dot-multiplying to Eq. (13) on both sides with \mathbf{w}_i yields

$$\begin{aligned} \mathbf{w}_i^T \delta \mathbf{p} = & j_{\theta i} \delta \theta_i + \mathbf{j}_{ai} \delta \mathbf{a}_i + j_{zi} \delta \alpha_i + j_{\beta i} \delta \beta_i + j_{bi} \delta b_i + \mathbf{j}_{Ai} \delta \psi_{Ai} + j_{di} \delta d_i \\ & + \delta l_i + j_{ri} \delta r_i + j_{\gamma i} \delta \gamma_i - \delta \phi r_i \mathbf{w}_i^T \mathbf{R}_z(\phi + \gamma_i) \mathbf{j} \end{aligned} \quad (14)$$

with

$$\begin{aligned} j_{\theta i} = & b_i \mathbf{w}_i^T \mathbf{R} \mathbf{j}; \quad \mathbf{j}_{ai} = \mathbf{w}_i^T; \quad j_{zi} = \mathbf{w}_i^T [\mathbf{k}] \mathbf{R} \mathbf{i} \\ j_{\beta i} = & b_i c \theta_i \mathbf{w}_i^T \mathbf{e}_i; \quad j_{bi} = \mathbf{w}_i^T \mathbf{h}_i; \quad \mathbf{j}_{Ai} = -b_i \mathbf{w}_i^T \mathbf{E}_i [\mathbf{R}_z(\theta_i) \mathbf{i}] \\ j_{di} = & \mathbf{w}_i^T \mathbf{e}_i; \quad j_{ri} = -\mathbf{w}_i^T \mathbf{R}_z(\phi + \gamma_i) \mathbf{i}; \quad j_{\gamma i} = -r_i \mathbf{w}_i^T \mathbf{R}_z(\phi + \gamma_i) \mathbf{j} \end{aligned} \quad (15)$$

Equation (14) can be rewritten in a vector form, namely,

$$\mathbf{J}_{xi} \delta \mathbf{x} = \mathbf{J}_{qi} \epsilon_{qi} \quad (16)$$

with

$$\mathbf{J}_{xi} = [\mathbf{w}_i^T \quad r_i \mathbf{w}_i^T \mathbf{R}_z(\phi + \gamma_i) \mathbf{j}] \quad (17)$$

$$\mathbf{J}_{qi} = [j_{\theta i} \quad \mathbf{j}_{ai} \quad j_{zi} \quad j_{\beta i} \quad j_{bi} \quad \mathbf{j}_{Ai} \quad j_{di} \quad 1 \quad \mathbf{j}_{Ci}] \quad (18)$$

where $\epsilon_{qi} = [\delta \theta_i, \delta \mathbf{a}_i^T, \delta \alpha_i, \delta \beta_i, \delta b_i, \delta \mathbf{y}_{Ai}^T, \delta d_i, \delta l_i, \delta c_i^T]^T$, and $\mathbf{j}_{Ci} = [j_{ri} \quad j_{\gamma i}] \mathbf{R}_{Ci}^{-1}$, \mathbf{R}_{Ci} and δc_i being defined as below

$$\begin{bmatrix} \delta c_{iX} \\ \delta c_{iY} \end{bmatrix} = \begin{bmatrix} \cos \gamma_i & -r_i \sin \gamma_i \\ \sin \gamma_i & r_i \cos \gamma_i \end{bmatrix} \begin{bmatrix} \delta r_i \\ \delta \gamma_i \end{bmatrix} \quad \text{or} \quad \delta \mathbf{c}_i = \mathbf{R}_{Ci} \begin{bmatrix} \delta r_i \\ \delta \gamma_i \end{bmatrix} \quad (19)$$

It is noted that δc_{iX} and δc_{iY} are the positioning errors of point C_i along X - and Y -axis, respectively, namely, the variations in the Cartesian coordinates of C_i in frame \mathcal{F}_p . Equations (16) can be written in a matrix form, namely,

$$\mathbf{J}_x \delta \mathbf{x} = \mathbf{J}_q \epsilon_q \quad (20)$$

with

$$\mathbf{J}_x = [\mathbf{J}_{x1}^T \quad \mathbf{J}_{x2}^T \quad \mathbf{J}_{x3}^T \quad \mathbf{J}_{x4}^T]^T \in \mathbb{R}^{4 \times 4} \quad (21a)$$

$$\mathbf{J}_q = \text{diag}[\mathbf{J}_{q1} \quad \mathbf{J}_{q1} \quad \mathbf{J}_{q3} \quad \mathbf{J}_{q4}] \in \mathbb{R}^{4 \times 56} \quad (21b)$$

$$\delta \mathbf{q} = [\delta \mathbf{q}_1^T \quad \delta \mathbf{q}_2^T \quad \delta \mathbf{q}_3^T \quad \delta \mathbf{q}_4^T]^T \in \mathbb{R}^{56 \times 1} \quad (21c)$$

As long as \mathbf{J}_x is not singular, the sensitivity matrix \mathbf{J} is obtained below

$$\delta \mathbf{x} = \mathbf{J} \boldsymbol{\epsilon}_q; \quad \mathbf{J} = \mathbf{J}_x^{-1} \mathbf{J}_q = \begin{bmatrix} \mathbf{J}_p \\ \mathbf{j}_\phi \end{bmatrix} \quad (22)$$

The sensitivity index of the EE pose to the variations in the k th design parameter of the same type, which is responsible for its pose error, i.e., $\delta \mathbf{q}_{(1,2,3,4)k}$, is defined by $\mu_{\lambda,k}$ below [11]:

$$\mu_{\lambda,k} = \sqrt{\sum_{i=1}^4 \sum_{n=1}^4 J_{in\lambda}^2}; \quad k = 1, \dots, 14, \quad \lambda \in \{x, y, z, \phi\} \quad (23)$$

where $J_{in\lambda}$ is the element in \mathbf{J} located in i th column and n th row. Hence, the sensitivity index of positioning error $\|\delta \mathbf{p}\|$ to the k th parameter is defined as:

$$\mu_k = \sqrt{\mu_{x,k}^2 + \mu_{y,k}^2 + \mu_{z,k}^2} \quad (24)$$

In order to evaluate the sensitivity globally, two aggregate sensitivity indices [11] of the position and orientation of the manipulator end-effector to variations in its geometric parameters and actuated joints are defined from Eq. (22), expressed as:

$$v_p = \frac{\|\mathbf{J}_p\|_2}{n_q}; \quad v_\phi = \frac{\|\mathbf{j}_\phi\|_2}{n_q} \quad (25)$$

where $\|\cdot\|$ denotes the 2-norm, and n_q is the number of variations that are considered. The smaller v_p and v_ϕ , the smaller the aggregate sensitivity of the EE pose of the manipulators to variations in its geometric parameters.

4 Numerical Analysis and Discussion

The sensitivity analysis is numerically illustrated with the asymmetrical robot in comparison with the symmetrical counterpart, for which the design parameters are given in Table 1, the length and angle being in the units of mm and $^\circ$, respectively. In order to approximate the maximum regular workspace, a super-ellipsoid is adopted to describe the workspace (WS), which can contain different shaped cuboid

Table 1 Geometric design parameters of the robots

	a_x	a_y	α	β	b	l	r	γ	d
Asymmetrical [5]	310	109	15	45	295	536	103	30	100
Symmetrical [4]	162.3	162.3	45	90	292.5	526.5	153	60	100

WS. The corresponding workspace with the rotation range of $\pm 45^\circ$ are shown in Fig. 8, from which it is seen that the asymmetrical robot admits a long and narrow workspace coincident with the PnP trajectory.

Figure 9 depicts the mean of the sensitivity coefficients of \mathbf{p} and ϕ with respect to the nominal geometric parameters throughout the workspace, defined by Eqs. (23) and (24), respectively. Due to the large link lengths, the position and orientation of the end-effector of the asymmetrical robot are very sensitive to the angular variations, particularly the actuated joints. Besides, contrary to orientation, the EE position is sensitive to the position of points A_i , variations in the lengths of

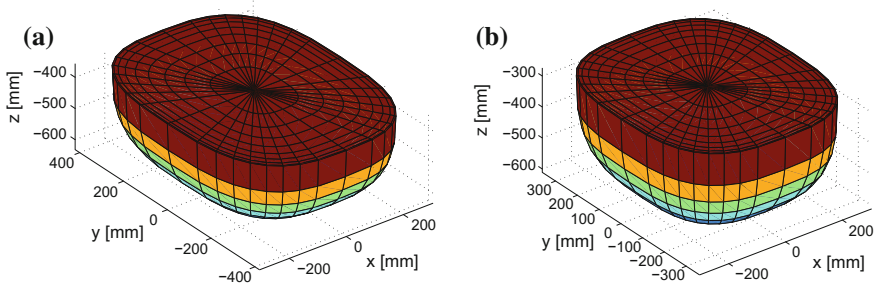
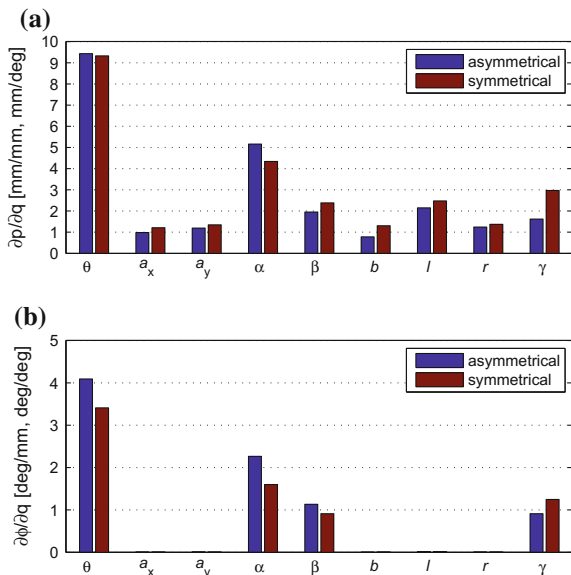


Fig. 8 Super-ellipsoidal workspace of the robots: **a** asymmetrical; **b** symmetrical

Fig. 9 Mean of sensitivity indices of \mathbf{p} and ϕ with respect to the nominal geometric parameters throughout the super-ellipsoidal workspace: **a** μ_p ; **b** μ_ϕ



the inner and outer arms b and l , and variation in the radius r of the mobile platform.

Due to the similar linkages, the sensitivity of EE pose of the symmetrical robot to the actuated joints and geometric parameters is similar to that of the asymmetrical one. Compared to the former, the pose of the symmetrical robot is less sensitive to the actuated joints and angle α . By contrast, the orientation of the asymmetrical robot is more sensitive to the variations, while the position of the symmetrical is more sensitive to the variations.

Aiming to carry out a comparative study between the asymmetrical and symmetrical robots, the sensitivity indices in Eq. (25) and pose errors are compared within a cuboid WS of $400 \times 600 \times 220 \text{ mm}^3$. In order to compare the sensitivity with respect to the workspace, the geometric parameters a_x , a_y , b , l , r and d are normalized by a normalizing factor [12] defined as

$$N_f = \left(\sqrt{a_x^2 + a_y^2} + r \right) / 2 \quad (26)$$

The isocontours of mean of the indices v_p and v_ϕ defined by Eq. (25) over the WS bottom cross-section of asymmetrical and symmetrical robots are displayed in Fig. 10. We can notice that the closer EE location to the central region of the workspace, the smaller the sensitivity of the MP pose to variations in the geometric parameters and active joints.

From Fig. 10a, it is seen that the indices corresponding to position of the asymmetrical robot is bounded between 0.1 and 0.15, which means that the asymmetrical robot admits a rectangular area with lower sensitivity indices evenly distributed. Figure 10b shows that the sensitivity indices associated with the orientation of the asymmetrical robot has close values along y -axis, particularly in the region of $|x| < 100 \text{ mm}$. Both the maximum values of v_p and v_ϕ occur at the WS corners.

Contrary to asymmetrical, the symmetrical robot has larger v_p but smaller v_ϕ at most workspace points, i.e., the position of the symmetrical robot is much more sensitive to the variations while its orientation is not so sensitive, which agrees with the results given in Figs. 9, 11 and Table 2.

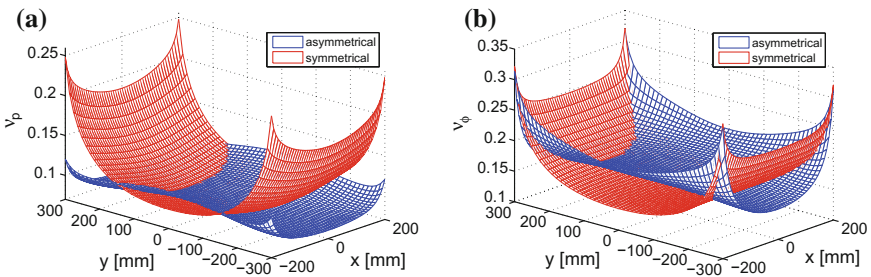


Fig. 10 Isocontours of the global sensitivity indices: **a** v_p ; **b** v_ϕ

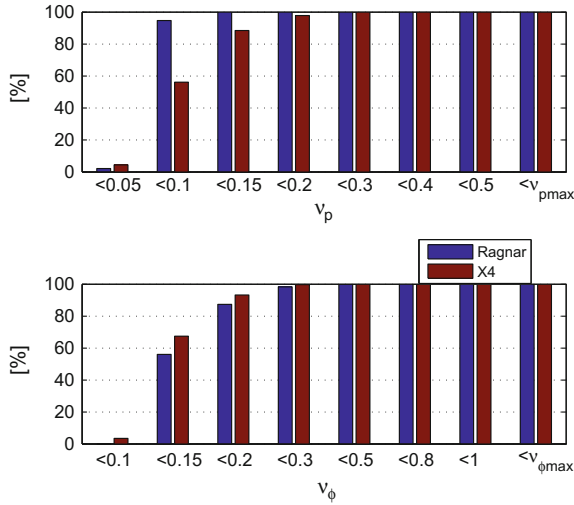


Fig. 11 Distributions of v_p and v_ϕ throughout the cuboid WS

Table 2 Maximum and mean values of sensitivity indices v_p and v_ϕ

	$v_{p,max}$	$v_{p,mean}$	$v_{\phi,max}$	$v_{\phi,mean}$
Asymmetrical	0.2194	0.0737	1.2260	0.1575
Symmetrical	0.5924	0.1006	0.9766	0.1415

Moreover, Eq. (22) can be used to compute the pose errors of the end-effector with known variations in design parameters. For instance, let the linear and angular tolerance be 0.02mm and 0.03°, respectively, the maximum pose errors of the asymmetrical and symmetrical robots throughout the workspace are visualized in Fig. 12. The error distributions are consistent with the isocontours of the sensitivity

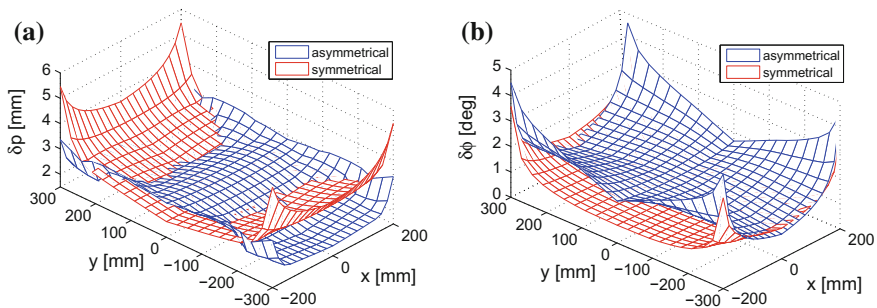


Fig. 12 Error comparison throughout the cuboid WS: **a** $\|\delta p\|_2$; **b** $\delta\phi$

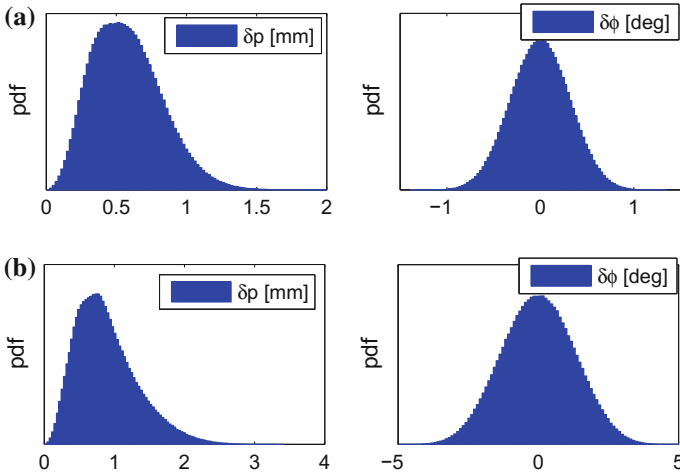


Fig. 13 Repartition of the pose errors of the asymmetrical robot with $\phi = \pi/4$: **a** $\mathbf{p} = [0, 0, -576]$; **b** $\mathbf{p} = [-200, -300, -576]$

indices in Fig. 10. It is noted that the asymmetrical robot has relatively higher positioning accuracy and lower orientation accuracy but acceptable for food handling industry that does not require very high accuracy. Moreover, the maximum pose errors of the two robots appear at the four corners on the bottom surface of the WS, where PnP motions rarely take place in these regions. The probability density function (pdf) of the pose errors of the asymmetrical robot at the center and corner on the bottom cross-section are shown in Fig. 13, respectively. Based on the previous analysis, the architecture of the asymmetrical robot still allows relatively better operational accuracy, particularly on the positioning accuracy, and outperforms the Quattro based robots in term of workspace shape and mounting space to better utilize the shop-floor space, leading to a more compact robot system in the production line.

5 Conclusions

This paper deals with the sensitivity analysis and comparison of two parallel Schönflies-motion robots with a single platform. The variational method was adopted to investigate the influence of the linear and angular variations in the manipulator components on the position and orientation of its end-effector as well as the nominal parameters. The position and orientation of the robots' end-effectors are very sensitive to variations in the angular parameters, particularly the actuated revolute joints. Based on two aggregate sensitivity indices, a comparative study

between the two robots was carried out, and the comparison shows that the asymmetrical robot still has relatively better kinematic performance.

Acknowledgments The support from Innovation Fund Denmark under the grant No. 137-2014-5 is greatly appreciated.

References

1. Krut S, Nabat V, Company O, Pierrot F (2004) A high-speed parallel robot for SCARA motions. *IEEE Int Conf Robot Autom* 4:4109–4115
2. Pierrot F, Nabat V, Company O, Krut S, Poignet P (2009) Optimal design of a 4-dof parallel manipulator: from academia to industry. *IEEE Trans Robot* 25(2):213–224
3. Altuzarra O, Şandru B, Pinto C, Petuya V (2011) A symmetric parallel Schönflies-motion manipulator for pick-and-place operations. *Robotica* 29:853–862
4. Xie F, Liu X (2015) Design and development of a high-speed and high-rotation robot with four identical arms and a single platform. *ASME J Mech Robot* 7(4):041015
5. Wu G, Bai S, Hjørnet P (2015) Parametric optimal design of a parallel Schönflies-motion robot under pick-and-place trajectory constraints. In: *IEEE/RSJ International Conference on Intelligent Robots and Systems (IROS)*, Hamburg, Germany, pp 3158–3163
6. Wu G, Bai S, Hjørnet P (2016) On the stiffness of three/four degree-of-freedom parallel pick-and-place robots with four identical limbs. In: *IEEE International Conference on Robotics and Automation*, Stockholm, Sweden, pp 861–866
7. Wang J, Masory O (1993) On the accuracy of a Stewart platform—part I, The effect of manufacturing tolerances. In: *IEEE International Conference on Robotics and Automation*, vol 1
8. Kim HS, Tsai LW (2003) Design optimization of a Cartesian parallel manipulator. *ASME J Mech Des* 125(1):43–51
9. Caro S, Binaud N, Wenger P (2009) Sensitivity analysis of 3-RPR planar parallel manipulators. *ASME J Mech Des* 131(12):121005
10. Wu G, Bai S, Kepler J, Caro S (2012) Error modeling and experimental validation of a planar 3-PPR parallel manipulator with joint clearances. *ASME J Mech Robot* 4(4):041008
11. Caro S, Wenger P, Bennis F, Chablat D (2006) Sensitivity analysis of the Orthoglide: a three-dof translational parallel kinematic machine. *ASME J Mech Des* 128(2):392–402
12. Liu XJ, Wang J, Pritschow G (2006) On the optimal kinematic design of the PRRRP 2-DOF parallel mechanism. *Mech Mach Theory* 41(9):1111–1130

Perception-Based Gait Planning for a Hexapod Robot Walking on Typical Structured Terrain

Xun Chai, Feng Gao and Yilin Xu

Abstract Legged robots have excellent terrain adaptability and can be used to accomplish rescuing and detecting tasks instead of human beings in harsh environment. This paper presents a framework developed to increase the autonomy and versatility of a hexapod robot. It combines terrain perception with four locomotion strategies, a flat-floor gait, a step-on gait, a step-down gait and a ditch-over gait. This way the robot can perceive the environment and distinguish four typical structured terrain, flat-floor step-on, step-down and ditch. Based on different terrain, the appropriate locomotion strategy is selected to be carried out. The terrain perception and the gait selection are performed autonomously. We present experiment trials of the Hexapod-III robot walking in structured environment including the flat-floor, step-on, step-down and ditch. The experiment results show that the robot has the ability to distinguish four typical structured terrain and pass through them autonomously.

Keywords Gait planning · Hexapod robot · Terrain perception

1 Introduction

In recent years, Fukushima nuclear power plant accident and other natural disasters like earthquakes, mudslides have prompted relevant research domains' awareness of importance and necessity of rescue robots. Compared with wheeled/tracked robots, legged robots only need some discrete footholds for locomotion on the

X. Chai · F. Gao (✉) · Y. Xu
State Key Laboratory of Mechanical System and Vibration, Shanghai
Jiao Tong University, Shanghai, China
e-mail: fengg@sjtu.edu.cn

X. Chai
e-mail: chaixun@sjtu.edu.cn

Y. Xu
e-mail: xuyilin@sjtu.edu.cn

ground, which makes legged robots more suitably operate in complex and rugged environments. In last few years, many legged robots are designed. Generally legged robots can be classified into three categories, biped robots, quadruped robots and hexapod robots. For the famous biped robots, see Petman [1], Atlas [2], ASIMO [3]. For the famous quadruped robots, see BigDog [4], HyQ [5], SILO4 [6]. For the famous hexapod robots, see Ambler [7], Athlete [8], DLR Crawler [9], RHex [10]. The number, the mechanism and the layout of legs need well-designed in order to satisfy the requirements of stability, load capacity, walking velocity, DOFS and control.

In structured environments, legged robots need to build terrain map with the help of necessary vision sensors mounted on them. Then legged robots can plan the gait to adapt various terrain based on the terrain map. Some studies have concerned about terrain adaption for legged robots. Matt zucker and Nathan Ratliff [11] presented a novel optimization method for a quadruped robot, which can walk on challenge terrains. Their method plans a set of footholds and dynamic body motions by thoroughly rooting in optimization. Estremera and Cobano [12] proposed a continuous free-crab gait planning method for a six-legged robot. Their method derived three control modules relying on two heuristic empirical rules. They [13] also presented a method to generate continuous free crab gaits for the quadruped robots on rough terrains. Their experimental results showed the SILO4 quadruped robot could perform stable and omnidirectional locomotion on rough terrains. Hoepflinger and Hutter [14] introduced a method to evaluate and estimate the mechanical robustness of footholds for legged robots in irregular terrain without using the human expert knowledge or human defined criteria. Haynes and Rizzi [15] developed a robust method allowing the specification, control and transition of the stepping pattern for a six-legged robot. Their method generated gaits by merging through controllers that imposed appropriately placed repellers and the torus of relative leg phases.

In this paper, a perception-based walking strategy for the Hexapod-III robot on typical structured terrain is presented. The structure of this paper is organized as follows. In Sect. 2, the system overview and the problem formulation are introduced briefly. Processes of terrain map modeling and structured terrain classifying are described in Sect. 3. In Sect. 4, walking strategies for four typical structured terrain are presented in detail. Motion planning for the legged robot is discussed in Sect. 5. The experimental results are presented in Sect. 6. Section 7 summarizes and concludes the paper.

2 System Overview and Problem Formulation

As Fig. 1 shows, the six-legged robot is called Hexapod-III, which has six legs symmetrically arranged around the body. Its leg is a parallel mechanism having three chains, two of which are constructed by the universal joint, prismatic joint and spherical joint, the other one is constructed by the universal joint and prismatic

Fig. 1 The Hexapod-III robot



joint. The linear movement of the prismatic joint is achieved by ball-bearing screw which is actuated by the motor. The control unit is an industrial computer running real-time Linux, which sends planned data to drivers via EtherCAT. The robot is equipped with a stereo camera, a six-axis force/torque sensor and an IMU.

As Fig. 2a shows, the robot has 18 inputs ($q_i, i = 1-18$), which are the prismatic positions. It has 24 outputs, 18 of which are the feet positions ($x_{F_i}, y_{F_i}, z_{F_i}, i = 1-6$), the other six outputs are the positions and orientations of the body ($x_B, y_B, z_B, \alpha_B, \beta_B, \gamma_B$).

During walking, four coordinate systems, the ground O_G , the stereo camera O_C , the body O_B and the foot O_F , exist all the time. Three transformation relationships T_C^R, T_R^G and T_R^F must be obtained. T_C^R is the transformation matrix from the stereo camera to the robot. The method of solving T_C^R has been presented in our previous work. T_R^G is the transformation matrix from the robot to the ground, which can be obtained from the body trajectory of the robot. T_R^F is the transformation matrix from the foot to the robot body which can be solved by the robot kinematics.

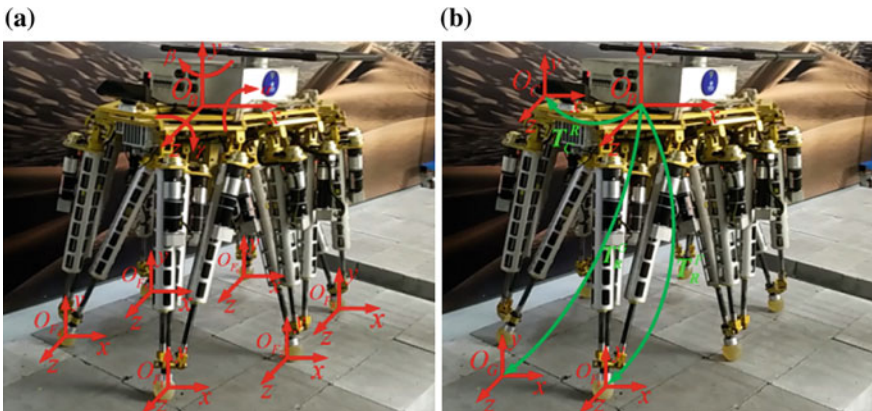


Fig. 2 a Inputs and outputs of the robot, b definition of the coordinate systems

3 Terrain Map Building and Terrain Classification

Accurate 3D coordinates of the terrain in front of the robot can be obtained from the depth image captured by the stereo camera. The raw terrain data consists of large amounts of point cloud, which spends too much storage space and takes a long time for the computer to process. Taking into account this issue, we decide to use a grid-type map to decrease the data amount and increase the updating and processing rate of the map. The grid-type map describes the terrain by using multiple square-shaped grids, and each grid stores the real height of the terrain.

Figure 3 shows the process of grid terrain map building. Firstly, the point cloud ${}^C P$ in O_C should be transformed in O_G by the following equation:

$${}^G P = T_R^G \cdot T_C^R \cdot {}^C P \quad (1)$$

Secondly, the point cloud ${}^G P$ is mapped into the corresponding grid by the following formulas:

$$\begin{aligned} x_G(i, j) &= (i - 60) \times 0.025 \\ z_G(i, j) &= j \times 0.025 \\ y_G(i, j) &= \frac{\sum_{n=1}^{n(i, j)} y_w(n)}{n(i, j)} \end{aligned} \quad (2)$$

Considering the capacity of Hexapod-III, the grid size is regulated as $0.025 \text{ m} \times 0.025 \text{ m}$, and the grid number is 120×120 . So the grid map represents the real terrain whose dimension is $3 \text{ m} \times 3 \text{ m}$. The grid height is obtained by

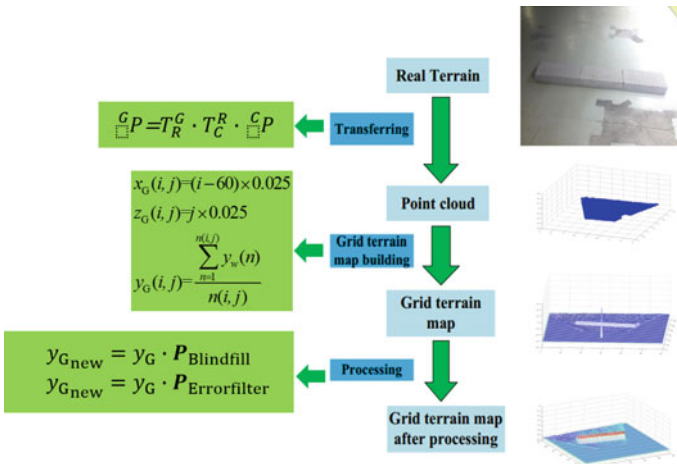
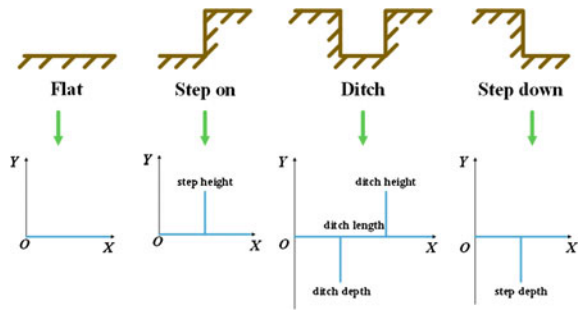


Fig. 3 Grid terrain map building

Fig. 4 Terrain classification



calculating the average height of the point cloud which are located in the same grid. Thirdly, two different kinds of wrong grid exists, which maybe influence the correctness of the map. One is the wrong data due to the outer noise and the sensor itself. The other one is the missing portion of the terrain caused by inevitable effect of occlusions in the sensors line of sight. The grid terrain map has to be processed further in order to exclude wrong grids as Fig. 3 shows. The processing algorithms are out of the scope of this article and won't be discussed here.

In this paper, we mainly focus on the classification of four common terrain in reality, the flat-floor, step-on, ditch, and step down. Based on the grid terrain map, we can extract the geometric features of the four terrain as Fig. 4 shows. For the flat-floor terrain, there is no rising and falling edges in the height direction. For the step-on terrain, there is only a rising edge in the height direction. The position and the height of the step-on terrain are decided by those of the rising edge. For the ditch terrain, there is a falling edge first, subsequently followed by a rising edge. The position of the ditch is decided by that of the falling edge. The length of the ditch is calculated by the differential position of the rising and falling edges. For the step-down terrain, there is only a falling edge in the height direction. The position and the depth of the step-down terrain are decided by those of the falling edge.

4 Walking Strategies

In this section, walking strategies are discussed in detail. The robot chooses the tripod waling gait, which is the fastest stable gait for the hexapod robot. The tripod walking gait enables the robot to have three nonadjacent feet touching with the ground all the time, the center of mass (COM) can be located in the support triangle easily as Fig. 5 shows.

For different terrain, the robot applies two different gait trajectories, the rectangular trajectory and the ellipse trajectory. The rectangular trajectory is typical but quite useful as shown in Fig. 6a. The determination of the rectangular trajectory only needs three parameters, the step length a , the height of the lifting foot b and the height of the falling foot c , which facilitates the planning process a lot. The

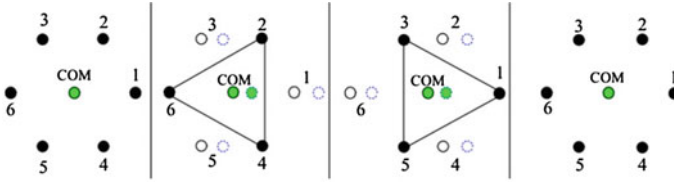


Fig. 5 The tripod walking gait

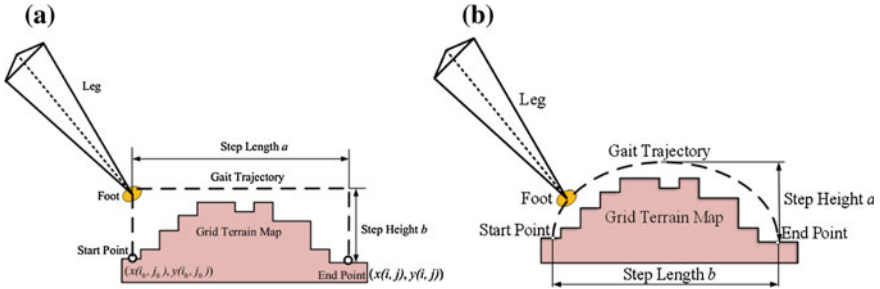


Fig. 6 a The rectangular trajectory, b the ellipse trajectory

rectangular gait is used on step-on and step down terrain, for it is easy to be planned to avoid the collision with the rising and falling edges. Ellipse trajectory is shown in Fig. 6b, which is smooth and has a shorter length compared to the rectangular trajectory. The ellipse trajectory is decided by two parameters the step length b and the step height a . It is used on flat-floor and ditch terrain, for it can satisfy the requirement of high walking speed and large workspace of the foot.

When the robot passes through the step-on, ditch and step down terrain, the detection error and the motion error may cause the robot to falling down and collision with the terrain. In order to ensure the robot’s safety, it is important for the robot to move to a safe pose. As Fig. 7 shows, the safe pose is defined as a pose where the robot trunk is far from the sides’ edge of the terrain and it is vertical to the front edge of the terrain. When the terrain is not a flat-floor after distinguishing, the edge of the terrain is detected and located. Then the robot will turn an appropriate angle to face the terrain vertically. If any foot of the robot is outside the terrain, it will move left or right to make its foot far away from the sides’ edge of the terrain.

The walking strategy on step-on and step-down terrain are substantially similar, the detailed walking process is shown in Fig. 8. The robot will detect the position and the height of the step-on terrain (the position and the depth of the step-down terrain), which has been described in detail above. Then the robot decides to use the rectangular trajectory. The robot will first move close to the step to ensure the position of the next foothold within the leg’s workspace. The robot will lift three nonadjacent feet, move them forward to a specified distance, then fall them down.

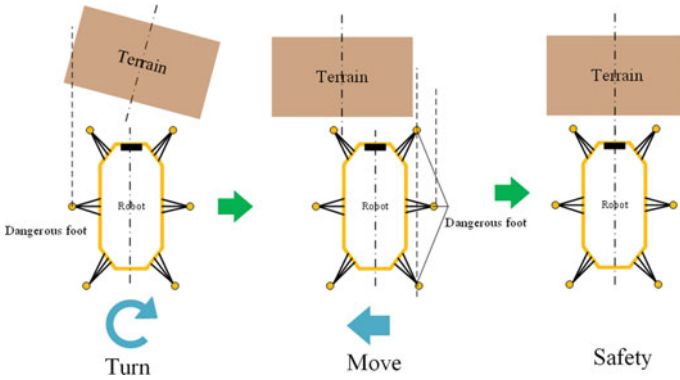


Fig. 7 Edge detection and pre-adjustment for safety

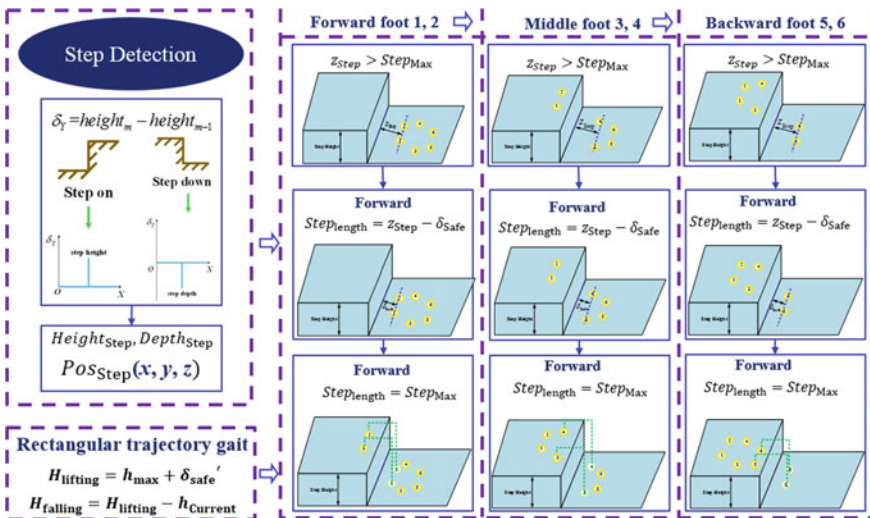


Fig. 8 Walking strategy on step-on and step-down terrain

Then the other three feet are motivated to move in the similar way. The robot will move its front two feet on or down the step, then the middle two feet, at last the back two feet. The step length, the foot lifting height and the foot falling height are calculated using following formulas.

$$\begin{aligned}
 Step_{length} &= Step_{max} \\
 H_{lifting} &= h_{max} + \delta'_{safe} \\
 H_{falling} &= H_{lifting} - h_{current}
 \end{aligned}
 \tag{3}$$

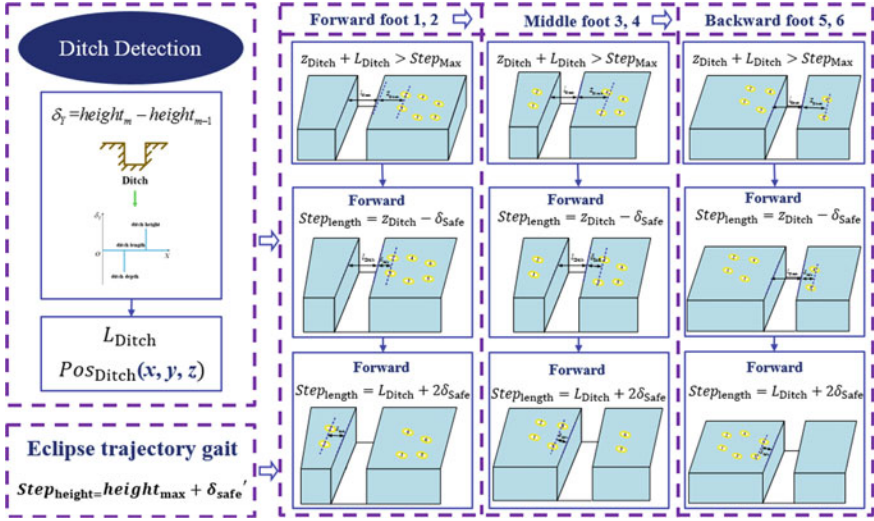


Fig. 9 Walking strategy on ditch terrain

where $\text{Step}_{\text{length}}$ is the step length, Step_{max} is the maximum step length within the foot's workspace. H_{lifting} is the foot lifting height, h_{max} is the maximum height of the terrain. For the step-down terrain, h_{max} is the maximum depth of the terrain. δ'_{safe} is the safety margin avoiding the collision of the terrain. H_{falling} is the foot falling height, h_{current} is the height of the next foothold.

The walking strategy on the ditch terrain is shown in Fig. 9. The robot will detect the position, and the length of the ditch first. Then it decides to use the ellipse trajectory. Before swinging its foot to the other side of the ditch, the robot will come close to the ditch in order to make sure the step length is longer than L_{Ditch} + ditch length. The robot will lift three nonadjacent feet, swing them to the planned footholds. Then it moves the other three feet in the same way. As Fig. 9 shows, the robot will first swing the front foot 1, 2 to the other side of the ditch. Then it comes close to the ditch and swings the medial foot 3 and 4 to the other side. At last it moves forward again and swings the back foot 5, 6 to the other side. The step length and the step height are calculated from following formulas:

$$\begin{aligned} \text{step}_{\text{length}} &= L_{\text{Ditch}} + 2\delta_{\text{Safe}} \\ \text{step}_{\text{height}} &= \text{height}_{\text{max}} + \delta'_{\text{Safe}} \end{aligned} \quad (4)$$

where L_{Ditch} is the length of the ditch, $\text{height}_{\text{max}}$ is the maximum height value of terrain within the ellipse trajectory. δ_{Safe} is the safe margin along the longitudinal direction, δ'_{safe} is the safe margin along the height direction.

Walking strategy on the flat-floor is basically the same to that on the ditch. The robot uses ellipse trajectory gait. The robot can walk with a high speed on the

flat-floor. So the step length can reach the maximum length within its workspace. And the step height can be obtained by adding a small safe margin to avoid little terrain bumps.

5 Motion Planning

After obtaining the gait trajectory, prismatic positions should be computed to control the robot to walk along the planned trajectory. Inverse kinematics is needed, and our previous work have finished the kinematics model of the robot [16].

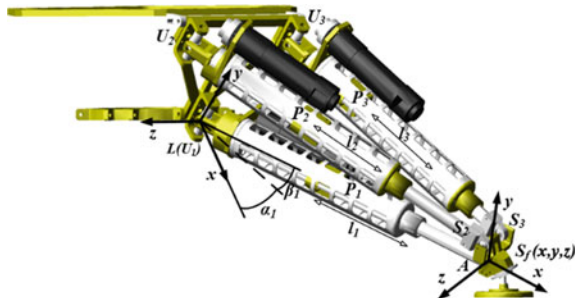
Figure 10 shows the kinematic model of single leg. The position of spherical joint S_f connecting the leg with the foot is obtained from the above section. U_1, U_2, U_3 are three universal joints connecting the leg with the body. S_1, S_2 are two spherical joints, which connects links with ankle joints. P_1, P_2, P_3 denote three prismatic joints, whose lengths are l_1, l_2, l_3 . The geometric constraint equation of inverse kinematics is represented as follows,

$$\begin{bmatrix} x \\ y \\ z \\ 1 \end{bmatrix} = {}^L A \begin{bmatrix} S_{fx} \\ S_{fy} \\ S_{fz} \\ 1 \end{bmatrix} \tag{5}$$

where ${}^L A$ is the transformation matrix from the ankle coordinate system (ACS) to the leg coordinate system (LCS). S_{fx}, S_{fy}, S_{fz} are coordinates of S_f with respect to ACS. (x, y, z) denotes the coordinates of S_f with respect to LCS. Formula (6) is the detailed expression of ${}^L A$,

$${}^L A = \begin{bmatrix} \cos \alpha_1 \cos \beta_1 & -\cos \alpha_1 \sin \beta_1 & \sin \alpha_1 & l_1 \cos \alpha_1 \cos \beta_1 \\ \sin \beta_1 & \cos \beta_1 & 0 & l_1 \sin \beta_1 \\ -\sin \alpha_1 \cos \beta_1 & \sin \alpha_1 \sin \beta_1 & \cos \alpha_1 & -l_1 \sin \alpha_1 \cos \beta_1 \\ 0 & 0 & 0 & 1 \end{bmatrix} \tag{6}$$

Fig. 10 Kinematic model of single leg



where α_1, β_1 are rotation angles of U_1 along two vertical directions, we can get the solution of the inverse kinematics by solving Eq. (5),

$$\begin{aligned}
 l_1 &= \sqrt{x^2 + y^2 + z^2 - S_{f_y}^2 - S_{f_z}^2 - S_{f_x}^2} \\
 \beta_1 &= \arcsin\left(\frac{y}{\sqrt{(l_1 + S_{f_x})^2 + S_{f_y}^2}}\right) - \arcsin\left(\frac{S_{f_y}}{\sqrt{(l_1 + S_{f_x})^2 + S_{f_y}^2}}\right) \\
 \alpha_1 &= \arctan\left(\frac{S_{f_x}x - [(l_1 + S_{f_x}) \cos \beta_1 - S_{f_y} \cos \beta_1]z}{[(1 + S_{f_x}) \cos \beta_1 - S_{f_y} \sin \beta_1]x + S_{f_z}}\right)
 \end{aligned} \quad (7)$$

${}^L A$ can be calculated by substituting α_1, β_1, l_1 into Eq. (6), and lengths l_2, l_3 of prismatic joints P_2, P_3 can be obtained from following equations,

$$\begin{aligned}
 l_2 &= \left| \overrightarrow{{}^L U_2} \overrightarrow{{}^L S_2} \right| = |{}^L A \cdot {}^A S_2 - {}^L U_2| \\
 l_3 &= \left| \overrightarrow{{}^L U_3} \overrightarrow{{}^L S_3} \right| = |{}^L A \cdot {}^A S_3 - {}^L U_3|
 \end{aligned} \quad (8)$$

where ${}^L U_2, {}^L U_3, {}^L S_2, {}^L S_3$ are positions of joints U_2, U_3, S_2, S_3 with respect to LCS respectively, and ${}^A S_2, {}^A S_3$ are positions of joints S_2, S_3 with respect to ACS respectively.

6 Experiments

In this section, experimental results are presented. Figure 11 shows the process of walking on the stair. The robot correctly detects the position and the height of the stair. Then it moves to the safe pose to guarantee safety. Before placing the feet on



Fig. 11 Snapshots of walking on step-on terrain



Fig. 12 Snapshots of walking on step-down terrain

the stair, it moves close to the stair to ensure that next footholds are within the workspace. And the robot trunk moves forward horizontally because of the accurate foot falling height.

Figure 12 shows the process of walking down the stair. The position and the depth of the stair are detected correctly. Then the robot moves to the safe pose. Before placing the feet on the ground, it moves close to the stair to ensure next footholds are within the workspace. From Fig. 12, we can see that the robot trunk maintains horizontally, which validates the walking strategy on step-down terrain.

Figure 13 shows the process of passing through the ditch. The position and the length of the ditch are calculated correctly. The robot uses the ellipse trajectory gait. Before swinging the feet to the other side of the ditch, it moves close to the nearer edge of the ditch to ensure the next step length is longer enough to pass the ditch safely. From Fig. 13, we can see that the robot passes through the ditch successfully.

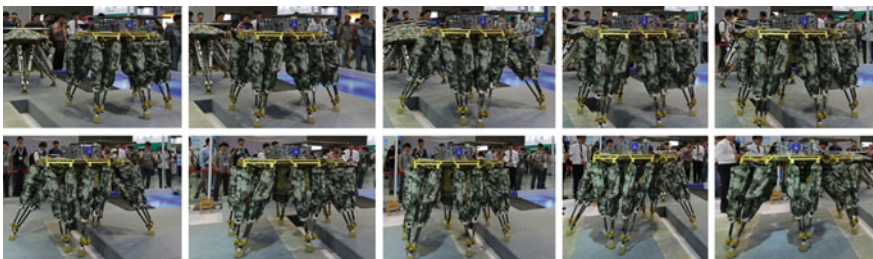


Fig. 13 Snapshots of passing through ditch

7 Conclusions

In this paper, we have presented a perception-based walking strategy for a hexapod robot on typical structured terrain. The walking strategy is based on the grid-type terrain map, which is modeled from point cloud captured by a stereo camera. The geometric feature of four typical structured terrain, the flat-floor, step-on, step-down and ditch are abstracted and detected from the grid-type map. In order to guarantee the robot safety, the pre-adjustment strategy is proposed. Then four walking strategies for different terrain are presented in detail. The motion planning method based on the robot kinematics is discussed too. At last, a serial of experiments are carried out and the results validate the practicability and theoretically of the proposed strategy.

Acknowledgments This study was supported by the National Basic Research Program of China (973 Program, No. 2013CB035501).

References

1. Nelson G et al (2012) Petman: a humanoid robot for testing chemical protective clothing. *J Robot Soc Japan* 30(4):372–377
2. Boston D http://www.bostondynamics.com/robot_Atlas.html
3. Hirose M, Ogawa K (2007) Honda humanoid robots development. *Philos Trans R Soc A: Math Phys Eng Sci* 365:9
4. Raibert M et al (2008) Bigdog, the rough-terrain quadruped robot. In *Proceedings of the 17th world congress*
5. Semini C, Tsagarakis NG, Guglielmino E, Focchi M, Cannella F, Caldwell DG (2011) Design of HyQ—a hydraulically and electrically actuated quadruped robot. *J Syst Control Eng* 225(6):19
6. Santos PGD, Gálvez JA, Estremera J, García E (2003) SILO4—a true walking robot for the comparative study of walking machine techniques. *IEEE Robot Autom Mag* 10(4):10
7. Krotkov E, Simmons R (1996) Perception, planning, and control for autonomous walking with the ambler planetary rover. *Int J Robot Res* 15(2):26
8. Wilcox BH et al (2007) ATHLETE: a cargo handling and manipulation robot for the moon. *J Field Robot* 24(5):421–434
9. Görner M, Wimböck T, Hirzinger G (2009) The DLR Crawler: evaluation of gaits and control of an actively compliant six-legged walking robot. *Ind Robot: Int J* 36(4):8
10. Haynes GC, Rizzi AA (2006) Gaits and gait transitions for legged robots. In *Proceedings of the IEEE international conference on robotics and automation*
11. Zucker M, Ratliff N et al (2011) Optimization and learning for rough terrain legged locomotion. *Int J Robot Res* 30(2):175–191
12. Estremera J, Cobano JA (2010) Continuous free-crab gaits for hexapod robots on a natural terrain with forbidden zones: an application to humanitarian demining. *Robot Auton Syst* 58(5):700–711
13. Estremera, J, de Santos PG (2005) Generating continuous free crab gaits for quadruped robots on irregular terrain. *IEEE Trans Robot* 21(6):1067–1076
14. Hoepflinger, MA, Hutter M (2013) Unsupervised identification and prediction of foothold robustness. In *IEEE international conference on robotics and automation*

15. Haynes G, Rizzi A, Koditschek D (2012) Multistable phase regulation for robust steady and transitional legged gaits. *Int J Robot Res* 21(14):1712–1738
16. Pan Y, Gao F (2013) A new 6-parallel-legged walking robot for drilling holes on the fuselage. *Proc Inst Mech Eng, Part C: J Mech Eng Sci* 228:753–764

Type Synthesis of N -Parallelogram-Based Surgical Arm with Remote Actuated Configuration

Fan Zhang, Xue Zhang, Lubin Hang, Cunyue Lu
and Tomonari Furukawa

Abstract Two remote actuated one rotational and one translational degree of freedom (1R1T DOF) surgical mechanisms are synthesized based on N -parallelogram linkages. The remote actuation of surgical arm keeps the bulky driving members away and saves the space. The surgical arms are also magnetic resonance imaging (MRI)-compatible in terms of noise reduction and space saving, since open MRI has narrow opening. The synthesis processes are implemented by combining the remote center motion (RCM) mechanism with the remote actuate 1R1T mechanisms. The N -parallelogram linkages play a key role in the synthesis of the novel remote actuate 1R1T mechanisms.

Keywords Minimally invasive surgery · Surgical arm · Remote center motion · Remote actuated configuration

F. Zhang (✉) · X. Zhang · L. Hang
Department of Mechanical Engineering, Shanghai University of Engineering Science,
Shanghai, China
e-mail: pdszhangfan@aliyun.com

X. Zhang
e-mail: zhangxue0857@163.com

L. Hang
e-mail: hanglb@126.com

C. Lu
School of Electronic Information and Electrical Engineering, Shanghai Jiao
Tong University, Shanghai, China
e-mail: lucunyue@163.com

T. Furukawa
Department of Mechanical Engineering, Virginia Tech, Blacksburg, USA
e-mail: tomonari@vt.edu

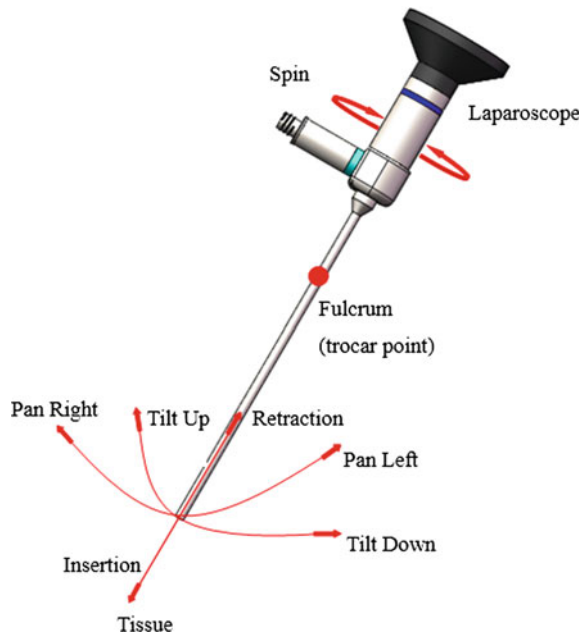
1 Introduction

In laparoscopic surgery [or Minimally Invasive Surgery (MIS)] [1–4], the surgeon performs the operation through small holes using long instruments and observing the internal anatomy with an endoscope camera. As shown in Fig. 1, surgical arms required for the endoscope holding robots need four-DOF to achieve the surgery-assistant operation [3, 4]: (1) insert along the tool spindle axis, (2) tilt and pan about the pivoting point, and (3) spin about the tool spindle axis.

Usually, existed surgical arms are actuated by wire and ball screw-motor pair. The wire-actuation mechanism eliminates backlash problems and promotes miniaturization. However, it also introduces modeling problems due to the flexibility and friction in the actuation lines. There often exists a shape discrepancy between the actual shape and the assumed ideal shape of one segment [5–7]. It is necessary to compensate the motion precision which relies on the online measurement [5]. After actuation compensation, the wire-driven robot can achieve with acceptable accuracy [7]. The commercial Da Vinci surgical system also implement the 6 DOF electro-magnetic sensor attached to the base of the two-segment continuum robot to compensate for the unknown shape of the passive segment [8].

The parallelogram-based mechanisms are recently developed to meet the required real-time dynamic respond and precision demanding for surgical arms [9–16]. In 2001, double parallelogram linkages are reported to be used as an RCM mechanism [17]. By investigating the structural characteristics of the parallelogram linkages, parallelograms are implemented to be multi-DOFs surgical arms: (1) Two

Fig. 1 Movement of endoscope: since the endoscope is limited due to the insertion site, the surgical arm is required to have four degrees of freedom



rotational DOF surgical arm [9]; (2) One rotational DOF and one translation DOF (1R1T) surgical arm [10, 13, 14]. For the 1R1T surgical arms, the end-effectors are to pivoted across the incision while insert along the tool spindle axis. Since the insert operation of the distal part is actuated by the motor located on the static base, the disadvantage of the high inertia problem result in ball screw and steering pod configuration is eliminated. It need less energy from the base motor to endure the weight of actuator and the screw. The robot need low inertia to achieve the high precision and human-robot interaction performance.

A reasonable type synthesis method of constructing 1R1T RCM mechanisms is introduced in this paper. The synthesis approach, investigated with the concept of “remote actuated mechanism” and features of “parallelogram linkage”, combining the RCM mechanism and 1R1T RCM mechanism, to generate the 1R1T remoted actuated mechanism. The synthesized mechanisms, featured by the configurations that all actuators are located on the static base, have the potential capacity on real-time respond and human-robot interaction performance.

2 Remote Actuated Mechanism

The remote actuated mechanisms, analogous to vertebrae and tendon, locate the actuators near or mounted at the static base [18]. The development of remote actuated mechanisms result in: (1) An actuator causes a magnetic and electrical noise and its effect on MRI is inverse proportional to the distance [18]; (2) the mechanism, required to meet the high dynamic respond and precision need, set the actuators distal from the kinematic joints which to be actuated; (3) it is necessary to provide elongate linkage structures to prompt miniaturization of the devices.

There are two successive application fields of remote actuated mechanism: laparoscopic surgical instruments [19–21] and palletizing robot [22–24]. The remote actuated tools ordinarily can be seen in the laparoscopic surgical instruments. The remote actuated design is helpful to miniaturize the diameter of the tools. The high payload ABB palletizing robots, originated from the patent [22], also applied the remote actuated configuration to meet the demanding requirement of the lightweight design and compact structure (Fig. 2).

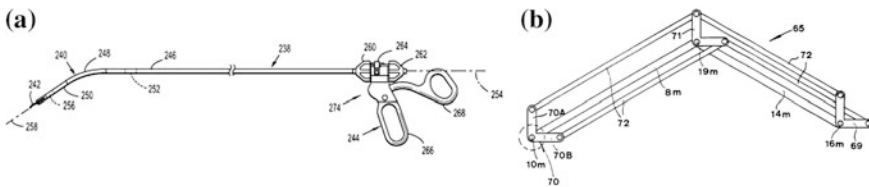


Fig. 2 The application of remote actuated mechanism. **a** Laparoscopic surgical instruments [21]; **b** The parallelogram-based structure of ABB palletizing robot [22]

The remote actuated surgical arm keeps the bulky driving members away and saves the space around the imaging area for the surgeon. This features promotes the surgical arms involve low loads and inertia, which promise capacity with respect to possible accelerations and speeds and accuracy with regard to path. Furthermore, it's very important because even Open MRI has narrow opening [18]. So the remote actuated surgical arm, featured with the actuators causing magnetic and electrical noise located on the static base, will promote MRI-compatibility of the surgical arm in terms of noise reduction and space saving.

In this paper, our major distribution is the proposed type synthesis approach of remote actuated 1R1T surgical arm, which is MRI-compatibility and having low load and inertia.

3 Parallelogram Linkages

The parallelogram linkages are firstly well-known for constructing three translational DOF delta robot [25]. The concept of parallelogram was latterly used in three DOF HALF robot manipulator [26], remote center motion manipulator [10, 13, 27–29].

Initially, the parallelogram linkage was raised great concern for the feature that the output link of the parallelogram remains the fixed orientation with the input link. The delta robot has three symmetric chain, in which the identical length links were connected by spherical joint to form a parallelogram. By this feature, the parallelogram guarantee the end-effector of delta robot remain the fixed orientation with the base. The typical applications include the pick-and-place robot [25] (Table 1).

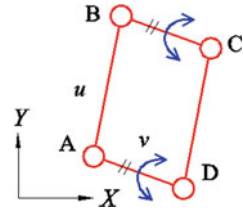
Two or more parallelogram linkages were subsequently combined to construct more complex mechanism. Connected by the pivot, the output link of 2nd parallelogram is at the fixed posture with the input link of the 1st parallelogram. This double-parallelogram linkage is the vital element of two translational DOF delta robot [30], to constraint three rotational DOFs of end-effector and guarantee only translational DOF for the end-effector. This concept of parallelogram was also utilizing in the palletizing robot [22–24].

In this paper, one interesting feature of parallelogram linkage is applied to synthesize the new 1R1T remote actuated surgical arm. As shown in Fig. 3, when

Table 1 The kinematic performance of parallelogram linkage

Linkage	Output link	Output link motion	DOF of output link (when link DC is fixed with the RCM mechanism)
Parallelogram	BC	To remain the fixed orientation with the input link AD	1 DOF

Fig. 3 The schematic graph of parallelogram linkage



the link DC of parallelogram is fixed with the RCM mechanism, the output links BC still has one DOF. It remains the fixed orientation with the input link AD.

In the following, this feature is going to be used to construct an approachable method to achieve the remote actuation transmission.

4 Type Synthesis of Parallelogram-Based 1R1T Remote Actuated Mechanism for Surgical Arm

The N -parallelogram linkage is used to synthesize the 1R1T remote actuated surgical arm in this paper. There is one fabrication accuracy about parallelogram should be considered: (1) the axes of all four joints need be parallel mutually; (2) the lengths between two of the four links need be equal [31]. This problem could be well solved by fabricating the parallelogram with high accuracy.

The remote actuated mechanisms could be synthesized by the type synthesis method of parallel mechanism. For parallel mechanisms, the end-effector is connected to the base through several chains of interconnected links. Therefore, the procedure of type synthesis of 1R1T remote actuated mechanism is:

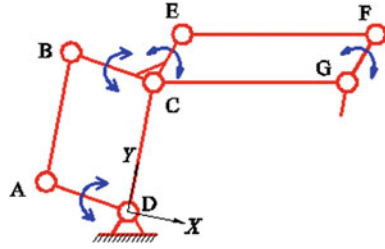
- (1) To synthesize the parallelogram-based remote actuated (RA) chain for 1R1T mechanism. The DOF of kinematic chain should not less than 1R1T DOF.
- (2) To combine the remote actuated chain with the RCM mechanism. The DOF of end-effector will be the intersection of the DOFs of all the kinematic chains.

4.1 Type Synthesis of Parallelogram-Based RA Chain for 1R1T Mechanism

A. Type synthesis of RA chain based on 1-parallelogram linkage

A 1-parallelogram linkage is divided into two parts to compatible with the revolute joints of RCM mechanism, as shown in Fig. 4, to transfer the actuated motion from the actuator located at the static base.

Fig. 4 The RA chain based on 1-parallelogram linkage



B. Type synthesis of RA chain based on 2-parallelogram linkage

Two parallelogram linkages are connected in serial, as shown in Fig. 5, forms a 2-parallelogram linkage.

When the input link AB of 2-parallelogram is fixed with the RCM mechanism, the output links MN will remain the fixed orientation with the RCM mechanism. In this case, link MN still have two planar DOFs in XY plane. If one of the two DOFs is active (actuated by motor), the rest of two DOFs will be positive and translate along the axis of rod (to achieve the controlled translational motion) under the constraints of the 2-parallelogram linkage (Table 2).

Fig. 5 The RA chain based on 2-parallelogram linkage

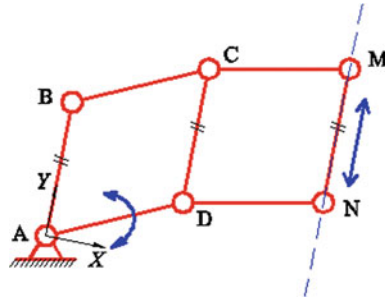


Table 2 The RA chain for 1R1T mechanism

Item	Input links	Output link	DOF of output link (when the input links are fixed with RCM mechanism)	Example
1-parallelogram-based chain	AD (link DC, CG are going to be fixed with the joints of RCM mechanism)	FG	1 DOF	Fig. 4
2-parallelogram-based chain	AD (link AB is going to be fixed with RCM mechanism)	MN	2 DOF	Fig. 5

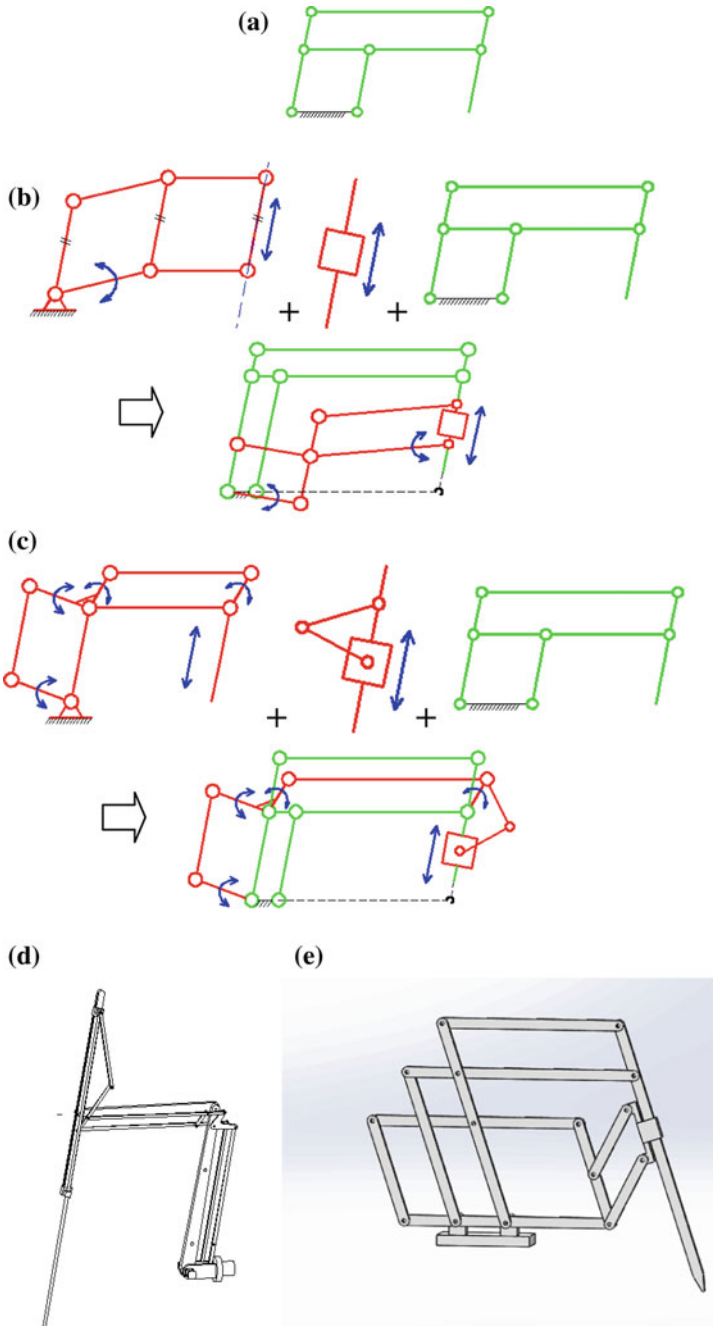


Fig. 6 Synthesized processes of the 1R1T remote actuated surgical arms. **a** RCM mechanism; **b** Processes of constructing the 1-parallelgram-based 1R1T remot ed actuated mechanism; **c** Processes of constructing the 2-parallelgram-based 1R1T remot ed actuated mechanism; **d** Prototype of the 1-parallelgram-based 1R1T remot ed actuated mechanism; **e** Prototype of the of 2-parallelgram-based 1R1T remot ed actuated mechanism

4.2 Type Synthesis of Parallelogram-Based 1R1T Mechanism

If a link of the mechanism can rotate around a fixed point distal from the mechanism, while there is no physical revolute joint at the fixed point, the mechanism is referred to as an RCM mechanism. Typical RCM mechanism is shown in Fig. 6a. The novel 1R1T remote actuated mechanisms for surgical robot are synthesized by combination the RA chain, prismatic joint with RCM mechanism. The mechanisms take full advantage of the remote center mechanism and remote actuated configuration.

5 Conclusion

The new N -parallelogram-based surgical arms with the remote actuated configuration are synthesized in this paper. The N -parallelogram linkages play a key role in the synthesis procedure.

The characteristics of the mechanisms include:

- (1) The actuators are mounted on the static base, which keeps the bulky driving members away and reduces the inertias.
- (2) The surgical arm is MRI-compatible in terms of noise reduction and space saving, since Open MRI has narrow opening.

Since the backlash problem of the reducer can be greatly reduced by adopting the precision gears or modified gear design, it is promising for N -parallelogram-based surgical arm with remote actuated configuration to be utilized for commercial application.

Appendix

Figures 7 and 8 show that the surgical arms with remote actuated configuration have the capability of inserting along the tool spindle axis and remote center motion.

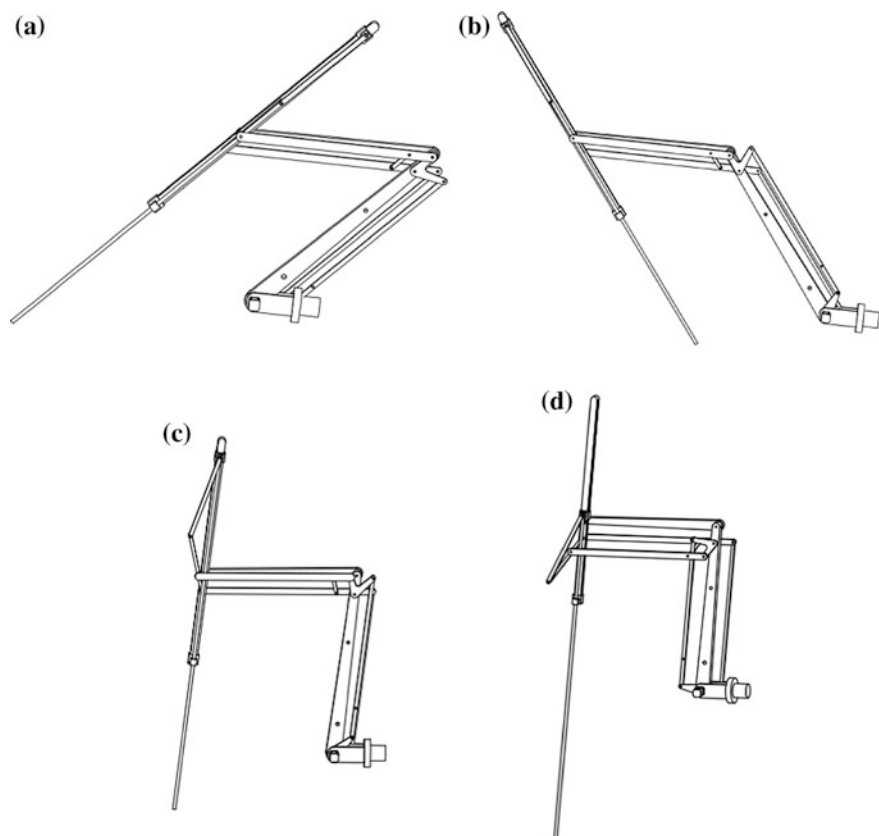


Fig. 7 The kinematic simulation of 1-parallelgram-based 1R1T remote actuated surgical arms: **a** and **b** show that the surgical arm can achieve the RCM. **c** and **d** show that the surgical arm can achieve the inserting motion

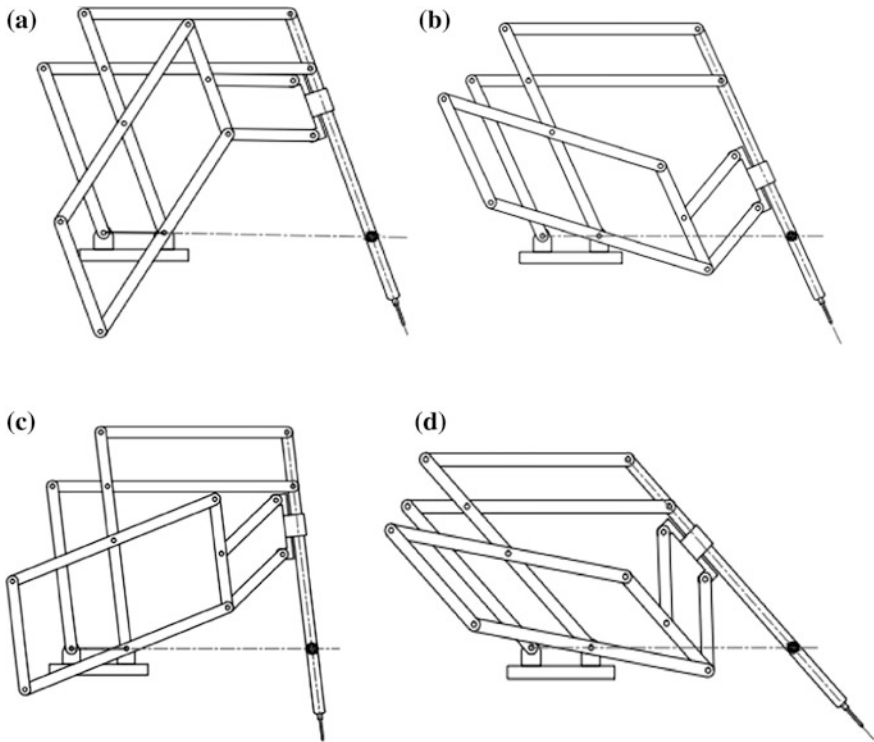


Fig. 8 The kinematic simulation of 1-parallelgram-based 1R1T remote actuated surgical arms: **a** and **b** show that the surgical arm can achieve the RCM. **c** and **d** show that the surgical arm can achieve the inserting motion

References

1. Mack MJ (2001) Minimally invasive and robotic surgery. *Jama* 285:568–572
2. Madhani AJ, Salisbury JK (1998) Wrist mechanism for surgical instrument for performing minimally invasive surgery with enhanced dexterity and sensitivity. Google Patents
3. D'Annibale A, Morpurgo E, Fiscon V, Trevisan P, Sovernigo G, Orsini C, Guidolin D (2004) Robotic and laparoscopic surgery for treatment of colorectal diseases. *Dis Colon Rectum* 47:2162–2168
4. Hagn U, Konietschke R, Tobergte A, Nickl M, Jörg S, Kübler B, Passig G, Gröger M, Fröhlich F, Seibold U (2010) DLR MiroSurge: a versatile system for research in endoscopic telesurgery. *Int J Comput Assist Radiol Surg* 5:183–193
5. Xu K, Simaan N (2006) Actuation compensation for flexible surgical snake-like robots with redundant remote actuation. In: *Proceedings 2006 IEEE international conference on robotics and automation, 2006, ICRA 2006*. IEEE, pp 4148–4154
6. Simaan N, Xu K, Wei W, Kapoor A, Kazanzides P, Taylor R, Flint P (2009) Design and integration of a telerobotic system for minimally invasive surgery of the throat. *Int J Robot Res* 28:1134–1153

7. Xu K, Zhao J, Fu M (2014) Development of the SJTU unfoldable robotic system (SURS) for single port laparoscopy
8. Donhowe CQ, Blumenkranz SJ, Duindam V (2013) Systems and methods for reducing measurement error in optical fiber shape sensors. Google Patents
9. Bai G, Qi P, Althoefer K, Li D, Kong X, Dai JS (2015) Kinematic analysis of a mechanism with dual remote centre of motion and its potential application. In: ASME 2015 international design engineering technical conferences and computers and information in engineering conference. American Society of Mechanical Engineers, pp V05BT08A011–V005BT008A011
10. Hadavand M, Mirbagheri A, Behzadipour S, Farahmand F (2014) A novel remote center of motion mechanism for the force-reflective master robot of haptic tele-surgery systems. *Int J Med Robot Comput Assist Surg* 10:129–139
11. Liu ST, Harewood L, Chen B, Chen C (2016) A skeletal prototype of surgical arm based on dual-triangular mechanism. *J Mech Robot* 8:041015
12. Schena B (2007) Robotic manipulator with remote center of motion and compact drive. Google Patents
13. Li J, Xing Y, Liu H, Wang S (2014) A Class of 2-degree-of-freedom planar remote center-of-motion mechanisms based on virtual parallelograms
14. Hadavand M, Mirbagheri A, Salarieh H, Farahmand, F (2011) Design of a force-reflective master robot for haptic telesurgery applications: robomaster1. In: 2011 annual international conference of the IEEE engineering in medicine and biology society. IEEE, pp 7037–7040
15. Lessard S, Bigras P, Bonev IA (2007) A new medical parallel robot and its static balancing optimization. *J Med Dev* 1:272–278
16. Li P, Yip HM, Navarro-Alarcon D, Liu Y, Tong CFM, Leung I (2013) Development of a robotic endoscope holder for nasal surgery. In: 2013 IEEE international conference on information and automation (ICIA). IEEE, pp 1194–1199
17. Blumenkranz SJ, Rosa DJ (2001) Manipulator positioning linkage for robotic surgery. Google Patents
18. Koseki Y, Koyachi N, Arai T, Chinzei K (2003) Remote actuation mechanism for MR-compatible manipulator using leverage and parallelogram-workspace analysis, workspace control, and stiffness evaluation. In: Proceedings ICRA'03. IEEE international conference on robotics and automation, 2003. IEEE, pp 652–657
19. Swayze JS, Huitema TW, Armstrong GA, Parihar SK, Korvick DL, Timm RW, Shelton IV, FE, Doll KR, Smith BW, Kelly WD (2014) Interchangeable tools for surgical instruments. Google Patents
20. Goble NM, Goble CC (1996) Laparoscopic surgical instrument. Google Patents
21. Piskun G, Shikhman O, Konik A, Rottenberg D, Battles C, Abrams M, Radziunas J, Ferreira D (2014) Laparoscopic instrument and related surgical method. Google Patents
22. Brogårdh T (2000) Device for relative movement of two elements. Google Patents
23. Chen W-S, Li H-Y (2011) Robot for handling object. Google Patents
24. Sutherland, I.E.: Robot arm structure. Google Patents (1990)
25. Pierrot F, Reynaud C, Fournier A (1990) DELTA: a simple and efficient parallel robot. *Robotica* 8:105–109
26. Liu X-J, Wang J, Gao F, Wang L-P (2001) On the analysis of a new spatial three-degrees-of-freedom parallel manipulator. *IEEE Trans Robot Autom* 17:959–968
27. Fu Y, Niu G, Pan B, Li K, Wang S (2013) Design and optimization of remote center motion mechanism of minimally invasive surgical robotics. In: 2013 IEEE international conference on robotics and biomimetics (ROBIO). IEEE, pp 774–779
28. Qu J, Chen W, Zhang J (2014) A parallelogram-based compliant remote-center-of-motion stage for active parallel alignment. *Rev Sci Instrum* 85:095112
29. Shusheng P, Guanghua Z (2009) Type synthesis for one-dimensional remote-center-of-motion mechanisms. *Chin J Mech Eng* 2:027

30. Huang T, Li Z, Li M, Chetwynd DG, Gosselin CM (2004) Conceptual design and dimensional synthesis of a novel 2-DOF translational parallel robot for pick-and-place operations. *J Mech Des* 126:449–455
31. Liu X-J, Wang J (2003) Some new parallel mechanisms containing the planar four-bar parallelogram. *Int J Robot Res* 22:717–732

Kinematics Analysis and Simulation of a Robot with Lower Extremity Exoskeleton

Maoyu Zhang, Yueri Cai and Shusheng Bi

Abstract The lower extremity exoskeleton is smart external power unit combined with the mechanical energy, which can enhance human body function. The progress, prospective and principle are introduced in brief. Based on the movement parameters of the several of joints of human extremity, the paper carried out the kinematics analysis and modeling the mechanical system of the lower extremity exoskeleton. Simulations of the mechanical system with MATLAB result in the motion trail in space structure. Comparing the motion with several points verifies the feasibility of the kinematical model established and the necessity of spatial motion analysis. Finally calculated the workspace and analyzed the influence of various parameters of the mechanism on the workspace. The study paves the way for the optimization design of the structure and the design and calculation of hydraulic drive system.

Keywords Lower extremity exoskeleton · Assisted mechanism · Spatial kinematical · Workspace

1 Introduction

Exoskeleton originally referred to the hard external structure providing living creatures with protection and support [1]. The lower extremity exoskeleton assist mechanism can be understood as man-machine combination of wearable equipment combined human intelligence with robot mechanical energy [2]. This feature makes it has a good application prospect in many areas: In the military field, lower extremity exoskeleton assisting robot can help improve individual soldier's combat capability; in civilian areas, the robot can be used for hiking, tourism, fire, disaster relief, etc.; in the medical field, the robot can be used for disabled assistance, medical rehabilitation, etc. [3].

M. Zhang (✉) · Y. Cai · S. Bi
School of Mechanical Engineering and Automation,
Beihang University, Beijing 100191, China
e-mail: 695291393@qq.com

© Springer Nature Singapore Pte Ltd. 2017
X. Zhang et al. (eds.), *Mechanism and Machine Science*,
Lecture Notes in Electrical Engineering 408,
DOI 10.1007/978-981-10-2875-5_17

The earliest study of exoskeleton system began in the 1960s. In 1962, the United States Air Force (USAF) required the Cornell Aeronautical Laboratory Inc. to conduct a feasibility research on the use of manpower amplifier system by using master-slave control mode. From 1960 to 1971, US General Electric Company began to develop a exoskeleton prototype based on master-slave control, called “Hardiman”, which was mainly used to relieve fatigue of the soldiers caused by long distance marching load. In 2004, University of California, Berkeley, developed the machine clothing that could make people easily carry heavy loads for long distance or heavy objects to go upstairs and downstairs—Berkeley Lower Extremity Exoskeleton (referred to as the BLEEX), the objective of the project was to develop exoskeleton that could heavily armed soldiers increase the load and improve the marching speed. The main part of BLEEX is a pair of stainless steel mechanical legs, and a small engine is equipped in the buttocks of the carriers to offer the power required for walking. An exquisite small folding steel frame extends from the rearward of the buttocks to be easy for soldiers to carry the military backpack, weapons and other items on the back. There are a number of research institutes in Japan engaged in the study of wearable assisted robot, which is mainly for civilian areas, and aimed at improving the ability to live independently and weight-bearing capacity of the elderly and people with disabilities. University of Tsukuba in Japan developed the world’s first commercial exoskeleton robot, namely the Hybrid Assistive Leg 3 (HAL3). This can help people to walk at a speed of 4 km per hour, and effortlessly climb the stairs. The domestic research on exoskeleton assistive robot has been started late and there’s no mature product on the market.

There’s even endless number of Kinematic analysis of lower extremity exoskeleton assistive mechanism. However, most of these studies are concentrated in the plane kinematics analysis, rather than the spatial kinematics analysis, or spatial kinematic analysis with less freedom. But exoskeleton mechanical mechanism needs to meet multiple kinds of walking requirements in the space according to different individuals’ walking habits. Meanwhile, the mechanical system is the basis of lower extremity exoskeleton assistive mechanism [4], as the carrier matrix of other systems, it complements other design systems. As a whole of overall structure, the mechanical system requires both the flexibility to follow the movement of the human body, not interfering with the body [5], and to provide human body with the impetus at the driven joints, which will not cause harm to humans due to the driving, there are very strict safety requirements. Therefore, it’s very necessary to guide the design of the mechanical system by motion information of each joint.

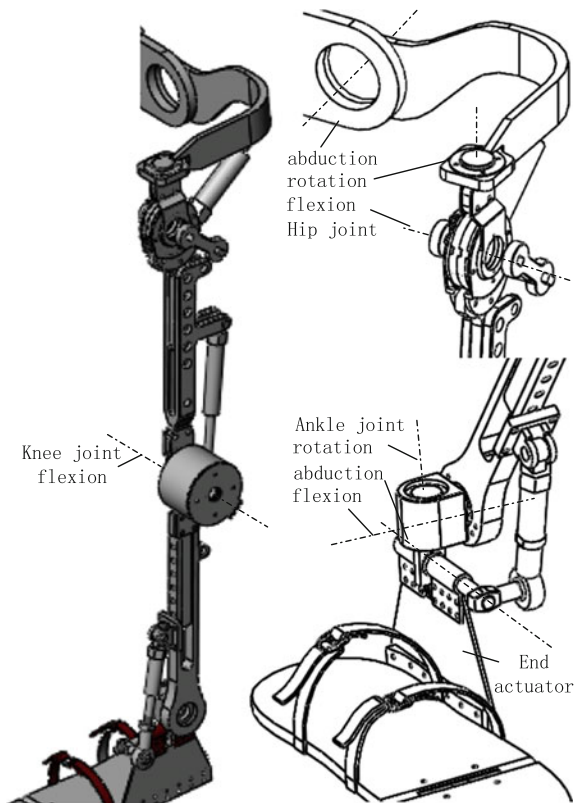
This thesis constructs a set of lower extremity exoskeleton assistive mechanism, and the mechanism is with a total of 14 freedoms. Considering that the mechanism is used for heavy load of individual soldier, electro-hydraulic drive is adopted accordingly. This thesis established the spatial kinematic model of the institution, and it simulates the parameters of each joint and spatial trajectory of the end actuator. This can be more effective verification of the correctness and feasibility of the mechanical system of the spatial kinematic model compared with the kinematic analysis of the sagittal plane of the drive joint.

2 Principle

Lower extremity exoskeleton assistive mechanisms is mainly composed by mechanical system, power system, control system and a variety of sensor systems to detect human action information [6].

The motion range of each joint in lower extremity varies in size and function, and each function varies in walking movements. According to the analysis of human lower extremity skeletal structure, hip joint and ankle joint are Ball and socket structure, which can be simplified as three-DOF joints composed of three revolute, and knee joint is complex and simplified as one-DOF revolute. As shown in Fig. 1, the mechanical structure is with a total of 14 freedoms, each leg has 7 freedoms. Of which, the hip joint comprises two passive freedoms and an active freedom, and the knee joint is an active freedom, the ankle joint includes two passive freedoms and one active freedom. The end actuator is in foot structure. The three active flexion and extension freedoms inside the sagittal plane is the main forward motion [7], the main role of internal and external rotation motion of the hip joint is to adjust the center balance of left and right sides of the body when adjusting

Fig. 1 Exoskeleton assistive structural diagram



the single leg support; the rotary motion of the hip joint is mainly used for changing the motion direction; flexion and extension of hip joint and knee joint directly affect stride length; the flexion and extension of the ankle joint is primarily used for regulating the stress points, internal and external rotation and rotation are mainly used to adjust force balance under the support state. Herewith, the hydraulic transmission is selected, so link rods on both sides of the active joints are connected to the hydraulic cylinder [8, 9].

3 Modeling and Simulation Analysis of Spatial Kinematics

Compared with the pure motion conducted only inside sagittal plane, spatial motion considers the influence of internal and external rotation and rotation of the hip joint while walking [10]. Different people have different walking habits, or habitual mention cross, or frequent inside and outside leg swing, and so on, which leads to mechanical leg tied in both legs not only need to meet freedom requirements to adapt to a variety of different individual walking habits, but also to meet the power demand. Therefore, it's critical to analyze the spatial trajectory of the end actuator.

3.1 *Obtaining of Lower Extremity Motion Data*

Seen from a biological perspective, the lower extremity motion of the human body takes joints as the fulcrum, the bones on both sides of joint is connected via ligaments, and then the skeletal motion around the articulation is driven by muscle contraction, thus to achieve walking and other movements [11]. There are a lot of methods to obtain the angle curve of each articulation: video capture, experiment obtaining or calculation.

Herewith, you can select the motion parameters of each joint through the simulation software. OpenSIM is the software that can be used by users for biological modeling, biomechanical analysis, a variety of the musculoskeletal modeling system and other operations. The software provides users with a variety of human skeleton model and sports model, the users can directly borrow or edit on this basis, thus to obtain the required data. Wherein, the legs model and walking motion model meet the design requirements of obtaining the motion parameters of each joint of human body lower extremity. As shown in Fig. 2, the human body lower extremity is within a walking cycle, and the motion angular displacement of respective freedom of the hip joint, knee joint and ankle joints are continuous function of time. In order to get the angular displacement of the different time spans corresponding to different joints through discretion, it can be used to calculate the homogeneous coordinates and trajectory curve of end actuator.

According to the CGA (Clinical Gait Analysis Data), hip flexion, knee flexion and ankle flexion all have big power consumptions while walking, otherwise the

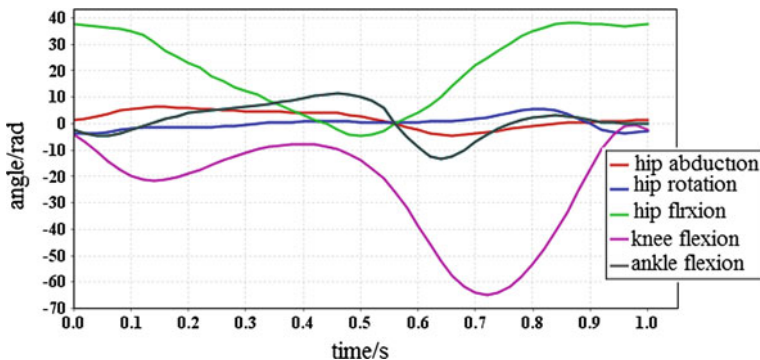


Fig. 2 Angular displacements of human body joints within walking cycle

other degrees of freedom all have very small power consumptions and thus remain un-actuated. Therefore, the flexion degree of freedom at hip is actuated, as is one flexion degree of freedom at knee, and the ankle plantar-dorsi flexion (in the sagittal plane) in each lower extremity exoskeleton leg.

3.2 Spatial Kinematics Modeling

The robot kinematics is mainly to study the mapping relationship between workspace and joint space [12]. Of which, the positive kinematics indicates the spatial space determined by the end actuator of the joint parameters, the trajectory planning of the end actuator can be conducted by changing the motion parameters of the joints, or the determined joint parameters can conduct the trajectory analysis of the end actuator.

As shown in Fig. 3, lower extremity exoskeleton assistive mechanism is composed by two left and right symmetrically mechanical legs, the corresponding structure is evenly symmetrical to motion parameters, herewith, the left leg is taken as an example for analysis.

D-H parameters table can be written according to the mechanism diagram of the mechanical system as shown in Table 1.

Figure 3 shows the kinematic model coordinate system of the mechanism, and the homogeneous coordinate transformation method is used to describe the phase posture between the link rods, thereby obtaining the position shape of each joint. In the Figure, $\{n_i\}$ is defined to represent the coordinate system $o_i - x_i y_i z_i (i = 1, 2, \dots, 7)$. Wherein, $\{n_0\}$ is the base coordinate system, and it is fixedly connected to link rod 1; $\{n_1\}\{n_2\}\{n_3\}$ respectively corresponds to abduction and outreaching, rotation, flexion and extension motion coordinate system of hip joint, which is connected to link rod 3; $\{n_4\}\{n_5\}$ respectively corresponds to the coordinate system of flexion and extension of knee and ankle joints, located in the center of the

Fig. 3 The mechanism diagram of lower extremity exoskeleton assistive mechanism

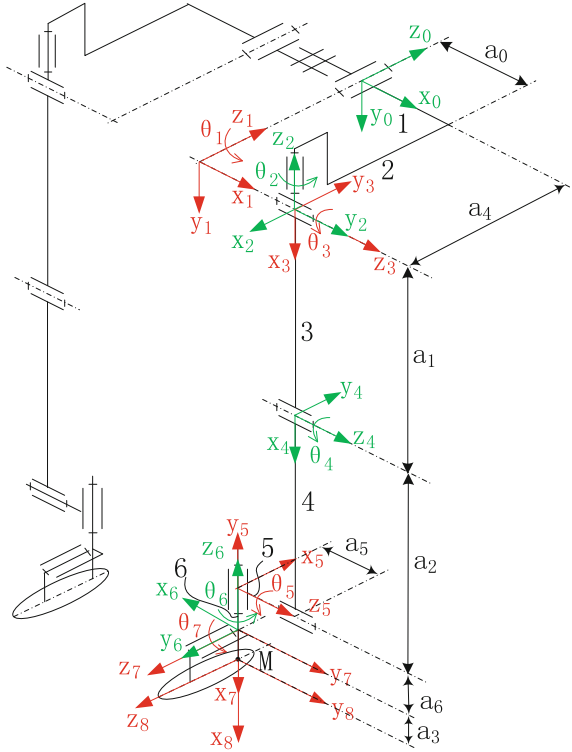


Table 1 D-H parameters table of single mechanical leg structure

i	a_{i-1}	α_{i-1}	d_i	θ_i
1	0	0	$-a_4$	$\theta_1(0)$
2	a_0	$\frac{\pi}{2}$	0	$\theta_2(\frac{-\pi}{2})$
3	0	$-\frac{\pi}{2}$	0	$\theta_3(\frac{\pi}{2})$
4	a_1	0	0	$\theta_4(0)$
5	a_2	0	$-a_5$	$\theta_5(\frac{\pi}{2})$
6	0	$-\frac{\pi}{2}$	$-a_6$	$\theta_6(\frac{\pi}{2})$
7	0	$-\frac{\pi}{2}$	0	$\theta_7(\frac{\pi}{2})$
8	a_3	0	0	0

joint, and are respectively attached to the leg link rod 4 and leg link rod 5; $\{n_6\}\{n_7\}$ represents coordinate system of the ankle joint rotation, adduction and outreach motion, which is fixedly connected to the link rod 6; $\{n_8\}$ is fixedly connected to the end actuator, $\theta_i(i = 1, 2, \dots, 7)$ is for the motion angle of articulation, in the sagittal motion plane, θ_3 is the flexion and extension angles of hip joint, θ_4 is the flexion and extension angles of knee joint; θ_5 is the flexion and extension angle of ankle joint; $a_j(j = 0, 1, \dots, 6)$ is the distance between two adjacent joints,

wherein a_0 representing a half of the waist width, a_1, a_2 respectively represent thigh length and calf length, a_3 represents the distance from the ankle joint center to feet.

According to D-H parameters table, the homogeneous coordinate transformation matrix T_{i-1}^i of coordinate system $\{n_{i-1}\}$ corresponds to the coordinates system $\{n_i\}$, thus to obtain homogeneous coordinate transformation of the coordinate system $\{n_i\}$ corresponding to the base coordinate system $\{n_0\}$:

$$T_0^i = T_0^1 T_1^2 \cdots T_{i-1}^i \quad (1)$$

According to Eq. (1), the homogeneous coordinates of the coordinate system $\{n_3\}$ corresponding to $\{n_0\}$ can be drawn as follows:

$$T_0^3 = T_0^1 T_1^2 T_2^3 \quad (2)$$

Since a variety of road conditions will be encountered during the walk, there's the need for timely turn or tilt feet, all these conditions lead to ankle having enough activity space in the rotation axis, internal and external rotation axis, namely the motion angle θ_6, θ_7 is not constant. However, since the two joints do not work when walking straightly on the flat ground, it's assumed here $\theta_6 = \theta_7 = \pi/2$. Thereby obtaining T_5^6, T_6^7 and T_7^8 , and T_0^8 is obtained according to Eq. (1).

It can be known from Fig. 1 that the center point M of the end actuator is located in the origin of coordinate system $\{n_8\}$, and therefore the homogeneous coordinate of point M in the coordinate system $\{n_8\}$ is as follows:

$$p_8 = (0 \quad 0 \quad 0 \quad 1)^T \quad (3)$$

Then the homogeneous coordinates of point M in the base coordinate system $\{n_0\}$ is as follows:

$$p^8 = T_0^8 p_8 = (f_1 \quad f_2 \quad f_3 \quad 1)^T \quad (4)$$

Wherein:

$$\begin{aligned} f_1 &= g_1(\theta_1, \theta_2, \theta_3, \theta_4, \theta_5, a_0, a_1, a_2, a_3, a_5, a_6) \\ f_2 &= g_2(\theta_1, \theta_2, \theta_3, \theta_4, \theta_5, a_0, a_1, a_2, a_3, a_5, a_6) \\ f_3 &= g_3(\theta_2, \theta_3, \theta_4, \theta_5, a_1, a_2, a_3, a_4, a_5, a_6) \end{aligned}$$

According to the structure proportion of design prototype in Fig. 1, taking the length of link rod as: $a_0 = 150$ mm, $a_1 = 440$ mm, $a_2 = 360$ mm, $a_3 = 90$ mm, $a_4 = 130$ mm, $a_5 = 20$ mm, $a_6 = 28.5$ mm. The joint angular displacement of $\theta_1, \theta_2, \theta_4, \theta_5$ and θ_5 at different moments is selected to obtain the position posture of the end actuator point M at the corresponding moment as shown in Table 2.

Table 2 Homogeneous coordinates of the end actuator point M in the base coordinate system at different moments

t/s	0.2	0.4	0.6	0.8	1
p^8	$\begin{bmatrix} 915.8 \\ 200.5 \\ -172 \\ 1 \end{bmatrix}$	$\begin{bmatrix} 975.1 \\ -25.2 \\ -141.4 \\ 1 \end{bmatrix}$	$\begin{bmatrix} 836.6, \\ -283.9 \\ -146.3 \\ 1 \end{bmatrix}$	$\begin{bmatrix} 805.1 \\ -44.7 \\ -90.4 \\ 1 \end{bmatrix}$	$\begin{bmatrix} 857.2 \\ 409.9 \\ -192.5 \\ 1 \end{bmatrix}$

3.3 Jacobian Matrix of the Mechanism

It can be seen from Eq. (4), the homogeneous coordinate system of point M mapping to the base coordinate system is:

$$(x_M \ y_M \ z_M \ 1)^T = (f_1 \ f_2 \ f_3 \ 1)^T \quad (5)$$

Then:

$$\begin{pmatrix} v_x \\ v_y \\ v_z \\ w_1 \\ w_2 \end{pmatrix} = \begin{pmatrix} \dot{f}_{1\theta_1} & \dot{f}_{1\theta_2} & \dot{f}_{1\theta_3} & \dot{f}_{1\theta_4} & \dot{f}_{1\theta_5} \\ \dot{f}_{2\theta_1} & \dot{f}_{2\theta_2} & \dot{f}_{2\theta_3} & \dot{f}_{2\theta_4} & \dot{f}_{2\theta_5} \\ \dot{f}_{3\theta_1} & \dot{f}_{3\theta_2} & \dot{f}_{3\theta_3} & \dot{f}_{3\theta_4} & \dot{f}_{3\theta_5} \\ 0 & 0 & 0 & 1 & 0 \\ 0 & 0 & 0 & 0 & 1 \end{pmatrix} \begin{pmatrix} \dot{\theta}_1 \\ \dot{\theta}_2 \\ \dot{\theta}_3 \\ \dot{\theta}_4 \\ \dot{\theta}_5 \end{pmatrix} \quad (6)$$

The obtained Jacobian matrix of the mechanism is:

$$J = \begin{pmatrix} \dot{f}_{1\theta_1} & \dot{f}_{1\theta_2} & \dot{f}_{1\theta_3} & \dot{f}_{1\theta_4} & \dot{f}_{1\theta_5} \\ \dot{f}_{2\theta_1} & \dot{f}_{2\theta_2} & \dot{f}_{2\theta_3} & \dot{f}_{2\theta_4} & \dot{f}_{2\theta_5} \\ \dot{f}_{3\theta_1} & \dot{f}_{3\theta_2} & \dot{f}_{3\theta_3} & \dot{f}_{3\theta_4} & \dot{f}_{3\theta_5} \\ 0 & 0 & 0 & 1 & 0 \\ 0 & 0 & 0 & 0 & 1 \end{pmatrix}_{5 \times 5} \quad (7)$$

The Jacobian matrix is a fifth-order square matrix, and the corresponding determinant is $|J| \neq 0$.

3.4 Verification of Spatial Kinematics

The kinematic model of the lower extremity exoskeleton assistive mechanism can be obtained through the Sect. 2.2, and the relationship between motion trajectory of the end actuator, each articulation motion parameters and link rod parameters can also be obtained accordingly. Now the motion simulation is conducted by using the

robot toolbox of MATLAB to verify the consistency of above kinematic model with the motion of human body lower extremity.

Determine the size of each link rod and establish the model, and the joint angular displacement data obtained from OpenSIM is considered as the drive parameters, simulation for simulation.

Analysis of the mainly existed errors:

- (1) The human body lower extremity motion mechanism is mainly analyzed by software OpenSIM, the corresponding motion data is also obtained by the software. The creation of the skeleton model, data processing and driven motion in the software are with certain error compared to the actual human body;
- (2) The quadratic error introduced when processing data obtained by the software, which mainly shows in the data error caused by the curve discretion and the effective value number of bits;
- (3) Human body joint is too complicated, and this only shows simple rotation, and therefore there's the error between the data obtained and model built due to simplified joints;

So, the creation of the spatial kinematic model of the lower extremity exoskeleton assistive mechanism is verified to be reasonable and correct.

It can be known from z direction displacement curve of Figs. 4 and 5 that the absolute displacement value of the spatial trajectory in the three axes of xyz is larger, wherein, z axis is perpendicular to the sagittal plane, and the corresponding absolute displacement value is directly related to the internal and external rotation

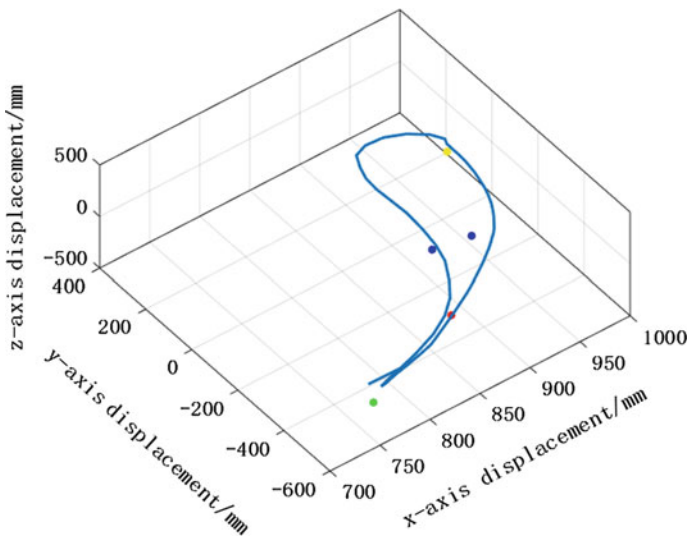
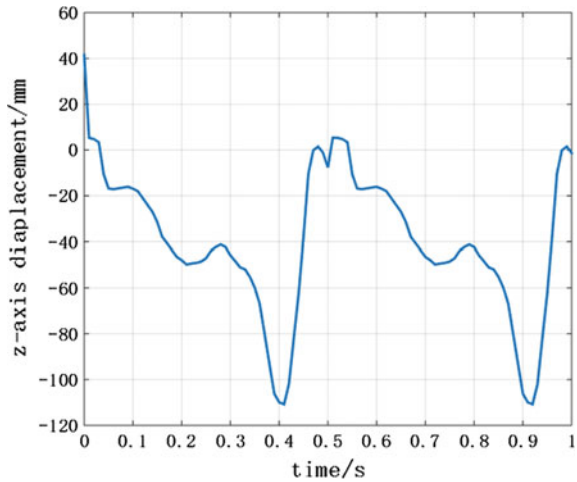


Fig. 4 End actuator center motion trajectory and kinematics to calculate coordinates

Fig. 5 End actuator center displaces to motion along the z-axis



motion of the hip joint and rotational motion, the maximum value is of about 150 mm.

It's visible that the end actuator has the significant displacement in the direction perpendicular to the sagittal plane, the pure displacement trajectory analysis inside the sagittal plane is not accurate enough, and therefore so it's critical to analyze the spatial motion trajectory of the end actuator.

4 Analysis of Workspace

4.1 Calculation of Workspace

Robot workspace refers to the range of activities with the coordinate origin of the end actuator reaching the maximum, and it is an important kinematics indicator used to measure the work capacity of the robot.

The relationship between position coordinate of point M , parameters of joints and link rod parameters can be obtained from Eq. (4), since the motion of each articulation angular displacement θ_i and length of the link rod a_i are known, the workspace of coordinate system origin M of the end actuator can be obtained through MATLAB editing the expression of f_i , as shown in Fig. 6.

The robot workspace is mainly determined by the robot configuration and structural parameters of the link rods, but also affected and restricted by their articulation motion range. It can be known from the analysis of Fig. 6 that the workspace of the structure is with the presence of empty and cavities. Therefore, this institution should avoid corresponding region during operation, thus to be placed within flexible workspace as far as possible.

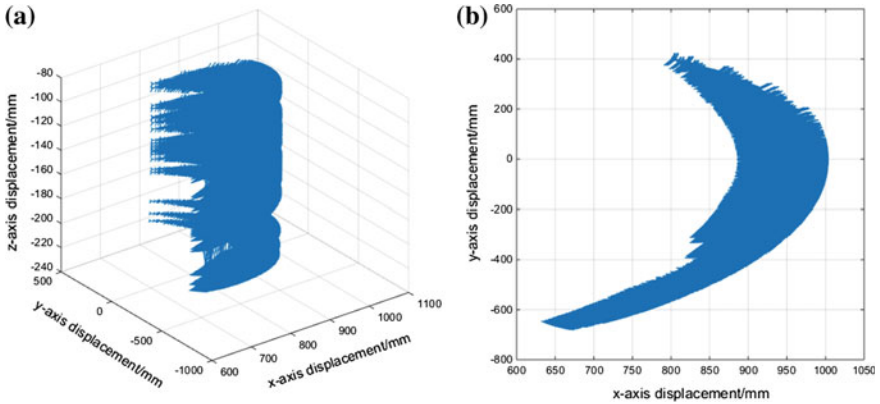


Fig. 6 Workspace of point M, **a** Workspace of point M in three-dimensional space, **b** Workspace of point M in xy plane

4.2 Workspace Analysis and Discussion

Robot kinematics is the basis of robot path planning, the given path motion of the end actuator in certain posture can be achieved through the positive solution and inverse solution of the institution position. It's assumed that two points in motion trajectory of the end actuator are taken as the initial point and end point of the corresponding linear motion trajectory, the initial velocity and initial acceleration is set to be known. The change curves of various joint angles can be drawn through the positive and inverse kinematics calculation, as shown in Fig. 7.

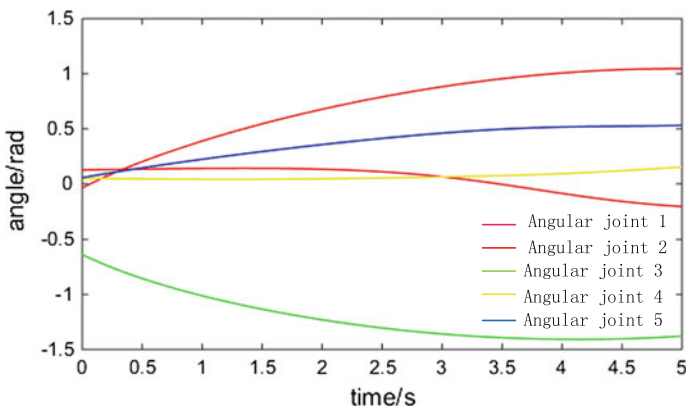


Fig. 7 Inverse solution of various joint angular displacements

5 Conclusion

This thesis created the spatial kinematic model of lower extremity exoskeleton assistive mechanical mechanism through the homogeneous coordinate transformation, and calculated and inverse analysis to verify correctness of the model. Furthermore, this thesis conducted the inverse solution of kinematics model, obtaining that there's no singular configuration in structural motion. Finally, there's simulation calculation of the workspace mechanism:

- (1) Construction of the spatial kinematic model of lower extremity exoskeleton assistive institution, and this thesis verified the correctness of the model through the theoretical calculations and MATLAB simulation and comparison.
- (2) Comparative analysis of the spatial motion trajectory of the end actuator and the motion trajectory of the sagittal plane. It can be known that the end actuator has larger spatial motion range in the perpendicular sagittal plane, which can't be ignored, it is critical to analyze the spatial motion trajectories.
- (3) Verifying the rationality of the joint layout. The joint structure in the mechanical system simplifies part of freedom with smaller motion range compared with the human body joints, but since the impact of the partial freedom on the overall motion is minimal, and therefore it can be ignored.
- (4) The inverse kinematics solution of the lower extremity exoskeleton assistive mechanism is conducted with the use of MATLAB, which verified that the mechanism did not have singular configuration. In addition, the workspace was constructed, which laid the foundation for further kinematics analysis, trajectory planning and optimization design.

The next step work will be the calculation and analysis of the force or torque required for driving the articulation motion. The points p_1 and p_2 connecting to the driven hydraulic cylinder on both ends of the link rods are taken to analyze the change law of linear distance between the two points in the walking motion, which is considered as the linear motion displacement of the hydraulic cylinder. With the use of the triangle similar principle, the hydraulic cylinder parameter is selected to calculate and obtain the torque curve provided by the hydraulic cylinder. The iterative calculation is conducted by comparing with the actually required torque and the torque provided by a hydraulic cylinder, until the provided torque is nearly greater than actually required torque. The above will be used to guide the hydraulic cylinder design and the driven system design.

References

1. Park Y (2013) Soft wearable motion sensing suit for lower limb biomechanics measurements. In: IEEE International Conference on Robotics and Automation
2. Mooney LM, Rouse EJ, Herr HM (2014) Autonomous exoskeleton reduces metabolic cost of walking. IEEE, NY

3. Wu BY, Yu Y, Xu DZ, et al. (2007) Kinematics analysis and simulation of a robot with wearable and power-assisted lower extremities. *Mech Sci Technol* (02):235–240(in Chinese)
4. Menguc Y, Park YL, Martinez-Villalpando E, Aubin P, Zisook M, Stirling L, Wood RJ, Walsh CJ (2013) Soft wearable motion sensing suit for lower limb biomechanics measurements. In: *IEEE international conference on robotics and automation*, 2013
5. Hal SY (2010) Hybrid assistive limb based on cybernics
6. Wa DQ, Xu YM, Bai YH (2011) Research and development of lower extremity rehabilitation exoskeletons. *J Clinical Rehabil Tissue Eng Res* 15(52): 9855–9858 (in Chinese)
7. Zhang ZH (2011) Research on lower extremity exoskeleton of power assist robot. Harbin Institute of Technology, Harbin (in Chinese)
8. Liang WY (2012) Research on wearable parallel assistive robot for hip joint power assist. University of Science and Technology of China, Anhui (in Chinese)
9. Yang JQ (2012) Research on the lower-limb exoskeleton assisted robot system. Harbin Engineering University, Harbin (in Chinese)
10. Zhi-jun YWJL (2013) Development of a wearable and portable rehabilitation exoskeleton robot. *J Integr Technol* (04):27–31 (in Chinese)
11. Chu A, Kazerooni H, Zoss A (2005) On the biomimetic design of the Berkeley lower extremity exoskeleton (BLEEX). In: *IEEE international conference on robotics and automation*
12. Zoss A, Kazerooni H, Chu A (2005) On the mechanical design of the Berkeley lower extremity exoskeleton (BLEEX). In: *IEEE international conference on intelligent robots and systems*
13. Zoss AB, Kazerooni H, Chu A (2006) Biomechanical design of the Berkeley lower extremity exoskeleton (BLEEX). *IEEE/ASME Trans Mechatron* 11(2):128–138

Equilibrium Conformation of Concentric-Tube Robots Under Loads Based on the Minimum Energy Principle

Long Huang, Changyan He, Yang Yang and Chenhan Guang

Abstract Concentric-tube robots, which consist of several pre-curved tubes, can achieve dexterous motion through axial rotation and translation of each component tube. Aiming at equilibrium conformation modeling of externally loaded concentric-tube robots, an equivalent conservative system is proposed to translate the force balance problem into the minimum potential energy configuration problem of the conservative system. Then, the optimal control theory is used to derive the differential equations for the equilibrium conformation. Finally, this model is visually evaluated through the simulation of a loaded two-tube robot, and the effects of the external loads on the vital parameters of the equilibrium conformation are analyzed.

Keywords Concentric-tube continuum robots · Equilibrium conformation · Minimum potential energy principle · Kirchhoff rod

1 Introduction

Concentric-tube robots, as a special type of continuum robots, are well-suited for minimally invasive surgeries [1–3]. Normally, a concentric-tube robot consists of several concentric Nitinol tubes with different curvatures. Through axial rotation and translation of each tube, the shape of the tubes' common backbone can be

L. Huang · C. He · Y. Yang (✉) · C. Guang
School of Mechanical Engineering and Automation, Beihang University,
Xueyuan Road 37, Haidian District, Beijing 100191, China
e-mail: yang_mech@126.com

L. Huang
e-mail: huanglongmech@buaa.edu.cn

C. He
e-mail: changyanhe@126.com

C. Guang
e-mail: guangchenhan@foxmail.com

altered, and consequently the pose of the robot's tip can vary within a certain range. Owing to the small diameter and simple structure, the concentric-tube robot can achieve dexterous motion under the narrow environment. Recent studies have already shown several potential clinic applications for these robots [4–7].

When the concentric-tube robot is used as a medical robot, a conventional task is to interact with the surrounding tissue. As a compliant mechanism, the robot will undergo a deformation during the interaction. Therefore, it is significant to study the precise equilibrium conformation of the robot subject to external loads. The general method adopted in prior researches is to analyze each tube with Newtonian mechanics and Kirchhoff rod theory, which is referred to as the geometrically exact model [8]. The processes of this method are as follows. First, the shape of each tube is described utilizing Kirchhoff rod theory; based on the linear constitutive equations, the relationship between moment and local curvature vector at arbitrary cross section for each tube need to be derived. Then, the force and moment balance equations for each tube are presented, and it is noteworthy that the unknown deformed shape of the tubes should be eliminated through the derivation of these equations. Furthermore, the equations about each tube's spin angle should also be deduced. Finally, by solving these equations, the equilibrium conformation can be obtained. The geometrically exact model is widely used to analyze both the concentric-tube robot and the cable-driven robot. Trivedi et al. [8] utilized geometrically exact Kirchhoff rod theory to model the shape of cable-driven robot under loads, and achieved high accuracy. Xu et al. [9] used four flexible rods instead of cables to build a small continuum robot, and they also used the geometrically exact model to derive the equilibrium conformation of the robot and furthermore achieve intrinsic force sensing. The models of these two cases are convenient to establish, since their components are under internal and external loads at discrete positions. However, the tubes in the concentric-tube robot are interacted continuously along the arc-length; therefore, the derivation of the geometrically exact model for the concentric-tube robot is more complicated [10, 11].

In order to avoid the complex interaction analysis of the tubes, this paper proposes an equivalent method which transform the force balance problem into the equilibrium problem of the conservative system. Then, applying the minimum potential energy principle of conservative system and the optimal control theory, the differential equations which describe the equilibrium conformation can be acquired. For clarity in deriving the equations, this paper focus on the shape modeling of the three-tube robot subject to concentrated forces at its tip, and the proposed method can also be used in the robot with arbitrary number of tubes subject to distributed forces and torques.

2 Description of the Concentric-Tube Robot

A concentric-tube robot usually comprises two or three Nitinol tubes, and achieves 3–6 degrees of freedom. These elastic tubes are assembled concentrically. Through axial rotation and translation of each component tube, the shape of the tubes’ common backbone can be altered, and consequently the position and pose of the robot’s tip can vary in a certain range. Nitinol is widely used in these robots due to its outstanding elasticity [12]. Figure 1 shows a concentric-tube robot consisting of three tubes.

3 Equivalent Conservative System for Concentric-Tube Robots Subject to External Forces

The widely used geometrically exact model always involves the complex force analysis of tubes. To simplify the model, this paper propose an alternative conservative system: a robot with an object hanging at its tip, as shown in Fig. 2; the weight of the object is the value of the external force F , and the direction of gravity is the direction of the external force. Since the weights of the tubes are neglected,

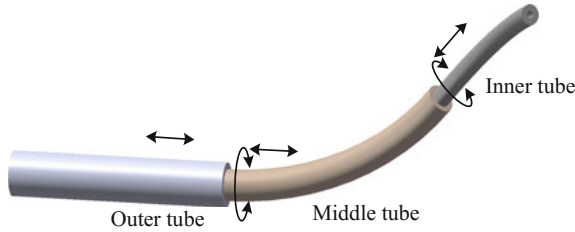


Fig. 1 A concentric-tube robot consisting of three tubes

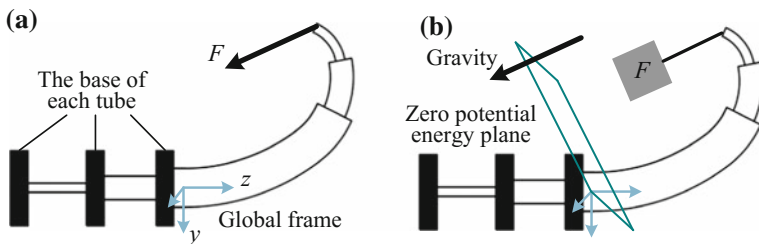


Fig. 2 The equivalent conservative system for the concentric-tube robot subject to an external force. The external force is replaced with an object hanging at the robot’s tip

the potential energy of this alternative system only includes the elastic energy of each tube and the gravitational potential energy of the object. Note that the zero potential energy plane passes through the origin of the global frame and it is perpendicular to the external force F .

4 Kinematic Model of Concentric-Tube Robots

4.1 Modeling Assumptions

Since all component tubes in the robot are long and thin, the basic assumptions of the Kirchhoff-rod theory are adopted in this paper: (1) the extension and transverse shear deformation of the tubes are neglected; (2) the linear constitutive equations for both bending and torsion are adopted.

In addition, for clarity in deriving the fundamental equations, the weights of tubes and friction between them are neglected. The tubes are considered to be strictly concentric. Experiments show that these aspects have little influence on the equilibrium conformation model [5, 10], and most of the prior models adopt these assumptions.

4.2 Geometric Descriptions of a Curving Tube

The undeformed curving backbone of a tube can be described by an arc-length parameterized curve $\mathbf{r}^*(s)$. And along this curve, the well-known Bishop frames [5] can be defined. By the convention of the Bishop frames, the z -axes are always in the instantaneous tangential direction of the curve, and the frames will not rotate around their z -axis along the curve. Therefore the Bishop frame is also known as the no-torsion frame. The Bishop frames $\{\mathbf{F}^*(s)\}$ for a undeformed tube can be described in the global frame $\{\mathbf{W}\}$ with a series of transformations $\mathbf{g}^*(s)$, which consist of position vectors $\mathbf{r}^*(s)$ and rotation matrices $\mathbf{R}^*(s)$ as

$$\mathbf{g}^*(s) = \begin{bmatrix} \mathbf{R}^*(s) & \mathbf{r}^*(s) \\ \mathbf{0}^T & 1 \end{bmatrix} \quad (1)$$

If the arc-length parameter s is replaced with time variable t , this can be considered as the homogeneous transformation description of rigid motion. Then drawing on the rigid motion theory [13], a twist can be defined as

$$\xi^*(s) = [\mathbf{v}^{*T}(s) \quad \boldsymbol{\omega}^{*T}(s)]^T = (\mathbf{g}^{*-1}(s)\dot{\mathbf{g}}^*(s))^\vee \quad (2)$$

where $\mathbf{v}^*(s) = \mathbf{e}_3 = [0 \ 0 \ 1]^T$ in this case, and $\boldsymbol{\omega}^*(s)$, implying the curvature of the rod (similar to the angular velocity of a rotation), is defined as the curvature vector in the local frame. In this paper, the dot over the variable represents the derivative of the variable with respect to arc-length s . The operator \mathbf{v} represents the transformation $\mathbf{R}^{4 \times 4}$ (or $\mathbf{R}^{3 \times 3}$) to \mathbf{R}^6 (or \mathbf{R}^3), given by the following equation

$$\begin{pmatrix} 0 & -a_3 & a_2 & b_1 \\ a_3 & 0 & -a_1 & b_2 \\ -a_2 & a_1 & 0 & b_3 \\ 0 & 0 & 0 & 0 \end{pmatrix}^\vee = (a_1 \ a_2 \ a_3 \ b_1 \ b_2 \ b_3)^T \quad (3)$$

Also, the inverse operation is denoted by \wedge . The detailed discussion on the related notations can be found in [13]. The relationship between $\boldsymbol{\omega}^*(s)$ and $\mathbf{R}^*(s)$ is as follows:

$$\boldsymbol{\omega}^*(s) = (\mathbf{R}^{*\top}(s) \dot{\mathbf{R}}^*(s))^\vee \quad (4)$$

The deformation of a pre-curved tube from its initial state to a new state corresponds to a variation of frames from $\{\mathbf{F}^*(s)\}$ to $\{\mathbf{F}(s)\}$, also corresponds to a variation from $\mathbf{g}^*(s)$ to $\mathbf{g}(s)$, and a variation from $\boldsymbol{\xi}^*(s)$ to $\boldsymbol{\xi}(s)$ (denoted by $\Delta \boldsymbol{\xi}(s)$). The new frames $\{\mathbf{F}(s)\}$ do not necessarily abide by the convention of the Bishop frames.

4.3 Kinematic Equations of Concentric-Tube Robots

The inputs of the concentric-tube robot are the translation and rotation of each component tube at the corresponding base. Let $s = a_i$ and $\theta_i(a_i)$ denote the translation and rotation inputs of the i th tube, also let $s = b_i$ denotes the arc-length location of the i th tube's tip, where i identifies the tubes from outer to inner. The shape of the concentric-tube robot can also be described by the Bishop frames $\{\mathbf{B}(s)\}$ along with other variables. The Bishop frame at the arc-length location $s = 0$, is set as the global frame $\{\mathbf{W}\}$. According to Sect. 3.2, $\{\mathbf{B}(s)\}$ can also be described in the global frame $\{\mathbf{W}\}$ with position vectors $\mathbf{r}(s)$ and rotation matrices $\mathbf{R}(s)$, which satisfy

$$\dot{\mathbf{r}}(s) = \mathbf{R}(s) \mathbf{e}_3 \quad (5)$$

$$\dot{\mathbf{R}}(s) = \mathbf{R}(s) \left((\omega_x \ \omega_y \ 0)^T \right)^\wedge \quad (6)$$

where $(\omega_x, \omega_y, 0)^T$ is the curvature vector of $\{\mathbf{B}(s)\}$. Since the tubes are assembled concentrically, the x - y components of each tube's curvature vector in the equilibrium conformation are equivalent respectively if they are expressed in a common

frame. When they are expressed in the robot’s Bishop frames, they all equals $(\omega_x, \omega_y)^T$, which is denoted by $\omega_{xy}(s)$. The frames $\{F_i(s)\}$ for each tube differ from the robot’s Bishop frames $\{B(s)\}$ by a rotation around the local z -axes; that is

$$\mathbf{R}_i(s) = \mathbf{R}(s)\mathbf{R}_z(\theta_i(s)) = \mathbf{R} \begin{bmatrix} \cos \theta_i(s) & \sin \theta_i(s) & 0 \\ \sin \theta_i(s) & \cos \theta_i(s) & 0 \\ 0 & 0 & 1 \end{bmatrix} \quad (7)$$

where $\mathbf{R}(s)$ and $\mathbf{R}_i(s)$ are rotation matrices of $\{B(s)\}$ and $\{F_i(s)\}$ with respect to $\{W\}$, $\theta_i(s)$ is the rotation angle from x -axes of $\{B(s)\}$ to x -axes of $\{F_i(s)\}$, and $\theta_i(a_i)$ is the aforementioned input angle of the i th tube at its base. Figure 3 shows the relationship of $\{F_i^*(s)\}$, $\{F_i(s)\}$ and $\{B(s)\}$.

Based on the above analysis, the x - y components of the i th tube’s curvature vector can be expressed as

$$\omega_{i,xy}(s) = \mathbf{R}_z(\theta_i(s))|_{xy}^T \omega_{xy}(s) \quad (8)$$

where

$$\mathbf{R}_z(\theta_i(s))|_{xy} = \begin{pmatrix} \cos \theta_i(s) & -\sin \theta_i(s) \\ \sin \theta_i(s) & \cos \theta_i(s) \end{pmatrix} \quad (9)$$

$$\omega_{i,xy}(s) = (\omega_{i,x}(s) \quad \omega_{i,y}(s))^T \in \mathbb{R}^2 \quad (10)$$

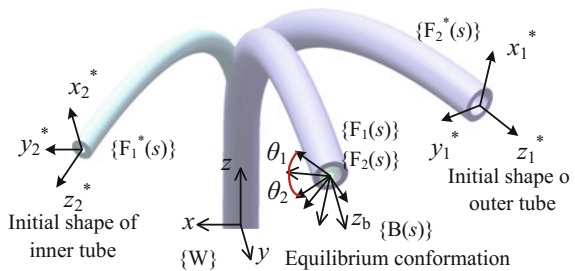
Besides, according to Eqs. (4) and (7), the third component of the i th tube’s curvature vector $(\omega_{i,z}(s))$ is equal to $\dot{\theta}_i(s)$. Define $\theta(s) = (\theta_1, \theta_2, \theta_3)^T$, and $\omega_z(s) = (\omega_{1,z}, \omega_{2,z}, \omega_{3,z})^T$, then we have

$$\dot{\theta}(s) = \omega_z(s) \quad (11)$$

The model of the concentric-tube robot should also include the linear constitutive relationship of Nitinol, which can be described in potential energy form as

$$E_i(s) = \int \frac{1}{2} (\omega_i - \omega_i^*)^T \mathbf{K}_i(s) (\omega_i - \omega_i^*) ds \quad (12)$$

Fig. 3 The tubes’ initial states and equilibrium states. In the equilibrium conformation, both tubes are bended and twisted



where $\boldsymbol{\omega}_i^*$ and $\boldsymbol{\omega}_i$ are the curvature vectors of the initial shape and the deformed shape respectively, and stiffness matrix $\mathbf{K}_i(s)$ can be expressed as

$$\mathbf{K}_i(s) = \begin{bmatrix} K_{i,xy}(s) & 0 & 0 \\ 0 & K_{i,xy}(s) & 0 \\ 0 & 0 & K_{i,z}(s) \end{bmatrix} \quad (13)$$

and $K_{i,xy}(s)$ is the bending stiffness of the i th tube in its x and y directions, and $K_{i,z}(s)$ is the torsional stiffness of the i th tube.

Normally, the lengths of the tubes in a robot are not equal. The outer tube is the shortest while the inner tube is the longest. For convenience, virtual tubes are added to the tips and the bases of the outer and the middle tubes, so that the tubes are fully overlapped over $[a_3, b_3]$. The virtual tubes at the bases are designated with infinite bending and torsional rigidity, and the virtual tubes at the tips are designated with zero bending and torsional rigidity. In this way, this fully overlapped model is equivalent to the original model.

5 Equilibrium Conformation of Concentric-Tube Robots

The static equilibrium configuration of a conservative system should conform to the minimum potential energy principle, which states that the total potential energy function is stationary at the static equilibrium configuration [11]. Therefore, the first variation of the potential energy function at the static equilibrium configuration should be zero. This problem can be solved utilizing the optimal control theory. According to the aforementioned alternative system, the total potential energy function is as follows:

$$J = -\mathbf{F}^T \mathbf{r}(b_3) + \int_{a_3}^{b_3} \sum_{i=1}^3 \frac{1}{2} (\boldsymbol{\omega}_i - \boldsymbol{\omega}_i^*)^T \mathbf{K}_i(s) (\boldsymbol{\omega}_i - \boldsymbol{\omega}_i^*) ds \quad (14)$$

The first part of the function J represents the gravitational potential energy of the object, and the integral term represents the bending and torsional energy along the arc-length of all tubes. Substituting (8) into (14) can eliminate $\boldsymbol{\omega}_i$ in the potential energy, and yields

$$J = -\mathbf{F}^T \mathbf{r}(b_3) + \int_{a_3}^{b_3} \frac{1}{2} \sum_{i=1}^3 \left(K_{i,z} (\dot{\theta}_i - \omega_{i,z}^*)^2 + K_{i,xy} \left| \mathbf{R}_z(\theta_i) \Big|_{xy}^T \boldsymbol{\omega}_{xy} - \boldsymbol{\omega}_{i,xy}^* \right|^2 \right) ds \quad (15)$$

where symbol $|\cdot|$ denotes the module of the vector, $\omega_{i,xy}^* \in \mathbb{R}^2$ is the x - y components of ω_i^* , $\omega_{i,z}^* \in \mathbb{R}$ is the third component of ω_i^* . For convenience, the term of gravitational potential energy is denoted by $\varphi(\mathbf{r})$, and the integrand term is denoted by Lagrangian function L .

The function J can be interpreted as the cost function of a control system with arc-length parameter s interpreted as time parameter t . Then we have its state vector and control vector as follows

$$\mathbf{x}(s) = (\mathbf{r}(s), \mathbf{R}(s), \boldsymbol{\theta}(s)) \in \mathbb{R}^3 \times \mathbb{R}^{3 \times 3} \times \mathbb{R}^3 \quad (16)$$

$$\mathbf{u}(s) = (\boldsymbol{\omega}_{xy}(s), \omega_z(s)) \in \mathbb{R}^2 \times \mathbb{R}^3 \quad (17)$$

and its state equations as (5), (6) and (11).

Therefore, drawing on the optimal control theory [14], the Hamiltonian function can be defined as:

$$\begin{aligned} H(\mathbf{x}, \mathbf{u}, \boldsymbol{\lambda}, s) = & \frac{1}{2} \sum_{i=1}^n \left(K_{i,z} (\omega_{i,z} - \omega_{i,z}^*)^2 \right) \\ & + \frac{1}{2} \sum_{i=1}^n \left(K_{i,xy} \left| \mathbf{R}_z(\theta_i) \Big|_{xy}^T \boldsymbol{\omega}_{xy} - \omega_{i,xy}^* \right|^2 \right) + \boldsymbol{\lambda}_r^T \mathbf{R} \mathbf{e}_z + \text{tr} \left(\boldsymbol{\lambda}_R^T \mathbf{R} \begin{bmatrix} \omega_x \\ \omega_y \\ 0 \end{bmatrix} \wedge \right) + \boldsymbol{\lambda}_\theta^T \omega_z \end{aligned} \quad (18)$$

where $\boldsymbol{\lambda} = (\boldsymbol{\lambda}_r^T, \boldsymbol{\lambda}_R^T, \boldsymbol{\lambda}_\theta^T)^T \in \mathbb{R}^3 \times \mathbb{R}^{3 \times 3} \times \mathbb{R}^3$ is the Lagrange multiplier. The component multipliers $\boldsymbol{\lambda}_r^T, \boldsymbol{\lambda}_R^T, \boldsymbol{\lambda}_\theta^T$ can be considered as the generalized forces on the generalized coordinates \mathbf{r}, \mathbf{R} and $\boldsymbol{\theta}$ respectively.

Obviously, this optimal control problem has the Bolza-type cost function, and it is under no terminal constraints. According to the fundamental optimal control theory [14], the first order necessary conditions for stationarity along entire trajectory include the canonical equations, the extreme conditions and the boundary conditions, as follows:

$$\begin{cases} \dot{\boldsymbol{\lambda}}_r = -\frac{\partial H}{\partial \mathbf{r}} = (0 \ 0 \ 0), \dot{\boldsymbol{\lambda}}_R = -\frac{\partial H}{\partial \mathbf{R}} = -\mathbf{e}_z \boldsymbol{\lambda}_r^T - \begin{bmatrix} \omega_x \\ \omega_y \\ 0 \end{bmatrix} \wedge \boldsymbol{\lambda}_R^T, \\ \dot{\boldsymbol{\lambda}}_\theta = -\frac{\partial H}{\partial \boldsymbol{\theta}} = \begin{pmatrix} K_{1,xy} \omega_{1,xy}^{*T} & \mathbf{R}_{d,1} \boldsymbol{\omega}_{xy} \\ K_{2,xy} \omega_{2,xy}^{*T} & \mathbf{R}_{d,2} \boldsymbol{\omega}_{xy} \\ K_{3,xy} \omega_{3,xy}^{*T} & \mathbf{R}_{d,3} \boldsymbol{\omega}_{xy}^T \end{pmatrix}^T \end{cases} \quad (19)$$

$$\begin{cases} \frac{\partial H}{\partial \omega_{xy}} = \sum_{i=1}^n K_{i,xy} (\omega_{xy} - \mathbf{R}_z(\theta_i) \omega_{i,xy}^*)^T + \begin{pmatrix} (\lambda_{\mathbf{R}\mathbf{R}}^T)_{23} - (\lambda_{\mathbf{R}\mathbf{R}}^T)_{32} \\ -(\lambda_{\mathbf{R}\mathbf{R}}^T)_{13} + (\lambda_{\mathbf{R}\mathbf{R}}^T)_{31} \end{pmatrix}^T = 0, \\ \frac{\partial H}{\partial \omega_z} = \begin{pmatrix} K_{1,z} (\omega_{1,z} - \omega_{1,z}^*) \\ K_{2,z} (\omega_{2,z} - \omega_{2,z}^*) \\ K_{3,z} (\omega_{3,z} - \omega_{3,z}^*) \end{pmatrix}^T + \lambda_\theta^T = 0 \end{cases} \quad (20)$$

$$\begin{cases} \mathbf{r}(a_3) = (0 \ 0 \ a_3)^T, \mathbf{R}(a_3) = \mathbf{I}, \boldsymbol{\theta}(a_3) = \boldsymbol{\theta}_{\text{base}}, \\ \lambda_r(b_3) = \frac{\partial \varphi}{\partial \mathbf{r}(b_3)} = -\mathbf{F}, \lambda_{\mathbf{R}}(b_3) = \frac{\partial \varphi}{\partial \mathbf{R}(b_3)} = 0, \lambda_\theta(b_3) = \frac{\partial \varphi}{\partial \boldsymbol{\theta}(b_3)} = 0 \end{cases} \quad (21)$$

where

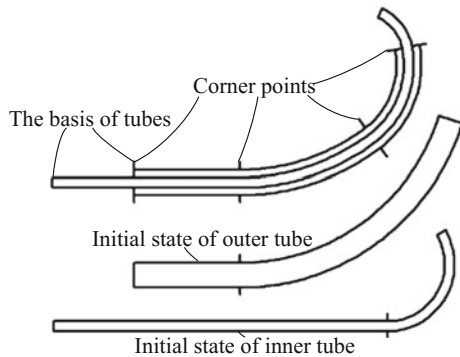
$$\mathbf{R}_{d,i} = \begin{bmatrix} -\sin \theta_i & \cos \theta_i \\ -\cos \theta_i & -\sin \theta_i \end{bmatrix} \quad (22)$$

$(\mathbf{A})_{ij}$ denotes the i th row and j th Column element of matrix \mathbf{A} , \mathbf{I} denotes the 3×3 identical matrix, $\boldsymbol{\theta}_{\text{base}} = \{\theta_1(a_3), \theta_2(a_3), \theta_3(a_3)\}^T$ is a column vector consists of the rotation angles of all tubes at the base.

In the above discussion, the admissible trajectories for the optimal control problem are assumed to be continuous and to have continuous first derivatives; that is, the trajectories are smooth. However, for concentric-tube robots, the trajectories are usually discontinuous at several discrete points owing to the following facts: (1) the precurvature of each tube is usually piecewise-constant along the full arc-length; e.g., a typical tube comprising a straight portion and a constant curvature portion; (2) owing to the aforementioned virtual tubes, the bending stiffness and torsional stiffness are also piecewise-constant along the full arc-length. These two kinds of points are shown in Fig. 4. They are both referred to as corner points.

Therefore, the admissible trajectories should satisfy the additional necessary conditions, as follows [14]:

Fig. 4 The corner points in a robot. The two corner points in the middle are emerged because of the pre-curvature mutation of the tubes. The first and the last corner points are emerged since the tubes are not fully overlapped



$$\begin{cases} \frac{\partial L}{\partial \dot{\mathbf{x}}}\big|_{s_j^-} = \frac{\partial L}{\partial \dot{\mathbf{x}}}\big|_{s_j^+} \\ (L - \dot{\mathbf{x}}^T \frac{\partial L}{\partial \dot{\mathbf{x}}})\big|_{s_j^-} = (L - \dot{\mathbf{x}}^T \frac{\partial L}{\partial \dot{\mathbf{x}}})\big|_{s_j^+} \end{cases} \quad (23)$$

where j is the number of the corner points, s_j is the arc-length location of corner point j . They are determined by the inputs of each tube.

In conclusion, the equilibrium conformation model of the robot comprises the differential Eqs. (19)–(20), boundary conditions (21) and corner point conditions (23) with respect to shape parameter set $\{\mathbf{r}(s), \mathbf{R}(s), \boldsymbol{\theta}(s)\}$. Normally, this various point boundary value problem (BVP) cannot be solved analytically. The common numerical methods for it include shooting method and difference method [15]. For a number of inputs, several corresponding configurations may emerge [16, 17]. The robot will take the configuration which is near its last configuration. Therefore we can take the parameters of its last configuration as the initial guess for the shooting processes. In addition, the stability of the configurations can be assessed utilizing methods in Ref. [17] in order to avoid snapping.

6 Numerical Examples

In this section, an intuitional two-tube robot is selected to demonstrate the effects of the external forces on the robot. Each tube's initial backbone shape is a section of a circle, and they are fully overlapped during the simulation. The processes of solving differential equations are implemented in Matlab using shooting method. It is assumed that both tubes not only have the same initial backbone shape and arc-length, but also have the same bending stiffness ($K_{i,xy}$) and torsional stiffness ($K_{i,z}$). The values of related parameters are listed in Table 1.

Figure 5 shows the equilibrium conformation under different loads when the outer and inner tubes were rotated to angles of -30° and 30° respectively. The unloaded equilibrium conformation lies on yz -plane, which agrees with the instinct. When the external force is applied to the robot's tip in y -direction, the updated equilibrium conformation still lies on yz -plane, as Fig. 5 shows. This is similar to the bending of a single cantilevered rod. Under the tip force of 5 N, the robot's tip is deflected from its initial position by about 30 mm.

Table 1 Parameters of the robot

Parameters	Values
Total arc-length (mm)	84
Pre-curvature (mm^{-1})	1/60
Curvature vector of the tubes' initial shape	(1/60, 0, 0)
Bending stiffness (Nm^2)	0.0202
Torsional stiffness (Nm^2)	0.0156

Fig. 5 The equilibrium conformation of the robot subject to different tip loads

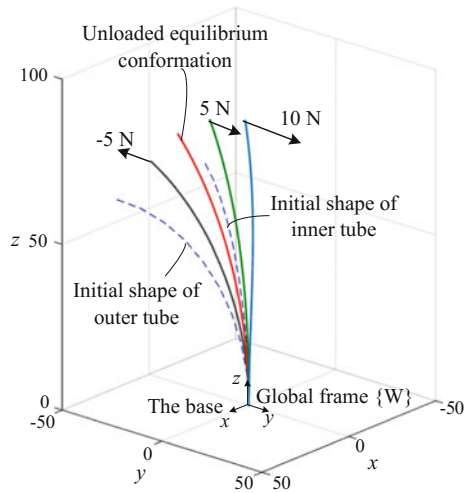
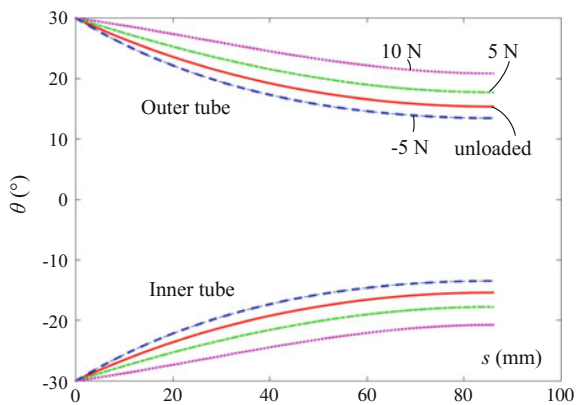


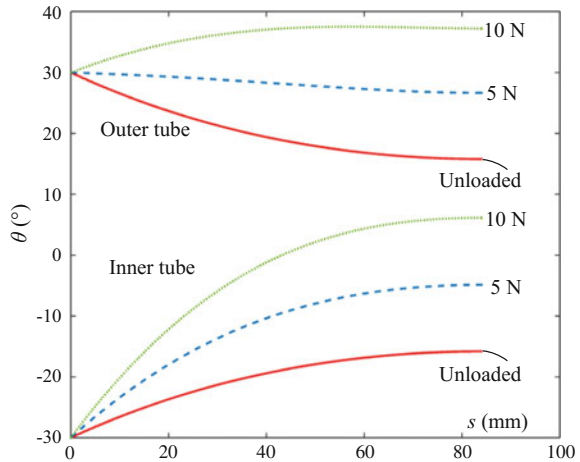
Fig. 6 The rotation angles of both tubes along the whole arc-length for the robot under y-direction tip forces



The rotation angles $\theta_1(s)$ and $\theta_2(s)$ of both tubes, which cannot be observed from the conformation figure, are also changed under loads. Figure 6 shows how the rotation angles vary along the whole arc-length in the loaded robot. At the common base of both tubes, the rotation angles of them are input angles. From the base to the tip, the outer tube twist about the local $-z$ -axes, while the inner tube twist about the local z -axes; therefore, the angle between $\{F_1(s)\}$ and $\{F_2(s)\}$ is decreasing. Also, the tip force in the $+y$ -direction, which tend to “straighten” the robot, will slowdown this trend, while the tip force in the $-y$ -direction will accelerate this trend.

If this robot is under $+x$ -direction tip forces, the rotation angles of both tubes along the whole arc-length are shown in Fig. 7. The rotation angles of both tubes are no longer symmetrical with respect to the line $\theta(s) = 0$. The load accelerates the increasing trend of the inner tube’s rotation angle, and slowdowns even reverses the decreasing trend of the outer tube’s rotation angle. Furthermore, In contrast with y -

Fig. 7 The rotation angles of both tubes along the whole arc-length for the robot under x -direction tip forces



direction tip forces, the effects of x -direction tip forces on the rotation angles are much larger, since the torque generated by x -direction tip forces are much larger.

7 Conclusions

This paper proposes an equivalent conservative system for the concentric-tube robot under loads, and utilizes the minimum potential energy principle and the optimal control theory to derive the equations of equilibrium conformation. Through numerical simulation, the effects of external forces on the robot's tip are analyzed, and the results show that the externally loaded concentric-tube robot will bend like a single cantilevered rod. The tip forces which tend to "straighten" the robot (i.e. in the $+y$ -direction) will slightly exaggerate the angle between the tubes' local frames at the tip, while the forces in the x -direction will affect the rotation angles of both tubes significantly. This model will facilitate the motion planning of the concentric-tube robot while it is performing an interactive task.

Acknowledgments The authors acknowledge the support from the National Natural Science Foundation of China (51175013).

References

1. Webster III RJ, Okamura AM, Cowan NJ (2006) Toward active cannulas: miniature snake-like surgical robots. In: IEEE/rsj international conference on intelligent robots and systems. IEEE Press, New York, pp 2857–2863

2. Sears P, Dupont P (2006) A steerable needle technology using curved concentric tubes. In: IEEE/rsj international conference on intelligent robots and systems. IEEE Press, New York, pp 2850–2856
3. Furusho J (2010) Curved multi-tube systems for fetal blood sampling and treatments of organs like brain and breast. *J Comput Assist Radiol Surg* 6:223–226
4. Rucker DC, Croom JM, Webster RJ III (2009) Aiming surgical lasers with an active cannula. *ASME J Med Devices* 3:027506–027510
5. Webster RJ III, Romano JM, Cowan NJ (2009) Mechanics of pre-curved-tube continuum robots. *IEEE Trans Robot* 25:67–78
6. Burgner J, Swaney PJ, Bruns TL, Clark MS, Rucker DC, Burdette EC (2012) An autoclavable steerable cannula manual deployment device: design and accuracy analysis. *ASME J Med Devices* 6:410071–410077
7. Swaney PJ, Croom JM, Burgner J, Gilbert HB, Rucker DC, Webster III RJ (2012) Design of a quadra manual robot for single-nostril skull base surgery. In: 2012 ASME dynamic systems and control conference. ASME Press, New York, pp 387–393
8. Trivedi D, Lotfi A, Rahn CD (2008) Geometrically exact models for soft robotic manipulators. *IEEE Trans Robot* 24:773–780
9. Xu K, Simaan N (2008) An investigation of the intrinsic force sensing capabilities of continuum robots. *IEEE Trans Robot* 24:576–587
10. Rucker DC, Jones BA, Webster RJ III (2010) A geometrically exact model for externally loaded concentric-tube continuum robots. *IEEE Trans Robot* 26:769–780
11. Antman SS (1976) *Nonlinear problems of elasticity*. Springer, Berlin
12. Berg BT (1995) Bending of superelastic wires, part I: experimental aspects. *ASME J Appl Mech* 62
13. Murray RM, Sastry SS, Li Z (1994) *A mathematical introduction to robotic manipulation*. CRC Press, Boca Raton
14. Bryson AE, Ho YC, Siouris GM (1975) *Applied optimal control: optimization, estimation, and control*. Halsted Press, New York
15. Kincaid D, Cheney W (1991) *Numerical analysis: mathematics of scientific computing*. Brooks/Cole Publishing Co., New York
16. Ha J, Park FC, Dupont PE (2015) Elastic stability of concentric tube robots subject to external loads. *IEEE Trans Biomed Eng* 26:1–13
17. Gilbert HB, Hendrick RJ, Webster RJ III (2015) Elastic stability of concentric tube robots: a stability measure and design test. *IEEE Trans Robot* 32:1–16

Double-Parameter Regression Design of Drive Trains for Lightweight Robotic Arms

Haibin Yin, Cheng Kong, Mingchang He and Shansheng Huang

Abstract This paper presents a new design approach for lightweight robotic arms. In this method, the drive trains and structural dimensions are parameterized as design variables, and a major objective is to minimize the total mass of robotic arms satisfying the constraint conditions. To solve the optimization problem, the relationship among mass, the moment of inertia and torque of drive trains are introduced as their power-density curves, which is the basis of the double-parameter regression design. In this design approach, there are two modules: structure optimization and drive trains optimization. The orthogonal design method is adopted to implement the structure optimization. The double-parameter regression design is used for drive trains optimization. Finally, a design example for a four degree of freedom (DOF) robotic arm is demonstrated to verify the validity of the proposed scheme.

Keywords Lightweight robotic arm · Structure optimization · Drive trains optimization · Double-parameter regression design

H. Yin (✉) · C. Kong · M. He · S. Huang
School of Mechanical and Electronic Engineering,
Wuhan University of Technology, Wuhan, Hubei, China
e-mail: chinaliuyin@whut.edu.cn

C. Kong
e-mail: kongcheng@whut.edu.cn

M. He
e-mail: hemingchang@whut.edu.cn

S. Huang
e-mail: huangshansheng@whut.edu.cn

H. Yin
School of Mechanical and Electronic Engineering,
Key Laboratory of Hubei Province for Digital Manufacturing, Wuhan, China

1 Introduction

As the development of robotics technology, the application of lightweight robotic arms plays a more and more important role in industrial production, service and space explorations etc. Due to the special requirements of work environment and tasks, they have to be energy efficiency and high load-weight ratio. This implies new design approaches have to be addressed to achieve these characteristic.

There are two main research directions to improve energy efficiency and load-weight ratio of lightweight robotic arms. On the one hand, some attempted to design desirable lightweight robotic arms by structure optimization. Hua presented a structural optimization for lightweight robotic using two kinds of new materials which are low-density and stiff [1]. However, the application of these materials is limited by their property of undesirable fabrication procedure and high-cost. Zhu proposed an integrated structure-control optimization method for a two-link flexible robotic arm, in which the structural and control parameters were optimized simultaneously [2]. Evolutionary optimization procedure was presented for optimization of the parameters of a manipulator in Ref. [3]. However, the methods mentioned in Refs. [2, 3] both took rarely consideration about the structural gesture and dimensions. Zhou proposed an optimized method for linkages of arms which regards the structural dimensions as variables [4]. There are two design variables for each linkage. But, given the limitation of the method mentioned in this paper, the process took too much time.

On the other hand, some believed drive trains optimization plays a key role in addressing a lightweight design. Cusimano [5, 6] presented a method for optimal selection of an electrical motor and transmission. This paper indicated the generalized moment of inertia of motor is a key parameter. But, this method is only applicable to the design of a single joint combing a motor and a gearbox. It does not address the discrete nature of the selection process. The drive trains optimize procedure was addressed for two joints in Ref. [7]. The algorithm mentioned in this paper is complex which requires approximately 700 evaluations to complete the optimization. It is also incapable in selection of components from a catalog. In Ref. [8], optimized selection of motors and gearboxes are done simultaneously for a robotic arm. But this method is confined by the limited catalog of commercially available components. DLR designed a 7-DOF lightweight robotic arm with customized drive trains to maximize the load-weight ratio [9]. In our previous work, the drive trains optimization is addressed though regression design proposed in Ref. [10]. However, the influence of the moments of inertia of drive trains is not considered in an appropriate way. The angular accelerations of all joints should not be regarded as a constant.

In this paper, an integrated optimization design was proposed to minimize the weight of robotic arms. The structure optimization is achieved using the orthogonal design method with the constraints of strength and stiffness. The drive trains optimization is executed by means of a new approach, called double-parameter regression design, presented in this paper based on the kinematics analysis and

dynamics analysis. For better reflect the influence of the moments of inertia of drive trains, the angular accelerations of joints are obtained according to the real work condition of robotic arms. An optimization example for a 4 DOF robotic arm shows the proposed approach can contribute to selecting the drive trains more accurately.

2 Problem Statement

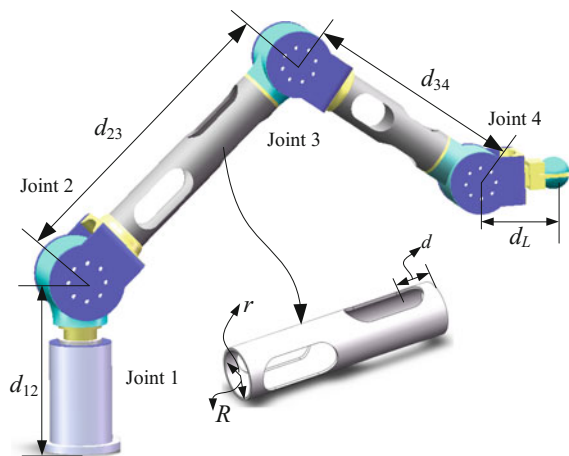
In this paper, a 4 DOF robotic arm will be designed for operation pick and position, shown in Fig. 1. In order to minimize the weight of designed robotic arm, the optimization will be executed in structure design and selection of drive trains. In this section, the structure optimization will be introduced firstly. The drive trains optimization will be illustrated with comparison to our previous study on drive trains optimization presented in Ref. [10].

2.1 Structure Optimization

In this part, the orthogonal design [11] is used to optimize the structure of designed robotic arm. The structure optimization is mostly acted on linkages because they focus the most mass of robotic arms. The optimization for joints structure is taken into account according to the assembly relationship between linkages and joints, drive trains and joints.

According to the relevant knowledge of mechanics of materials, there are four main factors affect the stiffness of robotic arms. They are regarded as design variables of structure. In order to find the optimal structure, the objective function $f_s(x_s)$ is defined as sum of the linkages mass m_{link} and joints mass m_{joint} , as shown in Eq. (1)

Fig. 1 The model of 4 DOF robotic arm



$$\begin{aligned} \min f_s(\mathbf{x}_s) &= (m_{link} + m_{joint}) \\ \mathbf{x}_s &= [d, \alpha, \beta, r] \end{aligned} \tag{1}$$

where $\mathbf{x}_s = [d, \alpha, \beta, r]$ is the vector of design variables of structure. d is the distance from end of linkage to center of semicircle of circular groove. α is the angle between director vectors of two slots. β is the angle between direction vector of joints and direction vector of the slot which is closer to end-effector. r is the inner radius of linkages. The width of slots w_1 , external radius R and length of linkage L and slot l_1 are regarded as constants. The design variables of structure are shown in Fig. 2.

The structure of robotic arm must be satisfied the constraints of strength and stiffness. The constraints are defined as

$$\sigma_{max} < \sigma_p, \tag{2}$$

$$\omega_{max} < \omega_p, \tag{3}$$

where σ_{max} is maximum stress of designed robotic arm. σ_p is the yield strength of material of designed robotic arm. ω_{max} is the maximum deformation of designed robotic arm. ω_p is the limit deformation of designed robotic arm.

2.2 Drive Trains Optimization

Beside the structure optimization, drive trains optimization also plays a significant role in minimizing the weight of robotic arms. In Ref. [8], the mass of the 5 DOF robotic arm was reduced by 38 % though the drive trains optimization. It implies that the further research in drive trains optimization needs to be done to achieve the goal of minimizing the weight of robotic arms.

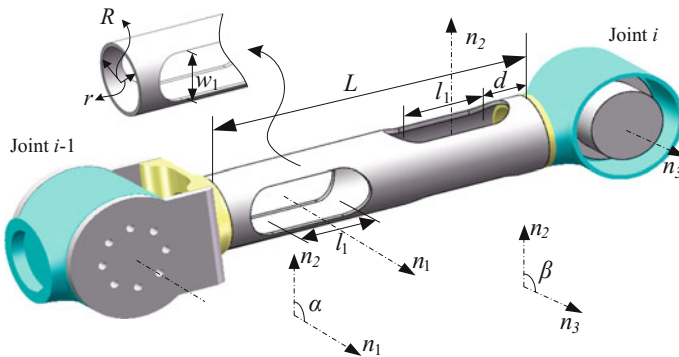


Fig. 2 Design variables of structure

In our previous work, the drive trains optimization was addressed based on the regression design proposed in Ref. [10]. However, angular accelerations of all joints should not be regarded as a constant in calculating the required torques of drive trains. The required torque of i th drive train $T_{d,i}$ is calculated by

$$T_{d,i}(t) = \tau_i(t) + J_{d,i}\ddot{\theta}_i(t)\rho_{d,i}^2\eta_{d,i} \quad (4)$$

where τ_i is the output torque of i th joint. $J_{d,i}$ is the moment of inertia of i th drive train. $\ddot{\theta}_i$ is the angular acceleration of i th joint. $\rho_{d,i}$ is the reduction ratio of i th drive train. $\eta_{d,i}$ is the efficiency of the i th drive train.

When the angular accelerations of all joints have obvious difference, big error will be occurred using the regression design to calculate the required torques of drive trains. In this paper, the further optimized method will be proposed for drive trains optimization. The moments of inertia of drive trains are taken into account with real angular accelerations to obtain the required torques of drive trains more accurately.

3 Double-Parameter Regression Design for Drive Trains

In this section, a new approach, called double-parameter regression design, is introduced for drive trains optimization. In our previous work [10], the regression of mass of drive trains is taken into account only based on the regression design. In previous section, it concluded that angular accelerations of all joints should not be handled as a constant to obtain the required torques of drive trains. It implies the moments of inertia of drive trains also need regression design.

3.1 Dynamic Model

The drive trains optimization will be studied based on the structure optimization mentioned in previous section. After the structure of robotic arm is determined, it is necessary to calculate the inverse dynamic for selection of drive trains. The dynamic model of designed robotic arm can be described as

$$\mathbf{M}(\boldsymbol{\theta})\ddot{\boldsymbol{\theta}} + \mathbf{h}(\boldsymbol{\theta}, \dot{\boldsymbol{\theta}}) + \mathbf{g}(\boldsymbol{\theta}) = \boldsymbol{\tau}, \quad (5)$$

where \mathbf{M} is the mass matrix, \mathbf{h} is a vector of Coriolis and centrifugal terms of the links, \mathbf{g} is the vector of gravitational forces, and $\boldsymbol{\tau}$ is the vector of joint torques.

The torque obtained from Eq. (5) is instantaneous value. In order to select the drive trains, the root mean square torque of i th joint T_{rms}^i is needed, which is calculated by

$$T_{rms}^i = \sqrt{\frac{1}{\Delta t} \int_0^{\Delta t} \tau_i^2 dt}, \quad i = 1, \dots, 4, \tag{6}$$

where Δt is the time of joint movement, τ_i is the instantaneous torque of i th joint.

In this section, the inverse dynamic is solved by the ADAMS based on Eq. (5). The root mean square of torque is obtained based on Eq. (6), to which the instantaneous torque is imported from ADAMS. It is a significant index for selection of drive trains.

3.2 Selection Criteria of Drive Trains

The drive train is consisted of motor and gearbox, shown in Fig. 3. The gearbox is used to increase the output torque of the drive train.

In order to guarantee the selected drive train is satisfied. The selection criteria of drive trains needs to be determined, listed as

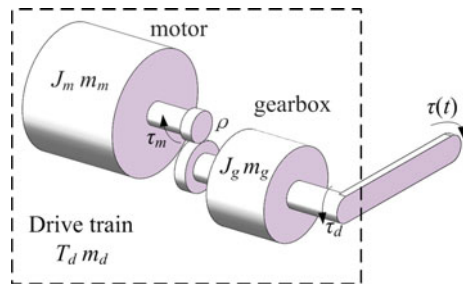
$$T_d \geq \tau_{d,rms}^i, T_d^{\max} \geq \tau_{d,p}^i, N_d^{\max} \geq n_{d,p}^i, \tag{7}$$

where T_d is the nominal torque of drive trains. T_d^{\max} and N_d^{\max} are the maximum torque and angular velocity of drive trains. $\tau_{d,rms}^i$ is the required root mean square torque of i th joint. $\tau_{d,p}^i$ and $n_{d,p}^i$ are the peak torque and angular velocity of i th joint.

3.3 The Process of Double-Parameter Regression Design

The objective of double-parameter regression design is to minimize the mass of drive trains satisfied the constraints (7). The objective function $f_d(x_d)$ can be defined as

Fig. 3 The model of drive train



$$\min f_d(\mathbf{x}_d) = \sum_{i=1}^4 m_d(u_{di}), \quad (8)$$

where $\mathbf{x}_d = [u_{d1}, u_{d2}, u_{d3}, u_{d4}]$ is the vector of design variables of drive trains optimization. m_d is the mass of drive trains. u_{di} is the rated torque of i th drive train.

In order to optimize the drive trains, the power-density curves are necessary, which reflects the relationships between torque and mass, the moment of inertia and mass of drive trains. It is believed the relationship between mass m_m and torque T_m of the motor are existed. Pettersson has concluded it in Ref. [7]. It can be described as

$$T_m = \frac{c_m \sqrt{r_m}}{\pi \rho_m} m_m, \quad (9)$$

where cooling conditions c_m and average density ρ_m are constants. r_m is stator radius. It implies the relationship between torque and mass of motors is positive correlation.

Based on Eq. (9), it implies the relationship between the mass m_d and torque T_d of drive trains is also certain positive correlation. This relationship can be formulated as

$$T_d = f_1(m_d), \quad (10)$$

where $m_d = m_m + m_g$, m_g is the mass of gearbox. $T_d = T_m \rho \eta$, ρ and η are the reduction ratio and efficiency of drive trains.

The relationship between inertia J_m and mass m_m of motor is described in Ref. [7] as

$$J_m = \frac{c_{m,j} r_m^2}{\pi \rho_m} m_m, \quad (11)$$

where $c_{m,j}$ is a constant for a specific motor type and is adjusted against data of existing motors in robotics.

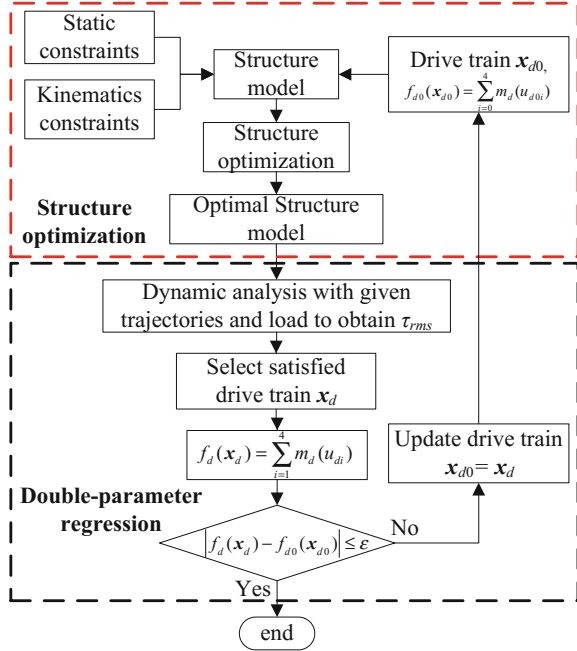
In order to take the moments inertia of drive trains into consideration, the relationship between inertia J_d and mass m_d of drive trains is also needed to be formulated. The positive correlation of J-m function can be formulated as

$$J_d = f_2(m_d), \quad (12)$$

where $J_d = J_m + J_g$, J_m is the inertia of motor, J_g is the equivalent inertia of gearbox reflected at the motor shaft.

Based on Eqs. (10) and (12), the double-parameter regression design for drive trains optimization can be executed based on the procedure shown in Fig. 4. The model of robotic arms is constructed by SOLIDWORKS, the static analysis and

Fig. 4 The procedure of double-parameter regression design



dynamic analysis are executed by ANSYS and ADAMS respectively. For start the optimization loop, the drive trains are initialized as $x_{d0} = [u_{d01}, u_{d02}, u_{d03}, u_{d04}]$. The optimal Structure model needs to be obtained through structure optimization when the drive trains are updated. The output torques of joints $\tau_{rms} = [\tau_1, \tau_2, \tau_3, \tau_4]$ can be calculated though the Adams based on Eq. (5). The rated torque of drive trains $x_d = [u_{d1}, u_{d2}, u_{d3}, u_{d4}]$ can be obtained according to the Eq. (4). The mass of drive trains can be determined based on Eq. (10). If the mass of drive trains $f_d(x_d)$ converges to small constant ϵ , the procedure of double-parameter regression design is completed. Otherwise, the drive trains need to be updated for the next iteration.

4 Discussion of Result

In this section, optimization design is conducted on a 4 DOF robotic arm, shown in Fig. 1. The reach space is up to 771 mm. The load is defined as 2 kg. The assembly dimensions of the robotic arm are defined as: $d_{12} = 224$ mm, $d_{23} = 393$ mm, $d_{34} = 293$ mm, $d_L = 85$ mm. Aluminum alloy (6061-T6) is chosen as the structure material and its yield strength is 270 Mpa. The limit deformation ω_p is set as 3 mm. The design variables of structure optimization is initialized as $x_s = [30, 0, 0, 28]$. The drive trains of robotic arm are initialized as $x_{d0} = [0, 0, 0, 0]$, the operation time of designed robotic arm is set as 4 s. Coefficient of convergence ϵ is set as 0.001.

4.1 Implementation of Structure Optimization

The structure optimization for robotic arms is solved based on orthogonal design. Levels of design variables of structure $x_s = [d, \alpha, \beta, r]$ is provided in Table 1.

Based on the design space listed in Table 1, the corresponding robotic model is constructed on SOLIDWORKS. The static analysis is executed on ANSYS. The variance analysis is used for simulation data obtained from ANSYS to find the optimal structure of robotic arm.

4.2 Implementation of Drive Trains Optimization

In this part, the drive trains optimization is solved based on the double-parameter regression design. The trajectories of joints are determined firstly. The candidate drive trains are selected based on the selection criteria of drive trains proposed in Sect. 3. The result of drive trains optimization is discussed with the comparison between double-parameter regression design and regression design.

Trajectories of Joints. The trajectories of joints have a significant influence to the required torque of joints. In this section, the trajectory of four joints is determined due to the specific purpose of designed robotic arm shown in the Fig. 5.

Combination of Drive Trains. In order to confirm the effectiveness of double-parameter regression design, drive trains need to be selected which are consisted of motors and gearboxes. The rough range of torques is obtained for selection of motors and gearboxes. In this example, the motors are selected from MAXON, listed in Table 2. Gearboxes are selected from Harmonic Drive, listed in Table 3.

In order to fit the power-density curves more accurately, the combination criteria is listed as

$$T_m i \eta \leq T_g, N_m / i \leq N_g^{max}, \min\{m_1, m_2, \dots, m_i\}, \tag{13}$$

where T_g is nominal torque of gearbox, N_g^{max} is the allowed maximum angular velocity of gearbox, $\min\{m_1, m_2, \dots, m_i\}$ is used to guarantee the mass of the selected drive train is minimum which satisfies the first two constraints (13).

The drive trains are combined based on the constraints (13), listed in Table 4. The index (1, a) represents the drive train is consisted of motor RE16 (4.5 W) and gearbox 14, listed in Tables 2 and 3. Based on the candidate drive trains listed in

Table 1 Levels of design variables of structure

Design variable	Range	Step size
d	[30, 50]mm	5
α	[0, 90]°	15
β	[0, 90]°	15
r	[28, 32]mm	1

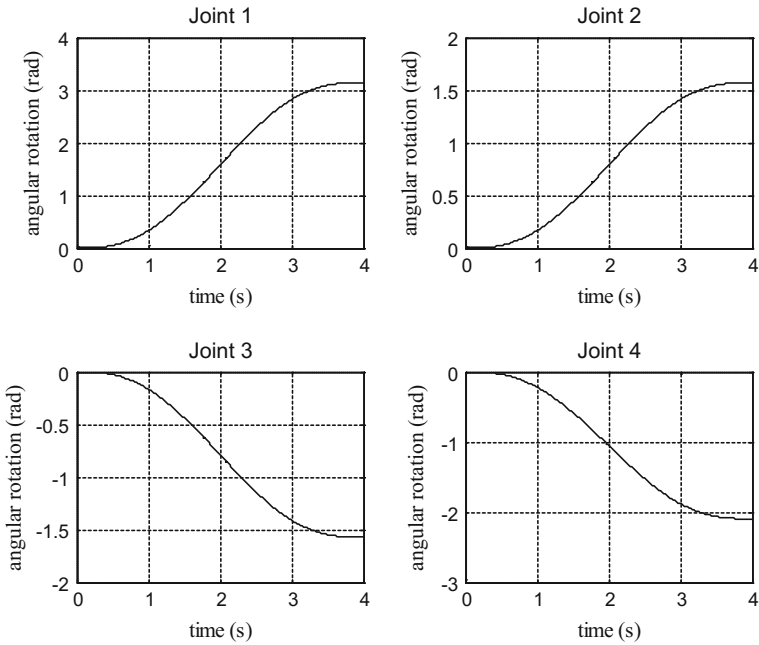


Fig. 5 Trajectories of four joints

Table 2 The candidate motors [12]

No.	Index	N_m (rpm)	T_m (mNm)	m_m (kg)	J_m (gcm ²)
1	RE16 (4.5 W)	3170	4.77	0.04	1.11
2	RE25 (20 W)	3430	32.3	0.115	13.9
3	RE35 (90 W)	2990	106	0.34	65.9
4	RE40 (150 W)	2700	187	0.48	123
5	RE50 (200 W)	2470	452	1.1	560

Table 3 The candidate gearboxes ($\rho = 100$) [13]

No.	Index	N_g^{max} (rpm)	T_g (Nm)	m_g (kg)	J_g (10^{-2} gcm ²)
a	14	8500	7.7	0.35	21
b	17	7300	27	0.46	54
c	20	6500	34	0.65	90
d	25	5600	75	1.2	282
e	32	4800	151	2.4	1090

Table 4, the power density curves of drive train can be fitted with interpolation algorithm.

Table 4 Candidate drive trains for fitting power density curve

No.	Index	N_d (rpm)	T_d (Nm)	m_d (kg)	J_d (gcm ²)
1	(1, a)	31.7	0.3339	0.39	22.11
2	(2, a)	34.3	2.261	0.465	34.9
3	(3, a)	29.9	7.42	0.69	86.9
4	(4, b)	27	13.09	0.94	177
5	(5, c)	24.7	31.64	1.75	650

Comparison between Two Methods. Based on the procedure shown in Fig. 4, the double-parameter regression design for drive trains optimization is executed using the dynamic analytic software ADAMS and FEA analytic software ANSYS. For better confirm the accuracy of double-parameter regression design, the regression design is also utilized for drive trains of designed robotic arm. The optimal structure of designed robotic arm is displayed in Table 5.

For better display the procedure of double-parameter regression design, the regression processes of joint 2 and 3 are shown in Fig. 6.

For confirming the accuracy of double-parameter regression design, the regression processes of joint 2 and 3 based on regression design are shown in Fig. 7.

From Figs. 6 and 7, the regression mass is different though two methods. It confirms the accuracy of double-parameter regression design. The optimal result of drive trains obtained from two methods are listed in Table 6.

From Table 6, the drive trains optimization based on regression design cannot reflect the real required torques of joints of robotic arms. It makes the selected drive trains redundant or insufficient. For example, if there is a candidate drive train

Table 5 Optimal result of structure

Design variable	d	α	β	r
Optimal value	50 mm	90°	90°	30 mm

Fig. 6 Double-parameter regression design of joint 2 and 3

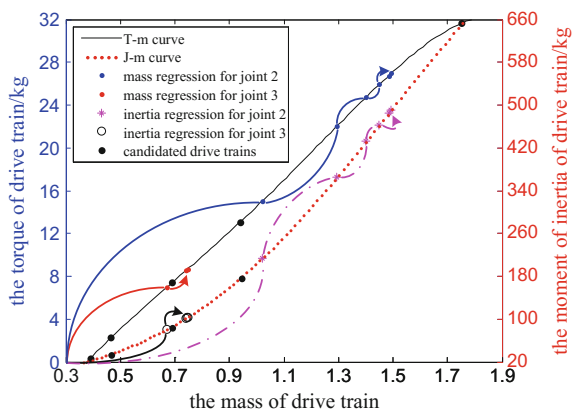


Fig. 7 Regression design of joint 2 and 3

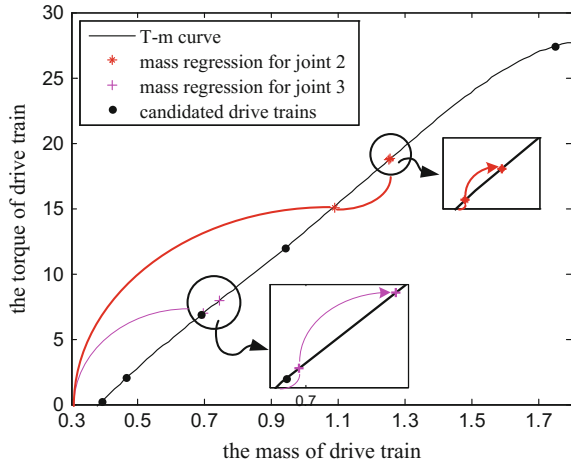


Table 6 Optimal result of drive train (unit N/m)

Method	u_{di}			
	Joint 1	Joint 2	Joint 3	Joint 4
Double-parameter regression	1.3122	26.7570	8.6782	1.3380
Regression design	1.2912	18.5261	7.9779	1.3436

which rated torque x_d is belong to (18.5261, 26.7570), the selected drive train of joint 2 based on the regression design will be insufficient. If there is a candidate drive train which rated torque x_d is belong to (1.3380, 1.3436), the selected drive train of joint 4 based on regression design will be redundant. This deficiency is solved by the double-parameter regression design which introduces the regression of the moment of inertia besides the mass regression.

The optimal result can be used to design the drive trains for lightweight robotic arms. However, due to the difficulty in manufacture specific drive trains, in the practice, drive trains of joints need to be adapted to available components from commercial catalog which discretely distribute on the power density curve. These drive trains close and exceeding to optimal result are chosen to guarantee them more reliable because of the reluctant capacity of them. For example, the optimal result of joint 1 is between (1, a) and (2, a), so the drive train (2, a) is selected as the optimal component in the practice. Based on this trade-off design, a 4 DOF robotic arm is constructed for further research shown in Fig. 8. The drive trains of four joints (waist, shoulder, elbow and wrist) are consisted of (2, a), (5, c), (4, b), and (2, a).

Fig. 8 4 DOF robotic arm

5 Conclusions

In this paper, a new design approach is proposed to design lightweight robotic arms. The structure optimization is achieved based on the orthogonal design. It is an effective algorithm for structure optimization which is not necessary to do all simulation experiment. It is benefit for saving the experimental time. The drive trains optimization is executed by means of double-parameter regression design.

The double-parameter regression design is an improved method for regression design. The example presented in Sect. 4 confirms precision of double-parameter regression design in drive trains optimization. The double-parameter regression design solved deficiency of regression design though the combination of regression of mass and the moment of inertia of drive trains.

However, the design of drive trains for lightweight robotic arms is still confined by the commercial available components. In the further study, the direction for optimization of lightweight robotic arms will focus on finding a series of theory to supporting the drive trains manufacture which is used in modular joints.

Acknowledgments Research was supported by National Natural Science Foundation of China under Grant 11202153 and 51575409.

References

1. Hua X, Guo S (2012) Design and simulation of light weight arm based on elderly/disabled life assist robot. In: 7th IEEE conference on industrial electronics and applications. IEEE Press, Singapore, pp 507–511
2. Zhu Y, Qiu J, Tani J (2001) Simultaneous optimization of a two-link flexible robot arm. *J Robot Syst* 18:29–38

3. Rout BK, Mittal RK (2010) Optimal design of manipulator parameter using evolutionary optimization techniques. *J Robotica* 28:381–395
4. Zhou L, Bai S (2015) A new approach to design of a lightweight anthropomorphic arm for service applications. *J Mech Robot* 7:031001
5. Cusimano G (2007) Optimization of the choice of the system electric drive-device—transmission for mechatronic applications. *J Mech Mach Theory* 42:48–65
6. Cusimano G (2003) A procedure for a suitable selection of laws of motion and electric drive systems under inertial loads. *J Mech Mach Theory* 38:519–533
7. Pettersson M, Olvander J (2009) Drive train optimization for industrial robots. *J IEEE Trans Robot* 25:1419–1424
8. Zhou L, Bai S, Hansen MR (2011) Design optimization on the drive train of a light-weight robotic arm. *Mechatronics* 21:560–569
9. Albu-Schäffler A, Haddadin S, Ott C, Stemmer A, Wimböck T, Hirzinger G (2007) The DLR lightweight robot: design and control concepts for robots in human environments. *J Industrial Robot* 34:376–385
10. Hai-bin Y, Ming-chang H, Shang-sheng H, Jun-feng L (2016) A new design on drive trains for light weight robotic arms. In: 6th international conference on machinery, materials science and engineering application (accepted)
11. Zhi-xing X, Da-quan H, Qing-gai S (1987) Optimization of the magnetic deflection system by the method of orthogonal design. *J Vacuum Sci Technol B* 5:153–155
12. Maxon Motor. Program 2016/17. Maxon Motor AG. Sachseln, Switzerland. Available at: <http://epaper.maxonmotor.com/>
13. Harmonic Drive. Engineering Data SHD-2SH Units. Harmonic Drive AG. Limburg/Lahn, Germany. Available at: http://harmonicdrive.de/produkte/media/catalog/category/2014_12_ED_1019647_SHD_2SH.pdf

Kinematics Analysis and Simulation of Two-Robot Coordination in Welding

Nianfeng Wang, Feiyue Zhang and Xianmin Zhang

Abstract This paper focus on two-robot coordinated welding process of complex spatial curve seam. A two-robot coordinated system is builded, kinematics analysis is given, and trajectory planning based on downhand welding constrains is provided. After that, a simulation platform based on OpenGL and VC++ is established. Finally, take the intersection curve seam of two cylinder for example, a motion simulation of two-robot coordinated welding is conducted. The results of simulation verify the correctness of kinematics analysis and the method of trajectory planning.

Keywords Coordinated welding · Trajectory planning · Motion simulation

1 Introduction

With the broadening application of robotic in welding industry, the welding requirements become more and more complex. Nowadays, a single robot is unable to meet the requirements of welding operation. For the complex curve seam in welding process, welding robot station is usually used to get the desired welding orientation and improve welding quality. The typical welding robot station mainly includes: robot-positioner station, dual-welding robot station, dual-welding robot and one positioner station. There are various research which focus on robot-positioner coordination of complex spatial curve seam welding process [1–3]. However, for two-robot welding coordination, the research are mostly focused on straight seam [4] or circular welds [5]. In these coordinated welding process, the relative orientation between two robot end-effector is unchanged. In Ref. [6],

N. Wang (✉) · F. Zhang · X. Zhang
Guangdong Province Key Laboratory of Precision Equipment and Manufacturing
Technology, South China University of Technology, Guangzhou 510640, Guangdong,
People's Republic of China
e-mail: menfwang@scut.edu.cn

a non-master/slave approach is employed for coordinated motion planning, a Solidworks-SimMechanics simulation platform is established, and a coordinated welding simulation of a steel curved pipe is given.

This paper focus on two-robot coordinated welding process of complex spatial curve seam. The two-robot coordinated system is built at the beginning, and its coordinated kinematics model is obtained by the motion constrains. After that, take downhand welding as the best welding position, a method of two-robot coordinated trajectory planning is given. Then a two-robot coordinated welding simulation platform which is based on OpenGL and VC++ is established. Finally, a coordinated welding simulation of an intersecting line is given and the simulation results indicate that the coordinated welding process can satisfy desired welding requirements.

2 Two-Robot Coordinated System and Kinematics Analysis

In order to realize the coordinated motion, one robot hold the workpiece and move it to desired position, the other hold the torch and move it to relative orientation and implement the welding task. A typical two-robot coordinated welding system is shown in Fig. 1, the symbol i indicates robot number. In a two-robot coordinated system, $i = 1, 2$; $i = 1$ indicates the clamping robot, $i = 2$ indicates the welding robot. $[R]$ represents the world coordinate system, $[R_i]$ represents the robot base coordinate system of the i th robot, $[E_i]$ represents the end-effector coordinate system of the i th robot, $[T_i]$ represents the tool coordinate system of the i th robot, $[u]$ represents the workpiece coordinate system, $[p]$ represents the welding points coordinate system. ${}^{R_i}T_{E_i}$ indicates the transformation matrix from $[E_i]$ to $[R_i]$, ${}^{E_i}T_{T_i}$ indicates the transformation matrix from $[T_i]$ to $[E_i]$, ${}^{T_i}T_u$ indicates the transformation matrix from $[u]$ to $[T_i]$, ${}^{T_i}T_p$ indicates the transformation matrix from $[p]$ to $[T_i]$, uT_p indicates the transformation matrix from $[p]$ to $[u]$, ${}^{R_1}T_{R_2}$ indicates the transformation matrix from $[R_2]$ to $[R_1]$. The base coordinate system of clamping robot $[R_1]$ is moved to the world coordinate system $[R]$ during coordinated motion.

During two-robot coordinated welding process, a closed kinematic chain which can be expressed as follow is formed.

$${}^{R_1}T_{E_1} \cdot {}^{E_1}T_{T_1} \cdot {}^{T_1}T_u \cdot {}^uT_p = {}^{R_1}T_{R_2} \cdot {}^{R_2}T_{E_2} \cdot {}^{E_2}T_{T_2} \cdot {}^{T_2}T_p \quad (1)$$

Decouple this closed kinematic chain, an opened kinematic chain of clamping robot and welding robot is obtained respectively. For clamping robot,

$${}^{R_1}T_p = {}^{R_1}T_{E_1} \cdot {}^{E_1}T_{T_1} \cdot {}^{T_1}T_u \cdot {}^uT_p \quad (2)$$

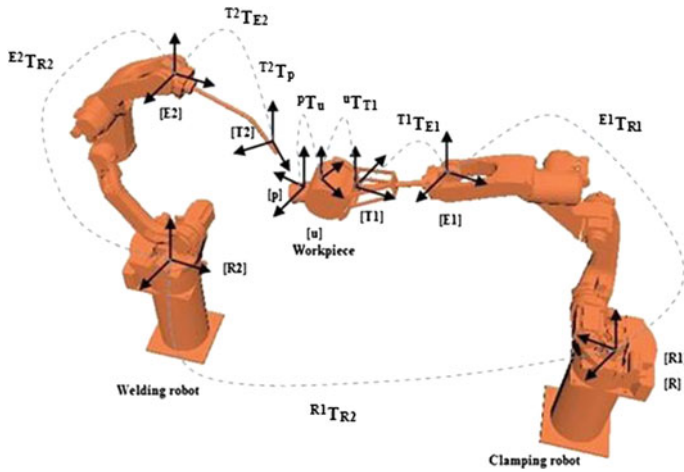


Fig. 1 Two-robot coordinated system

For welding robot,

$${}^R_1T_p = {}^R_1T_{R_2} \cdot {}^R_2T_{E_2} \cdot {}^{E_2}T_{T_2} \cdot {}^{T_2}T_p \tag{3}$$

In Eqs. 2 and 3, ${}^{E_1}T_{T_1}$ is depends on the fixture of the clamping robot, ${}^{E_2}T_{T_2}$ is depends on the torch of the welding robot, ${}^{T_1}T_u$ is decided by the assembly between the workpiece and the fixture of the clamping robot; ${}^R_1T_{R_2}$ is decided by the relative orientation between the clamping robot and the welding robot, which can be obtained through calibration. This article assumes that ${}^R_1T_{R_2}$ is known in simulation system. With these transformation matrixes are already known, as long as the desired welding orientation R_1T_p , the desired orientation between welding torch and welding points ${}^{T_2}T_p$ and the orientation of welding points uT_p are given, the transformation matrix from robot base coordinate system to robot end-effector coordinate system of clamping robot and welding robot are described as follow:

$${}^R_1T_{E_1} = {}^R_1T_p \cdot {}^uT_p^{-1} \cdot {}^{T_1}T_u^{-1} \cdot {}^{E_1}T_{T_1}^{-1} \tag{4}$$

$${}^R_2T_{E_2} = {}^R_1T_{R_2}^{-1} \cdot {}^R_1T_p \cdot {}^{T_2}T_p^{-1} \cdot {}^{E_2}T_{T_2}^{-1} \tag{5}$$

3 Constraint Relationship During Welding Process

During two-robot coordinated welding process, the clamping robot is used to move the welding points to the desired orientation which is suited to get better welding quality. To make the welding torch keep a certain orientation during welding

process, the welding robot is expected to move the welding torch considering the relative orientation between welding points and torch. In addition, there are motion constraints between welding torch and the welding points to ensure that the welding process is stable [7]. Since the depth of the welding puddle which is changed by gravity action greatly influences weld-forming, a desirable welding is downhand welding which means the welding direction of the seam should against the direction of gravity in every moment. What's more, two-robot coordinated welding station is a system with redundant degree of freedom. To resolve the redundancy, some additional conditions are provided.

- (1) The Z-axis of welding points coordinate system and the Z-axis of clamping robot base coordinate system should be in the same direction. Beside, the X-axis of welding points coordinate system and the Y-axis of clamping robot base coordinate system should be in the same direction. This is used to define the welding points orientation in world coordinate system.
- (2) To reduce energy using of clamping robot during positioning, the relative position between workpiece centre and clamping robot base coordinate system origin remain unchanged.

Form the first condition, the orientation of welding points in clamping robot base coordinate system which means the rotational matrix of R^1T_p is given by:

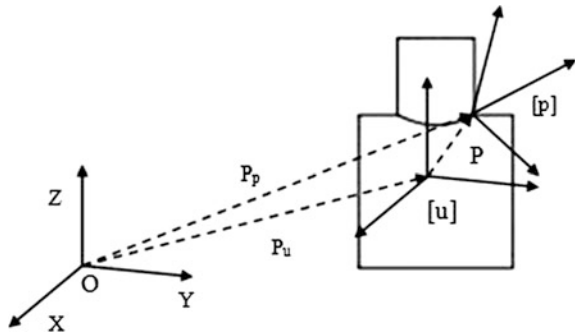
$$R_p = \begin{bmatrix} 0 & -1 & 0 \\ 1 & 0 & 0 \\ 0 & 0 & 1 \end{bmatrix} \tag{6}$$

According to Eq. 2, it can be obtained that:

$$P_p = R_u \cdot P + P_u \tag{7}$$

As show in Fig. 2, P_p represents the welding points position vector in world coordinate system, R_u represents the rotational matrix from workpiece coordinate system to world coordinate system, P represents the welding points position vector in workpiece coordinate system, P_u represents the origin position vector of

Fig. 2 The position of welding points



workpiece coordinate system in world coordinate system. From the second condition, it is easy to know P_u is a constant vector. With Eqs. 6 and 7, the transformation matrix from welding points coordinate system to world coordinate system ${}^{R1}T_p$ can be described as:

$${}^{R1}T_p = \begin{bmatrix} R_p & P_p \\ 0 & 1 \end{bmatrix} \quad (8)$$

Now that ${}^{R1}T_p$ is obtained, as long as the orientation of the points to be welded is certain, the transformation matrix from the clamping robot base coordinate system to end-effector coordinate system ${}^{R1}T_{E1}$ can be obtained by Eq. 4. Then, the six joint displacements of clamping robot can be calculated by inverse kinematics [8].

For welding robot, the relative orientation between torch and welding points should not be changed during welding task. This working orientation is determined by tilting angle, deflecting angle and drifting angle in the actual welding operation. Instead of discussing these welding technology, this paper defines the relative orientation between torch and welding points as follow: the X-axis of torch coordinate system and the X-axis of welding points coordinate system should be in the same direction; the Z-axis of torch coordinate system and the Z-axis of welding points coordinate system should be in the opposite direction. With this definition, the transformation matrix from welding torch coordinate system to welding points coordinate system ${}^{T2}T_p$ can be described as:

$${}^{T2}T_p = \begin{bmatrix} 1 & 0 & 0 & 0 \\ 0 & -1 & 0 & 0 \\ 0 & 0 & -1 & 0 \\ 0 & 0 & 0 & 1 \end{bmatrix} \quad (9)$$

Now that ${}^{R1}T_p$ and ${}^{T2}T_p$ is obtained, the transformation matrix from the welding robot base coordinate system to end-effector coordinate system ${}^{R2}T_{E2}$ can be obtained by Eq. 5. Then, the six joint displacements of welding robot can be calculated by inverse kinematics.

4 Establishment of Two-Robot Coordinated Simulation Platform

The robot models used in this paper are MOTOMAN-MH12, which is a multi-joint robot with 6 degree of freedom. Its D-H parameters are listed in Table 1.

Based on the environment of VC++6.0 and OpenGL, a 3D visualization simulation platform for two-robot coordinated motion is established. An OpenGL application which is used to read into and display the solid model built by SolidWorks is developed. The orientation of robot links are changing during simulation process, and the model of robot links are unchanged. To improve the

Table 1 D-H parameters of MOTOMAN-MH12 robot

Joint	$\theta/(\text{rad})$	$d/(\text{m})$	$a/(\text{m})$	$\alpha/(\text{rad})$
1	θ_1	0.45	0	0
2	θ_2	0	0.155	1.570796
3	θ_3	0	0.614	0
4	θ_4	0.64	0.2	1.570796
5	θ_5	0	0	1.570796
6	θ_6	-0.6002	0	1.570796

drawing efficiency, display list function of OpenGL is used. With this function, the property of robot links are saved, so that it only need to assign the position and orientation of model instead of rendering the whole graphic afresh. The steps of kinematics simulation are as follows:

- (1) Building the interface of OpenGL and Windows graphic based on VC++6.0, and setting up the drawing environment of OpenGL. After that, an OpenGL programming using VC++ is realized.
- (2) Establishing the 3D models of robot links and system parts by SolidWorks, and saving the models as STL documents.
- (3) Importing the STL documents into OpenGL, and assembling each part into a whole by scaling, translating, rotating and so on.
- (4) Realizing the actuation and simulation of the models according to the results of kinematics planning.

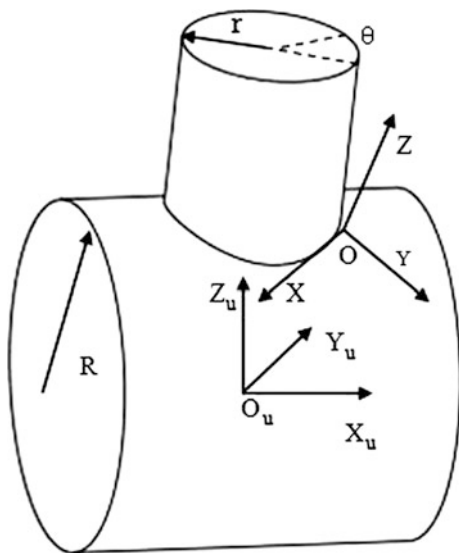
5 Motion Simulation for Intersecting Line

To verify kinematics analysis and trajectory planning of two-robot coordinated welding, here takes the intersection curve seam of two cylinder for example. The intersection curve seam to be welded is shown in Fig. 3. R represents the radius of horizontal cylinder, r represents the radius of vertical cylinder, $O_u-X_uY_uZ_u$ indicates workpiece coordinate system, $O-XYZ$ indicates welding points coordinate system. The equation of intersection curve can be expressed as:

$$\begin{cases} x = r \cdot \cos \theta \\ y = r \cdot \sin \theta \\ z = \sqrt{R^2 - r^2 \cdot \sin^2 \theta} \end{cases} \quad (10)$$

To meet the requirement that welding speed V_0 is constant, the arc length $dS(\theta)$ which is welding torch through in each interpolation cycle T should be the same. Thus,

Fig. 3 The workpiece to be welded



$$V_0 = \frac{dS(\theta)}{dt} = \frac{dS(\theta)}{d\theta} \cdot \dot{\theta} \quad (11)$$

According to the equation of intersection curve in Eq. 10, the arc length differential can be obtained:

$$dS(\theta) = \sqrt{(r \cdot \cos \theta)^2 + (r \cdot \sin \theta)^2 + (\sqrt{R^2 - r^2 \cdot \sin^2 \theta})^2} \cdot d\theta \quad (12)$$

With Eqs. 11 and 12, it is known that:

$$\dot{\theta} = \frac{V_0}{\sqrt{(r \cdot \cos \theta)^2 + (r \cdot \sin \theta)^2 + (\sqrt{R^2 - r^2 \cdot \sin^2 \theta})^2}} \quad (13)$$

So the displacements of angle in each interpolation cycle is:

$$\Delta\theta = \frac{V_0 \cdot \Delta T}{\sqrt{(r \cdot \cos \theta)^2 + (r \cdot \sin \theta)^2 + (\sqrt{R^2 - r^2 \cdot \sin^2 \theta})^2}} \quad (14)$$

Thus, the angle of each welding points can be calculated by:

$$\theta = \theta_0 + \frac{V_0 \cdot \Delta T}{\sqrt{(r \cdot \cos \theta)^2 + (r \cdot \sin \theta)^2 + (\sqrt{R^2 - r^2 \cdot \sin^2 \theta})^2}} \quad (15)$$

The position vector of welding points on intersection curve is expressed as: $\vec{p} = (x, y, z)$. The welding points coordinate system is defined as: the X-axis is the tangential direction of welding seam, the Z-axis is the angle bisector direction of two cylinder external normal line, the Y-axis is multiplication cross by X-axis to Z-axis. It is easy to know the tangent vector of welding seam is:

$$\vec{s} = (x', y', z') = \left(-r \cdot \sin \theta, r \cdot \cos \theta, \frac{-r^2 \cdot \sin \theta \cdot \cos \theta}{\sqrt{R^2 - r^2 \cdot \sin^2 \theta}} \right) \quad (16)$$

So the X-axis unit vector of welding points coordinate system is: $\vec{u} = \frac{\vec{s}}{|\vec{s}|}$. For horizontal cylinder, the external normal line direction of any point on intersection curve is:

$$\vec{n}_1 = (2x, 2y, 0) = (2r \cdot \cos \theta, 2r \cdot \sin \theta, 0) \quad (17)$$

For vertical cylinder, the external normal line direction of any point on intersection curve is:

$$\vec{n}_2 = (0, 2y, 2z) = (0, 2r \cdot \sin \theta, 2\sqrt{R^2 - r^2 \cdot \sin^2 \theta}) \quad (18)$$

The angle bisector direction of two cylinder external normal line is: $\vec{n} = \vec{n}_1 + \vec{n}_2$. So, the Z-axis unit vector of welding points coordinate system is: $\vec{w} = \frac{\vec{n}}{|\vec{n}|}$. The Y-axis unit vector of welding points coordinate system is the cross product of \vec{w} and \vec{u} : $\vec{v} = \vec{w} \times \vec{u}$. Substituting the angle calculated by Eq. 15 into Eqs. 16–18, the transformation matrix from welding points coordinate system to workpiece coordinate system is expressed as:

$${}^uT_p = \begin{bmatrix} \vec{u} & \vec{v} & \vec{w} & \vec{p} \\ 0 & 0 & 0 & 1 \end{bmatrix} \quad (19)$$

During simulation process, the following parameters are setting as: $R = 0.1$ m, $r = 0.05$ m, $v_0 = 0.04$ m/s, $T = 0.05$ s. The position vector of workpiece coordinate system origin is assigned as:

$$P_u = \begin{bmatrix} 1.2 \\ 0 \\ 0.3 \end{bmatrix} \quad (20)$$

In addition, it is known that:

$${}^{E1}T_{T1} = \begin{bmatrix} 1 & 0 & 0 & 0 \\ 0 & 1 & 0 & 0 \\ 0 & 0 & 1 & 0.163 \\ 0 & 0 & 0 & 1 \end{bmatrix} \quad (21)$$

$${}^{T1}T_u = \begin{bmatrix} 1 & 0 & 0 & 0 \\ 0 & 1 & 0 & 0 \\ 0 & 0 & 1 & 0.333 \\ 0 & 0 & 0 & 1 \end{bmatrix} \quad (22)$$

$${}^{E2}T_{T2} = \begin{bmatrix} 0.819 & 0 & -0.574 & -0.12 \\ 0 & -1 & 0 & 0 \\ -0.574 & 0 & -0.819 & 0.496 \\ 0 & 0 & 0 & 1 \end{bmatrix} \quad (23)$$

When Eqs. 1–23 are obtained, the six joint displacements of clamping robot and welding robot can be calculated respectively, then the models can be actuated and the motion simulation is realized.

The simulation process of two-robot coordinated welding for intersection line is shown in Fig. 4. View from the simulation process, the clamping robot and the welding robot are keep good fit while meeting the requirement of downhand welding at anytime, and the welding process is uniform and stable without collision. View from Figs. 5 and 6, the end-effector trajectories of clamping robot and welding robot are both continuous and closed spatial curve, and the relative trajectories of two-robot is absolutely intersection line. Figures 7 and 8 revealed that all the joint angle displacements are within robot working scope, and the six joints angle displacements curves are smooth.

Fig. 4 Simulation of two-robot coordinated welding



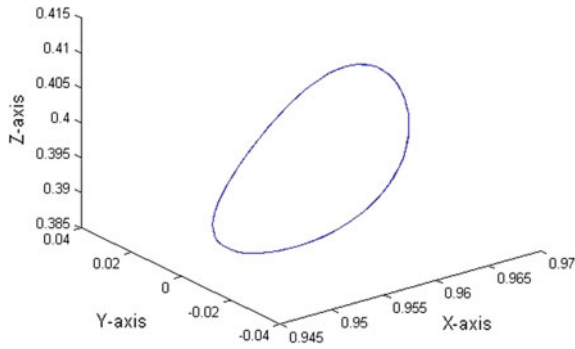


Fig. 5 End-effector trajectories of clamping robot

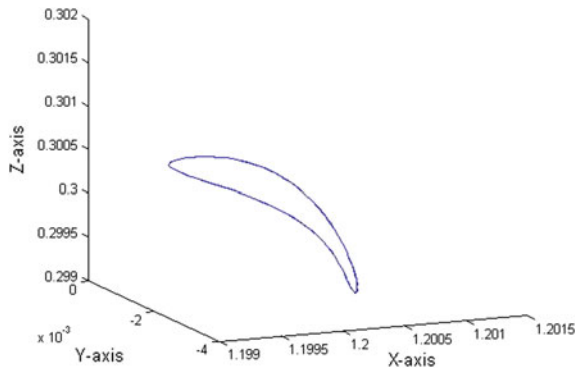


Fig. 6 End-effector trajectories of welding robot

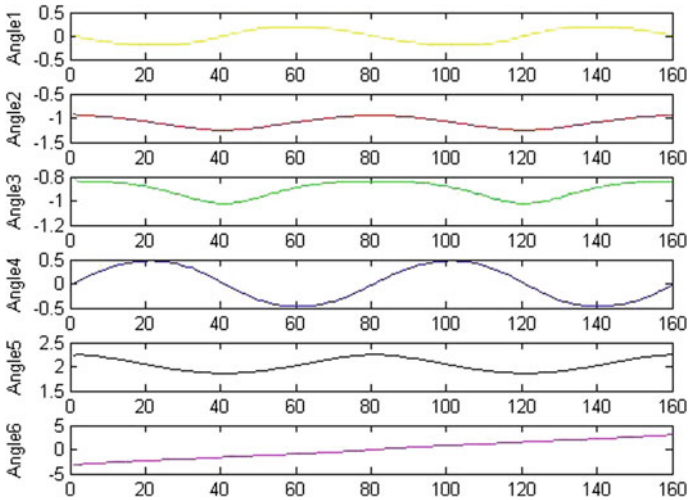


Fig. 7 Joints angle displacements of clamping robot

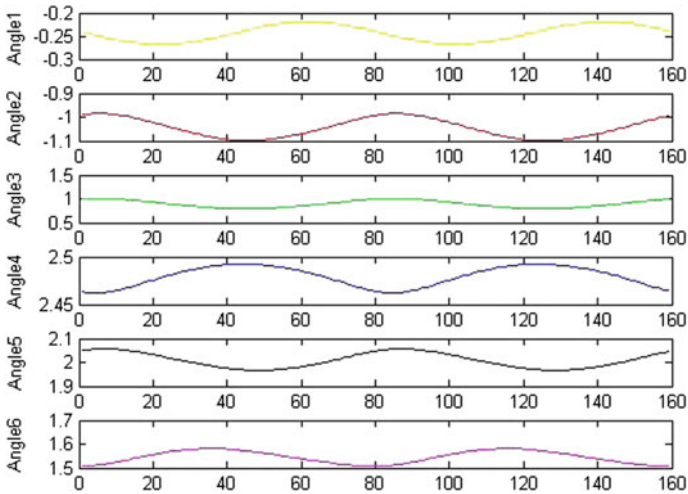


Fig. 8 Joints angle displacements of welding robot

6 Conclusions

This paper gives kinematics analysis of two-robot coordinated welding system, and proposes a method of two-robot coordinated trajectory planning which take downhand welding as the best welding position. Then, a simulation platform which is based on OpenGL and VC++ is established and a coordinated welding simulation of an intersecting line is given. Form the results of motion simulation, it can be concluded that the welding task of spatial complex curve seam is implemented by two-robot coordinated motion. The results of simulation win great satisfaction, so the kinematics analysis and the method of trajectory planning are verified.

Acknowledgments This work is supported by National Natural Science Foundation of China (Grant Nos. 51575187, 91223201), Science and Technology Program of Guangzhou (Grant No. 2014Y2-00217), Science and Technology Major Project of Huangpu District of Guangzhou (20150000661), Research Funds for the Central University(Fund No. 2015ZZ007).

References

1. Jouaneh MK, Wang X, Dornfeld DA (1990) Trajectory planning for coordinated motion of a robot and a positioning table. I. Path specification. In: IEEE transactions on robotics and automation. IEEE Press, Guangzhou, pp 735–745
2. He G, Gao H, Zhang G, Wu L (2005) Coordinated motion simulation in a robot arc off-line programming system. J Harbin Inst Technol, 813–815
3. Kang Y, Zhu D, Chen J (2005) Study on coordinative motion of arc-robot and positioner. Electr Weld Mach, 46–49

4. Zhang H, Zhang G, Cai C, Xiao J, Gao H (2011) Master-slave coordinated motion controlling of double-sided arc welding robots. *Trans China Weld Inst*, 25–28
5. Gan Y, Dai X (2011) Kinematic cooperation analysis and trajectory teaching in multiple robots system for welding. In: 16th IEEE conference on emerging technologies & factory automation (ETFa). IEEE Press, Piscataway, pp 1–8
6. Zhang T, Ouyang F (2012) Offline motion planning and simulation of two-robot welding coordination. *Front Mech Eng*, 81–92
7. Luh J, Zheng Y (1987) Constrained relations between two coordinated industrial robots for motion control. *Int J Robot Res*, 60–70
8. John J (2005) Introduction to robotics mechanics and control. China Machine Press

Development of Industrial Robot Teach Pendant Based on WinCE

Nianfeng Wang, Feiyue Zhang and Xianmin Zhang

Abstract This paper develops a kind of teach pendant based on embedded operating system Windows CE 6.0. Firstly, modular system structure is described based on the analysis of the basic functions of teaching system. Secondly, taking embedded computer as main controller, the human-machine interface is designed in MFC of Visual C++. After that, the key-press and touch screen are selected as input devices. By touching the screen or pressing the button, user can send functional commands to robot control system. Finally, the communication between teach pendant and host computer are carried out with Ethernet. Through testing, the design of teach pendant meets the requirements of six degrees of freedom industrial robot.

Keywords Teach pendant · Embedded computer · Ethernet communication

1 Introduction

Most industrial robots are programmed by teach-and-playback method because of its high repeatability positioning accuracy [1, 2]. As a tool of teaching programming, teach pendant has been an important part of the industrial robot control system. A teach pendant is a handheld device which is used with a robot controller to move, program, and run industrial robots. The user conveys the desired commands to robot controller and moves robot end-effector to the target positions through operating teach pendant. Robot controller records the corresponding joint angles in memory, then reads the memory and uses it for playback [3]. In addition, with teach pendant, the user can set robot parameters, view position information, get running status and alarm messages.

N. Wang (✉) · F. Zhang · X. Zhang
Guangdong Province Key Laboratory of Precision Equipment and Manufacturing
Technology, South China University of Technology,
Guangzhou 510640, Guangdong, People's Republic of China
e-mail: menfwang@scut.edu.cn

Generally, the research and design of teach pendant is completed by robot manufacturers and different corporations product various teach pendant. Therefore, the teach pendant and the program language are usually not exchangeable between different robots. With the increasing number of industrial robot, there are higher requirements of extending teach pendant for user [4]. To tackle this problem, it's a great significance to develop a kind of teach pendant for serial robot with simple operation, low cost and open source. Since the performance of teach pendant have a great impact on robot control system, a teach pendant should provides friendly human-machine interface and simple control method for user.

This paper designs and implements an open-sourced teach pendant for robot control system which is developed by laboratory. Based on the analysis of the basic functions of teach pendant, the implementation is divided into four modules which are System Monitoring, System Setting, Task Management, and Teaching Module respectively. Taking embedded computer as main controller, the development of teach system is based on Windows CE 6.0 operating system. The standard hardware devices are selected and the hardware platform of teaching system is established. Then the overall layout of the key-press is designed and the friendly human-machine interface is designed in MFC of Visual C++. After that the communication protocol between the teach pendant and the controller is realized by Ethernet. Periodic data and non-periodic data are exchange between teach pendant and host computer stable. Finally, the teach pendant has been tested on a six degrees of freedom industrial robot to verify the satisfaction of design requirements.

2 The Structure of Teach Pendant

A teach pendant is a handheld device for controlling a robot, it can perform basic functions such as manual control, teaching programming, executing robot programs, and halting robot in an emergency. The user can conveys commands to the end-effector and pauses or repeats the subtasks of whole operation. The two way communication between teach pendant and the controller provides a real time feedback data with detailed monitoring. A teach pendant is normally consists of main controller, display device, keyboard, enable switch and emergency stop switch.

2.1 *Basic Functions of Teach System*

As shown in Fig. 1, the expected functions of a teaching system are divided into the following four functional modules: Teaching Module, Task Management, System Setting and System Monitoring.

Teaching Module is used for teaching programming. During the process of teaching programming, the trajectory are divided into a series of characteristic

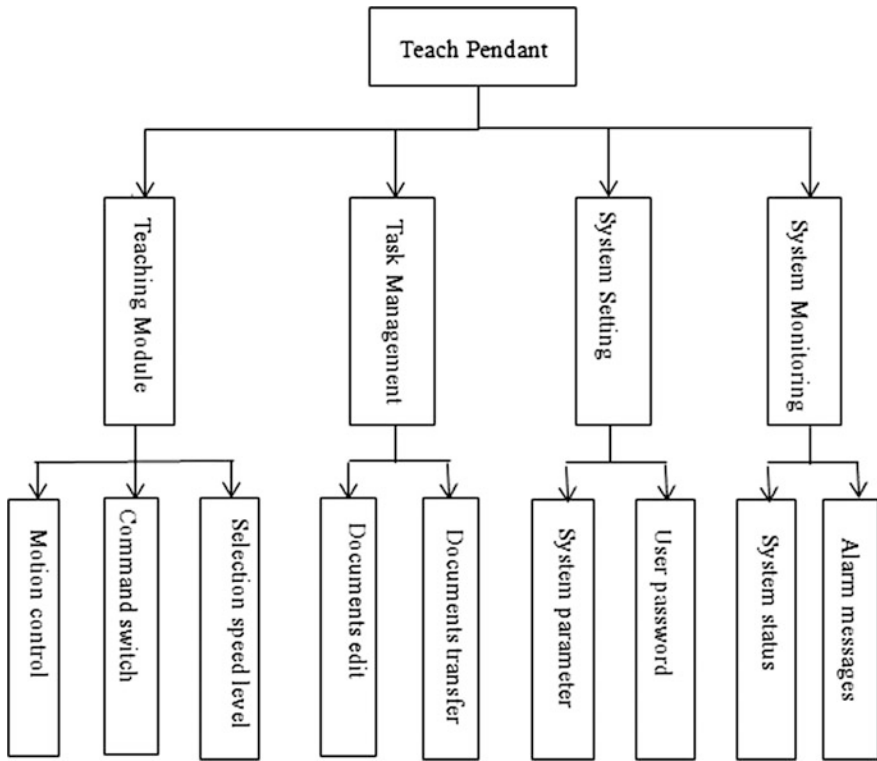


Fig. 1 Functions of teaching system

points according to the task requirements. The user controls robot to move to these characteristic points, and the control system gets the position messages. Apart from motion controlling of robot manually, teaching module is also used to provide interpolation methods and running speeds to achieve robot motion. Robot control system saves these messages as teaching programs and executes the programs by playback. Thus, the teaching partition should be included the functions of manual motion control and teaching program edition.

Task Management is used to manage the teaching program documents, including the functions of open a new document, open an existing document, save a document, delete a document. In addition, teaching programs are able to transfer to different devices which means personal PC can edit teaching programs and the programs of teach pendant are able to save to external devices.

System Setting is used to setup some parameters of control system such as position limitation, speed limitation, user password, and so on. What's more, the emergency stop button on robot teach pendant is the primary safety device of industrial robots. To make a convenient for user, enabling and emergency stop device are supposed to realize in teaching system.

System Monitoring is used to supervise the running status of robot control system, provide real-time information of robot position, speed, I/O status, and receive warning messages when robot control system break down. The I/O of the system consists of ac/dc inputs or outputs. Therefore, voltage or current are converted to control signals through the use of motion control card.

2.2 *Structure of Teach Pendant*

The relation between robot controller and teach pendant is host and slave computer, teach pendant is slave computer and robot controller is host computer. As slave computer, teach pendant consists of main controller, power module, input module, display module, communication module.

As the core of teaching system, main controller keep each module work coordinated, its functions mainly included responses input messages, gets the status of host computer, and transfers data bidirectionally. Main controller requires rapid data processing rate, convenient for redeveloping and small volume [5, 6]. Embedded computer can customize the operating system according to the development requirements, and it has good expansibility with different programming software. With standard interfaces and power module, using embedded computer would reduce the development difficulty and shorten developing period, so that the developer can focus on developing teaching system software. Based on these analysis, an embedded computer is used as main controller of teach pendant.

The input mode of teach pendant is mainly included key-press and touch screen. Input by pressing the key makes the operation more efficiency since all the functions are realized through the key instead of switching user interface. Input by touching the screen is more visual since it is easy to develop drag-and-drop commands. The teaching system developed in this paper is input by the combination of key-press and touch screen. For functional commands such as motion control and programs execution, user can sends the commands by pressing the key directly, which is more convenient and efficient. For non-functional commands such as setup parameters and program edition, it is simplifying the programming procedures and reducing the efforts in operation by touching the screen.

The communication between teach pendant and host computer is strict with the transfer speed and stability. Therefore, reliable communication and fast response speed are required for teaching system. Currently, the communication is mostly carried out with serial port, Ethernet or wireless. With standard Ethernet interface, embedded computer has the capability of creating sockets for communication, so it is easy to connect with other devices on same network. Take the advantages of TCP/UDP protocol, such as wide range application and high transmission speed, it's easy and fast to realize communication functions through Ethernet.

Based on these analysis, the design of teach pendant structure is shown in Fig. 2.

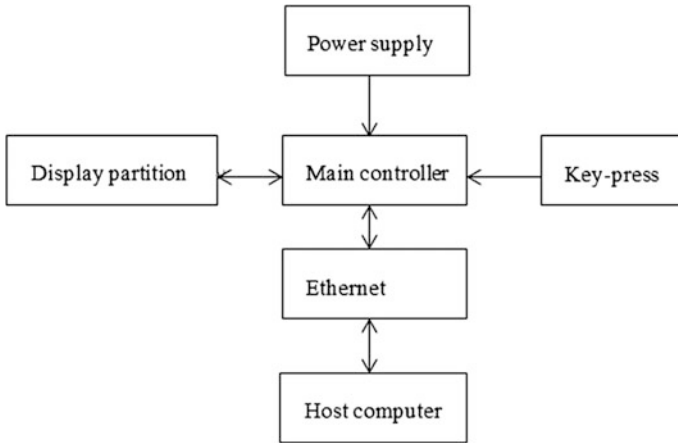


Fig. 2 Design of teach pendant structure

3 Hardware of Teach Pendant

With high performance of graphic engine, the embedded computer adopted in teach pendant is expected to meet higher requirements of performance and rapid processing rate. The embedded computer has a core hardware of ARM Cortex-A8 with 1 GHz dominant frequency. With the hardware headers interface such as GPIO, RAM, NandFlash, USB and Ethernet, embedded computer is enough for user to develop. In addition, embedded computer provides standard operating system facilities such as LCD output device and power module. The power module converts the power from the control cabinet to core board and LCD.

The embedded Operating System is customizable, portable, real time and low resources occupation. The core of Windows CE 6.0 system is customized, operating system image file is made, and the SDK used to debug MFC application is derived. Customizing Windows CE 6.0 according to the requirements of teaching system would reduce system expenditure and improve the running rate and real time of system.

The emergency stop device is the primary safety device of industrial robots. Considering the safety of operation, enable and emergency stop device are realized in teaching system. Two three-position enabling switches are located on the place where user touches the teach pendant. It requires the user turns on the switch while controlling robot, otherwise the robot won't move. The emergency stop device would cut the power supply of servo motor and stop the machine when emergency occur. Safety signals from enabling switch and emergency stop switch are sent to linking module through electric cable. The design of linking module is shown in Fig. 3. As input devices, touch screen and membrane buttons are accessible to user. The membrane buttons are divided into the partitions of interface switch keys,

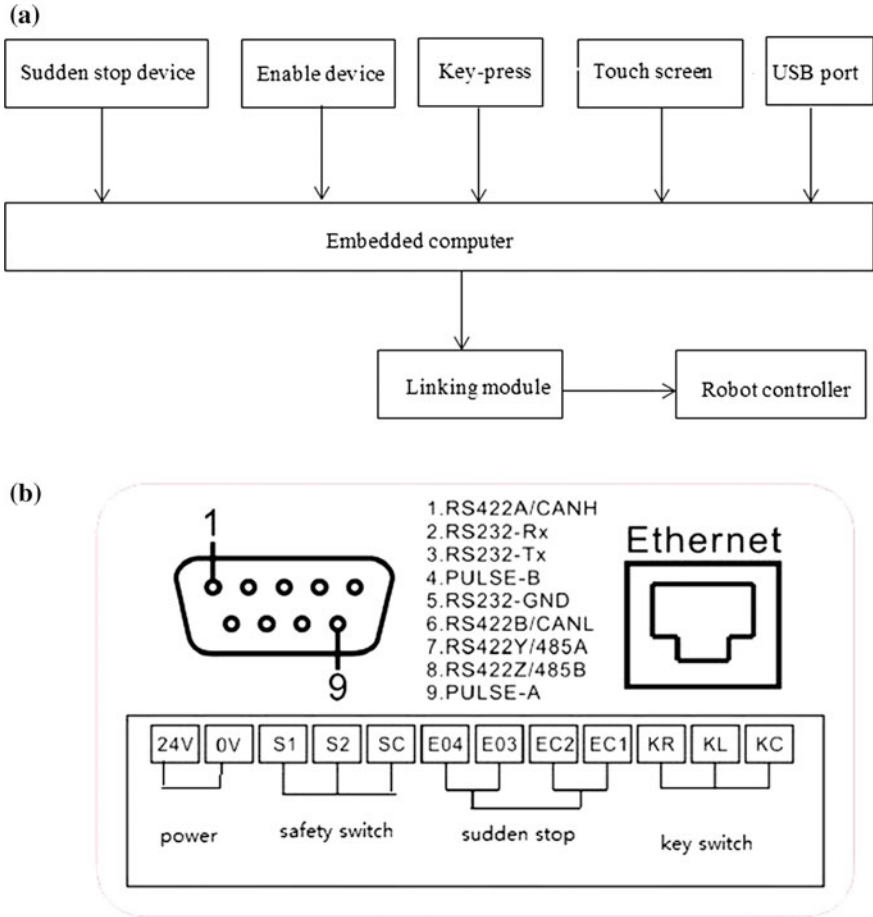


Fig. 3 Linking module of teach pendant

common function hotkeys and motion control keys. The appearance of teach pendant is shown in Fig. 4.

4 Design of Human-Machine Interface

The interaction between user and teach pendant is realized by the functions of input and display devices. By touching the screen or pressing the button, user can send commands to robot control system. There are functional input such as motion control, teach program execution, menu selection, speed level selection, and non-functional input such as program edition, documents naming, motion

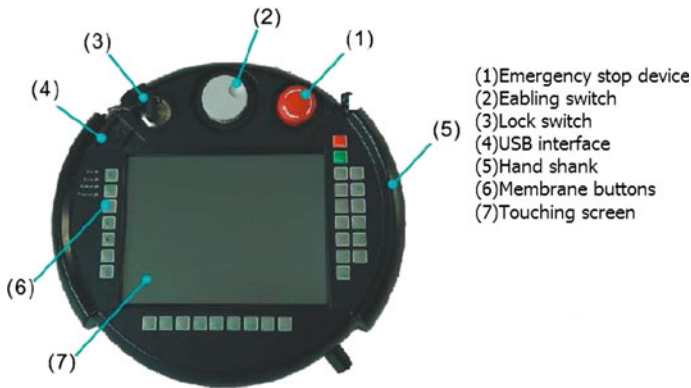
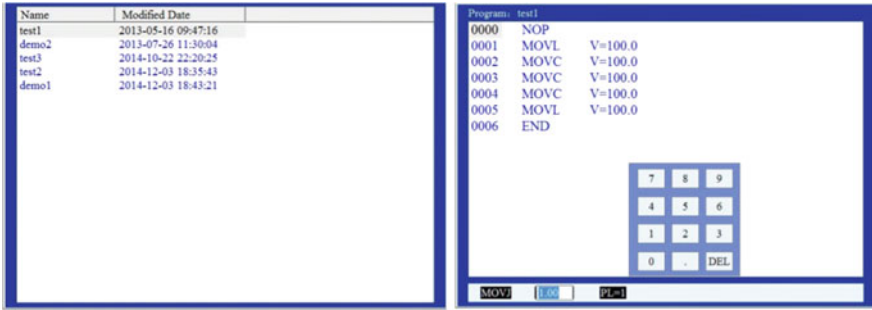


Fig. 4 Appearance of teach pendant

command selection, speed setup. For functional input, user sends the function commands by pressing the key directly. For non-functional input, user sends the commands by touching MFC button and visual keyboard. The display information are shown in software application interface. Based on graphic engine and MFC, the application interface of teach pendant is developed by Microsoft Visual Studio 2005.

4.1 Display Interface

According to the functions of teaching system, the basic interface is divided into seven menus, which included Program, I/O, Robot, Storage, Setting, System Information and Jog. The interface of Program included the submenus of Program Selection and Program Content. Program Selection shows all teaching program files in a list which included the information of file name and modified date. Files in the list can be selected by touching the screen or pressing the direction key. Program Content, which included the functions of inserting a new motion command and setup motion speed, is used to edit teaching programs. Different type of motion commands are switched by touching screen, and the speed value is input by virtual numeric keyboard. I/O is used to control and display system input and output status. User can converts the signals of ON/OFF to robot controller through pressing the MFC buttons. Robot is used to show the position messages of robot end-effector in real time. Storage is used to save, copy, backup and transfer teaching program files. Setting is used to setup control system parameters such as limitation of speed and position, user password. System Information is used to show the messages of system hardware version, running status, running speed and alarm messages. Jog is a manual control interface. It is mainly included the functions of single axis control,



(a) Program Selection

(b) Program Content



(c) Jog

Fig. 5 Software interface

jog speed level choice, return of origin position, switch of joint space to Cartesian space. The software interface is shown in Fig. 5.

4.2 Layout of Membrane Buttons

The membrane buttons are divided into the partitions of interface switch keys, common function hotkeys and motion control keys. Each membrane button has special key value. When pressing a button, teaching system gets key value and responses to commands according to key value. Seven interface switch keys are located on the left side of teach pendant operation panel. It is correspond to seven basic interfaces, and pressing one of them would enter corresponding interface. Common function hotkeys are located on downside, and its functions change according to current display interface. For example, when entering Program Content, its functions turn into inert a new motion command, run the program and so on; when entering Storage, its functions turn into copy, backup a teaching program and so on. Motion control keys are located on right side. User can controls

the robot by giving the commands of moving in X, Y, Z, RX, RY, RZ direction or S, L, U, R, B, T joint. Each time the user presses the keys, the related command is sent to the robot end-effector to take an incremental step in the relative direction. And there are keys used to run or stop a teach programs, return the robot to origin position and switch joint space to Cartesian space.

5 Communication with Host Computer

The communication between teach pendant and host computer is precondition of the whole control system running stability. Teach pendant exchanges data with host computer frequently through two way communication. The module of interface sends commands to robot controller and receives feedback from host computer. Host computer receives the commands form teach pendant and provides the data such as robot position, system running status and warning messages for teach pendant. Teach pendant and host computer are connected by network cable and communicated by Ethernet. The process of communication adopts server-client mode, and host computer is a server, teach pendant is a client. Teach pendant with fewer resource calling for host computer which has abundant resource, and host computer responses to teach pendant after received the asking. There are periodic data and non-periodic data during data transfer process. Non-periodic data which is sent by pressing a functional key is mainly included system parameters, I/O status, commands of motion control. Periodic data, which is updated by host computer and sent to teach pendant in real time, is mainly included robot position, running speed, running status and alarm messages. Since most transfer data are periodic data which have high requirements of real-time during communication, UDP protocol without connected, data confirmed and retransfer is selected as the protocol of Ethernet communication [7].

As shown in Fig. 6, the step of communicate with UDP protocol is described as follow:

1. Use `socket()` to establish an UDP socket, the second parameter is `SOCK_DGRAM`;
2. Initialize the value of `sockaddr_in` structure;
3. Use `bind()` to bind the IP and ports of socket;
4. Enter an infinite loop program, use `sendto()` and `recvform()` to send or receive data.

After create sockets for communication, it need to package and resolve transfer data. Figure 7 shows the structure of data frame. Periodic data is arranged one by one and saved in a transferring char which would send from host computer to teach pendant all the time until the host computer received a non-periodic data. When teach pendant receive a periodic data, it would assignment them to corresponding parameters and then display them. Non-periodic data is added a command type as

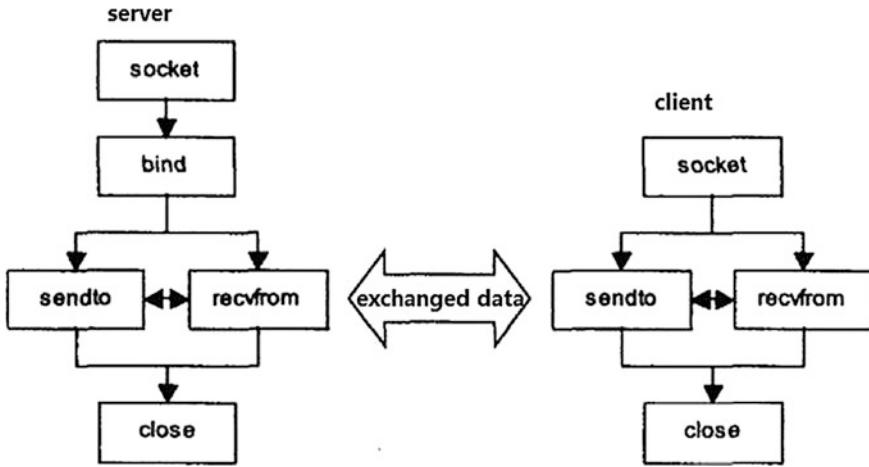
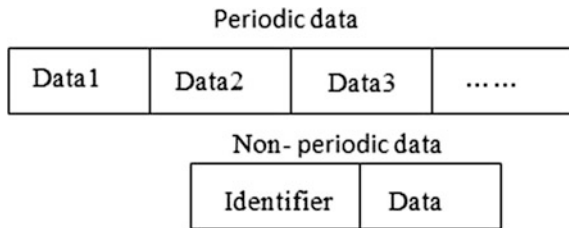


Fig. 6 UDP protocol

Fig. 7 Structure of data frame



an identifier in front of data value. When user presses a functional key, teach pendant sends a non-periodic data to host computer according to the key value. Host computer receives a non-periodic data, then executes special function according to the identifier.

6 Test of Teach Pendant

Based on laboratory self-developed six axis robot, test the performance of teach pendant. The test platform is shown in Fig. 8. First, connect the teach pendant and robot control cabinet by electric cable and network cable. Then, turn on the teach pendant and host computer, and setup the IP address. Pressing the key on left side, found that the display and switch of every interface is normal which proved the design of human-machine interface is good. Entering the Jog interface, push enable device, press the key to control single axis motion found that every joint is move according to the command. When press emergency stop device, the robot stop

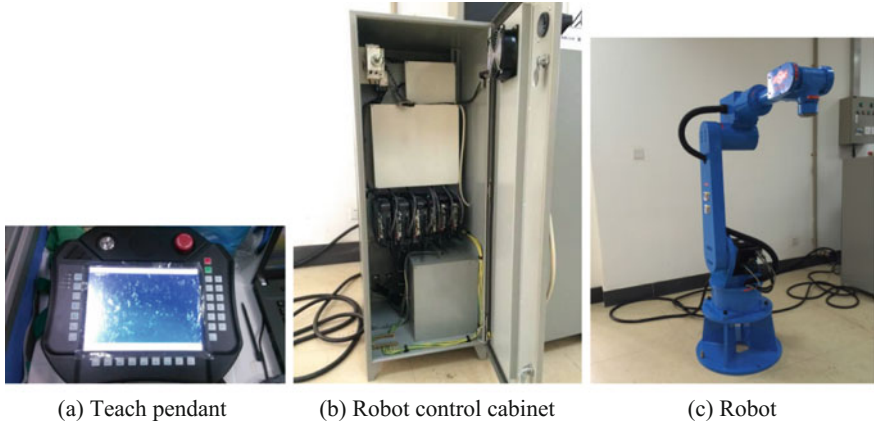


Fig. 8 Robot control system

moving. Switch to Robot interface after finished single axis control, the robot position of joint space and Cartesian space are display correctly. Form the test results, the hardware devices of teach pendant are running well, the interfaces are display fluent, and the communication between teach pendant and host computer are working stable.

7 Conclusions

Aiming at robot control system designed by laboratory, this paper develops a kind of teach pendant based on embedded operating system WinCE. Based on the analysis of the basic functions of the teach pendant, teaching system are divided into Teaching Module, Task Management, System Setting and System Monitoring. The hardware devices are selected and the hardware platform of teaching system is established. The human-machine Interface is designed in MFC of Visual C++. The key-press and touch screen are selected as input devices. The communication protocol between the teach pendant and the controller is realized by Ethernet. The teach pendant has been tested to verify the satisfaction of the design requirements.

Acknowledgments This work is supported by National Natural Science Foundation of China (Grant Nos. 51575187, 91223201), Science and Technology Program of Guangzhou (Grant No. 2014Y2-00217), Science and Technology Major Project of Huangpu District of Guangzhou (20150000661), Research Funds for the Central University (Fund No. 2015ZZ007).

References

1. Choi MH, Lee WW (2001) A force/moment sensor for intuitive robot teaching application. In: 2001 IEEE international conference on robotics & automation (ICRA). IEEE Press, Seoul Korea, pp 4011–4016
2. Shen T, Radmard S, Chan A (2013) Motion planning from demonstrations and polynomial optimization for visual servoing applications. In: 2013 IEEE/RSJ international conference on intelligent robots and systems (IROS). IEEE Press, Tokyo, pp 578–583
3. Fukui H, Yonejima S, Yamano M (2009) Development of teaching pendant optimized for robot application. In: 2009 IEEE workshop on advanced robotics and its social impacts (ARSO). IEEE Press, Tokyo, pp 72–77
4. Garcia E, Vergara S, Reyes F (2009) Development of a teach pendant for an ABB robot. In: 2009 international conference on electrical, communications, and computers (CONIELECOMP). IEEE Press, Cholula, pp 256–259
5. Sun J, Gao J, Zhang J (2007) Teaching and playback control system for parallel robot for ankle joint rehabilitation. In: 2007 IEEE international conference on industrial engineering and engineering management. IEEE Press, Singapore, pp 871–875
6. Yong Y, Huang Y, Chiba R (2013) Teaching-playback robot manipulator system in consideration of singularities. In: 2013 IEEE/ASME international conference on advanced intelligent mechatronics (AIM). IEEE Press, Wollongong, pp 453–458
7. Bishop S, Fairbairn M, Norrish M (2005) Rigorous specification and conformance testing techniques for network protocols, as applied to TCP, UDP, and sockets. In: 2005 conference on applications, technologies, architectures, and protocols for computer communications. New York, pp 265–276

On the Output Motion of PMSM Driving a Planar Underactuated 2R Manipulator

Jin Xie, Shicong Zhang and Zhaohui Liu

Abstract In this paper, a PMSM is connected to a planar underactuated 2R manipulator. Both two systems are nonlinear dynamic systems. It is deserted to learn the influence of coupling of nonlinear systems on the motion of the system. The coupling dynamic model is established, and simulation is carried out. The result shows that the coupling of nonlinear dynamic system certainly makes the bifurcation point changed, and even more disappeared. In addition to this, the coupling of nonlinear system intensifies the chaotic motion.

Keywords Nonlinear dynamics · PMSM · Planer underactuated 2R manipulator · Chaos controlling

1 Introduction

Planar underactuated 2R manipulator exhibits abundant nonlinear phenomenon, such as periodic motion and chaotic motion [1–3]. Lots of methods have been proposed to control the chaotic motion [4–6]. However, all these methods addressed the motion of two links without consideration of the actuator.

It is natural to think controlling the motion of the 2R manipulator with a permanent magnet synchronous motor (PMSM) for its high efficiency and performance, low noise and robustness. The dynamic model of PMSM is also a nonlinear system [7–10].

In this paper, the output shaft of PMSM is connected to the first joint of the manipulator directly forming an electro-mechanical system. The coupling of two

J. Xie (✉) · Z. Liu

School of Mechanical Engineering, Southwest Jiaotong University,
Chengdu 610031, People's Republic of China
e-mail: xj_6302@263.net

S. Zhang

Patient Examination Cooperation Sichuan Center of the Patinet Office,
Chengdu 610213, People's Republic of China

nonlinear systems results in a more complicated dynamic system and the output motion of PMSM is affected not only by the parameters of the motor but the parameters of the manipulator as well. On the other hand, the output motion of PMSM will determine the motion state of the manipulator.

This paper focuses on the influence of coupling between the motor and the manipulator on the output motion of the motor. This problem is of paramount value from the viewpoint of controlling chaos of 2R underactuated manipulator. The rest of this paper is organized as follows. Firstly, the dynamic characteristic of PMSM is discussed in Sect. 2. Then, following the establishment of the dynamic model of PMSM coupling with the manipulator, the impact of the parameters of the manipulator on the output motion of PMSM is analyzed in Sect. 3, and finally the conclusions are presented in Sect. 4.

2 Dynamic Analysis of PMSM

In this section, the dynamic model of PMSM is established, and simulation is carried out. With the results of simulation, it is shown that the output motion of PMSM may be chaotic or periodic dependent on the parameters of the motor.

2.1 The Dynamic Model of PMSM

The structure of PMSM and its equivalent circuit are shown in Fig. 1.

In the equivalent circuit of PMSM (Fig. 1b), R_s is the stator resistance, L is the inductance, i is the current, U is the supplied voltage and E is the back electromotive force. Assuming there is one pole-pair and air-gap field is well-distributed, we have following equations in the d, q rotating reference frames [11]

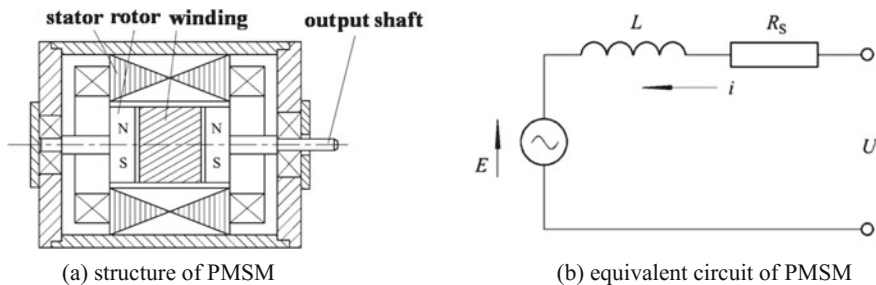


Fig. 1 The structure and equivalent circuit of PMSM

$$\begin{aligned} U_d &= R_s i_d + \frac{di_d}{dt} L - \omega L i_q \\ U_q &= R_s i_q + \frac{di_q}{dt} L - \omega L i_d - \omega \Psi \end{aligned} \quad (1)$$

where ω is the output angular velocity of PMSM, Ψ is permanent magnet flux. The condition of moment balance of output shaft gives

$$\Psi i_q = T_L + J \frac{d\omega}{dt} + B\omega \quad (2)$$

where T_L is load torque, J is rotary inertia of the rotor, and B is damping coefficient. Combining Eq. (1) with Eq. (2) yields the mathematic model of PMSM in the form

$$\begin{aligned} \frac{di_d}{dt} &= (U_d - R_s i_d + \omega L i_q) / L \\ \frac{di_q}{dt} &= (U_q - R_s i_q - \omega L i_d + \omega \Psi) / L \\ \frac{d\omega}{dt} &= (\Psi i_q - T_L - B\omega) / J \end{aligned} \quad (3)$$

Let

$$\begin{aligned} \tau &= \frac{L}{R_s}, t = \hat{t}, k = \frac{B}{\tau \Psi}, \gamma = \frac{\psi}{kL}, \sigma = \frac{B\tau}{J}, i_d = kx_1, \\ i_q &= kx_2, \omega = \frac{x_3}{\tau}, \hat{U}_d = \frac{U_d}{kR_s}, \hat{U}_q = \frac{U_q}{kR_s}, \hat{T}_L = \frac{\tau^2 T_L}{J}. \end{aligned}$$

The dimensionless dynamic equation of PMSM can be written as

$$\begin{aligned} \frac{dx_1}{d\hat{t}} &= \hat{U}_d - x_1 + x_2 x_3 \\ \frac{dx_2}{d\hat{t}} &= \hat{U}_q - x_2 - x_1 x_3 + \gamma x_3 \\ \frac{dx_3}{d\hat{t}} &= \sigma(x_2 - x_3) - \hat{T}_L \end{aligned} \quad (4)$$

2.2 The Output Angular Velocity of PMSM When $\hat{T}_L = 0$

There are five parameters in Eq. (4), they are $\hat{U}_d, \hat{U}_q, \hat{T}_L, \sigma, \gamma$. It is well known that any variation of these parameters will lead to a change in the state of output motion

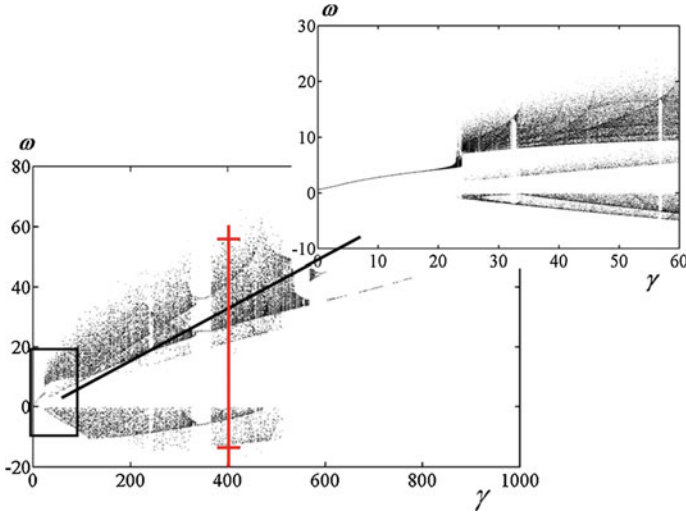


Fig. 2 Bifurcation diagram of output motion of PMSM

of PMSM. In this paper, we randomly chose parameter γ to represent the relationship between the parameter of the system and the output angular velocity of PMSM, ω . For other parameters, the method of analysis is along the similar lines.

In this subsection, we investigate the case in which $\hat{T}_L = 0$, i.e. the output shaft of PMSM is not connected to any device, so, there no exist any load. The simulation is carried out utilizing MATLAB with parameters $\hat{U}_d = 2$, $\hat{U}_q = 2$, $\sigma = 10$, $\tau = 15$, $J = 0.15$, and the initial condition $x_1 = x_2 = x_3 = 0.1$.

The outcomes of simulation are plotted in the (γ, ω) -plane, so-called bifurcation diagram, as shown in Fig. 2.

From Fig. 2, it can be seen that there are many bifurcation values at which the change of the motion state will appear. The lowest bifurcation value in Fig. 2 is 23.75 at which the output motion of PMSM transits from periodic motion into chaotic motion. Additionally, the span of output angular velocity varies with respect to the parameter γ . For example, the span is from -13.33 to 56.66 when $\gamma = 400$.

3 Dynamic Analysis of PMSM Driving Planar Underactuated 2R Manipulator

In this section, we connect PMSM with a planar underactuated 2R manipulator directly, as shown in Fig. 3.

We firstly establish the dynamic model of planar underactuated 2R manipulator. Then, couple it with the dynamic model of PMSM to form the dynamic model for

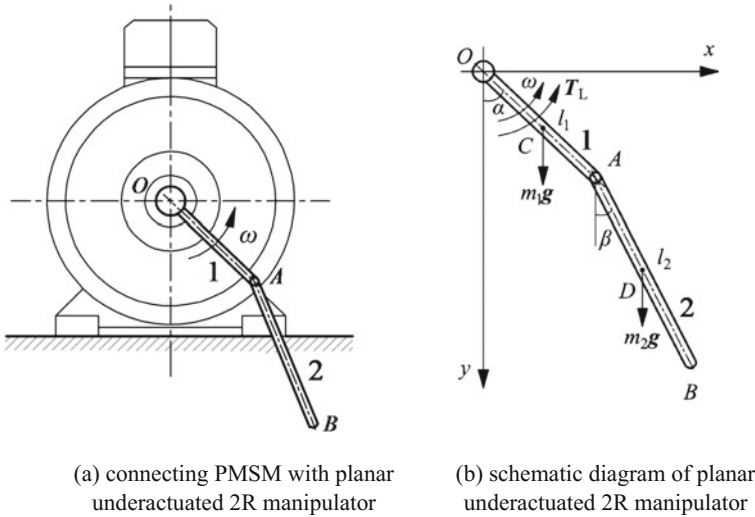


Fig. 3 PMSM driving the planar underactuated 2R manipulator

the whole system. Simulation is carried out in order to know how the coupling of two systems affects the output motion of PMSM.

3.1 The Dynamic Model of Planar Underactuated 2R Manipulator

As shown in Fig. 3b, the 2R manipulator possesses two degree of freedom. As joint O is connected to the output shaft of PMSM and joint A is free of actuation, known as passive joint, the manipulator is underactuated.

l_1, l_2 denote the lengths of Link 1 and Link 2, and m_1, m_2 denote the mass of Link 1 and Link 2 respectively. We assume that both links are rectangular solid of homogeneous density, the damping coefficient at joints O and A is C_p , and T_L is the driving torque provided by PMSM.

We construct the dynamic equation for the 2R manipulator with Lagrangian formulation [12].

The difference between the kinetic and potential energy of the system, known as Lagrangian, can be expressed as

$$\begin{aligned}
 L = \frac{1}{2} [& \left(\frac{1}{3}m_1 + m_2\right)l_1^2\dot{\alpha}^2 + \frac{1}{3}m_2l_2^2\dot{\beta}^2 + m_2l_1l_2\cos(\alpha - \beta)\dot{\alpha}\dot{\beta}] \\
 & + \frac{1}{2}m_1gl_1\cos\alpha + m_2g\left(l_1\cos\alpha + \frac{1}{2}l_2\cos\beta\right)
 \end{aligned}
 \tag{5}$$

At joint O , the actuator torque is $T_L - C_p \dot{\alpha}$, and at joint A , it is $-C_p \dot{\beta}$. After the substituting Lagrangian, L , and the actuator torques into Lagrangian formulation, the equations of motion for the planar underactuated 2R manipulator are then given by

$$\begin{aligned}
 & \left(\frac{1}{3}m_1 + m_2\right)l_1^2\ddot{\alpha} + \frac{1}{2}m_2l_1l_2\cos(\alpha - \beta)\ddot{\beta} + \frac{1}{2}m_2l_1l_2\dot{\beta}^2\sin(\alpha - \beta) \\
 & + \frac{1}{2}m_1gl_1\sin\alpha + m_2gl_1\sin\alpha - T_L + C_p\dot{\alpha} = 0 \\
 & \frac{1}{3}m_2l_2^2\ddot{\beta} + \frac{1}{2}m_2l_1l_2\cos(\alpha - \beta)\ddot{\alpha} - \frac{1}{2}m_2l_1l_2\dot{\alpha}^2\sin(\alpha - \beta) \\
 & + \frac{1}{2}m_2gl_2\sin\beta + C_p\dot{\beta} = 0
 \end{aligned} \tag{6}$$

3.2 Coupling Between PMSM and the Manipulator

In our case, the PMSM is connected with the manipulator by the output shaft of PMSM. So, the output angular velocity of PMSM is the input angular velocity of the manipulator, and the load torque of PMSM is the actuate torque of the manipulator. For simplify, the T_L is written as $m_2g[l_1 + l_2\sin\beta/2]$ without taking the influence of the angular velocity $\dot{\beta}$ into account for the reason that it is too small compared with influence of oher parameters.

For the purpose of consecution, let $x_4 = \beta$, $x_5 = \frac{d\beta}{dt}$, $x_6 = \zeta x_3 \hat{t}$. Combining Eq. (6) with Eq. (4) yields the following result:

$$\begin{aligned}
 \frac{dx_1}{dt} &= \hat{U}_d - x_1 + x_2x_3 \\
 \frac{dx_2}{dt} &= \hat{U}_q - x_2 - x_1x_3 + \gamma x_3 \\
 \frac{dx_3}{dt} &= \sigma(x_2 - x_3) - \hat{T}_L \\
 \frac{dx_4}{dt} &= x_5 \\
 \frac{dx_5}{dt} &= -\frac{3l_1}{2l_2}\cos(x_6 - x_4)\left[\sigma(x_2 - x_3) - \frac{\tau^2}{J}T_L\right] + \frac{3l_1}{2l_2}x_3^2\sin(x_6 - x_4) \\
 &\quad - \frac{3g\tau^2}{2l_2}\sin x_4 - \frac{3C_p\tau}{m_2l_2^2}x_5 \\
 \frac{dx_6}{dt} &= \zeta x_3
 \end{aligned} \tag{7}$$

3.3 The Output Motion of PMSM in the Coupling System

As foregoing discussion, both the model of PMSM and the manipulator are non-linear dynamic system. Integrating two such systems into one system creates a more complicated system. What we are interest in is how the output motion of PMSM is changed. To this end, we take the same parameters of PMSM as in Sect. 2, and set some parameters of the manipulator, $l_2 = 1.5$ m, $C_p = 0.05$, $\zeta = 0.75$, to carry out the simulation. The bifurcation diagrams for different lengths of Link 1 are shown in Fig. 4.

In Fig. 4a, it is hard to find the bifurcation value, but in Fig. 4b, c, the bifurcation values are obvious, they are almost 60. Additionally, the spans of output angular velocity of PMSM are larger than that shown in Fig. 2, when $\gamma = 400$, the span is from -22.73 to 54.54 as $l_1 = 0.8$ m, from -31.81 to 54.54 as $l_1 = 2.42$ m, and from -30.95 to 52.38 as $l_1 = 2.6$ m. The motion is the more chaotic, the lager the span is.

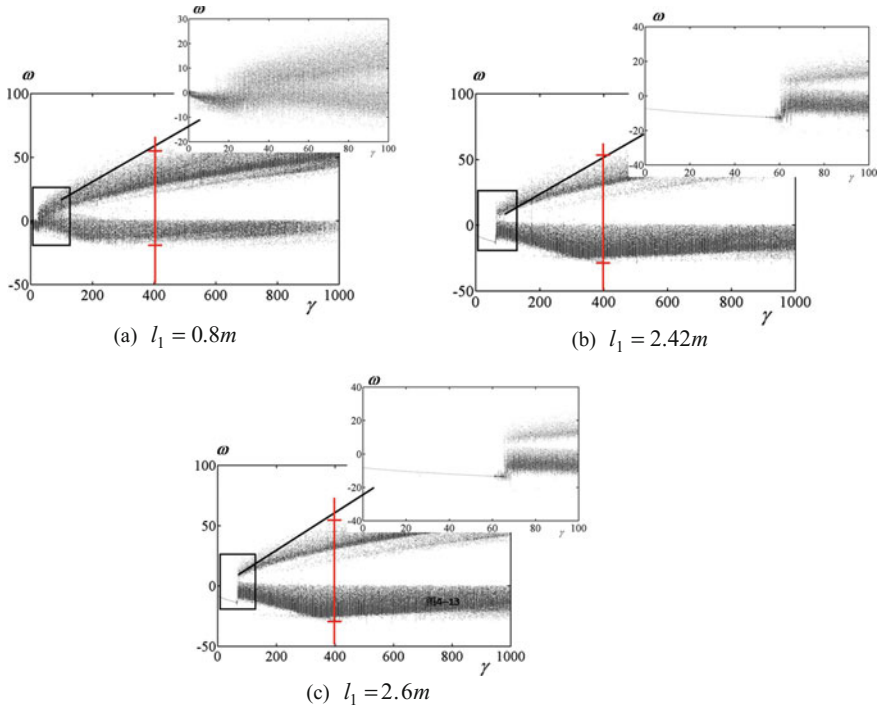


Fig. 4 Bifurcation diagram of output motion of PMSM in the coupling system

4 Conclusions

In this paper, two nonlinear dynamic systems, PMSM and planar underactuated 2R manipulator, are coupled. The outcome of simulation provides a real insight into such a complicated system.

Bifurcation point or bifurcation value plays an important role in controlling the chaos. With it, one can change the motion state from chaotic into periodic, or reversely, especially in the case when the motion is controllable, such as the system is driven by PMSM. While, the results of our study shows that the coupling of nonlinear dynamic system certainly makes the bifurcation point changed, and even more disappeared. So, it is possible to design a planar underactuated 2R manipulator driven by PMSM to generate or eliminate chaotic motion completely.

The coupling of nonlinear system intensifies the chaotic motion. This reveals a general rule for coupling of nonlinear system.

It should be noted that the conclusions drawn here are based on the results of simulation, theoretical and experimental certifications should be addressed in the future research.

Acknowledgments The authors would like to acknowledge the financial support of NSFC (National Natural Science Foundation of China) under the grant No. 51175437 and No. 51575457.

References

1. González-Hernández HG, Alvarez J, Alvarez-Gallegos J (2004) Experimental analysis and control of chaotic pendubot. *Int J Rob Res* 23(9):891–901
2. Xie J, Liu Zh-H, Chen Y (2013) Kinematic analysis of 2R planar underactuated manipulator with knowing the motion of the actuated joint. *Mach Des Res* 29 Supplementary Issue, 254–256 (in Chinese)
3. Freidovich L, Robertsson A et al (2013) Periodic motions of the pendubot via virtual holonomic constraints: theory and experiments. *Automatica* 44(3):785–791
4. Xin X, Tanaka S et al (2013) New analytical results of energy-based swing-up control for the pendubot. *Int J Non Linear Mech* 52:110–118
5. Xin X, Liu Y (2013) Reduced-order stable controllers for two-link underactuated planar robots. *Automatica* 49(7):2176–2183
6. Pongphut A, Sritheerawirojana U, Komine N, Sooraksa P (2006) Control of pendubot with chaotic perturbation. In: 1st IEEE conference on industrial electronics and applications, pp 446–450. Institute of Electrical and Electronics Engineers Computer Society, Singapore
7. Wei D-Q, Luo X-S, Wang B-H, Fang J-Q (2007) Robust adaptive dynamic surface control of chaos in permanent magnet synchronous motor. *Phys Lett A* 363(1–2):71–77
8. Su K-L, Li C-L (2014) Chaos control of permanent magnet synchronous motors via unidirectional correlation. *Optik* 125(14):3693–3696
9. Ataei M, Kiyomarsi A, Ghorbani B (2010) Control of chaos in permanent magnet synchronous motor by using optimal lyapunov exponents placement. *Phys Lett A* 374(41):4226–4230

10. Zribi M, Oteafy A, Smaoui N (2009) Controlling chaos in the permanent magnet synchronous motor. *Chaos Soliton Fract* 41(3):1266–1276
11. Krause PC, Wasynczuk O, Sudhuff SD (1995) *Analysis of electrical machinery*. IEEE Press, New York
12. Craig JJ (2005) *Introduction to robotics: mechanics and control*, 3rd edn. Pearson Education, Inc, Upper Saddle River

Fixed-Wing UAV Path Planning in a Dynamic Environment via Dynamic RRT Algorithm

Liang Lu, Chengxing Zong, Xinyu Lei, Bozhi Chen and Ping Zhao

Abstract This paper proposed a dynamic RRT algorithm that applied to fixed-wing UAV's path planning in dynamic three-dimensional environment. The tree structure of the dynamic RRT algorithm was expanded by adopting the constraint equations to satisfy fixed-wing UAV's actual dynamic constrains. In order to avoid collision with dynamic obstacles, corresponding locations of dynamic obstacles in the time of each step are considered in the algorithm. Also, B-spline was also used to interpolate the resulting optimal path for fixed-wing UAV. As a result, the algorithm could generate a smooth path that satisfy UAV's dynamic constrains in the three-dimensional environment with static and/or dynamic obstacles. The simulation results showed the effectiveness of proposed dynamic RRT algorithm, indicating that it could be applied to fixed-wing UAV's path planning in dynamic three-dimensional environment.

Keywords Path planning · Dynamic RRT · Fixed-Wing UAV · Dynamic obstacle avoidance

L. Lu · C. Zong · X. Lei · B. Chen · P. Zhao (✉)
Department of Mechanical Engineering, Hefei University of Technology, Hefei 230009,
China
e-mail: ping.zhao@hfut.edu.cn

L. Lu
e-mail: luliang92@mail.hfut.edu.cn

C. Zong
e-mail: 365717252@qq.com

X. Lei
e-mail: 1366118630@qq.com

B. Chen
e-mail: 1094532501@qq.com

1 Introduction

In the area of mobile robots, path planning is to find an obstacle-free path from the initial state to the goal state according to certain criteria in an environment with obstacles [1]. In the recent years, numbers of new algorithms have been proposed in the field of robotics, and a lot of effort is being expended on path planning [2, 3]. Especially, heuristic planning algorithms including A* [4, 5] and Dijkstra [6], and simpling-based planning algorithms including probabilistic roadmaps (PRM) [7] and rapidly exploring random trees (RRT) [8, 9] have been widely adopted to produce collision free path for kinds of Mobile Robots. Particularly, among these algorithms, most ones have been developed for application to Unmanned Aerial Vehicle (UAV).

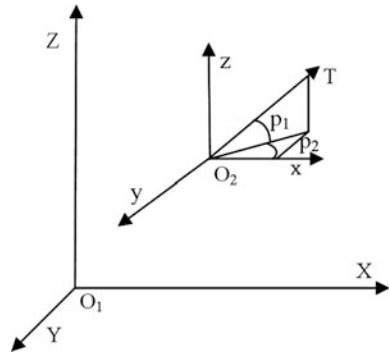
Lee et al. [10] proposed a spline-RRT*algorithm, which can produce a smooth path without any post-processing and can also handle the initial approach direction for the target UAV, but it cannot plan obstacle-free path in a dynamic environment. A dynamic RRT path planning algorithm was proposed in [11], which was applied in ALV (Automatic Land Vehicle). Yang et al. [12] use RRT algorithm to generate a collision free path in unknown environments and MPC (Model Predictive Control) to follow this path. All these above works have contributed to the path planning of mobile robots. However, it might be too complex to plan a path in a 3-dimensional environment with dynamic obstacles that follows a prescribed motion pattern. Unlike path planning in a environment with static obstacles, both the positions of mobile robot and obstacles at this moment and the changing environment at next moment should be considered in the algorithm. Based on the work and problems mentioned, A dynamic RRT algorithm is proposed in this paper, it plans a obstacle-free path for UAV successfully.

The paper is organized as follows: The path planning problem of a fixed-wing UAV in a dynamic environment is introduced and formulated in Sect. 2. The proposed algorithm is presented in Sect. 3. The results of the simulations for validating the proposed algorithm are described in Sect. 4. Section 5 is the conclusion.

2 Problem Formulation

This section mainly describes the path planning problem we are solving in this paper. First the mathematic model of fixed-wing UAV is introduced. Then the working environment of the fixed-wing UAV is introduced and constructed, consisting the fixed obstacles, dynamic obstacles and collision free space. At last, the dynamic constraints of flight routes are also described, which include minimum route leg length, maximum climbing/driving angle, maximum turning angle and maximum flight distance.

Fig. 1 Coordinates



2.1 Mathematic Model of Fixed-Wing UAV

In order to simplify the algorithm, the UAV is regarded as a mass point and the coordinates used by this paper are proposed as Fig. 1.

\$O_1XYZ\$ is earth fixed coordinate, \$O_2xyz\$ is carried normal earth fixed system. \$p_1\$ and \$p_2\$ are turning and climbing angles respectively. \$T\$ is the direction of goal.

According to the coordinates, model expression of turning and climbing are shown as follow. \$x_r, y_r, z_r\$ are relative displacements between UAV and destination points.

$$\begin{aligned}
 p_1 &= \arctan\left(\frac{y_r}{x_r + z_r}\right) \\
 p_2 &= -\arctan\left(\frac{z_r}{x_r}\right)
 \end{aligned}
 \tag{1}$$

2.2 Environment Model

This paper proposes a path planning approach for a fixed-wing UAV in a dynamic environment. As is shown in Fig. 2, the information of environment can be divided into 3 parts. One is fixed obstacle space OBS, another is dynamic obstacle space ROBS, which will move in the environment, following a prescribed motion. The rest is collision free space FREE. In some situations, the shape of obstacles can be very complicated, so we envelop these complicated obstacles with circles in 2-Dimensional space, and spheres in 3-dimensional space. In this way, the size of obstacles would be larger, but it increases the safety of flying path and reduces the complexity of algorithm.

After the establishment of environment model, we choose the start point and goal point of target UAV according to different flying missions. Then the initial direction of UAV is selected accordingly.

2.3 Flight Route's Constraints of UAV

In order to complete flight mission successfully, the flight route must satisfy the dynamic limitations of the fixed-wing UAV and mission scenario constraints. Particularly, different flight missions require different constraints on the resultant path. As is shown in [4, 13, 14]. In this paper, we consider about minimum route leg length, maximum driving/climbing angle, maximum turning angle and maximum flight distance.

- Minimum Route Leg Length L_{\min} : Due to the inertial of motion, aircraft will go along the previous direction for a certain distance before initiating a turn. We call it route leg length. Route leg length must larger than a minimum value so as to decrease navigation error.
- Maximum Turning Angle θ_{\max} : For the aircraft, there is an instantaneous maximum turning angle for the dynamic turning motion. In order to increase the safety of flight routes, a sharp climbing/driving angle should be avoided. This parameter is also referred as upper boundary limit of turning angle.
- Maximum Climbing/Driving Angle α_{\max} : The same definition as turning angle, there is also a maximum climbing/driving angle in horizontal direction. It can be either negative or positive, which is decided by aircraft's moving direction. The aircraft does not want to make sever turns in order to reduce the risk of collision. This parameter is also referred as upper/lower boundary limit of Climbing/Driving Angle.
- Maximum Flight Distance L_{\max} : Length of flight route is limited by airborne fuel or battery capacity. We call it maximum flight distance. The aircraft should accomplish its task within the maximum range. As a result, we should make the sum of every line-segment less or equal to the maximum flight distance.

$$\sum L_i \leq L_{\max} \quad i = 1, 2, 3, \dots, n - 1, n. \quad (2)$$

3 The Dynamic RRT Algorithm

This section describes the proposed dynamic RRT algorithm. The dynamic RRT algorithm is aimed specifically at path planning for fixed-wing UAVs operating in dynamic 3-dimensional environments. It can avoid dynamic obstacles which follows a certain prescribed motion because it is based on the dynamic RRT algorithm. It also satisfies UAV's dynamic limits like minimum route leg length, maximum climbing/driving angle and maximum turning angle and other mission scenario constraints like maximum flight distance.

3.1 Algorithm Overview

Unlike static environments, there are dynamic obstacles which follows a prescribed pattern of motion in dynamic environments. In order to avoid these dynamic obstacles, the dynamic RRT algorithm considers both the UAV’s and dynamic obstacles’ current locations over time. Then, it will generate a collision free path for UAV according to these different locations in different time. When a point generated by RRT algorithm cannot satisfy UAV’s constraints of turning and climbing/driving angle boundary limits, a new point that meets the above constraints is generated. Also, minimum route leg length and maximum flight distance will be considered by the connection between adjacent points.

3.2 Algorithm 1: Dynamic RRT

This algorithm is programmed in MATLAB and the pseudo code for the proposed algorithm is shown in Algorithm 1. Some important sub-functions and parameters are described below.

X_s : Starting position of path planning task.

X_g : End position of path planning task.

X_n : Current position of UAV.

SL: Step size of this dynamic RRT algorithm. In order to satisfy UAV’s dynamic constraints, we take L_{min} as step size of this algorithm.

T: The time that UAV takes from X_s to X_n .

tree: The set of all points of X_n .

$X_{node} = X_{near}(X_{node})$: Parent of the point X_{node} .

climbing(X_{near}, X_n) and **turning**($X_{near}(X_{near}), X_{near}, X_n$): These functions return climbing angle and turning angle when UAV flies from X_{near} to X_n . Climbing angle is the included angle of the direction vector and the horizontal plane and turning angle is the included angle of current path vector’s and last path vector’s projection on a horizontal plane.

constraintsfeasible($\alpha_{max}, \theta_{max}$): If the climbing angle or turning angle is larger than maximum climbing angle or maximum turning angle. This function will find a new point which can satisfy the above-mentioned constraints of angle. α and θ can be obtained by using the following equations.

$$\begin{cases} \alpha_{new} = -\alpha_{max} \times p, \theta = \theta_{max} \times p, & \alpha \leq 0 \\ \alpha_{new} = \alpha_{max} \times p, \theta = \theta_{max} \times p, & \alpha > 0 \end{cases} \quad (3)$$

$$p \in [0, 1]$$

$findX_n(X_{near}(X_{near}), X_{near}, SL, \alpha, \theta)$: This function obtains a new point which meets UAV's dynamic constraints by X_{near} , SL , α and θ . The following equations calculate the new point X_n .

We assume that the parent of X_{near} ($X_{near}(X_{near})$), X_{near} and X_n is $[x_1, y_1, z_1]$, $[x_2, y_2, z_2]$ and $[x, y, z]$.

$$\left\{ \begin{array}{l} x^2 + y^2 + z^2 = SL^2 \\ \frac{z}{\sqrt{x^2 + y^2 + z^2}} = \sin(\alpha) \\ \frac{(x-x_1)(x_1-x_2) + (y-y_1)(y_1-y_2)}{\sqrt{(x-x_1)^2 + (y-y_1)^2} \times \sqrt{(x_1-x_2)^2 + (y_1-y_2)^2}} = \cos(\theta) \end{array} \right. \quad (4)$$

The ways of collision checking of UAV and obstacles are described as follow. As for static obstacles, the function select n points of the path between parent and node. Once the distance between every selected point and centre of obstacles is smaller than 1.5 times the radius of the obstacle spheres, the algorithm will treat it as collision, and the flight from parent to node will be marked as infeasible. As for dynamic obstacles, first their locations at each point of time is determined according to their kinematical equations, then they are regarded as static obstacles at each point of the time that UAV flies from parent to node. They will be checked as the way of static obstacles at this point of time.

The procedure 1 finds a obstacle-free path in the given dynamic environment. It creates the dynamic environment. In the algorithm, each obstacle is enveloped with a sphere, which its center to be the coordinates of the obstacle's geometric center, and its radius to be the length between the furthest point on the obstacle to its geometric center. Then, tree will be built by the function of *extendtree* and *path* will be found by the function of *findpath*. If the length of *path* is less than upper boundary, algorithm finishes.

Procedure1: DynamicRRT

Input: X_s, X_g, SL, L_{max}

Output: path

```

1.   Flag0=0;
2.   While Flag0=0 do
3.       create dynamic environment
4.       if  $|X_s - X_g| \leq SL$  and no obstacles in  $X_g$  then
5.            $X_n = X_s$ 
6.           while  $|X_n - X_g| > SL$  do
7.               (tree,  $X_n$ , T) = extendtree (tree,  $X_s, X_g, SL, T$ )
8.           end
9.       end
10.      path = findpath (tree,  $X_s, X_g$ )
11.      if length of path  $< L_{max}$  then
12.          flag0=1
13.      end
14.  end

```

The first function of procedure1 builds tree of the dynamic RRT algorithm. It will generate a random point in obstacles-free space of the dynamic environment. Then, a new point is generated, same as in traditional RRT algorithm. If the new point do not satisfy UAV's dynamic constraints, another point which meets UAV's dynamic constraints will be generated by the functions of *constraintsfeasible* and *findX_n*. Then, the new generated point and parent of the point will be set as node and parent of the third function. If it is collision free between these two points, we add the new generated point to the tree.

function1: extendtree

Input: tree, X_s, X_g, SL, T

Output: tree, X_n, T

```

1.   Flag1=0;
2.   While Flag1=0 do
3.       Xrand=random point∈free space
4.       Xnear=nearestneighbor (tree, Xrand)
5.       Xn=newpoint (Xnear, Xrand)
6.       α=climbing (Xnear, Xn)
7.       θ=turning (Xnear (Xnear), Xnear, Xn)
8.       if α>αmax or θ >θmax then
9.           (α, θ)= constraintsfeasible (αmax, θmax)
10.      end
11.      Xn= find_Xn(Xnear, SL, α, θ)
12.      if no obstacles between Xnear and Xn then
13.          flag1=1

```

The second function finds the collision free path from the starting point to the goal. It will find the parent of the goal at first. Then, it will keep searching for the parent of the last point and this function will stop when the parent is starting point.

Function2: findpath

Input: X_s, X_g, tree

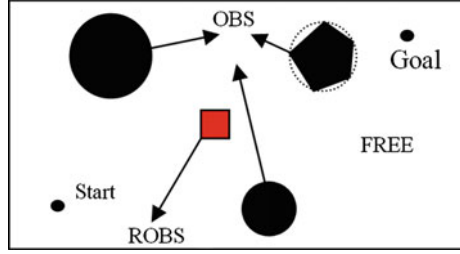
Output: path

```

1.   Flag2=0;
2.   Xnode=Xg
3.   while flag_2=0 do
4.       Xnode=findXnear (Xnode)
5.       put Xnode into path
6.       if Xnode=Xs then
7.           flag2=1
8.       end
9.   end

```

Fig. 2 Environment model



Till this step, the optimal path that obtained with our algorithm are consist by straight line-segments, e.g., a sequence of segments connecting the way points from the starting point to the goal point in our algorithm. However, in practical application the path generated for fixed-wing UAV should be smooth. Therefore in order to make the path smooth enough, we use B-spline curve to interpolate the resulting path. The reason is that B-spline curve has several advantages, e.g. [15–17]. It has convex null and its curvature is continuous. Coordinates of $n + 1$ points are given as $P_i(i = 0, 1, 2, \dots, n)$ and the formulation of n th order B-spline is shown as follow.

$$P(t) = \sum_{i=0}^n P_i F_{i,n}(t), t \in [0, 1] \tag{6}$$

$F_{i,n}(t)$ is basis function of n cubic B-spline:

$$F_{i,n}(t) = \frac{1}{n!} \sum_{j=0}^{n-1} (-1)^j C_{n+1}^j (t + n - i - j)^n \tag{7}$$

$$C_{n+1}^j = \frac{(n+1)!}{j!(n+1-j)!}$$

We use cubic B-spline in this paper. As a result, we obtained a smooth resulting path that satisfies the UAV’s dynamic constrains while avoiding collide with either dynamic obstacles or static obstacles.

4 Simulation

To illustrate the performance of the proposed algorithm, we create a three-dimensional dynamic environment and simulate the algorithm in MATLAB. The simulation results are shown in Fig. 3. Values of simulation parameters are listed in Table 1. Figure 4 shows climbing/driving angles and turning angles in the flight task. Figure 5 shows the path which is improved by B-spline interpolation.

In this case, two dynamic obstacles and three static obstacles are constructed. We give 4 periods of time, e.g. the total time of path planning is T . The first period of

Table 1 Values of the simulation parameters (South East Down coordinate system)

Parameter	Value
Starting point (m)	(0, 0, 0)
Goal point (m)	(60, 60, 60)
UAV's speed m/s	5
Maximum turning angle (deg)	30
Maximum climbing angle (deg)	45
Minimum road leg length (m)	5
Maximum flight distance (m)	500
Centre of static obstacles (m)	(70, 40, 20), (70, 10, 30), (50, 80, 50)
Centre of dynamic obstacles (m)	(20, 20, 30), (20, 60, 40) (T = 0)
Dynamic obstacles' speed (m/s)	(0.3, 0.3, -0.4), (1, -1, 0)

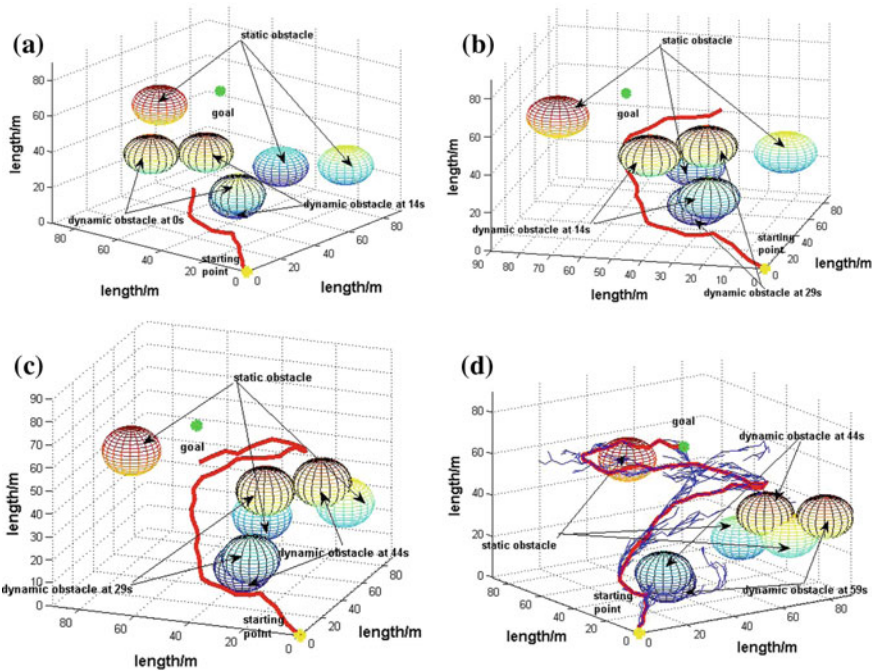


Fig. 3 Path planning using dynamic RRT at a three-dimensional dynamic environment. The *red line* indicates the resulting path, and the *blue line* in (d) shows the tree of the dynamic RRT algorithm. The total time of path planning is 59 s. **a–d** show path planning process from 0 to 14, 14 to 29, 29 to 44 and 44 to 59 s

time is $0-T/4$, the second period of time is $T/4-T/2$, the third period of time is $T/2-3 \times T/4$ and the fourth period of $3 \times T/4-T$. As can be seen from Fig. 3, in all the four periods of time, the path which is planned by above algorithm can avoid

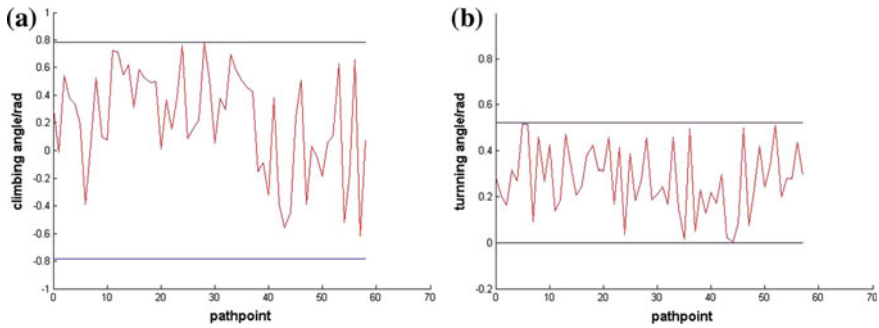


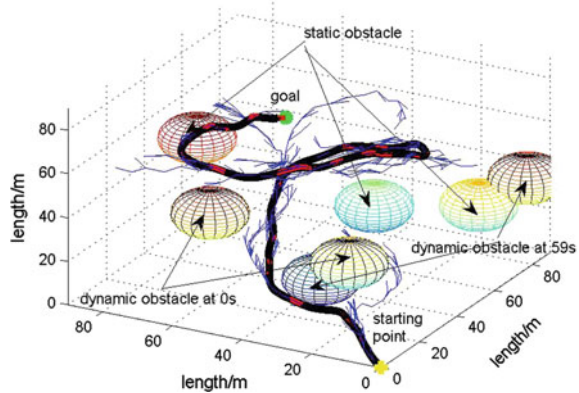
Fig. 4 The climbing angle and turning angle of every *straight line*-segment of path planning. The *blue lines* in (a) and (b) show the upper/lower boundaries of climbing angle and turning angle due to actual constraints

both dynamic obstacles and static obstacles. It demonstrates the feasibility of the proposed algorithm.

Figure 4 shows that every turning angle and climbing angle are within the upper and lower boundaries of climbing and turning angle. The length of the planned path is also calculated, which is 294.74 m. It is also shorter than the maximum flight distance. The figure shows that the proposed algorithm can satisfy UAV's dynamic constraints.

Now, we use B-spline curve to interpolate the resulting path so as to obtain a smooth resulting path. Figure 5 shows the path which is interpolated by B-spline. It can be found that the resulting path is a smooth curve that avoids collision with either dynamic obstacles or static obstacles. In addition, from the previous discussion we know that it also satisfies the actual dynamic constraints of UAV.

Fig. 5 The path which is interpolated by B-spline curve. The *black line* in the figure shows the interpolated path, which is significantly smoothed compared to Fig. 3



5 Conclusion

We have presented a dynamic RRT algorithm and applied to fixed-wing UAV's path planning. The proposed algorithm could handle both static and dynamic obstacles in three dimensional environment. The UAV's actual dynamic constrains have also been considered during the step of adding new point to the tree in our algorithm. B-spline interpolation is also adopted to smooth the resulting path. Thus in the end the algorithm can generate a smooth path which satisfy UAV's dynamic constrains. To evaluate the performance of proposed algorithm, simulations have been carried out and it has shown that the algorithm can find an obstacle-free path which satisfies UAV's actual dynamic constrains in dynamic three dimensional environment. Therefore, this algorithm provides one feasible approach for fixed-wing UAV's path planning in 3-dimensional environments with dynamic obstacles.

References

1. Hentschel M, Wagner B (2009) Adaptive path planning for long-term navigation of autonomous mobile robots. In: European conference on mobile robots, Ecmr'09, September. Mlini/dubrovnik, Croatia, pp 23–25
2. Jolly KG, Sreerama KR, Vijaya Kumar R (2009) A Bezier curve based path planning in a multi-agent robot soccer system without violating the acceleration limits. *Robot Auton Syst* 57:23–33
3. ŠKrljanc I, Klančar G (2010) Optimal cooperative collision avoidance between multiple robots based on Bernstein-Bézier curves. *Robot Auton Syst* 58:1–9
4. Zheng CG, Xu FJ, et al (2006) Online route planner for unmanned air vehicle navigation in unknown battlefield environment. In: IMACS multiconference on computational engineering in systems applications (CESA). IEEE Press, Beijing, pp 4–6
5. Kruusmaa M (2003) Global navigation in dynamic environments using case-based reasoning. *Auton Robots* 14(1):71–91
6. Medeiros FLL, Silva JDS (2010) A Dijkstra algorithm for fixed-wing UAV motion planning based on terrain elevation. In: da Rocha Costa AC, Vicari RM, Tonidandel F (eds) SBIA 2010. LNAI, vol 6404. Springer, Heidelberg, pp 213–222
7. Kavragi LE, Svestka P, Latombe JC, Overmars MH (1996) Probabilistic roadmaps for path planning in high-dimensional configuration spaces. *IEEE Trans Robot Autom* 12(4):566–580
8. Lavalley SM, Kuffner JJ (2000) Rapidly-exploring random tree: progress and prospects. *Algorithmic and Computational Robotics: New Directions*, New York, pp 293–308
9. Karaman S, Walter MR, Perez A et al (2011) Anytime motion planning using the RRT*. *IEEE international conference on robotics & automation*. IEEE Press, Shanghai, pp 1478–1483
10. Lee D, Song HJ, Shim DH (2014) Optimal path planning based on spline-RRT* for fixed-wing UAVs operating in three-dimensional environments. In: 14th IEEE international conference on control, automation and systems. IEEE Press, Gyeonggi-do, pp 835–839
11. Shan EZ, Dai B, Song JZ, Sun ZP (2009) An dynamic RRT path planning algorithm based on B-spline. In: 2nd IEEE international symposium on computational intelligence and design. IEEE Press, Changsha, pp 25–29

12. Yang K, Gan SK, Sukkarich S (2010) An efficient path planning and control algorithm for RUAV's in unknown and cluttered environments. *J Intell Rob Syst* 57:101–122
13. Yao P, Wang HL, Su ZK (2015) Real-time path planning of unmanned aerial vehicle for target tracking and obstacle avoidance in complex dynamic environment. *Aerosp Sci Technol* 47:269–279
14. Zhu LH, Cheng XH, Yuan FG (2016) A 3D collision avoidance strategy for UAV with physical constrains. *Measurement* 77:40–49
15. Wang WP, Helmut P, Liu Y (2006) Fitting B-spline curves to point clouds by curvature-based squared distance minimization. *ACM Trans Graph* 25(2):214–238
16. Kan EM (2010) Radar-aware path planning with B-spline trajectory generation for unmanned aerial vehicles (UAVs). *Int J Reasoning-Based Intell Syst* 2(3/4):226–236
17. Kan EM, Lim MH, Yeo SP et al (2011) Contour based path planning with B-spline trajectory generation for unmanned aerial vehicles (UAVs) over hostile terrain. *J Intell Learn Syst Appl* 03(3):122–130

Design and Modeling of an Omni-Directional Vector Thrust Hexarotor

MA Zhen-qiang, Dong Wen-han, Xie Wu-jie and Shao Peng-jie

Abstract In order to increase the flight speed of the conventional quadrotor UAV, meanwhile to keep horizontal attitude during the flight, a designing scheme of an omni-directional vector thrust hexarotor UAV is proposed in this paper. A new rotatable rotor is added in the center of the hexarotor UAV, which provides the omni-directional vector thrust by rotating centre on two orthogonal axes. The different flight modes, in which the rotatable rotor rotates to different angles, are analysed. The dynamic model is established and the PID controller to the vector thrust hexarotor is designed. The simulation results show that the designed omni-directional vector thrust hexarotor UAV can keep hovering and the horizontal attitude during the uniform speed flight.

Keywords Hexarotor · Thrust vector · Dynamic model · Flight mode · PID control

1 Introduction

The hexarotor is a kind of non-coaxial multi-rotor aircraft which can achieve vertical take-off and landing, which is suitable for the missions in middle or short distance [1–4]. Many kinds of designing and control theories of conventional rotorcraft are proposed. Two quadrotor dynamic models which are compared in simulation are introduced [5]. A new hexarotor with the structure of coaxial twin rotor is introduced in [6]. A PID + LQR controller is designed and the simulation results on the hexarotor demonstrate the effectiveness of the proposed attitude controller [7].

Many researches are already done in conventional rotorcraft. But conventional quadrotor flies forward through the body slopes a proper angle and the lift force has

M. Zhen-qiang (✉) · D. Wen-han · X. Wu-jie · S. Peng-jie
Engineering Institute of Aeronautics and Astronautics, Air Force Engineering University,
Xi'an 710038, China
e-mail: mazhenqiangnuaa@126.com

a forward component. So the forward thrust is small and the quadrotor can't keep horizontal and the quadrotor has low speed and low acceleration. In order to solve the problem, the rotatable rotor is added. A design of rotatable rotor aircraft is introduced in [8] and it flies successfully. Although rotatable rotor aircraft overcomes the problem of low speed and low acceleration, it has a complex structure with low safety and low stability.

An omni-directional vector thrust hexarotor is proposed in this paper. It can provide vector thrust in every direction when it keeps horizontal by rotating the tilt-rotor centre on two orthogonal axes.

2 Design of the Hexarotor

In Fig. 1, the omni-directional vector thrust hexarotor which is based on conventional quadrotor adds a coaxial twin rotor which can be tilted. In Fig. 2, the added coaxial twin rotor can be rotated centre on the perch which supports the motor, and the perch can be rotated center on the center of the perch. Combining the two rotating, the coaxial twin rotor can support vector thrust for conventional quadrotor through directing to optional direction. The angle between the adjacent arms of

Fig. 1 The omni-directional vector thrust hexarotor UAV

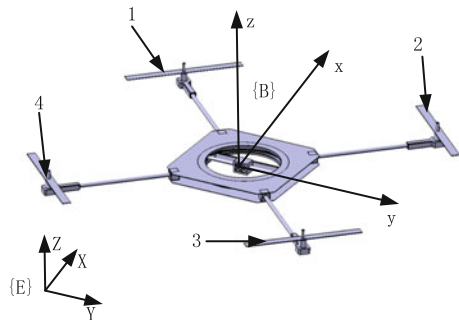
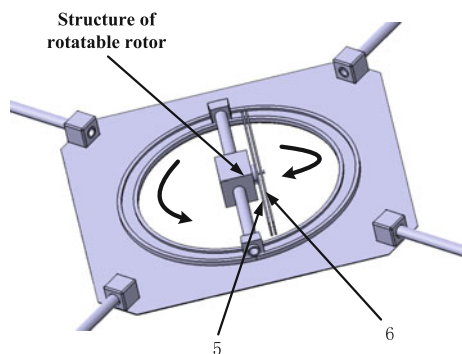


Fig. 2 Structure of rotatable rotor



force is 90°. Define the periphery rotors as the 1st rotor, the 2nd rotor, the 3rd rotor and the 4th rotor, and define the rotors which are in the center of the hexarotor as the 5th rotor and 6th rotor.

3 Hexarotor Dynamic Model

By Adding a coaxial twin rotor which can be tilted into the center of the conventional quadrotor, the omni-directional vector thrust hexarotor is almost symmetrical in structure and in mass, which means the mass of rotatable rotor can be ignored. Referencing to conventional quadrotor [9, 10] and we can suppose as follow:

Hypothesis 1: The gravity center of the omni-directional vector thrust hexarotor is always at the center tilting motor.

Hypothesis 2: The difference of rotational inertia caused by roll of the tilt-rotor can be ignored.

Hypothesis 3: The thrust of motor is proportional to the square of speed.

In e.g. [9], we can get the transition matrix R which is from the coordinate system B to the inertial frame E.

$$R = \begin{pmatrix} C_\psi C_\theta & C_\psi S_\theta S_\phi & C_\psi S_\theta C_\phi + S_\psi S_\phi \\ S_\psi C_\theta & S_\psi S_\theta S_\phi & S_\psi S_\theta C_\phi - S_\phi C_\psi \\ -S_\theta & C_\theta S_\phi & C_\theta C_\phi \end{pmatrix} \tag{1}$$

where, ϕ , θ and ψ are the yaw angle, the pitch angle and the roll angle in the coordinate system respectively.

According to the hypothesis 3, we can get the thrust of the hexarotor UAV in the coordinate system

$$\bar{F}_B = \begin{bmatrix} F_{Bx} \\ F_{By} \\ F_{Bz} \end{bmatrix} = \begin{bmatrix} k_t \sum_{i=5}^6 \omega_i^2 S_{\alpha_1} C_{\alpha_2} \\ k_t \sum_{i=5}^6 \omega_i^2 S_{\alpha_1} S_{\alpha_2} \\ k_t \sum_{i=1}^4 \omega_i^2 + k_t \sum_{i=5}^6 \omega_i^2 C_{\alpha_1} \end{bmatrix} \tag{2}$$

where, α_1 is the angle which the tilt-rotor rolls to y-axis, and α_2 is the angle which the tilt-rotor rolls to z-axis and k_t is the coefficient which is from force to the square of speed. According to $\bar{F}_E = R\bar{F}_B$, we can get the thrust of the hexarotor UAV in inertial system

$$\bar{F}_E = \begin{bmatrix} F_{Bx}C_\psi C_\theta + F_{By}C_\psi S_\theta S_\phi + F_{Bz}(C_\psi S_\theta C_\phi + S_\psi S_\phi) \\ F_{Bx}S_\psi C_\theta + F_{By}S_\psi S_\theta S_\phi + F_{Bz}(S_\psi S_\theta C_\phi - S_\phi C_\psi) \\ F_{By}C_\theta S_\phi - F_{Bx}S_\theta + F_{Bz}C_\theta C_\phi \end{bmatrix} \quad (3)$$

According to Newton's second law and considering resistance force in every direction, we can get an equation of the hexarotor

$$\begin{cases} \ddot{x} = [F_{Bx}C_\psi C_\theta + F_{By}C_\psi S_\theta S_\phi + F_{Bz}(C_\psi S_\theta C_\phi + S_\psi S_\phi) - K\dot{x}] / m \\ \ddot{y} = [F_{Bx}S_\psi C_\theta + F_{By}S_\psi S_\theta S_\phi + F_{Bz}(S_\psi S_\theta C_\phi - S_\phi C_\psi) - K\dot{y}] / m \\ \ddot{z} = [-F_{Bx}S_\theta + F_{By}C_\theta S_\phi + F_{Bz}C_\theta C_\phi - K\dot{z}] / m - g \end{cases} \quad (4)$$

where, K is the resistance coefficient. According to the relationship between Euler angle and angular velocity of the hexarotor, the following result can be obtained

$$\begin{bmatrix} \dot{\phi} \\ \dot{\theta} \\ \dot{\psi} \end{bmatrix} = \begin{bmatrix} (pC_\theta + qS_\phi S_\theta + rC_\phi S_\theta) / C_\theta \\ qC_\phi - rS_\phi \\ (qS_\phi + rC_\phi) / C_\theta \end{bmatrix} \quad (5)$$

where, p , q , r are the angular velocities when the hexarotor rolls to x-axis, y-axis and z-axis. The inertia matrix can be defined as follow

$$I = \begin{bmatrix} I_x & I_{xy} & I_{xz} \\ I_{xy} & I_y & I_{yz} \\ I_{xz} & I_{yz} & I_z \end{bmatrix} \quad (6)$$

Because of the hexarotor is nearly symmetrical in quality and structure, I_{xy} , I_{xz} and I_{yz} are relatively smaller than I_x , I_y and I_z . They can be ignored.

Through vector calculating, we can get the moment \bar{M} in the hexarotor coordinate system, which can be separated into M_x , M_y and M_z .

$$\begin{bmatrix} M_x \\ M_y \\ M_z \end{bmatrix} = \begin{bmatrix} \dot{p}I_x - rI_{xz} + qr(I_z - I_y) - pqI_{xz} \\ \dot{q}I_y + pr(I_x - I_z) + (p^2 + r^2)I_{xz} \\ \dot{r}I_z - \dot{p}I_{xz} + pq(I_y - I_x) + qrI_{xz} \end{bmatrix} \quad (7)$$

Through simplifying, we can get

$$\begin{bmatrix} \dot{p} \\ \dot{q} \\ \dot{r} \end{bmatrix} = \begin{bmatrix} [M_x + (I_y - I_z)qr] / I_x \\ [M_y + (I_z - I_x)rp] / I_y \\ [M_z + (I_x - I_y)pq] / I_z \end{bmatrix} \quad (8)$$

Nonlinear motion equations of the hexarotor can be obtained by combining the line motion equation and angular motion equation

$$\begin{cases}
\ddot{x} = [F_{Bx}C_\psi C_\theta + F_{By}C_\psi S_\theta S_\phi + F_{Bz}(C_\psi S_\theta C_\phi + S_\psi S_\phi) - K\dot{x}] / m \\
\ddot{y} = [F_{Bx}S_\psi C_\theta + F_{By}S_\psi S_\theta S_\phi + F_{Bz}(S_\psi S_\theta C_\phi - S_\phi C_\psi) - K\dot{y}] / m \\
\ddot{z} = [-F_{Bx}S_\theta + F_{By}C_\theta S_\phi + F_{Bz}C_\theta C_\phi - K\dot{z}] / m - g \\
\dot{p} = M_x + (I_y - I_z)qr] / I_x \\
\dot{q} = M_y + (I_z - I_x)rp] / I_y \\
\dot{r} = M_z + (I_x - I_y)pq] / I_z \\
\dot{\phi} = (pC_\theta + qS_\phi S_\theta + rC_\phi S_\theta) / C_\theta \\
\dot{\theta} = qC_\phi - rS_\phi \\
\dot{\psi} = (qS_\phi + rC_\phi) / C_\theta
\end{cases} \quad (9)$$

where, $\dot{p} \approx \ddot{\phi}$, $\dot{q} \approx \ddot{\theta}$, $\dot{r} \approx \ddot{\psi}$. Define U_1 , U_2 , U_3 , U_4 and U_5 as the input of the five independent control channels.

$$\begin{bmatrix} U_1 \\ U_2 \\ U_3 \\ U_4 \\ U_5 \end{bmatrix} = \begin{bmatrix} k_t (\omega_1^2 + \omega_2^2 + \omega_3^2 + \omega_4^2) \\ k_t (\omega_5^2 + \omega_6^2) \\ k_t (\omega_1^2 + \omega_4^2 - \omega_2^2 - \omega_3^2) \\ k_t (\omega_3^2 + \omega_4^2 - \omega_1^2 - \omega_2^2) \\ k_d (\omega_2^2 + \omega_4^2 - \omega_1^2 - \omega_3^2) \end{bmatrix} \quad (10)$$

where, U_1 is the input of the hexarotor at the vertical direction; U_2 is the input of the tilt-rotor; U_3 is the input of rolling motion; U_4 is the input of pitching motion and U_5 is the input of yawing motion. k_d is the torque coefficient which is from the rotational speed difference to torque.

Combining formula (9) and formula (10), we can get the nonlinear motion equation of hexarotor as follow

$$\begin{cases}
\ddot{x} = [U_2 S_{x_1} C_{x_2} C_\psi C_\theta + U_2 S_{x_1} S_{x_2} C_\psi S_\theta S_\phi + (U_1 + U_2 C_{x_1})(C_\psi S_\theta C_\phi + S_\psi S_\phi) - K\dot{x}] / m \\
\ddot{y} = [U_2 S_{x_1} C_{x_2} S_\psi C_\theta + U_2 S_{x_1} S_{x_2} S_\psi S_\theta S_\phi + (U_1 + U_2 C_{x_1})(S_\psi S_\theta C_\phi - S_\phi C_\psi) - K\dot{y}] / m \\
\ddot{z} = [-U_2 S_{x_1} C_{x_2} S_\theta + U_2 S_{x_1} S_{x_2} C_\theta S_\phi + (U_1 + U_2 C_{x_1})C_\theta C_\phi - K\dot{z}] / m - g \\
\dot{\phi} = lU_3 + (I_y - I_z)qr] / 2I_x \\
\dot{\theta} = lU_4 + (I_z - I_x)rp] / 2I_y \\
\dot{\psi} = U_5 + (I_x - I_y)pq] / I_z
\end{cases} \quad (11)$$

where, l is the distance between the two adjacent rotors.

4 Analysis of the Dynamic Model

The flight principle of the omni-directional vector thrust hexarotor is similar to the flight principle of conventional quadrotor which is introduced in [11, 12]. The function of the four periphery rotors is helping the hexarotor to keep steady. One of

the functions of the tilt-rotor in the center is supporting vector thrust for the hexarotor, the next one is increasing the maximum speed and the maximum acceleration of the hexarotor and the last one is helping the body to keep horizontal when the hexarotor flies. Analysis to the movement model is done when the tilt-rotor directs to different direction.

In Fig. 3a, when the tilt-rotor directs to z axis ($\alpha_1 = 0$, $\alpha_2 = 0$), all rotors provide lift force. On the condition that the horizontal velocity is zero, it hovers when the lift force equals to the gravity of the hexarotor; the hexarotor has downward acceleration when the lift force is smaller than the gravity of it and on the contrary, the hexarotor has upward acceleration. In Fig. 3b, the hexarotor pitches when the lift force of 1st rotor and the 4th rotor adds ΔF and the lift force of the 2nd rotor and the 3rd rotor decreases ΔF . In Fig. 3c, the hexarotor yaws when the speed of the two rotors in the center is difference.

In Fig. 3e, when the tilt-rotor directs to x axis ($\alpha_1 = 90^\circ$, $\alpha_2 = 0$), the four periphery rotors provide lift force for the hexarotor and help it to keep steady, and the tilt-rotor provides thrust in x direction. The acceleration of the hexarotor is increased by the tilt-rotor and it can help the the hexarotor to reach a speed in a shorter time and reach a larger maximal speed in x direction. Conventional quadrotor flies forward through the body slopes a proper angle and the lift force has a forward component. But the forward thrust is small and the quadrotor can't keep

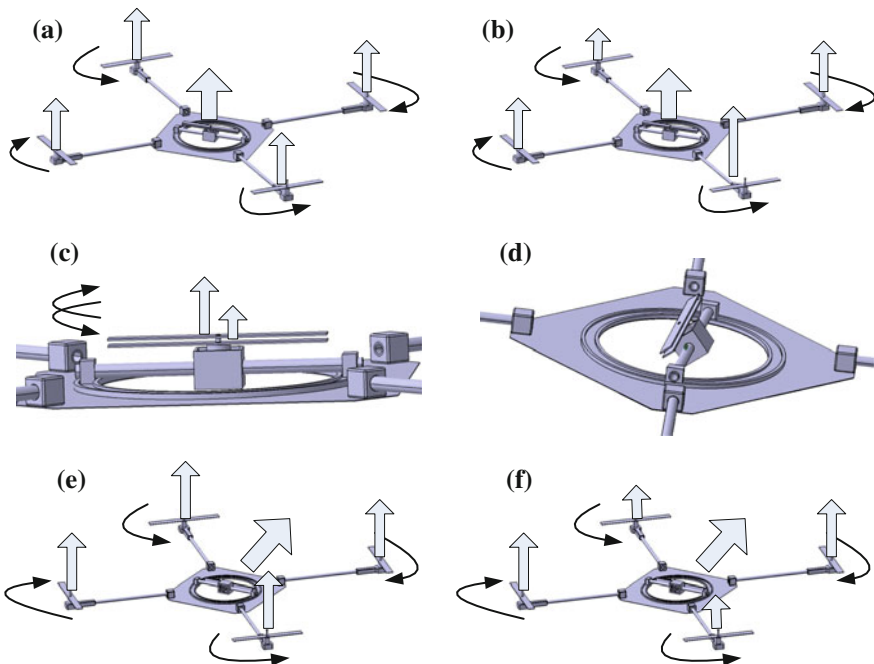


Fig. 3 Patterns of flight

horizontal and there is coupling between the forward speed and upward speed. The hexarotor has a larger forward speed because all the thrust produced by the tilt-rotor is in forward. And the body can keep horizontal when it flights forward. In Fig. 3f, the rotated speed of the 1st rotor and the 2nd rotor is in the same and the rotate speed of the 3rd rotor and the 4th rotor is in the same, but the rotated speed of the 1st rotor and the 3rd rotor is different, and then the hexarotor will yaw.

In Fig. 3d, when the tilt-rotor rolls the angle of α_1 centre on y-axis and the angle of α_2 center on z-axis (directing to arbitrary direction), it can provide larger thrust in the direction which the tilt-rotor directs to. And the direction of flight can be changed rapidly. The omni-directional vector thrust hexarotor has better motility than conventional hexarotor. The hexarotor can keep flight steady through adjusting the four periphery rotors when it is disturbed.

5 Design of the Controller and Simulations

The complex nonlinear and strong coupling system is divided into 5 independent control channels by defining U_1, U_2, U_3, U_4 and U_5 . The controller is composed of inside loop and outside loop. The inside loop controls the attitude of the hexarotor and the outside loop controls the location of the hexarotor.

In Fig. 4, where P_r is the hopeful location, θ_r is the hopeful pitch angle, ψ_r is the hopeful yaw angle and ϕ_r is the hopeful roll angle.

The parameters of the hexarotor UAV which are used in simulation see in Table 1.

The two often used flight models are that the tilt-rotor directs to z direction and x direction, so simulations to the two flight models have been done in this paper.

Two PID controllers are designed to the two models when the tile-rotor directs in z direction and in x direction. PID controller is a kind of feedback control which is

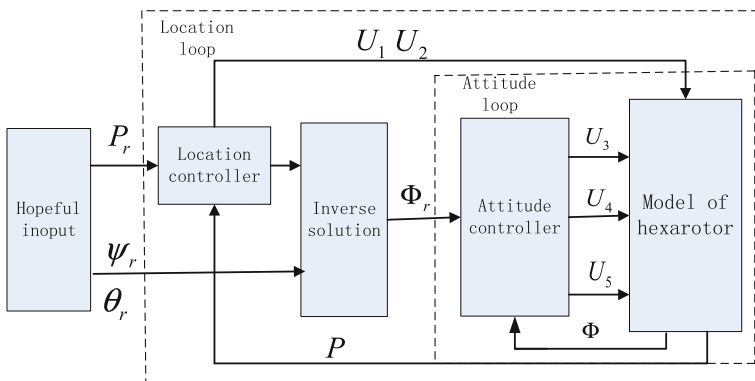


Fig. 4 Structure of control system

Table 1 Parameters of the hexarotor UAV

Parameters	Symbol	Value	Unit
Mass of hexarotor	m	1.2625	kg
Distance between the two adjacent rotor	l	0.642	m
Rotational inertia center on x axis	I_x	0.03151	kg m ²
Rotational inertia center on y axis	I_y	0.03152	kg m ²
Rotational inertia center on z axis	I_z	0.04975	kg m ²
Thrust coefficient	k_t	1.5e-05	Ns ²
Torque coefficient	k_d	2.8e-07	Nms ²
Drag coefficient	K	0.05	

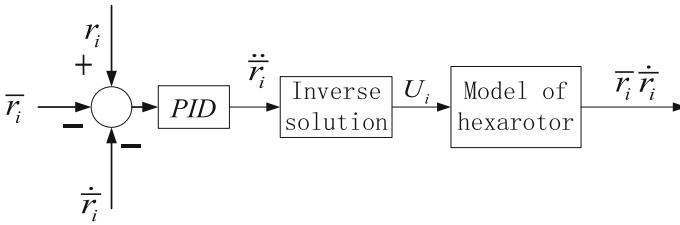


Fig. 5 Structure of PID controller

based on the difference between realy and target. The structure of PID controller sees in the Fig. 5.

Where, r_i is the hopeful location and angle, \bar{r}_i is the real feedback location and angle, $\dot{\bar{r}}_i$ is the real feedback speed and $\ddot{\bar{r}}_i$ is the acceleration and angular acceleration. Through solving (11), we can get

$$\begin{cases} U_1 = [G - U_2(D + E + F)]/C_\theta C_\phi \\ U_2 = C(G - H)/[C(D + E + F) - (A + B + C)C_\theta C_\phi] \\ U_3 = 2[\ddot{\phi}I_x - (I_y - I_z)qr]/l \\ U_4 = 2[\ddot{\theta}I_y - (I_z - I_x)rp]/l \\ U_5 = \ddot{\psi}I_z - (I_x - I_y)pq \end{cases} \quad (12)$$

where $A = S_{\alpha_1}C_{\alpha_2}C_\psi C_\theta$, $B = S_{\alpha_1}S_{\alpha_2}C_\psi S_\theta S_\phi$, $C = C_\psi S_\theta C_\phi + S_\psi S_\phi$, $D = -S_{\alpha_1}C_{\alpha_2}S_\theta$, $E = S_{\alpha_1}S_{\alpha_2}C_\theta S_\phi$, $F = C_{\alpha_1}C_\theta C_\phi$, $G = (\ddot{z} + g)m + K\dot{z}$, $H = (\ddot{x}m + K\dot{x})C_\theta C_\phi$.

A hovering control simulation is done when the tilt-rotor directs to z axis. Through bringing in the difference of location and angle, the controller revises the location and angle of the hexarotor. The hexarotor flies from the original point and the hopeful point is (10, 10, 10). The parameters of the PID controller see in Table 2 (Figs. 6, 7 and 8).

Table 2 Parameters of PID controllers

	<i>P</i>	<i>I</i>	<i>D</i>
x Channel	20	0.5	0.8
y Channel	1	0	1.53
z Channel	3	0	0.8
ϕ Channel	80	0	0.15
θ Channel	20	0	0.8
ψ Channel	30	0	0.88

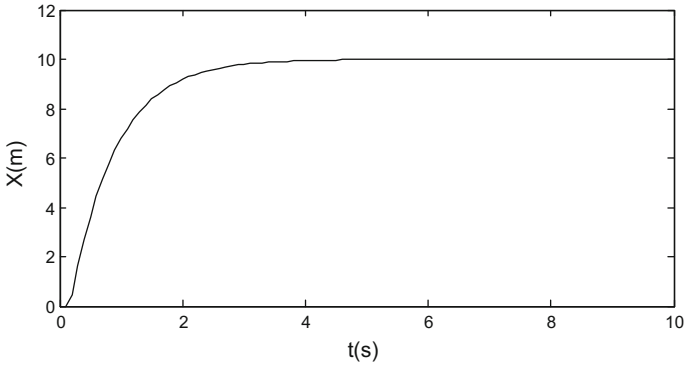


Fig. 6 Displacement in x direction

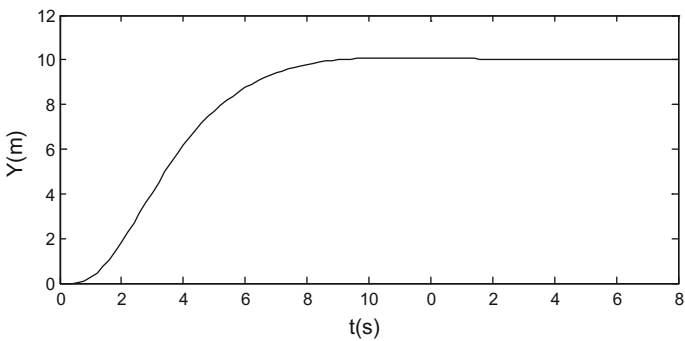


Fig. 7 Displacement in y direction

The simulation results show that the hexarotor can fly from the original point to the hopeful point in a short time and the dynamic performance of the time of adjusting and the overshoot amount is nice.

A constant speed simulation of the hexarotor is done when the tilt-rotor directs to x direction. The hexarotor flies from the original point to the height of 10 m and

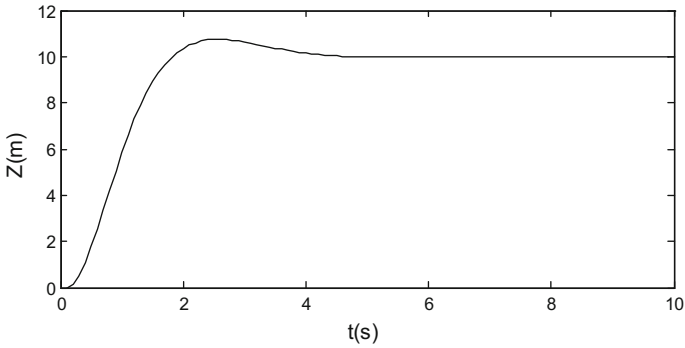


Fig. 8 Displacement in z direction

Table 3 Parameters of PID controllers

	<i>P</i>	<i>I</i>	<i>D</i>
x Channel	20	2	0
y Channel	1	0	5
z Channel	30	0	0.8
ϕ Channel	20	0	1
θ Channel	20	0	0.8
ψ Channel	30	0	0.88

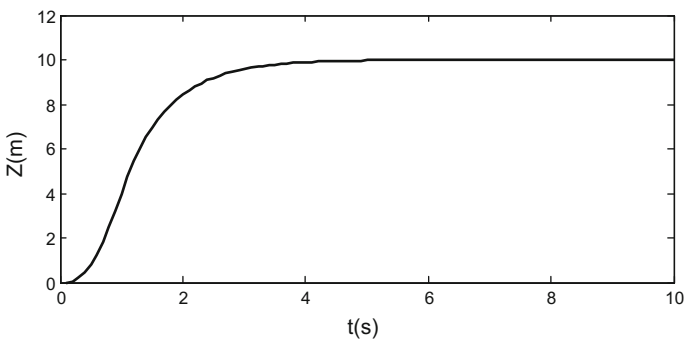


Fig. 9 Displacement in z direction

keeps 20 m/s flying. The parameters of the PID controller see in Table 3 (Figs. 9 and 10).

The simulation results show that the omni-directional vector thrust hexarotor can fly in hopeful route and the dynamic performance of the time of adjusting and the overshoot amount is nice.

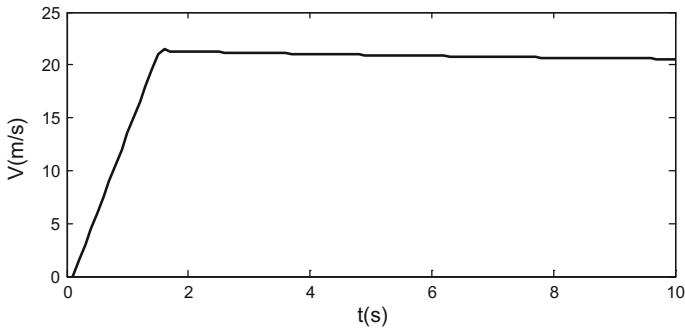


Fig. 10 Speed in x direction

6 Conclusions

To solve the problem that the conventional hexarotor has low speed and low acceleration, we design an omni-directional vector thrust hexarotor. The omni-directional vector thrust hexarotor can provide driving force to arbitrary direction and has strong mobility while the hexarotor keeps horizontal. The omni-directional vector thrust hexarotor dynamic model is established and simulations are carried out. The result of the simulations show that the omni-directional vector thrust hexarotor can keep steady when the tilt-rotor directs to x and z direction. It is meaningful to design a whole state controller for the omni-directional vector thrust hexarotor.

References

1. Yang CS, Yang Z, Xu DZ, Ge L (2012) Trajectory tracking control for novel six-rotor aircraft. *Syst Eng Electron* 10:2098–2105
2. Nie BW, Ma HX, Wang J, Wang JW (2007) Study on actualities and critical technologies of micro mini quadrotor. *Electron Opt Control* 06:113–117
3. Yue JL, Zhong QJ, Zhu HY (2010) Research progress and key technologies of micro quadrotor UAVs. *Electron Optics Control* 10:46–52
4. Angel E, Rosas A (2007) Path tracking control for an autonomous four rotor mini-helicopter. University of Calgary, Calgary, 09
5. de Rubio JJ, Cruz JHP, Zamudio Z, Salinas AJ (2014) Comparison of two quadrotor dynamic models. *IEEE Latin America Transactions*, America, June 4, pp 531–537
6. Zhang YS, Liu R (2010) Design of a new style six rotor-wings aircraft. *Mach Electron* 05: 64–66
7. Salim ND, Derawi D, Abdullah SS, Zamzuri H (2014) PID plus LQR attitude control for hexarotor MAV. In: *IEEE international conference on industrial technology (ICIT)*. Busan, Korea, pp 85–90, 26-Mar Feb 1 2014
8. Yanguo S, Huanjin W (2009) Design of flight control system for a small unmanned tilt rotor aircraft. *Chin J Aeronaut.* 22:250–256

9. Li J, Li Y (2011) Dynamic analysis and PID control for a quadrotor. In: Proceeding of the 2011 IEEE international conference on mechatronics and automation. Beijing, China, pp 573–578, 7–10 Aug 2011
10. Liu XJ (2009) Study and implementation of position and attitude estimation for four-rotor mini rotorcraft based on vision. Jilin University, Changchun
11. Huang YX (2014) Research on attitude control of quadrotor. Southwest jiaotong University, Leshan
12. Zhen HT, Qi XH, Xia MQ, Zhao HR (2012) Survey of flight control technology for quad-rotor unmanned helicopter. *Flight Dyn* 04:295–299

Energy Consumption of Trotting Gait for a Quadruped Robot

Xianbao Chen, Feng Gao, Chenkun Qi and Lin Wei

Abstract Battery driven robots have many advantages over combustion robots. They are clean, quiet, and can work in the airless or flammable environment. However, the limitation of the battery endurance is a great challenge. In order to increase the working hours of the battery driven quadruped robot, the energy expenditure of trotting gait under different gait parameters is studied. Firstly, the kinematic model of the quadruped robot and its gait planning method are introduced. Secondly, the dynamic model of the leg and the robot body are presented and the energy expenditures in the stance phase and the swing phase during trotting are analyzed. It can be proved that for any given trotting speed, the combination of the stride frequency and the stride length has great influence on the energy expenditure. Finally, experiments are presented to validate of the theory. The results show that by properly choosing the gait parameters the energy expenditure in trotting can be efficiently reduced.

Keywords Quadruped robot · Energy consumption · Trotting gait

X. Chen · F. Gao (✉) · C. Qi · L. Wei
State Key Laboratory of Mechanical System and Vibration,
Shanghai Jiao Tong University, Shanghai 200240, China
e-mail: fengg@sjtu.edu.cn

X. Chen
e-mail: xianbao@sjtu.edu.cn

C. Qi
e-mail: chenkunqi@sjtu.edu.cn

L. Wei
e-mail: weilinweilin@sjtu.edu.cn

1 Introduction

With the development of robot technology, more and more robots are able to walk outside the lab autonomously. Combustion robots can carry the fuel and travel for a long distance [1–4]. In many cases however, combustion engine is not the first choice due to the heat, vibration and the exhaust gas. Especially when the robot is working indoors or in the space, battery is a better option [5–7]. Electrical motor powered by battery is clean, quiet and its control system is stable and mature. But battery endurance is still a great challenge. The energy density of batteries is two orders of magnitude below that of liquid fuels [8, 9]. Increasing the amount of battery cells may help but the weight will become a problem. The most common method to save energy is to use springs during walking [10–12]. But the implementation of springs alone is not enough.

Walking pattern is the other way to reduce the energy expenditure. ALEXANDER [13] studied the energy saving mechanisms in walking and running. MINETTI [14] discovered the relationship between mechanical work and energy expenditure of locomotion horses. Although animal can freely choose their locomotion speed and locomotion gaits to save physical energy, legged robots can only be controlled by the operator and the speed is determined according to different tasks.

Under a certain speed, the resonant frequency is a very attractive theory to explain the energy efficiency of locomotion. HOYT [15] suggested that preferred stride frequency (PSF) of human walking was predictable using the resonant frequency of a force-drive harmonic oscillator (FDHO). Basically the model is related to the swing phase. Later he proposed another model [16] called the hybrid pendulum-spring model to consider both the swing phase and the stance phase. For some robots, however, the leg stiffness in the touchdown phase is hard to be estimated. On the other hand, the resonant frequency might be too fast or too slow for some robot under a certain working condition.

This paper intends to discuss how the gait parameters under a given trotting speed affect the energy consumption of a quadruped robot. Firstly, the kinematic model of the quadruped robot and its gait planning method are introduced. Secondly, the dynamic model of the leg and the robot body are presented and the energy expenditures in the stance phase and the swing phase during trotting are analyzed. It can be proved that for any given trotting speed, the combination of the stride frequency and the stride length has great influence on the energy consumption. Finally, experiments are presented to validate of the theory. The results reveal that these parameters may exert a tremendous influence on energy consumption. By properly choosing the gait parameters the energy consumption in trotting can be efficiently reduced.

This paper will be organized in six sections. In Sect. 2 the robot leg and its gait planning procedure will be briefly introduced. Section 3 will discuss the modeling of the robot leg. The energy consumption analysis will be introduced in Sect. 4, and the effects are presented by experiments in Sect. 5. Concluding remarks are given in Sect. 6.

2 Leg Mechanism and Gait Planning

The theory is implemented on a quadruped robot called the Baby Elephant [17–20] shown in Fig. 1. The robot uses a hybrid leg mechanism. In the sagittal plane, it is a parallel mechanism. Each cylinder drives one linkage connecting to the hip joint. The side movement is controlled by another hydraulic cylinder alone. In order to make it simple, the side cylinder will not be discussed.

As shown in Fig. 2 the origin O of the leg frame is set at the hip joint. Give the position of the foot tip P , the length of the left and right cylinder could be calculated as follows:

Fig. 1 Mechanical structure of the robot

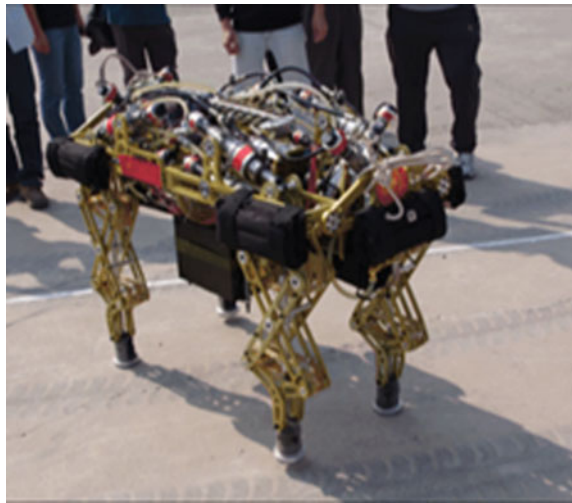


Fig. 2 Mechanism in the sagittal plane

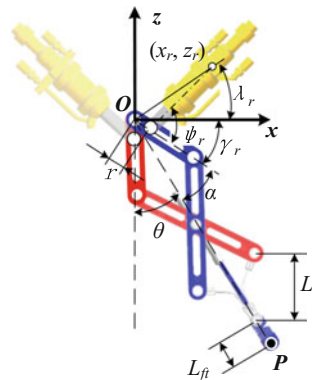
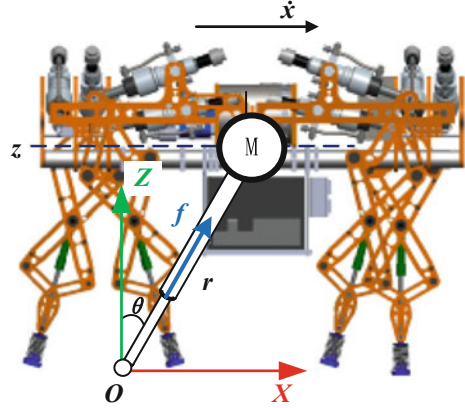


Fig. 3 Invert pendulum model of trotting gait



$$\begin{aligned} q_r^2 &= x_r^2 + z_r^2 + r^2 - 2r\sqrt{x_r + z_r} \cos(\lambda_r + \gamma_r) \\ q_l^2 &= x_l^2 + z_l^2 + r^2 - 2r\sqrt{x_l + z_l} \cos(\lambda_l + \pi - \gamma_l) \end{aligned} \quad (1)$$

In a trotting gait, the motion of the body can be regarded as an inverted pendulum with a prismatic joint along the stretch direction as shown in Fig. 3.

Forces can be applied on the prismatic joint. If the height of the body doesn't change during a trotting gait, the simplified dynamic model of the robot can be expressed as:

$$M\ddot{x} = f \sin \theta = \frac{Mg}{\cos \theta} \sin \theta \quad (2)$$

where M is the body mass, f is the contact force passes through the center of mass, θ is the swing angle of the leg. Solving Eq. (2) obtains the motion of the body as follows:

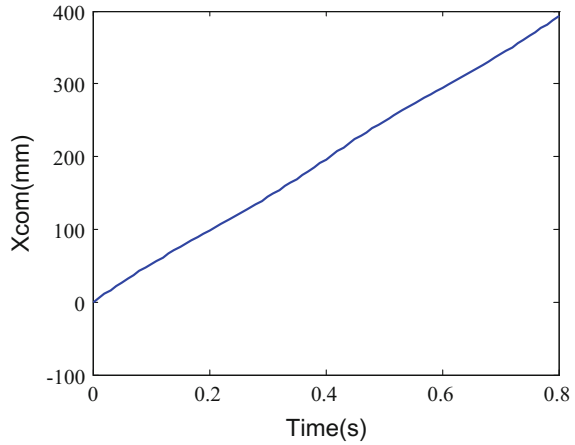
$$x(t) = x(0) \cosh\left(\frac{t}{T_c}\right) + T_c \dot{x}(0) \sinh\left(\frac{t}{T_c}\right) \quad (3)$$

$$\dot{x}(t) = \frac{x(0)}{T_c} \sinh\left(\frac{t}{T_c}\right) + \dot{x}(0) \cosh\left(\frac{t}{T_c}\right) \quad (4)$$

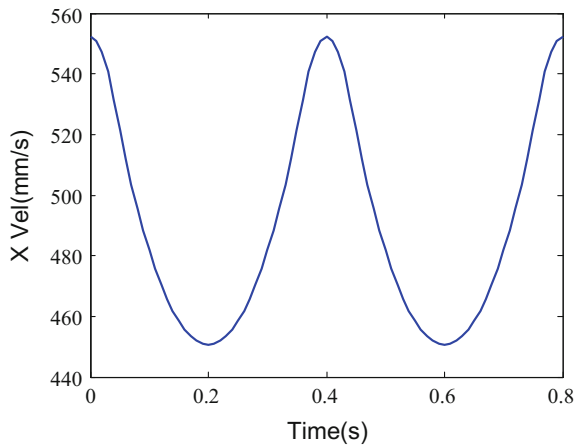
where $T_c = \sqrt{\frac{z}{g}}$, $\cosh\left(\frac{t}{T_c}\right) = \frac{e^{\frac{t}{T_c}} + e^{-\frac{t}{T_c}}}{2}$ and $\sinh\left(\frac{t}{T_c}\right) = \frac{e^{\frac{t}{T_c}} - e^{-\frac{t}{T_c}}}{2}$.

Figure 4 shows the displacement and the velocity of the robot body in the x direction. According to the gait planning, there is a decelerating phase and an accelerating phase when one pair of legs are in the stance phase. The robot is moving as an invert pendulum.

Fig. 4 Body trajectory and body velocity of the trotting gait



(a) Body Trajectory



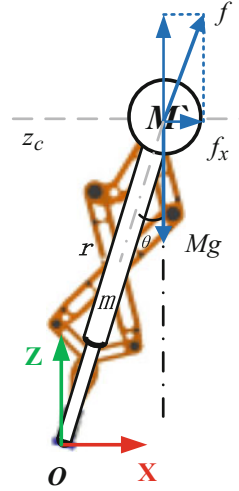
(b) Body Velocity

3 Modeling of the Robot Leg

According to the trotting gait planning, there are two phases of a single leg: the stance phase and the swing phase. In the modeling process, they can be modeled separately.

In the stance phase, the leg can be modeled as an inverted pendulum with half of the body mass M' at the mass center as shown in Fig. 5. This is because two legs are supporting the body in turns. According to the gait trajectories, there are very small velocities and accelerations in the z direction; the mechanical work is mostly used to push the body in the horizontal direction. In this phase, the leg moment of inertia can be ignored and its mass is added to the mass center M' .

Fig. 5 Leg model in the stance phase



The mechanical work from the touchdown moment to the neutral position can be expressed as:

$$W_{td2m} = \int_{t=0}^{\beta T/2} f_x(t) \dot{x}(t) dt \tag{5}$$

where β is the duty factor. Substituting Eq. (2) into (5) obtains

$$W_{td2mid} = \frac{M'g}{z} \int_{t=0}^{\beta T/2} \dot{x}(t)x(t) dt \tag{6}$$

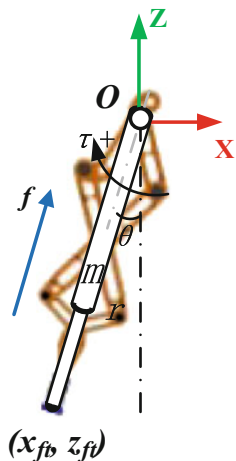
This equation can be rewritten as:

$$W_{td2mid} = \frac{M'gL_B^2}{8z} \tag{7}$$

where L_B is the stride length in the body frame. Springs at the foot tip are mainly used to reduce the impact. As a matter of fact, the effect of storing energy is very limited. The actuators do the major proportion of work. In order to focus on the effect of the gait parameters, the spring effect is not discussed. So the total energy expenditure in the stance phase is twice as much as W_{td2mid} :

$$W_{td} = \frac{M'gL_B^2}{4||z||} \tag{8}$$

Fig. 6 Leg model in the swing phase



It can be seen that for a given body height z , larger stride length leads to larger energy consumption.

In the swing phase, if the stride frequency is high, the mass and the moment of inertia can no longer be ignored. As shown in Fig. 6, the leg can be modeled as a simple physical pendulum with its length stretchable. Its dynamic model can be expressed as:

$$m\ddot{r} + mr_m\dot{\theta}^2 + mg \cos \theta + m\ddot{x} \sin \theta = f \quad (9)$$

$$I\ddot{\theta} - 2mr_m\dot{r}\dot{\theta} + mgr_m \sin \theta + m\ddot{x}r_m \cos \theta = \tau \quad (10)$$

where r_m represents the distance from the mass center to the rotating center, I represents the moment of inertia, m is the leg mass and τ is the equivalent torque to the rotating center. The actual moment of inertia of the robot leg can be calculated as:

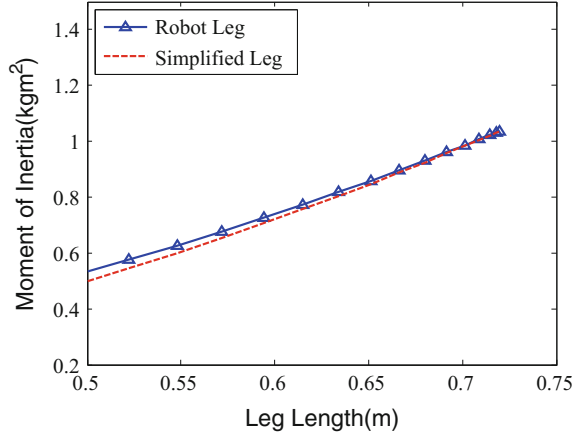
$$I_p = \frac{8}{3}m_{link}L^2 + 40m_{link}L^2 \cos^2 \alpha \quad (11)$$

where m_{link} is the mass of the link. The moment of inertia of a bar is:

$$I = \frac{mr^2}{3} \quad (12)$$

Substituting the actual mass of the link into the equations obtains the curves shown in Fig. 7. It can be seen that the simplified leg model makes very small difference with the actual leg.

Fig. 7 Leg moment of inertia



Multiply by \dot{r} on both side of Eq. (9) and $\dot{\theta}$ on both side of Eq. (10), add them up and then take the integral. The mechanical work in the swing phase can be expressed as:

$$W_{sw} = \int_{t=0}^T (f\dot{r} + \tau\dot{\theta}) dt \tag{13}$$

According to the foot tip trajectories, the actual numerical value can be obtained. For convenience, the energy consumption can be expressed as the mechanical work per unit distance which the body traverses:

$$W_{per_dist} = \frac{W_{sw} + W_{td}}{L_B} \beta \tag{14}$$

4 Energy Consumption Analysis

By substituting the parameters of the real robot into the Eq. (14), the energy consumption within a gait cycle can be computed. As shown in Fig. 9, the curve with triangles stands for the energy consumption for the stance legs. It is proportional to the step length. The curve with squares represents the energy consumption for the swing legs. For a given speed, the energy cost grows rapidly as the step length is close to zero. The solid curve represents the sum of the two curves. This curve represents the mechanical work of the robot when it goes through a unit distance.

Figure 9 extends the energy consumption curve in Fig. 8 to a surface by adding a speed coordinate axis. There are two peak values for a given range of speed.

Fig. 8 Energy consumption of a certain speed under different parameters

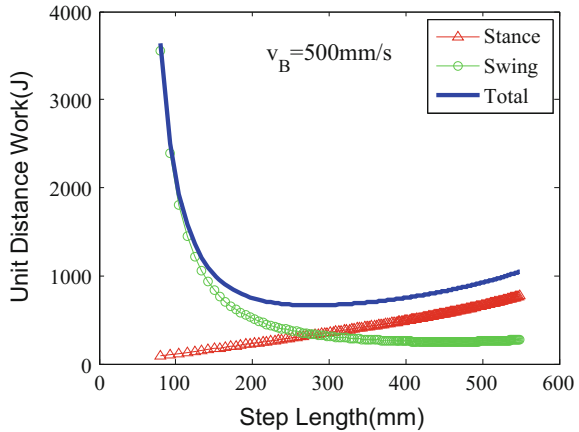
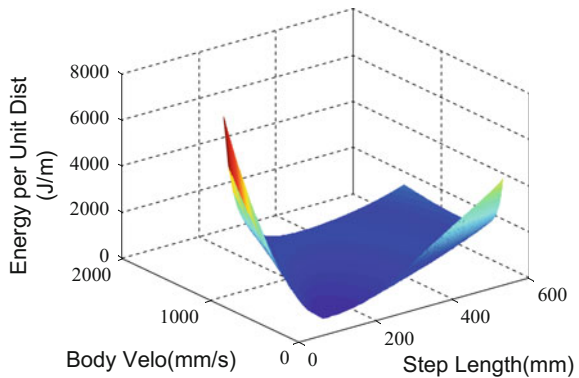


Fig. 9 Energy consumption surface of trotting



The first appears when the robot is moving fast but the step length is very small. The second one appears when the step length is very large but the robot is moving slowly.

It can be seen that the effects of the gait parameters on the energy consumption are remarkable. Improper combination of the step length and the step frequency will cause huge energy consumption. The minimum energy consumption value for every trotting speed corresponds to the optimal gait parameters.

5 Experiments on the Robot

In order to testify the theory, experiments of trotting with different gait parameters were carried out. The mass of the robot was 180 kg. The step height was 80 mm. The duty factor was 0.5. The robot walked for 10 times with the same speed of 0.5 m/s. The step length in the body frame changed from 100 to 400 mm.

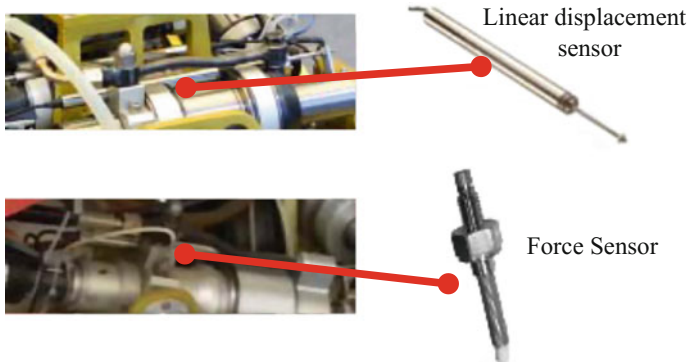


Fig. 10 Sensors on the robot

Force sensors and linear displacement sensors were configured on the actuators to measure the driving forces and positions as shown in Fig. 10. The step length range in the experiment was smaller because the robot became unstable when trotting with a relatively larger step length.

Using the force data and the velocity data from the sensors, the power of the actuators can be calculated. By integrating the output power in a step cycle, the mechanical work of the robot can be estimated. The experiments of the trotting gait are shown in Fig. 11. Figure 12 shows the mechanical work from the experimental data (curve with cycles) and its fitted curve (solid curve). The mechanical work in the experiments was larger due to the friction of the joints.

Although the results from theory deduction and the experiments were not exactly the same. The trend is clear. According to the data from the experiments, when the robot trotting at 0.5 m/s using a 100 mm step length, the energy consumption is about 2600 J/m. Comparing to the unit distance work 1100 J/m at the step length of 300 mm, approximately 57 % of energy can be reduced.

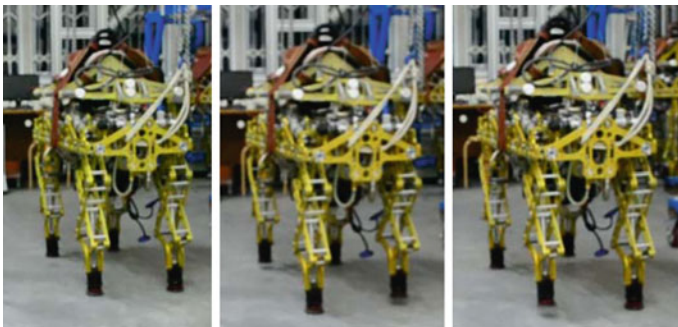
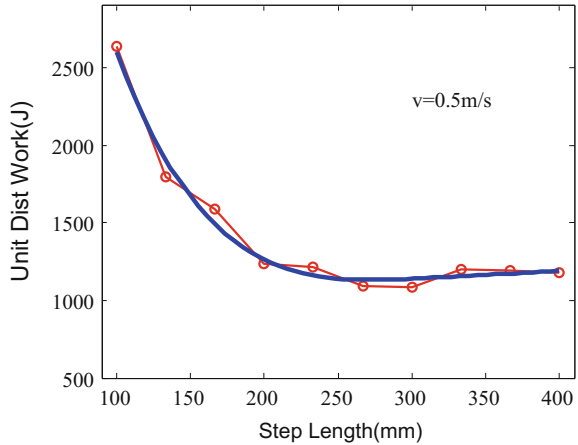


Fig. 11 Experiments of the trotting gait

Fig. 12 Experiment results of the trotting gait



As the step length increased, the energy consumption began to increase. But the effect is less remarkable. Because the robot became unstable and the constraint of the boundary of the workspace, the experiments stopped at the step length of 400 mm.

6 Conclusions

The paper shows how the combination of the gait parameters affects the energy consumption in trotting. The experiments proved the theory and it is concluded that at a given trotting speed there exists some optimal gait parameters which can reduce the energy consumption.

Endurance ability is very important for a hydraulic robot driven by battery. In the future, the fast-speed method to find the optimal gait parameters to minimize the energy consumption during trotting will be studied.

Acknowledgment Feng Gao supported by National Basic Research Program of China (973 Program, Grant No. 2013CB035501).

References

1. Raibert M, Blankespoor K, Nelson G et al (2008) Bigdog, the rough-terrain quadruped robot. In: Proceedings of the 17th world congress, pp 10823–10825
2. Semini C, Tsagarakis NG, Guglielmino E et al (2011) Design of HyQ—a hydraulically and electrically actuated quadruped robot. Proc Inst Mech Eng Part I: J Syst Control Eng 225 (6):831–849
3. Hyun DJ, Seok S et al (2014) High speed trot-running: implementation of a hierarchical controller using proprioceptive impedance control on the MIT Cheetah. J Rob Res 33 (11):1417–1445

4. Zhang J, Gao F, Han X et al (2014) Trot gait design and CPG method for a quadruped robot. *J Bionic Eng* 11(1):18–25
5. Iqbal J, Tahir AM (2012) Robotics for nuclear power plants—challenges and future perspectives[C]. In: 2012 2nd international conference on applied robotics for the power industry (CARPI), IEEE, pp 151–156
6. Murphy RR, Tadokoro S, Nardi D et al (2008) Search and rescue robotics. *Springer handbook of robotics*. Springer, Heidelberg, pp 1151–1173
7. Junyao G, Wei B, Jianguo Z (2008) Coal mine detect and rescue robot design and research. In: IEEE international conference on networking, sensing and control, 2008. ICNSC 2008, IEEE, pp 780–785
8. Fischer M, Werber M, Schwartz PV (2009) Batteries: higher energy density than gasoline? *Energy Policy* 37(7):2639–2641
9. Madden JD (2007) Mobile robots: motor challenges and materials solutions. *Science* 318(5853):1094–1097
10. Gregorio P, Ahmadi M, Buehler M (1997) Design, control, and energetics of an electrically actuated legged robot. *IEEE Trans Syst Man Cybern Part B: Cybern* 27(4):626–634
11. Ackerman J, Seipel J (2013) Energy efficiency of legged robot locomotion with elastically suspended loads. *IEEE Trans Rob* 29(2):321–330
12. Chen X, Gao F, Qi C et al (2014) Spring parameters design for the new hydraulic actuated quadruped robot. *J Mech Rob* 6(2):021003
13. Alexander RM (1991) Energy-saving mechanisms in walking and running. *J Exp Biol* 160(1):55–69
14. Minetti A, Ardigo L, Reinach E et al (1999) The relationship between mechanical work and energy expenditure of locomotion in horses. *J Exp Biol* 202(17):2329–2338
15. Holt KG, Hamill J, Andres RO (1991) Predicting the minimal energy costs of human walking. *Med Sci Sports Exerc* 23(4):491–498
16. Holt KG, Jeng SF, Ratcliffe R et al (1995) Energetic cost and stability during human walking at the preferred stride frequency. *J Mot Behav* 27(2):164–178
17. Zhang J, Gao F, Han X et al (2014) Trot gait design and CPG method for a quadruped robot. *J Bionic Eng* 11(1):18–25
18. Chen X, Gao F, Qi C et al (2013) Spring parameters design to increase the loading capability of a hydraulic quadruped robot. In: International conference on advanced mechatronic systems (ICAMEchS), IEEE, pp 535–540
19. Chen X, Gao F, Qi C et al (2015) Gait planning for a quadruped robot with one faulty actuator. *Chin J Mech Eng* 1–9
20. Gao F, Qi C, Sun Q et al (2014) A quadruped robot with parallel mechanism legs. In: 2014 IEEE international conference on robotics and automation (ICRA), IEEE, pp 2566–2566

Spatial Rolling Contact Pair Generating the Specified Relative Motion Between Links

Naoto Kimura and Nobuyuki Iwatsuki

Abstract Link mechanisms with single degree-of-freedom, in which links are connected with only lower pairs cannot completely generate the specified ideal output motion, and dimensional synthesis of them is very complicated. Therefore, we propose the spatial rolling contact pair (SRCP) which can generate the specified relative motion between links, and try to solve the above problems with the proposed SRCP. In order to design the SRCP, a method to specify relative spatial rolling motion between adjacent pairing elements and to determine shapes of both pairing elements which can generate that motion is proposed. An example of the SRCP is then designed and manufactured. The prototype of the SRCP is experimentally confirmed to generate the specified relative motion of pairing element. Finally, a spatial 4-bar mechanism having 1 DOF is synthesized with the SRCP. It can completely generate the specified output motion.

Keywords Link mechanism · Mechanism synthesis · Kinematic pair · Higher pair · Rolling contact

1 Introduction

Link mechanisms are composed of links and kinematic pairs such as revolute pairs, prismatic pairs and so on. In general, a link mechanism with 1 DOF cannot completely generate the specified output motion although the dimensional synthesis of the mechanism is very complicated. However if a suitable constraint between two

N. Kimura (✉)

School of Engineering, Tokyo Institute of Technology,
2-12-1 O-okayama Meguro-ku, Tokyo 152-8552, Japan
e-mail: kimura.n.ac@m.titech.ac.jp

N. Iwatsuki

Tokyo Institute of Technology, 2-12-1 O-okayama Meguro-ku, Tokyo 152-8552, Japan
e-mail: nob@mep.titech.ac.jp

pairing elements can be specified to generate the desired relative motion of the elements, a mechanism which can completely generate the specified output motion may be synthesized.

Takami et al. proposed kinematic pairs with from 1 to 4 DOF in which a pairing element slides in a curved pipe along an arbitrarily specified spatial curve [1]. However in case when the pair has 1 DOF, the spatial curve was limited to an arc, a straight line or an ordinary helix.

On the other hand, several researchers have proposed kinematic pairs having a rolling constraint. Kuntz [2] and Collins [3] proposed planar link mechanisms with circular rolling contact pairs. Jeanneau et al. [4], Cannon [5], and Halverson et al. [6] proposed a compliant rolling contact element (CORE). It is a circular rolling contact pair, and its pairing elements are connected by a compliant crossed flexure. Halverson et al. [7] proposed a bi-axial rolling contact joint consist of orthogonal two planar rolling contact joints with multiple curvatures. Montierth et al. [8] proposed an elliptical rolling contact joint. Conventional rolling contact pairs as described above have simple planar kinematic characteristics, and kinematic pairs having a desired spatial rolling constraint have not been proposed yet.

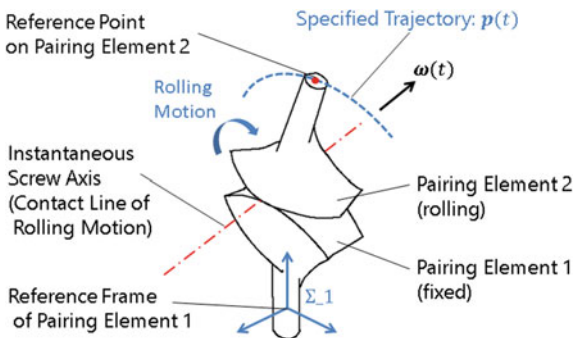
In this paper, we thus propose a spatial rolling contact pair (SRCP) which can generate the specified relative motion between two links. First, a constraint condition of spatial rolling motion is derived, and the method to specify the relative rolling motion satisfying the condition is proposed. Next, rolling motion surfaces of pairing elements generate the rolling motion is derived. Then, an example of the proposed SRCP is designed and is manufactured with additive production method. Finally, a spatial 4-bar link mechanism with 1 DOF is synthesized with the SRCP. It is confirmed that the synthesis with the proposed SRCP is easier than that with the conventional method and that the synthesized mechanism can completely generate the specified output motion.

2 Design of Rolling Motion Surfaces Generating the Specified Relative Motion

2.1 Specification of the Rolling Motion

Let's consider the case where a pairing element 2 is rolling on another pairing element 1 as shown in Fig. 1. Velocities on contact line of rolling motion of two pairing elements can be assumed as zero. Therefore, it can be considered that the instantaneous screw axis of the rolling motion corresponds to the contact line of the motion and the velocity in the axial direction is zero. The velocity $\dot{\mathbf{p}}(t)$ at the position $\mathbf{p}(t)$ on the rolling body and the angular velocity $\boldsymbol{\omega}(t)$ satisfy the following relationship:

Fig. 1 Relative spatial rolling motion between two pairing elements



$$\boldsymbol{\omega}(t) \cdot \dot{\boldsymbol{p}}(t) = 0, \tag{1}$$

where t is a parameter corresponding to time.

When a desired trajectory $\boldsymbol{p}(t)$ of the reference point on the pairing element 2 decided on the reference frame Σ_1 on the pairing element 1 is specified, the principal normal vector $\boldsymbol{n}(t)$ and the binormal vector $\boldsymbol{b}(t)$ of $\boldsymbol{p}(t)$ are calculated as

$$\boldsymbol{b}(t) = \frac{\dot{\boldsymbol{p}}(t) \times \ddot{\boldsymbol{p}}(t)}{|\dot{\boldsymbol{p}}(t) \times \ddot{\boldsymbol{p}}(t)|}, \quad \boldsymbol{n}(t) = \frac{\boldsymbol{b}(t) \times \dot{\boldsymbol{p}}(t)}{|\boldsymbol{b}(t) \times \dot{\boldsymbol{p}}(t)|}, \tag{2}$$

where $\boldsymbol{\omega}(t)$ should be given to satisfy Eq. (1). Therefore, it must be on the plane spanned by $\boldsymbol{n}(t)$ and $\boldsymbol{b}(t)$. Namely, $\boldsymbol{\omega}(t)$ is given as

$$\boldsymbol{\omega}(t) = \alpha(t)\boldsymbol{n}(t) + \beta(t)\boldsymbol{b}(t), \tag{3}$$

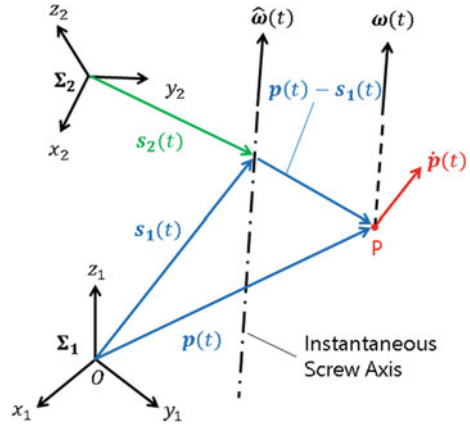
where $\alpha(t), \beta(t)$ are arbitrary real functions. The direction and the magnitude of $\boldsymbol{\omega}(t)$ is obtained by setting $\alpha(t), \beta(t)$ appropriately. In addition, the coordinate transformation matrix $\boldsymbol{R}_{1,2}(t)$ from the reference frame Σ_1 on the pairing element 1– Σ_2 on the pairing element 2, which represents the posture of the pairing element 2, is obtained by solving the following differential equation:

$$\dot{\boldsymbol{R}}_{1,2}(t) = [\boldsymbol{\omega}(t) \times] \boldsymbol{R}_{1,2}(t), \tag{4}$$

where $[\boldsymbol{\omega}(t) \times]$ is the matrix representing cross product operation of $\boldsymbol{\omega}(t) = [\omega_1 \ \omega_2 \ \omega_3]^T$, and is defined as

$$[\boldsymbol{\omega}(t) \times] = \begin{bmatrix} 0 & -\omega_3 & \omega_2 \\ \omega_3 & 0 & -\omega_1 \\ -\omega_2 & \omega_1 & 0 \end{bmatrix}. \tag{5}$$

Fig. 2 Schematic diagram of instantaneous screw motion composed of rotation around one axis and translation toward the axial direction



2.2 Derivation of Rolling Motion Surfaces

An instantaneous contact line of rolling motion is a segment of an instantaneous screw axis. Therefore, a ruled surface generated by a segment of an instantaneous screw axis is a rolling motion surface. Based on this idea, the rolling motion surface which can generate the specified rolling motion mentioned in Sect. 2.1 can be derived. Figure 2 is a schematic diagram of an instantaneous screw motion. In the system Σ_1 , since the velocity at the reference point on the pairing element 2 is generated by rotation around the instantaneous screw axis $s_1(t)$, the following equation is obtained.

$$[\omega(t) \times] p(t) - s_1(t) = \dot{p}(t) \tag{6}$$

Since $[\omega(t) \times]$ is not a regular matrix, $s_1(t)$ is calculated with a pseudo inverse matrix $[\omega(t) \times]^\#$ as

$$s_1(t) = p(t) - [\omega(t) \times]^\# \dot{p}(t) + u \hat{\omega}(t), \tag{7}$$

where u is an arbitrary real number, and $\hat{\omega}(t)$ is the unit vector in the same direction as $\omega(t)$. $s_1(t, u)$ has become the rolling motion surface of pairing element 1. On the other hand, the rolling motion surface of pairing element 2 is calculated as $s_2(t, u)$ described on Σ_2 and is represented

$$s_2(t, u) = R_{1,2}^{-1}(t)[s_1(t, u) - p(t)]. \tag{8}$$

Then, $s_2(t, u)$ in Σ_1 corresponds to $s_1(t, u)$ on Σ_1 in each moment. In addition, velocities on instantaneous screw axis are zero. Therefore, $s_2(t, u)$ is the rolling motion surface of pairing element 2. By the way, width and position of contact lines on each motion surfaces is determined by the range of the parameter u .

3 Design and Evaluation of the SRCP

3.1 Design of the SRCP

An example of the SRCP is designed with the method mentioned above. An ordinary helix shown below is given as the specified trajectory of the reference point on the pairing element 2.

$$\mathbf{p}(t) = [60 \cos(\frac{\pi t}{2}) \quad 60 \sin(\frac{\pi t}{2}) \quad 40t + 40]^T \quad (0 \leq t \leq 1) \tag{9}$$

An angular velocity of the rolling motion is also given as

$$\boldsymbol{\omega}(t) = \frac{\pi t}{2} \mathbf{n}(t), \tag{10}$$

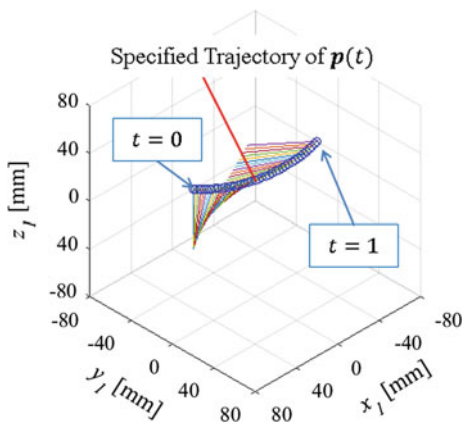
where $\mathbf{n}(t)$ denotes the principle normal vector of $\mathbf{p}(t)$. The motion of the pairing element 2 on Σ_1 is shown in Fig. 3. This motion looks like the twist motion of the pairing element 2 to the specified trajectory of $\mathbf{p}(t)$.

Based on this motion, rolling motion surfaces of both pairing elements are calculated as shown in Fig. 4. The range of the parameter u is $-30 \leq u \leq 0$. 3D-CAD models of pairing elements are illustrated in Fig. 5.

3.2 Prototype

The prototype of the designed SRCP manufactured with the FDM additive production is shown in Fig. 6. A rubber sheet was put between two pairing elements, and rubber bands were used to maintain contact between them. The rolling contact between two pairing elements is confirmed by visual experiment.

Fig. 3 Specified relative rolling motion of SRCP



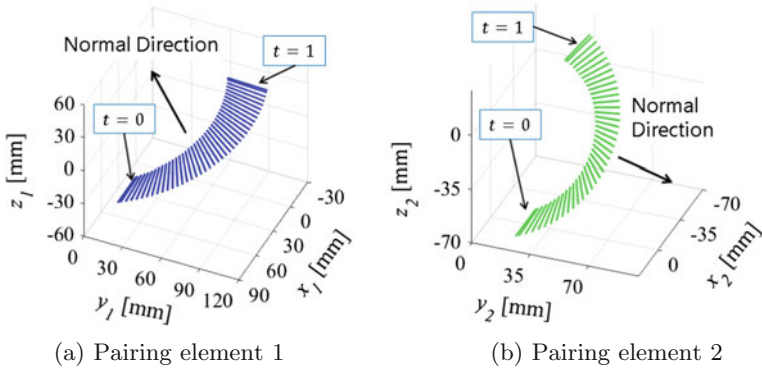


Fig. 4 Designed rolling motion surface of the SRCP

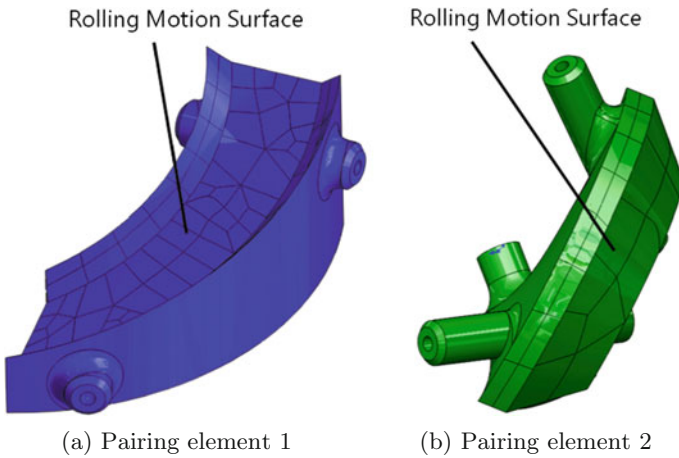


Fig. 5 3D-CAD models of pairing elements

Fig. 6 Prototype of the proposed rolling contact pair with elastic constraint

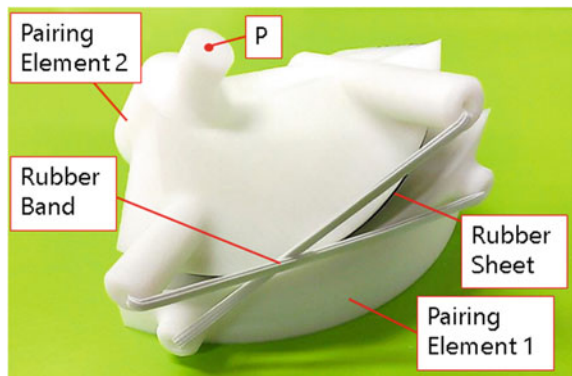


Fig. 7 Measurement of trajectory generated by pairing element with the 3D-CMM

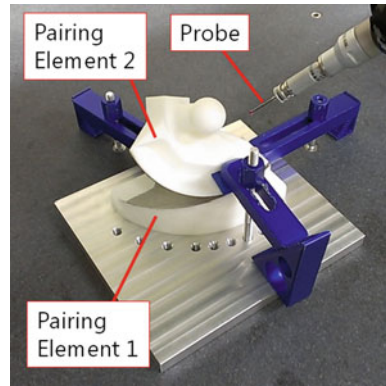
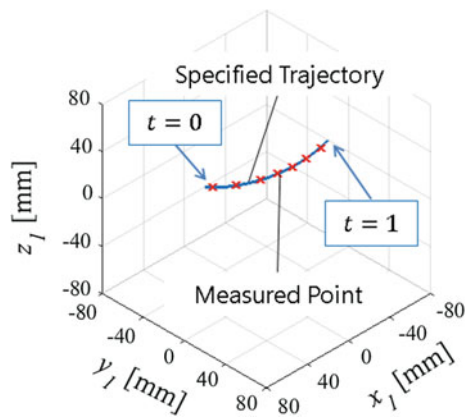


Fig. 8 The specified and measured trajectory of pairing element



To confirm the generated motion with the SRCP, the relative rolling trajectory of the SRCP is measured with 3D-CMM as shown in Fig. 7. The reference point on the pairing element 2 is in the center of the sphere in Fig. 7. Therefore, the trajectory of the reference point can be obtained by measuring several points on the sphere by the probe of 3D-CMM. Figure 8 shows the result of measurement. The mean value of the error between each measured points and the designed trajectory is approximately 1.31 [mm]. Since measured points were almost on the designed trajectory, it was confirmed that the SRCP could generate the specified trajectory.

4 Application of SRCP to Spatial 4-Bar Link Mechanism

In designing the proposed SRCP, a specified trajectory can be given to a reference point on a pairing element. However, desired postural change cannot be given because of the kinematic constraint represented in Eq. (1). Therefore, we consider

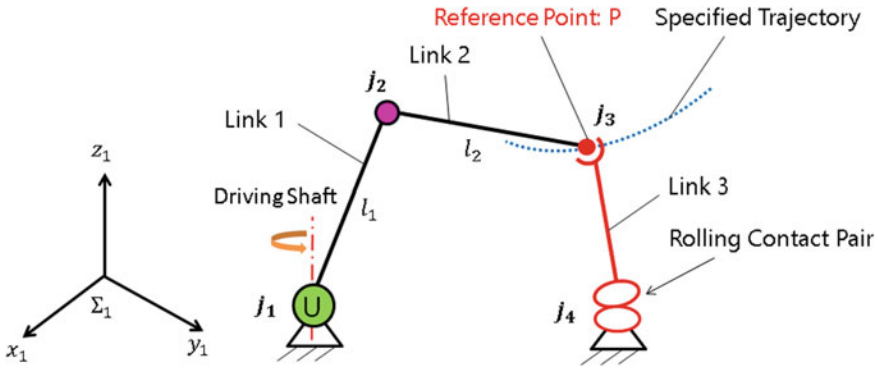


Fig. 9 An example of a spatial 4-bar link mechanism with the SRCP

to extract the translational motion of the SRCP by installing a spherical pair at the reference point on the pairing element.

An example of a spatial 4-bar link mechanism having 1 DOF with a SRCP is shown in Fig. 9. It is composed of a revolute pair (R), a universal joint (U), a spherical pair (S) and a SRCP (RC). The position of the spherical pair is the reference point P. Then, dimensional synthesis is carried out so that the point P can generate a desired trajectory.

The following vector is specified as the trajectory of the reference point.

$$p(t) = \begin{bmatrix} 100 \cos\left(\frac{\pi t}{2}\right) \\ 100 \sin\left(\frac{\pi t}{2}\right) \\ 30t + 60 \end{bmatrix} \quad (0 \leqq t \leqq 1) \tag{11}$$

Then, the mechanism is divided into the U-R-S chain and the S-RC chain. On the U-R-S chain, the maximum workspace of the point P is the sphere of which the center is at the position of U and the radius is the sum of the length of links: $l_1 + l_2$. If the specified trajectory is in the sphere, the point P can generate it. Therefore, the position of U to $j_1 = [0 \ 0 \ 60]^T$ [mm] and the length of links to $l_1 = l_2 = 60$ [mm] are set. In addition, to derive rolling motion surfaces of RC, the angular velocity is given as

$$\omega(t) = \frac{\pi}{3} n(t), \tag{12}$$

where $n(t)$ is the principal normal vector of $p(t)$. Rolling motion surfaces are derived as shown in Fig. 10. The parameter u is set as $-30 \leqq u \leqq 10$. If we synthesize a mechanism having 1 DOF with only lower pairs as usual, we have to determine mechanism dimensions by solving a complicated closed loop equation of the mechanism. However, by using the proposed SRCP, the mechanism can be synthesized easily.

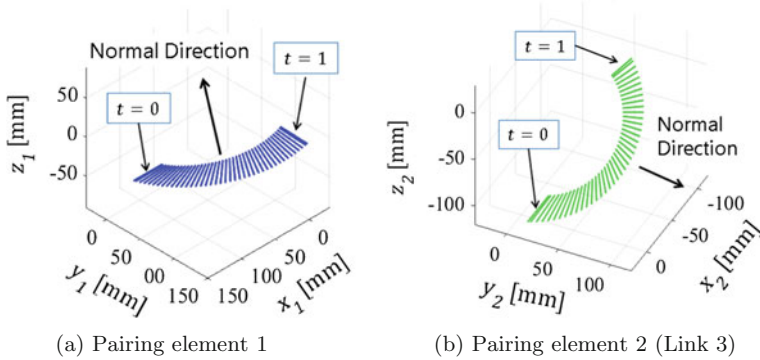


Fig. 10 Rolling motion surfaces of SRCP for the 4-bar link mechanism

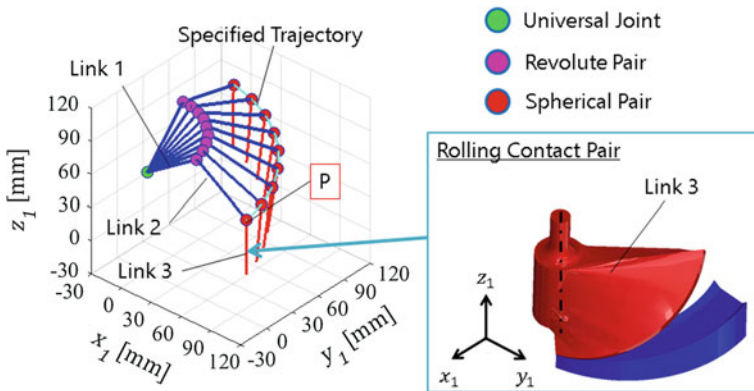


Fig. 11 Motion of the synthesized spatial 4-bar link mechanism with SRCP

The motion of the synthesized mechanism is shown in Fig. 11, and the 3D-CAD model of RC is shown on the right side in Fig. 11. The mechanism completely generated the specified trajectory.

5 Conclusions

In this paper, the spatial rolling contact pair (SRCP) which can generate the specified relative motion of links is proposed and designed. The obtained results are as follows.

- (1) Spatial rolling motion has the kinematic constraint that velocities of the rolling motion do not have the translational velocity components in the axial direction of the instantaneous screw axis. Therefore, by putting an angular velocity on

the normal surface of the trajectory, the motion of the pairing element rolling along the desired trajectory can be specified.

- (2) Rolling motion surfaces on pairing elements can be obtained as ruled surfaces of the instantaneous screw axis of the rolling motion.
- (3) An example of the SRCP is designed and manufactured with FDM additive production. The prototype is confirmed to maintain the rolling contact and to completely generate the specified relative motion with the experiment with 3D-CMM.
- (4) A spatial four-bar link mechanism with 1 DOF using the proposed SRCP is synthesized and is confirmed to completely generate the specified output motion.

In order to use the proposed SRCP effectively, pairing elements need to be constrained with suitable constraint elements. In the prototype in this paper, pairing elements are constrained with rubber bands. The optimum arrangement of elastic constraint on the point view of stable contact will be revealed in the next report.

References

1. Takami E, Iwatsuki N, Morikawa K (2003) Synthesis of multi-DOF pairs to generate relative displacement constraint described with mathematical function. In: *Proceeding of JSME annual meeting 2003*, No. 4, pp 153–154 (in Japanese)
2. Kuntz JP (1995) Rolling link mechanisms. PhD thesis, Delft University of Technology
3. Collins CL (2003) Kinematics of robot fingers with circular rolling contact joints. *J Robot Syst* 20(6):285–296
4. Jeanneau A, Herder J, Laliberte T, Gosselin C (2004) A compliant rolling contact joint and its application in a 3-dof planar parallel mechanism with kinematic analysis. In: *Proceedings of ASME 2004 design engineering technical conferences and computers and information in engineering conference (DETC'04)*, Paper No. DETC2004-57264
5. Cannon JR, Lusk CP, Howell LL (2005) Compliant rolling-contact element mechanisms. In: *Proceedings of ASME 2005 design engineering technical conferences and computers and information in engineering conference (DETC/CIE 2005)*, Paper No. DETC2005-84073
6. Halverson PA, Howell LL, Magleby SP (2010) Tension-based multi-stable compliant rolling-contact elements. *Mech Mach Theory* 45(2):147–156
7. Halverson PA, Howell LL, Bowden AE (2008) A flexure-based bi-axial contact-aided compliant mechanism for spinal arthroplasty. In: *Proceedings of the ASME 2008 international design engineering technical conferences and computers and information in engineering conference (IDETC/CIE)*, Paper No. DETC2008-50121
8. Montieth JR, Todd RH, Howell LL (2011) Analysis of elliptical rolling contact joints in compression. *J Mech Des* 133(3):031001

Experiment Study of Positioning Accuracy for a SCARA Robot

Yilong Tong, Yanjiang Huang, Lixin Yang, Changsheng Li and Xianmin Zhang

Abstract Repeated positioning accuracy is an important index for robot manipulator. To improve the performance of the robot manipulator, the repeated positioning accuracy in the different locations of robot workspace should be investigated. In this paper, we investigate the repeated positioning accuracy for a SCARA robot in different locations of robot workspace and investigate the repeatability when the robot moves in a continue path under different speeds. The experiment results show that the repeated positioning accuracy in different locations of robot workspace is different. The repeatability in continue path is good when the robot moves with an appropriate speed.

Keywords SCARA robot · Repeated positioning accuracy · Experiment study · Trajectory tracking

1 Introduction

Robot manipulator has been used in varied applications due to high speed and high accuracy. Normally, the repeated positioning accuracy is important for a robot manipulator, because this index can affect the task completion quality when using a

Y. Tong · Y. Huang · L. Yang · C. Li · X. Zhang (✉)
Guangdong Provincial Key Laboratory of Precision Equipment
and Manufacturing Technology, School of Mechanical
and Automotive Engineering, South China University of Technology,
Guangzhou 510640, China
e-mail: zhangxm@scut.edu.cn

Y. Tong
e-mail: yltong@scut.edu.cn

Y. Huang
e-mail: meijhuang@scut.edu.cn

L. Yang
e-mail: melxyang@scut.edu.cn

robot manipulator to complete a given task. Such as in welding task or assembly task, it is important to select the appropriate robot manipulator to complete the given task.

There are many factors can affect the repeated positioning accuracy, such as: (1) Manufacturing errors and assembly errors of robot components; (2) Calculation error on forward and inverse in kinematics and dynamics; (3) Transmission error; (4) The resolution of sensors and encoders causing error; (5) Control algorithm causing error; (6) Environment causing error; (7) Influence of different parameters of the trajectory planning, such as velocity. In previous study, many researchers have focused on the analysis of positioning accuracy [1]. Few researchers focused on the experimental study to analyze the positioning accuracy.

In this study, we analyzed the repeated positioning accuracy for SCARA robot based on experimental study. The repeated positioning accuracy in the different location of the robot workspace was analyzed. The repeatability in continue path was also conducted to evaluate the performance of the SCARA robot.

2 Kinematics

In this study, we used SCARA robot as the research object, as shown in Fig. 1. SCARA robot has three Rotary joints whose axis parallel to each other and a Prismatic joint. SCARA system compliant with the x, y direction, and has good stiffness in the Z-axis direction, this characteristic is particularly suitable for assembly work. Another feature of the SCARA robot is its series of two structures, which is similar to the human arm.

The specifications of the SCARA robot is shown in Table 1. The structure diagram of the SCARA robot is shown in Fig. 2. The θ_1 is the rotation of the joint 1, and the same, the θ_2, θ_3 stand for the rotation of joint 2 and joint 3, the θ_4 means

Fig. 1 The SCARA robot

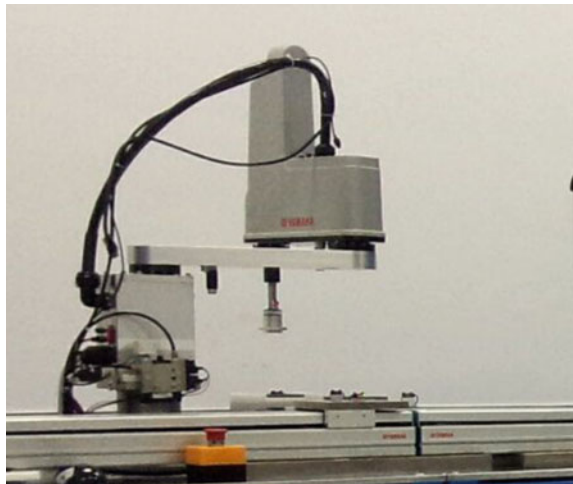
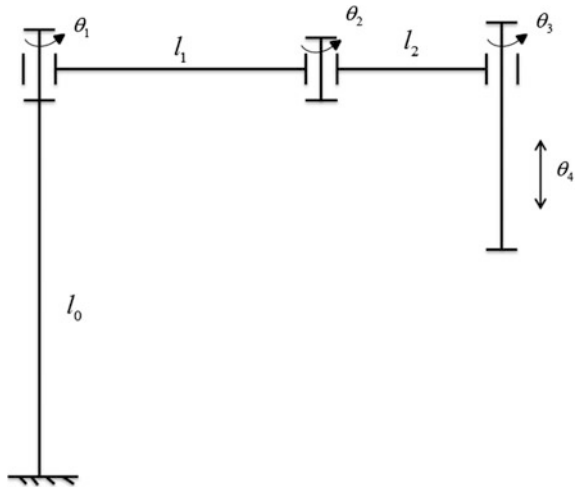


Table 1 Specifications of SCARA robot

	X axis	Y axis	Z axis	R axis
Arm length (mm)	350	250	150	–
Rotation range (°)	±140	±144	–	±360
Motor output AC (W)	200	150	50	100
Repeated accuracy (XYZ: mm) (R: °)	±0.01	±0.01	±0.01	±0.004
Maximum speed (XYZ: m/sec) (R: °/sec)	4.9	4.9	1.1	1020

Fig. 2 The structure diagram of the SCARA robot



the displacement of the joint 4. The l_0 is the height of the joint 1, the l_1 is the length of the arm 1, the l_2 is the length of the arm 2. Based on the specifications and structure diagram of the robot, we obtained the workspace of the robot, as shown in Fig. 3.

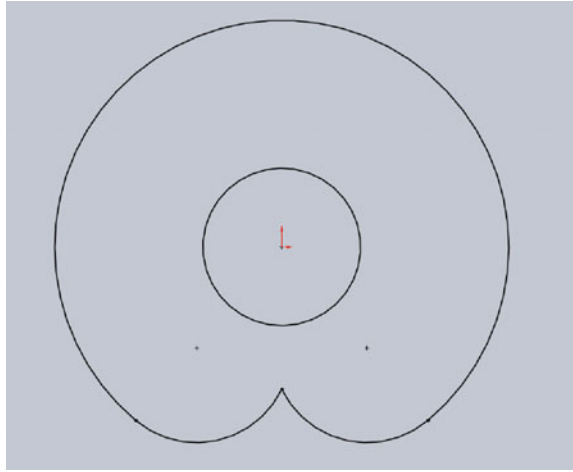
From the structure diagram, we can easily know the forward kinematics [2–5].

$$A = \begin{bmatrix} \cos \theta_{123} & -\sin \theta_{123} & 0 & -l_2 \sin \theta_{12} - l_1 \sin \theta_1 \\ \sin \theta_{123} & \cos \theta_{123} & 0 & l_2 \cos \theta_{12} + l_1 \cos \theta_1 \\ 0 & 0 & 1 & l_0 + \theta_4 \\ 0 & 0 & 0 & 1 \end{bmatrix} \quad (1)$$

As for the inverse kinematics, we can use the Paden-Kahan sub-problems algorithm which was first proposed by Paden and recorded in Kahan’s book. In the algorithm, there are three rules that should be adhered to. First, make the pure rotational and keep the distance unchanged; second, position remains unchanged; third, make the pure movement and keep the attitude unchanged. The inverse kinematics can be shown as below [6, 7].

Terminal Attitude: θ_2 (Z-axis),

Fig. 3 Workspace of SCARA robot



End position: $\theta_2, \theta_1, \theta_4$.

$$\theta_2 = \arccos \frac{x^2 + y^2 - (l_1^2 + l_2^2)}{2l_1l_2} \quad (2)$$

$$\theta_1 = \arccos \frac{x(l_2 \cos \theta_2 + l_1) + yl_2 \sin \theta_2}{-y(l_2 \cos \theta_2 + l_1) + xl_2 \sin \theta_2} \quad (3)$$

$$\theta_4 = z \quad (4)$$

To investigate the repeated positioning accuracy in different locations of the workspace, we did the experiment to test the repeated positioning accuracy in different locations of the workspace. The details about the experiment is described in the following section.

3 Experiment, Results and Discussion

The experiment setting is shown in Fig. 4. The position of the end-effector is derived through a laser tracker. Because it is difficult to attach the mirror ball of the laser tracker to the end-effector of robot, we attach the mirror ball of the laser tracker near the end-effector of robot [8, 9]. We obtain the position of the mirror ball in several positioning tests. The repeatability in the continue path is done by obtaining the discrete sampling trajectory points. In the repeated positioning accuracy test, the speed of robot is set to 20 % of the maximal speed. In the repeatability test, the speed of robot is set to 5 and 20 % of the maximal speed. The details are discussed in Sects. 3.1 and 3.2.



Fig. 4 The experiment setting

3.1 Repeated Positioning Accuracy

We tested the repeated positioning accuracy with 10 test points located in different locations in the workspace of the robot, as shown in Fig. 5. For each test point, the robot starts to move from the test point to an intermediate point, then return to the test point. The repeated positioning accuracy is tested when the robot returns to the test point. The intermediate points and test points are shown in Table 2. The robot

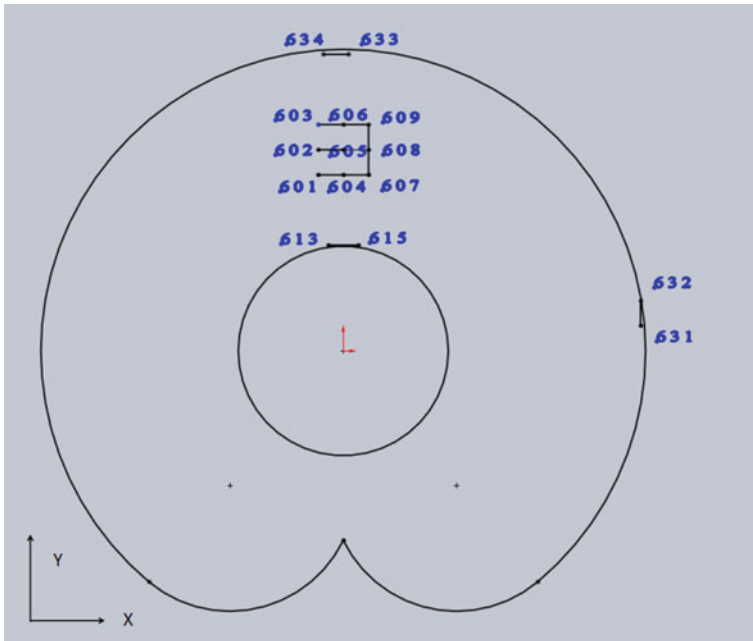


Fig. 5 Location of test points in robot workspace

Table 2 Test points and intermediate points in robot workspace

Test point 1	Test point 2	Test point 3	Test point 4	Test point 5
601(607)	602(608)	603(609)	604(610)	605(611)
Test point 6	Test point 7	Test point 8	Test point 9	Test point 10
606(612)	607(609)	633(634)	631(632)	613(615)

Note the number in () means the intermediate point. The location of the points are shown in Fig. 5. Because points 610, 611, and 612 are in Z axis, they are not shown in Fig. 5

repeatedly moves from the test point to the intermediate point and returns to the test point 6 times. The repeated positioning accuracy with 10 test points is shown in Fig. 6. From the results, we can find that the repeated positioning error is different in different locations of the workspace. The difference of repeated positioning error for different test points is not obvious, we think this may be caused by the low speed of robot and the short distance between the test point and intermediate point. The repeated positioning error in the robot moving direction is large, as shown in test points 5, 6, 7 in Fig. 6. The repeated positioning error in the edge the robot workspace is not worse than that in the center of the robot workspace.

3.2 Repeatability Test in Continue Path

In the repeatability test in continue path, we investigate the repeatability in continue path under different speeds of robot. The laser tracker collects the position data of the mirror ball with 100 Hz in the continue path. Figure 7 shows the repeatability in

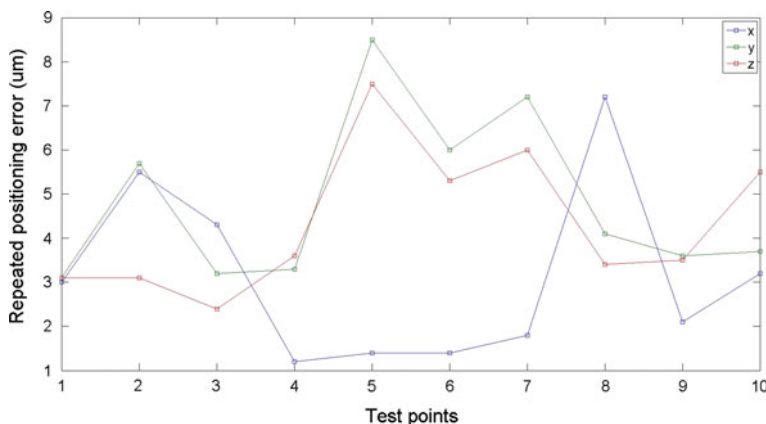
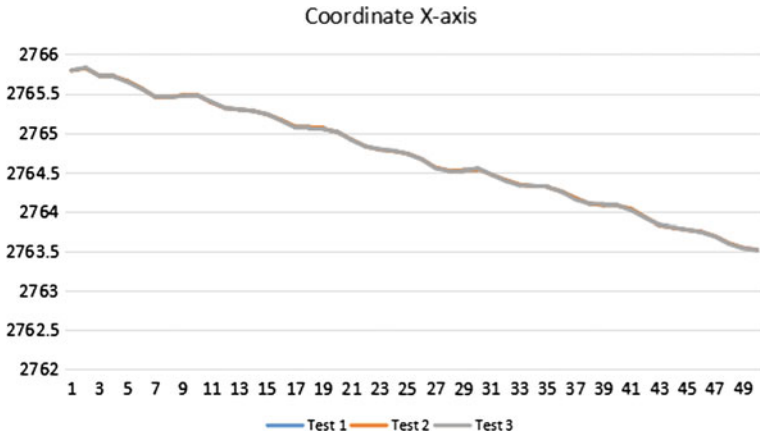
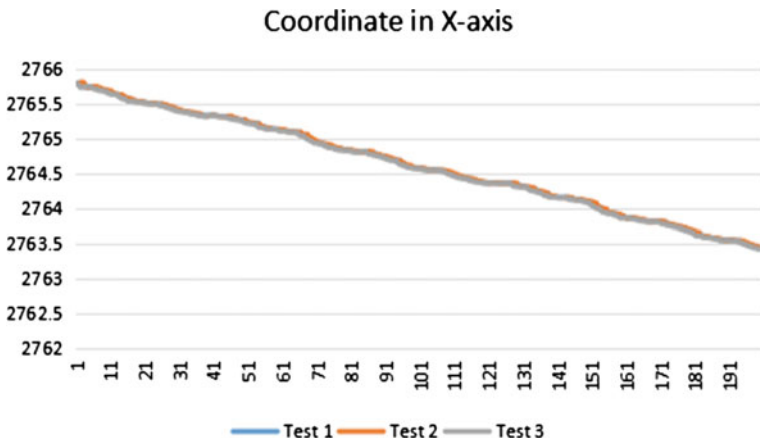


Fig. 6 Repeated positioning accuracy in different locations of robot workspace



(a) Robot moves with 20% of maximal speed



(b) Robot moves with 5% of maximal speed

Fig. 7 Repeatability in continue path with different robot speeds

the continue path with different speeds of robot with 3 tests. Due to the space of the paper, we only show the repeatability result in X-axis. From the results, we can find that when the robot speed is 20 % of the maximal speed, the repeatability in the continue path is better than that with 5 % of the maximal speed. This is because when robot moves under an appropriate speed, the robot may move smoothly, which may reduce the repeated positioning error. It is important to investigate that how the robot speed affects the repeatability in the continue path to obtain the appropriate speed for a robot.

4 Conclusion

In this paper, we investigated the repeated positioning accuracy of SCARA robot through experiment. The repeated positioning accuracy in the different locations of the robot workspace was investigated. The repeatability in continue path with different robot speeds was investigated. The experiment results show that the repeated positioning accuracy in the different locations of the robot workspace is different. The repeated positioning accuracy in the motion direction of the robot is larger than that in other directions. In the repeatability test in continue path, the repeatability is well when the robot moves with an appropriate speed. In future, the repeated positioning accuracy and trajectory tracking under varied speed and payload will be taken into account.

Acknowledgments This work was partially supported by the Scientific and Technological Project of Guangzhou (2015090330001), partially supported by the Fundamental Research Funds for the Central University (20152M004), partially supported by the Natural Science Foundation of Guangdong Province (2015A030310239).

References

1. Ma X (1991) Robot mechanisms. Machinery Industry Press, China
2. Liang Z, Su M, Changkun D (2011) Accuracy analysis of SCARA industrial robot based on screw theory. CSAE 2011.6
3. Stramigioli S, Bruynickx H (2001) Geometry and screw theory for robotics. Atutorial, ICRA
4. Davidson JK, Hunt KH (2004) Robots and screw theory: applications of kinematics and statics to robotics. Oxford University Press, London
5. Zhang L, Su M (2011) High accuracy analysis of SCARA industrial robot based on screw theory. ICMEE 2011.9
6. Park F, Bobrow J, Ploen S (1995) A lie group formulation of robot dynamics. Int J Robot Res 14(6):609–618
7. Nubiola A, Bonev IA (2013) Absolute calibration of an ABB IRB 1600 robot using a laser tracker. Robot Comput-Integr Manufact 29:236–245
8. Bai Y, Zhuang HQ, Roth ZS(2003) Experiment study of PUMA calibration using a laser tracking system. In: Proceedings of the IEEE international workshop on soft computing in industrial applications. Piscataway, IEEE, USA, pp 139–144

Part II
Mechanism Design

The Automatic Generation for Type Synthesis of Serial Mechanisms Based on POC Method

Chiyu Sun, Huiping Shen, Xiaorong Zhu, Anxin Liu, Lubin Hang and Tingli Yang

Abstract Serial mechanism type synthesis algorithms and their computer automation implementation were studied based on position and orientation characteristics (POC) set. Firstly, a new expression method for the dimension and direction of both translation and rotation for the serial mechanism end-reactor was proposed. The processes on algorithm and automation implementation of n-DOF serial mechanism using C Language were specifically described. Secondly, the program interface by Matlab which optimized the human-computer interaction was complete. Finally, taking the 4-DOF serial mechanism type synthesis as an example, the program can automatically generate 10 kinds of 1T3R serial mechanism, 23 kinds of 2T2R serial mechanism and 85 kinds of 3T1R serial mechanism. The user only needs to input the POC set of the mechanism which they want to create, and then the program can automatically generate the results, this operation has good usability and universality.

Keywords Serial mechanism · Position and orientation characteristics set · Computer automatic generation · Topology structure design · Type synthesis

C. Sun · H. Shen (✉) · X. Zhu · T. Yang
Research Center for Advanced Mechanism Theory, Changzhou University, 213016
Changzhou, People's Republic of China
e-mail: shp65@126.com

C. Sun
e-mail: 476885351@qq.com

C. Sun
Nanjing University of Technology and Engineering, 21000 Nanjing, People's Republic of China

A. Liu
School of Field Engineering PLA University, 21000 Nanjing, People's Republic of China

L. Hang
School of Mechanical Engineering, Shanghai University of Engineering Science, 201620
Shanghai, People's Republic of China

1 Introduction

Serial mechanism type synthesis is the basis of parallel mechanism type synthesis and hybrid mechanism type synthesis. Regarding to the methods for the topology structure design, there are 4 kinds of topology structure design method of parallel mechanisms currently, which is based on a linear transformation and evolution of morphological methods [1, 2], based on screw theory [3–6], based on displacement subgroups [7, 8], and based on Position and Orientation Characteristics (POC) set [9–17]. Compared with the other 3 methods for type synthesis, the method based on POC set has simple mathematical operation process, less algorithm rules and more clear geometric significance. At present, scholars at home and abroad use these methods to synthesize mechanisms artificially, and they have already got a number of serial mechanisms. But in theory, serial mechanism configuration is not complete because it has the characteristics of large, complex and diverse. And there are few related papers have published about computer assisted type synthesis.

The digital type synthesis dates back to 1963, Dobrjanskyj and Freudenstein [18] studied the automatic planar mechanism type synthesis based on the graph theory. There are less research about computer aided type synthesis of spatial parallel mechanism. Cao Wen-ao [19] proposed digital configuration of spatial parallel mechanism synthesis method based on screw theory, he derived the symmetric and asymmetric less degrees of freedom parallel mechanism constraint patterns and researched the type synthesis process in a given constraint mode; Ding [20] studied the 5-DOF computer aided type synthesis and established the movement structure database. Meng [21] construct a kind of computer aided parallel mechanism type synthesis architecture based on GF set.

A complete n-DOF serial mechanism type synthesis algorithms and automated generation program have been proposed based on the POC theory. Compared to other existing digital type synthesis method, our method is more simple and convenient, it is easy to understand and use, and is easy to operate, it is very practical, it provides a more convenient, powerful design platform for researchers.

2 Serial Mechanism Topology Structure Theory Based on POC Set

2.1 Common Dimensional Constraint Types of POC Set

Dimensional constraint type is one of the important elements of mechanism structure. Now we put the POC set of the common dimensional constraint types below as shown in Table 1, in order to facilitate the calculation of the serial mechanism POC set. Among them, the basic point of POC set (No.1–No.6) can be any point outside the axes of the end-reactor of the mechanism. And the basic point

Table 1 Common dimensional constraint types of POC set

Basic Types	$SOC\{-R//R-\}$ $SOC\{-R\perp P-\}$	$SOC\{-R//R//R-\}$, $SOC\{-R//R\perp P-\}$, $SOC\{-P\perp R\perp P-\}$.	$SOC\{-\diamond(P, P, \dots, P)-\}$
POC set	No. 1	No. 2	No. 3
	$\begin{bmatrix} t^1(\perp R) \cup t^1(\perp R) \\ r^1(/R) \end{bmatrix}$	$\begin{bmatrix} t^2(\perp R) \\ r^1(/R) \end{bmatrix}$	$\begin{bmatrix} t^2 \\ r^0 \end{bmatrix}$
	No. 1*	No. 2*	No. 3*
	$\begin{bmatrix} t^1(\perp R) \\ r^1(/R) \end{bmatrix}$	$\begin{bmatrix} t^2(\perp R) \\ r^1(/R) \end{bmatrix}$	$\begin{bmatrix} t^2 \\ r^0 \end{bmatrix}$
Basic types	$SOC\{-R//P-\}$	$SOC\left\{-\widehat{RR}-\right\}$	$SOC\left\{-\widehat{RRR}-\right\}$
POC set	No. 4	No. 5	No. 6
	$\begin{bmatrix} t^1(/P) \cup t^1(\perp R) \\ r^1(/R) \end{bmatrix}$	$\begin{bmatrix} t^2(\perp \rho) \\ r^2 \end{bmatrix}$	$\begin{bmatrix} t^2(\perp \rho) \\ r^3 \end{bmatrix}$
	No. 4*	No. 5*	No. 6*
	$\begin{bmatrix} t^1(/P) \\ r^1(/R) \end{bmatrix}$	$\begin{bmatrix} t^0 \\ r^2 \end{bmatrix}$	$\begin{bmatrix} t^0 \\ r^3 \end{bmatrix}$

of POC set (No.1*-No.6*) is on the axes of the end-reactor of the mechanism (or on the axis intersection point of several end-reactors).

3 Automation Algorithm of N-DOF Serial Mechanism Type Synthesis

We established the computer automatically generation algorithm, and the generation process is divided into two parts: (1) First, we established a set of numerical algorithms rules, we use these rules to describe the serial mechanism's structure constitution and the output dimension and the output direction of the end-reactor of the mechanism. (2) According to user's POC requirement, we program based on the mathematical algorithm of moving parts and generate all mechanism structure theoretically. Finally, we remove the plans which could not meet our requirements.

The essential of the serial mechanism computer automation type synthesis is a process including the mechanism component unit's construction, combination, evaluation and selection, and all these processes is finished by computer. After describe the expected mechanism, the system can generate a set of possible solutions. Then we can get a set of reasonable solutions according to the user's POC request. Therefore, the essence of serial mechanism type synthesis automation algorithm is using the numerical algorithms to describe the serial mechanism.

Serial mechanism is considered as a kind of organization form which is constraint by several common dimensional constraint types (as shown in Table 1). Therefore, the description method is: First, describe the first and the second dimensional constraint type of the serial mechanism, and combine them into a sub-SOC. Then combine the third dimensional constraint type and the first sub-SOC into the second sub-SOC. Therefore, a serial mechanism's (composed of n dimensional constraint type) end-reactor's dimension and direction output can be described by (n-1) composed sub-SOC.

Particularly, some serial mechanism can be composed of several dimensional constraint type and some single motion pair. Such as serial mechanism $SOC\{-\widehat{R\perp R}(\perp P)//\widehat{R\perp R}-\}$, it consists of two dimensional constraint types $SOC\{-\widehat{R\perp R}-\}$ and a single P pair. In this kind of circumstance, we can combine the dimensional constraint types into a sub-SOC first, then combine the single kinematic pair and the first sub-SOC into the second sub-SOC.

To transfer the serial mechanism end-reactor's dimension output and direction output at the same time, now we define the expression of sub-SOC:

$$\text{sub-SOC} = \begin{bmatrix} (X_t, Y_t), t^{Y_t}(\ast) \\ (X_r, Y_r), r^{Y_r}(\ast) \end{bmatrix} \quad (1)$$

Among them, t represents translation output; r represents rotation output; X represents sub-SOC output calculation variables, its evaluation method are given in Sect. 3.1. Y represents the dimension of the sub-SOC's output. t^{Y_t} and r^{Y_r} represent the translation output dimension and the rotation output dimension; (\ast) represents the output direction of the sub-SOC, its description method are given in Sect. 3.2.

3.1 The Expression of Serial Mechanism End-Reactor's Output Dimension

Now we propose a serial mechanism sub-SOC combination algorithm rule which based on the array (X, Y). We can use it to describe the serial mechanism end-reactor's output dimension. We use the dimensional constraint type as the basic unit to construct the serial mechanism. The construction step is below:

- (1) Combine the first and the second dimensional constraint type of the branch into a sub-SOC.
- (2) Determine the orientation relationship between the two dimensional constraint types, we can get the X value; then according to X, export the output dimension Y.
- (3) After complete the calculation of the first sub-SOC, combine the first sub-SOC and the kinematic pair next to it into a new sub-SOC and repeat the

calculation. Finally, we can get the Y value, and it is the output dimension of the branch.

The actual algorithm is below:

After connect the adjacent two dimensional constraint types, their POC output expression is below:

$$(X, Y)_1 = (X_1, Y_1) + (X_2, Y_2) \tag{2}$$

Among them, (X_1, Y_1) represents the output parameters of the first dimensional constraint; (X_2, Y_2) represents the output parameters of the second dimensional constraint type; (X, Y_1) represents the output parameters of the sub-SOC which was combined by the first and the second dimensional constraint type.

The X_1 value of the first kinematic pair is always 0, and we can determine X_2 according to the position relationship between the first and the second dimensional constraint type. In formula (2), if $X_2 = 0$, then $Y = \text{MAX}(Y_1, Y_2)$; if $X_2 = 1$, then $Y = Y_1 + Y_2$; the X which on the left side of the equation is always be 0. When the $Y > 3$, the Y value is still be 3.

Three adjacent dimensional constraint types can connect and become a new sub-SOC, and the expression of it is below:

$$(X, Y)_2 = (X, Y)_1 + (X_3, Y_3) \tag{3}$$

So, we can deduce the general formula, a serial mechanism composed of n dimensional constraint types can be represented by sub—SOC as:

$$(X, Y)_{n-1} = (X, Y)_{n-2} + (X_n, Y_n) \tag{4}$$

When the Y which is on the right side of the equation is 3, then, the y on the left will always equal 3. The operation must between two adjacent two kinematic pairs, and X always equal 0. The Y value which is in the result of the operation represents translation output dimension or rotation output dimension of the serial mechanism end-reactor.

Now a method will be given to determine the X value:

The common dimensional constraint types (as shown in Table 1) usually only contains R(P) pairs which have the same direction. For example, No. 1 SOC $\{-R||R-\}$ (as shown in Table 1) contains 2 R pairs, but they are parallel, so they have the same direction, this dimensional constraint type only contains R pairs with one direction. Another example, No. 2 SOC $\{-R||R\perp P-\}$ (as shown in Table 1), it contains 2 R pairs and 1 P pair, the 2 R pairs is parallel, they have the same direction, so the dimensional constraint type only contains R pairs with one direction and P pair of cause it just has one direction. At the same time, No. 2 SOC $\{-P\perp R\perp P-\}$ (as shown in Table 1) can be seen as an equivalent branch of SOC $\{-R||R\perp P-\}$, so it can be analyzed like SOC $\{-R||R\perp P-\}$. Therefore, we can get the conclusion, we can find the adjacent dimensional constraint types end-reactor’s output dimension rule by judging the direction relationship of the two

adjacent dimensional constraint types(both of them just has only one direction R/P pairs), then we can determine the X value.

To determine the X value, there have two situations: the X of the translation output dimension and the X of the rotation output dimension.

(1) Determine the X value of translation output:

The determination of the kinematic pair type of two adjacent dimensional constraint types can be divided into three kinds of circumstances:

(a) Both adjacent dimensional constraint types contain R pairs.

We need to judge the position relationship between the two R pairs, if they are parallel or collinear, then $X = 0$; if they are not parallel or collinear, then $X = 1$.

Particular case: when we meet $SOC\{-\widehat{RR}-\}$ and $SOC\{-\widehat{RRR}-\}$, $X = 1$.

(b) The two adjacent dimensional constraint types only contain P pairs.

We need to judge the position relationship between the two P pairs, if they are parallel or collinear, then $X = 0$; if they are not parallel or collinear, then $X = 1$.

(c) One of the adjacent dimensional constraint types only contains R pairs, another only contains P pairs.

We need to judge the position relationship between P pairs and R pairs, if they are vertical to each other, then $X = 0$, if they are not vertical to each other, then

$X = 1$. Particular case: when we meet $SOC\{-\widehat{RR}-\}$ and

$SOC\{-\widehat{RRR}-\}$, $X = 1$.

(2) Determine the X value of rotation output:

The determination of the kinematic pair type of two adjacent dimensional constraint types can be divided into three kinds of circumstances:

(a) Both adjacent dimensional constraint types contain R pairs.

We need to judge the position relationship between the two R pairs, if they are parallel or collinear, then $X = 0$; if they are not parallel or collinear, then $X = 1$.

Particular case: when we meet $SOC\{-\widehat{RR}-\}$ and $SOC\{-\widehat{RRR}-\}$, these dimensional constraint types contain R pairs with different directions, so when all R pairs are parallel to the same plane, then $X = 0$, if they are not, then $X = 1$.

(b) The two adjacent dimensional constraint types only contain P pairs.

$X = 0$.

(c) One of the adjacent dimensional constraint types only contains R pairs, another only contains P pairs.

$X = 0$.

Particular case: the serial mechanism can be composed of several dimensional constraint types and several single kinematic pairs, for example,

$SOC\{-\widehat{R\perp R}(\perp P)//\widehat{R\perp R}-\}$ is composed of two $SOC\{-\widehat{R\perp R}-\}$ and a P pair.

Table 2 The determination of X value (combination of dimensional constraint types and single kinematic pair) when the output between the adjacent kinematic pairs is 1T/1R

		Parallel	Intersect	Vertical	Free connect
Translation output T	R* and R	1	1	1	1
	R* and P	1	1	1	1
	P* and P	0	1	1	1
Rotation output R	R* and R	0	1	1	1
	R* and P	0	0	0	0
	P* and R	1	1	1	1
	P* and P	0	0	0	0

Table 3 The determination of X value (combination of dimensional constraint types and single kinematic pair) when the output between the adjacent kinematic pairs is 2T/2R

		Parallel	Intersect	Vertical	Free connect
Translation output T	R*R _n and R	0/1	1	1	1
	R*P* and R	1	1	1	1
	P*R* and R	1	1	1	1
	P*P _n and R	1	1	1	1
	R*R and P	1	1	0/1	1
	P*R* and P	1	1	1	1
	R*P* and P	0	1	1	1
	P*P _n and P	0	0/1	0/1	0/1
Rotation output R	R*R _n and R	0	0/1	0/1	1
	R*R _n and P	0	0	0	0

In this case, first we combine the dimensional constraint types into a sub-SOC, then, combine the kinematic pair and the sub-SOC together, so we get the second sub-SOC. The determination of X is shown in Tables 2 and 3.

X = 0, when the output between the adjacent kinematic pairs is 3T/3R.

The explanation of P*, P_n/R*, R_n in Tables 2 and 3 are detailed in Sect. 2.2.

3.2 The Expression of Serial Mechanism End-Reactor's Output Direction

Now we introduce the algorithmic rule of the serial mechanism sub-SOC combination process based on the array (X, Y). We can use that rule to describe the mechanism end-reactor's direction. We use the dimensional constraint type as the basic unit to construct the serial mechanism.

Cause the X value can represent the position relationship between the kinematic pair and the dimensional constraint type next to it, so we can use the X value and the directions of the front sub-SOC to describe the direction of the new sub-SOC.

Definition: Set the first kinematic pair of the branch for the direction foundation kinematic pair. If it is R pair, then the direction of its axis is R^* . If it is P pair, then the direction of its axis is P^* . Then we can describe the direction of the sub-SOC by R^* and P^* . P_n and R_n (in Tables 4 and 5) is also the direction foundation kinematic pair of the branch. P_n and R_n can be any P pair and R pair which has different directions with P^* and R^* . The max number of the direction foundation kinematic pair is 2, they can be P^* , P_n/R^* , R_n .

First, we discuss the direction of the translation output, the expression rule of serial mechanism end-reactor's translation output direction is shown in Table 4.

And then discuss the direction of the rotation output, the expression rule for serial mechanism end-reactor's rotation output direction is shown in Table 5.

Table 4 The expression of serial mechanism end-reactor's translation output direction

Combining form	The output of Sub-SOC	The value of X	Direction of translation
t^1 and t^1	$t^1(\parallel P^*)$	0	$t^1(\parallel P^*)$
		1	$t^2(\parallel \diamond(P^*, P_{\neg n}))$
	$t^1(\perp R^*)$	0	$t^1(\perp R^*)$
		1	$t^2(\perp R^*)$
t^1 and t^2	$t^1(\parallel P^*)$	0	$t^2(\parallel \diamond(P^*, P_{\neg n}))/t^2(\perp R^*)$
		1	t^3 (all directions)
	$t^1(\perp R^*)$	0	$t^2(\perp R^*)$
		1	t^3 (all directions)
t^1 and t^3	$t^1(\parallel P^*)$	0	t^3 (all directions)
		1	t^3 (all directions)
	$t^1(\perp R^*)$	0	t^3 (all directions)
		1	t^3 (all directions)
t^2 and t^1 t^2 and t^2	$t^2(\parallel \diamond(P^*, P_{\neg n}))$	0	$t^2(\parallel \diamond(P^*, P_{\neg n}))$
		1	t^3 (all directions)
	$t^2(\perp R^*)/t^2(\perp \rho)$	0	$t^2(\perp R^*)/$
		1	t^3 (all directions)
t^2 and t^3	$t^2(\parallel \diamond(P^*, P_{\neg n}))$	0	t^3 (all directions)
		1	t^3 (all directions)
	$t^2(\perp R^*)/t^2(\perp \rho)$	0	t^3 (all directions)
		1	t^3 (all directions)
t^3 and t^1 t^3 and t^2 t^3 and t^3	t^3	0	t^3 (all directions)
		1	t^3 (all directions)

Table 5 The expression of serial mechanism end-reactor’s rotation output direction

Combining form	The output of Sub-SOC	The value of X	Direction of rotation
r^1 and r^1	$r^1(\parallel R^*)$	0	$r^1(\parallel R^*)$
		1	$r^2(\parallel \diamond(R^*, R_{-n}))$
r^1 and r^2	$r^1(\parallel R^*)$	0	$r^2(\parallel \diamond(R^*, R_{-n}))$
		1	r^3 (all directions)
r^1 and r^3	$r^1(\parallel R^*)$	0	r^3 (all directions)
		1	r^3 (all directions)
r^2 and r^1 r^2 and r^2	$r^2(\parallel \diamond(R^*, R_{-n}))$	0	$r^2(\parallel \diamond(R^*, R_{-n}))$
		1	r^3 (all directions)
r^2 and r^3	$r^2(\parallel \diamond(R^*, R_{-n}))$	0	r^3 (all directions)
		1	r^3 (all directions)
r^3 and r^1 r^3 and r^2 r^3 and r^3	r^3	0	r^3 (all directions)
		1	r^3 (all directions)

4 Programming the Algorithm of N-DOF Serial Mechanism Type Synthesis

In order to obtain the serial mechanism which conformance to requirements of POC, We can divide the programming process into 4 steps:

- (1) If we want to obtain the limb which has certain POC set, the type and number of kinematic pair are certain. So, firstly, we should ensure the type and number of kinematic pair.
- (2) Ensure the common dimensional constraint type included in the serial mechanism.
- (3) According to the type and number of the kinematic pair in Step 1 and dimensional constraint type in Step 2, we can get possible combination plans which is consisted of dimensional constraint type and single kinematic pair reciprocally; farther, adding every orientation relation (parallel, intersect, vertical, free connection) into the combination plans to get all possible theoretical results which meet the requirement of POC set.
- (4) According to the eliminate principle and equivalent principle (shown in Sect. 3.4), we can eliminate the plan that does not meet the requirements, and get the final plan which meet the requirements. Its programming flow diagram is shown in Fig. 1, and is divided into 4 section as follows.

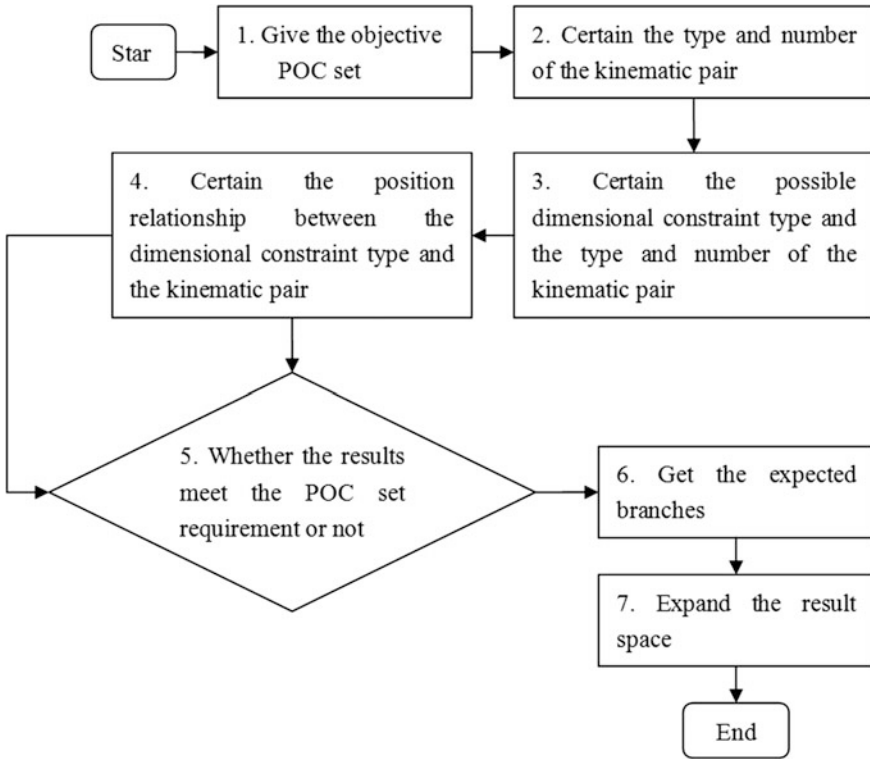


Fig. 1 Programming flow diagram

4.1 Determination of the Type and Number of the Kinematic Pairs

The first part of the program should certain the types and number of the kinematic pairs according to the equation (1), (2), (3). Users should input the number of translation and rotation of the objective POC set and the DOF of the branch, we can get the combination plans of P pairs and R pairs.

According to requirements above, programming by vc++6.0. The algorithm is easy and the specific program is omitted here.

4.2 Determination of the Possible Dimensional Constraint Type

Limited by the paper space, the algorithm of the program Step 2 is introduced particularly in literature [22], 4.3.2

4.3 *Determination of the Axis Relationship Between Every Combination Unit*

Limited by the paper space, the algorithm of the program Step 3 is introduced particularly in literature [22], 4.3.2

4.4 *Elimination of Wrong Plans and the Expanded Type of the Mechanism*

The major functions of the fourth part of the program are as follow:

- (1) Eliminate the plan which is repeated and can't meet the requirement according to the eliminate principle. Generate the mechanism which has equivalent kinematic pair and equivalent HSOC according to the equivalent principle (for example: RP can be seen as C, RRR can be seen as S).
- (2) The main program analyze the results from every subprogram, then output all serial mechanism structure which meet the requirements of the objective POC set input by users; and ensure the direction of translation/rotation output of every mechanism according to the algorithm of direction determination.

Then we introduce eliminate principle and equivalent principle easily as follows.

(1) Eliminate principle:

(1) Eliminate repeated plans.

(2) Eliminate plans which contain the incorrect kinematic pair connection ways:

① Multiple P pairs are parallel to each other;

② More than three R pairs are parallel to each other.

(2) Equivalent principle:

(1) Several kinematic pair can be replaced by an equivalent one.

① R pair parallel to P pair can be equivalent to a C pair.

② Three intersected R pairs can be equivalent to a S pair.

(2) Kinematic pairs can be replaced by equivalent sub parallel mechanism, such as P pair can be equivalent to HSOC $\{-P(4R)-\}$, the two structures have the same POC set output. And P||R can be equivalent to the structure HSOC $\{-P(4U)||R(4U)-\}$, the two structures have the same POC set output too.

5 The Human-Computer Interaction Interface

The process of interface operation is:

First, the user needs to enter the POC set requirements in the upper left of the interface (enter the number of translation independent element and the number of rotation independent element). For example, when we synthesize the 3T1R

(3 translation and 1 rotation) serial mechanism, we should enter ‘3’ in the input box ‘dim {M (t)}’, and enter ‘1’ in the input box ‘dim {M (r)}’. Click the ‘ok’ button right blew, we can get several combination plans which meet the POC set requirement in the right side of the interface

In Fig. 2 the program generate 4 plans, among them, ‘mr’ represents the number of R pairs which the objective mechanism may contains; ‘mp’ represents the number of P pairs which the objective mechanism may contains.

Then the program will generate mechanisms which meet the POC set requirement in four drop-down menu in the left blew of the interface automatically and output by symbol form.

Among then, the first drop-down menu of the first line menus can generate the serial mechanism which the basic point is not on the axis of the end-reactor kinematic pair, it can be any point outside the axis. And the drop-down menu beside it shows the expanded results which include C pairs, S pairs and U pairs. The first drop-down menu of the second line menus can generate the serial mechanism which the basic point is on the axis of the end-reactor kinematic pair. And the drop-down menu beside it shows the expanded results.

Users can click the ‘ok’ button which on the right side, get the structure diagram on the right of the interface according to their needs.

For example, user select the structure of ‘HSOC{-◇(P(3R-2P),P(3R-2P))-P∥R-}’, then click the ‘ok’ button, computer will generate the structure diagram on the right side of the interface.

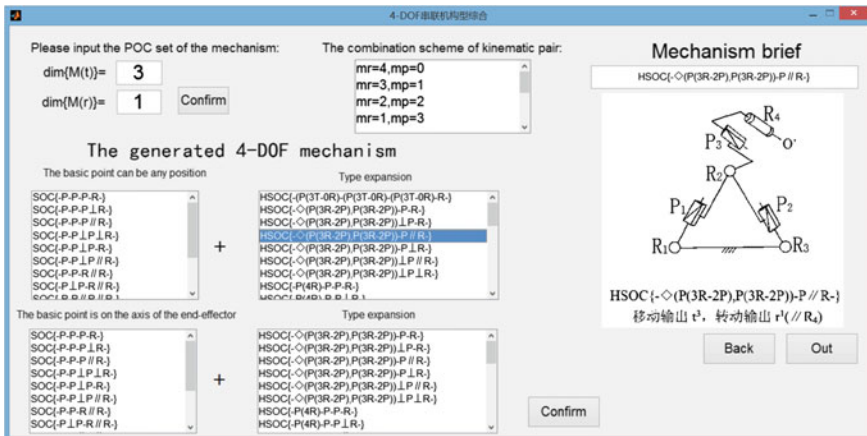


Fig. 2 Input the POC set requirement

6 Example: The Automation Generation of 4-DOF Serial Mechanism Synthesis

Our serial mechanism type synthesis program can synthesize 3-DOF, 4-DOF, 5-DOF serial mechanisms. Now we take the 4-DOF serial mechanism as an example, we can synthesize 1 [18] kinds of 4-DOF serial mechanism. Among them, there are 85 kinds of 3T1R mechanisms (72 % of the 4-DOF serial mechanisms); 23 kinds of 2T2R mechanisms (19 % of the 4-DOF serial mechanisms); 10 kinds of 1T3R mechanisms (9 % of the 4-DOF serial mechanisms). Limited by the paper space, the TABLE of 4-DOF serial mechanism generation is introduced particularly in literature [22], 5.3.4, Table 5.2.

7 Conclusions

- (1) A computer expression of sub-SOC is proposed and defined based on the POC set theory. And a set of numerical algorithms rules is established based on the sub-SOC expression. We can express the output dimension and direction of the serial mechanism end-reactor effectively, and it's convenient for computer recognition.
- (2) According to the expression of sub-SOC, we can use the VC++ to program the serial mechanism automation type synthesis algorithm; and program the interface by Matlab, finished the serial mechanism automation type synthesis generation.
- (3) The program we developed can synthesize 3-DOF, 4-DOF, 5-DOF serial mechanism. We can generate 31 kinds of 3-DOF mechanism (3 kinds of 3T0R, 21 kinds of 2T1R, 5 kinds of 1T2R and 2 kinds of 0T3R); 118 kinds of 4-DOF mechanism (85 kinds of 3T1R, 23 kinds of 2T2R and 10 kinds of 1T3R); 230 kinds of 5-DOF mechanism (203 kinds of 3T2R and 27 kinds of 3T2R).
- (4) We provide a serial mechanism design platform for mechanism researchers and our method is more convenient and powerful.

Acknowledgments This research is sponsored by the NSFC (Grant No. 51475050 and 51375062), Jiangsu Key Development Project (No. BE2015043) and Jiangsu Scientific and Technology Transformation Fund Project (No. BA2015098)

References

1. Gogu G (2007) Structural synthesis of fully-isotropic parallel robots with Schonflies motions via theory of linear transformations and evolutionary morphology. *Eur J Mech A Solids* 26:242–269

2. Gogu G (2004) Structural synthesis of fully-isotropic translational parallel robots via theory of linear transformations. *Eur J Mech A Solids* 23:1021–1039
3. Frisoli A, Checcacci F, Gosselin CM (2000) Synthesis by screw algebra of translating in-parallel actuated mechanisms. *Adv Robot Kinematics* 27:433–440
4. Hunt KH (1978) *Kinematic geometry of mechanisms*. Clarendon Press, Oxford
5. Kong X, Gosselin CM (2007) Type synthesis of parallel mechanisms. *Springer Tracts Adv Robot* 33:66–70
6. Huang Z, Li QC (2003) Type synthesis of symmetrical lower-mobility parallel mechanisms using the constraint-synthesis method. *Int J Robot Res* 22:55–79
7. Li QC, Huang Z, Herve JM (2004) Type synthesis of 3R2T 5-DOF parallel mechanisms using the lie group of displacements. *IEEE Trans Rob Autom* 20:173–180
8. Herve JM (1978) Analyse structurelle des mécanismes par groupe des déplacements. *Mech Mach Theory* 13:437–450
9. Yang T, Liu A, Luo Y et al (2012) *Theory and application of robot mechanism topology*. Science Press, Beijing, pp 17–150
10. Jin Q, Yang TL, Liu AX et al (2004) Theory for topology synthesis of parallel manipulators and its application to three-dimension-translation parallel manipulators. *ASME J Mech Des* 126:625–639
11. Yang TL, Jin Q et al (2002) Structural synthesis and classification of the 3DOF translational parallel robot mechanisms based on the units of single-opened-chain. *Chin J Mech Eng* 38 (8):31–36
12. Yang TL (2004) *Theory of robot mechanism topology*. Mechanical Industry Press, Beijing, pp 1–238
13. Yang T (1986) Kinematic structural analysis and synthesis of over-constrained spatial single loop chains. In: *Proceedings of the 19th Biennial mechanisms conference columbus: ASME*, 86-DET-189
14. Deng JM, Yu TZ, Shen HP et al (2012) Type synthesis for 6-DOF novel parallel mechanisms based on POC set method. *China Mech Eng* 23(21):2525–2640
15. Yu TZ, Shen HP, Deng JM et al (2012) Application of POC set method in structural synthesis of 3-translational parallel manipulator. *J Mach Des* 29(8):48–54
16. Yang TL, Jin Q, Liu AX et al (2001) A general method for structural synthesis of the degenerate-rank parallel robot mechanisms based on the units of single-opened-chain. *Mech Sci Technol* 20(3):321–325
17. Luo YF, Yao WK, Shi ZX et al (2011) Structural synthesis and classification of 2-translational and 2-rotation parallel manipulator based on POC approach. *Mach Tool Hydraulics* 39(3):22–25
18. Dobrjanskyj L, Freudenstein F (1967) Some applications of graph theory to structural analysis of mechanisms. *J Eng Indust ASME Trans Ser B* 89:153–158
19. Cao WS (2014) *Digital type synthesis theory of spatial multi-loop coupled mechanisms*. Yanshan University, Qinhuangdao
20. Ding Huafeng, Cao Wenao et al (2015) Computer-aided structural synthesis of 5-DOF parallel mechanisms and the establishment of kinematic structure databases. *Mech Mach Theory* 83:14–30
21. Xiangdun M, Feng G (2014) A framework for computer-aided type synthesis of parallel robotic mechanisms. *Mech Eng Sci* 0(0):1–9
22. Sun CY (2016) *Computer-aided serial mechanism type synthesis based on POC method*. Changzhou University, Changzhou

Dimensional Synthesis of a 2-PRS-PRRU Parallel Manipulator

Lingmin Xu, Qiaohong Chen, Junhua Tong and Qinchuan Li

Abstract This paper deals with the dimensional synthesis of a 2-PRS-PRRU (P, R, S and U standing for actuated prismatic, revolute, spherical and universal joint, respectively) parallel manipulator considering both dexterity and motion/force transmission. First, the inverse kinematic analysis of the parallel robot is presented. Next, the reciprocal of the condition number and the global conditioning index (GCI) based on a dimensionally homogeneous Jacobian matrix are used to evaluate the dexterity. Then, local transmission index (LTI) and good transmission workspace (GTW) are used for evaluation of the motion/force transmissibility of the 2-PRS-PRRU parallel manipulator. Finally, considering the GCI and GTW simultaneously, the parameter-finiteness normalization method is used to produce an optimal design. Both dexterity and motion/force transmission can be improved with the optimized link parameters.

Keywords Dimensional synthesis · Parallel manipulator · Dexterity · Motion/force transmission

L. Xu · J. Tong · Q. Li
Mechatronic Institute, Zhejiang Sci-Tech University, Hangzhou 310018,
Zhejiang Province, People's Republic of China
e-mail: xulingmin1993@163.com

J. Tong
e-mail: jhtong@zstu.edu.cn

Q. Li
e-mail: lqchuan@zstu.edu.cn

Q. Chen (✉)
School of Information, Zhejiang Sci-Tech University, Hangzhou 310018,
Zhejiang Province, People's Republic of China
e-mail: chen_lisa@zstu.edu.cn

1 Introduction

In recent decades, the lower-mobility parallel manipulator (PM), which has fewer than six degrees of freedom (DOFs), has attracted considerable attention in both the industrial and theoretical communities. Compared with 6-DOF PMs, these lower-mobility PMs are of several advantages, including simpler manufacturing and actuation, and lower cost of maintenance [1–4].

Dimensional synthesis of the PM is indispensable in optimal kinematic design, which aims at obtaining better performances in the reachable workspace. Based on the algebraic characteristics of the Jacobian matrix of a PM, several indices have been proposed and commonly used for evaluating kinematic performance of a PM, such as manipulability [5], condition number [6], etc. However, these Jacobian-based indices may not be effective when they are applied to PMs with combined types of mobility [7]. For PMs with this property, the units of the elements in the Jacobian matrix is inconsistent, which leads to unclear physical meanings and coordinate-dependence. This situations will subsequently cause erroneous interpretations. Much process have been made to deal with this inconsistency using scale factors or matrices [8–12]. And one widely adopted approach is to establish dimensionally homogeneous Jacobian matrix based on characteristic/natural length [8, 9].

Another type of index for evaluation of performance, is called the motion/force transmission characteristics, which is based on screw theory. This index illustrates the capability of transmission between the actuators and moving platform. In order to determine the motion/force transmissibility, many works have been made [13–15]. Particularly, Liu et al. [16, 17] developed a new local transmission index (LTI) which is consistent in physical meaning, frame-independence and scale-invariant.

Note that most works on dimensional synthesis of PMs consider only one performance index, for example, dexterity or motion/force transmissibility [10, 12, 16–18]. However, it is important to consider dexterity and motion/force transmissibility simultaneously in the dimensional synthesis of a PM. Unfortunately, this is a problem that has been addressed rarely.

In this paper, dimensional synthesis of the 2-PRS-PRRU PM [19] considering both dexterity and motion/force transmissibility is discussed. Here, the notations P, R, S and U denote actuated prismatic, revolute, spherical and universal joints, respectively. The paper is organized as follows. Section 2 introduces the 2-PRS-PRRU PM. The inverse kinematic analysis is performed in Sect. 3. Sections 4 and 5 discuss the dexterity and motion/force transmission, respectively. In Sect. 4, the dexterity analysis of the PM is performed in detail based on the dimensionally homogeneous Jacobian matrix. Based on the screw theory as foundation, the motion/force transmission performance with LTI and GTW are investigated in Sect. 5. Considering the distribution of GCI and GTW simultaneously, the

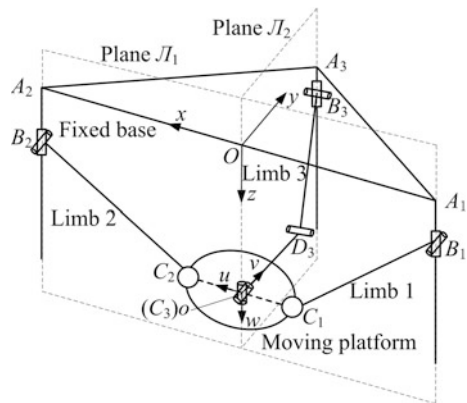
parameter-finiteness normalization method (PFNM) is used for optimal kinematic design in Sect. 6, and then the optimized design of the 2-PRS-PRRU PM with better GCI and GTW is derived. Finally, conclusions are presented in Sect. 7.

2 Description of the 2-PRS-PRRU PM

A prototype of 2-PRS-PRRU PM is shown in Fig. 1. The PM is composed of a fixed base, a moving platform and three actuated limbs. Limb 1 and 2 are two identical PRS limbs, and limb 3 is a PRRU limb. Limb 1 and 2 are coplanar and limited to within the plane J_1 , which is always perpendicular to the plane J_2 . The plane J_2 represents the symmetrical plane to which the limb 3 belongs. Beginning from the fixed base, the P joint connected to the slider is parallel to each other. For limb 1 and 2, the R joint is connected to the P joint, and the revolute axes of the two R joint are parallel to each other. Meanwhile, the revolute axes of R joints in limb 1 and 2 are perpendicular to the P joint. The PRS limbs are connected to the moving platform by S joint, which the centers are limited in plane J_1 . For limb 3, the revolute axes of the two R joints are parallel to each other. And the revolute axes of R joints are also perpendicular to plane J_2 . The first revolute axis of the U joint is parallel to the moving platform and limited in plane J_2 , the second revolute axis is perpendicular to the moving platform. The 2-PRS-PRRU PM are actuated by three P joints.

Let B_i ($i = 1, 2, 3$) denote the central points of the first R joints in each limbs, while the centers of the second R joints in limb 3 are denoted by D_3 . The centers of the S joints in limb 1 and 2 are denoted by C_1 and C_2 , respectively. And the centers of the U joint in limb 3 is denoted by C_3 , which lies in the middle of the line C_1C_2 . The sliders of limbs interest with the fixed base at points A_i ($i = 1, 2, 3$), which lie on the plane $A_1A_2A_3$, as shown in Fig. 1.

Fig. 1 Schematics of the 2-PRS-PRRU PM



The coordinate frames are established as shown in Fig. 1. A fixed reference coordinate frame $O\text{-}xyz$ is attached to the fixed base and the origin O is at the midpoint of line A_1A_2 . Let x -axis always point in the direction of OA_2 , y -axis point along OA_3 , and the z -axis point downward vertically. A moving coordinate frame $o\text{-}uvw$ is attached on the moving platform, and the origin o is coincide with point C_3 , as shown in Fig. 1. Let u -axis point in the direction of C_2C_3 and v -axis perpendicular to the line C_2C_3 . The w -axis is acting downward vertically with respect to the moving platform. The architectural parameters of the 2- $\underline{\text{PRS}}\text{-}\underline{\text{PRRU}}$ PM are defined as follows: $OA_1 = OA_2 = a=300$ mm, $OA_3 = h=250$ mm, $B_1C_1 = l_1 = 280$, $B_2C_2 = l_2 = 280$ mm, $B_3D_3 = l_3 = 225$ mm, $C_3D_3 = l_4 = 225$ mm, $C_1o = C_2o = r=120$ mm.

3 Inverse Position Analysis

The inverse kinematics of the 2 $\underline{\text{PRS}}\text{-}\underline{\text{PRRU}}$ PM involves the calculations of the actuated joint parameters (d_1, d_2, d_3) given the position and orientation parameters of the moving platform (α, β, P_z).

Because the rotation about w -axis is always equal to zero [4, 19], so the rotation matrix between the moving coordinate frames $o\text{-}uvw$ and the fixed coordinate frame $O\text{-}xyz$ is given by

$${}^o\mathbf{R}_o = \begin{bmatrix} c\alpha & s\alpha s\beta & s\alpha c\beta \\ 0 & c\beta & -s\beta \\ -s\alpha & c\alpha s\beta & c\alpha c\beta \end{bmatrix}, \quad (1)$$

where s and c denote \sin and \cos , respectively.

Meanwhile, the rotation matrix can also be obtained through the $u\text{-}v\text{-}w$ Euler angle, and the transformation mapping is given by

$${}^o\mathbf{R}_o = \begin{bmatrix} c\theta_3 c\theta_4 & -c\theta_3 s\theta_4 & s\theta_3 \\ s\psi s\theta_3 c\theta_4 + c\psi s\theta_4 & -s\psi s\theta_3 s\theta_4 + c\psi c\theta_4 & -s\psi c\theta_3 \\ -c\psi s\theta_3 c\theta_4 + s\psi s\theta_4 & c\psi s\theta_3 s\theta_4 + s\psi c\theta_4 & c\psi c\theta_3 \end{bmatrix}. \quad (2)$$

Apparently, the rotation matrices in Eqs. (1) and (2) are two different representations of the same orientations about moving platform, thus the following formulas can be obtained

$$\begin{cases} s\alpha c\beta = s\theta_3 \\ -s\beta = -s\psi c\theta_3 \end{cases}. \quad (3)$$

Using Eq. (3), the angle ψ can be calculated as follows

$$\psi = \arcsin\left(\frac{s\beta}{\sqrt{1 - (s\alpha c\beta)^2}}\right). \quad (4)$$

Thus, the inverse kinematics of 2-PRS-PRRU PM can be expressed as follows based on the geometrical conditions

$$\begin{cases} d_1 = P_z + rs\alpha - \sqrt{l_1^2 - (a - rc\alpha)^2} \\ d_2 = P_z - rs\alpha - \sqrt{l_2^2 - (a - rc\alpha)^2} \\ d_3 = P_z - l_4s\psi - \sqrt{l_3^2 - (h - l_4c\psi)^2} \end{cases}. \quad (5)$$

4 Velocity Analysis

The Jacobian matrix represents the mapping between the rates of the actuated joints $\dot{\mathbf{q}} = (\dot{d}_1 \ \dot{d}_2 \ \dot{d}_3)^T$ and the velocities of the moving platform $\dot{\mathbf{X}} = (\dot{\alpha} \ \dot{\beta} \ \dot{P}_z)^T$. By taking the derivative of Eq. (5) with respect to time leads to

$$\mathbf{J}_q \dot{\mathbf{q}} = \mathbf{J}_x \dot{\mathbf{X}}, \quad (6)$$

Where

$$\mathbf{J}_q = \begin{bmatrix} J_{q11} & 0 & 0 \\ 0 & J_{q22} & 0 \\ 0 & 0 & J_{q33} \end{bmatrix}, \quad \mathbf{J}_x = \begin{bmatrix} J_{x11} & J_{x12} & J_{x13} \\ J_{x21} & J_{x22} & J_{x23} \\ J_{x31} & J_{x32} & J_{x33} \end{bmatrix}, \quad J_{q11} = P_z + rs\alpha - d_1, \quad J_{q22} = P_z - rs\alpha - d_2, \\ J_{q33} = P_z - l_4s\psi - d_3, \quad J_{x11} = (P_z - d_1)rc\alpha + arsz, \quad J_{x12} = 0, \quad J_{x13} = P_z + rs\alpha - d_1, \\ J_{x21} = arsz - (P_z - d_2)rc\alpha, \quad J_{x22} = 0, \quad J_{x23} = P_z - rs\alpha - d_2, \quad J_{x31} = A\dot{Q} + B\dot{Q}, \quad J_{x32} = AR + BR, \\ J_{x33} = P_z - l_4s\psi - d_3, \quad A = (d_3 - P_z)l_4c\psi, \quad B = hl_4s\psi, \quad R = \frac{c\alpha}{1 - s^2\alpha c^2\psi}, \quad Q = \frac{szs\psi c\psi}{1 - s^2\alpha c^2\psi}$$

Thus, the velocity equation of the 2-PRS-PRRU PM can be established, and it is expressed as follows

$$\dot{\mathbf{q}} = \mathbf{J}_q^{-1} \mathbf{J}_x \dot{\mathbf{X}} = \mathbf{J} \dot{\mathbf{X}}, \quad (7)$$

where $\mathbf{J} = \mathbf{J}_q^{-1} \mathbf{J}_x$ is a 3×3 Jacobian matrix.

5 Dexterity Analysis

Based on the previous works [19], the 2-PRS-PRRU PM has combined types of mobility, i.e., two rotational DOFs and one translational DOF, which will cause the inconsistency of the units of the elements in the Jacobian matrix and erroneous interpretations. So it is necessary to obtain a new Jacobian matrix in which the dimensions of every elements are the same physical units. Considering the method proposed by Angeles et al. [8, 9], here the length of moving platform, r , is used as the characteristic/natural link length L to generate a new homogeneous Jacobian matrix. The function of the characteristic length L is to homogenize the original Jacobian matrix. And the homogeneous Jacobian matrix \mathbf{J}_h is then formulated as follows

$$\mathbf{J}_h = \mathbf{J} \text{diag}\left(\frac{1}{L} \quad \frac{1}{L} \quad 1\right) = \begin{bmatrix} \mathbf{F}_r & \mathbf{F}_t \end{bmatrix}, \quad (8)$$

where matrices \mathbf{F}_r and \mathbf{F}_t denote a 3×2 matrix and a 3×1 matrix, respectively. The matrix \mathbf{F}_r represents the mapping of the linear velocities to angular velocities $(\dot{d}_1, \dot{d}_2, \dot{d}_3 \mapsto \dot{\alpha}, \dot{\beta})$, while matrix \mathbf{F}_t corresponds to the mapping of the linear velocities to linear velocity $(\dot{d}_1, \dot{d}_2, \dot{d}_3 \mapsto \dot{P}_z)$.

5.1 Local Dexterity Index

The condition number of the Jacobian matrix is an important local dexterity index that can be used to describe the kinematic performance of a certain configuration. Reference [6] shows that the condition number c of the homogeneous Jacobian matrix can be defined as

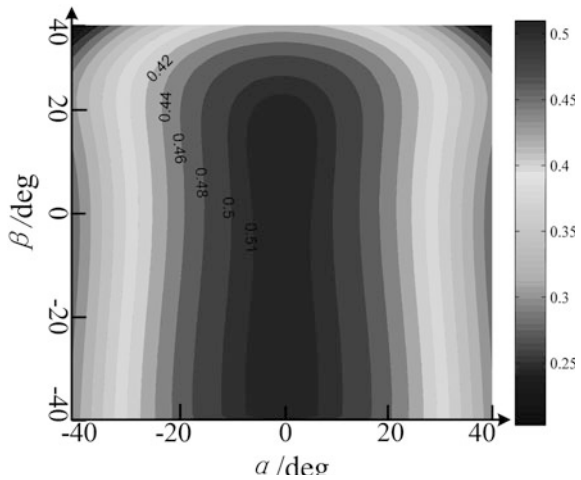
$$c = \|\mathbf{J}_h\| \cdot \|\mathbf{J}_h^{-1}\|, \quad (9)$$

where the notation $\|\cdot\|$ is defined as the 2-norm of the matrix.

The condition number can be used to illustrate the magnification between relative input errors and relative output error [7]. Condition number ranges from one to infinite. The closer the condition number is to unity, the better the kinematic performance of this configuration will be.

For clarity, we use the reciprocal of the condition number, i.e., $C = 1/c$ ($C \in [0, 1]$) in this paper. And the rotation ranges of moving platform are set as follows: $-40^\circ \leq \alpha \leq 40^\circ$, $-40^\circ \leq \beta \leq 40^\circ$. For 2-PRS-PRRU PM, the operating height P_z has no influence on the distribution of condition number. Based on the architecture parameters mentioned in Sect. 2, the distribution variations of the C for the 2-PRS-PRRU PM within orientation workspace different operating is shown in Fig. 2.

Fig. 2 Distributions of the reciprocal of the condition number for the 2-PRS-PRRU PM



5.2 Global Conditioning Index

Although the local dexterity index mentioned above shows the distribution of the kinematic performance characteristic, it can hardly be used to evaluate the global dexterity performance of the PM within the reachable workspace. The study of the global dexterity performance is also essential for dimensional synthesis of the mechanism. To describe the mechanism performance better, the global conditioning index (GCI) proposed by Gosselin et al. [20] is used to evaluate the global dexterity characteristic in this study. And the GCI is defined as

$$\eta = \frac{\int_W CdW}{W}. \tag{10}$$

Apparently, the purpose of calculating the GCI is to obtain the average performance over the whole reachable workspace (W). GCI ranges from zero to unity. And the closer the GCI is to unity, the better the global dexterity the PM has. The GCI of 2-PRS-PRRU PM is 0.426 through Eqs. (9) and (10).

6 Motion/Force Transmission Analysis

6.1 Local Transmission Index (LTI)

For dimensional synthesis of a PM, the motion/force transmission performance is crucially important. The motion/force transmission characteristic of a mechanism can be divided into two parts: input transmission performance and output transmission performance. The input transmission performance represents the efficiency

of power transmitted from the actuated joints to the limbs, while the output transmission performance represents the efficiency of power transmitted from the limbs to the moving platform. Readers are suggested to refer to [16, 17] for detailed introduction of LTI based on screw theory. Considering these two performances simultaneously, the motion/force transmission characteristics are then defined as

$$\lambda_i = \frac{|\$A_i \circ \$T_i|}{|\$A_i \circ \$T_i|_{\max}}, \tag{11a}$$

$$\eta_i = \frac{|\$O_i \circ \$T_i|}{|\$O_i \circ \$T_i|_{\max}}, \tag{11b}$$

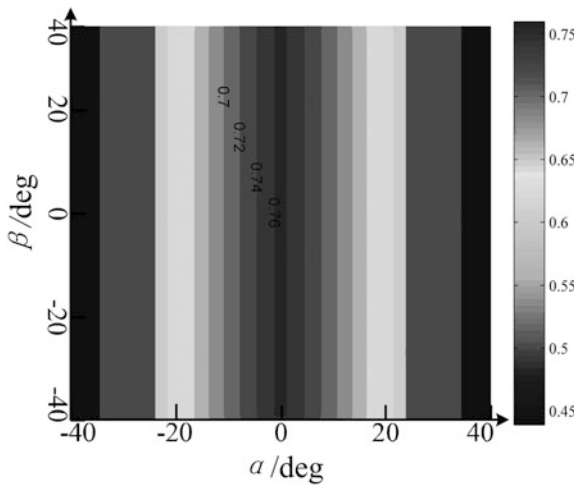
and

$$\Gamma = \min\{\lambda_i, \eta_i\}, \tag{11c}$$

where λ_i and η_i denote the input transmission index (ITI) and output transmission index (OTI) of the i th limb, respectively. $\$A_i$ denotes the input twist screw (ITS) of the i th limb. $\$O_i$ denotes the output twist screw (OTS) of the moving platform. And $\$T_i$ denotes the transmission wrench screw (TWS) of the i th limb. The range of Γ is from zero to unity, and a larger Γ indicates better motion/force transmissibility.

Based on the architecture parameters mentioned in Sect. 2, the LTI distribution of 2-PRS-PRRU PM in the orientation workspace can be obtained, as shown in Fig. 3. Because of the limbs arranged symmetrically, the distribution of the transmission characteristic is completely symmetrical with respect to angle α .

Fig. 3 LTI distribution of the 2-PRS-PRRU PM



6.2 Global Transmission Index

Similar to the condition number, the LTI represents the performance of the motion/force transmission in a single configuration, and thus can hardly be used to evaluate the global transmission performance of the robot. Therefore, it is necessary to define an index that can describe the performance in a set of poses. According to the definition of transmission angle [21], it is assumed that when $\Gamma \geq 0.7$ the manipulator has a relatively good motion/force transmissibility. And the region where $\Gamma \geq 0.7$ is defined as the good transmission workspace (GTW). Thus, the index can evaluate the global motion/force transmission of a PM, and is defined as

$$\sigma = \frac{\int_{S_G} dW}{\int_S dW}, \quad (12)$$

where W is the reachable workspace, S_G and S denote the area of GTW and overall possible workspace, respectively. Apparently, GTW ranges from zero to unity. And the closer the GTW is to unity, the better the transmission performance the parallel robot has. Accordingly, the value of GTW about 2-PRS-PRRU PM can be obtained, and it is 0.256.

7 Optimization of Design Parameters

The GCI and GTW of the 2-PRS-PRRU PM are both highly dependent on the design parameters, i.e., l_1, l_2, l_3, l_4, r, a and h , thus these two performance indices should be considered simultaneously for dimensional synthesis. Considering limitations of rotation angles, we restrict the motion capability as $\alpha \in [-40^\circ, 40^\circ]$, $\beta \in [-40^\circ, 40^\circ]$. Here, the parameter-finiteness normalization method (PFNM) proposed by Liu et al. [16, 17, 22] is used to optimize the design parameters. However, it is difficult to illustrate the performance of the 2-PRS-PRRU PM using the seven design parameters. Without loss of generality, we let the design parameters $l_1 = l_2 = l_3 = l_4, a = h$ be used as an example to illustrate the influence of the parameters. We can therefore obtain the 2-PRS-PRRU PM using the three design a, r and l_1 , and they are normalized as

$$D = \frac{l_1 + r + a}{3}, \quad (13)$$

where D is a normalized factor. Then the non-dimensional and normalized parameters e_1, e_2 and e_3 are deduced as

$$e_1 = \frac{l_1}{D}, e_2 = \frac{r}{D}, e_3 = \frac{a}{D}, \tag{14}$$

Considering the real application, the three normalized parameters should satisfy

$$0 < e_2 \leq e_3, 0 < e_3 < 3/2, 0 < e_1, e_2, e_3 < 3. \tag{15}$$

Using the method in [22], the parameter design space (PDS) can be obtained as shown in Fig. 4. The shaded area shown in Fig. 4a is the set of all possible points. For convenience, the chosen area can be transformed into plan view, as shown in Fig. 4b. The relationship between the parameters in spatial space (r_1, r_2, r_3) and those in plan space (s, t) can be described as follows

$$\begin{cases} e_1 = s \\ e_2 = \frac{3}{2} - \frac{\sqrt{3}}{2}t - \frac{s}{2} \\ e_3 = \frac{3}{2} + \frac{\sqrt{3}}{2}t - \frac{s}{2} \end{cases}, \text{ or } \begin{cases} s = e_1 \\ t = \frac{e_3 - e_2}{\sqrt{3}} \end{cases}. \tag{16}$$

The design steps required for performance optimization are as follows:

Step 1: Identify the optimal regions. The distributions of the GCI and GTW can be obtained, as shown in Fig. 5. Considering the dexterity and motion/force transmission characteristics of the mechanism, the region where $GCI \geq 0.45$ is regarded as having ideal dexterity, and the region where $GTW = 1$ is regarded as with desire motion/force transmission. The optimal design regions are shown in Fig. 6. Region **I** indicates that the GCI is good but GTW relatively poor. In region **II**, the GTW is relatively enlarged but GCI small. From the region **III**, we can find that the GCI and GTW both are better than values in two other regions.

Step 2: Select three groups of data points from each optimal region, **I**, **II**, and **III**. 9 groups of data points are chosen in this study. And the chosen parameters

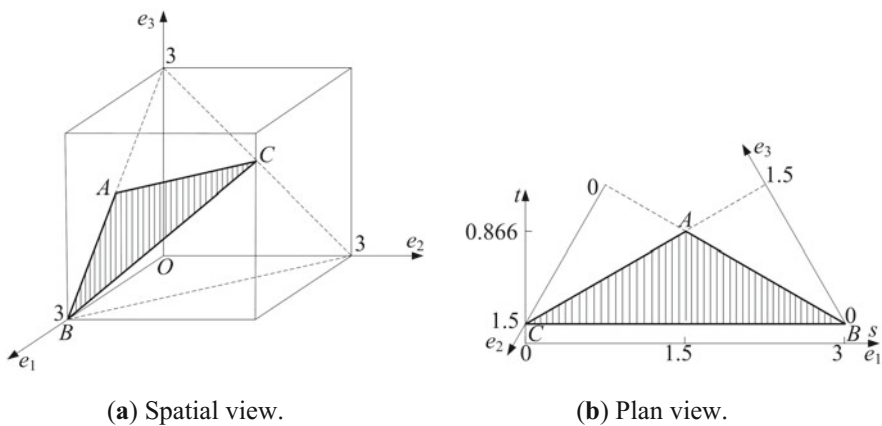


Fig. 4 Parameter design space model

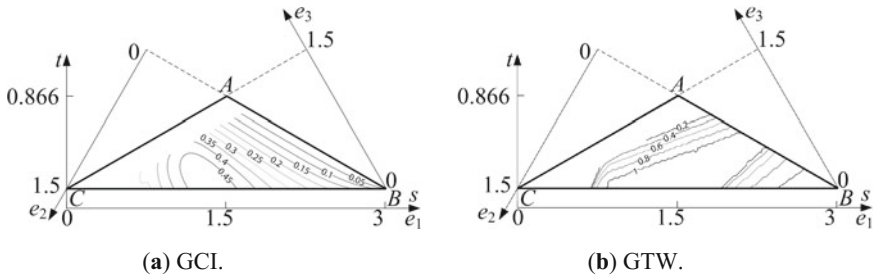


Fig. 5 Distribution of performances for the 2-PRS-PRRU PM

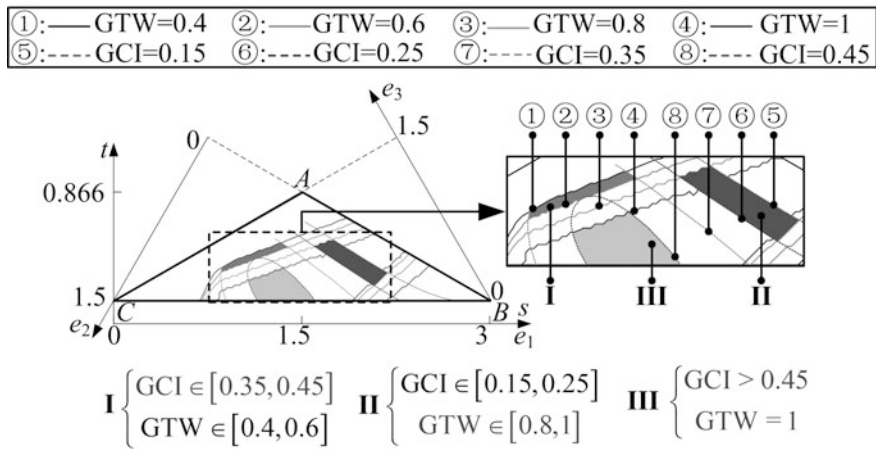


Fig. 6 Optimal design regions: I, II, and III

should be as far as possible from the bounds of the optimal region. Through Eq. (16), the non-dimensional parameters e_1 , e_2 and e_3 can be obtained. Using Eqs. (14) and (16), we can then obtain the three design parameters a , r and l_1 , and the two plan space parameters s and t , as listed in Table 1.

Table 1 GCI and GTW in the optimal design regions

Region	Group	s	t	e_1	e_2	e_3	l_1	r	a	GCI	GTW
I	1	1.14	0.36	1.14	0.62	1.24	285	155	310	0.442	0.492
	2	1.24	0.40	1.24	0.53	1.23	310	133	308	0.415	0.488
	3	1.32	0.40	1.32	0.49	1.19	330	123	298	0.390	0.586
II	4	1.70	0.44	1.70	0.27	1.03	425	68	258	0.196	0.892
	5	1.74	0.46	1.74	0.23	1.03	435	58	258	0.166	0.839
	6	1.68	0.40	1.68	0.31	1.01	420	78	253	0.231	0.946
III	7	1.10	0.14	1.10	0.83	1.07	275	208	268	0.458	1
	8	1.40	0.12	1.40	0.70	0.90	350	175	225	0.474	1
	9	1.32	0.16	1.32	0.70	0.98	330	175	245	0.480	1

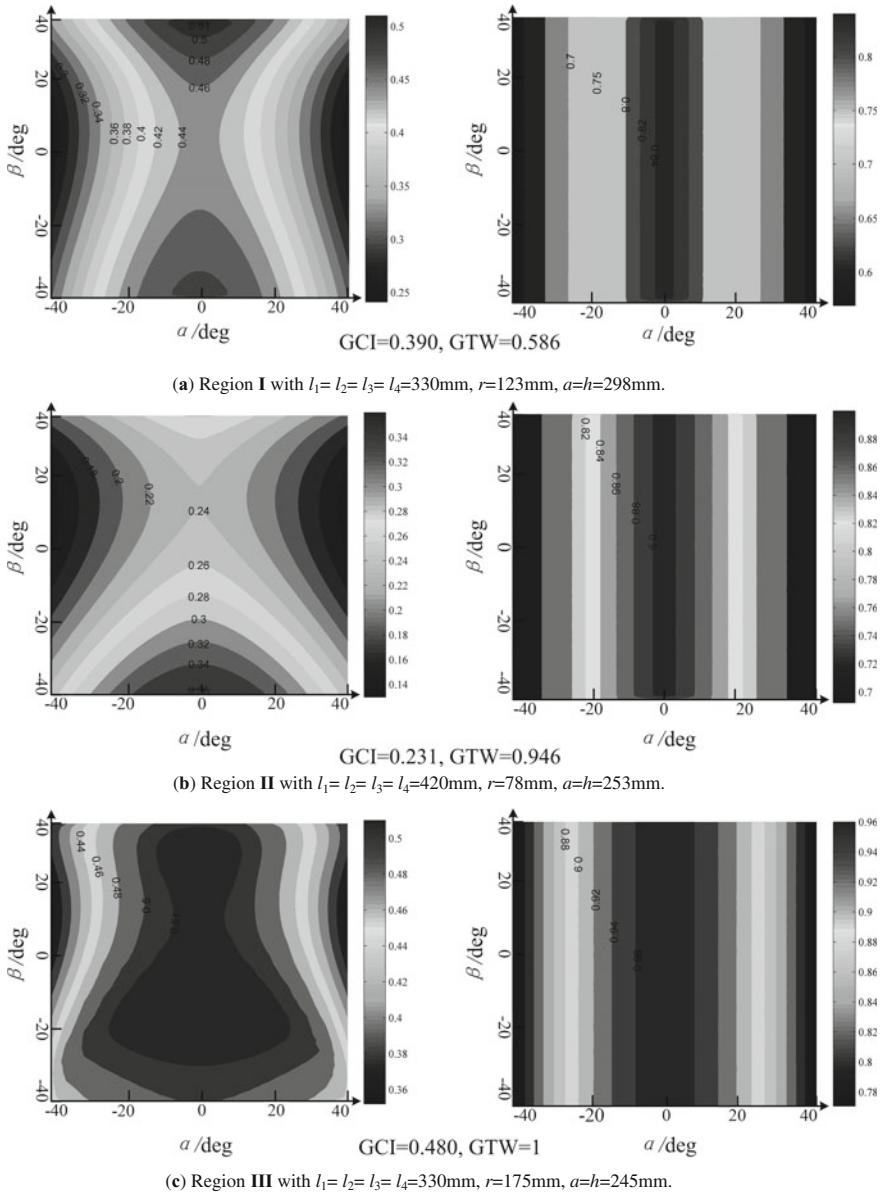
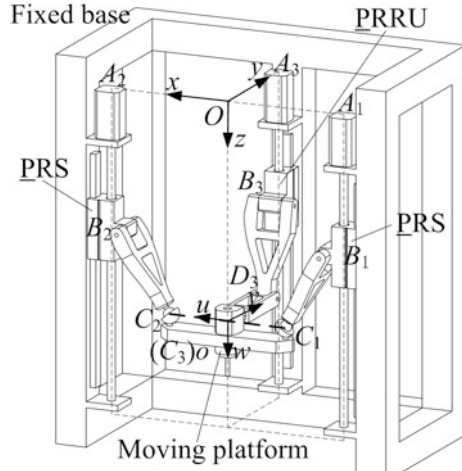


Fig. 7 Distributions of dexterity and motion/force transmission

Fig. 8 Schematic of the optimized 2-PRS-PRRU PM



Step 3: Determine the normalized factor D and dimensional parameters a, r, l_1 . The normalized factor D can be determined considering practical condition, and D is chosen as 250 mm in this study. For example, the design parameters in group “7” are chosen as the optimal results, i.e., $e_1 = 1.10, e_2 = 0.83, e_3 = 1.07$. Then the values of design parameters can be obtained using Eq. (16), i.e., $l_1 = l_2 = l_3 = l_4 = 275$ mm, $a = h = 268$ mm, $r = 208$ mm.

Step 4: Check whether the dimensional parameters obtained in Step 3 is suitable or not for an actual usage conditions. If it satisfies the actual assembly condition, the procedure is finished; otherwise, return to Step 3 to choose another group of data from the optimal region, and repeat Steps 3 and 4.

Figure 7 shows the comparisons of distributions of dexterity and motion/force transmission in region **I**, **II**, and **III**, where the design parameters in group “3”, “6” and “9” are chosen as examples. From Figs. 7a and b, we can find that the GCI in region **I** is 0.390, which is greater than 0.231 in region **II**, but the GTW in region **I** is 0.586, which is smaller than 0.946 in region **II**. As shown in Fig. 7c, the values of GCI and GTW in region **III** are 0.480 and 1, which are better than two other examples. It is demonstrated that the region **III** can be selected as the optimal region. Finally, based on information from the Fig. 6 and Table 1, the optimized manipulator can be obtained as shown in Fig. 8.

8 Conclusions

The dimensional synthesis of a 2-PRS-PRRU PM considering the dexterity and motion/force transmission simultaneously is presented, which is a key contribution of this paper. Local and global index of dexterity based on the homogenized Jacobian matrix including the reciprocal of the condition number and GCI are

obtained. The LTI and GTW of the 2-PRS-PRRU PM are obtained to evaluate the motion/force transmission characteristics. Finally, both good GCI and GTW of the 2-PRS-PRRU PM are achieved after optimizing the link parameters.

Acknowledgments The work is supported by the National Natural Science Foundation of China (NSFC) under Grant 51275479 and 51525004 and Natural Science Foundation of Zhejiang Province under Grant LZ14E050005.

References

- Hunt KH (1983) Structural kinematics of in-parallel-actuated robot arms. *J Mech Des* 105:705–712
- Merlet JP (2006) *Parallel robots*. Kluwer Academic Publishers
- Li QC, Hervé JM (2010) 1T2R parallel mechanisms without parasitic motion. *IEEE Trans Rob* 26:401–410
- Li QC, Hervé JM (2014) Type synthesis of 3-DOF RPR-equivalent parallel mechanisms. *IEEE Trans Rob* 30:1333–1343
- Stoughton RS, Arai T (1993) A modified Stewart platform manipulator with improved dexterity. *IEEE Trans Rob Autom* 9:166–173
- Angeles J, López-Cajún CS (1992) Kinematic isotropy and the conditioning index of serial robotic manipulators. *Int J Rob Res* 11:561–571
- Merlet JP (2006) Jacobian, manipulability, condition number, and accuracy of parallel robots. *J Mech Des* 128:199–206
- Ma O, Angeles J (1991) Optimum architecture design of platform manipulators. In: 5th international conference on advanced robotics, pp 1130–1135
- Angeles J (1992) The design of isotropic manipulator architectures in the presence of redundancies. *Int J Rob Res* 11:196–201
- Gosselin CM (1990) Dexterity indices for planar and spatial robotic manipulators. In: IEEE international conference on robotics and automation, pp 650–655
- Kim SG, Ryu J (2003) New dimensionally homogeneous Jacobian matrix formulation by three end-effector points for optimal design of parallel manipulators. *IEEE Trans Rob Autom* 19:731–736
- Shi J, Wang Y, Zhang G, Ding H (2013) Optimal design of 3-DOF PKM module for friction stir welding. *Int J Adv Manuf Tech* 66:1879–1889
- Ball RS (1998) *A treatise on the theory of screws*. Cambridge University
- Chen C, Angeles J (2007) Generalized transmission index and transmission quality for spatial linkages. *Mech Mach Theory* 42:1225–1237
- Sutherland G, Roth B (1973) A transmission index for spatial mechanisms. *J Eng Ind* 95:589–597
- Liu XJ, Wang LP, Xie FG, Bonev IA (2010) Design of a three-axis articulated tool head with parallel kinematics achieving desired motion/force transmission characteristics. *J Manuf Sci E-T ASME* 132:237–247
- Liu XJ, Wu C, Wang JS (2012) A new approach for singularity analysis and closeness measurement to singularities of parallel manipulators. *J Mech Rob* 4:61–68
- Fathah A, Ghasemi AH (2002) Isotropic design of spatial parallel manipulators. *Int J Rob Res* 811–824
- Li QC, Sun XD, Chen QH, Wu CY (2011) Kinematics and singularity analysis of 2-PRS-PRRU parallel mechanism. *Chin J Mech Eng* 47:21–27

20. Gosselin C, Angeles J (1991) A global performance index for the kinematic optimization of robotic manipulators. *J Mech Des* 113:220–226
21. Tao DC Applied linkage synthesis. Addison-Wesley Reading, MA
22. Liu XJ, Wang JS (2007) A new methodology for optimal kinematic design of parallel mechanisms. *Mech Mach Theory* 42:1210–1237

Synthesis of Two Primary Types of Walking Robot Legs

Da Xi and Feng Gao

Abstract Walking robots use legs to separate their bodies from tough terrain. There is few systematic method to accomplish specific structure design of robot legs. This paper provides a practical systematic design method based on generalized-function (GF) set theory. The process of the method includes type classification, number synthesis, limb decomposition and kinematic pair design. Two main types of robot legs are proposed to represent basic design targets. The number synthesis of the basic leg types are transferred to two linear Diophantine equations, actuation synthesis and constraint synthesis by name. According to practical requirements, feasible limb expressions and kinematic-pair design are proposed. Finally all the fifty-one leg types are synthesized and typical prototypes are realized to prove the validity of the design method.

Keywords Robot leg · Type synthesis · GF set · Linear diophantine equation

1 Introduction

Legged robots are widely used in complicated environments to adapt tough terrains. The leg-like structure of these robots makes it possible to separate bodies from obstacles. Thus the robots could maintain body stability on most of irregular terrains. In recent years, many legged robots have become hot topics in the field of robot research, such as BigDog [1, 2], Belepht [3, 4], PPHex [5–7] and other biomechanics [8, 9]. Leg structure is the key point of these robots. Well-designed robot legs will enhance operating performance under proper control program. But most current robot legs are lack of diligent design [10], which make it difficult to

D. Xi · F. Gao (✉)
State Key Laboratory of Mechanical System and Vibration,
Shanghai Jiao Tong University, Shanghai 200240, China
e-mail: fengg@sjtu.edu.cn

D. Xi
e-mail: x-deadog@sjtu.edu.cn

implement gait control and parts protection. It's a valuable topic to realize a specific robot leg design method to get better performance for walking robots.

The generalized-function set (GF set) theory was proposed by Gao and Yang to mathematically express the topological performance of the end-effectors [11–14]. The number synthesis equation was significantly analyzed in GF set theory to find various types for mechanism design.

This paper introduces a systematic type synthesis method for 3-DoF walking robot legs based on GF set theory. The paper is organized as follows. Section 2 sets the targets of synthesis, based on the analyses of the two main robot leg types. Section 3 provides the solutions of the number synthesis equations of actuators and constraints, which determine the GF expressions of limbs in Sect. 4. Section 5 raises some recommended limb designs of kinematic pairs. Typical design results of different limbs are illustrated in Sect. 6. Section 7 gives the conclusions.

2 Analyses of the Leg Mobility

Based on the relevant studies around the world, the DoF of legs are classified into two primary types (see Table 1).

Type R: Two rotational DoF are about the hip and one translational DoF is along the leg. This type of robot leg appears to be low level of anisotropy in horizontal directions. E.g., Raibert hopper [15, 16] and PPHex [7]. See Fig. 1a.

Type T: Foot moves in the sagittal plane which is located by an R-DoF about the hip. E.g., BigDog [2] and HyQ [17]. See Fig. 1b.

3 Number Synthesis

Mechanism parameters should satisfy the following integrated number synthesis equation [18], see Eq. (1).

$$\begin{cases} 2F_D + Q_r - C_o - \sum_{i=1}^N (q_i - 1) + \sum_{i=1}^N (c_i - 1) = 6 \\ c_i \leq 6 - F_D, \quad q_i \leq F_D + Q_r \end{cases} \quad (1)$$

where F_D is the dimension of the end-effector's characteristics, i.e., the quantity of nonzero elements in the GF set expression (F_D and DoF are equal in this paper). Q_r is the number of redundant actuators. C_o is the number of over-constraints. N is the

Table 1 GF expressions of type R and type T

Type	End-effector's DoF
R	$G_{F14}^{\parallel}(R_x, R_\beta, T_a, 0, 0, 0)$
T	$G_{F16}^{\parallel}(R_x, T_a, R_b, 0, 0, 0)$

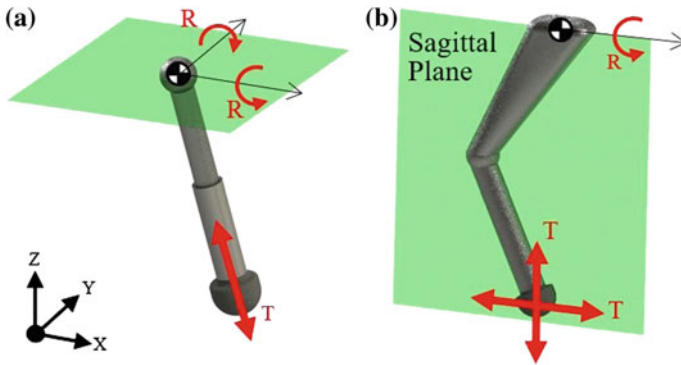


Fig. 1 Moving ability of the two main types of legs. a Type R, b Type T

total number of limbs. Within i th limb, c_i and q_i are the number of constraints and actuations, respectively.

3.1 Number Synthesis of Actuations

The actuation part of Eq. (1) is the number synthesis equation of actuations. It could be rewritten in the independent form, where $q_i = 0$ indicates the limb is passive (i.e., without actuators):

$$\begin{cases} N = F_D + Q_r - \sum_{i=1}^N (q_i - 1) \\ q_i \leq F_D + Q_r \end{cases} \quad (2)$$

In normal conditions, there is no more than one passive limb within the leg structure.

Set zero redundant actuation. Then the actuation number synthesis equation has the equivalent form:

$$\begin{cases} \sum_{j=1}^6 j \cdot n_{qj} = n_{q1} + 2n_{q2} + \dots + 6n_{q6} = F_D \\ \sum_{j=0}^6 n_{qj} = n_{q0} + n_{q1} + n_{q2} + \dots + n_{q6} = N \end{cases} \quad (3)$$

where n_{qj} is the number of limbs with j actuations, and

$$\begin{cases} n_{qj} \text{ are non-negative integers, } j = 0, 1, \dots, 6 \\ n_{q0} = 0, 1 \end{cases}$$

It is notable that:

$$N \leq n_{q0} + F_D. \tag{4}$$

The solution is expressed as an eight dimension vector:

$$[N, n_{q0}, n_{q1}, n_{q2}, n_{q3}, n_{q4}, n_{q5}, n_{q6}] \tag{5}$$

Equation (3) is called an constrained linear Diophantine Equation in combinatorics, solvability of which is included in Hilbert’s tenth problem.

In this paper, the solution (5) could be listed in sequence because of the specific parameters in the equation, and the analytical solving process is omitted.

For parallel/serial legs, $\sum qi = F_D = 3$, solutions are listed in Table 2.

Similarly, for multi-DoF part in hybrid legs, the local parameters satisfy $\sum qi = F_D = 2$.

The local solutions are listed in Table 3.

3.2 Number Synthesis of Constraints

The constraint part of the number synthesis equation (1) has the following equivalent form:

$$\begin{cases} \sum_{j=1}^6 j \cdot n_{cj} = n_{c1} + 2n_{c2} + \dots + 6n_{c6} = 6 - F_D + C_o \\ \sum_{j=0}^6 n_{cj} = n_{c0} + n_{c1} + n_{c2} + \dots + n_{c6} = N \end{cases} \tag{6}$$

where n_{cj} are non-negative integers, $j = 0, 1, \dots, 6$.

F_D and N are given as the design goal (Table 1) and the actuation number synthesis (Tables 2 and 3), respectively.

Table 2 Solutions of actuation number synthesis for parallel/serial legs

Index	[N, nqj], j = 0–6	Index	[N, nqj], j = 0–6
Q-1	[1, 0, 0, 0, 1, 0, 0, 0]	Q-4	[2, 1, 0, 0, 1, 0, 0, 0]
Q-2	[2, 0, 1, 1, 0, 0, 0, 0]	Q-5	[3, 1, 1, 1, 0, 0, 0, 0]
Q-3	[3, 0, 3, 0, 0, 0, 0, 0]	Q-6	[4, 1, 3, 0, 0, 0, 0, 0]

Table 3 Solutions of actuation number synthesis for hybrid legs

Index	[N, nqj], j = 0–6	Index	[N, nqj], j = 0–6
Q-7	[1, 0, 0, 1, 0, 0, 0, 0]	Q-9	[2, 1, 0, 1, 0, 0, 0, 0]
Q-8	[2, 0, 2, 0, 0, 0, 0, 0]	Q-10	[3, 1, 2, 0, 0, 0, 0, 0]

The solution of Eq. (6) could be expressed as an eight dimension vector:

$$[C, n_{c0}, n_{c1}, n_{c2}, n_{c3}, n_{c4}, n_{c5}, n_{c6}] \tag{7}$$

The equations are analyzed for different types (see Table 1) and connections (parallel/serial, hybrid) in the rest of the section.

In the process of synthesis, connection in series is a special case of that in parallel when $N = 1$. So here type R/T-P represents legs of type R/T in both parallel and serial connections. Additionally, type R/T-H represents legs of type R/T in hybrid connection. Details are shown in the tables of next section.

Without loss of generation, here goes the results of all types via the similar process in Sect. 3.1. The results are classified and listed in Sect. 4.

4 Limb Decomposition and Expression

For different leg mobility characteristics (type R or type T, see Table 1), the qualified limb expressions are listed in Tables 4, 5, 6 and 7. Tables 4 and 5 include expressions for type R structure, while Tables 6 and 7 include expressions for type T. For simplification, cases that $N > 3$ are omitted in the Table.

The abbreviations of GF sets in the tables correspond to the full-form 6-D expressions in Table 8 (Sect. 5).

5 Limb Design

Kinematic pairs and the actuation locations are listed in Table 8.

Table 4 Limb expression for type R-P

N	Limb 1	Limb 2	Limb 3	Limb 4
1	GF14			
3	GF14	GF1	GF1	
	GF8	GF2	GF2	
	GF14	GF2	GF2	
4	GF14	GF1	GF1	GF1
	GF8	GF2	GF1	GF1
	GF14	GF2	GF1	GF1
	GF8	GF2	GF2	GF1
	GF14	GF2	GF2	GF1
	GF8	GF2	GF2	GF2
	GF14	GF2	GF2	GF2

Table 5 Limb expression for type R-H

Hybrid limbs				Other limb
Parallel part			Series part	
Limb 1	Limb 2	Limb 3	Limb 4	Limb 5
GF18	GF1	GF1	GF7	
GF12	GF2	GF2	GF7	
GF18	GF2	GF2	GF7	
GF4	GF1	GF1	GF18	GF8/GF14
GF4	GF2	GF2	GF18	GF8/GF14
GF4	GF3	GF3	GF18	GF8/GF14
GF14	GF1	GF1	GF12	GF14
GF8	GF2	GF2	GF12	GF14
GF14	GF2	GF2	GF12	GF14

Table 6 Limb expression for type T-P

N	Limb 1	Limb 2	Limb 3	Limb 4
1	GF16			
3	GF16	GF1	GF1	
	GF16	GF2	GF2	
	GF10	GF3	GF3	
	GF16	GF3	GF3	
4	GF16	GF1	GF1	GF1
	GF16	GF2	GF1	GF1
	GF10	GF3	GF1	GF1
	GF16	GF3	GF1	GF1
	GF16	GF2	GF2	GF1
	GF16	GF2	GF2	GF2
	GF10	GF3	GF3	GF1
	GF10	GF3	GF2	GF2
	GF16	GF3	GF3	GF1
	GF16	GF3	GF2	GF2
	GF10	GF3	GF3	GF2
	GF16	GF3	GF3	GF2
	GF10	GF3	GF3	GF3
GF16	GF3	GF3	GF3	

Table 7 Limb expression for type T-H

Hybrid limbs				Other limb
Series part	Parallel part			
Limb 1	Limb 2	Limb 3	Limb 4	Limb 5
GF21	GF6	GF5		
GF21	GF6	GF6		
GF12	GF16	GF1	GF1	GF16
GF18	GF4	GF1	GF1	GF16
GF21	GF4	GF1	GF1	GF10/GF16

Table 8 Limb design for GF expressions

No.	Limb GF expression	DoF	Kinematic pair design
1	$G_{F1}^I(T_a, T_b, T_c, R_x, R_\beta, R_\gamma)$	6	<u>UPS</u> , <u>RUS</u>
2	$G_{F2}^I(T_a, T_b, T_c, R_x, R_\beta, 0)$	5	<u>RRU</u> [^] <u>R</u>
3	$G_{F3}^I(T_a, T_b, T_c, R_x, 0, 0)$	4	<u>RRU</u> [^]
4	$G_{F4}^I(T_a, T_b, T_c, 0, 0, 0)$	3	<u>P</u> [^] <u>U</u> , <u>R</u> [^] <u>U</u>
5	$G_{F5}^I(T_a, T_b, R_x, 0, 0, 0)$	3	<u>UR</u> , <u>RRR</u>
6	$G_{F6}^I(T_a, T_b, 0, 0, 0, 0)$	2	<u>RR</u> , <u>RP</u>
7	$G_{F7}^I(T_a, 0, 0, 0, 0, 0)$	1	<u>P</u>
8	$G_{F8}^II(R_x, R_\beta, R_\gamma, T_a, 0, 0)$	4	<u>SP</u>
9	$G_{F10}^II(R_x, R_\beta, T_a, T_b, 0, 0)$	4	<u>URR</u> , <u>URP</u> , <u>RR</u> [^] <u>U</u>
10	$G_{F12}^II(R_x, R_\beta, R_\lambda, 0, 0, 0)$	3	<u>S</u> , <u>RRR</u>
11	$G_{F14}^II(R_x, R_\beta, T_a, 0, 0, 0)$	3	<u>UP</u> , <u>RRP</u>
12	$G_{F16}^II(R_x, T_a, T_b, 0, 0, 0)$	3	<u>RPP</u> , <u>R</u> [^] <u>U</u> , <u>RRR</u>
13	$G_{F18}^II(R_x, R_\beta, 0, 0, 0, 0)$	2	<u>U</u> , <u>RR</u>
14	$G_{F21}^II(R_x, 0, 0, 0, 0, 0)$	1	<u>R</u>

6 Examples of Synthesis Results

Here several typical examples of the two primary types (i.e., type R and T) are illustrated and compared with some real robots to show the validity of the synthesis methodology.

For each limb expression in Sect. 4, take the corresponding kinematic form in Sect. 5 to get a final type of walking robot leg.

Three actuators distributed on each parallel limb perform as muscles in Fig. 2. The authors’ research team has realize a six-legged robot prototype using this kind of leg type [6].



Fig. 2 Leg model of R-P in 3-active-parallel limbs and the six-legged robot

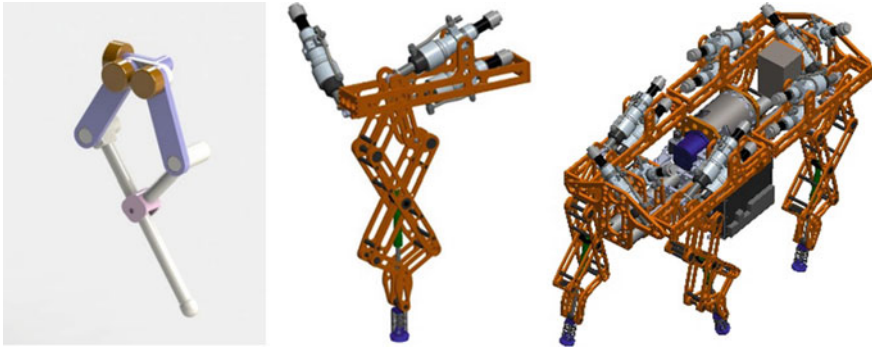


Fig. 3 Leg model of 3-DoF hybrid limb and the quadruped BabyElephant

The parallel revolute pairs are used to create the derivative translational characteristics in the sagittal plane in Fig. 3. The authors' research team has realized a quadruped prototype using this kind of leg [3]. Additional parallel links are used to increase the planer rigidity.

7 Conclusions

- (1) Robot legs of Type R fits omnidirectional moving platforms while type T plays a role of biomimetic mechanism. This classification of walking robot legs could fulfill the vast majority of leg functions in the up-to-date researches.
- (2) Number synthesis in GF set theory could be decomposed into two linear Diophantine Equations, which is never studied in the precious literatures.
- (3) Design results are illustrated with several robot models and real prototypes. The practical validity of the systematic design method is shown by these robots.

Acknowledgments Supported by National Basic Research Program of China (973 Program, Grant No. 2013CB035501).

References

1. Playter R, Buehler M, Raibert M (2006) BigDog. In: Defense and security symposium. International Society for Optics and Photonics, pp 62302O–62302O-6
2. Raibert M, Blankespoor K, Nelson G et al (2008) Bigdog, the rough-terrain quadruped robot. Proc 17th World Congress 17(1):10822–10825
3. Chen X, Gao F, Qi C et al (2014) Spring parameters design for the new hydraulic actuated quadruped robot. J Mech Robot 6(2):021003

4. Chen X, Gao F, Qi C et al (2015) Gait planning for a quadruped robot with one faulty actuator. *Chin J Mech Eng* 28(1):11–19
5. Pan Y, Gao F (2013) A new 6-parallel-legged walking robot for drilling holes on the fuselage. *Proc Inst Mech Eng, Part C: J Mech Eng Sci* 0954406213489068
6. Pan Y, Gao F (2013) Payload capability analysis of a new kind of parallel leg hexapod walking robot. In 2013 International conference on advanced mechatronic systems (ICAMechS). IEEE, pp 541–544
7. Pan Y, Gao F, Qi C et al (2016) Human-tracking strategies for a six-legged rescue robot based on distance and view. *Chin J Mech Eng* 1–12
8. Chen D, Liu Q, Dong L et al (2014) Effect of spine motion on mobility in quadruped running. *Chin J Mech Eng* 27(6):1150–1156
9. Lei J, Yu H, Wang T (2016) Dynamic bending of bionic flexible body driven by pneumatic artificial muscles (PAMs) for spinning gait of quadruped robot. *Chin J Mech Eng* 29(1):11–20
10. Quinn RD, Nelson GM, Bachmann RJ et al (2001) Insect designs for improved robot mobility. *Climbing Walk Robots: Biol Ind Appl* 59
11. Gao F, Zhang Y, Li W (2005) Type synthesis of 3-DOF reducible translational mechanisms. *Robotica* 23(02):239–245
12. Meng X, Gao F, Yang J (2012) The GF sets: a new kind of performance criterion of mechanisms. In: ASME 2012 international design engineering technical conferences and computers and information in engineering conference. American Society of Mechanical Engineers, pp 559–564
13. Yang P, Gao F (2012). Kinematical model and topology patterns of a new 6-parallel-legged walking robot. In: ASME 2012 international design engineering technical conferences and computers and information in engineering conference. American Society of Mechanical Engineers, pp 1197–1205
14. He J, Gao F, Meng X et al (2015) Type synthesis for 4-DOF parallel press mechanism using GF set theory. *Chin J Mech Eng* 28(4):851–859
15. Raibert MH, Brown HB, Chepponis M (1984) Experiments in balance with a 3D one-legged hopping machine. *Int J Robot Res* 3(2):75–92
16. Raibert MH (1990) Trotting, pacing and bounding by a quadruped robot. *J Biomech* 23:7983–8198
17. Semini C, Tsagarakis NG, Guglielmino E et al (2011) Design of HyQ—a hydraulically and electrically actuated quadruped robot. *Proc Inst Mech Eng, Part I: J Syst Control Eng* 0959651811402275
18. Meng X, Gao F, Ge QJ (2014) Number synthesis of parallel robotic mechanisms. *Mech Based Design Struct Mach* 42(2):211–228

POC Analysis of Parallel Mechanisms Based on Conformal Geometric Algebra Description Method

Chengwei Shen and Lubin Hang

Abstract Conformal geometric algebra (CGA), as an effective mathematical tool for geometric representation and computation, is introduced to position and orientation characteristics (POC) analysis of parallel mechanisms (PMs) in this paper. A group of six bivectors are derived in 5-dimensional conformal space to describe the joint axes and applied as independent bases to operation of mechanisms characteristics. Based on this, the POC and motion output characteristics of PMs can be obtained by the symbolic operation. Two types of PMs are analyzed by using this proposed method which shows conciseness and intuition.

Keywords Conformal geometric algebra · Position and orientation characteristics · Parallel mechanisms

1 Introduction

Over the past years, there have been a series of methods for type synthesis of parallel mechanisms (PMs). Huang [1–3] defines the mechanism constraint system and the limb constraint system based on the reciprocal screw theory and proposes the constraint-synthesis method for type synthesis of PMs. Hervé et al. [4, 5] introduce the Lie group algebraic structure of the set of rigid-body displacements to analysis of mechanisms and the full-cycle PMs can be obtained by the method based on the displacement subgroup. Gogu [6, 7] researches into the type synthesis with the linear transformation from the input space to the output space. Position and orientation characteristics (POC) sets [8–10] can be used to describe relative motion characteristics of any two mechanical links. It is critical to describe POC of parallel mechanisms (PMs) using an appropriate mathematical tool for application to the automatic derivation of type synthesis.

C. Shen · L. Hang (✉)

Shanghai University of Engineering Science, Shanghai, China
e-mail: hanglb@126.com

For the computerization of type synthesis, Gao [11] has developed an integrated software based on the GF sets. Ding [12] presents the character strings to represent the complete topological information of PMs for computer processing of type synthesis of both symmetrical and asymmetrical 5-DOF PMs. To describe the topological structure of mechanisms for the operation of synthesis, some other mathematical tools have been introduced in recent years. Grassmann-Cayley algebra [13, 14] is applied to singularity analysis of some types of PMs. Li [15] adopts the twists in the form of geometric algebra to describe the branches of PMs and proposes a mobility analysis approach for limited-DOF PMs based on the outer product operation. Husty et al. [16] introduce an algebraic approach via Study's kinematic mapping of the Euclidean group to reveal global kinematic behavior properties of 3-RPS parallel manipulator.

Conformal geometric algebra (CGA) [17], an effective mathematical tool for geometric representation and computation, has been widely applied in the field of robotics [18–20]. Still, CGA is rarely used for structure analysis of robot mechanisms. Based on the 3-dimensional Euclidean basis vectors $\{e_1, e_2, e_3\}$ and two additional basis vectors, $\{e_0\}$ representing the origin and $\{e_\infty\}$ representing the infinity, a group of bivectors $\{e_{23}, e_{31}, e_{12}, e_{1\infty}, e_{2\infty}, e_{3\infty}\}$ in 5-dimensional conformal space is derived and applied as the independent bases for the description and operation of joint axes in this paper. The union of each joint's characteristics is defined by the outer product operation for serial kinematic chains and the intersection of each limb's characteristics is defined by the shuffle product operation for parallel kinematic chains. Two parallel mechanisms' position and orientation characteristics are analyzed by this method, which shows conciseness and intuition.

2 POC Description Based on CGA

2.1 5-Dimensional Conformal Space

The fundamental operator in geometric algebra (GA) is geometric product [21], containing inner product and outer product, which can be expressed as

$$ab = a \cdot b + a \wedge b \quad (1)$$

As for the 3-dimensional Euclidean space \mathbf{R}^3 , it has a group of orthogonal basis vectors $\{e_1, e_2, e_3\}$. Here, we focus on the 5-dimensional conformal space that can be established via introducing two additional orthogonal basis vectors $\{e_+, e_-\}$ with positive and negative signature in Minkowski space to \mathbf{R}^3 , which is called as $\mathbf{G}^{4,1}$. These two additional vectors have the following properties

$$e_+^2 = 1, e_-^2 = -1, e_+ \cdot e_- = 0 \quad (2)$$

Another group of basis vectors $\{e_0, e_\infty\}$ with geometric meaning [22] can be defined as

$$e_0 = \frac{1}{2}(e_- - e_+), e_\infty = e_- + e_+ \tag{3}$$

where e_0 represents the 3-dimensional origin and e_∞ represents the infinity.

According to the above definition, $\{e_1, e_2, e_3, e_0, e_\infty\}$ is a group of basis vectors which forms the 5-dimensional conformal space and these five basis vectors have the following relation

$$e_1^2 = e_2^2 = e_3^2 = 1, e_0^2 = e_\infty^2 = 0, e_0 \cdot e_\infty = -1 \tag{4}$$

There are two representations of geometric entities in CGA [23], one is based on the inner product null space and the other is on the outer product null space. These two representations can be transformed each other by the dualization operator “*”, which can be expressed as

$$A^* = AI^{-1} = -AI = -A(e_0 \wedge e_1 \wedge e_2 \wedge e_3 \wedge e_\infty) \tag{5}$$

where I refers to the pseudoscalar of the whole 5-dimensional space.

Based on the inner product null space, the arbitrary plane can be described as

$$\pi_i = a_i e_1 + b_i e_2 + c_i e_3 + d_i e_\infty \tag{6}$$

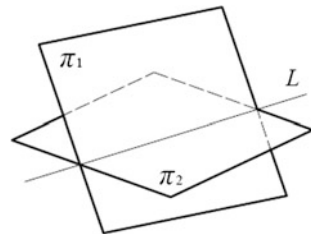
where (a_i, b_i, c_i) refers to the 3D normal vector of the plane π_i and d_i refers to the distance from the plane π_i to the origin. The line L can be generated by the intersection of two planes π_1 and π_2 via the outer product, as shown in Fig. 1, which is expressed as

$$L = (a_1 e_1 + b_1 e_2 + c_1 e_3 + d_1 e_\infty) \wedge (a_2 e_1 + b_2 e_2 + c_2 e_3 + d_2 e_\infty) \tag{7}$$

Furthermore, a line L in 5-dimensional conformal space can be define by

$$L = \alpha e_{23} + \beta e_{31} + \gamma e_{12} + p e_{1\infty} + q e_{2\infty} + r e_{3\infty} \tag{8}$$

Fig. 1 Line of intersection of planes



where the vector (α, β, γ) means the Euclidean direction of the line and (p, q, r) is the movement vector, which have the algebraic relation

$$\alpha \cdot p + \beta \cdot q + \gamma \cdot r = 0 \tag{9}$$

In Eq. (8), the e_{ij} refers to the 2-blade, which denotes the 2-dimensional plane that is directional but formless.

Based on the above derivation in 5-dimensional conformal space, any line can be identified by using these six 2-blades or bivectors $\{e_{23}, e_{12}, e_{31}, e_{1\infty}, e_{2\infty}, e_{3\infty}\}$ with $\{e_{23}, e_{12}, e_{31}\}$ for the orientation and $\{e_{1\infty}, e_{2\infty}, e_{3\infty}\}$ for the position. To extend this description of line to the joint axis and indicate the motion output characteristics of the moving link of the kinematic joint, these six bivectors can be applied as a group of independent bases, which constructs a new space and the pseudoscalar of this space can be expressed as

$$J = e_{23} \wedge e_{31} \wedge e_{12} \wedge e_{1\infty} \wedge e_{2\infty} \wedge e_{3\infty} \tag{10}$$

2.2 Description of Joint Axes

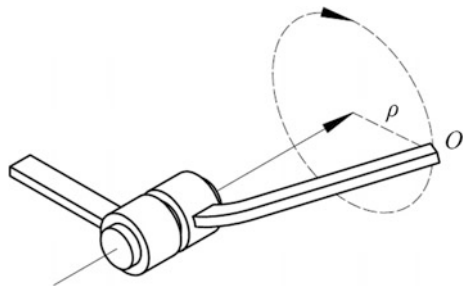
Based on the basis vectors of 5-dimensional conformal geometric algebra and the inner product expression of line, a group of unified basis bivectors $\{e_{23}, e_{31}, e_{12}, e_{1\infty}, e_{2\infty}, e_{3\infty}\}$ which can describe the POC of revolute and prismatic joint axes individually is proposed.

Revolute joint axis. The revolute joint is illustrated in Fig. 2. Point O on the moving link is chosen as origin e_0 . From the line definition using conformal geometric algebra, the axis l_R of a revolute joint can be described as

$$l_R = \alpha e_{23} + \beta e_{31} + \gamma e_{12} + p e_{1\infty} + q e_{2\infty} + r e_{3\infty} \tag{11}$$

where $\alpha e_{23} + \beta e_{31} + \gamma e_{12}$ means the moving link has one rotation around the axis of R pair and $p e_{1\infty} + q e_{2\infty} + r e_{3\infty}$ means the moving link also has a derivative translation perpendicular to the axis of R pair and radius vector ρ , i.e., $(p, q, r) = (\alpha, \beta, \gamma) \times \rho$.

Fig. 2 Revolute joint



In addition, the POC matrix of R pair can be defined as

$$M_R|_{CGA} = \begin{bmatrix} \alpha e_{23} + \beta e_{31} + \gamma e_{12} \\ \{pe_{1\infty} + qe_{2\infty} + re_{3\infty}\} \end{bmatrix} \text{ or } M_R|_{CGA} = \begin{bmatrix} \{\alpha e_{23} + \beta e_{31} + \gamma e_{12}\} \\ pe_{1\infty} + qe_{2\infty} + re_{3\infty} \end{bmatrix} \tag{12}$$

where {} refers to dependent motion.

Prismatic joint axis. The prismatic joint is illustrated in Fig. 3. Point O on the moving link is chosen as origin e_0 . The moving link can only translate without rotation, so its axis can be described by above three position bivectors as

$$l_P = le_{1\infty} + me_{2\infty} + ne_{3\infty} \tag{13}$$

where (l, m, n) refers to direction of P pair in Euclidean space and $l^2 + m^2 + n^2 = 1$. Furthermore, the POC matrix of P pair can be defined as

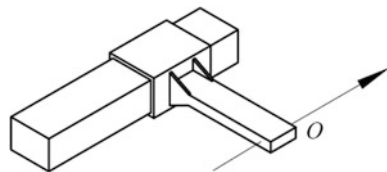
$$M_P|_{CGA} = \begin{bmatrix} 0 \\ le_{1\infty} + me_{2\infty} + ne_{3\infty} \end{bmatrix} \tag{14}$$

The position and orientation characteristics of the joint axis are corresponding to the motion output characteristics of the moving link, i.e., the expression of revolute joint axis indicates the rotation and dependent translation of its moving link, the expression of prismatic joint axis indicates the translation of its moving link. Generally speaking, the rotational link can be described by the line consisting of six bases $\{e_{23}, e_{12}, e_{31}, e_{1\infty}, e_{2\infty}, e_{3\infty}\}$ while the translational link can be described by the orientation consisting of three bases $\{e_{1\infty}, e_{2\infty}, e_{3\infty}\}$, once the origin e_0 is chosen.

2.3 Algorithm for Parallel Mechanisms

POC union for serial kinematic chains. For the serial kinematic chains, the motion output characteristics of the end-effector can be regarded as composition of position and orientation characteristics of every joint, which means the POC of the end-effector is the union of all of the joints' POC. The union of any two vectors

Fig. 3 Prismatic joint



A and B can be performed via the outer product [23], so the POC union of all joints' blades is defined as

$$\mathbf{M}_S|_{\text{CGA}} = \bigwedge_{i=1}^m \mathbf{M}_{J_i}|_{\text{CGA}} \quad (15)$$

where $\mathbf{M}_S|_{\text{CGA}}$ is the end-effector's POC blade in the form of CGA and $\mathbf{M}_{J_i}|_{\text{CGA}}$ is the set of the i th joint's POC blade in the form of CGA. Equation (15) is the equation of POC union for serial kinematic chains. Under these circumstances, the union for the serial mechanism is accomplished by the outer product operation and the result should be a polynomial of blades composed of proposed bases connected by “ \wedge ”s and “+”s.

POC intersection for parallel kinematic chains. A typical parallel mechanism has a base and a moving platform connected in parallel by several limbs. The movement of the moving platform is constrained by individual limbs. For the parallel kinematic chains, the motion output characteristics of the moving platform are the intersection of all limbs' characteristics and each limb can be considered as a serial kinematic chain. The intersection of any two vectors A and B is defined as the shuffle product [24], which can be obtained as

$$\mathbf{A} \vee \mathbf{B} = (\mathbf{A}^* \wedge \mathbf{B}^*) \mathbf{J}_{AB} \quad (16)$$

where \mathbf{J}_{AB} refers to the maximum subspace constructed by the bases belong to A and B . The operation of \mathbf{A}^* and \mathbf{B}^* is same as Eq. (10), which can be expressed as

$$\begin{cases} \mathbf{A}^* = \mathbf{A} \mathbf{J}_{AB}^{-1} = -\mathbf{A} \mathbf{J}_{AB} \\ \mathbf{B}^* = \mathbf{B} \mathbf{J}_{AB}^{-1} = -\mathbf{B} \mathbf{J}_{AB} \end{cases} \quad (17)$$

The POC intersection of all limbs' blades is defined as

$$\mathbf{M}_{Pa}|_{\text{CGA}} = \bigvee_{j=1}^n \mathbf{M}_{S_j}|_{\text{CGA}} \quad (18)$$

where $\mathbf{M}_{Pa}|_{\text{CGA}}$ is the moving platform's POC blade in the form of CGA and $\mathbf{M}_{S_j}|_{\text{CGA}}$ is the j th limb's POC blade in the form of CGA. Equation (18) is the equation of POC intersection for parallel kinematic chains.

According to Eq. (18), the motion output characteristics of the moving platform of parallel mechanism, or the intersection of limbs' motion output characteristics, can be obtained through the shuffle product operation. This direct symbolic computation avoids the geometric related operations that are required in the method based on POC sets. Corresponding to mechanism and machine theory, the pseudoscalar operated in Eq. (18) should be the maximal dimensional blade spanned by all limbs' POC blades.

3 3-RRC Parallel Mechanism

A type of 3-RRC parallel mechanism, as is shown in Fig. 4, is composed of a base and a moving platform connected by three RRC limbs. For each limb, the axes of R_{i1} , R_{i2} and C_{i3} are parallel to each other. The R_{11} and R_{12} joints located on the base are orthogonal, and so are the C_{13} and C_{23} joints located on the moving platform.

Establish the moving coordinate system. A moving coordinate system is created so that the origin e_0 is chosen at the intersection of axes of C_{13} and C_{23} joints. The axis e_1 coincides with the axis C_{13} and the axis e_2 coincides with the axis C_{23} , respectively.

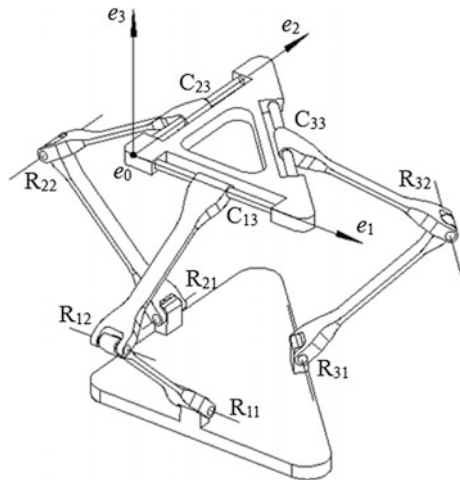
Obtain the POC blades of each limb. The POC blades of each limb should be the outer product of POC blades of every joint, which can expressed as

$$M_{S_i}|_{CGA} = M_{R_{i1}}|_{CGA} \wedge M_{R_{i2}}|_{CGA} \wedge M_{C_{i3}}|_{CGA} \tag{19}$$

According to the POC blades of R and P joint, Eq. (19) can be obtained as

$$\begin{cases} M_{S_1}|_{CGA} = (e_{23} + q_{11}e_{2\infty} + r_{11}e_{3\infty}) \wedge (e_{23} + q_{12}e_{2\infty} + r_{12}e_{3\infty}) \wedge e_{23} \wedge e_{1\infty} \\ M_{S_2}|_{CGA} = (e_{31} + p_{21}e_{1\infty} + r_{21}e_{3\infty}) \wedge (e_{31} + p_{22}e_{1\infty} + r_{22}e_{3\infty}) \wedge e_{31} \wedge e_{2\infty} \\ M_{S_3}|_{CGA} = (\alpha_{31}e_{23} + \beta_{31}e_{31} + p_{31}e_{1\infty} + q_{31}e_{2\infty} + r_{21}e_{3\infty}) \\ \quad \wedge (\alpha_{31}e_{23} + \beta_{31}e_{31} + p_{32}e_{1\infty} + q_{32}e_{2\infty} + r_{32}e_{3\infty}) \wedge (\alpha_{31}e_{23} + \beta_{31}e_{31}) \\ \quad \wedge (\alpha_{31}e_{1\infty} + \beta_{31}e_{1\infty}) \end{cases} \tag{20}$$

Fig. 4 3-RCC parallel mechanism



Coefficients in Eq. (20) are related to position and orientation of joints axes. Calculating Eq. (20) and neglecting the solar coefficients, then

$$\begin{cases} \mathbf{M}_{S_1}|_{CGA} = \mathbf{e}_{23} \wedge \mathbf{e}_{1\infty} \wedge \mathbf{e}_{2\infty} \wedge \mathbf{e}_{3\infty} \\ \mathbf{M}_{S_2}|_{CGA} = \mathbf{e}_{31} \wedge \mathbf{e}_{1\infty} \wedge \mathbf{e}_{2\infty} \wedge \mathbf{e}_{3\infty} \\ \mathbf{M}_{S_3}|_{CGA} = \mathbf{e}_{23} \wedge \mathbf{e}_{1\infty} \wedge \mathbf{e}_{2\infty} \wedge \mathbf{e}_{3\infty} + \mathbf{e}_{31} \wedge \mathbf{e}_{1\infty} \wedge \mathbf{e}_{2\infty} \wedge \mathbf{e}_{3\infty} \end{cases} \quad (21)$$

Establish the POC equation of parallel mechanism. The POC blade of the moving platform is the intersection of those of three limbs, which can be obtained according to the shuffle product mentioned in Eq. (18) as

$$\begin{aligned} \mathbf{M}_{Pa}|_{CGA} &= \mathbf{M}_{S_1}|_{CGA} \vee \mathbf{M}_{S_2}|_{CGA} \vee \mathbf{M}_{S_3}|_{CGA} \\ &= \mathbf{M}_{S_1}|_{CGA} \vee \mathbf{M}_{S_2}|_{CGA} \vee (\mathbf{M}_{S_1}|_{CGA} + \mathbf{M}_{S_2}|_{CGA}) \\ &= \mathbf{M}_{S_1}|_{CGA} \vee \mathbf{M}_{S_2}|_{CGA} \vee \mathbf{M}_{S_1}|_{CGA} + \mathbf{M}_{S_1}|_{CGA} \vee \mathbf{M}_{S_2}|_{CGA} \vee \mathbf{M}_{S_2}|_{CGA} \end{aligned} \quad (22)$$

The shuffle product of vectors means the intersection of them in the topological space, so the POC equation of this PM in the description of CGA can be described as

$$\mathbf{M}_{Pa}|_{CGA} = \mathbf{M}_{S_1}|_{CGA} \vee \mathbf{M}_{S_2}|_{CGA} \quad (23)$$

Obtain POC blade of the moving platform. Based on the blades of $\mathbf{M}_{S_1}|_{CGA}$ and $\mathbf{M}_{S_2}|_{CGA}$, the maximal dimensional blade \mathbf{J} spanned by them should be composed of \mathbf{e}_{23} , \mathbf{e}_{31} , $\mathbf{e}_{1\infty}$, $\mathbf{e}_{2\infty}$ and $\mathbf{e}_{3\infty}$, which can be expressed as

$$\mathbf{J} = \mathbf{e}_{23} \wedge \mathbf{e}_{31} \wedge \mathbf{e}_{1\infty} \wedge \mathbf{e}_{2\infty} \wedge \mathbf{e}_{3\infty} \quad (24)$$

Then the dualization of $\mathbf{M}_{S_1}|_{CGA}$ and $\mathbf{M}_{S_2}|_{CGA}$ can be obtained as

$$\begin{cases} \mathbf{M}_{S_1}^*|_{CGA} = -\mathbf{M}_{S_1}|_{CGA}(\mathbf{e}_{23} \wedge \mathbf{e}_{31} \wedge \mathbf{e}_{1\infty} \wedge \mathbf{e}_{2\infty} \wedge \mathbf{e}_{3\infty}) = \mathbf{e}_{31} \\ \mathbf{M}_{S_2}^*|_{CGA} = -\mathbf{M}_{S_2}|_{CGA}(\mathbf{e}_{23} \wedge \mathbf{e}_{31} \wedge \mathbf{e}_{1\infty} \wedge \mathbf{e}_{2\infty} \wedge \mathbf{e}_{3\infty}) = -\mathbf{e}_{23} \end{cases} \quad (25)$$

According to Eq. (16), Eq. (23) can be obtained by

$$\mathbf{M}_{Pa}|_{CGA} = (\mathbf{e}_{31} \wedge (-\mathbf{e}_{23}))(\mathbf{e}_{23} \wedge \mathbf{e}_{31} \wedge \mathbf{e}_{1\infty} \wedge \mathbf{e}_{2\infty} \wedge \mathbf{e}_{3\infty}) \quad (26)$$

The POC blade of the moving platform can be expressed as

$$\mathbf{M}_{Pa}|_{CGA} = \mathbf{e}_{1\infty} \wedge \mathbf{e}_{2\infty} \wedge \mathbf{e}_{3\infty} \quad (27)$$

Its POC matrix is

$$M_{Pa}|_{CGA} = \begin{bmatrix} 0 \\ \mathbf{e}_{1\infty} \wedge \mathbf{e}_{2\infty} \wedge \mathbf{e}_{3\infty} \end{bmatrix} \tag{28}$$

The result contains three translation bases connected by “ \wedge ”, which indicates that the moving platform of the 3-RRC parallel mechanism has three independent translation or full translation capability and no rotation.

4 3-RCRR Parallel Mechanism

The 3-RCRR parallel mechanism that nine joints (including C_{i2} , R_{i3} and R_{i4} , $i = 1, 2, 3$) intersect at a common point, and three R joints located on the base are perpendicular to the plane of the base and parallel to each other, which shown as Fig. 5.

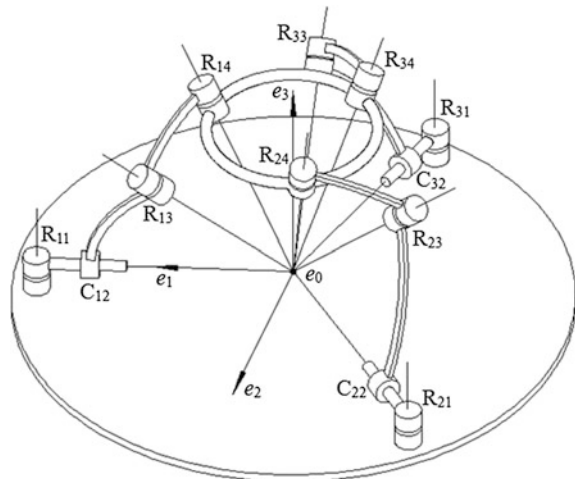
Establish the moving coordinate system. The intersection point of the axes of nine joints is selected as the origin e_0 and a moving coordinate system is established so that the axis e_1 coincides with the axis of C_{12} pair and the axis e_3 is perpendicular to the plane of the moving platform.

Obtain the POC blades of each limb. For the first limb $R_{11}C_{12}R_{13}R_{14}$, the POC blades of these three kinematic pairs can be expressed as

$$\begin{cases} M_{R_{11}}|_{CGA} = \mathbf{e}_{12} + q_{11}\mathbf{e}_{2\infty} \\ M_{C_{12}}|_{CGA} = \mathbf{e}_{23} \wedge \mathbf{e}_{1\infty} \\ M_{R_{13}}|_{CGA} = \alpha_{13}\mathbf{e}_{23} + \beta_{13}\mathbf{e}_{31} + \gamma_{13}\mathbf{e}_{12} \\ M_{R_{14}}|_{CGA} = \alpha_{14}\mathbf{e}_{23} + \beta_{14}\mathbf{e}_{31} + \gamma_{14}\mathbf{e}_{12} \end{cases} \tag{29}$$

where q_{11} is related to the position of R_{11} joint, $(\alpha_{13}, \beta_{13}, \gamma_{13})$ and $(\alpha_{14}, \beta_{14}, \gamma_{14})$ are the directional vectors of R_{13} and R_{14} joint axes, respectively. The POC blade of

Fig. 5 3-RCRR parallel mechanism



$R_{11}C_{12}R_{13}R_{14}$ is the outer product of each joint, neglecting the coefficient, which can be obtained as

$$\mathbf{M}_{S_1}|_{CGA} = \mathbf{e}_{23} \wedge \mathbf{e}_{31} \wedge \mathbf{e}_{12} \wedge \mathbf{e}_{1\infty} \wedge \mathbf{e}_{2\infty} \quad (30)$$

Similarly, the POC blades of other two limbs can be expressed as

$$\begin{cases} \mathbf{M}_{R_{21}}|_{CGA} = \mathbf{e}_{12} + p_{21}\mathbf{e}_{1\infty} + q_{21}\mathbf{e}_{2\infty} \\ \mathbf{M}_{C_{22}}|_{CGA} = (\alpha_{22}\mathbf{e}_{23} + \beta_{22}\mathbf{e}_{31}) \wedge (\alpha_{22}\mathbf{e}_{1\infty} + \beta_{22}\mathbf{e}_{2\infty}) \\ \mathbf{M}_{R_{23}}|_{CGA} = \alpha_{23}\mathbf{e}_{23} + \beta_{23}\mathbf{e}_{31} + \gamma_{23}\mathbf{e}_{12} \\ \mathbf{M}_{R_{24}}|_{CGA} = \alpha_{24}\mathbf{e}_{23} + \beta_{24}\mathbf{e}_{31} + \gamma_{24}\mathbf{e}_{12} \end{cases} \quad (31)$$

and

$$\begin{cases} \mathbf{M}_{R_{31}}|_{CGA} = \mathbf{e}_{12} + p_{31}\mathbf{e}_{1\infty} + q_{31}\mathbf{e}_{2\infty} \\ \mathbf{M}_{C_{32}}|_{CGA} = (\alpha_{32}\mathbf{e}_{23} + \beta_{32}\mathbf{e}_{31}) \wedge (\alpha_{32}\mathbf{e}_{1\infty} + \beta_{32}\mathbf{e}_{2\infty}) \\ \mathbf{M}_{R_{33}}|_{CGA} = \alpha_{33}\mathbf{e}_{23} + \beta_{33}\mathbf{e}_{31} + \gamma_{33}\mathbf{e}_{12} \\ \mathbf{M}_{R_{34}}|_{CGA} = \alpha_{34}\mathbf{e}_{23} + \beta_{34}\mathbf{e}_{31} + \gamma_{34}\mathbf{e}_{12} \end{cases} \quad (32)$$

Coefficients in Eqs. (31) and (32) are related to position and orientation of joints axes. Then the POC blades of $R_{21}C_{22}R_{23}R_{24}$ and $R_{21}C_{22}R_{23}R_{24}$ can be obtained as

$$\mathbf{M}_{S_2}|_{CGA} = \mathbf{M}_{S_3}|_{CGA} = \mathbf{e}_{23} \wedge \mathbf{e}_{31} \wedge \mathbf{e}_{12} \wedge \mathbf{e}_{1\infty} \wedge \mathbf{e}_{2\infty} \quad (33)$$

Establish the POC equation of parallel mechanism. The POC blade of the moving platform is shuffle product of POC blades of every limb, which can be expressed as

$$\mathbf{M}_{Pa}|_{CGA} = \mathbf{M}_{S_1}|_{CGA} \vee \mathbf{M}_{S_2}|_{CGA} \vee \mathbf{M}_{S_3}|_{CGA} \quad (34)$$

Obtain POC blade of the moving platform. In Eqs. (30) and (33), the POC blades of each limb are equal, so the result of Eq. (34) can be obtained without the selection of the maximal dimensional blade \mathbf{J} , which can be expressed as

$$\mathbf{M}_{Pa}|_{CGA} = \mathbf{e}_{23} \wedge \mathbf{e}_{31} \wedge \mathbf{e}_{12} \wedge \mathbf{e}_{1\infty} \wedge \mathbf{e}_{2\infty} \quad (35)$$

The POC matrix of the moving platform is

$$\mathbf{M}_{Pa}|_{CGA} = \begin{bmatrix} \mathbf{e}_{23} \wedge \mathbf{e}_{31} \wedge \mathbf{e}_{12} \\ \mathbf{e}_{1\infty} \wedge \mathbf{e}_{2\infty} \end{bmatrix} \quad (36)$$

The result contains five independent bases that three are rotation bases and other two are translation bases, which indicates that the moving platform of 3-RCRR PM can realize full rotation and two independent translation, which are situated on the plane of the base.

5 Conclusions

In this paper, a group of basis bivectors $\{e_{23}, e_{31}, e_{12}, e_{1\infty}, e_{2\infty}, e_{3\infty}\}$ which can describe position and orientation of revolute and prismatic joint axes individually is proposed. The motion characteristics of the moving link is described via the proposed basis bivector. The union and intersection operation of topological space are extended to position and orientation characteristics analysis of the kinematic chains. Two types of parallel mechanisms are analyzed by this method, which shows that this makes the description and derivation of POC for serial and parallel mechanisms more concise and intuitive. Due to the unity of this group of basis bivectors, they can be further applied to rigid body motion and kinematics analysis.

Acknowledgments The authors would like to acknowledge the financial support of the Natural Science Foundation of China (NSFC) under Grant 51475050 and also thank the reviewers for their suggestions and comments, which have helped to improve the quality of this paper.

References

1. Huang Z, Li Q (2002) General methodology for type synthesis of symmetrical lower-mobility parallel manipulators and several novel manipulators. *Int J Robot Res* 21(2):131–145
2. Huang Z, Li Q (2002) Type synthesis principle of minor-mobility parallel manipulators. *Sci China Ser E: Technol Sci* 45(3):241–248
3. Huang Z, Li Q (2003) Type synthesis of symmetrical lower-mobility parallel mechanisms using the constraint-synthesis method. *Int J Robot Res* 22(1):59–79
4. Hervé JM (1999) The Lie group of rigid body displacements, a fundamental tool for mechanism design. *Mech Mach Theory* 34(5):719–730
5. Li Q, Huang Z, Hervé JM (2004) Displacement manifold method for type synthesis of lower-mobility parallel mechanisms. *Sci China Ser E: Technol Sci* 47(6):641–650
6. Gogu G (2004) Structural synthesis of fully-isotropic translational parallel robots via theory of linear transformations. *Eur J Mech-A/Solids* 23(6):1021–1039
7. Gogu G (2005) Mobility and spatiality of parallel robots revisited via theory of linear transformations. *Eur J Mech-A/Solids* 24(4):690–711
8. Jin Q, Yang TL (2004) Theory for topology synthesis of parallel manipulators and its application to three-dimension-translation parallel manipulators. *J Mech Des* 126(4):625–639
9. Yang TL, Liu AX, Luo YF, Shen HP, Hang LB (2009) Position and orientation characteristic equation for topological design of robot mechanisms. *J Mech Des* 131(2):021001
10. Yang TL, Liu AX, Luo YF, Shen HP, Hang LB, Jin Q (2012) Theory and application of robot mechanism topology. Science Press, Beijing
11. Meng X, Gao F (2014) A framework for computer-aided type synthesis of parallel robotic mechanisms. *Proc Inst Mech Eng, Part C: J Mech Eng Sci* 228(18):3496–3504
12. Ding H, Cao W, Cai C, Kecskeméthy A (2015) Computer-aided structural synthesis of 5-DOF parallel mechanisms and the establishment of kinematic structure databases. *Mech Mach Theory* 83:14–30
13. Ben-Horin P, Shoham M (2009) Application of Grassmann-Cayley algebra to geometrical interpretation of parallel robot singularities. *International J Robot Res* 28(1):127–141
14. Amine S, Masouleh MT, Caro S, Wenger P, Gosselin C (2012) Singularity analysis of 3T2R parallel mechanisms using Grassmann-Cayley algebra and Grassmann geometry. *Mech Mach Theory* 52:326–340

15. Li Q, Chai X (2015) Mobility analysis of limited-DOF parallel mechanisms in the framework of geometric algebra. *ASME J Mech Robot* 8(4):041005
16. Schadlbauer J, Walter DR, Husty ML (2014) The 3-RPS parallel manipulator from an algebraic viewpoint. *Mech Mach Theory* 75:161–176
17. Hestenes D, Li H, Rockwood A (2001) New algebraic tools for classical geometry. In: *Geometric computing with Clifford algebras*. Springer, Berlin, pp 3–26
18. Wei Y, Jian S, He S, Wang Z (2014) General approach for inverse kinematics of nR robots. *Mech Mach Theory* 75:97–106
19. Kim JS, Jeong JH, Park JH (2015) Inverse kinematics and geometric singularity analysis of a 3-SPS/S redundant motion mechanism using conformal geometric algebra. *Mech Mach Theory* 90:23–36
20. Wei F, Wei S, Zhang Y, Liao Q (2016) Algebraic solution for the forward displacement analysis of the general 6-6 Stewart mechanism. *Chin J Mech Eng* 29(1):56–62
21. Hildenbrand D, Simos TE, Psihoyios G, Tsitouras C, Anastassi Z (2013) *Foundations of geometric algebra computing*. Springer, Berlin, Germany
22. Perwass CB, Hildenbrand D (2004) *Aspects of geometric algebra in euclidean, projective and conformal space—an introductory tutorial*
23. Dorst L, Mann S (2002) *Geometric algebra: a computational framework for geometrical applications*. *IEEE Comput Graphics Appl* 22(3):24–31
24. Selig JM (2005) *Geometric fundamentals of robotics*. Springer Science & Business Media, Berlin

Type Synthesis of the Hybrid Rotary Platform Mechanism with Three Degrees of Freedom

Yundou Xu, Liangliang Chen, Wennan Yan, Bei Wang
and Yongsheng Zhao

Abstract To improve the carrying capacity, a novel hybrid mechanism for rotary platform with three degrees of freedom (DOFs) is proposed, the serial mechanism is located on the moving platform (MP) of the parallel mechanism (PM), but its actuation system are located on the base, and the rolling motion is transferred by a motion transferring chain. The constraint wrench imposed on the upper MP of the hybrid rotary platform is analyzed, the type synthesis of the motion transferring chain was carried out using the constraint-synthesis method based on reciprocal screw theory. The relationship between input of the transferring chain and output of the upper MP is established, then the principle of transferring rolling motion by the motion transferring chain is explained. Finally, based on the motion transferring chain after optimization, two hybrid mechanisms for the rotary platform with three DOFs are obtained, which can meet the demands presented above.

Keywords Type synthesis · Hybrid mechanism · Screw theory

1 Introduction

The rotary platform with three degrees of freedom (DOFs) has very large applications in many occasions, such as attitude adjustment and self-stabilizing of platforms on ships and planes, CNC rotary table, medical instruments, positioning

Y. Xu · L. Chen · W. Yan · B. Wang · Y. Zhao
Parallel Robot and Mechatronic System Laboratory of Hebei Province,
Qinhuangdao 066004, Hebei, China

Y. Zhao (✉)
Key Laboratory of Advanced Forging and Stamping Technology and
Science of Ministry of National Education, Yanshan University,
Qinhuangdao 066004, Hebei, China
e-mail: yszhao@ysu.edu.cn

of camera and telescope, as well as the position tracking of the antenna and solar [1, 2] and other fields.

In many of these occasions, the platform not only need to meet the large carrying capacity, but also require a large range of rolling, but the rotary platforms with three DOFs that meet simultaneously these two indexes are very few. Such as the 3-UPU spherical PM designed by Karouia et al. [3], the 3-RRS spherical PM designed by Di Gregorio [4], for which the condition that the axes of multiple revolute pairs intersect at a certain point should be satisfied, the 3UPS/S spherical PM proposed by Merlet [5] in his monograph, a kind of pyramid PM with three DOFs proposed by Huang et al. [6], all these mechanisms effectively increase the carrying capacity but fail to realize the large range of rolling motion. For this reason, some scholars adopt the hybrid mechanism that the PM and serial mechanism are serially connected, so as to realize the large carrying capacity and large range of rolling simultaneously, Wu et al. [7] proposed an asymmetric hybrid mechanism with three DOFs, in which the PM is the 2-RRR + RRS + RUR mechanism, and the rolling motion is realized by the revolute pair arranged over the PM; Hong et al. [8] proposed a hybrid mechanism with three DOFs, in which the PM is the 2-PUS + U mechanism, and the rolling motion is realized by the revolute pair arranged under the PM, Li [9] also used a hybrid mechanism as a heavy-load rotational swing test platform with three axes, in which the PM is the 2-UPS + RRS + S mechanism, and the rolling motion is realized by the revolute pair installed on the PM (R, P, U and S represent the revolute, prismatic, universal and spherical pairs respectively). In summary, for the above-mentioned hybrid mechanisms, either actuation system of the serial mechanism is arranged over the PM, in this case the actuation system will be the load of the PM; or the actuation system is located below the PM, in such case the whole PM will be the load of the actuation system, thus the carrying capacity of these hybrid mechanism is restrained. In view of the above statements, a novel hybrid parallel mechanism is presented to further improve the carrying capacity, in which the serial mechanism is located over the MP of the PM, but its actuation system are located on the base, and the rolling motion is transferred by a motion transferring chain, and the type synthesis of the motion transferring chain was carried out.

2 The Scheme of Hybrid Mechanism for the Rotary Platform with Three DOFs

2.1 The Selection of the PM

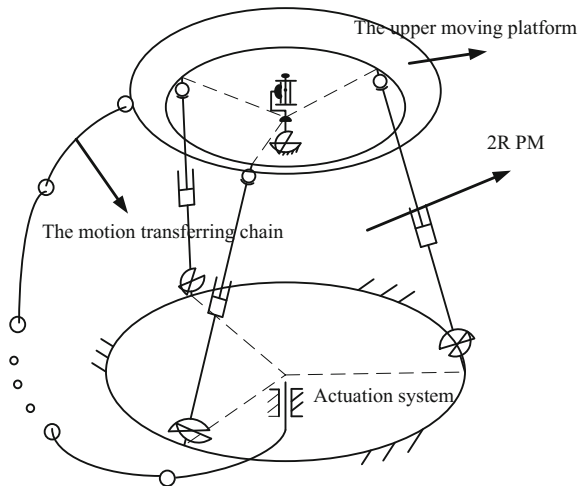
The two-rotational-degrees-of-freedom (2R) PM with two continuous rotational axes (CRAs) has a simple kinematic model. It is therefore easy to implement trajectory planning, parameter calibration, and motion control, which allows for a

very variety of application prospects, so a 2R-PM with two CRAs will be chosen to complete the yawing and pitching motion. There are two kinds of typical 2R-PMs with two CRAs, one is the two DOFs spherical PM [10, 11], the other kind of 2R-PM contains a constrained branch composed of only a U joint [12, 13]. The two DOFs spherical PM has strict assembly requirements that the axes of the revolute pair intersect at a certain point, so the 2R-PM contains a constrained branch composed of only a U joint is selected. In such mechanisms, 2UPS/U PM has the advantages of simple structure and wide application, as the specific situation of the load of the platform is uncertain when selecting of 2R-PM as a rotary simulation platform, and to avoid offset load, an UPS unconstrained branch is symmetrically arranged based on 2UPS/U PM, thus the 3UPS/U 2R-PM is obtained as the main load-bearing component, which realize the yawing and pitching motion.

2.2 The Arrangement of the Actuation System

When the PM is determined, the rolling platform is arranged at the top of the MP of the PM, and through R joints connected the MP with the rolling platform to achieve the rolling motion, while its actuation system is placed over the base and is connected with the base through R joints whose axis pass through the center of the U joints within the constrained branch of the PM, and the actuation system is connected with the rolling platform through the motion transferring chain (Fig. 1).

Fig. 1 The diagram of the novel hybrid platform mechanism



3 Type Synthesis of the Motion Transferring Chain

3.1 Introduction of the Constraint-Synthesis Method Based on Screw Theory

In the screw theory, a unit screw is given by a dual vector,

$$\mathcal{S} = [\mathcal{S}^T \quad \mathcal{S}_0^T]^T = \begin{bmatrix} \mathbf{S} \\ \mathbf{r} \times \mathbf{S} + h\mathbf{S} \end{bmatrix} \quad (1)$$

where \mathbf{S} denotes the unit vector along the screw axis, \mathbf{r} denotes the position vector of any point on the screw axis, and h is the pitch of the screw.

A screw, $\mathcal{S}_r = [\mathcal{S}_r^T \quad \mathcal{S}_{0r}^T]^T$, and a set of screws, $\mathcal{S}_1 \mathcal{S}_2 \dots \mathcal{S}_n$, are said to be reciprocal if they satisfy condition:

$$\mathcal{S}_j \circ \mathcal{S}_r = \mathcal{S}_j \cdot \mathcal{S}_{0r} + \mathcal{S}_r \cdot \mathcal{S}_{0j} = 0 \quad (j = 1, 2, \dots, n) \quad (2)$$

where “ \circ ” represents reciprocal product, and \mathcal{S}_j represents the j th screw of the screw set.

We call the screw a twist if it represents an instantaneous motion of a rigid body. We call the screw a wrench if it represents a force and a coaxial couple acting on a rigid body. The unit screw associated with a prismatic joint (P) or a couple is given by $[\mathbf{0}^T \quad \mathbf{S}^T]^T$, and the unit screw associated with a revolute joint (R) or a force is given by $[\mathcal{S}^T \quad (\mathbf{r} \times \mathbf{S})^T]^T$. Other types of joint can be formed by combining these two basic joints. For example, a spherical joint (S) is equivalent to three intersecting but not coplanar revolute joints, a cylindrical joint (C) to a prismatic joint in concentric with a revolute joint.

If a set of screws, $\mathcal{S}_1 \mathcal{S}_2 \dots \mathcal{S}_n$ represent the joint twists associated with a supporting limb of a parallel manipulator, then \mathcal{S}_r , reciprocal to the joint twists, represents the constraint wrench imposed on the moving platform by the supporting limb of the parallel manipulator. The motion of the moving platform is completely determined by combined effect of all the constraint wrenches of each limb of the parallel manipulator.

Type synthesis procedures of the constraint-synthesis method based on screw theory is given as follows. First of all, according to the required mechanism twist system, calculate the mechanism constraint system that is reciprocal to the mechanism twist system. And then determine all the limb constraint systems according to the mechanism constraint system, each limb twist system can then be obtained from the limb constraint systems correspondingly. Next, construct the limb kinematic chains according to the limb twist systems. Finally, distribute all the limb kinematic chains properly so as to guarantee that the combination of all the limb constraint systems is equal to the desired mechanism constraint system.

3.2 The Analysis of the Motion Transferring Chain

In order to achieve the yawing, pitching, and rolling three-dimension rotation movement, there are two requirements that the motion transferring chain need to satisfy:

- (1) It should follow the yawing and pitching motion of the 2R-PM;
- (2) It can transfer the rolling motion generated by the actuation system to the rolling MP of the hybrid mechanism, so as to achieve the rolling.

According to the conditions (1) and (2), based on the reciprocal screw theory, it can be obtained that the motion transferring chain can provide up to three linearly independent constrained forces which all pass through the center of the U joint within the constrained branch; According to condition (2), the transferring process of the rolling motion can be simplified as that the actuation system of the rolling mechanism outputs an actuation wrench acting on the transferring chain and generates an effective transferring wrench, thus the energy is transferred from the input to the output through transferring wrench.

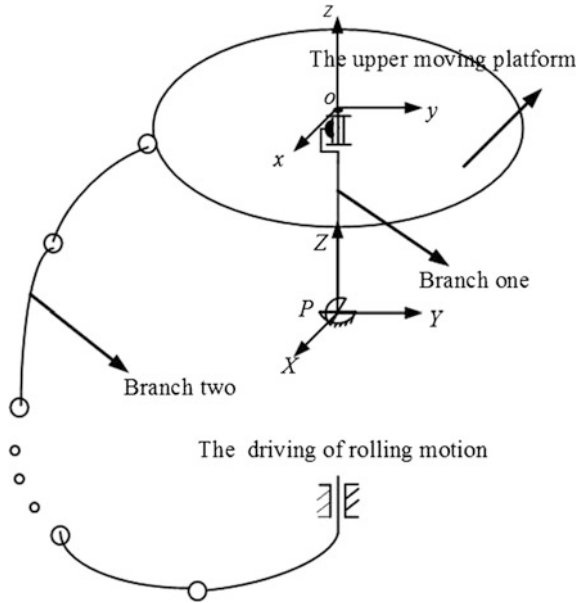
The transferring wrench of the motion transferring chain can be specifically divided into two aspects:

- (1) It is the force line vector, it exists component in the tangential direction of the rolling MP, particularly when the component is zero, the mechanism is unable to transfer the rolling motion at the instant, that is, the mechanism is in the “dead point” position;
- (2) It is the couple, according to the principle of coordinate transformation, the effect of the couple can be equivalent to the force line vector acting on the center point of the pair that connects the rolling MP and the motion transferring chain, similarly, the force line vector is decomposed in the tangential direction of the rolling MP. In brief, the transferring wrench can always be equivalent to the force line vector acting on the center point of the pair that connects the rolling MP and the motion transferring chain.

To simplify the analysis, as the UPS branch provides no constraints to the MP of the PM, the 3-UPS + U PM is equivalent to a single U pair, and the schematic diagram is shown in Fig. 2. This mechanism can be considered as a PM with two branches, one kinematic chain is composed by a U joint and an R joint, and the other is composed of the motion transferring chain.

The coordinate system of the branch: P - XYZ is established at the center point of U joint, and the coordinate system of Branch one and two are coincident, with X -axis pointing along the direction of the rotating shaft connected by the U joint within branch one to the rolling MP, and Y -axis pointing along the direction of the rotating shaft connected by the U joint within branch one to the base respectively, and the direction of Z -axis is determined by the right-hand rule. The moving coordinate system: o - xyz is established at the center of the rolling MP. In the initial state, the moving coordinate system is parallel to the coordinate system of the branch.

Fig. 2 The simplified mechanism of the hybrid platform mechanism



Based on the reciprocal screw theory, the constraint wrench imposed on the upper MP provided by the branch one can be obtained as:

$$\begin{cases} \mathcal{S}_{11}^r = (1 & 0 & 0 & 0 & 0 & 0) \\ \mathcal{S}_{12}^r = (0 & 1 & 0 & 0 & 0 & 0) \\ \mathcal{S}_{13}^r = (0 & 0 & 1 & 0 & 0 & 0) \end{cases} \quad (3)$$

As the upper MP can achieve three-dimension rotation, based on the reciprocal screw theory, the constraint force of the upper MP which all pass through the origin of coordinate system of the branch must satisfy the following formula:

$$\begin{cases} \mathcal{S}_{21}^r = (l_1 & m_1 & n_1 & 0 & 0 & 0) \\ \mathcal{S}_{22}^r = (l_2 & m_2 & n_2 & 0 & 0 & 0) \\ \mathcal{S}_{23}^r = (l_3 & m_3 & n_3 & 0 & 0 & 0) \end{cases} \quad (4)$$

where, l_i, m_i, n_i represent any nonzero constant.

Therefore, the constraint wrench imposed on the upper MP provided by the branch two can be divided into four kinds: one is providing the three linearly independent constraint force line vectors, second is providing two of the three linearly independent constraint line vectors, the third is providing one of the three linearly independent constraint line vectors, four is providing no constraints. Because when the branch provides one or two constraint force line vectors which pass through a certain point, it is complex [14], it will not be studied here. What follows is a detailed analysis about the branch two when it provides three linearly independent constraint force line vectors and provides no constraints, respectively.

3.2.1 The Branch Two Providing Three Constraints

When the constraint force line vectors provided by the branch two are $\$_{21}^r$, $\$_{22}^r$ and $\$_{23}^r$, the typical kinematic chain provides the above three constraint line vectors is the RRR spherical sub-chain, denoted as (RRR), whose axes all pass through the center of the U joint of the branch one, and the mechanism is shown in Fig. 3.

At this time, the upper MP is acted upon by six force line vectors which all pass through the center of U pair of the branch one, it can be obtained that the DOFs of the platform is three rotations.

In the same way, the branch two can complete the transmission of the rolling motion, the transferring wrench of RRR spherical sub-chain is obtained as:

$$\mathcal{S} = (0 \quad 0 \quad 0 \quad \mathbf{u}_1 \times \mathbf{u}_2) \tag{5}$$

The transferring wrench is a couple, whose axis is $\mathbf{u}_1 \times \mathbf{u}_2$, and \mathbf{u}_1 indicates the direction of the passive R pair within chain (RRR); \mathbf{u}_2 indicates the direction of the other passive R pair within chain (RRR).

The effect of the transferring couple is equivalent to the force line vector acting on the center point of the pair that connects the upper MP and the motion transferring chain. Obviously, the force line vector exists component in the tangential direction of the upper MP, and it can realize the rolling motion.

Fig. 3 The hybrid platform mechanism with (RRR) motion transferring chain

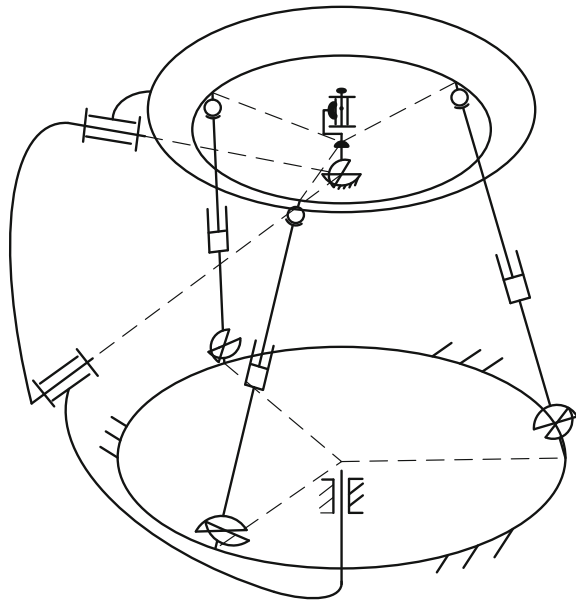
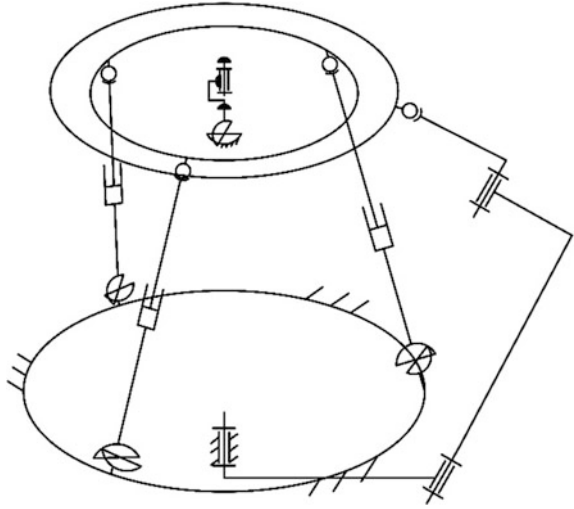


Fig. 4 The hybrid platform mechanism with RRRS motion transferring chain



3.2.2 The Branch Two Providing no Constraints

When the branch does not provide constraints, only by changing the types, the order of arrangement and the axes of joints in any branch with six DOFs, at the same time maintaining six independent DOFs, the unconstrained chains can be obtained. The RRRS branch is the typical and relatively simple kind of branch, in which the axis of the first R joint coincide with Z axis, which is the actuated joint, and the other two axes of the R joints are parallel to each other and parallel to the XY plane.

Similarly, based on the reciprocal screw theory, the transferring wrench of the RRRS branch is the constraint force line vector which passes through the center of the spherical joint, and its direction is parallel to the axes of the rear two R joints. Obviously, the transferring force of the branch above exists component in tangential direction of the platform, and the transfer of the rolling motion can be completed (Fig. 4).

4 Conclusion

- (1) A novel kind of hybrid mechanism for rotary platform with three DOFs is proposed, upon the MP of PM is a revolute pair connected to the rolling MP, and the rolling MP is driving through a motion transferring chain. As a result, parallel mechanism and the actuation of the rolling mechanism will not become each other's load, which improves the carrying capacity.
- (2) Based on the principle of reciprocal screw theory, first the constraint wrench that need to be provided by the motion transferring chain is analyzed, then

according to different constraint wrench conditions, a variety of the motion transferring chains are obtained, and two branches with better performances are obtained, which are RRR spherical sub-chain and RRRS chain.

Acknowledgments This research was sponsored by the National Natural Science Foundation of China under Grant No. 51405425, the Science and technology project of Hebei Province under Grant No. 15211819, and the Independent Research Program Topics of Young Teachers in Yanshan University under Grant No. 13LGA001.

References

1. Dunlop GR, Jones TP (1999) Position analysis of a two DOF PM—the Canterbury tracker. *J. Mech Mach Theory* 34(4):599–614
2. Rolland L (2010) Synthesis of two DOFs parallel robots for solar tracking, from the Drawing Board until Prototyping Stage. C. In: 21st International workshop on nuclear and renewable energy, Ankara
3. Karouia M, Herve JM (2000) A three-DOF tripod for generating spherical rotation. In: C. Advances in robot kinematics. Kluwer Academic Publishers, Dordrecht, pp 395–402
4. di Gregorio R (2004) The 3-RRS wrist: a new, simple and non-overconstrained spherical parallel manipulator. *J Mech Design* 126(5):850–855
5. Merlet JP (2006) Parallel robot. Springer, The Netherlands, pp 35–37
6. Huang Z (1996) Kinematic characteristics analysis of three DOFs in-parallel actuated pyramid mechanisms. *J Mech Mach Theory* 31(8):1009–1018
7. Wu G, Caro S, Wang J (2015) Design and transmission analysis of an asymmetrical spherical parallel manipulator. *J Mech Mach Theory* 94:119–131
8. Hong Z, Zhang Z (2014) Dimensional synthesis of a novel three DOFs hybrid manipulator based on stiffness. *Chin J Mech Eng* 25(5):619–629
9. Li J, Zhang J, Cai D (2006) High precision, heavy load three-axis rotating sway test system platform: CN200520023093.6. P. authorization day: 2006-09-13
10. Gosselin CM, Caron F (1999) Two-degree-of-freedom spherical orienting device: US 5966991. P. 1999-10-19
11. Hervé JM (2006) Uncoupled actuation of pan-tilt wrists. *J IEEE Trans Robot* 22(1):56–64
12. Carricato M, Parenti-Castelli V (2004) A novel fully decoupled two-degrees-of-freedom parallel wrist. *Int J Robot Res* 23(6):661–667
13. Zeng DX, Huang Z (2011) Type synthesis of the rotational decoupled PM based on screw theory. *Sci China Technol Sci* 41(5):585–591
14. Kong X, Gosselin CM (2006) Type synthesis of three-dof UP-equivalent parallel manipulators using a virtual-chain approach. In: Lenarčič J, Roth B (eds) *Robot kinematics: mechanisms and motion*. Springer, The Netherlands, pp 123–132

Conceptual Design and Analysis of a 6-Axis Double Delta Robot Towards High Acceleration

Guanglei Wu

Abstract In this paper, a 6-axis parallel robot for pick-and-place operations is introduced based on the double structures of the Delta robot. Differing from the current 6-axis Delta robot, all the actuators are mounted on a base platform, which can reduce the inertia for high dynamic performance. Besides the 3-axis translation of the Delta robot, this robot's three rotations of the end-effector are realized by the relative movements of the two sub-platforms in three directions, but without significant structural complexity compared to the existing gearbox of Delta robot. The kinematic problems are studied to reveal that the workspace volume of the robot is similar to the existing design. The simplified dynamic model is established and the simulation results show that the robot can have the 100G acceleration maximally subject to the specifications of the current commercial actuator and gearbox.

Keywords Delta robot · 6-axis · Pick-and-place · Screw pair · Bevel gear

1 Introduction

Parallel pick-and-place (PnP) robots are one class of popular robots in material handling, of which the types are diverse, from 2 degrees of freedom (dof) planar robot to general 6-dof FANUC Delta robot. The most widely used parallel robots, in the light industries of food handling and electronic board assembly [1], produce three translations and one rotation [2–7], also known as Schönflies motion [8] or SCARA motion [9], such as the Delta robot as shown in Fig. 1a. On the other hand, 6-axis motion, namely, three translations and three rotations, are needed in some industrial applications, for instance, the FANUC 6-axis Delta robot displayed in Fig. 1b.

G. Wu (✉)

School of Mechanical Engineering, Dalian University of Technology, Dalian, China
e-mail: gwu@dlut.edu.cn

G. Wu

Department of Mechanical and Manufacturing Engineering, Aalborg University,
9220 Aalborg, Denmark



Fig. 1 The Delta robots. **a** ABB FlexPicker [10]. **b** FANUC M-3iA/6A [11]

The FANUC M-3iA/6A robot [11] adopts the structure of the translational Delta robot [12], for which three additional are mounted on the parallelogram close to the ends of the three actuated links, with the axis of rotation parallel to the parallelogram in each limb, respectively. In each limb, a RU chain, composed of an actuated revolute joint in series with a passive universal joint and connected to the manipulated platform by a passive revolute joint, is adopted to transfer actuator rotation to rotation relative to the manipulated platform, where the three rotations are achieved by the combined rotations or independent rotation of the RU chains through a complex gearbox. However, as noted by Pierrot et al. [13], it is difficult to design a lightweight passive prismatic joint with a long service life. As the RU chain is long, it raises the stability problem when this long chain undergoes high-speed rotations around the axes of the U joint [14]. Furthermore, the floating actuators mounted in the robot linkages will decrease the dynamic performance due to the increased inertia in the high-speed motion.

In light of the previous issues, a 6-axis double Delta robot is introduced in this paper, for which all the actuators are mounted on a base platform to reduce the inertia. This robot's three rotations of the end-effector are realized by the relative movements of the two sub-platforms in three directions, wherein a similar gearbox inherits from 6-axis Delta robot. In this work, the kinematics of the robot is developed and the workspace is analyzed. Moreover, the simplified dynamic model is established and the simulation results show that the robot can have the 100G acceleration maximally subject to the specifications of the current commercial actuator and gearbox.

2 Manipulator Architecture

The general structure of the robot under study is described in Fig. 2, consisting of two translational Delta robots as shown in Fig. 2a. The orientational difference between the two robots is 60° and their base planes have a vertical offset. The two mobile platforms, namely, sub-platforms 1 and 2, are connected through a gearbox as the rotation unit with the detailed structure displayed in Fig. 2b.

As illustrated in Fig. 2b, when sub-platform 1 rotates relatively to sub-platform 2, the gearbox on the latter will rotate around the vertical axis. A successive rotation of the end-effector around a horizontal axis can be realized by the translation of sub-platform 1 relative to the sub-platform 2, along the linear guide horizontally, where the screw pair 1 transforms the linear motion into rotation, subsequently, the rotation being transferred to the end-effector via the bevel gear transmission. Similarly, the third rotation around the axis of rotation of the end-effector can be achieved through screw pair and bevel gear transmission, where the motion is generated by the relative translation of the sub-platform 1 along the vertical axis.

Figure 3 illustrates kinematic structure of the robot as well as the gearbox. The global coordinate frame \mathcal{F}_b is built with the origin located at the geometric center of the base frame, namely, point O , where the x -axis is perpendicular to the axes of rotation of the first actuator in the first Delta robot and the second actuator in the second one. The moving coordinate frame \mathcal{F}_p in Fig. 3b is attached to the end-effector and the origin is at the end, namely, point P , where X -axis is parallel to x -axis in the home configuration. Here and after, vectors \mathbf{i} , \mathbf{j} and \mathbf{k} represent the unit vectors of x -, y - and z -axis, respectively. The orientation of the i th actuator in the first and second Delta robots, respectively, are described by unit vectors \mathbf{u}_i and \mathbf{r}_i :

$$\mathbf{u}_i = [-\sin \eta_i \quad \cos \eta_i \quad 0]^T; \quad \mathbf{r}_i = [-\sin \zeta_i \quad \cos \zeta_i \quad 0]^T \quad (1)$$

where $\eta_i = 2(i-1)\pi/3$, $\zeta_i = \eta_i + \pi/3$, $i = 1, 2, 3$. Moreover, unit vectors \mathbf{v}_i and \mathbf{w}_i are parallel to the segments $A_i\overline{B}_i$ and $\overline{B}_i\overline{C}_i$, respectively, namely, the unit vectors along the active link and parallelogram in the i th limb of the first Delta robot. Likewise, the same interpretation of unit vectors \mathbf{s}_i and \mathbf{t}_i are applicable to the second Delta robot.

The kinematic parameters of the gearbox are depicted in Fig. 3b. The orientation of the end-effector follows the Euler convention $Z-X-Z$, where the three successive rotations are denoted by Euler angles $\alpha \in [0, \infty)$, $\beta \in [0, 2\pi]$ and $\gamma \in [0, 2\pi]$. The gear transmission ratios for the last two rotations are both equal to 1, and the leads of the two screw pairs 1 and 2 are represented by h_1 and h_2 , respectively.

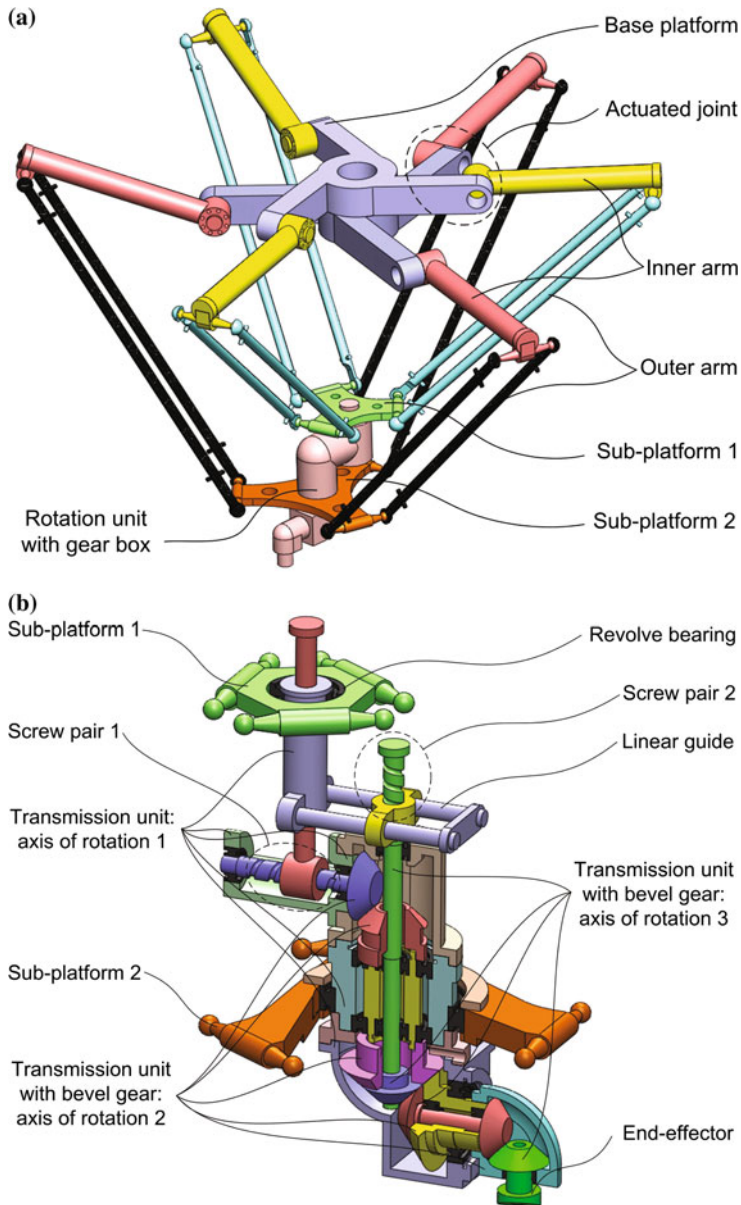


Fig. 2 The CAD model of the double Delta robot. **a** Architecture. **b** Gearbox

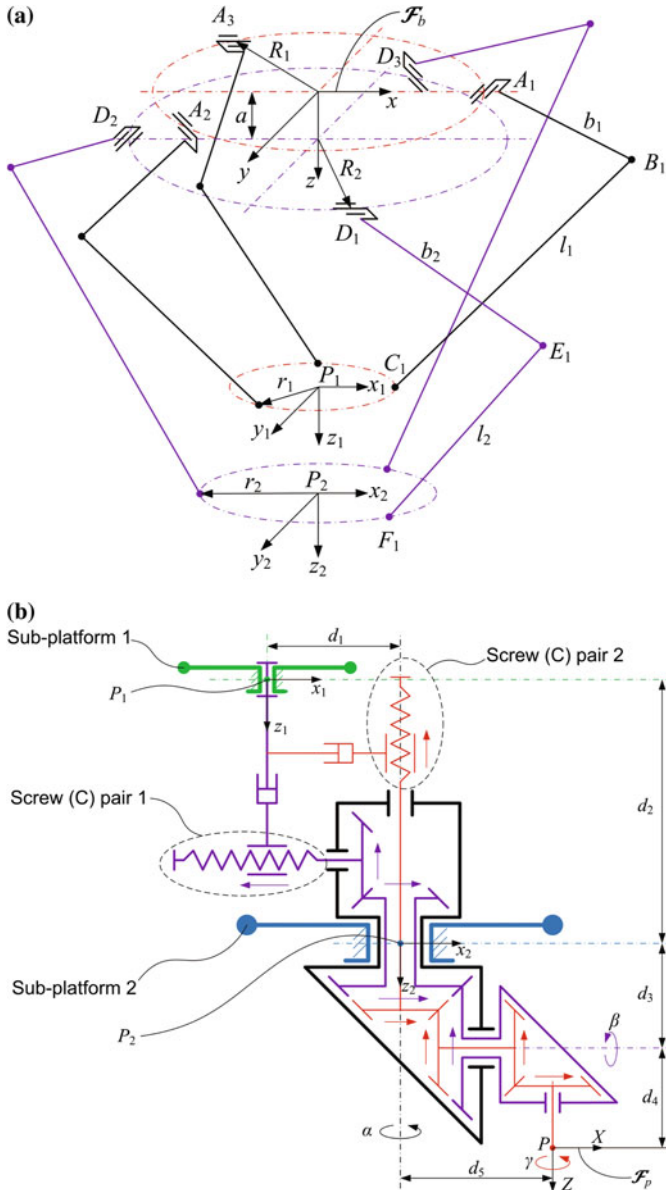


Fig. 3 The kinematic structure of the robot. **a** Double Delta robot. **b** Home configuration of the mobile platform

3 Kinematic Analysis of the Robot

Under the coordinate systems in Fig. 3a, the position vectors of points A_i and D_i in frame \mathcal{F}_b are denoted by

$$\mathbf{a}_i = R_1[\cos \eta_i \quad \sin \eta_i \quad 0]^T; \quad \mathbf{d}_i = R_2[\cos \zeta_i \quad \sin \zeta_i \quad a]^T \quad (2)$$

and the position vectors of points B_i and C_i are derived as

$$\mathbf{b}_i = b_1 \mathbf{v}_i + \mathbf{a}_i; \quad \mathbf{v}_i = \mathbf{R}_z(\eta_i) \mathbf{R}_y(\theta_i) \mathbf{i} \quad (3)$$

$$\mathbf{e}_i = b_2 \mathbf{s}_i + \mathbf{d}_i; \quad \mathbf{s}_i = \mathbf{R}_z(\zeta_i) \mathbf{R}_y(\phi_i) \mathbf{i} \quad (4)$$

where θ_i and ϕ_i are the angles of rotation of motors from a reference position for the first and second Delta robots, respectively.

According to Fig. 3b, the homogeneous transformation from the frame (x_2, y_2, z_2) on the sub-platform 2 to the end-effector frame \mathcal{F}_p is:

$$\mathbf{T} = \mathbf{T}_1 \mathbf{T}_2 \mathbf{T}_3 \quad (5)$$

with

$$\begin{aligned} \mathbf{T}_1 &= \begin{bmatrix} \mathbf{R}_z(-\alpha) & d_3 \mathbf{k} \\ \mathbf{0} & 1 \end{bmatrix} \begin{bmatrix} \mathbf{I}_3 & d_5 \mathbf{i} \\ \mathbf{0} & 1 \end{bmatrix}; \\ \mathbf{T}_2 &= \begin{bmatrix} \mathbf{R}_x(-\beta) & \mathbf{0} \\ \mathbf{0} & 1 \end{bmatrix} \begin{bmatrix} \mathbf{I}_3 & d_4 \mathbf{k} \\ \mathbf{0} & 1 \end{bmatrix}; \\ \mathbf{T}_3 &= \begin{bmatrix} \mathbf{R}_z(-\gamma) & \mathbf{0} \\ \mathbf{0} & 1 \end{bmatrix} \end{aligned} \quad (6)$$

where \mathbf{I}_3 is the 3×3 identity matrix. Thus, the rotation matrix of the end-effector will be described by

$$\mathbf{Q} = \mathbf{R}_z(-\alpha) \mathbf{R}_x(-\beta) \mathbf{R}_z(-\gamma) \quad (7)$$

3.1 Inverse Geometry

Let the robot end-effector pose be denoted by $\mathbf{x} = [\mathbf{p}^T \quad \boldsymbol{\xi}^T]^T$, $\mathbf{p} = [x \quad y \quad z]^T$, $\boldsymbol{\xi} = [\alpha \quad \beta \quad \gamma]^T$, subsequently, the Cartesian coordinates of point P_2 of sub-platform 2 can be derived as

$$\mathbf{p}_2 = \begin{bmatrix} x_2 \\ y_2 \\ z_2 \end{bmatrix} = \begin{bmatrix} x - d_5 \cos \alpha - d_4 \sin \alpha \sin \beta \\ y + d_5 \sin \alpha - d_4 \cos \alpha \sin \beta \\ z - d_3 - d_4 \cos \beta \end{bmatrix} \quad (8)$$

and the Cartesian coordinates of point P_1 of sub-platform 1 are expressed as

$$\mathbf{p}_1 = \begin{bmatrix} x_1 \\ y_1 \\ z_1 \end{bmatrix} = \begin{bmatrix} x - d_5 \cos \alpha - \cos \alpha (d_1 + h_1 \beta / (2\pi)) - d_4 \sin \alpha \sin \beta \\ y + d_5 \sin \alpha + \sin \alpha (d_1 + h_1 \beta / (2\pi)) - d_4 \cos \alpha \sin \beta \\ z - d_2 - d_3 - d_4 \cos \beta - h_2 \gamma / (2\pi) \end{bmatrix} \quad (9)$$

The inverse geometry of the robot can be solved from the following kinematic constraints:

$$\|\mathbf{c}_i - \mathbf{b}_i\| - l_1 = 0; \quad \|\mathbf{f}_i - \mathbf{e}_i\| - l_2 = 0 \quad (10)$$

where \mathbf{c}_i and \mathbf{f}_i , respectively, are the Cartesian coordinates of points C_i and F_i in the global frame \mathcal{F}_b :

$$\mathbf{c}_i = \mathbf{p}_1 + r_1 [\cos \eta_i \quad \sin \eta_i \quad 0]^T; \quad \mathbf{f}_i = \mathbf{p}_2 + r_2 [\cos \zeta_i \quad \sin \zeta_i \quad 0]^T \quad (11)$$

Let $\mathbf{m}_i = [m_{ix} \quad m_{iy} \quad m_{iz}]^T = \mathbf{c}_i - \mathbf{a}_i$, the angular displacement of the i th actuated joint of the first robot is solved as

$$\theta_i = 2 \tan^{-1} \frac{-I_i \pm \sqrt{I_i^2 + J_i^2 - K_i^2}}{K_i - J_i} \quad (12)$$

with

$$I_i = 2b_1 m_{iz}, \quad J_i = -2b_1 (m_{ix} \cos \eta_i - m_{iy} \sin \eta_i), \quad K_i = \|\mathbf{m}_i\|^2 + b_1^2 - l_1^2 \quad (13)$$

By the same token, the inverse geometry of the second robot is:

$$\phi_i = 2 \tan^{-1} \frac{-U_i \pm \sqrt{U_i^2 + V_i^2 - W_i^2}}{W_i - V_i} \quad (14)$$

with

$$U_i = 2b_2 n_{iz}, \quad V_i = -2b_2 (n_{ix} \cos \zeta_i - n_{iy} \sin \zeta_i), \quad W_i = \|\mathbf{n}_i\|^2 + b_2^2 - l_2^2 \quad (15)$$

where $\mathbf{n}_i = [n_{ix} \quad n_{iy} \quad n_{iz}]^T = \mathbf{f}_i - \mathbf{d}_i$.

3.2 Kinematic Jacobian Matrix

Differentiating Eq. (10) with respect to time leads to

$$\mathbf{w}_i^T \dot{\mathbf{p}} + \dot{\alpha} \mathbf{w}_i^T \mathbf{w}_\alpha + \dot{\beta} \mathbf{w}_i^T \mathbf{w}_\beta + \dot{\gamma} \mathbf{w}_i^T \mathbf{w}_\gamma = \dot{\theta}_i l_1 \mathbf{w}_i (\mathbf{u}_i \times \mathbf{v}_i) \quad (16)$$

$$\mathbf{t}_i^T \dot{\mathbf{p}} + \dot{\alpha} \mathbf{t}_i^T \mathbf{t}_\alpha + \dot{\beta} \mathbf{t}_i^T \mathbf{t}_\beta = \dot{\theta}_i l_2 \mathbf{t}_i (\mathbf{r}_i \times \mathbf{s}_i) \quad (17)$$

with

$$\mathbf{w}_\alpha = \begin{bmatrix} d_5 \sin \alpha + \sin \alpha (d_1 + h_1 \beta / 2\pi) - d_4 \cos \alpha \sin \beta \\ d_5 \cos \alpha + \cos \alpha (d_1 + h_1 \beta / 2\pi) + d_4 \sin \alpha \sin \beta \\ 0 \end{bmatrix} \quad (18a)$$

$$\mathbf{w}_\beta = [-h_1 \cos \alpha / 2\pi - d_4 \cos \beta \sin \alpha \quad h_1 \sin \alpha / 2\pi - d_4 \cos \alpha \cos \beta \quad d_4 \sin \beta]^T \quad (18b)$$

$$\mathbf{w}_\gamma = [0 \quad 0 \quad -h_2 / 2\pi]^T \quad (18c)$$

$$\mathbf{t}_\alpha = [d_5 \sin \alpha - d_4 \cos \alpha \sin \beta \quad d_5 \cos \alpha + d_4 \sin \alpha \sin \beta \quad 0]^T \quad (18d)$$

$$\mathbf{t}_\beta = [-d_4 \cos \beta \sin \alpha \quad -d_4 \cos \alpha \cos \beta \quad d_4 \sin \beta]^T \quad (18e)$$

where $\dot{\mathbf{p}} = [\dot{x} \quad \dot{y} \quad \dot{z}]^T$ and $\mathbf{w}_i = (\mathbf{c}_i - \mathbf{b}_i) / l_1$, $\mathbf{t}_i = (\mathbf{f}_i - \mathbf{e}_i) / l_2$. Equation (16) can be cast in a matrix form, namely,

$$\mathbf{J}_x \dot{\mathbf{x}} = \mathbf{J}_q \dot{\mathbf{q}} \quad (19)$$

with

$$\mathbf{J}_x = [\mathbf{j}_1 \quad \mathbf{j}_2 \quad \mathbf{j}_3 \quad \mathbf{j}_4 \quad \mathbf{j}_5 \quad \mathbf{j}_6]^T; \quad \dot{\mathbf{x}} = [\dot{x} \quad \dot{y} \quad \dot{z} \quad \dot{\alpha} \quad \dot{\beta} \quad \dot{\gamma}]^T \quad (20a)$$

$$\mathbf{J}_q = \text{diag}[q_{11} \quad q_{22} \quad q_{33} \quad q_{44} \quad q_{55} \quad q_{66}]^T; \quad (20b)$$

$$\dot{\mathbf{q}} = [\dot{\theta}_1 \quad \dot{\theta}_2 \quad \dot{\theta}_3 \quad \dot{\phi}_1 \quad \dot{\phi}_2 \quad \dot{\phi}_3]^T$$

where \mathbf{J}_x and \mathbf{J}_q are the forward and inverse Jacobians, respectively, and

$$\mathbf{j}_i = [\mathbf{w}_i^T \quad \mathbf{w}_i^T \mathbf{w}_\alpha \quad \mathbf{w}_i^T \mathbf{w}_\beta \quad \mathbf{w}_i^T \mathbf{w}_\gamma]^T, \quad \mathbf{j}_{i+3} = [\mathbf{t}_i^T \quad \mathbf{t}_i^T \mathbf{t}_\alpha \quad \mathbf{t}_i^T \mathbf{t}_\beta \quad 0]^T \quad (21a)$$

$$q_{ii} = l_1 \mathbf{w}_i^T (\mathbf{u}_i \times \mathbf{v}_i), \quad q_{i+3i+3} = l_2 \mathbf{t}_i^T (\mathbf{r}_i \times \mathbf{s}_i) \quad (21b)$$

Table 1 Geometric design parameters (unit: mm) of the double Delta robot

R_1, R_2	r_1	r_2	b_1, b_2	l_1, l_2	a	h_1, h_2	d_1	d_2	d_3	d_4	d_5
265	60	100	300	800	180	20	60	180	70	40	80

3.3 Workspace Analysis

The workspace of the robot can be obtained from the common volume of the two Delta robots, whose workspace is determined by the common volume of three tori [5] that are the functions of the link lengths, actuator position/orientations and manipulator pose, which can be geometrically visualized by virtue of some commercial CAD softwares, such as SolidworksTM.

With the geometric parameters in Table 1, the reachable workspace of one limb can be readily visualized, subsequently, the workspace of the sub-platform for one limb is obtained by an offset with the platform radius. To this end, the reachable translational workspace is the common volume of all the limbs with offsets according to the end-effector's geometric parameters, as displayed in Fig. 4a. A regular workspace with $\alpha \in [0, \infty)$ is identified, which is slightly smaller compared to the Delta robot [11]. The numerical searching method is also adopted to approximate the workspace for comparison, as demonstrated in Fig. 4b.

4 Dynamic Model of 6-Axis Delta Robot

In order to simplify the dynamic model, the centers of mass of the links are supposed to be coincident to their geometric centers, and the joint friction and the rotation of the outer arms are neglected. Based on these assumptions, the dynamic model is derived by means of the Lagrange equations below

$$\frac{d}{dt} \left(\frac{\partial L}{\partial \dot{\mathbf{q}}} \right) - \frac{\partial L}{\partial \mathbf{q}} + \mathbf{C}_q^T \boldsymbol{\lambda} = \mathbf{Q}_{ex} \quad (22)$$

where $L \equiv T - V$ is the Lagrangian of the system, including the mobile platform and the six limbs, and $\mathbf{q} = [\boldsymbol{\theta}^T \quad \boldsymbol{\phi}^T \quad \mathbf{x}^T]^T$. Moreover, $\mathbf{Q}_{ex} = [\boldsymbol{\tau}^T, \mathbf{0}]^T \in \mathbb{R}^{12}$ is the vector of external forces and vector $\boldsymbol{\tau} = [\tau_{11} \quad \tau_{12} \quad \tau_{13} \quad \tau_{21} \quad \tau_{22} \quad \tau_{23}]^T$ characterizes the actuator torques. Matrix $\mathbf{C}_q = [\mathbf{J}_q \quad -\mathbf{J}_x]$ is the system's constraint Jacobian. Moreover, $\boldsymbol{\lambda} = [\lambda_1 \quad \lambda_2 \quad \lambda_3 \quad \lambda_4 \quad \lambda_5 \quad \lambda_6]^T$ is a vector of Lagrange multipliers.

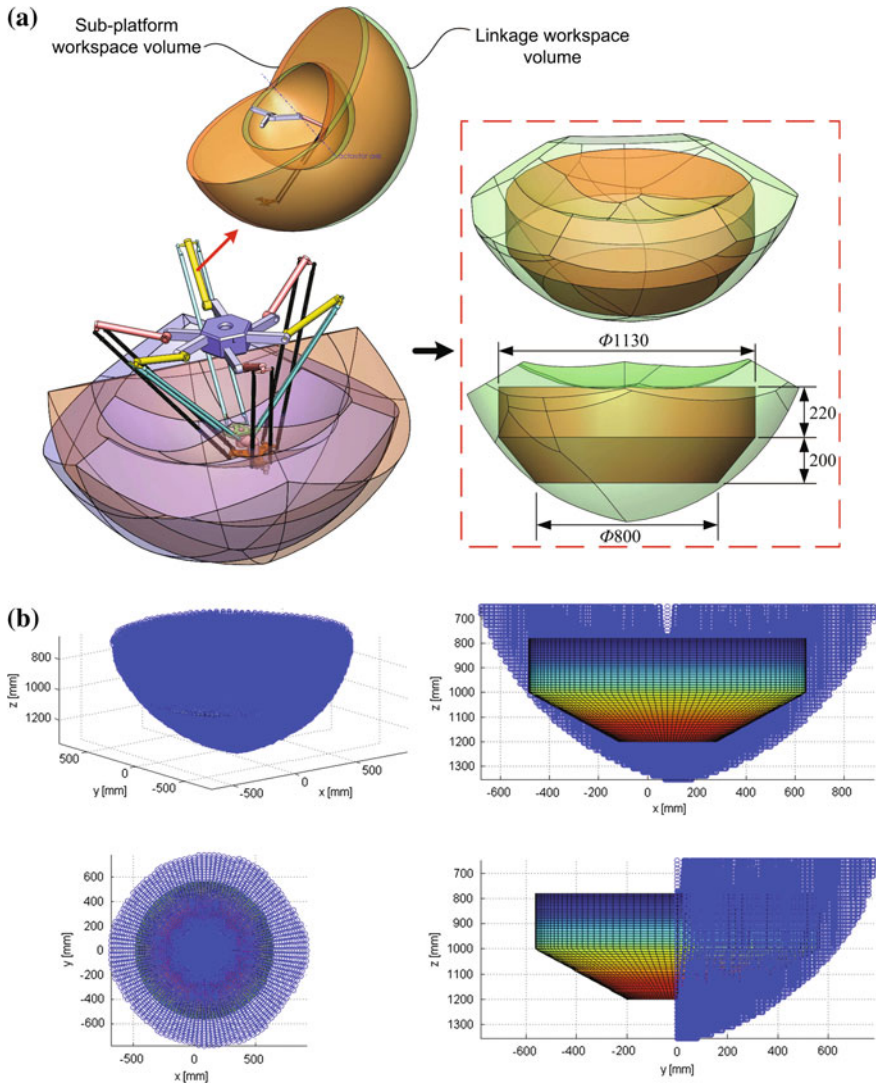


Fig. 4 The translational and regular workspace of the 6-axis Delta robot with $\alpha = \beta = \gamma = 0$. **a** CAD representation. **b** Numerical

The kinetic and potential energies are calculated below:

$$T = \sum_{i=1}^3 \left[\frac{1}{2} I_b (\dot{\theta}_i^2 + \dot{\phi}_i^2) + \frac{1}{8} m_l \|\dot{\mathbf{b}}_i + \dot{\mathbf{c}}_i\|^2 + \frac{1}{8} m_l \|\dot{\mathbf{f}}_i + \dot{\mathbf{e}}_i\|^2 \right] + \frac{1}{2} \dot{\mathbf{x}}^T \mathbf{M}_p \dot{\mathbf{x}} \quad (23a)$$

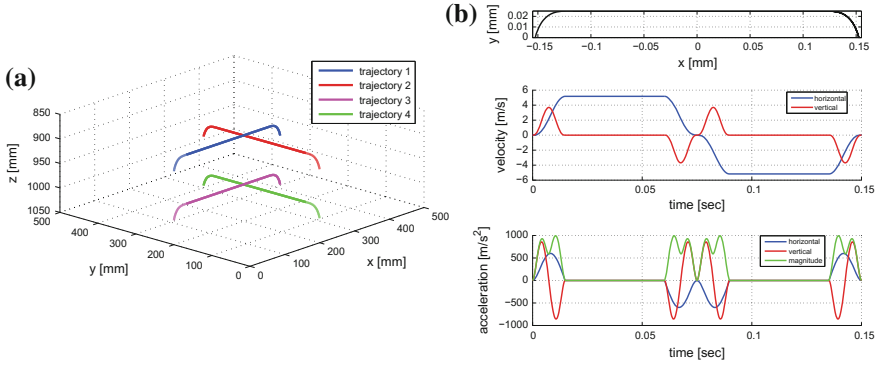


Fig. 5 The pick-and-place trajectories for dynamic simulation. **a** Trajectories in workspace. **b** Motion profiles

$$V = \frac{1}{2} \sum_{i=1}^3 [m_b(\mathbf{b}_i + \mathbf{d}_i + \mathbf{e}_i) + m_l(\mathbf{b}_i + \mathbf{c}_i + \mathbf{e}_i + \mathbf{f}_i)] \cdot \mathbf{g} + (m_p + m_e)\mathbf{p}^T \mathbf{g} \quad (23b)$$

where I_b and m_b are the moment of inertia and mass of the inner arm, respectively, and m_l , m_p and m_e are the masses of the outer arm, the mobile platform and the payload. Moreover, $\mathbf{M}_p = \text{diag}[m_p \ m_p \ m_p \ I_x + m_e d_5^2 \ I_\beta + m_e d_4^2 \ I_\gamma]$ is the mass matrix of the mobile platform, I_x , I_β and I_γ being the mass moments of inertia around the three axes of rotation for α , β and γ , respectively. Terms $\dot{\mathbf{b}}_i$ and $\dot{\mathbf{c}}_i$ stand for the velocities of points B_i and C_i , respectively, which can be calculated with known $\dot{\theta}_i$, $\dot{\phi}_i$ and $\dot{\mathbf{x}}$. A similar dynamic modeling procedure has been developed and validated in the previous work [15, 16].

Substituting Eq. (23a) into Eq. (22), the terms in the equation of motion for this system can be derived. As reported by Corbel et al. [17], the six-limb parallel robot can reach up to 100G acceleration. Hence, the dynamic simulation is conducted with four trajectories based an energy-minimized pick-and-place motion profiles of 25 mm × 305 mm × 25 mm without rotations, where the motion profiles are shown in Fig. 5. With the mass properties in Table 2, the maximum requirements of the speed and torques on the actuators are shown in Fig. 6, which implies that the current commercial actuator and gearbox can meet the robot’s high dynamic performance to reach to the 100G acceleration.

Table 2 The mass and moment of inertia of the robot for dynamic simulation

m_b (kg)	I_b (kg · m ²)	m_l (kg)	m_e (kg)	m_p (kg)	I_x (kg · m ²)	I_β (kg · m ²)	I_γ (kg · m ²)
2.5	0.075	0.42	5	5	0.032	0.016	0.004

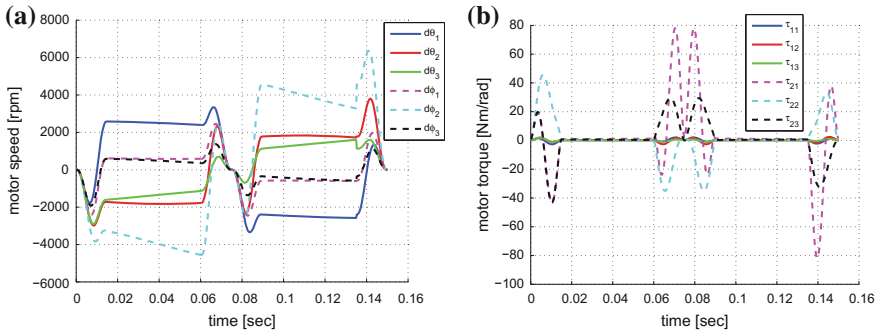


Fig. 6 The maximum requirement on actuators with gearbox of reduction ratio 50. **a** Maximum speed along trajectory 1. **b** Maximum torque along trajectory 4

5 Conclusions

This paper introduces a 6-axis double Delta robot for pick-and-place operations with high acceleration. Different from its 6-axis counterpart, all the actuators of this robot are mounted on a base platform, which can reduce the inertia for high dynamic performance. In comparison with the current design of the gearbox, this robot's three rotations of the end-effector are realized by the relative movements of the two sub-platforms in three directions, but without significantly increasing the structural complexity. The inverse kinematics is studied and the workspace is analyzed to show that the workspace volume of the robot is similar to the existing design. The simplified dynamic model is established and the simulation results show that the robot can have the 100G acceleration maximally subject to the specifications of the current commercial actuator and gearbox.

Acknowledgments The reported work is supported by the Fundamental Research Funds for the Central Universities.

References

1. Adept: Adept Quattro Parallel Robots. <http://www.adept.com/products/robots/parallel/quattro-s650h/general>
2. Pierrot F, Reynaud C, Fournier A (1990) DELTA: a simple and efficient parallel robot. *Robotica* 8(2):105–109
3. Krut S, Nabat V, Company O, Pierrot F (2004) A high-speed parallel robot for SCARA motions. *IEEE Int Conf Robot Autom* 4:4109–4115
4. Kong X, Gosselin C (2004) Type synthesis of 3T1R 4-dof parallel manipulators based on screw theory. *IEEE Trans Robot Autom* 20(2):181–190
5. Altuzarra O, Şandru B, Pinto C, Petuya V (2011) A symmetric parallel Schönflies-motion manipulator for pick-and-place operations. *Robotica* 29:853–862

6. Xie F, Liu X (2015) Design and development of a high-speed and high-rotation robot with four identical arms and a single platform. *ASME J Mech Robot* 7(4):041015
7. Wu G, Bai S, Hjørnet P (2016) On the stiffness of three/four degree-of-freedom parallel pick-and-place robots with four identical limbs. In: *IEEE international conference on robotics and automation*, Stockholm, Sweden, pp 861–866
8. Angeles J, Caro S, Khan W, Morozov A (2006) Kinetostatic design of an innovative Schönflies-motion generator. *Proc Inst Mech Eng Part C J Mech Eng Sci* 220(7):935–943
9. Pierrot F, Nabat V, Company O, Krut S, Poignet P (2009) Optimal design of a 4-dof parallel manipulator: from academia to industry. *IEEE Trans Robot* 25(2):213–224
10. ABB: IRB 360 FlexPicker. <http://new.abb.com/products/robotics/industrial-robots/irb-360>
11. FANUC: M-3iA/6A Delta robot. <http://www.fanuc.eu/se/en/robots/robot-filter-page/m3-series/m-3ia-6a>
12. Clavel R (1990) Device for the movement and positioning of an element in space. US Patent 4,976,582
13. Pierrot F, Company O, Krut S, Nabat V (2006) Four-dof PKM with articulated travelling-plate. In: *Proceedings of parallel kinematics seminar (PKS'06)*, Chemnitz, Germany, pp 25–26
14. Gosselin C, Isaksson M, Marlow K, Laliberté T (2016) Workspace and sensitivity analysis of a novel nonredundant parallel SCARA robot featuring infinite tool rotation. *IEEE Robot Autom Lett* 1(2):776–783
15. Wu G, Bai S, Hjørnet P (2015) Design analysis and dynamic modeling of a high-speed 3T1R pick-and-place parallel robot. In: Bai S, Ceccarelli M (eds) *Mechanisms and machine science: recent advances in mechanism design for robotics*, vol 33, pp 285–295
16. Wu G, Bai S, Hjørnet P (2015) Parametric optimal design of a parallel Schönflies-motion robot under pick-and-place trajectory constraints. In: *IEEE/RSJ international conference of intelligent robotics system*, Hamburg, Germany, pp 3158–3163
17. Corbel D, Gouttefarde M, Company O, Pierrot F (2010) Actuation redundancy as a way to improve the acceleration capabilities of 3T and 3T1R pick-and-place parallel manipulators. *ASME J Mech Robot* 2(4):041002

Design and Analysis of a Precise Adjustment Mechanism for Lithography Objective Lens Based on Slit Diaphragm Flexure

Shize Dong, Kang Guo, Xianling Li, Huanan Chen and Mingyang Ni

Abstract An adjustment mechanism with three degrees of freedom (θ_x - θ_y - Z) based on slit diaphragm flexure is designed to meet the requirement of high precise adjustment and guidance accuracy for the application in lithography objective lens. The stiffness formulas of the adjustment mechanism are derived by elastic mechanics, and verified by finite element simulation. The effect of the adjusting force acts on the surface figure of the optical element is also analyzed. The results show that the stiffness ratio between the radial direction and axial direction is 1534.6, the error between the theoretical value and simulation value of the axial stiffness is 6.07 %, and 8.33 % for the radial stiffness, which indicates the validity of the stiffness calculation. During the axial adjustment process, the adjusting force mainly introduces defocus, spherical and trefoil aberration. However, during the tilt adjustment process, the adjusting force mainly introduces astigmatism, coma and trefoil aberration.

Keywords Lithography objective lens · Adjustment mechanism · Slit diaphragm flexure · Guidance accuracy · Surface figure

S. Dong (✉) · K. Guo · X. Li · H. Chen · M. Ni
State Key Laboratory of Applied Optics, Engineering Research Center
of Extreme Precision Optics, Changchun Institute of Optics,
Fine Mechanics and Physics, Chinese Academy of Science,
Changchun 130033 China
e-mail: ultra_create@163.com

K. Guo
e-mail: guok@sklao.ac.cn

S. Dong
University of Chinese Academic of Sciences, Beijing 100049, China

1 Introduction

Lithography is the main process for manufacturing the grand scale integrated circuit. The development of lithography is represented by the progress of the lithography objective lens [1, 2]. Adjustment mechanism, which is a component of the lithography objective lens, is used to accurately adjust the relative position between the optical elements, for compensating the aberration of the lens optical system, such as field curvature, astigmatism, distortion and spherical aberration [3].

With the accuracy improvement of the lithography objective lens, the precision of the adjustment mechanism is required to achieve the level of nanometer even sub-nanometer. The traditional adjustment mechanism, such as lead-screw nut mechanism, cam mechanism and etc., couldn't be used in the lithography objective lens, because of their drawbacks of friction, backlash, need for lubrication and lower precision. In recent years, according to the requirements of the precise adjustment for the optical element, the flexible mechanism, actuating by piezo-electric actuators, receives a better application in the field of fine adjustment [4].

Hale et al. [5, 6] developed a mechanism to finely align optics for extreme ultraviolet lithography. The mechanism is a small motion parallel link manipulator with flexure joints, and the high accurate adjustment in three degrees of freedom (θ_x - θ_y - Z) is achieved by precisely controlling the piezo screws. Chen et al. [7] designed an ultra-precision radial spoke diaphragm flexure stage for guiding an objective lens along the optical axis in a high performance microscope. Cox et al. [8] designed a two precision mirror gimbal using slit diaphragm flexures to provide two-axis precision mirror alignment for the Gamma Reaction History diagnostic system in the Neutron Imaging System. Vukobratovich et al. [9] proposed two types of slit diaphragms for many precision motion applications in optical engineering: a two axis gimbal for rotation and a linear flexure for translation. Peng et al. [10] designed a precision adjustment mechanism with flexure hinges and lever for lithography lens. Guo et al. [11] presented a precision axial adjustment mechanism based on 6-PSS type parallel mechanism to realize the adjustment stroke in micrometer size and the accuracy in nanometer size for optical element in lithography objective lens.

Most of the researches use flexible adjustment mechanisms to achieve high adjustment accuracy, but few researches focus on the guidance accuracy of the adjustment mechanism. High guidance accuracy promotes the adjustment mechanism with better motion decoupling and better mobility constrain in the non-movement direction. For the application of the lithography objective lens, if the guidance accuracy of the adjustment mechanism exceeds 1 μm (translation) and 1 arcsec (tilt), it will degrade the wavefront aberration of the lens optical system with a magnitude of 0.2 nm (root mean square value). This paper presents a precise adjustment mechanism for lithography objective lens based on slit diaphragm flexure. The mechanism not only has high adjusting accuracy, but also owns high guidance accuracy. In this paper, the axial stiffness and radial stiffness, which are the major influence factors of the guidance accuracy, are analyzed. The impact of the adjusting force on the surface figure of the optical element is also investigated.

2 The Conceptual Model of the Slit Diaphragm Flexure

In this paper, the adjustment mechanism for lithography objective lens is composed of slit diaphragm flexure, inner barrel and out barrel, as shown in Fig. 1. The adjustment mechanism can be easily fabricated from a single workblank by turning, milling, drilling, wire cutting and other processes. Since the slit diaphragm flexure and the barrels are with monolithic structure, it does not require assembly, which is benefit for the improvement of mechanical precision.

When the adjustment mechanism operates, the outer barrel is fixed, the slit diaphragm flexure is driven by three actuators, which are evenly distributed under the flexible structure, and the output shafts of the actuators are connected to the flexible structure at points A, B and C, as shown in Fig. 1. Under the action of three actuators, the slit diaphragm flexure deforms elastically, and the optical element, which is mounted on the inner barrel, moves with the inner barrel. By controlling the driving force of the three actuators, the optical element can not only translate along the optical axis, but also tilt against the plane that perpendicular to the optical axis. Namely, the adjustment mechanism can realize the three degrees of freedom motion (θ_x - θ_y - Z). The distribution of the points A, B and C is shown in Fig. 2. Assign δ_A , δ_B , and δ_C represent the output displacement of A, B and C, respectively, the axial displacement and the angular displacement of the optical element can be calculated as:

$$\begin{aligned} \delta_z &= \frac{1}{3}(\delta_A + \delta_B + \delta_C) \\ \theta_x &= \frac{2\delta_A - \delta_B - \delta_C}{2a} \\ \theta_y &= \frac{\delta_B - \delta_C}{b} \end{aligned} \tag{1}$$

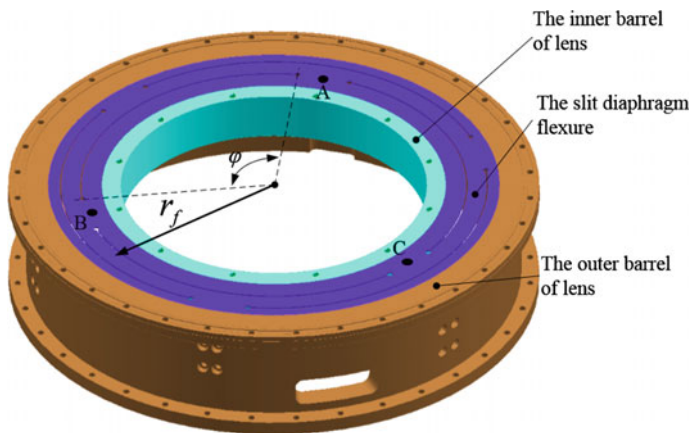
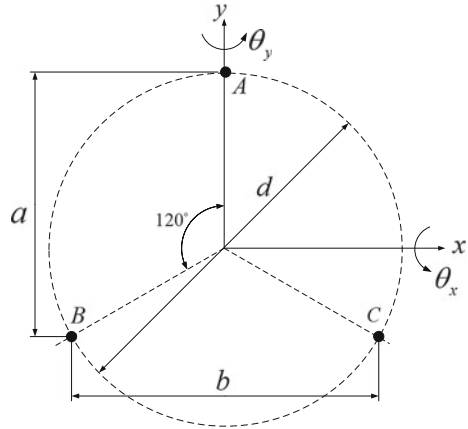


Fig. 1 The structure of the adjustment mechanism based on slit diaphragm flexure

Fig. 2 The sketch of evenly distributed actuators



According to Eq. 1, in order to achieve high adjustment accuracy of the adjustment mechanism, three piezoelectric actuators with high-resolution should be applied to driving the slit diaphragm flexure.

The slit diaphragm flexure can be regarded as constituted by a number of curved beams with rectangular cross-section, connected in parallel and series. According to the number of curved beams and their connection types, the slit diaphragm flexure can be defined as $a \times b$ type, as shown in Fig. 3. Where ‘ a ’ represents the number of the curved beams in the radial direction, the connection type of the curved beams is in series. ‘ b ’ represents the number of the curved beams in the circumferential direction, the connection type of the curved beams is in parallel. After the preliminary analysis, it is found that when the number of the curved beams in the radial direction is one, the adjustment mechanism expresses higher guidance accuracy. Therefore, the 1×3 type slit diaphragm flexure is investigated in this research.

3 The Theoretical Analysis of the Slit Diaphragm Flexure

There are three degrees of freedom (θ_x - θ_y - Z) existing in the adjustment mechanism. In the process of adjusting, the in-plane movement should be constrained in order to reduce the coupling error and improve the guidance accuracy of the adjustment



Fig. 3 The conceptual model of silt diaphragm flexure. **a** 1×3 type, **b** 2×3 type, **c** 3×3 type

mechanism. The key method to constrain the in-plane movement is to improve the radial stiffness of the adjustment mechanism. If the radial stiffness of the adjustment mechanism is much higher than its axial stiffness, coupled displacement error can be suppressed. Therefore, the guidance accuracy of adjustment mechanism is highly influenced by the axial stiffness and radial stiffness. The stiffness analysis of the slit diaphragm flexure is given out in this section.

The basic model element of the slit diaphragm flexure is the curved beam with both ends fixed, as shown in Fig. 4. Based on the stress function of elastic mechanics [12, 13], the stiffness of the curved beam with both ends fixed is analyzed.

The external force F_a is applied to the midpoint of the arc length of the curved beam along the axial direction. The arc length of the curved beam is $l = \varphi r_f$. The elastic modulus of the curved beam is E . Then, the deflection equation of the curved beam with both ends fixed is taken as:

$$\delta_a = \begin{cases} \frac{F_a r_f^3}{2Eh^3} \left[-2\theta^3 + \frac{3}{2}\varphi\theta^2\right], & 0 \leq \theta \leq \frac{\varphi}{2} \\ \frac{F_a r_f^3}{2Eh^3} \left(2\theta^3 - \frac{9}{2}\varphi\theta^2 + 3\varphi^2\theta - \frac{1}{2}\varphi^3\right), & \frac{\varphi}{2} \leq \theta \leq \varphi \end{cases} \quad (2)$$

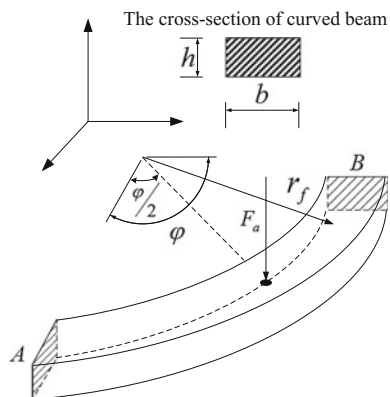
According to Eq. 2, the maximal deflection of the curved beam appears at the action point of F_a , where $\theta = \varphi/2$. It is also the connect point between the slit diaphragm flexure and the inner barrel. The maximal value of δ_a is expressed as:

$$\delta_{amax} = \frac{F_a(\varphi r_f)^3}{16Ebh^3}. \quad (3)$$

Then the axial stiffness of the curved beam is taken as:

$$k_a = \frac{F_a}{\delta_{amax}} = \frac{16Ebh^3}{(\varphi r_f)^3} \quad (4)$$

Fig. 4 The curved beam element with both ends fixed



The main body of the slit diaphragm flexure is composed of three curved beams in parallel. Therefore, the axial stiffness of the slit diaphragm flexure can be calculated as:

$$k_A = 3k_a = \frac{48Eb^3h^3}{(\varphi r_f)^3} \quad (5)$$

The radial stiffness of the slit diaphragm flexure k_R is represented by the radial stiffness k_r and the tangential stiffness k_t of the curved beam. The radial stiffness is taken as:

$$k_R = \frac{5}{4} \left(3k_r + \frac{k_t}{3} \right) \quad (6)$$

Where:

$$k_r = \frac{192EI_r}{l^3} = \frac{16Eb^3h}{(\varphi r_f)^3}, k_t = \frac{4Eb^3h}{l} = \frac{4Eb^3h}{\varphi r_f} \quad (7)$$

Bringing Eq. 7 into Eq. 6:

$$k_R = \frac{5}{4} \left(\frac{48Eb^3h}{(\varphi r_f)^3} + \frac{4Eb^3h}{3\varphi r_f} \right) \quad (8)$$

The stroke of the slit diaphragm flexure is constrained by the yield stress of material. The internal stress of the curved beam is expressed as:

$$\begin{aligned} \sigma_\theta &= \begin{cases} \frac{3F_a r_f}{bh^3} \left(2\theta - \frac{\varphi}{2} \right) z, & 0 \leq \theta \leq \frac{\varphi}{2} \\ -\frac{3F_a r_f}{bh^3} \left(2\theta - \frac{3}{2}\varphi \right) z, & \frac{\varphi}{2} \leq \theta \leq \varphi \end{cases} \\ \sigma_z &= 0 \\ \tau_{\theta z} &= \begin{cases} \frac{3F_a}{h^3} \left(\frac{1}{4}h^2 - z^2 \right), & 0 \leq \theta \leq \frac{\varphi}{2} \\ -\frac{3F_a}{h^3} \left(\frac{1}{4}h^2 - z^2 \right), & \frac{\varphi}{2} \leq \theta \leq \varphi \end{cases} \end{aligned} \quad (9)$$

Where, z is the axial height of the curved beam. The Von mises stress of the curved beam is calculated as:

$$\tilde{\sigma} = \sqrt{3 \times \frac{1}{6} \left[(\sigma_\theta - \sigma_z)^2 + \sigma_z^2 + \sigma_\theta^2 + 6\tau_{\theta z}^2 \right]} \quad (10)$$

Equation 10 is a constraint condition for the dimension optimization of the adjustment mechanism.

4 Design and Simulation of the Adjustment Mechanism

4.1 Optimal Design of the Adjustment Mechanism

To ensure the adjustment mechanism with high guidance accuracy, the slit diaphragm flexure is optimized. The stiffness ratio between the radial and axial direction is set as the objective function, the dimension parameters of the curved beam are set as the variables. The material of the adjustment mechanism is stainless steel, the optimized geometrical parameters and specifications of the adjustment mechanism are shown in Table 1.

According to the optimized dimensions, the assembly model is established, as shown in Fig. 5. Multi-flexural brackets are used to support the optical element in order to reduce the effect of the adjusting force on the surface figure of the optical element.

4.2 Adjustment Stroke Analysis of the Adjustment Mechanism

The simulation analysis of the adjustment mechanism for lithography objective lens based on slit diaphragm flexure is implemented by ANSYS software. In this research, the piezoelectric actuator for the adjustment mechanism can provide 30 N output force to deform the slit diaphragm flexure and balance the gravity of the inner barrel and other components connected to it. According to the working

Table 1 The optimized geometrical parameters and specifications of the adjustment mechanism

b	h	φ	r_f	k_A	k_R	σ	k_R/k_A
13 mm	1.25 mm	112°	139.5 mm	15.46 N/mm	23,147 N/mm	250 MPa	1497.7

Fig. 5 The assembly model of the adjustment mechanism

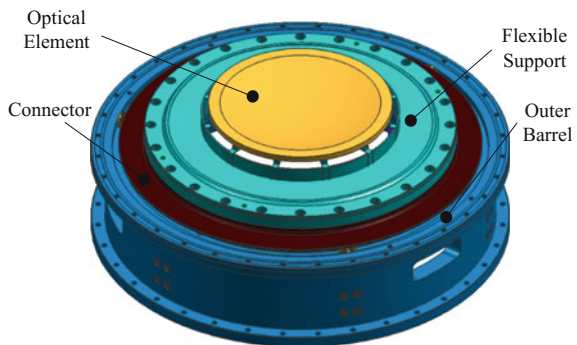


Table 2 The simulation results of the adjustment stroke of the adjustment mechanism

Motion	Force applied at point A	Force applied at point B	Force applied at point C	Von mises stress	Adjustment stroke
Z	30 N	30 N	30 N	85.58 Mpa	999.2 μm
θ_x	30 N	23.03 N	23.03 N	69.57 Mpa	4.7 mrad
θ_y	25.35 N	30 N	20.71 N	93.15 Mpa	5.5 mrad

principle of the adjustment mechanism described in Sect. 2, the adjustment stroke and the maximum Von mises stress of the adjustment mechanism are acquired by applying different axial force on the three action points, as shown in Table 2.

4.3 The Stiffness Analysis of the Adjustment Mechanism

Without considering the action of the gravity, the axial stiffness of the adjustment mechanism is analyzed by applying the axial force on the action points. Making the driving force alterable from 3 N to 30 N, the approximately linear relationship between driving force and axial displacement can be obtained. After fitting-linear, the axial stiffness of the adjustment mechanism is $k_{A_ansys} = 16.45$ N/mm. The same process is implemented to investigate the radial stiffness of the adjustment mechanism. The force is applied perpendicular to the axial direction on the action points, and altered from 3 N to 24 N. And the radial stiffness of the adjustment mechanism is $k_{R_ansys} = 25,250$ N/mm.

According to the simulation results of the adjustment mechanism, the ratio between the radial and axial stiffness can be deduced as:

$$ratio_{ansys} = \frac{k_{R_ansys}}{k_{A_ansys}} = 1534.6 \tag{11}$$

Comparison of the theoretical and simulation value of the stiffness of the adjustment mechanism is shown in Table 3. The error between the theoretical value and the simulation value are less than 10 %. The ratio between the radial and axial stiffness is relatively large. Therefore, coupled displacement error can be suppressed in the radial direction, and the adjustment mechanism can acquire high guidance accuracy.

Table 3 Comparison of the theoretical and simulation value of the stiffness of the adjustment mechanism

Item	The axial stiffness (N/mm)	The radial stiffness (N/mm)	The stiffness ratio
The theoretical value	15.46	23,147	1497.7
The simulation value	16.45	25,250	1534.6
The relative tolerance (%)	6.07	8.33	2.41

5 Effect of the Adjustment Mechanism on the Surface Figure of the Optical Element

The adjustment mechanism of the lithography objective lens not only possess high guidance accuracy, but also need to reduce the effect of the adjusting force on the surface figure of optical element during adjustment procedure. In the process of adjusting the position of the optical element, if the adjusting force causes significant change of the surface figure of the optical element, the change of the position and the surface figure will be coupled in the lens optical system, which will make the strategy complex to compensate the wavefront aberration of the lens optical system and increase the difficulty and uncertainty of the adjusting process. Therefore, the effect of the adjusting force on the surface figure of the optical element cannot be ignored in the application of the lithography objective lens.

5.1 Effect of the Axial Adjustment on the Surface Figure of the Optical Element

In this research, the axial stroke of the adjustment mechanism for the lithography objective lens is required to reach 200 μm , therefore, this paper investigates the effect of the adjustment mechanism under the stroke of $\pm 200 \mu\text{m}$. When the displacement is within $[-200 \mu\text{m}, 200 \mu\text{m}]$, the 37 order normalized Fringe Zernike polynomial coefficients of the upper and lower surface figure of the optical element is shown in Fig. 6.

When the axial adjustment stroke is $-200, 0$ and $200 \mu\text{m}$, the root mean square (RMS) value of the surface figure of the optical element is 4.01, 3.26 and 4.61 nm, respectively. The amplitude of variation of the RMS value is about 40 % before and

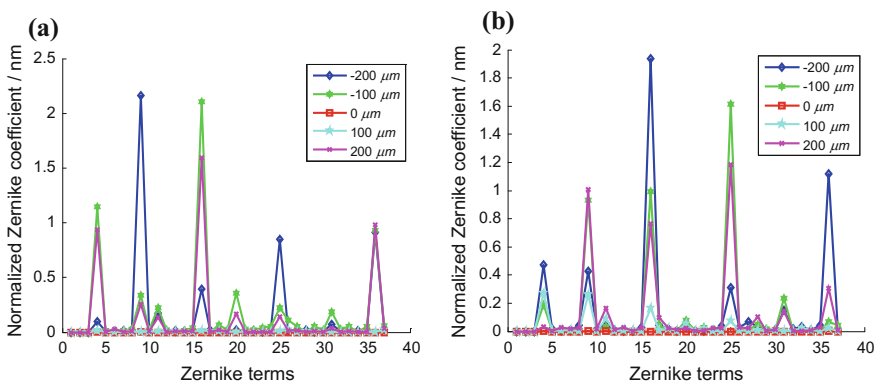


Fig. 6 Normalized Zernike terms for the surface figure of the optical element under axial adjustment. **a** The upper surface, **b** the lower surface

after adjusting. Moreover, as shown in Fig. 6, among the Fringe Zernike polynomial coefficients of the upper and lower surface figure of the optical element, the terms sensitive to the adjusting force are Z_4 (Defocus), Z_9 (Pri Spherical), Z_{11} (Pri Trefoil-X), Z_{16} (Sec Spherical), Z_{20} (Sec Trefoil-Y), Z_{25} (Ter Spherical), Z_{31} (Ter Trefoil-Y) and Z_{36} (Qua Spherical). Therefore, during the axial adjustment process, the adjusting force mainly introduces defocus, spherical and trefoil aberration. The largest terms are the primary spherical aberration (the upper surface) with a variation of 2.16 nm and the second spherical aberration (the lower surface) with a variation of 1.94 nm.

5.2 Effect of the Tilt Adjustment on the Surface Figure of the Optical Element

When the adjustment mechanism tilt about X axis, the 37 order normalized Fringe Zernike polynomial coefficients of the upper and lower surface figure of the optical element is shown in Fig. 7.

When the tilt stroke about X axis is 0 and 3.8 mrad, the RMS value of the surface figure of the optical element is 3.26 and 3.73 nm, respectively. The amplitude of variation of the RMS value is about 15 % before and after adjusting. Moreover, as shown in Fig. 7, among the Fringe Zernike polynomial coefficients of the upper surface figure of the optical element, the terms sensitive to the adjusting force are Z_5 (Pri Astig.-X), Z_8 (Pri Coma-Y) and Z_{11} (Pri Trefoil-Y). The sensitive terms of the lower surface figure include Z_6 (Pri Astig.-X), Z_8 (Pri Coma-Y), Z_{15} (Sec Coma-Y), Z_{20} (Sec Trefoil-Y), Z_{24} (Ter Coma-Y), Z_{31} (Ter Trefoil-Y) and Z_{35} (Qua Coma-Y). Therefore, during the tilt adjustment process about the X axis, the adjusting force mainly introduces astigmatism, coma and trefoil aberration, and the largest terms

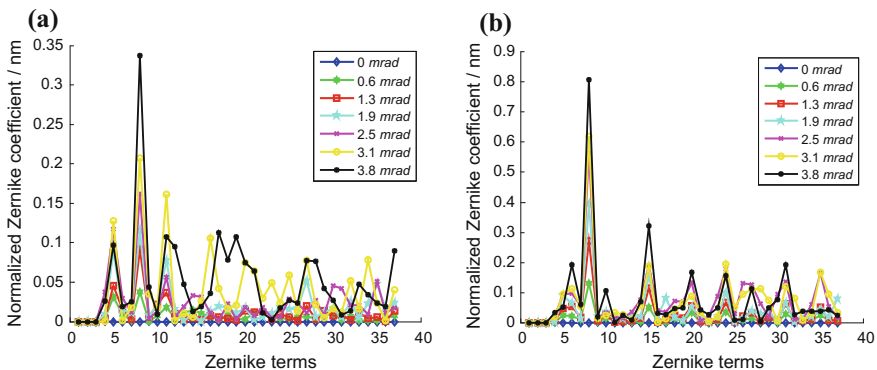


Fig. 7 Normalized Zernike terms for the surface figure of the optical element under tilt adjustment about X axis. **a** The upper surface, **b** the lower surface

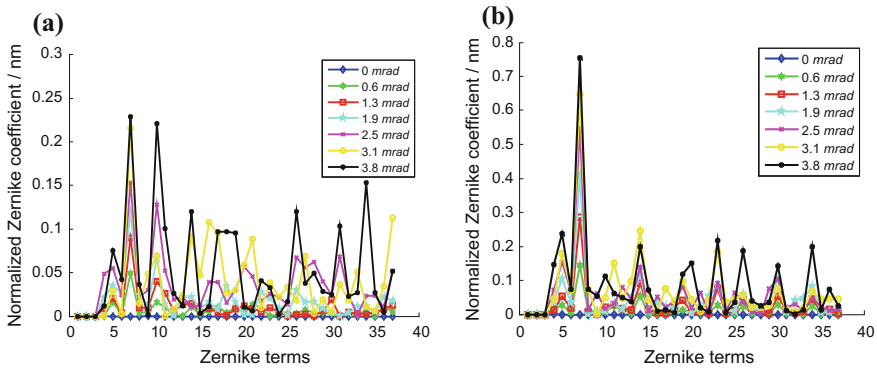


Fig. 8 Normalized Zernike terms for the surface figure of the optical element under tilt adjustment about *Y* axis. **a** The upper surface, **b** the lower surface

are the primary coma aberration (the upper surface) with a variation of 0.34 nm and the primary coma aberration (the lower surface) with a variation of 0.81 nm.

When the adjustment mechanism tilt about *Y* axis, the 37 order normalized Fringe Zernike polynomial coefficients of the upper and lower surface figure of the optical element is shown in Fig. 8.

When the tilt stroke about *Y* axis is 0 and 3.8 mrad, the RMS value of the surface figure of the optical element is 3.26 and 3.75 nm, respectively. The amplitude of variation of the RMS value is about 15 % before and after adjusting. Moreover, as shown in Fig. 8, among the Fringe Zernike polynomial coefficients of the upper surface figure of the optical element, the terms sensitive to the adjusting force are Z_7 (Pri Coma-X) and Z_{10} (Pri Trefoil-X). The sensitive terms of the lower surface figure include Z_5 (Pri Astig.-X), Z_7 (Pri Coma), Z_{14} (Sec Coma-X), Z_{23} (Ter Coma-X), Z_{30} (Ter Trefoil-X) and Z_{34} (Qua Coma-X). Therefore, during the tilt adjustment process about the *Y* axis, the adjusting force mainly introduces astigmatism, coma and trefoil aberration. The largest term is the primary coma aberration (the lower surface) with a variation of 0.76 nm.

6 Conclusion

An adjustment mechanism with three degrees of freedom ($\theta_x\text{-}\theta_y\text{-}Z$) for lithography objective lens is designed, based on slit diaphragm flexure. The ratio between the radial and axial stiffness of the adjustment mechanism is up to 1534.6. The relatively large stiffness ratio can suppress the coupled displacement error in the radial direction, and ensure high guidance accuracy. With the conceptual model of the slit diaphragm flexure, the stiffness of flexible structure is analyzed based on elastic mechanic. The dimensions of the adjustment mechanism are optimized, and the stiffness of the adjustment mechanism is analyzed by finite element simulation.

The results show that, the stiffness error between the theoretical value and the simulation value is within 10 %, which indicates the validity of the stiffness calculation. The axial adjustment stroke of the adjustment mechanism is 999.2 μm , and the tilt adjustment stroke about the x axis is ± 4.7 and ± 5.5 mrad about the y axis. The effect of the adjusting force on the surface figure of the optical element is analyzed additionally. It is shown that the defocus, spherical and trefoil aberration are sensitive to the adjusting force during axial adjustment process, and the largest terms are the primary spherical aberration and second spherical aberration, the introduced value is 2.16 and 1.94 nm respectively. However, during the tilt adjustment process, the astigmatism, coma and trefoil aberration are sensitive to the adjusting force, and the largest term is the primary coma aberration, the introduced value is 0.81 nm. In conclusion, the introduced aberration is relatively small.

Acknowledgments This work was supported in part by the National Science and Technology Major Project of China (Grant No. 2009ZX02205).

References

1. Matsuyama T, Ohmura Y, Williamson DM (2006) The lithographic lens: its history and evolution. *Proc SPIE* 6154:615403–615414
2. Miura T, Murakami K, Suzuki K et al (2006) Nikon EUVL development progress summary. *Proc SPIE* 6151:615105–615110
3. Sugisaki K, Oshino T, Murakami K et al (2000) Assembly and alignment of three-aspherical-mirror optics for extreme ultraviolet projection lithography. *Proc SPIE* 3997: 751–758
4. Yu J, Hao G, Chen G, Bi S (2015) State-of-art of compliant mechanisms and their applications. *J Mech Eng* 13:53–68 (in Chinese)
5. Hale L, Jensen S, Malsbury T, et al. (1998) Three-degree-of-freedom optic mount for extreme ultraviolet lithography. Office of Scientific and Technical Information Technical Reports
6. Hale L (1999) Principles and techniques for designing precision machines. Office of Scientific and Technical Information Technical Reports, pp 352–358
7. Chen SC, Golda D, Herrmann A, et al. (2004) Design of an ultra precision diaphragm flexure stage for out-of-plane motion guidance. In: ASME 2004 international design engineering technical conferences and computers and information in engineering conference, pp 1015–1021
8. Cox B, Kaufman M (2011) Design considerations of a slit diaphragm flexure used in a precision mirror gimbal. *Proc SPIE*. 8125, 81250R–81211
9. Vukobratovich D, Richard RM, McNiven JP, et al. (1995) Slit diaphragm flexures for optomechanics. *Proc SPIE*. 2542:2–10
10. Peng H, Sun Z (2014) Design and analysis of a precision axial adjusting mechanism for optical elements in lithographic lens. *Acta Photonica Sinica* 4:113–117 (in Chinese)
11. Guo K, Gong Y (2013) Precise axial adjustment mechanism with 6-PSS type of optical elements. *Optics Precis Eng* 10:2648–2655 (in Chinese)
12. Timoshenko SP, Woinowsky-Krieger S (1959) *Theory of plates and shells*. McGraw-hill, China
13. Xu Z (1990) *Elastic mechanics*. Higher Education Press, Beijing, China

A Rolling Triangular-Bipyramid Robot Covering Bennett Linkage

Ran Liu and Yan-an Yao

Abstract In this paper, a novel rolling triangular-bipyramid robot constructed based on a well-known Bennett linkage and a RSR chain is proposed. The two components connected by hinging RSR chain on two opposite axes of the Bennett linkage, and the R joints are perpendicular to the two axes, respectively. The robot has two degrees of freedom, and one actuator mounted at one of the R joint of the Bennett linkage while the other mounted at the R joint of the junction. By the analysis of kinematics, the robot can be folded into a narrow structure, which is easy to store and carry. Further, the rolling motion and path analysis are discussed. Finally, the simulation based on a 3D model was carried out to verify the feasibility of the proposed concept.

Keywords Triangular-bipyramid · Bennett linkage · Rolling robot

1 Introduction

Territorial mobile robots have many locomotion modes, such as walking, rolling, sliding and crawling. Rolling locomotion is an effective mode that has been used widely for the high mobility on the flat ground [1]. Spherical robot is a typical rolling mechanism with spherical geometrical shape. Its rolling locomotion is realized by rotating the entire outer surface of the spherical construction with the actuators inside [2]. Different from spherical robots, some rolling robots realize the rolling function by deforming their geometry shapes. Hamlin et al. [3] proposed the concept of concentric multilink spherical (CMS) joint on the nodes that intersect multiple links. Both tetrahedron and octahedron structures were built with this joint.

R. Liu (✉) · Y. Yao
School of Mechanical, Electronic and Control Engineering,
Beijing Jiaotong University, 100044 Beijing, China
e-mail: 14116360@bjtu.edu.cn

Y. Yao
e-mail: yayao@bjtu.edu.cn

Curtis et al. [4] introduced TET walker which formed with a set of telescopic struts. It moves by the coordination of extension or shrink of the telescopic links.

Triangular bipyramid is a common polyhedron formed by joining two tetrahedrons on their mirror face base-to-base. According to different construction methods, the design concepts of triangular-bipyramid robot mainly contain modularization and parallel-based construction. Ding et al. [5] designed a pneumatic triangular bipyramid with the module of pneumatic cylinder, which moved along dynamic rolling locomotion. Besides, based on the concept of parallel mobile mechanism, Tian et al. [6–8] developed a series of rolling robots appear as triangular bipyramid. And they all had one thing in common is that the robots were constructed with two identical nodes and three identical branch chains. As a result, the robot usually has two kinds of motions, one is that with single-DOF (Degrees Of Freedom) but the rolling directions could not be controlled, another is a flexible turning robot with three DOFs.

Bennett-based linkages comprise a major linkage family among the various single-loop overconstrained spatial linkages. Bennett linkage is usually used as the homogenous construct unit to form different overconstrained linkages [9]. But the heterogeneous Bennett-based linkage is rarely. According to the excellent folding function, the Bennett linkage is used as the module to form large-scale folding structures [10]. However, there is little intersection between the Bennett linkage and rolling robot, either the triangular-bipyramid structure.

In totally different way, this paper using the folding and single-DOF properties of the Bennett linkage substitute two branch chains of the triangular-bipyramid robot, and by hinging the third chain with RSR structure to present a novel rolling triangular-bipyramid robot with two DOFs. The robot has a large deformation capability. The dynamic rolling locomotion is analyzed to plan the straight rolling and turning motion. Finally, the simulations are carried out to express the motion more clearly.

2 Mechanism Design and Rolling Principle

2.1 Mechanism Design

Bennett linkage is a classical overconstrained linkage, which appears as a single-loop spatial mechanism consisting of four links that connected to each other with revolute joints. RSR chain is a familiar symmetrical chain. Connect these two elements by hinging the RSR chain on the separate axes of the Bennett linkage, where each of the R joints on the chain is perpendicular to the corresponding axis. See in Fig. 1, the triangular-bipyramid rolling robot with a Bennett linkage (ABCD) and a RSR chain (AEC) is constructed.

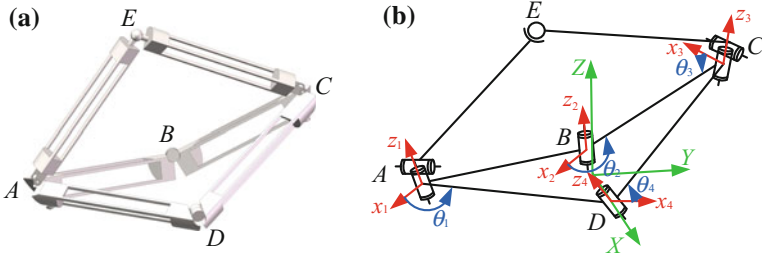


Fig. 1 3D model and sketch diagram of the robot

2.2 Mobility Analysis

It is well know that the Bennett linkage is single-DOF, thus the motion of point A and C on it could be further simplified as driving by a revolute joint, see in Fig. 2. The simplified mechanism is a non-overconstrained configuration, so that the mobility of it satisfied the Grübler-Kutzbach mobility condition [11]. Therefore,

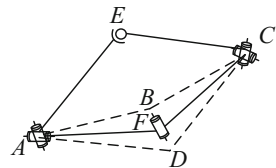
$$M = 6(n - 1) - \sum_{i=1}^g (6 - f_i) \tag{1}$$

where n is the number of links, g is the number of joints, and f_i is the DOF of the i -th joint. Substituting the parameter values for the robot, $M = 6 \times 3 - 16 = 2$. The triangular-bipyramid rolling robot has two DOFs.

2.3 Rolling Motion Analysis

Because of the asymmetry of the robot, there are three different states of the robot, including Bennett supporting (State I), Bennett link I and RS link supporting (State II) and Bennett link II and RS link supporting (State III), see in Fig. 3. In the three states, the robot all has three feasible tipping directions.

Fig. 2 The simplified configuration



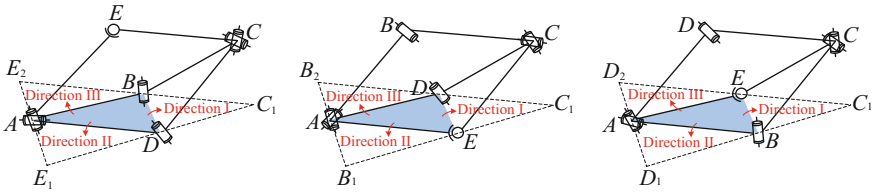


Fig. 3 Rolling feasibility of the three different states

3 Kinematics of the Robot

3.1 Kinematics of the Bennett Linkage

The Bennett linkage is a skewed linkage of four links having the axes of R joints neither parallel nor concurrent, its behavior is better illustrated by the schematic diagram shown in Fig. 4a. We choose an equilateral linkage whose linkage lengths are equal to each other, and the twist angles of opposite sides are supplementary angles.

The coordinate frame $O\text{-}XYZ$ is built in Fig. 4b. The origin O is the midpoint of nodes B and D . BD is the positive coordinate direction of X -axis, AO is the positive coordinate direction of Y -axis, Z -axis is determined by the right-hand screw rule.

The relationships between θ_i ($i = 2, 3, 4$) and input angle θ_1 are acquired with the geometry conditions of the Bennett linkage in [12], as shown in Eqs. (2)–(4).

$$\theta_2 = 2 \arctan \left(\frac{1}{\cos \alpha \tan \frac{\theta_1}{2}} \right) \tag{2}$$

$$\theta_3 = \theta_1 \tag{3}$$

$$\theta_4 = 2\pi - 2 \arctan \left(\frac{1}{\cos \alpha \tan \frac{\theta_1}{2}} \right) \tag{4}$$

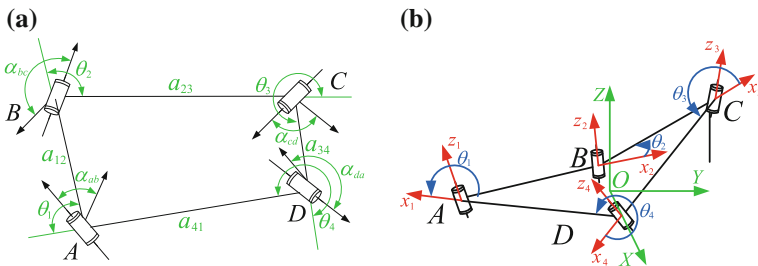


Fig. 4 Sketch diagram of the Bennett linkage and the coordinate system

The position coordinates of the four nodes $A-D$ are expressed as follows.

$$(x_A, y_A, z_A)^T = \left(0, -a \sin \frac{\theta_1}{2}, 0 \right)^T \quad (5)$$

$$(x_B, y_B, z_B)^T = \left(-a \cos \frac{\theta_1}{2}, 0, 0 \right)^T \quad (6)$$

$$(x_C, y_C, z_C)^T = \left(0, a \sin \frac{\theta_1}{2} \cos \angle C, a \sin \frac{\theta_1}{2} \sin \angle C \right)^T \quad (7)$$

$$(x_D, y_D, z_D)^T = \left(a \cos \frac{\theta_1}{2}, 0, 0 \right)^T \quad (8)$$

where, α is the twist angle of α_{ab} ; a is the length of each link; $\angle C$ is the dihedral angle of $\angle C-BD-y$. And it is the supplementary angle of dihedral angle of $\angle C_1$ ($\angle C-BD-A$), which could be solved by the dihedral angle formula in Eq. (9). And $\angle C$ is obtained in Eq. (10).

$$\begin{aligned} \cos \angle C_1 &= \frac{\cos \angle ADC - \cos \angle ADB \cos \angle CDB}{\sin \angle ADB \sin \angle CDB} = \frac{\cos(\theta_4 - \pi) - \cos \frac{\theta_1}{2} \cos(\pi - \frac{\theta_3}{2})}{\sin \frac{\theta_1}{2} \sin(\pi - \frac{\theta_3}{2})} \\ &= \frac{1 + \cos \theta_1 + 2 \cos \theta_2}{\cos \theta_1 - 1} \end{aligned} \quad (9)$$

$$\cos \angle C = \cos(\pi - \angle C_1) = -\cos \angle C_1 = \frac{1 + \cos \theta_1 + 2 \cos \theta_2}{1 - \cos \theta_1}. \quad (10)$$

3.2 Mounting a RSR Chain on the Bennett Linkage

The mounting strategy is that mount the RSR chain on the Bennett linkage with hinging link AE and CE on node A and C , separately. The initial position of E is set in the plane of OAC expressed as E_0 , see in Fig. 5. Q is the midpoint of AC , and the length of L_{EQ} is expressed in Eq. (11). δ is the angle between CA and Y -axis, which is obtained in Eq. (12). And φ is the next input angle that representing the dihedral angle of $\angle E_0-AC-E$. Then the position coordinates of node E could be acquired through the inputs in Eq. (13).

$$L_{EQ} = \sqrt{a^2 - \left(\frac{(x_C - x_A)^2 + (y_C - y_A)^2 + (z_C - z_A)^2}{4} \right)} \quad (11)$$

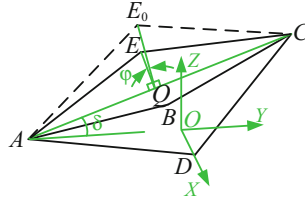


Fig. 5 Position coordinates of node E in O-XYZ coordinate system

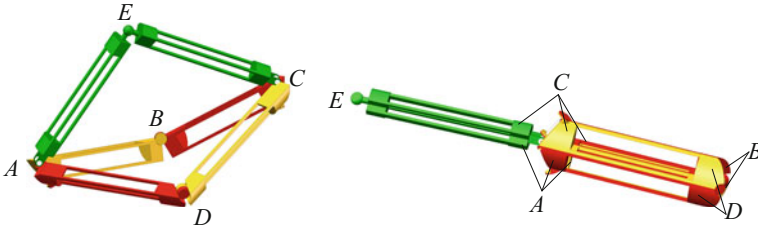


Fig. 6 Folding capability of the robot

$$\delta = \arctan \frac{z_C - z_A}{y_C - y_A} \tag{12}$$

$$(x_E, y_E, z_E)^T = \left(L_{EQ} \sin \varphi, -L_{EQ} \cos \varphi \sin \delta + \frac{y_A + y_C}{2}, L_{EQ} \cos \varphi \cos \delta + \frac{z_A + z_C}{2} \right)^T \tag{13}$$

According to the folding of Bennett linkage, when $\theta_1 = 180^\circ$, $\varphi = 0^\circ$, the robot folds into a stick, see in Fig. 6.

4 Locomotion Analysis

Because of the triangular-bipyramid rolling robot is symmetric with respect to the plane BDE all the time, so that the center mass of it would be always in this plane. Thus, no matter which points landing on the ground, the projection of the center mass of the robot would not go beyond the supporting area. Then the dynamic rolling locomotion is discussed in this section. The feasibility of achieving the rolling motions are shown based on the ZMP analysis.

4.1 Rolling Locomotion of State I

ZMP (Zero Moment Point) can be considered as the center of pressure at the feet (Supporting area) on the ground [13]. If ZMP is out of the supporting area, then the robot will lose the dynamic balance and tips over the corresponding supporting edge.

When the robot is in State I, there are three feasible rolling directions. Using the analysis similar to Kim et al. [14] and Takanishi et al. [15], ZMP can be expressed as follows.

$$x_{ZMP} = \frac{\sum_{i=0}^n m_i(\ddot{z}_i + g_z)x_i - \sum_{i=0}^n m_i\ddot{x}_iz_i}{\sum_{i=0}^n m_i(\ddot{z}_i + g_z)}. \quad (14)$$

$$y_{ZMP} = \frac{\sum_{i=0}^n m_i(\ddot{z}_i + g_z)y_i - \sum_{i=0}^n m_i\ddot{y}_iz_i}{\sum_{i=0}^n m_i(\ddot{z}_i + g_z)} \quad (15)$$

where, m_i is the mass of link i ; $(\ddot{x}_i, \ddot{y}_i, \ddot{z}_i)^T$ are the acceleration of link i ; g_z is the gravitational acceleration ($g_z = -9.8 \text{ m/s}^2$); $(x_i, y_i, z_i)^T$ is the mass center of link i .

Let ω_1, α_1 and ω_2, α_2 be the angular velocity and acceleration of θ_1 and φ , respectively. Based on the position coordinates of the nodes in Eqs. (5)–(7) and Eq. (13), the $(\ddot{x}_i, \ddot{y}_i, \ddot{z}_i)^T$ are expressed as follows.

$$(\ddot{x}_A, \ddot{y}_A, \ddot{z}_A)^T = \left(0, -\frac{a}{4} \left(2\alpha_1 \cos \frac{\theta_1}{2} - \omega_1^2 \sin \frac{\theta_1}{2} \right), 0 \right)^T \quad (16)$$

$$(\ddot{x}_B, \ddot{y}_B, \ddot{z}_B)^T = \left(\frac{a}{4} \left(2\alpha_1 \sin \frac{\theta_1}{2} + \omega_1^2 \cos \frac{\theta_1}{2} \right), 0, 0 \right)^T \quad (17)$$

$$(\ddot{x}_C, \ddot{y}_C, \ddot{z}_C)^T = \begin{pmatrix} 0 \\ a \left(\begin{array}{l} \frac{\alpha_1}{2} \cos \frac{\theta_1}{2} \cos \angle C - \frac{\omega_1^2}{4} \sin \frac{\theta_1}{2} \cos \angle C + \frac{\omega_1}{2} \cos \frac{\theta_1}{2} \cos \angle C \\ -\frac{\omega_1}{2} \cos \frac{\theta_1}{2} \cos \angle C - \sin \frac{\theta_1}{2} \cos \angle C \end{array} \right) \\ a \left(\begin{array}{l} \frac{\alpha_1}{2} \cos \frac{\theta_1}{2} \sin \angle C - \frac{\omega_1^2}{4} \sin \frac{\theta_1}{2} \sin \angle C + \frac{\omega_1}{2} \cos \frac{\theta_1}{2} \sin \angle C \\ -\frac{\omega_1}{2} \cos \frac{\theta_1}{2} \sin \angle C - \sin \frac{\theta_1}{2} \sin \angle C \end{array} \right) \end{pmatrix} \quad (18)$$

$$(\ddot{x}_D, \ddot{y}_D, \ddot{z}_D)^T = \left(-\frac{a}{4} \left(2\alpha_1 \sin \frac{\theta_1}{2} + \omega_1^2 \cos \frac{\theta_1}{2} \right), 0, 0 \right)^T \quad (19)$$

$$(\ddot{x}_E, \ddot{y}_E, \ddot{z}_E)^T = \begin{pmatrix} \ddot{L}_{EQ} \sin \varphi + 2\dot{L}_{EQ}\omega_2 \cos \varphi + L_{EQ}\alpha_2 \cos \varphi - L_{EQ}\omega_2^2 \sin \varphi \\ \ddot{L}_{EQ} \cos \varphi \sin \delta + \dot{L}_{EQ}\omega_2 \sin \varphi \sin \delta - \dot{L}_{EQ}\dot{\delta} \cos \varphi \cos \delta + \dot{L}_{EQ}\omega_2 \sin \varphi \sin \delta \\ + L_{EQ}\alpha_2 \sin \varphi \sin \delta + L_{EQ}\omega_2^2 \cos \varphi \sin \delta + L_{EQ}\omega_2 \dot{\delta} \sin \varphi \cos \delta - \dot{L}_{EQ}\dot{\delta} \cos \varphi \cos \delta \\ - L_{EQ}\dot{\delta} \cos \varphi \cos \delta + L_{EQ}\dot{\omega}_2 \sin \varphi \cos \delta + L_{EQ}\dot{\delta}^2 \cos \varphi \sin \delta + \frac{\ddot{y}_C + \ddot{y}_A}{2} \\ \ddot{L}_{EQ} \cos \varphi \cos \delta - \dot{L}_{EQ}\omega_2 \sin \varphi \cos \delta - \dot{L}_{EQ}\dot{\delta} \cos \varphi \sin \delta - \dot{L}_{EQ}\omega_2 \sin \varphi \cos \delta \\ - L_{EQ}\alpha_2 \sin \varphi \cos \delta - L_{EQ}\omega_2^2 \cos \varphi \cos \delta + L_{EQ}\omega_2 \dot{\delta} \sin \varphi \sin \delta - \dot{L}_{EQ}\dot{\delta} \cos \varphi \sin \delta \\ - L_{EQ}\dot{\delta} \cos \varphi \sin \delta + L_{EQ}\dot{\omega}_2 \sin \varphi \sin \delta - L_{EQ}\dot{\delta}^2 \cos \varphi \cos \delta + \frac{\ddot{z}_C + \ddot{z}_A}{2} \end{pmatrix} \quad (20)$$

The supporting area in State I is $\triangle ABD$, when ZMP is beyond the supporting area, the mechanism will tip over. In the initial state, $\theta_1 = 120^\circ$, $\varphi = 0^\circ$. For $\omega_1 < 0$ and $\alpha_1 < 0$, $\angle BAD$ will increase, then the ZMP goes beyond the supporting area, the robot will tipping to Direction I along supporting edge of BD . Figures 7 and 8 show the ZMP curve and the process of tipping to direction I. For $\omega_1 > 0$, $\alpha_1 > 0$, $\angle BAD$ will decrease. At that time, if $\omega_2 > 0$, $\alpha_2 > 0$, then the ZMP will goes beyond supporting area along edge AD . If $\omega_2 < 0$, $\alpha_2 < 0$, the ZMP will goes

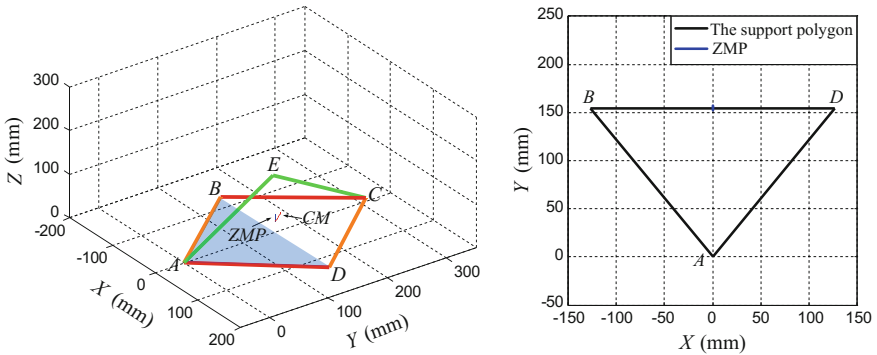


Fig. 7 The plot of ZMP when the robot tipping to direction I

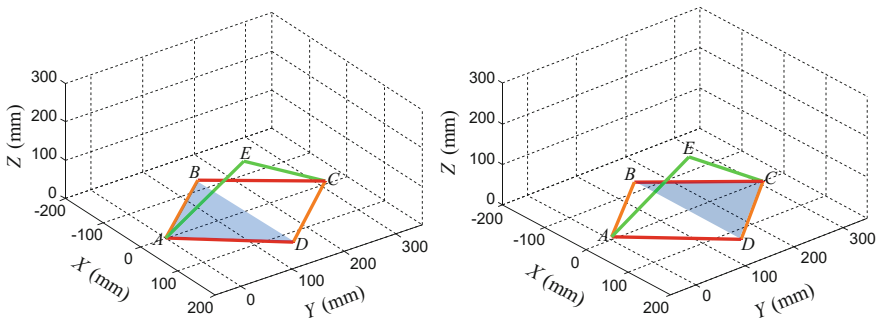


Fig. 8 The tipping process of tipping to direction I

beyond supporting area along edge AB . Figures 9 and 10 show the ZMP curve and the process of tipping to direction II.

Rolling locomotion in State II and State III are similar to State I. However, if the rolling principle is not roll back to the last step, then the rolling in the three states only have two effective directions.

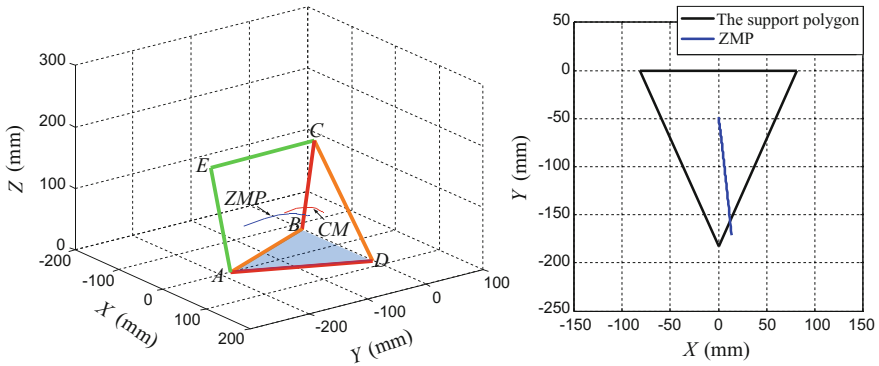


Fig. 9 The plot of ZMP when the robot tipping to direction II

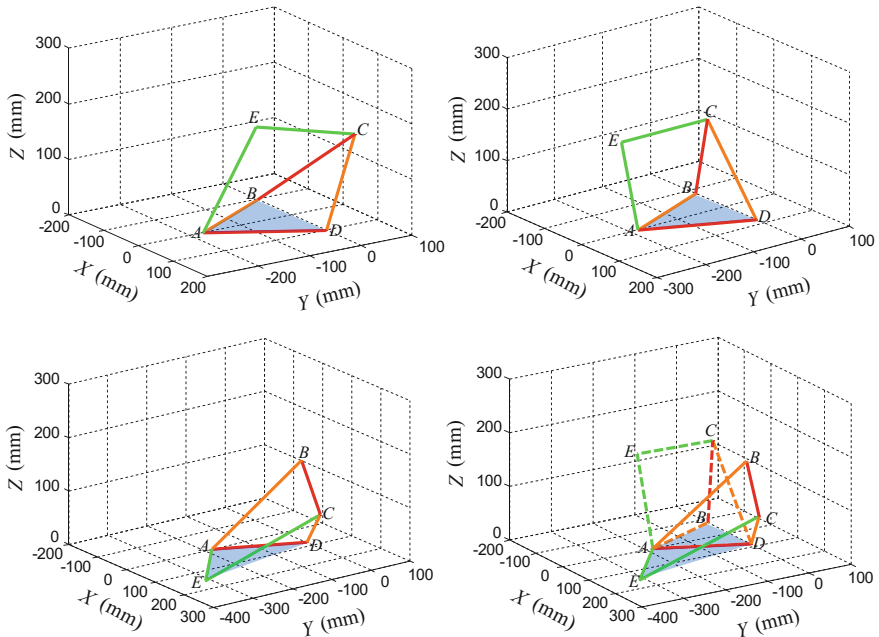


Fig. 10 The process of tipping to direction II

4.2 Straight and Turning Path

According to the locomotion analysis, the moving path of the robot is a serial of triangles. In this triangular grid (see in Fig. 11), the robot would easily get the straight and turning motion. As Fig. 12a–b show, the path planning of straight moving is carried out. Eight steps rolling make up a cycle, then the robot return to the initial state and rolling forward for $2\sqrt{3}a$. Repeat the cycle motion, the robot could go in the straight. In addition, according to the locomotion analysis, if the robot need turn to another direction, the turning angle is 60° . Figure 12c–d show the examples of turning motion.

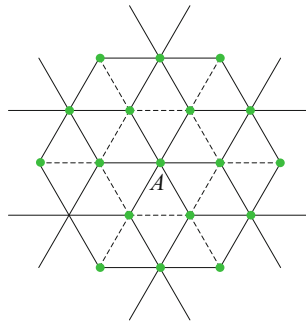


Fig. 11 The supporting triangle grid

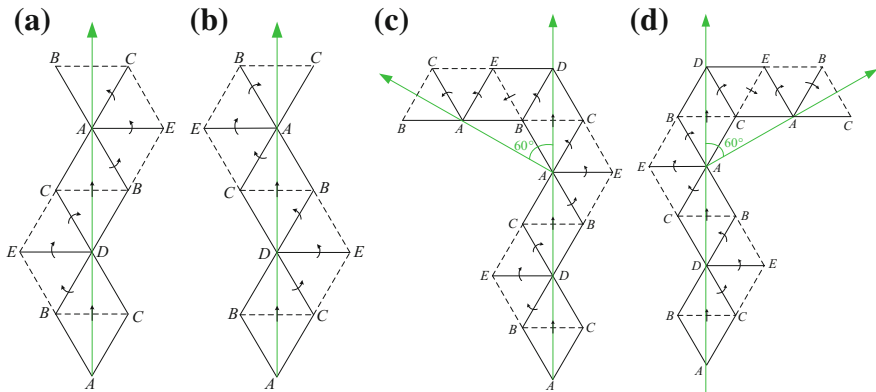


Fig. 12 Straight rolling cycle and turning motion

5 Simulation of the Movement

To verify the feasibility of the robot, the dynamical model was set up and the rolling functions were simulated in the software.

Figure 13 shows the straight rolling locomotion. In this process, M_1 and M_2 are driven synchronously to control θ_1 and φ . By a certain control strategy, the robot could roll in straight by tipping eight times to return to its initial state. Figure 13 is corresponding to the locomotion shown in Fig. 12b.

When the robot is to switch its direction, both turning to left and right are feasible. Without the loss of generality, the simulation is carried out by assuming that it turns right. Figure 14 illustrates the turning motion of the robot. Each time,

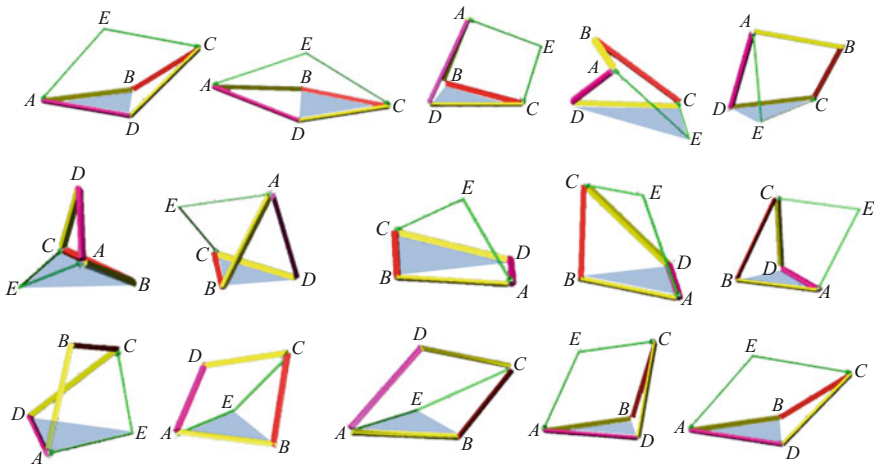


Fig. 13 Straight rolling locomotion

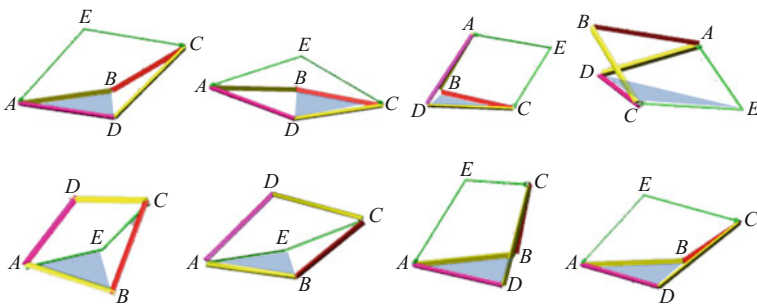


Fig. 14 Turning locomotion

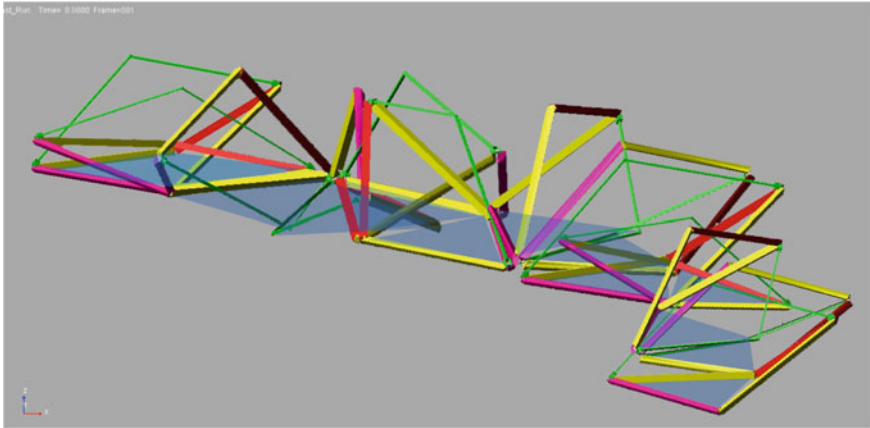


Fig. 15 Simulation of straight rolling and turning correspond to Fig. 13b

the robot could turn 60° . The simulation is corresponding to the turning motion shown in Fig. 12d.

Figure 15 is the successive moving locomotion of a cycle straight rolling and a direction switching. For the ignorance of friction in the theoretical analysis, the simulation and the theoretical trajectories are not exactly the same. However, the rolling motion is consistent in these two results. Thus, it reveals that the robot could realize the expected motion.

6 Conclusions

This paper proposed a rolling triangle-bipyramid robot, which was formed by a Bennett linkage and a RSR chain with two DOFs. By kinematic analysis, the robot has a flexible folding function that it could fold into a stick. Further, the rolling locomotion is analyzed, the result shows that with proper dynamic conditions, the mechanism was able to roll along straight line and switch its directions with 60° every time. A series of simulations were carried out that verify the feasibility of the robot.

In the future, there are two issues should be done to improve the robot: First, the optimal size of the linkages will be analyzed to increase the rolling smoothness; Second, based on the first issue, manufacture a prototype to test the dynamic property of the robot, which benefits to the control of dynamic rolling.

Acknowledgments This work was supported by National Natural Science Foundation of China (51405013), Science and Technology Special Project of Beijing (Z161100003216024).

References

1. Armour RH, Vincent JFV (2006) Rolling in nature and robotics: a review. *J Bion Eng* 3:195–208
2. Mojabi P (2002) Introducing August: a novel strategy for an omnidirectional spherical rolling robot. In: *Proceedings of the 2002 IEEE international conference on robotics and automation*, vol 4. Washington, D.C., USA, pp 3527–3533
3. Hamlin GJ, Sanderson AC (1994) A novel concentric multilink spherical joint with parallel robotics applications. In: *Proceedings of the 1994 IEEE international conference on robotics and automation*, vol 2. San Diego, Chile, pp 1267–1272
4. Curtis S, Brandt M, Bowers G et al (2007) Tetrahedral robotics for space exploration. *IEEE Aerosp Electron Syst Mag* 22:22–30
5. Ding W, Kim SC, Yao YA (2012) A pneumatic cylinder driving polyhedron mobile mechanism. *Front Mech Eng* 7:55–65
6. Tian YB, Guo YZ, Liu CH et al (2011) Single-DOF mobile linkage with possibility orientation movements. *J Mech Eng* 47:28–34
7. Tian YB, Yao YA (2015) Dynamic rolling analysis of triangular-bipyramid robot. *Robotica* 33:884–897
8. Tian YB, Yao YA (2012) Constructing rolling mechanisms based on tetrahedron units. *Adv Reconfigurable Mech Robots I* 21:221–232
9. Song CY, Chen Y, Chen IM (2013) A 6R linkage reconfigurable between the line-symmetric Bricard linkage and the Bennett linkage. *Mech Mach Theory* 70:278–293
10. Chen Y, You Z (2005) Mobile assemblies based on the Bennett linkage. In: *Proceedings of the royal society of London A: mathematical, physical and engineering sciences*, vol 461. London, Britain, pp 1229–1245
11. Gogu G (2005) Mobility of mechanisms: a critical review. *Mech Mach Theory* 40:1068–1097
12. Chen Y, You Z (2012) Spatial overconstrained linkages—the lost jade. In: *Proceeding of HMMS 2012 Explorations in the History of Machines and Mechanisms*, vol 15, pp 535–550
13. Vukobratovic M, Frank AA, Juricic D (1970) On the stability of biped locomotion. *IEEE Trans Biomed Eng* 17:25–36
14. Kim J, Chung WK, Youm Y et al (2002) Real-time ZMP compensation method using motion for mobile manipulators. In: *Proceedings of the 2002 IEEE international conference on robotics and automation*, vol 2. Washington, D.C., USA, pp 1967–1972
15. Takanishi A, Tochizawa M, Takeya T et al (1989) Realization of dynamic biped walking stabilized with trunk motion under known external force. In: *Proceedings of the 4th international conference on advanced robotics*, vol 21. Columbus, Ohio, pp 299–310

Mechanical Design and Dynamics Simulation of Locust-Inspired Straight Line Four-Bar Jumping Mechanism

Xiaojuan Mo, Wenjie Ge, Shaocong Wang and Donglai Zhao

Abstract By the observation and analysis of video took in the take-off phase of locust, it is concluded that hind limb plays an important role in jumping process. The trajectory of the end of tibiae approximately a straight line through the centroid of body, which explains the outstanding jumping performance and high energy utilization rate of locust jumping. The knee joint angle of hind limb changes from 10° to 140° during take-off. We proposed locust-inspired straight line four-bar jumping mechanism actuated by a micro motor, and it mimics trajectory of the end of tibiae, knee joint angle range and ground reaction force very well. Both dynamics simulation results and experimental results show that the designed jumping mechanism mimics the movement of hind limb very well during take-off.

Keywords Straight line · Trajectory · Jumping performance · Ground reaction force

1 Introduction

With robotic applications continuing to expand, there are more and more demands for robots that can adapt to non-structural environments. Presently, mobile robots can be divided into wheeled, crawler and multi-legged; all of these robots work very well in different environments, but all these traditional movement modes have

X. Mo · W. Ge (✉) · S. Wang · D. Zhao
School of Mechanical Engineering, Northwestern Polytechnical University,
Xi'an, China
e-mail: gwj@nwpu.edu.cn

X. Mo
e-mail: momo152562@mail.nwpu.edu.cn

S. Wang
e-mail: wangshaocong@mail.nwpu.edu.cn

D. Zhao
e-mail: dl_zhao@mail.nwpu.edu.cn

trouble to overcome obstacles that quite larger than their own. At the same time, it can be seen that frogs, kangaroos and locusts use jumping as their main movement modes to overcome big obstacles in nature, which inspires us to mimic movement models of those animals to design jumping robots. To adapt to complex environment, micro robots are more convenient to operate and can get more environmental information through group collaboration. Existing jumping robots can be divided into two kinds, continuous and intermittent. The former are mainly used for theoretical research while hopping robots oriented to practical application are usually intermittent hopping robots [1–4].

As a typical representative animal of intermittent jumping, locusts have moderate size and three kinds of compound movement models including crawling, jumping and flying, which gives us a lot of inspirations, such as developing micro jumping robots, combing jumping with crawling to improve efficiency, combing flying with jumping to solve landing and orientation changing problem. What's more, locusts have moderate size and longer take-off time comparing to other insects. And locusts widely exist in nature, so it is convenient to obtain and observe [5–7].

There are many scholars that choose locusts as the bionic object of the mobile robot research at home and abroad, and have made a wealth of research results. Professor Paolo Dario of Scuola Superiore Sant'Anna firstly proposed to use cams of quick-return characteristics, and developed "Grillo" series miniature jumping robots based on this [8–10]; Micro Kovac of Federal Polytechnic Institute in Lausanne developed a 5 cm 7 g jumping robot on the basis of robots "Grillo", which can jump over the obstacles that are 27 times its own size. Designer added the orientation-changing and take-off angle adjusting function for the jumping robots and designed a frame structure for the robots to solve the landing and resetting problem. In the later works they designed a pair of wings to help the jumping robot improve jump distance, reduce the landing speed and avoid landing buffer and resetting mechanism design [11–13]. V. Zaitsev of Tel Aviv University in Israel et al. proposed a new jumping mechanism based on torsion spring and rope lock-release mechanism which mimics the important role of strong hind limb and the semi-lunar process (SLP) in take-off phase. Designed robot mimics the jumping performance of locusts perfectly, which weighs 22.6 g, jumps 3.1 m in height and 3 m in distance, but this robot cannot realize take-off angle changing, orientation changing, landing buffer and resetting; so this robots need further improvement [14].

Chen, a professor of Beihang University, built an experimental platform to study the mechanism of locust movement during take-off and landing, designed a locust-inspired wheeled jumping robot and proposed energy distribution principle during landing phase. This principle provides basis for leg spring selection during mechanism design of bionic robots [15, 16]. Zhang, doctoral candidate of Southeast University proposed a locust-inspired jumping robot based on cam with quick-return characteristics, and designed method of localization, group-decision making and cooperation while multi-jumping robots work together [17, 18].

Zhen, of Zhejiang University studied the jumping mechanism of locust and designed four-bar jumping robots based on incomplete gear-rack mechanism, and the improved rope-lock mechanism effectively improved the energy utilization rate and jumping height of jumping robots [19].

In this paper, we designed a locust-inspired linear four-bar jumping mechanism which mimics the straight line trajectory of the end of tibiae and the angle range between femur and tibiae. Firstly, we analyzed the jumping mechanism of locusts combing the video filmed in take-off phase and calculated the contact force between foot and ground. Then, we designed the locust-inspired jumping mechanism and got one group optimized dimension parameters of four-bar mechanism which can achieve the straight line trajectory of the end of the tibiae and the angle range between femur and tibiae. Finally, we designed incomplete gear mechanism which can achieve energy locking and releasing, optimized fixed position of linear spring and stiffness coefficient, established the virtual prototype with dynamic analysis software to verify designed mechanism and built experimental prototype to verify simulation results.

2 Biological Observation and Analysis

In nature, animals such as frogs, kangaroos and a variety of insects like locusts, crickets use jumping as the main mode of movement. Animal researchers studied the jumping mechanism from the point of biomechanics and anatomy, and provided us precious locusts jumping video. Locusts were chosen as bionic object in our research work. Professor Burrows of the University of Cambridge studied the jumping mechanism of locusts systematically and deeply. And he divided animals' jumping mechanism into two kinds, lever and ejection. Jumping mechanism of locusts has the characteristics of both lever and ejection [20]. The videos analyzed in this thesis are provided by professor Burrows of University of Cambridge, and here we express our gratitude to professor of Burrows for his generous sharing.

2.1 *Locust Morphology Observation*

The insects are arthropods in which the body, the center of movement, is divided into head, thorax and abdomen. Locusts have three pairs of legs and wings. The jumping legs are hind legs which can be divided into femur, tibiae and tarsus as shown in Fig. 1. The strong femurs of jumping legs and the slender tibiae make locusts have strong ability of jumping. Before take-off of locusts, it stores the energy in semi-lunar process which works like a spring by the coordinated movement of femur and tibiae. During jumping phase, by rapid release of stored energy, locusts realize jumping while mid legs and fore legs play an important role

Fig. 1 Locust morphology

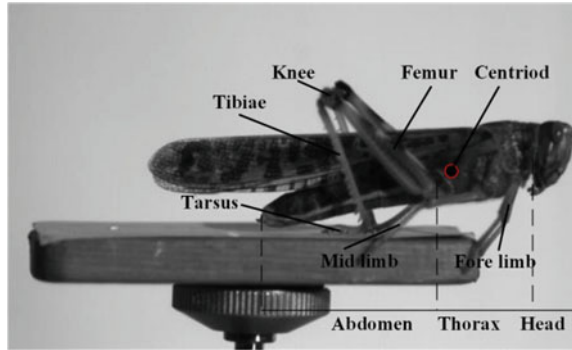


Table 1 The average morphology parameters of locust hindlimb

Body part	Length (mm)
Hindlimb, femur	23.15
Hindlimb, tibiae	22.04
Hindlimb, tarsus	6.52
Body	47.45

mainly in adjusting take-off angle and direction. The videos provided by professor Burrows were filmed by 1000 frames/s high speed camera; and the female locusts in the video weighs 2.5 g; related dimension parameters were shown in Table 1.

2.2 *Jumping Analysis at Take-off Stage*

We selected one clear and complete take-off video from the videos provided by professor Burrows, extracted key joint position using related software to analyze the jumping mechanism and concluded that the take-off phase of locusts lasts about 30 ms; the take-off angle is about 40°. In order to better understand the jumping mechanism of locusts, we recorded the important joint angle like θ_1 between tibiae and ground, knee joint angle θ_2 , θ_3 between body and femur during take-off phase. Fitted angle curve is illustrated in Fig. 2. In take-off phase, knee joint angle θ_2 becomes larger and larger; and ground force makes body continue to accelerate and finally left the ground and realize jumping.

Because the jumping mainly relates to the hind legs, the fore legs and mid legs are omitted in the simplified model and the quality of the fore legs and mid legs are merged into the body mass. In the simplified model, the body is simplified as a rigid body; the centriod is located in point S; femur is connected with the body by the joint C. We simplify the femur and tibiae as rigid rods, and simplified the knee joint as hinge B. In the take-off phase, the tarsus contacts with the ground so we simplified the tarsus with ground as a whole, the joint between tarsus and tibiae as hinge A. Simplified theoretical model is shown in Fig. 3.

Fig. 2 The joint angles of hindlimb

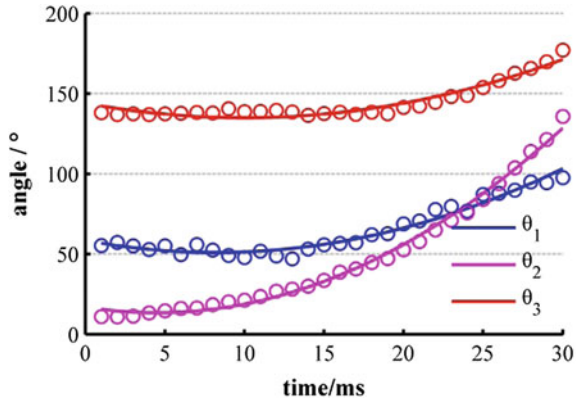
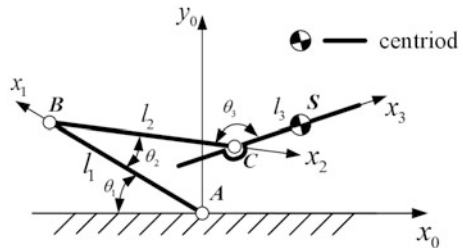


Fig. 3 Theoretical model of locust movement



According to the D-H method we established the X-Y reference coordinate system on the ground as Fig. 3 shown, and built up base coordinate system x_0-y_0 in the fixed hinge A and coordinate axes are parallel to the reference coordinate system. Because hinge A is fixed on the ground, the base coordinate system is fixed too. We established dynamic coordinate systems x_1-y_1 , x_2-y_2 , x_3-y_3 in the joint B, C, centroid S respectively, of which the x-axis positive direction is the direction of rods; z axis is perpendicular to the paper plane outward, and determined the joint angle positive direction based on right hand rule. θ_1 , θ_2 , θ_3 represents the angles between the links respectively, l_1 , l_2 , l_3 represents the length of femur bar AB, tibiae bar BC and the length between point C and centroid S respectively.

The transformed rotational matrix of coordinate system x_2-y_2 relative to coordinate system x_1-y_1 is:

$${}^1T_2 = \begin{bmatrix} \cos(180^\circ + \theta_2) & -\sin(180^\circ + \theta_2) & 0 & l_2 \bullet \cos(180^\circ + \theta_2) \\ \sin(180^\circ + \theta_2) & \cos(180^\circ + \theta_2) & 0 & l_2 \bullet \sin(180^\circ + \theta_2) \\ 0 & 0 & 1 & 0 \\ 0 & 0 & 0 & 1 \end{bmatrix} \quad (1)$$

Therefore, centroid coordinates in coordinate system x_0 - y_0 can be expressed as:

$$\begin{aligned}
 P_0 &= {}^0T_1 \bullet {}^1T_2 \bullet P_2 \\
 &= \begin{bmatrix} -l_3 \bullet \cos(\theta_1 - \theta_2 - \theta_3) + l_2 \bullet \cos(\theta_1 - \theta_2) - l_1 \bullet \cos\theta_1 \\ l_3 \bullet \sin(\theta_1 - \theta_2 + \theta_3) - l_2 \bullet \sin(\theta_1 - \theta_2) - l_1 \bullet \sin\theta_1 \\ 0 \\ 1 \end{bmatrix} \quad (2)
 \end{aligned}$$

So centroid position at take-off phase can be expressed as:

$$\begin{cases} x_S = -l_3 \bullet \cos(\theta_1 - \theta_2 + \theta_3) + l_2 \bullet \cos(\theta_1 - \theta_2) - l_1 \bullet \cos\theta_1 \\ y_S = l_3 \bullet \sin(\theta_1 - \theta_2 + \theta_3) - l_2 \bullet \sin(\theta_1 - \theta_2) - l_1 \bullet \sin\theta_1 \end{cases} \quad (3)$$

The displacement L_S , velocity V_S and acceleration a_S of centroid can be solved by the above formula:

$$\begin{cases} L_S = \sqrt{x_S^2 + y_S^2} \\ v_S = dL_S/dt = \sqrt{(\dot{x}_S)^2 + (\dot{y}_S)^2} \\ a_S = dv_S/dt = \sqrt{(\ddot{x}_S)^2 + (\ddot{y}_S)^2} \end{cases} \quad (4)$$

Ground contact force can be gotten from acceleration a_S , F is expressed as

$$F = m(a_S + g \sin\theta) \quad (5)$$

We substituted the angle θ_1 , θ_2 , θ_3 calculated from high speed video into the formula (5), and got centroid trajectory and acceleration curve of simplified model at take-off phase, as shown in Figs. 4 and 5. The acceleration is substituted into formula (6) and the contact force curve during the jumping process is got.

Fig. 4 Centroid trajectory

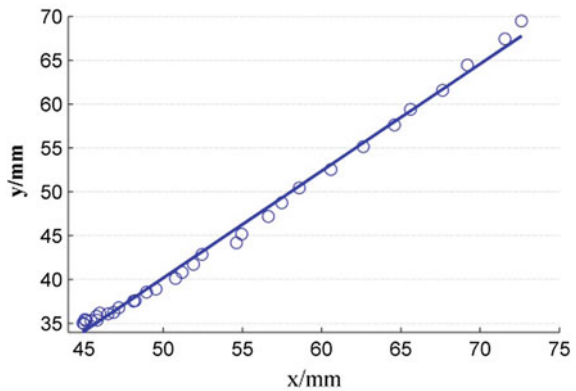
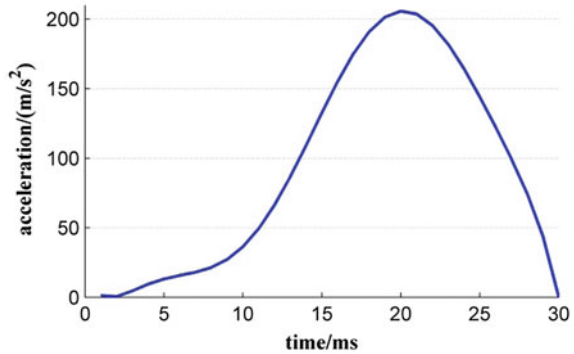


Fig. 5 Acceleration during take-off



By the analysis results of experimental data, it can be known that take-off phase lasts about 30 ms. At take-off phase, fore legs and mid legs left the ground first, the joint of hind legs will continue to rotate until the hind legs left the ground. It is concluded from the analysis result that θ_1 changes from 40° to 100° , θ_2 changes from 10° to 140° , θ_3 keeps unchangeable in the first 20 ms and gradually increases to 160° – 180° . With the increase of θ_2 , femur muscle is fully contracted and drives the movement of tibiae. Range of θ_3 will be different with the take-off angle changing. During the whole take-off phase, the trajectory of centroid of locusts is approximately a straight line. As the acceleration curve shown in Fig. 3, it is concluded that the contact force increased gradually to maximum value and then decreased. This variation trend makes locust jumping efficient, smooth and steady.

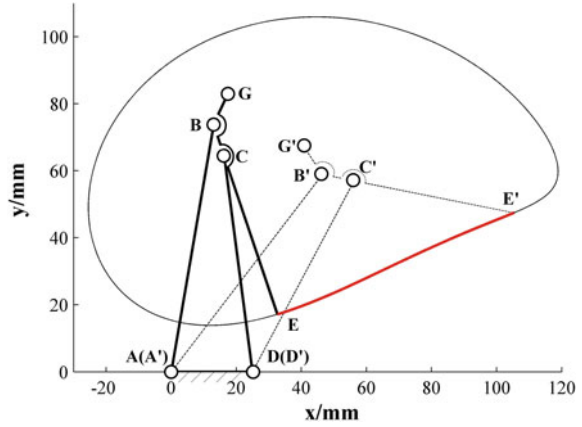
In sum, there are slight difference between the centroid position and displacement curve calculated from simplified model and that of biological prototype, but the variation trend is consistent. The error maybe caused by the following two factors: (1) there are errors in points marking of locust joints in jumping video processing; (2) the simplified model supposed centroid position is fixed relative to body while centroid position is changing because hind legs changes from curling up to stretching in locust jumping.

3 Jumping Mechanism Design and Analysis

3.1 Design of the Bio-Inspired Jumping Mechanism

The mechanism design of bio-inspired jumping legs needs to conform to two conditions: (1) the angle between two connecting rods working as femur and tibiae can change from 10° to 140° ; (2) centroid trajectory should be approximately a straight line in the jumping phase, so the distal of tibiae trajectory should be a straight line relative to body which is reference frame in calculation. Because

Fig. 6 Simplified model of bio-locust hopping mechanism



four-bar mechanism can achieve a variety of complex movement, the straight line trajectory of tibiae distal can be achieved by optimizing the length of bars. At the same time, the parameters of the four-bar mechanism is relative fewer which makes the mechanism design become easier, so the four-bar mechanism is chosen to mimic locust jumping legs. In simplified jumping mechanism, bar AD is fixed on the locust body; bar AB is femur; bar BC is tibia; and bar CD is auxiliary bar as Fig. 6 shown.

Initial values of links dimensions are got through calculation software of four-bar mechanism coupler curve which developed by professor Ge Wenjie, which has already applied for software copyright. The optimization result is got with the aim that the trajectory is a linear straight line passes the hip which is shown in the analyses results of locust jumping process. Line AE is supposed as the ideal trajectory line of the end of tibiae. If we suppose equation of line AE is L and $D_{E'_i \rightarrow L}$ is the distance between point E'_i and line L , we choose N positions of the end of tibiae at take of stage, the optimization goal is

$$\min \sum_1^N D_{E'_i \rightarrow L}^2 \tag{6}$$

Robots body works as a reference, which means bar AD is selected as rack. The four-bar mechanism parameters are optimized combining hind legs proportion of locust biological prototype. Optimization results shows proportion that $\overline{AD} : \overline{AB} : \overline{BC} : \overline{CD} : \overline{BE}$ equals to 1:3:0.4:2.6:2.4 should be kept to ensure the trajectory of point E is approximately a straight line. As the red line shown in Fig. 6, the trajectory of the distal point E of the tibiae bar is approximately a straight line passing through point A while bar AD works as reference frame. $ABCDE$ represents the beginning position of robots jumping, $A'B'C'D'E'$ represents the end position of

robots jumping, and the knee angle change from 29° to 117° which mimic the angle range of locust jumping very well.

Extension spring is chosen as energy storage element based on leg structure of jumping robots. In energy storage phase, tibiae are driven back to femurs while the spring is extended to storage energy. When the lock mechanism is released suddenly, tibiae are driven by the spring force to kick the ground quickly. Extension spring is chosen as the energy storage element in the four-bar mechanism while one end of the spring is fixed at point D , and other end of the spring is fixed at point G which is located in extended plane of bar BE . The position G is optimized with the optimization aim are minimum output torque of motor and maximum elongation of extension spring. Bar GB and BE 's length and installation convenience are took into consideration. The optimized result is shown in Fig. 6, $\angle GBC$ equals to 135° , \overline{BG} equals to \overline{BC} , of which the length of DG change from 83 mm at the beginning to 69 mm in the end of jumping and the elongation rate of the spring is 1.2.

In robots overall design, micro DC motor with speed reducer that is 6 mm in diameter and 21 mm in length is chosen in order to reduce the overall size and weight. The output speed of the motor is 30000 r/min, after gear reducer output speed is reduced to 40 r/min. The ratios of gear transmission are both determined by gear reducer output velocity and the hypothetical jumping preparation time. The ADAMS simulation results show that knee angle range is 120° while angle range between femur bar and body is 40° . Gear reducer output velocity is 40 r/min, the hypothetical jumping preparation time is 4 s, full period is 36 s, so the final output gear of femur bar is $5/3$ r/min, so reduction ratio of gear transmission is 24. We choose tri-step gear reducer with the reduction ratios are 2.8, 2.8, and 3 separately while modulus of standard gears is 0.5. The transmission mechanism is shown in Fig. 7.

We designed the frame, established three-dimensional model of robot as shown in Fig. 8, and determined mechanism parameters based on the biological model as shown in Table 2. In Fig. 8, two jumping legs are of symmetrical structure, and driven by a set of driven system synchronously.

Fig. 7 Transmission mechanism

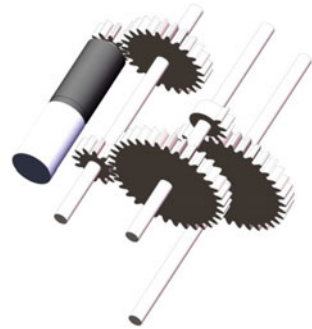


Fig. 8 Solidworks model of bio-locust jumping robot



Table 2 The structure size parameters

Parameter	Value
Bar AD/mm	25
Bar AB/mm	75
Bar BC/mm	10
Bar CD/mm	65
Bar BE/mm	60
$k/(N/mm)$	0.5

3.2 Kinematics Simulation and Experiment

Three-dimensional model established in Solidworks is imported into ADAMS. Materials properties, necessary markers, contacts and constraints are set up simulated. The elasticity of spring added in the model is 0.5 N/mm while the payload is 20 N. The simulation results of jumping process are shown in Fig. 9.

From Figs. 10, 11, 12 and 13, the following results can be obtained. The vertical displacement of robot's centroid is 380.4863 mm, and the horizontal displacement of robot's centroid is 1700.681 mm. The vertical velocity and the horizontal at the take-off point are 2646.607 and 3090.248 mm/s. It indicates that our design is feasible. During the take-off phase of the jumping robot, both the horizontal and

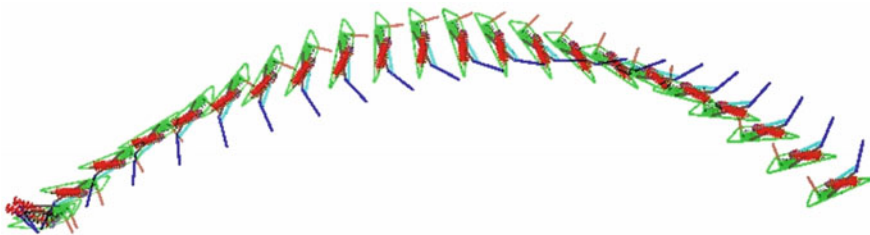


Fig. 9 The jumping process by simulation

Fig. 10 The horizontal displacement of the robot centroid

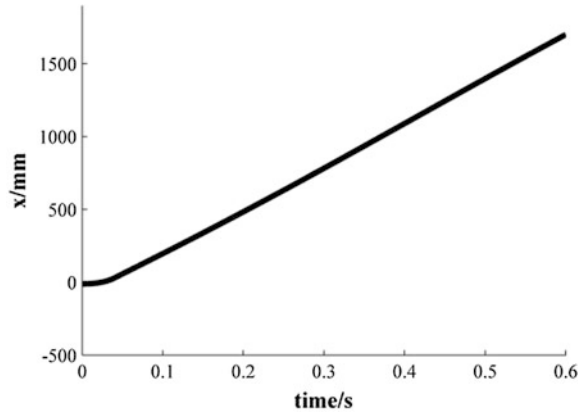


Fig. 11 The vertical displacement of the robot centroid

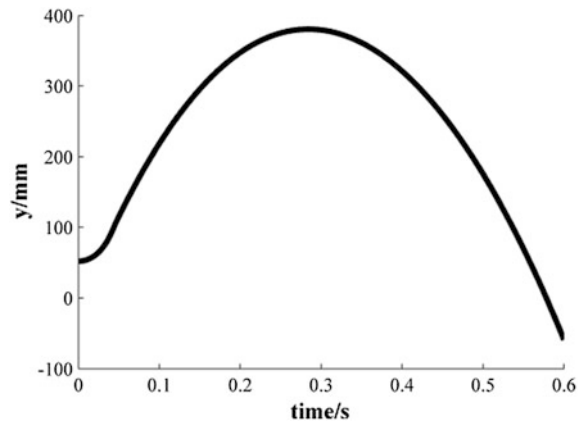


Fig. 12 The horizontal velocity of the robot centroid

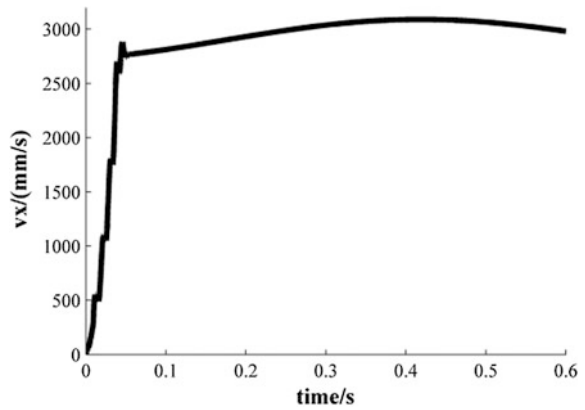


Fig. 13 The vertical velocity of the robot centroid

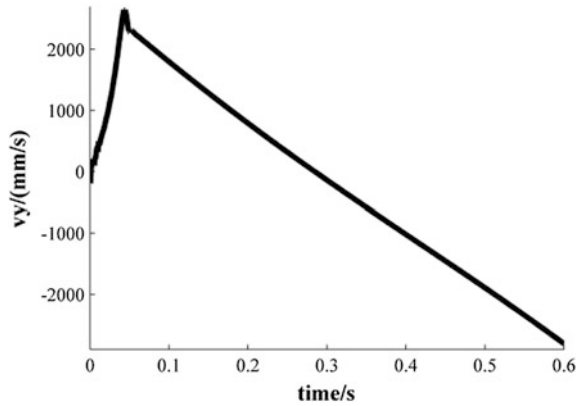
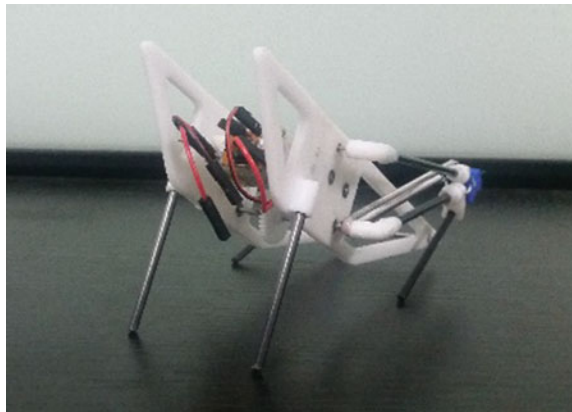


Fig. 14 Experimental prototype



vertical velocity increases sharply as shown in Figs. 12 and 13 but the displacement increase slowly as the initial velocity is zero. After the take-off phase, the robot follows the parabola so the horizontal velocity keeps stable and vertical velocity decrease to zero and then increase as shown in Figs. 12 and 13.

The frame of jumping robots was printed by 3D printer with PLA material; the legs were made by carbon fiber material with sufficient strength and toughness; the micro coreless DC motor and 3.7 V lithium battery is chosen. The prototype is shown in Fig. 14.

From the screenshot of jumping video of experimental prototype, it is known that jumping height is of about 2.5 times of body size and the jumping distance is of about 3 times of body size. The jumping performance of jumping robots is ideal.

4 Conclusion

The design of the straight line four-bar jumping mechanism gets inspiration from the locust's jumping leg. Based on the video provided by professor Burrows, biological kinematic analysis of the locust jumping mechanism is made. And a similar ground reaction force is get, compared to the biological analysis. The mechanical design is deliberated and kinematics simulation and experimental prototype are conduct to verify our design, which shows a feasible scheme.

In this paper, the jumping mechanisms are proposed based on the characteristics of locust such as the knee angle range during the jumping process and linear trajectory of the end of tibiae. At the same time, the mechanism proposed in this paper use the incomplete gears to achieve the goal of energy locking and releasing of the four-bar linkage mechanism and only use a micro motor which avoid the complex multi-motor coordinated control.

Our future work will concentrate on fabricating refined prototype and conducting experiments to test the jumping performance of it. Then the parameters that influence the performance will be studied and a self-righting mechanism is necessary to be added for posture recovery.

Acknowledgments In this thesis, the video used in the jumping mechanism analysis of locusts is provided by professor Burrows of university of Cambridge. Here we express our gratitude to professor of Burrows for his generous sharing.

References

1. Raibert MH (1986) Legged robots that balance. *J IEEE Expert* 1(4):89
2. Alexander RM (1995) Leg design and jumping technique for humans, other vertebrates and insects. *J Philos Trans R Soc B Biol Sci* 347(1321):235–248
3. James RS, Navas CA, Herrel A (2007) How important are skeletal muscle mechanics in setting limits on jumping performance? *J of Exp Biol* 210:923–933
4. Raibert MH (1993) Legged robots. *J Commu ACM* 29(6):499–514
5. Chen D, Yin J et al (2011) Bionic mechanism and kinematics analysis of hopping robot inspired by locust jumping. *J Bion Eng* 8(4):429–439
6. Chen D, Zhang Z, Chen K (2016) Legs attitudes determination for bionic locust robot based on landing buffering performance. *J Mech Mach Theory* 99:117–139
7. Zhao K, Yin J, Chen D et al (2012) Design and kinematics simulation for bionic crank-slider mechanism of jumping robot. *IEEE international conference on robotics and biomimetics*, pp 796–801
8. Scarfogliero U, Stefanini C, Dario P (2007) Design and development of the long-jumping “grillo” mini robot. *IEEE international conference on robotics and automation*, pp 467–472
9. Scarfogliero U, Stefanini C, Dario P (2006) A bioinspired concept for high efficiency locomotion in micro robots: the jumping robot grillo. *IEEE international conference on robotics and automation*, pp 4037–4042
10. Scarfogliero U, Stefanini C, Dario P (2009) The use of compliant joints and elastic energy storage in bio-inspired legged robots. *J Mech Mach Theory* 44(3):580–590
11. Kovac M (2010) Bioinspired jumping locomotion for miniature robotics. EPFL

12. Kovac M, Fuchs M, Guignard A et al (2008) A miniature 7 g jumping robot. IEEE international conference on robotics and automation, pp 373–378
13. Kovac M, Guignard A, Nicoud JD et al (2007) A 1.5 g SMA-actuated microglider looking for the light. IEEE international conference on robotics and automation, pp 367–372
14. Zaitsev V, Gvirsman O, Ben HU et al (2015) A locust-inspired miniature jumping robot. J Bioinspiration Biomimetics 10(6):066012
15. Chen K, Chen D, Zhang Z et al (2015) Design and analysis of the locust-inspired jumping robot leg. J Chin Sci Pap 10:1127–1130
16. Chen D, Zhang Z, Chen K (2015) Energy allocation in landing buffering process for biomimetic locust mechanism. J Mech Eng 13:196–202
17. Zhang J, Song G, Li Y et al (2013) A bio-inspired jumping robot: modeling, simulation, design, and experimental results. J Mechatron 23(8):1123–1140
18. Zhang J, Zhu Y, Wang H et al (2010) Design of a bio-inspired jumping robot for rough terrain. 2010 IEEE international conference on environmental science and information application technology (ESIAT), pp 40–43
19. Zhen Y (2013) Study on bio-jumping mechanism inspired from locust's take-off jumping mechanism. Zhejiang University
20. Bennet-Clark HC (1975) The energetics of the jump of the locust *Schistocerca gregaria*. J Exp Biol 63(1):53–83

A Novel Ventricular Assist Miniscule Maglev Nutation Pump: Structure Design, 3D Modelling and Simulation

Fengxiang Lin, Ligang Yao, Rongye Zheng, Wenjian Li
and Changsheng Fang

Abstract The ventricle assist device has emerged as an important therapeutic option in the treatment of both acute and chronic heart failure. The blood pumps, the major components of ventricle assist devices, have also progressed to the third generation. The magnetic levitation technologies have been applied into the third generation blood pumps. This paper proposes a novel miniscule maglev nutation pump with Magnetic bearing based on nutation principle. The calculation formula of magnetic force is established on the basis of the research for the operational principle of the magnetic bearing. Through establishing and solving the equations, the structural dimension and magnetization intensity of the magnetic bearing are obtained. Then, the three-dimensional model of the nutation pump is established. Furthermore, the structure design, manufacturing and assembling of the pump is completed. Finally, the simulation of the maglev nutation pump is carried out. And the effectiveness of the miniscule maglev nutation pump is verified.

Keywords Ventricle assist device · Nutation pump · Maglev · Manufacturing · Simulation

1 Introduction

Heart failure is the most challenging epidemic cardiovascular disease faced by the people in 21st century and causes the major death of human beings in global [1]. The best way to survive the lives of the end-stage heart failure patients is the heart transplant. Due to the amount of the heart donors is too small, and no effective immunosuppressive drugs are found for resolving the human tissue immune rejection after heart transplantation [2], it has become a trend that transplanting the heart with the artificial heart pump rather than the human body heart. Artificial heart

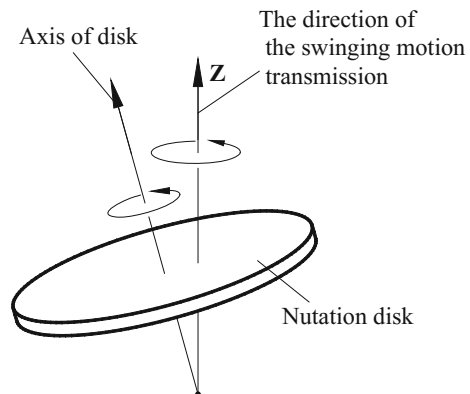
F. Lin (✉) · L. Yao · R. Zheng · W. Li · C. Fang
School of Mechanical Engineering and Automation, Fuzhou University, Fuzhou, China
e-mail: 526126877@qq.com

pumps make the blood flow in the body of patients to accomplish some of the functions of the heart of human being by mechanical movement. However, almost all of the artificial heart pumps suffer from hemolysis problems [3]. At present, the heart pump has developed to the third generation, which is based on the maglev technology [4–6]. The maglev heart pump is a hot research topic of artificial heart pumps. The maglev heart pumps are favorite for the properties including low thrombosis, less hemolysis, high energy efficiency ratio and long life [7]. In the view of the questions that continuous pumps have a high blade speed which could damage blood cells and cause hemolysis [8], reference [9] proposes a novel miniscule nutation pump for the heart-assist. This nutation pump has largely reduced the rotating speed under the same pump size and flow rate. In this paper, we introduce the magnetic bearing structure into the nutation pump, aiming at reducing the noise and friction. A novel miniscule maglev nutation pump for the heart-assist is proposed. The structure design including force analysis and mathematical modeling has been carried out. A prototype is also successfully made. And through the simulation for the maglev nutation pump, the feasibility of the structure of maglev nutation pump was validated.

2 The Principle of the Novel Miniscule Maglev Nutation Pump

The novel ventricular assist miniscule maglev nutation pump is based on the theory of nutation motion. Nutation motion is simple and clever. It can be described as the axis of a nutation disk has an angle with the space axis Z, and the disk rotates around the space axis with self rotating shown in Fig. 1 [10]. We introduce the magnetic bearing structure into the nutation pump which can be making the nutation disk suspension. In the process of the nutation disk doing swing motion, the magnetic bearing can provide enough magnetic flux to ensure stability.

Fig. 1 Nutation motion



3 The Design and Manufacture of the Novel Miniscale Maglev Nutation Pump

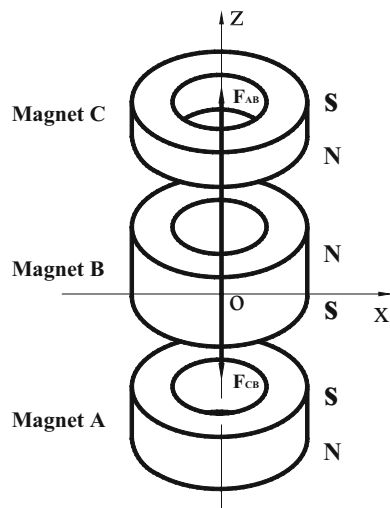
3.1 The Design Background of the Magnetic Suspension Structure

Magnetic suspension bearing is a new type of non—contact bearing which uses magnetic field to realize the suspension of moving parts [11]. According to the different ways of providing the magnetic, magnetic bearings can be divided into passive magnetic bearings (PMB) such as permanent maglev, active magnetic bearing (AMB) such as electromagnetic levitation and active passive hybrid magnetic bearing (HMB). Passive magnetic bearings do not need the active electronic control system which can save the power consumption, and reduce complex control system components. Since the structure of the novel ventricular assist miniscale maglev nutation pump is compact and small, it is suitable to adopt the passive magnetic suspension bearing, so that the structure of the bearing will be compact and robust.

3.2 Determine the Structure of the Magnetic Suspension Bearing

The magnetic bearing structure of the novel ventricular assist miniscale maglev nutation pump is shown in Fig. 2. The magnetic suspension bearing consists of three pieces of circular permanent magnets, the magnetic pole shapes the

Fig. 2 The structure of the magnetic suspension bearing



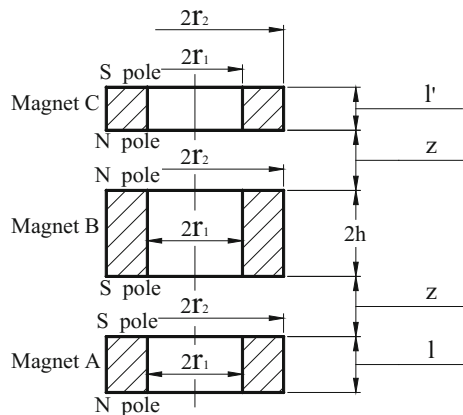
magnetization intensity, and the magnetization direction distributed along the axial of magnet A, magnet B and magnet C are identical. The arrangements of magnetic poles are shown in Fig. 2 and are keeping in the coaxial direction. There are only axial size differences among magnet A, magnet B and magnet C with the largest magnet B and the smallest magnet C. The direction of the magnetic force F_{AB} is upward of magnet A acting on magnet B, the direction of the magnetic force F_{CB} is downward of magnet C acting on magnet B, and the F_{AB} is greater than F_{CB} . And the resultant force can be expressed by F , the calculation formula is $F = F_{AB} - F_{CB}$. As a result, the resultant of the magnetic force is upward which can eliminate axial force of gravity.

The size of the magnetic structure of the magnetic suspension bearing can be solved by the equation $F = G$. Where G is required to balance the gravity of the nutation disk and sleeve including magnet B, the calculation formula is $G = G_{disk} + G_{sleeve} + G_{MagnetB} = 0.0405 \text{ N}$. It can be obtained the bearing size initially as shown in Fig. 3, $r_1 = 1.1 \text{ mm}$, $r_2 = 2.05 \text{ mm}$, $l' = 1 \text{ mm}$, $z = 2.6 \text{ mm}$, $h = 1 \text{ mm}$, $l = 1.5 \text{ mm}$.

Magnetic suspension bearing assembly is shown in Fig. 4. The magnet C and the magnet A are respectively fixed on the upper cover and the lower cover by the adhesive, the installation process must keeping the magnets coaxial.

As shown in Fig. 5, the magnet B is fixedly connected with the sleeve 1 and sleeve 2 by the adhesive, to ensure that the central axis of the magnet B is coincident with the square hole of the sleeve. The diameter of the magnet B is a little larger than that of the sleeve, the motor shaft and the square hole of the sleeve are matched with the small clearance. When the motor shaft drives the sleeve to rotate, the magnetic pole position of the magnet B remains unchanged, keeping the magnets coaxial when the nutation disk is working.

Fig. 3 Size diagram of the magnetic suspension bearing structure



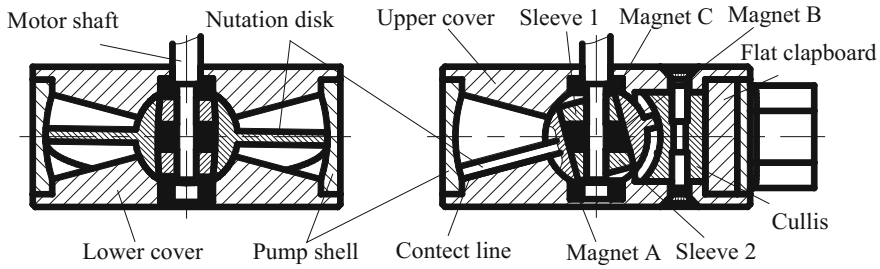
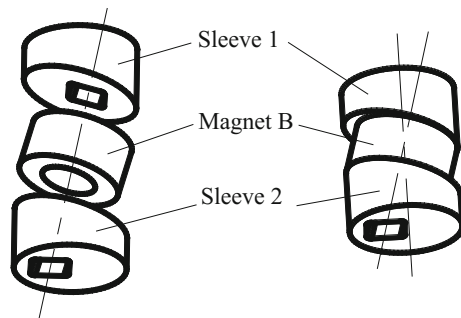


Fig. 4 Section view of the maglev nutation pump

Fig. 5 Sleeve assembly diagram



3.3 Manufacture of the Pump

The parts of the nutation pump are processed by CNC because of the absence of the forming tool and special machine tool. And NdFeB is selected as the material of the magnetic bearings. In order to prevent the magnetic bearing from adsorbing on the pump body, the material of the pump body is non-magnetic. Physical processing is only a preliminary experiment; as a result, stainless steel 304 is selected as the material of the pump body. Tips for manufacturing are listed as followed: (1) Ensure the processing precision. (2) Tilt angle of upper and under covers is slightly larger than tilt angle of sleeve, which can avoid interference. (3) For avoiding contact and friction, there is small gap between edge of nutation disk and inner spherical surface of shell. (4) A transition fit between the magnet slot and the magnet are set. (5) The motor shaft is processed into square with its size 1.5×1.5 mm.

The machining parts are shown in Fig. 6, the assembling is shown in Fig. 7. The pump has been manufactured, and the experiment has been carried out. With the limitation in space, we have not discussed the experiment in this paper.

Fig. 6 Parts drawing of pump



Fig. 7 Assembly drawing of pump



4 The Simulation of the Novel Ventricular Assist Miniscule Maglev Nutation Pump

4.1 3D Modeling of Pump

As shown in Fig. 8, the new miniscule nutation pump consists of pump body and drive motor. The pump body is composed of an upper cover, a magnet A, sleeve 1, a magnet B, sleeve 2, a nutation disk, a flat clapboard, a cullis, a pump shell, a magnet C, a lower cover and lock screws as shown in Fig. 9.

Fig. 8 Component of pump

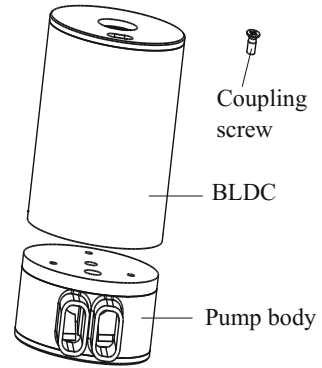
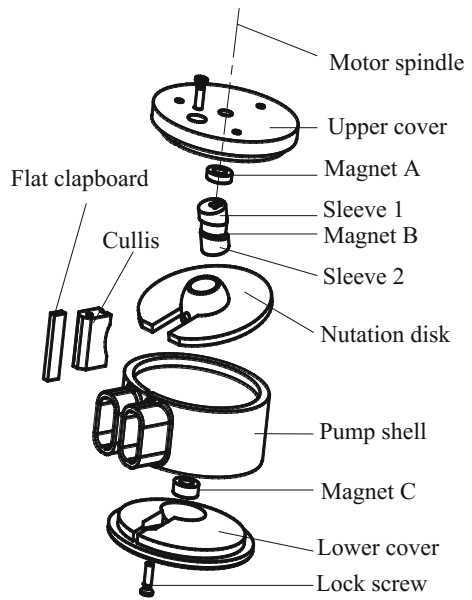
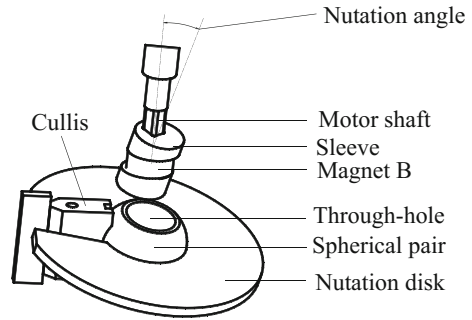


Fig. 9 Pump body assembly diagram



Where in Fig. 10, the motor shaft is fixed to the sleeve with incline axis (the tilt angle is nutation angle), and there is a through-hole in the spherical pair of the nutation disk. In order to prevent the motor shaft idling in the sleeve, the structure of the motor shaft is designed to be square. During the working time, the motor drives the sleeve rotation and the sleeve drives the nutation disk doing swing motion.

Fig. 10 Drive of sleeve

4.2 Simulation of the Pump

The Motion simulation module in SOLIDWORKS can simulate the energy consumption of the motor in real time. The module can set the movement rule of the pump. At the same time, force loading and moment loading of the pump, then the energy loss of the motor are obtained by simulation. The magnetic suspension bearing of the maglev nutation pump eliminates the gravity of the moving parts, so the nutation disk is mainly influenced by the fluid force. The principal vector and principal moment of the fluid acting on the nutation disk is three-dimensional space. Import the principal vector and principal moment of X, Y, Z deviator. Nutation disk is cycle operation and according to the analysis of an operation period of nutation disk. The time span of a cycle is 0.015 s, the real time changing curves of the principal vector and principal moment are shown in Figs. 11 and 12.

The real time changing curves of the motor energy in the maglev nutation pump are shown in Fig. 13. Due to the complex interaction produced by fluid in the pump body, there are fluctuations in the working power, the average power is about 4 W in a cycle, maximum up to 5.2 W.

5 Conclusions

This paper presents a novel ventricular assist miniscule maglev nutation pump with passive magnetic bearing structure. The design background and working principle of the magnetic suspension bearing are analyzed, and the axial suspension of the moving parts is realized by the repulsive force among the three ring permanent magnets. A theoretical method is used to derive the formula for calculating the magnetic force of the magnetic structure. The gravity of the moving parts is calculated and the magnetization intensity of the magnetic suspension bearing is determined by the equation. Three dimensional model of heart pump was built by using 3D software, and the prototype of the heart pump was processed according to the determined dimensions. It is concluded that the resultant force of the middle

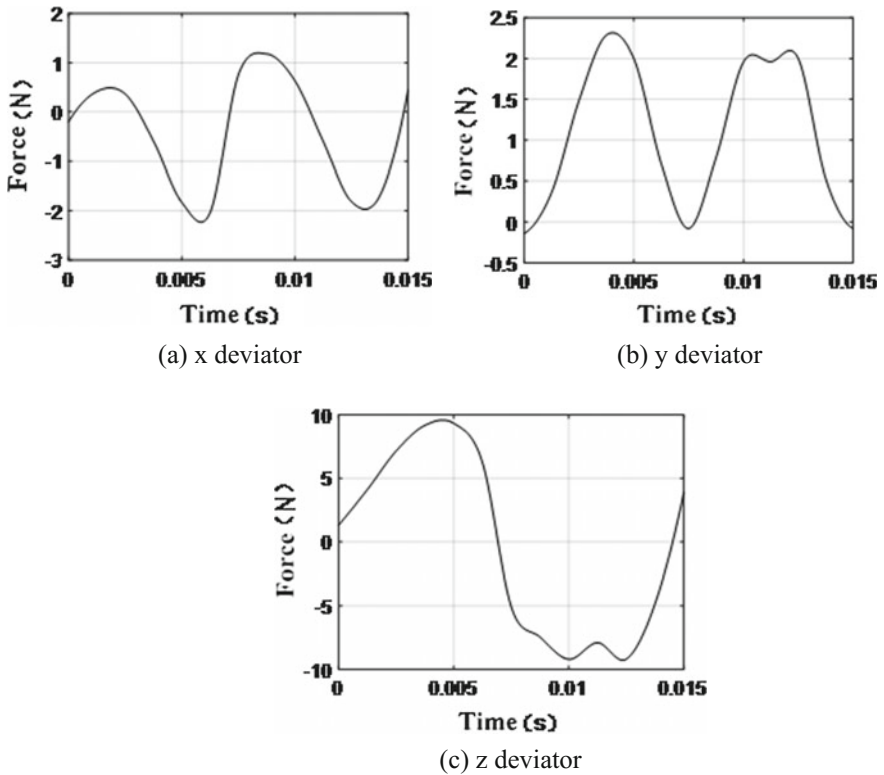


Fig. 11 Principal vector

magnet is nearly equal to the gravity of the moving parts, the magnetic structure is proved to meet the design requirements. Finally, the simulation of the maglev nutation pump is carried out. And the effectiveness of the miniscule maglev nutation pump is verified. The magnetic nutation heart pump does not increase the volume of the pump and ensures existing rotation speed and flow rate based on the ventricular assist miniscule nutation pump. The axial suspension of moving parts is realized, which reduces the friction and noise, and the performance of the pump is improved.

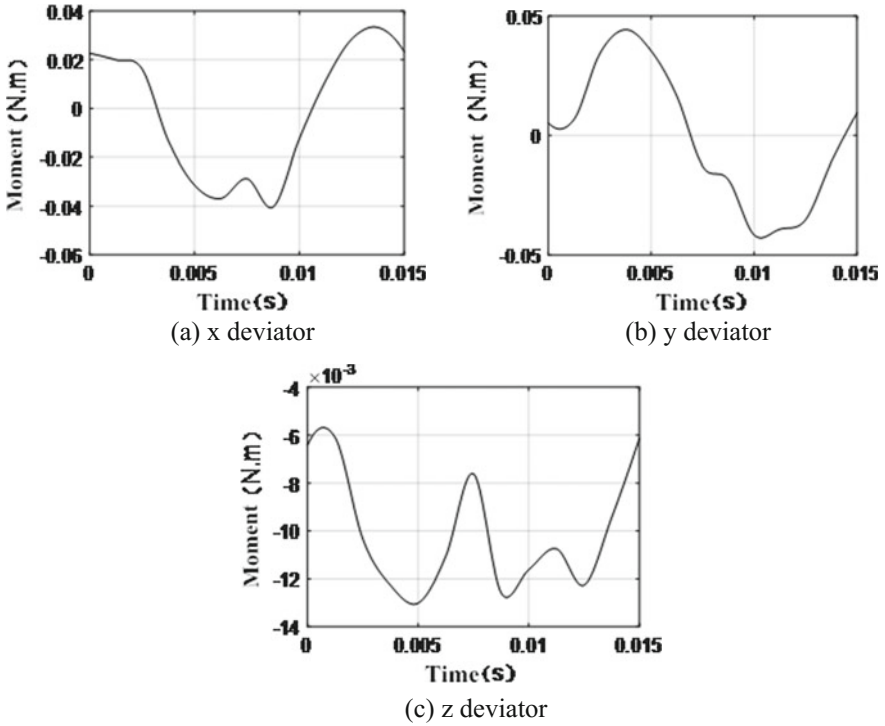
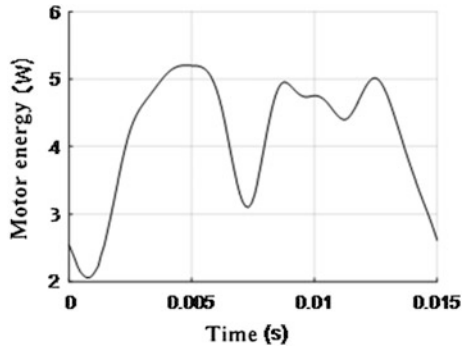


Fig. 12 Principal moment

Fig. 13 Motor energy consumption



References

1. Qu Z (2008) Modern mechanic circulation support for heart failure. Scientific and Technological Literature Publishing House, Beijing, pp 9–10
2. Mozaffarian D, Benjamin EJ, Go AS (2015) Heart disease and stroke statistics–2015 update: a report from the American Heart Association. *Circulation* 131:e29–322

3. Han W, Han BX, Wang HY, Shen ZJ (2013) Numerical analysis of the internal flow field in screw centrifugal blood pump based on CFD. *52(3):032020*
4. Schmitto JD, Hanke JS, Rojas SV (2015) First implantation in man of a new magnetically levitated left ventricular assist device (Heart mate III). *J Heart Lung Transplant 34(6):858–860*
5. Hoshi H, Shinshi T, Takatani S (2006) Third-generation blood pumps with mechanical noncontact magnetic bearings. *Artif Organs 30(5):324–338*
6. Yang S, Liu SQ, Guan Y (2010) Study on drive motor for axial-flow magnetic-levitation artificial heart pump. *Chin Mech Eng 21(8):893–896*
7. Guo LH, Zhang JM, Zhao L, Liu XC (2011) Experimental study of hydrodynamic in vitro of an implantable magnetic levitation blood pump. *J Biomed Eng Res 30(2):82–85*
8. Chen ZS, Yao ZH, Zhu LL, Zhang XW (2013) Hemolysis analysis of axial blood pump with various structure impellers. *J Mech Med Biol 13(4):1484–1497*
9. Shen HW (2014) Feasibility analysis and design of a novel ventricular assist miniscule nutation pump. Fuzhou University, Fu Zhou
10. He JY, Yao LG, Shen HW, Zheng RY (2015) Feasibility analysis and design of a novel ventricular assist miniscule nutation pump. *Procedia CIRP 36:273–278*
11. Zhang WY, Zhu HQ, Yuan Y (2015) Study on key technologies and applications of magnetic bearings. *Trans Chin Electrotech Soc 30(12):12–20*

A Novel Mechanism for Winding Foaming Resin on Embedment Used in Aerospace

Wuxiang Zhang, Keqing Zhang and Xilun Ding

Abstract The embedment, wound by foaming resin, is an important component widely utilized in the honeycomb sandwich structure to connect with equipment. However, the wound embedment is still manufactured manually nowadays and the productivity is low. In this paper, an automatic winding mechanism is developed, which consists of foaming resin feeding, transmitting, cutting mechanism, and embedment positing and driving mechanism. Especially, embedment positing and driving mechanism which is the key part of the whole mechanism is designed and analyzed. Different experiments are provided to demonstrate the validation of the mechanism.

Keywords Foaming resin strip · Embedment · Motion analysis · Force analysis

1 Introduction

Conventionally, the threaded hole in an embedment is used as the connection of honeycomb sandwich structures. As a kind of foam rubber, the foaming resin is usually used in the honeycomb sandwich structure to fill in the blanks, and splice metal alloy and carbon fiber composite [1]. The foaming resin is wrapped on embedment and connects with the honeycomb. During the fabrication process, the foaming resin strip is wound on embedment and the winding diameter equals to diameter of the flange [2]. Nowadays, no equipment can meet this demand. Due to the adhesive and soft characteristics of the foaming resin, the wound embedment is

W. Zhang (✉) · K. Zhang · X. Ding
School of Mechanical Engineering and Automation, Beihang University,
Beijing, People's Republic of China
e-mail: zhangwuxiang@buaa.edu.cn

K. Zhang
e-mail: zhangkeqing@buaa.edu.cn

X. Ding
e-mail: xlding@buaa.edu.cn

still manually manufactured. Consequently, the foaming resin strip may be polluted and it is difficult to guarantee that the length of foaming resin strip of each wound embedment is uniform. Similar equipment used to winding other particular strip often adopts the method that a motor drives the winding axis directly, and in some other equipment, a friction roller drives the winding axis [3, 4]. The product made by hand is of poor quality, but the design of similar equipment doesn't apply to wind foaming resin on embedment.

This paper firstly introduces the technological requirements of the equipment, then demonstrates the integral mechanism and concentrates on the kinematic and force analysis of the clamping and rotating integrated mechanism. Finally, this paper presents some experiments with the developed equipment and draws some conclusions.

2 Technological Requirements

As shown in Fig. 1, the shape of embedment made of aluminum alloy is a cylinder with a flange on one side or each side. H is the height of the embedment, and h indicates the height of the foaming resin strip. To ensure a continuous work, the machine needs to connect strips autonomously during the transmitting process, and prevent strips from either plastic deformation due to even a small extra force or sticking to adjacent objects. A steady tension of the foaming resin strip should be maintained during the winding process. A flat end face of the final wrapped embedment is required [5].



Fig. 1 Appearance of the embedment before and after winding

3 Mechanism Design

Automatic winding mechanism for foaming resin strip consists of foaming resin feeding, transmitting, cutting mechanism, and embedment positing and driving mechanism (Fig. 2).

Each foaming resin strip is stored in one groove. Ten parallel long grooves are equidistantly installed on a metal panel. The metal panel is fixed on the block of the linear slide unit which can move in the Y-axis. The first groove is located when the metal panel triggers the limit switch. With a sheet installed on its piston rod, the air cylinder is fixed behind the linear slide unit used to push the foaming resin strip in the X-axis. When the whole strip is out of the groove, the linear slide unit will drive the metal panel to locate the next groove. Then, the air cylinder pushes out another strip for supplement.

The foaming resin strip is between two rollers when be pushed out of the groove. Installed on the output shaft of the servo motor which changes the rotational speed to match the winding speed, the rollers transmit the foaming resin strip by the friction force. The connection between the end of the former strip and the beginning of the later strip, realized by the pressure between two rollers, ensures a continuous transmitting of the strips.

The cutting mechanism consists of an immobile cutter blade and a removable cutter blade. The removable cutting blade can move in Y axis driven by an air cylinder. When the length of the strip transferred through the cutting mechanism is proper, the removable cutting blade slides fast and cuts the strip. The pressing mechanism of the foaming resin strip is an air cylinder which presses the strip on

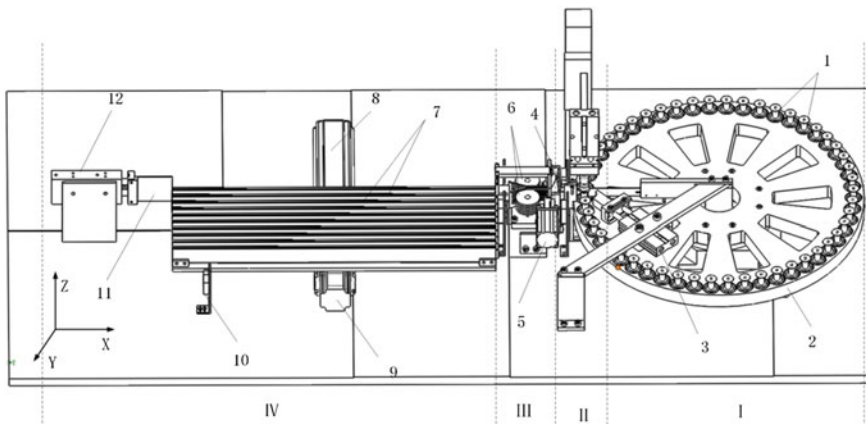


Fig. 2 Schematic diagram of the automatic winding machine (1 embedment, 2 circular panel, 3 air cylinder for pressing, 4 cutting mechanism, 5 air cylinder for driving cutter blade, 6 a pair of rollers, 7 groove for storing strip, 8 linear slide, 9 stepper motor, 10 limit switch, 11 sheet, 12 air cylinder)

the cylindrical surface of the embedment when the beginning end of the strip approaches the embedment.

Fifty identical stepped holes are located equally along a circle on the upper surface of a circular panel. From the bottom-up in Z-axis, a thrust ball bearing, a rotatable support, a silicone shim and a positioning tool is installed. The thrust ball bearing ensures the rotation of the rotatable support and embedment under the action of load along Z-axis, and rotational torque is transferred from the drive motor to the embedment. The silicone shim is placed between the upper surface of the rotatable support and the lower surface of the embedment for increasing friction. Each kind of embedment can be coaxial with the holes by the positioning tool assisting. Proximity switch, mounted on the table, is used to locate the first embedment by detecting the mark on the underside of the circular panel. On the basis of that, the next embedment can be located through the constant angle rotation of the circular panel driven by electric rotary table.

4 Design and Analysis of Clamping and Rotating Integrated Mechanism

Due to the special design requirements and basing on the storing and positing mechanism of the embedment, a clamping and rotating integrated mechanism of the embedment is desired. Although mechanisms with similar functions already exist, the special requirements proposed by the winding mechanism for foaming resin cannot be satisfied.

For instance, the vacuum chuck requires large adsorption area to generating enough adsorption force and an unstable air supply may cause clamping failure. Besides, falling debris can block air pipe [6]. Mechanical clamps, such as the scroll chuck, have a large scale and need a big clamping length, and the rotating axis cannot be installed automatically without manual or robotic support [7]. This paper focuses on designing an integrated mechanism to clamp and rotate the embedment on the circular panel. Kinematic and dynamic characters of the mechanism are analyzed based on the design.

4.1 Detailed Design of the Integrated Mechanism

An air cylinder with a 1-dof rotatable rod on its piston is used for clamping the upper surface of the embedment. The lower surface of the embedment is supported by the rotatable support. Under the circular panel, another air cylinder is mounted, and a servo motor is installed on the piston rod of the air cylinder. When the circular panel is rotating, piston rods of the upper and lower air cylinders must be retracted to avoid hindering the rotation. The piston rod of the upper air cylinder extend once

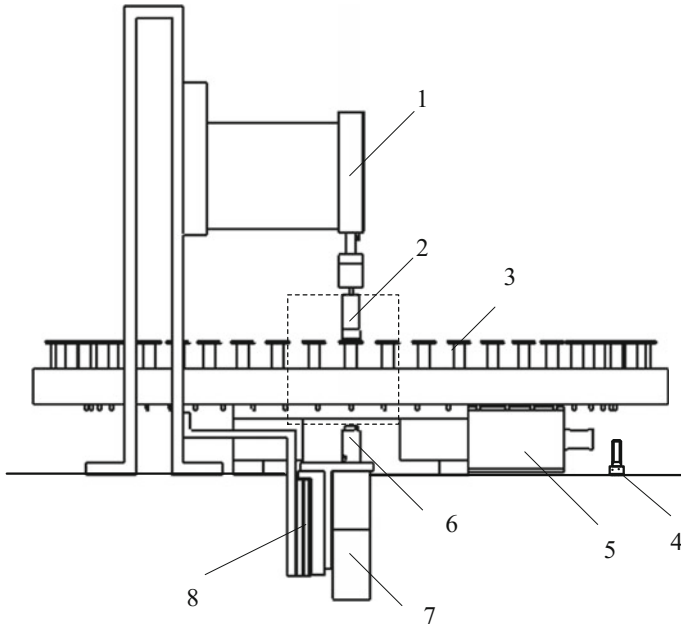
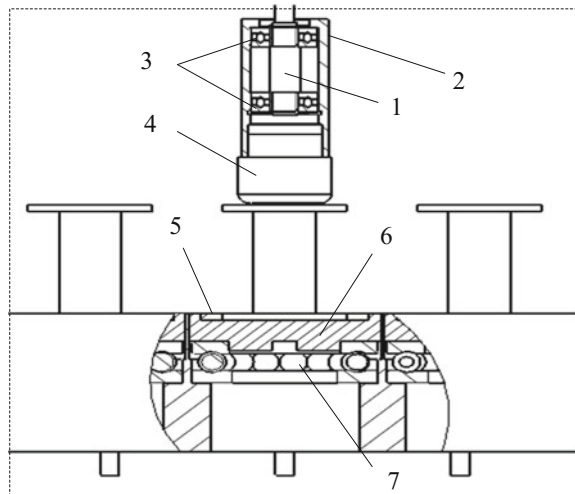


Fig. 3 Clamping and rotating integrated mechanism of embedment (1 upper air cylinder, 2 rotatable rod, 3 embedment, 4 proximity switch, 5 electric rotary table, 6 cylinder with a boss, 7 servo motor, 8 lower air cylinder)

Fig. 4 Details of the clamping structure (1 inner shaft of the rotatable rod, 2 rotatable outer part, 3 thrust ball bearing, 4 flexible part, 5 positing tool, 6 rotatable support, 7 thrust ball bearing)



the next embedment is placed. Then, the piston rod of the lower air cylinder raises the motor which is used to drive the embedment to rotate. A cylinder with a boss on upper face is installed on the output shaft of the motor (Figs. 3 and 4).

Corresponding with the boss, there is a slot on the bottom surface of the rotatable support. When the lower air cylinder extends, the boss of the cylinder presses the bottom surface of the rotatable support. After rotating a certain angle, the boss aligns with the slot on the vertical plane. Under the pressure of the piston, the motor rises and the boss is chucked by the slot. Then the rotatable support and the embedment rotate together driven by servo motor.

4.2 Kinematic and Force Analysis

Since the pressure of cylinder is much larger than gravity of each part, the latter is ignored in force analysis. As shown in Figs. 5 and 6, the shaded part of the figure indicates the boss and the other part indicates the lower surface of the rotatable support. Analysis of 1/4-circle rotation process is enough to understand the total process as the two parts both have symmetrical structures. Before the boss has embedded the slot, the torque of the motor must be smaller than sum of friction torques of all bearings.

When the boss embeds the slot, the lower air cylinder reaches its limit in Z axis direction, the upper surface of the boss is lower than the slot. And the motor doesn't supply support force to the rotatable support.

The diameter and width of the boss is 10 and 3 mm respectively, and the width of the slot is 4 mm. For easier calculation, the coordinate system is established with the rotation center as the origin. Y axis is parallel to the side of the boss.

S_1 and S_2 indicate the contact areas, and T_1 and T_2 indicate the friction moments. F_{dn} indicates the vertical force exerting on the rotatable support by the motor. Due to the different expression, the rotation process is divided into two stages.

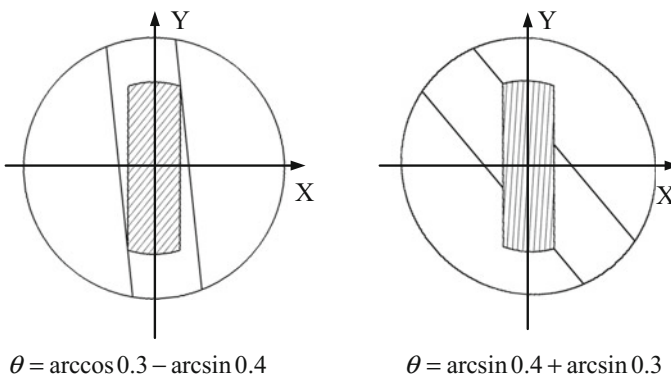


Fig. 5 The first stage of rotation

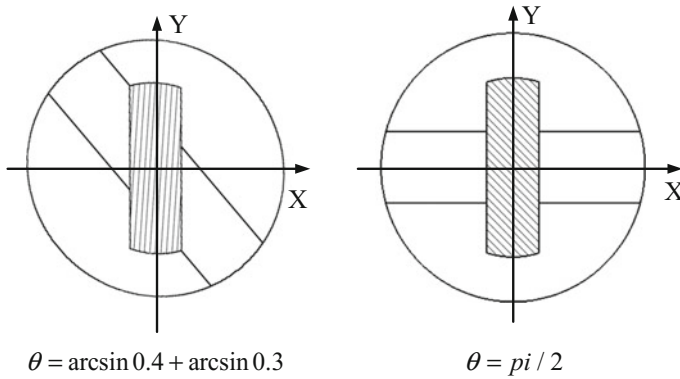


Fig. 6 The second stage of rotation

$$S_1 = 2 \times \int_{-\frac{3}{2}}^{\sqrt{21} \sin \theta - 2 \cos \theta} \sqrt{25 - x^2} - \left(x \cot \theta + \frac{2}{\sin \theta} \right) dx \tag{1}$$

$$T_1 = \frac{\mu_{dn} F_{dn}}{S_1} \int_{-\frac{3}{2}}^{\frac{3}{2}} \int_{x \cot \theta - \frac{2}{\sin \theta}}^{\sqrt{25 - x^2}} 2 \sqrt{x^2 + y^2} dy dx \tag{2}$$

$$S_2 = 2 \times \int_{-\frac{3}{2}}^{\frac{3}{2}} \sqrt{25 - x^2} - \left(x \cot \theta + \frac{2}{\sin \theta} \right) dx \tag{3}$$

$$T_2 = \frac{\mu_{dn} F_{dn}}{S_2} \int_{-\frac{3}{2}}^{\frac{3}{2}} \int_{x \cot \theta - \frac{2}{\sin \theta}}^{\sqrt{25 - x^2}} 2 \sqrt{x^2 + y^2} dy dx \tag{4}$$

Figure 7 shows the connect area and the torque changing with the rotation angle by (1-4).

It can be seen clearly from the figure, the angle can be given by,

$$\theta = \arccos 0.3 - \arcsin 0.4 \tag{5}$$

The largest friction torque can be calculated as,

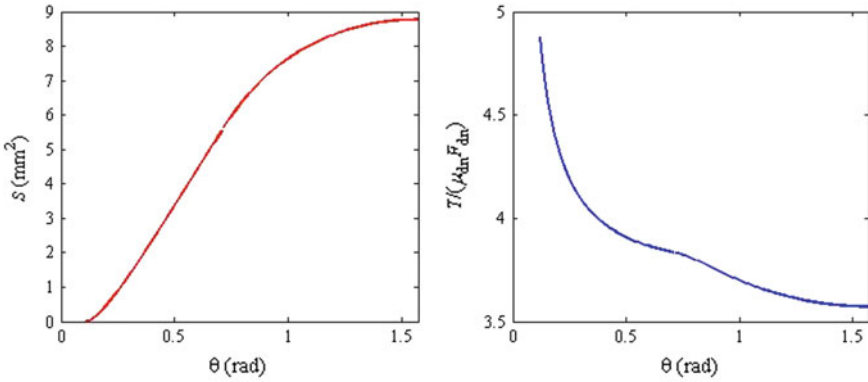


Fig. 7 Contacting area and torque needed with the angle

$$T = 3.8659 \times \mu F_{dn} \quad (6)$$

Thus, we calculate the bearing friction torque according to,

$$M_f = \mu_{bear} \frac{d}{2} F_{up}, \quad (7)$$

where M_f denotes friction torque, μ_{bear} is friction coefficient, d means bearing bore diameter, and F_{up} is load. For a thrust ball bearing,

$$\mu_{bear} = 0.004. \quad (8)$$

The torque balance equation is given by,

$$\mu_{bear} F_{up} \frac{d}{2} + \mu_{bear} (F_{up} - F_{dn}) \frac{D}{2} = 3.8659 \times \mu_{dn} F_{dn}, \quad (9)$$

where F_{up} is the vertical force exerting on the upper surface of the embedment, d is the bore diameter of the thrust ball bearing in the rotation support, D is the bore diameter of the thrust ball bearing under the rotation support, and μ_{dn} is the coefficient of friction between the rotation support and the boss.

Before the boss is clamped into the slot, the friction torque must be less than the sum of the bearing friction torques,

$$F_{dn} < \frac{\mu_{bear} (F_{up} (\frac{D+d}{2}) - F_{dn} \frac{D}{2})}{3.8659 \mu_{dn}}. \quad (10)$$

After the boss is clamped into the slot, the driving torque can be calculated as,

$$T = M_f + (J\omega)' + Fr, \quad (11)$$

where J is the rotary inertia of the winding embedment, ω is the angular velocity, F is the tension on the strip, and r is the radius of the winding embedment.

Before the boss is clamped into the slot, the force equilibrium equation is given by,

$$F_{up} = F_{dn} + F_p. \quad (12)$$

After the boss is clamped into the slot, the force equations are,

$$F_{up} = F_p, \quad (13)$$

$$F_{dn} = 0. \quad (14)$$

The sudden change of the T and F_p signals the beginning of the rotation of the embedment.

5 Experiment

Figure 8 shows the platform, the foaming resin feeding, transmitting, cutting mechanism is in a constant temperature and humidity box which is used to prevent the strip sticking to adjacent objects. The HMI (Human machine interface) is installed on the table beside the circular panel by which the worker can manipulate the machine. The cutting moment, the control of the winding length and the tension on the foaming resin strip and many factors affect the final diameter and incremental weight, so in this experiment, the two parameters are measured.

Experiments are performed for validating the design and proving the reliable operation of the machine. Figure 9 shows an example of the experiments. Two parameters, the final diameter and the incremental weight, have been examined during the course of experiments. Each time, 50 embedments put on the circular panel are wound. Data are retrieved by measuring 50 wound embedded parts, and variation range of the weight and diameter are smaller than 0.5 g and 1 mm respectively, and the result satisfies the proposed requirements.



Fig. 8 The experimental platform

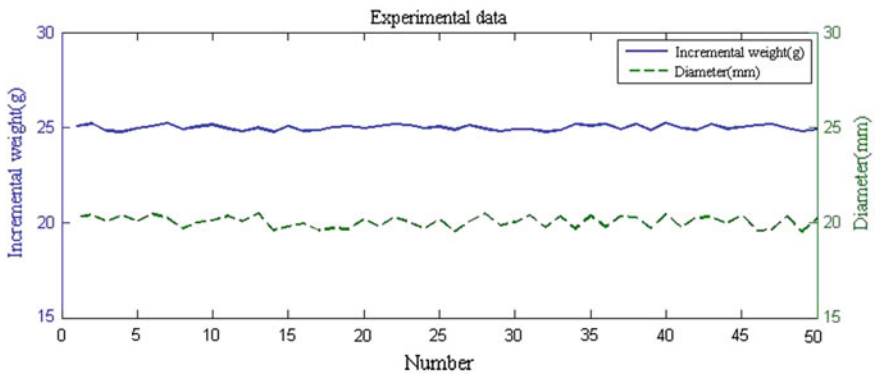


Fig. 9 The experimental data

6 Conclusions

This article has presented a novel mechanism for winding foaming resin on the astronautics embedment. By the kinematic and force analysis of the novel clamping and rotating integrated mechanism, range of the force is given. Some experimental results are reported to validate the performance of the mechanism.

- (1) The mechanism consists of foaming resin feeding, transmitting, cutting mechanism, and embedment positing and driving mechanism.
- (2) The clamping and rotating integral mechanism works reliably, and the rotation of the embedment synchronizes with the motor during the winding process.
- (3) The mechanism can be adjusted to adapt to different diameters and heights of embedment.

Acknowledgements The authors gratefully acknowledge the support of the National Natural Science Foundation of China.

References

1. Fa YY, Chen XH (2012) Finite element analysis of honeycomb sandwich in pull-off damage. *Mater Mech Eng* 36(10):86–96
2. Zhao YF (2014) Application of High-Performance Adhesives and Saelants in Aerospace Industry 32(6):446–450
3. Qin LN (2009) Design and research of cloth wind-up in loom. Soochow University
4. Wang YZ, Zhou XQ, Huang J et al (2013) Mechanical analysis of loom's roll-up mechanism and its tension control system. *J Text Res* 34(11):141–156
5. Zhang LH, Han Y, Wo XY et al (2006) Analysis on process defects of honey comb sandwich. *Spacecraft Recovery Remote Sens* 27(01):57–61
6. Wei Y, Wu AM (2008) Design of a Vacsorb Jig System. *Telecommun Eng* 48(04):107–110
7. Yang HY, Zhou C (2007) Self-centering hydraulic power chuck: current status and trends. *China Mech Eng* 18(02):244–251

Mechanism Design and Analysis for a Lightweight Manipulator Based on Topology Optimization Methods

Hongchuan Zhang, Yanjiang Huang, Zhuowen Mo
and Xianmin Zhang

Abstract In this paper we designed a lightweight manipulator which is installed on a kind of mobile robot—turtlebot. Firstly, we select the configuration of the robot. Then, we optimized the best mechanism of the robot to obtain the large workspace with small size of robot. And then we did the statics analysis and design main link with topology optimization method. Finally, we made a comparison among the side topology optimization beam, traditional I-beam and the structure combined with these two shapes together. Based on the comparison results, we can conclude that: (1) Traditional configuration of palletizing robot is a good configuration to realize lightweight design. (2) The strategy of combine those two optimal shape together can be a solution to achieve 3D-optimization.

Keywords Lightweight · Mechanism design · Topology optimization

1 Introduction

With the development of robotics [1], robots are used more and more widely, more and more work needs to be replaced by robot. But in many place especially in factory or laboratory the robots are always the fixed manipulator. We have to set the task into the place of working space which is not convenient, so a light weight, small size, compact structure, low moment of inertia mobile manipulator is a urgent demand [2].

H. Zhang · Y. Huang (✉) · Z. Mo · X. Zhang (✉)
Guangdong Provincial Key Laboratory of Precision Equipment
and Manufacturing Technology, School of Mechanical and Automotive Engineering,
South China University of Technology, Guangzhou 510640, China
e-mail: mehuangyj@scut.edu.cn

X. Zhang
e-mail: zhangxm@scut.edu.cn

H. Zhang
e-mail: transbrainwsh@foxmail.com

In the previous studies, a large number of researchers and companies focused on the mobile manipulator, many types of manipulator have been developed [3–7]. A lightweight hyper-redundant, deployable binary mobile robot was designed in the paper [3]. The paper [4] designed a humanoid mobile manipulator for service tasks. A leg-wheel hybrid mobile platform was bought up in the paper [5]. A tiny mobile robot platform for large-scale ad hoc sensor networks [6]. A mobile robot with an articulated body has been shown in the paper [7]. It can be found from these papers that most configurations of mobile manipulators are based on a gripper installed on a movable platform [8]. The advantage of this configuration of mobile manipulators is the simple structure and compact design while the disadvantage is the limited flexibility. In order to increase the flexibility, the gripper can be replaced by a lightweight robot arm [9].

In this paper, we aim to design a lightweight manipulator to put on the mobile robot—turtlebot. The manipulator will be designed to handle the objectives on the ground or around the mobile robot. We first optimize the mechanism to attain the large workplace with the small size. And then, we analysis the statics stress of manipulator and design main link with topology optimization method. Finally, the comparisons between the side topology optimization beam, traditional I-beam and the structure combined with two shapes together are conducted to select the optimal configuration. According to the optimal links we will design the manipulator and print it by 3D-printer.

The mechanism design and main link topology optimization is described in Sect. 2. The comparisons and result analysis is presented in Sect. 3 and the conclusions are presented in Sect. 4.

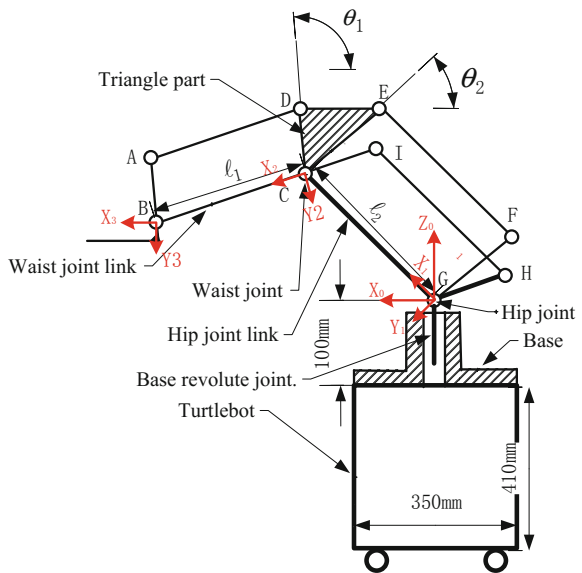
2 Mechanism Design

Firstly, we decide the configuration and the size of the manipulator. Due to the high center of gravity and unstable motion performance of the turtlebot [10], the size of driver and the overall size of the manipulator will be limited. This configuration is shown in Fig. 1. In order to have a high workload with low power motor, the traditional configuration of palletizing robot [11] is a good choice. There are three reasons for it: The first, no drive hangs at the end of any arm, it means that the load on motor can be reduced greatly. Surely, load on the first drive rod (GC) is amplified by the lever (BCI), but the amplification ratio is small, thus, gear reduction mechanism can be added on the point G to compensate the amplified focus. The second, this palletizing robot has a good flexibility. Compared with the traditional SCARA robot [12], palletizing can be able to stretch to the higher space than robot. Working space of this configuration is larger and the shape can be designed according to actual working environment. The pose of end effector remains unchanged so that it is easy to develop into 6-axis manipulator if a 3-degree

gripper is installed on the end. The last, static stress analysis of each link is simple. The focus of load is only act on motive link and the moment of load is only act on pose-holding mechanism.

The dimension of this mechanism can be optimized by GA (genetic algorithm) [13] to achieve a large working space with a small linkage size. Kinematic model of this configuration is also shown in Fig. 1, volume of working space can be judged by the area of the end effector [14] since the first base revolute joint is perpendicular to others. The first objective function is shown in Formulate 1. As this manipulator is aimed at handling objects on the ground, the projected area of the working space on the plane (XZ) ought to be as large as possible. The second optimization target can be set by projected area of the working space on the ground. Thus, the second objective function (v) is shown in Formulate 2. In the above description, l_{sg} is the length of projection which is reflected on the ground of the workspace and l_{sum} is the sum of all linkage design variable. Design variables are classified into two types: linkage design variables and angular design variables. Linkage design variables are the length of hip joint link and the length of waist joint link: l_1 and l_2 . Angular design variables are the shape of triangle part: θ_1 and θ_2 . The area of working space is mainly affected by linkage design variables and the shape of working space is mainly affected by shape of triangle. Take geometry constraint of this mechanism into consideration, we can establish functional relations between workspace area and all design variables. Length of projection (l_{sg}) can be also calculated if the workspace cross-sectional on plane XZ be worked out. Because both optimization functions are at the same scale, traditional weight coefficient transformation method can be used to compute the pareto solution [15]. The working space function is shown in Formula 4 and the functional relations are

Fig. 1 Kinematic model of manipulator



described in Formula 3. Compared with single objective optimization results in NO. 6–7, as shown in Table 1, the pareto results NO. 1–5 not only have larger workspace area but also shorter size and larger cross-section on the ground. In order to achieve lightweight design of this manipulator, we choose the result NO. 5 which has the smallest ℓ_{sum} . The workspace with this parameter is shown in Fig. 2.

The first objective function:

$$\mu = \frac{S_w}{\ell_{sum}^2} \tag{1}$$

Table 1 Results of optimization

Result		Design variables					Objective function		
No.		ℓ_1	ℓ_2	θ_1	θ_2	ℓ_{sum}	F	μ	v
Pareto	1	430.20	590.50	26.30	116.90	1020.70	0.59	0.64	0.54
	2	482.30	610.40	15.00	158.80	1092.70	0.61	0.63	0.59
	3	566.40	633.00	26.10	130.70	1198.20	0.62	0.60	0.64
	4	399.70	588.20	16.60	111.90	987.90	0.58	0.63	0.53
	5	379.80	629.30	14.0	107.60	1009.10	0.58	0.58	0.58
Single	6	403.70	344.30	35.70	124.60	748.00	0.36	0.72	0
	7	285.60	814.80	30.10	136.70	1100.40	0.50	0.32	0.68

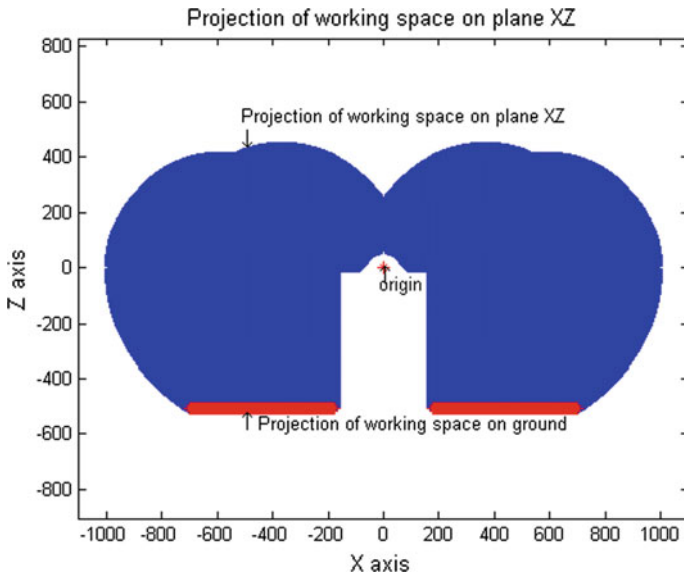


Fig. 2 Projection of workspace on plane XZ

The second objective function:

$$v = \frac{\ell_{sg}}{\ell_{sum}} \tag{2}$$

Design variables are $\ell_1, \ell_2, \theta_1, \theta_2$. The whole objective-function is Formula 1.

$$F = \omega_1\mu + \omega_2v \tag{3}$$

Here, $\ell_{sum} = \ell_1 + \ell_2$

Working space function:

$$s_w = \iint_{\Omega_1 \cap \Omega_2 \cap \Omega_3 \cap \Omega_4} ds \tag{4}$$

Here,

$$\begin{cases} \Omega_1 = \{(x, z) | x \geq 0, z \in R, \ell_1^2 - \ell_2^2 \leq x^2 + z^2 \leq \ell_1^2 + \ell_2^2\} \\ \Omega_2 = \{(x, z) | \theta_2 \leq \theta_{GC} \leq \theta_2 + \pi\} \\ \Omega_3 = \{(x, z) | \theta_{BC} - \pi \leq \theta_{BC} \leq \theta_{GC}\} \\ \Omega_4 = \{(x, z) | \theta_2 - \pi \leq \theta_{BC} \leq \theta_2\} \end{cases}$$

Secondly, we design main components by topological optimization method [16] to aim at the high stiffness with light weight of the link [17]. At the beginning of optimization, the statics stress sustained analysis is shown in the Formula 5–10. Rod BC and CG take full force of load on B point, meanwhile, Rod BA, AD, EF, FG and triangle part DCE bearing the full moment to B by load because parallelogram mechanism ABCD and EFGC are mainly keeping the posture of effector. Figure 3 is used to show the force tendency of each joint. The max torques of actuating arms (GC and CB) are equal to 1.899 and 3.1465 N m if the workload of manipulator is set about 5 N. Take dynamics performance [18] into account, driving torque can be set about 3.836 and 5.376 N m since these two types of motors can be bought directly. After sustained analysis, the topology optimization design regions and the results are shown in Fig. 4. Since the matrix is out of memory for the whole link, as is shown above, the connecting rod is divided into several sections for topology optimization. The quality ratio of resection is 0.5, and the focus F_1 and F_2 satisfy law of leverage.

Stress sustained analysis of main components:

$${}^2f_2 = \begin{bmatrix} f_x \\ f_y \\ 0 \end{bmatrix} \tag{5}$$

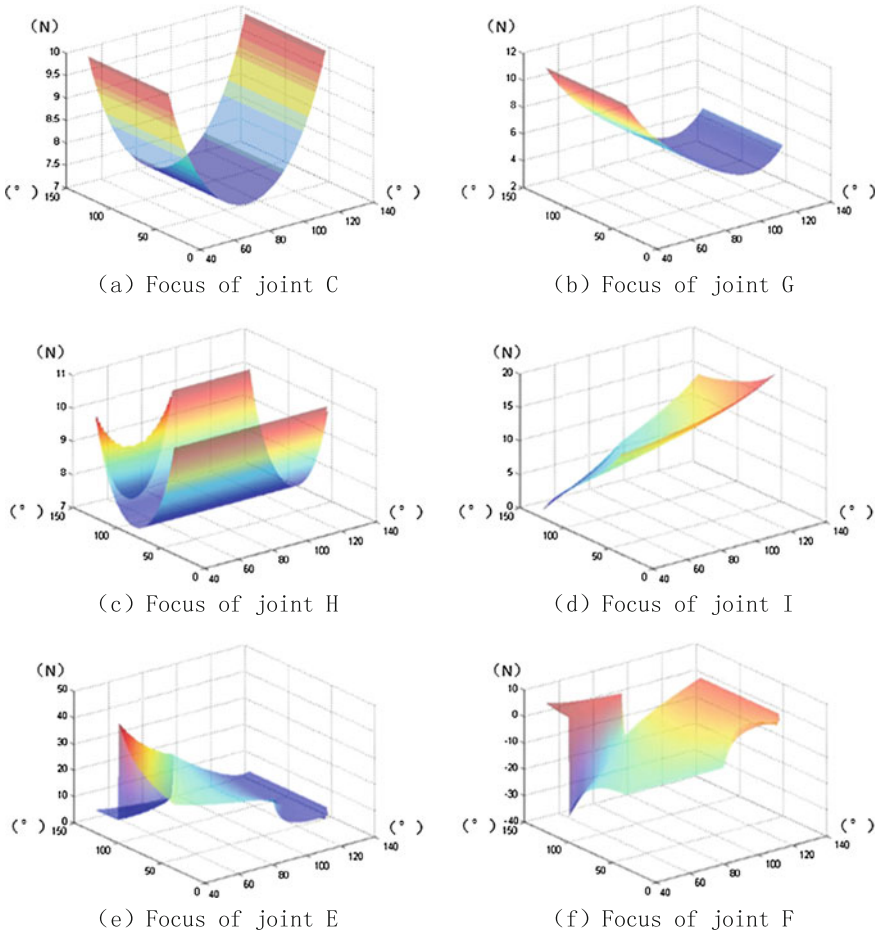


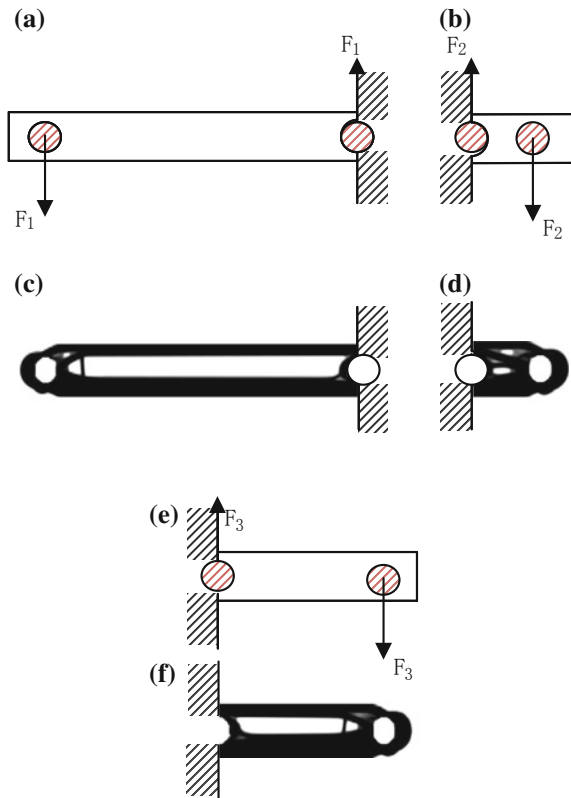
Fig. 3 Force tendency of main joints

$${}^2n_2 = l_2 \cdot \widehat{X}_2 \times \begin{bmatrix} f_x \\ f_y \\ 0 \end{bmatrix} = \begin{bmatrix} 0 \\ 0 \\ l_2 \cdot f_y \end{bmatrix} \quad (6)$$

$${}^1f_1 = \begin{bmatrix} c_2 & s_2 & 0 \\ s_2 & c_2 & 0 \\ 0 & 0 & 1 \end{bmatrix} \begin{bmatrix} f_x \\ f_y \\ 0 \end{bmatrix} = \begin{bmatrix} c_2 \cdot f_x - s_2 \cdot f_y \\ s_2 \cdot f_x + c_2 \cdot f_y \\ 0 \end{bmatrix} \quad (7)$$

$${}^1n_1 = \begin{bmatrix} 0 \\ 0 \\ l_2 \cdot f_y \end{bmatrix} + l_1 \cdot \widehat{X}_1 \times {}^1f_1 = \begin{bmatrix} 0 \\ 0 \\ l_1 \cdot s_2 \cdot f_x + l_1 \cdot c_2 \cdot f_y + l_2 \cdot f_y \end{bmatrix} \quad (8)$$

Fig. 4 Topology optimization results of main link



$$\tau_1 = \ell_1 \cdot s_2 \cdot f_x + (\ell_2 + \ell_1 \cdot c_2) \cdot f_y \tag{9}$$

$$\tau_2 = \ell_2 \cdot f_y \tag{10}$$

3 Result Analysis

The topology optimization in Sect. 2 focus on the side of link, whereas, the best cross-sectional shape of bending section is I-beam which has been widely used to make steel roll [19]. If we take two optimal designs into consideration, another two constructions can be put forward (Call it combined optimal rod I and II). Combined optimal rod I is the intersection of these two shape extension bodies. Combined optimal rod II is the union of these two shape extension bodies. These four types of constructions are shown in Fig. 5. As it is hard to make those constructions at the same quality, we have to propose a parameter η to evaluate the quality of construction and the stiffness together. Parameter η relates to the volume and the

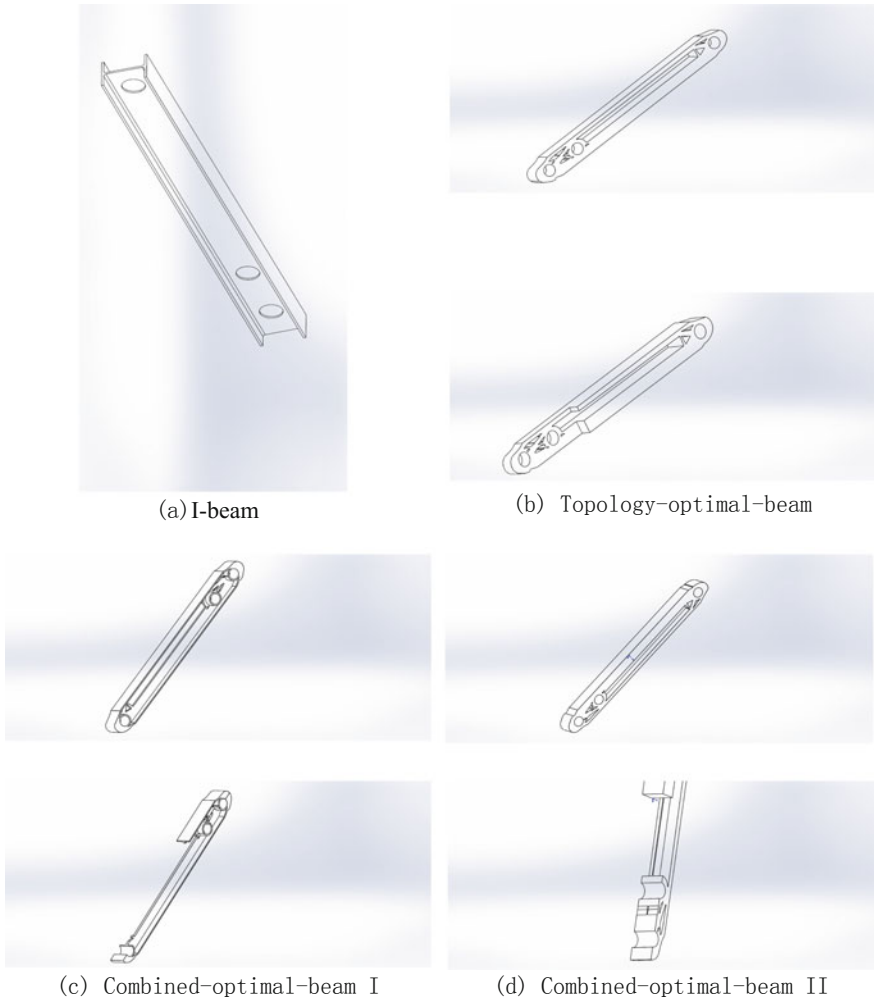


Fig. 5 Four type constructions

maximum deformation of the end. The volume (V) reflects the quality of link as we suppose the density is uniform. The stiffness is characterized by the maximum deformation of the end (ζ). If we aim at achieving high stiffness with the low quality, parameter η should be lower. Parameter η is shown in Formula 11. The analysis results are shown in Fig. 6. All links are designed in the same cuboid chamber with the same dimension and same position of bearing holes. The comparison is shown in Table 2. From the table, we can find that Combined-optimal-beam II not only has the smallest deformation but also minimum η . In the way, combined-optimal-beam II seems to be the best optimal link in 3D design cuboid chamber, but we can't prove that because it is hard to maintain all

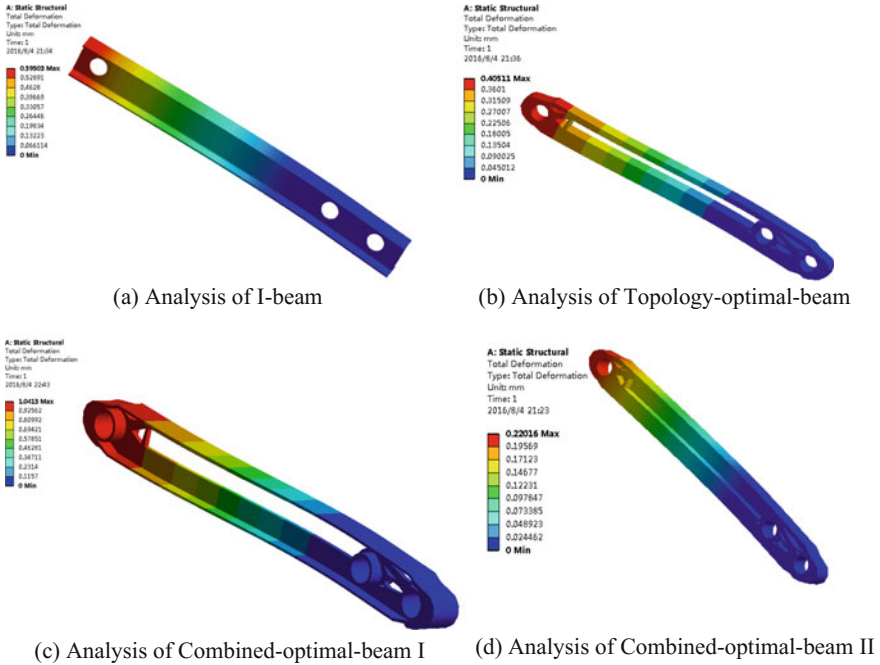


Fig. 6 Topology optimization results of main link

Table 2 Comparison of each construction

Construction	Volume (mm ³ × 10 ⁶)	Deformation (mm)	η (× 10 ²)
I-beam	0.57	0.39	0.99
Topology-optimal-beam	2.16	0.81	1.04
Combined-optimal-beam I	0.83	1.04	0.98
Combined-optimal-beam II	2.22	0.22	0.29

structures at the same quality in topology optimization [20]. Of course, during this light-weight design model, we choose the structure of combined-optimal-beam II.

$$\eta = \sqrt[3]{V} \cdot \zeta \tag{11}$$

The primary design of the manipulator is presented in Fig. 7. Since all the analyses of this paper are based on the 3D printer material C/PLA, the arm won't be too heavy and the stiffness of the manipulator can meet the working requirement well.

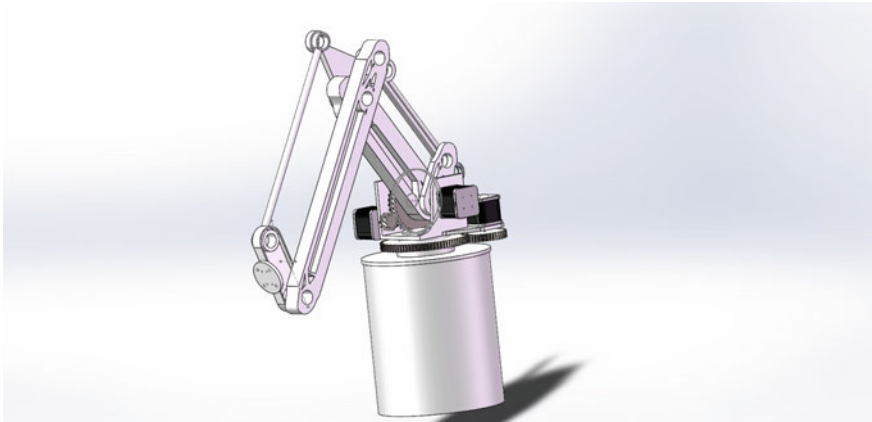


Fig. 7 The primary design of the manipulator

4 Conclusion

This paper designed a lightweight manipulator with the configuration of traditional palletizing robot which is installed on one kind of mobile robot. The main function of the manipulator is to carry and handle the object on the ground. To achieve the light-weight design, mechanism is optimized by GA. Then, structures of main links are designed by topological optimization. At last, the comparison of topological optimization link, traditional I-beam and the structure link which take these two structures together is conducted to realize the optimal design of main rods.

From the comparison we can concluded that:

- (1) Traditional configuration of palletizing robot is a good configuration to realize the light-weight manipulator.
- (2) In the topological optimization of link, combining the best topology shape of side with the best shape of cross-section is a strategy to attain the 3D-optimization of link but it is not sure to be the best.

Acknowledgments This work was partially supported by the Scientific and technological project of Guangzhou (2015090330001), partially supported by the Fundamental Research Funds for the Central University (20152M004), partially supported by the Natural Science Foundation of Guangdong Province (2015A030310239).

References

1. Paul RP (1981) Robot manipulators: mathematics, programming, and control: the computer control of robot manipulators. Richard Paul, 1981
2. Critchlow AJ (1985) Introduction to robotics. Macmillan, New York

3. Sujan VA, Dubowsky S (2004) Design of a lightweight hyper-redundant deployable binary manipulator. *J Mech Des* 126(1):29–39
4. Bischoff R (1997) Hermes—a humanoid mobile manipulator for service tasks. In: Proceedings of the FSR'97 international conference on field and service robots, Canberra, December 1997
5. Shen SY, Li CH, Cheng CC et al (2009) Design of a leg-wheel hybrid mobile platform. In: 2009 IEEE/RSJ international conference on intelligent robots and systems. IEEE, pp. 4682–4687
6. Sibley GT, Rahimi MH, Sukhatme GS (2002) Robomote: a tiny mobile robot platform for large-scale ad-hoc sensor networks. In: Proceedings of the IEEE international conference on robotics and automation, 2002 (ICRA'02). IEEE, vol 2, pp 1143–1148
7. Hirose S, Morishima A (1990) Design and control of a mobile robot with an articulated body. *Int J Robot Res* 9(2):99–114
8. Ryu D, Cho C, Kim M et al (2003) Design of a 6 DOF haptic master for teleoperation of a mobile manipulator. In: Proceedings of the IEEE international conference on robotics and automation, 2003 (ICRA'03). IEEE, vol 3, pp 3243–3248
9. Hirzinger G, Butterfass J, Fischer M et al (2000) A mechatronics approach to the design of light-weight arms and multifingered hands. In: Proceedings of the IEEE international conference on robotics and automation, 2000 (ICRA'00). IEEE, vol 1, pp 46–54
10. Boucher S (2012) Obstacle detection and avoidance using TurtleBot platform and Xbox Kinect. Department of Computer Science, Rochester Institute of Technology 56
11. Li X, Liu J (2011) Research and application situation, problems and solutions of palletizing robots. *Packag Eng* 3:029
12. Makino H, Furuya N. SCARA robot and its family[C] Proc. 3rd Int. Conf. on Assembly Automation. 1982: 433–444
13. Nelder JA, Patil GP, Teugels JL et al (1974) Statistical training and research/formation et recherche statistiques. *Int Stat Rev/Rev Internationale de Statistique* 42(1):79–87
14. Merlet JP (2012) Parallel robots. Springer Science & Business Media, 2012
15. Huang Y, Gueta LB, Chiba R et al (2013) Selection of manipulator system for multiple-goal task by evaluating task completion time and cost with computational time constraints. *Adv Robot* 27(4):233–245
16. Sigmund O (2001) A 99 line topology optimization code written in Matlab. *Struct Multi Optim* 21(2):120–127
17. Xianmin Z (2003) Topology optimization of compliant mechanisms. *Chin J Mech Eng* 39(11):47–51
18. Lee CSG (1982) Robot arm kinematics, dynamics, and control. *Computer* 15(12):62–80
19. Chandra R, Chopra I (1991) Experimental and theoretical analysis of composite I-beams with elastic couplings. *AIAA J* 29(12):2197–2206
20. Wang NF, Tai K (2010) Target matching problems and an adaptive constraint strategy for multiobjective design optimization using genetic algorithms. *Comput Struct* 88(19):1064–1076

Synthesis of Branch Type Lower Limb Assistive Device

Yue Sun and Dar-Zen Chen

Abstract Design of a portable branch type lower limb orthosis for persons with impairments of motor system is presented. Since the hip joint has relation movement to human trunk, unlike most exoskeleton type of lower limb orthosis, considers the hip joint as a plane pair and knee joint as a revolute joint. Topological synthesis of the branch type lower limb assistive device according to the kinematic behavior of the human lower limb is accomplished. And the partition coefficient is applying on optimizing design for spring parameters.

Keywords Branch type · Lower limb assistive device · Hip joint · Partition coefficient

1 Introduction

The post-operative patients typically suffer from the motor system impairments, resulting in the lower limb disability and affecting their daily life activities. Those with lower limb problems usually use a crutch or a walker to support their body weights during gait Agrawal and Fattah proposed two non-robotic leg orthosis, GBO [1] and GBEO [2] composed of a primary planar two-link serial linkage for gait training based on the gravity-balancing techniques. Although many lower limb orthoses or exoskeletons, such as ALEX [3], LOPES [4] and Lokomat [5] had been developed to guide the gait pattern of locomotion, such devices are complex and uniquely designed for gait training rehabilitation in hospitals. Design of a lower limb orthosis without actuators and compatible with the kinematic behavior of the lower limb for elderly, post-operative and muscle weakness patients is proposed. According to the studies of Kadaba et al. [6] and Sutherland et al. [7], the rotation of the pelvis induces the relative motion of the hip joint with respect to the human trunk. The kinematic interference between the orthosis and the human lower limb

Y. Sun · D.-Z. Chen (✉)

Department of Mechanical Engineering, National Taiwan University, Taipei 10617, Taiwan
e-mail: dzchen@ntu.edu.tw

can be minimized and discomfort can be eliminated. Since no article has designed the lower limb assistive device with branch type mechanism, a methodology is addressed to design and optimize the branch type lower limb assistive device in this paper. Topological synthesis of the branch type lower limb assistive device according to the kinematic behavior of the human lower limb is first accomplished. And the partition coefficient is applying on optimizing design for spring parameters.

2 Kinematic Modeling of Human Lower Limb

2.1 The Coordinate System of Human Lower Limb

In order to design branch type lower limb assistive device without motion incompatibility, the anatomical structure and kinesiology of human lower limb have to be investigated first. The coordinate system of a human can be described by three anatomically aligned axes: axis of superior/inferior (SI), axis of anterior/posterior (AP) and axis of medial/lateral (ML). The axes of SI and AP form the sagittal plane, on which the side view is projected. The axes of SI and ML form the frontal plane, on which the front view is projected. The axes of AP and ML form the transverse plane, on which the top view is projected. The sagittal plane, frontal plane and transverse plane are referred to as the three cardinal planes of a human body (Fig. 1).

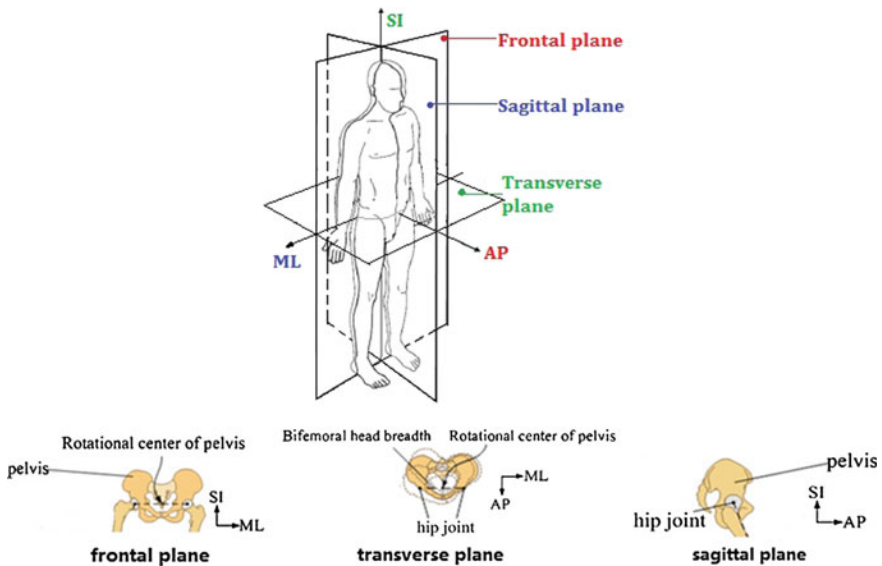


Fig. 1 The coordinate system of a human

According to the human anatomy and kinematics of the lower limbs, seen the rotation of pelvis during walking will cause position of hip joint changed with respect to the trunk. Assistive device and lower limbs occurs interference during walking. The displacement of each joint to origin point can be seen as the displacement to human body backbone. The rotations of hip joint and knee joint in sagittal plane are called flexion/extension, the rotation of hip joint in frontal plane is called abduction/adduction, the rotation of knee joint in frontal plane is called valgus/varus, the rotations of hip joint and knee joint in transverse plane are called medial/lateral rotation. While the lower limb is in motion, the pelvis exhibit a complex motion with respect to the body trunk, where the rotation in the sagittal plane is called posterior/anterior tilt, in frontal plane is called up/down obliquity and in transverse plane is called medial/lateral rotation.

2.2 Simplifications of Human Lower Limb Model

Movement of hip joint is produced by rotation of the following three plane: α (sagittal plane), β (frontal plane), γ (transverse plane) (Fig. 2).

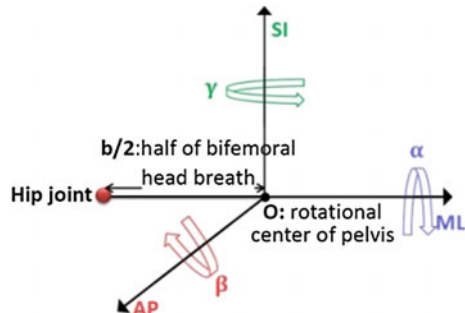
Define the rotational center of pelvis as original point O and b is the length of bifemoral head breath. The distance between hip joint and rotation center of pelvis is 1/2 of bifemoral head breath. The initial of hip joint is $(0, \frac{b}{2}, 0)$. The displacement vector of hip joint after rotation is (L_{AP}, L_{ML}, L_{SI}) .

$$L_{AP} = \frac{1}{2} b \cos \beta \sin \gamma \tag{1}$$

$$L_{ML} = \frac{1}{2} b (1 - \cos \beta \cos \gamma) \tag{2}$$

$$L_{SI} = \frac{1}{2} b \sin \beta \tag{3}$$

Fig. 2 Movement of hip joint during gait



Normal walking can be divided into two phases: as the foot is in contact with the ground is referred to as the stance phase, while the foot swings in the air is referred to as the swing phase. Figure 3 shows the full gait cycle of the right lower limb. At 0 % of the cycle, the heel of the right lower limb begins to contact with the ground; at 10 % of the cycle, the foot is flat; at 50 % of the cycle, the heel is pulled off the ground; at 60 % of the cycle, the toe is completely off the ground; at 80 % of the cycle, the right leg is swung ahead of the left leg and at the 100 % of the cycle, the terminal swing of the right leg is completed. The gait cycle from 0 to 60 % is

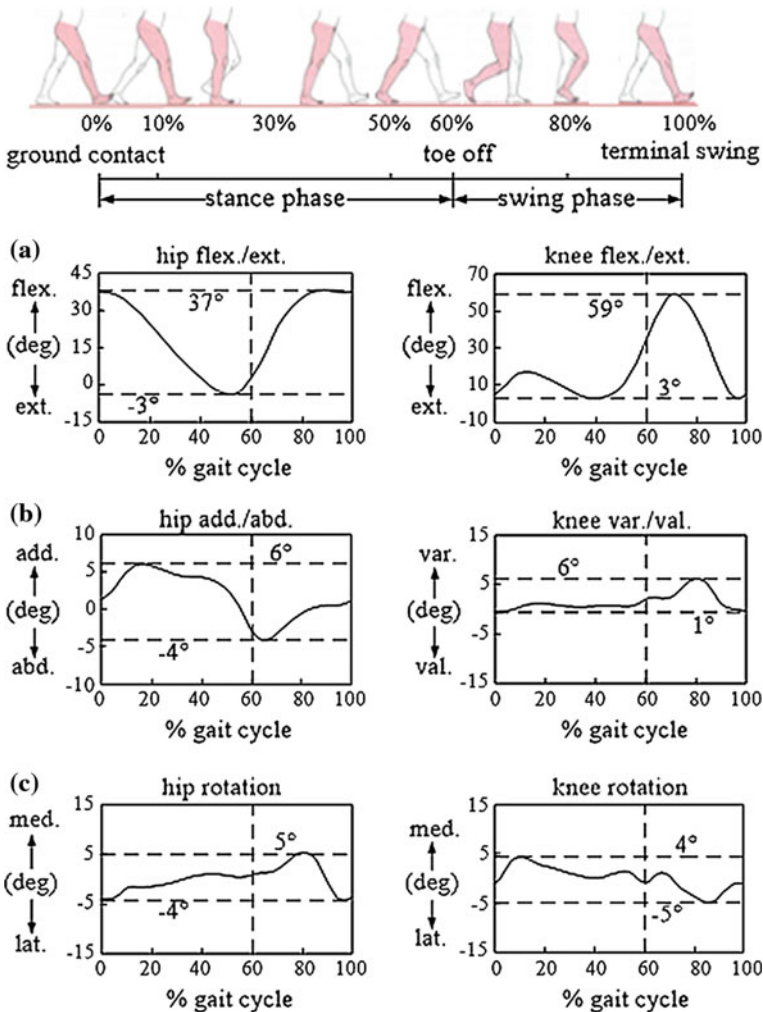


Fig. 3 The displacement to trunk of body during gait

Table 1 The description of displacement in gait

Phase	Stance phase			Swing phase		
	Min	Max	Difference	Min	Max	Difference
α	14°	16°	2°	14°	16°	2°
β	-3°	4°	7°	-4°	0°	4°
γ	-4°	3°	7°	-4°	1°	5°
L_{SI}	-0.0262b	0.0349b	0.0611b	-0.0349b	0	0.0349b
L_{AP}	-0.0019b	0.0019b	0.0038b	-0.00243b	0.00243b	0.00486b
L_{ML}	-0.0348b	0.0261b	0.0609b	-0.0348b	0.00873b	0.04353b

For healthy adults, the width of pelvic is in a direct ratio with stature H . $b = 0.191H$
 Where $H = 170$ cm $b \approx 32$ cm

referred to as the stance phase of normal walking, while that from 60 to 100 % is referred to as the swing phase.

Because of assistive devices fixed on the body in different ways, the best way to describe the motion also changes. The movement of hip joint is described by two ways: angle and displacement.

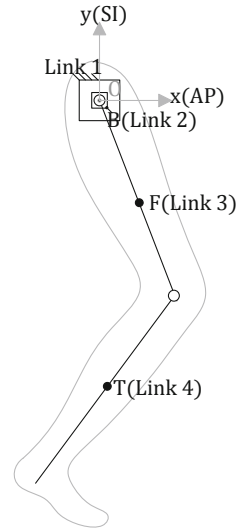
The description of angle during stance phase is the variation of α is 2°. Compared with β and γ , it is negligible. And during the swing phase the variation of α is 2°. Compared with β and γ , it is negligible. The description of displacement is as Table 1. L_{SI} and L_{ML} are both more than 2 cm, L_{AP} is less than 2 mm. L_{AP} is less than 1/10 of the other variation of directions. Therefore L_{SI} and L_{ML} are needed to be considered, but L_{AP} is negligible. And during swing phase, L_{SI} and L_{ML} are both more than 1 cm, L_{AP} is less than 2 mm. L_{AP} is less than 1/5 of the other variation of directions. Therefore L_{SI} and L_{ML} are needed to be considered, but L_{AP} is negligible.

2.3 Kinematic Modeling of Human Lower Limb

For design of branch type planar assistive device, displacement of SI and AP in the plane Sagittal plane is needed to be considered. In the past research, the movement of hip joint is considered. But the movement of hip joint is complicated. According Agrawal the design of GBO [1] and GBEO [2] consider 2DOF movement of hip joint. It doesn't solve the motion of hip joint in sagittal plane. It just focuses on the gravity-balancing during walking. According Banala [8], the design of ALEX solves the motion of hip joint. But the mechanism isn't portable, it needs a support. And according the Krut [9], the design of Moon Walk consider 3DOF movement of hip joint. But it solves the motion of hip joint on SI depended on motion on AP axis.

The lower limb is considered as constituted with linkages B, F and T. Linkage B which is regarded as hip joint can move in sagittal plane within limits. It can be regarded as planar joint (Fig. 4).

Fig. 4 The lower limb is considered as constituted with linkages



3 Topological Synthesis of Lower Limb Assistive Device

3.1 Selection of Lower Limb Assistive Device

According to Grubler and Kutzbach criterion

$$F = \lambda(n - j - 1) + \sum_i f_i \tag{4}$$

where F is the degree of freedom of the mechanism, λ is the degree of freedom of the space in which a mechanism is intended to function, n is the number of links, j is the number of joints, and f_i is the degree of freedom possessed by joint i . In order to make the lower limb orthosis is simple, the number of links of mechanisms is as less as possible, $(n, j) = (7, 8)$ is chosen.

The rules to choose kinematic chains is that the hip or the knee joint can be placed in any loop with at least four joints, while both hip and knee joints can only be placed in a loop with at least five joints. So, the $(7, 8)$ chain as shown in Fig. 5 is excluded, because neither hip nor knee joint can be placed in the three-joint loop. The rules are proposed to design branch and type planar assistive device. There is one and only one revolute joint connected ground with hip joint. And the mechanism isn't single chain. Mechanism of type (a) are all single chain, and type (b) cannot configure the hip joint and knee joint. The hip joint and knee joint is identified on admissible kinematic chains of the lower limb orthosis as Fig. 6.

Fig. 5 Admissible kinematic chains of the lower limb orthosis

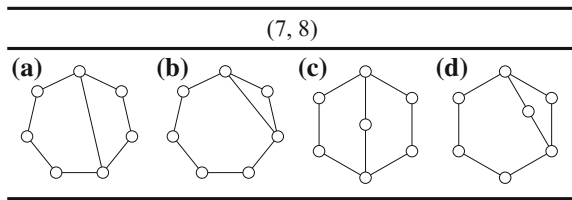
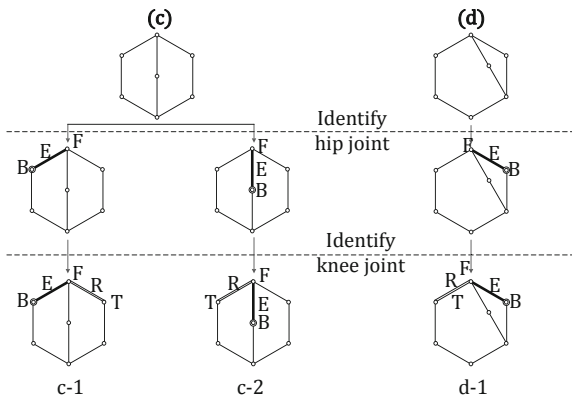


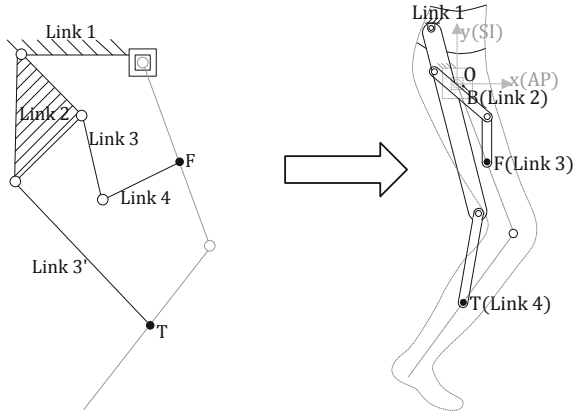
Fig. 6 Identify hip joint and knee joint



3.2 The Diagram of the Lower Limb Assistive Device

First consider design c-2 achieve balancing, since the K_{14} and K_{15} should be zero, $\lambda_{14} = 1$ and $\lambda_{15} = 1$ are required, However, by $\lambda_{14} = 1$ and $\lambda_{15} = 1$ the components K_{23} , K_{24} , K_{25} , K_{34} , and K_{35} becomes non-zero matrix, therefore, $\lambda_{24} = 1$ and $\lambda_{25} = 1$, those springs are called basic springs. Since the overall design equations are provided by non-zero off-diagonal components of \mathbf{K} , each component provide two design equations, hence, there are eighteen design equations, $n_e = 18$. Since these basic springs aren't mono-articular spring, therefore, there are sixteen available design parameters. c-2 is the most appropriate branch type mechanism assistive devices, because it's the only choice which conform the DOF of lower limb after separate the mechanism into main part and branch part. So the diagram of the lower limb assistive device is as Fig. 7. And the mechanism is a branch type planar mechanism.

Fig. 7 The diagram of the lower limb assistive device



4 Design of Branch Type Lower Limb Assistive Device

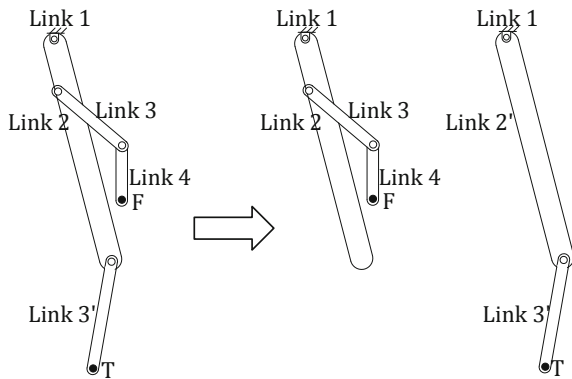
4.1 Gravity-Balancing Technique with Spring Only

Suppose the assistive device is installed in the mass center of lower limb, it can be treated as a point with mass attached to the link connected to it. So the whole is a branch type mechanism. Link 2 is the overlapping portion of main part and branch part. So the G_{12} is shared by two parts (Fig. 8).

The equations of gravity balance of main part with partition coefficient E_2 are as below:

$$k^{14}a_{14}r_2 \cos \alpha_{14} + k^{13}a_{13}r_2 \cos \alpha_{13} = -(1 - E_2)m_2g s_2 \sin \delta_2 \quad (5)$$

Fig. 8 The branch type lower limb assistive device



$$k^{14}a_{14}r_2 \sin \alpha_{14} + k^{13}a_{13}r_2 \sin \alpha_{13} = (1 - E_2)[m_2gs_2 \cos \delta_2 + m_3gr_2 + (m_4 + m_f)gr_2] \quad (6)$$

$$k^{13}a_{13}b_{13} \cos(\alpha_{13} - \beta_{13}) + k^{14}a_{14}r_3 \cos \alpha_{14} = m_3gs_3 \sin \delta_3 \quad (7)$$

$$k^{13}a_{13}b_{13} \sin(\alpha_{13} - \beta_{13}) + k^{14}a_{14}r_3 \sin \alpha_{14} = m_3gs_3 \cos \delta_3 + (m_4 + m_f)gr_3 \quad (8)$$

$$k^{14}a_{14}b_{14} \cos(\alpha_{14} - \beta_{14}) = (m_4 + m_f)gr_3 \quad (9)$$

$$k^{14}a_{14}b_{14} \sin(\alpha_{14} - \beta_{14}) = (m_4 + m_f)gr_3 \quad (10)$$

$$k^{14}r_2r_3 - k^{24}a_{24}r_3 \cos(-\alpha_{24}) + k^{13}b_{13}r_2 \cos \beta_{13} = 0 \quad (11)$$

$$-k^{24}a_{24}r_3 \sin(-\alpha_{24}) + k^{13}b_{13}r_2 \sin \beta_{13} = 0 \quad (12)$$

$$k^{14}b_{14}r_2 \cos \beta_{14} = k^{24}a_{24}b_{24} \cos(\beta_{24} - \alpha_{24}) \quad (13)$$

$$k^{14}b_{14}r_2 \sin \beta_{14} = k^{24}a_{24}b_{24} \sin(\beta_{24} - \alpha_{24}) \quad (14)$$

$$k^{14}a_{14}b_{14} \sin(\alpha_{14} - \beta_{14}) = (m_4 + m_f)gr \quad (15)$$

$$k^{14}b_{14} \sin \beta_{14} = -k^{24}b_{24} \sin \beta_{24} \quad (16)$$

The equations of gravity balance of branch part with E_2 are as below:

$$k^{13'}a'_{13}r'_2 \cos \alpha'_{13} = -E_2m_2gs_2 \sin \delta_2 \quad (17)$$

$$k^{13'}a'_{13}r'_2 \sin \alpha'_{12} = E_2[m_2gs_2 \cos \delta_2 + m'_3gr_2 + (m'_4 + m_f)gr_2] + (m'_3 + m_t)gr_2^b \quad (18)$$

$$k^{13'}a'_{13}b'_{13} \cos(\alpha'_{13} - \beta'_{13}) = (m'_3 + m_t)gs_3^b \sin \delta_3^b \quad (19)$$

$$k^{13'}a'_{13}b'_{13} \sin(\alpha'_{13} - \beta'_{13}) = (m'_3 + m_t)gs_3^b \cos \delta_3^b \quad (20)$$

$$k^{13'}r'_2b'_{13} \cos \beta'_{13} = k^{23}a'_{23}b'_{23} \cos(\alpha'_{23} - \beta'_{23}) \quad (21)$$

$$k^{13'}r'_2b'_{13} \sin \beta'_{13} = -k^{34}a'_{23}b'_{23} \sin(\alpha'_{23} - \beta'_{23}) \quad (22)$$

The E_v is partition ratio of main part G_{1v} shared by branch part. The spring influenced by E_v which can be observed directly by stiffness block is defined as direct influence spring. All springs of branch type statically balanced mechanism are related. For the branch type lower limb assistive device, E_2 is applied to optimize the spring configuration, which tends the spring constants to average.

4.2 Anthropometric of Human Lower Limb

Based on the 1969 study of Clauser et al. [10] and the database provided by NASA in 1978 [11], the masses of thigh and shank can be evaluated by linear regression equations, such as (Table 2):

$$m_t = 0.0452\rho_1 + 0.82 \tag{23}$$

$$m_f = 0.0452\rho_1 + 0.82 \tag{24}$$

$$s_t = 0.335\rho_5 - 0.159\rho_6 + 11.267 \tag{25}$$

$$s_f = 0.227\rho_2 + 0.989\rho_3 - 0.033\rho_4 - 13.362 \tag{26}$$

where ρ_i is anthropometric parameters.

The mass and location of mass center of femur and tibia of small, mid and larger size objects can be obtained (Table 3).

Aluminum alloy 6061 is chosen as material of all links of lower limb orthosis. The mass center locations of all links are assumed to be at the mid-length of each link. Density of aluminum alloy 6061 is 2700 kg/m^3 . The width and thickness of all links of lower limb orthosis are assumed as W and T . Therefore mass of links of lower limb orthosis can be expressed as function of link-length: $m_n = 2700 \times W \times T \times r_n$.

Mass of links is much less than tibia or femur, and the orthosis is connected with mass center of them. Therefore the mass center of links which attached to tibia or femur are assumed to be near the junction with lower limb. Constraint equations of lower limb extension during swing phase:

$$(r'_2 + r'_3)^2 \geq (t_{y,l} - l_{1y})^2 + (t_{x,u} - l_{1x})^2 \tag{27}$$

$$(r'_2 + r'_3)^2 \geq (t_{y,l} - l_{1y})^2 + (t_{x,l} - l_{1x})^2 \tag{28}$$

Table 2 The masses of thigh and shank

Anthropometric parameters	Symbol	Small	Mid	Large
Total body weight (kg)	ρ_1	63.3	81.5	97.7
Trochanteric height (cm)	ρ_2	87.2	94.6	102.5
Knee breadth/bone (cm)	ρ_3	9.6	10.5	11.4
Iliac crest (fat) (cm)	ρ_4	7.5	19.5	31.3
Tibiale height (cm)	ρ_5	43.4	48.0	52.6
Calf cir. (cm)	ρ_6	28.9	32.7	36.5

Table 3 The mass and location of mass center of femur and tibia

Mass and location of mass	Symbol	Small	Mid	Large
Mass of tibia (kg)	m_t	3.7	4.5	5.2
Mass of femur (kg)	m_f	6.3	8.4	10.3
COM of tibia w.r.t. knee joint (cm)	s_t	21.2	22.1	23.1
COM of femur w.r.t. hip joint (cm)	s_f	15.7	17.9	20.1

$$(r_2 + r_3 + r_4)^2 \geq (f_{y,l} - l_{ly})^2 + (f_{x,u} - l_{lx})^2 \tag{29}$$

$$(r_2 + r_3 + r_4)^2 \geq (f_{y,l} - l_{ly})^2 + (f_{x,l} - l_{lx})^2 \tag{30}$$

4.3 Optimal Design of Lower Limb Assistive Device

To keep the installation of springs remaining unchanged installation as much as possible, apply E_v to change the installation. To reduce the different among springs, the goal of optimization is decrease the variance of all springs. Objective function of optimization is $F(E_2) = V(k^{ij})$, where $V(k^{ij})$ is the variance of all springs. With the partition coefficient changes, spring constant is changed. Select the range of $[-1, 1]$ to adjust the E_2 . The change of all spring constant is as Fig. 9.

According the design equation, constraint conditions and parameters of human body, the optimized result is $F(0.175) = 7.420 \times 10^5$. And the initial value is $F(0) = 1.038 \times 10^6$. Compared with the initial value, the variance of springs is reduced, so the spring constant is tended to average.

Fig. 9 The optimizing of variance of springs

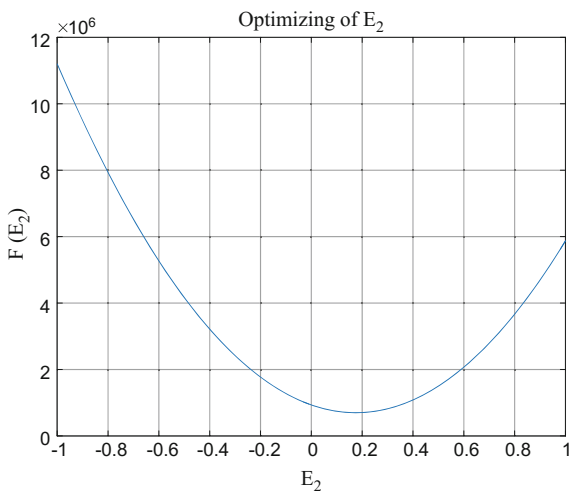


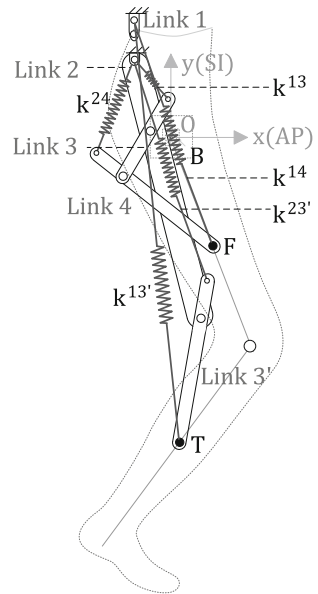
Table 4 The mass and dimension properties of the mechanism

Link i	Length (m)	s_i (m)	Mass(kg)
Link 2	0.60	0.30	1.422
Link 3	0.10	0.10	0.237
Link 4	0.20	0.10	0.473
Link 3'	0.20	0.20	0.473
F	–	–	8.400
T	–	–	4.500

Table 5 The spring constant and design parameters

ij	k^{ij} (N/m)	a_{ij} (m)	b_{ij} (m)
13	1083.79	0.005	0.100
14	836.20	0.087	0.020
24	482.91	0.115	0.200
13'	928.43	0.050	0.082
23'	406.21	0.050	0.200

Fig. 10 The branch type assistive device



The mass and dimension properties of the mechanism are shown in Table 4. The spring constant and design parameters for this example are tabulated in Table 5. The branch type assistive device is illustrated as Fig. 10.

5 Conclusions

Design of a branch type lower limb assistive device for persons with motor system impairments is presented. In this orthosis, the movement of the hip joint due to the rotation of the pelvis and the working space of the lower limb during walking is considered, such that the discomfort induced by the motion incompatibility between the orthosis and the human lower limb can be alleviated. The orthosis is also capable of compensating the gravitational effect of the human lower limb and the orthosis during the swing phase. Based on the anthropometric data for the middle-size subjects, the design optimization is accomplished and the simulated results show the concept of the branch type gravity-balancing assistive device is feasible. The partition coefficient is applied to optimize the spring configuration. Based on free body diagram of human thigh and shank, the locational error of interfacial point is estimated, and method for reduce the locational error is presented. Design of a device to switch on and off the spring forces between the swing phase, and the prototyping, testing, and evaluation of the lower limb assistive device will be implemented in the near future.

References

1. Agrawal SK, Fattah A (2004) Theory and design of an orthotic device for full or partial gravity-balancing of a human leg during motion. *IEEE Trans Neural Syst Rehabil Eng* 12:157–165
2. Agrawal SK, Banala SK, Fattah A, Sangwan V, Krishnamoorthy V, Scholz JP et al (2007) Assessment of motion of a swing leg and gait rehabilitation with a gravity balancing exoskeleton. *IEEE Trans Neural Syst Rehabil Eng* 15:410–420
3. Banala SK, Kim SH, Agrawal SK, Scholz JP (2009) Robot assisted gait training with active leg exoskeleton (ALEX). *IEEE Trans Neural Syst Rehabil Eng* 17:2–8
4. Dollar AM, Herr H (2008) Lower extremity exoskeletons and active orthoses: challenges and state-of-the-art. *IEEE Trans Rob* 24:144–158
5. Jezernik S, Colombo G, Keller T, Frueh H, Morari M (2003) Robotic orthosis lokomat: a rehabilitation and research tool. *Neuromodulation (Technology at the neural interface)* 6: 108–115
6. Kadaba MP, Ramakrishnan H, Wootten M (1990) Measurement of lower extremity kinematics during level walking. *J Orthop Res* 8:383–392
7. Sutherland DH, Olshen R, Cooper L, Woo SL (1980) The development of mature gait. *J Bone Joint Surg Am* 62:336–353
8. Banala SK, Agrawal SK, Fattah A, Krishnamoorthy V, Hsu W-L, Scholz J et al (2006) Gravity-balancing leg orthosis and its performance evaluation. *IEEE Trans Rob* 22:1228–1239
9. Krut S, Benoit M, Dombre E, Pierrot F (2010) Moonwalker, a lower limb exoskeleton able to sustain bodyweight using a passive force balancer. In: 2010 IEEE international conference on robotics and automation (ICRA), 2010, pp 2215–2220
10. Clauser CE, McConville JT, Young JW (1969) Weight, volume, and center of mass of segments of the human body. DTIC Document 1969
11. A. S. Book (1978) Vol. 1: Anthropometry for designers, NASA Reference Publication 1024

On Passive Limbs in the Design of Parallel Mechanisms

Xu Wang, Weizhong Guo and Feng Gao

Abstract Passive limbs in parallel mechanisms can be introduced during type synthesis in order to reduce the possibility of redesigning or to decrease the complexity of the latter control strategy. In this paper, to find out more influences passive limbs can have on the performance of parallel mechanisms, using the theory of reciprocal screws, a united modeling framework of parallel mechanisms with passive limbs and without passive limbs is established first and then the performance comparison is carried out between parallel mechanisms with passive limbs and without passive limbs. All the performance indexes are calculated based on Jacobian matrices. The comparison results indicate that parallel mechanisms with passive limbs perform better in architecture dexterity, linear velocity isotropy, angular velocity isotropy, force isotropy, torque isotropy, maximum values of torque, linear deformation isotropy, angular deformation isotropy and maximum values of angular deformation.

Keywords Parallel mechanism · Passive limb · Reciprocal screws · Performance comparison

1 Introduction

For the research and development of parallel mechanisms (PMs), simple type synthesis is not enough and there is a lack of usage of limb structures with good performance, reasonable actuators distribution and appropriate constraint assign-

X. Wang · W. Guo · F. Gao (✉)
State Key Laboratory of Mechanical Systems and Vibration,
Shanghai Jiao Tong University, Shanghai 200240, China
e-mail: fengg@sjtu.edu.cn

X. Wang
e-mail: saddy_xgd@sjtu.edu.cn

W. Guo
e-mail: wzguo@sjtu.edu.cn

ment. Consideration of these factors can reduce the possibility of redesigning or decrease the complexity of the latter control strategy. Fortunately, there exists a kind of limb structure with good performance which can be called passive limbs (PLs), among today's PMs. However, there is no specific research on PLs.

PLs are those limbs who provide constraints but do not possess any active joints. At present, there are four classes of PMs with PLs. The structure of the first class is like n $\underline{\text{SPS}}/\underline{\text{UPS}}/\underline{\text{RUS}}/\underline{\text{PSS}}\text{-XXX}$, such as SKM400 by Ponisch [1], 3SPS-UP by Neumann [2], cable-controlled mechanism by Landsberger [3, 4], GEC Tetrabot by Dwolatzky [5], 3UPS-PU by Fattah [6], 4PUS-1PS by Abbasnejad [7] and 2PSS-U by Carricato [8], where n , S, P, U, R, and XXX represent the number of $\underline{\text{SPS}}/\underline{\text{UPS}}/\underline{\text{RUS}}/\underline{\text{PSS}}$ -limbs, spherical joints, prismatic joints, universal joints, revolute joints and PL, respectively. The active joints are underlined. This class of PMs have characteristics as: (1) The DOFs of the end-effector are directly determined by XXX-limb [7], thus the type synthesis can be easier, such as motion constraint generator method by Kuo [9]; (2) The total number of limbs is one more than DOFs, so the constraints can be stripped from the active limbs while it also means the increasement in manufacturing cost and possibility of interference between limbs [10]; (3) The performances of this class of PMs in global condition number, working space and stiffness matrix condition number maybe better according to the comparison between 3SPS-UP and 3UPU by Joshi [11]; (4) This class of PMs are easy to be reproduced. Because the structure of each active limb is identical, so it is convenient for manufacturing and assembling [12]; (5) Although one of the active limbs can be removed, loading the active force on PL, the driving uniformity will lose [13]; (6) This class of PMs have larger loading capacity, and PL can effectively remove the redundant self-motion of the moving platform [14, 15].

The structure of the second class is like n SPS/ $\underline{\text{UPS}}/\underline{\text{RUS}}/\underline{\text{PSS}}\text{-}n\text{XXX}$, such as 3SPS-3PRS by Lippmeier [16], where n represents the number of ALs or PLs. This class has characteristics as: (1) Because the original one PL is decomposed into n PLs with the same structure, purchasing costs of materials will increase while the load applied on PLs can be more symmetrical; (2) If the n ALs are removed, the rest of the body is still a PM with some advantages relative to the serial mechanisms remained, thus the configuration choices can be more flexible; (3) Over constraints are inevitable, which is not conducive to assembling, so there is a higher requirement for machining precision.

The structure of the third class is like r SPS/ $\underline{\text{UPS}}/\underline{\text{RUS}}/\underline{\text{PSS}}\text{-XXX}$, such as Ankle Rehabilitation Device by Saglia [17], where $r > \text{DOFs}$. This class has characteristics as: (1) For ankle rehabilitation device which needs only two degrees of rotation freedom, using 3 ALs with uniform distribution is more loading reasonable; (2) The use of redundant actuation is to completely eliminate the singularity and to improve the dexterity [17].

The structure of the last class is decoupled PMs (DPMs), such as 2PSS-U by Carricato [8] and U-RRU-SPS by Zeng [18]. This class has characteristics as:

(1) During type synthesis, PMs with 2 DOFs can be evolved from a planar four bar mechanism, providing another drive by adding an AL, one of the remaining two limbs with constraints acting as a PL and finally allowing the whole mechanism to be partly DPMs [18]; (2) Sometimes completely DPMs can be generated using PLs, which leads to more direct kinematics and easier analysis of singularity problem [8].

This paper is organized as follows. Firstly, using the theory of reciprocal screws, a united modeling framework of parallel mechanisms with passive limbs and without passive limbs is established to deduce the Jacobian of constraints and the Jacobian of actuations. Then, the performance comparison is carried out between two types of PMs, with PLs (3SPS-UP and 3SPS-3PRS) and without PLs (2SPS-UP and 3PRS).

To facilitate the discussion, the parallel mechanisms with passive limbs and without passive limbs are named as “PMWPL” and “PMWOPL”, respectively.

2 A United Modeling Framework of PMWPL and PMWOPL

Up to present, according to Chap. 1, the most common type of PMWPL is $n\text{SPS-}m\varepsilon$, where $n = \text{DOFs}$ and ε is a set of various type of PLs with the total number of PLs being m . To find out more influences PLs can have on the performance of PMs, a corresponding PMWOPL which is evolved from $n\text{SPS-}m\varepsilon$ by removing out m ALs and making the a_j^{th} joint (it is practical that at most one active joint can be used for each limb [19]) on the j^{th} PL active, is introduced for comparison. The type of PMWOPL is donated by $(n-m)\text{SPS-}m\zeta$, where ζ is a set of various type of limbs and these limbs are donated by cALs(ALs with constraints). In order to maintain the DOFs unchanged, the following relationship must be realized:

$$5 \geq n \geq m \geq 2. \quad (1)$$

Here, “ $m \geq 2$ ” can guarantee that if $n = m$, with m ALs removed, the final mechanism can also be a parallel one. A generalized schematic diagram of PMWPL is shown in Fig. 1a. The moving platform (MP) and the based platform (BP) are connected by n scalable ALs ($S_i^B S_i^M, i = 1, \dots, n$) and m PLs ($B_j M_j, j = 1, \dots, m$). We suppose that the connectivity of the j^{th} PL is equal to c_j . Obviously, the connectivity of each AL is equal to 7. Figure 1b is the schematic diagram of the corresponding PMWOPL.

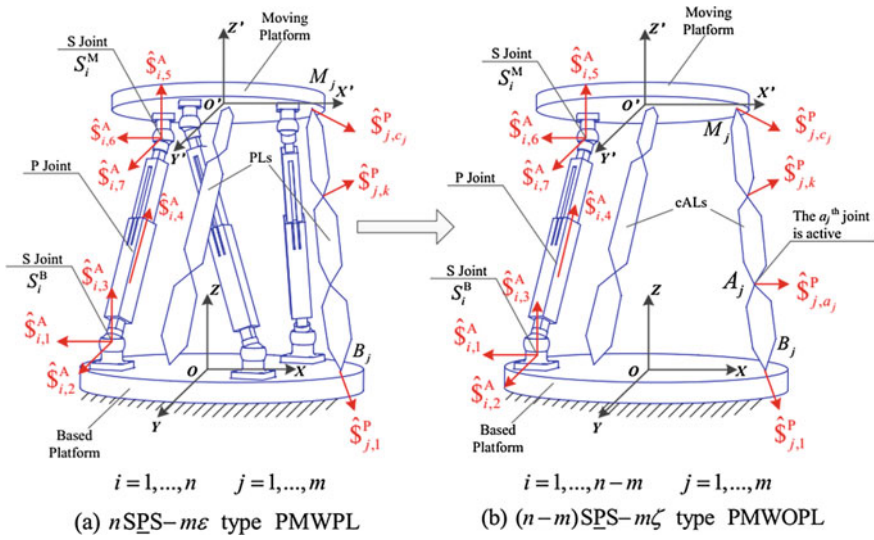


Fig. 1 The types of PMWPL and PMWOPL discussed in this paper

2.1 Jacobian of PMWPL

To perform a velocity analysis of PMWPL, Jacobian matrices need to be built for both ALs and PLs. Inspired by the method in [20], making use of the theory of reciprocal screws, the Jacobian matrix of the constraining PLs is presented first. The instantaneous velocity $\hat{\$}_{MP}$ of MP can be expressed as a linear combination of instantaneous unit joint twists plotted in Fig. 1a:

$$\hat{\$}_{MP} = (\vec{\omega}^T \quad \vec{v}^T)^T = \dot{\theta}_{j,1}^P \hat{\$}_{j,1}^P + \dots + \dot{\theta}_{j,k}^P \hat{\$}_{j,k}^P + \dots + \dot{\theta}_{j,c_j}^P \hat{\$}_{j,c_j}^P, \quad (2)$$

where $\vec{\omega}$ and \vec{v} are the angular velocity and linear velocity from $O' - X'Y'Z'$ to $O - XYZ$, respectively. $\dot{\theta}_{j,k}^P$ and $\hat{\$}_{j,k}^P$ are the joint velocity and the instantaneous unit twist of the R/P joint in the PL, respectively.

We then suppose that there exists no redundant constraints on every PL so those wrenches that are reciprocal to all the joint twists of the j^{th} PL form a $(6 - c_j)$ -system, which can be denoted by $\hat{\$}_{j,q}^{P,r} = \begin{bmatrix} a_{j,q}^{P,r} \\ b_{j,q}^{P,r} \end{bmatrix}$ ($q = 1, \dots, 6 - c_j$). Taking the orthogonal product of both sides of Eq. (2) with $\hat{\$}_{j,q}^{P,r}$ yields the *Jacobian of constraints* as:

$$J_P \hat{\mathbb{S}}_{MP} = 0, \tag{3}$$

where

$$J_P = \begin{bmatrix} \vdots & \vdots \\ \left(b_{j,1}^{P,r}\right)^T & \left(a_{j,1}^{P,r}\right)^T \\ \vdots & \vdots \\ \left(b_{j,6-c_j}^{P,r}\right)^T & \left(a_{j,6-c_j}^{P,r}\right)^T \\ \vdots & \vdots \end{bmatrix}. \tag{4}$$

Next, the similar method is applied to ALs to deduce the *Jacobian of actuations* as:

$$J_A \hat{\mathbb{S}}_{MP} = \vec{q}_a, \tag{5}$$

where

$$J_A = \begin{bmatrix} \left(o\vec{S}_1^M \times \vec{\mathbb{S}}_{1,4}^A\right)^T & \left(\vec{\mathbb{S}}_{1,4}^A\right)^T \\ \vdots & \vdots \\ \left(o\vec{S}_n^M \times \vec{\mathbb{S}}_{n,4}^A\right)^T & \left(\vec{\mathbb{S}}_{n,4}^A\right)^T \end{bmatrix} \vec{q}_a = \left[\dot{\theta}_{1,4}^A \quad \cdots \quad \dot{\theta}_{n,4}^A\right]^T. \tag{6}$$

2.2 *Jacobian of PMWOPL*

As mentioned above, PMWOPL derives from PMWPL by removing out m ALs and making one joint on each PL active and ultimately leading to the whole structure as:

$$(n - m) \underline{SPS} - \underbrace{\dots \underline{P} \dots \underline{R} \dots}_{\text{cAL } 1} - \dots - \dots - \underbrace{\dots \underline{P} \dots \underline{R} \dots}_{\text{cAL } m},$$

where the R joints in cAL can also be active, depending on the particular structure of this cAL. For instance, the R joint connecting cAL and BP is more adaptable to be chosen as an actuation. Supposing that the a_{ii}^{th} joint in the i^{th} cAL is P and the a_{jj}^{th} joint in the jj^{th} cAL is R, then we can get:

$$J_{\text{cAL}} \hat{\mathbb{S}}_{MP} = \vec{q}_{a,\text{cAL}}. \tag{7}$$

and

$$J_{AL} \hat{\mathcal{S}}_{MP} = \vec{q}_{a,AL}, \tag{8}$$

where

$$J_{cAL} = \begin{bmatrix} \vdots & \vdots \\ \left({}^O\vec{A}_{ii} \times \vec{\mathcal{S}}_{ii,a_{ii}}^P \right)^T & \left(\vec{\mathcal{S}}_{ii,a_{ii}}^P \right)^T \\ \vdots & \vdots \\ \left(\vec{\mathcal{S}}_{jj,a_{jj}}^P \right)^T & \vec{0} \\ \vdots & \vdots \\ \left(b_{ii,1}^{P,r} \right)^T & \left(a_{ii,1}^{P,r} \right)^T \\ \vdots & \vdots \\ \left(b_{ii,6-c_{ii}}^{P,r} \right)^T & \left(a_{ii,6-c_{ii}}^{P,r} \right)^T \\ \vdots & \vdots \end{bmatrix}, \vec{q}_{a,cAL} = \begin{bmatrix} \vdots \\ \dot{\theta}_{ii,a_{ii}}^P \\ \vdots \\ \dot{\theta}_{jj,a_{jj}}^P \\ \vdots \\ 0 \\ \vdots \\ 0 \\ \vdots \end{bmatrix}, \tag{9}$$

and

$$J_{AL} = \begin{bmatrix} \left({}^O\vec{\mathcal{S}}_1^M \times \vec{\mathcal{S}}_{1,4}^A \right)^T & \left(\vec{\mathcal{S}}_{1,4}^A \right)^T \\ \vdots & \vdots \\ \left({}^O\vec{\mathcal{S}}_{n-m}^M \times \vec{\mathcal{S}}_{n-m,4}^A \right)^T & \left(\vec{\mathcal{S}}_{n-m,4}^A \right)^T \end{bmatrix}, \vec{q}_{a,AL} = \left[\dot{\theta}_{1,4}^A \quad \dots \quad \dot{\theta}_{n-m,4}^A \right]^T. \tag{10}$$

The *Jacobian of actuations* J_A consists of J_{AL} and the first m' rows of J_{cAL} , where m' equals to the number of nonzero rows of $\vec{q}_{a,cAL}$. The *Jacobian of constraints* J_P comes from

$$\begin{bmatrix} J_{AL} \\ J_{cAL} \end{bmatrix} = \begin{bmatrix} J_A \\ J_P \end{bmatrix}. \tag{11}$$

3 Case Studies

In this section, performance comparison is carried out between two types of PMs, which are PMs with PLs (3SPS-UP and 3SPS-3PRS) and without PLs (2SPS-UP [21] and 3PRS [22]), in terms of architecture dexterity, velocity isotropy, velocity maximum values, loading isotropy, loading maximum values, deformation isotropy, deformation maximum values, actuation forces maximum values and

constraint forces maximum values. All these performance indexes are calculated based on Jacobian matrices [23] deduce in Chap. 2.

3.1 Comparison of 3SPS-uP and 2SPS-uP

In 3SPS-UP as shown in Fig. 2a, MP and BP are connected by three scalable ALs ($S_i^B S_i^M, i = 1, 2, 3$) and one scalable PL ($B_j M_j, j = 1$). Between PL and MP is the fixed perpendicular joint. S_i^B and S_i^M are the three vertexes of an equilateral triangle with geometry center $O(B_j)$ and $O'(M_j)$, respectively. 3SPS-UP has 3 DOFs, and the end-effector can rotate around two axes and translate along another axis. When the position of the end-effector is given, the orientation of the end-effector can be determined [24].

Based on 3SPS-UP which is PMWPL, if one of the ALs is removed, a new parallel mechanism can be created, namely 2SPS-UP which is PMWOPL. In 2SPS-UP, $B_j M_j$ becomes cAL, thus there exists no PLs. The coordinate system of 2SPS-UP is the same as 3SPS-UP which is shown in Fig. 2b.

Figure 3 shows the comparison of LCI at some height between 3SPS-UP and 2SPS-UP and Table 1 shows the comparison of GCI between 3SPS-UP and 2SPS-UP. Analysis of LCI and GCI indicates that 3SPS-UP has better architecture

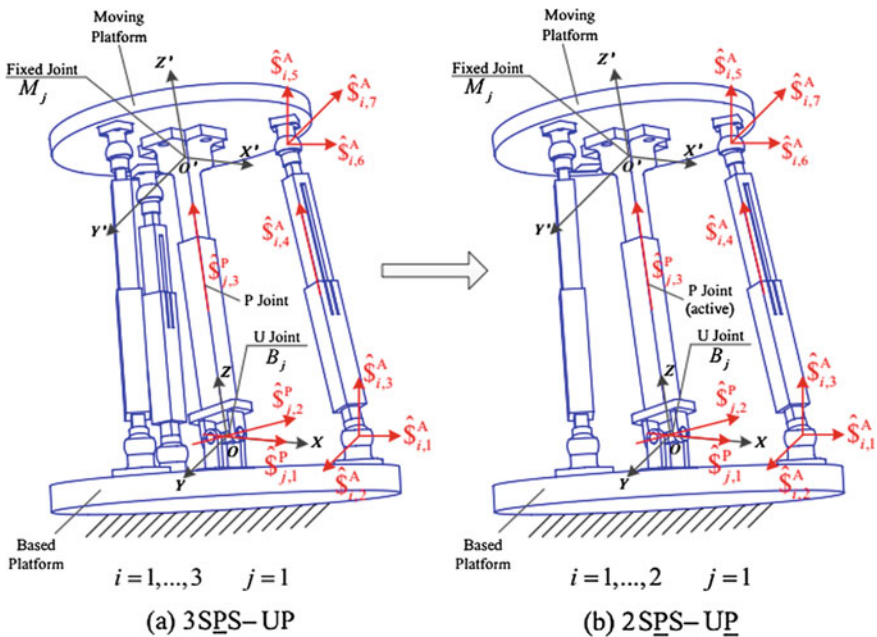


Fig. 2 Generalized schematic diagrams of 3SPS-UP and 2SPS-UP

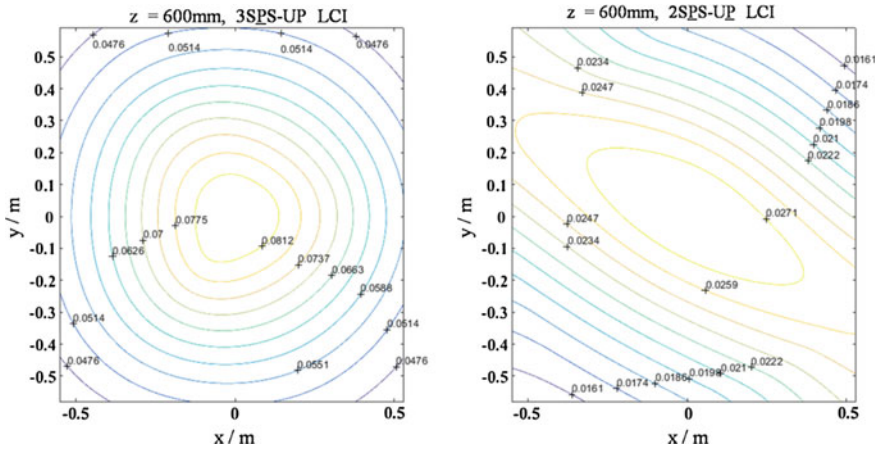


Fig. 3 The comparison of LCI at some height between 3SPS-UP and 2SPS-UP

Table 1 The comparison of GCI between 3SPS-UP and 2SPS-UP

Mechanism type	GCI
3SPS-UP	0.0666
2SPS-UP	0.0238

dexterity than 2SPS-UP under the same configuration and the same mechanism dimension.

To compare the velocity performance between 3SPS-UP and 2SPS-UP, choose enough sections at different heights, and at each section, calculate the velocity indexes which include mean values of velocity isotropy and mean values of maximum velocity. Figures 4 and 5 show the comparison of velocity indexes between 3SPS-UP and 2SPS-UP.

As for payload indexes, stiffness indexes and force indexes, the processes of comparison are same with that of velocity indexes mentioned above and will not be demonstrated here in detail.

3.2 Comparison of 3SPS-3PRS and 3PRS

In 3SPS-3PRS, as shown in Fig. 6a, MP and BP are connected by three scalable ALs ($S_i^B S_i^M, i = 1, 2, 3$) and three scalable PLs ($B_j M_j, j = 1, 2, 3$). Based on 3SPS-3PRS which is PMWPL, if all of the ALs are removed, a new parallel mechanism can be created, namely 3PRS which is PMWOPL. In 3PRS, the P joint in each $B_j M_j$ becomes active, thus there exists no PLs. The coordinate system of 3PRS is the same as 3SPS-3PRS, which is shown in Fig. 6b.

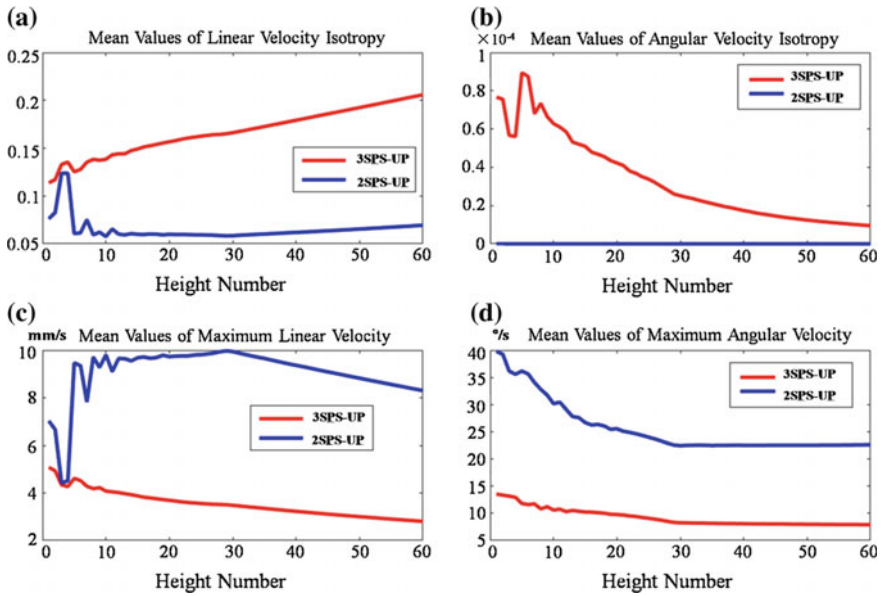


Fig. 4 The tendency comparison of velocity indexes between 3SPS-UP and 2SPS-UP

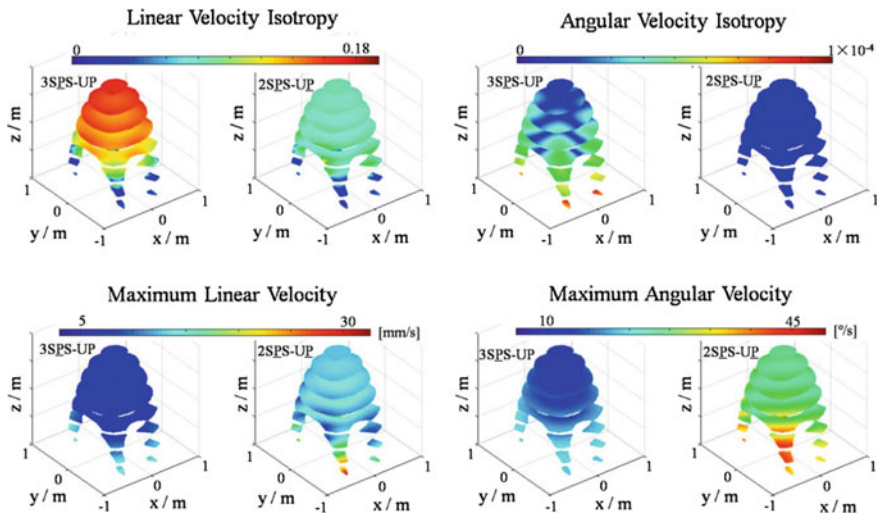


Fig. 5 The global view of velocity indexes between 3SPS-UP and 2SPS-UP

As for the indexes comparison, the processes are same with that in Sect. 3.1 and will not be demonstrated here in detail.

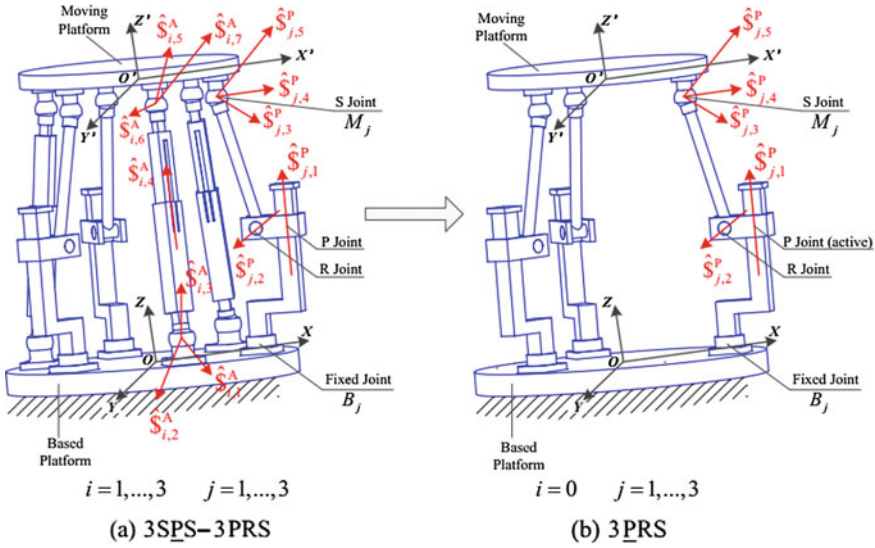


Fig. 6 Generalized schematic diagrams of 3SPS-3PRS and 3PRS

3.3 The Comprehensive Comparison

Influence of PLs on the performance of PMs can be obtained by finding out the unchangeable comparison results in Sects. 3.1 and 3.2. Finally the performances which are better with PLs and which are better without PLs are listed in Table 2, where “↓” represents that the global value of the corresponding index goes down from PMWPL to PMWOPL and vice versa. Taking the second line of Table 2 as an example, it means that 3SPS-UP and 3SPS-3PRS perform better than 2SPS-UP and 3PRS in isotropy of linear velocity (big-friendly index), respectively.

Table 2 The comprehensive comparison

Group No.	1		2	
Mechanism type	3SPS-UP	2SPS-UP	3SPS-3PRS	3PRS
Contains PLs or Not	Yes	No	Yes	No
Architecture Dexterity (BF ^{ah})*	↓ (-64.2643%)		↓ (-83.0233%)	
Isotropy	LV (BF)*	↓ (-65.1136%)	↓ (-100%)	
	AV (BF)*	↓ (-100%)	↓ (-100%)	
Maximum values	LV (BF)	↑ (+186.1109%)	↓ (-68.4590%)	
	AV (BF)	↑ (+175.3132%)	↑ (+1179.8%)	
Isotropy	F (BF)*	↓ (-62.5498%)	↓ (-100%)	
	T (BF)*	↓ (-100%)	↓ (-100%)	

(continued)

Table 2 (continued)

<i>Group No.</i>		1	2
<i>Mechanism type</i>		3SPS-UP	2SPS-UP 3SPS-3PRS 3PRS
<i>Contains PLs or Not</i>		Yes	No
<i>Maximum values</i>	<i>F</i> (BF)	↑ (+0.0462%)	↑ (+8.4534)
	<i>T</i> (BF)*	↓ (-5.0612%)	↓ (-47.2460%)
<i>Isotropy</i>	<i>LD</i> (BF)*	↓ (-88.4298%)	↓ (-100%)
	<i>AD</i> (BF)*	↓ (-100%)	↓ (-100%)
<i>Maximum values</i>	<i>LD</i> (SF ^a)	↑ (+744.2535%)	↓ (-55.8966%)
	<i>AD</i> (SF)*	↑ (+667.2251%)	↑ (+7708.8%)
<i>Maximum values</i>	<i>AF</i> (SF)	↑ (+190.0224%)	↓ (-21.1452%)
	<i>CF</i> (SF)	↑ (+0.0160%)	↓ (-17.8809%)

* refers to the indexes which perform better in PMWPL for both Group 1 and Group 2
^a*BF* and *SF* refer to “big-friendly” index and “small-friendly” index, respectively
LV Linear velocity; *AV* Angular velocity; *LD* Linear deformation; *AD* Angular deformation;
F Force; *T* Torque; *AF* Actuation force; *CF* Constraint force

4 Conclusions

In this paper, using a united modeling framework, the comparison of the performance of two groups of parallel mechanisms is carried out. Each group contains two parallel mechanisms with same DOFs, and the difference is whether it contains PLs or not. The comprehensive comparison results indicate that PMs with PLs perform better in architecture dexterity, linear velocity isotropy, angular velocity isotropy, force isotropy, torque isotropy, maximum values of torque, linear deformation isotropy, angular deformation isotropy and maximum values of angular deformation.

Acknowledgments The authors thank the partial financial supports under the projects from the National Natural Science Foundation of China (Grant No. 51275284, 51323005), and the Research Fund of State Key Lab of MSV, China (Grant No. MSV-ZD-2016-08).

References

1. Ponisch A (2003) Machine-tool milling center: U.S. Patent 6,540,458. 1 Apr 2003
2. Neumann KE (1988) Robot: U.S. Patent 4,732,525. 22 Mar 1988
3. Landsberger SE (1984) Design and construction of a cable-controlled, parallel link manipulator. Massachusetts Institute of Technology
4. Landsberger SE, Sheridan TB (1987) Parallel link manipulators: U.S. Patent 4,666,362. 19 May 1987
5. Dwolatzky B, Thornton GS (1988) The GEC Tetrabot-a serial-parallel topology robot: control design aspects. Control, Control 88., International conference on. IET, pp 426–431
6. Fattah A, Kasaei G (2000) Kinematics and dynamics of a parallel manipulator with a new architecture. Robotica 18(05):535–543

7. Abbasnejad G, Daniali HM, Fathi A (2011) Architecture optimization of 4PUS+1PS parallel manipulator. *Robotica* 29(05):683–690
8. Carricato M, Parenti-Castelli V (2004) A novel fully decoupled two-degrees-of-freedom parallel wrist. *Int J Robot Res* 23(6):661–667
9. Kuo CH, Dai JS (2013) Task-oriented structure synthesis of a class of parallel manipulators using motion constraint generator. *Mech Mach Theory* 70:394–406
10. Joshi SA, Tsai LW (2003) The Kinematics of a Class of 3-dof, 4-legged Parallel Manipulators. *J Mech Des* 125(1):52–60
11. Joshi S, Tsai LW (2003) A comparison study of two 3-DOF parallel manipulators: one with three and the other with four supporting legs. *IEEE Trans Robot Autom* 19(2):200–209
12. Zhang D, Gosselin CM (2001) Kinetostatic modeling of N-DOF parallel mechanisms with a passive constraining leg and prismatic actuators. *J Mech Des* 123(3):375–381
13. Zhang D, Gosselin CM (2002) Kinetostatic modeling of parallel mechanisms with a passive constraining leg and revolute actuators. *Mech Mach Theory* 37(6):599–617
14. Lu Y, Hu B, Liu PL (2007) Kinematics and dynamics analyses of a parallel manipulator with three active legs and one passive leg by a virtual serial mechanism. *Multibody SysDyn* 17(4):229–241
15. Lu Y, Hu B (2007) A unified method to find active forces and passive wrench of some parallel manipulators with n SPS active legs and a passive leg. *Proc Inst Mech Eng Part C: J Mech Eng Sci* 221(4):467–478
16. Lippmeier WC, Wilkinson TT, Ausdenmoore RM (1992) Support for a translating nozzle vectoring ring: U.S. Patent 5,174,502. 29 Dec 1992
17. Saglia JA, Tsagarakis NG, Dai JS et al (2009) A high performance redundantly actuated parallel mechanism for ankle rehabilitation. *Int J Robot Res*
18. Zeng D, Huang Z, Lu W (2007) A family of novel 2 DOF rotational decoupled parallel mechanisms. *Mechatronics and Automation, 2007. ICMA 2007. International conference on. IEEE*, pp 2478–2483
19. Zhang D (2009) *Parallel robotic machine tools*. Springer Science & Business Media
20. Joshi SA, Tsai LW (2002) Jacobian analysis of limited-DOF parallel manipulators. *ASME 2002 international design engineering technical conferences and computers and information in engineering conference. American Society of Mechanical Engineers*, pp 341–348
21. Huang T, Li M, Zhao XM et al (2005) Conceptual design and dimensional synthesis for a 3-DOF module of the 2SPS-UP-a novel 5-DOF reconfigurable hybrid robot. *IEEE Trans Robot* 21(3):449–456
22. Tsai MS, Shiau TN, Tsai YJ et al (2003) Direct kinematic analysis of a 3-PRS parallel mechanism. *Mech Mach Theory* 38(1):71–83
23. Wu M, Zhang D, Zhao X (2007) Conceptual design and kinematic performance evaluation of a new asymmetrical parallel robot. *Mechatronics and Automation, 2007. ICMA 2007. International conference on. IEEE*, pp 2854–2859
24. Siciliano B (1999) The 3SPS-UP robot: inverse kinematics, manipulability analysis and closed-loop direct kinematics algorithm. *Robotica* 17(04):437–445

The Application of Stewart Parallel Mechanism in Auricular Prosthesis Forming

Ruiqin Guo, Haiyan Gu and Qizhe Xu

Abstract Auricular prosthesis is a kind of artificial auricle of repairing physiological defect. This paper studies the problem of forming curve and machining method in auricular prosthesis forming, and puts forward a quick forming method of combining parallel mechanism and NC machine tool. The mathematical model and motion reverse equation of parallel mechanism are established and the structural parameters of Stewart parallel mechanism were designed. Finally, Matlab Software is used in an example to figure out motion function curve of each branch, which verifies the feasibility of this method. In addition, it lays the foundation for further studies of control of parallel mechanism.

Keywords Auricular prosthesis forming · Stewart parallel mechanism · Forming curve · Simulation analysis

1 Introduction

Auricular prosthesis [1], as well as called artificial ear, is using kinds of artificial materials and methods to restore the normal shape and part of physiological function of the ears. The whole auricular defect in clinic is a relatively common disease [2], and as one of the most important organs of head, the morphological abnormality of auricle has a great impact on patient's psychological and social interaction [3]. Auricular prosthesis is the main repairing method in medicine. There are two main methods to make auricular prosthesis: the traditional fabrication method and the 3D printing auricular prosthesis forming method. The traditional fabrication method is carving wax manually and using resin or silicone to make auricular prostheses [4, 5], but this method has many shortcomings such as complex

R. Guo (✉) · H. Gu · Q. Xu
School of Mechanical and Energy Engineering, Tongji University, Shanghai, China
e-mail: ruiqin_guo@tongji.edu.cn

fabrication processes, too many human factors, high technical and experiential requirements for carving and the long production cycle. Computer aided forming method uses CT scanning and image processing to construct three dimensional model of auricular prosthesis, and finish the design and fabrication through 3D printing and NC machining. However, due to poor bio-compatibility and inconsistent color with human, the 3D printing auricular prosthesis forming method still couldn't meet the requirement of patients [6]. With the rapid development of computer and numerical machining technology in recent years, it makes traditional auricle rapid casting forming and cartilage rapid prototyping become possible, which attracts many relevant scholars.

Rapid auricular moulding is casting mould through machining, and rapid prototyping of using patients' own cartilage is machining directly. The key technology of these two methods is rapid machining forming.

Owing to the irregular space surface, it requires high flexibility and space posture of the mechanical processing equipment and requires relatively low displacement working space. Auricular prosthesis rapid forming is mainly influenced by two factors, one is reasonable forming path planning, and the other is rapid adjustment of the position and orientation of machining equipment.

Stewart parallel mechanism is a complex mechanism with multiple DOF, and it has been applied in the fields of aerospace, driving simulation, medicine and mechanical machining due to the advantages of short kinematic chains, flexible space posture, quick dynamic response speed and high motion accuracy etc. [7–13]. Therefore, the parallel mechanism is proposed to be applied on the research of auricular prosthesis forming and to study the forming curve of auricle and the posture working space planning of Stewart parallel mechanism combining the morphological characteristics of human ears.

2 The Forming Curve and the Establishment of Mathematical Model of Auricular Prosthesis Forming

2.1 Analysis of Auricular Features

In medicine, human ear is defined to be composed of the external ear, middle ear and inner ear, of which the external ear is exposed to be seen. External ear is a complex and irregular space surface as shown in Fig. 1.

Auricular prosthesis is mainly restyling the external ear, which mainly consists of helix, fossae helicis, antihelix, fossae triangularis, cymba conchae, cristae helicis, anthelix, cavum conchae, antilobium and earlobe etc. There are differences between human ears. The visual appearance of external ear is much influenced by the size of the external ear, helix, concha and the shape of the earlobe, and other parts just has few effects on the visual appearance. Therefore, the following characteristics

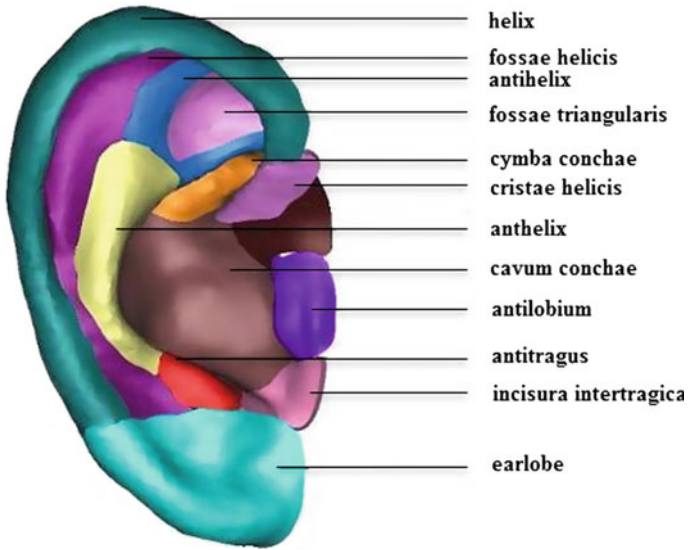
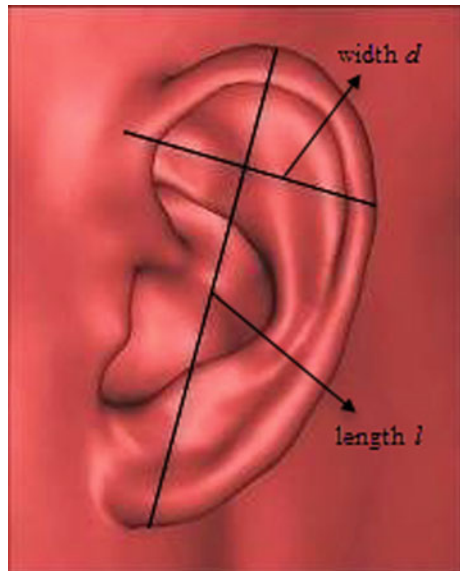


Fig. 1 Structural characteristics of ear

should be taken into considered to study the auricular prosthesis forming: auricular length l , width d and helix thickness h as shown in Fig. 2. For convenience, they are represented as $E = \{W, G\}$, $W = \{l, d, h\}$. In auricular prosthesis forming, size characteristic parameter W should be figured out and shape characteristic parameter G should be taken into considered.

Fig. 2 Parameter characteristics of ear



2.2 Motion Design of Auricular Prosthesis Forming

According to three-dimensional scanning picture of the human ear shown in Fig. 2, the external ear is composed of multiple intersected space surface with two types of spatial location characteristics: The first type of space surface is like that the fossae helicis, antihelix and so on have changed little in the Z-axis direction; The second type of space surface is like that there must be a large angel between it and xy plane as well as the helix, earlobe, cavum conchae and so on should meet the desired shape.

According to the surface characteristics of the human ear described above, three axis NC machine tool and Stewart parallel mechanism are used in auricular prosthesis forming, and its motion scheme has 9 DOF which is shown in Fig. 3. The direction of auricular prosthesis blank thickness coincides with the Z axis. The first type of space surface can be achieved from three axis NC machine tool (x, y, z) coordinates; The second type can be realized by following, first is to form an xy plane trace by three-axis machine (x, y) coordinates, and then Stewart parallel mechanism is used to adjust the attitude to ensure the relative position between machined surface and the tool axis to form a space surface. The tool processing point is expressed as $P(x, y, z)$. The Static platform of Stewart parallel mechanism is fixed with machine tool, the blank is placed on the moving platform, moving synchronously with it. Then, the adjustment of posture of forming curved surfaces can be achieved. The posture of moving platform of Stewart parallel mechanism is expressed as $\{P, Q\} = \{x, y, z, \alpha, \beta, \gamma\}$. There is no coupling relationship between the three axis NC machine tool and Stewart parallel mechanism, which could be controlled respectively. In the following, it is mainly discussed about the forming curve problem of forming the second type of space surface, including figuring out the size and shape characteristic parameters.

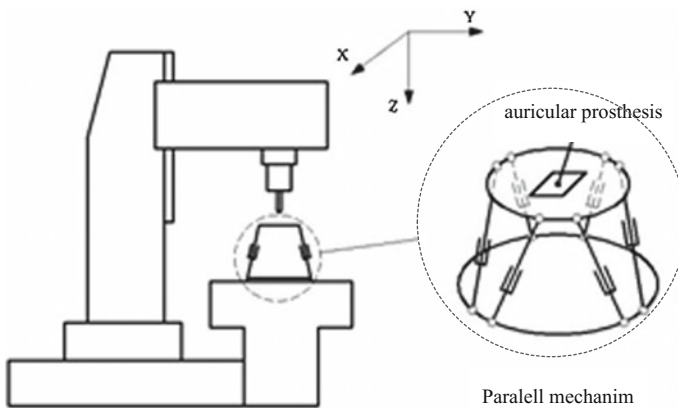


Fig. 3 Motion scheme of auricular prosthesis forming

2.3 Curve Planning of Auricular Prosthesis Forming

2.3.1 Size Characteristic of Forming Curve

Due to individual differences, the values of characteristic parameters W and G are different. The basic dimension of external ear of general people can be obtained from analysis of a large number of sample. Data collection is carried out on 513 Han Nationality Youth to get the statistical data of the characteristic parameters W about the young people in our country by statistical analysis [14].

Carry out the weighted averages of data listed in Table 1 with Eq. (1)

$$\bar{x} = \frac{x_1w_1 + x_2w_2 + \dots + x_nw_n}{w_1 + w_2 + \dots + w_n} \tag{1}$$

Then, the weighted average values of size characteristic parameter W can be figured out as follows:

$$\bar{l} = 5.9 \text{ cm}, \quad \bar{d} = 3.1 \text{ cm}, \quad h' = 0.8 \text{ cm} \tag{2}$$

The size characteristic parameters shown in Eq. (2) could be taken as the medians of general auricular prosthesis, and the size difference of individual auricle could be adjusted by shape characteristic forming curve.

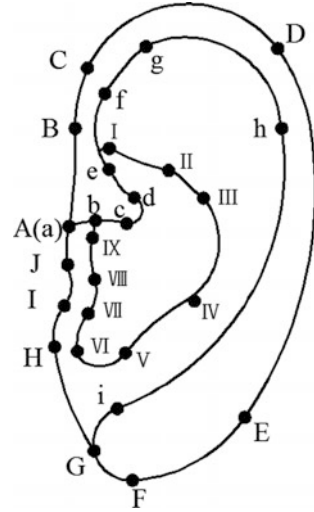
2.3.2 Shape Characteristic Curve Planning of Auricular Prosthesis Forming

During the process of auricular prosthesis forming, the shape characteristic parameter G determined the outline of the ear shape. According to the human ear of general characteristics shown in Fig. 2, the planar shape characteristics curve can be obtained to describe auricular prosthesis forming through curve fitting. The shape of auricular prosthesis forming curve can be divided into three closed curve shown in Fig. 4, and they are curve $L_1(ABCDEFGHIJA)$, $L_2(abcdefghiGHIJa)$ and $L_3(I-IX bcdeI)$.

Table 1 The measuring results of the auricular length, width and thickness (cm)

		Length l			Width d			Helix thickness h		
		Max	Min	Average	Max	Min	Average	Max	Min	Average
Male	Left	7.12	4.80	6.06	4.00	2.06	3.10	9.40	7.20	8.20
	Right	7.44	4.62	5.93	3.75	2.42	3.06	9.30	7.20	8.25
Female	Left	7.05	4.83	5.89	3.94	2.54	3.10	8.67	6.80	7.82
	Right	6.85	4.67	5.77	3.60	2.20	3.00	8.75	7.05	7.87

Fig. 4 Curve model of auricular prosthesis forming



According to Fig. 4, it can be obtained that:

- (1) Curve L_1 forms the overall size and global shape feature of auricular prosthesis;
- (2) The closed area between Curve L_1 and L_2 forms the shape of helix and earlobe;
- (3) The closed area between Curve L_2 and L_3 forms the shape of fossae helices, fossa triangularis, antihelix and so on;
- (4) Curve L_3 forms the shape of cavum conchae.

According to the above analysis, the combination of these three curves can generate the basic shape of external ear.

2.3.3 The Establishment of Mathematical Model of Auricular Prosthesis Forming Curve

According to the shape characteristics obtained from curve fitting shown in Fig. 4, shape curves are all irregular curves, so it's hard to accurately represent the shape characteristics of the human ear with a mathematical analysis formula. Therefore, human ear can be regarded as fitting curve of multistage rule curves when the auricular prosthesis forming curve modeling is carried out, namely:

$$f(x, y) = \sum_{i=1}^n f_i(x, y) \tag{3}$$

In the above formula, f_i is the function expression of i th segment curve, n is the number of segment curves; n is determined both by forming precise and forming speed of auricular prosthesis.

According to the fundamental principle of curve simplification described above, simplify the irregular curve of auricular prosthesis shown in Fig. 4, fit multi-point curve approximately and establish mathematical model based on linear or circular plane curve, in order to achieve the characteristic curve to approximately express the real shape. These shape characteristic curves and envelope curve form Helix, concha and earlobe, etc. And there is a certain angel between the envelope curve in the direction of Z -axis and xy plane. Therefore, the math model f is needed to be figured out as well as the angle Q between xy plane and Helix, concha, etc.

In order to establish the mathematical model f of each curve, construct the coordinate system shown in Fig. 5.

1. Curve L_1

The curve L_1 shown in Fig. 5a can be approximately considered as composition of L_2 Arc curves of ABCDEFGHIJA based on the multi-point curve fitting method, and the parameter equation of forming curve can be expressed as follows:

$$f_1(x, y) = \sum_{i=1}^{10} f_{1i}(x, y) \tag{4}$$

$$f_{1i}(x, y) = O_{1i} + r_{1i}\theta_{1i} \tag{5}$$

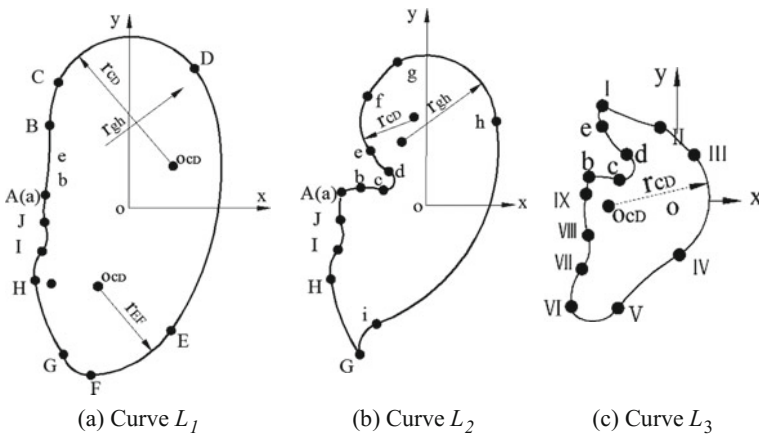


Fig. 5 Curves of auricular prosthesis forming

In two equations above: $i = 1, 2, \dots, 10, i_{1i} \{AB, BC, CD, \dots, JA\}$, of which the value of r_{1i} and θ_{1i} can be obtained simultaneously.

2. Curve L_2

Similarly, the curve L_2 shown in Fig. 5b can be approximately considered as composition of L_3 Arc curves of abcdefghiGHIJa based on the multi-point curve fitting method, and the parameter equation of forming curve can be expressed as follows:

$$f_2(x, y) = \sum_{j=1}^{13} f_{2j}(x, y) \tag{6}$$

$$f_{2j}(x, y) = O_{2j} + r_{2j}\theta_{2j} \tag{7}$$

In two equations above: $j = 1, 2, \dots, 13, j_{2j} \{ab, bc, cd, \dots, Ja\}$, of which the value of r_{2j} and θ_{2j} can be obtained simultaneously.

3. Curve L_3

The curve L_3 shown in Fig. 5c can be approximately considered as composition of L_3 Arc curves of I–IX bcdeI based on the multi-point curve fitting method, and the parameter equation of forming curve can be expressed as follows:

$$f_3(x, y) = \sum_{k=1}^{13} f_{3k}(x, y) \tag{8}$$

$$f_{3k}(x, y) = O_{3k} + r_{3k}\theta_{3k} \tag{9}$$

In two equations above: $k = 1, 2, \dots, 13, k_{2k} \{I II, II III, \dots, de, eI\}$, of which the value of r_{3k} and θ_{3k} can be obtained simultaneously.

The general expression of the forming curve equation is given by Eqs. (2)–(7), and the parameter value of each equation can be achieved from following factors, such as the size of external ear of patient、differences between shapes and patients’ aesthetic sense of auricular prosthesis. All these factors can be adjusted to adapt to the different needs of people. The value of inclination Q_{1i} of each helix curve is from 19° to 30° . For those patients with unilateral defects of the external ear, their value of inclination Q_{1i} can be measured from three-dimensional model by ear CT scanning.

3 Motion Reverse Solution and Parameter Design of Stewart Parallel Mechanism

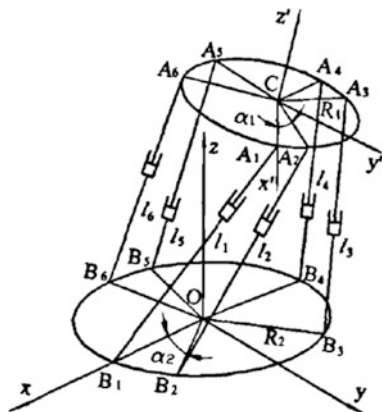
3.1 The Establishment of Motion Reverse Solution of Stewart Parallel Mechanism During Auricular Prosthesis Forming

The general Stewart parallel mechanism is shown in Fig. 6. The lower platform is a fixed platform and the upper platform is a moving platform. During the processing of auricular prosthesis forming, the auricular prosthesis blank is placed on the moving platform, and the posture of moving platform is changed to meet the requirements of blank posture of auricle surface forming. According to the working principle of Stewart parallel mechanism, the movement of moving platform comes from the movement of parallel mechanism actuating cylinders, which move according to certain motion laws. Therefore, the relationship between platform movement and actuating cylinders movement should be found out to get inverse position equation of Stewart parallel mechanism.

To establish the movement and Static coordinate system coordinate system shown in Fig. 6. The coordinates of six hinge points $A_i (i = 1, 2, \dots, 6)$ of moving platform in the moving coordinate system are $A'_i = (x'_{Ai}, y'_{Ai}, z'_{Ai})^T$, and the coordinates of six hinge points $A_i = (x_{Ai}, y_{Ai}, z_{Ai})^T$ of static platform in the fixed coordinate system are $B_i = (x_{Bi}, y_{Bi}, z_{Bi})^T$. Euler angle azimuth vector representation $Q = (\alpha, \beta, \gamma)^T$ is used in this paper. The transformation for an arbitrary vector A'_i in the moving coordinate system to the vector A_i in the fixed coordinate system can be expressed as:

$$A_i = P + TA'_i \tag{10}$$

Fig. 6 Stewart parallel mechanism



In Eq. (10), P is the static coordinate point of C, which is the origin point in moving coordinate system, $T = R_{z,\gamma}R_{y,\beta}R_{x,\alpha}$. In this case, length vector of six actuators in a fixed coordinate system can be expressed as:

$$\mathbf{l}_i = \mathbf{A}_i - \mathbf{B}_i \quad (i = 1, 2, \dots, 6) \quad (11)$$

Therefore, inverse position equation of Stewart parallel mechanism can be expressed as follows:

$$l_i = \sqrt{(x_{Ai} - x_{Bi})^2 + (y_{Ai} - y_{Bi})^2 + (z_{Ai} - z_{Bi})^2} \quad (i = 1, 2, \dots, 6) \quad (12)$$

Equation (12) is the inverse position equation of Stewart parallel mechanism, and it is the independent explicit equation for posture $P(x, y, z, \alpha, \beta, \gamma)$ about 6 parameters of moving platform. According to the requirements of inclination Q and the shape characteristics of auricular prosthesis forming curve, posture parameter $P(x, y, z, \alpha, \beta, \gamma)$ of relative moving platform can be obtained. And then, the motion law of 6 actuating cylinders can be achieved based on the inverse position equation shown in Eq. (12). When actuating cylinders move according to given motion laws, the parallel mechanism will move simultaneously to meet the requirements of posture curve of auricular prosthesis forming.

3.2 Parameter Design of Stewart Parallel Mechanism

During the processing of auricular prosthesis forming, the auricular prosthesis blank is placed on the moving platform. The workspace of moving platform represents the changeable posture range in the space of the auricular prosthesis blank. Big workspace is beneficial to the motion planning of auricular prosthesis forming and control of moving platform. Stewart is semi-symmetrical mechanism as shown in Fig. 6, and it has some main parameters: radius R_1 and R_2 of moving and static platform; hinge angle α_1 and α_2 of moving and static platform; the origin length l_i of actuating cylinder when moving platform is parallel to static platform. According to literature research [15], when $R_1 = 1$, $R_2/R_1 = 1.4-2.24$, $l_i/R_1 = 1.6-2.6$, the moving platform will get much larger workspace with a larger value of $|\alpha_2 - \alpha_1|$.

Based on statistical analysis of the morphology of auricular prosthesis in the previous section, the overall structure parameters of auricle length l, width d and thickness h are respectively 5.9 cm, 3.1 cm and 1.6 cm. Therefore, the radius R_1 of moving platform of Stewart parallel mechanism is chosen as 6 cm, the corresponding radius R_2 of static platform is 10 cm and the length of actuator cylinders l_i ($i = 1, 3, 5$) is 12 cm.

When the static platform is parallel to moving platform, the distance H between them can be expressed as follows:

Table 2 Structure parameters of Stewart parallel mechanism

No.	Structure parameters	Symbol	Unit	Value
1	Radius of moving platform	R1	cm	6
2	Radius of static platform	R2	cm	10
3	Length of actuating cylinders	li (i = 1, 3, 5)	cm	12
		li (i = 2, 4, 6)	cm	13.02
4	Distance between moving and static platform	H	cm	11.31
5	Hinge angle of the moving platform	α_1	degree	68°
6	Hinge angle of the static platform	α_2	degree	30°

$$H = \sqrt{l_1^2 - (R_2 - R_1)^2} \tag{13}$$

Putting the values of Table 2 into Formula (13), the distance between moving and fixed platform can be solved: $H = 8\sqrt{2}$ cm = 11.31 cm. Meanwhile, the length of the remaining three actuator cylinders li (i = 2, 4, 6) can be obtained, the formula can be expressed as:

$$l_i = \sqrt{(R_1 \cos \alpha_1 - R_2 \cos \alpha_2)^2 + (R_1 \sin \alpha_1 - R_2 \sin \alpha_2)^2 + H^2} \quad (i = 2, 4, 6) \tag{14}$$

Putting the concrete values into formula (14), the length l_i (i = 2, 4, 6) of the remaining three actuating cylinders of Stewart parallel mechanism is 13.02 cm.

In summary, when the static platform is parallel to moving platform, the selected structure parameters are shown in Table 2.

The values in Table 2 are the theoretical parameters, which meet the requirement of auricular prosthesis forming. When they can't meet the requirement of structural design, those values could be amplified proportionally, with little effect on the working space.

4 Examples of Auricular Prosthesis Forming

4.1 The Establishment of Mathematical Model of Auricular Prosthesis Forming

Taking the CT scanning picture of human ear as an example shown in Fig. 2, the mathematical model of forming curve can be established based on above methods shown in Fig. 3. And then, the mathematical model of curve L_1 , L_2 and L_3 can be built on basis of specific expression (4)–(9) of correlation curve and inclination Q formed by space surface of each curve. Finally, the values of parameters in mathematical model of curve L_1 , L_2 and L_3 can be presented in Tables 3, 4 and 5.

Table 3 Mathematical model of forming curve L_1

$$f_{1i}(x, y) = O_{1i} + r_{1i}\theta_{1i}$$

i	O_{1i}	r_{1i}	θ_{1i}	Q_{1i}
1	(-92.52, 13.16)	77.62	10°	0
2	(8.36, 14.56)	23.28	21°	0
3	(0.41, 16.73)	15.13	118°	0
4	(-36.65, 4.89)	54.2	56°	0
5	(-8.27, -14.56)	19.8	52°	0
6	(7.45, 29.33)	5.01	81°	0
7	(15.96, 11.58)	33.99	26°	0
8	(-11.3, -14.85)	6.56	51°	0
9	(-19.83, -7.95)	4.41	55°	0
10	(-2.28, -3.05)	13.81	28°	0

Table 4 Mathematical model of forming curve L_2

$$f_{2j}(x, y) = O_{2j} + r_{2j}\theta_{2j}$$

j	O_{2j}	r_{2j}	θ_{2j}	Q_{2j}
1	(-11.23, -11.4)	12.26	37°	23
2	(-7.69, 2.23)	1.84	163°	23
3	(-4.75, 8.71)	5.28	56°	23
4	(-3.24, 13.24)	9	70°	0-23
5	(14.02, 2.57)	29.29	17°	0
6	(0, 12.67)	12.93	112°	0
7	(-21.59, 8.1)	35	78°	0
8	(10.61, -42.6)	5.01	81°	0

Table 5 Mathematical model of forming curve L_3

$$f_{3k}(x, y) = O_{3k} + r_{3k}\theta_{3k}$$

k	O_{3k}	r_{3k}	θ_{3k}	Q_{3k}
1	(5.61, 41.2)	34.52	14°	30
2	(17.3, 23.24)	24.44	14°	30
3	(-1.37, -2.83)	7.68	131°	30
4	(-7.71, -28.4)	19.46	35°	30
5	(-11.63, -14.6)	4.28	107°	0-30
6	(-7.96, -16.03)	6.72	47°	0
7	(-16.96, -8.65)	4.92	57°	0
8	(-1.57, -3.75)	11.23	29°	0
9	(-55.97, 7.3)	44.28	3°	0

4.2 Solution of Motion Reverse Equation of Parallel Mechanism

Suppose that the forming curve coordinate system o-xyz of auricular prosthesis shown in Fig. 2 overlaps with moving platform coordinate system c-xyz. When the machine tool processes along auricular prosthesis forming curve shown in Tables 3, 4 and 5, according to the requirement of space surface inclination Q formed by each curve, the relationship between forming curve and moving platform posture parameters (α, β, γ) of parallel mechanism can be expressed as follows:

$$Q(\phi) = Q(\alpha, \beta, \gamma) \tag{15}$$

The motion law of parallel mechanism actuating cylinder of auricular prosthesis forming can be obtained by using Matlab software and establishing the simultaneous equations of Eqs. (10), (12) and (15). The parallel mechanism actuating cylinders are changing in condition of different forming curves, the changing rules shown in Figs. 7 and 8 are representing the mechanism processes along curve L_2 from d to I and along L_3 from I to V respectively. The three dimensional picture of auricular prosthesis can be obtained by means of forming curve of curve forming described above, with its boundary rounded.

Compared auricular prosthesis picture after processing shown in Fig. 9 with relative ear CT scanning shown in Fig. 2, the exterior of auricular prosthesis processed according to space surface forming method has been more close to the shape of actual ear. Therefore, it is meaningful and important to make further forming curve of auricular prosthesis partial characteristics on basis of space surface forming research. On this way, it will meet the finer forming requirements of auricular prosthesis in medicine.

Fig. 7 The length changing curve of actuating cylinder l_i when the forming curve L_2 (defghi) is forming ($i = 1, 2, \dots, 6$)

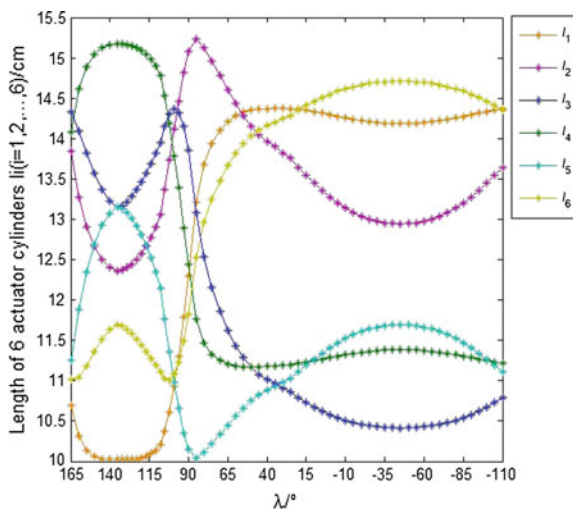


Fig. 8 The length changing curve of actuating cylinder l_i when the forming curve L_3 (I II III IV V) is forming ($i = 1, 2, \dots, 6$)

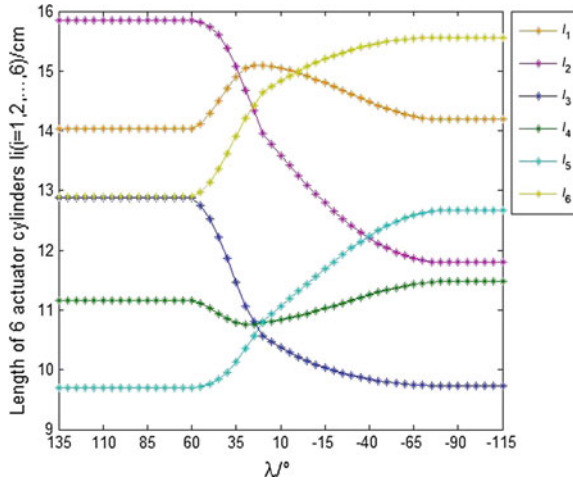


Fig. 9 Three dimensional picture of auricular prosthesis with boundary rounded



During the forming process of auricular prosthesis, the length of Stewart parallel mechanism is changing at the same time, and the maximum changing length is shown in Tables 6 and 7 respectively.

As shown in Tables 6 and 7, it can be achieved that the maximum displacement of six actuating cylinders of parallel mechanism $\Delta l_i \leq 4.348$ cm when the forming

Table 6 The maximum changing length of actuating cylinder l_i when the forming curve L_2 (defghi) is forming

l_i	l_1	l_2	l_3	l_4	l_5	l_6
l_{imax}	14.373	15.238	14.363	15.171	13.149	14.71
l_{imin}	10.025	12.356	10.412	11.169	10.038	11.007
Δl_i	4.348	2.882	3.951	4.002	3.111	3.703

Table 7 The maximum changing length of actuating cylinder l_i when the forming curve L_3 (I II III IV V) is forming

l_i	l_1	l_2	l_3	l_4	l_5	l_6
l_{imax}	15.092	15.851	12.873	11.475	12.665	15.562
l_{imin}	14.026	11.797	9.7321	10.755	9.6926	12.888
Δl_i	1.066	4.054	3.1409	0.72	2.9724	2.674

curve L_2 is forming from d to i clockwise; the maximum displacement of six actuating cylinders of parallel mechanism $\Delta l_i \leq 4.058$ cm when the forming curve L_3 is forming from I to V clockwise, and the length changing of actuating cylinder is $\Delta l_i < 12$ cm. In this way, the length of actuating cylinder can meet the requirement of structure when parallel mechanism is adjusting its moving platform. At the same time, the motion simulation of virtual prototype shows that there is no interference during the forming motion of parallel mechanism. Therefore, Stewart parallel mechanism can both meet the demands of motion and structure of auricular prosthesis forming.

5 Conclusion

This paper puts forward a practical method for auricular prosthesis rapid prototyping with parallel mechanism. Based on the study of auricular characteristics, this paper gives the method to establish auricular prosthesis forming curve and build the mathematical model of forming curve by piecewise function. The structure parameters of parallel mechanism can be designed according to the relationship between the structure parameters and workspace of Stewart parallel mechanism. Finally, the calculation method of motion reverse of parallel mechanism can be obtained. The example of auricular prosthesis forming shows that parallel mechanism can meet requirements of both position and posture of auricular prosthesis forming. And the study also lays foundation for research on drive and motion control system of parallel mechanism.

References

1. Liu H, Wang G, Li Q (2005) The research status of auricular prosthesis making technique based on CT and rapid prototyping technology. *J Clin Otorhinolaryngol Head Neck Surg* 16:759–760
2. Zhang Z (2007) Artificial auricle-auricular prosthesis. *Chin ENT News Rev* 4:19
3. Zhang Z, Zhen YQ, Liu X et al (2008) Auricular prostheses by osseointegration technique for auricular defect after trauma. *Chin Arch Otolaryngol Head Neck Surg* 10:559–561
4. Zhao Z, Xue B, Xu T et al (2013) Auricle reconstruction assisted by an expander using porous silicon auricle frame. *Chin J Med Aesthetics Cosmetol* 19(6):37–40
5. Guo Y, Li Y, Dong D et al (2005) Design and manufacture of false ear based on CAD and RP technology. *Mod Manuf Eng* 02:144–146
6. Lv T, Wang H, Han Z (2013) Research progress in auricular reconstruction. *Med Recapitulate* 19(12):2180–2182
7. Patel YD, George PM (2012) Parallel manipulators applications—a survey. *Mod Mech Eng* 2 (3):57–64
8. Hou Y, Xinzhe HU, Zeng D et al (2014) Biomimetic shoulder complex based on 3-PSS/S spherical parallel mechanism. *Chin J Mech Eng* 28(1):29–37
9. Altuzarra O, Pinto C, Avilés R (2004) A practical procedure to analyze singular configurations in closed kinematic chains. *IEEE Trans Rob* 20(06):929–940
10. Guo RQ, Gu HY, Hu W (2015) Research on avoiding singularity of linkage mechanism by self-adaptive structure. In: *Proceedings of the 14th IFToMM world congress, 2015*
11. Liu K, Wang C, Fang D et al (2015) Design of multi-gripper flexible stretch forming machine based on parallel mechanism. *Forging Stamping Technol* 40(07):87–91
12. Liu Z, Pan C, Wang Y et al (2015) Study on control of flight simulator stewart platform and its load by joint simulation. *Mach Tool Hydraulics* 2015(03):72–75
13. Zhou C, Fang Y, Ye W et al (2016) Performance analysis of 6-RRS over-redundant actuation flight simulator. *J Mech Eng* 52(01):34–40
14. Yang Y, Wu H (1988) Anatomical study of auricle. *Chin J Anat* 1988(01)
15. Guo R (2007) Singularity analysis and investigation on avoiding singularity method for parallel mechanisms. Tongji University, Shanghai

Modeling and Optimal Control of Rescue Quadruped Robot with High Payload

Nan Hu, Shaoyuan Li, Dan Huang and Feng Gao

Abstract Timely and efficient rescue missions in nuclear power plant accidents require operating robots to work under high payload typically more than 300 lb. Dynamics of the high payload quadruped robots driven by hydraulic cylinder with parallel designed legs are typically studied by commercial software due to its complexity to establish proper models. This paper proposes a kinematics model and an approximate dynamics model to describe the velocity and the force of the hydraulic cylinder, which are then used to characterize the energy requirement for rescuing walking performance. Furthermore, the models are used to optimally design the step length and height in robot rescue mission that balances the trade off between the energy consumption in robotic motion due to limited battery capacity and the requirement for timely rescuing. We applied Nelder-Mead algorithm to solve for the optimal pair of length and height.

Keywords Quadruped robot · Trajectory planning · Trot gait

N. Hu · S. Li (✉)

Department of Automation, Shanghai Jiao Tong University,
Shanghai 200240, China
e-mail: syli@sjtu.edu.cn

N. Hu

e-mail: smrw5655095@sjtu.edu.cn

D. Huang

School of Aeronautics and Astronautics, Shanghai Jiao Tong University,
Shanghai 200240, China
e-mail: huangdan@sjtu.edu.cn

F. Gao

School of Mechanical Engineering, Shanghai Jiao Tong University,
Shanghai 200240, China
e-mail: fengg@sjtu.edu.cn

© Springer Nature Singapore Pte Ltd. 2017

X. Zhang et al. (eds.), *Mechanism and Machine Science*,

Lecture Notes in Electrical Engineering 408,

DOI 10.1007/978-981-10-2875-5_43

1 Introduction

The energy demand around the world is project to growth in the next 20 years. It is expected that the amount of nuclear power plant, which is the most environmentally friendly way of producing electricity on a large scale, will also increase in the near future. Although the construction standard of the nuclear power plants is very high, with the irresistible natural disasters, such as earthquake and man-made damages, serious nuclear accidents may happen in the plants. Fukushima Daiichi Nuclear Power Plant accident happened on March 11, 2011 brought huge damage to the humanity and the society. Due to the strong nuclear radiation intensity, rescuing missions requires deploying by groups of robots that can react timely and consistently [1–4]. And this has aroused numerous attention to developing disaster rescue robot for different purposes. Wheeled robots are developed to quickly gather environment information of disaster site as it moves flexibly and fast [5]. Flight robot such as UAVs are developed to search the wounded and navigate the robots on the ground in [6–9]. Legged robots such as BigDog [10], HyQ [11], and KOLT [12] are developed for missions that requires tasking on irregular terrains.

Tasking consistently requires the rescue robot to be energy efficient and saving due to its limited capacity of carrying the battery. We need to make the rescue robot finish missions as more as possible with the same battery before back to replacement. A high-speed gallop gait using an evolutionary search method is designed to improve the energy efficiency of the robot [13]. Though the gallop gait is energy efficient, it can not be used on some irregular terrains in disaster site because the robot is unstable with the gallop gait in this environment. The energy efficiency can also be improved by minimizing torques occurring at crucial actuators in a quadruped robot [14], by searching an allowable ZMP region in a biped robot [15], and by adjusting the foot positions of the hexapod robot [16]. These various designs may not be capable of holding high payload in irregular terrains, and thus are questionable for practical considerations. Energy efficiency should be jointly solved with time optimal control since the nuclear disaster site is radioactive and less rescue time means less damage. Wheel-leg robots is preferably studied and used for its flexibility of transformation under different terrains [17, 18]. Due to its limitation of carrying payload, it cannot be used for large scale rescue mission.

The contribution of the paper is the synergy of design, modelling, and control of a quadruped robot that specifically work for high payload scenario. Considering that the robot is used to transport heavy goods and rescue equipments, we develop a novel quadruped robot having parallel leg structures, see Fig. 1. Compared with the series leg structure of almost all existing quadruped robots, robots with parallel legs are driven by hydraulic pump providing more powerful power than DC motor, and thus work under heavy payload [19]. In order to verify different control algorithms designed for the robot in the simulation software, we build and verify a kinematic and a dynamic model of the robot based on the Baby Elephant Robot we developed [20]. Upon model validation, we proceed to minimize the total rescue costs that contains the trade off between (i) the energy consumption of robot to reach a desired

destination of rescue, and (ii) the time it takes to reach the specified destination. The solution to the problem is an optimal pair of step height and step length gotten by Nelder-Mead Method [21].

This paper proceeds as follows. Section 2 gives the background of our robot platform and defines the energy and time metric in the optimization problem. Section 3 describes the kinematic and dynamic models of the quadruped robot and figures out the velocity and force of the hydraulic cylinder. The Nelder-Mead Method is applied in Sect. 5 to jointly minimize the energy consumption and mission time. Section 6 concludes.

2 Problem Formulation

2.1 *Baby Elephant Robot*

The quadruped robot we have developed for rescue mission is called Baby Elephant Robot as shown in Fig. 1. The Baby Elephant Robot is about 1.2 meters long, 0.5 meters wide, and 1 m tall. It weighs about 250 lb and can carry loads more than 300 lb. Each leg of the robot has three degrees. Each DOF is controlled by a separate hydraulic actuator which can guarantee the robot powerful and reliable.

Fig. 1 The baby elephant robot with hydraulic pump is design to carry high payload. It has decoupled design of the motion and the power



2.2 Problem Definition

Robot rescue problem requires timely execution as well as that the robot to be able to perform time consistently. Since the energy that a robot can carry is fixed, energy efficiency movement planning needs to be considered. We formulate the optimal motion planning control problem for the quadruped robot as the problem to solve the trade off between robot movement energy efficiency and swiftness.

Energy Efficiency Since most of the battery energy is consumed by the hydraulic cylinders to make the feet of the robot perform desired walking motion, we calculate the energy consumed by the hydraulic cylinders as the total energy consumption in one walking cycle.

$$E = \int_T \sum_{i=1}^{12} P_{cy,i}(t) dt = \int_T \sum_{i=1}^{12} (F_{cy,i}(t) v_{cy,i}(t)) dt, \quad (1)$$

where i is the index of the hydraulic cylinder, T is the single walking cycle duration, $F_{cy,i}(t)$ is the driving force, and $v_{cy,i}(t)$ is the velocity of hydraulic cylinder.

Value of Rescue Time The nuclear radiation increases as the rescue time increases from the quadruped robot. It is well know that he nuclear radiation is released with radioactive decay and he amount of substance $m(t)$ at time t is [22].

$$m(t) = m_0 e^{rt}, \quad (2)$$

where r is decay rate and m_0 is initial substance value. The total nuclear radiation dose Q released from a accident by time t can be calculated as

$$Q = X m_0 (1 - e^{rt}), \quad (3)$$

where X is the radiation dose released by per unit mass radioactive decay.

Constraints Physical geometric constraints are required to guarantee feasible walking motions for the robot in real environments. In the Baby Elephant Robot, the angle θ and the angle α showed in Fig. 2 have physical limits which are given by

$$\begin{aligned} \frac{1}{12} \pi \leq \theta \leq \frac{11}{12} \pi, \\ 0 \leq \alpha \leq \frac{5}{12} \pi. \end{aligned} \quad (4)$$

In order to get the geometric constraints, we need to solve for the geometric relationships that we will derive in Sect. 3. Basing on geometric relationships in the Eq. (9), we have the constraints for the step pitch ΔX in X axis direction as well as the step height ΔZ in Z axis direction as follows.

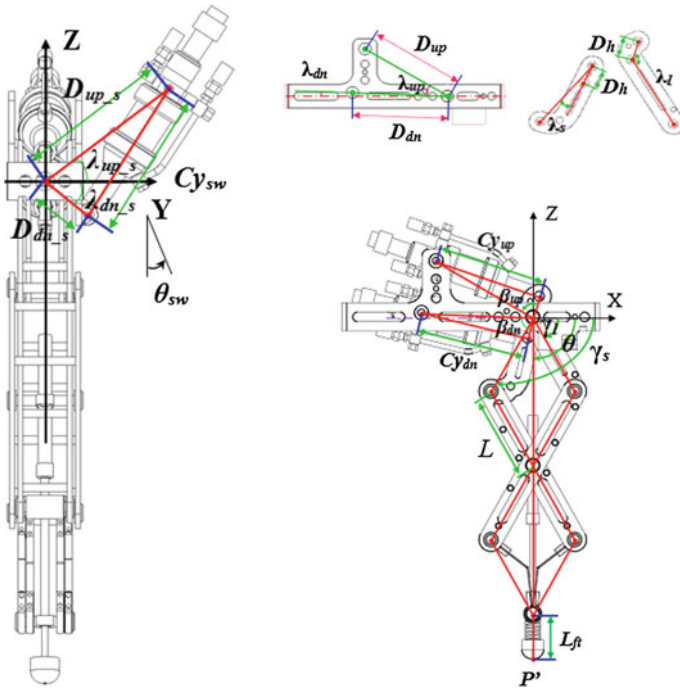


Fig. 2 The left figure and the right figure is the leg in coronal plane from front view and the leg in sagittal plane from the side view respectively. Every alphabetic character in the figure presents the corresponding size of the parts of the leg

$$\begin{aligned}
 \Delta X &\leq (4L + L_{ft}) \sin\left(\frac{5}{12}\pi\right), \\
 \Delta Z &\leq [(4L + L_{ft}) - (4L \cos\left(\frac{5}{12}\pi\right) + L_{ft}) \cos\left(\frac{5}{12}\pi\right)].
 \end{aligned}
 \tag{5}$$

To this end, we define the optimal planning of the robot rescue problem as follows. Given our robot performs a rescue mission in a distance D , our goal is to solve for an optimal pair of step pitch ΔX and step height ΔZ to minimize the summed costs of the energy consumption in (1) and the radiation dose release in (3) satisfying (5).

3 Kinematic and Dynamic Models of the Quadruped Robot

We build an approximate kinematic and dynamic model of the robot in order to have an analytical expression of (1). Based on the approximate model we will

calculate velocity $v_{cy,i}(t)$ and force $F_{cy,i}(t)$ of the hydraulic cylinder to solve for the energy consumption is one operating cycle.

3.1 Computing $v_{cy,i}(t)$ of the Hydraulic Cylinder

Figure 2 demonstrates the mechanical structure of robot leg. The origin frame of the leg is set at the hip joint. Given the foot tip position $P_b(x_p, y_p, z_p)$, the coordinate of the foot tip on the sagittal plane can be derived from the transform matrix below.

$$\theta_{sw} = -\arctan\left(\frac{y_p}{z_p}\right), \quad (6)$$

$$P(x, 0, z) = R_x(\theta_{sw}) \cdot P_b(x_p, y_p, z_p), \quad (7)$$

where R_x is the transform matrix from the frame fixed with the body to the frame rotate with the sagittal plane.

$$R_x = \begin{bmatrix} 1 & 0 & 0 \\ 0 & \cos \theta_{sw} & \sin \theta_{sw} \\ 0 & -\sin \theta_{sw} & \cos \theta_{sw} \end{bmatrix}. \quad (8)$$

On the sagittal plane in Fig. 2, based on the paper [25] and [26], we get the equations below based on geometric relationships.

$$\begin{aligned} L_p &= \sqrt{x^2 + z^2}, \\ L_{p'} &= L_p - L_{ft}, \\ \theta &= \frac{\pi}{2} - \arctan \frac{x}{z}, \\ \alpha &= \arccos\left(\frac{L_{p'}}{4L}\right), \\ \begin{cases} \gamma_l = \theta - \alpha \\ \gamma_s = \theta + \alpha, \end{cases} \\ \beta_{up} &= \pi - (\lambda_l - \gamma_l) - \lambda_{up}, \\ \beta_{dn} &= \pi + \lambda_s - \gamma_s + \lambda_{dn}, \\ \beta_{sw} &= \lambda_{up_s} + \lambda_{dn_s} - \theta_{sw}. \end{aligned} \quad (9)$$

The length of the cylinder can be gotten as follows

$$Cy_{dn}^2 = D_{dn}^2 + D_h^2 - 2D_{dn}D_h \cos(\beta_{dn}), \tag{10}$$

$$Cy_{up}^2 = D_{up}^2 + D_h^2 - 2D_{up}D_h \cos(\beta_{up}), \tag{11}$$

$$Cy_{sw}^2 = D_{dn_s}^2 + D_{up_s}^2 - 2D_{dn_s}D_{up_s} \cos(\beta_{sw}).$$

We assume the robot walks in a straight line and for simplicity let $Cy_{sw} = 0$. Computing the derivatives of (12) and (13), we get the Jacobin matrix

$$Cy_{dn}^2 = D_{dn}^2 + D_h^2 - 2D_{dn}D_h \cos(\beta_{dn}), \tag{12}$$

$$Cy_{up}^2 = D_{up}^2 + D_h^2 - 2D_{up}D_h \cos(\beta_{up}), \tag{13}$$

$$Cy_{sw}^2 = D_{dn_s}^2 + D_{up_s}^2 - 2D_{dn_s}D_{up_s} \cos(\beta_{sw}). \tag{14}$$

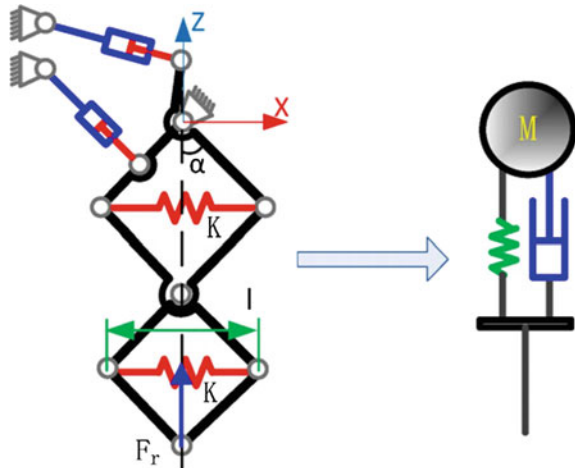
where Cy_{dn} , Cy_{up} and Cy_{sw} is the length of down, up and swing cylinder as shown in Fig. 3 respectively. And β_{dn} , β_{up} , β_{sw} are given in [25] and [26].

We assume the robot walks in a straight line so Cy_{sw} is constant, then we don't consider Cy_{sw} here, and for simplicity let $Cy_{sw} = 0$. Computing the derivatives of (12) and (13), we get the Jacobin matrix

$$\begin{bmatrix} v_{dn} \\ v_{up} \end{bmatrix} = \begin{bmatrix} \dot{C}y_{dn} \\ \dot{C}y_{up} \end{bmatrix} = \frac{1}{AB} [D] \begin{bmatrix} -A & B \\ -B & -B \end{bmatrix} [R'_y(\theta)] \begin{bmatrix} v_{px} \\ v_{pz} \end{bmatrix}, \tag{15}$$

where $A = 8L \sin(\alpha)$, $B = 4L \cos(\alpha)$,

Fig. 3 Spring system of the leg



$$[D] = \begin{bmatrix} \frac{D_{dn}D_h \sin(\beta_{dn})}{C_{ydn}} & 0 \\ 0 & \frac{D_{up}D_h \sin(\beta_{up})}{C_{yup}} \end{bmatrix},$$

$$R_y(\theta) = \begin{bmatrix} \sin \theta & \cos \theta \\ -\cos \theta & \sin \theta \end{bmatrix}.$$

Each leg of the robot is controlled by the up and down cylinder as shown in Fig. 2. The $v_{dn,j}$ and $v_{up,j}$ we get from (15) (where j is the leg j and $j = 1, 2, 3, 4$) are the $v_{cy,i}(t)$.

3.2 Computing the Force of the Hydraulic Cylinder

We can get the static force Jacobin by transforming (15) as follows.

$$\begin{bmatrix} F_{cydn} \\ F_{cyup} \end{bmatrix} = \frac{4L}{D_h} R_y(\theta) \begin{bmatrix} \frac{C_{ydn} \cos \alpha}{D_{dn}D_h \sin(\beta_{dn})} & \frac{C_{ydn} \sin \alpha}{D_{dn}D_h \sin(\beta_{dn})} \\ \frac{C_{yup} \cos \alpha}{D_{up}D_h \sin(\beta_{up})} & \frac{C_{yup} \sin \alpha}{D_{up}D_h \sin(\beta_{up})} \end{bmatrix} \begin{bmatrix} F_t \\ F_r \end{bmatrix}, \quad (16)$$

where F_r is the radial force which usually goes through the hip joint, and F_t is the tangential force perpendicular to F_r . To simplify the problem, the leg weight and the inertia are neglected here.

We applied the spring system on the leg of the robot to promote the energy deficiency. Figure 3 shows how the spring system is configured on the leg.

According to the principle of virtual work, we have

$$F_r \cdot \delta z = 2K\Delta l \cdot \delta l, \quad (17)$$

where δz and δl are the vertical virtual displacements of foot tip and the horizontal virtual displacement of the spring, respectively. K is the stiffness coefficient of spring. And

$$\begin{cases} z = -4L \cos \alpha \\ l = 2L \sin \alpha, \end{cases} \quad (18)$$

where l is the length of the spring. Computing the derivative of (18), we have

$$\frac{\delta z}{\delta l} = 2 \tan \alpha. \quad (19)$$

Based on (17) and (19), we solve for F_r

$$F_r = \frac{K(2L \sin \alpha - l_{initial})}{\tan \alpha}, \tag{20}$$

where $l_{initial}$ is the initial length of the spring.

Paper [23] suggests the contact force between the foot tip and ground is normally aligned with radial direction of the leg except for acceleration and deceleration in the process of walking. And the tangential force F_t is usually very small under a constant walking speed. Hence we let

$$F_t = 0. \tag{21}$$

Finally we solve for $F_{cy,dn}, F_{cy,up}$ by substituting F_r and F_t in (20) and (21) to (16).

3.3 Gait and Foot Trajectory Planning

Gait is a pattern of discrete foot placements performed in a given sequence. The gaits of the quadruped robots are classified into static gaits and dynamics gaits. Static gaits contain crawl and wave. Dynamic gaits include trot, pace and gallop. In this paper, we choose trotting gait for the quadruped robot because its high energy efficiency and simplicity of control [26].

We use Bezier curve to design the trajectory of robot’s feet which can guarantee the robot walk stably and make the trajectory of the robot similar to that of an animal. The Bezier curve is given as follows [25].

$$B(t) = \sum_{i=0}^n C_n^i P_i (1-t)^{n-i} t^i. \tag{22}$$

Constraints in (24) can guarantee the velocity and acceleration of foot be zero when foot leaving and landing on the ground. Since we have six constraints to design the foot trajectory, we choose a five order Bezier curve to define the foot trajectory on X axis orientation from Eq. (22) as follows.

$$X(t) = P_0(1-t)^5 + 5P_1(1-t)^4t + 10P_2(1-t)^3t^2 + 10P_3(1-t)^2t^3 + 5P_4(1-t)t^4 + P_5t^5, \tag{23}$$

We let the T be the time of one walking period and set the duty factor here is 0.5 which means a leg will take only $0.5T$ to complete its own motion. Equation (23) is subject to the following constraints.

$$\begin{aligned}
\text{Position : } & \begin{cases} X(0) = X_0 \\ X(0.5T) = X_0 + \Delta X, \end{cases} \\
\text{Velocity : } & \begin{cases} \dot{X}(0) = 0 \\ \dot{X}(T) = 0, \end{cases} \\
\text{Acceleration : } & \begin{cases} \ddot{X}(0) = 0 \\ \ddot{X}(T) = 0, \end{cases}
\end{aligned} \tag{24}$$

where X_0 is the start position of robot's foot on X axis orientation while ΔX is the step pitch on X axis orientation. So we can get the coefficient P_0 to P_5 from (23) to (24). Letting $X_0 = 0.5m$, $T = 0.65s$, we have

$$\begin{aligned}
X(t) = 0.5 + 291.3t^3 \cdot \Delta X - 1344.5t^4 \cdot \Delta X + 1654.8t^5 \cdot \Delta X \\
(0 \leq t \leq 0.325).
\end{aligned} \tag{25}$$

Similarly letting start position of robot's foot on Z axis $Z_0 = 0$ be zero, and assuming that the robot walks in a straight line with $Y(t) = 0$, we get the foot trajectory $Z(t)$ as follows

$$Z(t) = \begin{cases} 2330.5t^3 \cdot \Delta Z - 21511.9t^4 \cdot \Delta Z + 52953.6t^5 \\ \cdot \Delta Z (0 \leq t \leq 0.1625) \\ \Delta Z - 2330.5(t - 0.1625)^3 \cdot \Delta Z + 21511.9(t - 0.1625)^4 \\ \cdot \Delta Z - 52953.6(t - 0.1625)^5 \cdot \Delta Z (0.1625 \leq t \leq 0.325). \end{cases} \tag{26}$$

Computing the derivatives of (25) and (26), we get v_{px}, v_{pz}

$$\begin{aligned}
v_{px} = \dot{X}(t) = 873.9t^2 \cdot \Delta X - 86047.6t^3 \cdot \Delta X + 258.5t^4 \cdot \Delta X \\
(0 \leq t \leq 0.325),
\end{aligned} \tag{27}$$

$$v_{pz} = \dot{Z}(t) = \begin{cases} (6991.5t^2 \cdot -86047.6t^3 \cdot + 264761.3t^4) \\ \cdot \Delta Z (0 \leq t \leq 0.1625) \\ -6991.5(t - 0.1625)^2 \cdot \Delta Z + 86047.6(t - 0.1625)^3 \\ \cdot \Delta Z - 264761.3(t - 0.1625)^4 \\ \cdot \Delta Z (0.1625 \leq t \leq 0.325). \end{cases} \tag{28}$$

Using v_{px}, v_{pz} above, we can get the $v_{cy,dn}, v_{cy,up}$ in (15) that is used to solve the energy consumption defined in (1).

3.4 Robot Energy Consumption

Basing on (1), (15), and (16), we have the total energy consumed by the robot in one walking cycle as follows

$$\begin{aligned}
 E &= \int_T \sum_{i=1}^{12} (F_{cyi}(t)v_{cyi}(t))dt \\
 &= \int_T \sum_{j=1}^{12} (F_{cypj}(t)v_{cypj}(t) + F_{cydnj}(t)v_{cydnj}(t) \\
 &\quad + F_{cyswj}(t)v_{cyswj}(t))dt
 \end{aligned} \tag{29}$$

where j is the leg index. As $v_{cysw,j} = 0$, the energy consumed by the diagonal legs is symmetrical and a leg takes $0.5T$ to complete its own motion in one period. Equivalently, the energy E can be expressed as follows

$$E = 4 \int_{0.5T} (F_{cyp}(t)v_{cyp}(t) + F_{cydn}(t)v_{cydn}(t))dt. \tag{30}$$

4 Optimal Solution of ΔX and ΔZ

4.1 Monetary Metric Objection Function

We solve the trade off between minimizing the energy consumption in (1) and the radiation dose release in (3). For small value of ΔX , we have less energy consumption but longer execution time for the robot to walk from starting point to the destination. Hence the radiation dose release Q will increase. We unify the metrics of E and Q into monetary metric cost minimization. Specifically, we assume that it costs us K_E per unit energy the robot consumes, and it increases us rescue cost K_Q with per unit radiation dose release increase from the accident. The objective function is therefore defined as follows

$$F(\Delta X, \Delta Z) = K_E E_t + K_Q Q, \tag{31}$$

Suppose the total traveling distance of the rescue mission is D and our robot walks in a constant velocity. Based on (3) and (30), Eq. (31) is equivalent to

$$\begin{aligned}
 F(\Delta X, \Delta Z) &= K_Q X m_0 (1 - e^{-\frac{D}{\Delta X}}) + \frac{4DK_E}{2\Delta X} \int_{0.5T} (F_{cyp}(t)v_{cyp}(t) \\
 &\quad + F_{cydn}(t)v_{cydn}(t))dt.
 \end{aligned} \tag{32}$$

4.2 Nelder-Mead Algorithm

Equation (32) is nonlinear scalar function of two variables that can be solved by Nelder-Mead algorithm. The Nelder-Mead algorithm is also known as the flexible polyhedron algorithm which is a multi-dimensional, nonlinear minimization and unconstrained algorithm [21]. This method requires a starting point $(\Delta X_0, \Delta Z_0)$, and then it can find an optimal point $(\Delta X^*, \Delta Z^*)$ to minimize the objective function (32). It can expressed by

$$\text{minimize}_{\Delta X, \Delta Z} F(\Delta X, \Delta Z) \rightarrow (\Delta X^*, \Delta Z^*), \tag{33}$$

Simulation parameters are $D = 300, K_Q = 100, X = 50, m_0 = 500, r = -0.4,$ and $K_E = 2.$ We apply (33) to compute ΔX and ΔZ and minimize the objective function $F(\Delta X, \Delta Z).$ We start the Nelder-Mead Method with the initial point $\Delta X_0 = 0.1, \Delta Z_0 = 0.2,$ the optimal solution is $\Delta X^* = 0.2659, \Delta Z^* = 0.0602,$ and the minimum cost function $F^*(\Delta X, \Delta Z)$ is 25,939 dollar.

In order to verify the ΔX^* and ΔZ^* we get above is the global optimal solution, we figure out the rescue cost with all the feasible ΔX and ΔZ with the constraints in Eq. (5). Figure 4 shows the rescue cost with $\Delta X \in [0.2, 0.3]$ and $\Delta Z \in [0, 0.1].$ Figure 5 shows the contour line of rescue cost with different ΔX and $\Delta Z.$ We can see from Figs. 4 and 5 that the cost function $F(\Delta X, \Delta Z)$ is convex, and the optimal point is $\Delta X^{*'} = 0.26, \Delta Z^{*'} = 0.062.$ It exits an error about 2.2 % of optimal ΔX and an error about 2.9 % of optimal ΔZ between the real value and the calculation

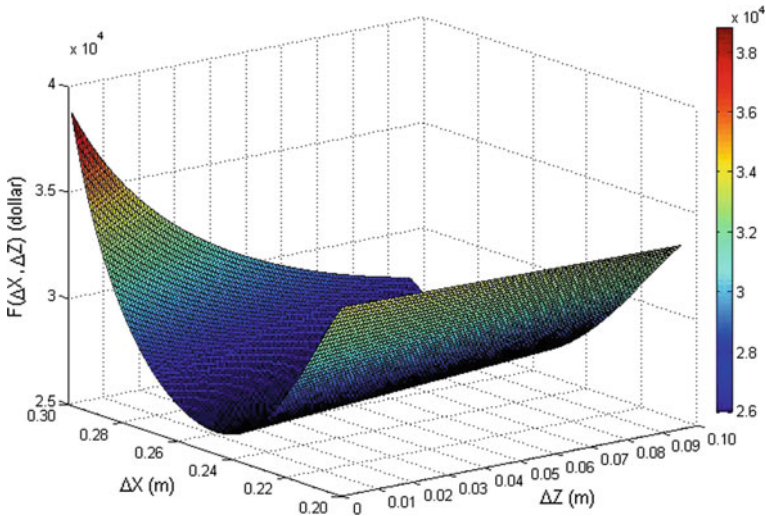


Fig. 4 The rescue cost with different feasible ΔX and $\Delta Z.$ ΔZ represents possible step height in $(0, 0.1],$ ΔX represent possible step pitch in $[0.2, 0.3],$ and the vertical axis denotes the total system cost in (31). The optimal solution is $(\Delta X, \Delta Z) = (0.26, 0.062)$

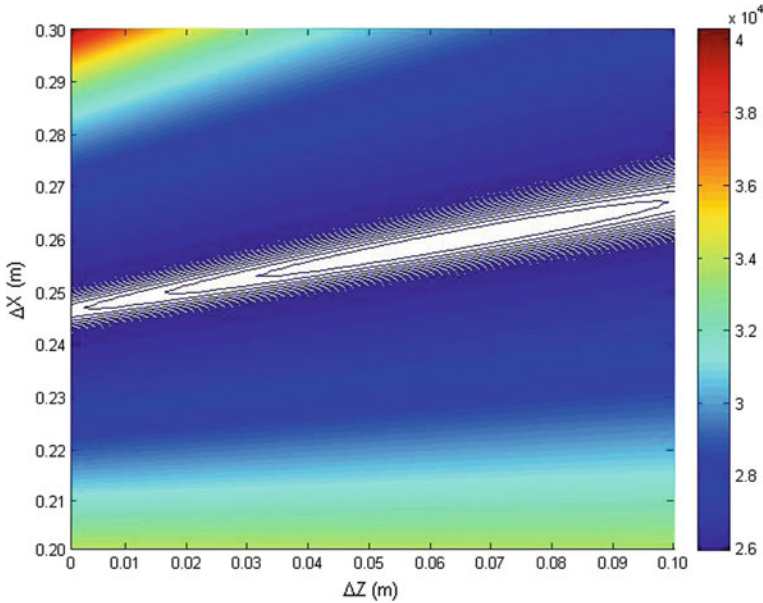


Fig. 5 The contour plot of rescue cost with different pairs of ΔX and ΔZ . Numerically it is shown that the cost function is convex and is more significantly impacted by ΔX than ΔZ . This can be explained since the energy consumption and the radiation dose release both decided by ΔX while ΔZ has no relation with the radiation dose release

value using the Nelder-Mead Method. It is a normal numerical calculation error of Matlab, which can be acceptable.

5 Conclusion

As minimizing the energy consumption and the execution time are both important in robot rescue missions, this paper solves the trade off between the two physical units for optimal rescue planning. The solution to this problem requires that we build a quadruped robot platform with high payload and formulate approximate kinematic and dynamic model of the robot. In the end numerical algorithm is used to solve for the optimal step pitch and height for the motion planning problem.

Acknowledgments This work is supported by National Basic Research Program of China (973 Program-2013CB035500), China Scholarship Council, and the National Nature Science Foundation of China (61233004, 61221003, 61074061, 61104091).

References

1. Murphy RR, Peschel J, Arnett C, Martin D (2012) Projected needs for robot-assisted chemical, biological, radiological, or nuclear (CBRN) incidents. In: 2012 International symposium on safety, security, and rescue robotics, Austin, pp 1–4
2. Nagatani K, Kiribayashi S, Okada Y, Tadokoro S, Nishimura T, Yoshida T, Koyanagi E, Hada Y (2011) Redesign of rescue mobile robot Quince—toward emergency response to the nuclear accident at Fukushima Daiichi Nuclear Power Station on March 2011. In: Proceedings of the 2011 IEEE international symposium on safety, security and rescue robotics, Kyoto, pp 13–18
3. Sugisaka M (2011) Working robots for nuclear power plant disasters. In: 5th IEEE international conference on digital ecosystems and technologies, Daejeon, pp 358–361
4. Shimizu M, Takahashi T (2014) Simulated environment for wirelessly controlled robots using the natural behavior of radio waves. In: 2014 IEEE international symposium on safety, security, and rescue robotics, Hokkaido, pp 1–6
5. Chiu Y, Shiroma N, Igarashi H, Stao N, Inami M, Matsuno F (2005) FUMA: environment information gathering wheeled rescue robot with one-DOF arm. In: Proceedings of the 2005 IEEE international workshop on safety, security and rescue robotics, Kobe, pp 81–86
6. Goodrich MA, Lin L, Morse BS (2012) Using camera-equipped mini-UAVS to support collaborative wilderness search and rescue teams. In: International conference on collaboration technologies and systems, Denver, pp 638
7. Almurib HAF, Nathan PT, Kumar TN (2011) Control and path planning of quadrotor aerial vehicles for search and rescue. In: 2011 Proceedings of SICE annual conference, Tokyo, pp 700–705
8. Dhaliwal SS, Ramirez-Serrano A (2009) Control of an unconventional VTOL UAV for search and rescue operations within confined spaces based on the MARC control architecture. In: 2009 IEEE international workshop on safety, security and rescue robotics, Denver, pp. 1–6
9. Tomic T, Schmid K, Lutz P, Domel A, Kassecker M, Mair E, Grix IL, Ruess F, Suppa M, Burschka D (2012) Toward a fully autonomous UAV: research platform for indoor and outdoor urban search and rescue. *IEEE Robot Autom Mag* 19(3):46–56
10. Raibert M, Blankespoor K, Nelson G, Playter R, the BigDog Team: BigDog, the rough-terrain quadruped robot. In: Proceeding of 17th IFAC world congress, Seoul, pp 10822–10825
11. Semini C, Tzagarakis NG, Guglielmino E, Focchi M, Cannella F, Caldwell DG (2011) Design of HyQ-a hydraulically and electrically actuated quadruped robot. *Proc IMechE Part I J Syst Control Eng* 225(6):831–849
12. Nichol JG, Singh SPN, Waldron KJ, Palmer LR, Orin DE (2004) System design of a quadrupedal galloping machine. *Int J Robot Res* 23(10–11):1013–1027
13. Chae G, Park J (2007) Galloping trajectory optimization and control for quadruped robot using genetic algorithm. In: 2007 IEEE international conference on robotics and biomimetics, Sanya, pp 1166–1171
14. Thomson T, Sharf I, Beckman B (2012) Kinematic control and posture optimization of a redundantly actuated quadruped robot. In: 2012 IEEE international conference on robotics and automation, Saint Paul, pp 1895–1990
15. Shin H, Kim B (2014) Energy-efficient gait planning and control for biped robots utilizing the allowable ZMP region. *IEEE Trans Rob* 30(4):986–993
16. Gonzales de Santos P, Garcia E, Ponticelli R, Armada M (2009) Minimizing energy consumption in hexapod robots. *Adv Robot* 23(6):681–704
17. Kim Y, Jung G, Kim H, Cho K, Chu C (2014) Wheel transformer: a wheel-Leg hybrid robot with passive transformable wheels. *IEEE Trans Rob* 30(6):1487–1498
18. Kleiner A, Kummerle R (2007) Genetic MRF model optimization for real-time victim detection in search and rescue. In: Proceedings of the 2007 IEEE/RSJ international conference on intelligent robots and systems, San Diego, pp 3025–3030

19. Tian X, Gao F, Chen X, Qi C (2013) Mechanism design and comparison for quadruped robot with parallel-serial leg. *J Mech Eng* 49(6):81–88
20. Gao F, Qi C, Sun Q, Chen X, Tian X (2014) A quadruped robot with parallel mechanism legs. In: 2014 IEEE international conference on robotics and automation, Hongkong, pp 2566
21. Lagarias JC, Reeds JA, Wright MH, Wright PE (1998) Convergence properties of the Nelder-Mead simplex method in low dimensions. *SIAM J Optim* 9(1):112–147
22. L'Annunziata MF (1998) Handbook of radioactivity analysis. Academic Press, New York
23. Pontzer H (2005) A new model predicting locomotor cost from limb length via force production. *J Exp Biol* 208:1513–1524
24. Palmer III LR, David OE (2007) Force redistribution in a quadruped running trot. In: IEEE international conference on robotics and automation, pp 4343–4348
25. Hu N, Li S, Huang D, Gao F (2014) Crawling gait planning for a quadruped robot with high payload walking on irregular terrain. In: The 19th IFAC world congress, vol 47(3), Cape Town, pp 2153–2158
26. Hu N, Li S, Huang D, Gao F (2014) Trotting gait planning for a quadruped robot with high payload walking on irregular terrain. In: International joint conference on neural networks, Beijing, pp 581–587

A Contrastive Study on the Force Analysis of the Active and Passive Overconstrained Parallel Mechanisms

Yundou Xu, Wenlan Liu, Jinwei Guo, Yongsheng Zhao, Jiantao Yao and Bo Han

Abstract This paper reveals that the distinction between the statically indeterminate force problem of the active overconstrained parallel mechanisms (PMs), i.e., the redundantly actuated PMs, and that of the passive overconstrained PMs is the displacement coordination condition. For the redundantly actuated PMs, the displacement consists of the input displacements of the actuators and the elastic deformations of the system. While for the passive overconstrained PMs, it just refers to the elastic deformations of the system. Besides, taking the typical 2RPR+P redundantly actuated mechanism as an example, the relationship between the input displacement and the driving force/torque of an actuator under the position and torque control modes are discussed. The results will provide an important theoretical guidance for the control of the redundantly actuated mechanisms.

Keywords Redundantly actuated PM · Driving force distribution · Passive overconstrained PM · Force analysis · Coordination condition

Y. Xu · W. Liu · J. Guo · Y. Zhao (✉) · J. Yao · B. Han
Parallel Robot and Mechatronic System Laboratory of Hebei Province,
Qinhuangdao 066004, Hebei, China
e-mail: yszhao@ysu.edu.cn

Y. Xu
e-mail: ydxu@ysu.edu.cn

W. Liu
e-mail: wenlanl@163.com

J. Guo
e-mail: 1473733099@qq.com

J. Yao
e-mail: jtyao@ysu.edu.cn

B. Han
e-mail: 1440731168@qq.com

Y. Xu · Y. Zhao · J. Yao
Key Laboratory of Advanced Forging and Stamping Technology
and Science of Ministry of National Education, Yanshan University,
Qinhuangdao 066004, Hebei, China

1 Introduction

The redundantly actuated parallel mechanisms (PMs) have received widespread attention for the merits of eliminating kinematic singularities [1, 2], enhancing carrying capacity [3] and improving motion accuracy [4]. The redundant constraints rise in this kind of PMs since the number of the driving joints is larger than the degrees of freedom (DOFs) of the mechanisms. In view that all driving forces/torques of this kind of PMs can be given actively on the basis of the optimal goals, the redundantly actuated PMs can also be called as the active overconstrained PMs. There exist another kind of overconstrained PMs relative to the active overconstrained PMs, i.e., the passive overconstrained PMs, in which the constraints imposed on the moving platform by the supporting limbs are linear dependent [5, 6]. For this kind of overconstrained PMs, the constraint forces/moments can not be given actively. The passive overconstrained PMs have been widely applied in the occasions of high load bearing [7] for the characteristics of simple structure, high rigidity and high precision [8].

Due to the existence of the redundant constraints, the force analysis of both the redundantly actuated PMs and the passive overconstrained PMs belong to the statically indeterminate problem. Therefore, a certain number of supplementary equations are required to solve the driving forces/torques and constraint forces/moments. For the redundantly actuated PMs, there are theoretically an infinite number of solutions for their driving forces/torques distribution problem. Nevertheless, the uncoordinated driving force distribution will lead to the generation of larger internal forces or even destroy the mechanism in practical application. Therefore, the driving forces/torques of this kind of PMs can be distributed according to different optimization goals. A new method for solving the inverse dynamics and internal force of the redundantly actuated PM was proposed under the condition of considering the elastic deformation of limbs [9]. Harada et al. [10] studied a strategy of driving force distribution in order to achieve the goal of force balance of each limb. Nokleby et al. [11] proposed a method to determine the driving force of the non-redundantly and redundantly actuated parallel robots by using scaling factor. Wojtyra et al. [12–14] solved the constraint reaction forces in joints of the redundant constraint mechanism. Besides, the driving forces/torques of the redundantly actuated mechanism is optimized in [15–18]. For the passive overconstrained PMs, the force analysis of this kind of mechanisms has also received extensive attention from the domestic and foreign scholars, since it contributes to the design, manufacture and control of the mechanisms. The statically indeterminate force problem of the passive overconstrained PMs has unique solution, which can not be arbitrarily distributed. A general method for force analysis of the passive overconstrained PMs was proposed in [19]. By applying the reciprocal-screw theory, the kinetostatics of the 4-R (CRR) Parallel Manipulator with overconstraints is presented in [20]. Bonnemains et al. [21] analyzed the dynamics of an overconstrained PKM with compliances: the Tripteor X7. Sapio et al. [22] studied the method for motion control and computation of the constraint

forces. Vertechy et al. [23] analyzed the static and stiffness of the PM with the US and UPS limbs. Based on the Newton-Euler method, the inverse dynamic model of the overconstrained mechanism is constructed in [24]. Li et al. [25] explored deformation compatibility conditions and twist/wrench mapping models of the two-DOF overconstrained PM considering gravitational effects.

All of the above mentioned literatures focused on the methods for force analysis of the redundantly actuated mechanisms and the passive overconstrained mechanisms, but no research has been carried out about the essential difference of the statically indeterminate force problem between the two kinds of overconstrained mechanisms. Therefore, this paper mainly studies the differences in the force analysis of the two kinds of overconstrained PMs. Taking the typical 2RPR+P redundantly actuated mechanism as an example, the mechanism on the driving forces/torques distribution is analyzed, in the condition of considering and without considering the system stiffness. Besides, the future works are put forward.

2 Coordination Conditions of Both the Overconstrained PMs

It is assumed that the stiffness of the moving platform of both the redundantly actuated PMs and the passive overconstrained PMs is much larger than that of all supporting limbs, as a result, the moving platform can be regarded as a rigid body. In order to ensure that each limb and the moving platform are always connected, the displacements of all limbs should meet a certain coordination relationship. For the redundantly actuated PMs, the displacement coordination condition contains the input displacements of the actuators and the elastic deformations of the system. While for the passive overconstrained PMs, the displacement coordination condition just refers to the elastic deformations of the system.

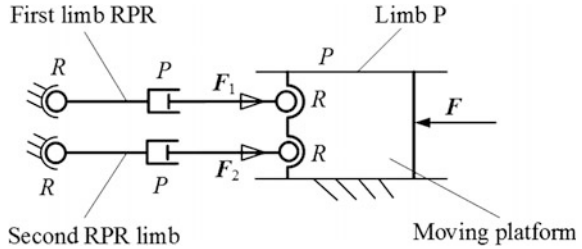
Taking the 2RPR+P redundantly actuated PM shown in Fig. 1 as an example, in which the axes of the two RPR supporting limbs and the P limb are parallel. The displacement coordination condition of this mechanism is that the displacements of the two limbs are completely equal during the moving process of the mechanism. Here, the displacement includes two parts. One part is the input displacement of the i th ($i = 1, 2$) actuator, and the other part is the tension and compression elastic deformation of the corresponding limb. The displacement coordination condition of the 2RPR+P mechanism can be expressed as

$$d_1 + \delta_1 = d_2 + \delta_2. \quad (1)$$

where, d_i and δ_i represent the magnitudes of the input displacement and the tension and compression elastic deformation of the i th limb, respectively.

When the actuation joints of the 2RPR+P mechanism are locked, it becomes a passive overconstrained mechanism. For this 2RR+P passive overconstrained PM, the displacement coordination condition reduces to $\delta_1 = \delta_2$. Let k_i denote the

Fig. 1 Schematic diagram of the 2RPR+P redundantly actuated PM



stiffness of the i th limb, then the magnitude F_i of the constraint force supplied by the i th limb can be formulated by $F_i = k_i \delta_i$. Sequentially, combining the force/moment equilibrium equation of the moving platform, i.e., $F = F_1 + F_2$, the unique solutions of the constraint forces imposed on the moving platform by the two limbs can be solved, where F denotes the magnitude of the external force exerted on the moving platform along the axial direction of the three limbs. Therefore, from the perspective of the displacement coordination, it can be said to some extent that the passive overconstrained mechanism is a special case of the active overconstrained mechanisms (i.e., the redundantly actuated mechanisms).

3 Driving Forces/Torques Distribution of the Redundantly Actuated PMs

3.1 Driving Forces/Torques Distribution Without Considering the Stiffness of the System

Generally speaking, the control mode of actuators can be categorized into three types: position, speed and torque control mode. The influences of the position and torque control modes on the driving forces/torques distribution of the redundantly actuated mechanisms are only discussed in this paper.

When the stiffness of the system is not considered, the displacement coordination condition of the redundantly actuated mechanisms only contains the input displacements of the actuators. For the 2RPR+P redundantly actuated mechanism, the displacement coordination condition can be formulated as: $d_1 = d_2$.

In the position control mode of the actuators, the input displacements are given directly. The displacement coordination condition (i.e., $d_1 = d_2$) of the 2RPR+P mechanism is always met.

1. Assuming that the driving force F_i is not determined by the input displacement of the i th actuator, the driving forces of the two limbs can be arbitrarily distributed as long as the force equilibrium equation (i.e., $F = F_1 + F_2$) of the moving platform is satisfied.

2. Assuming that the driving force F_i of the i th actuator is determined by its input displacement, the relationship might as well be denoted by

$$F_i = A_i d_i, \quad (2)$$

where A_i is a coefficient.

Substituting Eq. (2) into the force equilibrium equation of the moving platform of the 2RPR+P mechanism yields

$$A_1 d_1 + A_2 d_2 = F. \quad (3)$$

Combining Eq. (3) and the displacement coordination equation of the mechanism leads to

$$d_1 = d_2 = \frac{F}{A_1 + A_2}. \quad (4)$$

Thus, the driving force F_i of the i th actuator can be derived by substituting Eq. (4) into Eq. (2), as following:

$$F_i = \frac{A_i F}{A_1 + A_2}. \quad (5)$$

which shows that the driving forces of the two limbs can be uniquely solved in this case. In other words, if the driving force of the i th actuator is determined by its input displacement, the driving forces of the 2RPR+P mechanism can not be distributed arbitrarily, which is inconsistent with the general phenomena that the driving forces/torques of the redundantly actuated PMs can be distributed arbitrarily according to different optimization goals.

3. Assuming that the driving force of the actuator within the non-redundant limb (the first RPR limb) is determined by its input displacement, while that within the redundant limb (the second RPR limb) has nothing with the input displacement, the following equations can be obtained:

$$\begin{cases} F_1 = A_1 d_1 \\ F_2 = F - A_1 d_1 \end{cases}, \quad (6)$$

which indicate the driving forces can be distributed arbitrarily through changing the input displacement of the actuator within the non-redundant limb.

In the torque control mode of the actuators, the driving forces are given directly.

1. Assuming that the input displacement d_i of the i th actuator is followed, in other words, it is not determined by the driving force, the displacement coordination condition ($d_1 = d_2$) of the 2RPR+P mechanism is always met. Therefore, in this case, the driving forces of the two limbs can also be arbitrarily distributed.

2. Assuming that the input displacements of the actuators are determined by the driving forces, i.e., $d_i = F_i/A_i$, the two driving forces are uniquely solved by combining the displacement coordination equation and the force equilibrium equation of the mechanism, as shown in Eq. (5).
3. Assuming that the input displacement d_1 of the actuator within the first RPR limb is determined by its driving force f_1 , while the input displacement d_2 within the second RPR limb is followed, the displacement coordination condition ($d_1 = d_2$) can always be satisfied. Therefore, in this assumption, the driving forces of the 2RPR+P redundantly actuated PM can also be arbitrarily distributed on the condition that the force equilibrium equation of the mechanism is met.

3.2 Driving Forces/Torques Distribution Considering the Stiffness of the System

When the stiffness of the system is taken into consideration, the displacement coordination condition of the redundantly actuated mechanisms is shown in Eq. (1).

1. Under the first assumption described in the position control mode of the actuators in Sect. 3.1, the displacement coordination condition shown in Eq. (1) can be rearranged as

$$\frac{F_1}{k_1} - \frac{F_2}{k_2} = d_2 - d_1. \quad (7)$$

On the basis of the force equilibrium equation of the mechanism, the two driving forces of the 2RPR+P mechanism can be arbitrarily distributed, since Eq. (7) is always satisfied.

2. Under the second assumption described in the position control mode of the actuators in Sect. 3.1, as shown in Eq. (2), the following equations can be gotten

$$\begin{cases} A_1 d_1 + A_2 d_2 = F \\ d_1 + \frac{A_1 d_1}{k_1} = d_2 + \frac{A_2 d_2}{k_2} \end{cases} \quad (8)$$

from which we can get

$$\begin{cases} F_1 = \frac{k_1 A_1 (k_2 + A_2)}{k_1 A_1 (k_2 + A_2) + k_2 A_2 (k_1 + A_1)} F \\ F_2 = \frac{k_2 A_2 (k_1 + A_1)}{k_1 A_1 (k_2 + A_2) + k_2 A_2 (k_1 + A_1)} F \end{cases} \quad (9)$$

It can be seen from Eq. (9) that the two driving forces can not be distributed arbitrarily in this assumption.

3. Under the third assumption described in the position control mode in Sect. 3.1, Eq. (1) can be rearranged as

$$\frac{A_1 d_1}{k_1} + d_1 = \frac{F_2}{k_2} + d_2. \quad (10)$$

If the two driving forces are distributed arbitrarily under the condition that $F_1 + F_2 = F$, Eq. (10) is always met. Consequently, in this case, the driving forces can be distributed arbitrarily through changing the input displacement of the actuator within the non-redundant limb.

In the torque control mode of the actuators, once the driving force is given, the elastic deformation of the corresponding limb can be computed by $\delta_i = F_i/k_i$.

1. Under the first assumption described in the torque control mode of the actuators in Sect. 3.1, the displacement coordination condition shown in Eq. (1) can always be satisfied. Thus, the driving forces have an infinite number of solutions.
2. Under the second assumption described in the torque control mode in Sect. 3.1, Eq. (1) turns to

$$\frac{F_1}{A_1} + \frac{F_1}{k_1} = \frac{F_2}{A_2} + \frac{F_2}{k_2}. \quad (11)$$

Combining Eq. (11) and the force equilibrium equation of the mechanism Eq. (9) can be obtained, so the solutions of the driving forces are unique in this situation.

3. Under the third assumption described in the torque control mode in Sect. 3.1, Eq. (1) can be rearranged as

$$\frac{F_1}{A_1} + \frac{F_1}{k_1} = d_2 + \frac{F_2}{k_2}. \quad (12)$$

If the two driving forces are distributed arbitrarily satisfying the force equilibrium equation of the mechanism, Eq. (12) is always met since the input displacement d_2 is followed. Therefore, there are also an infinite number of solutions for the driving force distribution.

4 Conclusions

This paper analyzes the differences between the statically indeterminate force problem of the redundantly actuated PMs and that of the passive overconstrained PMs. The main conclusions reached are as follows:

1. The coordination conditions of both the overconstrained PMs are different. The redundantly actuated PMs satisfy the displacement coordination including the input displacements of the actuators and the elastic deformation of the system, while the passive overconstrained PMs need to meet the elastic deformation coordination.
2. Under the conditions of considering and without considering the system stiffness, the relationship between the driving force and the input displacement of an actuator in the position and torque control modes is discussed.

Based on the discussions demonstrated in this paper, future works are suggested: the experiment system of the 2RPR+P redundantly actuated mechanism need to be established, then, the magnitudes of the driving forces of the mechanism are respectively measured through switching the position and torque control modes of the actuators. On the basis of the experimental data the relationship between the input displacement and the driving force of an actuator under different control modes can be derived, which will greatly contribute to the control of the redundantly actuated mechanisms.

Acknowledgments This research was sponsored by the National Natural Science Foundation of China under Grant 51275439 and Grant 51675458.

References

1. Dasgupta B, Mruthunjaya TS (1998) Force redundancy in parallel manipulators: theoretical and practical issues. *Mech Mach Theory* 33:727–742
2. Firmani F, Podhorodeski RP (2004) Force-unconstrained Poses for a redundantly-actuated planar parallel manipulator. *Mech Mach Theory* 39:459–476
3. Zhao YJ, Gao F, Li WM, Liu W, Zhao XC (2009) Development of a 6-DOF parallel seismic simulator with novel redundant actuation. *Mechatronics* 19:422–427
4. Zhao YJ, Gao F (2009) Dynamic performance comparison of the 8PSS redundant parallel manipulator and its non-redundant counterpart—the 6PSS parallel manipulator. *Mech Mach Theory* 44:991–1008
5. Fang YF, Tsai LW (2004) Enumeration of a class of overconstrained mechanisms using the theory of reciprocal screws. *Mech Mach Theory* 39:1175–1187
6. Huang Z, Li QC (2003) Type synthesis of symmetrical lower-mobility parallel mechanisms using the constraint-synthesis method. *Int J Rob Res* 22:59–79
7. Mavroidis C, Roth B (1995) Analysis of overconstrained mechanisms. *J Mech Des Trans ASME* 117:69–74
8. Merlet JP (2000) *Parallel robots*. Kluwer, London
9. Xu YD, Yao JT, Zhao YS (2012) Inverse dynamics and internal forces of the redundantly actuated parallel manipulators. *Mech Mach Theory* 51:172–184
10. Harada T, Nagase M (2010) Impedance control of a redundantly actuated 3-DOF planar parallel link mechanism using direct drive linear motors. In: *IEEE international conference on robotics and biomimetics, ROBIO Tianjin, China, December*, pp 501–506
11. Nokleby SB, Fisher R, Podhorodeski RP, Firmani F (2004) Force capabilities of redundantly-actuated parallel manipulators. *Mech Mach Theory* 40:578–599

12. Fraczek J, Wojtyra M (2011) On the unique solvability of a direct dynamics problem for mechanisms with redundant constraints and coulomb friction in joints. *Mech Mach Theory* 46:312–334
13. Wojtyra M, Fraczek J (2012) Joint reactions in rigid or flexible body mechanisms with redundant constraints. *Bull Pol Acad Sci Tech Sci* 60:617–626
14. Wojtyra M (2005) Joint reaction forces in multibody systems with redundant constraints. *Multibody Syst Dyn* 14:23–46
15. Jiang Y, Li TM, Wang LP (2015) Dynamic modeling and redundant force optimization of a 2-DOF parallel kinematic machine with kinematic redundancy. *Rob Comput Integr Manuf* 32:1–10
16. Wu J, Chen XM, Li TM, Wang LP (2013) Optimal design of a 2-DOF parallel manipulator with actuation redundancy considering kinematics and natural frequency. *Rob Comput Integr Manuf* 29:80–85
17. Boudreau R, Nokleby S (2012) Force optimization of kinematically-redundant planar parallel manipulators following a desired trajectory. *Mech Mach Theory* 56:138–155
18. Wu J, Li TM, Xu BQ (2013) Force optimization of planar 2-DOF parallel manipulators with actuation redundancy considering deformation. *Proc Inst Mech Eng, Part C J Mech Eng Sci* 227:1371–1377
19. Xu YD, Liu WL, Yao JT, Zhao YS (2015) A method for force analysis of the overconstrained lower mobility parallel mechanism. *Mech Mach Theory* 88:31–48
20. Huang Z, Zhao Y, Liu JF (2010) Kinetostatic analysis of 4-R (CRR) parallel manipulator with overconstraints via reciprocal-screw theory. *Adv Mech Eng* 1–11
21. Bonnemains T, Chanal H, Bouzgarrou BC, Ray P (2013) Dynamic model of an overconstrained PKM with compliances: the Tripteur X7. *Rob Comput Integr Manuf* 29:180–191
22. Sapiro DV, Srinivasa N (2015) A methodology for controlling motion and constraint forces in holonomically constrained systems. *Multibody Syst Dyn* 33:179–204
23. Vertechy R, Parenti-Castelli V (2007) Static and stiffness analyses of a class of over-constrained parallel manipulators with legs of type US and UPS. In: *Proceedings of the IEEE international conference on robotics and automation*. Roma, Italy, April, pp 561–567
24. Bi ZM, Kang BS (2014) An inverse dynamic model of over-constrained parallel kinematic machine based on Newton–Euler formulation. *J Dyn Syst Meas Control Trans ASME* 136:1–9
25. Li B, Li YM, Zhao XH (2016) Stiffness analysis of a 2-DoF over-constrained RPM with an articulated traveling platform. *Mech Mach Theory* 96:165–178

Parallel Manipulator of a Class RoboMech

Zhumadil Baigunchekov, Maksat Kalimoldayev, Sayat Ibrayev, Myrzabai Izmambetov, Talgat Baigunchekov, Batyr Naurushev and Nadira Aisa

Abstract A mechanical system, having the property of the manipulating robot as a manipulation of the moving object according to its given laws of motion, and the property of the mechanism as a simple control of motion according to the given laws of motions of drives, is called parallel manipulator of a class RoboMech. Parallel manipulators of a class RoboMech work under certain structural schemes and geometrical parameters of their links. In this paper the methods of structural and kinematic synthesis of 2-DOF five-bar parallel manipulator RoboMech1 are considered.

Keywords Manipulating robot · Mechanism · RoboMech · Structural and kinematic synthesis

Z. Baigunchekov (✉) · S. Ibrayev · M. Izmambetov · T. Baigunchekov · B. Naurushev · N. Aisa

Kazakh National Research Technical University after K.I. Satpayev,
Almaty, Kazakhstan
e-mail: bzh47@mail.ru

M. Izmambetov
e-mail: myrza_62@mail.ru

T. Baigunchekov
e-mail: talgat.baigunchekov@gmail.com

B. Naurushev
e-mail: batyr_n@mail.ru

N. Aisa
e-mail: nadira.aisa@gmail.com

M. Kalimoldayev
Institute of Informatics and Computing Technologies, Almaty, Kazakhstan
e-mail: mnk@ipic.kz

1 Introduction

The actuating mechanism of most manipulating robots is 2-DOF serial manipulator, reproducing the given laws of motion the end-effector's point [1]. The inverse kinematics is solved and the control system is developed when the manipulating robots are designed on the base of serial manipulator. The possible irregularity and reversibility of rotation of the links obtained from the solution of the inverse kinematic are the disadvantages of the serial manipulator.

In this paper the problems of structural and kinematic synthesis of the parallel manipulator of a class RoboMech are considered. A mechanical system having the property of the manipulating robot as a manipulation of the moving object according to its given laws of motion and the property of mechanism as a simple control of motion according to the given laws of motion of drives, is called parallel manipulator of a class RoboMech. Because the parallel manipulators of a class RoboMech are designed according to the given laws of motions of the end-effectors and drives, they work under certain structural schemes and geometrical parameters of their links.

Many works are devoted of structural and kinematic synthesis of mechanisms [2–6]. For structural and kinematic synthesis of the parallel manipulator of a class RoboMech the modular method is used [7–10]. According to the modular method the parallel manipulator is formed from the actuating and closing kinematic chains representing the structural modules. A kinematic chain realizing the given laws of motions of the input and output links is called the actuating kinematic chain (AKC). A kinematic chain forming the parallel manipulator by connecting the links of the AKC is called a closing kinematic chain (CKC). In the considered parallel manipulator which is called RoboMech1, 2-DOF serial manipulator and the dyad with revolute kinematic pairs are AKC and CKC respectively.

2 Structural Synthesis

Let consider the 2-DOF serial manipulator (Fig. 1). The disadvantages of this serial manipulator are possible irregularity and reversibility of rotation of links 1 and 2 derived from the solution of inverse kinematics that worse its dynamics. If we connect the link BP of this serial manipulator with a base by the binary link CD with revolute kinematic pairs, we get a manipulator with 1-DOF (fixed-sequence manipulator) or four-bar path generation mechanism $ABCD$ (Fig. 2) which provides a given laws of motion of the point P .

In this case, the coordinates $x_C^{(2)}$ and $y_C^{(2)}$ of the point (joint) C in the coordinate system Bx_2y_2 must be such that the point C moves along the arc of the circle with center D and radius l_{CD} . In this case, the coordinates $x_C^{(2)}$ and $y_C^{(2)}$ of the point C in the coordinate system Bx_2y_2 of the link 2, the coordinates X_D and Y_D of the joint D in absolute coordinate system OXY and the length l_{CD} of the link CD are the determined

Fig. 1 2-DOF serial manipulator

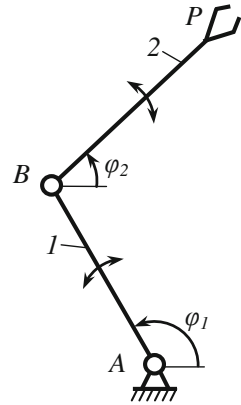
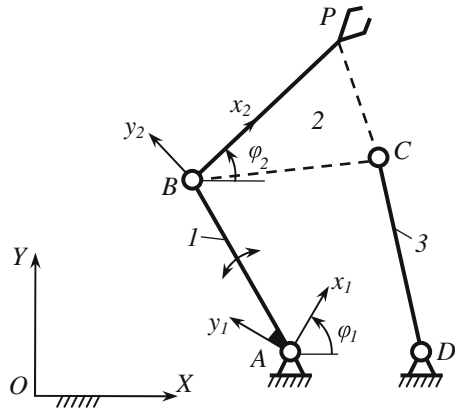


Fig. 2 Four-bar path generation mechanism



parameters of the binary link CD . In the considered case the values of the angle φ_1 of the link l are the same that they are defined by the solution of inverse kinematics, i.e. their possible irregularity and reversibility are saved. To eliminate this case, we can set the value of the angle φ_1 uniform and to the extent necessary. This case occurs under certain conditions when the coordinates $x_B^{(1)}$ and $y_B^{(1)}$ of the point B in the coordinate system Ax_1y_1 of the link l should be such that this point was the center of the circle on which the point P lies and having a radius l_{BP} in the relative motion of the point P relative to the moving coordinate system Ax_1y_1 of the link l . In this case the coordinates X_A, Y_A of the joint A in the absolute coordinate system OXY , the coordinates $x_B^{(1)}$ and $y_B^{(1)}$ of the joint B in the coordinate system Ax_1y_1 of the link l and the length l_{BP} of the link BP are the defined parameters of the serial manipulator ABP . Thus, the formed manipulator or the four-bar path generation mechanism $ABCD$ according to the given laws of motions of the point P and the input link l works under certain geometrical parameters of the links. The disadvantage of this manipulator is that the point P reproduces one stereotyped trajectory, so this manipulator (mechanism) is used in the machine-automats.

To eliminated the noted disadvantage of the considered manipulator it is possible to form a manipulator with 2-DOF. For this purpose we connect the link BP of the serial manipulator ABP with a base by the dyad CDE with the input joint E (Fig. 3).

The formed 2-DOF five-bar 5R parallel manipulator reproduces the series trajectories of the point P . The principal difference of the formed 2-DOF five-bar 5R parallel manipulator from the known parallel manipulator similar structure [1] is that the angles φ_1 and φ_4 of the formed parallel manipulator are not determined by solving the inverse kinematics, these angles are set by designer. Consequently, a control system is simplified substantially or control system is absent practically.

The formed five-bar 5R parallel manipulator has the property of the manipulating robot as a manipulation of the moving object according to its given lows of motion and property of the mechanism as a simple control of motion according to the given lows of motions of the drives.

Therefore, this manipulator is called the parallel manipulator of a class RoboMech. Manipulators of a class RoboMech work on the principle of functionally independent drives. For example, in the considered parallel manipulator, which is called RoboMech1, the drive of the first input link 1 reproduces the series trajectories of the point P , and the drive of the second input link 4 puts the point P from one trajectory to another. Figure 4 shows M series of motion of the output point P , and this point has N finitely separated positions in each series of trajectories.

3 Kinematic Synthesis

RoboMech1 works at certain values of the geometric parameters of the links. Let consider the kinematic synthesis of RoboMech1. The coordinates X_{Pij} and Y_{Pij} , ($i = 1, 2, \dots, N; j = 1, 2, \dots, M$) of the point P correspond to the N and M given values of the angles φ_{1i} and φ_{4j} respectively. We proceed from the double indexation i and j of the parameters $X_{Pij}, Y_{Pij}, \varphi_{1i}, \varphi_{4j}$ to one indexation k , ($k = 1, 2,$

Fig. 3 Five-bar 5R manipulator

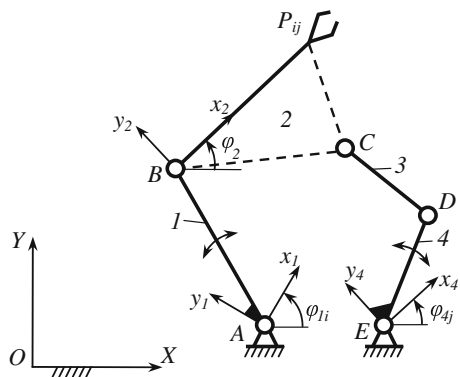
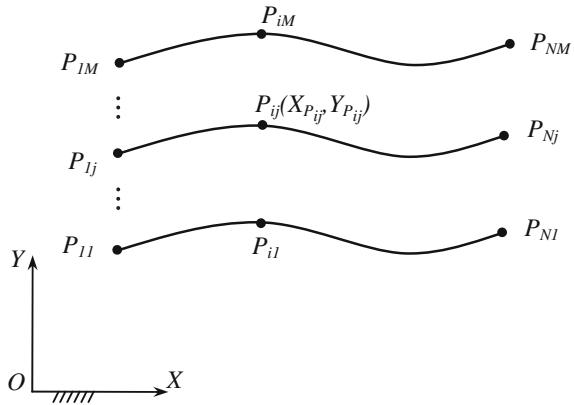


Fig. 4 M series of motion of the output point P



..., N·M). According to the modular synthesis the kinematic synthesis of RoboMech1 consists of kinematic syntheses its structural modules, i.e. the serial manipulator ABC and the dyad CDE.

3.1 Kinematic Synthesis of the Kinematic Chain ABP

The considered kinematic chain ABP (Fig. 3) has the following geometric parameters: $X_A, Y_A, x_B^{(1)}, y_B^{(1)}, l_{BP}$, where $[X_A, Y_A]^T$ and $[x_B^{(1)}, y_B^{(1)}]^T$ —coordinates of the radius-vectors $\mathbf{R}_A, \mathbf{r}_B^{(1)}$ of the joints A and B in the coordinate systems OXY and Ax_1y_1 respectively, l_{BP} —length of the link BP. These parameters are called the approximating parameters and they are denoted by the vector $\mathbf{P}_1 = [X_A, Y_A, x_B^{(1)}, y_B^{(1)}, l_{BP}]^T$.

The constraint equation to optimize the desired parameters will be obtained from loop—closure equation of the contour OABPO

$$\mathbf{R}_A + \Gamma(\varphi_{1k})\mathbf{r}_B^{(1)} + \mathbf{l}_{BP} - \mathbf{R}_{P_k} = \mathbf{0}, \tag{1}$$

where

$$\Gamma(\varphi_{1k}) = \begin{bmatrix} \cos\varphi_{1k} & -\sin\varphi_{1k} \\ \sin\varphi_{1k} & \cos\varphi_{1k} \end{bmatrix}, \quad \mathbf{l}_{BP} = [l_{BP}\cos\varphi_{2k}, l_{BP}\sin\varphi_{2k}]^T.$$

We exclude the angle φ_{2k} from the Eq. (1) and obtain

$$(\mathbf{R}_A + \Gamma(\varphi_{1k})\mathbf{r}_B^{(1)} - \mathbf{R}_{P_k})^2 - l_{BP}^2 = 0. \tag{2}$$

The synthesis problem for the considered kinematic chain ABP is to determine the vector \mathbf{P}_1 of parameters approximately realizing the constraint equations

$$\Delta_k(\mathbf{P}, X_{P_k}, Y_{P_k}, \varphi_{1k}) = 0, \quad k = 1, 2, \dots, K. \tag{3}$$

Then we can formulate the problem of quadratic approximation as follow

$$S(\mathbf{P}_1) = \sum_{k=1}^K [\Delta_k(\mathbf{P}_1)]^2 \Rightarrow \min_{\mathbf{P}_1} S. \tag{4}$$

By next non-generation change of variables

$$\begin{aligned} p_1 &= X_A, \quad p_2 = Y_A, \quad p_4 = x_B^{(1)}, \quad p_5 = y_B^{(1)}, \\ p_3 &= (X_A^2 + Y_A^2 + x_B^{(1)2} + y_B^{(1)2} - l_{BP}^2)/2 \end{aligned}$$

the function $\Delta_k(\mathbf{P}_1)$ is expressed linearly by groups of parameters

$$\mathbf{q}^{(1)} = [p_1, p_2, p_3]^T, \quad \mathbf{q}^{(2)} = [p_4, p_5, p_3]^T$$

in the following form

$$0.5 \cdot \Delta_k^l(\mathbf{P}_1) = \mathbf{g}_k^{(l)T} \cdot \mathbf{q}^{(l)} - g_{0k}^{(l)}, \quad l = 1, 2. \tag{5}$$

This property of the function (3) simplifies the solution of the problem of minimizing the function (4) which depends on five parameters.

A necessary condition for the minimum of function $S(\mathbf{P}_1)$ on the parameters $\mathbf{q}^{(l)}$

$$\frac{\partial S(\mathbf{P}_1)}{\partial \mathbf{q}^{(l)}} = \mathbf{0} \tag{6}$$

leads to a system of leaner equation

$$\mathbf{H}^{(l)}(\mathbf{X}) \cdot \mathbf{q}^{(l)} = \mathbf{h}^{(l)}(\mathbf{X}), \quad l = 1, 2, \tag{7}$$

where $\mathbf{X} = \mathbf{P} \setminus \mathbf{q}^{(l)}$, and

$$\mathbf{H}^{(l)} = \sum_{k=1}^K \begin{bmatrix} g_{1k}^{(l)2} & g_{1k}^{(l)} \cdot g_{2k}^{(l)} & g_{1k}^{(l)} \\ g_{1k}^{(l)} \cdot g_{2k}^{(l)} & g_{2k}^{(l)2} & g_{2k}^{(l)} \\ g_{1k}^{(l)} & g_{2k}^{(l)} & 1 \end{bmatrix}, \quad \mathbf{h}^{(l)} = \sum_{k=1}^K \begin{bmatrix} g_{1k}^{(l)} \cdot g_{0k}^{(l)} \\ g_{2k}^{(l)} \cdot g_{0k}^{(l)} \\ g_{0k}^{(l)} \end{bmatrix}. \tag{8}$$

Here $\mathbf{g}_k^{(l)} = [g_{1k}^{(l)}, g_{2k}^{(l)}, g_{3k}^{(l)}]^T, g_{0k}^{(l)}$ —coefficients of the linear forms (5), where $g_{3k}^{(l)} = 1$ for all $k = 1, 2, \dots, K$.

Thus, the problem of quadratic approximation (4) can be solved by the method of leaner iterations at each step of which one of two groups of parameters $\mathbf{q}^{(l)}$ is defined.

3.2 Kinematic Synthesis of the Kinematic Chain EDC

At known geometrical parameters of the kinematic chain ABP and coordinates of the point P the orientation φ_{2k} of the coordinate system Bx_2y_2 of the link 2 can be defined by formula

$$\varphi_{2k} = \arctg(Y_{P_k} - Y_{B_k}, X_{P_k} - X_{B_k}). \tag{9}$$

The considered kinematic chain EDC has the following geometrical parameters: $x_C^{(2)}, y_C^{(2)}, x_D^{(4)}, y_D^{(4)}, X_E, Y_E, l_{DC}$, where $x_C^{(2)}, y_C^{(2)}, x_D^{(4)}, y_D^{(4)}, X_E, Y_E$ —coordinates of the joints C, D, E in the coordinate systems Bx_2y_2, Dx_4y_4, OXY respectively, l_{DC} —length of the link DC . These parameters of synthesis are denoted by the vector $\mathbf{P}_2 = [x_C^{(2)}, y_C^{(2)}, x_D^{(4)}, y_D^{(4)}, X_E, Y_E, l_{DC}]^T$.

The constraint equation for optimization of the designed parameters to be obtained from loop-closure equation of the contour $OEDCPO$

$$(\mathbf{R}_E + \Gamma(\varphi_{4k})\mathbf{r}_D^{(4)} - \mathbf{R}_{P_k} - \Gamma(\varphi_{2k})\mathbf{r}_C^{(2)})^2 - l_{DC}^2 = \mathbf{0}. \tag{10}$$

The problem of kinematic synthesis of the considered kinematic chain EDC is to determine the vector \mathbf{P}_2 of parameter synthesis approximately realizing the constraint equations

$$\Delta_k(\mathbf{P}_2, X_{P_k}, Y_{P_k}, \varphi_{2k}, \varphi_{4k}) = 0, \quad k = 1, 2, \dots, K.$$

Then the problem of quadratic approximation is formulated as follow

$$S(\mathbf{P}_2) = \sum_{k=1}^K [\Delta_k(\mathbf{P}_2)]^2 \Rightarrow \min_{\mathbf{P}_2} S. \tag{11}$$

By the following non-generation change of variables

$$p_1 = X_E, \quad p_2 = Y_E, \quad p_4 = x_D^{(4)}, \quad p_5 = y_D^{(4)}, \quad p_5 = x_C^{(2)}, \quad p_6 = y_C^{(2)},$$

$$p_3 = (X_E^2 + Y_E^2 + x_D^{(4)2} + y_D^{(4)2} + x_C^{(2)2} + y_C^{(2)2} - l_{CD}^2)/2$$

the function $\Delta_k(\mathbf{P}_2)$ is expressed linearly by groups of parameters

$$\mathbf{q}^{(1)} = [p_1, p_2, p_3]^T, \quad \mathbf{q}^{(2)} = [p_4, p_5, p_3]^T, \quad \mathbf{q}^{(3)} = [p_6, p_7, p_3]^T$$

in the following form

$$0.5 \cdot \Delta_k^l(\mathbf{P}_2) = \mathbf{g}_k^{(l)T} \cdot \mathbf{q}^{(l)} - g_{0k}^{(l)}, \quad l = 1, 2, 3. \tag{12}$$

In this case also the necessary condition for the minimum of function $S(\mathbf{P}_2)$ on the parameters $\mathbf{q}^{(l)}$ leads to a system of linear equation of the form (7). Thus, the define of seven synthesis parameters of the kinematic chain ECD is also carried out by the method of linear iterations at each step iterations one of three groups of unknown parameters is determined.

4 Numerical Example

As an example, the parallel manipulator RoboMech1 which output point P reproduces the series of horizontal trajectories is synthesized (Fig. 5). In this parallel manipulator, the motion of the point P on each series of the trajectory is performed by the rotation of the first input link AB , and the transition of the output point P from one trajectory to another is performed by the second input link ED . In the result of kinematic synthesis the following geometrical parameters are obtained: $X_A = -0.621$ m, $Y_A = 0.475$ m, $X_E = -0.577$ m, $Y_E = 0.094$ m, $l_{AB} = 1.418$ m, $l_{BP} = 1.443$ m, $l_{ED} = 0.329$ m, $l_{DC} = 1.771$ m, $l_{BC} = 0.365$ m, $l_{CP} = 1.092$ m.

Figures 6 and 7 show the trajectories and the diagrams of changing the coordinates X_P and Y_P of the output point P in depending of the angle of rotation φ_1 of the first input link AB for three series of its trajectory, corresponding to three positions ($\varphi_4 = 0^\circ, 8^\circ, \text{ and } 16^\circ$) of the second input link ED . The angle φ_1 is changed in the interval $[55^\circ; 130^\circ]$.

Fig. 5 Parallel manipulator RoboMech1

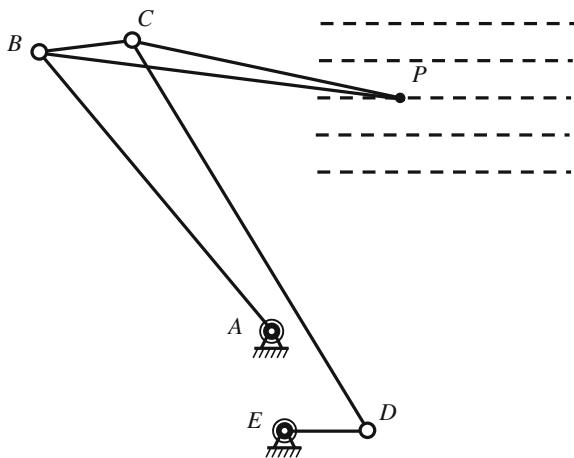


Fig. 6 Three series of trajectories of the output point P

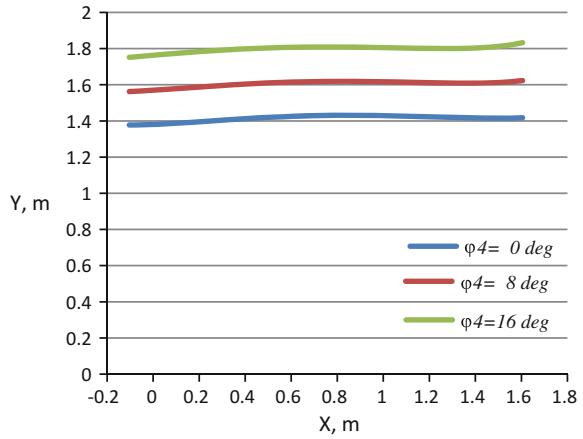
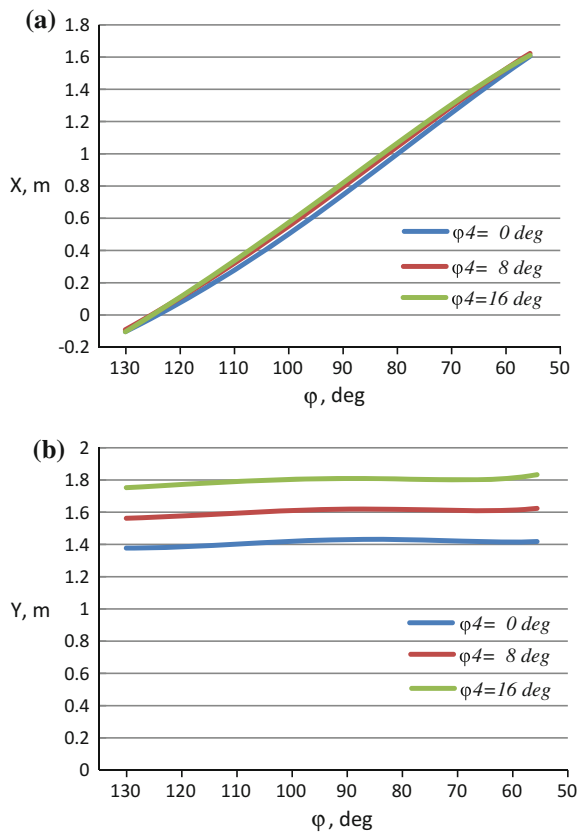


Fig. 7 The diagrams of changing the coordinates X_P and Y_P of the output point P



5 Conclusions

A mechanical system, having the property of the manipulating robot as a manipulation of the moving object according to its given laws of motion and the property of the mechanism as a simple control of motion according to the given laws of motions of drives, is called parallel manipulator of a class RoboMech. The principle of formation of RoboMech is developed according to which the RoboMech is formed from the actuating and closing kinematic chains representing the structural modules. A kinematic chain realizing the given laws of motions of the input and output links is called the actuating kinematic chain (AKC). A kinematic chain forming the parallel manipulator by connecting the links of the AKC is called a closing kinematic chain (CKC). On the base of this principle the RoboMech1 is formed, the structural modules of which are 2-DOF serial manipulator and the dyad with revolute joints. Parallel manipulators of a class RoboMech work at certain values of the geometrical parameters of the links, because the laws of motions of the input and output links are given simultaneously. According to the module principle the kinematic synthesis of the RoboMech1 consists of kinematic synthesis of its structural modules, i.e. 2-DOF serial manipulator and the dyad. The methods of kinematic synthesis of the RoboMech1 structural modules are developed and the numerical example is presented.

References

1. Tsai L-W (1999) Robot analysis. The mechanics of serial and parallel manipulators. A Wiley-Interscience Publication, Hoboken
2. Erdman A, Sandor G (1997) Mechanism design: analysis and synthesis, vol 1. Prentice Hall, New Jersey
3. Mallik AK, Ghosh A, Ditttrich G (1994) Kinematic analysis and synthesis of mechanisms. CRC Press, Boca Raton
4. Hunt KH (1990) Kinematic geometry of mechanisms. Dover, Mineola
5. Gupta KC, Roth BA (1975) General approximation theory for mechanisms synthesis. ASME J Appl Mech 42:451–457
6. Al-Dwairi AF, Kikin AB (2004) Multipurpose for least-squares synthesis of linkages. In: Proceedings of the eleventh world congress in mechanisms and machine sciences, Tianjin, China, 1–4 Apr 2004, vol 1, pp 181–185
7. Joldasbekov UA, Baigunchekov ZZ, Ibraev SM (1995) Modular approach for synthesizing of planar one-DOF and adjustable mechanisms of high classes. In: Proceedings of the ninth IFToMM world congress on TMM. Milan, Italy, vol 1
8. Baigunchekov ZZ et al (1996) Modular synthesis of spatial manipulating devices of high classes. In: Proceeding of the twelfth international conference on CAD/CAM robotics and factories of the future. Middlesex University, London, UK, pp 685–690

9. Baigunchekov ZZ et al (2000) The basis of structural and parametric synthesis of the parallel manipulators with functionally independent drives. Part I&II. In: Proceedings of the 16th international conference on gearing, transmissions and mechanical systems, The Nottingham Trent University, UK, pp 1–19 (2000)
10. Baigunchekov Z, Kalimoldayev M, Utenov M, Arymbekov B, Baigunchekov T (2016) Structural and dimensional synthesis of parallel manipulator with two end-effectors. Robotics and mechatronics. Springer, Berlin, pp 15–23 (2016)

Unified Description of DOF of Crank Group Mechanism Based Screw Theory

Yansong Liu, Jujiang Cao and Sheng Ren

Abstract The link truss was defined by analyzing the kinematics of the basic unit of the crank group mechanism, and summarized the structure unity in the crank group mechanisms with different topological structure. The calculation method was given for the number of the public constraints, that of the redundant constraints, and the DOF of the crank group mechanism with any number of crank by screw theory. The results show that the method reduces the number of the mechanism members, avoids the tedious calculations and achieves the unified description of DOF of the crank group mechanism with any number of the cranks based the link truss and the screw theory.

Keywords Crank group mechanism · Degrees of freedom (DOF) · Screw theory · Link truss

1 Introduction

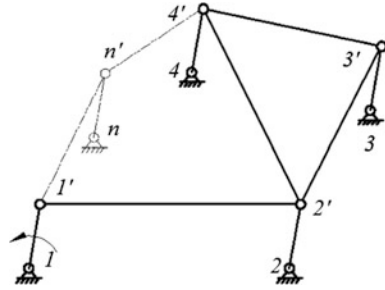
Crank group mechanism has been widely applied to realize synchronous transmission mechanism, such as special drill press [1], packaging equipment, printing machinery, etc. [2–4]. Figure 1 is a diagram of the crank group mechanism.

Y. Liu (✉) · J. Cao · S. Ren
College of Mechanical and Electrical Engineering, Shaanxi University
of Science and Technology, Xi'an 710021, China
e-mail: yansong_liu@qq.com

J. Cao
e-mail: jjcao@sust.edu.cn

S. Ren
e-mail: 412776507@qq.com

Fig. 1 Diagram of the crank group mechanism



In crank-group mechanism, all cranks have the same length and movement phase, and any two cranks and corresponding link constitute a parallelogram mechanism [5–7]. So crank-group mechanism is one kind of planar mechanism. For the calculation of DOF of planar mechanism, many factors should generally be considered, such as composite hinge, partial freedom, virtual constraint [8: 17–21], etc. For the different occasions and strength requirements, the crank number and link number are different in crank group mechanism, and the determination of composite hinge, virtual constraint and effective member are more complex, so the calculation of DOF of crank-group mechanism is more difficult using conventional methods such as Chebychev formula [9].

The corrected formula *Grübler – Kutzbach* (shorted as *G-K*) formula is proved to be correct by the theory and practical application [10, 11]. However, the calculation of DOF of the crank-group mechanism showed by Fig. 1 is still very difficult, when the number of crank is uncertain, and link structure is complex by G-K formula.

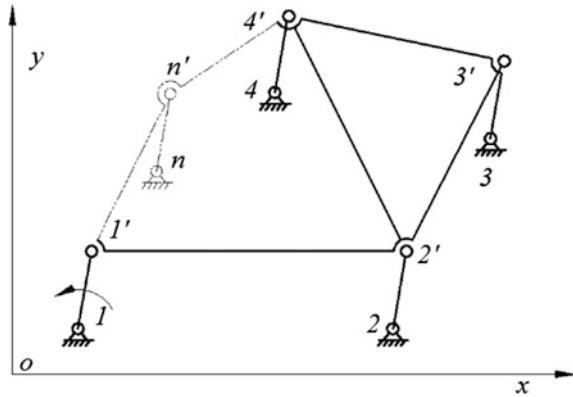
In this paper, the concept of link truss is raised, and the structure of crank-group mechanism is simplified by analyzing the movement characteristics of the basic unit of crank-group mechanism. Unified description of DOF of crank group mechanism is given by screw theory and G-K formula.

2 Simplifying Crank Group Mechanism

Parallelogram mechanism is the basic unit of crank-group mechanism showed by Fig. 1, such as unit 1'2'2. Assuming that the crank 11' is the driving crank, and its angular velocity is ω , the angular velocity of the crank 22' is also ω , and the angular velocity of the link 1'2' is 0. The velocity of any point on the link 1'2' is expressed by formula (1) [8: 60–61].

$$\begin{cases} v_x = -r\omega \sin \theta \\ v_y = r\omega \cos \theta \end{cases} \quad (1)$$

Fig. 2 Diagram of crank group mechanism based on link truss



Formula (1) shows that all links only translate in parallelogram mechanism, and the links' velocity is only related to the active crank's length r and angular velocity ω . All links have the same motion based on the characteristics of the crank-group mechanism group, so all links can be seen as a motion member named link truss. Figure 2 shows the diagram of crank-group mechanism based on link truss.

The number of the members of crank-group mechanism is $(p + 2)$, assuming the number of the cranks is p based on link truss. Composite hinge does not exist on the hinge joint in crank-group mechanism simplified. Crank mechanism can be regarded as a special parallel mechanism. In this parallel mechanism, the link truss is moving platform, the rack is static platform, and one crank is a kinetic limb. The calculation of DOF of crank-group mechanism is simplified describing the mechanism of motion and constraints of the mechanism based on screw theory.

3 Motion Screw System and Constraint Screw System of Crank-Group Mechanism

3.1 Introduction of Screw Theory

Formula (2) shows any rotation expressed with a screw [12].

$$\mathcal{S} = \begin{bmatrix} \mathbf{S} \\ S_0 \end{bmatrix} \tag{2}$$

In formula (2), \mathbf{S} is rotation direction vector, S_0 is line moment of \mathbf{S} , $S_0 = \mathbf{r} \times \mathbf{S}$, \mathbf{r} is position vector of \mathbf{S} , and $\mathbf{S} \cdot S_0 = 0$.

If the reciprocity product of two screw is 0, namely

$$\mathcal{S}_1 \circ \mathcal{S}_2 = 0 \tag{3}$$

Formula (3) shows two screws are inverse screws each other, in other words, if one screw represents the movement of the object, other one represents constraints imposed on the object.

3.2 Motion Screw System and Constraint Screw System of Crank Group Mechanism

In Fig. 2, crank mechanism can be regarded as a special parallel mechanism, and any crank mn' is a kinetic limb. The coordinates of point n are (x_n, y_n) in coordinate system xoy , and the coordinates of point n' are (x_0, y_0) . Two movement screws of kinetic limb mn' constitute one movement screw system, namely

$$\begin{aligned} \mathcal{S}_n &: (0 \ 0 \ 1; \ y_n \ -x_n \ 0) \\ \mathcal{S}_{n'} &: (0 \ 0 \ 1; \ y_n + y_0 \ -x_n - x_0 \ 0) \end{aligned} \tag{4}$$

Any inverse screw can be represented as

$\mathcal{S}^r : (L^r, M^r, N^r; P^r, Q^r, R^r)$, namely

$$\begin{cases} \mathcal{S}_n \circ \mathcal{S}^r = 0 \\ \mathcal{S}_{n'} \circ \mathcal{S}^r = 0 \end{cases} \tag{5}$$

That is

$$\begin{cases} R^r + L^r y_n - M^r x_n = 0 \\ R^r + L^r (y_n + y_0) - M^r (x_n + x_0) = 0 \end{cases} \tag{6}$$

All the solution screws of formula (6) constitute the inverse screw system of formula (4), namely

$$\begin{aligned} \mathcal{S}_1^r &: (0 \ 0 \ 1; \ 0 \ 0 \ 0) \\ \mathcal{S}_2^r &: (0 \ 0 \ 0; \ 1 \ 0 \ 0) \\ \mathcal{S}_3^r &: (0 \ 0 \ 0; \ 0 \ 1 \ 0) \\ \mathcal{S}_4^r &: (x_0 \ y_0 \ 0; \ 0 \ 0 \ x_n y_0 - y_n x_0) \end{aligned} \tag{7}$$

For mechanism, inverse screw system of movement screw system is its constraint screw system.

4 DOF of Crank Group Mechanism

DOF of crank-group mechanism can be calculated by screw theory and the corrected G-K formula [13] showed formula (8).

$$M = d(m - g - 1) + \sum_{i=1}^g f_i + v \tag{8}$$

In formula (8), d is the order number of the mechanism, $d = 6 - \lambda$, and λ is public constraint number of the mechanism. For the parallel mechanism, λ is the number of public constraint screw on moving platform applied by all kinetic limbs.

In the constraint screw system applied by all kinetic limb showed by formula (7), the first three are exactly the same screws, and the fourth screw is related with the location of kinetic limb. λ is 3 for the crank group mechanism with p kinetic limbs (with p cranks), so

$$d = 6 - 3 = 3 \tag{9}$$

m is the number of the members of the mechanism, and is calculated by formula (10) based on link truss.

$$m = p + 2 \tag{10}$$

g is the number of the kinematic pairs of the mechanism for the crank group mechanism with p cranks, and is calculated by formula (11).

$$g = 2p \tag{11}$$

f_i is DOF of No. i kinematic pair. Because the kinematic pairs of crank group mechanism are all revolute pairs, f_i is 1. DOF of all revolute pairs of crank-group mechanism with p cranks is calculated by formula (12).

$$\sum_{i=1}^g f_i = 2p \tag{12}$$

v is the number of the parallel redundant constraints [14], and calculated by formula $v = t - k$. In this formula, t is $qp - \lambda p$, and qp is the number of all constraint screws applied by all kinetic limbs. λp is the number of public constraint screws applied by all kinetic limbs. k is the number of independent constraint screws in t constraint screws.

Formula (7) shows the constraint screw system on moving platform supplied by one kinetic limb, and its rank is 4. Each kinetic limb has 4 linearly independent constraint screws, so $qp = 4p$. Formula (7) shows that the first three are public constraint screws, the total number of public constraint screws is $\lambda p = 3p$,

so $t = qp - \lambda p = p$. Formula (13) shows the screw system composed of this p constraint screws.

$$\begin{aligned}
 \mathcal{S}_1^r &: (x_0 \quad y_0 \quad 0; \quad 0 \quad 0 \quad x_1y_0 - y_1x_0) \\
 \mathcal{S}_2^r &: (x_0 \quad y_0 \quad 0; \quad 0 \quad 0 \quad x_2y_0 - y_2x_0) \\
 \mathcal{S}_3^r &: (x_0 \quad y_0 \quad 0; \quad 0 \quad 0 \quad x_3y_0 - y_3x_0) \\
 &\dots \\
 \mathcal{S}_p^r &: (x_0 \quad y_0 \quad 0; \quad 0 \quad 0 \quad x_py_0 - y_px_0)
 \end{aligned} \tag{13}$$

The screw system's rank is 2 showed by formula (13), that is, this screw system is a screw system with only 2 independent constraint screws, namely, $k = 2$. v is calculated by formula (14).

$$v = t - k = p - 2 \tag{14}$$

Formula (15) shows DOF of crank-group mechanism calculated by solving the simultaneous equation composed of formulas (8)–(10), (12) and (14).

$$\begin{aligned}
 M &= d(m - g - 1) + \sum_{i=1}^g f_i + v \\
 &= 3(p + 2 - 2p - 1) + 2p + p - 2 \\
 &= 1
 \end{aligned} \tag{15}$$

The DOF is 1 for crank-group mechanism with any number of cranks.

5 Conclusion

Crank-group mechanism is regarded as a special parallel mechanism and the DOF is calculated based on the definition of link truss. The calculation methods of the public constraint number, the order number, and the number of the parallel redundant constraints of the mechanism are analyzed by screw theory.

The DOF of crank-group mechanism is uniformly described by screw theory and corrected G-K formula. The DOF of crank-group mechanism is 1. The moving feasible of crank-group mechanism is proved by this calculation, and if an independent rotation is applied to any one crank, crank-group mechanism has the determined motion.

Acknowledgments This work is supported by the NSFC (Grant No. 51175313).

References

1. Wenxin LU (1996) Design and application of single-link and multi-crank mechanism in crank driving for multi-axle box. *J Changzhou Ind Technol Coll (Natural Science Edition)* 9(2):46–51 (in Chinese)
2. Wang Y, Cao J (2013) Study on the motion feature of crank-group driving mechanism. *J Mech Transm* 37(10):79–81 (in Chinese)
3. Ren S, Cao J, Liu Y (2015) Inertia force balance of crank-group driving mechanism based on crank unit. *J Light Ind Mach* 33(1):8–10 (in Chinese)
4. Barton LO (2008) Mechanism analysis of a trisector. *J Mech Mach Theory* 43(2):115–122
5. Wang Y, Cao J (2013) The overview of crank-group driving mechanism. *J Mech Transm* 37(4):134–136 (in Chinese)
6. Liu Z, Feng Z (1990) Theoretical study of integral balancing of first-order reciprocal inertia of small-sized single-cylinder horizontal engine. *J Agric Mach* 3:23–28 (in Chinese)
7. Ren S, Cao J (2014) DOF analysis of crank-group drive mechanism based on the theory of parallel mechanism. *J Mach Des Res* 30(4):14–16 (in Chinese)
8. Lvzhong MA, Xie J, Yin X (2015) Theory and design of machines and mechanisms. Machinery Industry Press, Beijing, pp 60–61 (in Chinese)
9. Han Q, Li T (2015) A new universal formula of degree of freedom for planar mechanism. *J Mech Transm* 39(3):153–157 (in Chinese)
10. Huang Z, Liu J, Zeng X (2009) The general method of DOF of mechanism based on the constraint screw. *J Sci Chin* 39(1):84–93 (in Chinese)
11. Cai H, Fu O, Liao M (2011) Comparable study and application on new and old formulas of calculating DOFs of mechanisms and structures. *Chin Mech Eng* 22(1):35–38 (in Chinese)
12. Guo S, Fang Y, Yue C (2009) Structure synthesis of single closed-loop multi-degree of freedom of over-constrained mechanism based on screw theory. *J Mech Eng* 45(11):38–45 (in Chinese)
13. Lu W, Zhang L, Zeng X, Zhang Y (2014) Research on application of GOM formula—a novel mobility formula. *Chin Mech Eng* 25(17):2283–2289 (in Chinese)
14. Zheng H, Yongsheng Z, Tieshi Z (2014) Higher spatial organization, 2nd edn. Higher Education Press, Beijing, pp 121–122 (in Chinese)

An Introduction to the Reconstruction Model of Antikythera Mechanism

Jian-Liang Lin and Hong-Sen Yan

Abstract Antikythera mechanism is known as the oldest astronomical calculator in ancient Greece. With the development of modern science and technology, the inscriptions, functions and exterior appearance are decoded from the surviving fragments. The corresponding reconstruction designs of interior structure and physical models are continuously presented. This work introduces an assembly process of physical model that is one of 48 feasible reconstruction designs presented by Yan and Lin. Firstly, the geometric constraints of interior subsystems are concluded so as to generate the reconstruction designs with complete interior structure. Then, a detail design procedure of reconstruction model is presented. Through this systematic procedure, teeth calculations are resolved based on the concluded teeth relations. Gear sizes and gear models of lost structures are reconstructed, and space arrangements can be finished by graphical method. Finally, the simulation model and its corresponding physical model re built to confirm the operation of reconstruction design.

Keywords Antikythera mechanism · Reconstruction design · Assembly design · Physical model

1 Introduction

Antikythera mechanism is the oldest astronomical calculator in the ancient Greece. The mechanical device was discovered in 1900–01 as a group of fragments and has no confirmed historical records now. The lost mechanical device deeply attracts many scholars so that it is gradually decoded through a serious of reconstruction

J.-L. Lin (✉)

Exhibition Collection, National Science and Technology Museum, Kaohsiung, Taiwan
e-mail: golduser007@gmail.com

H.-S. Yan

Department of Mechanical Engineering, National Cheng Kung University,
No.1, University Road, Tainan 70101, Taiwan

research. Until now, the functions of the device are defined to demonstrate the cyclic motions of the sun, the moon and five planets, to display the moon phase, to calculate the calendars, and to predict the eclipses by the interior gear trains. In the historical development of reconstruction research, Price [1, 2], Edmunds and Morgan [3], Wright [4–14], Antikythera Mechanism Research Project (AMRP) held by Freeth et al. [15–17], Evans et al. [18, 19], and Yan and Lin [20–25] presented their conceptual reconstruction designs of the interior structure so as to satisfy the existing evidence and the decoded functions. Figure 1 is the complete concept of reconstruction design by Yan and Lin. The design is divided into six subsystems including the date subsystem, the calendrical calculation subsystem, the eclipse prediction subsystem, the lunar subsystem, the solar subsystem and the planetary subsystem. And the mechanism to display the moon phase is over the front dial [25].

Except for decoding the inscriptions, the functions and the mechanisms, the building of reconstruction models is necessary. Constructing simulation and solid models is helpful to confirm the standard of science and technology at the time of Antikythera mechanism. It is contributed to investigate the historical development of manufacture in the ancient time. The reconstruction of Antikythera mechanism has to satisfy the evidence discovered from the excavation. The detail designs of

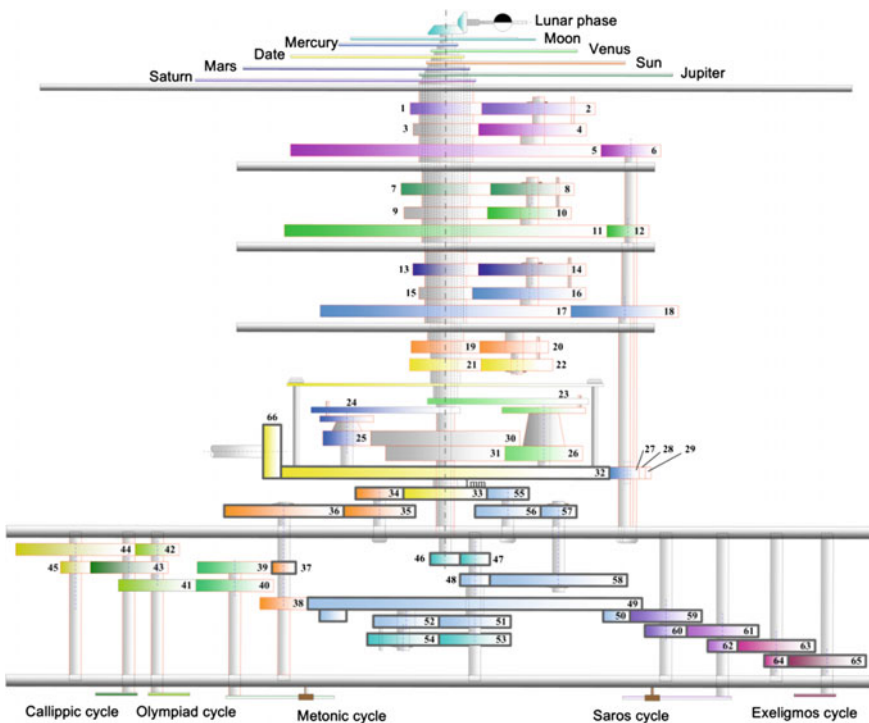


Fig. 1 A existing reconstruction design [20]

mechanical elements are based on the constraints of the existing geometric and the concluded gear ratios. Here, the paper introduces the reconstruction work of a simulation model and its solid model based on the reconstruction design presented by Yan and Lin as shown in Fig. 1 [19]. The possible teeth and gear sizes are concluded so as to confirm the engagement of gear trains by the models. Finally, the possibility of reconstruction design is verified.

2 Historical Developments of Reconstruction Models

The model construction of Antikythera mechanism is varied with the decoding of excavation. The first physical model was reconstructed by I. Theofanidis, as shown in Fig. 2a [26, 27]. This model is unworkable and preserved in National Archaeological Museum in Athens today. Theofanidis indicated that Antikythera mechanism was a navigational computing device with the features of a planetarium and an astrolabe. The interior gear trains were used to generate the motions of the sun, the moon and planets [27]. The second reconstruction model was presented by D. Price as shown in Fig. 2b [1, 2]. The mechanism was defined as an ancient mechanical computer. The front dial was a concentric dial. The upper back dial and the lower back dial had four concentric annuli respectively. The third physical

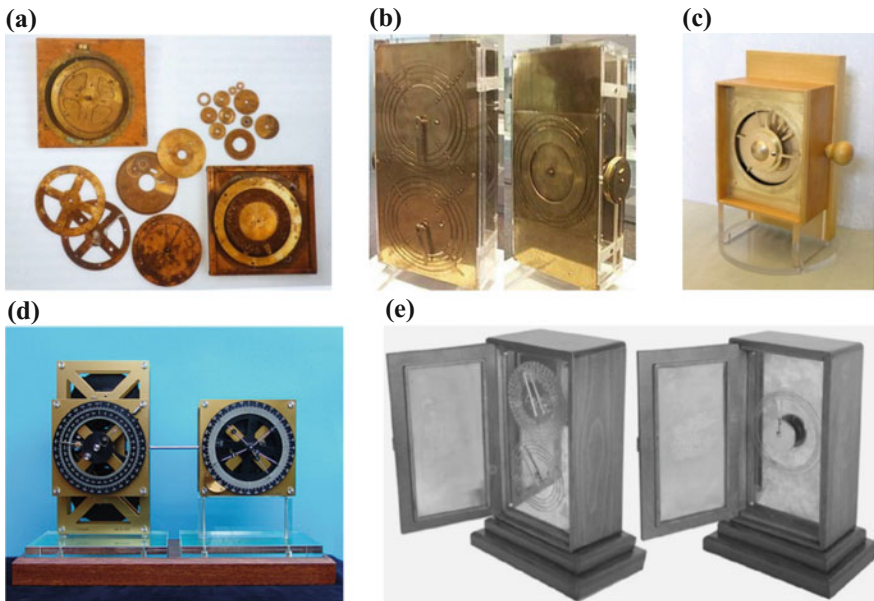


Fig. 2 Existing reconstruction models **a** Model by Theofanidis [26, 27] **b** Model by Price [1, 2] **c** Model by Wright [4–14] **d** Model by Tatjana van Vark [17] **e** Model by Efstathiou et al. [28]

model was reconstructed by A. Bromley and F. Percival [3]. This is a partial reconstruction of Antikythera mechanism through altering the function of the handle in Price's model. The improvement resulted that one complete rotation of the handle would correspond to a single day, which was the most obvious astronomical unit in his viewpoint. However, the types of dials are different from Antikythera mechanism known today, and the functions of dials are, too.

The following reconstruction model was presented by M. Wright through integrating the findings of the AMRP and his own research, as shown in Fig. 2c [4–14]. The back dials were corrected as spiral dials. The lost mechanisms were reconstructed in accordance with the concept of planetariums. The front dial could display the sun, the moon and five planets known to antiquity. Also, the gear train to demonstrate the moon phase was built in the reconstruction model. Next, D. Kriaris and M. Vicentini built new models with some variations, respectively [17, 27]. Tatjana van Vark made an impressive model, as shown in Fig. 2d [17]. The model focused on the essence of Antikythera mechanism, but detached from the standard of ancient artifact. This model added the parts of planetariums based on the AMRP research. The research group held by J.H. Seiradakis and K. Efstathiou developed the reconstruction model by their measurements of all gears found in the fragments, as shown in Fig. 2e [28]. They determined the root angle, the module and the chord length of all gears, and calculated the axial distances of all cooperating gears. Therefore, the model could be accurately manufactured by CAD tools.

3 Geometric Constraints

The reconstruction works [20–25] by Yan and Lin showed all feasible reconstruction designs of the unclear and lost subsystems. For a complete interior mechanism composed of the surviving structure and the reconstruction designs of the unclear and lost subsystems, some constraints for the assembly work of these subsystems are identified, especially for the lost solar subsystem and the lost planetary subsystem.

3.1 *Driving Power of Lost Structures*

To identify the driving power of lost structures and simplify the reconstruction designs, it is hypothesized that the mechanisms of the lost structures are driven by the output power of the existing structures. One mechanism of the lost structures driven by another mechanism of the lost structures is not considered. In previous research [20, 23, 24], three possible conditions with single driving power are identified. And, the arrangement of driving power absolutely affects the reconstruction designs of the lost structures.

3.2 Gear Sizes

The resulting gear ratios are the key points for the reconstructing Antikythera mechanism. For the lost structures, the reconstructed gears must not only satisfy the concluded teeth calculation relations but also avoid the interference [15–17, 20]. Therefore, the geometric constraints to match the known positions and the limited space are concluded. The mechanisms for the sun and the planets are the lost structures, and its geometric constraints should be introduced.

When the design shown in Fig. 3a is used to demonstrate the solar motion, the link 4 (K_T) is the carrier of planetary gear train and plays the deferent of epicyclic model. Based on the data of Table 1, the rate of link 4 should be once a tropical year. By kinematic analysis of gear trains, the link 2 (K_I) is an idle gear, and the link 4 must have the 224 teeth (the same to the surviving no.32 gear shown in Fig. 1). As a result, the output shaft of link 3 (K_O) for the solar motion cannot be coaxial with the shaft of the surviving no.32 gear for the daily motion, regardless of the size

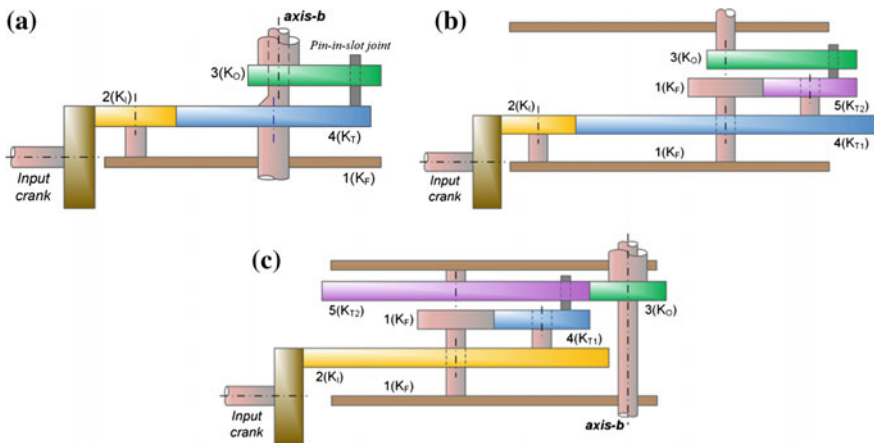


Fig. 3 Partial reconstruction designs of lost subsystem [20, 23, 24]

Table 1 Information of epicyclic system [29]

Datum		Deferent		Epicycle	
Planets		Period (tropical year)	Radius (arbitrary unit)	Period (tropical year)	Radius (arbitrary unit)
Inferior planets	Mercury	1	60	0.241	22.5
	Venus	1	60	0.615	43.16
Superior planets	Mars	1.88	60	1	39.5
	Jupiter	11.862	60	1	11.5
	Saturn	29.458	60	1	6.5

of link 2 (K_I). The design shown in Fig. 3a is unfeasible for the solar motion. In the same way, it is found that the teeth of the link 4 (K_{T1}) shown in Fig. 3b should be several times the teeth of the surviving no.32 gear (shown in Fig. 1) by the kinematic analysis of gear trains, when the design shown in Fig. 3b demonstrates the superior planets. This result is unreasonable and the space is not enough to contain such a big gear.

3.3 *Types of Planets*

For superior planets and inferior planets, there was only a geometric model, i.e., the epicyclic model, to introducing these planetary motions in the astronomy of ancient Greece, based on the historical records. Based on the periods of planets shown in Table 1, inferior planets and superior planets have the consistence respectively in the period of deferent and the period of epicycle. Furthermore, Antikythera device was the astronomical model to demonstrate the development of astronomy at that time. Therefore, it is logically believed that the mechanisms of inferior planets are constructed by the same design concept, also the superior planets are.

3.4 *Epicyclic System of Superior Planets*

Here, the interference of mechanical elements and the limited space are presented to conclude the geometric constraints again.

When the design shown in Fig. 3c is applied to superior planets, the link 2 (K_I) is the input link and regarded as the deferent of epicyclic model. This input link must engage with the contrate gear (no.66 gear) to transmit power. However, the deferent of superior planets have different rates as shown in Table 1, and the contrate gear can engage with only one gear. As a result, the mechanisms respectively for Mars, Jupiter and Saturn cannot be achieved simultaneously.

To conclude above geometric constraints, several design concepts for assembling a whole reconstruction design are unfeasible. In previous reconstruction research [20–25], 48 feasible reconstruction designs with complete interior structure are generated by Yan and Lin. The design shown in Fig. 1 is one of 48 feasible reconstruction designs.

4 *Systematic Design Procedure*

This work presents a systematic assembly procedure of the reconstruction design of the whole interior structure to build the simulation or physical model, as shown in Fig. 4. Following this procedure, the detail design of gears including the teeth, gear

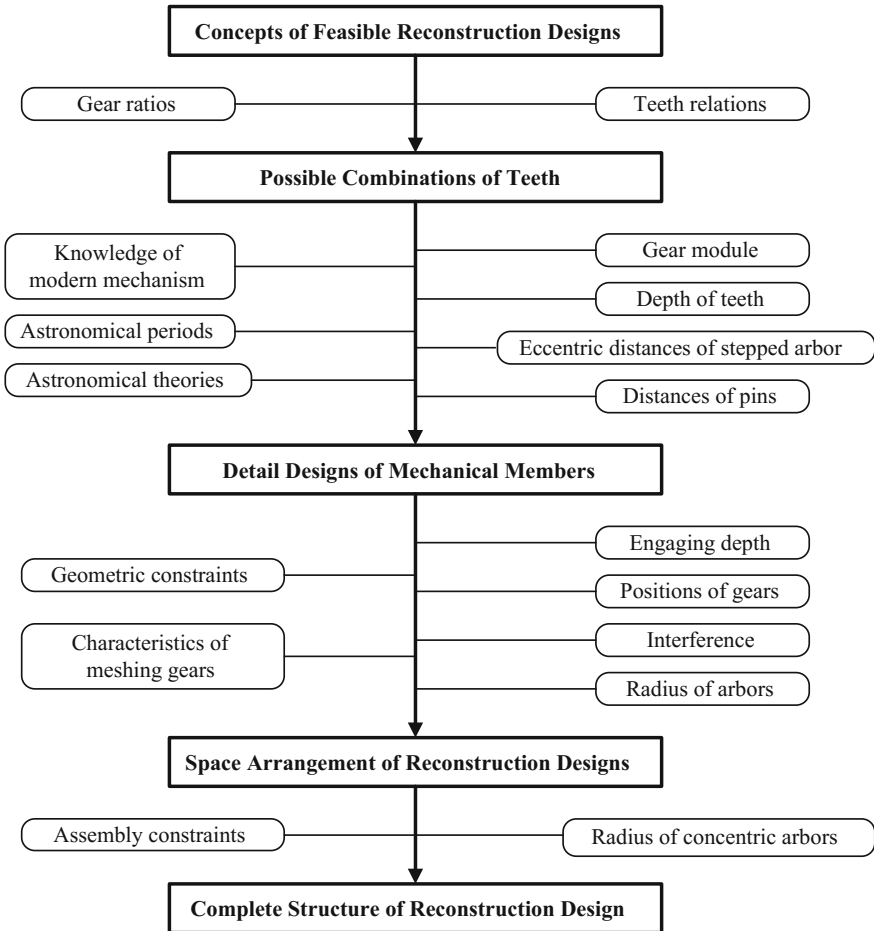


Fig. 4 A systematic design procedure of mechanical elements [20]

module and gear sizes can be obtained. Considering the interference, the orientation work of gears can be done by the graphic method. Finally, the simulation or physical model of reconstruction design can be generated.

4.1 Teeth Calculations

In the following, the teeth designs of the incomplete (calendrical) and lost (solar and planetary) subsystems are proposed in detail.

Calendrical Subsystem. Except for the known gear ratios (three display astronomical cycles), there are two surviving gears respectively with 60 teeth and 15 teeth. The relations of teeth calculation, Eqs. (1)–(3), are concluded [20, 21].

$$\frac{T_{37}}{T_{39}} = \frac{15}{53} \quad (1)$$

$$\frac{T_{40}}{T_{41}} = \frac{19}{20} \quad (2)$$

$$\frac{T_{42}}{T_{44}} \times \frac{T_{45}}{T_{43}} = \frac{1}{19} \quad (3)$$

where the subscript is the number of gears shown in Fig. 1.

Although these conditions are able to reconstruct simulation or solid models, the amount of the teeth calculation results is numerous. In order to appropriately estimate all teeth of each feasible design and size gears, the following constraints are assumed by the direct evidences:

1. The gear ratio of a gear joint should be 5 at most.
2. It is optimal that the calculated teeth should appear in the existing discovery.
3. The calculated teeth of the reconstruction design are constrained between 10 and 120. Thus, these reconstructed gears can fit the space of the mechanism.

According to Eqs. (1)–(3) and the above mentioned constraints of gear sizes, a set of possible teeth numbers is generated as follows:

$$(T_{39}, T_{40}, T_{41}, T_{42}, T_{43}, T_{44}, T_{45}) = (53, 57, 60, 24, 114, 120, 30)$$

Solar Subsystem. For the solar subsystem included in the reconstruction design, the relation of teeth calculation is concluded as follows [20, 23]:

$$\frac{T_{20} \times T_{21}}{T_{19} \times T_{22}} = 1 \quad (4)$$

Through try and error and considering the surviving gears (such as the gears of the lunar subsystem), a set of teeth is determined for a solid model by Eq. (4):

$$(T_{19}, T_{20}, T_{21}, T_{22}) = (60, 60, 61, 61)$$

Planetary Subsystem. Whatever the solar subsystem and however the planetary subsystem, the design process of mechanical elements should be the same. Teeth calculation is related to the required gear ratios. Space constraints are related to interference between mechanical elements. Eccentric distance is related to the model of celestial bodies, specific planet and its periods. Unfortunately, there were no definite historical records for the parameters of the geometric model of celestial bodies, including the radius of the period of the epicycle and the deferent radius.

Even though it is believed that the planets' periods are known in the era and applied for Apollonius' epicyclic system. Here, the parameters of Ptolemy's model, as listed in Table 1 [29], are used so as to restore the lost planetary subsystem. It means that the reconstruction model of the lost planetary subsystem emphasizes the configuration design and the results are merely approximate values. Equations (5)–(12) are the concluded relations of teeth calculations for different planets [20, 24].

$$\text{Mercury} \quad \frac{T_{30}}{T_{25}} = \frac{\omega_e}{\omega_d} \quad (5)$$

$$\text{Venus} \quad \frac{T_{31}}{T_{26}} = \frac{\omega_e}{\omega_d} \quad (6)$$

$$\text{Mars} \quad \frac{T_{13} \times T_{16} - T_{14} \times T_{15}}{T_{14} \times T_{15}} = \frac{\omega_d}{\omega_e}; \quad (7)$$

$$\frac{T_{17} \times T_{27}}{T_{32} \times T_{18}} = \frac{\omega_{year}}{\omega_d + \omega_e} \quad (8)$$

$$\text{Jupiter} \quad \frac{T_7 \times T_{10} - T_8 \times T_9}{T_8 \times T_9} = \frac{\omega_d}{\omega_e}; \quad (9)$$

$$\frac{T_{11} \times T_{28}}{T_{32} \times T_{12}} = \frac{\omega_{year}}{\omega_d + \omega_e} \quad (10)$$

$$\text{Saturn} \quad \frac{T_1 \times T_4 - T_2 \times T_3}{T_2 \times T_3} = \frac{\omega_d}{\omega_e}; \quad (11)$$

$$\frac{T_5 \times T_{29}}{T_{32} \times T_6} = \frac{\omega_{year}}{\omega_d + \omega_e} \quad (12)$$

where ω_d is the rate of deferent; ω_e is the rate of epicycle; ω_{year} means once a tropical year. For each planet, the rates of the deferent and the epicycle are listed in Table 1.

Based on these relations, the comparisons of surviving gears, and Ptolemy's planetary parameters, five sets of approximate teeth results respectively for Mercury, Venus, Mars, Jupiter and Saturn are estimated arbitrarily as follows:

Mercury	$(T_{30}, T_{32}, T_{25}) = (92, 224, 22)$
Venus	$(T_{31}, T_{32}, T_{26}) = (64, 224, 40)$
Mars	$(T_{13}, T_{14}, T_{15}, T_{16}, T_{17}, T_{18}, T_{27}) = (54, 94, 36, 96, 215, 30, 20)$
Jupiter	$(T_7, T_8, T_9, T_{10}, T_{11}, T_{12}, T_{28}) = (62, 60, 60, 63, 215, 31, 30)$
Saturn	$(T_1, T_2, T_3, T_4, T_5, T_6, T_{29}) = (55, 100, 50, 94, 215, 30, 30)$

4.2 Detail Designs of Gears

In order to reconstruct the lost and incomplete gears, the gear module of modern mechanisms (the basis for determining the sizes of gears) is applied. There were measurement errors in detecting surviving gears. And, the gear modulus of surviving gears are variable, not exactly consistent. The gear module of no.32 gear (the biggest gear in the surviving evidence) is estimated at about 0.58 for example. Hence, we forced to define the appropriate gear modules for a pair of engaging gears so as to restore the lost structures. Except for gear modulus, the teeth shape is triangular and the teeth depth is reasonably defined about 1.2 mm in accordance with the surviving evidence. And thus, the lost and incomplete gears are built successfully. Table 2 shows the data of reconstruction model of the solar subsystem.

For reconstructed gear trains, the geometric positions and their resulting distances are related to the radius ratio of the epicyclic model and the distance ratio of eccentric model. The eccentric model is applied to demonstrate the motions of Mercury and Venus. The carrier is the deferent, and the planet gear is the epicycle. For the applied planetary gear train, the center distance between the sun gear and the planet gear is the radius of deferent and the distance between the pin and the center of gear with pin is the radius of epicycle.

Furthermore, the demonstrations of Mars, Jupiter and Saturn also apply the epicyclic model, but are similar to the design of the lunar subsystem. The eccentric distance of the stepped arbor (the gear between the planet gear with a pin and the gear with a slot) is the radius of epicycle. The distance between the pin and the center of gear with pin is the radius of deferent.

As to the solar motion, its demonstration applies the eccentric model. The ratio of the radius of deferent and the eccentric distance is $1/24$. The radius of deferent should be regarded as the distance between the pin and the center of gear with a pin. The eccentric distance of the model is the eccentric distance of the stepped arbor, i.e., the gear between the planet gear with a pin and the gear with a slot.

Table 2 Information of reconstructed gears (lost planetary subsystem-Saturn)

No.	Teeth	Radius of pitch circle (mm)	Radius of addendum circle (mm)	Radius of dedendum circle (mm)	Module	Pin positions—from the center of gear (mm)
1	55	15.13	15.73	14.53	0.55	–
2	100	27.50	28.10	26.90	0.55	–
3	50	14.38	14.98	13.78	0.58	–
4	94	27.03	27.63	26.43	0.58	11.31
5	215	64.08	64.68	63.48	0.60	–
6	30	8.94	9.54	8.34	0.60	–

To conclude above and based on the information of Table 1, the following is the detail design of mechanisms respectively for Mercury, Venus, Mars, Jupiter, Saturn and the sun.

- Mercury: center distance = 32.8 mm, pin radius = 12.3 mm
- Venus: center distance = 29.9 mm, pin radius = 21.5 mm
- Mars: eccentric distance = 6.3 mm, pin radius = 9.5 mm
- Jupiter: eccentric distance = 1.8 mm, pin radius = 9.5 mm
- Saturn: eccentric distance = 1.2 mm, pin radius = 11.3 mm
- Sun: eccentric distance = 0.6 mm, pin radius = 14.4 mm

4.3 Space Arrangement

One basic work of reconstructing a simulation or physical model is the orientation of gear shafts in gear trains. The whole reconstruction design shown in Fig. 1 is regarded as a complicated gear train including six plates as frames. From top to down, it is clear that the fifth plate is the most complicated one. Also, its resulting simultaneously affects the orientation work of gear shafts in other plates and the positions of the exterior dials, either the front dials or the back dials. In other words, once the orientation work of the fifth plates is finished, all gear shafts of the reconstruction design is almost determined. Depending on the graphic method, the gear shafts including the calendrical subsystem, the lunar subsystem and the eclipse prediction subsystem are located in the fifth plates, as shown in Fig. 5.

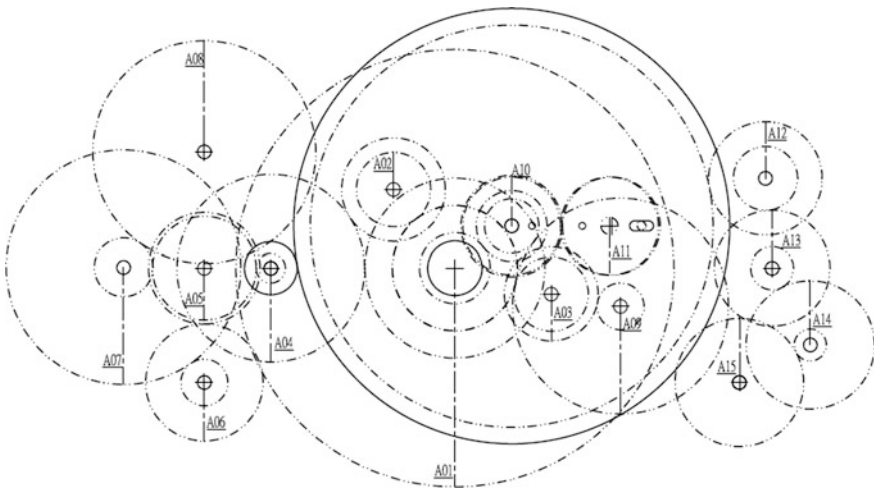


Fig. 5 2D positions of gears on the fifth plate [20]

Following this systematic procedure and inspecting the interference, the detail designs of gears and mechanical elements are resolved. Especially for the sizes of concentric arbors, they should be strong enough to support the weights of most gears. After solving the above problems, the corresponding reconstruction model can be built.

5 Building a Physical Model

For the compound gears, the positions of gears on their shafts are determined by considering the ability of manufacturing and the convenience of assembly. It affected the height of the reconstruction model. Through choosing the appropriate distance above or under gears, a 3D model of the reconstruction design model is presented, as shown in Fig. 6a, for verification in advance. Its animation clearly shows the operation of the mechanism and the demonstration of the pointers on the dials. Then, the physical model is reconstructed as shown in Fig. 6b. In this reconstruction model, the wooden case cover of the Antikythera device is removed in order to show clearly the reconstructed interior gear trains. Indeed, the building of the simulation and physical models are very helpful in describing the complete

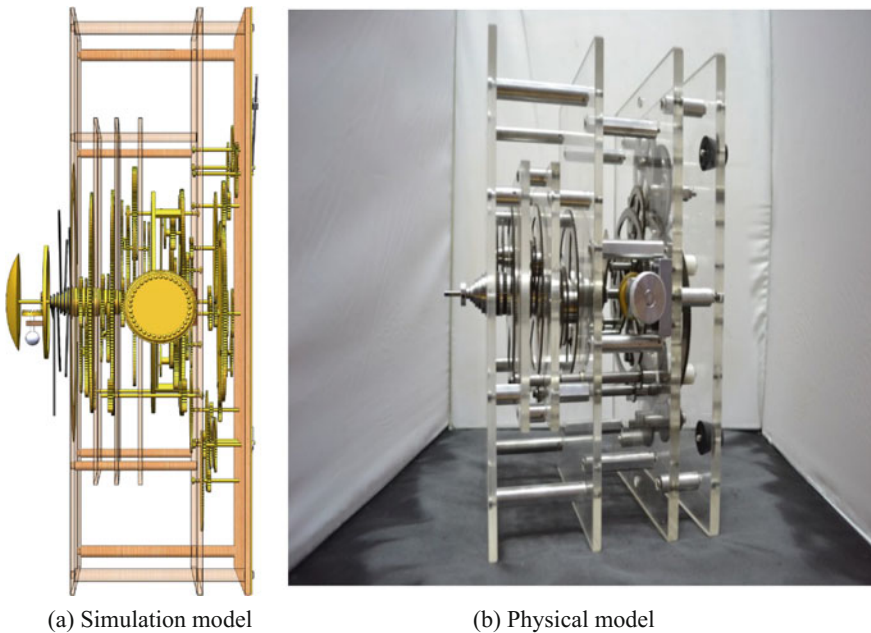


Fig. 6 A reconstruction model by Lin and Yan **a** Simulation model **b** Physical model

concept of Antikythera astronomical calculator. In a word, the work of building 3D mechanisms is able to precisely prove the feasibility of the obtained reconstruction designs.

6 Conclusions

The reconstruction research of Antikythera mechanism develops more than 100 years until now. With decoding the inscriptions and detecting the surviving fragments, several different reconstruction designs are continuously presented. The building of solid or physical models is a direct way to prove the feasibility of conceptual reconstruction designs. This work introduces the assembly work of physical model in detail. By geometric constraints of subsystems, 48 complete reconstruction designs are presented, and one of them is used to reconstruct the corresponding solid model. A systematic design procedure of mechanical elements is presented. Based on this procedure, teeth calculations, gear sizes, gear models and space positions are resolved. The simulation and physical models are successfully reconstructed. This is a new physical model of Antikythera mechanism.

Acknowledgments The authors are grateful to the National Science Council (TAIWAN, ROC) under Grant NSC 99-2221-E-006-253 for the financial support of this work.

References

1. Price D, de S (1959) An ancient greek computer. *Sci Am* 60–67
2. Price D, de S (1974) Gears from the Greeks: the Antikythera mechanism—a calendar computer from ca. 80 BC. *Trans Am Phil Soc New Ser* 64:1–70; reprinted by Science History Publications, New York (1975)
3. Edmunds M, Morgan P (2000) The Antikythera mechanism: still a mystery of Greek astronomy? *Astron Geophys* 41:6.10–6.17
4. Wright MT, Bromley AG (2001) Towards a new reconstruction of the Antikythera mechanism. In: *Proceedings of the conference extraordinary machines and structures in antiquity*, Patras
5. Wright MT (2002) A planetarium display for the Antikythera mechanism. *Horological J* 144 (5):169–173
6. Wright MT (2002) In the steps of the master mechanic. In: *Proceedings of the conference: ancient Greece and the modern world*. University of Patras, pp 86–97
7. Wright MT (2003) Epicyclic gearing and the Antikythera mechanism: part 1. *Antiquarian Horol* 27:270–279
8. Wright MT (2004) The scholar, the mechanic and the Antikythera mechanism. *Bull Sci Instrum Soc* 80:4–11
9. Wright MT (2005) The Antikythera mechanism: a new gearing scheme. *Bull Sci Instrum Soc* 85:2–7
10. Wright MT (2005) Epicyclic gearing and the Antikythera mechanism: part 2. *Antiquarian Horol* 29:51–63

11. Wright MT (2005) Counting months and years: the upper back dial of the Antikythera mechanism. *Bull Sci Instrum Soc* 87:8–13
12. Wright MT (2006) The Antikythera mechanism and the early history of the moon phase display. *Antiquarian Horol* 29(3):319–329
13. Wright MT (2006) Understanding the Antikythera mechanism. In: *Proceedings of the conference on ancient Greek technology*. Athens, pp 49–60
14. Wright MT (2007) The Antikythera mechanism reconsidered. *Interdisciplinary Sci Rev* 32(1):27–43
15. Freeth T et al (2006) Decoding the ancient Greek astronomical calculator known as the Antikythera mechanism. *Nature* 444:581–591
16. Freeth T et al (2008) Calendars with olympiad display and eclipse prediction on the Antikythera mechanism. *Nature* 454:614–617
17. Freeth T et al (2005) Antikythera mechanism research project (website), <http://www.antikythera-mechanism.gr/>. Accessed 13 July
18. Evans J, Carman CC, Thorndike AS (2010) Solar anomaly and planetary displays in the Antikythera mechanism. *J Hist Astron* 42:1–39
19. Evans J, Carman CC (2014) *Mechanical astronomy: a route to the ancient discovery of epicycles and eccentrics*. Alexandria, through Baghdad: surveys and studies in the ancient Greek and medieval islamic mathematical sciences in Honor of J.L. Berggren. Springer
20. Lin J-L, Yan H-S (2015) *Decoding the mechanisms of Antikythera astronomical device*. Springer, Beijing. ISBN:978-3-662-48445-6
21. Yan H-S, Lin J-L (2011) Reconstruction synthesis of the calendrical subsystem of Antikythera mechanism. *ASME Trans J Mech Des* 133(2):021004
22. Yan H-S, Lin J-L (2012) Reconstruction synthesis of the lunar subsystem with an unexplained feature of Antikythera mechanism. *Proc Inst Mech Eng Part C J Mech Eng Sci* 226(4):1053–1067
23. Yan H-S, Lin J-L (2013) Reconstruction synthesis of the lost interior structure for the solar anomaly motion of the Antikythera mechanism. *Mech Mach Theory* 70:354–371
24. Yan H-S, Lin J-L (2012) Reconstruction synthesis of the lost subsystem for the planetary motions of Antikythera mechanism. *ASME Trans J Mech Des* 134(1):011003
25. Lin J-L, Yan H-S (2015) Decoding the moon phase display device over the front dial of the Antikythera mechanism. *Chin J Mech Eng* 28(4):676–683. Also in *IFTtoMM Asian conference on mechanism and machine science (Asian-MMS 2014)*, Tanjing, China, 9–14 July
26. Kaltsas N, Vlachogianni E, Bouyia P (2012) *The Antikythera shipwreck: the ship, the treasures, the mechanism*. Hellenic Ministry of Culture and Tourism, National Archaeological Museum, Athens
27. Jones A (2012) *The Antikythera mechanism and the public face of Greek science*. Lecture in *Proceedings of science from Antikythera to the square kilometre array: lessons from the ancients*, Kerastari, Greece, 12–15 June 2012
28. Efstathiou K, Basiakoulis A, Efstathiou M, Anastasiou M, Seiradakis JH (2012) Determination of the gears geometrical parameters necessary for the construction of an operational model of the Antikythera mechanism. *Mech Mach Theory* 52:219–231
29. Ptolemy C (1998) *Almagest (100)*. English edition: Ptolemy C (1998) *Ptolemy's Almagest* (trans: Toomer GJ). Princeton University Press, USA

Mobility Analysis of Generalized Mechanisms via Screw Algebra

Tuanjie Li, Hanqing Deng and Lei Zhang

Abstract Compared with traditional mechanisms, a new class of mechanism considering both the rigid and the flexible elements is proposed to satisfy the demands of modern engineering in this paper. This class of mechanism is named as generalized mechanism, and they consists of generalized links and kinematic pairs. First, based on screw algebra, we derive the motion spaces of generalized links and the constraint spaces of generalized kinematic pairs. Then, we analyze the minimal and maximal mobilities of generalized links, as well as the minimal and maximal constraints of generalized kinematic pairs. Finally, three formulas for calculating the degree of freedom (DOF) of generalized mechanisms are established. The analytical results show that the DOF of each generalized mechanism is not unique, but an interval value. The real DOF of generalized mechanisms depends on both the links' materials, the magnitude and direction of external loads.

Keywords Generalized mechanism · Degree of freedom · Screw algebra · Motion space · Constraint space

1 Introduction

With the development of society and the evolution of science and technology, the demands of mechanisms have been more and more emphasized recently [1]. The development of mechanisms has displayed the diversification and practicality. Several new classes of mechanisms have been proposed, such as parallel mechanisms [2, 3], compliant mechanisms [4], tensegrity mechanisms [5], metamorphic mechanisms [6], overconstrained parallel mechanisms [7], and cable-driven parallel mechanisms [8], etc. In order to satisfy the demands of modern engineering, the

T. Li (✉) · H. Deng · L. Zhang
School of Electromechanical Engineering, Xidian University,
P.O. Box 188, Xi'an 710071, China
e-mail: tjli888@126.com

configurations of mechanisms, the types of links and kinematic pairs have been changed.

Various links and kinematic pairs have been applied in practical engineering. For example, due to the applications of flexible links and hinges, compliant mechanisms emerged with the characteristics of high precision, friction-free motion, wear-free motion, no assembly requirement, and no need of lubrication. These characteristics lead to the wide development of micro-electromechanical systems (MEMS) [8]. Based on the rigid-flexible combination, the cable-driven parallel mechanisms have advantages of both the stiffness of rigid links and the flexibility of cables. In medical mechanisms, springs and cables are widely used in rehabilitated robots [9]. They have several desirable characteristics over rigid-link parallel mechanisms: reduced end-effector weight and inertia, enlarged reachable workspace, ease of transportation, and high reconfigurability [10]. Typical applications include the telemanipulator for cardiac surgery (ARTEMIS) [11, 12], the Anubis scope [13] and the Spider surgery system [14]. In the space deployable mechanisms, flexible links, springs, cables and pre-tensioned joints are also widely used because of their advantages of light-weight, high precision and high availability. For instance, the supporting structure of the Wrap-Rib Antenna [15] is completely made by flexible winding ribs. The folding articulated square truss (FAST) [16] of the international space station is a deployable mast which is actuated by the strain energy stored in flexible links. And the deployment is controlled by the diagonal bracing cables on each face of the units. The same situation also occurred in the space deployable antennas [17], such as AstroMesh [18], Energia-GPI-Space (EGS) [19], and Engineering Test Satellite VIII (ETS-VIII) [20]. The new members such as flexible links, springs and cables, have played important roles in satisfying the engineering requirements.

In the fields of mechanisms, scholars have made great contributions to analyze the DOF of mechanisms [21], such as Chebyshev, Grübler, Kutzbach, Moroskine, Hervé, Angeles and Gosselin, and Huang, etc. The studies of DOF include planar mechanisms, spatial mechanisms, parallel mechanisms, compliant mechanisms, and metamorphic mechanisms, etc. Many methods have been proposed for calculating DOFs, including the C-G-K formula, the rank calculation of the matrix of mechanical homogeneous equations, the application of screw theory [22], the algebraic-group-structure-theory of displacement groups, and the kernel dimensionality of zero-dimension by using the Jacobian Matrix. So far, there remains no universal and admissible computational formula. Furthermore, the DOF calculation methods above are appropriate for the ideal rigid links and kinematic pairs. In practical engineering, not all mechanisms can be considered as ideal, how to analyze and calculate the DOFs of mechanisms containing flexible elements becomes very essential. To address the problem that compliant mechanisms are treated as structures without any DOF in traditional mechanisms, Her [23] redefined the DOF of compliant mechanisms and established a method for calculating the DOF of mechanisms which contain flexible links, according to the effects of link characteristics on DOF. Chen et al. [24] calculated the DOFs by means of the C-G-K formula with the equivalent of pseudo-rigid-body. Su et al. [25–27]

analyzed the motion and constraint spaces of flexible links via screw algebra, and the mobilities of compliant mechanisms. But these methods are difficult to use for the mechanisms including springs and cables.

Therefore, it is necessary to define a new class of mechanism considering both the rigid and flexible elements to satisfy the engineering requirements, as well as the definition and calculation of the DOF. The layout of the paper is as follows. The generalized mechanisms are defined in Sect. 2. Based on screw theory, motion spaces of generalized links and constraint spaces of generalized kinematic pairs are derived in Sect. 3. In this section we analyze the minimal and maximal mobilities of generalized links, as well as the minimal and maximal constraints of generalized kinematic pairs. Three formulas for DOF calculation are then established. And the numerical simulations to illustrate the feasibility and effectiveness of the proposed method are given in Sect. 4. Finally, some conclusions are summed up in Sect. 5.

2 Definition of Generalized Mechanisms

As an expansion of traditional mechanism, generalized mechanism is defined as:

Definition 2.1 *The generalized links*, as the expansion of the traditional rigid links, contain all links which are capable to transform motions and forces, including rigid links, flexible links, springs, and cables, etc.

Definition 2.2 *The generalized kinematic pairs*, as the expansion of the traditional pairs, contain all kinematic pairs which connect different links and offer constraints, including not traditional pairs but pre-tensioned joints, compliant hinges, etc.














Definition 2.3 *The generalized mechanism* is a class of mechanism consisted of generalized links and generalized kinematic pairs.

There exist some differences between traditional mechanisms and generalized mechanisms in the links and kinematic pairs, briefly as follows.

- (a) Flexible links, including blade flexures and wire flexures, etc., come from compliant mechanisms. They play the roles of links or flexible hinges in some conditions, and transform motions and forces by means of deformations.
- (b) Both torsion springs and helical springs are applied in generalized mechanisms. A torsion spring is generally combined with a revolute pair to form a pre-tensioned revolute joint. While the helical spring can act as an independent link or a pre-tensioned prismatic joint combined with a prismatic pair.
- (c) Cables have advantages of good flexibility and high load capacity. They can work well for transforming the motion and force at very small space.

Several typical generalized links and kinematic pairs are listed in Table 1.

Table 1 Typical generalized links and kinematic pairs

Generalized links	Skeleton diagrams	Generalized kinematic pairs	Skeleton diagrams
Rigid link		Revolute pair	
Flexible link		Prismatic pair	
Helical spring		Pre-tensioned prismatic joint	
Torsion spring		Pre-tensioned revolute joint	
Cable		Compliant hinge	
		Solid joint	
		Spherical pair	
		Sphere-pin pair	

3 Mobility of Generalized Mechanisms

3.1 Screw Algebra

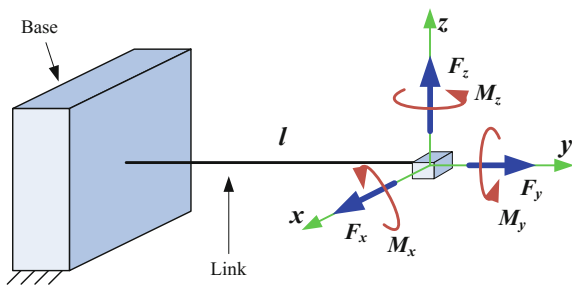
In screw theory, every motion and constraint can be denoted by a twist $\hat{T} = (\theta_x \theta_y \theta_z; \delta_x \delta_y \delta_z)^T$ and a wrench $\hat{W} = (F_x F_y F_z; M_x M_y M_z)^T$. When a twist is reciprocal to a wrench, their reciprocal product equals zero, that is

$$\hat{T} \circ \hat{W} = F_x \delta_x + F_y \delta_y + F_z \delta_z + M_x \theta_x + M_y \theta_y + M_z \theta_z = 0. \tag{1}$$

3.2 Motion Spaces of Generalized Links

A generalized link is shown in Fig. 1, with the length l , and the sectional diameter d . Three direction forces (F_x, F_y, F_z) and moments (M_x, M_y, M_z) are applied to one endpoint, the other endpoint is fixed. The deformation of a generalized link is:

Fig. 1 Motion space analysis of generalized links



$$\hat{T} = \mathbf{C}\hat{W}. \tag{2}$$

where \mathbf{C} is the compliance matrix.

When consider the effects of F_x, F_y, F_z, M_x, M_y and M_z respectively, the motion space of a generalized link can be derived as:

$$[T] = [\hat{T}_{F_x} \hat{T}_{F_y} \hat{T}_{F_z} \hat{T}_{M_x} \hat{T}_{M_y} \hat{T}_{M_z}]Q. \tag{3}$$

where, $\hat{T}_{F_x}, \hat{T}_{F_y}, \hat{T}_{F_z}, \hat{T}_{M_x}, \hat{T}_{M_y}$ and \hat{T}_{M_z} are 6-by-1 vectors, which are the respective effects of the external loads F_x, F_y, F_z, M_x, M_y and M_z . \mathbf{Q} is the transform matrix that makes $[T]$ formed by $E_1 = [1\ 0\ 0\ 0\ 0\ 0]^T, E_2 = [0\ 1\ 0\ 0\ 0\ 0]^T, \dots, E_6 = [0\ 0\ 0\ 0\ 0\ 1]^T$.

The deformation of a generalized link is produced by external loads. It is obviously that the number of external mobilities is the rank of the motion space $rank([T])$.

(1) Rigid links

For a rigid link, the elastic modulus is infinity, i.e. $\mathbf{C} = \mathbf{0}$. The rigid link does not deform under the condition. There is no additional motion mobility in the rigid link.

(2) Flexible links

When the link shown in Fig. 1 is a flexible links, the deformation is as Eq. (4).

$$\hat{T} = \mathbf{C}\hat{W} = \begin{bmatrix} 0 & 0 & \frac{l^2}{2EI_x} & \frac{l}{EI_x} & 0 & 0 \\ 0 & 0 & 0 & 0 & \frac{l}{GJ} & 0 \\ -\frac{l^2}{2EI_z} & 0 & 0 & 0 & 0 & \frac{l}{EI_z} \\ \frac{l^3}{3EI_z} & 0 & 0 & 0 & 0 & -\frac{l^2}{2EI_z} \\ 0 & \frac{l}{EA} & 0 & 0 & 0 & 0 \\ 0 & 0 & \frac{l^3}{3EI_x} & \frac{l^2}{2EI_x} & 0 & 0 \end{bmatrix} \begin{Bmatrix} F_x \\ F_y \\ F_z \\ - \\ M_x \\ M_y \\ M_z \end{Bmatrix} = \begin{Bmatrix} \theta_x \\ \theta_y \\ \theta_z \\ - \\ \delta_x \\ \delta_y \\ \delta_z \end{Bmatrix}. \tag{4}$$

where E and G are the elastic modulus and shear modulus, A is the cross sectional area, I_x, I_z are the moments of inertia, J is the torsional moment inertia.

When EA, EI and GJ are close in magnitude, the deformations cannot be neglected. The motion space of flexible link is as Eq. (5):

$$[T_1] = [\hat{T}_{F_x} \hat{T}_{F_y} \hat{T}_{F_z} \hat{T}_{M_x} \hat{T}_{M_y} \hat{T}_{M_z}]\mathbf{Q}_1 = [E_1\ E_2\ E_3\ E_4\ E_5\ E_6]. \tag{5}$$

where, the full rank of $[T_1]$ indicates six relative motions in the free endpoint, which offers six external mobilities. The effects of F_x, F_y, F_z, M_x, M_y and M_z are:

$$\begin{aligned} \hat{T}_{F_x} &= -\frac{F_x l^2}{2EI_z} (0 \ 0 \ 1; \ -\frac{2l}{3} \ 0 \ 0)^T, \quad \hat{T}_{F_y} = \frac{F_y l}{EA} (0 \ 0 \ 0; \ 0 \ 1 \ 0)^T, \\ \hat{T}_{F_z} &= \frac{F_z l^2}{2EI_x} (1 \ 0 \ 0; \ 0 \ 0 \ \frac{2l}{3})^T, \\ \hat{T}_{M_x} &= \frac{M_x l}{EI_x} (1 \ 0 \ 0; \ 0 \ 0 \ \frac{l}{2})^T, \quad \hat{T}_{M_y} = \frac{M_y l}{GJ} (0 \ 1 \ 0; \ 0 \ 0 \ 0)^T, \\ \hat{T}_{M_z} &= \frac{M_z l}{EI_z} (0 \ 0 \ 1; \ -\frac{l}{2} \ 0 \ 0)^T. \end{aligned}$$

When $d \ll l$, we can obtain $l/EA \ll l/EI_x = l/EI_z$ and $l/EA \ll l/GJ$. The deformation affected by F_y can be neglected, and the motion space is:

$$[T_2] = [\hat{T}_{F_x} \ \hat{T}_{F_z} \ \hat{T}_{M_x} \ \hat{T}_{M_y} \ \hat{T}_{M_z}] \mathbf{Q}_2 = [E_1 \ E_2 \ E_3 \ E_4 \ 6]. \tag{6}$$

$rank([T_2]) = 5$ indicates five relative motions, which offers five external mobilities. The motion space in Eq. (6) is the same as the description in [27].

(3) Spring links

When the link shown in Fig. 1 is a helical spring, the deformation is as follows.

$$\hat{T} = \mathbf{C}\hat{W} = \begin{bmatrix} 0 & 0 & 0 & 0 & 0 & 0 \\ 0 & 0 & 0 & 0 & 0 & 0 \\ 0 & 0 & 0 & 0 & 0 & 0 \\ 0 & 0 & 0 & 0 & 0 & 0 \\ 0 & 1/K_1 & 0 & 0 & 0 & 0 \\ 0 & 0 & 0 & 0 & 0 & 0 \end{bmatrix} \begin{Bmatrix} F_x \\ F_y \\ F_z \\ - \\ M_x \\ M_y \\ M_z \end{Bmatrix} = \begin{Bmatrix} 0 \\ 0 \\ 0 \\ - \\ 0 \\ \delta_y \\ 0 \end{Bmatrix}. \tag{7}$$

where, K_1 is the tension and compression stiffness of the helical spring.

It is noted that just F_y affects the spring on the δ_y direction, and the motion space is:

$$[T_3] = [\hat{T}_{F_y}] K_1 / F_y = E_5. \tag{8}$$

The spring link offers one external mobility since $rank([T_3]) = 1$. While K_1 is much larger, the relatively axial translation can be neglected without any mobility.

If the link is a torsion spring with y-axis as the rotation axis, the motion space is:

$$[T_4] = [\hat{T}_{M_y}] K_2 / (M_y l) = E_2. \tag{9}$$

where, K_2 is the flexural rigidity of the torsion spring.

The torsion spring offers one external mobility. Similarly, when K_2 is much larger, the relatively rotation can be neglected resulting in no mobility.

(4) Cable link

When the link shown in Fig. 1 is a cable link, the deformation is as Eq. (10), since the cable can just bear tension in the axial direction.

$$\hat{T} = \mathbf{C}\hat{W} = \begin{bmatrix} 0 & 0 & \infty & \infty & 0 & 0 \\ 0 & 0 & 0 & 0 & \infty & 0 \\ \infty & 0 & 0 & 0 & 0 & \infty \\ \infty & 0 & 0 & 0 & 0 & \infty \\ 0 & f_c \frac{l}{EA} & 0 & 0 & 0 & 0 \\ 0 & 0 & \infty & \infty & 0 & 0 \end{bmatrix} \begin{Bmatrix} F_x \\ F_y \\ F_z \\ - \\ M_x \\ M_y \\ M_z \end{Bmatrix} = \begin{Bmatrix} \infty \\ \infty \\ \infty \\ - \\ \infty \\ \delta_y \\ \infty \end{Bmatrix}. \tag{10}$$

Where $f_c = \begin{cases} 1, & \text{The cable is tensioned.} \\ \infty, & \text{The cable is slack.} \end{cases}$ is the flag of a cable link.

When the cable is slack, there is no constraint, the motion space is as Eq. (11); When the cable is tensioned, $l/EA \ll \infty, F_y l/EA \rightarrow 0$, the motion space is as Eq. (12):

$$[T_5] = [E_1 E_2 E_3 E_4 E_5 E_6]. \tag{11}$$

$$[T'_5] = [E_1 E_2 E_3 E_4 E_6]. \tag{12}$$

As seen from Eqs. (11) and (12), the motion space of the cable depends on its status in the axis direction. The mobility in this direction is thus defined as:

$$F_{st} = \begin{cases} 0, & \text{The cable is tensioned.} \\ 1, & \text{The cable is slack.} \end{cases} \tag{13}$$

In summary, motion spaces of generalized links have been analyzed above. And the mobilities caused by the deformations are summarized in Table 2. In the table, d is the order of the mechanism. ‘‘Additional mobility’’ is the mobilities caused by the deformations. n is the number of kinematic pairs connected to the link.

3.3 Constraint Spaces of Generalized Kinematic Pairs

As shown in Fig. 2, two rigid links connect to generalized kinematic pairs and $(F_x, F_y, F_z, M_x, M_y, M_z)$ are applied to the free endpoint respectively. By analyzing the relative motion between the two rigid links, the motion spaces can be derived, and the constraint spaces are thus obtained by Eq. (1). So the number of additional constraint of generalized kinematic pairs can be obtained by $rank([W])$.

(1) Pre-tensioned revolute joints

When the generalized kinematic pair shown in Fig. 2 is a pre-tensioned revolute joint, the deformation of pre-tensioned revolute joint is:

Table 2 Mobilities of the generalized links

Items	Rigid link	Flexible link	Helical spring	Torsion spring	Cable
Minimal mobility	d	d	d	d	d
Additional mobility	Translation x	\times	\times	\times	$\sqrt{\quad}$
	Translation y	\times	$\sqrt{\quad}$	\times	\times
	Tension	\times	$\sqrt{\quad}$	\times	$\sqrt{\quad}$
	Compression	\times	$\sqrt{\quad}$	\times	$\sqrt{\quad}$
	Translation z	\times	\times	$\sqrt{\quad}$	$\sqrt{\quad}$
	Rotation x	\times	$\sqrt{\quad}$	\times	$\sqrt{\quad}$
	Rotation y	\times	$\sqrt{\quad}$	\times	$\sqrt{\quad}$
Rotation z	\times	$\sqrt{\quad}$	\times	\times	$\sqrt{\quad}$
Sum	0	$d(n-1)$	$(n-1)$	$(n-1)$	$(d-1 + F_{st})(n-1)$
Maximal mobility	d	dn	$d+n-1$	$d+n-1$	$dn + (n-1)(F_{st} - 1)$

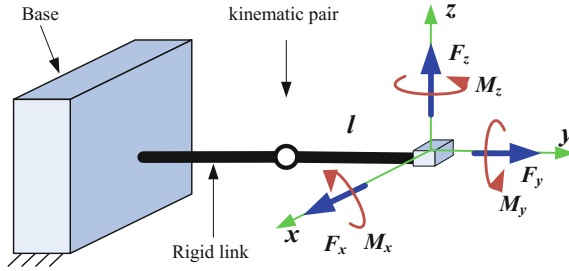


Fig. 2 Constraint space analysis of generalized kinematic pairs

$$\hat{T} = \mathbf{C}\hat{W} = \begin{bmatrix} 0 & 0 & l^2/K_2 & l/K_2 & 0 & 0 \\ 0 & 0 & 0 & 0 & 0 & 0 \\ 0 & 0 & 0 & 0 & 0 & 0 \\ 0 & 0 & 0 & 0 & 0 & 0 \\ 0 & 0 & 0 & 0 & 0 & 0 \\ 0 & 0 & l^3/K_2 & l^2/K_2 & 0 & 0 \end{bmatrix} \begin{Bmatrix} F_x \\ F_y \\ F_z \\ - \\ M_x \\ M_y \\ M_z \end{Bmatrix} = \begin{Bmatrix} \theta_x \\ 0 \\ 0 \\ - \\ 0 \\ 0 \\ \delta_z \end{Bmatrix}. \quad (14)$$

When the value of K_2 is appropriate, F_z and M_x have effects on θ_x and δ_z directions of the pre-tensioned revolute joint, respectively.

$$[T_6] = [\hat{T}_{F_z} \hat{T}_{M_x}] \begin{bmatrix} 2K_2/F_z l^2 \\ -K_2/M_x l \end{bmatrix} = (1 \ 0 \ 0; \ 0 \ 0 \ l)^T. \quad (15)$$

where, $\hat{T}_{F_z} = F_z l^2 / K_2 (100; 00l)^T$ is linearly correlated with $\hat{T}_{M_x} = M_x l / K_2 (100; 00l)^T$. The motion space and constraint space of the pre-tensioned revolute joint is obtained as Eqs. (16) and (17).

$$[T_7] = E_1. \quad (16)$$

$$[W_7] = [E_1 \ E_2 \ E_3 \ E_5 \ E_6]. \quad (17)$$

When K_2 is much larger, the torsion spring of the pre-tensioned revolute joint acts as a constraint, the relative rotation between the two rigid links can be neglected, then the relative mobility is zero. It is noted that constraints of pre-tensioned revolute joints are greatly affected by the factors of material. According to these factors, a pre-tensioned revolute joint offers five or six constraints.

(2) Pre-tensioned prismatic joints

When the generalized kinematic pair shown in Fig. 2 is a pre-tensioned prismatic joint, the deformation is as Eq. (18), and the constraint space is as Eq. (19):

$$[T_8] = [\hat{T}_{F_y}]K_1/F_y = E_5. \tag{18}$$

where $\hat{T}_{F_y} = F_y/K_1(000; 01)^T$.

$$[W_8] = [E_1 E_3 E_4 E_5 E_6]. \tag{19}$$

When K_1 is much larger, the helical spring of the pre-tensioned prismatic joint acts as a constraint. So, a pre-tensioned prismatic joint offers five or six constraints.

Similarly, a compliant hinge offers five or six constraints like a pre-tensioned revolute joints. And the solid joint has six constraints without doubt. The constraint spaces of the spherical pair and sphere-pin pair can be obtained by the same method.

The constraints of generalized kinematic pairs are summarized in Table 3. d is the order of the mechanism. ‘‘Additional constraint’’ is the constraints caused by the deformations. The minimal constraint does not consider the constraints caused by the deformations, while the maximal constraint does. ‘‘T $x/y/z$ ’’ and ‘‘R $x/y/z$ ’’ denote the translations and rotations in x , y or z directions, respectively. ‘‘R’’, ‘‘P’’, ‘‘P-R’’, ‘‘P-T’’, ‘‘CH’’, ‘‘Solid’’, ‘‘SP’’ and ‘‘S-PP’’ denote the revolute joint, prismatic joint, pre-tensioned revolute joint, pre-tensioned prismatic joint, compliance hinge, solid joint, spherical pair and sphere-pin pair, respectively. ‘‘•’’ indicates that the generalized kinematic pair offers an additional constraint in one of the directions.

3.4 DOF Calculation

IFTtoMM terminology defines the mobility or the DOF as the number of independent co-ordinates needed to define the configuration of a kinematic chain or mechanism. It is noted from the above analysis that both mobilities and constraints of generalized links and kinematic pairs are greatly affected by factors of the physical dimension, material and external loads. Therefore, based on this definition

Table 3 Constraints of generalized kinematic pairs

Items	R	P	P-R	P-P	CH	Solid	SP	S-PP
Minimal	$d - 1$	$d - 1$	$d - 1$	$d - 1$	$d - 1$	d	$d - 3$	$d - 2$
Additional	T x	×	×	×	•	×	×	×
	T y	×	×	×	•	×	×	×
	T z	×	×	×	•	×	×	×
	R x	×	×	•	×	•	×	×
	R y	×	×	•	×	•	×	×
	R z	×	×	•	×	•	×	×
	Sum	0	0	1	1	1	0	0
Maximal	$d - 1$	$d - 1$	d	d	d	d	$d - 3$	$d - 2$

and the characteristics of generalized mechanisms, the DOF of generalized mechanisms is redefined with the minimal and maximal DOFs.

Definition 3.1 *The minimal DOF of generalized mechanisms, also called rigid DOF, is the number of independent co-ordinates needed to define the configuration of a kinematic chain or mechanism after rigidifying all elements.*

Definition 3.2 *The maximal DOF of generalized mechanisms is the sum of minimal DOF and additional mobilities offered by deformations of flexible elements.*

Referred to the DOF calculation method of traditional mechanisms, that is

$$F = \sum_{i=1}^{n_m} Mo_i - \sum_{j=1}^{n_p} Co_j + v - \zeta. \tag{20}$$

where, Mo_i is the mobility offered by the i th movable link, Co_j is the constraints offered by the j th pairs. n_m and n_p are the numbers of movable links and kinematic pairs, respectively. v and ζ are the redundant constraint and the local degree of freedom, respectively, which can be calculated by Huang [22].

Combining with Tables 2 and 3, the minimal and maximal DOFs of generalized mechanisms are expressed as follows.

$$F_{min} = \sum_{i=1}^{n_m} \min\{Mo_i\} - \sum_{j=1}^{n_p} \max\{Co_j\} + v - \zeta. \tag{21}$$

$$F_{max} = \sum_{i=1}^{n_m} \max\{Mo_i\} - \sum_{j=1}^{n_p} \min\{Co_j\} + v - \zeta. \tag{22}$$

where, $\min\{Mo_i\}$ and $\max\{Mo_i\}$ are the minimal and maximal mobilities offered by the i th movable link, respectively. $\min\{Co_j\}$ and $\max\{Co_j\}$ are the minimal and maximal constraints offered by the j th kinematic pairs, respectively.

The maximal DOF may be calculated by the sum of the minimal DOF and the additional mobilities offered by the flexible elements, that is

$$F_{max} = F_{min} + \sum_{i=1}^{n_m} AMo_i + \sum_{j=1}^{n_p} ACo_j. \tag{23}$$

where, AMo_i is the additional mobility offered by the i th generalized link, and ACo_j is the additional constraints offered by the j th generalized kinematic pair.

In order to calculate the mobilities of generalized links conveniently, the minimal and maximal mobility of the i th generalized link is denoted by an interval variables \widetilde{Mo}_i , and the minimal and maximal constraints of the j th generalized kinematic pairs is also denoted by \widetilde{Co}_j . According to the operational rule of interval

variables, the minimal and maximal DOFs of generalized mechanisms can be calculated as:

$$\tilde{F} = [F_{min}, F_{max}] = \sum_{i=1}^{n_m} \tilde{M}O_i - \sum_{j=1}^{n_p} \tilde{C}O_j + v - \xi. \tag{24}$$

where, the DOF of generalized mechanisms, \tilde{F} , is also an interval variable, and the lower and upper bounds of \tilde{F} are the corresponding minimal and maximal DOFs, respectively.

In summary, the procedures of DOF calculation for generalized mechanisms are as follows. (a) For new links and kinematic pairs, analyze the motion and constraint spaces and obtain both the minimal and maximal mobilities and constraints. (b) Analyze the order of mechanisms d , redundant constraint v , and local degree of freedom ξ . (c) Calculate the DOF with Eqs. (20)–(24).

4 Numerical Examples

4.1 Example 1

The mechanism shown in Fig. 3a is a spatial four-bar mechanism of a sewing machine. Some variations are applied to Fig. 3b, c to make it become generalized mechanisms. By calculating the DOFs from Fig. 3a–c, we can analyze the evolution of generalized mechanisms and the change of the DOFs. Based on screw theory, the twist system of the mechanism shown in Fig. 3a is obtained:

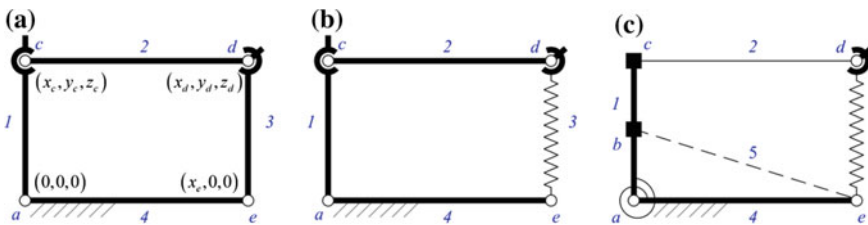


Fig. 3 Spatial generalized mechanisms

$$\begin{cases} T_a = (0 & 0 & 1; & 0 & 0 & 0)^T \\ T_{cx} = (1 & 0 & 0; & 0 & z_c & -y_c)^T \\ T_{cy} = (0 & 1 & 0; & -z_c & 0 & x_c)^T \\ T_{cz} = (0 & 0 & 1; & y_c & -x_c & 0)^T \\ T_{dy} = (0 & 1 & 0; & -z_d & 0 & x_d)^T \\ T_{dz} = (0 & 0 & 1; & y_d & -x_d & 0)^T \\ T_e = (0 & 0 & 1; & 0 & -x_e & 0)^T \end{cases} . \quad (25)$$

Obviously, there is no common constraint. So the order is $d = 6$. And $v = 0, \zeta = 0$. Also, there is no flexible element, so the minimal and the maximal DOFs are equal.

$$F_{min} = F_{max} = 6 \times 3 - 5 \times 2 - 4 - 3 + 0 - 0 = 1. \quad (26)$$

Compared with Fig. 3a, the mechanism shown in Fig. 3b changes the rigid link 3 to a helical spring, the DOFs are:

$$\begin{aligned} F_{min} &= 6 \times 3 - 5 \times 2 - 4 - 3 + 0 - 0 = 1 \\ F_{max} &= 1 + 1 = 2. \end{aligned} \quad (27)$$

Without considering the deformation of the helical spring, the mechanism shown in Fig. 3b can be equivalent to a spatial four-bar mechanism whose rigid DOF is 1. However, the deformation of the helical spring offers the relatively axial translation, which makes the mechanism satisfy the length condition of the crank-rocker mechanism in arbitrary link size, i.e. $L_2 + L_3 \leq L_1 + L_4$. The mechanism is thus changed into a special crank-rocker mechanism with an enlarged work space.

Based on Fig. 3b, the twist system of the mechanism in Fig. 3c is composed of T_a, T_{dy}, T_{dz} and T_e , which are the same as Eq. (25). And the common wrenches is:

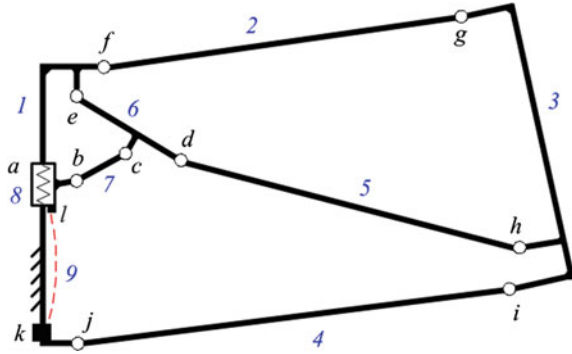
$$\begin{cases} W_1 = (0 & 0 & 0; & 1 & 0 & 0)^T \\ W_2 = (0 & 1 & 0; & 0 & -x_d & 0)^T \end{cases} . \quad (28)$$

It is noted that the number of common constraints in the mechanism is 2, the order is $d = 6 - 2 = 4$. And $v = 0, \zeta = 0$. Then DOFs of the mechanism is:

$$\begin{aligned} F_{min} &= (6 - 2) \times 4 - (5 - 2) \times 2 - (4 - 2) - (6 - 2) - (6 - 2) \times 2 + 0 - 0 = -4 \\ F_{max} &= -4 + (5 + F_{st} - 2) + 1 + (6 - 2) + 1 = 5 + F_{st}. \end{aligned} \quad (29)$$

It is noted that due to the number of common constraints is 2, the mobilities of flexible link and the cable are [4, 8] and [4, 7 + F_{st}], in which F_{st} is the cable mobility that limits the work space. The constraints of the solid joint, revolute pair and pre-tensioned revolute pair are 4, 3 and [3, 4], respectively.

Fig. 4 Deployable unit of ETS-VIII



4.2 Example 2

As shown in Fig. 4, the generalized mechanism is a deployable unit of the large deployable reflector antenna, ETS- VIII [20]. The pre-tensioned prismatic joint *a* assembled in member 1 is the deployment driver. The spring drives the antenna by member 8, and the cable (member 9) is used for controlling the development. And the DOFs are calculated in Eq. (30).

$$\tilde{F} = (3 \times 8 + [3, 5 + F_{st}]) - ([2, 3] + 2 \times 9 + 3 \times 2) - 3 = [-3, F_{st}]. \quad (30)$$

It is noted from Eq. (30) that the minimal DOF of the deployable unit is -3 , because of the rigidity of the pre-tensioned prismatic joint and the triangle constituted by members 1, 8 and 9, which makes it become a statically indeterminate structure. And the maximal DOF is the cable mobility which controls the development.

5 Conclusions

A new kind of mechanism named the generalized mechanism is first defined in this paper. Then the minimal and the maximal DOFs of generalized mechanisms are developed. Some conclusions are summed up as follows.

Based on screw theory, both the minimal and maximal mobilities of generalized links and the constraints of generalized kinematic pairs are analyzed by the motion spaces and constraint spaces. And then three formulas are established for calculating the DOFs of the generalized mechanisms.

Both the mobilities of generalized links and the constraints of kinematic pairs are affected by the physical dimension, material and the external loads. And the DOFs of the generalized mechanisms are thus affected by the above factors. The DOF of a generalized mechanism is always not a unique value, but an interval value.

The generalized links such as flexible links, springs and cables are able to enlarge, limit and control the work space of the generalized mechanisms.

Acknowledgments This project is supported by National Natural Science Foundation of China (Grant No. 51375360).

References

1. McCarthy JM (2013) 21st century kinematics. Springer, Berlin
2. Gogu G (2009) Structural synthesis of parallel robots: part I: methodology. Springer, Oshawa
3. Howell LL (2001) Compliant mechanisms. Wiley, New York
4. Dai JS, Jones JR (1999) Mobility in metamorphic mechanisms of foldable/erectable kinds. *J Mech Des* 121(3):375–382
5. Baker JE (1978) Overconstrained 5-bars with parallel adjacent joint axes—I method of analysis. *Mech Mach Theory* 13(2):213–218
6. Arsenault M, Gosselin CM (2006) Kinematic, static and dynamic analysis of a planar 2-DOF tensegrity mechanism. *Mech Mach Theory* 41(9):1072–1089
7. Zhang D (2010) Parallel robotic machine tools. Springer, Oshawa
8. Howell LL, McLain TW, Baker MS, Lott CD (2006) MEMS/NEMS handbook, techniques and applications. Springer, New York
9. Ying M, Sunil K (2012) Design of a cable-driven arm exoskeleton (CAREX) for neural rehabilitation. *IEEE Trans Rob* 28(4):922–931
10. Darwin L, Denny O, Saman KH (2013) Generalized modeling of multilink cable-driven manipulators with arbitrary routing using the cable-routing matrix. *IEEE Trans Rob* 29(5):1102–1113
11. Hermann R (1999) ARTEMIS: a telemanipulator for cardiac surgery. *Eur J Cardiothorac Surg* 16(2):S106–S111
12. Schurr MO, Buess G, Neisius B, Voges U (2000) Robotics and telemanipulation technologies for endoscopic surgery. *Surg Endosc* 14(4):375–381
13. Parag WD, Michele D, Joel L, Jacques M (2011) Minimally invasive single-site surgery for the digestive system: a technological review. *J Minim Access Surg* 7(1):40–51
14. Haber GP, Autorino R, Laydner H, Yang B, White MA, Hillyer S, Altunrende F, Khanna R, Spana G, Wahib I, Fareed K, Stein RJ, Kaouk JH (2012) SPIDER surgical system for urologic procedures with laparoendoscopic single-site surgery: from initial laboratory experience to first clinical application. *Eur Urol* 61(2):415–422
15. Tibert G (2002) Deployable tensegrity structures for space applications. Royal Institute of Technology, Stockholm
16. Miura K, Miyazaki Y (1990) Concept of the tension truss antenna. *AIAA J* 28(6):1098–1104
17. Li TJ (2012) Deployment analysis and control of deployable space antenna. *Aerosp Sci Technol* 18(1):42–47
18. Thomson MW (1999) The astromesh deployable reflector. In: Proceedings of IEEE of antennas and propagation society international symposium, pp 1516–1519
19. Gulyaev VI, Gaidaichuk VV, Chernyavskii AG, Scialino L (2003) Dynamic behavior of a large deployable reflector. *Int Appl Mech* 39(9):1084–1088
20. Meguro A, Tsujihata A, Hamamoto N, Homma M (2000) Technology status of the 13 m aperture deployment antenna reflectors for engineering test satellite VIII. *Acta Astronaut* 47(2–9):147–152
21. Gogu G (2005) Mobility of mechanisms: a critical review. *Mech Mach Theory* 40(9):1068–1097

22. Huang Z, Li QC (2003) Type synthesis of symmetrical lower-mobility parallel mechanisms using the constraint-synthesis method. *Int J Robot Res* 22(1):59–79
23. Her I, Midha A (1987) A compliance number concept for compliant mechanisms, and type synthesis. *J Mech Des* 109(3):348–357
24. Chen GM, Li DL (2010) Degree of freedom of planar compliant mechanisms. *J Mech Eng* 46(13):48–53
25. Su HJ, Dorozhkin DV, Vance JM (2009) A screw theory approach for the conceptual design of flexible joints for compliant mechanisms. *J Mech Robot* 105(4):469–484
26. Su HJ, Tari H (2010) Realizing orthogonal motions with wire flexures connected in parallel. *J Mech Des* 132(12):121002–121008
27. Su HJ (2011) Mobility analysis of flexure mechanisms via screw algebra. *J Mech Robot* 3(4):04101–041010

Research on the Mechanism of Alternating Temperatures on Space Bearing Preload

Fengping Ning, Jiantao Yao, Ruiqin Li and Yongsheng Zhao

Abstract The main purpose of this paper is to research the influence of alternating temperatures on space bearing and to provide theoretical guidance for establishing the model of the preload and determining initial preload. Considering the assembly tolerance of the bearing and the thermal deformation of shaft-bearing system, the prediction model of the preload is established and verified by experiment. The laws are revealed that how the mechanical property changes with the alternating temperatures. As alternating temperatures increasing, the interference of the outer ring decreases and the inner ring increases. Compared with the situation without considering the interference, the variation of the preload is larger when the interference is considered. The preload increases with the axial load increasing. Furthermore, the preload decreases with the initial interference when the alternating temperature is above room temperature. The range of the preload is studied to ensure the reliable operation of the revolute joint in spacecraft mechanism.

Keywords Alternating temperatures · Bearing · Preload · Failure · Reliability

1 Introduction

With the rapid development of the spacecraft mechanism technology, the structure and motion performance of mechanism become more and more complicated [1–3]. Meanwhile, the reliability requirements are increasingly improved. As one of the

F. Ning (✉) · R. Li
School of Mechanical and Power Engineering, North University of China,
Taiyuan 030051, China
e-mail: ning_fengping@163.com

J. Yao · Y. Zhao
Parallel Robot and Mechatronic System Laboratory, Yanshan University,
066004 Qinhuangdao, China

most basic components of spacecraft mechanism, preload has a significant effect on the performance of spacecraft mechanism. Alfares [4] and Gunduz [5] studied the influence of preload on dynamics performance, stability and modal characteristics of shafting. The thermal deformation of spindle and bearing leads to the change in preload under alternating temperature. Bearing may not be able to meet the preload requirements. Thus, the research on the mechanism of alternating temperatures on preload has a special meaning to ensure the reliable operation of mechanism in the extreme conditions of high-low temperature and alternating temperatures.

Bossmanns [6] predicted the temperature distribution of the spindle system by using the thermal-mechanical coupling model. Lin [7] constructed the temperature mutation preload model on this basis. And based on this model, Hu [8] predicted the thermal preload variation of angular contact ball bearing at different speeds. Following this model, Gao [9] did the corresponding research in their own studies.

Considering the working conditions, Kim [10, 11] established a comprehensive model to forecast the thermal and mechanical properties of the spindle-bearing system. Yang [12] proposed the design methods that can automatically adjust the preload. Wu [13] designed a device to meet the needs of aerospace bearings in different working conditions, the preload of which is adjustable. However, the temperature change will lead to changes in bearing assembly tolerances and further changes in preload, which are not taken into consideration in above studies.

Considering the bearing assembly tolerance and shaft-bearing system thermal deformation, this paper focused on the shaft-bearing system of spacecraft mechanism. The influence of alternating temperatures on the mechanism of preload and the mechanical properties of bearing axial stiffness are studied, and the variation of preload at different temperatures is verified by experiment.

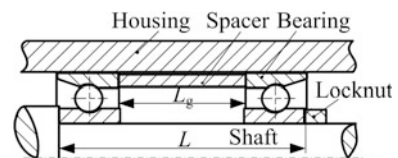
2 Deformation Analysis of Shaft-Bearing System

2.1 Bearing Deformation Under Assembly Pressure

Bearings are usually used in interference fit, mounted on the shaft or housing to avoid the fretting corrosion [14]. Figure 1 is the shaft-bearing system, in which the assembly mode between the inner ring and the shaft is interference fit, and the assembly mode between the outer ring and the housing is transition fit.

Assume that the bearing ring is thin-wall ring while analyzing the deformation of rings under assembly pressure [14]. If the interference of the inner ring is I_i , the

Fig. 1 The shaft-bearing system



inner radius of inside ring and inner raceway are R_i and r_i , respectively, then the swelling increment of inner raceway that caused by the assembly pressure will be

$$u_{i0} = \frac{R_i r_i I_i / (r_i^2 - R_i^2)}{\left[\left(\frac{r_i^2 + R_i^2}{r_i^2 - R_i^2} + \mu_b \right) + \frac{E_b}{E_s} (1 - \mu_s) \right]} \tag{1}$$

where, E_b and E_s refer to elastic modulus of bearing and spindle. Likewise, μ_b and μ_s refer to Poisson’s ratio of bearing and spindle, respectively.

In the same way, if the interference of the outer ring is I_o , the outer radius of outside ring and the radius of outer raceway are R_o and r_o , respectively, then the swelling increment of outer raceway that caused by the assembly pressure will be

$$u_{oi} = \frac{R_o r_o I_o / (R_o^2 - r_o^2)}{\left[\frac{E_b}{E_h} \left(\frac{R_h^2 + r_h^2}{R_h^2 - r_h^2} + \mu_h \right) + \left(\frac{R_o^2 + r_o^2}{R_o^2 - r_o^2} - \mu_b \right) \right]} \tag{2}$$

where, E_h and μ_h respectively refer to elastic modulus and Poisson’s ratio of bearing housing, and, r_h and R_h stand for the inner and outer surface radius of the housing.

The initial radial clearance and initial contact angle of bearings will change under the assembly pressure. The radial clearance reduction that caused by the compression on bearing inner and outer ring will be

$$\Delta u_r = u_{oi} + u_{i0} \tag{3}$$

After assembly, the contact angle becomes

$$\alpha_1 = \arccos^{-1} \left[1 - \frac{u_r - \Delta u_r}{2BD_w} \right] \tag{4}$$

where, BD_w is the distance between the curvatures centers of the inner and outer raceway.

2.2 Thermal Deformation of Spindle-Bearing System

The friction heat of space bearing that operating at the light load and low speed is both little and negligible. Alternating temperatures becomes the main reason leading to the thermal deformation in spindle-bearing system. Space bearings are usually installed at room temperature. It will cause corresponding thermal deformation when it works at space environment, which is ΔT higher than room temperature.

Bearings will show the linear expansion and changes in structural parameters with the ambient temperature. The deformation amount of the inner raceway radius is

$$\Delta r_i = \alpha_b r_i \Delta T \quad (5)$$

where, α_b represents thermal expansion coefficient of bearing material.

The deformation amount of the outer raceway radius is

$$\Delta r_o = \alpha_b r_o \Delta T \quad (6)$$

The deformation amount of the rolling ball diameter is

$$\Delta D_w = \alpha_b D_w \Delta T \quad (7)$$

By the Eqs. (5)–(7), it obtains the reduction of the initial radial clearance.

$$\Delta u_{r1} = \alpha_b u_r \Delta T \quad (8)$$

Width variation of bearings after thermal deformation is given as follow:

$$B' = (1 + \alpha_b \Delta T) B \quad (9)$$

In the fitting position, the inner diameter of the bearing inner ring and the spindle diameter are D_i and d_s . The deformation can be calculated as follows, respectively

$$\Delta D_i = \alpha_b D_i \Delta T \quad (10)$$

$$\Delta d_s = \alpha_s d_s \Delta T \quad (11)$$

where, α_s represents the thermal expansion coefficient of shaft material.

According to the deformation coordination, the variable quantity of interference where bearing and spindle fit each other after the thermal deformation becomes

$$\Delta I_{iT} = (\alpha_s - \alpha_b) D_i \Delta T \quad (12)$$

Similarly, the variable of interference at the fitting area of outer ring is given by

$$\Delta I_{oT} = (\alpha_b - \alpha_h) D_o \Delta T \quad (13)$$

where, α_h represents the thermal expansion coefficient of housing material.

For the spindle-bearing system, L is the original spindle length and the length after thermal deformation becomes

$$L' = (1 + \alpha_s \Delta T)L \tag{14}$$

The length of spacer between bearings after thermal deformation becomes

$$L'_g = (1 + \alpha_g \Delta T)L_g \tag{15}$$

where, α_g represents the thermal expansion coefficient of spacer material.

3 Influence of Alternating Temperatures on Bearing Preload

As is shown in Fig. 2, it keeps certain pressure and elastic deformation between the ball and two rings. Meanwhile, the relative axial movement is produced between inner and outer rings under the preload force. The relationship between the radial clearance and axial deflection of bearing can be given by the following formula

$$\left(\frac{u_a}{2} + \delta_a\right)^2 + \left(BD_w - \frac{u_r}{2}\right)^2 = (BD_w + \delta_n)^2 \tag{16}$$

where, δ_a and δ_n represent an axial deflection and a normal deflection, respectively.

The relationship between the axial deflection δ_a and the actual contact angle α is

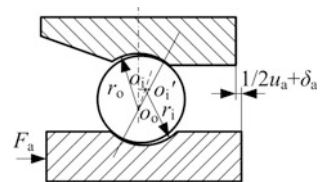
$$\delta_a = BD_w(\cos \alpha_0 \tan \alpha - \sin \alpha) \tag{17}$$

Both the assembly tolerance and the shapes will change in alternating temperatures, leading to the change in the compression deformation of balls and then the preload.

When the ambient temperature changes, the variation of radial clearance is Δu_{r1} , the distance between the curvature centers of the inner and outer raceway becomes BD_w' and the variable of interference at the fitting area of outer ring which are ΔI_{iT} and ΔI_{oT} , respectively. Combining the two Eqs. (1) and (2) yields the variable of the inner and outer raceway are Δu_{io} and Δu_{oi} . Therefore, the radial clearance in alternating temperatures can be given as follow

$$u_{rT} = u_r + \Delta u_{r1} - \Delta u_{io} - \Delta u_{oi} \tag{18}$$

Fig. 2 Angular contact ball bearing under preload



The bearing contact angle turns to be

$$\alpha_T = \arccos^{-1} \left[1 - \frac{u_{rT}}{2BD'_w} \right] \quad (19)$$

Substituting u_{rT} into Eq. (16) yields the relationship between the radial clearance and axial deflection of bearing in alternating temperatures

$$\left(\frac{u'_{aT}}{2} + \delta'_a \right)^2 + \left(BD'_w - \frac{u'_{rT}}{2} \right)^2 = (BD'_w + \delta'_n)^2 \quad (20)$$

Combined with Figs. 1 and 2, the geometric relationship among the spindle length, bearing width and spacer length can be given by

$$L = L_g + 2B - 2 \left(\frac{1}{2} u_a + \delta_a \right) \quad (21)$$

where, u_a refers to the radial clearance and δ_a refers to the axial deformation amount at room temperature.

The above geometric relationship after thermal deformation becomes

$$L' = L'_g + 2B' - 2 \left(\frac{1}{2} u_{aT} + \delta'_a \right) \quad (22)$$

where, δ'_w refers to the axial deformation amount after thermal deformation.

Substituting BD'_w into (17) yields the actual contact angle

$$\delta'_a = BD'_w (\cos \alpha_T \tan \alpha'_T - \sin \alpha'_T) \quad (23)$$

The relation between preload and the actual contact angle after thermal deformation obey the following equation

$$\frac{F'_{aT}}{ZK_n (BD'_w)^{3/2}} = \sin \alpha'_T \left(\frac{\cos \alpha_T}{\cos \alpha'_T} - 1 \right)^{3/2} \quad (24)$$

where, K_n represents the load-displacement coefficient.

Considering the assembly tolerance of the bearing and the thermal deformation, the prediction model of the preload in alternating temperatures is established.

4 Bearing Preload Test System

Experimental research on the influence of alternating temperatures on bearing preload was conducted to verify the theoretical analysis. Bearing preload test system is shown in Fig. 3, which consists of bearing preload test device, DC power supply, signal acquisition system, high-low temperature laboratory box and data display, etc.

The bearing preload test device is shown in Fig. 4, the “back to back” mode was taken to install bearing pairs. Fitting mode between the bearing and the main shaft is interference fit. Replacing the sleeve between the bearing pairs with sensor 2, sensor 1 is installed between the bearing and the locknut. The orientation and axial preload of bearings can be adjusted by the locknut. Sensor 1 is used for measuring the axial force applied by the locknut. Sensor 2 plays the role of spacer, measuring the actual bearing preload between the bearing pairs at the same time.

There exists friction at the fitting area. In other words, the actual preload applied on the bearing has something to do with the tightening torque and bearing friction. The shaft-bearing test system without housing was used to study the influence of

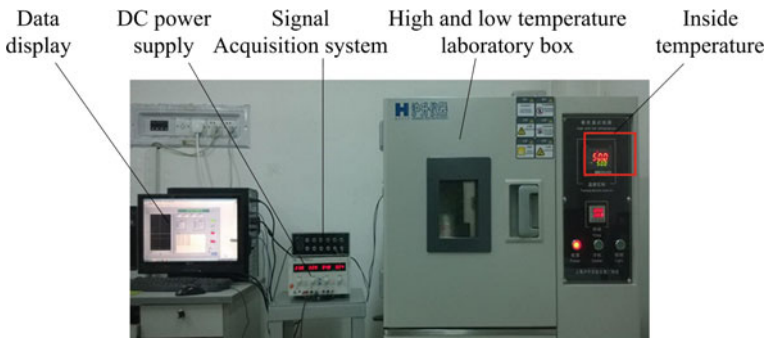


Fig. 3 Bearing preload test system

Fig. 4 Bearing preload test device

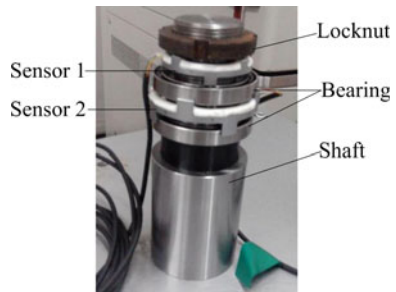


Table 1 Physical properties of the materials [15]

Material	Elastic modulus (GPa)	Poisson's ratio	Thermal expansion coefficient ($10^{-6}\text{m}^{\circ}\text{C}$)
9Cr18	200	0.30	10.5
TC4	110	0.33	9
40CrNiMoA	210	0.29	12.8

Table 2 Geometric parameters of angular contact ball bearing (NSK71807C)

Parameters	Value
D_i (mm)	35
D_o (mm)	47
d_i (mm)	37.694
d_o (mm)	43.976
d_m (mm)	40.835
B (mm)	7
D_w (mm)	3.135
Z	25

assembly tolerance and alternating temperatures on preload. If the friction between the spindle and bearings is the only factor brought, the preload will be

$$F_a = F - f \quad (25)$$

where, F refers to the axial force applied by lock nut, but f refers to the bearing friction between shaft and bearing, which is related to the assembly tolerance.

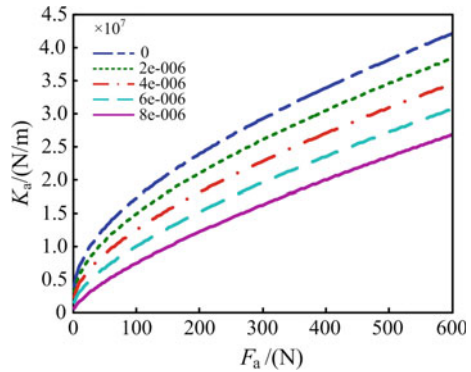
The bearing designation in the test system is angular contact ball bearings (71807C), which is made of 9Cr18. The materials of the spindle and the sensor are TC4 and 40CrNiMoA, respectively. Physical properties of the materials in shaft-bearing test system are shown in Table 1. Geometric parameters of the angular contact ball bearing (NSK71807C) are shown in Table 2.

5 Results of Simulation and Test

The variation of mechanical properties is analyzed with the dual effect of assembly tolerance and alternating temperatures. The change rules of the axial stiffness and preload are also studied by taking the shaft-bearing system as the research object.

The change rule of the stiffness which follows the change of axial preload in different inner ring assembly tolerances situations is shown in Fig. 5. The axial stiffness increases with the axial preload when the assembly tolerance keeps the same. However, the increasing amplitude will shrink gradually. Both the radial clearance and the contact angle will decrease as a result of the increase in the

Fig. 5 Relation between axial stiffness and preload



interference, which is the reason why the inner ring interference increases while the axial stiffness decreases with the same axial preload. The larger the interference is, the huger the axial preload is required for the same bearing to reach the same axial stiffness.

In the spindle-bearing system, assume interference of the inner ring and the outer ring is 5 and 1.5 μm , respectively. The change rule of interference following the variation of alternating temperatures is shown in Fig. 6. The interference of inner ring decreases with the rise of temperature, but the interference fit of outer ring shows the opposite trend. The thermal expansion coefficient of bearing material (9Cr18) is bigger than the spindle and housing materials (TC4). The failure on connections between the inner ring and the spindle, even loose phenomenon, will occur at extreme high temperature if the initial interference of inner ring is less than a certain value. Simultaneously, the failure on connections between the outer ring and housing will occur at extreme low temperature. The failure mechanism is that the assembly pressure is close to zero, even that fretting wear occurs in contact area.

The relation between alternating temperatures and preload is shown in Fig. 7. If the initial preload is set 150 N, the compression deformation of roller ball will increase, but the axial preload will show a totally opposite trend with the increasing

Fig. 6 Effect of alternating temperatures on the assembly tolerance

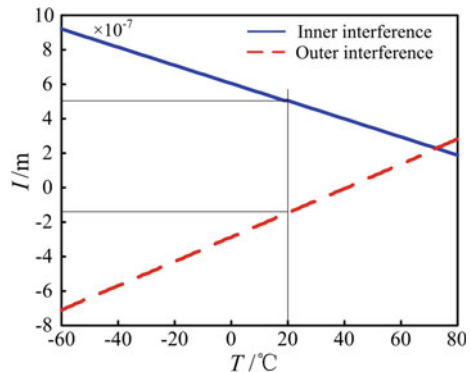
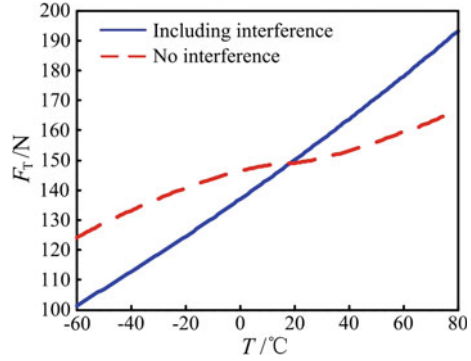


Fig. 7 Relation between alternating temperatures and preload



alternating temperature. Compared with the situation without considering the interference, the variable of axial preload will increase under the influence of alternating temperatures when the interference is taken into consideration. The interference at the fitting area changes in alternating temperatures, leading to the thermal deformation in spindle-bearing system, and then the corresponding change in preload.

Figure 8 shows the simulation and experimental results alternating temperature influence on the preload. There is deviate between the theoretical and experimental data, but the experiment data verify correctness of the theoretical analysis. It can be seen from Fig. 8 that the bearing interference responds to the change in temperature, which will lead to the corresponding change in preload. The reason why the experimental results deviate from the simulation results at high and low temperatures is that the bearing friction at the fitting area responds to changes with alternating temperatures as well.

In engineering practices, the axial preload increases with the rise of temperature for the bearing pairs installed with “back to back” mode. The reason is that the temperature of spindle and the bearing inner ring higher than outer ring and spacer, which results in thermal deformation of shaft larger than the sum of outer ring and spacer. In spacecraft mechanism, when temperature increases, the sum of

Fig. 8 Result of test and simulation

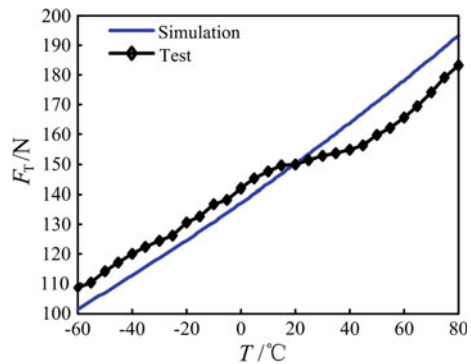
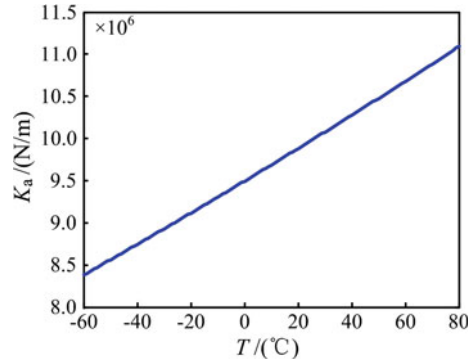


Fig. 9 Effect of alternating temperatures on axial stiffness



thermal deformation of the spacer in length and the bearing outer ring in width is larger than the change of spindle in width, which results in the increasing of the preload. Similarly, while temperature decreases, preload becomes smaller.

The effect of alternating temperatures on axial stiffness is shown in Fig. 9 when the initial preload is set 150 N. As seen in the figure, both the axial preload and the axial stiffness increase when alternating temperature rises.

6 Conclusion

The influence of assembly tolerance, alternating temperatures and axially mounted load and axial stiffness of mechanical properties was simulated, and then the experiment was conducted on the effect of alternating temperatures on preload.

- (1) The inner ring interference increases but the axial stiffness decreases with the same axial preload. The larger the interference is, the more hugely the axial preload is required for the same bearing to reach the same axial stiffness.
- (2) The increase of alternating temperatures result in increasing of interference of outer ring, and it is opposite in inner ring. If the initial interference of inner ring is chosen inappropriately, the connections failure will occur at extreme temperature, scilicet loose phenomenon at contact surface.
- (3) For the bearing pairs installed with “back to back” mode, the axial preload increases with the rise of alternating temperatures. Compared with no considering the interference, the variable of axial preload will increase more under the influence of alternating temperatures when the interference is taken into consideration.
- (4) The axial stiffness on bearings increases when alternating temperatures rises. While alternating temperature is above room temperature, the preload decreases with the initial interference increasing. The change rule of the preload will turn to the opposite if the alternating temperature is below room temperature.

Acknowledgments This research was financially supported by the Major State Basic Research Development Program of China (973 program) under Grant 2013CB733000 and Research Fund of North University of China under Grant XJJ2016003.

References

1. Yu DY, Yang JZ, et al. (2011) The spacecraft mechanism technology. China Science and Technology Press, Beijing, pp 27–31
2. Chen YS, Zhang HB (2011) Review and prospect on the research of dynamics of complete aero-engine systems. *Acta Aeronautica Et Astronautica Sinica* 32(8):1371–1391
3. Wang Z, Guo WC (2014) Analysis on the relationship between bearing preload of space arm compensation mechanism and system stiffness. *Chin Optics* 7(6):989–995
4. Alfares MA, Elsharkawy AA (2003) Effects of axial preloading of angular contact ball bearings on the dynamics of a grinding machine spindle system. *J Mater Process Technol* 136(1):48–59
5. Gunduz A, Dreyer JT, Singh R (2012) Effect of bearing preloads on the modal characteristics of a shaft-bearing assembly: experiments on double row angular contact ball bearings. *Mech Syst Signal Process* 31:176–195
6. Bossmanns B, Tu JF (1999) A thermal model for high speed motorized spindles. *Int J Mach Tools Manuf* 39(9):1345–1366
7. Lin CW, Tu JF, Kamman J (2003) An integrated thermo-mechanical-dynamic model to characterize motorized machine tool spindles during very high speed rotation. *Int J Mach Tools Manuf* 43(10):1035–1050
8. Hu T, Yin GF, Deng CY (2014) Integrated thermo-mechanical model and analysis of angular contact ball bearing. *J Sichuan Univ (Engineering Science Edition)* 46(4):189–198
9. Gao SH, Meng G, Long XH (2010) Stability prediction in high-speed milling including the thermal preload effects of bearing. *Proc Inst Mech Eng Part E: J Process Mech Eng* 224(1):11–22
10. Kim SM, Lee SK (2001) Prediction of thermo-elastic behavior in a spindle-bearing system considering bearing surroundings. *Int J Mach Tools Manuf* 41(6):809–831
11. Kim SM, Lee SK, Lee KJ (2002) Effect of bearing surroundings on the high-speed spindle-bearing compliance. *Int J Adv Manuf Technol* 19(8):551–557
12. Yang QD, Wang KS, Meng LX et al (2008) Design method of automatic adjustment of bearing preload based on thermal characteristic of materials. *Chin J Mech Eng* 44(9):183–187
13. Wu C, Liu XH (2007) Study on the active preload technology of space rolling bearing. *Sci Technol Eng* 7(17):4538–4539
14. Harris TA, Kotzalas MN (2006) Essential concepts of bearing technology: rolling bearing analysis. CRC press, Boca Raton
15. Yan MG (2002) China aviation materials handbook, Volume 4 Titanium copper alloy, 2nd edn. China standard press, Beijing, pp 705–709

Development of a Continuously Statically Balanced Tablet Computer Stand

Hsu-Kai Tsai, You-Shen Chen and Chin-Hsing Kuo

Abstract This paper presents the design and prototype of a tablet computer stand able to be statically balanced at any operation angle. First, we introduce the mechanism design of the stand, in which the cylindrical cam, damper and spring are used. Then, we verify the static balancing condition of the proposed mechanism via its force equations. Last, we built a prototype, testing that the stand can support the tablet computer in any inclined angle and can automatically return back to original place when it is not in use.

Keywords Gravity compensation · Statically balanced mechanism · Static balancing · Monitor stand

1 Introduction

Tablet computer stand is a mechanical device for supporting tablet computers or monitors steadily staying, i.e., being statically balanced, on table at specific angles. A continuously supported tablet computer stand is a mechanism able to support the tablet computer or monitor staying at any inclined angle within the specified range of motion, that is, the stand mechanism is statically balanced. Figure 1 shows a commercially available continuously supported tablet computer stand.

Two issues are generally discussed when designing continuously supported tablet computer stands, that are, the functions of static balancing and automatic return. For static balancing, there are already various designs disclosed in patent

H.-K. Tsai (✉) · Y.-S. Chen · C.-H. Kuo

Department of Mechanical Engineering, National Taiwan University of Science and Technology, 43, Sec. 4, Keelung Rd, Taipei 106, Taiwan
e-mail: m10403101@mail.ntust.edu.tw

Y.-S. Chen
e-mail: b10031008@mail.ntust.edu.tw

C.-H. Kuo
e-mail: chkuo717@mail.ntust.edu.tw

Fig. 1 Continuously supported tablet computer stand [1]



documents. For example, Xue [2] raised a mechanism that a spring in the stand can expand outward to hold and bring a gear to produce a blocking force at the demanded inclined angle. Chang and Yeh [3] proposed a bi-axis mechanism with blocking cams. One of the axis can rotate up to 360° and lock at some specific angle due to its profile design. Chen [4] presented a mechanism that the friction force produced by plastic sleeve is used to make the tablet staying at any angle.

For automatically returning, there are two kinds of stands for this purpose. Lin [5] used a cam mechanism to generate the returning force for the stand. Huang et al. [6] made a compression spring working with the cam for stand returning motion. On the other hand, Ahn et al. [7] designed an outer shell shape for a cam, in which the outer shell will compress the inner spring to produce demanded force for automatically returning. In summary, the above three patents all apply cams to transform a rotational motion to a translational motion for actuating a tensile or compressive spring. Then, the spring will be compressed or stretched to provide returning force for the target object. On the other hand, Kang et al. [8] applied gear train to produce a blocking force for locking the stand in required position. Lin [9] and Yi et al. [10] filed two patents in which the profile of a cam and the oil in sleeve can achieve the returning motion and slow down the stand in case hitting the tablet. Jiang [11] applied protrusion as latch and gasket to make the mechanism return automatically and slowly in specific range of degrees.

One common approach for making mechanisms statically balanced is the employment of springs. For example, Nathen [12] proposed the fundamental concept of using one spring to balance a rotating hinged body. Herder [13] summarized a couple of spring-based approaches for static balancing. Gosselin [14] introduced several balancing methods that apply the springs into spatial parallel mechanisms. Kuo and Lai [15] mentioned a multi-degree-of-freedom manipulator with attached springs for balancing purpose in operating room. The static balancing technique has also been successfully used for monitor stands. Hsiu et al. [16] proposed a design which using the springs, pulleys and wires to balance lifting desktop monitors.

The objective of this work is to design a torsional-spring tablet computer support that possesses the functions of static balancing and automatic returning. In what follows, the design concept is introduced first. Then, a design example of the proposed mechanism is provided with and without considering friction. Finally, a prototype is manufactured and tested.

2 Mechanism Design

The mechanism we designed is a one-axis design as shown in Fig. 2. The name of each part as list in Table 1. We apply two-set pivots with a U shape stand to be our statically balanced mechanism. The main idea is that the washer can provide torsional spring a pre-loading angle to make it compensating the weight of the tablet computer. And, the cams are the main part to provide a range of specific angle for dampers to work, which can be rotated by the stand. The working procedure of the mechanism is introduced below.

In the beginning state, as shown in Fig. 3, the torsion spring (Part 11) will constantly give a force to the stand because of the pre-compressed angle imposed by Part 2. In the standing state, the tablet monitor, the stand and the table together form a triangle. When the stand (Part 16) rotates, the torsional spring will be tightened so as to drive the cylindrical cam (Part 5) toward the fixed cam (Part 4).

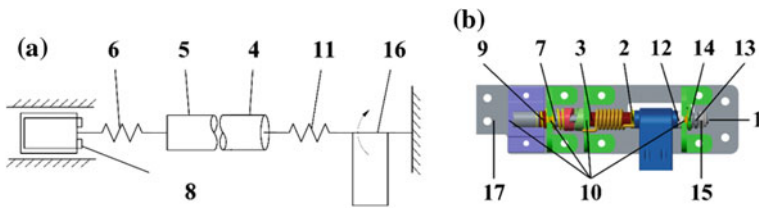


Fig. 2 Schematic diagram of one side of rotating tablet stand. a Concept. b CAD model

Table 1 Main mechanical parts of the proposed design in Fig. 2

No.	Name	No.	Name
1	Main axle	2	Washer
3	Sleeve	4	Fixed cam
5	Cylindrical cam	6	Compressed spring
7	Axial linking part	8	Damper
9	Damper part	10	Fixture
11	Torsional spring	12	Washers with bumps
13	Washer	14	Blocking washer
15	Nut	16	Stand leg
17	Base (attached to the tablet)		

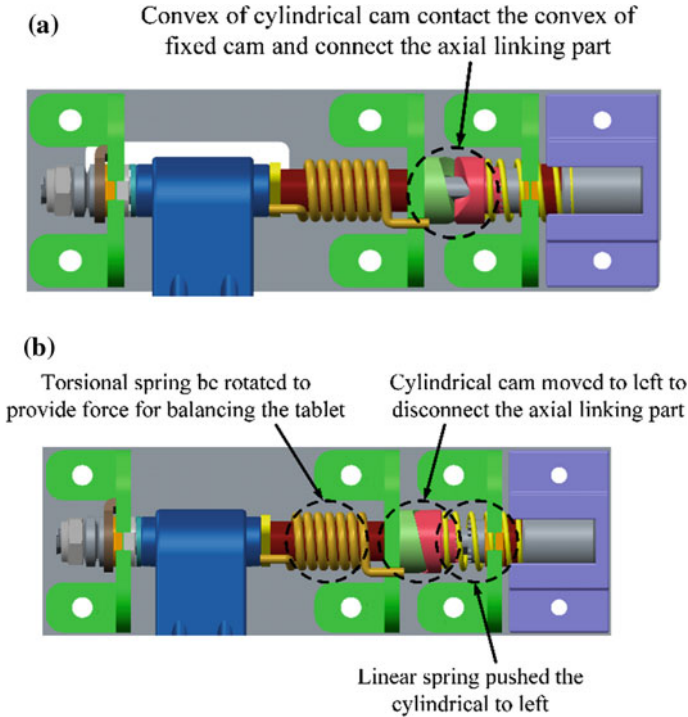


Fig. 3 Operation states. **a** Beginning state. **b** Standing state

In this state, the mechanical system is statically balanced. When the stand off the table, the stand doesn't have the weight force from tablet. Therefore, the torsional spring will force the stand starting to return back because the statically balanced condition is changed. When the stand is closed to the tablet monitor, the damper (Part 8) will start to rotate because of the gear surface of the axial linking part (Part 7) attached to damper linking part (Part 9). Owing to the function of the damper, the returning force can be reduced. As a result, the whole operation can be divided to two states, which are explained as follows.

2.1 Beginning State (Fig. 3a)

When the mechanism is in the beginning state, the stand (Part 16) is mainly pushed by the returning force of torsion spring (Part 11). The compressed spring (Part 6) is also pre-compressed in this state. As shown in Fig. 3a, the convex surfaces of the fixed cam (Part 4) and the cylindrical cam (Part 5) are contacted with each other. The gear surface of the cylindrical cam is to be inserted into axial linking part (Part 7).

2.2 Standing State (Fig. 3b)

As shown in Fig. 3b, when the mechanism is in the standing state, the stand is still mainly pushed by the torsional spring. In this state, the tablet monitor can stand on table or any flat surface. The range of inclined angle is limited by the blocking washer (Part 14). Because of the rotation, the convex of the cylindrical cam is in the concave of the cylindrical cam. Therefore, the cylindrical cam can close to cylindrical cam and lose the contact with the axial linking part. At the standing state, the mechanism will not contact with the axial linking part (Part 7). We use this mechanism to accomplish the purpose of automatic return. When the stand off the table, the stand will start to return back and the cylindrical cam will rotate. Until the cam rotates to a particular angle, the gear side of the cylindrical cam will be inserted into the axial linking part to actuate the damper (Part 9).

3 Static Balancing

3.1 Mathematic Model

As shown in Fig. 4, Part 1 is ground, part 2 is tablet computer, and part 3 is the stand support. θ_1 is the angle between tablet and vertical line, which is also known as working angle. θ_2 is the angle between tablet and stand support. The length of tablet monitor is assumed 0.3 m. The weights of the tablet and the stand are assumed 5.16 and 0.343 kg, respectively.

FBD of the monitor. The free-body diagram (FBD) of the monitor is shown in Fig. 5a. When the resultant and the resultant moment are zero, the system of the tablet monitor is statically balanced. The force and moment equations of the monitor is as Eqs. (1–3). F_{f12} is the friction between the table and the tablet

Fig. 4 The dimension of the stand (Unit: cm)

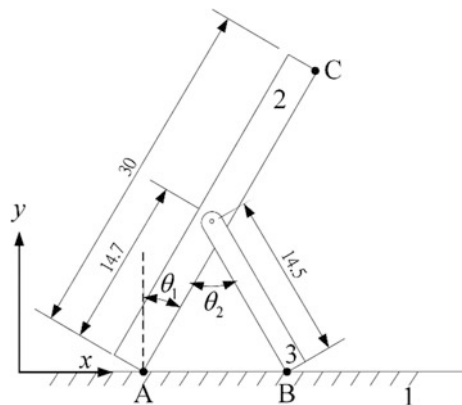
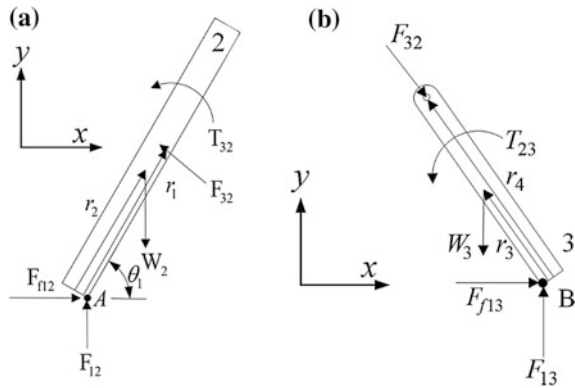


Fig. 5 Free-body diagrams. **a** Monitor. **b** Stand



monitor, F_{12} is the magnitude of the reaction force between the table and the tablet monitor, F_{32x} is the force-component of the stand to tablet monitor along the x -axis direction. F_{32y} is the force-component of stand to tablet monitor along the y -axis direction. W is the weight of tablet monitor. T_{32} is a moment applied by the torsional spring. And μ is the friction coefficient between table and tablet monitor.

$$\sum F_x = F_{32x} + F_{f12} = F_{32x}F_{12}\mu = 0. \tag{1}$$

$$\sum F_y = F_{32y} + F_{12} - W_2 = 0. \tag{2}$$

$$\sum M_A = (r_{1x}F_{32y} - r_{1y}F_{32x}) - W_2r_{2x} + T_{32} = 0. \tag{3}$$

FBD of the stand. The FBD of the stand is shown in Fig. 5b. The way of carrying out is as monitor. The force and moment equations of the stand is as Eqs. (4–6).

$$\sum F_x = F_{23x} + F_{13}\mu = 0. \tag{4}$$

$$\sum F_y = F_{23y} + F_{13} - W_3 = 0. \tag{5}$$

$$\sum M_B = (r_{4x}F_{23y} - r_{4y}F_{23x}) - W_3r_{3x} + T_{23} = 0. \tag{6}$$

Static balancing of whole system. Equations (1–6) forms a system of equations with six unknown variables F_{12} , F_{13} , F_{32} , F_{23} , T_{32} and T_{23} . Because F_{32} and F_{23} are with the same value but different direction, we consider these are the same variable. T_{32} and T_{23} are the same variables as same reason. Therefore, the unknown we want to figure out becomes to F_{12} , F_{13} , F_{23x} , F_{23y} and T_{23} . The other parameters will be

place into real data to get the answer of unknown parameters. T_{32} will be the value that we want. According to the relation between T_{32} and angle, we can know that for static balance how much force we need to input to select the match spring.

3.2 Design Example

Here we provide a numerical example to illustrate our design. The design parameters are given in Table 2. The weights and dimensions of tablet, stand and friction coefficient are given by following the practical needs. Based on these parameters, we can solve the equations list in Sect. 3.1 and the result is shown as Fig. 6. The curve in Fig. 6 is about working degree θ_3 (the angle between vertical line and tablet monitor) to required torsion torque. The value of torsion torque is getting large as the working degrees increasing. This trend is as same as the weight torque. So, compensation force can truly compensate the weight of tablet. The red line is the fitting line and its equation is $y = 0.0239x + 0.8393$. According to this equation, we can get the value K (the coefficient of elastic of spring) is 0.0239 N/m, the slope rate of this fitting line. Then, according to the K value, we can figure out the pre-pressed angle of torsional spring at working angle 15° is 52° .

Table 2 Known parameters of the mechanisms

Parameter	W_2	W_3	r_1	r_4	μ
Value	5.16 kg	0.343 kg	0.145 m	0.147 m	0.5

Fig. 6 Balancing situation of the design example

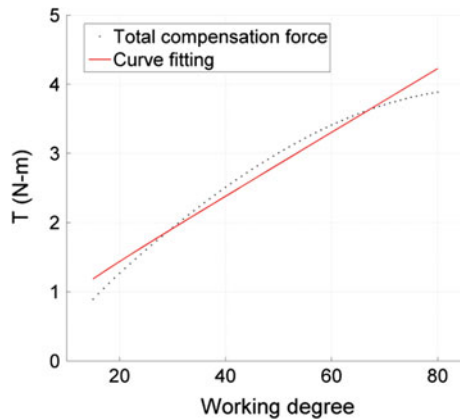
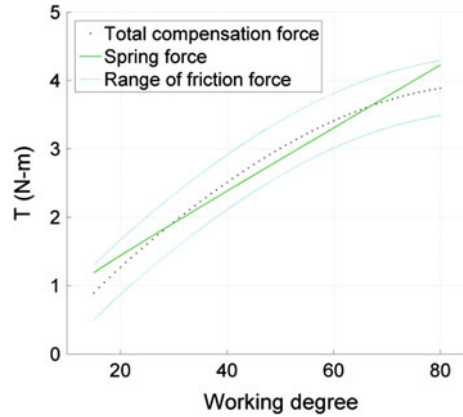


Fig. 7 Balancing situation when friction force is considered



3.3 Friction Compensation

In reality, the friction force can be used to compensate the imperfect balancing. Figure 7 shows the situation when friction is considered in the present design in Sect. 3.2. In our model, the average friction force that produces at pivot point is about 0.4 N-m. Since the friction force is always against the motion of the body, we shift the curve of spring force up and down by 0.4 N-m to represent the total balancing force made by spring and friction. As a result, the balancing for computer weight is bounded by two curves (the “range of friction force” in Fig. 7). As long as the whole curve of “total compensation force” is bounded between these two curves, the mechanism will be statically balanced in reality.

4 Prototype

After the selection of size and materials and verification of static balancing, we are going to manufacture a prototype according to these data. Using 3D drafting software Pro/E to draw part graphs including stand, spring, torsion spring, cams, dampers, fixed parts, washers etc. Then, export to engineering graphics to factory to produce each part and we assemble them.

Based on the design result in Sect. 3, a CAD model of the proposed tablet computer stand is generated as Fig. 8. Accordingly, we built a prototype as Fig. 9 and tested that the stand can balance the weight of the computer in a range of inclined angles between 15° to 80°.

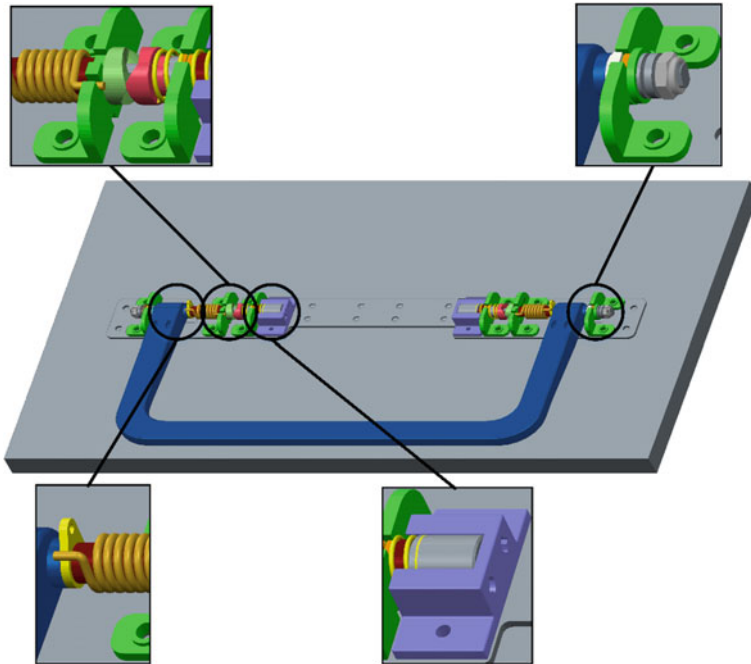
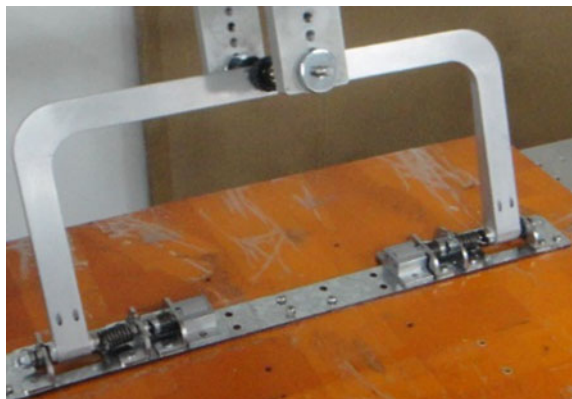


Fig. 8 CAD model of creative design of a torsional-spring tablet computer support. The picture on the left bottom corner shows the means to pre-load the torsion spring to compensate the weight of tablet. In this way, the torsion spring force can balance the weight of tablet to accomplish the static balance

Fig. 9 Prototype of the proposed tablet computer stand



5 Conclusions

We have presented the design of a continuously statically balanced tablet computer stand which can support the tablet computer staying at any angle in working space and return automatically. A new mechanism made by torsional spring, cylindrical cam and damper was devised. According to the configuration of this new mechanism, the equations of static balancing were figured out. Via the illustration of the provided numerical example, the stiffness of the torsional spring was identified from the force and moment equations. Accordingly, a prototype was manufactured and was tested, for which the mock computer can be balanced with an inclined angle between 15 and 80°. The future work would be the design for the stand returning speed, which can return fast but would not impact the monitor.

References

1. Jetart Technology Co., <http://www.jetart.com>
2. Xue H-Z (1995) Hinge can position at any angle. R.O.C. Patent No. 279578
3. Chang J-H, Yeh C-Y (2006) Pulley latch biaxial hinge. R.O.C. Patent No. M442005
4. Chen K-H (2009) Hinge can position at any angle. R.O.C. Patent No. M362286
5. Lin D (2000) Position hinge having a cam block. U.S. Patent No. 6,108,868
6. Huang C, Yang SY, Wang TH (2002) Hinge assembly. U.S. Patent No. 8,266,766
7. Ahn SH, Kim WT, Hwang HG, Cho PJ (2007) Portable terminal with hinge apparatus. U.S. Patent No. 8,437,146
8. Kang SI, Bae JG, Kim YC (2004) One step automatic hinge device and information terminal. U.S. Patent No. 6,925,684
9. Lin M-H (2007) Hinge. R.O.C. Patent No. M327626
10. Yi T-H, Yang S-Y, Lin M-H, Liang W-C, Chien C-H (2007) Hinge (II). R.O.C. Patent No. M327626
11. Chiang Y-C (2009) Positioning automatic closing of the hinge. R.O.C. Patent No. 364893
12. Nathen RH (1985) A constant force generation mechanism. *ASME J Mech Transm Autom Design* 107(4):508–512
13. Herder JL (1996) Design of spring force compensation system. *Mech Mach Theory* 33(1–2): 151–161
14. Gosselin C (2008) Gravity compensation, static balancing and dynamic balancing of parallel mechanisms. In: Wang L, Xi F (eds) *Smart devices and machines for advanced manufacturing*. Springer, London
15. Kuo C-H, Lai S-J (2015) Design of a novel statically balanced mechanism for laparoscope holders with decoupled positioning and orientating manipulation. *ASME J Mech Robot* 8 (1):015001
16. Hsiu W-H, Syu F-C, Kuo C-H (2015) Design and implementation of a new statically balanced mechanism for slider-type desktop monitor stands. *Proc Inst Mech Eng, Part C: J Mech Eng Sci* 229(9):1671–1685

Part III
Compliant Mechanism

The Local Optimum in Topology Optimization of Compliant Mechanisms

Qi Chen and Xianmin Zhang

Abstract The local optimum is widespread in topology optimization of compliant mechanisms due to the non-convex objective function. And sometimes the result is far always from the global optimum. A scheme composed of two steps is proposed to avoid most of the local optimum in topology optimization of compliant mechanisms in this article. Unlike the traditional method which starts from a uniform guess, the second step of the scheme starts from the upper bound of the objective function which is the objective function of the global optimum in some cases. The numerical example indicates that this method is useful. The theoretical upper bounds of the objective function in two formulations are deduced. And it is pointed out that in some cases, topology optimization of compliant mechanisms is a process to find a rigid-body mechanism with a certain geometrical advantage. And the geometrical advantage is depended on the boundary condition.

Keywords Local optimum · Compliant mechanisms · Topology optimization

1 Introduction

A compliant mechanism transmits the applied forces from specified input ports to output ports by elastic deformation of its comprising material, fulfilling required kinematic functions analogous to a rigid-body mechanism [1]. There are two major design methods for compliant mechanisms: pseudo-rigid-body mechanism synthesis and continuum structure optimization.

A number of techniques have been developed to design the compliant mechanisms by continuum structure optimization. Simplified isotropic material with penalization (SIMP) [2, 3] is a fundamental method and will be discuss in this

Q. Chen · X. Zhang (✉)

Guangdong Provincial Key Laboratory of Precision Equipment
and Manufacturing Technology, South China University of Technology,
Guangzhou, China
e-mail: zhangxm@scut.edu.cn

article. Many objective function of the optimization problem are proposed. Two formulations will be discussed. They are the mechanical advantage (MA) formulation and the output displacement formulation. The output displacement formulation includes an input spring to model the actuator's stiffness [4]. The output displacement is the objective function. The mechanical advantage (MA) formulation applies constrain on the input displacement [5]. The mechanical advantage is the objective function.

The objective function which maximizes mechanical or geometrical advantage [6] is found to be a non-convex function [7]. And most of the topology optimization method updates the design viable according to the sensitive analysis. Thus, the result of the topology optimization of compliant mechanisms is usually the local optimum but not a global one. Sometimes, the result is far always from the global optimum. This is a serious problem. However, the researches about the local optimum in topology optimization of compliant mechanisms are rare.

Similar researches about the local optimum aim to deal with the structural topology optimization problem [8]. The structural topology optimization problems are modeled using material interpolation, e.g. simplified isotropic material with penalization, to produce almost solid-and-void designs. But the problems become non convex due to the use of these techniques when penalty factor is bigger than 1. The penalty continuation in structural topology optimization is used to avoid the local optimum in many researches [9, 10]. This method increases the penalty factor from 1 to a maximum number during topology optimization. The penalty continuation is reported to be helpful in topology optimization of compliant mechanisms [11, 12]. Instead of OC and MMA, GCMMA is proposed to update the design variable to avoid the local optimum [13]. However, the global optimal solution cannot always be obtained by continuation with respect to the penalization parameter and how far is the result away from the global optimum remains unknown. The theoretical upper bounds of the objective function in two formulations are deduced in this article. And the upper bound is equal to the global optimum when the stiffness of the spring is small.

In this article, the scheme composed of two steps is proposed to avoid most of the local optimum and find the solution next to the global optimum in topology optimization of compliant mechanisms. The scheme composed of two steps is based on the following discoveries. The theoretical upper bound of the objective function exists and is equal to the global optimum when the stiffness of the spring is very small. And in this case, topology optimization of compliant mechanisms is a process to find a rigid-body mechanism with a certain geometrical advantage. And the geometrical advantage is depended on the boundary condition.

The paper is organized as follows. Section 2 discusses the theoretical upper bounds of the objective function. Section 3 discusses the essence of topology optimization of compliant mechanisms in some cases. Section 4 introduces the scheme composed of two steps to avoid most of the local optimum. Section 5 is the discussion and conclusion.

2 The Theoretical Upper Bound of the Objective Function

The theoretical upper bound of the objective function in the output displacement formulation is deduced here. An input spring is introduced to model the actuator's stiffness. The mathematical model is given as

$$\begin{aligned} \max_{0 \leq x \leq 1} &: \Delta_{out} \\ \text{s.t.} &: \mathbf{F}_{in} - \mathbf{K}\mathbf{U} = \mathbf{0} \\ &V(\mathbf{x}) \leq V_0 \end{aligned} \quad (1)$$

where Δ_{out} is the displacement of the output node. \mathbf{F}_{in} is the force vector applied on the input node. \mathbf{U} is the displacement vector. $V(\mathbf{x})$ is the volume factor. \mathbf{K} is the stiffness matrix and is given by

$$\mathbf{K} = \mathbf{K}_S + \mathbf{K}_{in} + \mathbf{K}_{out} \quad (2)$$

where \mathbf{K}_S is the sum of stiffness matrix of all continuum elements. \mathbf{K}_{in} is the stiffness matrix of input spring. \mathbf{K}_{out} is the stiffness matrix of output spring.

The norm of the input force vector $\|\mathbf{F}_{in}\|$ can be divided into two parts and can be given as

$$\|\mathbf{F}_{in}\| = F_{ink} + F_{ins} \quad (3)$$

where F_{ink} is applied to the input spring and is given as

$$F_{ink} = K_{in}\Delta_{in} \quad (4)$$

where K_{in} is the stiffness of input spring. Δ_{in} is the displacement of the input node. F_{ins} is applied to the compliant mechanisms. Compliant mechanisms store the energy when they are deformed. Thus, the input energy is bigger than the output energy.

$$F_{ins}\Delta_{in} \geq F_{out}\Delta_{out} \quad (5)$$

η is introduced as the energy transport efficiency and is given by

$$\eta = \frac{F_{out}\Delta_{out}}{F_{ins}\Delta_{in}} \quad (6)$$

r is defined as the geometrical advantage and is given by

$$r = \frac{\Delta_{out}}{\Delta_{in}} \quad (7)$$

Then, the objective function can be deduced by a combination of Eq. 1–7

$$\Delta_{out} = \frac{F_{in}}{\frac{K_{in}}{r} + \frac{K_{out}}{\eta}} \quad (8)$$

when

$$r = \sqrt{\frac{\eta K_{in}}{K_{out}}} \quad (9)$$

The objective function is maximized. If the Young's modulus of the material is large while the stiffness of input and output spring is small, the compliant mechanism is close to the rigid-body mechanism and the energy transport efficiency η is close to 1. The objective function reaches the theoretical upper bound and is given as

$$\Delta_{out} = \frac{F_{in}}{2\sqrt{K_{in}K_{out}}} \quad (10)$$

The theoretical upper bound of the objective function in the output displacement formulation is deduced. In this case, the topology optimization of compliant mechanisms is a process to find a rigid-body mechanism with a certain geometrical advantage. And the geometrical advantage is depended on the stiffness of input spring and output spring as given in Eq. 9.

If there is no relationship between the energy transport efficiency and the geometrical advantage, then the objective function is maximized when the energy transport efficiency is equal to 1. This deduction is corresponded to the theory in other researches [14, 15].

In the MA formulation, constrain on the input displacement is applied. The mathematical model is given as

$$\begin{aligned} \max_{\mathbf{0} \leq \mathbf{x} \leq \mathbf{1}} : & \quad MA(\mathbf{x}) = \frac{\|\mathbf{F}_{out}\|}{\|\mathbf{F}_{in}\|} = \frac{K_{out}\Delta_{out}}{\|\mathbf{F}_{in}\|} \\ s.t. : & \quad \mathbf{F}_{in} - \mathbf{K}\mathbf{U} = \mathbf{0} \\ & \quad V(\mathbf{x}) \leq V_0 \\ & \quad \Delta_{in} \leq \Delta_{max} \end{aligned} \quad (11)$$

where Δ_{max} is the upper bound of the input displacement. \mathbf{K} is the stiffness matrix and is given by

$$\mathbf{K} = \mathbf{K}_S + \mathbf{K}_{out} \quad (12)$$

the output displacement can be deduced as

$$\Delta_{out} = \min \left\{ \frac{\eta F_{in}}{r K_{out}}, r \Delta_{max} \right\} \quad (13)$$

and the objective function is given by

$$MA = \min \left\{ \frac{\eta}{r}, \frac{K_{out}}{F_{in}} r \Delta_{max} \right\} \quad (14)$$

If $\eta \approx 1$, MA will reach the maximum value when the geometrical advantage

$$r = \sqrt{\frac{F_{in}}{\Delta_{max} K_{out}}} \quad (15)$$

The maximum value, which is the theoretical upper bound of the objective function, is given by

$$MA = \sqrt{\frac{\Delta_{max} K_{out}}{F_{in}}} \quad (16)$$

The theoretical upper bound of the objective function in the MA formulation is deduced above. In this case, the topology optimization of compliant mechanisms is a process to find a rigid-body mechanism with a certain geometrical advantage. And the geometrical advantage is depended on Eq. (15).

3 The Essence of Topology Optimization of Compliant Mechanisms

When the Young's modulus of the material is large and the stiffness of input and output spring is small, topology optimization of compliant mechanisms is a process to find a rigid-body mechanism with a certain geometrical advantage. And the geometrical advantage is depended on the boundary condition.

A numerical example is illustrated. It is an inverter design problem. The boundary condition is showed as Fig. 1. Term E is the Young's modulus of the material, μ is the Poisson ratio. t is the thickness and V_0 is the volume factor.

The design domain is discretized. The 105 line MATLAB code [4] is used to solve this problem. And the result of this problem is showed in Fig. 2.

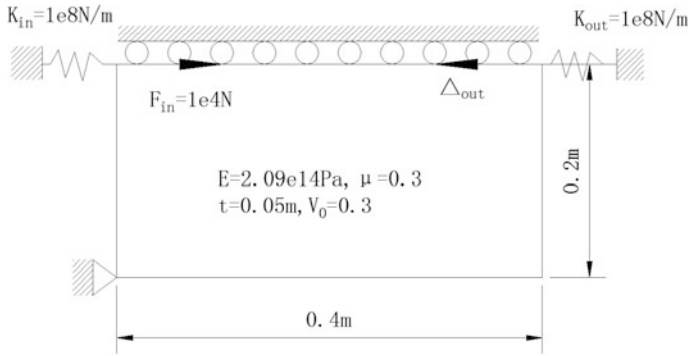


Fig. 1 The boundary condition of the inverter design problem

Fig. 2 The result of the inverter design problem



The objective function of the result is 0.04996 mm. And the result is in accordance with Eq. (10) because

$$\Delta_{out} = \frac{F_{in}}{2\sqrt{K_{in}K_{out}}} = 0.05 \text{ mm} \tag{17}$$

A check of the geometrical advantage r in this problem is done for further validation. The geometrical advantage r should be equal to 1 when the objective function is maximized in this problem according to Eq. (9). A rigid-body mechanism is extracted from Fig. 2 and is showed in Fig. 3.

The geometrical advantage r from the kinematic analysis is given by

$$r = \frac{\dot{\Delta}_{out}}{\dot{\Delta}_{in}} = 0.9804 \approx 1 \tag{18}$$

The result is nearly the same as that in Eq. (9).

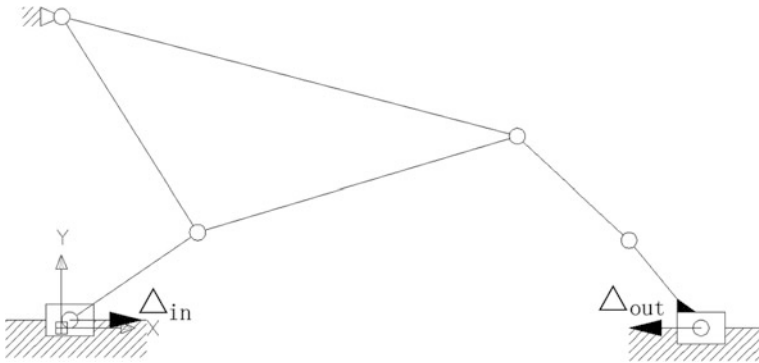


Fig. 3 Kinematic sketch of the rigid-body mechanism(*upper half*)

This numerical example indicates that in some cases the essence of topology optimization of compliant mechanisms is a process to find a rigid-body mechanism with a certain geometrical advantage. And the geometrical advantage is depended on the boundary condition. This phenomenon occurs when the Young’s modulus of the material is large and the stiffness of input and output spring is small.

4 The Scheme Composed of Two Steps to Avoid Most of the Local Optimum

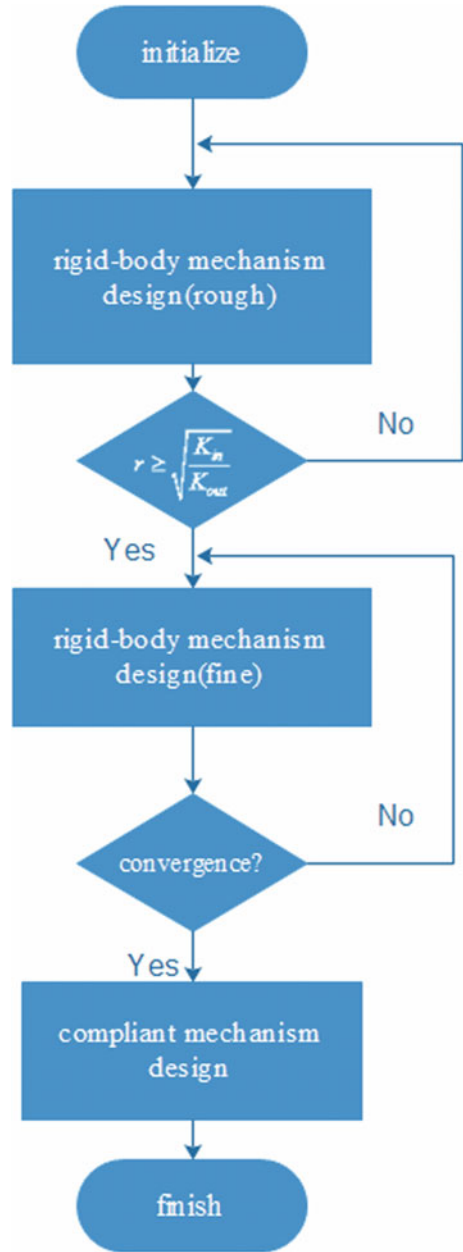
Now that the upper bound of the objective function is deduced, evaluating the problem of the local optimum becomes an easier task. A method is proposed to find the solution next to the global optimum in topology optimization of compliant mechanisms.

This scheme is composed of two steps. The first step is to find a rigid-body mechanism with a certain geometrical advantage r . The geometrical advantage is given by Eqs. (9) or (15). In order to find the rigid-body mechanisms by topology optimization, the Young’s modulus is magnified and the stiffness of output spring is reduced. The second step is topology optimization of compliant mechanisms. The Young’s modulus and the stiffness of output spring the same as the original problem, but the initial guess is the result of the first step instead of the uniform density. The flow chart is showed in Fig. 4.

An example is used for illustration. The boundary condition of the inverter design problem is showed in Fig. 5. The objective function is the output displacement. And the result of the 105 line MATLAB code is showed in Fig. 6. This result is used for comparison.

When the proposed scheme is used, the first step is to find a rigid-body mechanism. The best geometrical advantage is equal to 20 in this problem according to Eq. (9). The Young’s modulus is magnified 1000 time and the stiffness of the

Fig. 4 The flow chart of the scheme composed of two steps



output spring is set to be 625 N/m. Then, the program starts until the geometrical advantage reaches 20 as showed in Fig. 7a. The rough rigid-body mechanism design problem is finished. In order to get a reasonable result, the stiffness of the

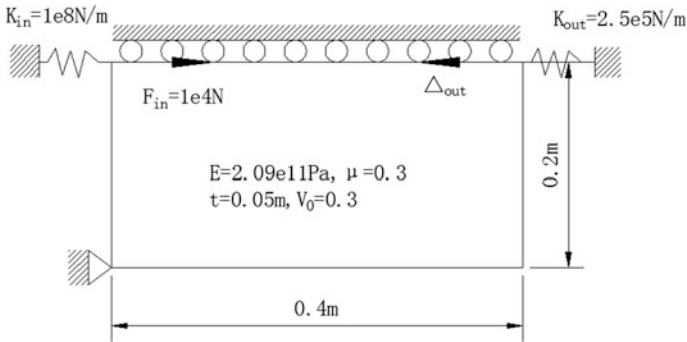
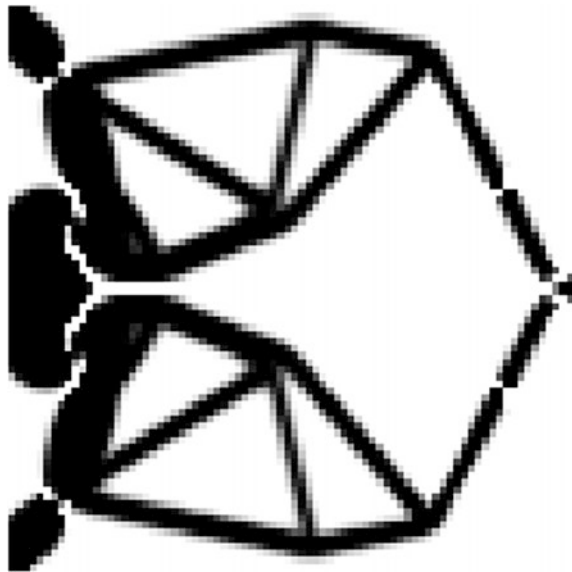


Fig. 5 The boundary condition of the inverter design problem

Fig. 6 The result of the 105 line MATLAB code, the output displacement is 0.408 mm



output spring is then set to be the same as the original problem. Then, a fine rigid-body mechanism whose geometrical advantage is next to 20 is got. The rigid-body mechanisms is showed in Fig. 7b. That is the first step. The second step is to find a compliant mechanism from the rigid-body mechanism. The Young's modulus is set to be 2.09e11 Pa. The final result is showed in Fig. 7c.

Comparison between the traditional method starts from the uniform guess and the proposed method in this article is showed in Table 1 and discussed below.

The traditional 105 line MATLAB code finds the result that the output displacement is 0.408 mm. The proposed method finds the result that the output displacement is 0.832 mm. There are great differences between these two results and both of them are local optimum. The upper bound of the output displacement is

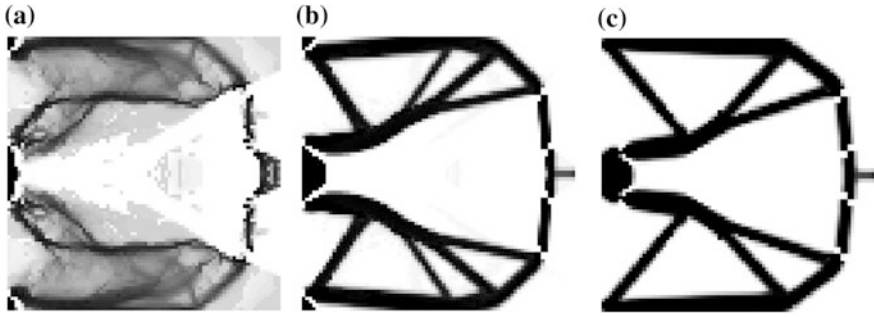


Fig. 7 **a** The geometrical advantage is 19.19. **b** The reasonable rigid-body mechanism. The objective function is equal to 1.00 mm and is next to the upper bound 1 mm in Eq. (10). **(c)** The result of the topology optimization of inverter, the output displacement is 0.832 mm. And the geometrical advantage is 12.8864

Table 1 Comparison between the traditional method and the scheme composed of two steps

Objective function	The traditional method	Scheme in this article	Upper bound
Output displacement (mm)	0.408	0.832	1

1 mm in this problem. However, it is not the result of global optimum because the soft material always stores energy and makes the energy transport efficiency η lower than 1.

5 Discussion and Conclusion

In output displacement formulation, the objective function is a function of two variable in Eq. (8). They are energy transport efficiency and the geometrical advantage. If the energy transport efficiency is close to 1, the output displacement is depended on the geometrical advantage. In this case, topology optimization of compliant mechanisms is a process to find a rigid-body mechanism with a certain geometrical advantage. And the objective function reaches the upper bound. Similar phenomenon occurs in MA formulation. The existence of the output spring and input spring is important. The problem will become ill-condition if one of their stiffness is zero. Because there won't be a certain geometrical advantage which maximizes the output displacement as given in Eq. (9).

In future research, the analysis of the other objective function, e.g. efficiency formulation [16], Characteristic Stiffness (CS) Formulation [17] and Artificial I/O Spring Formulation [18], should be done. The quantity relation between the stiffness of spring and the Young's modulus when a rigid body mechanism is design should be pointed out.

In conclusion, three discoveries are discussed in this article. First, the theoretical upper bounds of the objective function in two formulations are deduced. Second, it is pointed out that in some cases, topology optimization of compliant mechanisms is a process to find a rigid-body mechanism with a certain geometrical advantage. And the geometrical advantage is depended on the boundary condition. Third, based on the above discoveries, a method is proposed to find the solution next to the global optimum in topology optimization of compliant mechanisms. The numerical example indicates that this method is useful.

Acknowledgments This work was supported by the National Natural Science Foundation of China (Grant Nos. U1501247, 91223201), and the Scientific and Technological Research Project of Dongguang (Grant No. 2015215119). These supports are greatly acknowledged.

References

1. Wang MY (2009) A kinetoelastic formulation of compliant mechanism optimization. *J Mech Robot* 1(2):021011
2. Wang F, Lazarov BS, Sigmund O (2011) On projection methods, convergence and robust formulations in topology optimization. *Struct Multi Optim* 43(6):767–784
3. Sigmund O (2007) Morphology-based black and white filters for topology optimization. *Struct Multi Optim* 33(4–5):401–424
4. Bendsoe MP, Sigmund O (2013) *Topology optimization: theory, methods, and applications*. Springer, Berlin
5. Sigmund O (1997) On the design of compliant mechanisms using topology optimization*. *J Struct Mech* 25(4):493–524
6. Saxena A, Ananthasuresh G (2000) On an optimal property of compliant topologies. *Struct Mult Optim* 19(1):36–49
7. Lau G, Du H, Lim M (2001) Convex analysis for topology optimization of compliant mechanisms. *Struct Mult Optim* 22(4):284–294
8. Sigmund O, Petersson J (1998) Numerical instabilities in topology optimization: a survey on procedures dealing with checkerboards, mesh-dependencies and local minima. *Struct Optim* 16(1):68–75
9. Li L, Khandelwal K (2015) Volume preserving projection filters and continuation methods in topology optimization. *Eng Struct* 85:144–161
10. Watada R, Ohsaki M, Kanno Y (2011) Non-uniqueness and symmetry of optimal topology of a shell for minimum compliance. *Struct Multi Optim* 43(4):459–471
11. Rojas-Labanda S, Stolpe M (2015) Automatic penalty continuation in structural topology optimization. *Struct Multi Optim* 52(6):1205–1221
12. Deaton JD, Grandhi RV (2014) A survey of structural and multidisciplinary continuum topology optimization: post 2000. *Struct Multi Optim* 49(1):1–38
13. Rojas-Labanda S, Stolpe M (2015) Benchmarking optimization solvers for structural topology optimization. *Struct Multi Optim* 52(3):527–547
14. Zhu B, Zhang X (2012) A new level set method for topology optimization of distributed compliant mechanisms. *Int J Numer Meth Eng* 91(8):843–871
15. Zhu B, Zhang X, Wang N (2013) Topology optimization of hinge-free compliant mechanisms with multiple outputs using level set method. *Struct Multi Optim* 47(5):659–672
16. Hetrick J, Kota S (1999) An energy formulation for parametric size and shape optimization of compliant mechanisms. *J Mech Des* 121(2):229–234

17. Chen S, Wang MY (2007) Designing distributed compliant mechanisms with characteristic stiffness. In: ASME 2007 international design engineering technical conferences and computers and information in engineering conference. American Society of Mechanical Engineers
18. Rahmatalla S, Swan CC (2005) Sparse monolithic compliant mechanisms using continuum structural topology optimization. *Int J Numer Meth Eng* 62(12):1579–1605

Minimizing the Difference Between Two Output Performances to Avoid de Facto Hinges in Topology-Optimized Compliant Mechanisms

Benliang Zhu, Xianmin Zhang, Sergej Fatikow and Jinglun Liang

Abstract This paper presents a method for mathematically formulating the *compliant mechanisms topology optimization problem* aimed at automatically eliminating the de facto hinges. The underlying idea is to augment the traditional kinematic objective with a difference between two cases of output displacements of the mechanism: one without spring and one with. A formulation is developed by using the weighting method. An adaptive scheme for setting the weighting factor is proposed. Several numerical examples are studied to demonstrate the validity of the proposed method.

Keywords Compliant mechanism · De facto hinge · Topology optimization · SIMP · Weighted sum method

1 Introduction

A compliant mechanism is defined as a mechanism which gain its mobility from the flexibility of at least parts of its members [1, 2]. Over the past decade, design of compliant mechanisms using continuum topology optimization methods has undergone considerable development. The topology optimization problem for the synthesis of compliant mechanisms has been formulated in many different ways [3–7].

B. Zhu · X. Zhang (✉)

Guangdong Province Key Laboratory of Precision Equipment and Manufacturing Technology, South China University of Technology, Guangzhou 510640, China
e-mail: zhangxm@scut.edu.cn

S. Fatikow

Department of Computing Science, University of Oldenburg, Uhlhornsweg 84, A1, Oldenburg 26111, Germany

J. Liang

School of Mechanical Engineering, Dongguan University of Technology, Dongguan 523808, China

© Springer Nature Singapore Pte Ltd. 2017

X. Zhang et al. (eds.), *Mechanism and Machine Science*,

Lecture Notes in Electrical Engineering 408,

DOI 10.1007/978-981-10-2875-5_52

However, one of the unsolved issues is that the created mechanisms are strongly related to de facto hinges although that was not the intent [8–10].

Great efforts have been made by various researchers who attempted to remove these hinges to obtain compliant mechanisms with distributed compliance. Extra constrains [11–15] and the filtering methods [16, 17] are often employed into the optimization process. However, these schemes appear to have a limit success on preventing de facto hinges [16, 17]. In addition, some novel geometric representation schemes have been investigated to inherently avoid topological anomalies [18, 19]. Hybrid Discretization method [20, 21] has been developed for achieving distributed compliant mechanisms. However, it requires re-meshing of the design domain and thus it is computationally expensive.

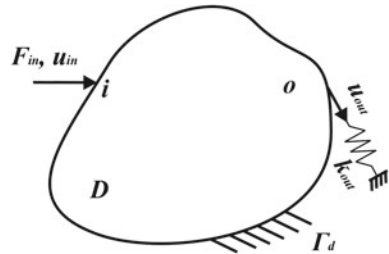
The reason causing de facto hinges lied behind the mathematical formulations [8, 9, 22, 23]. In order to formulate the design problem that can inherently prevent de facto hinges, new formulations have been proposed, including the intrinsic characteristic formulation [10], the artificial I/O spring formulation [5] and the input-output mean compliances formulation [24, 25].

2 Motivation

Figure 1 illustrates a schematic of a monolithic compliant mechanism design problem. The design domain D with a fixed boundary Γ_d is loaded with an input force F_{in} with its displacement magnitude u_{in} at the input port i . It is desired to have an output performance, e.g., u_{out} , at the output port o . A spring k_{out} is attached to the output port to imitate the workpiece. An assumption of a force/displacement relationship, i.e. $F_{out} = k_{out}u_{out}$, at the output port is often necessary. Without using this condition, it is difficult to achieve a mechanism design in which the input and output ports are even connected [3, 9].

Most of the current force-deflection type formulations simultaneously maximize the deformation at the output port and maximize the overall stiffness of the structure which is measured by using the strain energy. As a result, a rigid-body linkage with revolute joints is the true optimum because it can generate large output deformation

Fig. 1 The design domain for topology optimization of compliant mechanisms



and has zero strain energy. Thus, de facto hinges are inevitable. In this study, we are motivated to develop an alternative mathematical formulation aimed at inherently avoiding the de facto hinges.

3 A Difference Reducing Method

We first use an example to illustrate the underlying idea of the proposed method. Considering a compliant mechanism with de facto hinges shown in Fig. 2a, we consider two load cases: (I) the spring k_{out} is attached to the output port and the resulting output displacement is denoted as u_{o1} ; (II) the spring k_{out} is eliminated and the resulting output displacement is denoted as u_{o1f} .

Let us use $\Delta u_{out}^{hinged} = |u_{o1} - u_{o1f}|$ to indicate the difference between u_{o1} and u_{o1f} . For the hinged compliant mechanism, Δu_{out}^{hinged} will approach extremely large as the hinge parts undergo essential rigid-body rotation of the second load case.

A smaller output displacement difference will be obtained if the compliant mechanism is free of de facto hinges (as shown in Fig. 2b) as a certain level of energy will be stored inside the mechanism. Let us use $\Delta u_{out}^{hinge-free} = |u_{o2} - u_{o2f}|$ to indicate the difference obtained from the mechanism in Fig. 2b. Thus

$$\Delta u_{out}^{hinge-free} < \Delta u_{out}^{hinged} \tag{1}$$

This means, hinged compliant mechanism corresponds to a large Δu_{out} , whereas hinge-free compliant mechanism corresponds to a small one. Conversely, if Δu_{out} can be reduced, de facto hinges can be prevented.

Think of the spring as an obstacle, which is pushed with a compliant mechanism. Reducing the performance difference is actually equivalent to lowering the effect of

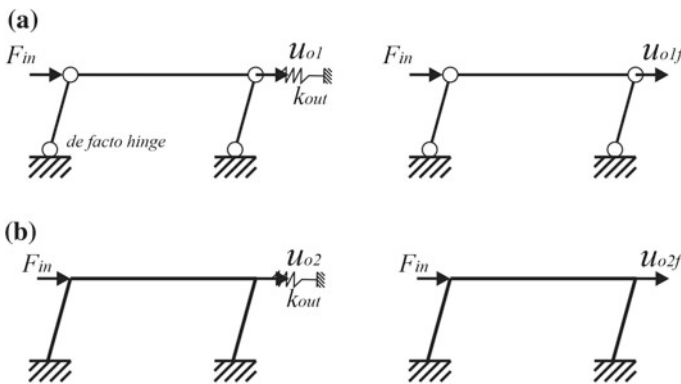


Fig. 2 Two kinds of compliant mechanisms: **a** contains de facto hinges and **b** free of de facto hinges

the obstacle. If the output performance of a mechanism is hardly changed whether it is blocked by an obstacle, the mechanism has to be stiff enough (free of de facto hinges).

3.1 An Alternative Formulation

Here, we can describe our method as follows: (I) obtain the displacements u_{out}^a (without spring) and u_{out}^b (with spring) respectively from two load cases. (II) maximize u_{out}^b to obtain *compliant* mechanism and minimize Δu_{out} to make it hinge-free. Δu_{out} can be expressed as

$$\Delta u_{out} = |u_{out}^a - u_{out}^b| \quad (2)$$

A multi-objective optimization problem is considered. Using the weighting method, an alternative optimization model Q for topology optimization of hinge-free compliant mechanisms can be formulated as

$$\begin{aligned} Q: \quad & \text{Minimize : } J = \omega \Delta u_{out} - (1 - \omega) u_{out}^b \\ & \text{Subject to : } V \leq V_{max} \\ & \quad \quad \quad u_{in} \leq u_{in}^{max} \end{aligned} \quad (3)$$

where V and u_{in} indicate the maximal material usage and the displacement at the input port, respectively.

For the implementation of Q , since the best definition for ω is problem dependent, we therefore propose an adaptive way to assign this value, based on the value of ω of the previous iteration. In the $(k + 1)^{th}$ iteration, the value of ω^{k+1} can be set to

$$\omega^{k+1} = \frac{1}{1 + \frac{|(u_{out}^b)^k|}{|\Delta u_{out}^k|}} \quad (4)$$

With a decreasing of Δu_{out} and an increasing of u_{out}^b , ω will be gradually enlarged. Thus, the weight of Δu_{out} is increased. This can minimize Δu_{out} to prevent de facto hinges meanwhile avoiding setting ω artificially. During each iteration, the ω is constant. Therefore

$$\frac{\partial \omega}{\partial x} = 0 \quad (5)$$

where x is the design variable matrix. This makes the sensitivity of the proposed method easy to compute.

Although for the implementation of the proposed method, an extra equilibrium equation needs to be solved to obtain u_{out}^a , it does not occupy much CPU time. This will be quantitatively demonstrated in Sect. 5.

4 Solution Algorithm

Incorporating the SIMP method [26, 27], Q can be rewritten as

$$\underset{x}{\text{Minimize}} : J = \omega |\mathbf{L}^T \mathbf{U}_{out}^a - \mathbf{L}^T \mathbf{U}_{out}^b| - (1 - \omega) \mathbf{L}^T \mathbf{U}_{out}^b \quad (6)$$

$$\text{Subject to} : \sum_{e=1}^N v_e x_e \leq V_{\max} \quad (7)$$

$$u_{in} \leq u_{in}^{\max} \quad (8)$$

$$\mathbf{K}_a \mathbf{U}_{out}^a = \mathbf{F}_{in} \quad (9)$$

$$\mathbf{K}_b \mathbf{U}_{out}^b = \mathbf{F}_{in} \quad (10)$$

$$0 < x_{\min} \leq x_e \leq 1 \quad (11)$$

$$e = 1, 2, \dots, N \quad (12)$$

where \mathbf{L} is a unit load vector consisting of zero except for position i with an entry of $\mathbf{L}_i = 1$, and \mathbf{U}_{out}^a is the displacement vector generated by the load vector \mathbf{F}_{in} applied at the input port with a spring fixed at the output port of the design domain. \mathbf{U}_{out}^b is the displacement vector generated by the load vector \mathbf{F}_{in} applied at the input port without a spring fixed at the output port of the design domain. The stiffness matrixes \mathbf{K}_a and \mathbf{K}_b depend on the stiffness E_e in element e which can be written as

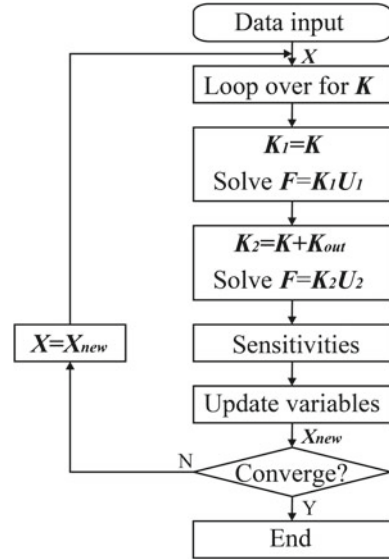
$$\mathbf{K}_a = \sum_e^N \mathbf{K}_e(E_e) = \mathbf{K} \quad (13)$$

$$\mathbf{K}_b = \sum_e^N \mathbf{K}_e(E_e) + \mathbf{K}_{out} = \mathbf{K} + \mathbf{K}_{out} \quad (14)$$

where \mathbf{K}_e is the element stiffness matrix in the global level. \mathbf{K}_{out} is the artificial spring stiffness k_{out} in the global level.

The flowchart of the optimization is shown in Fig. 3. The filtering method [27] is employed to prevent the checkerboard patterns, and the optimal criteria method [28, 29] is employed to update the design variables.

Fig. 3 The flowchart of the proposed optimization procedure



5 Numerical Examples

The artificial material properties are described as: Young's modulus for the solid material is $E = 1$ and Poisson's ratio $\nu = 0.3$. The densities are restricted by a lower bound $x_{min} = 10^{-3}$. The power law mixing rule with $p = 3$ is used in the computations. The design domain is discretized by using 100×100 finite elements.

5.1 Compared with Conventional Spring Model: Displacement Inverter

The design domain is shown in Fig. 4. The maximal material usage is restricted to 20 %. The upper limit of the input displacement u_{in}^{max} is set to 10.

For both the conventional spring model and the proposed method, the same spring $k_{out} = 10^{-3}k_b$ is used where k_b is the *bounding spring value* [5]. Figure 5 reveals that the traditional method gives lumped compliant mechanism, whereas the proposed method gives distributed compliant mechanism. The hinge-free compliant mechanism performs smaller compliance than the design containing de facto hinges. However, the hinged designs are so fragile that they could fail immediately when being loaded. Therefore, the performance of a compliant mechanism that relies on de facto hinges is not necessarily achievable. Further, in order to obtain

Fig. 4 The design domain of the displacement inverter

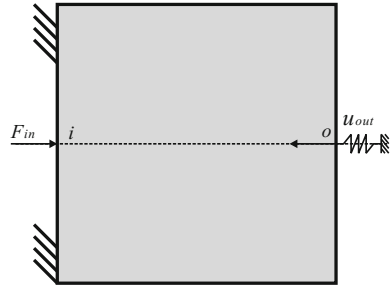
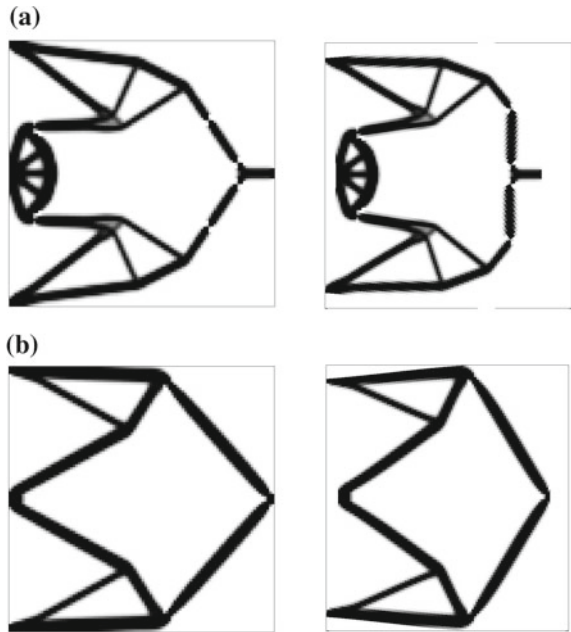


Fig. 5 The optimized topologies of the displacement inverter obtained using: **a** the conventional spring model, **b** Q



compliant mechanisms that have higher compliance characteristics, an alternative way is to impose more restrictive material usage constraint value [5].

For implementation of Q , ω is dynamically changed during the optimization process. The convergence history of ω is shown in Fig. 6. It reveals that, with the increasing of u_{out} and the decreasing of Δu_{out} , ω can vary dynamically and be enlarged and thus the lumped compliance is prevented.

The average CPU time of one optimization iteration when using different methods is compared in Table 1 where \mathbf{T} is the overall CPU time of each optimization iteration, $t_{\mathbf{K}}$ is the time of assembling of \mathbf{K} , $t_{\mathbf{U}_1}$ is the time of calculating \mathbf{U}_1 , $t_{\mathbf{U}_2}$ is the time of calculating \mathbf{U}_2 , t_{sa} is the time of sensitivity analysis, and t_x is the time of updating variables.

Fig. 6 The convergence history of ω

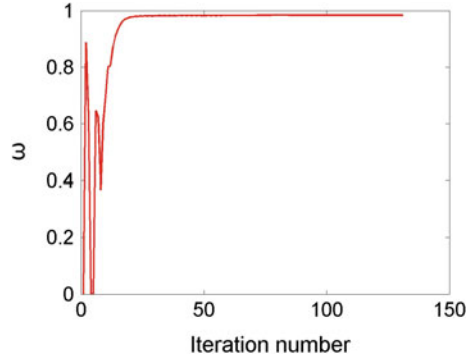


Table 1 The values of the average CPU times(s) in each iteration obtained using the conventional spring method and the proposed method

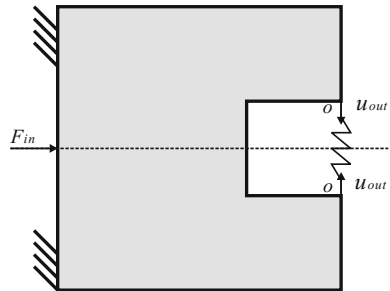
	$t_{\mathbf{K}}$	t_{U_1}	t_{U_2}	t_{sa}	t_x	\mathbf{T}
Conventional	4.2136	–	0.0914	0.0993	0.0247	4.4290
Proposed	4.1988	0.0372	0.0901	0.1024	0.0242	4.4527

The assembling of \mathbf{K} is the most CPU time consuming step no matter which method is used. For using the proposed method, the costing CPU time of each iteration is a little larger than the traditional method. However, it does not influence the computational efficiency very much as the establishment of \mathbf{K} is only needed once.

5.2 Effect of the k_{out} : Push Gripper

The design domain and boundary conditions are shown in Fig. 7. The gap size of the design domain is 30×30 . The upper limit of the input displacement u_{in}^{max} is set to 10. The maximum material usage constraint V_{max} is set to 0.2.

Fig. 7 The design domain of the push gripper



The effect of different k_{out} upon the resulting optimal configurations is examined in this section. Four cases are studied where k_{out} is respectively set to $10^{-1}k_b$, $10^{-2}k_b$, $10^{-3}k_b$ and $10^{-4}k_b$.

Fig. 8 The optimized topologies of the push gripper obtained using Q :
a $k_{out} = 10^{-1}k_b$;
b $k_{out} = 10^{-2}k_b$;
c $k_{out} = 10^{-3}k_b$;
d $k_{out} = 10^{-4}k_b$

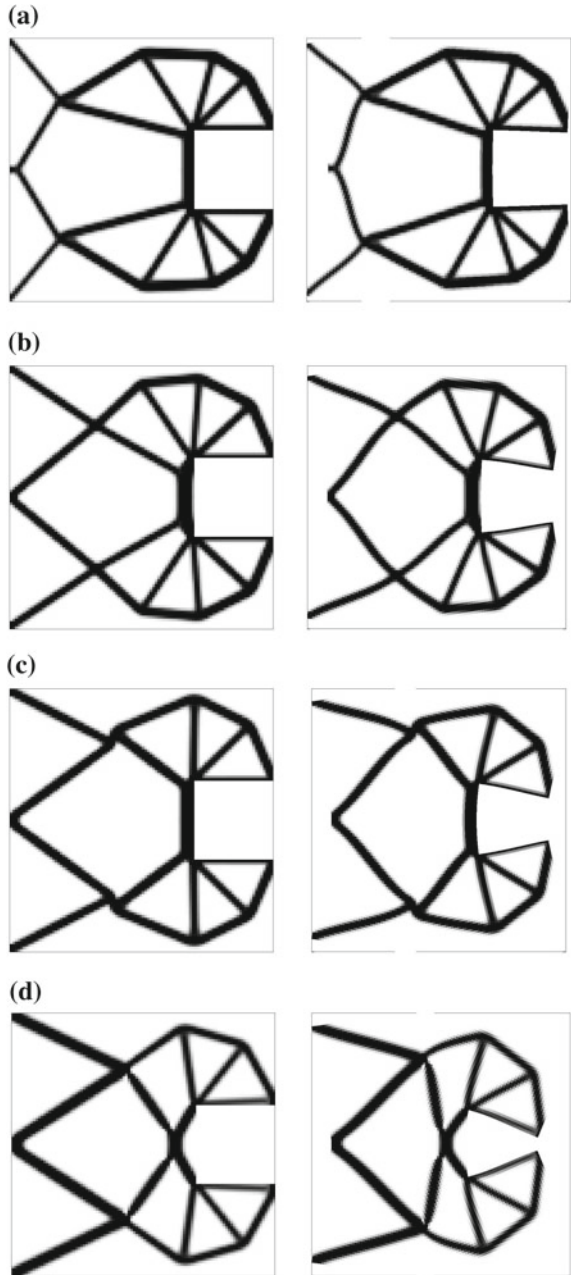


Figure 8 shows the optimized configurations for each case. All of the obtained configurations are free of de facto hinges. The respective deformed configurations of these designs show the mechanisms functioning with well-distributed elastic deformation when they are loaded. For implementation of Q , hinge-free compliant mechanisms can be obtained no matter k_{out} is set to be large or small.

6 Conclusions

In this study, a new method for topology synthesis of hinge-free compliant mechanisms is presented. In the method, the objective function is augmented by minimizing the difference between two output performances. Numerical examples show that hinge-free compliant mechanisms can be obtained. Further, the proposed method is very easy for application.

Other aspects of the method need further investigation, such as the proposed method could be generalized for using other objective functions, such as the geometrical advantage and the mechanical advantage.

Acknowledgments This research was supported by the China Postdoctoral Science Foundation Funded Project (2016M590772), the National Science Foundation of China (51605166, 51275174, U1501247, 91223201), the Natural Science Foundation of Guangdong Province (Grant No. S2013030013355), the Scientific and Technological Project of Guangzhou (Grant No. 2015090330001), and the Science and Technology Planning Project of Guangdong Province (Grant No. 2014B090917001). The Natural Science Foundation of Guangdong (2015A030310415), Doangguan Industrial Science and Technology Development Project (2015222119) and Dongguan Social Science and Technology Development Project (2013108101011).

References

1. Howell LL (2001) Compliant mechanisms. Wiley, Hoboken
2. Bendsoe MP, Sigmund O (2003) Topology optimization: theory, methods and applications. Springer, Berlin
3. Sigmund O (1997) On the design of compliant mechanisms using topology optimization. *Mech Struct Mach Int J* 25(4):493–524
4. Nishiwaki S, Min S, Yoo J, Kikuchi N (2001) Optimal structural design considering flexibility. *Comput Methods Appl Mech Eng* 190(34):4457–4504
5. Rahmatalla S, Swan CC (2005) Sparse monolithic compliant mechanisms using continuum structural topology optimization. *Int J Numer Meth Eng* 62(12):1579–1605
6. Chen SK (2007) Compliant mechanisms with distributed compliance and characteristic stiffness: a level set method. PhD thesis, The Chinese University of Hong Kong, China
7. Zhu B, Zhang X (2012) A new level set method for topology optimization of distributed compliant mechanisms. *Int J Numer Meth Eng* 91(8):843–871
8. Yin L, Ananthasuresh GK (2003) Design of distributed compliant mechanisms. *Mech Based Des Struct Mech* 31(2):151–179

9. Deepak SR, Dinesh M, Sahu DK, Ananthasuresh GK (2009) A comparative study of the formulations and benchmark problems for the topology optimization of compliant mechanisms. *ASME J Mech Robot* 1:1–8
10. Wang MY, Chen S (2009) Compliant mechanism optimization: analysis and design with intrinsic characteristic stiffness. *Mech Based Des Struct Mach Int J* 37(2):183–200
11. Petersson J, Sigmund O (1998) Slope constrained topology optimization. *Int J Numer Meth Eng* 41(8):1417–1434
12. Yoon GH, Kin YY, Bendsøe MP, Sigmund O (2004) Hinge-free topology optimization with embedded translation-invariant differentiable wavelet shrinkage. *Struct Multi Optim* 27(3):139–150
13. Duysinx P, Bendsøe MP (1998) Topology optimization of continuum structures with local stress constraints. *Int J Numer Meth Eng* 43(8):1453–1478
14. Poulsen TA (2003) A new scheme for imposing a minimum length scale in topology optimization. *Int J Numer Meth Eng* 57:741–760
15. Wang N, Zhang X (2012) Compliant mechanisms design based on pairs of curves. *sci China Technol Sci* 55(8):2099–2106
16. Luo Z, Chen L, Yang J, Zhang Y, Abdel-Malek K (2005) Compliant mechanism design using multi-objective topology optimization scheme of continuum structures. *Struct Multi Optim* 30(2):142–154
17. Sigmund O (2007) Morphology-based black and white filters for topology optimization. *Struct Multi Optim* 33(4–5):401–424
18. Wang N, Tai K (2008) Design of grip-and-move manipulators using symmetric path generating compliant mechanisms. *J Mech Des* 130(11):11230501–11230509
19. Wang N, Tai K (2010) Design of 2-dof compliant mechanisms to form grip-and-move manipulators for 2d workspace. *J Mech Des* 132(3):03100701–03100709
20. Zhou H (2010) Topology optimization of compliant mechanisms using hybrid discretization model. *ASME J Mech Des* 132(11):111003–111010
21. Kim JE, Kim YY, Min S (2005) A note on hinge-free topology design using the special triangulation of design elements. *Commun Numer Methods Eng* 21(12):701–710
22. Luo J, Luo Z, Chen S, Tong L, Wang MY (2008) A new level set method for systematic design of hinge-free compliant mechanisms. *Comput Methods Appl Mech Eng* 198(2):318–331
23. Wang MY (2009) A kinetoelastic formulation of compliant mechanism optimization. *ASME J Mech Robot* 1(2):02101101–02101110
24. Zhu B, Zhang X, Wang N (2012) Topology optimization of hinge-free compliant mechanisms with multiple outputs using level set method. *Struct Multi Optim* 47(5):659–672
25. Zhu B, Zhang X, Wang N, Fatikow S (2014) Topology optimization of hinge-free compliant mechanisms using level set methods. *Eng Optim* 46:580–605
26. Bendsøe MP, Sigmund O (1999) Material interpolation schemes in topology optimization. *Arch Appl Mech* 69(9–10):635–654
27. Sigmund O (2001) A 99 line topology optimization code written in matlab. *Struct Multi Optim* 21(2):120–127
28. Bendsøe MP (1989) Optimal shape design as a material distribution problem. *Struct optim* 1(4):193–202
29. Yin L, Yang W (2001) Optimality criteria method for topology optimization under multiple constraints. *Comput Struct* 79(20–21):1839–1850

Topology Optimization of Compliant Mechanism Based on Minimum Manufacturing Constraints

Zhang Yonghong, Sang Yang, Ge Wenjie and Xu Lei

Abstract The objective of this paper is to demonstrate a method for the topology optimization of compliant mechanism. The proposed method employs the minimum manufacturing constraints to realize the non-linearly mapping between the qualities of nodes and unit volume fraction in order to void the narrow hinge-like section in compliant mechanism which is difficult to be manufactured. The method and implementation are illustrated through numerical experiment of compliant grasper. The result shows that minimum structure size could be controlled by the topology optimization including the non-linearly mapping method. At the same time, the use of the minimum manufacturing constraints reduces the maximum stress level of grasper, and makes the stress distribution tends to be homogenization. But this method would reduce the output displacement of the structure in a certain extent.

Keywords Complaint mechanism · Manufacturing constraints · Topology optimization · Flexible grasper

Z. Yonghong · S. Yang (✉) · G. Wenjie · X. Lei
School of Mechanical Engineering, Northwestern Polytechnical University,
Xi'an 710072, Shaanxi, China
e-mail: gwj@nwpu.edu.cn

Z. Yonghong
e-mail: zhangyonghong@nwpu.edu.cn

G. Wenjie
e-mail: sangyanggood@mail.nwpu.edu.cn

X. Lei
e-mail: xulei@mail.nwpu.edu.cn

1 Introduction

In contrast to traditional mechanism that rely on movable joint in order to perform their function, the compliant mechanism is defined by Howell as a mechanism that utilize the deformation of the flexible members to transfer force, motion and energy [1]. Compliant mechanism has the innate abilities that they are easy to fabricate, exhibit low wear and low friction, and have a built-in restoring force. So it become popular in mechanical design. Topology optimization is often used in synthesizing the compliant mechanism. But in the topology optimization process the narrow weak hinge-like section are often present in compliant mechanism that are also called checkerboard and mesh dependence and other numerical instability phenomenon, which leads to poor manufacturing ability and the reduction of the reliability of the calculation results [2–4]. To deal with the problem, many techniques including the global perimeter constraint method [5], the slope constrained method [6], the local stress constraints scheme [7], the minimum length scale constraint method [8], the upper-bound constraint approach [9] have been proposed. Another approach is to employ filtering schemes. Luo et al. devised a density-sensitivity duplicate filtering scheme to control hinges in final design [10], Sigmund presented a morphology-based density filtering scheme for controlling grey scale transitions between solid and void regions to generate manufacturable solutions by constraining minimum length scale of structural feature sizes [11]. In addition, Benliang Zhu and Xianmin Zhang et al. presented a two-step elastic modeling method (TsEM) for the topology optimization of compliant mechanisms, based on the TsEM method, an alternative formulation be developed and incorporated with the level set method, which can improve the computational efficiency and eliminate de facto hinges effectively [12], Junzhao Luo and Zhen Luo et al. presented a new level set-based method to realize shape and topology optimization of hinge-free compliant mechanisms, which used a quadratic energy functional in image processing applications be introduced in the level set method to control the geometric width of structural components in the created mechanism, the result showed that the method can eliminate numerical difficulties in most conventional level set method [13], Guest et al. presented a method for imposing a minimum length scale on structural members using nodal variables-based projection approach [14]. However, there are relatively few studies on the general optimal structure considering difficulty in the process of manufacture.

With the development of 3D printer, the design method of compliant mechanism objecting to the 3D printer has been proposed. Gaynor et al. introduced the combinatorial SIMP to design compliant mechanism [15], employing a min-max formulation that optimize a larger projection and small projection of the same design variable while considering size of droplet of 3D printer. The experimental result exhibited that the method considering the minimum feature constraint could ensure the final compliant mechanism easy to be manufactured. Guest et al. proposed minimum feature constraint in topology optimization [16], he used a regular Heaviside the mapping method that is independent of mesh density, the result

shows that it can control the minimum feature size and the middle density unit and the checkerboard phenomenon. Sigmund et al. [17] proposed a topology optimization method that including the manufacturing factors. The use of Heaviside mapping method can achieve the topology shape of the “fill” and “Corrosion” and effectively reduce the appearance of single joint.

In this article, based on the Heaviside step function of non-linearly mapping method that employs minimum manufacturing constraints, with the cell density being taken as the design variable, the topology optimization of compliant mechanism is carried on. The optimality criteria method [18–20] is the topology optimization technique. The compliant grasper was synthesized, and its properties were analyzed.

2 Design Formulation Based on Non-linearly Mapping Method

2.1 Nonlinearly Mapping Technique in Topology Optimization

In this paper, a specific combination of the topology optimization of compliant mechanism and nonlinearly mapping method is proposed. In the topology optimization process the narrow weak hinge-like section are often present in compliant mechanism, so the mapping between the qualities of elements and unit volume fraction is defined to eliminate the weak section. In the mapping scheme the minimum size parameter r_{min} is introduced to represent the lower limit of minimum component size in the final topology.

As shown in Fig. 1a, r_{min} is the radius of the circular domain. The units located in the sub region Ω_{ω}^e will be used to calculate the volume fraction e . With grid refinement, r_{min} and Ω_{ω}^e will not change, as shown in Fig. 1b.

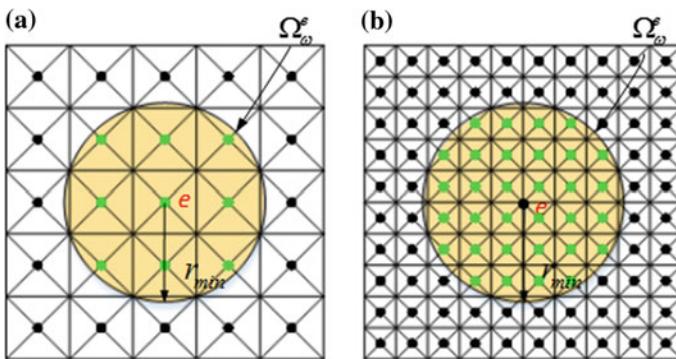


Fig. 1 The mapping scheme of the centroid of the grid map

In nonlinear mapping method, $\tilde{\rho}_e(\boldsymbol{\rho})$ is used to represent the weighted average of the unit volume fraction within the Ω_{ω}^e , so

$$\tilde{\rho}_e = \frac{\sum_{i \in S_e} \rho_i \omega(\mathbf{x}_i - \bar{\mathbf{x}}^e)}{\sum_{i \in S_e} \omega(\mathbf{x}_i - \bar{\mathbf{x}}^e)} \tag{1}$$

Among them, $\omega(\mathbf{x}_i - \bar{\mathbf{x}}^e)$ is the weight function, if \mathbf{x} belongs to Ω_{ω}^e , then $\omega(\mathbf{x}_i - \bar{\mathbf{x}}^e)$ equals to $(r_{min} - r)/r_{min}$, and unit volume fraction can be expressed as the form of Heaviside step function.

$$\bar{\rho}_e = \begin{cases} 1 & \text{if } \tilde{\rho}_e(\boldsymbol{\rho}) > \rho_i^{\min} \\ \bar{\rho}_e^{\min} & \text{if } \tilde{\rho}_e(\boldsymbol{\rho}) = \rho_i^{\min} \end{cases} \tag{2}$$

In order to be used for continuum topology optimization problems, the Heaviside step function is regularized to ensure the continuous of ρ_i with respect to the gradient of $\bar{\rho}_e$, which will be achieved through an exponential function.

$$\bar{\rho}_e = 1 - e^{-\beta \tilde{\rho}_e(\boldsymbol{\rho})} + \zeta^e(\boldsymbol{\rho}) \tag{3}$$

In the formula, the parameters of the β are expressed by the curvature of the regularization, shown in the Fig. 2 and the $\zeta^e(\boldsymbol{\rho})$ is corrected by the boundary of the unit volume fraction:

$$\zeta^e = \tilde{\rho}_e(\boldsymbol{\rho}) e^{-\beta} \tag{4}$$

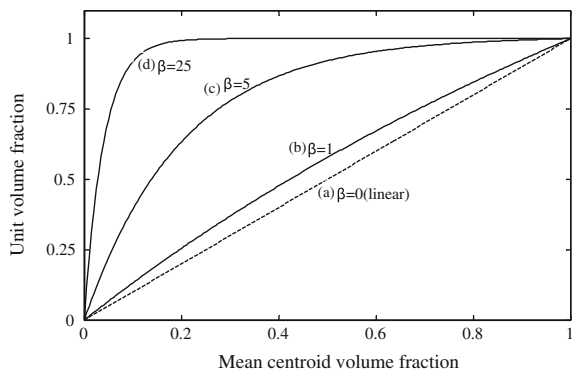
The ρ_i^{\min} can be adjusted depending on the values of β on the boundary.

$$\bar{\rho}_e^{\min} \cong 1 - e^{-\beta \rho_i^{\min}} + \rho_i^{\min} e^{-\beta} \tag{5}$$

In above equation, the third item is approximately equal to 0, the ρ_i^{\min} are as follows:

$$\rho_i^{\min} = -\frac{1}{\beta} \ln(1 - \bar{\rho}_e^{\min}) \tag{6}$$

Fig. 2 The regular Heaviside step function under different β values



2.2 The Model of Topology Optimization of Compliant Mechanisms with Minimum Manufacturing Constraints

The topology optimization of compliant mechanism employed nonlinear mapping method. Different from the design of Guest [16], the design variable of this paper is the volume fraction of elements, but not the volume fraction of nodes. The design objective of topology optimization is output displacement. Based on SIMP method [21, 22]. The model of topology optimization is followed:

$$\left\{ \begin{array}{l} \text{Maximize} \\ \mathbf{x}=(x_1, x_2, \dots, x_i)^T \in \mathbb{R}^n, i=1, \dots, N : f(\mathbf{x}) = \mathbf{L}^T \mathbf{U} \\ \text{Subject to :} \left\{ \begin{array}{l} \mathbf{K}(\mathbf{x}) \mathbf{U} = \mathbf{F} \\ \mathbf{K}(\mathbf{x}) \tilde{\mathbf{U}} = \mathbf{L} \\ \sum_{e=1}^N \bar{x}_e(\mathbf{x}) v_e \leq V^* \\ 0 < x_i^{\min} \leq x_i \leq 1 \end{array} \right. \end{array} \right. \quad (7)$$

where \mathbf{x} is the design variable, x_i is the unit relative density, \mathbf{F} is the input force matrix, \mathbf{K} is whole stiffness matrix, \mathbf{U} is displacement vector of nodes, \mathbf{L} is the adjoint matrix load vector, $\tilde{\mathbf{U}}$ is displacement vector of each node related to \mathbf{L} , v_e is the volume of first unit e , \bar{x}_e is the relative density of the mapping unit, V^* is the desired volume, x_i^{\min} is a unit relative density of the minimum, N is the total number of units in the discrete design domain.

2.3 Sensitivity Analysis

The sensitivity of objective function is provided using the adjoint matrix method in this section. The sensitivity of objective function in Eq. (7) with respect to a change in design variable x_e is expressed as:

$$\frac{\partial u_{out}}{\partial \bar{x}_e} = \mathbf{L}^T \frac{\partial \mathbf{U}}{\partial \bar{x}_e} = -\mathbf{L}^T \mathbf{K}^{-1} \frac{\partial \mathbf{K}}{\partial \bar{x}_e} \mathbf{U} \quad (8)$$

Substituting the equation $\mathbf{K} \tilde{\mathbf{U}} = \mathbf{L}$ to Eq. (8), and according to the finite element stiffness matrix assembly principle and artificial material density model, the sensitivity of the output point displacement u with respect to a change in design variable is obtained as:

$$\frac{\partial u_{out}}{\partial \bar{x}_e} = -\tilde{\mathbf{U}}^T \frac{\partial \mathbf{K}}{\partial \bar{x}_e} \mathbf{U} = -\sum_{e=1}^N P(\bar{x}_e(\mathbf{x}))^{p-1} \tilde{\mathbf{u}}_e^T \mathbf{k}_0^e \mathbf{u}_e \quad (9)$$

Based on the nonlinear mapping method, the expression is followed:

$$\bar{x}_e = 1 - e^{-\beta \tilde{x}_e(\mathbf{x})} + \zeta^e(\mathbf{x}) \tag{10}$$

$$\zeta^e = \tilde{x}_e(\mathbf{x})e^{-\beta} \tag{11}$$

$$\tilde{x}_e = \frac{\sum_{i \in S_e} x_i \omega(\mathbf{x}_i - \bar{\mathbf{x}}^e)}{\sum_{i \in S_e} \omega(\mathbf{x}_i - \bar{\mathbf{x}}^e)} \tag{12}$$

According the Eqs. (10), (11) and (12), the output displacement of point u_{out} with respect to design variables x_j are deduced:

$$\frac{\partial u_{out}}{\partial x_j} = - \sum_{e=1}^N p(\bar{x}_e(\mathbf{x}))^{p-1} \bar{\mathbf{u}}_e^T \mathbf{k}_e^e \mathbf{u}_e \frac{\partial \bar{x}_e}{\partial x_j} \tag{13}$$

2.4 Implementation Process of Topology Optimization

The topology optimization of complaint mechanism based on the optimization criterion method is shown in Fig. 3.

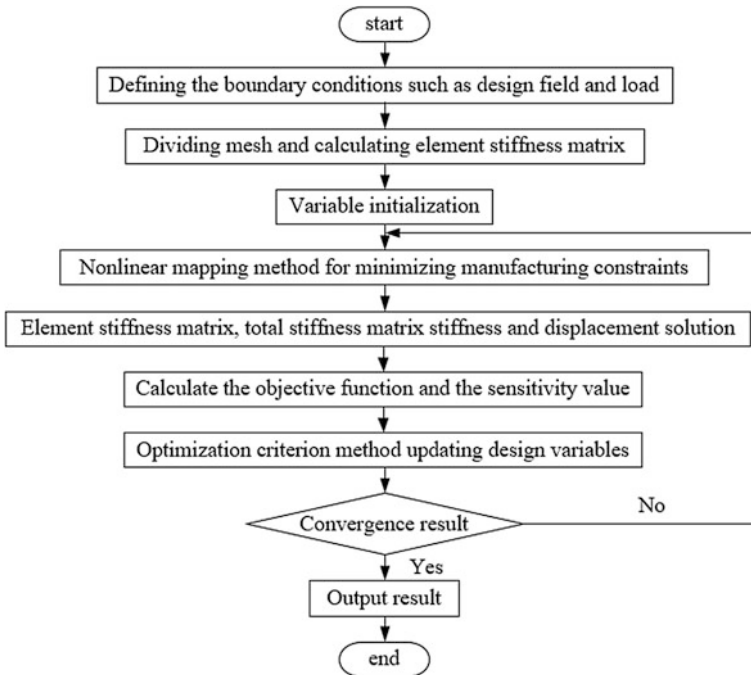
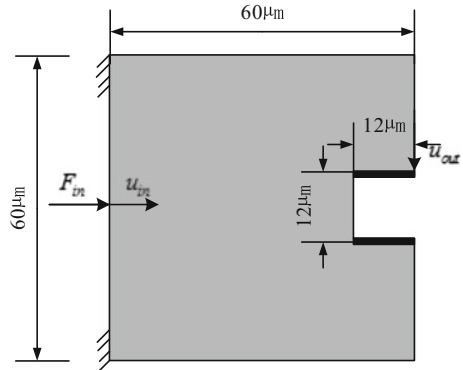


Fig. 3 Topology optimization flow chart

Fig. 4 Design domain



3 Case Study: Micro Flexible Grasper

As illustrated in Fig. 4, the design domain is $60\ \mu\text{m} \times 60\ \mu\text{m}$ with $12\ \mu\text{m} \times 12\ \mu\text{m}$ gap in the middle of right-side of the space. The displacements are fixed at the top and bottom points on the left side of the design domain. A force of $1000\ \mu\text{N}$ is applied at middle of left side. Virtual springs are applied at the input and output nodes. The objective the study is to maximize the output displacement. At the same time, the desired volume fraction is less than 30 %.

The material properties are that of silicon with $E = 160\ \text{GPa}$, $\mu = 0.22$. Exploiting symmetry, only half the domain is modeled. While using SIMP, the penalty factor p is 3, the minimum size constraint parameter β is 5.

The following study is on the relationship between the minimum size r_{min} and the final topological structures.

3.1 Grasper-Topology-Optimized Solution

The topology optimized solutions of grasper are presented in Figs. 5 and 6. The black rectangle at the upper right corner of each figure represents the lower size

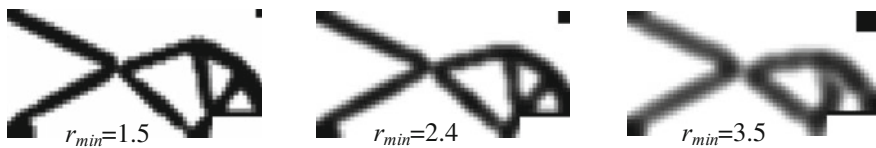


Fig. 5 Topological structures with different sizes (mesh number 30×60)

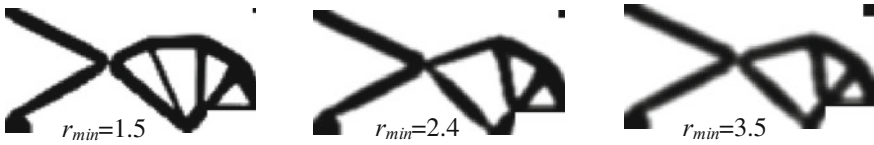


Fig. 6 Topological structures with different sizes (mesh number 50×100)

limit of the structure under different size constraints. When taking the r_{min} respectively as 1.5, 2.4 and 3.5, different final topological shape could be designed.

By analyzing the topological grasper, the conclusion could be get that with the increase of r_{min} , the size of the minimum flexible hinge of the topological structure section more than the lower size limit of the structure at the upper right corner of each figure, especially the flexible hinge in the middle of grasper and the larger the r_{min} the stronger the hinge. Therefore, the nonlinear mapping method can control the size of topological structure by r_{min} component size. Meanwhile, with the increase of r_{min} , gray-scale elements appear in the structure boundary, it can be decreased by increase the mesh number and select appropriate r_{min} , such as Fig. 6. In order to suppress the gray-scale elements, Fuchs et al. proposed a sum of the reciprocal variables (SRV) to constraint for 0/1 topological design [23]. Wang et al. proposed a bilateral filtering for structural topology optimization [24]. Long et al. proposed a modified optimality criterion method for gray elements suppression [25] and so on, the suppression of gray-scale elements need further studies.

3.2 Stress Analysis of Grasper

Stress distribution are shown in Fig. 7, and the stress variances of grasper designed with and without minimum manufacture constraints are shown in Table 1.

When r_{min} is 1.5, the maximum stress of the grasper is 0.057 GPa, r_{min} is 3.5, the maximum stress of the grasper is 0.041 GPa. The results show that while r_{min} increasing the maximum stress of the grasper is decreasing. This is because that the increase of r_{min} makes the smallest part thick and makes the stress concentration decrease.

As shown in Table 1, in addition, the stress variances of grasper designed with minimum manufacturing constraints are generally smaller than that of grasper designed without the manufacture constraint. And the stress distributions of grasper designed with minimum manufacture constraints are uniform, it is better to avoid the stress concentration, so the failure probability structure could be reduced.

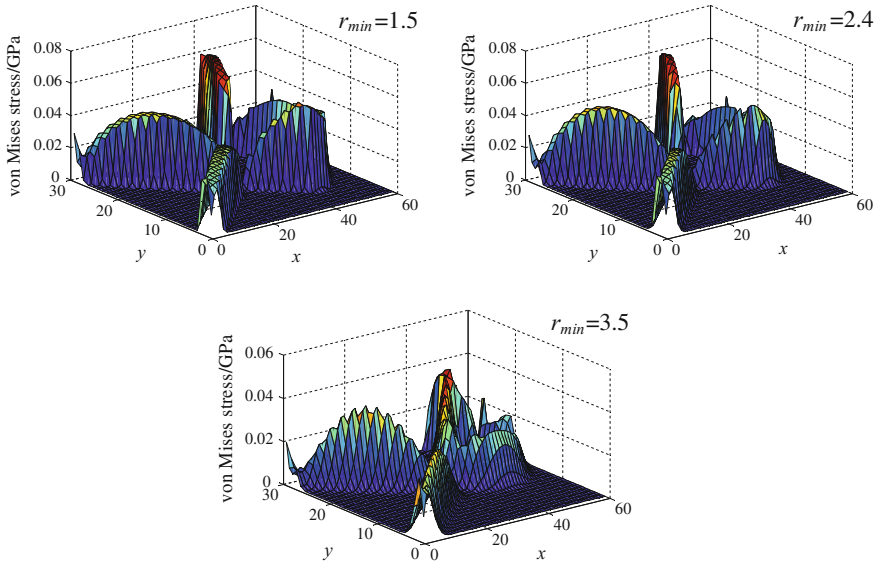


Fig. 7 The stress distribution under the minimum size constraint (mesh 30×60)

Table 1 Variance of stress value under different constraint conditions

Manufacturing constraints	Yes	No
$r_{min} = 1.5$	1.98	2.48
$r_{min} = 2.4$	1.39	1.85
$r_{min} = 3.5$	0.75	0.95

3.3 Output Displacement Analysis of Grasper

The reasonable output displacement of grasper is desired. As shown in Fig. 8, the output displacement's curves are illustrated with the development of computational process when minimum size constraints r_{min} respectively are 1.5, 2.4 and 3.5.

Taking compare between the three output displacement curves in Fig. 8, the result could be deduced that as the r_{min} value increase, output displacements of graspers decrease. Employing the method of nonlinear mapping by r_{min} to control the minimum size, to a certain extent, will reduce the flexible grasper displacement value of the output point.

The output displacement with and without minimum size constraint are illustrated in Table 2. The data in the table shows that the output displacement with minimum size constraint are accordingly smaller than that without minimum size constraint.

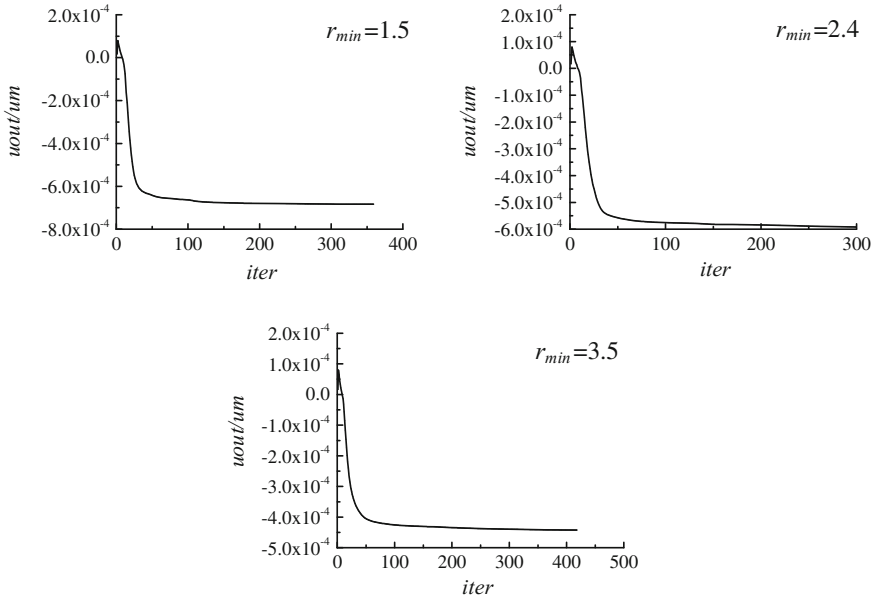


Fig. 8 Output point displacement

Table 2 The output point displacement with and without minimum size constraint

Manufacturing constraints	Yes	No	Decrease percentage
$r_{min} = 1.5$	6.83	7.47	8.58
$r_{min} = 2.4$	5.91	6.54	9.62
$r_{min} = 3.5$	4.42	4.92	10.16

4 Conclusion

A method that employs the non-linearly mapping method to realize minimal size constraints in topology optimization, combined with SIMP, is explored in this paper. Its viability is demonstrated through numerical experiment-grasper. Stress and the output displacement are analyzed.

The experimental results of the compliant grasper show that non-linearly mapping method with r_{min} is able to control the size of the smallest topology section effectively. The topological structure section become thick, especially the flexible hinge in the middle of grasper that is helpful to manufacture. The maximum stress level of grasper could be reduced by employing minimal size constraints, and the stress distribution tend to be homogenization which avoid the phenomenon of stress concentration.

Future work will focus on the research related to manufacture and extending the current formulation to design larger size mechanisms.

Acknowledgments Authors gratefully acknowledge the funding support of National Natural Science Foundation of China for this work under the research fund number 51375383.

References

1. Howell LL (2001) *Compliant mechanisms*. Wiley, New York
2. Jog CS, Haber RB (1996) Stability of finite element models for distributed-parameter optimization and topology design. *J Comput Methods Appl Mech Eng* 130:203–226
3. Sigmund O, Petersson J (1998) Numerical instabilities in topology optimization: a survey on procedures dealing with checkerboards, mesh-dependencies and local minima. *J Struct Optim* 16:68–75
4. Diaz A, Sigmund O (1995) Checkerboard patterns in layout optimization. *J Struct Optim* 10:40–45
5. Haber RB, Jog CS, Bendsoe MP (1996) A new approach to variable-topology shape design using a constraint on perimeter. *J Struct Optim* 11:1–12
6. Petersson J, Sigmund O (1998) Slope constrained topology optimization. *Int J Numer Meth Eng* 41:1417–1434
7. Duysinx P, Bendsoe MP (1998) Topology optimization of continuum structures with local stress constraints. *Int J Numer Methods Eng* 43:1453–1478
8. Poulsen TA (2003) A new scheme for imposing a minimum length scale in topology optimization. *Int J Numer Methods Eng* 57:741–760
9. Yin L, Ananthasuresh GK (2001) Design of distributed compliant mechanisms. *Mech Based Des Struct Machines* 31:151–179
10. Luo Z, Chen LP, Yang JZ, Zhang YQ, Abdel-Malek K (2005) Compliant mechanism design using a multi-objective topology optimization scheme of continuum structures. *J Struct Multi Optim* 33:142–154
11. Sigmund O (2007) Morphology-based black and white filters for topology optimization. *J Struct Multi Optim* 33:401–424
12. Zhu B, Zhang X, Fatikow S (2014) Level set-based topology optimization of hinge-free compliant mechanisms using a two-step elastic modeling method. *J Mech Des* 136(3):031007
13. Luo J, Luo Z, Chen S et al (2008) A new level set method for systematic design of hinge-free compliant mechanisms. *J Comput Methods Appl Mech Eng* 198(2):318–331
14. Guest JK, Prevost JH, Belytschko T (2004) Achieving minimum length scale in topology optimization using nodal design variables and projection functions. *Int J Numer Methods Eng* 61:238–254
15. Gaynor AT, Meisel NA, Williams CB et al (2014) Multiple-material topology optimization of compliant mechanisms created via polyjet three-dimensional printing. *J Manufact Sci Eng* 136:061015
16. Guest JK, Prevost JH, Belytschko T (2004) Achieving minimum length scale in topology optimization using nodal design variables and projection functions. *Int J Numer Methods Eng* 61:238–254
17. Sigmund O (2009) Manufacturing tolerant topology optimization. *J Acta Mechanica Sinica* 25(2):227–239
18. Zhou M, Rozvany GIN (1992) DCOC: an optimality criteria method for large systems, part I: theory. *J Struct Optim* 5:12–25
19. Zhou M, Rozvany GIN (1993) DCOC: an optimality criteria method for large systems, part II: algorithm. *J Struct Optim* 6:250–262
20. Rozvany GIN, Sobieski JS (1992) New optimality criteria methods: forcing uniqueness of the adjoint strains by corner-rounding at constraint intersections. *J Struct Optim* 4:244–246

21. Sigmund O (1999) Design of material structures using topology optimization. PhD thesis, Department of Solid Mechanics, Technical University of Denmark, Denmark, vol 169, pp 31–42
22. Rietz A (2001) Sufficiency of a finite exponent in SIMP (power law) methods. *J Struct Multidisc Optim* 21:159–163
23. Fuchs MB, Jiny S, Peleg N (2005) The SRV constraint for 0/1 topological design. *J Struct Multidisc Optim* 30:320–326
24. Wang MY, Wang SY (2005) Bilateral filtering for structural topology optimization. *Int J Numer Meth Eng* 63:1911–1938
25. Long K, Zhao HW (2010) A modified optimality criterion method for gray elements suppression. *J Comput Aided Des Comput Graph* 22:2197–2201

A Boundary Reconstruction Algorithm Used in Compliant Mechanism Topology Optimization Design

Nianfeng Wang, Hao Guo, Chaoyu Cui, Xianmin Zhang and Kai Hu

Abstract This paper proposes a boundary reconstruction algorithm for the compliant mechanism topology optimization design. The gray units resulted from the numerical instability after topology optimization makes the interpretation of optimal material distribution and subsequent manufacturing difficult, which need to be eliminated. The proposed algorithm in this paper is composed of three steps which are contraction of gray units, search and move of boundary units and smoothness of the boundary. Several simulations have been taken to verify the effectiveness of this algorithm. The simulation demonstrates that the algorithm is effective.

Keywords Compliant mechanism · Topology optimization · Boundary reconstruction

1 Introduction

Topology optimization design is a mathematical method that optimizes the material layout in a given space, implemented by using the finite method for the analysis [1] and has a good performance in the field of automatic design and material optimization [2–4]. Many methods utilized in topology optimization have been developed during last several decades, mainly including homogenization method [5, 6], Solid Isotropic Material with Penalization [7], level set method [8, 9], Ground Structure approach [10] and Evolution algorithm [11]. The above men-

N. Wang (✉) · H. Guo · C. Cui · X. Zhang · K. Hu
Guangdong Provincial Key Laboratory of Precision Equipment
and Manufacturing Technology, School of Mechanical
and Automotive Engineering, South China University of Technology,
Guangzhou 510640, China
e-mail: menfwang@scut.edu.cn

H. Guo
e-mail: ahguohaostu@gmail.cn

tioned topology optimization methods have a wide range of applications in structural design especially in the field of compliant mechanism design [12–14].

The beginning of topology optimization design in compliant mechanism filed can be dated back to year 1994 when Ananthasuresh creatively utilized homogenization optimization method to design a compliant mechanism [15]. Compliant mechanism topology optimization has been developed remarkably afterwards both in theoretical studies and practical applications. Sigmund [16] proposed a method based on continuum-type topology optimization techniques for the design of compliant mechanism. Pederson [17] proposed evolution algorithm to design compliant mechanism in the idea of recognizing empty material as 0 and solid material as 1 to represent the material distribution. Du [18] used element-free Galerkin method for the optimal design of compliant mechanisms with geometrically non-linearity, this method is more capable of handling large deformation. Yin and Ananthasuresh [19] illustrated a continuous peak function utilized for material interpolation. Wang [20–26] developed a topology method by using theory of pairs of curves. Other researches, such as Alonso [27], Takezawa [28], Jin [29] have developed variant novel and practical methods in the field of compliant mechanism design.

Among mentioned methods above, SIMP method acts as the most popular and useful method in the field of compliant mechanisms design. However, experiments have shown that most popular topology optimization methods have the same undesirable characters: they may result in the feature of gray units whose density is between 0 and 1, which makes the interpretation of optimal material distribution and subsequent manufacturing difficult. Serval methods have been proposed to deal with numerical instabilities feature in topology optimization. Haber [30] proposed a method called perimeter method to control the number of holes and establish the characteristic length scale, however, the value of perimeter can only be confirmed by experiment which results in the difficulty in application. Hu [31] proposed a crossing sensitivity filter method to improve the distribution of gray units. Anderson [32] utilized polygonal finite elements to deal with this feature. These methods generally improve gray units during the process of handling the problem of checkerboard pattern and mesh dependence feature [16]. Few methods have been proposed to eliminate gray units and most of them are complex which result in the low efficiency during the solution [33].

In this paper, a new boundary reconstruction algorithm is proposed to address the problem mentioned above based on the SIMP method. This algorithm is composed of three steps. In the first step, gray units are contracted to insure that there is at most one-layer gray unit in outermost layer. In the second step, gray units are moved according to the direction of solid material to insure the volume of gray units equal to 1. In the last step, smoothing algorithm is utilized in the boundary to obtain an ideal boundary.

2 Topology Optimization Based on SIMP Method

The alternative method among topology optimization used in this paper is the so-called “power-law method” or SIMP method (Solid Isotropic Material with Penalization). The design domain is discretized into finite element in which material properties are assumed constant. Each element is assigned a relative material density x_e range from 0 to 1 that determines its Young’s modulus E_e :

$$E_e(x_e) = E_{\min} + x_e^p(E_0 - E_{\min}) \tag{1}$$

where E_0 is the stiffness of the material and E_{\min} is a very small stiffness to prevent singular of stiffness matrix. p is the penalization factor which typically takes $p = 3$. For a compliant mechanism design, the mathematical formulation can be written as:

$$\begin{aligned} \min_{\mathbf{x}} : c(\mathbf{x}_i) &= -\mathbf{U}_i^T \mathbf{K} \mathbf{U}_{\text{in}} = -\sum_{e=1}^N E(\mathbf{x}_e) (\mathbf{u}_2^e)^T \mathbf{k}^e \mathbf{u}_1^e \\ \text{s.t.} : &\begin{cases} \mathbf{K} \mathbf{U}_{\text{in}} = \mathbf{F}_{\text{in}} \\ \mathbf{K} \mathbf{U}_i = \mathbf{F}_i \\ \frac{V(\mathbf{x}_i)}{V_0} = f_i \\ 0 < x_{\min} \leq \mathbf{x}_i \leq 1 \end{cases} \quad (i = 1, 2, \dots, M) \end{aligned} \tag{2}$$

where c is the compliance, \mathbf{U} and \mathbf{F} are the displacement vector and force vector, \mathbf{K} is the global stiffness matrix, \mathbf{u}_1^e and \mathbf{u}_2^e are the element displacement vectors result from the input force and output force, \mathbf{k}^e is the element stiffness matrix, $V(x_i)$ and V_0 are the material volume and design domain volume, f_i is the volume fraction, \mathbf{x}_i is the density of every single element between x_{\min} and 1. The process of compliant mechanism topology optimization design is shown in Fig. 1.

3 Boundary Reconstruction Algorithm

SIMP method has been widely used in mechanism design and model optimization due to its simple algorithm and high efficiency. However, for a given the design domain in Fig. 2a to optimize a MBB beam, the optimized configuration shown in Fig. 2b has many gray units in the boundary which can be clearly observed. The optimized configuration will be difficult for the processing and manufacturing. Therefore, this paper proposed a new boundary reconstruction algorithm to address this problem. The algorithm is composed of three steps: contraction of gray units, search and move of boundary units and smoothness of the boundary.

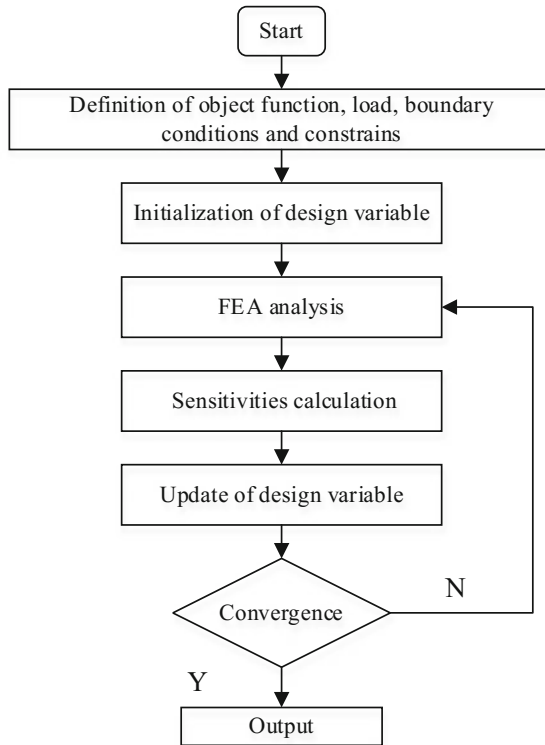


Fig. 1 Process of compliant mechanism topology optimization design

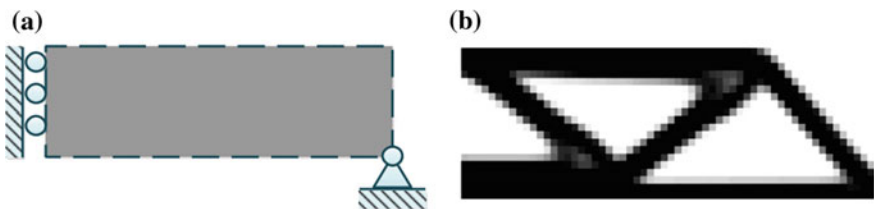


Fig. 2 **a** The design domain of MBB beam. **b** The configuration obtained by topology optimization design

3.1 Contraction of Gray Units

For an optimized configuration of MBB beam shown in Fig. 2b, there are more than one layer gray units in the outermost layer. The procedure primarily taken into account is the contraction of gray units to insure there are at most one layer in the outermost layer meanwhile not result in the looseness of configuration and the occurrence of holes.

The main idea of contraction of gray units is to specify relative precedence according to their distance to solid units. Every gray unit has four directions which are left, right, up and down and they belong to different union $\{E_n, E_{n-1}, E_{n-2}, \dots, E_1\}$ which the precedence is from low to high. For a gray unit N in union of lower precedence $E_n (n \geq 1)$, it can move to a nearest gray unit M in union $\{E_{n-1}\}$. If unit M can accommodate N which means $V(M) + V(N) \leq 1$, the volume of unit M will be update to $V(M) + V(N)$ and the volume of unit N will be updated to 0. Then, volume of unit $V(M)$ will move to a nearest unit in union $\{E_{n-2}\}$ until the unit in a union of high procedure can be updated to 1. If unit $E_{n-1}(1)$ can't accommodate N which means $V(M) + V(N) \geq 1$, the volume of unit M will be update to 1 and volume of unit N will be updated to $V(M) + V(N) - 1$. Then, volume of unit $V(M)$ will move to nearest unit $E_{n-1}(2)$ in union $\{E_{n-1}\}$. After several movements, neither one layer or none gray units will be occurring in the boundary layer. The process of this algorithm is shown in Fig. 3 and the result after contraction of gray units is shown in Fig. 4.

It can be observed from Fig. 4 that there is only one layer gray units or the solid units in the boundary, which conforms to the expected result.

3.2 Boundary Search and Move

Boundary of configuration has only one layer gray units after contraction. These gray units can be used to insure new boundary. Four defined boundaries here which

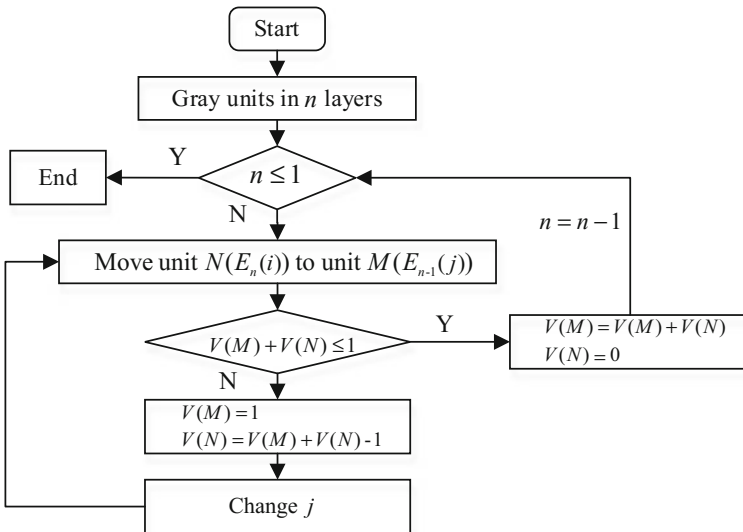


Fig. 3 Process of contraction of gray units

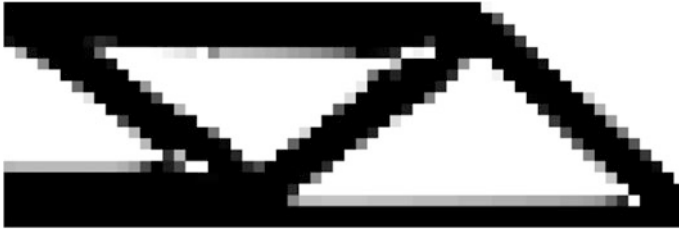


Fig. 4 Configuration after contraction of gray units

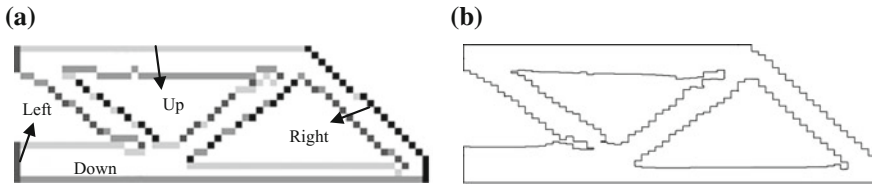


Fig. 5 **a** The search and move of MBB beam boundary. **b** New boundary after secondarily contract

are up, down, left and right shown in Fig. 5a. All the gray units in the boundary are secondarily contracted to the solid units in the negative direction of the boundary to make volume of the unit in the boundary equals to 1. Consequently, the gray units are eliminated after secondary contraction. The result is shown in Fig. 5b.

3.3 Smooth Boundary

Configuration obtained has many sawtooth units which will be difficult for the processing and manufacturing which shown in Fig. 6a. Therefore, sawtooth units should be handled to obtain smooth and continuous boundary. The smooth algorithm contains two steps. In the first step, the boundary is divided into many segments, depending on whether solid units in boundary are adjacent. In the second step is shown in Fig. 6b, two solid units are as a whole unit which can be smoothed by cubic spline curve.

Finally, the smooth boundary of MBB beam can be obtained by using the smooth algorithm, which is shown in Fig. 7.

Simulation was taken to compare the performance of old configuration and new configuration. The strain energy of new MBB beam obtained by FEA simulation is 19.830 and the strain energy of old configuration is 20.35. The error between two configurations is 2.63 % which is accord with the design intention.

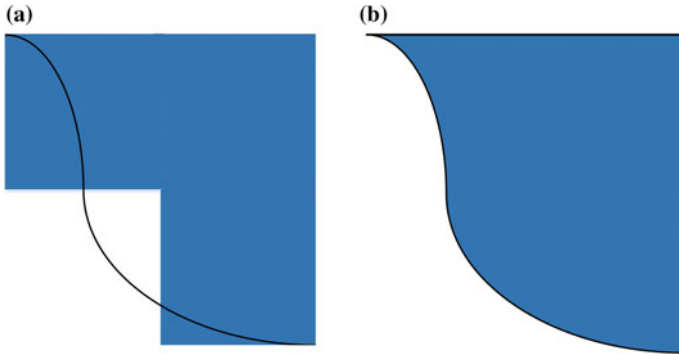


Fig. 6 **a** The old boundary contains sawtooth. **b** The new boundary obtained by interpolation of cubic spline curve


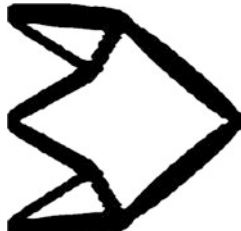


Fig. 7 Smooth boundary of MBB beam

4 Boundary Reconstruction of Compliant Mechanism

To verify the boundary reconstruction algorithm mentioned above, numerical simulations are carried out on several compliant mechanisms of single material and double material which shown in Tables 1 and 2.

Table 1 Compare of output with different compliant mechanisms (single material)

Result by topology optimization (a)	Result by boundary reconstruction (b)	Output (a)	Output (b)	Error %
		1.6998	1.6834	0.262

(continued)

Table 1 (continued)

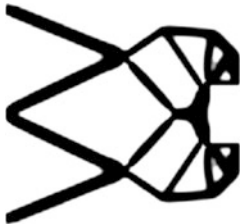
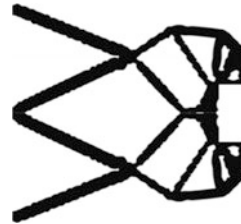
Result by topology optimization (a)	Result by boundary reconstruction (b)	Output (a)	Output (b)	Error %
		1.5384	1.5333	0.332

Table 2 Compare of output with different compliant mechanisms (double material)

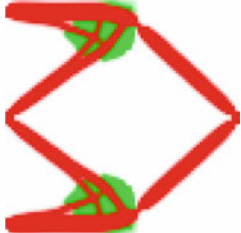
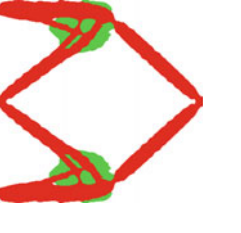
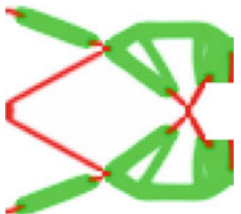
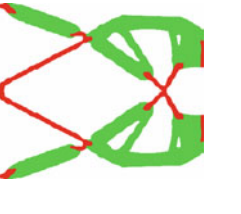
Result by topology optimization (a)	Result by boundary reconstruction (b)	Output (a)	Output (b)	Error %
		1.3518	1.3541	0.18
		1.9100	1.9070	0.16

Table 1 shows the configuration of inverter and gripper of single material. Table 2 shows the configuration of inverter and gripper of double material which represented in different color. Given a certain input, the output can be obtained from the simulation.

It can be observed from Tables 1 and 2 that the error between configuration old and new configuration is very small which can illustrate the effectiveness of the boundary reconstruction algorithm.

5 Conclusion

In conclusion, this paper proposed an effective boundary reconstruction algorithm used in compliant mechanism topology optimization design. The boundary reconstruction algorithm is composed of three steps which are introduced in detail.

The simulation shows a good performance of this method which means the method is effective. We believe this method will play a practical role in the processing and manufacturing of compliant mechanism.

Acknowledgments The authors would like to gratefully acknowledge the reviewers' comments. This work is supported by National Natural Science Foundation of China (Grant Nos. 51575187, 91223201), Science and Technology Program of Guangzhou (Grant No. 2014Y2-00217), Science and Technology Major Project of Huangpu District of Guangzhou (20150000661), Research Project of State Key Laboratory of Mechanical System and Vibration (MSV201405), the Fundamental Research Funds for the Central University (Fund No. 2015ZZ007) and Natural Science Foundation of Guangdong Province (S2013030013355).

References

1. Bendsoe MP, Sigmund O (2013) *Topology optimization: theory, methods, and applications*. Springer Science & Business Media
2. Zhu JH, Zhang WH, Xia L (2015) Topology optimization in aircraft and aerospace structures design. *Arch Comput Methods Eng*, 1–28
3. Rezaie R, Badrossamay M, Ghaie A et al (2013) Topology optimization for fused deposition modeling process. *Procedia CIRP* 6:521–526
4. Yu Y, Jang IG, Kwak BM (2013) Topology optimization for a frequency response and its application to a violin bridge. *Struct Multi Optim* 48(3):627–636
5. Bendsoe MP, Kikuchi N (1988) Generating optimal topologies in structural design using a homogenization method. *Comput Methods Appl Mech Eng* 71(2):197–224
6. Suzuki K, Kikuchi N (1991) A homogenization method for shape and topology optimization. *Comput Methods Appl Mech Eng* 93(3):291–318
7. Bendsoe MP, Sigmund O (1999) Material interpolation schemes in topology optimization. *Arch Appl Mech* 69(9–10):635–654
8. Wang MY, Wang X, Guo D (2003) A level set method for structural topology optimization. *Comput Methods Appl Mech Eng* 192(1):227–246
9. Zhu B, Zhang X, Wang N (2013) Topology optimization of hinge-free compliant mechanisms with multiple outputs using level set method. *Struct Multi Optim* 47(5):659–672
10. Hassani B, Hinton E (2012) *Homogenization and structural topology optimization: theory, practice and software*. Springer Science & Business Media
11. Huang X, Xie M (2010) *Evolutionary topology optimization of continuum structures: methods and applications*. Wiley
12. Zhang X (2003) Topology optimization of compliant mechanisms. *Chin J Mech Eng* 39(11):47–51
13. De Leon DM, Alexandersen J, Fonseca JSO et al (2015) Stress-constrained topology optimization for compliant mechanism design. *Struct Multi Optim* 52(5):929–943
14. Chen G, Li D (2010) Degree of freedom of planar compliant mechanisms. *J Mech Eng* 46(13):48–53
15. Ananthasuresh G K, Kota S, Kikuchi N (1994) Strategies for systematic synthesis of compliant MEMS. In: *Proceedings of the 1994 ASME winter annual meeting*, pp 677–686
16. Sigmund O, Petersson J (1998) Numerical instabilities in topology optimization: a survey on procedures dealing with checkerboards, mesh-dependencies and local minima. *Struct Optim* 16(1):68–75
17. Parsons R, Canfield SL (2002) Developing genetic programming techniques for the design of compliant mechanisms. *Struct Multi Optim* 24(1):78–86

18. Du Y, Chen L (2009) Topology optimization for large-displacement compliant mechanisms using element free Galerkin method. *Int J CAD/CAM* 8(1)
19. Yin L, Ananthasuresh GK (2001) Topology optimization of compliant mechanisms with multiple materials using a peak function material interpolation scheme. *Struct Multi Optim* 23(1):49–62
20. Wang NF, Zhang XM (2012) Compliant mechanisms design based on pairs of curves. *Sci Chin Technol Sci* 55(8):2099–2106
21. Wang NF, Zhang XM (2015) Topology optimization of compliant mechanisms using pairs of curves. *Eng Optim* 47(11):1497–1522
22. Wang NF, Tai K (2008) Design of grip-and-move manipulators using symmetric path generating compliant mechanisms. *J Mech Des* 130(11):112305
23. Wang NF, Yang YW (2009) Structural design optimization subjected to uncertainty using fat Bezier curve. *Comput Methods Appl Mech Eng* 199(1):210–219
24. Wang NF, Tai K (2010) Design of 2-DOF compliant mechanisms to form grip-and-move manipulators for 2D workspace. *J Mech Des* 132(3):031007
25. Wang NF, Tai K (2010) Target matching problems and an adaptive constraint strategy for multi objective design optimization using genetic algorithms. *Comput Struct* 88(19):1064–1076
26. Wang NF, Zhang XM, Yang YW (2013) A hybrid genetic algorithm for constrained multi-objective optimization under uncertainty and target matching problems. *Appl Soft Comput* 13(8):3636–3645
27. Alonso C, Ansola R, Querin OM (2014) Topology synthesis of multi-material compliant mechanisms with a sequential element rejection and admission method. *Finite Elem Anal Des* 85:11–19
28. Takezawa A, Yoon GH, Jeong SH et al (2014) Structural topology optimization with strength and heat conduction constraints. *Comput Methods Appl Mech Eng* 276:341–361
29. Jin M, Zhang X (2016) A new topology optimization method for planar compliant parallel mechanisms. *Mech Mach Theory* 95:42–58
30. Haber RB, Jog CS, Bendsøe MP (1996) A new approach to variable-topology shape design using a constraint on perimeter. *Struct Optim* 11(1–2):1–12
31. Hu SB, Chen LP, Zhang YQ et al (2009) A crossing sensitivity filter for structural topology optimization with chamfering, rounding, and checkerboard-free patterns. *Struct Multi Optim* 37(5):529–540
32. Pereira A, Talischib C, Menezesa IFM et al (2010) Checkerboard-free topology optimization using polygonal finite elements. *Mecánica Computacional* 29:1525–1534
33. Suresh K (2010) A 199-line Matlab code for Pareto-optimal tracing in topology optimization. *Struct Multi Optim* 42(5):665–679

Topology Optimization of Thermally Actuated Compliant Mechanisms Using Node Design Variables

Jinqing Zhan, Liangming Long and Zhichao Huang

Abstract The topology optimization method of thermally actuated compliant mechanisms using node design variables method is presented. The projection function within defined sub-domain is used to represent the relationship of node design variables and node density variables in the method. It can impose the minimum length scale control during topological design. The topology optimization model of thermally actuated compliant mechanism is established by maximizing the output displacement and restricting the structure volume. The adjoint approach is applied to perform the design sensitivity analysis, and the method of moving asymptotes is adopted to solve the topology optimization problem. The numerical examples are presented to show that the proposed method can avoid the de facto hinges in the obtained thermally actuated compliant mechanism.

Keywords Compliant mechanisms · Thermal loads · Topology optimization · Node design variables

1 Introduction

Compliant mechanisms can transmit force and motion through its elastic deformation of flexible member [1–3]. It has many advantages such as a simple structure, simplified manufacture processes, reduced friction, reduced assembly time, high

J. Zhan (✉) · L. Long · Z. Huang
School of Mechatronics and Vehicle Engineering, East China Jiaotong University,
Nanchang 330013, China
e-mail: zhan_jq@126.com

L. Long
e-mail: long_lm@126.com

Z. Huang
e-mail: hzcosu@163.com

precision, high reliability, light weight and miniaturization. It has been widely used in biological engineering micromanipulation, micro-electro-mechanical systems and optical fiber alignment. Topological design of compliant mechanisms only needs to specify design domain and the input and output position, without a known rigid-link mechanism. Thus, the method has drawn more and more attentions.

In recent years, topology optimization of compliant mechanisms applied input force have been made great development. Topology optimization of thermally actuated compliant mechanisms becomes one of the research hotspots due to their good controllability [4]. The topology optimization method has been used to electro-thermo-mechanical actuators with geometrical nonlinearities including multiple materials [5]. Yin [6] presented a new material interpolation scheme for topology optimization problem of electro-thermally actuated compliant micro-mechanisms. Du [7] suggested a new topology optimization method which the element-free method is applied to design thermally actuated compliant mechanisms with geometrical nonlinearities. Luo [8] used level set methods to perform shape and topology optimization of electro-thermally actuated compliant mechanisms. Ansola [9, 10] integrated an additive strategy to evolutionary optimization method for topological design of thermally actuated compliant mechanisms including uniform and non-uniform temperature fields. However, de facto hinges usually occur in the created mechanisms while thermally actuated compliant mechanisms are designed using topology optimization. The hinges results in high stress concentration and poor fatigue reliability. Heo [11] developed a topology optimization method of thermally actuated compliant mechanisms with minimum length scale control. Compared to the amount of literature on hinge-free compliant mechanisms [12], research on topological design of thermally actuated compliant mechanisms with hinge free are relatively few.

In this study, we proposed a new method for topology optimization of thermally actuated mechanisms using node design variables method in order to avoid generating the de facto hinges in the created mechanisms. Within defined sub-domain, the projection function independent on element mesh is adopted to represent the relationship of node design variables and node density variables. It can impose the minimum length scale control during topological design to avoid one-node connecting hinges. The topology optimization model of thermally actuated compliant mechanism was established by maximizing the output displacement and restricting the structure volume. The adjoint approach is utilized to solve the sensitivity of objective function and constraints, and the method of moving asymptotes is adopted as strategy for the topology optimization problem.

2 Optimization Formulations of Thermally Actuated Compliant Mechanisms

2.1 The Node Design Variables Method

The displacement field of each point in design domain and element density field are denoted as Q4/Q4 implementation, as shown in Fig. 1. The displacement for each point of an element and element densities are approximated using bi-linear interpolation function in the implementation method. Compared to the material interpolation model of element density method, the material density for each point of an element is not uniform in the implementation model. Therefore, the displacement and element densities are expressed by

$$u_e = \sum_{i=1}^m N_i u_i \quad \rho_e = \sum_{i=1}^m N_i \rho_i \tag{1}$$

where u_e represents the displacement of any point in an element, N_i denotes the shape function related to node i , u_i denotes the displacement vector of node i , m is the node number of each element, ρ_e is the element density and ρ_i is the node density related to node i .

The projection function independent on element mesh independent is adopted in the node design variables method. It represents the relationship of the node design variables and the node density variables within defined sub-domain. The minimum length scale control can be achieved during topological design of thermally actuated compliant mechanisms using the projection function. The projection can be expressed as using the maximum function [13, 14]

$$\rho_i = \max_{j \in \Omega_i} (d_j) \tag{2}$$

where ρ_i denotes the material density of node i , d_j represents the node design variable corresponding to node j , and Ω_i is the sub-domain associated with node i .

Fig. 1 Q4/Q4 Interpolation method

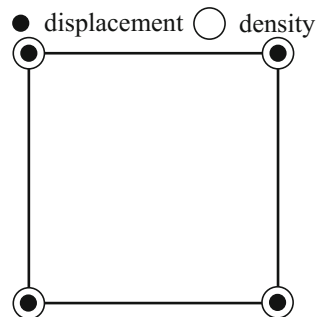
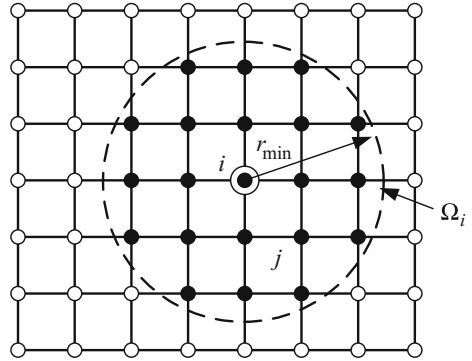


Fig. 2 Sub-domain corresponding to the node i



The sub-domain Ω_i associated with node i is defined as a circle with its center located at the node i . The radius r_{\min} of the circle equals half of defined minimum length size of structural members during topological design of thermally actuated compliant mechanisms, as shown in Fig. 2. The distant between node j and node i in the sub-domain Ω_i must meet the following equation

$$r = |r_i - r_j| < r_{\min} \quad j \in \Omega_i \tag{3}$$

where r represents the distant between node i and node j , r_i is defined as the distant between node i and the reference point, and r_j is defined as the distant between node j and the reference point. The parameter r_{\min} can be defined to determines the minimum length scale of the obtained compliant mechanisms.

2.2 Optimization Model

The output displacement at the output point is maximized to meet the flexibility requirement and obtain desired motion. The output displacement u_{out} can be defined using the dummy load method. A unit dummy load \mathbf{F}_2 is applied at the output point in the desired direction, as shown in Fig. 3, and the displacement u_{out} can be expressed by

$$u_{out} = \mathbf{F}_2 \mathbf{U} \tag{4}$$

where \mathbf{U} represents the nodal displacement subjected to thermal load.

The objective function of the topology optimization problem is developed by maximum the output displacement. The material volume is defined as the constraint. The node design variables method is applied to avoid generating de facto hinges during topological design of thermally actuated compliant mechanisms. The optimization model can be written as

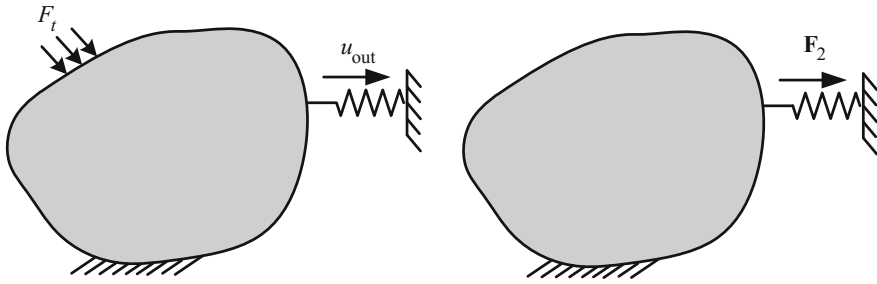


Fig. 3 Design domain for thermally actuated compliant mechanism

$$\begin{aligned}
 & \text{Minimize } -u_{\text{out}}(\mathbf{d}) \\
 & \quad \quad \quad d_1, d_2, \dots, d_M \\
 & \text{Subject to :} \\
 & \left\{ \begin{array}{l} \rho_i = f(\mathbf{d}) \\ \rho_e = \sum_{i=1}^N N_i \rho_i \\ \mathbf{F}_t(T) = \mathbf{K}\mathbf{U} \\ \sum_{e=1}^N V_e \rho_e - V^* \leq 0 \\ 0 < d_{\min} \leq d_j \leq 1, \quad j = 1, 2, \dots, M \end{array} \right. \quad (5)
 \end{aligned}$$

where \mathbf{d} refers to the design variables, f represents the projection function, N_i denotes the shape function associated with node i , N is the number of nodes of each element. \mathbf{K} is the global stiffness matrix of structure, \mathbf{F}_t denotes the thermal stress load which is related to the nodal temperature T subjected to thermal load. V_e refers to the element volume, V^* is the allowed material volume ratio, and M denotes the total number of node. d_{\min} is the lower bound on the node design variables which is taken to be a small positive value in order to avoid singularity of the global stiffness matrix during the finite element analysis.

2.3 Sensitivity Analysis and Solution Technique

To apply the gradient-based algorithm, the sensitivities of objective and constraint with respect to the design variables are need to be solved. The sensitivity of the objective can be obtained following a Lagrange multiplier approach. The lagrangian using Eq. (5) for the problem can be expressed as

$$L = -\mathbf{F}_2^T \mathbf{U} + \lambda(\mathbf{K}\mathbf{U} - \mathbf{F}_t) \quad (6)$$

where λ refers to the Lagrangian multiplier vectors for the elastic problems.

The sensitivity of objective for the problem can be expressed by

$$\frac{\partial L}{\partial d_i} = \sum_{j \in S_i} \frac{\partial L}{\partial \rho_j} \quad (7)$$

where S_i is the set of nodes mapped from the node design variable d_i .

Firstly, the sensitivity with respect to the node density is solved:

$$\frac{\partial L}{\partial \rho_j} = -\mathbf{F}_2^T \frac{\partial \mathbf{U}}{\partial \rho_j} + \lambda^T \left(\frac{\partial \mathbf{K}}{\partial \rho_j} \mathbf{U} - \frac{\partial \mathbf{F}_t}{\partial \rho_j} \right) + \lambda^T \frac{\partial \mathbf{U}}{\partial \rho_j} \mathbf{K} - \lambda^T \frac{\partial \mathbf{F}_t}{\partial T} \frac{\partial T}{\partial \rho_j} \quad (8)$$

The thermo stress load \mathbf{F}_t with respect to the nodal temperature is zero because the uniform temperature fields is considered in this study. Thus, Eq. (7) is rewritten as

$$\frac{\partial L}{\partial \rho_j} = (-\mathbf{F}_2^T + \lambda^T \mathbf{K}) \frac{\partial \mathbf{U}}{\partial \rho_j} + \lambda^T \left(\frac{\partial \mathbf{K}}{\partial \rho_j} \mathbf{U} - \frac{\partial \mathbf{F}_t}{\partial \rho_j} \right) \quad (9)$$

To remove the sensitivity terms $\partial \mathbf{U} / \partial \rho_j$, the following expression should be zero:

$$-\mathbf{F}_2^T + \lambda^T \mathbf{K} = 0 \quad (10)$$

From Eqs. (7) and (9), we get

$$\frac{\partial L}{\partial d_i} = \sum_{j \in S_i} \frac{\partial L}{\partial \rho_j} = \sum_{j \in S_i} \lambda^T \left(\frac{\partial \mathbf{K}}{\partial \rho_j} \mathbf{U} - \frac{\partial \mathbf{F}_t}{\partial \rho_j} \right) \quad (11)$$

According to the relationship between the node densities and the element densities, we got

$$\begin{aligned} \frac{\partial \mathbf{K}}{\partial \rho_j} &= \sum_{e=1}^N \int_{\Omega_e} \frac{\partial \mathbf{K}_e}{\partial \rho_e} \frac{\partial \rho_e}{\partial \rho_j} d\Omega_e = \sum_{e=1}^N \int_{\Omega_e} \frac{\partial \mathbf{K}_e}{\partial \rho_e} N_i d\Omega_e \\ &= \sum_{e=1}^N \int_{\Omega_e} p \rho_e^{p-1} \mathbf{K}_e N_i d\Omega_e \end{aligned} \quad (12)$$

where \mathbf{K}_e refers to the element stiffness matrix, P is the penalization parameter which is set equal to 3.

The sensitivity of the constraint with respect to the node design variables can be written as

$$\frac{\partial V}{\partial d_i} = \sum_{j \in S_i} \frac{\partial V}{\partial \rho_j} = \sum_{j \in S_i} \sum_{e=1}^N \int_{\Omega_e} N_i d\Omega_e \tag{13}$$

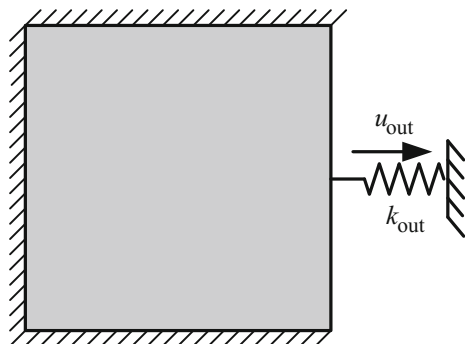
The Method of Moving Asymptotes (MMA) [15] is flexible to solving the complicated optimization problem. MMA is applied to update the design variables during the topological design of thermally actuated compliant mechanisms.

3 Numerical Example

This example demonstrates the topological design of a clamped thermal actuator subjected to uniform thermal effects. The design domain and boundary conditions for the problem are shown in Fig. 4. The output port is prescribed at the center point of the right side. Due to the symmetric nature of this problem, only the half the design domain is modeled. The design domain is meshed with 120×60 four node plane finite elements in a 60 mm by 30 mm region. The artificial material properties are set as: Young’s modulus for solid material E is 100 GPa, thermal expansion coefficient α is $2 \times 10^{-5} \text{ K}^{-1}$, and Poisson’s ratio μ is 0.3. The allowed material volume ratio is given as 25 %. The artificial springs with stiffness are set to $k_{\text{out}} = 100 \text{ N/m}$ at output port, and the compliant mechanisms is actuated by a uniform rise at the temperature of $\Delta K = 100$.

The optimal thermally actuated compliant mechanism are obtained by the node design variables method as shown in Fig. 5a, while Fig. 5b represents the optimal mechanisms obtained by variable density method with sensitivity filter. The de facto hinges occurs in the obtained compliant mechanism, as shown in Fig. 5b. The hinges can lead to high stress concentration and poor fatigue reliability. Thus, the thermally actuated compliant mechanisms is not useful in real applications. In

Fig. 4 Design domain and boundary conditions



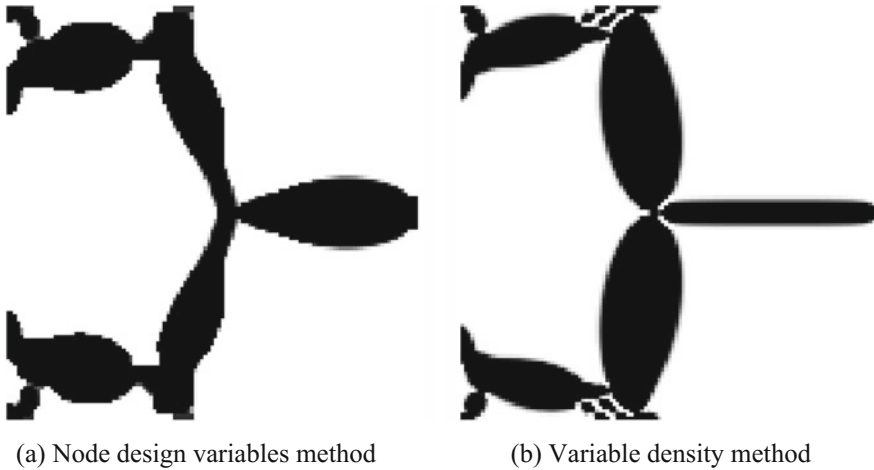


Fig. 5 Optimal compliant mechanisms obtained by different methods

addition, the topological structure of the optimal mechanism appears checkerboard phenomenon that cause the thermal actuator to be not convenient for manufacturing.

Compared Fig. 5a with Fig. 5b, de facto hinges are completely avoided in the topological structure of thermally actuated compliant mechanisms. The result shows that the minimum length scale constraint can be achieved to eliminate the de facto hinges in the thermally actuated compliant mechanisms using the projection function method. Meanwhile, the topological structure of thermally actuated compliant mechanisms has distinct topology. It is greatly meaningful and economical for manufacturing. It can be seen that the proposed method can result in similar topological result of compliant mechanisms as reported in the literature [7]. Thus, the node design variables method can be applied to design thermally actuated compliant mechanisms with hinge-free successfully.

4 Conclusions

A new topology optimization method of thermally actuated compliant mechanisms using the node design variables method is presented. The node design variables method apply projection function to represent the relationship of node design variables and node density variables. The adjoint approach is applied to perform the design sensitivity analysis, and the method of moving asymptotes is adopted to solve the topology optimization problem. The numerical examples are presented to show that the minimum length scale control can be achieved using the node design variables method to avoid generating the de facto hinges in the created thermally

actuated compliant mechanism. Meanwhile, the optimal thermally actuated compliant mechanism has distinct topology which is greatly meaningful and economical for fabrication.

Acknowledgement This research was supported by the National Natural Science Foundation of China (51305136), the Natural Science Foundation of Jiangxi, China (20151BAB206032) and the Science and Technology Plan Projects of Jiangxi Provincial Education Department (GJJ150547). This supports are greatly acknowledged.

References

1. Howell LL (2001) Compliant mechanisms. Wiley, New York
2. Bendsoe MP, Sigmund O (2003) Topology optimization: theory, methods and applications. Springer, Berlin
3. Zhan JQ, Zhang XM (2011) Topology optimization of compliant mechanisms with geometrical nonlinearities using the ground structure approach. *Chin J Mech Eng* 24:257–263
4. Jonsmann J, Sigmund O, Bouwstra S (1999) Compliant thermal microactuators. *Sens Actuators A* 76:3463–3469
5. Sigmund O (2001) Design of multi-physics actuators using topology optimization. Part 1: one-material structures. *Comput Methods Appl Mech Eng* 190:6577–6604
6. Yin LZ, Ananthasuresh GK (2002) A novel topology design scheme for the multi-physics problems of electro-thermally actuated compliant micromechanisms. *Sens Actuators A* 97–98:599–609
7. Du YX, Luo Z, Tian QH, Chen LP (2009) Topology optimization for thermo-mechanical compliant actuators using mesh-free methods. *Eng Comput* 41:753–772
8. Luo Z, Tong LY (2009) Shape and topology optimization for electrothermo-mechanical actuators using level set methods. *J Comput Phy* 228:3173–3181
9. Ansola R, Vegueria E, Canales J (2010) An element addition strategy for thermally actuated compliant mechanism topology optimization. *Eng Comput* 27:694–711
10. Ansola R, Vegueria E, Canales J, Alonso C (2012) Evolutionary optimization of compliant mechanisms subjected to non-uniform thermal effects. *Finite Elem Anal Des* 57:1–14
11. Heo S, Yoon GH, Kim YY (2008) Minimum scale controlled topology optimization and experimental test of a micro thermal actuator. *Sens Actuators A* 141:603–609
12. Zhu BL, Zhang XM, Wang NF (2012) A new level set method for topology optimization of distributed compliant mechanisms. *Int J Numer Methods Eng* 91:843–871
13. Guest JK, Prevos JH, Belytschko T (2004) Achieving minimum length scale in topology optimization using nodal design variables and projection functions. *Int J Numer Methods Eng* 61:238–254
14. Chau HL (2006) Achieving minimum length scale and design constraint in topology optimization: a new approach. Master's thesis, University of Illinois at Urbana-Champaign, Urbana
15. Svanberg K (1987) The method of moving asymptotes: a new method for structural optimization. *Int J Numer Methods Eng* 42:359–373

Design of Bistable Pinned-Pinned Arches with Torsion Springs by Determining Critical Points

Safvan Palathingal and G.K. Ananthasuresh

Abstract This paper describes a simplified method to analyze and design a bistable pinned-pinned arch with torsion springs at the pin (revolute) joints. Finite, but not zero, values of torsion spring constants offer the dual advantage of being amenable to monolithic compliant bistable arches wherein torsion springs are realized with equivalent revolute flexures; and giving enhanced range of travel between the stable states and reduced switching forces. However, the equilibrium equations become intractable for analytical solution unlike the extreme cases of fixed-fixed and pinned-pinned arches. Therefore, a new method for analyzing and designing novel bistable arches is presented here by determining critical points in the force-displacement curve. First, the equilibrium equations for post-buckling analysis are derived by writing the deflected profile as a linear combination of the buckling mode shapes of the corresponding straight beam with torsion springs at the pinned ends. These equations are then used to find the critical points with maximum, minimum, and zero forces. The critical points not only provide an approximate view of the bistable force-displacement curve but also enable synthesis of arches with desired behaviour. By using this semi-analytical method, we present an example of an arch with reduced switching force, large switch-back force, and enhanced travel between the two stable states.

Keywords Compliant monolithic bistable mechanisms · Buckling modes · Optimization · Revolute flexures

S. Palathingal (✉) · G.K. Ananthasuresh
Indian Institute of Science, Bangalore, India
e-mail: safvan@mecheng.iisc.ernet.in
URL: <http://www.iisc.ac.in/>

G.K. Ananthasuresh
e-mail: suresh@mecheng.iisc.ernet.in

1 Introduction

Arches with two force-free stable equilibrium positions are called bistable arches. Bistable arches, also known as curved-beam bistable mechanisms, find application at multiple length-scales. Micro-relays [1, 2], electromagnetic actuator [3], micro-valves [4] and mechanical memory components [5] are examples of bistable micro devices. Retractable devices [6], rear trunk-lids of cars [7], circuit breakers and easy-chairs [8, 9] are examples of macro-scale bistable devices.

A buckled column is one of the simplest bistable arches. It can be toggled between the two states by applying a transverse force [12, 13]. This arch relies on the pre-stress in the buckled column to achieve its bistability. Precise pre-stress is hard to realize during bulk-manufacturing as well as in microfabrication. Another class of bistable arches with small flexure joints have been studied in [14–18]. These arches have relatively rigid regions and their compliance come from the flexures. Such arches are not very efficient since the entire arch does not contribute to the compliance and flexures are prone to failure. Hence, it is beneficial to pursue fully-compliant monolithic bistable arches that do not rely on pre-stress for their bistability.

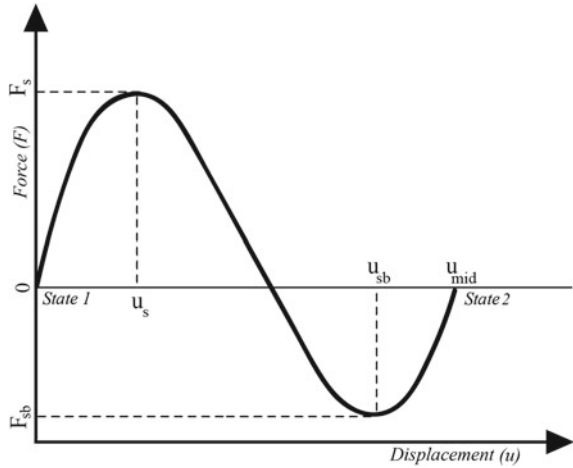
One way of achieving bistability without pre-stress is to make the fundamental buckling mode shape as the as-fabricated profile. Analysis of such arches under fixed-fixed boundary condition has been treated by [19, 20]. They employ post-buckling analysis of curved beams for fixed-fixed boundary conditions and obtained a monolithic fully-compliant bistable arch. On the other hand, [22] reported exact bistable characteristics of arches with pinned-pinned boundary conditions. In our previous work, [10], we presented the design of monolithic bistable arches by generalizing the boundary conditions from fixed-fixed to pinned-pinned with torsional (Fig. 1) and linear springs at the joints. By changing the boundary conditions, we could reduce the switching force and increase the travel between the stable states as compared to bistable arches with fixed-fixed boundary conditions.

In this paper, we present a computationally efficient method to design bistable arches by determining critical points on the force-displacement curve. The characteristic force-displacement curve of a bistable arch is shown in Fig. 2. State 1 is the as-fabricated force-free equilibrium state and State 2 the stressed but force-free equilibrium state. Switching force, F_s , is the force required to switch from State 1 to State 2; switch-back force, F_{sb} , is the force required to switch back to state 1 and travel, u_{mid} , is the distance the midpoint of the arch moves between the two states. Generally, points on force-displacement curve corresponding to F_s , F_{sb} and u_{mid} are

Fig. 1 Pinned-pinned bistable arch with torsion springs



Fig. 2 Characteristic force-displacement behavior of bistable mechanisms



sufficient for designing a bistable arch. Furthermore, by examining the values of F_s and F_{sb} , bistability of the arch can be checked. Hence, these three points are identified as the critical points on the force-displacement curve. This approach simplifies the design methodology to find the optimal bistable design parameters pertaining to size, arch shape, and cross-section dimensions.

2 Analysis of Pinned-Pinned Bistable Arches with Torsion Springs

An initially straight beam, pinned with a torsional spring at both ends is subjected to an axial force and its buckling mode shapes are calculated. In post-buckling analysis, a linear combination of the buckling modes is taken as the as-fabricated profile of the bistable arch and then it is subjected to a transverse actuating force. The potential energy of the system is found and minimized to obtain equilibrium equations. Critical points are obtained from the equilibrium equations, which can be used to check if the arch is bistable and then optimize the geometry of the arch.

2.1 Buckling and Post-buckling Analysis

Buckling Analysis A pinned-pinned beam with torsion springs is shown in Fig. 3. The governing differential equation and boundary conditions are given by [21].

Fig. 3 Reduced boundary condition beam to find mode shapes



$$EI \frac{d^4 w}{dx^4} + P \frac{d^2 w}{dx^2} = 0 \tag{1}$$

$$EI \frac{d^2 w}{dx^2} \Big|_{x=0} = \kappa_A \frac{dw}{dx} \Big|_{x=0} \tag{2}$$

$$EI \frac{d^2 w}{dx^2} \Big|_{x=L} = -\kappa_B \frac{dw}{dx} \Big|_{x=L} \tag{3}$$

where p is the axial load, w the transverse displacement of the beam perpendicular to the axial force, E the Young's Modulus, I the second moment of area of the cross section, κ_A the stiffness of torsional spring at the left end and κ_B the stiffness of torsional spring at the right end. As derived in our earlier work [10], the transcendental equation for the non-trivial buckled configuration can be written as

$$\begin{aligned} \frac{4\kappa_B}{M^3 EI} \sin^2\left(\frac{ML}{2}\right) - \left[\frac{\kappa_B}{\kappa_A M^2} - \frac{\kappa_B L}{M^2 EI} - \frac{EIL}{\kappa_A} - \frac{1}{M^2} \right] \sin(ML) \\ = \left[\frac{L}{M} - \frac{\kappa_B L}{\kappa_A M} \right] \cos(ML) \end{aligned} \tag{4}$$

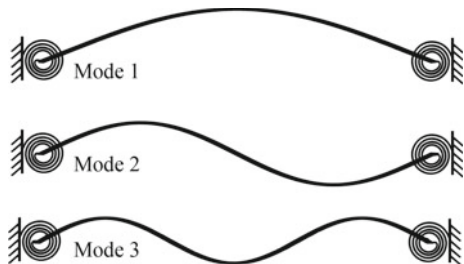
where

$$M^2 = \frac{N^2}{L^2} \tag{5}$$

$$N^2 = \frac{PL^2}{EI} \tag{6}$$

For $\kappa_A = \kappa_B = 0.0525$ Nm/rad, the mode shapes shown in Fig. 4 can be obtained from Eq. 4.

Fig. 4 First three buckling modes for $\kappa_A = \kappa_B = 0.00525$ Nm/rad



Post-buckling Analysis: The choice of as-fabricated shape of the element dictates its bistability. In [19], the authors proved that bistability exists when the first buckling mode for the fixed-fixed boundary condition with restricted asymmetric mode is used as the as-fabricated, stress-free geometric profile. In [22], bistability of a sin-curved arch which is the first mode for the pinned-pinned boundary condition is analysed. Any profile that is a linear combination of the buckling modes for a given boundary condition can be taken as the as-fabricated geometric profile of the bistable element ($h(x)$):

$$h(x) = \sum_{j=1}^{\infty} a_j w_j(x) \quad (7)$$

where w_j s are the mode shapes, and a_j s are their corresponding weights. Particular values of a_j s give rise to a unique arch. Post-buckling analysis is used to check bistability of the arch profile corresponding to the selected a_j s.

The deformed shape (w) of the bistable beam can also be approximated as a linear combination of the mode shapes.

$$w(x) = \sum_{j=1}^{\infty} A_j w_j(x) \quad (8)$$

In order to determine the force-displacement curve of the element, we minimize the potential energy of the element with respect to the A_j s. The potential energy is given by

$$PE = SE_b + SE_c + WP_f + \frac{1}{2} \kappa_A \left(\frac{dw}{dx} \Big|_{x=0} \right)^2 + \frac{1}{2} \kappa_B \left(\frac{dw}{dx} \Big|_{x=L} \right)^2 \quad (9)$$

where SE_b is the strain energy associated with the bending of the element, SE_c is the strain energy associated with deformation due to compression and WP_f is the work potential due to transverse force f . The strain energy due to bending is given by

$$SE_b = \frac{EI}{2} \int_0^L \left(\frac{d^2 \bar{w}}{dx^2} - \frac{d^2 w}{dx^2} \right)^2 dx \quad (10)$$

where L is the span of the arch. The work potential due to the transverse force f is given by

$$WP_f = -f u_{mid} \quad (11)$$

where u_{mid} is the deflection under the application of force f acting vertically downwards at the mid-point of the beam. It is given by

$$u_{mid} = h\left(\frac{L}{2}\right) - w\left(\frac{L}{2}\right) \quad (12)$$

The strain energy due to the axial force p is given by

$$SE_c = - \int_{\bar{s}}^s p d(s - \bar{s}) \quad (13)$$

where p is the axial force, s the length of the beam as it deforms and \bar{s} the as-fabricated length of the beam. They are given by:

$$p = Ebt\left(1 - \frac{s}{\bar{s}}\right) \quad (14)$$

$$s = \int_0^L \sqrt{1 + \left(\frac{dw}{dx}\right)^2} dx \approx \int_0^L \left[1 + \frac{1}{2} \left(\frac{dw}{dx}\right)^2\right] dx \quad (15)$$

$$\bar{s} = \int_0^L \left[1 + \frac{1}{2} \left(\frac{dh}{dx}\right)^2\right] dx \quad (16)$$

For static equilibrium, we need:

$$\frac{\partial PE}{\partial A_j} = 0 \quad (17)$$

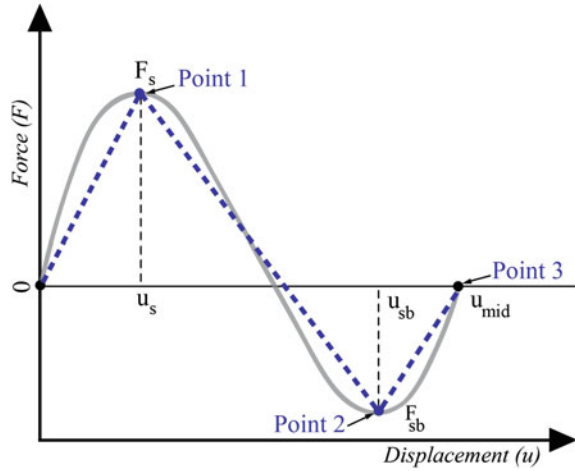
Upon solving Eq. 17, after substituting for u from Eq. 12, we get the force-displacement relationship. This analysis is mathematically tedious and in fact unnecessary from a design point of view. Hence, we developed a numerical technique described next. Note that only first three modes are used in the approximations in Eqs. 7 and 8 as results were found to be in good agreement with finite element analysis (FEA).

2.2 Critical-Point Method

A bistable force-displacement curve gives three important design parameters: switching force, switch-back force, and distance of travel between two stable states. These parameters correspond to three critical points on the curve as shown in Fig. 5. These points can be determined as described next.

First point: Force (F_s) at this point is the minimum force required to switch the bistable arch to the second stable state. Switching from the first stable state to the second can either happen with a completely symmetric deformation (symmetric switching) or with a partially asymmetric deformation (asymmetric switching); this is dependent on the as-fabricated shape of the arch. F_s is dependent on the mode of

Fig. 5 Critical points on a force-displacement curve



switching of the bistable arch. Equation 17 satisfies both symmetric switching and asymmetric switching conditions. So, it is important to identify the mode of switching between these two for a given arch. This can be done numerically by solving for two switching forces: one assuming symmetric switching (F_{ss}) and other assuming asymmetric switching (F_{as}). Once F_{ss} and F_{as} are determined, F_s and thereby the nature of switching can be assessed.

Figure 6a shows a case where a bistable arch prefers asymmetric switching over symmetric switching. Critical points are joined using dotted straight lines for visual association; they do not imply linear interpolation. It can be observed that asymmetric switching reduces F_s . There can be also cases where asymmetric switching is preferred but with $F_s = F_{ss}$ as shown in Fig. 6b.

F_{ss} is the point where the force is maximum w.r.t. to the displacement on the force-displacement curve. It can be found by maximizing the force F satisfying equilibrium equations. The finite variable optimization statement to obtain F_{ss} can

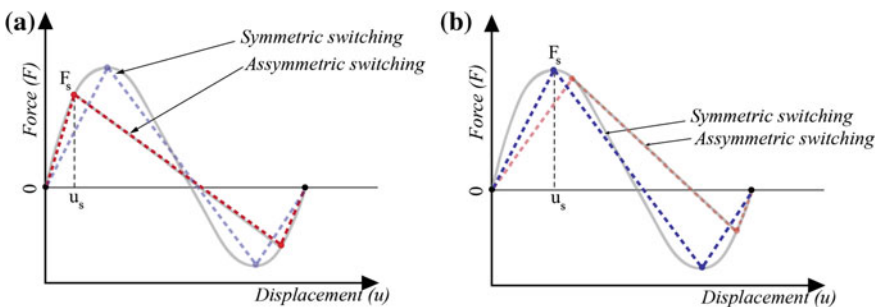


Fig. 6 Two cases of symmetric and asymmetric switching

be written as an optimization problem, which is solved numerically, say, Newton-Raphson or any other method.

$$\begin{aligned}
 & \text{Maximize } F \\
 & \quad A_1, A_2, A_3 \\
 & \text{Subject to} \\
 & A_1 : \frac{dPE}{dA_1} = 0 \\
 & A_2 : \frac{dPE}{dA_2} = 0 \\
 & A_3 : \frac{dPE}{dA_3} = 0
 \end{aligned} \tag{18}$$

Asymmetric switching force corresponds to the point when the arch begins to deflect asymmetrically. This is one of the points where multiple solutions exist for Eq. 17 with respect to A_2 , i.e.,

$$\frac{d^2PE}{d^2A_2} = 0 \tag{19}$$

F_{as} is found by solving Eqs. 19 and 17 numerically using the Newton-Raphson method. Initial values of A_1, A_2, A_3 and F are taken as a_1, a_2, a_3 and 0 respectively; these values correspond to State 1 of the arch. From F_{ss} and F_{as} , switching force F_s is found by comparing travel corresponding to points F_{ss} and F_{as} .

Second point: Switch-back force, F_{sb} is the minimum amount of force required to switch a bistable arch from State 2 to State 1. F_{sb} can also be thought as a measure of bistability. The larger the switch-back force, the higher the stability in the second stable state. Similar to F_s , F_{sb} depends also on the nature of switching. We proceed by solving for two different F_{sb} s, corresponding to symmetric and asymmetric switching. Equations for finding the first and second points are the same, but taking the initial condition as State 2 in the numerical method gives the second point. While implementing the critical-point algorithm, the third point(State 2) is determined before the second point and is used as the initial guess for finding the second point.

Third point: This point corresponds to the second force-free equilibrium state of the arch. Since $F = 0$, at this point, we have three equations in three unknowns, which can be solved numerically. The numerical method does not converge to the point corresponding to unstable force-free equilibrium state, which also satisfies the same equations, because of the numerical instability algorithm may face at this point.

Figure 7 compares the critical-point method to FEA for the parameters given in Table 1. It can be observed that critical points obtained from aforementioned technique are in good agreement with critical points on the force-displacement curve. Incidentally, in this case approximate linearly interpolated curve matches quite well with the FEA solution, which is not true in general.

Fig. 7 Comparison of critical-point method and FEA for pinned-pinned boundary conditions

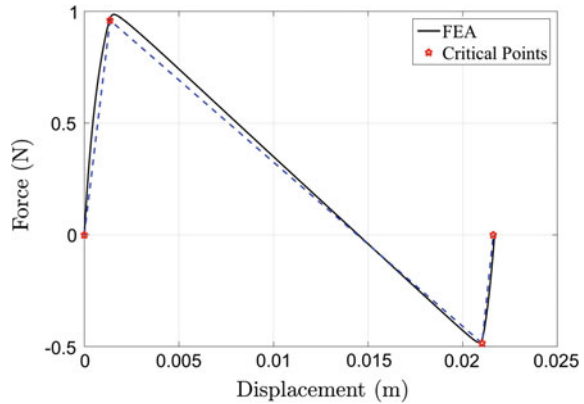


Table 1 Geometric and material parameters

Sl. No	Parameter	Value	Unit
1	Length (L)	125	mm
2	Height (h_{mid})	11	mm
3	Thickness (t)	1	mm
4	Depth (b)	5	mm
5	Young's modulus (E)	$2.1 * 10^9$	N/m ²

3 Optimal Design of Pinned-Pinned Bistable Arches with Torsion Springs

Bistable arches of different profiles can be made by taking a weighted combination of first three buckling mode shapes, or more if desired for given boundary conditions. We explore how the shape of the profile is related to the bistable characteristics. Once boundary conditions are identified, an analysis similar to that described in the previous section can be used to obtain the critical points for any bistable profile. Critical points give the bistable characteristics we want to optimize for. Some arches explored have been synthesized and compared with finite element simulations in [10].

To illustrate the approach, pinned-pinned boundary conditions with torsion spring of $\kappa_A = \kappa_B = 0.00525$ Nm/rad are used. A compliant revolute flexure of this κ value is realizable using split-tube flexure as shown in [11]. We assume that the profile of the arch will be a weighted combination of buckling modes for the given boundary conditions. Here, a_1, a_2 and a_3 are the unknown weights to be optimized. An arch is not bistable for any combination of a_1, a_2 and a_3 . Each point in the shaded region of the feasible space shown in Fig. 8 gives the combination of a_1, a_2 and a_3 that are bistable. The feasible space is computed by critical-point method, described in the previous section, over combinations of $\frac{a_2}{a_1}$ and $\frac{a_3}{a_1}$, and checking for bistability. Arches are bistable for a broader range of $\frac{a_3}{a_1}$ ratios as compared to $\frac{a_2}{a_1}$. The

loss of bistability beyond certain combinations of mode shapes can be understood better by analyzing the dependence of the switch-back force on as-fabricated shape.

The design space for designing and optimizing is constructed by plotting the bistable parameters: switching force (F_s), switch-back force (F_{sb}) and travel at the midpoint (u_{mid}), in the feasible space shown in Fig. 8. In the plot, F_s, F_{sb} , and u_{mid} are normalized using:

$$\bar{F} = \frac{FL^3}{Elh_{mid}} \tag{20}$$

$$\bar{u}_{mid} = \frac{u_{mid}}{h_{mid}} \tag{21}$$

where, $h_{mid} = h(L/2)$. Switching force reduces as $\frac{a_3}{a_1}$ and $\frac{a_2}{a_1}$ ratios increase. As we move towards the end of the feasibility region, F_{sb} approaches zero. This agrees with the intuitive understanding of switch-back force, as low values of F_{sb} imply that even a slight disturbance can bring the arch back from the second to the first equilibrium state. A bistable arch with maximum F_s , optimal design profile A in Fig. 8, is the one where $\frac{a_3}{a_1}$ and $\frac{a_2}{a_1}$ ratios are zero. The profile B has the highest switch-back force, F_{sb} , making it the most stable bistable arch in the feasible space. Largest travel at the midpoint, u_{mid} , is for the profile C. All the points corresponding to these three optimal profiles are indicated in the feasible and design spaces. The design space is a quick tool to select the right shape for the desired bistable behaviour and boundary conditions.

From a design perspective, it would be advantageous to select a profile that reduces F_s and increases F_{sb} and u_{mid} . One such design, profile B, has been modeled and 3D printed as shown in Fig. 9. The torsion springs at the pin joints are realized by compound split-tube flexures.

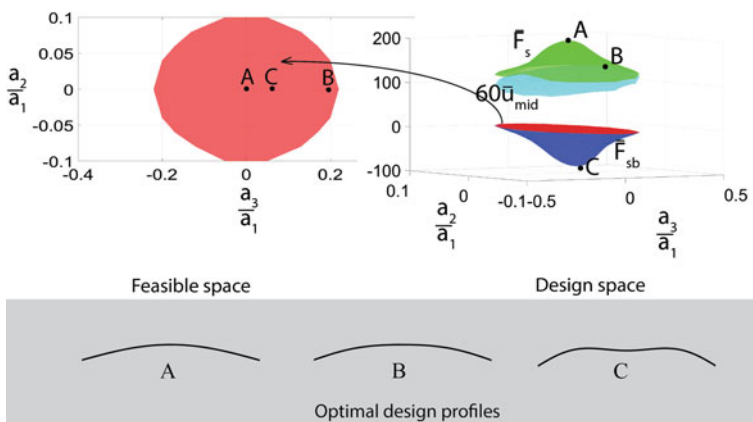


Fig. 8 Feasible and design spaces for pinned-pinned boundary conditions with $\kappa_A = \kappa_B = 0.00525$ Nm/rad

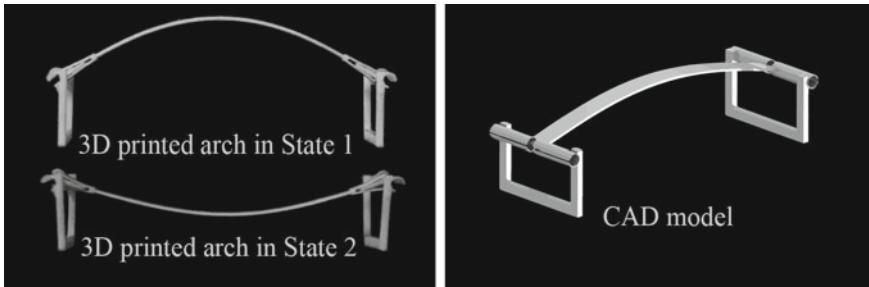


Fig. 9 3D printed (Objet Connex) bistable arch with revolute flexures

4 Summary

A critical point-based method to design pinned-pinned bistable arches with torsion springs at the joints has been presented. The motivation for developing bistable arches with torsion-spring boundary condition was to make them amenable for monolithic construction and positive lithography-based miniaturization. While pinned-pinned joints are difficult to realize at the micro-scale, pinned-pinned joints with torsional springs can be realised using revolute flexures. Such a bistable arch with compound split-tube flexures at the pinned-pinned ends is fabricated as an example.

It was found that including higher mode shapes in the as-fabricated geometric profile can lead to improved designs. Three profiles that maximize the switching force, switch-back force and travel at the midpoint were obtained from the design space. Furthermore, a design-space-based approach for designing bistable arch shape for any values of torsional stiffness of the springs at the pinned-pinned ends is also presented.

Acknowledgments The authors thank D. Sarojini for valuable discussions and M. Varun for his help in fabrication. Financial support from the Department of Science and Technology (DST) under the Technology Initiative for the Disabled and the Elderly (TIDE) programme, is also gratefully acknowledged.

References

1. Qiu J, Lang JH, Slocum AH, Weber AC (2005) A bulk-micromachined bistable relay with u-shaped thermal actuators. *J Microelectromech Syst* 14(5):1099–1109
2. Gomm T, Howell LL, Selfridge RH (2002) In-plane linear displacement bistable microrelay. *J Micromech Microeng* 12(3):257
3. Park S, Hah D (2008) Pre-shaped buckled-beam actuators: theory and experiments. *Sens Actuators, A* 148(1):186–192

4. Wagner B, Quenzer H, Hoerschelmann S, Lisee T, Juerss M (1996) Bistable microvalve with pneumatically coupled membranes. In: Micro electro mechanical systems, 1996, MEMS'96, proceedings. An investigation of micro structures, sensors, actuators, machines and systems. IEEE, the ninth annual international workshop on, IEEE, pp. 384–388
5. Hälgl B (1990) On a nonvolatile memory cell based on micro-electro-mechanics. In: Micro electro mechanical systems, 1990. proceedings, an investigation of micro structures, sensors, actuators, machines and robots. IEEE, pp 172–176
6. Ohsaki M, Tsuda S, Watanabe H (2013) Optimization of retractable structures utilizing bistable compliant mechanism. *Eng Struct* 56:910–918
7. Zhang S, Chen G (2011) Design of compliant bistable mechanism for rear trunk lid of cars. In: *Intelligent robotics and applications*, Springer, pp 291–299
8. Darshan S, Lassche TJ, Herder JL, Ananthasuresh GK (2015) A compliant two-port bistable mechanism with application to easy-chair design. 14th World Congress in Mechanism and Machine Science, Taipei, Taiwan, October 25–30, 2015
9. Sarojini D, Lassche T, Herder J, Ananthasuresh G (2016) Statically balanced compliant two-port bistable mechanism. *Mech Mach Theory* 102:1–13
10. Palathingal S, Sarojini D, Katti AN, Ananthasuresh GK (2015) A generalized method to investigate the bistability of curved beams using buckling analysis, 2nd international and 17th national conference on machines and mechanisms, iNaCoMM 73
11. Goldfarb M, Speich JE (1999) A well-behaved revolute flexure joint for compliant mechanism design. *J Mech Des* 121(3):424–429
12. Vangbo M (1998) An analytical analysis of a compressed bistable buckled beam. *Sens Actuators, A* 69(3):212–216
13. Saif MTA (2000) On a tunable bistable mems-theory and experiment. *J Microelectromech Syst* 9(2):157–170
14. Jensen BD, Howell LL (2003) Identification of compliant pseudo-rigid-body four-link mechanism configurations resulting in bistable behavior. *J Mech Des* 125(4):701–708
15. Zhao J, Jia J, He X, Wang H (2008) Post-buckling and snap-through behavior of inclined slender beams. *J Appl Mech* 75(4):041020
16. Wu C-C, Lin M-J, Chen R (2012) Bistable criterion for mechanically bistable mechanism. In: *Micro electro mechanical systems (MEMS), 2012 IEEE 25th international conference on*, IEEE, pp 396–399
17. Li G, Chen G (2014) A function for characterizing complete kinetostatic behaviors of compliant bistable mechanisms. *Mech Sci* 5(2):67–78
18. Jensen BD, Howell LL (2004) Bistable configurations of compliant mechanisms modeled using four links and translational joints. *J Mech Des* 126(4):657–666
19. Qiu J, Lang JH, Slocum AH (2004) A curved-beam bistable mechanism. *J Microelectromech Syst* 13(2):137–146
20. Cazottes P, Fernandes A, Pouget J, Hafez M (2009) Bistable buckled beam: modeling of actuating force and experimental validations. *J Mech Des* 131(10):101001
21. Simitsep GJ, Hodges DH (2006) *Fundamentals of structural stability*, Butterworth-Heinemann
22. Chen J-S, Ro W-C, Lin J-S (2009) Exact static and dynamic critical loads of a sinusoidal arch under a point force at the midpoint. *Int J Non-Linear Mech* 44(1):66–70

Optimal Design of a Novel Compliant Orthogonal Displacement Amplification Mechanism Considering Static and Dynamic Properties

Weilin Chen and Xianmin Zhang

Abstract In micro-manipulation, orthogonal displacement amplification mechanism (DAM) is important for obtaining parallel grasping movement. In this paper, the optimal design of a novel compliant orthogonal DAM, which can be used for the actuators with typical unidirectional movement, is presented. The optimal problem is formulated with considering the static and dynamic properties of the proposed mechanism. With predetermining the fabrication limit and customers' requirements, all the other dimensions of the proposed orthogonal DAM can be automatically determined by the optimal process. A design example is used to verify the optimal process. The iteration process verifies the effectiveness and stability of the optimal process. Finite element analysis (FEA) is used to verify the design results. The effect of large deflection nonlinearity to the orthogonal movement transformation accuracy is discussed.

Keywords Optimal design · Compliant mechanism · Orthogonal displacement amplification mechanism · Static and dynamic properties

1 Introduction

Recently, micro-grasping system has become a key device in many fields, such as micro-particle handling [1], optical fibers assembling [2] and cell manipulation [3]. The basic structure of micro-grasping system consists of actuator, intermediate mechanism and grasping ends. A typical case is that for obtaining parallel grasping movement, the movement of the grasping ends should be perpendicular to the output displacement of actuator [4–6]. Meanwhile, the movement of the grasping

W. Chen · X. Zhang (✉)

Guangdong Provincial Key Laboratory of Precision Engineering and Manufacturing Technology, South China University of Technology, Guangzhou 510640, China
e-mail: zhangxm@scut.edu.cn

W. Chen

e-mail: wlchen1@outlook.com

ends generally need to be amplified compared with that of the actuator [5, 7–9]. For these reasons, the intermediate mechanism generally needs to be designed as an orthogonal displacement amplification mechanism (DAM).

Several kinds of orthogonal DAMs are presented in the previous researches. Bridge-type mechanism [10] is the widely used orthogonal DAM, in which full symmetric structure and bidirectional symmetric input forces/displacements are required to reduce the parasitic movement at the output port. Therefore, bridge-type mechanism is used for the actuator with bidirectional symmetric movement, such as piezoelectric stack actuator. The static model, optimization [11], dynamic test [12] and development [13, 14] of bridge-type mechanism have been presented. A novel orthogonal DAM without requiring bidirectional symmetric input forces/displacements is proposed in our previous research [15]. The undetermined parameters are introduced and the corresponding design equations have been derived. The proposed orthogonal DAM can be used for the actuator with bidirectional symmetric movements or typical unidirectional movement, such as lateral comb electrostatic actuator [4], arrays of electrostatic actuators [7], and chevron electrothermal actuator [16]. However, the optimal design of the proposed DAM has not been presented.

In this paper, the optimal problem of the proposed compliant orthogonal DAM [15] will be formulated in Sect. 2, in which the static and dynamic properties will be considered to model the objective function and the constraints. With predetermining the fabrication limit and customers' requirements, all the other dimensions of the proposed orthogonal DAM can be automatically determined by the optimal process. In Sect. 3, a design example will be used to verify the optimal process and the simulation results will be discussed.

2 Optimal Problem

The proposed orthogonal DAM is a triangulation amplification-based mechanism (as shown in Fig. 1a), in which the output displacement depends on the displacement amplification ratio Q and the input displacement e_{in} . In the situation that the value of Q is predetermined, larger output displacement can be obtained as e_{in} increases.

The actuator of the proposed compliant orthogonal DAM (as shown in Fig. 1b) is of typical unidirectional linear movement. The relationship between e_{in} and the unidirectional linear movement of the actuator without external load applied at the output port e_a is:

$$e_{in} = \frac{k_a}{k_a + k_{in}} \cdot e_a = \frac{1}{1 + \frac{k_{in}}{k_a}} \cdot e_a, \quad (1)$$

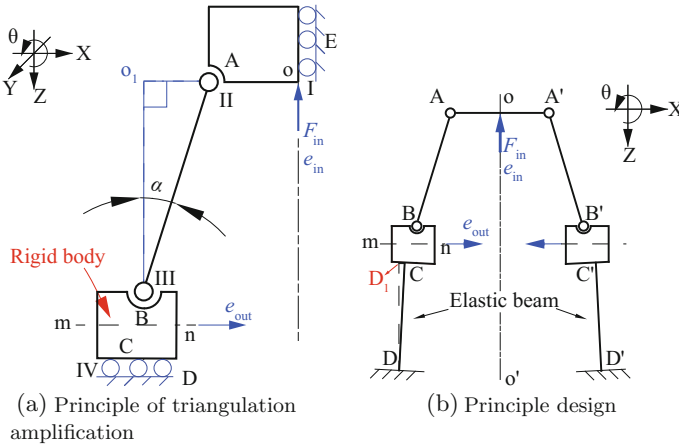


Fig. 1 The proposed compliant orthogonal DAM [15]

where e_a is only related to the driven voltage. For a certain actuator, the stiffness k_a is a constant. According to Eq. 1, if the input stiffness k_{in} is minimized, e_{in} can be maximized.

The optimization of k_{in} should be constrained by the static and dynamic properties as well as the requirements for miniaturization. The proposed orthogonal DAM is satisfied with small deflection assumption and Euler-Bernoulli beam assumption, which introduces a static constraint to the optimization. The natural frequency of the mechanism f_q should be larger than the threshold f_{qmin} to resist the vibration. The size of the proposed orthogonal DAM mainly depends on the length L_2 , as shown in Fig. 2b. In terms of miniaturization, L_2 should be smaller than a predetermined upper limit L_{max} . Moreover, the parameters L_2, t, r should be satisfied with the fabrication limit. Therefore, the optimal problem of the proposed orthogonal DAM is shown as follows:

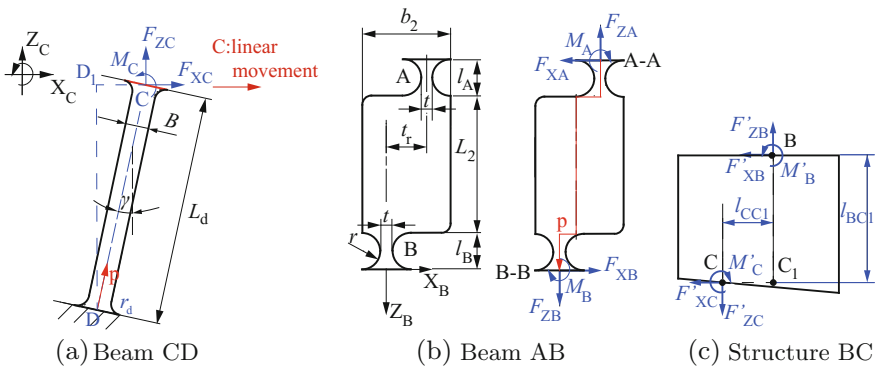


Fig. 2 Specific structure of beams CD and AB as well as rigid body BC [15]

$$\begin{aligned}
 \min \quad & k_{in}(\text{design variables} : L_2, t, r) \\
 \text{s.t.} \quad & \text{static constraint} \\
 & \text{dynamic constraint} : f_q \geq f_{qmin} \\
 & \text{miniaturization} : L_2 \leq L_{max} \\
 & \text{fabrication limit} t \geq t_{min}, r \geq 0, L_2 \geq 0
 \end{aligned} \tag{2}$$

2.1 Modeling of the Objective Function

According to the relation between compliance and stiffness, the objective function can be transformed into:

$$\min \frac{1}{C_{in}} = \frac{1}{\frac{e_{in}}{F_{in}}} \tag{3}$$

The input structure AA' can be viewed as a beam, as shown in Fig. 3. According to Castigliano's second theorem, the input displacement e_{in} is:

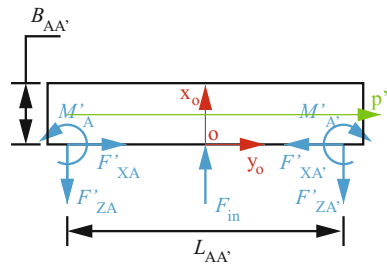
$$e_{in} = x_o = \frac{\partial V_{AA'}}{\partial F_{in}} + x_{oA} \tag{4}$$

For the constant cross-sectional beam AA', Euler-Bernoulli beam theory is used to derive the strain energy $V_{AA'}$.

$$V_{AA'} = \int_0^{L_{AA'}} \frac{(F_{AA'})^2}{2EA_{AA'}} dp' + \int_0^{L_{AA'}} \frac{(M_{AA'})^2}{2EI_{AA'}} dp', \tag{5}$$

where $L_{AA'}$ is used to control the overall width of the DAM, which is predetermined according to the customers' requirement. The parameters $EA_{AA'}$ and $EI_{AA'}$ are axial stiffness and the bending stiffness respectively. According to the force equilibrium, the axial force $F_{AA'}$ equals F_{XB} .

Fig. 3 Load analysis of the input structure AA'



For linear elastic beam AB, the compliance matrix connects the generalized displacements at point B with the loads that are applied at the same point:

$$\begin{pmatrix} X_B \\ Z_B \\ \theta_B \end{pmatrix} = \begin{pmatrix} S_{XB-FXB} & S_{XB-FZB} & S_{XB-MB} \\ S_{ZB-FXB} & S_{ZB-FZB} & S_{ZB-MB} \\ S_{\theta B-FXB} & S_{\theta B-FZB} & S_{\theta B-MB} \end{pmatrix} \begin{pmatrix} F_{XB} \\ F_{ZB} \\ M_B \end{pmatrix} \quad (6)$$

On one hand, substitute the displacement boundary condition $\theta_B = 0$ into Eq. (6), the relation among the loads F_{ZB} , F_{XB} , M_B is established:

$$M_B = -\frac{S_{\theta B-FZB}}{S_{\theta B-MB}} \cdot F_{ZB} + \left(-\frac{S_{\theta B-FZB}}{S_{\theta B-MB}}\right) \cdot F_{XB}, \quad (7)$$

On the other hand, the relation among the loads F_{ZB} , F_{XB} , M_B can be established by the load equilibrium of beam AB as well:

$$M_B = -M_A + F_{XB}(l_A + L + l_B) + F_{ZB}t_r. \quad (8)$$

According to moment distribution method, in the statically indeterminate structure shown in Fig. 1b, $M_A \rightarrow 0$.

With the combination of Eqs. (7), (8) and $M_A \rightarrow 0$, the relation between F_{XB} and F_{ZB} can be constructed:

$$F_{XB} = -\frac{\phi_1}{\phi_2} F_{ZB} = -\frac{1}{2} \cdot \frac{\phi_1}{\phi_2} \cdot F_{in}, \quad (9)$$

where $\phi_1 = S_{\theta B-FZB} + S_{\theta B-MB}t_r$, $\phi_2 = S_{\theta B-FXB} + S_{\theta B-MB}(l_A + L + l_B)$.

Considering $M_A \rightarrow 0$, the bending moment $M_{AA'}$ can be derived as:

$$M_{AA'} = \begin{cases} \frac{F_{in}}{2} \cdot p', & 0 < p' < \frac{L_{AA'}}{2} \\ \frac{F_{in}}{2} \cdot (L_{AA'} - p'), & \frac{L_{AA'}}{2} < p' < L_{AA'} \end{cases}. \quad (10)$$

Equations (5), (9) and (10) lead to that the deformation of the input structure $\partial V_{AA'}/\partial F_{in}$ can be expressed as a function of F_{in} :

$$\frac{\partial V_{AA'}}{\partial F_{in}} = w_1 \cdot F_{in} = \left(\frac{L_{AA'}}{4EB_{AA'}h(\frac{\phi_2}{\phi_1})^2} + \frac{(L_{AA'})^3}{4Eh(B_{AA'})} \right) \cdot F_{in}. \quad (11)$$

Similar to Eq. (6), the displacement-load relation at point A can be described by compliance matrix method. Substituting Eq. (9), $M_A \rightarrow 0$ as well as the force equilibrium of beam AB into the displacement-load relation at point A, Z_A which equals x_{oA} can also be expressed as a function of F_{in} :

$$Z_A = x_{oA} = w_2 \cdot F_{in} = \frac{1}{2} (S_{ZA-FZA} - S_{ZA-FXA} \cdot \frac{\phi_1}{\phi_2}) \cdot F_{in}, \tag{12}$$

The compliances $S_{\theta B-FZB}$, $S_{\theta B-FXB}$, $S_{\theta B-MB}$, S_{ZA-FZA} , S_{ZA-FXA} above can be derived by Castigliano’s second theorem.

With the combination of Eqs. (3), (4), (11) and (12), the objective function can be modelled as: $\min 1/(w_1 + w_2)$.

2.2 Modeling the Static Constraint

On one hand, the proposed orthogonal DAM is satisfied with the assumption of Euler-Bernoulli beam. Naturally, fixed-guided beams CD and C’D’ are Euler-Bernoulli beam. Whether beam AB is an Euler-Bernoulli beam can be verified by a strain energy-based evaluation error Δ_{error} , which is defined as [17]:

$$\Delta_{error} = \frac{\frac{\partial}{\partial F_{XB}} \alpha \int_0^{L_{AB}} \frac{F_s^2}{2GA_{AB}} dp}{\frac{\partial}{\partial F_{XB}} \left(\int_0^{L_{AB}} \frac{F_s^2}{2EA_{AB}} dp + \int_0^{L_{AB}} \frac{M_a^2}{2EI_{AB}} dp \right)} \cdot 100 \% . \tag{13}$$

For the rectangular cross section, the shearing coefficient α is 6/5. The parameters F_s , F_a , M_a are shearing force, axial force, and bending moment respectively. The parameter G denotes the shearing elastic module. When Δ_{error} is small enough, such as $\Delta_{error} < 2 \%$, beam AB is an Euler-Bernoulli beam.

On the other hand, the proposed orthogonal DAM is satisfied with small deflection assumption, which should be considered when the lower limit $\Delta_{error-1}$ is set. The set of $\Delta_{error-1}$ will be further discussed in Sect. 3.

Therefore, the static constraint can be expressed as: $\Delta_{error-1} \leq \Delta_{error} < 2 \%$.

2.3 Further Modeling the Dynamic Constraint

The model of f_q has been presented in our previous research [15], which indicates the model is related to the undetermined parameters of beam CD **a**. Thus, obtaining the reasonable value of **a** should be considered when the dynamic constraint is further modelled.

In beam CD, the undetermined parameters can be set as the length L_d , the width B as well as the inclined angle θ , as shown in Fig. 2a. In our previous research, the design equations of the undetermined parameters have been derived:

$$\Gamma_{XC-FZC}(\mathbf{a})g + \Gamma_{XC-FXC}(\mathbf{a}) + \Gamma_{XC-MC}(\mathbf{a})f_1g + \Gamma_{XC-MC}(\mathbf{a})f_2 = -q, \tag{14}$$

$$g(\mathbf{a}) = -j, \tag{15}$$

$$f_1(\mathbf{a}) + \frac{f_2(\mathbf{a})}{g(\mathbf{a})} = l_{CC1} + \frac{l_{BC1}}{j} + i_1 + \frac{i_2}{j}, \tag{16}$$

where Γ is the compliance of beam CD related to \mathbf{a} , and f_1, f_2, g are the functions of $\Gamma(\mathbf{a})$. The parameters q, j, i_1, i_2 are the functions of the compliance S . The formulation of these parameters can be found in our previous work [15].

However, using the design Eqs. (14)–(16), the calculated results of the undetermined parameters \mathbf{a} are only satisfied with the displacement boundary conditions and load equilibrium equations, whereas the calculated results which are not fit for the fabrication or are too large can not be avoided automatically.

Based on the load equilibrium of output structure BC (as shown in Fig. 2c), as well as Eqs. (7) and (9), $M_C - F_{ZC}$ relation can be obtained:

$$M_C = [(i_1 + l_{CC1}) - \frac{\phi_1}{\phi_2}(i_2 + l_{BC1})]F_{ZC}, \tag{17}$$

where l_{BC1} is predetermined by the requirement for the size of the output port. For determining the reference range of l_{CC1} , another formulation of $M_C - F_{ZC}$ will be obtained in terms of the displacement-load relation of beam CD ignoring the filleted corners as well as the displacement boundary conditions $Z_C = 0, \theta = 0$:

$$M_C = \frac{L_d}{2[-1 + (\frac{L_d}{B})^2] \sin \theta} F_{ZC}. \tag{18}$$

In Euler-Bernoulli beam CD, the ratio of length to width $L_d/B \gg 1$. Therefore, the coefficient of Eq. (18) is positive, further leading to that the coefficient of Eq. (17) is positive, which determines the range of l_{CC1} :

$$l_{CC1} > -i_1 + \frac{\phi_1}{\phi_2}(i_2 + l_{BC1}), \tag{19}$$

where the right side is the lower limit l_{CC1-l} . The value of B will be reduced as the decrease of l_{CC1} , and gradually approaches to the fabrication limit B_1 .

The further modeling of the dynamic constraint considering obtaining the reasonable value of \mathbf{a} is shown in Fig. 4.

In Fig. 4, the vector \mathbf{p} contains all the predetermined parameters, including (1) the fabrication limit: the radius of the filleted corners r_d , as well as, t_{min} ; (2) the customers' requirements: the thickness of the mechanism h , the width of the output port l_{BC1} , the theoretical displacement amplification ratio Q_t as well as $f_{qmin}, L_{max}, L_{AA'}, \Delta_{error-1}$ and the material. The vector v_0 contains all the initial values of the design variables.

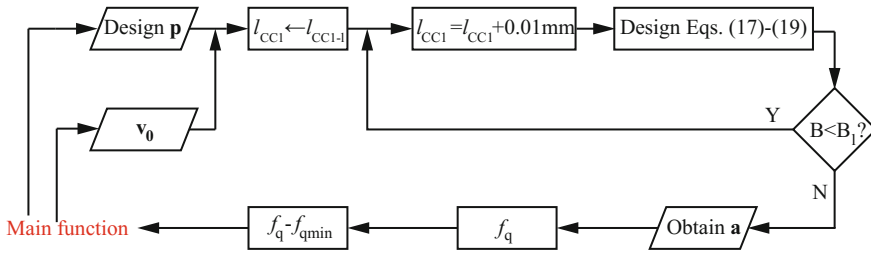


Fig. 4 Further modeling of the dynamic constraint

3 Design Examples and Finite Element Analysis (FEA)

In this section, a design example will be used to verify the optimal process. The movement accuracy and the displacement amplification ratio in the design results will be evaluated in terms of small deflection-based and large deflection-based FEA. The movement direction accuracy of the output structure BC can be evaluated by the parameters δ , ζ , which are defined as:

$$\delta = \left| \frac{(Z_B + Z_{C1})/2}{(X_B + X_{C1})/2} \right| \cdot 100\%, \quad \zeta = \frac{|X_B - X_{C1}|}{l_{BC1}} / |X_{C1}|. \quad (20)$$

where δ is used to evaluate the Z-axis parasitic movement of output structure BC, and ζ is used to evaluate the corresponding rotation parasitic movement.

The predetermined parameters of the design example are shown in Table 1. The parameter $\Delta_{error-1}$ is set as 1.10, 1.20, 1.30, 1.40 % respectively to analyze its effect to the large deflection error.

All the other dimensions are automatically determined by solving the optimal problem, including the key dimensions of beam AB \mathbf{o} , l_{CC1} , and the undetermined parameters of beam CD \mathbf{a} , as shown in Table 2. Note that in beam AB, the distance t_r and the width b_2 are the function of \mathbf{o} . The constraint optimal problem is solved by MATLAB “fmincon” function.

Take 1.30 % group for example, as shown in Fig. 5. Using different initial value v_0 , as the increase of the iteration steps, the value of k_{in} finally decreases to the same minimum value 2.68 N/ μm , which is converged. Similar results can be obtained in other groups. Therefore, the optimal problem with complex dynamic constraint can be solved stably and the results are effective.

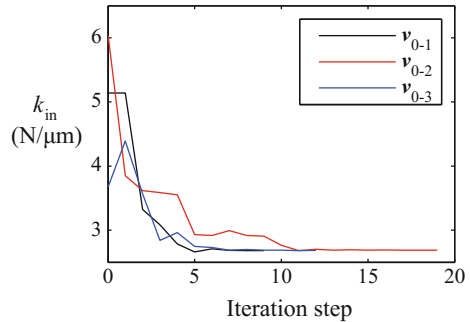
Table 1 Predetermined parameters \mathbf{p} of the design example

Fabrication limit (mm)			Customers' requirements						
r_d	t_{min}	B_1	h (mm)	l_{BC1} (mm)	Q_t	f_{qmin} (Hz)	L_{max} (mm)	$L_{AA'}$ (mm)	Material
0.25	0.25	0.20	1.00	2.00	8.00	2000	12.00	10.40	Al-alloy

Table 2 Optimal design results

$\Delta_{error-1}$ (%)	o			a			
	L_2 (mm)	t (mm)	r (mm)	l_{CC1} (mm)	L_d (mm)	B (mm)	γ
1.10	9.07	0.25	0.74	0.26	6.03	0.20	0.10
1.20	9.88	0.25	0.67	0.26	5.57	0.20	0.10
1.30	10.76	0.25	0.61	0.28	5.72	0.22	0.10
1.40	11.78	0.25	0.55	0.29	5.51	0.23	0.09

Fig. 5 Iteration process to solve the optimal problem ($\Delta_{error-1} = 1.3\%$)



The FEA results of 1.30 % group are illustrated in Fig. 6. The direction of the input force F_{in} is vertical towards up. Qualitatively, in the small deflection-based FEA results, the output structure is move horizontally and the orthogonal movement transformation is verified. The movement of the output structure can be applied to construct parallel grasping. Similar results can be obtained in the large deflection-based FEA results, in which the orthogonal movement transformation accuracy is reduced. The input stiffness of the design result is 2.52 $N/\mu m$. The error between the converged value and the FEA result is 6.35 %.

The quantitative results are listed in Table 3. In the situation of small deflection FEA, the value of Q is larger than 4.7, which verifies the displacement amplification of the design results. The error due to Z-axis translational parasitic movement δ is smaller than 0.30 %. Table 3 shows that as in the situation of small deflection-based FEA, as $\Delta_{error-1}$ decreases, the resulting Δ_{error} decreases and further the error due to rotation parasitic movement ζ reduces as well, which conform to small deflection assumption and Euler-Bernoulli beam assumption.

In the large deflection-based FEA, the value of δ is smaller than 2.5 %, which is much better than the traditional bridge-type DAM driven by an unidirectional force as well. The parameter ξ is used to evaluate the effect of large deflection nonlinearity to ζ , which is defined in Table 3. Further, the FEA results of ξ in four design groups are illustrated in Fig. 7. For each group, $\xi - F_{in}$ relation can be fitted by an exponential function $\xi = a \cdot \exp(-c \cdot F_{in}(N)) + d$. According to this fitting equation, if ξ is required to be smaller than 0.3, the input force F_{in} should be smaller than 0.68 N (Group 1.1 %), 0.99 N (Group 1.2 %), 2.79 N (Group 1.3 %), 8.54 N (Group 1.4 %) respectively. Therefore, if the proposed mechanism needs to be used

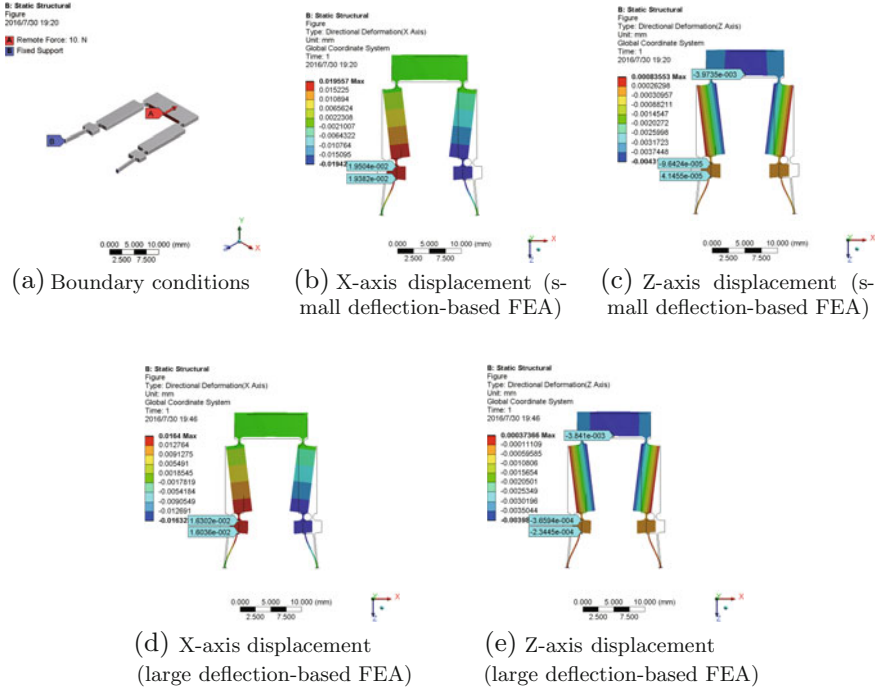
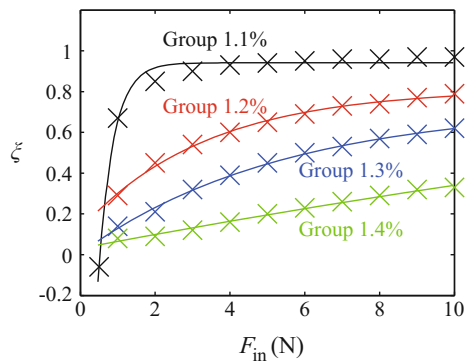


Fig. 6 FEA results of 1.30 % group

Table 3 Small deflection-based and large deflection-based FEA results ($F_{in} = 10\text{ N}$)

$\Delta_{error-1}$ (%)	ζ_{small} (μ rad/ μ m)	ζ_{large} (μ rad/ μ m)	$\xi = (\zeta_{large} - \zeta_{small}) / \zeta_{large}$	Δ_{error} (%)	δ_{small} (%)	δ_{large} (%)	Q_{small}	Q_{large}
1.10	0.37	12.40	0.97	1.10	0.19	2.46	5.15	4.23
1.20	2.82	13.15	0.79	1.20	0.27	2.27	4.98	4.17
1.30	3.17	8.39	0.62	1.30	0.15	1.86	4.90	4.21
1.40	4.93	7.36	0.33	1.40	0.10	1.58	4.75	4.18

Fig. 7 ξ - F_{in} relation of the design results



in larger range of input force with acceptable large deflection nonlinearity, $\Delta_{\text{error}-1}$ should be larger as well.

4 Conclusion

This paper presents the optimal design of a novel compliant orthogonal DAM with considering the static and dynamic properties. The proposed orthogonal DAM can be used for the actuators with bidirectional symmetric movement or typical unidirectional movement. The objective function to minimize the input stiffness is formulated. The static constraint is modelled with considering the large deflection nonlinearity. The dynamic constraint is modelled with obtaining the reasonable value of the undetermined parameters in the proposed orthogonal DAM. With the predetermined fabrication limit and customers' requirements, all the other nine dimensions of the proposed orthogonal DAM can be automatically determined by the optimal process. A design example is used to verify the optimal process. The iteration process in MATLAB shows that using different initial value, as the increase of the iteration steps, the input stiffness finally decreases to the same converged value $2.68 \text{ N}/\mu\text{m}$, which verifies the effectiveness and stability of the optimal process. The converged value of the input stiffness approaches to the FEA value: $2.52 \text{ N}/\mu\text{m}$ (error: 6.35 %). FEA results verify the orthogonal movement transformation and displacement amplification of the proposed mechanism in the situation of small deflection. Small deflection assumption should be considered when the lower limit of the evaluating parameter $\Delta_{\text{error}-1}$ is predetermined in the optimal process. As $\Delta_{\text{error}-1}$ is reduced, the orthogonal movement transformation accuracy in the range of small deflection is improved, whereas the range of the input force with acceptable large deflection nonlinearity is reduced.

Acknowledgments This research is supported by the National Natural Science Foundation of China (Grant No. U1501247, 91223201), the Natural Science Foundation of Guangdong Province (Grant No. S2013030013355), the Scientific and Technological Project of Guangzhou (Grant No. 2015090330001), and the Science and Technology Planning Project of Guangdong Province (Grant No. 2014B090917001). The authors gratefully acknowledge these support agencies.

References

1. Blideran MM, Bertsche G, Henschel W, Kern DP (2006) A mechanically actuated silicon microgripper for handling micro- and nanoparticles. *Microelectron Eng* 83(4):1382–1385
2. Chen W, Shi X, Chen W, Zhang J (2013) A two degree of freedom micro-gripper with grasping and rotating functions for optical fibers assembling. *Rev Sci Instrum* 84(11):115111–115111–10
3. Han K, Sang HL, Moon W, Park JS (2006) Fabrication of the micro-gripper with a force sensor for manipulating a cell. In: SICE-ICASE, 2006. International joint conference. pp 5833–5836

4. Bazaz SA, Khan F, Shakoor RI (2011) Design, simulation and testing of electrostatic soft grippers based microgripper integrated with capacitive contact sensor. *Sens Actuators, A* 167:44–53
5. Hoxhold B, Buttgenbach S (2010) Easily manageable, electrothermally actuated silicon micro gripper. *Microsyst Technol* 16:1609–1617
6. Xiao S, Li Y, Zhao X (2011) Optimal design of a novel micro-gripper with completely parallel movement of gripping arms. In: 2011 IEEE conference on robotics, automation and mechatronics (RAM), IEEE, pp 35–40
7. Millet O, Bernardoni P, Regnier S, Bidaud P, Collard D, Buchaillet L (2003) Micro gripper driven by sdas coupled to an amplification mechanism. In: *Transducers, solid-state sensors, actuators and microsystems, 12th international conference on, 2003, vol 1, IEEE*, pp 280–283
8. Zubir MNM, Shirinzadeh B, Tian Y (2009) A new design of piezoelectric driven compliant-based microgripper for micromanipulation. *Mech Mach Theory* 44:2248–2264
9. Kim DH, Lee MG, Kim B, Sun Y (2005) A superelastic alloy microgripper with embedded electromagnetic actuators and piezoelectric force sensors: a numerical and experimental study. *Smart Mater Struct* 14:1265–1272
10. Pokines BJ, Garcia E (1998) A smart material microamplification mechanism fabricated using ligaments. *Smart Mater Struct* 7(1):105
11. Lobontiu N, Garcia E (2003) Analytical model of displacement amplification and stiffness optimization for a class of flexure-based compliant mechanisms. *Comput Struct* 81(32):2797–2810
12. Ham YB, Jang SK, Oh SJ, Jeon EC, Park JH, Yun SN, Choi SG (2012) Piezoelectrically driven dispensing head for encapsulation of light emitting diode chip. *Jpn J Appl Phys* 51(9):539–545
13. Kim JH, Kim SH, Kwak YK (2003) Development of a piezoelectric actuator using a three-dimensional bridge-type hinge mechanism. *Rev Sci Instrum* 74(5):2918–2924
14. Xu Q, Li Y (2011) Analytical modeling, optimization and testing of a compound bridge-type compliant displacement amplifier. *Mech Mach Theory* 46(2):183–200
15. Chen W, Zhang X, Fatikow S (2016) Design, modeling and test of a novel compliant orthogonal displacement amplification mechanism for the compact micro-grasping system. *Microsyst Technol* 1–14
16. Carlson K, Andersen KN, Eichhorn V, Petersen DH, Molhave K, Bu IYY, Teo KBK, Milne WI, Fatikow S, Boggild P (2007) A carbon nanofibre scanning probe assembled using an electrothermal microgripper. *Nanotechnology* 18:1–7
17. Lobontiu N (2002) *Compliant mechanisms: design of flexure hinges*. CRC Press, New York

A Novel Bridge-Type Compliant Mechanism with Metastructures for Broadband Vibration Suppression

Xiaomeng Jiang, Zhong Chen, Wenqiang Cao and Xianmin Zhang

Abstract Vibration suppression on precision equipments always attracts great attention in industry and academic field. In order to reduce the vibration, many measures are taken in the past few decades. In general, vibration suppression can be classified as either active or passive mode. However, both of them achieve their own vibration-suppression function by attaching external members, which has some shortcomings of the complexity of production assembly. In order to improve vibration-suppression performance of a compliant amplifier, a novel compliant mechanism with metastructures is designed. The metastructures as shock-absorbed unit inserted in the amplifier's members can have capabilities of vibration suppression for their host structures. The different configurations of the metastructures in the host members are presented. Their frequency response functions are obtained using ABAQUS software, respectively. Through comparisons between their response functions, it indicates that the vibration-absorbing metastructures orienting along horizontal direction, which vibration-suppression direction is consistent with the output direction, have excellent performance of broadband suppression when their natural frequency keep highly coincident with the first order modal frequency of the compliant mechanism.

Keywords Broadband vibration suppression · Metastructures

1 Introduction

As we know, the needs for precision equipments become more and more urgent than ever due to the development of modern industry, such as medical, industrial, aerospace, biotechnology and other fields, which all are payed attention on the

X. Jiang · Z. Chen (✉) · W. Cao · X. Zhang
Guangdong Provincial Key Laboratory of Precision Equipment and Manufacturing
Technique, School of Mechanical and Automotive Engineering, South China University
of Technology, Guangzhou, China
e-mail: mezhchen@scut.edu.cn

© Springer Nature Singapore Pte Ltd. 2017
X. Zhang et al. (eds.), *Mechanism and Machine Science*,
Lecture Notes in Electrical Engineering 408,
DOI 10.1007/978-981-10-2875-5_58

701

influence of equipment vibration to their precision [1, 2]. In order to achieve the purpose of vibration suppression, a large number of researches are conducted. The major measures to reduce vibration can be classified as active and passive vibration control [3]. Active vibration control need some embedded actuators for vibration suppression, which energy consumptions depend on external energy. Passive vibration control don't need external energy, actuators and a control system, but usually adopt additional damping structure to consume vibration energy. Unfortunately, both of them are taken after the structure is fabricated, which will increase the complexity of the production assembly and reduces the production efficiency. Besides, they cannot be applied to some smaller size of structures.

With the development of 3D printing technology [4], especially the publication of the 3D printing of pure metal [5], a suitable solution can be adopted is to design a vibration-absorbing metastructure, a kind of oscillators, which are designed uniquely to be insert to its host structure. Usually the metastructures are designed and fabricated as a whole. And there are large numbers of researches and applications focusing on the vibration suppression with metastructures recently [6, 7]. Hobeck et al. [3] designed a rod inserted into the beam to implement the vibration suppression of the beam with some rods [8]. Xiao et al. extended to study the flexural wave propagation in locally resonant beams with multiple periodic arrays of attached spring-mass resonators [9]. Zhu et al. [10] adopted a uniquely designed array of chiral oscillators to achieve the broadband vibration suppression [10]. Sun studied theoretically broadband damping characteristics of partial array of resonant beam [11]. Baravelli et al. presented a structural concept for high stiffness and high damping performance by designing the resonating lattice to resonate at selected frequency [12]. Brittany presented an experimental study of optimized numerical simulations on a metastructure created for the purpose of broadband vibration suppression [13].

However, the above mentioned researches only use some simple structures like cantilever beam, that whether it can be applied in a complicated structures may be further investigated. So the paper focuses on broadband vibration suppression with metastructures for a complicated structure: a bridge-type compliant mechanism. In order to realize broadband vibration suppression of the compliant amplifier, the paper puts forward some configurations of vibration-absorbing metastructure, and verifies their performance of broadband vibration suppression based on ABAQUS software, respectively.

2 Structure Design

In order to analyze the vibration-suppression effect of the absorbers, this paper presents a design which is to insert the absorbers into a stiff body at the output end of a bridge-type compliant mechanism. all the absorbers are same, a kind of metastructure, and every absorber is designed as a cantilever beam with a tip mass

as illustrated in Fig. 1c. if hollowing directly the output end of the mechanism for adding the absorbers, it will reduce its stiffness. Hence, a clapboard is added inside of the output member, as shown in Fig. 1a, b.

The vibration-suppression effect of the absorbers is heavily influenced by the consistence of first order modal frequency between the absorber and the compliant amplifier with the absorbers which has the compact size, 40×21 mm. All of the absorbers and the complaint amplifier are made of stainless steel, which the elastic modulus and the Poisson’s ratio equals to 2.06×10^{11} Pa and 0.3, respectively. The first order vibration mode of the compliant mechanism with the absorbers usually is a kind of back-forward motion of the output member along the output direction. Hence, in order to meet the requirements, the dimensions of the absorbers are designed carefully for adjusting its first order natural frequency. According to the analysis, the dimension 1–6 of the absorber equals to 0.15, 0.46, 2, 1.5, 2 and 3 mm, respectively. The four absorbers are fabricated in the output member of the compliant amplifier. Meanwhile, their dimensions are kept in consistence to reduce influences in evaluation of vibration suppression and make it more easily fabricated.

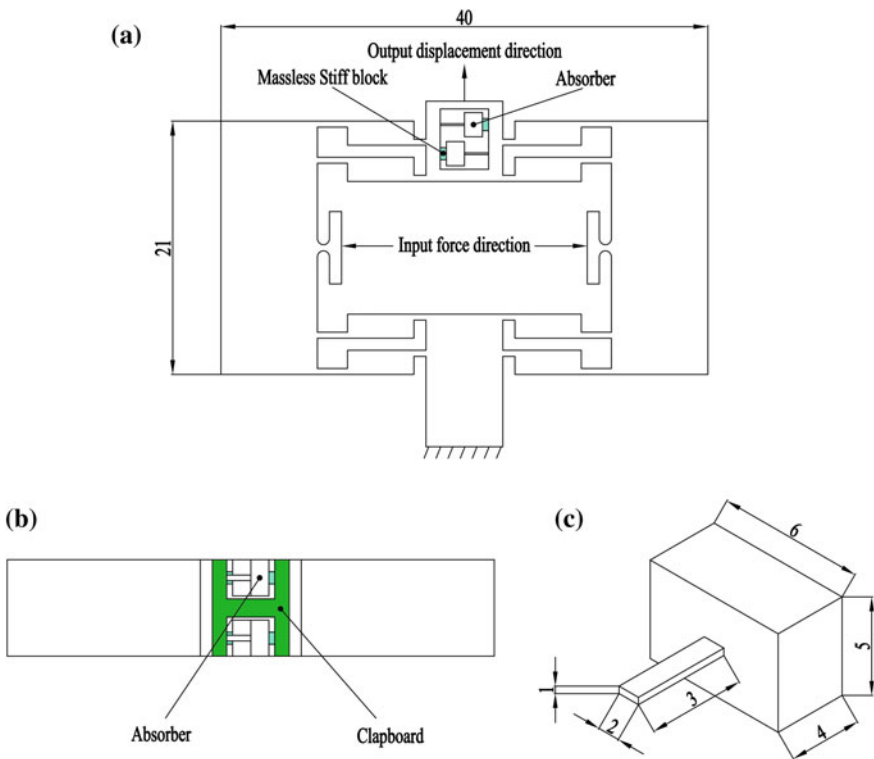


Fig. 1 Bridge-type compliant mechanism with absorbers in **a** the front view and **b** the top view and **c** its embedded absorber

3 Evaluation of Vibration Suppression

3.1 Preliminary Vibration Suppression

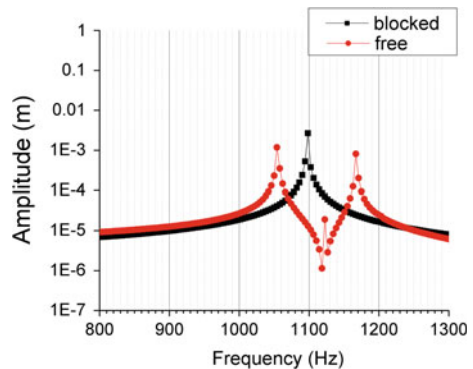
In order to evaluate the vibration suppression effect using the absorbers embedded in the compliant mechanism, two kinds of configurations of the absorbers are set beforehand, which include absorbers in blocked as Fig. 1a and absorbers in free as removing the massless stiff blocks from Fig. 1a. When implementing dynamical analysis, the blocks are set at massless stiff state, and these blocks can restrain the vibration of the absorbers. Then their frequency response functions are obtained using scanning stimulus in ABAQUS software, as fixing the lowest end of the mechanism, then loading a stimulus unit-force in different frequencies in scanning mode on the input end of the mechanism, and recording the output displacements. Comparisons of these frequency response functions are conducted, as shown in Fig. 2.

From Fig. 2, we can observe that the vibration at the design frequency of 1097 Hz is suppressed, which is the first order modal frequency of the mechanism in blocked state. And the shock absorption bandwidth is about 90 Hz. The result suggests that the four absorbers, which are not blocked, can eliminate the peak of the output displacement at the design frequency and effectively suppress the vibration of the whole mechanism in a certain bandwidth.

3.2 Superimposed Vibration Suppression

In above section, it has been proved that the absorbers embedded into the bridge-type compliant mechanism have a good performance of vibration suppression. However, whether the bandwidth of vibration suppression of the absorbers can be enhanced by inserting more absorbers to the other rigid bodies of the mechanism is unknown. However, the output end of the mechanism has no more

Fig. 2 Frequency response function of the output end of the mechanism in free and blocked state



space to configure more absorbers. Only both side rigid blocks can be used to embedded more absorbers. In order to keep its static performance of the mechanism unchanged, eight symmetrical absorbers are embedded into the both side bodies. It is obvious that the side beams vibrate along the direction of the input force more easily than along output direction, but it is still necessary to evaluate the performance of vibration suppression under different orientations of the absorbers when embedded in the both side beams.

Thus, there are two different layouts of the absorbers in horizontal and vertical orientations, which remain along input axis and output axis, respectively. In order to confirm exactly which layout has better performance of vibration suppression, many dynamical simulations are implemented under different condition of absorbers as shown in Fig. 3. In Fig. 3 there are eight configurations, which *horizontal-all blocked* means that all absorbers are blocked, *horizontal-side blocked* means that only the absorbers in both side beams are blocked, *horizontal-half blocked* means that only half of the absorbers in any side beam are blocked, *horizontal-all free* means that all absorbers in both side beams are free, and other configurations in vertical orientation like that in horizontal orientation.

Like the above section, their frequency response functions are obtained under configuration (b), (c), (d) in horizontal orientation and (f), (g), (h) in vertical orientation, respectively, as shown in Fig. 4.

From Fig. 4a, b, c, we can get information of bandwidth of vibration suppression of *horizontal-side blocked*, *horizontal-half blocked*, and *horizontal-all free* which are approximately 90, 120, and 145 Hz. And this indicates that it can enhance the performance of vibration suppression by adding more absorbers to the mechanism when the absorbers in the side beams are inserted along horizontal orientation. However, from Fig. 4d, e, f, the bandwidth of vibration suppression of *vertical-side blocked*, *vertical-half blocked*, and *vertical-all free* are approximately 90, 90, and

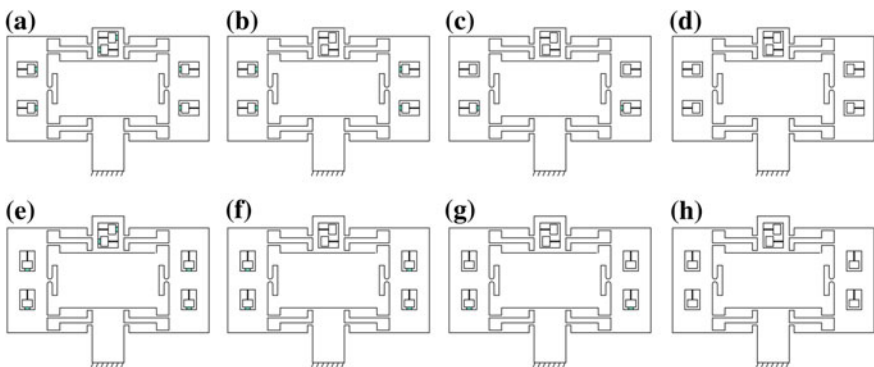


Fig. 3 Bridge-type compliant mechanism with absorbers in different free or blocked state: **a** horizontal-all blocked **b** horizontal-side blocked **c** horizontal-half blocked **d** horizontal-all free **e** vertical-all blocked **f** vertical-side blocked **g** vertical-half blocked **h** vertical-all free

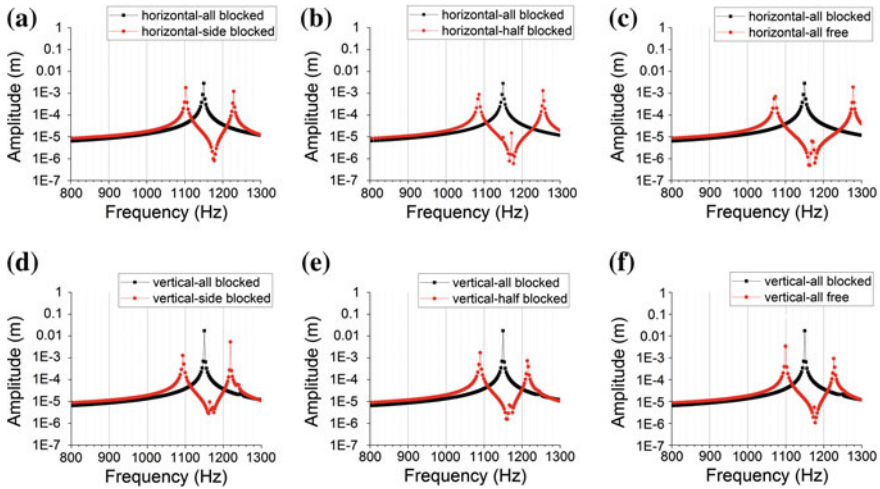


Fig. 4 Comparisons of the frequency response functions under the different configurations of the absorbers

90 Hz. And this indicates that it cannot enhance the performance of vibration suppression after inserting more absorbers to the mechanism when the absorbers in the side beams are inserted along vertical orientation.

3.3 Further Discussions

In above two sections, it has been discussed whether the bridge-type compliant mechanism which embeds some absorbers can have a better performance of vibration suppression and whether it can enhance the performance of vibration suppression when inserting more absorbers to the host mechanism. But all of them are based on the following premise that the absorbers must approximately keep same of first order modal frequency with the bridge-type compliant mechanism. Thus, if changing the first order frequency of the absorbers, it will lead to a little impact on the first order modal frequency of the mechanism. Will the vibration-suppression effect of the absorbers be weaken? Aiming at the issue, the following discussions are carried out.

According to Sect. 3.1, a best performance of vibration suppression is obtained when the absorbers are configured as in Fig. 3d. So we choose the model in Fig. 3d to start a discussion firstly. By changing the dimension 1 and the dimension 2 in Fig. 1c, the first order modal frequency of the absorber can be changed as we need. And their frequency response functions are obtained while the dimension 1, 2 are changed, as shown in Fig. 5, which include four kinds of models, *free1-free4*. From Fig. 5, it is obvious that the absorbers with different dimension 1, 2 have a

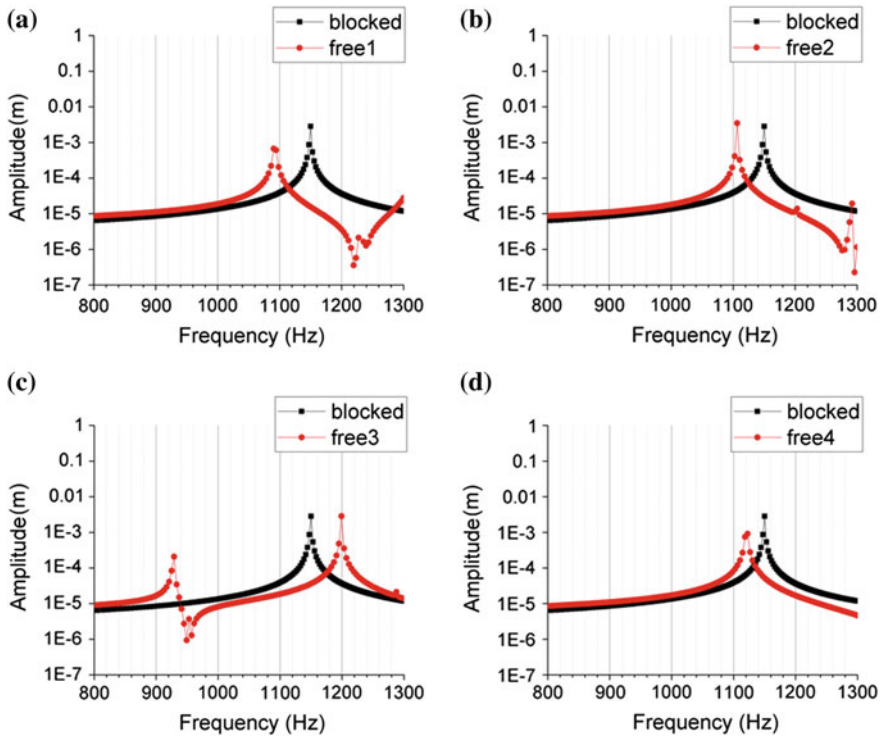


Fig. 5 Comparisons of the frequency response functions when changing the natural frequency of the absorbers

little impact on the first order modal frequency of the bridge-type compliant mechanism. So we can evaluate the performance of vibration suppression when dimension 1, 2 of the absorber are changed.

After analyzing all frequency response functions in Fig. 5, we can easily draw a conclusion that performance of vibration suppression of the absorbers depend on its first order modal frequency. And it becomes more and more weak, when its first order modal frequency deviates more heavily from the design frequency of the bridge-type compliant mechanism. Even when the frequency deviation increase at a certain extent, its vibration-suppression effect will disappear.

4 Conclusion

The paper analyzes the performance of vibration suppression of the absorbers, a kind of metastructure, embedded into a bridge-type compliant mechanism. When the first order modal frequency of the absorbers equals to the one of the compliant amplifier, the absorbers can reach best performance of vibration suppression. Their

vibration-suppression effect can be enhanced by adding more absorbers into both side beam of the mechanism in horizontal orientation. And their vibration-suppression effect has a key relation with deviation degree between first order modal frequency of the absorbers and their host structure. When their first order modal frequency deviates more largely from the design frequency, their effect will become weaker until it has no vibration-suppression effect nearly.

Acknowledgment The work described in this paper is supported by the Natural Science Foundation of Guangdong Province (2016A030313481), the Scientific and Technological Research Project of Guangdong Province (2015B020239001, 2014B090917001), the National Natural Science Foundation of China (U1501247).

References

1. Rivin Eugene I (1995) Vibration isolation of precision equipment. *Precis Eng* 17(1):41–56
2. DeBra D (1992) B: vibration isolation of precision machine tools and instruments. *Ann CIRP* 41(2):711–718
3. Hobeck JD, Inman DJ (2015) Magnetoelastic metastructures for passive broadband vibration suppression. In: *Active and passive smart structures and integrated systems 2015*, 9 Mar 2015–12 Mar 2015. SPIE Press, San Diego
4. Pham DT, Gault RS (1998) A comparison of rapid prototyping technologies. *Int J Mach Tool Manuf* 38(10):1257–1287
5. Visser CW, Pohl R, Sun C (2015) Toward 3D printing of pure metals by laser-induced forward transfer. *Adv Mater* 27(27):4087–4092
6. Chen JS, Sharma B, Sun CT (2011) Dynamic behaviour of sandwich structure containing spring-mass resonators. *Compos Struct* 93(8):2120–2125
7. Abdeljaber O, Avci O, Inman DJ (2016) Optimization of chiral lattice based metastructures for broadband vibration suppression using genetic algorithms. *J Sound Vib* 369:50–62
8. Hobeck JD, Inman DJ (2015) 3D printing of metastructures for passive broadband vibration suppression. In: *20th international conference on composite materials*. Copenhagen
9. Xiao Y, Wen J, Wen X (2012) Broadband locally resonant beams containing multiple periodic arrays of attached resonators. *Phys Lett A* 376(16):1384–1390
10. Zhu R, Liu XN, Hu GK, Sun CT, Huang GL (2014) A chiral elastic metamaterial beam for broadband vibration suppression. *J Sound Vib* 333(10):2759–2773
11. Sun H, Du X, Pai PF (2010) Theory of metamaterial beams for broadband vibration absorption. *J Sound Vib* 21(11):1085–1101
12. Baravelli E, Ruzzene M (2013) Internally resonating lattices for bandgap generation and low-frequency vibration control. *J Sound Vib* 332(25):6562–6579
13. Essink BC, Inman DJ (2016) Optimized 3D printed chiral lattice for broadband vibration suppression. Mains, Michael, Cham

Design of Micro-positioning Stage with Large Stroke Based on Novel Compliant Parallel Mechanism

Qinghua Lu and Youcai Zhang

Abstract Compliant mechanism is widely used in the fields of precision mechanical engineering for the advantages such as no friction losses, no need for lubrication, no assembly. However, its stroke is limited by the type of compliant joint, the size and performance of materials. In this paper, a novel compliant parallel mechanism with high precision and large stroke is proposed, which is composed of a parallel mechanism with full compliant joints. The curved planar compliant unit based on the hammer orchid's compliant joints is viewed as the object, and a compliant parallel mechanism is designed through the analysis of the curved planar model method and the finite element. The analysis results show the curved planar compliant unit in compliant parallel mechanism has better performance. According to the analysis results of different types of the curved planar compliant unit, a novel parallel micro-positioning stage with three degrees of freedom is designed, which has the advantages of high precision and large stroke.

Keywords Compliant joint · Parallel · Micro-positioning · Large stroke

1 Introduction

High performance compliant parallel mechanisms can provide precise positioning and movement, which had attracted the attention of many countries around the world [1]. The good performance of compliant mechanism is mainly shown in: reduce the cost of compliant mechanism and improve the performance of compliant mechanism [2]. Compliant joints had a limited working space and restrictions on the scope of cubic micron, meanwhile related to the reasonable design of compliant parallel mechanism [3]. For the compliant parallel mechanisms, Sun designed the parallel micro-positioning stage based on the novel Hooke hinge [1]. Zhao studied on the large deformation of the curved compliant element [4]. Zhang took the

Q. Lu (✉) · Y. Zhang

School of Mechanical and Electrical Engineering, Foshan University, Foshan, China
e-mail: qhlu@fosu.edu.cn

Fig. 1 The motion of Orchid

performance testing and optimization of 5-DOF hybrid parallel mechanism [5]. Horacio presented the large deformation of semi circular hinge in planar compliant mechanism [6]. Hesselbach presented a DELTA parallel mechanism using compliant joints made of a superelastic alloy (CuAlNiFe) [7]. Horie presented a 2-DOF translational robot using a large-deflection deformable joints that are made of superelastic metal (Ni-Ti) [8]. Clavel presented a 3-DOF parallel mechanism with brace-shaped compliant joints(2-DOF rotation and 1-DOF translation) [9]. Li Yuan presented a kinetic model of planar compliant parallel robot based on semi circular compliant joint [10]. In previous studies, most of the parallel mechanisms could work in the small space, but the effect was not good in a wider range of working space.

This paper presented a novel compliant parallel mechanism inspired by the orchid as shown in Fig. 1 and proposed the deformation of the joint under different combinations and used it in the design of a 3-DOF compliant parallel micro-positioning stage with high precision and large stroke. It had large working space, which had certain significance to the study of the compliant parallel mechanisms.

2 Compliant Joint Model

In order to study the performance of compliant joints, some nonlinear finite element analyses were taken on it. According to the orchid's model, a compliant joint with three-dimensional simplified model was established as shown in Fig. 2. The middle of the compliant joint is extracted to analyze in this paper. As described above, the joints would subject to the horizontal force, vertical force and couple respectively, its deformation analytical model as shown in Fig. 3.

When different loads were applied, the curved planar compliant unit could be changed, and the curvature could be predicted [11–13]. According to the theory of Bernoulli-Euler, the curvature of a semi-circular beam in Cartesian coordinates can be given by [14]:

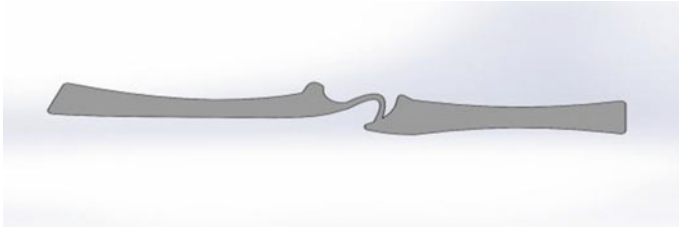
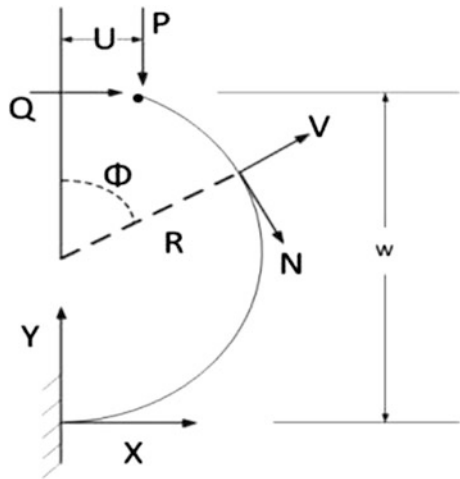


Fig. 2 Compliant joint model

Fig. 3 The analytical model of compliant joint



$$\kappa = \frac{1}{\rho} = \frac{M}{EI} = \frac{d\theta}{ds} = \frac{d^2y/dx^2}{[1 + (dy/dx)^2]^{1/2}} \tag{1}$$

2.1 Vertical Deformation

To calculate the displacement caused by vertical load P, an expression for the curvature to the beam based on formulas (1) is developed. When the internal moment at a distance x from the origin is given by: $M = -P(u - x)$, considering the initial curvature $1/R$, and get formulas (2) can be given by [6]:

$$\kappa = \frac{d\theta}{ds} = -\frac{P}{EI}(u - x) + \frac{1}{R} \tag{2}$$

Differentiating with respect to s

$$\frac{d\kappa}{ds} = \frac{d^2\theta}{ds^2} = \frac{P}{EI} \left(\frac{dx}{ds} \right) = \frac{P}{EI} \cos \theta \quad (3)$$

The second derivative of the angle θ with respect to the length s can be expanded as follows:

$$\frac{d^2\theta}{ds^2} = \frac{d}{ds} \left(\frac{d\theta}{ds} \right) = \frac{d\kappa}{d\theta} \kappa = \frac{d}{d\theta} \left(\frac{\kappa^2}{2} \right) \quad (4)$$

Combined with formula (3) and formula (4)

$$\frac{d}{d\theta} \left(\frac{\kappa^2}{2} \right) = \frac{P}{EI} \cos \theta \quad (5)$$

Applying boundary conditions, at $x = u$ and $y = w$, and taking $\theta = \theta_0$ as the initial angle of the beam and solving for κ results in

$$\kappa = \sqrt{\left(\frac{1}{R} \right)^2 + \frac{2P}{EI} (\sin \theta - \sin \theta_0)} \quad (6)$$

The displacement of the y direction is derived as follows:

$$\kappa = \frac{d\theta}{ds} = \frac{d\theta}{dy} \frac{dy}{ds} = \frac{d\theta}{dy} \sin \theta \quad (7)$$

Integrating both sides

$$w = \sqrt{\frac{EI}{2P}} \int_0^{\theta_0} \frac{\sin \theta d\theta}{\sqrt{(1/R)^2 \frac{EI}{2P} + (\sin \theta - \sin \theta_0)}} \quad (8)$$

In the x direction:

$$u = \sqrt{\frac{EI}{2P}} \int_0^{\theta_0} \frac{\cos \theta d\theta}{\sqrt{(1/R)^2 \frac{EI}{2P} + (\sin \theta - \sin \theta_0)}} \quad (9)$$

2.2 Horizontal Deformation

To calculate the displacement caused by horizontal load Q , an expression for the curvature to the beam based on formulas (1) is developed. When the internal moment at a distance y from the origin is given by: $M = -Q(w - y)$, considering the initial curvature $1/R$, and get formulas (10) can be given by [6]:

$$\kappa = \frac{d\theta}{ds} = -\frac{Q}{EI}(w - y) + \frac{1}{R} \quad (10)$$

Differentiating with respect to s

$$\frac{d\kappa}{ds} = \frac{d^2\theta}{ds^2} = \frac{Q}{EI} \left(\frac{dy}{ds} \right) = \frac{Q}{EI} \sin \theta \quad (11)$$

According to (5) can be obtained:

$$\frac{d}{d\theta} \left(\frac{\kappa^2}{2} \right) = \frac{Q}{EI} \sin \theta \quad (12)$$

Applying boundary conditions, at $x = u$ and $y = b$, and taking $\theta = \theta_0$ as the initial angle of the beam and solving for κ results in

$$\kappa = \sqrt{\left(\frac{1}{R} \right)^2 + \frac{2Q}{EI} (-\cos \theta + \cos \theta_0)} \quad (13)$$

The displacement of the y direction is derived as follows:

$$w = \sqrt{\frac{EI}{2Q}} \int_0^{\theta_0} \frac{\sin \theta d\theta}{\sqrt{\left(\frac{1}{R} \right)^2 \frac{EI}{2Q} + (-\cos \theta + \cos \theta_0)}} \quad (14)$$

In the x direction:

$$u = \sqrt{\frac{EI}{2Q}} \int_0^{\theta_0} \frac{\cos \theta d\theta}{\sqrt{\left(\frac{1}{R} \right)^2 \frac{EI}{2Q} + (-\cos \theta + \cos \theta_0)}} \quad (15)$$

2.3 Finite Element Analysis of Compliant Joint

According to the above theoretical model, the large deformation performance of different combinations of compliant joints was verified, which provided an effective basis for the design of compliant parallel micro-positioning stage. The compliant joint combinations are shown in Fig. 4.

The mechanism parameters of three forms compliant joints: Radius $R = 10\text{ mm}$, arc length $C = 30\text{ mm}$, thickness $t = 0.5\text{ mm}$. All the selected materials were spring steels as shown in Table 1, other materials were stainless steels.

Under the action of horizontal load Q and vertical load P , the three finite element models were compared as shown in Figs. 5 and 6.

By seen Figs. 5 and 6 data analysis, single joint deformation was obviously better than the other two symmetrical double joint, and could achieve mm scope.

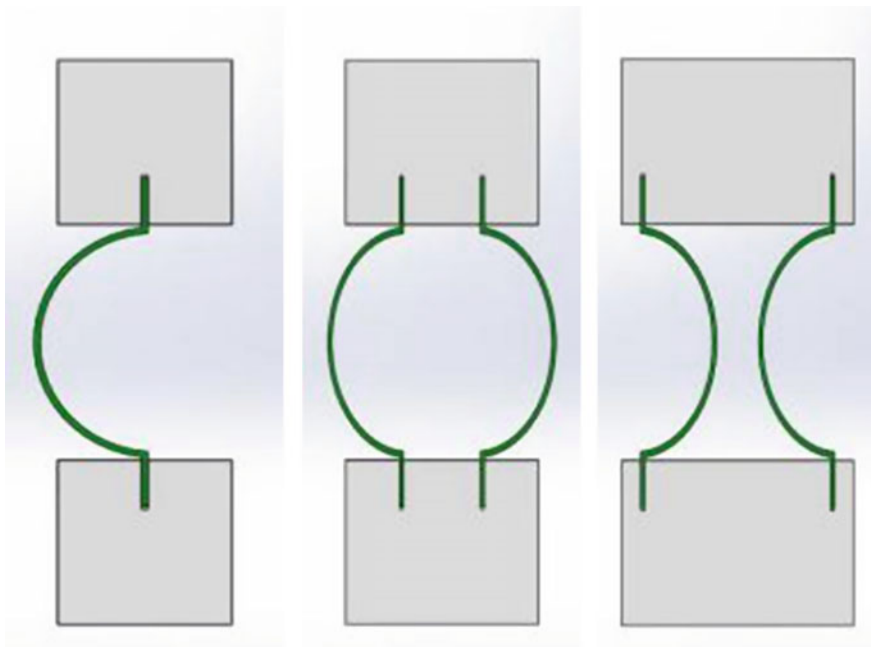


Fig. 4 The type of compliant joint

Table 1 Performance parameter of spring steel

Elastic modulus $E / (\text{Pa})$	Yield stress $\sigma_s / (\text{Pa})$	Shear modulus $G / (\text{Pa})$	Density $\rho / (\text{kg} / \text{m}^3)$	Poisson's ratio μ
$2.07\text{E} + 11$	$1.18\text{E} + 09$	$8.13\text{E} + 10$	7730	0.27

Fig. 5 Displacement under horizontal load Q

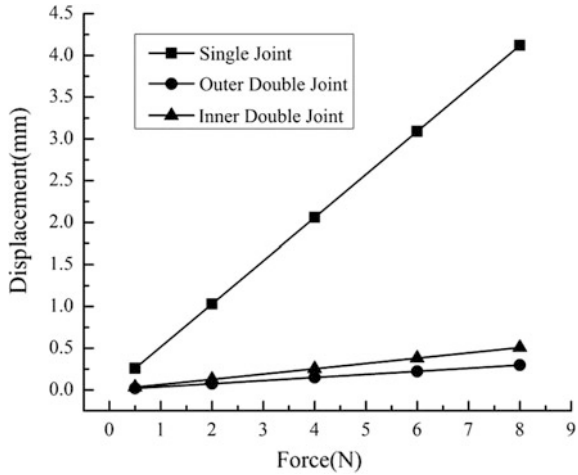
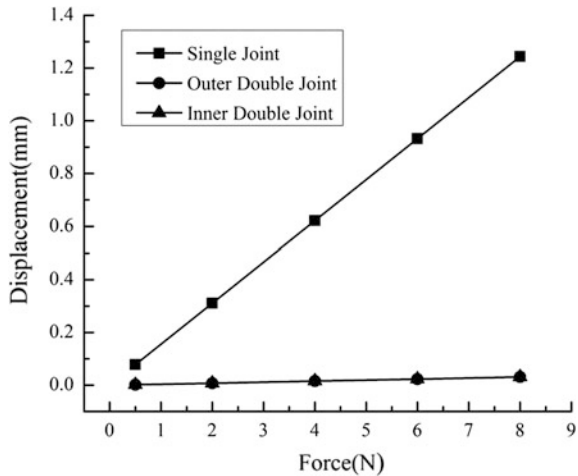


Fig. 6 Displacement under vertical load P



The results showed that the single compliant joint had good deformation performance and could be used as the design of micro-positioning stage with large deformation.

3 Compliant Parallel Micro-positioning Stage

According to the comparative analysis on three forms of compliant joint, single compliant joint was selected and constructed PRRRR compliant kinematic chains as shown in Fig. 7.

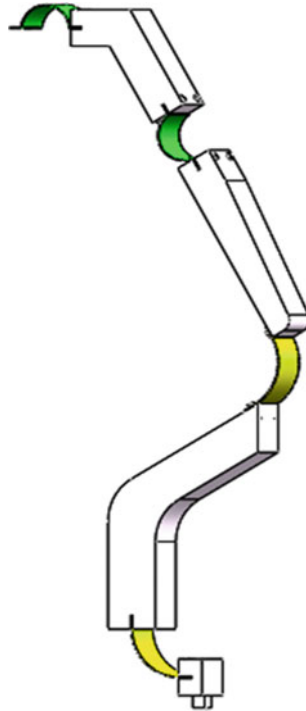
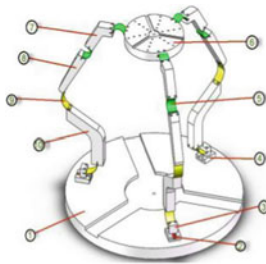


Fig. 7 PRRRR compliant kinematic chains



- 1.static stage 2.drive 3.sliding mechanism 4.rail 5.compliant 1
- 6.moving stage 7.rigid body 1 8.rigid body 2 9.compliant 2 10.rigid body 3

Fig. 8 Compliant parallel micro-positioning stage model

A PRRRR compliant kinematic chain proposed by Fig. 7 was constructed in a 3-DOF parallel micro-positioning stage as shown in Fig. 8. The compliant parallel micro-positioning stage was composed of a static stage and moving stage, three

chains composed by the compliant joints, drive, rigid components and three branch chains had the identical geometrical condition.

The movement pair composed of the spatial mechanism had the revolute pair, the prismatic pair, the screw pair, the cylindrical pair, the spherical pair, the plane pair and the Hooke hinge [15].

According to the modified Kutzbach-Grubler formula for the general mechanism of general freedom [16].

$$M = d \times (n - g - 1) + \sum_{i=1}^g f_i + v \tag{16}$$

In this paper, The dynamic model of compliant parallel micro-positioning stage as shown in Fig. 9, which contained 14 components, 15 motion pairs (3 prismatic pairs, 12 revolute pairs), without parallel redundant constraints, the stage had a degree of freedom as follows:

$$M = d \times (n - g - 1) + \sum_{i=1}^g f_i + v = 6 \times (14 - 15 - 1) + 15 = 3$$

According to the above model analysis, the initial condition of the compliant parallel micro-positioning stage was parallel to the static stage. Three degrees of freedom motion of the moving stage could be achieved when the driver was driven to the three compliant joints which are uniformly distributed at the bottom [17], and its structural parameters as shown in Table 2.

In this paper, ANSYS was used to simulate the deformation and motion of the 3-DOF compliant parallel micro-positioning stage. In the process of simulation, the static stage, the moving stage and the rigid components were made of stainless

Fig. 9 Compliant parallel micro-positioning stage structure

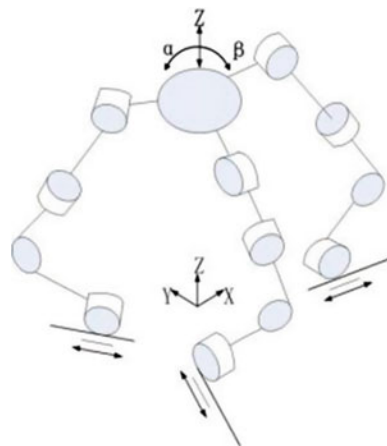
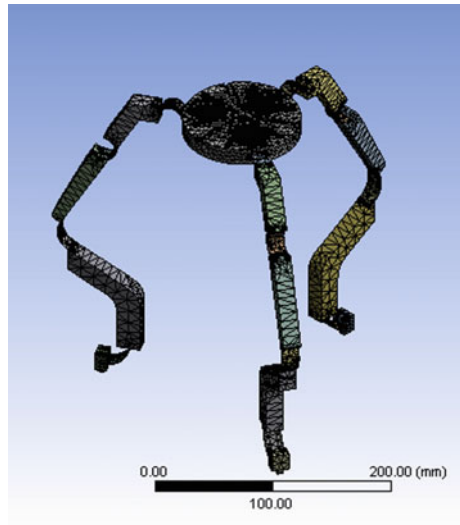


Table 2 Structural parameters of compliant parallel micro positioning stage

	Length (mm)	Thickness (mm)	Material
Moving stage	100	15	Duralium
Static stage	300	20	Cast iron
	Radius (mm)	Section (mm ²)	Material
Compliant 1	10	15 × 0.5	Spring steel
Compliant 2	20	15 × 0.5	Spring steel

Fig. 10 Structure and meshing



steels, and the other two kinds of compliant joints were made of spring steels. And then the meshing as shown in Fig. 10. Because the maximum stroke of the micro displacement actuator was 15 mm, the displacement load of the bottom sliding stroke was 2 mm. After a series of meshing, adding constraints and loads, solving, and obtain the total deformation and stress of the single load, double load, triple load as shown in Figs. 11 and 12.

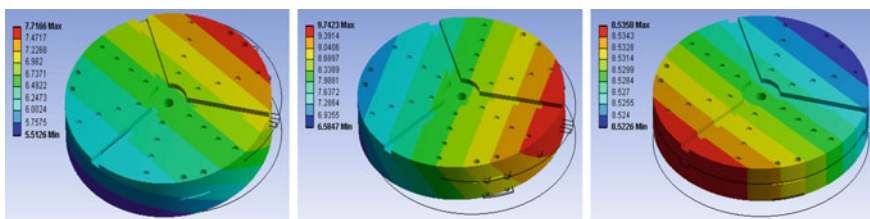


Fig. 11 Displacement under different loads

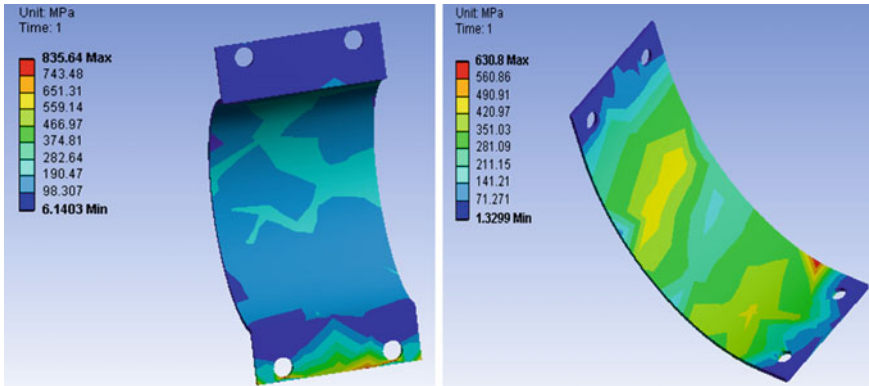


Fig. 12 Stress of compliant joints

It was concluded from the above two figure that when the displacement load was applied to the bottom sliding stroke 2 mm, the moving stage could output the displacement of 9 mm, and the stress at the joints was less than the yield strength ($\sigma_s = 1.18E + 09\text{Pa}$), so compliant parallel micro-positioning stage satisfied the requirements of the design of large stroke.

4 Conclusions

In this paper, mathematical analysis and finite element method were used to analyze the output displacement of compliant joints in different combinations to find the correlation between the compliant joints and the load in different combinations that could provide a reasonable suggestion for the design of a large deformation micro positioning stage based on compliant joint.

- (1) In the case of the same load, the deformation of the single joint was obviously better than that the other two kinds of symmetric double joints, and could achieve the scale of mm. The results showed that the single compliant joint had good deformation performance and could be used as a joint foundation for the design of micro-positioning stage with large deformation.
- (2) In the case of the application of horizontal load, the single joint showed a better deformation performance, could provide a reasonable suggestion for the design of a large deformation micro-positioning stage based on compliant joint.

- (3) In the case of using the single compliant joints, a 3-DOF compliant parallel micro positioning stage had been designed that could initially achieve the requirements of large stroke and high accuracy, which can provide the effective references for the design of the micro-positioning stage.

Acknowledgments This research was supported by the Natural Science Foundation of Guangdong Province under grants 2014A030313616, the Science and Technology Planning Project of Guangdong Province (2015B010101015) and the Science and Technology Innovation Project of Foshan (2015AG10018).

References

1. Sun W (2014) The theoretical and experimental study of novel large-stroke compliant parallel mechanism. South China University Technology (in Chinese)
2. Li Y, Yu YQ (2016) Feasibility analysis of compliant joints instead of traditional joints in the parallel robot. Trans Chin Soc Agric Mach 4 (in Chinese)
3. Chen GM (2015) Handbook of compliant mechanisms. High Education Press (in Chinese)
4. Zhao SS, Bi SS, Zong GH et al (2009) New large-deflection flexure pivot based on curved flexure element. J Mech Eng 45(4):8–12 (in Chinese)
5. Zhang D, Gao Z (2015) Performance analysis and optimization of a five-degrees-of-freedom compliant hybrid parallel micromanipulator. Rob Comput Integr Manuf 34:20–29
6. Ahuett-Garza H, Chaides O, Garcia PN et al (2014) Studies about the use of semicircular beams as hinges in large deflection planar compliant mechanisms. Precis Eng 38(4):711–727
7. Raatz A, Wrege J, Burisch A et al (2006) Compliant parallel robots. Precision assembly technologies for mini and micro products, Springer, USA, pp 83–92
8. Horie M, Kobayashi F, Ikegami K et al (1996) Characteristic analysis of pantograph mechanisms with superelastic hinges. Trans Jpn Soc Mech Eng C 62:2403–2408
9. Pham P, Regamey YJ, Fracheboud M et al (2005) Orion minangle: a flexure-based, double-tilting parallel kinematics for ultra-high precision applications requiring high angles of rotation. ISR Proc
10. Li Y, Yu YQ (2015) Dynamic model of parallel robot with compliant joints. Trans Chin Soc Agric Mach 46(7):345–353 (in Chinese)
11. Kozuka H, Arata J, Okuda K et al (2013) A compliant-parallel mechanism with bio-inspired compliant joints for high precision assembly robot. Procedia Cirp 5(1):175–178
12. Huang PT (2012) Research on the structure and design for planar three-DOF compliant micro-positioning platform. Shandong University of Technology (in Chinese)
13. Ma L, Xie W, Liu B, (2014) Design of micro-positioning stage with flexure hinge. Opt Precis Eng 22(2):338–345 (in Chinese)
14. Li YM, Xiao X, Tang H (2013) Design and analysis of a novel 3-DOF large stroke micro-positioning platform. J Mech Eng 49(19):48–54 (in Chinese)
15. Hu JF, Xu GY (2014) The design and properties of a novel 4-DOF compliant parallel mechanism. Mech Sci Technol Aerosp Eng 33(4):496–500 (in Chinese)

16. Huang Z (2004) The kinematics and type synthesis of lower-mobility parallel manipulators. In: Proceedings of the 11th World Congress in Mechanism and Machine Science, 2004, Tianjin, China, 65–76
17. Howell LL, Midha A (1995) Parametric deflection approximations for end-loaded, large-deflection beams in compliant mechanisms. *J Mech Des* 117(1):156–165

Design of a 3DOF Precision Positioning Stage Based on Corrugated Flexible Units

Nianfeng Wang, Zhiyuan Zhang, Xianmin Zhang and Luming Cui

Abstract Flexure hinge has been widely used in micro-positioning stages and medical applications to take the place of mechanical joints. In this paper, a planar three degree of freedom (DOF) precision positioning stage is designed with corrugated flexible units, which offers great improvement over traditional flexible hinge in terms of large range of motion. A first order displacement amplification mechanism is led into the stage to amplify the displacement and the stage is actuated by piezo actuator. Then the simulation and analysis of the stage are conducted by finite element analysis (FEA) via ANSYS, which validate the characteristic of large displacement of the stage and eliminating stress concentration effects.

Keywords Precision positioning stage · Corrugated flexible units · 3DOF · FEA

1 Introduction

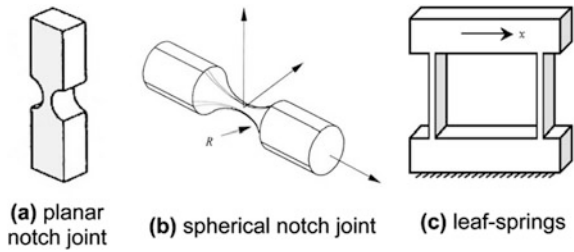
With the constant development of medical equipment, communication equipment, circuits and some other interrelated technologies, the requirements for precision and ultra-precision positioning technology has become more and more strict, and a nanoscale resolution or repeatability becomes more important.

Since the micro-positioning stage based on flexure hinges has quite a lot of advantages, such as no lubrication, no noise, fewer parts and more compact, the stage has been widely used in many industrial applications, including biological science, micro-grippers, scanning probe microscopy [1–3] and so on. And in the

N. Wang (✉) · Z. Zhang · X. Zhang · L. Cui
Guangdong Provincial Key Laboratory of Precision Equipment and Manufacturing
Technology, School of Mechanical and Automotive Engineering,
South China University of Technology, Guangzhou 510640, China
e-mail: menfwang@scut.edu.cn

Z. Zhang
e-mail: 805541375@qq.com

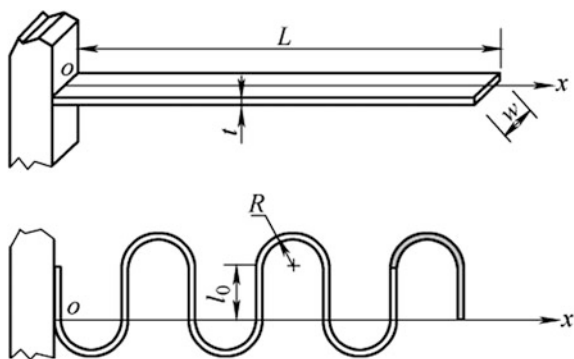
Fig. 1 Basic flexible joint components



early 1965s, PAROS gave out the simplified calculation formula of a circular arc shape flexible hinge [4], today this kind of flexible hinge, which is also called notch-type flexible joints (Fig. 1a, b) [5], has been well understood by many researchers and designers and gets lots of applies in the field of high-precision and small-displacement mechanisms [6]. Another primary flexure hinge is leaf spring (Fig. 1c). It's just like a four-bar linkage and composed of sets of parallel flexible beams. And this kind of joints is widely applied in medical instrumentation [7] and MEMS devices [8]. Wang [9–12] have used periodically corrugated cantilever beam (Fig. 2) to design compliant joints and established the pseudo-rigid-body model of it. This corrugated flexure unit with semi-circular segment and straight segment connected end to end somehow overcome the disadvantage of limited range of motion for its large flexibility obtained from longer overall length on the same span. With the corrugated flexure beam (CF beam), a XY micro-positioning stage is designed and the static and modal analysis of the stage are conducted by finite element analysis (FEA) via Workbench.

In this paper, we propose a planar three degree of freedom precision positioning stage using corrugated flexible units. On the basis of 3-PRR rigid model with three chains 120° apart from each other, we take the place of traditional notch joints with corrugated flexible units and a first order displacement amplification mechanism, whose fulcrum is also a corrugated flexible unit is led into the stage. And then, the FEA model is given out to assist determining the position of the fulcrum. After that, 65Si2Mn is chosen as the material of the stage. And simulation and analysis of the

Fig. 2 Straight cantilever beam and corrugated cantilever beam



stage with corrugated flexible units and notch-type joints are carried out respectively.

2 The Design of 3DOF Precision Positioning Stage

2.1 The Model of 3DOF Positioning Stage

In order to set up a positioning stage with three degrees of freedom, we take the 3-PRR rigid model as shown in Fig. 3 [13] into account. The three chains are 120° apart from each other and this symmetric structure decreases the influence of the temperature and disturbance from the outside environment. On this basis, a first order displacement amplification mechanism is led into the model to increase the displacement of the stage.

According to reference [14], and because the deformation of the stage mainly produced by flexure hinges, the deformation of link bar can be ignored and treated as rigid body, as shown in Fig. 4. The relationship between input and output can be described by following matrix:

$$GX_{in} = \begin{bmatrix} a_{11} & a_{12} & a_{13} \\ a_{21} & a_{22} & a_{23} \\ a_{31} & a_{32} & a_{33} \end{bmatrix} \begin{bmatrix} d_1 \\ d_2 \\ d_3 \end{bmatrix} = X_{out} \tag{1}$$

where G is a 3 × 3 transfer function matrix, X_{in} is the input matrix and X_{out} is the output matrix, and $a_{ij}(i = 1, 2, 3; j = 1, 2, 3)$ are all constants and d_i represent the input values. From the equations above, we can get the output values as long as we

Fig. 3 3-PRR rigid model

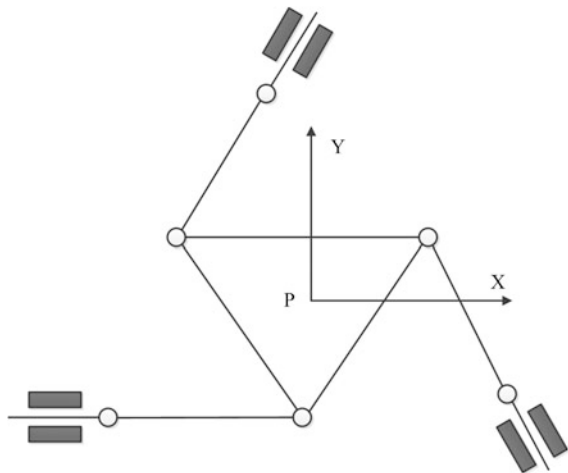
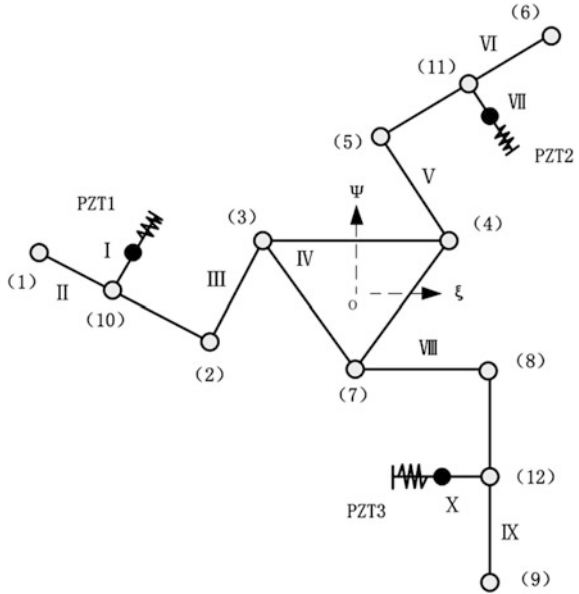


Fig. 4 Model of precision positioning stage



know the input values, and if three input values are equal, the center stage will get a rotational movement in the plane.

2.2 Design of 3 DOF Positioning Stage Using Corrugated Flexible Units

Employing the corrugated flexible units as flexure hinges, the whole stage is designed as shown in Fig. 5, and the joints are all actuated by piezo actuators in three directions. The displacement is transferred by the first order displacement amplification mechanism from the actuators to the center stage, and then three Laser Displacement Sensor measure the motion of the center stage.

Import this model into FEA software, ANSYS, to check out the feasibility. The force and fixed support are applied as actual situation, and the result is shown in Fig. 6. The color in Fig. 6 show the size of the displacement, and the red represent large displacement, the blue represent small displacement. From this perspective, the input displacement is larger than the output one, and it's obviously not match the goal of positioning stage. Taking into account of the fulcrum of the first order displacement amplification mechanism, the stiffness of the fulcrum is quite small and as a result, the largest displacement of the stage is not lie in the center of it. More importantly, it's quite difficult to keep the input force vertical to the input stage, and the shift may cause unavoidable input error. Therefore, an improved model is proposed. As shown in Fig. 7, a structure of double corrugated flexible

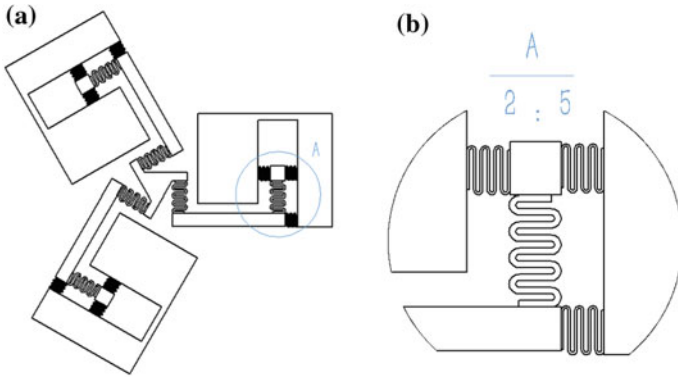


Fig. 5 Three DOF positioning stage with corrugated flexible units

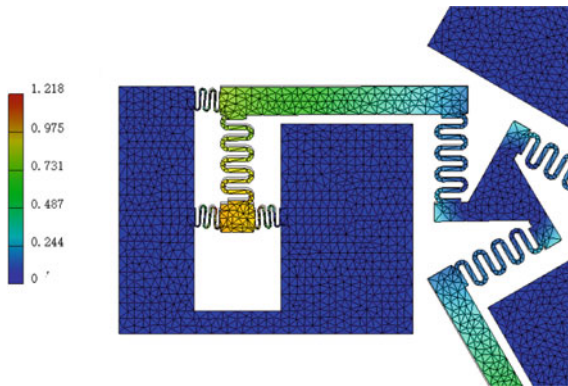


Fig. 6 The result of FEA via ANSYS

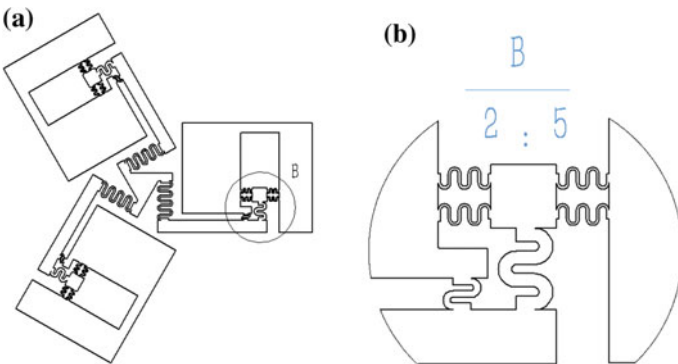


Fig. 7 The structure of double corrugated flexible units

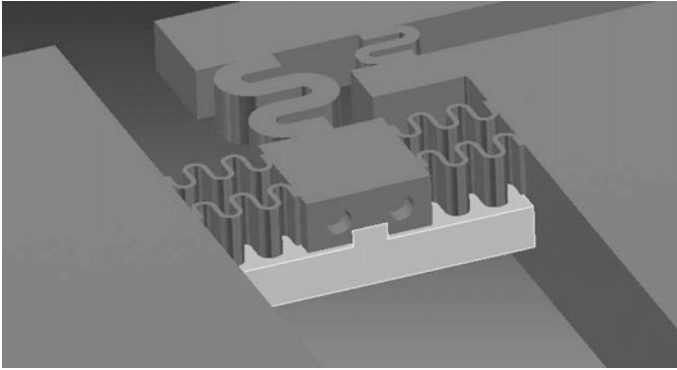


Fig. 8 The guide with dovetail under the input stage

units is introduced to restrict the rotating shift of input stage and keep input force be vertical to the input stage. Also the fulcrum of the first order displacement amplification mechanism is modified to cater the goal of displacement amplification. In addition, a guide with dovetail is added under the input stage to guarantee the input stage moving only in the vertical direction, as shown in Fig. 8.

3 Simulation and Analysis

The material of precision positioning stage accounts for a large proportion in influencing the property of the stage, and it requires high fatigue strength and yield strength, as well as high stiffness. At the same time, when forced, it should generate elastic deformation. Considering various factors mentioned above and compare the materials list in Table 1, we select 65Si2Mn as the material of the platform, and the property parameters of 65Si2Mn are listed in Table 2.

Take the place of corrugated flexible units with notch-type joints as a fulcrum and then import the two models into ANSYS. Apply the same fix support and loads, and also the same meshing. The results are illustrated in Fig. 9. In Fig. 9, three same 200 N forces are applied in every direction of the two stages to get a pure rotational movement. From Fig. 9a, c we can get the conclusion that the two stages

Table 1 The property parameters of some materials

Materials	Elastic Modulus (GPa)	Yield limit (MPa)	Density (kg/m ³)	Market price (RMB/kg)
Beryllium alloy	128	1170	8300	260
Titanium alloy	114	1170	4400	310
Aluminum alloy	71.7	34	2710	50
Spring steel	210	1641	7800	15

Table 2 The property parameters of 65Si2Mn

Property	Density	Poisson's ratio	Young's modulus
values	$\rho = 7850 \text{ kg} \cdot \text{m}^{-3}$	$\nu = 0.3$	$E = 210 \text{ GPa}$

can achieve a goal of amplifying the displacement. Further in detail, the displacement of 3DOF positioning stage based on all corrugated flexible units reaches to 671.69 μm while another stage with a notch-type fulcrum gets a displacement of 640.5 μm . That is to say, the 3DOF positioning stage based on all corrugated flexible units obtains larger displacement in output stage, but the disparity is relatively small. Comparing Fig. 9b, d, the equivalent stress of notch-type fulcrum concentrates on the center of notch-type joints while the equivalent stress of corrugated flexible fulcrum is uniformly distributed in curved portion and largely eases the stress concentration.

Table 3 is the simulation data report forms of the stage with all CF units in ANSY. Firstly, compared to the average yield strength spring steel, $S_y = 1641 \text{ MPa}$, the maximum equivalent stress is 487.656 MPa, and obviously it suffices the security strength of materials. Secondly, the extreme position in the X

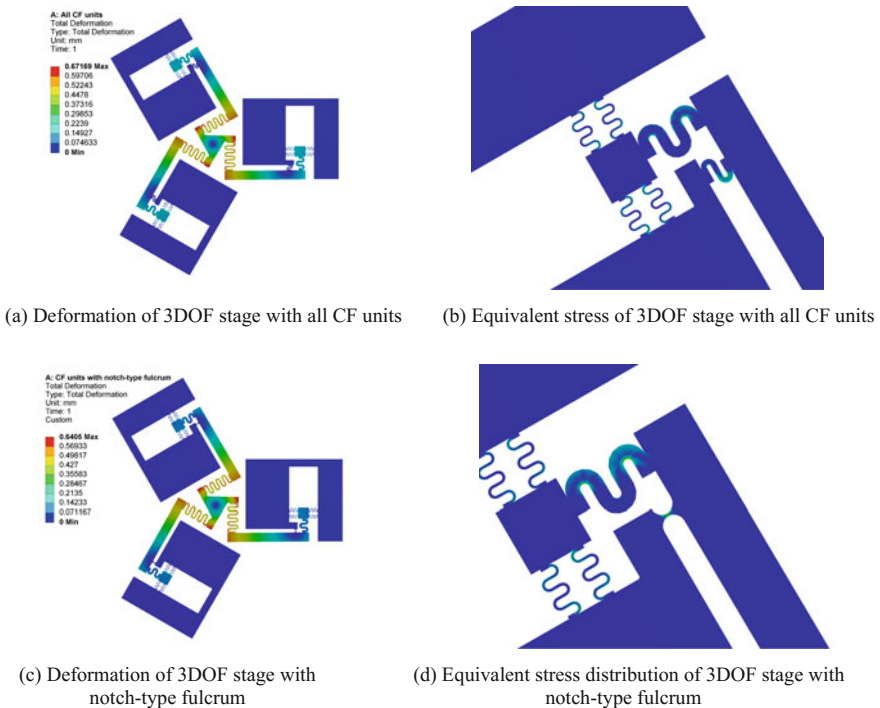


Fig. 9 Deformation and equivalent stress analysis of two kinds of 3DOF stage

Table 3 Simulation data report forms of ANSYS result

Name	Minimum	Maximum
Volume	203,309 mm ³	
Weight	1.59598 kg	
Mises equivalent stress	0.0002899 MPa	487.656 MPa
The first principal stress	-155.417 MPa	347.605 MPa
The third principal stress	-558.595 MPa	60.9061 MPa
Displacement	0 mm	0.676884 mm
Safety factor	0.42448 ul	15ul
Stress XX	-501.28 MPa	320.053 MPa
Stress XY	-237.509 MPa	208.477 MPa
Stress XZ	-24.8098 MPa	29.9408 MPa
Stress YY	-544.088 MPa	316.047 MPa
Stress YZ	-29.0776 MPa	35.564 MPa
Stress ZZ	-184.482 MPa	98.7652 MPa
X displacement	-0.667815 mm	0.53829 mm
Y displacement	-0.63116 mm	0.526358 mm
Z displacement	-0.00103052 mm	0.000896717 mm
Equivalent strain	0.00000000134969 ul	0.00222061 ul
The first principal strain	0.0000118803 ul	0.00154738 ul
The third principal strain	-0.00254529 ul	0.00000576862 ul
Strain XX	-0.00218795 ul	0.00142384 ul
Strain XY	-0.00154381 ul	0.0013551 ul
Strain XZ	-0.000161264 ul	0.000194615 ul
Strain YY	-0.00238741 ul	0.00143431 ul
Strain YZ	-0.000189004 ul	0.000231166 ul
Strain ZZ	-0.000419773 ul	0.000545216 ul

direction is $-667.815 \mu\text{m} \sim +538.29 \mu\text{m}$, and even through it's not the absolute value of the center platform, a large displacement of the center platform in X direction can be obtained with a decomposition. Similarly, the extreme position in the Y direction is $-631.16 \mu\text{m} \sim +526.358 \mu\text{m}$. The positioning errors in X and Y axis are about 36 and 12 μm . In Z direction, the extreme position is $-1.03 \mu\text{m} \sim +0.896 \mu\text{m}$ and this is mainly caused by the gravity of itself. Obviously this error will have some small impact on the positioning accuracy of the platform, but the impact on the overall positioning is quite small.

Further, take the place of every corrugated flexible unit in the positioning stage with notch-type joints, and analysis it with same fixed support and force in ANSYS. Three same forces of 200 N are also given in every input stage to get a rotational movement of the center stage. Figure 10 shows the final result. Largest displacement of this stage can only reach 103.23 μm and this is quite smaller than the stage based on all corrugated flexible units. This is caused by the high stiffness of notch-type joints in input stages. And the stress focus on the center of the

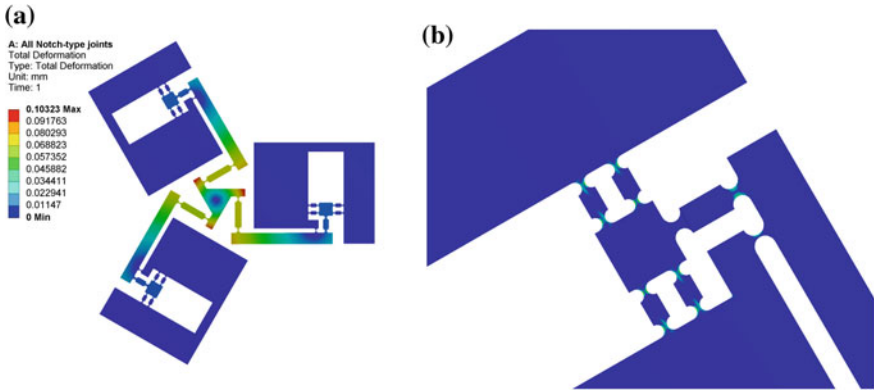


Fig. 10 **a** is deformation of 3DOF stage with all notch-type joints, **b** is equivalent stress distribution of 3DOF stage with all notch-type joints

notch-type joints and it may cause damage in it. This leads to the conclusion that the precision positioning stage based on all corrugated flexible units can get a relatively good and larger displacement.

4 Conclusion

In conclusion, a planar 3DOF precision positioning stage actuated by piezo actuators is proposed in this paper. The stage possesses a relatively large displacement with the help of CF units and a first order displacement amplification mechanism. The comparison between the precision positioning stage with all corrugated flexible units and the stage with notch-type fulcrum are carried out via ANSYS, and these two kinds of positioning stage gain large displacement in output stage. Through introducing corrugated flexible units, the stress concentration is largely eased. Compared to traditional 3DOF positioning stage with all notch-type joints, the stage with CF units gets larger more displacement. In future works, the relationship between input and output will be deduced and optimization of the stage will be carried to get a better decoupling property, and the stage will be manufactured using Wire cut Electrical Discharge Machining (WEDM) to verify the result of ANSYS.

Acknowledgments The authors would like to gratefully acknowledge the reviewers' comments. This work is supported by National Natural Science Foundation of China (Grant Nos. 51575187, 91223201), Science and Technology Program of Guangzhou (Grant No. 2014Y200217), Science and Technology Major Project of Huangpu District of Guangzhou (20150000661), Research Project of State Key Laboratory of Mechanical System and Vibration (MSV201405), the Fundamental Research Funds for the Central University (Fund No. 2015ZZ007) and Natural Science Foundation of Guangdong Province (S2013030013355).

References

1. Verma S, Kim WJ, Shakir H (2005) Multi-axis maglev nanopositioner for precision manufacturing and manipulation applications. *IEEE Trans Ind Appl* 41(5):1159–1167
2. Leang KK, Fleming AJ (2009) High-speed serial-kinematic SPM scanner: design and drive considerations. *Asian J Control* 11(2):144–153
3. Schitter G, Astrom KJ, DeMartini BE, Thurner PJ, Turner KL, Hansma PK (2007) Design and modeling of a high-speed AFM-scanner. *IEEE Trans Control Syst Technol* 15(5):906–915
4. Paros JM (1965) How to design flexure hinges. *Mach Des* 37:151–156
5. Trease BP, Moon YM, Kota S (2005) Design of large-displacement compliant joints. *J Mech Des* 127(4):788–798
6. Lobontiu N, Paine J (2002) Design of circular cross-section corner-filletted flexure hinges for three-dimensional compliant mechanisms. *ASME J Mech Des* 124(3):479–484
7. Smith ST (2000) *Flexures: elements of elastic mechanisms*. CRC Press
8. Saggere L, Kota S, Crary SB (1994) A new design for suspension of linear microactuators. In: *Proceedings, DSC-Vol 55-2, dynamic systems and control, vol 2, 1994 international mechanical engineering congress and ex-position, Chicago, IL, 6–11 Nov 1994*, pp 671–675
9. Wang N, Zhang X (2012) Compliant mechanisms design based on pairs of curves. *Sci China Technol Sci* 55(8):2099–2106
10. Wang N, Liang X, Zhang X (2014) Pseudo-rigid-body model for corrugated cantilever beam used in compliant mechanisms. *Chin J Mech Eng* 27(1):122–129
11. Wang N, Liang X, Zhang X (2015) Stiffness analysis of corrugated flexure beam used in compliant mechanisms. *Chin J Mech Eng* 28(4):776–784
12. Wang N, Liang X, Zhang X (2014) Design and analysis of a novel XY micro-positioning stage used corrugated flexure beams. In: *International conference on intelligent robotics and applications*. Springer International Publishing, pp 586–595
13. Wang NF, Tai K (2010) Design of 2-DOF compliant mechanisms to form grip-and-move manipulators for 2D workspace. *J Mech Des* 132(3):031007
14. Wang H, Zhang X (2008) Input coupling analysis and optimal design of a 3-DOF compliant micro-positioning stage. *Mech Mach Theory* 43(4):400–410
15. Du Y, Li T, Jiang Y, Wang H (2016) Design and analysis of a 2-degree-of-freedom flexure-based micro-motion stage. *Adv Mech Eng* 8(3):1687814016638301
16. Yi BJ, Chung GB, Na HY, Kim WK, Suh IH (2003) Design and experiment of a 3-DOF parallel micromechanism utilizing flexure hinges. *IEEE Trans Robot Autom* 19(4):604–612
17. Lobontiu N, Paine JS, O'Malley E, Samuelson M (2002) Parabolic and hyperbolic flexure hinges: flexibility, motion precision and stress characterization based on compliance closed-form equations. *Precis Eng* 26(2):183–192
18. Hao G, Kong X (2012) A novel large-range XY compliant parallel manipulator with enhanced out-of-plane stiffness. *J Mech Des* 134(6):061009
19. Xu Q (2014) Design and development of a compact flexure-based precision positioning system with centimeter range. *IEEE Trans Ind Electron* 61(2):893–903
20. Zettl B, Szyszowski W, Zhang WJ (2005) Accurate low DOF modeling of a planar compliant mechanism with flexure hinges: the equivalent beam methodology. *Precis Eng* 29(2):237–245
21. Li Y, Xiao S, Xi L, Wu Z (2014) Design, modeling, control and experiment for a 2-DOF compliant micro-motion stage. *Int J Precis Eng Manuf* 15(4):735–744
22. Sardan O, Eichhorn V, Petersen DH, Fatikow S, Sigmund O, Bøggild P (2008) Rapid prototyping of nanotube-based devices using topology-optimized microgrippers. *Nanotechnology* 19(49):495503

23. Aten QT, Jensen BD, Howell LL (2012) Geometrically non-linear analysis of thin-film compliant MEMS via shell and solid elements. *Finite Elem Anal Des* 49(1):70–77
24. Su HJ, Dorozhkin DV, Vance JM (2009) A screw theory approach for the conceptual design of flexible joints for compliant mechanisms. *J Mech Robot* 1(4):041009

Part IV
Reconfigurable Mechanism

A Deployable Robot Based on the Bricard Linkage

Hao Shang, Dawei Wei, Rongjie Kang and Yan Chen

Abstract A large variety of transformable robots were proposed in the past decades, which were mainly based on reconfigurable mechanisms. Meanwhile, deployable structures have been extensively applied to various fields, such as aerospace industry, civil engineering, and medical engineering. This paper presents a new method to integrate deployable structures to the design of transformable robots. A threefold-symmetric Bricard linkage is analyzed and used as the body structure of the robot. Gait control is then achieved by using the deploying and folding motion of the Bricard linkage. Experimental results show that the robot is capable of moving through limited space with single degree-of-freedom (DOF).

Keywords Threefold-symmetric bricard linkage · Deployable robot · Gait control

1 Introduction

In recent years, there has been a growing interest in the development of transformable robots, which can adjust their configurations to adapt to multiple tasks and uncertain environment. Such robots have been widely applied to areas such as reconnaissance, rescue missions, and space applications [1].

H. Shang · D. Wei · R. Kang (✉) · Y. Chen

Key Laboratory of Mechanism Theory and Equipment Design of Ministry of Education, Tianjin University, Tianjin 300072, China
e-mail: rjkang@tju.edu.cn

H. Shang
e-mail: shanghao@tju.edu.cn

D. Wei
e-mail: wdw03@tju.edu.cn

Y. Chen
e-mail: yan_chen@tju.edu.cn

H. Shang · D. Wei · R. Kang · Y. Chen
School of Mechanical Engineering, Tianjin University, 300072 Tianjin, China

Reconfigurable robots are a kind of transformable robots built from modules that can be connected in different ways to form different morphologies for different purposes [3]. Since the Reconfigurable Modular Manipulator System (RMMS) was invented in 1988 [2], many kinds of reconfigurable robots have appeared successively.

Chain-type reconfigurable robots were a typical class of reconfigurable robots, such as the PolyPod robot [4] and later its descendent PolyBot [5] and CONRO [6] shown in Fig. 1a.

Another class of reconfigurable robots is the lattice-type robots. Early two-dimensional lattice-type robots include the Fracta and Metamorphic robots [7, 8]; the first three-dimensional lattice-type robots were the Molecule shown in Fig. 1b and the 3-D-Unit [9, 10].

Chain-type and lattice-type robots have evolved to the hybrid reconfigurable robots. The recent generation of self-reconfigurable robots, including M-TRAN III, ATRON shown in Fig. 1c, and SuperBot, are all of the hybrid type [1, 11, 12].

In the last decade, a new kind of transformable robots based on metamorphic mechanisms was presented. Dai [13] proposed the concept of metamorphic palm. As shown in Fig. 1d, a robotic hand in which the palm section enables it to achieve a wide range of movement was designed. Ding [14, 15] proposed a novel design of metamorphic hybrid wheel-legged rover mechanism.

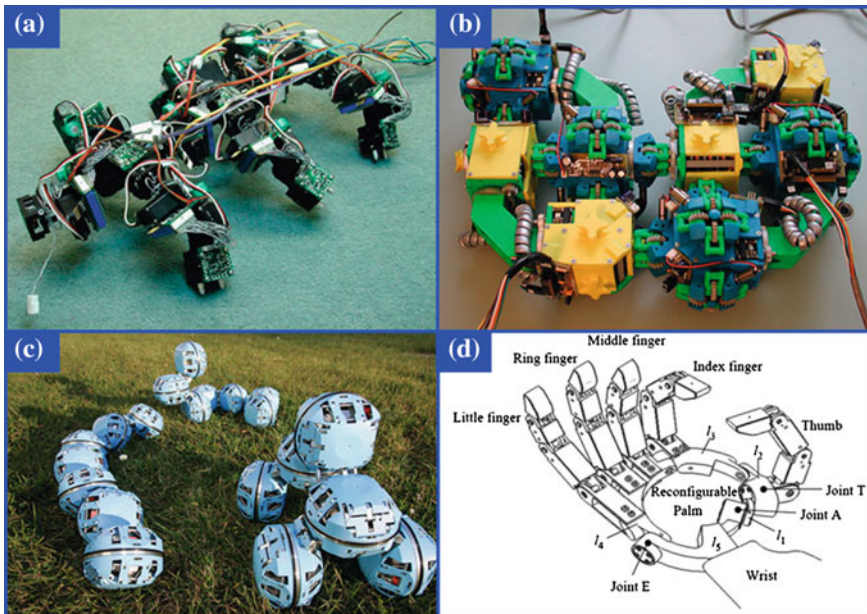


Fig. 1 Transformable robot **a** CONRO **b** Molecule **c** ATRON **d** metamorphic palm

However, the above-mentioned robots are not able to change their size significantly, which is important for passing through constrained environment.

Meanwhile, since the first overconstrained mechanism was proposed by Sarrus [16], a number of overconstrained mechanisms have been proposed by some researchers including Bennett in 1903 [17, 18], Bricard in 1926 [19], Myard in 1931 [20], Goldberg in 1943 [21], Waldron in 1968 [22], and Wohlhart in 1987 [23]. After that the overconstrained mechanisms, especially Bennett and Bricard linkages, were applied to deployable structures by Chen [24, 25, 26]. A large variety of deployable structures were used in engineering fields. Catherine used the Hoberman mechanism to design reconfigurable antenna and solar arrays [27]. Wohlhart also developed a deployable polyhedron by using a set of planar linkages [28]. Gantes [29], Hanaor [30] and Pellegrino [31] et al. applied to the civil engineering structures.

Although deployable structures have achieved great progress in the fields of aerospace industry, civil engineering, and medical engineering, there were seldom applications in the design of transformable robots.

The aim of this paper is to use the deployable structure to develop a novel transformable robot. The threefold-symmetric Bricard linkage is adopted here due to its large expansion ratio and single DOF moving ability that allows for easy control. The presented robot can change its configuration to go through a narrow gap either perpendicular or parallel to the ground.

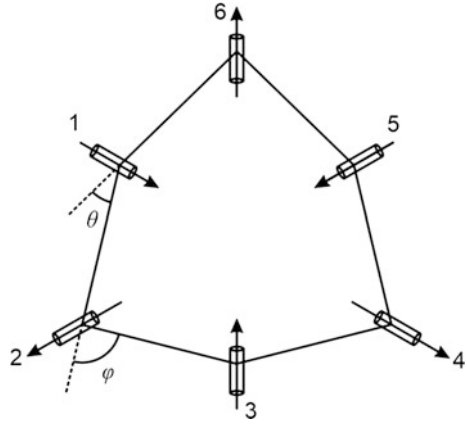
The paper is organized as follows. Section 2 shows the analysis of geometrical properties of the threefold-symmetric Bricard linkage. Section 3 presents the design of the robot including the mechanism analysis, gaits generation and control system. Section 4 presents the experimental results, and Sect. 5 gives the conclusion and discussion.

2 Bricard Linkage

The Bricard linkage is the only 6R overconstrained linkage independent from other linkages. There are six distinct types of Bricard linkages in the family of Bricard linkage. They were discovered and reported by Bricard [32]. In 2005, Chen et al. [33] presented a kinematic analysis of a new linkage called *Threefold-symmetric Bricard linkage*, which was obtained by combining the general plane-symmetric and trihedral Bricard linkage, and pointed out the possibility of applying this linkage to deployable structures.

The configuration of this linkage is shown in Fig. 2. It has three symmetric planes and threefold-rotational symmetry. Each link of the linkage is perpendicular to the two axes of adjacent revolute joints it connects.

Fig. 2 Threefold-symmetric Bricard linkage



The threefold-symmetric Bricard linkage satisfies the following conditions:

$$\begin{cases} a_{12} = a_{23} = a_{34} = a_{45} = a_{56} = a_{61} = l, \\ \alpha_{12} = \alpha_{34} = \alpha_{56} = \alpha, \quad \alpha_{23} = \alpha_{45} = \alpha_{61} = 2\pi - \alpha, \\ R_i = 0 (i = 1, 2, 3, 4, 5, 6) \\ \theta_1 = \theta_3 = \theta_5 = \theta \\ \theta_2 = \theta_4 = \theta_6 = \varphi \end{cases} \quad (1)$$

where a_{jk} is the length of a link between two adjacent axes of revolute j and k , α_{jk} is the twist angle between axes of adjacent revolute joints j and k ($j, k = 1, 2, 3, 4, 5, 6$), and R_i is the offset between endpoints of two links connected by one revolute joint along the axis i . θ_i is the rotation angle about axis of joint i .

The closure equation of this threefold-symmetric linkage is then obtained by

$$\cos^2 \alpha + \sin^2 \alpha (\cos \theta + \cos \varphi) + (1 + \cos^2 \alpha) \cos \theta \cos \varphi - 2 \cos \alpha \sin \theta \sin \varphi = 0 \quad (2)$$

The structure when $l = 500$ mm, $\alpha = 2\pi/3$ as shown in Fig. 3 is chosen to build the model of the deployable robot.

The reasons for selecting these parameters can be listed as follows:

1. For $0 \leq \alpha < \pi/3$, or $2\pi/3 < \alpha \leq \pi$, the movement of linkages is not continuous. Thus, the linkage is physically blocked in the positions where all links crossed at the center when either θ or φ reaches π or $-\pi$. When $\pi/3 \leq \alpha \leq 2\pi/3$, the linkage keeps moving continuously [33].
2. When $\alpha = \pi/3$ or $\alpha = 2\pi/3$, the movement of the linkages has a kinematic bifurcation, which means the number of instantaneous (infinitesimal) degrees of freedom increases. Although we took some measures to prevent this robot movement curve passing the bifurcation point in this paper. By taking advantage of kinematic bifurcation, there is an infinite possibility with the future to develop the robot that will have more ways in transformation.

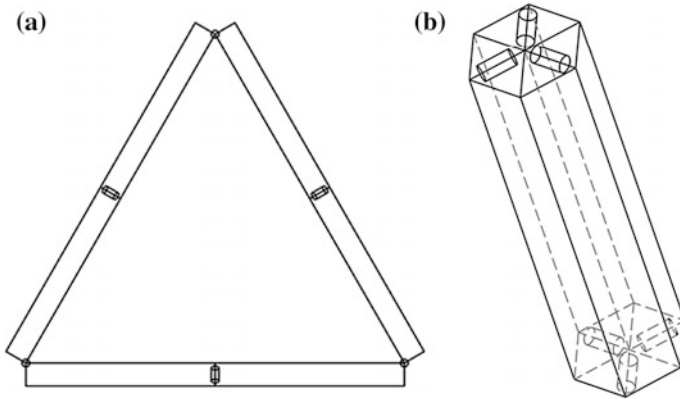


Fig. 3 The structure which is applied to the robot **a** The deployed configuration; **b** The folded configuration

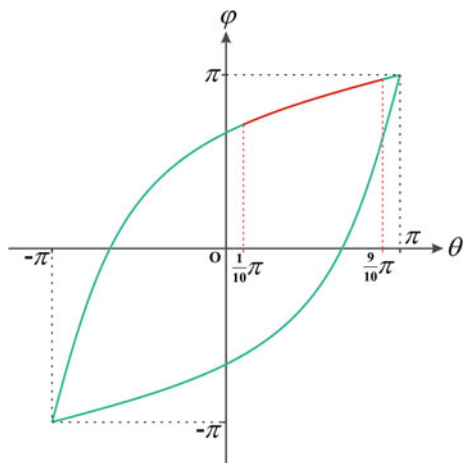
3. In fact, for $\alpha = \pi / 3$ and $\alpha = 2\pi / 3$, the linkages have the same kinematic properties. So we chose one of it.
4. To adapt to the size of other parts that constituted the robot, $l = 500$ mm was selected.

Substituting $\alpha = 2\pi/3$ into Eq. (2), we can reach the input–output equation:

$$\frac{1}{4} + \frac{3}{4}(\cos \theta + \cos \varphi) + \frac{5}{4}\cos \theta \cos \varphi + \sin \theta \sin \varphi = 0 \quad (3)$$

Figure 4 shows the input–output curve (green color) determined by Eq. (3). According to Figs. 3 and 4, the properties for the threefold-symmetric linkage when $\alpha = 2\pi/3$ are as follows. Firstly, it appears that only one of the six revolute

Fig. 4 θ versus φ for the threefold-symmetric linkage for $\alpha = 2\pi/3$



variables can be free. Thus, this threefold-symmetric linkage has one degree of finite mobility. Secondly, it can be flattened to form a planar equilateral triangle with side length 21. Additionally, the linkage keeps moving continuously.

However, as shown in Fig. 4, the point at $(\theta, \varphi) = (\pi, \pi)$ is the point of bifurcation. This means the linkage has 2 DOF in this point, which causes the unexpected motion. Meanwhile, when $(\theta, \varphi) = (0, 2\pi/3)$, the linkage is in the deployed configuration. It's difficult to change the linkage structure to the folded configuration because of the overload torque. So as shown in Fig. 4, the curve in red color, in which θ varies from $\pi/10$ to $9\pi/10$, is used for the robot to perform walking motions.

The reasons for applying this linkage to the robot are that the linkage has single DOF and simple structure, which make the actuation and control easy and feasible. Moreover, the linkage has a large expansion ratio, meaning that it can change its size significantly.

3 Design of the Deployable Robot

Based on the above analysis this section presents the design of the deployable robot using the threefold-symmetric Bricard linkage. In the first part, the mechanical design of the robot is elaborated in detail. Two gaits of the robot are presented in the second part. The final part discusses a double closed loop control system applied to the robot.

3.1 *The Mechanical Design*

To build a lightweight, flexible and high strength deployable robot, carbon fiber tubes are used to form the robot body. The “feet”, constituted with a steel frame and wheels, play a significant role in supporting the body, walking and transforming. The transmission gears, battery and the DC-motor are located inside the steel frame. Meanwhile, the angle sensor is assembled collinearly with the joint axis to monitor the rotation angle θ , which is the parameter of the linkage as shown in Fig. 2, and the control module (CMOD) is fixed on the robot body. In addition, Omni-directional wheels are used to achieve a batter gait. The robotic prototype is shown in Fig. 5.

The robot has an extensive ability of transformation. The bottom area of the robot varies from 0.027–0.73 m² with the height between 0.68–0.2 m. Therefore, the robot has an expansion ratio of 27.04 (defined as ratio of bottom area of the deployed and folded form).

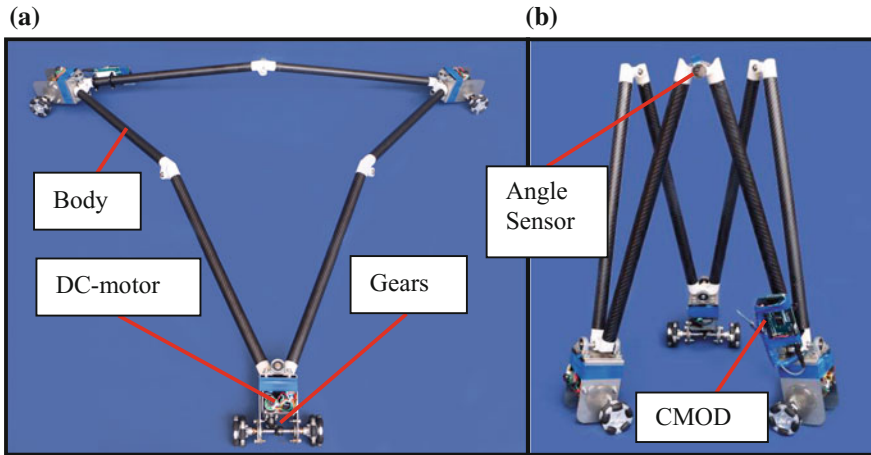


Fig. 5 The robotic prototype **a** the deployed configuration; **b** the folded configuration

3.2 Gait of the Robot

The robot is actuated by three DC-motors, while it has single DOF. We designed two kinds of gaits to achieve walking.

One is simply to change the configuration of the robot's body, called deployed-folded gait. As the structure has good symmetry and single DOF, the deployed-folded gait is performed by activating the three motors at the same time with identical rotating speed. As shown in Fig. 6a, in the deployed configuration, the three feet move outward synchronously to the deployed form. In the folded configuration they move inversely to the folded form. In this gait the robot will not walk but change its size and height.

The other gait is designed for the robot to walk in a specific direction, called directional gait. In this gait one motor is locked and the others are activated in sequence at identical rotating speed. So that the robot moves forward.

As shown in Fig. 6b, at the beginning, the foot 2 is locked while the feet 1 and 3 move outward. The centroid of the robot moves from the point s_1 to s_2 . Then the foot 2 and foot 3 move inward while the foot 1 is locked, and the centroid of the robot moves from the point s_2 to s_3 . Afterwards the robot deploys with the foot 3 locked, and the robot moves from s_3 to s_4 . Finally, the robot folds with the foot 1 locked, and moves from s_4 to s_5 . During a circle of all steps, the robot completes a forward motion from s_1 to s_5 .

In the directional gait, the motors are not allowed for delay to ensure synchronization. Therefore, a self-locking motor is selected. Meanwhile, the composite force of the working feet exerted by the robot body is not parallel to the motion of the wheels. Therefore, there exists a friction perpendicular to the movement of the feet. Omni-directional wheels are employed in case of lateral slip.

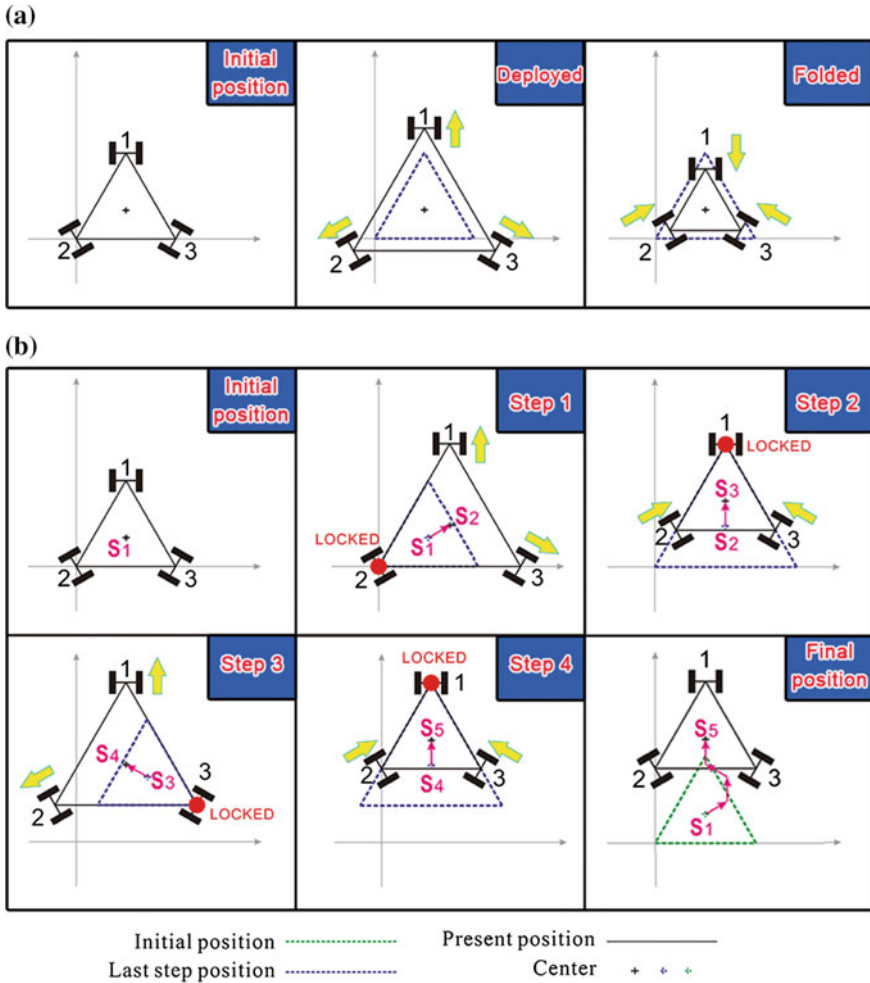


Fig. 6 The forward gait a the deployed-folded gait b the directional gait

3.3 The Control System Design

The robotic control system consists of a host computer, an on-board micro-computer (Arduino Mega 2560), three DC motors with transmission system, three electromagnetic encoders on the motors, and an angle sensor on one joint of the linkage, Fig. 5b.

Control commands, like walking direction and speed, are sent by the host computer and received by the on-board micro-computer via a Bluetooth module. The micro-computer then converts the control commands to level signals and PWM

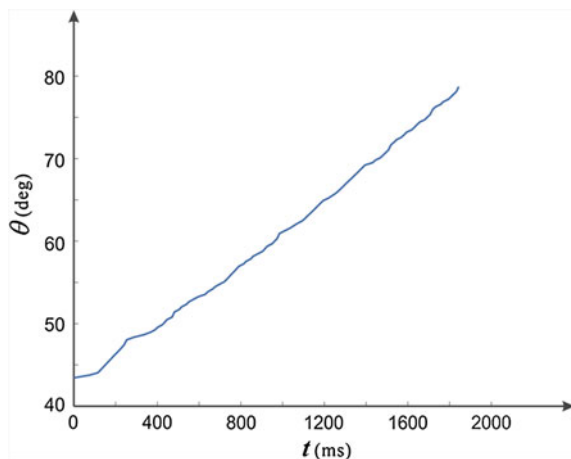
signals to drive the three motors. The rotating speed of the motors are fed back to the micro-computer to form a velocity control loop with a PID algorithm while the angle θ is fed back to the micro-computer to form a position control loop. The angle θ is also sent back to the host computer to show the position of the robot to the operator.

4 Experiment

In order to illustrate the performance of the robot, two experiments were conducted. One is to test the folding motion of the robot, in which the rotation angle θ , which is the supplement of the angle between the axes linked by the joint fixed with the angle sensor, increases from 43° to 77° . As shown in Fig. 7, the rotation angle θ goes up with a constant rate after 0.3 s. This indicates that the motion of the robot reaches stability in a short time with no strong vibration, which reflects an effective control strategy.

The second experiment is to test the ability of the robot to pass narrow gaps. Two kinds of circumscribed paths are established as shown in Fig. 8. The first, in Fig. 8a, is a 400 mm high gap. The robot deploys to a position where θ reaches 150° and then advances in the directional gait during which the height varies from 0.2 to 0.3 m. To pass through the second path shown in Fig. 8b whose width is 600 mm, the robot folds to an extent that θ is 30° and keeps moving in the directional gait with its width fluctuating from 0.4 to 0.5 m. The experiment demonstrates high adaptability of the robot to variable and limited space.

Fig. 7 θ versus t in the folding process



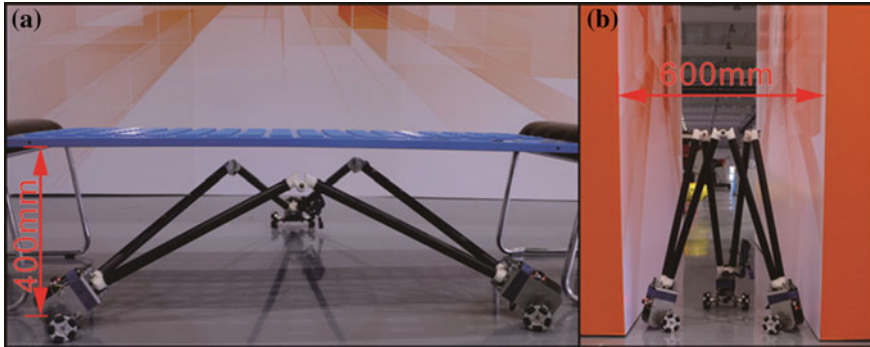


Fig. 8 Field condition of the passing experiment **a** a horizontal gap; **b** a vertical gap

5 Conclusion and Discussion

In this paper, a new deployable robot based on threefold-symmetrical Bricard linkage is proposed. It is a single-DOF robot with two unique gaits achieved by the deploying and folding movements of the structure. DC motors are assembled on its feet to actuate the robot. A rotating speed-angle double loop control system is applied to the robot to improve its control performance. The robot exhibits good adaptability when passing through limited space.

Future work will involve exploring other forms of Bricard linkages applicable to deployable robots, which can fulfill tasks like stair climbing, and focus on its control stability.

Acknowledgments The financial supports from the Natural Science Foundation of China (Project No. 51275334 and 51375329), and Tianjin Municipal Science and Technology Department Program (Grants No. 14JCYBJC19300) are greatly acknowledged.

References

1. Salemi B, Moll M, Shen WM (2006) Superbot: a deployable, multi-functional, and modular self-reconfigurable robotic system. *IEEE international conference on intelligent robots and systems*, pp 3636–3641
2. Schmitz D, Khosla P, Kanade T (1988) The CMU reconfigurable modular manipulator system. technical report
3. Støy K (2015) *Reconfigurable robots*. Springer, Berlin Heidelberg
4. Yim M (1998) *Locomotion with a unit-modular reconfigurable robot*. Stanford University
5. Duff DG, Yim M, Roufas K (2001) Evolution of polybot: a modular reconfigurable robot. *Proceedings of the harmonic drive international symposium*
6. Castano A, Chokkalingam R, Will P (2000) Autonomous and self-sufficient CONRO modules for reconfigurable robots. *international symposium on distributed autonomous robotic systems*

7. Murata S, Kurokawa H, Kokaji S (1994) Self-assembling machine. In: IEEE international conference on robotics and automation. proceedings, pp 441–448
8. Chirikjian GS (1994) Kinematics of a metamorphic robotic system. IEEE international conference on robotics and automation. pp 449–455
9. Kotay K, Rus D, Vona M, Mcgray C (1998) The self-reconfiguring robotic molecule. In: IEEE international conference on robotics and automation, pp 424–431
10. Murata S, Kurokawa H, Yoshida E, Tomita K (1998) A 3-D self-reconfigurable structure. In: IEEE international conference on robotics and automation, pp 432–439
11. Kurokawa H, Tomita K, Kamimura A, Kokaji S, Hasuo T (2008) Distributed self-reconfiguration of M-TRAN III modular robotic system. *Int J Robot Res* 27 (3–4):373–386
12. Stergaard EH, Kassow K, Beck R, Lund HH (2006) Design of the ATRON lattice-based self-reconfigurable robot. *Auton Rob* 21(2):165–183
13. Wei G, Dai JS, Wang S, Luo H (2011) Kinematic analysis and prototype of a metamorphic anthropomorphic hand with a reconfigurable palm. *Int J Humanoid Rob* 8(3):459–479
14. Wang Z, Ding X, Rovetta A (2007) Structure design and locomotion analysis of a novel robot for lunar exploration. *Iftomm world congress*
15. Ding XL, Kun XU (2009) Design and analysis of a novel metamorphic wheel-legged rover mechanism. *Zhongnan Daxue Xuebao* 40:91–101
16. Sarrus PTC (1853) Note sur la transformation des mouvements rectilignes alternatifs, en mouvements circulaires; et reciproquement. *Academie des sciences*. pp 1036–1038
17. Bennett GT (1903) A new mechanism. *Engineering* 76:777–778
18. Bennett GT (1914) The skew isogram mechanism. *Proc Lond Math Soc* 13(1):151–173
19. Bricard R (1926) *Leçons de cinématique*: Gauthier-Villars
20. Myard FE (1931) Contribution à la géométrie des systèmes articulés. *Bull Soc Math France* 59:183–210
21. Goldberg M, Goldberg M (1943) New five-bar and six-bar linkages in three dimensions. *Trans ASME*
22. Waldron KJ (1968) Hybrid overconstrained linkages. *J Mech* 3(2):73–78
23. Wohlhart K (1987) A new 6R space mechanism. In: *Proceedings of the seventh world congress on the theory of machines and mechanisms*, Sevilla, Spain, pp. 193–198
24. Chen Y, You Z (2006) Square deployable frames for space applications. Part 1: theory. *Proc Inst Mech Eng Part G J Aerosp Eng* 220(4):347–354
25. Chen Y, You Z (2007) Square deployable frames for space applications. Part 2: realization. *Proc Inst Mech Eng Part G J Aerosp Eng* 221(1):37–845
26. Chen Y, You Z (2007) Curved-profile deployable structures based on Bennett linkages. In: *AIAA/ASME/ASCE/AHS/ASC structures, structural dynamics, and materials conference*
27. Faist KA, Wiens GJ (2010) Parametric study on the use of Hoberman mechanisms for reconfigurable antenna and solar arrays. In: *Aerospace conference, 2010 IEEE*, pp. 1–8
28. Wohlhart K (2004) *Polyhedral zig-zag linkages*. Springer, Netherlands
29. Gantes CJ, Connor JJ, Logcher RD, Rosenfeld Y (1989) Structural analysis and design of deployable structures. *Comput Struct* 32(3–4):661–669
30. Hanaor A, Levy R (2001) Evaluation of deployable structures for space enclosures. *Int J Space Struct* 16(4):211–229
31. Pellegrino S (2001) Deployable structures in engineering. In: *Deployable structures*
32. Bricard R (1897) Mémoire sur la théorie de l'octaèdre articulé. *J Math Pures Appl* 3 (5):11–148
33. Chen Y, You Z, Tarnai T (2005) Threefold-symmetric Bricard linkages for deployable structures. *Int J Solids Struct* 42(8):2287–2301

Configuration Design and Kinematics Research of Scissor Unit Deployable Mechanism

Jianfeng Li, Sanmin Wang, Changjian Zhi and Yuantao Sun

Abstract Scissor unit deployable mechanism is widely used in aerospace and architecture, and the configuration design and kinematics analysis are two important problems that need to be solved in the application process. The first order and second order influence coefficient matrices are derived by coordinate transform. Kinematics analysis model and its calculating examples are presented, and the displacement, velocity and acceleration of all the hinged points are calculated. Moreover, the numerical example is used to verify the effectiveness of analysis method which also presented in this paper.

Keywords Scissor unit deployable mechanism · Configuration design · Influence coefficient matrices · Kinematics analysis model

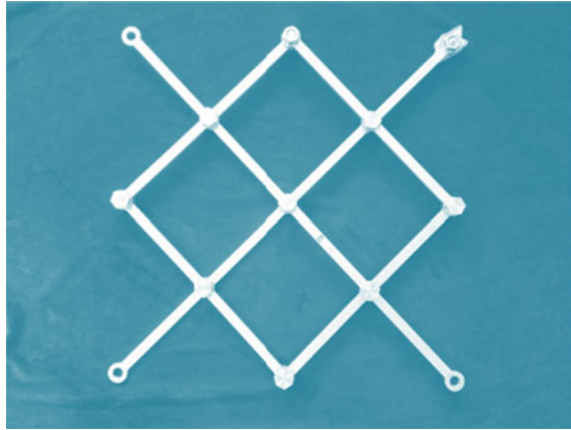
1 Introduction

Deployable mechanism presents contractility and develop ability characters, which allows convenient transport and storage, so as to widely applied on various areas, such as aviation, aerospace, civil engineering, and so on [1–3]. The first of application of deployable mechanism is the design of “mobile theater” by Pinero [4], and then Escriing et al. [5] designed an indoor swimming pool cover of Seville, Spain. In 1970s, NASA and Cambridge university’s research on developable antenna promoted the development and application of deployable mechanism theories. On the basis of the equilibrium matrix theory, Calladine and Pellegrino of Cambridge University research the stability of deployable mechanism [6]. Chen [7] derived the

J. Li (✉) · S. Wang · C. Zhi · Y. Sun
School of Mechanical Engineering, Northwestern Polytechnical University,
Xi’an, Shanxi 710072, People’s Republic of China
e-mail: jevonslivip@163.com

J. Li · S. Wang · C. Zhi · Y. Sun
178# Northwestern Polytechnical University, 127 West Youyi Road,
Xi’an Shanxi 710072, People’s Republic of China

Fig. 1 The experimental scissor unit plane deployable mechanism



kinematics differential equation for unfold process analysis by using null space basis of constraint Jacobian matrix. Zhang [8] adopting multi-body kinematics theory, combined with finite element method and Lagrange equation, established multi flexible-body kinematics equation for deployable mechanism.

In this paper, takes plane unit that consists of four scissor units as research object, Fig. 1 shows the plane deployable mechanism, which consists of four scissor units. The plane unit of experimental deployable mechanism is presented in figure, and dynamic model of scissor unit deployable mechanism is built on the basis of Cartesian coordinate.

2 Configuration Design

Scissor unit consists of two central mutually hinged and rotatable link members, a number of basic scissor link units are linked each other on terminal hinged point to compose basic piece unit plane deployable mechanism. In this paper, taking a hinged surface developable structure that consists of four scissor unit as an example to express the process of deduction.

The schematic diagram of Scissor unit surface developable mechanism is shown in Fig. 2, surface unit and serial number that assigned to hinged points of deployable mechanism is depicted in the figure.

Taking the surface developable mechanism that consists of four scissor units as an example, serial number of each hinged point is shown in Fig. 2, the first term of i and j subscript represents the scissor unit number, the second term of i and j subscript represents the hinged point number, α and β are geometric parameters, the first term of link length l subscript represents scissor unit number, the second term of link length l subscript represents link number.

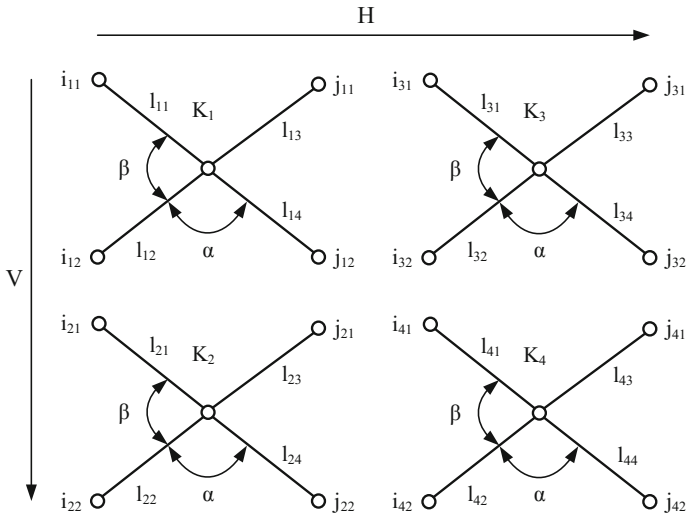


Fig. 2 The schematic diagram of scissor unit surface developable mechanism

The geometrical conditions that this plane of scissor units needs to satisfy (on V direction) are:

$$i_{11}j_{11} = i_{12}j_{12} = i_{21}j_{21} = i_{22}j_{22} \tag{1}$$

Since links are taken as rigid body on configuration design, thus

$$i_{12}j_{12} = i_{21}j_{21} \tag{2}$$

Then it is concluded that

$$l_{12}^2 + l_{14}^2 - 2l_{12}l_{14} \cos \alpha = l_{21}^2 + l_{23}^2 - 2l_{21}l_{23} \cos \alpha \tag{3}$$

Simultaneous solving the above equations, it is obvious that there are multiple solutions. This article selects a case as an example to carry out analysis, namely the lengths l of each link are equivalent conditions.

3 Kinematics Investigation

3.1 Influence Coefficient Method

Mechanism kinematic influence coefficient is proposed by Prof. Tesar and Dufy etc., and the influence coefficient method involves establishing 1-step exercise

coefficient matrix and 2-step exercise coefficient matrix, the former refers to Jacobian matrix, and the latter refers to Hessian matrix [9–12].

For the deployable mechanism showed in above picture, if exercise is input by single-degree-of-freedom kinematic pair, which can be revolute pairs or movement pairs, then the position of mechanism’s any pole is determined. Pole’s position can be described by hinged point coordinates and pole’s angular position, thus

$$\begin{aligned} \Phi_i &= f_1(\varphi_1 \varphi_2 \dots \varphi_N) \\ X_i &= f_2(\varphi_1 \varphi_2 \dots \varphi_N) \\ Y_i &= f_3(\varphi_1 \varphi_2 \dots \varphi_N) \end{aligned} \tag{4}$$

where, Φ_i, X_i, Y_i refers to the angular position of reference frame and X, Y coordinate of reference point that selected for position determination of the i-th pole. Since the input motion parameter $\varphi_1, \varphi_2, \dots, \varphi_N$ varying with time. The coordinates of Certain pole on deployable mechanism can be signed by $U_i\{\Phi_i, X_i, Y_i\}^T$, and deduce from (4),

$$U = f(\varphi_1 \varphi_2 \dots \varphi_N) \tag{5}$$

$$\dot{U} = \sum_{N=1}^N \frac{\partial U}{\partial \varphi_N} \dot{\varphi}_N \tag{6}$$

A first order partial derivative is defined as the first order influence coefficient, and can be described by matrix by

$$\dot{U} = [J] \dot{\varphi} \tag{7}$$

where, the matrix J is called the first order influence coefficient.

$$[J] = \left[\frac{\partial U}{\partial \varphi_1} \quad \frac{\partial U}{\partial \varphi_2} \quad \dots \quad \frac{\partial U}{\partial \varphi_N} \right]_{1 \times N} = \begin{bmatrix} \frac{\partial f_1}{\partial \varphi_1} & \dots & \frac{\partial f_1}{\partial \varphi_N} \\ \vdots & & \vdots \\ \frac{\partial f_3}{\partial \varphi_1} & \dots & \frac{\partial f_3}{\partial \varphi_N} \end{bmatrix} \in R^{3 \times N} \tag{8}$$

$$\dot{\varphi} = \left[\dot{\varphi}_1 \quad \dot{\varphi}_2 \quad \dots \quad \dot{\varphi}_N \right]_{N \times 1}^T \tag{9}$$

Formula (8) illustrate the 1-step exercise coefficient matrix, namely Jacobi matrix.

Accordingly, the second order partial derivative can be calculated from Eq. (6), written as

$$\ddot{U} = \sum_{p=1}^N \sum_{q=1}^N \frac{\partial^2 U}{\partial \varphi_p \partial \varphi_q} \dot{\varphi}_p \dot{\varphi}_q + \sum_{N=1}^N \frac{\partial U}{\partial \varphi_N} \ddot{\varphi}_N \tag{10}$$

Define the second derivative $\partial^2 U / \partial \varphi_p \partial \varphi_q$ as the second order kinematic influence coefficient, then formula (10) can be expressed by

$$\ddot{U} = \dot{\varphi}^T [H] \dot{\varphi} + [J] \ddot{\varphi} \tag{11}$$

where

$$\begin{aligned} \ddot{\varphi} &= \left\{ \ddot{\varphi}_1 \ \ddot{\varphi}_2 \ \cdots \ \ddot{\varphi}_N \right\}_{N \times 1}^T \\ [H] &= \begin{bmatrix} \frac{\partial^2 U}{\partial \varphi_1 \partial \varphi_1} & \cdots & \frac{\partial^2 U}{\partial \varphi_1 \partial \varphi_N} \\ \vdots & & \vdots \\ \frac{\partial^2 U}{\partial \varphi_N \partial \varphi_1} & \cdots & \frac{\partial^2 U}{\partial \varphi_N \partial \varphi_N} \end{bmatrix} \end{aligned} \tag{12}$$

The matrix H is called the second order influence coefficient.

3.2 Kinematics of Each Point

Before the research of kinematics of mechanism, proper fixed coordinate system and movement coordinate system should be established. The simplified form of kinematics equation can reduce the complicity of equation solving, and shorten the calculation time.

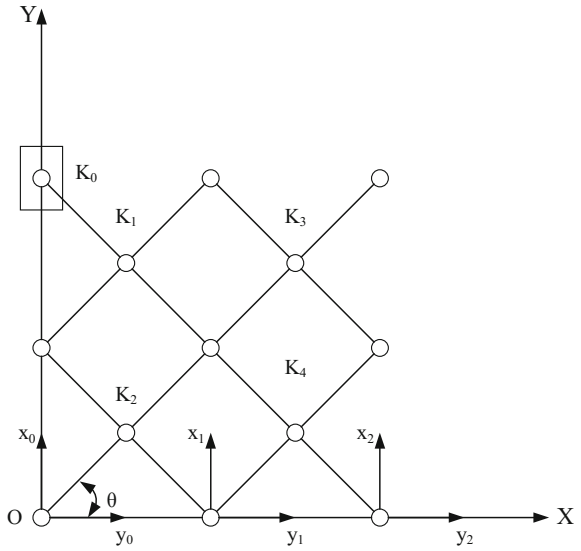
Taking the scissor unit deployable mechanism that shown in Fig. 3 as an example, Assuming the support pole's length are equivalent, and when deploy the mechanism, which connects the support structure through revolute pairs at i_{12} , i_{22} , j_{22} and j_{42} , and articulate with a slide block K_0 by revolute pairs, then the slide block move along the OY shaft, and mechanism deploy along the OX direction. The origin of fixed coordinate system $\sum XOY$ is located on the center of articulated point i_{22} , OX axis is consistent with the direction of $i_{22}j_{22}$, OY axis is established according to principle of Cartesian coordinates.

From the geometrical relationship of scissor unit deployable mechanism and coordinate, for any deploy angle θ , the coordinate transformation matrix from coordinate system of movement unit coordinate system $\sum x_i o_i y_i$ to fixed coordinate system can be described by formula (13)

$$R_{oi} = \begin{pmatrix} 1 & 0 \\ 0 & 1 \end{pmatrix} \tag{13}$$

Because the configuration of surface deployable mechanism's each unit is the same, thus

Fig. 3 The scissor unit surface deployable mechanism



$$i_{(2t)2}j_{(2t)2} = l \cos(\theta)(t = 1, 2, \dots, N) \tag{14}$$

The origin of movement unit coordinate system $\sum x_t o_t y_t$ corresponding to the x point of fixed coordinate system $\sum XOY$, and x 's coordinate is

$$x_{ot} = t i_{(2t)2} j_{(2t)2} = t l \cos \theta \tag{15}$$

The coordinate transformation matrix from coordinate system $\sum x_t o_t y_t$ to fixed coordinate system $\sum XOY$ is

$$T_{ot} = \begin{pmatrix} x_{o(t-1)} \\ 0 \end{pmatrix} = \begin{pmatrix} 2tl \cos \theta \\ 0 \end{pmatrix} = t T_o \tag{16}$$

where, $T_o = (2l \cos \theta \ 0)^T$, T_o 's first and second order derivative derivation of θ respectively is

$$\begin{bmatrix} \dot{T}_o \\ \dot{\theta} \end{bmatrix} = -2l (\sin \theta \ 0)^T \tag{17}$$

$$\begin{bmatrix} \ddot{T}_o \\ \ddot{\theta} \end{bmatrix} = -2l (\cos \theta \ 0)^T \tag{18}$$

Using formula (16) can acquire T_{ot} 's first and second order derivative of θ respectively is

$$[\overset{\bullet}{T}_{ot}]_{\theta} = t[\overset{\bullet}{T}_o]_{\theta} \tag{19}$$

$$[\overset{\bullet\bullet}{T}_{ot}]_{\theta\theta} = t[\overset{\bullet\bullet}{T}_o]_{\theta\theta} \tag{20}$$

Assuming ${}^o r_M^t$ represent M point's radius vector of unit mechanism in fixed coordinate system $\sum x_t o y_t$, and ${}^t r_M^t$ represent M point's radius vector of unit mechanism in movement unit coordinate system, then

$${}^o r_M^t = T_{ot} + R_{ot} {}^t r_M^t = T_{ot} + {}^t r_M^t \tag{21}$$

Using formula (21) to get the first and second order derivation of time, can obtain the velocity and acceleration of M point:

$${}^o v_M^t = \overset{\bullet}{o} r_M^t = \overset{\bullet}{T}_{ot} + {}^t \overset{\bullet}{r}_M^t \tag{22}$$

$${}^o a_M^t = \overset{\bullet\bullet}{o} r_M^t = \overset{\bullet\bullet}{T}_{ot} + {}^t \overset{\bullet\bullet}{r}_M^t \tag{23}$$

According to coordinate translation variables and M point's coordinate, it is available that

$$v_M^t = {}^o J_{Mt}^t \omega \tag{24}$$

$$a_M^t = {}^o J_{Mt}^t \delta + {}^o H_{Mt}^t \omega^2 \tag{25}$$

$${}^o J_{Mt}^t = v_M^t / \omega = d\left(\overset{\bullet}{T}_{ot} + {}^t \overset{\bullet}{r}_M^t\right) / d\theta = \left[\overset{\bullet}{T}_{ot}\right]_{\theta} + \left[{}^t \overset{\bullet}{r}_M^t\right]_{\theta} = t\left[\overset{\bullet}{T}_o\right]_{\theta} + \left[{}^t \overset{\bullet}{r}_M^t\right]_{\theta} \tag{26}$$

$$\begin{aligned} {}^o H_{Mt}^t &= d({}^o J_{Mt}^t) / d\theta = d^2\left(\overset{\bullet}{T}_{ot} + {}^t \overset{\bullet}{r}_M^t\right) / d\theta^2 = \left[\overset{\bullet}{T}_{ot}\right]_{\theta\theta} + \left[{}^t \overset{\bullet}{r}_M^t\right]_{\theta\theta} \\ &= t\left[\overset{\bullet}{T}_o\right]_{\theta\theta} + \left[{}^t \overset{\bullet}{r}_M^t\right]_{\theta\theta} \end{aligned} \tag{27}$$

${}^o J_{Mt}^t$ is the first order influence coefficient of line movement, ${}^o H_{Mt}^t$ is the second order influence coefficient of line movement. Where, $\left[{}^t \overset{\bullet}{r}_M^t\right]_{\theta} = d\left({}^t \overset{\bullet}{r}_M^t\right) / d\theta$, $\left[{}^t \overset{\bullet}{r}_M^t\right]_{\theta\theta} = d^2\left({}^t \overset{\bullet}{r}_M^t\right) / d\theta^2$.

From above reasoning, the displacement, velocity and acceleration of surface deployable mechanism's any point can be obtained. In other words, only needs to calculate the displacement, velocity and acceleration of five points: $i_{11}, i_{12}(i_{21}), i_{22}, j_{32}(j_{21}), j_{22}$.

4 Illustrative Example

Taking the scissor unit surface deployable mechanism as an example, adopt pole length $l = 600$ mm, $r = 2$ mm, pole mass $m = 1$ kg, density $\rho = 7800$ kg/m³, driven force that exerted on y axis direction through hinge point i_{11} is $F = -60$ N, the initial value of fixed coordinate system is $\theta_0 = (\pi - 0.1)rad$, Displacement, velocity and acceleration of each hinge point and constraint force of articulated link chain are shown in Figs. 4, 5, 6, 7, 8 and 9.

Fig. 4 The displacement curve of hinge point on x direction

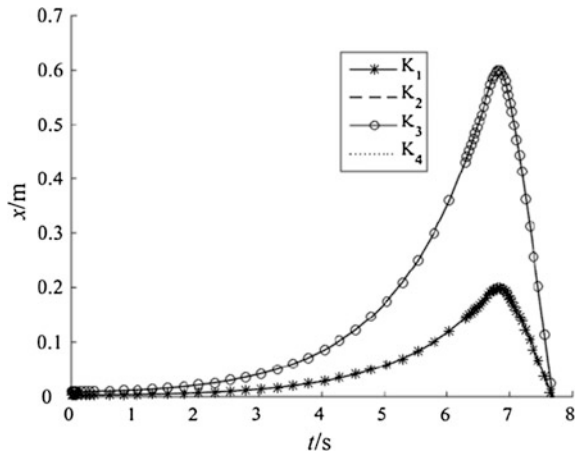


Fig. 5 The displacement curve of hinge point on y direction

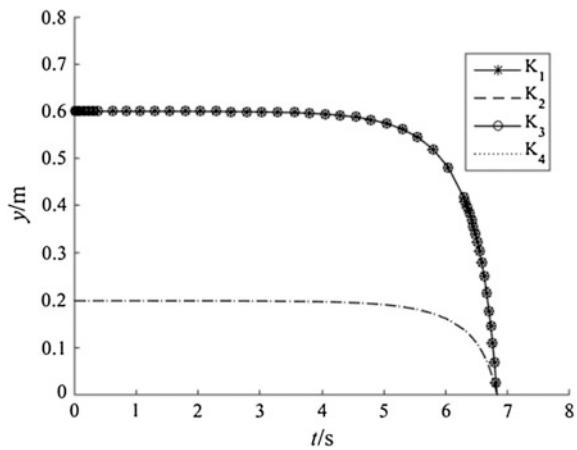


Fig. 6 The velocity curve of hinge point on x direction

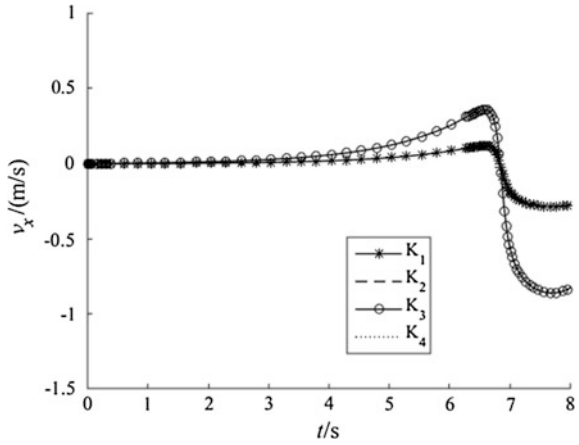


Fig. 7 The velocity curve of hinge point on y direction

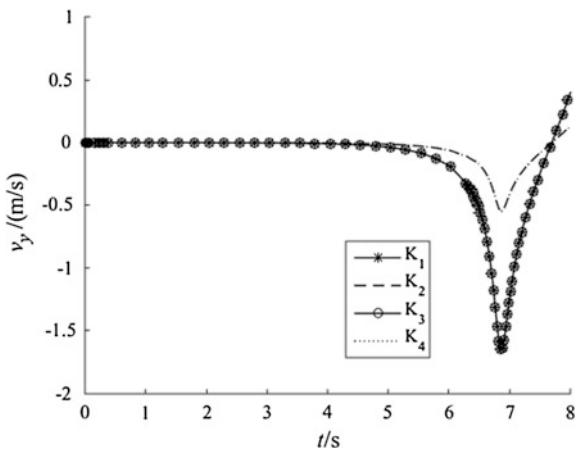


Fig. 8 The acceleration curve of hinge point on x direction

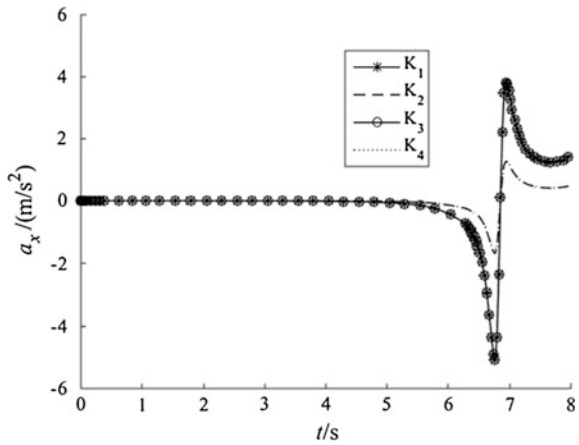
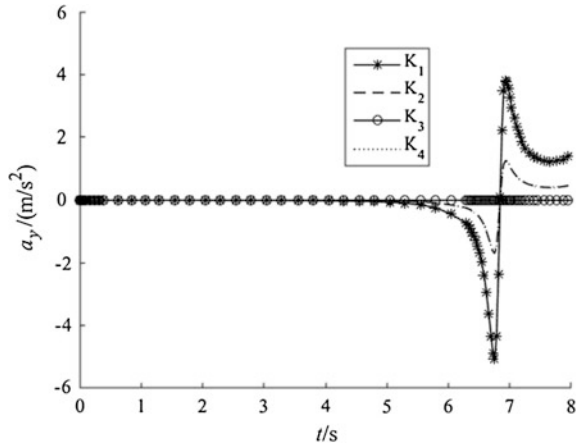


Fig. 9 The acceleration curve of hinge point on y direction



5 Conclusion

- (1) After hinge point i_{11} exerts driven force F on y direction, surface deployable mechanism complete deployment with varying acceleration. When the configuration angle $\theta \gg 0$, the angular acceleration of each component approximate to unchanging, deploy with approximate uniform angular acceleration, the linear acceleration of each component also approximate to unchanging, move with approximate uniform acceleration of each component approximate to unchanging.
- (2) From analysis of Figs. 4, 5, 6, 7, 8 and 9, When the configuration angle θ of unit mechanism approach to π , the angular acceleration of each component increase rapidly, the angular velocity vary fast, the linear acceleration of each component increase rapidly, the linear velocity vary fast, then cause larger constraint force on hinges.
- (3) According to the surface deployable mechanism, Illustrative example of kinematic analysis is given. By means of the coordinate transformation, the function of the displacement of each unit mechanism on the generalized coordinates is obtained. The displacement, velocity and acceleration of each hinge point are calculated, and the correctness of the method is verified.

Acknowledgments The authors gratefully acknowledge the financial support of the National Natural Science Foundation of China (Grant No. 51175422).

References

1. Yan C, Zhong Y, Tarnai T (2005) Threefold-symmetric bricard linkages for deployable structures. *Int J Solids Struct* 42(8):2287–2301
2. Gan WW, Pellegrino S (2006) Numerical approach to the kinematic analysis of deployable structures forming a closed loop. *Proc Inst Mech Eng Part C* 220(7):1045–1056
3. Liew JYR, Krishnapillai A (2009) Deployable structures: US, US 20090199503 A1 2009
4. Pinero EP (1961) A reticular movable theatre. *Architects' J* 134:299
5. Escrig F, Brebbia CA (1996) *Mobile and rapidly assembled structures II*, 1st edn. Computational and Mechanics Publications, Southampton
6. Calladine CR, Pellegrino S (1991) First-order infinitesimal mechanisms. *Int J Solids Struct* 27(4):505–515
7. Chen X (2000) Deployment Simulation and dynamic response analysis and structures design for deployable trusses. Zhejiang University, HangZhou (in Chinese)
8. Chong Zhang, Sanmin Wang, Yuan Ru (2007) On elasto dynamic characteristics of space deployable mechanism. *Mech Sci Technol Aerosp Eng* 26(11):1479–1482
9. Thomas M, Tesar D (1982) Dynamic modeling of serial manipulator arms. *J Dyn Syst Meas Control* 104(9):218–227
10. Freeman RA, Tesar D (1982) The generalized coordinate selection for the dynamics of complex planar mechanical system. *J Mech Des* 104:207–217
11. Duffy J (1980) *Analysis of mechanisms and robot manipulators*. Wiley, New York
12. Mohamed MG, Duffy J (1985) A direct determination of the instantaneous kinematics of fully-parallel robot manipulators. ASME paper 84-DET-114

The Design and Simulation of a New Time-Controlled Spring Driven Hinge for Deployable Structures

Qi'an Peng, Sanmin Wang and Changjian Zhi

Abstract Driving hinge, the core part of deployable structure, is commonly used in aerospace nowadays. This paper describes the design process of a new type of time controlled spring driven hinge. In this process, on the one hand, we derive a new transmission ratio distribution method in the transmission system, with which we could get the minimum center distance by optimizing the design. Given all other conditions are fixed, the hinge get smaller size due to the design under the optimal transmission ratio we derived. On the other hand, inspired by clock timing device, we design a new time-controlled system and research the relationship between timekeeping time and transmission ratio to improve the preciseness and controllability of deploying time. At last, we create 3D model and timing function with simulation method to prove the fact that time-controlled system is precise enough to control deploying time.

Keywords Time-controlled spring driven hinge · Design · Simulation

1 Introduction

Thanks to the development of aerospace and technology, deployable structure [1–4], a new type space structure has been applied in reflectors and antennas of telecommunications and Earth observation. Deployable structure could shrink to small size when it is not working thus it could be conveniently stored in spacecraft. When the spacecraft reaches the appointed position, the deployable structure items

Q. Peng (✉) · S. Wang · C. Zhi
School of Mechanical Engineering, Northwestern Polytechnical University,
Xi'an 710072, People's Republic of China
e-mail: pengqian0530@mail.nwpu.edu.cn

S. Wang
e-mail: wangsami@nwpu.edu.cn

C. Zhi
e-mail: zhichangjiannwpu@163.com

could stretch to start to work and satisfy mission's request. The core of the space deployable structure is its drive hinge. Function of the driving hinge determines stability, reliability and working life of the deployable structure, thus indirectly determines the success of the mission.

So far, people have designed a lot of new hinges, and keep researching and improving the function of hinges. For example, Pellegrino [5] at Cambridge designs a new type hinge called tape spring hinge, further Zhejiang University Wang [6] researches the tape hinge, Southeast University Chen [7] designs a new synchronization hinge. Although hinges have been greatly improved in lot of aspects such as self-deploying, self-locking and synchronization, most of them are designed for ground use not for space use which has stricter requirement. Thus, the unsophisticated hinges design slows down the development of deployable structure. At the same time, the design process of hinges mentioned above doesn't consider the size limitation of space device.

This paper, combining the above two points, introduces the design process of a new type time-controlled spring-loaded hinge. In drive design part, we propose a new distribution scheme of gear ratio to get the hinge's minimum center distance based on optimal design [8, 9], and ratios which can fully utilize limited space can be obtained by this distribution scheme, so by the way the hinge's size becomes smaller under the other conditions unchanged. And in time-controlled design part, we design a new type device enlightened by clock timing device to reduce the impact and because of finding out the relationship between timing time and ratios, so deployable timing is more precise and controllable. In the end, we create 3D model and timing function with simulation method to prove the fact that time-controlled system is precise enough to control deploying time.

2 Design of a New Time-Controlled Spring Driven Hinge

The entire transmission system can be divided into two parts: drive part and time-controlled part. The spring, as a prime mover in drive part, is mainly used to transfer torque; time-controlled part drives intermittent motion mechanism at the end through a series of increasing transmission gears, mainly used to control movement time in driver link.

The graphic design schematic diagram of the new time-controlled spring driven hinge is shown in Fig. 1.

Gear 8 for the shaft gear, and the lower end of the gear is equipped with spring. Drive link is made up of gear 1 to gear 8, which is used to transfer the torque from the spring to the shaft 1. And time control link is made up of gear 5 to gear 12, and gear 11 and gear 12 make up intermittent motion mechanism, which can control the spring relaxation time, control the movement velocity of spring drive unit, and avoid the impact of antenna deployment in place.

According to the design requirements, the graphic design schematic diagram (Fig. 1) is converted into more specific three-dimensional structural diagram, as

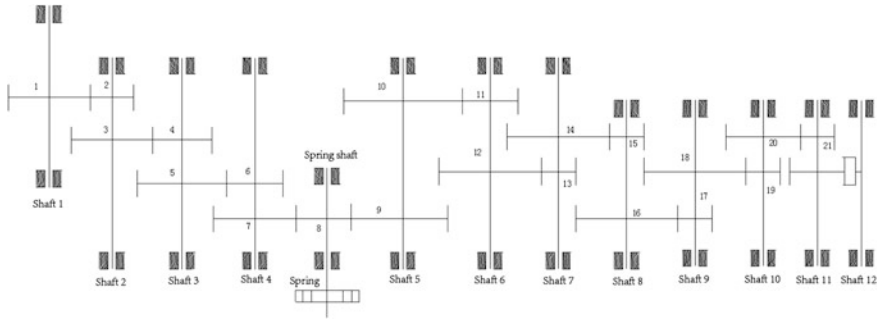
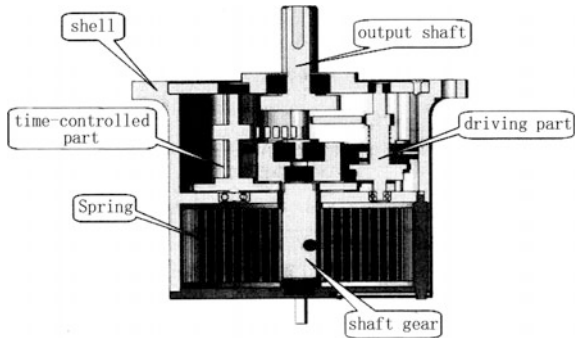


Fig. 1 Structural scheme of the hinge

Fig. 2 Space structural representation



shown in Fig. 2. It is based on the graphic design schematic diagram of the hinge, and gives more detailed structure of the hinge. In the Fig. 2, driving part is composed of the drive link and spring shaft to shaft 1 (namely output shaft). Similarly, time-controlled part is made of time control link and corresponding shafts. And both parts are loaded into the shell.

The hinges used in space are strictly limited to its size, quality. Therefore, in the case of the limited size, through a reasonable position distribution method the driving part and time-controlled part are loaded into the shell.

2.1 Design of Driving Part

The driving part of the hinge is composed of transmission parts such as gears, bearings and clutches. The total efficiency of the drive link depends on the efficiency of the transmission parts, so we need to determine the efficiency of driving parts firstly.

We can obtain the efficiency of transmission parts in the system, and calculate the transmission efficiency (η) between the two adjacent level. Then by the mission requirements, the output torque (T_1) and the total transmission ratio (i) can be known, then by a optimization method, the minimum center distance is used as the main target parameter, and the drive ratio ($i_{21}, i_{43}, i_{65}, i_{87}$) of the drive part can be obtained. The method is introduced as follows in detail:

The center distance of each pair of gears is:

$$a = \frac{m(z + z')}{2} \tag{1}$$

where a is the center distance, m is the cylindrical gear modulus, z, z' is the number of gear teeth.

The sum equation of the center distance of the drive part is the Eq. (2):

$$\begin{aligned} a_{sum} &= \sum_{i=1}^4 a_i = a_1 + a_2 + a_3 + a_4 \\ &= \frac{m_1(z_1 + z_2)}{2} + \frac{m_2(z_3 + z_4)}{2} + \frac{m_3(z_5 + z_6)}{2} + \frac{m_4(z_7 + z_8)}{2} \end{aligned} \tag{2}$$

Transmission ratio is defined as

$$i_{i+1i} = \frac{z_i}{z_{i+1}} \tag{3}$$

Equation (2) can be simplified as the Eq. (4).

$$a_{sum} = r_2 i_{21} + r_4 i_{43} + r_6 i_{65} + r_8 i_{87} + (r_2 + r_4 + r_6 + r_8) \tag{4}$$

where r_2, r_4, r_6, r_8 is gear radius correspondingly.

The Eq. (4) is used as the main objective function to obtain the minimum value, and the corresponding solution is the optimal solution, so the optimal model (Eq. (5)) is obtained.

$$\begin{cases} \min a_{sum} = r_2 i_{21} + r_4 i_{43} + r_6 i_{65} + r_8 i_{87} + c \\ st : i_{21} i_{43} i_{65} i_{87} = i \end{cases} \tag{5}$$

where $c = r_2 + r_4 + r_6 + r_8$ is constant.

The Eq. (6) was obtained by using the optimal design method.

$$f(i_{21}, i_{43}, i_{65}, i_{87}) = r_2 i_{21} + r_4 i_{43} + r_6 i_{65} + r_8 i_{87} + c + M(i_{21} i_{43} i_{65} i_{87} - i)^2 \tag{6}$$

where M is penalty factor.

And the best ratio (Eq. (7)) can be obtained.

$$i_{21} = \sqrt[4]{\frac{ir_4r_6r_8}{r_2^3}}, i_{43} = \sqrt[4]{\frac{ir_2r_6r_8}{r_4^3}}, i_{65} = \sqrt[4]{\frac{ir_2r_4r_8}{r_6^3}}, i_{87} = \sqrt[4]{\frac{ir_2r_4r_6}{r_8^3}} \tag{7}$$

From the above we can see that the hinge has a size limit, set the radius (R) of its shell. Geometric relations are got:

$$\begin{cases} r_1 + 2r_2 < R \\ r_3 + r_4 < 2(\sqrt{2} - 1)R \\ r_5 + r_6 < 2(\sqrt{2} - 1)R \\ 2r_7 + r_8 < R \end{cases} \Rightarrow \begin{cases} \sqrt{4}ir_2r_4r_6r_8 + 2r_2 < R \\ \sqrt{4}ir_2r_4r_6r_8 + r_4 < 2(\sqrt{2} - 1)R \\ \sqrt{4}ir_2r_4r_6r_8 + r_6 < 2(\sqrt{2} - 1)R \\ 2\sqrt{4}ir_2r_4r_6r_8 + r_8 < R \end{cases} \tag{8}$$

Because of gear speed reducer drive, each transmission ratio should be greater than 1.

$$\begin{cases} i_{21} > 1 \\ i_{43} > 1 \\ i_{65} > 1 \\ i_{87} > 1 \end{cases} \Rightarrow \begin{cases} r_2 < \frac{R}{3} \\ r_4 < (\sqrt{2} - 1)R \\ r_6 < (\sqrt{2} - 1)R \\ r_8 < \frac{R}{3} \end{cases} \tag{9}$$

Combined with the constraint conditions can choose r_2, r_4, r_6, r_8 rightly, at all levels to get the optimal velocity ratio.

The power and torque formula can be found in the literature.

$$T = 9549 \frac{P}{n} \tag{10}$$

where T is the torque in a shaft of transmission part of time-controlled spring driven hinge, P is the power transmitted on the shaft, n is rotation speed of the shaft.

By the Eq. (10), T is inversely proportional to n , so there are:

$$T_i = \frac{T_{i+1}}{\eta \times i_{+1i}} \tag{11}$$

with $i = 1, 2, 3, 4$.

After getting the torque, by using the classic gear design method [8] we calculate the various parameters of gears: module m and the number of teeth z , and here the modulus m and the number of teeth z need to meet the constraint conditions of transmission ratio.

2.2 Design of Time-Controlled Part

The time-controlled part of the hinge is composed of passing motion parts such as gears, bearings and clutches, and intermittent movement parts. And in order to make the development process smooth and reliable, also should meet the time-controlled requirements of use in space, intermittent moving parts, which is composed of a balance pendulum and a riding wheel, reference from a clock timing device and is the core of the whole time-controlled part.

Time-controlled part is mainly composed by three parts: a prime mover (as a power source), a gear train and a governor (i.e. swing), in this article the mover is a torsional spring, and deployable time (t) mainly depends on the structural parameters of the above three parts:

$$t = \frac{8K\varphi\theta}{\delta_q} \sqrt{\frac{KJ(1-\beta)}{M_D\delta_q(1+\beta)}} \quad (12)$$

where K is the gear ratio of time-controlled part; φ is the rotation angle of the prime mover in the whole timing process; θ is the half of the angular displacement of the balance pendulum in the engagement process; J is the rotational inertia of the balance pendulum; β is speed recovery coefficient; M_D is driving moment effected on the riding wheel; δ_q is a rotary angular displacement of a tooth of the riding wheel.

According to the above formula, the moment of inertia of the balance pendulum can be obtained when the swing frequency (f) of the balanced pendulum is known, with $K = 1$, $\varphi = \delta_q$, $t = 1/f$. After determining appropriate time (t), gear train transmission ratio of time-controlled part can be obtained by the Eq. (12), through optimizing design method, the time-controlled part also make the smallest center distance as the main target parameter, so transmission ratios can be obtained at all levels. But compared with driving gear system design, the time-controlled part of the gear train just translates motion, instead transfers torque, so this paper only considers the design to meet the gear ratio and if the design of gear is difficult to manufacture, thus do not need to use classical design method of gear.

3 Simulation and Analysis

3.1 Calculation of Key Design Parameters and 3D Modeling

Assuming that the required output torque at the output end is $T_1 \geq 12 \text{ N} \cdot \text{m}$, that the total transmission ratio is $i = 8$, that deployment time is $t_b = 90 \text{ s}$, that unilateral deployment angle is 90° , that by Eqs. (7), (8) and (9) we can obtain the gear transmission ratios of the driving part at all levels, as shown in Table 1.

Table 1 Gear ratios at all levels

Gear pair	i_{87}	i_{65}	i_{43}	i_{21}
Gear ratio	1.60	1.71	2.08	1.40

Table 2 Torque of each shaft

Shaft number	Spring shaft	4	3	2	1
Torque ($N \cdot m$)	1.85	2.81	4.57	9.02	12

Table 3 z and m of each Gear of Driving part

Gear no.	1	2	3	4	5	6	7	8
z	14	10	25	12	24	14	32	20
m	1.5	1.5	1	1	0.8	0.8	0.6	0.6

Table 4 z and m of each gear of time-controlled part

Gear no.	9	10	11	12	13	14	15
z	28	36	12	40	12	40	12
m	0.6	0.5	0.5	0.4	0.4	0.3	0.3
Gear no.	16	17	18	19	20	21	
z	40	12	40	12	50	12	
m	0.3	0.3	0.3	0.3	0.25	0.25	

And by the Eq. (8) we can obtain the shaft torque of driving part (Table 2).

According to the classic gear design method in literature [8], the tooth number (z) and modulus (m) of each gear can be obtained (Table 3).

Set the rotation angle of the spring in the deployment process $\phi = 720^\circ$. The angular displacement of the pendulum in the engagement process is $2\theta = 15^\circ$. The number of riding wheel teeth is 13. By the Eq. (12), the total transmission ratio of the time-controlled part of the gear system is $K = 231$. With the optimal design method, the total transmission ratio is distributed to all levels, so the gear tooth number (z) and modulus (m) of the time-controlled part can be calculated out (Table 4).

On the basis of the above design parameters, the graphic design schematic diagram (Fig. 1) and three-dimensional structural diagram (Fig. 2), by using 3D modeling software to model, the three-dimensional structural diagram is converted into a certain specific 3D model and its drive part, time-controlled part and the whole 3D model, as shown in Fig. 3.

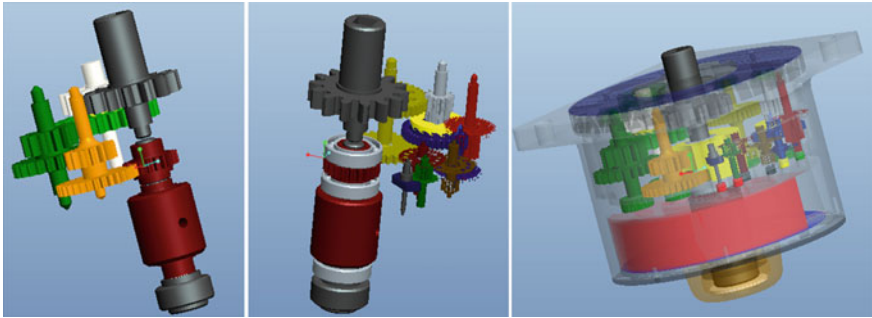


Fig. 3 3D model of the new time-controlled spring driven hinge

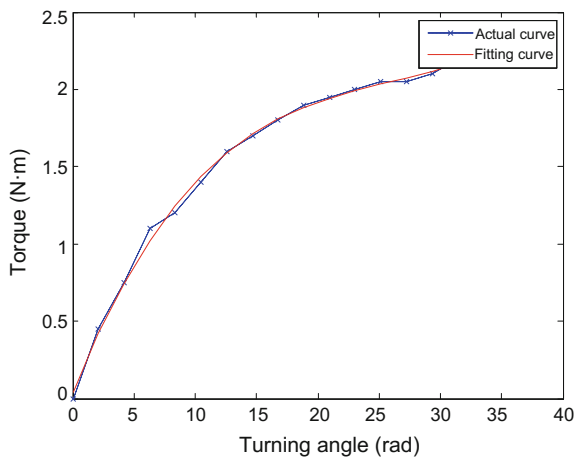
3.2 Motion Simulation

Through the experiment, the characteristic curve of torsion spring can be obtained as shown in Fig. 4.

Due to the requirements of the output torque is more than $12 \text{ N} \cdot \text{m}$, so it is required that the input torque of the spring shaft is not less than $1.85 \text{ N} \cdot \text{m}$. When the rotation angle is greater than 18 rad (from Fig. 5), and the corresponding torque is $1.85 \text{ N} \cdot \text{m}$, while rising curve flattens, similar to a straight line. So $T = a\theta + c$ can be used to fit, and intercept $18\text{--}30 \text{ rad}$'s straight line as input characteristic curve.

The model and the input characteristic curve are introduced into the classical kinematics simulation software Adams to carry on the movement simulation, but due to the limitations of computer performance and simulation time, don't need to simulate the whole operation process of the mechanism, so the simulation time is only 5 s of the start time. The simulation results are shown Figs. 5, 6, 7 and 8.

Fig. 4 The characteristic curve



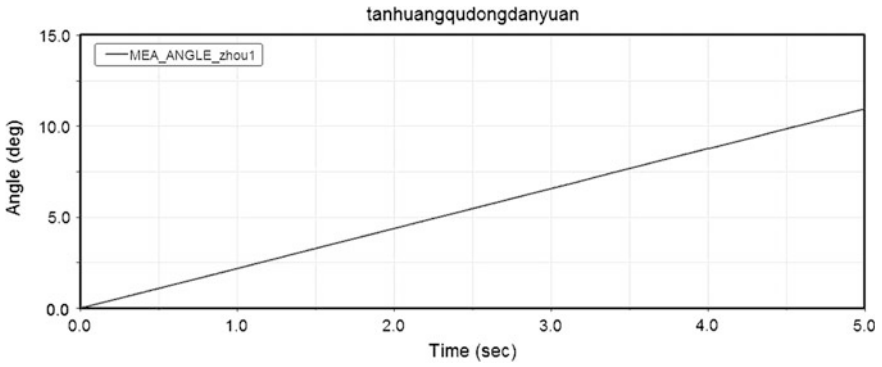


Fig. 5 Angular displacement curve of the output shaft

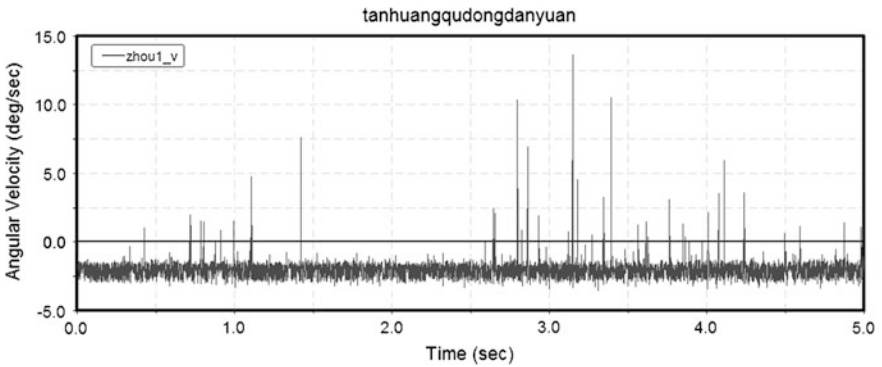


Fig. 6 Angular velocity curve of the output shaft

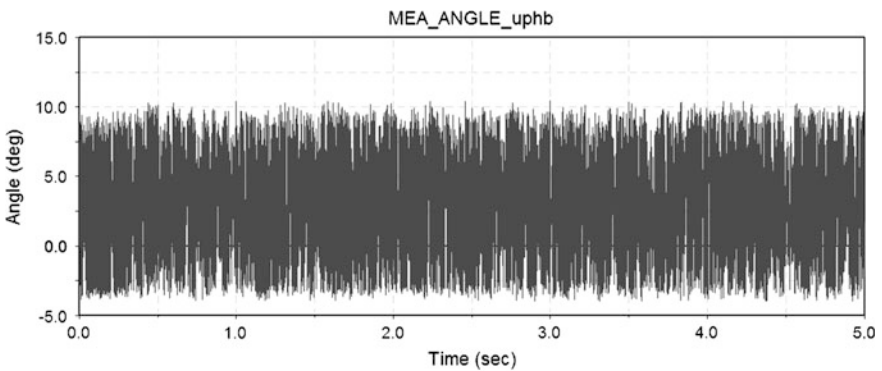


Fig. 7 Balance pendulum angular displacement curve

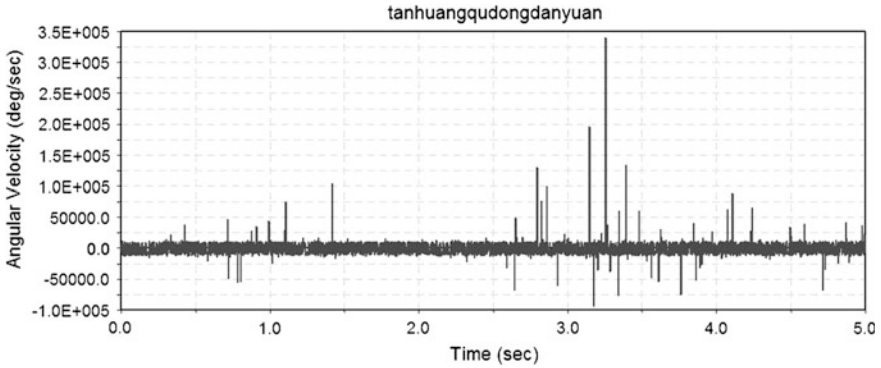


Fig. 8 Balance pendulum angular velocity curve

3.3 Analysis and Discussion

From the simulation results, in the course of the hinge movement, all of the shafts and the bearings will not interfere, and the hinge can normally motion.

From Fig. 5 we can see that although the angular velocity of the output shaft is a reciprocating wave vector, at macro level output shaft angular displacement appears to be a relatively smooth straight line, and small fluctuations in angular velocity does not affect the hinge's normal use, and will not lead direction to change. Velocity fluctuations are mainly due to impact between the balance pendulum and riding wheel of the time-controlled part. But the collision frequency between the balancing pendulum and riding wheel is very high. Therefore, at macro level displacement curve of the output shaft is a relatively smooth straight line.

From angular displacement curve of the output shaft, the output shaft has been turned around 10.95° in 5 s, launch speed is slightly larger than the required expansion speed of 2 degrees/s, but in the error range. Through the angular displacement simulation results, the balance pendulum swing angle, which is slightly less than initial set value 15° , can be acquired. By Eq. (12), in the other conditions unchanged, the balancing pendulum angular displacement in the meshing process decreasing will cause deployable time of the time-controlled part to shorten accordingly. It can be modified to get a more precise deployment time, also can change the moment of inertia by changing the shape or mass of the balance swing, which makes the deployment time more close to the time required.

Observing the output shaft and the balance pendulum angular velocity curve, both of the angular velocity basically fluctuate in a certain range, but sometimes will appear to beat, which is due to the presence of certain error between part modeling and simulation. Therefore, simulation results of the kinematics characteristic curve have obvious beating.

4 Conclusions

From detailed introduction of three aspects of design ideas, design principles and design steps for the new time-controlled spring driving hinge used for deployable structure, conclusions can be obtained as follow:

1. In the design of the driving part, the transmission ratios are:

$$i_{21} = \sqrt[4]{\frac{i r_4 r_6 r_8}{r_2^3}}, i_{43} = \sqrt[4]{\frac{i r_2 r_6 r_8}{r_4^3}}$$

$$i_{65} = \sqrt[4]{\frac{i r_2 r_4 r_8}{r_6^3}}, i_{87} = \sqrt[4]{\frac{i r_2 r_4 r_6}{r_8^3}}$$

meanwhile they must meet these constraint conditions:

$$\begin{cases} \sqrt[4]{i r_2 r_4 r_6 r_8} + 2r_2 < R \\ \sqrt[4]{i r_2 r_4 r_6 r_8} + r_4 < 2(\sqrt{2} - 1)R \\ \sqrt[4]{i r_2 r_4 r_6 r_8} + r_6 < 2(\sqrt{2} - 1)R \\ 2\sqrt[4]{i r_2 r_4 r_6 r_8} + r_8 < R \end{cases} \begin{cases} r_2 < \frac{R}{3} \\ r_4 < (\sqrt{2} - 1)R \\ r_6 < (\sqrt{2} - 1)R \\ r_8 < \frac{R}{3} \end{cases}$$

2. A new time-controlled device is designed, and relationship between timing-time and structural parameters is

$$t = \frac{8K\varphi\theta}{\delta_q} \sqrt{\frac{KJ(1 - \beta)}{M_D\delta_q(1 + \beta)}}$$

3. Through motion simulation, the new hinge can work normally, it means that the new distribution scheme avoids the interference between gears and the shell successfully, and from simulation results, it is known that expansion speed is 2.19 degrees/s, so time-controlled device can work, and slow down expansion speed to reduce impact.

Acknowledgments The authors gratefully acknowledge the financial support of the National Natural Science Foundation of China (Grant No. 51175422).

References

1. Santiago-Prowald J, Baier H (2013) Advances in deployable structures and surfaces for large apertures in space. *Ceas Space J* 5:89–115
2. Amyotte E, Martins C (2012) *Space antenna handbook*. Wiley, New York
3. De Temmerman N (2007) *Design and analysis of deployable bar structures for mobile architectural applications*. Vrije Universiteit Brussel, Brussel

4. Pellegrino S (Ed.) (2014) Deployable structures, vol 412. Springer, New York
5. Watt A, Pellegrino S (2002) Tape-spring rolling hinges. In: Proceedings of the 36th aerospace mechanisms symposium, Glenn Research Center
6. Wang J, Guan FL, Zhou ZG (2007) Design and analysis of tape hinge for deployable structures. *J Astronaut* 3(28):720–727
7. Chen Y (2014) Morphology and kinematic folding analysis and application research on novel symmetric deployable structures. Southeast University, Nanjing
8. Shi Y (2011) The optimal design of the drive train. *Acad Forum*, 303–313
9. Duan JL, Li JH (2016) Pure electric vehicle power system transmission ratio optimization design. *Electron Tech* 4:228–230

The Configuration Design and Kinematic Analysis of the Deployable Mechanism Based on Bennett Linkage

Changjian Zhi, Sanmin Wang, Jianfeng Li and Qi'an Peng

Abstract Bennett linkage can be applied to build kinds of spatial deployable mechanism, and they have been used in the aviation fields, shelters fields and so on. The paper derives the transformation formula of the adjacent Bennett linkage units and puts forward a deployable mechanism configuration design method based on Bennett linkage. The coordinate transformation theory is applied to build the kinematic analysis model of this deployable mechanism, and an example is provided to verify the kinematic analysis model. The effects of the parameters of Bennett linkage on the kinematics of the deployable mechanism and its scale are researched.

Keywords Bennett linkage · Deployable mechanism · Configuration design · The coordinate transformation theory · Kinematics

1 Introduction

Bennett linkage is a very important spatial over-constrained mechanism, and its application prospect is very vast. It can be used in the field of deployable antenna, solar panel, building, shelter and so on. The coordinate transformation theory is an analysis tool of the force and kinematic in common use. It can simplify the analysis process to some extent while it is applied to the kinematic analysis of deployable mechanisms. In the configuration design fields of the deployable mechanism, Chen and You [1, 2] have a great contribution on it, and they built the single-layer and multi-layer structures based on Bennett linkage. Melin [3] researched the

C. Zhi (✉) · S. Wang · J. Li · Q. Peng
School of Mechanical Engineering, Northwestern Polytechnical University,
Xi'an 710072, People's Republic of China
e-mail: zhichangjiannwpu@163.com

C. Zhi · S. Wang · J. Li · Q. Peng
Northwestern Polytechnical University, 178# 127 West Youyi Road,
Xi'an Shanxi 710072, People's Republic of China

deployable structure proposed by Chen in detail, and try to apply it in shelters. Wang [4] built a basic module using the scissor Bennett linkage, and it is used to construct a large scale deployable structure. Yang et al. [5] built a deployable Bennett network in a saddle surface and researched its configuration properties. In the field of the kinematic analysis, Lee [6] and Zhi et al. [7] analyzed the kinematics of Bennett linkage. Wang [4] and Yang et al. [5] studied the kinematics of the deployable mechanism built by themselves using the D-H method.

According to the characteristic of Bennett linkage the array configuration method building deployable mechanism is proposed. Using this method builds a single degree L-form deployable mechanism. The transformation matrix of the adjacent Bennett linkage units is derived to build the kinematic analysis model of the deployable mechanism. Finally, the effect of the parameters of Bennett linkage on the scale and kinematic range of the deployable mechanism is researched.

2 The Coordinate Transformation Theory

When a coordinate system rotates α about x -axis, rotates β about y -axis or rotates γ about z -axis whose rotation directions are all anticlockwise, the specific process can be seen in Fig. 1. Their transformation matrixes equations are as follows [8]:

$$\begin{aligned}
 \mathbf{R}_x &= \begin{bmatrix} 1 & 0 & 0 \\ 0 & \cos(\alpha) & -\sin(\alpha) \\ 0 & \sin(\alpha) & \cos(\alpha) \end{bmatrix}, \mathbf{R}_y = \begin{bmatrix} \cos(\beta) & 0 & \sin(\beta) \\ 0 & 1 & 0 \\ -\sin(\beta) & 0 & \cos(\beta) \end{bmatrix}, \mathbf{R}_z \\
 &= \begin{bmatrix} \cos(\gamma) & -\sin(\gamma) & 0 \\ \sin(\gamma) & \cos(\gamma) & 0 \\ 0 & 0 & 1 \end{bmatrix} \tag{1}
 \end{aligned}$$

In the formula (1), although all the rotation angles α , β and γ are plus, the locations of minus in the rotation transformation matrixes are different. In the traditional method, if we want to estimate the location of minus, the right-hand rule and other methods are needed. It makes the estimating process more difficult. In order to solve this problem, we improve the right-hand rule. Assume that x , y and z are real

Fig. 1 The rotation transformation of a coordinate system rotating about the different axes

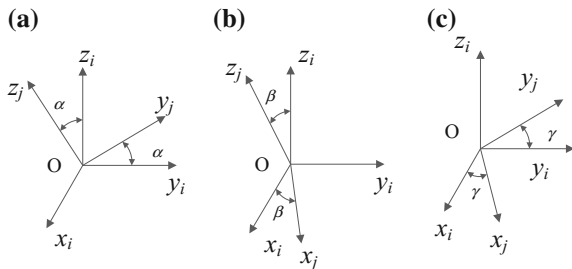


Table 1 The value of the rotation angle of the a coordinate system rotating about the different axes

Rotating about x-axis		Rotating about y-axis		Rotating about z-axis	
$y \rightarrow z$	$z \rightarrow y$	$x \rightarrow z$	$z \rightarrow x$	$x \rightarrow y$	$y \rightarrow x$
α	$-\alpha$	β	$-\beta$	γ	$-\gamma$

numbers, they satisfy the relationship $x < y < z$. When a coordinate system rotates about x -axis, y -axis or z -axis, if the rotation direction is from large to small, the rotation angle is plus and the minus locates before the top-right symbol ‘sin’. On the contrary, the rotation angle is minus and the minus locates before the bottom-left symbol ‘sin’. According to this method, when the value of the rotation angle is decided, the rotation transformation matrix is assured. Its specific process can be simplified by Table 1.

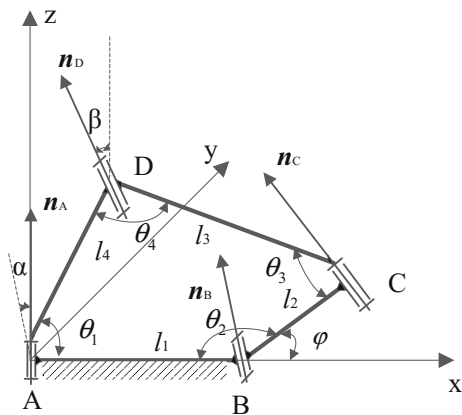
The translation of the origin of a coordinate system can be expressed as: $\mathbf{d} = [d_x \ d_y \ d_z]^T$. The translation and rotation in the coordinate transformation can be expressed by the homogeneous coordinate. It can be written as [8]:

$$T = \begin{bmatrix} R & \mathbf{d} \\ \mathbf{0} & 1 \end{bmatrix} \tag{2}$$

3 The Configuration Design of the Deployable Mechanism

The 4 axes of kinematic pairs of Bennett linkage are unparallel, and Fig. 2 is its schematic diagram. $\mathbf{n}_A, \mathbf{n}_B, \mathbf{n}_C$ and \mathbf{n}_D are respectively the direction vectors of the joints A, B, C and D. The angle between \mathbf{n}_A and \mathbf{n}_B is α , and the angle between \mathbf{n}_C and \mathbf{n}_D is the same as. The angle between \mathbf{n}_B and \mathbf{n}_C is β , the same as between \mathbf{n}_D and \mathbf{n}_A . Assume that the link 1 is the fixed link, the Cartesian coordinate system A - xyz is built up with A as its origin. The x axis is coinciding with link 1 and z axis

Fig. 2 The schematic diagram Bennett linkage



is coinciding with the axis direction of the kinematics pair A. Bennett linkage satisfies the following geometrical conditions [7]: 1, $l_1 = l_3$, $l_2 = l_4$, 2, $\frac{\sin(\alpha)}{l_1} = \frac{\sin(\beta)}{l_2}$.

In Fig. 2 the angle between link 4 and link 1 is θ_1 , the angle between link 1 and link 2 is θ_2 , the angle between link 2 and link 3 is θ_3 , and the angle between link 3 and link 4 is θ_4 . According to the geometrical conditions of Bennett linkage, we can get $\triangle ABC \cong \triangle CDA$ and $\triangle BCA \cong \triangle CAD$. Therefore, the angles satisfy: $\theta_1 = \theta_3$ and $\theta_2 = \theta_4$. θ_1 and θ_2 can be represented as the interior angle of Bennett linkage. φ is the angle between link 1 and the x axis. In order to identify these angles in the deployable mechanism, θ_1 , θ_2 and φ are called as the driving angle, the interior output angle, and the exterior output angle of the Bennett linkage. θ_2 and φ satisfy the following equation:

$$\varphi = \pi - \theta_2 \quad (3)$$

All kinematic pair coordinates of Bennett linkage are as follows [7]: A (0, 0, 0), B (l_1 , 0, 0), C ($l_1 + l_2 \cos(\varphi)$, $l_2 \cos(\alpha) \sin(\varphi)$, $l_2 \sin(\alpha) \sin(\varphi)$), D ($l_2 \cos(\theta_1)$, $l_2 \sin(\theta_1)$, 0). Since the length of CD is l_1 , we can get the following equation:

$$\cos(\theta_1) \cos(\varphi) + (l_1/l_2)(\cos(\theta_1) - \cos(\varphi)) + \cos(\alpha) \sin(\theta_1) \sin(\varphi) = 1 \quad (4)$$

According to half-angle formula, solving the Eq. (4) can obtain the following roots:

$$\varphi = 2 \tan^{-1} \left(\frac{-f_2(\theta_1) \pm \sqrt{f_2^2(\theta_1) - f_1(\theta_1)f_3(\theta_1)}}{f_1(\theta_1)} \right) \quad (5)$$

where

$$\begin{aligned} f_1(\theta_1) &= (l_1/l_2 - 1)(\cos(\theta_1) + 1) \\ f_2(\theta_1) &= \cos(\alpha) \sin(\theta_1) \\ f_3(\theta_1) &= (l_1/l_2 + 1)(\cos(\theta_1) - 1) \end{aligned}$$

Similarly, substitute the formula (3) into (4), the expression of solution can be obtained:

$$\theta_2 = 2 \tan^{-1} \left(\frac{-h_2(\theta_1) \pm \sqrt{h_2^2(\theta_1) - h_1(\theta_1)h_3(\theta_1)}}{h_1(\theta_1)} \right) \quad (6)$$

where

$$\begin{aligned} h_1(\theta_1) &= (l_1/l_2 + 1)(\cos(\theta_1) - 1) \\ h_2(\theta_1) &= \cos(\alpha) \sin(\theta_1) \\ h_3(\theta_1) &= (l_1/l_2 - 1)(1 + \cos(\theta_1)) \end{aligned}$$

There are two different Bennett linkage forms corresponding to the two solutions in the formulas (5) and (6) [7]. One is an open form mechanism, the other is a cross form.

Due to the first and second derivative of formula (4), the following relations can be written as

$$\begin{cases} \dot{\varphi} = \frac{h_1}{h_2} \dot{\theta}_1 \\ \ddot{\varphi} = \frac{h_1 \ddot{\theta}_1 + h_3 \dot{\theta}_1^2 + h_4 \dot{\varphi} \dot{\theta}_1 + h_5 \dot{\varphi}^2}{h_2} \end{cases} \quad (7)$$

where

$$\begin{aligned} h_1 &= \cos(\alpha) \cos(\theta_1) \sin(\varphi) - \sin(\theta_1) \cos(\varphi) - (l_1/l_2) \sin(\theta_1) \\ h_2 &= \cos(\theta_1) \sin(\varphi) - (l_1/l_2) \sin(\varphi) - \cos(\alpha) \sin(\theta_1) \cos(\varphi) \\ h_3 &= -\cos(\alpha) \sin(\theta_1) \sin(\varphi) - \cos(\theta_1) \cos(\varphi) - (l_1/l_2) \sin(\theta_1) \\ h_4 &= 2 \cos(\alpha) \cos(\theta_1) \cos(\varphi) + 2 \sin(\theta_1) \sin(\varphi) \\ h_5 &= (l_1/l_2) \cos(\varphi) - \cos(\alpha) \sin(\theta_1) \sin(\varphi) - \cos(\theta_1) \cos(\varphi) \end{aligned}$$

Bennett linkage can be applied to build the deployable mechanism by the array way. In this paper, all Bennett linkages which are used to build the deployable mechanism are the same. The specific deployable mechanisms based on Bennett linkage can be classified into 3 forms. The first is the row array (Fig. 3a), the second is the column array (Fig. 3b), and the third is the mixed array (Fig. 3c). The number of Bennett linkage applied to build row array and column array deployable mechanism is unlimited. The scale of the mixed array is related to the geometrical condition of Bennett linkage, which needs the specific analysis. In order to simplify the expression, the m rows and n columns deployable mechanism can be written as $m \times n$.

The basic form of the deployable mechanisms based on Bennett linkage is built by two units which have a common link. It has 2 sorts: one is the transverse connection whose common length is l_2 seeing in the Fig. 4a, the other is the vertical connection whose common length is l_1 seeing in the Fig. 4b.

Fig. 3 The schematic diagram of the deployable mechanism based on Bennett linkage

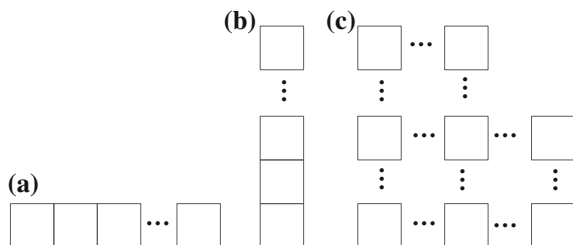


Fig. 4 Two sorts deployable mechanism based on Bennett linkage

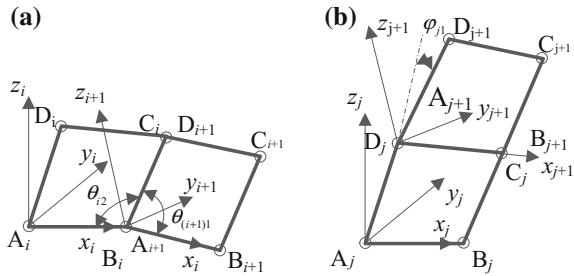
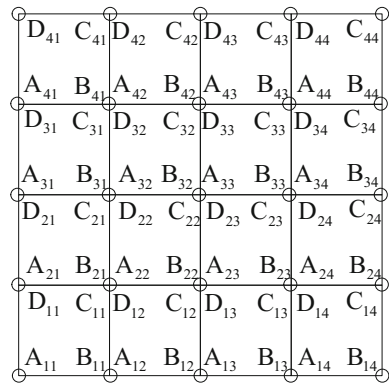


Fig. 5 The 4×4 deployable mechanism



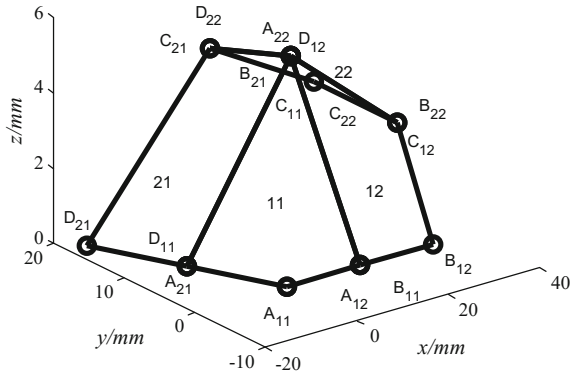
4 and 16 Bennett linkages can be used to build the 2×2 and 4×4 (seeing Fig. 5) deployable mechanism respectively. The right and bottom sides of the 2×2 and 4×4 deployable mechanism keep in the straight lines by using the designed kinematic pairs, and both of them mobility is 1. Since the constrained profile is similar to the letter L, this kind of deployable mechanisms are called as the L deployable mechanism.

4 The Kinematic Analysis of the Deployable Mechanism

In the deploying process, when the driving interior angle is greater than π , links in the deployable mechanisms may interfere with each other. In Fig. 6, the driving angle of the unit 22 of the 2×2 L deployable mechanism is greater than π , and some links interfere with each other.

All displacements of kinematic pairs in the deployable mechanism can be obtained by the row transformation matrix and the column transformation matrix. Assume that the adjacent units in Fig. 4a locates in the e th row in the deployable

Fig. 6 The 2×2 L deployable mechanism



mechanism. The origin of the local coordinate $A_i-x_iy_iz_i$ is A_i , its x -axis is coinciding with link A_iB_i and its z -axis is coinciding with the axis n_{A_i} . Transforming the coordinate system i to $i + 1$ needs 3 procedures. The first procedure is translating the origin from $(0, 0, 0)$ to $(l_1, 0, 0)$. The second procedure is rotating α about x -axis. The third procedure is rotating δ_i about z -axis. The e th row transformation matrix from the coordinate system i to $i + 1$ is expressed as:

$$T_{R^{(i)(i+1)}}^e = \begin{bmatrix} \cos(\delta_i) & -\sin(\delta_i) & 0 & l_1 \\ \sin(\delta_i) \cos(\alpha) & \cos(\delta_i) \cos(\alpha) & -\sin(\alpha) & 0 \\ \sin(\delta_i) \sin(\alpha) & \cos(\delta_i) \sin(\alpha) & \cos(\alpha) & 0 \\ 0 & 0 & 0 & 1 \end{bmatrix} \quad (8)$$

where δ_i is the angle between the vectors A_iB_i and $A_{i+1}B_{i+1}$, $\delta_i = \varphi_i - \theta_{(i+1)1}$.

Assume that the adjacent units in Fig. 4b locates in the f th column in the deployable mechanism. The origin of the local coordinate $A_f-x_fy_fz_f$ is A_f , its x -axis is coinciding with link A_fB_f and its z -axis is coinciding with the axis n_{A_f} . Transforming the coordinate system j to $j + 1$ needs 4 procedures. The first procedure is translating the origin from $(0, 0, 0)$ to $(l_2 \cos(\theta_j), l_2 \sin(\theta_j), 0)$. The second procedure is rotating θ_j about z -axis. The third procedure is rotating β about x -axis. The third procedure is rotating $-\varphi_j$ about x -axis. The f th column transformation matrix from the coordinate system j to $j + 1$ is expressed as:

$$T_{C^{(j)(j+1)}}^f = \begin{bmatrix} u_{11} & u_{12} & -\sin(\theta_j) \sin(\beta) & l_2 \cos(\theta_j) \\ u_{21} & u_{22} & \cos(\theta_j) \sin(\beta) & l_2 \sin(\theta_j) \\ \sin(\varphi_j) \sin(\beta) & -\cos(\varphi_j) \sin(\beta) & \cos(\beta) & 0 \\ 0 & 0 & 0 & 1 \end{bmatrix} \quad (9)$$

where

$$\begin{aligned}
 u_{11} &= \cos(\theta_j) \cos(\varphi_j) + \sin(\theta_j) \sin(\varphi_j) \cos(\beta) \\
 u_{12} &= \cos(\theta_j) \sin(\varphi_j) - \sin(\theta_j) \cos(\varphi_j) \cos(\beta) \\
 u_{21} &= \sin(\theta_j) \cos(\varphi_j) - \cos(\theta_j) \sin(\varphi_j) \cos(\beta) \\
 u_{22} &= \sin(\theta_j) \sin(\varphi_j) + \cos(\theta_j) \cos(\varphi_j) \cos(\beta)
 \end{aligned}$$

For the L deployable mechanism, if we choose different routes, although the expression of the coordinate transformation matrix from the local coordinate system pq to the global coordinate system 11 is different, their final results is the same. If we choose the p th row and the first column as its route, the coordinate transformation matrix can be written as:

$$\mathbf{T}_{pq} = \mathbf{T}_{C(1)(2)}^1 \mathbf{T}_{C(2)(3)}^1 \cdots \mathbf{T}_{C(q-1)(q)}^1 \mathbf{T}_{R(1)(2)}^p \mathbf{T}_{R(2)(3)}^p \cdots \mathbf{T}_{R(p-1)(p)}^p \quad (10)$$

The displacement, velocity, and acceleration of an arbitrary kinematic pair P in the row p column q unit can be written as:

$$\mathbf{P}_{11} = \mathbf{T}_{pq} \mathbf{P}_{pq} \quad (11)$$

$$\dot{\mathbf{P}}_{11} = \dot{\mathbf{T}}_{pq} \mathbf{P}_{pq} + \mathbf{T}_{pq} \dot{\mathbf{P}}_{pq} \quad (12)$$

$$\ddot{\mathbf{P}}_{11} = \ddot{\mathbf{T}}_{pq} \mathbf{P}_{pq} + 2\dot{\mathbf{T}}_{pq} \dot{\mathbf{P}}_{pq} + \mathbf{T}_{pq} \ddot{\mathbf{P}}_{pq} \quad (13)$$

\mathbf{P} can represents the kinematic pairs A, B, C and D. Formulas (10), (11), (12) and (13) produce the kinematic analysis model. It can be used to solve the displacements, velocities, and accelerations of all kinematic pairs in the deployable mechanism.

5 Illustrative Example

Take as an example the 4×4 deployable mechanism to analyze its kinematics. The parameters of Bennett linkage are as follows: $l_1 = 36$ mm, $l_2 = 12$ mm and $\alpha = \pi/6$. Assume that the unit 11 is the driving unit and the link $A_{11}B_{11}$ is the fixed link, the driving machine is fixed on the kinematic pair A_{11} . In order to keep the efficiency and stabilization of the deployment, the motion of the driving can be classified into 3 stages: boost phase, uniform phase and decelerating phase. The specific motion is expressed as:

$$\theta = \begin{cases} \frac{1}{2}\alpha_1 t^2 & (0 \leq t \leq \frac{T}{6}) \\ \frac{\alpha_1 T t}{6} - \frac{\alpha_1 T^2}{72} & (\frac{T}{6} < t \leq \frac{2T}{3}) \\ \frac{1}{2}\alpha_1 T t - \frac{\alpha_1 T^2}{8} - \frac{\alpha_1 t^2}{4} & (\frac{2T}{3} < t \leq T) \end{cases} \quad (14)$$

The motion range of the driving unit is $[0 \pi]$, and its angle acceleration is $\alpha_1 = 0.1 \text{ rad.s}^{-1}$. Figure 7 shows the 4×4 L deployable mechanism which is deploying. The points $A_{11}, B_{11}, A_{12}, B_{12}, A_{13}, B_{13}, A_{14}$ and B_{14} lie on a line, and the points $A_{11}, B_{11}, A_{21}, B_{21}, A_{31}, B_{31}, A_{41}$ and B_{41} lie on a line. The driving angles, the interior output angles and the exterior output angles of the units of the deployable mechanism in the first row and in the first column can be solved by the formulas (5) and (6). The driving angle, the interior output angle and the exterior output angle of the unit of the deployable mechanism in row 2 column 2 can be solved by the formula (5) and $\theta_1^{11} + \theta_2^{12} + \theta_2^{21} + \theta_1^{22} = 2\pi$. The other angles of the deployable mechanism can be solved in sequence. The angular velocities and accelerations of the previous angles can be solved by the formula (7) by the previous order.

For the 4×4 L deployable mechanism, the motion parameters of the units locating on the diagonal is the most typical. Figures 8, 9 and 10 provide us with the angular displacements, velocities and accelerations of the driving angle of the units locating on the diagonal respectively. The parameters of the Bennett linkage have effects on the motion of the L deployable mechanism. When the parameters are given, its scale and motion range are decided. The parameters provided in the paper can keep the driving angle of all units changing slowly, and its angular velocities and accelerations have no abrupt change. Therefore, it won't cause the great impact forces. Since the range of the driving angles of all units satisfy $[0 \pi]$, it won't cause the links interfering with each other.

Fig. 7 The 4×4 L deployable mechanism in deploying

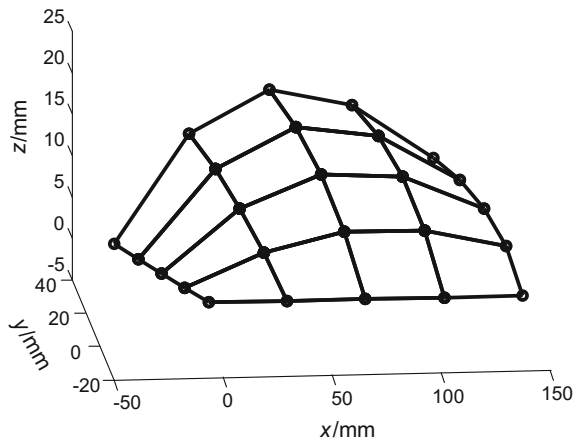


Fig. 8 The angular displacements of the driving angle of the units on the diagonal in the motion range

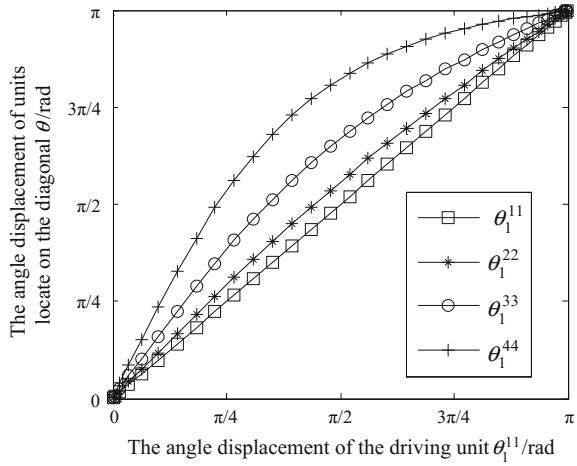


Fig. 9 The angular velocities of the driving angle of the units on the diagonal in the motion range

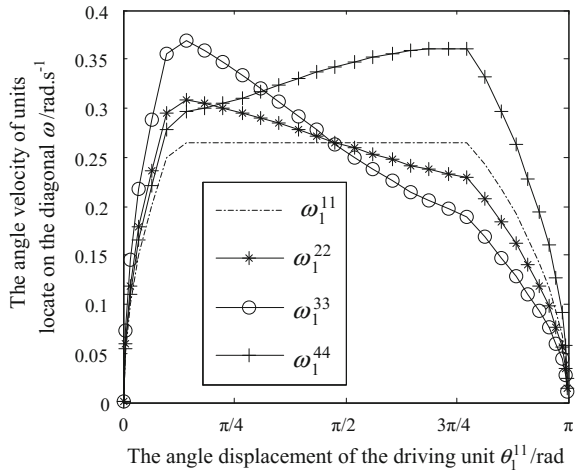
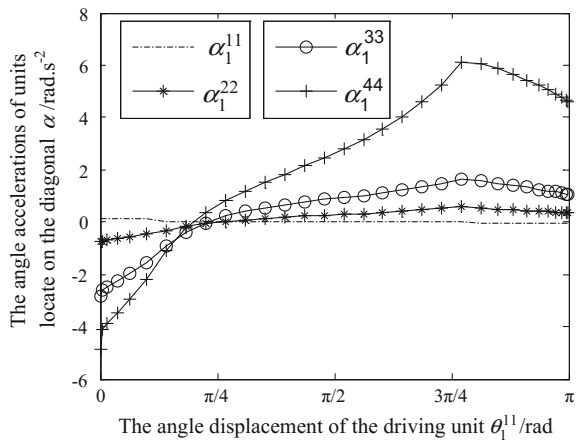


Fig. 10 The angular accelerations of the driving angle of the units on the diagonal in the motion range



Figures 11, 12 and 13 provide us with the displacements, velocities and accelerations of the kinematic pairs C of all units locating on the diagonal respectively. In Figs. 11 and 12, the displacements and velocities change slowly, therefore, they run smoothly. In Fig. 13, the accelerations of the kinematic pair C⁴⁴ in the x-axis direction changes the fastest near the initial phase. The farther away from the driving unit, the change range of the acceleration of the kinematic pairs C is the larger. Although the acceleration of the kinematic pairs of the deployable mechanism in the x-axis direction near the initial phase changes fast, their change directions are consistent. Therefore, the inertia forces are large at this moment, but they won't cause the large impact forces.

Fig. 11 The displacements of the kinematic pairs C of the units on the diagonal in the motion range

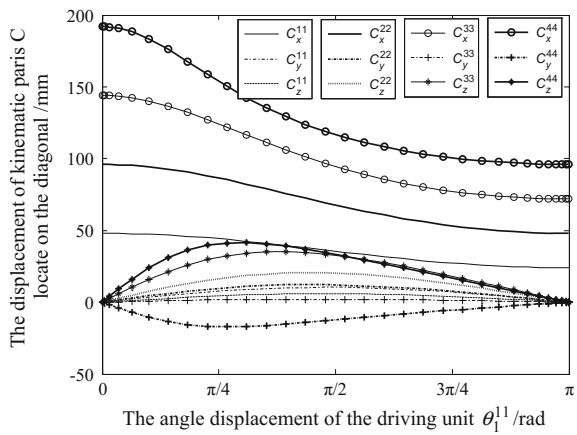


Fig. 12 The velocities of the kinematic pairs C of the units on the diagonal in the motion range

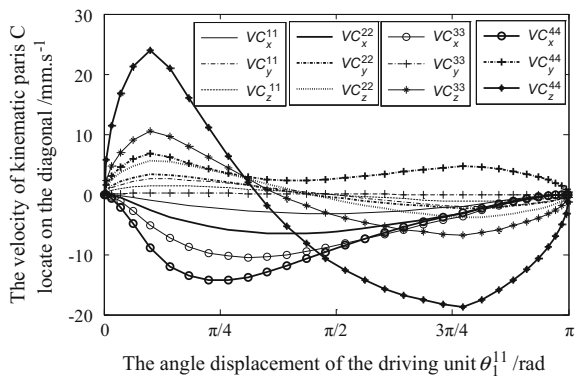
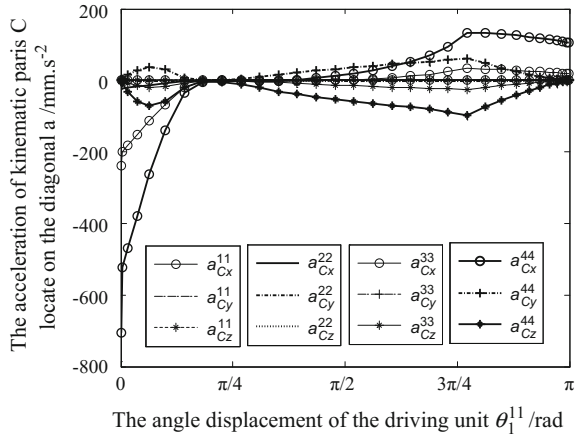


Fig. 13 The accelerations of the kinematic pairs C of the units on the diagonal in the motion range



6 Conclusions

1. A new method estimating the plus or minus of the rotational angle based on the coordinate transformation theory of the spatial mechanism is proposed.
2. The array configuration method is applied to build the deployable mechanism. Using this method builds the row array deployable mechanism, the column array deployable mechanism, the mixed array deployable mechanism and a single degree L-form deployable mechanism.
3. The transformation formula of the adjacent Bennett linkage units is derived, and it is used to build the kinematic analysis model of this deployable mechanism. The kinematics of the 4×4 L deployable mechanism are analyzed by this model. The effects of the parameters of Bennett linkage on building a deployable mechanism are discussed. Once the parameters of Bennett linkage is suitable, it can be used to build a large scale deployable mechanism.

Acknowledgments The authors gratefully acknowledge the financial support of the National Natural Science Foundation of China (Grant No. 51175422).

References

1. Chen Y, You Z (2005) Mobile assemblies based on the Bennett linkage. Proc Roy Soc Lond A Math Phys Eng Sci Roy Soc 461(2056):1229–1245
2. Chen Y (2003) Design of structural mechanisms. University of Oxford, Oxford
3. Melin NOB (2004) Application of Bennett mechanisms to long-span shelters. University of Oxford, Oxford
4. Wang W (2011) Assembling and analysis of large special deployable and networks based on Bennett linkage. Harbin Institute of Technology, Master Degree Dissemination, Shen Zhen

5. Yang F, Li J, Chen Y, et al (2015) A deployable Bennett network in saddle surface. In: Proceedings of the 14th IFToMM World Congress. Taiwan, pp 428–434
6. Lee C (1995) Kinematic analysis and dimensional synthesis of Bennett 4R mechanism. *JSME Int J Ser C Dyn Control Robot Des Manufact* 38(1):199–207
7. Zhi C, Wang S, Sun Y et al (2015) Kinematic and dynamic characteristics analysis of Bennett's linkage. *J Harbin Inst Technol* 22(3):95–100
8. Murray RM, Li Z, Sastry SS et al (1994) A mathematical introduction to robotic manipulation. CRC press, Boca Raton

Design and Analysis of the Scissors Double-Ring Truss Deployable Antenna Mechanism

Bo Han, Yundou Xu, Jiantao Yao, Wenlan Liu, Xiangbin Li
and Yongsheng Zhao

Abstract With the development of the aerospace industry, large deployable antennas have been widely applied in various spacecrafts, in order to improve the stiffness of the ring truss deployable antenna, this paper proposed a scissors double-ring truss deployable antenna mechanism. The double-ring truss mechanism is divided into a plurality of hexahedral deployable units, and the geometric conditions for the double-ring form of the scissors double-ring truss mechanism is investigated with the consideration of the effects of joint size. Based on the screw theory, the degree of freedom (DOF) of the hexahedral deployable unit is analyzed, the result showed that it only has one DOF, the simulation model of the double-ring truss is built and the deployable feature of the whole truss mechanism is verified through the deploying process.

Keywords Scissors · Double-ring truss · Deployable antenna · Screw theory

B. Han · Y. Xu · J. Yao · W. Liu · X. Li · Y. Zhao (✉)
Parallel Robot and Mechatronic System Laboratory of Hebei Province,
Yanshan University, Qinhuangdao 066004, Hebei, China
e-mail: yszhao@ysu.edu.cn; 1657774223@qq.com

B. Han
e-mail: 1440731168@qq.com

Y. Xu
e-mail: ydxu@ysu.edu.cn

J. Yao
e-mail: jtyao@ysu.edu.cn

W. Liu
e-mail: wenlanl@163.com

X. Li
e-mail: 1250403481@qq.com

Y. Xu · J. Yao · Y. Zhao
Key Laboratory of Advanced Forging & Stamping Technology and Science of Ministry
of National Education, Yanshan University, Qinhuangdao 066004, Hebei, China

1 Introduction

The space deployable and foldable mechanism can be applied to a variety of spacecrafts such as communication satellite platforms, space station, space telescopes and so on, an important application of the large scale space deployable and foldable mechanism in the field of aerospace is used to the deployment and support mechanism of the large diameter antenna. The mesh deployable antenna, which has a reflective surface formed by the tensioned cable net structure, is widely applied in large diameter antennas [1]. At present, the large diameter space deployable antennas mainly include the rib deployable antenna [2], truss deployable antenna [3] and the ring truss deployable antenna [4].

The ring truss deployable antenna has high folded rate and light weight, and its weight does not increase in proportion with the increase of the diameter, this characteristics makes it to be the ideal form of the large diameter antenna. The United States launched the Astro Mesh deployable antenna in 2000 [5], which is a single ring deployable antenna composed by a plurality of planar diagonal stretching units, the diameter of this antenna is 12.25 meters (m). Escrig F proposed the Pactruss double-ring truss deployable mechanism in 1985 [6], the Pactruss mechanism is a double-ring truss mechanism which is also composed by the planar diagonal stretching units, but it needs synchronous gears in the node positions to ensure the synchronization of the movement. Datashvili L et al. developed a double-ring deployable truss which has a 6 m diameter [7], the basic unit is composed by two scissors mechanisms which are spaced apart from each other at a certain height, the upper and lower ends of the two scissors mechanisms are fixed in the vertical rods. Xu and Guan developed a truss deployable antenna which is composed by tetrahedron units [8], they also developed a double-ring truss deployable antenna [9], and the structure of the double-ring truss is the same as that of the Pactruss mechanism proposed by Escrig F. Shi et al. proposed a slider-crank planar deployable mechanism unit and designed a single ring truss and a double-ring truss based on the unit, they also developed the prototypes [10].

The deployment and support mechanism of the large diameter antenna needs high stiffness and folded rate, and there should be less prismatic joints to avoid the cold welding phenomenon in space, but almost all the previously proposed deployable mechanisms have these limitations more or less. Hence, we propose a scissors double-ring truss deployable antenna mechanism, it has high structure stiffness, the joints in the mechanism are all revolute joints, the movement of the whole truss is synchronous and there are no synchronous gears in the node positions, this characteristics can perfectly meet the needs of large diameter truss antenna, and makes it have a good application prospect in the field of aerospace.

2 Configuration Design of the Scissors Double-Ring Truss Deployable Antenna Mechanism and the Division of the Units

The scissors double-ring truss deployable antenna mechanism is shown in Fig. 1, it includes the inner ring truss, the outer ring truss and a plurality of connection units, the basic unit of the inner ring truss and the outer ring truss is a scissors 7R mechanism, the connected unit is a scissors 5R mechanism.

As shown in Fig. 1, in the planar projection of the double-ring truss deployable antenna mechanism, it can be seen as a bicyclic ring which is connected by a plurality of isosceles trapezoids, so the whole truss can be divided into a plurality of hexahedral deployable units which have the isosceles trapezoid cross-section. The hexahedral deployable unit is shown in Fig. 2, each hexahedral deployable unit includes an inner scissors 7R mechanism, an outer scissors 7R mechanism and two connected scissors 5R mechanisms, and they are connected by the node components.

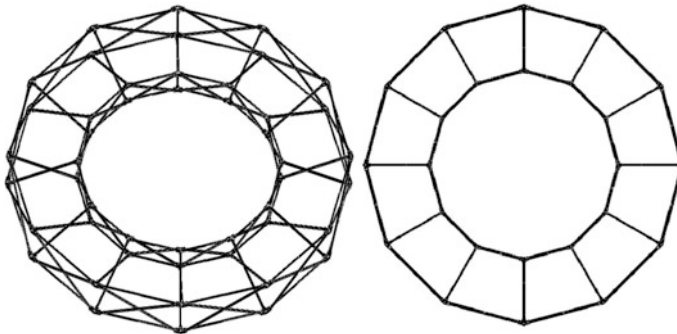


Fig. 1 The double-ring truss deployable antenna mechanism

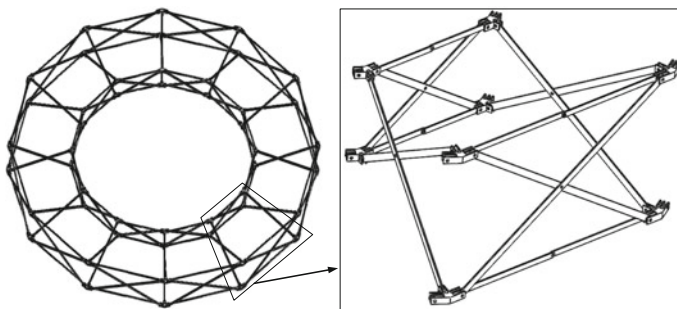


Fig. 2 The double-ring truss and hexahedral deployable unit

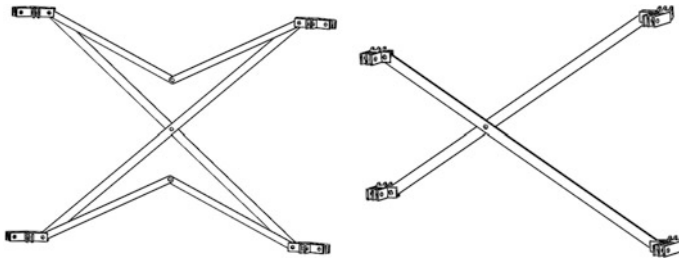


Fig. 3 The scissors 7R mechanism and the scissors 5R mechanism

The inner scissors 7R mechanism and the outer scissors 7R mechanism have the same structure, only their sizes are different. The scissors 7R mechanism and the scissors 5R mechanism are shown in Fig. 3, the scissors 7R mechanism is centrosymmetric, but the scissors 5R mechanism is a non-symmetrical mechanism.

Both the scissors 7R mechanism and the scissors 5R mechanism are planar mechanisms, as shown in Fig. 4, the scissors 7R mechanism can be divided into a symmetrical scissors 5R mechanism and two 3R mechanisms, the 3R mechanism is a planar 3 DOFs mechanism, it provides no constraints to the planar mechanisms [11], the two 3R mechanism can be seen as unconstrained branches, they can not affect the DOFs and the geometric conditions for the double-ring form of the double-ring truss mechanism, so they can be neglected in the subsequent analysis, and the scissors 7R mechanism can be simplified to a symmetrical scissors 5R mechanism in the follow derivation processes.

The folded and deployed states of the scissors double-ring truss deployable antenna mechanism is shown in Fig. 5, the scissors double-ring truss has high structure stiffness, there is no synchronous gear and compound hinge in this mechanism, the inner ring truss is always lower than the outer ring truss during the folding and deploying processes, so the cable net can be connected on the outer ring truss, the area of the cable net will be greatly increased.

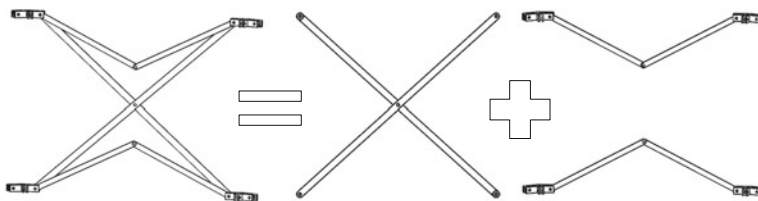


Fig. 4 The scissors 7R mechanism and its components

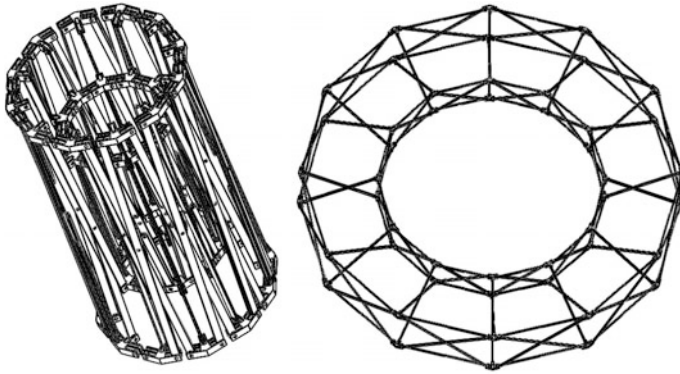
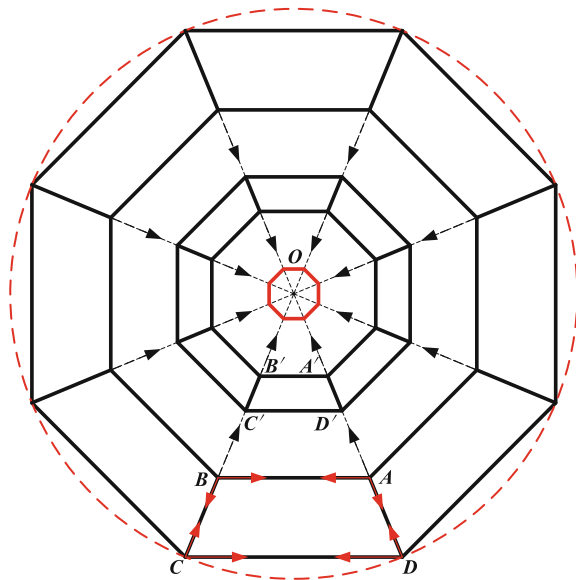


Fig. 5 Folded and deployed states of the scissors double-ring truss deployable antenna mechanism

3 Analysis of the Geometric Conditions for the Double-Ring Form of the Scissors Double-Ring Truss Mechanism

The scissors double-ring truss deployable antenna mechanism only has one form of movement, it can only fold or deploy, the folding process schematic is shown in Fig. 6, each node component moves to the center of the double-ring truss.

Fig. 6 Folding process schematic of the scissors double-ring truss mechanism



As shown in Fig. 6, the two nodes on each side of the unit $ABCD$ moves closer to each other, the unit $ABCD$ turns to the unit $A'B'C'D'$, then continue to fold to the center, the folding process of the other units are the same as that of the unit $ABCD$. Herein, we take the unit $ABCD$ as an example, considering the size of the node components, and neglect the 3R mechanisms in the scissors 7R mechanism, to analyze the geometric conditions for the double-ring form of the scissors double-ring truss mechanism.

To ensure the scissors mechanisms can be formed to the hexahedral deployable unit and the whole double-ring truss, the lengths and the angles of the scissors rods are shown in Fig. 7, the length of the inner scissors mechanism rod is $2l$ and the length of the outer scissors mechanism rod is $2L$ in Fig. 7a, b, the revolute joints located at the intermediate position of the two scissors mechanisms, the length of the connected scissors mechanism rod is $l + L$ in Fig. 7c, the revolute joint divides the rod into two sections, the lengths are l and L . The left side of Fig. 7c is connected to the inner scissors mechanism rods in Fig. 7a and the right side of Fig. 7c is connected to the outer scissors mechanism rods in Fig. 7b, so the angles

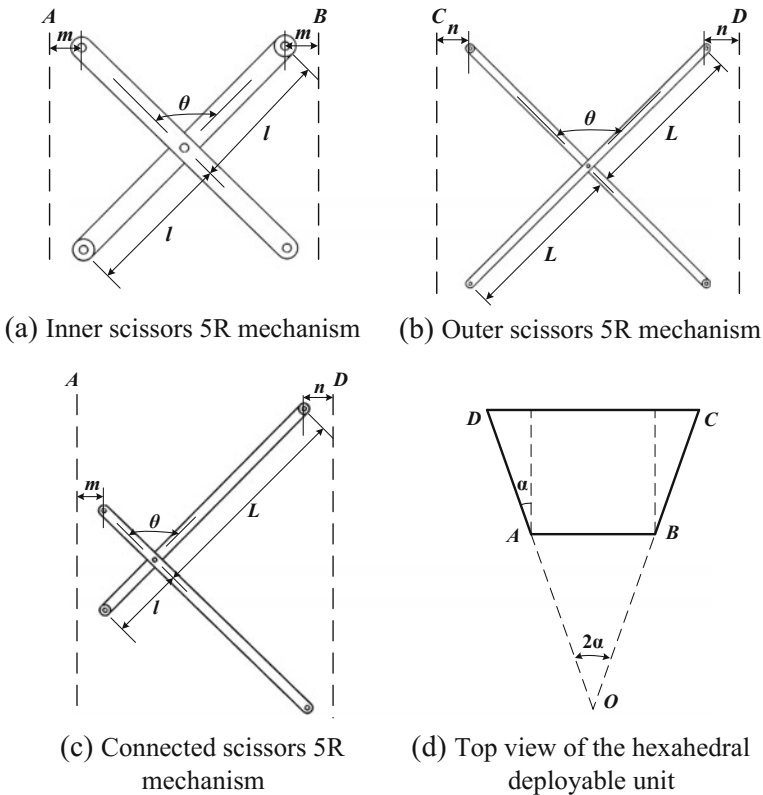


Fig. 7 Basic mechanism units of the scissors double-ring truss mechanism

of the two rods in Fig. 7a–c are identical, the value of the angle is θ . There are only two different types of node components which are lying on the inner ring truss and the outer ring truss, the distances of the axes of the revolute joints to the node components center are m and n respectively, as shown in Fig. 7a–c. Figure 7d is the top view of the hexahedral deployable unit, the cross-section $ABCD$ is an isosceles trapezoid, and the central angle corresponding to the unit is 2α .

The projected rod lengths, shown in Fig. 7d, have the following expressions:

$$\begin{aligned} CD &= AB + 2AD \sin \alpha \\ AD &= (AB + CD)/2 \end{aligned} \tag{1}$$

Expressing AB and CD in terms of l, L, θ, m and n :

$$\begin{aligned} AB &= 2l \sin(\theta/2) + 2m \\ CD &= 2L \sin(\theta/2) + 2n \end{aligned} \tag{2}$$

From Eqs. (1) and (2), we can conclude the following equation:

$$\frac{AB}{CD} = \frac{1 - \sin \alpha}{1 + \sin \alpha} = \frac{l \sin(\theta/2) + m}{L \sin(\theta/2) + n} \tag{3}$$

Equation (3) can be written as:

$$l \sin(\theta/2) + m = L \sin(\theta/2) \frac{1 - \sin \alpha}{1 + \sin \alpha} + n \frac{1 - \sin \alpha}{1 + \sin \alpha} \tag{4}$$

It is a very complex equation, instead of looking for a general solution, we are interested in the particular solution that makes the first term on the left side equal to the corresponding term on the right side, and also the second term equal to the corresponding second term. Hence, instead of solving Eq. (4), we can solve the following equations:

$$l \sin(\theta/2) = L \sin(\theta/2) \frac{1 - \sin \alpha}{1 + \sin \alpha}, m = n \frac{1 - \sin \alpha}{1 + \sin \alpha} \tag{5}$$

From Eq. (5), we can conclude the proportional relationship:

$$\frac{l}{L} = \frac{1 - \sin \alpha}{1 + \sin \alpha}, \quad \frac{m}{n} = \frac{1 - \sin \alpha}{1 + \sin \alpha} \tag{6}$$

The α in Eq. (6) is related to the amount of the hexahedral deployable units in the whole double-ring truss mechanism, if the total number of the hexahedral units is N , we can get the following equation:

$$2\alpha = 360/N \quad (7)$$

Substituting Eq. (7) into Eq. (6), we can get the final relationship:

$$\frac{l}{L} = \frac{1 - \sin(180/N)}{1 + \sin(180/N)}, \quad \frac{m}{n} = \frac{1 - \sin(180/N)}{1 + \sin(180/N)} \quad (8)$$

Equation (8) is the geometric conditions for the double-ring form of the double-ring truss deployable antenna mechanism, from the two equations we can see that the two proportional relationships are identical, and they are related to the amount of the hexahedral deployable units in the double-ring truss deployable antenna mechanism.

4 DOFs Analysis of the Deployable Unit and the Simulation of the Double-Ring Truss Deployable Antenna Mechanism

The double-ring truss deployable antenna mechanism is highly symmetrical, it contains a plurality of hexahedral deployable units, so we can analyze the DOFs of the single hexahedral deployable unit to get the motion properties, then analyze the folding and deploying processes of the whole double-ring truss mechanism.

4.1 DOFs Analysis of the Hexahedral Deployable Unit

The hexahedral deployable unit without 3R mechanisms is shown in Fig. 8, $A-H$ represent the eight node components, M , N , P and Q represent the revolute joints. Each node component is connected with two scissors mechanisms, the vertically adjacent two node components can be considered as a parallel mechanism which consists of two RRR branches.

As shown in Fig. 9, the node component H connects with the node component C through the two branches HNC and HPC , both the two branches are RRR branches. Establish the coordinate system $O-XYZ$, the origin O is located at the center of the node component C , the X axis is along the connection line between C and D , the Z axis is vertical upward (along the connection line between C and H), the Y axis is determined by right hand rule. The DOFs of the node component H will be analyzed by using the screw theory [12].

Fig. 8 The hexahedral deployable unit without 3R mechanisms

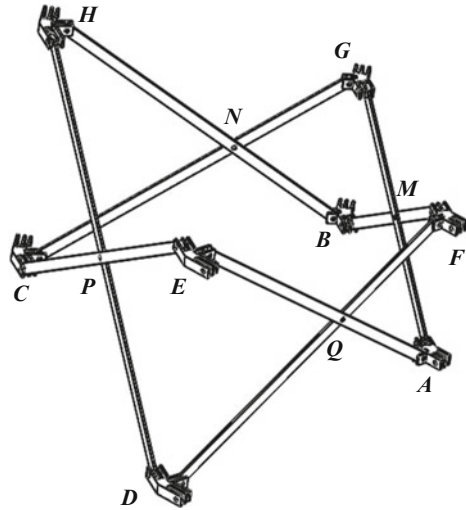
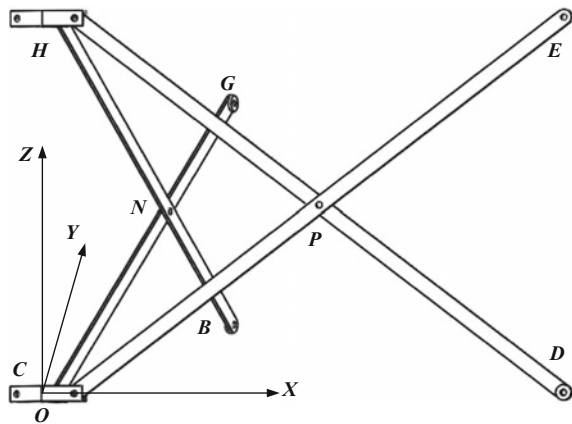


Fig. 9 The branches between the node components *C* and *H*



The kinematic twists of the *HPC* branch can be identified as:

$$\begin{aligned}
 \mathcal{S}_{11} &= (0 \ 1 \ 0; \ 0 \ 0 \ a) \\
 \mathcal{S}_{12} &= (0 \ 1 \ 0; \ -b \ 0 \ c) \\
 \mathcal{S}_{13} &= (0 \ 1 \ 0; \ -d \ 0 \ e)
 \end{aligned}
 \tag{9}$$

Through the kinematic twists of the *HPC* branch, the constraint wrenches of the *HPC* branch can be obtained as follows:

$$\begin{aligned}
 \$_{11}^r &= (0 \ 0 \ 0; \ 1 \ 0 \ 0) \\
 \$_{12}^r &= (0 \ 0 \ 0; \ 0 \ 0 \ 1) \\
 \$_{13}^r &= (0 \ 1 \ 0; \ 0 \ 0 \ 0)
 \end{aligned} \tag{10}$$

The $\$_{11}^r$ is a constraint couple along the X axis, the $\$_{12}^r$ is a constraint couple along the Z axis, the $\$_{13}^r$ is a constraint force which passes through the origin O and along the Z axis.

In the same way, the constraint wrenches of the HNC branch are gotten as follows:

$$\begin{aligned}
 \$_{21}^r &= (0 \ 0 \ 0; \ 0 \ 1 \ 0) \\
 \$_{22}^r &= (0 \ 0 \ 0; \ 0 \ 0 \ 1) \\
 \$_{23}^r &= (1 \ 0 \ 0; \ 0 \ 0 \ 0)
 \end{aligned} \tag{11}$$

The $\$_{21}^r$ is a constraint couple along the Y axis, the $\$_{22}^r$ is a constraint couple along the Z axis, the $\$_{23}^r$ is a constraint force which passes through the origin O and along the Z axis.

From Eqs. (10) and (11), the constraint wrenches of the node component H can be obtained:

$$\begin{aligned}
 \$_1^r &= (0 \ 0 \ 0; \ 1 \ 0 \ 0) \\
 \$_2^r &= (0 \ 0 \ 0; \ 0 \ 0 \ 1) \\
 \$_3^r &= (0 \ 1 \ 0; \ 0 \ 0 \ 0) \\
 \$_4^r &= (0 \ 0 \ 0; \ 0 \ 1 \ 0) \\
 \$_5^r &= (1 \ 0 \ 0; \ 0 \ 0 \ 0)
 \end{aligned} \tag{12}$$

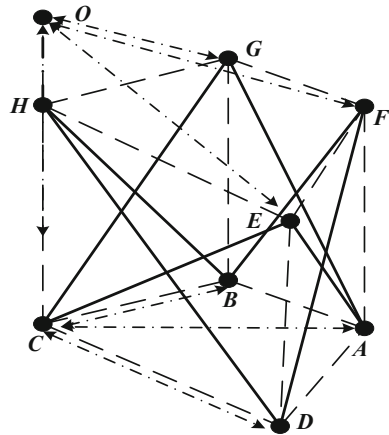
By solving the reciprocal screws of the constraint wrenches in Eq. (12), we can conclude the kinematic twist of the H component:

$$\$ = (0 \ 0 \ 0; \ 0 \ 0 \ 1) \tag{13}$$

The $\$$ represents the translational movement along the Z axis, which means that the node component H can only translate along the connection line of CH , hence, as shown in Fig. 8, the node components A and F , B and G , C and H , D and E can only translate along their connection lines at any time, since the scissors 5R mechanism is a planar mechanism which only has one DOF, so the whole hexahedral deployable unit only has one DOF.

Simplified the node components in the hexahedral deployable unit to ideal points, and make C as the fixed point, the relative trajectories of the node components in the process of folding and deploying are shown in Fig. 10, the double arrow dot chain lines represent the trajectories of the node components, dotted lines are the outer contour of the hexahedral deployable unit, when the hexahedral

Fig. 10 The trajectories of the nodes components in the folding and deploying processes



deployable unit folded, the point *A*, *B* and *D* move to the point *C* and the point *E*, *F*, *G* and *H* move to the point *O*, the whole hexahedral deployable unit folded into the space straight line *AO*, the hexahedral deployable unit only has one DOF.

In the double-ring truss deployable antenna mechanism, each node component is shared by two adjacent hexahedral deployable units, the vertically adjacent two node components are connected by three scissors mechanisms, they can be considered as a 3-RRR parallel mechanism, since the 3-RRR parallel mechanism has the same DOF properties as the 2-RRR parallel mechanism, so either the single hexahedral deployable unit or the hexahedral deployable unit in the whole double-ring truss only has one DOF, the DOF properties of the whole double-ring truss are the same as that of the hexahedral deployable unit, it also only has one DOF.

4.2 Deploying Process Simulation Verification of the Double-Ring Truss Deployable Antenna Mechanism

In order to verify the deployable feature of the double-ring truss deployable antenna mechanism, the three-dimensional model of the whole double-ring truss is built in the Solidworks software to simulate the deploying process.

The amount of the hexahedral deployable units is 12, the length of the outer scissors rod is 600 mm, through the relationship in Eq. (8) we can calculate that the length of the inner scissors rod is 353.27 mm, and the length of the connection scissors rod is 476.64 mm, the deploying process is shown in Fig. 11.

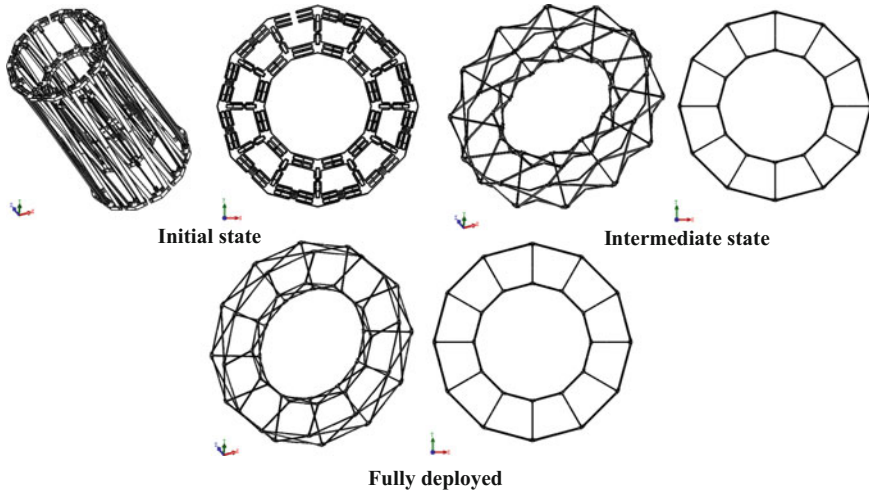


Fig. 11 The deploying process of the double-ring truss

5 Conclusion

A scissors double-ring truss deployable antenna mechanism is proposed in this paper, and it is divided into a plurality of hexahedral deployable units. The geometric conditions for the double-ring form of the scissors double-ring truss mechanism is investigated with the consideration of the effects of joint size, it showed that the proportional relationships of the rods and joint sizes of the inner ring truss and the outer ring truss are related to the amount of the hexahedral deployable units in the double-ring truss deployable antenna mechanism. The DOFs of the hexahedral deployable unit is analyzed based on the screw theory, the result showed that it only has one DOF, the simulation model of the double-ring truss is built and the deployable feature of the whole double-ring truss mechanism is verified through the deploying process.

The scissors double-ring truss deployable antenna mechanism has high stiffness, and it only has one DOF, the whole truss mechanism can fold and deploy without synchronous gears, and the cable net can be connected on the outer ring truss, this characteristics makes it have a good application prospect in the field of space deployable antenna.

Acknowledgments This research was sponsored by the National Natural Science Foundation of China under Grant 51675458 and Grant 51275439.

References

1. Li TJ (2012) Deployment analysis and control of deployable space antenna. *Aerosp Sci Technol* 18:42–47
2. Liu MZ, Gao GF (2003) Advances in the study on structure for space deployable antenna. *Yuhang Xuebao* 24:82–87
3. Chu ZR, Deng ZQ, Qi XZ et al (2014) Modeling and analysis of a large deployable antenna structure. *Acta Astronaut* 95:51–60
4. Li TJ, Wang Y, Wei JR et al (2009) Structural frequency prediction of large deployable antenna in space. *Hangkong Xuebao* 30:1648–1654
5. Meguro A, Tsujihata A, Hamamoto N et al (2000) Technology status of the 13 m aperture deployment antenna reflectors for engineering test satellite VIII. *Acta Astronaut* 47:147–152
6. Escrig F (1985) Expandable space structures. *Int J Space Struct* 1:79–91
7. Datashvili L, Endler S, Wei B et al (2013) Study of mechanical architectures of large deployable space antenna apertures: from design to tests. *Ceas Space J* 5:169–184
8. Xu Y, Guan FL (2013) Structure–electronic synthesis design of deployable truss antenna. *Aerosp Sci Technol* 26:259–267
9. Xu Y, Guan FL, Chen JJ et al (2012) Structural design and static analysis of a double-ring deployable truss for mesh antennas. *Acta Astronaut* 81:545–554
10. Shi C, Guo HW, Liu RQ et al (2015) Formulations for dynamics of annular deployable truss for mesh antennas. In: *Proceedings of the 14th IFToMM world congress*. IFToMM, Taiwan (2015)
11. Xu YD, Yao JT, Zhao YS (2013) Simple methods for distinguishing instantaneity of mobility of the overconstrained parallel mechanism based on the geometric constraint conditions. *Jixie Gongcheng Xuebao* 49:10–16
12. Liu SC, Chen ZM, Liu JF et al (2011) Force analysis of single ring spatial RSUR mechanism based on screw theory. *Jixie Gongcheng Xuebao* 47:23–28

Deployable Mechanism Design for Span Morphing Wing Aircraft

Binbin Gao, Rongjie Kang and Yan Chen

Abstract Compared with traditional aircrafts, span morphing wing aircrafts can change their span according to different flight conditions and missions to improve flight performances. Also, it has advantages in storage and transportation. In this paper, a single-degree-of-freedom (SDOF) mechanism based on Sarrus linkages is presented and applied to the construction of a span morphing wing aircraft. Computational Fluid Dynamics (CFD) simulation shows that the deployable mechanism generates slight influence on the drag coefficient while having a relatively strong influence on the lift coefficient and lift to drag ratio. Finite Element Model (FEM) methods are used to analyze the mechanical properties of the mechanism during flight. The results indicate that the maximum stress 45.5 Mpa occurs at the link connected to the base link. A series of flight experiments were conducted to prove that the mechanism enables the span change smoothly and improves the flight performances effectively.

Keywords Span morphing wing aircraft · Deployable mechanism · Computational fluid dynamics simulation · Finite element model

B. Gao · R. Kang · Y. Chen
Key Laboratory of Mechanism Theory and Equipment Design of Ministry of Education,
Tianjin University, Tianjin 300072, China
e-mail: gaobinbin@tju.edu.cn

Y. Chen
e-mail: yan_chen@tju.edu.cn

B. Gao · R. Kang (✉) · Y. Chen
School of Mechanical Engineering, Tianjin University, Tianjin 300072, China
e-mail: rjkang@tju.edu.cn

1 Introduction

Inspired by nature, people found that birds change their gestures to get a better performance according to different flight conditions. More than 100 years ago, the Wright brothers successfully controlled flight by pulling on cables to twist the wing [1], which brought the first morphing wing aircraft to the world. Morphing wing have attracted great attention among the world since the Defense Advanced Research Projects Agency (DARPA) carried out Morphing Aircraft Structures (MAS) Program between 2002 and 2007 [2–4].

Particularly, as a type of morphing wing, span morphing wing can improve the properties of an aircraft and form a multi-role aircraft. The changes of span have influences on maneuverability, payload, voyage and specific fuel consumption of an aircraft. In consideration of economy, using one multi-role span morphing wing aircraft to replace several types of aircrafts tailored for specific missions saves production cost largely. Also, it brings benefits to the storage and transportation of the aircraft [4, 5].

The first span morphing wing concept was presented by an American aircraft designer named Vincent in 1929 and in the same year, he designed and manufactured a morphing aircraft GX-3 which could change its span and camber simultaneously [6]. Previous researches on span morphing wing included telescoping wing aircraft [7, 8], the Lockheed Martin's Z-wing concept [9, 10], the modular variable geometry truss mechanism configuration [11, 12] and so on. Most of the above concepts require multi-degree-of-freedom (MDOF) movement, in other words, more than one actuators are needed to achieve wing morphing. For the Lockheed Martin's Z-wing concept, the span morphing wing consists of an inner panel and an outboard panel. The span changes by folding the inner panel to the fuselage. There are two actuators in the leading edge flap, one actuator between the inner panel and fuselage while the other one between the inner panel and outboard panel. For the modular variable geometry truss mechanism configuration, eight actuators were used to control each module, as the number of modules increases, the number of actuators increases accordingly. The use of a large numbers of actuators will decrease payload, increase specific fuel consumption, narrow voyage, bring a complex control system to an aircraft. Additionally, the rigidities of MDOF mechanisms are usually insufficient, which means unexpected deformations may occur in the wing structure. To solve the above problems, a single-degree-of-freedom (SDOF) mechanism is required for span morphing wing aircraft.

Traditional SDOF mechanisms for span morphing wing aircraft include screw rod and guide rail, gear and rack, the scissor mechanism configuration. Chen et al. [13] presented a span morphing wing aircraft driven by screw rod and guide rail. The active wing is attached to a slider on the guide rail. The rotation of the screw rod causes the slider to translate which enables the active wing to move relatively to the fixed wing. The screw rod and guide rail mechanism can change the span accurately. However, there are slight deformations at the wing that may cause issues

on the relative displacements between the screw rod and the nut, the guide rail and the slider, even making the slider stuck. In 2005, Alemayehu et al. [14] designed a span morphing wing aircraft based on the gear and rack mechanism. The active wing is attached to the rack. This design can make the active wing translate smoothly, efficiently and reliably. But large space is needed to install the mechanism in the direction perpendicular to the wing surface and the length of the span is restricted by the size of the rack. Wang [15] changed the span by the scissor mechanism which consists of scissor units assembled in series. This design is simple and reliable, and the driving force is small. However, the rigidity of the mechanism will decrease greatly if the number of units increases.

In 2012, Wang et al. [16] presented a novel design based on a SDOF over-constrained mechanism, the Sarrus linkage, for span-changing aircrafts. The outboard wing was attached to one end of the deployable mechanism, and the other end of the mechanism was fixed to the inner wing. The mechanism was driven by a servo and the span of aircraft can change from minimum 1.43 m to maximum 1.77 m. The reference area changes 23.5 % accordingly. The space required for installation is small and the mechanism is of high folding ratio. As each links are connected by revolute joints, the driving moment is small. Since the mechanism is overconstrained, the morphing wing is of high rigidity.

However, many problems were found through later flight tests. Firstly, the connection between the mechanism and the inner wing is not firm, where deformations were easy to take place. Secondly, the folding ratio for the span (23.5 %) is not large enough. Thirdly, as the outboard wing takes more load, the driving moment for the mechanism increases greatly. To solve the above problems, a new generation of span morphing wing aircraft is designed and manufactured in this paper. To decrease the deformation in the connection, a specific connector is designed to connect the inner wing and deployable mechanism. To improve the changing ratio of reference area to 50 %, which is a standard for span morphing wing aircraft [17], the number of the Sarrus units in the deployable mechanism triples. To reduce the driving moment for the mechanism, rolling bearings are applied to all revolute joints.

This paper is organized as follows: Sects. 2 and 3 presents the design and simulated analysis of the morphing wing using Sarrus linkages, respectively; a series of experiments are then carried out to test the performance of the span morphing wing aircraft in Sect. 4; and the conclusions are given in Sect. 5.

2 Morphing Wing Mechanism Design

The new morphing wing aircraft is based on a multi-segmented Sarrus linkages. As shown in Fig. 1, this mechanism consists of four parallelogram units connected by three Sarrus linkages.

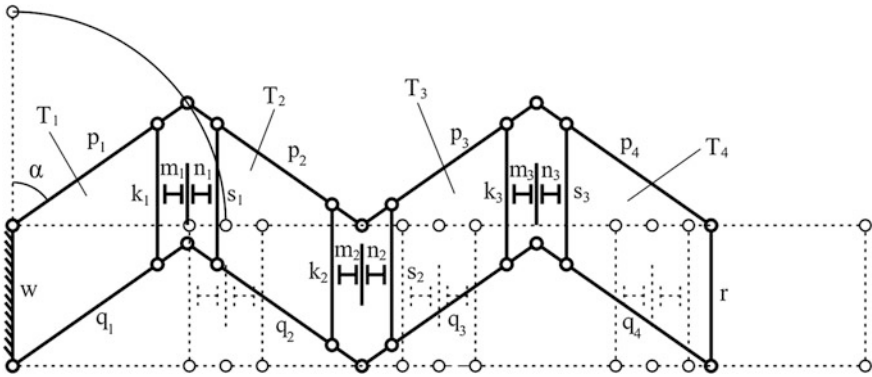


Fig. 1 Schematic of the span morphing wing mechanism

In this mechanism, the links $w, k_1, s_1, k_2, s_2, k_3, s_3, r$ have the same length,

$$l_w = l_{k_1} = l_{s_1} = l_{k_2} = l_{s_2} = l_{k_3} = l_{s_3} = l_r = \delta \tag{1}$$

Also, the links $p_1, q_1, p_2, q_2, p_3, q_3, p_4, q_4$ have the same length,

$$l_{p_1} = l_{q_1} = l_{p_2} = l_{q_2} = l_{p_3} = l_{q_3} = l_{p_4} = l_{q_4} = l \tag{2}$$

The unit T_1 formed by w, p_1, k_1, q_1 and T_4 formed by r, p_4, s_3, q_4 are identical, the unit T_2 formed by s_1, p_2, k_2, q_2 and T_3 formed by s_2, p_3, k_3, q_3 are the same. Two units T_1 and T_2 are connected by linking p_1, p_2 and q_1, q_2 respectively with two revolute joints. The links k_1 and s_1 are connected to two identical the links m_1 and n_1 by a revolute joint, respectively. The other ends of links m_1 and n_1 are connected to each other by a revolute joint. The first Sarrus linkage consists of the links $p_1, k_1, m_1, p_2, s_1, n_1$, so the mechanism formed by the units T_1 and T_2 is SDOF. Rotating the link p_1 around the link w can make the link k_2 translate in the direction perpendicular to link w . In the same way, the units T_2 and T_3, T_3 and T_4 are connected by the Sarrus linkages, so the deployable mechanism is SDOF, the mechanism can be extended by rotating any link in it.

According to Eqs. (1) and (2), the mechanism becomes symmetrical about the middle line that connects the p_2 - p_3 joint and the q_2 - q_3 joint. In the mechanism, the rotational motion of link p_1 would result in the linear motion of link r , and the direction of this linear motion is always perpendicular to the link w , link w is connected to the inner wing by a specific connector and the outboard wing is fixed to the link r .

Define α as the driving angle between the links p_1 and w , t as the thickness of the links w, r , and D as the instantaneous displacement of r from w , when p_1 is driven around the revolute joint between w and p_1 . Due to the symmetry of the mechanism with respect to the middle line, it can be found that

$$D = 4l \sin \alpha + 2t \tag{3}$$

Taking the derivative of (3), the velocity of link r is

$$V = \frac{dD}{d\alpha} 4l \cos \alpha \tag{4}$$

In Eqs. (3) and (4) the driving angle α is between 0° and 90° .

A three-dimensional model is created in SOLIDWORKS 2014, where $\delta = 0.055$ m, $l = 0.085$ m, $t = 0.004$ m. To improve the strength and reduce the weight of the deployable structure, the links $p_1, q_1, p_2, q_2, p_3, q_3, p_4, q_4$ are designed to be an I-shape beam. Besides, unnecessary supports are removed from all links. All the sharp corners of the links are rounded in order to avoid possible stress concentrations. The extension process of the mechanism is shown in Fig. 2. The rotation angle α for the four gestures correspond to $0^\circ, 30^\circ, 60^\circ, 90^\circ$.

When the mechanism fully extends, the maximum displacement D_{max} is 0.34 m. When the mechanism fully folds, as shown in Fig. 2a, there are seven revolute joints placed one by one along the extending direction. Every joint has a size of 0.008 m, so the minimum displacement D_{min} is 0.056 m. This mechanism is designed to be attached to a prototyped aircraft with a reference area A_0 of 0.27 m² and chord length C of 0.257 m. The instantaneous reference area A can be calculated by

$$A = A_0 + 2DC \tag{5}$$

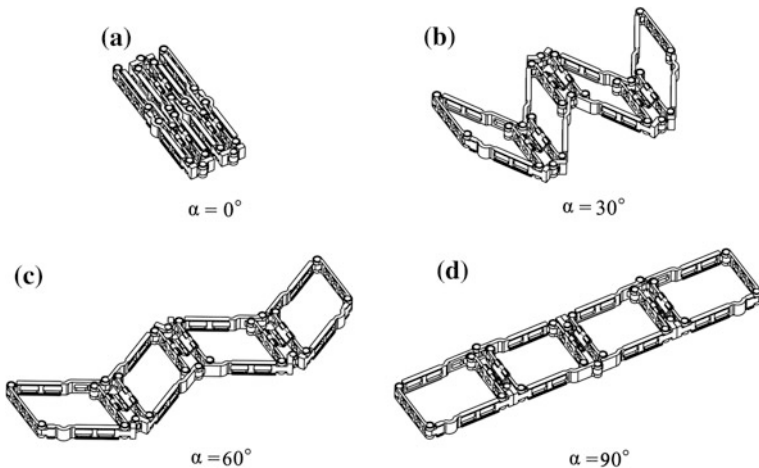
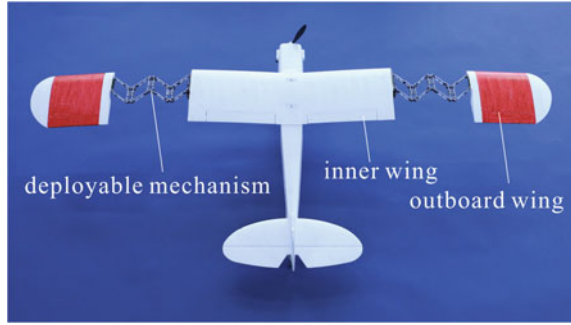


Fig. 2 Extension process of the deployable mechanism

Fig. 3 The prototyped airplane with morphing wing mechanism installed



When the mechanism fully folds, it can be found that

$$A_{min} = A_0 + 2D_{min}C \approx 0.2988 \text{ m}^2 \quad (6)$$

When the mechanism fully extends, it can be found that

$$A_{max} = A_0 + 2D_{max}C \approx 0.4489 \text{ m}^2 \quad (7)$$

Thus, the reference area changing ratio is

$$\psi = \frac{A_{max} - A_{min}}{A_{min}} = 0.5023 \quad (8)$$

The maximum reference area changing ratio for the span morphing aircraft is 50.23 %, which is larger than 50 %.

Figure 3 shows the prototype of the span morphing wing aircraft. To illustrate the deployable mechanism clearly, the covering skin is removed. During real flights, rigid skin is attached to the inner wing. The section shape of the rigid skin is the same as the outboard wing and the section size of the rigid skin is a little bit larger than the outboard wing to ensure the smooth movement and the adequate lift.

3 Simulations and Analyses

The CFD simulations were carried out to study the aerodynamic performances of the span morphing wing. Since the payload, the maneuverability and the voyage of an aircraft are highly affected by the wing parameters, such as the lift coefficients, the drag coefficients and the lift to drag ratios, it is necessary to change the wing span to optimize these parameters according to the flight conditions and missions. Above parameters are also related to the angle of attack (AOA), so the changes of the parameters with respect to different AOA need to be compared. The FEM

analyses were then used to locate the maximum stresses and to improve the design of the deployable mechanism.

3.1 Computational Fluid Dynamics Simulations

Seven models with the driving angles of 0°, 10°, 20°, 30°, 40°, 60°, 90° are set up in CATIA V5, and then these models are put into GAMBIT for meshing. In the end, these models are imported into FLUENT, a plug-in from ANSYS 15.0, which is used for CFD simulation. In simulations, the Spalart-Allmaras (SA) model is chosen to set up the turbulence model. Assuming that the flight tests are carried out at sea level and the air temperature is 288.15 K, the designed air speed is $U = 12$ m/s, the air density is $\rho = 1.225$ kg/m³, the air viscosity is $\mu = 1.789 \times 10^{-5}$ pa.s. The Reynolds number can be obtained by

$$Re = \frac{\rho UC}{\mu} = 2.11 \times 10^5 \tag{9}$$

Figure 4 shows that for a certain model, when the AOA increases, both the lift coefficient and the drag coefficient get larger. The lift coefficient curves approximate a straight line while the drag coefficient curves approximate a quadratic curve.

On the other hand, for the same AOA, the increasing span result in growing lift coefficients, though the growth are small. Table 1 presents the changes of the lift coefficients in percentage relative to the folding condition. As the AOA gets larger, the percent changes get smaller.

Though the lift coefficient changes very small, the lift force increases greatly as span gets larger.

$$F_L = \frac{1}{2} C_L A \rho U^2 \tag{10}$$

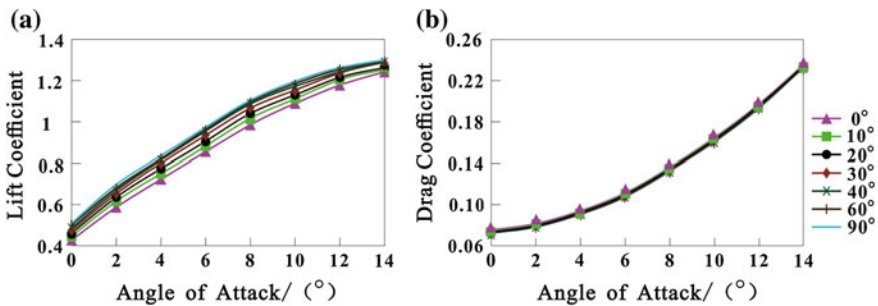


Fig. 4 Relationship between **a** the lift coefficients and the angles of attack, **b** the drag coefficients and the angles of attack

Table 1 Percentage changes in the lift coefficients under different spans

Changes of lift coefficients (%)	Degree of expansion (°)					
	AOA (°)	10	20	30	40	60
0	3.3	6.2	8.8	10.6	13.7	15.0
2	4.2	6.7	8.8	11.0	12.9	14.0
4	2.8	5.6	8.7	10.0	10.3	12.0
6	2.6	4.8	7.5	9.7	10.5	11.5
8	2.4	4.4	6.5	8.0	8.8	9.3
10	1.4	2.8	4.6	6.2	7.1	8.2
12	2.0	2.7	4.0	4.3	5.2	5.8
14	0.06	1.3	3.0	3.1	3.4	3.7

where F_L is the lift force and C_L stands for the lift coefficient, based on other parameters being hold, 50 % increase in the reference area A will result in at least 50 % increase in the lift force. Combining Eqs. (5) and (10), it indicates that, there is a linear relationship between lift force F_L and D , as shown in Eq. (11).

$$F_L = \frac{1}{2} C_L (A_0 + 2DC) \rho U^2 \quad (11)$$

Unlike the lift coefficients, as shown in Table 2, the drag coefficients for a constant AOA decreases slowly when the mechanism extends. In conclusion, airfoil shape rather than span morphing, dominates the values of the lift and drag coefficients.

Using the drag coefficient C_D to replace the lift coefficient C_L in Eq. (10), the ideal drag force F_D is

$$F_D = \frac{1}{2} C_D A \rho U^2 \quad (12)$$

Table 2 Percentage changes in the drag coefficients under different spans

Changes of drag coefficients (%)	Degree of expansion (°)					
	AOA (°)	10	20	30	40	60
0	-2.1	-4.7	-4.7	-5.4	-5.6	-5.8
2	-3.1	-4.5	-4.6	-4.7	-4.7	-6.2
4	-2.0	-2.5	-3.1	-4.6	-4.8	-5.0
6	-1.2	-2.6	-3.7	-4.1	-4.4	-5.1
8	-1.0	-2.2	-2.5	-2.9	-2.9	-3.9
10	-0.8	-2.6	-3.2	-3.3	-3.5	-3.7
12	-1.0	-1.1	-1.6	-1.7	-2.5	-3.4
14	-0.5	-0.8	-1.0	-1.2	-1.4	-1.6

Fig. 5 Relationship between the lift to drag ratios and the angles of attack

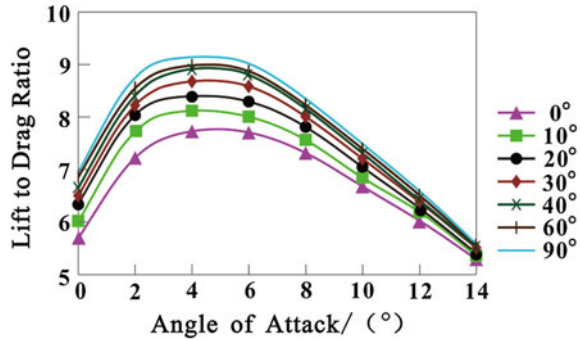


Table 3 Percentage changes in the lift to drag ratios under different spans

Changes of L/D (%)	Degree of expansion (°)					
	10	20	30	40	60	90
AOA (°)	10	20	30	40	60	90
0	5.5	11.3	14.2	16.9	20.5	22.1
2	7.5	11.8	14.0	16.5	18.5	21.5
4	4.9	8.2	12.1	15.3	16.0	17.8
6	3.8	7.6	11.6	14.4	15.5	17.4
8	3.5	6.7	9.2	11.1	12.0	13.8
10	2.2	5.6	8.0	9.8	11.0	12.3
12	3.1	3.9	5.7	6.0	7.9	9.4
14	1.1	2.1	4.0	4.4	4.9	5.4

Combining Eqs. (5) and (12), as shown in Eq. (13), above linear relationship can be applied to drag force F_D and D as

$$F_D = \frac{1}{2} C_D (A_0 + 2DC) \rho U^2 \tag{13}$$

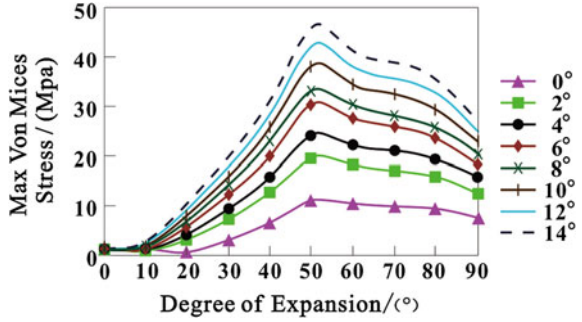
Figure 5 shows that, for a certain span, the lift to drag ratio increases first and then decreases, as the AOA increases. Though the changes of the lift coefficients and drag coefficients change slightly when the mechanism extends, there is a significant increase in the lift to drag ratio L/D . The maximum L/D 9.15 occurs when AOA is closed to 5° and the mechanism fully extends.

Table 3 shows the details of the changes. It indicates that, the influence of the span morphing on the lift to drag ratio gets less as the AOA increases.

3.2 Finite Element Model Analyses

From CFD simulations, the lift coefficient and the drag coefficient for each model under different AOA have been obtained. Combining (11) and (13), the lift and drag

Fig. 6 Relationship between the maximum stresses and the driving angles



forces are derived. In this section, 10 models are built with the driving angles of 0°, 10°, 20°, 30°, 40°, 50°, 60°, 70°, 80°, 90°. They are meshed in fore treatment software HYPERMESH. FEM analyses are carried out on morphing mechanism to find the maximum stresses and locating their positions with commercial finite element method (FEM) software ABAQUS 6.13. Assuming the aluminum T6061 is used to fabricate the morphing mechanism. For the boundary conditions, the lift force, drag force as well as the gravity are applied to the wing surface, and a fixed support is applied at the wing root. The driving link on the mechanism is set to have no rotation.

Figure 6 shows the changes of the maximum stresses for 10 models under different AOA. Ignoring several points with large deviation, the maximum stresses increases as AOA get larger. In other words, the increasing AOA results in a rapid growth of lift force and drag force, which causes a large deformation in the mechanism. However, for a constant AOA, as the mechanism extends, the maximum stresses increases first and then decreases. The peak point occurs when the driving link angle is around 50°. The reason may be that a mechanical disadvantage occurs when the driving angle chose to 50°.

All maximum stresses occur at the link next to the base link, which is the thinnest part of the linkage, as shown in Fig. 7. The whole mechanism can be considered as a cantilever beam. The largest value among all maximum stresses is

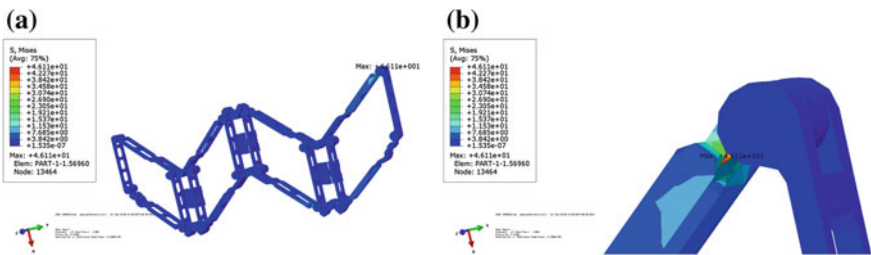


Fig. 7 The maximum stress observed in the structure with 50° extension under 14° angle of attack: **a** overall view of the stress distribution in the mechanism; **b** zoomed view of the position of where the maximum stress occurred

45.5 Mpa when the mechanism has an extension of 50° and the AOA is 14° . It indicates that, Aluminum T6061 with a yielding stress 275 Mpa is safe enough for the prototype of the span morphing wing aircraft.

4 Flight Performance

To assess the performances of the span morphing prototyped plane after refitted, a series of experiments were conducted under similar wind condition. A micro-camera is affixed to a rigid portion of the fuselage and directed towards the morphing wing to record the movement of the wing. Figure 8 shows the flight tests.

The experiments were carried out with the driving angles of 0° , 30° , 90° , which correspond to the dash configuration, the intermediate configuration, the loiter configuration [10], and focus on the performances of takeoff distance, stability and maneuverability. The takeoff distances are measured under different configurations with full throttle and maximum elevator deflection. The results show that the loiter configuration needs a takeoff distance within 10 m to take off and the dash configuration needs more than 15 m. The stability includes flight stability and landing stability. Experiments show that the loiter configuration has better stability than the other two configurations. A mutational wind condition brings more risk to the dash configuration during flight. The loiter configuration allows for an easier landing. Though the loiter configuration has worse stability, it has better maneuverability. When the plane needs to turn around, the turning radius of the dash configuration is much smaller. For the same thrust, the dash configuration has a larger speed and acceleration than other two configurations.

The voyage, the maneuverability and the load weight of the plane improve a lot after applying the deployable mechanism to the wing. However, there are also limitations of the plane. Its deadweight increases from 0.85 to 1.5 kg i.e. its inertia increases and its maneuverability gets worse.

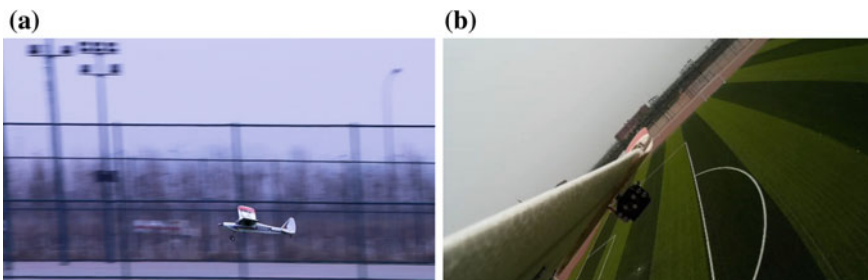


Fig. 8 Photos for flight performance tests: **a** video snapshot from the ground; **b** video snapshot from the on-board camera

5 Conclusion and Discussion

In this paper, a deployable mechanism based on the Sarrus linkages is presented to construct a span morphing wing aircraft. The design of the mechanism is investigated with a brief kinematics analyses. To analyze the influence of span morphing on aerodynamic performances of the prototyped aircraft, CFD simulations were carried out. FEM analyses were used to help to select the appropriate material for the deployable mechanism. And a series of experiments were then conducted to test the design.

It was found that the changes of span have slight influences on the lift coefficient and the drag coefficient while can improve the lift force and drag force by 50 %. It proves that the mechanism is able to improve the aerodynamic performance of a span morphing wing aircraft.

The maximum stress occurs when the mechanism is semi-expanded. The yielding stress of the selected material Aluminum T6061 is much larger than the maximum stress 45.5 Mpa, which indicates that material is safe enough in the span morphing wing aircraft.

In the future, small sensors and data acquisition devices will be used to measure and record the command input and aircraft response during flight. In that case, the performance of the span morphing wing aircraft can be parameterized. Also, the weight of the plane must be reduced to decrease its inertia and improve its maneuverability. Then the rigidity of the wing needs to be enhanced to reduce deformations in the outboard wing and improve the performances of the span morphing wing aircraft.

Acknowledgments The authors acknowledge the supports of the National Natural Science Foundation of China (Project No. 51275334 and 51375329).

References

1. Bowman J, Sanders B, Cannon B (2007) Development of next generation morphing aircraft structures. In: 48th AIAA/ASME/ASCE/AHS/ASC structures, structural dynamics, and materials conference, 1730. AIAA Press, Honolulu
2. Love MH, Zink PS, Stroud RL (2007) Demonstration of morphing technology through ground and wind tunnel tests. In: 48th AIAA/ASME/ASCE/AHS/ASC structures, structural dynamics, and materials conference, 1729. AIAA Press, Honolulu
3. Weisshaar TA (2013) Morphing aircraft systems: history perspectives and future challenges. *J Aircr* 50(2):337–353
4. Rodriguez AR (2007) Morphing aircraft technology survey. In: 45th AIAA aerospace sciences meeting and exhibit, 1258. AIAA Press, Reno
5. Bowman J, Sanders B, Weisshaar TA (2002) Evaluating the impact of morphing technologies on aircraft performance. In 43rd AIAA/ASME/ASCE/AHS/ASC structures, structural dynamics, and materials conference, 1631. AIAA Press, Denver
6. Rodriguez AR (2002) The contributions of Vincent Justus Burnelli. In: 41st AIAA aerospace sciences meeting and exhibit, 292. AIAA Press, Reno

7. Blondeau J, Pines DJ (2003) Design development and testing of a morphing aspect ratio wing using an inflatable telescopic spar. In: 44th AIAA/ASME/ASCE/AHS/ASC structures, structural dynamics, and materials conference. AIAA Press, Norfolk
8. Neal DA, Johnston CO (2004) Design and wind-tunnel analysis of a fully adaptive aircraft configuration. In: 45th AIAA/ASME/ASCE/AHS/ASC structures, structural dynamics, and materials conference. AIAA Press, California
9. Baldelli DH, Lee DH, Hopper D (2007) Practical modeling, control and simulation of an aeroelastic morphing UAV. In: 48th AIAA/ASME/ASCE/AHS/ASC structures, structural dynamics, and materials conference, 2236. AIAA Press, Honolulu
10. Ivanco TG, Scott RC, Love MH (2007) Validation of the Lockheed martin morphing concept with wind tunnel testing. In: 48th AIAA/ASME/ASCE/AHS/ASC structures, structural dynamics, and materials conference, 2235. AIAA Press, Honolulu
11. Moosavian A, Xi FF, Hashemi SM (2013) Design and motion control of fully variable morphing wings. *J Aircr* 50(4):1189–1201
12. Moosavian A, Xi FF, Hashemi SM (2014) Optimal configuration design for the variable geometry wing-box. *J Aircr* 51(3):811–823
13. Chen X (2012) Design of an axially telescoping wing control system and nonlinear vibration experiment research. Beijing University of Technology, Beijing, China
14. Alemayehu D, Leng M, McNulty R (2005) Virginia Tech morphing wing team spring 2005 final report, 2005
15. Wang LJ (2014) The scheme design of the UAV morphing wing and simulation analysis. Harbin Institute of Technology, Harbin, China
16. Wang Q, Chen Y, Tang H (2012) Mechanism design for aircraft morphing wing. In: 53rd AIAA/ASME/ASCE/AHS/ASC structures, structural dynamics, and materials conference, 1608. AIAA Press, Honolulu
17. Ramrakhyani DS, Lesieutre GA, Frecker M (2005) Aircraft structural morphing using tendon-actuated compliant cellular trusses. *J Aircr* 52(6):1615–1621

Part V
Kinematics

Kinematics and Singularity of a 4-DOF Parallel Mechanism with Passive Spherical Joints

Binbin Peng, Wenchen Zhen, Xiangqian Wang, Kaituo He and Song FU

Abstract This paper presents a 4-DOF (3T1R: three-translational and one rotational degrees of freedom) parallel mechanism with passive spherical joints, which has better stiffness than the other ones with just prismatic and revolute joints. Firstly, structure description is given. And a complete study regarding motion characteristics is done by analytical method. Then the kinematics of the 4-DOF parallel manipulator, which includes inverse and forward solutions, is studied in detail by numerical method. The Jacobian matrix of the parallel manipulator is also derived. Based on the Jacobian matrix, singularity analysis of the parallel mechanism has been described clearly. All prismatic actuators of the 4-DOF parallel manipulator are parallel to each other, enables it to have an independent Z motion—only limited by the stroke of the prismatic actuators. So the parallel manipulator has the identical performance along the direction of the actuated linear slides. The 4-DOF parallel manipulator is characterized by elevated dynamical capabilities having its actuators at base.

Keywords Parallel manipulator · Motion characteristics · Position analysis · Singularity

1 Introduction

Parallel mechanisms have been known for their increased rigidity, better accuracy, higher load and dynamical capacities as compared to their competent serial mechanisms. The advantages of such mechanisms are quite sufficient to be the motive behind the increasingly interest in these mechanisms, in which they have been under extensive research in the last decades.

B. Peng (✉) · W. Zhen · X. Wang · K. He · S. FU
School of Mechanical Engineering, Nanjing University of Science and Technology,
Nanjing 210094, China
e-mail: pengbinbin2013@126.com

© Springer Nature Singapore Pte Ltd. 2017
X. Zhang et al. (eds.), *Mechanism and Machine Science*,
Lecture Notes in Electrical Engineering 408,
DOI 10.1007/978-981-10-2875-5_67

In fact, regarding some tasks 4-DOF (3T1R) parallel mechanisms are sufficient. In others, where another rotation is required it can be provided either by the table or by an additional actuator in series with the parallel mechanism (forming a hybrid mechanism). The 3T1R parallel mechanisms can be mainly divided into two types, fully-parallel robots and series-parallel robots (hybrid robots). In this work, the first type will be deeply studied. Many 3T1R fully-parallel mechanisms exist in literature. The RRP+2UPU [1] with 3 legs rotates about the axis which is perpendicular to the moving platform, and no singularity would occur in the reachable workspace if the size of the moving platform is different from that of the base. However, only one rotational actuator is installed on the base, which influences its stability and vibration. The redundant parallel mechanism in [2] (large operational workspace and rotational capability, no singularity) rotates about the axis which is parallel to the moving platform. However, it has two parallelogram arms with revolute joints, which has an effect on the rigidity because the bars will bear the bending moment. The articles [3] and [4] introduce several 3T1R parallel mechanisms with kinematic chains consisting of revolute, prismatic or universal joints which bear a lot of torque. The other 3T1R parallel mechanisms with no passive spherical joints such as [5] (4-DOF Schonflies motions) and [6] (five 4-DOF operation modes) also have the same problems like stability and rigidity. Here to point out a famous family of mechanisms, which are the H4 in [7], the I4 in [8], the Par4 in [9] with its industrialized version Adept Quattro [10] (it is the fastest industrial pick-and-place robot with high acceleration in a short cycle time), they have interesting articulated traveling plates and their rotation axis are all perpendicular to the moving platform respectively. The principle of H4 is the base of the above family of machines, which is shown in Fig. 1a. Based on the H4, many 3T1R non-over-constrained parallel mechanisms in [11] are constructed based on screw theory, some of the mechanisms which contain multiple revolute joints in each chain are more suitable for application in light load. As demonstrated in the article [7], the performance and

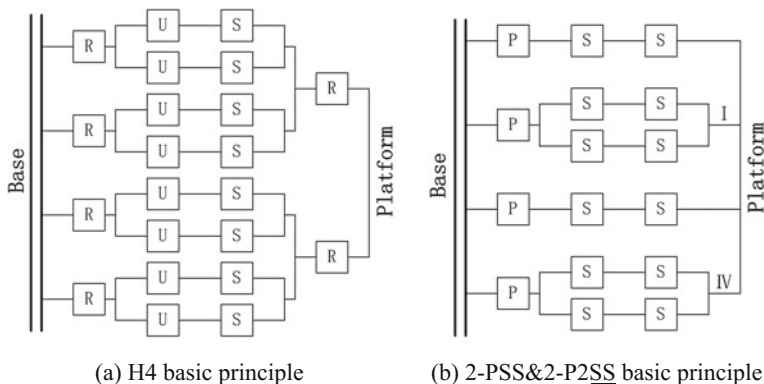


Fig. 1 Basic principles of two parallel mechanisms

characteristics of the mechanism have a great relationship with the arrangement mode of the chains, which can be got from the example not compatible with the condition in section VI of the article [7].

At the end of the paper [7], an asymmetrical $P-(U-S)_2/P-U-S$ H4 was simply given (simple structure, no detailed analysis), and its two $P-(U-S)_2$ chains are adjacent. In this work, a symmetrical 4-DOF parallel mechanism is presented, denoted to $2-PSS\&2-P2SS$ (P denotes the prismatic joint, S denotes the spherical joint), whose rotation axis is parallel to the moving platform. Every strut of the mechanism is the true two-force bar which can avoid bending moments when under the action of external force for its passive spherical joints. It will give the mechanism the highest rigidity. The mechanism is also characterized by elevated dynamical capabilities and better stability having its actuators at base. Meanwhile, the mechanism has simple structure and convenient control.

The paper introduces a 4-DOF parallel mechanism with passive spherical joints in Sect. 2. Then Sect. 3 describes the study of motion characteristics. The analysis of position is detailed in Sect. 4. Section 5 presents the singularity analysis of this mechanism. The paper ends with Sect. 6 giving the conclusions.

2 Structure Description of the Parallel Mechanism

The basic principle of the 4-DOF (3T1R) parallel mechanism with passive spherical joints proposed is shown in Fig. 1b with its model in Fig. 2a. There are four independent kinematic chains between the base and the moving platform, and each chain is actuated (prismatic joint are actuated and their position are being measured, while spherical joint are passive). Chains (I) and (IV) (see Fig. 2b, where the spherical joints are expressed by geometrical points A_i and B_i), are two same composite legs (each composite leg is the same as the spatial parallelogram in DELTA, which is described here for $P2SS$ chain), and they are relative, which cooperate with the other two same single chains (two PSS chains) to position and control the platform.

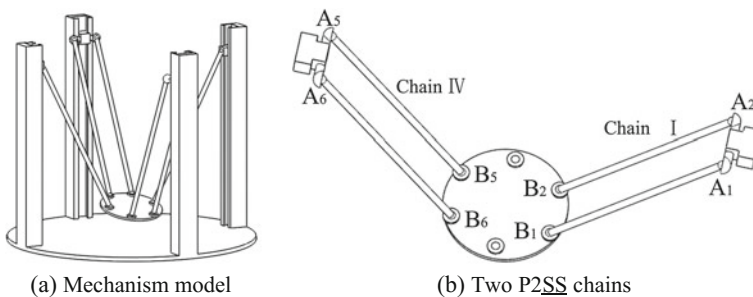


Fig. 2 $2-PSS\&2-P2SS$ parallel mechanism

From Fig. 1, one can know that the 4-DOF parallel mechanism presented has no any passive revolute joint compared with the general parallel mechanism H4. The difference between the 4-DOF parallel mechanism presented and the asymmetrical H4 is the two same composite legs of the parallel mechanism in this paper are connected to the moving platform with interval, while the two composite legs of the asymmetrical H4 are connected adjacent to the moving platform. Another important geometrical structure conditions of the parallel mechanism presented in this paper are needed to point out, which are $\overline{A_1A_2} = \overline{A_6A_5}$ and $\overline{B_1B_2} = \overline{B_6B_5}$. It can be seen from the Fig. 2b. The two geometrical structure conditions are very important for analyzing the motion characteristic of the 4-DOF (3T1R) parallel mechanism with passive spherical joints. It will be given in the Sect. 3 of this paper in detail.

The 4-DOF parallel mechanism with passive spherical joints consists of four actuators along the same direction (Z-axis). It is quite clear that this mechanism can move along the direction of Z-axis independently of the other motions. This motion along Z is only limited by the available stroke for the prismatic actuators.

3 Motion Characteristics of the 4-DOF Parallel Mechanism

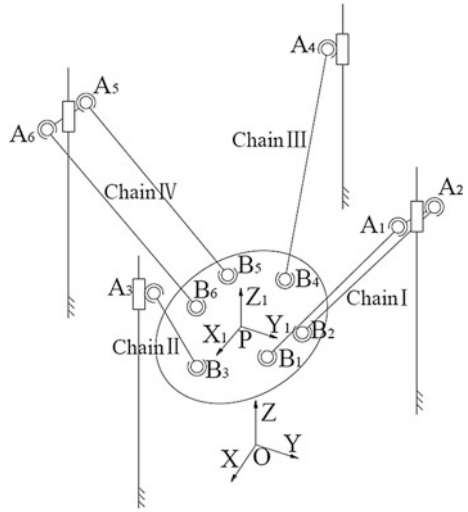
The current section is dedicated to the study of motion characteristics. First the mathematical model is established. Then the detailed solution procedure is given by using geometrical structure condition.

3.1 Modeling

Let O-XYZ and P- $X_1Y_1Z_1$ denote the coordinate frames fixed on the base and moving platform respectively. O is located at the center of the base. The schematic diagram of mechanism is depicted in Fig. 3.

The different geometrical elements of the mechanism will be defined before studying motion characteristics, as well as position and singularity. The following notations are used: L_i ($i = 1-6$) is the length of the i th strut of extremities A_i and B_i . Point A_i and point B_i are the connection points of the strut A_iB_i and their coordinates $\mathbf{A}_i = (x_{ai}, y_{ai}, z_{ai})^T$ and $\mathbf{B}_i = (x_{bi}, y_{bi}, z_{bi})^T$ are expressed in the base frame of the mechanism. Note that the coordinates of the point B_i expressed in moving frame of the parallel mechanism are $\mathbf{B}_{i1} = (x_{B_i}, y_{B_i}, z_{B_i})^T$ ($i = 1-6$). The position and pose of the mechanism are $\mathbf{P}_t = (x, y, z)^T$ and $\mathbf{P} = (x, y, z, \alpha, \beta, \gamma)^T$ respectively. The input of the parallel mechanism is $\mathbf{I} = (z_{a1}, z_{a2}, z_{a3}, z_{a4}, z_{a5}, z_{a6})^T$. Rotational matrix of the platform frame with respect to the fixed base frame can be expressed as follows (α, β, γ are the rotational angle; $\alpha, \beta, \gamma \in (-90^\circ, +90^\circ)$)

Fig. 3 The schematic diagram of the parallel mechanism



$$\begin{aligned}
 T_{ZYX} &= Rot_Z(\alpha)Rot_Y(\beta)Rot_X(\gamma) = \begin{pmatrix} d_{11} & d_{12} & d_{13} \\ d_{21} & d_{22} & d_{23} \\ d_{31} & d_{32} & d_{33} \end{pmatrix} \\
 &= \begin{pmatrix} \cos \alpha \cos \beta & \cos \alpha \sin \beta \sin \gamma - \sin \alpha \cos \gamma & \sin \alpha \sin \gamma + \cos \alpha \sin \beta \cos \gamma \\ \sin \alpha \cos \beta & \cos \alpha \cos \gamma + \sin \alpha \sin \beta \sin \gamma & \sin \alpha \sin \beta \cos \gamma - \sin \gamma \cos \alpha \\ -\sin \beta & \cos \beta \sin \gamma & \cos \beta \cos \gamma \end{pmatrix} \tag{1}
 \end{aligned}$$

Geometrical structure conditions of the mechanism can be written as follows

$$\begin{aligned}
 L_1 = L_2 = L_3 = L_4 = L_5 = L_6, \quad z_{a1} = z_{a2}, \quad z_{a5} = z_{a6}, \quad y_{a1} = x_{a3} = -x_{a4} = -y_{a6}, \\
 x_{a1} = -x_{a2} = -x_{a5} = x_{a6}, \quad x_{B1} = -x_{B2} = -x_{B5} = x_{B6}, \quad y_{a3} = y_{a4} = y_{B3} = y_{B4} = 0, \\
 \overline{B_1B_2} / \overline{B_5B_6}, \quad \overline{A_1A_2} / \overline{A_5A_6}, \quad |\overline{B_1B_2}| = |\overline{B_5B_6}| = |\overline{A_1A_2}| = |\overline{A_5A_6}|, \quad z_{ai} > z_{bi}
 \end{aligned}$$

3.2 Solution Procedure

Giving the position P_t of the parallel mechanism, and then the coordinates of B_i can be got as follows

$$\mathbf{B}_i = T_{ZYX} \mathbf{B}_{ti} + \mathbf{P}_t \quad (i = 1-6) \tag{2}$$

The length of strut A_iB_i can be expressed as

$$(x_{ai} - x_{bi})^2 + (y_{ai} - y_{bi})^2 + (z_{ai} - z_{bi})^2 = L_i^2 \quad (i = 1-6) \quad (3)$$

The mechanism has two composite legs [chain (I) and chain (IV)], from chain (I), one may obtain

$$(x_{a1} - x_{b1})^2 + (y_{a1} - y_{b1})^2 + (z_{a1} - z_{b1})^2 = L_1^2 \quad (4)$$

$$(x_{a2} - x_{b2})^2 + (y_{a2} - y_{b2})^2 + (z_{a2} - z_{b2})^2 = L_2^2 \quad (5)$$

$$(x_{a1} - x_{a2})^2 + (y_{a1} - y_{a2})^2 + (z_{a1} - z_{a2})^2 = |\overline{A_1A_2}|^2 \quad (6)$$

$$(x_{b1} - x_{b2})^2 + (y_{b1} - y_{b2})^2 + (z_{b1} - z_{b2})^2 = |\overline{B_1B_2}|^2 \quad (7)$$

But at all times, there are

$$\begin{pmatrix} x_{a1} - x_{a2} \\ y_{a1} - y_{a2} \\ z_{a1} - z_{a2} \end{pmatrix} = \begin{pmatrix} |\overline{A_1A_2}| \\ 0 \\ 0 \end{pmatrix}, \quad \begin{pmatrix} x_{b1} - x_{b2} \\ y_{b1} - y_{b2} \\ z_{b1} - z_{b2} \end{pmatrix} = \begin{pmatrix} \frac{|\overline{B_1B_2}|}{|\overline{B_1B_2}|} d_{11} \\ \frac{|\overline{B_1B_2}|}{|\overline{B_1B_2}|} d_{21} \\ \frac{|\overline{B_1B_2}|}{|\overline{B_1B_2}|} d_{31} \end{pmatrix} \quad (8)$$

Equation (5) minus Eq. (4) produces

$$\begin{pmatrix} |\overline{A_1A_2}| - |\overline{B_1B_2}| d_{11} \\ -|\overline{B_1B_2}| d_{21} \\ -|\overline{B_1B_2}| d_{31} \end{pmatrix}^T \begin{pmatrix} (x_{a1} + x_{b1}) - (x_{a2} + x_{b2}) \\ (y_{a1} + y_{b1}) - (y_{a2} + y_{b2}) \\ (z_{a1} + z_{b1}) - (z_{a2} + z_{b2}) \end{pmatrix} = 0 \quad (9)$$

Equation (7) minus Eq. (6) produces

$$\begin{pmatrix} |\overline{A_1A_2}| - |\overline{B_1B_2}| d_{11} \\ -|\overline{B_1B_2}| d_{21} \\ -|\overline{B_1B_2}| d_{31} \end{pmatrix}^T \begin{pmatrix} (x_{a1} + x_{a2}) - (x_{b1} + x_{b2}) \\ (y_{a1} + y_{a2}) - (y_{b1} + y_{b2}) \\ (z_{a1} + z_{a2}) - (z_{b1} + z_{b2}) \end{pmatrix} = 0 \quad (10)$$

Equation (10) plus Eq. (9) produces

$$\begin{pmatrix} |\overline{A_1A_2}| - |\overline{B_1B_2}| d_{11} \\ -|\overline{B_1B_2}| d_{21} \\ -|\overline{B_1B_2}| d_{31} \end{pmatrix}^T \begin{pmatrix} x_{a1} - x_{b2} \\ y_{a1} - y_{b2} \\ z_{a1} - z_{b2} \end{pmatrix} = 0 \quad (11)$$

Equation (10) minus Eq. (9) produces

$$\begin{pmatrix} |\overline{A_1A_2}| - |\overline{B_1B_2}|d_{11} \\ -|\overline{B_1B_2}|d_{21} \\ -|\overline{B_1B_2}|d_{31} \end{pmatrix}^T \begin{pmatrix} x_{a2} - x_{b1} \\ y_{a2} - y_{b1} \\ z_{a2} - z_{b1} \end{pmatrix} = 0 \quad (12)$$

The following vectors are defined for clarity

$$N = (|\overline{A_1A_2}| - |\overline{B_1B_2}|d_{11}, -|\overline{B_1B_2}|d_{21}, -|\overline{B_1B_2}|d_{31}) \quad (13)$$

$$\overline{B_2A_1} = (x_{a1} - x_{b2}, y_{a1} - y_{b2}, z_{a1} - z_{b2})^T \quad (14)$$

$$\overline{B_1A_2} = (x_{a2} - x_{b1}, y_{a2} - y_{b1}, z_{a2} - z_{b1})^T \quad (15)$$

Then Eqs. (11) and (12) can be written as

$$N \cdot \overline{B_2A_1} = 0, \quad N \cdot \overline{B_1A_2} = 0 \quad (16)$$

The method is equally applicable to the chain (IV). This calculation procedure will not be discussed here for brevity. In chain (IV), the following vectors are defined:

$$N_1 = (|\overline{A_5A_6}| - |\overline{B_5B_6}|d_{11}, -|\overline{B_5B_6}|d_{21}, -|\overline{B_5B_6}|d_{31}) \quad (17)$$

$$\overline{B_5A_6} = (x_{a6} - x_{b5}, y_{a6} - y_{b5}, z_{a6} - z_{b5})^T \quad (18)$$

$$\overline{B_6A_5} = (x_{a5} - x_{b6}, y_{a5} - y_{b6}, z_{a5} - z_{b6})^T \quad (19)$$

Then the following relations can be found:

$$N_1 \cdot \overline{B_5A_6} = 0, \quad N_1 \cdot \overline{B_6A_5} = 0 \quad (20)$$

From geometrical structure condition, there is

$$N = N_1 \quad (21)$$

That is,

$$N \cdot \overline{B_5A_6} = 0, \quad N \cdot \overline{B_6A_5} = 0 \quad (22)$$

Note that Eqs. (16) and (22) mean if the vector $N \neq \mathbf{0}$, it is only possible that all the vectors $\overline{B_2A_1}$, $\overline{B_1A_2}$, $\overline{B_5A_6}$ and $\overline{B_6A_5}$ are in the same plane, we name this plane pl (II). It is obvious that the plane does not exist except in their singular configurations. So $N = \mathbf{0}$ and then there are

$$\begin{cases} d_{11} = \cos \alpha \cos \beta = 1 \\ d_{21} = \sin \alpha \cos \beta = 0 \\ d_{31} = -\sin \beta = 0 \end{cases} \quad (23)$$

Equation (23) leads to

$$\alpha = \beta = 0$$

Therefore, the parallel mechanism presented in this paper can perform four motions x , y , z and γ (rotation about X -axis).

4 Position Analysis

In this work, the 4-DOF parallel mechanism presented can be regarded as the generalized 6-PSS parallel mechanism substituted the four PSS chains for the two P2SS chains. In order to convenient for the analysis of position, the parallel mechanism is converted into a virtual 6-PSS parallel mechanism first. Then the inverse and direct geometric models are established based on 6-PSS parallel mechanism (six-dimensional). In order to ensure the alternative inverse and direct geometric models are adapted to the structure requirement of the 4-DOF parallel mechanism presented in this paper, the two inputs are synchronous, which is $z_{a1} = z_{a2}$ and $z_{a5} = z_{a6}$. Thus the kinematics of the 4-DOF parallel mechanism can be analyzed with the help of the alternative inverse and direct geometric models of the 6-PSS parallel mechanism.

4.1 The Inverse Geometric Model (IGM)

The inverse geometric model for parallel robots is usually easy to determine and 4-DOF parallel mechanism is not an exception of this idea. From the Eq. (3), it can be obtained

$$z_{ai} = z_{bi} \pm \sqrt{L_i^2 - (y_{bi} - y_{ai})^2 - (x_{bi} - x_{ai})^2} \quad (i = 1-6) \quad (24)$$

As long as the term within the square root is positive, two real solutions for each z_{ai} are possible. The choice depends on the assembly mode chosen. In our case, we will choose to have the actuator to be above the platform, meaning

$$z_{ai} = z_{bi} + \sqrt{L_i^2 - (y_{bi} - y_{ai})^2 - (x_{bi} - x_{ai})^2} \quad (i = 1-6) \quad (25)$$

4.2 The Direct Geometric Model (DGM)

Unlike serial robots, the direct geometric model of a parallel manipulator is most often difficult to be determined analytically. However, with this mechanism it is easy to establish its model.

Equation (3) can be differentiated with respect to $x, y, z, \alpha, \beta, \gamma$, which leads to

$$(x_{ai} - x_{bi})\dot{x}_{bi} + (y_{ai} - y_{bi})\dot{y}_{bi} + (z_{ai} - z_{bi})\dot{z}_{bi} = (z_{ai} - z_{bi})\dot{z}_{ai}, \quad (i = 1-6) \quad (26)$$

The following vectors are defined for simple

$$\mathbf{M}_O = (\dot{x}, \dot{y}, \dot{z}, \dot{\alpha}, \dot{\beta}, \dot{\gamma})^T \quad (27)$$

$$\mathbf{M}_I = (\dot{z}_{a1}, \dot{z}_{a2}, \dot{z}_{a3}, \dot{z}_{a4}, \dot{z}_{a5}, \dot{z}_{a6})^T \quad (28)$$

Rearranging Eq. (26) yields an equation of the form

$$\mathbf{A} \cdot \mathbf{M}_O = \mathbf{B} \cdot \mathbf{M}_I \quad (29)$$

If the inverse of \mathbf{A} exists, there is

$$\mathbf{M}_O = \mathbf{A}^{-1} \mathbf{B} \cdot \mathbf{M}_I = \mathbf{J} \cdot \mathbf{M}_I \quad (30)$$

Matrix \mathbf{J} (6×6) is the mapping matrix of speed from drive joint to the output of the moving platform. A simple numerical method is given below when the inverse of \mathbf{J} exists. (ε : the given calculation accuracy.)

- Step 1: Giving the initial pose of the robot \mathbf{P} .
- Step 2: Getting the input \mathbf{I}_n corresponding to the output \mathbf{P} through IGM.
- Step 3: Then we get the new pose of the robot: $\mathbf{P}_o = \mathbf{P} + \mathbf{J}(\mathbf{I}_n - \mathbf{I})$
- Step 4: If $\|\mathbf{I}_n - \mathbf{I}\| > \varepsilon$, then go back to Step 3, or the new pose of the robot \mathbf{P}_o is the real solution.

For verifying the analysis in the Sect. 3 of this paper, the parameters (Table 1) and numerical method above are used to study the motion of parallel mechanism. Figure 4 shows the change of pose for the 4-DOF parallel mechanism as function of

Table 1 The dimensional parameters of structure (unlabeled units: m)

y_{B1}	x_{B3}	x_{B4}	y_{B6}	y_{a1}	L_i	$ A_1 A_2 $
0.22	0.1	-0.1	-0.1	0.75	0.88	0.12

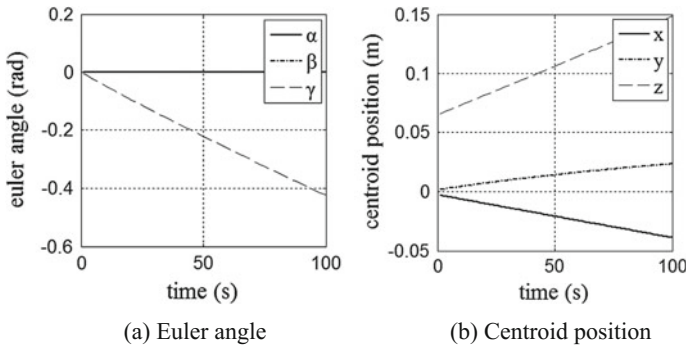


Fig. 4 Motion curve of the parallel mechanism

the time given the six inputs additional $z_{a1} = z_{a2}$ and $z_{a5} = z_{a6}$. That is the two inputs are synchronous.

Figure 4a shows the values (α and β) are always zero with the change of time. Figure 4 also shows the 4-DOF parallel mechanism presented in this paper can perform four motions x , y , z and γ (rotation about X-axis). The same result of motion characteristics can be got as studied in Sect. 3. Thus the motion of the 4-DOF parallel mechanism is verified by analytical method and numerical method.

5 Singularity Analysis

An important step in the study of a parallel mechanism is investigating the presence of singularities. This situation is present when the square diagonal matrix \mathbf{J} is non-invertible, which is expressed mathematically as

$$\det(\mathbf{J}) = \det(\mathbf{A}^{-1}\mathbf{B}) = 0 \tag{31}$$

This can be divided into two kinds of situations as follows

- (a) $\det(\mathbf{B}) = 0 \Leftrightarrow (z_{a3} - z_{b3})(z_{a1} - z_{b1})(z_{a4} - z_{b4})(z_{a6} - z_{b6}) = 0$, the equation simply implies that we have serial type singularity when one of the arms is in the XY plane. If the pose that might lead to such a case exists, such pose will obviously be at the envelope of the XY geometrically accessible workspace.
- (b) $\det(\mathbf{A}) = 0$

$$\det(\mathbf{A}) = k_1 \det(\mathbf{A}_{3 \times 3}) = 0 \tag{32}$$

where

$$\mathbf{A}_{3 \times 3} = \begin{bmatrix} x_{a3} - x_{b3} & y_{a3} - y_{b3} & z_{a3} - z_{b3} \\ (x_{a1} - x_{b1}) - k(x_{a6} - x_{b6}) & (y_{a1} - y_{b1}) - k(y_{a6} - y_{b6}) & (z_{a1} - z_{b1}) - k(z_{a6} - z_{b6}) \\ x_{a4} - x_{b4} & y_{a4} - y_{b4} & z_{a4} - z_{b4} \end{bmatrix}$$

$$k_1 = -(y_{a6} - y_{b6})y_{B6} \sin \gamma + (z_{a6} - z_{b6})y_{B6} \cos \gamma$$

$$k = \frac{-(y_{a1} - y_{b1})y_{B1} \sin \gamma + (z_{a1} - z_{b1})y_{B1} \cos \gamma}{-(y_{a6} - y_{b6})y_{B6} \sin \gamma + (z_{a6} - z_{b6})y_{B6} \cos \gamma}$$

The reason for $k_1 \neq 0$ is given here. If $k_1 = 0$, then

$$\tan \gamma = \frac{z_{a6} - z_{b6}}{y_{a6} - y_{b6}} \quad (33)$$

This relation simply implies that vector $\overline{B_6A_6}$ is in the X_1Y_1 plane when $k_1=0$. Such pose does not exist in application because of poor mechanical properties and geometrical structure condition.

From relation (32), there is

$$\det(\mathbf{A}_{3 \times 3}) = 0 \quad (34)$$

This means that matrix $\mathbf{A}_{3 \times 3}$ is rank deficient. In other words, matrix $\mathbf{A}_{3 \times 3}$ is not linearly independent. In case of composite arms (they are parallelogram arms in this case), vectors \mathbf{m}_1 and \mathbf{m}_4 are along the mid-axis of the parallelograms respectively. The following vectors are given

$$\mathbf{m}_1 = (x_{a1} - x_{b1}, y_{a1} - y_{b1}, z_{a1} - z_{b1}) \quad (35)$$

$$\mathbf{m}_2 = (x_{a3} - x_{b3}, y_{a3} - y_{b3}, z_{a3} - z_{b3}) \quad (36)$$

$$\mathbf{m}_3 = (x_{a4} - x_{b4}, y_{a4} - y_{b4}, z_{a4} - z_{b4}) \quad (37)$$

$$\mathbf{m}_4 = (x_{a6} - x_{b6}, y_{a6} - y_{b6}, z_{a6} - z_{b6}) \quad (38)$$

$$\mathbf{m}_{p1} = \frac{\mathbf{m}_2 + \mathbf{m}_3}{2}, \quad \mathbf{m}_{p2} = \frac{\mathbf{m}_1 + \mathbf{m}_4}{2} \quad (39)$$

Matrix $\mathbf{A}_{3 \times 3}$ is not linearly independent means vectors $\mathbf{m}_1 - k\mathbf{m}_4$, \mathbf{m}_2 and \mathbf{m}_3 are in the same plane.

If the moving platform is symmetric ($y_{B1} = -y_{B6}$, $x_{B3} = -x_{B4}$), matrix $\mathbf{A}_{3 \times 3}$ is rank deficient when the 4-DOF parallel mechanism is at the pose $\mathbf{P} = (0, 0, 0, 0, 0, 0)^T$ ($k = -1 \Rightarrow \mathbf{m}_{p1} = \mathbf{m}_{p2} \Rightarrow \det(\mathbf{A}_{3 \times 3}) = 0$).

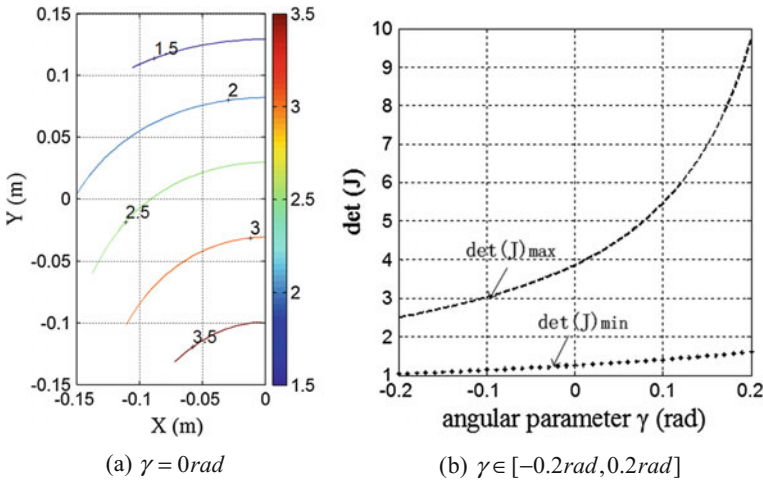


Fig. 5 The variation of the determination of Jacobian matrix

A major characteristic of this kind of singularity is the platform is symmetric. In order to avoid this kind of singularity, one can increase the length of y_{B1} or use the method of trajectory planning. In this case, the former will be chosen and used the parameters in Table 1 to do numerical verification.

Hence, the mechanism which is optimized by methods proposed will avoid singularities within the XY geometrically accessible region, and if not, this would not happen except at boundary of this region.

It is important to note that in what follows, the XY region rather than talking about the XYZ region will be taken into account, simply due to the fact that Z motion can be provided independently of the other X, Y and γ motions. Figure 5 gives the operation performance of the parallel mechanism when the moving platform is not symmetric (Table 1). Figure 5a shows the variation of the index $\det(\mathbf{J})$ as function of the position (x, y) when $\gamma = 0$ rad. It has been shown half of the workspace due to symmetry with respect to the X-axis. A set of values $\det(\mathbf{J})_{\max}$ and $\det(\mathbf{J})_{\min}$ can be obtained in this figure. One can obtain a series of values $\det(\mathbf{J})_{\max}$ and $\det(\mathbf{J})_{\min}$ when $\gamma \in [-0.2 \text{ rad}, 0.2 \text{ rad}]$. Figure 5b shows the variation of indexes $\det(\mathbf{J})_{\max}$ and $\det(\mathbf{J})_{\min}$ as function of the angular parameter γ . The value $\det(\mathbf{J}) \in (1, 10)$ shows the 4-DOF parallel mechanism has no singularity in the workspace at any pose.

6 Conclusions

In this paper, a 4-DOF (3T1R) parallel mechanism with passive spherical joints whose rotation axis is parallel to the moving platform is presented. Analytical method and numerical method has been used to study the motion characteristics of

the 4-DOF parallel mechanism based on the geometrical structure. Both of the two methods verify the parallel mechanism can perform four motions x , y , z and γ (rotation about X-axis). Both the inverse and direct geometric models have been established by a virtual 6-PSS parallel mechanism and a complete analysis of the singularities has been presented finally.

The workspace of this parallel mechanism along Z direction is independent of the other motions and only limited by the available stroke of the linear actuators, which is one of its major advantages. Another advantage of this 4-DOF parallel mechanism is having its workspace symmetric with respect to XZ plane, free of collisions. Besides, the simplicity of the design, the actuation at base, and the high stiffness of the mechanism (with passive spherical joints) will contribute to the high dynamical performance capabilities and enhance accuracy and precision. This 4-DOF parallel mechanism can have some good applications like the parallel machine tools, medical bed, and so on.

Acknowledgments This work is financially supported by the National Natural Science Foundation of China (51275243).

References

1. Yi L, Shi Y, Huang Z, Jianping Y, Li S, Tian X (2009) Kinematics/ statics of a 4-DOF over-constrained parallel manipulator with 3 legs. *Mech Mach Theory* 44:1479–1506
2. Shayya S, Krut S, Company O, Baradat C, Pierrot F (2013) A Novel (3T-1R) redundant parallel mechanism with large operational workspace and rotational capability. In: 2013 IEEE/RSJ international conference on intelligent robots and systems (IROS), Tokyo, Japan, 3–7 Nov 2013
3. Kong X, Gosselin CM (2004) Type synthesis of 3T1R 4-DOF parallel manipulators based on screw theory. *IEEE Trans Robot Autom* 20(2):181–190
4. Li QC, Huang Z (2003) Type synthesis of 4-DOF parallel manipulators. In: Proceedings of the 2003 IEEE international conference on robotics and automation, Taipei, Taiwan, Sept 2003, pp 755–560
5. Kim SM, Kim W, Yi B-J (2009) Kinematic analysis and design of a new 3T1R 4-DOF parallel mechanism with rotational pitch motion. In: 2009 IEEE/RSJ international conference on intelligent robots and systems (IROS), St. Louis, USA, 11–15 Oct 2009
6. Kong X (2016) Reconfiguration analysis of a 4-DOF 3-RER parallel manipulator with equilateral triangular base and moving platform. *Mech Mach Theory* 98:180–189
7. Pierrot F, Company O (1999) H4: a new family of 4-dof parallel robots. In: Proceedings of the IEEE/ASME international conference on advanced intelligent mechatronics, Atlanta, USA, 1999, pp 508–513
8. Krut S, Company O, Benoit M, Ota H, Pierrot F (2003) I4: a new parallel mechanism for Scara motions. In: Proceedings of the 2003 international conference on robotics and automation, Taipei, Taiwan, Sept 2003, pp 1875–1880
9. Nabat V, Company O, Krut S, Rodriguez M, Pierrot F (2005) Par4: very high speed parallel robot for pick-and-place. In: Proceedings of the IEEE international conference on intelligent robots and systems (IROS'05), Edmonton, Alberta, Canada, Aug 2005

10. Pierrot F, Nabat V, Company O, Krut S (2008) From Par4 to Adept Quattro. In: Proceedings of the robotic systems for handling and assembly—3rd international colloquium of the collaborative research center SFB 562, Braunschweig, Germany, 2008
11. Guo S, Fang Y, Qu H (2012) Type synthesis of 4-DOF nonoverconstrained parallel mechanisms based on screw theory. *Robotica* 30:31–37

Static Performance Analysis of an Exechon-like Parallel Kinematic Machine

Tengfei Tang, Jun Zhang and Marco Ceccarelli

Abstract A performance index of local dexterity stiffness index (LDSI) is proposed to consider both kinematic dexterity and static rigidity characteristics of a parallel kinematic machine (PKM). Based on the proposed index, the static performance of an Exe-Variant PKM module is predicted in a quick manner. Since the proposed LDSI is a dimensional index, a dimensionless global index is further presented to optimize the geometric parameters of the PKM module. An optimal searching algorithm is used to obtain reasonable radii of the moving platform and the fixed base of Exe-Variant PKM.

Keywords Exechon · Parallel kinematic machine · Dexterity · Static performance

1 Introduction

Due to their conceptual advantages of high rigidity and high dynamics, parallel kinematic machines (PKMs) have been regarded as a promising alternative solution for high speed machining in aeronautic and automotive industries. Though numerous versions of PKMs have been proposed and investigated in the past decades, a few of them have achieved commercial success. By checking through

T. Tang (✉)
School of Mechanical Engineering, Anhui University of Technology,
Ma'anshan 243032, China
e-mail: tengfei413zm@163.com

J. Zhang
School of Mechanical Engineering and Automation,
Fuzhou University, Fuzhou 350116, China
e-mail: zhang_jun@tju.edu.cn

M. Ceccarelli
Laboratory of Robotics and Mechatronics, University of Cassino and South Latium,
Via Di Biasio 43, 03043 Cassino (Fr.), Italy
e-mail: ceccarelli@unicas.it

those ‘unsuccessful’ PKMs, one may find that they usually adopt too many passive joints in their structural design which will arouse geometric discrepancy and deformations under a force or thermal load. With the motivation of reducing the number of the passive joints and un-actuated degrees of freedom of a PKM, Neumann [1] proposed the 5-DOF Exechon machine tool. As one of the most successfully applied PKMs, Exechon machine tool has attracted intensive attentions from the research society [2–6].

Inspired by the commercial success of the Exechon machine tool, the authors recently proposed a novel Exechon-like PKM named Exe-Variant by adopting the concept of mechanism variation [7]. As shown in Fig. 1a, the proposed Exe-Variant is designed as 5-DOF machining tool for high speed machining of metal materials. For this purpose, good dexterity and high rigidity are demanded at the early design stage of Exe-Variant PKM. However, the evaluation for the comprehensive performances of both dexterity and rigidity of this kind of PKM still remains a challenge unless a reasonable performance index can be proposed. Following this track, this paper proposes a performance index named local dexterity stiffness index (LDSI) as inspired by the proposition of local dexterity index (LDI) [8, 9]. The proposed index of LDSI integrates both the local dexterity [10–12] and the static stiffness [13, 14] of a PKM. Based on this index, the static performance of Exe-Variant PKM is evaluated and analyzed through out the entire workspace in an efficient manner. Since LDSI is a dimensional index, a global dimensionless index can be defined by the ratio of mean and standard deviation of the LDSI is proposed to obtain optimal geometric parameters of a PKM module. Furthermore, the process of optimization can be described by a searching algorithm with the variation of radii of the moving platform and the fixed base.

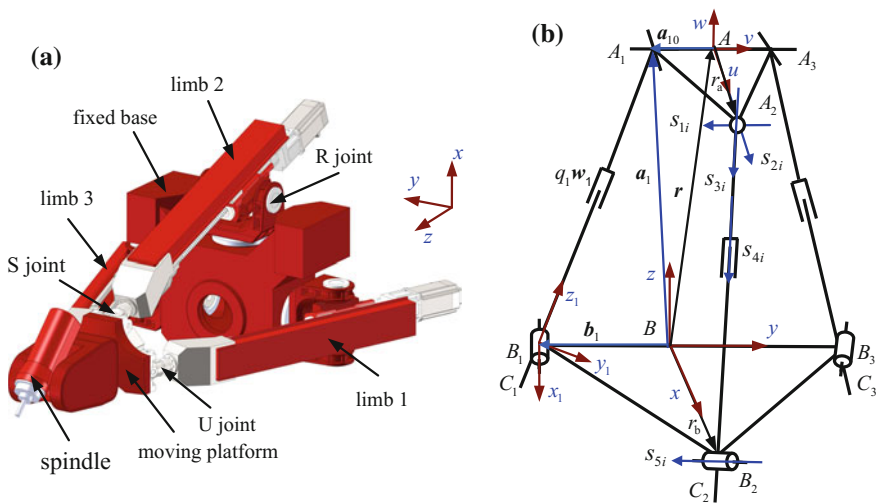


Fig. 1 a Structure of Exe-Variant; b schematic diagram of Exe-Variant PKM

The remaining of this paper is organized as follows. In Sect. 2, the structure of Exe-Variant is briefly described followed by inverse kinematic definitions. In Sect. 3, the performance index LDSI is proposed on the basis of local dexterity formulation and static stiffness formulation. In Sect. 4, the static performance of this PKM is predicted with the index of LDSI and a global dimensionless index is proposed to optimize the geometric parameters of the PKM module through a searching algorithm. Finally, conclusions are drawn in Sect. 5 to close the paper.

2 Structural Description and Inverse Kinematic Definitions

As shown in Fig. 1a, Exe-Variant is a hybrid serial-parallel machine tool, consisting of a parallel structure to locate the position of the moving platform and a serial structure to orient an electrical driven spindle. Herein, Limb 1 (and limb 3) connects the fixed base to the moving platform by a passive revolute (R) joint, an active prismatic (P) joint and a passive universal (U) joint in sequence. Limb 2 connects the fixed base to the moving platform by a passive revolute (R) joint, an active prismatic (P) joint and a passive spherical (S) joint in sequence. Therefore, the topological architecture behind the proposed Exe-Variant PKM is a $2R\underline{P}U&1R\underline{P}S$ parallel mechanism which consists of two identical $R\underline{P}U$ limbs and one $R\underline{P}S$ limb, where the underline P denotes an active prismatic joint driven by a lead screw linear actuator.

Since it is driven independently by three servomotors, the moving platform of Exe-Variant PKM can achieve one translation along z axis and two rotations about x and y axes [7]. When two rotational motions of the serial part are added in, Exe-Variant can achieve 5-axis machining ability. When compared to its counterpart of serial structure, the 1T2R parallel part of Exe-Variant looks complex. Therefore, the following will only focus on the parallel part of the machine tool.

The schematic diagram of Exe-Variant PKM is depicted in Fig. 1b.

As shown in Fig. 1b, each limb connects the moving platform to the fixed base through two passive joints whose geometric centers are denoted as A_i and B_i ($i = 1, 2, 3$), respectively. For derivation convenience, reference coordinate frames need to be defined at first. A global Cartesian coordinate system $B-xyz$ is fixed at the centre of B_1B_3 with x axis paralleling to BB_2 and y axis paralleling to B_1B_3 , while z axis is determined by the right hand rule. Similarly, a moving platform body fixed Cartesian coordinate system $A-uvw$ is attached to the moving platform with u axis paralleling to AA_2 and v axis paralleling to A_1A_3 , while w is determined with the right-hand rule. A limb reference coordinate frame $B_i-x_iy_iz_i$ ($i = 1, 2, 3$) is established at the centre of the i th passive joint B_i with x_i coincident with x axis and z_i preferred to be projecting from B_i to A_i while y_i is determined with the right-hand rule. For clarity, only one limb reference frame in limb 1 is depicted in Fig. 1b.

With the above coordinates setting, one may derive the transformation matrix between the body-fixed frames and the global coordinate system with considering of kinematics.

The transformation matrix of $A-uvw$ with respect to $B-xyz$ is ${}^B T_A$ and can be expressed as

$${}^B T_A : \text{Trans}(A - uvw \rightarrow B - xyz) \tag{1}$$

Similarly, one may denote the transformation matrix of $B_i-x_iy_iz_i$ with respect to $B-xyz$ as

$${}^B T_{B_i} : \text{Trans}(B - x_iy_iz_i \rightarrow B - xyz) \tag{2}$$

The detailed inverse kinematic analysis of Exe-Variant can be found in Ref. [7].

3 Static Performance

3.1 Local Dexterity Formulation

According to Refs. [8, 15], the dimensionally homogeneous Jacobian of Exe-Variant PKM can be formulated as

$$\mathbf{J}_{pa0} = \left[\mathbf{J}_{pa0} \mathbf{A} \mathbf{d}_{g_R}^T (\mathbf{J}^T \mathbf{J})^{-1} \mathbf{J}_a^T \right]^{-1} \tag{3}$$

where \mathbf{J}_{pa0} denotes a 3×6 matrix that's formed by three linearly independent row vectors where each row represents a twist of one feature point on the moving platform; $\mathbf{A} \mathbf{d}_{g_R}^T = \begin{bmatrix} {}^B T_A & 0 \\ 0 & {}^B T_A \end{bmatrix}$ is the transformation matrix of the body-fixed coordinate system with respect to the global coordinate system; \mathbf{J} is known as the generalized Jacobian of the manipulator and can be expressed as

$$\mathbf{J} = \begin{bmatrix} \mathbf{J}_a \\ \mathbf{J}_c \end{bmatrix} \tag{4}$$

$$\mathbf{J}_a = \begin{bmatrix} \mathbf{s}_{4,1}^T & \left(\mathbf{a}_1 \times \mathbf{s}_{4,1} \right)^T \\ \mathbf{s}_{4,2}^T & \left(\mathbf{a}_2 \times \mathbf{s}_{4,2} \right)^T \\ \mathbf{s}_{4,3}^T & \left(\mathbf{a}_3 \times \mathbf{s}_{4,3} \right)^T \end{bmatrix} \tag{5}$$

$$\mathbf{J}_c = \begin{bmatrix} \mathbf{s}_{5,1}^T/q_1 & (\mathbf{a}_1 \times \mathbf{s}_{5,1})^T/q_1 \\ \mathbf{s}_{5,2}^T/q_2 & (\mathbf{a}_2 \times \mathbf{s}_{5,2})^T/q_2 \\ \mathbf{s}_{5,3}^T/q_3 & (\mathbf{a}_3 \times \mathbf{s}_{5,3})^T/q_3 \end{bmatrix} \tag{6}$$

where $\mathbf{s}_{j,i}$ ($i = 1-3, j = 1-5$) is a unit vector along the j th 1-DOF joint of the i th limb shown in the Fig. 1b. \mathbf{a}_i denotes the vector of point A_i in the frame B -xyz; q_i represents the distance between A_i and B_i of the i th limb; $\mathbf{a}_i = \mathbf{a}_{i0} \cdot {}^B\mathbf{T}_A$, $\mathbf{a}_{i0} = r_p [\cos \alpha_i \quad \sin \alpha_i \quad 0]^T$ denotes the position vector of point A_i in the frame A -uvw; r_p and r_b represent the circumcircle radii of the moving platform and the fixed base, respectively; α_i denotes the position angle, and $\alpha_1 = -\pi/2, \alpha_2 = 0, \alpha_3 = \pi/2$.

Based on the proposed dimensionally homogeneous Jacobian of Exe-Variant PKM, one can obtain the local dexterity (v) for determining the kinematic accuracy and the dexterous regions as [8]

$$v = \frac{1}{\|\mathbf{J}_{pa}\| \cdot \|\mathbf{J}_{pa}^{-1}\|} \tag{7}$$

where the values of v vary from zero to one while its higher values indicate higher accurate motion as well as better kinematic performance generated at given instance.

3.2 Local Stiffness Formulation

In order to formulate the local stiffness expression of Exe-Variant PKM, a kinetostatic model proposed by the authors in Ref. [16] is adopted with minor modifications. The PKM system is divided into three limb assembly subsystems, a platform subsystem and a base subsystem. Revolute, universal and spherical joints are simplified into virtual lumped springs with equivalent stiffness at their center points. Limb body is discredited into spatial beam elements with corresponding cross-section according to its geometry. The platform and fixed base are treated as rigid bodies due to their higher rigidity.

After introducing the deformation compatibility conditions into the equilibrium equations of subsystems, the static governing equations of the system can be formulated and expressed as

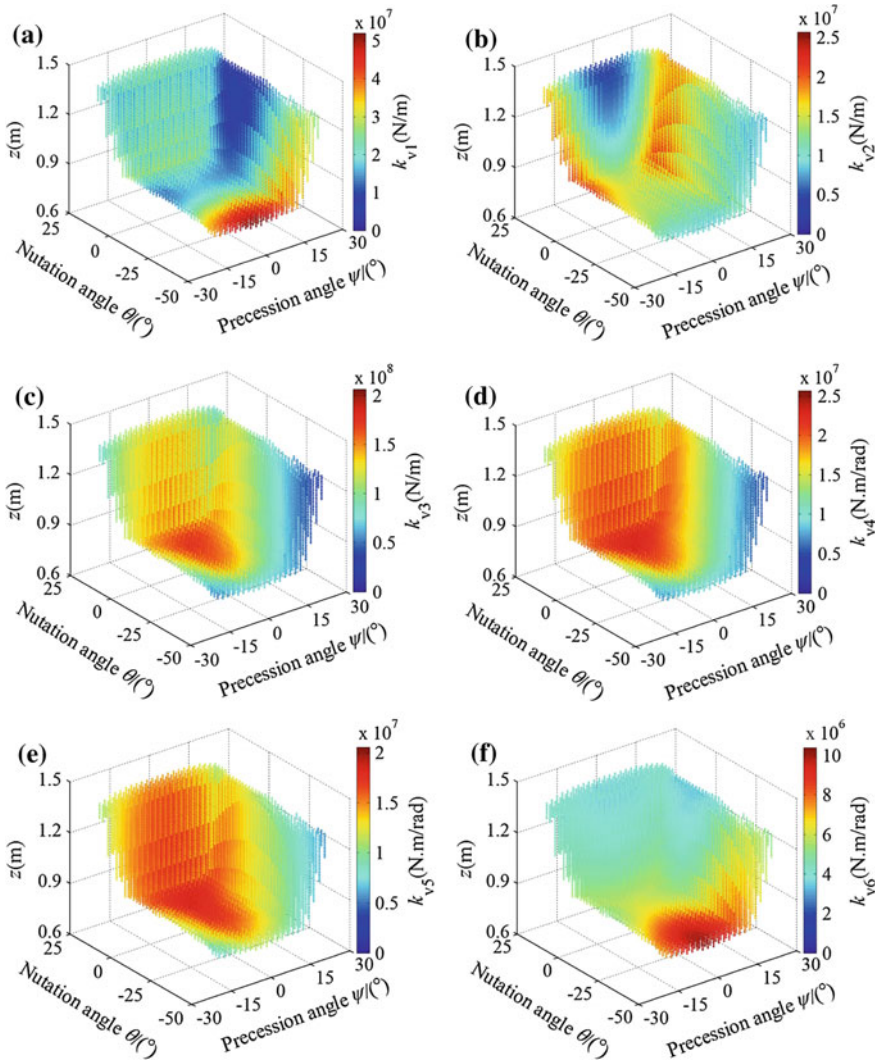


Fig. 2 The distribution of LDSI throughout the entire workspace: **a** along u axis, **b** along v axis, **c** along w axis, **d** about u axis, **e** about v axis, and **f** about w axis

$$\tilde{\mathbf{K}} \tilde{\mathbf{U}} = \tilde{\mathbf{F}} \tag{8}$$

where $\tilde{\mathbf{K}}$ is the global stiffness matrix; $\tilde{\mathbf{U}}$ and $\tilde{\mathbf{F}}$ are the general coordinates and external loads vectors. The global stiffness matrix is given by

$$\tilde{\mathbf{K}} = \begin{bmatrix} \mathbf{K}_{1,1} & & & \mathbf{K}_{1,4} \\ & \mathbf{K}_{2,2} & & \mathbf{K}_{2,4} \\ & & \mathbf{K}_{3,3} & \mathbf{K}_{3,4} \\ \mathbf{K}_{4,1} & \mathbf{K}_{4,2} & \mathbf{K}_{4,3} & \mathbf{K}_{4,4} \end{bmatrix} \quad (9)$$

Equation (9) formulates the global stiffness matrix, from which it can be observed that it is non-diagonal. This indicates that the stiffness of the moving platform is coupled with those of the limb substructures. Therefore, the stiffness of the platform in the body fixed frame $A-uvw$ can be expressed according to the duality of compliance as

$$\mathbf{K}_p = \mathbf{T}_0^T \mathbf{C}_p^{-1} \mathbf{T}_0 = \mathbf{T}_0^T \left[\tilde{\mathbf{K}}^{-1} \Big|_{(H-18n) \times (H-18n)} \right]^{-1} \mathbf{T}_0 \quad (10)$$

where $\mathbf{T}_0 = \text{diag} \left[{}^B\mathbf{T}_A \quad {}^B\mathbf{T}_A \right]$.

The detailed elements in the above matrix and vectors are not listed here due to page limitation. Readers can find the detailed derivation in our previous publication [16].

3.3 A Performance Index

With the local dexterity index ν defined in Eq. (7) and the static stiffness matrix \mathbf{K}_p in Eq. (10), a performance index named local dexterity stiffness index (LDSI) is proposed by taking the inspiration from local dexterity index (LDI) [8]. The proposed index LDSI can be expressed as six independent forms for the principle stiffness values of a PKM are given along (about) u , v , and w directions at any given configuration. Following shows the expressions of six independent forms of LDSI that denote the static performance of a PKM along (about) u , v , and w directions, respectively.

$$\text{LDSI} = k_{vi} = \nu k_i \quad (i = 1, 2, 3, 4, 5, 6) \quad (11)$$

where k_i denotes the principle stiffness value along (about) u , v , and w directions at any given configuration of the PKM.

From the above expression of LDSI, it can be found that this index has the same dimension of stiffness matrix while the local dexterity can be regarded as a dimensionless factor representing the kinematic features in corresponding directions. LDSI can be interpreted as the static rigidity multiplies with a weighting factor of dexterity denoting the kinematic performance of a parallel mechanism. The most useful advantage of the proposed index is that LDSI considers both the dexterity and stiffness performance while avoiding the allocation of weighting factors between dexterity and stiffness.

4 Performance Evaluation

In this section, an Exe-Variant PKM is taken as an example to demonstrate the performance evaluation process by using LDSI. The major dimensional parameters of the PKM module are shown in Table 1. Herein, r_p and r_b represent the circumference radii of the moving platform and the fixed base, respectively; q_{max} and q_{min} represent the maximum and the minimum distances between A_i and B_i ; z_{max} and z_{min} represent the maximum and the minimum of the z coordinates of the moving platform.

The stiffness coefficients of three perpendicular axes of joints in their local frames can be calculated through ANSYS software. Table 2 gives the equivalent spring constants of the three translational and the three torsional virtual spring components of passive joints at A_i and B_i in the i th limb of the Exe-Variant module.

With the above parameters, the following static performance predictions are worked out. Figure 2 shows the six LDSI k_{vi} along (about) u , v , and w axes throughout the entire workspace. Table 3 gives the minimal and maximal values of six LDSI k_{vi} , respectively.

As shown in Fig. 2, the values of LDSI about u and v axes are more homogeneously distributed over the entire workspace while the others of LDSI are either concentrated or decentralized in a region of the workspace with higher values. In addition, Table 3 shows that the values of LDSI along u and v axes are much smaller than those along w axis while values about u and v axes are much larger than that about w axis, implying that Exe-Variant PKM claims the ‘strongest’ static performance along the w direction and the ‘weakest’ static performance about the w direction over the entire workspace. For example, the LDSI along u axis claims the maximal value of 1.79×10^8 and a minimal value of 3.03×10^7 while LDSI about u axis claims the maximal value of 1.01×10^7 and a minimal value of 3.00×10^6 throughout the entire workspace.

For further observations, the distributions of LDSI values at a given work plane of $z = 1.2$ m are given in Fig. 3.

Table 1 Dimensional parameters of the Exe-Variant PKM in Fig. 1

r_p (m)	r_b (m)	q_{min} (m)	q_{max} (m)	z_{max} (m)	z_{min} (m)
0.2	0.4	0.76	1.46	0.6	1.4

Table 2 The stiffness coefficients of joints in local frames for Exe-Variant PKM in Fig. 1

k_{ux} (N/ μ m)	k_{uy} (N/ μ m)	k_{uz} (N/ μ m)	k_{uw} (MN m/rad)	k_{sx} (N/ μ m)	k_{sy} (N/ μ m)
365	524	1006	19	365	524
k_{sz} (N/ μ m)	k_{r1x} (N/ μ m)	k_{r1y} (N/ μ m)	k_{r1z} (N/ μ m)	k_{r1v} (MN m/rad)	k_{r1w} (MN m/rad)
524	24	24	618	19	19
k_{r2x} (N/ μ m)	k_{r2y} (N/ μ m)	k_{r2z} (N/ μ m)	k_{r2u} (MN m/rad)	k_{r2v} (MN m/rad)	k_{r2w} (MN m/rad)
112	207	105	24	21	21

Table 3 The maximal and minimal values of six LDSI k_{vi} along (about) u , v , and w axes throughout the entire workspace

LDSI	k_{v1} (N/m)	k_{v2} (N/m)	k_{v3} (N/m)	k_{v4} (N m/rad)	k_{v5} (N m/rad)	k_{v6} (N m/rad)
Maximum	5.14×10^7	2.17×10^7	1.79×10^8	2.40×10^7	1.95×10^7	1.01×10^7
Minimum	3.97×10^6	2.93×10^6	3.03×10^7	4.49×10^6	5.52×10^6	3.00×10^6

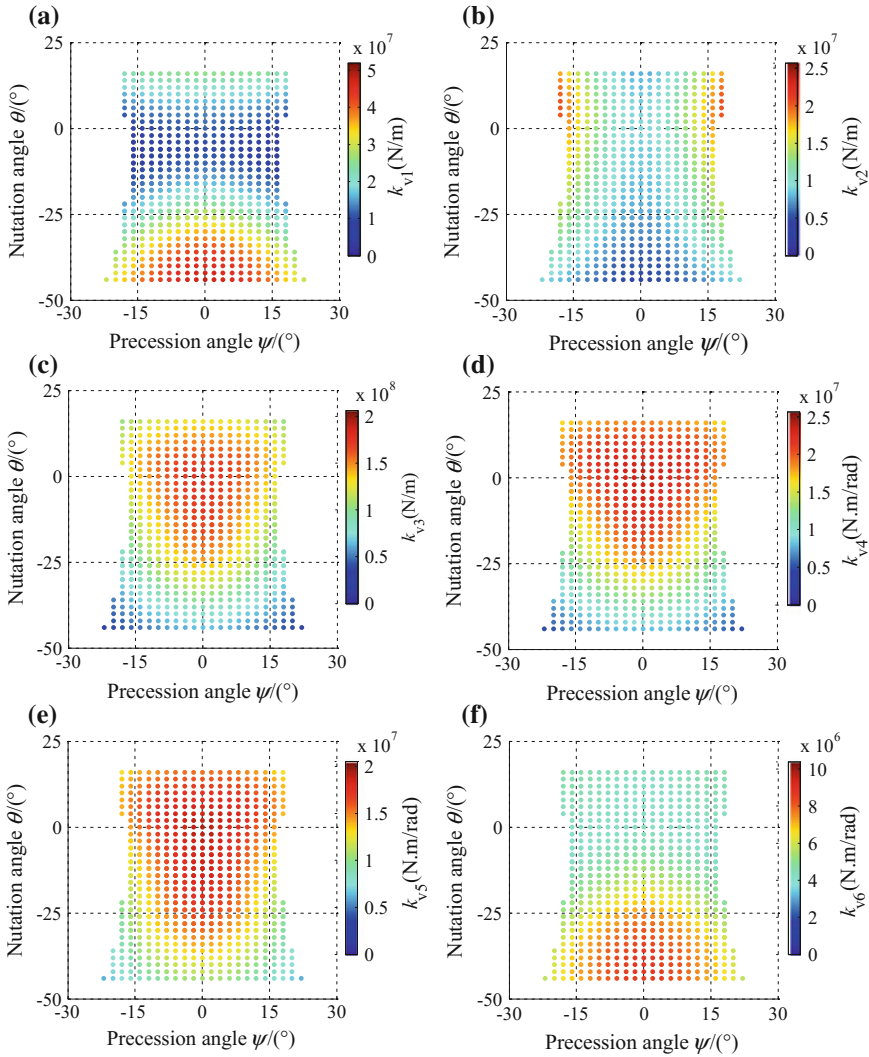


Fig. 3 The distributions of LDSI at a given work plane of $z = 1.2$ m: **a** along u axis, **b** along v axis, **c** along w axis, **d** about u axis, **e** about v axis, and **f** about w axis

It can be observed that LDSI values are axisymmetric over entire workspace, which is in accordance with the structural features that limb 1 and limb 3 are symmetrical with respect to limb 2. For example, the LDSI along u axis claims the maximal value of 4.67×10^7 at the position $\theta = -44^\circ$, $\psi = 0^\circ$ while the LDSI along v axis achieves the maximal value of 1.99×10^7 at position $\theta = 8^\circ$, $\psi = 20^\circ$ and $\theta = 8^\circ$, $\psi = -20^\circ$.

Noticing that LDSI is a dimensional index, one may think that it is difficult to use LDSI for global performance evaluation. In order to avoid this problem, a dimensionless global index LDSI_{gl} is proposed and defined as the ratio of mean and standard deviation of the LDSI.

$$\text{LDSI}_{\text{gl}} = \sum_{i=1}^6 \frac{\bar{x}_i}{\sigma_i} \quad (i = 1, 2, 3, 4, 5, 6) \quad (12)$$

where \bar{x}_i and σ_i ($i = 1, 2, 3, 4, 5, 6$) are defined as mean and standard deviation of LDSI along (about) u , v , and w axes, respectively. They are expressed as following

$$\bar{x}_i = \frac{1}{n} \sum_{j=1}^n k_{vin}; \quad \sigma_i = \sqrt{\frac{1}{n} \sum_{j=1}^n (k_{vin} - \bar{x}_i)^2} \quad (i = 1, 2, 3, 4, 5, 6) \quad (13)$$

From Eq. (12), a higher value of LDSI_{gl} means better static performance of a PKM.

With the above global index, an optimal design may be conducted to achieve better static performance by choosing propitiate geometric parameters of the PKM module. For simplicity, this paper only takes the radii of the moving platform and the fixed base as optimal design variables. The optimal design can be described by the following mathematical problem

$$\text{Max} : \text{LDSI}_{\text{gl_max}}(r_p, r_b) = \max\{\max\{\text{LDSI}_{\text{gl_m,n}}\}\} \quad (14)$$

where $\text{LDSI}_{\text{gl_max}}$ represents the maximal value of the dimensionless index $\text{LDSI}_{\text{gl_m,n}}$ which varies with respect to the optimal design variables r_p and r_b .

The optimal procedure of the searching algorithm is described in Fig. 4.

Herein, the variation intervals of the radii of the moving platform and the fixed base are set as $r_p = [0.2, 0.4]$ m and $r_b = [0.4, 0.8]$ m while $r_{p\text{min}} = 0.2$ m, $r_{p\text{max}} = 0.4$ m and $r_{b\text{min}} = 0.4$ m, $r_{b\text{max}} = 0.8$ m; the increments of radii are set as $\Delta p = 0.05$ m and $\Delta b = 0.10$ m. When the radii r_p and r_b are given, the reachable workspace of the PKM can be calculated through a process demonstrated in our previous paper [7]. The obtained reachable workspace is used to evaluate the LDSI throughout the entire workspace based on formulations and expressions proposed in Sect. 3. Then the LDSI_{gl} can be calculated through \bar{x}_i and σ_i ($i = 1, 2, 3, 4, 5, 6$) which are defined through the values of LDSI along (about) u , v , and w axes,

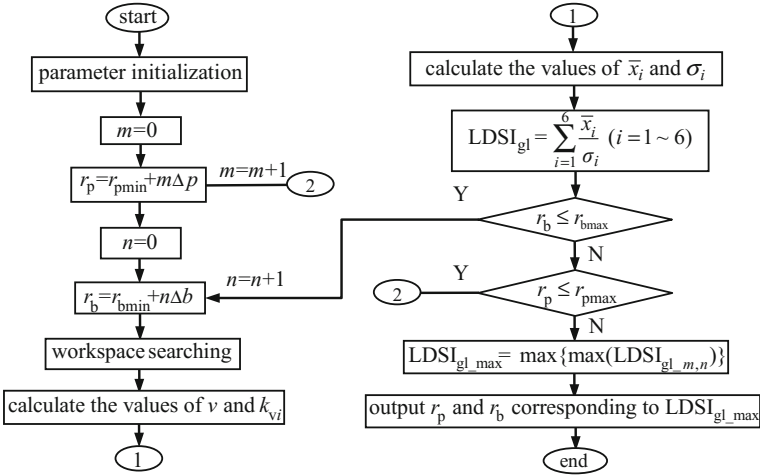


Fig. 4 Searching algorithm for optimal radii of the platform and the base

respectively. Finally, the optimal radii of the platform and the base are presented corresponding to the $LDSI_{gl_max}$ as well as the searching process is at the end.

The optimal results are calculated in Fig. 5.

As can be observed from Fig. 5, the PKM module achieves the most excellent static performance with $r_p = 0.20$ m and $r_b = 0.40$ m, while the maximal value of dimensionless index $LDSI_{gl_max}$ is 20.046. Further analyses reveal that under this condition the value of \bar{x}_i/σ_i in each individual direction is 1.865, 2.802, 3.548, 3.512, 4.987, and 3.421, respectively. Since a higher value of $LDSI_{gl}$ means better static performances of a PKM, the above values may indicate that the static performances along u and v axes need to be strengthened when the Exe-Variant machine tool is designed for high speed machining.

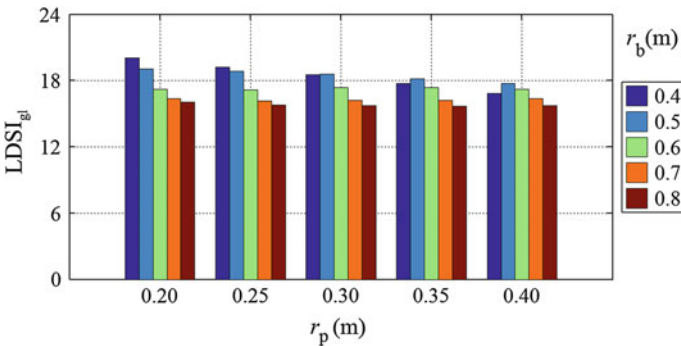


Fig. 5 The calculated values of optimal results $LDSI_{gl}$ with respect to r_p and r_b

5 Conclusions

To summarize the contributions of this paper, the following conclusions can be drawn:

- (1) A comprehensive performance index LDSI is proposed to consider both the kinematic dexterity and static rigidity characteristics of a PKM. Based on the proposed index, the static performances of Exe-Variant PKM module are predicted in an efficient manner.
- (2) A dimensionless global index is further presented to evaluate the overall static performance of a PKM throughout its workspace while avoiding the allocation of weighting factors between the dexterity and rigidity.
- (3) With the proposed global index, an optimal design is carried out to obtain reasonable radii of the moving platform and the fixed base of Exe-Variant PKM.
- (4) The proposed index and searching algorithm are expected to be applied for structural optimization and performance enhancement of other Exechon-like machine tools.

Acknowledgments This work was jointly supported by Open Fund of State Key Laboratory for Manufacturing Systems Engineering (Xi'an Jiaotong University) with Grant No. sklms-2015004 and National Natural Science Foundation of China (NSFC Grant No. 51375013). The first author also would like to acknowledge for Innovation Research Fund for Postgraduates of Anhui University of Technology (Grant No. 2015032).

References

1. Neumann KE (2006) Exechon concept. *Parallel Kinematic Mach Res Pract* 33:787–802
2. Zoppi M, Zlatanov D, Molfino R (2010) Kinematics analysis of the Exechon tripod. In: ASME 2010 international design engineering technical conferences and computers and information in engineering conference, pp 1381–1388. American Society of Mechanical Engineers
3. Bi ZM (2014) Kinetostatic modeling of Exechon parallel kinematic machine for stiffness analysis. *Int J Adv Manuf Technol* 71(1–4):325–335
4. Zlatanov D, Zoppi M, Molfino R (2012) Constraint and singularity analysis of the Exechon tripod. In: ASME 2012 international design engineering technical conferences and computers and information in engineering conference, pp 679–688. American Society of Mechanical Engineers
5. Jin Y, Bi ZM, Liu HT, Higgins C, Price M, Chen WH, Huang T (2015) Kinematic analysis and dimensional synthesis of Exechon parallel kinematic machine for large volume machining. *J Mech Robot* 7(4):041004
6. Zhao Y, Jin Y, Zhang J (2015) Kinetostatic modeling and analysis of an Exechon parallel kinematic machine (PKM) module. *Chin J Mech Eng* 29(1):33–44
7. Tengfei T, Yanqin Z, Jun Z, Yan J (2016) Conceptual design and workspace analysis of an Exechon-inspired parallel kinematic machine. In: *Advances in reconfigurable mechanisms and robots II*. Springer International Publishing, pp 445–453

8. Gosselin CM (1992) The optimum design of robotic manipulators using dexterity indices. *Robot Auton Syst* 9(4):213–226
9. Huang T, Whitehouse DJ, Wang J (1998) The local dexterity, optimal architecture and design criteria of parallel machine tools. *CIRP Ann Manuf Technol* 47(1):346–350
10. Klein CA, Blaho BE (1987) Dexterity measures for the design and control of kinematically redundant manipulators. *Int J Robot Res* 6(2):72–83
11. Kim JO, Khosla PK (1991) Dexterity measures for design and control of manipulators. In: *Intelligence for mechanical systems, proceedings IROS'91, IEEE/RSJ international workshop on Intelligent robots and systems '91*. IEEE, pp 758–763
12. Gosselin CM, Angeles J (1991) A global performance index for the kinematic optimization of robotic manipulators. *J Mech Des* 113:220–226
13. Ceccarelli M, Carbone G (2002) A stiffness analysis for CaPaMan (Cassino parallel manipulator). *Mech Mach Theory* 37(5):427–439
14. Carbone G (2006) Stiffness performance of multibody robotic systems. In: *2006 IEEE international conference on automation, quality and testing, robotics, vol 2*, pp 219–224. IEEE
15. Liu H, Huang T, Chetwynd DG (2011) A method to formulate a dimensionally homogeneous Jacobian of parallel manipulators. *IEEE Trans Robot* 27:150–156
16. Zhang J, Zhao Y, Jin Y (2016) Kinetostatic-model-based stiffness analysis of Exechon PKM. *Robot Comput Integr Manuf* 37(C):208–220 (2016)

Motion Analysis of a 2-DoF Planar Mechanism

Ziming Chen, Xuedan Wei, Xiaomeng Liu, Dongliang Cheng and Peng Huang

Abstract Planar mechanisms with two degrees of freedom (2-DoF) have been studied extensively. In this research, a 2-DoF planar mechanism is proposed and analyzed. This mechanism has a axisymmetric structure that the lower part and the upper part are identical and symmetrical with each other during the motion. The end effector of this mechanism can translate continuously along the direction perpendicular to the axis of symmetry of this mechanism and rotate continuously about any point on the axis of symmetry. The forward and inverse kinematics solutions are derived which can be used for further analysis of this mechanism.

Keywords Planar mechanism · 2-DoF · Axisymmetry · Continuous rotation

1 Introduction

Planar mechanisms with two degrees of freedom (2-DoF) have been studied extensively. The most famous 2-DoF planar mechanism is the five-bar mechanism (also called as 5R mechanism). Liu et al. [1, 2] researched on the kinematics, singularity, workspace and the optimum design of planar 5R symmetric parallel mechanism. Joubair et al. [3, 4] analyzed the structure optimization and dynamics of the planar five-bar mechanism. Campos et al. [5] optimized the five-bar mechanism for large workspace. The five-bar mechanism also can be used to design a compliant mechanism [6].

Gao et al. [7] applied the space dimension design theory to the mechanism design of the planar 2-DoF parallel mechanisms. Huang et al. [8] presented the

Z. Chen (✉) · X. Wei · X. Liu · D. Cheng · P. Huang
School of Mechanical Engineering, Yanshan University,
Qinhuangdao 066004, China
e-mail: chenzm@ysu.edu.cn

Z. Chen · X. Wei · X. Liu · D. Cheng · P. Huang
Hebei Provincial Key Laboratory of Parallel Robot and Mechatronic System,
Yanshan University, Qinhuangdao 066004, China

kinematic optimal design of 2-DoF PMs with a mirror symmetrical geometry. Liu et al. [9] designed a planar 2-DoF mechanism with three parallelogram that can be used as a spray-painting robot. Huang et al. used the planar 1R1T mechanism as part of the remote center-of-motion mechanism [10, 11]. Li et al. designed a 2-DoF Planar remote center-of-motion mechanisms based on virtual parallelograms.

A 2-DoF planar mechanism is proposed and analyzed in this paper. This mechanism has an axisymmetric structure during the motion. The motion characteristics of this mechanism is analyzed. In the end, the forward and inverse kinematics solutions are derived.

2 Mobility Analysis

As shown in Fig. 1, the end effector DE is connected to the base AB by three branches which are branch AFE , branch BCD and branch AGE . All these branches are RRR chains, which is made up by three revolute joints (R joint) and two links with the same length. Between the points C and F , there is another RPR chain consists of two links, two R joints and a prismatic joint (P joint). The middle R joint of the branch AGE is connected to the above mentioned RPR chain by a slider at point G . So, point G is always sliding on the line CF .

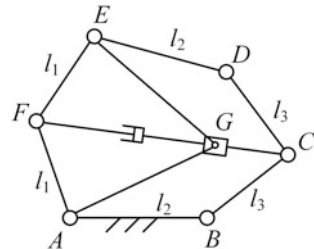
This mechanism contains ten movable links, five multiple revolute joints at points A, C, E, F and G , two simple revolute joints at points B and D , and two prismatic joints on the line CF . So there are fourteen lower pairs and no higher pairs. According to the mobility formula of planar mechanisms, the mobility of this mechanism is

$$F = 3n - 2p_l - p_h = 3 \times 10 - 2 \times 14 - 0 = 2$$

where F is the mobility of the planar mechanism; n is the number of the links exclude the base; p_l is the number of the lower pairs; p_h is the number of the higher pairs.

Because the mobility is two, this mechanism only needs two actuators. Two cranks AF and BC are chosen as the actuated links in this research.

Fig. 1 The planar mechanism



3 Motion Characteristics

The mobility of this mechanism is two, which means the motion of the end effector is restricted. In this section, the restricted motion will be found out and the motion characteristics of this mechanism will be analyzed.

It is easy to find that this planar mechanism has an axisymmetric kinematic structure. The structure can be divided into two identical parts by the axis of symmetry. The links DE and AB are always symmetrical about the line CF .

If line CF is fixed, this mechanism can transfer the same motion of link AB to the link DE . So, this structure can be used as a motion tracking mechanism [10]. In this research, we focus on this mechanism with the link AB fixed on the base.

3.1 Motion Property of Two Axisymmetric Links

In order to get the motion characteristics of this planar mechanism, we can simplify it as two axisymmetric links AB and DE . Link AB is fixed, and link DE is movable, as shown in Fig. 2. Their axis of symmetry is l .

In order to preserve the line symmetry of these two links, the motion of the link DE is restricted and has the following two properties:

Property 1 The movable link DE can only translate along the direction which is perpendicular to the axis of symmetry l .

Property 2 The movable link DE can only rotate about the point that lies on the axis of symmetry l .

Proof of Property 1 As shown in Fig. 3, because link AB and link DE are symmetrical with respect to the line l at the initial configuration. A reference frame OXY is attached on the fixed link AB , where the coordinate origin O lies on the axis of symmetry l and the X axis coincides with the axis of symmetry l .

So, at the initial configuration, the coordinates of points A , B , D and E are

$$\begin{cases} A(A_x, A_y) = (x_1, -y_1) \\ B(B_x, B_y) = (x_2, -y_2) \\ D(D_x, D_y) = (x_2, y_2) \\ E(E_x, E_y) = (x_1, y_1) \end{cases} \quad (1)$$

Fig. 2 Two axisymmetric links

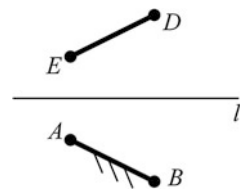
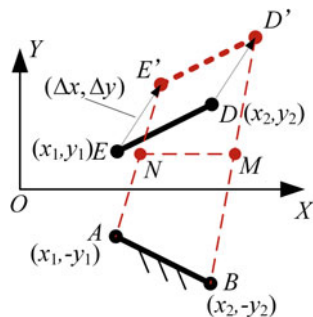


Fig. 3 Proof of Property 1



If the link DE translates from the initial position by the distance $(\Delta x, \Delta y)$ and reaches the final position $D'E'$, the coordinates of D' and E' will be

$$\begin{cases} D'(D'_x, D'_y) = (x_2 + \Delta x, y_2 + \Delta y) \\ E'(E'_x, E'_y) = (x_1 + \Delta x, y_1 + \Delta y) \end{cases} \quad (2)$$

After the translation, the links AB and $D'E'$ are still symmetrical with each other. So, the following geometric conditions should be matched.

$$\begin{cases} \overrightarrow{AE'} // \overrightarrow{BD'} \\ \overrightarrow{MN} \perp \overrightarrow{AE'} \end{cases} \Rightarrow \begin{cases} \frac{E'_y - A_y}{E'_x - A_x} = \frac{D'_y - B_y}{D'_x - B_x} \\ (M_x - N_x, M_y - N_y) \cdot (A_x - E'_x, A_y - E'_y) = 0 \end{cases} \quad (3)$$

where M and N are the midpoints of line segment BD' and AE' , respectively. Their coordinate can be represented as

$$\begin{cases} M(M_x, M_y) = \left(\frac{D'_x + B_x}{2}, \frac{D'_y + B_y}{2} \right) \\ N(N_x, N_y) = \left(\frac{E'_x + A_x}{2}, \frac{E'_y + A_y}{2} \right) \end{cases} \quad (4)$$

Substituting the coordinates of the points in Eqs. (1), (2) and (4) into Eq. (3), the following equations can be obtained.

$$\begin{cases} \frac{2y_2 + \Delta y}{\Delta x} = \frac{2y_1 + \Delta y}{\Delta x} \\ \Delta x \cdot (x_1 - x_2) = 0 \end{cases} \quad (5)$$

It can be simplified as

$$\begin{cases} \Delta x \cdot (y_1 - y_2) = 0 \\ \Delta x \cdot (x_1 - x_2) = 0 \end{cases} \quad (6)$$

If $(y_1 - y_2) = (x_1 - x_2) = 0$, the point D and E will coincide with each other. So, the only possible solution of Eq. (6) is $\Delta x = 0$, which means the link DE can not translate along the direction parallel to the axis of symmetry l .

So, in order to keep the two links axisymmetric with each other, the link DE can only translate along the direction perpendicular to the axis of symmetry l .

Proof of Property 2 As shown in Fig. 4, the link DE rotates about the point $P(P_x, P_y)$ by the angle θ , and reaches the final position $D'E'$.

The coordinates transformation equation are

$$\begin{cases} \overrightarrow{OD'} = \mathbf{R}_{(\theta)} \overrightarrow{PD} + \overrightarrow{OP} \\ \overrightarrow{OE'} = \mathbf{R}_{(\theta)} \overrightarrow{PE} + \overrightarrow{OP} \end{cases} \tag{7}$$

where $\mathbf{R}_{(\theta)}$ is the rotation matrix of rotating about the Z axis by angle θ

$$\mathbf{R}_{(\theta)} = \begin{bmatrix} \cos \theta & -\sin \theta \\ \sin \theta & \cos \theta \end{bmatrix} \tag{8}$$

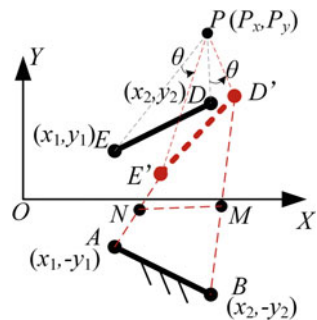
So, the coordinates of $D'(D'_x, D'_y)$ and $E'(E'_x, E'_y)$ can be obtained

$$\begin{cases} D'_x = P_x + (D_x - P_x) \cos \theta - (D_y - P_y) \sin \theta \\ D'_y = P_y + (D_x - P_x) \sin \theta + (D_y - P_y) \cos \theta \\ E'_x = P_x + (E_x - P_x) \cos \theta - (E_y - P_y) \sin \theta \\ E'_y = P_y + (E_x - P_x) \sin \theta + (E_y - P_y) \cos \theta \end{cases} \tag{9}$$

Substituting the coordinates of the points in Eqs. (1), (2) and (7) into Eq. (3), the following equations can be obtained.

$$\begin{cases} P_y \cdot (2x_1 \sin^2 \frac{\theta}{2} - 2x_2 \sin^2 \frac{\theta}{2} + y_1 \sin \theta - y_2 \sin \theta) = 0 \\ P_y \cdot (y_2 - y_1 + y_1 \cos \theta - y_2 \cos \theta + x_1 \sin \theta - x_2 \sin \theta) = 0 \end{cases} \tag{10}$$

Fig. 4 Proof of Property 2



It is easy to find that the solution of Eq. (10) is $P_y = 0$, which means the rotation center P should lie on the axis of symmetry l .

So, in order to keep the two links axisymmetric with each other after the rotation, link DE can only rotate about the point that lies on the axis of symmetry l .

3.2 Motion Characteristics of the 2-DoF Planar Mechanism

From the result of mobility analysis, we have known that the motility of this planar mechanism is two, which means the motion of the end effector is restricted. Based on the Property 1 introduced above, it can be found that the end effector can not move along the direction parallel to the axis of symmetry. So, one translational motion of this mechanism has been restricted, and it is a 1R1T planar mechanism.

The remaining translational mobility of the end effector is the translation along the direction perpendicular to the axis of symmetry. Besides, Eq. (6) shows that the distance δy does not affect the symmetry of the mechanism. So, it can be concluded that the end effector can translate continuously along this direction.

This mechanism also has a rotational mobility. Based on Property 2, we can know that the end effector can rotate about any point that lies on the axis of symmetry of this mechanism. In addition, from Eq. (10), it can be found that the value of angle θ does not affect the symmetry of this mechanism, which means the end effector can rotate continuously about any point on the axis of symmetry.

4 Kinematics Analysis

According to the motion characteristics of this planar mechanism, the end effector DE can translate along the normal direction of line CF and rotate about any point on the line CF . So, as shown in Fig. 5, the configuration of the end effector DE can be expressed by angle φ formed by DE and X axis, and the distance d of point O and

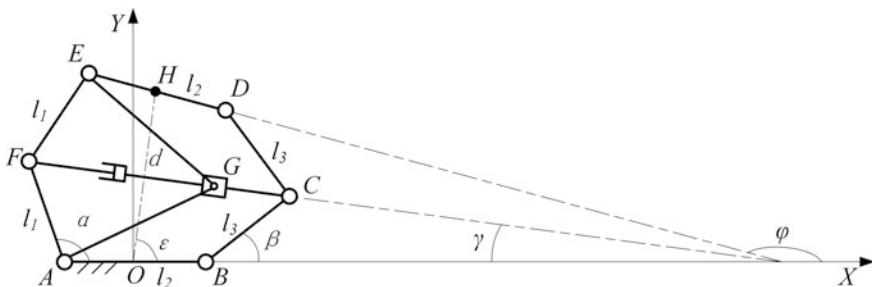


Fig. 5 Parameters of the mechanism

H , while O is the midpoint of AB and H is the midpoint of DE . The actuated parameters are α and β which represent the angle formed by FA , BC with X axis, respectively.

A coordinate system OXY is attached on the base with the origin at point O and the X axis is coaxial with line AB . For the convenience of calculation, let the length of links FA , AB , BC be l_1 , l_2 , l_3 .

So, the coordinates of the points A and B are

$$\begin{cases} A(A_x, A_y) = (-\frac{1}{2}l_2, 0) \\ B(B_x, B_y) = (\frac{1}{2}l_2, 0) \end{cases} \tag{11}$$

4.1 Forward Kinematics

So the problem of the forward kinematics is to calculate the parameters φ and d when the driving angles α and β are known.

The coordinates of the points C and F can be expressed as

$$\begin{cases} C(C_x, C_y) = (\frac{1}{2}l_2 + l_3 \cos \beta, l_3 \sin \beta) \\ F(F_x, F_y) = (-\frac{1}{2}l_2 + l_1 \cos \alpha, l_1 \sin \alpha) \end{cases} \tag{12}$$

The equation of the straight line on the line segment CF can be obtained by using the coordinates of points C and F

$$\frac{y - F_y}{C_y - F_y} = \frac{x - F_x}{C_x - F_x} \tag{13}$$

Substituting the coordinates of the points in Eq. (12) into Eq. (13), the standard form equation of line CF can be obtained

$$Jx + Ky + L = 0 \tag{14}$$

In which

$$\begin{aligned} J &= l_3 \sin \beta - l_1 \sin \alpha \\ K &= l_1 \cos \alpha - l_2 - l_3 \cos \beta \\ L &= \frac{1}{2}l_1l_2 \sin \alpha + \frac{1}{2}l_2l_3 \sin \beta + l_1l_3 \sin \alpha \cos \beta - l_1l_3 \sin \beta \cos \alpha \end{aligned}$$

Because point H and O are symmetrical with respect to the line CF , the coordinate of point $H(H_x, H_y)$ can be obtained

$$\begin{cases} H_x = \frac{-2JL}{J^2 + K^2} \\ H_y = \frac{-2KL}{J^2 + K^2} \end{cases} \quad (15)$$

So the length of OH is

$$d = \frac{2|L|}{\sqrt{J^2 + K^2}} \quad (16)$$

Angles φ and γ have the following relationship

$$\varphi = 180^\circ - 2\gamma \quad (17)$$

Angle γ can be obtained by the coordinates of point C and F

$$\gamma = \arctan \frac{F_y - C_y}{F_x - C_x} = \arctan \frac{l_1 \sin \alpha - l_3 \sin \beta}{l_1 \cos \alpha - l_2 - l_3 \cos \beta} \quad (18)$$

According to Eq. (17), angle φ is

$$\varphi = 180^\circ - 2 \arctan \frac{l_1 \sin \alpha - l_3 \sin \beta}{l_1 \cos \alpha - l_2 - l_3 \cos \beta} \quad (19)$$

Therefore, when the driving angles α and β are known, the configuration of the end effector DE can be obtained by Eqs. (16) and (19).

4.2 Inverse Kinematics

The problem of the inverse kinematics is to calculate the driving angles α and β when the parameters of the end effector (φ and d) are known.

According to the geometrical relationship shown in Fig. 5, we have

$$\varepsilon = 90^\circ - \gamma = 90^\circ - \frac{1}{2}(180^\circ - \varphi) = \frac{\varphi}{2} \quad (20)$$

Then the coordinates of point $H(H_x, H_y)$ can be solved as

$$\begin{cases} H_x = d \cdot \cos \varepsilon = d \cdot \cos \frac{\varphi}{2} \\ H_y = d \cdot \sin \varepsilon = d \cdot \sin \frac{\varphi}{2} \end{cases} \quad (21)$$

The equation of the perpendicular bisector of OH can be written as follows

$$y - \frac{1}{2}H_y = k(x - \frac{1}{2}H_x) \quad (22)$$

where k represents the slope of perpendicular bisector

$$k = -\frac{H_x}{H_y} = -\cot \frac{\varphi}{2} \quad (23)$$

Point F lies on the circle whose center is point A and the radius is l_1 . So, the equation of this circle is

$$\left(x + \frac{1}{2}l_2\right)^2 + y^2 = l_1^2 \quad (24)$$

The coordinate of point $F(F_x, F_y)$ can be obtained by solving Eqs. (22) and (24)

$$\begin{cases} F_x = \frac{1}{2} \left(\pm \sin \frac{\varphi}{2} \sqrt{-d^2 - 2dl_2 \cos \frac{\varphi}{2} + 4l_1^2 - l_2^2 \cos^2 \frac{\varphi}{2}} - l_2 \sin^2 \frac{\varphi}{2} + d \cos \frac{\varphi}{2} \right) \\ F_y = \frac{1}{2} \left(d \sin \frac{\varphi}{2} + l_2 \sin \frac{\varphi}{2} \cos \frac{\varphi}{2} \mp \cos \frac{\varphi}{2} \sqrt{-d^2 - 2dl_2 \cos \frac{\varphi}{2} + 4l_1^2 - l_2^2 \cos^2 \frac{\varphi}{2}} \right) \end{cases} \quad (25)$$

Point C lies on the circle whose center is point B and the radius is l_3 . So, the equation of this circle is

$$\left(x - \frac{1}{2}l_2\right)^2 + y^2 = l_3^2 \quad (26)$$

The coordinate of point $C(C_x, C_y)$ can be obtained by solving Eqs. (22) and (26)

$$\begin{cases} C_x = \frac{1}{2} \left(l_2 \sin^2 \frac{\varphi}{2} \mp \sin \frac{\varphi}{2} \sqrt{-d^2 + 2dl_2 \cos \frac{\varphi}{2} + 4l_3^2 - l_2^2 \cos^2 \frac{\varphi}{2}} + d \cos \frac{\varphi}{2} \right) \\ C_y = \frac{1}{2} \left(d \sin \frac{\varphi}{2} - l_2 \sin \frac{\varphi}{2} \cos \frac{\varphi}{2} \pm \cos \frac{\varphi}{2} \sqrt{-d^2 + 2dl_2 \cos \frac{\varphi}{2} + 4l_3^2 - l_2^2 \cos^2 \frac{\varphi}{2}} \right) \end{cases} \quad (27)$$

Using the coordinates of C and F , the actuated angles α and β can be easily obtained.

5 Conclusions

A planar mechanism with two-degree-of-freedom is proposed and analyzed. This mechanism has an axisymmetric structure that the lower part and the upper part are identical and symmetrical with each other. In order to analyze the motion characteristics of the end effector, the mechanism can be simplified as two axisymmetric links and the motion properties of this simplified links are studied. The results show that the end effector can translate continuously along the direction perpendicular to the axis of symmetry of the base and the end effector and rotate continuously about

any point on the axis of symmetry l . In the end, the forward and inverse kinematics solutions are derived which can be used for further analysis of this mechanism.

Acknowledgments The work reported here is supported by National Natural Science Foundation of China (Grant No. 51305381) and the Joint Specialized Research Fund for the Doctoral Program of Higher Education (Grant No. 20131333120006).

References

1. Liu X-J, Wang J, Pritschow G (2006) Performance atlases and optimum design of planar 5R symmetrical parallel mechanisms. *Mech Mach Theory* 41:119–144
2. Liu X-J, Wang J, Pritschow G (2006) Kinematics, singularity and workspace of planar 5R symmetrical parallel mechanisms. *Mech Mach Theory* 41:145–169
3. Joubair A, Bonev IA (2013) Comparison of the efficiency of five observability indices for robot calibration. *Mech Mach Theory* 70:254–265
4. Joubair A, Slamani M, Bonev IA (2013) Kinematic calibration of a five-bar planar parallel robot using all working modes. *Robot Comput Integr Manuf* 29:15–25
5. Campos L, Bourbonnais F, Bonev IA et al (2010) Development of a five-bar parallel robot with large workspace. In: ASME 2010 international design engineering technical conferences (IDETC 2010), Montreal, QC, Canada
6. Tanik E (2016) Analysis and design of an underactuated compliant five-bar mechanism. *Mech Mach Theory* 102:123–134
7. Gao F, Zhang XQ, Zhao YS et al (1996) A physical model of the solution space and the atlas of the reachable workspace for 2-DoF parallel planar manipulators. *Mech Mach Theory* 31:173–184
8. Huang T, Li M, Li Z et al (2004) Optimal kinematic design of 2-DoF parallel manipulators with well-shaped workspace bounded by a specified conditioning index. *IEEE Trans Robot Autom* 20:538–543
9. Liu X-J, Li J, Zhou Y (2015) Kinematic optimal design of a 2-degree-of-freedom 3-parallelogram planar parallel manipulator. *Mech Mach Theory* 87:1–17
10. Huang L, Yang Y, Xiao J et al (2015) Type synthesis of 1R1T remote center of motion mechanisms based on pantograph mechanisms. *J Mech Des* 138:014501
11. Li J, Zhang G, Xing Y et al (2014) A class of 2-degree-of-freedom planar remote center-of-motion mechanisms based on virtual parallelograms. *J Mech Robot* 6:031014

DOF and Kinematic Analysis of a Deployable Truss Antenna Assembled by Tetrahedral Elements

Wenlan Liu, Yundou Xu, Yongsheng Zhao, Jiantao Yao, Bo Han and Liangliang Chen

Abstract Deployable structure has played a more and more important role in the large-caliber antennas. This paper deals with the degree of freedom (DOF) and kinematics of a kind of deployable truss antenna composed of tetrahedral elements. Firstly, based on the reciprocal screw theory the DOF of one tetrahedral element is analyzed. Then, the equivalent mechanism of the minimum composite unit of the deployable truss antenna is obtained according to the characteristic of the DOF of the tetrahedral element. Sequentially, the DOF of the deployable truss antenna is derived. Further, the analytical expressions of the positions and velocities of the connection nodes of the antenna during its deploying/folding process are formulated by resorting to the coordinate transformation matrices. Finally, the correctness of the kinematic analysis of the deployable truss antenna is verified by simulation based on the Adams software.

Keywords Deployable structure · Truss antenna · Degree of freedom · Kinematic analysis · Screw theory

W. Liu · Y. Xu (✉) · Y. Zhao · J. Yao · B. Han · L. Chen
Parallel Robot and Mechatronic System Laboratory of Hebei Province,
Qinhuangdao 066004, Hebei, China
e-mail: ydxu@ysu.edu.cn

W. Liu
e-mail: wenlanl@163.com

Y. Zhao
e-mail: yszhao@ysu.edu.cn

J. Yao
e-mail: jtyao@ysu.edu.cn

B. Han
e-mail: 1440731168@qq.com

L. Chen
e-mail: 1307152110@qq.com

Y. Xu · Y. Zhao · J. Yao
Key Laboratory of Advanced Forging and Stamping Technology and Science
of Ministry of National Education Yanshan University, Qinhuangdao 066004, Hebei, China

1 Introduction

Demand for the large-caliber antennas is increasing with the rapid development of the aerospace science and technology. However, the caliber of antennas is severely restricted by limited volume of the launch vehicle. As a result, spatial deployable structures have been widely applied in the large-caliber antennas [1, 2], which have the advantages including higher precision, smaller launch volume and higher reliability for deployment. Basically, deployable antennas can be divided into three categories: mesh, solid surface and inflatable antennas, among which the mesh antenna is the most common type.

The mesh antenna is mainly composed of a reflective metallic mesh and a deployable supporting structure. For this kind of antennas, the most critical part is the deployable supporting structure. There is a large amount of literatures focusing on the deployable structures at present. Wang et al. [3] proposed a two-step topology structure synthesis approach to design novel pyramid deployable truss structures. A structure-electronic synthesis design method of antennas is given in [4]. The literatures [5–8] paid attention to the configuration design of polyhedral linkage for deployable truss structure. Zheng et al. [9] proposed a new conceptual structure design for large deployable spaceborne antennas based on a folded fixed truss hoop reflector. You [10] demonstrated a generic solution for construction of deployable structures in any shape of rotational symmetry. The optimization of antennas was demonstrated in [11, 12]. Besides, Yu et al. [13] accomplished the motion analysis of deployable structures using the finite particle method. Moore-Penrose generalized inverse method is applied to the kinematic analysis of deployable toroidal spatial truss structures for large mesh antenna [14]. Xu et al. [15, 16] addressed the structural design, kinematic and static analysis of a double-ring deployable antenna. What's more, Li et al. [17] used the absolute nodal coordinate formulation to analyze the flexible body dynamics of deployable structures under different temperatures to simulate space environments. Afterwards, Li [18] presented the kinematic, dynamic analysis and control methods of a hoop deployable antenna.

To sum up, most of the above-mentioned literatures focused on the structural design, kinematic and dynamic analysis of deployable structures. There are few investigations on the methods for degree of freedom (DOF) analysis of the deployable structures applied in the antennas. It is well known that getting the number of the DOFs for mechanisms is the most fundamental understanding to a mechanism. However, deployable antenna structure is constituted by a large number of deployable elements through some regular structural topology, which increases the complexity and difficulty of the mobility analysis for this kind of deployable structures. In this work, the DOF of a deployable structure assembled by tetrahedral elements for space truss antennas is analyzed based on the reciprocal screw theory, and the correctness of the mobility analysis is verified by simulation.

2 DOF Analysis of the Deployable Truss Antenna

2.1 Structure of the Deployable Truss Antenna

The deployable truss antenna consists of a large number of basic tetrahedral elements, as shown in Fig. 1. Each tetrahedral element contains four connection nodes, three swing-struts with identical length, and three foldable and deployable struts. Both ends of the struts are connected to the nodes by revolute joints (R), and each foldable and deployable strut is made up of two struts with identical length connected by an R joint, as shown in Fig. 2. For the purpose of analysis, the tetrahedral element shown in Fig. 2 is denoted by $H-ABC$, where the letter H represents the top node and the other letters denote the three nodes located at the undersurface of the tetrahedral element. The axes of all R joints of the tetrahedral element $H-ABC$ are respectively denoted by S_i ($i = 1, 2, \dots, 15$). Then, the geometric characteristics of the S_i can be expressed as: $S_1 \parallel S_2 \parallel S_3 \perp AB$, $S_4 \parallel S_5 \parallel S_6 \perp AC$, $S_7 \parallel S_8 \parallel S_9 \perp BC$, $S_{10} \parallel S_{11} \perp AH$, $S_{12} \parallel S_{13} \perp CH$, and $S_{14} \parallel S_{15} \perp BH$. Besides, the S_{11} , S_{13} and S_{15}

Fig. 1 Deployable truss antenna

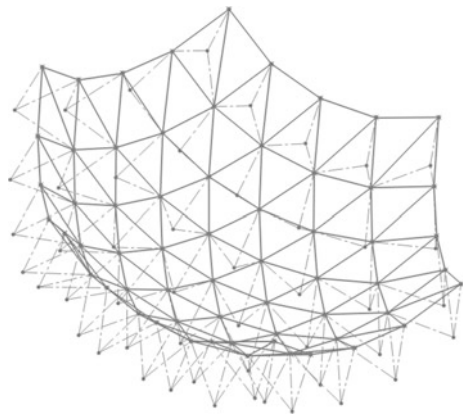


Fig. 2 Schematic diagram of the tetrahedral element

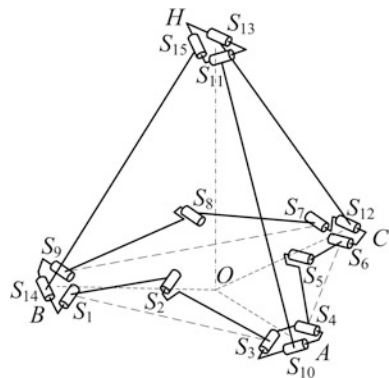


Fig. 3 Schematic diagram of the minimum composite unit

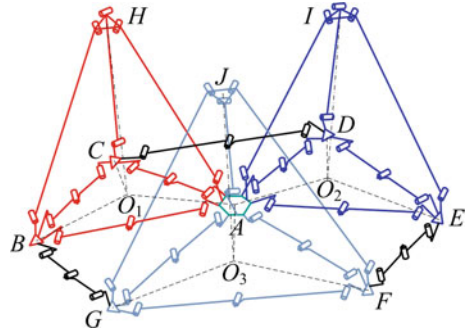
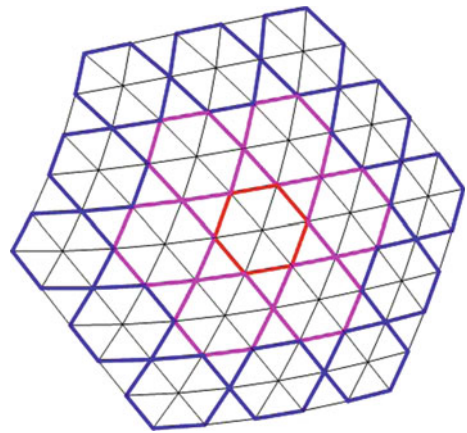


Fig. 4 Reflecting surface of the antenna spliced by the minimum composite units



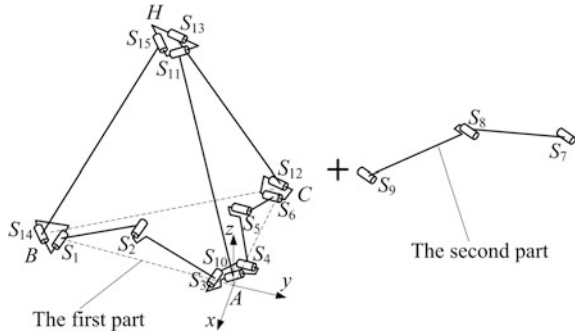
are coplanar and perpendicular to the planes AOH , COH and BOH , respectively, where the point O represents the circumcenter of the triangle ABC .

The minimum composite unit of the deployable truss antenna is constituted by three tetrahedral elements, as shown in Fig. 3. Then the whole deployable truss antenna shown in Fig. 1 can be obtained by extending the minimum composite units from the central axis of the antenna. The reflecting surface of the antenna spliced by the minimum composite units is shown in Fig. 4, in which the triangle planes are the undersurface of the tetrahedral elements and the color hexagons represent the minimum composite units.

2.2 DOF Analysis of the Tetrahedral Element

In order to analyze the DOF of the tetrahedral element, it is firstly divided into two parts in this section, as shown in Fig. 5. Then, the DOF of the first part is derived

Fig. 5 Two parts of the tetrahedral element



based on the reciprocal screw theory. Finally, the DOF of the tetrahedral element can be obtained after considering the constraint influence of the second part.

The first part of the tetrahedral element can be regarded as a parallel mechanism (PM) composed of a fixed node A, a moving node B, and two supporting limbs. One limb connects the node B to the node A by three R joints (i.e., S₁, S₂ and S₃), denoted by the limb RRR. The other limb consists of a closed-loop kinematic chain containing seven R joints (i.e., S₄, S₅, S₆, S₁₂, S₁₃, S₁₁ and S₁₀) and a serial chain RR (i.e., S₁₄ and S₁₅), denoted by the limb (7R)-RR. A fixed coordinate frame Ax-yz is attached to the center of the node A, with x-axis perpendicular to the BA, y-axis pointing along the BA, and z-axis determined by the right-hand rule, as shown in Fig. 5.

The closed-loop kinematic chain in the limb (7R)-RR can also be treated as a PM containing a fixed node A, a moving node H, two supporting limbs, RR (i.e., S₁₀ and S₁₁) and RRRRR (i.e., S₄, S₅, S₆, S₁₂ and S₁₃). The constraint wrenches imposed on the node H by the limbs RR and RRRRR can be expressed in the Ax-yz as

$$\begin{cases} \mathcal{S}_{r1}^H = (0 \ 0 \ 0 \ 0 \ 0 \ 1)^T \\ \mathcal{S}_{r2}^H = (0 \ 0 \ 0 \ -b_4 \ a_4 \ 0)^T \\ \mathcal{S}_{r3}^H = (x_{11} - x_{10} \ y_{11} - y_{10} \ z_{11} - z_{10} \ y_{10}z_{11} - y_{11}z_{10} \ x_{11}z_{10} - x_{10}z_{11} \ x_{10}y_{11} - x_{11}y_{10})^T, \\ \mathcal{S}_{r4}^H = (a_4 \ b_4 \ 0 \ -b_4z_{10} \ a_4z_{10} \ x_{10}b_4 - a_4y_{10})^T \\ \mathcal{S}_{r5}^H = (0 \ 0 \ 0 \ b_5c_2 \ -a_5c_2 \ a_5b_2 - a_2b_5)^T \end{cases} \tag{1}$$

where, (a₂ b₂ c₂), (a₄ b₄ 0) and (a₅ b₅ 0) denote the direction vectors of the S₄, S₁₀ and S₁₂, (x₁₀ y₁₀ z₁₀) and (x₁₁ y₁₁ z₁₁) represent the position vectors of the centers of the joints S₁₀ and S₁₁, respectively.

The twist of the node H which is reciprocal to the constraint wrenches shown in Eq. (1) is solved as

$$\mathcal{S}_m^H = (0 \ 0 \ 0 \ b_4(z_{11} - z_{10}) \ -a_4(z_{11} - z_{10}) \ b_4(x_{10} - x_{11}) + a_4(y_{11} - y_{10}))^T, \quad (2)$$

where, \mathcal{S}_m^H represents a translation perpendicular to both the \mathcal{S}_{10} and the $\mathcal{A}H$.

It can be known from Eq. (2) that the closed-loop kinematic chain within the limb (7R)-RR is equivalent to a translation joint P, so that the limb (7R)-RR can be substituted by the limb PRR. The constraint wrenches imposed on the node B by the limb PRR can be obtained as

$$\begin{cases} \mathcal{S}_{r1}^1 = (0 \ 0 \ 0 \ 0 \ 0 \ 1)^T \\ \mathcal{S}_{r2}^1 = (0 \ 0 \ 0 \ b_4 \ a_4 \ 0)^T \\ \mathcal{S}_{r3}^1 = (a \ 0 \ c \ (y_{10} + y_{14})c/2 \ az_{10} - ((y_{14} - y_{10})a_4 / (2b_4) + x_{10})c \ -(y_{10} + y_{14})a/2)^T \end{cases}, \quad (3)$$

where, $a = b_4(x_{11} - x_{10}) - a_4(y_{11} - y_{10})$, $c = b_4(z_{11} - z_{10})$, and $y_{10} + y_{14} = y_{11} + y_{15}$, \mathcal{S}_{r1}^1 represents the constraint couple parallel to the z -axis, \mathcal{S}_{r2}^1 is the constraint couple located in the plane xAy and perpendicular to the \mathcal{S}_{14} , and \mathcal{S}_{r3}^1 denotes the constraint force passing through the point $(\frac{(y_{14} - y_{10})a_4}{2b_4} + x_{10} \ \frac{y_{10} + y_{14}}{2}z_{10})$ and along the direction $(a \ 0 \ c)$, in which $(x_{10} \ y_{14} \ z_{10})$ and $(x_{11} \ y_{15} \ z_{11})$ represent the position vectors of the centers of the joints S_{14} and S_{15} , respectively.

Similarly, the constraint wrenches imposed on the node B by the limb RRR can be derived as

$$\begin{cases} \mathcal{S}_{r1}^2 = (0 \ 0 \ 0 \ 0 \ 1 \ 0)^T \\ \mathcal{S}_{r2}^2 = (0 \ 0 \ 0 \ -c_1 \ 0 \ a_1)^T \\ \mathcal{S}_{r3}^2 = (a_1 \ 0 \ c_1 \ y_1c_1 \ 0 \ -a_1y_1)^T \end{cases}, \quad (4)$$

where, $(a_1 \ 0 \ c_1)$ denotes the direction vector of the \mathcal{S}_1 , $(x_1 \ y_1 \ 0)$ represents the position vector of the center of the joint S_1 , \mathcal{S}_{r1}^2 represents the constraint couple parallel to the y -axis, \mathcal{S}_{r2}^2 is the constraint couple located in the plane xAz and perpendicular to the \mathcal{S}_1 , and \mathcal{S}_{r3}^2 is the constraint force passing through the point $(0 \ y_1 \ 0)$ and parallel to the \mathcal{S}_1 .

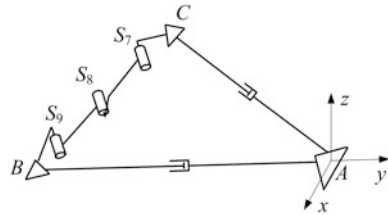
By combining Eqs. (3) and (4) all constraint wrenches suffered by the node B can be obtained. According to the reciprocal screw theory the twist of the node B can be derived as

$$\mathcal{S}_m^B = (0 \ 0 \ 0 \ 0 \ 1 \ 0)^T, \quad (5)$$

where \mathcal{S}_m^B represents a translation along the y -axis, which shows that the node B has a translational DOF with respect to the fixed node A .

As similar as the above solving process, it can be known that the node C also has a translational DOF with respect to the node A . On the condition of considering the

Fig. 6 Equivalent mechanism of the tetrahedral element



constraint influence of the second part of the tetrahedral element, the tetrahedral element can be equivalent to the mechanism shown in Fig. 6. It can be easily obtained that the number of the DOFs of the equivalent mechanism is one.

2.3 DOF of the Deployable Truss Antenna

According to the analysis in Sect. 2.2 the equivalent mechanism of the minimum composite unit shown in Fig. 2 can also be formulated, as shown in Fig. 7.

Assuming that the foldable and deployable strut BG is removed from the equivalent mechanism shown in Fig. 7 and the joint connecting the node B to the node A is selected as the actuated joint, then the nodes C, D, E, F and G will move as the movement of the node B , as shown in Fig. 8. According to the characteristic of the DOF of the tetrahedral element there exist the following relations:

$$\frac{AB_1}{AB} = \frac{AC_1}{AC} = \frac{AD_1}{AD} = \frac{AE_1}{AE} = \frac{AF_1}{AF} = \frac{AG_1}{AG}. \tag{6}$$

Fig. 7 Equivalent mechanism of the minimum composite unit

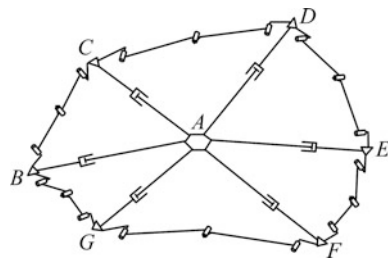
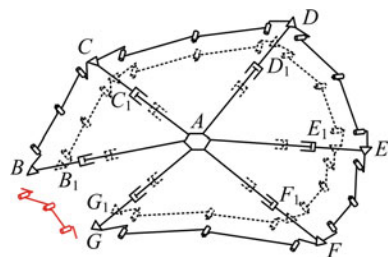


Fig. 8 Configuration of the mechanism shown in this figure after movement



From Eq. (6) it can be gotten that $\frac{AB_1}{AB} = \frac{AG_1}{AG}$, which will not be restricted after connecting the foldable and deployable strut BG to the nodes B and G . Therefore, the minimum composite unit also has one DOF.

Based on the structural topology relationship of the minimum composite unit, we can derive that the number of the DOFs of the whole deployable truss antenna shown in Fig. 1 also is one. That is to say, only the positions of the connection nodes of the deployable truss antenna are changing during its deploying/folding process, but their orientations keep constant.

3 Kinematic Analysis of the Deployable Truss Antenna

3.1 Position and Velocity Analysis of the Tetrahedral Element

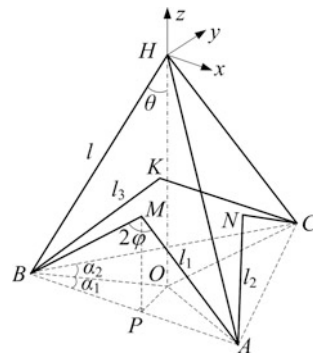
It can be known from the analysis mentioned in Sect. 2 that the orientations of the connection nodes are unchangeable during the deploying/folding process of the antenna. Consequently, the kinematic sketch shown in Fig. 9 is used to analyze the position and velocity variations of the nodes of the tetrahedral element.

As shown in Fig. 9, a reference coordinate system $H-xyz$ is attached to the node H with x -axis parallel to the BA and z -axis along the OH . Then the following equation can be obtained:

$$BP = l_1 \sin \varphi, BO = AO = CO = \frac{l_1}{\cos \alpha_1} \sin \varphi, PO = l_1 \tan \alpha_1 \sin \varphi, \quad (7)$$

where, $\cos \alpha_1 = l_1 \sin(\alpha_1 + \alpha_2)/l_2$, $\cos(\alpha_1 + \alpha_2) = (l_1^2 + l_3^2 - l_2^2)/(2l_1l_3)$, l_1 , l_2 and l_3 represent the length of the struts AM (BM), AN (CN) and BK (CK), respectively, φ denotes half of the angle between the BM and AM , α_1 (α_2) is the constant angle between the BO and BA (BC).

Fig. 9 Kinematic sketch of the tetrahedral element



Besides, there exists that

$$\sin \theta = \frac{BO}{BH} = \frac{l_1}{l \cos \alpha_1} \sin \varphi, \quad OH = l \cos \theta, \quad (8)$$

in which l denotes the length of the swing-struts HA , HB and HC .

Then the position vectors of the nodes A , B and C expressed in the H -xyz can be derived as

$$\begin{cases} \mathbf{P}_A = (l_1 \sin \varphi - l_1 \tan \alpha_1 \sin \varphi - l \cos \theta)^T \\ \mathbf{P}_B = (-l_1 \sin \varphi \quad -l_1 \tan \alpha_1 \sin \varphi \quad -l \cos \theta)^T \\ \mathbf{P}_C = (l_1 \cos \beta \sin \varphi / \cos \alpha_1 \quad l_1 \sin \beta \sin \varphi / \cos \alpha_1 \quad -l \cos \theta)^T \end{cases}, \quad (9)$$

where $\beta = 2\alpha_2 + \alpha_1$.

The angular velocities of the swing-struts HA , HB and HC can be computed by

$$\begin{cases} \boldsymbol{\omega}_{HA} = \mathbf{r}_1 \dot{\theta} = (\sin \alpha_1 \quad \cos \alpha_1 \quad 0)^T \dot{\theta} \\ \boldsymbol{\omega}_{HB} = \mathbf{r}_2 \dot{\theta} = (\sin \alpha_1 \quad -\cos \alpha_1 \quad 0)^T \dot{\theta}, \\ \boldsymbol{\omega}_{HC} = \mathbf{r}_3 \dot{\theta} = (-\sin \beta \quad \cos \beta \quad 0)^T \dot{\theta} \end{cases} \quad (10)$$

where, \mathbf{r}_1 , \mathbf{r}_2 and \mathbf{r}_3 represent the unit normal vectors of the planes AOH , BOH and COH , respectively, and $\dot{\theta}$ can be gotten by taking the derivative of Eq. (8) with respect to time as

$$\dot{\theta} = \frac{l_1 \cos \varphi}{l \cos \alpha_1 \cos \theta} \dot{\varphi}. \quad (11)$$

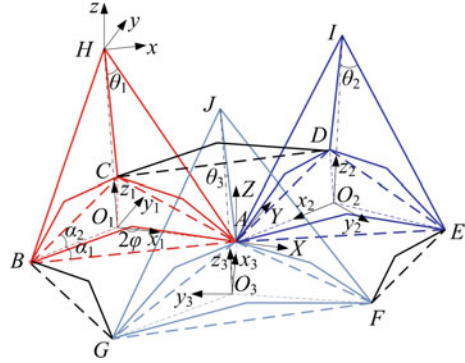
On the basis of Eqs. (9) and (10) the velocities of the nodes A , B and C can be calculated as

$$\begin{cases} \mathbf{V}_A = \boldsymbol{\omega}_{HA} \times \mathbf{P}_A = (-l \cos \theta \cos \alpha_1 \quad l \cos \theta \sin \alpha_1 \quad -l_1 \sin \varphi (\tan \alpha_1 \sin \alpha_1 + \cos \alpha_1))^T \cdot \frac{l_1 \cos \varphi}{l \cos \alpha_1 \cos \theta} \dot{\varphi} \\ \mathbf{V}_B = \boldsymbol{\omega}_{HB} \times \mathbf{P}_B = (l \cos \theta \cos \alpha_1 \quad l \cos \theta \sin \alpha_1 \quad -l_1 \sin \varphi (\tan \alpha_1 \sin \alpha_1 + \cos \alpha_1))^T \cdot \frac{l_1 \cos \varphi}{l \cos \alpha_1 \cos \theta} \dot{\varphi} \\ \mathbf{V}_C = \boldsymbol{\omega}_{HC} \times \mathbf{P}_C = -(l \cos \theta \cos \beta \quad l \cos \theta \sin \beta \quad \frac{l_1 \sin \varphi}{\cos \alpha_1})^T \cdot \frac{l_1 \cos \varphi}{l \cos \alpha_1 \cos \theta} \dot{\varphi} \end{cases}. \quad (12)$$

3.2 Position and Velocity Analysis of the Minimum Composite Unit

The kinematic sketch of the minimum composite unit is shown in Fig. 10. A reference coordinate system A -XYZ is attached to the node A with Z -axis being

Fig. 10 Kinematic sketch of the minimum composite unit



vertically placed and X -axis located in the plane AO_1H and having an angle γ_1 with respect to the AO_1 . Three body-fixed coordinate frames $O_j-x_jy_jz_j$ ($j = 1,2,3$) are assigned at the circumcenters O_j of the triangles ABC , ADE and AFG , with x_j -axis coinciding with the O_1A , O_2A and O_3A , and z_j -axis point along the O_1H , O_2I and O_3J , respectively, and y_j -axis are determined by the right-hand rule.

In the light of the analysis in Sect. 3.1 the position vectors of the nodes B , C and H expressed in the $O_1-x_1y_1z_1$ are

$$\begin{cases} {}^{O_1}P_H = (0 \quad 0 \quad l \cos \theta_1)^T \\ {}^{O_1}P_B = {}^{O_1}R \cdot {}^H P_B + {}^{O_1}P_H = l_1 \sin \varphi (M_1 \quad -2 \sin \alpha_1 \quad 0)^T \\ {}^{O_1}P_C = {}^{O_1}R \cdot {}^H P_C + {}^{O_1}P_H = l_1 \sin \varphi (M_2 \quad \cos \beta \tan \alpha_1 + \sin \beta \quad 0)^T \end{cases}, \quad (13)$$

in which, $M_1 = \tan \alpha_1 \sin \alpha_1 - \cos \alpha_1$ and $M_2 = \cos \beta - \sin \beta \tan \alpha_1$, ${}^H P_B$ and ${}^H P_C$ represent the position vectors of the nodes B and C expressed in the H - xyz , respectively, ${}^{O_1}R$ is the orientation matrix of the H - xyz with respect to the $O_1-x_1y_1z_1$, which can be formulated by ${}^{O_1}R = R(z, \alpha_1)$.

By resorting to the coordinate transformation matrix the position vectors of the nodes B , C and H can be expressed in the A - XYZ as

$$\begin{cases} {}^A P_H = {}^A_{O_1}R \cdot {}^{O_1}P_H + {}^A P_{O_1} \\ {}^A P_B = {}^A_{O_1}R \cdot {}^{O_1}P_B + {}^A P_{O_1}, \\ {}^A P_C = {}^A_{O_1}R \cdot {}^{O_1}P_C + {}^A P_{O_1} \end{cases}, \quad (14)$$

where, ${}^A_{O_1}R$ is the orientation matrix of the $O_1-x_1y_1z_1$ with respect to the A - XYZ , which can be computed by ${}^A_{O_1}R = R(Y, \gamma_1)$, and ${}^A P_{O_1}$ is the position vector of the point O_1 expressed in the A - XYZ , which can be calculated by

$${}^A\mathbf{P}_{O_1} = -{}^A_{O_1}\mathbf{R}{}^{O_1}\mathbf{P}_A = -{}^A_{O_1}\mathbf{R}(\mathbf{A}O_1 \quad 0 \quad 0) = \begin{pmatrix} -\frac{l_1\cos\gamma_1}{\cos\alpha_1}\sin\varphi & 0 & \frac{l_1\sin\gamma_1}{\cos\alpha_1}\sin\varphi \end{pmatrix}. \quad (15)$$

Substituting Eqs. (13) and (15) into Eq. (14) yields

$$\begin{cases} {}^A\mathbf{P}_H = \left(l\sin\gamma_1\cos\theta_1 - \frac{l_1\cos\gamma_1}{\cos\alpha_1}\sin\varphi & 0 & l\cos\gamma_1\cos\theta_1 + \frac{l_1\sin\gamma_1}{\cos\alpha_1}\sin\varphi \right)^T \\ {}^A\mathbf{P}_B = l_1\sin\varphi \left(M_1\cos\gamma_1 - \frac{\cos\gamma_1}{\cos\alpha_1} & -2\sin\alpha_1 & \frac{\sin\gamma_1}{\cos\alpha_1} - M_1\sin\gamma_1 \right)^T \\ {}^A\mathbf{P}_C = l_1\sin\varphi \left(M_2\cos\gamma_1 - \frac{\cos\gamma_1}{\cos\alpha_1} & \cos\beta\tan\alpha_1 + \sin\beta & \frac{\sin\gamma_1}{\cos\alpha_1} - M_2\sin\gamma_1 \right)^T \end{cases}. \quad (16)$$

Then taking the derivative of Eq. (16) with respect to time and taking Eq. (11) in mind leads to

$$\begin{cases} {}^A\mathbf{V}_H = \left(-\sin\gamma_1\tan\theta_1 - \cos\gamma_1 & 0 & \sin\gamma_1 - \cos\gamma_1\tan\theta_1 \right)^T \frac{l_1}{\cos\alpha_1}\cos\varphi\dot{\varphi} \\ {}^A\mathbf{V}_B = \left(M_1\cos\gamma_1 - \frac{\cos\gamma_1}{\cos\alpha_1} & -2\sin\alpha_1 & \frac{\sin\gamma_1}{\cos\alpha_1} - M_1\sin\gamma_1 \right)^T l_1\cos\varphi\dot{\varphi} \\ {}^A\mathbf{V}_C = \left(M_2\cos\gamma_1 - \frac{\cos\gamma_1}{\cos\alpha_1} & \cos\beta\tan\alpha_1 + \sin\beta & \frac{\sin\gamma_1}{\cos\alpha_1} - M_2\sin\gamma_1 \right)^T l_1\cos\varphi\dot{\varphi} \end{cases}, \quad (17)$$

which just are the velocity vectors of the nodes H , B and C during the deploying/folding process of the minimum composite unit.

In the same way, the position and velocity vectors of the remaining nodes of the minimum composite unit can be derived. Thus, in view of the structural topology relationship of the minimum composite units and the coordinate transform matrices, the kinematic analysis of the whole antenna can be easily accomplished.

4 Numerical Calculation and Simulation Verification

4.1 Verification on the DOF Analysis

The simulation model of a deployable truss spherical antenna composed of 27 tetrahedral elements is shown in Fig. 11. On the condition that one of the R joints of the 27 tetrahedral elements is actuated, the deployable truss antenna can be completely folded, as shown in Fig. 12, which effectively verifies the correctness of the DOF analysis of the deployable truss antenna.

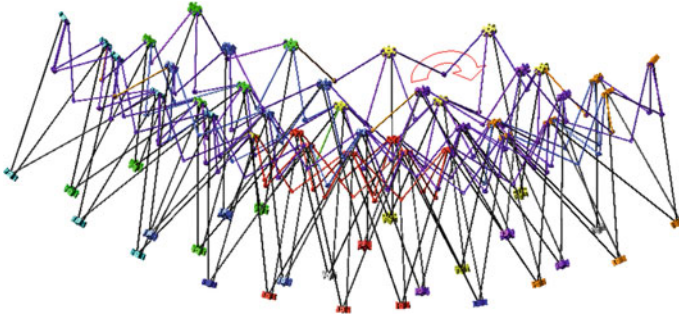


Fig. 11 Deployable truss antenna composed of 27 tetrahedral elements

Fig. 12 Folded configuration of the antenna



4.2 Verification on the Kinematic Analysis

A set of structure parameters of the minimum composite unit are given as: $l = 0.59$ m, $l_1 = l_2 = 0.250376$ m, $l_3 = 0.25$ m, and $\gamma_1 = \gamma_2 = \gamma_3 = 3.623^\circ$, where γ_2 (γ_3) represents the angle between the O_2A (O_3A) and the plane XAY . The minimum composite unit is folded from the initial configuration with $\varphi_0 = 66.829^\circ$. Let $\varphi = \varphi_0 - 0.5^\circ t$, then the simulation values of the positions and velocities of all nodes can be measured by the Adams software. The theoretical value and simulation result of the position variation of the node F and that of the velocity variation of the node I are given in Fig. 13 as representatives.

It can be seen from Fig. 13 that the simulation results and the theoretical values of the nodes F and I are basically consistent, and the errors between the theoretical values and the simulation ones of all nodes are less than 2 %, which effectively shows the correctness of the kinematic analysis of the deployable truss antenna.

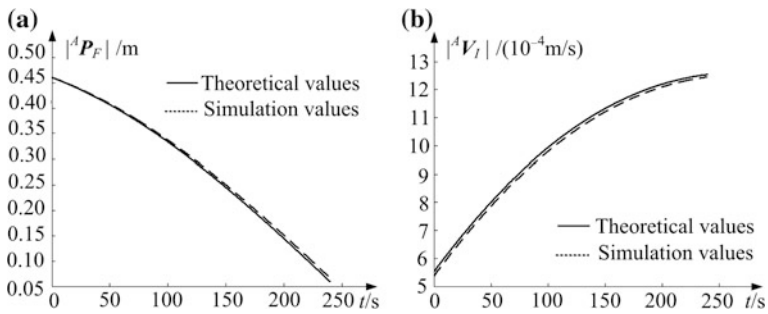


Fig. 13 **a** Position variation of the node F , **b** Velocity variation of the node I

5 Conclusions

In this work, an approach based on the reciprocal screw theory for the DOF analysis of the deployable truss antenna assembled by tetrahedral elements is presented, which greatly reduces the complexity and difficulty on the mobility analysis of this kind of mechanisms with multiple coupling-loops. The tetrahedral element is divided into a PM and a serial kinematic chain. On the basis of the numbers and characteristic of the DOF of the divided PM, the tetrahedral element with multiple coupling-loops is converted to a single-loop mechanism, as a result, the minimum composite unit of the antenna is also simplified, which contributes to the investigation on the DOF of the whole deployable truss antenna. In addition, according to the topological relationship of the antenna and the coordinate transformation matrices the position and velocity vectors of the connection nodes of the antenna during its deploying/folding process are derived. What's more, the simulation model of a deployable truss spherical antenna composed of 27 tetrahedral elements is built, and the simulation results on the DOF and kinematics of the antenna indicate the correctness of the theoretical analysis.

In view of the folded configuration of the deployable truss antenna shown in Fig. 13, future works are suggested: if the tetrahedral element mentioned in this paper is applied to the curved antenna, such as, parabolic or spherical antenna, a portion of R joints of the tetrahedral element need to be changed in order to achieve a smaller stowed volume.

Acknowledgments This research was sponsored by the National Natural Science Foundation of China under Grant 51675458 and Grant 51275439.

References

1. Cherniavsky AG, Gulyayev VI, Gaidaichuk VV, Fedoseev AI (2005) Large deployable space antennas based on usage of polygonal pantograph. *J Aerosp Eng* 18:139–145
2. Fazli N, Abedian A (2011) Design of tensegrity structures for supporting deployable mesh antennas. *Sci Iran* 18:1078–1087
3. Wang Y, Deng ZQ, Liu RQ, Yang H, Guo HW (2014) Topology structure synthesis and analysis of spatial pyramid deployable truss structures for satellite SAR antenna. *Chin J Mech Eng Engl Ed* 27:683–692
4. Xu Y, Guan FL (2013) Structure–electronic synthesis design of deployable truss antenna. *Aerosp Sci Technol* 26:259–267
5. Gosselin CM, Gagnon-Lachance D (2006) Expandable polyhedral mechanisms based on polygonal one-degree-of-freedom faces. *Proc Inst Mech Eng Part C J Mech Eng Sci* 220:1011–1018
6. Kiper G, Söylemez E, Kişisel A (2008) A family of deployable polygons and polyhedral. *Mech Mach Theory* 43:627–640
7. Wei GW, Ding XL, Dai JS (2011) Geometric constraint of an evolved deployable ball mechanism. *J Adv Mech Des Syst Manuf* 5:302–314
8. Ding XL, Yang Y, Dai JS (2013) Design and kinematic analysis of a novel prism deployable mechanism. *Mech Mach Theory* 63:35–49
9. Zheng F, Chen M (2015) New conceptual structure design for affordable space large deployable antenna. *IEEE Trans Antennas Propag* 63:1351–1358
10. You Z (2000) Deployable structure of curved profile for space antennas. *J Aerosp Eng* 13:139–143
11. Dai L, Guan FL, Guest James K (2014) Structural optimization and model fabrication of a double-ring deployable antenna truss. *Acta Astronaut* 94:843–851
12. Tanaka H (2006) Design optimization studies for large-scale contoured beam deployable satellite antennas. *Acta Astronaut* 58:443–451
13. Yu Y, Luo YZ (2009) Motion analysis of deployable structures based on the rod hinge element by the finite particle method. *Proc Inst Mech Eng Part C J Aerosp Eng* 223:955–964
14. Zhao ML, Guan FL (2005) Kinematic analysis of deployable toroidal spatial truss structures for large mesh antenna. *J Int Assoc Shell Spatial Struct* 46:195–204
15. Xu Y, Guan FL, Zheng Y, Zhao ML (2012) Kinematic analysis of the deployable truss structures for space applications. *J Aerosp Technolog Manage* 4:453–462
16. Xu Y, Guan FL, Chen JJ, Zheng Y (2012) Structural design and static analysis of a double-ring deployable truss for mesh antennas. *Acta Astronaut* 81:545–554
17. Li TJ, Wang Y (2009) Deployment dynamic analysis of deployable antennas considering thermal effect. *Aerosp Sci Technol* 13:210–215
18. Li TJ (2012) Deployment analysis and control of deployable space antenna. *Aerosp Sci Technol* 18:42–47

Displacement Analysis of a 6R Serial Robot Mechanism Using Conformal Geometric Algebra

Xiguang Huang and Dishuo Zhao

Abstract In this paper, we present a novel method for displacement analysis of a 6R serial robot mechanism based on conformal geometric algebra (CGA) method. The forward displacement problem of the mechanism is solved using motor and the inverse displacement problem is solved in a geometrically very intuitive way by handling intersections of spheres, circles, and planes, etc. in CGA. It is shown that this method has the advantages of simple computation and geometrical intuition.

Keywords Displacement analysis · 6R serial robot · Conformal geometric algebra

1 Introduction

The inverse displacement analysis of serial robot manipulators is a fundamental problem in the automatic control of robot manipulators. The inverse displacement problem, which is to compute the joint displacements given the position and orientation of the end-effector, is very difficult. The motion planning and control of a serial robot calls for the solution of the inverse displacement. There have been many literatures on the closed-form solutions for the inverse displacement analysis of serial robot mechanisms. Pieper [1] developed closed-form solutions for the case where any three consecutive axes intersect in a common point. Roth [2] showed that the number of solutions of the general serial 6R mechanism problem was an upper bound of 32. Subsequently, many excellent researchers studied the kinematics community the inverse displacement analysis problem of general 6R mechanism attracted until Li [3] gave the exact solution in lower dimensions by reducing the problem to a 16 degree polynomial. This work was simplified and extended by Raghavan [4]. Manocha [5] formulated this problem as an eigenvalue problem and improved the stability and accuracy of the algorithm. Manfred [6] presented an easy

X. Huang (✉) · D. Zhao

School of Mechanical and Materials Engineering, North China University of Technology,
Beijing 100041, China
e-mail: marchbupt@126.com

solution to give the necessary insight into the geometric structure of the 6R mechanism by using the classical multi-dimensional geometry. Qiao [7] transformed the homogeneous matrix to the form of double quaternion and obtained 16 solutions from resultant matrix by linear algebra and Dixon resultant elimination. In this paper, we present a novel method for displacement analysis of a 6R serial robot mechanism based on conformal geometric algebra.

The organization of the paper is as follows: Sect. 2 presents a brief introduction about the foundation of CGA. Section 3 shows the forward displacement problem of the mechanism is solved using motor that describing a rigid-body motion in CGA. Section 4 demonstrates the computation of the inverse displacement problem of a 6R serial robot mechanism by CGA. This framework appears promising for dealing with kinematics problems. Section 5 illuminates a numerical example of inverse kinematics of a 6R serial robot to verify the presented method, and a set of real solution are obtained. Finally, Sect. 6 provides conclusions of this study.

2 Conformal Geometric Algebra

Conformal geometric algebra (CGA) is a new tool for geometric representation and computation [8, 9]. There are three kinds of products in geometric algebra: geometric product, outer product and inner product. For two vectors \mathbf{u} and \mathbf{v} , the geometric product can be defined as

$$\mathbf{uv} = \mathbf{u} \cdot \mathbf{v} + \mathbf{u} \wedge \mathbf{v} \tag{1}$$

where $\mathbf{u} \cdot \mathbf{v}$ denotes the inner product and $\mathbf{u} \wedge \mathbf{v}$ denotes the outer product.

Blades are the basic computational elements and geometric entities of the geometric algebra. The n -blades can be written as

$$\mathbf{I} = e_1 \wedge e_2 \wedge e_3 \cdots \wedge e_n \tag{2}$$

where \mathbf{I} is called the pseudo-scalar and e_i denotes the basic vector i . The inverse of a blade \mathbf{A} is defined by \mathbf{A}^{-1} . The dual operation of a blade \mathbf{A} is defined as

$$\mathbf{A}^* = \mathbf{A}/\mathbf{I} = \mathbf{AI}^{-1} \tag{3}$$

where \mathbf{A}^* denotes the dual of \mathbf{A} .

A geometric algebra \mathbf{G}_n is an n -dimensional vector space with the basic vectors e_1, e_2, \dots, e_n . CGA uses the three Euclidean basis vectors e_1, e_2, e_3 and two additional basis vectors e_+, e_- , with the properties

$$\begin{cases} e_i^2 = 1, i = 1, 2, 3 \\ e_{\pm}^2 = -1 \\ e_i \cdot e_+ = e_i \cdot e_- = 0, i = 1, 2, 3 \end{cases} \tag{4}$$

A null basis $\{e_0, e_\infty\}$ can be introduced by

$$\begin{cases} e_0 = \frac{1}{2}(e_- - e_+) \\ e_\infty = e_- + e_+ \\ e_0^2 = e_\infty^2 = 0, e_0 \cdot e_\infty = -1 \end{cases} \tag{5}$$

with e_0 represents the 3D origin, and e_∞ represents infinity.

CGA provides a great variety of basic geometric entities to compute with, namely points, spheres, planes, circles, lines, and point pairs, as listed in Table 1. In the table, \mathbf{X} and \mathbf{n} are marked bold to represent 3D entities, with \mathbf{X} indicating a point and \mathbf{n} indicating the normal vector of a plane.

The operator $\mathbf{R} = e^{-\frac{\theta}{2}\mathbf{L}}$ describes a rotor, where $\mathbf{L} = n_1 \wedge n_2$ is the rotation axis, and θ is the rotation angle. \mathbf{R} can also be written as

$$\mathbf{R} = \cos\left(\frac{\theta}{2}\right) - \mathbf{L} \sin\left(\frac{\theta}{2}\right) \tag{6}$$

The operator $\mathbf{T} = e^{-\frac{1}{2}\mathbf{t}e_\infty}$ describes a translator, where \mathbf{t} is a vector. \mathbf{T} can also be written as

$$\mathbf{T} = 1 - \frac{1}{2}\mathbf{t}e_\infty \tag{7}$$

A Rigid-Body motion, including both a rotation and a translation, is described by a motor \mathbf{M}

$$\mathbf{M} = \mathbf{R}\mathbf{T} \tag{8}$$

where \mathbf{R} being a rotor and \mathbf{T} being a translator.

So the Rigid-Body motion of the object \mathbf{o} can be described as

$$\mathbf{o}' = \mathbf{M}\mathbf{o}\tilde{\mathbf{M}} \tag{9}$$

Table 1 Entities in conformal geometric algebra

Entities	INPS representation	OPNS representation
Point	$\mathbf{P} = \mathbf{X} + \mathbf{X}^2 e_\infty / 2 + e_0$	
Sphere	$\mathbf{S} = \mathbf{P} - r^2 e_\infty / 2$	$\mathbf{S}^* = \mathbf{X}_1 \wedge \mathbf{X}_2 \wedge \mathbf{X}_3 \wedge \mathbf{X}_4$
Plane	$\boldsymbol{\pi} = \mathbf{n} + d e_\infty$	$\boldsymbol{\pi}^* = \mathbf{X}_1 \wedge \mathbf{X}_2 \wedge \mathbf{X}_3 \wedge e_\infty$
Circle	$\mathbf{Z} = \mathbf{S}_1 \wedge \mathbf{S}_2$	$\mathbf{Z}^* = \mathbf{X}_1 \wedge \mathbf{X}_2 \wedge \mathbf{X}_3$
Line	$\mathbf{l} = \boldsymbol{\pi}_1 \wedge \boldsymbol{\pi}_2$	$\mathbf{l}^* = \mathbf{X}_1 \wedge \mathbf{X}_2 \wedge e_\infty$
Point pair	$\mathbf{P}_P = \mathbf{S}_1 \wedge \mathbf{S}_2 \wedge \mathbf{S}_3$	$\mathbf{P}_P^* = \mathbf{X}_1 \wedge \mathbf{X}_2$

where \tilde{M} denoting the reverse of M .

In CGA, the two points of a point pair Pp^* can be extracted by

$$p_{\pm} = -\frac{\pm\sqrt{Pp^* \cdot Pp^*} + Pp^*}{e_{\infty} \cdot Pp^*} \tag{10}$$

And the angle θ is computed by the formula

$$\cos(\theta) = \frac{o_1^* \cdot o_2^*}{|o_1^*| |o_2^*|} \tag{11}$$

with o_i ($i = 1, 2$) being lines or planes, θ being the angle between line and line or plane and plane.

3 The Forward Displacement Analysis

A six degree of freedom 6R serial Spray Painting robot is shown in Fig. 1 and the structure diagram of the robot mechanism is shown in Fig. 2. The robot has six revolute joints, among which the joint $Z_1, Z_2,$ and Z_3 determine 6 the position of the end-effector, in addition the joint $Z_4, Z_5,$ and Z_6 determine the orientation where the consecutive three axes intersect in a common point. The end-effector and the position of the tool are fixed at the same point. $L_1, L_2,$ and L_3 denote the lengths of the three links respectively.

The forward displacement analysis of a serial robot manipulator is to determine the position and orientation of the end-effector given the joint positions, i.e. the angles of the revolute joints and the displacements of the prismatic joints.

From Eq. (8), the forward kinematics can be described by

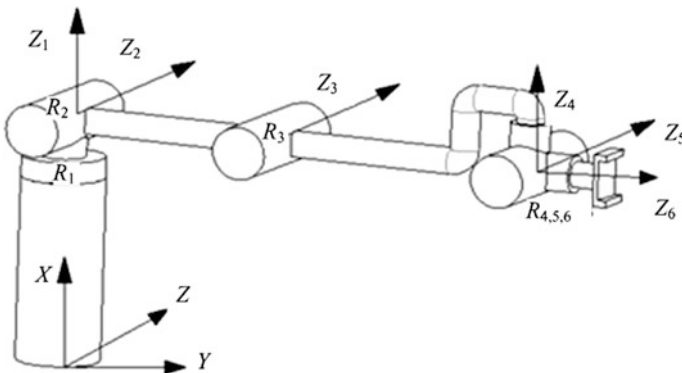


Fig. 1 A six degree of freedom 6R serial Spray Painting robot

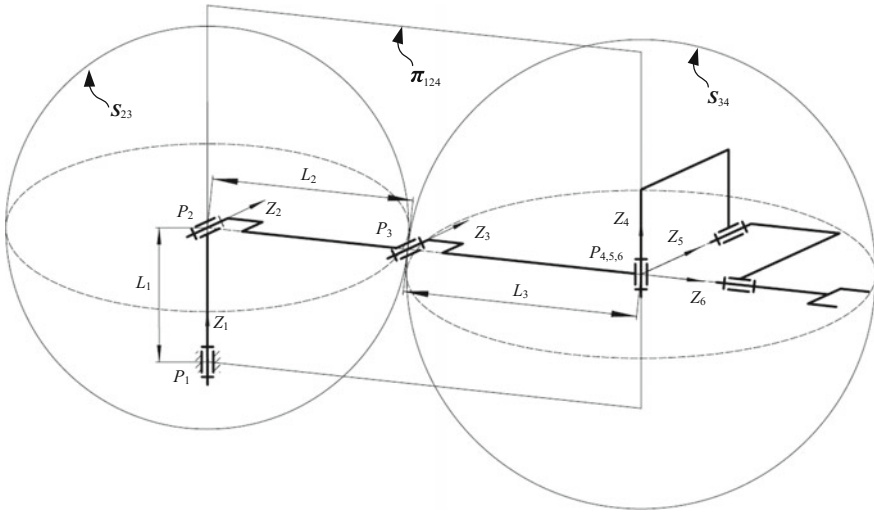


Fig. 2 The structure diagram of the 6R serial robot mechanism

$${}^0M = {}^0M_1M_2M_3M_4M_5M_6M_t \tag{12}$$

where 0M represents the end-effector's pose with respect to the base of the robot, iM_j notes the pose of the joint j with respect to the joint i . The descriptions of iM_j are given as following

$$\begin{aligned}
 {}^1_0M &= R_{\theta_1}T_{L_1}, R_{\theta_1} = \cos\left(\frac{\theta_1}{2}\right) - e_{23} \sin\left(\frac{\theta_1}{2}\right), T_{L_1} = 1 - \frac{1}{2}L_1e_1e_\infty \\
 {}^2_1M &= R_{\theta_2}T_{L_2}, R_{\theta_2} = \cos\left(\frac{\theta_2}{2}\right) - e_{12} \sin\left(\frac{\theta_2}{2}\right), T_{L_2} = 1 - \frac{1}{2}L_2e_2e_\infty \\
 {}^3_2M &= R_{\theta_3}T_{L_3}, R_{\theta_3} = \cos\left(\frac{\theta_3}{2}\right) - e_{12} \sin\left(\frac{\theta_3}{2}\right), T_{L_3} = 1 - \frac{1}{2}L_3e_2e_\infty \\
 {}^3_4M &= R_{\theta_4}, R_{\theta_4} = \cos\left(\frac{\theta_4}{2}\right) - e_{23} \sin\left(\frac{\theta_4}{2}\right) \\
 {}^4_5M &= R_{\theta_5}, R_{\theta_5} = \cos\left(\frac{\theta_5}{2}\right) - e_{12} \sin\left(\frac{\theta_5}{2}\right) \\
 {}^5_6M &= R_{\theta_6}, R_{\theta_6} = \cos\left(\frac{\theta_6}{2}\right) + e_{13} \sin\left(\frac{\theta_6}{2}\right) \\
 {}^6_tM &= 1
 \end{aligned}$$

Knowing the values of L_1 , L_2 , and L_3 and the input values of $\theta_1 \sim \theta_6$, the position P_t of the end-effector can be obtained by Eq. (9)

$$P_t = \begin{pmatrix} 0 \\ 1 \end{pmatrix} \mathbf{M} P_1 \begin{pmatrix} 0 \\ 1 \end{pmatrix} \tilde{\mathbf{M}} \tag{13}$$

From Eq. (9), X_t , Y_t , and Z_t can be easily calculated as following

$$\begin{cases} X_t = \begin{pmatrix} 0 \\ 1 \end{pmatrix} \mathbf{M} e_1 \begin{pmatrix} 0 \\ 1 \end{pmatrix} \tilde{\mathbf{M}} \\ Y_t = \begin{pmatrix} 0 \\ 1 \end{pmatrix} \mathbf{M} e_2 \begin{pmatrix} 0 \\ 1 \end{pmatrix} \tilde{\mathbf{M}} \\ Z_t = \begin{pmatrix} 0 \\ 1 \end{pmatrix} \mathbf{M} e_3 \begin{pmatrix} 0 \\ 1 \end{pmatrix} \tilde{\mathbf{M}} \end{cases} \tag{14}$$

where X_t , Y_t , and Z_t represent the x -axis, y -axis, z -axis of the coordinates system of the end-effector. Equations (14) and (15) can indicate the position and orientation of the end-effector.

4 The Inverse Displacement Analysis

The inverse displacement problem is to determine the angle $\theta_1 \sim \theta_6$ given the end-effector's position P_t and orientation X_t, Y_t and Z_t . In the following steps, we calculate the joint point P_2, P_3 and P_4 , where joint point P_4, P_5 and P_6 coincide in the same one point. Then, all joint angle $\theta_1 \sim \theta_6$ of each joint can be obtained using the inner product in CGA.

4.1 Computation of the Joint Positions

Firstly, joint point P_2 can be get by moving joint point P_1 along vector L_1 . From Table 1, the position of the joint point P_2 can be get

$$P_2 = L_1 e_1 + \frac{1}{2} L_1 e_\infty + e_0 \tag{15}$$

Referring to the Fig. 1, joint points P_4, P_5 and P_6 coincide in the same one point and the three positions of joint point P_4, P_5 and P_6 equals the end-effector's position P_t . From Table 1, we get

$$P_4 = P_t = P_{tx} e_1 + P_{ty} e_2 + P_{tz} e_3 + \frac{1}{2} (P_{tx}^2 + P_{ty}^2 + P_{tz}^2) e_\infty + e_0 \tag{16}$$

Referring to Fig. 2, the joint point P_3 has to lie on the sphere S_{23} with center joint P_2 and with the length L_2 as the radius. From Table 1, we get

$$S_{23} = P_2 - \frac{1}{2}L_2^2e_\infty \tag{17}$$

Since the joint point P_3 also has to lie on the sphere S_{43} with center joint P_4 and with the length L_3 as the radius. From Table 1, we get

$$S_{43} = P_4 - \frac{1}{2}L_3^2e_\infty \tag{18}$$

Since the joint point P_3 also has to lie in the plane π_{124} which can be defined with the help of the joint point P_1, P_2 and P_4 that line on it. From Table 1, we get

$$\pi_{124} = P_1 \wedge P_2 \wedge P_4 \wedge e_\infty \tag{19}$$

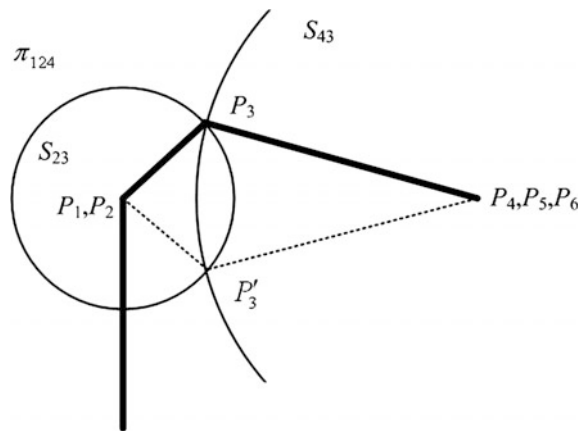
Referring to Fig. 2, the position of the joint point P_3 can be calculated as the intersection of the sphere S_{23}, S_{43} and the plane π_{124} . We can get the point pair Pp_3 about the joint point P_3 and the

$$Pp_3 = S_{23} \wedge S_{43} \wedge \pi_{124} \tag{20}$$

Referring to Fig. 3, there are two results responding to two different configurations of the robot. Among two points only P_3 is applicable from the point of view of mechanics. We have to choose the proper one by Eq. (10)

$$P_3 = \frac{\sqrt{Pp_3^* \cdot Pp_3^*} + Pp_3^*}{e_\infty \cdot Pp_3^*} \tag{21}$$

Fig. 3 Computation of the joint point P_3



4.2 Computation of the Joint Angles

Referring to Fig. 2, the angle θ_1 is between the plane π_{124} and the plane π_{xoy} . By Eq. (11), we get

$$\cos \theta_1 = \frac{\pi_{124}^* \cdot \pi_{xoy}^*}{|\pi_{124}^*| \cdot |\pi_{xoy}^*|} \tag{22}$$

where, $\pi_{124} = P_1 \wedge P_2 \wedge P_4 \wedge e_\infty$, $\pi_{xoy} = e_3 I_c^{-1}$.

Referring to Fig. 2, the angle θ_2 is between the line l_{23} and the line l_{proc} that is the projection of l_{23} in the plane π_{234} obtained by moving the plane π_{yoz} along X -axis by L_1 , we get

$$\cos \theta_2 = \frac{l_{23}^* \cdot l_{proc}^*}{|l_{23}^*| \cdot |l_{proc}^*|} \tag{23}$$

where, $l_{23} = P_2 \wedge P_3 \wedge e_\infty$, $\pi_{234} = e_1 + L_1 e_\infty$, $l_{proc} = \frac{\pi_{234}^* \cdot l_{23}^*}{\pi_{234}^*}$.

The angle θ_3 is between the line l_{23} and the line l_{34} , we get

$$\cos \theta_3 = \frac{l_{23}^* \cdot l_{34}^*}{|l_{23}^*| \cdot |l_{34}^*|} \tag{24}$$

where, $l_{34} = P_3 \wedge P_4 \wedge e_\infty$.

Referring to Fig. 2, the axis Y_6 in the 6th coordinate system is the same with the axis Y_1 in the coordinate system of the end-effector that is known in the inverse displacement analysis, yields by Eq. (14)

$$Y_1 = ({}^0_5M) e_2 ({}^0_5\tilde{M}) \tag{25}$$

In Eq. (9), making corresponding coefficients of the left equate with the right ends equal, so a quadratic equations in terms of two unknown variables θ_4 , and θ_5 can be obtained and the value of the angle θ_4 , and θ_5 can be computed by Gauss elimination simply.

The axis Y_1 in the coordinate system of the end-effector also can be obtained using 0_tM by Eq. (14), yields

$$Y_1 = ({}^0_tM) e_2 ({}^0_t\tilde{M}) \tag{26}$$

Substituting $\theta_1, \theta_2, \theta_3, \theta_4$, and θ_5 into Eq. (26) with only a unknown θ_6 . The value of the angle θ_6 can be obtained easily.

5 Numerical Example

In this section, we validate the new algorithm with a numerical example to verify the presented method. The input geometrical parameters of the Spray Painting robot are given as: $L_1 = 0.8, L_2 = 1.2, L_3 = 1.4$. Given a set of joint values: $\theta_1 = 11.12^\circ, \theta_2 = -10.57^\circ, \theta_3 = -24.51^\circ, \theta_4 = -35.16^\circ, \theta_5 = 142.02^\circ, \theta_6 = 13.25^\circ$.

The position P_{tx}, P_{ty} , and P_{tz} and the orientation X_t, Y_t , and Z_t of the end-effector are computed by Sect. 3 as follows

$$\begin{aligned}
 P_{tx} &= 1.824799997, P_{ty} = 2.281600001, P_{tz} = 0.448600000 \\
 X_t &= -0.422189627e_1 + 0.822663280e_2 - 0.380763766e_3 \\
 Y_t &= -0.873978690e_1 - 0.257881491e_2 + 0.411896085e_3 \\
 Z_t &= 0.240659856e_1 + 0.506677672e_2 + 0.827865067e_3
 \end{aligned}$$

Based on the values of $P_{tx}, P_{ty}, P_{tz}, X_t, Y_t$, and Z_t , the homogenous transformation matrix T , represents the end-effector's pose with respect to the base of the robot, can be obtained easily

$$T = \begin{bmatrix} -0.422189627 & -0.873978690 & 0.240659856 & 1.824799997 \\ 0.822663280 & -0.257881491 & 0.506677672 & 2.281600001 \\ -0.380763766 & 0.411896085 & 0.827865067 & 0.448600000 \\ 0 & 0 & 0 & 1 \end{bmatrix}$$

According to the inverse displacement algorithm proposed in Sect. 4, we get eight solutions of the inverse displacement of the robot as shown in Table 2. All solutions have been verified by the forward displacement analysis.

Table 2 Eight real solutions of the robot

No.	θ_1	θ_2	θ_3	θ_4	θ_5	θ_6
1	11.1234027	-36.997899	24.5129213	128.294726	54.6653395	170.750206
2	11.1234027	-36.997899	24.5129213	-51.705277	125.334662	-9.2497993
3	11.1234027	-10.570249	-24.512921	144.838235	37.9831318	-166.75318
4	11.1234027	-10.570249	-24.512921	-35.161762	142.016862	13.2468134
5	-168.87659	-169.42975	24.5129213	35.1617620	-142.01686	-166.75318
6	-168.87659	-169.42975	24.5129213	-144.83823	-37.983131	13.2468134
7	-168.87659	-143.00210	-24.512921	51.7052771	-125.33466	170.750206
8	-168.87659	-143.00210	-24.512921	-128.29472	-54.665339	-9.2497993

6 Conclusions

This paper presents a novel method based on the conformal geometric algebra to solve the displacement problem of a 6R Spray Painting robot. We make use of CGA to structure the problem and use the geometric information or properties to reduce the problem to some geometric computation. The forward displacement problem of the mechanism is solved using motor and the inverse displacement problem is solved in a geometrically very intuitive way by handling intersections of spheres, circles, and planes, etc. in CGA. A numerical example is demonstrated to show that this method has the advantages of simple computation and geometrical intuition.

Acknowledgments This work is partially supported by a National Natural Science Foundation of China (51105003) and NCUT Youth Talent Support Program (XN070016).

References

1. Pieper D (1968) The kinematics of manipulators under computer control. Ph.D. thesis: Stanford University, Stanford, America
2. Roth B, Rastegar J, Scheinman V (1973) On the design of computer controlled manipulators. In: First CISM-IFTMM symposium on theory and practice of robots and manipulators, pp 93–113
3. Lee HY, Liang CG (1988) Displacement analysis of the general spatial 7-link 7R mechanism. *Mech Mach Theory* 23(3):219–226
4. Raghavan M, Roth B (1990) Inverse kinematics of the general 6R manipulator and related linkages. *ASME J Mech Des* 115(3):228–235
5. Manocha D, Canny J (1994) Efficient inverse kinematics for general 6R manipulators. *IEEE Trans Robot Autom* 5(9):648–657
6. Manfred LH, Martin P, Schrocher H (2007) A new and efficient algorithm for the inverse kinematics of a general serial 6R manipulator. *Mech Mach Theory* 42:66–81
7. Qiao S, Wei S, Liao Q (2010) Inverse kinematic analysis of the general 6r serial manipulators based on double quaternions. *Mech Mach Theory* 45(2):193–199
8. Li HB, Hestenes D, Rockwood A (2001) Spherical conformal geometry with geometric algebra. In *Geometric computing with clifford algebras*. Springer, Heidelberg, pp 61–76
9. Li HB, Hestenes D, Rockwood A (2001) A universal model for conformal geometries of euclidean, spherical and double-hyperbolic spaces. In: *Geometric computing with clifford algebras*. Springer, Heidelberg, pp 77–104

The Kinematics of a 3-DOF Mechanism for Wave Energy Converter

Weixing Chen and Feng Gao

Abstract As we all know, oceans have great wave power, and many types of wave energy converters (WECs) have been invented so far. Oscillating body systems are a major class of WECs which almost only have one degree of freedom (DOF). This paper presents a 3-DOF mechanism which can extract the wave power from any wave directions. The 3-DOF mechanism mainly consists of a four-bar linkage and a spherical joint, which are used to capture the heave motion and the pitch and roll motions of the oscillating body respectively. The power conversion principle of the WEC is proposed and the kinematics of the mechanism is derived.

Keywords WEC · Principle · 3-DOF mechanism · Kinematics

1 Introduction

Ocean is a huge reservoir of renewable energy, such as wave power, tidal power, ocean current power, ocean thermal power, salinity gradient power, etc. Of these types of energy, wave power is deemed as the most notable form [1]. The research enthusiasm of the WEC is raised since the Duck proposed by Salter in 1974 [2]. So far, few systems have reached full-scale stage, such as OPT and Pelamis.

There are three WEC systems classified by working principles [3], including the oscillating water column [4, 5], the oscillating body system [6–9] and the over-topping device [10, 11]. Among the various technologies, the oscillating body systems have been researched widely in the recent years. They generally extract wave power through relative motion between two bodies, almost of them oscillate in only one direction [12, 13]. The power absorption performances of numerous

W. Chen · F. Gao (✉)

State Key Laboratory of Mechanical System and Vibration, Shanghai Jiao Tong University,
Shanghai 200240, China
e-mail: fengg@sjtu.edu.cn

W. Chen

e-mail: cwxsjtu@163.com

WECs have been numerically studied [14]. The results show that the capture width ratio of almost existing oscillating systems is not satisfactory.

It is well known that the oscillating body has six DOFs in the random ocean waves. When the oscillating body is axisymmetric, only heave, pitch and roll motions have the restoring force (moments), which benefit for the power absorption. Because the restoring force (moments) can make the body itself return to the equilibrium position without external force (moments). However, some mechanisms being able to harvest the three motion's mechanical energy have not appeared.

This paper focuses on the principle of the 3-DOF mechanism for wave energy converter. The power conversion principle of the mechanism is first introduced. Subsequently, the kinematics of the mechanism is derived. The mechanism can absorb and deliver the three motions of the floating body.

2 Conversion Principle

The 3-DOF WEC is shown in Fig. 1, and the 3-DOF mechanism for the wave power converter is shown in Fig. 2. β is the wave direction. The oscillating body has three motions including heave, roll and pitch. The body can rotate around point O and oscillate up and down. The roll and pitch motions are achieved by the spherical joint, and the heave motion is realized by the four-bar linkage. The

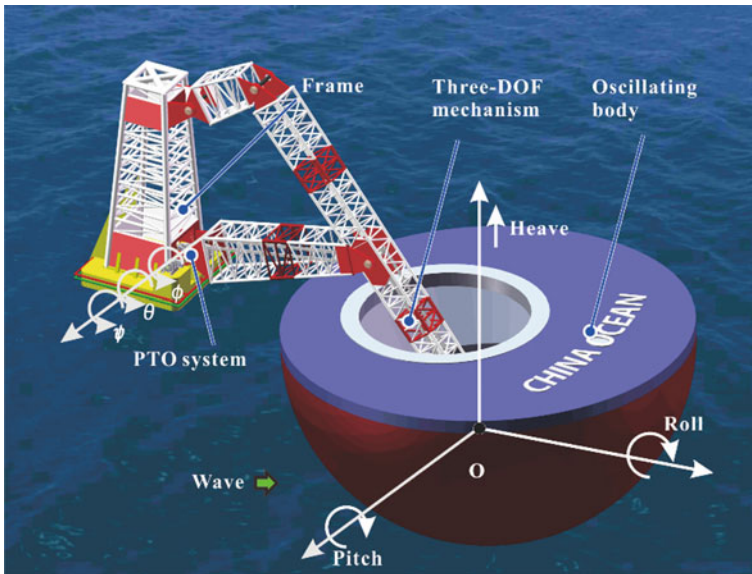


Fig. 1 Schematic of the 3-DOF WEC

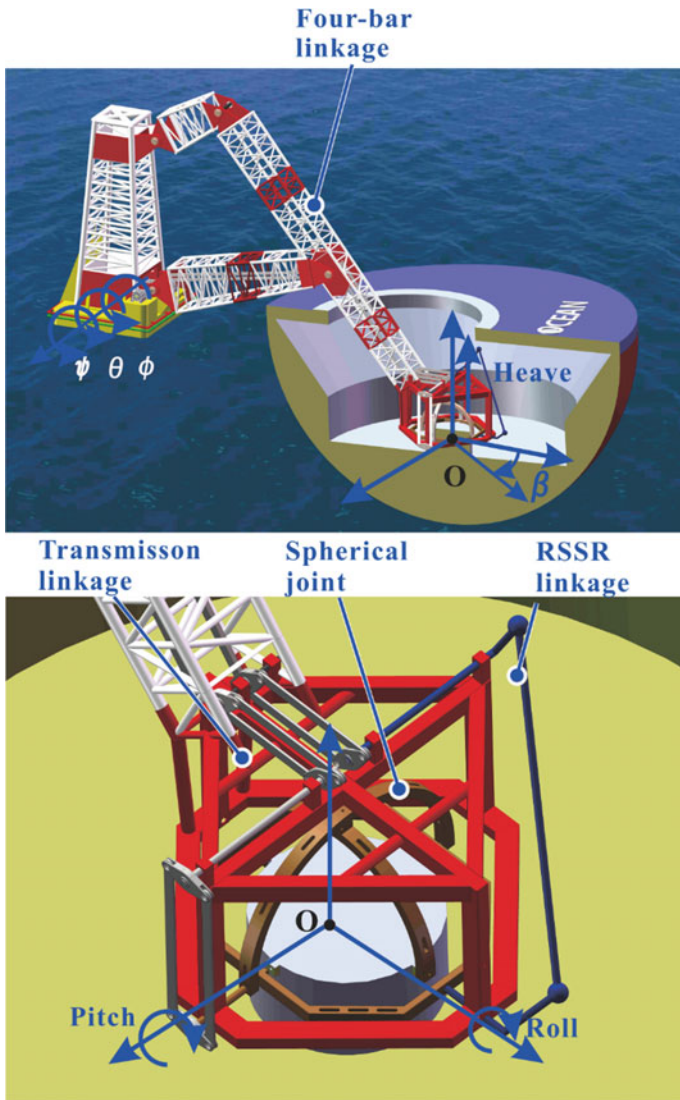


Fig. 2 Schematic of the 3- DOF mechanism for wave energy converter

mechanism can deliver the random reciprocating motions of the body to the reciprocating rotations (ψ , θ and ϕ) of the mechanism relative to the frame. Then rotational mechanical energy can transform into hydraulic energy through PTO systems, which are simplified as constant torques in this study. Finally, the hydraulic energy can be converted into electrical energy through hydraulic motor and electrical generator.

3 Kinematics

The 3-DOF mechanism is composed of the spherical joint, the four-bar linkage and the RSSR (revolute pair—spherical pair—spherical pair—revolute pair) linkage. The spherical joint delivers rotational energy of the oscillating body, and the translation energy is collected by the four-bar linkage. The RSSR linkage is used to change the transmission direction. It is necessary to discuss the kinematics of the mechanism.

The four-bar linkage is shown in Fig. 3. The wave forces act on the point O through the body and drive the motion of the four-bar linkage. θ is the output of the linkage. The θ and θ_2 can be expressed as:

$$\theta = 2 \arctan \frac{B_\theta + \sqrt{A_\theta^2 + B_\theta^2 - C_\theta^2}}{A_\theta - C_\theta} \tag{1}$$

$$\theta_2 = \arctan \frac{B_\theta + l_3 \sin \theta_3}{A_\theta + l_3 \cos \theta_3} \tag{2}$$

where

$$A_\theta = l_4 - l_1 \cos \theta_h \tag{3}$$

$$B_\theta = -l_1 \sin \theta_h \tag{4}$$

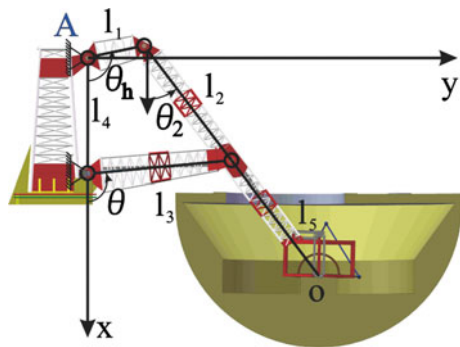
$$C_\theta = (A_\theta^2 + B_\theta^2 + l_3^2 - l_2^2) / (2l_3) \tag{5}$$

The vertical position of the point O is given:

$$L_{Ox} = l_1 \cos \theta_h + (l_2 + l_5) \cos \theta_2 \tag{6}$$

The horizontal position of the point O is given:

Fig. 3 The schematic of the four-bar linkage



$$L_{Oy} = l_1 \sin \theta_h + (l_2 + l_5) \sin \theta_2 \tag{7}$$

when the length of l_1 is equal to 12 m; the length ratio is satisfied $l_1 : l_2 : l_3 : l_4 : l_5 = 2 : 5 : 5 : 4 : 5$; θ_h is in the interval $[80^\circ, 280^\circ]$, the trajectory of the point O is close to a straight line, which is shown in Fig. 4.

The simplified two-DOF spherical joint is shown in Fig. 5, which is composed of five spatial components and five revolute joints. The body 4 can rotate around the point O induced by waves. The α_y and α_z work as the output. The moving frame $\{i_x i_y i_z\}$ is fixed in the body, and the fixed frame is $\{j_x j_y j_z\}$.

The reference frames used in the analysis are shown in Fig. 5. First, the body rotates around i_z axis θ_z degree, then rotates around i_y axis θ_y degree. The rotating matrix $\{i_x i_y i_z\}$ relative to $\{j_x j_y j_z\}$ can be described as :

$$R = R_z R_y = \begin{bmatrix} \cos \theta_y \cos \theta_z & -\sin \theta_z & \sin \theta_y \cos \theta_z \\ \cos \theta_y \sin \theta_z & \cos \theta_z & \sin \theta_y \sin \theta_z \\ -\sin \theta_y & 0 & \cos \theta_y \end{bmatrix} \tag{8}$$

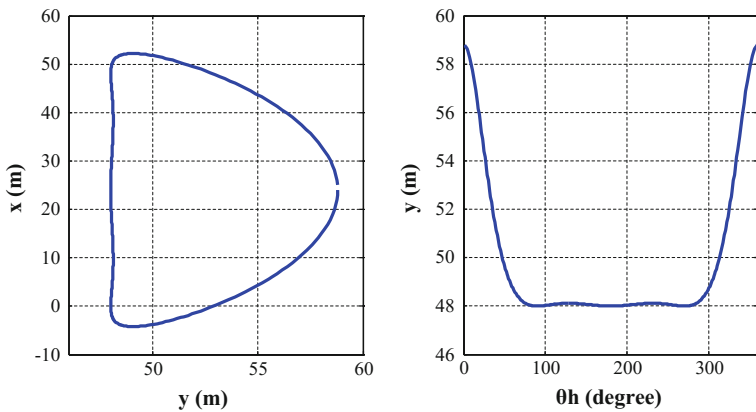
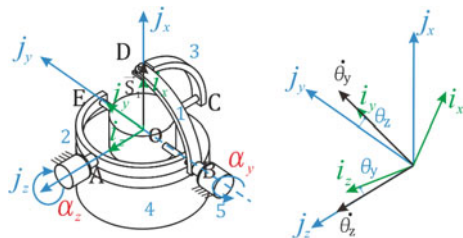


Fig. 4 The trajectory of the point O in the left and the y coordinate of the point O changed with θ_h in the right

Fig. 5 The simplified spherical joint and reference frames



where

$$R_z = \begin{bmatrix} \cos \theta_z & -\sin \theta_z & 0 \\ \sin \theta_z & \cos \theta_z & 0 \\ 0 & 0 & 1 \end{bmatrix} \tag{9}$$

$$R_y = \begin{bmatrix} \cos \theta_y & 0 & \sin \theta_y \\ 0 & 1 & 0 \\ -\sin \theta_y & 0 & \cos \theta_y \end{bmatrix} \tag{10}$$

i_y axis relative to the fixed frame $\{j_x j_y j_z\}$ can be expressed as

$$i_y = R \begin{bmatrix} 0 \\ 1 \\ 0 \end{bmatrix} = \begin{bmatrix} -\sin \theta_z \\ \cos \theta_z \\ 0 \end{bmatrix} \tag{11}$$

i_z axis relative to the fixed frame $\{j_x j_y j_z\}$ can be expressed as:

$$i_z = R \begin{bmatrix} 0 \\ 0 \\ 1 \end{bmatrix} = \begin{bmatrix} \sin \theta_y \cos \theta_z \\ \sin \theta_y \sin \theta_z \\ \cos \theta_y \end{bmatrix} \tag{12}$$

Meanwhile, the joint E revolute α_y , the joint A revolute α_z , \vec{S}_1 is the unit vector, which is in the body fixed moving frame then

$$\vec{S}_1 = \begin{bmatrix} \cos \alpha_y & 0 & \sin \alpha_y \\ 0 & 1 & 0 \\ -\sin \alpha_y & 0 & \cos \alpha_y \end{bmatrix} \begin{bmatrix} 1 \\ 0 \\ 0 \end{bmatrix} = \begin{bmatrix} \cos \alpha_y \\ 0 \\ -\sin \alpha_y \end{bmatrix} \tag{13}$$

$$i_y = \begin{bmatrix} \cos \alpha_z & -\sin \alpha_z & 0 \\ \sin \alpha_z & \cos \alpha_z & 0 \\ 0 & 0 & 1 \end{bmatrix} \begin{bmatrix} 0 \\ 1 \\ 0 \end{bmatrix} = \begin{bmatrix} -\sin \alpha_z \\ \cos \alpha_z \\ 0 \end{bmatrix} \tag{14}$$

Comparing Eq. (11) and Eq. (14), the relationship of the α_z and θ_z is obtained:

$$\alpha_z = \theta_z \tag{15}$$

S_1 and i_z is always vertical, so

$$\vec{S}_1 \cdot i_y = 0 \tag{16}$$

That is

$$\sin \theta_y \cos \theta_z \cos \alpha_y - \cos \theta_y \sin \alpha_y = 0 \tag{17}$$

Hence, the forward position solution of the joint can be written as:

$$\begin{cases} \alpha_z = \theta_z \\ \alpha_y = \arctan\left(\frac{\sin \theta_y \cos \theta_z}{\cos \theta_y}\right) \end{cases} \tag{18}$$

Some linkages are needed to change the transmission direction of the output of the roll motion (α_y). Here the RSSR linkage is introduced, which is presented in Fig. 6. The homogeneous transformation matrix from frame $\{x_1y_1z_1\}$ to frame $\{x_0y_0z_0\}$ is given:

$${}^0_1T = \begin{bmatrix} \cos \gamma_1 & -\sin \gamma_1 & 0 & 0 \\ \sin \gamma_1 & \cos \gamma_1 & 0 & 0 \\ 0 & 0 & 1 & -e_0 \\ 0 & 0 & 0 & 1 \end{bmatrix} \tag{19}$$

The homogeneous transformation matrix from frame $\{x_3y_3z_3\}$ to frame $\{x_0y_0z_0\}$ is given:

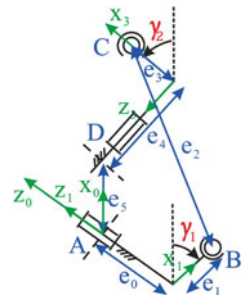
$${}^0_3T = \begin{bmatrix} \cos \gamma_2 & -\sin \gamma_2 & 0 & e_5 \\ 0 & 0 & -1 & e_4 \\ \sin \gamma_2 & \cos \gamma_2 & 0 & 0 \\ 0 & 0 & 0 & 1 \end{bmatrix} \tag{20}$$

Point B in frame $\{x_1y_1z_1\}$ is expressed as

$${}^1B = [e_1 \quad 0 \quad 0 \quad 1]^T \tag{21}$$

Point B in frame $\{x_0y_0z_0\}$ is expressed as

Fig. 6 Schematic of the RSSR linkage



$${}^0B = {}^0_1T^1B = \begin{bmatrix} \cos \gamma_1 & -\sin \gamma_1 & 0 & 0 \\ \sin \gamma_1 & \cos \gamma_1 & 0 & 0 \\ 0 & 0 & 1 & -e_0 \\ 0 & 0 & 0 & 1 \end{bmatrix} \begin{bmatrix} e_1 \\ 0 \\ 0 \\ 1 \end{bmatrix} = \begin{bmatrix} e_1 \cos \gamma_1 \\ e_1 \sin \gamma_1 \\ -e_0 \\ 1 \end{bmatrix}$$

Point C in frame $\{x_3y_3z_3\}$ is:

$${}^3C = [e_3 \quad 0 \quad 0 \quad 1]^T \tag{22}$$

Point C in frame $\{x_0y_0z_0\}$ is:

$${}^0C = {}^0_3T^3C = \begin{bmatrix} \cos \gamma_2 & -\sin \gamma_2 & 0 & e_5 \\ 0 & 0 & -1 & e_4 \\ \sin \gamma_2 & \cos \gamma_2 & 0 & 0 \\ 0 & 0 & 0 & 1 \end{bmatrix} \begin{bmatrix} e_3 \\ 0 \\ 0 \\ 1 \end{bmatrix} = \begin{bmatrix} e_3 \cos \gamma_2 + e_5 \\ e_4 \\ e_3 \sin \gamma_2 \\ 1 \end{bmatrix} \tag{23}$$

The length of the BC bar is invariant so

$$(x_B - x_c)^2 + (y_B - y_c)^2 + (z_B - z_c)^2 = e_2^2 \tag{24}$$

Substituting the coordinates of point B and point C in the frame $\{x_0y_0z_0\}$ into Eq. (25), and simplifying

$$M \sin \gamma_2 + N \cos \gamma_2 + P = 0 \tag{25}$$

where

$$M = 2e_0e_3 \tag{26}$$

$$N = 2e_3e_5 - 2e_1e_3 \cos \gamma_1 \tag{27}$$

$$P = e_0^2 + e_1^2 + e_3^2 + e_4^2 + e_5^2 - e_2^2 - 2e_1e_5 \cos \gamma_1 - 2e_1e_4 \sin \gamma_1 \tag{28}$$

Substituting $\sin \gamma_2 = \frac{2 \tan(\frac{\gamma_2}{2})}{1 + \tan^2(\frac{\gamma_2}{2})}$ and $\cos \gamma_2 = \frac{1 - \tan^2(\frac{\gamma_2}{2})}{1 + \tan^2(\frac{\gamma_2}{2})}$ into Eq. (26) and considering the configuration, then

$$\gamma_2 = 2 \arctan \frac{M - \sqrt{M^2 + N^2 - P^2}}{N - P} \tag{29}$$

When the scale parameters of the RSSR linkage are determined ($e_0 : e_1 : e_2 : e_3 : e_4 : e_5 = 3 : 1 : 5 : 1 : 4 : 2$), the relationship of the γ_1 and γ_2 is depicted in Fig. 7.

The outputs (ψ and ϕ) delivered by the parallel spherical joint, the RSSR linkage and the other transmission linkage shown in Fig. 8 are satisfied: $\dot{\psi} = \dot{\alpha}_z$ and $\dot{\phi} = \dot{\gamma}_2$.

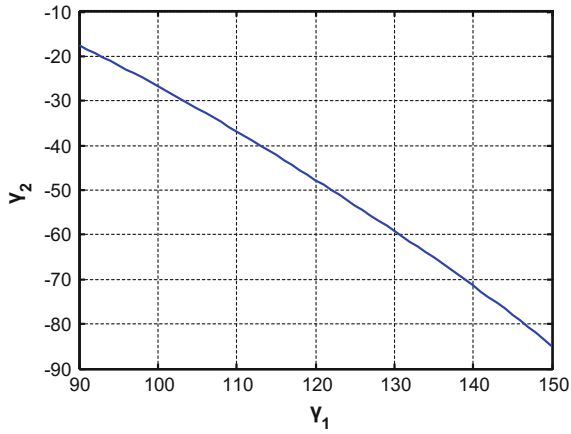


Fig. 7 The relationship of the input and output of the RSSR linkage

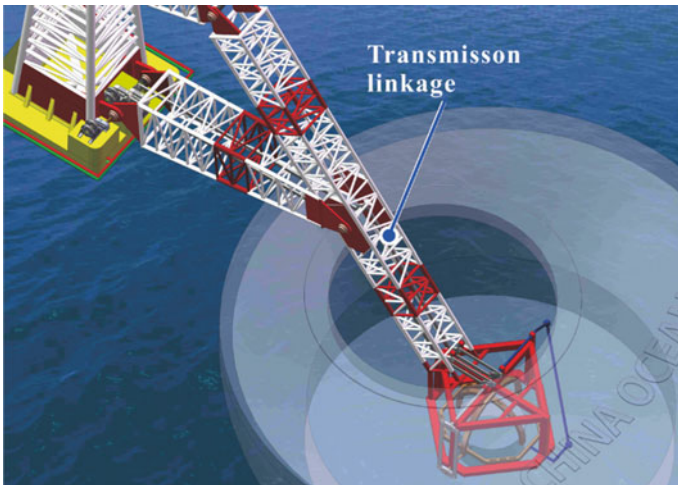


Fig. 8 Schematic of the transmission linkage

So the three reciprocating rotations θ , ψ and ϕ drive the PTO systems to export hydraulic energy.

4 Conclusions

This paper presents a 3-DOF mechanism to extract the wave power. The power conversion principle of the WEC is first proposed, and the kinematics of the mechanism are derived. The mechanism can absorb and deliver the three motions of the floating body

Acknowledgments This research was supported by National Natural Science Foundation of China (Grant No. 51335007)

References

1. Isaacs JD, Schmitt WR (1980) Ocean energy: forms and prospects. *Science* 207(4428):265–273
2. Salter SH (1974) Wave power. *Nature* 249(5459):720–724
3. de Falcão AFO (2010) Wave energy utilization: a review of the technologies. *Renew Sustain Energy Rev* 14(3):899–918
4. Masuda Y (1986) An experience of wave power generator through tests and improvement. In: *Hydrodynamics of ocean wave-energy utilization*. Springer, Berlin, pp 445–452
5. Brito-Melo A, Neuman E, Sarmiento AJNA (2008) Full-scale data assessment in OWC Pico plant. *Int J Offshore Polar Eng* 18(1):27–34
6. Josset C, Babarit A, Clément A (2007) A wave-to-wire model of the SEAREV wave energy converter. *Proc Inst Mech Eng Part M: J Eng Marit Environ* 221(2):81–93
7. Hansen RH, Kramer MM (2011) Modelling and control of the Wavestar prototype. *Proc EWTEC*
8. Bracco G, Giorcelli E, Mattiazzo G (2011) ISWEC: A gyroscopic mechanism for wave power exploitation. *Mech Mach Theory* 46(10):1411–1424
9. Henderson R (2006) Design, simulation, and testing of a novel hydraulic power take-off system for the Pelamis wave energy converter. *Renew Energy* 31(2):271–283
10. Kofoed JP et al (2006) Prototype testing of the wave energy converter wave dragon. *Renew Energy* 31(2):181–189
11. Vicinanza D, Frigaard P (2008) Wave pressure acting on a seawave slot-cone generator. *Coast Eng* 55(6):553–568
12. Ruellan M et al (2010) Design methodology for a SEAREV wave energy converter. *IEEE Trans Energy Convers* 25(3):760–767
13. Eriksson M, Isberg J, Leijon M (2005) Hydrodynamic modelling of a direct drive wave energy converter. *Int J Eng Sci* 43(17):1377–1387
14. Babarit A et al (2012) Numerical benchmarking study of a selection of wave energy converters. *Renew Energy* 41:44–63

Isomorphism Identification of Planar Multiple Joint Kinematic Chains by Circuit Analysis Method

Yanhua Zou, Peng He, Dawei Xu and Jun Li

Abstract In this paper, isomorphism identification algorithm of planar multiple joint kinematic chains by circuit analysis method has been presented. Firstly, topological model is introduced. Then, corresponding equivalent circuit model is established to obtain node voltage sequence; By the solved node voltage sequence, an algorithm to identify isomorphic kinematic is obtained. Lastly, examples are carried out to show this useful method.

Keywords Isomorphism identification · Planar multiple joint kinematic chain · Circuit analysis method · Node voltage sequence

1 Introduction

Isomorphism identification is one of indispensable steps in the structural synthesis of kinematic chains, so a lot of studies have been done in this field. Until now, many methods have been presented for planar simple joint kinematic chains [1–9]. So far, isomorphism identification studied most is about those planar simple joint chains, and identification technique for this kind of chains is comparatively mature. However, besides simple joint chains, planar kinematic chains also include multiple joint kinematic chains. This type kinematic chain can be used in a lot of mechanism design problems. As we know, isomorphism identification methods used in the simple joint chains are always not satisfied multiple joint kinematic chains. In the field of isomorphism identification of multiple joint kinematic chains, adjacent chain table method was introduced in the paper [10]. Song [11] presented the spanning tree method of identifying isomorphism and topological symmetry for

Y. Zou (✉) · P. He · D. Xu · J. Li
Quanzhou Institute of Equipment Manufacturing, Haixi Institutes,
Chinese Academy of Science, Quanzhou, People's Republic of China
e-mail: Zouyh@fjirsm.ac.cn

Y. Zou
Expo Boulevard of Jinjiang, Quanzhou, Fujian, People's Republic of China

multiple joint kinematic chains, but this method was not easily achieved by computer. Liu [12] presented a representation and isomorphism identification of planar multiple joint kinematic chains based on the converted adjacent matrix, but converted adjacent matrix not only increased the order of matrix, but also added the complexity of isomorphism identification process. So from the researches above, to find a useful method to solve the problem of isomorphism identification of planar multiple joint kinematic chains is existing research content and further study is necessary.

In this paper, an algorithm based on the equivalent circuit analysis for isomorphism identification of planar multiple joint is presented. Firstly, weighted-double color contracted graph (WDCCG) and corresponding weighted adjacency matrix (WAM) are introduced to describe multiple joint kinematic chains. Corresponding equivalent circuit model (ECM) of the WDCCG is established, then use circuit analysis method to obtain the node voltages of every vertex in WDCCG. The solved node voltage sequence (NVS) is used to determine correspondence vertices of two isomorphism identification kinematic chains. Then an algorithm to determine isomorphism of planar multiple joint kinematic chains is proposed.

2 Topological Model and Adjacency Matrix

2.1 Topological Model

In this paper, a weighted double color contracted graph (WDCCG) is introduced to represent the topological structure of kinematic chains. The WDCCG model which wiped off all of the simple joints and simple joint links form the multiple joint kinematic chain can improve the efficiency of isomorphism identification. The graph is established as follows: solid vertices “●” denote multiple joint links and hollow vertices “○” denote multiple joints. If two multiple-joint links are connected by simple joints and simple joint links, connect two corresponding solid vertices with a weighted edge (weighted value equal to the number of simple joints between two vertices). If one multiple-joint link is connected with one multiple-joint or two multiple-joints are connected by simple joints and simple joint links, connect them with a weighted edge as well (weighted value also equal to the number of simple joints between two vertices). For example, Fig. 1c is the WDCCG of multiple-joint kinematic chain as showed in Fig. 1a.

2.2 Adjacency Matrix

Obviously, a multiple joint kinematic chain and its WDCCG are one-to-one correspondent with each other. The WDCCG of a kinematic chain can be represented

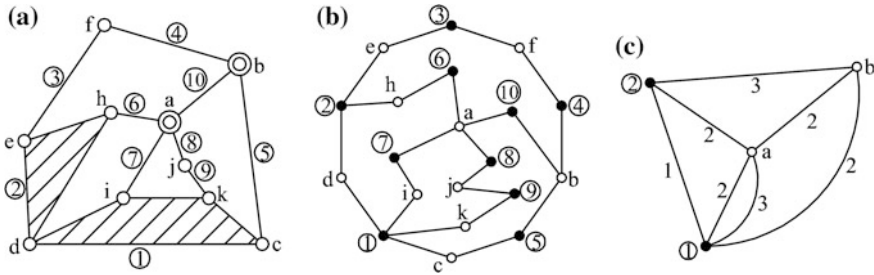


Fig. 1 A multiple joint kinematic chain and its TM described

by a vertex-vertex weighted-adjacency-matrix (WAM) while the elements of WAM are defined as follows:

$$A = [d_{ij}]_{n \times n} = \begin{cases} (d_{ij}) = (m_{ij1}, m_{ij2}, \dots, m_{ijk}) & i \neq j \\ (d_{ij}) & i = j \end{cases} \quad (1)$$

where n is the number of vertices in WDCCG.

When $i = j$: if vertex is hollow vertex, then $d_{ij} = 0$; Otherwise the vertex is solid vertex then $d_{ij} = 1$.

When $i \neq j$: if two vertices are not connected directly, then $d_{ij} = 0$; Otherwise the two vertices are connected directly by k weighted edges, then $d_{ij} = m_{ij1}, m_{ij2}, \dots, m_{ijk}$, ($m_{ij1} \geq m_{ij2} \geq \dots \geq m_{ijk}$, m_{ijk} is the weighted value of k -th edge).

For example, the WAM A of a multiple joint kinematic chain as showed in Fig. 1c can be expressed as follow:

$$A = \begin{matrix} & \begin{matrix} 1 & 2 & a & b \end{matrix} \\ \begin{matrix} 1 \\ 2 \\ a \\ b \end{matrix} & \begin{bmatrix} (1) & (1) & (2) & (2, 3) \\ (1) & (1) & (3) & (2) \\ (2) & (3) & (0) & (2) \\ (2, 3) & (2) & (2) & (0) \end{bmatrix} \end{matrix}$$

3 Equivalent Circuit Analysis

As we know, when two multiple joint kinematic chains are isomorphic, their WDCCG are exactly the same, their vertices and edges are in one-to-one correspondence with each other, and the vertices, edges in correspondence keep the same incidence and weighted relation. According to this definition, the necessary and sufficient condition for isomorphism of kinematic chains is that they have same WAM, i.e., $A = A'$.

Equivalent circuit model (ECM) of WDCCG is established by its each edge, which is replaced by a conductance that equal to the weighted value of corresponding edge m_{ij} .

Theorem 1 If two WDCCG corresponding to the kinematic chains are isomorphic, then their corresponding ECM are identical.

For example, two isomorphism multiple joint kinematic chains are showed in Fig. 2a, b, their WDCCG showed in Fig. 2c, d, respectively. According to the description above, their corresponding ECM are showed in Fig. 3a, b, respectively. There are two identical circuits and nodes of this two ECM are in one-to-one correspondence.

Complete excitation (CE) of an ECM is established as follows: In an ECM with n nodes, firstly, set a node $(n + 1)$ to be a reference node, then connect the reference node $(n + 1)$ with every other nodes $n_i, (i = 1, 2, \dots, n)$ of the ECM whose conductance values equal to the sum of weighted values of the node edges. Secondly, apply the same current source 1A between node $(n + 1)$ and other nodes $n_i, (i = 1, 2, \dots, n)$ of the ECM, respectively, in directions of the currents going from node $(n + 1)$ to other nodes $n_i, (i = 1, 2, \dots, n)$, respectively.

According to circuit theory, two identical circuits under the same CE have the same response. And their node voltages can be solved by the nodal method of circuit analysis. The nodal method of circuit analysis can be expressed as follows: in a circuit network, choose a node as a reference node, the voltage difference between each node and the reference node is known as the node voltage of the node. For a circuit network with n nodes, which has $(n - 1)$ node voltages, if the node n as the reference node, the nodal voltage equation can be expressed as:

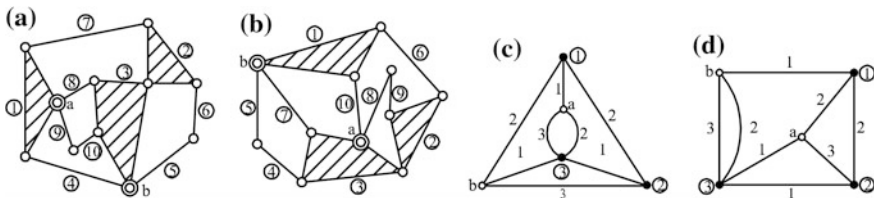
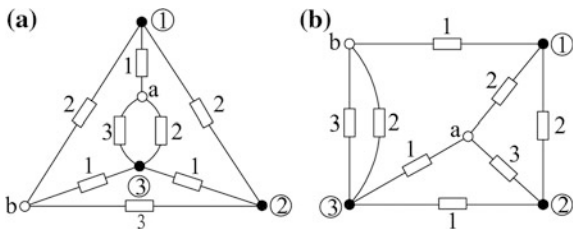


Fig. 2 Two multiple joint kinematic chains and their WDCCG

Fig. 3 ECM corresponding to two WDCCG of Fig. 2c, d, respectively



$$\begin{bmatrix} G_{11} & G_{12} & \cdots & G_{1(n-1)} \\ G_{21} & G_{22} & \cdots & G_{2(n-1)} \\ \vdots & \vdots & \ddots & \vdots \\ G_{(n-1)1} & G_{(n-1)2} & \cdots & G_{(n-1)(n-1)} \end{bmatrix} \begin{bmatrix} v_{n1} \\ v_{n2} \\ \vdots \\ v_{n(n-1)} \end{bmatrix} = \begin{bmatrix} I_{sn1} \\ I_{sn2} \\ \vdots \\ I_{sn(n-1)} \end{bmatrix} \quad (2)$$

where: $G_{ii}(i = 1, 2, \dots, n - 1)$ is called the self admittance of a node i , the value of which is the sum of the admittance of all branches that are connected to the node i ;

$G_{ij}(i = 1, 2, \dots, n - 1; j = 1, 2, \dots, n - 1)$ is called the mutual admittance of node i and node j , whose value is the sum of the branch admittance between node i and node j ;

$I_{sni}(i = 1, 2, \dots, n - 1)$ is called the algebraic sum of the current source for the inflow node i (inflow is positive, outflow is negative).

For example, an ECM with 4 nodes which are showed in Fig. 4a. Apply the CE of reference node 5 as showed in Fig. 4b. By nodal method of circuit analysis Eq. (2), node voltages v_1, v_2, v_3 and v_4 can be expressed as follows:

$$\begin{bmatrix} G_1 + G_4 + G_6 & -G_4 & 0 & -G_1 \\ -G_4 & G_2 + G_4 + G_5 + G_7 & -G_5 & -G_2 \\ 0 & -G_5 & G_3 + G_5 + G_8 & -G_3 \\ -G_1 & -G_2 & -G_3 & G_1 + G_2 + G_3 + G_9 \end{bmatrix} \begin{bmatrix} v_1 \\ v_2 \\ v_3 \\ v_4 \end{bmatrix} = \begin{bmatrix} 1 \\ 1 \\ 1 \\ 1 \end{bmatrix} \quad (3)$$

Then the node voltages v_1, v_2, v_3 and v_4 can be obtained by solving the above Eq. (3). Therefore, the following conclusion can be obtained.

Theorem 2 If two WDCCGs corresponding to the same type of kinematic chains are isomorphic, their two corresponding ECM N and N' can be established and excited by the same CE as above, respectively. Then the node voltages of each correspondence nodes of two ECM N and N' are the same.

Fig. 4 An ECM with 4 nodes and its CE by reference node 5

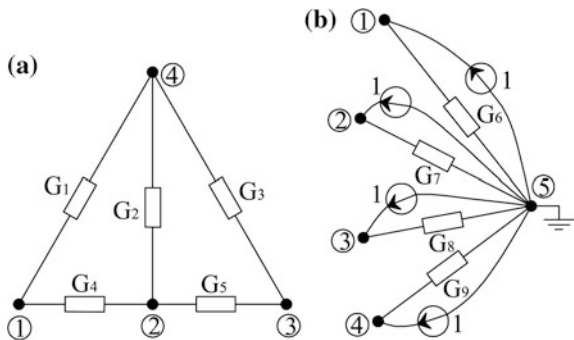
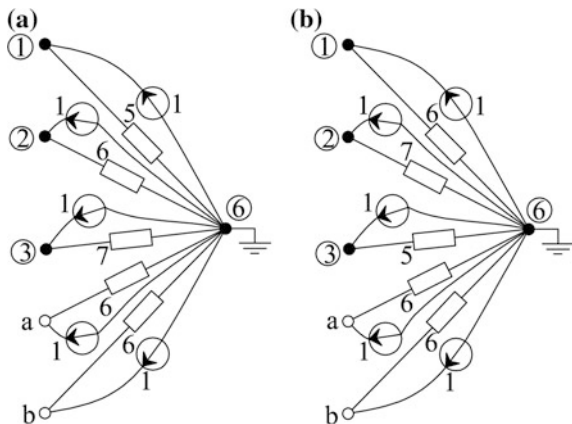


Fig. 5 Two ECM with the same CE, respectively



For example, two identical ECM N and N' with 5 nodes as showed in Fig. 3a, b. Apply same CE of reference node 6 which is showed in Fig. 5a, b, respectively. And their corresponding WAM are A and A' can be obtained as follows:

$$A = \begin{matrix} & \begin{matrix} 1 & 2 & 3 & a & b \end{matrix} \\ \begin{matrix} 1 \\ 2 \\ 3 \\ a \\ b \end{matrix} & \begin{bmatrix} (1) & (2) & (0) & (1) & (2) \\ (2) & (1) & (1) & (0) & (3) \\ (0) & (1) & (1) & (2,3) & (1) \\ (1) & (0) & (2,3) & (0) & (0) \\ (2) & (3) & (1) & (0) & (0) \end{bmatrix} \end{matrix}$$

$$A' = \begin{matrix} & \begin{matrix} 1 & 2 & 3 & a & b \end{matrix} \\ \begin{matrix} 1 \\ 2 \\ 3 \\ a \\ b \end{matrix} & \begin{bmatrix} (1) & (1) & (2) & (3) & (0) \\ (1) & (1) & (0) & (1) & (2,3) \\ (2) & (0) & (1) & (2) & (1) \\ (3) & (1) & (2) & (0) & (0) \\ (0) & (2,3) & (1) & (0) & (0) \end{bmatrix} \end{matrix}$$

By nodal method of circuit analysis, equations about node voltages v_1, v_2, v_3, v_a and v_b can be expressed respectively as follows:

$$\begin{bmatrix} 10 & -2 & 0 & -1 & -2 \\ -2 & 12 & -1 & 0 & -3 \\ 0 & -1 & 14 & -5 & -1 \\ -1 & 0 & -5 & 12 & 0 \\ -2 & -3 & -1 & 0 & 12 \end{bmatrix} \begin{bmatrix} v_1 \\ v_2 \\ v_3 \\ v_a \\ v_b \end{bmatrix} = \begin{bmatrix} 1 \\ 1 \\ 1 \\ 1 \\ 1 \end{bmatrix} \tag{4}$$

Table 1 Node voltages of two ECM with same CE

Vertex type		Hollow vertex		Solid vertex		
Figure 5a	Vertex code	<i>a</i>	<i>b</i>	1	2	3
	Node voltage	0.1627	0.1691	0.1839	0.1691	0.1537
Figure 5b	Vertex code	<i>a</i>	<i>b</i>	1	2	3
	Node voltage	0.1691	0.1627	0.1691	0.1537	0.1839

$$\begin{bmatrix} 12 & -1 & -2 & -3 & 0 \\ -1 & 14 & 0 & -1 & -5 \\ -2 & 0 & 10 & -2 & -1 \\ -3 & -1 & -2 & 12 & 0 \\ 0 & -5 & -1 & 0 & 12 \end{bmatrix} \begin{bmatrix} v_1 \\ v_2 \\ v_3 \\ v_a \\ v_b \end{bmatrix} = \begin{bmatrix} 1 \\ 1 \\ 1 \\ 1 \\ 1 \end{bmatrix} \tag{5}$$

Then node voltages v_1, v_2, v_3, v_a and v_b of two ECM can be obtained by solving the above Eqs. (4) and (5), respectively, showed in Table 1.

From the theorem 2, node voltages of each correspondence node in this two ECM are the same as follows: ($v_a = v_b = 0.1627, v_b = v_a = 0.1691, v_1 = v_3 = 0.1839, v_2 = v_1 = 0.1691, v_3 = v_2 = 0.1537$). When arrange the obtained node voltages in descending order with the same node voltages staying together, this set are called the node voltage sequence (NVS) and denoted as:

$$NVS = [(v_1, v_2, \dots, v_{n_1}), (v_{(n_1+1)}, v_{(n_1+2)}, \dots, v_n)] (v_1 \geq v_2 \geq v_{n_1}; v_{(n_1+1)} \geq v_{(n_1+2)} \geq \dots \geq v_n) \tag{6}$$

where: The variables v_1, v_2, \dots, v_{n_1} represent node voltages of hollow vertex.

The variables $v_{(n_1+1)}, v_{(n_1+2)}, \dots, v_n$ represent node voltages of solid vertex.

If two identical ECM stimulated by the same CE as above, then the NVS in correspondence are same. For example, two identical ECM as showed in Fig. 5a, b, the NVS and vertex codes can be obtained respectively, as follows:

$$\begin{aligned}
 NVS(a) &= [(v_b, v_a), (v_1, v_2, v_3)] = [(0.1691, 0.1627), (0.1839, 0.1691, 0.1537)] \\
 NVS(b) &= [(v_a, v_b), (v_3, v_1, v_2)] = [(0.1691, 0.1537), (0.1839, 0.1691, 0.1627)]
 \end{aligned}$$

If the NVS of two ECM are not the same, then the two WDCCG are not isomorphic. On the contrary, if they are the same, correspondence vertices in these two WDCCG can be determined by the element values of NVS. Then perform the row exchanges of WAM A' to determine if they are isomorphic. Because the NVS can reduce the number of row exchanges to several or only just one, this is a very effective method. For example, by the NVS(a) and NVS(b) of two ECM showed in Fig. 3a, b, the vertices in correspondence are ($a-b, b-a, 1-3, 2-1, 3-2$), then through exchanging the row of WAM A' , we obtain $A = A'$, which are isomorphic.

4 Algorithm

Here, a direct algorithm is given to determine isomorphism of planar multiple joint, and it can be expressed as follows:

Step 1: Input the vertex codes and WAM A, A' of two WDCCGs corresponding to the kinematic chains.

Step 2: Assign vertices codes of A and A' in two groups: the hollow vertexes to be the first group and the solid vertexes to be another group.

Step 3: Calculate NVS(a), NVS(b) and their vertex codes of the two ECMs with the same CE, respectively. Compare NVS(a) and NVS(b): if equivalence cannot be seen, it is determined that they are not isomorphic and program stops; Otherwise, it is determined that they could be isomorphic. Then check the NVS(a) and NVS(b) to see if the values in two vertex code groups are all distinct: If yes, go to Step 4; If no, go to Step 6.

Step 4: Take the NVS(a), NVS(b) and their vertex codes to determine the correspondence of vertices according to the values that are in correspondence.

Step 5: According to the corresponding vertices obtained and the vertex codes to form new WAM A'_1 , rewrite WAM A' . If $A = A'_1$, it is determined that they are isomorphic; otherwise, they are not isomorphic and program stops.

Step 6: According to the corresponding vertices obtained, the NVS(a) and NVS(b) have same values in the corresponding two vertex code groups. Just adjust the position order of vertices of the same group in A' to obtain vertex codes to from new adjacency matrix A'_1 . If $A = A'_1$, it is determined that they are isomorphic and program stops; If $A \neq A'_1$, keep on adjusting the position order of the aforementioned vertices in A' of the vertex code groups for all possibilities. And if $A \neq A'_1$ always, it is determined that they are not isomorphic and program stops.

5 Examples

Example 1: Two 10-link multiple joint kinematic chains are showed in Fig. 6a, b. Their corresponding WDCCGs are depicted in Fig. 6c, d, respectively. The direct process to determine isomorphism of this two kinematic chains can be expressed as follows.

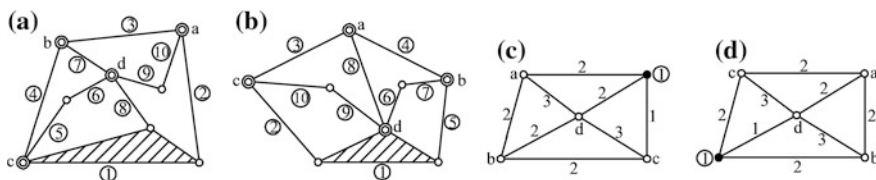


Fig. 6 Two 10-link multiple joint kinematic chains and their WDCCGs

Step 1: Input their corresponding vertex codes and WAM A, A' as follows:

$$A = \begin{matrix} & 1 & a & b & c & d \\ \begin{matrix} 1 \\ a \\ b \\ c \\ d \end{matrix} & \begin{bmatrix} (1) & (2) & (0) & (1) & (3) \\ (2) & (0) & (2) & (0) & (3) \\ (0) & (2) & (0) & (2) & (2) \\ (1) & (0) & (2) & (0) & (3) \\ (2) & (3) & (2) & (3) & (0) \end{bmatrix} \end{matrix}$$

$$A' = \begin{matrix} & 1 & a & b & c & d \\ \begin{matrix} 1 \\ a \\ b \\ c \\ d \end{matrix} & \begin{bmatrix} (1) & (0) & (2) & (2) & (1) \\ (0) & (0) & (2) & (2) & (2) \\ (2) & (2) & (0) & (0) & (3) \\ (2) & (2) & (0) & (0) & (3) \\ (1) & (2) & (3) & (3) & (0) \end{bmatrix} \end{matrix}$$

Step 2: Evidently, $A \neq A'$. Assign vertices codes of A and A' in two groups (a): $[(a, b, c, d), (1)]$ and (b): $[(a, b, c, d), (1)]$.

Step 3: Calculate NVS(a), NVS(b) and their vertex codes of two ECMs with the same CE, respectively, as follows:

$$NVS(a) = [(v_c, v_b, v_a, v_d), (v_1)] = [(0.1551, 0.1546, 0.1451, 0.1275), (0.1700)]$$

$$NVS(b) = [(v_a, v_b, v_c, v_d), (v_1)] = [(0.1538, 0.1459, 0.1459, 0.1308), (0.1714)]$$

Compare NVS(a) and NVS(b) and equivalence cannot be seen. It is determined that they are not isomorphic and program stops.

Example 2: Two 11-link multiple joint kinematic chains are showed in Fig. 7a, b. Their corresponding WDCCGs are described in Fig. 7c, d, respectively. The direct process to determine isomorphism of this two kinematic chains, as follows.

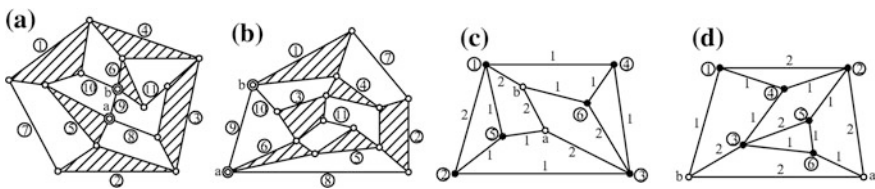


Fig. 7 Two 11-link multiple joint kinematic chains and their WDCCGs

Step 1: Input their corresponding vertex codes and WAM A, A' as follows:

$$A = \begin{matrix} & \begin{matrix} 1 & 2 & 3 & 4 & 5 & 6 & 7 & 8 \end{matrix} \\ \begin{matrix} 1 \\ 2 \\ 3 \\ 4 \\ 5 \\ 6 \\ 7 \\ 8 \end{matrix} & \left[\begin{matrix} (1) & (2) & (0) & (1) & (1) & (0) & (0) & (2) \\ (2) & (1) & (1) & (0) & (1) & (2) & (0) & (0) \\ (0) & (1) & (1) & (1) & (0) & (0) & (1) & (0) \\ (1) & (0) & (1) & (1) & (0) & (1) & (0) & (0) \\ (1) & (1) & (0) & () & (1) & (0) & (1) & (0) \\ (0) & (0) & (2) & (1) & (0) & (1) & (0) & (1) \\ (0) & (0) & (2) & (0) & (1) & (0) & (0) & (2) \\ (2) & (0) & (0) & (0) & (0) & (1) & (2) & (0) \end{matrix} \right] \end{matrix}$$

$$A' = \begin{matrix} & \begin{matrix} 1 & 2 & 3 & 4 & 5 & 6 & 7 & 8 \end{matrix} \\ \begin{matrix} 1 \\ 2 \\ 3 \\ 4 \\ 5 \\ 6 \\ a \\ b \end{matrix} & \left[\begin{matrix} (1) & (2) & (0) & (1) & (0) & (0) & (0) & (1) \\ (2) & (1) & (0) & (1) & (1) & (0) & (2) & (0) \\ (0) & (0) & (1) & (1) & (2) & (1) & (0) & (2) \\ (1) & (1) & (1) & (1) & (0) & (0) & (0) & (0) \\ (0) & (1) & (2) & (0) & (1) & (1) & (0) & (0) \\ (0) & (0) & (1) & (0) & (1) & (1) & (1) & (0) \\ (0) & (2) & (0) & (0) & (0) & (1) & (0) & (2) \\ (1) & (0) & (2) & (0) & (0) & (0) & (2) & (0) \end{matrix} \right] \end{matrix}$$

Step 2: Evidently, $A \neq A'$. Assign vertices codes of A and A' in two groups (a): $[(a, b), (1, 2, 3, 4, 5, 6)]$ and (b): $[(a, b), (1, 2, 3, 4, 5, 6)]$.

Step 3: Calculate NVS(a), NVS(b) and their vertex codes of two ECMs with the same CE, respectively, as follows:

$$\begin{aligned}
 \text{NVS}(a) &= [(v_a, v_b), (v_5, v_4, v_2, v_6, v_1, v_3)] = [(0.2084, 0.2056), \\
 &\quad (0.743, 0.2727, 0.2348, 0.2347, 0.2023, 0.1995)] \\
 \text{NVS}(b) &= [(v_b, v_c), (v_6, v_4, v_5, v_1, v_3, v_2)] = [(0.2084, 0.2056), \\
 &\quad (0.743, 0.2727, 0.2348, 0.2347, 0.2023, 0.1995)]
 \end{aligned}$$

Compare NVS(a) and NVS(b) and equivalence can be seen. So the node voltages in two vertex code groups are all distinct, go to step 4.

Step 4: Take the NVS(a), NVS(b) and their vertex codes to determine the corresponding vertices of two WDCCGs as follows: $(a-b, b-a, 1-3, 2-5, 3-2, 4-4, 5-6, 6-1)$.

Step 5: According to the corresponding vertices obtained and the vertex codes to form new WAM A_1' , rewrite WAM A' . Then we have: $A = A_1'$, so they are isomorphic and program stops.

6 Conclusions

In this paper, a weighted-double-color-contracted-graph (WDCCG) and a weighted-adjacency-matrix (WAM) are introduced to describe the planar multiple joint. Then isomorphism identification method are carried out by the equivalent-circuit-models (ECMs) of WDCCGs with the same complete-excitation (CE). Finally, an algorithm to identify isomorphic kinematic chains is obtained. It is an efficient and easy method to be realized by computer.

Acknowledgments This project is supported by the Fujian province science and technology major projects (No. 2015HZ0001)

References

1. Uicker JJ, Raicu A (1975) A method for the identification of and recognition of equivalence of kinematic chains. *Mech Mach Theory* 10:375–383
2. Yan HS, Hall AS (1982) Linkage characteristic polynomials: assembly, theorems, uniqueness. *ASME J Mech Des* 104:11–20
3. Ambekar A, Agrawal V (1987) Canonical numbering of kinematic chains and isomorphism problem: min code. *Mech Mach Theory* 22:453–461
4. Chu JK, Cao WQ (1994) Identification of isomorphism among kinematic chains and inversions using link's adjacent chain table. *Mech Mach Theory* 9:53–58
5. Rao AC (2000) Application of fuzzy logic for the study of isomorphism, inversions, symmetry, parallelism and mobility in kinematic chains. *Mech Mach Theory* 35:1103–1116
6. He PR, Zhang WJ, Li Q (2005) Some further development on the eigensystem approach for graph isomorphism detection. *J Franklin Inst* 342:657–673
7. Cubillo JP, Wan JB (2005) Comments on mechanism kinematic chain isomorphism identification using adjacent matrices. *Mech Mach Theory* 40:131–139
8. Ding HF, Huang Z (2007) A unique representation of the kinematic chain and the atlas database. *Mech Mach Theory* 42:637–651
9. Kong FG, Li Q, Zhang WJ (1999) An artificial neural network approach to mechanism kinematic chain isomorphism identification. *Mech Mach Theory* 34:271–283
10. Chu JK (1992) The structural and dimensional characteristics of planar linkages. Press of Beihang University of China, Beijing, BJ, pp 44–51
11. Song L, Yang J, Cao WQ (2001) Spanning tree method of identifying isomorphism and topological symmetry to planar kinematic chain with multiple joint. *Chin J Mech Eng* 14: 27–31
12. Liu JG, Yu DJ (2012) Representations and isomorphism identification of planar kinematic chains with multiple joints based on the converted adjacent matrix. *Chin J Mech Eng* 48: 15–21

Automatic Synthesis of Planar Simple Joint Kinematic Chains by Single Kinematic Chain Adding Method

Yanhua Zou, Peng He, Dawei Xu and Jun Li

Abstract An automatic topological structural synthesis algorithm has been proposed for planar-simple-joint-kinematic-chains (PSJKC) in this paper. The corresponding incident-matrix(IM)s of PSJKCs with special input parameters can be formed with the single kinematic chain adding method with the help of single-color-topological-graph(SCTG). And based on the procedure for the SCTG automatic drawing, an automatic topological structural synthesis algorithm of PSJKCs with specified degree-of-freedom(DOF) F and number of links n can be synthesized in batch.

Keywords Planar simple joint kinematic chain · Topological structural synthesis · Single kinematic chain adding method · Single color topological graph

1 Introduction

Structural synthesis is the first and most important stage in the mechanical conceptual design progress [1, 2]. It is the original innovation of mechanical systems and provides large numbers of optional structure types when new mechanisms are created. The structural synthesis of planar mechanisms aims at generating a complete list of kinematic structures of mechanisms with specified input parameters, which are free from isomorphic kinematic chains. Since 1960s, structural synthesis of kinematic chains has been attracted by many scholars to research on [3–11], but structure synthesis of PSJKCs has lingered at a relatively low level in terms of automation in the past. Therefore, developing a more effective method for automatic topological structural synthesis for all possible kinds of PSJKCs is urgently

Y. Zou (✉) · P. He · D. Xu · J. Li
Quanzhou Institute of Equipment Manufacturing, Haixi Institutes, Chinese Academy of Science, Beijing, People's Republic of China
e-mail: Zouyh@fjirsm.ac.cn

Y. Zou
Expo Boulevard of Jinjiang, Quanzhou, Fujian, People's Republic of China

desired, which would directly export final kinematic structures in topological graphs and would give designers a better visual understanding of the kinematic chains. Thus it makes concept design more convenient.

An automatic topological structural synthesis algorithm has been advanced for PSJKCs in this paper. The IMs of the PSJKCs with independent loops D can be formed by subsequently adding single open chain to the basic chain. In this way, the topological structures of simple joint kinematic chains with specified DOF F and number of links n can be automatically synthesized in batch.

2 Automatic Synthesis of IMs from PSJKCs

2.1 Single Color Topological Graph

It is very meaningful to study PSJKC to be represented by SCTG description or IM representation [5, 6]. The SCTG model is established as follows: solid vertices indicate the joints of a kinematic chain meanwhile the edges denote the links of a kinematic chain and connect the corresponding solid vertexes. For example, a PSJKC showed in Fig. 1a can be represented by the SCTG model showed in Fig. 1b.

The PSJKC also can be described as link-joint incident-matrix (IM) A and the elements of IM A are defined as follows:

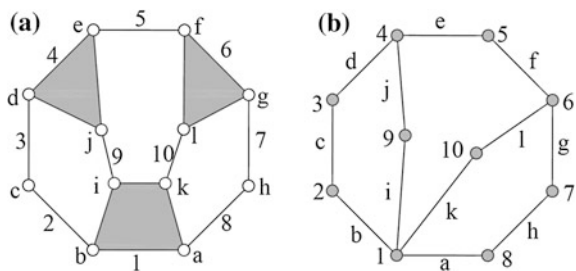
$$A = [a_{ij}]_{n \times m} \tag{1}$$

where n is the number of links and m indicates the number of joints. If link i and joint j are coincident, $a_{ij} = 1$ otherwise $a_{ij} = 0$.

2.2 Automatic Synthesis of IMs

An IM of PSJKC with independent loops D can be formed by subsequently adding O_j , ($j = 2, \dots, D$) to a basic C_1^{14} . For example, the process to form an IM of 10-link

Fig. 1 A PSJKC and its single color topological graph



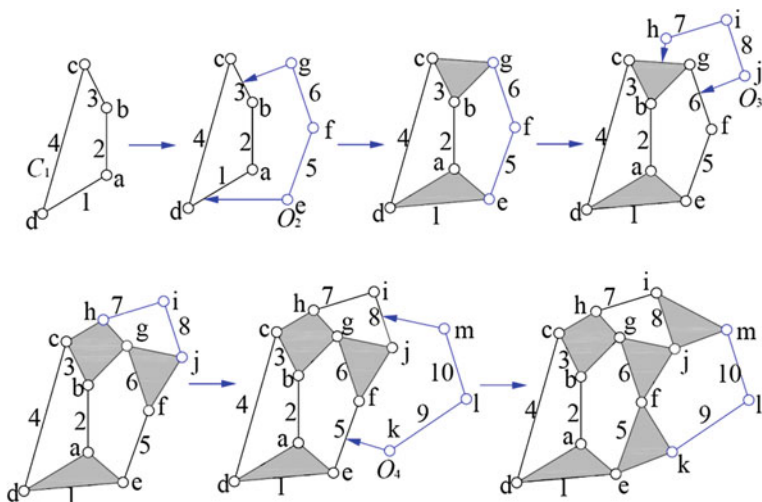


Fig. 2 The process to form a 10-link 1-DOF PSJKC IM

1-DOF PSJKC with independent loops $D = 4$ as showed in the Fig. 2. The first step is to choose $C_1(1-a-2-b-3-c-4-d)$ to form the kinematic chain IM $A_{(4 \times 4)}$ with one independent loop; After that, both ends of the $O_2(e-5-f-6-g)$ are added to link 1 and 3 to form the kinematic chain IM $A_{(6 \times 7)}$; Then both ends of the $O_3(h-7-i-8-j)$ are added to link 3 and 6 to form the kinematic chain IM $A_{(8 \times 10)}$; Finally, both ends of the $O_4(k-9-l-10-m)$ are added to link 5 and 8 to form the kinematic chain IM $A_{(10 \times 13)}$, which meets the requirements.

Supposed that a PSJKC has independent loops D , the number of links and joints $[(m_1, n_1); (m_2, n_2); \dots; (m_D, n_D)]$ of the C_1, O_2, \dots, O_D are determined in the following measures. At the beginning, in all loops of the kinematic chain, choose the one with the minimum number of links as the first independent loop. So the number (m_1, n_1) of C_1 are determined. Then from those remaining O_2, O_3, \dots, O_D constructing the second independent loop, which still contains the minimum number of links, the number (m_2, n_2) of the second O_2 is obtained. By this logo, for the remaining O_j, O_{j+1}, \dots, O_D constructing the j th independent loop, which contains the minimum number of links, the number (m_j, n_j) of the O_j is obtained. This process can proceed until independent loops D of $[(m_1, n_1); (m_2, n_2); \dots; (m_D, n_D)]$ for C_1, O_2, \dots, O_D are constructed.

Synthesize all the IMs of the PSJKCs corresponding to input synthesis task. Firstly, it is very important to determine the number of link-joint distribution sets. For the PSJKCs, if the Degree-of-Freedom(DOF) F and the number of links n are obtained, its independent loops D and the number of joints m can be obtained by:

$$m = [3(n - 1) - F]/2 \tag{2}$$

$$D = m - n + 1 \tag{3}$$

The number of link-joint distribution sets can be obtained as follows:

Step 1: Determine the value of (m_1, n_1)

For simple joint kinematic chains, notice that the number of link n_1 of C_1 must be larger than 4 and the first independent loop must be the shortest one. So the following equation can be obtained according to the graph theory:

$$\begin{cases} 4 \leq n_1 \leq \text{Int}[2(3D - 1)/D] \\ m_1 = n_1 \end{cases} \tag{4}$$

Step 2: Determine the values of (m_2, n_2)

According to the discussion above on the algorithm to determine the number of links of each independent loop, the addition of second O_2 to the first loop C_1 should not produce a loop which contains the number of links smaller than that in the first loop, therefore:

$$\begin{cases} n_2 \geq \text{Int}(n_1/2) \\ n_1 + n_2 \leq n \\ m_1 + m_2 \leq m \\ m_2 = n_2 + 1 \end{cases} \tag{5}$$

Step j: Determine the values of (m_D, n_D) , $(j = 3, 4, \dots, (D - 1))$

For the same argument in the determination of the values (m_2, n_2) of O_2 , the addition of O_j to the existing $(j - 1)$ independent loop kinematic chain should not produce a loop containing the number of links smaller than that in any $(j - 1)$ independent loops. The values of (m_j, n_j) must be satisfied as follows:

$$\begin{cases} n_j \leq n_{(j-1)} \leq \dots \leq n_2 \\ n_1 + n_2 + \dots + n_j \leq n \\ m_1 + m_2 + \dots + m_j \leq m \\ m_j = n_j + 1, (j = 3, \dots, D) \end{cases} \tag{6}$$

Step D: Determine the values of (m_D, n_D)

As above, the (m_D, n_D) must be satisfied:

$$\begin{cases} n_D \leq n_{(D-1)} \leq \dots \leq n_2 \\ n_1 + n_2 + \dots + n_D = n \\ m_1 + m_2 + \dots + m_D = m \\ m_j = n_j + 1, (j = 2, \dots, D) \end{cases} \tag{7}$$

So if the parameters F, n of a structural synthesis task are given, it is easy to obtain all the possible distribution sets: $[(m_1, n_1); (m_2, n_2); \dots; (m_D, n_D)]_k$, (k is the number of the joint-link distribution sets).

For the link-joint distribution sets: $[(m_1, n_1); (m_2, n_2); \dots; (m_D, n_D)]$, we can determine all the IMs of PSJKCs in the following steps:

Step 1: Develop the incident matrix A for the first independent loop. This can be done by the first C_1 according to the values (m_1, n_1) . So have:

$$\begin{cases} A(n_1, m_1) = 1 \\ A(i, i) = 1 \\ A(i + i, i) = 1 \end{cases}, i = (1, 2, \dots, n_1 - 1) \quad (8)$$

Step 2: Develop the IMs for the two independent loops. This is done by adding the sketched O_2 to any group of link-link of the first independent loop from the first group to the last group and it can determine the isomorphic IMs to form all the IMs of 2-th independent loop. Firstly, sketch all the groups of two links: (v_{2a}^e, v_{2b}^e) of first independent loop, which meets condition that the minimum number of links between those two links (v_{2a}^e, v_{2b}^e) is not bigger than n_1 . For one group of two links (v_{2a}^e, v_{2b}^e) , the IM A_e of second independent loop can be formed as follows:

1. If $n_2 = 0$,

$$\begin{cases} A_e(v_{2a}^e, m_1 + 1) = 1 \\ A_e(v_{2a}^e, m_1 + 1) = 1 \end{cases} \quad (9)$$

2. If $n_2 \geq 1$,

$$\begin{cases} A_e(v_{2a}^e, m_1 + 1) = 1 \\ A_e(v_{2b}^e, k_2 + 1) = 1 \\ A_e(i, i) = 1 \\ A_e(i, i + 1) = 1 \end{cases}, i = (n_1, n_1 + 1, \dots, k_1) \quad (10)$$

$$\text{where: } \begin{cases} k_1 = n_1 + n_2 \\ k_2 = m_1 + m_2 - 1 \end{cases}$$

Step j: Develop all the IMs for the j independent loops. For the incident matrix of the $(j - 1)$ th independent loop, sketch the O_j and add it to any group of the link-link: (v_{ja}^e, v_{jb}^e) , (e is the number of groups) from the first group to the last group to determine the isomorphic IMs. Operate just like this: choose all IMs of the $(j - 1)$ independent loops from the first to last to obtain all the IMs of j independent loops, (A_1, A_2, \dots, A_e) . For the IM A_e of $(j - 1)$ th independent loop, only the group (v_{ja}^e, v_{jb}^e) can be chosen meanwhile the addition of O_j on them does not produce a loop with the number of links smaller than that in the any independent loop before. Firstly, sketch all groups of two links: (v_{ja}^e, v_{jb}^e) of $(j - 1)$ th independent loop A_e , which meets the condition that the minimum number of links between those two links are supposed not to be bigger than that in $(j - 1)$ th independent loops. For the group of two links: (v_{ja}^e, v_{jb}^e) , the j th independent loop IM A_e can be formed as follows:

1. If $n_j = 0$,

$$\begin{cases} A_e(v_{ja}^e, \phi_j + 1) = 1 \\ A_e(v_{jb}^e, \phi_j + 1) = 1 \end{cases} \tag{11}$$

2. If $n_j \geq 1$,

$$\begin{cases} A_e(v_{ja}^e, \phi_j + 1) = 1 \\ A_e(v_{jb}^e, k_2 + 1) = 1 \\ A_e(i, i) = 1 \\ A_e(i, i + 1) = 1 \end{cases}, i = (\phi_j + 1, \phi_j + 2, \dots, k_1) \tag{12}$$

Where: $\begin{cases} \phi_j = n_1 + n_2 + \dots + n_{(j-1)} \\ \phi_j = m_1 + m_2 + \dots + m_{(j-1)} \\ k_1 = \phi_j + n_j \\ k_2 = \phi_j + m_j - 2 \end{cases}$, ϕ_j : represents the number of links in

$(j - 1)$ independent loops; ϕ_j represents the number of simple joints in the $(j - 1)$ independent loops.

According to the step j , repeat the steps until all the IMs (A_1, A_2, \dots, A_e) of D independent loops are obtained. Then all the IMs are formed corresponding to the link- joint distribution sets.

3 SCTG Automatic Drawing

In this section, a direct algorithm is given for automatically drawing the SCTG by IM A in the Matlab7.0, which can be expressed as follows:

Step 1: Input the IM A of the PSJKC.

Step 2: Achieve the vertex-vertex adjacency-matrix (AM) DA corresponding to SCTG by IM A , the elements of (AM) DA are defined as follows:

$$DA = [b_{ij}]_{(n \times n)} \tag{13}$$

Where: if $i = j$, then $b_{ij} = 0$; if $i \neq j$ and the vertices i and j are adjacent, then $b_{ij} = 1$, otherwise $b_{ij} = 0$.

Step 3: Obtain the characteristic-loop(CL) of SCTG by (AM) DA . As we know, in the SCTG of a PSJKC, the number of independent loops $D = m - n + 1$, and the total number of its loops is $T = 2^D - 1$ at most. Try to find the loop which goes through all the vertices whose vertex-degrees are more than 3. It contains largest number of vertices in a SCTG and this kind loop is called CL of a kinematic chain. Plenty of PSJKCs have showed that there always exist a few elements of CL, or only one.

Here, a direct algorithm is given to search for CL by the (AM) DA of a DCTG, which can be expressed as follows:

Step 3.1: Try to find all the permutation and combination of any two adjacency vertices of (AM) DA: $[(v_{11}, v_{12}); (v_{21}, v_{22}); \dots; (v_{i1}, v_{i2})]$;

Step 3.2: For the first combination (v_{11}, v_{12}) , use the Depth-First-Traversal method to form a recursive program to search all the roads from v_{11} to v_{12} for all the loops passing the two root vertices (v_{11}, v_{12}) ;

Step 3.3: Increase i by 1 and repeat *Step 3.2* to find loops passing the two root vertices (v_{i1}, v_{i2}) . Link them until the last combination of two adjacency vertices is processed to get all the loops $[L_1, L_2, \dots, L_T]$ of the DCTG.

Step 3.4: Find the CL by choosing the loops which both past all the vertices whose vertex-degree is more than 3 and contain the largest number of vertices from the all loops $[L_1, L_2, \dots, L_T]$. Such CLs are generally only a few, or even one.

Step 4: Automatically draw of the SCTG by AM DA and CL. It is known that the SCTG can be drawn in many different ways. And the characteristic graph of a non-fractionated graph is gotten in the following steps:

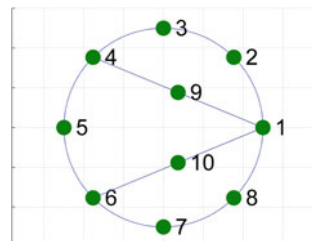
Step 4.1: Draw the CL as the outmost loop in the form of a sharing circle. Specific drawing method can be expressed as follows: If the characteristic-loop has n_1 vertices, draw a circle whose center is $(0, 0)$ and radius is $R = 5$. Then its perimeter is divided into n_1 average parts by vertices. According to the coordinate formula of this circle to obtain the coordinates of each vertex on the CL, draw the vertices of the CL ordered by vertex coordinates.

Step 4.2: Draw remaining vertices inside the CL on the sub simple chains. Specific drawing way can be expressed as follows: firstly, based on the CL and DA, find out all the sub simple chains $(SSC_1, SSC_2, \dots, SSC_{D-1})$ on which both the start and end vertices are by the Depth-First-Traversal method. Secondly, draw a line by both start and end vertices to form a corresponding sub simple chain. If a sub simple chain has n_2 vertices, the line can be divided equally into $(n_2 + 1)$ segments to obtain the coordinates of each vertex on this sub simple chain; do just link this above until all the sub simple chains and vertices are determined. If the coordinates of vertices are same, adjust the corresponding coordinates of relative vertices until all the vertices do not coincide. Lastly, draw all the vertices in corresponding sub simple chains by the order of coordinates.

Step 4.3: Set corresponding color and label of each vertex in SCTG by DA. The rule to determine the color of each vertex can be expressed as follows: draw the vertices in dark green. The label of each vertex can be determined according to the ranks of DA, where the link vertices are labeled by the ordered number: $(1, 2, 3, \dots, n)$.

For example, the process to generate SCTG of a PSJKC as showed in the Fig. 1a, can be obtained which is showed in the Fig. 3.

Fig. 3 Automatically drawn SCTG of a 10-link 1-DOF PSJKC



4 Synthesis Algorithm

A general algorithm is given for automatic topological structural synthesis of PSJKCs, which can be expressed as follows:

Step 1: Input the parameter value: n and F to obtain the value of independent loops D and the number of revolute joints m . Then, according to the previous discussion, calculate the link-joint distribution set denoted by: $[(m_1, n_1); (m_2, n_2); \dots; (m_D, n_D)]_k$, (k is the number of the joint-link distribution sets).

Step 2: When $k = 1$, for the first distribution set: $[(m_1, n_1); (m_2, n_2); \dots; (m_D, n_D)]_k$, we can get all the corresponding IMs of PSJKCs: (A_1, A_2, \dots, A_e) ;

Step 3: Increase k by 1 and repeating *Step 2* until the last distribution set of k is processed. Then determine the isomorphic kinematic chains and immovable kinematic chains generated from *Step 2* to get all the corresponding IMs: (A_1, A_2, \dots, A_b) , (b is the number of the PSJKCs of synthesis task);

Step 4: Use the link-joint IMs: (A_1, A_2, \dots, A_b) to automatically draw corresponding SCTG of each PSJKC one by one.

By this algorithm, the topological structure of PSJKCs with specified DOF F and the number of links n can be synthesized in batch. Example 3, for the automatic topological structural synthesis of 10-link 1-DOF PSJKCs, all the 230 structural types of SCTGs can be obtained, among which the corresponding 24 structural types are depicted in the Fig. 4.

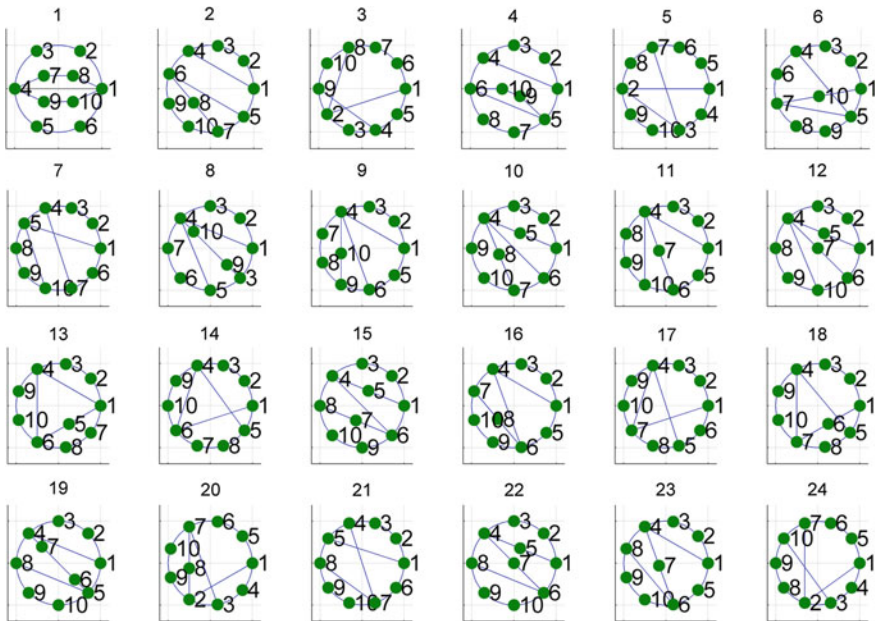


Fig. 4 Automatic synthesis of 24 types of 10-link 1-DOF PSJKCs

5 Conclusions

In this paper, an automatic topological structural synthesis algorithm has been proposed for the PSJKCs. By the general algorithm for automatic topological structural synthesis of PSJKCs with independent loops D , if the DOF F and the number of links n are specified, all corresponding topological structures of PSJKCs can be synthesized in batch.

Acknowledgments This project is supported by the Fujian province science and technology major projects (No.2015HZ0001)

References

1. Dai JS (1999) Mobility in metamorphic mechanisms of foldable/erectable kinds. *Trans ASME J Mech Des* 121:375–382
2. Liu XJ, Wang JS, Pritschow G (2005) A new family of spatial 3-DOF fully-parallel manipulators with high rotational capability. *Mech Mach Theory* 40:475–494
3. Rao AC (1997) Hamming number technique-II: generation of planar kinematic chains. *Mech Mach Theory* 32:489–499
4. Manolescu NI (1968) For a united point of view in the study of the structural analysis of kinematic chains and mechanisms. *J Mech* 3:149–169
5. Tuttle ER, Peterson SW, Titus JE (1989) Further application of group theory to the enumeration and structural analysis of basis kinematic chains. *ASME J Mech Trans Autom Des* 11:494–497
6. Yan HS, Hwang YW (1990) Number synthesis of kinematic chains based on permutation groups. *Math Comput Model* 13:29–42
7. Yang TL, Yao FH (1988) Topological characteristics and automatic generation of structural analysis and synthesis of plane mechanisms. Part II: application. *Am Soc Mech Eng Des Eng Div* 15:85–190
8. Butcher EA, Hartman C (2005) Efficient enumeration and hierarchical classification of planar simple jointed kinematic chains: application to 12- and 14-bar single degree-of-freedom chains. *Mech Mach Theory* 40(9):1030–1050
9. Sunkari RP, Schmidt LC (2006) Structural synthesis of planar kinematic chains by adapting a McKay-type algorithm. *Mech Mach Theory* 41:1021–1030
10. Ding HF, Zhao J, Huang Z (2008) Unified structural synthesis of planar simple and multiple joint kinematic chains. *Mech Mach Theory* 45:555–568
11. Chu JK, Zou YH (2014) An algorithm for structural synthesis of planar simple and multiple joint kinematic chains. *Proc Inst Mech Eng Part C: J Mech Eng Sci* 228(12):2178–2192

A Novel Geometric Modeling and Solution Method for Forward Displacement Analysis of 6-3 Stewart Platforms

Ying Zhang, Qizheng Liao, Shimin Wei, Feng Wei and Duanling Li

Abstract In this paper, we propose a novel modeling and solution method for the forward displacement analysis of 6-3 Stewart platforms based on Conformal Geometric Algebra (CGA). First of all, one of three unknown vertices on the moving platform is expressed with the angle that measuring the elevation of a triangular face relative to the base reference system. Then, the other two unknown vertices are established with the aforementioned angle and the scale ratio based on CGA. Finally, a 16th-degree univariate polynomial equation is reduced from two geometric constraint equations by constructing a 4 by 4 Sylvester resultant matrix. At last, a numerical example is deployed to verify the procedure. The novelty of this paper lies in that only one step elimination procedure is required to derive the 16th-degree polynomial equation and the modeling formulation and the elimination procedure can be understood with geometric intuition.

Keywords Forward displacement analysis · 6-3 Stewart platforms · Conformal geometric algebra · Sylvester resultant

Y. Zhang (✉) · Q. Liao · S. Wei · F. Wei · D. Li
School of Automation, Beijing University of Posts and Telecommunication,
Beijing 100086, China
e-mail: graduate_yingzh@bupt.edu.cn

Q. Liao
e-mail: qzliao@bupt.edu.cn

S. Wei
e-mail: wsmly@bupt.edu.cn

F. Wei
e-mail: weif@bupt.edu.cn

D. Li
e-mail: liduanling@bupt.edu.cn

1 Introduction

The Stewart platform [1] is a fully parallel, six-degree-of-freedom manipulator that generally consists of a base platform, a moving platform and six legs connected to each other in parallel. The Stewart platforms have been successfully used in a wide variety of fields and industries, ranging from astronomy to flight simulators, and are becoming increasingly popular in the machine-tool industry [2]. From the 1980s, the Stewart platforms have attracted wide interests from researchers and engineers due to their advantages of simplicity, high stiffness, large load capacity, quick dynamic response and excellent accuracy.

Given the lengths of the six legs, the forward displacement problem is to find the position and orientation of the moving platform with respect to a base platform. The problem has been considered a challenging problem, which involves highly non-linear algebraic equations. There are two main approaches to solve these equations: numerical schemes and closed-form solutions. A closed-form solution provides more information about the geometric and kinematic behavior over a numerical solution and the closed-form univariate polynomial equation has significant theoretical values as it is fundamental to many other kinematic problems. Hence obtaining a closed-form solution to the forward displacement analysis is more desirable in most cases.

In this paper, we will revisit the forward displacement analysis of 6-3 Stewart platforms, whose six legs meet in a pair-wise fashion at three-points in the moving triangular platform. Numerous researchers have worked on this problem. Hunt [3] stated that the maximum number of assembly modes for the problem was 16 by geometrical proof. Griffis and Duffy [4] obtained a closed-form solution to the problem based on the use of the input-output equation of spherical four-bar mechanisms. However, their approach is not suitable to the general 6-3 Stewart platforms, for which the six spherical points on the base platform are not restricted to lie in a plane. Innocenti et al. [5] reduced the problem to the solution of a non-linear system of three quadratic equations by the study of its equivalent mechanism, i.e., a 3-RS mechanism, from the forward kinematic viewpoint. Later on, Liang et al. [6] and Merlet [7] also solved this problem by the approach similar to the method proposed by Innocenti. The modeling method aforementioned is all formulated algebraically and non-geometrically based on the geometric and kinematic constraint.

In the paper, we will model this problem geometrically based on Conformal Geometric Algebra (CGA). CGA [8–10] is a new tool for geometric representation and computation. CGA provides a new model dealing with projective and kinematic geometry which is not based on pure point concepts, but points and spheres, leading to a new stratification hierarchy. CGA is coordinate-free. CGA subsumes Euclidean Geometric Algebra (EGA) and Projective Geometric Algebra (PGA). In this paper, we will model this problem in the conformal space by the intersection, extension and incidence of geometric entities, i.e., spheres, points, lines, planes,

circles and point pairs etc. CGA has been applied to solve the kinematic problem of the serial mechanisms [11, 12].

The rest of the paper is organized as follows. In Sect. 2, the definition, the geometric entities and the operations of CGA are introduced. In Sect. 3, the kinematic and geometric modeling is established by using CGA. Section 4 proposes the elimination procedure and reduces to a 16th-degree univariate polynomial equation. In Sect. 5, a numerical example is provided to verify our new kinematic method. At last, a conclusion is given.

2 Conformal Geometric Algebra

CGA is a very convenient model to do Euclidean geometry. In this section, CGA with its so-called “conformal model” of 3-dimensional (3D) Euclidean geometry will be introduced.

2.1 Notations and Basic Computations in CGA

The 5D CGA $\mathbb{R}^{3+1,1}$ is derived from a 3D Euclidean vector space \mathbb{R}^3 and a 2D Minkowski vector space $\mathbb{R}^{1,1}$. CGA has five orthonormal bases $\{e_1, e_2, e_3, e_+, e_-\}$, defined by the properties

$$e_i^2 = 1, i = 1, 2, 3, \tag{1}$$

$$e_+^2 = 1, e_-^2 = -1, \tag{2}$$

$$e_i \cdot e_+ = e_i \cdot e_- = e_+ \cdot e_- = 0. \tag{3}$$

where $\{e_1, e_2, e_3\}$ are the three orthonormal base vectors in EGA and $\{e_+, e_-\}$ are the two orthogonal bases in Minkowski vector space.

In addition, a null basis can now be introduced by the vectors

$$e_0 = \frac{1}{2}(e_- - e_+), \tag{4}$$

$$e_\infty = e_+ + e_-, \tag{5}$$

with the properties

$$e_0^2 = e_\infty^2 = 0, e_\infty \cdot e_0 = -1. \tag{6}$$

where e_0 is the conformal origin and e_∞ is the conformal infinity.

The three most often used products of CGA are the outer, the inner and the geometric product. The geometric product consists of an outer (denoted by “ \wedge ”) and an inner (denoted by “ \cdot ”) product, whose roles are to increase or to decrease the grade of the algebraic entities, respectively. The geometric product of two multi-vectors A and B is denoted as AB . **Blades** are the basic computational elements and the basic geometric entities of the geometric algebra.

The inner (\cdot) and outer (\wedge) products of two vectors u, v are defined as

$$u \cdot v = \frac{1}{2}(uv + vu), \tag{7}$$

$$u \wedge v = \frac{1}{2}(uv - vu). \tag{8}$$

Here, $\alpha = u \cdot v$ represents a scalar, which is a 0-blade, (blade of grade zero), $B = u \wedge v$ represents a bivector, which is a 2-blade. The grade of a blade is simply the number of vectors that “wedged” together give the blade.

As extension, the inner product of an r -blade $u_1 \wedge \dots \wedge u_r$ with an s -blade $v_1 \wedge \dots \wedge v_s$ can be defined recursively by

$$\begin{aligned} & (u_1 \wedge \dots \wedge u_r) \cdot (v_1 \wedge \dots \wedge v_s) \\ &= \begin{cases} ((u_1 \wedge \dots \wedge u_r) \cdot v_1) \cdot (v_2 \wedge \dots \wedge v_s) & \text{if } r \geq s \\ (u_1 \wedge \dots \wedge u_{r-1}) \cdot (u_r \cdot (v_1 \wedge \dots \wedge v_s)) & \text{if } r < s \end{cases}, \end{aligned} \tag{9}$$

with

$$\begin{aligned} (u_1 \wedge \dots \wedge u_r) \cdot v_1 &= \sum_{i=1}^r (-1)^{r-i} u_1 \wedge \dots \wedge u_{i-1} \wedge (u_i \cdot v_1) \wedge u_{i+1} \wedge \dots \wedge u_r, \\ u_r \cdot (v_1 \wedge \dots \wedge v_s) &= \sum_{i=1}^s (-1)^{i-1} v_1 \wedge \dots \wedge v_{i-1} \wedge (u_r \cdot v_i) \wedge v_{i+1} \wedge \dots \wedge v_s. \end{aligned}$$

The blades of highest grade are n -blades, called *pseudoscalars* P . Pseudoscalars differ from each other by a nonzero scalar only. There exist two unit n -blades, called the *unit pseudoscalars* $\pm I$, where $I_E(e_{123})$ and $I_C(e_{+-123}$ or $e_{\infty 0123})$ represent the unit pseudoscalars of the algebras for the Euclidean and conformal space respectively.

We define the dual X^* of an r -blade X by

$$X^* = XI^{-1}, \tag{10}$$

where I^{-1} is the inverse of I . It follows, that the dual of an r -blade is an $(n-r)$ -blade.

2.2 Geometric Entities in CGA

Compared to 3D EGA, the 5D CGA provides a greater variety of basic geometric entities to compute with. In CGA, the spheres are the basic entities from which the other entities are derived. The primitive geometric entities in CGA consist of spheres, points, lines, planes, circles and point pairs. The definition of the geometric entities with respect to the inner product null space, their dual representation with respect to the outer product null space and their grades are given in Table 1. The detailed derivation is referred to the paper [9]. In Table 1, \underline{x} is marked bold italic and it represents the entity in 3D EGA and \underline{X} is the representation of a geometric entity in 5D CGA. For example, the basic entities, spheres \underline{S} , containing the center \underline{p} and the radius ρ is represented by $\underline{S} = \underline{p} + \frac{1}{2}(\underline{p}^2 - \rho^2)\underline{e}_\infty + \underline{e}_0$. The point $\underline{X} = \underline{x} + \frac{1}{2}\underline{x}^2\underline{e}_\infty + \underline{e}_0$ is nothing more than a degenerate sphere with radius $\rho = 0$, which can easily be seen from the representation of a sphere.

The inner product between both normalized points is calculated as

$$\begin{aligned} \underline{X}_1 \cdot \underline{X}_2 &= \left(\underline{x}_1 + \frac{1}{2}\underline{x}_1^2\underline{e}_\infty + \underline{e}_0 \right) \cdot \left(\underline{x}_2 + \frac{1}{2}\underline{x}_2^2\underline{e}_\infty + \underline{e}_0 \right) = -\frac{1}{2}(\underline{x}_1^2 + \underline{x}_2^2) + \underline{x}_1 \cdot \underline{x}_2 \\ &= -\frac{1}{2}(\underline{x}_1 - \underline{x}_2)^2 = -\frac{1}{2}d_{12}, \end{aligned} \tag{11}$$

where, d_{12} denotes the Euclidean distance between two points. From Eq. (11), it can be seen that $\underline{X} \cdot \underline{X} = 0$. Similarly, the inner product between the point and the sphere, $\underline{X} \cdot \underline{S} = -\frac{1}{2}((\underline{x} - \underline{p})^2 - \rho^2)$, can be used to identify whether a point is inside or outside of a sphere.

Table 1 The entities and their dual representations in CGA

Entity	Representation	Grade	Dual representation	Grade
Sphere	$\underline{S} = \underline{p} + \frac{1}{2}(\underline{p}^2 - \rho^2)\underline{e}_\infty + \underline{e}_0$	1	$\underline{S}^* = \underline{A} \wedge \underline{B} \wedge \underline{C} \wedge \underline{D}$	4
Point	$\underline{X} = \underline{x} + \frac{1}{2}\underline{x}^2\underline{e}_\infty + \underline{e}_0$	1	$\underline{X}^* = \underline{e}_\infty \wedge \underline{X}$	4
Plane	$\underline{P} = n\underline{I}_E - d\underline{e}_\infty$ $n = (\underline{a} - \underline{b}) \wedge (\underline{a} - \underline{c})$ $d = (\underline{a} \wedge \underline{b} \wedge \underline{c})\underline{I}_E$	1	$\underline{P}^* = \underline{e}_\infty \wedge \underline{A} \wedge \underline{B} \wedge \underline{C}$	4
Line	$\underline{L} = r\underline{I}_E + \underline{e}_\infty m\underline{I}_E$ $r = \underline{a} - \underline{b}$ $m = \underline{a} \wedge \underline{b}$	2	$\underline{L}^* = \underline{e}_\infty \wedge \underline{A} \wedge \underline{B}$	3
Circle	$\underline{Z} = \underline{S}_1 \wedge \underline{S}_2$	2	$\underline{Z}^* = \underline{A} \wedge \underline{B} \wedge \underline{C}$	3
Point pair	$\underline{PP} = \underline{S}_1 \wedge \underline{S}_2 \wedge \underline{S}_3$	3	$\underline{PP}^* = \underline{A} \wedge \underline{B}$	2

Note In this table, both representations after dualization of geometric entities are not identical and differ from each other by a nonzero scale ratio only. The representations of points and spheres with respect to the inner product null space are their normalized representatives. The normalization of the points can be achieved simply by dividing $-\underline{e}_\infty \cdot \underline{X}$

In this paper, the inner product, the outer product and the dual operation are important. In the next section, we will model this problem based on CGA.

3 Kinematic and Geometric Modeling Based on CGA

A 6-3 Stewart platform $A_1A_2A_3A_4A_5A_6-B_1B_2B_3$, shown in Fig. 1, has six SPS (S: spherical joint, P: prismatic joint) legs meeting in a pair-wise fashion at three-points in the moving triangular platform. The six leg lengths l_i ($i = 1, 2, \dots, 6$) provided by prismatic joint in every leg are six inputs to control the position and orientation of the moving platform. For the base platform, the six joints are not restricted to lie in a plane.

3.1 The Representation of Vertex B_1 with Variable θ

According to Ref. [5], in Fig. 1, the point B_1 can be only located on a circle with axis A_1A_2 . Therefore we can replace the two SPS links A_1B_1 and A_2B_1 by one RPS (R: Revolute joint) link A_0B_1 where point A_0 denotes the foot point on A_1A_2 with respect to point B_1 . Now, clearly the forward displacement analysis of 6-3 Stewart platform is equivalent to the equivalent one seen in Fig. 2, where one revolute pair is introduced in place of two legs converging at point B_1 .

Then we attach the fixed coordinate frame $O: X-Y-Z$ to the base. The coordinates of A_i ($i = 1, 2, \dots, 6$) and the coordinates of B_i ($i = 1, 2, 3$) in the fixed reference frame are denoted by $a_i = (a_{ix}, a_{iy}, a_{iz})^T$ and $b_i = (b_{ix}, b_{iy}, b_{iz})^T$ respectively, where the coordinates of points A_i are known. The distances between points B_i ($i = 1, 2, 3$) are denoted by r_i ($i = 1, 2, 3$) and they are known.

Fig. 1 The geometric model of a 6-3 Stewart platform

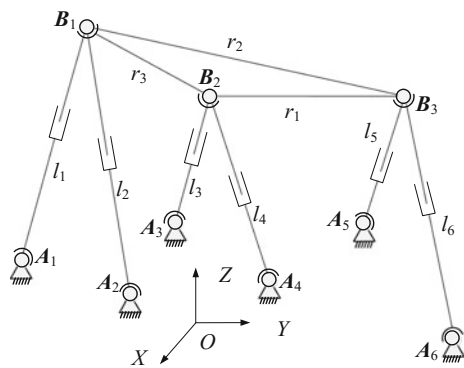
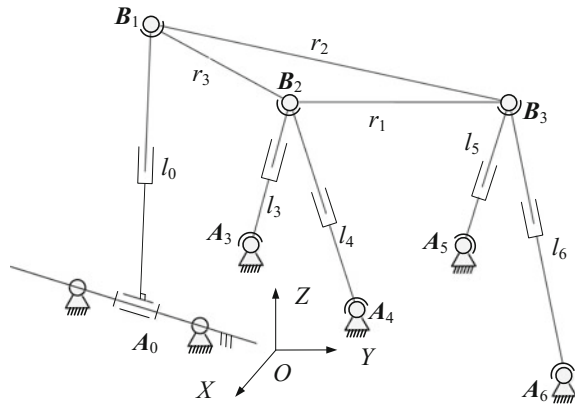


Fig. 2 The equivalent geometric model of a 6-3 Stewart platform



One variable θ is introduced to denote the dihedral angles between the triangles $\triangle A_1B_1A_2$ and the base plane. Now the coordinate of the point B_1 in Euclidean space in the fixed frame can be written as follows,

$$b_1 = (\beta)(\alpha)(\theta)(l_0, 0, 0)^T + a_0, \tag{12}$$

where, (β) , (α) and (θ) denotes the rotation matrix with axis Y , X and Z respectively, and l_0 represents the distance between the points B_1 and A_0 , i.e., $l_0 = |B_1A_0|$, which can be determined by using the sine law for a planar triangle $\triangle A_1B_1A_2$.

Introducing the Euler equations $\cos \theta = (e^{i\theta} + e^{-i\theta})/2$ and $\sin \theta = (e^{i\theta} - e^{-i\theta})/(2i)$, where, i denotes the imaginary unit, according to the list in Table 1, the point B_1 can be represented by CGA as

$$\underline{B}_1 = b_1 + \frac{1}{2}b_1^2e_\infty + e_0. \tag{13}$$

3.2 The Representation of Vertices B_2 and B_3 with Variable θ and λ

For the vertex B_2 on the moving platform, it can be seen from Fig. 2 that it is one of the point pair, the intersection of three spheres \underline{S}_1 , \underline{S}_2 and \underline{S}_3 , i.e., the sphere \underline{S}_1 with the center at point \underline{B}_1 and the radius r_3 , the sphere \underline{S}_2 with the center at point \underline{A}_3 and the radius l_3 and the sphere \underline{S}_3 with the center at point \underline{A}_4 and the radius l_4 . And therefore, the point pair \underline{B}_{b_2} of grade 3 can be expressed as

$$\underline{\mathbf{B}}_{b2} = \underline{\mathbf{S}}_1 \wedge \underline{\mathbf{S}}_2 \wedge \underline{\mathbf{S}}_3, \tag{14}$$

where, the three spheres $\underline{\mathbf{S}}_1, \underline{\mathbf{S}}_2$ and $\underline{\mathbf{S}}_3$ can be represented as follows,

$$\underline{\mathbf{S}}_1 = \underline{\mathbf{S}}_{B_1B_2} = \underline{\mathbf{B}}_1 - \frac{1}{2}r_3^2e_\infty, \underline{\mathbf{S}}_2 = \underline{\mathbf{S}}_{A_3B_2} = \underline{\mathbf{A}}_3 - \frac{1}{2}l_3^2e_\infty, \underline{\mathbf{S}}_3 = \underline{\mathbf{S}}_{A_4B_2} = \underline{\mathbf{A}}_4 - \frac{1}{2}l_4^2e_\infty,$$

and the other two centers can be expressed as follows,

$$\underline{\mathbf{A}}_3 = \mathbf{a}_3 + \frac{1}{2}a_3^2e_\infty + \mathbf{e}_0, \underline{\mathbf{A}}_4 = \mathbf{a}_4 + \frac{1}{2}a_4^2e_\infty + \mathbf{e}_0.$$

According to Eq. (10), the dual $\underline{\mathbf{B}}_{b2}^*$ of the point pair $\underline{\mathbf{B}}_{b2}$ by

$$\underline{\mathbf{B}}_{b2}^* = \underline{\mathbf{B}}_{b2} \mathbf{I}_C^{-1} = -\underline{\mathbf{B}}_{b2} \mathbf{e}_{+123}, \tag{15}$$

According to the expression in Table 1, the dual representation of the point pair $\underline{\mathbf{B}}_{b2}$ can be expressed by

$$\underline{\mathbf{B}}_{b2}^* = \eta \underline{\mathbf{B}}_{21} \wedge \underline{\mathbf{B}}_{22}, \tag{16}$$

The vertex \mathbf{B}_2 can be reduced from the point pair $\underline{\mathbf{B}}_{b2}^*$ as

$$\begin{aligned} \{\underline{\mathbf{B}}_{21}, \underline{\mathbf{B}}_{22}\} &= \frac{1}{2} \left(\frac{2(e_\infty \cdot \underline{\mathbf{B}}_{b2}^*) \cdot \underline{\mathbf{B}}_{b2}^*}{(e_\infty \cdot \underline{\mathbf{B}}_{b2}^*) \cdot (e_\infty \cdot \underline{\mathbf{B}}_{b2}^*)} \pm \lambda (e_\infty \cdot \underline{\mathbf{B}}_{b2}^*) \right) \\ &= \frac{(e_\infty \cdot \underline{\mathbf{B}}_{b2}^*) \cdot \underline{\mathbf{B}}_{b2}^*}{(e_\infty \cdot \underline{\mathbf{B}}_{b2}^*) \cdot (e_\infty \cdot \underline{\mathbf{B}}_{b2}^*)} \pm \frac{\lambda (e_\infty \cdot \underline{\mathbf{B}}_{b2}^*)}{2}, \end{aligned} \tag{17}$$

where $\lambda = \frac{1}{\eta}$.

Equation (17) is different from the equation in Ref. [10], and in this paper, we introduce a scale ratio λ to avoid the extraneous roots in the solution procedure.

Substituting $t_1 = e_\infty \cdot \underline{\mathbf{B}}_{b2}^*, t_2 = (e_\infty \cdot \underline{\mathbf{B}}_{b2}^*) \cdot (e_\infty \cdot \underline{\mathbf{B}}_{b2}^*) = t_1 \cdot t_1, t_3 = (e_\infty \cdot \underline{\mathbf{B}}_{b2}^*) \cdot \underline{\mathbf{B}}_{b2}^* = t_1 \cdot \underline{\mathbf{B}}_{b2}^*$, the vertex \mathbf{B}_2 can be expressed by as

$$\underline{\mathbf{B}}_2 = \{\underline{\mathbf{B}}_{21}, \underline{\mathbf{B}}_{22}\} = \frac{t_3}{t_2} \pm \frac{\lambda t_1}{2}, \tag{18}$$

where t_1 is a vector of grade 1, t_2 is a scalar and t_3 is also a vector of grade 1.

According to the inner product of two identical points equal to zero, the first constraint equation is obtained as

$$\underline{\mathbf{B}}_2 \cdot \underline{\mathbf{B}}_2 = 0 \Leftrightarrow \left(\frac{t_3}{t_2} \pm \frac{\lambda t_1}{2}\right) \cdot \left(\frac{t_3}{t_2} \pm \frac{\lambda t_1}{2}\right) = \frac{t_3^2}{t_2^2} + \frac{\lambda^2}{4} t_2 \pm \frac{\lambda t_1 \cdot t_3}{t_2} = 0. \tag{19}$$

According to Eqs. (9) and (16), we have the following expressions,

$$t_1 \cdot t_3 = t_1 \cdot \left(t_1 \cdot \underline{\mathbf{B}}_{b2}^*\right) = \eta t_1 \cdot (t_1 \cdot (\underline{\mathbf{B}}_{21} \wedge \underline{\mathbf{B}}_{22})) = 0, \tag{20}$$

$$t_3 \cdot t_3 = \left(t_1 \cdot \underline{\mathbf{B}}_{b2}^*\right) \cdot \left(t_1 \cdot \underline{\mathbf{B}}_{b2}^*\right) = -(t_1 \cdot t_1) \left(\underline{\mathbf{B}}_{b2}^* \cdot \underline{\mathbf{B}}_{b2}^*\right) = -t_2 D, \tag{21}$$

where we have used

$$t_1 \cdot (\underline{\mathbf{B}}_{21} \wedge \underline{\mathbf{B}}_{22}) = (t_1 \cdot \underline{\mathbf{B}}_{21}) \underline{\mathbf{B}}_{22} - (t_1 \cdot \underline{\mathbf{B}}_{22}) \underline{\mathbf{B}}_{21}, t_1 \wedge \underline{\mathbf{B}}_{b2}^* = 0, \\ \left(t_1 \wedge \underline{\mathbf{B}}_{b2}^*\right) \cdot \left(t_1 \wedge \underline{\mathbf{B}}_{b2}^*\right) = \left(\underline{\mathbf{B}}_{b2}^* \wedge t_1\right) \cdot \left(t_1 \wedge \underline{\mathbf{B}}_{b2}^*\right) = (t_1 \cdot t_1) \left(\underline{\mathbf{B}}_{b2}^* \cdot \underline{\mathbf{B}}_{b2}^*\right) + \left(t_1 \cdot \underline{\mathbf{B}}_{b2}^*\right) \cdot \left(t_1 \cdot \underline{\mathbf{B}}_{b2}^*\right) = 0.$$

and $D = \underline{\mathbf{B}}_{b2}^* \cdot \underline{\mathbf{B}}_{b2}^*$.

Substituting Eq. (20) and (21) into Eq. (19), we have

$$\frac{D}{t_2} + \frac{\lambda^2}{4} t_2 = 0, \tag{22}$$

where Eq. (22) is the first equation with two variables λ and θ .

For the vertex $\underline{\mathbf{B}}_3$ on the moving platform, it can be seen from Fig. 2 that it is the intersection point of four spheres $\underline{\mathbf{S}}_4, \underline{\mathbf{S}}_5, \underline{\mathbf{S}}_6$ and $\underline{\mathbf{S}}_7$, i.e., the sphere $\underline{\mathbf{S}}_4$ with the center at point $\underline{\mathbf{A}}_1$ and the radius r_2 , the sphere $\underline{\mathbf{S}}_5$ with the center at point $\underline{\mathbf{A}}_5$ and the radius l_5 the sphere $\underline{\mathbf{S}}_6$ with the center at point $\underline{\mathbf{A}}_6$ and the radius l_6 and the sphere $\underline{\mathbf{S}}_7$ with the center at point $\underline{\mathbf{B}}_2$ and the radius r_1 . And therefore, the vertex $\underline{\mathbf{B}}_3$ of grade 4 can be expressed as

$$\underline{\mathbf{B}}_3 = \underline{\mathbf{S}}_4 \wedge \underline{\mathbf{S}}_5 \wedge \underline{\mathbf{S}}_6 \wedge \underline{\mathbf{S}}_7, \tag{23}$$

where, the four spheres $\underline{\mathbf{S}}_4, \underline{\mathbf{S}}_5, \underline{\mathbf{S}}_6$ and $\underline{\mathbf{S}}_7$ can be represented as follows,

$$\underline{\mathbf{S}}_4 = \underline{\mathbf{S}}_{B_1 B_3} = \underline{\mathbf{B}}_1 - \frac{1}{2} r_2^2 e_\infty, \underline{\mathbf{S}}_5 = \underline{\mathbf{S}}_{A_5 B_3} = \underline{\mathbf{A}}_5 - \frac{1}{2} l_5^2 e_\infty, \\ \underline{\mathbf{S}}_6 = \underline{\mathbf{S}}_{A_6 B_3} = \underline{\mathbf{A}}_6 - \frac{1}{2} l_6^2 e_\infty, \underline{\mathbf{S}}_7 = \underline{\mathbf{S}}_{B_2 B_3} = \underline{\mathbf{B}}_2 - \frac{1}{2} r_1^2 e_\infty,$$

and the centers can be expressed as follows,

$$\underline{\mathbf{A}}_5 = \mathbf{a}_5 + \frac{1}{2} \mathbf{a}_5^2 e_\infty + \mathbf{e}_0, \underline{\mathbf{A}}_6 = \mathbf{a}_6 + \frac{1}{2} \mathbf{a}_6^2 e_\infty + \mathbf{e}_0.$$

According to Eq. (10), the dual $\underline{\mathbf{B}}_3^*$ of the point $\underline{\mathbf{B}}_3$ by

$$\underline{\mathbf{B}}_3^* = \underline{\mathbf{B}}_3 \mathbf{J}_C^{-1} = -\underline{\mathbf{B}}_3 \mathbf{e}_{+123} = \underline{\mathbf{S}}_7 \cdot \underline{\mathbf{B}}_{b_3}^*, \tag{24}$$

where $\underline{\mathbf{B}}_{b_3}^* = -(\underline{\mathbf{S}}_4 \wedge \underline{\mathbf{S}}_5 \wedge \underline{\mathbf{S}}_6) \mathbf{e}_{+123}$ and it is a bivector with grade 2.

According to the inner product of two identical points equal to zero, the second constraint equation is obtained as

$$\underline{\mathbf{B}}_3^* \cdot \underline{\mathbf{B}}_3^* = 0 \Leftrightarrow (\underline{\mathbf{S}}_7 \cdot \underline{\mathbf{B}}_{b_3}^*) \cdot (\underline{\mathbf{S}}_7 \cdot \underline{\mathbf{B}}_{b_3}^*) = 0, \tag{25}$$

Expanding Eq. (25), we can obtain the following equation with two variables λ and θ as

$$\frac{\lambda^2}{4} U \cdot U + \lambda \left(\pm \frac{1}{t_2} V \cdot U \mp \frac{r_2^2}{2} W \cdot U \right) + \left(\frac{1}{t_2^2} V \cdot V + \frac{r_4^2}{4} W \cdot W - \frac{r_2^2}{t_2} W \cdot V \right) = 0, \tag{26}$$

where $U = t_1 \cdot \underline{\mathbf{B}}_3^*$, $V = t_3 \cdot \underline{\mathbf{B}}_3^*$, $W = e_\infty \cdot \underline{\mathbf{B}}_3^*$, and U , V and W are all vectors of grade 1.

Equations (22) and (26) are two kinematic constraint equations for the forward displacement analysis of 6-3 Stewart platforms. Equation (22) and Eq. (26) are quadratic equations in variable λ . In the next section, we will derive the univariate polynomial equation in symbolic form for this problem.

4 Solution Procedure

In this section, we will firstly eliminate the variable λ from Eqs. (22) and (26) by Sylvester resultant method, and then we will derive an univariate polynomial equation and finally, we will substitute back and solve the coordinates of the points in the moving platform.

4.1 Elimination of the Variable λ

By analyzing Eqs. (22) and (26), it can be seen that the degrees of Eqs. (22) and (26) in λ is 2 and 1. Before we eliminate the variable λ , we rearrange Eqs. (22) and (26) in λ as follows,

$$c_{12}\lambda^2 + c_{10} = 0, \tag{27}$$

$$c_{22}\lambda^2 + c_{21}\lambda + c_{20} = 0, \tag{28}$$

where, $c_{12} = \frac{D}{4}$, $c_{10} = \frac{D}{t_2}$, $c_{22} = \frac{1}{4}U \cdot U$, $c_{21} = \pm \frac{1}{t_2}V \cdot U \mp \frac{r_2^2}{2}W \cdot U$ and $c_{20} = \frac{1}{t_2^2}V \cdot V + \frac{r_2^4}{4}W \cdot W - \frac{r_2^2}{t_2}W \cdot V$.

According to the Sylvester resultant method, the elimination of Eqs. (27) and (28) in the variable λ can be written as:

$$\begin{bmatrix} c_{12} & 0 & c_{10} & 0 \\ 0 & c_{12} & 0 & c_{12} \\ c_{22} & c_{21} & c_{20} & 0 \\ 0 & c_{22} & c_{21} & c_{20} \end{bmatrix} \begin{bmatrix} \lambda^3 \\ \lambda^2 \\ \lambda \\ 1 \end{bmatrix} = \mathbf{0}_{4 \times 1}. \tag{29}$$

Equation (29) can simply be written as:

$$\mathbf{M}[\lambda^3 \quad \lambda^2 \quad \lambda \quad 1]^T = \mathbf{0}_{4 \times 1}, \tag{30}$$

where \mathbf{M} is a coefficient matrix.

According to Sylvester resultant elimination, Eqs. (27) and (28) have common zeros if the determinant of the matrix \mathbf{M} equals 0, i.e.,

$$\det = |\mathbf{M}| = 0. \tag{31}$$

Expanding Eq. (31), we can obtain the equation as

$$\begin{aligned} \det &= c_{12}^2c_{20}^2 + c_{10}c_{12}c_{21}^2 - 2c_{10}c_{12}c_{20}c_{22} + c_{10}^2c_{22}^2 \\ &= \frac{1}{t_2^2}C_{-2} + \frac{r_2^2}{t_2}C_{-1} + C_0 = 0, \end{aligned} \tag{32}$$

where,

$$\begin{aligned} C_{-2} &= \frac{D}{4}(V \cdot U)^2 - \frac{D}{8}(U \cdot U)(V \cdot V) + \frac{D^2}{16}(U \cdot U)^2 + \frac{1}{16}(V \cdot V)^2, \\ C_{-1} &= -\frac{1}{8}(V \cdot V)(C \cdot V) - \frac{D}{4}(V \cdot U)(C \cdot U) + \frac{D}{8}(W \cdot V)(U \cdot U), \\ C_0 &= \frac{t_2^2 r_2^8}{256}(W \cdot W)^2 + \frac{r_2^4}{16}(W \cdot V)^2 + \frac{r_2^4}{32}(V \cdot V)(W \cdot W) - \frac{r_2^6 t_2}{32}(W \cdot V)(W \cdot W) \\ &\quad + \frac{D r_2^4}{16}(W \cdot A)^2 - \frac{D r_2^4}{32}(W \cdot W)(U \cdot U). \end{aligned}$$

It can be seen that there exists the terms t_2^{-2} and t_2^{-1} in Eq. (32), and therefore it is not easy to see its highest degree. In the next subsection, we will expand and simplify Eq. (32) and derive a 16th-degree univariate polynomial equation.

4.2 An Univariate Equation in Variable $e^{i\theta}$

For the term C_{-2} , it can be expanded and rewritten as

$$C_{-2} = -\frac{1}{4}t_2^2E^2DF + \frac{1}{16}t_2^2(DF - G \cdot G + E^2)^2, \tag{33}$$

where we use $(U \wedge V) \cdot (U \wedge V) = (U \cdot V)^2 - (U \cdot U)(V \cdot V)$, $U \wedge V = -t_2E\underline{\mathbf{B}}_{b_3}^*$, $D(U \cdot U) + V \cdot V = t_2(DF - G \cdot G + E^2)$, and $E = \underline{\mathbf{B}}_{b_2}^* \cdot \underline{\mathbf{B}}_{b_3}^*$, $F = \underline{\mathbf{B}}_{b_3}^* \cdot \underline{\mathbf{B}}_{b_3}^*$, $G = \underline{\mathbf{B}}_{b_2}^* \wedge \underline{\mathbf{B}}_{b_3}^*$.

For the term C_{-1} , it can be expanded and rewritten as

$$C_{-1} = -\frac{1}{8}t_2(DF - G \cdot G + E^2) - \frac{D}{4}t_2EHF, \tag{34}$$

where we use $(U \wedge V) \cdot (U \wedge W) = (U \cdot V)(U \cdot W) - (U \cdot U)(V \cdot W)$, $U \wedge W = -H\underline{\mathbf{B}}_{b_3}^*$, and $H = (t_1 \wedge e_\infty) \cdot \underline{\mathbf{B}}_{b_3}^*$.

Substituting Eqs. (33) and (34) into Eq. (32), it yields to

$$\begin{aligned} \det &= -\frac{1}{4}E^2DF + \frac{1}{16}(DF - G \cdot G + E^2)^2 - \frac{r_2^2}{8}(DF - G \cdot G + E^2) \\ &\quad - \frac{r_2^2}{4}DEHF + C_0 \\ &= 0 \end{aligned} \tag{35}$$

It can be seen that Eq. (35) is a polynomial equation in variable $e^{i\theta}$.

4.3 Back Substitution

Solving Eq. (35), all the 16 solutions for $e^{i\theta}$ can be gotten. Substituting $e^{i\theta}$ into Eqs. (22) and (26), linear equation in variable λ can be obtained by using Euclidean algorithm and λ can be solved directly.

After two variables are obtained, the point \mathbf{B}_1 can be directly gotten from Eq. (12). The points \mathbf{B}_2 and \mathbf{B}_3 can be obtained from Eqs. (18) and (24) by dividing their magnitudes $-e_\infty \cdot \underline{\mathbf{B}}_2$ and $-e_\infty \cdot \underline{\mathbf{B}}_3$ respectively.

Table 2 Input data

$O-X-Y-Z$	A_1	A_2	A_3	A_4	A_5	A_6
a_{ix}	50	-25	80	-50	48	36
a_{iy}	0	-2	20	-20	15	31
a_{iz}	100	40	50	70	68	-93
The distances r_i between the points B_i	$r_1 = 135, r_2 = 190, r_3 = 141$					
The lengths of six legs l_i	$l_1 = 76, l_2 = 160, l_3 = 139, l_4 = 55, l_5 = 128, l_6 = 21$					

Table 3 Real solutions

i	$e^{i\theta}$	λ		B_1	B_2	B_3
1	0.4371 -0.8994i	0.006058	X	79.5353	-26.0942	-70.9222
			Y	-45.8809	-68.9457	54.3104
			Z	152.9018	62.3955	94.3853
2	0.7572 -0.6532i	0.006078	X	68.8676	-47.0215	21.2493
			Y	-33.0062	21.0886	137.0612
			Z	165.8073	106.4396	95.7395
3	0.2969 +0.9549i	-0.004463	X	82.5389	-48.8261	14.0067
			Y	51.0783	24.7276	-108.359
			Z	145.9154	101.9852	71.8847
4	0.03977 +0.9992i	-0.0009328	X	90.9016	-40.7763	-6.7822
			Y	53.3944	6.2851	-100.5172
			Z	135.3847	117.4237	74.2180

5 Numerical Example

In order to validate the solution procedure, the input data of the numerical example is given in Table 2 and the same data as Ref. [5]. Due to the space limitation, the real solutions are only given in Table 3.

6 Conclusion

The paper presents a novel modeling and solution method for the forward displacement analysis of 6-3 Stewart platforms based on CGA. Two kinematic equations with two variables are formulated for two vectices in the moving platform by using CGA. The 16th-degree univariate polynomial equation is derived by constructing a 4 by 4 Sylvester resultant matrix and it is smaller in size than those existed. The two kinematic equations have explicit geometric meaning and the real solutions are easily obtained. Compared with the previously methods in the literature, the main contribution of the paper lies in that the modeling formulation and

the elimination procedure for this problem can be understood with geometric intuition and only one step elimination procedure is required to derive the 16th-degree polynomial equation.

Acknowledgments The authors acknowledge funding provided by the Fundamental Research Funds for the Central Universities (No. 2016RC28), the National Natural Science Foundation of China (No. 51375059 and No. 51375058), the joint project of scientific research and cultivation of students, the Special Fund for Agro-scientific Research in the Public Interest of China (No. 201313009-06), the National Key Technology R&D Program of the Ministry of Science and Technology of China (No. 2013BAD17B06) and Beijing Municipal Natural Science Foundation of China (No. 3162021) for this research.

References

1. Stewart D (1965) A platform with six degree of freedom. *Proc Inst Mech Eng (Part I)* 180 (1):371–386
2. Merlet JP (2006) *Parallel robots*. Springer, Dordrecht
3. Hunt KH (1983) Structural kinematics of in parallel actuated robot arms. *Trans ASME J Mech Trans Autom Des* 105:705–712
4. Griffis M, Duffy J (1989) A forward displacement analysis of a class of Stewart platforms. *J Rob Syst* 6(6):703–720
5. Innocenti C, Parenti-Castelli V (1990) Direct position analysis of the Stewart platform mechanism. *Mech Mach Theory* 25(6):611–621
6. Liang CG, Rong H (1991) The forward displacement solution to a Stewart platform type manipulator. *Chin J Mech Eng* 27(2):26–30 Chinese edition
7. Merlet JP (1992) Direct kinematics and assembly modes of parallel manipulators. *Int J Robot Res* 11(2):150–162
8. Li H (2005) Conformal geometric algebra—a new framework for computational geometry. *J Comput Aided Des Comput Graph* 17(11):2383–2393
9. Rosenhahn B, Sommer G (2005) Pose estimation in conformal geometric algebra part I: the stratification of mathematical spaces. *J Math Imaging Vis* 22:27–48
10. Hildenbrand D, Fontijne D, Perwass C et al (2004) Geometric algebra and its application to computer graphics. *Eurographics 2004 tutorial*, pp 1–49
11. Hildenbrand D, Zamora J, Bayro-Corrochano E (2008) Inverse kinematics computation in computer graphics and robotics using conformal geometric algebra. *Adv Appl Clifford Algebras* 18(3–4):699–713
12. Kim JS, Jeong JH, Park JH (2015) Inverse kinematics and geometric singularity analysis of a 3-SPS/S redundant motion mechanism using conformal geometric algebra. *Mech Mach Theory* 90:23–36

Structural Conditions of Two Types of 3-DOF Parallel Mechanisms with Zero-Torsion Characteristics

Jiexin Zou and Jingjun Yu

Abstract The tilt-and-torsion angles are used for representations of the orientation workspace of parallel mechanisms (PMs). For the zero-torsion PMs, it needs only two angles to represent the orientation workspace. However, there are few studies about the structural conditions of zero-torsion PMs. This paper deals with the derivation of structural conditions of two types of three-degree-of-freedom (3-DOF) parallel mechanisms with zero-torsion characteristics. The PMs include a class of 3-[PP]S PMs and the 3-RSR one, both of which have been widely used as the orientational stages. The structural conditions of these PMs that satisfies zero-torsion characteristics have been derived from a conventional kinematics-based approach. The results indicates that the zero-torsion 3-[PP]S PMs have at least the characteristic of z -axial symmetry, while the zero-torsion 3-RSR PM should be mirror-symmetrical in structure.

Keywords Parallel mechanism · Symmetry · Zero torsion

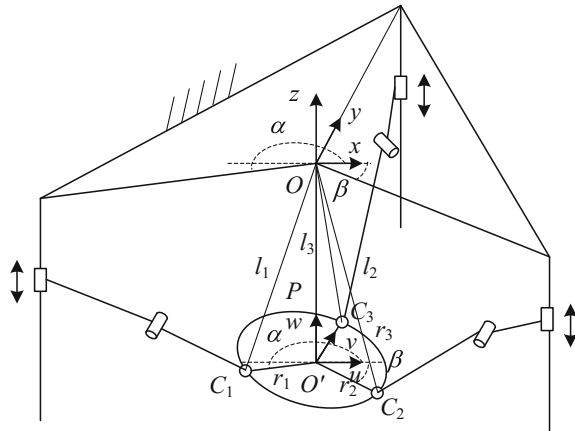
1 Introduction

As it became clear that hexapods are too complex for machining applications, industry and academia have spent considerable efforts on investigating parallel mechanisms (PMs) with less than six degrees of freedom (DOF) [1], since the late 1990s. Among all these PMs, the most popular ones are undoubtedly the groups of 3-DOF parallel mechanisms, such as a family of 3-[PP]S PMs [2] and the 3-RSR PM. A 3-[PP]S parallel mechanism, whose moving platform is attached to three legs via spherical joints (Fig. 1) and has two rotational and one translational DOFs, constrains the centers of the spherical joints to move in three vertical planes

J. Zou · J. Yu (✉)
Robotics Institute, Beihang University, Beijing, China
e-mail: jjyu@buaa.edu.cn

J. Zou
e-mail: za2153@126.com

Fig. 1 3-PRS parallel mechanism



intersecting at a common line. The family of 3-[PP]S parallel mechanisms include 3-PPS PM, 3-RRS PM, 3-RPS PM and 3-PRS PM. The 3-RSR parallel mechanism is symmetrical about the mid-plane that passes through the centers of the spherical joints. The axis of upper revolute pair and that of lower revolute pair are coplanar with respect to each leg of the 3-RSR parallel mechanism.

There is a large number of literatures on 3-[PP]S PMs and the 3-RSR one. A 3-PPS parallel mechanism was proposed in Ref. [3]. Kinematics of the 3-RPS architecture was analyzed in Refs. [4–8]. Two different designs related to the 3-PRS PMs were studied in Refs. [9, 10], and the latter is well known through the patented Z3 Head by DS Technology [11]. A 3-RRS PM was investigated in Ref. [12]. Both the forward and inverse kinematics of the 3-RSR PM are investigated in Refs. [13–15].

In Ref. [16], the exponential submanifolds are used to investigate the geometric properties of zero-torsion parallel kinematics machines. Wu et al. claimed that all zero-torsion parallel mechanisms are symmetrical around the z -axis and proved that the Omni-wrist III and the 3-RSR PM are both the zero-torsion parallel mechanisms. But the proposed method seems too complex and not easy to understand without the knowledge of differential manifolds.

In this paper, the authors apply a conventional kinematics-based approach to deduce that the structural conditions of the 3-[PP]S PMs and the 3-RSR PM are zero-torsion parallel kinematics machines. In Sect. 2, the structural condition that all 3-[PP]S PMs are resorted to the family of zero-torsion PMs is derived. In the next section, the structural condition that the 3-RSR PM being a zero-torsion one are also deduced. Finally, conclusions are drawn in Sect. 4.

2 3-[PP]S PM and z -Axial Symmetry

When it comes to the necessary and sufficient condition that the 3-[PP]S PM belongs to be a zero-torsion one, the derivation procedure is listed as follows.

Take the 3-PRS PM as an example (Fig. 1). Let O - xyz be the fixed coordinate system and O' - uvw be the moving coordinate system. Three P joints are parallel to the z -axis, and three legs constrain the centers of the S joints to move in three vertical planes. The angle between the plane of leg 1 and x -axis is α , the angle between the plane of leg 2 and x -axis is β , and the x -axis is perpendicular to the plane of leg 3. Let C_1, C_2, C_3 denote the centers of the S joints respectively. The distances between C_1, C_2, C_3 and O' are represented with r_1, r_2, r_3 , and the distances between C_1, C_2, C_3 and O are l_1, l_2, l_3 . In the initial moment, the moving platform is parallel to the fixed platform, and the x -axis, y -axis, z -axis are parallel to the u -axis, v -axis, w -axis respectively. The z -axis coincides with the w -axis at its initial position. Denote $\mathbf{p} = (x \ y \ z)^T$ and \mathbf{p} is the vector along OO' expressed in the fixed coordinate system, $\mathbf{l}_i = (l_{ix} \ l_{iy} \ l_{iz})^T$ and \mathbf{l}_i are the vectors along OC_i expressed in the fixed coordinate system, and $\mathbf{a}_i = (a_{ix} \ a_{iy} \ a_{iz})^T$ and \mathbf{a}_i are the vectors along $O'C_i$ expressed in the fixed coordinate system.

Here the T&T angle method [17] is used to represent the orientation of the moving platform, and the resultant rotational matrix in terms of T&T angles is written directly, which is

$$\begin{aligned} \mathbf{T} &= \mathbf{T}_{ZYZ} = \mathbf{R}_Z(\phi)\mathbf{R}_Y(\theta)\mathbf{R}_Z(\psi - \phi) \\ &= \begin{bmatrix} c\phi c\theta c(\psi - \phi) - s\phi s(\psi - \phi) & -c\phi c\theta s(\psi - \phi) - s\phi c(\psi - \phi) & c\phi s\theta \\ s\phi c\theta c(\psi - \phi) + c\phi s(\psi - \phi) & -s\phi c\theta s(\psi - \phi) + c\phi c(\psi - \phi) & s\phi s\theta \\ -s\theta c(\psi - \phi) & s\theta s(\psi - \phi) & c\theta \end{bmatrix} \end{aligned} \quad (1)$$

where s^* denotes $\sin(^*)$ and c^* denotes $\cos(^*)$.

Considering that the centers of three S joints are constrained to move in three vertical planes, thus three constraint equations can be derived as

$$\begin{cases} l_{1y} = l_{1x} \tan \alpha \\ l_{2y} = l_{2x} \tan \beta \\ l_{3x} = 0 \end{cases} \quad (2)$$

Let \mathbf{a}'_i be the vectors along $O'C_i$ expressed in the moving frame, that is

$$\begin{cases} \mathbf{a}'_1 = (a'_{1x} \ a'_{1y} \ a'_{1z})^T = (r_1 \cos \alpha \ r_1 \sin \alpha \ 0)^T \\ \mathbf{a}'_2 = (a'_{2x} \ a'_{2y} \ a'_{2z})^T = (r_2 \cos \beta \ r_2 \sin \beta \ 0)^T \\ \mathbf{a}'_3 = (a'_{3x} \ a'_{3y} \ a'_{3z})^T = (0 \ r_3 \ 0)^T \end{cases} \quad (3)$$

According to the vector relationship of $\mathbf{l}_i = \mathbf{a}_i + \mathbf{p}$, it can be obtained as

$$\begin{cases} l_{1x} = x + \mathbf{T}_{11}a'_{1x} + \mathbf{T}_{12}a'_{1y} = x + r_1c\alpha(c\phi c\theta c(\psi - \phi) - s\phi s(\psi - \phi)) \\ \quad + r_1s\alpha(-c\phi c\theta s(\psi - \phi) - s\phi c(\psi - \phi)) \\ l_{1y} = y + \mathbf{T}_{21}a'_{1x} + \mathbf{T}_{22}a'_{1y} = y + r_1c\alpha(s\phi c\theta c(\psi - \phi) + c\phi s(\psi - \phi)) \\ \quad + r_1s\alpha(-s\phi c\theta s(\psi - \phi) + c\phi c(\psi - \phi)) \end{cases} \quad (4)$$

$$\begin{cases} l_{2x} = x + \mathbf{T}_{11}a'_{2x} + \mathbf{T}_{12}a'_{2y} = x + r_2c\beta(c\phi c\theta c(\psi - \phi) - s\phi s(\psi - \phi)) \\ \quad + r_2s\beta(-c\phi c\theta s(\psi - \phi) - s\phi c(\psi - \phi)) \\ l_{2y} = y + \mathbf{T}_{21}a'_{2x} + \mathbf{T}_{22}a'_{2y} = y + r_2c\beta(s\phi c\theta c(\psi - \phi) + c\phi s(\psi - \phi)) \\ \quad + r_2s\beta(-s\phi c\theta s(\psi - \phi) + c\phi c(\psi - \phi)) \end{cases} \quad (5)$$

$$\begin{cases} l_{3x} = x + \mathbf{T}_{12}a'_{3y} = x + r_3(-c\phi c\theta s(\psi - \phi) - s\phi c(\psi - \phi)) \\ l_{3y} = y + \mathbf{T}_{22}a'_{3y} = y + r_3(-s\phi c\theta s(\psi - \phi) + c\phi c(\psi - \phi)) \end{cases} \quad (6)$$

By substituting Eqs. (4)–(6) into Eq. (2), it can be obtained as

$$\begin{aligned} & y + r_1c\alpha(s\phi c\theta c(\psi - \phi) + c\phi s(\psi - \phi)) + r_1s\alpha(-s\phi c\theta s(\psi - \phi) + c\phi c(\psi - \phi)) \\ & = [x + r_1c\alpha(c\phi c\theta c(\psi - \phi) - s\phi s(\psi - \phi)) + r_1s\alpha(-c\phi c\theta s(\psi - \phi) - s\phi c(\psi - \phi))] \tan \alpha \end{aligned} \quad (7)$$

$$\begin{aligned} & y + r_2c\beta(s\phi c\theta c(\psi - \phi) + c\phi s(\psi - \phi)) + r_2s\beta(-s\phi c\theta s(\psi - \phi) + c\phi c(\psi - \phi)) \\ & = [x + r_2c\beta(c\phi c\theta c(\psi - \phi) - s\phi s(\psi - \phi)) + r_2s\beta(-c\phi c\theta s(\psi - \phi) - s\phi c(\psi - \phi))] \tan \beta \end{aligned} \quad (8)$$

$$x + r_3(-c\phi c\theta s(\psi - \phi) - s\phi c(\psi - \phi)) = 0 \quad (9)$$

According to the Eq. (7), it can be obtained as

$$x = r_3(\cos \phi \cos \theta \sin(\psi - \phi) + \sin \phi \cos(\psi - \phi)) \quad (10)$$

Substitution of Eq. (10) into Eq. (7) yields

$$\begin{aligned} y & = -r_1c\alpha(s\phi c\theta c(\psi - \phi) + c\phi s(\psi - \phi)) - r_1s\alpha(-s\phi c\theta s(\psi - \phi) + c\phi c(\psi - \phi)) \\ & \quad + [(c\phi c\theta s(\psi - \phi) + s\phi c(\psi - \phi))r_3 + r_1c\alpha(c\phi c\theta c(\psi - \phi) - s\phi s(\psi - \phi))] \tan \alpha \\ & \quad + r_1s\alpha \tan \alpha (-c\phi c\theta s(\psi - \phi) - s\phi c(\psi - \phi)) \end{aligned} \quad (11)$$

Substitution of Eqs. (10) and (11) into Eq. (8) yields

$$\begin{aligned}
 & -r_1 c\alpha (s\phi c\theta c(\psi - \phi) + c\phi s(\psi - \phi)) - r_1 s\alpha (-s\phi c\theta s(\psi - \phi) + c\phi c(\psi - \phi)) \\
 & \quad + [(c\phi c\theta s(\psi - \phi) + s\phi c(\psi - \phi))r_3 + r_1 c\alpha (c\phi c\theta c(\psi - \phi) - s\phi s(\psi - \phi))] \tan \alpha \\
 & \quad + r_1 s\alpha \tan \alpha (-c\phi c\theta s(\psi - \phi) - s\phi c(\psi - \phi)) \\
 & \quad + r_2 c\beta (s\phi c\theta c(\psi - \phi) + c\phi s(\psi - \phi)) + r_2 s\beta (-s\phi c\theta s(\psi - \phi) + c\phi c(\psi - \phi)) \\
 & = [(c\phi c\theta s(\psi - \phi) + s\phi c(\psi - \phi))r_3 + r_2 c\beta (c\phi c\theta c(\psi - \phi) - s\phi s(\psi - \phi))] \tan \beta \\
 & \quad + r_2 s\beta \tan \beta (-c\phi c\theta s(\psi - \phi) - s\phi c(\psi - \phi))
 \end{aligned} \tag{12}$$

Sufficient condition: In terms of the zero-torsion property, it can be found that $\psi = 0$. Assume that $r_1 = r_2 = r_3 = r$, and substitute it into Eq. (12), and the equation can be simplified as

$$\begin{aligned}
 & r(\cos \theta - 1)\sin \phi \cos \phi [\tan \beta - \tan \alpha + \cos \beta - \cos \alpha + \sin \alpha \tan \alpha - \sin \beta \tan \beta] \\
 & \quad + r(\cos \theta - 1)(\cos^2 \phi - \sin^2 \phi)(\sin \alpha - \sin \beta) = 0
 \end{aligned} \tag{13}$$

In the alternative form, it can be written as

$$A \sin(2\phi) + B \cos(2\phi) = 0 \tag{14}$$

where,

$$\begin{aligned}
 A &= \frac{1}{2}(\tan \beta - \tan \alpha + \cos \beta - \cos \alpha + \sin \alpha \tan \alpha - \sin \beta \tan \beta), \\
 B &= \frac{1}{2}(\sin \alpha - \sin \beta).
 \end{aligned}$$

Because ϕ is a continuous variable, it is concluded that $A = 0$ and $B = 0$. When $B = 0$, $\alpha = \pi - \beta$. And then substitute it into $A = 0$, that is

$$\sin \alpha \tan \alpha - \tan \alpha - \cos \alpha = 0 \tag{15}$$

By solving Eq. (15), it can be obtained as

$$\alpha = 7\pi/6, \quad \beta = -\pi/6 \tag{16}$$

Above all, the zero-torsion 3-PRS parallel mechanism must be symmetrical around z -axis.

Necessary condition: Since the parallel mechanism is symmetrical around z -axis, it can deduced that $\alpha = 7\pi/6$ and $\beta = -\pi/6$. Assume that $r_1 = r_2 = r_3 = r$ and substitute it into Eq. (12), it can be obtained as

$$\sqrt{3}r(\cos \theta + 1) \sin \psi = 0, \quad \psi = 0. \tag{17}$$

Thus the 3-PRS parallel mechanism is definitely a zero-torsion one.

3 3-RSR PM and Mirror Symmetry

The 3-RSR PM (Fig. 2) is mirror symmetrical about the mid-plane that passes through the centers of S joints. For each leg, the axis of the upper and lower revolute pairs are coplanar, and it means that they are parallel to each other or intersecting on the mid-plane. This mirror-symmetry ensures that the 3-RSR PM is a zero-torsion one.

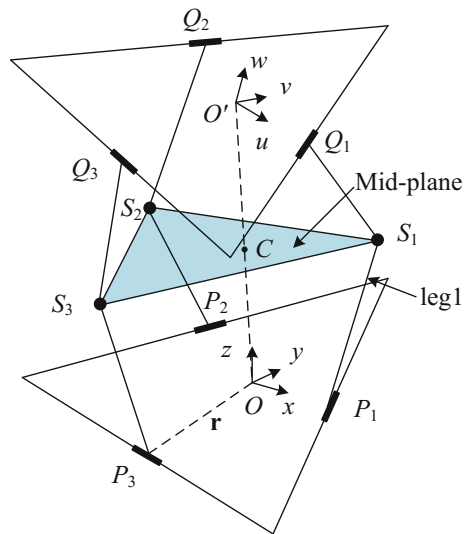
The derivation procedure is listed as follows.

Let O - xyz be the fixed coordinate system and O' - uvw be the moving coordinate system. The x -axis coincides with the line OP_1 and the u -axis coincides with the line $O'Q_1$. Let C be the midpoint of OO' . Assume that the coordinate of point O' in the fixed frame is denoted as $(x_{O'} \ y_{O'} \ z_{O'})^T$. So the coordinate of point C in the fixed frame is $(0.5x_{O'} \ 0.5y_{O'} \ 0.5z_{O'})^T$. Let r denote the magnitude of OP_i and $O'Q_i$. Assume that

$$x_{O'}^2 + y_{O'}^2 + z_{O'}^2 = p^2 \tag{18}$$

where p is a continuous variable.

Fig. 2 3-RSR parallel mechanism



Since the 3-RSR PM is symmetrical about the mid-plane, OO' is always perpendicular to the mid-plane and the point C is located on the mid-plane. Thus the equation relating to the mid-plane can be formulated as

$$x_{O'}x + y_{O'}y + z_{O'}z - \frac{1}{2}p^2 = 0 \quad (19)$$

When applying T&T angles to represent the orientation of the moving platform, the rotational matrix can be written as

$$\mathbf{R} = \begin{bmatrix} c\varphi c\theta c(\psi - \varphi) - s\varphi s(\psi - \varphi) & -\cos \varphi c\theta s(\psi - \varphi) - s\varphi c(\psi - \varphi) & c\varphi s\theta \\ s\varphi c\theta c(\psi - \varphi) + c\varphi s(\psi - \varphi) & -s\varphi c\theta s(\psi - \varphi) + c\varphi c(\psi - \varphi) & s\varphi s\theta \\ -s\theta c(\psi - \varphi) & s\theta s(\psi - \varphi) & c\theta \end{bmatrix} \quad (20)$$

The position vector of O' is $t = (x_{O'} \ y_{O'} \ z_{O'})$, and the corresponding homogeneous transformation matrix is written as

$$\mathbf{T} = \begin{bmatrix} \mathbf{R} & \mathbf{t} \\ \mathbf{0} & \mathbf{1} \end{bmatrix} = \begin{bmatrix} c\varphi c\theta c(\psi - \varphi) - s\varphi s(\psi - \varphi) & -c\varphi c\theta s(\psi - \varphi) - s\varphi c(\psi - \varphi) & c\varphi s\theta & x_{O'} \\ s\varphi c\theta c(\psi - \varphi) + c\varphi s(\psi - \varphi) & -s\varphi c\theta s(\psi - \varphi) + c\varphi c(\psi - \varphi) & s\varphi s\theta & y_{O'} \\ -s\theta c(\psi - \varphi) & s\theta s(\psi - \varphi) & c\theta & z_{O'} \\ 0 & 0 & 0 & 1 \end{bmatrix} \quad (21)$$

and the adjoint transformation of \mathbf{T} is written in a form of $6 * 6$ matrix, namely,

$$\mathbf{Ad} = \begin{bmatrix} \mathbf{R} & \mathbf{0} \\ \hat{\mathbf{t}}\mathbf{R} & \mathbf{R} \end{bmatrix} \quad (22)$$

where $\hat{\mathbf{t}}$ is the antisymmetric matrix of \mathbf{t} .

It is worth mentioning that, in the leg 1, the axis of upper revolute pair and that of upper revolute pair are coplanar, the two twists representing the upper revolute pair and the lower one are therefore reciprocal to each other according to the screw theory [18].

The twist of upper rotation pair expressed in the moving frame is formulated as

$$\xi_{O'_1} = (0 \ 1 \ 0 \ 0 \ 0 \ r)^T \quad (23)$$

The twist of upper rotation pair expressed in the fixed coordinate system is thus deduced, namely,

$$\xi_{Q_1} = \mathbf{Ad}\xi_{Q'_1} = \begin{pmatrix} -c\varphi c\theta s(\psi - \varphi) - s\varphi c(\psi - \varphi) \\ -s\varphi c\theta s(\psi - \varphi) + c\varphi c(\psi - \varphi) \\ s\theta s(\psi - \varphi) \\ z_{O'}s\varphi c\theta s(\psi - \varphi) - z_{O'}c\varphi c(\psi - \varphi) + y_{O'}s\theta s(\psi - \varphi) + rc\varphi s\theta \\ -z_{O'}c\varphi c\theta s(\psi - \varphi) - z_{O'}s\varphi c(\psi - \varphi) - x_{O'}s\theta s(\psi - \varphi) + rs\varphi s\theta \\ x_{O'}(-s\varphi c\theta s(\psi - \varphi) + c\varphi c(\psi - \varphi)) + y_{O'}(c\varphi c\theta s(\psi - \varphi) + s\varphi c(\psi - \varphi)) + rc\theta \end{pmatrix} \quad (24)$$

In addition, the twist of lower revolute pair expressed in the fixed coordinate system can be written as

$$\xi_{P_1} = (0 \quad 1 \quad 0 \quad 0 \quad 0 \quad r)^T \quad (25)$$

The coordinate of point Q_1 expressed in the fixed coordinate system is written as

$$\mathbf{OQ}_1 = \begin{pmatrix} r(c\varphi c\theta c(\psi - \varphi) - s\varphi s(\psi - \varphi)) + x_C \\ r(s\varphi c\theta c(\psi - \varphi) + c\varphi s(\psi - \varphi)) + y_C \\ -rs\theta c(\psi - \varphi) + z_C \end{pmatrix} \quad (26)$$

and the coordinate of point P_1 expressed in the fixed coordinate system is

$$\mathbf{OP}_1 = (r \quad 0 \quad 0)^T \quad (27)$$

According to the above formulations, the parameterized equation of the axis of upper revolute pair can be obtained as

$$\begin{cases} x = r(c\varphi c\theta c(\psi - \varphi) - s\varphi s(\psi - \varphi)) + x_{O'} + (-c\varphi c\theta s(\psi - \varphi) - s\varphi c(\psi - \varphi))t \\ y = r(s\varphi c\theta c(\psi - \varphi) + c\varphi s(\psi - \varphi)) + y_{O'} + (-s\varphi c\theta s(\psi - \varphi) + c\varphi c(\psi - \varphi))t \\ z = r(-s\theta c(\psi - \varphi)) + z_{O'} + (s\theta s(\psi - \varphi))t \end{cases} \quad (28)$$

and the parameterized equation of the axis of lower revolute pair is

$$\begin{cases} x = r \\ y = s \\ z = 0 \end{cases} \quad (29)$$

From Eqs. (28) and (29), one can obtain the coordinate of the intersecting point between the axis of lower revolute pair and that of upper revolute pair $(x \quad y \quad z)^T$. And then substitute it into Eq. (11), one yields

$$\begin{aligned}
 &2x_{O'}^2s\theta s(\psi - \varphi) + 2y_{O'}^2s\theta s(\psi - \varphi) - p^2s\theta s(\psi - \varphi) \\
 &\quad + 2ry_{O'}c\varphi s\theta - 2rx_{O'}s\varphi s\theta + 2x_{O'}z_{O'}s\varphi c(\psi - \varphi) \\
 &\quad + 2x_{O'}z_{O'}c\varphi c\theta s(\psi - \varphi) + 2y_{O'}z_{O'}s\varphi c\theta s(\psi - \varphi) \\
 &\quad - 2y_{O'}z_{O'}c\varphi c(\psi - \varphi) = 0
 \end{aligned} \tag{30}$$

Equation (30) can be written in an alternative form, namely,

$$\begin{aligned}
 &(2x_{O'}^2s\theta + 2y_{O'}^2s\theta - p^2s\theta + 2x_{O'}z_{O'}c\varphi c\theta + 2y_{O'}z_{O'}s\varphi c\theta)s(\psi - \varphi) \\
 &\quad + (2x_{O'}z_{O'}s\varphi - 2y_{O'}z_{O'}c\varphi)c(\psi - \varphi) + (2ry_{O'}c\varphi s\theta - 2rx_{O'}s\varphi s\theta) = 0
 \end{aligned} \tag{31}$$

Considering the mirror-symmetry property in the 3-RSR mechanism, the aforementioned equation is always established as,

$$\begin{cases}
 2x_{O'}^2s\theta + 2y_{O'}^2s\theta - p^2s\theta + 2x_{O'}z_{O'}c\varphi c\theta + 2y_{O'}z_{O'}s\varphi c\theta = 0 \\
 2x_{O'}z_{O'}s\varphi - 2y_{O'}z_{O'}c\varphi = 0 \\
 2ry_{O'}c\varphi s\theta - 2rx_{O'}s\varphi s\theta = 0
 \end{cases} \tag{32}$$

By Combining Eq. (10) with Eq. (14), it can be obtained as

$$x_{O'} = p \cos \varphi \sin(\theta/2), \quad y_{O'} = p \sin \varphi \sin(\theta/2), \quad z_{O'} = p \cos(\theta/2) \tag{33}$$

With the substitution of Eq. (33) into Eq. (24), one yields

$$\xi_{Q_1} = \begin{pmatrix} -c\varphi c\theta s(\psi - \varphi) - s\varphi c(\psi - \varphi) \\ -s\varphi c\theta s(\psi - \varphi) + c\varphi c(\psi - \varphi) \\ s\theta s(\psi - \varphi) \\ -pc\varphi c(\theta/2)c(\psi - \varphi) + ps\varphi c(\theta/2)s(\psi - \varphi) + rc\varphi s\theta \\ -ps\varphi c(\theta/2)c(\psi - \varphi) - pc\varphi c(\theta/2)s(\psi - \varphi) + rs\varphi s\theta \\ ps(\theta/2)c(\psi - \varphi) + rc\theta \end{pmatrix} \tag{34}$$

According to the reciprocal screw system theory, the reciprocal product $\xi_{Q_1} \circ \xi_{P_1}$ is equal to zero. Thus it can be deduce that

$$\cos(\theta/2)(2r\sin(\theta/2)(\sin \varphi + \sin(\psi - \varphi) - p \sin \psi) = 0 \tag{35}$$

Notice that θ is a continuous variable, it is concluded that

$$\sin \varphi + \sin(\psi - \varphi) = 0, \quad \sin \psi = 0 \tag{36}$$

Equation (36) means that $\psi = 0$. So the 3-RSR mechanism with mirror-symmetry characteristic is definitely a zero-torsion PM.

4 Conclusions

In this paper, a conventional kinematics-based approach is used to prove the structural conditions of two types of zero-torsion parallel mechanisms, i.e. the 3-[PP]S PMs and the 3-RSR PM. As for the family of 3-[PP]S parallel mechanisms, z-axial symmetry is the necessary and sufficient condition of being a zero-torsion mechanism. However, for the 3-RSR parallel mechanism, the existence of mid-plane can ensure its zero-torsion property.

Acknowledgments The authors would like to thank National Natural Science Foundation of China (NSFC) for the financial support under Grant No. 51575017.

References

1. Merlet JP (2006) *Parallel robots*, 2nd edn. Springer, The Netherlands
2. Bonev IA (2002) *Geometric analysis of parallel mechanisms*. Laval University, Quebec
3. Liu XJ, Pruscsek P, Pritschow G (2004) A new 3-DoF parallel mechanism with full symmetrical structure and parasitic motions. In: *Proceedings of the intelligent manipulation and grasping international conference*, Genova, Italy, pp 389–394
4. Lee KM, Shah DK (1988) Kinematic analysis of a three-degree-of-freedom in-parallel actuated manipulator. *IEEE J Robot Autom* 4(3):354–360
5. Buruncuk K, Tokad Y (1999) On the kinematics of a 3-DOF Stewart platform. *J Robotic Syst* 16(2):105–118
6. Kim HS, Tsai LW (2003) Kinematic synthesis of a spatial 3-RPS parallel manipulator. *ASME J Mech Des* 125:92–97
7. Liu CH, Cheng S (2004) Direct singular positions of 3RPS parallel manipulators. *ASME J Mech Des* 126:1006–1016
8. Sokolov A, Xirouchakis P (2006) Singularity analysis of a 3-DOF parallel manipulator with R-P-S joint structure. *Robotica* 24(1):131–142
9. Carretero JA, Nahon MA, Podhorodeski RP (2000) Workspace analysis and optimization of a novel 3-DOF parallel manipulator. *IEEE J Robot Autom* 15(4):178–188
10. Tsai MS, Shiau TN, Tsai YJ, Chang TH (2003) Direct kinematic analysis of a 3-PRS parallel mechanism. *Mech Mach Theory* 38(1):71–83
11. Wahl J (2000) Articulated tool head. WIPO Patent No. WO 00/25976
12. Li J, Wang J, Chou W, Zhang Y, Zhang Q (2001) Inverse kinematics and dynamics of the 3-RRS parallel platform. In: *Proceedings of the IEEE international conference on robotics and automation*, Seoul, Korea, pp 2506–2511
13. Dunlop GR, Jones TP (1997) Position analysis of a 3-DOF parallel manipulator. *Mech Mach Theory* 32(8):903–920
14. Zhou B, Fang H, Ren L, Feng ZR (2000) Closed-form direct position kinematics solution for a 3-RSR platform manipulator. In: *Proceedings of the 3rd world congress on intelligent control and automation*, pp 1289–1294
15. Fang HR, Fang YF, Hu M (2003) Forward position analysis of a novel three DOF parallel mechanism. In: *Proceedings of the 11th world congress in mechanism and machine science*, 18–21 Aug 2003

16. Wu YQ, Li ZX, Shi JB (2010) Geometric properties of zero-torsion parallel kinematics machines. In: IEEE/RSJ international conference on intelligent robots and systems, pp 2307–2312
17. Bonev IA, Ryu J (1999) Orientation workspace analysis of 6-DOF parallel manipulators. In: Proceedings of the ASME 1999 design engineering technical conferences, Las Vegas, NV
18. Ball RS (1998) The theory of screws. Cambridge University Press, Cambridge

Kinematics and Stiffness Characteristics of 3-PRP Planar Parallel Mechanism

Yuting Du, Ruiqin Li and Qianwen Dong

Abstract This paper presents a kind of 3-PRP planar parallel mechanism (PPM). The kinematics property of 3-PRP PPM is analyzed. Its motion constraint equations are derived to analyze the positive and inverse kinematics of the mechanism using the coordinate transformation method. The positive and inverse kinematics of position are derived on the basis of kinematic analysis of the moving platform. It can figure out the velocity, acceleration of the moving platform and also the Jacobian matrix. The stiffness of 3-PRP PPM and stiffness components along the direction of X axis and Y axis and orientation angle θ are derived using the new conservative coordinate conversion stiffness matrix. The stiffness mapping curves inside workspace are drawn under the situation that orientation angle is given using Matlab software. The stiffness characteristics of 3-PRP PPM is analyzed based on the stiffness mapping curve.

Keywords 3-PRP · Planar parallel mechanism · Kinematics · Stiffness

1 Introduction

The stiffness is an important index describing the characteristics of parallel mechanisms. Exploring the stiffness mapping and stiffness characteristics of parallel mechanisms and the influence of the stiffness variation on the performance of the mechanism, has important significance on stiffness control, structure design and parameter selection of parallel mechanisms [1].

Gosselin et al. [2] presented a stiffness mapping matrix of 3-RPR Planar Parallel Mechanism (PPM for short) and analyzed the influence on stiffness characteristics for different structure parameters. Li et al. [3, 4] studied the stiffness of 3-RPR and 3-PRR PPM. The stiffness matrices of the two mechanisms were deduced by using

Y. Du · R. Li (✉) · Q. Dong

School of Mechanical and Power Engineering, North University of China,
Taiyuan 030051, People's Republic of China
e-mail: liruiqin@nuc.edu.cn

conservative congruence transformation stiffness matrix. The distribution diagrams of stiffness mapping of the two mechanisms with different structure parameters were obtained by using Matlab. Wu [5] obtained new conservative congruence transformation stiffness matrix of 3-RPR PPM.

Wu et al. [6] studied the stiffness of 3-PPR PPM. The translation stiffness and rotation stiffness are expressed by using graphical representation. Dong et al. [7] analyzed the stiffness in the direction of non-function of 3-PRR micro-motion manipulator.

In this paper, configuration and coordinates of 3-PRP PPM are described in Sect. 2. The kinematics and Jacobian matrix are deduced in Sect. 3. The stiffness matrix are solved in Sect. 4. Stiffness mapping and stiffness characteristics are displaced in Sects. 5 and 6, respectively. Conclusions are drawn in Sect. 7.

2 Configuration and Coordinates of 3-PRP PPM

As shown in Fig. 1, 3-PRP PPM is composed of moving platform, base and three limbs. Each limb has two prismatic pairs and one revolute pair. The 3-PRP PPM is symmetrical distribution. Three sliders connected to the base are driving links. The center P of the moving platform is the output reference point. Figure 1a is the initial position of the mechanism. Figure 1b is the general position of the mechanism. The moving platform of 3-PRP PPM has two translations and one rotation.

In Fig. 1, the static coordinate system $O-XY$ is connected to the base. The origin O is located at the geometric center of the base. The moving coordinate system $P-xy$ is connected to the moving platform. The origin P is located at the geometric center P of the moving platform. $M_i (i = 1, 2, 3)$ is the initial positions of three prismatic pairs. The included angle between the three mobile guide in the base and X axis in $O-XY$ is $\theta_i = 0^\circ, 120^\circ, 240^\circ (i = 1, 2, 3)$, respectively.

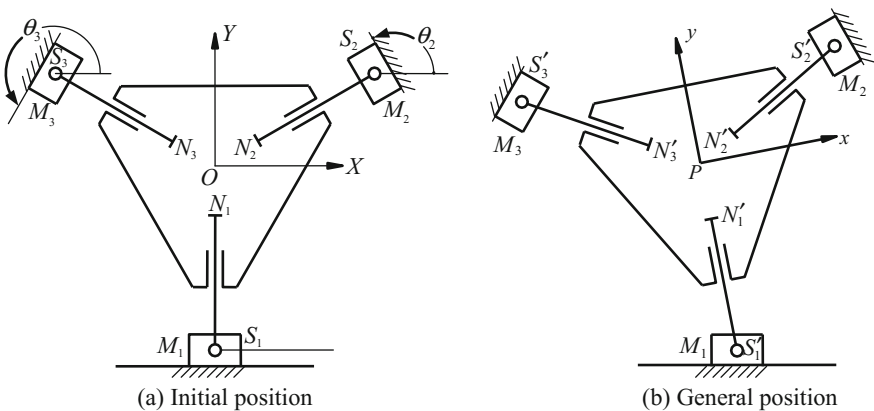


Fig. 1 Configuration of 3-PRP PPM. **a** Initial position **b** general position

Table 1 The structure parameters of 3-PRP PPM

Parameters limb	Link $N_i S_i/\text{mm}$	Prismatic pair/mm	Input quantity q_i/mm	Output quantity/mm
Limb 1	100	100	150	130
Limb 2	100	100	150	130
Limb 3	100	100	150	130

In Fig. 1b, the coordinates of the center P of the moving platform in $O-XY$ is (x_p, y_p) . The included angle between the corresponding axes in $P-xy$ and $O-XY$ is θ_p . $\mathbf{p} = (x_p, y_p, \theta_p)^T$ represents the position and orientation of the moving platform.

Supposing the driving position variable $\mathbf{q} = (q_1, q_2, q_3)^T$. The length of link $N_i S_i$ is h . The length of the OS_i in the initial position is l_i . The length of PS'_i in the general position is l'_i . The structure parameters of 3-PRP PPM are shown in Table 1.

3 Kinematics and Jacobian Matrix of 3-PRP PPM

The forward kinematics is that given the input quantity $\mathbf{q} = (q_1, q_2, q_3)^T$ to solve the output quantity $\mathbf{p} = (x_p, y_p, \theta_p)^T$.

The point S'_i in $O-XY$ can be expressed as follows.

$${}^o S'_i = \begin{bmatrix} x_p + l'_i \sin(\theta_i + \theta_p) \\ y_p - l'_i \cos(\theta_i + \theta_p) \end{bmatrix} = \begin{bmatrix} q_i \cos \theta_i + l_i \sin \theta_i \\ q_i \sin \theta_i - l_i \cos \theta_i \end{bmatrix} \quad (1)$$

Expanding Eq. (1), yields

$$l'_i \sin(\theta_i + \theta_p) = q_i \cos \theta_i + l_i \sin \theta_i - x_p \quad (2a)$$

$$l'_i \cos(\theta_i + \theta_p) = -q_i \sin \theta_i + l_i \cos \theta_i + y_p \quad (2b)$$

Eliminating the variable l'_i , yields

$$\cos(\theta_i + \theta_p)x_p + \sin(\theta_i + \theta_p)y_p - q_i \cos \theta_p + l_i \sin \theta_p = 0 \quad (3)$$

Let $A_i = \cos(\theta_i + \theta_p)$, $B_i = \sin(\theta_i + \theta_p)$, $D_i = -q_i \cos \theta_p + l_i \sin \theta_p$

Simplifying Eq. (3), the equations of the forward position/orientation solutions are expressed as follows.

$$\begin{cases} A_1 x_p + B_1 y_p + D_1 = 0 & \text{(a)} \\ A_2 x_p + B_2 y_p + D_2 = 0 & \text{(b)} \\ A_3 x_p + B_3 y_p + D_3 = 0 & \text{(c)} \end{cases} \quad (4)$$

In the 3-PRP PPM, A_i, B_i has nothing to do with the input variables q_i , thus

$$D_1 + D_2 + D_3 = 0 \tag{5}$$

Substituting D_i into Eq. (5), yields

$$a \sin \theta_p + b \cos \theta_p = 0 \tag{6}$$

where $a = 3l_i, b = -q_1 - q_2 - q_3$.

Solving Eq. (6), yields

$$\theta_p = 2 \tan^{-1} \frac{a \pm \sqrt{a^2 + b^2}}{b} \tag{7}$$

Solving Eq. (4a) and (b), yields

$$\begin{cases} x_p = \frac{2\sqrt{3}}{3}(e - f) \\ y_p = \frac{2\sqrt{3}}{3}(k - m) \end{cases} \tag{8}$$

where

$$\begin{aligned} e &= -q_2 \sin \theta_p \cos \theta_p + l_i \sin^2 \theta_p, \\ f &= -q_1 \sin(120^\circ + \theta_p) \cos \theta_p + l_i \sin(120^\circ + \theta_p) \sin \theta_p, \\ k &= -q_1 \cos(120^\circ + \theta_p) \cos \theta_p + l_i \cos(120^\circ + \theta_p) \sin \theta_p, \\ m &= -q_2 \cos^2 \theta_p + l_i \sin \theta_p \cos \theta_p. \end{aligned}$$

Inverse kinematics is to calculate the input values $\mathbf{q} = (q_1, q_2, q_3)^T$ in the static coordinate system of 3-PRP PPM under given the output position/orientation values $\mathbf{p} = (x_p, y_p, \theta_p)^T$ of the moving platform.

From Eq. (3), the input values q_i can be obtained.

$$q_i = \frac{\cos(\theta_i + \theta_p)x_p + \sin(\theta_i + \theta_p)y_p + l_i \sin \theta_p}{\cos \theta_p}, \quad (i = 1, 2, 3) \tag{9}$$

Jacobian matrix expresses the velocity mapping relationship between input and output of the PPM. Jacobian matrix can be used to solve the moving velocity of the PPM. It is also the prerequisite conditions to analyze the performances of the PPM such as singularity, dexterity and stiffness, etc.

The constraint equation is established as follows.

$$F(\mathbf{p}, \mathbf{q}) = 0 \tag{10}$$

where \mathbf{q} represents the input quantity of the mechanism.

\mathbf{p} represents the output quantity of the mechanism.

Differentiating Eq. (10) with respect to time, yields

$$\mathbf{J}_p \dot{\mathbf{p}} = \mathbf{J}_q \dot{\mathbf{q}} \quad (11)$$

where $\mathbf{J}_p = \frac{\partial \mathbf{F}}{\partial \mathbf{p}}$, $\mathbf{J}_q = \frac{\partial \mathbf{F}}{\partial \mathbf{q}}$, $\dot{\mathbf{q}} = (\dot{q}_1, \dot{q}_2, \dot{q}_3)^T$ represents driving velocity, $\dot{\mathbf{p}} = (\dot{x}_p, \dot{y}_p, \dot{\theta}_p)^T$ represents velocity vector of the moving platform.

Equation (11) can be rewritten as

$$\dot{\mathbf{q}} = \mathbf{J} \dot{\mathbf{p}} \quad (12)$$

where $\mathbf{J} = \mathbf{J}_p^{-1} \mathbf{J}_q$ is called the Jacobian matrix of 3-PRP PPM.

The coordinates of the point N'_i is

$$\begin{cases} x_{N'_i} = x_p + (l'_i - h) \sin(\theta_i + \theta_p) \\ y_{N'_i} = y_p - (l'_i - h) \cos(\theta_i + \theta_p) \end{cases} \quad (13)$$

The coordinates of the point S'_i is

$$\begin{cases} x_{S'_i} = q_i \cos \theta_i + l_i \sin \theta_i \\ y_{S'_i} = q_i \sin \theta_i - l_i \cos \theta_i \end{cases} \quad (14)$$

According to link length constraint condition of link $\overline{N'_i S'_i}$, the following equation can be obtained.

$$(x_{N'_i} - x_{S'_i})^2 + (y_{N'_i} - y_{S'_i})^2 = h^2 \quad (15)$$

Substituting the coordinates of N'_i , S'_i , into Eq. (15), yields

$$\begin{aligned} & [x_p + (l'_i - h) \sin(\theta_i + \theta_p) - q_i \cos \theta_i - l_i \sin \theta_i]^2 + [y_p - (l'_i - h) \cos(\theta_i + \theta_p) - q_i \sin \theta_i + l_i \cos \theta_i]^2 \\ & = h^2 \end{aligned} \quad (16)$$

Differentiating Eq. (16) with respect to time, yield

$$\begin{aligned} & [x_p + (l'_i - h) \sin(\theta_i + \theta_p) - q_i \cos \theta_i - l_i \sin \theta_i] [\dot{x}_p + \dot{\theta}_p (l'_i - h) \cos(\theta_i + \theta_p) - \dot{q}_i \cos \theta_i] \\ & + [y_p - (l'_i - h) \cos(\theta_i + \theta_p) - q_i \sin \theta_i + l_i \cos \theta_i] [\dot{y}_p + \dot{\theta}_p (l'_i - h) \sin(\theta_i + \theta_p) - \dot{q}_i \sin \theta_i] = 0 \end{aligned} \quad (17)$$

Let

$$\begin{aligned} a_{ix} &= x_p + (l'_i - h)s(\theta_i + \theta_p) - q_i c\theta_i - l_i s\theta_i, \\ a_{iy} &= y_p - (l'_i - h)c(\theta_i + \theta_p) - q_i s\theta_i + l_i c\theta_i, \\ e_{ix} &= (l'_i - h)\sin(\theta_i + \theta_p), \quad e_{iy} = (l'_i - h)\cos(\theta_i + \theta_p). \end{aligned}$$

Thus, Eq. (17) can be rewritten as

$$\begin{aligned} & \begin{bmatrix} a_{1x} & a_{1y} & a_{1x}e_{1y} + a_{1y}e_{1x} \\ a_{2x} & a_{2y} & a_{2x}e_{2y} + a_{2y}e_{2x} \\ a_{3x} & a_{3y} & a_{3x}e_{3y} + a_{3y}e_{3x} \end{bmatrix} \begin{bmatrix} \dot{x}_p \\ \dot{y}_p \\ \dot{\theta}_p \end{bmatrix} \\ &= \begin{bmatrix} a_{1x}c\theta_1 + a_{1y}s\theta_1 & 0 & 0 \\ 0 & a_{2x}c\theta_2 + a_{2y}s\theta_2 & 0 \\ 0 & 0 & a_{3x}c\theta_3 + a_{3y}s\theta_3 \end{bmatrix} \begin{bmatrix} \dot{q}_1 \\ \dot{q}_2 \\ \dot{q}_3 \end{bmatrix} \end{aligned} \quad (18)$$

Thus,

$$\mathbf{J}_p = \begin{bmatrix} a_{1x} & a_{1y} & a_{1x}e_{1y} + a_{1y}e_{1x} \\ a_{2x} & a_{2y} & a_{2x}e_{2y} + a_{2y}e_{2x} \\ a_{3x} & a_{3y} & a_{3x}e_{3y} + a_{3y}e_{3x} \end{bmatrix} = \begin{bmatrix} b_{11} & b_{12} & b_{13} \\ b_{21} & b_{22} & b_{23} \\ b_{31} & b_{32} & b_{33} \end{bmatrix} \quad (19)$$

$$\mathbf{J}_q = \begin{bmatrix} a_{1x}c\theta_1 + a_{1y}s\theta_1 & 0 & 0 \\ 0 & a_{2x}c\theta_2 + a_{2y}s\theta_2 & 0 \\ 0 & 0 & a_{3x}c\theta_3 + a_{3y}s\theta_3 \end{bmatrix} = \begin{bmatrix} n_1 & 0 & 0 \\ 0 & n_2 & 0 \\ 0 & 0 & n_3 \end{bmatrix} \quad (20)$$

where $n_1 = a_{1x}c\theta_1 + a_{1y}s\theta_1$, $n_2 = a_{2x}c\theta_2 + a_{2y}s\theta_2$, $n_3 = a_{3x}c\theta_3 + a_{3y}s\theta_3$.

Substituting $\mathbf{J}_p, \mathbf{J}_q$ into $\mathbf{J} = \mathbf{J}_p^{-1}\mathbf{J}_q$, the Jacobian matrix \mathbf{J} can be expressed as

$$\mathbf{J} = \mathbf{J}_p^{-1}\mathbf{J}_q = \begin{bmatrix} \frac{b_{11}}{n_1} & \frac{b_{12}}{n_1} & \frac{b_{13}}{n_1} \\ \frac{b_{21}}{n_2} & \frac{b_{22}}{n_2} & \frac{b_{23}}{n_2} \\ \frac{b_{31}}{n_3} & \frac{b_{32}}{n_3} & \frac{b_{33}}{n_3} \end{bmatrix} \quad (21)$$

4 Stiffness Matrix of 3-PRP PPM Based on Conservation Congruence Transformation

The stiffness can be divided into two kinds of link stiffness and section stiffness [3]. The magnitude of the link stiffness is proportional to the force/moment exerted on the link and linear displacement and angular displacement caused by the

force/moment. The elastic modulus or shear modulus of the section stiffness is related with the sectional area of links or inertia moments exerted on the links.

The displacement of the moving platform of the multi-DOF mechanism is the mode of the unit vector force \mathbf{F} . When the mode of the displacement of the moving platform is a unit vector, the mode of the force \mathbf{F} is equal to singular value of the matrix. From this, \mathbf{K} can be defined as the stiffness matrix of the mechanism. The stiffness matrix can describe the stiffness of the PPM. The stiffness matrix represents the relationship between the external force or external moment exerted on the moving platform and the displacement of the moving platform.

The stiffness matrix of the mechanism can be solved by kinematic constraint equations of the mechanism. The stiffness of any point in the workspace of the PPM can be solved by the stiffness matrix.

$$\mathbf{K}_c = \mathbf{J}^T \mathbf{K}_j \mathbf{J} \quad (22)$$

where \mathbf{K}_j represents joint stiffness matrix.

Equation (22) only considers the influence of the internal forces in the mechanism, doesn't consider the influence of the external force. The external force will lead to deformation of the links. Considering two influencing factors, the stiffness matrix based on conservation coordination transformation can be expressed as follows [8].

$$\mathbf{K}_c = \mathbf{K}_G + \mathbf{J}^T \mathbf{K}_j \mathbf{J} = \mathbf{K}_G + \mathbf{S}_j \quad (23)$$

For the 3-PRP PPM, the expression of \mathbf{K}_G can be rewritten as

$$\mathbf{K}_G = \begin{bmatrix} \frac{\partial \mathbf{J}^T}{\partial x_p} \mathbf{T} & \frac{\partial \mathbf{J}^T}{\partial y_p} \mathbf{T} & \frac{\partial \mathbf{J}^T}{\partial \theta_p} \mathbf{T} \end{bmatrix} \quad (24)$$

where $\mathbf{T} = [T_1, T_2, T_3]^T$ is driving force or driving moment. The relationship between \mathbf{T} and external force or moment $\mathbf{F} = [f, m_3]^T$ can be expressed as follows.

$$\mathbf{F} = \mathbf{J}^T \mathbf{T} \quad (25)$$

Because 3-PRP PPM is acted only by external forces, not by the impact of the moment, \mathbf{T} and \mathbf{F} only represent the driving forces and external forces of the 3-PRP PPM.

Supposing the joint stiffness matrix is

$$\mathbf{K}_j = \begin{bmatrix} k_{11} & 0 & 0 \\ 0 & k_{22} & 0 \\ 0 & 0 & k_{33} \end{bmatrix} \quad (26)$$

From the Jacobian matrix of 3-PRP PPM in Eq. (21), the following expression can be obtained.

$$\mathbf{J}_{1i} = \frac{b_{1i}}{n_1}, \mathbf{J}_{2i} = \frac{b_{2i}}{n_2}, \mathbf{J}_{3i} = \frac{b_{3i}}{n_3} \quad (i = 1, 2, 3) \quad (27)$$

Because $\mathbf{p} = \mathbf{p}(\mathbf{q}) = (x_p, y_p, \theta_p)^T$, g and j can be obtained, then \mathbf{K}_G and \mathbf{S}_J can be further obtained.

$$g_{i1} = \frac{\partial}{\partial x_p} \left(\frac{b_{1i}}{n_1} T_1 + \frac{b_{2i}}{n_2} T_2 + \frac{b_{3i}}{n_3} T_3 \right) \quad (28)$$

$$g_{i2} = \frac{\partial}{\partial y_p} \left(\frac{b_{1i}}{n_1} T_1 + \frac{b_{2i}}{n_2} T_2 + \frac{b_{3i}}{n_3} T_3 \right) \quad (29)$$

$$g_{i3} = \frac{\partial}{\partial \theta_p} \left(\frac{b_{1i}}{n_1} T_1 + \frac{b_{2i}}{n_2} T_2 + \frac{b_{3i}}{n_3} T_3 \right) \quad (30)$$

$$j_{1i} = \frac{b_{11}b_{1i}}{n_1^2} k_{11} + \frac{b_{21}b_{2i}}{n_2^2} k_{22} + \frac{b_{31}b_{3i}}{n_3^2} k_{33} \quad (31)$$

$$j_{2i} = \frac{b_{12}b_{1i}}{n_1^2} k_{11} + \frac{b_{22}b_{2i}}{n_2^2} k_{22} + \frac{b_{32}b_{3i}}{n_3^2} k_{33} \quad (32)$$

$$j_{3i} = \frac{b_{13}b_{1i}}{n_1^2} k_{11} + \frac{b_{23}b_{2i}}{n_2^2} k_{22} + \frac{b_{33}b_{3i}}{n_3^2} k_{33} \quad (33)$$

where g_{i1}, g_{i2}, g_{i3} are the elements of the matrix \mathbf{K}_G ; j_{1i}, j_{2i}, j_{3i} are the elements of the matrix \mathbf{S}_J .

Supposing $K_{cxp}, K_{cyp}, K_{c\theta p}$ are the elements of the stiffness matrix \mathbf{K}_e in the X, Y, θ direction of 3-PRP PPM, respectively, thus

$$K_{cxp} = g_{11} + j_{11} = \frac{\partial}{\partial x_p} \left(\frac{b_{11}}{n_1} T_1 + \frac{b_{21}}{n_2} T_2 + \frac{b_{31}}{n_3} T_3 \right) + \frac{b_{11}^2}{n_1^2} k_{11} + \frac{b_{21}^2}{n_2^2} k_{22} + \frac{b_{31}^2}{n_3^2} k_{33} \quad (34)$$

$$K_{cyp} = g_{22} + j_{22} = \frac{\partial}{\partial y_p} \left(\frac{b_{12}}{n_1} T_1 + \frac{b_{22}}{n_2} T_2 + \frac{b_{32}}{n_3} T_3 \right) + \frac{b_{12}^2}{n_1^2} k_{11} + \frac{b_{22}^2}{n_2^2} k_{22} + \frac{b_{32}^2}{n_3^2} k_{33} \quad (35)$$

$$K_{c\theta p} = g_{33} + j_{33} = \frac{\partial}{\partial \theta_p} \left(\frac{b_{13}}{n_1} T_1 + \frac{b_{23}}{n_2} T_2 + \frac{b_{33}}{n_3} T_3 \right) + \frac{b_{13}^2}{n_1^2} k_{11} + \frac{b_{23}^2}{n_2^2} k_{22} + \frac{b_{33}^2}{n_3^2} k_{33} \quad (36)$$

5 Stiffness Mapping of 3-PRP PPM

Stiffness mapping is an important parameter in the stiffness control of the parallel mechanism. It shows the transformation relation between the joint stiffness and the rectangular coordinate space. The distribution diagrams of the stiffness mapping can clearly reflect the specific situation and the characteristics of the stiffness distribution.

Solving Eqs. (34)–(36) using Matlab, the stiffness mapping distribution of 3-PRP PPM can be obtained.

(1) The distribution of the stiffness mapping when $T_i = 0$ and $k_{ii} = 1$.

When $T_i = 0$ and $k_{ii} = 1 (i = 1, 2, 3)$, 3-PRP PPM is not affected by external forces. The distribution of the stiffness mapping of 3-PRP PPM are shown in Fig. 2.

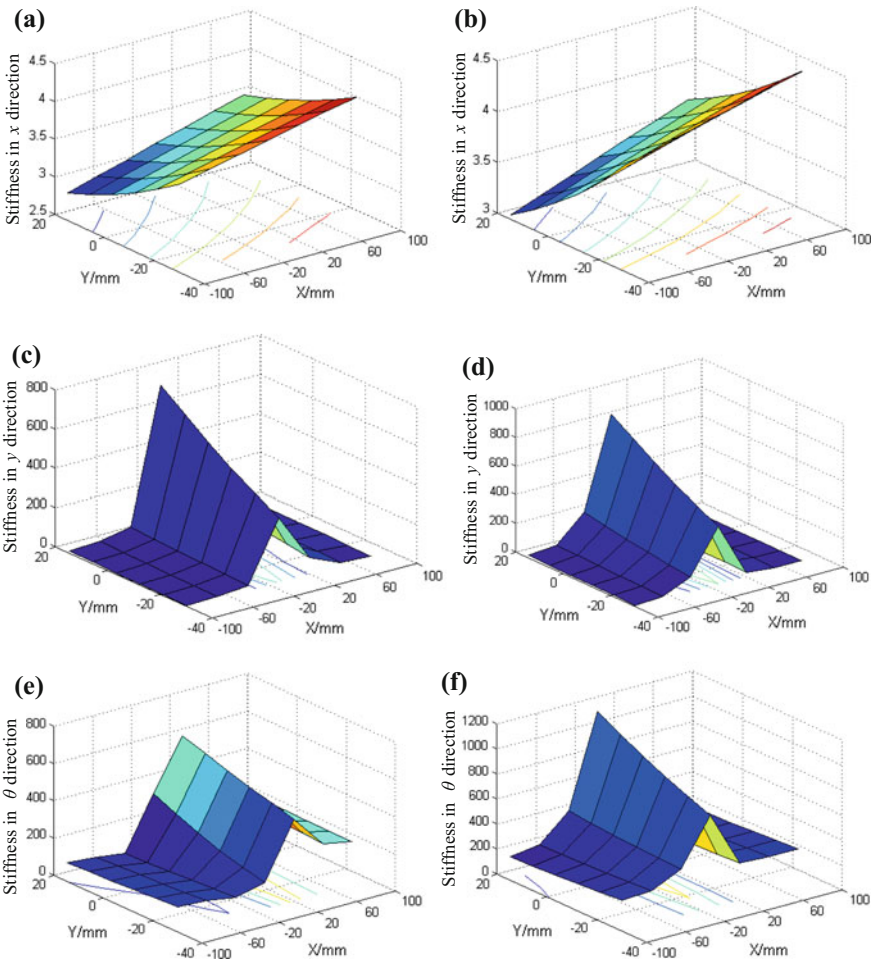


Fig. 2 Distribution of the stiffness mapping of 3-PRP PPM when $T_i = 0$ and $k_{ii} = 1 (i = 1, 2, 3)$

Figures 2a and b show the distribution of the stiffness mapping along X direction when the orientation angles $\theta_p = 0$ and $\theta_p = \pi/2$, respectively.

Figures 2c and d show the distribution of the stiffness mapping along Y direction when the orientation angles $\theta_p = 0$ and $\theta_p = \pi/2$, respectively.

Figures 2e and f show the distribution of the stiffness mapping in θ direction when the orientation angles $\theta_p = 0$ and $\theta_p = \pi/2$, respectively.

(2) The distribution of the stiffness mapping when $T_i = 1$ and $k_{ii} = 0$.

When $T_i = 1$ and $k_{ii} = 0 (i = 1, 2, 3)$, 3-PRP PPM is influenced by external force. The distribution of the stiffness mapping are shown in Fig. 3.

Figures 3a and b show the distribution of the stiffness mapping in X direction when the orientation angles $\theta_p = 0$ and $\theta_p = \pi/2$, respectively.

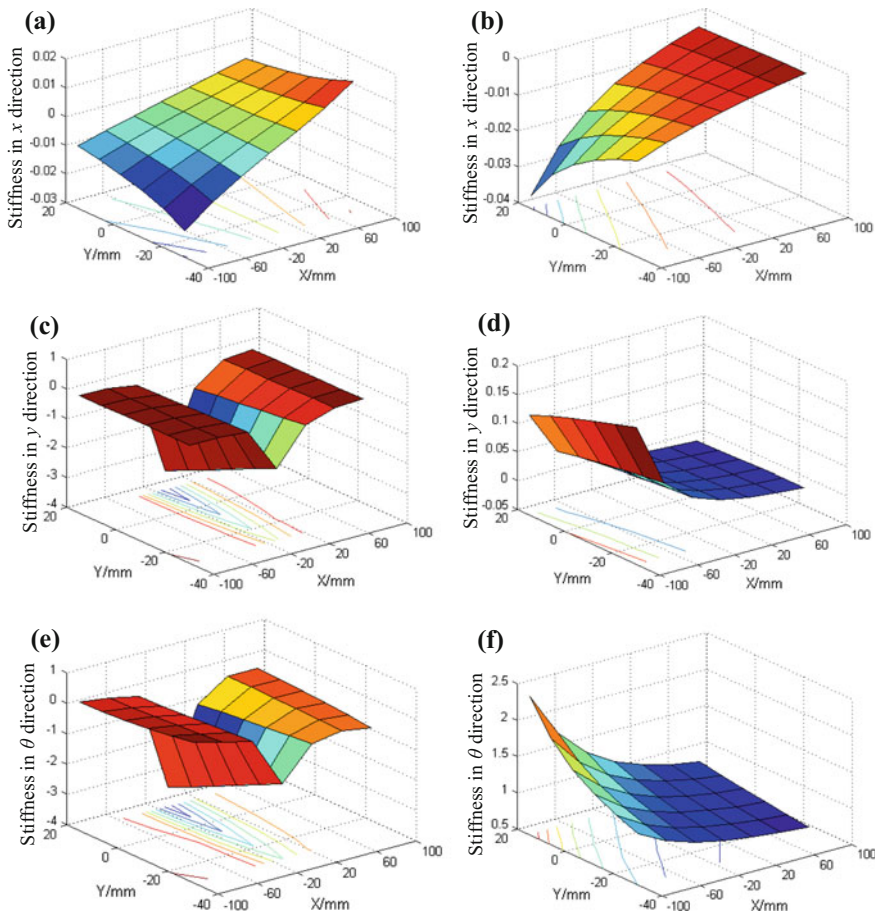


Fig. 3 Distribution of stiffness mapping of 3-PRP PPM when $T_i = 1$ and $k_{ii} = 0 (i = 1, 2, 3)$

Figures 3c and d show the distribution of the stiffness mapping in Y direction when the orientation angles $\theta_p = 0$ and $\theta_p = \pi/2$, respectively.

Figures 3e and f show the distribution of the stiffness mapping in θ direction when the orientation angles are $\theta_p = 0$ and $\theta_p = \pi/2$, respectively.

(3) Distribution of stiffness mapping when $T_i = 1$ and $k_{ii} = 1$.

3-PRP PPM is influenced by external forces and internal forces when $T_i = 1$ and $k_{ii} = 1 (i = 1, 2, 3)$. The distribution of stiffness mapping is shown in Fig. 4.

Figures 4a and b show the distribution of stiffness mapping along X direction when the orientation angles $\theta_p = 0$ and $\theta_p = \pi/2$, respectively.

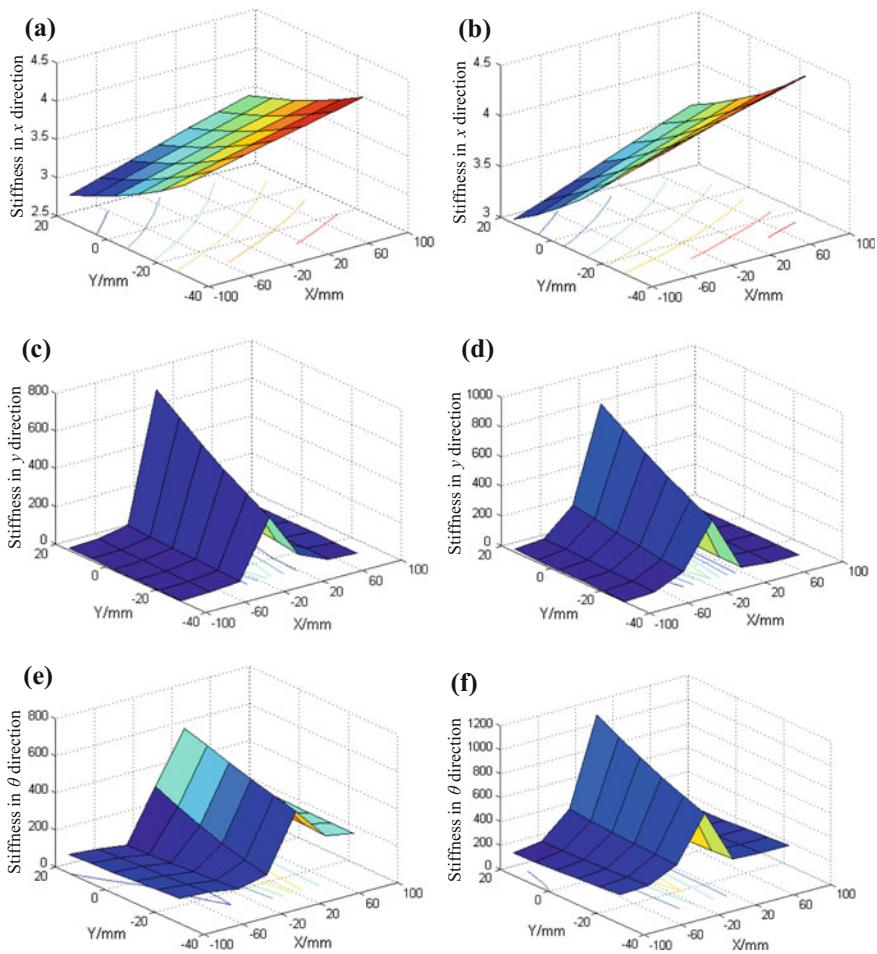


Fig. 4 Distribution of stiffness mapping of 3-PRP PPM when $T_i = 1$ and $k_{ii} = 1 (i = 1, 2, 3)$

Figures 4c and d show the distribution of stiffness mapping along Y direction of when orientation angles $\theta_p = 0$ and $\theta_p = \pi/2$, respectively.

Figures 4e and f show the distribution of stiffness mapping in θ direction of when orientation angles $\theta_p = 0$ and $\theta_p = \pi/2$, respectively.

6 Stiffness Characteristics of 3-PRP PPM

From Eqs. (34) to (36) and Fig. 2, 3 and 4, the following results can be obtained.

(1) The stiffness of 3-PRP PPM is a function proportional to the driving force T and k_i . (2) The variation law of the \mathbf{S}_J .

In Figs. 2a and b, the stiffness in X direction is proportional to the b_{i1} and increases with increasing b_{i1} . The stiffness of 3-PRP PPM is inversely proportional to n_i and decreases with increasing n_i . In the workspace, the stiffness in X direction increases with increasing the value x of the moving platform and decreases with increasing the value y of the moving platform. When the orientation angle $\theta_p = \pi/2$, the stiffness in X direction is similar to the stiffness after rotating a certain angle in an anticlockwise direction when the orientation angle $\theta_p = 0$.

In Figs. 2c and d, the stiffness in Y direction is proportional to b_{i2} and increases with increasing b_{i2} . The stiffness is inversely proportional to n_i and decreases with increasing n_i . In the workspace, the stiffness in Y direction first increases and then decreases with increasing the value x of the moving platform. The maximum value is reached at approximately 145 mm. When the orientation angle $\theta_p = \pi/2$, the stiffness in Y direction is similar to the stiffness after rotating a certain angle in an anticlockwise direction when the orientation angle $\theta_p = 0$.

In Figs. 2e and f, the stiffness in θ direction is proportional to b_{i3} and increases with increasing b_{i3} . The stiffness is inversely proportional to n_i and decreases with increasing n_i . In the workspace, the stiffness in θ direction first increases and then decreases with increasing the value x of the moving platform. The maximum value is reached at approximately 145 mm.

(3) The variation law of the \mathbf{K}_G

In Figs. 3a and b, the stiffness in X direction is inversely proportional to n_i and decreases with increasing n_i . In the workspace, the stiffness in X direction increases with increasing the value x of the moving platform. When the orientation angle $\theta_p = \pi/2$, the stiffness in X direction is similar to the stiffness after rotating a certain angle in an anticlockwise direction when the orientation angle $\theta_p = 0$.

In Figs. 3c and d, the stiffness in Y direction is inversely proportional to n_i and decreases with increasing n_i . In the workspace, the stiffness in Y direction first decreases and then increases with increasing the value x of the moving platform. The maximum value is reached at approximately 140 mm. When the orientation angle $\theta_p = \pi/2$, the stiffness in X direction is similar to the stiffness after rotating a certain angle in an anticlockwise direction when the orientation angle $\theta_p = 0$.

In Figs. 3e and f, the stiffness in θ direction is inversely proportional to n_i and decreases with increasing n_i . In the workspace, the stiffness in θ direction in Fig. 3e first decreases then increases with the values x of the moving platform. The maximum value is reached at approximately 140 mm. The stiffness decreases with increasing the value y of the moving platform.

The stiffness in θ direction decreases with increasing the value x of the moving platform and increases with increasing the value y of the moving platform in Fig. 3f.

(4) Stiffness matrix of 3-PRP PPM

The stiffness of 3-PRP PPM is analyzed by the comparison of the position stiffness matrix not affected by external force and the position stiffness matrix affected by external force.

In Figs. 4a and b, the stiffness in X direction is proportional to b_{i1} and n_i . In the workspace, the stiffness in X direction increases with increasing the value x of the moving platform and decreases with increasing the value y of the moving platform. When the orientation angle $\theta_p = \pi/2$, the stiffness in X direction is similar to the stiffness after rotating a certain angle in an anticlockwise direction when the orientation angle $\theta_p = 0$.

In Figs. 4c and d, the stiffness in Y direction is proportional to b_{i2} and n_i . In the workspace, the stiffness in Y direction first increases and then decreases with increasing the value x of the moving platform. The maximum value is reached at approximately 140 mm. When the orientation angle $\theta_p = \pi/2$, the stiffness in X direction is similar to the stiffness after rotating a certain angle in an anticlockwise direction when the orientation angle $\theta_p = 0$.

In Figs. 4e and f, the stiffness in θ direction is proportional to b_{i3} and n_i . In the workspace, the stiffness in θ direction first increases and then decreases with increasing the value x of the moving platform. The maximum value is reached at approximately 140 mm. The stiffness increases with increasing the value y of the moving platform.

7 Conclusions

This paper deduced the stiffness components along the X , Y , θ directions of 3-PRP PPM based on new conservative congruence transformation stiffness matrix. The distribution diagrams of stiffness mapping in the workspace with different orientation angles are drawn based on MATLAB. According to obtained the distribution diagram of stiffness mapping of 3-PRP PPM, the variation laws of the stiffness are analyzed. The stiffness of 3-PRP PPM is a function relative to the mechanism configuration. The stiffness of the mechanism is not only affected by the external forces but also is proportional to the joint stiffness. The influence of the external forces not only displays the magnitudes of the external forces, but also displays the action directions of the external forces.

Acknowledgments The authors gratefully acknowledge the financial and facility support provided by the National Natural Science Foundation of China (Grant No. 51275486).

References

1. Li RQ, Guo WZ (2014) Research progress on theory and application of modern mechanisms. Higher education press, Beijing (in Chinese)
2. Gosselin CM (1990) Martin Jean. Stiffness mapping for parallel manipulators. *IEEE Trans Robot Autom* 6(3):377–382
3. Li SJ, Gosselin CM (2009) Stiffness analysis of 3-RPR planar parallel mechanism to the stiffness control. *Appl Mech Mater* 16–19:786–790
4. Li SJ, Meng QL (2009) Stiffness characteristics of 3-PRR planar parallel mechanism based on CCT stiffness matrix. *J Northeast Univ (Nat Sci)*, 30(6):865–868 (in Chinese)
5. Wu ZH (2013) Research on characteristics for 3-RPR three degree of freedom parallel mechanism. North University of China, Taiyuan
6. Wu GL, Bai SP, Kepler JA (2012) Stiffness analysis and comparison of 3-PPR Planar parallel manipulators with actuation compliance. In: ASME 2012 11th biennial conference on engineering systems design and analysis, vol 3, Nantes, France, pp 255–264
7. Dong Y, Gao F, Yue Y (2011) Stiffness and workspace analysis of 3-PRR micro-motion manipulator. *Mach Des Res* 27(2):15–18 (in Chinese)
8. Chen SF, Kao I (2000) The conservative congruence transformation for joint and cartesian stiffness matrices of robotic hands and fingers. *Int J Robot Res* 19(9):835–847

Topology Optimization of 3-DOF Peristaltic Structure Based on Vector Continuous Mapping Matrix

Zhu Dachang and Feng Yanping

Abstract A method for topology optimization of peristaltic structure with vector continuous mapping matrix using SIMP method is presented in this paper. The focus of this paper is on how to keep the differential motion consistency. As the conventional joints/hinges are no longer needed after topology optimization, therefore, we renamed this kind of structure as peristaltic structure. In the proposed method, the vector continuous mapping matrix is build as stress/strain transfer direction conditions for topology optimization of peristaltic structure, and SIMP method used for multi-inputs and multi-outputs which decided by parallel prototype mechanisms. Some numerical examples are presented to illustrate the validity of the proposed method.

Keywords Peristaltic structure · Topology optimization · Vector continuous mapping matrix

1 Introduction

Substantial researchers have been spent on the design of Micro/Nano equipments in recent years. Flexure joints are typically manufactured monolithically, therefore, avoid assemble errors. In terms of operation, flexure joints have little friction loss and do not require lubrication. The generate smooth and continuous displacement without backlash. So flexure joints are usually used to compose the structure of Micro/Nano equipments which named as compliant mechanisms [1, 2]. However, compliant mechanisms can not finish multi-dimensional motion characteristic in

Z. Dachang (✉)

School of Mechanical and Electric Engineering, Guangzhou University,
Guangzhou 510006, People's Republic of China
e-mail: zdc98998@gzhu.edu.cn

F. Yanping

School of Innovation and Entrepreneurship, Guangzhou University,
Guangzhou 510006, People's Republic of China

© Springer Nature Singapore Pte Ltd. 2017

X. Zhang et al. (eds.), *Mechanism and Machine Science*,

Lecture Notes in Electrical Engineering 408,

DOI 10.1007/978-981-10-2875-5_78

spatial. To overcome the shortcoming, the structure of parallel mechanisms with flexure joints are investigated which called as compliant parallel mechanism. Yun [3] presented the design and modeling of a new 6-DoF 8-PSS/SPS compliant dual redundant parallel robot with wide-range flexure joints, and the kinematics model of the macro parallel mechanism system via the stiffness model and Newto-Raphson method are adapted to build the dynamic's model for the micro-motion system. Wei [4] proposed a compliant ultra-precision parallel position based on the coarse/fine dual architecture, and flexure hinges are adopted as compliant passive joints. Choi [5] proposed a compliant parallel mechanism for two translations and applied to a XY fine motion stage driven by piezo actuators, and four flexure-based prismatic joint chains are arranged in four sides of a target platform to implement the compliant parallel mechanism. Gao and Zhang [6] designed a novel three DoF compliant parallel mechanism and its performance characterization is analyzed which affects the application potential. Treatments of the characterization and design of compliant parallel mechanisms may also be found in other literatures [7–9]. By using the flexure hinges instead of the conventional rigid joints, although this kind of structure compose method have spatial multi-dimensional motion characteristics, but the whole stiffness is decent obviously. It is important to design a perfect structure satisfy the two subjects: high stiffness and multi-dimensional operation ability.

In terms of high stiffness, topology optimization method is proposed for compliant mechanism. Topology optimization approach is advantageous because it does not require a rigid-link mechanism configuration as a starting point, and can be used to design single-piece fully compliant mechanisms. Ever since Bendsøe introduced the homogenization method [10], many topology optimization methods have been developed such as the solid isotropic material with the penalization (SIMP) method [11], the ground structure method [12] and level set based method [13], etc. Although topology optimization has been a matured tool for optimization design problem, most of them are focusing on the single input-output conditions. In reality, parallel compliant mechanism with multiple inputs and outputs are widely used in the fields of micro-positioning and micro-manipulation. The relationship between multiple I/O are vector mapping matrix with certainly connection. Zhu et al. [14, 15] presented a hinge-free compliant mechanism which has one input and two outputs based on level set method. Yong et al. [16] presented a wavelet-based topology optimization formulation by implicitly imbedding wavelet shrinkage method into optimization formulation based on SIMP method. Topology optimization methods for parallel compliant mechanisms may also be found in other literatures [17–19]. In those methods, compared with conventional parallel prototype mechanisms, the motion characteristics of designed structure are ambiguity. On the other hand, the mechanism has not been included the hinge form after the topology optimization process, in this case, we called this structure as peristaltic structure in this paper.

In this study, we proposed a new method for topology optimization of planar 3-DoF peristaltic structure based on differential kinematic vector continuous mapping matrix with conventional prototype parallel mechanism. The remainder of

this paper is organized as follows. In Sect. 2, the differential kinematic vector continuous mapping matrix with conventional prototype parallel mechanism is build. In Sect. 3, the optimization problems of design peristaltic structure are proposed based on SIMP method. The shape sensitivity analysis is applied to obtain the displacement field for the optimization which combined with the vector mapping matrix. In Sect. 4, numerical examples are presented to demonstrate the effectiveness of the proposed method. Finally, conclusions are developed.

2 Differential Kinematic with Vector Continuous Mapping Matrix

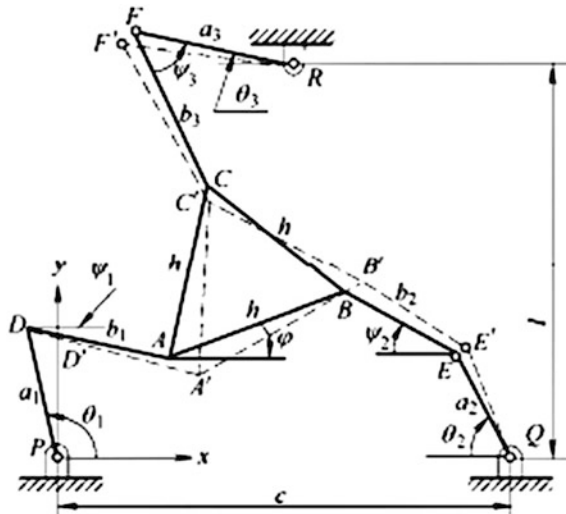
In order to keep the differential kinematic characteristics with the prototype of parallel mechanism, the differential kinematic equations with vector continuous mapping of micro-elastic deformation mechanism should be set. Without loss of generality, we select the 3-RRR prototype of planar parallel mechanism as an example. As shown in Fig. 1, the structure of 3-RRR prototype planar parallel mechanism is established.

Constraint equations may be described as

$$x_B = x_A + h \cos \varphi, \quad y_B = y_A + h \sin \varphi \tag{1}$$

$$x_C = x_A + h \cos\left(\varphi + \frac{\pi}{3}\right), \quad y_C = y_A + h \sin\left(\varphi + \frac{\pi}{3}\right) \tag{2}$$

Fig. 1 3-RRR planar parallel prototype mechanism



Vector equations of the limb PDA may be described as

$$OA = OP + PD + DA \tag{3}$$

where $x_p = y_p = 0$

Substituting (1), (2) into (3), we get

$$x_A - a_1 \cos \theta_1 = b_1 \cos(\theta_1 + \psi_1), \quad y_A - a_1 \sin \theta_1 = b_1 \sin(\theta_1 + \psi_1) \tag{4}$$

Considering two other limbs, we can get

$$c - a_2 \cos \theta_2 - b_2 \cos \psi_2 = x_A + h \cos \varphi, \quad a_2 \sin \theta_2 + b_2 \sin \psi_2 = y_A + h \sin \varphi \tag{5}$$

$$x_A + h \cos \left(\varphi + \frac{\pi}{3} \right) = \frac{1}{2}c - a_3 \cos \theta_3 - b_3 \cos \psi_3, \quad y_A + h \sin \left(\varphi + \frac{\pi}{3} \right) = 1 - a_3 \sin \theta_3 - b_3 \sin \psi_3 \tag{6}$$

Assumed that the displacement of each limb are equal to infinitesimal and may defined as $\theta'_i = \theta_i + \Delta\theta_i, i = 1, 2, 3$, and then (4)–(6) can be rewritten as following with infinite displacement.

$$\begin{aligned} x'_A - a_1 \cos(\theta_1 + \Delta\theta_1) &= b_1 \cos((\theta_1 + \psi_1) + (\Delta\theta_1 + \Delta\psi_1)) \\ y'_A - a_1 \sin(\theta_1 + \Delta\theta_1) &= b_1 \sin((\theta_1 + \psi_1) + (\Delta\theta_1 + \Delta\psi_1)) \end{aligned} \tag{7}$$

$$\begin{aligned} x'_B &= c - a_2 \cos(\theta_2 + \Delta\theta_2) - b_2 \cos(\psi_2 + \Delta\psi_2) = x'_A + h \cos(\varphi + \Delta\varphi) \\ a_2 \sin(\theta_2 + \Delta\theta_2) + b_2 \sin(\psi_2 + \Delta\psi_2) &= y'_A + h \sin(\varphi + \Delta\varphi) \end{aligned} \tag{8}$$

$$\begin{aligned} x'_C &= x'_A + h \cos \left(\left(\varphi + \frac{\pi}{3} \right) + \Delta\varphi \right) = \frac{1}{2}c - a_3 \cos(\theta_3 + \Delta\theta_3) - b_3 \cos(\psi_3 + \Delta\psi_3) \\ y'_C &= y'_A + h \sin \left(\left(\varphi + \frac{\pi}{3} \right) + \Delta\varphi \right) = 1 - a_3 \sin(\theta_3 + \Delta\theta_3) - b_3 \sin(\psi_3 + \Delta\psi_3) \end{aligned} \tag{9}$$

Let $\Delta x = x'_A - x_A$ and $\Delta y = y'_A - y_A$, and then the three parameters can be defined as output displacement of moving platform. The relationship between active joint displacement and task displacement is the given by (4)–(9), and the vector continuous mapping matrix between the joints and task displacement can be formulated as following.

$$\begin{bmatrix} \Delta x \\ \Delta y \\ \Delta \varphi \end{bmatrix} = J_D \begin{bmatrix} \Delta \theta_1 \\ \Delta \theta_2 \\ \Delta \theta_3 \end{bmatrix} \tag{10}$$

where

$$J_D = \begin{bmatrix} \frac{a_1 s \psi_1 (s(\alpha) s \psi_2 + s(\gamma) s \psi_3)}{-M} & \frac{a_2 s(\beta) s(\sigma) s(\alpha)}{-M} & \frac{a_3 s(\beta) s(\gamma) s(\theta_3 - \psi_3)}{M} \\ \frac{a_1 s \psi_1 (s(\alpha) s \psi_2 c \psi_2 + s(\gamma) c \psi_3)}{M} & \frac{a_2 c(\beta) s(\sigma) s(\alpha)}{M} & \frac{a_3 c(\beta) s(\gamma) s(\theta_3 - \psi_3)}{-M} \\ \frac{a_1 s \psi_1 s(\psi_3 - \psi_2)}{hM} & \frac{a_2 s(\theta_2 - \psi_2) s(\psi_3 - \theta_1 - \psi_1)}{hM} & \frac{a_3 s(\theta_3 - \psi_3) s(\psi_2 - \theta_1 - \psi_1)}{hM} \end{bmatrix}$$

$$\alpha = \varphi + \frac{\pi}{3} - \psi_3, \beta = \theta_1 + \psi_1, \gamma = \varphi + \psi_2, \sigma = \theta_2 - \psi_2, s(\cdot) = \sin(\cdot), c(\cdot) = \cos(\cdot)$$

$$M = s\left(\varphi + \frac{\pi}{3} - \psi_3\right) s(\theta_1 + \psi_1 - \psi_2) + s(\varphi + \psi_2) s(\theta_1 + \psi_1 - \psi_3)$$

3 Topology Optimization of 3-DoF Peristaltic Structure

3.1 SIMP Model of Topology Optimization with Vector CMM

The motion characteristic of 3-DoF peristaltic structure has three input parameters and three output parameters respectively. By using the vector continuous mapping matrix (CMM), the model of SIMP is build as

$$\begin{aligned} \min \quad C &= \sum_{i=1}^3 \sum_{j=1}^3 \tilde{U}_j^T K U_i = \sum_{e=1}^N \sum_{i=1}^3 \sum_{j=1}^3 \tilde{U}_{ej}^T \rho_e^p K_E U_{ei} \\ \text{s.t.} \quad K \tilde{U}_j &= F_j \quad K U_i = F_i \quad F_j = J_D F_i \quad i, j = 1, 2, 3 \\ \int_{\Omega} \rho_e d\Omega &\leq V \quad 0 \leq \rho_{\min} \leq \rho_e \leq 1 \quad e = 1, 2, \dots, N \end{aligned} \tag{11}$$

where U_j is companion displacement vector, K is whole post optimality stiffness of peristaltic structure, U_i is the displacement with actual load, V is post optimality volume of peristaltic structure, F_i is $i^{\#}$ actual load, U_{ei} is the unit displacement vector under the $i^{\#}$ actual load, F_j is $j^{\#}$ virtual load, \tilde{U}_{ej} is the unit displacement vector under the $j^{\#}$ virtual load, K_E is unit stiffness, ρ_e is unit density, p is penalty factor and satisfy $p \geq \max\left\{\frac{2}{1-\nu^p}, \frac{4}{1+\nu^p}\right\}$.

3.2 Sensitivity Analysis

Sensitivity analysis in topology optimization includes the sensitivity of objective function and constraint function. Differentiating the two functions with respect to design variables, we can derive the direction of iterative update during topology optimization process.

(1) Sensitivity analysis of objective function

Differentiating (11) with respect to density yields

$$\begin{aligned} \frac{\partial C}{\partial \rho_e} = & \left(\frac{\partial \left(\sum_{j=1}^3 \tilde{U}_j^T \right)}{\partial \rho_e} \mathbf{K} + \sum_{j=1}^3 \tilde{U}_j^T \frac{\partial \mathbf{K}}{\partial \rho_e} \right) \sum_{i=1}^3 U_i \\ & + \sum_{j=1}^3 \tilde{U}_j^T \left(\frac{\partial \mathbf{K}}{\partial \rho_e} \sum_{i=1}^3 U_i + \mathbf{K} \frac{\partial \left(\sum_{i=1}^3 U_i \right)}{\partial \rho_e} \right) - \sum_{j=1}^3 \tilde{U}_j^T \frac{\partial \mathbf{K}}{\partial \rho_e} \sum_{i=1}^3 U_i \end{aligned} \quad (12)$$

From a macro perspective, without loss of generality, we assumed that the I/O is unconcerned with design variables, and then differentiating (11) with respect to design variables, we get

$$\frac{\partial \mathbf{K}}{\partial \rho_e} \sum_{j=1}^3 \tilde{U}_j^T + \mathbf{K} \frac{\partial \left(\sum_{j=1}^3 \tilde{U}_j^T \right)}{\partial \rho_e} = \frac{\partial \left(\sum_{j=1}^3 F_j \right)}{\partial \rho_e} = 0 \quad (13)$$

$$\frac{\partial \mathbf{K}}{\partial \rho_e} \sum_{i=1}^3 U_i + \mathbf{K} \frac{\partial \left(\sum_{i=1}^3 U_i \right)}{\partial \rho_e} = \frac{\partial \left(\sum_{i=1}^3 F_i \right)}{\partial \rho_e} = 0 \quad (14)$$

Substituting (13), (14) into (12), we get

$$\frac{\partial C}{\partial \rho_e} = - \sum_{j=1}^3 \tilde{U}_j^T \mathbf{K} \sum_{i=1}^3 U_i \quad (15)$$

Substituting the $\mathbf{K} = \sum_{e=1}^N \rho_e^p \mathbf{K}_E$ into (15), the computational formula for objective function sensitivity analysis is given by

$$\frac{\partial C}{\partial \rho_e} = \sum_{e=1}^N \sum_{i=1}^3 \sum_{j=1}^3 p \tilde{U}_j^T \rho_e^{p-1} K_E U_i \tag{16}$$

(2) Sensitivity analysis of constraint function

Differentiating the volume function with respect to the density, sensitivity of constraint function can be derived as

$$\frac{\partial V}{\partial \rho_e} = \frac{\partial (\int_{\Omega} \rho_e dV)}{\partial \rho_e} = 1 \tag{17}$$

We find that the sensitivity of constraint function is constant. It denotes that the direction of iterative update of volume with design variables is assured.

3.3 Solution with Optimization Model

We apply Lagrange multiplier to construct the Lagrange function which including objective function and constraint function simultaneously. By solving the extreme value of the Lagrange function, the optimization value of objective function can be derived. The optimization criterion algorithm is proposed for iterative update which described as

$$\rho_e^{(k+1)} = \begin{cases} \min \{ (m+1)\rho_e^{(k)}, 1 \} \\ \max \{ (1-m)\rho_e^{(k)}, \rho_{\min} \} \\ (D_e^{(k)})^\zeta \rho_e^{(k)} \\ \min \{ (m+1)\rho_e^{(k)}, 1 \} \leq (D_e^{(k)})^\zeta \rho_e^{(k)} \leq \max \{ (1-m)\rho_e^{(k)}, \rho_{\min} \} \end{cases} \tag{18}$$

where $\rho_e^{(k)}$ is the iteration value of k step, $\rho_e^{(k+1)}$ is the iteration value of k + 1 step, and m is the mobile limit constant and m is a appropriate constraint to design variables for stability the iteration process. Based on literature [10], its range may be selected between 0.1 and 0.3, ζ is damping factor and range of 0.4–0.5, and $D_e^{(k)}$ is expressed as following.

$$D_e^{(k)} = \frac{p \rho_e^{(p-1)} \sum_{j=1}^3 \tilde{U}_j^T K_E \sum_{i=1}^3 U_i \Delta E}{\Lambda^{(k)} V_E} = (\max(0, -\frac{\partial C}{\partial \rho_e})) / \Lambda^{(k)} V_E \tag{19}$$

where $\Lambda^{(k)}$ is the Lagrange multiplier with volume constraint of k step iteration and the update of Lagrange multiplier is adapted double convex linear programming algorithm, V_E is the unit volume of k step iteration.

3.4 Heaviside Filter

We adapt Heaviside function to modify the linear filter for peristaltic structure. As the minimum filter radius, if $\tilde{\rho}_e > 0$, then $\bar{\rho}_e = 1$, otherwise, $\tilde{\rho}_e = 0$, $\bar{\rho}_e = 0$.

The resulting of linear filter can be given by

$$\tilde{\rho}_i = \sum_j \omega_{ij} \rho_j, \sum_j \omega_{ij} = 1 \tag{20}$$

where ω_{ij} is the filter weight factor of the j unit to the i unit.

To get the better discrete 0/1 distribution optimization results, and decent the middle density unit, second weight calculation equation and Heaviside function are adopted as following.

$$\omega_{ij} = \begin{cases} \frac{r_{\min} - d(i, j)}{\sum_{k \in N_i} (r_{\min} - d(i, k))} & j \in N_i \\ 0 & j \notin N_i \end{cases}, N_i = \{J: (r_{\min} - d(i, j)) \geq 0\} \tag{21}$$

where $d(i, j)$ is the displacement between i unit and j unit, and r_{\min} is the minimum filter radius.

4 Design Conditions and Simulations for Peristaltic Structure

Based on linear elastic relationship between force and displacement, the three-DoF of peristaltic structure has been changed to force output, shown as Fig. 2.

Assumed that the topology optimization yield of peristaltic structure is a square with size 12×12 , and the number of discrete grid is 120×120 , the elastic modulus of solid material is 2×10^{11} Pa, the elastic modulus of holes are 10^{-3} Pa, Poisson's ratio is 0.3, optimum volume ratio is 0.3, minimum filter radius is 1.5, input force F_{in1} is 1000 N, input force F_{in2} is 1000 N, input force F_{in3} is 1000 N. Based on the relationship between input forces and output forces which denoted as, the output forces can be solved as $F_{out1} = 365N$, $F_{out2} = 1680N$, $F_{out3} = 1130N$, respectively. The optimization was run for 180 iterations, and the topology optimized structure of peristaltic structure is shown as Fig. 3, and the iterative process of the optimization is shown as Fig. 4.

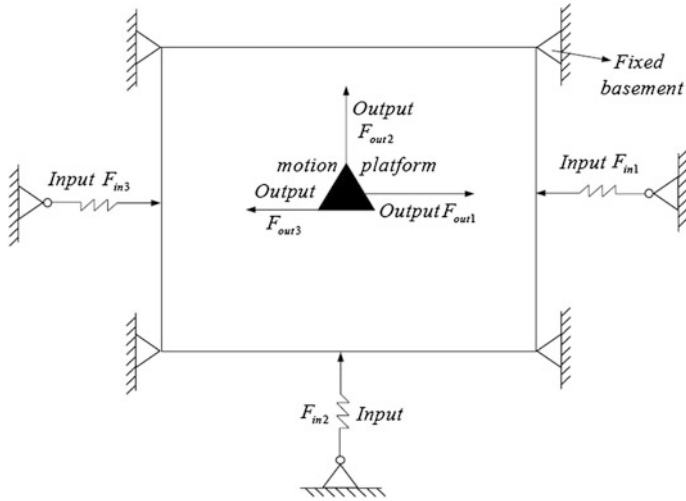


Fig. 2 Design conditions for peristaltic structure with topology optimization method

Fig. 3 Topology optimization structure of peristaltic mechanism



And then, Ansys software is used for static simulations of peristaltic structure. The differential displacement of direction and are shown as Fig. 5a and b with the maximum value and respectively. The differential rotational displacement of direction is shown as Fig. 5c with the maximum value.

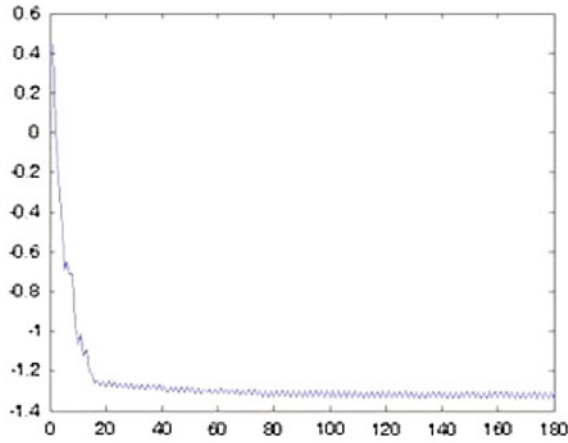


Fig. 4 Convergence curve of optimization process of the peristaltic structure

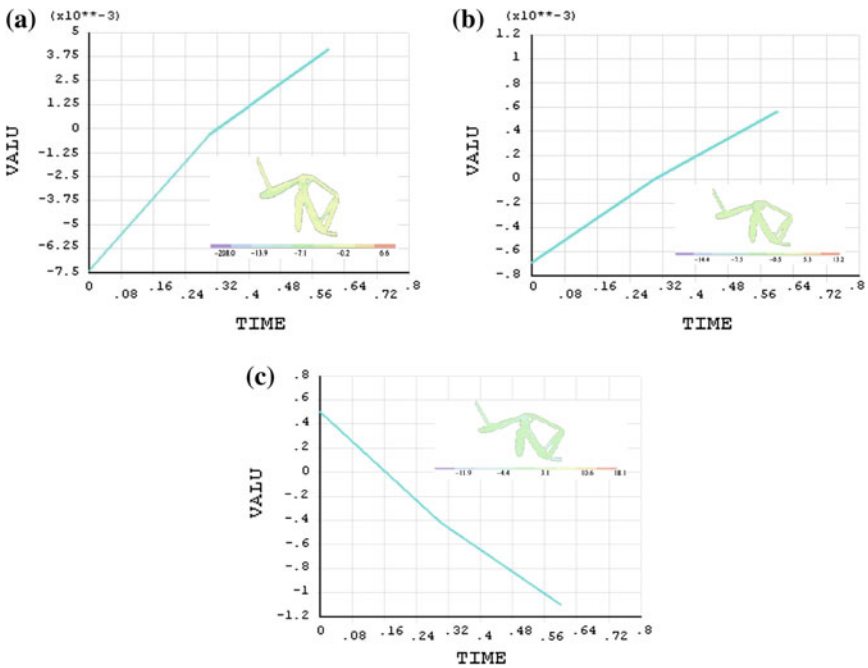


Fig. 5 Differential displacement of peristaltic structure **a** with direction x; **b** with direction y; **c** with direction z

5 Conclusions

In this study, we presented a new formulation for synthesis of peristaltic structure with vector continuous mapping matrix based on topology optimization method. In proposed method, the vector continuous mapping matrix, derived with parallel prototype mechanism, is taken into account to make the peristaltic structure to keep the same kinematic characteristic with parallel prototype mechanism. By doing so, we proposed a new topology optimization method combined SIMP with vector continuous mapping matrix to synthesis peristaltic structure. Numerical simulations with vector continuous mapping matrix are presented for illustrating the validity of the presented method.

References

1. Howell LL (2001) *Compliant mechanism*. Wiley, New York
2. Wojciech B, John WG, Satyandra K et al (2011) Design and fabrication of miniature compliant hinges for multi-material compliant mechanisms. *Int J Adv Manuf Technol* 57:437–452
3. Yun Y, Li Y (2010) Design and analysis of a novel 6-DoF redundant actuated parallel robot with compliant hinges for high precision positioning. *Nonlinear Dyn* 61:829–845
4. Wei D, Zhijiang D, Lining S, Bo Z (2006) A compliant ultra-precision 6-DoF parallel positioner based on the coarse/fine dual architecture. In: *Proceedings of the 1st IEEE international conference on nano/micro engineered and molecular systems*, Jan 18–21, Zhuhai, China, pp 488–492
5. Choi KB, Lee JJ, Kim GH, Lim HJ (2012) A compliant parallel mechanism with flexure-based joint chains for two translations. *Int J Precision Eng Manuf* 13(9):1625–1632
6. Gao Z, Zhang D (2014) Simulation driven performance characterization of a spatial compliant parallel mechanism. *Int J Mech Mater Des* 10:227–246
7. Dachang Z, Pei L, Xiangfu C (2013) Structure design of a 3-DOF UPC type rotational fully spatial compliant parallel manipulators. *Int J Advancements Comput Technol* 5:70–81
8. Dan Z, Zhen G (2015) Performance analysis and optimization of a five-degrees-of-freedom compliant hybrid parallel manipulator. *Robot Comput Integr Manuf* 34:20–29
9. Guangbo H, Haiyang L (2015) Design of 3-legged XYZ compliant parallel manipulators with minimized parasitic rotations. *Robotica* 33(4):787–806
10. Bendse MP, Kikuchi N (1988) Generating optimal topologies in structural design using a homogenization method. *Comput Methods Appl Mech Eng* 71(2):197–224
11. Bendse MP, Sigmund O (1999) Material interpolation schemes in topology optimization. *Arch Appl Mech* 69(9–10):635–654
12. Frecker MI, Ananthasuresh GK, Nishiwaki S, Kikuchi N, Kota S (1997) Topology synthesis of compliant mechanisms using multi-criteria optimization. *J Mech Des* 119(2):238–245
13. Allaire G, Jouve F, Toader AM (2004) Structural optimization using sensitivity analysis and a level set method. *J Comput Phys* 194(1):363–393
14. Zhu B, Zhang X, Wang N (2013) Topology optimization of hinge-free compliant mechanisms with multiple outputs using level set method. *Struct Multidisc Optim* 47:659–672
15. Zhu B, Zhang X, Fatikow S (2014) A multi-objective method of hinge-free compliant mechanism optimization. *Struct Multidisc Optim* 49:431–440
16. Jones J (2000) *Contact mechanics*. Cambridge University Press, Cambridge

17. Guangbo H, Haiyang L (2015) Conceptual designs of multi-degree of freedom compliant parallel manipulators composed of wire-beam based compliant mechanisms. *Proc Inst Mech Eng Part C J Mech Eng Sci* 229(3):538–555
18. Guozhan L, Joo TT, Guilin Y et al (2015) Integrating mechanism synthesis and topological optimization technique for stiffness-oriented design of a three-DoF flexure-based parallel mechanism. *Precis Eng J Int Societies Precis Eng Nanotechnol* 39:125–133
19. Beroz J, Awar S, Hart AJ (2014) Extensible-link kinematic model for characterizing and optimizing compliant mechanism. *J Mech Des* 136(3):031008

Vision-Aided Online Kinematic Calibration of a Planar 3RRR Manipulator

Hai Li, Xianmin Zhang, Lei Zeng and Heng Wu

Abstract In this paper, we propose an automatic approach for the online kinematic calibration of a planar 3RRR manipulator. This method utilizes a camera as the global sensor to measure pose of the end effector. After the visual measuring system obtains enough pose data, an algorithm based on the implicit model is performed for the kinematic calibration. Finally, the calibration result is sent to the controller to compensate the geometric model of the manipulator. All these mentioned steps are implemented automatically without human intervene. Experiment studies on a real system have shown the effectiveness and the convenience of the present method.

Keywords Vision-aided · Kinematic calibration · 3RRR manipulator · Automatic

1 Introduction

Kinematic calibration is widely used in robotics to improve the absolute accuracy of manipulators. In other words, the basic goal of calibration is to find a more precise kinematic model of the manipulator. Usually, four steps are included in the calibration procedure [1, 2]. Firstly, developing a kinematic model. Secondly, measuring a sequence of poses with different configurations. Thirdly, identifying the accurate parameters of the models with proper optimized algorithm. Fourthly, compensating the controller with the optimized parameters. Due to the advantages of high stiffness, high speed, and compact structure, parallel mechanisms have drawn many researchers' attention. Plenty of research about the kinematic calibration of parallel manipulators has been done in recent decades. Zhuang et al. present a method used for calibration of Gough-Stewart, measuring setup used in

H. Li · X. Zhang (✉) · L. Zeng · H. Wu
Guangdong Province Key Laboratory of Precision Equipment
and Manufacturing Technology, South China University of Technology,
Guangzhou 510640, China
e-mail: zhangxm@scut.edu.cn

this method is theodolite [3]. Joubair et al. [4, 5] carry out calibrations for a planar PM and a five bar mechanism with the measuring setup of coordinate measurement machine (CMM) and measurement arm (MA). Kim presents a calibration for a Cartesian PM using a ballbar [6]. Except commercial measurement setups mentioned above, vision-based equipment also has widely used in this area. Renaud et al. [7] propose a calibration method for a H4 PM with a vision-based metrology. Daney et al. [8] propose an optimized pose choosing strategy and realize the calibration for a Gough-Stewart PM with a vision-based device. Traslosheros et al. [9] realize the calibration of a delta PM with a camera attached at the end effector.

An obvious drawback for the calibration methods mentioned above is that this procedure is done before the use of the manipulator, which may cause the calibration result inaccurate when the manipulators are loaded or continuously running. In addition, as the measurement setup and the manipulator are two separated systems, data transfer between these two systems is inconvenient and always needs aiding from human. Hence, the entire procedure is inefficiency and non-automatic. In order to make the calibration procedure easy to implement and fully automatic, an effective way is to integrate a measurement sensor that can communicate with the controller of the manipulator. The ideal sensor has the following characteristics: full pose measurement ability, low price, open access for data acquisition. Compare the common measuring setups mentioned above, it can be found out that only vision sensor can satisfy these requirements for system integration.

In this paper, a scheme that combines vision sensor and controller of the planar 3 RRR parallel manipulator is proposed. Utilize the convenient of the combined system, automatic online kinematic calibration of the manipulator is realized. In Sect. 2, vision-based online pose measurement is present in detail. Kinematic calibration of 3RRR is introduced in Sect. 3. Section 4 is the experiment. Section 5 is the conclusion.

2 Vision-Aided Pose Measurement

2.1 System Scheme

The pose of the mobile platform can be measured by camera through recognizing low-level geometric features on it, such as the points or the lines [10]. In practical, point feature is more commonly used. As the 3RRR have three degree of freedoms in the motion plane, so theoretically two markers are enough. However, more marker points will make the measurement more robust to noise. A system schematic diagram is shown in Fig. 1. In this scheme, optical axis of the camera is set to be perpendicular to the base platform. Mobile platform can move to the desired pose under the control of the controller, and its actual pose can be measured through the camera and sent to the controller immediately. Hence, the automatic online calibration can be realized.

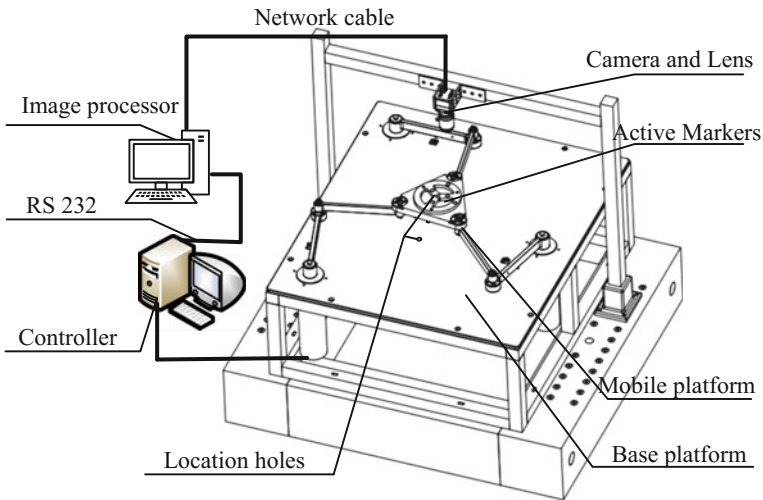


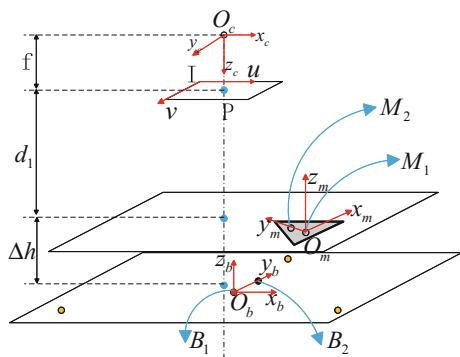
Fig. 1 System setup

In this section, we outline the main principles of the vision-aided online measuring system, the planar 3RRR manipulator used in this system is the one proposed in reference [11].

2.2 Define the Coordinate Frames

To measure the pose of the moving platform by the camera, the first thing is to confirm the coordinate frames. Four frames are included in this system, as shown in Fig. 2. The following notations are used in this paper.

Fig. 2 Schematic diagram of the systemic coordinate



- $R_b(O_b, x_b, y_b, z_b)$ is the base coordinate of the PPM with its origin at location hole B_1 and y-axis coincident with B_1B_2 .
- $R_m(O_m, x_m, y_m, z_m)$ is the coordinate on the mobile platform with its origin at the location hole M_1 and y-axis direction of M_1M_2 .
- $R_c(O_c, x_c, y_c, z_c)$ is the camera coordinate with its origin at the optical center O_c .
- $O_i - UV$ is the coordinate of the image plane with its origin at the top-left corner of the image.
- IP, MP, BP is short for image plane, mobile plane and base plane, respectively.
- jT_i is the transformation from frame R_i to R_j .

All these frames are right-handed coordinate and their Z-axes are parallel and perpendicular to the base plane. B_1, B_2 and M_1, M_2 are the location holes on the base plane and mobile platform, respectively. Focal length of the lens is f , distance from IP to MP and MP to BP are $d, \Delta h$, respectively. As B_1 and M_1 are the centroids of the base platform and mobile platform respectively, components in bT_m represent the pose of the mobile platform under the frame of base coordinate.

2.3 Pose Measuring in Base Frame

From the classic pin-hole camera model, we can obtain the projective transformation equation from world space to image space as following [12]:

$$\begin{pmatrix} u \\ v \\ 1 \end{pmatrix} = sK[R, T] \begin{pmatrix} X \\ Y \\ Z \\ 1 \end{pmatrix} \tag{1}$$

where K is the 3×3 intrinsic parameter matrix of the camera, R and T are 3×3 rotation matrix and the 3×1 translation vector respectively from frame of the world to frame of camera. This projection equation is defined to an arbitrary factor s .

For this system, as BP, MP, IP are parallel to each other and Z-axis component of the points on the plane is zero, so the projective from MP to IP or BP to IP can be uniformly simplified as:

$$\begin{pmatrix} u \\ v \\ 1 \end{pmatrix} = sKA \begin{pmatrix} X \\ Y \\ 1 \end{pmatrix} = sK \begin{bmatrix} \cos \theta & -\sin \theta & t_x \\ -\sin \theta & -\cos \theta & t_y \\ 0 & 0 & 1 \end{bmatrix} \begin{pmatrix} X \\ Y \\ 1 \end{pmatrix}. \tag{2}$$

Matrix A represents the simplified transformation relation from reference frame to camera frame. Three parameters are included in this matrix. Once the intrinsic

parameter matrix K and more than two known points are obtained, then A can be solved out with Eq. (2).

After obtaining cT_b and mT_b , pose expressed in base frame can be written as ${}^cT_b \cdot {}^mT_b^{-1}$. Intrinsic parameter matrix of the camera can be gotten from using the camera calibration with the methods proposed in reference [13]. Known points can be obtained from using the active markers as shown in the following experiment.

2.4 Discussions of This Measuring Method

Three main kinds of errors are included in this measuring scheme, the lens distortion, uncertainty of the intrinsic parameters of the camera, and the installation error of the camera. To improve the absolute measuring accuracy of this system, calibration of this system with the help of another high-precision setup is necessary. All these problems will be solved and presented in our next paper.

3 Kinematic Calibration

The manipulator used here is the one proposed in literature [11]. It is designed as the macro manipulator in the macro-micro manipulates system. Main target of this manipulator is realizing rapid precision positioning at the accuracy of $10\ \mu\text{m}$ with the load of micro positioning platform. Once the manipulator is loaded, its kinematic parameters need to be re-calibrated.

In this section, kinematic model of this mechanism will be introduced firstly, and then is the calibration model. Parameter identification also will be simply discussed.

3.1 Closed Loop Vector Equation of the 3RRR

Figure 3 is the schematic diagram of 3RRR. As shown in this figure, A_i , B_i , C_i represent the revolute joints. A_iB_i and B_iC_i are the active and passive links, respectively. Their corresponding designed length are a_i and b_i . Orientation angles of A_iB_i and B_iC_i in base frame are θ_i and γ_i . Origins of frame R_b and R_m are the centroids of $A_1A_2A_3$ and $C_1C_2C_3$, respectively. Designed value of OA_i and $O'C_i$ are d_i and c_i , their corresponding orientation angles are α_i and β_i . (i represents the number of the chains, its value is set from 1 to 3.)

To better display the mathematical model of this mechanism, a branch is taken out separately, as shown in Fig. 4. Utilizing the close-loop vectors [14], an equation that includes kinematic model can be obtained as following:

Fig. 3 Schematic diagram of 3RRR

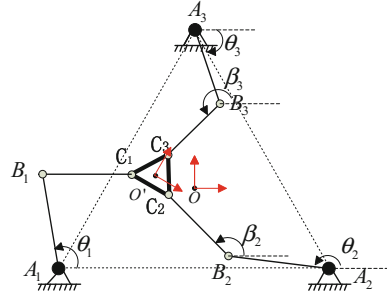
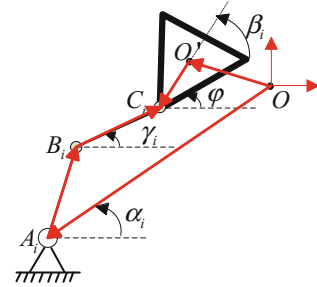


Fig. 4 Mathematical model of a branch



$$\vec{OO'} + \vec{O'C_i} - \vec{OA_i} - \vec{A_iB_i} - \vec{B_iC_i} = 0. \tag{3}$$

Suppose a pose of the mobile platform is $(x^j, y^j, \varphi^j)^T$, and the coordinates of A_i and C_i in the base frame are $(x_{A_i}, y_{A_i})^T$ and $(x_{C_i}, y_{C_i})^T$, respectively. According Eq. 3 and the orientation angles mentioned before, a new equation can obtain as following:

$$\begin{bmatrix} x^j \\ y^j \end{bmatrix} + \begin{bmatrix} \cos \varphi^j & -\sin \varphi^j \\ \sin \varphi^j & \cos \varphi^j \end{bmatrix} \begin{bmatrix} x_{C_i} \\ y_{C_i} \end{bmatrix} - \begin{bmatrix} x_{A_i} \\ y_{A_i} \end{bmatrix} - \begin{bmatrix} \cos \theta_i^j \\ \sin \theta_i^j \end{bmatrix} a_i - \begin{bmatrix} \cos \gamma_i^j \\ \sin \gamma_i^j \end{bmatrix} b_i = 0 \tag{4}$$

After multiplying the vector $(\cos \gamma_i^j, \sin \gamma_i^j)$ at both sides of this equation, this equation is simplified as a single equation that includes all the geometric parameters and the pose. In addition, it can be simplified as:

$$\psi_i(\kappa_i, v_i^j) = 0. \tag{5}$$

where $\kappa_i = (x_{A_i}, y_{A_i}, a_i, b_i, x_{C_i}, y_{C_i})$, represents the geometric parameters of the i th branch of the manipulator, $v_i^j = (x^j, y^j, \varphi^j, \theta_i^j)$, represents the j th pose and the corresponding input angles.

3.2 Kinematic Calibration Method

Equation 5 is reasonable under the ideal conditions. However, if take the manufacturing, installation, and load into consideration, this equation will not be equal. This means that the geometric parameters of the manipulator are inaccurate compared with the designed value. Once pose of the manipulator has been measured, a rational way to identify the real parameters of this PM is to find out the optimized solution of the following equation:

$$\min \sum_{i=1}^3 \sum_{j=1}^N \|\psi_i(\kappa_i, \tilde{v}_i^j)\|^2 \quad (6)$$

where N is the number of pose. Since there are 18 parameters that need to identify, at least 6 different poses are required. Appropriate increasing of the number of the poses can improve the accuracy and robustness of the result. This is a non-linear optimize problem, which can be solved by the least square method, Levenberg-Marquardt method, or kalman-based method, etc. In this paper, the Levenberg-Marquardt algorithm is chosen as the method for this problem.

4 Experiment

To test the effectiveness of the proposed approach, a real system is constructed as shown in Fig. 5. The vision system consists of a CMOS camera (Tendency Dalsa, Genie TS M2048) with the resolution of 2048×2048 , a prime lens (Kowa, LM16SC) with the focus length of 16 mm, and an image processor (IP) (Intel(R) Core(TM) i7-4770MQ, CPU 2.40 GHz, RAM 8 GB). As mentioned before, manipulator used here is the one proposed in literature [11], its control system is built base on a motion control card from Galil (DMC-1886PCI). The controller of the robot and the measuring system communicate with interface of RS232. To decrease the time for image processing, active markers (AMs) are designed and used as shown in this figure.

Experiment includes several steps as shown in the following. First, a set of pose are choosing as the target measurement pose. Second, the corresponding input angle will be calculated by the inverse kinematic of the mechanism and sent to the controller. Once the mobile platform reach to each of the target configuration, the actual pose will be measured by the vision system. After all the poses are measured and recorded, the kinematic calibration proposed in Sect. 3 will be implemented, and the results will be sent to the controller automatically. Finally, automatic online calibration is finished. The calibration results are shown in Table 1.

After obtaining the compensate values of the kinematic model, a set of 49 poses are measured with the designed model and the compensated model, respectively. These 49 poses are evenly distributed in a square workspace with the side length of

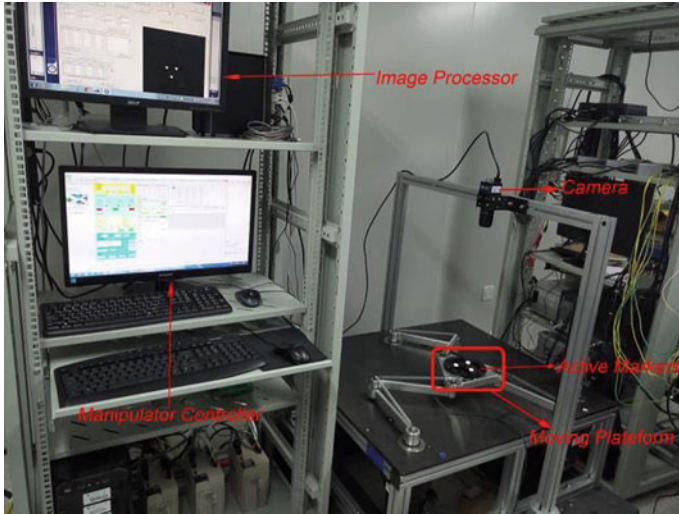


Fig. 5 Experiment setups

Table 1 Kinematic calibration results

i	Value					
	x_{Ai}	y_{Ai}	a_i	b_i	x_{Ci}	y_{Ci}
1	-346.2670	-199.8231	244.9540	241.8785	-97.1206	-56.1790
2	346.4335	-200.0030	244.9333	242.0029	96.9359	-55.9968
3	-0.0830	400.1246	245.0377	242.0304	0.0838	111.8724

120 mm, as shown in Fig. 6a. The numbers on the top of the poses represent the pose number. Figure 6b shows the corresponding positioning error. From this figure, we can find out that after compensation, the absolute accuracy of the robot has been improved from 0.12 to 0.04 mm.

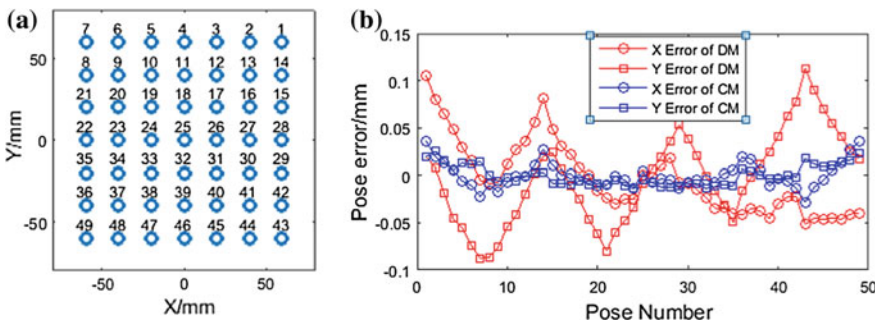


Fig. 6 Positioning accuracy of the manipulator

5 Conclusion

Vision-based measurement has the advantages of low cost, easy integration, and the ability of full pose measurement. To make the kinematic calibration of the planar parallel robot become more effective and automatic, a parallel manipulator combined with a vision-based measuring device is proposed. With the help of the vision technique, pose of the mobile platform can be measured rapidly and efficiently, and thus the automatic kinematic calibration can be realized by the communication between the vision system and the robot controller. Experiment results have shown the effectiveness of this method. After calibration, the maximum positioning error has decreased from 0.12 to 0.04 mm.

Acknowledgments This research was supported by the National Natural Science Foundation of China (Grant no. U1501247), the Scientific and Technological Research Project of Guangdong Province (2015B020239001), and the Scientific and Technological Research Project of Dongguang (Grant No.2015215119). These supports are greatly acknowledged.

References

1. Elatta AY et al (2004) An overview of robot calibration. *Inf Technol J* 3(1):74–78
2. Roth ZS, Mooring BW, Ravani B (1987) An overview of robot calibration. *IEEE J Robot Autom RA-3*(5):377–385
3. Hanqi Z, Jiahua Y, Masory O (1998) Calibration of Stewart platforms and other parallel manipulators by minimizing inverse kinematic residuals. *J Robot Syst* 15(7):395–405
4. Joubair A, Slamani M, Bonev IA (2012) Kinematic calibration of a 3-DOF planar parallel robot. *Ind Robot Int J* 39(4):392–400
5. Joubair A, Slamani M, Bonev IA (2013) Kinematic calibration of a five-bar planar parallel robot using all working modes. *Robot Comput Integr Manuf* 29(4):15–25
6. Kim HS (2005) Kinematic calibration of a Cartesian parallel manipulator. *Int J Control Autom Syst* 3(3):453
7. Renaud P et al (2006) Simplifying the kinematic calibration of parallel mechanisms using vision-based metrology. *IEEE Trans Rob* 22(1):12–22
8. Daney D et al (2006) Interval method for calibration of parallel robots: vision-based experiments. *Mech Mach Theory* 41(8):929–944
9. Traslosheros A et al (2011) A method for kinematic calibration of a parallel robot by using one camera in hand and a spherical object. In: IEEE 15th international conference on advanced robotics (ICAR)
10. Zou H, Notash L (2001) Discussions on the camera-aided calibration of parallel manipulators. In: CCToMM Symposium, 2001. Saint-Hubert, Canada
11. Gao M, Zhang X, Wu Z (2011) Optimum design of a 3-RRR planar parallel manipulator with a singularity-free workspace. In: Yin ZY et al (eds) *Applied mechanics and materials*, pp 606–610
12. Hartley R, Zisserman A (2003) *Multiple view geometry in computer vision*. Cambridge university press, Cambridge

13. Zhengyou Z (1999) Flexible camera calibration by viewing a plane from unknown orientations. In: Proceedings of the seventh IEEE international conference on computer vision, Kerkyra, Greece, vol 1, pp 666–73
14. Peng SZTX (2009) Self-calibration method of planar flexible 3-RRR parallel manipulator. *J Mech Eng* 45(3):150–155

Workspace Analysis and Application of the PRRRP Decoupled Parallel Mechanism

Shuwei Qu and Ruiqin Li

Abstract The workspace of parallel mechanism determines the work region of a mechanism and directly correlates with the synthesis of the mechanism for desired performance characteristics. This paper investigates the issues of decoupled properties of the PRRRP parallel mechanism. Based on the geometrical relation among the parameters, the reachable workspace atlases are drawn. The closed-form solutions are presented according to the decoupled properties of the parallel mechanism. The relationships are analyzed among the parameters. The oscillating angle of the output link is analyzed and the relationships are given. Based on those foundations, the optimized structure is presented. The optimized mechanism can be used as plating and carving machines. The experiment verifies the correctness and effectiveness of the method.

Keywords Decoupled parallel mechanism · Workspace · Optimization

1 Introduction

Workspace is an important index to measure the performance of the mechanism. It correlates with the configuration of the mechanism for desired performance characteristics, and reflects the working ability of the mechanism. Parallel mechanisms have some advantages in dynamic behavior, stiffness, accuracy, compactness and load carrying capacity compared with serial mechanisms. Coupled parallel mechanisms bring about some limitations, such as difficulty to solve workspace, high nonlinear relationship between input and output, difficulties in static and dynamic analysis, and the development of control system, which restrict its application fields [1].

S. Qu · R. Li (✉)

School of Mechanical and Power Engineering, North University of China,
Taiyuan 030051, China
e-mail: liruiqin@nuc.edu.cn

S. Qu

e-mail: shuweiqu1222@nuc.edu.cn

Decoupled parallel mechanism has a one-to-one correspondence relationship between the input and output variables, and attracts many scholars' interests.

Current available methods for workspace analysis are divided into two types. One is geometric method, which is a visual technique. Li and Dai [2] presented the workspace atlas of planar seven-bar mechanisms. Gallant et al. [3] proposed a geometric method to study the n-RRRR and the n-RRPR manipulators for the dexterous workspace. Kaloorazi et al. [4] used a geometric approach to obtaining the maximal singularity-free regions of a planar 3-DOF parallel mechanisms. Wang et al. [5] proposed a geometric approach to solving the stable workspace of quadruped bionic robot. Tsai et al. [6] developed reachable workspace according to geometric properties of the characteristics of workspace boundaries for a symmetrical Stewart-Gough manipulator. However, this method has a common disadvantage of ignoring mechanical interference and other physical constraints.

The other kind of method is closed-form solutions, which is convenient for analysis. Lee et al. [7] presented a closed-form solutions for the radii of the inscribed and circumscribed circles of the positional workspace for a hexapod parallel mechanism. Wang et al. [8] presented a unified algorithm for determining the reachable and dexterous workspace of parallel manipulators. Sánchez et al. [9] proposed an integrated method to analyze the workspace of Schönflies parallel manipulator. Gauthier et al. [10] presented higher-order continuation for the determination of robot workspace boundaries. Zhang et al. [11] proposed workspace investigation of a novel 2-DOF parallel manipulator. But the equation dimensions and the parameters higher than three are the major drawbacks for this method.

In this paper, a PRRRP decoupled parallel mechanism with two degree of freedom is proposed. Its topology configuration and decoupled properties are presented in Sect. 2. The reachable workspace atlases are drawn and the areas of the reachable workspace are calculated in Sect. 3. The oscillating angle of the output link is analyzed with algorithm method in Sect. 4. Section 5 the optimized PRRRP decoupled parallel mechanism with the variable link-length and its application are discussed. Finally, the conclusions are drawn in Sect. 6.

2 Configuration of the PRRRP Parallel Mechanism

2.1 Topology Configuration

As shown in Fig. 1, the PRRRP parallel mechanism contains three revolute pairs (R_1 , R_2 and R_3) and two prismatic pairs (P_1 and P_2). Link 2 is selected as the output link. P_1 and P_2 are two driving sliders. The point A is the output point.

Figure 1a indicates the initial position of the PRRRP parallel mechanism. Two sliders are in the lowest position. The static coordinate system O - xy is established at

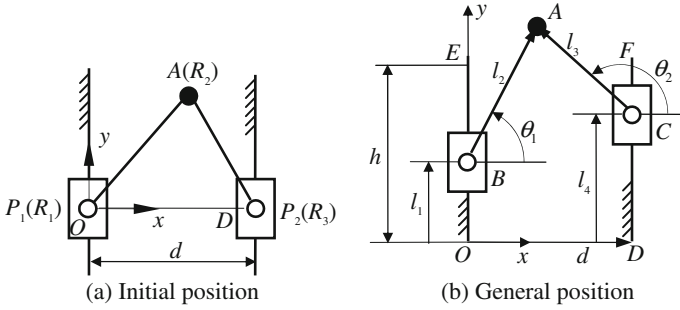


Fig. 1 The initial position and general position of the PRRRP decoupled parallel mechanism

the initial position of the mechanism. The coordinate origin O is located at the center of the revolute pair R_1 . y axis is aligned with the guide of the slider P_1 .

Figure 1b indicates the general position of the PRRRP parallel mechanism. The structure parameters of the mechanism include: the length l_2 of link BA , the length l_3 of link AC , the distance d between the guides of two sliders P_1, P_2 .

The variation ranges of the motion parameters l_1 and l_4 are $l_1 \in [0, h], l_4 \in [0, h]$.

2.2 Decoupled Property of the PRRRP Parallel Mechanism

The link l_2 is the output link. The movement of link l_2 can be regarded as the combination of translation along y axis and rotation around the rotational axis of joint R_1 . P_1 and P_2 are driving sliders, respectively. From the geometry in Fig. 1b, a closed-loop vector equation can be written as follows

$$r_A = \mathbf{l}_1 + \mathbf{l}_2 = d + l_4 + l_3 \tag{1}$$

Expanding Eq. (1), the coordinates of the output point A can be expressed as follows:

$$\begin{cases} x_A = l_2 \cos \theta_1 = d + l_3 \cos \theta_2 \\ y_A = l_1 + l_2 \sin \theta_1 = l_4 + l_3 \sin \theta_2 \end{cases} \tag{2}$$

Eliminating the passive angle θ_2 from Eq. (2), yields

$$\theta_1 = 2 \arctan \left(\frac{B_0 \pm \sqrt{A_0^2 + B_0^2 - C_0^2}}{A_0 + C_0} \right) \tag{3}$$

where,

$$\begin{aligned} A_0 &= dl_2 \\ B_0 &= 2(l_1 - l_4), \\ C_0 &= l_3^2 + d^2 - l_2^2 - (l_1 - l_4)^2 \end{aligned}$$

where, the parameters l_1 and l_4 are displacements of the driving sliders P_1 and P_2 , respectively.

The position and orientation of link l_2 can be expressed as follows

$$\begin{cases} y_B = l_1 \\ \theta_1 = 2 \arctan \left(\frac{B_0 \pm \sqrt{A_0^2 + B_0^2 - C_0}}{A_0 + C_0} \right) \end{cases} \quad (4)$$

Equation (4) indicates that the mechanism is a decoupled parallel mechanism about the position and orientation of link l_2 when the sliders P_1 and P_2 are selected as the two driving links.

3 Reachable Workspace of the PRRRP Parallel Mechanism

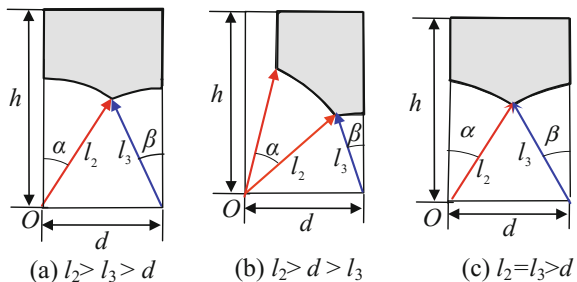
The reachable workspace is defined as a set of the output point A that can reach.

According to the different relationship between the structure parameters l_2 , l_3 and d , there exist two situations of the output workspace of point A .

3.1 Situation 1: l_2 Is the Longest Link

Figure 2 gives atlas when l_2 is the longest link according to geometrical relation of the parameters, as follows.

Fig. 2 The atlas of the reachable workspace when l_2 is the longest link



1. When $l_2 > l_3 > d$, as shown in Fig. 2a, the area S of the reachable workspace of point A can be expressed as follows

$$S = h \times d - \frac{1}{2}l_2^2\alpha - \frac{1}{2}l_3^2\beta - \frac{1}{2}dl_3 \cos \beta \tag{5}$$

In Eq. (5), the following expression holds.

$$\begin{cases} l_2 \sin \alpha + l_3 \sin \beta = d \\ l_2 \cos \alpha = l_3 \cos \beta \end{cases} \tag{6}$$

where, the angles α, β are expressed as radians.

2. When $l_2 > d > l_3$, as shown in Fig. 2b, the area S of the reachable workspace of point A is

$$S = h \times d - \frac{1}{2}l_2^2\alpha - \frac{1}{2}l_3^2\beta - \frac{1}{2}dl_3 \cos \beta - \frac{1}{2}(h + h')(d - l_3) \tag{7}$$

where, $h' = h - l_2 \sin\left(\arccos\frac{d-l_3}{l_2}\right)$, $\left(0 \leq \arccos\frac{d-l_3}{l_2} \leq \frac{\pi}{2}\right)$.

In Eq. (7), the following expression holds.

$$l_2 \sin\left(\arccos\frac{d-l_3}{l_2}\right) + l_3 \sin \beta = d \tag{8}$$

3. When $l_2 = l_3 > d$, as shown in Fig. 2c, the area S of the reachable workspace of point A is

$$S = h \times d - l_2^2\alpha - \frac{1}{2}dl_2 \cos \alpha \tag{9}$$

In Eq. (9), the following expression holds.

$$2l_2 \sin \alpha = d \tag{10}$$

3.2 Situation 2: d Is the Longest Link

Figure 3 gives atlas when d is the longest link according to geometrical relation of the parameters, as follows.

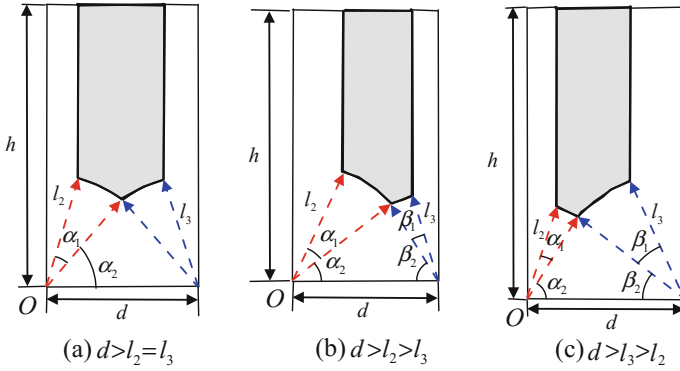


Fig. 3 The atlas of reachable workspace when d is the longest link

1. When $d > l_2 = l_3$, as shown in Fig. 3a, the area S of the reachable workspace of point A is

$$S = h \times d - l_2^2 \alpha_1 - \frac{1}{2} d l_2 \sin \alpha_2 - (h + h_1)(d - l_2) \tag{11}$$

where, $h_1 = h - l_2 \cos\left(\arcsin \frac{d}{l_2} - 1\right)$, $\left(0 \leq \arcsin \frac{d}{l_2} - 1 \leq \frac{\pi}{2}\right)$.

In Eq. (11), the following expression holds.

$$\begin{cases} l_2 \cos \alpha_2 = \frac{1}{2} d \\ l_2 \cos(\alpha_1 + \alpha_2) = d - l_2 \end{cases} \tag{12}$$

2. When $d > l_2 > l_3$, as shown in Fig. 3b, the area of the reachable workspace of point A is

$$\begin{aligned} S = h \times d - \frac{1}{2} l_2^2 \alpha_1 - \frac{1}{2} l_3^2 \beta_1 - \frac{1}{2} l_2 d \sin \alpha_2 \\ - \frac{1}{2} (2h - h_2)(d - l_3) - \frac{1}{2} (2h - h_3)(d - l_2) \end{aligned} \tag{13}$$

where, $h_2 = h - l_2 \cos\left(\arcsin \frac{d-l_3}{l_2}\right)$, $\left(0 \leq \arcsin \frac{d-l_3}{l_2} \leq \frac{\pi}{2}\right)$.

$$h_3 = h - l_3 \cos\left(\arcsin \frac{d-l_2}{l_3}\right), \left(0 \leq \arcsin \frac{d-l_2}{l_3} \leq \frac{\pi}{2}\right).$$

In Eq. (13), the following expression holds.

$$\begin{cases} l_2 \cos \alpha_2 + l_3 \cos \beta_2 = d \\ l_2 \sin \alpha_2 = l_3 \sin \beta_2 \\ l_2 \cos(\alpha_1 + \alpha_2) = d - l_3 \\ l_3 \cos(\beta_1 + \beta_2) = d - l_2 \end{cases} \quad (14)$$

When $d > l_3 > l_2$, as shown in Fig. 3c, the reachable workspace of point A is the same as the model of Fig. 3b.

4 The Oscillating Angle of the Output Link

The oscillating angle of the output link l_2 for the PRRRP decoupled parallel mechanism also has two kinds of situations according to the geometry parameter relations. Figure 4a gives the atlas of the oscillating angle when l_2 is the longest link. Figure 4c shows the d is the longest link.

When l_2 is the longest link, one situation is $l_2 > l_3 > d$, the oscillating angle is

$$\theta = \frac{\pi}{2} - \arccos \frac{d}{l_2} \quad (15)$$

where, $0 \leq \arccos \frac{d}{l_2} \leq \frac{\pi}{2}$.

The other situation is $l_2 > d > l_3$, as shown in Fig. 4b, the oscillating angle is

$$\theta = \frac{\pi}{2} - \arccos \frac{d}{l_2} - \arcsin \frac{d - l_3}{l_2} \quad (16)$$

where, $0 \leq \arccos \frac{d}{l_2} \leq \frac{\pi}{2}$, $0 \leq \arcsin \frac{d - l_3}{l_2} \leq \frac{\pi}{2}$.

When $d > l_2 > l_3$, as shown in Fig. 4c, the oscillating angle is

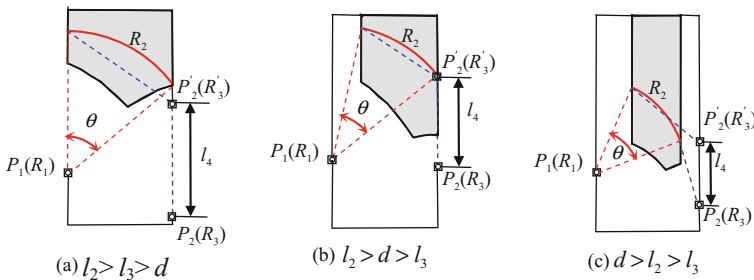


Fig. 4 The atlas of the oscillating angle of the output link

$$\theta = \frac{\pi}{2} - \arccos \frac{l_2 - d}{l_2} - \arcsin \frac{d - l_3}{l_2} \tag{17}$$

where, $0 \leq \arccos \frac{l_2 - d}{l_2} \leq \frac{\pi}{2}$, $0 \leq \arcsin \frac{d - l_3}{l_2} \leq \frac{\pi}{2}$.

The relationship of the oscillating angle of output link with the structure parameters were shown in Figs. 5, 6 and 7.

Figure 5 shows the oscillating angle is larger with the ratio of d and l_2 . The largest angle is 1.5 rad. But the oscillating angle is smaller with the ratio of $d-l_3$ and l_2 . The largest angle is 1 rad.

When, the ratio of d and l_2 with the ratio of $d-l_3$ and l_2 between [0.5–0.6], the oscillating angle is largest which is near by 0.5 rad, as shown in Fig. 6.

In Fig. 7, the structural constraint conditions of each curve are shown in Table 1.

As can be seen from Fig. 7, under the situation of l_2 equal to l_3 , the oscillating angle of the output link is changed faster than the other situations.

Fig. 5 The relationship of the oscillating angle with the ratio d and l_2

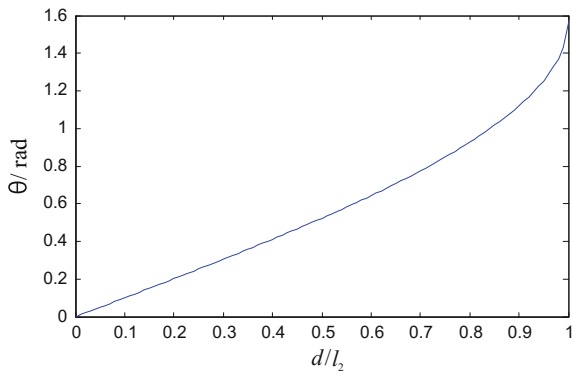


Fig. 6 The relationship of the oscillating angle with relation of the parameters

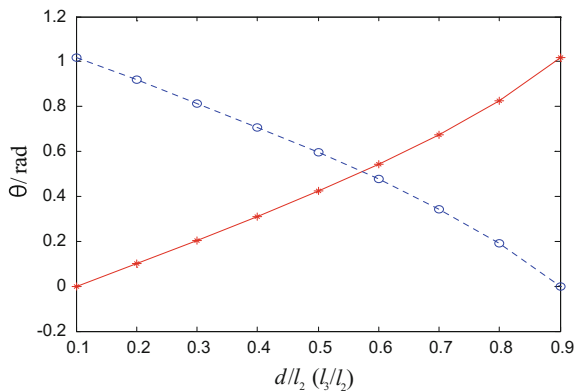


Fig. 7 The relationship of the oscillating angle with relation of the parameters

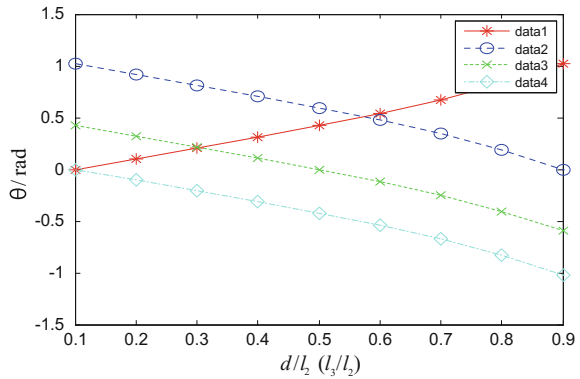


Table 1 The structural constraint conditions

Curve	Data 1	Data 2	Data 3	Data 4
Structural constraint condition	$l_2 = l_3$	$\frac{d-l_2}{l_2} = 0.1$	$\frac{d-l_2}{l_2} = 0.5$	$\frac{d-l_2}{l_2} = 0.8$

5 The PRRRP Decoupled Parallel Mechanism with Controlled Variable Link-Length Structure

5.1 The Structure of the Controlled Variable Link-Length PRRRP Decoupled Parallel Mechanism

The reachable workspace and the oscillating angle of the PRRRP mechanism are related to the structure parameters l_2, l_3 , and d . When $l_2 > l_3 > d$ or $l_3 > l_2 > d$, the reachable workspace is largest. If the length of links l_2 and l_3 are variable, the mechanism can enlarge the reachable workspace of the output point A. The variable link-length structure was shown in Fig. 8a. The assembly model was shown in Fig. 8b.

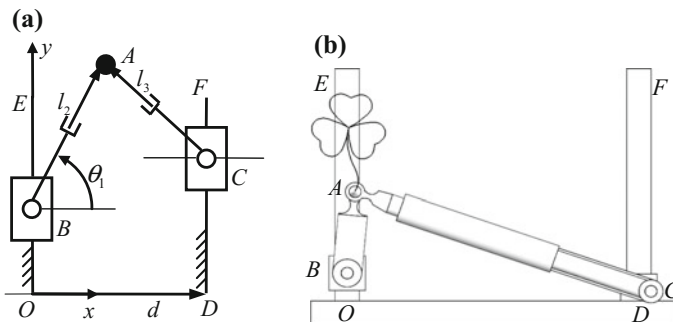


Fig. 8 The variable link-length structure of the PRRRP mechanism

5.2 Application of the Controlled Variable Link-Length PRRRP Mechanism

The controlled variable link-length PRRRP mechanism can be used plane plating and carving. The size can be changed with the parameters l_2 and l_3 .

The flower pattern in Fig. 8b was carved using the variable link-length PRRRP mechanism. The diameter of the flower pattern is 25 mm. The structure parameters of the mechanism were shown in Table 2.

The output parameters of the driving slider P_1 were shown in Figs. 9, 10 and 11. From Fig. 9, the flower pattern is basically symmetrical. The velocity changes with the shape of the flower pattern, the more smooth the more quickly. In the center of the flower pattern, the acceleration reaches the maximum value.

Table 2 The structure parameters of the variable link-length mechanism (mm)

Parameter	d	l_2	l_3	h
Value	120	40	80 ~ 140	80

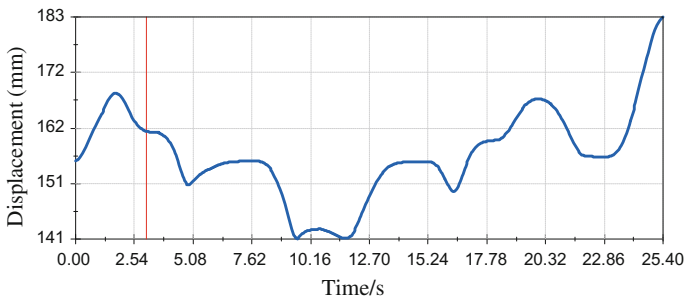


Fig. 9 The displacement variation law of the driving slider P_1

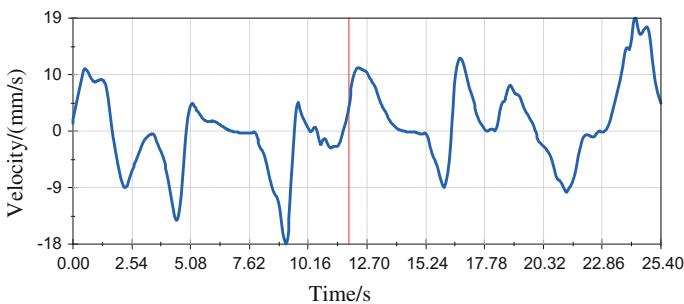


Fig. 10 The velocity variation law of the driving slider P_1

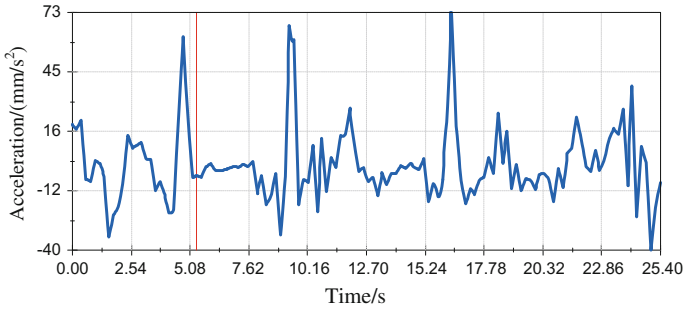


Fig. 11 The acceleration variation law of the driving slider P_1

The output parameters of the driving slider P_2 are shown in Figs. 12, 13 and 14. From Fig. 12, the displacement stroke of the driving slider P_2 is almost 45 mm. The velocity is opposite with that of the driving slider P_1 , the more smooth the more quickly. In the center of the flower pattern, there also exist three extreme points of the acceleration.

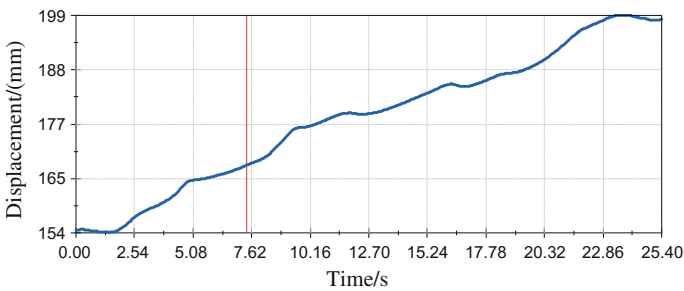


Fig. 12 The displacement variation law of the driving slider P_2

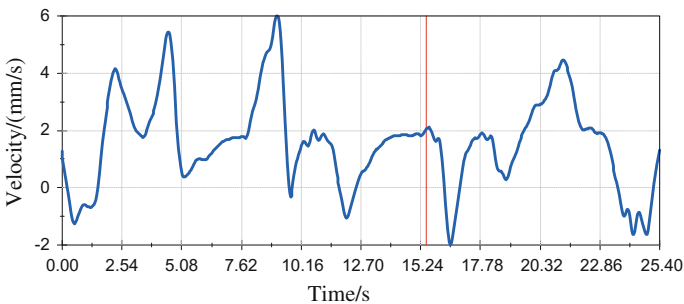


Fig. 13 The velocity variation law of the driving slider P_2

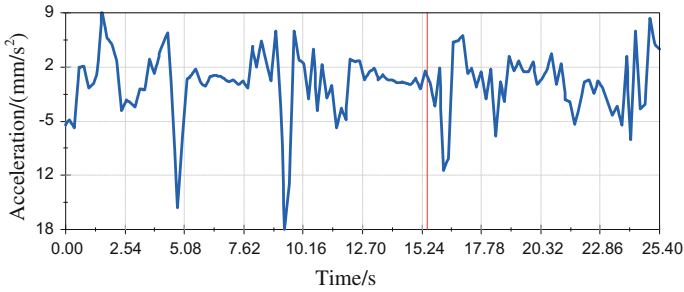


Fig. 14 The acceleration variation law of the driving slider P_2

6 Conclusions

1. The configuration of the PRRRP parallel mechanism is presented. The decoupled properties of the manipulator are analyzed. The workspace is analyzed from closed-form according to the decoupled properties.
2. The reachable workspace and the oscillating angle of the output link are analyzed using closed vector equations based on the atlas which is the relationships of the structure parameters.
3. The charts of the oscillating angle with the structure parameters were given according to the closed-loop vector equations. The charts of Fig. 5 show the oscillating angle is larger with the ratio of d and l_2 . When the ratio d and l_2 with the ratio l_3 and l_2 between [0.5–0.6] the oscillating angle is largest. The oscillating angle changed faster when l_2 equal l_3 .
4. The optimized structure is presented according to the relationship of the parameter. The optimized mechanism can be used as plating and carving machines.
5. The experiment verifies the design method is correct and effective.

Acknowledgments The authors gratefully acknowledge the financial and facility support provided by the National Natural Science Foundation of China (Grant No. 51275486).

References

1. Zeng DX, Hou YL, Lu WJ et al (2010) Comparative analysis of characteristics of the coupled and decoupled parallel mechanisms. *Chin J Mech Eng* 23(4):468–476
2. Li RQ, Dai JS (2012) Workspace atlas and stroke analysis of seven-bar mechanisms with the translation-output. *Mech Mach Theory* 47(1):117–134
3. Gallant A, Boudreau R, Gallant M (2012) Geometric determination of the dexterous workspace of n-RRRR and n-RRPR manipulators. *Mech Mach Theory* 51:159–171

4. Kaloorazi M-HF, Masouleh MT, Stéphane C (2015) Determination of the maximal singularity-free workspace of 3-DOF parallel mechanisms with a constructive geometric approach. *Mech Mach Theory* 84:25–36
5. Wang LW, Du WL, Mu XQ et al (2016) A geometric approach to solving the stable workspace of quadruped bionic robot with hand-foot-integrated function. *Robot CIM-INT Manuf* 37:68–78
6. Tsai KY, Lo IT, Lin PJ (2014) Compatible reachable workspaces of symmetrical Stewart-Gough parallel manipulators. *Mech Mach Theory* 77:111–121
7. Lee TC, Perng MH (2007) Analysis of simplified position and 5-DOF total orientation workspaces of a hexapod mechanism. *Mech Mach Theory* 42:1577–1600
8. Wang ZF, Ji SM, Li YB et al (2010) A unified algorithm to determine the reachable and dexterous workspace of parallel manipulators. *Robot CIM-INT Manuf* 26:454–460
9. Jesús JC-S, José MR-M, Hugo VP-M (2016) An integrated study of the workspace and singularity for a Schönflies parallel manipulator. *J Appl Res Technol* 14(1):9–37
10. Gauthier H, Charpentier I, Renaud P (2016) Higher-order continuation for the determination of robot workspace boundaries. *CR Mec* 344:95–101
11. Zhang C, Zhang LY (2013) Kinematics analysis and workspace investigation of a novel 2-DOF parallel manipulator applied in vehicle driving simulator. *Robot CIM-INT Manuf* 29:113–120

The Workspace Analysis and Simulation of a Novel Dexterous Hand FZU-I

Fanlei Chen, Ligang Yao, Chen Peng, Changsheng Fang and Wenjian Li

Abstract Manipulator is an important bridge to connect robot and environment. However the current manipulators that have been put into productions are accompanied by the poor flexibility, low operating performance, single grasp mode and other defects. In order to solve these problems, improve the flexibility of dexterous hand and lay the foundation for the later control experiment of dexterous hand, this paper will further analyze the working performance of the dexterous hand FZU-I. In this paper, the researches of the dexterous hand FZU-I include: introduce the overall structure, determine the range of motion of each base joint, obtain the workspace of finger-tip by using the forward and inverse kinematics model and MATLAB, analyze and compare the intersection space between thumb base joint under three different configurations and index finger. Through the above researches, it not only verify the feasibility of the forward and inverse kinematics solving model, but also analyzes the working performance of the dexterous hand FZU-I to some extent.

Keywords Dexterous hand · MATLAB · Workspace · Simulation

1 Introduction

With the development of manufacturing technology, Multi-DOF dexterous hand will gradually replace the artificial manufacturing, under the premise of satisfying the basic motion performance of the robot, the robot finger mechanism is the most important executive mechanism of the robot [1].

At present, the main research areas of the robot hand at home and abroad are divided into two types, namely, the full drive dexterous hand and the under-actuated dexterous hand [2]. The full drive dexterous hands started early and had a greater advantage in the humanoid and flexibility, such as Robonaut hand,

F. Chen (✉) · L. Yao · C. Peng · C. Fang · W. Li
School of Mechanical Engineering and Automation, Fuzhou University, Fuzhou, China
e-mail: cff766@163.com

UBV hand, Stanford/JPI hand, DLR II hand, etc [3–6]. However, the disadvantages of this system are: multiple driving elements, higher cost, difficult to achieve miniaturization and lightweight, and much more for scientific experiments rather than the actual use of industry. By comparison, the under-actuated dexterous hand, though starts late, but in recent years it has developed rapidly, such as the four-finger under-actuated dexterous hand designed by Ma et al. [7, 8]. The development prospect of the under-actuated dexterous hand is relatively better for its simple structure, less driving parts, simple control and lower cost, which has become the focus of the practical research.

The analysis of workspace is necessary, it not only provides utility theoretical foundation for overall structure design of dexterous hand and kinematics calculation, but also is easy to set the parameters of control system and to avoid accidents. This paper aims to introduce the structure of dexterous hand FZU-I, analyze the range of motion of base joint and obtain the workspace. Then different intersection spaces are compared through kinematics simulation to choose the most excellent thumb configuration.

2 Dexterous Hand FZU-I

This part proposes a novel dexterous hand called FZU-I to achieve the characteristics of small size, simple transmission setup and compact structure. The FZU-I is designed with compliant transmission mechanism between the middle phalanx and distal phalanx. With the least transmission gear and coupled mechanism who has two joints but its input is given by only one motor, this allocation can enable the hand to be as small as normal Chinese hand, and the control system could be much easier. Its size is as small as 67 mm width and 172 mm length.

The overall structure of the dexterous hand FZU-I is shown in Fig. 1. The dexterous hand FZU-I adopts a built-in motor drive, characterized by high transmission precision, flexible movement and so on. In order to expand the application range of dexterous hand and improve the stability of grasping force, FZU-I configures a total of four mechanical fingers and ten drive motors, the configuration layout is shown in Fig. 1.

The dexterous hand FZU-I's thumb, index finger and middle finger each has three joints with three DOFs, the base joint (MP) with two DOFs. Therefore the near knuckle is driven by two motors installed in the mechanical palm. The middle knuckle has one DOF and one coupling between middle knuckle and far knuckle, the coupling rate of the distal interphalangeal joint (DIP) and the proximal interphalangeal joint (PIP) is 2:1. So the middle knuckle and far knuckle are driven by one motor installed in the near knuckle.

The dexterous hand FZU-I's ring finger has three joints with one DOF, coupling transmission in each joint, only a motor is required to complete the three joint drive. The purpose of the configuration of the ring finger is to match middle finger grasping to enhance grasping strength of the dexterous hand FZU-I, through the

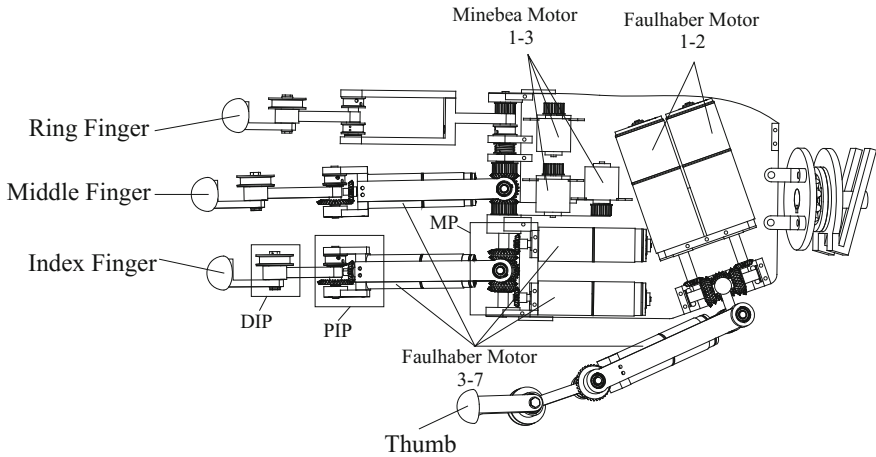


Fig. 1 Overall structure of the dexterous hand

overrunning clutch and flexible transmission mechanism between the middle finger and ring finger.

3 The Constraint Analysis of Workspace

On structure of the dexterous hand FZU-I base joint, there are certain constraints in each joint. In order to set parameters of the control system and avoid the accident, each joint needs to meet certain critical conditions. First, in view of the flexion/extension motion of dexterous hand FZU-I base joint, as shown in Fig. 2. Because the movement of finger is limited by the installation of palm board and back board, the flexion/extension motion of finger must be within a certain range.

According to Fig. 2, the geometric relations can be given as,

$$DE + DC = EC \tag{1}$$

$$DE = AB \cos \alpha \tag{2}$$

$$DC = (AB \sin \theta + AE) \tan \alpha \tag{3}$$

where $AB = 7 \text{ mm}$, $AE = 6 \text{ mm}$, $EC = 7.7 \text{ mm}$.

Simultaneous equations above: $\alpha = 6.27^\circ$.

Because the fingers do not need to bend to the back, combining above calculations, the range of finger's flexion/extension is available: $0^\circ\text{--}96.27^\circ$, for the sake of safety, set $0^\circ\text{--}90^\circ$.

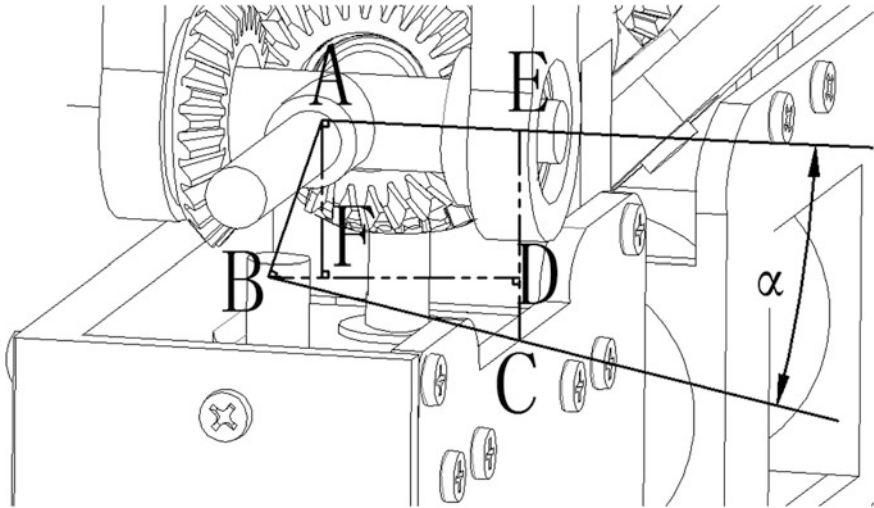


Fig. 2 The limitation of flexion/extension motion of base joint

Second, in view of the adduction/abduction motion of dexterous hand FZU-I base joint, as shown in Fig. 3. Because the movement of finger is limited by the bearing seat, the adduction/abduction motion of finger must be within a certain range.

As shown in Fig. 3, finger at abduction movement process, θ expresses the included angle between the critical position and bearing seat, OO_1 expresses base joint axis.

According to Fig. 3, the geometric relations can be given as,

$$BC + CH = BH \tag{4}$$

$$OH + AO_1 = AB \tag{5}$$

$$BC + CO \cos \theta = BH \tag{6}$$

Fig. 3 The limitation of adduction/abduction motion of base joint

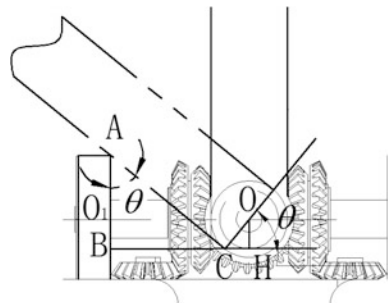


Table 1 The critical scope of motion

Motion	Thumb	Index finger	Middle finger	Ring finger
MP adduction/abduction	-40°-40°	-30°-30°	-10°-10°	0
MP flexion/extension	0-90°	0-90°	0-90°	0-90°
PIP flexion/extension	0-90°	0-90°	0-90°	0-90°
DIP flexion/extension	0-45°	0-45°	0-45°	0-45°

$$CO \sin \theta + AO_1 = BC \cot \theta \tag{7}$$

where $AO_1 = 5\text{mm}$, $CO = 3 \text{ mm}$.

Simultaneous equations above: $\theta = 50.62^\circ$.

In order to guarantee the safety of dexterous hand FZU-I, we should limit the range of thumb’s adduction/abduction motion $[-40^\circ, 40^\circ]$.

For the index finger, because its fingertip space among other fingers and range of adduction/abduction motion are both small, most digital-opposition motions of finger are completed by thumb, we should limit the range of index finger’s adduction/abduction motion $[-30^\circ, 30^\circ]$.

For the middle finger, used to cooperate with index finger when grasping something, thus we should limit the range of middle finger’s adduction/abduction motion $[-10^\circ, 10^\circ]$.

For the ring finger, there is only one degree of freedom and it can’t undertake adduction/abduction motion. It not only simplify the structure and control, but also keep the dexterity of whole dexterous hand and reduce the number of motors the overall weight of dexterous hand.

According to the similar calculation method we can get the critical conditions of scope of motion as shown in Table 1. The inverse kinematics should meet the critical condition.

4 The Simulation of Workspace

4.1 Workspace of Single Finger

Workspace of the dexterous hand is an index for evaluating the flexibility of dexterous hand. The larger the workspace of the dexterous hand is, the greater both the movement range of fingertip and the operational range to object are. And the ability of posture adjustment will be stronger.

According to the dexterous hand forward kinematics equation $g(\theta)$ or T , and considering constraints of base joint for adduction/abduction motion. MATLAB is used to calculate each finger’s movements, the point cloud on base joint coordinate system of fingertips’ workspace are available, as shown in Figs. 4 and 5. “*ab*”

Fig. 4 Index finger

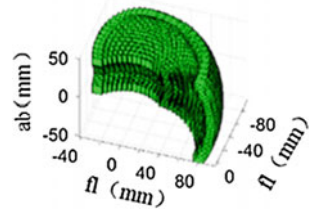
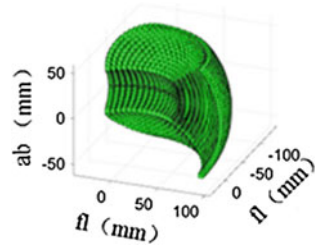


Fig. 5 Thumb



denotes adduction/abduction motion and “*fl*” denotes Flexion/Extension motion. Its shape is similar to the watermelon peel, the same as the results of literature [9].

4.2 Intersection Space

Thumb fingertip’s intersection space is an important indicator to measure the precise grasping performance of the dexterous hand; and the grasping performance is measured in the space position of palm. The single finger coordinates must be mapped to the palm space coordinate system. Through simulation, three kinds of thumb base joint’s workspace in the coordinates system of palm are available, and then obtain the intersection space. As shown in Figs. 6, 7 and 8. Respectively denote the first kind of thumb base joint’s intersection space, and the second one

Fig. 6 First configuration

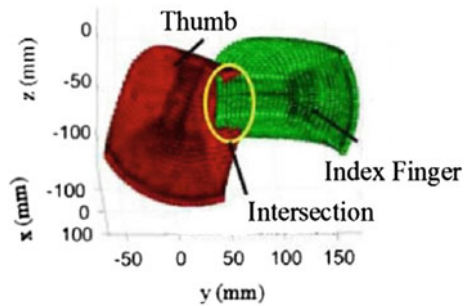


Fig. 7 Second configuration

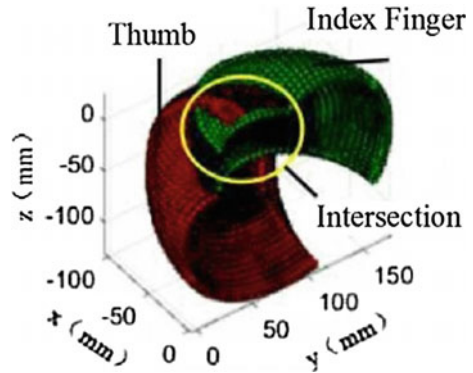
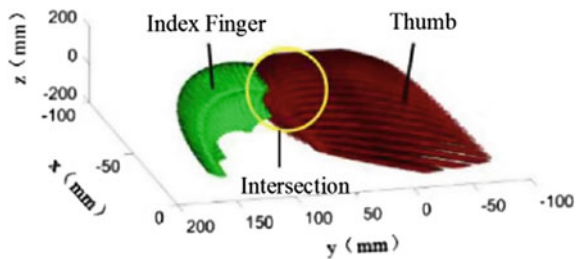


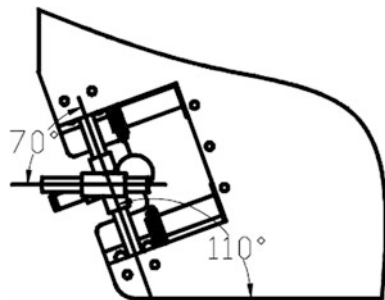
Fig. 8 Third configuration



and the third one. The intersection space between index finger and thumb, which is shown in Fig. 8, is larger.

From the above, the workspace and intersection space of three kinds of thumb configurations are similar. Although it is difficult to solve the inverse kinematics to the third kind of configuration, the digital opposition coefficient between thumb and forefinger is larger and method to solve the inverse kinematics will be easier through MATLAB, so we choose the third configuration mode. As shown in Fig. 9, in third configuration mode, the deviation angle between two axes in thumb base joint is 70° and the vertical distance between two axes is 10 mm, the deviation angle between thumb-pedestal and palm is 110° .

Fig. 9 Third configuration mode



5 Conclusion

The dexterous hand FZU-I is characterized with symmetric structure in basal joint, coupled mechanism between middle and distal phalanx, compliant mechanism among the fingers. The differential structure enables the fingers bearing larger fingertip force and two axes in the base joint cross orthogonally at one point make the FZU-I more dexterous.

This paper briefly introduces the overall structure of dexterous hand FZU-I, and then analyzes the workspace constraints of base joint. After that we proceed to utilize the kinematics model to simulate and obtain the intersection space between thumb and index finger. Finally, this paper optimizes the thumb base joint's structure and chooses the third configuration mode.

Acknowledgment The authors acknowledge the support of the Fujian Provincial Industrial Robot Basic Components Technology Research and Development Center under Grant No. 2014H21010011.

References

1. Wang GJ, Liang XC, Jiang JD (2004) The present development situation and tendency of robot joints. *Mech Transm*, 17–19
2. Luo JL (2008) The integrated design and application research of variable constraints and mechanical adaptive structure. Chongqing University
3. Loucks CS (1987) Modeling and control of the Stanford/JPL hand. In: *Proceedings of the 1987 IEEE international conference on robotics and automation*. Raleigh, NC. 573–578
4. Palli GU, Scarcia C, Melchiorri Vassura G (2012) Development of robotic hands: the UB hand evolution. In: *2012 IEEE/RSJ international conference on intelligent robots and systems*, Portugal, pp 5456–5457
5. Butterfass J, Grebenstein M, Liu H (2001) DLR-Hand II: next generation of a dexterous robot hand. In: *Proceedings of the 2001 IEEE international conference on robotics and automation*, Seoul, Korea, pp 109–114
6. Bridgwater LB, Ihrke CA (2012) The robonant 2 hand-designed to do work with tools. In: *2012 IEEE international conference on robotics and automation*, USA, pp 3425–3430
7. Ma RR, Dollar AM (2014) An underactuated hand for efficient finger-gaiting-based dexterous manipulation. In: *IEEE international conference on robotics and biomimetics*, pp 2214–2219
8. Stuart HS, Wang SQ, Gardineer BA (2014) Compliant under actuated hand with suction flow for underwater mobile manipulation. In: *IEEE international conference on robotics and automation*, pp 6691–6697
9. Liu MJ, Cui JK (2006) The 3-D modeling of fingers' workspace. *J USST (University of Shanghai for Science and Technology)*, 95–98

Real-Time Solutions to the Forward Kinematics of a 2RSS + RRR Parallel Mechanism

Hongdong Zhang, Yuru Zhang and Dangxiao Wang

Abstract In this paper, we propose a new parallel mechanism designed for haptic interface. The haptic device consists of a 2RSS + RRR parallel mechanism with 3 degrees of freedom. In general, the control of haptic devices requires a high servo rate up to 1 kHz which demands a fast and real-time solution to the forward kinematics. Newton–Raphson method is one of the most efficient solutions to achieve real time requirement. However, its efficiency relies deeply on initial value of iterations. We present a methodology to overcome this limitation. We first model the forward kinematics of 2RSS + RRR as an 8th-degree polynomial equation in one unknown. We then propose two methods for determining the initial value to reduce the iterations and computing time. The numerical examples in the paper demonstrate that average time of 0.15 ms (6.7 kHz) for the solutions is achieved with an accuracy of 0.001 mm. The methodology proposed in this paper is general and can be applied to other applications requiring real time solutions to forward kinematics of parallel mechanisms.

Keywords Parallel mechanism · Forward kinematics · Real-time · Newton-Raphson

1 Introduction

Parallel mechanisms have found many applications in different areas, such as aircraft simulation, force-torque sensor, CNC machine, haptic device, etc. It is well known that forward kinematics of parallel mechanisms is, in general, highly nonlinear and difficult to solve in real time. This issue is specifically challenging when a parallel mechanism is used for haptic devices. This is because the control of haptic devices often requires high update rate. In order to provide realistic force feedback, a common practice in the design of haptic devices is to set the update rate of the

H. Zhang · Y. Zhang (✉) · D. Wang
Beihang University, No. 37 Xueyuan Rd., Haidian, Beijing, China
e-mail: yuru@buaa.edu.cn

© Springer Nature Singapore Pte Ltd. 2017
X. Zhang et al. (eds.), *Mechanism and Machine Science*,
Lecture Notes in Electrical Engineering 408,
DOI 10.1007/978-981-10-2875-5_82

995

control loop as 1 kHz [1, 2], which requires that the solution to the forward kinematics of a parallel mechanism must be found within less than 1 ms.

Various numerical methods have been applied to solve forward kinematics of parallel mechanisms [3–5]. A fast, robust and practical algorithm was presented specially to solve the forward kinematics of Stewart Platform [3]. The Newton-Raphson method was modified to overcome the tendency to fail when the constraint equations become poorly conditioned. Based on the simultaneous solution of three constraint equations, 0.2 ms were taken at regular configurations and 0.22 ms when the platform was near to a singularity. Another modified Newton-Raphson method [4] based on Taylor's series was proposed and the solutions could be obtained requiring just a few iteration steps. However, calculation time was not mentioned in the paper.

Many efforts have been made to convert the nonlinear equations of forward kinematics to high degree polynomial with one unknown so that forward kinematics solutions could be obtained more quickly [6–9]. A mono-dimensional-search algorithm was reported to the forward kinematics solution of the general 6-6 fully parallel mechanism in [6]. All the real solutions, free from extraneous, of the forward kinematics could be found out through this method relied on a high degree polynomial in one unknown. A kinematic mapping, i.e., to map three-dimensional motions into a seven-dimensional quasi-elliptic space, was introduced in [7] and finally a univariate 40th-degree polynomial was obtained. A quaternion to represent the transformation matrix was introduced in [8]. A concise closed-form solution to the forward kinematics of the Stewart platform was obtained and as a result, only univariate quadratic equations were required to solve. Gröbner bases were used by Gan [9] to analyze the forward kinematics of the general 6-6 Stewart mechanism, which was reduced to a 40th-degree polynomial equation in one unknown. However, calculation time was not mentioned in these papers.

Other techniques to find forward kinematics solutions include neural networks, genetic algorithm and hybrid strategy. Yee [10] used a BP network to recognize the relationship between input values and output of the forward kinematics problem. It took about 1 ms to find the forward kinematics solution with an average accuracy of 0.009 units by performing several iterations. However, long hours were required for training before implementation. A genetic algorithm was presented in [11]. Although, this method converged to a solution within a broader search domain compared to the Newton-Raphson scheme, it took about 12–15 times longer, average 10 ms, than Newton-Raphson method to find the forward kinematics solution. Kang [12] employed the RBF neural network, which has a universal approximation capability, to model the forward kinematics of a hybrid structure robot. Although this method avoids the geometric parameters measurement in the real robot, a relative long time (6.84 ms) was spent on obtaining solutions to the forward kinematics with an average position error of 0.0986 mm. A hybrid strategy to solve forward kinematics in parallel manipulators was reported in [13]. A modified form of multilayered perceptron with back propagation learning was used to predict the initial position of the forward kinematic for the standard Newton-Raphson numerical technique. The hybrid strategy could achieve an

accuracy of about 0.01 mm and 0.01° in the position and orientation parameters in less than two iterations and 20 ms of execution time.

In this paper, we propose a new 3-DoF parallel mechanism for a haptic device, which has two RSS chains and one RRR chain. To achieve the frequency of control loop higher than 1 kHz, we model the forward kinematics of the parallel mechanism as an 8th-degree polynomial equation in one unknown. Newton–Raphson method is applied and the initial value of iterations is carefully studied to obtain highly efficient and accurate solution of the forward kinematics.

2 Description for the 2RSS + RRR Parallel Mechanism

The schematic representation of the 2RSS + RRR parallel mechanism is illustrated in Fig. 1. This mechanism includes two RSS limbs (R: revolute joint; S: spherical joint) with an actuator at the first revolute joint for each limb and one RRR limb with an actuator at the first revolute joint. The geometric characteristics associated with the components of all limbs are as follows (the nomenclature is showed in Table 1): A plane p can be determined by C, O_0C, O_1O_2 and the axes of the joints R_1 and R_2 , in which the line $(O_1O_2) \perp (O_0C)$ and the axes of R_1 and R_2 are parallel to O_0C . The axis of R_3 is parallel to O_1O_2 and has a distance of c from O_3 to the plane p . The points of O_1, O_2, M_1 and M_2 are in the same plane. The axis of R_4 is parallel to R_3 and simultaneously perpendicularly intersects the axis of R_5 . It should be noted that a U (Universal) joint is assimilated by R_4 and R_5 . Besides, the line $(P_1P_2) \perp (QM_3)$.

Fig. 1 The 2RSS + RRR parallel mechanism

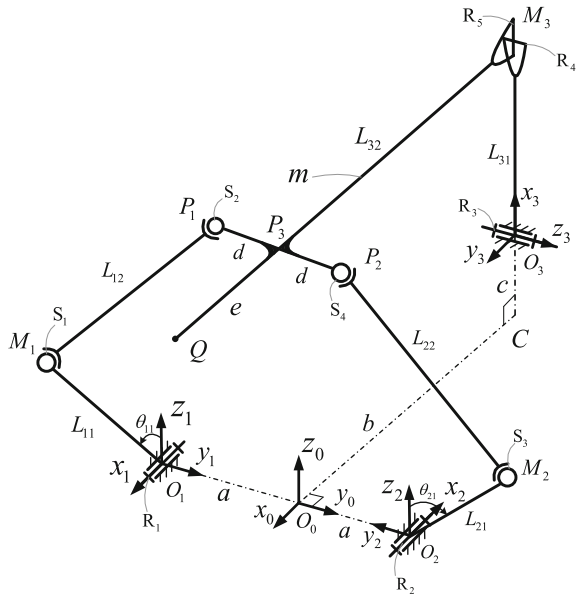


Table 1 Nomenclature

Letters	Definitions
m	The moving platform
Q	The reference point fixed on the moving platform
$R_i, i = 1, 2, 3, 4$	The revolute joints
$S_i, i = 1, 2, 3$	The spherical joints
$P_i, M_i, i = 1, 2$	The center point of the joints S_i
M_3	The intersection of axes of R_4 and R_5
P_3	The intersection of P_1P_2 and MQ
a	The length of O_0O_1 and O_0O_2
b	The length of O_0C
c	The length of CO_3
d	The length of P_1P_3 and P_2P_3
e	The length of P_3Q
$L_{i1}, i = 1, 2, 3$	The length of O_iM_i
$L_{i2}, i = 1, 2, 3$	The length of M_iP_i
L_{33}	The length of M_3Q
$O_0-x_0y_0z_0$	The coordinate system fixed on the ground
$O_i-x_iy_iz_i, i = 1, 2, 3$	The coordinate systems fixed on the joints $R_i (i = 1, 2, 3)$
$O_{3i}-x_{3i}y_{3i}z_{3i}, i = 1, 2, 3$	The D-H coordinate systems of the RRR limb
$O_Q-x_Qy_Qz_Q$	The coordinate system of Q fixed on m
q_pT	The homogeneous coordinate transformation from p to q
$\theta_{i1}, i = 1, 2, 3$	The rotational angles of R_1, R_2 and R_3
θ_{32}, θ_{33}	The rotational angles of R_4 and R_5
$s\theta, c\theta$	$\sin\theta, \cos\theta$
$//, \perp$	Parallel constraint and perpendicular constraint

To determine mathematically the relative positions of all limbs, three coordinate systems $O_i-x_iy_iz_i (i = 1, 2, 3)$ of the limbs and a coordinate system $O_0-x_0y_0z_0$ fixed on the ground are established, as Fig. 1 shows. The homogeneous coordinate transformation matrices from $O_0-x_0y_0z_0$ to $O_i-x_iy_iz_i$ are

$${}_{O_0}T_1 = \begin{bmatrix} 1 & 0 & 0 & 0 \\ 0 & 1 & 0 & -a \\ 0 & 0 & 1 & 0 \\ 0 & 0 & 0 & 1 \end{bmatrix}, {}_{O_0}T_2 = \begin{bmatrix} -1 & 0 & 0 & 0 \\ 0 & -1 & 0 & a \\ 0 & 0 & 1 & 0 \\ 0 & 0 & 0 & 1 \end{bmatrix}, {}_{O_0}T_3 = \begin{bmatrix} 0 & 1 & 0 & -b \\ 0 & 0 & 1 & 0 \\ 1 & 0 & 0 & c \\ 0 & 0 & 0 & 1 \end{bmatrix} \tag{1}$$

Consisting of a revolute joint and two spatial joints, the first and second limbs, which have more than six degrees of freedom, apply no constraint to the moving platform m . However, the third limb, which has three revolute joints and three

degrees of freedom, applies three independent constraints to m . Consequently, through the graphical approach [14], we can conclude that the moving platform m has three degrees of freedom.

3 Forward Kinematics

In this section, we modeled the forward kinematics of the 2RSS + RRR parallel mechanism. Specially, for the haptic device, we only need to obtain the coordinate of Q when given the angles of active joints. To achieving this goal, we firstly led the first constraint equation by modeling the kinematics of the RRR limb on D-H method. Then, another two constraint equations were led based on the kinematics of the two RSS limbs. An 8th-degree polynomial equation in one unknown for the forward kinematics of the 2RSS + RRR parallel mechanism was finally obtained. Upon solving the one unknown of the high-order polynomial equation, the coordinate of Q will be easily calculated.

Firstly, we focus our attention to the kinematics model of the RRR limb. Referring to Fig. 2, the D-H parameters of the third limb, which are given in Table 2, can be obtained. Applying the D-H convention, the four transformation matrices are led as follows:

Fig. 2 D-H coordinate systems of the RRR limb

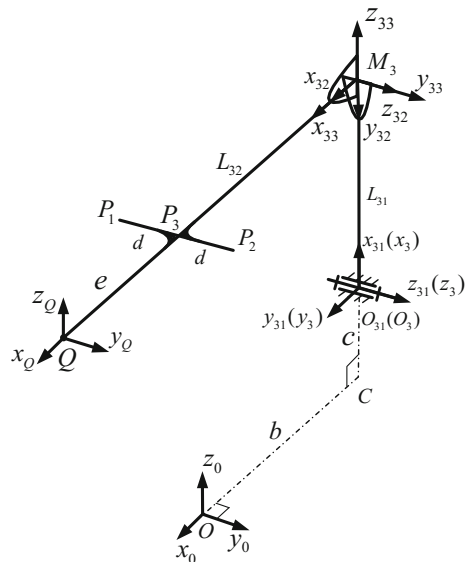


Table 2 D-H parameters of the RRR limb

i	a_{i-1}	α_{i-1}	d_i	θ_i
1	0	0	0	θ_{31}
2	L_{31}	0	0	θ_{32}
3	0	90°	0	θ_{33}
4 (Q)	L_{32}	0	0	0

$$\begin{aligned}
 {}_{O_3}^{O_{31}}T &= \begin{bmatrix} c\theta_{31} & -s\theta_{31} & 0 & 0 \\ s\theta_{31} & c\theta_{31} & 0 & 0 \\ 0 & 0 & 1 & 0 \\ 0 & 0 & 0 & 1 \end{bmatrix} & {}_{O_{32}}^{O_{33}}T &= \begin{bmatrix} c\theta_{33} & -s\theta_{33} & 0 & 0 \\ 0 & 0 & -1 & 0 \\ s\theta_{33} & c\theta_{33} & 0 & 0 \\ 0 & 0 & 0 & 1 \end{bmatrix} \\
 {}_{O_{32}}^{O_{33}}T &= \begin{bmatrix} c\theta_{33} & -s\theta_{33} & 0 & 0 \\ 0 & 0 & -1 & 0 \\ s\theta_{33} & c\theta_{33} & 0 & 0 \\ 0 & 0 & 0 & 1 \end{bmatrix} & {}_{O_{33}}^{O_{34}}T &= \begin{bmatrix} 1 & 0 & 0 & L_{32} \\ 0 & 1 & 0 & 0 \\ 0 & 0 & 1 & 0 \\ 0 & 0 & 0 & 1 \end{bmatrix}
 \end{aligned} \tag{2}$$

Thus, the forward kinematics equations for the third limb, which are with respect to the joints variables and the design variables, can be obtained:

$${}_0^Q T = {}_{O_0}^{O_3} T {}_{O_3}^{O_{31}} T {}_{O_{31}}^{O_{32}} T {}_{O_{32}}^{O_{33}} T {}_{O_{33}}^Q T \tag{3}$$

where ${}_0^Q T$ is the homogeneous coordinate transformation matrix from the coordinate system of $O_0-x_0y_0z_0$ to $O_Q-x_Qy_Qz_Q$, from which we can obtain the first constraint equation of the forward kinematics:

$$\begin{cases} x = L_{31}s\theta_{31} + L_{33}s(\theta_{31} + \theta_{32})s\theta_{33} - b \\ y = L_{33}s\theta_{33} \\ z = L_{31}c\theta_{31} + L_{33}c(\theta_{31} + \theta_{32})c\theta_{33} + c \end{cases} \tag{4}$$

where (x, y, z) is the coordinate of Q in $O_0-x_0y_0z_0$.

To calculate x, y and z from (4), the values of θ_{32} and θ_{33} need to be calculated first. Thus, the other two following constraint equations are led:

$$\begin{cases} L_{12}^2 = |P_1M_1|^2 \\ L_{22}^2 = |P_2M_2|^2 \end{cases} \tag{5}$$

where $|P_iM_i|$ ($i = 1, 2$) are the distances between P_i and M_i .

Referring to Fig. 1, the coordinates of M_i (x_{Mi}, y_{Mi}, z_{Mi}) ($i = 1, 2$) can be expressed as follows:

$$\begin{bmatrix} x_{M1} \\ y_{M1} \\ z_{M1} \end{bmatrix} = \begin{bmatrix} 0 \\ -a - L_{11}s\theta_{11} \\ L_{11}c\theta_{11} \end{bmatrix}, \quad \begin{bmatrix} x_{M2} \\ y_{M2} \\ z_{M2} \end{bmatrix} = \begin{bmatrix} 0 \\ a + L_{21}s\theta_{21} \\ L_{21}c\theta_{21} \end{bmatrix} \tag{6}$$

According to the D-H parameters of the RRR limb shown in Table 1, the coordinates of $P_i (x_{P_i}, y_{P_i}, z_{P_i}) (i = 1, 2)$ in $O_0-x_0y_0z_0$ can be obtained:

$$\begin{bmatrix} x_{P1} \\ y_{P1} \\ z_{P1} \end{bmatrix} = \begin{bmatrix} L_{31}s\theta_{31} - b + ds\theta_{33}s(\theta_{31} + \theta_{32}) + L_{32}c\theta_{33}s(\theta_{31} + \theta_{32}) \\ L_{32}s\theta_{33} - dc\theta_{33} \\ c + L_{31}c\theta_{31} + ds\theta_{33}c(\theta_{31} + \theta_{32}) + L_{32}c\theta_{33}c(\theta_{31} + \theta_{32}) \end{bmatrix} \quad (7)$$

$$\begin{bmatrix} x_{P2} \\ y_{P2} \\ z_{P2} \end{bmatrix} = \begin{bmatrix} L_{31}s\theta_{31} - b - ds\theta_{33}s(\theta_{31} + \theta_{32}) + L_{32}c\theta_{33}s(\theta_{31} + \theta_{32}) \\ L_{32}s\theta_{33} + dc\theta_{33} \\ c + L_{31}c\theta_{31} - ds\theta_{33}c(\theta_{31} + \theta_{32}) + L_{32}c\theta_{33}c(\theta_{31} + \theta_{32}) \end{bmatrix} \quad (8)$$

Substituting all the coordinates (6), (7) and (9) into Eq. (5), we can get

$$\begin{cases} k_1 + k_2s\theta_{33} + k_3c\theta_{33} + c\theta_{32}(k_4c\theta_{33} + k_5s\theta_{33}) + s\theta_{32}(k_6c\theta_{33} + k_7s\theta_{33}) = 0 \\ r_1 + r_2s\theta_{33} + r_3c\theta_{33} + c\theta_{32}(r_4c\theta_{33} + r_5s\theta_{33}) + s\theta_{32}(r_6c\theta_{33} + r_7s\theta_{33}) = 0 \end{cases} \quad (9)$$

where k_i and $r_i (i = 0-7)$ are with respect to $\theta_{11}, \theta_{21}, \theta_{31}$ and other design variables.

Equation (10) can be derived from (9) as follows:

$$\begin{cases} w_1 + w_2c\theta_{32} + w_3s\theta_{32} = 0 \\ v_1 + v_2c\theta_{32} + v_3s\theta_{32} = 0 \end{cases} \quad (10)$$

where all of w_i and v_i share a common factor of θ_{33} .

If $\theta_{11} = \theta_{21}$, we can know $\theta_{31} = 0$ by symmetry of the parallel mechanism. If $\theta_{11} \neq \theta_{21}$, we can lead the 8th-degree polynomial equation of the forward kinematics from Eq. (10) by applying the tangent half-angle substitution, $t = \tan(\theta_{33}/2)$, as follows:

$$\sum_{i=0}^8 q_i t^i = 0 \quad (11)$$

where $q_i (i = 0-8)$ are in terms of $\theta_{11}, \theta_{21}, \theta_{31}$ and other design variables.

The variable of t in Eq. (11) can be calculated through the Newton-Raphson approach which is discussed in Sect. 4. Upon obtaining t , it turns out that θ_{33}, θ_{32} can be obtained:

$$\begin{aligned} \theta_{33} &= 2 \arctan(t) \\ \theta_{32} &= \begin{cases} \cos^{-1}\left(\frac{w_3v_1 - w_1v_3}{w_2v_3 - w_3v_2}\right), & \text{when } \theta_{11} \neq \theta_{21} \\ \arccos\left(\frac{-2\alpha\beta + \sqrt{(2\alpha\beta)^2 - 4(\alpha^2 + 1)(\beta^2 - 1)}}{2(\alpha^2 + 1)}\right), & \text{when } \theta_{11} = \theta_{21} \end{cases} \end{aligned} \quad (12)$$

where $\alpha = -w_2/w_3, \beta = -w_1/w_3$.

In (12), the extraneous root of θ_{32} is avoided. Consequently, substituting θ_{11} , θ_{21} , θ_{31} , θ_{32} , θ_{33} and other design variables into Eqs. (3) and (4), we can obtain the coordinate of the reference point Q .

Concerns should be raised here that an important but also difficult problem is how to solve Eq. (11) rapidly and accurately. Although the Newton-Raphson method, one of the most efficient solutions, can be used, its efficiency relies deeply on initial value of iterations. To overcome this limitation, we proposed two methods of determining the initial value of iterations, which are described in the next section.

4 Analysis of Real-Time Forward Kinematics

Aiming to reduce the iterations and computing time, we describe two methods for determining the initial value of iterations in the Newton-Raphson method. The first method uses the solution of the previous step as the initial value to calculate t ($t = \tan(\theta_{33}/2)$). The second method determines the initial value of iterations according to the symmetry of this parallel mechanism. In the light of simulation results, the pros and cons of the two methods are discussed in the following sections. The values of all parameters for simulations are as follows: maximum velocity of Q $v_Q = 2$ m/s, servo rate $f = 1$ kHz, $a = 50$ mm, $b = 135.5$ mm, $c = 45$ mm, $d = 15$ mm, $e = 50$ mm, $L_{11} = L_{21} = 70$ mm, $L_{12} = L_{22} = 164$ mm, $L_{31} = 100$ mm, $L_{32} = 135.5$ mm, $L_{33} = 185.5$ mm, $0^\circ \leq \theta_{11} \leq 103^\circ$, $0^\circ \leq \theta_{21} \leq 103^\circ$, $-20^\circ \leq \theta_{31} \leq 20^\circ$, $0^\circ < \theta_{32} < 180^\circ$, $-90^\circ < \theta_{33} < 90^\circ$, $-1 < t < 1$.

4.1 First Method

To test the validity of the first method, simulations whose results are partly shown in Fig. 3 are conducted with Matlab. We firstly use the coordinates of points on designed trajectories to calculate angles of actuators based on the inverse kinematics. Considering the maximum velocity of $v_Q = 2$ m/s and the servo rate $f = 1$ kHz, the distance between adjacent two points on the designed trajectories should be 2 mm. We then use the calculated angles of actuators to obtain solutions to the forward kinematics by the first method. The efficiency of the first method can be validated by comparing coordinates of designed trajectories with coordinates of calculated points. Most of the simulated trajectories can be tracked correctly by the first method, except the two kinds of trajectories shown in Fig. 3.

The trajectory in Fig. 3a is a line which can be described as: the y coordinate varies from -30 to 30 with an interval of 2 . The x is 50 and z 145 . The coordinate of starting point is $(50, -30, 145)$. As Fig. 3a illustrates, the trajectory fails to be tracked upon passing through the plane of YOZ . The wrong solutions are far away from the trajectory. In fact, we found that all of simulated trajectories which go

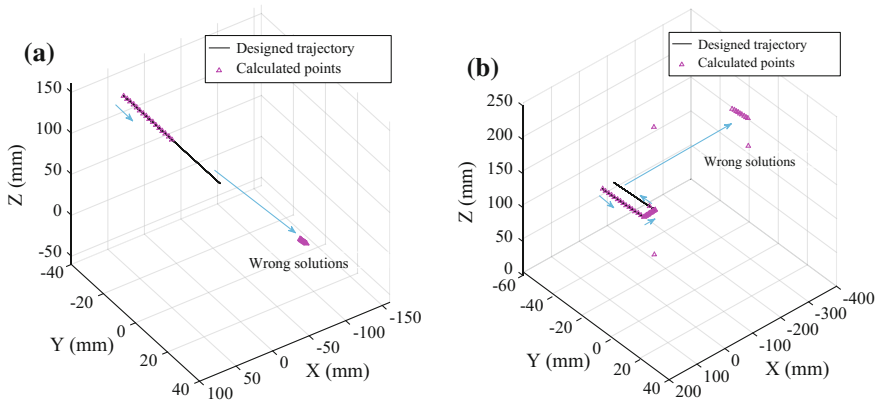


Fig. 3 Simulations of two trajectories which have wrong solutions by the first method: **a** miscalculated when going through the plane of *YOZ*; **b** wrong solutions exist when moving away from where it is close to the plane of *YOZ*

through the plane of *YOZ* are miscalculated. Once one solution is wrong, all of the following points will fail to be tracked.

Wrong solutions also occur in the second kind of trajectories which are like “U” as Fig. 3b shows. The designed trajectory, which is very close to but not through the plane at the bottom of “U”, is tracked successfully when moving to the plane of *YOZ*. However, miscalculations exist when moving along the negative *Y* axis away from where the trajectory is very close to the plane of *YOZ*.

Based on the simulation results above, we can conclude that the first method works at most of points but fails in some cases, e.g. when the trajectories pass through or move away from the plane of *YOZ*. This result is related to the symmetry of the parallel mechanism and the characters of Eq. (11). The reasons are discussed in the next section.

4.2 Second Method

The second method determines the initial value by the value of $|\theta_{11} - \theta_{21}|$, which is based on the characters of Eq. (11) partly shown in Fig. 4. Equation (11) is an equation of t , θ_{11} , θ_{21} , θ_{31} and other designed variables, in which t ($t = \tan(\theta_{33}/2)$) is the one unknown and the coefficients of the equation are determined by other variables. There are three characters of $f(t)$ making the second method work. As one example of the first character shown in Fig. 4a, we found that when given the value $|\theta_{11} - \theta_{21}|$ and θ_{31} , the desired roots of all curves are very close to each other even though θ_{21} varies from 10° to 50° (correspondingly θ_{11} varies from 60° to 100°). This character is not limited just to the values of $|\theta_{11} - \theta_{21}|$ and θ_{31} . Figure 4b shows one case of the second character that the desired root is slightly affected

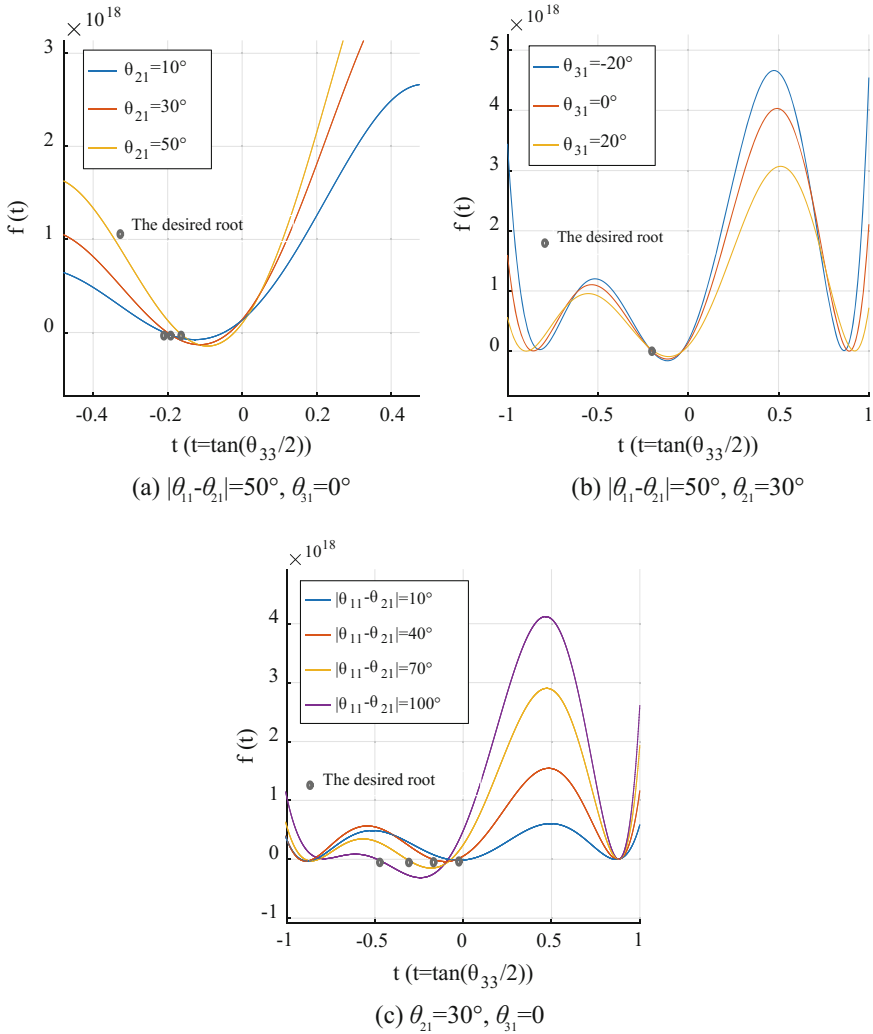


Fig. 4 Distribution of solutions of Eq. (11): **a, b** solutions depend slightly on θ_{21} and θ_{31} ; **c** solutions depend largely on $|\theta_{11} - \theta_{21}|$. The smaller $|\theta_{11} - \theta_{21}|$ is, the nearer to zero the solution gets

when the values of $|\theta_{11} - \theta_{21}|$ and θ_{21} are given although θ_{31} varies over a wide range from -20° to 20° .

The third character should also be noted that there is always another undesired root close to the desired root which is generally approximate to zero, as Fig. 4c illustrates. Furthermore, the smaller the value of $|\theta_{11} - \theta_{21}|$ is, the more close to each other the two roots are. As a result, both of the roots are more approximate to zero. That is why wrong solutions often exist by the first method when the

Table 3 Initial value of t ($t = \tan(\theta_{33}/2)$)

$ \theta_{11} - \theta_{21} $ ($^\circ$)	t_0 ($\theta_{11} < \theta_{21}$)	t_0 ($\theta_{11} > \theta_{21}$)
(0, 1]	0.00873	-0.00873
(1, 2]	0.01746	-0.01746
(2, 5]	0.04366	-0.04366
(5, 10]	0.08748	-0.08748
(10, 20]	0.13165	-0.13165
(20, 30]	0.17633	-0.17633
(30, 40]	0.22169	-0.22169
(40, 60]	0.26795	-0.26795
(60, 90]	0.31530	-0.31530
(90, 100]	0.36397	-0.36397

trajectories are close to or go through the plane of YOZ . When the value of $|\theta_{11} - \theta_{21}|$ is very small, Q is close to the plane of YOZ and the two roots are approximate. If the variation of θ_{33} (correspondingly means t) is large during a servo cycle, wrong solutions are usually obtained because the initial value (the solution of the previous step) is more close to the undesired root.

Based on the three characters above, the initial values of t_0 for Newton-Raphson method according to the value of $|\theta_{11} - \theta_{21}|$ are listed as shown in Table 3. To validate the second method, we choose the ones which have wrong solutions (in Fig. 3) as the testing trajectories using the initial values in Table 3. As shown in Fig. 4a, both of trajectories are tracked successfully. Besides, we randomly select eighty points in the workspace of the parallel mechanism to test the second method. All of the points can be calculated correctly as Fig. 5b illustrates. It demonstrates that the second method can not only calculate continuous trajectories but also discrete points in the workspace.

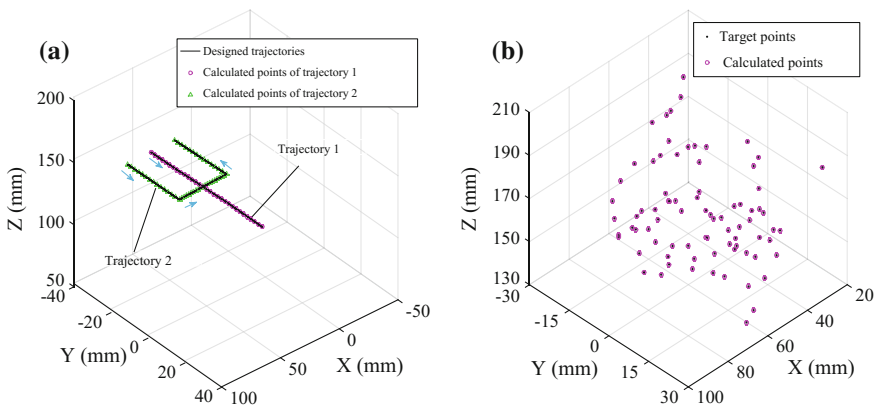


Fig. 5 Simulations of the second method: **a** two kinds of continuous trajectories both can be tracked successfully; **b** no wrong solution exists for random discrete points in the workspace

4.3 Results, Comparison and Discussion

In Sects. 4.1 and 4.2, we talked about the validity of the proposed methods of determining the initial values. In addition to this, we paid more attention to the computing time of the two methods. As known, computing time is related to configuration of CPU, initial value and tolerance of the unknown variables, etc. The simulations in this paper were all conducted on a 3-GHz computer with the Intel Core 2 Duo CPU and 4G RAM.

Considering smaller tolerance of t ($t = \tan(\theta_{33}/2)$) will cost more computing time, we conducted a simulation using the data in Fig. 5b based on the second method to find the relationship between the tolerance of t and the error of solutions. Referring to the simulation result shown in Fig. 6, we finally select 10^{-8} as the tolerance of t , which can obtain an average accuracy of 0.00099 mm and a maximum error of 0.03 mm at the these points.

Using the tolerance of 10^{-8} , we simulated the average computing time of three continuous trajectories based the two proposed methods. Comparing the results shown in Table 4, we can conclude that generally less computing time costs by the first method than the second method, especially in case that the variation of t is very

Fig. 6 Simulation of the maximum and average errors of solution with the tolerance of t : the smaller the tolerance of t is, the smaller the error of solution gets

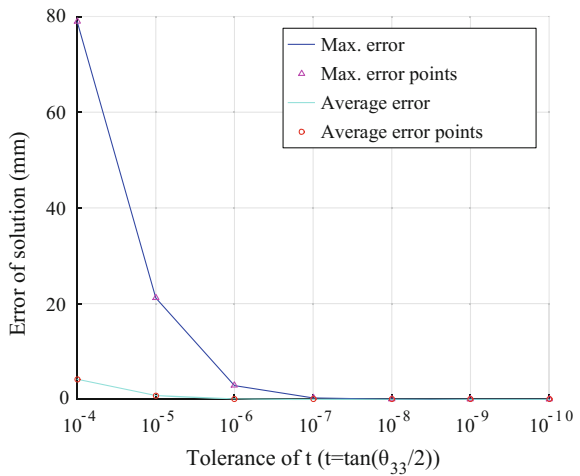


Table 4 Comparison between the two methods

Trajectory	Method	Average time (ms)	Average iteration	Average error (mm)	Maximum error (mm)	Wrong solution
1	1st	0.12	6	1×10^{-13}	5×10^{-13}	No
	2nd	0.15	7	1×10^{-4}	2×10^{-4}	No
2	1st	0.15	7	3×10^{-5}	4×10^{-4}	Yes
	2nd	0.15	7	2×10^{-4}	1×10^{-3}	No
3	1st	0.025	2	9×10^{-14}	2×10^{-13}	No
	2nd	0.12	6	9×10^{-14}	2×10^{-13}	No

small in a servo cycle as the trajectory 3 does. With the same tolerance of t , a higher accuracy of solutions can usually be obtained by the first method with the highest accuracy of up to 0.0002 mm.

However, as mentioned above, wrong solutions often exist by the first method in some cases which must be avoided in practical occasions. As the trajectories have to be continuous, if one solution is wrong, all of the following points will fail to be calculated correctly. Although more computing time and iterations cost, the second method are robust because right positions can be calculated without the influence of the solution of the previous step, which is quite different from the first method. Besides, even though with a lower accuracy, the second method can also work in many practical cases whose demands are not high.

It is worth considering to calculate solutions to the forward kinematics using both of the methods. For example, in the case that trajectories are far from the plane of YOZ , we can use the first method and in other cases, the second method can be used. As a result, both of a high accuracy and less computing time can be obtained in the workspace of the parallel mechanism.

5 Conclusions

We proposed a new parallel mechanism for the design of haptic devices. The forward kinematics of the parallel mechanism can be modeled as an 8th-degree polynomial equation in one unknown. To meet the control requirement of 1 kHz update rate, we proposed two methods to determine the initial value in the Newton-Raphson scheme for the forward kinematics. The first method uses the solution of the previous step as the initial value for iterations. An accuracy of about 0.0004 mm was obtained with the computing time of 0.15 ms. However, wrong solutions existed in some occasions. The second method determines the initial value according to the value of $|\theta_{11} - \theta_{21}|$. This method is robust comparing to the first method. The computing time same with the first method was obtained but with a lower accuracy of 0.001 mm. Higher computing efficiency and accuracy may be obtained by combining both of the two methods.

References

1. Mohand-Ousaid A, Millet G, Regnier S, Haliyo S, Hayward V (2012) Haptic interface transparency achieved through viscous coupling. *Int J Robot Res* 31(3):319–329
2. Zhang YR, Li CB, Wang DX et al (2015) Task oriented method for designing haptic devices. *J. Mech Eng* 51(13):212–217
3. McAree PR, Daniel RW (1996) A fast, robust solution to the stewart platform forward kinematics. *J Rob Syst* 13(7):407–427
4. Ku DM (1999) Direct displacement analysis of a Stewart platform. *Mech Mach Theory* 34:453–465

5. Akcali ID, Mutlu H (2006) A novel approach in the direct kinematics of Stewart platform mechanisms with planar platforms. *ASME J Mech Des* 128:252–263
6. Innocenti C, Parenti-Castelli V (1993) Forward kinematics of the general 6-6 fully parallel mechanism: an exhaustive numerical approach via a mono-dimensional-search algorithm. *ASME J Mech Des* 115:932–937
7. Husty ML (1996) An algorithm for solving the direct kinematics of general Stewart-Gough platforms. *Mech Mach Theory* 31(4):365–380
8. Ji P, Wu HT (2001) A closed-form forward kinematics solution for the 6–6 Stewart platform. *IEEE Trans Robot Automat* 17(4):522–526
9. Gan DM, Liao QZ, Dai JS et al (2009) Forward displacement analysis of the general 6-6 Stewart mechanism using Gröbner bases. *Mech Mach Theory* 44:1640–1647
10. Yee CS, Lim KB (1997) Forward kinematics solution of Stewart platform using neural networks. *Neurocomputing* 16:333–349
11. Boudreau R, Turkkkan N (1996) Solving the forward kinematics of parallel manipulators with a genetic algorithm. *J Rob Syst* 13(2):111–125
12. Kang RJ, Chanal H, Dai JS, Ray P (2015) Comparison of numerical and neural network methods for the kinematic modeling of a parallel-serial structure robot. *J Mech Eng Sci, Proc Inst Mech Eng, Part C* 229(6):1162–1171
13. Parikh PJ, Lam SSY (2005) A hybrid strategy to solve the forward kinematics problem in parallel manipulators. *IEEE Trans Robot* 21(1):18–25
14. Yu JJ, Pei X, Zong GH (2014) Graphical approach to creative design of mechanical devices. Science Press, Beijing, China

A Step Identification Method for Kinematic Calibration of a 6-DOF Serial Robot

Huaiyan Tang, Zhenya He, Yexin Ma and Xianmin Zhang

Abstract In order to improve the kinematic calibration accuracy, this paper proposes a step identification method for link 6-DOF serial robot. Firstly, kinematic model of serial robot was established based on the D-H parameter method. And then, a step identification method (SIM) for robot calibration was presented, including the offset of sphere-cally mounted reflection (SMR) and Frame offset, and the robot parameters. Finally, a calibration experiment was carried out to verify the effectiveness of the proposed identification method. The results demonstrate that the accuracy of robot have an improvement of 50.31 % after calibration. Hence, the step identification method established in this study is feasible and efficient.

Keywords Serial robot · Kinematic calibration · Step identification method · Laser tracker

1 Introduction

With the rapid development of technologies, manufacturing and other industries have moved towards the road of intelligent. The most important of automatic manufacturing is the manufacturing and optimization technology of the robot.

H. Tang · Z. He (✉) · Y. Ma · X. Zhang
Guangdong Provincial Key Laboratory of Precision Equipment and Manufacturing
Technology, School of Mechanical and Automotive Engineering, South China University of
Technology, Guangzhou 510640, China
e-mail: mezhyhe@scut.edu.cn

H. Tang
e-mail: medaisy.thy@mail.scut.edu.cn

X. Zhang
e-mail: zhangxm@scut.edu.cn

Z. He
State Key Laboratory of Fluid Power and Mechatronic Systems, Zhejiang University,
Hangzhou 310027, China

Furthermore, due to the intelligent transfer of industrial production and manufacturing, the industrial robot is becoming one of the key equipment to improve the production efficiency, and the level of intelligent manufacturing, and reduce the costs. At present, most of the industrial robots are of high repeatability. The absolute accuracy, however, is relatively poor. As robot accuracy is the important standard of its quality, the robot kinematic calibration must be performed before industrial applications.

Errors can be classified into different types according to the source and characteristics. The errors caused by the factors which are related to the geometry of the robot is called geometric error. Among the factors that affect the accuracy of the robot, the geometric error occupies about 80 % of the proportion. Thus the robot kinematics calibration is mainly to study the geometric error caused by manufacturing error, installation error, and encoder error and so on. We mainly study the geometric error model in this paper.

Geometrical calibration is usually divided into four steps: modeling, measurement, parameter identification, error compensation [1]. The most common calibration model is D-H model based on homogeneous transformation matrix [2], but it's not suitable for robot with parallel joint axis due to the singularity problem. Hayati et al. [3] modified the D-H model by introducing a rotation about the Y-axis of the parallel joint axes. Later, researchers have proposed S model using six parameters [4], POE model based on exponential accumulation [5], CPC model [6], the differential model [7], and so on. A measurement method is crucial for the efficiency and accuracy of the calibration. Measuring instruments can be divided into two types according to measuring scale. Instruments with large scale include laser tracker, CMM systems [8–10] etc. These ways perform high accuracy with high cost; the small-scale measurement includes visual measurement system, sonar sensors [11, 12] etc. Furthermore, some use homemade tools for measurement. Joubair [13] used a special plate with metal ball and triangular tactile probe; Ballbar Albert and Nubiola [14] measured posture through the telescopic ballbar and homemade fixed disk. Parameter Identification can get the approximate parameters of the kinematic model based on the measured data. The most common methods include least squares [15], maximum likelihood method [16], and extended Kalman filter [17] and so on. Omodei et al. [18] compared the linear iteration, least squares method, extended Kalman filter using the measured tracking error data, conclude that extended Kalman filter method has faster convergence speed and better stability. The offset of SME and base frame offset are often ignored in traditional kinematic calibration methods.

Therefore, this paper will focus on the kinematic calibration of serial robots to improve the accuracy of robots. To this end, Sect. 2 of the paper will establish the kinematic model of serial robot based on the D-H parameter method. Section 3 will present a new method, namely step identification method (SIM), to calibrate the serial robots using laser tracker system. In order to verify the feasibility of the present method, Sect. 4 will carry out a calibration experiment on a 6-DOF serial robot. Finally, the paper will end with a brief conclusion as presented in Sect. 5.

2 Kinematic Model

The most widely used kinematic model for robots is the D-H model, in which 3 fixed parameters and 1 joint variable are used to describe the location of each link relative to its neighbors, described by a_{i-1} , d_i and α_{i-1} for link i . However, D-H model is no longer suitable when the adjacent axes are parallel. In this case, the modified D-H model adding a rotation parameter (β_i) for nearly parallel axes is introduced to solve this problem.

According to D-H notation, a frame, attached to each link, is defined. The link frames are named by number according to the link to which they are attached. That is, frame $\{i\}$ is attached rigidly to link i . The convention used to locate frame on the links is shown as follows: The Z_i -axis of frame $\{i\}$, called Z_i , is coincident with the joint axis i . The origin of frame $\{i\}$ is located where the a_i perpendicularly intersects the joint i axis. X_i points along a_i in the direction from joint i to joint $i + 1$. The relationship of the two links is shown in Fig. 1.

To explain the modeling approach based on the modified D-H model, let's take a 6-DOF serial robot as an example. And the coordinate system of the robot is shown in Fig. 2. In D-H model, the transformation matrix from the frame $\{i\}$ to the frame $\{i - 1\}$ is described as follow.

$$\begin{aligned}
 {}^{i-1}T_i &= Rot_X(\alpha_{i-1})Trans_X(a_{i-1})Rot_Z(\theta_i)Trans_Z(d_i) \\
 &= \begin{pmatrix} c\theta_i & -s\theta_i & 0 & a_{i-1} \\ s\theta_i c\alpha_{i-1} & c\theta_i c\alpha_{i-1} & -s\alpha_{i-1} & -s\alpha_{i-1}d_i \\ s\theta_i s\alpha_{i-1} & c\theta_i s\alpha_{i-1} & c\alpha_{i-1} & c\alpha_{i-1}d_i \\ 0 & 0 & 0 & 1 \end{pmatrix} \tag{1}
 \end{aligned}$$

Similarly, in modified D-H model, the transformation matrix can be written as:

Fig. 1 The relationship of the two adjacent axes

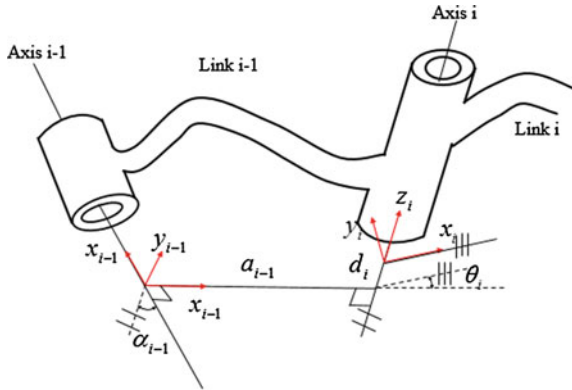
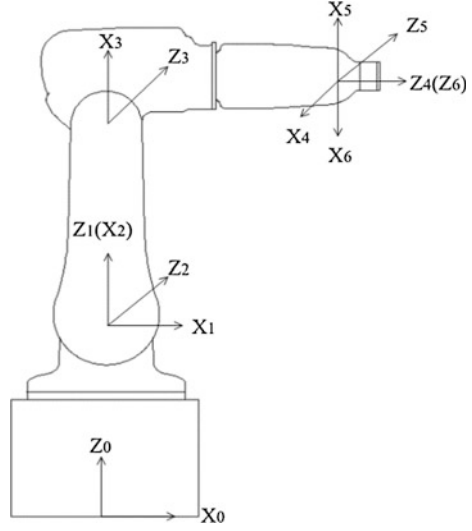


Fig. 2 The D-H coordinate system



$$\begin{aligned}
 {}^{i-1}\mathbf{T}_i &= \begin{pmatrix} c\theta_i & -s\theta_i & 0 & a_{i-1} \\ s\theta_i c\alpha_{i-1} & c\theta_i c\alpha_{i-1} & -s\alpha_{i-1} & -s\alpha_{i-1}d_i \\ s\theta_i s\alpha_{i-1} & c\theta_i s\alpha_{i-1} & c\alpha_{i-1} & c\alpha_{i-1}d_i \\ 0 & 0 & 0 & 1 \end{pmatrix} \begin{pmatrix} c\beta_i & 0 & s\beta_i & 0 \\ 0 & 1 & 0 & 0 \\ -s\beta_i & 0 & c\beta_i & 0 \\ 0 & 0 & 0 & 1 \end{pmatrix} \\
 &= \begin{pmatrix} c\theta_i c\beta_i & -s\theta_i & c\theta_i s\beta_i & a_{i-1} \\ s\theta_i c\alpha_{i-1} c\beta_i + s\alpha_{i-1} s\beta_i & c\theta_i c\alpha_{i-1} & s\theta_i c\alpha_{i-1} s\beta_i - s\alpha_{i-1} c\beta_i & -s\alpha_{i-1} d_i \\ s\theta_i s\alpha_{i-1} c\beta_i - c\alpha_{i-1} s\beta_i & c\theta_i s\alpha_{i-1} & s\theta_i s\alpha_{i-1} s\beta_i + c\alpha_{i-1} c\beta_i & c\alpha_{i-1} d_i \\ 0 & 0 & 0 & 1 \end{pmatrix} \tag{2}
 \end{aligned}$$

where, $c\alpha$ is shorthand for $\cos \alpha$, $s\alpha$ for $\sin \alpha$, and so on.

For the 6-DOF serial robot, the overall transformation between first link and the last link is the ${}^0\mathbf{T}_6$ by matrix multiplication of the individual link matrices, which can be written as:

$${}^0\mathbf{T}_6 = {}^0\mathbf{T}_1 {}^1\mathbf{T}_2 {}^2\mathbf{T}_3 {}^3\mathbf{T}_4 {}^4\mathbf{T}_5 {}^5\mathbf{T}_6 \tag{3}$$

The robot transformation relates points expressed in the end-effector coordinate system to those of same points in the world coordinate system. Where a frame $\{tcp\}$ has been attached to the end-effector, the ${}^6_{tcp}\mathbf{T}$ is the transformation matrix respect to the orientation and position of the frame $\{tcp\}$ in the frame $\{6\}$. The correctness of the model is verified by the forward kinematics and inverse kinematic.

3 Principle of the Identification Method

In traditional method, the errors of the robot itself are usually considered, but some installation errors are ignored. And the influence of the installation errors is greater than the robot itself. Therefore, these errors are taken into account in this paper.

Due to the experimental needs, a connecting component is added at the end-effector, as shown in Fig. 3. Hence, the offset between the end-effector which and sphere-cally mounted reflection (SMR) of the laser tracker must be taken into account. This offset is determined only by measurement or simple geometric calculations in traditional method. Similarly, a frame attached to the center of the SMR is defined, named frame $\{7\}$, and a transformation matrix T_7 is used to describe the orientation and position of the frame $\{7\}$ in the frame $\{tcp\}$. In addition, it is difficult to find the base frame of the robot, so there is a deviation between the base frame $\{0'\}$ established by laser tracker and the actual base frame $\{0\}$ of the robot, which can also be expressed by a transformation matrix T_0 .

Compared to errors of the robot itself, these two sets of errors are obviously larger than the robot parameters. To improve the accuracy of the calibration, the two sets of errors and the robot parameters need to be identified respectively. Therefore, this paper presents a step identification method (SIM) for robot calibration.

3.1 Identification of the SMR and Frame Offset

First, we identify the parameters in T_7 . Compared to the position deviation, machining accuracy of the connecting component and the SMR base is relatively high. So only the position deviations are considered. T_7 can be assumed as:

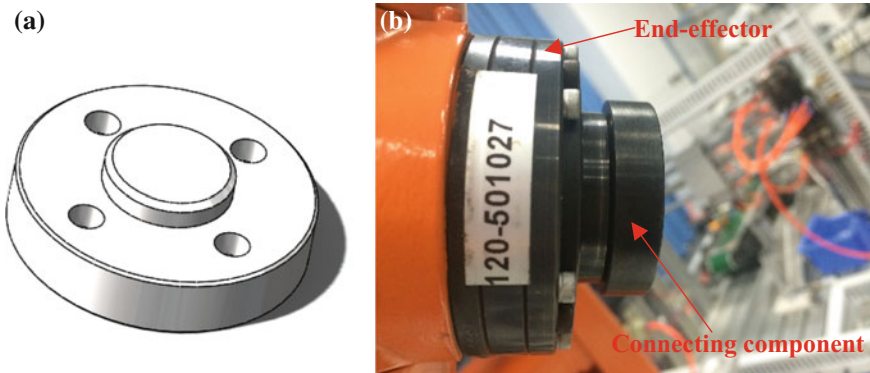


Fig. 3 Connecting component between the end-effector and the SMR: **a** the 3D model, **b** installation on the robot

$$\mathbf{T}_7 = \begin{pmatrix} 1 & 0 & 0 & p_{x_7} \\ 0 & 1 & 0 & p_{y_7} \\ 0 & 0 & 1 & p_{z_7} \\ 0 & 0 & 0 & 1 \end{pmatrix} \quad (4)$$

$$\mathbf{P}_7 = [p_{x_7} \quad p_{y_7} \quad p_{z_7} \quad 1]^T$$

where p_{x_7} , p_{y_7} and p_{z_7} are unknown.

To fast identify the \mathbf{T}_7 , a new method, only one axis moving during measurement, is presented. Furthermore, in order to avoid the influence of the non-coincidence of the frames and the errors inducing by other links, the axis near the end-effector is controlled to move during measurement. Assuming that the fifth axis is chosen to rotate when identifying the \mathbf{T}_7 . According to the forward kinematics an equation can be written as:

$$|\mathbf{P}_{t_1} - \mathbf{P}_{t_2}| = \left| \mathbf{T}_0 \mathbf{T}_1(\theta_1) \mathbf{T}_2(\theta_2) \mathbf{T}_3(\theta_3) \mathbf{T}_4(\theta_4) \mathbf{T}_5(\theta_{5-1}) \mathbf{T}_6(\theta_6) \mathbf{T}_{tcp} \mathbf{P}_7 \right. \\ \left. - \mathbf{T}_0 \mathbf{T}_1(\theta_1) \mathbf{T}_2(\theta_2) \mathbf{T}_3(\theta_3) \mathbf{T}_4(\theta_4) \mathbf{T}_5(\theta_{5-2}) \mathbf{T}_6(\theta_6) \mathbf{T}_{tcp} \mathbf{P}_7 \right| \quad (5)$$

where \mathbf{P}_{t_1} represents the position measured the laser tracker in the first point, \mathbf{P}_{t_2} represent the position measured by the laser tracker in the second point. Where θ_{5-1} represent the first value of θ_5 , θ_{5-2} represent the second values of θ_5 .

In addition, the position vector between the two points is invariable, no matter relative to the frame $\{0'\}$ or the frame $\{5\}$. Hence, according to the matrix operation, another equation can be written as:

$$\left| \mathbf{T}_0 \mathbf{T}_1(\theta_1) \mathbf{T}_2(\theta_2) \mathbf{T}_3(\theta_3) \mathbf{T}_4(\theta_4) \mathbf{T}_5(\theta_{5-1}) \mathbf{T}_6(\theta_6) \mathbf{T}_{tcp} \mathbf{P}_7 \right. \\ \left. - \mathbf{T}_0 \mathbf{T}_1(\theta_1) \mathbf{T}_2(\theta_2) \mathbf{T}_3(\theta_3) \mathbf{T}_4(\theta_4) \mathbf{T}_5(\theta_{5-2}) \mathbf{T}_6(\theta_6) \mathbf{T}_{tcp} \mathbf{P}_7 \right| \quad (6) \\ = \left| \mathbf{T}_5(\theta_{5-1}) \mathbf{T}_6(\theta_6) \mathbf{T}_{tcp} \mathbf{P}_7 - \mathbf{T}_5(\theta_{5-2}) \mathbf{T}_6(\theta_6) \mathbf{T}_{tcp} \mathbf{P}_7 \right|$$

By comparing the formulas (5) and (6), it can be written as:

$$\left| \mathbf{T}_5(\theta_{5-1}) \mathbf{T}_6(\theta_6) \mathbf{T}_{tcp} \mathbf{P}_7 - \mathbf{T}_5(\theta_{5-2}) \mathbf{T}_6(\theta_6) \mathbf{T}_{tcp} \mathbf{P}_7 \right| = |\mathbf{P}_{t_1} - \mathbf{P}_{t_2}| \quad (7)$$

Being controlled the fifth axis to rotate, 15 points are selected and measured by laser tracker. A set of equations can be obtained according to the 15 positions. Then the unknowns of the \mathbf{P}_7 can be identified by the least-square method with the help of Matlab Software.

Secondly, the parameters in \mathbf{T}_0 can be identified. Due to the poor accuracy of the platform used to install the robot, the orientation and position of the frame $\{0'\}$ relative to the frame $\{0\}$ must be taken into account. According to the Z-Y-X Euler angles, \mathbf{T}_0 can be assumed as:

$$T_0 = \begin{pmatrix} c\gamma_1c\gamma_2 & c\gamma_1s\gamma_2s\gamma_3 - s\gamma_1c\gamma_3 & c\gamma_1s\gamma_2c\gamma_3 + s\gamma_1s\gamma_3 & P_{x_0} \\ s\gamma_1c\gamma_2 & s\gamma_1s\gamma_2s\gamma_3 + c\gamma_1c\gamma_3 & s\gamma_1s\gamma_2c\gamma_3 - c\gamma_1s\gamma_3 & P_{y_0} \\ -s\gamma_2 & c\gamma_2s\gamma_3 & c\gamma_2c\gamma_3 & P_{z_0} \\ 0 & 0 & 0 & 1 \end{pmatrix} \quad (8)$$

According to the forward kinematics, we can get an equation as follow:

$$T_0T_1T_2T_3T_4T_5T_6T_{tcp}P_7 = P_{t_i} \quad (9)$$

where, the parameters in T_0 is unknown, and the other matrixes are known. 20 points are selected among the workspace, the positions of the selected points are measured by the laser tracker system. The parameters in the T_0 can be identified based on the least-square method using Matlab Software.

3.2 Identification of Robot Parameters

The next step is to identify the other deviations about the robot itself. The positions of the points by laser tracker need to transfer to the base frame of the robot at first. The relationship can be written as:

$$T_1T_2T_3T_4T_5T_6T_{tcp}Q = T_0^{-1}(P_{t_i} - P_7) \quad (10)$$

where multiply $Q = [0 \ 0 \ 0 \ 1]^T$ is in order to extract the fourth columns which express the nominal position of the robot.

The 2 axis parallel to the 3, which must be taken into account when making error modeling in calibration. Thus the differential model in calibration was established according to the D-H model and the modified D-H model. Δa_i , $\Delta \alpha_i$, Δd_i , $\Delta \beta_i$ and $\Delta \theta_i$ are described the deviation between the nominal parameters and actual parameters. The robot kinematics is analyzed in details, and the position error model of the robot is derived, as shown as the follow.

$$\Delta p = \sum_{i=0}^5 \left(\frac{\partial p}{\partial \alpha_i} \right) \Delta \alpha_i + \sum_{i=0}^5 \left(\frac{\partial p}{\partial a_i} \right) \Delta a_i + \sum_{i=1}^6 \left(\frac{\partial p}{\partial \theta_i} \right) \Delta \theta_i + \sum_{i=1}^6 \left(\frac{\partial p}{\partial d_i} \right) \Delta d_i + \frac{\partial p}{\partial \beta_2} \Delta \beta_2 = J_\delta \Delta \delta \quad (11)$$

where,

$$J_\delta = \begin{bmatrix} \frac{\partial p_x}{\partial \alpha_0} & \cdots & \frac{\partial p_x}{\partial \alpha_5} & \cdots & \cdots & \frac{\partial p_x}{\partial d_1} & \cdots & \frac{\partial p_x}{\partial d_6} & \frac{\partial p_x}{\partial \beta_2} \\ \frac{\partial p_y}{\partial \alpha_0} & \cdots & \frac{\partial p_y}{\partial \alpha_5} & \cdots & \cdots & \frac{\partial p_y}{\partial d_1} & \cdots & \frac{\partial p_y}{\partial d_6} & \frac{\partial p_y}{\partial \beta_2} \\ \frac{\partial p_z}{\partial \alpha_0} & \cdots & \frac{\partial p_z}{\partial \alpha_5} & \cdots & \cdots & \frac{\partial p_z}{\partial d_1} & \cdots & \frac{\partial p_z}{\partial d_6} & \frac{\partial p_z}{\partial \beta_2} \end{bmatrix}_{3 \times 25}$$

$$\Delta \delta = (\Delta \alpha_0 \dots \Delta \alpha_5, \Delta a_0 \dots \Delta a_5, \Delta \theta_1 \dots \Delta \theta_6, \Delta d_1 \dots \Delta d_6, \Delta \beta_x)^T$$

$$\Delta p = T_0^{-1}(P_{t_i} - P_7) - T_1T_2T_3T_4T_5T_6T_{tcp}Q$$

The robot is conducted to walk 20 points in the workspace, and the positions are measured by the laser tracker system. The parameters in the $\Delta\delta$ can be identified based on the least-square method using Matlab Software.

4 Experiment and Results

To verify the feasibility of the method, a calibration experiment on ABB IRB 120 robot was conducted based on Leica laser tracker system, as shown in Fig. 4. According to the specification of laser tracker, the precision of laser tracker is 10 μm . The experiment was performed at ambient temperature.

According to D-H model, a set of four D-H parameters extracted from the model is illustrated in Table 1. The resulting link-transformation matrices are:

$$T_1 = {}^0T_1 = \begin{pmatrix} c\theta_1 & -s\theta_1 & 0 & 0 \\ s\theta_1 & c\theta_1 & 0 & 0 \\ 0 & 0 & 1 & d_1 \\ 0 & 0 & 0 & 1 \end{pmatrix} \quad T_2 = {}_2T = \begin{pmatrix} c(\theta_2 - \pi/2) & -s(\theta_2 - \pi/2) & 0 & 0 \\ 0 & 0 & 1 & 0 \\ -s(\theta_2 - \pi/2) & -c(\theta_2 - \pi/2) & 0 & 0 \\ 0 & 0 & 0 & 1 \end{pmatrix}$$

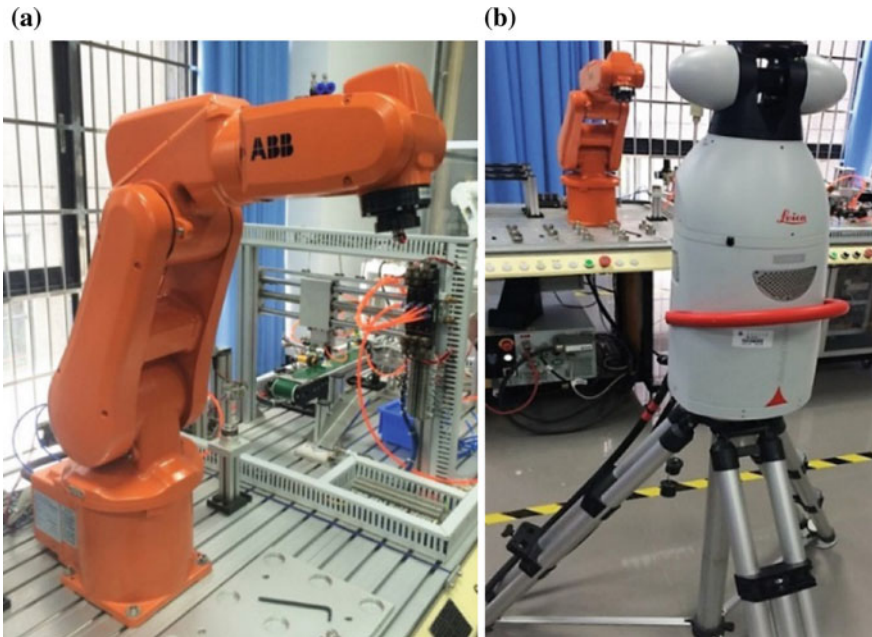


Fig. 4 The calibration experiment of the robot based on Laser tracker: **a** ABB IRB120 robot, **b** Leica laser tracker system

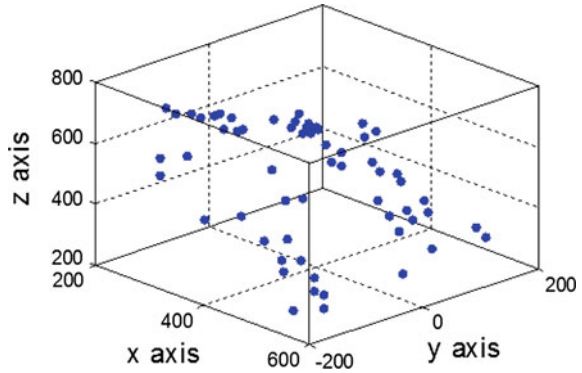
$$\begin{aligned}
\mathbf{T}_3 = {}^2_3\mathbf{T} &= \begin{pmatrix} c\theta_3 & -s\theta_3 & 0 & a_2 \\ s\theta_3 & c\theta_3 & 0 & 0 \\ 0 & 0 & 1 & 0 \\ 0 & 0 & 0 & 1 \end{pmatrix} & \mathbf{T}_4 = {}^3_4\mathbf{T} &= \begin{pmatrix} c\theta_4 & -s\theta_4 & 0 & a_3 \\ 0 & 0 & 1 & d_4 \\ -s\theta_4 & -c\theta_4 & 0 & 0 \\ 0 & 0 & 0 & 1 \end{pmatrix} \\
\mathbf{T}_5 = {}^4_5\mathbf{T} &= \begin{pmatrix} c\theta_5 & -s\theta_5 & 0 & 0 \\ 0 & 0 & -1 & 0 \\ s\theta_5 & c\theta_5 & 0 & 0 \\ 0 & 0 & 0 & 1 \end{pmatrix} \\
\mathbf{T}_6 = {}^5_6\mathbf{T} &= \begin{pmatrix} c(\theta_6 + \pi) & -s(\theta_6 + \pi) & 0 & 0 \\ 0 & 0 & 1 & 0 \\ -s(\theta_6 + \pi) & -c(\theta_6 + \pi) & 0 & 0 \\ 0 & 0 & 0 & 1 \end{pmatrix} \\
\mathbf{T}_{tcp} = {}^6_{tcp}\mathbf{T} &= \begin{pmatrix} 1 & 0 & 0 & 0 \\ 0 & 1 & 0 & 0 \\ 0 & 0 & 1 & d_6 \\ 0 & 0 & 0 & 1 \end{pmatrix} \\
{}^0_{tcp}\mathbf{T} = {}^0_1\mathbf{T}_2^1\mathbf{T}_3^2\mathbf{T}_4^3\mathbf{T}_5^4\mathbf{T}_6^5\mathbf{T}_{tcp}^6\mathbf{T} &= \begin{pmatrix} n_x & o_x & a_x & n_x \\ n_y & o_y & a_y & n_y \\ n_z & o_z & a_z & n_z \\ 0 & 0 & 0 & 1 \end{pmatrix}
\end{aligned}$$

First, the frame of the laser tracker system was established. Then the fifth axis of the robot was conducted to move to 15 different points, and the actual and nominal positions of the points were record, respectively. The set of data was used to identify \mathbf{T}_7 . Similarly being controlled the arbitrary axis rotation of the robot, make the end-effector move to 60 points, and record the position. The points were shown in Fig. 5. The points were divided into two groups, one group including 30 points

Table 1 The ABB IRB 120 robot nominal D-H parameters

Link	α_{i-1}	a_{i-1}	θ_i	d_i
1	0	0	θ_1	290
2	$-\pi/2$	0	$\theta_2 - \pi/2$	0
3	0	270	θ_3	0
4	$-\pi/2$	70	θ_4	302
5	$\pi/2$	0	θ_5	0
6	$-\pi/2$	0	$\theta_6 + \pi$	0
TCP	0	0	0	72

Fig. 5 The points in the workspace



was used to calibration, and the rest of the points were used to verify the result of the calibration.

According to the method in Sect. 2, the identified T_7 and T_0 are as follows:

$$T_7 = \begin{pmatrix} 1 & 0 & 0 & -0.3092 \\ 0 & 1 & 0 & -0.2732 \\ 0 & 0 & 1 & 18.0101 \\ 0 & 0 & 0 & 1 \end{pmatrix}$$

$$T_0 = \begin{pmatrix} 1.0000 & -0.0005 & -0.0030 & 0.2988 \\ 0.0005 & 1.0000 & -0.0012 & 0.9270 \\ 0.0030 & 0.0012 & 1.0000 & -6.6116 \\ 0 & 0 & 0 & 1.0000 \end{pmatrix}.$$

The deviation of the Δa_i , $\Delta \alpha_i$, Δd_i , $\Delta \beta_i$ and $\Delta \theta_i$ are shown in Table 2.

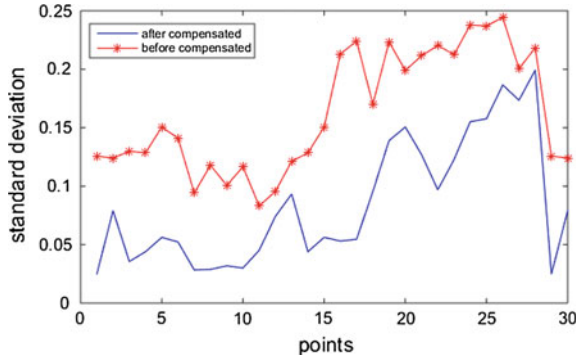
Then the errors were compensated into the Kinematic model, and compared the results with the previous results, as is shown in Fig. 6.

After calibration, the maximum error changed from 0.2369 to 0.1992 mm; the minimum error changed from 0.0831 to 0.0248 mm; the average error changed from 0.1590 to 0.0790 mm. The average absolute accuracy of the robot was

Table 2 Errors of each parameter

Link	$\Delta a_{i-1}/\text{mm}$	$\Delta \alpha_{i-1}/\text{rad}$	$\Delta d_i/\text{mm}$	$\Delta \theta_i/\text{rad}$	$\Delta \beta_i$
1	0.057	-0.0002	0.0299	-0.0037	0
2	0.5164	-0.0008	-0.0506	0.0095	0.0004
3	0.0601	-0.0044	0.0195	0.0076	0
4	0.0665	-0.0028	-0.0175	0	0
5	-0.3555	0.0010	-0.0267	0	0
6	0.1303	0.0046	-0.0105	0	0

Fig. 6 The result of calibration



improved 50.31 %. The experimental results show that the step identification method is effective in improving the accuracy of the robot.

5 Conclusion

Step identification method for link 6-DOF serial robot is proposed in this paper. The method consists of two steps. One step is to identify the SMR and frame offset, and the other step is to identify the robot parameters. An experiment was carried out on an ABB IRB120 robot to verify the feasibility of the proposed method. The results show that the accuracy of this method is higher than that of traditional calibration method, and the accuracy of robot improves 50.31 % after calibration. Furthermore, the proposed method retains the advantages of traditional method that the error model is simple and easy to realize.

Acknowledgments This work was supported by the Natural Science Foundation of Guangdong Province (Nos. 2016A030310408), the National Natural Science Foundation of China (No. U1501247), the China Postdoctoral Science Foundation (No. 2015M580718), the Open Foundation of the State Key Laboratory of Fluid Power and Mechatronic Systems (No. GZKF-201506), and the Fundamental Research Funds for the Central Universities (No. 2015ZM043).

References

1. Elatta AY, Gen LP, Zhi FL et al (2004) An overview of robot calibration. *Inf Technol J* 3 (1):74–78
2. Denavit J (1955) A kinematic notation for lower-pair mechanisms based on matrices. *Trans ASME J Appl Mech* 22:215–221
3. Hayati SA (1983) Robot arm geometric link parameter estimation. In: *The 22nd IEEE conference on decision and control*. IEEE, New York, pp 1477–1483

4. Stone HW (2012) Kinematic modeling, identification, and control of robotic manipulators. Springer Science and Business Media, Berlin
5. Okamura K, Park FC (1996) Kinematic calibration using the product of exponentials formula. *Robotica* 14(04):415–421
6. Zhuang H, Roth ZS, Hamano F (1992) A complete and parametrically continuous kinematic model for robot manipulators. *IEEE Trans Robot Autom* 8(4):451–463
7. Park IW et al (2011) Laser-based kinematic calibration of robot manipulator using differential kinematics. *IEEE/ASME Trans Mechatron* 99:1–9
8. Nubiola A, Bonev IA (2013) Absolute calibration of an ABB IRB 1600 robot using a laser tracker. *Robot Comput Integr Manuf* 29(1):236–245
9. Lightcap C, Hamner S, Schmitz T et al (2008) Improved positioning accuracy of the PA10-6CE robot with geometric and flexibility calibration. *IEEE Trans Rob* 24(2):452–456
10. Nubiola A, Slamani M, Joubair A et al (2014) Comparison of two calibration methods for a small industrial robot based on an optical CMM and a laser tracker. *Robotica* 32(03):447–466
11. Du G, Zhang P (2013) Online robot calibration based on vision measurement. *Robot Comput Integr Manuf* 29(6):484–492
12. Stone HW, Sanderson AC (1987) A prototype arm signature identification system. In: *Proceedings of 1987 IEEE international conference on robotics and automation*, vol 4. IEEE, New York, pp 175–182
13. Joubair A, Bonev IA (2015) Kinematic calibration of a six-axis serial robot using distance and sphere constraints. *Int J Adv Manuf Technol* 77(1–4):515–523
14. Nubiola A, Bonev IA (2014) Absolute robot calibration with a single telescoping ballbar. *Precis Eng* 38(3):472–480
15. Wang P, Liao Q, Zhuang Y et al (2006) Simulation and experimentation for calibration of general 7R serial robots. *Robot* 28(5):483–487 (in Chinese)
16. Renders JM, Rossignol E, Becquet M et al (1991) Kinematic calibration and geometrical parameter identification for robots. *IEEE Trans Robot Autom* 7(6):721–732
17. Du G, Zhang P (2014) Online serial manipulator calibration based on multisensory process via extended Kalman and particle filters. *IEEE Trans Ind Electron* 61(12):6852–6859
18. Omodei A, Legnani G, Adamini R (2000) Three methodologies for the calibration of industrial manipulators: experimental results on a SCARA robot. *J Robotic Syst* 17(6):291–307

Part VI
Dynamics of Machinery

Dynamic Characteristics of Planetary Transmission with Thin-Walled Ring Gear on Elastic Supports under Different Working Conditions

Jianying Li and Qingchun Hu

Abstract A lumped parameter-rigid elastic coupled dynamic model of two-stage planetary transmission for a hybrid car is established through inter-stage coupled method, after including the elasticity of the ring gear of planet set II and simplifying its elastic supports. Analyzing the relative displacement of various components and considering the time-varying mesh stiffness of each stage gear pairs, the equations of motion are obtained. On this basis, the influences of different working conditions on the dynamic characteristics of two-stage planetary transmission are discussed by the theoretical analysis and experimental testing. The simulation results show the influence trendies of each stage dynamic mesh forces by the input rotational speeds are opposite, but the influence trendies are the same by the load torques; simultaneously, each stage dynamic mesh forces have been affected by the load torque more than the input rotational speed. The vibration experimental results have good consistencies with the theoretical analysis.

Keywords Elastic supports · Thin-walled ring gear · Vibration testing · Working conditions

1 Introduction

The internal combustion engine, the generator/motor are usually used as power sources in a hybrid car, in order to solve this multi-power sources coupled problem, a planetary gears mechanism is often used as key part of its transmission system [1, 2]. However, the planetary gear vibration and noise have been critical factors which affect transmission system performance. Although wide studies on this problem are

J. Li (✉) · Q. Hu
School of Mechanical and Automotive Engineering,
South China University of Technology, Guangzhou 510640, China
e-mail: lijianying519@163.com

Q. Hu
e-mail: huqingchunscut@163.com

carried out in the academic field, which mainly involve dynamic modeling, natural frequency analysis, dynamic response solving, parameters stability and experiment verifications [3–13], only the changing mesh and support stiffness are considered as modeling, meanwhile the gears and carrier are regarded as rigid bodies, some scholars have pointed out the elasticity of the ring gear should be taken into account in certain situations, especially the ring gear is a thin-walled structure [14–17].

Because of thin-walled ring gear, its elastic deformations have influences on dynamic characteristics of transmission system, so the thin-walled ring gear is no longer regarded as a rigid body as modeling. This problem is discussed by the researchers, Wu [18] studied the nonlinear dynamic characteristics of planetary gears having an elastic ring gear through the method of multiple scales, Zhang et al. [19, 20] pointed out the elasticity of the ring gear has a certain influence on the dynamic characteristics of planetary gears. However, they mainly aimed at single-stage planetary gears transmission. The linear dynamic characteristics of multi-stage planetary gear transmission (the ring gears are regarded as the rigid bodies) were studied by Xiao and Zhao et al. [21, 22], and they analyzed the dynamic characteristics of planetary gears train used in driving cutter-head of shield tunneling machine. Qin et al. [23] studied the dynamic characteristics of planetary gear system of wind turbines, but the study on the dynamic characteristics of two-stage planetary transmission including elastic continuum ring gear has not been reported presently.

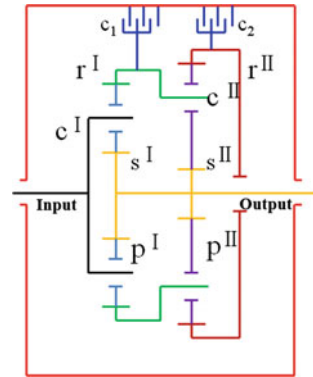
In view of the problem above and practical application for a hybrid car, a dual-clutch and dual-speed planetary gears mechanism (see Fig. 1) of a hybrid car coupled-system is taken as a research subject in this paper, the ring gear uses a thin-walled structure and the clutch friction plates are used as its elastic supports. A lumped parameter-rigid elastic coupled dynamic model of two-stage planetary transmission is established, the supports of the ring gear are represented as an elastic foundation with radial and tangential distributed stiffness in this paper, where the ring gear is modeled as an elastic continuum body, each stage sun, carrier and planets are regarded as rigid bodies. On this basis, the influences of different working conditions on the dynamic characteristics of two-stage planetary transmission are analyzed by the theoretical analysis and experimental testing, it can be provided guidance for dynamic design of two-stage planetary transmission with thin-walled ring gear on elastic supports.

2 Dynamic Model of Planetary Transmission with Thin-Walled Ring Gear on Elastic Supports

2.1 Modeling Assumptions

The diagram of two-stage planetary gears mechanism for a hybrid car is shown in Fig. 1. It is composed of planet set I and II, clutches c_1 , c_2 and shell. The sun of

Fig. 1 The diagram of two-stage planetary gears mechanism for a hybrid car



planet set I(s^I) and II(s^{II}) connect together, the ring gear of planet set I(r^I) and the carrier of planet set II(c^{II}) connect together. Clutch c_1 controls r^I and c^{II} . Clutch c_2 only controls the ring gear of planet set II(r^{II}). The carrier of planet set I(c^I) is the input, the sun of planet set I and II ($s^I - s^{II}$) is the output.

There are following assumptions as modeling in this paper:

- (1) The ring gear of planet set II is modeled as elastic continuum body and in inextensible plane vibration condition. Each stage sun, carrier and planets are regarded as rigid bodies; the planets are identical and equally spaced.
- (2) The bearing stiffness of the sun, carrier and planets are linear stiffness, the supports of the ring gear of planet set II are represented as an elastic foundation with uniform radial and tangential distributed stiffness per unit length k_{rbs} and k_{rns} .
- (3) All ring-planet and sun-planet mesh stiffness are time-varying. The damping, friction and transmission errors of two-stage planetary gears mechanism are neglected.

2.2 Dynamic Model

Based on the above assumptions, the dynamic models of two-stage planetary transmission are shown in Fig. 2, which are modeled relative to the co-moving coordinate of each stage carrier. Unless specially indicating, $i = I, II$ represent planet set I and II, respectively. $n = 1, 2, \dots, N_i$, where N_I, N_{II} represent numbers of planets of planet sets I and II. The two-stage planetary transmission dynamic model is established through inter-stage coupled method based on the translation-torsional dynamic model of planet set I (see Fig. 2a), in which the deformations and elastic

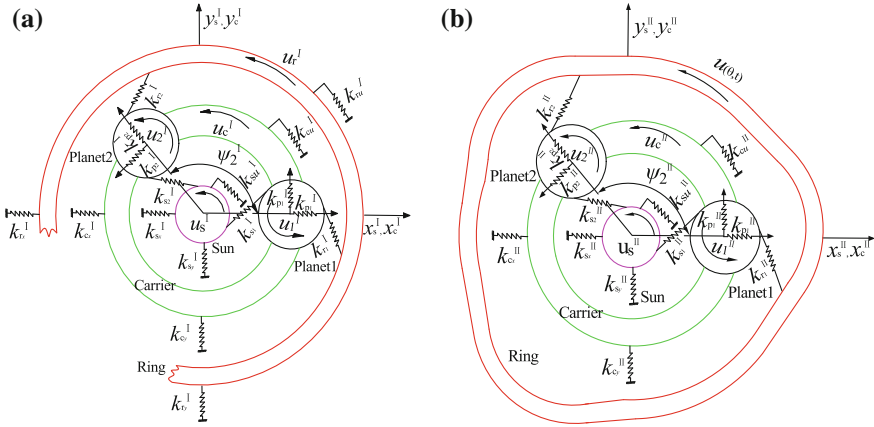


Fig. 2 Dynamic model of two-stage planetary transmission with thin-walled ring gear on elastic supports

supports of the ring gear of planet set II are considered (see Fig. 2b). x_h^i, y_h^i, u_h^i , ($h = s, c, r$) are translational and torsional displacements of component h of planet set i (the sun, carrier and ring gear), respectively. θ_h^i is angular displacement of component h of planet set i , and $u_h^i = r_h^i \theta_h^i$, where r_h^i is base radius of component h of planet set i (r_c^i is radius of the circle passing through planet centers). x_n^i, y_n^i, u_n^i are translational and torsional displacements of the n th planet of planet set i , respectively. $u(\theta, t)$ is tangential displacement of the ring gear of planet set II, its radial displacement is determined by the inextensibility condition $w(\theta, t) = -\partial u / \partial \theta$. In what follows, $u(\theta, t)$ is abbreviated as u .

The displacement along mesh line of the sun and n th planet is

$$\delta_{sn}^i = -x_s^i \sin \psi_{sn}^i(t) + y_s^i \cos \psi_{sn}^i(t) - x_n^i \sin \alpha_s^i - y_n^i \cos \alpha_s^i + u_s^i + u_n^i. \quad (1)$$

As including the elasticity of the ring gear of planet set II, the displacement along mesh line of the ring gear and n th planet has changed, it can be obtained according to the deformation compatibility condition [18, 20]

$$\delta_m^{\text{II}} = u(\theta, t) - \delta_n^{\text{II}}. \quad (2)$$

$$u(\theta, t) = v(\theta, t) + U_1(t)e^{i\theta} + U_{-1}(t)e^{-i\theta} + U_0(t). \quad (3)$$

where $v(\theta, t)$ is elastic deformation of the ring gear of planet set II. U_1, U_{-1} and U_0 represent the rigid body motion of the ring gear of planet set II, and

$$v(\theta, t) = \sum_{m=\pm 2}^{\pm \infty} V_m(t)e^{im\theta} \approx \sum_{m=\pm 2}^{\pm JN_{II}} V_m(t)e^{im\theta}. \tag{4}$$

J is an arbitrary integer, the right terms of Eq. (4) is composed of JN orders nodal diameter components of the ring gear of planet set II.

For yielding the full expansion of Eq. (2), assuming

$$x_r^{II} = -i(U_1 - U_{-1}), y_r^{II} = U_1 + U_{-1}, u_r^{II} = U_0 \cos \alpha_r^{II}. \tag{5}$$

Substituting Eqs. (3–5) into Eq. (2) yield the equation of the displacement along mesh line of the ring gear and n th planet of planet set I and planet set II

$$\delta_m^{II} = \left(v \cos \alpha_r^{II} + \frac{\partial v}{\partial \theta} \sin \alpha_r^{II} \right) \Big|_{\theta=\psi_n^{II}} - x_r^{II} \sin \psi_m^{II}(t) + y_r^{II} \cos \psi_m^{II}(t) + u_r^{II} + x_n^{II} \sin \alpha_r^{II} - y_n^{II} \cos \alpha_r^{II} - u_n^{II}. \tag{6}$$

$$\delta_m^I = -x_r^I \sin \psi_m^I(t) + y_r^I \cos \psi_m^I(t) + u_r^I + x_n^I \sin \alpha_r^I - y_n^I \cos \alpha_r^I - u_n^I. \tag{7}$$

For expressing conveniently, δ_m^I and δ_m^{II} are written δ_m^i .

The radial and tangential deformations of the n th planet bearing

$$\delta_{nr}^i = y_n^i + x_c^i \cos \psi_n^i(t) - y_c^i \sin \psi_n^i(t). \tag{8}$$

$$\delta_{nt}^i = y_n^i + x_c^i \sin \psi_n^i(t) - y_c^i \cos \psi_n^i(t) - u_c^i. \tag{9}$$

where $\psi_n^i(t)$ is the n th planet location of planet set i with x axis positive direction. $\psi_n^i(t) = \omega_c^i t + 2\pi(n - 1) / N_i$. $\psi_{rn}^i(t) = \psi_n^i(t) + \alpha_r^i$, $\psi_{sn}^i(t) = \psi_n^i(t) - \alpha_s^i$, where α_r^i , α_s^i is pressure angle of the ring gear and sun gear of planet set i , respectively.

The differential equations of motion of two-stage planetary transmission are

$$M\ddot{a} + Ka = F. \tag{10}$$

where $M = \text{diag}[M^I, M_e, M^{II}]$ is equivalent mass matrix, $M_e = PR \left(1 - \frac{\partial^2}{\partial \theta^2} \right)$ represents equivalent mass of the ring gear of planet set II, $a = [U^I, v, U^{II}]^T$ is generalized coordinates vector; $K(t)$ is time-varying stiffness matrix (see Appendix for details), F is force vector, $F = [F^I, \mathbf{0}, F^{II}]$.

$$\begin{aligned}
 \mathbf{M}^I &= \text{diag}(m_r^I, m_r^I, I_r^I / (r_r^I)^2, m_c^I, m_c^I, I_c^I / (r_c^I)^2, \\
 &\quad m_s^I, m_s^I, I_s^I / (r_s^I)^2, m_1^I, m_1^I, I_1^I / (r_1^I)^2 \cdots m_n^I, m_n^I, I_n^I / (r_n^I)^2), \\
 \mathbf{M}^{II} &= \text{diag}(m_r^{II}, m_r^{II}, I_r^{II} / (r_r^{II})^2, m_c^{II}, m_c^{II}, I_c^{II} / (r_c^{II})^2, \\
 &\quad m_s^{II}, m_s^{II}, I_s^{II} / (r_s^{II})^2, m_1^{II}, m_1^{II}, I_1^{II} / (r_1^{II})^2 \cdots m_n^{II}, m_n^{II}, I_n^{II} / (r_n^{II})^2), \\
 \mathbf{U}^I &= [x_r^I, y_r^I, u_r^I, x_c^I, y_c^I, u_c^I, x_s^I, y_s^I, u_s^I, x_1^I, y_1^I, u_1^I \cdots x_n^I, y_n^I, u_n^I]^T, \\
 \mathbf{U}^{II} &= [x_r^{II}, y_r^{II}, u_r^{II}, x_c^{II}, y_c^{II}, u_c^{II}, x_s^{II}, y_s^{II}, u_s^{II}, x_1^{II}, y_1^{II}, u_1^{II} \cdots x_n^{II}, y_n^{II}, u_n^{II}]^T, \\
 \mathbf{F}^I &= [\frac{T_r^I}{r_r^I}, \frac{T_c^I}{r_c^I}, \frac{T_s^I}{r_s^I}, 0, \dots, 0]^T, \\
 \mathbf{F}^{II} &= [\frac{T_r^{II}}{r_r^{II}}, \frac{T_c^{II}}{r_c^{II}}, \frac{T_s^{II}}{r_s^{II}}, 0, \dots, 0]^T.
 \end{aligned}$$

where m_h^i, I_h^i are mass and moment of inertia of component h of planet set i ; m_n^i, I_n^i are mass and moment of inertia of the n th planet of planet set i ; $k_{sn}^i(t), k_m^i(t)$ are time-varying mesh stiffness of the sun, ring gear with the n th planet of planet set i ; $k_{h'j}^i$ ($h' = c, s, j = x, y, u$) is bearing stiffness and torsional stiffness of component h' of planet set i (the carrier and sun gear), k_{rj}^I is bearing stiffness and torsional stiffness of the ring gear of planet set I; k_{rus}, k_{rbs} are tangential and radial stiffness with units length of the ring gear of planet set II; k_{pn}^i is bearing stiffness of the n th planet; k_{ssu}^i is coupling torsional stiffness of the sun gear of planet set I with the sun gear of planet set II; k_{cru}^i is coupling torsional stiffness of the ring gear of planet set I with the carrier of planet set II; T_h^i is external torque of component h of planet set i ; r_c is connecting shaft radius of the ring gear of planet set I with the carrier of planet set II, r_b is connecting shaft of the sun gear of planet set I with the sun gear of planet set II.

The internal and external time-varying mesh stiffness with the n th planet of planet set i $k_{sn}^i(t), k_m^i(t)$

$$k_{sn}^i(t) = \bar{k}_{sn}^i + k_{1n}^i(t), k_m^i(t) = \bar{k}_m^i + k_{2n}^i(t). \tag{11}$$

$\bar{k}_{sn}^i, \bar{k}_m^i$ are internal and external average mesh stiffness with the n th planet of planet set i ; $k_{1n}^i(t), k_{2n}^i(t)$ are internal and external mesh stiffness variations with the n th planet of planet set i

$$\begin{aligned}
 k_{1n}^i(t) &= 2\mu^i \sum_{l=1}^{\infty} \left(a_{sn}^{i(l)} \sin l\omega_m^i t + b_{sn}^{i(l)} \cos l\omega_m^i t \right), \\
 k_{2n}^i(t) &= 2\varepsilon^i \sum_{l=1}^{\infty} \left(a_{rn}^{i(l)} \sin l\omega_m^i t + b_{rn}^{i(l)} \cos l\omega_m^i t \right).
 \end{aligned} \tag{12}$$

$$\begin{aligned}
 a_{sn}^{i(l)} &= \frac{2}{l\pi} \sin[l\pi(c_s^i + 2\gamma_{sn}^i)] \sin(l\pi c_s^i), \\
 b_{sn}^{i(l)} &= \frac{2}{l\pi} \cos[l\pi(c_s^i + 2\gamma_{sn}^i)] \sin(l\pi c_s^i).
 \end{aligned}
 \tag{13}$$

$$\begin{aligned}
 a_m^{i(l)} &= \frac{2}{l\pi} \sin[l\pi(c_r^i + 2\gamma_{sr}^i + 2\gamma_{rm}^i)] \sin(l\pi c_r^i), \\
 b_{rm}^{i(l)} &= \frac{2}{l\pi} \cos[l\pi(c_r^i + 2\gamma_{sr}^i + 2\gamma_{rm}^i)] \sin(l\pi c_r^i).
 \end{aligned}
 \tag{14}$$

$k_{1n}^i(t)$, $k_{2n}^i(t)$ with peak to peak amplitudes $2\mu^i$, $2\varepsilon^i$; contact ratios c_s^i , c_r^i ; mesh frequency ω_m^i ; internal and external mesh phasing γ_{rm}^i , γ_{sn}^i ; the phasing between internal and external meshes for a given planet γ_{sr}^i . Each stage internal and external mesh stiffness fluctuation curves with the n th planet of two-stage planetary transmission with thin-walled ring gear on elastic supports can be seen from Figs. 3 and 4.

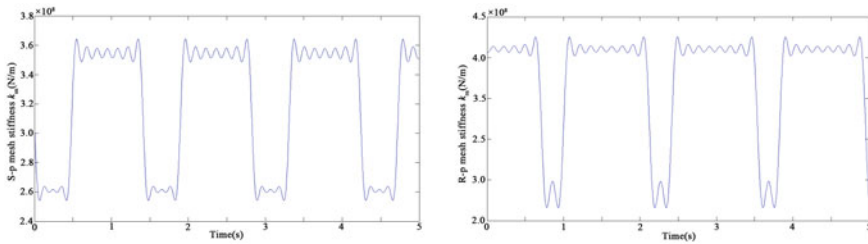


Fig. 3 The internal and external time-varying mesh stiffness of planet set I

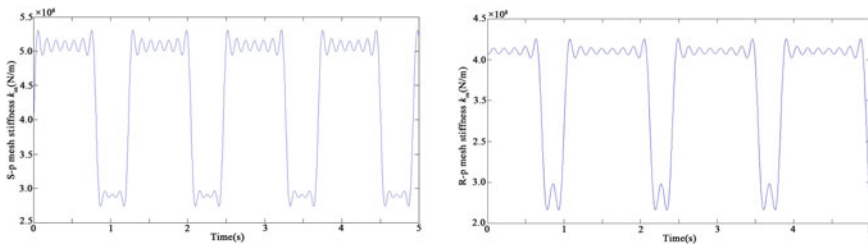


Fig. 4 The internal and external time-varying mesh stiffness of planet set II

3 Influences of Working Conditions on Dynamic Mesh Forces of Planetary Transmission with Thin-Walled Ring Gear on Elastic Supports

In order to understand the influences of different working conditions on each gear pairs dynamic mesh forces of two-stage planetary transmission, the Runge-Kutta method is used for numerical solutions of Eq. (10) and numbers of each stage planet are 4, the numerical simulation parameters are shown in Table 1. The results of numerical simulation show that the influence trendies of the working conditions on the sun-planet and ring-planet dynamic mesh forces of planet set I and II are

Table 1 Parameters of two-stage planetary transmission with thin-walled ring gear on elastic supports

	Parameters	Ring gear	Carrier	Sun gear	Planet
Planet set I	Teeth	83	–	33	25
	Pitch diameter (mm)	103.75	–	41.25	31.25
	Base diameter (mm)	97.49	72.5	38.76	29.37
	Modulus (mm)	1.25	–	1.25	1.25
	Pressure angle (°)	20°	20°	20°	20°
	Mass (kg)	0.547	0.573	0.106	0.064
	Moment of inertia (kg mm ²)	933.060	552.328	18.443	6.963
	Bearing stiffness (N/μm)	170	109	126	108
	Torsional stiffness (N/μm)	$k_{su}^I = k_{cu}^I = 0 \quad k_{ru}^I = 15750$			
	Mesh stiffness (N/μm)	$\bar{k}_m^I = 373.5 \quad \bar{k}_{st}^I = 322.8$			
	Tooth width (mm)	17	–	17	17
Planet set II	Teeth	83	–	33	25
	Pitch diameter (mm)	103.75	–	41.25	31.25
	Base diameter (mm)	97.49	72.5	38.76	29.37
	Modulus (mm)	1.25	–	1.25	1.25
	Pressure angle (°)	20°	20°	20°	20°
	Mass (kg)	0.741	0.613	0.143	0.086
	Moment of inertia (kg mm ²)	1277.185	730.328	27.812	11.145
	Bearing stiffness (N/μm)	0.31	109	126	108
	Torsional stiffness (N/μm)	$k_{su}^{II} = k_{ru}^{II} = 0 \quad k_{cu}^{II} = 6850$			
	Mesh stiffness (N/μm)	$\bar{k}_m^{II} = 505.3 \quad \bar{k}_{st}^{II} = 433.8$			
	Tooth width mm	23	–	23	23
Coupling stiffness (N/μm)	$k_{ssu}^I = k_{ssu}^{II} = 151.0 \quad k_{cru}^I = k_{cru}^{II} = 5630$				
Contact ratios	$c_s^I = c_s^{II} = 1.66 \quad c_r^I = c_r^{II} = 1.79$				

roughly similar, so only the ring-planet dynamic mesh forces of planet set I and II are listed below, respectively.

The influences of the input rotational speeds on each stage ring-planet dynamic mesh forces are solved through the Runge-Kutta method under the load torque $T_s^I = 10 \text{ Nm}$, the input rotational speeds n_c^I is 100, 200 and 300 r/min, respectively. Shown in Fig. 5, the blue dotted lines and the red solid lines represent the influences of different input rotational speeds on the ring-planet dynamic mesh forces of planet set I and II, respectively. Seen from Fig. 5, with the increasing of the input rotational speeds, the ring-planet dynamic mesh forces of planet set I increase first and then decrease and their amount of change are all small. That is, the peak values of the blue dotted lines in turn are 270, 280 and 260 N from Fig. 5a–c. The meshing states between the ring gear and the planet gears of planet set I transform from the short time single side impact to the elimination gear teeth off. Meanwhile the ring-planet dynamic mesh forces of planet set II decrease first and then increase and their amount of change are also small when the input rotational speeds increase, the double sides impact phenomenon occurs between the ring gear and the planet gears of planet set II, the time change of the meshing states of the elimination gear teeth off is not obvious.

The influences of the load torques on each stage ring-planet dynamic mesh forces are studied through the Runge-Kutta method under the input rotational speed

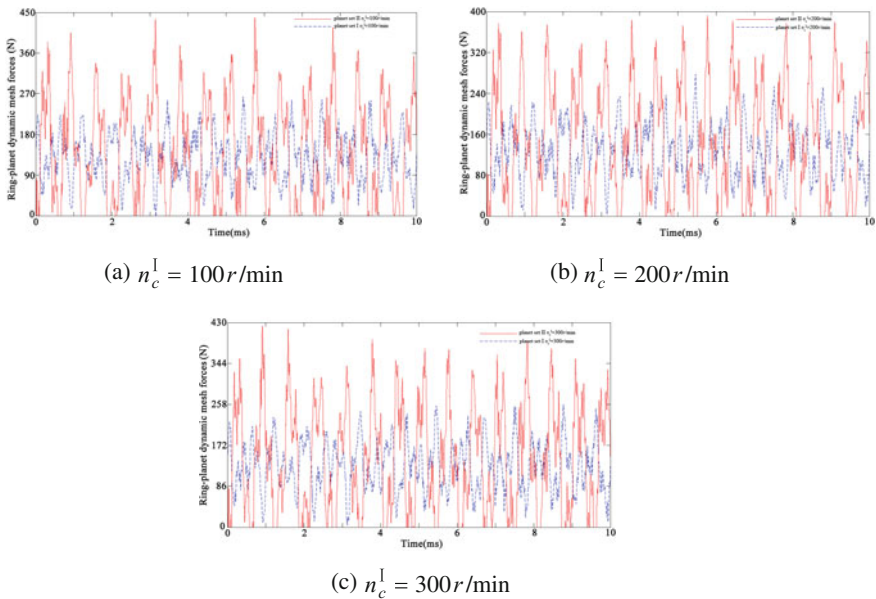


Fig. 5 Influences of input rotational speeds n_c^I on ring-planet dynamic mesh forces

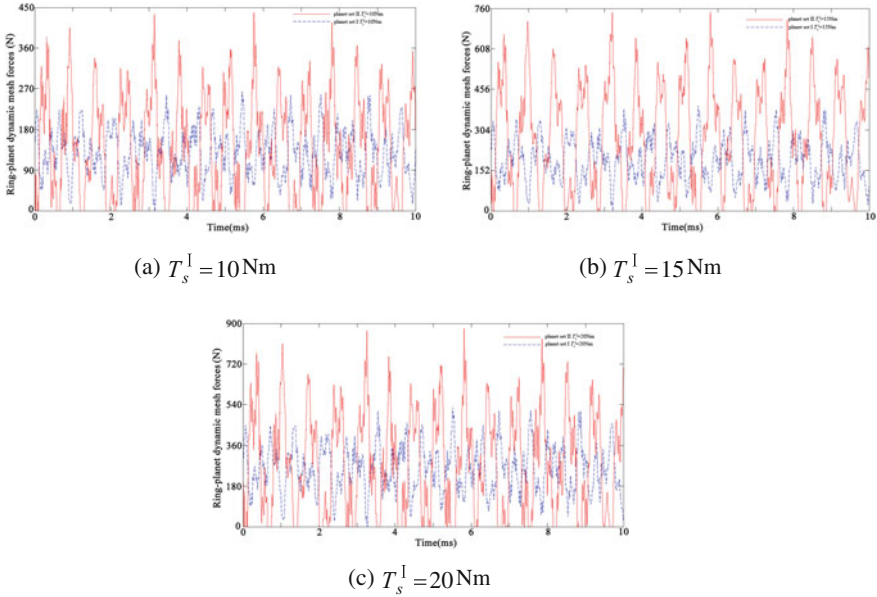


Fig. 6 Influences of load torques T_s^I on ring-planet dynamic mesh forces

$n_c^I = 100\text{ r/min}$, the load torques T_s^I is 10, 15 and 20 Nm, respectively. Shown in Fig. 6, the blue dotted lines and the red solid lines represent the influences of different load torques on the ring-planet dynamic mesh forces of planet set I and II, respectively. Seen from Fig. 6, with the increasing of the load torques, the ring-planet dynamic mesh forces of planet set I increase, the peak values of the blue dotted lines in turn are 270, 400 and 545 N from Fig. 6a–c. The meshing states between the ring gear and the planet gears of planet set I also transform from the short time single side impact to the elimination gear teeth off. Simultaneously, with the increasing of the load torques, the ring-planet dynamic mesh forces of planet set II also increase, the double sides impact phenomenon occurs between the ring gear and planet gears of planet set II, the time change of the meshing states of the elimination gear teeth off is also not obvious.

Compared Fig. 5 with Fig. 6, it can be known that each stage ring-planet dynamic mesh forces have been affected by the load torque more than the input rotational speed, but the meshing state and meshing time between the ring gear and the planet gears are similar.

4 Vibration Testing Experiments

4.1 Vibration Testing Platform

For verifying the theoretical analysis above, the vibration experiments of two-stage planetary gears box exemplified in Table 1 have been tested. The vibration testing platform is composed of motor, torque and speed sensors, tested two-stage planetary gears box, acceleration sensors, elastic coupling, magnetic loader and other components. 1#, 2# and 3#, 4# are the vibration testing points at the input shaft bearing, the ring gear of planet set I and II, the output shaft bearing of two-stage planetary gears box, respectively (shown in Fig. 7). The vibration testing sampling frequency is 10,000 Hz, where $f_m, f_k (k = r, c, s, p)$ are mesh fundamental frequency and rotating frequency of each stage component k under different working conditions.

4.2 Experimental Testing and Analysis

The vibration experiments affected by the input rotational speeds are tested under the load torque $T_s^I = 10 \text{ Nm}$, the input rotational speeds n_c^I is 100, 200 and 300 r/min, respectively. The vibration acceleration time-domain curves of each stage ring gear of two-stage planetary gears box are shown in Figs. 8a and 9a. As shown in Figs. 8a and 9a, with the increasing of the input rotational speeds, the vibration acceleration peaks of the ring gear of planet set I in turn are 11.55, 12.01

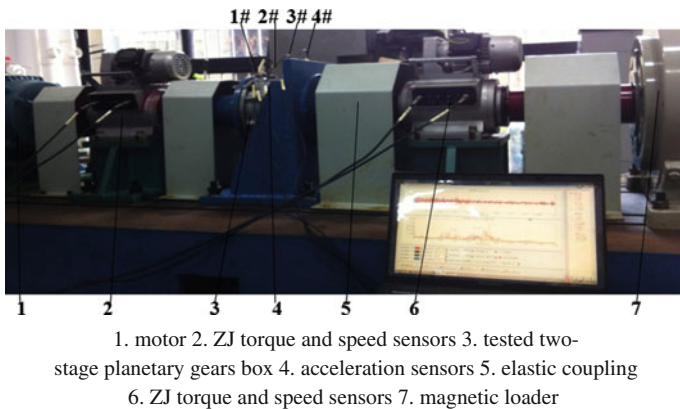
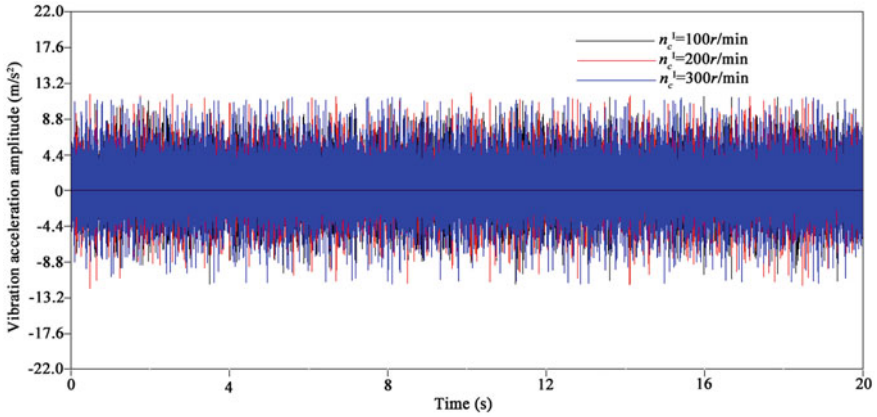
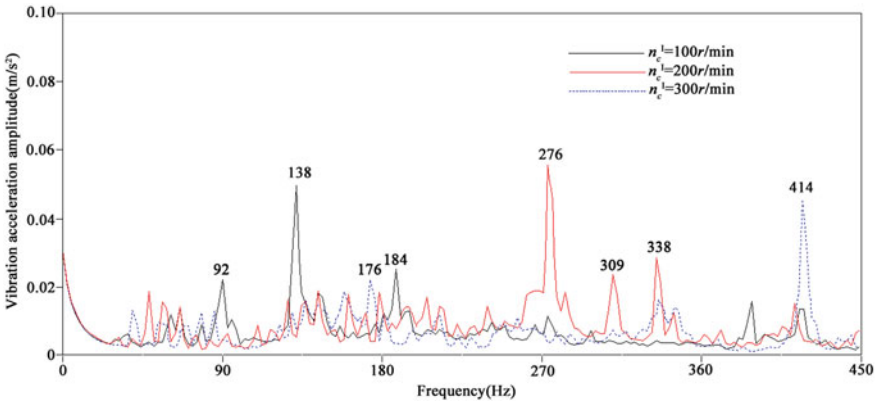


Fig. 7 Vibration testing platform of two-stage planetary gears box



(a) Time-domain curves

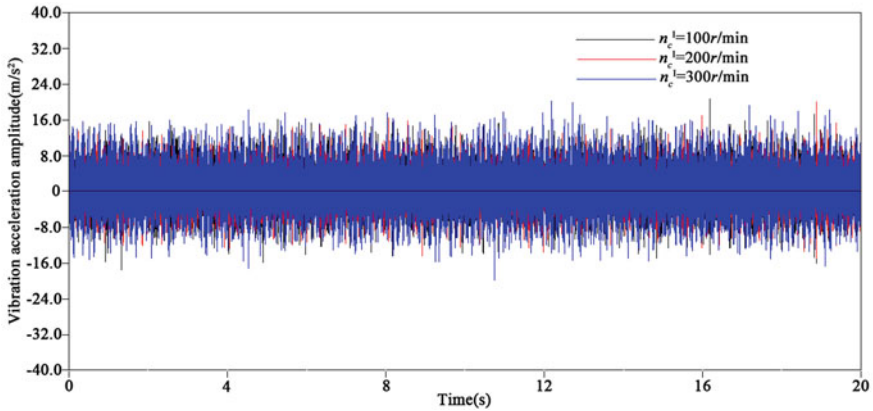


(b) Frequency-domain curves

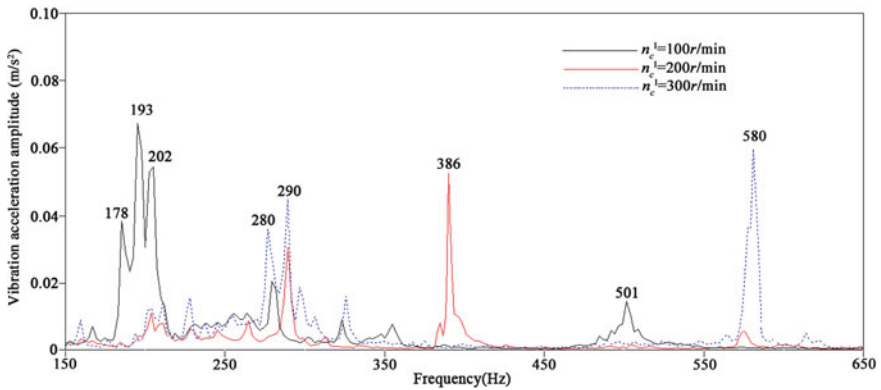
Fig. 8 Dynamic responses of the ring gear of planet set I versus input rotational speeds n_c^I

and 11.49 m/s^2 ; the vibration acceleration peaks of the ring gear of planet set II in turn are 20.64 , 20.10 and 20.16 m/s^2 . That is, the dynamic response of the ring gear of planet set I increases first and then decreases, nevertheless, the dynamic response of the ring gear of planet set II decrease first and then increase when the input rotational speeds increase.

The corresponding frequency spectra are refined in Figs. 8b and 9b. Seen from Fig. 8b, there are the vibration acceleration peaks of the ring gear of planet set I at the mesh fundamental frequency 138 , 276 and 414 Hz and they increase first and then decrease in a small extent when the input rotational speeds increase from 100 to 300 r/min . The combination frequencies 92 Hz ($f_m - f_p - 2f_s - 2f_c$) and 184 Hz



(a) Time-domain curves



(b) Frequency-domain curves

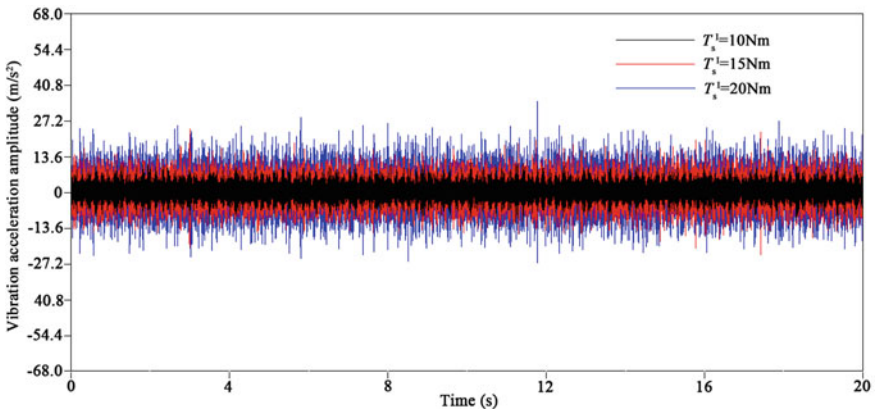
Fig. 9 Dynamic responses of the ring gear of planet set II versus input rotational speeds n_c^1

$(f_m + f_p + 2f_s + 2f_c)$ appear under the working conditions $T_s^1 = 10 \text{ Nm}$, $n_c^1 = 100 \text{ r/min}$; The combination frequencies 309 Hz ($f_m + f_p + 2f_c - 3f_s$) and 338 Hz ($f_m + f_p$) appear under the working conditions $T_s^1 = 10 \text{ Nm}$, $n_c^1 = 200 \text{ r/min}$; The combination frequency 176 Hz ($f_m + f_s + f_c - 3f_p$) appears under the working conditions $T_s^1 = 10 \text{ Nm}$, $n_c^1 = 300 \text{ r/min}$. The rotating frequencies of the carrier of planet set I appear in the frequency range of 1–5 Hz under different working conditions.

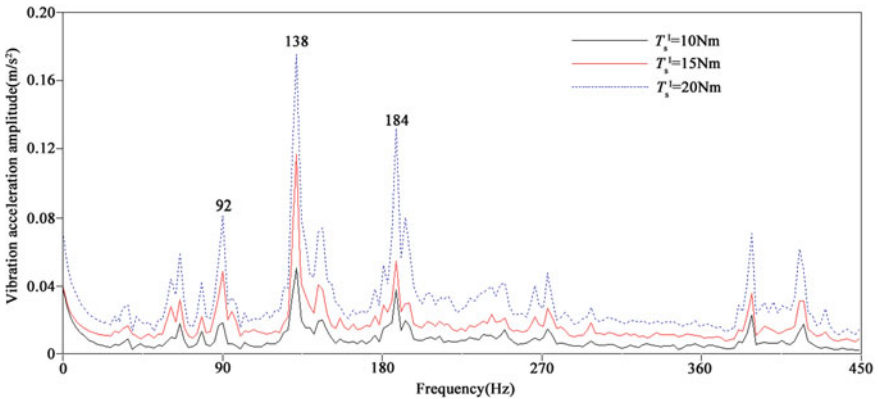
Seen from Fig. 9b, there are the vibration acceleration peaks of the ring gear of planet set I at the mesh fundamental frequency 193, 386 and 580 Hz and they decrease first and then increase in a small extent when the input rotational speeds

increase from 100 to 300 r/min. The combination frequencies 178 Hz ($f_m + 2f_s + 2f_r - f_p$), 202 Hz ($f_m + 2f_s - 2f_r$) and 501 Hz ($2f_m + 3f_p + 3f_s + 2f_r$) appear under the working conditions $T_s^I = 10\text{ Nm}$, $n_c^I = 100\text{ r/min}$; The combination frequency 290 Hz ($f_m + 2f_s + f_r - 2f_p$) appears under the working conditions $T_s^I = 10\text{ Nm}$, $n_c^I = 200\text{ r/min}$; The combination frequency 280 Hz ($f_m + 2f_r - 3f_p - 2f_s$) and half times mesh fundamental frequency 290 Hz ($1/2f_m$) appear under the working conditions $T_s^I = 10\text{ Nm}$, $n_c^I = 300\text{ r/min}$.

The vibration experiments affected by the load torques are tested under the input rotational speed $n_c^I = 100\text{ r/min}$, the load torques T_s^I is 10, 15 and 20 Nm, respectively. The vibration acceleration time-domain curves of each stage ring gear of two-stage planetary gears box are shown in Figs. 10a and 11a. As shown in

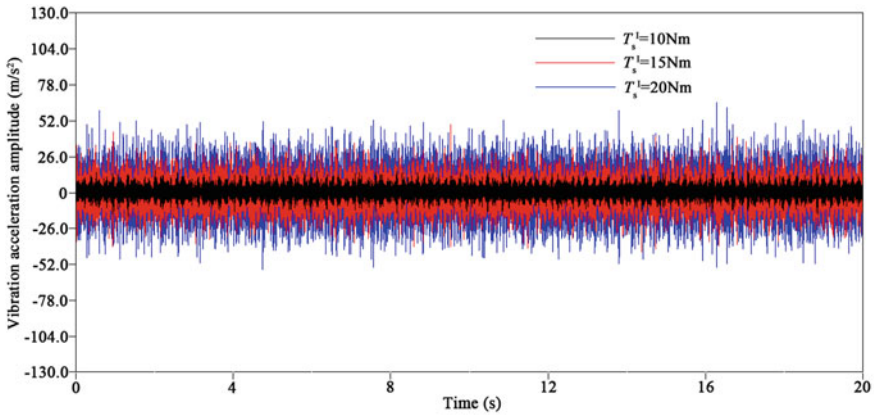


(a) Time-domain curves

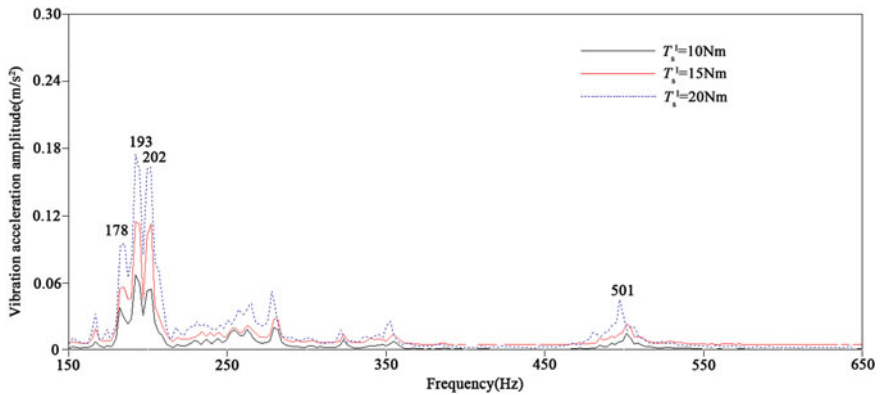


(b) Frequency-domain curves

Fig. 10 Dynamic responses of the ring gear of planet set I versus load torques T_s^I



(a) Time-domain curves



(b) Frequency-domain curves

Fig. 11 Dynamic responses of the ring gear of planet set II versus load torques T_s^1

Figs. 10a and 11a, with the increasing of the load torques, the vibration acceleration peaks of the ring gear of planet set I in turn are 11.55, 24.07 and 34.54 m/s^2 ; the vibration acceleration peaks of the ring gear of planet set II in turn are 20.64, 49.22 and 65.23 m/s^2 . That is, the dynamic responses of the ring gear of planet set I and II all increase when the load torques increase.

The corresponding frequency spectra are refined in Figs. 10b and 11b. Seen from Fig. 10b, there are the vibration acceleration peaks of the ring gear of planet set I at the mesh fundamental frequency 138 Hz and the combination frequencies 92 Hz ($f_m - f_p - 2f_s - 2f_c$), 184 Hz ($f_m + f_p + 2f_s + 2f_c$) appear when the input

rotational speed $n_c^I = 100 \text{ r/min}$, the load torques T_s^I is 10, 15 and 20 Nm, respectively. Seen from Fig. 11b, there are the vibration acceleration peaks of the ring gear of planet set II at the mesh fundamental frequency 193 Hz and the combination frequencies 178 Hz ($f_m + 2f_s + 2f_r - f_p$), 202 Hz ($f_m + 2f_s - 2f_r$), 501 Hz ($2f_m + 3f_p + 3f_s + 2f_r$) appear when the input rotational speed $n_c^I = 100 \text{ r/min}$, the load torques T_s^I is 10, 15 and 20 Nm, respectively.

5 Conclusions

- (1) The lumped parameter-rigid elastic coupled dynamic model of two-stage planetary transmission for a hybrid car is established through inter-stage coupled method, where the supports of the ring gear of planet set II are represented as an elastic foundation with radial and tangential distributed stiffness, the ring gear of planet set II is modeled as an elastic continuum body and each stage sun, carrier and planets are regarded as rigid bodies. After analyzing the relative displacement of various components and considering the time-varying position angle of the planet gear and mesh stiffness of internal and external gear pairs, the differential equations of motion of two-stage planetary transmission are obtained. On this basis, the influences of different working conditions on each stage ring-planet dynamic mesh forces of two-stage planetary transmission are analyzed. With the increasing of the input rotational speeds, the ring-planet dynamic mesh forces of planet set I increase first and then decrease, but contrary to planet set II; With the increasing of the load torques, the ring-planet dynamic mesh forces of planet set I and II all increase. Simultaneously, each stage ring-planet dynamic mesh forces have been affected by the load torque more than the input rotational speed.
- (2) The acceleration data of two-stage planetary transmission box are tested by using the vibration testing platform and the corresponding refined frequency spectra are analyzed. The vibration testing experiments show that the vibration responses of planet set I and II by the working condition are not exactly the same, with the increasing of the input rotational speeds, the vibration intensities of planet set I increase first and then decrease, but contrary to planet set II; The vibration responses of planet set I and II all increase when the load torques increase.

Appendix

$$\mathbf{K}(t) = \begin{bmatrix} \mathbf{K}_{11} & \mathbf{K}_{12} & \mathbf{K}_{13} \\ \mathbf{K}_{21} & \mathbf{K}_{22} & \mathbf{K}_{23} \\ \mathbf{K}_{31} & \mathbf{K}_{32} & \mathbf{K}_{33} \end{bmatrix}$$

$$\mathbf{K}_0^i(t) = \begin{bmatrix} \sum_{n=1}^{N_i} (\mathbf{K}_{r1}^n)^i + (\mathbf{K}_{rb})^i & & & & (\mathbf{K}_{r2}^1)^i & \dots & (\mathbf{K}_{r2}^{N_i})^i \\ & \sum_{n=1}^{N_i} (\mathbf{K}_{c1}^n)^i + (\mathbf{K}_{cb})^i & & & (\mathbf{K}_{c2}^1)^i & \dots & (\mathbf{K}_{c2}^{N_i})^i \\ & & \sum_{n=1}^{N_i} (\mathbf{K}_{s1}^n)^i + (\mathbf{K}_{sb})^i & & (\mathbf{K}_{s2}^1)^i & \dots & (\mathbf{K}_{s2}^{N_i})^i \\ & & & & (\mathbf{K}_{pp}^1)^i & & \\ & & & & & \ddots & \\ & & & & & & (\mathbf{K}_{pp}^{N_i})^i \end{bmatrix}$$

symmetric

$$(\mathbf{K}_{r1}^n)^i = k_m^i(t) \begin{bmatrix} \sin^2 \psi_m^i & -\cos \psi_m^i \sin \psi_m^i & -\sin \psi_m^i \\ & \cos^2 \psi_m^i & \cos \psi_m^i \\ \text{symmetric} & & 1 \end{bmatrix};$$

$$(\mathbf{K}_{r2}^n)^i = k_m^i(t) \begin{bmatrix} -\sin \psi_m^i \sin \alpha_r^i & \sin \psi_m^i \cos \alpha_r^i & \sin \psi_m^i \\ \cos \psi_m^i \sin \alpha_r^i & -\cos \psi_m^i \cos \alpha_r^i & -\cos \psi_m^i \\ \sin \alpha_r^i & -\cos \alpha_r^i & -1 \end{bmatrix};$$

$$(\mathbf{K}_{r3}^n)^i = k_m^i(t) \begin{bmatrix} \sin^2 \alpha_r^i & -\cos \alpha_r^i \sin \alpha_r^i & -\sin \alpha_r^i \\ & \cos^2 \alpha_r^i & \cos \alpha_r^i \\ \text{symmetric} & & 1 \end{bmatrix};$$

$$\mathbf{K}_{rb}^I = \text{diag}(k_{rx}^I, k_{ry}^I, k_{ru}^I + k_{cru}^I \frac{(r_e^I)^2}{(r_r^I)^2});$$

$$\mathbf{K}_{rb}^{II} = \pi \text{diag}(k_{rbs} + k_{rus}, k_{rbs} + k_{rus}, \frac{2k}{\cos^2 \alpha_r^{II}});$$

$$(\mathbf{K}_{c1}^n)^i = k_{pn}^i \begin{bmatrix} 1 & 0 & -\sin \psi_n^i \\ & 1 & \cos \psi_n^i \\ \text{symmetric} & & 1 \end{bmatrix};$$

$$(\mathbf{K}_{c2}^n)^i = k_{pn}^i \begin{bmatrix} -\cos \psi_n^i & \sin \psi_n^i & 0 \\ -\sin \psi_n^i & -\cos \psi_n^i & 0 \\ 0 & -1 & 0 \end{bmatrix};$$

$$(\mathbf{K}_{c3}^n)^i = \text{diag}(k_{pn}^i, k_{pn}^i, 0);$$

$$\mathbf{K}_{cb}^I = \text{diag}(k_{cx}^I, k_{cy}^I, k_{cu}^I);$$

$$\mathbf{K}_{cb}^{II} = \text{diag}(k_{cx}^{II}, k_{cy}^{II}, k_{cu}^{II} + k_{cru}^{II} \frac{(r_e^{II})^2}{(r_c^{II})^2});$$

$$(\mathbf{K}_{s1}^n)^i = k_{sn}^i(t) \begin{bmatrix} \sin^2 \psi_{sn}^i & -\cos \psi_{sn}^i \sin \psi_{sn}^i & -\sin \psi_{sn}^i \\ & \cos^2 \psi_{sn}^i & \cos \psi_{sn}^i \\ \text{symmetric} & & 1 \end{bmatrix};$$

$$(\mathbf{K}_{s2}^n)^i = k_{sn}^i(t) \begin{bmatrix} \sin \psi_{sn}^i \sin \alpha_s^i & \sin \psi_{sn}^i \cos \alpha_s^i & -\sin \psi_{sn}^i \\ -\cos \psi_{sn}^i \sin \alpha_s^i & -\cos \psi_{sn}^i \cos \alpha_s^i & \cos \psi_{sn}^i \\ -\sin \alpha_s^i & -\cos \alpha_s^i & 1 \end{bmatrix};$$

$$(\mathbf{K}_{s3}^n)^i = k_{sn}^i(t) \begin{bmatrix} \sin^2 \alpha_s^i & \cos \alpha_s^i \sin \alpha_s^i & -\sin \alpha_s^i \\ & \cos^2 \alpha_s^i & -\cos \alpha_s^i \\ \text{symmetric} & & 1 \end{bmatrix};$$

$$\mathbf{K}_{sb}^I = \text{diag}(k_{sx}^I, k_{sy}^I, k_{su}^I + k_{ssu}^I \frac{(r_b^I)^2}{(r_s^I)^2});$$

$$\mathbf{K}_{sb}^{II} = \text{diag}(k_{sx}^{II}, k_{sy}^{II}, k_{su}^{II} + k_{ssu}^{II} \frac{(r_b^{II})^2}{(r_s^{II})^2});$$

$$(\mathbf{K}_{pp}^{N_i})^i = (\mathbf{K}_{r3}^{N_i})^i + (\mathbf{K}_{c3}^{N_i})^i + (\mathbf{K}_{s3}^{N_i})^i;$$

$$\mathbf{K}_{11} = \mathbf{K}_0^I;$$

$$\mathbf{K}_{12}\mathbf{a} = \mathbf{0}_{3N_1 + (9 \times JN_{II})};$$

$$\mathbf{K}_{13}\mathbf{a} = \begin{bmatrix} (\mathbf{K}_{13})_{3 \times 6} & \mathbf{0} \\ \mathbf{0} & (\mathbf{K}_{13})_{9 \times 9} \end{bmatrix}_{(3N_1 + 9) \times (3N_{II} + 9)}, \quad (\mathbf{K}_{13})_{3 \times 6} = -k_{cru}^I \frac{(r_e^I)^2}{r_r^I}, \quad (\mathbf{K}_{13})_{9 \times 9} = -k_{ssu}^I \frac{(r_b^I)^2}{r_s^I};$$

$$\mathbf{K}_{21}\mathbf{a} = \mathbf{0}_{JN_{II} \times (3N_1 + 9)};$$

$$\mathbf{K}_{22}\mathbf{a} = [k_{bend}L_1 + \left(k_{rus} - k_{rbs} \frac{\partial^2}{\partial \theta^2}\right)R / k_m^{II}(t) + k_m^{II}(t)L_2]_{JN_{II} \times N_{II}};$$

$$k_{bend} = EI_a / R^3(1 - \nu^2), \quad L_1 = -\left(\frac{\partial^6}{\partial \theta^6} + 2\frac{\partial^4}{\partial \theta^4} + \frac{\partial^2}{\partial \theta^2}\right),$$

$$L_2 = -\sum_{n=1}^{N_{II}} \left[\left(\sin^2 \alpha_r^{II} \frac{\partial^2}{\partial \theta^2} - \cos^2 \alpha_r^{II} \right) \delta(\theta - \psi_n^{II}) + \left(\sin \alpha_r^{II} \frac{\partial}{\partial \theta} + \cos \alpha_r^{II} \right) \sin \alpha_r^{II} \frac{\partial \delta(\theta - \psi_n^{II})}{\partial \theta} \right],$$

- $\delta(\theta - \psi_n^{\text{II}})$ Dirac function;
- E Young's modulus of the ring gear of planet set II, $E = 2.07 \times 10^{11}$,
- ν Poisson's ratio of the ring gear of planet set II, $\nu = 0.3$,
- R neutral radius of the ring gear of planet set II,
- I_a area moment of inertia of the ring gear of planet set II,
- P mass density per unit length of the ring gear of planet set II.

$$k_{rus} = 0 \text{ N/m}, k_{rbs} = 10^5 \text{ N/m};$$

$$\mathbf{K}_{23}\mathbf{a} = [k_m^{\text{II}}(t) \left[\cos \alpha_r^{\text{II}} \delta(\theta - \psi_n^{\text{II}}) - \sin \alpha_r^{\text{II}} \frac{\partial \delta(\theta - \psi_n^{\text{II}})}{\partial \theta} \right] \delta_n^{\text{II}}]_{JN_{\text{II}} \times (3N_{\text{II}} + 9)};$$

$$\mathbf{K}_{31}\mathbf{a} = \begin{bmatrix} (\mathbf{K}_{31})_{6 \times 3} & \mathbf{0} \\ \mathbf{0} & (\mathbf{K}_{31})_{9 \times 9} \end{bmatrix}_{(3N_{\text{II}} + 9) \times (3N_{\text{II}} + 9)}, (\mathbf{K}_{31})_{6 \times 3} = -k_{cru}^{\text{II}} \frac{(r_e^{\text{II}})^2}{r_c^{\text{II}}}, (\mathbf{K}_{31})_{9 \times 9} = -k_{ssu}^{\text{II}} \frac{(r_b^{\text{II}})^2}{r_s^{\text{II}}};$$

$$\mathbf{K}_{32}\mathbf{a} = k_m^{\text{II}}(t) \left[\sum_{n=1}^{N_{\text{II}}} \left(\mathbf{b}_r \chi|_{\theta=\psi_n^{\text{II}}} \right) \quad \mathbf{0} \quad \mathbf{0} \quad \mathbf{b}_p \chi|_{\theta=\psi_1} \quad \cdots \quad \mathbf{b}_p \chi|_{\theta=\psi_{N_{\text{II}}}} \right]_{(3N_{\text{II}} + 9) \times JN_{\text{II}}}^{\text{T}},$$

$$\mathbf{b}_r = (-\sin \psi_m^{\text{II}}, \cos \psi_m^{\text{II}}, 1)^{\text{T}}, \mathbf{b}_p = (\sin \alpha_r^{\text{II}}, -\cos \alpha_r^{\text{II}}, -1)^{\text{T}};$$

$$\mathbf{K}_{33} = \mathbf{K}_0^{\text{II}}.$$

References

1. Sun YT, Zhang HT (2011) Hybrid vehicle research situation and development prospect. J Heilongjiang Inst Technol 25(2):13–16 (in Chinese)
2. Luo YT, Chen YS (2012) Dynamic modeling and analysis of power coupling system with two-stage planetary gear trains for hybrid system. J Mech Eng 48(5):70–75 (in Chinese)
3. Kahraman A (1994) Natural modes of planetary gear trains. J Sound Vib 173(1):125–130
4. Song YM, Xu WD, Zhang C et al (2006) Modified torsional model development and natural characteristics analysis of 2 K-H epicyclic gearing. J Mech Eng 42(5):16–21 (in Chinese)
5. Duan FH, Hu QC, Xie CX (2010) Dynamic behavior for planetary geared system with plastic gear. J Mech Eng 46(1):62–67 (in Chinese)
6. Lin J, Parker RG (1999) Analytical characterization of the unique properties of planetary gear free vibration. ASME J Vib Acoust 121(3):316–321
7. Ericson TM, Parker RG (2013) Natural frequency clusters in planetary gear vibration. J Vib Acoust 135:061002-1–13
8. Kiracofe DR, Parker RG (2007) Structured vibration modes of general compound planetary gear systems. J Vib Acoust 129(1):1–16
9. Cooley CG, Parker RG (2012) Vibration properties of high-speed planetary gears with gyroscopic effects. J Vib Acous 134:061014-1–11
10. Lin J, Parker RG (2002) Planetary gear parametric instability caused by mesh stiffness variation. J Sound Vib 249(1):129–145
11. Cooley CG, Parker RG (2013) Mechanical stability of high-speed planetary gears. Int J Mech Sci 69:59–71
12. Ericson TM, Parker RG (2013) Planetary gear modal vibration experiments and correlation against lumped parameter and finite element models. J Sound Vib 332:2350–2375
13. Ericson TM, Parker RG (2014) Experimental measurement of the effects of torque on the dynamic behavior and system parameters of planetary gears. Mech Mach Theory 74:370–389

14. Hidaka T, Terauchi Y, Nagamura K (1979) Dynamic behavior of planetary gear (7th report, influence of the thickness of the ring gear). *Bull JSME* 22(170):1142–1149
15. Vaujany JP, Kim HC (1996) Effects of rim and web on stresses of internal cylindrical gears. *ASME Design Eng Division* 88(1):73–80
16. Kahraman A, Vijayakar S (2001) Effect of internal gear flexibility on the quasi-static behavior of a planetary gear set. *Trans ASME J Mech Design* 123(3):408–415
17. Kahraman A, Kharazi AA, Umrani M (2003) A deformable body dynamic analysis of planetary gears with thin rims. *J Sound Vib* 262:752–768
18. Wu XH (2010) Vibration of planetary gears having an elastic continuum ring gear. The Ohio State University, The Ohio State
19. Zhang J, Song YM, Wang JJ (2009) Dynamic modeling for spur planetary gear transmission with flexible ring gear. *J Mech Eng* 45(12):29–36 (in Chinese)
20. Zhang J, Liu XZ, Jiao Y, Song YM (2014) Vibration analysis of planetary gear trains based on a discrete-continuum dynamic model. *J Mech Eng* 50(15):104–112 (2014) (in Chinese)
21. Xiao ZM, Qin DT, Wang JH et al (2010) Study on torsional dynamic of 3-stage planetary gears of main reducer used in driving cutterhead of shield tunneling machine. *China Mech Eng* 21(18):2176–2182 (in Chinese)
22. Zhao Y, Qin DT (2013) Dynamic characteristics of multi-stage planetary gear train in shield machine cutter driver. *J Chongqing Univ* 36(6):26–34 (in Chinese)
23. Qin DT, Yang J, Zhou ZG et al (2013) Dynamic characteristic of planetary gear system of wind turbines under varying load. *China Mech Eng* 24(3):295–301 (in Chinese)

Stiffness Modeling of Parallel Manipulator with Articulated Traveling Plate

Tao Sun, Hao Wu, Binbin Lian, Panfeng Wang and Yimin Song

Abstract Parallel manipulator (PM) with articulated travelling plate (ATP) has drawn more and more attention from industry and academia. In order to characterize stiffness of PMs with ATP in an explicit and accurate manner, a semi-analytical stiffness modeling method is proposed. Resorting to superposition principle, compliance matrix of the whole PM can be formulated by the parallel limbs and ATP step-by-step. In the formulation of compliance of two substructures, n -DoF ($n \leq 6$) virtual springs are firstly applied to describe component deformations. Then, deformation superposition, twist/wrench mapping model, virtual work principle and Hooke's Law are adopted. Wrenches of parallel limbs become single wrenches within each limb, combination wrenches from opposite limbs due to the effect of ATP. This stiffness modeling method is exemplified and verified by a one translational and three rotational (1T3R) PM with ATP. Results from finite element analysis software indicate that proposed stiffness modeling method is with high accuracy.

Keywords Parallel manipulators · Articulated traveling plate · Stiffness modeling · Virtual springs · Jacobian matrix · Twist and wrench mapping model

T. Sun · H. Wu · B. Lian · P. Wang · Y. Song (✉)

Key Laboratory of Mechanism Theory and Equipment Design of Ministry of Education,
Tianjin University, Tianjin 300354, China
e-mail: ymsong@tju.edu.cn

T. Sun
e-mail: stao@tju.edu.cn

H. Wu
e-mail: whao@tju.edu.cn

B. Lian
e-mail: lianbinbin@tju.edu.cn

P. Wang
e-mail: panfengwang@tju.edu.cn

1 Introduction

In the industrial areas such as food packaging, medicine, and semiconductor manufacturing, the family of parallel manipulators (PMs) with articulated traveling plate (ATP) have proven great efficiency in high speed pick-and-place operations [1–3]. Unlike single platform of common PMs, ATP is composed of two or more in-parts and one out-part [4]. Additional motions can be obtained from relative movements of in-parts, which enable PMs to have larger range of motions. Due to superior motion capability, PMs with ATP have great potential to enlarge their commercial applications, for instance, tracking mechanism [5], docking equipment [6] or machine tools. Analysis and design of PMs with ATP have also attracted more and more attention.

Stiffness evaluates deformations caused by external payloads and directly affects accuracy of PMs [7–9]. Thus, stiffness modeling is one of the most fundamental analyses in the development of PMs with ATP. Referring to stiffness modeling of PMs, semi-analytical approach is recognized as the most effective method. It obtains compliance matrix of components by FEA software, then achieves stiffness of PMs by analytical computation [10–24]. Semi-analytical stiffness modeling is also regarded as virtual joint method (VJM). The core idea is adding virtual springs to elastic deformations of components [11]. And stiffness model of PMs is formulated by applying deformation superposition principle, mapping matrix, Hooke's Law to virtual work equation [19]. Concerning denotation of virtual springs, semi-analytical approach can be roughly divided into two categories, i.e. single degree-of-freedom (DoF) spring [16–23] and 6-DoF spring [10, 11, 24].

For the first category, compliance of virtual springs is usually in scalar form. And mapping matrix between joint space and operated space (Jacobian matrix) are adopted. This method can be traced back to 1990. Gosselin [16] employed linear spring to describe actuator compliance and formulated stiffness models of planar 3-DoF and spatial 6-DoF parallel mechanisms by Jacobian matrix. Note that stiffness along/about constrained directions of lower mobility PMs cannot be obtained through overall Jacobian matrix. Ceccarelli [17], Zhang [18] and Li [19, 20] applied overall Jacobian matrix to the stiffness modeling of CaPaMan, Tripod-based PM, 3-PUU and 3-PRC PMs. Herein, P, U, R, C denote actuated prismatic joint, universal joint, revolute joint and cylindrical joint. This adopted Jacobian matrix is able to unify PM performance analysis including kinematic, stiffness, accuracy and dynamic [5]. However, only diagonal elements of compliance matrix are selected when concerning compliance of virtual joint. The scalar compliance of virtual spring corresponds to limb force or moment. Coupling effects between linear and angular compliance are neglected, which might lower the accuracy of stiffness model of PMs.

For the second category, compliance matrix denoted by 6-DoF virtual spring is applied. It addresses more effort on high accuracy of stiffness model since the coupling items are included. Pashkevich [10, 11] formulated mapping models between each component and end reference point of Orthoglide PM. Then he

employed 6-DoF virtual springs to describe deformations of components. From the point of elastic energy, 6-DoF virtual springs within the same limb are adopted to calculate energy of the whole mechanism by Taghvaeipour [24]. Mapping relations from components to end reference point are considered in generalized displacements of virtual springs. It is summarized that 6-DoF virtual spring provides complete deformations of components to end effector. The stiffness model is more accurate. But the mapping matrix fails to characterize the deformation transmissions from limbs to mechanism. And effects of passive joints have to be evaluated separately, which makes calculation process complicated.

Inspired by above literature review, a new stiffness modeling method is proposed. The idea is to integrate advantages of the two semi-analytical approaches and fix their defects. That is (1) to describe the compliance of component by n -DoF spring ($n \leq 6$) considering the effect of passive joint, and (2) to employ Jacobian matrix between joint space and operated space. Taking the special structure of ATP into account, how to apply this stiffness modeling method to a general PM with ATP is the main target of this article.

Having outlined the state-of-art, this paper is organized as follow: Sect. 2 investigates a general procedure for stiffness modeling of PM with ATP, then one translational and three rotational (1T3R) PM with ATP is picked out as an example to demonstrate the stiffness modeling procedure. Mechanism description is introduced in Sect. 3, while its stiffness modeling is formulated in Sect. 4. Case study and verification by finite element analysis (FEA) software are implemented in Sect. 5 before the conclusions are drawn in Sect. 6.

2 Stiffness Modeling Procedure of PM with ATP

Figure 1 shows a PM with ATP from initial location to a general configuration. The motion of out-part (regarded as moving platform) can be divided into two phases. Phase 1: Rotation and translation caused by limbs. End reference point O' is from the initial state $O'(0)$ to state $O'(1)$. Phase 2: Rotation or translation independently by relative motion of in-parts. Point O' is from state $O'(1)$ to state $O'(2)$.

Thus, motion of point O' is contributed by both the limbs and the in-parts. Similarly, when exerting external forces on point O' , corresponding internal forces are from limbs and in-parts. Therefore, compliance matrix of point O' is contributed by the parallel limbs and ATP. Since motions and forces of ATP are independent from limbs, step-by-step strategy [25] is adopted. And stiffness modeling procedure of PM with ATP can be summarized as: firstly formulate compliance model of point O' (C_L) by regarding the input parts and output part as rigid bodies, then establish compliance model of point O' (C_P) by assuming that limbs are rigid, finally add the two compliance models by deformation superposition principle.

Drawing mainly on screw theory, twist/wrench mapping model of limbs are computed considering the effect of ATP. And several reference frames needs to be

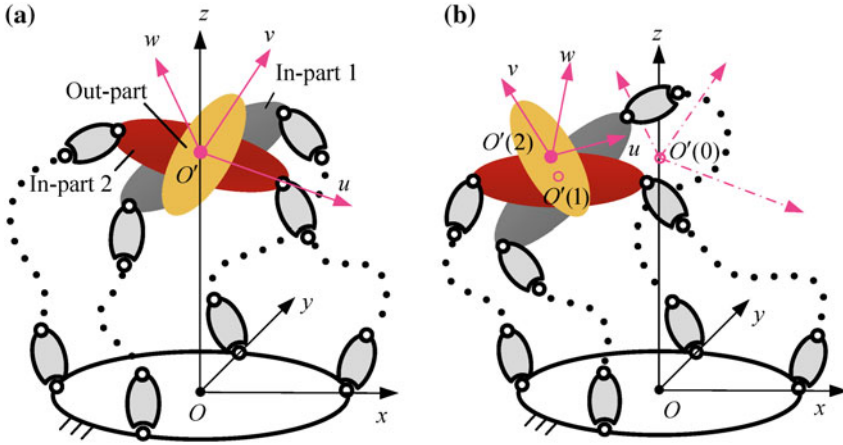


Fig. 1 PM with ATP **a** at initial location, **b** at a general configuration

assigned to deal with n -DoF virtual springs. Therefore, formulation of C_L can be carried out as follow.

- (1) Formulate twist/wrench mapping model of parallel limbs taking joints in ATP into account.
- (2) Assign instantaneous reference frame to point O' and component reference frame to each component.
- (3) Obtain compliance matrices of n -DoF ($n \leq 6$) virtual springs by FEA software in the component reference frame.
- (4) Add compliance matrices within the same limb in instantaneous reference frame and then obtain compliance matrix of limb by superposition principle.
- (5) Calculate C_L by twist/wrench mapping models, Hooke's law and virtual work principle.

Similarly, twist/wrench transmission of ATP are investigated, and reference frames are established to address n -DoF virtual springs. Thus, formulation of C_P is implemented as follow.

- (1) Determine all twist/wrench transmission routes from the in-parts to point O' .
- (2) Establish route reference frame and acquire compliance matrices of n -DoF ($n \leq 6$) virtual springs by means of FEA software.
- (3) Take the sum of compliance matrices within the same route and calculate stiffness matrix of the route in the moving reference frame.
- (4) Obtain C_P utilizing transformation matrix, Hooke's law and virtual work principle.

The effect of joints in ATP is addressed in the formulation of C_L and C_P . n -DoF ($n \leq 6$) virtual springs are employed to provide complete information of component compliance matrix. And the Jacobian matrix between joint space and operated

space is adopted. With the step-by-step strategy, explicit mapping relations and complete component deformations can be applied to the semi-analytical stiffness modeling of PM with ATP. The obtained stiffness model is believed to be highly accurate.

3 Mechanism Description

A pose-adjusting PM with ATP (called PaQuad PM) is taken as an example. The virtual prototype of PaQuad PM is as shown in Fig. 2a. PaQuad PM is composed of a fixed base, an ATP and four identical $\underline{P}RS$ limbs. Herein S denotes spherical joint. ATP consists of in-part 1, in-part 2 and out-part. The in-part 1 connects to out-part through helical (H) joint, whereas the in-part 2 joints to out-part by R joint. The axis of H joint and R joint in ATP are collinear. The $\underline{P}RS$ limbs link to fixed base and ATP by \underline{P} joint and S joint. Herein, \underline{P} joint is designed to be combination of screw/nut, guide/slider and sliding saddle. The R joint and S joint are connected by bar. S joint is composed of three mutually perpendicular R joint components. Note that relative translation of in-part 1 and in-part 2 results in rotation of H joint, i.e.

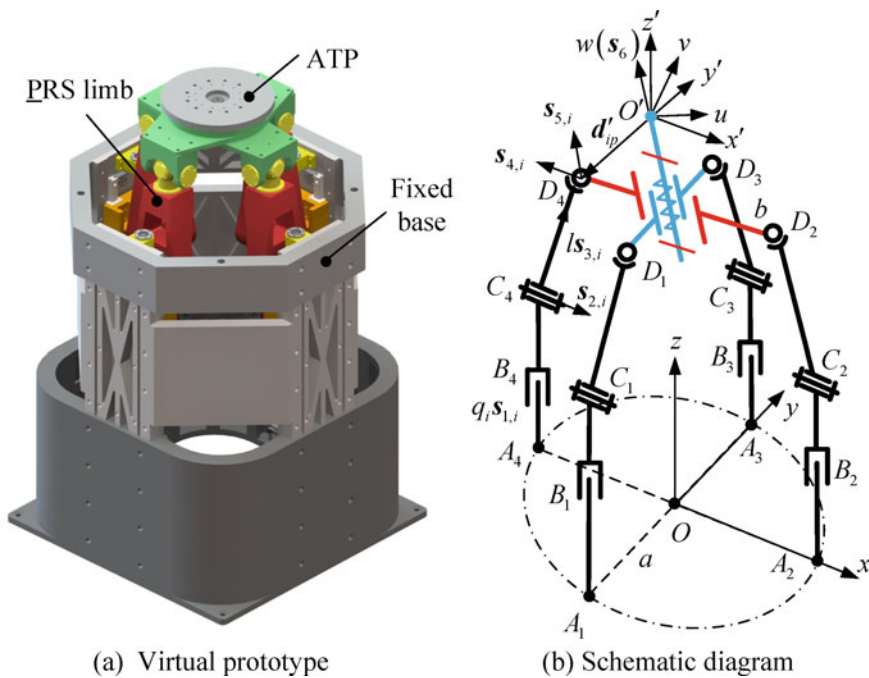


Fig. 2 Virtual prototype and schematic diagram of PaQuad PM

the rotation of out-part. Combining with two rotations and one translation formulated by the \underline{P} RS limbs, PaQuad PM has the capability of 1T3R motions [9].

In order to describe motions of PaQuad PM, some denotations and coordinate frames are defined as shown in Fig. 2b. The plane of fixed base is formed by connecting points A_i ($i = 1, \dots, 4$), which are symmetrically distributed on the circle with center point O and radius a . Point B_i , C_i and D_i ($i = 1, \dots, 4$) denote centers of \underline{P} joint, R joint and S joint. The lengths of in-part 1 and in-part 2 are both $2b$ and the initial distance is e . The moving distance of \underline{P} joint and the length of bar are represented by q_i and l . A fixed reference frame $O - xyz$ is assigned to point O , of which x -axis is collinear with OB_2 and z -axis is vertical to the fixed base. Similarly, moving reference frame $O' - uvw$ is attached to the point O' of out-part. Its w -axis points to the same direction with H joint, and u -axis is parallel to D_4D_2 at initial location. Meanwhile, instantaneous frame $O' - x'y'z'$ is fixed to point O' and their axes are parallel to those of frame $O - xyz$. Inverse position analysis of PaQuad PM can be referred to [9].

4 Stiffness Modeling of PaQuad PM

Referring to Sect. 2, stiffness modeling procedure of PaQuad PM involves determination of C_L and C_P . Therefore,

$$C = C_L + C_P, K = C^{-1}. \quad (1)$$

where C , K are compliance and stiffness matrix of PaQuad PM.

Considering deformations of components, two basic assumptions are made as follow: (1) the friction within joints are neglected, (2) All of the moving components satisfy the linear superposition principle.

4.1 Determination of C_L

Due to the effect of joints in ATP, actuation and constraint wrenches of limbs have transferred into single and combination wrenches. Single wrench is converted from wrenches within each limb. Combination wrench is formulated by the constraint wrenches in the opposite limbs. Referring to [9], the twist and wrench mapping model of PaQuad PKM can be established as follow.

$$\$_i = J_x^{-1} J_\rho \rho, (J_x^{-1} J_\rho)^T \$_w = f. \quad (2)$$

where,

$$\begin{aligned}
 \mathbf{J}_x &= \begin{bmatrix} \mathbf{J}_{xs} \\ \mathbf{J}_{xc} \end{bmatrix}, \mathbf{J}_\rho = \begin{bmatrix} \mathbf{J}_{\rho a} & \mathbf{0} \\ \mathbf{0} & \mathbf{0} \end{bmatrix}, \mathbf{J}_{xs} = \begin{bmatrix} \hat{\$}_{ws,1}^T \\ \hat{\$}_{ws,2}^T \\ \hat{\$}_{ws,3}^T \\ \hat{\$}_{ws,4}^T \end{bmatrix}, \mathbf{J}_{xc} = \begin{bmatrix} \hat{\$}_{wc,1}^T \\ \hat{\$}_{wc,2}^T \end{bmatrix} \\
 \mathbf{J}_{\rho a} &= \begin{bmatrix} \hat{\$}_{ws,1}^T \hat{\$}_{ta,1} & 0 & 0 & 0 \\ 0 & \hat{\$}_{ws,2}^T \hat{\$}_{ta,2} & 0 & 0 \\ 0 & 0 & \hat{\$}_{ws,3}^T \hat{\$}_{ta,3} & 0 \\ 0 & 0 & 0 & \hat{\$}_{ws,4}^T \hat{\$}_{ta,4} \end{bmatrix}, \boldsymbol{\rho} = \begin{pmatrix} \rho_{ta} \\ \mathbf{0} \end{pmatrix}, \\
 \boldsymbol{\rho}_{ta} &= \begin{pmatrix} \rho_{ta,1} \\ \rho_{ta,2} \\ \rho_{ta,3} \\ \rho_{ta,4} \end{pmatrix}
 \end{aligned}$$

$$\hat{\$}_{ws,i}^T = \hat{\$}_{w,lc,i}^T - k_i \hat{\$}_{w,la,i}^T, \hat{\$}_{wc,1}^T = \hat{\$}_{w,lc,1}^T - l_1 \hat{\$}_{w,lc,3}^T, \hat{\$}_{wc,2}^T = \hat{\$}_{w,lc,2}^T - l_2 \hat{\$}_{w,lc,4}^T$$

As mentioned in Sect. 2, component reference frame are firstly assigned to derive the component compliance matrices by FEA software. And then effects of passive joints are eliminated, finally the component compliance matrices are transferred to the instantaneous reference frame $O' - x'y'z'$. Therefore, compliance matrix of i th PRS limb $\bar{C}_{L,i}$ in frame $O' - x'y'z'$ can be formulated as

$$\bar{C}_{L,i} = \mathbf{T}_{pi} \bar{C}_{pi} \mathbf{T}_{pi}^T + \mathbf{T}_{bi} \bar{C}_{bi} \mathbf{T}_{bi}^T + \mathbf{T}_{si} \bar{C}_{si} \mathbf{T}_{si}^T. \tag{3}$$

where \bar{C}_{pi} , \bar{C}_{bi} , \bar{C}_{si} are the compliance matrices of P joint component, R joint component and S joint component in each component reference frame. \mathbf{T}_{pi} , \mathbf{T}_{bi} , \mathbf{T}_{si} are the transmission matrices from each component to point O' in frame $O' - x'y'z'$.

$$\begin{aligned}
 \mathbf{T}_p &= \begin{bmatrix} \mathbf{R}_p^{-1} & \mathbf{R}_p^{-1} \cdot [-\mathbf{l}_p \times] \\ \mathbf{0} & \mathbf{R}_p^{-1} \end{bmatrix}, \mathbf{T}_b = \begin{bmatrix} \mathbf{R}_b^{-1} & \mathbf{R}_b^{-1} \cdot [-\mathbf{l}_b \times] \\ \mathbf{0} & \mathbf{R}_b^{-1} \end{bmatrix}, \\
 \mathbf{T}_s &= \begin{bmatrix} \mathbf{R}_s^{-1} & \mathbf{R}_s^{-1} \cdot [-\mathbf{l}_s \times] \\ \mathbf{0} & \mathbf{R}_s^{-1} \end{bmatrix}
 \end{aligned}$$

herein, \mathbf{R}_p , \mathbf{R}_b , \mathbf{R}_s are the rotating matrix of frame $O' - x'y'z'$ with respect to component frames. $[-\mathbf{l}_p \times]$, $[-\mathbf{l}_b \times]$, $[-\mathbf{l}_s \times]$ are skew symmetrical matrices. \mathbf{l}_p , \mathbf{l}_b , \mathbf{l}_s are vectors from each center to point O' .

Taking \underline{P} joint component as example, compliance matrix of component in component reference frame is obtained by FEA software. Unit force/moment along/about each axis is applying on the output point and the compliance matrix is formulated as

$$\bar{C}_{pi} = \begin{bmatrix} \frac{\Delta p_x(f_x)}{f_x} & \frac{\Delta p_x(f_y)}{f_y} & \dots & \frac{\Delta p_x(\tau_z)}{\tau_z} \\ \frac{\Delta p_y(f_x)}{f_x} & \frac{\Delta p_y(f_y)}{f_y} & \dots & \frac{\Delta p_y(\tau_z)}{\tau_z} \\ \vdots & \vdots & \dots & \vdots \\ \frac{\Delta \varphi_z(f_x)}{f_x} & \frac{\Delta \varphi_z(f_y)}{f_y} & \dots & \frac{\Delta \varphi_z(\tau_z)}{\tau_z} \end{bmatrix}_{6 \times 6} \quad (4)$$

where f_x, f_y, τ_z denote unit force/moment along/about the corresponding axis, each column represents linear/angular deformation resulted from unit force/moment. The linear compliance is obtained directly from FEA software while angular compliance is derived from rotation matrix determined by SVD-based solution [26].

When the in-parts and out-part are regarded as rigid bodies, virtual work equation at point O' for each limb can be formulated as

$$\mathbf{\$}_w^T \mathbf{\$}_t = \mathbf{f}_i^T \Delta_i \quad (5)$$

where $\mathbf{\$}_w, \mathbf{\$}_t$ are external wrench and corresponding deformations. \mathbf{f}_i, Δ_i are the single wrench and deformations in i th PRS limb.

According to twist mapping model in Eq. (2) and Hooke's law, one can obtain

$$\mathbf{\$}_{ws,i}^T \mathbf{\$}_t = \Delta_i, \quad \bar{C} \mathbf{f}_i = \Delta_i \quad (6)$$

Substituting Eq. (6) into Eq. (5), and taking inversion yields

$$\mathbf{K}_{Ls,i} = \mathbf{\$}_{ws,i} \left(\mathbf{\$}_{ws,i}^T \bar{C}_{L,i} \mathbf{\$}_{ws,i} \right)^{-1} \mathbf{\$}_{ws,i}^T \quad i = 1, 2, \dots, 4. \quad (7)$$

Similarly, taking combination wrenches from opposite limbs into account, corresponding stiffness matrices can be obtained by virtual work equation and Hooke's Law.

$$\mathbf{K}_{Lc,j} = \mathbf{\$}_{wc,j} \left[\mathbf{\$}_{wc,j}^T \left(\bar{C}_{Lj}^{-1} + \bar{C}_{Lj+1}^{-1} \right)^{-1} \mathbf{\$}_{wc,j} \right]^{-1} \mathbf{\$}_{wc,j}^T \quad j = 1, 2. \quad (8)$$

Therefore, the compliance matrix of PRS limbs when regarding component in ATP are rigid can be formulated as

$$\mathbf{C}_L = \left(\sum_{i=1}^4 \mathbf{K}_{Ls,i} + \sum_{j=1}^2 \mathbf{K}_{Lc,j} \right)^{-1} \quad j = 1, 2. \quad (9)$$

4.2 Determination of C_P

As is shown in Fig. 3, the contribution of ATP is analyzed by regarding components in PRS limbs as rigid body. There are two routes from the two in-parts to reference point O' , in the meanwhile, the in-parts are connected by C joint. Thus, the two routes can be determined as (1) from in-part 1 through H joint to center screw finally out-part, (2) in-part 2 plus in-part 1 with C joint through R joint to out-part.

Compliance matrix of route 1 in frame $O' - x'y'z'$ can be formulated as

$$\bar{C}_{r,1} = T_{I1,1}C_{I1,1}T_{I1,1}^T + T_{cs}C_{cs}T_{cs}^T. \tag{10}$$

where $T_{I1,1}$, T_{cs} are transmission matrices of in-part 1, center screw to point O' in frame $O' - x'y'z'$. $C_{I1,1}$ represents the compliance matrix of in-part 1 that connects to H joint. C_{cs} is compliance matrix of center screw.

Similarly, the compliance matrix of route 2 in moving reference frame $O' - uvw$ is computed as

$$\bar{C}_{r,2} = T_{I1,2}C_{I1,2}T_{I1,2}^T + T_{I2}C_{I2}T_{I2}^T + T_{be}C_{be}T_{be}^T. \tag{11}$$

where, $T_{I1,2}$, T_{I2} , T_{be} are transmission matrices of in-part 1, in-part 2 and bearing (R joint) to point O' in frame $O' - x'y'z'$. $C_{I1,2}$, C_{I2} , C_{be} are compliance matrices of components in component frames.

Therefore, compliance matrix of ATP when regarding components in PRS limb are rigid is as follow.

$$C_P = \left(\bar{C}_{r,1}^{-1} + \bar{C}_{r,2}^{-1} \right)^{-1}. \tag{12}$$

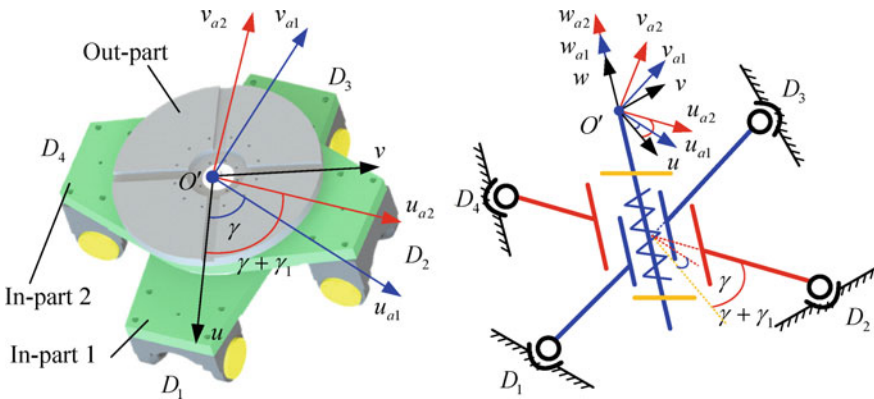


Fig. 3 ATP and corresponding component reference frames

5 Verification

Case study is carried out to verify the stiffness modeling in Sect. 4. Dimensional parameters and prescribed workspace of PaQuad PM are as shown in Table 1. The virtual prototype and built on the basis of engineering experience. And the distribution of linear and angular stiffness within prescribed workspace is as shown in Fig. 4. FEA software (SAMCEF by SAMTECH Inc.) is applied to the verification of stiffness modeling of PaQuad PM in Sect. 4. PaQuad PM is assumed to be made of steel. Tetrahedron elements are employed in SEMCEF. Unit force and moment are exerted to point O' . Four typical configurations in the prescribed workspace are chosen, whose rotating angles α, β, γ are $(0^\circ, 0^\circ, 0^\circ), (15^\circ, 0^\circ, 0^\circ), (0^\circ, 15^\circ, 0^\circ), (15^\circ, 15^\circ, 0^\circ)$ and the z value is 1200 mm.

Tables 2 and 3 show the linear and angular deformations of reference point O' in the fixed frame obtained from theoretical and FEA simulation. It can be concluded that the variation tendency of the theoretical values is similar to that of the FEA values. The errors are in an acceptable range (within 5 %), which indicates the correctness of theoretical stiffness model.

Table 1 Dimensional parameters and workspace of PaQuad PM (unit: rad or mm)

Dimensional parameters					Prescribed workspace			
a	b	l	P_h	e_0	α	β	γ	z
286	260	541	10	0	$\pm \frac{2}{9}\pi$	$\pm \frac{2}{9}\pi$	$\pm \pi$	(850, 1350)

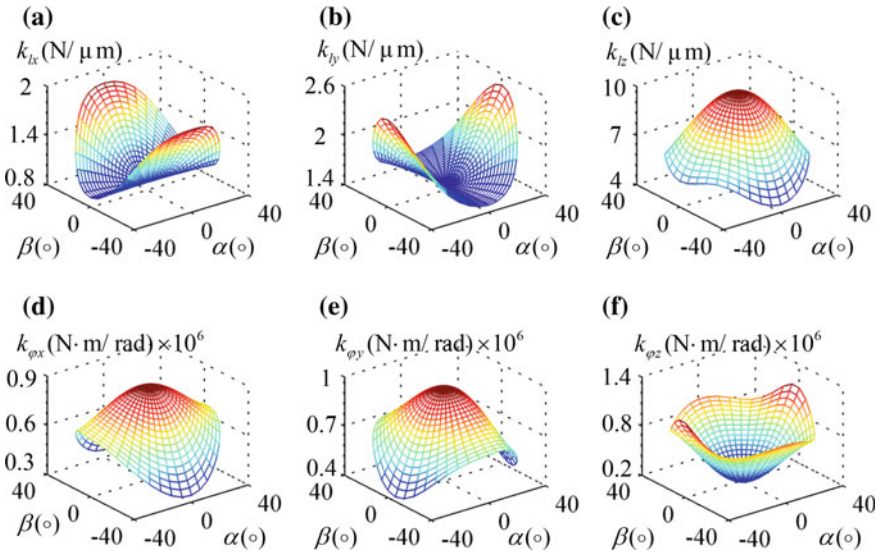


Fig. 4 Stiffness distribution of point O' in frame $O - xyz$

Table 2 Linear stiffness between theoretical and FEA simulations (unit: N/ μm)

$z = 1200$		k_{lx}	k_{ly}	k_{lz}
$(0^\circ, 0^\circ, 0^\circ)$	Theoretical	0.8902	1.5010	9.5890
	FEA	0.9253	1.5157	9.7219
	Error	4.38 %	1.05 %	1.39 %
$(15^\circ, 0^\circ, 0^\circ)$	Theoretical	0.8892	1.7290	7.7160
	FEA	0.9271	1.7657	7.9312
	Error	4.26 %	2.12 %	2.79 %
$(0^\circ, 15^\circ, 0^\circ)$	Theoretical	1.1735	1.5030	7.1475
	FEA	1.2178	1.5268	7.3812
	Error	3.78 %	1.58 %	3.27 %
$(15^\circ, 15^\circ, 0^\circ)$	Theoretical	1.0865	1.6761	5.9326
	FEA	1.1365	1.7316	6.1039
	Error	4.60 %	3.31 %	2.89 %

Table 3 Angular stiffness between theoretical and FEA simulations (unit: Nm/rad)

$z = 1200$		$k_{\phi x} \times 10^6$	$k_{\phi y} \times 10^6$	$k_{\phi z} \times 10^6$
$(0^\circ, 0^\circ, 0^\circ)$	Theoretical	0.8935	0.9820	0.4702
	FEA	0.9204	0.9919	0.4803
	Error	3.01 %	1.01 %	2.15 %
$(15^\circ, 0^\circ, 0^\circ)$	Theoretical	0.8371	0.7161	0.5551
	FEA	0.8613	0.7428	0.5635
	Error	2.89 %	3.73 %	1.51 %
$(0^\circ, 15^\circ, 0^\circ)$	Theoretical	0.6969	0.9216	0.5036
	FEA	0.7117	0.9476	0.5135
	Error	2.12 %	2.82 %	1.97 %
$(15^\circ, 15^\circ, 0^\circ)$	Theoretical	0.6698	0.7005	0.7914
	FEA	0.6927	0.7183	0.8297
	Error	3.42 %	2.54 %	4.84 %

6 Conclusions

Aiming at the accurate and explicit stiffness model of PMs with ATP, this paper proposes a general procedure by means of step-by-step strategy. Drawing on screw theory, twist/wrench mapping matrices and n -DoF ($n \leq 6$) virtual springs are applied. The conclusions are as follow.

- (1) Contribution of parallel limbs is investigated. Twist/wrench mapping matrices are firstly analyzed considering joints in ATP. Then component reference frames are assigned for obtaining component compliance matrix by FEA software. Finally compliance matrix of the limbs is calculated through deformation superposition principle, twist/wrench mapping model, Hooke's law and virtual work equation.

- (2) Contribution of ATP is studied. Twist/wrench transmission routes are firstly analyzed. Component reference frames are then established for compliance of components by FEA software. Finally the compliance matrix of ATP is obtained by deformation superposition of each route, Hooke's law and virtual work equation.
- (3) Compliance model of PM with ATP is achieved by superposition of the two compliance matrices from limbs and ATP. The stiffness modeling procedure is exemplified by a 1T3R PM with ATP. And the theoretical stiffness values are verified by FEA software at some typical configurations. It indicates that the proposed stiffness modeling approach is highly accurate.

Acknowledgments This research work was supported by National Natural Science Foundation of China (NSFC) under Grant No. 51205278, 51475321 and 51305293.

References

1. Pierrot F, Nabat V, Krut S et al (2009) Optimal design of a 4-DOF parallel manipulator: from academia to industry. *IEEE Trans Robot*, 213–224
2. Nabat V, del la O, Rodriguez M, Company O et al (2005) Par4: very high speed parallel robot for pick-and-place. In: *Proceedings of IEEE/RSJ international conference on intelligent robots and systems (IROS'05)*, pp 1202–1207. Alberta, Canada
3. Wu JB, Yin ZP, Xiong YL (2006) Singularity analysis of a novel 4-dof parallel manipulator H4. *Int J Adv Manuf Technol* 29:294–802
4. Sun T, Song YM, Gao H et al (2015) Topology synthesis of a 1-translational and 3-rotational parallel manipulator with an articulated traveling plate. *ASME J Mech Rob* 7(3), 031015-1–031015-9
5. Sun T, Lian BB, Song YM (2016) Stiffness analysis of a 2-DoF over-constrained RPM with an articulated traveling platform. *Mech Mach Theory* 96:165–178
6. Song YM, Gao H, Sun T et al (2014) Kinematic analysis and optimal design of a novel 1T3R parallel manipulator with an articulated travelling plate. *Robot Com-Int Manuf* 30(5):508–516
7. El-Khasawneh BS, Ferreira PM (1999) Computation of stiffness bounds for parallel link manipulators. *Int J Mach Tools Manuf* 39(2):321–342
8. Zhang D, Xi FF, Mechefskec CM et al (2004) Analysis of parallel kinematic machine with kinetostatic modelling method. *Robot Com-Int Manuf* 20(2):151–165
9. Bi ZM (2014) Kinetostatic modeling of Exechon parallel kinematic machine for stiffness analysis. *Int J Adv Manuf Technol* 71:325–335
10. Klimchik A, Chablat D, Pashkevich A (2014) Stiffness modeling for perfect and non-perfect parallel manipulators under internal and external loadings. *Mech Mach Theory* 79:1–28
11. Pashkevich A, Klimchik A, Chablat D (2011) Enhanced stiffness modeling of manipulators with passive joints. *Mech Mach Theory* 46(5):662–679
12. Deblaise D, Hernot X, Maurine P (2006) A systematic analytical method for PKM stiffness matrix calculation. In: *Proceedings of the 2006 IEEE international conference on robotics and automation, Florida, USA*, pp 4213–4219
13. Wu J, Wang JS, Wang LP et al (2009) Study on the Stiffness of a 5-DOF Hybrid Machine Tool with Actuation Redundancy. *Mech Mach Theory* 44(2):289–305
14. Cammarata A., Condorelli SR (2013) An algorithm to study the elastodynamics of parallel kinematic machines with lower kinematic pairs. *J Mech Robot* 5(1):011004-1–011004-9

15. Sung KH, Lipkin H (2014) Stiffness of parallel manipulators with serially connected legs. *J Mech Robot* 6(3):031001-1–031001-9
16. Gosselin CM (1990) Stiffness mapping for parallel manipulators. *IEEE Trans Robot Autom* 6(3):377–382
17. Ceccarelli M, Carbone GA, Wang LP et al (2002) Stiffness analysis for CaPaMan (Cassino parallel manipulator). *Mech Mach Theory* 37(5):427–439
18. Xi F, Zhang D, Xu Z, Mechefske CM (2003) A comparative study on tripod units for machine tools. *Int J Mach Tools Manuf* 43(7):721–730
19. Li YM, Xu QS (2008) Stiffness analysis for a 3-PUU parallel kinematic machine. *Mech Mach Theory* 43(2):186–200
20. Li YM, Xu QS (2008) An investigation on mobility and stiffness of a 3-DOF translational parallel manipulator via screw theory. *Robot Com-Int Manuf* 24(3):402–414
21. Xi FF, Zhang D, Mechefske C (2004) Global kinetostatic modelling of tripod-based parallel kinematic machine. *Mech Mach Theory* 39(4):357–377
22. Dai JS, Ding XL (2006) Compliance analysis of a three-legged rigidly-connected platform device. *J Mech Des* 128(4):755–764
23. Majou F, Gosselin CM, Wenger P et al (2007) Parametric stiffness analysis of the orthoglide. *Mech Mach Theory* 42(3):296–311
24. Taghvaeipour A, Angeles J, Lessard L (2012) On the elastostatic analysis of mechanical systems. *Mech Mach Theory* 58:202–216
25. Lian BB, Sun T, Song YM et al (2015) Stiffness analysis and experimental of a novel 5-DoF parallel kinematic machine considering gravitational effects. *Int J Mach Tools Manuf* 95:82–96
26. Klimchik A, Pashkevich A, Chablat D (2013) CAD-based approach for identification of elasto-static parameters of robotic manipulators. *Finite Elem Anal Des* 75:19–30

The Vibration Control of Stick-Slip Actuated Precision Positioning Structure

Yunzhi Zhang, Xianmin Zhang and Qinghua Lu

Abstract As one of the inherent defects of stick-slip actuation, violent vibrations exist at the end of each driving cycle, which will affect the positioning accuracy of stick-slip actuated structure seriously. In order to analysis and decrease these vibrations, a prototype of stick-slip actuated precision positioning structure is built in this paper, which is made up by piezoelectric ceramic, compliant platform, basement and cylinder slider. In order to decrease the vibration of basement, a new type of band elimination filter is proposed and integrated into the control system. Then, the vibration of slider is reduced by feedforward input shaping method, which is integrating a specific sinusoidal voltage signal into the input signal of piezoelectric ceramic. Finally, the moving stability and driving efficiency of stick-slip actuated structure are improved obviously by applying these vibration control methods.

Keywords Vibration control · Stick-slip actuation · Precision positioning structure · Band elimination filter · Feedforward input shaping

1 Introduction

Stick-slip actuation is one kind of precision positioning method, which has been described in many research works [1–4], and has a nano scale step in one actuation cycle. The illustrative diagram of stick-slip actuation movement is shown in Fig. 1. The classical stick-slip actuation structure is made up by three parts: piezoelectric

Y. Zhang · Q. Lu
Foshan University, Foshan, Guangdong, China
e-mail: scutdongri@163.com

Q. Lu
e-mail: qhlu@fosu.edu.cn

X. Zhang (✉)
South China University of Technology, Guangzhou, Guangdong, China
e-mail: xmzhang@scut.edu.cn

ceramic, basement and slider. Basement is glued with piezoelectric ceramic, and slider is laid onto the basement. The movement of stick-slip actuation in one drive cycle can be divided into three steps:

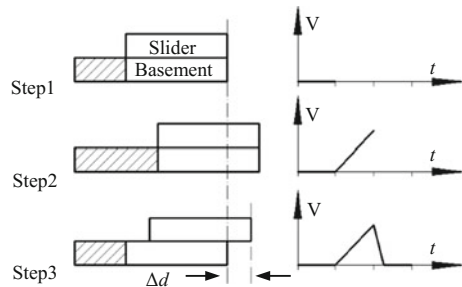
- Step 1: the structure stays in a relaxed state, no voltage is input to the piezoelectric ceramic, so that no deformation is happened, the basement and slider are both in a relatively static state.
- Step 2: a slowly rising voltage signal is input to the piezoelectric ceramic, so that the piezoelectric ceramic will extend slowly. Because of the low speed, the slider will move forward with basement together.
- Step 3: when the piezoelectric ceramic is long enough, the voltage will decrease to zero in a short time, so the piezoelectric ceramic will be compressed to the initial length soon. Since the basement is glued with piezoelectric ceramic, it will move back too. The slider will move forward a short distance, because of its inertia.

After these three steps above, a net step in nano scale is formulated. If keep inputting the saw tooth like voltage signal, the slider will move forward step by step.

Although this kind of actuation method has a high positioning accuracy, it still has two defects, which will disturb the positioning accuracy and driving efficiency hardly. The first defect is backlash. When basement move back fast, the friction force between the contact surfaces will drive the slider decelerate first and then move back for a short distance. If the amount of backlash is too large, the driving efficiency of structure will be very low. The second defect is vibration. Vibrations will happen when the contact situation between slider and basement changes, such as the moment basement start moving back and the moment of each driving cycle's end. Large amount of vibrations will make the stick-slip actuated structure unstable and out of control. So, compared with backlash decreasing, vibration control is more important to improve the performance of stick-slip actuated structure.

In order to research the stick-slip actuation method, a prototype structure is made in part 2, then a new band elimination filter is proposed to decrease the vibration of basement in part 3, in order to control the vibration of slider, a feedforward input shaping method is used in part 4, at last, the performance of stick-slip actuated structure after vibration control is examined, and the vibration control methods proposed in this paper are proved to be effective.

Fig. 1 The illustrative diagram of stick-slip actuation



2 The Prototype of Stick-Slip Actuated Structure

In order to research the stick-slip actuation method, a prototype of stick-slip actuated structure is built (Fig. 2).

This structure is made up by piezoelectric ceramic, compliant platform, basement and slider. The cylinder slider is made by stainless steel and plated by chrome. Slider is supported by four ruby spheres, which are fixed onto the basement. The basement, which is made by aluminum alloy, is fixed on the compliant platform, and can move along a single direction with the compliant platform together.

The compliant platform is driven by a stack type piezoelectric ceramic, the maximum extension of which is about 60 μm .

The structure of compliant platform is shown in Fig. 3, which can move in a single direction.

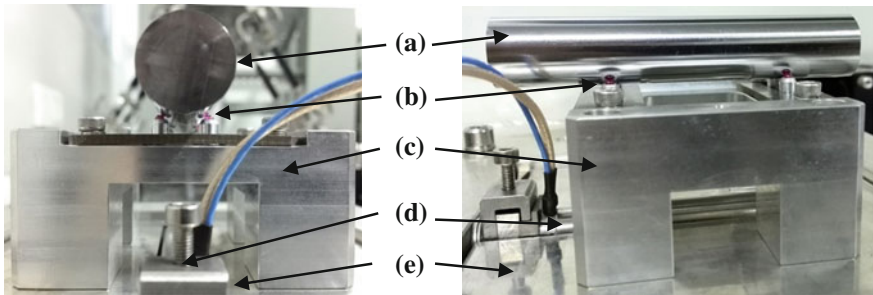


Fig. 2 The prototype of stick-slip actuated structure. **a** The cylinder slider is made by stainless steel and plated by chrome. **b** Four ruby spheres are fixed onto the basement to support the slider. **c** The basement is made by aluminum alloy, which is fixed onto a single degree of freedom compliant platform, and can move with the compliant platform together. **d** A stack type piezoelectric ceramic, which can drive the compliant platform move forward and backward. **e** Compliant platform

Fig. 3 The structure of compliant platform

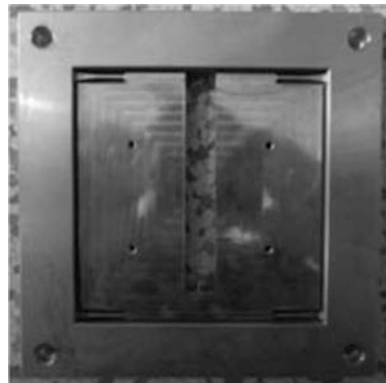




Fig. 4 The experiment system of stick-slip actuated structure. **a** Controller of piezoelectric ceramic. **b** dSPACE 1104, which can convert the digital control signal into analog signal. **c** Laser interferometer, the measurement accuracy is 1 nm. **d** The prototype of stick-slip actuated structure

The whole control and measurement system of this structure is shown in Fig. 4. The piezoelectric ceramic is controlled by dSPACE 1104, the control signal is produced by MATLAB Simulink, and the displacements of basement and slider can be captured by Renishaw XL-80 laser interferometer.

3 The Reduction of Basement Vibration

As shown in Fig. 5a, a saw tooth like voltage signal is input to the piezoelectric, then the basement moves forward slowly and backward fast, the displacement of basement captured by laser interferometer is shown in Fig. 5b.

As shown in the curves above, violent vibrations exist at the end of each driving cycle, whose amplitudes even equal to the stroke of piezoelectric. In order to analysis the modal of basement, a step voltage signal is input to the piezoelectric ceramic, the step response and frequency spectrum of basement are shown in Fig. 6.

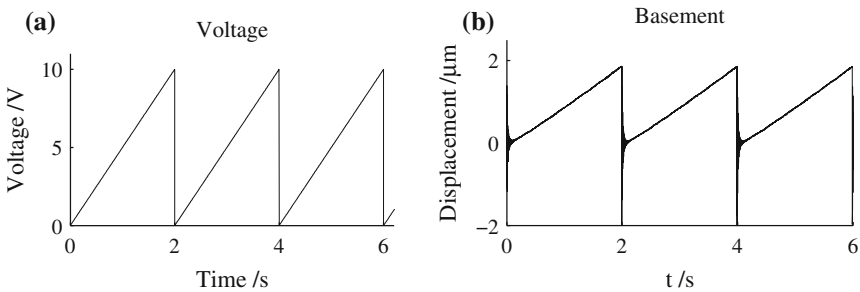


Fig. 5 The saw tooth like voltage signal and the displacement of basement

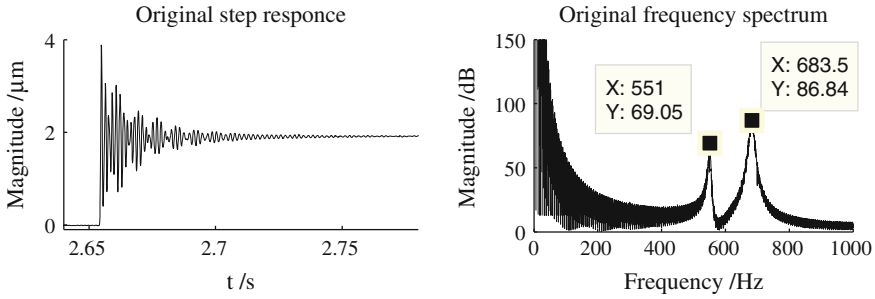


Fig. 6 The step response and the frequency spectrum of basement

As shown above, basement vibrates hardly at two frequencies (551 and 683.5 Hz). In order to decrease these vibrations, the modal of basement is identified first and a new band elimination filter is designed and integrated into the control system then.

3.1 Modal Identification of Basement

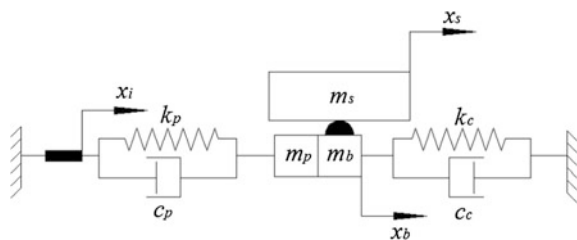
The dynamic diagrammatic sketch of prototype structure is shown in Fig. 7, where the piezoelectric ceramic and compliant platform can be indicated by spring-damper system, k_p , c_p , k_c and c_c are the stiffness and damping coefficient of piezoelectric ceramic and compliant platform respectively. x_i , x_b and x_s are the displacement of input, basement and slider respectively. m_p , m_b and m_s are the mass of piezoelectric ceramic, basement and slider respectively.

Only consider the kinematics of basement, and ignore the effect of slider, the dynamic equation of basement can be proposed as follows.

$$k_p(x_i - x_b) + c_p(\dot{x}_i - \dot{x}_b) - k_c x_b - c_c \dot{x}_b = (m_p + m_b)\ddot{x}_b \tag{1}$$

After Laplace transforming and combining like items, the transfer function of basement can be described by Eq. (2).

Fig. 7 The dynamic diagrammatic sketch of prototype structure



$$G(s) = \frac{c_p s + k_p}{(m_p + m_b)s^2 + (c_p + c_c)s + (k_p + k_c)} \quad (2)$$

If $M = m_p + m_c$, $K = k_p + k_c$, $C = c_p + c_c$, Eq. (2) can be simplified as follows.

$$G(s) = \frac{k_p}{K} \left(\frac{c_p}{k_p} s + 1 \right) \frac{K}{Ms^2 + Cs + K} \quad (3)$$

Since the damping coefficient of piezoelectric ceramic is far less than stiffness, and the stiffness of compliant platform is far less than piezoelectric, the value of c_p/k_p and k_p/K can be approximately calculated as $c_p/k_p \approx 0$ and $k_p/K \approx 1$. So Eq. (3) can be simplified as the following equation.

$$G(s) = \frac{K}{Ms^2 + Cs + K} \quad (4)$$

So that, the basement can be described as a classical second-order oscillating system. The modal of basement is identified then based on the least square method, and the identification result is shown as follows.

$$G(s) = 2.368 \times 10^{-4} \times \frac{1.843 \times 10^7}{s^2 + 239.9s + 1.843 \times 10^7} \quad (5)$$

3.2 A New Type of Band Elimination Filter

According to the transfer function of basement, a new type of band elimination filter is designed based on the filter in [5], which can be described by Eq. (6).

$$H(s) = \frac{s^2 + 239.9s + 1.843 \times 10^7}{1.843 \times 10^7 (s^2 + 4.34 \times 10^{-4}s + 1)} \quad (6)$$

Integrate this band elimination filter into the control system of the prototype structure (Fig. 8), input the same step signal to the piezoelectric ceramic again, the step response and frequency spectrum are indicated by Fig. 9.

As shown in Fig. 9, the vibrations of basement at frequencies of 551 and 683.5 Hz have been decreased obviously.

Integrate this band elimination filter into the control system of prototype structure, and input the same saw tooth like voltage signal (Fig. 5a) again, the displacement curve of basement captured by laser interferometer is shown in Fig. 10.

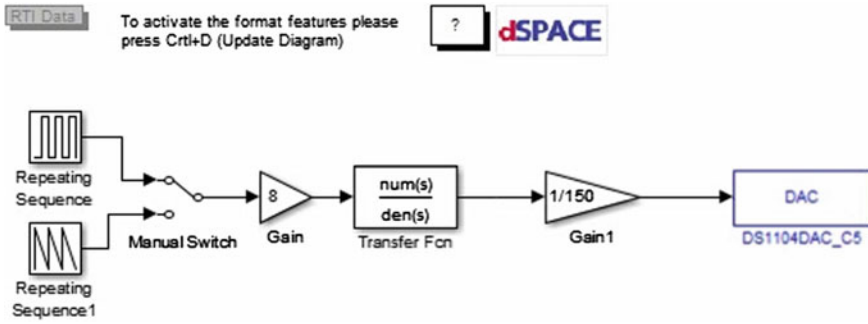


Fig. 8 The Simulink diagram of control system with the band elimination filter

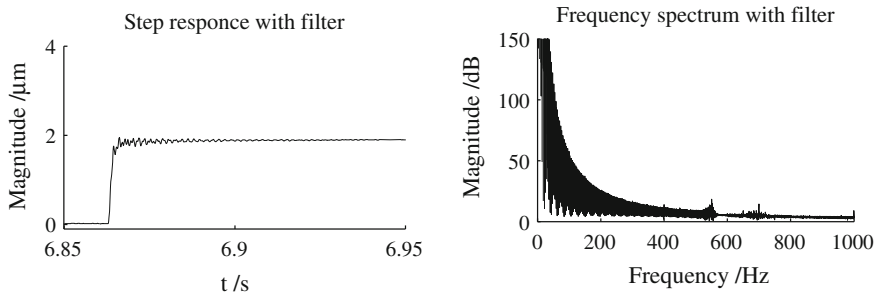
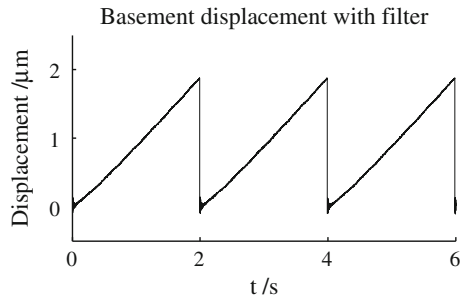


Fig. 9 The step response and the frequency spectrum of basement with band elimination filter

Fig. 10 The displacement of basement with band elimination filter



Compared with Fig. 5b, the vibrations of basement at the end of each driving cycle have been decreased successfully. This band elimination filter is proven to be useful for controlling the basement’s vibrations of prototype stick-slip actuated structure.

4 Vibration Reduction of Slider

As declared before, the prototype structure is combined by piezoelectric ceramic and compliant platform. Since the difference of stiffness between piezoelectric ceramic and compliant platform, when the driving voltage drop fast, the piezoelectric ceramic and compliant platform will move back in a different velocity, and result in a separation between them. When the piezoelectric ceramic extend again in the next driving cycle, impact will happen between the piezoelectric ceramic and compliant platform, and result in a new vibration.

So, in order to make sure the piezoelectric ceramic and compliant platform contact with each other during the whole driving cycle, the driving voltage signal is changed from positive, which is rising slowly and dropping fast, to negative, which is rising fast and dropping slowly.

Input this negative saw tooth voltage signal (Fig. 11a) to the piezoelectric ceramic, the displacement of slider captured by laser interferometer is shown in Fig. 11b.

As shown above, some vibrations exist at the end of each driving cycle, and the step size of slider cannot be stable because of these vibrations.

Some methods of controlling the vibrations of slider have been proposed so far.

In [6], a method is proposed that, the basement has been driven to the central position before the vibration of slider happens, to decrease the amount of vibrations. Since the basement and piezoelectric ceramic in [6] are stuck together, the method mentioned above can work. Since the basement and piezoelectric ceramic are separate with each other, this method is not fit for the prototype structure in this paper.

In order to analysis the vibration characteristics of slider, a step signal is input to the structure, and the step response and frequency spectrum of slider are proposed (Fig. 12).

As shown in Fig. 12, obvious vibrations happen at the frequency of 389 Hz. In order to reduce these vibrations, a specific sinusoidal voltage signal ($V = A \sin(\omega t + \varphi)$) is integrated into the control signal of piezoelectric ceramic, where $A = 0.425 \text{ V}$, $\varphi = 1.43\pi$, $\omega = 2\pi \times 389 \text{ rad/s} = 2444.16 \text{ rad/s}$.

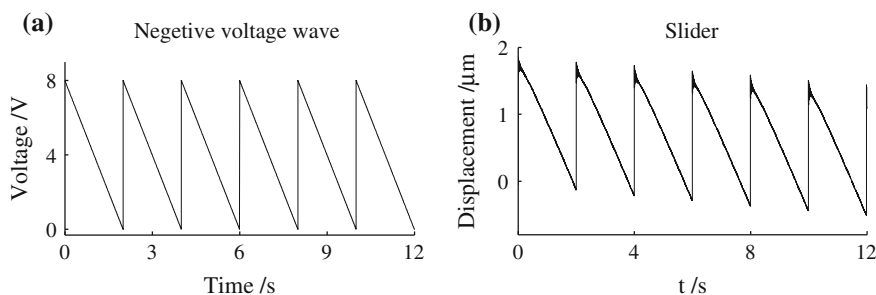


Fig. 11 **a** The negative saw tooth voltage signal. **b** The displacement curve of slider

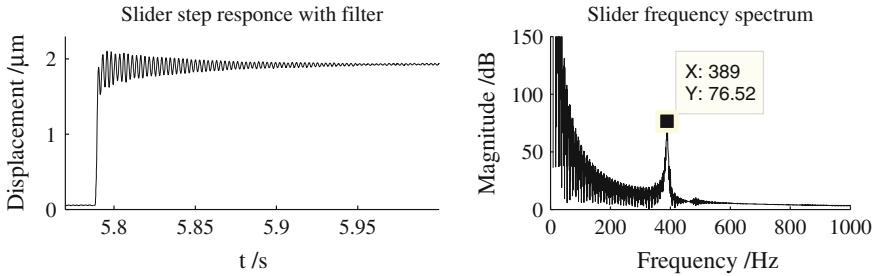


Fig. 12 The step response and frequency spectrum of slider

The Simulink diagram of control system with the sinusoidal signal is shown in Fig. 13.

Input the step signal integrated with the specific sinusoidal signal (Fig. 14) to the piezoelectric ceramic, the step response and frequency spectrum of slider are shown in Fig. 15.

Compare Figs. 15 with 12, the vibrations at frequency of 389 Hz are reduced obviously.

Integrate this sinusoidal signal to a negative saw tooth like voltage signal (Fig. 16a), and input it to the piezoelectric ceramic, the displacement of slider captured by laser interferometer is shown in Fig. 16b.

Compared Figs. 16b with 11b, not only the vibrations at the end of each driving cycle are reduced obviously, the step size of slider is also enlarged. Therefore, the moving stability and drive efficiency of the stick-slip actuated structure are both improved by this vibration control method.

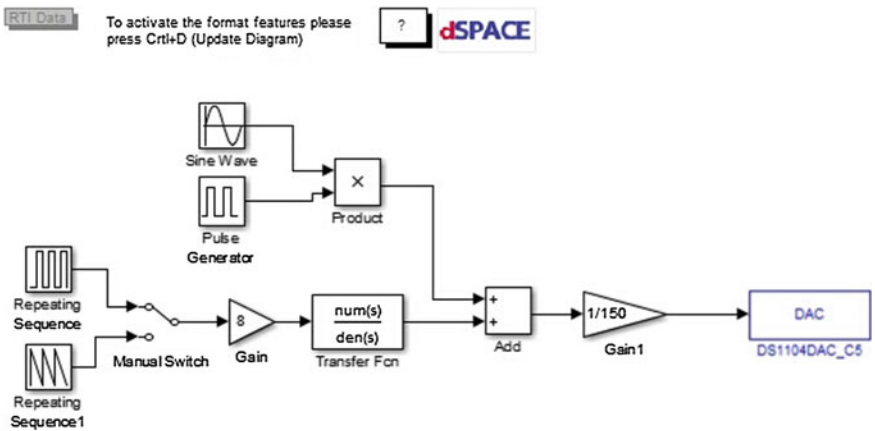


Fig. 13 The Simulink diagram of control system with the sinusoidal signal

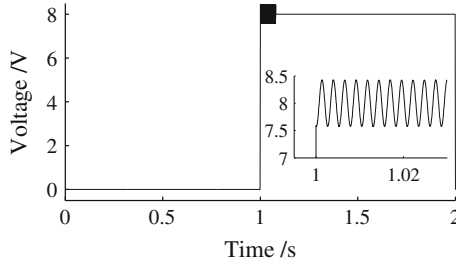


Fig. 14 The step signal integrated with sinusoidal signal and its local magnification

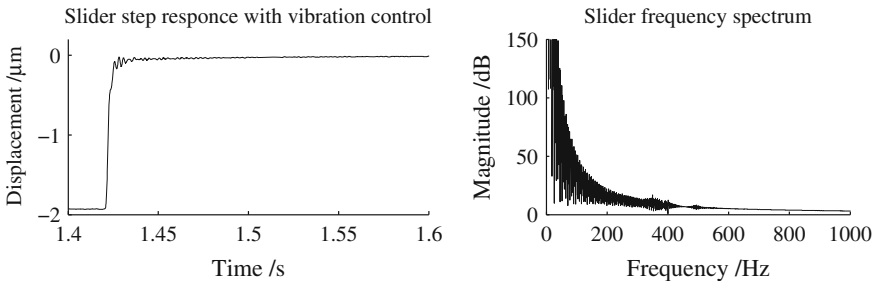


Fig. 15 The step response and frequency spectrum of slider

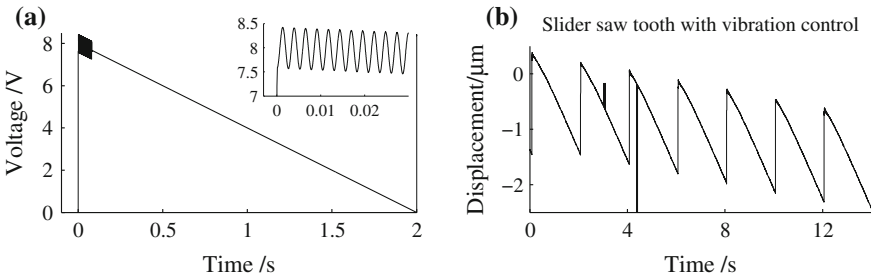


Fig. 16 a The negative saw tooth like signal integrated with sinusoidal signal and its local magnification. b The displacement curve of slider

5 Conclusion

A prototype of stick-slip actuated precision positioning structure is built in this paper, which is made up by piezoelectric ceramic, compliant platform, basement and cylinder slider. This structure is driven by saw tooth like voltage signal, and has nano scale positioning accuracy and micro scale stroke.

In the process of driving, both the basement and slider oscillate hardly at the end of each driving cycle, these vibrations will influence the moving stability and driving efficiency of stick-slip actuated structure seriously.

The basement of this prototype structure has been proved to be a second-order oscillating system, and the transfer function of basement is proposed then. According to this transfer function, a new type of band elimination filter has been proposed and integrated into the control system, and the vibrations of basement are decreased successfully.

Based on the step response and frequency spectrum of slider, a specific sinusoidal voltage signal is integrated into the driving voltage signal. As a result, the vibrations of slider have been reduced successfully by this input shaping method.

With these vibrations control methods above, the moving stability and driving efficiency of stick-slip actuated structure have been improved obviously.

Acknowledgments This research work was supported by the National Natural Science Foundation of China (91223201), the Natural Science Foundation of Guangdong Province (S2013030013355), the Natural Science Foundation of Guangdong Province under grants 2014A030313616, the Science and Technology Planning Project of Guangdong Province (2015B010101015) and the Science and Technology Innovation Project of Foshan City (2015AG10018).

References

1. Edeler C, Meyer I, Fatikow S (2011) Modeling of stick-slip micro-drives. *J Micro-Nano Mechatron* 6:65–87
2. Peng JY, Chen XB (2011) Modeling of piezoelectric-driven stick-slip actuators. *IEEE/ASME Trans Mechatron* 16:394–399
3. Zhang QS, Chen XB, Yang Q et al (2012) Development and characterization of a novel piezoelectric-driven stick-slip actuator with anisotropic-friction surfaces. *Int J Adv Manuf Technol* 61:1029–1034
4. Kim S, Kim SH (2001) A precision linear actuator using piezoelectrically driven friction force. *Mechatronics* 11:969–985
5. Yang H, Fan Y, Shu H (2004) An improved digital filter for restraining mechanical resonance frequency. *Opto-Electron Eng* 31:30–32
6. Nguyen HX (2014) Simulation, validation and optimization of stick-slip drives for nanorobotic applications. Carl von Ossietzky Universität, Oldenburg
7. Zhong B, Sun L, Chen L et al (2011) The dynamics study of the stick-slip driving system based on LuGre dynamic friction model. In: *The 2011 IEEE international conference on mechatronics and automation*, pp 584–589
8. Bergander A, Breguet JM, Schmitt C et al (2000) Micropositioners for microscopy applications based on the stick-slip effect. In: *Proceedings of 2000 international symposium on micromechatronics and human science*, pp 213–216
9. Zhong B, Wang Z, Chen L, Sun L (2011) Current development of trans scale precision positioning technology based on the stick slip effect. *Piezoelectr Acoustoopt ICS* 33:479–485
10. Bergander A, Breguet JM (2003) Performance improvements for stick-slip positioners. In: *2003 International symposium on micro mechatronics and human science*, pp 59–66
11. Rong W, Zhang S, Yu M, Sun L (2011) A 3D stick-slip nanopositioner for nanomanipulation. In: *Proceedings of the 2011 IEEE international conference on mechatronics and automation*, pp 195–199

Dynamics Analysis of a Modular Reconfigurable Parallel Robot

Qisheng Zhang, Ruiqin Li and Jingjing Liang

Abstract The paper studies the dynamic performance of a Modular Reconfigurable Parallel (MRP) robot with four different configurations. Finite element models of the MRP robot of each configuration are established using ANSYS Workbench software. The modal is analyzed. The first six natural frequencies and corresponding modes are acquired under four configurations. Based on modal analysis, the harmonic response of the MRP robot is analyzed under each configuration. The response curves of the three main motion directions along x , y , z axes are obtained under each configuration. Furthermore, the characteristics on harmonic response of the robot are discussed. The resonance frequency, resonance amplitude and the main vibration direction of each configuration are calculated. The weaker links of the robot system can be found out through the analysis of the dynamic characteristics. The robot's anti-vibration performance under the action of external force is verified. Some suggestions are given by analyzing the cause of weaker links. The results can be reference to the structure improvement, optimum design and dynamic design on the MRP robot system.

Keywords Modular reconfigurable parallel robot · Modal analysis · Harmonic response

Q. Zhang · R. Li (✉) · J. Liang
School of Mechanical and Power Engineering, North University of China,
Taiyuan 030051, China
e-mail: liruiqin@nuc.edu.cn

Q. Zhang
e-mail: 1020709642@qq.com

J. Liang
e-mail: 94419179@qq.com

1 Introduction

Modular Reconfigurable Parallel (MRP for short) robot consists of many modules. The modules, such as frame, moving platform and joints, etc., have different size and functional characteristics. The MRP robot has an ability of flexibility. It can be changed to varied types of parallel robot by simply and quickly assembling and disassembling among modules like building blocks [1]. Therefore, it has a wide range of application and can better meet the demands of different applications. However, carrying capacity, working speed, driving performance and dynamic stiffness of MRP robot are unsatisfactory due to its own structure. These factors affect the robot's dynamic performance. In order to make the MRP robot has better reconfigurable ability, strong processing capacity and good operating performance, it is important to study the dynamic performance of the MRP robot.

Dynamic characteristic analysis includes modal analysis, harmonic response analysis and random vibration. Modality is one of the inherent vibration characteristics of mechanical structure. Each modality has a specific inherent frequency, damping ratio and modal shape [2, 3]. The purpose of modal analysis is to restrain or avoid the resonance phenomenon. Harmonic response analysis is used to confirm the steady state response when the forces applied to the structure of MRP robot changing according to the variation of harmonic law. Its purpose is to get the curves of displacements of the structure on the frequency response and verify that the system can overcome the harmful effect caused by resonance and other force vibration [4].

The MRP robot consists of many modules with elastic parts, which have the characteristics of nonlinear, varying with time, structure coupling, and so on. Therefore, the dynamic system of the MRP robot is a multi-elastic system. Finite element analysis is usually used to analyze the dynamic performance in the process of optimum design of the MRP robot, which is convenient to solve and can accurately reflect the dynamic characteristics [5]. The accurate models of the mechanical system can be established, and the natural frequency, mode shape and strain contour of each order mode of the system can be obtained by using finite element analysis software. The results of finite element analysis are able to identify the frequency and the weaker parts of the system which are easy to cause resonance [6–8].

In the paper, the dynamic characteristics of a type of MRP robot with four different configurations will be analyzed by using ANSYS Workbench software. The purpose is to get dynamic characteristics of the whole MRP robot system. At first, the first six order natural frequencies, vibration mode and harmonic response rules of each configuration will be analyzed. Then, the changing rules of each configuration are obtained.

2 Structure of the MRP Robot

The basic module units of the MRP robot includes frame, moving platform, Hooke hinge, connecting rod and moving module, vertical pillar, etc. The MRP robot can change into four types of parallel robot, i.e. 6-PSS slider type, 6-PSS scissors type, 3-Delta slider type and 6-SPS telescopic type, as shown in Fig. 1a–d. The origin of coordinate of each type robot locates in the mid-point of moving platform. The z axis is perpendicular to the surface of the moving platform. The x axis is perpendicular to an edge of hexagon at the bottom of the frame.

In Fig. 1a, 6-PSS slider configuration consists of frame, six limbs and moving platform. Each limb consists of two sets of Hooke hinges, one connecting rod and one pair of driving modules. There are three sets of vertical pillars fixed at the top of the frame. Two sets of driving modules are fixed into each pillar.

In Fig. 1b, 6-PSS scissors configuration consists of frame, six limbs and moving platform. Each limb consists of two sets of Hooke hinges, one connecting rod and one pair of driving modules. The driving modules are fixed at the top of the frame with an angle of 60° between each other.

In Fig. 1c, 3-Delta configuration consists of frame, three limbs and moving platform. Each limb consists of four sets of Hooke hinges, two connecting rods and one pair of driving modules. There are three sets of vertical pillars fixed at the top of the frame. One set of driving modules is fixed into each pillar.

In Fig. 1d, 6-SPS telescopic configuration consists of frame, six limbs and moving platform. Each limb consists of two sets of Hooke hinges, one connecting rod and one pair of driving module. One end of each driving module is fixed on the top frame by Hooke hinge, the other side is fixed to moving platform with parts of ball screw socket within the bar, which makes the length of the limb variable.

Under each configuration, driver modules are driven by servo motors. The motors make ball screw moving. The ball screw makes the wire mother slide along

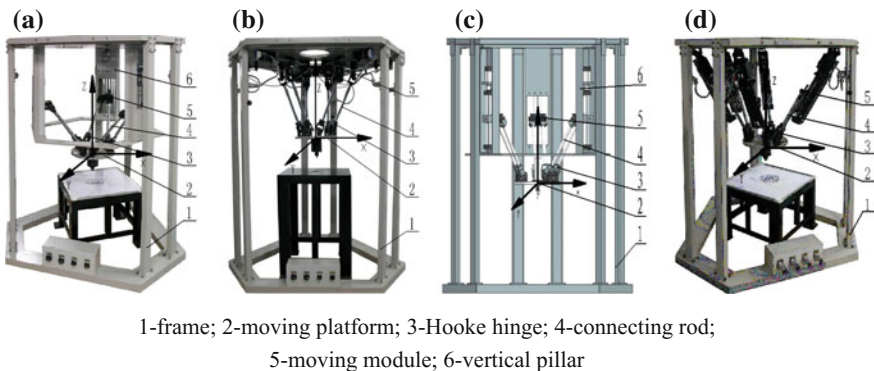


Fig. 1 Four types of the MRP robot

the central axis of the ball screw. The moving platform can achieve the desired trajectory through cooperative movement of the limb.

3 Dynamics Analysis

The transmission system of the robot is driven by servo motors, which includes elastic parts such as linkages, Hook joints and bearings. Existing of these parts will make the machine tool vibration, severely reduce the machining precision and the surface quality of the work-pieces, which caused by the high speed of motor, cutting forces changes in real-time and environmental factors. At the same time, vibration can also reduce the processing efficiency, speed up the tool wear. It will affect the stability of the whole machine cutting movement. Therefore, the dynamic characteristics should be considered in the process of designing precision machine tools [9, 10].

3.1 Modal Analysis

It is not necessary to find out all the natural frequencies and modes, but the frequencies of the system under working condition, when the modal analysis is carried out. Only the natural frequency consistent with the loading frequency can cause resonance system. Through finite element analysis can find out the region of frequency possible cause resonance. In the process of processing, the quality of the work-pieces can be effectively improved by avoiding resonance region excited by the external forces. The structure vibration can be expressed as the linear superposition of each order mode. The vibration caused by lower order modes has higher influence on the structure. Thus the low-order modal of the structure plays a decisive role in the dynamic characteristics. Therefore, the dynamics characteristics analysis of the structure usually takes 1st-order to 6th-order mode.

In the following section, the natural frequencies and vibration modes of four different configurations will be analyzed. The frequencies that may cause resonance under each configuration will also be analyzed.

3.1.1 6-PSS Slider Configuration

Figure 2 is the cloud chart of each order vibration mode of 6-PSS slider configuration. From Fig. 2, the natural frequency of each mode can be obtained as shown in Table 1.

The displacement of the 6th-order modal is the biggest, which occurs at the bottom of the vertical pillars. Its influence is largest on the dynamic of the whole robot system. It directly affects the machining precision and surface quality of the

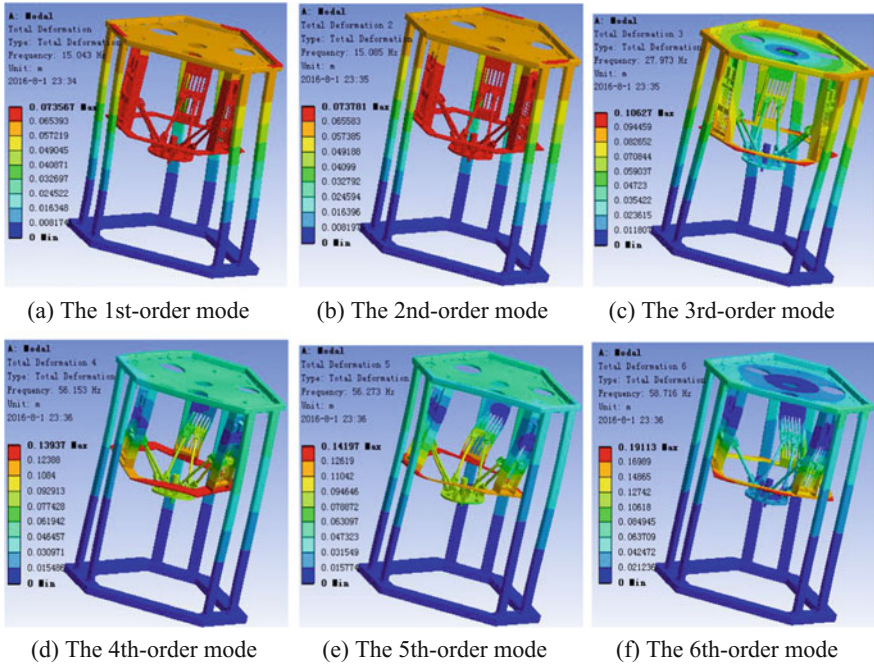


Fig. 2 The first six vibration modes of the 6-PSS slider configuration

Table 1 The inherent frequency and vibration mode

Order	f/Hz	Modal description
1	15.043	The frame, vertical pillars and moving pairs swing from left to right along x direction
2	15.085	The frame vibrates from down to up along the z axis. The vertical pillars swing from left to right around z axis
3	27.973	The frame and vertical pillars twist around z axis
4	56.153	The frame vibrates from down to up along the z axis. The limbs twist around z axis and cause the vertical pillars shrink
5	56.273	The limbs swing and twist around z axis
6	58.716	The vertical pillars and the frame swing back and forth along x direction

work-pieces. The robot’s transmission system is also installed on the vertical pillars, some of whose parts consist of elastic parts and have less stiffness such as lead screws, bearings, Hook hinges. Therefore, in the process of structure design, it is necessary to strengthen the stiffness of the vertical pillars and improve the stiffness of the lead screw. It is best to connect the column and frame as a whole to reduce the system errors. The vibration amplitude of ball screws is relatively large. Thus the connection between them and the moving platform are weaker points. Attention should be paid to ensure their stiffness in the design process.

3.1.2 6-PSS Scissors Configuration

Figure 3 is the cloud chart of each order vibration mode of 6-PSS scissors configuration. From Fig. 3, the natural frequency and vibration characteristic of each mode can be obtained, as shown in Table 2.

The displacement of the 6th-order modal is the largest occurred at Hooke hinges where the limbs are connected to the moving platform. In addition, the amplitude of the limbs is also relatively large. Therefore, in the process of processing, vibration will be excited at action of force on the surface of work-pieces, which will cause resonance of the limbs. It will causes severe vibration of the whole system and

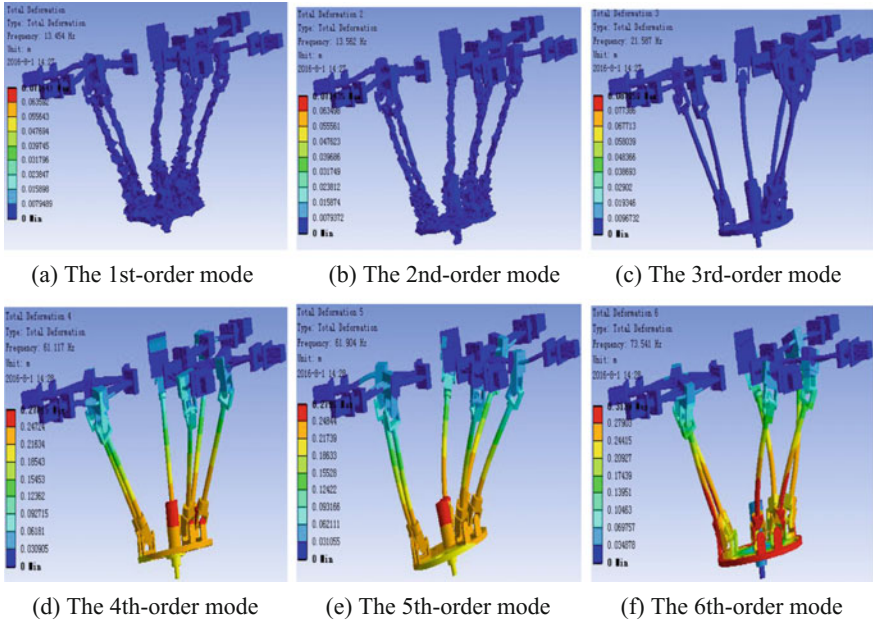


Fig. 3 The first six vibration modes of 6-PSS scissors configuration

Table 2 The inherent frequency and vibration mode

Order	f/Hz	Modal description
1	13.454	The frame vibrates from down to up along the z axis. Each limb twists around its own axis
2	13.562	The frame vibrates from down to up along the z axis. Each limb twists around its own axis. The moving platform twists around z axis
3	21.527	Each limb twists around its own axis. The frame swings from left to right along x direction
4	61.117	Six limbs and the frame vibrate from down to up along the z axis
5	61.904	Six limbs swing around z axis
6	73.541	Limbs swing around z axis. Each limb vibrates around its own axis

affect the processing precision and surface quality of work-pieces. It even causes damage to the screw of the driving system. Thus in this configuration, the stiffness of each limb and Hooke hinge are the key points in designing the weak links. The ball screw will affect the entire processing precision at the action of force in z direction, which will endure bending deformation. Therefore, the bending strength of screw should be considered when designing the transmission system.

3.1.3 3-Delta Configuration

Figure 4 is the cloud chart of each order vibration mode of 3-Delta configuration. From Fig. 4, the natural frequency, maximum displacement and vibration characteristics of each mode can be obtained, as shown in Table 3.

The displacement of the 4th-order modal is the biggest occurred at the bottom of the vertical pillars. Thus, it greatly affects the dynamic characteristics of this configuration and directly affects precision and surface quality of work-pieces. Moving modules of this type robot is also installed in the vertical pillars which consist of many elastic parts such as ball screw, bearing with less stiffness. Therefore, in the process of structure design, it is necessary to increase the stiffness of the elastic parts of each moving modules by replacing perfect material and improve the stiffness of pillars. The best way is to fix vertical pillars to the robot body [11].

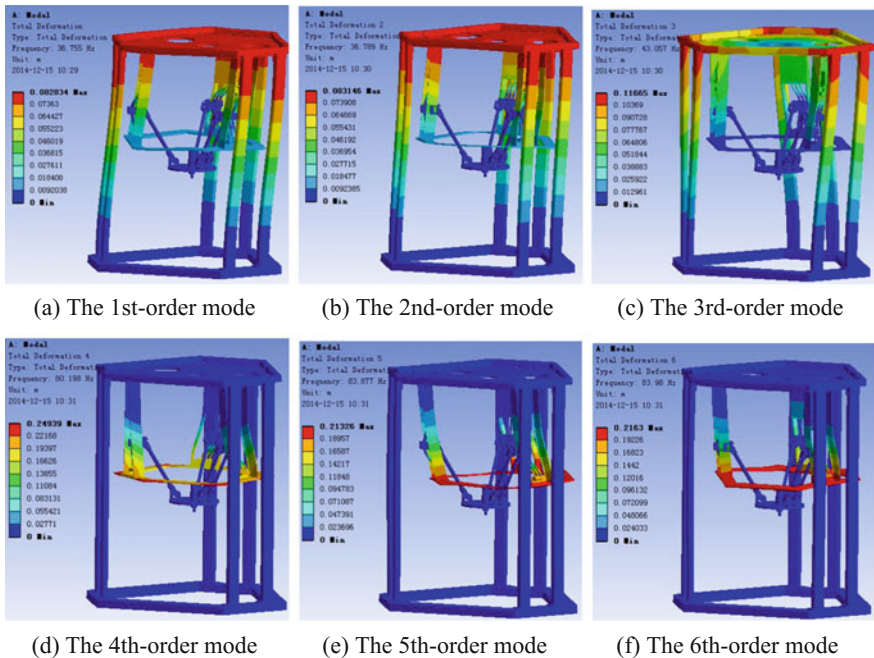


Fig. 4 The first six order vibration modes of 3-Delta configuration

Table 3 The inherent frequency and vibration mode

Order	f/Hz	Modal description
1	36.755	The frame and body oscillate around the x axis
2	36.789	The frame and body oscillate around the y axis
3	43.057	The frame and body twist around the z axis
4	80.198	The vertical pillars and sliding pairs twist around the z axis
5	83.877	The pillar swings along the x axis
6	83.98	The pillar swings along the y axis

3.1.4 6-SPS Telescopic Configuration

Figure 5 is the cloud chart of each order vibration mode of 6-SPS telescopic configuration. From Fig. 5, the natural frequency, maximum displacement and vibration characteristics of each mode can be obtained, as shown in Table 4.

The displacement of the 5th-order modal is the biggest, which occurs at the position the telescopic prismatic module connect to the Hooke hinges of the frame. So stiffness of these parts may not enough to support the system well working, and it is weak points of this configuration. Therefore, the hinges' stiffness will affect the overall stiffness.

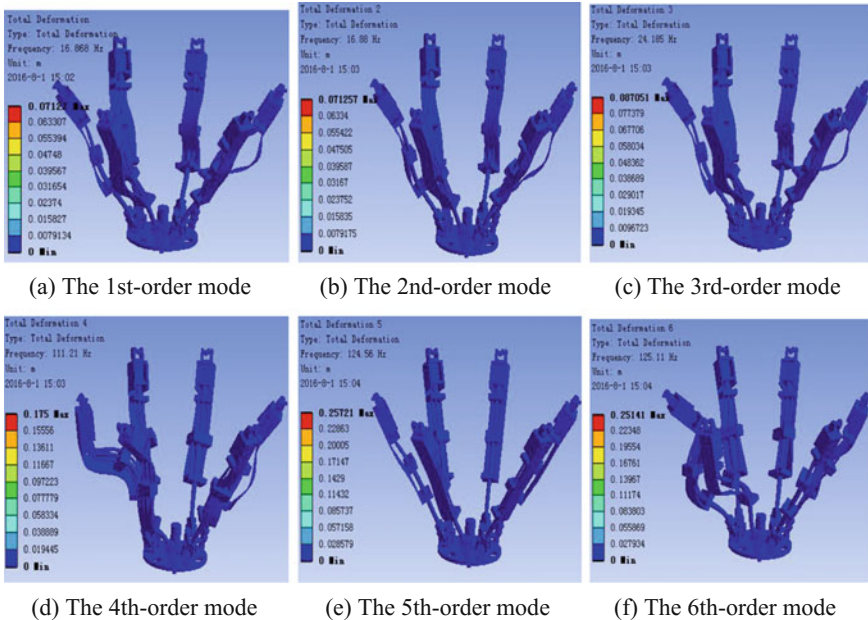


Fig. 5 The first six vibration modes of the 3-Delta parallel robot system

Table 4 The inherent frequency and vibration mode

Order	f/Hz	Modal description
1	16.868	The vertical pillars twist around z axis. Each limb stretch out and draw back along its own axis and vibrates around its own axis
2	16.88	The frame vibrates from bottom to top around z axis. Each limb stretch out and draw back along its own axis and vibrates around its own axis
3	24.185	The frame, each limb and the moving platform twist around z axis
4	111.21	The frame and moving platform twist around z axis. Each limb bending vibrates around the axis
5	124.56	The vertical pillars and limb vibrates from bottom to top around z axis
6	125.11	The frame, limb interval vibrates from bottom to top

3.1.5 Results of Modal Analysis

- (1) With the increasing of the order number, the energy will decrease that stimulate the high-order vibration. Thus the vibration is not easy to be inspired. Under all configurations, the deformation of the connecting rod and the frame can be neglected.
- (2) The natural frequencies of different configurations have certain change, but they are not big. Under each configuration, the upper part deformation is large, the lower part's is small, from down to top gradually increased, which accordance with the actual situation. It is reasonable.
- (3) The difference of natural frequency of the 1st-order and the 2nd-order of all configurations are small which prone to resonance, so do the 4th-order and the 5th between 6-PSS slider configuration and 6-PSS scissors configuration, the 5th-order and the 6th-order between 3-Delta configuration and 6-SPS telescopic configuration. It will result in greater dynamic stress and cause the robot system violent vibration. At the place in the center of the Hooke hinges and the ball screw of prismatic pairs connect to moving platform will appear bending fatigue cracks for weaken of stiffness parts. Therefore, it is important to avoid the sensitive frequencies of all configurations to avoid resonance.

3.2 Harmonic Response Analysis

Harmonic response analysis is used to calculate the structure vibration force with a certain frequency range of the displacement response, and get the system dynamic response and excitation frequency curve.

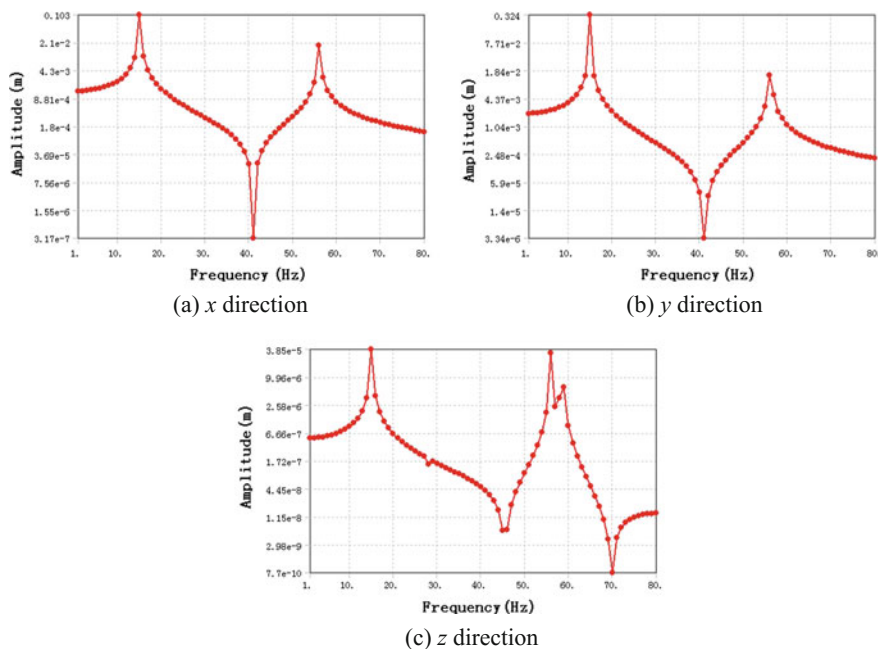


Fig. 6 Amplitude frequency curves of 6-PSS slider configuration

3.2.1 6-PSS Slider Configuration

Under the 6-PSS slider configuration, the amplitude frequency curves of the center point of the moving platform are shown in Fig. 6. The horizontal coordinate represents the frequency. The vertical coordinate represents the response displacement.

From Fig. 6, the system response reaches its maximum and the response displacement has changed dramatically, when the excitation frequencies along *x*, *y*, *z* directions are around 16 Hz. Thus, the resonance occurring in around 16 Hz should be avoided. The stiffness along *z* axis is the main stiffness. The spatial frequency response along *x*, *y* directions are very large. Thus the stiffness along *x*, *y* directions are insufficient. In these directions, the force acting on the screw of ball screw, which are elastic parts and have weaker compressive stiffness. The dynamic performance of the configuration can be improved by increasing the screw of the compressive stiffness, or let the prismatic pairs and moving platform at an angle.

3.2.2 6-PSS Scissors Configuration

Under the 6-PSS scissors configuration, the amplitude frequency curves of the center point of the moving platform are shown in Fig. 7. The horizontal coordinate represents the frequency. The vertical coordinate represents the response displacement.

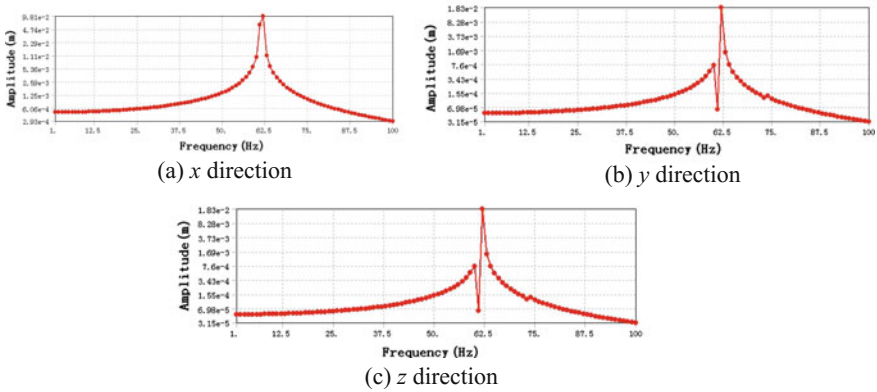


Fig. 7 Amplitude frequency curves of 6-PSS scissors configuration

From Fig. 7, the system response reaches its maximum and response displacement has changed dramatically, when the excitation frequency along x, y, z directions is around 61 Hz. Thus the resonance occurring around 61 Hz should be avoided. There is little difference among the response along three directions. Thus the stiffness is very near. This configuration has good dynamic performance.

3.2.3 3-Delta Configuration

Under 3-Delta configuration, the amplitude frequency curves of the center point of the moving platform are shown in Fig. 8. The horizontal coordinate represents the frequency. The vertical coordinate represents the response displacement.

From Fig. 8, the system response reaches its maximum and response displacement has changed dramatically, when the excitation frequency along x, y, z

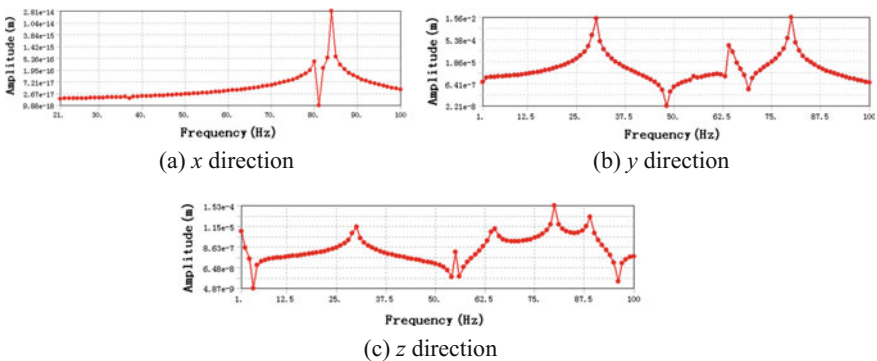


Fig. 8 Amplitude frequency curves of 6-SPS telescopic configuration

directions is around 79 Hz. The main phenomenon is vertical pillars twist around the z axis. Thus the dynamic performance of the system structure can be improved by increasing the stiffness of pillars and the stiffness of ball screw of moving modules [11]. The processing precision of the configuration can be improved through improving the dynamic stiffness in three directions.

3.2.4 6-SPS Telescopic Configuration

Under 6-SPS telescopic configuration, the amplitude frequency curves of the center point of the moving platform are shown in Fig. 9. The horizontal coordinate represents the frequency, and the vertical coordinate represents the response displacement.

From Fig. 9, the system response reaches its maximum and the response displacement has changed dramatically, when the excitation frequency along x, y, z directions is around 125 Hz. Under 6-SPS telescopic configuration, the response gradually increases before reaching the resonance frequency. Of all the four configurations, the range of frequency the configuration is the widest. It has a widest working range. There is little difference among the response along three directions. Therefore, the stiffness is very near.

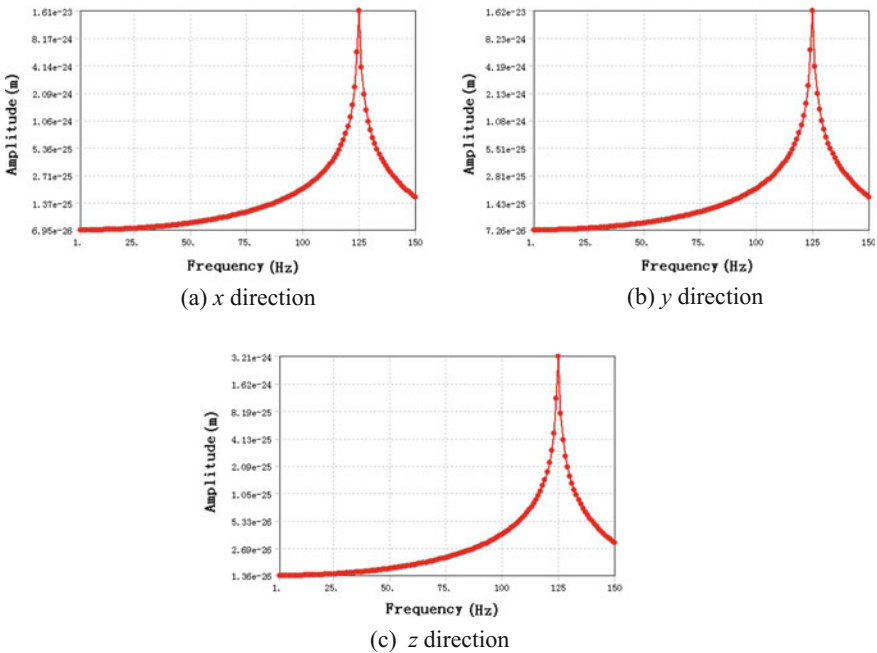


Fig. 9 Amplitude frequency curves of 6-SPS telescopic configuration

3.2.5 Summary of Harmonic Response Analysis

- (1) In four configurations, the ball screw of the prismatic pairs has influence on the response. Improving the compressive stiffness of wire rod can improve the overall stiffness of the MRP robot.
- (2) 6-SPS telescopic configuration has the largest workspace, working frequency and better stiffness performance.

The overall stiffness and dynamic performance can be improved using the following methods:

- (1) Using large bending stiffness lead screw as prismatic pairs.
- (2) Improving the support stiffness of the linkage to obtain a good anti-vibration effect.
- (3) Making the frequency of exciting force far away from the natural frequency by using materials with larger stiffness.

4 Conclusions

- (1) Through modal analysis, the differences among natural frequencies are obtained. The first six order natural frequencies and vibration modes under each configuration are obtained. The key factors and the weaker links of each configuration are determined, which affects the overall dynamic performance. The improvement method is proposed.
- (2) Harmonic response of the MRP robot is analyzed. The frequency range of each configuration is obtained. The results show that the response of the robot moving platform along x , y and z directions is relatively large in the first six orders. 6-SPS telescopic configuration has largest workspace, the widest working frequency and the best stiffness performance.
- (3) The dynamic characteristics analysis of the MRP robot provides a basis for improving and optimizing the system structure. The results provide a theoretical basis for the design of the robot system with higher precision.

Acknowledgments The authors gratefully acknowledge the financial and facility support provided by the National Natural Science Foundation of China (Grant No. 51275486).

References

1. Jiang Y, Wang H, Pan X et al (2011) Autonomous online identification of configurations for modular reconfigurable robot. *Chin J Mech Eng* 47(15):17–24 (in Chinese)
2. Lv D, Zeng DJ, Yu XY et al (2012) Finite element modal analysis of V8 engine crankshaft based on ANSYS workbench. *Mach Des Manuf* 8:11–13 (in Chinese)

3. Zhang L, Lin JL, Xiang HY (2011) Modal analysis and experiment. Tsinghua University Press, Beijing
4. Liu CL, Luo XL (2013) The modal and harmonic response analysis of connection rod of a six cylinders compressor by ANSYS. *Mach Des Manuf* 3:26–29 (in Chinese)
5. Ju F, Choo YS, Cui FS (2006) Dynamic response of tower crane induced by the pendulum motion of the payload. *Int J Solids Struct* 43(2):376–389
6. Hu Y, Li B, Wang Z et al (2007) Analysis of kinematics and dynamics for a novel hybrid kinematics machine. *J Adv Mech Des Sys Manuf* 1(1):58–69
7. Li YP, Zhong PS, Gong W et al (2013) Modal analysis of picking chip head based on ANSYS workbench. *Mach Tool Hydra* (in Chinese)
8. Cai L, Ma SM, Zhao YS, et al (2011) Modal analysis and experimental research on heavy load angularly deflecting milling head. *J Vib Shock* 30(7):250–255 (in Chinese)
9. Ge ZH, Ma WJ, Zhang KK et al (2011) Mechanism design and dynamic analysis of Hybrid Cam-Linkage Mechanical Press. *Key Eng Mater* 474–476:803–806
10. Dang XZ, Zhou LS, Liang D (2013) Dynamic performance analysis and simulation of hybrid-driven seven-bar mechanical press with double cranks. *Adv Mater Res* 834–836: 1327–1332
11. Zhang QS, Li RQ, Tian YL (2015) Dynamic performance analysis of 3-Delta type parallel robot. In: Proceedings of the 14th IFToMM world congress, mechanics department, National Taiwan University

Inversion Study of Current Parameters Based on Attitude Data of Subsurface Buoy System

Z.Y. Chang, Y.M. Fang and Z.Q. Zheng

Abstract Subsurface buoy system is one of the most important devices to measure information of ocean environment. The profile of current can be measured by Acoustic Doppler Current Profilers (ADCP) mounted on the subsurface buoy system. However, the variation of position and orientation of ADCP can affect the precision of measurement. In this paper, current profile is retrieved from the attitude data of subsurface buoy system based on a practical case. Firstly, the dynamical analysis model of the subsurface buoy system and the cable equation are established by using polygonal approximation method of lumped mass. Secondly, according to the design parameters of surface buoy and the model, the equilibrium equations of nodes of the subsurface buoy system are built. In addition, the fitting function of depth and currents velocity is obtained by MATLAB. The simulation model of subsurface buoy system is established by using the force and lumped mass method, and the simulation of whole system is given to verify the attitude of the system based on the ADAMS software. Through the method of the inversion analysis, the current profile is obtained. This study has an important significance for determining the accurate information validation of current.

Keywords Subsurface buoy system · Attitude · Current profile · Fitting function · Inversion analysis · Polygonal approximation method

Z.Y. Chang (✉) · Y.M. Fang · Z.Q. Zheng
Department of Mechanical Engineering, College of Engineering,
Ocean University of China, Qingdao, China
e-mail: zongyuchang@qq.com

Z.Y. Chang · Z.Q. Zheng
Key Lab of Ocean Engineering of Shandong Province, Qingdao, China

© Springer Nature Singapore Pte Ltd. 2017
X. Zhang et al. (eds.), *Mechanism and Machine Science*,
Lecture Notes in Electrical Engineering 408,
DOI 10.1007/978-981-10-2875-5_88

1083

1 Introduction

As a carrier of marine research and marine environmental monitoring equipment, subsurface buoy system has many special advantages, such as long observation period good concealed performance, less vulnerable to the influence meteorological conditions. And it can work for fixed point and multiple parameters profile observation and be widely used in the fields of marine scientific research, marine comprehensive utilization, national defense development and so on [1–3]. Since the performances of subsurface buoy system depend on many complex factors of the marine environment, equipment parts and cables suffered environmental forces, the composition and distribution form of the cable, depth of sea water and so on. Therefore, it has become an important research topic to design and analyze a potential system to ensure its high reliability and good adaptability.

The current research of the subsurface buoy system mainly focuses on the stability of the subsurface buoy system. Based on the statics analysis method, some scholars analyzed and calculated the force and attitude of the subsurface buoy in the water, considering that the subsurface buoy system may be destroyed or moved by the external actions such as the waves and currents, and so on [4–8]. Ge et al. [9] established the submerged buoy cable motion model in deep sea using the lumped mass method to calculate the dynamic tension and configuration of ocean cables, and the static computation and dynamics simulation of submerged buoy were proposed by using the MATLAB computer program. Tjavaras et al. [10] studied the nonlinear dynamic response of mooring buoy under linear wave excitation. And on this basis, the strange attractors and bifurcation phenomena were obtained by applying Poincare map. Chang et al. [11] developed the model for submersible buoy moored by extensible cable and excited by surface, found snap phenomena and its chaotic characteristics under severe wave condition. Guo et al. [12] analyzed the vertical movement characteristics in the process of floating-up by means of mathematical modeling.

In view of the insufficiency of the reliability caused by the failure model [13] of the subsurface buoy system, this paper carries out the inversion analysis of the current parameters based on the dynamic analysis of the subsurface buoy system and the existing measured data of the subsurface buoy position.

2 Dynamic Analysis of the Subsurface Buoy System

Figure 1 shows the simplified dynamic analysis model of the subsurface buoy system under the action of currents by using polygonal approximation method of lumped mass.

Fig. 1 Model of the subsurface buoy system

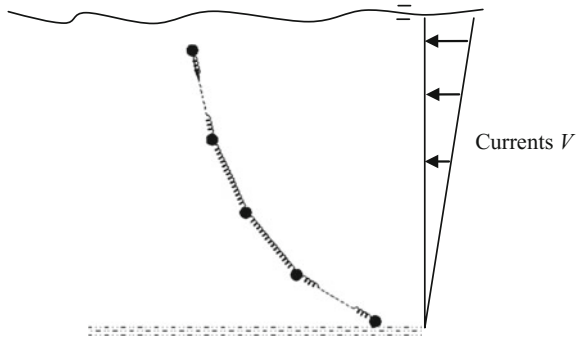
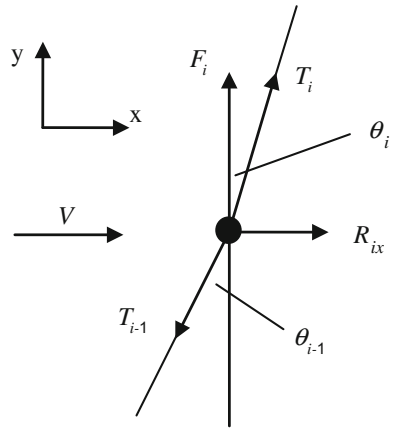


Fig. 2 Diagram of force acting on one node



Taking the forces acting on a node of the system as an example, a single node is acted by four forces: F_i , T_i , T_{i-1} and current force represented by R_{ix} . The diagram of force is shown in Fig. 2.

According to Fig. 2, this force distribution can be expressed by the following set of equations:

$$T_{i-1} \sin \theta_{i-1} = T_i \sin \theta_i + R_{ix} \tag{1}$$

$$T_{i-1} \cos \theta_{i-1} = T_i \cos \theta_i + F_i \tag{2}$$

From Eqs. (1) and (2)

$$R_{ix} = (F_i + T_i \cos \theta_i) \tan \theta_{i-1} - T_i \sin \theta_i \tag{3}$$

3 Inversion Analysis of Currents Parameters

3.1 Procedure of the Inversion Analysis Method

This inversion analysis method is performed according to a practical engineering case. Firstly, according to the current force, the current velocity will be calculated and the fitting function of depth-velocity can be obtained by MATLAB. Secondly, the subsurface buoy motion model is established by using the lumped mass method. And the simulation of whole system is given to verify the attitude of the system based on the ADAMS software. At last, the current profile will be determined by comparing the results between simulation and reality and adjusting the parameters of simulation until it has a high agreement between the simulation and reality. A flow chart of the inversion analysis method is shown in Fig. 3. Where, E is the elastic modulus of Kevlar lanyard in the system.

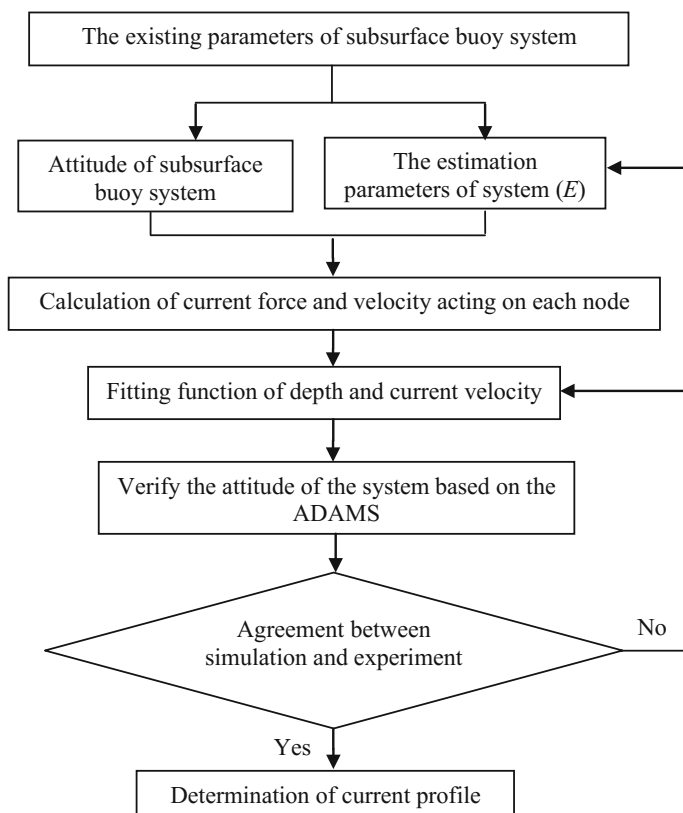


Fig. 3 The flow chart of the analysis method

3.2 The Existing Database of the Subsurface Buoy System

As is shown in Table 1, we know the components and the partial measured data of the subsurface buoy system, consisting of the initial depth of each node without ocean currents and the lowest and deepest depth of each node under the action of ocean current, represented by H_0 , H_{min} , H_{max} , respectively. In addition, the net-buoyancy of each part in water is known, using notation F_i .

Assume that the length of each piece of Kevlar lanyard is not changed from the lowest depth position of nodes to the deepest depth position. Then, the attitude of subsurface buoy system, described in Fig. 4, was drawn in AutoCAD, according to the data in Table 1.

Table 2 shows the position of each node of the subsurface buoy system at the deepest depth position.

In addition, we can get the data of each segment of Kevlar lanyard, which is shown in the following Table 3.

Where, L_{i0} is the initial length of Kevlar lanyard between the two adjacent nodes; L_i is the stressed length of Kevlar lanyard in water; ΔL_i is the elongation of each segment of Kevlar lanyard; T_{i0} is the tension of each Kevlar lanyard in water when the system is in the lowest depth position.

Based on the characteristics of lanyard, we can get the following formula:

$$K_i \cdot \Delta L_i = T_i \tag{4}$$

In addition

$$K_i = EA/L_i \tag{5}$$

Table 1 The existing parameters of subsurface buoy system

Components	Parameters			
	H_0 (m)	H_{min} (m)	H_{max} (m)	F_i (N)
Main floating body	400	437	1104	1313.2
Floating ball group 1	700	652	1407	764.4
Floating ball group 2	1000	961	1709	980
CTD	1250	1218	1961	-19.6
Floating ball group 3	1500	1476	2212	764.4
Releaser	1800	1813	2514	352.8
Anchor	5800	5800	5800	-17,000

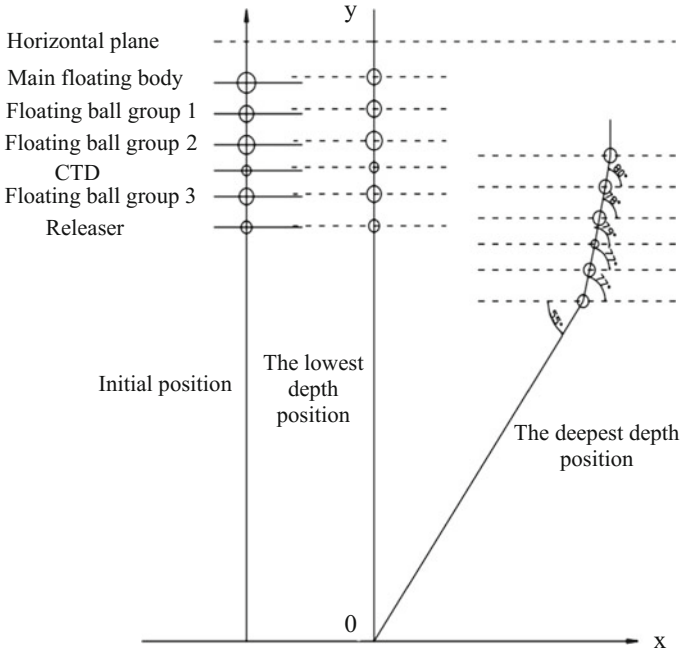


Fig. 4 Approximate attitude of the subsurface buoy system

Table 2 Position parameters of each node at the deepest depth position

Position parameters	Nodes					
	Main floating body	Floating ball group 1	Floating ball group 2	CTD	Floating ball group 3	Releaser
Displacement in current direction x (m)	2606	2551	2485	2435	2375	2305
Depth H (m)	-1104	-1407	-1709	-1961	-2212	-2514

Table 3 Data of each segment of Kevlar lanyard

No.	L_{i0} (m)	L_i (m)	ΔL_i (m)	T_{i0} (N)
1	300	304	4	1313.2
2	300	306	9	2077.6
3	250	257	7	3057.6
4	250	257	7	3038
5	300	310	10	3802.4

3.3 Fitting Function of Depth-Currents Velocity

Currents force can be given by the following Formula:

$$R_{ix} = \frac{1}{2} \rho_w C_{Di} A_x V_{ix} |V_{ix}| \tag{6}$$

where, ρ_w is the density of seawater, C_{Di} is drag coefficient, V_{ix} is the current velocity in horizontal direction, A_x is the effective cross-sectional area, which is calculated by the following formula:

$$A_x = L_i d_i \sin \theta_{i-1} + A_{ix} \tag{7}$$

where, L_i is the length of each segment, d_i is the diameter of lanyard, A_{ix} is the cross-sectional area of the floating body in the direction of motion.

The forces acting on each node can be calculated by Eq. (3) and the angles in Fig. 4, which are listed in Table 4.

From Formulas (6) and (7)

$$V_{ix} = \sqrt{\frac{2R_i}{\rho_w C_{Di} (L_i d_i \sin \theta_{i-1} + A_{ix})}} \cdot \frac{R_{ix}}{|R_{ix}|} \tag{8}$$

Then, the hydrodynamic parameters of each node are shown in Table 5.

Assuming that the variation of the current velocity along the depth direction is linear attenuation, the changing currents are divided into many small uniform flow layers, using the theory of finite element. Based on the hypothesis, the current velocity can be described by the following formula:

$$V_{ix} = \lambda H_i + C \tag{9}$$

where λ is ratio coefficient, C is a constant.

Table 4 Forces acting on each of node

Forces (N)	Nodes					
	Main floating body	Floating ball group 1	Floating ball group 2	CTD	Floating ball group 3	Releaser
F_i	1313.2	764.4	980	-19.6	764.4	352.8
T_i	0	1345	2146	3178	3169	3982
T_{i-1}	1345	2146	3178	3169	3982	1291
R_{ix}	231.6	210.1	152.7	107	176.5	900

Table 5 Hydrodynamic parameters of each node

Parameters	Nodes					
	Main floating body	Floating ball group 1	Floating ball group 2	CTD	Floating ball group 3	Releaser
Depth H_i (m)	400	700	1000	1250	1500	1800
L_i (m)	300	300	250	250	300	4000
A_x (m ²)	3	2.8	2.4	1.8	2.8	14
C_{Di}	0.7	0.8	0.7	0.7	0.8	1.2
R_{ix} (N)	231.6	210.1	152.7	107	176.5	900
V_{ix} (m/s)	0.47	0.45	0.42	0.40	0.39	0.32

According to the values of H_i and V_{ix} in Table 6, the fitting function (10) of depth-current velocity can be obtained by MATLAB.

$$V_{ix} = P_1 H_i + P_2 \tag{10}$$

where $P_1 = 1/9466$ and $P_2 = 0.53$.

3.4 Verification of Equilibrium Attitude of the System

The model of the system is established by using the lumped mass method. In order to have a high accuracy of simulation in ADAMS software, the lower 4000 m Kevlar lanyard is divided into 5 segments, and the net weight of each segment is concentrated to one node. So the simplified model of system consists of 11 nodes, and the adjacent two nodes are connected by a variable force, which is changed with the distance between the two nodes. The variable force replaces the elongation of lanyard between the two nodes, which is expressed by the following formula:

$$T_i = \frac{EA}{L_{i0}} \Delta L_i \tag{11}$$

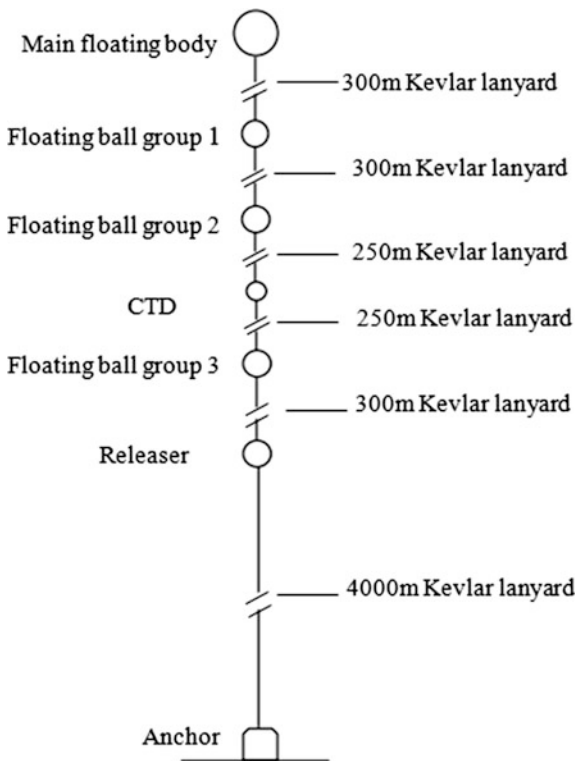
where, ΔL_i is the elongation of each segment of the Kevlar lanyard, and the values of ΔL_i are automatically measured by ADAMS.

Figure 5 shows the structure of system before simplified, and Fig. 6 shows the force-lumped mass model established in ADAMS.

Table 6 Parameters of each node of the simplified model

Parameters	Nodes										
	11	10	9	8	7	6	5	4	3	2	1
A_{ix} (m ²)	3	2.8	2.4	1.8	2.8	5.6	4.8	4.8	4.8	4.8	0
C_{Di}	0.7	0.8	0.7	0.7	0.8	1.2	1.2	1.2	1.2	1.2	-
F_i (N)	1313.2	76.4	980	-19.6	764.4	352.8	-320	-320	-640	-640	-17,000
V'_{ix} (m/s)	0.49	0.46	0.42	0.40	0.37	0.34	0.26	0.17	0.09	0.002	0
R'_i (N)	257.3	239.9	155.8	102.8	159.2	399.7	193.4	86.6	22.1	0.01	0

Fig. 5 The structure of the subsurface buoy system



According to the fitting function (10) and formula (6), the current velocities and current forces of each node can be obtained. Table 6 shows the parameters of each node of the simplified model.

In the ADAMS simulation, the forces in Table 6 are applied to each node, and the equilibrium attitude of the submarine buoy system at the deepest depth position is simulated. Figure 7 shows the attitude of the submarine buoy system at the deepest depth position.

Table 7 shows the position parameters of each buoy at the deepest depth position. Where ΔX and ΔH are respectively the deviations of the displacement in current direction and the depth of each node compared with the values in Table 2. If the deviations are relatively large, we can adjust the parameters (E) of simulation or the fitting function (10) until it has a high agreement between the simulation and reality. According to the data of Table 7, the largest deviation is 22 m, and the

Fig. 6 The force-lumped mass model

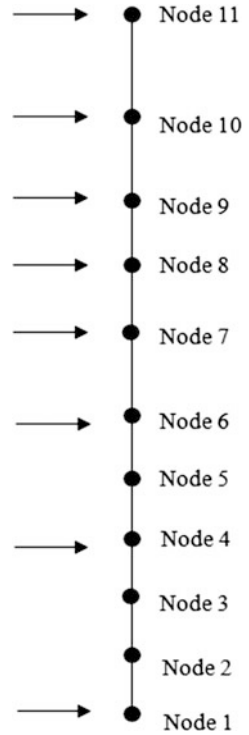


Table 7 The simulated position parameters of each buoy at the deepest depth position

Position parameters	Nodes					
	Main floating body	Floating ball group 1	Floating ball group 2	CTD	Floating ball group 3	Releaser
X' (m)	2615	2564	2501	2452	2394	2336
ΔX	+9	+13	+16	+17	+19	+21
H' (m)	-1126	-1425	-1724	-1976	-2225	-2506
ΔH	-22	-18	-15	-15	-13	+8

deviation rate is less than ten percent. So we consider that the result of simulation is accurate. The current profile is obtained according to the fitting function (10), as shown in Fig. 8.

Fig. 7 The attitude of each node at the deepest depth position

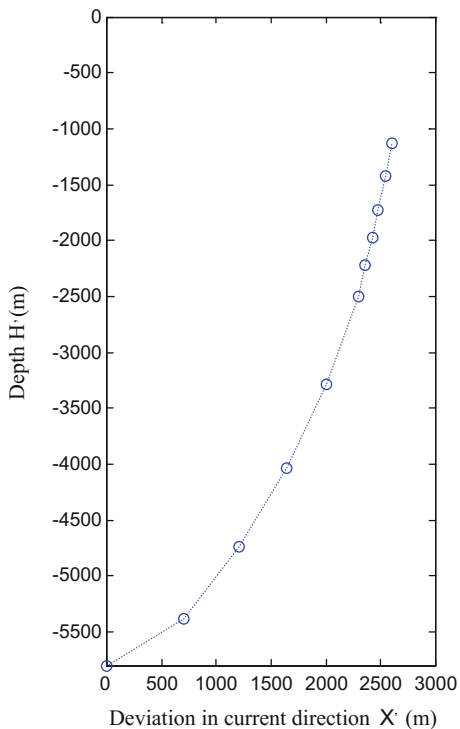
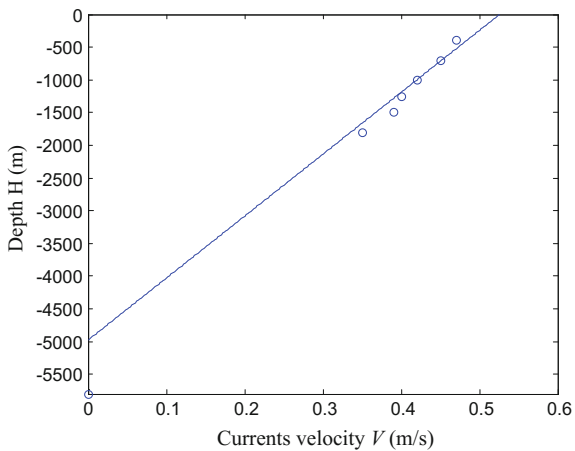


Fig. 8 Current profile



4 Conclusion

This article provides a method of inversion study of current parameters based on attitude data of subsurface buoy system through a practical case. And the current profile is obtained through the inversion analysis method. This method is proved to be practicable by comparing the results between the simulation and experiment data. This study has an important significance for determining the accurate information validation of current.

References

1. Li FQ, Zhang XM, Zhang P et al (2004) The design and application of marine submersible buoy system. *Ocean Technol* 23(1):17–21 (in Chinese)
2. Mao ZS (2001) Application and development of marine submersible buoy. *Mar Sci China* 4:57–58
3. Yang KH (1989) On the role of subsurface mooring system in oceanographic research in China. *Ocean Technol China* 8(1):82–93 (in Chinese)
4. Wang MW (2001) Static analysis and attitude calculation of marine submersible. *Ocean Technol* 20(4):39–47 (in Chinese)
5. Lan ZG et al (2008) The design and attitude analysis of a subsurface buoy for deep sea current profiling. *Mar Sci* 32(8):21–24 (in Chinese)
6. Hou GL, Zhang Y, Sun JC et al (2010) Analysis of attitude variation for submersible buoy system. *Ocean Technol* 29(3):38–43 (in Chinese)
7. Liu YQ, Sheng YF, Wang JQ et al (2010) Static analysis and attitude calculation of marine submersible buoy system and its application development. *Ocean Technol* 3:34–37 (in Chinese)
8. Ma L, Zhang HX, Zhang XB et al (2015) Attitude simulative analysis and optimal allocation suggestions for the deep-sea submersible buoy system. *Ocean Technol* 6:47–53 (in Chinese)
9. Ge DH, Zhu H, Chen JH et al (2014) Motion simulation study of deep-sea submerged buoy system. *J Dalian Marit Univ* 40(1):25–28 (in Chinese)
10. Tjavaras AA, Zhu Q, Liu Y et al (1998) The mechanics of highly-extensible cables. *J Sound Vib* 213(4):709–737
11. Chang ZY et al (2009) Nonlinear dynamic behavior of moored buoy excited by free surface waves. *China Ocean Eng* 23:585–592
12. Guo YQ, Li XL, Xiong XJ (2015) Mathematical modeling and result validation of mooring vertical movement in the course of floating-up. *Coast Eng* 34(2):11–23 (in Chinese)
13. Wu ZR (1985) Research on reliability of potential target system. *Ocean Technol* (3) (in Chinese)

Dynamic Modeling of Spherical 5R Parallel Mechanism for Spherical Plain Bearing Running-in Equipment

Yilei Zheng, Weidong Guo and Yan Xie

Abstract Spherical plain bearing plays a significant role in the national defense military, aerospace, robotics and other cutting-edge fields. Running-in test should be conducted prior to use which can significantly reduce friction coefficient, minimize torque ripple, improve reliability and increase lifecycle. Based on the requirement for spherical plain bearing running-in equipment, this paper conducts the feasibility analysis of application of spherical 5R parallel mechanism in spherical plain bearing running-in equipment. According to the geometric constraint conditions, a simple kinematic model is derived. Then the dynamic model is established based on the Lagrange method. Combining with a specific prototype, the reachable workspace and kinematic characteristics are analyzed, and the effective inertia varying with the configurations of mechanism is also discussed. Finally, dynamic simulation is implemented to verify the correctness of the dynamic model by using ADAMS software. The derived model can provide theoretical basis in dynamic optimal design, driving unit lectotype and control model establishment.

Keywords Spherical plain bearing · Running-in · Spherical 5R parallel mechanism · Dynamics · Lagrange method

Y. Zheng · W. Guo (✉) · Y. Xie
Robotics Institute, Beihang University, Beijing 100191, China
e-mail: guowd@buaa.edu.cn

Y. Zheng
e-mail: yileizheng@126.com

Y. Xie
e-mail: xieyan@buaa.edu.cn

1 Introduction

Spherical plain bearing typically consists of both a spherical inner ring and a spherical outer ring, which permits not only angular swing around a central point in two orthogonal directions within a specified angular limit but also rotation around the same point along z axis without angular limit. It possesses many virtues such as compact structure, miniaturization, large bearing capacity and impact resistance, etc., which lays the foundation for its application in gimbal, wrist of robot, transmission of car, dexterous eyes and other cutting-edge fields [1, 2].

Running-in test should be conducted prior to use which can fully run-in the contact face between inner and outer rings, significantly reduce friction coefficient and minimize torque ripple, thus make the installed bearing into a good working condition directly. Running-in test is of crucial significance to improve the performance, enhance the reliability and prolong the lifecycle. By far, the research hotspots of bearing running-in equipment mainly lie in rolling bearing with a single rotation DOF (axis Z). Apparently, existing bearing running-in equipment [3–6] is rarely able to achieve efficient running-in for the spherical plain bearing with a 3-DOF spherical motion. Therefore, the core issue to design a spherical plain bearing running-in equipment lies in choosing a mechanism with the spherical plain bearing motion characteristics.

Spherical 5R parallel mechanism, also known as spherical five-bar parallel mechanism, is constructed by connecting links with hinged joints such that the axis of each hinge intersects at a fixed point. Major applications are involved in the antenna pointing, operation of laser beam and minimally invasive surgery [7–10], etc. The kinematics and dynamics analysis, as the foundation of application, have been extensively studied in recent years. The relationship among effective workspace, singularity characterization, kinetostatic performance and force transmission capability has been systematically revealed in references [11–15] which helps designers have an anticipated knowledge of the workspace shape and other characteristics. Beyond that, Dong [16] adopted a visual graphic approach to analyze its DOF, workspace and singularity and further established a simple kinematic model. Zhang and Li [17, 18] analyzed the kinematics, error sensitivity, trajectory planning and motion control by D-H coordinate method. But the research in [18] about dynamics of 5R parallel manipulator is primary. Fang [19] made a deep research in respect of inertia force balance condition to achieve a better dynamic performance. And the relationship between the input conditions and driving torque is also discussed. In general, previous studies of spherical 5R mechanism are mainly focused on the kinematic analysis, and the dynamic research is rarely involved. The existing process of forward and inverse kinematics is basically based on the D-H parameters, which leads to a complicated dynamic model. And the intrinsic relationship between input torque and mechanism configuration has not been announced. Therefore, adopting an appropriate method to establish an accurate and succinct dynamic model is the prerequisite for figuring out the influence factors of input torque.

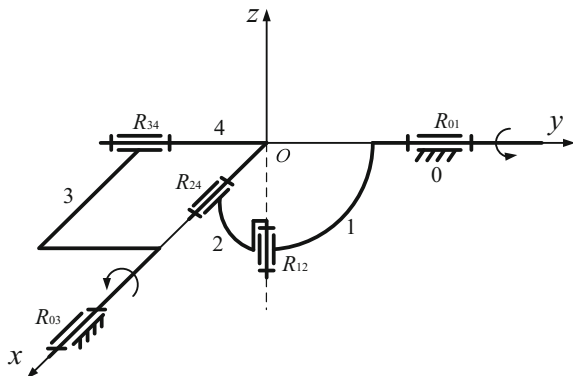
The purpose of this paper is to analyze the feasibility of application of spherical 5R parallel mechanism in spherical plain bearing running-in equipment in terms of kinematics and dynamics characteristics. The whole paper is organized as follows: Sect. 2 derives a simple kinematic model according to the geometric constraint conditions. The dynamic model is established based on the Lagrange method in Sect. 3. And in Sect. 4, the reachable workspace and kinematic characteristics are analyzed combining with a specific prototype. Meanwhile, the effective inertia varying with the configurations of mechanism is also discussed which could be beneficial to research attempting to increase the dynamic performance. Further, dynamic simulation is implemented to verify the correctness of the dynamic model by using ADAMS software. Finally, conclusions are given.

2 Kinematic Modeling

The architecture of spherical 5R parallel mechanism is illustrated in Fig. 1. It consists of a base platform (No. 0), a mobile platform (No. 4) and three links (No. 1, 2, 3), which can be classified into two limbs actuated by two rotary actuators separately. The two limbs of the mechanism are arranged at 90 degrees. One limb is composed by link 1 and 2, including three revolute joints R_{01} , R_{12} , R_{24} , and the other limb is link 3, including two revolute joints R_{03} , R_{34} . All axes of revolute joints intersect at the fixed point O , the center of both base platform and mobile platform.

Different from the general configuration, this study defines that the intersection angle between adjacent revolute joints is at 90° . As shown in Fig. 1, the global coordinate O - xyz is attached to the base platform at point O and x/y axes are along the axes of R_{03} , R_{01} separately which also denotes two active revolute joints of this mechanism. Let θ_1 and θ_2 be the actuation angle of R_{01} and R_{03} , respectively. Then defines the unit normal vector of mobile platform as $\mathbf{n}_M = (x_M, y_M, z_M)^T$, and the

Fig. 1 Schematic diagram of spherical 5R parallel mechanism



unit vector of axis of R_{24} as $\mathbf{OR}_{24} = (x, y, z)^T$. Therefore, the unit vector of the axes of R_{12} and R_{34} expressed in the global coordinate frame can be written as

$$\mathbf{OR}_{12} = (\sin \theta_1, 0, -\cos \theta_1)^T \quad (1)$$

$$\mathbf{OR}_{34} = (0, -\cos \theta_2, \sin \theta_2)^T \quad (2)$$

Further, vector \mathbf{n}_M can be expressed as

$$\mathbf{n}_M = \mathbf{OR}_{34} \times \mathbf{OR}_{24} \quad (3)$$

Therefore, the unit normal vector (x_M, y_M, z_M) of the mobile platform can be obtained by Eq. (3)

$$\begin{cases} x_M = -z \cos \theta_2 - y \sin \theta_2 \\ y_M = x \sin \theta_2 \\ z_M = x \cos \theta_2 \end{cases} \quad (4)$$

Vector \mathbf{OR}_{12} and \mathbf{OR}_{34} are both always vertical to vector \mathbf{OR}_{24} in the motion process of this mechanism. Then this geometric constraint condition can be represented as

$$\begin{cases} \mathbf{OR}_{12} \cdot \mathbf{OR}_{24} = 0 \\ \mathbf{OR}_{34} \cdot \mathbf{OR}_{24} = 0 \end{cases} \quad (5)$$

The above equation can be simplified as

$$\begin{cases} x \sin \theta_1 - z \cos \theta_1 = 0 \\ -y \cos \theta_2 + z \sin \theta_2 = 0 \end{cases} \quad (6)$$

Notably, $|\mathbf{OR}_{24}|^2 = x^2 + y^2 + z^2 = 1$ is a default condition.

Hence, the forward kinematics of this mechanism can be derived by Eqs. (4) and (6)

$$\begin{cases} x_M = -\frac{\sin \theta_1}{k} \\ y_M = \frac{\cos \theta_1 \sin \theta_2 \cos \theta_2}{k} \\ z_M = \frac{\cos \theta_1 \cos^2 \theta_2}{k} \end{cases} \quad (7)$$

where $k = \sqrt{\sin^2 \theta_1 + \cos^2 \theta_1 \cos^2 \theta_2}$

Similarly, the actuation angle θ_1 and θ_2 can be solved when the vector $\mathbf{n}_M = (x_M, y_M, z_M)$ is given:

$$\begin{cases} \cos \theta_1 = \frac{1-x_M^2}{\sqrt{x_M^4 + (z_M^2 - 2)x_M^2 + 1}} \\ \cos \theta_2 = \sqrt{\frac{z_M^2}{1-x_M^2}} \end{cases} \quad (8)$$

3 Dynamic Modeling

3.1 Mechanical Energy of Driving Links

Link 1 and 3 are defined as driving links which are directly actuated by rotary actuators fixed to the base. The position of link 1 and 3 can be solely determined by the actuation angle θ_1 and θ_2 , respectively. Therefore, \mathbf{C}_1 and \mathbf{C}_3 which denote the centroid vector of link 1 and 3 expressed in the global coordinate frame can be written as

$$\mathbf{C}_1 = (l_{1y}, \sin \theta_1, l_{1x}, -l_{1y} \cos \theta_1)^T \quad (9)$$

$$\mathbf{C}_3 = (l_{3y}, -l_{3x} \cos \theta_2, l_{3x} \sin \theta_2)^T \quad (10)$$

where l_{1x} and l_{1y} refer to the distance from the centroid of link 1 to axes y and z , respectively. Similarly, l_{3x} and l_{3y} refer to the distance from the centroid of link 3 to axes y and x . These parameters are determined by the geometric size and mass distribution of link 1 and 3.

Let \mathbf{C}_1 and \mathbf{C}_3 be $\mathbf{C}_1 = (x_1, y_1, z_1)^T$, $\mathbf{C}_3 = (x_3, y_3, z_3)^T$, then the potential energy of link 1 and 3 can be expressed as

$$\begin{cases} P_1 = m_1 g z_1 \\ P_3 = m_3 g z_3 \end{cases} \quad (11)$$

where m_1 and m_3 are the mass of link 1 and 3.

Since driving link 1 and 3 only possesses pure rotational characteristics, the kinetic energy of link 1 and 3 can be simplified as

$$\begin{cases} K_1 = \frac{1}{2} J_1 \dot{\theta}_1^2 \\ K_3 = \frac{1}{2} J_3 \dot{\theta}_2^2 \end{cases} \quad (12)$$

where $\dot{\theta}_1$ and $\dot{\theta}_2$ are angular velocity of link 1 and 3. J_1 is the moment of inertia of link 1 around axis y , and J_3 is the moment of inertia of link 3 around axis x .

3.2 Mechanical Energy of Passive Links

Link 2 and the mobile platform 4 are defined as passive links, which are actuated by driving links indirectly. Connecting link coordinate $R_{12}-x_2y_2z_2$ is attached to the link 2 at point R_{12} with axis y_2 coincided with y and axis z_2 coincided with vector $OR_{12}O$ as shown in Fig. 2. Then the transform matrix from the global coordinate to the coordinate $R_{12}-x_2y_2z_2$ can be written as

$$S_2 = R(z, \frac{\pi}{2})T(OR_{12})R(x, -\theta_1)R(z, -\beta) \tag{13}$$

And the corresponding rotation matrix obtained from Eq. (13) can be written as

$$R_2 = R(z, \frac{\pi}{2})R(x, -\theta_1)R(z, -\beta) \tag{14}$$

where β is the angle between link 1 and 2, the value of which varies with the position of the mechanism.

n_1 , the normal vector of link 1, can be obtained by cross product of vector OR_{12} and OR_{01}

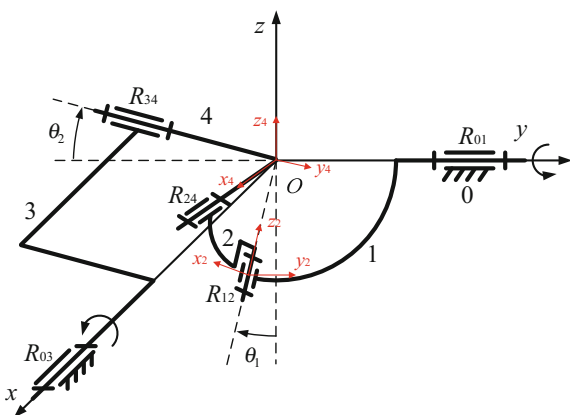
$$n_1 = OR_{12} \times OR_{01} \tag{15}$$

Similarly, n_2 , the normal vector of link 2, can be expressed by vector OR_{12} and OR_{24}

$$n_2 = OR_{12} \times OR_{24} \tag{16}$$

Then the value of β is the supplementary angle relative to the angle between n_1 and n_2

Fig. 2 Coordinate diagram of spherical 5R parallel mechanism



$$\beta = \pi - \arccos \frac{|\vec{n}_1 \cdot \vec{n}_2|}{|\vec{n}_1| \cdot |\vec{n}_2|} \tag{17}$$

C'_2 , which refers to the centroid vector of link 2 in the coordinate $R_{12-x_2y_2z_2}$, can be expressed as

$$C'_2 = (l_{2x}, l_{2y}, l_{2z})^T \tag{18}$$

Then C_2 , the centroid vector of link 2 in the global coordinate, will be expressed as

$$C_2 = S_2 C'_2 \tag{19}$$

Especially, the corresponding operator matrix of angular velocity can be obtained by \dot{R}_2 and R_2^{-1}

$$\begin{pmatrix} 0 & -\omega_{z2} & \omega_{y2} \\ \omega_{z2} & 0 & -\omega_{x2} \\ -\omega_{y2} & \omega_{x2} & 0 \end{pmatrix} = \dot{R}_2 R_2^{-1} \tag{20}$$

where ω_{x2} , ω_{y2} and ω_{z2} represent the angular velocity of link 2 around axes x_2 , y_2 and z_2 , respectively. The values can be derived by Eqs. (13)–(20):

$$\begin{cases} \omega_{x2} = \dot{\beta} \sin \theta_1 \\ \omega_{y2} = -\dot{\theta}_1 \\ \omega_{z2} = -\dot{\beta} \cos \theta_1 \end{cases} \tag{21}$$

The mobile coordinate $O-x_4y_4z_4$ is attached to the mobile platform at point O with axis x_4 coincided with vector OR_{24} and axis y_4 coincided with vector $R_{34}O$ as shown in Fig. 2. Then the transform matrix from the global coordinate to the mobile coordinate $O-x_4y_4z_4$ can be expressed as

$$R_4 = R(x, -\theta_2)R(z, -\varphi) \tag{22}$$

where φ is the angle between link 3 and mobile platform 4, which can be derived by the angle between vector OR_{24} and OR_{03}

$$\begin{cases} \sin \varphi = \frac{|OR_{24} \times OR_{03}|}{|OR_{24}| \cdot |OR_{03}|} \\ \cos \varphi = \frac{|OR_{24} \cdot OR_{03}|}{|OR_{24}| \cdot |OR_{03}|} \end{cases} \tag{23}$$

C'_4 , which refers to the centroid vector of the mobile platform in the mobile coordinate $O-x_4y_4z_4$, can be expressed as

$$C'_4 = (l_{4x}, l_{4y}, l_{4z})^T \tag{24}$$

Then C_4 , the centroid vector in the global coordinate can be expressed as

$$C_4 = R_4 C'_4 \tag{25}$$

The corresponding operator matrix of angular velocity can be derived by \dot{R}_4 and R_4^{-1}

$$\begin{pmatrix} 0 & -\omega_{z4} & \omega_{y4} \\ \omega_{z4} & 0 & -\omega_{x4} \\ -\omega_{y4} & \omega_{x4} & 0 \end{pmatrix} = \dot{R}_4 R_4^{-1} \tag{26}$$

where ω_{x4} , ω_{y4} and ω_{z4} represent the angular velocity of the mobile platform around axes x_4 , y_4 and z_4 , respectively. The values can be solved by Eqs. (22)–(26):

$$\begin{cases} \omega_{x4} = -\dot{\theta}_2 \\ \omega_{y4} = -\dot{\varphi} \cos \theta_2 \\ \omega_{z4} = \dot{\varphi} \sin \theta_2 \end{cases} \tag{27}$$

Let C_2 and C_4 be $C_2 = (x_2, y_2, z_2)^T$, $C_4 = (x_4, y_4, z_4)^T$, then the potential energy of link 2 and 4 is written as

$$\begin{cases} P_2 = m_2 g z_2 \\ P_4 = m_4 g z_4 \end{cases} \tag{28}$$

where m_2 and m_4 are the mass of link 2 and 4.

Since link 2 and mobile platform 4 not only possess rotational but also translational characteristic, the kinetic energy is expressed as

$$\begin{cases} K_2 = K_2^R + K_2^T \\ K_4 = K_4^R + K_4^T \end{cases} \tag{29}$$

$$K_2^R = \frac{1}{2} J_{2x} \omega_{x2}^2 + \frac{1}{2} J_{2y} \omega_{y2}^2 + \frac{1}{2} J_{2z} \omega_{z2}^2$$

$$K_4^R = \frac{1}{2} J_{4x} \omega_{x4}^2 + \frac{1}{2} J_{4y} \omega_{y4}^2 + \frac{1}{2} J_{4z} \omega_{z4}^2$$

$$K_2^T = \frac{1}{2} m_2 (\dot{x}_2^2 + \dot{y}_2^2 + \dot{z}_2^2)$$

$$K_4^T = \frac{1}{2} m_4 (\dot{x}_4^2 + \dot{y}_4^2 + \dot{z}_4^2)$$

where J_{2x} , J_{2y} and J_{2z} is the moment of inertia of link 2 around axes x_2 , y_2 and z_2 ; J_{4x} , J_{4y} and J_{4z} is the moment of inertia of mobile platform 4 around axes x_4 , y_4 and z_4

z_4 , respectively. $\dot{x}_2, \dot{y}_2, \dot{z}_2$ and $\dot{x}_4, \dot{y}_4, \dot{z}_4$ denote the translational velocity of the centroids of link 2 and 4 along the corresponding axes.

3.3 Dynamic Modeling

Combining Eqs. (11) and (28), the total potential energy of the parallel mechanism can be represented by

$$P = P_1 + P_2 + P_3 + P_4 \tag{30}$$

Combining Eqs. (12) and (29), we can also derive the total kinetic energy of the parallel mechanism

$$K = K_1 + K_2 + K_3 + K_4 \tag{31}$$

Then Lagrange function L can be constructed as

$$L = K - P \tag{32}$$

The input torque $\tau = (\tau_1 \ \tau_2)^T$ acting upon the driving links 1 and 3 can be derived by applying Lagrange equation when a part of driving system of force is conservative force

$$\frac{d}{dt} \frac{\partial L}{\partial \dot{\theta}} - \frac{\partial L}{\partial \theta} = \tau \tag{33}$$

where $\theta = (\theta_1 \ \theta_2)^T$ is denoted as actuation angle of R_{01} and R_{03} , $\dot{\theta} = (\dot{\theta}_1 \ \dot{\theta}_2)^T$ is denoted as angular velocity of R_{01} and R_{03} .

Since the potential energy P is independent of $\dot{\theta}$, the first part of Eq. (33) can be rewritten as follows according to derivative rule of compound function

$$\frac{d}{dt} \frac{\partial L}{\partial \dot{\theta}} = \frac{\partial^2 K}{\partial \dot{\theta} \partial \dot{\theta}} \dot{\theta} + \frac{\partial^2 K}{\partial \dot{\theta}^2} \ddot{\theta} \tag{34}$$

where $\ddot{\theta} = (\ddot{\theta}_1 \ \ddot{\theta}_2)^T$ is denoted as angular acceleration of R_{01} and R_{03} .

Hence, the input torque can be reorganized as

$$\tau = \frac{\partial^2 K}{\partial \dot{\theta} \partial \dot{\theta}} \dot{\theta} + \frac{\partial^2 K}{\partial \dot{\theta}^2} \ddot{\theta} - \frac{\partial L}{\partial \theta} \tag{35}$$

We can reduce Eq. (35) to a general form

$$\mathbf{M}(\boldsymbol{\theta})\ddot{\boldsymbol{\theta}} + \mathbf{C}(\boldsymbol{\theta}, \dot{\boldsymbol{\theta}})\dot{\boldsymbol{\theta}} + \mathbf{G}(\boldsymbol{\theta}, \dot{\boldsymbol{\theta}}) = \boldsymbol{\tau}$$

where $\mathbf{M}(\boldsymbol{\theta})$ is the inertia matrix, $\mathbf{C}(\boldsymbol{\theta}, \dot{\boldsymbol{\theta}})$ is the coriolis and centrifugal matrix, $\mathbf{G}(\boldsymbol{\theta}, \dot{\boldsymbol{\theta}})$ is the gravity matrix. $\mathbf{M}(\boldsymbol{\theta})$ occupies the main component of input torque and plays a lead role in the system especially when there is a sharp change in angular velocity. Since $\mathbf{M}(\boldsymbol{\theta})$ is an important parameter for estimating of input torque, selection of servo motor and simplification of control model, it is necessary to analyze the influence factors of $\mathbf{M}(\boldsymbol{\theta})$ thoroughly.

$\mathbf{M}(\boldsymbol{\theta})$ can be further expanded as

$$\mathbf{M}(\boldsymbol{\theta}) = \frac{\partial^2 K}{\partial \dot{\boldsymbol{\theta}}^2} = \begin{bmatrix} M(\boldsymbol{\theta})_{11} & M(\boldsymbol{\theta})_{12} \\ M(\boldsymbol{\theta})_{12} & M(\boldsymbol{\theta})_{22} \end{bmatrix} \quad (36)$$

As implied in Eq. (36), $\mathbf{M}(\boldsymbol{\theta})$ is the function of θ_1 and θ_2 , which determined by the position of the parallel mechanism. $M(\boldsymbol{\theta})_{12}$ reflects the coupling relationship between the input torques, the values of which can affect the stability of control system directly. $M(\boldsymbol{\theta})_{11}$ and $M(\boldsymbol{\theta})_{22}$ are denoted as effective inertia of the system, the average values of which in the workspace can be used to estimate equivalent load inertia of servo motor.

4 Case Study

4.1 Workspace Analysis

Considering the specific requirement for spherical plain bearing running-in equipment, the prototype of a spherical 5R parallel mechanism is demonstrated in Fig. 3. Details of the structural parameters are listed in Table 1. The theoretical reachable workspace can be obtained according to the kinematic equations and movement interference, as shown in Fig. 4a. By comparing with simulation results obtained by ADAMS shown in Fig. 4b, the theoretical and simulation workspace have been verified to be consistent, which belong to a part of a spherical surface. However, the minor difference lies in the existence of tip region in the both sides of theoretical workspace. This results from the fact that some approximations are adopted to simplify the movement interference. Although actual actuation angle limits vary with the posture of mechanism, they are treated as constants in theoretical analysis.

The comparison between theoretical and simulation workspace verifies the correctness of the kinematic model and proves that the spherical 5R parallel mechanism can operate freely where $\theta_1 \in (-50.6^\circ$ to $50.6^\circ)$, $\theta_2 \in (-16.4^\circ$ to $16.7^\circ)$ which meets the swing angle requirement (-15° to 15°) of spherical plain bearing running-in equipment.

Fig. 3 Diagram of the mechanism prototype

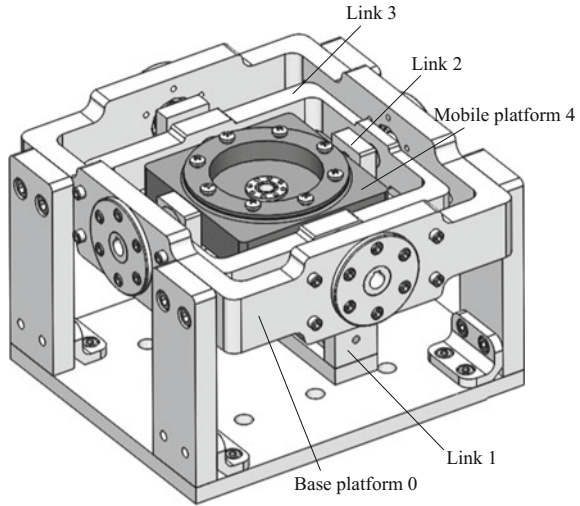


Table 1 Structural parameters of the prototype

Parameter (unit)	Specification relative to local coordinate	Value
L_{1x} (m)	x Coordinate of centroid -1	1.7×10^{-3}
L_{1y} (m)	y Coordinate of centroid -1	1.2×10^{-6}
L_{1z} (m)	z Coordinate of centroid -1	-7.3×10^{-7}
L_{2x} (m)	x Coordinate of centroid -2	-3.3×10^{-6}
L_{2y} (m)	y Coordinate of centroid -2	-3.6×10^{-7}
L_{2z} (m)	z Coordinate of centroid -2	25.9×10^{-3}
L_{3x} (m)	x Coordinate of centroid -3	2.0×10^{-6}
L_{3y} (m)	y Coordinate of centroid -3	2.4×10^{-3}
L_{3z} (m)	z Coordinate of centroid -3	-62.9×10^{-3}
L_{4x} (m)	x Coordinate of centroid -4	0
L_{4y} (m)	y Coordinate of centroid -4	0
L_{4z} (m)	z Coordinate of centroid -4	2.3×10^{-3}
m_1 (kg)	Mass of 1	3.16
m_2 (kg)	Mass of 2	1.67
m_3 (kg)	Mass of 3	2.38
m_4 (kg)	Mass of mobile platform	3.62
J_1 (kg m ²)	Moment of inertia around $R_{01} - 1$	1.95×10^{-6}
J_3 (kg m ²)	Moment of inertia around $R_{03} - 3$	1.36×10^{-6}
J_{2x} (kg m ²)	Moment of inertia around $x_2 - 2$	1.87×10^{-3}
J_{2y} (kg m ²)	Moment of inertia around $y_2 - 2$	9.80×10^{-3}
J_{2z} (kg m ²)	Moment of inertia around $z_2 - 2$	8.38×10^{-3}
J_{4x} (kg m ²)	Moment of inertia around $x_4 - 4$	7.64×10^{-3}
J_{4y} (kg m ²)	Moment of inertia around $y_4 - 4$	7.70×10^{-3}
J_{4z} (kg m ²)	Moment of inertia around $z_4 - 4$	1.47×10^{-2}

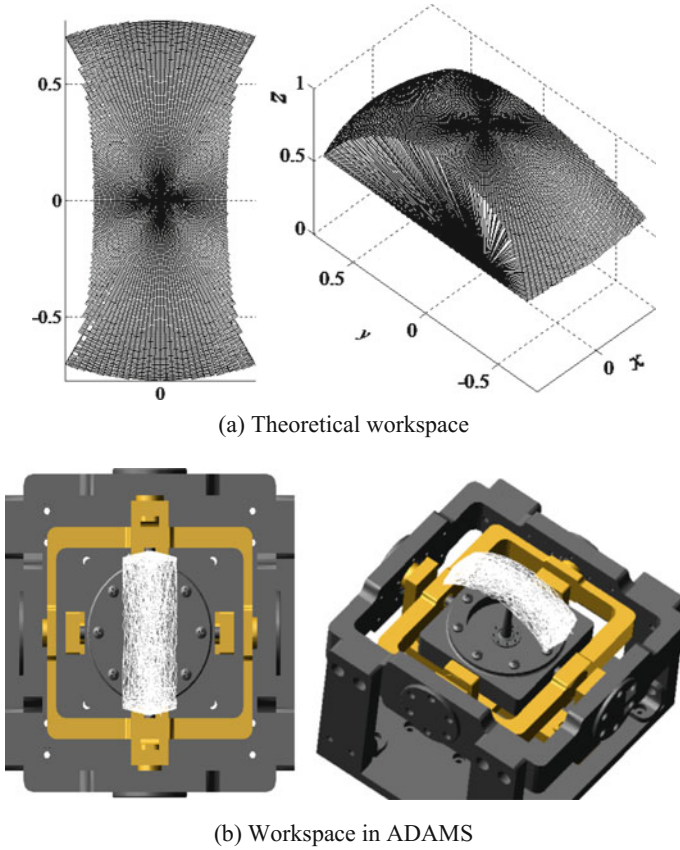


Fig. 4 Workspace of the prototype

4.2 Kinematics Analysis and Simulation

Assuming that the peak of vector n_M moves along a circle, the radius of which is set at 0.2, as shown in Fig. 5, we can derive the normal unit vector of mobile platform n_M

$$\begin{cases} x_M = 0.2 \sin t \\ y_M = 0.2 \cos t \\ z_M = \sqrt{1 - x_M^2 - y_M^2} \end{cases} \quad (37)$$

Substituting Eq. (37) into Eqs. (8)–(10), (19) and (25), we can obtain the actuation angle curves and centroid position curves of each link, as shown in Figs. 6 and 7, which are consistent with the simulation results measured from ADAMS.

Fig. 5 Trajectory of the mobile platform

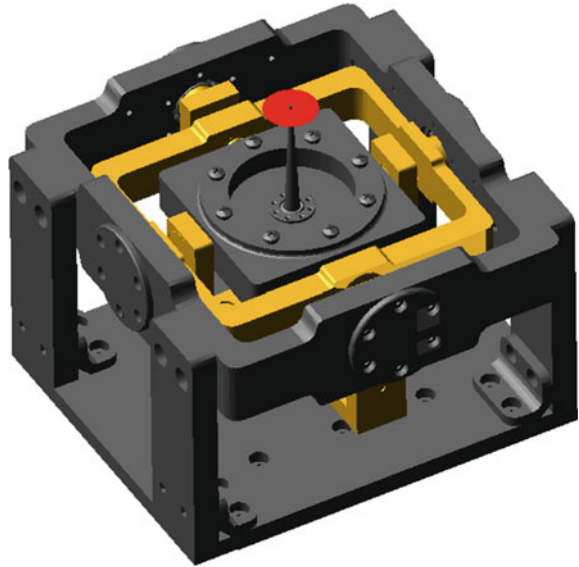
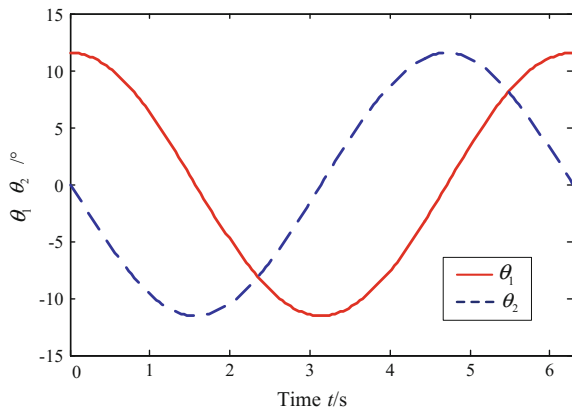


Fig. 6 Actuation angle



4.3 Dynamic Analysis and Simulation

(A) Inertia matrix

Figure 8 shows the effective inertia M_{11} , M_{22} and coupling inertia M_{12} associated with the actuation angles θ_1 , θ_2 . Obviously, M_{11} , M_{22} and M_{12} are continuous function with actuation angles θ_1 and θ_2 within the workspace.

- (1) The effective inertia M_{11} , the shape of which exhibits some sort of symmetry, will increase rapidly when the values of θ_1 and θ_2 are close to the

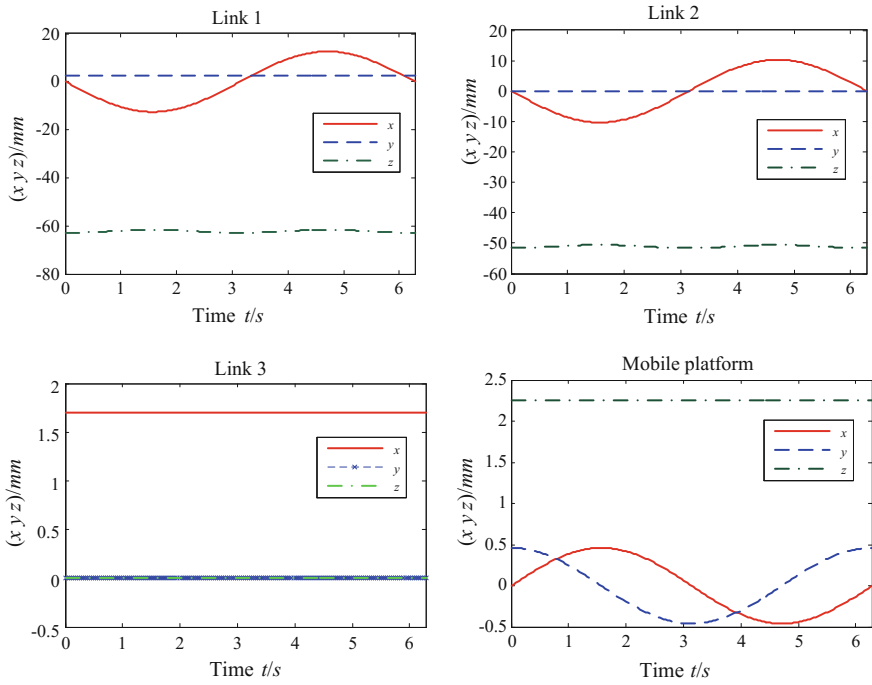


Fig. 7 Centroid position

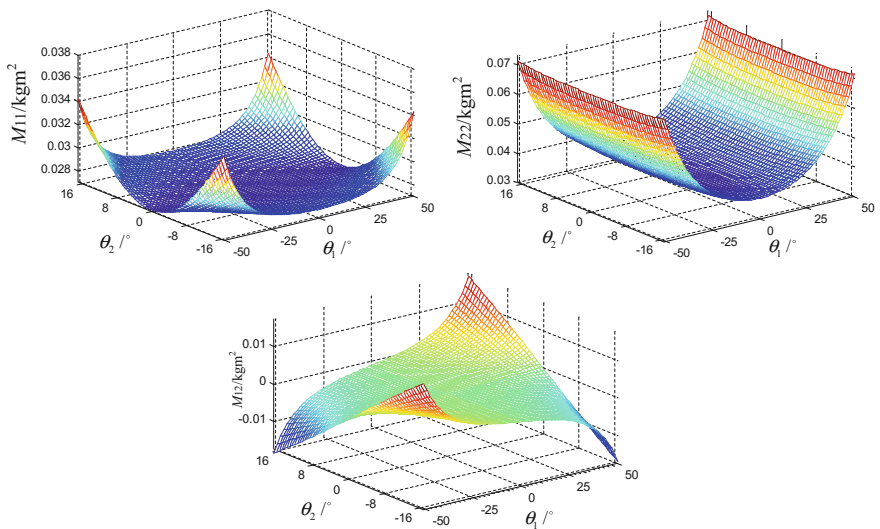


Fig. 8 Effective inertia and coupling inertia of the prototype

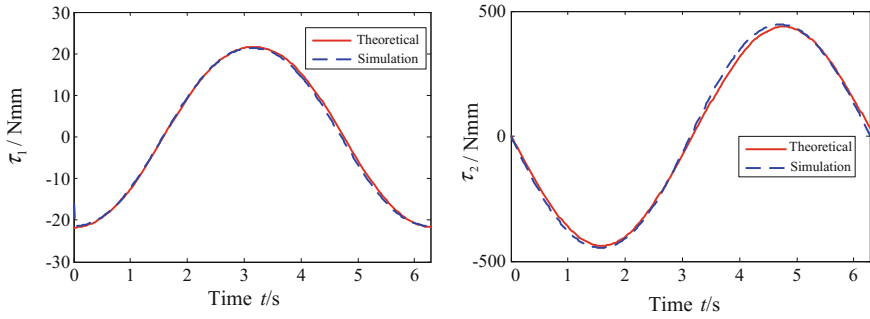


Fig. 9 Input torque of the prototype

maximum, which will lead to a steep increasing of the input torque τ_1 . However, supposing that the values of θ_1 and θ_2 are set less than half of their maximum values, the effective inertia M_{11} will remain steady. Therefore, the extreme position should be avoided in the motion control.

- (2) The effective inertia M_{22} , the shape of which is analogous to a parabolic surface, mainly depends on the value of θ_1 which means that it will not fluctuate despite a sharp change of θ_2 when θ_1 is a constant. Nevertheless, the value of M_{22} will reach a peak with the value of θ_1 approaching to its maximum. The peak value is almost twice as much as that in initial position. It indicates that the input torque τ_2 is mainly associated with actuation angle θ_1 rather than θ_2 , which may have practical importance.
- (3) The coupling inertia M_{12} is also symmetric within the workspace. The average value is close to zero, which reflects the driving torques of two limbs are decoupled. But the coupling extent will become increasingly evident when the values of θ_1 and θ_2 are close to their maximum. Since the value of coupling inertia M_{12} is very small compared with that of effective inertia M_{11}, M_{22} , it accounts for a minor proportion in the driving torques τ_1, τ_2 . However, it is not negligible when applied in precise control.

(B) Input torque

The theoretical input torques τ_1 and τ_2 obtained from Eq. (35) are described by solid lines shown in Fig. 9. Compared with the simulation results measured via ADAMS described by dotted lines, the proposed dynamic model is verified. Meanwhile, it has been found that the average value of input torque τ_1 is much larger than that of τ_2 . The maximum value of input torque τ_1 can support for the driving unit lectotype.

5 Conclusions

In this study, spherical 5R parallel mechanism with two rotational DOF around a fixed point is applied to meet the requirement for spherical plain bearing running-in equipment. Combining the kinematic and dynamic analysis, the application feasibility of the spherical 5R parallel mechanism in spherical plain bearing running-in equipment is verified. The main conclusions are drawn as follows:

- (1) A simple kinematic model is derived according to the geometric constraint conditions. Further, the dynamic model is established based on the Lagrange method, which is concise and straightforward contrast to the existing model established by D-H coordinate method.
- (2) The theoretical workspace considering the movement interference are given with adopting some reasonable simplifications, which may provide practical guidance on designing a mechanism prototype with appropriate workspace.
- (3) The effective inertia and coupling inertia, major factors of input torques, varying with the configurations of mechanism are discussed which show that rational ranges of actuation angles are vital to reduce the input torques fluctuation and coupling.
- (4) Verified by the dynamic simulation in ADAMS software, the derived dynamic model can provide theoretical basis in dynamic optimal design, driving unit lectotype and control model establishment.

References

1. Tang ZQ (2008) A review on the development of spherical plain bearing. *Mech Eng* 07:72–73
2. Spherical plain bearings. <http://www.astbearings.com/spherical-plain-bearings.html>
3. Staley JH (1923) Engine-bearing burning-in and running-in machine. *US* 1,452,446, 1923
4. Sikora J (2002) Bearing testing machine with rotating load vector. Institute of Aviation
5. Xu LP, Li LJ (2015) Design of hydraulic loading system for the little loading bearing testing machine. *Appl Mech Mater* 490–494
6. Qiu YP, Shen XJ (2011) Research progress of wear performance test for spherical bearings. *Bearings* 06:56–61
7. Larochelle P (2007) Synthesis of part orienting devices for spatial assembly tasks. *Adv Robot Kinematics: Anal Des* 79–87
8. Lum MJH, Rosen J, Sinanan MN et al (2006) Optimization of a spherical mechanism for a minimally invasive surgical robot: theoretical and experimental approaches. *IEEE Trans Biomed Eng* 1440–1445
9. Lum MJH, Rosen J, Sinanan MN et al (2004) Kinematic optimization of a spherical mechanism for a minimally invasive surgical robot. *IEEE Robot Autom* 829–834
10. Caron F, Gosselin CM (1999) Two degree-of-freedom spherical orienting device. *US* 5,966,991, 1999
11. Cervantes-Sánchez JJ, Hernández-Rodríguez JC et al (2004) On the 5R spherical, symmetric manipulator: workspace and singularity characterization. *Mech Mach Theory* 409–429
12. Daneshmand M et al (2016) Optimal design of a spherical parallel manipulator based on kinetostatic performance using evolutionary techniques. *J Mech Sci Technol* 1323–1331

13. Wu C, Liu XJ et al (2009) Force transmission analysis of spherical 5R parallel manipulators. In: ASME international conference on reconfigurable mechanisms and robots, pp 331–336
14. Zhang LJ et al (2006) Analysis of the workspace of 2-DOF spherical 5R parallel manipulator. In: IEEE international conference on robotics and automation, pp 1123–1128
15. Kohli D, Khonji A (1994) Grashof-Type rotatability criteria of spherical five-bar linkages. *J Mech Des* 99–104
16. Dong X et al (2012) Geometric approach for kinematic analysis of a class of 2-DOF rotational parallel manipulators. *Chin J Mech Eng* 241–247
17. Li YQ (2012) Theory analysis and experiment research of spherical 2-DOF parallel manipulator. Yanshan University, China
18. Zhang LJ, Li YQ et al (2009) Dynamic analysis of spherical 5R parallel manipulator. *Int Conf Mechatron Autom* 1510–1514
19. Fang X (2009) Design and analysis of tracking parallel mechanism. Shanghai Jiaotong University, China

Dynamic Modeling and Analysis of Sucker Rod Pumping System in a Directional Well

Dong-yu Wang and Hong-zhao Liu

Abstract The sucker rod dynamic model including the influences of rod-fluid-tubing viscous friction and rod-tubing Coulomb friction is developed. Considering the influences of the liquid inertia and plunger-barrel friction, down-hole boundary conditions are determined. To improve the velocity and preciseness of simulation and prediction, a hybrid algorithm is proposed for solving the wave equation. This algorithm combines the implicit differential method applied in homogeneous sucker rod with the variable step differential method applied in the boundary node of composite sucker rod. Based on the model and the algorithm, the computer programs predicting the polished rod dynamometer card of sucker rod pumping system in a directional well are written. The results of simulation and prediction show that the modeling method is effective and the reliability of the model is verified. The model can provide a reference for pumping well fault diagnosis.

Keywords Dynamic modeling · Rod pumping system · Directional well · Plunger-barrel friction · Polished rod load

1 Introduction

The method of extracting oil from formation can be divided into two kinds [1]: natural flowing production method and the artificial lift oil production method, 85 % worldwide the crude oil relies on artificial lift oil production method. Sucker rod pumping method is the earliest artificial lift oil production method, which is one of most widely used methods [2]. As early as the beginning of the oil industry, this method for production began to be taken advantage of. Sucker rod pumping equipment consists of the following three parts: pumping unit, sucker rod and

D. Wang (✉) · H. Liu

School of Mechanical and Precision Instrument Engineering,
Xi'an University of Technology, Xi'an 710048, China
e-mail: dongyu-wang@qq.com

oil-well pump. As the most important part in lift equipment [3, 4], pumping unit has been the emphasis of the research. Polished rod dynamometer card is a load graphics which can reflect polished rod load of pumping unit changed with the displacement. With the use of polished rod dynamometer card, polished rod load can be obtained, which can calculate the balance of pumping unit, the reducer output shaft torque and motor power [5]. As the measured polished rod dynamometer card can only be obtained in the actual operation process of the pumping unit, it is mainly for pumping well fault diagnosis [6–9]. In conclusion, the prediction of the polished rod load is very necessary.

In 1963, Gibbs [10] developed a new method for predicting the behavior of sucker rod pumping systems. A wave equation of sucker rod was established, and polished rod dynamometer card could be calculated for various downhole pump conditions. Later Gibbs [11] summarized the methods for design and analysis of rod pumping installations. A completely general diagnostic method had been developed from mathematical solution of a boundary value problem based on the wave equation. In 1983, Doty and Schmidt [12] presented an improved model for predicting the behavior of sucker rod pumping installations. This model incorporated the dynamics of the liquid columns as well as sucker rod through a system of partial differential equations. In 1992, Wang et al. [13] studied three-dimensional vibration of sucker rod, tubing and liquid column in the sucker rod pumping system comprehensively. The simulation results showed that the developed model was much superior over the existing one-dimensional or two-dimensional models. This model could be also used for predicting dynamic parameters and well site diagnosis. In 2012, Luan et al. [14] developed a prediction model for a new deep-rod pumping system. The new one-dimensional vibration model took into account the structure of the side-flow pump. The results of dynamometer card analysis showed that mathematical model of side-flow pumping system and its computer programs could successfully model deep sucker rod performance.

There are two main problems in the existing models. The first problem to be solved is to improve the accuracy of the predicted results. In order to simplify the solving process, some influence factors are ignored. Therefore, the liquid inertial load acting on the plunger as well as plunger-barrel friction are considered in downhole boundary conditions. The other problem is the limitations of the method for solving models. As the existing models mentioned above are solved by means of explicit differential method with the aid of computers, the stability conditions of explicit difference scheme of the equations must be satisfied to ensure stable solutions. In order to remove the restriction of stability conditions, a hybrid algorithm is proposed for solving the wave equation. This algorithm combines the implicit differential method applied in homogeneous sucker rod with the variable step differential method applied in the boundary node of composite sucker rod. Then the predicted polished rod dynamometer card can be obtained.

2 Mathematical Model

2.1 Wave Equation

In a pumping cycle, sucker rod moves up and down in the tubing. In order to truly describe the deformations of sucker rod, the nonlinear influences of geometry and contact should be considered. At the same time, dynamical influences, such as various frictional resistances and inertia forces, should not be ignored. The key problem of dynamic modeling and analysis of sucker rod pumping system is the establishment of the axial vibration wave equation of sucker rod. Therefore, the micro unit of sucker rod is taken as research object. Figure 1 shows a multistage sucker rod. Polished rod location is chosen as the origin, and along the downward direction of the axis of sucker rod is positive.

$u(x, t)$ is assumed as the displacement along the depth direction in section position x of sucker rod at time t . In this case, natural coordinate system and cartesian coordinate system are built. Forces distribution of micro unit are shown in Fig. 2.

In any position x of sucker rod, the micro unit is acted on by seven forces as follows:

An axial force of the micro unit acting on the upper cross-section is $F_{(x,t)}$, which is given by

$$F_{(x,t)} = E_r A_r \left(\frac{\partial u}{\partial x} \right)_x \tag{1}$$

where E_r is modulus of elasticity of sucker rod, and A_r is cross-sectional area of sucker rod.

An axial force of the micro unit acting on the lower cross-section is $F_{(x+\Delta x,t)}$ which is given by

Fig. 1 Schematic diagram of multistage sucker rod

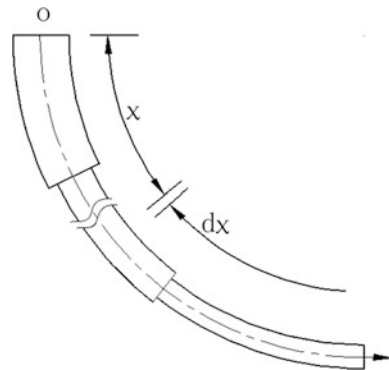
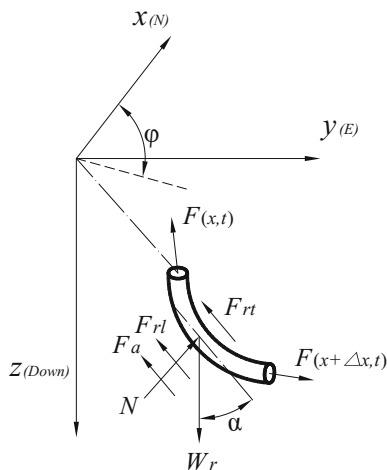


Fig. 2 Force schematic diagram of sucker rod micro unit



$$F_{(x+\Delta x,t)} = E_r A_r \left(\frac{\partial u}{\partial x} \right)_{x+\Delta x} \tag{2}$$

The function of F_a is the inertia force of the micro unit. The equation for F_a is

$$F_a = \rho_r A_r \left(\frac{\partial^2 u}{\partial t^2} \right) \Delta x \tag{3}$$

where ρ_r is sucker rod density.

F_{rl} is defined to be the viscous force acting on the micro unit. This force has the representation

$$F_{rl} = v_e \frac{\partial u}{\partial t} \Delta x \tag{4}$$

where v_e is viscous damping coefficient per unit length of sucker rod.

N is support reaction force acting on the micro unit from tubing. This force is given by

$$N = \sqrt{\left(F_{(x,t)} \frac{d\alpha}{dx} - q'_r \sin \alpha \right)^2 + \left(F_{(x,t)} \sin \alpha \frac{d\varphi}{dx} \right)^2} \tag{5}$$

where α is deviation angle and φ is hole azimuth angle.

F_{rt} is frictional force between tubing and sucker rod. The relationship between F_{rt} and N is given by

$$F_{rt} = \delta f N \Delta x \tag{6}$$

where δ determines the direction of the force. δ is equal to -1 if the sucker rod is operating on the upstroke, otherwise equal to $+1$. f is friction coefficient between tubing and sucker rod.

W_r is gravity of sucker rod. The equation for W_r is

$$W_r = \rho'_r A_r g \Delta x \tag{7}$$

where ρ'_r is relative density. ρ'_r and ρ_r are related by the equation,

$$\rho'_r = \rho_r - \rho_L$$

where ρ_L is fluid density.

According to the balance condition of axial forces, wave equation of sucker rod can be obtained that:

$$\frac{\partial^2 u}{\partial t^2} = a^2 \frac{\partial^2 u}{\partial x^2} - c \frac{\partial u}{\partial t} - \delta h N_{(x)} + g' \cos \theta \tag{8}$$

where

$$a = \sqrt{E_r / \rho_r}, \quad c = v_e / \rho_r A_r, \quad h = f / \rho_r A_r, \quad g' = \rho'_r g / \rho_r$$

This equation is valid for each region of sucker rod that has constant taper. If, at some point, sucker rod changes size, then Eq. 8 must be modified.

2.2 Surface Boundary Conditions

The movement on the top of sucker rod is decided by the motion of polished rod of the pumping unit. That is

$$u(0, t) = U_0 \tag{9}$$

In the design and calculation of conventional beam pumping unit, the ratio of polished rod displacement and stroke is often used, which is named the location factor of pumping unit. It is obtained by

$$\overline{PR} = \frac{U_0}{S} = \frac{\psi_b - \psi}{\psi_b - \psi_t} \tag{10}$$

where U_0 is polished rod displacement and S is polished rod stroke.

Figure 3 is the mechanism sketch of conventional beam pumping unit. It can be seen that ψ is the angle between C and K, where C is the back arm length of beam and K is the distance between the support center of beam and the output shaft center of the gear reducer. In a pumping process, the value of ψ changes with the changes of t ,

$$\psi = \psi(t) \tag{11}$$

When the polished rod is in the lowest position, ψ are endowed with the minimum value, which is named ψ_t . ψ_t has the representation

$$\psi_t = \arccos\left(\frac{C^2 + K^2 - (P - R)^2}{2CK}\right) \tag{12}$$

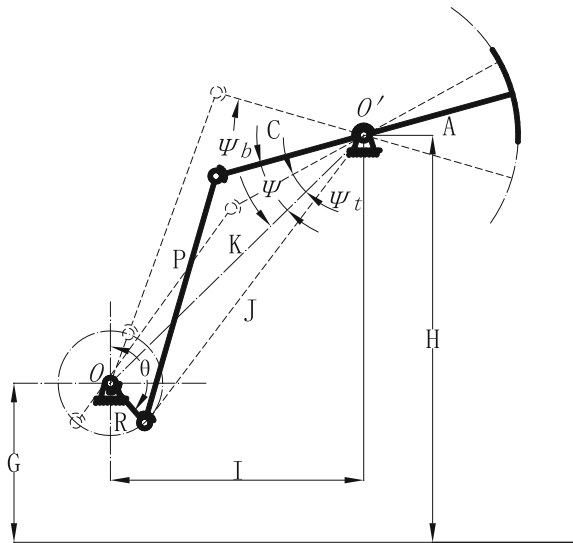
where P is length of sucker rod S, and R is radius of crank.

When the polished rod is in the highest position, ψ are endowed with the maximum value, which is named ψ_b . ψ_b has the representation

$$\psi_b = \arccos\left(\frac{C^2 + K^2 - (P + R)^2}{2CK}\right) \tag{13}$$

Geometric parameters of pumping unit are determined, if the type of pumping unit is selected. Substituting the values of ψ_t and ψ_b calculated by geometric parameters into Eq. 10, the motion of polished rod of the pumping unit is obtained.

Fig. 3 Mechanism sketch of conventional beam pumping unit



2.3 Downhole Boundary Conditions

The most important boundary condition in sucker rod problem is the one which describes the operation of downhole pump. Undoubtedly, the mathematical description of the downhole pump has been the greatest difficulty in analytical treatment of the sucker-rod system. Many attempts have been made to formulate explicit expressions which describe its behavior, but unfortunately these expressions have proved inadequate when applied over the range of conditions encountered in practice. Gibbs gave an expression to describe the pump condition as

$$\alpha u(L, t) + \beta \frac{\partial u(L, t)}{\partial x} = p(t) \tag{14}$$

wherein the parameters α , β and $p(t)$ depend upon the type of pump operation to be simulated.

Obviously, Eq. 14 does not consider the influences of the liquid inertial force and plunger-barrel friction force. In practice, those influences are important, which should not be ignored. For this purpose, the pump condition is improved as

$$\alpha u(L, t) + \beta \frac{\partial u(L, t)}{\partial x} + \gamma \frac{\partial^2 u(L, t)}{\partial t^2} + \kappa \frac{\partial u(L, t)}{\partial t} = p(t) \tag{15}$$

In Eq. 15, the third item represents the liquid inertial force acting on the plunger. γ is equal to the mass of liquid if the liquid inertial force acts on the plunger, otherwise is zero. The fourth item represents plunger-barrel friction force. κ is given as

$$\kappa = 2\pi\mu L_p \ln\left(\frac{R_p}{R_b}\right) \tag{16}$$

where μ is the dynamic viscosity of the well liquid, L_p , R_p and R_b is the length of plunger, the radius of plunger and barrel respectively.

2.4 Initial Condition

The initial condition have to be determined in the first place when Eq. 8 need to be solved. In order to facilitate calculation, the initial condition is assumed as follows: At the moment of $t = 0$, motor start turning and polished rod is in the lowest position. At this time, the whole sucker rod is in a stationary state. It means that:

$$u(x, 0) = 0, \quad \dot{u}(x, 0) = 0 \tag{17}$$

3 Numerical Solution Technique

3.1 Difference Scheme of Homogeneous Rod

In homogeneous rod, the node of equal step Δx is selected along axial direction of sucker rod, then sucker rod is divided into m units and i is defined as the subscript notation, $i = 1, 2, \dots, m$. The node of equal step Δt is selected along the time direction, and j is defined as the subscript notation, $j = 1, 2, \dots, n$. Thus, $u_{i,j}$ is defined as the i node displacement of rod string at j time.

In the node (i, j) , central difference quotient formulas are used to approximate $\partial^2 u / \partial t^2$ and $\partial u / \partial t$. Further more, the weighted average formula of central difference quotient in $j - 1, j$ and $j + 1$ layers is used to approximate $\partial^2 u / \partial x^2$. Thus Eq. 8 can be simplified as

$$\begin{aligned}
 &-\frac{a^2}{4\Delta x^2} u_{i-1,j+1} + \left(\frac{a^2}{2\Delta x^2} - \frac{c}{2\Delta t} - \frac{1}{\Delta t^2} \right) u_{i,j+1} + \frac{a^2}{4\Delta x^2} u_{i+1,j+1} \\
 &= 2a_1 (u_{i+1,j} - u_{i-1,j}) + a_2 u_{i,j} + a_1 (u_{i+1,j-1} - u_{i-1,j-1}) + a_3 u_{i,j-1} - b_{i,j}
 \end{aligned} \tag{18}$$

where

$$\begin{aligned}
 a_1 &= -\frac{a^2}{4\Delta x^2}, & a_2 &= -\frac{a^2}{\Delta x^2} + \frac{2}{\Delta t^2}, \\
 a_3 &= -\frac{a^2}{\Delta x^2} - \frac{c}{2\Delta t}, & b_{i,j} &= \delta_{i,j} h_i N_{i,j} - g'_j \cos \theta
 \end{aligned}$$

3.2 Difference Scheme of Multistage Rod

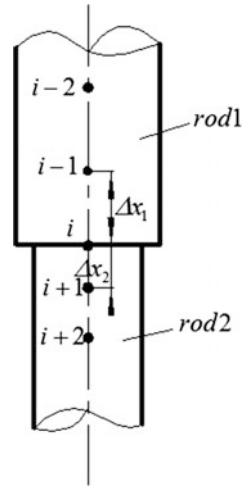
In order to establish differential form of multistage rods by equal step length difference, the equivalent density and elastic modulus, etc. must be calculated before the solving processing. In the meantime, the mixed units are converted into a uniform unit. During the equivalent process, it may produce certain errors. To reduce the errors, variable step length difference is used to establish differential form of multistage rods.

Take the two stage rod for example. Δx_1 is chosen to be the axial step of the first homogeneous rod, while Δx_2 is chosen to be the axial step of the second homogeneous rod. In this case, as shown in Fig. 4, wave equations of the first and second sucker rod can be described as:

$$\frac{\partial^2 u}{\partial t^2} = a_l^2 \frac{\partial^2 u}{\partial x^2} - c_l \frac{\partial u}{\partial t} - \delta h_l N + g'_l \cos \theta \tag{19}$$

where l is equal to 1 or 2.

Fig. 4 Sketch map of sucker rod interface



According to Taylor formula, $u_{i-1,j}$ and $u_{i+1,j}$ can be expanded into the following equations

$$u_{i-1,j} = u_{i,j} - \left(\frac{\partial u}{\partial x}\right)_{i1} \Delta x_1 + \left(\frac{\partial^2 u}{\partial x^2}\right)_{i1} \frac{1}{2} (\Delta x_1)^2 \tag{20}$$

$$u_{i+1,j} = u_{i,j} + \left(\frac{\partial u}{\partial x}\right)_{i2} \Delta x_2 + \left(\frac{\partial^2 u}{\partial x^2}\right)_{i2} \frac{1}{2} (\Delta x_2)^2 \tag{21}$$

The following continuous conditions should be satisfied at i point of two-stage rod joint.

$$F(i,j)_1 = F(i,j)_2 \tag{22}$$

$$u(i,j)_1 = u(i,j)_2 \tag{23}$$

Combined the Eq. 19 through Eq. 23, the difference equation of different material in the joint of different rod diameters can be given by

$$u_{i,j+1} = \frac{(2b_1 + b_2 - v_2 - v_1) - b_1 u_{i,j} + v_2 u_{i+1,j} + v_1 u_{i-1,j}}{b_1 + b_2} - \frac{r_1 (\delta_{i,j} h_{1i} N_{i,j} - g'_{1j} \cos \theta_i) + r_2 (\delta_{i,j} h_{2i} N_{i,j} - g'_{2j} \cos \theta_i)}{b_1 + b_2} \tag{24}$$

where

$$b_1 = \frac{(\Delta x E_r A_r)_1}{2(a_1 \Delta t)^2} + \frac{(\Delta x E_r A_r)_2}{2(a_2 \Delta t)^2}, \quad b_2 = \frac{(\Delta x E_r A_r c)_1}{2a_1^2 \Delta t} + \frac{(\Delta x E_r A_r c)_2}{2a_2^2 \Delta t}$$

$$r_i = \frac{(\Delta x E_r A_r)_i}{2a_i^2}, \quad v_i = \frac{(E_r A_r)_i}{\Delta x_i}, \quad i = 1, 2$$

4 Instance Calculation and Analysis

In order to prove the correctness of dynamic model (including Eqs. 8, 9, 15 and Eq. 17), two wells named well L2111 and L2517 from Liao He oilfield have been chosen to do the experiments. Equipment parameters of sucker rod pumping system have been given in Table 1.

According to the type of pumping unit in Table 1, we learned that the geometric parameters of pumping unit are: R = 1.04 m, P = 4 m, C = 2.905 m, A = 4.81 m, I = 2.8 m, H = 6 m, G = 2 m. With the help of those above geometric parameters, Eq. 10 can be solved to obtain the location factor, the dimensionless velocity and the dimensionless acceleration of the pump unit under each angle, which are showed in Fig. 5.

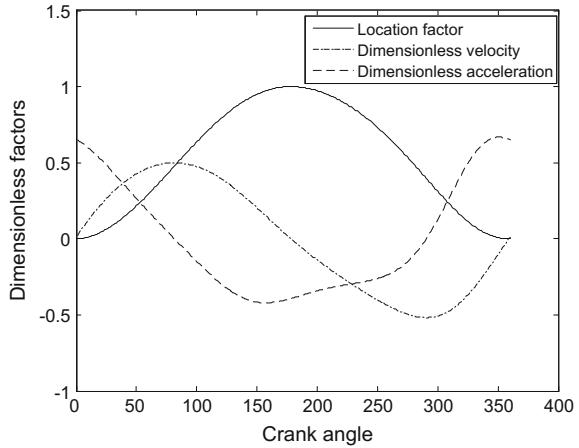
As can be seen from Fig. 5, the position factor curve of pumping unit is similar to normal distribution. The position factor in a cycle uniformly changes from 0 to 1, then back to 1 uniformly again. Dimensionless velocity curve is similar to sine curve. In the process of upstroke, in which the crank angle varies from 0° to 180°, the dimensionless velocity is positive and maximum speed appears when crank angle is 82°. In the process of downstroke, the dimensionless velocity is negative and minimum speed appears when crank angle is 290°. Dimensionless acceleration curve seems to be an irregular curve. The minimum acceleration appears when crank angle is 157°. In the process of varying from 157° to 275°, the acceleration increases slowly. Acceleration is bumped up after the 275°, and the maximum value is arrived at 351°.

In the process of solving Eq. 8, Δx and Δt are the parameters which need to be selected. In order to ensure the accuracy of the calculation, sucker rod is divided into 400. For the well L2111, Δx = 4.435 m. For the well L2517, Δx = 4.4275 m.

Table 1 Equipment parameters of sucker rod pumping system

NO.	Pumping unit type	Parameters of sucker rod	Parameters of pump
L2111	CYJ12-4.8-73HB	φ 19 * 814 m + φ 22 * 603 m + φ 25 * 554 m	φ 44 mm * 1997 m
L2517	CYJ12-4.8-73HB	φ 19 * 710 m + φ 22 * 890 m + φ 25 * 174 m	φ 38 mm * 1801 m

Fig. 5 Position factor, the dimensionless velocity and dimensionless acceleration curves changed with crank angle



If explicit difference scheme is selected to solve Eq. 8, Δt needs to satisfy the stability conditions. For the well L2111, Δt need to be less than 0.000765 s. For the well L2517, Δt need to be less than 0.000763 s. Obviously the value of Δt is so small that the number of stored data is approximately 14 million. Using the proposed method, Δt can be valued at 0.068 and 0.06. The number of stored data is just 144 thousand, which are hundredth of those from explicit difference scheme. By means of the proposed method, the displacements of sucker rod at any position at any time are obtained. And then the polished rod dynamometer card can be obtained.

Figures 6 and 7 respectively describe the polished rod dynamometer cards of well L2111 and L2517. It is not hard to see from the figures that, the predicted polished rod dynamometer cards of two methods are similar. They both match with

Fig. 6 Polished rod dynamometer cards of well L2111

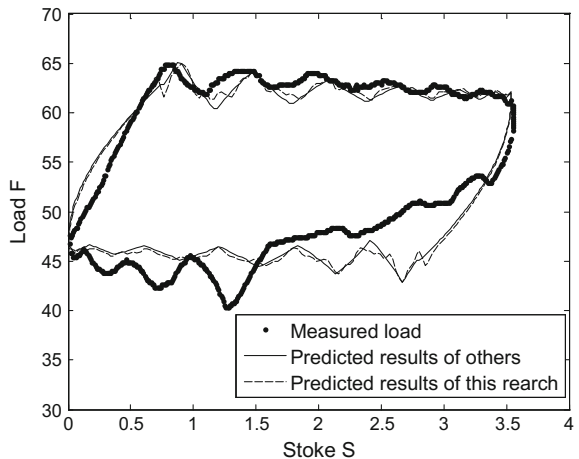
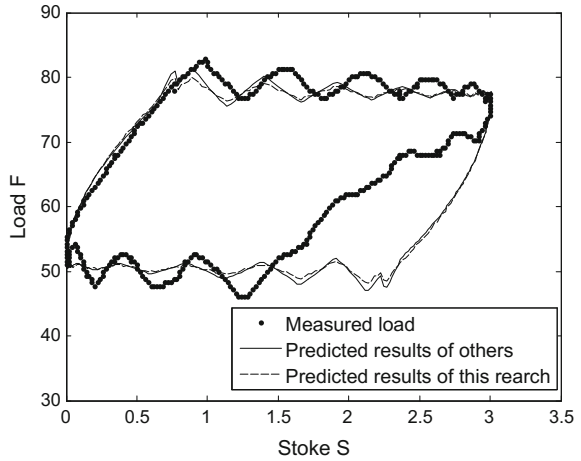


Fig. 7 Polished rod dynamometer cards of well L2111



the measured polished rod dynamometer card. However, from the view point of the opening moments of the standing valve and the travelling valve, the maximum and minimum loads, the predicted result with sufficient consideration of liquid inertial load and plunger-barrel friction is more accordant with practical circumstances. In the process of downstroke, the predicted curves of two models fall faster than the actual case. The reason of this phenomenon is that there are gases in the oil well. Affected by gas, the standing valve can not open in time, which causes that the liquid load can not be transferred.

5 Conclusion

1. An improved dynamic model of sucker rod pumping system in a directional well is established. This model considers the influence of rod-fluid-tubing viscous friction and rod-tubing Coulomb friction. In the meanwhile, the liquid inertial load acting on the plunger as well as plunger-barrel friction are considered in downhole boundary conditions.
2. In the process of solving the model, the implicit differential method is applied in homogeneous sucker rod, while the variable step differential method is applied in the boundary node of composite sucker rod.
3. Two wells from Liao He oilfield are chosen to do the experiments. The predicted result with sufficient consideration of liquid inertial load and plunger-barrel friction is more accordant with practical circumstances. Application of the hybrid algorithm solve the problem of stability conditions and computational efficiency has been greatly improved.

Acknowledgments The financial support of National Natural Science Foundation of China (51275404) and data support of Liao He Oilfield are grate-fully acknowledged.

References

1. Wang XF (2005) Research in the present and developing status of the oil producing internationally. *J China Min Mag* 14(5):4–6 (in Chinese)
2. Wu YJ, Liu ZJ, Zhao GX (1994) Pumping unit. Petroleum Industry Press, Beijing (in Chinese)
3. Fang RJ, Zhu WB (2011) Analysis of the history, present situation and development trend of pumping unit. *J Drilling Prod Technol* 34(2):60–63 (in Chinese)
4. Dong SM, Li BS (1996) Design of Sucker rod pumping system in horizontal well. Petroleum Industry Press, Beijing (in Chinese)
5. Chen PY, Yao CD, Dong SM (2013) Simulation model of polished rod indicator diagram based on measured electrical power of pumping unit. *J Petrol Mach* 41(11):91–95 (in Chinese)
6. Moises GVL, Andrade SFA, Garcia ACB (2010) Sucker-rod pumping failures diagnostic system. In: SPE annual technical conference and exhibition, pp. 1–12. Society of Petroleum Engineers, Florence
7. Liu SP, Raghavendra CS, Liu YT et al (2011) Automatic early fault detection for rod pump systems. In: SPE annual technical conference and exhibition, pp. 1–11. Society of Petroleum Engineers, Denver
8. Horowitz G, Faundez E, Maestri M et al (2014) Fault diagnosis in oil wells. In: SPE annual technical conference and exhibition, pp. 1–9. Society of Petroleum Engineers, Amsterdam
9. Reges GD, Schnitman L, Reis R et al (2015) A new approach to diagnosis of sucker rod pump systems by analyzing segments of downhole dynamometer cards. In: SPE artificial lift conference—Latin America and Caribbean, pp 1–13. Society of Petroleum Engineers, Salvador
10. Gibbs SG (1963) Predicting the behavior of sucker-rod pumping systems. *J Petrol Technol* 15 (7):769–778
11. Gibbs SG (1982) Nable corp: a review of methods for design and analysis of rod pumping installations. *J Petrol Technol* 34(12):2931–2940
12. Doty DR, Schmitd Z (1983) An improved model for sucker rod pumping. *J Soc Petrol Eng* 23 (01):33–41
13. Wang GW, Rahman SS, Yang GY (1992) An improved model for the sucker rod pumping system. In: 11th Australasian fluid mechanics conference, pp 1137–1140. The Australasian Fluid Mechanics Society, Hobart
14. Luan GH, He SL, Yang Z (2012) A prediction model for a new deep-rod pumping system. *J Petrol Sci Eng* 80(1):75–80

Dynamics Modeling, Control System Design and Simulation of Manipulator Based on Lagrange Equation

Da-quan Li, Hua-jie Hong and Xian-liang Jiang

Abstract To improve the servo performance of the manipulator and further obtain higher motion accuracy, dynamics equation of the series manipulator is developed based on Lagrange dynamics method. Simultaneously, the control algorithm is studied to ensure the error system is globally asymptotically stable near the equilibrium point. With full consideration of the dynamic characteristics of the system, a controller is designed and the control system simulation model is established subsequently. The simulation results show that the controller designed in this paper has good dynamic and static performances, the manipulator system can follow the control directives effectively with the tracking error of joint angles limited to 10^{-5} rad. Methods of dynamics modeling, controller design and control system simulation are universal to the multi-degree-of-freedom series manipulators, which has a certain reference value for the research of similar mechanisms.

Keywords Manipulator · Lagrange equation · Control system · Simulation

1 Introduction

With the rapid development of microelectronic technology, sensor technology, control theory and machinery manufacturing technology, the automation and intelligence of manufacturing industry are gradually improved and higher requirements to digital performance of manufacturing equipment are also put forward. As the typical joint type robots, manipulators have been widely used in

D. Li (✉) · H. Hong · X. Jiang
College of Mechatronics Engineering and Automation,
National University of Defense Technology, Changsha 410073, China
e-mail: lidaquan1993@163.com

H. Hong
e-mail: opalqq@163.com

X. Jiang
e-mail: 15616196400@163.com

industrial production with the advantages of compact structure, small space occupation, large movement space and so on. Therefore, it is an important research direction in the field of mechanical arms to establish its dynamic model and explore the general method of controller design.

Methods on dynamics modeling, control and simulation of manipulators are in varied forms, and the related research is also a lot. In paper [1], the kinematic model of the robot manipulator is established by D-H parameters. Based on the Newton-Euler iterative dynamics algorithms, the forward and inverse dynamic simulation is done by Robotics Toolbox in MATLAB; Paper [2] and [3] simplify the multi-input and strongly coupled manipulator as a single output decoupled servo control system in the process of modeling and controller design, which ignore its dynamic characteristics. The control structure is shown in Fig. 1. Under the control principle $\tau = K_p(\theta_d - \theta) - K_v\dot{\theta}$, its control quality is limited because of the idealized assumption; Based on the principle of multi-rigid body kinematics and Lagrange dynamics equations of the manipulator, paper [4] obtains its Jacobian matrix and proposes the 3D simulation model to analyze the dynamical characteristics.

As shown in Fig. 2, the input of the controller is set as the error between the expected and actual position in the structure of classical manipulators control system, and the joint torque which is the output controls manipulator to track the command signal, so that the end-effector is expected to reach the desired position. In other words, the controller is a method to adjust the joint torque when error exists between the desired trajectory and the actual one.

To achieve precise control of the manipulator system, the first target is to establish a precise dynamic model of the corresponding object. As a multi-rigid-body system, its dynamic analysis is a complex problem of non-free

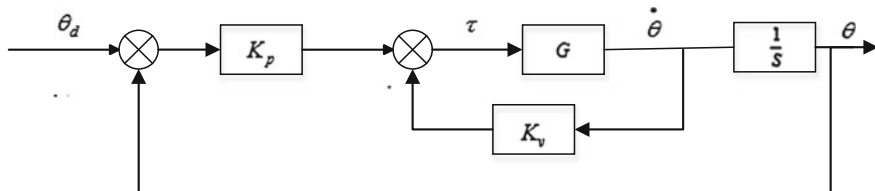


Fig. 1 The diagram of decoupled control system of the manipulator

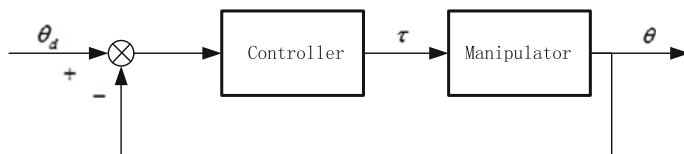


Fig. 2 Simplified diagram of manipulators control system

particle system. The Generalized Equations of Dynamics, which is set up based on d'Alembert's Principle and the PRINCIPLE of virtual displacement, describes the motion of the system in Cartesian coordinates. The manipulator is regarded as a system consisting of n particles, where the mass of the particle is m_i , the position vector relative to the inertial system is r_i , the acceleration of the particle is a_i and the restriction of the complete constraint between the particles is $g_j(r_1 \dots r_n) = 0$. The specific form of the equation is shown in Formula (1),

$$\sum_{i=1}^n f_i^e \cdot \delta r_i + \sum_{i=1}^n (-m_i a_i) \cdot \delta r_i = 0 \tag{1}$$

in which f_i^e and δr_i are defined as the external force and virtual displacement of particles respectively. It is complicated to analyze the practical problems applying the aforementioned approach. Lagrange dynamics method describes the motion of the system with fewer variables in form of generalized coordinates, which simplifies the Generalized Equations of Dynamics and has been widely used in solving the dynamic problem of particle system with mutual constraints. The Lagrange function takes the form of $L = T - V$, where T is the total kinetic energy and the total gravitational potential energy of the system is defined by V . Then in the generalized coordinates, Lagrange dynamic equation [5, 6] takes the following form:

$$\frac{d}{dt} \frac{\partial L}{\partial \dot{q}} - \frac{\partial L}{\partial q} = Y \tag{2}$$

Thereinto, Y is composition of forces except for gravity.

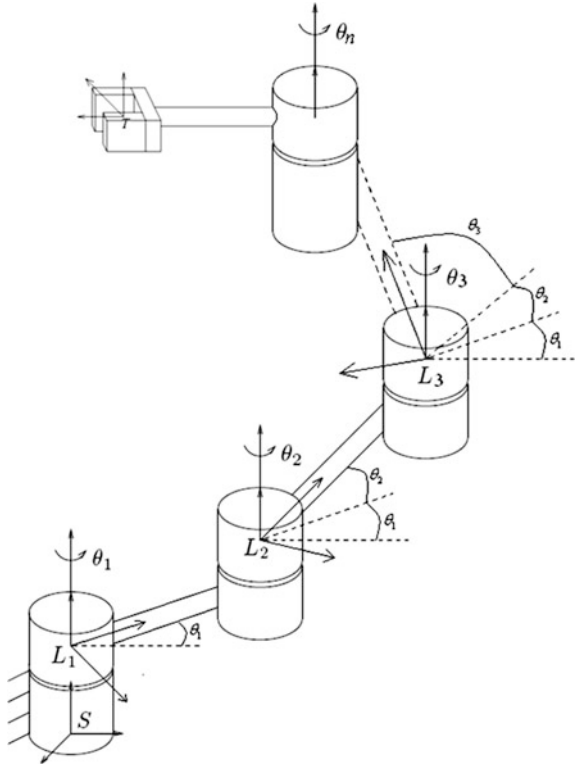
2 Dynamics Model of the Manipulator System

For the N-DOF manipulator system (shown in Fig. 3), the body-fitted coordinate system of arm i is established as L_i . Based on the screw theory, for a N-DOF manipulator whose joint angles are given as $\theta_1, \theta_2, \dots, \theta_n$, the homogeneous coordinate matrix of the end-effector relative to base coordinate can be expressed as $g_{st}(\theta) = e^{\tilde{\xi}_1 \theta_1} e^{\tilde{\xi}_2 \theta_2} g_{st}(0)$, in which $g_{st}(0)$ represents the homogeneous matrix of the work coordinate system T relative to the base coordinate system S when $\theta = 0$ and $\tilde{\xi}_i$ is the motion screw of the rigid body i in the base coordinate system S at the initial time.

Therefore, the total kinetic energy of the manipulator is:

$$T = \sum_{i=1}^n T_i = \frac{1}{2} \sum_{i=1}^n \left(V_{sl_i}^b \right)^T \Psi_i V_{sl_i}^b \tag{3}$$

Fig. 3 The manipulator model of N-DOF



Ψ_i and $V_{sl_i}^b$ stand for the inertia matrix of rigid body i and the velocity screw of joint i in the base coordinate system. While $V_{sl_i}^b = J_{sl_i}^b \cdot \dot{\theta}$ and the Jacobian matrix is $J_{sl_i}^b = [\zeta_{1,l_i}^* \ \cdots \ \zeta_{i,l_i}^* \ 0, \dots, 0]$, the kinetic energy equation of rigid body can be rewritten as:

$$T = \frac{1}{2} \sum_{i=1}^n \dot{\theta}^T J_i^T \Psi_i J_i \dot{\theta} = \frac{1}{2} \dot{\theta}^T \left(\sum_{i=1}^n J_i^T \Psi_i J_i \right) \dot{\theta} \tag{4}$$

Define the inertia matrix as following:

$$M = \sum_{i=1}^n J_i^T \Psi_i J_i \tag{5}$$

Consequently,

$$T = \frac{1}{2} \dot{\theta}^T M(\theta) \dot{\theta} \tag{6}$$

The total potential energy of the manipulator is:

$$V = \sum_{i=1}^n mgh_i(\theta) \quad (7)$$

And $h_i(\theta)$ is the height of the centroid of rigid body i .

The Lagrange function of the manipulator can be expressed as:

$$\begin{aligned} L(\theta, \dot{\theta}) &= T(\theta, \dot{\theta}) - V(\theta) = \frac{1}{2} \dot{\theta}^T M(\theta) \dot{\theta} - \sum_{i=1}^n mgh_i(\theta) \\ &= \frac{1}{2} \sum_{i,j=1}^n M_{ij}(\theta) \dot{\theta}_i \dot{\theta}_j - \sum_{i=1}^n mgh_i(\theta) \end{aligned} \quad (8)$$

The dynamic model of the N-DOF manipulator is finally obtained:

$$M(\theta) \ddot{\theta} + C(\theta, \dot{\theta}) \dot{\theta} + N(\theta) = \tau \quad (9)$$

Where

$$\begin{aligned} M(\theta) &= \sum_{i=1}^n J_i^T \Psi_i J_i, \quad J_i = [\xi_{1,i}^* \quad \dots \quad \xi_{i,i}^* \quad 0 \quad \dots \quad 0] \\ C_{ij}(\theta, \dot{\theta}) &= \sum_{k=1}^n \frac{1}{2} \left(\frac{\partial M_{ij}(\theta)}{\partial \theta_k} + \frac{\partial M_{ik}(\theta)}{\partial \theta_j} - \frac{\partial M_{kj}(\theta)}{\partial \theta_i} \right) \dot{\theta}_k \\ N(\theta) &= \frac{\partial V}{\partial \theta} \end{aligned}$$

θ is the angular displacement, $M(\theta)$ is the inertia matrix, $C(\theta, \dot{\theta})$ represents the centrifugal force and Coriolis force, $N(\theta)$ is the gravity item and τ is the joint torque.

3 Research on Control Algorithm of Manipulator System

The control objective of the system is to track the desired joint trajectory $\theta_d(t)$ so that the error converges to 0. According to the Lyapunov stability theory, the evaluation of control algorithm for the controller is equivalent to the evaluation on the stability of the controlled system. And research on the stability of controlled system is also equivalent to the study on the performance of the error system when the error $\theta = \theta_d - \theta = 0$ [7, 8]. The error system can be expressed as the following equation,

$$\begin{cases} \dot{e}_1 = e_2 \\ \dot{e}_2 = -M^{-1}(\theta) \left(C(\theta, \dot{\theta})e_2 + Q(\theta) - \tau \right) \end{cases} \quad (10)$$

in which $Q(\theta) = M(\theta)\ddot{\theta}_d + C(\theta, \dot{\theta})\dot{\theta} + N(\theta)$ and the inertia matrix $M(\theta)$ is a positive definite matrix.

3.1 Proportional Control

With the control algorithm $\tau = -K_p e_1$, where K_p is a positive definite matrix. The error system can be rewritten as:

$$\begin{cases} \dot{e}_1 = e_2 \\ \dot{e}_2 = -M^{-1}(\theta) \left(C(\theta, \dot{\theta})e_2 + Q(\theta) + K_p e_1 \right) \end{cases} \quad (11)$$

The zero $e = 0$ is not the equilibrium point of the system and the error does not converge to 0.

3.2 Proportional Control with Offset

Rewriting the error system with the control algorithm adjusted to $\tau = -K_p e_1 + Q(\theta)$:

$$\begin{cases} \dot{e}_1 = e_2 \\ \dot{e}_2 = -M^{-1}(\theta) \left(C(\theta, \dot{\theta})e_2 + K_p e_1 \right) \end{cases} \quad (12)$$

The error system is an autonomous system, and the zero point $e = 0$ is a balance point of the system. Constructing a Lyapunov function:

$$V(e) = \frac{1}{2} \begin{bmatrix} e_1 \\ e_2 \end{bmatrix}^T \begin{bmatrix} K_p & 0 \\ 0 & M(\theta) \end{bmatrix} \begin{bmatrix} e_1 \\ e_2 \end{bmatrix} \quad (13)$$

The function $V(e)$ is globally positive definite and satisfies $\|e\| \rightarrow \infty \Rightarrow V(e) \rightarrow \infty$. Its differential function,

$$\dot{V}(e, \dot{e}) = 0 \quad (14)$$

is globally negative semi-definite. According to the Lyapunov stability theorem, it is known that the equilibrium point is globally stable, but it is not sure whether the joint trajectory of the controlled manipulator can reach the fixed point θ_d .

3.3 PD Control with Offset

Similarly, under the control of joint torque $\tau = -K_p e_1 - K_v e_2 + Q(\theta)$, the error system can be expressed as follows:

$$\begin{cases} \dot{e}_1 = e_2 \\ \dot{e}_2 = -M^{-1}(\theta) \left(C(\theta, \dot{\theta}) e_2 + K_p e_1 + K_v e_2 \right) \end{cases} \quad (15)$$

The error system is an autonomous system, and the zero point $e = 0$ is the equilibrium point of the system. Constructing a Lyapunov function:

$$V(e) = \frac{1}{2} \begin{bmatrix} e_1 \\ e_2 \end{bmatrix}^T \begin{bmatrix} K_p & 0 \\ 0 & M(\theta) \end{bmatrix} \begin{bmatrix} e_1 \\ e_2 \end{bmatrix} \quad (16)$$

The function $V(e)$ is globally positive definite and satisfies $\|e\| \rightarrow \infty \Rightarrow V(e) \rightarrow \infty$. Its differential function:

$$\dot{V}(e) = -e_2^T K_v e_2 \quad (17)$$

$\Rightarrow \dot{V} \leq 0, \forall e_2$. Furthermore, $\dot{V}(e) = 0$, only when $e_2 = 0$.

Under the Lyapunov stability theorem, the system is globally stable at the equilibrium point.

Further considering the set

$$R = \{e | e_2 = 0\} \quad (18)$$

Consequently, the largest invariant set in R is:

$$M = \{e = 0\} \quad (19)$$

By the Russell globally invariant set theorem, the equilibrium point $e = 0$ is globally asymptotically stable and the joint trajectory of controlled is able to arrive at the given one θ_d .

3.4 Stable Torque Control Algorithm

Further modifying the control algorithm and obtaining the error system with $\tau = -M(\theta)(K_p e_1 + K_v e_2) + Q(\theta)$:

$$\begin{cases} \dot{e}_1 = e_2 \\ \dot{e}_2 = -K_p e_1 - K_v e_2 \end{cases} \quad (20)$$

According to the proof above, the zero $e = 0$ is the balance point of the system. Constructing the Lyapunov function,

$$V(e, \dot{e}) = \frac{1}{2} \begin{bmatrix} e \\ \dot{e} \end{bmatrix}^T \begin{bmatrix} K_p & \varepsilon I \\ \varepsilon I & I \end{bmatrix} \begin{bmatrix} e \\ \dot{e} \end{bmatrix} \tag{21}$$

where ε is a sufficiently small positive. It is easy to prove that the Lyapunov function $V(e, \dot{e})$ is globally positive definite and satisfies $\|e\| \rightarrow \infty \Rightarrow V(e) \rightarrow \infty$. Its differential function,

$$\dot{V}(e, \dot{e}) = - \begin{bmatrix} e \\ \dot{e} \end{bmatrix}^T \begin{bmatrix} \varepsilon K_p & \frac{1}{2} \varepsilon K_v \\ \frac{1}{2} \varepsilon K_v & K_v - \varepsilon I \end{bmatrix} \begin{bmatrix} e \\ \dot{e} \end{bmatrix} \tag{22}$$

is globally negative definite.

In summary, based on the Lyapunov stability theorem, the system is globally asymptotically stable near the equilibrium point $e = 0$ under the control law shown in Eq. 23,

$$\tau = -M(\theta)(K_p e - K_v \dot{e}) + N(\theta) + M(\theta)\ddot{\theta}_d + C(\theta, \dot{\theta}) \tag{23}$$

which means that the actual trajectory of the manipulator can be expected to coincide to the desired one [9]. Therefore, in order to achieve effective and accurate control, the dynamic performance of the system must be taken into consideration in the process of controller design (Fig. 4).

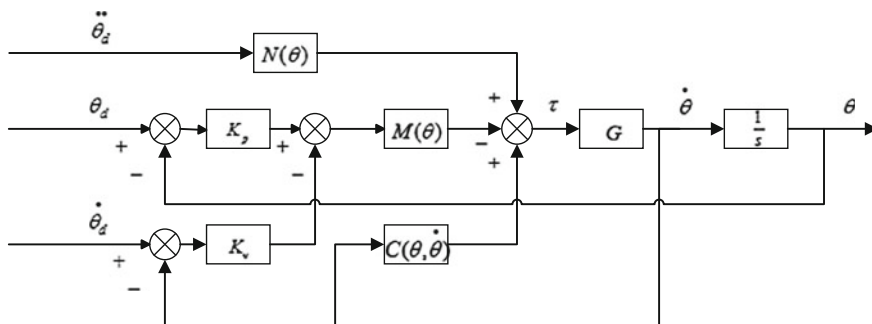


Fig. 4 The diagram of control system of the manipulator with dynamic characteristics

4 System Modeling and Simulation Based on MATLAB/Simulink

4.1 Simulation of the Manipulator Dynamics Model

With the subject investigated shown in Fig. 5, the dynamic model of the manipulator is established in MATLAB/Simulink based on Lagrange dynamics modeling method [10]. The studied control algorithm is applied to design a controller. Finally, the control effect is evaluated by simulation.

The main parameters of each part of the object are given in Table 1.

A dynamic model of the system is established in MATLAB/Simulink, as shown in Fig. 6.

The process of model building is as follows:

- (1) Choosing any point on the rotation shafts of joints q_1, q_2, q_3 and their angular velocity of rotation $\omega_1, \omega_2, \omega_3, \omega_4$, the joint spinors ζ are obtained;
- (2) Obtaining of the inertia matrix $M(\theta)$:

$$M(\theta) = \sum_{i=1}^4 J_i^T \Psi_i J_i, \quad \Psi_i = \text{diag}(m_i, m_i, m_i, I_{xi}, I_{yi}, I_{zi}) \quad (24)$$

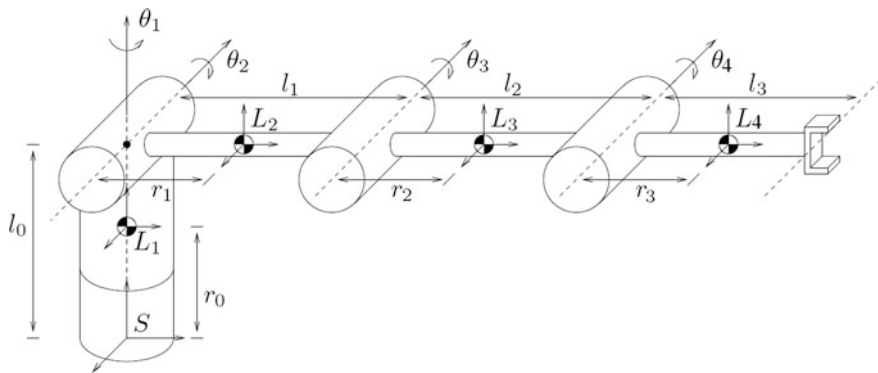


Fig. 5 Model of 4-DOF manipulator

Table 1 Parameter table of the model

	Mass (kg)	Centroid coordinates (m)	Moment of inertia (kg. m ²)
Arm 1	0.5	(0, 0, 0.075)	$\text{diag}\{0.0014, 0.0014, 0.0025\}$
Arm 2	1.4	(0, 0.15, 0.1)	$\text{diag}\{0.0108, 0.0006, 0.0108\}$
Arm 3	1.4	(0, 0.45, 0.1)	$\text{diag}\{0.0108, 0.0006, 0.0108\}$
Arm 4	0.2	(0, 0.63, 0.1)	$\text{diag}\{1.05 \times 10^{-4}, 9 \times 10^{-5}, 1.05 \times 10^{-4}\}$

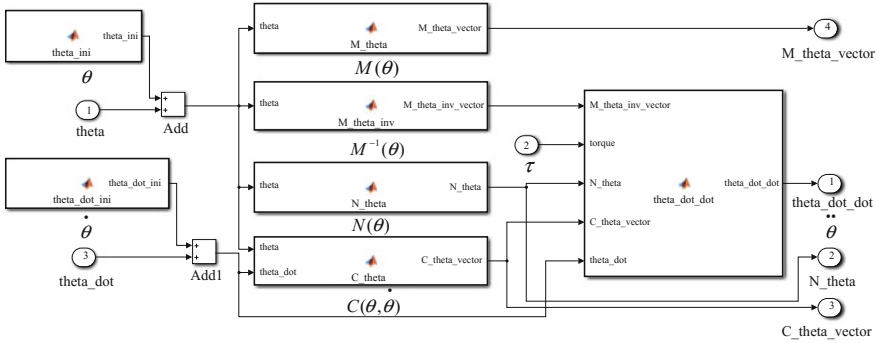


Fig. 6 Dynamic model of 4-DOF manipulator based on MATLAB/Simulink

(3) Obtaining of the Coriolis matrix $C(\theta, \dot{\theta})$:

$$C_{ij}(\theta, \dot{\theta}) = \frac{1}{2} \sum_{k=1}^3 \left(\frac{\partial M_{ij}(\theta)}{\partial \theta_k} + \frac{\partial M_{ik}(\theta)}{\partial \theta_j} - \frac{\partial M_{kj}(\theta)}{\partial \theta_i} \right) \dot{\theta}_k \quad (25)$$

(4) Calculating $N(\theta) = \frac{\partial V}{\partial \theta}$.

The overall simulation design of the manipulator with four degrees of freedom is shown in Fig. 7. The system is mainly composed of a trajectory planning module named Path_planning, a controller module and a dynamic model module. The purpose of path planning is to provide the expected position and motion state of the robot arm. The specific indicators are characterized by $\theta_d, \dot{\theta}_d$ and $\ddot{\theta}_d$.

Based on the torque control algorithm given above, a joint torque controller with the input parameters $\theta_d, \dot{\theta}_d, \ddot{\theta}_d, M(\theta), C(\theta, \dot{\theta}), N(\theta)$ is established. Therein the output parameter is torque τ . Parameters θ and $\dot{\theta}$ are the feedback of the system.

4.2 Results and Analysis

To verify the effect of the control system, the expected motion trajectory and joint motion state of the arms are needed. Here a numerical example is used for path planning. The system simulation results are given by Figs. 8, 9 and 10.

The simulation time is set to 15 s. Figures 8 and 9 respectively show the expected joint angle curves of the given manipulator and the expected trajectory of the end-effector. Specifically, the four curves in Fig. 8 show the desired joint angles $\theta_{1d}, \theta_{2d}, \theta_{3d}$ and θ_{4d} of the subject investigated. The trajectory in Fig. 10 is obtained by the forward kinematics equation of the manipulator system based on the given joint angles. As shown in Fig. 10, the angle errors are limited within a

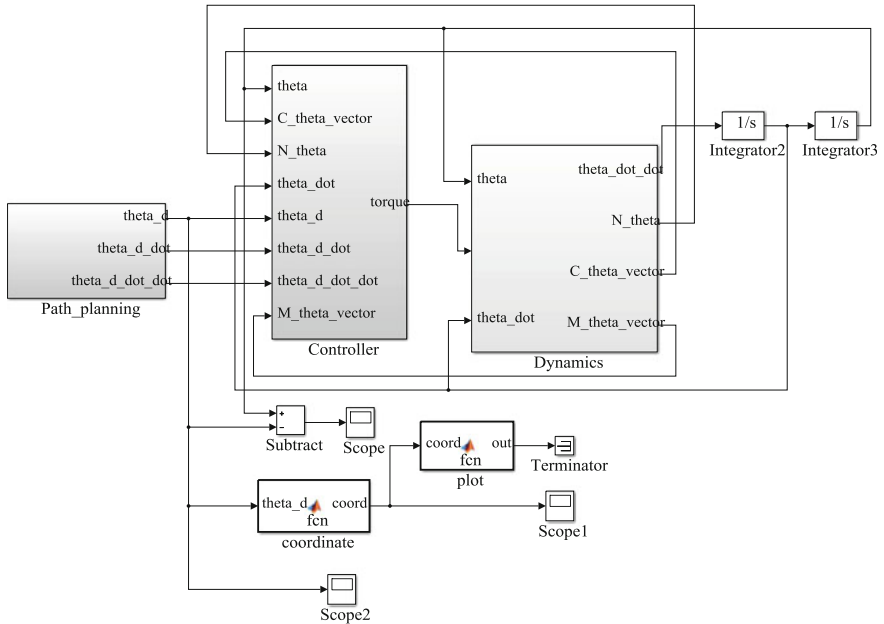


Fig. 7 The simulation model of a 4-DOF manipulator

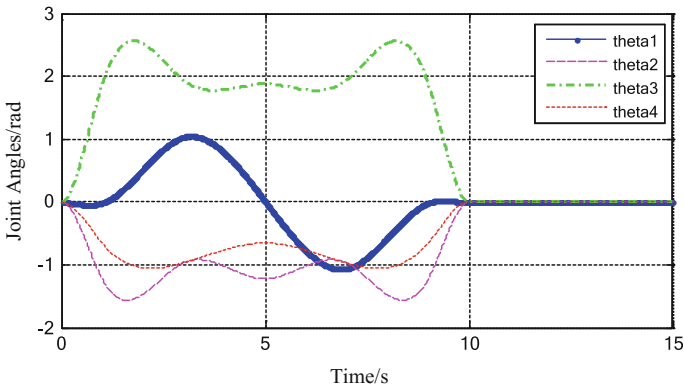


Fig. 8 The expected joint angle curves of the manipulator

reasonable range during the whole simulation and the maximal value is no more than 1×10^{-5} rad with the designed controller, which indicates an excellent dynamical control performance.

Integrating the simulation results, the designed controller can meet the control requirements of the manipulator and effectively track the position command, which is stable, accurate and quick.

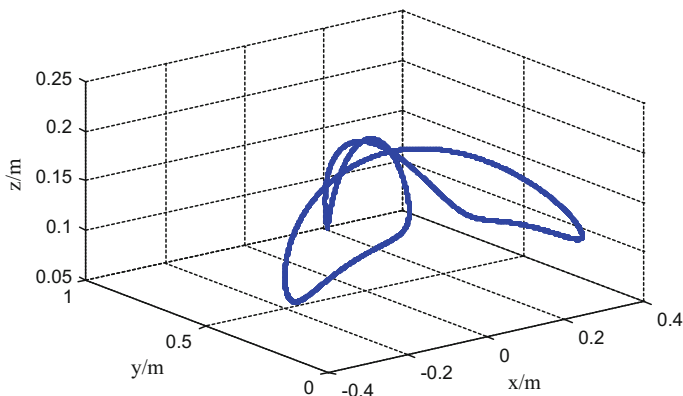


Fig. 9 The expected trajectory of the manipulator end-effector

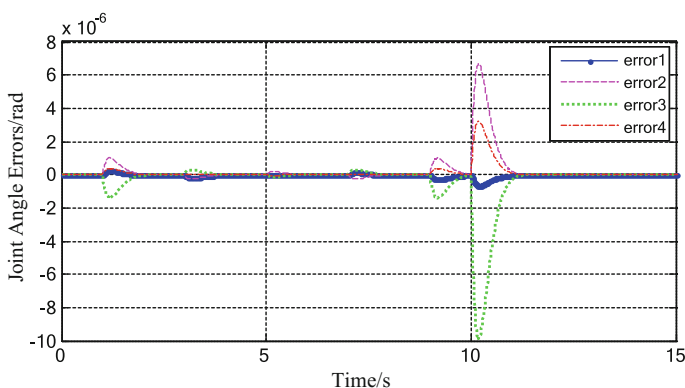


Fig. 10 The joint angle error curves

5 Conclusion

Lagrange dynamics method can simplify the dynamic analysis of the non-free particle system, so the dynamic equation of the system is established with the manipulators. According to the attained model, the control algorithm of the system is further studied. In the previous research, the controller design and simulation analysis simplify the multi-input and strongly coupled complex system into an ideal system of single-input and single-output, which neglects its dynamic characteristics and affect the performance of the system.

To validate the model's accuracy and the validity of the control algorithm, whole control system is built and simulated with its dynamic performance in full consideration. The studied manipulator with the designed joint torque controller can steadily, accurately and quickly follow the instruction, which greatly improves its

servo performance. The methods of modeling, controller design and simulation in this paper are of general significance to multi-degree-of-freedom manipulators, which has a certain reference value for the research of similar mechanisms.

References

1. Ren C-x (2012) Simulation and analysis for five-DOF robot manipulators movement and control. South China University of Technology, Guangzhou
2. Ma R-q, Hao S-h, Zheng W-f, Hao M-h, Song B-y (2010) Research on coordinated simulation of robot arm based on MATLAB and ADAMS. *Mach Des Manuf* (4):93–95
3. Zong X-p, Li Y-y (2009) The two degree of freedom manipulator control simulation based on ADAMS and MATLAB. *Microcomput Inf (Embedded Syst SOC)* 25(12–2):29–30
4. Wang W-x, Xiao S-d, Meng W, Meng X-y, Zhang W-h (2009) Dynamic modeling simulation of mechanic arm based on virtual prototype. *Appl Res Comput* 26(1):105–107
5. Muryay RM, Li Z-x, Sastry SS (1994) A mathematical introduction to robotic manipulation. CRC Press, Florida, pp 155–158
6. Nike SB (2011) Introduction to robotics: analysis, control, application. Wiley, Hoboken, NJ, pp 147–169
7. Lei J, Huang J-j (2014) Control law design for the nonlinear base on the first Lyapunov method. *J Yunnan Minzu University (Sci Technol)* 23(4):262–265
8. Choset HM (2005) Principles of robot motion: theory, algorithms, and implementations. MIT Press, Cambridge, pp 356–372
9. Zhang S-y, Gao L-q (2006) Modern control theory. Tsinghua University Press, Beijing, pp 162–177
10. Sun L, Ma J, Ruan X-g (2010) Trajectory planning and simulation of 6-DOF manipulator. *Control Eng China* 17(3):388–392

The Dynamic Characteristics Analysis of the Vertical Milling-Turning Machining Center

Jialin Li, Yidu Zhang, Qiong Wu and Hanjun Gao

Abstract The dynamic modeling and the dynamic characteristics analysis of the vertical milling-turning machining center is studied in this paper. Firstly, Finite Element Method (FEM) model of the machining center is established, and the modal of the machining center is obtained by ANSYS software. Secondly, the theory of the modal testing is illustrated, and the modal parameters, including both natural frequency and model of vibration of the machining center are got by using the hammer-hitting method. The result of the modal testing is analyzed and compared with the finite element analysis results. Also the two results offer a theoretical basis to the subsequent dynamic characteristics analysis and dynamic optimization design.

Keywords Vertical milling-turning machining center · Dynamic characteristics analysis · FEM · Modal analysis

J. Li · Y. Zhang (✉) · Q. Wu · H. Gao
State Key Laboratory of Virtual Reality Technology and Systems,
Beihang University, Beijing, People's Republic of China
e-mail: ydzhang@buaa.edu.cn

J. Li
e-mail: lijialin@buaa.edu.cn

Q. Wu
e-mail: wuqlc@buaa.edu.cn

H. Gao
e-mail: gao.hanjun@buaa.edu.cn

J. Li · Y. Zhang · Q. Wu · H. Gao
School of Mechanical Engineering and Automation,
Beihang University, Beijing, People's Republic of China

© Springer Nature Singapore Pte Ltd. 2017
X. Zhang et al. (eds.), *Mechanism and Machine Science*,
Lecture Notes in Electrical Engineering 408,
DOI 10.1007/978-981-10-2875-5_92

1 Introduction

Machine tool is the basic equipment of the manufacturing industry, which is the strategic industry and has a great role in both national welfare and national defense construction [1]. Milling-turning machining center can manufacture complex shapes in a single set-up, significantly reducing the time and the cost of preparing fixtures as well as improving the efficiency of the production and the accuracy of machining. The dynamic characteristics analysis of the vertical milling-turning machining center can assist in improving the production efficiency, machining accuracy and the life of the machining center directly. Therefore, it is of great significance to analyze the dynamic characteristics analysis of the machining center [2].

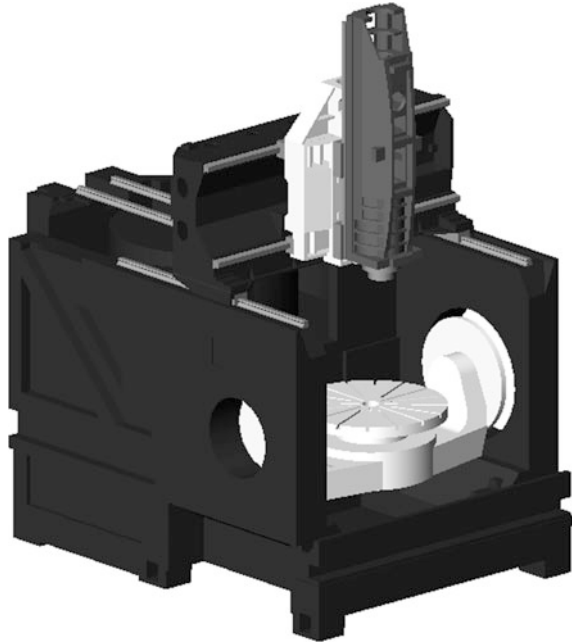
There are three research methods of the dynamic characteristics analysis of the mechanical structure, including theoretical research method, experimental method and the method of theory analysis combined with test [3]. Theoretical research method uses some numerical techniques to establish the model of the machining center, which is a simplified method to some degree. The result of the modal obtained in experimental method will be analyzed and verified. The above two methods both have limitations. The method of theory analysis combined with test which fully utilizes their respective advantages aims to use the result obtained by modal testing to correct the FEM model of the machining center. Kruszewski [4] put forward the concept of the dynamic modeling at the first time in 1975 and got the result of the modal testing by using the hammer-hitting method. The result of the modal testing is analyzed and compared with the result of theoretical research. Berczynski and Gutowski [5] and Ahmadi [6] apply rigid body dynamics theory to the dynamic modeling. In this paper, Finite Element Method (FEM) model of the machining center is established, and the modal of the machining center is obtained by ANSYS software. And then, the theory of the modal testing is elaborated, and the modal parameters containing both natural frequency and mode of vibration of the machining center are got by using the hammer-hitting method. The result of the modal testing is analyzed and compared with the finite element analysis result. Also the two results provide a theoretical basis to the subsequent dynamic characteristics analysis and dynamic optimization design.

2 Modeling and Simulation

2.1 Geometrical Modeling

The geometrical model of the machining center is established by 3D CAD software owing to the convenience of modeling with complicated shape parts compared to the ANSYS software, which will be subsequently imported into ANSYS software.

Fig. 1 The geometrical model of machining center



Considering the complex structure and the finite element calculation efficiency, it is not convenient to model all tiny features. Therefore, the model of the structure is simplified, by expurgating some features such as bosses and chamfers and filling up others such as grooves, contributing to the efficiency of modeling and the quality of the finite element mesh. The geometrical model of the vertical milling-turning machining center is shown in Fig. 1.

2.2 FEM Modeling

The main processes of the FEM modelling of the machining center are: (1) Defining material model behavior (2) Selecting element types (3) Meshing (4) Defining loads (5) Simulation.

(1) Defining material model behavior

Defining the material of the model is needed, including Elastic modulus, poisson's ratio and density of the material. The material of the model is shown in Table 1.

Table 1 The material properties of the model

Material	Density (kg/m ³)	Elastic modulus (GPa)	Poisson's ratio
HT250	7000	110	0.27
S-45	7800	206	0.30
Concrete	2600	37	0.0476

(2) Selecting element types

There are some cavities with stiffeners which can enhance the structure strength and reduce weight in the main place of the machining center such as the spindle and the beam. Therefore, the SOLID285 is selected.

(3) Meshing

Meshing, the base of finite element simulation, is the key step, whose quality affect the computational efficiency and computational accuracy directly. The method of manual intervention for meshing is adopted, which is benefit to the accuracy of the finite element analysis.

(4) Defining loads

Boundary conditions of finite element analysis should be set fixed joint between the bottom of the machining center and the ground, according to the actual conditions on the test field. Therefore, displacement constraints are added to the bottom of the machining center.

(5) Simulation

After Finite Element Method (FEM) model of the machining center is established, the modal of the machining center is finally obtained. The first six order of natural frequencies from FEM are shown in Table 2. The first six order of mode of vibration from FEM are shown in Fig. 2.

3 Model Testing and Simulation

3.1 Theory of the Modal Testing

The dynamic characteristics analysis of the machining center can be obtained with the method of theory analysis combined with test, which is the trend of the research

Table 2 The first six order natural frequencies from FEM

Order	Frequency (Hz)
1	75.187
2	78.421
3	106.75
4	117.46
5	149.72
6	159.60

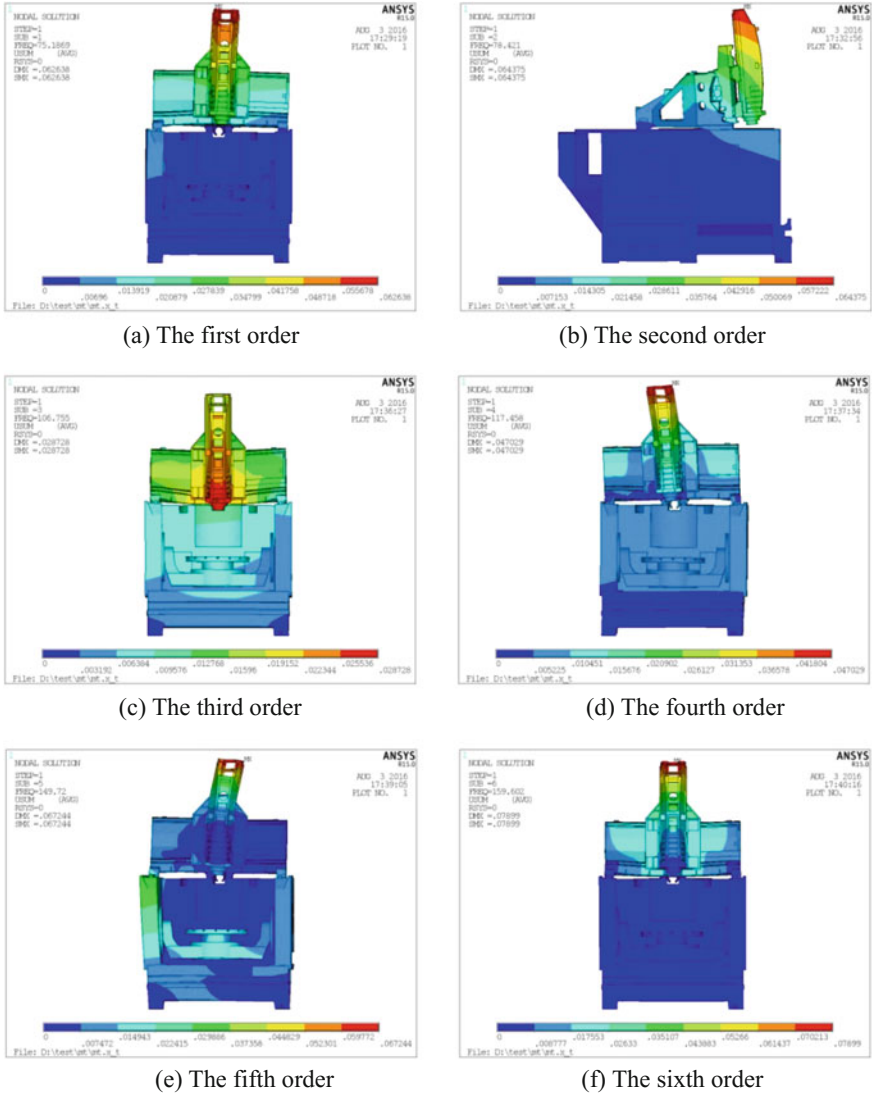


Fig. 2 The first six order of mode of vibration from FEM

on dynamic characteristics [7]. The theory analysis and the modal testing both have some advantages. It is an important means of solving the dynamic characteristic of some complicated structures by taking advantages of the strengths of each. It is a method of estimating characteristic parameters for continuous spectrum of response signal of damped free vibration. The free vibration of the machining center can be

obtained by using the test hammer to give effective excitation of the structure. Acceleration signal of the machining center is recorded through the high-sensitivity sensors stuck to the machining center, which contains some different frequency information. The natural frequency can be gained directly by using transfer function got from the force signal and the acceleration signal. The connection of experimental equipment is shown in Fig. 3.

Experimental Modal Analysis (EMA) involves two testing approaches, SIMO and MIMO. In the first, there are two measuring plans. The first one is fixing the hammering point and then moving the sensor. The second one is fixing the sensor, and then moving the hammering point. They all belong to SIMO. According to hypothesis of reciprocity, others are MIMO. This modal experiment adopts the first plan. The final results can be gained by fixing the sensor and moving the hammering point. Compared with the MIMO, the advantage of SIMO is cheaper and time-efficiency, although it is not easy to measure all points and identify close modal effectively.

Establishing the Dynamics Equations through experimental data is called system identification. In the case of knowing the forms of the equation, estimating parameters through experimental data is called parameter identification. Modal analysis belongs to the second, based on the actual structure which can be described by the modal model. And then estimate parameters through experimental data. The key to identify its basic modal Parameters is getting the Eigenvector of Vibration.

Normally, the dynamic damped vibration systems model can be expressed by Formula (1). The modal parameters can be gained through the transfer function, and it can be expressed by Formula (2).

$$[M]\{\ddot{x}\} + [C]\{\dot{x}\} + [K]\{x\} = \{f\} \quad (1)$$

Fig. 3 The sketch of the connection of experimental equipment



where, $[M]$ is mass matrix, $[C]$ is damping matrices, $[K]$ is stiffness matrix, $\{x\}$ is Deformation Vector, $\{f\}$ is excitation force vector.

$$H_{ij}(\omega) = \frac{X_i(\omega)}{F_j(\omega)} = \sum_{r=1}^n \frac{\varphi_{ri}\varphi_{rj}}{m_r[(\omega_r^2 - \omega^2) + 2j\xi_r\omega_r\omega]} \tag{2}$$

where, $H_{ij}(\omega)$ is transfer function, $X_i(\omega)$ is the response of point i , $F_j(\omega)$ is the excitation force of point j , n is the total order of Recognition mode, φ_{ri} , φ_{rj} respectively is the r order vibration model of i , j , m_r is the mass of model, ξ_r is damping ratios of model, ω_r is the frequency of model.

3.2 Experimental Process and Results

Firstly, adjust the machining center to the working condition. And then stick the accelerometer to the bottom of the spindle with a permanent. Finally, debug the

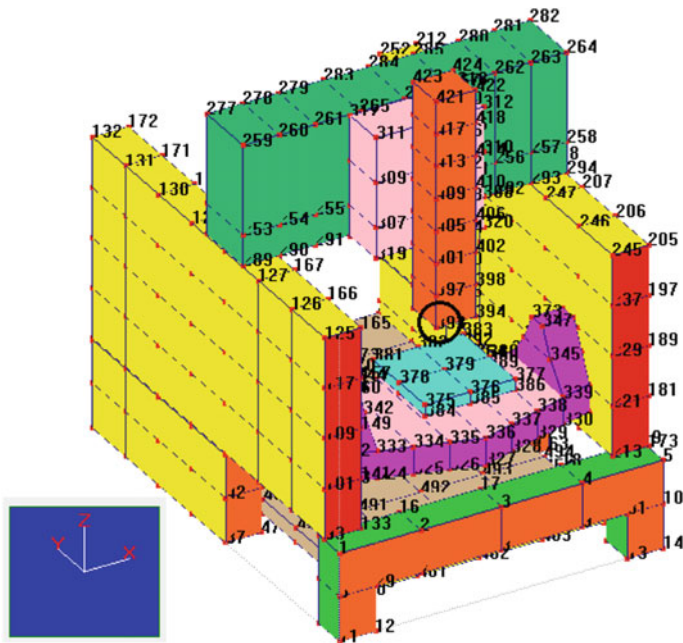


Fig. 4 Dynamic model of the machining center



Fig. 5 The position of the accelerometer

equipment, set the parameter. This experiment totally knocked 539 points, and each position knocks three times. The structure of transducer and the number of measuring position is expressed by Figs. 4 and 5.

The modal testing results by using DASP software are shown in the following table. The first six order of natural frequencies from testing are shown in Table 3. The first six order of modal of vibration from testing are shown in Fig. 6. Compared with the results of FEM, the natural frequencies from experiment is lower than the frequencies from FEM. Detail data representation as Table 4.

Table 3 The first six order natural frequencies from EMA

Order	Frequency (Hz)
1	53.592
2	57.287
3	74.609
4	78.387
5	95.014
6	125.796

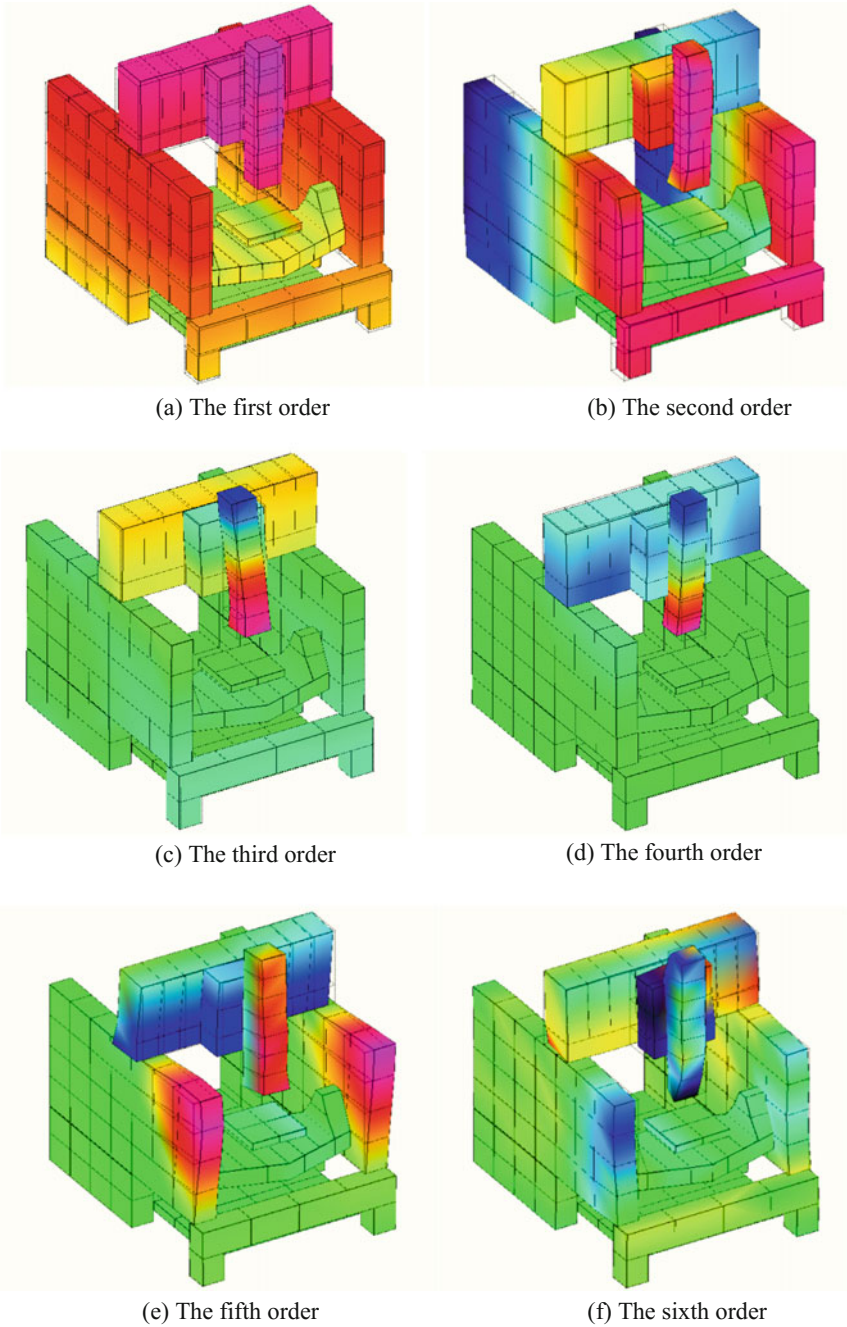


Fig. 6 The first six order of mode of vibration from EMA

Table 4 The first six order natural frequencies from FEM and EMA

Order	Frequency of FEM (Hz)	Frequency of EMA (Hz)
1	75.187	53.592
2	78.421	57.287
3	106.75	74.609
4	117.46	78.387
5	149.72	95.014
6	159.60	125.796

4 Conclusions

Based on the three-dimensional model, the finite element simulated model of the vertical milling-turning machining center is obtained. And then we can get the first six order natural frequencies of the co-whole system. At the same time, the testing results are gained which is compared with the results from FEM. While the frequency of machine from FEM simulative analysis is higher than the frequency from experimental analysis, the distribution of the two is similar. Because we didn't take the characteristics of the machining center's joints into consideration, so the result from FEM is higher.

References

1. Chenjin (2013) The dynamic characteristics analysis of CKX53280 Milling-turning Machine based on conjoint interfaces. Huazhong University of Science and Technology, Wuhan. 陈金. 基于结合面的CKX53280铣车床整机动态特性分析[D]. 武汉: 华中科技大学, 2013
2. Tanwenjie, Zuozhengxing, Liuyutong et al (2000) Analysis of dynamic characteristics of machine tool as a whole. *Jixie Sheji* 2000(10):24–25. 覃文洁, 左正兴, 刘玉桐, 等. 机床整机的动态特性分析[J]. *机械设计*, 2000(10):24–25
3. Zhangfei (2012) Study on static and dynamic characteristics and optimization of high-speed machining center worktable system. Shaanxi University of Science and Technology, Xian. 张菲. 高速加工中心工作台系统的静动态特性分析及优化设计[D]. 西安: 陕西科技大学, 2012
4. Kruszewski J (1975) The rigid finite element method. Arkady, Warszawa
5. Berczynski S, Gutowski P (2006) Identification of the dynamic models of machine tool supporting systems. *J Vibr Control*
6. Ahmadi K (2007) Modelling machine tool dynamics using a distributed parameter toolholder joint interface. *Int J Mach Tools Manuf*
7. Litao (2008) The dynamic characteristic analysis of the MB4250-2 high-precision control vertical honing machine. Shanghai Jiao Tong University, Shanghai. 李涛. CKX53280MB4250-高精度立式珩磨机床的动态特性分析[D]. 上海: 上海交通大学, 2008

Dynamic Modeling and Simulation of Q-Baller—A Spherical Wheeled Robot

Jiamin Wang and Yuyi Lin

Abstract In this paper we present the dynamic modeling of Q-Baller—a Spherical Wheeled Robot (Ball-Bot) design. A low cost prototype is constructed to verify the theoretical derivation. Low cost is achieved by using inexpensive structural design and electronic components, which, however, increases the difficulty for control. The Ball-Bot's dynamic model is important for the later studied and design suitable controller. Simulations are performed to test the design concepts, which includes detailed system modeling, noisy environment setup and the human machine interface. The results of the simulation reveal some potential problems of the current design and the improvements needed in both mechanical components and controller designs. The simulations also prepare us for improving the Ball-Bot prototype and future experiments.

Keywords Spherical wheeled robot · Dynamic modeling · Modern control · Real time simulation · Noisy simulation environment · Human machine interface

1 Introduction

To develop low cost mechatronic or robotic products that involves control issues can be quite challenging—inaccessibility of high-end or professional processors and sensors; lack of manufacturing accuracy in prototyping; shortage of human resources and experimental environment. These challenges may bring any ambitious but not well-funded project to a halt.

Since 2005 when Carnegie Mellon University (CMU) accomplished the first Spherical Wheeled Robot—a robot that can maintain balance standing on and moving around with a ball, several spherical wheeled robot designs as shown in Fig. 1 have been introduced. Inspired by these predecessors, we have been

J. Wang (✉) · Y. Lin
University of Missouri, Columbia, MO, USA
e-mail: jw2gd@mail.missouri.edu

Y. Lin
e-mail: liny@missouri.edu

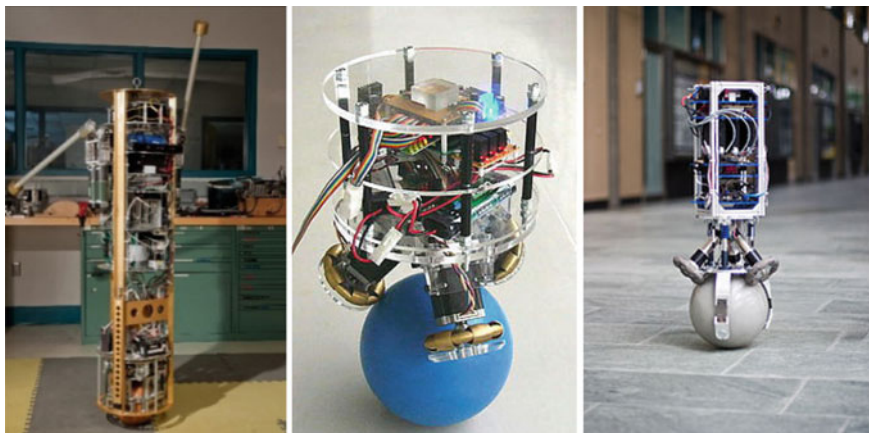


Fig. 1 *Left* the CMU Ball-Bot [1]; *Middle* the BallIP [2]; *Right* the Rezero [3]

developing a Spherical Wheeled Robot starting from 2015. Our design costs less than most of the current Spherical Wheeled Robots on the market. In addition to adopting reasonable mechanical design structure, the electronic components we use are, in most cases, less advanced than those in the other designs which, however, posed a different and more complex control task.

We performed detailed modeling and simulations to better understand the design and its potential problems. Our system model has combined mechanical electronics dynamics, and involves detailed parameters to derive random models for uncertainty simulation. Simulation processes include a noisy environment and a real-time human machine interface to facilitate a more realistic study of Ball-Bot dynamics. The process helps us better understand our control task and prepare for a suitable controller design. The study also helps us figure out the improvements to be made to our current design.

2 The Q-Baller Design

Our basic design goal is to design a Ball-Bot with great dynamic performance and possibly the lowest cost. Presented in Fig. 2 is our current Ball-Bot design named Q-Baller. The robot is about $300 \times 300 \times 400 \text{ mm}^3$ in size, and 8 kg in weight. Q-Baller has 4 friction drive system to provide symmetric control performance. The spherical wheel is made from an iron spherical shell with a high traction coating. We also have a four-bearing system, which serves to secure the frictional surface contact and allow addition add-ons for future uses. All structural parts are sheet metal providing sufficient strength with low material and manufacture cost.

Instead of using high-end and expensive servo motors, we adopt four brushed DC motors without any speed feedback sensors (rotary encoders) in our design.

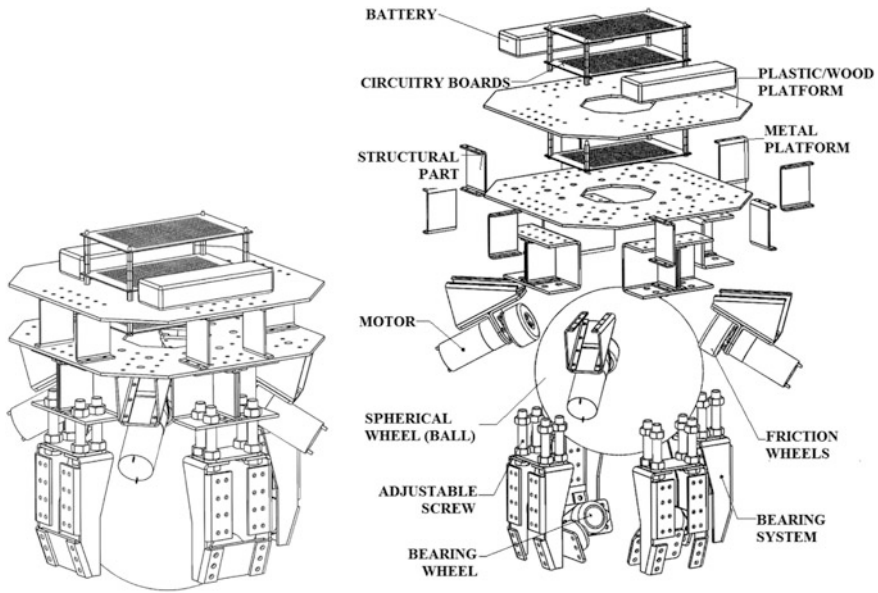


Fig. 2 Q-baller spherical wheeled robot design

These motors have less control accuracy, but are less expensive than the servo motors, and can generate greater power compared to the stepper motors of the same size. Rotary velocity feedback can be installed as add-ons if necessary.

Since DC motors require only the simplest control hardware, the electronic circuitry of Q-Baller has also been minimized, leaving the gyroscope/accelerometer sensor currently the only sensor in our robotic system (Fig. 3). A Bluetooth device provides communication between the Ball-Bot and the microcontroller. The control

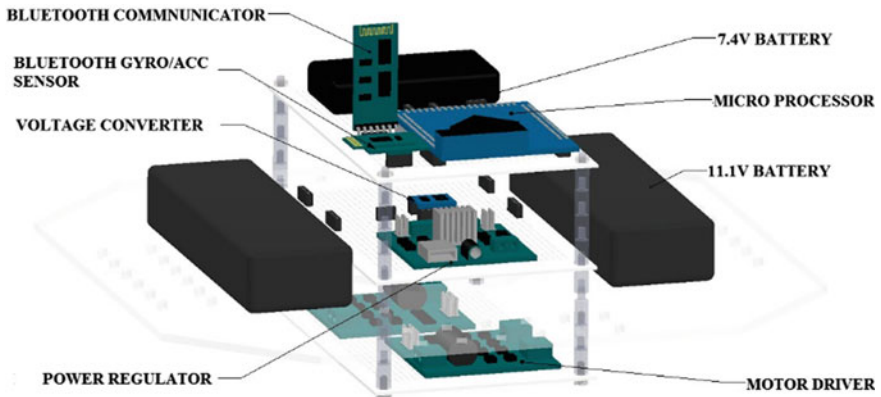


Fig. 3 Electronic system of Q-Baller

programs are processed by a 32-bit microprocessor, which sends a control signal to drive the motor through the motor driver module boards.

Some features of this ball-bot are:

1. Without highly reliable feedback and powerful processors, the control sensitivity, accuracy and frequency is limited. Many complicated control methods cannot be used due to the calculation limitation.
2. No guarantee exists that the friction surfaces have good contact. Since the DC motors are controlled without any state feedback, DC motor outputs may not be stable and identical, causing uncertainties in the system.
3. The prototype may not be the same as approximated ones from ideal modeling due to differences in manufacturing accuracies and actual component properties.

As a result, simulations must check the design feasibility before prototyping. Even though the simulation results may be limited, they may help improve the Q-Baller design, control algorithm and programming.

3 Dynamic Analysis

The Cartesian coordinate frames of the system used in the modeling process are depicted in Fig. 4. The ground coordinate frame (Frame G) will be set up by the time the robot starts running. Frame O's origin is at the center of the ball and it takes form after the orientation conversion around the Z axis (Yawing) from Frame G. Similarly, the Local Frame L takes form after the Pitching and Rolling of the coordinate system. The origins of Frame O and Frame L are both located at the

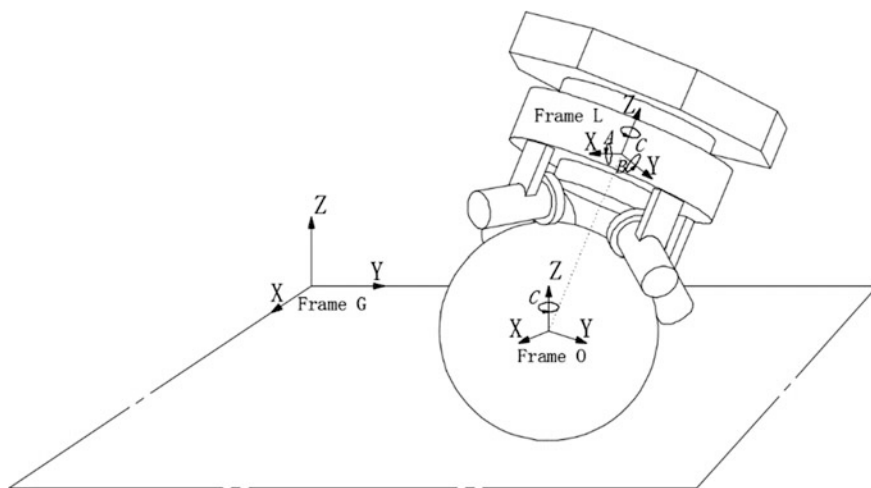


Fig. 4 Different coordinate frames of the system

center of the ball, while in Fig. 4 Frame L is moved away only for clearer presentation purpose.

Figure 5 describes vectors of forces and geometries in the system: \vec{V}_M stands for the vector pointing from the origin to the center of mass of the robot body; \vec{V}_R and \vec{V}_W points from the origin to the contact point of the ground and one of the friction Omni-Wheels respectively; \vec{V}_m and \vec{V}_r stands for the positive direction of the rotary velocity and the positive translational velocity direction at the contact point on the Omni-Wheel from one of the motors respectively; \vec{T}_m is the actuating torque effect on the robot body from one of the motors; \vec{F}_G is the gravity force of the Ball-Bot's body (origins from the Center of Mass of the body); and $\vec{T}_d, \vec{F}_d, \vec{T}_D, \vec{F}_D$ are the 4 exterior perturbation torques and forces acting on the body and the ball (which are under Frame G) which will be used as process noises during simulation. (Note that $\vec{V}_w, \vec{V}_m, \vec{V}_r$ and \vec{T}_m are sets of 3×4 matrixes because there are 4 motors in total, and direction vectors are unit vectors.)

To adopt a Lagrangian Method [4], we first choose the generalized coordinates according to the assumptions: (1). the Ball-Bot will always be on the ground; (2). there is no slipping between any of the contact surfaces; (3). the body never loses contact with the ball. The coordinate vectors chosen only include 5 states in total:

$$q = [A \ B \ C \ X \ Y]^T \tag{1}$$

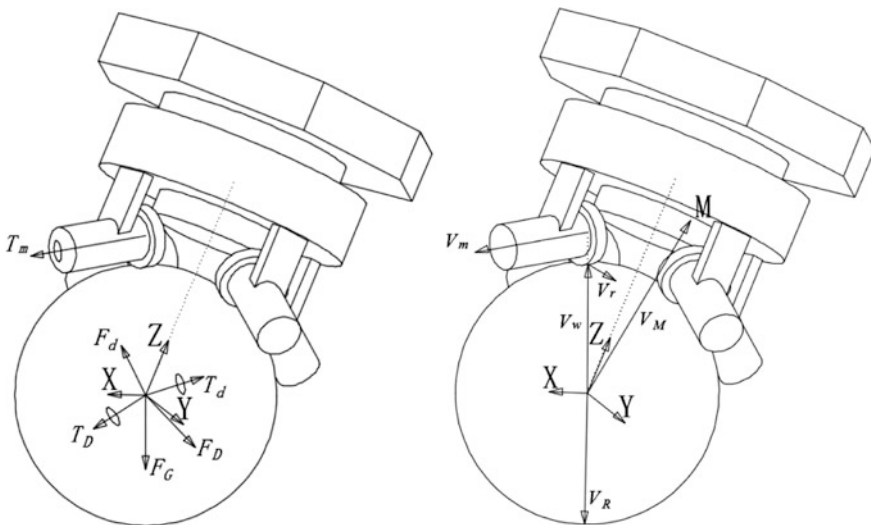


Fig. 5 Force and geometric vectors of the system

As shown in (1), A, B, C are the Euler Angles describing the rotation of the robot body around axis X (Rolling), Y (Pitching), Z (Yawing) in Frame L, and X, Y are the accumulated distance of the Ball-Bot traveled along X and Y directions in Frame O which are derived from the rotation of the ball. Some of the terms are derived from the coordinate vectors. Here are the terms for the Lagrange Equations:

$$W_{B-L} = M_J [\dot{A} \quad \dot{B} \quad \dot{C}]^T \tag{2}$$

$$W_{b-O} = \left[-\frac{\dot{Y}}{R} \quad \frac{\dot{X}}{R} \quad 0 \right]^T \tag{3}$$

$$V_G = C_L^G V_O = C_L^G * [\dot{X} \quad \dot{Y} \quad 0]^T \tag{4}$$

Here R is the radius of the ball, which is a scalar value. C_L^G is the coordinate conversion matrix from the local to the ground frame. The other coordinate conversion matrixes are similar (For example: C_X^Y is the coordinate transformation matrix from X frame to Y frame.) M_J is the Jacobian Matrix transforming the Euler Angle rates to the angular velocity of the robot body. Some of these conversion matrixes are shown below in (5), (6) [5, 6]:

$$M_J = \begin{bmatrix} 1 & 0 & -\sin(B) \\ 0 & \cos(A) & \sin(A) \cos(B) \\ 0 & -\sin(A) & \cos(A) \cos(B) \end{bmatrix} \tag{5}$$

$$C_L^G = \begin{bmatrix} \cos(C) & -\sin(C) & 0 \\ \sin(C) & \cos(C) & 0 \\ 0 & 0 & 1 \end{bmatrix} \begin{bmatrix} \cos(B) & 0 & \sin(B) \\ 0 & 1 & 0 \\ -\sin(B) & 0 & \cos(B) \end{bmatrix} \begin{bmatrix} 1 & 0 & 0 \\ 0 & \cos(A) & -\sin(A) \\ 0 & \sin(A) & \cos(A) \end{bmatrix} \tag{6}$$

According to the Lagrangian formulation, we have the following equations which govern the motion of the Ball-Bot’s entire mechanical system [4, 6]:

$$T_L = \frac{1}{2} V_G^T (M + m) V_G \tag{7}$$

$$T_R = \frac{1}{2} (W_{B-L}^T J_B W_{B-L}) + \frac{1}{2} (W_{b-O}^T J_b W_{b-O}) \tag{8}$$

$$T_C = M (V_G^T C_L^G) (W_{B-L} \times V_M) \tag{9}$$

$$V = -F_G C_L^G V_M \tag{10}$$

$$L = T_L + T_R + T_C - V \tag{11}$$

$$Q_I = W_{b-o}^T C_L^O (T_W + C_G^L T_d) + W_{B-L}^T (-T_W + C_G^L T_D) + V_G^T (F_D + F_d) \tag{12}$$

$$Q_D = \frac{1}{2} V_G^T (C_L^G B_{BL} + B_{bL}) V_G + \frac{1}{2} (W_{B-L}^T B_{BR} W_{B-L}) + \frac{1}{2} (W_{b-o}^T B_{bR} W_{b-o}) \tag{13}$$

And finally the Lagrange Equation:

$$\frac{d}{dt} \left(\frac{\partial L}{\partial \dot{q}_i} \right) - \left(\frac{\partial L}{\partial q_i} \right) = \left(\frac{\partial(Q_I dt)}{\partial(dq_i)} \right) - \left(\frac{\partial Q_D}{\partial \dot{q}_i} \right) \text{ (for } i = 1, 2, \dots, 5) \tag{14}$$

Here $T_L + T_R + T_C$ make up the kinematic energy of the whole system including translation, rotary movement plus the coupling effect since the rotary coordinate of the robot body does not origin from its center of mass; V accounts for the potential energy from the non-conservative forces—the gravity forces, for which the Zero-Potential-Level is set at the horizontal plane that goes through the center of the ball; Q_I stands for the virtual work caused by internal and exterior inputs; and Q_D is the energy dissipation term according to Rayleigh Dissipation Function caused by viscosity dampers in the system. (M , J and B terms are translational inertias, rotary inertias and viscosity dampers measured in the components' local frames.)

The following part is the modeling of the mechatronic system and the constraints to complete the modeling of the whole mechatronic system. According to the geometry of the robot system, the working torque T_W as the sum of the motor outputs acting on the ball:

$$T_W = -\frac{R}{r} T_m * [1 \quad 1 \quad 1 \quad 1]^T \tag{15}$$

where each motor's torque T is determined by the dynamics of the DC motor [7, 8]:

$$\frac{T_{s_0} U}{U_0} - T = J_w \dot{\omega} + b_w \omega + \frac{60 T_{s_0}}{2\pi n_{0_0}} \omega \tag{16}$$

Equation (16) has omitted the fast dynamics from the inductances in the motor, and it is simplified by the free spin velocity n_{0_0} , stalling torque T_{s_0} and nominal voltage U_0 according to the typical steady performance plot of DC motors.

According to the nonslip condition, the contact point velocity at the friction wheel and the ball should be identical. Thus, for each motor the velocity equation should be:

$$\omega_j = V_{r_j}^T ((C_O^L W_{b-o}) \times V_{W_j} - W_{B-L} \times V_{W_j}) / r \tag{17}$$

where V_{XX_j} is the j th column of the V_{XX} matrix, and $j = 1, 2, 3, 4$. The equations couple the electronic systems of the motors with the mechanical system of the robot. Governing equations therefore can be rearranged into the standard form:

$$x = [A \ B \ C \ X \ Y \ \dot{A} \ \dot{B} \ \dot{C} \ \dot{X} \ \dot{Y}]^T \tag{18}$$

$$u = [U_{x+y+} \ U_{x+y-} \ U_{x-y-} \ U_{x-y+}]^T \tag{19}$$

$$v = [T_D^T \ F_D^T \ T_d^T \ F_d^T]^T \tag{20}$$

And the standard ODE functions are:

$$\dot{x} = f(x, u, v) \tag{21}$$

$$y = g(x, w) \tag{22}$$

where u is the input of the system, v is the process noise, y is the output (or measurement) of the system, and $w(x)$ is the measurement noise. This completes the system model with detailed dynamics including exterior perturbations and possible errors.

In order to study the effect of potential uncertainty that may occur because of modeling inaccuracies, we generated two different sets of governing equations based on 2 different property setups—the standard model whose properties are acquired from 3D modeling, and a randomly generated model whose properties are presumed unknown.

The system generally presents strong nonlinearity at most of the areas. However, when linearized at the point $x^T = [0 \ \dots \ 0]_{1 \times 10}$ (zero point) and presented in State-Space Form, the ideal system characteristic matrix A_{SS} and B_{SS} for $\dot{X}_{SS} = A_{SS}X_{SS} + B_{SS}U_{SS}$ [9] would be:

$$A_{SS} = \begin{bmatrix} 0 & 0 & 0 & 0 & 0 & 1 & 0 & 0 & 0 & 0 \\ 0 & 0 & 0 & 0 & 0 & 0 & 1 & 0 & 0 & 0 \\ 0 & 0 & 0 & 0 & 0 & 0 & 0 & 1 & 0 & 0 \\ 0 & 0 & 0 & 0 & 0 & 0 & 0 & 0 & 1 & 0 \\ 69.27 & 0 & 0 & 0 & 0 & -8.23 & 0 & 0 & 0 & -81.08 \\ 0 & 67.60 & 0 & 0 & 0 & 0 & -8.04 & 0 & 79.12 & 0 \\ 0 & 0 & 0 & 0 & 0 & 0 & 0 & -3.98 & 0 & 0 \\ 0 & -5.17 & 0 & 0 & 0 & 0 & 1.11 & 0 & -11.12 & 0 \\ 5.30 & 0 & 0 & 0 & 0 & -1.13 & 0 & 0 & 0 & -11.27 \end{bmatrix} \tag{23}$$

$$B_{SS} = \begin{bmatrix} 0 & 0 & 0 & 0 & 0 & 9.68 & -9.44 & -5.68 & 1.32 & 1.34 \\ 0 & 0 & 0 & 0 & 0 & -9.68 & -9.44 & 5.68 & 1.32 & -1.34 \\ 0 & 0 & 0 & 0 & 0 & -9.68 & 9.44 & -5.68 & -1.32 & -1.34 \\ 0 & 0 & 0 & 0 & 0 & 9.68 & 9.44 & 5.68 & -1.32 & 1.34 \end{bmatrix}^T \tag{24}$$

Matrixes in (23) and (24) indicate the symmetric characteristic of the Q-Baller design. They also present the weak bonds between states and low nonlinearity around the zero point. The zero point is also an equilibrium point, which would be a good choice for designing a linear controller.

4 Controller Design

We presume that the random model properties cannot be acquired, along with the unidentified process and measurement noise that will take place in real practice. So the controller design is only based on the ideal standard model. The preliminary simulation only deploys a standard PID linear controller [9] to the system. Gain scheduling method [10] may take place when PID at a single operating point is insufficient to cover the required controllable areas. The system flowchart is presented in Fig. 6 Left.

We used a LQR designer [11] to find the initial parameters for the PID controller, These values optimize the control performance by minimizing a cost function ($J = \int_0^\infty (x^T Qx + u^T Ru) dt$) which balances performance and energy conservation. The PID controller will later be adjusted to enhance performance.

Linear controllers are only effective in vicinity areas, and may fail when the system goes beyond certain boundaries. The Gain Scheduling Method [10] is adopted to solve this problem especially when the Q-Baller is required to operate at high speed. We have effectively chosen several equilibrium points which provide enough coverage for the required velocity control areas. The idea is depicted in the right side of Fig. 6, where you can see that each small circle indicates the approximate effectiveness boundary of an operating point. Generally, a linear controller performs better in the vicinity of the zero point, but may have problems away from the zero point. A good algorithm should be circumspective and smooth to avoid drastic jumps in parameters during scheduled zone switches.

5 Simulation Layout

The simulation loop is shown in the flowchart in Fig. 7. In addition to discretize the originally continuous control model into code loops, we have added simulation modules for the sensor and filters along with noise generators. We have also separated the numerical integration process and included a time lag feature in the program to add realistic challenges to the control problem.

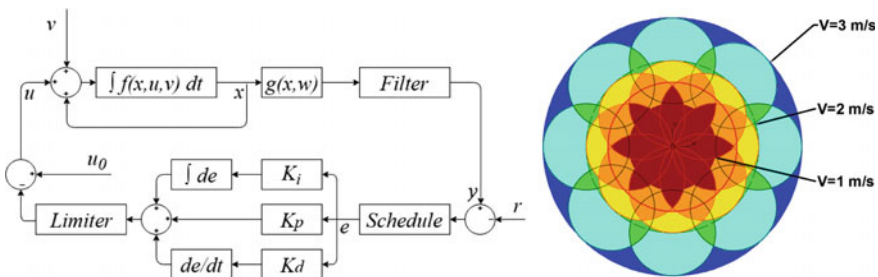


Fig. 6 Left control system flowchart; Right gain scheduling tiers

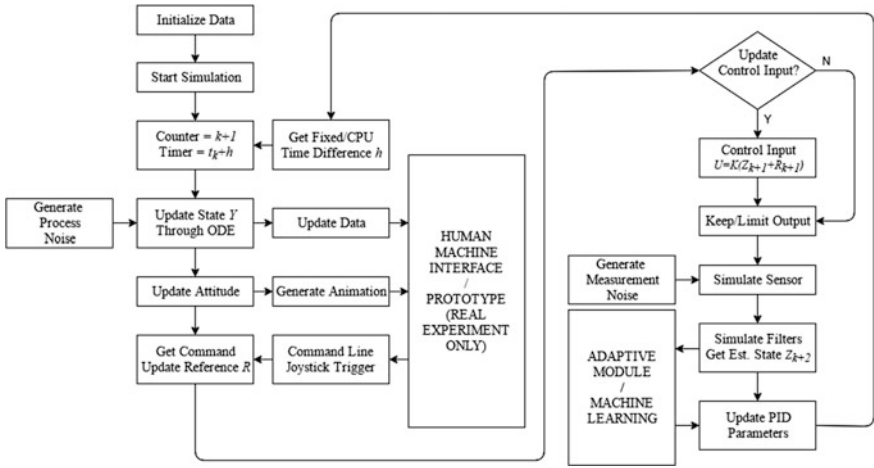


Fig. 7 Simulation flowchart

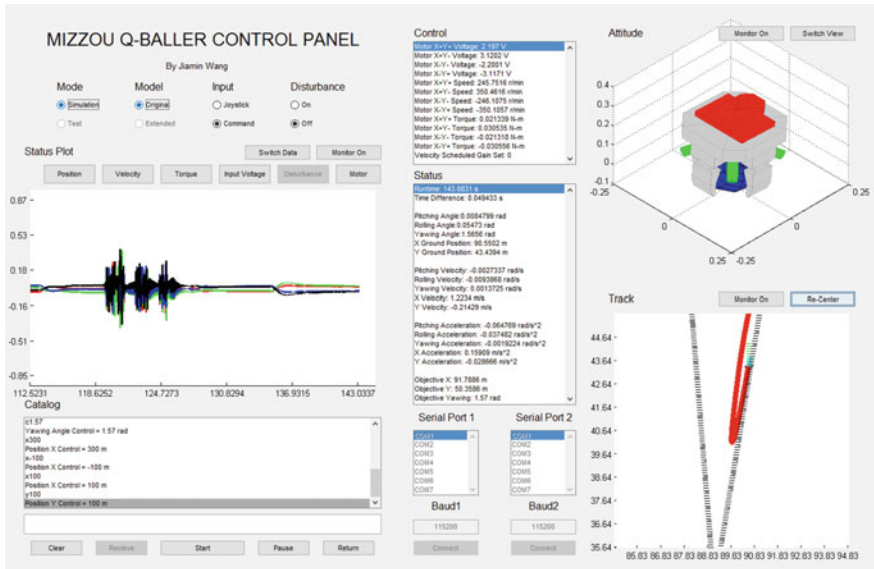


Fig. 8 MATLAB GUI human machine interface for Q-Baller

A Human Machine Interface based on MATLAB GUI has been constructed to support real time simulation as shown in Fig. 8. The interface is able to generate real time plotting, 3D animation and trajectory recording. In addition to type-in commands we use a gaming joystick as a more convenient alternative input. The interface will also be modified into an experimental interface for the Q-Baller after

prototyping is completed, facilitating observation, comparing models, data collecting and possibly recognizing dynamic pattern.

Adaptive and machine learning modules are something we have just started working on. Future planned improvements include adaptive control and neural network techniques to improve the controller design for maneuvering a prototype whose model is vastly different from the ideal one we established before.

6 Some Results and Conclusion

Currently we are able to control the ideal model well under noiseless condition. We also realized that PD controller would be enough for position control, but Integral Control has to be included during velocity control to eliminate static error. Under noiseless conditions, a velocity controller can cover up to 3 m/s in any direction on the horizontal plane with Gain Scheduling.

However, the situation becomes very different with noise. A random model simulation shows this with reference following at low speed noise. The sensor feedback frequency is 50 Hz and the control input update frequency is 25 Hz. Both process and measurement noise are generated randomly with amplitudes realistically set. The feedbacks are digitally filtered and later used in state estimation through a Discrete Kalman Filter presented from (25) to (30) [13]:

$$x_{n+1,n} = Ax_n + B(u_n + v) \tag{25}$$

$$E = y_n - Cx_n - Du_n \tag{26}$$

$$P_{n+1,n} = AP_nA^T + Q_n \tag{27}$$

$$K_n = P_{n+1,n}C^T(CP_{n+1,n}C^T + R_n)^{-1} \tag{28}$$

$$P_{n+1} = (I - K_nC)P_{n+1,n} \tag{29}$$

$$x_{n+1} = x_{n+1,n} + K_nE \tag{30}$$

where x is the state estimation through integration of gyroscope sensor data; y is the measurement of Pitch and Roll angle through accelerometer data; Initial parameters P, Q, R are empirically determined which can be either fixed or variable [13].

Kalman filters are very useful tools when dealing with the digital signal feedback from a gyroscope/accelerometer under noisy conditions for pitch and roll states. As displayed in Fig. 9 Left, the Kalman Filter successfully kept the rolling angle from drifting away during numerical integration. However, Fig. 9 Right shows the integrals of accelerometer (displacement and velocity) are not reliable due to the truncation error and amplification of noise.

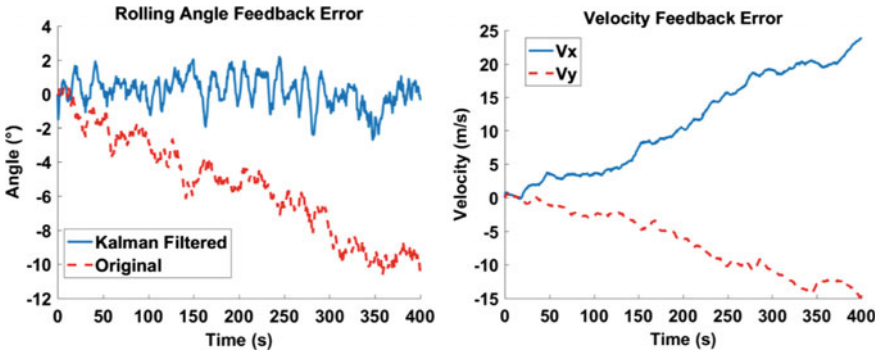


Fig. 9 Left performance of kalman filter; Right accelerometer data integration

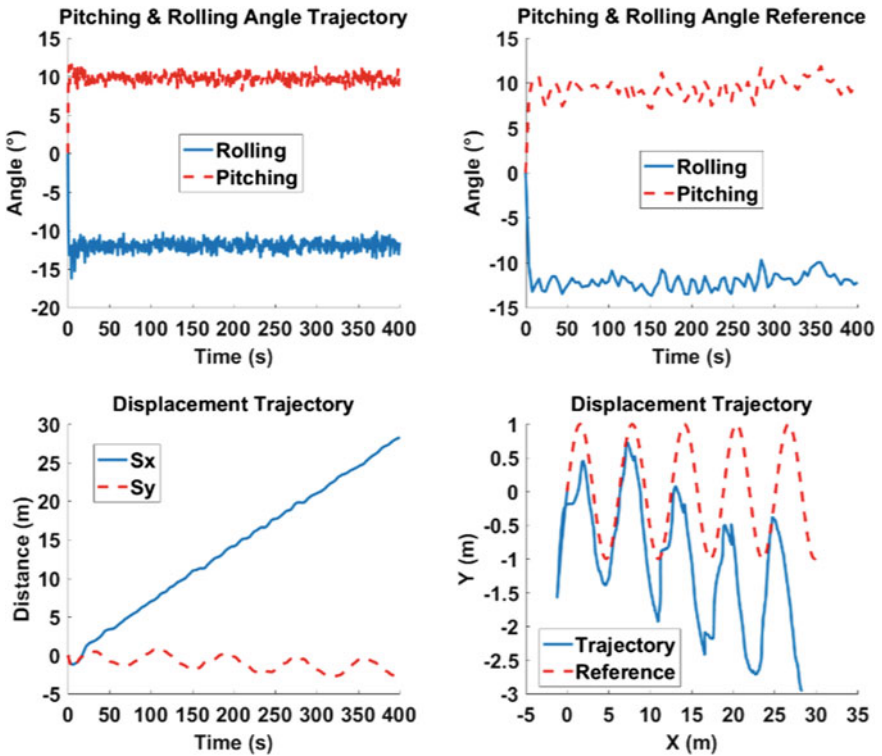


Fig. 10 Trajectory following simulation under noisy condition

Here we adopted some simple adaptive control algorithm. Assuming that the displacement and velocity feedback of Q-Baller are reliable (directly updated by ODE), and we use sensor simulator for Pitch, Roll and Yaw feedbacks, then the robot can be stably controlled as shown in Fig. 10. The adaptive control mainly

works on adjusting the Pitch and Roll references so as to eliminate static error in position control caused by inaccurate modeling. The angle references tend to converge to 9 and -12 degrees respectively, indicating that those may be the ‘Zero Point’ States of this random model.

It is also easy to see that the Q-Baller cannot follow the trajectory well, and starts to deviate toward $-Y$ direction. The phenomenon results from the lack of a Kalman Filter for Yawing to eliminate error accumulation.

Based on these results we have reached the following conclusions about the current Q-Baller design, control program and simulation:

1. Controllers and filters should be further improved for better product control performance.
2. Rotary encoders should be installed to monitor spherical wheel rotations. Rotary encoders provide more accurate translational velocity and position feedback.
3. A magnetometer should be installed to form a Kalman Filter along with the gyroscope sensor to eliminate Yawing errors
4. The current simulation has not yet been perfected since features like friction surfaces are very complicated to model. More accurate simulation should be made before experimenting on the prototype to possibly reveal more problems.

7 Conclusion and Future Plans

The simulation results we have acquired so far indicated that our design needs further improvement. The results have also shown us that our design may be feasible if better refined and controlled. Better structural design obviously will lead to better control conditions, while control theory would certainly help optimizing the product design. Simulation serves as the bond and facilitates the mutual improvement between product design and controller design.

For the moment Our Ball-Bot is already being prototyped and will be tested in the near future. As mentioned previously we will try some more complicated control algorithms and refine the current PID controller. Simulation will help us predict more problems before actually getting our hands on the robot. Our final goal would be successfully developing a Q-Baller software system with excellent control performance.

Acknowledgments The authors thank Dr. Ming Xin, Dr. Qingbin Tong, Mr. Zhengwei Nie from Department of Mechanical & Aerospace Engineering, University of Missouri—Columbia for their supports in fields of mechanical, control and signal process engineering. The authors also thank Mr. Yueqi Yu from Department of Electronic and Computer Engineering for his support in fields of electronic and computer engineering. Finally, the authors thank Dr. Peter Hodges for proof reading the manuscript.

References

1. Lauwers TB, Kantor GA, Hollis RL (2006) A dynamically stable single-wheeled mobile robot with inverse mouse-ball drive. In: IEEE international conference on robotics and automation. pp 2884–2889
2. Kumagai M, Ochiai T (2008) Development of a robot balancing on a ball. In: International conference on control (Seoul, Korea: Automation and Systems). pp 433–438
3. Doessegger S, Fankhauser P, Gwerder C, Huessy J, Kaeser J, Kammermann T, Limacher L, Neunert M (2010) Rezero, focus project report. Autonomous Systems Lab, ETH Zurich
4. Greenwood DT (1987) Principle of dynamics, 2nd edn. Pearson Education, Upper Saddle River. ISBN-13: 978-0137099818
5. Kim P (2013) Rigid body dynamics for beginners: euler angles & quaternions. CreateSpace Independent Publishing Platform ISBN-13: 978-1493598205
6. Raffo GV, Ortega MG, Rubio FR (2010) An integral predictive/nonlinear H^∞ control structure for a quadrotor helicopter. *Automatica* 46(1):29–39
7. Emhemed AAA, Mamat RB (2012) Modelling and simulation for industrial DC motor using intelligent control. In: International symposium on robotics and intelligent sensors 2012 (IRIS 2012), *Procedia Engineering* vol 41, pp 420–425
8. Hao Y, Miao M, Luo X (2009) Electric drive control (Chinese edition). Huazhong University of Science and Technology Press, Wuhan. ISBN-13: 978-560958620
9. Ogata K (2009) Modern control engineering, 5th edn. Pearson Education, Upper Saddle River. ISBN-13: 978-0136156734
10. Khalil HK (2002) Nonlinear systems, 3rd edn. Pearson Education, Upper Saddle River. ISBN-13:978-9332542037
11. Naidu DS (2012) Optimal control systems, 1st edn. CRC Press, Boca Raton. ISBN-13: 978-0849308925
12. Kalman RE (1960) A new approach to linear filtering and prediction problems. *Trans ASME J Basic Eng* 82(Series D):35–45
13. Feng B, Fu M, Ma H, Xia Y, Wang B (2014) Kalman filter with recursive covariance estimation—sequentially estimating process noise covariance. *IEEE Trans Ind Electron* 54 (1):6253–6263

Stiffness Analysis and Measurement Method for a 3-DOF Cable-Driven Joint Module

Kaisheng Yang and Guilin Yang

Abstract A modular cable-driven manipulator that consists of a number of cable-driven joint modules can produce intrinsically-safe motions due to its light-weight structure. In this paper, a stiffness analysis and measurement method is proposed for a 3-DOF six-cable cable-driven spherical joint module (CSJM) based on the group theory and differential geometry. A measurement simulation is carried out to validate the presented algorithms. It is shown that the stiffness matrix obtained from measurement simulation are equivalent to the theoretical stiffness matrix.

1 Introduction

Cable-driven manipulators are a special class of parallel manipulators, in which the moving platforms are driven by cables instead of rigid links [1–4]. Utilizing light-weight driving cables and the base-mounted actuators, a cable-driven manipulator has low moving mass and movement of inertia. Such characteristics make the cable-driven manipulator intrinsically safe. Besides, as the driving cables can pull but cannot push, a cable-driven manipulator is always a redundantly actuated system.

K. Yang · G. Yang (✉)

Zhejiang Provincial Key Laboratory of Robotics and Intelligent Manufacturing Equipment Technology, Ningbo Institute of Material Technology and Engineering, Chinese Academy of Sciences, Zhenhai District, Ningbo, Zhejiang, People's Republic of China
e-mail: glyang@nimte.ac.cn

K. Yang

e-mail: yangkaisheng@nimte.ac.cn; yksh001@163.com

K. Yang

Zhejiang Marine Development Research Institute, Dinghai District, Zhoushan, Zhejiang, People's Republic of China

© Springer Nature Singapore Pte Ltd. 2017

X. Zhang et al. (eds.), *Mechanism and Machine Science*,

Lecture Notes in Electrical Engineering 408,

DOI 10.1007/978-981-10-2875-5_94

In robotics literatures, various design analysis issues of cable-driven manipulators have been addressed. Stump [5] proposed the closed form of the workspace boundary of cable-actuated parallel manipulators based on convex analysis. Chen [6] analyzed the workspace of the cable-driven parallel robot under the tension restraint. Khajepour [7] analyzed the bounded cable tensions for cable-driven parallel manipulators.

To simplify the design of cable-driven manipulators, Lim [8] proposed a novel modular cable-driven manipulator that consists of a number of cable-driven joint modules. For the purpose of stiffness regulation, a tension distribution algorithm is proposed for the cable-driven joint module based on gradient projection method [9]. However, it is still a challenging issue to experimentally evaluate the stiffness of cable-driven manipulators.

In this paper stiffness analysis and measurement method is proposed for a 3-DOF six-cable cable-driven spherical joint module (CSJM) based on the group theory and differential geometry, which is useful to experimentally study the stiffness of cable-driven joint modules as well as modular cable-driven manipulators.

2 3-Dof Cable-Driven Spherical Joint Module Design

The conceptual design of a 3-DOF six-cable cable-driven spherical joint module (CSJM) (see [10] for details) is shown in Fig. 1. This CSJM consists of a base and a moving-platform, which are connected together by a 3-DOF passive spherical joint. The moving-platform is driven by six cables. As shown in Fig. 2, in the home pose

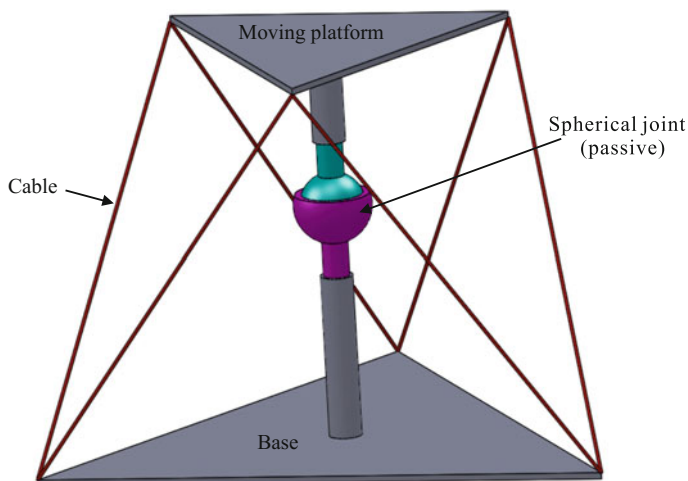


Fig. 1 Home position of CSJM

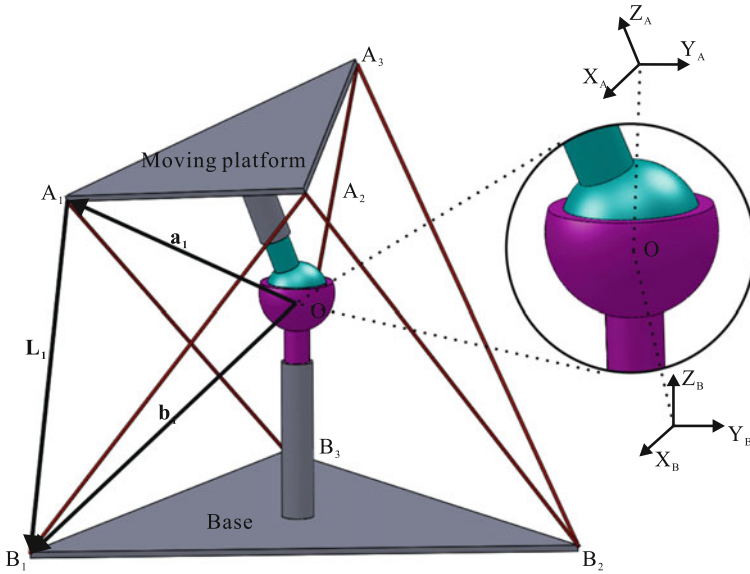


Fig. 2 Arbitrary position of CSJM

of the CSJM, the base and the moving-platform are parallel to each other. The edges of the moving-platform are also parallel to the diagonally opposite ones of the base, i.e., $A_1A_2 // B_2B_3$, $A_2A_3 // B_3B_1$ and $A_3A_1 // B_1B_2$.

Let the stiffness of the cable be $k_c (\frac{N}{m})$ per unit meter. The relationship between the change of the cable tension Δt_c and the change of the cable length Δl_c is given by:

$$\Delta t_c = k_c \Delta l_c \tag{1}$$

3 Stiffness Analysis of the CSJM Module

3.1 Rotational Motion and SO(3)

In the 3-DOF six-cable cable-driven spherical joint module (as shown in Fig. 2), frame B (called base frame) represents the frame attached to the base of the module with Z axis being perpendicular to the base and the Y axis being parallel to the edge B_1B_2 of the base. Frame A (called moving frame) represents the local frame attached to the moving-platform with the Z axis being perpendicular to the moving-platform and the Y axis being parallel to the edge A_3A_1 of the moving-platform. The origins of both frames are located at the center of the spherical joint denoted by O , and both frames coincide with each other when the CSJM is at the home position.

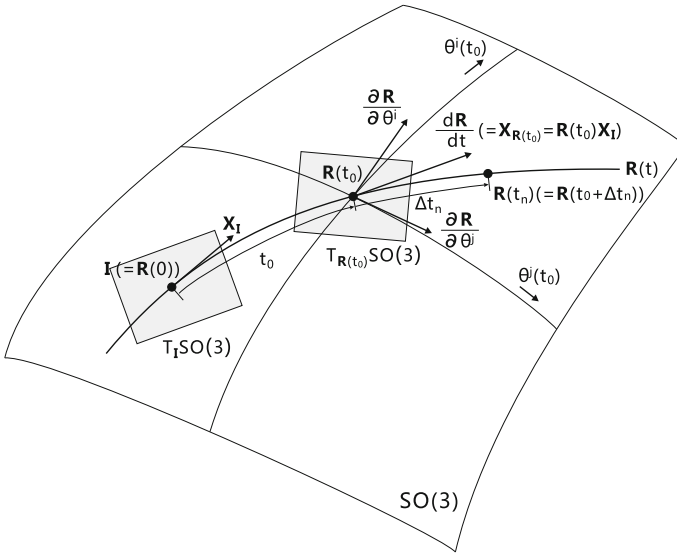


Fig. 3 A curve in $SO(3)$

When the moving-platform take a pure rotational motion with respect to the base, the orientation of the moving-platform with respect to the base can be described by a rotation matrix $\mathbf{R} \in \mathbb{R}^3$, which is an element of Lie group $SO(3)$. Then the motion of the moving-platform with respect to the base can be described by a curve $\mathbf{R}(t)$ on Lie group $SO(3)$, which is a differentiable manifold. The time derivative $\frac{d\mathbf{R}(t)}{dt}$ is an element (a vector) of the tangent space to $SO(3)$ at $\mathbf{R}(t)$, denoted as $T_{\mathbf{R}(t)}SO(3)$, which maps moving-frame coordinates of a given point into its velocity, expressed in base-frame coordinates [11]. The curve $\mathbf{R}(t)$ is shown in Fig. 3.

On the Lie group $SO(3)$, the tangent space at the group identity element I (i.e., $\mathbf{R}(0)$) has the structure of a Lie algebra, which is denoted as $so(3)$.

Let $\boldsymbol{\omega}_1 = [1, 0, 0]^T$, $\boldsymbol{\omega}_2 = [0, 1, 0]^T$ and $\boldsymbol{\omega}_3 = [0, 0, 1]^T$, then $\hat{\boldsymbol{\omega}}_1, \hat{\boldsymbol{\omega}}_2, \hat{\boldsymbol{\omega}}_3$ consist the basis twists of $so(3)$, where $\hat{\boldsymbol{\omega}}_1, \hat{\boldsymbol{\omega}}_2, \hat{\boldsymbol{\omega}}_3$ represent instantaneous rotation about the Cartesian axes X, Y and Z , respectively. The mapping between $\boldsymbol{\omega} \in \mathbb{R}^3$ and $\hat{\boldsymbol{\omega}} \in \mathbb{R}^{3 \times 3}$ is given below:

$$\boldsymbol{\omega} = \begin{pmatrix} \omega_1 \\ \omega_2 \\ \omega_3 \end{pmatrix} \rightarrow \hat{\boldsymbol{\omega}} = \begin{pmatrix} 0 & -\omega_3 & \omega_2 \\ \omega_3 & 0 & -\omega_1 \\ -\omega_2 & \omega_1 & 0 \end{pmatrix} \tag{2}$$

When the moving-platform of the CSJM take a rotation with respect to the base, the rotation matrix $\mathbf{R}(t)$ can be expressed by the Product-of-Exponentials (POE) formula:

$$\mathbf{R}(t) = e^{\hat{\omega}_1 \theta^1(t)} e^{\hat{\omega}_2 \theta^2(t)} e^{\hat{\omega}_3 \theta^3(t)} \tag{3}$$

where $\theta^1(t)$, $\theta^2(t)$ and $\theta^3(t)$ are the angular displacement about the Cartesian axes X , Y and Z , respectively. $\theta^i(t)(i = 1, 2, 3)$ are called *the canonical coordinates of the second kind*.

Consider the tangent vector of the curve $\mathbf{R}(t)$, denoted as $\mathbf{X}_{\mathbf{R}(t)}$. It can be obtained by differentiating $\mathbf{R}(t)$, i.e.,

$$\mathbf{X}_{\mathbf{R}(t)} = \frac{d\mathbf{R}}{dt}(\theta^1(t), \theta^2(t), \theta^3(t)) = \sum_{i=1}^3 \frac{\partial \mathbf{R}}{\partial \theta^i} \frac{d\theta^i}{dt} \tag{4}$$

Denote $\mathbf{\Omega}_i \triangleq \frac{\partial \mathbf{R}}{\partial \theta^i}$ and $x^i \triangleq \frac{d\theta^i}{dt}$, then

$$\mathbf{X}_{\mathbf{R}(t)} = \sum_{i=1}^3 x^i \mathbf{\Omega}_i \tag{5}$$

$T_{\mathbf{R}(t)}SO(3)$ is a *left invariant vector field*, so $\mathbf{X}_{\mathbf{R}(t)} = \mathbf{R}(t)\mathbf{X}_I$, where $\mathbf{X}_I \in T_I SO(3)$ and $\mathbf{X}_{\mathbf{R}(t)} \in T_{\mathbf{R}(t)}SO(3)$. Since $\mathbf{X}_I = \sum_{i=1}^3 x^i \mathbf{\omega}_i$, it can be concluded that $\mathbf{\Omega}_i = \mathbf{R}(t)\mathbf{\omega}_i$, especially, at the identity element I , $\mathbf{\Omega}_i = \mathbf{\omega}_i$.

In robotics, a twist \mathbf{T} is an element of the tangent space $T_I SO(3)$, and a wrench \mathbf{W} is an element of the cotangent space $T_I^* SO(3)$, which is the dual space of the tangent space $T_I SO(3)$. The wrench \mathbf{W} can be expressed as

$$\mathbf{W} = \sum_{j=1}^3 w_j \boldsymbol{\lambda}^j \tag{6}$$

where $\boldsymbol{\lambda}^i$ is the basis of the cotangent space $T_I^* SO(3)$. The basis of the tangent space $T_I SO(3)$ $\mathbf{\omega}_i$ and the basis of the cotangent space $T_I^* SO(3)$ $\boldsymbol{\lambda}^j$ satisfies

$$\langle \mathbf{\omega}_i, \boldsymbol{\lambda}^j \rangle = \delta_i^j = \begin{cases} 1 & (i = j) \\ 0 & (i \neq j) \end{cases} \tag{7}$$

In this paper, the Cartesian coordinate is considered, then $\mathbf{\omega}_i = \boldsymbol{\lambda}^i$. Let $\boldsymbol{\Lambda}^i$ be the basis of the cotangent space $T_{\mathbf{R}(t)}^* SO(3)$, then $\boldsymbol{\Lambda}^i \triangleq \mathbf{R}(t)\boldsymbol{\lambda}^i = \mathbf{R}(t)\mathbf{\omega}_i = \mathbf{\Omega}_i$.

3.2 Cartesian Stiffness Matrix on $SO(3)$

Broadly speaking, the Cartesian stiffness matrix describes the relationship between the small changes in the components of a force and the small displacements caused

along the basis twists. In this paper, the change of the force $\mathbf{F} \in \mathbb{R}^3$ acting on the moving-platform along a basis twist $\mathbf{\Omega}_j$ at location \mathbf{R} can be described by the covariant derivative $\nabla_{\mathbf{\Omega}_j} \mathbf{F}$. Then the components k_{ij} of the stiffness matrix $\mathbf{K} \in \mathbb{R}^{3 \times 3}$ can be described by the following equation:

$$k_{ij} = -\langle \nabla_{\mathbf{\Omega}_j} \mathbf{F}, \mathbf{\Omega}_i \rangle \tag{8}$$

The negative sign in front of the parenthesis in (8) is used to conform to the definition of the stiffness matrix in other literatures.

In Cartesian Coordinates, a force \mathbf{F} is an element of the cotangent space $T_{\mathbf{R}(t)}^* SO(3)$, which can be expressed as

$$\mathbf{F} = \sum_{i=1}^3 f_i \mathbf{\Lambda}^i = f_i \mathbf{\Omega}_i \tag{9}$$

According to the definition of the covariant derivative, $\nabla_{\mathbf{\Omega}_j} \mathbf{F}$ can be expressed as

$$\nabla_{\mathbf{\Omega}_j} \mathbf{F} = \frac{\partial}{\partial \theta^j} \sum (f_k \mathbf{\Omega}_k) = \sum_{k=1}^3 \left(\frac{\partial f_k}{\partial \theta^j} \mathbf{\Omega}_k + f_k \frac{\partial \mathbf{\Omega}_k}{\partial \theta^j} \right) \tag{10}$$

According to the definition of the covariant derivative,

$$\nabla_{\mathbf{\Omega}_j} \mathbf{\Omega}_k = \frac{\partial \mathbf{\Omega}_k}{\partial \theta^j} \tag{11}$$

Substituting the result of (10) and (11) into the (8), the components of the stiffness matrix can be expressed as

$$\begin{aligned} k_{ij} &= -\left\langle \sum_{k=1}^3 \left(\frac{\partial f_k}{\partial \theta^j} \mathbf{\Omega}_k + f_k \frac{\partial \mathbf{\Omega}_k}{\partial \theta^j} \right), \mathbf{\Omega}_i \right\rangle \\ &= -\left(\frac{\partial f_i}{\partial \theta^j} + \sum_{k=1}^3 \langle f_k \nabla_{\mathbf{\Omega}_j} \mathbf{\Omega}_k, \mathbf{\Omega}_i \rangle \right) \end{aligned} \tag{12}$$

Given two vectors $\mathbf{X}, \mathbf{Y} \in T_{\mathbf{R}} SO(3)$, which is the left-invariant tangent space on Lie group $SO(3)$. They satisfy $\nabla_{\mathbf{X}} \mathbf{Y} = \frac{1}{2} [\mathbf{X}, \mathbf{Y}]$. Then

$$k_{ij} = -\left(\frac{\partial f_i}{\partial \theta^j} + \frac{1}{2} \sum_{k=1}^3 \langle f_k [\mathbf{\Omega}_j, \mathbf{\Omega}_k], \mathbf{\Omega}_i \rangle \right) \tag{13}$$

4 Stiffness Measurement Method

4.1 Experiment Design

The measurement method of the stiffness matrix is necessary for the manipulator, which can be used to the position compensation and so on. For the variable-stiffness manipulator, there have different stiffness at the same location, so it is important to estimate the stiffness at the same location. Some methods were proposed in both robotics [12, 13] and biomechanics [14–16] to estimate the stiffness at some location based on perturbations and force measurements at some nearby, known locations. Among these methods, some methods applied a known perturbing force to the manipulator under analysis and then measured the resultant displacement, while some methods imposed a known displacement and then measured the resultant force. These methods have different procedures, but the final sets of measured data are similar in the sense that a series of {force, displacement} measurement pairs are available for several locations surrounding the starting position. In this paper, a known force is exerted and the resultant displacement is measured.

In order to estimate the stiffness of the CSJM at a given location $\mathbf{R}(t_0)$, several external forces are exerted to pull the moving platform of the CSJM from a location $\mathbf{R}(t_0)$ to N peripheral locations $\mathbf{R}(t_n)(n = 1, 2, \dots, N)$ for a small displacement, where $t_n = t_0 + \Delta t_n$. The location $\mathbf{R}(t_0)$ is a static status of the CSJM, and $\mathbf{R}(t_n)$ is another static status of the CSJM after an external force is exerted on the moving platform of the CSJM. Based on the analysis above, an numerical algorithm is proposed to estimate the stiffness of the CSJM at location $\mathbf{R}(t_0)$.

4.2 Stiffness Analysis Algorithm

Let $\mathbf{F}(\mathbf{R}(t))$ be the external force exerted on the moving-platform of the CSJM at location $\mathbf{R}(t)$. The external force $\mathbf{F}(\mathbf{R}(t))$ can be measured by a sensor mounted on the moving-platform during the experiment. As shown in Fig. 3, $\mathbf{R}(t_n)$ can be expressed as

$$\mathbf{R}(t_n) = \mathbf{R}(t_0 + \Delta t_n) = \mathbf{R}(t_0)e^{\hat{\mathbf{V}}_n \Delta t_n} \quad (14)$$

where $\hat{\mathbf{V}}_n \in T_{\mathbf{R}(t)}SO(3)$ and its can be expressed as

$$\hat{\mathbf{V}}_n = \sum_{i=1}^3 \alpha_n^i \hat{\boldsymbol{\omega}}_i = \sum_{i=1}^3 v_n^i \hat{\boldsymbol{\Omega}}_i \quad (15)$$

where $\hat{\mathbf{V}}_n$ is an unit vector.

The inverse of the exponential map is the *logarithmic map* $\log: SO(3) \rightarrow so(3)$. For Lie group $SO(3)$ with Riemannian metric [17], the distance between the elements $\mathbf{R}(t_n), \mathbf{R}(t_0) \in SO(3)$ can be computed by the following equation

$$\hat{\mathbf{V}}_n \Delta t_n = \log((\mathbf{R}(t_0))^T \mathbf{R}(t_n)) \tag{16}$$

Since $\hat{\mathbf{V}}_n$ is an unit vector, i.e., $|\hat{\mathbf{V}}_n| = 1$, then the distance between $\mathbf{R}(t_n)$ and $\mathbf{R}(t_0)$ can be simplified to the following equation

$$\Delta t_n = \|\log((\mathbf{R}(t_0))^T \mathbf{R}(t_n))\| \tag{17}$$

According to the definition of the directional derivative, when Δt_n is small enough, $D_{\mathbf{V}_n} f_i$ can be approximated as

$$\begin{aligned} D_{\mathbf{V}_n} f_i &\triangleq \lim_{\Delta t_n \rightarrow 0} \frac{f_i(\mathbf{R}(t_n))|_{\mathbf{R}(t_0)} - f_i(\mathbf{R}(t_0))|_{\mathbf{R}(t_0)}}{\Delta t_n} \\ &\simeq \frac{f_i(\mathbf{R}(t_n))|_{\mathbf{R}(t_0)} - f_i(\mathbf{R}(t_0))|_{\mathbf{R}(t_0)}}{\|\log((\mathbf{R}(t_0))^T \mathbf{R}(t_n))\|} \end{aligned} \tag{18}$$

where $f_i(\mathbf{R}(t_n))|_{\mathbf{R}(t_0)}$ denotes the i th component of the external force \mathbf{F} at location $\mathbf{R}(t_n)$ under the frame at location $\mathbf{R}(t_0)$. and $f_i(\mathbf{R}(t_0))|_{\mathbf{R}(t_0)}$ denotes the i th component of the external force \mathbf{F} at location $\mathbf{R}(t_0)$ under the frame at location $\mathbf{R}(t_0)$.

According to (15) and the linear property of the directional derivative, $D_{\mathbf{V}_n} f_i$ can be expressed as

$$D_{\mathbf{V}_n} f_i = \sum_{j=1}^3 (v_n^j \frac{\partial f_i}{\partial \theta^j}) \tag{19}$$

Let $[u_j^n] \in \mathbb{R}^{3 \times N}$ be the pseudo-inverse of $[v_n^j] \in \mathbb{R}^{N \times 3}$, i.e., $[u_j^n] \triangleq [v_n^j]^+$ ($j = 1, 2, 3$ and $n = 1, 2, \dots, N$). Then

$$[D_{\mathbf{V}_n} f_i] = [v_n^j] \left[\frac{\partial f_i}{\partial \theta^j} \right] \tag{20}$$

$$\left[\frac{\partial f_i}{\partial \theta^j} \right] = [u_j^n] [D_{\mathbf{V}_n} f_i] \tag{21}$$

where $[D_{\mathbf{V}_n} f_i] \in \mathbb{R}^{N \times 1}$ and $\left[\frac{\partial f_i}{\partial \theta^j} \right] \in \mathbb{R}^{3 \times 1}$.

The stiffness matrix expressed in (13) can be written as

$$\begin{aligned}
 K_{ij} &= - \left(\left[\frac{\partial f_i}{\partial \theta^j} \right] \right)_{i,1} + \frac{1}{2} \sum_{k=1}^3 \langle f_k[\boldsymbol{\Omega}_j, \boldsymbol{\Omega}_k], \boldsymbol{\Omega}_i \rangle \\
 &= - \left([u_j^n][D_{V_n} f_i] \right)_{i,1} + \frac{1}{2} \sum_{k=1}^3 \langle f_k[\boldsymbol{\Omega}_j, \boldsymbol{\Omega}_k], \boldsymbol{\Omega}_i \rangle
 \end{aligned}
 \tag{22}$$

where $([\cdot])_{i,j}$ represents an element of the matrix in row i and column j .

Finally, the numerical estimation for stiffness matrix of the CSJM can be computed by submitting (18) into (22).

$$\begin{aligned}
 K_{ij} &= - \left([u_j^n] \left[\frac{f_i(\mathbf{R}(t_n))|_{\mathbf{R}(t_0)} - f_i(\mathbf{R}(t_0))|_{\mathbf{R}(t_0)}}{\|\log((\mathbf{R}(t_0))^T \mathbf{R}(t_n))\|} \right] \right)_{i,1} \\
 &\quad + \frac{1}{2} \sum_{k=1}^3 \langle f_k(\mathbf{R}(t_0))|_{\mathbf{R}(t_0)}[\boldsymbol{\Omega}_j, \boldsymbol{\Omega}_k], \boldsymbol{\Omega}_i \rangle
 \end{aligned}
 \tag{23}$$

5 Measurement Simulation Example

The CSJM module shown in Fig. 4 is employed for the simulation, with the dimensions given in Table 1.

For an arbitrary location $\mathbf{R}(t)$, as shown in Fig. 2, let \mathbf{a}_{kp} ($p = 1, 2, 3$) denote the position vector of the k th ($k = 1, 2, \dots, 6$) cable attachment point A_p on the

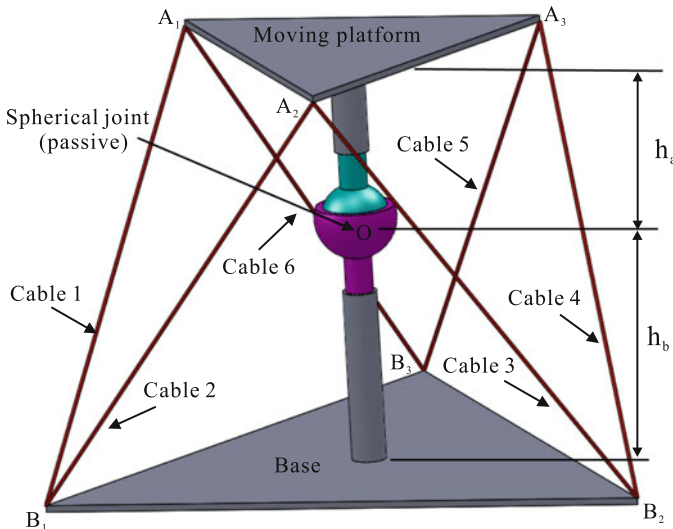


Fig. 4 Dimension of the module CSJM

Table 1 Dimension of the CSJM for simulation

Dimension	Length (m)
A_1A_2	0.1
A_2A_3	0.1
A_3A_1	0.1
B_1B_2	0.2
B_2B_3	0.2
B_3B_1	0.2
h_a	0.08
h_b	0.08

moving-platform with respect to the base frame B and vector \mathbf{b}_{kq} ($q = 1, 2, 3$) denote the position vector of the k th ($k = 1, 2, \dots, 6$) cable attachment point B_q on the base with respect to the base frame B . According to the vector loop-closure equation, the cable vector \mathbf{L}_k ($k = 1, 2, \dots, 6$), which goes along the k th cable from point A_p to point B_q , can be written as:

$$\mathbf{L}_k = \overrightarrow{A_p B_q} = \overrightarrow{OB_q} - \overrightarrow{OA_p} = \mathbf{b}_{kq} - \mathbf{a}_{kp} = \mathbf{b}_{kq} - R^A \mathbf{a}_{kp} \tag{24}$$

where ${}^A \mathbf{a}_{kp}$ is the position vector of the start point A_p of the k th cable vector \mathbf{L}_k with respect to the moving frame A , \mathbf{b}_{kq} is the position vector of the end point B_q of the k th cable vector \mathbf{L}_k with respect to the base frame B , and $\mathbf{L}_k = [L_{kx}, L_{ky}, L_{kz}]^T$ is the cable vector of the k th cable with respect to the base frame B .

For the simulation, the location $\mathbf{R}(t_0)$ of CSJM corresponds to the position of the moving-platform when the coordinates $\theta^1 = 0.1745rad(\simeq 10^\circ)$, $\theta^2 = 0.3491rad(\simeq 20^\circ)$ and $\theta^3 = 0.5236rad(\simeq 30^\circ)$. According to (24), the cable length vector of the k th cable can be computed when the CSJM is at location $\mathbf{R}(t_0)$. The result is listed in Table 2.

According to (1), the deformations of the cable can be computed with the given cable tensions of CSJM. The result is listed in Table 3, where Δl_{ck} is deformations of the k th ($k = 1, 2, \dots, 6$) cable at location R_0 under the given cable tension.

Table 2 Cable length at location R_0

Number k	Cable length vector \mathbf{L}_k			Cable length $\ \mathbf{L}_k\ $ (m)
1	0.030	-0.030	-0.144	0.150220
2	-0.016	-0.118	-0.142	0.185751
3	-0.017	0.082	-0.142	0.164821
4	0.077	0.088	-0.176	0.211172
5	-0.096	-0.012	-0.176	0.200691
6	-0.143	0.070	-0.144	0.214539

Table 3 VSD deformation at location R_0

Number k	Cable tension t_k (N)	Deformation of cable Δl_{ck} (m)
1	10	0.0050
2	15	0.0075
3	8	0.0040
4	12	0.0060
5	10	0.0050
6	14	0.0070

5.1 Measurement Simulation

As shown in the Fig. 2, for an 3-DOF cable-driven manipulator module driven by 6 cables, the kinetostatic equilibrium analysis of the moving-platform yields:

$$\mathbf{W} = \mathbf{S}\mathbf{T} \quad (25)$$

where $\mathbf{W} \in \mathbb{R}^3$ is the external wrench, $\mathbf{T} \in \mathbb{R}^6$ is the cable tension vector, $\mathbf{S} \in \mathbb{R}^{3 \times 6}$ is the structure matrix of the module.

For the structure matrix $\mathbf{S} = [\mathbf{s}_1, \mathbf{s}_2, \dots, \mathbf{s}_3] \in \mathbb{R}^{3 \times 6}$, the component \mathbf{s}_i can be computed as

$$\mathbf{s}_i = \mathbf{a}_p \times \frac{\mathbf{L}_i}{L_i} \in \mathbb{R}^3 \quad (26)$$

where \mathbf{a}_p and \mathbf{L}_i are described in base frame ($p = 1, 2, 3; i = 1, 2, \dots, 6$).

According to [10], the stiffness of the CSJM Module can be expressed by the traditional method of analysis,

$$\mathbf{K}_{module} = \mathbf{S}\mathbf{K}_c\mathbf{S}^T + \sum_{k=1}^6 (-t_k) \otimes \mathbf{H}_k^{2nd} \quad (27)$$

where $\mathbf{K}_{module} \in \mathbb{R}^{3 \times 3}$ is the stiffness of the CSJM Module described in the base frame, $\mathbf{K}_c = \text{diag}[k_{c1}, k_{c2}, \dots, k_{c6}] \in \mathbb{R}^{6 \times 6}$ is a diagonal matrix, k_{ci} is the stiffness of the i th ($i = 1, 2, \dots, 6$) cable, $\mathbf{S} \in \mathbb{R}^{3 \times 6}$ is the structure matrix of the module, t_k is the tension of the k th cable, $\mathbf{H}^{2nd} \in \mathbb{R}^{6 \times (3 \times 3)}$ is the second-order influence coefficient array, \mathbf{H}_k^{2nd} is the k th component of \mathbf{H}^{2nd} , \otimes represents the *Kronecker product* of tensors.

In (27), the first part of the stiffness $\mathbf{S}\mathbf{K}_c\mathbf{S}^T$ can be considered as the part which is caused by the stiffness of the cables, the second part of the stiffness $\sum_{k=1}^6 (-t_k) \otimes \mathbf{H}_k^{2nd}$ can be considered as the part which is caused by the tension of the cables. The second part $\sum_{k=1}^6 (-t_k) \otimes \mathbf{H}_k^{2nd}$ is always much smaller than the first part $\mathbf{S}\mathbf{K}_c\mathbf{S}^T$, so

Table 4 Theory stiffness

K_{the}	24.8204	0.9621	-5.3179
Eigenvalue	0.9621	24.8782	0.9133
	-5.3179	0.9133	10.5747
	26.7985	24.7511	8.7236

the first part SK_cS^T always be the approximation to the stiffness of the module K_{module} . i.e.,

$$K_{module} \simeq SK_cS^T \tag{28}$$

At the certain location $R(t_0)$, the structure matrix of the CSJM module can be computed by using (26)

$$S = \begin{pmatrix} 0.0798 & 0.0256 & -0.0466 & -0.0501 & -0.0049 & 0.0261 \\ 0.0392 & 0.0514 & 0.0579 & 0.0188 & -0.0630 & -0.0242 \\ 0.0087 & -0.0457 & 0.0387 & -0.0127 & 0.0071 & -0.0376 \end{pmatrix} \tag{29}$$

In this paper, the stiffness of the cable is constant, i.e., $k_{ci} = 2000 \left(\frac{N}{m}\right)$, then $K_c = diag\{2000, 2000, 2000, 2000, 2000, 2000\}$ with the unit N/m. According to (28), the approximation of the stiffness K_{module} can be computed, the result is list in Table 4.

When the external force F is exerted on the moving-platform of the module at location $R(t_0)$, the moving-platform will have a small displacement to a location $R(t_n)$ around the location $R(t_0)$ along the directions v_n . W represents the corresponding wrench to the external force F , where $F = R(t_0)W$. The changes of the external force ΔF and the corresponding wrench for this measurement simulation ΔW are listed in Table 5. The coordinates of the external force ΔF are under the moving-frame, and the ones of the wrench ΔW are under the base-frame.

In the traditional method, the change of the wrench ΔW and the change of the twist of the moving-platform $\Delta \xi$ in the base frame can be described as (Table 6).

$$\Delta W = K_{the} \Delta \xi \tag{30}$$

According to (23), the stiffness of the module can be measured. The result is listed in Table 7.

5.2 Discussion

In this measurement simulation, there is no pre-load on the moving-platform before the external force F is exerted, i.e., $F(R(t_0))|_{R(t_0)} = 0$. The theoretical stiffness matrix K_{the} and the measured stiffness matrix K_{mea} are different, but the

Table 5 External forces and wrenches

No. n	External force ΔF (N)			Wrench ΔW (N)		
1	1	0	0	0.8138	0.5438	-0.2049
2	-1	0	0	-0.8138	-0.5438	0.2049
3	0	1	0	-0.4698	0.8232	0.3188
4	0	-1	0	0.4698	-0.8232	-0.3188
5	0	0	0.4	0.1368	-0.0653	0.3702
6	0	0	-0.4	-0.1368	0.0653	0.3702
7	0.8	0.5	0	0.4161	0.8467	-0.0045
8	0.8	-0.5	0	0.8860	0.0235	-0.3233
9	-0.8	0.5	0	-0.8860	-0.0235	0.3233
10	-0.8	-0.5	0	-0.4161	0.8467	0.0045
11	0.6	0	0.3	0.5909	0.2774	0.1547
12	0.6	0	-0.3	0.3857	0.3753	-0.4005
13	0.5	0.3	0.2	0.3343	0.4862	0.1783
14	0.5	0.3	-0.2	0.1975	0.5515	0.1919
15	0.6	-0.5	0.3	0.8258	-0.1342	-0.0047
16	0.6	-0.5	-0.3	0.6206	-0.0363	-0.5599
17	-0.6	0.5	0.4	-0.5864	0.0200	0.6525
18	-0.6	0.5	-0.4	0.8600	0.1506	-0.0878

Table 6 The directions and displacements under base frame

No. n	Direction V_n			Displacement $ \theta_n $ (rad)
1	-0.9985	-0.0244	-0.0486	0.0376
2	0.9985	0.0244	0.0486	0.0376
3	-0.0221	-0.9859	-0.1660	0.0414
4	0.0221	0.9859	0.1660	0.0414
5	-0.0160	-0.0603	-0.9981	0.0457
6	0.0160	0.0603	0.9981	0.0457
7	-0.8146	-0.5651	-0.1309	0.0374
8	-0.8312	0.5533	0.0556	0.0356
9	0.8312	-0.5533	-0.0556	0.0356
10	0.8146	0.5651	0.1309	0.0374
11	-0.5464	-0.0619	-0.8352	0.0422
12	-0.5530	0.0381	0.8323	0.0398
13	-0.5515	-0.4002	-0.7319	0.0352
14	-0.6334	-0.3844	0.6716	0.0295
15	-0.5270	0.4149	-0.7417	0.0429
16	-0.4509	0.4596	0.7652	0.0477
17	0.3736	-0.3961	-0.8388	0.0571
18	0.4403	-0.3306	0.8348	0.0518

Table 7 Measurement stiffness

K_{mea}	26.6609	-0.5323	-0.3952
Eigenvalue	-0.5323	24.7399	-1.4852
	-0.3952	-1.4852	8.8724
	26.7985	24.7511	8.7236

eigen-values of the two stiffness matrices are same. The reason is that the measured stiffness matrix and the theoretical stiffness matrix are described in different frames, one is in moving frame and one is in base frame. After an orthogonal transformation of the measured stiffness matrix, the two stiffness matrices can both be described in the base frame, then they will be the same. This result shows that the measurement method is valid. When there is some pre-load on the moving-platform before the external force exerted, the stiffness matrices K_{the} and K_{mea} , the eigen-values of the two stiffness matrices will be different.

6 Conclusions

In this paper, a stiffness measurement method as well as the computation algorithm is proposed for the CSJM module. With the theoretical stiffness matrix of the CSJM module, the stiffness measurement experiment is simulated. Simulation results shown that the measured stiffness matrix is real symmetric. Although it looks different from the theoretical stiffness matrix, the eigen-values of these two stiffness matrices are the same. The reason is that the measured stiffness matrix and the theoretical stiffness matrix are described in different coordinate frames. Hence, the stiffness analysis and measurement method can be employed to experimentally study the stiffness of the CSJM module.

Acknowledgments The authors wish to thank Professors Domenico Campolo of Nanyang Technological University, Singapore, for his valuable comments. The authors also gratefully acknowledge the funding support for this project from the National Natural Science Foundation of China.

Research supported by the National Natural Science Foundation of China (Project code: 51475448).

References

1. Chen W, Chen Q, Zhang J et al (2007) Inverse kinematic analysis for cable-driven humanoid arm. *Chin J Mech Eng* 43(4):12–20
2. Brackbill EA, Mao Y, Agrawal SK et al (2009) Dynamics and control of a 4-DOF wearable cable-driven upper arm exoskeleton. In: *Proceedings of IEEE international conference on robots and automation, Kobe, Japan, 12–17 May 2009*, pp 2300–2305

3. Yang G, Lin W, Mustafa SK et al (2005) Kinematic design of a 7-DOF cable-driven humanoid arm: a solution-in nature approach. In: Proceedings of IEEE international conference on advanced intelligent mechatronics, California, USA, 24–28 July 2005, pp 444–449
4. Chunping SUI, Mingyang ZHAO (2006) Statics and stiffness study on a 3-DOF parallel wire driven flexible manipulator. *Chin J Mech Eng* 42(6):205–210
5. Stump E, Kumar RV (2004) Workspace delineation of cable-actuated parallel manipulators. In: Proceedings of ASME international design engineering technical conference, Salt Lake City, USA, Sept 2004, pp 1303–1310
6. Weihai C, Yangyi Y, Xingming W et al (2011) Tension restrained workspace analysis for cable-driven parallel robot. *J Beijing Univ Aeron Astronaut* 37(7):817–821
7. Khajepour A, Hassan M (2011) Analysis of bounded cable tensions in cable-actuated parallel manipulators. *IEEE Trans Rob* 27(5):891–900
8. Lim WB, Yeo SH, Yang G et al (2013) Design and analysis of a cable-driven manipulator with variable stiffness. In: Proceedings of IEEE international conference on robotics and automation, Karlsruhe, Germany, 6–10 May 2013, pp 4519–4524
9. Lim W, Yeo S, Yang G (2014) Optimization of tension distribution for cable-driven manipulators using tension-level index. *IEEE/ASME Trans Mechatron* 19(2):676–683
10. Yang K, Yang G, Wang J et al (2015) Design analysis of a 3-DOF cable-driven variable-stiffness joint module. In: Proceedings of IEEE international conference on robotics and biomimetics, Zhuhai, China, 6–9 Dec 2015, pp 529–534
11. Murray RM, Li Z, Sastry SS (1994) A mathematical introduction to robotic manipulation. CRC Press, Boca Raton
12. Alici G, Shirinzadeh B (2005) Enhanced stiffness modeling, identification and characterization for robot manipulators. *IEEE Trans Rob* 21(4):554–564
13. Ceccarelli M, Carbone G (2002) A stiffness analysis for CaPaMan (CassinoParallel Manipulator). *Mech Mach Theory* 37(5):427–439
14. Perreault EJ, Kirsch RF, Crago PE (2004) Multijoint dynamics and postural stability of the human arm. *Exp Brain Res* 157(4):507–517
15. Pisano F, Miscio G, Del Conte C et al (2000) Quantitative measures of spasticity in post-stroke patients. *Clin Neurophysiol* 111(6):1015–1022
16. Rijnveld N, Krebs HI (2007) Passive wrist joint impedance in flexion-extension and abduction-adduction. In: Proceeding IEEE international conference on rehabilitation robotics, Noordwijk, The Netherlands, pp 43–47
17. do Carmo MP (1992) Riemannian geometry. Birkhauser, Boston

Part VII
Joint Clearance

Elastodynamics of a Rigid-Flexible 3-RRR Mechanism with Joint Clearances

Xuchong Zhang and Xianmin Zhang

Abstract The purpose of this paper is to analyze the elastodynamics of a rigid-flexible planar 3-RRR parallel mechanism with multiply joint clearances. In order to reduce the global system coordinates, the nature coordinate is used to model the rigid link, while the absolute nodal coordinate formulation is employed to model the flexure link. Full description of the revolute joint with clearance is given, a continuous dissipative Hertz contact model is applied to describe the contact phenomenon in the joint. Two-step Bathe integration method is utilized to solve the nonlinear system motion equations. Detailed comparisons are made among the systems under different situations. Results demonstrate that the methodology can represent the dynamic performances of the system with link flexibility and joint clearance well.

Keywords Elastodynamics · Joint clearance · 3-RRR mechanism · Contact model

1 Introduction

Joint clearances are unavoidable due to manufacturing tolerances, assembling, wear and material deformation [1], Link flexibility also plays an important role in the dynamic performances of the mechanical system. The joint clearances and link flexibility can cause vibration and noise, decreasing the service life or even leading to failure of the mechanism [2]. Due to the increasing requirements for high

X. Zhang (✉)
School of Design, South China University of Technology,
Guangzhou 510006, China
e-mail: sdxczhang@scut.edu.cn

X. Zhang
Guangdong Provincial Key Laboratory of Precision Equipment
and Manufacturing Technology, South China University of Technology,
Guangzhou 510640, China
e-mail: zhangxm@scut.edu.cn

precision and high speed of the mechanism, it is necessary to establish a methodology to model the multibody system with both joint clearances and link flexibility.

The subject of modeling the real joints with clearance has drawn the attentions of a large amount of researchers over the last few decades, which can be mainly divided into three categories: kinematical analysis [3, 4], dynamic analysis and experimental studies. In the area of dynamic analysis of mechanisms with joint clearances, Dubowsky and Freudenstein [5] are the pioneers. They firstly proposed a mathematical model of an elastic mechanical joint with clearance and derived the dynamical equations of motion. The most representative works in this topic is done by Ravn [6] and Flores [7–10]. They developed a continuous analysis approach for rigid multibody system with joint clearance, which is easy to integrate the contact force model into the system motion equations. This methodology allows not only to get the overall dynamic performance of the multibody system, but also to provide detailed characteristics the joint with clearance. Zhao [11] proposed a numerical approach for the modeling and prediction of wear at revolute clearance joints in flexible multibody systems by integrating the procedures of wear prediction with multibody dynamics. Realized that the revolute joint with clearance is always simplified into two parts, which cannot represent the realistic case well, Xu [12] gave a full description of the deep-groove ball bearing with clearance in a rigid planar slider-crank mechanism.

It is noticeable that, very few researchers study the mechanism with more than one degree of freedom. The 3-RRR parallel mechanism is widely used in industry applications and laboratory researches for its high moving velocity and wide range of motion [13, 14], but none of the researches has taken the joint clearances along with link flexibility into consideration in such mechanism. The main purpose of this paper is to establish a general computational methodology for analyzing the planar rigid-flexible multibody system with multiply joint clearances.

The Absolute Nodal Coordinate Formulation (ANCF) is implemented to describe the deformation of the flexible link [15]. The deformation modes of the flexure multibody system with joint clearance are associated with high frequencies, in which the explicit integration methods can be very inefficient or even fail [16]. For such a stiff system, implicit integration methods are much more efficient than explicit methods. The most popular implicit integrators are the generalized- α method, Newmark method and HHT method, but these methods may become unstable for long time simulation. To overcome this limitation, Bathe [17] proposed a two-step implicit time integration method for the large deformation system with long time durations.

This paper is organized as follows: In Sect. 2, the planar rigid and flexible beams are briefly introduced. In Sect. 3, a 3-RRR planar parallel mechanism with rigid-flexible links and multiply clearance joints is modeled. In Sect. 4, full description of the joint clearance is presented, in which the contact force model with

damping is incorporated. In Sect. 5, the computational strategy for the solution of the system motion equations is described. After that, simulation results are obtained and discussed. Finally, the main conclusions are drawn.

2 Planar Rigid and Flexible Beam Element

This section will present the model of rigid and flexible beams, as shown in Fig. 1.

2.1 Rigid Beam

For the rigid beam, the coordinates of the link is described using Natural Coordinates (NC) [18], see Fig. 1a. The coordinates of the link in global coordinate system are defined as

$$\mathbf{q} = [\mathbf{r}_i, \mathbf{r}_j]^T = [x_i, y_i, x_j, y_j]^T \tag{1}$$

There exists the following constraint equation

$$\Phi = (x_i - x_j)^2 + (y_i - y_j)^2 - l^2 = 0 \tag{2}$$

The location of generic point along the central axis of the link is

$$\mathbf{r} = \begin{bmatrix} X \\ Y \end{bmatrix} = \begin{bmatrix} x_i + (x_j - x_i)x/l \\ y_i + (y_j - y_i)x/l \end{bmatrix} = \mathbf{S}_r \mathbf{q} \tag{3}$$

where X and Y denote the position coordinates defined in the global coordinate system, x denotes the nodal coordinate along the beam central line, l denotes the element length. S_r is the shape function

$$\mathbf{S}_r = \begin{bmatrix} 1 - x/l & 0 & x/l & 0 \\ 0 & 1 - x/l & 0 & x/l \end{bmatrix} \tag{4}$$

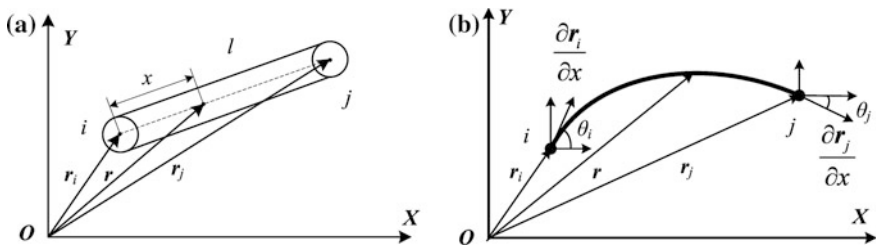


Fig. 1 Planar beam element. **a** Rigid beam based on NC; **b** Flexible beam based on ANCF

The mass matrix of the rigid beam can be obtained by using the principle of virtual work [18]. It is expressed as

$$\mathbf{M}_r^e = \rho \int_V \mathbf{S}_r^T \mathbf{S}_r dV \tag{5}$$

in which ρ is the density and V is the volume of the beam.

2.2 Flexible Beam

The planar ANCF-based deformable beam element is described by two nodes [15], as shown in Fig. 1b. The coordinates of an arbitrary point along the central axis of the beam can be defined by the third-order polynomials in the global coordinates, that is

$$\mathbf{r} = \begin{bmatrix} X \\ Y \end{bmatrix} = \begin{bmatrix} a_0 + a_1x + a_2x^2 + a_3x^3 \\ b_0 + b_1x + b_2x^2 + b_3x^3 \end{bmatrix} = \mathbf{S}\mathbf{q} \tag{6}$$

where X and Y denote the position coordinates defined in the global coordinate system, x denotes the nodal coordinate along the beam central line. \mathbf{S} is the shape function. The absolute nodal coordinate \mathbf{q} for node i and j can be expressed as

$$\mathbf{q} = \left[r_{i1}, r_{i2}, \frac{\partial r_{i1}}{\partial x}, \frac{\partial r_{i2}}{\partial x}, r_{j1}, r_{j2}, \frac{\partial r_{j1}}{\partial x}, \frac{\partial r_{j2}}{\partial x} \right]^T \tag{7}$$

The vector $\mathbf{r}_m = [r_{m1}, r_{m2}]^T (m = i, j)$ indicates the position coordinates defined in the global coordinate system, the angle θ_m indicates the beam cross section orientation, which can be expressed by the vector $\frac{\partial \mathbf{r}_m}{\partial x} = \left[\frac{\partial r_{m1}}{\partial x}, \frac{\partial r_{m2}}{\partial x} \right]^T$. According to the conventional finite element method, the element shape function can be obtained by

$$\mathbf{S} = [S_1 \mathbf{I}_2 S_2 \mathbf{I}_2 S_3 \mathbf{I}_2 S_4 \mathbf{I}_2] \tag{8}$$

where \mathbf{I}_2 is the identity matrix of size two and $S_1 = 1 - 3\xi^2 + 2\xi^3$, $S_2 = l(\xi - 2\xi^2 + \xi^3)$, $S_3 = 3\xi^2 - 2\xi^3$, $S_4 = l(-\xi^2 + \xi^3)$, in which $\xi = x/l$.

By using the Newton-Euler formulation [15], the element equations of motion are as follows

$$\mathbf{M}^e \ddot{\mathbf{q}} + \mathbf{F}^e = \mathbf{Q}^e \tag{9}$$

where \mathbf{Q}^e represents the element generalized force vector, \mathbf{M}^e denotes the element constant mass matrix

$$\mathbf{M}^e = \int_V \rho \mathbf{S}^T \mathbf{S} dV \tag{10}$$

ρ is density and V is the volume. \mathbf{F}^e denotes the element elastic force vector, which is expressed as [15]

$$\begin{aligned} \mathbf{F}^e &= \left(\frac{\partial U_l}{\partial \mathbf{q}}\right)^T + \left(\frac{\partial U_t}{\partial \mathbf{q}}\right)^T = \int_0^l EA \varepsilon \mathbf{S}_l \mathbf{q} dx + \int_0^l EIS''^T \mathbf{S}'' \mathbf{q} dx \\ &= \left(\int_0^l EA \varepsilon \mathbf{S}_l dx\right) \mathbf{q} + \left(\int_0^l EIS''^T \mathbf{S}'' dx\right) \mathbf{q} = \mathbf{K}_t \mathbf{q} + \mathbf{K}_s \mathbf{q} \end{aligned} \tag{11}$$

where

$$\begin{aligned} \mathbf{K}_t &= \int_0^l EA \varepsilon \mathbf{S}_l dx = EA \int_0^l \frac{1}{2} (\mathbf{q}^T \mathbf{S}_l \mathbf{q} - 1) \mathbf{S}_l dx \\ &= \frac{1}{2} EA \int_0^l \mathbf{S}_l \mathbf{q} \mathbf{q}^T \mathbf{S}_l dx - \frac{1}{2} EA \int_0^l \mathbf{S}_l dx = \mathbf{K}_{t1} + \mathbf{K}_{t2} \end{aligned} \tag{12}$$

To improve the computation efficiency, Garcia-Vallejo [19] firstly proposed an invariant matrix method to calculate the elastic force and the tangent matrix of the elastic force. Based on the following matrix transformation

$$(\mathbf{S}_l \mathbf{q} \mathbf{q}^T \mathbf{S}_l)_{ij} = \mathbf{q}^T (\mathbf{S}_l)_{,i} (\mathbf{S}_l)_{,j} \mathbf{q} \tag{13}$$

The element of \mathbf{K}_{t1} can be expressed as

$$(\mathbf{K}_{t1})_{ij} = \mathbf{q}^T \left(\frac{1}{2} EA \int_0^l (\mathbf{S}_l)_{,i} (\mathbf{S}_l)_{,j} dx \right) \mathbf{q} = \mathbf{q}^T \mathbf{C}_{t1}^{ij} \mathbf{q} \tag{14}$$

where \mathbf{C}_{t1}^{ij} is called the constant matrix of \mathbf{K}_{t1} .

When solving the motion equations of the multibody system in an interactive way, that is, in an implicit way, the derivation of the elastic force respect to generalized coordinates will be used. It can be expressed as [19]

$$\left(\frac{\partial \mathbf{F}^e}{\partial \mathbf{q}}\right)_{ij} = \frac{\partial (\mathbf{F}^e)_i}{\partial \mathbf{q}_j} = (\mathbf{K}_t + \mathbf{K}_{t2} + \mathbf{K}_{t1})_{ij} + \sum_k^8 \sum_s^8 \mathbf{q}_s \left(\mathbf{C}_{t1}^{ik} + (\mathbf{C}_{t1}^{ik})^T \right)_{sj} \mathbf{q}_k \tag{15}$$

which will be the most time consuming part in simulation.

3 Modeling of the 3-RRR Mechanism

This section will describe the configuration and motion equations of a planar 3-RRR parallel mechanism. The mechanism is a symmetry structure which is composed by the fixed platform $A_1A_2A_3$, the moving platform $C_1C_2C_3$, three driving links A_iB_i ($i = 1-3$) and three passive links B_iC_i . Joints A_1, A_2 and A_3 are actuators, the backlash of the motor and reducer are not considered in the analysis. Joint B_1, B_2, B_3 and C_1, C_2, C_3 are revolute joints with clearance, as is shown in Fig. 2.

The global coordinate system XOY is fixed at the center of the fixed platform. All the driving links are treated as rigid, and all the passive links are treated as flexible. Each rigid link is described by one NC beam element, while each flexible link is described by one ANCF beam element. The combination use of these two coordinates can share the same coordinates and lower the global coordinates of the system. Particularly, the moving platform is treated as rigid, and described by the reference point coordinates $[x_o, y_o, \theta_o]$. Thus there are totally 27 generalized coordinates in the system. 24 coordinates to describe the flexible links and 3 coordinates to describe the moving platform, as labeled in the Fig. 2b.

3.1 Without Joint Clearance

Let l_1 and l_2 denote the length of active link AB and passive link BC , while let l_3 and l_4 denote the radius of the circumscribed circle of the moving and fixed platform. The constraint equations introduced by the rigid links and revolute joints are expressed as, take the first chain $A_1B_1C_1$ as an example,

$$\Phi_{q,1} = \begin{bmatrix} (q_1 - x_{A1})^2 + (q_2 - y_{A1})^2 - l_1^2 \\ x_o + l_3 \cos(\theta + 7\pi/6) - q_5 \\ y_o + l_3 \sin(\theta + 7\pi/6) - q_6 \end{bmatrix} = \mathbf{0} \tag{16}$$

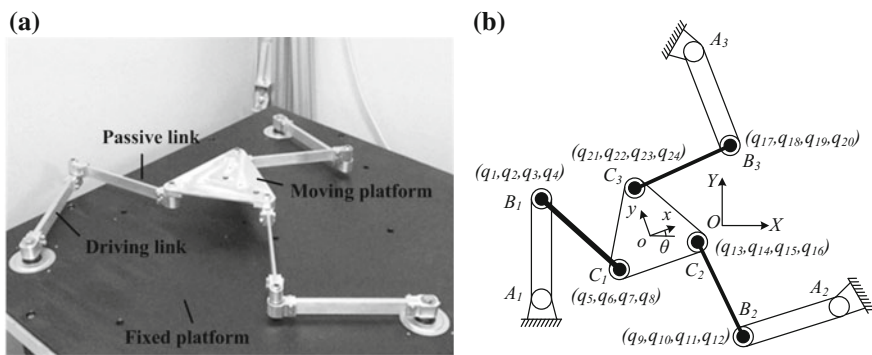


Fig. 2 Geometry and global coordinates of the 3-RRR mechanism. a Geometry structure; b Global coordinates

In the simulation, the expected motion of the moving platform is given, the input angles can be easily obtained by the inverse kinematics of the ideal rigid mechanism. The goal is to calculate the real motions of the moving platform considering link flexibility and joint clearance. The dynamic equations of the system are needed.

Based on the ANCF, the assembly of the elements can be carried out by the conventional finite element method. The element nodal can be easily transformed into the flexible multibody system generalized coordinates. Without considering the damping of the system, the Newton-Euler equations for the rigid-flexible multibody system in Cartesian coordinates can be written as

$$M\ddot{q} + \Phi_q^T \lambda + F_e = F \quad (17)$$

where M is the system mass matrix, λ is the Lagrange multiplier, F_e denotes the system elastic force vector, F is the external force vector.

3.2 With Joint Clearances

When considering the joint clearances, the constraints in the clearance joints are lost. Moreover, in the simulation, the inputs are given, so the position of joint B in driving link can be easily obtained, there is no need to form the constraint equations. The motion equations of the system with joint clearances are written as

$$M\ddot{q} + F_e = F_d + F_c \quad (18)$$

where F_d is the driving force vector, F_c is the contact force vector which is introduced by the clearance joints. The key procedure is to describe the contact forces, which will be presented in the following section.

4 Modeling of the Clearance Joint

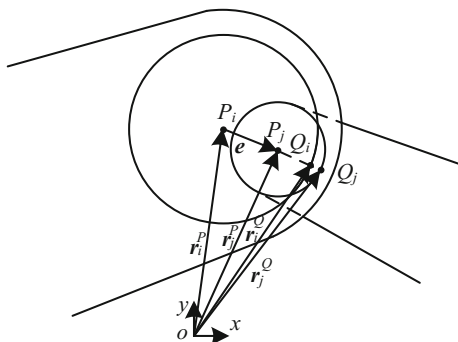
4.1 Geometry Description

In order to bring the contact forces of the clearance joints into the system motion equations, it is necessary to develop the joint clearance model. Figure 3 shows a typical revolute clearance joint.

The center of bearing and journal are marked as P_i and P_j , the eccentricity vector which connects P_i and P_j is calculated by

$$e = r_j^P - r_i^P \quad (19)$$

Fig. 3 Geometry of the revolute joint with clearance



The unit vector of the eccentricity vector can be written as

$$n = e/e \tag{20}$$

in which e is the magnitude of eccentricity vector, $e = \sqrt{e^T e}$. The clearance size is

$$\delta = e - c \tag{21}$$

where c is the radial clearance $c = R_i - R_j$. Negative of δ means that there is no contact between the journal and the bearing. Thus the detection of the instant of contact is when the sign of penetration changes between the two discrete moments in time, and such accurate moment can be found by using the Newton-Raphson method.

The contact points are denoted as Q_i and Q_j , their global coordinates and velocities are evaluated as

$$\begin{cases} r_k^Q = r_k^P + R_k n \\ \dot{r}_k^Q = \dot{r}_k^P + R_k \dot{n} \end{cases} \tag{22}$$

where $k = i, j$. The relative velocity is projected onto the plane of collision and onto the normal plane of collision, obtaining a relative tangential velocity v_t and a relative normal velocity v_n .

$$\begin{cases} v_n = (\dot{r}_j^Q - \dot{r}_i^Q)^T n \\ v_t = (\dot{r}_j^Q - \dot{r}_i^Q)^T t \end{cases} \tag{23}$$

4.2 Contact Force Models

Knowing the penetration depth and relative velocity, the normal and tangential forces F_n and F_t are obtained. Lankarani-Nikravesh contact force model is largely

used for mechanical contacts owing to its simplicity and easiness in implementation in a computational program, and also because this model accounts for the energy dissipation during the impact process [20]. The expression of the model is

$$F_n = K\delta^n \left(1 + \frac{3(1 - c_e^2)}{4} \frac{\dot{\delta}}{\dot{\delta}^{(-)}} \right) \tag{24}$$

where the generalized stiffness K can be evaluated by

$$K = \frac{4}{3(\delta_i + \delta_j)} \left(\frac{R_i R_j}{R_i - R_j} \right)^{\frac{1}{2}} \tag{25}$$

in which $\delta_k = (1 - \nu_k^2)/E_k$ ($k = i, j$), ν_i, E_i, R_i and ν_j, E_j, R_j are the Poisson’s ratio, the Yong’s modulus and radii of the journal and bearing respectively. $\dot{\delta}$ is the relative penetration velocity and $\dot{\delta}^{(-)}$ is the initial impact velocity. c_e is the restitution coefficient, the exponent n is set to 1.5 for metallic surfaces.

The modified Coulomb’s friction law presented by Ambrósio [21] is used here, which is given by

$$F_t = \begin{cases} 0 & \text{if } v_t \leq v_0 \\ -c_f \frac{v_t - v_0}{v_1 - v_0} F_n & \text{if } v_0 \leq v_t \leq v_1 \\ -c_f F_n & \text{if } v_t \geq v_1 \end{cases} \tag{26}$$

where c_f is the coefficient of friction, v_0 and v_1 is the given tolerance for the velocity. Using the NC and ANCF method, there is no need to transform these forces into the center of the mass of each body.

5 Solving the Equations of Motion

The process of the integration of the Differential Algebraic Equations (DAEs) of motion for a flexible multibody system with joint clearance is different from that of ideal rigid body system. The high frequency responses are stimulated both by the continuous high frequency contact forces and by the finite element discretization. The Bathe integration method [17] is a composite scheme which calculates the unknown displacements, velocity and accelerations by dividing the time step h into two equal sub-steps $h/2$. For the first sub-step, the well-known trapezoidal rule is used, while for the second sub-step, the three-point Euler backward formula is used. The Newton interaction approach is used to solve the nonlinear equations in each sub-step. The interested readers can refer to Ref. [17] for details. The whole computational scheme can be illustrated in a flowchart shown in Fig. 4.

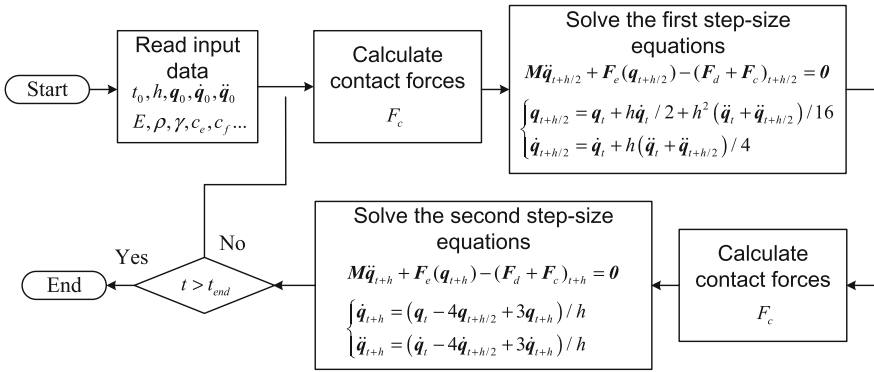


Fig. 4 Flowchart of the computational scheme

6 Results and Discussions

The geometric parameters of the 3-RRR mechanism are listed in Table 1, the material of all the parts are Aluminum. In the simulation, the preset trajectory of the moving platform is a circle with radius 0.1 m

$$\begin{cases} q_{25} = 0.1 \cos(2\pi t) \text{ m} \\ q_{26} = 0.1 \sin(2\pi t) \text{ m} \\ q_{27} = 0 \text{ rad} \end{cases} \quad (27)$$

At the start of the simulation, $t = 0$ s, the journal and bearing centers are defined coincident. The initial positions and velocities necessary to start the dynamic analysis are obtained from the kinematic simulation of the 3-RRR mechanism without considering link flexibility and joint clearance.

Four simulations are carried out to make comparisons, as are shown in Table 2. That is, Case 1: Rigid passive links without joint clearance; Case 2: Flexible passive links without joint clearance; Case 3: Rigid passive links with joint clearance; Case 4: Flexible passive links with joint clearance. In the simulations, the joint clearance size is taken to be 0.02 mm, which is a normal clearance size in a typical bearing with nominal dimensions. For flexible beams, the Young’s module of the passive links is set to be 7 GPa for Aluminum. Figures 5, 6, 7, 8 and 9 illustrates the simulation results of the system which are taken for two full cycles after the system steady running.

Table 1 Geometry parameters of the 3-RRR mechanism

Member	Driving link	Passive link	Moving stage	Fixed stage
Length (m)	0.245	0.242	0.112	0.4
Width (m)	0.015	0.005	–	–
Height (m)	0.03	0.03	0.01	–

Table 2 Parameters for different cases

Case	1	2	3	4
Clearance size (mm)	None	None	0.02	0.02
Young's modulus of passive links (Pa)	Rigid	7e9	Rigid	7e9

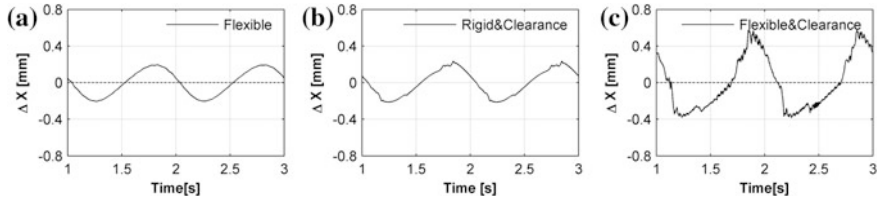


Fig. 5 Displacement errors of the moving platform along axis-x. **a** Case 2; **b** Case 3; **c** Case 4

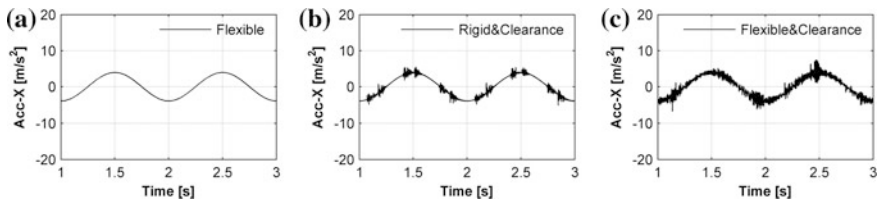


Fig. 6 Moving accelerations of the moving platform along axis-x. **a** Case 2; **b** Case 3; **c** Case 4

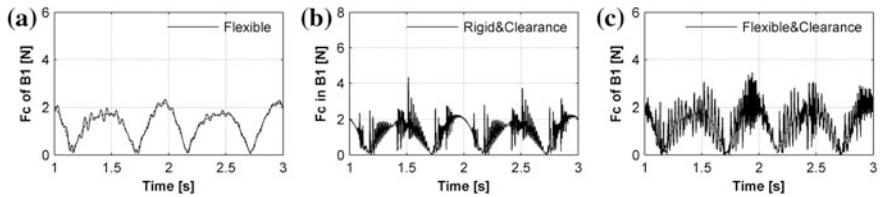


Fig. 7 Contact forces of clearance joint B1. **a** Case 2; **b** Case 3; **c** Case 4

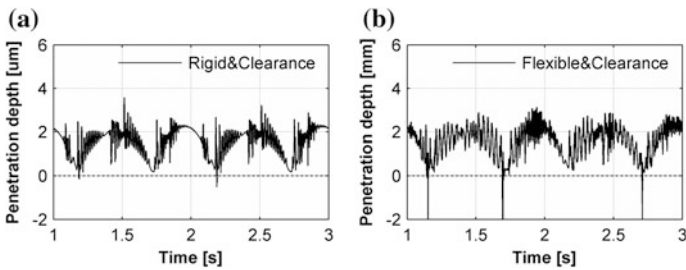


Fig. 8 Penetration depths of clearance joint B1. **a** Case 3; **b** Case 4

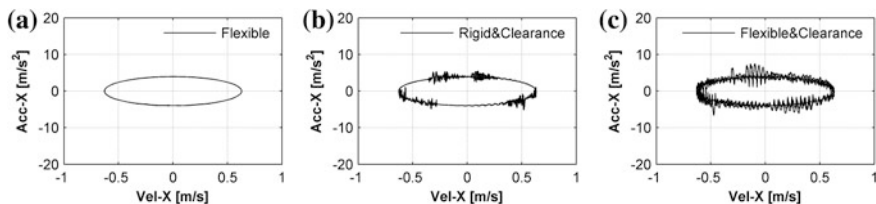


Fig. 9 Poincare maps for different cases. **a** Case 2; **b** Case 3; **c** Case 4

Figure 5 shows the displacement errors of the moving platform along axis-x direction in different cases. In Fig. 5a for Case 2, the positioning error of the platform along axis-x is around ± 0.2 mm, these values are caused by the deformation of the passive link, and they are influenced by the stiffness of the flexible links. In Fig. 5b for Case 3, the errors are around ± 0.2 mm, and these values will be influenced by the clearance size of the joints. In Fig. 5c for Case 4, it has the largest deviation and can be seen as the composition of Case 2 and Case 3. It indicates that both the flexure of the link and the joint clearance are the important influence factors of positioning accuracy.

In Fig. 6, the accelerations of the moving platform along axis-x for different cases are plotted, which show that these accelerations are very different with their ideal values. In Fig. 6a for Case 2, the acceleration is slightly vibrated when the link flexibility is taken into consideration. In Fig. 6b for system with joint clearances, the acceleration curve presents high frequency vibrations, which is caused by the impact of journal and bearing in clearance joints, and these vibrations will make the system unstable and difficult to control. Moreover, the vibration amplitude get larger and the frequency get higher when both link flexibility and joint clearances are taken into consideration, which can be observed in Fig. 6c.

The same phenomena can also be observed in the curves of the contact forces represented in Fig. 7. It is certain that the high peaks of acceleration curve and the contact force curve occur at the same time. The enlarged contact forces will decrease the service life of the components, or even lead to failure of the mechanism.

The penetration depths of the clearance joint are plotted in Fig. 8. The positive value means the journal and bearing contact with each other, while the passive value means they separate with each other. It shows that for most of the time, the joint components keep contact.

The Poincare map is often used to highlight the nonlinear behavior of systems. The acceleration-x and velocity-x of moving stage are chosen to plot the Poincare map. In Fig. 9a, periodic motion is presented in flexible system. Figure 9b, c shows a non-periodic motion of the moving stage, since the curve does not repeat from cycle to cycle. It indicates that the collision between the joint components will cause chaotic motion of the multibody system.

7 Conclusions

In this paper, the dynamic analysis of a planar 3-RRR parallel mechanism is presented. Both the joint and the link flexibility are taken into consideration. The rigid driving links are molded using NC while the flexure passive links are molded using ANCF, in order to lower the global system coordinates. The continuous dissipative contact force model is employed to describe the contact phenomenon in joint clearance. Comparisons are made between the systems with and without joint clearances.

Simulation results show that the positioning accuracy of the moving platform are apparently affected by both the joint clearance and link flexibility. When the joint clearances are considered, the system performs high frequency responses, and the enlarged contact forces can decrease the service life of the mechanism. It also shows that the joint components keep contact with each other for most of the time. On the other side, the mechanism is influenced by the link flexibility in a smoother way. The 3-RRR mechanism with the flexible links is a periodical system, but it becomes non-periodical when the joint clearances are taken into consideration, as the joint clearance and link flexibility interact with each other in a nonlinear way. The future work shall focus on the control of such a complex system.

Acknowledgments This research was supported by the Natural Science Foundation of Guangdong Province (Grant no. 2016A030310420), the National Natural Science Foundation of China (Grant nos. U1501247), and the Scientific and Technological Research Project of Guangdong Province (2015B020239001). These supports are greatly acknowledged.

References

1. Flores P (2004) Dynamic analysis of mechanical systems with imperfect kinematic joints. PhD Thesis, University of Minho, Guimaraes, Portugal
2. Tian Q, Sun Y, Liu C (2013) Elastohydrodynamic lubricated cylindrical joints for rigid-flexible multibody dynamics. *Comput Struct* 114:106–120
3. Parenti-Castelli V, Venazi S (2005) Clearance influence analysis on mechanisms. *Mech Mach Theory* 40:1316–1329
4. Erkaya S, Uzmay I (2009) Determining link parameters using genetic algorithm in mechanisms with joint clearance. *Mech Mach Theory* 44:222–234
5. Dubowsky S, Freudenstein F (1971) Dynamic analysis of mechanical systems with clearances Part I: formation of dynamic model. *Trans ASME J Eng Ind* 93:305–309
6. Ravn P (1998) A continuous analysis method for planar multibody systems with joint clearance. *Multibody SysDyn* 2:1–24
7. Flores P (2010) A parametric study on the dynamic response of planar multibody systems with multiple clearance joints. *Nonlinear Dyn* 61:633–653
8. Flores P (2009) Modeling and simulation of wear in revolute clearance joints in multibody systems. *Mech Mach Theory* 44:1211–1222
9. Flores P, Ambrosio J, Claro JCP (2006) A study on dynamics of mechanical systems including joints with clearance and lubrication. *Mech Mach Theory* 41:247–261

10. Flores P, Koshy CS, Lankarani HM (2011) Numerical and experimental investigation on multibody systems with revolute clearance joints. *Nonlinear Dyn* 65:383–398
11. Zhao B, Zhang ZN, Dai XD (2013) Modeling and prediction of wear at revolute clearance joints in flexible multibody systems. *Proc Inst Mech Eng Part C: J Mech Eng Sci* 4:1–13
12. Xu LX, Yang YH, Li YG, Li CN, Wang SY (2012) Modeling and analysis of planar multibody systems containing deep groove ball bearing with clearance. *Mech Mach Theory* 56:69–88
13. Zhang XC, Zhang XM, Chen Z (2014) Dynamic analysis of a 3-RRR parallel mechanism with multiple clearance joints. *Mech Mach Theory* 78:105–115
14. Zhang XC, Zhang XM (2016) A comparative study of 3-RRR and 4-RRR mechanisms with joint clearances. *Robot Comput-Int Manuf* 40:24–33
15. Shabana AA (2005) *Dynamics of multibody systems*, 3rd edn. Cambridge University Press, New York
16. Flores P, Machado M, Seabra E, Sliva MT (2011) A parametric study on the Baumgarte stabilization method for forward dynamics of constrained multibody systems. *Trans ASME, J Comput Nonlinear Dyn* 6(1):1–9
17. Bathe KJ (2007) Conserving energy and momentum in nonlinear dynamics: a simple implicit time integration scheme. *Comput Struct* 85:437–445
18. Garcia DJJ, Bayo E (1994) *Kinematic and dynamic simulation of multibody systems: the real-time challenge*. Springer, New York
19. Garcia-Vallejo D, Mayo J, Escalona JL, Dominguez J (2004) Efficient evaluation of the elastic forces and the Jacobian in the absolute nodal coordinate formulation. *Nonlinear Dyn* 35:313–329
20. Lankarani HM, Nikravesh PE (1994) Continuous contact force models for impact analysis in multibody systems. *Nonlinear Dyn* 5:193–207
21. Ambrósio JAC (2002) Impact of rigid and flexible multibody systems: deformation description and contact models. *Virtual Nonlinear Multibody Syst* 2:15–33

Accuracy Analysis of a 3-DOF Mechanism with Joint Clearances Under Different Working Modes

Xuchong Zhang and Xianmin Zhang

Abstract This paper presents an analytical investigation on the positioning accuracy of a planar 3DOF 3-RRR parallel mechanism with multiply joint clearances, in which eight working modes of the mechanism are included. The joint clearance is treated as a mass-less virtual link in the analysis. Assuming that the clearance size is much smaller than the geometric size of the mechanism, a simplified expression of the output errors is obtained by the kinematic analysis of the planar 3-RRR parallel mechanism. The error boundary for a given position of the mechanism and the maximum error distribution in the whole workspace is plotted out. The results show that the proposed method is an efficient way to predicate the positioning error of the 3-RRR mechanism with joint clearances under different working modes.

Keywords 3-RRR mechanism · Joint clearance · Accuracy analysis · Working modes

1 Introduction

Parallel robots are increasingly used for precision positioning, in which accuracy is of great importance in such application. The pose errors of a parallel mechanism are due to many factors [1–4]: manufacturing and assembling tolerances, flexibility of the links, input uncertainties and the clearances between the joint components. The manufacturing and assembly errors are considered predictable and can be compensated by calibration; the flexibility can be eliminated by adopting more rigid

X. Zhang (✉)

School of Design, South China University of Technology, Guangzhou 510006, China
e-mail: sdxczhang@scut.edu.cn

X. Zhang

Guangdong Provincial Key Laboratory of Precision Equipment and Manufacturing Technology, South China University of Technology, Guangzhou 510640, China
e-mail: zhangxm@scut.edu.cn

structures; the input uncertainties are determined by the actuators; while the influence of joint clearances are stochastic and unavoidable.

In this paper, we address the problem of computing the accuracy of a planar parallel mechanism in the presence of joint clearances. Several methods have been developed to evaluate the accuracy of serial and parallel mechanisms. Yu et al. [5] showed a simple geometric approach to compute the exact local maximum position and orientation error caused by actuator inaccuracies, this method only works for special planar parallel mechanisms. Briot and Bonev [6, 7] presented an interval analysis method which is based on a detailed error analysis of the parallel robots, in which the Hessian matrix is used. In these two studies, only the input error is taken into consideration.

For the purpose of predicting the influences of the joint clearance on the output errors, Innocenti [8] and Parenti-Castelli and Venanzi [9, 10] used the virtual work method to determine the position of the end-effector when a given external load is applied. After that, Venanzi and Parenti-Castelli [11–13] presented a general methodology for the computation of maximum position error in planar and spatial parallel manipulators both with revolute joints and prismatic pairs. Using the similar method, Chebbi et al. [14] analyzed the singularity of the mechanism and studied the effects of the joint clearances on the parallel robot accuracy, Altuzarra et al. [15] analyzed the location of the discontinuities in the workspace due to clearances in the parallel mechanisms. The virtual work method is efficient, but not applicable to overconstrained parallel manipulators. To overcome this, Meng et al. [16] proposed an error prediction model that is applicable to planar or spatial parallel manipulators that are either over constrained or non over constrained.

Other researchers' work are that, Tsai and Lai [17, 18] described a screw theory method for determining the transmission quality of closed-loop linkages, which is based on the static equilibrium of the linkage. Frisoli et al. [19] performed a method based on screw theory for the estimation of position accuracy in spatial parallel manipulators with revolute joint clearance, in which a 2-step procedure for the computation of the maximum pose error is defined. Jawale and Thorat [20] investigated the positional error in 5R mechanism with joint clearance, in which inverse kinematics and forward kinematics of the mechanism are performed. Voglewede and Uphoff [21] predicted the end-effectors displacement error for a 3-RRR and some special parallel mechanisms with joint clearance. In the above studies, the effects of input uncertainties and joint clearances are not taken into consideration at the same time. Based on the theory of envelope, Chen et al. [22] presented a unified approach to predict the accuracy performance of the general planar parallel manipulators both due to the input uncertainties and joint clearances, however, without experimental verification. In the aspect of the experimental studies of the positioning accuracy, Wu et al. [23] performed experiments to validate the error model of a planar 3-PPR parallel manipulator with joint clearances and configuration errors.

This paper is dedicated to present a simple method to calculate the positioning errors of the 3-RRR planar mechanism in the presence of joint clearances under different working modes. This paper is organized as follows. The 3-RRR mechanism without joint clearances is presented and modeled in Sect. 2. The joint clearance is modeled in Sect. 3. The error prediction model is established in Sect. 4. The simulation results are obtained and discussed in Sect. 5. The conclusions are made in Sect. 6.

2 Kinematic Model of the 3-RRR Mechanism Without Joint Clearances

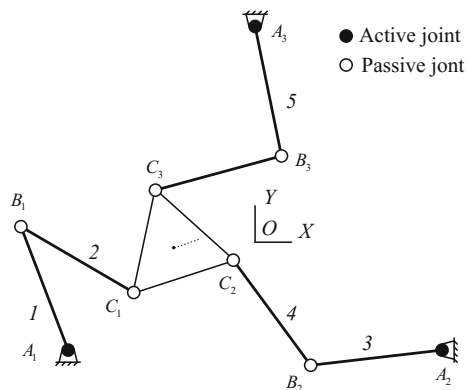
In this section, the kinematic model of the mechanism without joint clearance is established. Figure 1 shows the configuration of the 3-RRR parallel mechanism [24, 25], it is a symmetrical structure which is represented by the base platform $A_1A_2A_3$, the driving link A_iB_i , the passive link B_iC_i and the moving platform $C_1C_2C_3$. In this paper, only the clearance existing at the passive revolute joints $B_1B_2B_3$ and $C_1C_2C_3$ are considered, while the inputs are treated as ideal. The global coordinate system are defined in the figure, the pose of the moving platform are defined as $[x_o, y_o, \theta_o]$, in which x_o and y_o is the position of the mass center of moving platform, and θ_o is the rotational angle of the moving platform.

The kinematic constraint equations of the mechanism are

$$\begin{cases} l_{2i-1} \cos \theta_{2i-1} + l_{2i} \cos \theta_{2i} = x_o + l_o \cos(\theta_o + \pi/6 + 2\pi i/3) - x_{Ai} \equiv m_i \\ l_{2i-1} \sin \theta_{2i-1} + l_{2i} \sin \theta_{2i} = y_o + l_o \sin(\theta_o + \pi/6 + 2\pi i/3) - y_{Ai} \equiv n_i \end{cases} \quad (1)$$

in which $i = 1-3$. For the inverse kinematics of the mechanism, the given parameters are outputs $[x_o, y_o, \theta_o]$, the inputs are to be solved. Eliminating θ_{2i} , one can obtain

Fig. 1 Kinematic model of the 3-RRR mechanism



$$(m_i - l_{2i-1} \cos \theta_{2i-1})^2 + (n_i - l_{2i-1} \sin \theta_{2i-1})^2 = l_{2i}^2 \tag{2}$$

This equation can be rewritten in the form

$$m_i \cos \theta_{2i-1} + n_i \sin \theta_{2i-1} = (l_{2i}^2 - l_{2i-1}^2 + m_i^2 + n_i^2) / 2l_{2i-1} \equiv p_i \tag{3}$$

Using the tangent half-angle formulation

$$\cos \theta = \frac{1 - \tan^2(\theta/2)}{1 + \tan^2(\theta/2)}, \quad \sin \theta = \frac{2 \tan(\theta/2)}{1 + \tan^2(\theta/2)} \tag{4}$$

The input angles can be solved

$$\theta_{2i-1} = 2 \tan^{-1} \left(\frac{n_i \pm \sqrt{m_i^2 + n_i^2 - p_i^2}}{m_i + p_i} \right) \tag{5}$$

There are two solutions for each chain, corresponding that $A_i B_i$ is lay on the left (marked as +) or right (marked as -) hand of the line $A_i C_i$. The passive link angle θ_{i2} can be solved by substituting Eq. (5) into Eq. (1). There are totally eight working modes of the planar parallel 3-RRR mechanism, as shown in Fig. 2, named as (a) +++, (b) ++-, (c) +-+, (d) +--, (e) -++, (f) -+-, (g) -+-, (h) ---, respectively.

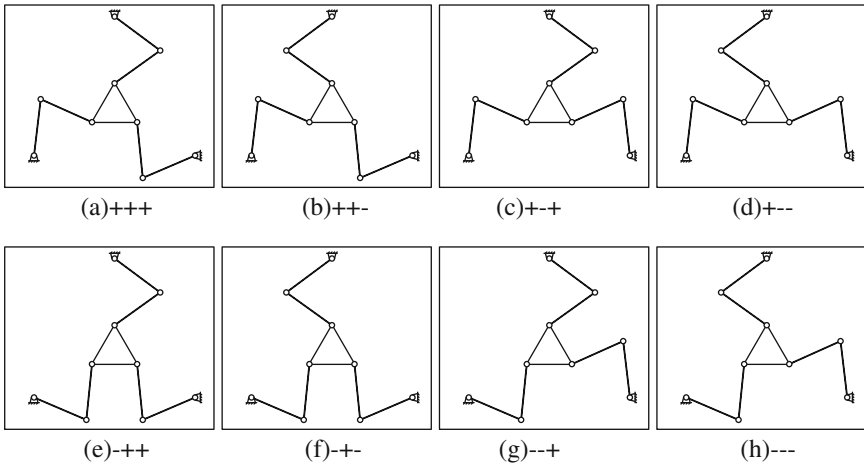


Fig. 2 Eight working modes of the 3-RRR mechanism

3 Joint Clearance Model

The joint clearance is treated as virtual link when modeling as shown in Fig. 3a. The bearing and journal are assumed to be ideal circle, with radius R_B and R_J respectively. The joint clearance size is calculated by

$$c = R_B - R_J \tag{6}$$

Considering the joint clearance, the journal can move freely within the bearing. The clearance can be described by two parameters, the length of the virtual link r and the contact angle α , and the boundary of their values are

$$r \in [0, c]; \quad \alpha \in [0, 2\pi) \tag{7}$$

When the joint clearance is equivalent as virtual link, the passive link of the 3-RRR mechanism BC is equivalent as $B'C'$, as shown in Fig. 3b. Thus

$$l_{2i} - (r_{2i-1} + r_{i2}) \leq l'_{2i} \leq l_{2i} + (r_{2i-1} + r_{i2}) \tag{8}$$

Which means that the joint clearance lead to the length error of passive link, expressed as

$$\Delta l_{i2} = l'_{i2} - l_{i2} \in [-(r_{i1} + r_{i2}), (r_{i1} + r_{i2})] \ll l_{i2} \tag{9}$$

It is notable that the joint clearance size is much small than the link length of the mechanism.

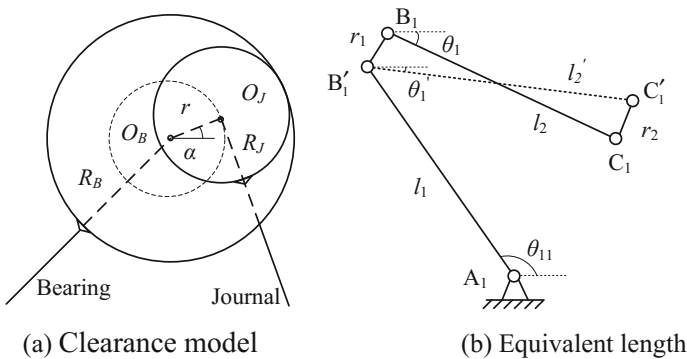


Fig. 3 Joint clearance models

4 Error Modeling of the 3-RRR Mechanism with Joint Clearances

In this paper, only the clearances in passive joints are considered, that is, the geometrical dimensions and inputs are ideal of the mechanism. The deviation of the kinematical constraint equations respect to is

$$\begin{cases} \Delta l_{2i} \cos \theta_{2i} - l_{2i} \sin \theta_{2i} \Delta \theta_{2i} = \Delta x_o - l_o \sin(\theta_o + \pi/6 + 2\pi i/3) \Delta \theta_o \\ \Delta l_{2i} \sin \theta_{2i} + l_{2i} \cos \theta_{2i} \Delta \theta_{2i} = \Delta y_o + l_o \cos(\theta_o + \pi/6 + 2\pi i/3) \Delta \theta_o \end{cases} \quad (10)$$

They can be written in the matrix form

$$\begin{bmatrix} 1 & 0 & l_o \sin(\theta_o + \theta_{13}) & -l_2 \sin \theta_2 & 0 & 0 \\ 0 & 1 & -l_o \cos(\theta_o + \theta_{13}) & l_2 \cos \theta_2 & 0 & 0 \\ 1 & 0 & l_o \sin(\theta_o + \theta_{23}) & 0 & -l_4 \sin \theta_4 & 0 \\ 0 & 1 & -l_o \cos(\theta_o + \theta_{23}) & 0 & l_4 \cos \theta_4 & 0 \\ 1 & 0 & l_o \sin(\theta_o + \theta_{33}) & 0 & 0 & -l_6 \sin \theta_6 \\ 0 & 1 & -l_o \cos(\theta_o + \theta_{33}) & 0 & 0 & l_6 \cos \theta_6 \end{bmatrix} \begin{bmatrix} \Delta x_o \\ \Delta y_o \\ \Delta \theta_o \\ \Delta \theta_2 \\ \Delta \theta_4 \\ \Delta \theta_6 \end{bmatrix} \\ = \begin{bmatrix} \cos \theta_2 & 0 & 0 \\ \sin \theta_2 & 0 & 0 \\ 0 & \cos \theta_4 & 0 \\ 0 & \sin \theta_4 & 0 \\ 0 & 0 & \cos \theta_6 \\ 0 & 0 & \sin \theta_6 \end{bmatrix} \begin{bmatrix} \Delta l_2 \\ \Delta l_4 \\ \Delta l_6 \end{bmatrix} \quad (11)$$

One can obtain the outputs error $[\Delta x_o, \Delta y_o, \Delta \theta_o]$ of the moving platform caused by the joint clearances by this equation. The left matrix of the equation is defined as transform matrix J .

5 Results and Discussions

Determinations of the transform matrix J in the whole workspace with $\theta_o = 0$ under different working modes are drawn in Fig. 4, these values are scaled to make them feasible to read. It can be observed that these eight working modes can be divided into two types, the first type is that all the directions of driving links are the same, including (a) +++ and (h) ---; the second type is that one of the directions of driving links is different from the other two links, including (b)–(g). Within the same working mode type, the distributions of the determinations of the transform matrix are similar, but with different signals and directions.

The first simulation is to know the error boundary of the moving platform with the influence of joint clearance. While considering maximum pose error in all set of combinations of joint clearance, all clearance virtual links are rotated from 0 to 2π

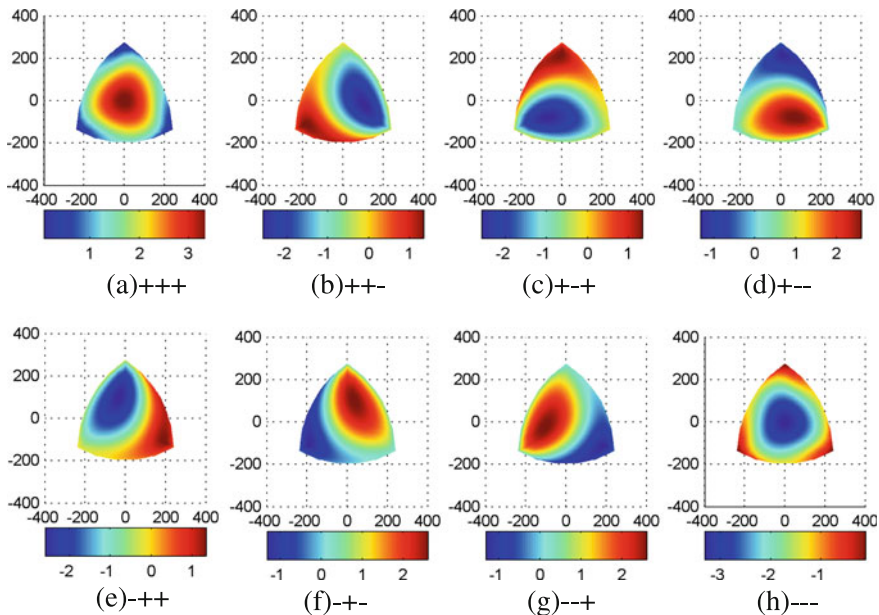


Fig. 4 Determinations of the transform matrix J under different working modes

rad independently, and the pose errors are calculated for each combination one by one.

The length of the active link is 245 mm, the length of the passive link is 242 mm, the radius of the moving platform is 120 mm and the radius of the fixed platform is 400 mm. The joint clearance size is set to be 0.01 mm for a typical journal-bearing with nominal dimensions. The expected configuration of the moving platform is [0 mm, 0 mm, 0 rad], the results are plotted in Figs. 5 and 6.

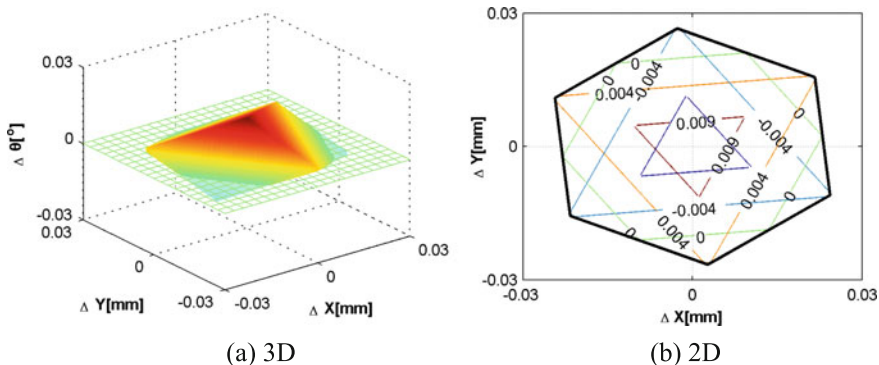


Fig. 5 Error boundary of the platform under working mode +++

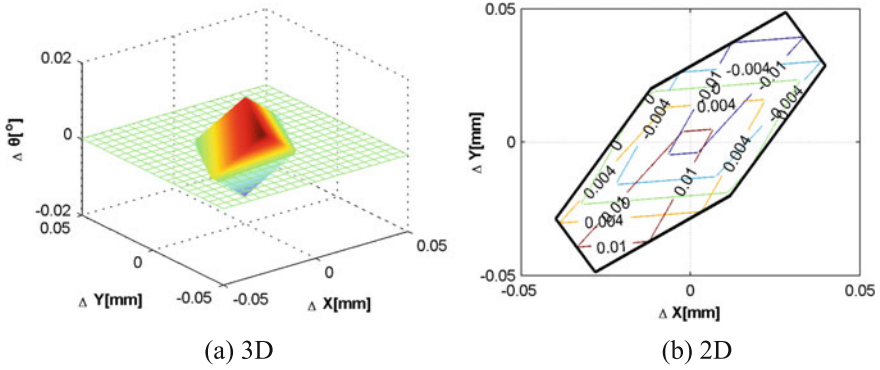


Fig. 6 Error boundary of the platform under working mode ++-

In Fig. 5, the working mode of the mechanism is +++ . It can be observed that, the errors caused by the joint clearances can be modeled as an uncontrollable three dimensional space, with Δx_o varies from about -0.02 to 0.02 mm, Δy_o varies from about -0.02 to 0.02 mm and $\Delta\theta_o$ varies from about -0.01 to 0.01 m rad. Moreover, different $\Delta\theta_o$ corresponds to different translation error areas. The positioning error and the joint clearance size are in the same orders of magnitude.

In Fig. 6, the working mode of the mechanism is ++- . It can be observed that, the uncontrollable space is different from that of +++ . Δx_o varies from about -0.04 to 0.04 mm, Δy_o varies from about -0.05 to 0.05 mm and $\Delta\theta_o$ varies from about -0.01 to 0.01 m rad. These results indicate that the working mode influences the error distribution obviously.

To better understand the mechanism, it is import to know the maximum pose error distribution in the whole workspace. The expected angle of the moving platform is still set to be 0 rad, the maximum pose error of the moving platform caused by joint clearances is calculated point by point over the whole workspace. Figures 7 and 8 show the maximum error of the mechanism under two different

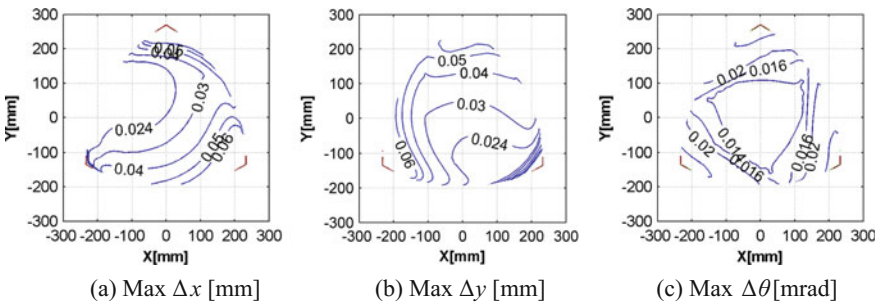


Fig. 7 Maximum error distributions of the platform under working mode +++

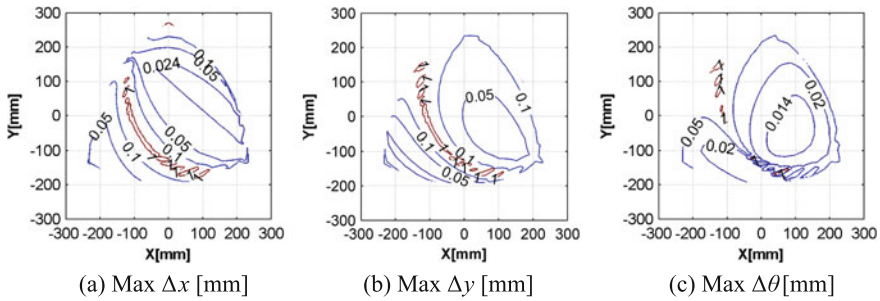


Fig. 8 Maximum error distributions of the platform under working mode ++-

working modes +++ and ---, respectively. These show that the position of the moving platform has a large influence on the pose error of it, leading to the pose error different from place to place. The error distribution trend is very similar with the determinant of Transform matrix \mathbf{J} , that is, most of the errors are very small, but when the mechanism is close to its singular configurations, the maximum errors increase dramatically and become unacceptable.

6 Conclusions

In this paper, the influence of joint clearance on the positioning accuracy of a 3-RRR mechanism is investigated. A simplified transform model is obtained by deviating the kinematical equations of the 3-RRR planar parallel mechanism. The maximum error distribution in the whole workspace is calculated, showing that the pose error is sensitive to the position of the moving platform; singular configuration can lead to an unacceptable pose error. It also shows that the mechanism performance different positioning ability under different working modes.

The study indicates that the proposed method is an efficient way to predicate the kinematic accuracy of the planar mechanical system with presence of joint clearances. This method can be applied to any planar mechanism with revolute joints. It is advisable that the joint clearance should be minimized, the working mode should be carefully selected and the singular configurations must be avoided.

Acknowledgments This research was supported by the Natural Science Foundation of Guangdong Province (Grant no. 2016A030310420), the National Natural Science Foundation of China (Grant nos. U1501247), the Scientific and Technological Project of Guangzhou (Grant no. 2015090330001), and the Scientific and Technological Research Project of Guangdong Province (2015B020239001). These supports are greatly acknowledged.

References

1. Chun HG, Kwon SJ, Tak T (2008) Multibody approach for tolerance analysis and optimization of mechanical systems. *J Mech Sci Technol* 22:276–286
2. Vaidya AM, Padole PM (2010) A performance evaluation of four bar mechanism considering flexibility of links and joints stiffness. *Open Mech Eng J* 4:16–28
3. Flores P, Ambrosio J, Claro JCP (2006) A study on dynamics of mechanical systems including joints with clearance and lubrication. *Mech Mach Theory* 41:247–261
4. Flores P (2009) Modeling and simulation of wear in revolute clearance joints in multibody systems. *Mech Mach Theory* 44:1211–1222
5. Yu A, Bonev IA, Zsombor-Murray P (2008) Geometric approach to the accuracy analysis of a class of 3-dof planar parallel robots. *Mech Mach Theory* 43:364–375
6. Briot S, Bonev IA (2008) Accuracy analysis of 3-dof planar parallel robots. *Mech Mach Theory* 43:445–458
7. Briot S, Bonev IA (2010) Accuracy analysis of 3t1r full-parallel robots. *Mech Mach Theory* 45:659–706
8. Innocenti C (2002) Kinematic clearance sensitivity analysis of spatial structures with revolute joints. *ASME J Mech Des* 124:52–57
9. Parenti-Castelli V, Venanzi S (2002) On the joint clearance effects in serial and parallel manipulators. In: *Proceedings of the workshop on fundamental issues and future research directions for parallel mechanisms and manipulators*, pp 215–223
10. Parenti-Castelli V, Venanzi S (2002) A new deterministic method for clearance influence analysis in spatial mechanisms. In: *Proceedings of the 2002 ASME international mechanical engineering congress and exposition*
11. Venanzi S, Parenti-Castelli V (2005) A new technique for clearance influence analysis in spatial mechanism. *ASME J Mech Des* 127:446–455
12. Parenti-Castelli V, Venanzi S (2005) Clearance influence analysis on mechanisms. *Mech Mach Theory* 40:1316–1329
13. Parenti-Castelli V, Venanzi S (2005) Kinetostatic modeling of the clearance-affected prismatic pair. *J Robot Syst* 22(9):487–496
14. Chebbi AH, Affi Z, Romdhane L (2009) Prediction of the pose errors produced by joints clearance for a 3-UPU parallel robot. *Mech Mach Theory* 44:1768–1783
15. Altuzarra O, Aginaga J, Hernandez A, Zabalza I (2011) Workspace analysis of positioning discontinuities due to clearance in parallel manipulators. *Mech Mach Theory* 46:577–592
16. Meng J, Zhang DJ, Li ZX (2009) Accuracy analysis of parallel manipulators with joint clearance. *ASME J Mech Des* 131(011012):1–9
17. Tsai MJ, Lai TH (2004) Kinematic sensitivity analysis of linkage with joint clearance based on transmission quality. *Multibody Syst Dyn* 39:1189–1206
18. Tsai MJ, Lai TH (2008) Accuracy analysis of a multi-loop linkage with joint clearances. *Multibody Syst Dyn* 43:1141–1157
19. Frisoli A, Solazzi M, Pellegrinetti D, Bergamasco M (2011) A new screw theory method for the estimation of position accuracy in spatial parallel manipulators with revolute joint clearances. *Mech Mach Theory* 46:1929–1949
20. Jawale HP, Thorat HT (2012) Investigation of positional error in two degree of freedom mechanism with joint clearance. *ASME J Mech Robot* 4:011002-1–011002-17 (2012)
21. Voglewede P, Uphoff I (2004) Application of workspace generation techniques to determine the unconstrained motion of parallel manipulators. *ASME J Mech Des* 126:283–290
22. Chen GL, Wang H, Lin ZQ (2013) A unified approach to the accuracy analysis of planar parallel manipulators both with input uncertainties and joint clearance. *Multibody Syst Dyn* 64:1–17

23. Wu G, Bai S, Kepler JA, Caro S (2012) Error modelling and experimental validation of a planar 3-ppr parallel manipulator with joint clearances. *ASME J Mech Robot* 4(4):041011-1–041011-8 (2012)
24. Zhang XC, Zhang XM, Chen Z (2014) Dynamic analysis of a 3-RRR parallel mechanism with multiple clearance joints. *Mech Mach Theory* 78:105–115
25. Zhang XC, Zhang XM (2016) A comparative study of 3-RRR and 4-RRR mechanisms with joint clearances. *Robot Comput-Integr Manuf* 40:24–33

Dynamic Response and Stability Analysis of a Parallel Mechanism with Clearance in Revolute Joint

Yulei Hou, Guoning Jing, Yi Wang, Daxing Zeng and Xuesong Qiu

Abstract The clearances in kinematic pair are inevitable, which will affect the accuracy and stability of the mechanism directly. A two rotational decoupled parallel mechanism RU-RPR is taken as the research object. Considering the clearance existing in the revolute pair, the dynamics equations are established. Then the effects of clearance on the dynamic characteristics of the mechanism are researched. Meanwhile, a spring is added to the mechanism, and its influences on the dynamic of the mechanism are analyzed. In order to further improve the dynamic response of the mechanism, the genetic algorithm is applied to optimize the related parameters of the spring. The research contents possess theoretical guidance significance on improvement of the dynamic characteristics and control of the chaotic motion of the parallel mechanism with clearances.

Keywords Parallel mechanism · Clearance · Dynamics · Stability · Optimization

Y. Hou (✉) · G. Jing · Y. Wang · D. Zeng · X. Qiu
School of Mechanical Engineering, Yanshan University,
Qinhuangdao 066004, China
e-mail: ylhou@ysu.edu.cn

G. Jing
e-mail: 931949991@qq.com

Y. Wang
e-mail: 474633785@qq.com

D. Zeng
e-mail: roboms@ysu.edu.cn

X. Qiu
e-mail: qxsong@ysu.edu.cn

1 Introduction

Due to the existence of the friction and wear which bring about error in the process of design, manufacture, installation, there will always produce clearance in the kinematic pairs of mechanism [1]. And the existence of the clearance will have great influence on the performance of the mechanism [2], resulting in shock vibration, reducing the work efficiency and the accuracy [3], and even cause the failure of the mechanism.

In recent years, the dynamic of the mechanism with clearance were widely studied by many scholars. A new hybrid contact force model was proposed by Bai and Zhao [4]. The effect of lubrication on the dynamic performance of the mechanism with clearance was analyzed by Flores et al. [5]. Zhang et al. [6], took the planar 3-RRR parallel mechanism with multiple clearances as the research object, and analyzed the influence of different loads, velocities and trajectories on the accuracy and stability of the mechanism.

The effect of the clearance on the accuracy and stability of the mechanism can not be ignored, so it is very significant to study how to eliminate the effect of clearance on the performance of the mechanism. Varedi et al. [7], optimized the mass of the slider-crank mechanism with clearance to reduce the vibration and improve the stability of the mechanism. Olyaei and Ghazavi [8], added a disturbance to the slider-crank mechanism with clearance, and transformed the mechanism from the chaotic motion into periodic motion state. Zhang et al. [9], optimized the high speed and heavy load mechanism with clearance based on the ADAMS simulation analysis software.

Stability of the dynamic response of the mechanism with clearance is one of important research contents, while the bifurcation diagram [10] can reflect the stability of mechanism with the change of sensitive parameters. In Ref. [11], the bifurcation diagram of the slider-crank mechanism with clearance was drawn, and the corresponding stable region was studied. In Ref. [12], the chaos control method of the under actuated planar five bar mechanism was analyzed, and the bifurcation diagram of the mechanism with the change of system parameter variation was drawn. In Ref. [13], the bifurcation and chaos phenomena of the planetary reversing mechanism under the action of rotation and torque were studied.

In this paper, taking RU-RPR parallel mechanism with the revolute pair clearance as the research object, the dynamics equations are established and numerical simulated, the spring is added and the genetic algorithm is applied to optimize the related parameters. In addition, the chaotic characteristics of the mechanism and the influence on the dynamic stability are analyzed.

2 Dynamic Modeling of RU-RPR Parallel Mechanism with Clearance

2.1 Structural Composition of RU-RPR Parallel Mechanism

Figure 1 is the structural composition of RU-RPR decoupled parallel mechanism [14]. It can be seen that the mechanism is composed of a fixed base, a moving platform and two limbs which connect the fixed base and moving platform. The first limb consists of a revolute pair and a hooke joint connected in turn, and the second limb consists of a revolute pair, a prismatic pair and another revolute pair connected in turn. The mechanism has two rotational degrees of freedom.

As shown in Fig. 1, θ and γ are the input angles, while α and β are the output angles. There is a one-to-one correspondence between θ and α , the relationship between γ and β is also one-to-one correspondence. Therefore the two rotational degrees of freedom of the RU-RPR parallel decoupled mechanism are independent of each other. So for the study of the clearance in the revolute pair D (F denotes the journal center in the clearance), the rotation of the moving platform around z_0 axis (vertical direction) should be considered, and the rotation of the moving platform around y_0 axis can be ignored temporarily. At this point, the mechanism is equivalent to a planar four bar mechanism with revolute pair clearance, as shown in Fig. 2.

Fig. 1 Structure diagram of RU-RPR two rotation decoupled parallel mechanism

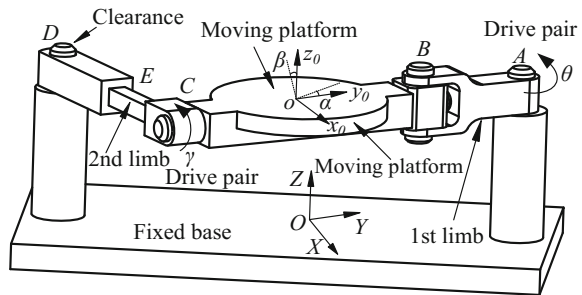
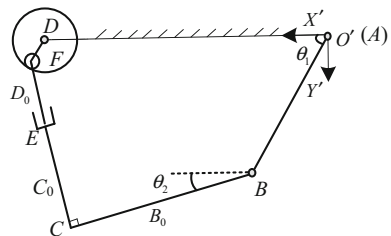


Fig. 2 Equivalent mechanism diagram of the RU-RPR parallel mechanism with clearance



2.2 Establishment of the Dynamic Equations of the Parallel Mechanism with Clearance

As shown in Fig. 2, the planar coordinate system $X'O'Y'$ is established for the equivalent mechanism, and the relevant parameters are defined as follows: l is the distance between C and F ; l_1 , l_2 and l_5 are the length of bar AB , bar BC and bar AD respectively; B_0 , C_0 and D_0 are the center of mass of bar BC , bar CE and bar EF ; l_{s2} , l_{s3} and l_{s4} are the length of B_0B , C_0C and D_0F ; θ_1 , θ_2 are the angles between the bar AB , bar BC and the positive direction of X' axis respectively; J_1 is the moment of inertia of bar AB around the axis A ; J_{s2} , J_{s3} and J_{s4} are the moment of inertia of bar BC , bar CE and bar EF around the axis which through the center of mass and parallel to the normal of $X'O'Y'$ plane, respectively; m_2 , m_3 , m_4 are the mass of bar BC , bar CE and bar EF , respectively; x , y are the offset coordinate component of the axis center F relative to the bearing axis center D along X' direction and Y' direction, respectively.

As the existence of the rotation clearance at D point, in addition to the rotational degree of freedom, there increase two relative motion degrees of freedom for the bearing and shaft of the revolute pair. The generalized coordinates of the mechanism are selected as follows: x , y and the drive angle θ_1 of bar AB .

When there is no clearance in the mechanism, the closed equations are as follows

$$\begin{cases} l_1 \cos \theta_1 + l_2 \cos \theta_{20} + l_0 \sin \theta_{20} - l_5 = 0 \\ l_1 \sin \theta_1 + l_2 \sin \theta_{20} - l_0 \cos \theta_{20} = 0 \end{cases} \quad (1)$$

where, θ_{20} is the rotation angle of bar BC , l_0 is the distance of CF .

When there has clearance in the mechanism, the closed equations are as follows

$$\begin{cases} l_1 \cos \theta_1 + l_2 \cos \theta_2 + l \sin \theta_2 - x - l_5 = 0 \\ l_1 \sin \theta_1 + l_2 \sin \theta_2 - l \cos \theta_2 - y = 0 \end{cases} \quad (2)$$

According to the perturbation coordinate method, the rotation angle of the moving platform and the bar length can be regarded as adding a small disturbance value to the normal value, then the following equations can be obtained as

$$\begin{cases} l = l_0 + \Delta l \\ \theta_2 = \theta_{20} + \Delta \theta_2 \end{cases} \quad (3)$$

Using the equivalent infinitesimal concepts, simultaneous Eqs. (1)–(3) can be simplified, and the following equations can be obtained as

$$\begin{bmatrix} (l_2 \cos \theta_{20} + l_0 \sin \theta_{20})/l_0 & (l_2 \sin \theta_{20} - l_0 \cos \theta_{20})/l_0 \\ \cos \theta_{20}/l_0 & \sin \theta_{20}/l_0 \end{bmatrix} \begin{Bmatrix} x \\ y \end{Bmatrix} = \begin{Bmatrix} \Delta l \\ \Delta \theta_2 \end{Bmatrix} \quad (4)$$

Based on the geometric relationships, the X' component and Y' component of the mass center coordinates of the bar BC , CE and EF can be calculated respectively and the Lagrange equations of motion can be expressed as

$$\frac{d}{dt} \left(\frac{\partial L}{\partial \dot{q}_j} \right) - \frac{\partial L}{\partial q_j} = Q_j (j = 1, 2, 3) \tag{5}$$

where, Q_j is the generalized force corresponding to the generalized coordinate q_j in non-conservative systems, and q_1, q_2, q_3 denote x, y and θ_1 , respectively. Q_j can be expressed as

$$Q_j = \sum_{i=1}^4 F_i \frac{\partial r_i}{\partial q_j} + M_i \frac{\partial \varphi_i}{\partial q_j} \tag{6}$$

where, F_i and M_i are the external force and the external moment acting on the center of mass of the object i , respectively; r_i and φ_i are the moving displacement and rotation angle of the center of mass of the object i , respectively.

Substituting Eq. (6) into Eq. (5), the dynamic equations of RU-RPR parallel mechanism with clearance can be obtained.

2.3 Establishment of the Contact Force Model in the Revolute Pair Clearance

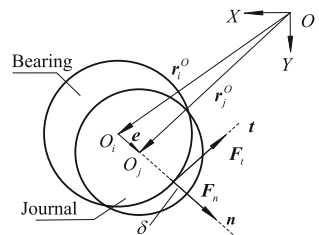
The clearance model of the revolute pair is shown in Fig. 3, O_i and O_j are the centers of the bearing and the journal, respectively. r_i^O and r_j^O are the position vectors of the center of the bearing and the journal in the static coordinate system, respectively.

The clearance vector and its unit normal vector can be expressed as

$$e = r_j^O - r_i^O \tag{7}$$

$$n = e / e \tag{8}$$

Fig. 3 Clearance model of the revolute pair



where, $e = \sqrt{e^T e}$. The depth of penetration between the bearing and the journal can be written as

$$\delta = e - c \quad (9)$$

where c is the clearance value, and $c = R_i - R_j$. When δ is positive, the bearing is in contact with the journal. On the contrary, the bearing and the journal are separated.

The Lankarani-Nikravesh contact force model [15] is used to calculate the normal contact force. This model not only involves the energy loss during the collision, but also concerns the material properties, the local elastic deformation and the velocity of the collision [16]. The normal contact force F_n of the journal to bearing is shown as follows

$$F_n = K\delta^n \left(1 + \frac{3(1 - c_e^2)}{4} \frac{\dot{\delta}}{\dot{\delta}^{(-)}} \right) \quad (10)$$

where, c_e is the restitution coefficient, $\dot{\delta}^{(-)}$ is the initial impact velocity at the beginning of each contact process, $\dot{\delta}$ is the relative penetration velocity, the stiffness coefficient K is shown as follows

$$K = \frac{4}{3(\delta_i + \delta_j)} \sqrt{\frac{R_i R_j}{R_i - R_j}} \quad (11)$$

where, $\delta_k = (1 - \nu_k^2)/E_k$ $k = i, j$, ν_k and E_k represent Poisson ratio and the elastic modulus, respectively. The subscript i and j represent the bearing and the journal respectively.

Adopting the modified Coulomb friction law proposed by AMBRÓSIO [17], the tangential contact force is expressed as follows

$$F_t = -c_f c_d F_n \text{sgn}(v_t) \quad (12)$$

where, c_f is the friction coefficient, v_t is relative tangential velocity of collision, c_d is the correction coefficient.

The impact force of the journal to bearing can be expressed as

$$\mathbf{f}_i = F_n \mathbf{n} + F_t \mathbf{t} \quad (13)$$

3 Dynamic Numerical Simulation of Parallel Mechanism with Clearance

Due to the existence of clearance, there are two different phases: contact and non-contact, in the motion process of the mechanism. Considering the collision time is very short, the variable step size fourth-order Runge-Kutta method [18] is used to carry out numerical integration to ensure the efficiency and accuracy of the calculation.

The material of RU-RPR mechanism is selected as 45 steel, and the relevant parameters can be obtained as: $l_1 = 130$ mm, $l_2 = 308$ mm, $l_{s2} = 154$ mm, $l_{s3} = 80$ mm, $l_{s4} = 54$ mm, $l_5 = 524$ mm, $J_1 = 7.351 \times 10^{-3}$ kg m², $J_{s2} = 6.160 \times 10^{-2}$ kg m², $J_{s3} = 5.772 \times 10^{-3}$ kg m², $J_{s4} = 3.008 \times 10^{-3}$ kg m², $m_2 = 8.516$ kg, $m_3 = 1.161$ kg, $m_4 = 1.405$ kg.

The dynamic simulation parameters of the mechanism are shown in Table 1. The bar *AB* and bar *BC* are collinear in the initial position and the driven angular velocity $\omega = 10\pi$ rad/s. The MATLAB software is used to program and calculate, and the simulation result of the mechanism is obtained as shown in Fig. 4.

The dynamic response curve of RU-RPR parallel mechanism with clearance is shown in Fig. 5, in which Fig. 5a–c are the contact force curve, driving torque curve and the axis trajectory, respectively. Poincare mapping [19] can be used to easily identify the chaos. Figure 5d shows Poincare mapping of the mechanism and five hundred mapping points are calculated. A point or a small number of discrete points, closed curves, and the dense points on a certain area with fractal structure on the Poincare mapping represent periodic motion, quasi periodic motion and chaotic motion, respectively. Both the contact force curve in Fig. 5a and the drive torque curve in Fig. 5b have high frequency oscillation and large fluctuation, and the maximum fluctuation amplitude are 8000 N and 1243 N m, respectively.

From Figs. 4 and 5, the existence of clearance leads to the decrease of the stability of the mechanism, and makes the dynamic response of RU-RPR mechanism with clearance in a state of instability.

Table 1 Dynamic simulation parameters of RU-RPR mechanism

Parameter	Value	Parameter	Value
Bearing radius R_i (mm)	15	Clearance c (mm)	0.5
Recovery coefficient c_e	0.9	Friction coefficient c_f	0.02
Elastic modulus E_i, E_j (GPa)	200	Poisson ratio ν_i, ν_j	0.3
Integral step error δ_m (m)	0.000001	Integral step d_t (s)	0.00001

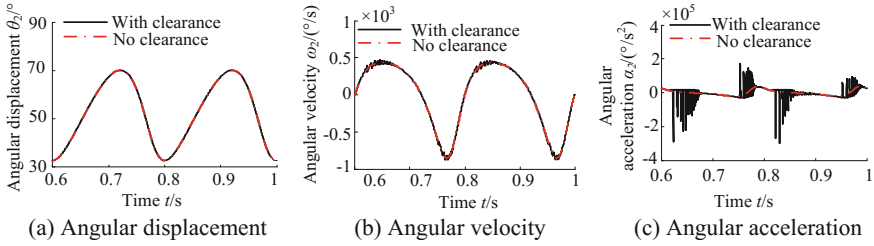


Fig. 4 Kinematic analysis of the RU-RPR parallel mechanism with clearance

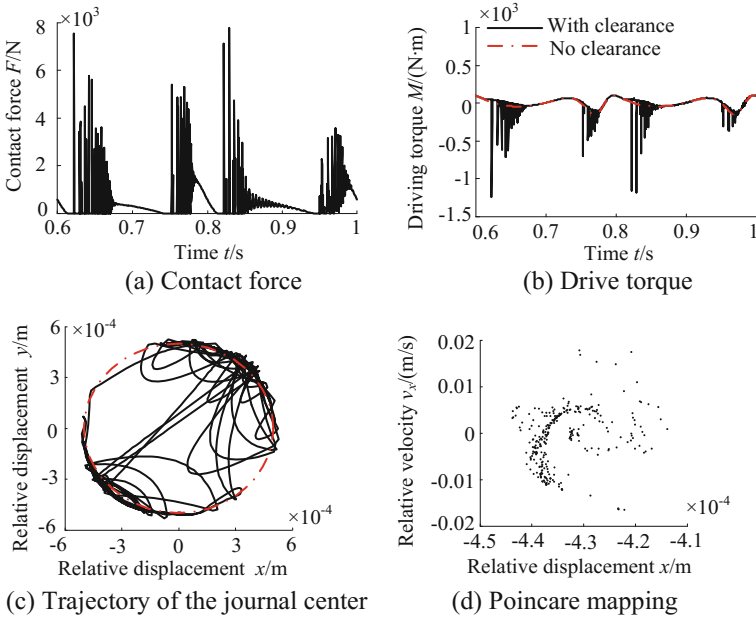


Fig. 5 Dynamic response of RU-RPR parallel mechanism with clearance

4 Dynamic Response Analysis of Parallel Mechanism with Clearance

4.1 Effect of Adding Spring on the Dynamic Characteristics of the Mechanism

In order to reduce the impact between the journal and the bearing and improve the dynamic response stability of the mechanism, a spring is added between the center of mass of the bar EF and a certain point O_1 in the connection of $O'D$, as shown in Fig. 6. The spring is set to be a cylindrical helical tension spring, which works in

the tensile state and can not bear the pressure. The length of the $O'O_1$ is set as d , the initial length of the spring is L_{s0} , the stiffness coefficient is k_s , the length of the spring is L_s .

The initial parameters of the spring may be set as $d = 0.13$ m, $L_{s0} = 0.15$ m, $k_s = 1000$ N/m, meanwhile, the other simulation parameters are consistent with the previous section, then the numerical solution can be solved by using MATLAB software and the results are as shown in Fig. 7.

From the comparison between Figs. 7 and 5, it can be found that the collision between the bearing and the journal is reduced, and the maximum amplitude of the contact force fluctuation declines from 8000 N to 2051 N which decreased by 74.4 %, the maximum amplitude of the driving torque fluctuation declines from 1243 to 294 N m which decreased by 76.3 %. Through the comparison between Figs. 7c and 5c, it can be found that the journal moves close to the edge of the bearing, and the impact phenomenon becomes weak. While Fig. 7d shows that the mechanism changes from chaos to periodic motion with addition of the spring. As a whole, the stability of the dynamic response of the mechanism is enhanced by adding the spring.

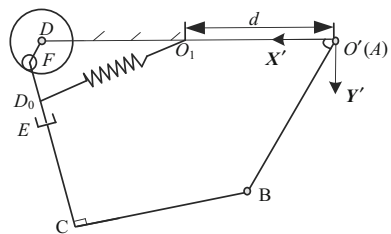
4.2 Parameter Optimization on the Dynamic Response of the Mechanism

In order to further improve the stability of the dynamic response of RU-RPR parallel mechanism, the genetic algorithm is used to optimize the related parameters of the spring.

In this paper, the purposes of optimization mainly focus on two aspects. On the one hand, to control or eliminate the adverse effects caused by the kinematic pair clearance, and improve the stability of the dynamic response of the mechanism. On the other hand, it is to minimize the driving torque of the joint of the mechanism. Thus, the penetration depth between the journal and the bearing is selected as the optimization goal, and the objective function expression is as follows

$$S = \frac{1}{\sum_{n=1}^s (r - c)^2} \tag{14}$$

Fig. 6 Equivalent mechanism diagram of RU-RPR parallel mechanism with spring



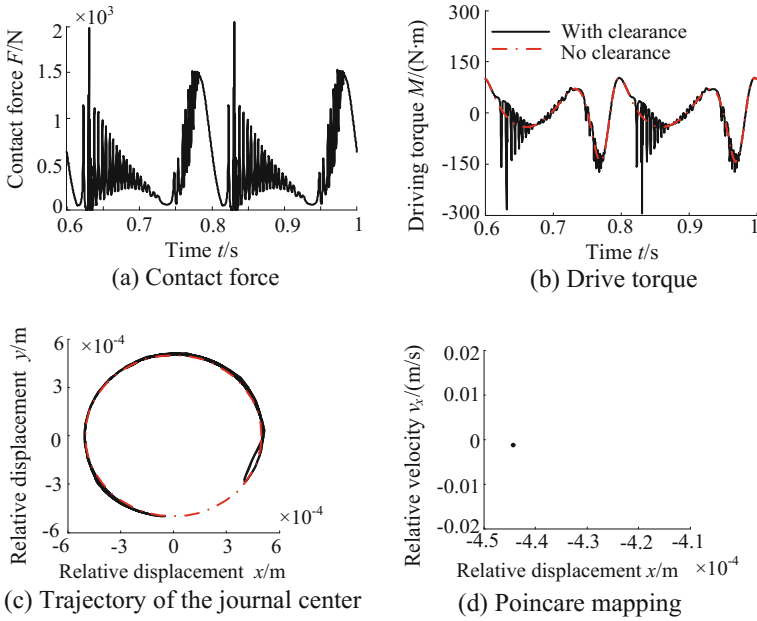


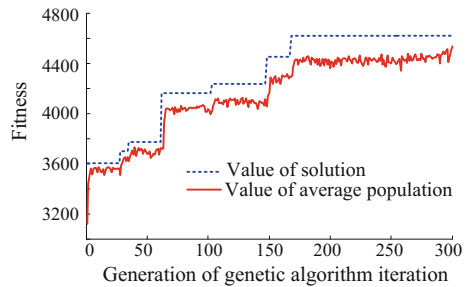
Fig. 7 Dynamic response of RU-RPR parallel mechanism with spring

where, r is the distance between the bearing center and the journal center, c is the clearance size, s indicates the number of selected samples.

The parameters d , k_s and L_{s0} are selected as the optimization parameters. In order to ensure the spring is always in a state of tension, it needs to maintain a certain distance between D_0 and O_1 . Then the scope of the variable is set as follows: d [0, 0.26] m, k_s [500, 1500] N/m, L_{s0} [0.05, 0.25] m. Setting maximum objective function as the optimization goal, the genetic algorithm optimization is performed, and the track diagram of the optimization performance of genetic algorithm is shown as Fig. 8.

The optimized parameters of the spring are as follows: $d = 0.067$ m, $k_s = 526$ N/m, $L_{s0} = 0.178$ m. Adopting the consistent simulation parameters, the

Fig. 8 Track diagram of the optimization performance of genetic algorithm



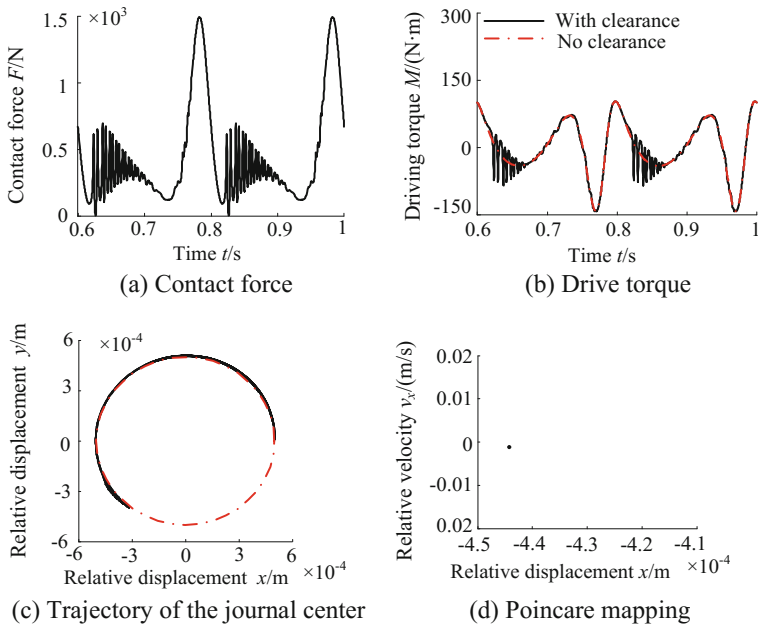


Fig. 9 Dynamic response of RU-RPR parallel mechanism after optimization

dynamics numerical simulation of the mechanism is carried out, and the results are shown in Fig. 9.

Compared Fig. 9a with Fig. 7a, it can be found that the degree of the high-frequency oscillation decreased obviously. From the comparison between Figs. 9b and 7b, it can be found that the range and degree of high frequency oscillation of the driving torque is also reduced. Comparing Fig. 9c, d with Fig. 7c, d respectively, it can be found that the impact phenomenon of the clearance between the journal and the bearing is weakened, the journal tends to slide along the inner wall of the bearing, and the mechanism is in a steady state of periodic motion. In conclusion, the dynamic response stability of RU-RPR parallel mechanism with clearance is further enhanced through the optimization.

4.3 Stability Analysis of Dynamics Response of the Mechanism

To analysis the dynamic response of the mechanism with the change of the parameters, the bifurcation diagrams of the mechanism with the change of driving speed is drawn in the following section. Here divide two kinds of cases: no spring in RU-RPR parallel mechanism and has spring in the mechanism. Selecting the

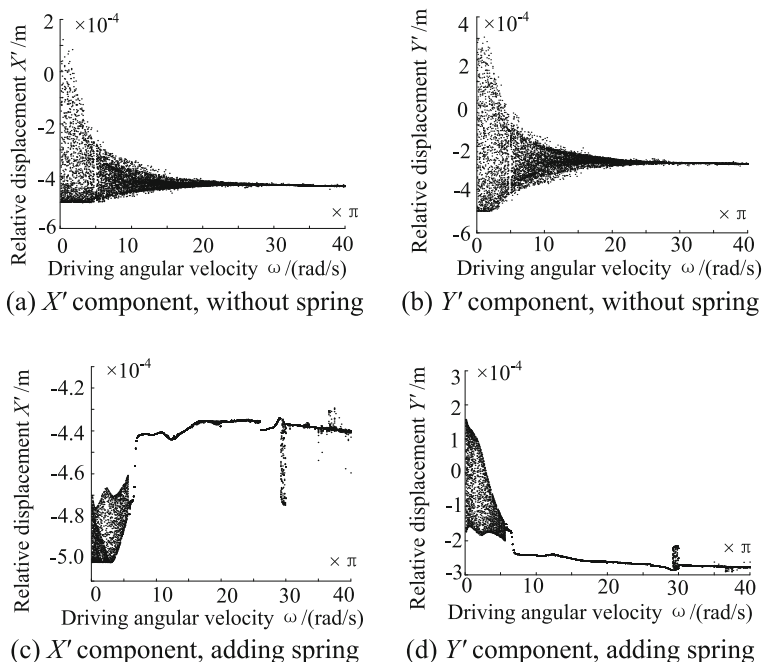


Fig. 10 Bifurcation diagram of RU-RPR parallel mechanism

driving speed ω as the variable parameter, the bifurcation diagrams of the relative displacement of the journal center respect to the bearing center in X' direction and Y' direction are drawn respectively, as shown in Fig. 10.

Figure 10a, b represent the bifurcation diagrams of the relative displacement x in X' direction and the relative displacement y in Y' direction of the rotation pair clearance of RU-RPR parallel mechanism without spring, respectively. And it can be seen that the size of the drive speed has great influence on the dynamics stability of the mechanism. With the increase of the drive speed, the chaos phenomenon is weakened, and the mechanism changes from the chaotic motion to the periodic state. Moreover, the trend of the bifurcation diagram of the relative displacement x in X' direction and the relative displacement y in Y' direction of the rotation pair clearance is consistent. When the value of the drive speed is greater than 25π , the mechanism has turned into the periodic motion.

Figure 10c, d represent the bifurcation diagrams of the relative displacement x in X' direction and the relative displacement y in Y' direction of the rotation pair clearance of RU-RPR parallel mechanism with the spring, respectively. As is shown in the figures, the values of the two figures are different, but the change rule is consistent. With the drive speed increased from 0.1π to 7π , the degree of chaos

phenomenon decrease gradually. When the drive speed value increased from 7π to 29π , the bifurcation diagram appear single line, which means the mechanism is in the state of periodic motion and the dynamic response of the mechanism is stable. When the value of the drive speed is greater than 29π , the bifurcation diagram become complex, and the stability of the dynamic response of the mechanism decrease.

Comparing the bifurcation diagrams of RU-RPR parallel mechanism without and adding spring in Fig. 10, it can be found that for the mechanism adding spring, when the value of the drive speed is about 10π , the dynamic response of is significantly more stable than the mechanism without spring. When the drive speed of the value is in $[0.1\pi, 29\pi]$, the stability of dynamic response of the mechanism adding spring is enhanced. While when the drive speed of the value is greater than 29π , the stability of the mechanism adding spring is worse than that without spring.

Overall, the optimization of the mechanism has a significant effect on improving the stability of the dynamic response, however it should be noted that the impact of the spring parameters on the dynamic response stability of the mechanism is more complex and not linear, the selection of the optimal drive speed under certain parameters should be determined with the consideration of the specific conditions.

5 Conclusions

The dynamics equations of RU-RPR parallel mechanism with clearance in revolute joint were established by the Lagrange method, the Lankarani-Nikravesh contact force model and the modified Coulomb friction laws were used to calculate the normal and tangential contact forces, respectively. The numerical solution was solved by the variable step Runge-Kutta method. The results show that for the existence of clearance, the dynamics response stability of the mechanism becomes weak, and the angular acceleration, the contact force and the drive torque curve fluctuate violently.

Spring was added in RU-RPR parallel mechanism and the genetic algorithm was used to optimize the parameters. The analysis results show that the dynamic response stability of the mechanism is improved obviously. The bifurcation diagrams of the mechanism with the change of the drive speed were drawn by the Poincare section method, and the effectiveness of adding springs and parameters optimization for improvement of the stability of the mechanism have been further verified.

Acknowledgments This study was supported by National Natural Science Foundation of China (51205339, 51305384), China Postdoctoral Science Foundation (2013M541199).

References

1. Flores P (2004) Dynamic analysis of mechanical systems with imperfect kinematic joints. Universidade Do Minho, Portugal
2. Bai ZF (2011) Research on dynamic characteristics of mechanism with joint clearance. Harbin Institute of Technology, Harbin
3. Yu YQ, Tian H (2015) Error and compensation of parallel robot with joint clearances. *Opt Precis Eng* 23(5):1331–1339
4. Bai ZF, Zhao Y (2013) A hybrid contact force model of revolute joint with clearance for planar mechanical systems. *Int J Non-Linear Mech* 48(1):15–36
5. Flores P, Ambrosio J, Claro JCP et al (2006) A study on dynamics of mechanical systems including joints with clearance and lubrication. *Mech Mach Theory* 41(3):247–261
6. Zhang XC, Zhang XM, Chen Z (2014) Dynamic analysis of a 3-RRR parallel mechanism with multiple clearance joints. *Mech Mach Theory* 78(8):105–115
7. Varedi SM, Daniali HM, Dardel M et al (2015) Optimal dynamic design of a planar slider-crank mechanism with a joint clearance. *Mech Mach Theory* 86(1):191–200
8. Olyaei AA, Ghazavi MR (2012) Stabilizing slider-crank mechanism with clearance joints. *Mech Mach Theory* 53(3):17–29
9. Zhang ZL, Wu SJ, Zhang HB et al (2013) Stability analysis and optimal design of high-speed and high-load driving mechanism with joint clearance based on multi-body dynamics. American Society of Mechanical Engineering. International Mechanical Engineering Congress and Exposition. ASME, California, pp 1–13
10. Tang YG, Chang ZY, Dong XG et al (2013) Nonlinear dynamics and analysis of a four-bar linkage with clearance. *Front Mech Eng* 8(2):160–168
11. Rahmanian S, Ghazavi MR (2015) Bifurcation in planar slider–crank mechanism with revolute clearance joint. *Mech Mach Theory* 91(5):86–101
12. He JB, Xie J, Chen Y et al (2013) Control and anti-control of chaotic motion for a under-actuated planar five-bar mechanism. *Mech Sci Technol Aerosp Eng* 32(1):1–5
13. Ma HT, Xue DL (2013) Bifurcation and chaos of planetary reverse system to external excitation. *China Mech Eng* 24(23):3129–3133, 3339
14. Hou YL, Zeng DX, Zhang ZY et al (2012) A novel two degrees of freedom rotational decoupled parallel mechanism. *Appl Mech Mater* 215–216:293–296
15. Lankarani HM, NIKRAVESH PE (1994) Continuous contact force models for impact analysis in multibody systems. *Nonlinear Dyn* 5(2):193–207
16. Flores P, Ambrósio J, Claro JCP et al (2006) Influence of the contact—impact force model on the dynamic response of multi-body systems. *Proc Inst Mech Eng Part K J Multi-body Dyn* 220(1):21–34
17. Ambrósio J (2003) Impact of rigid and flexible multibody systems: deformation description and contact models. *Virtual Nonlinear Multibody Syst* 103:57–81
18. Flores P, Ambrósio J (2010) On the contact detection for contact-impact analysis in multibody systems. *Multibody Syst Dyn* 24(1):103–122
19. Chen YS (1993) Bifurcation and chaos theory of nonlinear vibration system. Higher Education Press, Beijing

Chaos Suppression for Joint Clearances Based on Trajectory Planning of Robotic Mechanisms

Wanghui Bu, Chenguang Yang, Duyu Chen, Hangyu Zhou, Jia Hu and Yinfan Hou

Abstract Robotic mechanisms have been widely used, and the clearances existing in mechanism joints decrease the positioning accuracy and bring about the impact between joint elements. In this paper, the chaos caused by joint clearances is investigated, and a novel approach to suppress the chaos based on the trajectory planning of the robotic mechanism is presented. The dynamics of the robotic mechanism with joint clearances is analyzed, and the model of the worn revolute joint is established. Furthermore, the allowable abrasion depth is derived to suppress chaos for the worn joints.

Keywords Manipulator · Clearance · Chaos · Trajectory planning

1 Introduction

Robotic mechanisms have been widely used, and their positioning accuracy and dynamic performance are crucial for successfully performing robotic tasks. However, the clearances existing in the joints of a robotic mechanism decrease the accuracy of the mechanism and bring about the impact between joint elements. Even worse, the longer the mechanism works, the larger the clearance becomes. The clearance may induce the relative motion of the two joint elements into the chaotic status, which intensifies the impact and abrasion of the joint.

Many researchers studied the effects of joint clearances on positioning accuracy [1–5] and mechanism dynamics [6–10]. To attenuate the negative effects caused by the clearances, many methods have been presented. Especially Bu et al. [11]

W. Bu (✉) · C. Yang · D. Chen · H. Zhou · J. Hu · Y. Hou
School of Mechanical Engineering, Tongji University, Shanghai 201804, China
e-mail: buwanghui@tongji.edu.cn

proposed a novel approach based on trajectory planning to avoid the detachment of joint elements. In the following of this paper, the chaos caused by joint clearances will be investigated and be suppressed by the trajectory planning of the robotic mechanism. Furthermore, the allowable abrasion depth will be derived to suppress chaos for the worn joints.

2 Dynamics of Robotic Mechanisms with Joint Clearances

The planar PRR robotic mechanism with clearances is shown in Fig. 1, and its structural and kinematic parameters are listed in Table 1. Note that the two revolute joints are with clearances, while the prismatic joint is ideal. The robotic world frame is established as follows: the axis x is to the right, while the axis y is downward along link 1, as shown in Fig. 1.

Let F_{C1x} and F_{C1y} be the components along axes x and y for the reaction force at joint C_1 ; F_{C2x} and F_{C2y} be the components of the reaction force at joint C_2 . Let \ddot{s}_{2x} and \ddot{s}_{2y} be the components along axes x and y for the centroid acceleration of link 2; Let \ddot{s}_{3x} and \ddot{s}_{3y} be the components of the centroid acceleration of link 3. The reaction forces can be obtained using Newton's law as follows.

$$F_{C1x} = m_2\ddot{s}_{2x} + m_3\ddot{s}_{3x} \tag{1}$$

$$F_{C1y} = m_2\ddot{s}_{2y} + m_3\ddot{s}_{3y} - m_2g - m_3g \tag{2}$$

$$F_{C2x} = m_3\ddot{s}_{3x} \tag{3}$$

Fig. 1 The planar PRR robotic mechanism

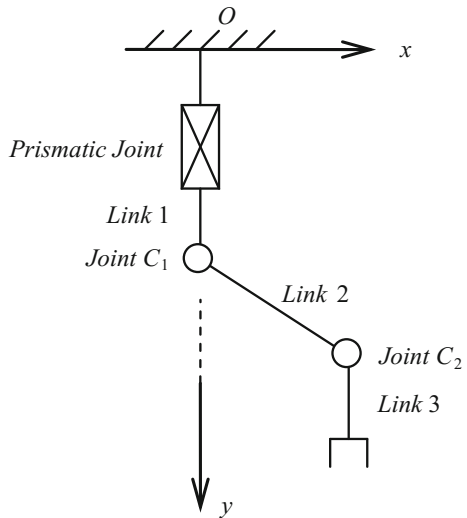


Table 1 Structural and kinematic parameters of the PRR robotic mechanism

Physical quantity	Symbol	Value
Length of link 2	l_2	0.8 m
Centroid positon in link 2	l_{2c}	0.4 m
Centroid positon in link 3	l_{3c}	0.2 m
Clearance in joint C_1	L_{C1}	0.00001 m
Clearance in joint C_2	L_{C2}	0.00001 m
Mass of link 2	m_2	12 kg
Mass of link 3	m_3	6 kg
Acceleration of gravity	g	9.8 N/s ²
Initial position of the prismatic joint	q_{1o}	0 m
Initial position of the joint C_1	q_{2o}	0°
Initial position of the joint C_2	q_{3o}	0°
End position of the prismatic joint	q_{1e}	0.8 m
End position of the joint C_1	q_{2e}	30°
End position of the joint C_2	q_{3e}	-150°

$$F_{C2y} = m_3\ddot{s}_{3y} - m_3g \tag{4}$$

The centroid accelerations of links 2 and 3 can be obtained by the kinematic relation between displacements and accelerations as follows.

$$s_{2x} = l_{2c} \cos \theta_2 + L_{C1} \cos \alpha_{C1} \tag{5}$$

$$s_{2y} = q_1 + l_{2c} \sin \theta_2 + L_{C1} \sin \alpha_{C1} \tag{6}$$

$$s_{3x} = l_2 \cos \theta_2 + l_{3c} \cos \theta_3 + L_{C1} \cos \alpha_{C1} + L_{C2} \cos \alpha_{C2} \tag{7}$$

$$s_{3y} = q_1 + l_2 \sin \theta_2 + l_{3c} \sin \theta_3 + L_{C1} \sin \alpha_{C1} + L_{C2} \sin \alpha_{C2} \tag{8}$$

where q_1 denotes displacement of the prismatic joint; α_{C1} and α_{C2} denote two angles of virtual links at joints C_1 and C_2 .

Suppose the stiffness of the revolute joints with clearances is $k = 10^6$ N/m; the normal dumping is $C_n = 600$ Ns/m. The reaction forces of two revolute joints can be obtained as follows.

$$F_{C1} = (k \cdot \delta_{C1} + c_n \cdot v_{C1n}) \cdot \text{Sign}[\text{Sign}(\delta_{C1}) + 1] \tag{9}$$

$$F_{C2} = (k \cdot \delta_{C2} + c_n \cdot v_{C2n}) \cdot \text{Sign}[\text{Sign}(\delta_{C2}) + 1] \tag{10}$$

where δ_{C1} and δ_{C2} denote the displacements between the joint elements for the two revolute joints, and they are derived as follows.

$$\delta_{C1} = \sqrt{e_{2x}^2 + e_{2y}^2} - L_{C1} \quad (11)$$

$$\delta_{C2} = \sqrt{e_{3x}^2 + e_{3y}^2} - L_{C2} \quad (12)$$

and

$$e_{2x} = p_{2x} \quad (13)$$

$$e_{2y} = p_{2y} - q_1 \quad (14)$$

$$e_{3x} = p_{3x} - [p_{2x} + l_2 \cdot \cos(90^\circ + q_2)] \quad (15)$$

$$e_{3y} = p_{3y} - [p_{2y} + l_2 \cdot \sin(90^\circ + q_2)] \quad (16)$$

where p_{2x} and p_{2y} denote coordinates of joint C_1 described in the world frame; p_{3x} and p_{3y} denote coordinates of joint C_2 described in the world frame.

The normal velocities v_{C1n} and v_{C2n} in Eqs. (9) and (10) can be derived as follows.

$$v_{C1n} = \dot{e}_{2x} \cos \alpha_{C1} + \dot{e}_{2y} \sin \alpha_{C1} \quad (17)$$

$$v_{C2n} = \dot{e}_{3x} \cos \alpha_{C2} + \dot{e}_{3y} \sin \alpha_{C2} \quad (18)$$

where α_{C1} and α_{C2} denote two angles of virtual links at joints C_1 and C_2 , and can be solved as follows.

$$\alpha_{C1} = \arctan \frac{e_{2x}}{e_{2y}} \quad (19)$$

$$\alpha_{C2} = \arctan \frac{e_{3x}}{e_{3y}} \quad (20)$$

The sign function in Eqs. (9) and (10) satisfies the following equations.

$$\text{Sign}(x) = -1, \quad x < 0 \quad (21)$$

$$\text{Sign}(x) = 0, \quad x = 0 \quad (22)$$

$$\text{Sign}(x) = 1, \quad x > 0 \quad (23)$$

Therefore $\text{Sign}[\text{Sign}(\delta_{C1}) + 1]$ means the value is 0 when $\delta_{C1} \geq 0$, and the value is 1 when $\delta_{C1} < 0$.

3 Trajectory Planning to Suppress Chaos Caused by Clearances

The trajectory of the PRR mechanism can be described in the joint space, as (q_1, q_2, q_3) . The initial and end positions of the mechanism are given as (q_{1o}, q_{2o}, q_{3o}) and (q_{1e}, q_{2e}, q_{3e}) respectively, which are listed in Table 1. The trajectory between the initial and end positions can be presented by the quintic polynomial function as follows.

$$q_k = A_{k,5}t^5 + A_{k,4}t^4 + A_{k,3}t^3 + A_{k,2}t^2 + A_{k,1}t + A_{k,0} \tag{24}$$

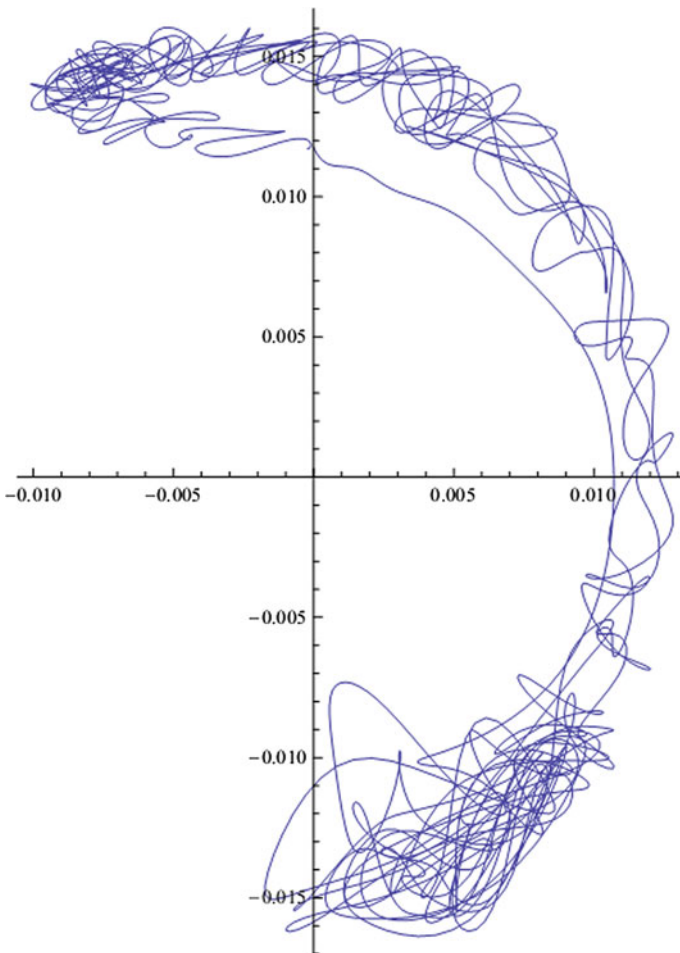


Fig. 2 The relative motion path of the two joint elements for joint C_1 when $T_p = 0.3$ s

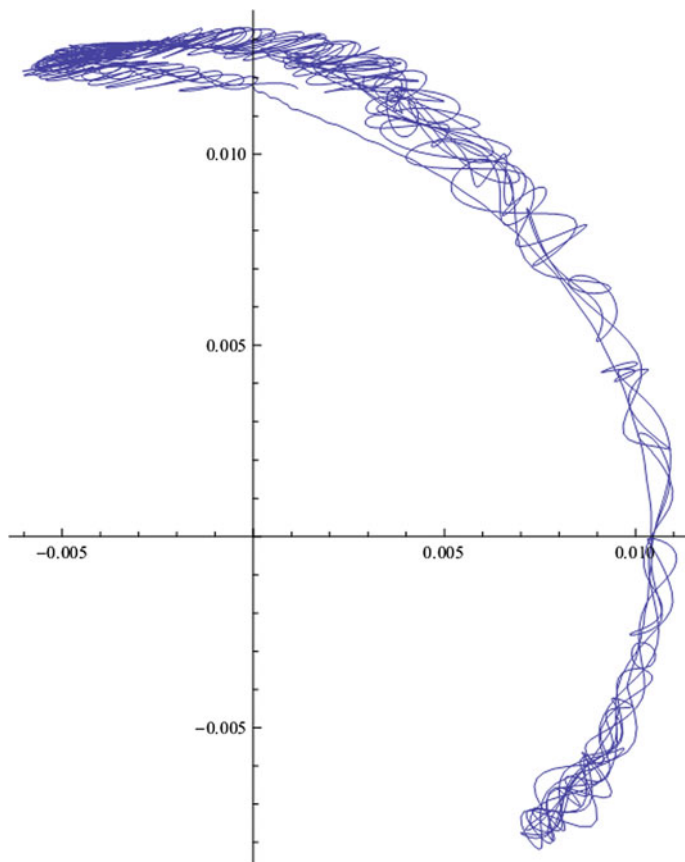


Fig. 3 The relative motion path of the two joint elements for joint C_1 when $T_p = 0.5$ s

where $k = 1, 2, 3$; and the coefficients satisfy the following equations.

$$A_{k,0} = q_{ko} \quad (25)$$

$$A_{k,1} = 0 \quad (26)$$

$$2A_{k,2} = 0 \quad (27)$$

$$A_{k,5}T_p^5 + A_{k,4}T_p^4 + A_{k,3}T_p^3 + A_{k,2}T_p^2 + A_{k,1}T_p + A_{k,0} = q_{ke} \quad (28)$$

$$5A_{k,5}T_p^4 + 4A_{k,4}T_p^3 + 3A_{k,3}T_p^2 + 2A_{k,2}T_p + A_{k,1} = 0 \quad (29)$$

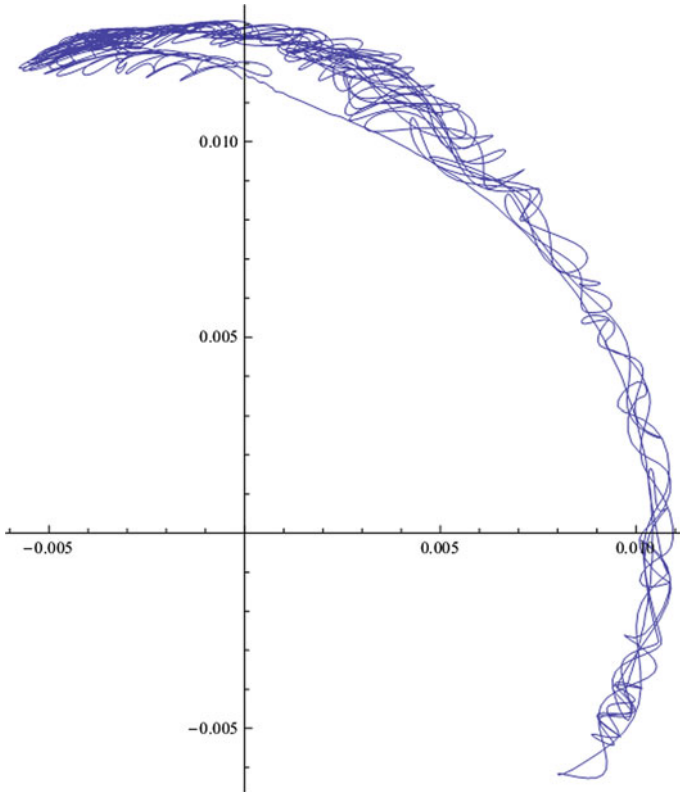


Fig. 4 The relative motion path of the two joint elements for joint C_1 when $T_p = 0.53$ s

$$20A_{k,5}T_p^3 + 12A_{k,4}T_p^2 + 6A_{k,3}T_p + 2A_{k,2} = 0 \tag{30}$$

Hence

$$A_{k,2} = 0 \tag{31}$$

$$A_{k,3} = \frac{10(q_{ke} - q_{ko})}{T_p^3} \tag{32}$$

$$A_{k,4} = -\frac{15(q_{ke} - q_{ko})}{T_p^4} \tag{33}$$

$$A_{k,5} = \frac{6(q_{ke} - q_{ko})}{T_p^5} \tag{34}$$

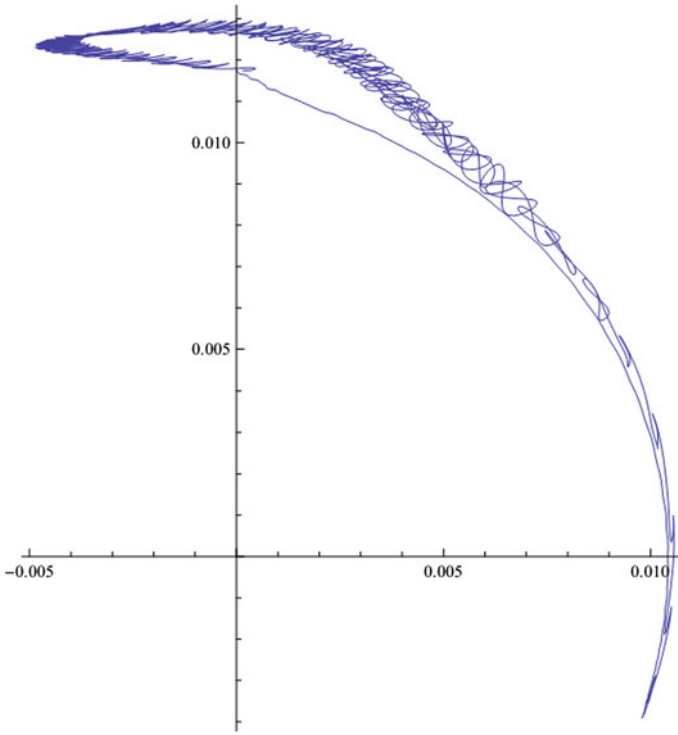


Fig. 5 The relative motion path of the two joint elements for joint C_1 when $T_p = 0.535$ s

where T_p denotes the time interval for the PRR mechanism moving along the trajectory.

When T_p equals 0.3, 0.5, 0.53, 0.535, 0.54, 0.545 s, respective, the relative motion paths of the two joint elements for joint C_1 are solved and shown in Figs. 2, 3, 4, 5, 6 and 7.

It can be found from Figs. 2, 3, 4, 5, 6 and 7 that the relative motion of the two joint elements appears chaos when $T_p < 0.54$ s, and the chaos can be suppressed if T_p equals 0.545 s.

4 Modeling of the Worn Revolute Joint

The revolute joint with clearance is comprised of a shaft and a sleeve, and the sleeve is a little larger than the shaft. After working for a time span, the revolute joint will be worn. Usually the material of the shaft is harder than the material of the sleeve, which indicates that the abrasion occurs first in the sleeve. The worn

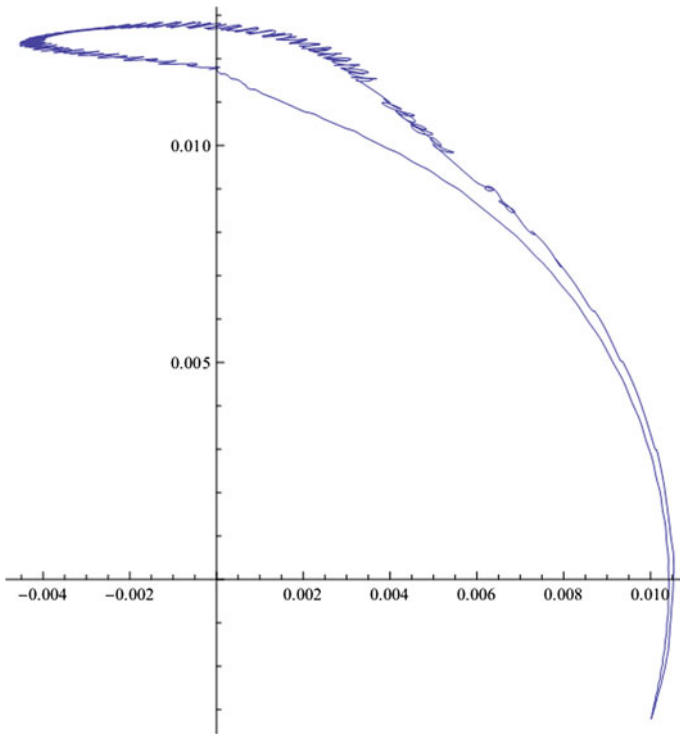


Fig. 6 The relative motion path of the two joint elements for joint C_1 when $T_p = 0.54$ s

revolute joint can be modeled by four parameters, such as the radius of the shaft r , the radius of the sleeve R , the abrasion depth δ , and the abrasion angle θ .

Figure 8 shows the worn sleeve when $r = 10$ mm, $R = 10.01$ mm, $\delta = 1.5$ mm, $\theta = 75^\circ$. In Fig. 8, the dashed line denotes the profile of the unworn sleeve, and the solid line denotes the shape of the worn sleeve.

5 Allowable Abrasion for the Revolute Joint to Suppress Chaos

The time interval of the trajectory planning is given as $T_p = 1.0$ s, and the structural parameters of the worn revolute joint are $r = 10$ mm, $R = 10.01$ mm, and $\theta = 75^\circ$. When δ equals 0, 0.01, 0.05, 0.09, 0.093, 0.095 mm, respectively, the relative motion paths of the two joint elements for joint C_1 are solved and shown in Figs. 9, 10, 11, 12, 13 and 14.

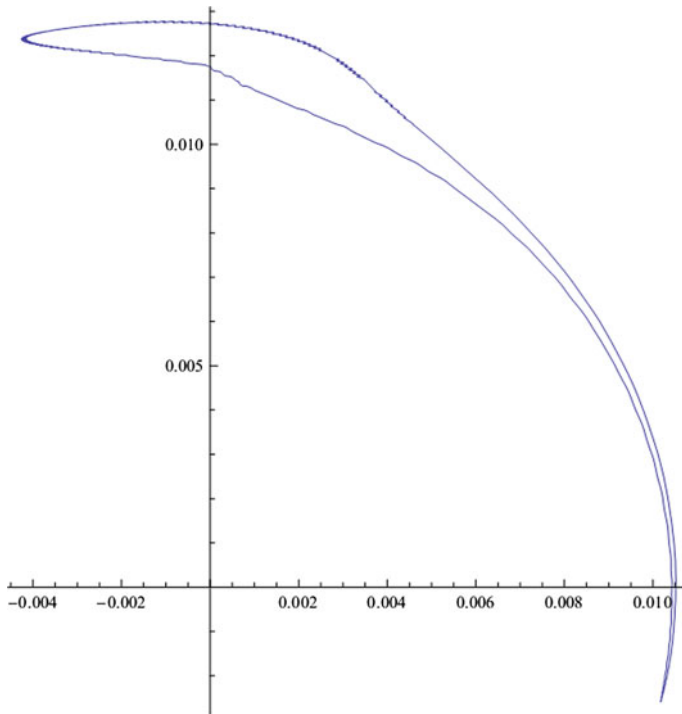


Fig. 7 The relative motion path of the two joint elements for joint C_1 when $T_p = 0.545$ s

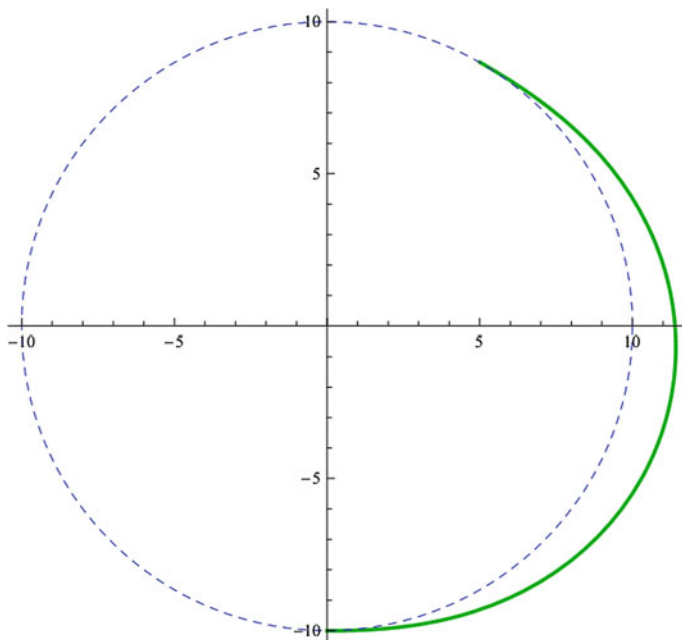


Fig. 8 The worm sleeve when $r = 10$ mm, $R = 10.01$ mm, $\delta = 1.5$ mm, $\theta = 75^\circ$

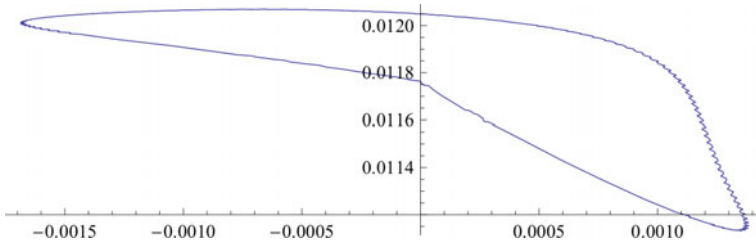


Fig. 9 The relative motion path of the two joint elements for joint C_1 when $T_p = 1$ s, $r = 10$ mm, $R = 10.01$ mm, $\theta = 75^\circ$, $\delta = 0$ mm

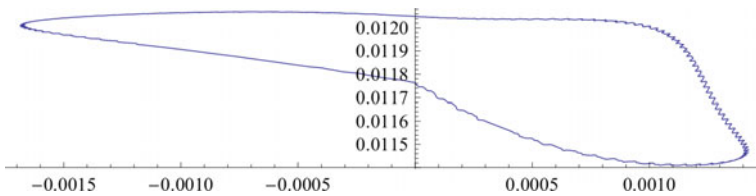


Fig. 10 The relative motion path of the two joint elements for joint C_1 when $T_p = 1$ s, $r = 10$ mm, $R = 10.01$ mm, $\theta = 75^\circ$, $\delta = 0.01$ mm

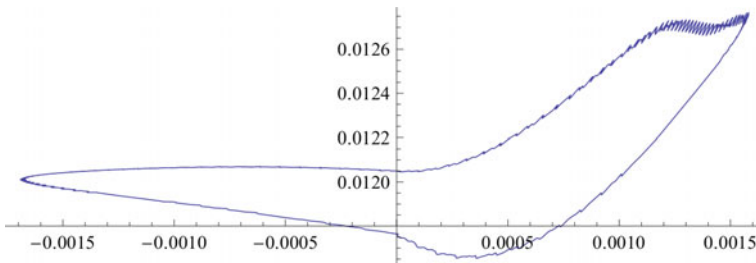


Fig. 11 The relative motion path of the two joint elements for joint C_1 when $T_p = 1$ s, $r = 10$ mm, $R = 10.01$ mm, $\theta = 75^\circ$, $\delta = 0.05$ mm

It can be found from Figs. 9, 10, 11, 12, 13 and 14 that, for $T_p = 1.0$ s, the relative motion of the two joint elements appears chaos when the abrasion depth $\delta > 0.09$ mm, and the chaos can be suppressed if $\delta < 0.05$ mm. Therefore the allowable abrasion for the revolute joint to suppress chaos is 0.05 mm when the time interval of the trajectory planning is $T_p = 1.0$ s.

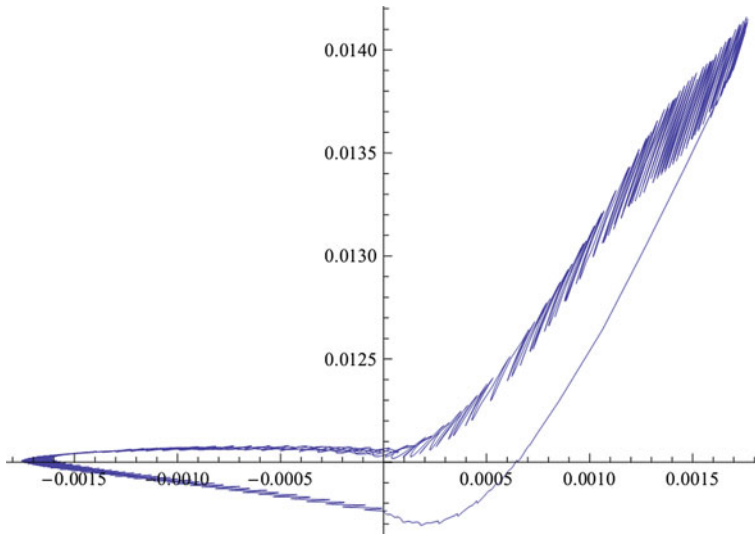


Fig. 12 The relative motion path of the two joint elements for joint C_1 when $T_p = 1$ s, $r = 10$ mm, $R = 10.01$ mm, $\theta = 75^\circ$, $\delta = 0.09$ mm

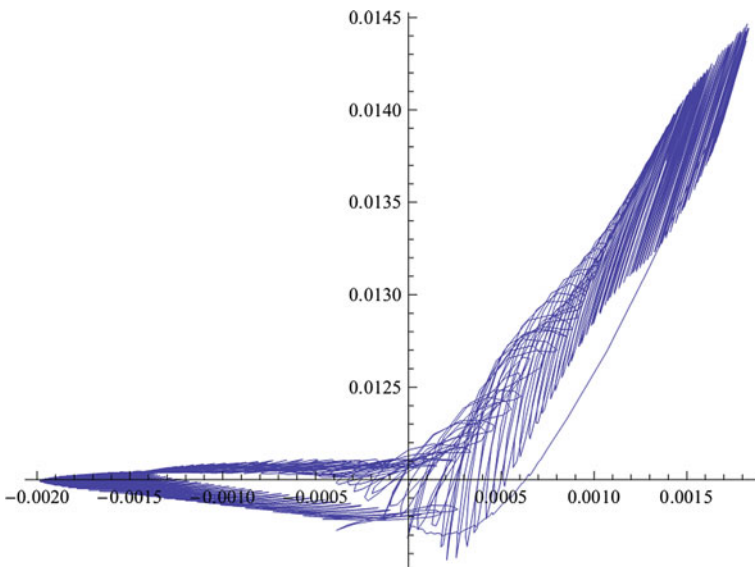


Fig. 13 The relative motion path of the two joint elements for joint C_1 when $T_p = 1$ s, $r = 10$ mm, $R = 10.01$ mm, $\theta = 75^\circ$, $\delta = 0.093$ mm

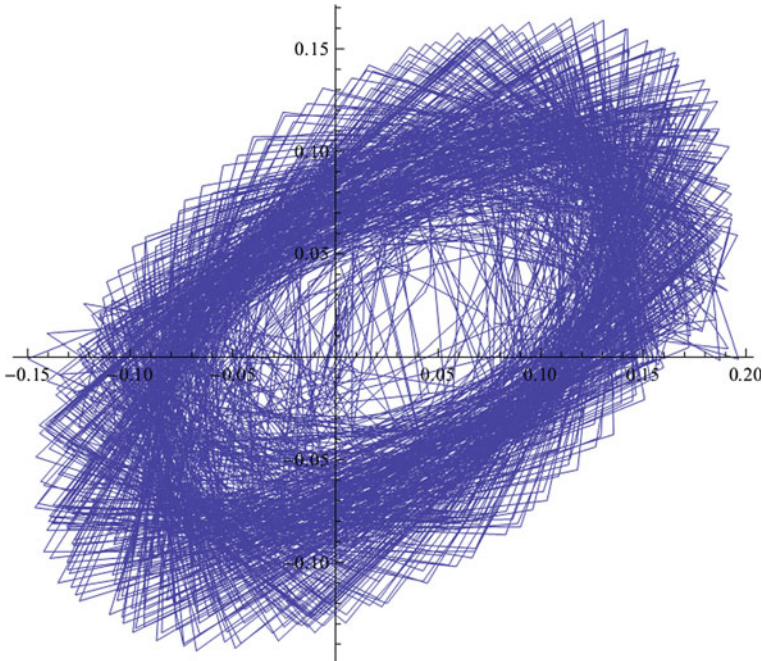


Fig. 14 The relative motion path of the two joint elements for joint C_1 when $T_p = 1$ s, $r = 10$ mm, $R = 10.01$ mm, $\theta = 75^\circ$, $\delta = 0.095$ mm

6 Conclusions

In this paper, the dynamics of the PRR robotic mechanism with revolute joint clearances is analyzed, and the chaos caused by joint clearances is investigated. A novel approach based on the trajectory planning of the robotic mechanism is presented to suppress the chaos. It can be found that the relative motion of the two joint elements appears chaos when the time interval of the trajectory planning is less than a threshold, and the chaos can be suppressed if the time interval is equal to or greater than the threshold.

Furthermore, the dynamics model of the worn revolute joint is established, and the allowable abrasion depth is derived to suppress chaos for the worn joints. It can be found that the relative motion of the two joint elements appears chaos when the abrasion depth is greater than a threshold, and the chaos can be suppressed if the abrasion depth is equal to or less than the threshold. In this way, the allowable abrasion for the revolute joint to suppress chaos can be obtained for a given time interval of the trajectory planning.

Acknowledgments This work was supported in part by the National Natural Science Foundation of China under Grants 51475331 and 51005199, and the Fundamental Research Funds for the Central Universities.

References

1. Wu WD, Rao SS (2007) Uncertainty analysis and allocation of joint tolerances in robot manipulators based on interval analysis. *Reliab Eng Syst Saf* 92:54–64
2. Wu WD, Rao SS (2004) Interval approach for the modeling of tolerances and clearances in mechanism analysis. *J Mech Des Trans ASME* 126:581–592
3. Huang T, Chetwynd DG, Mei JP, Zhao XM (2006) Tolerance design of a 2-DOF overconstrained translational parallel robot. *IEEE Trans Rob* 22:167–172
4. Venanzi S, Parenti-Castelli V (2005) A new technique for clearance influence analysis in spatial mechanisms. *J Mech Des Trans ASME* 127:446–455
5. Volgewede P, Ebert-Uphoff I (2004) Application of workspace generation techniques to determine the unconstrained motion of parallel manipulators. *J Mech Des Trans ASME* 126:283–290
6. Flores P, Ambrosio I, Claro JCP, Lankarani HM (2007) Dynamic behavior of planar rigid multi-body systems including revolute joints with clearance. *Proc Inst Mech Eng Part K J Multi-Body Dyn* 221:161–174
7. Flores P, Ambrosio I, Claro JCP, Lankarani HM, Koshy CS (2006) A study on dynamics of mechanical systems including joints with clearance and lubrication. *Mech Mach Theory* 41:247–261
8. Liu CS, Zhang K, Yang R (2007) The FEM analysis and approximate model for cylindrical joints with clearances. *Mech Mach Theory* 42:183–197
9. Alshaer BJ, Nagarajan H, Beheshti HK, Lankarani HM, Shivaswamy S (2005) Dynamics of a multibody mechanical system with lubricated long journal bearings. *J Mech Des Trans ASME* 127:493–498
10. Papadopoulos CA, Nikolakopoulos PG, Gounaris GD (2008) Identification of clearances and stability analysis for a rotor-journal bearing system. *Mech Mach Theory* 43:411–426
11. Bu W, Liu Z, Tan J, Gao S (2010) Detachment avoidance of joint elements of a robotic manipulator with clearances based on trajectory planning. *Mech Mach Theory* 45:925–940

Effects of Body Flexibility on Dynamics of Mechanism with Clearance Joint

Zheng Feng Bai, Xin Shi and Ping Ping Wang

Abstract In this paper, the dynamics characteristics of flexible mechanical system with clearance joint are investigated. The constraints of clearance joint are modeled as contact force constraints. The normal and tangential contact forces in clearance joints are modeled using a new nonlinear continuous contact force model and a modified friction force model, respectively. The flexible body is modeled by modal expansion method. Then, a planar slider-crank mechanism with clearance and flexible link is utilized as demonstrative application example to perform the investigation. The effects of body flexibility on dynamics of slider-crank mechanism with clearance are presented and discussed. The main results indicate that clearance has significant effects on dynamics responses of mechanism system. However, the body flexibility will deaden the contact and impact in clearance joints and has buffer effects for the mechanism with clearance.

Keywords Clearance joint · Flexible body · Mechanical system · Dynamics characteristics

1 Introduction

In general dynamic analysis of mechanical systems it is assumed that the kinematic joints are ideal or perfect, that is, clearance effects are neglected. However, in a real mechanical kinematical joint a clearance is always existence due to assemblage, manufacturing errors and wear. These clearances in joints cause impact loads, modify the dynamic response of the system and eventually lead to important

Z.F. Bai (✉) · X. Shi
Department of Mechanical Engineering, Harbin Institute of Technology,
Weihai 264209, Shandong, China
e-mail: baizhengfeng@126.com

P.P. Wang
Department of Astronautics Engineering, Harbin Institute of Technology,
Harbin 150001, Heilongjiang, China

deviations of the outcomes [1–6]. Several works were carried out to study the dynamic responses of particular mechanisms with clearance theoretically and experimentally, such as four-bar mechanism systems. Moreover, the dynamic responses of mechanism systems are affected by the deformation of the flexible elements. However, some of these works were limited only to the rigid case, that is, the structural flexibility of bodies is neglected.

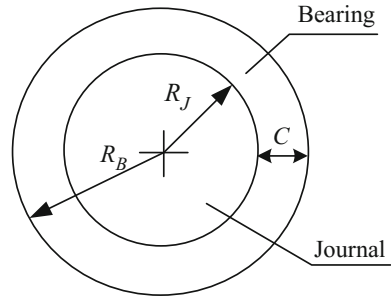
Stoenescu and Marghitu [7] studied the dynamics response of a planar rigid-link mechanism with a sliding joint clearance and indicate that high crank speeds lead to nonlinear characteristics of the mechanism with clearance. Erkaya and Uzmay [8, 9] studied the dynamic characteristics of planar mechanisms with revolute clearance joints theoretically and experimentally. Flores [10] studied the clearance effects on a planar slider-crank mechanism with different initial parameters, including the clearance size, clearance number and crank speed. Bai and Zhao [11] presented a new hybrid contact force model for revolute joint with clearance. The planar four-bar mechanism with a revolute clearance joint is used as a general numerical example to illustrate the methodology. Muvengei et al. [12] investigated the different motion modes of a slider-crank mechanism with two revolute joints. In conclusion, there are a great deal of researches on kinematics and dynamics analysis of mechanism with clearance. However, these works were limited only to the rigid case and most researches are based on the assumption of rigid multibody dynamics, that is, the body flexibility is not considered, and the findings may be limited to the rigid case of mechanism system with clearance. This is contrary to a realistic situation in which body flexibility is neglected.

In this paper, the dynamics responses of planar flexible mechanical system with revolute clearance joint are investigated using a computational method. The constraints of clearance joint are modeled as contact force constraints. The normal and tangential contact forces in clearance joints are modeled using a nonlinear continuous contact force model and a modified tangential friction force model, respectively. Consideration of structural flexibility of bodies, the flexible body is modeled by modal expansion method. Then, the dynamics equations of mechanism with clearance joint and flexible bodies are established using Lagrange multiplier method. Finally, a planar slider-crank mechanism with revolute clearance joint and flexible link is utilized as demonstrative application example to perform the investigation. The dynamics characteristics of slider-crank mechanism with clearance and flexible link are presented and discussed.

2 Modeling of Revolute Joint with Clearance

In this section, the model of a revolute joint in the presence of clearance is established. Figure 1 depicts a revolute joint with clearance. The radius of bearing and journal in revolute clearance joint are R_B and R_J , respectively. The difference between their radii is defined as the radial clearance. Thus, the radial clearance is expressed as:

Fig. 1 Schematic of revolute joint with clearance



$$c = R_B - R_J \tag{1}$$

It is known that the motion of mechanism with clearance always includes contact/impact process and the constraints of clearance joint are modeled as contact force constraints. Therefore, to evaluate efficiently the contact forces between the bearing and journal in a revolute joint with clearance, special attention must be given to the numerical description of the contact model [13–15]. In this paper, the revolute clearance joint is considered as dry contact and friction. A new nonlinear contact force model proposed by Bai and Zhao [13] is used for contact modeling of journal and bearing in revolute clearance joint. This new nonlinear contact force model accounts for both the elastic and damping effects and can be expressed as:

$$F_n = K_n \delta^n + D_{\text{mod}} \dot{\delta} \tag{2}$$

where K_n is the nonlinear stiffness coefficient, depending on the geometry of the contact surfaces, contact process and their physical properties. D_{mod} is the modified damping coefficient. δ is the deformation and $\dot{\delta}$ is the relative deformation velocity. Therefore, the first term in the right-hand side of Eq. (2) represents the elastic force based on the Hertz contact law, while the second term accounts for the damping force due to energy dissipation.

For journal and bearing contact in clearance join, K_n is expressed as:

$$K_n = \frac{1}{8} \pi E^* \sqrt{\frac{2\delta(3(R_B - R_J) + 2\delta)^2}{(R_B - R_J + \delta)^3}} \tag{3}$$

where E^* is compound elastic modulus and can be expressed as:

$$\frac{1}{E^*} = \frac{1 - \nu_i^2}{E_i} + \frac{1 - \nu_j^2}{E_j} \tag{4}$$

The modified damping coefficient, D_{mod} is expressed as:

$$D_{\text{mod}} = \frac{3K_n(1 - c_e^2)e^{2(1-c_e)}\delta^n}{4\dot{\delta}^{(-)}} \tag{5}$$

where ν is the Poisson ratio of contact bodies, E is the Young modulus of contact bodies, c_e is coefficient of restitution and $\dot{\delta}^{(-)}$ is initial relative velocity of the impact point.

Further, for tangential contact of clearance joint, the modified Coulomb friction model [11] is used to represent the friction response in clearance joint and the modified Coulomb friction model is expressed as Eq. (6):

$$F_t = -\mu(v_t)F_n \frac{v_t}{|v_t|} \tag{6}$$

where the dynamic friction coefficient $\mu(v_t)$ is given as Eq. (7):

$$\mu(v_t) = \begin{cases} -\mu_d \text{sign}(v_t) & \text{for } |v_t| > v_d \\ -\left\{ \mu_d + (\mu_s - \mu_d) \left(\frac{|v_t| - v_s}{v_d - v_s} \right)^2 \left[3 - 2 \left(\frac{|v_t| - v_s}{v_d - v_s} \right) \right] \right\} \text{sign}(v_t) & \text{for } v_s \leq |v_t| \leq v_d \\ \mu_s - 2\mu_s \left(\frac{v_t + v_s}{2v_s} \right)^2 \left(3 - \frac{v_t + v_s}{v_s} \right) & \text{for } |v_t| < v_s \end{cases} \tag{7}$$

where v_t is relative sliding velocity. μ_d and μ_s are dynamic and static friction coefficient, respectively. v_s and v_d are the given bounds for the tangential critical velocity.

3 Flexible Body Discretization Modeling

In realistic situation, the body flexibility of mechanism system cannot be neglected. The flexibility of bodies usually introduces an infinite number of degrees of freedom (DOF). The discretization procedures can truncate the number of DOF to a finite number, such as assumed modes or finite element. Therefore, the discretization procedures can be used to provide approximate description of the mechanism system with flexible bodies. In this paper, modal expansion method was used to realize the discretization processing of the flexible bodies.

Therefore, flexible body is modeled by modal expansion method and the deformation of flexible link can be represented as

$$u_f = \Phi \tau_f \tag{8}$$

where u_f is the deformation of flexible body. Φ is the modal matrix and τ_f is the modal coordinate matrix, $\tau_f = [\tau_1 \tau_2 \dots \tau_n]^T$. n is the number of mode order considered in the modeling of flexible body. Modal expansion method usually truncate small elastic deformation mode of flexible body to improve the computational efficiency.

4 Application Example: Slider-Crank Mechanism

In order to study the combined effect of joint clearance and flexible link on dynamics characteristics of mechanical system, a slider-crank mechanism with a revolute clearance joint and a flexible link is used to represent the investigation. The dynamic simulations are carried out with rigid link and flexible link of slider-crank mechanism with clearance joint, respectively. The dynamic responses of slider-crank with clearance obtained with rigid link are compared with that of flexible link.

Figure 2 depicts the configuration of the planar slider-crank mechanism. A revolute clearance joint exists between the connecting rod and slider, and the clearance size is 0.5 mm. Other joints are considered as ideal joint, that is, no clearances in these joints. In the dynamics simulation, the connecting rod is considered as rigid and flexible link, respectively. Crank and slider are considered as rigid bodies. Initially, the journal and bearing centers are coincident. The material and geometric properties of the bodies in slider-crank mechanism are listed in Table 1 and the parameters used in the dynamic simulations are given in Table 2.

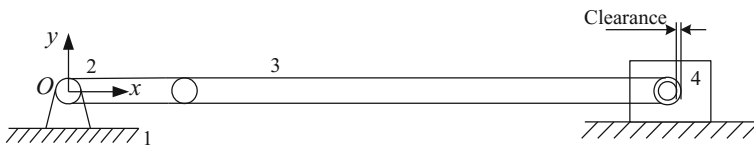


Fig. 2 Planar slider-crank mechanism with clearance

Table 1 Material and geometric properties of the slider-crank mechanism

Body	Length (m)	Width (m) × depth (m)	Young’s modulus (GPa)	Density (kg/m ³)	Poisson’s ratio
Crank	0.06	0.02 × 0.02	207	7801	0.29
Connection rod	0.4	0.02 × 0.004	71.705	2740	0.33
Sliding block	0.04	0.04 × 0.04	207	7801	0.29

Table 2 Simulation parameters for the slider-crank mechanism

Restitution coefficient	0.9
Dynamic friction coefficient	0.01
Input speed of the crank (rpm)	600
Initial position	0
Initial velocity (°/s)	0

The simulation results of slider-crank mechanism considering clearance with rigid and flexible connecting rod are as following. Note that the results are plotted for two full crank rotations after steady-state has been reached.

Figure 3 presents the dynamics characteristics of slider-crank mechanism with clearance for rigid and flexible link. Figure 3a shows that the position curves of slider are almost completely a coincidence between the ideal mechanism without clearance and real mechanism with clearance for both rigid and flexible link. Figure 3b shows that the effects of clearance on slider velocity are obvious when connection rod is considered as rigid link. The velocity of slider is vibration with higher amplitude. However, when the connection rod is modeled as flexible link,

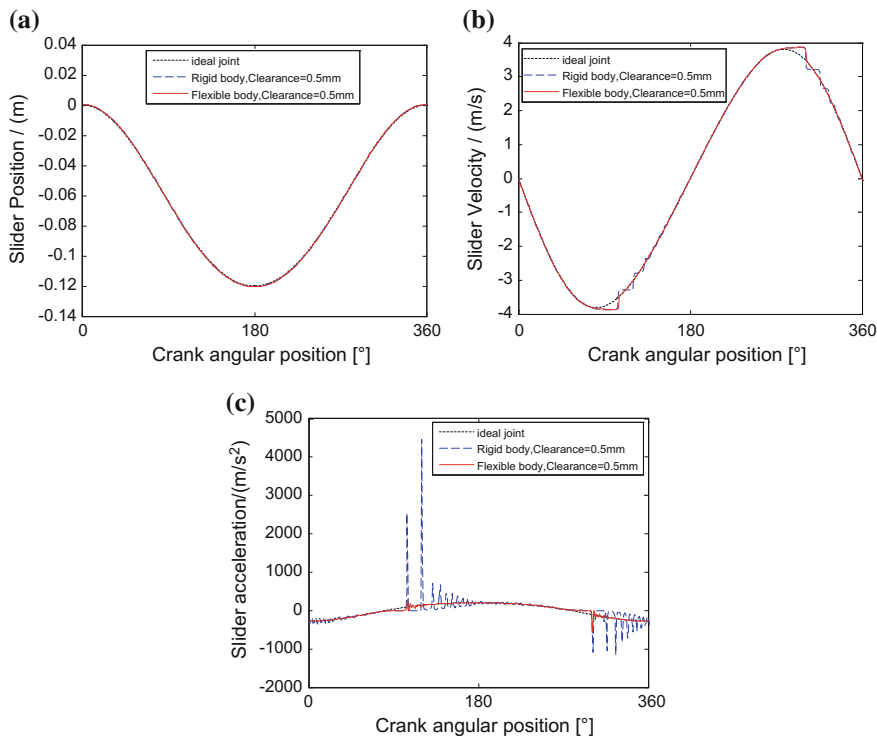
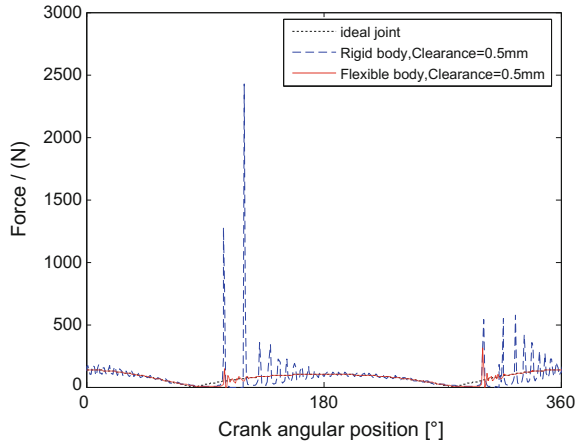


Fig. 3 Dynamics characteristics of slider-crank mechanism with clearance: **a** slider position; **b** slider velocity; **c** slider acceleration

Fig. 4 Contact forces in clearance joint



the velocity of slider is less vibration. Figure 3c shows that the acceleration of slider is significant differences between the dynamic responses of mechanism when modeled as rigid link without clearance, rigid link with clearance joint, and flexible link with clearance joint. When the connection rod is modeled as rigid link, the acceleration of slider is vibration with very high peaks due to the existence of clearance. However, in contrast to the acceleration of rigid slider-crank mechanism with clearance, in the case of a flexible link, the vibration of slider acceleration is depression and the vibration peaks are reduced obviously compared to the case where the connection rod is modeled as rigid link. It indicates that the effects of clearance on the acceleration of the slider are obviously differences between the dynamic responses of the mechanism when modeled with rigid and flexible link.

Figure 4 shows the contact forces in clearance joint when slider-crank mechanism model as rigid and flexible link. It shows that the impacts between journal and bearing decrease and the peaks of contact forces are reduced when connection rod is model as flexible link. Therefore, the link flexibility will deaden the contact and impact in clearance joints and has buffer effects for the mechanism with clearance, which is very close to the ideal case of mechanism system.

5 Conclusions

In this work, the dynamics responses of flexible mechanical system with clearance joint are investigated. The normal and tangential contact forces in clearance joints are modeled using a nonlinear contact force model and a modified friction force model, respectively. Consideration of structural flexibility of body, the flexible body is modeled by modal expansion method. A planar slider-crank mechanism with clearance and flexible link is utilized to perform the investigation.

The results show that clearance has less effect on position of slider for both rigid and flexible link of mechanism system. The effects of clearance on slider velocity are obvious when connection rod is considered as rigid link. The velocity of slider is vibration with higher amplitude. However, when considering the link flexibility, the velocity of slider is less vibration. Moreover, when ignore the link flexibility, the acceleration of slider is obviously vibration with high peaks for the rigid mechanism with clearance. However, considering the link flexibility, the vibration of slider acceleration is depression and the vibration peaks are reduced obviously.

The impacts between journal and bearing decrease and the peaks of contact forces are reduced when connection rod is model as flexible link. Therefore, the link flexibility will deaden the contact and impact in clearance joints and has buffer effects for the mechanism with clearance, which is very close to the ideal case of mechanism system. It indicates that when dynamics analysis of mechanism with clearance, the flexibility of bodies in mechanism cannot be ignore.

Acknowledgment This work was supported by the National Natural Science Foundation of China (Grant No.: 51305093), the Natural Science Foundation of Shandong Province (Grant No.: ZR2013EEQ004) and the China Postdoctoral Science Foundation funded project (Grant Nos. 2012M520723; 2014T70317). Project supported by the National Key Basic Research Program of China (No. 2013CB733000) are also gratefully acknowledged.

References

1. Flores P, Ambrosio J, Claro JCP, Lankarani HM, Koshy CS (2006) A study on dynamics of mechanical systems including joints with clearance and lubrication. *Mech Mach Theory* 41:247–261
2. Bai ZF, Liu YQ, Sun Y (2015) Investigation on dynamic responses of dual-axis positioning mechanism for satellite antenna considering joint clearance. *J Mech Sci Technol* 29(2): 453–460
3. Flores P (2009) Modeling and simulation of wear in revolute clearance joints in multibody systems. *Mech Mach Theory* 44(6):1211–1222
4. Bai ZF, Zhao Y (2012) Dynamics modeling and quantitative analysis of multibody systems including revolute clearance joint. *Precision Eng* 36:554–567
5. Mukras S, Kim NH, Mauntler NA, Schmitz TL, Sawyer WG (2010) Analysis of planar multibody systems with revolute joint wear. *Wear* 268:643–652
6. Oeden JCG (2005) Analysis of clearance in multibody system. *Multibody Syst Dyn* 13: 401–420
7. Stoenescu ED, Marghitu DB (2003) Dynamic analysis of a planar rigid-link mechanism with rotating slider joint and clearance. *J Sound Vib* 266:394–404
8. Erkaya S, Uzmay I (2008) A neural-genetic (NN-GA) approach for optimizing mechanisms having joints with clearance. *Multibody Syst Dyn* 20(1):69–83
9. Erkaya S, Uzmay I (2009) Investigation on effect of joint clearance on dynamics of four-bar mechanism. *Nonlinear Dyn* 58(1–2):179–198
10. Flores P (2010) A parametric study on the dynamic response of planar multibody systems with multiple clearance joints. *Nonlinear Dyn* 61:633–653
11. Bai ZF, Zhao Y (2012) Dynamic behaviour analysis of planar mechanical systems with clearance in revolute joints using a new hybrid contact force model. *Int J Mech Sci* 54:190–205

12. Muvengei O, Kihiu J, Ikua B (2013) Dynamic analysis of planar rigid-body mechanical systems with two-clearance revolute joints. *Nonlinear Dyn* 73:259–273
13. Bai ZF, Zhao Y (2013) A hybrid contact force model of revolute joint with clearance for planar mechanical systems. *Int J Nonlinear Mech* 48:15–36
14. Liu CS, Zhang K, Yang L (2006) Normal force-displacement relationship of spherical joints with clearances. *ASME J Comput Nonlinear Dyn* 1:160–167
15. Koshy CS, Flores P, Lankarani HM (2013) Study of the effect of contact force model on the dynamic response of mechanical systems with dry clearance joints-computational and experimental approaches. *Nonlinear Dyn* 73:325–338

The Dynamics Modeling of Serial Robot with Joint Clearance Based on the Massless Link Method

Chanyuan Chen, Lixin Yang, Yanjiang Huang, Haopeng Zhou, Jinying Zhang and Xianmin Zhang

Abstract A general and comprehensive dynamics modeling of serial robot with clearance in joint is presented throughout this work. The key point in this paper is to treat the joint clearance as a massless link, which directly relate to the dynamics modeling of the mechanism. Using the massless link method, combined with the Lagrange method and the D'Alembert's principle, a computational methodology for purpose of solving the clearance angle, is presented. With the clearance size calculated, the terminal position of robot manipulator can be derived, which provides a reference for subsequent robot control.

Keywords Massless link method · Dynamics modeling · Clearance angle

1 Introduction

Machinery industry is developing towards the direction of high precision, high reliability and long life. Hence the study on improving the working precision of industrial robot is essential and necessary to the modern industrial production.

The mechanism analysis of multibody system in the past tend to regard the hinge as ideal hinge, while ignoring the inevitable joint clearance. As a result of the need of clearance fit, manufacturing errors, imperfections and material deformation, the

C. Chen · L. Yang · Y. Huang · H. Zhou · J. Zhang · X. Zhang (✉)
Guangdong Provincial Key Laboratory of Precision Equipment and Manufacturing
Technology, School of Mechanical and Automotive Engineering, South China
University of Technology, Guangzhou 510640, China
e-mail: zhangxm@scut.edu.cn

C. Chen
e-mail: 18814105651@163.com

L. Yang
e-mail: melxyang@scut.edu.cn

Y. Huang
e-mail: mehuangyj@scut.edu.cn

existence of joint clearance in mechanism become unavoidable [1–4]. The existence of clearance in the machine joints leads to the degradation of the overall system performance. Increasingly accuracy requirements for the modern industry demand that the influence of the joint clearance can not be ignored.

Systematic research into the dynamics of mechanism with joint clearance can be traced back to the early 1970s, before which, most of the studies only studied the motion error analysis of mechanism with clearance. American scholar Dubowsky et al. proposed an Impact Pair Model in 1971, and investigated the dynamic characteristics of the mechanical systems with joint clearance [5–9]. Based on their research, many scholars published a considerable amount of experimental and theoretical works associated with joint clearance, formed a relatively complete research system. In the research methods proposed by the researchers by now, the description method of joint clearance can be divided into the following three categories: (1) ‘a two-mode model’ [7, 10], which holds that the pairing elements exist two states, that is, contact and free movement; (2) ‘a three-state model’ [11], as the name implies, in this modeling strategy exists three phases, the contact, freedom, and collision contact phase; (3) the continuous contact model [12, 13], assuming that the pairing element always keep contact with each other when it works [14].

The ‘two-state model’ can calculate the impact of the collision in this model. The ‘three-state model’ is more coincide with the actual situation. However, the accurate transition time between these states and the motion parameters are difficult to determine. In addition, both these two models are instable in the numerical calculation computation, and hard to apply to dynamics analysis of mechanism that considers more clearance.

Advantage of continuous contact model is no need to consider the transition between different states, which greatly simplifies the analysis and the calculation process, making it more suitable for application in the analysis of multibody system or mechanism with multi-clearance. Some physical parameters of moving pairs are ignored, resulting in not truly reflecting the contact characteristics of the joints with clearance in the mechanism, so further studies are needed. However, due to the joint clearance is relatively small, some studies believe that the collision and separation time of the pairing elements is very short, mainly in contact state. Assuming the contact surface of motion pair do not have deformation, therefore, using a massless link [15, 16] instead of joint clearance, the equivalent to adding a degree of freedom to the mechanism with ideal joints. This kind of modeling method is pretty simple, and greatly simplifies the analysis work.

2 Dynamics Modeling of Serial Robot System with Clearance

Actually, the revolute joints in a robot manipulator should be count as clearance joints.

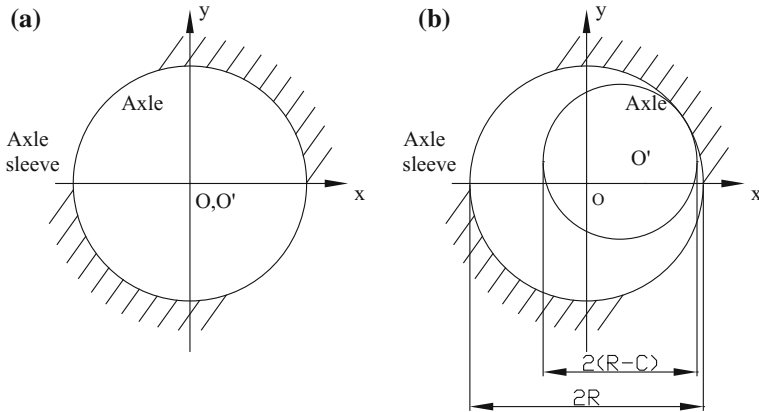


Fig. 1 Model of ideal and actual rotating hinge with clearance: **a** the ideal rotating hinge; **b** the actual rotating hinge

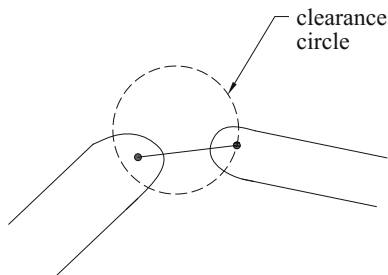
The classical approach which is the so-called zero-clearance approach, regards that the center of the bearing and journal that connecting two components are coincident, as shown in (a) of Fig. 1. The introduction of clearance in joint separates them. Figure 1b depicts the difference in radius between the bearing and journal generates the clearance in joint, and two kinematic constraints are removed when two degrees of freedom are introduced instead. As the key point of establishing the dynamics model for robot manipulator with clearance is to incorporate the clearance model and the robot dynamics model, which needs to rationally describe the joint clearance.

2.1 Description Method of Joint with Clearance

The serial robot studied in this paper has five degrees of freedom, which means that's a multi-body dynamics problem. As we all know, the multi-body dynamics is nonlinear and complex, so the description of the clearance should occurs to be easy to analysis. In the modeling methods mentioned in this paper, it is clear that the continuous contact model is the most simple to analysis and more suitable for dynamic analysis of the multi-body system with clearance.

In order to reflect the dynamics influence of joint clearance, regarding the joint clearance as a massless link in this paper. The length of this link indicates the size of the joint clearance like Fig. 2 shows, which varies with the relative position of the bearing and journal. Each joint clearance adds an additional degree of freedom to the mechanism. The rotation angle of this linkage can be described as clearance angle, when mutated means that the separation between motion pair elements occurred. Therefore, this model can describe the movement of joint with clearance in a certain extent.

Fig. 2 Revolute clearance joint modeled by massless link approach



2.2 Kinematics Description of Serial Robot with Joint Clearance

Before having the dynamics modeled of the robot with joint clearance, kinematics modeling about the serial robot should be carried out on the first. The mechanism studied in this paper is a serial robot with five degrees of freedom. For the convenience of analysis, only considering the first joint as a clearance joint while taking the other joints as ideal joints. When analyze mechanism with clearance in other joint or in multi-joints, this case can be referred. As clearance exists in the first joint, regarding the clearance as a massless link with the length equal to one half of the clearance size. It adds a degree of freedom to this system and turns the 5-DOF system to a system with six degree of freedom. Denote the length of the clearance link as l_1 , the angle between the link and X-axis of the base coordinate system as θ_1 . In this model, take the link as the clearance of joint, the clearance angle as the contact position of the bearing and journal.

In the science of kinematics, it studies the position, the velocity, the acceleration, and all higher order derivatives of the position variables (with respect to time or any other variable). Figure 3 demonstrates the configuration of the robot manipulator system, which consists of five rotation shafts and a massless link on behalf of the clearance existing in the first joint. Namely, the kinematics modeling of 5-DOF robot with joint clearance can be regarded as the modeling of a 6-DOF robot with ideal joints.

The Denavit-Hartenberg notation was used in the kinematics modeling, Table 1 shows the corresponding parameters of this robot. The parameter l_2 to l_6 represent the length of the second link to sixth link respectively while the parameter l_1 means the length of the clearance link, and the parameter θ_2 to θ_6 on behalf of the link twist of each link while θ_1 means the clearance angle. Have all this parameters prepared, it is possible to compute the individual transformations ${}^{i-1}T_i$ for each link.

Fig. 3 Configuration and coordinate system of serial robot with clearance in the first joint

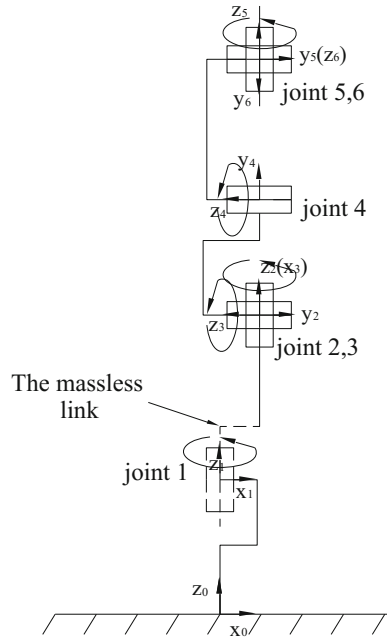


Table 1 The D-H parameters of the 5-R serial robot with clearance in the first joint

Link num.	Link twist	Link length	Joint angle (initial value)	Link offset
1	0	0	$\theta_1(0)$	100
2	0	l_1	$\theta_2(-\pi/2)$	245
3	$\pi/2$	l_2	$\theta_3(\pi/2)$	0
4	0	l_3	$\theta_4(-\pi/2)$	0
5	$-\pi/2$	l_4	$\theta_5(0)$	448
6	$-\pi/2$	l_5	$\theta_6(0)$	0

The velocity of a particle on the link i can be expressed as

$${}^0v_i = \frac{d}{dt}({}^0r_i) = \frac{d}{dt}({}^0T_i^i r_i) = \left[\sum_{j=1}^i \left(\frac{\partial {}^0T_i}{\partial \theta_j} \dot{\theta}_j \right) \right] i r_i \tag{1}$$

where the symbol ${}^i r_i$ means the particle's coordinate in the frame of joint i , the partial derivation of 0T_i to θ_i can be further expressed as

$$\frac{\partial {}^{i-1}T_i}{\partial \theta_i} = Q_i {}^{i-1}T_i \tag{2}$$

With all the preparations above, 0v_i can be converted as

$$\begin{cases} U_{ij} = \frac{\partial T_i}{\partial \theta_j} = \begin{cases} {}^0T_1{}^1T_2 \dots {}^{j-2}T_{j-1}Q_j{}^{j-1}T \dots {}^{i-1}T_i & j \leq i \\ 0 & j > i \end{cases} \\ {}^0v_i = \left[\sum_{j=1}^i (U_{ij}\dot{\theta}_j) \right] {}^i r_i \end{cases} \quad (3)$$

Similarly, 0a_i can be expressed like this

$${}^0a_i = \frac{d}{dt}({}^0v_i) = \sum_{j=1}^i \left[\sum_{k=1}^i ({}^0T_{k-1}Q_k{}^{k-1}T_{j-1}Q_j{}^{j-1}T_i\dot{\theta}_k) \dot{\theta}_j + U_{ij}\ddot{\theta}_j \right] {}^i r_i \quad (4)$$

The expressions of coordinate transformation, velocity and acceleration, almost describe all the properties of robot kinematics. It is the groundwork for the followed dynamic analysis.

2.3 Dynamics Modeling of Serial Robot with Joint Clearance

On the basis of kinematics analysis, the dynamic analysis is carried out. The main task of dynamic analysis is to discuss the relationship between the driving torque and the motion of components in mechanism.

Langrangian dynamic formulation is an “energy-based” approach to dynamics. In this method, the entire system is regarded as a unified object. It establishes the dynamical equations based on the generalized coordinate by the view of energy, so as to avoid the complex computing of power, velocity, acceleration vectors. The Lagrange method is suitable for multi-constraint processing. Therefore, the Lagrange method is the most widely used dynamic modeling method for multi-body system at present.

The langrangian dynamic formulation provides a method of deriving dynamic equations from a scalar function called Langrangian, which is defined as the difference between the kinetic and the potential energy of the mechanical system. It can be described as

$$L = K - U \quad (5)$$

In this formula, K represents the kinetic energy of the system with clearance, including translation and rotational kinetic energy, and U indicates the potential energy of the system with clearance. The equations of motion for the manipulator are then given by

$$\tau_i = \frac{d}{dt} \frac{\partial L}{\partial \dot{\theta}_i} - \frac{\partial L}{\partial \theta_i} = \frac{d}{dt} \frac{\partial K}{\partial \dot{\theta}_i} - \frac{\partial K}{\partial \theta_i} + \frac{\partial U}{\partial \theta_i} \quad (6)$$

The total potential energy of the system can be expressed as

$$U = \sum_{i=2}^6 -m_i g ({}^0T_i^i r_i) + \frac{1}{2} k \delta^2 \quad (7)$$

the first part in the formula indicates the gravitational potential energy, the second part means the spring damping potential energy produced in the process of collision caused by clearance in the first joint.

The kinetic energy of particle j on the link i is described as

$$\begin{aligned} dK_j &= \frac{1}{2} dm ({}^0v_j)^2 \\ &= \frac{1}{2} Trace \left(\sum_{p=1}^i \sum_{r=1}^i \frac{\partial {}^0T_i^i}{\partial \theta_p} r_p dm ({}^i r_p)^T \left(\frac{\partial {}^0T_i^i}{\partial \theta_r} \right)^T \dot{\theta}_p \dot{\theta}_r \right) \end{aligned} \quad (8)$$

the computing method of *Trace* can be described as

$$Trace \left(\begin{bmatrix} \dot{x}_i \\ \dot{y}_i \\ \dot{z}_i \end{bmatrix} \cdot [\dot{x}_i \quad \dot{y}_i \quad \dot{z}_i] \right) = \dot{x}_i^2 + \dot{y}_i^2 + \dot{z}_i^2$$

By doing integral computation on the kinetic energy of all particles on the link i , the total kinetic energy of link i is obtained.

$$\begin{aligned} K_i &= \int_i dK_p = \frac{1}{2} Trace \left(\sum_{p=1}^i \sum_{r=1}^i \frac{\partial {}^0T_i^i}{\partial \theta_p} J_i \left(\frac{\partial {}^0T_i^i}{\partial \theta_r} \right)^T \dot{\theta}_p \dot{\theta}_r \right) \\ J_i &= \int_i {}^i r_p ({}^i r_p)^T dm \end{aligned} \quad (9)$$

According to the total kinetic energy and potential energy of the robot, the driving torque of each joint of the robot can be obtained as

$$\begin{aligned} \tau_i &= \sum_{p=i}^n \sum_{j=1}^p \sum_{k=1}^p Trace \left(U_{ijp} J_p U_{ip}^T \right) \dot{\theta}_j \dot{\theta}_k \\ &+ \sum_{p=i}^6 \sum_{j=1}^p Trace \left(U_{pj} J_p U_{ip}^T \right) \ddot{\theta}_j - \sum_{p=i}^6 (m_p g^T U_{ip}^p r_p) + I_i \ddot{\theta}_i \end{aligned} \quad (10)$$

Using the formulas above, the driving torque can be calculated under the given parameters such as θ_i , $\dot{\theta}_i$ and $\ddot{\theta}_i$.

3 Algorithm Founding for Solving Clearance Angle

In the study of robot with clearance, it is important to figure out the relative position between the bearing and journal. Only after the position is counted can other parameters be calculated. The clearance angle reflects the position, so it is critical to establish the equation to calculate the clearance angle with the help of the formulas above.

The following Fig. 4 reveals the force and torque loaded on the link i , the point C_i indicates the center of mass. According to the force balance equation, the formula obtained of link i can be expressed as

$$\begin{cases} F_i = f_{i-1,i} - f_{i,i+1} \\ N_i = \tau_{i-1} - \tau_i + r_{C,i-1} \times f_{i-1,i} + r_{C,i} \times (-f_{i,i+1}) \end{cases} \quad (11)$$

the symbol F_i and N_i means the resultant force and moment loaded on this link, which can be calculated by the dynamic static analysis method (the so-called D'Alembert's principle):

$$\begin{cases} F_i = m_i \dot{v}_{C_i} - m_i g \\ N_i = {}^{C_i}I \dot{\omega}_i + \omega_i \times {}^{C_i}I \omega_i \end{cases} \quad (12)$$

In order to figure out the value of the clearance angle, it is essential to establish the solving equations. As the first link of the robot is a massless link, which means its mass and rotational inertia comes to be zero, making the formulas above simpler. Another key point is τ_1 equals to zero, as the massless link has no driving torque. Then the following equation is obtained.

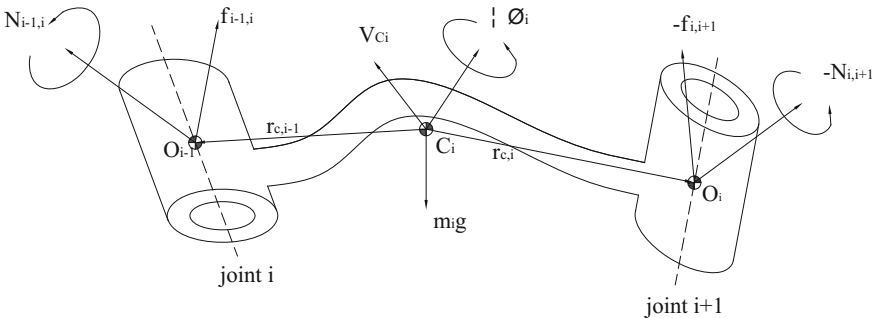


Fig. 4 Force diagram of the link i of the robot

$$\tau_2 + (-r_{C,1} + r_{C,i}) \times f_{1,2} = 0 \tag{13}$$

Using the expressions relevant to τ_2 and $f_{1,2}$, formula (13) can be derived as

$$\begin{aligned} & \left(\sum_{i=2}^6 \text{Trace}(U_{i1} J_i U_{i2}^T) + H_1 \sum_{i=2}^6 m_i U_{i1}^i r_i \right) \ddot{\theta}_1 = -I_2 \ddot{\theta}_2 - H_1 \sum_{i=2}^6 E \\ & + \sum_{i=2}^6 m_i g^T U_{i2}^i r_i - \sum_{i=2}^6 \sum_{p=2}^i \text{Trace}(U_{ip} J_i U_{i2}^T) \ddot{\theta}_p \\ & - \sum_{i=2}^6 \sum_{p=1}^i \sum_{j=1}^i \text{Trace}(U_{ijp} J_i U_{i2}^T) \dot{\theta}_j \dot{\theta}_p \end{aligned} \tag{14}$$

where

$$\begin{aligned} H_1 &= [1 \ 0 \ 0 \ 0] \cdot (-r_{C,1} + r_{C,i}) \cdot [0 \ 1 \ 0 \ 0] - [0 \ 1 \ 0 \ 0] \cdot (-r_{C,1} + r_{C,i}) \cdot [1 \ 0 \ 0 \ 0], \\ E &= m_i \left(Q_1 \dot{\theta}_1 \sum_{k=1}^i ({}^0 T_{k-1} Q_k^{k-1} T_i \dot{\theta}_k)^i r_i + \sum_{j=2}^i \left(\sum_{k=1}^i ({}^0 T_{k-1} Q_k^{k-1} T_{j-1} Q_j^{j-1} T_i \dot{\theta}_k) \dot{\theta}_j + U_{ij} \ddot{\theta}_j \right)^i r_i - g \right) \end{aligned}$$

Since it is too sophisticated to work out the analytical solution of differential Eq. (14) about the clearance angle, then the function Ode45 of Matlab would be the access to its numerical solution. Ode is a series functions of Matlab devoted to solving the numerical solution of differential equations, in which the Ode45 function is the preferred method.

Under the aid of function Ode45 in Matlab, the numerical solutions of the clearance joint can be obtained. As the clearance angle has been calculated, the displacement of robot manipulator is supposed to be figured out.

4 Dynamic Simulation of Robot with Clearance

4.1 The Parameters of the Simulation

The simulation object in this work is a five DOF robot whose first joint is assumed to be a joint with clearance as Fig. 2 shows. The first link is a massless link which represents the clearance exists in the first joint. The mass properties of the robot system are shown as the following Table 2. It also presents the assignments of the parameters attached to the robot in the simulation. Combined with all the given parameters, using the modeling method referred above, the relevant results are supposed to achieve.

Table 2 The parameters of the robot system in dynamic simulation

Link num.	Mass (kg)	Rotation speed (rad/s)
1	0	Passive
2	0.593	$\pi/6$
3	1.461	$\pi/6$
4	1.260	$\pi/6$
5	0.134	$\pi/6$
6	0.762	$\pi/6$

4.2 Simulation Results

In order to obtain the related parameters in the movement of the 5-axis robot with clearance contained in the first joint, first and foremost is to figure out the clearance angle. Making use of the differential equations deduced above, and set the clearance size l_1 as 0.1 mm, the clearance joint θ_1 and its velocity $\dot{\theta}_1$ would be worked out as shown in the following (a) and (b) of Fig. 5 separately.

With the results received, the location of the end of robot manipulator relate to the global coordinate system can be inferred. The following Fig. 6 indicates coordinates of the end of manipulator under different clearance sizes. These figures shows that the location curves of robot manipulator with different clearance are almost coincidence. It declares that the clearance size has slight effects on the displacement of the serial robot manipulator. Since the size of joint clearance is very small relative to the components of the mechanism, according to the relevant knowledge of kinematics, it can be speculated that the displacement transferred to the end manipulator is unobvious.

As the massless link method belongs to the continuous contact model, that is, it supposing the bearing and journal always contact. Therefore, this method is more applicable to joints like the second joint. When clearance exists in this kind of

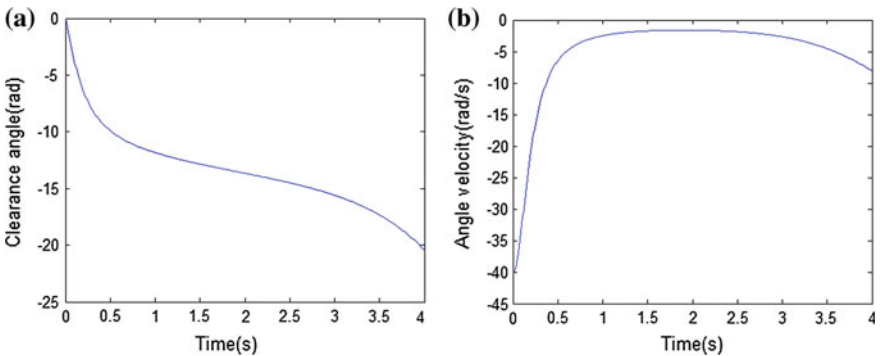


Fig. 5 Clearance angle and velocity of the robot manipulator with joint clearance: **a** is clearance angle; **b** is clearance angle velocity

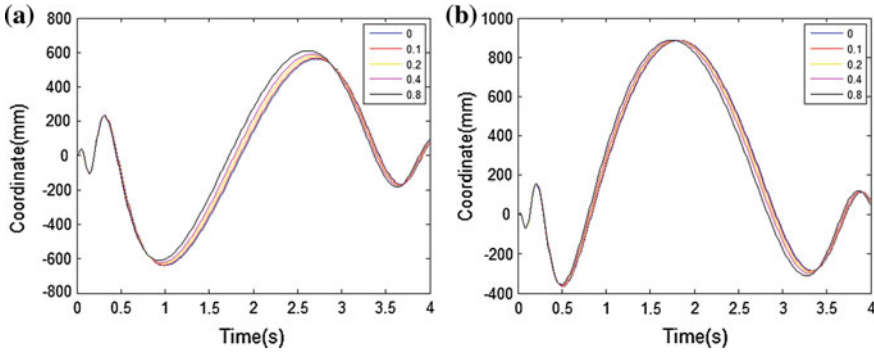


Fig. 6 Displacement of the robot manipulator related to the origin of global coordinate system: **a** is the coordinate of x direction under different clearance size; **b** is the coordinate of y direction under different clearance size

joints, the bearing and journal can maintain contact in a certain angle under the action of gravity.

With the data obtained, the offset error of the actual position and ideal position can be inferred, which can be applied to the following study of motion control. Using movement control, the error can be compensated, so as to improve the position precision of the robot displacement.

5 Conclusions

In this paper, the dynamic simulation about 5-axis robot with clearance is being studied. By the use of the D-H method, the motion relationship between the various links of the robot was signified, in the other hand, the dynamics equation was established with the application of Lagrange method combined with the D'Alembert's principle. Based on the formulations built above, the computational methodology for purpose of solving the clearance angle, considering the joint clearance as massless link, is presented. After obtaining the value of the clearance angle, almost all the dynamics and kinematics parameters can be figured out, here in this paper, the location of the robot manipulator was derived. However without considering the elastic deformation in the joint with clearance and the clearance size was set too single, leading to the results not so accurate. In the future work, these factors can be taken into consideration for better consequences.

In short, the massless link method is a relatively simple modeling method. With the application of this method, it is relatively simple to work out the kinematic and kinetic parameters, and reflect the effect of joint clearance in a certain extent. Overall, this is a high cost-effective method.

Acknowledgments This research was supported by the National Natural Science Foundation of China (Grant no. U1501247), the Scientific and Technological Research Project of Guangdong Province (2015B020239001), and the Scientific and Technological Research Project of Dongguang (Grant No. 2015215119). These supports are greatly acknowledged.

References

1. Erkaya S, Uzmay I (2009) Investigation on effect of joint clearance on dynamics of four-bar mechanism. *Nonlinear Dyn* 58(1–2):179–198
2. Flores P, Ambrósio J (2004) Revolute joints with clearance in multibody systems. *Comput Struct* 82(17):1359–1369
3. Flores P, Ambrósio J, Claro JCP et al (2006) A study on dynamics of mechanical systems including joints with clearance and lubrication. *Mech Mach Theory* 41(3):247–261
4. Flores P, Ambrósio J, Claro JP (2004) Dynamic analysis for planar multibody mechanical systems with lubricated joints. *Multibody Sys Dyn* 12(1):47–74
5. Dubowsky S, Freudenstein F (1971) Dynamic analysis of mechanical systems with clearances—part 1: formation of dynamic model. *J Eng Ind* 93(1):305–309
6. Dubowsky S, Freudenstein F (1971) Dynamic analysis of mechanical systems with clearances—part 2: dynamic response. *J Eng Ind* 93(1):310–316
7. Dubowsky S, Gardner TN (1975) Dynamic interactions of link elasticity and clearance connections in planar mechanical systems. *J Eng Ind* 97(2):652–661
8. Dubowsky S, Prentis JM, Valero RA (1979) On the development of criteria for the prediction of impact in the design of high speed systems with clearances. In: *Proceedings of the fifth world congress on theory of machines and mechanisms*, pp 968–971
9. Dubowsky S, Norris M, Aloni E et al (1984) An analytical and experimental study of the prediction of impacts in planar mechanical systems with clearances. *J Mech Transm Autom Des* 106(4):444–451
10. Wang Y, Wang Z (1996) Dynamic analysis of flexible mechanisms with clearances. *J Mech Des* 118(4):592–594
11. Soong K, Thompson BS (1990) A theoretical and experimental investigation of the dynamic response of a slider-crank mechanism with radial clearance in the gudgeon-pin joint. *J Mech Des* 112(2):183–189
12. Seneviratne LD, Earles SWE, Fenner DN (1996) Analysis of a four-bar mechanism with a radially compliant clearance joint. *Proc Inst Mech Eng Part C J Mech Eng Sci* 210(3): 215–223
13. Furuhashi T, Morita N, Matsuura M (1978) Research on dynamics of four-bar linkage with clearances at turning Pairs: 1st report, general theory using continuous contact model. *Bull JSME* 21(153):518–523
14. Zhao ZK, Wang YT (2009) Dynamic analysis and experiment research of mechanism with clearance. Dalian University of Technology, Dalian
15. Ting KL, Zhu J, Watkins D (2000) The effects of joint clearance on position and orientation deviation of linkages and manipulators. *Mech Mach Theory* 35(3):391–401
16. Erkaya S, Uzmay I (2009) Determining link parameters using genetic algorithm in mechanisms with joint clearance. *Mech Mach Theory* 44(1):222–234
17. Bai Z, Tian H, Zhao Y (2010) Dynamics modeling and simulation of mechanism with joint clearance. *J Harbin Inst Technol* 17(5):706–710

Part VIII
Gear and Transmissions

A Precise FE Model of a Spur Gear Set Considering Eccentric Error for Quasi-static Analysis

Huimin Dong, Chu Zhang, Xiwei Wang and Delun Wang

Abstract This paper presents a quasi-static FE contact model of a spur gear set with consideration of eccentric error. In the precise model, the nodes of contact and target surface can be mated as one-to-one at any instant by means of the instantaneous contact lines mesh generating method of engaged gears. This node-to-node contact FE model can fulfill static/dynamic/quasi-static FE analysis precisely, even with manufacturing and assembly error embedded. In the quasi-static FE contact model, the rotation of wheel with consideration of assembly eccentric error is set through the instantaneous mated position function, which ensures the solving convergence and preciseness. A gear set is used as an example to investigate the influence of gear eccentricity and elastic deformation acted by load on transmission accuracy. The case study illustrates that the presented quasi-static FE contact analysis model is easier convergence and more precise; the elastic deformation enlarges the TE which cannot be neglected in the FE analysis.

Keywords Quasi-static finite element method · Node-to-node model · Eccentric error

1 Introduction

Gear drive is one of the fundamental components of rotating machines and is widely used in modern industry. Many scholars tried to establish precise models to study on the transmission characteristics of gear drives, either by the theoretical or simulation method. Theoretical method [1–4] is based on rigid theory without considering elastic deformation of gears, which could not satisfy the high precision gear drive requirement. With the rapid development of computational technology and software, finite element (FE) method is widely applied to study the transmission

H. Dong (✉) · C. Zhang · X. Wang · D. Wang
School of Mechanical Engineering, Dalian University of Technology, Dalian 116024, China
e-mail: donghm@dlut.edu.cn

characteristics of gear drives with considering the elastic deformation, due to the fact that it can provide fast, accurate and effective numerical analysis.

The main influence factor for the accuracy of gear drive FE analysis is the modeling method. The modeling method directly impacts accuracy due to the complicated shape of the involute and the import error from other aided design software. The grid quality is an important part of the FE modeling and the commonly used mesh generation methods are mapping method, node connection element method, topology decomposition method, geometric decomposition method and scanning method [5–9]. The grid density is required to balance the accuracy and the computation time. Wang [10] proposed the practical right angle coordinate equation of involute profile instead of polar equation in traditional calculation. Yang [11] established a pair of gear contact FE model, and studied the relationship between the density of the grid and the contact stress by means of changing the density of the mesh. Mao [12] used the APDL language to obtain precise gear modeling in the FE software directly to avoid the import error.

Gear contact analysis is mainly based on static and dynamic FE method, few on quasi-static method [13–15]. The static FE method is time-saving but the result of each meshing position is independent. The dynamic method can well reflect the process of gear transmission, but is time-consuming. The solution requires very small time load step, and the convergence is difficult. The quasi-static method simulates a low-speed motion process, and each step of the calculation is conducted on the basis of the previous results, so the quasi-static method can reflect the process of gear transmission more accurately relative to the static method.

In the process of gear installation, assembly eccentric error is inevitable, which leads to periodically changing transmission ratio. Wu [16] derived a formula for calculating the time-varying speed ratio with eccentric error. Zhang [17] analyzed the influence of the eccentric error on the gear transmission by using the dynamic FE method. Li [18] investigated the effects of machining errors, assembly errors and tooth modifications on loading capacity.

With the development of FE method, many scholars have investigated the accurate modeling method but rarely involved in node programming. The calculation of FE method is based on the nodes, and it is more accurate in the case of node-to-node contact condition. In previous studies for the influence of the assembly eccentric error on transmission accuracy, the gears are assumed as rigid bodies, and the effect of elastic deformation is not considered.

In this paper, we provide an effective method to program the nodes of contact and target surface to be one-to-one at any instant. The precise FE model is established and the eccentric error is embedded for the quasi-static transmission analysis. For the first time, we calculate the instantaneous mated position function, which is the rotation condition in the quasi-static FE analysis and investigate the influence of eccentricity error on transmission accuracy considering elastic deformation.

2 Precise FE Contact Model

The mesh generation is vital which is the basis of FE calculation, especially the mated position. The calculation of FE model is based on the nodes, so we need to program the nodes and take the effective method to achieve a precise FE model.

2.1 Instantaneous Contact Point

We use the instantaneous contact line mesh generating method to get the node coordinates on the involute of pinion and wheel.

Three rectangular coordinate systems need to be established. One fixed coordinate $S(O - xy)$ on the frame, with its origin O on the rotary center of the pinion and its y axis coincides with the line between the two rotary centers; the two rotating coordinates $S_1(O_1 - x_1y_1)$ and $S_2(O_2 - x_2y_2)$ fixed with the two gears and the y axis is the symmetry line of tooth thickness respectively. The initial position of S_1 coincides with the S and the initial angle between S_2 and center line is φ_0 . The gears are initially engaged at point N_0 and the coordinate of N_0 is (x_{N0}, y_{N0}) . φ_0 and (x_{N0}, y_{N0}) can be calculated by the gear conjugate principle.

Figure 1 shows an arbitrary meshing position of the gear set. The rotation angle of the pinion is θ and the rotation angle of the wheel is φ . a is the length of the installation center distance O_1O_2 . The projection of contact line is the contact point on the end surface due to spur gear and N is the instant contact point.

The coordinates of B_1 and B_2 in the global coordinate system S are (x_{B11}, y_{B11}) and (x_{B21}, y_{B21}) , which can be obtained by simultaneous equations:

$$\begin{cases} x_{B11}^2 + y_{B11}^2 = r_a^2 \\ x_{B21}^2 + y_{B21}^2 = r_a^2 \\ y_{B11} = x_{B21} \tan \alpha' + z_1 a / z_1 + z_2 \quad i = 1, 2. \end{cases} \tag{1}$$

where r_a is the radius of addendum circle, α' is the meshing angle, z_1 is the tooth number of pinion and z_2 is the tooth number of wheel.

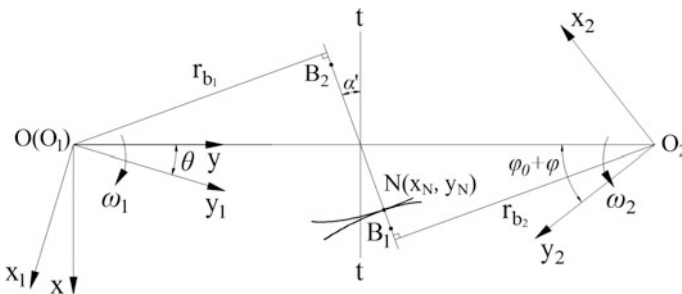


Fig. 1 Geometric model of a gear pair for instantaneous contact

The coordinate of N in the global coordinate system is:

$$\begin{cases} x_N = x_{N_0} + r_{b1} \theta \cos \alpha' \\ y_N = y_{N_0} + r_{b1} \theta \sin \alpha' \end{cases} \quad x_{B_1} \leq x_N \leq x_{B_2}. \tag{2}$$

We can obtain the coordinates of node N on the involute in their own rotating coordinate system by establishing the transformation matrix:

$$M_{10} = \begin{bmatrix} \cos \theta & \sin \theta & 0 \\ -\sin \theta & \cos \theta & 0 \\ 0 & 0 & 1 \end{bmatrix}. \tag{3}$$

$$M_{20} = \begin{bmatrix} -\cos(\varphi_0 + \varphi) & \sin(\varphi_0 + \varphi) & a \sin(\varphi_0 + \varphi) \\ -\sin(\varphi_0 + \varphi) & -\cos(\varphi_0 + \varphi) & a \cos(\varphi_0 + \varphi) \\ 0 & 0 & 1 \end{bmatrix}. \tag{4}$$

where M_{10} is the transformation matrix from the global coordinate system to the rotating coordinate system of the pinion and M_{20} is the transformation matrix from the global coordinate system to the rotating coordinate system of the wheel.

N is a point on the actual meshing line, and the coordinate of each node at any instant contact position can be obtained.

2.2 The Node-to-Node Contact FE Model

The spur gear parameters selected in this paper are shown in Table 1 to establish a pair of contact model.

The steps of construction for the node-to-node FE model are presented as follow:

- (1) Get the coordinates of key points on addendum circle, transition curve, dedendum circle directly by curve equation. Get the coordinates of key points on involute by the instantaneous contact line method.
- (2) The contact area needs to be refined. Based on the Hertz contact theory and the related paper [5], the thickness of the gear contact area is the double of half width.

Table 1 Parameters and material properties

Gears parameter	Pinion	Wheel
No. of teeth	18	18
Modulus (mm)	2.5	2.5
Normal angle (°)	20	20
Face width (mm)	20	20
Modification coefficient	0	0
Young’s modulus (Gpa)	206	206
Poisson’s ratio	0.3	0.3

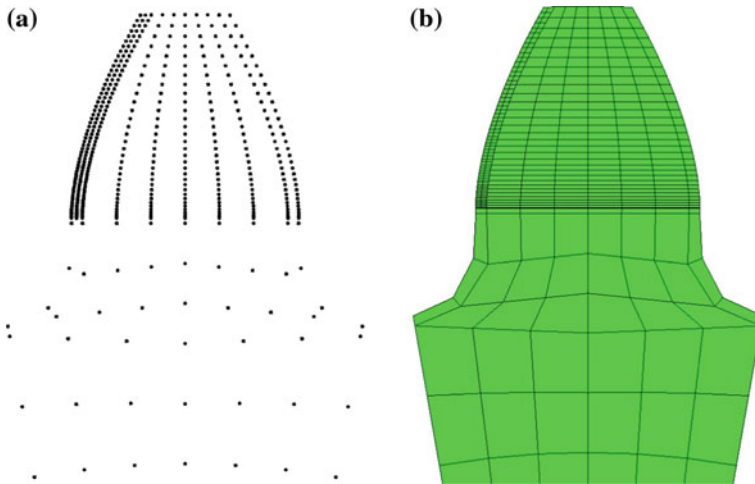


Fig. 2 End surface modeling: **a** end surface nodes **b** end surface elements

- (3) Generate nodes of gears in ANSYS 14.0 by reading the coordinates of nodes obtained in the previous steps (shown in Fig. 2a).
- (4) Based on the node connection element method, generate the elements of gear end surface (shown in Fig. 2b).
- (5) Stretch the 2D model into 3D model, and then revolve as well as copy the 3D model to generate a complete gear model.
- (6) Rotate the two gears to the initial meshing state by calculation (shown in Fig. 3) and when rotating a certain angle, the node-to-node contact model is also set up (shown in Fig. 4).

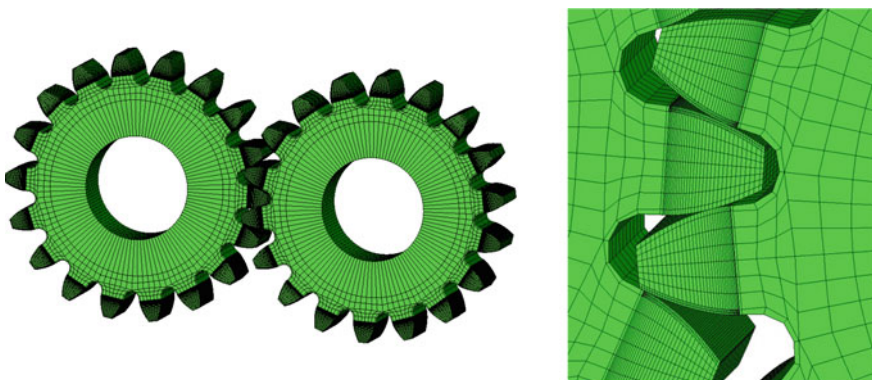


Fig. 3 FE contact model of meshing pair and enlarged the engagement

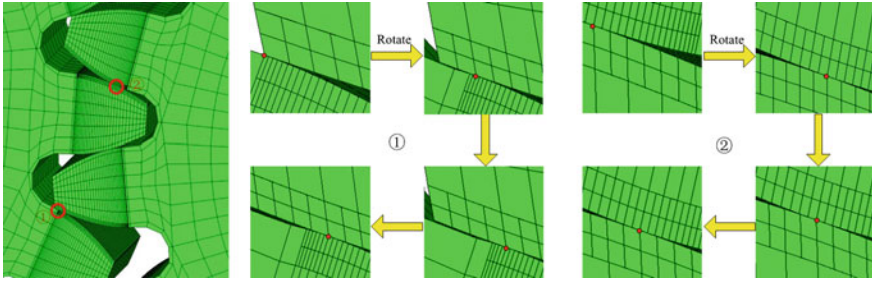


Fig. 4 The node-to-node contact FE model

3 Quasi-static FE Model

Quasi-static FE analysis is to simulate the process of gear pair engagement with lower speed operating. For ensuring analysis accuracy adopting the node-to-node contact FE model, the processes need to hold:

- (1) In the whole period of quasi-static contact process, the mesh of one-sided tooth profiles participating in engagement needs be refined. The nodes on the contact and target region are respectively defined as one group. One group chooses CONTA 174 element type and the other chooses TARGE 170 element type to establish contact pairs (shown in Fig. 5).
- (2) Couple the refinement area with the non- refinement area for the transfer of the force.
- (3) Use the mass21 element to establish the revolute joints at the center of gear and the nodes of gear inner ring are coupled with revolute joints. In this way, the gear inner ring moves as a rigid body with the six degrees of freedom.
- (4) Pinion and wheel are connected with body-ground revolute joints. The joint of the pinion runs with a constant rotation velocity 0.2 rad/s while the joint of the wheel runs with a rotational velocity $0.2/i_{12}$ rad/s (i_{12} is the transmission ratio). A 10 Nm torque is applied on the wheel (shown in Fig. 6).
- (5) Extract the transmission error caused by the elastic deformation at a short time interval where the nodes are one-to-one.

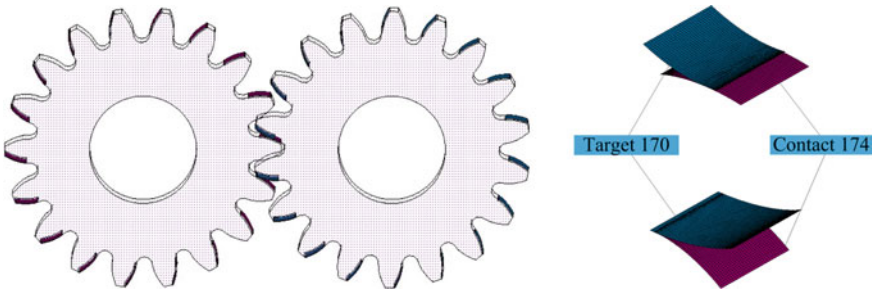


Fig. 5 Contact pair definition and enlarged the contact area

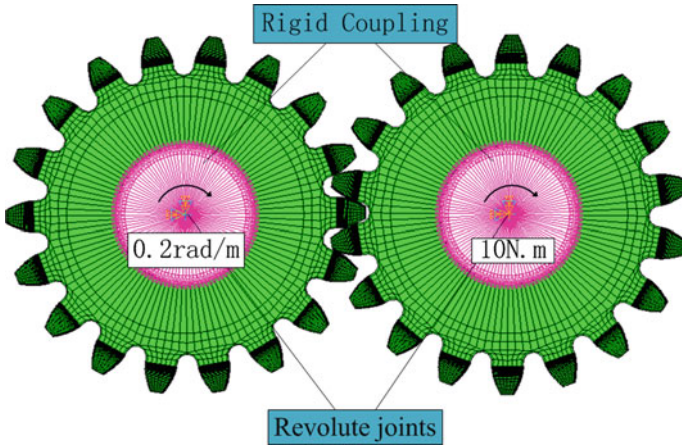


Fig. 6 Definition of boundary conditions

4 Eccentric Error Model

The eccentricity of a gear pair will cause the center distance of the gear set fluctuating as well as the time-varying transmission ratio which will influence the accuracy of transmission.

4.1 Rigid Body Eccentric Error Model

The arbitrary meshing position of standard pinion and wheel is as shown in Fig. 7 and the pinion is eccentrically installed. O_1 and O_2 are respectively the installation center of pinion and wheel. O'_1 is the base circle center and P' is tangent point of instantaneous pitch circles.

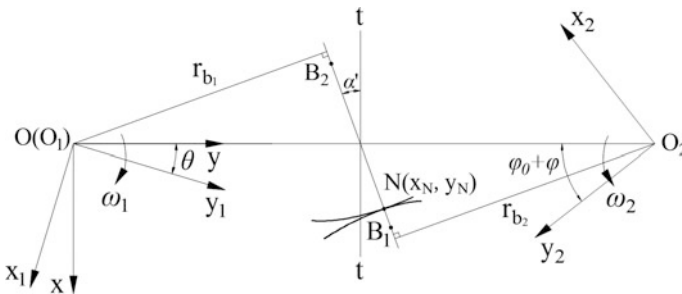


Fig. 7 Eccentric error model

Assume that the standard center distance is $O_1^oO_2$, and a is the length of $O_1^oO_2$. P_o is the instant center of initial position. The ideal transmission ratio is:

$$i_{12}^0 = \frac{z_2}{z_1} = \frac{O_2P_o}{O_1P_o}. \tag{5}$$

The center distance and pressure angle are time-varying, and meet the following conditions:

$$a \cos \alpha = a' \cos \alpha'. \tag{6}$$

$$a' = \sqrt{(\Delta e \sin \theta)^2 + (a + \Delta e - \Delta e \cos \theta)^2}. \tag{7}$$

where, a' is the instant center distance and α' is the instant pressure angle.

According to the geometric relations and the gear conjugate principle, we can get:

$$\begin{cases} \frac{O_2P'}{O_1^oO_2} = \frac{O_2P_o}{O_2O} \\ O_2P = O_2P(\cos \lambda - \sin \lambda \tan \alpha') \\ \cos \lambda = \frac{OO_2 - \Delta e \cos \theta}{O_1^oO_2} \\ \sin \lambda = \frac{\Delta e \sin \theta}{O_1^oO_2} \end{cases}. \tag{8}$$

By solving the simultaneous equations, we can get the transmission ratio error Δi_{12} :

$$O_2P = \frac{z_2}{z_1 + z_2} \frac{(\Delta e \sin \theta)^2 + (a + \Delta e - \Delta e \cos \theta)^2}{a + \Delta e - \Delta e \cos \theta - \Delta e \tan \alpha' \sin \theta}. \tag{9}$$

$$\Delta i_{12} = \frac{OO_2}{OO_2 - O_2P} - \frac{O_1O_2}{O_1P_o} = \frac{a + \Delta e}{a + \Delta e - O_2P} - \frac{z_1 + z_2}{z_1}. \tag{10}$$

The instantaneous mated position function (PF) of the wheel related to the rotation of pinion can be calculated:

$$PF = z_1\theta/z_2 + \int_0^\theta \Delta i_{12}. \tag{11}$$

4.2 Eccentric Gear Finite Element Analysis

The elastic deformation is considered in the FE analysis. The FE analysis of eccentric gear is similar to the ideal model accept the eccentricity and time-varying rotational velocity of the wheel:

- (1) The pinion is selected to be the eccentric gear and the assembly eccentricity is set.
- (2) The rotation angle of the wheel is set according to the instantaneous mated position function. If the transmission ratio error is ignored, the contact surface will be embedded in the target surface, which will caused difficulties in convergence and precise calculation.
- (3) Although the eccentricity makes nodes misplaced, the distance between the nodes is so small that the effect can be ignored.

5 The Finite Element Analysis Results

5.1 The Node-to-Node Model Validation

In order to verify the accuracy of the node-to-node model, we compare the stress at the pitch circle of FEA with that of Hertz theoretical calculation.

The theoretical result at the pitch point based on theory of Hertz contact is 268.2 MPa and the result of finite element model is 260.315 MPa as shown in the

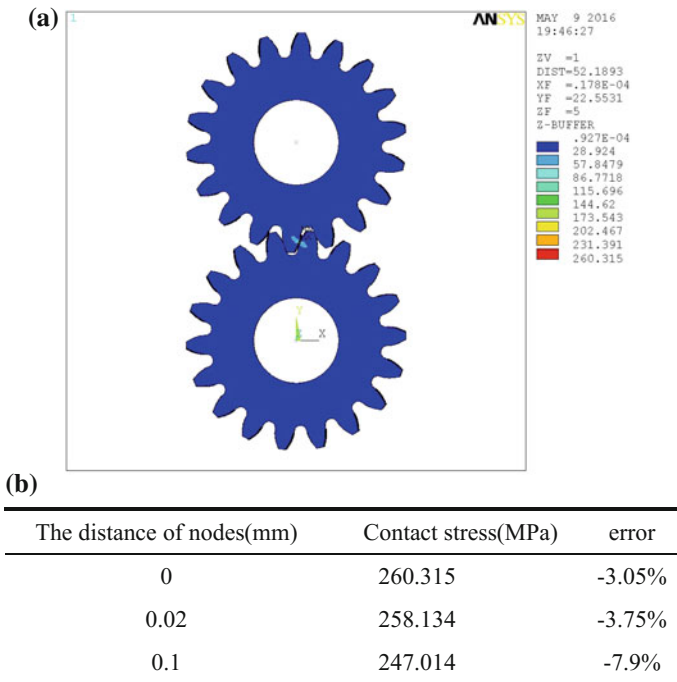


Fig. 8 FE calculation results: a stress cloud b sensitivity analysis of the node-to-node model

Fig. 8a, with merely difference of -3.05% . Then we conduct the sensitivity analysis of the node-to-node model as shown in the Fig. 8b. Therefore the accuracy of the node-to-node model by means of sensitivity analysis is verified.

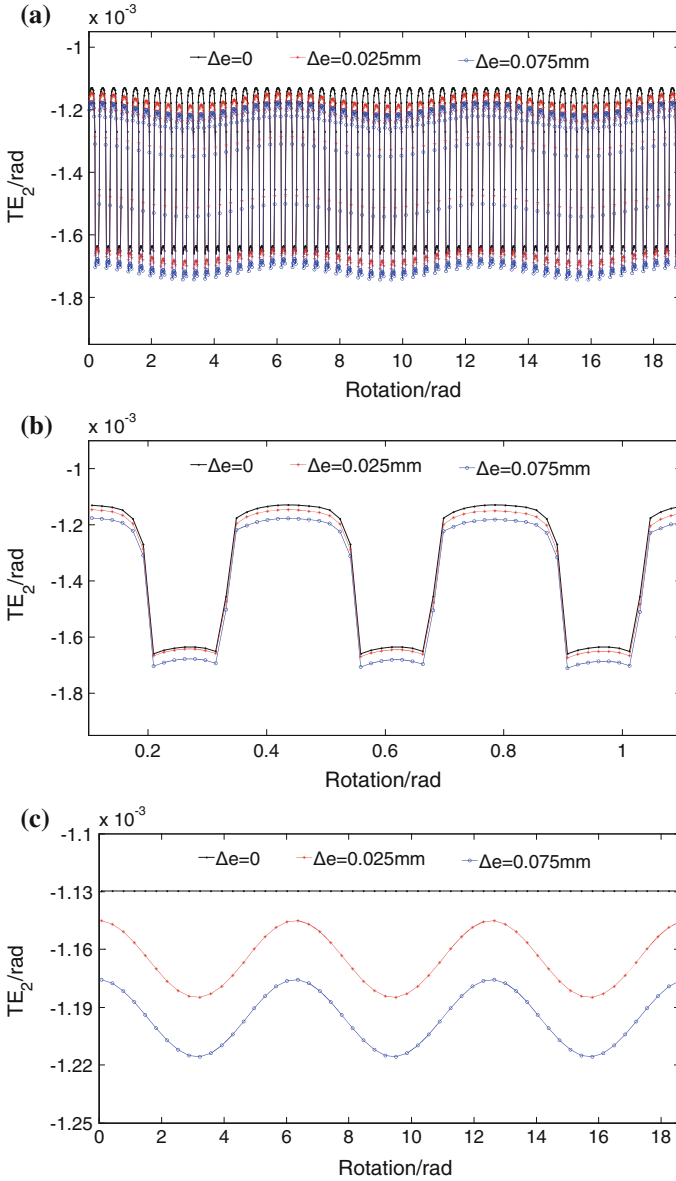


Fig. 9 TE caused by elastic deformation: **a** TE₂ in multiple period **b** partial view of TE₂ **c** the peak of TE₂ in each tooth frequency period

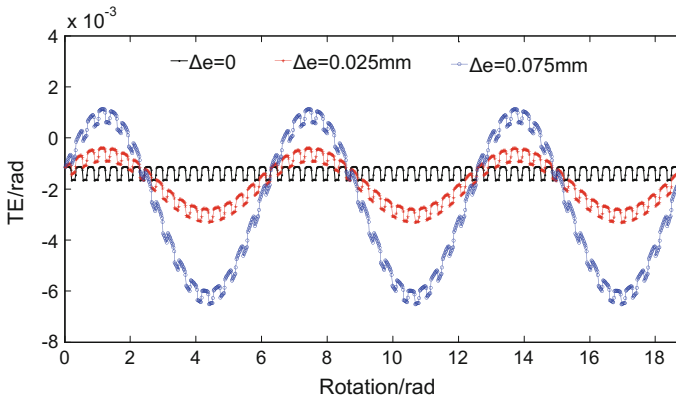


Fig. 10 Comprehensive TE

5.2 The Influence of Assembly Eccentric Error

The assembly eccentric error is the eccentricity between the base circle center and the installation center. The eccentricity tolerance of Grade 6 and Grade 8 gear is 0.025 and 0.075 mm. We take three sets of gear as the case study and their eccentricity Δe is 0, 0.025 and 0.075 mm, respectively.

The transmission ratio error Δi_{12} calculated by the theory method is not the minimum at the angle of zero and the maximum at the angle of π . The ideal drive position is not at the angle of $\pi/2$ while at $\varphi = \pi/2 - \alpha - \theta$, which leads to asymmetry.

TE is the difference between ideal angle and actual angle of the wheel and it is a cumulative process from initial position to a certain instant. The mated position phase difference function for the wheel is $TE_1 = PF - \varphi/i_{12}$.

The TE caused by the elastic deformation (TE_2) is extracted by the quasi-static FE method (shown in Fig. 9a). The single tooth interval is wide due to the increase of the center distance (shown in Fig. 9b). The obvious phenomenon proves the correctness of the calculation. The sine wave of the TE_2 shown in Fig. 9c is due to the variation of center distance during eccentric rotation.

We can get the comprehensive transmission error $TE = TE_1 + TE_2$ shown in Fig. 10 which illustrates that the effect of elastic deformation for the precise gear set is large enough to affect the transmission accuracy and cannot be neglected.

6 Conclusion

The new method presented in this paper, constructing a spur gear set eccentric error model combining with node-to-node FE contact mesh generation, can achieve more accurate results for quasi-static FE analysis, which is proofed by comparing with Hz

contact theory. The quasi-static FE contact model is more accurate through setting the instantaneous mated position function as the rotation condition which avoid the embedding error due to the change of the transmission ratio.

The effect of gear eccentric error with gear elastic deformation on TE makes the peak of TE in each tooth frequency period fluctuate, not symmetrical about the ideal value. The elastic deformation enlarges the transmission error which reflects the working condition precisely.

Acknowledgments This work was financially supported by the National Natural Science Foundation of China (No. 51375065).

References

1. Velez P, Maatar M (1996) A mathematical model for analyzing the influence of shape deviations and mounting errors on gears dynamic behavior. *J Sound Vib* 191(5):629–660
2. Zhao J, Li R (1984) Gears strength design data. Machinery Industry Press, Beijing
3. Xianbo Z (1982) Error and strength of gears. Machinery Industry Press, Beijing
4. Hertz H (1882) Uber die Berührung fester elastischer Korpe. *Journal Fur Die Reine Und angewandte Mathematik* 92:156–171
5. Chengzhong Gu, Xinyue Wu (2008) A review of FEM and trend of development. *J Front Comput Sci Technol* 2(3):248–259
6. Lv J, Wang Z, Wang Z (2001) Generation of finite element hexahedral mesh and its trend of development. *J Harbin Inst Technol* 33(4):485–490
7. Wei H, Zhou B (1997) The choice of adaptive finite element mesh automatic generation method. *J Southwest Jiaotong Univ* 32(5):477–482
8. Yu H, Zhao K (2004) Finite element mesh automatic subdivision. *High Voltage Eng* 30(5):4–5
9. Blacker T (2001) Automated conformal hexahedral meshing constraints, challenges and opportunities. *Eng Comput* 17(3):201–210
10. Wang Y, Yu Q, Jiang Y (2002) The practical rectangular coordinate equation research on gear tooth profile of involute. *J Mech Transm*
11. Yang S (2003) Gear contact finite element analysis. *J Comput Mech* 20(2):189–194
12. Mao K (2006) An approach for powertrain gear transmission error prediction using the non-linear finite element method. *Proc Inst Mech Eng Part D J Automobile Eng* 220(220):1455–1463
13. Ma Y, Qiao F (2013) Research on contact characteristics of gear with profile error based on an accurately modeling method by ANSYS. *J Mech Transm* 11:38–42
14. Kahraman A, Ozguven HN, Houser DR, Zakrajsek JJ (1990) Dynamic analysis of geared rotors by finite elements. *J Mech Des* 114(3):507–514
15. Zhan J, Fard M, Jazar R (2015) A quasi-static FEM for estimating gear load capacity. *Measurement* 75:40–49
16. Wu C (1982) The gear transmission error caused by eccentric error. *J Southeast Univ* 4:133–145
17. Zhang Y, Wang Q, Ma H, Huang J, Zhao C (2013) Dynamic analysis of three-dimensional helical geared rotor system with geometric eccentricity. *J Mech Sci Technol* 27(11):3231–3242
18. Li S (2007) Effects of machining errors, assembly errors and tooth modifications on loading capacity, load-sharing ratio and transmission error of a pair of spur gears. *Mech Mach Theory* 42(6):698–726

Velocity Ratio Variation Device Without Interruption and Control System for Automatic Ratio Change

Masaharu Komori and Yukihiko Kimura

Abstract Velocity ratio variation device is used to realize a wide range of speed or torque. However, the conventional ratio variation device cannot transmit torque and rotation from the input shaft to the output shaft during the velocity ratio variation process and interruption of torque and rotation occurs. In order to solve this problem, the authors proposed a novel ratio variation system using noncircular gears. It can transmit torque and rotation without interruption even in the changing process of velocity ratio. In this report, a control system for automatic ratio change of the proposed ratio variation system is described. A ratio variation system with a different setup of components is constructed and the effectiveness is investigated experimentally.

Keywords Ratio variation · Transmission

1 Introduction

Some types of machines require a wide range of speed or torque. The range of speed or torque of a motor is wide but limited. If the velocity ratio between the input shaft and the output shaft can be changed, it is possible to realize a wide range of speed or torque. A velocity ratio variation system is an effective method in this point. In the industrial fields, ratio variation systems using gears (geared transmission) are widely used. Geared transmissions have an advantage in efficiency. Therefore, there have been many studies [1–3] on geared transmissions. In a geared transmission, changing process of the working gear pairs is necessary to change the velocity ratio of the transmission. However, in this process, torque transmission is interrupted from the input shaft to the output shaft. Besides, the rotation of shaft is

M. Komori (✉) · Y. Kimura

Department of Mechanical Engineering and Science, Kyoto University,
Kyotodaigakukatsura, Nishikyo-ku, Kyoto-shi, Kyoto 615-8540, Japan
e-mail: komorim@me.kyoto-u.ac.jp

not transmitted between the input shaft and the output shaft. This is an important problem for machines.

In order to solve this problem, the authors proposed a novel ratio variation system called uninterrupted transmission system, that can transmit torque and rotation without interruption even during velocity ratio change [4–8]. Uninterrupted transmission system uses a noncircular gear pair that can realize the velocity ratios of two gear pairs. In this paper, a control system for automatic gear change of uninterrupted transmission system is described. In addition, an uninterrupted transmission system with a different setup of input shaft, output shaft, and clutches is investigated and the effectiveness is verified experimentally.

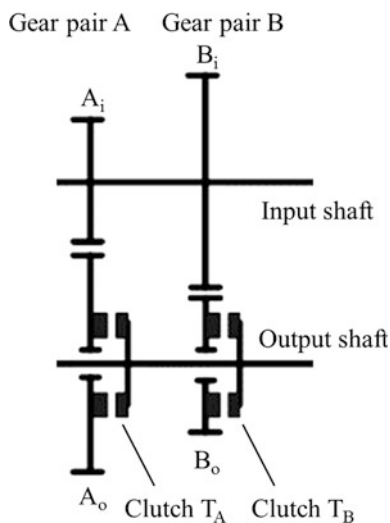
2 Uninterrupted Transmission System

2.1 Problem of the Conventional Transmission

A schematic model of a conventional transmission is shown in Fig. 1. Input shaft, output shaft, gear pairs A and B, and two clutches T_A and T_B are used. Gears A_i and B_i are fixed to the input shaft. Clutch T_A or T_B connects a gear to the output shaft. If gear A_o or B_o is connected to the output shaft by engaging clutch T_A or T_B , the gear and the output shaft rotate together. In contrast, the gear is free from the rotation of the output shaft if the clutch is disengaged.

Velocity ratio is defined as the rotational velocity of the output shaft divided by that of the input shaft. Under the engagement of clutch T_A , the velocity ratio between the input and output shafts is the same as that of gear pair A. This condition is called the first ratio condition. When clutch T_B is engaged, the velocity

Fig. 1 Schematic model of a conventional transmission



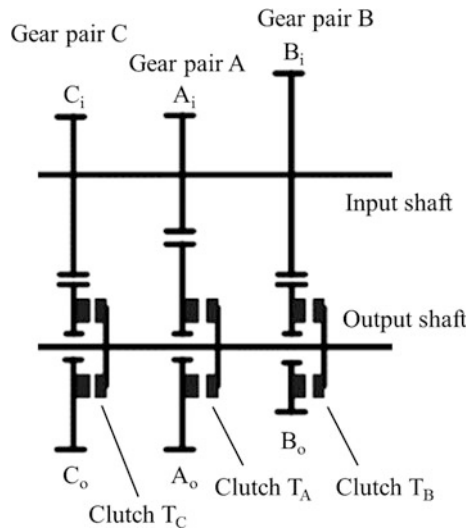
ratio is the same as that of gear pair B. This condition is called the second ratio condition. Changing process from the first ratio condition to the second ratio condition is as follows. Clutch T_A is engaged but clutch T_B is disengaged in the initial state. It is impossible to engage clutches T_A and T_B simultaneously because the velocity ratio of gear pair A and that of gear pair B are different. Therefore, clutch T_A is disengaged and then clutch T_B is engaged in the changing process from the first ratio condition to the second ratio condition. An interval exists between the disengagement of clutch T_A and the engagement of clutch T_B . This means that no clutch is engaged and torque and rotation are not transmitted in this interval. This is interruption problem of torque and rotation of the conventional transmission.

2.2 Structure of Uninterrupted Transmission System

A schematic model of proposed uninterrupted transmission system [4–8] is shown in Fig. 2. The right side in Fig. 2 is similar to the conventional transmission in Fig. 1 but gear pair C and clutch T_C are set in this transmission. Gear pair C is a noncircular gear pair. Gear C_i is fixed to the input shaft. Gear C_o is free from the rotation of the output shaft but it rotates together with the output shaft when clutch T_C is engaged.

r_A is the velocity ratio of gear pair A and r_B is that of gear pair B. The pitch curve of gear pair C and the pitch circles of gear pairs A and B are shown in Fig. 3. The pitch curve of gear pair C is divided into four parts (section a, b, c and d). It has the same form as gear pair A in section a, and in section b, it has the same form as gear pair B. In contrast, the pitch curve smoothly connects sections a and b in sections c

Fig. 2 Schematic model of uninterrupted transmission system



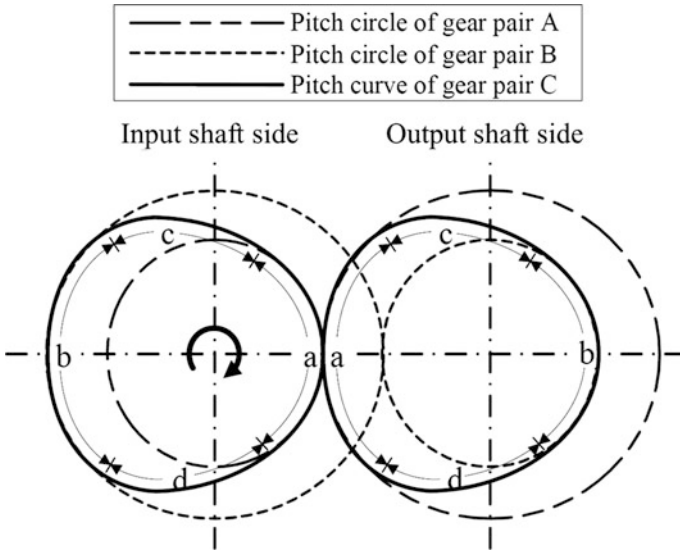


Fig. 3 Pitch curve of gear pair C

and d. If gear pair C meshes in section a, the meshing condition is the same as that of gear pair A and the velocity ratio is r_A . On the other hand, the meshing condition is the same as that of gear pair B and the velocity ratio is r_B if gear pair C meshes in section b. When gear pair C rotates in the direction shown in Fig. 3, the meshing section changes from a to c. In section c, the meshing condition changes from the meshing of gear pair A to that of gear pair B and the velocity ratio changes from r_A to r_B . In contrast, if gear pair C meshes in section d, the velocity ratio changes from r_B to r_A .

2.3 Velocity Ratio Variation Process

The velocity ratio variation from r_A to r_B is explained here. In the initial state, the velocity ratio is r_A . Clutch T_A is engaged and clutches T_B and T_C are disengaged. Gear C_i rotates with the input shaft and gear C_o rotates freely from the output shaft. After gear pair C begins meshing in section a, clutch T_C is engaged. In section a, the pitch curve of gear pair C has the same form as gear pair A and the velocity ratio of gear pair C is identical with that of gear pair A. Thus, clutch T_C can be engaged while clutch T_A is engaged. Gear pairs A and C transmit the rotation in this state. Next, the clutch T_A is disengaged while the clutch T_C is engaged. Under this state, gear pair C transmits the rotation. Then the meshing section changes to section c and the velocity ratio between the input and output shafts changes from r_A to r_B due to the change of the velocity ratio of gear pair C. After gear pair C begins meshing

in section b, clutch T_B is engaged while clutch T_C is engaged. In this state, the velocity ratio of gear pair C is the same as that of gear pair B. Thus, clutch T_B can be engaged while clutch T_C is engaged and gear pairs B and C transmit the rotation. After clutch T_B is engaged, clutch T_C is disengaged while clutch T_B is engaged. In this state, gear pair B transmits the rotation and the velocity ratio is r_B . This is the process of the velocity ratio variation.

At least one of the clutches is engaged in this process. Therefore, torque and rotation are not interrupted even during ratio variation process.

3 Manufacture of Experimental Device

Experimental device is manufactured in this section.

3.1 Overview of the Experimental Device

Figure 4 shows the system of the experimental device. Figure 5 shows the transmission part and Fig. 6 shows the schematic model of the transmission. The fundamental component of the transmission is the same as that shown in Fig. 2 but clutches T_A , T_B , and T_C are set on the input shaft. There is a possibility to use the structure shown in Fig. 6 but this structure of the uninterrupted transmission system is not investigated. In this paper, the effectiveness of this structure is verified experimentally. Clutch T_{C2} is equipped in this experiment device. However, it is always engaged and therefore gear C_o always rotates with the output shaft. A motor is connected to the input shaft.

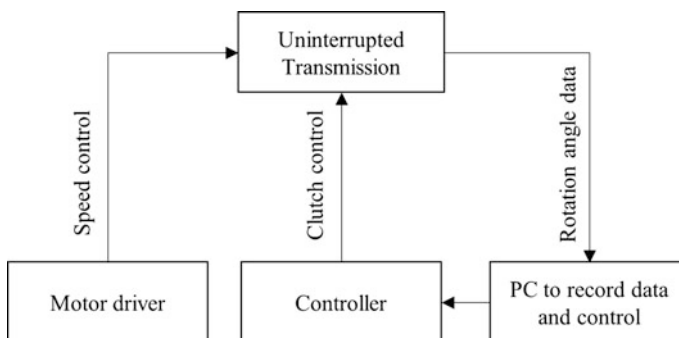


Fig. 4 System of the experimental device

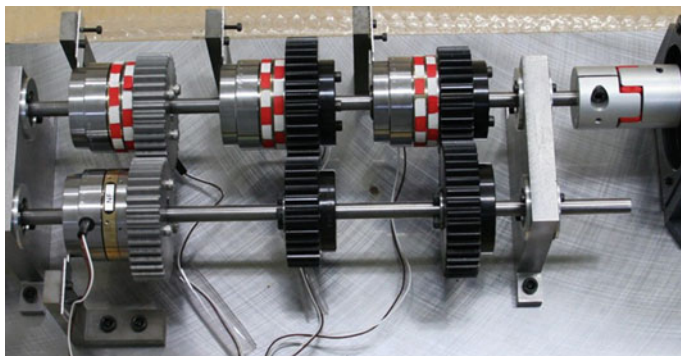
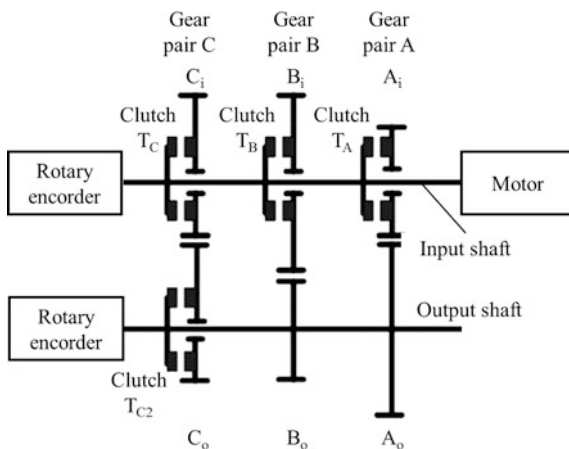


Fig. 5 Manufactured uninterrupted transmission

Fig. 6 Schematic model of the uninterrupted transmission used for the experiment



3.2 Clutches and Gears

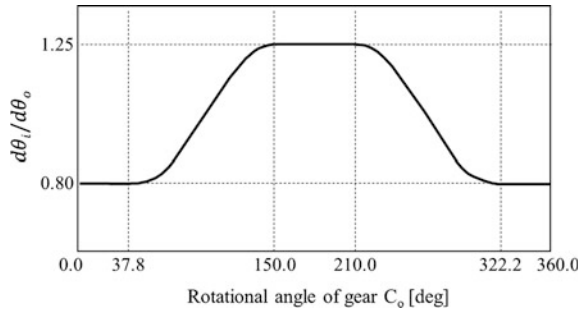
Electromagnetic tooth clutch is used in this experiment. The rotor of the clutch is fixed to the shaft using a key and the stator is fixed to the base part of the experimental device. When an electric current is supplied to the coil, the armature and the rotor are connected and the clutch gets engaged. Conversely, if the electric current is cut, the armature is returned by a spring and the clutch becomes disengaged.

Table 1 shows the specification of the gear pairs A and B used in this experiment. The gears are standard gears. Figure 7 shows the velocity ratio of the non-circular gear pair C for the experiment. The rotational angle of the output shaft is θ_o , and that of the input shaft is θ_i . The material is S45C, module is 2, and tooth number is 36.

Table 1 Specification of gears used for the experiment

	A_i, B_o	A_o, B_i
Module	2	2
Tooth number	32	40
Pitch circle diameter (mm)	64	80
Tooth width (mm)	20	20
Pressure angle (°)	20	20
Material	S45C	S45C

Fig. 7 Velocity ratio of the noncircular gear pair C for the experiment



3.3 Motor and Recording System

In this experimental device, a stepping motor and reduction gears are used. Rotational speed of the stepping motor is set by a motor driver. A rotary encoder is equipped to each shaft to measure the rotational angle. The rotary encoder is connected to a PC to display and record the rotational angle of each shaft.

3.4 Control System

A control panel is used to control each clutch. Figure 8 shows the circuit diagram of the control panel. In the control panel, a relay board connected to the PC switches the flow of an electric current. This PC is connected to the rotary encoder and the relay board and therefore it is possible to control the clutches based on the measured rotational angle of the shafts.

Rotation angle to switch the clutches must be determined to change velocity ratio while rotating the shafts. Table 2 shows the relationship between rotation angle and clutch control.

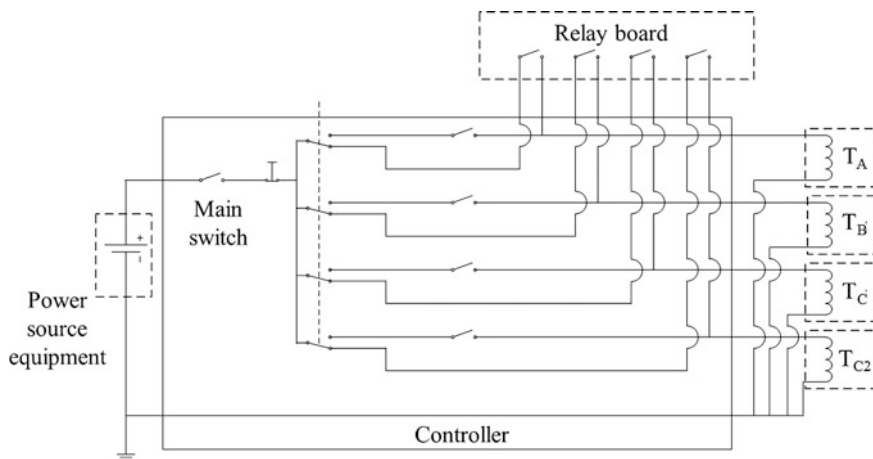


Fig. 8 Circuit diagram of the experimental device

Table 2 Relationship between shaft angle and clutch control from the 1st ratio condition to the 2nd ratio condition

Rotation angle of the output shaft	T_A	T_B	T_C
1st ratio condition	On	Off	Off
330.0°	Gear pair C gets in the 1st ratio condition		
340.0°	On	Off	On
15.0°	Off	Off	On
30.0°	Gear pair C begins ratio change		
142.2°	Gear pair C gets in the 2nd ratio condition		
170.0°	Off	On	On
190.0°	Off	On	Off
217.8°	Gear pair C begins ratio change		
2nd ratio condition	Off	On	Off

Control program is developed based on the above algorithm. Figure 9 shows the display to control the program. Rotation angle of the shafts, condition of the clutches, switch for the rotary encoder, switch for manual or automatic ratio change, and switch for manual control of the clutches are shown on the display. In this program, manual and automatic control of the clutches is possible using this display on the PC.

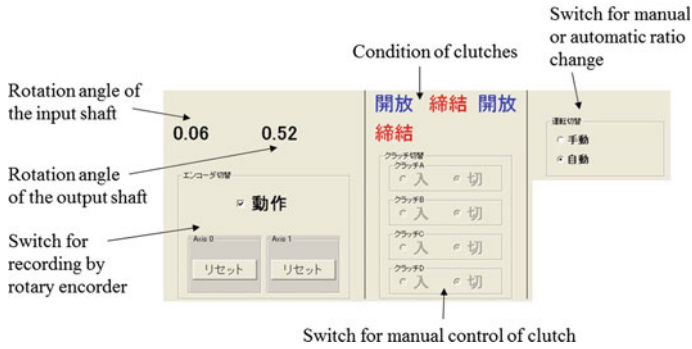


Fig. 9 Display to control the program

4 Experiment

4.1 Preparation for Experiment

The following items are performed before the experiment.

1. Clutch T_{c2} is engaged after it is confirmed that the marks on the noncircular gears match as shown in Fig. 10.
2. The output shaft is rotated by 180° and the meshing condition of the noncircular gear pair becomes the same as that of gear pair B.
3. It is confirmed that clutches T_A , T_B , and T_C can get engaged.

Figure 11 shows the meshing condition of the noncircular gear pair. In (a), the meshing condition of the noncircular gear pair is the same as that of gear pair A and, in (b), it is the same as that of gear pair B.

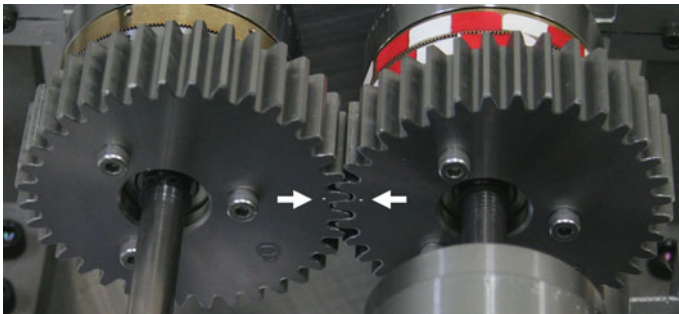


Fig. 10 Marks on the noncircular gear

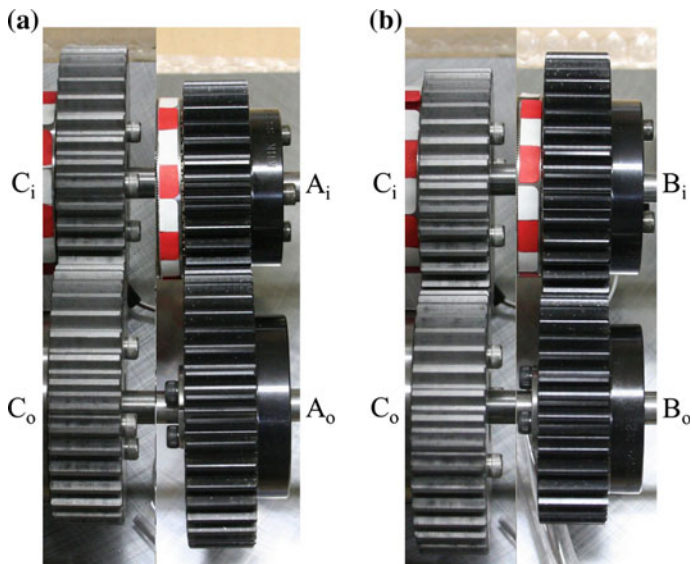


Fig. 11 Meshing condition of the noncircular gear pair (gear pair C)

4.2 Experiment

A load is applied to the output shaft and the ratio change from the 1st ratio to the 2nd ratio is performed in this experiment. A weight is attached to an end of a rope and the other end of the rope is wound onto the output shaft. A load is applied to the output shaft by hanging the weight as shown in Fig. 12. The loaded torque is 0.11 Nm.

Fig. 12 Method to apply a load to the shaft

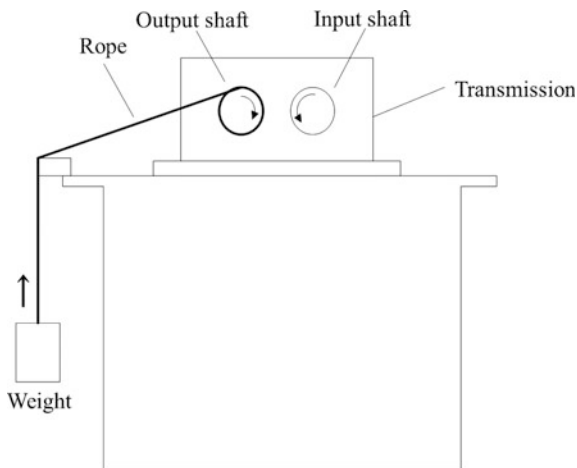


Fig. 13 Result of the experiment of the velocity ratio change

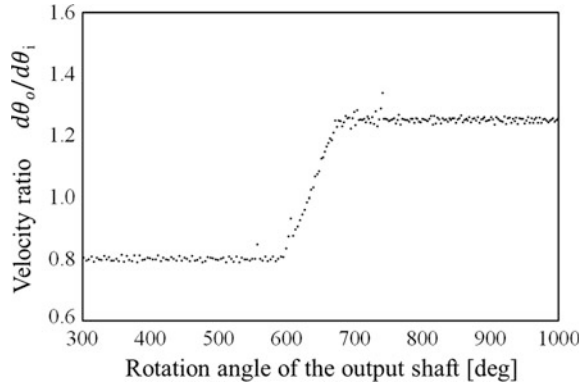


Figure 13 shows the measured velocity ratio when the ratio is changed. The velocity ratio is calculated from the rotary encoders attached to the shafts. The rotational speed of the input shaft is 5.6 rpm. The result shows that the velocity ratio is smoothly changed during the ratio variation process without any interruption.

4.3 Discussion

In the conventional transmission, torque and rotation cannot be transmitted during the velocity ratio change. Therefore, the velocity ratio might not change smoothly and might become zero or negative under loaded condition. On the other hand, the experimental result of the manufactured uninterrupted transmission in Fig. 13 shows smooth change of velocity ratio. This result means that the proposed system can change velocity ratio without torque interruption and can transmit the rotation precisely even during velocity ratio change. The effectiveness of the proposed structure of the uninterrupted transmission and control system is verified by this experimental result.

5 Conclusion

Some types of machines require a wide range of speed or torque and a velocity ratio variation device is used to realize it. However, the conventional ratio variation device cannot transmit torque and rotation from the input shaft to the output shaft during the velocity ratio variation process and interruption of torque and rotation occurs. In order to solve this problem, the authors proposed a novel ratio variation system called uninterrupted transmission system using a noncircular gear pair. In this paper, a control system for automatic ratio change of the proposed ratio

variation system was described. Developed control program based on switching algorithm of clutches was explained. The uninterrupted transmission with a different setup of input shaft, output shaft, and clutches was constructed. The experimental results showed that the constructed transmission system can change velocity ratio smoothly without interruption and the effectiveness was verified.

References

1. Nozaki Y, Tanaka Y, Tomomatsu H, Tsukamoto H, Hanji F (2004) Toyota's new six-speed automatic transmission A761E for RWD vehicles, SAE technical paper, 2004-01-0650
2. Gama Froreicio D, Resis Assis E, Ferreira Amendola C (2004) The manual transmission automated—gearshift quality comparison to a similar manual system, SAE technical paper, 2004-01-3363
3. Tseng C, Hsieh M (2005) Analysis and optimization of clutch actuator on automated manual transmission system, SAE technical paper, 2005-01-1782
4. Komori M, Kang J, Kimura Y (2010) Study on the ratio variable system to transmit power and motion continuously. *Des Eng* 45(10):512–519
5. Komori M, Kang J, Takeoka F, Kimura Y, Onodera Y (2011) Geometrical analysis of noncircular gear for ratio variation system and modifying method of ratio variation. *Des Eng* 46(7):402–409
6. Kang J, Komori M, Takeoka F, Onodera Y (2011) Multi-speed ratio variable system to transmit power and motion continuously. *Trans JSME C* 77(782):3871–3880
7. Kang J, Komori M, Zhang S, Sugiyama K (2012) Control method for output speed during velocity ratio change under high rotational speed using an uninterrupted transmission system. *J Adv Mech Des Syst Manufact* 6(7):1281–1297
8. Kang J, Komori M (2013) Uninterrupted transmission system for realizing high flexibility in design of angular velocity ratio. *J Adv Mech Des Syst Manufact* 7(2):140–155

An Elastic Transmission Model of Spur Gears for TE Analysis

Huimin Dong, Zhipeng Li and Delun Wang

Abstract This paper presents an elastic transmission model of spur gear (2-D) sets by means of combination with the kinematic geometry and elastic theory of gearing for analysis of transmission error (TE). Based on conventional contact condition between a teeth pair, an elastic contact mathematic equation is established, whose elastic deformation is caused by contact, bending and torsion of gears. The elastic contact equation involves time-varying center distance. For double tooth pairs contact, a compatibility equation is comprehensively established to implement continuously transformation. A spur gear (2-D) set is used as example to analyze the influences of the elastic deformation and center distance of the gears on the contact position and TE. The case study shows that the method of using mathematical model to study the gears TE presented in this paper is reliable. The work lays the theoretical foundation for further accuracy analysis and design.

Keywords Transmission error · Conjugate contact · Errors and elasticity

1 Introduction

Transmission error and its characteristics of a gear drive are important technical indexes to evaluate the accuracy of gear drives. Because of the presence of machining errors on component surfaces and component deformations, there is deviation between the real rotational angle and the ideal rotational angle of the output shaft, defined as transmission error (TE). There are many factors to influence TE of gear transmission system, such as manufacturing errors, assembly errors, the time-varying stiffness of the gears and other errors.

Surveying available literatures, many researches on TE of gears were conducted by setting up the mathematical physical model, FEM and the experimental observation and statistical method [1–16]. Koide [1] established a mathematical models

H. Dong (✉) · Z. Li · D. Wang
School of Mechanical Engineering, Dalian University of Technology, Dalian 116024, China
e-mail: donghm@dlut.edu.cn

considered the elastic deformations of components and the gear eccentricity. Shi et al. [2] studied the gear integrated error treated the geometric errors of the gear profile as the errors on the line of action without load. Tang [3] established a new model to calculate TE of the gear set with considering the bending, torsion, contact stiffness of gears and the influence of them in the view of mechanics. The TE model neglected the error of the gear profile and the influence of the components of the shafts and the bearings.

Tesfahunegn et al. [4] established a FEM considering the influence of the gear tooth profile shape, bending of the gears and contact stress. Hua [5] established the refined FEM. Hao [6] established the accurate(refined) model of helical gear. The refined model, the coordination between the degree of refinement and computation time, how to express the gear profile error should be considered. Vexet et al. [7, 8] established a quasi-static model of gears, in which the shape of the gear profile and the elasticity the shafts and the bearings were considered, and the mesh stiffness was assumed to be equivalent to the stiffness of contact line. The model above is much more complicated, it also neglected time-varying center distance, and it spends much longer calculating time.

Lin and Zhu [9, 10] studied the probability and statistics calculation method to calculate TE of gear system. The establishment of the model was relatively simple, the results indicated that the probability of the error of the gear was maximum. Hotait [11] used the experimental method to study the effect of shaft eccentricity on the load distribution of gears and on gear teeth bending, the theoretical predictions were compared with experimental results.

This paper is to set up an elastic transmission model of spur gear (2-D) sets with consideration of elastic deformation and time-varying center distance to investigate the influence of elastic deformations of the gears on the meshing characteristics, and the influence of single and double teeth pair alternating mating on the meshing characteristics, as well as the influence of time-varying center distance of a pair of gears.

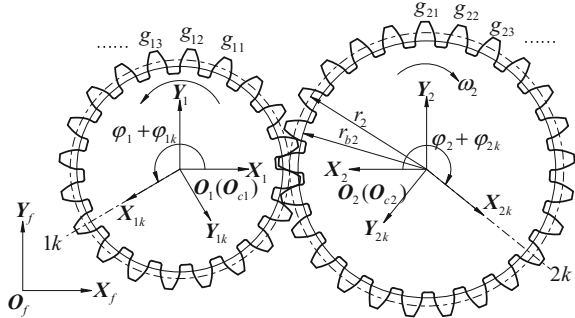
2 Elastic Conjugate Contact Model

We mainly study the elastic conjugate model of a pair of 2-D spur gears without considering the change of the tooth along the tooth width.

Coordinate Frame Definition:

For convenience to establish the model, we set up some coordinate system: one fixed coordinate system $\{O_f; X_f, Y_f, Z_f\}$, two moving coordinate systems $\{O_i; X_i, Y_i, Z_i\}$ $i = 1, 2$ attached to the gears, and local tooth auxiliary coordinate system $\{O_{ik}; X_{ik}, Y_{ik}, Z_{ik}\}$ attached to each tooth of the gear, shown in Fig. 1. g_{ij} represents the j th gear tooth of the i th gear; axis X_{ik} is consistent with the k th tooth midline. φ_{1k} represents the angle between X_{1k} and X_1 ; $i = 1, 2$ represent the driving gear 1 and driven gear 2.

Fig. 1 Definition of coordinate system for gears



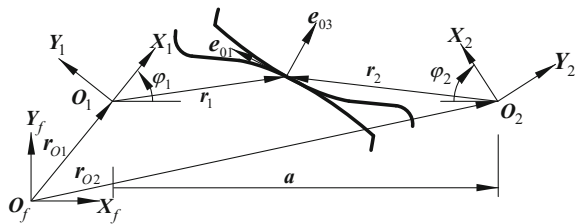
To investigate the status of a pair of tooth profile, we set up Frenet frame $\{r_i; e_1^{(i)}, e_2^{(i)}, e_3^{(i)}\}$ $i = 1, 2$ on each tooth profile/surface (in Fig. 2), in which $e_1^{(i)}, e_2^{(i)}$ and $e_3^{(i)}$ are the unit vector along the tangent direction, along the tooth width direction and the unit normal vector of the tooth profile.

Tooth meshing equation for perfect tooth pair, the tooth profile contact of a pair of gears driving can be seen as a conjugate surface, that is, the tooth profile meshing meets the contact condition and the tangency condition. We firstly consider that the gears are rigid, which is no error and distortion and the center distance between the two gears is ideal center distance, as shown in Fig. 2. The conjugate contact equation can be written as:

$$\left. \begin{aligned} r_1 - r_2 &= a \\ e_{03} &= e_{03}^{(1)} = e_{03}^{(2)} \\ r_1 &= r_1(u_1); r_2 = r_2(u_2) \end{aligned} \right\} \quad (1)$$

where r_1, r_2 are the theoretical meshing point vectors of gear 1, 2 in the fixed coordinate system $\{O_f; X_f, Y_f, Z_f\}$; a is the center distance vector; $e_{03}^{(1)}, e_{03}^{(2)}$ are unit normal vectors of meshing points of gear 1, 2.

Fig. 2 Ideal conjugate contact model



2.1 Elastic Conjugate Meshing Equations

Elastic deformation of gear teeth and wheel always exists due to load action. Because of the deformation, the contact position at the engaged zone deviates from ideal position, shown in Fig. 3. The gear meshing still meets the conjugate condition under the influence of elastic deformation and center distance error of gears. Let r_1^* and r_2^* be the actual meshing points of the radius, $a + \Delta a$ be the time varying center distance, e_3^* be the unit normal vector at the meshing point, the elastic conjugate meshing equations can be written as:

$$\left. \begin{aligned} r_1^* - r_2^* &= a + \Delta a \\ e_3^* &= e_3^{(1)*} = e_3^{(2)*} \end{aligned} \right\} \tag{2}$$

In Fig. 3, the $\delta\varphi_{Ei}$ and $\delta\varphi_{ai}$ ($i = 1, 2$) are the deviational angle, i.e. TE, caused by the elastic deformation of gear- i and center distance deviation of gears, respectively. The $\delta\varphi_{Ei}$ is TE caused by total of contact pair deformation, tooth bending and torsional deformation of gear body. According to the content of the document [12] the center distance of the gear can be obtained as a function of Δa (φ), where φ is the rotation angle of the input shaft.

Let the deviation of tooth profile along the line of action caused by contact deformation, tooth bending and torsional deformation of the gear body be h_{ci} , h_{bi} and h_{ti} respectively, the effect on the tooth profile and position is shown in Fig. 4.

As shown in Fig. 4, the twisting of gear tooth rotates around the O_{bi} point. The rotation of the wheel body revolves around the center of the O_i . l_{ci} represents a vector from the O_{bi} along the meshing point. The bending of the gear teeth and the twist of the gear don't affect the shape of the tooth profile, but it will make the tooth around the center of some rotation $\delta\varphi_{bi}$ and $\delta\varphi_{ti}$. h_{bi} is the bending deformation along the line of action and h_{ti} is the torsional deflection along the line of action. Contact does not affect the rotation of the gear teeth, but will make the tooth profile deformation is $h_{ci}(u_i)$. Elastic deformation makes the angle error of gear is $\delta\varphi_{Ei}$.

Fig. 3 Effect of elastic deformation on meshing situation

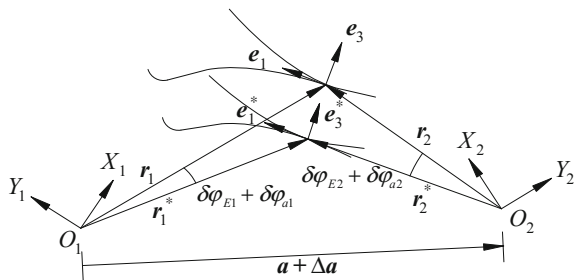
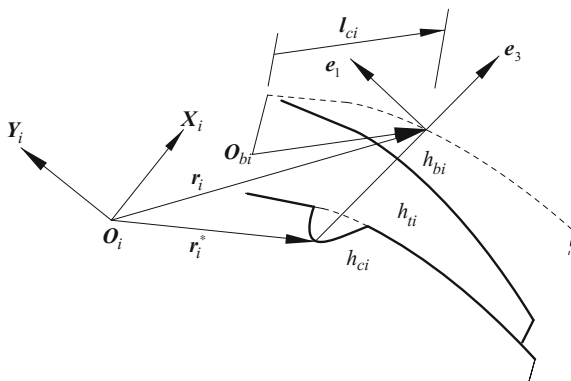


Fig. 4 Elastic deformation on tooth profile



Due to the deformation error of the gear tooth, the tooth profile equation becomes $r'_i = r_i(u_i) + h_{ci}(u_i)e_3^{(i)}$. According to the kinematic theory [13]

$$dr'_i = dr_i(u_i) + dh_{ci}(u_i)e_3^{(i)} + h_{ci}(u_i)de_3^{(i)} \tag{3}$$

where $dr_i(u_i)$ is differential of theoretical profile and $dh_{ci}(u_i)e_3^{(i)} + h_{ci}(u_i)de_3^{(i)}$ is differential of tooth profile error caused by elastic deformation.

$$\left. \begin{aligned} dr_i &= e_1^{(i)} \sigma_1^{(i)} \\ de_3^{(i)} &= e_1^{(i)} w_1^{(i)} \\ w_1^{(i)} &= c_{11}^{(i)} \sigma_1^{(i)} \end{aligned} \right\} \tag{4}$$

where $\sigma_1^{(i)}$ is the error component along the $e_1^{(i)}$ direction; $c_{11}^{(i)}$ is the opposite number of normal curvature along $e_1^{(i)}$ direction.

$$\left. \begin{aligned} dh_{ci}(u_i) &= h_{ci1}(u_i) \sigma_1^{(i)} \\ h_{ci1}(u_i) &= \frac{dh_{ci}(u_i)}{\sigma_1^{(i)}} \end{aligned} \right\} \tag{5}$$

Bring the formula (4), (5) into the (3) and rearranging to get a plane expressed by $\sigma_1^{(i)}$.

$$\left. \begin{aligned} dr'_i &= r'_{i1} \sigma_1^{(i)} \\ r'_{i1} &= (1 + h_{ci} c_{11}^{(i)}) e_1^{(i)} + h_{ci1} e_3^{(i)} \end{aligned} \right\} \tag{6}$$

The normal vector of the contact point of the actual tooth profile is:

$$\mathbf{e}'_3 = -h_{ci1}\mathbf{e}_1 + \mathbf{e}_3 \tag{7}$$

Elastic conjugate meshing equations can be written as:

$$\left. \begin{aligned} \mathbf{r}_i^* &= \mathbf{M}_i(\delta\varphi_{Ei} + \delta\varphi_{fi})(\mathbf{r}_i + \delta\mathbf{r}_i) + \mathbf{M}_i(\delta\varphi_{bi})(\mathbf{l}_{ci} + \delta\mathbf{r}_i) + h_{ci}\mathbf{e}_3 \\ \mathbf{e}_3^{(i)*} &= \mathbf{M}_i(\delta\varphi_{Ei} + \delta\varphi_{fi} + \delta\varphi_{bi})(\mathbf{e}'_3 + \delta\mathbf{e}'_3) \end{aligned} \right\} \tag{8}$$

$\mathbf{M}(\delta\varphi)$ represents the rotation matrix of the rotating shaft of the gear and its rotation angle is $\delta\varphi$. Since the rotation angle is small, the rotation matrix can be written as:

$$\left. \begin{aligned} \mathbf{M}(\varphi_i + d\varphi_i) &= \begin{pmatrix} c(\varphi_i + d\varphi_i) & -s(\varphi_i + d\varphi_i) & 0 \\ s(\varphi_i + d\varphi_i) & c(\varphi_i + d\varphi_i) & 0 \\ 0 & 0 & 1 \end{pmatrix} = \mathbf{M}(\varphi_i)\mathbf{M}(d\varphi_i) \\ \mathbf{M}(\delta\varphi_i) &= \begin{pmatrix} c\delta\varphi_i & -s\delta\varphi_i & 0 \\ s\delta\varphi_i & c\delta\varphi_i & 0 \\ 0 & 0 & 1 \end{pmatrix} = \mathbf{E} + \begin{pmatrix} 0 & -1 & 0 \\ 1 & 0 & 0 \\ 0 & 0 & 0 \end{pmatrix} \delta\varphi_i = \mathbf{E} + \boldsymbol{\lambda}\delta\varphi_i; \boldsymbol{\lambda} = \begin{pmatrix} 0 & -1 & 0 \\ 1 & 0 & 0 \\ 0 & 0 & 0 \end{pmatrix} \end{aligned} \right\} \tag{9}$$

$$\mathbf{M}(\varphi_i + \delta\varphi_i) \cdot \mathbf{R}_i = \mathbf{M}(\varphi_i) \cdot \mathbf{r}_i + \mathbf{k} \times \mathbf{r}_i \delta\varphi_i \tag{10}$$

The Eqs. (7), (9) and (10) are brought into (8) and then Eq. (11) can be obtained.

$$\left. \begin{aligned} \mathbf{r}_i^* &= \mathbf{r}_i + \delta\mathbf{r}_i + h_{ci}\mathbf{e}_3 + \mathbf{k}_i \times \mathbf{r}_i(\delta\varphi_{Ei} + \delta\varphi_{fi}) + \mathbf{k}_i \times \mathbf{l}_{ci}\delta\varphi_{bi} \\ \mathbf{e}_3^{(i)*} &= \mathbf{e}_3 - h_{ci1}\mathbf{e}_1 + \delta\mathbf{e}_3 + \mathbf{k}_i \times \mathbf{e}_3(\delta\varphi_{Ei} + \delta\varphi_{fi} + \delta\varphi_{bi}) \end{aligned} \right\} \tag{11}$$

The Eqs. (10) and (11) are brought into the elastic and error conjugate equations to obtain Eq. (12).

$$\left. \begin{aligned} \delta\mathbf{r}_1 - \delta\mathbf{r}_2 + (h_{c1} - h_{c2})\mathbf{e}_3 + \mathbf{k}_1 \times \mathbf{r}_1(\delta\varphi_{E1} + \delta\varphi_{f1}) + \mathbf{k}_1 \times \mathbf{l}_{c1}\delta\varphi_{b1} - \mathbf{k}_2 \times \mathbf{r}_2(\delta\varphi_{E2} + \delta\varphi_{f2}) - \mathbf{k}_2 \times \mathbf{l}_{c2}\delta\varphi_{b2} &= \mathbf{0} \\ \delta\mathbf{e}_3^{(1)} - \delta\mathbf{e}_3^{(2)} + (h_{c21} - h_{c11})\mathbf{e}_1 + \mathbf{k}_1 \times \mathbf{e}_3(\delta\varphi_{E1} + \delta\varphi_{f1} + \delta\varphi_{b1}) - \mathbf{k}_2 \times \mathbf{e}_3(\delta\varphi_{E2} + \delta\varphi_{f2} + \delta\varphi_{b2}) &= \mathbf{0} \end{aligned} \right\} \tag{12}$$

\mathbf{l}_{ci} can be obtained by meshing point position; Eq. 12 known parameters \mathbf{l}_{ci} , $\delta\varphi_{bi}$, $\delta\varphi_{fi}$ and h_{ci} can get $\sigma_1^{(1)}$, $\sigma_1^{(2)}$, $\delta\varphi_{E1}$ and $\delta\varphi_{E2}$.

2.2 Gear Elastic Deformation Equations

The angle error caused by elastic deformation of gear teeth is $\delta\varphi_{Ei}$. Due to the elasticity of the gear and the torsion of the shaft, elastic deformation has an influence on the rotation angle error of the gear. The calculation methods of three kinds of deformations of gear can be obtained according to the Refs. [14–16]. \mathbf{l}_{ci}

can be calculated according to the Ref. [17]. The bending stiffness of the gear teeth, the contact stiffness and the torsion of the gear wheel are different for K_{bi} , K_{ci} and K_{ti} .

$$\left. \begin{aligned} h_{ci} &= \frac{F_{Hi}}{K_{ci}} \\ \delta\varphi_{ti} &= \frac{F_{Hi}}{K_{ti}} \\ \delta\varphi_{bi} &= \frac{F_{Hi}}{K_{bi}} \end{aligned} \right\} \tag{13}$$

$$\left. \begin{aligned} K_{ci} &= E \frac{B}{0.58 \left(\ln \left(\frac{2c_1}{a} \right) + \ln \left(\frac{2c_2}{a} \right) - 0.429 \right)} \\ K_{ti} &= \frac{E}{(\cos \alpha_m)^2} \frac{B}{\frac{s_F^2}{s_F} + \frac{1}{s_F} + 1.4(1 + 0.249(\tan \alpha_m)^2)} \\ K_{bi} &= \frac{E}{(\cos \alpha_m)^2} \frac{B}{10.92 \int_0^{l_{ci}} \frac{(l_{ci}-x)^2}{(2y)^3} dx + 3.1 \left(1 + 0.294(\tan \alpha_m)^2 \int_0^{l_{ci}} \frac{dx}{2y} \right)} \end{aligned} \right\} \tag{14}$$

where a represents the Hertz contact radius, $a = 1.52 \sqrt{\frac{F_H}{E(\rho_1 + \rho_2)B}}$; ρ_1 and ρ_2 represent the radius of curvature of the contact point. α_m represents the pressure angle of the contact point. s_F represents the root circle tooth thickness. E = Young’s modulus; B = face width; $2y$ = tooth thickness of x .

Taking the rotation angle of the driving gear as the standard, so $\delta\varphi_{E1} = 0$. $\delta\varphi_{E2}$, $\sigma_1^{(1)}$ and $\sigma_1^{(2)}$ can be obtained by Eq. (12).

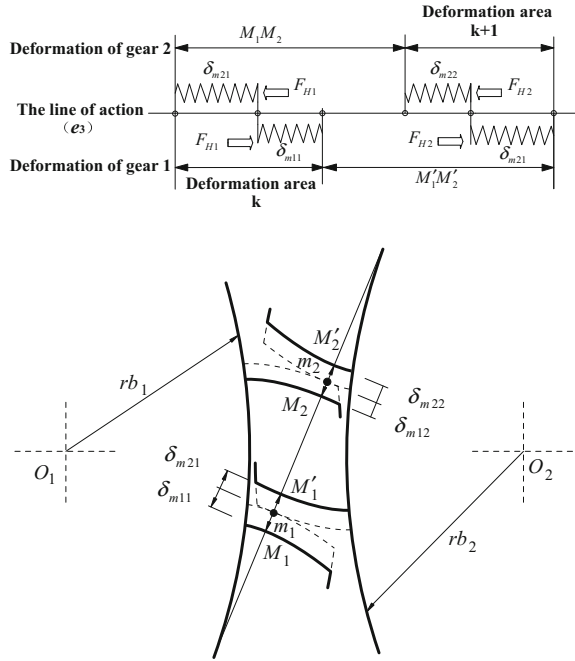
h_{ci} can be obtained through the gear meshing force; the gear tooth is simplified as the cantilever beam model, so that the rotation angle $\delta\varphi_{bi}$ can be solved and the rotation axis is the center line of the gear teeth. The force model of the wheel body is simplified to the hollow shaft model, so that the torsion angle $\delta\varphi_{ti}$ can be obtained.

2.3 Compatibility Equation of Double Tooth Pairs Contact

For double tooth pairs meshing, the double pairs should meet compatibility contact condition. Under the action of meshing force, the contact points of the gears are m_1 and m_2 , respectively. The elastic deformation of the gear is in the direction of the meshing line. Elastic deformation includes the contact deformation of the gear, the bending of the gear and the twisting of the gear. The elastic deformation of the gear teeth at the contact point is δm_{ij} , in which $i = 1, 2$ represent the driving gear and driven gear and $j = 1, 2$ represent the meshing point 1, 2. Elastic deformation of gear at meshing point can be calculated according to the meshing force and the stiffness of contact points, elastic deformation can be written as:

$$\delta m_{ij} = \frac{F_{Hj}}{K_{ij}} \tag{15}$$

Fig. 5 Elastic deformation of double teeth



As shown in Fig. 5, F_{Hj} represents the meshing force and K_{ij} represents the composite stiffness of contact point (Fig. 5).

As the elastic deformation at the meshing point is in the direction of the meshing line, according to the deformation compatibility equation, the relationship between the elastic deformation and the forces of the two gears at the meshing point is:

$$\left. \begin{aligned} F_H \cdot r_{b2} &= T_O \\ F_{H1} + F_{H2} &= F_H \\ \delta_{m11} + \delta_{m21} &= \delta_{m12} + \delta_{m22} \\ \delta_{mij} &= \frac{F_{Hj}}{K_{ij}} \end{aligned} \right\} \quad (16)$$

F_{H1} and F_{H2} can be obtained by Eq. 16. To judge whether the gear teeth are in contact with Eq. 17.

$$F_{Hi} = \sum_{j=1}^2 F_{Hj} H_{contj} \left\{ \begin{aligned} H_{contj} &= 1 && \text{if } j = i \wedge F_{Hj} \geq 0 \\ H_{contj} &= 0 && \text{if } j = i \wedge F_{Hj} < 0 \\ H_{contj} &= 0 && \text{if } j \neq i \wedge F_{Hj} \geq 0 \\ H_{contj} &= 1 && \text{if } j \neq i \wedge F_{Hj} < 0 \end{aligned} \right. \quad (17)$$

which is compatibility equation, where H_{cont1} is defined as contact factor, which is equal to 0 if gear teeth are disengaged, thus the contact force of the gear teeth can be

obtained. F_{Hi} can be calculated by Eq. 17. F_{H1} and F_{H2} are brought into Eq. 13 and then $\delta\varphi_{bi}$, $\delta\varphi_{ti}$ and h_{ci} can be obtained.

3 Case Studies

The parameters and material properties of the gears are shown in the following Table 1.

The center distance error of the floating axis model can be obtained according to the content of related Ref. [12]. The center distance error function can be written as: $\Delta a = \Delta a(\varphi)$.

The meshing force F_H can be obtained by the input torque; under the condition of single tooth contact: $F_{Hi} = F_H$, in the case of double tooth contact F_{Hi} can be obtained through the compatibility equation; bring gear parameters, Young’s modulus, position of theoretical meshing point, pressure angle and radius of curvature at the meshing point into Eq. 14 and rearranging to get K_{ci} , K_{bi} and K_{ti} . F_{Hi} , K_{ci} , K_{bi} and K_{ti} can be brought into Eq. 13 can be obtained $\delta\varphi_{bi}$, $\delta\varphi_{ti}$ and h_{ci} . Finally, $\delta\varphi_{E2}$, $\sigma_1^{(1)}$ and $\sigma_1^{(2)}$ can be obtained by using Eq. 12.

For a pair of gear transmission, the variation law of the transmission error is studied under the influence of the errors and the elasticity. Firstly, the transmission error of the gear is calculated under the action of the elasticity of the gears; Secondly, the influence of time varying center distance is considered.

As shown in Fig. 6, it shows that elastic deformation of gears under loads is the most important impact on the transmission error of ideal gears model, and the elastic deformation of gears is decided by meshing stiffness. Therefore, the changes of TE are seemed like the changes of engagement stiffness (show in Fig. 6).

Table 1 Parameters and material properties of gears pair

Gears parameter	Gear	Wheel
No. of teeth	25	25
Modulus (mm)	4	4
Normal angle (°)	20	20
Addendum coefficient	1	1
Input torque (Nm)	260	–
Face width (mm)	30	25
Modification coefficient	0	0
Young’s modulus (Gpa)	206	206
Poisson’s ratio	0.3	0.3
Headspace coefficient	0.25	0.25
s_F (mm)	7.3	7.3

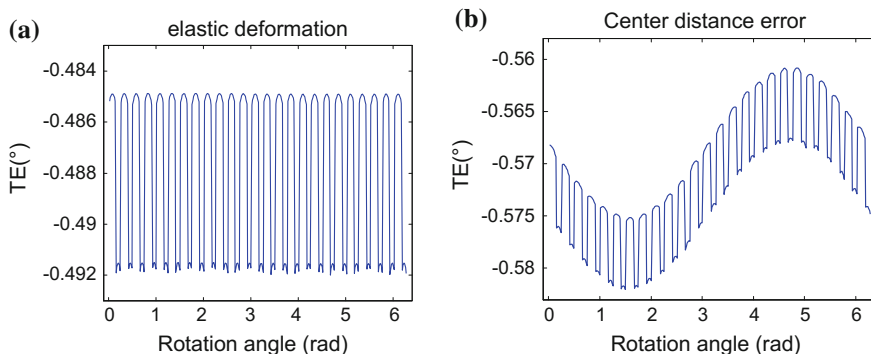


Fig. 6 The influence of elasticity and deformation on the error of the rotation angle: **a** effect of elastic deformation on TE **b** influence of center distance error on TE

The center distance error can cause the meshing clearance, which can result in the transmission error. And the greater the center distance is, the greater TE is.

It shows that meshing point position change caused by elastic deformation of gear (shown in Fig. 7). Numerical value represents the meaning of the difference between the position of the actual meshing point and theoretical meshing point. The numerical value of the mutation is caused by two reasons. The first reason is that the TE is mutation; Therefore Figs. 6a and 7a are similar. Another reason is that the curvature radius of the single and double teeth contact is changed, so the position of the meshing point can be changed.

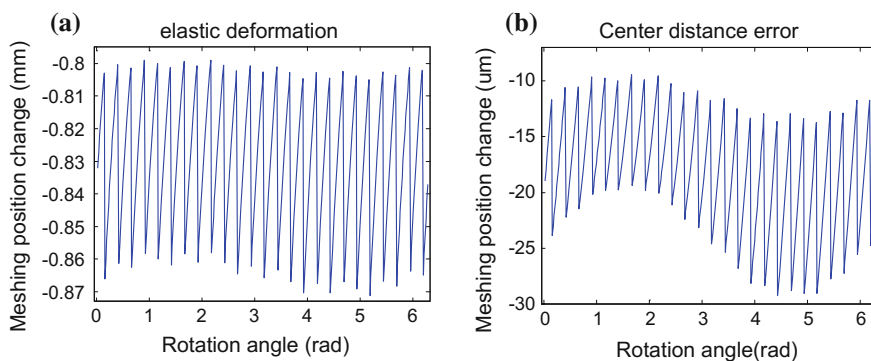


Fig. 7 The influence of the error on the position of the meshing point: **a** influence of elastic deformation on meshing point **b** the influence of center distance error on the meshing point

4 Conclusion

- (1) The transmission model of spur gears presented in this paper first deals with the elastic deformations and time-varying center distance of gears by using theoretical method. This work expands the traditional gear meshing theory.
- (2) The established elastic meshing mathematic equation and the compatibility equation can comprehensively analyze the contact position and TE of spur gears, not only effect of the contact, bending and torsion deflection of gears, but also of time-varying center distance of gears.
- (3) The case studies demonstrate that the theoretical model presented in this paper is correct and feasible.

Acknowledgments This work was financially supported by the National Natural Science Foundation of China (No. 51375065).

References

1. Koide T, Oda S, Matsuura S, Kubo A (2003) Equivalent misalignment of gears due to deformation of shafts, bearings and gears (Model Proposal and Development of Calculation Program). *JSME Int J Ser C Mech Syst Mach Elem Manuf* 46(4):1563–1571
2. Shi Z, Kang Y (2012) Gear pair integrated error and its measurement method. *J Tianjin Univ* 45(02):128–134
3. Jinyuan T (2008) New calculation model of gear transmission error. *J Mech Transm* 32(06):13–14
4. Tesfahunegn YA, Rosa F, Goral C (2010) The effects of the shape of tooth profile modifications on the transmission error, bending, and contact stress of spur gears. *Proc Inst Mech Eng Part C J Mech Eng Sci* 224(8):1749–1758
5. Hua X, Moyan X, Guansheng C (2015) Precise modeling and simulation analysis of the straight bevel gear train. *J Mech Transm* 10:72–76
6. Hao D (2011) Finite element modeling method for precise contact analysis of helical gears. *J Dalian Univ Technol* 51(6):825–831
7. Vexlex P, Maatar M (1996) A mathematical model for analyzing the influence of shape deviations and mounting errors on gear dynamic behaviors. *J Sound Vib* 191(5):629–660
8. Vexlex P, Bruyere J, Houser DR (2011) Some analytical results on transmission errors in narrow-faced spur and helical gears: influence of profile modifications. *J Mech Des* 133(3): 586–599
9. Lin C, Zhu J (2011) The calculation of transmission error of gear. *Machinery* 38(8):10–13
10. Li WEI, Xiumei QI (2006) Analysis of distribution law of dynamic load along meshing line of spur gear drive. *Mech Eng Autom* 06:63–66
11. Hotait MA, Talbot D, Kahraman A (2008) An investigation of the influence of shaft misalignment on bending stresses of helical gears with lead crown. *Gear Technol* 25(8)

12. Dong H, Wang D, Li Z, Wang Z, Yu S (2016) Kinematic geometry model of a spur gear drive supported by floating shafts. In: The 4th joint international conference on multibody system dynamics
13. Liu J (1978) Theory of meshing. Dalian University of Technology Press, Dalian
14. Li R, Zhao Q (1984) Gear strength design data. Machinery Industry Press
15. Comell RW (1981) Compliance and stress sensitivity of spur gear teeth. *J Mech Des* 103 (2):447–459
16. Liu H (2004) Mechanics of materials, 4th edn. Higher Education Press, Beijing
17. Pu L, Ji M (2006) Machine design, 8th edn. Higher Education Press, Beijing

Configuration Synthesis of Compound Gear Trains Based on State-Space Approach

Jun Qiu, Huimin Dong, Yali Ma, Shangkun Xu and Delun Wang

Abstract This paper presented a new method for configuration synthesis of compound gear trains based on state-space approach [1]. This method first proposed a basic gear train unit (BGU) with two degrees of freedom, and a state equation is established to describe the transformation of kinematic, dynamic and structure information from input to output terminal. Then the dual vectors and a special state-space are defined by means of state equation. The operational rules of dual vectors in state-space were discussed and described using formulas, which revealed the relationship between the series-parallel connections of BGUs and transform path of dual vectors in state-space. The new method transformed the configuration synthesis of compound gear trains into the path planning of dual vectors under constraints in state-space. And it is more efficient to distinguish isomorphism and more convenient to achieve computer programming. Finally, an example of speed-increasing gearbox of semi-direct drive wind generator is given to show the process of configuration synthesis based on state-space approach.

Keywords Compound gear trains · Configuration synthesis · Conceptual design · State-space

1 Introduction

Gear train is one of the most common forms of transmission in mechanical engineering, which transfers kinematic, dynamic and structure information from input to output terminal by gear meshing. They are commonly used in fields of aerospace, heavy industry, wind dynamic equipment and so on, which have the transmission requirements of low-speed or high-speed, heavy-load and dynamic split, and usually are designed to complex compound gear trains. Configuration synthesis is an important innovation means of gear trains.

J. Qiu (✉) · H. Dong · Y. Ma · S. Xu · D. Wang
School of Mechanical Engineering, Dalian University of Technology, Dalian 116024, China
e-mail: qiu jun@mail.dlut.edu.cn

Researchers had made a lot of studies about configuration synthesis of gear trains. One of the important approaches is based on the graph and topology theory. Buchsbaum [2] first proposed the method of graph theory to solve the conceptual design problem of planetary gear trains, but there are isomorphic problems in the topology graph; Freudenstein [3] used the rotation graph to solve the problem of isomorphism determination; Furthermore, Hsu [4] summarized the advantages and disadvantages of the previous gear train graph and then proposed the standard substitution graph and new rotation graph. Another common method is based on configuration synthesis of links which get through low pair replacing high pair. Rao [5–7] proposed a six link one degree of freedom onwards model to achieve conceptual design of planetary gear train; Peiwen [8] and Huaiwen [9] studied the application of kinematic chain with single joint in design of gear trains. In other respects, Dazhun [10] first proposed a specific correlation matrix to describe the epicyclic gear train; Yang [11] proposed gear units and their combinations to describe the epicyclic gear train.

However, the compound gear train easily forms complex polycyclic transfer paths of kinematic and dynamic. All the models for gear trains focused more on topological relation among gears, but not the information transferred by gear trains. It is difficult to establish a unified mathematical model for configuration synthesis, configuration optimization and quantitative analysis. Wang [1] presented an approach to automated conceptual design of mechanical system by means of state-space based on control theory. And then, in a series of research [12–14], serial mechanism, parallel mechanism and multi degree-of-freedom mechanism is modeling by the same method. Based on previous efforts, this paper focuses on presenting a new unified mathematical model for compound gear trains based state-space approach and trying to achieve the configuration synthesis of compound gear trains efficiently. Configuration optimization and quantitative analysis by this method will be presented in another article.

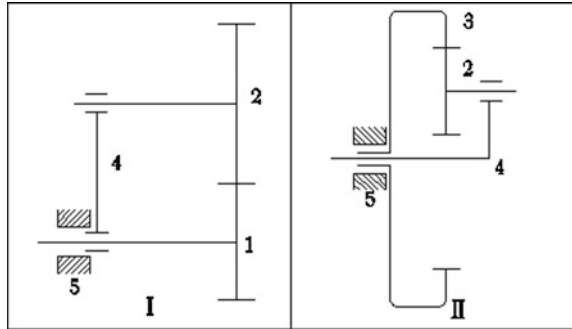
2 BGU and State-Space

2.1 Basic Gear Train Unit

Any compound gear train can be viewed as a combination of inner and outer gear meshing unit. In order to discuss the characteristics of transmission of compound gear trains, basic gear train unit (BGU) is defined as a pair of external or internal gear mesh with two degrees-of-freedom in Fig. 1.

BGU changes the rotate speed, torque and position and orientation from input to output terminal. That is the change of kinematic, dynamic and structure characteristics information which is collectively known as state-characteristics from input to output terminal in the transient.

Fig. 1 Basic gear train unit



This paper takes the expression strategy of “Dual vectors-Matrixes-Equations” to explain the relationship of state-characteristics between the input and output terminal, and explore a new method for configuration synthesis of compound gear trains by searching the operation rules of dual vectors in state-space. The dual vectors composed of input and output state-characteristics are the basis and premise to research the transform of state-characteristics, which is composed of kinematic factors, dynamic factors and structure factors.

Kinematic factors: The kinematic of every component in BGU is continuous, stable, and linear correlation. A rotate speed vector ω is defined to describe the kinematic factors of BGU.

Dynamic factors: The torque of every component in BGU is continuous, stable, and linear correlation. A torque vector M is defined to describe the dynamic factor of BGU.

Structure factors: The position and direction of rotation center of every component in BGU can be described with a position and orientation vector called structure vector r .

The state-characteristics of input and output terminal can be expressed by sequential collections of minimum number of kinematic, dynamic and structure eigenvalues in the form of multi-dimensional vector, which is called eigenvector. The input eigenvector R_i and the output eigenvector R_o are dual vectors, which can be written as $R_i R_o$.

$$R_i = (\omega_i \quad M_i \quad r_i)^T$$

$$R_o = (\omega_o \quad M_o \quad r_o)^T$$

The relationship between the input and output dual vectors of BGU can be expressed as follow equation, which is called state equation.

$$R_o = A_1 \cdot R_{i1} \oplus A_2 \cdot R_{i2} \tag{1}$$

where A_1 and A_2 are the $n \times n$ transformation matrix, n is the dimension of eigenvector.

The matrix form of the state equation of BGU is shown as below

$$\begin{pmatrix} \omega_o \\ M_o \\ r_o \end{pmatrix} = \begin{pmatrix} \lambda_{\omega 1} & \mathbf{0} & \mathbf{0} \\ \mathbf{0} & \lambda_{M1} & \mathbf{0} \\ \mathbf{0} & \mathbf{0} & \lambda_{r1} \end{pmatrix} \begin{pmatrix} \omega_{i1} \\ M_{i1} \\ r_{i1} \end{pmatrix} \oplus \begin{pmatrix} \lambda_{\omega 2} & \mathbf{0} & \mathbf{0} \\ \mathbf{0} & \lambda_{M2} & \mathbf{0} \\ \mathbf{0} & \mathbf{0} & \lambda_{r2} \end{pmatrix} \begin{pmatrix} \omega_{i2} \\ M_{i2} \\ r_{i2} \end{pmatrix} \quad (2)$$

where $\lambda_{\omega i}$, $\lambda_{M i}$, $\lambda_{r i}$ respectively are the transformation submatrix of rotate speed vector, torque vector and structure vector, they constitute the transformation matrix A_i .

The condition of the addition between two eigenvectors is that they have the same structure vector. And the result of the addition is that rotate speed vector and torque vector are added respectively and the structure vector remaining unchanged, which is different from normal vector addition. So a new sign of operation ‘ \oplus ’ is defined to describe the addition among eigenvectors.

For example, if $\begin{pmatrix} \omega_3 \\ M_3 \\ r_3 \end{pmatrix} = \begin{pmatrix} \omega_1 \\ M_1 \\ r_1 \end{pmatrix} \oplus \begin{pmatrix} \omega_2 \\ M_2 \\ r_2 \end{pmatrix}$, there is $\begin{cases} r_3 = r_1 = r_2 \\ \omega_3 = \omega_1 = \omega_2 \\ M_3 = M_1 + M_2 \end{cases}$.

1. The function of gear teeth number (z) is used to express the transition of rotate speed vector, as follows

$$\omega_o = \lambda_{\omega 1}(\alpha(z_k)) \cdot \omega_{i1} + \lambda_{\omega 2}(\alpha(z_k)) \cdot \omega_{i2} \quad (3)$$

where z_k is the gear tooth number of component k ; $\alpha(z_k)$ is the eigenvalue of rotate speed vector transformation submatrix.

2. The function of rotate speed (ω) is used to express the transition of torque vector, as follows

$$M_o = \lambda_{M1}(\beta(\omega_k)) \cdot M_{i1} + \lambda_{M2}(\beta(\omega_k)) \cdot M_{i2} \quad (4)$$

where ω_k is the rotate speed of component k ; $\beta(\omega_k)$ is the eigenvalue of torque vector transformation submatrix.

3. The coordinate transformation equation is used to express the transition of structure vector, as follows

$$r_o = \lambda_{r1} \cdot r_{i1} \oplus \lambda_{r2} \cdot r_{i2} \quad (5)$$

Under the specified coordinates, the rotate speed vector, the torque vector and the structure vector can be decomposed to the coordinate axes, as follows

$$\begin{aligned} \omega &= (\omega_x \quad \omega_y \quad \omega_z)^T \\ \mathbf{M} &= (M_x \quad M_y \quad M_z)^T \\ \mathbf{r} &= (X \quad Y \quad Z \quad x \quad y \quad z \quad 1)^T \end{aligned}$$

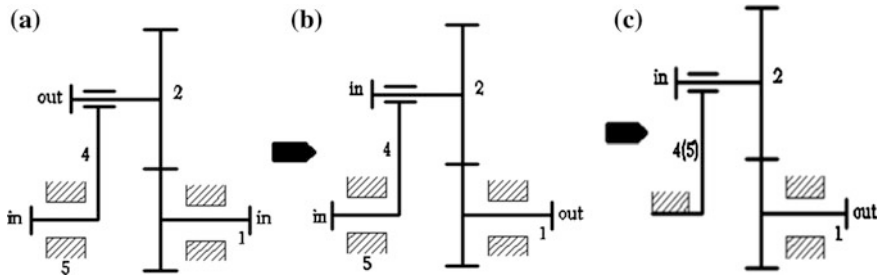


Fig. 2 Conversion of GBU

Different gear train unit can be obtained from BGU’s conversion through the method of kinematic inversion, for example in Fig. 2.

According to the Eq. (1), the state equation of a two degree-of-freedom unit shown in Fig. 2a as below

$$R_2 = A_1 \cdot R_1 \oplus A_2 \cdot R_4 \tag{6}$$

where A_i is a reversible matrix, so the state equation of the two degree of freedom unit shown in Fig. 2b as below

$$R_1 = -A_1^{-1} \cdot A_2 \cdot R_4 \oplus -A_1^{-1} \cdot R_2 \tag{7}$$

If the planet carrier is fixed, the state transformation equation of the one degree-of-freedom unit shown in Fig. 2c as (7), however the rotate speed vector of R_4 is 0, so it simplified to

$$R_1 = -A_1^{-1} \cdot R_2 \tag{8}$$

The state equation clearly describes the internal relations among different gear meshing units, which can realize different transformation of state-characteristics from input to output terminal.

2.2 The Connection of BGUs

Any compound gear train is formed according to certain rules by the connections of BGUs after their conversions. The BGU can be expressed by lines with arrows and block diagrams to explain the connection between gear BGUs in more intuitive (Figs. 3 and 4).

Through analysis of different gear trains, there are two typical connection relationships between two BGUs: series connection and parallel connection. The feature of series connection is that the output component of previous BGU and the

Fig. 3 The diagram of one degree of freedom BGU



Fig. 4 The diagram of two degree-of-freedom BGU

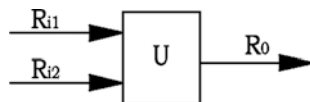


Fig. 5 The series connection

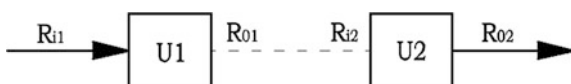
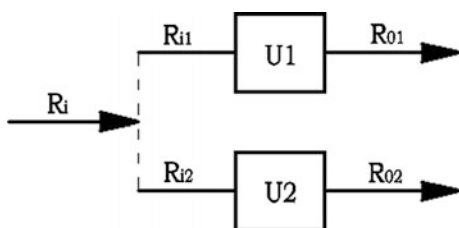


Fig. 6 The parallel connection



input component of rear BGU are merged, and the state-characteristics are transferred through the combined component in serial mode, shown in Fig. 5. The feature of parallel connection is that the input component or the output components of two BGUs are merged, and the state-characteristics are transferred through the combined component in parallel mode shown in Fig. 6.

The conditions for the components which are going to merge through series or parallel connection are that their rotate speed and structure vectors must be same, but their torque must be balanced.

Two BGUs are connected through series connection in Fig. 5, the state equation as follows

$$R_{o2} = A_2 \cdot R_{i2} = A_2 \cdot C \cdot R_{o1} = A_2 \cdot C \cdot A_1 \cdot R_{i1} \tag{9}$$

where C is the gear unit series adjacency matrix as shown below.

$$C = \begin{bmatrix} E & 0 & 0 \\ 0 & -E & 0 \\ 0 & 0 & E \end{bmatrix}$$

Two BGUs are connected through parallel connection in Fig. 6, the transformation equation as follows

$$\begin{cases} \mathbf{R}_{o1} = \mathbf{A}_1 \cdot \mathbf{R}_{i1} = \mathbf{A}_1 \cdot \mathbf{C}_{s1} \cdot \mathbf{R}_i \\ \mathbf{R}_{o2} = \mathbf{A}_2 \cdot \mathbf{R}_{i2} = \mathbf{A}_2 \cdot \mathbf{C}_{s2} \cdot \mathbf{R}_i \end{cases} \quad (10)$$

where C_{s1} and C_{s2} are gear unit parallel adjacency matrix, as shown below.

$$C_{s1} = \begin{bmatrix} E & 0 & 0 \\ 0 & t_1 & 0 \\ 0 & 0 & E \end{bmatrix} \quad C_{s2} = \begin{bmatrix} E & 0 & 0 \\ 0 & t_2 & 0 \\ 0 & 0 & E \end{bmatrix}$$

where $t_1 + t_2 = -E$.

2.3 State-Space of BGUs

The state-space is a collection of all possible states in the system, and its coordinate axis is the state parameters. The state-space of BGUs takes parameters of state-characteristics as the coordinate axes. Any eigenvector of BGU is one vector in this state-space. In addition, the input and output eigenvectors of BGU are dual vectors in this state-space. **The important conclusion is that the BGU, the dual vectors and the transformation matrix are one to one correspondence.** The dual vectors or transformation matrix can express the BGU, so a series of dual vectors or transformation matrixes can describe the gear trains.

What kind of operation rules for dual vectors in state-space and what kind of physical meaning for the rules are necessary to discuss. The dual vectors for one degree of freedom GBU are represented as $\mathbf{R}_i\mathbf{R}_o$, and for two degrees of freedom d GBU are represented as $\mathbf{R}_{i1}\mathbf{R}_{i2}\mathbf{R}_o$.

Set $B_iB_o, C_iC_o, D_iD_o, E_iE_o, B_iC_iD_o$ belongs to the state-space Σ ; the dual vectors have the following operational rules:

1. Multiplication.

$$B_iB_o \times C_iC_o = B_iC_iD_o$$

2. Commutative law of multiplication.

$$B_iB_o \times C_iC_o = C_iC_o \times B_iB_o$$

3. Addition.

$$B_iB_o + C_iC_o = B_iC_o$$

4. Associative law of addition.

$$\mathbf{B}_i\mathbf{B}_o + \mathbf{C}_i\mathbf{C}_o + \mathbf{D}_i\mathbf{D}_o = \mathbf{B}_i\mathbf{B}_o + (\mathbf{C}_i\mathbf{C}_o + \mathbf{D}_i\mathbf{D}_o)$$

5. Commutative law of addition.

$$\mathbf{B}_i\mathbf{B}_o + \mathbf{C}_i\mathbf{C}_o = -(\mathbf{C}_i\mathbf{C}_o + \mathbf{B}_i\mathbf{B}_o)$$

6. Distributive law of multiplication.

$$\mathbf{B}_i\mathbf{B}_o \times (\mathbf{C}_i\mathbf{C}_o + \mathbf{D}_i\mathbf{D}_o) = \mathbf{B}_i\mathbf{B}_o \times \mathbf{C}_i\mathbf{C}_o + \mathbf{B}_i\mathbf{B}_o \times \mathbf{D}_i\mathbf{D}_o$$

7. Scalar multiplication.

$$k \cdot \mathbf{B}_i\mathbf{B}_o \in \mathbf{M}, \text{ where } k \text{ is real number}$$

8. Reversibility.

$$(\mathbf{B}_i\mathbf{B}_o)^{-1} = \mathbf{B}_o\mathbf{B}_i$$

The rule 1 indicates that the operation rule of the dual vectors of two degrees of freedom BGU; the rule 2 indicates that the dual vectors of two degrees of freedom gear unit are equal; the rule 3 indicates that the operation rule of the dual vectors in series connection; the rule 4 and 5 indicate that all the dual vectors in the series connection are equal; the rule 6 indicates that the operation rule of the dual vectors of compound connection; the rule 7 indicates that the state eigenvectors is the inherent attributes of gear unit, nothing to do with size; the rule 8 indicates that the state eigenvector is reversible, and the BGU is reversible.

All the above operation rules illustrate that the dual vectors form a specific state-space. The operation rules of the dual vectors indicate that the feature of series and parallel connections of BGUs. These rules are the basis of configuration synthesis of gear train through dual vectors operation.

3 Configuration Synthesis of Compound Gear Trains

Configuration synthesis of compound gear trains is to design a conceptual of gear train to meet the transmission performance constraints. Essentially it is path planning from input to output terminal under constraints.

3.1 Path Planning of Two BGUs

Path planning of two BGUs is the basis of the synthesis of compound gear trains. According to 1.4, **the state equation is the transformation path of dual vectors of gear trains in the state-space**. So the path planning of two BGUs is equal to establish the state equation of two BGUs in series or parallel connection. The DOF of gear train will change with combination of component merged in series or parallel connection as follows

$$Dof = Dof_1 + Dof_2 - n \tag{11}$$

where Dof_1 and Dof_2 are respectively the DOF of two BGUs; n is the number of merged components.

Considering that the degree of freedom of gear train is no more than 2, the connection forms of two BGUs can be summarized as shown as Tables 1 and 2, which is called the basic connection form.

3.2 Path Planning of Multi-BGUs

Path planning of multi-BGUs is to establish the state equation of multi-BGUs in series or parallel connection as follows

$$R_o = A^* \cdot R_i \tag{12}$$

Table 1 The series connection

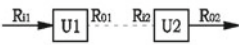
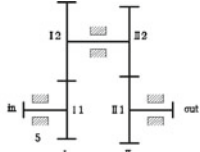
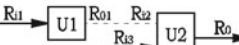
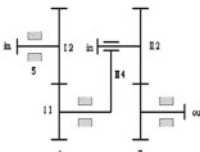
Series connection	Example	State equation
		$R_o = A_2 \cdot C \cdot A_1 \cdot R_i$
		$R_o = A_{21} \cdot C \cdot A_1 \cdot R_{i1} \oplus A_{22} \cdot R_{i2}$

Table 2 The parallel connection

Parallel connection	Example	State equation
		$R_{o1} = A_1 \cdot C_{S1} \cdot R_{i1}$ $R_{o2} = A_2 \cdot C_{S2} \cdot R_{i2}$
		$R_o = A_{21} \cdot C \cdot A_1 \cdot C_{S1} \cdot R_i$ $\oplus A_{22} \cdot C_{S2} \cdot R_i$
		$R_o = A_{21} \cdot C \cdot (A_{11} \cdot R_{i2} \oplus A_{12} \cdot C_{S1} \cdot R_{i1})$ $\oplus A_{22} \cdot C_{S2} \cdot R_{i1}$

where A^* is the total transformation matrix of gear train; R_i is the eigenvector of input terminal; R_o is the eigenvector of output terminal.

The transformation matrix and the state equation are corresponded one by one, so the path planning of multi-BGUs in the state-space is to decompose the total transform matrix.

Any gear train can be divided into several BGUs according to basic connection form. The total transformation matrix can be decomposed according the basic connection form as follows.

$$A^* = A_2 \cdot A_1 \tag{13}$$

$$A^* = A_{21} \cdot A_1 \oplus A_{22} \tag{14}$$

$$A^* = \begin{bmatrix} A_1 \cdot C_{S1-1} \\ A_2 \cdot C_{S2-1} \end{bmatrix} \tag{15}$$

$$A^* = A_{21} \cdot A_1 \cdot C_{S1-1} \oplus A_{22} \cdot C_{S1-2} \tag{16}$$

$$A^* = A_{21} \cdot (A_{11} \oplus A_{12} \cdot C_{S1-1}) \oplus A_{22} \cdot C_{S1-2} \tag{17}$$

3.3 The Constraints of Configuration Synthesis

The configuration of compound gear trains is composed of multi-BGUs in series or parallel connection under the performance constraints of DOF, kinematic, dynamic and structure etc.

1. The constraint of DOF is determined by the number of input terminal, and it determines the initial basic connection form in Tables 1 and 2.
2. The constraint of kinematic is the rotate speed changing from input to output terminal, and it is determined by the eigenvalue of the rotate speed transformation submatrix of each BGU.

$$i = f(\alpha_k)$$

where i is the constraint of kinematic; α_k is the eigenvalue of the rotate speed transformation submatrix.

3. The constraint of dynamic is the torque changing from input to output terminal, and it is determined by the eigenvalue of the torque vector transformation submatrix of each BGU.

$$j = f(\beta_k)$$

where j is the constraint of dynamic; β_k is the eigenvalue of the torque vector transformation submatrix.

4. The constraint of structure is structure vector changing from input to output terminal, and it is determined by the eigenvalue of the structure vector transformation submatrix of each BGU.

$$k = f(\gamma_k)$$

where k is the constraint of structure; γ_k is the eigenvalue of the structure vector transformation submatrix.

According to the design requirements, determine the constraints of DOF, kinematic, dynamic and structure. Then when the total transformation matrix is decomposed, take a full consideration about all the constraints.

4 An Example

The speed-increasing gearbox is the core component of WTGS. The weight, bearing capacity and reliability of the gearbox is determined by transmission configuration. So configuration synthesis of the speed-increasing gearbox directly determines the technological level of the WTGS. This paper takes the configuration

synthesis of 6 MW semi-direct drive wind generator gearbox as an example to explain the process of configuration synthesis by means of state-space.

1. Design requirements of gear trains.

The number η_i ; the speed ω_i , the torque M_i and the position and orientation r_i of input terminal; the number η_o , the speed ω_o , the torque M_o and the position and orientation r_o of output terminal.

2. Input and output eigenvectors.

$$\begin{aligned} R_i &= (\omega_i \quad M_i \quad r_i)^T \\ R_o &= (\omega_o \quad M_o \quad r_o)^T \end{aligned}$$

3. Total transfer equation.

$$R_o = A^* \cdot R_i$$

4. Constraints.

Kinematic constraint: same direction and speed up.

$$i = f(\alpha_k) > 1;$$

Dynamic constraint: reverse direction and reduced.

$$j = f(\beta_k) \subset (-1 \quad 0);$$

Structure constraint: concentric constraint. $k = f(\gamma_k) = \begin{bmatrix} T & & \\ & E & \\ & & 1 \end{bmatrix};$

Other constraint: power flow

$$g = f(\alpha_k) > 0.$$

5. The decomposition of total transform matrix

(a) The number of units

The number of units is random; generally, however the form of semi-direct drive wind generator gearbox is 4 K, so choose unit number is 4.

(b) The initial matrix decomposition

The number of input shaft $\eta_i = 1$, the number of output shaft $\eta_o = 1$, there are two kinds of initial matrix decomposition shown as below:

$$\begin{aligned} \text{i: } \mathbf{A}^* &= \mathbf{A}_2 \cdot \mathbf{A}_1 \\ \text{ii: } \mathbf{A}^* &= \mathbf{A}_{21} \cdot \mathbf{A}_1 \cdot \mathbf{C}_{s1-1} \oplus \mathbf{A}_{22} \cdot \mathbf{C}_{s1-2} \end{aligned}$$

The submatrices corresponding can be decomposed one by one until the number of submatrices meets the unit number. Take the decomposition of matrix **ii** as interpretation.

(c) The submatrix decomposition

According to the basic connection form, the matrix \mathbf{A}_1 in **ii** can be decomposed as formula (13) and (16), the matrix \mathbf{A}_2 can be decomposed as formula (14) and (17). **ii1** is decomposed from \mathbf{A}_1 according to (14) and **ii2** is decomposed from \mathbf{A}_2 according to (14).

$$\begin{aligned} (\text{ii2})\mathbf{A}^* &= \mathbf{A}_{2-21}\mathbf{A}_{2-1}\mathbf{A}_1\mathbf{C}_{s1-1} \oplus \mathbf{A}_{2-22}\mathbf{C}_{s1-2} \\ (\text{ii1})\mathbf{A}^* &= \mathbf{A}_{21}\mathbf{A}_{1-1}\mathbf{A}_{1-2}\mathbf{C}_{s1-1} \oplus \mathbf{A}_{22}\mathbf{C}_{s1-2} \end{aligned}$$

According to the basic connection form, the matrix \mathbf{A}_{1-1} and \mathbf{A}_{1-2} in **ii** can be decomposed as formula (13) and (16), the matrix \mathbf{A}_2 can be decomposed as formula (14) and (17). **ii11** is decomposed from \mathbf{A}_{1-2} according to (14) and **ii12** is decomposed from \mathbf{A}_2 according to (14).

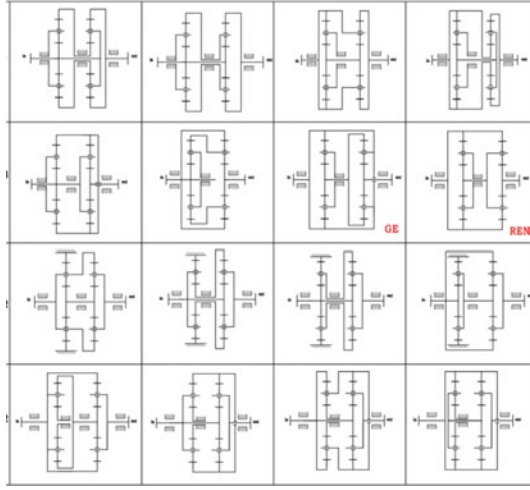
$$\begin{aligned} (\text{ii11})\mathbf{A}^* &= \mathbf{A}_{21}\mathbf{A}_{1-1}\mathbf{A}_{1-2-1}\mathbf{A}_{1-2-2}\mathbf{C}_{s1} \oplus \mathbf{A}_{22}\mathbf{C}_{s2} \\ (\text{ii12})\mathbf{A}^* &= \mathbf{A}_{2-21}(\mathbf{A}_{2-11} \oplus \mathbf{A}_{2-12}\mathbf{C}_{s2-1})\mathbf{A}_{1-1}\mathbf{A}_{1-2}\mathbf{C}_{s1-1} \oplus \mathbf{A}_{22}\mathbf{C}_{s2-2}\mathbf{C}_{s1-2} \end{aligned}$$

In summary, the decomposition of total transformation matrix can get the initial configurations without the constraints of unit connection and transmission performance. Different transform paths can be generated as much as possible with this method.

6. BGU's conversion

In the transform paths, the BGU's conversion (in Sect. 2.1) is restrained by the connection of BGU (in Sect. 2.2) and the constraints of configuration synthesis (in Sect. 3).

A lot of different state transformation equation can be obtained. And they have the same basic equation as shown as (18), but the differences are the transformation matrixes and eigenvalues.

Table 3 Part results of transmission configurations of 6 MW semi-direct drive wind generator

$$\mathbf{R}_o = (\mathbf{A}_{2-21}(\mathbf{A}_{2-11} \oplus \mathbf{A}_{2-12} \mathbf{C}_{s2-1}) \mathbf{A}_{1-1} \mathbf{A}_{1-2} \mathbf{C}_{s1-1} \oplus \mathbf{A}_{22} \mathbf{C}_{s2-2} \mathbf{C}_{s1-2}) \mathbf{R}_i \quad (18)$$

According to the formula (18), part of transmission configurations of 6 MW semi-direct drive wind generator gearbox are shown in Table 3. And how to evaluate the result of configuration synthesis will be presented in another article.

5 Conclusions

1. This paper presents a unified mathematical model to describe the gear trains using the dual vectors and state transformation matrix, which can express the information of kinematic, dynamic and structure of BGUs clearly; it is convenient to achieve configuration synthesis, configuration optimization and quantitative analysis.
2. The state-space of gear trains and its operational rules revealed the relationship between the series-parallel connections of BGUs and the computation paths of dual eigenvectors, which is the basic of configuration synthesis of compound gear trains.
3. An example of speed-increasing gearbox is given to show the process of configuration synthesis under constraints. The configuration synthesis of compound gear trains based on state-space approach is more efficient to distinguish isomorphism and more convenient to achieve computer programming.

Acknowledgments The authors want to acknowledge the financial support from National Natural Science Foundation of China (No. 51375065), National Key Technology Research and Development Program of the Ministry of Science and Technology of China (No. 2012BAA01B05).

References

1. Wang D, Zhang D, Ma Y (2003) New Approach to automated conceptual design of mechanical system by means of state-space. *J Mech Eng* 39(3):548–553
2. Buchsbaum F, Freudenstein F (1970) Synthesis of kinematic structure of geared kinematic chains and other mechanisms. *J Mech* 5(3):357–392
3. Freudenstein F (1971) An application of boolean algebra to the kinematic of epicyclic drives. *ASME J Engl Ind* 93B:176–182
4. Hsu CH, Lam KT (1992) A new graph representation for the automatic kinematic analysis of planetary spur-gear trains. *J Mech Des* 114(1):196–200
5. Rao AC, Raju DV (1991) Application of the hamming number technique to detect isomorphism among kinematic chains and inversions. *Mech Mach Theory* 26(1):55–75
6. Rao AC, Prasad Raju Pathapati VVNR (2000) Loop based detection of isomorphism among chains, inversions and type of freedom in multi degree of freedom chain. *J Mech Des* 122(1):31–42
7. Prasad Raju Pathapati VVNR, Rao AC (2002) A new technique based on loops to investigate displacement isomorphism in planetary gear trains. *J Mech Des* 124(4):662–675
8. Peiwen A, Huang M, Lin J (2001) A method of innovative synthesis of epicyclic gear trains based on kinematic chain with single joints. *Mech Des Res* 01:44–46
9. Xu H, Huang M, Xiang C (2003) A method for innovative synthesis of epicyclic gear trains based on pairs-replaying. *Mech Sci Technol* 22(S2):145–148
10. Dazhun X (1984) Application of graph theory to analysis and synthesis of epicyclic gear trains. *J Dalian Univ Technol* 04
11. Yang S, Duan X (2003) An elementary unit-combined method for creative design of epicyclic gear train. *Mech Sci Technol* 22(05):761–763
12. Zhang D, Ma Y, Wang D (2003) Mechanical system movement transmission and transformation matrix analysis method. *China Mech Eng* 14(1): 4–8
13. Zhang L, Wang D (2006) New approach to automated conceptual design of hybrid mechanical system by means of characteristic state-space. *J Mech Eng* 42(12):26–35
14. Ma Y, Zhang Y (2015) Kinematic characteristic state models for basic units of compound gear train. *China Mech Eng* 15:1999–2003

Identification and Modification of Closed Defect of the Location Function for N -Lobed Noncircular Gears

Xin Zhang and Shouwen Fan

Abstract A general formulation of the identification and modification method of closed defect for the location function of N -lobed noncircular gears (N -LNGs) is proposed. The method is forced to satisfy closed condition of the location function by introducing two modification parameters: proportional parameter and controllable parameter. Controllable parameter can be improved based on the minimization of the maximum modification error. In particular, in order to modified the closed defect without the introduction of new design defect: pitch curves interference defect, controllable modification parameter is further verified and improved by the relationship of curvature radius between internal gear pitch curve and external gear pitch curve for N -lobed internal meshing noncircular gears. This identification and modification method is implemented in several numerical examples, and simulation results demonstrate that the closed defect of the location function for N -LNGs can be effectively identified and modified.

Keywords Location function · Closed defect · Pitch curve interference · Noncircular gear · Identification · Modification

1 Introduction

Since noncircular gears possess excellent transmission performance between two parallel axes with a variable transmission ratio, they are already applied to mechanical equipments: Maltese mechanism, packaging machinery, printing machinery, textile machinery, gear shaper and fluid flowmeter [1–4]. Most of these noncircular gears applications are elliptical gears and eccentric gears, which are

X. Zhang (✉) · S. Fan
School of Mechatronics Engineering, University of Electronic
Science and Technology of China, Chengdu, Sichuan 611731, China
e-mail: zhangxin891221@163.com

S. Fan
e-mail: shouwenfan@263.net

constructed by the existing closed and smoothed curves as the pitch curves of N -lobed noncircular gears (N -LNGs). For instance, Wei H. [5] develops an elliptical interpolation algorithm for elliptical gears on the basis of the principle of central angle division of an arc. Hector F.Q.R. and Salvador C.F. et al. [6] put forward a design approach of pitch curves for N -LNGs on the basis of Bézier and B-spline nonparametric curve. A general generation method of N -lobed elliptical gears from a basic ellipse was proposed in Ref. [7], and the synthesis of N -lobed or high-order elliptical gears and their rack by means of a conjugate shaper cutter with an involute tooth profile was obtained in Refs. [8–13].

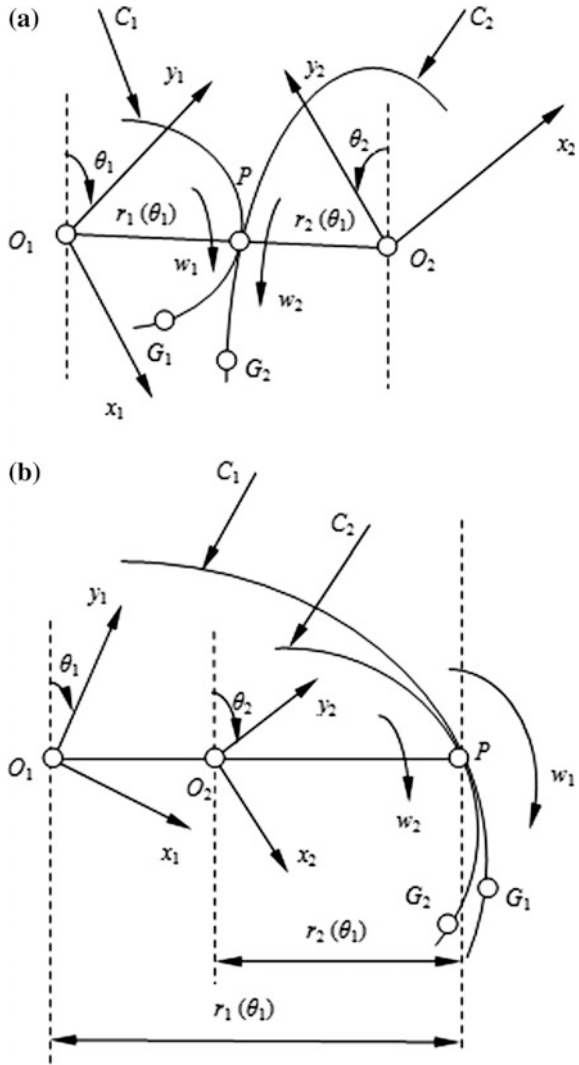
However, the location function of above N -LNGs is obtained after the determination of pitch curves, which is often inconsistent with practical application. In practical, the design of N -LNGs is often need to satisfy the specific location function between driving and driven noncircular gears. Namely, the pitch curves are determined by the location function. In order to realize the continuous transmission, the design of N -LNGs on the basis of location function require that the location function is a periodic function and should also satisfy the closed condition [4]. The location function is not always satisfy the closed condition in practical application, so an effective identification and modification model and method are necessary for the location function.

Aiming at above problem, an identification and modification method of closed defect of the location function for N -LNGs is proposed by resorting to modification parameters: proportional parameter and controllable parameter. Controllable parameter can be improved based on the minimization of the maximum modification error. In particular, in order to avoid the occurrence of the pitch curve interference for N -LIMNGs, the condition without pitch curve interference is firstly given. Meanwhile, the controllable parameter is further improved so that the pitch curves without interference defect for N -LIMNGs. Some numerical results are shown to validate the proposed formulation.

2 Identification Principle and Method of Closed Defect of the Location Function for N-LNGs

As shown in Fig. 1, pitch curves C_1 and C_2 of N -lobed noncircular gears are rolling on each other without sliding. Moving coordinate systems $\Gamma_1(O_1-x_1y_1)$ and $\Gamma_2(O_2-x_2y_2)$ are attached, each to its corresponding N_1 -lobed driving and N_2 -lobed driven noncircular gears, respectively. Angle θ_1 rotates about x_1 -axis with the angular speed of w_1 , while angle θ_2 rotates about x_2 -axis at w_2 . Assuming P_0 is starting meshing point($\theta_1 = 0, \theta_2 = 0$), P is a instantaneous meshing point that driving gear rotated angle θ_1 and its corresponding driven gear rotated angle θ_2 . This moment, the starting point P_0 is moved to point G_1 and G_2 . According to the design rules of the pitch curves for gear pair, namely, the location function $\theta_2 = F(\theta_1)$ is known condition. So, the transmission ratio i_{12} of N -lobed noncircular gears can be expressed as:

Fig. 1 Meshing relationships of N -lobed noncircular gears: **a** External meshing **b** Internal meshing



$$i_{12} = \frac{w_1}{w_2} = \frac{d\theta_1}{d\theta_2} = \frac{1}{F'(\theta_1)} \tag{1}$$

According to the meshing principle, relative velocity of the instantaneous meshing point P for N -LNGs should be zero, namely $w_2 \times \overline{O_1P} = w_1 \times \overline{O_2P}$. Assuming radius vectors $\overline{O_1P} = r_1(\theta_1)$ and $\overline{O_2P} = r_2(\theta_1)$, we have:

$$\frac{w_1}{w_2} = \frac{\overline{O_2P}}{\overline{O_1P}} = \frac{r_2(\theta_1)}{r_1(\theta_1)} \tag{2}$$

Along with Eq. (1), one obtains:

$$\frac{r_2(\theta_1)}{r_1(\theta_1)} = \frac{1}{F'(\theta_1)} \tag{3}$$

The pitch curves roll without slip, therefore:

$$d\theta_2 = \frac{r_1(\theta_1)}{r_2(\theta_1)} d\theta_1 \tag{4}$$

Taking Eqs. (1)–(3) into consideration, after integrating both sides of Eq. (4) from $\theta_1 = 0$ to $\theta_1 = 2\pi/N_1$, we obtain:

$$\frac{2\pi}{N_2} = \int_0^{\frac{2\pi}{N_1}} \frac{r_1(\theta_1)}{r_2(\theta_1)} d\theta_1 = \int_0^{\frac{2\pi}{N_1}} F'(\theta_1) d\theta_1 \tag{5}$$

Equation (5) is the closed condition of pitch curves for N -lobed noncircular gears. Equation (5) is usually not satisfied. Therefore, Eq. (5) can be used as the identification method of closed defect of the location function for N -LNGs.

Assume that the center distance between points O_1 and O_2 is A_0 ($A_0 > 0$). Because the difference between $r_1(\theta_1)$ and $r_2(\theta_1)$ at their contact point P is a constant that equals the center distance A_0 , then the relationship between pitch curves and center distance is shown in Table 1.

Along with the Eqs. (3)–(4), pitch curve equations $r_1(\theta_1)$ and $r_2(\theta_1)$ of N_1 -lobed driving and N_2 -lobed driven noncircular gears can be obtained, respectively. Their computational formulas are shown in Table 2.

Table 1 The relationship between pitch curves and center distance for N -LNGs

External meshing	Internal meshing	
	$r_1(\theta_1)$ is external gear pitch curve $r_2(\theta_1)$ is internal gear pitch curve	$r_2(\theta_1)$ is external gear pitch curve $r_1(\theta_1)$ is internal gear pitch curve
$r_1(\theta_1) + r_2(\theta_1) = A_0$	$r_1(\theta_1) - r_2(\theta_1) = A_0$	$r_2(\theta_1) - r_1(\theta_1) = A_0$

Table 2 The formulas of pitch curve equations $r_1(\theta_1)$ and $r_2(\theta_1)$ of N_1 -lobed driving and N_2 -lobed driven noncircular gears

External meshing	Internal meshing	
	$r_1(\theta_1)$ is external gear pitch curve $r_2(\theta_1)$ is internal gear pitch curve	$r_2(\theta_1)$ is external gear pitch curve $r_1(\theta_1)$ is internal gear pitch curve
$r_1(\theta_1) = \frac{A_0 F'(\theta_1)}{F'(\theta_1) + 1} \begin{cases} r_2(\theta_1) = \frac{A_0}{F'(\theta_1) + 1} \\ \theta_2 = F(\theta_1) \end{cases}$	$r_1(\theta_1) = \frac{A_0 F'(\theta_1)}{F'(\theta_1) - 1} \begin{cases} r_2(\theta_1) = \frac{A_0}{F'(\theta_1) - 1} \\ \theta_2 = F(\theta_1) \end{cases}$	$r_1(\theta_1) = \frac{A_0 F'(\theta_1)}{1 - F'(\theta_1)} \begin{cases} r_2(\theta_1) = \frac{A_0}{1 - F'(\theta_1)} \\ \theta_2 = F(\theta_1) \end{cases}$

3 Modification Method of Closed Defect of the Location Function for N-LNGs

Assume that the numbers of pitch curve lobes N_1 and N_2 for N -lobed noncircular gears are known. Due to Eq. (5) is not necessarily established, the location function of N -LNGs has closed design defect. Therefore we add two modification parameters to modify the original $F(\theta_1)$ and force the two sides equal:

$$\frac{2\pi}{N_2}a + b = \int_0^{\frac{2\pi}{N_1}} F'(\theta_1) d\theta_1, (a, b \neq 0 \text{ and } a \neq 1) \tag{6}$$

where a and b are, respectively, proportional modification parameter and controllable modification parameter of the closed design defect, N_1 and N_2 are the numbers of pitch curve lobes of driving and driven noncircular gear for N -LNGs, and we have:

$$\begin{cases} a = \frac{N_2 \int_0^{\frac{2\pi}{N_1}} F'(\theta_1) d\theta_1 - bN_2}{2\pi} \\ b = \int_0^{\frac{2\pi}{N_1}} F'(\theta_1) d\theta_1 - \frac{2\pi}{N_2}a \end{cases} \tag{7}$$

Rearrange Eq. (7) to:

$$\frac{2\pi}{N_2} = \int_0^{\frac{2\pi}{N_1}} \left(\frac{F'(\theta_1)}{a} - \frac{bN_1}{2a\pi} \right) d\theta_1 \tag{8}$$

Assume that the original $\theta_2 = F(\theta_1)$ is composed of the change function $f(\theta_1)$ and constant C , namely:

$$\theta_2 = F(\theta_1) = f(\theta_1) + C \tag{9}$$

The modified location function $\theta_{2m}(\theta_1)$ can be obtained by Eqs. (8)–(9)

$$\theta_{2m} = \frac{1}{a}f(\theta_1) - \frac{bN_1}{2a\pi}\theta_1 + c \tag{10}$$

where c is an unsolved integration constant.

3.1 Modification Method of Closed Defect of the Location Function for N -Lobed External Meshing Noncircular Gears

In order to guarantee the continuous rotary motion of the noncircular gears, the location function $\theta_2 = F(\theta_1)$ of N -lobed external meshing noncircular gears should satisfy the following conditions:

$$\begin{cases} \theta_1 = 0, F(\theta_1) = 0 \\ \forall \theta_1 \in [0, 2\pi/N_1], F'(\theta_1) > 0 \\ F'(\theta_1) = F'(\theta_1 + 2\pi/N_1) \end{cases} \quad (11)$$

where N_1 is the number of pitch curve lobes of driving external meshing noncircular gears, respectively. Without additional exception, the original location function $\theta_2 = F(\theta_1)$ has satisfied these conditions.

According to Eq. (11), rearrange Eq. (9) to:

$$\theta_2 = F(\theta_1) = f(\theta_1) - f(0) \quad (12)$$

Along with Eqs. (10)–(11), we have:

$$\begin{cases} c = -\frac{1}{a}f(0) \\ \forall \theta_1 \in [0, 2\pi/N_1], \frac{1}{a}f'(\theta_1) - \frac{bN_1}{2a\pi} > 0 \end{cases} \quad (13)$$

The modified location function $\theta_{2m}(\theta_1)$ can be expressed as:

$$\theta_{2m} = \frac{1}{a}f(\theta_1) - \frac{bN_1}{2a\pi}\theta_1 - \frac{1}{a}f(0), \frac{1}{a}f'(\theta_1) - \frac{bN_1}{2a\pi} > 0 \quad (14)$$

Further, in order to better analyze the error, the error function $e(\theta_1)$ can be established by Eqs. (12)–(14):

$$\begin{aligned} e(\theta_1) &= \theta_{2m} - \theta_2 \\ &= \frac{1-a}{a}f(\theta_1) - \frac{bN_1}{2a\pi}\theta_1 + \frac{a-1}{a}f(0), \frac{1}{a}f'(\theta_1) - \frac{bN_1}{2a\pi} > 0 \end{aligned} \quad (15)$$

And the first-order derivative of the error function $e(\theta_1)$ can be obtained:

$$e'(\theta_1) = \frac{1-a}{a}f'(\theta_1) - \frac{bN_1}{2a\pi}, \frac{1}{a}f'(\theta_1) - \frac{bN_1}{2a\pi} > 0 \quad (16)$$

Assuming $\theta_{11}, \theta_{12}, \dots$ are solutions of the equation $e'(\theta_1) = 0$ at $\theta_1 \in [0, 2\pi/N_1]$. The maximum e_{\max} of the Eq. (15) can be expressed as:

$$e_{\max} = \max\{|e(0)|, |e(\theta_{11})|, |e(\theta_{12})|, \dots, |e(2\pi/N_1)|\} \tag{17}$$

In order to obtain the minimize of the maximum e_{\max} for the error function $e(\theta_1)$, the following objective function has been established according to Eqs. (15)–(17):

$$\min f_e(b) = \min(e_{\max}), \frac{1}{a}f'(\theta_1) - \frac{bN_1}{2a\pi} > 0 \tag{18}$$

According to Table 2 and Eqs. (14)–(18), modification parameters a and b can be solved and makes the maximum e_{\max} of the error function $e(\theta_1)$ is minimal. Pitch curve equations $r_1(\theta_1)$ and $r_2(\theta_1)$ of N_1 -lobed driving and N_2 -lobed driven external meshing noncircular gears can be calculated, respectively:

$$r_1(\theta_1) = \frac{A_0\theta'_{2m}}{1 + \theta'_{2m}}, \frac{1}{a}f'(\theta_1) - \frac{bN_1}{2a\pi} > 0 \tag{19}$$

$$\begin{cases} r_2(\theta_1) = \frac{A_0}{1 + \theta'_{2m}} \\ \theta_{2m} = \frac{1}{a}f(\theta_1) - \frac{bN_1}{2a\pi}\theta_1 - \frac{1}{a}f(0) \end{cases}, \quad \frac{1}{a}f'(\theta_1) - \frac{bN_1}{2a\pi} > 0 \tag{20}$$

3.2 Modification Method of Closed Defect of the Location Function for N -Lobed Internal Meshing Noncircular Gears

According to Table 2, the location function $\theta_2 = F(\theta_1)$ of N -lobed internal meshing noncircular gears should also satisfy the following conditions:

$$\begin{cases} \theta_1 = 0, F(\theta_1) = 0 \\ \forall \theta_1 \in [0, \frac{2\pi}{N_1}], F'(\theta_1) > 1 \text{ or } 0 < F'(\theta_1) < 1 \\ F'(\theta_1) = F'(\theta_1 + 2\pi/N_1) \end{cases} \tag{21}$$

where N_1 is the numbers of pitch curve lobes of driving noncircular gear for N -LIMNGs, respectively. When $r_1(\theta_1)$ is external gear pitch curve and $r_2(\theta_1)$ is internal gear pitch curve, the first-order derivative of location function $F'(\theta_1) > 1$, otherwise $0 < F'(\theta_1) < 1$. Without additional exception, the original location function $\theta_2 = F(\theta_1)$ has satisfied these conditions.

According to Eq. (21), rearrange Eq. (9) to:

$$\theta_2 = F(\theta_1) = f(\theta_1) - f(0) \tag{22}$$

Along with Eqs. (21)–(22), we have:

$$\begin{cases} c = -\frac{1}{a}f(0) \\ \forall \theta_1 \in [0, \frac{2\pi}{N_1}], \frac{1}{a}f'(\theta_1) - \frac{bN_1}{2a\pi} > 1 \text{ or } 0 < \frac{1}{a}f'(\theta_1) - \frac{bN_1}{2a\pi} < 1 \end{cases} \quad (23)$$

The modified location function $\theta_{2m}(\theta_1)$ can be expressed as:

$$\begin{cases} \theta_{2m} = \frac{1}{a}f(\theta_1) - \frac{bN_1}{2a\pi}\theta_1 - \frac{1}{a}f(0), \\ s.t. \frac{1}{a}f'(\theta_1) - \frac{bN_1}{2a\pi} > 1 \text{ or } 0 < \frac{1}{a}f'(\theta_1) - \frac{bN_1}{2a\pi} < 1 \end{cases} \quad (24)$$

Further, in order to better analyze the error, the error function $e(\theta_1)$ can be established by Eqs. (22)–(24):

$$\begin{cases} e(\theta_1) = \theta_{2m} - \theta_2 = \frac{1-a}{a}f(\theta_1) - \frac{bN_1}{2a\pi}\theta_1 + \frac{a-1}{a}f(0), \\ s.t. \frac{1}{a}f'(\theta_1) - \frac{bN_1}{2a\pi} > 1 \text{ or } 0 < \frac{1}{a}f'(\theta_1) - \frac{bN_1}{2a\pi} < 1 \end{cases} \quad (25)$$

And the first-order derivative of the error function $e(\theta_1)$ can be obtained:

$$\begin{cases} e'(\theta_1) = \frac{1-a}{a}f'(\theta_1) - \frac{bN_1}{2a\pi}, \\ s.t. \frac{1}{a}f'(\theta_1) - \frac{bN_1}{2a\pi} > 1 \text{ or } 0 < \frac{1}{a}f'(\theta_1) - \frac{bN_1}{2a\pi} < 1 \end{cases} \quad (26)$$

Assuming $\theta_{11}, \theta_{12}, \dots$ are solutions of the equation $e'(\theta_1) = 0$ at $\theta_1 \in [0, 2\pi/N_1]$. The maximum e_{\max} of the Eq. (25) can be expressed as:

$$e_{\max} = \max\{|e(0)|, |e(\theta_{11})|, |e(\theta_{12})|, \dots, |e(2\pi/N_1)|\} \quad (27)$$

In order to obtain the minimize of the maximum e_{\max} for the error function $e(\theta_1)$, the following objective function has been established according to Eqs. (25)–(27):

$$\begin{cases} \min_f e(b) = \min(e_{\max}), \\ s.t. \frac{1}{a}f'(\theta_1) - \frac{bN_1}{2a\pi} > 1 \text{ or } 0 < \frac{1}{a}f'(\theta_1) - \frac{bN_1}{2a\pi} < 1 \end{cases} \quad (28)$$

According to Table 2 and Eq. (24), the pitch curve equations $r_1(\theta_1)$ and $r_2(\theta_1)$ of N_1 -lobed driving and N_2 -lobed driven internal meshing noncircular gears can be calculated:

$$\begin{cases} r_1(\theta_1) = \frac{A_0\theta_{2m}}{\theta_{2m}^2-1} \\ r_2(\theta_1) = \frac{A_0}{\theta_{2m}^2-1} \\ \theta_{2m} = \frac{1}{a}f(\theta_1) - \frac{bN_1}{2a\pi}\theta_1 - \frac{1}{a}f(0) \end{cases}, \quad \frac{1}{a}f'(\theta_1) - \frac{bN_1}{2a\pi} > 1 \quad (29)$$

Fig. 2 The relationship of curvature radius between internal gear pitch curve and external gear pitch curve for *N*-LIMNGs

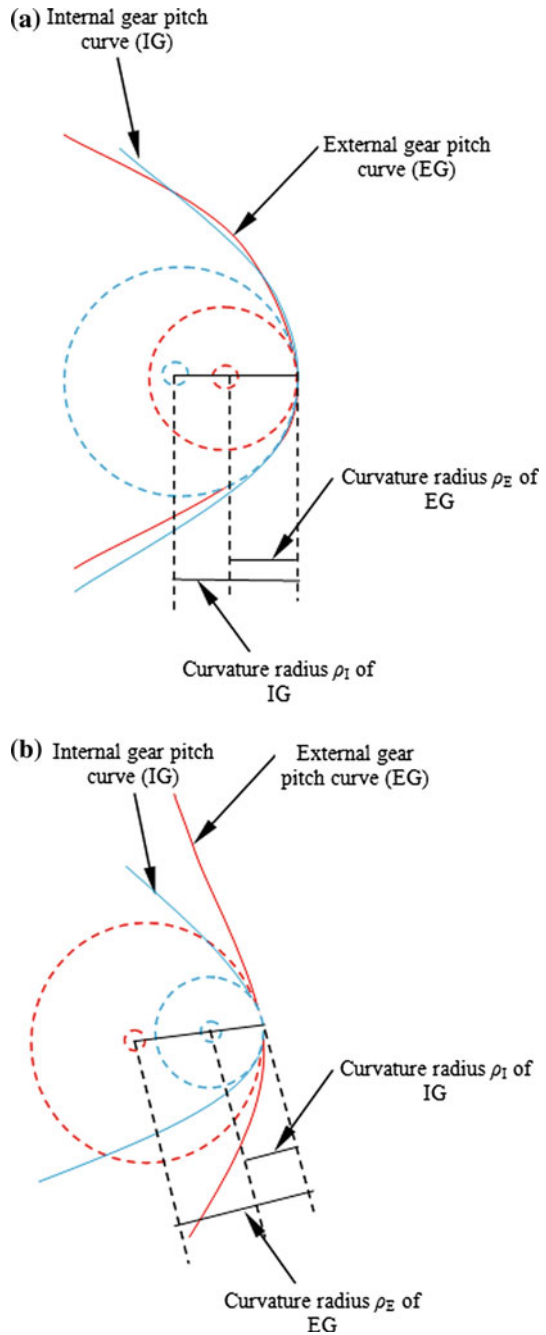


Table 3 The relationship of curvature radius between pitch curves $r_1(\theta_1)$ and $r_2(\theta_1)$ for N -LIMNGs

Internal meshing	
$r_1(\theta_1)$ is external gear pitch curve $r_2(\theta_1)$ is internal gear pitch curve	$\forall \theta_1 \in [0, 2\pi/N_1],$ $\frac{[r_2^2 + (\frac{dr_2}{d\theta_{2m}})^2]^{3/2}}{r_2^2 + 2(\frac{dr_2}{d\theta_{2m}})^2 - r_2 \frac{d^2 r_2}{d\theta_{2m}^2}} \leq \frac{[r_1^2 + (\frac{dr_1}{d\theta_1})^2]^{3/2}}{r_1^2 + 2(\frac{dr_1}{d\theta_1})^2 - r_1 \frac{d^2 r_1}{d\theta_1^2}}$
$r_2(\theta_1)$ is external gear pitch curve $r_1(\theta_1)$ is internal gear pitch curve	$\forall \theta_1 \in [0, 2\pi/N_1],$ $\frac{[r_2^2 + (\frac{dr_2}{d\theta_{2m}})^2]^{3/2}}{r_2^2 + 2(\frac{dr_2}{d\theta_{2m}})^2 - r_2 \frac{d^2 r_2}{d\theta_{2m}^2}} \geq \frac{[r_1^2 + (\frac{dr_1}{d\theta_1})^2]^{3/2}}{r_1^2 + 2(\frac{dr_1}{d\theta_1})^2 - r_1 \frac{d^2 r_1}{d\theta_1^2}}$

Table 4 The curvature radius relationship represented by location function for N -LIMNGs

Internal meshing	
$r_1(\theta_1)$ is external gear pitch curve $r_2(\theta_1)$ is internal gear pitch curve	$\forall \theta_1 \in [0, 2\pi/N_1],$ $\begin{cases} (\theta'_{2m})^3(\theta'_{2m} - 1) - (\theta''_{2m})^2 + \theta'_{2m}\theta''_{2m} < 0 \\ \theta'_{2m} - 1 > 0 \end{cases}$ or $\begin{cases} (\theta'_{2m})^2(\theta'_{2m} - 1) - 2(\theta''_{2m})^2 + \theta'_{2m}\theta''_{2m} > 0 \\ \theta'_{2m} - 1 > 0 \end{cases}$
$r_2(\theta_1)$ is external gear pitch curve $r_1(\theta_1)$ is internal gear pitch curve	$\forall \theta_1 \in [0, 2\pi/N_1],$ $\begin{cases} (\theta'_{2m})^3(1 - \theta'_{2m}) + (\theta''_{2m})^2 - \theta'_{2m}\theta''_{2m} > 0 \\ 0 < \theta'_{2m} < 1 \end{cases}$ or $\begin{cases} (\theta'_{2m})^2(1 - \theta'_{2m}) + 2(\theta''_{2m})^2 - \theta'_{2m}\theta''_{2m} < 0 \\ 0 < \theta'_{2m} < 1 \end{cases}$

or

$$\begin{cases} r_1(\theta_1) = \frac{A_0\theta'_{2m}}{1-\theta'_{2m}} \\ r_2(\theta_1) = \frac{A_0}{1-\theta'_{2m}} \\ \theta_{2m} = \frac{1}{a}f(\theta_1) - \frac{bN_1}{2a\pi}\theta_1 - \frac{1}{a}f(0) \end{cases}, \quad 0 < \frac{1}{a}f'(\theta_1) - \frac{bN_1}{2a\pi} < 1 \quad (30)$$

However, the pitch curve interference may occur at the meshing points of N -lobed internal meshing noncircular gears. Namely, the curvature radius of internal gear pitch curve is more than the curvature radius of external gear pitch curve, as shown in Fig. 2a. In order to avoid the occurrence of the pitch curve interference, referring to Fig. 2b, we know that the relationship of curvature radius between pitch curves $r_1(\theta_1)$ and $r_2(\theta_1)$ of N_1 -lobed driving and N_2 -lobed driven internal meshing noncircular gears is shown in Table 3. Along with Eqs. (29)–(30), the curvature radius relationship represented by location function is shown in Table 4.

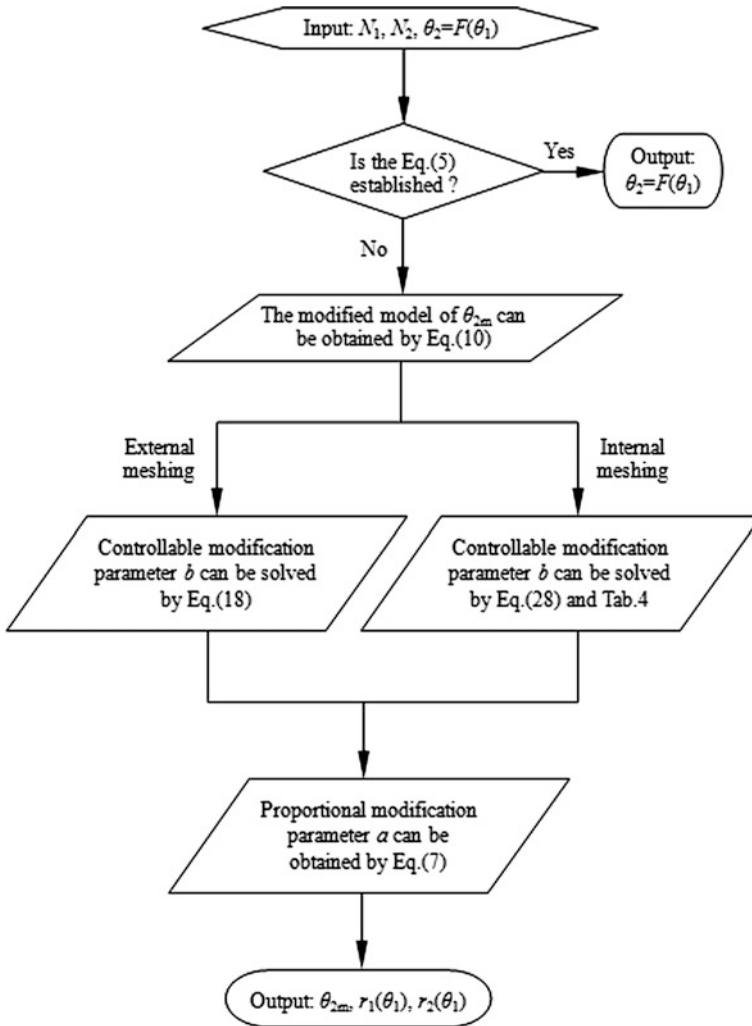


Fig. 3 Flow chart of the identification and modification algorithm for closed defect

4 Algorithm

An identification and modification algorithm of closed defect of the location function for N -LNGs was produced using the foregoing formulation. Referring to the algorithm flow chart of Fig. 3, the input data are the numbers of pitch curve lobes N_1 and N_2 , the original location function $\theta_2 = F(\theta_1)$ for N -LNGs, respectively.

If original location function θ_2 does not satisfy the Eq. (5), then the modification model θ_{2m} can be obtained by Eq. (10). The controllable modification parameter b of external meshing gears or internal meshing gears can be, respectively, solved

Table 5 Identification and modification model of an external meshing location function

Original location function	Identification model	Modification parameters relationship	Modification model (θ_{2m})
$3\theta_1 - \frac{\cos(2\theta_1)}{2} + \frac{1}{2},$ $\begin{cases} f(\theta_1) = 3\theta_1 - \frac{\cos(2\theta_1)}{2} \\ f(0) = -\frac{1}{2} \end{cases}$	$2\pi/3 \neq \int_0^{\frac{\pi}{6}} (3 + \sin(2\theta_1)) d\theta_1 = 3\pi$	$\begin{cases} a = \frac{9\pi - 3b}{2\pi} \\ b = \frac{9\pi - 2a\pi}{3} \end{cases}$	$\frac{2}{3}\theta_1 + \frac{\pi(1 - \cos(2\theta_1))}{3(3\pi - b)}$ <p style="text-align: center;"><i>s.t.</i> $b \neq 3\pi$</p>

Table 6 The solution and selection of modification parameters

Min $f_c(b)$	Constraint condition of parameter b	Selection of modification parameters	Modified location function	Figures
$\frac{7\pi}{3}$	$b < 2\pi, \quad b \neq 0$ or $b > 4\pi$	$a = 6,$ $b = -\pi$	$\frac{2}{3}\theta_1 + \frac{1-\cos(2\theta_1)}{12}$	Figure 4a
		$a = -3,$ $b = 5\pi$	$\frac{2}{3}\theta_1 - \frac{1-\cos(2\theta_1)}{6}$	Figure 4b

Fig. 4 Original location function and modified location function of an external meshing noncircular gears

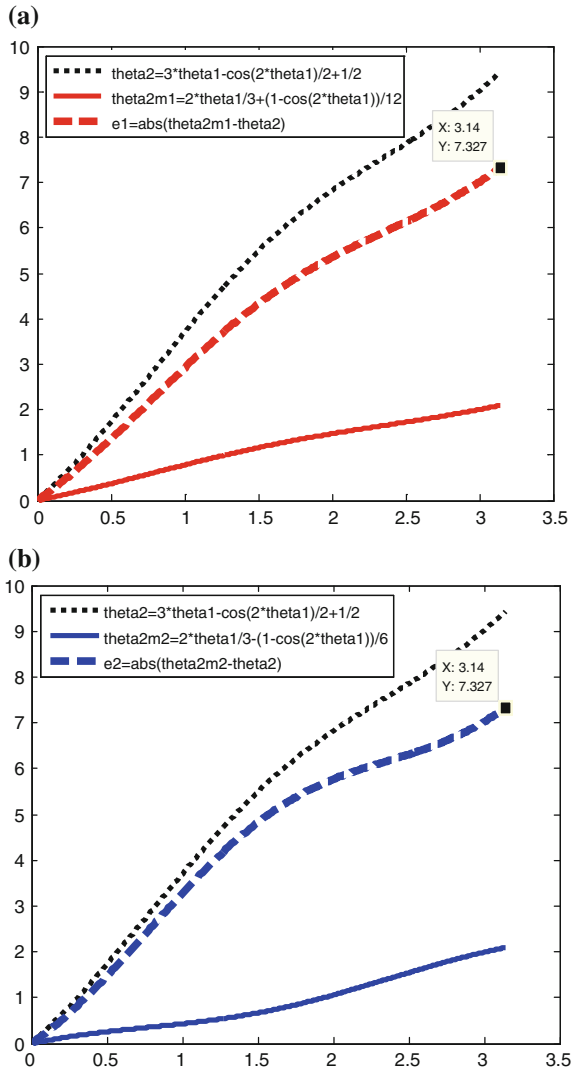


Table 7 Modified location function and closed pitch curves in Fig. 5

Modified location function	Center distance	Closed pitch curves	Figures
$\frac{2}{3}\theta_1 + \frac{1-\cos(2\theta_1)}{12}$	$A_0 = 5$	$r_{1a}(\theta_1) = \frac{5(4 + \sin(2\theta_1))}{10 + \sin(2\theta_1)}$, $r_{2a}(\theta_1) = \frac{30}{10 + \sin(2\theta_1)}$	Figure 5a
$\frac{2}{3}\theta_1 - \frac{1-\cos(2\theta_1)}{6}$		$r_{1b}(\theta_1) = \frac{5(2 - \sin(2\theta_1))}{5 - \sin(2\theta_1)}$, $r_{2b}(\theta_1) = \frac{15}{5 - \sin(2\theta_1)}$	Figure 5b

Fig. 5 Two samples of the closed pitch curves for N -lobed external meshing noncircular gears

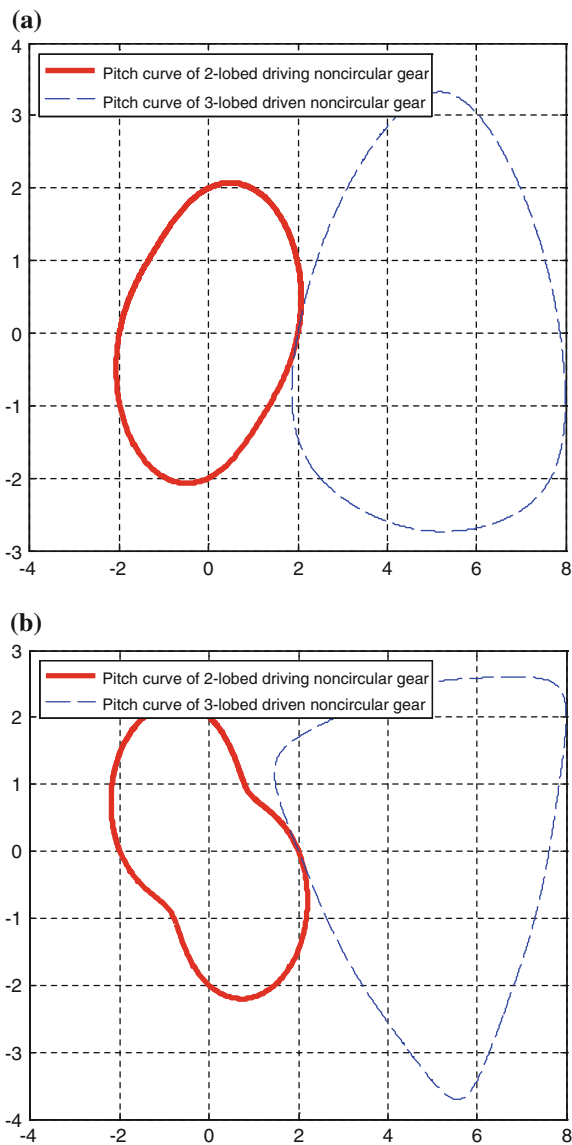


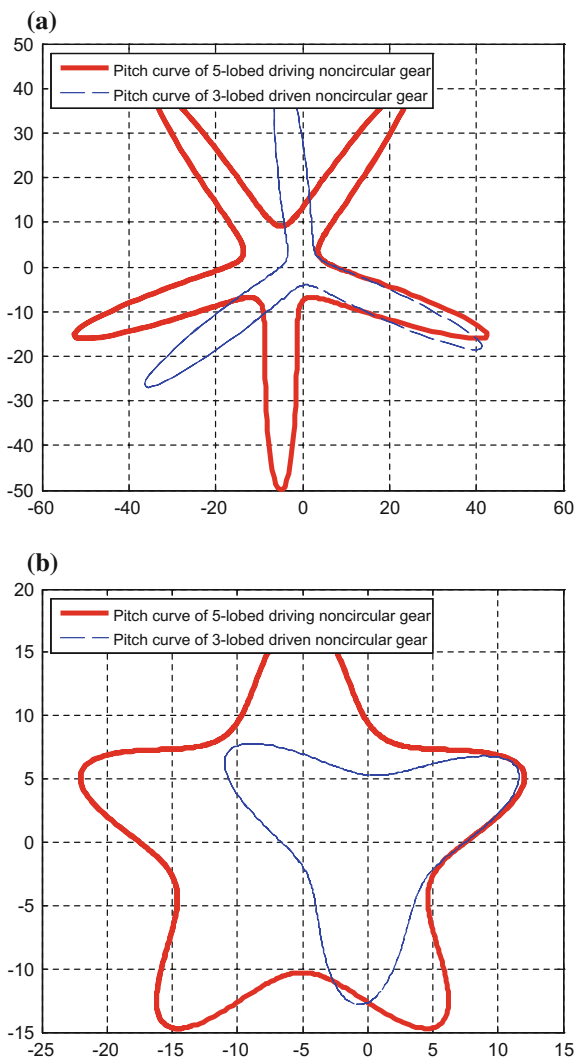
Table 8 Identification and modification model of an internal meshing location function

Original location function	Identification model	Modification parameters relationship	Modification model (θ_{2m})
$4\theta_1 - \frac{\cos(5\theta_1)}{5} + \frac{1}{5},$ $\left\{ \begin{array}{l} f(\theta_1) = 4\theta_1 - \frac{\cos(5\theta_1)}{5} \\ f(0) = -\frac{1}{5} \end{array} \right.$	$2\pi/3 \neq \int_0^{\frac{2\pi}{3}} (4 + \sin(5\theta_1)) d\theta_1 = \frac{8\pi}{5}$	$\left\{ \begin{array}{l} a = \frac{3(8\pi - 5b)}{10\pi} \\ b = \frac{24\pi - 10a\pi}{15} \end{array} \right.$	$\frac{5}{3}\theta_1 + \frac{2\pi(1 - \cos(5\theta_1))}{3(8\pi - 5b)}$ $s.t. b \neq \frac{8\pi}{5}$

Table 9 The feasible region of controllable modification parameter b

Min $f_c(b)$	Constraint condition of parameter b
$\frac{14\pi}{15}$	$b < \frac{3\pi}{5}$ and $b \neq 0$ or $b > \frac{13\pi}{5}$

Fig. 6 Two samples of the closed pitch curves with interference defect for N -lobed internal meshing noncircular gears



by Eq. (18) or Eq. (28) and Table 4. The proportional modification parameter a can be obtained by Eq. (7). The modified location function θ_{2m} and its corresponding pitch curves $r_1(\theta_1)$ and $r_2(\theta_1)$ can be solved by the modification parameters a and b .

5 Examples

The proposed identification and modification method was implemented in MATLAB to run several illustrative examples.

Case 1: Example on the design of an external meshing location function $F(\theta_1) = 3\theta_1 - \frac{\cos(2\theta_1)}{2} + \frac{1}{2}$ for 2-lobed driving and 3-lobed driven external meshing noncircular gears, namely, $N_1 = 2$ and $N_2 = 3$.

According to Eqs. (5)–(10), its identification and modification model is shown in Table 5. In order to minimize the maximum e_{max} of the error function $e(\theta_1)$, the values of parameters a , b and their corresponding modified location function θ_{2m} are, respectively, depicted in Table 6 and Fig. 4 by resorting to Eqs. (11)–(20).

Table 7 and Fig. 5 are two samples of the closed pitch curves for N -lobed external meshing noncircular gears based on the modified location function in Table 6.

Table 10 Corresponding parameters with interference defect of closed pitch curves in Fig. 6

Modification parameters	Modified location function	Center distance	Pitch curves
$a = 9/5,$ $b = 2\pi/5$	$\frac{5}{3}\theta_1 + \frac{1-\cos(5\theta_1)}{9}$	$A_0 = 5$	$r_{1a}(\theta_1) = \frac{25(3 + \sin(5\theta_1))}{6 + 5\sin(5\theta_1)}$ $r_{2a}(\theta_1) = \frac{45}{6 + 5\sin(5\theta_1)}$
$a = -18/5,$ $b = 4\pi$	$\frac{5}{3}\theta_1 - \frac{1-\cos(5\theta_1)}{18}$		$r_{1b}(\theta_1) = \frac{25(6 - \sin(5\theta_1))}{12 - 5\sin(5\theta_1)}$ $r_{2b}(\theta_1) = \frac{90}{12 - 5\sin(5\theta_1)}$

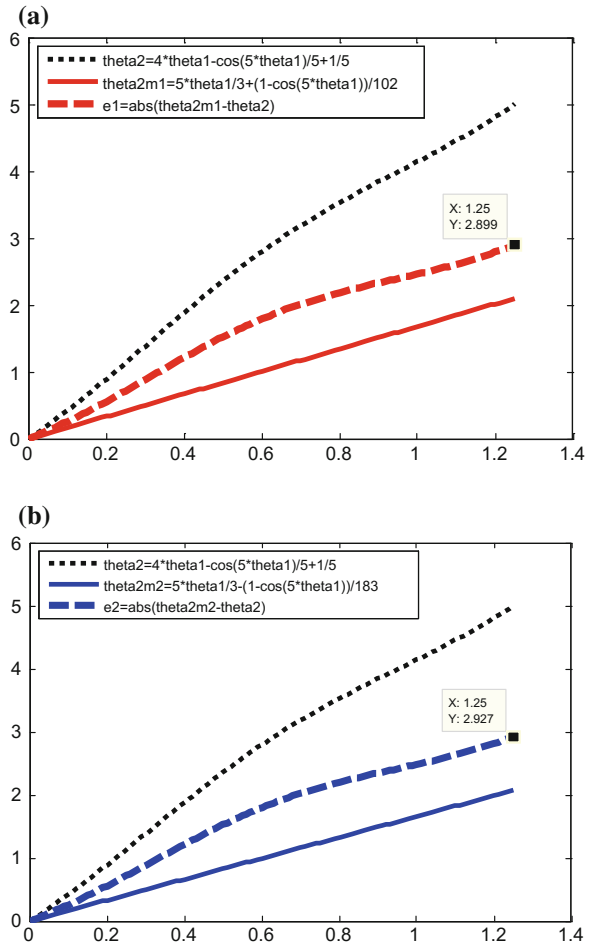
Table 11 The improved feasible region of controllable modification parameter b

Min $f_c(b)$	Constraint condition of parameter b
$\frac{14\pi}{15}$	$b < \frac{8}{5}\pi - \frac{213.1653}{5} (\approx \frac{-59.8526}{5}\pi)$ or $b > \frac{8}{5}\pi + \frac{213.1653}{5} (\approx \frac{75.8526}{5}\pi)$

Table 12 The solution and selection of modification parameters

Original location function	Modification parameters	Modified location function	Figures
$4\theta_1 - \frac{\cos(5\theta_1)}{5} + \frac{1}{5}$	$a = 102/5, b = -60\pi/5$	$\frac{5}{3}\theta_1 + \frac{1-\cos(5\theta_1)}{102}$	Figure 7a
	$a = -183/5, b = 130\pi/5$	$\frac{5}{3}\theta_1 - \frac{1-\cos(5\theta_1)}{183}$	Figure 7b

Fig. 7 Original location function and modified location function of an internal meshing noncircular gears



Case 2: Example on the design of an internal meshing location function $F(\theta_1) = 4\theta_1 - \frac{\cos(5\theta_1)}{5} + \frac{1}{5}$ for 5-lobed driving and 3-lobed driven internal meshing non-circular gears, namely, $N_1 = 5$ and $N_2 = 3$. $r_1(\theta_1)$ is external gear pitch curve and $r_2(\theta_1)$ is internal gear pitch curve. Its identification and modification model is shown in Table 8 by resorting to Eqs. (5)–(10).

Before considering the interference condition, the feasible region of controllable modification parameter b is shown in Table 9 by minimizing the maximum e_{\max} of the error function $e(\theta_1)$ according to Eqs. (21)–(28). Two examples of pitch curves with interference for internal meshing gears are shown in Fig. 6 based on the feasible region. Its corresponding parameters are depicted in Table 10.

In order to modified the closed defect without the introduction of new design defect: pitch curves interference defect, the improved feasible region of controllable

Fig. 8 Two samples of the closed pitch curves without interference defect for N -lobed internal meshing noncircular gears

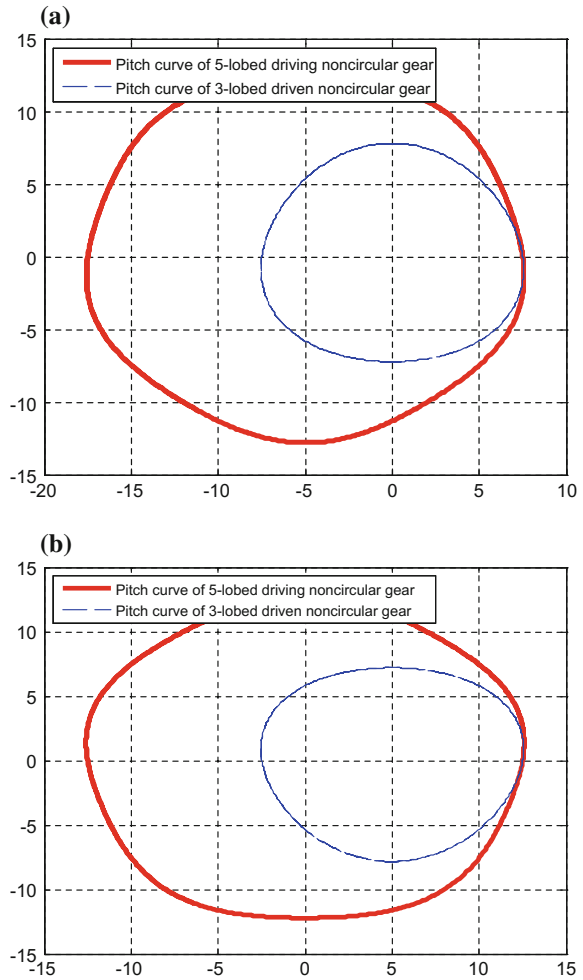


Table 13 Modified location function and closed pitch curves without interference defect in Fig. 8

Modified location function	Center distance	Closed pitch curves	Figures
$\frac{5}{3}\theta_1 + \frac{1-\cos(5\theta_1)}{102}$	$A_0 = 5$	$r_{1a}(\theta_1) = \frac{25(34 + \sin(5\theta_1))}{68 + 5\sin(5\theta_1)}$	Figure 8a
		$r_{2a}(\theta_1) = \frac{510}{68 + 5\sin(5\theta_1)}$	
$\frac{5}{3}\theta_1 - \frac{1-\cos(5\theta_1)}{183}$		$r_{1b}(\theta_1) = \frac{25(61 - \sin(5\theta_1))}{122 - 5\sin(5\theta_1)}$	Figure 8b
		$r_{2b}(\theta_1) = \frac{915}{122 - 5\sin(5\theta_1)}$	

Table 14 Identification and modification model of an internal meshing location function

Original location function	Identification model	Modification parameters relationship	Modification model (θ_{2m})
$\frac{1}{2}\theta_1 + \frac{\sin(4\theta_1)}{16}, \begin{cases} f(\theta_1) = \frac{1}{2}\theta_1 + \frac{\sin(4\theta_1)}{16} \\ f(0) = 0 \end{cases}$	$2\pi/5 \neq \int_0^{2\pi} \left(\frac{1}{2} + \frac{\cos(4\theta_1)}{4} \right) d\theta_1 = \frac{\pi}{4}$	$\begin{cases} a = \frac{5(\pi - 4b)}{8\pi} \\ b = \frac{5\pi - 8a\pi}{20} \end{cases}$	$\frac{4}{5}\theta_1 + \frac{\pi\sin(4\theta_1)}{10(\pi - 4b)}$ <p style="text-align: center;"><i>s.t.</i> $b \neq \frac{\pi}{4}$</p>

Table 15 The feasible region of controllable modification parameter b

Min $f_c(b)$	Constraint condition of parameter b
$\frac{3\pi}{20}$	$b < -\frac{\pi}{4}$ or $b \geq \frac{9\pi}{4}$

Fig. 9 Two samples of the closed pitch curves with interference defect for N -lobed internal meshing noncircular gears

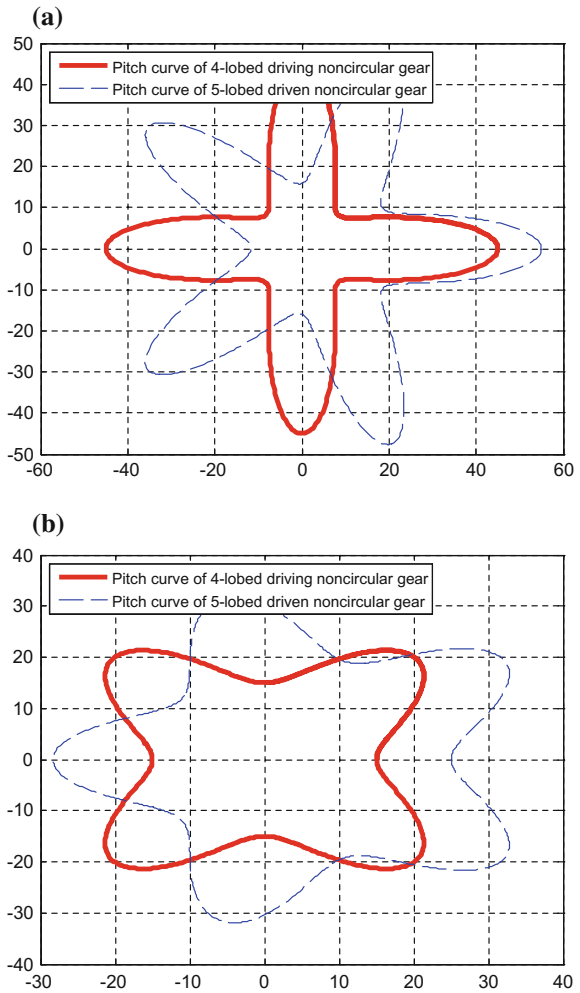


Table 16 Corresponding parameters with interference defect of closed pitch curves in Fig. 9

Modification parameters	Modified location function	Center distance	Pitch curves
$a = 5/2,$ $b = -3\pi/4$	$\frac{4}{5}\theta_1 + \frac{\sin(4\theta_1)}{40}$	$A_0 = 5$	$r_{1a}(\theta_1) = \frac{5(8 + \cos(4\theta_1))}{2 - \cos(4\theta_1)}$ $r_{2a}(\theta_1) = \frac{50}{2 - \cos(4\theta_1)}$
$a = -5,$ $b = 9\pi/4$	$\frac{4}{5}\theta_1 - \frac{\sin(4\theta_1)}{80}$		$r_{1b}(\theta_1) = \frac{5(16 - \cos(4\theta_1))}{4 + \cos(4\theta_1)}$ $r_{2b}(\theta_1) = \frac{100}{4 + \cos(4\theta_1)}$

Table 17 The improved feasible region of controllable modification parameter b

Min $f_e(b)$	Constraint condition of parameter b
$\frac{3\pi}{20}$	$b < \frac{1}{4}\pi - \frac{154.0495}{4} (\approx -\frac{48.0355}{4}\pi)$ or $b > \frac{1}{4}\pi + \frac{154.0495}{4} (\approx \frac{50.0355}{4}\pi)$
$\frac{20}{20}$	

Table 18 The solution and selection of modification parameters

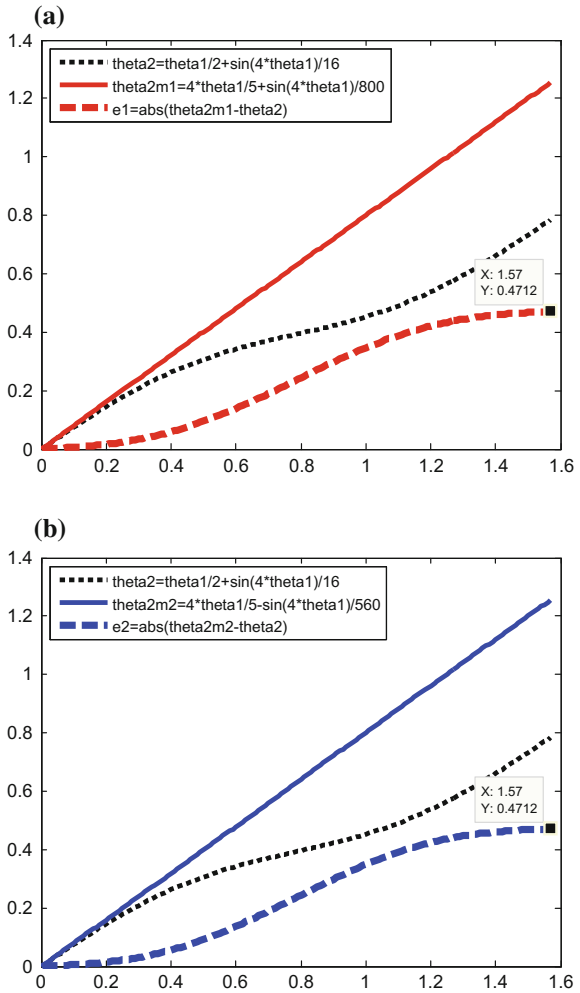
Original location function	Modification parameters	Modified location function	Figures
$\frac{1}{2}\theta_1 + \frac{\sin(4\theta_1)}{16}$	$a = 50, b = -79\pi/4$	$\frac{4}{5}\theta_1 + \frac{\sin(4\theta_1)}{800}$	Figure 10a
	$a = -35, b = 57\pi/4$	$\frac{4}{5}\theta_1 - \frac{\sin(4\theta_1)}{560}$	Figure 10b

modification parameter b is shown in Table 11 according to Eq. (29) and Table 4. The values of parameters a, b and their corresponding modified location function θ_{2m} are, respectively, depicted in Table 12 and Fig. 7. Figure 8 and Table 13 are two samples of the closed pitch curves without interference defect for N -lobed internal meshing noncircular gears based on the modified location function in Table 12.

Case 3: Example on the design of an internal meshing location function $F(\theta_1) = \frac{1}{2}\theta_1 + \frac{\sin(4\theta_1)}{16}$ for 4-lobed driving and 5-lobed driven internal meshing noncircular gears, namely, $N_1 = 4$ and $N_2 = 5$. $r_2(\theta_1)$ is external gear pitch curve and $r_1(\theta_1)$ is internal gear pitch curve. Its identification and modification model is shown in Table 14 by resorting to Eqs. (5)–(10).

Before considering the interference condition, the feasible region of controllable modification parameter b is shown in Table 15 by minimizing the maximum e_{max} of the error function $e(\theta_1)$ according to Eqs. (21)–(28). Two examples of pitch curves with interference for internal meshing gears are shown in Fig. 9 based on the feasible region. Its corresponding parameters are depicted in Table 16.

Fig. 10 Original location function and modified location function of an internal meshing noncircular gears



In order to modified the closed defect without the introduction of new design defect: pitch curves interference defect, the improved feasible region of controllable modification parameter b is shown in Table 17 according to Eq. (30) and Table 4. The values of parameters a , b and their corresponding modified location function θ_{2m} are, respectively, depicted in Table 18 and Fig. 10. Figure 11 and Table 19 are two samples of the closed pitch curves without interference defect for N -lobed internal meshing noncircular gears based on the modified location function in Table 18.

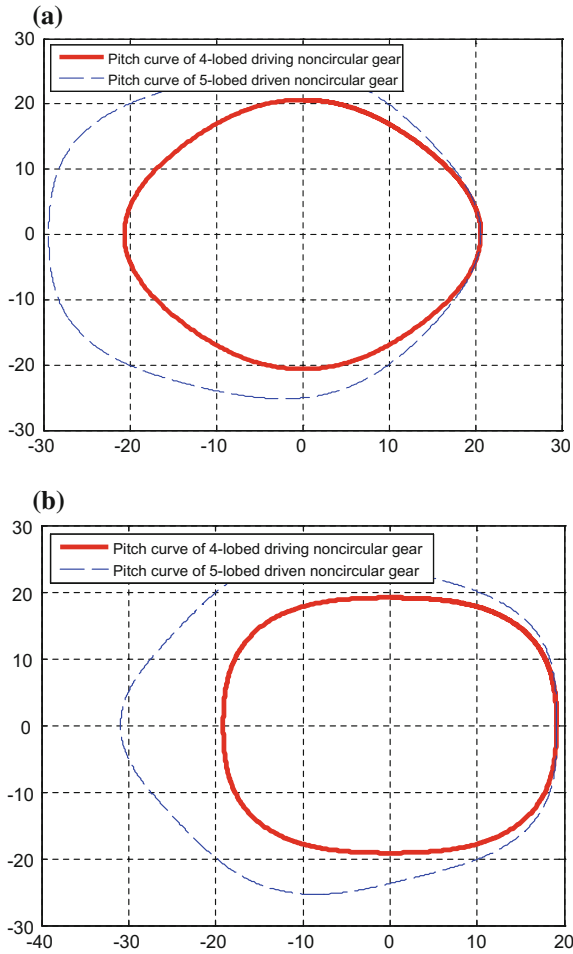


Fig. 11 Two samples of the closed pitch curves without interference defect for N -lobed internal meshing noncircular gears

Table 19 Modified location function and closed pitch curves without interference defect in Fig. 11

Modified location function	Center distance	Closed pitch curves	Figures
$\frac{4}{5}\theta_1 + \frac{\sin(4\theta_1)}{800}$	$A_0 = 5$	$r_{1a}(\theta_1) = \frac{5(160 + \cos(4\theta_1))}{40 - \cos(4\theta_1)}, r_{2a}(\theta_1) = \frac{1000}{40 - \cos(4\theta_1)}$	Figure 11a
$\frac{4}{5}\theta_1 - \frac{\sin(4\theta_1)}{560}$		$r_{1b}(\theta_1) = \frac{5(112 - \cos(4\theta_1))}{28 + \cos(4\theta_1)}, r_{2b}(\theta_1) = \frac{700}{28 + \cos(4\theta_1)}$	Figure 11b

6 Conclusions

An identification and modification algorithm on the design of location function for N -lobed noncircular gears was proposed to obtain a reshaping location function without closed defect. Based the reshaping location function, the closed pitch curves can be obtained. This design method is helpful to avoid the occurrence of pitch curves interference defect for N -lobed internal meshing noncircular gears, which have negative influence on transmission performance. The proposed algorithm was implemented in MATLAB, the feasibility and validity are verified through several design examples of location function for N -lobed noncircular gears.

Acknowledgments The authors are grateful for financial support from National Natural Science Foundation of China [grant number: 51175067].

References

1. Stefano Z, Christian MF, Marco F (2012) A method for the design of ring dampers for gears in aeronautical applications. *ASME J Mech Des* 134(9):091003.1–091003.10
2. Figliolini G, Angeles J (2003) The synthesis of elliptical gears generated by shaper-cutters. *ASME J Mech Des* 125:793–801
3. Yan J, Yang DCH, Tong SH (2008) On the generation of analytical noncircular multilobe internal pitch curves. *ASME J Mech Des* 130(8):092601.1–092601.8
4. Litvin FL, Fuentes A (2004) *Gear geometry and applied theory*. Cambridge University Press, Cambridge
5. Wei H (2002) Interpolation algorithm based on central angle division. *Int J Mach Tools Manuf* 42:473–478
6. Hector FQR, Salvador CF, Liuisa JN (2007) The synthesis of a N -lobe noncircular gear using Bézier and B-spline nonparametric curve on the design of its displacement law. *ASME J Mech Des* 129:982–985
7. Figliolini G, Lanni C, Ceccarelli M (2000) On the kinematic synthesis of non-circular gears. *Int J Gear Trans* 3:90–98
8. Bair BW (2002) Computer aided design of elliptical gears. *ASME J Mech Des* 124:787–793
9. Chang SL, Tsay CB (1998) Computerized tooth profile generation and undercut analysis of non-circular gears manufactured with shaper cutters. *ASME J Mech Des* 120:92–99
10. Lin C, Hou YJ, Gong H et al (2012) Tooth profile design and manufacture of high-order elliptical bevel gear. *Chin J Mech Eng* 23(3):253–258
11. Zhang GZ, Han J, Liu YY (2014) Gear hobbing machining method and its principle for higher-order elliptic gears. *Comput Integr Manuf Syst* 20(5):1106–1113
12. He JL, WU XT (2004) Kinematic characteristics and gear pair design for deformed elliptical geared linkage mechanism. *Chin J Mech Eng* 40(1):62–65
13. Danieli G (2000) Analytical description of meshing of constant pressure angle teeth profiles on a variable radius gear and its applications. *ASME J Mech Des* 122:123–129

Part IX
MISC: Sensor, Actuator, Linkage,
and Cam

Design of a Maximally Regular Acceleration Sensor Based on Generalized Gough-Stewart Platforms

Zhizhong Tong, Hongzhou Jiang, Hui Zhang and Jingfeng He

Abstract An analytical formulation and a new routine are presented to design a maximally regular acceleration sensor based on a generalized Gough-Stewart platform. The Jacobian matrix considering the measuring point is constructed symbolically and also acceleration mapping matrix done. Optimal indices and coupling evaluation are proposed to qualify performances of the sensor. Subsequently, the singular values of the acceleration Jacobian matrix are solved analytically to evaluate acceleration transmission. The conditions for the maximally regular acceleration are expressed in close-form. Based on the analytical formulation, an optimal design routine is put forward to determine a family of orthogonal and maximally regular acceleration sensor. With the aid of numerical examples, the acceleration-coupling is investigated and the results illustrate that the proposed design method is effective.

Keywords Acceleration sensor · Gough-Stewart platform · Isotropy · Circular hyperboloids · Coupling analysis

1 Introduction

Gough-Stewart parallel manipulators have been employed in a wide variety of areas such as manipulation, matching, control, tracking, haptic force feed-back, etc. When considering the implementation of parallel mechanisms in the field of sen-

Z. Tong (✉) · H. Jiang · H. Zhang · J. He
Department of Mechatronics Engineering, Harbin Institute of Technology,
Harbin 150001, China
e-mail: tongzhizhong@hit.edu.cn

H. Jiang
e-mail: Jianghz@hit.edu.cn

H. Zhang
e-mail: huizhang@hit.edu.cn

J. He
e-mail: hjfeng@hit.edu.cn

sors, the Gough-Stewart structure has become an alternative solution for certain applications including force/torque sensors and acceleration sensors. An acceleration sensor with orthogonal or isotropic performance has better sensitivity and higher accuracy without doubt, however, it has been researched scarcely any.

A lot of theoretical and experimental investigations on the 6-dof force/torque sensors with Gough-Stewart platforms were carried out in-depth by many researchers [1–5]. In general, few works focused on the 6-dof acceleration sensors with parallel structures. Xu et al. derived a symbolic expression to evaluate the acceleration isotropy of a Stewart platform-based acceleration sensor [6]. An E-type linear accelerometer with three dimensions was developed to measure the applied force from the upper limb [7]. However, the decoupling process was difficult and non-standard due to its unique and complex structure. To obtain a decoupled configuration with compact elements, Gao et al. presented a multidimensional acceleration sensor through the novel architecture of 3RRPRR fully decoupling parallel mechanism [8]. For its special mechanism, only linear acceleration can be sensitive. Theoretically, orthogonality is interesting for geometry of mechanism; so many design approaches have been presented. Jafari and McInroy explored various properties of the inverse Jacobian matrix to design orthogonal GSPMs among all the possible geometries [9, 10]. A class of orthogonal Gough-Stewart parallel manipulators was generated by Jafari and Yi et al. [11–13].

As can be seen from the literature survey, the movable platform is served as the inertial mass of the sensor. The measuring point is generally over the geometric center of the platform. What is more, an analytical formulation considering the measuring point has not been proposed to guide theoretical analysis so that an orthogonal structure is hardly to be found for a given requirement. It is a significant work, which would lead to a novel design routine and easily hunt for a family of orthogonal and maximally regular acceleration sensor. These interesting problems attract us to make an attempt. This work concerns about the comprehensive exploration from conceptual design to prototype. In this paper, we will evaluate the acceleration transmission capability for being realistic using a hypercube instead of a hyperboloid, i.e., maximally regular acceleration.

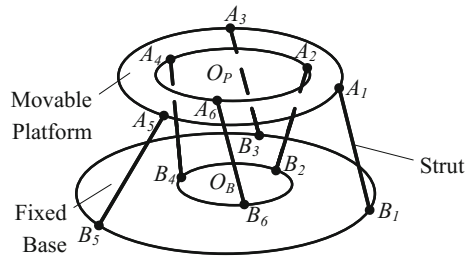
2 Problem Descriptions

2.1 *Jacobian Matrix*

A generalized Gough-Stewart platform (GGSP), as a variant kind of Gough-Stewart platforms, has been considered a well-established option and been well-studied [11–14], as shown in Fig. 1.

Mathematically, it can be expressed using double circular hyperboloids by [14, 15]

Fig. 1 Schematic diagram of a GGSP



$$\frac{x - r_1 \cos \alpha}{-r_1 \sin \alpha} = \frac{y - r_1 \sin \alpha}{-r_1 \cos \alpha} = \frac{z - a_{1z}}{c_1} \tag{1}$$

$$\frac{x - r_2 \cos \alpha}{-r_2 \sin \alpha} = \frac{y - r_2 \sin \alpha}{-r_2 \cos \alpha} = \frac{z - a_{2z}}{c_2} \tag{2}$$

where r_1 and r_2 are the throat radius of the hyperboloids respectively, and a_{1z} and a_{2z} are distances from the center of the hyperboloids to the frame origin. c_1 and c_2 can be called the shape parameters of the hyperboloids respectively and α as the sweep angle.

Accordingly, the Jacobian matrix is defined by

$$\mathbf{J}(\alpha) = [\mathbf{p}_1(\alpha) \quad \mathbf{p}_2(\alpha - \frac{2}{3}\pi) \quad \mathbf{p}_1(\alpha + \frac{2}{3}\pi) \quad \mathbf{p}_2(\alpha + \frac{2}{3}\pi) \quad \mathbf{p}_1(\alpha - \frac{2}{3}\pi) \quad \mathbf{p}_2(\alpha)]^T \tag{3}$$

$$\mathbf{p}_1(\theta) = [-k_{a1} \sin \theta \quad k_{a1} \cos \theta \quad k_{c1} \quad -a_{1z}k_{a1} \cos \theta + r_1k_{c1} \sin \theta \quad -a_{1z}k_{a1} \sin \theta - r_1k_{c1} \cos \theta \quad r_1k_{a1}]^T \tag{4}$$

$$\mathbf{p}_2(\theta) = [-k_{a2} \sin \theta \quad -k_{a2} \cos \theta \quad k_{c2} \quad -a_{2z}k_{a2} \cos \theta - r_1k_{c2} \sin \theta \quad a_{2z}k_{a2} \sin \theta - r_2k_{c2} \cos \theta \quad -r_2k_{a2}]^T \tag{5}$$

where the vectors of $\mathbf{p}_1(\theta)$ and $\mathbf{p}_2(\theta)$ are the unitary Plücker coordinates of straight lines 1 and 6 respectively. θ represents the rotation angle along z-axis. $k_{a1} = \frac{r_1}{\sqrt{r_1^2 + c_1^2}}$, $k_{c1} = \frac{c_1}{\sqrt{r_1^2 + c_1^2}}$, $k_{a2} = \frac{r_2}{\sqrt{r_2^2 + c_2^2}}$ and $k_{c2} = \frac{c_2}{\sqrt{r_2^2 + c_2^2}}$.

2.2 Acceleration Mapping Matrix

For the special case of a GGSP based accelerometer, the movable platform is preponderant compared with the inertia mass of the struts and serves as the inertia mass of the sensor. Each strut serves as an elastic measuring instrument and sustains tensile strain or compressive strain along its axis. Neglecting the Coriolis/centripetal

term and the gravity of the struts, the dynamics equation can be given in the following simplified form

$$\mathbf{J}^T \mathbf{f}_a = \mathbf{M}_t \ddot{\mathbf{x}} \quad (6)$$

where $\mathbf{f}_a = [f_1 \ f_2 \ f_3 \ f_4 \ f_5 \ f_6]^T$ represents the vector composed of the reacting force on the six struts caused by the inertia mass of the movable platform. \mathbf{M}_t denotes the inertia matrix of the movable platform.

Rewriting (6), the generalized acceleration of the movable platform is given with

$$\ddot{\mathbf{x}} = \mathbf{M}_t^{-1} \mathbf{J}^T \mathbf{f}_a \quad (7)$$

In order to clarify physical conceptions, we introduce the following definition.

Definition 1 $\mathbf{M}_t^{-1} \mathbf{J}^T$, defined as the acceleration mapping matrix, indicates the acceleration transmission capacity from the space of active joints to the space of the mass, which relates the generalized force developed by the struts to the generalized acceleration of the movable platform.

Let \mathbf{G} denote the acceleration mapping matrix, then we have

$$\mathbf{G} = \mathbf{M}_t^{-1} \mathbf{J}^T \quad (8)$$

For the convenience of analysis, the coordinates can be selected along the principal axes of the platform. Consequently, \mathbf{M}_t is decoupled and diagonal. That is $\mathbf{M}_t = \text{diag}(m \ m \ m \ I_{xx} \ I_{yy} \ I_{zz})$. I_{xx} , I_{yy} and I_{zz} are three rotational inertia components.

2.3 Acceleration Optimal Indices

Factually, using isotropy to describe the acceleration transmission capability is inappropriate. In this paper, we evaluate the acceleration transmission capability for being realistic using a hypercube instead of a hyperellipsoid, i.e., maximally regular acceleration. The term of a maximally regular parallel manipulator was presented by Merlet to define the isotropic robots [16]. Assuming 1 as a bound, then the force satisfies $\|\mathbf{f}_a\| \leq 1$. If we use the 2-norm, then it means they are not independent. For example, one of them is 1, and then the others should all become 0. The infinite norm should be a more realistic norm. With this norm, the force is restricted to lie in a 6-dimensional hypercube in the joint space. The hypercube in the joint space is thus mapped into the acceleration hypercube in the working space, which includes the acceleration hyperellipsoid. Consequently, such a manipulator is far from isotropy and can NEVER be obtained. We prefer the term of maximally regular, instead of the word isotropy to avoid the confusion of the concept of isotropy. Hence, we focus on the maximally regular acceleration sensor.

The singular values of \mathbf{GG}^T are used to be indices, which can be given by

$$\boldsymbol{\sigma} = \sqrt{\boldsymbol{\lambda}_{\mathbf{GG}^T}} \tag{9}$$

where $\boldsymbol{\lambda}_{\mathbf{GG}^T} = [\lambda_{\mathbf{GG}^T1} \ \lambda_{\mathbf{GG}^T2} \ \lambda_{\mathbf{GG}^T3} \ \lambda_{\mathbf{GG}^T4} \ \lambda_{\mathbf{GG}^T5} \ \lambda_{\mathbf{GG}^T6}]$.

To obtain an optimal design with a maximally regular acceleration, we introduce optimal performance factors. One factor is the ratio of the maximal singular value and the minimal one. Translational accelerations and rotational accelerations are not dimensionally homogenous, thus the optimal performance factors are discussed respectively and formulated by

$$\text{Minimizing } k_v = \frac{\max(\boldsymbol{\sigma}_v)}{\min(\boldsymbol{\sigma}_v)}, \quad k_\omega = \frac{\max(\boldsymbol{\sigma}_\omega)}{\min(\boldsymbol{\sigma}_\omega)} \tag{10}$$

where $\boldsymbol{\sigma}_v$ are the singular values of the translation accelerations, while $\boldsymbol{\sigma}_\omega$ are the singular values of the rotation accelerations.

In Eq. (10), if $k_v = 1$, then a GGSP based sensor is maximally regular with translational accelerations. Rotational accelerations are maximally regular when $k_\omega = 1$. If $k_v = 1$ and $k_\omega = 1$, a GGSP based sensor is fully maximally regular.

2.4 Acceleration-Coupling Evaluation

The acceleration mapping matrix will not be a diagonal matrix at overall workspace, and the acceleration-coupling characteristics cannot be neglected. It becomes to weaken the acceleration transmission performance and to decrease measuring precision. Thus, in this paper an acceleration-coupling factor is an important measure to quantify exactly its influence. Local norm-coupling factor (LNCF) is defined to cover the acceleration matrix

$$\mathbf{CI}_{\text{LNCF}} = \sum_{i=1}^6 \sum_{j=1}^6 w_{i,j} \frac{\mathbf{GG}^T(i,j)}{\sqrt{\mathbf{GG}^T(i,i)}\sqrt{\mathbf{GG}^T(j,j)}} \quad (i \neq j) \tag{11}$$

where $w_{i,j}$ is a weighted coefficient in the range from 0 to 1 and $\sum_{i=1}^6 \sum_{j=1}^6 w_{i,j} = 1 \quad (i \neq j)$.

Merlet proposed an iso-stiffness curve to analyze stiffness mapping [16]. Similarly, a locus with a constant LNCF value, denoted by an iso-LNCF curve, can be introduced to investigate acceleration performance. It is straightforward to identify a working configuration where the acceleration matrix fits the requirements.

3 Analytical Design of Maximally Regular Acceleration Sensors

In general, a good acceleration sensor is designed for measuring all sensitive acceleration components in the similarly isotropic mode. A maximally regular acceleration sensor may be preferred from the view of practice. In this section, we will derive fully analytical formulations.

3.1 Orthogonal Conditions

The orthogonal analysis of a GGSP presented by Jiang et al. [14] can be introduced into the design. As a consequence, the orthogonal conditions, formulated by the parameters of double circular hyperboloids, are

$$r_1 k_{a1} k_{c1} = r_2 k_{a2} k_{c2} \quad (12)$$

$$k_{a1}^2 a_{1z} = -k_{a2}^2 a_{2z}, \quad (13)$$

According to the previous research [14, 15], the orthogonal conditions are determined according to the measuring center. It is significant that an acceleration sensor can be designed to meet the requirement with a given measuring point.

3.2 Analytical Formulations

When a GGSP based sensor is orthogonal, the eigenvalues of the matrix \mathbf{GG}^T can be derived directly, and the indices can be summarized as below

$$\sigma_1 = \frac{\sqrt{3}}{\sqrt{2}} \frac{1}{m} \sqrt{k_{a1}^2 + k_{a2}^2} \quad (14)$$

$$\sigma_2 = \frac{\sqrt{3}}{\sqrt{2}} \frac{1}{m} \sqrt{k_{c1}^2 + k_{c2}^2} \quad (15)$$

$$\sigma_3 = \frac{\sqrt{3}}{m} \sqrt{k_{c1}^2 + k_{c2}^2} \quad (16)$$

$$\sigma_4 = \frac{\sqrt{3}}{\sqrt{2}} \frac{1}{I_{xx}} \sqrt{r_1^2 k_{c1}^2 + a_{1z}^2 k_{a1}^2 + r_2^2 k_{c2}^2 + a_{2z}^2 k_{a2}^2} \quad (17)$$

$$\sigma_5 = \frac{\sqrt{3}}{\sqrt{2}I_{yy}} \frac{1}{\sqrt{r_1^2 k_{c1}^2 + a_{1z}^2 k_{a1}^2 + r_2^2 k_{c2}^2 + a_{2z}^2 k_{a2}^2}} \tag{18}$$

$$\sigma_6 = \frac{\sqrt{3}}{I_{zz}} \sqrt{r_1^2 k_{a1}^2 + r_2^2 k_{a2}^2} \tag{19}$$

A fully maximally regular sensor is hardly to be realized due to dimensional nonuniformity between translations and rotations. An engineering length can be introduced to overcome this problem [17]. In this paper, we denote it by L_{scale} .

Let $\sigma_v = L_{scale} \sigma_{\sigma}$, summarizing (12–19) as

$$\begin{cases} \frac{4L_{scale}^2 I_{xx}^2}{3m^2} = r_1^2 k_{c1}^2 + a_{1z}^2 k_{a1}^2 + r_2^2 k_{c2}^2 + a_{2z}^2 k_{a2}^2 \\ \frac{2L_{scale}^2 I_{zz}^2}{3m^2} = r_1^2 k_{a1}^2 + r_2^2 k_{a2}^2 \end{cases} \tag{20}$$

Rewriting (20) as functions of r_2^2/r_1^2 and k_{c2}^2 , yields

$$\begin{cases} a_{2z}^2 = \frac{9(1-k_{c1}^2)}{4(3k_{c1}^2+1)} \left(\frac{4I_{xx}^2}{3m^2 L_{scale}^2} - \frac{I_{zz}^2}{m^2 L_{scale}^2} \frac{k_{c1}^2}{(k_{c1}^2+1/3)} \right) \left(\frac{2}{3} + \left(\frac{r_1^2}{r_2^2} - 1 \right) k_{c1}^2 \right) \\ r_2^2 = \frac{I_{zz}^2}{m^2 L_{scale}^2} \frac{k_{c1}^2}{(k_{c1}^2+1/3)} \end{cases} \tag{21}$$

Once we choose arbitrary r_1/r_2 , then r_2 , a_{2z} and a_{1z} can be determined accordingly. Based on this mathematical description in close-form, a family of fully maximally regular acceleration sensors based on GGSPs can be synthesized.

Remark If a standard Gough-Stewart parallel manipulator is expected to be fully maximally regular, $I_{zz} = 2I_{xx} = 2I_{yy}$ must be met. In practice, it is hardly to be realized because of the strictly physical restriction. However, it is feasible for a sensor based on a GGSP.

4 Numerical Verifications

With the aid of numerical cases, the presented algorithm could be verified. Considering the mechanical feasibility, it is necessary to ensure intersections among components. Table 1 gives the parameters of the inertia matrix of the platform.

Table 1 Parameters of the inertia matrix of the platform

Variable	Description	Value	Unit
m	Mass of platform	4	Kg
I_{xx}	Moment of inertia of the platform around x-axis	0.08	Kg m ²
I_{yy}	Moment of inertia of the platform around y-axis	0.08	Kg m ²
I_{zz}	Moment of inertia of the platform around z-axis	0.104	Kg m ²

Obviously, the frame is selected to coincide with the orientation of the principle axes of the movable platform.

Therefore, we have generated an optimal architecture at general neutral configuration, and the surface equations of double hyperboloids have the form as

$$\begin{cases} S_{1,t_i} : \frac{x^2 + y^2}{0.1061^2} - \frac{(z + 0.0382)^2}{0.1501^2} = 1 \\ S_{2,t_i} : \frac{x^2 + y^2}{0.1061^2} - \frac{(z - 0.0382)^2}{0.0751^2} = 1 \end{cases} \quad (22)$$

According to Eq. (28) the architecture is obtained by setting $H_2 = -0.2$ m and $\alpha = 10^\circ$. The verified architecture is shown schematically in Fig. 2.

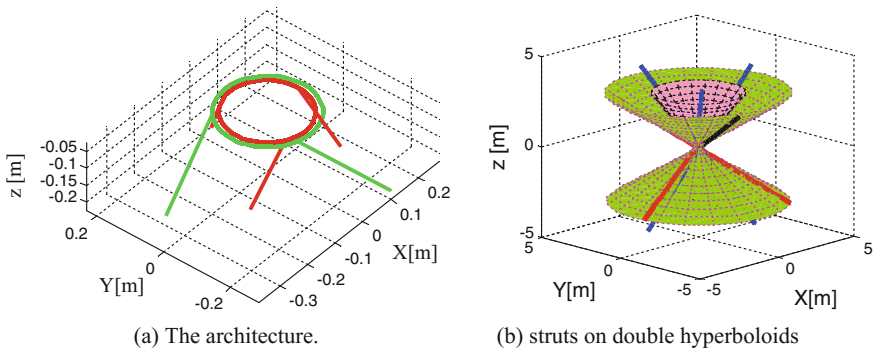
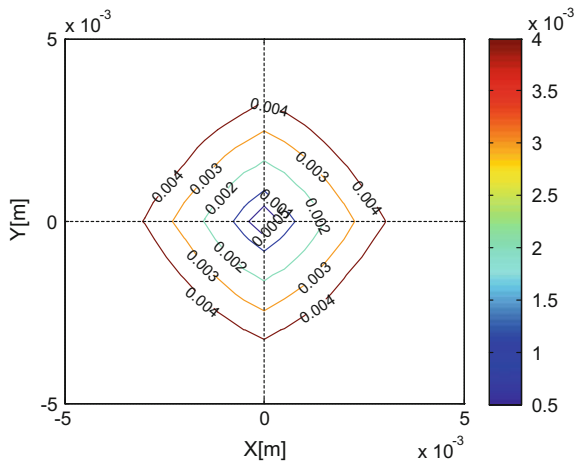


Fig. 2 Schematic of the reconfiguration mechanism for the numerical case

Fig. 3 The iso-LNCF curves at neutral configuration



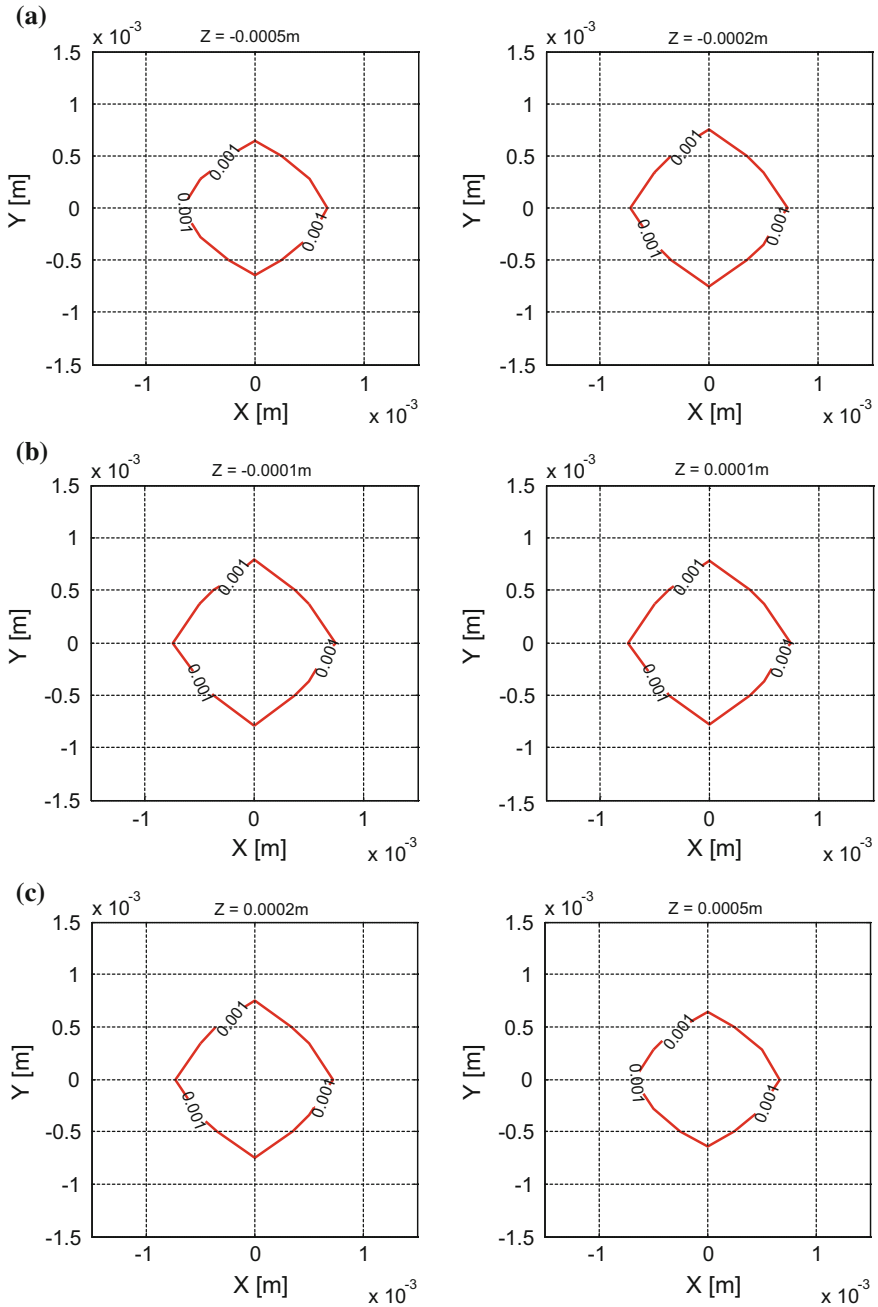


Fig. 4 The iso-LNCF curves at different cross-sections ($CI_{LNCF} = 0.1 \%$)

The maximally regular acceleration sensor operates with optimal performances but only at the neutral configuration. Therefore, the coupling has to be addressed for high precision measuring.

In Fig. 3, iso-LNCF curves for the maximally regular acceleration sensor, at neutral configuration, is illustrated schematically. It is interesting that the obtained sensor has better isotropic performance and possesses low acceleration-couplings. As a consequence, the orthogonal point coincides with the measuring center. Combining the mechanism geometry and the design of flexible joints and elastic struts, it is accessible to fabricate the maximally regular acceleration sensor with high accuracy.

If the required coupling measure, evaluated by LNCF, is 0.1 %, then in the following, estimations using iso-LNCF curve is demonstrated, in order to quantify acceleration-coupling over the global workspace. Figure 4 illustrates the iso-LNCF curves in deferent planar horizontal cross-sections of the small workspace near the neutral pose. Obviously the locus areas are approximately invariant at all cross-sections of the small workspace. Furthermore, a locus covered by the iso-LNCF curves can be used to bound a high-precision working area. It implies that the sensor exhibits better performances including uniformity and working stability. Moreover, with respect to specific iso-LNCF, a volume can be determined, which seems adapted to certain tasks with required accuracy and workspace. It becomes more evident that the presented method is validated and significant.

5 Conclusions

In this paper, we have presented a fully analytical formulation for a family maximally regular acceleration sensor. The routine is qualitatively different from the previous researches.

The acceleration mapping matrix is constructed by the descriptions of double circular hyperboloids. New indices are presented to evaluate the acceleration transmission capability for being realistic using a hypercube instead of a hyperboloids, i.e., maximally regular acceleration. To qualify acceleration-coupling at overall workspace, local norm-coupling factor and iso-LNCF curves are introduced reasonably. Numerical examples are carried out to evaluate the effectiveness of the proposed design method. The results show that the maximally regular acceleration sensor possesses better performances. The design method is effective for a highly accurate sensor.

Our future work includes investigating and extending this routine to more general parallel manipulators, for example, unsymmetrical parallel manipulators.

Acknowledgments This work is financially supported by the National Natural Science Foundation of China (Grant No. 51575121). The authors wish to thank the anonymous reviewers.

References

1. Ranganath R, Nair PS, Mruthyunjaya TS, Ghosal A (2004) A force–torque sensor based on a Stewart platform in a near-singular configuration. *Mech Mach Theory* 39(9):971–998
2. Ferraresi C, Pastorelli S, Sorli M, Zhmud N (1995) Static and dynamic behavior of a high acceleration Stewart platform-based force/torque sensor. *J Robot Syst* 12(10):883–893
3. Sorli M, Zhmud N (1993) Investigation of force and moment measurement system for a robotic assembly hand. *Sens Actuators, A* 37–38:651–657
4. Hou YL, Zeng DX, Yao JT, Kang KJ, Lu L, Zhao YS (2009) Optimal design of a hyperstatic Stewart platform-based force/torque sensor with genetic algorithms. *Mechatronics* 19:199–204
5. Yao JT, Hou YL, Wang H, Zhao YS (2008) Isotropic design of Stewart platform-based force sensor. *Lect Notes Comput Sci* 5315:723–732
6. Xu Y, Zhao X, Gao F, Zhang J (2005) Design and analysis of a novel 6-axis acceleration sensor. *Mach Des Res (Chinese)* 1(25):48–52
7. Gao Z, Song B, Liu M, Song GM, Sun WQ, Ge YJ (2009) Design and application of a multidimensional acceleration sensor for coaching of shot-put athletes. *Sens Actuators, A* 149:213–220
8. Gao Z, Zhang D (2010) Design, analysis and fabrication of a multidimensional acceleration sensor based on fully decoupled compliant parallel mechanism. *Sens Actuator, A* 163:418–427
9. McInroy JE, Jafari F (2006) Finding symmetric orthogonal Gough-Stewart platforms. *IEEE Trans Robot* 22(5):880–889
10. Ukidve CS, McInroy JE, Jafari F (2006) Orthogonal Gough-Stewart platforms with optimal fault tolerant manipulability. In: *Proceedings of the 2006 IEEE international conference on robotics and automation*, pp 3801–3806
11. Yi Y, McInroy JE, Jafari F (2005) Generating classes of locally orthogonal Gough-Stewart Platforms. *IEEE Trans Robot Automat* 21(5):812–820
12. Yi Y, McInroy JE, Jafari F (2004) Optimum design of a class of fault-tolerant isotropic Gough–Stewart platforms In: *IEEE international conference on robotics and automation*, vol 5, New Orleans, LA, April 2004, pp 4963–4968
13. Yi Y, McInroy JE, Jafari F (2004) Generating classes of orthogonal Gough–Stewart platforms. In: *IEEE international conference on robotics and automation*, vol 5, New Orleans, LA, April 2004, pp 4969–4974
14. Jiang HZ, Tong ZZ, He JF (2010) Dynamic isotropy design of a class of Gough-Stewart parallel manipulators lying on a circular hyperboloid of one sheet. *Mech Mach Theory* 46(3):358–374
15. Jiang HZ, He JF, Tong ZZ (2010) Dynamic isotropic design for modified Gough-Stewart platforms lying on a pair of circular hyperboloids. *Mech Mach Theory* 46(9):1301–1315
16. Merlet JP (2006) Jacobian, manipulability, condition number, and accuracy of parallel robots. *J Mech Des* 128:199–205
17. Angeles Jorge (2006) Is there a characteristic length of a rigid-body displacement? *Mech Mach Theory* 41:884–896

A Multi-objective Design Optimization of a Centrifugal Cooling Fan on a TEFC Motor

Qi Lu, Fei Zhen, Martin Kefer and Maria Nylander

Abstract A design optimization method of a centrifugal fan on a totally-enclosed fan-cooled (TEFC) motor was studied in this paper. A multi-objective optimization problem was formulated which is to decrease noise level of fan and to increase air flow rate at the same time. Two design variables, namely fan diameter (D) and blade height (H), were investigated. Responses surface models were established based on design of experiments to identify the mathematical relationships between fan performances and the design parameters. These models were later used in optimization. As a result, a Pareto front was obtained which illustrated the optimal trade-offs that can be achieved in design. The Pareto front was then experimentally verified on an in-house test rig by using acoustic holography techniques.

Keywords Design optimization · Centrifugal cooling fan design · Fan noise

1 Introduction

A Totally Enclosed Fan-Cooled (TEFC) electrical motor, is probably the most commonly used motor in many applications, such as pumps, blowers, compressors, just to name a few. As indicated by its name, A TEFC motor usually has a fan on the non-drive end of the motor for cooling purpose. In many cases, a centrifugal fan

Fei Zhen and Maria Nylander were interns of ABB Corporate Research China at the time of this work.

Q. Lu (✉) · M. Kefer
ABB Corporate Research China, Shanghai, China
e-mail: qi.lu@cn.abb.com

F. Zhen
College of Mechanical Engineering, Zhejiang University,
Hangzhou, Zhejiang, China

M. Nylander
Department of Earth Sciences, Uppsala University, Uppsala, Sweden

with straight blades is often adopted as the cooling fan, simply because it has to guarantee the cooling performance when the motor is operating in both clockwise and counter-clockwise directions.

In practice of motor design, the centrifugal fan is considered as a critical component as it must produce a great amount of air to cool down the motor and to prevent it from overheating. The more air a fan can produce, the better a motor performs from thermal perspectives. However, it is also observed that a centrifugal fan may also generate high noise level together with high air volume. The noise issue becomes even more critical for high-speed motors (e.g. 2-pole motors). Therefore, optimization of the centrifugal fan regarding air flux and noise level is of great interest in design. Specifically, the objective of the design optimization is to decrease fan noise level, and at the same time maintain a large volume of air flow.

To deal with the design problems of a centrifugal fan, many studies have been conducted in the past. Computational fluid dynamics (CFD) models were developed to identify the critical design parameters (e.g. geometrical parameters in [1] and number of blade in [2]) affecting fan efficiency. An experimental study was carried out in [3] which revealed that the distance between the impeller and volute tongue was of great importance to the noise level of the centrifugal fan.

The aero-acoustic property of a centrifugal fan was also studied by simulation in publications [4–8]. In the simulations, noise models (e.g. Lawson's equation in [4], and Ffowcs-Williams-Hawkings (FWH) equation in [5–8]) were established together with the CFD models to identify the sources of noise. The studies focused on different types of fans, and the sources of noise varied from the force acting on the fan volute [4], aerodynamic interaction between impeller and volute tongue of fan [5], unsteady forces on the blades [6], and effects blade passing frequency [7, 8]. Then, various proposals were made based on the simulation results in order to design a low-noise fan.

The idea of optimization was proposed in [9] for the design of a swept bladed fan. In the study, noise level, fan efficiency and fan capacity were investigated. The authors focused on a great amount of input parameters by using a knowledge-based method combined with the centrifugal fan theory. Their result showed that the number of blade, was the main parameter that separated a high efficiency fan from a low noise level fan.

Instead of a knowledge-based optimization, this paper proposes a model-based method for design optimization of a centrifugal fan on a TEFC motor. The goal is to make a trade-off between air flux and noise level. In the paper, a multi-objective optimization is setup in terms of air flux and noise level which are modeled as responses to two main parameters, namely, fan diameter (D) and blade height (H). The same method, as used in this paper, has already been applied in [10], although for optimizing electrical design of a motor. It should be noted that the focus of this paper is to utilize the optimization methodology in the design of centrifugal cooling fan. The development of optimization algorithm is out of scope of this study.

2 Design Variables and Design Objectives

A typical centrifugal fan used on a TEFC motor is presented in Fig. 1. The centrifugal fan has straight blades since the fan should be able to cool down the motor both clockwise and counterclockwise.

Although many geometrical parameters are needed to fully describe a straight-blade centrifugal fan, this study only considers the centrifugal fan diameter (D) and the blade height (H) as the design variables as they are the most critical parameters in terms of noise and air flow. Figure 1 shows the definition of the two design variables. However, the optimization method presented in this paper, with only two design variables, is generic and should be applicable to other cases involving more design variables.

Meanwhile, four responses of the two design variables are investigated in this study. The first two responses are relevant in order to optimize the centrifugal fan, whence a multi-objective optimization problem is formulated as follows:

- To minimize noise level
- To maximize air flow flux

The other two responses were used as references:

- Total pressure of the fan
- Fan efficiency

3 Fan Design Optimization

A typical optimization is an iterative process. It requires to compute the values of responses in each iteration which will be computationally costly in practice. In order to reduce computational cost, response surfaces models for each responses which established based on a few samples in design of experiments will be used for optimization.

Fig. 1 A TEFC motor with in between centrifugal fan, and its design parameters



3.1 Design of Experiments (DOE)

In order for the response surface models to “look like” the real physical model, the DOE must make the design variables spread over the entire range of values. This can be achieved by many mature algorithms, and partial fractional algorithm is used in this study. Figure 2 shows the distribution of the samples derived from the partial fractional algorithm. The whole range of values appears to be covered by the implementation of the six samples.

The values of all four responses corresponding to the DOE samples are presented in Table 1. It should be mentioned that both design variables and responses are dimensionless due to the confidential regulation of the company. The design variables are scaled with respect to the range of values and the responses are scaled with respect to the values of a benchmark fan.

Fig. 2 The sampling distribution of design variables after DOE

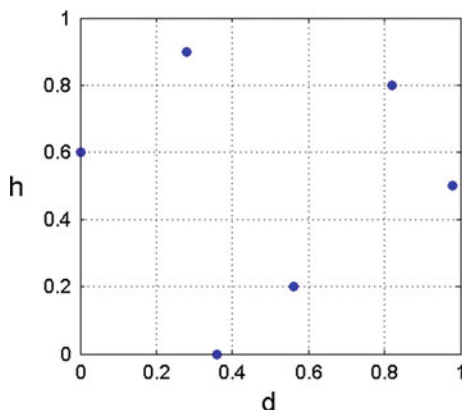


Table 1 The six samples of design variables after DOE and their responses

d	h	Noise	Total Pressure	Air flux	Efficiency
0	0.6	0.9725	0.4846	0.7326	0.7378
0.28	0.9	1.0125	0.6327	0.8491	0.8392
0.36	0	0.9733	0.6326	0.7925	0.7797
0.56	0.2	0.9758	0.7401	0.8704	0.8566
0.82	0.8	1.0158	0.8687	0.9967	0.986
0.98*	0.5	1	1	1	1
0	0.6	0.9725	0.4846	0.7326	0.7378

*This is a benchmark fan design

3.2 Response Surface Models (RSM)

A RSM is a numerical model established based on DOE samples. It is an approximation to the original physical relationship between the design variables and their responses. In order to reach a RSM with high fidelity, it is essential that the DOE has its design variables spread over the entire range of values.

In this study, multiple methods have been employed to establish the RSMs for all four responses. As a result, different RSMs are established as mathematical approximations to the original physical relations, but they are numerically very close to each other. More importantly, when applying these RSMs in the optimization, not much differences are observed (see Sect. 5 for more discussions). This indicates these RSMs are more or less equivalent from a perspective of optimization. Therefore, only the RSMs resulted from 1st order Least Square Regression (LSR) method are presented in Fig. 3.

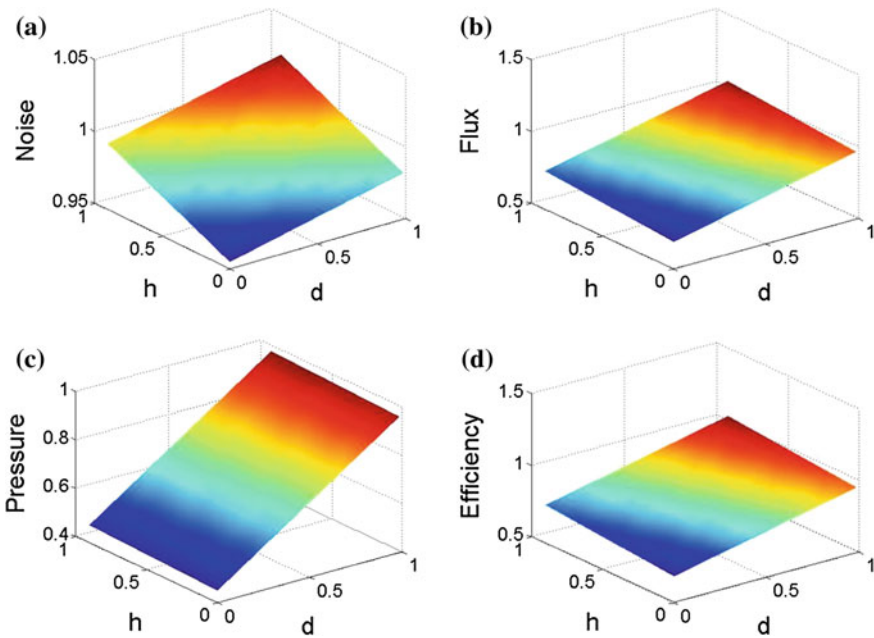


Fig. 3 Response surface models of **a** Noise, **b** Air flux, **c** Total pressure, and **d** Efficiency

3.3 Optimization

Based on the RSMs as presented in Fig. 3, a multi-objective optimization is conducted by using multi-objective genetic algorithm (MOGA). The optimization leads to a Pareto front showing the Pareto-efficient (i.e. “best”) trade-offs between air flux and noise level as illustrated in Fig. 4. In this case, the Pareto front has a broken-line shape. This is because the RSMs are established by using 1st order LSR algorithm which results in linear RSMs, and Pareto front as well. Since the choices on the Pareto front is the “best” that can be achieved, it helps a designer to make trade-offs with restricted attentions.

Based on this particular optimization result, a few fan designs are selected for experimental verification. The design variables of these designs are presented in Table 2.

Fig. 4 The optimization results in a broken-line-shape Pareto front based on the RSMs using 1st order LSR algorithm

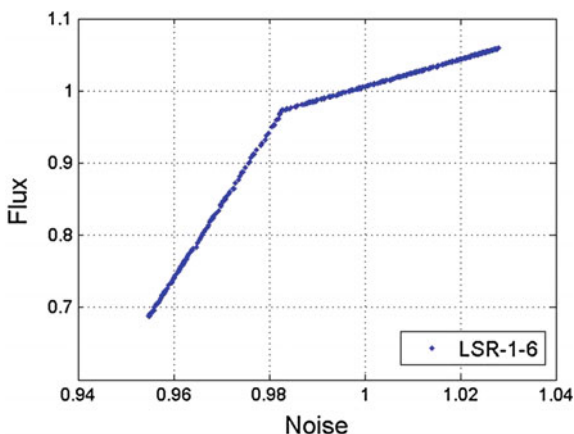


Table 2 Design variables of the new fans in verification

No.	d	h	Expected relation with Pareto front
1	0.5	0	On Pareto front
2	0.28	0.275	Off Pareto front
3	0.64	0.4	Off Pareto front
4	1	0	On Pareto front
5	0.98	0.5	Benchmark, almost on Pareto front
6	1	0.9	Almost on Pareto front

4 Experimental Verification

Based on the optimization result, a few fan designs are selected for experimental verification. The design variables of these fans are presented in Table 2. The new designs of centrifugal fans are fabricated using 3D printing techniques.

The lab experiments are performed in an in-house test rig, illustrated in Fig. 5. The idea is to measure the near field noise by acoustic holography technology using an industrial robot with a set of microphones at its end effector. The air flow rate at the fan outlet is measured by an air velocity meter and convert to air flux to compare with the optimization results. The development of the test rig is presented in [11].

The results of the verification experiments are plotted in Fig. 6 together with the Pareto front from Fig. 4. The performance of the new fan designs seems to be close to the predicted Pareto front.

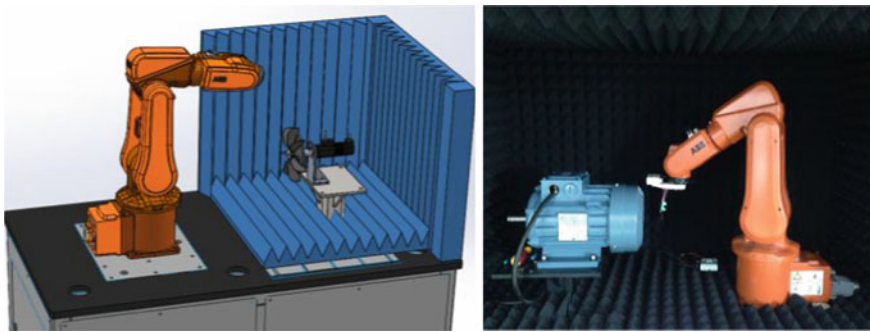
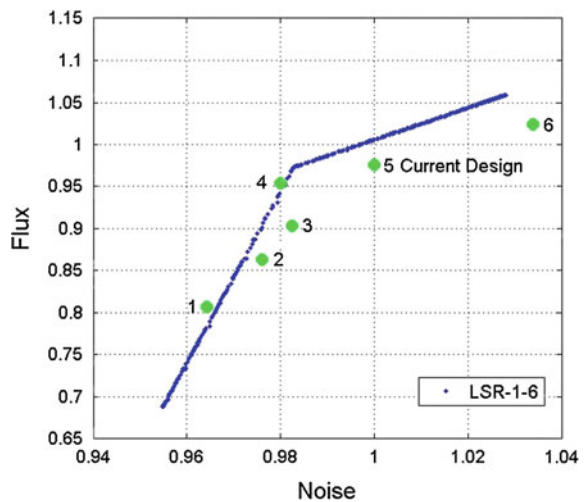


Fig. 5 Concept and implementation of the test rig

Fig. 6 Experimental verification of Pareto front



5 Discussion

In this paper a multi-objective optimization problem was applied. However, to formulate a single-objective optimization problem, which is to minimize noise with air flow rate constraints, was also possible. Though, solving a multi-objective problem was assumed to lead to more meaningful results for designers.

- DOE sampling

The result of DOE sampling has a great impact on the fidelity of RSMs, and the quality of optimization as well. In order to have a RSM that represents the real physical models in good fidelity, the DOE samples should be so well distributed that they cover the entire range of values of design variables. In this case, only two design variables were involved, and it is shown in Fig. 2 that 6 DOE samples resulted from partial fractional algorithm has larger enough coverage to obtain a high-fidelity RSM. The numbers of samples may also contribute to the fidelity, but it is not as important as the coverage of samples. This was illustrated by a comparison of optimization with 6 DOE samples (as in Fig. 2), and that with 12 DOE samples. The Pareto front resulted from these two cases are very close to each other (as shown Fig. 7).

- Algorithms of RSM

The algorithm of RSM also plays a role in optimization. A few algorithms were studied, namely, 1st order LSR, 2nd order LSR, 1st order moving least square (MLSR), and 2nd order MLSR. These algorithms led to various RSMs as approximation to physical models. The resultant Pareto fronts based on these RSMs

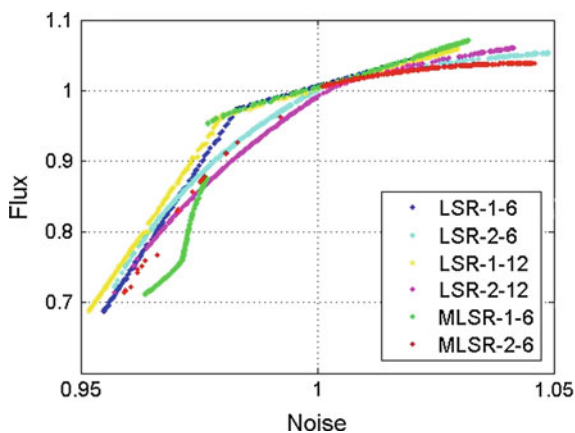


Fig. 7 The Pareto fronts based on various RSMs obtained by different algorithms and DOE samples (*LSR-1-6* 1st order LSR with 6 samples; *LSR-2-6* 2nd order LSR with 6 samples; *LSR-1-12* 1st order LSR with 12 samples; *LSR-2-12* 2nd order LSR with 12 samples; *MLSR-1-6* 1st order MLSR with 6 samples; and *MLSR-2-6* 2nd order MLSR with 6 samples)

are also plotted in Fig. 7. Of course, they are different, but still quite close to each other. As a consequence, the simplest RSM algorithm (i.e. 1st order LSR) is preferred from application point of view. Particularly, linear RSMs, which is obtained by 1st order LSR, are much easier to implement into design practice than other RSMs. Therefore, only the optimization based on linear RSM were proposed in this study.

6 Conclusion

This paper has presented a design optimization method for a centrifugal cooling fan on a TEFC motor. The objective is to achieve optimal design of the fan in terms of its noise level and air flux.

The results of the lab experiments resemble with the achieved Pareto front, which indicates that the design optimization based on RSM and DOE has been a successful method.

The outcomes of the study can be directly used in design practice. On one hand, the linear RSMs gives direct relationships between design variables and fan performances, which is regarded as know-how in practice. On the other hand, the Pareto front can advantageously be adapted when making trade-offs in design of centrifugal fans.

In addition, the study presented in this paper can be regarded as method development for motor fan design optimization. Although the method was only exercised on a two-variable optimization problem, it was generic and therefore applicable to other design optimization problems involving more design variables.

References

1. Chen YC, Chen CL, Dong Q (2003) CFD modeling for motor fan system. In: IEEE international conference of electric machines and drives, vol 2
2. Singh OP, Khilwani R, Sreenivasulu M, Kannan M (2011) Parametric study of centrifugal fan performance: experiments and numerical simulation. *Int J Adv Eng Technol* 1:33–50
3. Suarez SV, Tajadura RB, Morros CS, Garcia BP (2008) Reduction of the aerodynamic tonal noise of a forward-curved centrifugal fan by modification of the volute tongue geometry. *Appl Acoust* 69:225–232
4. Liu Q, Qi D, Mao Y (2006) Numerical calculation of centrifugal fan noise. *J Mech Eng Sci* 220(8):1167–1177
5. Younsi M, Bakir F, Kouidri S, Rey R (2007) Numerical and experimental study of unsteady flow in a centrifugal fan. *J Power Energy* 221(7):1025–1036
6. Wong IYW, Leung RCK, Law AKY (2011) Unsteady flow dynamics and acoustic of two-outlet centrifugal fan design. In: *Proceeding of the sixth international conference on fluid mechanics*, vol 1376, pp 467–469
7. Cho Y, Moon YJ (2003) Discrete noise prediction of variable pitch cross-flow fans by unsteady Navier Stokes computations. *J Fluids Eng* 125(3):543–550

8. Tajadura RB, Suarez SV, Cruz JPH (2008) Noise prediction of a centrifugal fan: numerical results and experimental validation. *J Fluid Eng* 130(9)
9. Chon Y, Kim KI, Kim K (1993) A knowledge-based system for centrifugal fan blade design. *Eng Appl Artif Intell* 6(5):425–435
10. Kim HH, Kim DK, Lee YJ, Kim BT (2010) Efficiency optimization design of a BLDC motor driving fans. In: *International conference in electrical machines and systems (ICEMS)*, pp 1147–1152
11. Kefer M, Lu Q (2016) Acoustic holography—a robot application. In: *2016 international conference on real-time computing and robotics (RCAR 2016)*, Angkor Wat, Cambodia, 6–10 June

Research on Slope Climbing Capacity of a Close Chain Five-Bow-Shaped-Bar Linkage

Lian-qing Yu, Yuan-yuan Mei, Yu-jin Wang and Chang-lin Wu

Abstract Slope climbing capacity of a close chain five-bow-shaped-bar linkage and minimum friction coefficient during climbing are analyzed. First, the analysis model of slope climbing for the closed linkage is established, and the CG position kinematics model on slope is built with homogeneous transformation matrix. Secondly, the static analysis model is established to get the active joint angle along with a certain slope under the geometrical constraint of the slope, and the graph between the maximum slope and roll angle is obtained by using numerical method. Thirdly, the minimum static friction coefficients curve is figured out by the force relationship. Then, motion planning is conducted by the constant CG offset for uniform climbing, thereby solving the active joint trajectory. Finally, slope climbing experiments are carried out to verify the correctness of analysis results.

Keywords A close chain five-bow-shaped-bar linkage · Constant CG offset · Slope climbing · Joint trajectory

1 Introduction

Slope climbing capacity is an important indicator of overcoming obstacles about moving mechanism. Sun et al. design a series of BYQ rolling spherical and variable structure spherical robots and Yue et al. also have granted many research results about climbing the status and the performance [1–7]. Kinetic analysis to determine

L. Yu (✉) · Y. Mei
School of Mechanical Engineering and Automation,
Wuhan Textile University, 430073 Wuhan, Hubei,
People's Republic of China
e-mail: yulianqing@163.com

Y. Wang · C. Wu
School of Mechanical Science and Engineering,
Huazhong University of Science and Technology,
430074 Wuhan, Hubei, People's Republic of China

the basis for the moment equilibrium equation is to obtain the spherical robot climbing conditions. When the friction between the slope and the robot is large enough, the robot will only roll without slipping in the process of the slope. Maximum slope of the spherical robot is only related to its structure parameters. However, the study about the climbing performance of moving linkage is rarely reported at home and abroad. In this article, a close chain five-bow-shaped-bar linkage mechanism with the outer contour of the arc will be analyzed by the slope, and consider the impact that the outer contour of the arc has on the slope climbing capacity. The interference between the outer contour of the arc and the bow-shaped-bar may occur in the process of the slope, which can become the geometrical constraint of the slope.

This article discusses the roll angle changes from 0 to 360 about the slope climbing capacity of the institution. Creating the static analysis model, let the active joints initiative between the critical angle position and the slope stability without interference constraints, to observe the changes between the maximum slope angle of a close chain five-bow-shaped-bar linkage with roll angle and radius of the circle of the joint, and to calculate the minimum static friction coefficients by the force relationship. Then, motion planning is conducted by a constant CG offset for uniform climbing, thereby solving the active joint trajectory. Finally, the slope climbing experiments are carried out to verify the correctness of analysis results.

2 Kinematic Model of a Five-Bow-Shaped-Bar Linkage on Slope

2.1 Mechanical Structure of a Five-Bow-Shaped-Bar Linkage

A close chain five-bow-shaped-bar linkage consists of five identical bow-shaped-bar module which linked end to end in series, bow-shaped-bar module including parts around an arc plate, a support annex, DC motor and gear and other components. Though the balanced weight method, weight each bow-shaped-bar module mass m_i equally and the CG is at the midpoint of the adjacent modules of the connection joints. When the five joint angles are all 108, a close chain five-bow-shaped-bar linkage outer contour is circular and the CG coincides with the centre. It's solid model shown in Fig. 1.

2.2 Kinematics Analysis of CG

So ${}^{i-1}\mathbf{T}_i$ represents homogeneous transformation matrix of the adjacent bar; ${}^j\mathbf{T}_i$ represents homogeneous transformation matrix of link coordinates $x_i y_i$ with

Fig. 1 Solid Model of the Five-bow-shaped-bar Linkage. 1 flange 2 shaft 3 umbrella bevel gear 4 bevel gear 5 motor bearings 6 right arched plate 7 left arched plate 8 motor 9 angle sensor

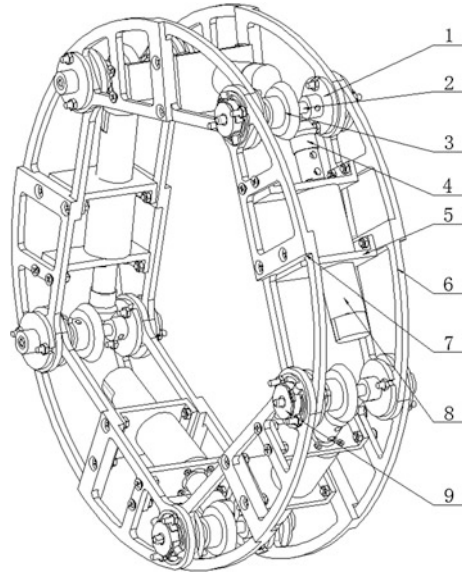
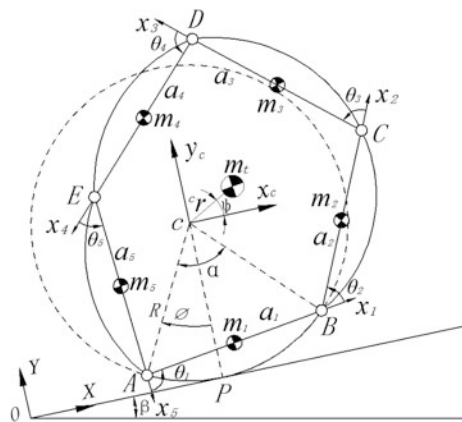


Fig. 2 CG kinematic model of a close chain five-bow-shaped-bar linkage on slope



touchdown club members coordinate, j represents touchdown bow-shaped-bar ($j = 1, 2, \dots, 5$); ${}^i\mathbf{T}_i$ is a unit matrix; and a touchdown bow-shaped-bar coordinate system in $x_c y_c$ homogeneous coordinate transformation is ${}^c\mathbf{T}_j$:

$${}^j\mathbf{T}_i = {}^j\mathbf{T}_{j+1} {}^{j+1}\mathbf{T}_{j+2} \dots {}^{i-1}\mathbf{T}_i; \quad {}^i\mathbf{T}_j = ({}^j\mathbf{T}_i)^{-1}; \quad {}^i\mathbf{T}_i = \mathbf{I}_{4 \times 4};$$

$${}^c\mathbf{T}_j = \mathbf{Rot}(z_c, \frac{2j-1}{2}\alpha - \varphi) \cdot \mathbf{Trans}(R s_{\alpha/2}, -R c_{\alpha/2}, 0) \quad , i, j = 1, 2, \dots, 5 \quad (1)$$

Five module of a close chain five-bow-shaped-bar linkage has the same configuration parameters and mass distribution. Therefore, each rod has the equal mass m_i , the equal chord a_i , the equal bow-shaped-bar corresponding central angle α_i and the

same homogeneous coordinates \mathbf{b}_i about CG position of each rod in its own link coordinate system, namely:

$$m_i = m_t/5 \quad a_i = 2R \sin(\alpha_i/2) \quad \alpha_i = 2\pi/5 \quad \mathbf{b}_i = \left[-\frac{a_i}{2} \ 0 \ 0 \ 1\right]^T \quad i = 1, 2, \dots, 5 \tag{2}$$

According to coordinate homogeneous transformation relations of bars CG, in the five-link rod, member j ($j = 1, 2, \dots, 5$) is touching the ground phase, the CG of bow-shaped-bar i representing m_i in the coordinate system of $x_c c y_c$ about the position vector can be expressed as:

$${}^c \mathbf{r}_i = {}^c \mathbf{T}_j {}^j \mathbf{T}_i \mathbf{b}_i \quad (i, j = 1, 2, \dots, 5). \tag{3}$$

Further, according to the CG composition theorem, the total center of mass m_t of a five-link can get the position vector in the coordinate system $x_c c y_c$:

$${}^c \mathbf{r} = \frac{1}{m_t} \sum_i^{i=5} m_i {}^c \mathbf{r}_i. \tag{4}$$

Expand the formula to a rolling cycle period to get different stages of the five-link at the rod touching the ground, the center of mass in the $x_c c y_c$ coordinates can be expressed as:

$$j, {}^c \mathbf{r} = \frac{m_i}{m_t} {}^c \mathbf{T}_j \mathbf{b}_i \sum_{i=1}^5 {}^j \mathbf{T}_i \quad (j-1)\alpha \leq \varphi \leq j\alpha, \quad j = 1, 2, \dots, 5. \tag{5}$$

From (5), a CG coordinate can be written as specific forms of a tumbling cycle. In planar motion of five-link, the coordinates of the center of mass in the z_c axis direction are zero and z_c axis coordinates are ignored writing in the specific formula. Because a close chain five-bow-shaped-bar linkage consists of five identical bow-shaped-bar with end to end modules in series, each module touch the ground one by one in the course of the campaign, so j at value in 1 to 5 followed by cycle, for example, when $j = 1, j + 1$ value 2, $j - 1$ value 5. When the bow-shaped-bar of j is touching, according to the homogeneous coordinate transform, the specific coordinates of combines center of mass m_t in translation coordinate system $x_c c y_c$ is:

$$j, {}^c \mathbf{r} = \left[\begin{array}{l} \left\{ \begin{array}{l} -\frac{3a}{10} c(\varphi - \frac{2j-1}{2}\alpha + \theta_j) + \frac{3a}{10} c(\varphi - \frac{2j-1}{2}\alpha - \theta_{j+1}) + \frac{a}{10} c(\varphi - \frac{2j-1}{2}\alpha - \theta_{(j+1)(j+2)}) \\ -\frac{a}{10} c(\varphi - \frac{2j-1}{2}\alpha + \theta_{(j-1)j}) - \frac{a}{2} c(\varphi - \frac{2j-1}{2}\alpha) - R s(\varphi - j\alpha) \end{array} \right\} \\ \left\{ \begin{array}{l} \frac{3a}{10} s(\varphi - \frac{2j-1}{2}\alpha + \theta_j) - \frac{3a}{10} s(\varphi - \frac{2j-1}{2}\alpha - \theta_{j+1}) - \frac{a}{10} s(\varphi - \frac{2j-1}{2}\alpha - \theta_{(j+1)(j+2)}) \\ + \frac{a}{10} s(\varphi - \frac{2j-1}{2}\alpha + \theta_{(j-1)j}) + \frac{a}{2} s(\varphi - \frac{2j-1}{2}\alpha) - R c(\varphi - j\alpha) \end{array} \right\} \end{array} \right] \tag{6}$$

From (6), $c_\phi = \cos\phi; s_\phi = \sin\phi; c_\alpha = \cos\alpha; s_\alpha = \sin\alpha; \theta_{ij} = \theta_i + \theta_j$.

3 Climbing Model and Solution

3.1 Stability Constraints of Critical Position

When the bow-shaped-bar is in the critical position of climbing, the constrained model is shown in Fig. 3, and the contact point P will be coincided with the joints of the robot. In the time that the joint is touch downing, the constraint is imposed on the joints at both ends of the rod to ensure the angle of the joint being 72° . The constraint is a necessary condition to keep the tumbling motion going on consecutively and steadily. But, at same time, the number of system degree of freedom is also reduced by the constraint.

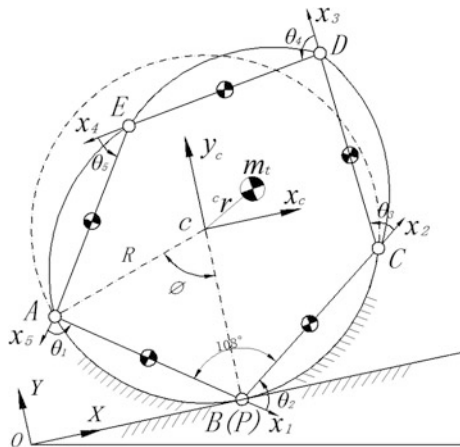
When the bow-shaped-bar is constrained by the critical position, the agency has only one degree of freedom. Then the constraint model of the critical point of the bow-shaped-bar in a rolling cycle is mathematically described as:

$$\theta_{k+1} = 72^\circ, \quad \varphi = k\alpha, \quad k = 1, 2, \dots, 5. \tag{7}$$

3.2 Constrained by the Slope with No Interference

Figure 4 show the interference model between the slope and a close chain five-bow-shaped-bar linkage. There are two contact points between the bow-shaped-bar and the slope in the model: P_1, P_2 or P_1, P_3 , which brings negative effects to mechanical properties of the joint drive and dynamic-rollover's continuity and stability. The meaning about non-interference constraint is that there is only one point between the bow-shaped-bar and the slope when different bow-shaped-bar touch the ground. When the bow-shaped-bar has two contact-points, the two

Fig. 3 Constraint model of critical position on slope



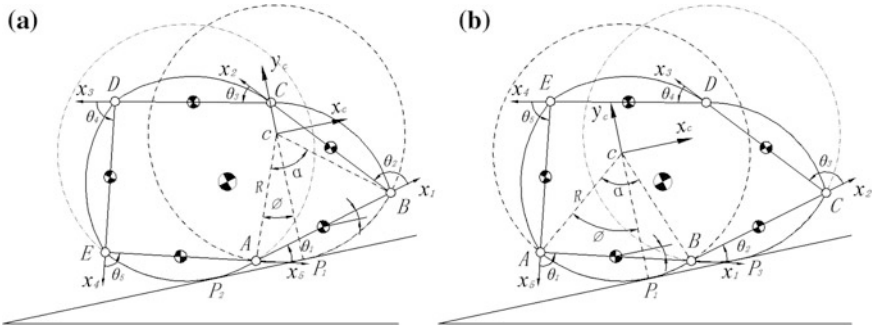


Fig. 4 The interference constraint model of a five-bow-shaped-bar linkage on slope

symmetric contact point is relative to the middle joints, as shown in Fig. 4a that two symmetric contact point is relative to the joint A and as shown in Fig. 4b that two symmetric contact point is relative to the joint B.

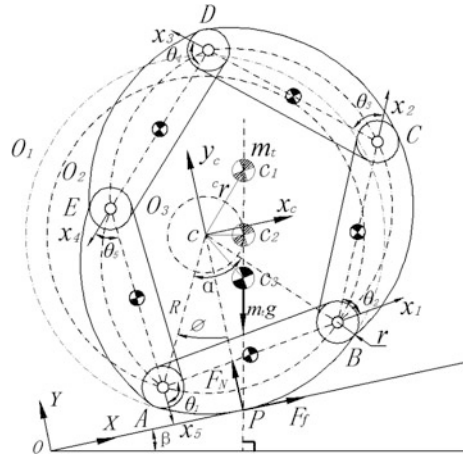
A close chain five-bow-shaped-bar linkage consists of five identical bow-shaped-bar end to end modules in series. Each module contacts the slope side by side in the course of the campaign, so j is valued in 1 to 5 by cycle. For example, when j is valued 2, $j + 1$ is valued 3; when j is valued 5, $j + 1$ is valued 1. According to the relational between the model and the geometry, it is said that the range of constraint of the active joint will be got, when the bow-shaped-bar j contacts the slope:

$$j, \begin{cases} \theta_j = 72^0, & 47^0 < \theta_{j+1} < 114^0; \\ 2\left(\frac{2j-1}{2}\alpha - \varphi\right) \leq \theta_j \leq 151^0, & 0 < \theta_{j+1} \leq \pi - \arccos\left(\frac{1-2\cos\theta_j}{\sqrt{5-4\cos\theta_j}}\right); \\ 2\left(\frac{2j-1}{2}\alpha - \varphi\right) \leq \theta_{j+1} \leq 151^0; \\ \frac{\pi}{2} + \frac{\theta_{j+1}}{2} - \arccos\left(\frac{4\sin^2(\theta_{j+1}/2)-3}{4\sin(\theta_{j+1}/2)}\right) < \theta_j \leq \frac{\pi}{2} + \frac{\theta_{j+1}}{2} - \arccos\left(\frac{4\sin^2(\theta_{j+1}/2)+3}{8\sin(\theta_{j+1}/2)}\right) \\ 47^0 < \theta_j < 114^0, \theta_{j+1} = 72^0; \end{cases} \begin{cases} \varphi = (j-1)\alpha \\ (j-1)\alpha < \varphi \leq (2j-1)\alpha/2 \\ (2j-1)\alpha/2 \leq \varphi < j\alpha \\ \varphi = j\alpha \quad j = 1, 2, \dots, 5 \end{cases} \quad (8)$$

3.3 Analysis Uniform Slope Climbing of Five-Bow-Shaped-Bar Linkage

As showed in Fig. 5, the model of the close chain five-bow-shaped-bar linkage slope climbing uniform stress analysis, in which the vector of system center in the translation coordinates $x_c c y_c$ is ${}^c\mathbf{r}$. Unlike the center of kinematic model in Fig. 2, the introduced r is an joint radius of entity bow-shaped-bar and the joint radius of circle is equal to each other, the circle O_1 is the outer circle contour of entity bow’s ground-touched bow-shaped-bar while circle O_2 is the virtual circle. Because the gravity, friction and slopes support force are in balance when slope climbing in a

Fig. 5 Five-link uniform climbing analysis model on slope



constant speed, the gravity extension line that the system suffered through P . F_f is the minimum static friction, which direction is upward along the slope and coefficient is u ; F_N is positive pressure the five-link suffered and the direction is perpendicular to slope; β is the inclined slope angle.

Figure 5 shows that system center is on the plumb-line which the over-slope contact point P is perpendicular to the horizontal surface. We call the plumb-line equilibrium line or borderline. The coordinates of contact point P is $(0, -R-r)$, the equilibrium line's expression in coordinate system $x_c y_c$ is:

$$y_c = x_c \cot \beta - R - r, \quad x_c \geq 0. \tag{9}$$

In order to meet the bow slope climbing, The coordinates of system center is in the linear programming right of the equilibrium line. So get the simplification:

$$\beta \leq \arctan \left(\frac{{}^c x_t}{{}^c y_t + R + r} \right). \tag{10}$$

As can be seen from (10), under certain circumstances of the radius R , the greatest impact on the slope angle is the ratio of the the mass center in ${}^c y_t$ axis offset and in ${}^c x_t$ axis offset. Although the joint radius r is also determined when the experimental prototype determined, the joint radius r still effects the maximum slope angle. Then the optimal model of maximum slope climbing is established:

$$\begin{aligned} \max \beta &= f(r, \varphi, \theta_1, \theta_2) \\ \text{s.t. } \beta &\leq \arctan \left(\frac{{}^c x_t}{{}^c y_t + R + r} \right). \end{aligned} \tag{11}$$

Within the scope of active joints expressed in formula (7) and (8), the change curve of maximum slope climbing of bow-shaped-bar with roll angle and the radius of joint circle can be obtained by the two-dimension search algorithm(see Fig. 6).

Figure 6a shows the roll angle of 0 to 72 change curve and 6b shows the roll angle in a range of 0–360 motion cycle graph.

According to the relationship such as $u = \tan\beta$ between the slope and the minimum static friction coefficient, the change curve of the bow-shaped-bar minimum static friction coefficient with roll angle and radius of the joint circle (see Fig. 7). Figure 7a shows the roll angle of 0 to 72 change curve and 7b shows the roll angle in a range of 0 to 360 motion cycle graph.

As the roll angle changes from 0 to 72, showed in Fig. 6a, 7a, the slope climbing capacity of a closed chain bow five-link and the minimum static friction coefficients are negative associated with the radius of joint circle, increases first and then decreases with the roll angle and reaches the maximum value when the roll angle is 36. When the radius of joint circle is zero and roll angle is 36, the theoretical slope climbing of the bow-shaped-bar up to 54.1 and the friction coefficient could up to 1.38. However, the practical application needs a certain the radius of joint circle, taking $r = 0.15R$ as an example into illustrate: when the roll angle is 36, the bow-shaped-bar slope climbing up to the maximum about 47.9, friction coefficient reaches the maximum about 1.11; when the roll angle is 72, the bow-shaped-bar slope climbing reaches the minimum about 12.6. Figure 6b, 7b shows the curve

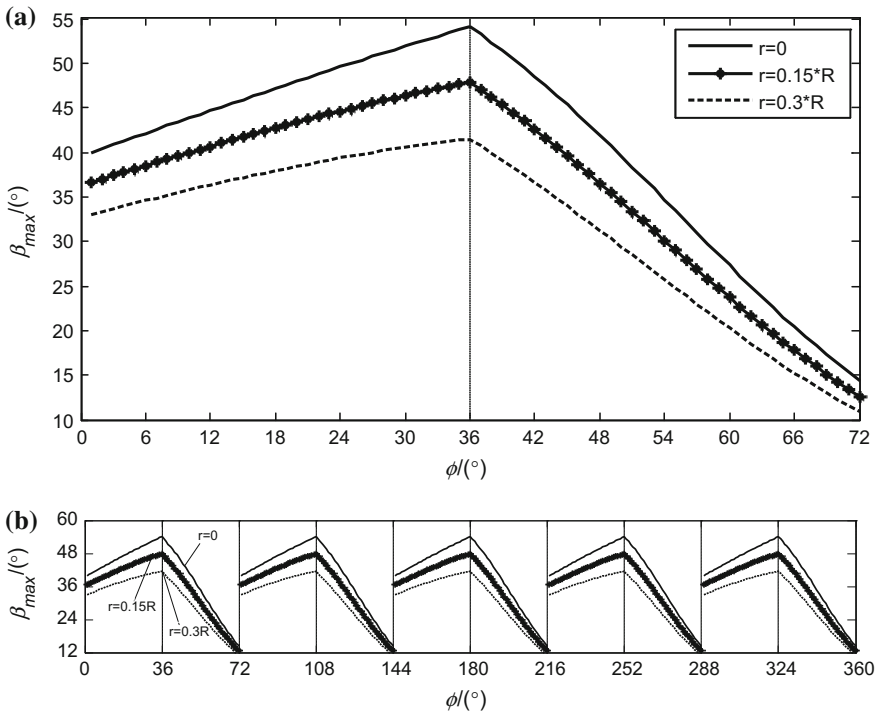


Fig. 6 Five-link maximum slope climbing graph

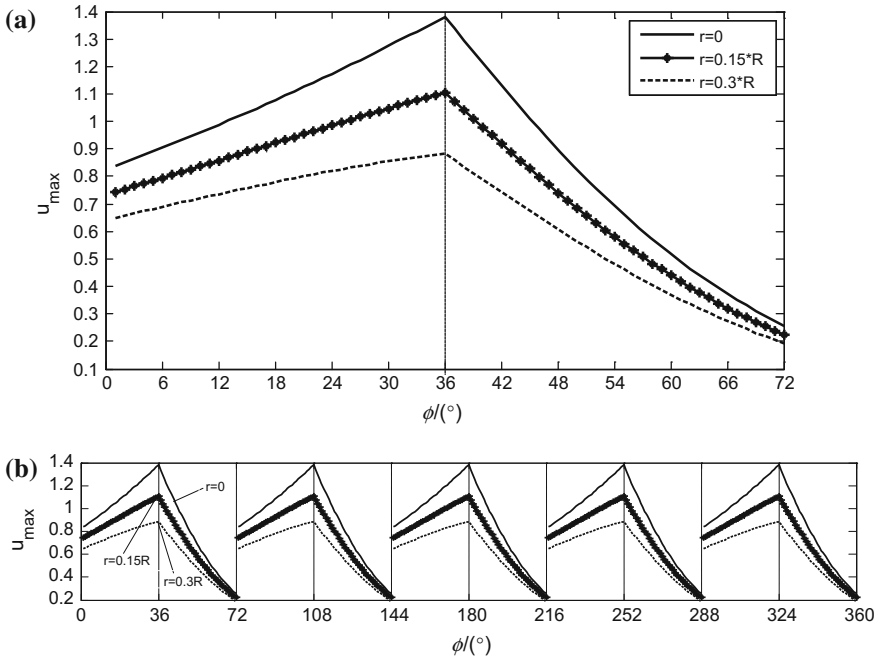


Fig. 7 Five-link slope climbing showing the minimum static friction coefficients

graph between the maximum slope climbing and the minimum static friction coefficients within a five-link motion period. A jump occurs when the roll angle $n \times 72^\circ$, which is due to stability constraints of critical position.

4 Motion Planning Process of Constant CG Offset Climbing

Gravity offset torque depends on the CG offsets L and offset angle ψ . The strategy of constant CG offset in uniform rolling motion planning is more appropriate [8–11]. In order to achieve a constant speed climbing, climbing critical location constraints must be taken into account as shown in Fig. 6b, the bow-shaped-bar slope climbing reach the minimum about 12.6° , when the roll angle is $n \times 72^\circ$ within a movement cycle. A constant offset of CG climbing process can be achieved when the slope is at the minimum, then the system of CG is represented as the point of contact c_3 of the circle O_3 and balance line as shown in Fig. 5, and the coordinate in $x_c y_c$ expressed as:

$${}^c x_t = (R + r) \sin \beta \cos \beta; {}^c y_t = -(R + r) \sin^2 \beta \tag{12}$$

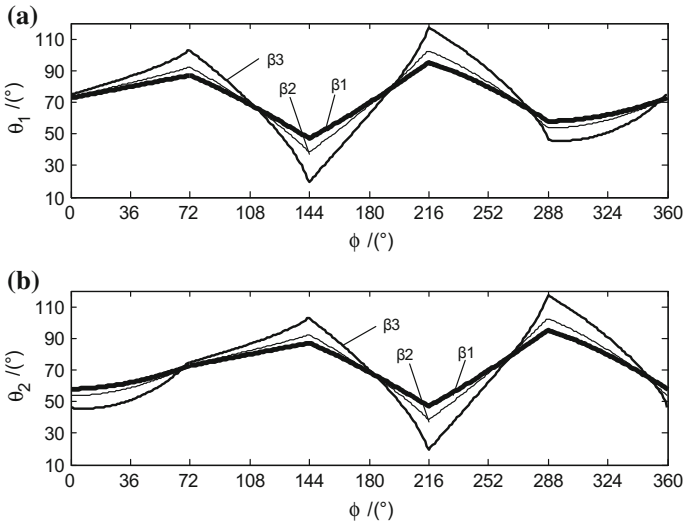


Fig. 8 CG offset constant uniform climbing active joint trajectory

So we take the minimum slope of bow-shaped-bar greatest slope climbing as the maximum climbing at a constant speed climbing of the bow in practical application. Slope climbing values as follows: $\beta_1 = 6^\circ$, $\beta_2 = 10^\circ$, $\beta_3 = 12^\circ$, the roll angle's value is continuous range from $(0, 360^\circ]$. Bring the three slope value into the formula (11) respectively, then put the coordinate of center of mass that solved into Eq. (6), the unique solution of active joint angle can be get finally. Use the least square method to obtain the vary scene of active joints θ_1 and θ_2 within a rolling cycle, as shown in Fig. 8.

Figure 8 shows: the change of active joint angle exhibit periodicity when use the planning strategies of a constant CG offset, and the slope climbing is positive correlation with the opening angle of the active joint. It is easy to find that the two active joint angle have a same variation regularity and joint angle of the trajectory curve θ_2 phase behind θ_1 joint angle trajectory curve with 72, which is the characteristics of symmetrical design agency. Further, when the roll angle is 72, the joint B touch the ground, then the three tracks curves is all through 72, thus ensure the stability of the closed five-link chain bow roll.

5 Experiment of Slope Climbing Capacity

In order to verify the analysis conclusion, we made a physical prototype of a close chain five-bow-shaped-bar linkage, the main structural parameters is: $a = 200$ mm, $R = 170$ mm, $r = 0.15R = 25.5$ mm and the quality of each rod segment is 312 g.

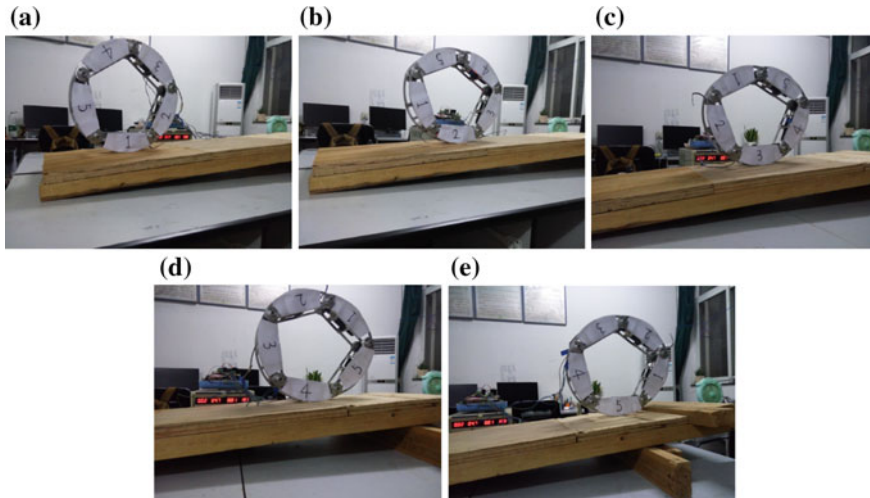


Fig. 9 $\beta_I = 6^\circ$ constant CG offset for uniform climbing process on slope

With the slope being $\beta_I = 6^\circ$, the roll angle being φ changes form 0 to 360, uniform climbing experiment are designed by active joint trajectory of uniform climbing of bow-shaped-bar system CG offset within a movement cycle. As showed in Fig. 9. Given the initial velocity, a close chain five-bow-shaped-bar linkage has realized constant CG uniform climbing process, the climbing cycle experiment results verify the correctness of the theoretical analysis.

6 Conclusions

The optimization model of the maximum gradient of uniform slope climbing is established. According to the relationship between the slope climbing and the static friction coefficient, the minimum static friction coefficients is the same as the change trend of the maximum slope.

The maximum slope of practical application bar reach 12.6 degrees, which is the minimum value of a cycle of slope climbing, and constant CG offset uniform climbing process can be realized in the slope of the minimum values. Use the least square method to obtain the unique solution of active joints in a rolling cycle. Finally, the correctness of the theoretical analysis is verified by experiments. In this paper, the theoretical analysis and the experiment of slope climbing capacity of a close chain five-bow-shaped-bar linkage provides the theoretical basis of the motion planning process and a theoretical reference for the structure design, the motion planning and control in unstructured environment.

Acknowledgments The paper writing is supported by the National Natural Science Foundation of China (Grant no. 51275363, 11072181).

References

1. Yamawaki T, Mori O, Omata T (2003) Nonholonomic dynamic rolling control of reconfigurable 5R closed kinematic chain robot with passive joints. In: Proceedings of the 2003 IEEE international conference on robotics and automation, vol 2(3), pp 4054–4059
2. Zhang L, Ma S, Li B, Zhang Z (2009) Research on climbing capacity of self-reconfiguration modular exploration robots system. *China Mech Eng* 20(13):1551–1555
3. Flynn LL, Jafari R, Mukherjee R (2010) Active synthetic-wheel biped with torso. *IEEE Trans Rob* 26(5):816–826
4. Zhiwei S, Hanxu S, Qingxuan J, Yan heng Z, Wei Z, Zhuo Y (2012) Motion analysis of a spherical robot with climbing ability. *Robot* 34(2):152–158
5. Liangqing W, Hanxu S, Qingxuan J (2007) Research on the climbing and jumping of a spherical rolling robot. *J Beijing Univ Posts Telecommun* 30(2):11–14
6. Hanxu S, Wei Z, Yanheng Z (2013) Mechanical analysis about a new kind of variable structure spherical mobile robot. *J Mech Eng* 49(19):40–47
7. Ming Y, Zongquan D (2009) Dynamic modeling and optimal controller design of a spherical robot in climbing state. *J Mech Eng* 45(11):46–50
8. Phipps CC, Shores BE, Minor MA (2008) Design and quasi-static locomotion analysis of the rolling disk biped hybrid robot. *IEEE Trans Rob* 24(6):1302–1314
9. Ligu S, Liyuan Z, Yanqiong F (2016) Climbing motion of a track-wheel hybrid mobile robot. *J Harbin Eng Univ* 37(2):266–270
10. Lianqing Y, Xiaojun L, Yujin W, Changlin W (2014) Quasi-static locomotion planning for rolling mechanism of close chain five-bow-shaped-bar linkage. *J Huazhong Univ Sci Tech (Nat Sci Ed)* 42(6):33–37
11. Halme A, Schonberg T, Wang Y (1996) Motion control of a spherical mobile robot. *IEEE Trans Rob* 9(96):259–264

Multi-objective Optimization Design of Automated Side Loader of Arm Actuator

Binlin Yi and Jiangnan Liu

Abstract During the process of loading rubbish for the automated side loader (ASL), the accuracy of the trajectory of key point and the motion smoothness of mechanism are the key factors to reduce the scatter of rubbish. In order to optimize the deviation of the trajectory of key point and the standard deviation of the angular velocity of the trash barrel, the optimization model of automated side arm actuator (ASAA) is established. According to the constraint conditions of mechanism, the minimum deviation of the key-point trajectory and the minimum standard deviation of the angular velocity are taken as the optimization targets, while mechanism parameters are regarded as design variables. A mathematical optimization model about key-point trajectory and motion smoothness is built for the ASAA, which is solved by the optimization method based on interior point algorithm, and the optimization results are verified by a simulation experiment. The results show that the performance of optimized ASAA is greatly improved.

Keywords Automated side arm · Trajectory of key point · Motion smoothness · Multi-objective optimization

1 Introduction

The automated side arm (ASA) is an important part of the automated side loader (ASL), whose main function is automatically grasp and dump the trash barrel [1]. ASA mechanism as the actuator of rotating, telescopic movement which mainly be composed of a pair of parallel double-rocker mechanism. The trajectory deviations of key point and motion smoothness of ASAA are major factors for reducing the scattering of rubbish during the feeding process. It has important practical

B. Yi · J. Liu (✉)

State Key Laboratory of Advanced Design and Manufacturing for Vehicle Body,
Hunan University, Changsha, People's Republic of China
e-mail: liujiangnan@hnu.edu.cn

significance to optimize the ASAA of the key-point trajectory deviation and motion smoothness for decreasing the scattering of rubbish.

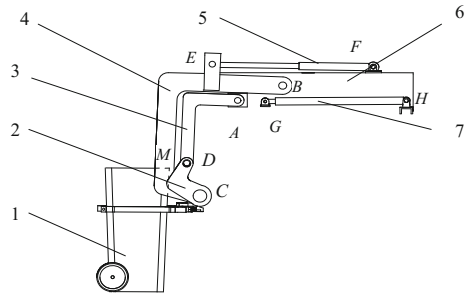
Many scholars have studied the trajectory optimization and the motion smoothness of the mechanism. In Barnard et al. [2], Lenarčič and Wingers' [3] papers, a optimization method using Lamé curve trajectory is developed, which has taken planar five bar mechanism as an example and comparing the different trajectory curve. It is proved that the motion law in terms of residual vibration and impact point accuracy has a better performance. A trajectory optimization method based upon B spline curves is also presented for a series manipulator [4–6]. As discussed in Ullah et al. [7], Yu et al. [8], Mullineux et al. [9] s' studies, a closed trajectory optimization method based on Fourier transform is proposed, which is suitable for the series parallel manipulator, and it can avoid solving the complex nonlinear equation. But Fourier transform is not suitable for open path curve, therefore, Galan-Marín et al. [10], Sun. et al. [11] put forward a open trajectory optimization method based on wavelet transform that applicable to a series-parallel arm. Heuristic optimization algorithms are generally used because they are simple and effective, but there is still room for improvement in convergence speed and global search capability [12]. Wang et al. [13] proposed an improved differential evolution algorithm for the problem of the convergence speed and the global searching ability, which has better convergence speed and global searching ability.

In Korayem et al. [14, 15], Jiang et al. [16] and Hu et al. [17] s' studies, a trajectory optimization method based on dynamic characteristics is proposed by combining trajectory optimization and the characteristics of multi body dynamics. A further study is carried out by Ghasemi et al. [18], Bamdad et al. [19] and Barnett et al. [20] in which a combination of dynamic characteristics, trajectory and working time of the optimization method is put forward. The research of trajectory optimization [2–20] in literature is concentrated in a given trajectory curve, applying interpolation to optimize the given trajectory curve and other factors, but do not consider the coupling relation between component angle and the trajectory curve.

In order to optimize the motion smoothness and the force transmission of the spatial mechanism, the hybrid genetic algorithm is applied to optimize the spatial mechanism, and the optimization results are better than the results of the single application genetic algorithm [21]. Taking the parallel manipulator as the research object, a method of trajectory optimization method for the insertion of transition arcs is proposed in H Shen et al.'s paper aiming at the problems such as vibration and instability of the mechanical hand [22]. All of these studies have focused on the multi objective optimization of the given trajectory and the dynamic characteristics of the mechanism, which rarely involve the multi objective optimization of the combining of the critical -point trajectory and the motion smoothness of the trajectory curve.

In this study, taking ASAA as the research object, considering the key-points trajectory and motion smoothness factors, the multiple objective optimization mathematical model is established in the absence of the desired trajectory, which is based on the deviation of the key-points trajectory and the smoothness of the mechanism. By using the interior point algorithm and combining with the linear weighting, the multi-objective optimization is carried out on ASAA.

Fig. 1 Mechanism diagram of ASA



2 The Mechanism of ASA

A schematic diagram of ASA mechanism is represented in Fig. 1. The short side links (3) are connected to the telescopic frame (6) through the hinges. A pair of pivoting links of the short side links is connected to connecting rods (2). The connecting rods are in turn connected at their lower ends to the long side links (4) which are turned by the turning hydraulic cylinder (5), and the upper side of the long side links is connected to the telescopic frame. The telescopic frame is driven by a telescopic ram (7) hooked to the shoveling box (not shown). The point *M* in the graph is the midpoint of the barrel eaves. Lateral movement is driven by the telescopic ram and dumping of the trash barrel driven by the turning hydraulic cylinder.

3 The Mathematical Model of ASAA

In order to obtain the relationship between the objective functions, the nonlinear constraint functions and the four-bar mechanism parameters, a mathematical model of the ASAA is built with its parameters as independent variables, the key-point path and the output of connecting rod angular velocity as dependent variables. The specific process is as follows: firstly, by the location analysis of ASAA, the function relation between the key point path and the independent variable is derived. Then, based on the velocity analysis, the relation between the output angular velocity and the input angular velocity is obtained.

3.1 The Position Analysis of ASAA

The key-point trajectory includes the position of the key point and the angle of the connecting rod. As to ensure the critical point position deviation in an allowable range, the position of ASAA is analyzed. Position analysis includes the analysis of initial position and the analysis of the key-points position. First, based on the initial position analysis of ASAA, a functional relationship between the parameter of the

non independent and the independent variable is deduced. Then through the key-point position analysis of ASAA, the functional expression of key-point position is gotten. Finally, it could deduce the function relationship between the point trajectory of the arbitrary angle and arguments by combining the initial position analysis and the key-point position analysis.

The scattering of rubbish mainly occurs in the feeding process for ASA. Turning of the trash barrel is driven by the connecting rod CD and the point M is midpoint of the barrel eaves, so MCD is one component. When the position of ASAA is analyzed, the four-bar mechanism $ABCD$ and the related point M are selected for analysis. Taking point B as the origin, the analysis diagram of mechanism location is built as shown in Fig. 2.

The Position Analysis of Initial Point M . The Point M and B are also fixed points, that is to say $|BM|$ and $\angle MBY$ are the constant and $|CM|, \angle MBY$ are non-independent parameters. The function relation between the non-independent parameters and the independent variables is derived by theoretical calculation:

Setting: $|BM| = l_6, \angle MBY = \theta_6(0), |CM| = 5, \angle MCD = \theta_5$

By the geometric relationship, it is easy to get

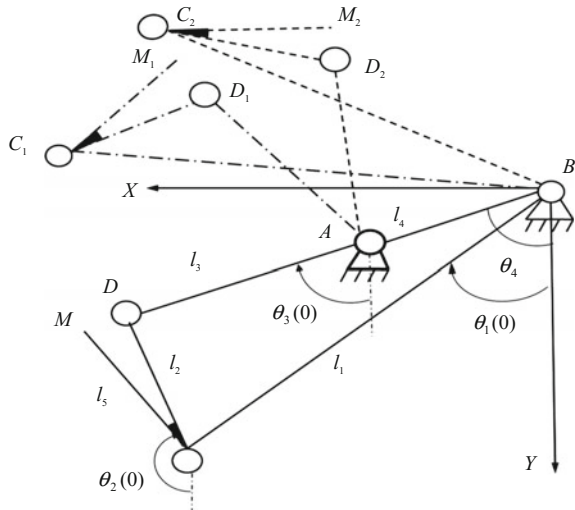
$$\begin{aligned} X_c &= l_1 \sin \theta_1(0) \\ Y_c &= l_1 \cos \theta_1(0) \end{aligned} \tag{1}$$

$$X_{m0} = X_c + l_5 \cos(\theta_2(0) - \theta_5) \tag{2}$$

On the basis of Eq. (2), the θ_5 could be written in the following form

$$\theta_5 = \theta_2(0) - \arccos \frac{X_{m0} - X_c}{l_5} \tag{3}$$

Fig. 2 Analysis diagram of mechanism location



In triangular BCM , Using the cosine law

$$\cos(\theta_6(0) - \theta_1(0)) = \frac{l_6^2 + l_1^2 - l_5^2}{2l_6l_1} \tag{4}$$

On the basis of Eq. (4), the l_5 could be expressed as the following form

$$l_5 = \sqrt{l_6^2 + l_1^2 - 2l_6l_1 \cos(\theta_6(0) - \theta_1(0))} \tag{5}$$

The Position Analysis of Key Points M_1, M_2 . In the whole trajectory of the ASAA, there are several key-points associated with connecting rod angle. The deviation of several key-points path has a significant impact on the scatter of rubbish in the process of loading litter. When the trash barrel is filled with rubbish and the trash barrel turns 70° , the X and Y direction still do not reach the feeding mouth which will cause rubbish scattered. In addition, when the trash barrel turns 135° and the trash barrel turned too high, which will also affect the rubbish scattered.

(1) The calculation of point M_1

As shown in Fig. 2, M_1 represents the location of the linkage rotating 70° , in the meantime, θ'_1 represents the angle of the long side link. By the geometric relationship of coordinates, it is easy to get

$$\begin{aligned} X_c &= l_1 \sin \theta'_1 \\ Y_c &= l_1 \cos \theta'_1 \end{aligned} \tag{6}$$

$$\begin{aligned} X_{m1} &= X_{c1} + l_5 \sin(\theta_2(0) + 70^\circ - \angle MC_1D_1) \\ Y_{m1} &= X_{c1} + l_5 \cos(\theta_2(0) + 70^\circ - \angle MC_1D_1) \end{aligned} \tag{7}$$

The optimization of mechanism in an iterative progress:

$$\angle MCD = \angle MC_1D_1 = \theta_5 \tag{8}$$

Substituting Eqs. (6), (5) and (3) into Eq. (7), Point M_1 is determined as Eq. (9).

$$\begin{aligned} X_{m1} &= g_0(\theta_1(0), \theta_2(0), \theta'_1, \theta_4, l_1, l_2, l_3, l_4) \\ Y_{m1} &= g_1(\theta_1(0), \theta_2(0), \theta'_1, \theta_4, l_1, l_2, l_3, l_4) \end{aligned} \tag{9}$$

where (g_0, g_1) is a function. The subsequent emergence of f_i and g_i are said to be functions of a certain relationship. Equation (9) indicates that the key point trajectory M_1 is related to the above 8 variables, but $l_1, l_2, l_3, l_4, \theta_1(0), \theta_4$ can be identified a four-bar mechanism and its initial position, therefore, the between $\theta_2(0), \theta'_1$ and $l_1, l_2, l_3, l_4, \theta_1(0), \theta_4$ function relation must be deduced.

Using the plural vector position equation of the four-bar mechanism [23]

$$A \sin \theta_2 + B \cos \theta_2 + C = 0 \quad (10)$$

Based on Eq. (10), the θ_2 is obtained as follow form

$$\theta_2 = 2 \arctan \left[\frac{A_1 \pm \sqrt{A_1^2 + B_1^2 - C_1^2}}{B_1 - C_1} \right] \quad (11)$$

where

$$\begin{aligned} A_1 &= 2l_2(l_1 \sin \theta_1 - l_4 \sin \theta_4) \\ B_1 &= 2l_2(l_1 \cos \theta_1 - l_4 \cos \theta_4) \\ C_1 &= l_1^2 + l_2^2 + l_4^2 - l_3^2 - 2l_1l_4 \cos(\theta_1 - \theta_4) \end{aligned}$$

Equation (11) in the type of \pm number, according to the initial installation of the mechanism can be identified as the + number.

Equation (11) also could be expressed as following form

$$\theta_1 = 2 \arctan \left[\frac{A_2 \pm \sqrt{A_2^2 + B_2^2 - C_2^2}}{B_2 - C_2} \right] \quad (12)$$

where

$$\begin{aligned} A_2 &= 2l_1(l_2 \sin \theta_2 - l_4 \sin \theta_4) \\ B_2 &= 2l_1(l_2 \cos \theta_2 - l_4 \cos \theta_4) \\ C_2 &= l_1^2 + l_2^2 + l_4^2 - l_3^2 - 2l_1l_4 \cos(\theta_2 - \theta_4) \end{aligned}$$

Equation (12) in the type of \pm number, according to the initial installation of the mechanism can be identified as the—number.

$\theta_1(0), \theta_2(0) + 70^\circ$ are substituted into Eq. (11), (12) respectively, so the $\theta_2(0)$ and θ'_1 could be derived as follow form

$$\theta_2(0) = f(\theta_1(0), \theta_4, l_1, l_2, l_3, l_4) \quad (13)$$

$$\theta'_1 = f_1(\theta_2(0), \theta_4, l_1, l_2, l_3, l_4) \quad (14)$$

Replacing $\theta_2(0)$ with $f_1(\theta_2(0), \theta_4, l_1, l_2, l_3, l_4)$, Eq. (14) could be expressed as

$$\theta'_1 = f_2(\theta_1(0), \theta_4, l_1, l_2, l_3, l_4) \quad (15)$$

Substituting Eqs. (6), (5), (13) and (3) into Eq. (9), key point trajectory M_1 could be written in the following form

$$\begin{aligned} X_{m1} &= g_0(\theta_1(0), \theta_4, l_1, l_2, l_3, l_4) \\ Y_{m1} &= g_1(\theta_1(0), \theta_4, l_1, l_2, l_3, l_4) \end{aligned} \tag{16}$$

(2) The calculation of point M_2

As shown in Fig. 2. M_2 is the location of the linkage rotating 135° . Because the analysis of 135° position of linkage is similar to the analysis of 70° position of linkage, therefore, key point M_2 could be determined as in the following form

$$\begin{aligned} X_{m2} &= g_2(\theta_1(0), \theta_4, l_1, l_2, l_3, l_4) \\ Y_{m2} &= g_3(\theta_1(0), \theta_4, l_1, l_2, l_3, l_4) \end{aligned} \tag{17}$$

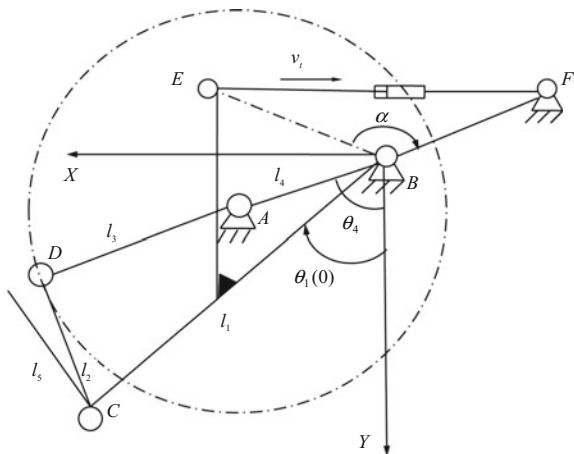
3.2 The Velocity Analysis of ASAA

The scatter of litter is mainly occurred in the process of loading rubbish for ASL. The motion smoothness of ASAA is an important influencing factor for the scatter of rubbish, so it is necessary for ASAA to analyze velocity. Velocity analysis includes two parts: deducing the nonlinear function of the input angular velocity and the output angular velocity.

(1) The calculation of input angular velocity ω_1

As shown in Fig. 3, the B, E, F initial position stay relatively the same, that is to say ω_1 is only a function of time t .

Fig. 3 Kinematic diagram of ASAA



Because BCE is the same component, the $\omega_1(t)$ is expressed as the following form

$$\omega_1(t) = \dot{\theta}_1(t) = -(\angle B\dot{E}F) \tag{18}$$

In triangular BEF , using the cosine law

$$\cos \angle BEF = \frac{|BE|^2 + |BF|^2 - |EF|^2}{2|BE||BF|} \tag{19}$$

Based on Eq. (19), the $\angle BEF$ is obtained as follow form

$$\angle BEF = \arccos \frac{|BE|^2 + |BF|^2 - |EF|^2}{2|BE||BF|} \tag{20}$$

$|BE|, |BF|$ are constants and the length of the hydraulic cylinder is only changed with time t , so $|EF|$ can be described as the following form

$$|EF| = l_0 - v_t t \tag{21}$$

where l_0 is the initial length of hydraulic cylinder.

Substituting Eqs. (20), (21) and (13) into Eq. (18), the $\omega_1(t)$ is expressed as the following form

$$\omega_1(t) = v_t(l_0 - vt) \frac{1}{\sqrt{1 - \left(\frac{|BE|^2 + |BF|^2 - (l_0 - vt)^2}{2|BE||BF|}\right)^2}} \tag{22}$$

Then the Eq. (22) is integrated for t , the $\theta_1(t)$ could be written in the following form

$$\theta_1(t) = \int_0^t \omega_1(t) = f_4(t) + \theta_1(0) \tag{23}$$

(2) The calculation of input angular velocity ω_2

The Eq. (11) is taken a derivative with respect to t , so ω_2 could be obtained by the derivation rule of compound function

$$\omega_2 = \frac{2}{(B_1 - C_1)^2 + (A_1 + \sqrt{A_1^2 + B_1^2 - C_1^2})} \left[(B_1 - C_1)(A_1' + \frac{A_1 A_1' + B_1 B_1' - C_1 C_1'}{\sqrt{A_1^2 + B_1^2 - C_1^2}}) - (A_1 + \sqrt{A_1^2 + B_1^2 - C_1^2})(B_1' - C_1') \right] \tag{24}$$

where

$$A'_1 = \omega_1 m, B'_1 = -\omega_1 t, C'_1 = \omega_1 p \tag{25}$$

where

$$\begin{aligned} m &= 2l_1 l_2 \cos \theta_1 & t &= 2l_1 l_2 \sin \theta_1 \\ p &= 2l_1 l_4 (\sin \theta_1 \cos \theta_4 - \cos \theta_1 \sin \theta_4) \end{aligned} \tag{26}$$

Substituting Eqs. (25), (26) into Eq. (24), ω_2 is expressed as the following form

$$D = \frac{2}{(B_1 - C_1)^2 + (A_1 + \sqrt{A_1^2 + B_1^2 - C_1^2})} \left[(B_1 - C_1) \left(m + \frac{A_1 m + B_1 t - C_1 p}{\sqrt{A_1^2 + B_1^2 - C_1^2}} \right) + (A_1 + \sqrt{A_1^2 + B_1^2 - C_1^2}) (t + p) \right] \tag{27}$$

4 The Optimization Analysis of Mechanism

4.1 Design Variables

Figure 3 shows the kinematical principle of ASAA. The analysis of above indicates that the key-point trajectory and the motion smoothness of ASAA are merely related to $l_1, l_2, l_3, l_4, \theta_1(0)$, and θ_4 . Therefore, they can be taken as the design variables of mechanism optimization.

4.2 Constraint Function

The mechanism optimization algorithm in this paper allows the definition of a number of linear and nonlinear constraints to satisfy ASAA property, link dimensions, bounds of design variables et al.

- (1) Constraints for property.

Aiming at decreasing the scattering of rubbish in the loading process, the horizontal and vertical coordinates of the key point M_1 could only change within certain limits. When the connecting link is rotated 70° , the minimum value of X_{m1} should be greater than 0.618 m which is the horizontal coordinate of feeding port, and X_{m1} do not be 0.085 m far away from the horizontal coordinate of feeding port. At the same time, Y_{m1} should be 0.24 m far away from the vertical coordinate of feeding port at least. When the connecting link is rotated 135° , Y_{m1} should also be 0.24 m

far away from the vertical coordinate of feeding port at least. These constrains are written as the following form

$$\begin{aligned} 0.618 &\leq X_{m1} \\ X_{m1} - 0.618 &\leq 0.085 \end{aligned} \quad (28)$$

$$0.24 + Y_{m1} \leq 0 \quad (29)$$

$$0.24 + Y_{m2} \leq 0 \quad (30)$$

(2) Constraints for link dimensions.

With different dimension relations of links, the mechanism has the different operation characteristics. To satisfy the operation requirement of ASAA, l_2 link is the shortest, l_1 link is the longest and l_3 link should be longer than l_4 link. Moreover, the point A should be kept in the plane of the telescopic frame, whose height is 0.1 m. Therefore, the link dimension constraints could be written as the following inequalities

$$\begin{aligned} l_3 &\leq l_1, l_4 \leq l_3, l_2 \leq l_4 \\ l_4 \cos \theta_4 &\leq 0.1 \end{aligned} \quad (31)$$

(3) Constraints for bounds of design variables.

In order to avoiding the external obstacle in the loading process, the design variables of mechanism can only change within certain limit. The lower and upper bounds of the design variables are as follow

$$\begin{aligned} 31^\circ &\leq \theta_1(0) \leq 40^\circ, 70^\circ \leq \theta_4 \leq 80^\circ \\ 0.800 &\leq l_1 \leq 1, 0.200 \leq l_2 \leq 0.300 \\ 0.45 &\leq l_3 \leq 0.550, 0.250 \leq l_4 \leq 0.350 \end{aligned} \quad (32)$$

4.3 Objective Function

When the trash barrel is rotated 70° and 135° , the trajectory deviations U_1 and U_2 seriously affect the scattering of litter in the loading process. Additionally, the motion smoothness of ASAA U_3 is the other important impact factor about the scattering of rubbish. Therefore, this is a multi-objective optimization problem. The linear weight method [24] is used to translating the multi-objective optimization into single-objective optimization in this paper. On account of their different units, the dimensionless method is applied to U_1 , U_2 , and U_3 . Applying the relevant target values of the existing ASAA as the initial values of optimization, the objective

function is established by dividing each target value at each iteration by the initial value respectively and linear weighting. The objective function F is determined as follow form

$$F = u_1 \frac{U_1}{U_{10}} + u_2 \frac{U_2}{U_{20}} + u_3 \frac{U_3}{U_{30}} \quad (33)$$

where $u_1 \sim u_3$ are weight factors.

Objective Function U_1, U_2 . The objective function U_1 represents the horizontal coordinate deviation between the middle point of the edge of trash barrel and reference point M'_1 , when the trash barrel is rotated 70° . The objective function U_2 represents the vertical coordinate deviation between the trash barrel and the feeding port, when the trash barrel is rotated 135° . The objective function U_1 and U_2 of the key-point trajectory could be expressed by

$$U_1 = (X_{m1} - 0.618) \times 100\% \quad (34)$$

$$U_2 = -(Y_{m2} + 0.24) \times 100\% \quad (35)$$

Objective Function for the Smoothness of Motion U_3 . Using the standard deviation to analyze the angular velocity of the connecting link ω_2 , the standard deviation represents the fluctuation of the average angular velocity of the connecting link. Consequently, the standard deviation of the angular velocity of the connecting link ω_2 in the loading process should be as small as possible. The objective function U_3 of the smoothness of motion is calculated as follow form

$$U_3 = \sqrt{\frac{1}{n} \sum_i^n (\omega_{2i} - \overline{\omega_2})^2} \quad (36)$$

There are 59 points within the effective rotation angle β , which are selected for calculating.

5 Optimization Calculation

The optimization of this paper is a multi objective nonlinear optimization problem. The trajectory of key point and motion smoothness make a difference to the rubbish scattered, so the above weight factor: $u_1 = u_2 = 0.33, u_3 = 0.34$. ASAA parameters are shown in Table 1.

Taking the optimization method based on interior point algorithm to optimize multi-objective function f and getting the main target optimization iterative curve after 31 iterations, as shown in Fig. 4, objective function f of the optimal value is 0.816 which is compared with the initial value optimized 17.8 %. Variables of

Table 1 Parameters of ASAA

Names	Numerical value	Names	Numerical value
$v_f/m/s$	0.15	α	151°
$l_6(0)/m$	0.809	β	87°
$\theta_6(0)$	53°	U_{10}	0.096
$ BF /m$	0.814	U_{20}	0.128
$ BE /m$	0.481	U_{30}	7.098

Fig. 4 Iteration curve

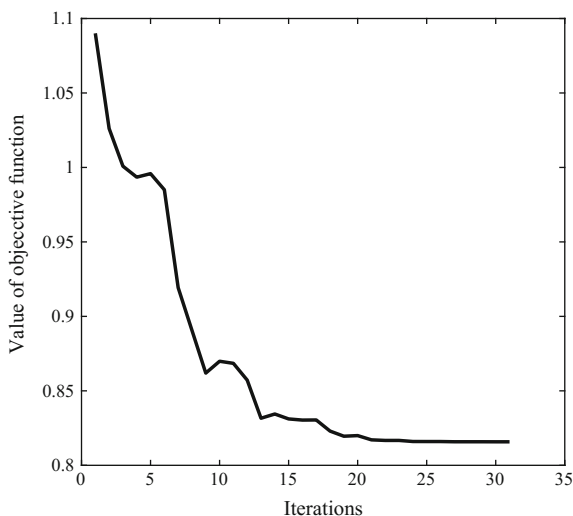


Table 2 Variable values of initial design and optimal design

Variable	l_1/m	l_2/m	l_3/m	l_4/m	$\theta_1(0)$	θ_4
Original	0.842	0.240	0.482	0.300	36°	70°
Optimized	0.960	0.292	0.550	0.292	31.5°	70.0°

Table 3 Optimization of each single objective and multi-objective

Objective functions	F	U_1	U_2	U_3
Original	1.000	1.000	1.000	1.000
Optimized	0.822	0.859	0.977	0.636

optimal design are shown in Table 2. Optimization values of each single objective and multi-objective are shown in Table 3.

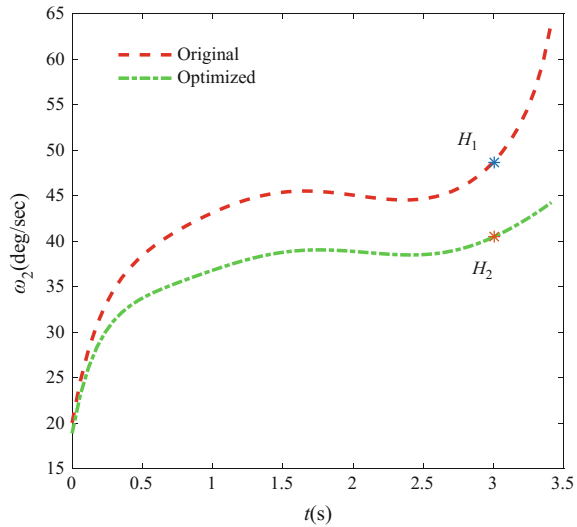
From the Table 3, it can be seen that the optimal value of the target U_2 and U_1 are 0.859 and 0.977, which are decreased by 14.1 and 2.3 % respectively.

The coordinate values of the optimized trajectory are obtained by the values of the optimized design variables substituted into optimization mathematical model. The coordinates of the key points M_1 , M_2 and the ideal key points are shown in Table 4. The optimized key points are more close to the ideal point.

Table 4 Theoretical coordinates of the key points and ideal points

Parameters	Original coordinate	Optimized coordinate	Ideal coordinate
Point M_1	(0.71, -0.209 m)	(0.70, -0.260 m)	(0.61, -0.240 m)
Point M_2	(0.50, -0.368 m)	(0.48, -0.365 m)	(Unlimited, 0.3400 m)

Fig. 5 Optimized angular velocity ω_2 and original



The optimal value of the target U_3 as shown in Table 3 is 0.636, which is decreased by 36.4 %. The optimized angular velocity curve and original as shown in Fig. 5, the slope of the optimized angular velocity is gentler and better. H_2 and H_1 respectively indicate the optimized theoretical angular velocity and original when it reaches 3 s.

6 The Verification of Optimization Results

Firstly, in order to verify the rationality of the optimization mathematical model and the optimization result, the simulation model is established. The result of simulation consists of the data of trajectory curve about the point M and angular velocity and angle about connecting rod, and the optimal curve and original are obtained. As illustrated in Fig. 6, points M_1, M_2 and M_1^1 et al. are marked. In Fig. 7, points like h_1, h_2, P_1 et al. are also marked. The details are as below figures.

As illustrated in Fig. 6, M_1, M_2 are the corresponding points when connecting rod turns 70° and 135° respectively. Likewise, M_1^1, M_2^1 are the corresponding ideal points when connecting rod turns 70° and 135° respectively.

Fig. 6 Optimized trajectory curve and original

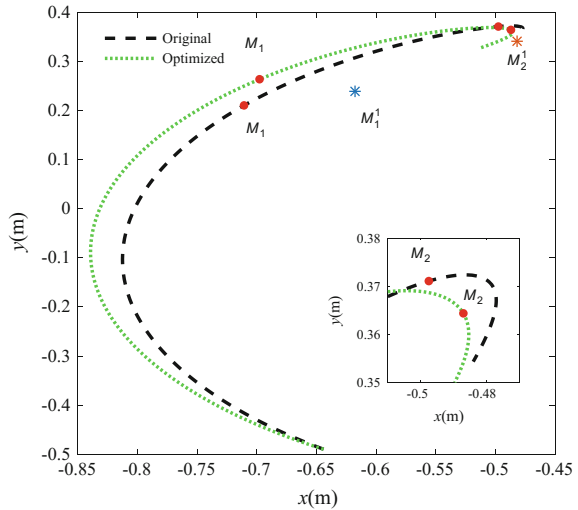
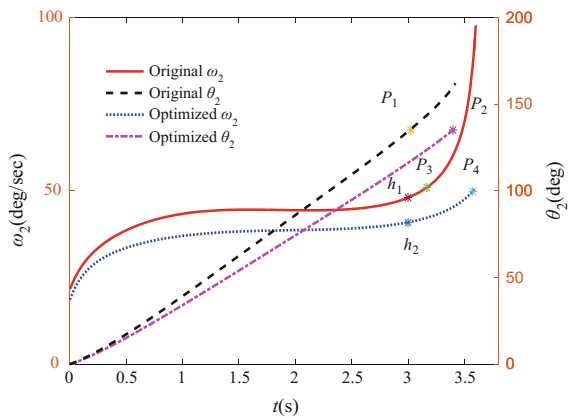


Fig. 7 Optimized linkage angular velocity ω_2 and angle and original



As illustrated in Fig. 7, h_1 , h_2 are the corresponding angular velocities of simulation test when it reaches 3 s. In addition, P_1 , P_2 are the corresponding original and optimal points when connecting rod turns 135° . P_3 , P_4 are the corresponding points of original and optimal angular velocity when connecting rod turns 135° .

6.1 The Verification of Trajectory Optimization Results

Because of the planar motion of trash barrel, the trajectory described in this paper includes not only the trajectory curve, but also the rotation angle of the trash barrel. The relationship between trajectory coordinates and the turning angle of trash barrel

Table 5 Test values of trajectory coordinates and angles

Original				Optimized		
Angle	70°	90°	135°	70°	90°	135°
X/m	0.713	0.639	0.500	0.699	0.613	0.499
Y/m	-0.208	-0.290	-0.371	-0.262	-0.331	-0.365

could be obtained from Figs. 6 and 7. Now selecting the trash barrels flip 70°, 90° and 135° for trajectory analysis, the specific situation as shown in Table 5:

Combination with Tables 4 and 5, the maximum error of the analytical solution and the experimental solution of the critical point trajectory is occurred in the Y coordinates of the original M_2 points, which is 2.04 %. The value is within the rational range, which proves the accuracy of the mathematical model of the trajectory deviation.

Seen from the Table 5 and Fig. 6, during the trash barrel from 70° turning to 90°, the non-optimized X direction position of the trash barrel mouth has not reached the 0.618 which is the feeding mouth X coordinate. The optimized trash barrel horizontal position could be reached 0.618 which is the feeding mouth X coordinate, when the trash barrels is not rotated to 90°. In the Y direction, when the trash barrel turns 70°, the height of the optimized position is higher than the position of the feed port. Furthermore, when trash barrel rolls over from 70° to 135°, the original of incremental is 0.163 and optimized incremental is 0.102, so the optimized ASAA effectively reduced trash barrels vertical increment. Therefore, the optimized trajectory is more ideal than the original.

6.2 The Verification of Motion Smoothness Optimization Results

The motion smoothness is relevant to the variation of angular velocity ω_2 . Based on Figs. 5 and 7, it is easy to get the relation between operation time t and angular velocity of trash barrel ω_2 . Accordingly, the motion smoothness is verified by selecting angular velocity ω_2 , when ASAA operates for 0s and 3s. The details are as below Table 6.

Table 6 Error analysis of angular velocity ω_2

Names	Original		Optimized	
	t/s	ω_2 (deg/s)	t/s	ω_2 (deg/s)
Experimental solution	0	20.06	0	18.89
	3	48.07	3	40.97
Theoretic solution	0	19.87	0	18.98
	3	49.23	3	40.97

It can be seen from the Table 6, the biggest error between experimental result and theoretic result about angular velocity ω_2 is occurred in 3s, and the error is 2.36 %. The error is within the rational range which effectively verifies the precision of motion smoothness about the mathematical model.

Based on Fig. 7, when the connecting rod turns from 0° to 135° , the whole angular velocity curve of the optimized mechanism is gentler, and the movement stability is more ideal.

Above all, the error between experimental solution and theoretic solution is minor, which effectively verify the precision of the mathematical model. After optimization, the trajectory curve and motion smoothness are improved greatly which effectively reduces the scattering of rubbish during the loading process.

7 Conclusion

In this paper, the mathematical model of the key-point trajectory deviation and motion smoothness of ASAA have been established, and a method of using the standard deviation of the angular velocity of the output component was proposed to describe the smoothness of the turning motion. Combined the mathematical model with the actual engineering constraints, an optimization mathematical model has been established. The optimization method based on interior point algorithm has been used to solve the multi objective optimization problem, and the optimized results show that key-point trajectory deviations and motion smoothness are improved obviously. The experimental results obtained by simulation are compared with the theoretical solutions. The consistency is good, and the rationality of the optimization model and the optimization results are verified.

Acknowledgment This project was supported by Central State-Owned Capital Operating Budget Expenditure Items (No. 10502500514001).

References

1. Goedken KD (2015) Automated load arm mechanism for front forks of refuse collection truck, US20150030419 (2015)
2. Barnard CJ, Briot S, Caro S (2012) Trajectory generation for high speed pick and place robots. In: 11th ASME 2012, Biennial conference on engineering systems design and analysis. ASME press, Nantes, France, pp 165–174
3. Lenarčič J, Wenger P (2010) Advances in robot kinematics: analysis and design. Springer, Berlin
4. Gasparetto A, Zanotto V (2007) A new method for smooth trajectory planning of robot manipulators. Mech Mach Theory 42:455–471
5. Gasparetto A, Lanzutti A, Vidoni R, Zanotto V (2012) Experimental validation and comparative analysis of optimal time-jerk algorithms for trajectory planning. Robot Com-Inte Manuf 28:164–181

6. Liu H, Lai X, Wu W (2013) Time-optimal and jerk continuous trajectory planning for robot manipulators with kinematic constraints. *Robot Com-Inte Manuf* 29:309–317
7. Ullah I, Kota S (1997) Optimal synthesis of mechanisms for path generation using fourier descriptors and global search method. *J Mech Des* 119:504–510
8. Yu HY, Tang DW, Wang ZX (2007) Study on a new computer path synthesis method of a four-bar linkage. *Mech Mach Theory* 42:383–392
9. Mullineux G (2011) Atlas of spherical four-bar mechanisms. *Mech Mach Theory* 46:1811–1823
10. Galán-Marín G, Alonso FJ, Castillo JMD (2009) Shape optimization for path synthesis of crank-rocker mechanisms using a wavelet-based neural network. *Mech Mach Theory* 44:1132–1143
11. Sun J, Liu W, Chu J (2015) Dimensional synthesis of open path generator of four-bar mechanisms using the haar wavelet. *J Mech Des* 137:8–9
12. Lin WY, Hsiao KM (2016) A new differential evolution algorithm with a combined mutation strategy for optimum synthesis of path-generating four-bar mechanisms. *P. I. Mech Eng C-J Mech* 203–210:1989–1996
13. Wang C, Fang Y, Sheng G (2015) Multi-objective optimization of a parallel ankle rehabilitation robot using modified differential evolution algorithm. *Chin J Mech Eng* 28:702–715
14. Korayem MH, Azimirad V, Vatanjou H, Korayem AH (2012) Maximum load determination of nonholonomic mobile manipulator using hierarchical optimal control. *Robotica* 30:53–65
15. Korayem MH, Bamdad M, Tourajizadeh H, Korayem AH, Bayat S (2012) Analytical design of optimal trajectory with dynamic load-carrying capacity for cable-suspended manipulator. *Int J Adv Manuf Tech* 60:317–328
16. Jiang X, Gosselin C (2015) Trajectory generation for three-degree-of- freedom cable-suspended parallel robots based on analytical integration of the dynamic equations. *J Mech Robot* 8:041001-1–7 (2015)
17. Hu Q, Zhang J (2015) Dynamics and trajectory planning for reconfigurable space multibody robots. *J Mech Des* 137:092304-1–12
18. Ghasemi MH, Kashiri N, Dardel M (2012) Time-optimal trajectory planning of robot manipulators in point-to-point motion using an indirect method. *P I Mech Eng C-J Mech* 226:473–484
19. Bamdad M (2013) Time-energy optimal trajectory planning of cable-suspended manipulators. In: Pott A, Bruckmann T (eds). *MMS*, vol 12. Springer, Heidelberg, pp 41–51
20. Barnett E, Gosselin C (2013) Time-optimal trajectory planning of cable-driven parallel mechanisms for fully-specified paths with G^1 discontinuities. *J Dyn Syst-T ASME* 137:071007-1–12
21. Perez-Gracia A, Yihun Y, Bosworth KW (2014) Link-based performance optimization of spatial mechanisms. *J Mech Des* 136:122303-1–11
22. Sun H, Li JQ (2010) *Theory of machines and mechanisms*. Northwestern Polytechnical University Press, Xi-an
23. Chen J, Fei Q, Pang X (2014) Mechanism optimal design of backhoe hydraulic excavator working device based on digging paths. *J Mech Sci Technol* 28:213–222
24. He CH, Shen XL, Zhou HJ (2014) Stability analysis of dense phase pneumatic conveying of pulverized coal at high pressure. *CIESC J* 65:820–828

Optimal Design of Parallel Mechanism for Automobile Electro-Coating Conveyor

Suhua Yao, Guoqin Gao and Zhiming Fang

Abstract Poor mechanism rigidity are prone to big terminal deformation as one exerts certain external force. In order to make the terminal deformation within acceptable range, work space needs to be optimized first with suitable global rigidity evaluation index. For the purpose, Global Stiffness Index (GSI), is defined in the paper. Dimensionless work space of the parallel mechanism is optimized based on the GSI, combined with the Upper Limit of the Jacobian matrix condition number and Maximum Tolerated Deformation. Within the dimensionless work space, terminal deformation does not exceed tolerated value, at the same time, the level of average deformation can reach average requirement. Link length, a parameter of the parallel mechanism, is later obtained with real length of work space divided by the dimensionless length of work space. Optimal design results are computed according to specific design requirements to the parallel mechanism in the automobile electro-coating conveyor. The simulation verifications show that the optimal design to parallel mechanism is in accord with design requirements. The design results are also used to develop a prototype for further research.

Keywords Parallel mechanism · Global stiffness index · Optimal design · Work space

1 Introduction

Parallel mechanisms have higher bearing capacity than serial ones. By taking this advantage, two same parallel mechanisms are installed on the automobile electro-coating conveyor to cooperatively support Car Body-in-white by up-and-down

S. Yao · G. Gao (✉) · Z. Fang
School of Electrical and Information Engineering, Jiangsu University,
212013 Zhenjiang, People's Republic of China
e-mail: gqgao@ujs.edu.cn

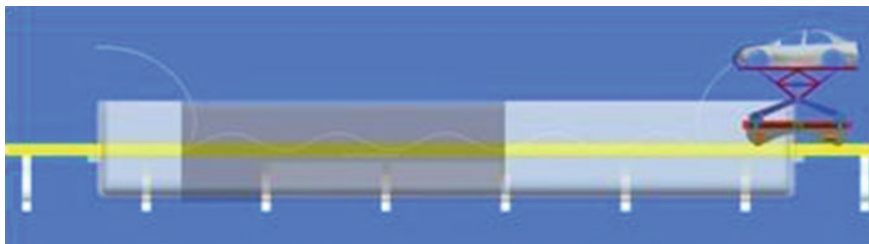


Fig. 1 Electro-coating process track route

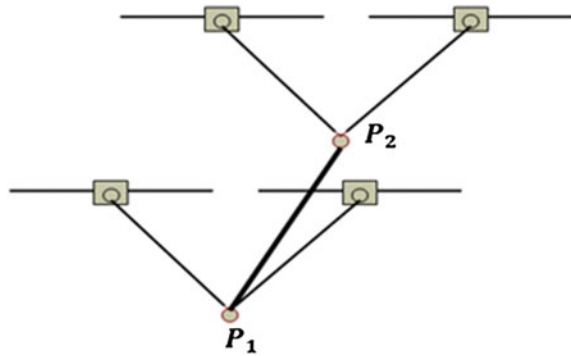
movements on end-effectors to eliminate air bag. The electro-coating process track route is Fig. 1.

To decrease the terminal deformation that reduces the end-effectors precision in overload situation, work space must be designed to satisfy certain rigidity requirement. Considering that high-strength material is used in parallel mechanism, the terminal deformation which is caused by stress can be ignored. So the effect on terminal deformation caused by elastic deformation in active joints is only considered in the paper.

Since mechanism rigidity affects terminal deformation, the rigidity or the static stiffness can be a primary consideration in optimal design of parallel mechanism. Optimal design needs to select a suitable global evaluation index based on rigidity to design parameters of mechanism. Many researchers have contributed to this. Kim and Tsai [1] used diagonal elements of the stiffness matrix of two norm as the stiffness evaluation index in 3-DOF parallel mechanism, Xu and Li [2, 3] respectively choose the average value and the minimum of determinant of the stiffness matrix within work space of 3-PUU parallel mechanism as indicators. Zhang and Gosselin [4] select weight sum of the diagonal elements of the stiffness matrix for Tricept mechanism. No matter how local rigidity evaluation index is defined, it can always reflect terminal deformation to some degree. However, the single global rigidity evaluation index based on above local stiffness evaluation index has some certain defects in optimal design. Because global rigidity evaluation index is mean value of stiffness evaluation index in the work space, the selection to work space has no criteria and thus causes computational complexity by trial-and-error method. In order to avoid trial-and-error method in optimal design, Global Stiffness Index is used to optimize the parameters of the parallel mechanism in the paper, combined with the Upper Limit of the Jacobian matrix condition number and Maximum Tolerated Deformation.

The paper is organized as follows. Section 2 introduces design requirements. Section 3 gives kinematics solutions, Jacobian matrix and the definition of

Fig. 2 Parallel mechanisms of automobile electro-coating conveyor



Work Space. Section 4 shows optimal design to the parallel mechanism. Section 5 gives optimal design results and verification. Finally, Sect. 6 offers conclusions, followed by acknowledgements, respectively.

2 Design Requirements

Two same parallel mechanisms are used to realize 200 mm up-down movement to eliminate air bag with a beam linked to each terminal in vertical direction in Fig. 2 the average terminal deformation or Global Stiffness Index, Maximum Tolerated Deformation and condition number of the Jacobian matrix are required to achieve respectively less than 1.38×10^{-5} mm/N, 2.45×10^{-5} mm/N and 2.0 in work space.

As the most important functional part in automobile electro-coating conveyor, the optimal design to parallel mechanisms is the key but challenging to conveyor.

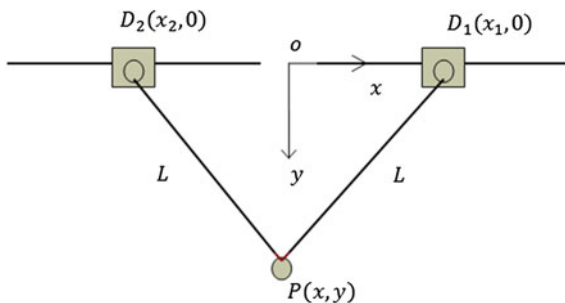
The parallel mechanism is horizontally actuated with only one geometric parameter, i.e., the link length of each of the two legs. In appearance, the link length is solely designed, while the key problem in the design is the determination of not the link length but the work space. The following paper will demonstrate how to design work space and further determine the link length.

3 Kinematics Solutions, Jacobian Matrix and the Definition of Work Space

3.1 Kinematics Solutions and Jacobian Matrix

Assuming that fixed frame O - xy is attached to base of one side of lifting parallel mechanism, in Fig. 3, coordinates of the active joints $D1$ and $D2$ are respectively $(x1, 0)$ and $(x2, 0)$, coordinate of the terminal P is (x, y) .

Fig. 3 Parallel mechanism of lifting mechanism



With constraint relation of $PD_i = L$, there are kinematics inverse solutions Eq. (1) and kinematics forward solutions Eq. (2).

$$\begin{cases} x_1 = x + \sqrt{L^2 - y^2} \\ x_2 = x - \sqrt{L^2 - y^2} \end{cases} \quad (1)$$

$$\begin{cases} x = (x_1 + x_2)/2 \\ y = \sqrt{L^2 - \frac{1}{4}(x_1 - x_2)^2} \end{cases} \quad (2)$$

Jacobian matrix of parallel mechanism Eq. (3) is induced from Eq. (2).

$$J = \begin{bmatrix} \frac{\partial x}{\partial x_1} & \frac{\partial x}{\partial x_2} \\ \frac{\partial y}{\partial x_1} & \frac{\partial y}{\partial x_2} \end{bmatrix} = \begin{bmatrix} \frac{1}{2} & \frac{1}{2} \\ -\frac{\sqrt{L^2 - y^2}}{2y} & \frac{\sqrt{L^2 - y^2}}{2y} \end{bmatrix} \quad (3)$$

3.2 Definition of Work Space

Common parallel mechanism is multi-dimensional planar or spatial area, however, the two same parallel mechanism installed on the automobile electro-coating conveyor only do up-and-down movements along y-axis with no displacement of x-axis, i.e., $x = (x_1 + x_2)/2 = 0$, in other words, the parallel mechanism in the paper has a constraint condition with $x = 0$, so the work space in the paper degenerates from two-dimensional area to one-dimensional interval along y-axis.

To prevent confusion, the work space in the paper is specifically defined as an interval along y-axis. So, the work space has certain length, the length of the work space is actually the length of interval.

4 Optimal Design to the Parallel Mechanism

4.1 The Definition of GSI

In the operational coordinate space, the relationship between the output displacement vector and the operational force of the planar or spatial mechanism is given in Eq. (4), with consideration of the active joint elasticity by Gosselin [11]. In the operational coordinate space, there is

$$\delta x = (J^T K_J J) F = M F \tag{4}$$

where δx and F are the operational force vector and the output displacement vector, respectively, $K_J = \text{diag}(k_1, k_2, \dots, k_n)$ is active joint stiffness diagonal matrix, J is Jacobi matrix, $M = J^T K_J J$ is stiffness matrix of mechanism.

Supposing that $\|F_2\| = 1$, $\|\delta x_2\|$, i.e., the length of output displacement vector δx , which reflects the degree of terminal deformation of one pose, is not greater than $\max(\sqrt{\text{eigenvalue}(M^T M)})$ or the square root of maximum eigenvalue of $M^T M$ by

$$\|\delta x\|_2 = \|M F\|_2 \leq \|M\|_2 \|F\|_2 = \|M\|_2 = \max\left(\sqrt{\text{eigenvalue}(M^T M)}\right) = D \tag{5}$$

where $\|\cdot\|_2$ is 2-norm of vector or matrices.

D is a local index that reflects the degree of terminal deformation in one pose. In the parallel mechanism of Fig. 3, there is Eq. (6) induced by Eqs. (3) and (5).

$$D = \begin{cases} \frac{1}{2}k & y > \frac{\sqrt{2}L}{2} \\ \frac{(L^2 - y^2)k}{2y^2} & y \leq \frac{\sqrt{2}L}{2} \end{cases} \tag{6}$$

where $k_1 = k_2 = k$ is active joint stiffness coefficient and D is only related to variable y .

In order to reflect the average degree of terminal deformation in the work space, η_D , which denotes average value of D , is defined as Global Stiffness Index(GSI), expressed by

$$GSI = \eta_D \tag{7}$$

η_D , as average value of D in work space of (y_2, y_1) , can be expressed by

$$\eta_D = \frac{\int_{y_2}^{\frac{\sqrt{2}L}{2}} \frac{(L^2 - y^2)k}{2y^2} dy + \int_{\frac{\sqrt{2}L}{2}}^{y_1} \frac{1}{2} k dy}{y_1 - y_2} \tag{8}$$

4.2 The Optimization of Dimensionless Work Space

It's known that the reciprocal of the condition number of the Jacobian matrix of parallel mechanism can be used to evaluate singularity [1, 5, 6], control deformation [1, 6, 8–10], dexterity [6–9], it must be kept as large as possible. Since that, the condition number of the Jacobian matrix of parallel mechanism may be kept within certain value. Moreover, the condition number of matrix is mathematically used in numerical analysis to estimate the error generated in the solution of a linear system of equations by the error on the data [12], therefore, condition number of the Jacobian matrix of parallel mechanism should also be less than one Upper Limit.

Assume that condition number of the Jacobian matrix of parallel mechanism $\kappa = \|J\| \|J^{-1}\|$, where $\|\cdot\|$ denotes the Euclidean norm of the matrix, which is defined with $\|J\| = \sqrt{\frac{1}{2}tr(J^T J)}$.

To the parallel mechanism in the paper, the condition number of Jacobian matrix is induced to Eq. (9) with Eq. (3).

$$\kappa = \frac{L^2}{2y\sqrt{L^2 - y^2}} \tag{9}$$

Supposing Upper Limit of the condition number of the Jacobian matrix is κ_0 , y_1 and y_2 of the work space along y-axis axis can be resolved with Eq. (10) by Eq. (9).

$$\begin{cases} y_1 = y_{1_B}L = \frac{L}{\sqrt{2\kappa_0}} \sqrt{\kappa_0 + \sqrt{\kappa_0^2 - 1}} \\ y_2 = y_{2_B}L = \frac{L}{\sqrt{2\kappa_0}} \sqrt{\kappa_0 - \sqrt{\kappa_0^2 - 1}} \end{cases} \tag{10}$$

where $\begin{cases} y_{1_B} = \frac{1}{\sqrt{2\kappa_0}} \sqrt{\kappa_0 + \sqrt{\kappa_0^2 - 1}} \\ y_{2_B} = \frac{1}{\sqrt{2\kappa_0}} \sqrt{\kappa_0 - \sqrt{\kappa_0^2 - 1}} \end{cases}$.

As $y \in (y_2, y_1)$, $\kappa \leq \kappa_0$. Obviously, $\kappa_0 > 1$ and $\begin{cases} y_1 < \frac{\sqrt{2}}{2}L \\ y_2 > \frac{\sqrt{2}}{2}L \end{cases}$.

Though $\kappa \leq \kappa_0$ in the work space (y_{2_LAC}, y_{1_LAC}) , D can still too big to accept. For this reason, Maximum Tolerated Deformation, denoted as σ_{max} , is used as an indicator in the paper. The work space that $D > \sigma_{max}$ cannot be accepted as a part of the work space of (y_2, y_1) . In other words, the work space of $y < \sqrt{\frac{1}{\frac{2\sigma_{max}}{k} + 1}}L$ resolved by Eq. (11) should be removed from (y_2, y_1) .

$$\frac{(L^2 - y^2)k}{2y^2} > \sigma_{max} \tag{11}$$

For the work space that satisfies $\kappa \leq \kappa_0$ and $D < \sigma_{max}$ is $\left(\sqrt{\frac{1}{2\sigma_{max}^k + 1}}L, y_1 \right)$, there is

$$\eta_D = \frac{\int_{y_1}^{y_1} \sqrt{\frac{1}{2\sigma_{max}^k + 1}}L Ddy}{y_1 - \sqrt{\frac{1}{2\sigma_{max}^k + 1}}L} = \frac{\int_{\frac{\sqrt{2}L}{2}}^{\frac{\sqrt{2}L}{2}} \frac{(L^2 - y^2)k}{2y^2} dy + \int_{\frac{\sqrt{2}L}{2}}^{y_1} \frac{k}{2} dy}{y_1 - \sqrt{\frac{1}{2\sigma_{max}^k + 1}}L} \tag{12}$$

Supposing $\alpha = \sqrt{\frac{1}{2\sigma_{max}^k + 1}}$, there is

$$\eta_D = \frac{1}{2}k - \frac{\sqrt{2\kappa_0}(\alpha - \sqrt{2} + \frac{1}{2\alpha})}{\alpha\sqrt{2\kappa_0} - \sqrt{\kappa_0 + \sqrt{\kappa_0 + \sqrt{\kappa_0^2 - 1}}}} \tag{13}$$

From Eq. (13), η_D is independent of actual length L , so link length L can be assumed as an dimensionless unity, i.e., $L = 1$.

Supposing Global Stiffness Index (*GSI*) of the parallel mechanism in the paper is satisfied with Eq. (14), η_D needs to be satisfied with $\eta_D < \zeta$.

$$GSI < \zeta \tag{14}$$

If σ_{max} is given, α is achieved. Supposing $\eta_D = \zeta$, Upper Limit κ_0 can be resolved by Eq. (13), and then dimensionless work space (α, y_{1_B}) and dimensionless work space length along y-axis $|\alpha - y_{1_B}|$ is determined. In dimensionless work space (α, y_{1_B}) , $\eta_D < \zeta$, $D < \sigma_{max}$ and $\kappa \leq \kappa_0$.

4.3 Determination of Link Length of the Parallel Mechanism

From Sect. 4.2, it is easy to know that the actual work space that satisfies $\eta_D < \zeta$, $D < \sigma_{max}$ and $\kappa \leq \kappa_0$ is $(\alpha, y_{1_B})L$, and thus work space length is $|\alpha - y_{1_B}|L$, provided with the link length is L .

Provided that actual work space length is G , there is

$$G = |\alpha - y_{1_B}|L \tag{15}$$

Therefore, the optimal design formula to L is

$$L = \frac{G}{|\alpha - y_{1_B}|} \tag{16}$$

5 Optimal Design Results and Verification

In the parallel mechanism, active joint stiffness $k = 1.6 \times 10^{-5}$ mm/N. Based on the design requirement of mechanism tolerated deformation $\sigma_{max} = 2.45 \times 10^{-5}$ mm/N, $\alpha = 0.496$.

Based on the design requirement of $\eta_D < 1.38 \times 10^{-5}$ mm/N, Upper Limit of the condition number of the Jacobian matrix $\kappa_0 = 1.2750 < 2.0$ according to Eq. (13). With the value of $\kappa_0, y_{1_B} = 0.9, |\alpha - y_{1_B}| = 0.404$, the optimal design length L is 495 mm by Eq. (16) with task work space (245.52, 445.52) mm. By Eq. (1) and the constraint condition with $x = 0$, active joint coordinate $D_1 : x_1 \in (215.72, 429.82)$ mm, active joint coordinate $D_2 : x_2 \in (-429.82, -215.72)$ mm.

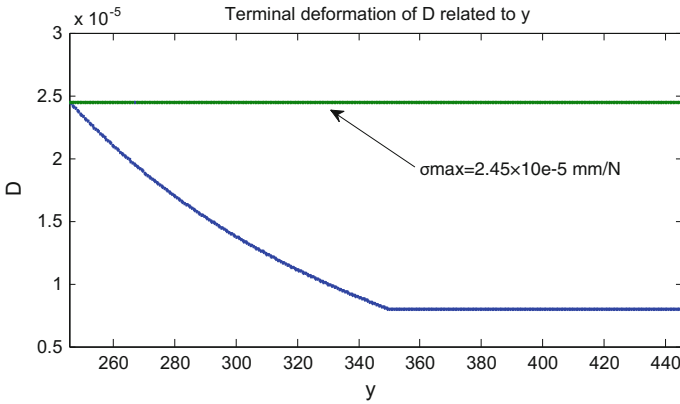


Fig. 4 Curve of the terminal deformation

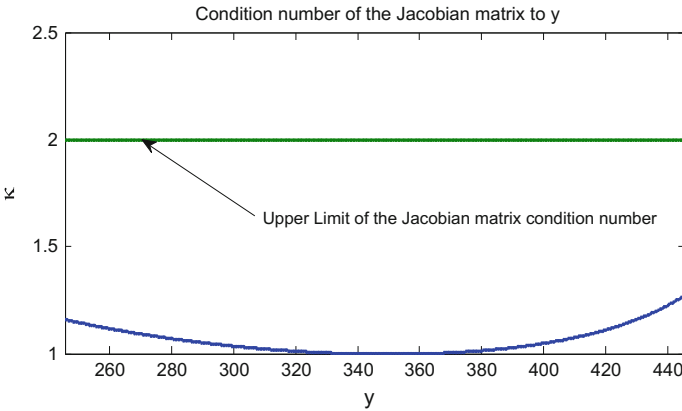


Fig. 5 Curves of Jacobian matrix condition number



Fig. 6 Electro-coating conveyor with two same parallel mechanisms

There will be some verification as follows. Bringing task work space (245.52, 445.52) mm into Eqs. (6) and (9), respectively, one will make two curves of the D and κ with use of matlab simulation in Figs. 4 and 5. From Figs. 4 and 5, one can see that $D < 2.45 \times 10^{-5}$ mm/N and $\kappa < 2.0$. Bring task work space (245.52, 445.52) mm into Eq. (8), one obtains $\eta_D = 1.16 \times 10^{-5}$ mm/N $< 1.38 \times 10^{-5}$ mm/N.

The verifications show that the optimal design to parallel mechanism is in accord with design requirements.

Optimal design results are used to develop a prototype of electro-coating conveyor with two same parallel mechanisms in Fig. 6, which will be use for further research.

6 Conclusions

In order to meet terminal deformation requirements in parallel mechanism, Global Stiffness Index, combined with Upper Limit of condition number of Jacobi matrix and maximum tolerated deformation is defined in the paper. Dimensionless work space of the parallel mechanism is optimized based on the GSI, combined with the Upper Limit of the Jacobian matrix condition number and Maximum Tolerated Deformation. Optimal link length of parallel mechanism is obtained with real length of work space divided by the dimensionless length of work space. Optimal design results of the parallel mechanism are computed with design requirements of parallel mechanism for automobile electro-coating conveyor. The simulation verifications show that the optimal design to parallel mechanism is in accord with design requirements. The design results are used to develop a prototype for following control research.

Acknowledgments This work was financially supported by the National Natural Science Foundation of China (Grant No. 51375210), the Priority Academic Program Development of Jiangsu Higher Education Institutions, Zhenjiang Municipal Industry Key Technology R&D Program (Grant No. GY2013062), Science and Technology Program of Jingkou, Zhenjiang, China (Grant No. jkGY2013002), and Graduate innovation program of Jiangsu Province (Grant No. CXLX13_667).

References

1. Kim HS, Tsai LW (2003) Design optimization of a cartesian parallel mechanism. *ASME J Mech Des* 125(1):43–51
2. Xu Q, Li Y (2006) GA-based architecture optimization of a 3-PUU parallel mechanism for stiffness performance. In: Proceedings of the 6th world congress on intelligent control and automation, Dalian, China, 2006, pp 9099–9103
3. Xu Q, Li Y (2006) Stiffness optimization of a 3-DOF parallel kinematic machine using particle swarm optimization. In: Proceedings of the 2006 IEEE international conference on robotics and biomimetics, Kunming, China, pp 1169–1174
4. Zhang D, Gosselin CM (2002) Kinestostatic analysis and design optimization of the Tricept machine tool family. *ASME J Manuf Sci Eng* 124:725–733
5. Gosselin CM, Angeles J (1989) The optimum kinematic design of a spherical three degree-of-freedom parallel mechanism. *ASME J Mech Transm Autom Des* 111:202–207
6. Arsenault M, Boudreau R (2006) Synthesis of planar parallel mechanisms while considering workspace, dexterity, stiffness and singularity avoidance. *ASME J Mech Des* 128:69–78
7. Gosselin CM (1992) The optimum design of robotic mechanisms using dexterity indices. *Rob Autom Syst* 9:213–226
8. Stoughton RS, Arai T (1993) A modified stewart platform mechanism with improved dexterity. *IEEE Trans Rob Autom* 9(2):166–173
9. Carretero JA et al (2000) Kinematic analysis and optimization of a new three degree-of-freedom spatial parallel mechanism. *ASME J Mech Des* 122:17–24
10. Ryu J, Cha J (2001) Optimal architecture design of parallel mechanisms for best deformation. In: Proceedings of 2001 IEEE/RSJ international conference on intelligence robots and systems, Mani, IEEE, New York, pp 1281–1286
11. Gosselin CM (1990) Stiffness mapping for parallel mechanism. *IEEE Trans Robot Autom* 6 (3):377–382
12. Strang G (1976) *Linear algebra and its application*. Academic Press, New York

Design and Simulation of a Dual-Piezo-Driven Actuator Utilizing the Bridge-Type Mechanism

Junyang Wei, Xianmin Zhang and Sergej Fatikow

Abstract In this paper, a dual-piezo-driven actuator with a configuration based on the bridge-type amplification mechanism is presented. The configuration should enable the actuator to be driven with diverse friction drive principles for operations under different conditions. Numerical simulations of the actuator based on a basic mathematical model applying the DTC-MRD friction model, and the FEA of the bridge-type mechanism deformation are carried out for analyzing the feasibility of the design.

Keywords Actuator · Friction drive · Compliant mechanism · Dual piezo

1 Introduction

With the development of microsystem technology and nanotechnology, research topics in the field of nanohandling have drawn more and more attention of the industry and research institutes in recent decades. Among several nanohandling approaches [1], top-down approach is one that utilizes precision positioning systems and their manipulation tools to physically achieve handling goals. To ensure the high performance of top-down nanohandling approach's process, the actuation of the positioning systems is not trivial. Applying piezoelectric actuators has

J. Wei (✉) · S. Fatikow

Division Microrobotics and Control Engineering, University of Oldenburg,
26129 Oldenburg, Germany
e-mail: junyang.wei@uni-oldenburg.de

S. Fatikow

e-mail: sergej.fatikow@uni-oldenburg.de

X. Zhang · S. Fatikow

Guangdong Provincial Key Laboratory of Precision Equipment
and Manufacture Technology, South China University of Technology,
510641 Guangzhou, People's Republic of China
e-mail: zhangxm@scut.edu.cn

© Springer Nature Singapore Pte Ltd. 2017

X. Zhang et al. (eds.), *Mechanism and Machine Science*,

Lecture Notes in Electrical Engineering 408,

DOI 10.1007/978-981-10-2875-5_111

become one of the trends due to the benefits of compact size, high dynamics, high accuracy and large output force. However, because of the limited elongation of the piezoelectric effect (around 0.1 %), special methods are usually applied for achieving cross-scale movement with high positioning accuracy.

One commonly known method is applying the friction-drive principles, which could be further divided into different types such as the Stick-slip-drive principle, the Inchworm-drive principle and the Ultrasonic-drive principle. A positioning system with high precision, high speed, high force, cross-scale working range and miniaturization is an ambitious vision. Yet, it is a common sense that such requirements cannot be satisfied simultaneously by applying one single actuation principle, as actuators based on different principles have different driving properties. Thus, they are generally tailored for different applications.

The Stick-slip-drive actuator as an example, has the advantages of simple structure, simple control, high actuation speed and high positioning resolution. However, the output force capability of stick-slip drive, usually within the range of single-digit Newton, is far from efficient for some applications. On the contrary, the inchworm actuator is especially suited for high-force-required situations, yet it has drawbacks of low speed and low working frequency, due to a relatively complex structure. Thus, applications that require operations under different conditions such as high actuation speed and high output force, pose challenges for the actuator design.

Concerning this issue, an actuator with a special configuration for applying different actuation principles would be a potential solution. The key to the configuration is the feasibility of changing the normal preload force of the contact surfaces and the guarantee of horizontal movement generation. In [2] a so-called “pull-push” actuator is proposed, enabling two degrees of freedom within the same bulk material. The actuator is able to function in Stick-slip mode and ultrasonic mode [3]. The PiezoWalk linear motor from Physik Instrumente uses piezoelectric actuators in groups to generate walking-like feed movement, producing feed forces up to 600 N at 2 mm/s as claimed [4]. Besides of changing the configuration of piezoelectric material itself, it is also of interest to introduce mechanism into actuators, as it diversifies greatly the actuation movements. A piezoelectric linear motor developed in [5] reaches high linear forces up to 2000 N at a speed of 1 mm/s, with the help of an axis clamping system. The authors in [6] take advantage of parallelogram-type flexure hinge mechanism to generate lateral motion. The maximum output force is 3.43 N while the maximum speed 14.25 mm/s.

Based on the state of the art evaluation, a dual-piezo-driven configuration utilizing bridge-type amplification mechanism is considered for development of a novel actuator that is capable of applying different actuation principles. In the scope of this paper, the basic principle of the actuator will be described and simulations focusing on its feasibility will be carried out based on the mathematical model.

2 Actuator Configuration

2.1 Configuration Analysis

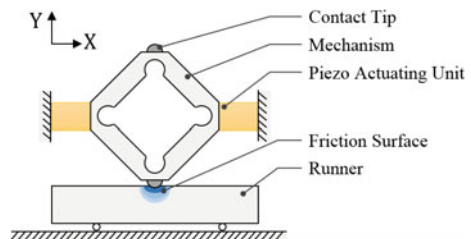
As shown in Fig. 1, the actuator mainly consists of a runner and one or more driving components. Each driving component includes two actuating units, i.e. piezoelectric stacks, and a symmetrical bridge-type amplification mechanism which is in the form of compliant mechanism corresponding to the piezoelectric stacks. Controlling of the elongations of the two actuating units determines the movement of the driving points, i.e. the contact tips. The runner driven by the driving component with the contact tips, produces the output of the actuator in the X-axis direction. Both contact tips in one driving unit engage in the actuation simultaneously. Such configuration guarantees the driving component is under force balance in the Y-axis direction with forces only from the runner. This means that no shear force is implied on the grounded end of the component, which is important to avoid potential damage to the piezoelectric stacks.

As known, applying bridge-type mechanism for multi-DoFs movement is no secret in the field of precision positioning. Their purpose is usually either providing a preload to the piezoelectric stack or amplifying the output displacement. In most cases the mechanism is actuated with an actuating unit embedded in the center of it and next connected with other actuators. Compared to that, the configuration proposed has the following benefits:

(a) Avoidance of asymmetric bidirectional output property

For devices utilizing compliant mechanism and piezoelectric stack, asymmetric bidirectional output property is an issue. The reason to this issue, on one hand, is because of the nonlinear property of the piezoelectric stack due to the bonding material, e.g. glue. This factor reduces the stiffness of the stack especially when a tensile force is applied. On the other hand, a compliant mechanism is an elastic potential energy storage element. It respectively does negative and positive work while the piezoelectric stack elongates and contracts, which varies the bidirectional output property. Benefited from the symmetric structure, the proposed configuration theoretically counteracts the factors mentioned above.

Fig. 1 Schematic of the actuator. Only one side of the runner is illustrated. The actual runner has contact with both of the contact tips on the bridge-type mechanism



(b) Improved stiffness

The configuration in essence is a parallel mechanism, which reduces the inertia of the mechanism and improve the dynamic property. Also, the configuration can be regarded as a simple support beam structure, which means higher stiffness of the structure and leads to higher driving frequency, i.e. higher output speed of the actuator.

2.2 Actuation Principles

As mentioned in Sect. 1, the actuator is able to apply different actuation principles. The operations will be presented in the following.

(a) Stick-slip-drive principle

As shown in Fig. 2a, to start up, one of the actuating units elongates until certain indentation depth on the contact surface is reached to provide a suitable preload. Then both actuating units are energized slowly and simultaneously, with one elongating and the other contracting. This causes the compliant mechanism to move forwards horizontally while maintaining its deformation, i.e. the preload, unchanged. Consequently, the runner moves with the contact tip due to the friction, known as the “stick” phase. Next, the compliant mechanism moves backwards with a same operation except the actuating units are energized sharply. Due to that, the runner

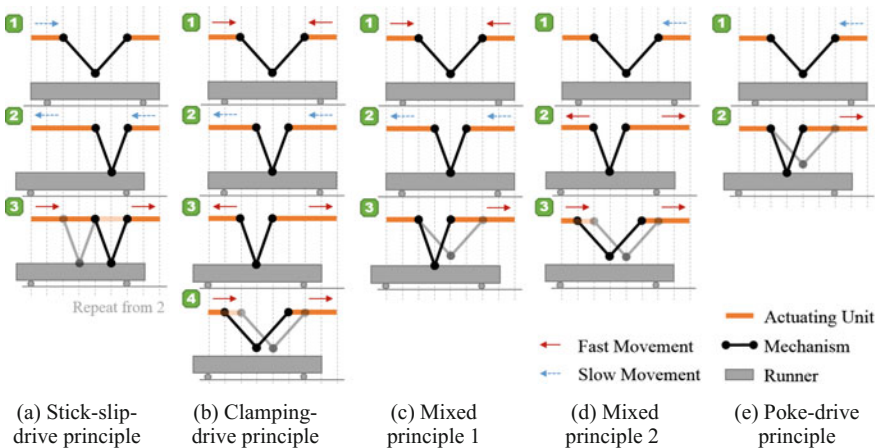


Fig. 2 Diagram of the different actuation principles in single cycle. The numbers represent the operation sequence. Only one half of the mechanism is illustrated for simplicity in the diagram. The initial place of the contact tip is assumed to be slightly above the contact surface without preload

could not follow the quick movement because of the inertia force. This is known as the “slip” phase. Via this operation cycle, a net movement of the runner is then generated and by repeating the continuous output displacement is achieved.

(b) “Clamping-drive” principle

The actuation starts with clamping the runner, as both actuating units elongate towards each other and cause a high normal force on the surface to hold the runner. After clamping, the compliant mechanism and the runner are driven forwards as the same operation in the “stick” phase of the Stick-slip drive. Finally, the actuating units contract in inverse direction to release the runner and then the compliant mechanism is driven back to the original position. The operation cycle is demonstrated in Fig. 2b. With two driving components operating this principle in turns, the Inchworm-drive principle is achieved.

(c) “Poke-drive” principle

When only one actuating unit elongates, the contact tip will be driven both horizontally and vertically, which “pokes” the runner forwards. This principle is also defined as the “IFc type” in [7]. Regarding the proposed configuration, the operation of this drive principle is the simplest (Fig. 2e).

(d) Other drive principles

As shown in Fig. 2c, d, it would be of interest to explore drive principles mixed by the former principles. In essence, the driving component is a 2-DoFs mechanism, which should theoretically generate arbitrary movement track within its working space, e.g. an elliptical movement track to perform a quasi-ultrasonic actuation. For this purpose, the kinematic model would be helpful to further investigate the potential capabilities of this actuator.

3 Mathematical Modelling

The proposed actuator can be regarded as a nonlinear dynamical systems, considering the issues of hysteresis and creep of the piezoelectric material, the nonlinear deformation of the compliant mechanism, the friction on the contact surface and so on. Such a complex system would pose great challenge to the modelling. Hence, it is reasonable to develop a model from scratch for exploratory study. In this paper, the proposed actuator is simplified into a basic mathematical model that is separated into three portions. The model is based on the following assumptions:

- (a) The input displacements of the piezoelectric material are ideal. Nonlinear factors are not involved. The input forces of the piezoelectric material are always large enough.

- (b) Dynamic properties of both the piezoelectric material and the compliant mechanism are omitted. Only the kinematic model of the driving component is considered.
- (c) The contact tips are absolutely rigid and the surfaces of the runner in contact are elastic continuums.

3.1 Model of the Driving Component

Adopting the pseudo-rigid-body theory [8], from the bridge-type mechanism geometry yields the equations of the forward kinematic model of the driving component:

$$X_{p1} = X_{p2} = \frac{1}{2}X_A + \frac{1}{2}X_B \tag{1}$$

$$Y_{p1} = -Y_{p2} = L \left[\sqrt{1 - \left(\frac{X_B - X_A}{2L} + \cos \theta_0 \right)^2} - \sin \theta_0 \right] \tag{2}$$

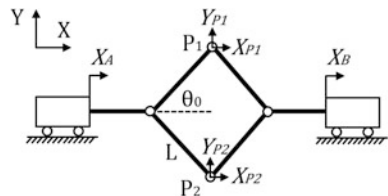
Equations (1) and (2) then yield the equations of the inverse kinematic model, which are:

$$X_A = X_{p1} + L \cos \theta_0 - \sqrt{L^2 - (Y_{p1} + L \sin \theta_0)^2} \tag{3}$$

$$X_B = X_{p1} - L \cos \theta_0 + \sqrt{L^2 - (Y_{p1} + L \sin \theta_0)^2} \tag{4}$$

Where X_A and X_B are the input displacements, X_{p1} , Y_{p1} , X_{p2} , Y_{p2} , are the movements of the two contact tips P_1 , P_2 in X and Y axis separately. L represents the lengths of the four bars of the bridge-type mechanism and θ_0 is the initial angle between the bar and the X axis. The schematic is illustrated in Fig. 3.

Fig. 3 Schematic of the driving component



3.2 Friction Model

Friction modelling is one key portion for establishing a convincing mathematical model. From the well-known Coulombs friction model to Dahl model [9], LuGre model [10], elastoplastic model [11], etc., detail aspects of the friction phenomenon are gradually represented as the friction models are being improved. Still, these models do not consider the geometry in the micro scale on the friction surface, which involves contact theories.

For the proposed actuator, micro-scale details should not be ignored as the displacement of the indentation on the surface as preload is unneglectable compared to the displacement range of the driving component. Therefore, a DTC-MRD model (Dynamic Tangential Contact model based on the Method of Reduction of Dimensionality) [12], is adopted for the modelling of the actuator.

According to the Hertz's theory, the normal force produced by a rigid sphere that is indented into an elastic half-space is given by:

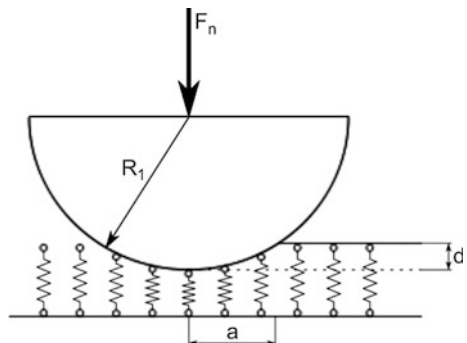
$$F_n = \frac{4}{3} E_e R^{0.5} d^{1.5} \tag{5}$$

where E_e is the effective Young's modulus, R is the sphere radius and d is the indentation depth. Concerning the applied tangential force, the contact region $a = \sqrt{Rd}$, could be further divided into a stick region and a slip region with the separation circle with a radius c . Here the friction is considered as the Coulombs friction. In the stick region, the friction force remains static friction force and in the slip region the friction is assumed as the kinetic friction. When $c = 0$ the sphere is about to slip, with a maximal tangential displacement given by:

$$u_{max} = \frac{3\mu F_n}{4G_e a} \tag{6}$$

where μ is the friction coefficient and G_e is the effective shear modulus. Applying the method of reduction of dimensionality [13], the 3D contact could be mapped to a one dimensional contact with equivalent springs as shown in Fig. 4. The normal

Fig. 4 Schematic of the method of reduction of dimensionality [12]



stiffness Δk_z and the tangential stiffness Δk_x of each spring, of which the distance between each other is Δx , are defined as:

$$\Delta k_z = E_e \Delta x, \Delta k_x = G_e \Delta x \quad (7)$$

With the displacement input from the driving component, friction force F_f is generated by summing up the force of each spring.

3.3 Dynamic Model of the Runner

The DoF of the runner is restricted in one direction, with displacement X . The runner is simplified into a simple mass M , with the friction force F_f between one contact tip and the runner. The number of the contact tips is n . For force estimation, a spring with stiffness K is added to represent the external load for the system. One end of the spring is fixed on the ground and the other on the runner. The schematic is shown in Fig. 5. Based on the Newton's second law, we have:

$$M\ddot{X} = nF_f - KX \quad (8)$$

4 Simulation and Analysis

In this section, a case study of the actuator will be simulated and analyzed. Figure 6 shows the CAD model of an early prototype design. Based on the design, the dimensions and the physical parameters of the mathematical model for the actuator are set as in Table 1:

4.1 FEA Verification of the Model of the Driving Component

Figure 7 shows a FEA (Finite Element Analysis) result of the bridge-type mechanism deformation. As the stiffness of the piezoelectric stack is assumed to be infinite, an input displacement series within the input displacement range is applied vertically on the left side face of the mechanism directly. The face on the opposite

Fig. 5 Abstracted model of the runner. For displacement estimation of the actuator, $K = 0$

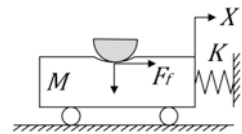


Fig. 6 Prototype design

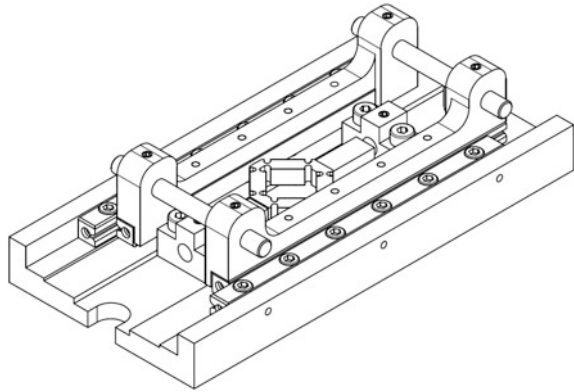


Table 1 Parameter values for simulation of the mathematical model

Parameter	Value	Unit
Initial angle	$\pi/4$	rad
Equivalent bar-length of the mechanism	7.6	mm
Input displacement range	0–8	μm
Radius of the contact tips	0.5	mm
Young’s modulus of the contact tips	345	Gpa
Poisson’s ratio of the contact tips	0.3	/
Young’s modulus of the runner surface	69	Gpa
Poisson’s ratio of the runner surface	0.35	/
Friction coefficient	0.3	/
Mass of the runner	5	g

side is fixed. Then, in another scenario two forces are applied on the output ends to represent the normal reactive forces from the runner. The values of the forces are calculated via Eq. (5) using the simulated output displacements from the former scenario. These results are shown in Table 2, compared with the kinematic model. As can be seen, results from both scenarios fits the mathematical model decently (6, 8 %). Notice that the vertical displacement error of Scenario 2 is relatively high, which implies in reality the vertical displacement is not likely to be precise as expected due to the limited stiffness of the compliant mechanism.

A modal analysis of the bridge-type mechanism is also applied, indicating the first resonate frequency of 21131.5 Hz. This should guarantee that the actuator is capable of functioning under actuation signal at hundreds’ frequency without exciting the resonance that could undermine the performance.

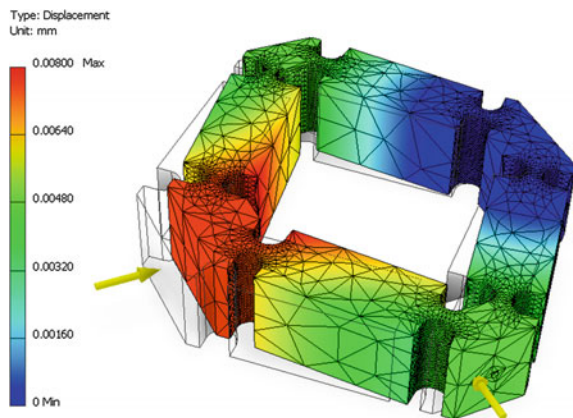


Fig. 7 Deformation result with an 8 μm input

Table 2 Comparison of FEA results and the model values

Input	Model	Scenario 1		Scenario 2	
Value (μm)	Value (μm)	Value (μm)	Relative error (%)	Value (μm)	Relative error (%)
(1, 0)	(0.5, 0.5)	(0.486, 0.482)	3.19	(0.481, 0.467)	5.17
(2, 0)	(1.0, 1.0)	(0.943, 0.936)	6.05	(0.956, 0.922)	6.08
(3, 0)	(1.5, 1.5)	(1.415, 1.404)	6.03	(1.425, 1.366)	6.95
(4, 0)	(2.0, 2.0)	(1.887, 1.872)	6.02	(1.895, 1.809)	7.38
(5, 0)	(2.5, 2.5)	(2.359, 2.340)	6.02	(2.374, 2.255)	7.39
(6, 0)	(3.0, 3.0)	(2.830, 2.808)	6.03	(2.867, 2.715)	6.93
(7, 0)	(3.5, 3.5)	(3.302, 3.275)	6.04	(3.325, 3.135)	7.67
(8, 0)	(4.0, 4.0)	(3.774, 3.743)	6.04	(3.801, 3.572)	7.79

4.2 Numerical Simulation of the Actuator

The simulation of the mathematical model of the actuator is carried out in Matlab/Simulink. Actuation signals with a frequency at 250 Hz, a slop rate of 50 mm/s are chosen.

Concerning the output force performance, Fig. 8 shows a typical Stick-slip-drive displacement curve with external load from the spring. Net movements of the Stick-slip drive and the micro residual vibration phenomenon are well reflected. As the output displacement increases, the external load accordingly increases until it reaches a force balance status with the maximum output force of the actuator. Thus, the actuator is blocked from driving further. The simulation applying

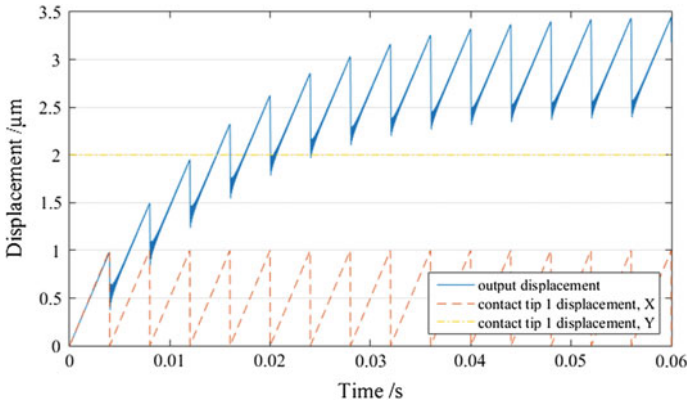


Fig. 8 Displacement curve of the stick-slip drive

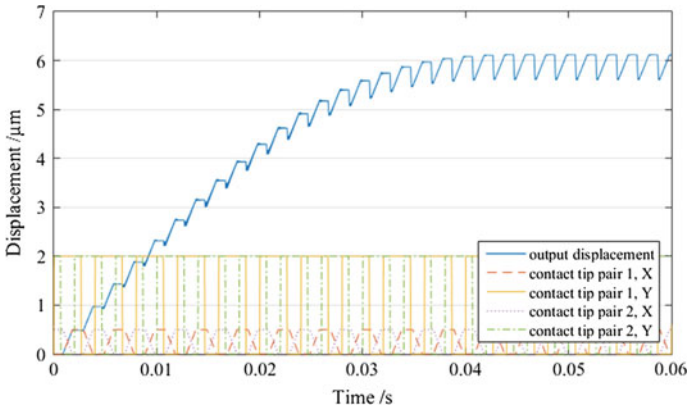


Fig. 9 Displacement curve of the inchworm drive

inchworm-drive principle exhibits a similar displacement curve trend, as shown in Fig. 9.

Both simulations are applied with the same maximum indentation depth of the contact tips. Their total actuation amplitude per period and the numbers of the each's contact tips are also equal (in inchworm-drive partly doubled).

It is obvious that the output force capacity of the inchworm drive principle overwhelms the one of the Stick-slip drive. The increase of the friction force by either changing the number of contact tips (Fig. 10a) or increasing the indentation depth does enhance well the output force of inchworm drive. However, for Stick-slip drive it is not necessary a plus effect. Focusing on output force generation, given an indentation depth of 5 μm and the contact tips number of two, an

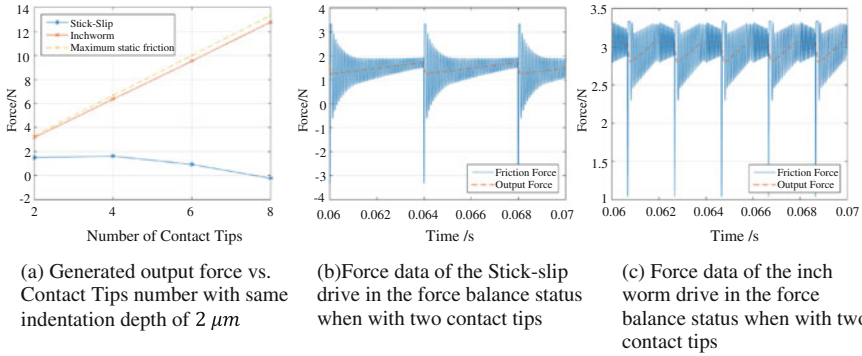


Fig. 10 Output force tendency regarding different contact tips number, with example force data

output force of 11.15 N can be obtained theoretically applying the Inchworm-drive principle (Higher output force is also achievable).

Regarding the speed performance, an indentation depth of $0.25\ \mu\text{m}$ and an actuation signal with an amplitude of $8\ \mu\text{m}$ which is the maximum distance in the X-axis direction in the mechanism workspace, are considered. An output speed of 1.78 mm/s is achieved applying the Stick-slip-drive principle by simulation consequently. Simulation with higher actuation frequencies leads to higher output speeds in the results, despite of factors that would possibly weaken the speed performance in reality.

Simulation of the “Poke-drive” principle is also carried out. With an input amplitude of $2\ \mu\text{m}$, the actuator generates an output speed of 0.10 mm/s, which is lower than the one of the Stick-slip drive under same input amplitude. According to the model, the reason is that the friction force generated at the beginning of the stick phase is very small, which leads to slow deceleration the backlash movement of the runner (compared to the Stick-slip drive) and cause a smaller net movement.

5 Conclusion and Outlook

This paper presents a dual-piezo-driven actuator with a configuration based on the bridge-type amplification mechanism. A mathematical model adopting the DTC-MRD model is developed. In the case study, the FEA results of the compliant mechanism agree with the kinematic model with relative errors less than 8%, which means the contact tips should be able to perform in movement tracks decently as expected. The actuator should be able to realize an output force of 11.15 N in inchworm mode and an output speed of 1.78 mm/s in theory as an example, which demonstrates the idea that the proposed configuration is capable to function utilizing different driving principles and hence would be suitable for

application that required operation under diverse conditions such as high actuation speed and high output force.

In the future, prototype experiments will be carried out to evaluate the conception and more detailed models especially concerning the dynamic character of the driving component would be concerned to further investigate and control the operations. An obvious question is whether the driving component would behave as expected especially under high actuation frequency and high preload. The compromise between the characters of the compliant mechanism (stiffness, geometrical configuration) and the output performance of the actuator is however at the moment not clarified.

Acknowledgments This work has been sponsored by the China Scholarship Council. The authors thank for the support.

References

1. Fatikow S (2007) Automated nanohandling by microrobots. Springer Science & Business Media
2. Bergander A et al (2003) Monolithic piezoelectric push-pull actuators for inertial drives. In: Proceedings of 2003 international symposium on micromechatronics and human science, 2003. MHS 2003. IEEE
3. Breguet J-M et al (2007) Applications of piezo-actuated micro-robots in micro-biology and material science. In: 2007 International conference on mechatronics and automation. IEEE
4. Physik Instrumente Website, <https://www.physikinstrumente.com/>
5. Ferrier N, Markovic M, Perriard Y (2012) Evaluation of an electromechanical clamping system for its integration in a piezoelectric linear motor for the generation of high linear forces. In: 15th international conference on electrical machines and systems
6. Li J et al (2015) Design and experimental performances of a piezoelectric linear actuator by means of lateral motion. Smart materials and structures, pp 1–5
7. Driesen W (2008) Concept, modeling and experimental characterization of the modulated friction inertial drive (MFID) locomotion principle: application to mobile microrobots. Citeseer
8. Howell LL (2001) Compliant mechanisms. Wiley, New York
9. Karnopp D (1985) Computer simulation of stic-slip friction in mechanical dynamical systems. J Dyn Syst Meas Contr 107:420–436
10. De Wit CC et al (1995) A new model for control of systems with friction. IEEE Trans Autom Control 40(3):419–425
11. Dupont P et al (2002) Single state elastoplastic friction models. IEEE Trans Autom Control 47(5):787–792
12. Teidelt E et al (2012) Modeling of the dynamic contact in stick-slip microdrives using the method of reduction of dimensionality. Физическая мезомеханика 15(4)
13. Popov VL (2013) Method of reduction of dimensionality in contact and friction mechanics: a linkage between micro and macro scales. Friction 1(1):41–62

A Novel Method of Fault-Location in Long Power Cable

Jianwei Mi, Ximing Men, Xiaoli Fang and Libin Fan

Abstract In the case of malfunction in power cables, it is feasible to obtain the location information of fault point by using reflection phenomenon of traveling waves occurred during transmission due to the fact that the characteristic impedance of fault point changes. However, the energy attenuation and distortion of traveling waves in fault detection of long power cable become the key influence factors of extracting fault reflection signal, which ultimately affect the measurement accuracy. Therefore, by employing the successive optimized high-frequency pulse signal instead of the single pulse signal used in the traditional testing equipment for the long power cable fault-detection, this paper proposes a signal processing method based on digital non-coherent pulses accumulation to calculate the fault location by accumulating reflected signal. The simulated results show that this method can effectively improve the Signal to Noise Ratio (SNR), threshold detection level of the fault signal, and also enhance the detection capability of the fault location in long power cable.

Keywords Successive high-frequency pulse signal · Pulse accumulation · Fault location · Long power cable

1 Introduction

With the development of economy in China, the long power cable plays an increasingly important role in power transmission. If the fault point can not be quickly and accurately located when the malfunctions occur, there will be not only

J. Mi (✉) · X. Men · X. Fang · L. Fan
Key Laboratory of Electronic Equipment Structure Design,
Ministry of Education of China, Xidian University, No. 2 South Taibai Road,
Xi'an 710071, People's Republic of China
e-mail: jwmi@xidian.edu.cn

© Springer Nature Singapore Pte Ltd. 2017
X. Zhang et al. (eds.), *Mechanism and Machine Science*,
Lecture Notes in Electrical Engineering 408,
DOI 10.1007/978-981-10-2875-5_112

1419

excessive time and financial cost for cable maintenance [1], but also considerable inconvenience to the users and dramatical economic losses to the industry.

At present, the fault location method based on the time-domain characteristics of the fault traveling wave is effective and has found practical engineering applications among the power cable fault location methods [2]. It attracts wide attention since its advent as a result of its advantages in theory, such as the high range accuracy, the high reliability, and the good stability. Its basic principle is that the speed is close to the speed of light when the traveling wave propagates in the cable, and it will also produce the refraction and reflection phenomenon when the waves encounters the fault points or nodes with an mismatched impedance. By recording the launch time and the time when the traveling wave reflects back to the launch point, one can calculate the time difference between the two moments and finally obtain the fault location according to the speed and the running time of the traveling wave [3]. However, when the traveling wave propagates in the power cable, the energy will attenuate exponentially with the increase of transmission distance. On the other hand, the traveling wave will have a serious distortion. These two points described above are the main factors affecting the measurement accuracy of the method. Subsequently, many power researchers committed to the investigation on precise recognition of the reflected wave [4–6], such as filtering out the interference signal by setting the threshold voltage. Typical interference signal is the reflected signal of nodes, but it fails to exclude the clutter signal which has the same magnitude as the fault signal, so it barely filters out the interference signal completely. Furthermore, some scholars eliminate the pulse interference by the correlation method which is analyzing the correlation between the incident signal and the received signal. It is considered as the useful fault signal when the two signals have the similar pulse width. But the actual cable is a lossy transmission line and the reflected wave has a significant distortion compared with the incident wave: the width increases, the correlation of incident wave and reflected wave reduces greatly, so this method has a bigger error for solving problem of the fault location.

Therefore, it is desired to explore a more stable algorithm to improve the solution precision of cable fault location. Then, after the thorough analysis of fault location method based on the time-domain characteristics of the fault traveling wave, one can notice that the single pulse signal is difficult to become the incident wave used for the long power cable fault-detection due to the serious waveform distortion and energy limitation. Therefore, by utilizing the successive high-frequency pulse signal with a certain width instead of the single pulse signal as the incident wave which is used for the long power cable fault-detection, this paper proposes a signal processing method based on digital non-coherent pulses accumulation, which calculates the fault location using the reflected signal's multiple accumulation by means of the digital non-coherent pulses accumulation.

2 Cable Model and Its Refraction and Reflection Characteristics of Traveling Wave

2.1 Mathematical Model of the Cable

The cable equivalent model can be divided into the lumped parameter model and the distributed parameter model. The cable is equivalent to a simple circuit consisting of resistors and other components in the lumped parameter model, which can not express the transient process of the traveling wave on the cable. And the cable is equivalent to a circuit composed of innumerable second-order circuit in series in the distribution model. The model can express the specific transient process and transmission characteristics of traveling wave during transmission according to the different impedance of per unit length of cable, which is more consistent to the actual transmission characteristics of long cables. In addition, it can be divided into the lossy model [7] and the non-destructive model according to the presence of loss in the traveling wave transmission process in distributed cable model. The difference between the two models lies in that the non-destructive model can not express the attenuation characteristics in traveling wave transmission, but it is easy to be analyzed and solved while the lossy model is opposite. Therefore, this paper uses the distributed lossy cable model which is closer to the actual cable to analyze and solve problems, as shown in Fig. 1.

According to Fig. 1, one can get the differential equation of the model, as the Eq. (1).

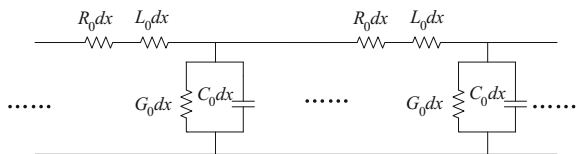
$$\begin{cases} -\frac{\partial u}{\partial x} = R_0 i + L_0 \frac{\partial i}{\partial t} \\ -\frac{\partial i}{\partial t} = G_0 u + C_0 \frac{\partial u}{\partial x} \end{cases} \quad (1)$$

In the equation, u and i are respectively the voltage and current along the cable. R_0, L_0, G_0, C_0 are respectively the original distribution parameters of cable (distributed resistance, distributed inductance, distributed conductance, distributed capacitance).

By simplifying the Eq. (1), one can obtain the steady-state solution shown in the Eq. (2).

$$U_{(x,t)} = U_{(x,t)}^+ + U_{(x,t)}^- = \sqrt{2}U_1^+ e^{-\beta x} \sin(\omega t - \alpha x) + \sqrt{2}U_1^- e^{\beta x} \sin(\omega t + \alpha x + \varphi^-) \quad (2)$$

Fig. 1 The distributed cable model



In the formula, ω is the angular frequency for power supply, U_1^+ and U_1^- are the integral constant, α and β are determined by the Eq. (3).

$$\gamma = \beta + j\alpha = \sqrt{Z_0 Y_0}, \quad Z_0 = R_0 + j\omega L_0, \quad Y_0 = G_0 + j\omega C_0 \quad (3)$$

It can be found by the Eq. (2) that the steady-state solution of the model is composed of two parts which are U_1^+ and U_1^- . U_1^+ is called the forward direction traveling wave and U_1^- is called the reverse traveling wave. This paper only set U_1^+ as an example to study the propagation law of voltage along the transmission line.

The propagation characteristics of traveling wave in the transmission line can be summarized as the propagation speed and the degree of attenuation of wave. Wave propagates with speed v and attenuates exponentially with $e^{-\beta x}$ times in the transmission line. The loss of traveling wave in the cable is determined by the decay constant β .

2.2 The Analysis About the Refraction and Reflection Characteristics of Traveling Wave

If two cables with different characteristic impedance are connected, as shown in Fig. 2, there will be refracted wave U_q and reflected wave U_f when the incident wave passes the connection point. The reflected wave U_f transmits along the opposite direction of the incident wave U_0 , while the refracted wave U_q transmits along the direction of the incident wave U_0 .

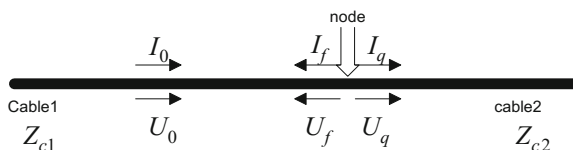
In the Fig. 2, Z_{c1} and Z_{c2} are respectively the characteristic impedance of transmission line 1 and transmission line 2. The calculation formula of the characteristic impedance is Eq. (4).

$$Z_{c1}, Z_{c2} = Z_c = \sqrt{(R_0 + j\omega L_0)/(G_0 + j\omega C_0)} \quad (4)$$

According to Ref. [8], the solution formula of refracted voltage and reflected voltage is shown as Eq. (5).

$$\begin{cases} U_q = \frac{2Z_{c2}}{Z_{c1} + Z_{c2}} U_0 \\ U_f = \frac{Z_{c2} - Z_{c1}}{Z_{c1} + Z_{c2}} U_0 \end{cases} \quad (5)$$

Fig. 2 The refraction and reflection characteristics of traveling wave



Its special circumstances can be summarized as follows:

- (1) When the end of the infinitely long cable breaks, that is to say Z_{c2} is infinite. U_q equals to $2U_0$, and U_f equals to U_0 .
- (2) When the end of the infinitely long cable is short-circuited, that is to say Z_{c2} is zero. U_q equals to zero, and U_f equals to $-U_0$.

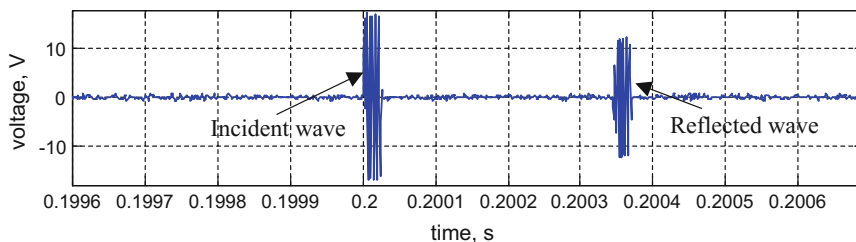
3 Analysis and Optimization of the Incident Signal

3.1 Analysis of the Problems in Single Pulse Signal

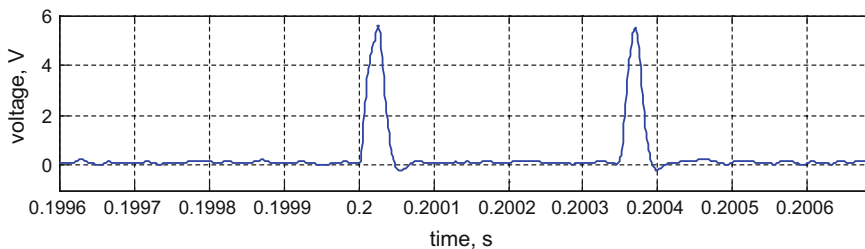
At present, the incident wave is the single pulse signal used in the cable fault detection method based on the time-domain. To shorten the measuring blind area and increase the measurement length, the pulse width is generally 0.2–2 μs [9]. But the voltage amplitude will exponentially attenuate along with the cable length in transmission process and the waveform will have serious distortion. It is difficult to detect the fault traveling wave from the long cable fault. In order to improve the energy of traveling wave, there are two methods can be used. One is to increase the amplitude of the transmitted pulse voltage, but the voltage amplitude can not be increased indefinitely due to the limitation of cable pressure parameters [10] and existing high-voltage pulse generating technologies. The other is to increase the width of transmitted pulse, but it can not reduce the influence of waveform distortion towards fault signal recognition. And too wide pulse width will generate interference between the incident wave and the reflected wave. Therefore, we should seek a more ideal waveform as the incident wave to detect faults in the long cable.

3.2 The Incident Wave of Successive High-Frequency Pulse Signal

Considering the advantages and disadvantages of the single pulse signal as the incident wave in the cable fault location, this paper resolves to use the successive high-frequency pulse signal with a certain width as the incident wave, which consists of a number of positive and negative polarity single pulse signals and has the same energy as the single pulse signal with the same amplitude and pulse width. From the fact mentioned above, the reflected wave will generate pulse signals with different polarity due to different types of faults when the incident wave is the single pulse signal. Similarly, the reflected wave will be the high-frequency signal when the incident wave is the successive high-frequency pulse signal with a certain width. The single pulse signal is difficult to be accurately detected due to waveform



(a) The original reflection waveform



(b) The waveform after envelope detection

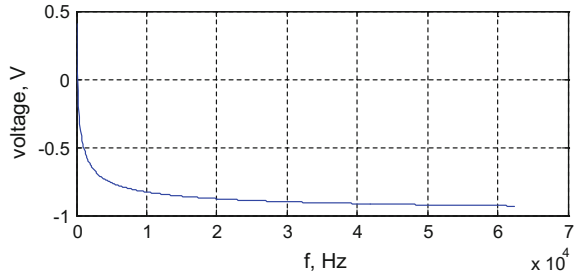
Fig. 3 The reflection waveform of successive high-frequency pulse signal

distortion. But when the reflected wave is the high-frequency signal with a certain width, the signal is composed of multiple single pulse distorted waveforms and there are mutual influences between each single pulse signal. A more inerratic signal can be obtained after the signal is envelope detected. The problem that the waveform is difficult to be detected caused by single pulse distortion can be solved with this method, as shown in Fig. 3. It can be seen from Fig. 3 that the incident wave using the successive high-frequency pulse signal can effectively reduce the influence of waveform distortion towards detecting the reflected wave. In addition, selecting the appropriate width of the incident wave should be considered when using the successive high-frequency pulse signal as the incident wave so as not to generate interference between the incident wave and the reflected wave, but also need to take the energy loss of wave in the transmission process into account.

3.3 The Frequency Optimization of the Successive High-Frequency Pulse Signal

Z_c described in Eq. (4) is the characteristic impedance of cable, which is related to the power frequency ω and increases with the increase of ω . However, in a certain fault condition, Z_{c2} in Eq. (5) is fixed and is the characteristic impedance of the fault point, and Z_{c1} is the characteristic impedance of normal cable. The characteristic impedance Z_{c1} increases with the increase of ω , while the fault point

Fig. 4 The relationship between the reflected voltage and power frequency



impedance Z_{c2} does not change. According to the relationship in Eq. (5), U_0 is set to 1 V and the fault type is a low-resistance fault. Thus, the change trend of the reflected voltage U_f on power frequency can be obtained, as shown in Fig. 4. With the increase of power frequency, the voltage reflection coefficient approaches to -1 , which means a negative total reflection occurs. Therefore, when the power amplitude does not change and frequency increases, the amplitude of the reflected voltage is closer to the power amplitude but has the opposite polarity and its energy is closer to the power energy.

From the propagation constant in Eq. (2), we can know that attenuation coefficient β determines the degree of attenuation of traveling wave with the propagation length, namely the propagation characteristics of traveling wave is: wave propagates with speed v and attenuates exponentially with $e^{-\beta x}$ times in the transmission line. The attenuation coefficient β increases with the increase of the power frequency ω . The value of β hardly changes when ω is less than 20π KHz; the value of β will increase sharply when ω is greater than 20π KHz, and the amplitude attenuation will accelerate [8].

Therefore, it should comprehensively consider the effect of change of power frequency toward the voltage amplitude attenuation and the relationship between the amplitude of the reflected voltage and the amplitude of the incident voltage. Adjusting the frequency of the incident wave to be about 20π KHz is relatively appropriate.

4 Pulse Accumulation Method Used for Fault Detection

4.1 Pulse Accumulation Method

The common solutions are using the Neyman-Pearson criterion in radar signal detection. The specific method is to compare the reflected signal received by radar with a given threshold voltage. When the amplitude of the reflected signal is greater than the threshold voltage, it is considered that the target object is detected. Otherwise, the target does not exist. Obviously, selecting the appropriate threshold voltage can improve the accuracy of detecting target, and the SNR of radar signal

has a great influence on selecting the threshold level. So some scholars proposed to use the pulse accumulation method to improve the SNR, and thus improving the detection accuracy of radar [11].

Similarly, the phenomenon of reflection of cable fault has similarities with radar, so the method of accumulation of multiple pulses can also effectively improve the SNR of reflected wave, and thus the detection accuracy of cable fault is improved. The accumulation can be finished before envelope detection, which is called the predetection integration or intermediate frequency integration. There is strict phase relationship when the signal is accumulated with intermediate frequency integration, that is to say, the signal is coherent and it is also known as the coherent integration [12]. In addition, the accumulation can be carried out after the envelope detection, which is called the post detection integration or the video integration. The accumulation after detection does not need to have strict phase relationship between signals, so it is also known as the non-coherent integration.

The fault reflection pulse signal in the cable is periodic and time-dependent while the noise signal is random and time-irrelevant, so that the accumulation of multiple pulse signals can effectively improve the SNR. Supposing that a reflected signal $R(t)$ is composed of the noise signal $N(t)$ and the fault signal $S(t)$, and the ratio of signal to noise is shown in Eq. (6).

$$\left[\frac{S}{N}\right]_1 = \frac{[S(t)]^2}{E\{[N(t)]^2\}} \tag{6}$$

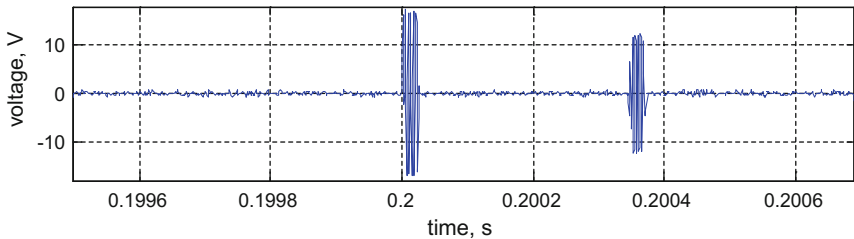
One can get the SNR in Eq. (7) by accumulating the reflected fault waveforms through M times.

$$\begin{aligned} \left[\frac{S}{N}\right]_M &= \frac{[M \times S(t)]^2}{E\left\{\sum_{i=1}^M [N_i(t)]^2\right\}} = \frac{M^2 \times [S(t)]^2}{E\left\{\sum_{i=1}^M [N_i(t)]^2\right\} + E\left[\sum_{i \neq j}^M [N_i(t)][N_j(t)]\right]} \\ &= M \times \left[\frac{S}{N}\right]_1 \end{aligned} \tag{7}$$

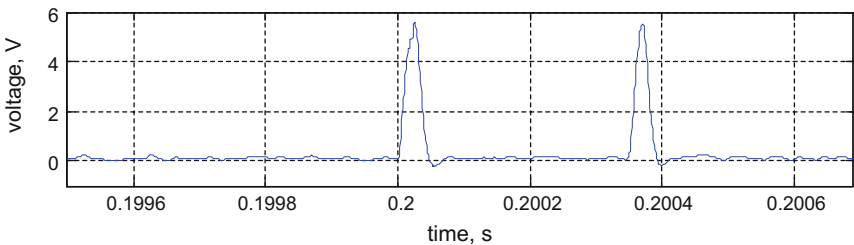
According to the Eq. (7), it can be observed that SNR is improved M times when the fault waveform is accumulated M times. But the SNR obtained by accumulating reflected signals M times after the envelope detection can not reach M times [13]. That is the reason why the non-linear function of envelope detection which increases the interaction between signal and noise and affects the SNR at the output when the reflected signal passes the detector. However, the non-coherent integration does not have the strict requirements of phase parameters and is easier to be implemented in engineering, and it has no requirements for the phase parameters of the reflected wave in fault detection. Therefore, the non-coherent integration after envelope detection is used in this paper.

4.2 Simulation Analysis

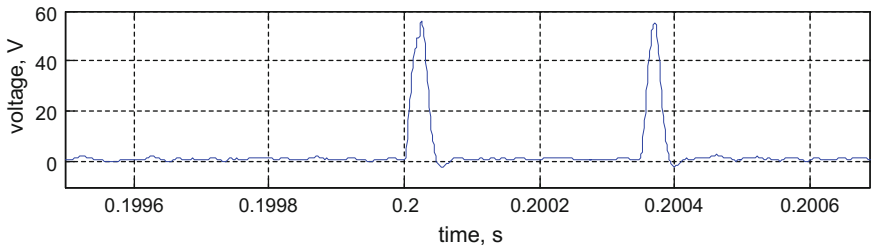
The successive high-frequency pulse signal is used as the incident wave and its width of signal is less than the reflected cycle of the fault wave, so as not to generate interference between the incident wave and reflected wave. A reflected signal will be produced due to impedance mismatch when the incident wave passes the fault point and the signal can form relatively regular wide-pulse signal after the envelope detection in the source. But the reflection signal has a low SNR and a relatively low voltage threshold set, which is difficult to distinguish between the noise signal and the useful fault signal. Therefore, the scheme implemented in this paper is to record and store the reflected signal obtained after the envelope detection. After a while, the successive high-frequency pulse signal is launched once again at the source. And then to record the reflected signal obtained after the envelope detection and to



(a) The original fault reflection waveform



(b) Waveform after the envelope detection



(c) Waveform of the video accumulation by 10 times

Fig. 5 Waveform of pulse accumulation by 10 times

Table 1 The measurement errors of different fault distance

Fault distance (km)	Time between the incident wave and reflected wave (s)	Distance measurement (km)	Measurement error (%)	Measurement error of traditional methods (%)
50	0.000343	49.857	-0.2860	-0.3090
100	0.000691	100.160	0.1605	0.4902
150	0.001036	150.168	0.1121	0.5274
200	0.001381	200.295	0.1475	0.4475
400	0.002761	400.206	0.0515	0.4902

accumulate and store the reflected signal and the reflected signal obtained last time. It needs to perform 10 times circularly as above and superimposes the signals obtained by sampling 10 times, and then a set of reflected waveforms will be got after the pulse is accumulated 10 times. It can be observed that the SNR is significantly improved and the useless interference signal can be filtered out by increasing the voltage threshold. The fault location of faulted cable can be accurately determined according to the time difference between the reflected signal and the incident signal. The simulation waveforms are shown in Fig. 5.

The fault distance and measurement error calculated using the pulse accumulation method under the condition of different fault distance are shown in Table 1.

It can be obtained after analyzing the simulation results that the fault reflection signal after the envelope detection and accumulation by 10 times can significantly improve the SNR, which plays an important role in accurately identifying the fault signal. The results show that the fault location of cable can be accurately determined with this method according to the simulations of different fault distance.

5 Conclusion

This paper analyzes the refraction and reflection characteristics of the single pulse signal at the fault point in detail on the basis of the refraction and reflection principles of traveling wave, and accordingly proposes a fault detection method based on digital non-coherent pulses accumulation. The method employs the successive high-frequency pulse signal instead of the single pulse signal as the incident wave, and superimposes the reflected signal many times by using the pulse accumulation method after the envelope detection. Some meaningful conclusions can be summarized as follows:

- (1) Adoption of the successive high-frequency pulse signal as the incident wave improves the resolution of the reflected signal and thus improves the detection capability of the fault location;

- (2) Using the non-coherent pulse accumulation method is able to improve the SNR of the fault signal, identifies the fault waveform clearly, obtains a relatively accurate fault distance and finally solves the problem that is difficult to be detected due to the serious attenuation and distortion of signal when the signal transmits in the long distance.

Acknowledgments This work is partially supported by National Natural Science Foundation of China under Grant Nos. 51490660 and 51405362. The authors also gratefully acknowledge the helpful comments and suggestions of the reviewers, who have improved the presentation.

References

1. Cun JJ, Liang ZP, Sun YX (2001) Summary of power cable fault location technology and application. *J High Voltage Eng* 27:40–43
2. Xu M, Bai CT, Qin YN, Liao XH (2007) Method of power cable fault automatic location based on low voltage pulse. *J Relay* 35:37–40
3. Bo ZQ, Weller G (1999) Accurate fault location technique for distribution system using fault-generated high-frequency transient voltage signals. *J IEE Proc Gener Transm Distrib* 146:73–79
4. Shehab-Eldin EH, McLaren PG (1988) Travelling wave distance protection—problem areas and solutions. *J IEEE Trans Power Delivery* 3:894–902
5. Christopoulos C, Tomas D, Wright Prof A (1989) Signal processing and discriminating techniques incorporated in a protective scheme based on traveling wave. *J IEE Proc* 136:278–288
6. Zhang DB, Zhang DH, Wang TH (2005) Cable fault location based on the apparent traveling wave velocity. *J High Voltage Eng* 31:79–86
7. Sun T, Liu ZH, Jiang ZJ (2005) Method of computing sinusoidal steady-state solutions of lossy uniform transmission lines. *J Chongqing Univ (Nat Sci Ed)* 28:69–72
8. Lin S, He ZY, Chen J (2012) A single terminal fault location method based on time-frequency characteristic of traveling wave. *J Power Syst Technol* 36:258–264
9. Xu M, Zheng WQ (2009) Development of low voltage pulse generator based on MCU. *J Electr Power Autom Equip* 29:119–142
10. Holt TA, Lara MB (2009) Compact Marx generators modified for fast rise time. *J IEEE Int Pulsed Power Conf* 35:1197–1200
11. Shen PL, Li CC, Yin CY (2006) Employing pulse accumulation method to improve the ranging performance of anticollision radar. *J Chongqing University (Nat Sci Ed)* 29:29–31
12. Tian C, Wen SL, Du ZY (2015) Long time coherent integration algorithm for moving targets with high order motion. *J Syst Eng Electr* 37:1229–1236
13. He Y, Peng YN (2000) Performance analysis of distributed OS-CFAR detection with noncoherent integration of multiple pulses. *J Electr* 22:747–752

The Study Status of the Key Techniques About the Toroidal Drive

Yanhua Zhang, Jujiang Cao and Beibei Liu

Abstract The origin and the characteristic of the toroidal drive is reviewed in this paper. The toroidal drive combines rolling contact technique with planet worm drive. The drive has many advantages such as high load-carrying capacity, a wide range of transmission ratios, noiselessness and so on. And the study status of the key techniques about the toroidal drive is summarized, which including the mesh theory, manufacturing techniques, load-carrying capacity and other study works. And then the future trends of the toroidal drive is discussed.

Keywords Toroidal drive · Study status · Future research direction

1 Introduction

Mechanical transmission is an important part of mechanical engineering technology, which marks the level of mechanical engineering technology. To meet the needs of the machine's power and speed, it is important to research and development the mechanical transmission system. The toroidal drive combines rolling contact technique with planet worm drive. It is the frontier in the mechanical drive field [1, 2].

Y. Zhang (✉) · J. Cao · B. Liu
College of Mechanical & Electrical Engineering, Shaanxi University of Science
and Technology, Xian 710021, China
e-mail: zhangyanhua@sust.edu.cn

J. Cao
e-mail: jjcao@sust.edu.cn

B. Liu
e-mail: 1037745948@qq.com

2 The Toroidal Drive

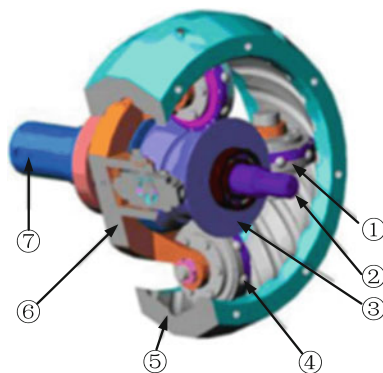
The toroidal drive was proposed by M.R. Kuehnle in 1965 [3]. In the early 80s, the first test prototype was made by the Coulter Company of the United States and a research team led by professor H1Peeken which were sent by the Aachen University of the Former West Germany [4]. From the traditional point of view, this kind of transmission mechanism is mainly composed of two parts; (a) the central input worm assembly, which including center worm, wheelset and planets carrier. (b) a stator of toroidal shape, which consists of two and a half piece of curved parts [5]. The toroidal drive of the structure diagram is shown in Fig. 1.

The input worm rotates each planet about its own axis. The planets have balls or rollers instead of teeth. Each planet meshes with the toroidal grooves in the stator. Because the planets are rotating, and the stator is fixed, the planets are forced to process in a toroidal path. The rotor is the output. The movement of the cylindrical gear, cycloidal gear and planetary gear transmission is carried in the same plane. And the movement of worm drive and helical gear transmission is carried in the two rotation plane. But the toroidal drive movement is carried in three plane of the three directions circular motion at the same time. Then the toroidal drive offers a number of advantages such as high load-carrying capacity, a wide range of transmission ratios, noiselessness, compactness and high operating efficiencies.

3 The Status of the Key Technology

When the toroidal drive was proposed, it was researched extensively by the scholars both at home and abroad. So far, the mainly research about the toroidal drive has the following several aspects. Some researchers have studied the mesh theory, and some researchers have studied the manufacturing techniques, and some researchers have studied the load-carrying capacity of the toroidal drive, and so on.

Fig. 1 The structure composition of the toroidal drive including: ① wheelset, ② input axis, ③ center worm, ④ roller, ⑤ toroidal, ⑥ planets carrier, ⑦ output axis



3.1 The Research of Meshing Theory Figures

The researches of China have performed much of research in the meshing theory of the toroidal drive [6–10]. The tooth surface equations of toroidal and worm, and the equations of contact line and spiral are described by the Refs. [6, 7]. In the Refs. [9], there is a breakthrough in the meshing theory of the toroidal drive. Not only the three different shape of planetary gear tooth of contact line were solved and compared, but also the root cutting boundary was discussed. And based on the stator normal sections surface, the fly-cutting was design. Then the practical manufacturing process and the meshing theory of the toroidal stator linked closely. At present, the research of meshing characteristics for this kind of drive, should be explored that how the various meshing parameters effect on the toroidal drive working efficiency. The date which can used to the design and manufacturing was obtained by the combination of the meshing theory and the practical manufacturing process.

3.2 The Research of Manufacturing Techniques

In the research of manufacturing technology, the possibility and the accuracy of toroidal surface manufacturing are the main research. Table 1 shows the main directions of the research on the manufacturing techniques of toroidal drive.

Among the seven directions shown in the Table 1, general machine tools processing is the uppermost concern of researchers. The main purpose of their research is investigating machining methods by remodeling general machine tools. Based on the principle of dual generating method, Cierniak et al. tried to remodel hobbing machine for machining toroidal. Their research work could increase the machining efficiency. They tried to divide toroidal into two parts and machined separately in their work. But the shortage of the machining process led to the difficulty of improving manufacturing precision [11]. In order to overcome the shortcomings mentioned above, domestic researchers improved the generating method for machining toroidal. A processing method of “simultaneous processing of the spiral groove of each part of toroidal” was put forth. Their work improved the manufacturing precision. Based on the research achievement of their work, the first toroidal drive prototype at home was made [9, 12]. Although this processing method became the most successful method of machining toroidal, two reasons lead to the need to further improve manufacturing method. First, the surface quality and precision is still not ideal. The reason is that cutting speed is too low to achieve high surface quality. Second, the dimension of toroidal is limited by the motion space of grinding head.

Beside toroidal surface, the study work about the manufacturing process of other components of toroidal drive, such as intermediate worm, was carried out by researchers at home and abroad [13, 14].

Table 1 Machining methods of toroidal

Machining process		Advantage	Shortage	Application
Non cutting methods	Precision casting	Reducing machining amount	Only suitable for synthetic material, such as Nylon 6	Suitable for small power transmission
	Powder metallurgy	High surface hardness, high wear resistance, long life and less machining amount	Need large forming pressures. Pressures distribution is always inhomogeneous	Suitable for small power transmission
	Precision forging	Less machining amount	Need large forming pressures Mold cost is high	Mass-producing small toroidal drive reducer
	Electrochemical forming	Toroidal dimension is limited by the size of electrolytic cell	Separate manufacture technique can be applied Precision is low	Mass-producing small toroidal drive reducer
Cutting methods	CNC machining	High precise	High machine cost	Small quantity producing and mass-producing
	Special machine tools processing	High production efficiency	High machine cost	Mass-producing
	General machine tools processing	Low machine cost	Low precise	Mass-producing

3.3 The Study of Load-Carrying Capacity

Improving the load capacity has important value for the popularization and application of toroidal drive. Peeken et al. researched on the load distribution and the pitting corrosion of toroidal drive. Based on the result of their work, a computation formula for load distribution was established. In their research work, experimental study was carried out to determine the load distribution and the influence between allowable torque and the material for toroidal [15, 16]. Their work involves innovative significance for the load capacity study of toroidal drive. Tooten et al. analyzed detailed the offset loading in toroidal drive transmission. Furthermore, according to the results of their study, some suggestions for toroidal drive design were proposed [17].

Some studies about the load capability of toroidal drive also have been done by domestic researchers. Yang Chuanmin provided a new method for analyzing the transmission efficiency of toroidal drive. By considering the effect of helix angle, a formula, which includes helix angle as an independent variable, was also presented

for calculating transmission efficiency [18]. Xu Lizhong carried out research on the load distribution and the contact stress of toroidal drive. Based on the results of his work, calculation formulas for determining the load distribution and contact stress were obtained [19].

Although some achievements were obtained by domestic researchers, the open published literatures about the load capability study of toroidal drive are insufficient in China. All in all, the research of the load capability of toroidal drive is at the starting stage. It's an urgent need for the popularization and application of toroidal drive in domestic to study load capability from the perspective of material science, tribology and mechanism dynamics.

3.4 The Study of Other Works

Besides the research reviewed above, some researches on other fields of toroidal drive were carried out at home and abroad. These mainly involves design theory and method and transmission efficiency.

Yao Ligang, Xu Xiaojun and Li Huamin researched on the computer-aided design technique for toroidal drive and developed corresponding CAD system [20]. In order to decrease machining difficulty, the design theory of toroidal drive were researched. And some new toroidal drives were invented [10]. These works enriched the design theory of toroidal drive. Cierniak et al. carried out their study on the working resistance of planetary gear in toroidal drive [21]. Some Chinese researchers studied on the friction and lubrication between components and relationship between efficiency and influence factor [22–24]. Their works is helpful to increase the efficiency of toroidal drive.

4 Discussion and Future Trends

The review above shows that the existing research on toroidal drive involves two main aspects: meshing theory and machining methods. Despite lots of achievements have been obtained, a number of areas could still benefit considerably from further investigation. These include the following:

- Simulation analysis methods is one of the important methods for studying the dynamical characteristic of toroidal drive. Although some achievements have been accumulated in dynamical characteristic research at home and abroad, deeper investigations are still needed on a more precise model.
- Increasing load bearing ability is significant for the popularization and application of toroidal drive. More research work on load capability of toroidal drive must be carried out from the perspective of material science, tribology and mechanism dynamics.

- It is significant to improve structure design, which can improve the processing efficiency and the stability of toroidal drive. More work can be done to optimizing structure design of toroid.
- For having complicated structure, the toroidal is much difficult to processing. Improving the precision and efficiency of toroidal processing remains to be further investigated.

Although some achievements have been accumulated in kinematic and dynamic characteristics research at home and abroad, deeper investigations are still needed.

References

1. Hong M, Yao L (2013) Study current state and prospect of the toroidal planet worm drive system. *J Mech Transm* 37(06):129–132 (in Chinese)
2. Qin D (2003) History and progress of science and technology on mechanical transmission. *Chin J Mech Eng* 39(12):37–43 (in Chinese)
3. Kuehnle MR (1966) Transmission. United States Patent Office 3,174,354 1966
4. Kuehnle MR, Peeken H, Troeder C et al (1981) The toroidal drive. *J Mech Eng* 32(02):32–39
5. Xu L (2006) General review of the study on the toroidal drive. *J Eng Sci* 2(06):84–88 (in Chinese)
6. Wang J (1986) Toroidal drive and its engagement principle. *J Dalian Inst Technol* 25(04):57–62 (in Chinese)
7. Xu X, Zhang Y, Tang D (1995) The study on the meshing theory of toroidal planet wormgear drive with ball tooth. *J Harbin Inst Technol* 27(01):123–126 (in Chinese)
8. Xu L, Wang L, Zhao Y (1997) Study on engagement features for toroidal drive. *J Trans Chin Soc Agric Mach* 28(04):139–143 (in Chinese)
9. Yao L (1996) The study of toroidal drive for meshing analyzing and manufacturing method. D. Harbin Institute of Technology (in Chinese)
10. Ma Q, Cai Y (2010) The study of meshing principle for magnetic toroidal transmission. *J Mach Des Manuf* 02:132–134 (in Chinese)
11. Cierniak S, Quint M (1983) Qualitätskontrolle der Zahn2 flanken des Toroidgetriebe2Stators. *J. VDI—Z* 125(07):233–236
12. Yao L, Xu X, Li H (1996) Toroidal drive stator research by envelope method processing. *J Mech Transm* 20(03):24–26 (in Chinese)
13. Cierniak S, Quint M, Kretzer W (1982) Drei-Koordinaten-Meßtechnik zur Kontrollerraumlich gekrummter Zahn-flanken. *J Werkstatt Betrieb* 115(11):721–723
14. Zhang C, Xu X, Dong S (1999) The numerical simplified method of processing toroidal drive worm on the NC milling machine. *J Mech Transm* 23(02):133–15 (in Chinese)
15. Peeken H, Troeder C, Tooten KH (1984) Berechnung und Messung der Lastverteilung im Toroidgetriebe. *J Konstruktion* 36(3):81–86
16. Peeken H, Cierniak S, Troeder C (1980) Walzfestigkeiten moderner Werkstoffe der Walzpaarung “Kuge-Kugellaufrinne”. *J Konstruktion* 362(3):89–95
17. Tooten KH (1985) Optimierung des Kraftübertragungsverhaltens in Getrieben mit Walzkon-takten. *J Antriebstechnik* 24(7):49–55
18. Yang C (1997) The efficiency of screw ring gear. *J Mech Des* 02:35–38 (in Chinese)
19. Xu L, Zhao Y (1998) Study on meshing features and contact stresses for roller toroidal drive. *Chin J Eng Des* 01:35–37 (in Chinese)
20. Yao L, Xu X, Li H (1995) The intelligent CAD system for toroidal drive. In: *Proceedings of 18th international conference on computer in engineering, China*, pp 181–184

21. Cierniak S (1981) Rollverhalten von Kugeln zwischen geschrankten Rinnen. *J Konstruktion* 33(04):155–158
22. Xu L, Yang Y, Huang Z (2002) EHD condition for toroidal drive. *Chin J Mech Eng* 38 (09):114–117 (in Chinese)
23. Xu L, Huang Z (2002) Friction theory for toroidal drive. *J Eng Sci* 4(03):63–67
24. Tan Y, Yang S, Wang L et al (2010) Pressure angle of toroidal drive with cylindrical teeth. *J Mech Eng* 46(21):29–34 (in Chinese)

Motion Control of Pneumatic Muscle Actuator Using Fast Switching Valve

Shenglong Xie, Jiangping Mei, Haitao Liu and Panfeng Wang

Abstract Considering the nonlinear and time-varying phenomena existing in pneumatic muscle actuators (PMAs), this paper deals with the modeling of tracking control of PMA using fast switching valves. A close-loop control scheme combined with feed-forward and feedback controllers is proposed to achieve high accuracy trajectory tracking control. First, the static model of the PMA is established using the data obtained from isometric experiment, and the dynamic model is developed based on the polytropic equation. Then, the hysteresis model and its inverse model is established, in which the air mass flow rate through the fast switching valve is evaluated using the Sanville equation. The PWM signal used to control the fast switching valves is generated referring to the pulse signal modulation method. Sequentially, the trajectory tracking control models of the PMA are derived by means of close-loop control scheme, which are implemented in the environment of MATLAB/Simulink. Finally, the simulation result is compared with the experiment result. The results indicate that the control model can achieve satisfactory performance and accuracy, which validates the feasibility of the proposed model and control scheme, providing an effective approach for high accuracy trajectory tracking control of PMA.

Keywords Fast switching valve · Pneumatic muscle actuator · Hysteresis identification · Tracking control

1 Introduction

Pneumatic muscle actuators (PMA) possess several advantages over servo-motors, such as simple structure, compactness, high power-to-weight ratio, etc. [1], which have been widely used in medical rehabilitation robots, bionic robots, and orthotics.

S. Xie · J. Mei · H. Liu (✉) · P. Wang

Key Laboratory of Mechanism Theory and Equipment Design, Ministry of Education, Tianjin University, Tianjin 300072, China
e-mail: liuht@tju.edu.cn

However, the hysteresis [2], threshold pressures [3], creep [4], compliance [5], and low bandwidth [6] make the design of the corresponding controller complicated. Especially, since the hysteresis may cause energy loss and reduce the contracting force, there will be errors in tracking control. Therefore, it has to establish a precise hysteresis model to improve the dynamic behavior of a PMA [7].

Typically, there are two types of electro-pneumatic valves to control the fluid flow of a PMA, i.e. the continuously acting servo/proportional valves and the on-off switching valves [8]. Although the servo/proportional valve has high control accuracy, it is expensive and tends to be bulky compared to the on-off switching (or fast switching) valve [9]. Therefore, the trajectory control methods of PMA utilizing fast switching valves have been extensively studied in recent years. Kimura [10] applied feedback linearization control method to deal with the nonlinearity caused by hysteresis of the PMA, which was verified by the experiment of a single pneumatic muscle system. Repperger [11] developed a three-element phenomenological model for the PMA, and introduced a variable structure controller based on feedback linearization control method to predict its response. However, the feedback linearization method requires an accurate model and all states, if there were uncertain parameters or unmodeled dynamic characteristics, the robustness of the control system could not be ensured. Based on the three-element phenomenological model, Amato [12] used the robust control strategy to study the trajectory tracking control of a robotic arm actuated by PMAs. Zhu [13] presented an adaptive robust posture controller to compensate the parametric uncertainties and uncertain nonlinearities of a parallel manipulator actuated by PMAs. Although these proposed controllers can effectively handle the nonlinearities caused by the friction forces of PMAs, they are unable to compensate the rapid change uncertain quantities. Shen [14] developed a sliding model controller, of which the effectiveness is demonstrated experimentally by step response and sinusoidal tracking at different frequencies. However, due to the inertia, delay, and measurement errors of the system, this controller will generate high frequency vibration, and the gas consumption is large. Therefore, there is still a need to further investigate the precision tracking control of PMA using fast switching valves.

In consideration of this issue, this paper deals with the motion control of PMA using fast switching valve. The rest of this paper is organized as follows. In Sect. 2 the experimental system is briefly introduced. In Sect. 3, the static model, dynamic model, and hysteresis model of the PMA are systematically derived. Then, a close-loop control scheme is proposed to achieve high accuracy trajectory tracking control of the PMA, and the simulation is carried out in the environment of MATLAB/Simulink in Sect. 4 before conclusions are drawn in Sect. 5.

2 System Description

Figure 1 shows the schematic diagram of the pneumatic muscle actuator. The components used here are given in Table 1. The air compressor connects the fast switching valve with throttle valve and reservoir. The fast switching valve 1 is inlet

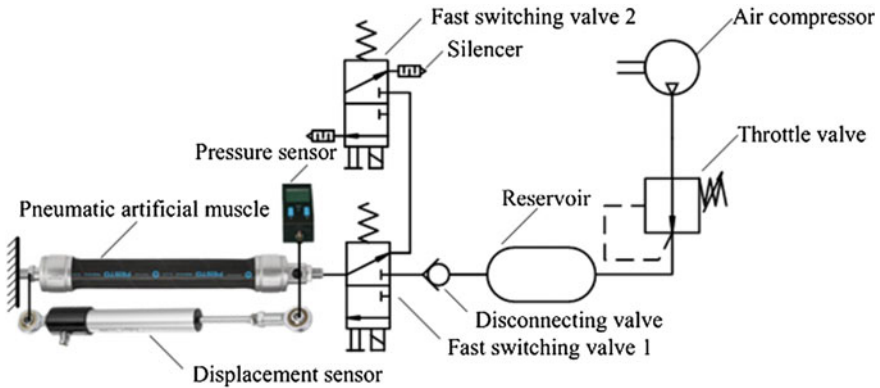


Fig. 1 Schematic diagram of the pneumatic muscle actuator

valve, called inlet valve for short; the fast switching valve 2 is exhaust valve, called exhaust valve for short. Without the excitation of the solenoid, the valve will keep closed due to return spring. The working process is as follows. Initially, the PMA connects with the external environment, and the internal pressure of PMA is equal to atmospheric pressure. When the inlet valve is open, the compressed air flows into the PMA while the exhaust valve is closed, resulting in the contraction of the PMA. When the PMA reaches the desired position, the inlet and exhaust valves are closed at the same time, then the PMA keeps the compressed air inside and maintains the current state. When inlet valve is closed and exhaust valve is open, the compressed air is discharged through the exhaust valve. During this process, fast switching valves are controlled by PWM signals. In the beginning, the inlet valve is fully opened to let the PMA quickly reach the desired position; when it is approaching to the desired position, the duty cycle of PWM is reduced proportionally to the displacement deviation. When the displacement deviation is smaller than a given value, the duty cycle of PWM is set zero to avoid the PMA oscillating around the desired position.

3 Modeling

3.1 Static Model of PMA

The static model of a PMA gives a nonlinear relationship between the contracting force, the applied pressure, and the PMA length. There are several methods for developing static models of a PMA, such as geometry analysis, the principle of energy conservation, and empirical method. These models always rely on simplifying assumptions, for example, neglecting of the rugby-ball shape forms at either end of the PMA or the thickness of the PMA bladder, etc. These assumptions

Table 1 Components used in the system

Component	Type	Company
PMA	DMSP-20-500N-RM-CM	Festo
Displacement sensor	TEX 0150 415 002 205	Novotechnik
Pressure sensor	SDE1-D10-G2-WQ4-L-PU-M8-G5	Festo
Fast switching valve	MHE2-MS1H-3/2G-QS-4-K	Festo
Data acquisition card	PCI-6254-779071-01	National Instruments

results in the inconsistency of predicted result and practical measurement, and make the precise position control of pneumatic muscle hard to be achieved. Therefore, in this paper, the static model is established by means of isometric experiment.

Figure 2 shows the measured data of contracting force F_{const} against internal pressure P at different constrained lengths x . It can be seen that for a given length the variation of P vs. F_{const} is nearly linear, but the slopes are varied for x . It indicates that the contracting force can be formulated as a linear function of the internal pressure and length [15]

$$F_{const} = a(x)P + b(x) \tag{1}$$

where $a(x)$ and $b(x)$ are the slope and the intercept, respectively. $a(x)$ and $b(x)$ can be evaluated as follows

$$\begin{cases} a(x) = \sum_{i=0}^2 a_i x^i \\ b(x) = \sum_{j=0}^3 b_j x^j \end{cases} \tag{2}$$

where a_i and b_j are the coefficients of the polynomial function.

Fig. 2 Contracting force via the internal pressure at different constrained lengths

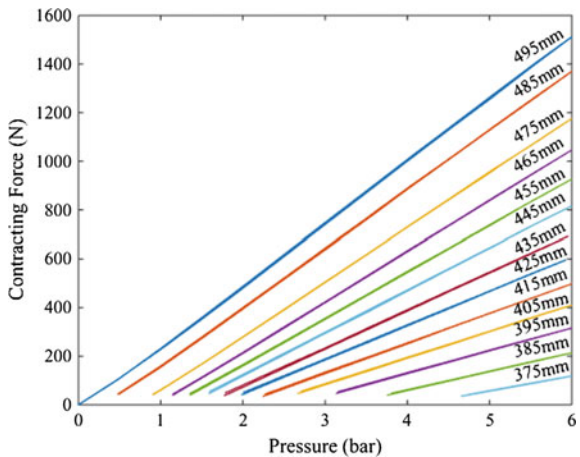
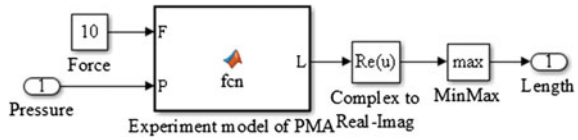


Fig. 3 Block-diagram of PMA’s static characteristic model



These coefficients can be obtained by using the least squares curve fitting tools in MATLAB, and are given as follows

$$\begin{cases} a(x) = 0.000953x^2 + 0.7979x - 370.7 \\ b(x) = 0.0004561x^3 - 0.5668x^2 + 234.6x - 32560 \end{cases} \quad (3)$$

Substituting Eq. (3) into Eq. (1), one can obtain the static model of PMA. Based on this model, the variation of the length of the PMA vs. its internal pressure can be obtained once given the load and internal pressure using the block-diagram shown in Fig. 3.

3.2 Dynamic Model of PMA

Since the PMA is constructed by an elastic nylon material rubber covered by a mesh of inextensible threads, it can be assumed that during charging and discharging process are in isothermal and adiabatic states. The relationship of the mass of air, muscle volume, and internal pressure obeys the polytropic gas law [16]

$$P \left(\frac{V}{m} \right)^k = \text{const} \quad (4)$$

where P and V are the inner pressure and volume of PMA; m is the air mass inside the PMA; k is the polytropic exponent. Taking the total differential of Eq. (4) leads to

$$\dot{P}V + kP\dot{V} = kPV \frac{\dot{m}}{m} \quad (5)$$

Then, substituting the ideal gas law

$$PV = mRT \quad (6)$$

into Eq. (4) results in

$$\dot{P} = \frac{k}{V} (\dot{m}RT - P\dot{V}) \quad (7)$$

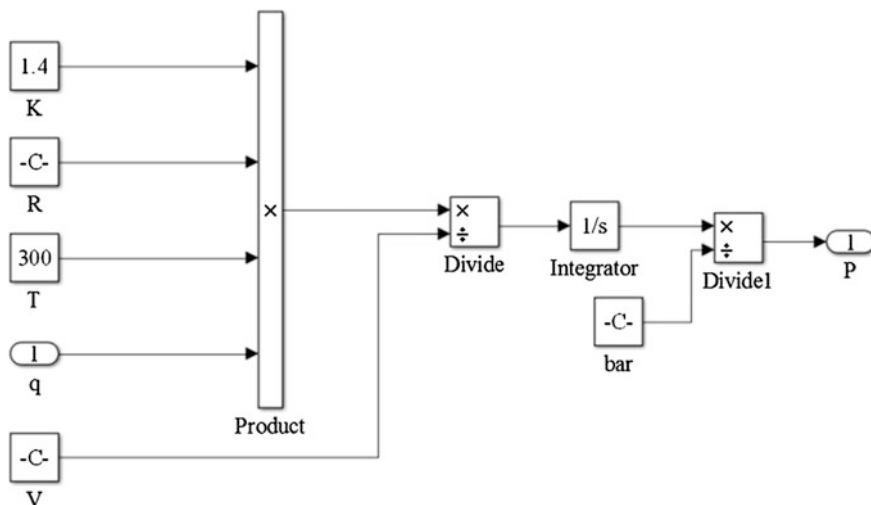


Fig. 4 Block-diagram of PMA’s dynamic characteristic model

From Eq. (7), the corresponding Simulink block-diagram can be developed as shown in Fig. 4, where the input is the air mass flow rate and the output is the internal pressure of PMA. Assuming that the volume of PMA is constant during charging and discharging, then $P\dot{V} \equiv 0$ and the internal pressure of PMA can be obtained by taking integration of Eq. (7).

3.3 Hysteresis Model of PMA

In this section, the Prandtl-Ishlinskii (P-I) model [17] will be used to derive the hysteresis of the PMA. It has two advantages: first, it is simpler compared with other models because it only consist of linear play operators; second, the inverse PI model can be obtained analytically, which is easier for realization of hysteresis compensation. The elementary operator of the PI model is linear play operator, which can be mathematically illustrated by Fig. 5.

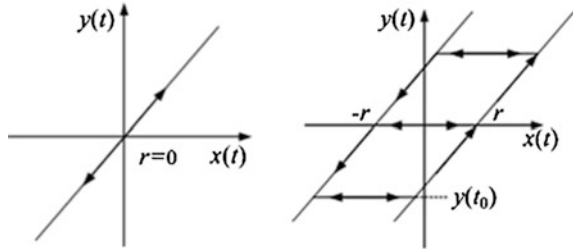
Its *i*th linear play operator can be expressed as

$$y_i(k) = \max\{x(k) - r_i, \min\{x(k) + r_i, y_i(k - 1)\}\} \tag{8}$$

while the initial condition is

$$y_i(0) = \max\{x(0) - r_i, \min\{x(0) + r_i, y_{i0}\}\} \tag{9}$$

Fig. 5 Linear-play operator



The output of PI model is

$$y(k) = \sum_{i=1}^n \omega_i y_i(k) = \sum_{i=1}^n \omega_i \max\{x(k) - r_i, \min\{x(k) + r_i, y_i(k - 1)\}\} \tag{10}$$

$$= \omega^T \mathbf{H}_r [x(k), \mathbf{y}_0]$$

where \mathbf{H}_r denotes the linear play operator; $\omega = [\omega_1, \dots, \omega_n]^T$ is the weighting vector; $\mathbf{r} = [r_1, \dots, r_n]^T$ is the threshold vector; x and y are the input and output of the operator, respectively; \mathbf{y}_0 is the initial state; k is the sampling number of the operator; and n is the number of the linear play operator.

To determine the parameters of PI model, the threshold vector \mathbf{r} is firstly determined by the following equation

$$r_i = \frac{i}{n+1} \max\{|x(t)|\} \quad i = 1, \dots, n \tag{11}$$

Then, using the least square method (LSM) the weighting vector ω can then be determined. Figure 6 shows the comparison of the pressure/length hysteresis characteristics obtained from the experiment and the PI model using the identified parameters. The result clearly shows that the PI model can effectively characterize the hysteresis loop of the PMA.

From Eq. (8), the inverse model of PI model can be formulated as

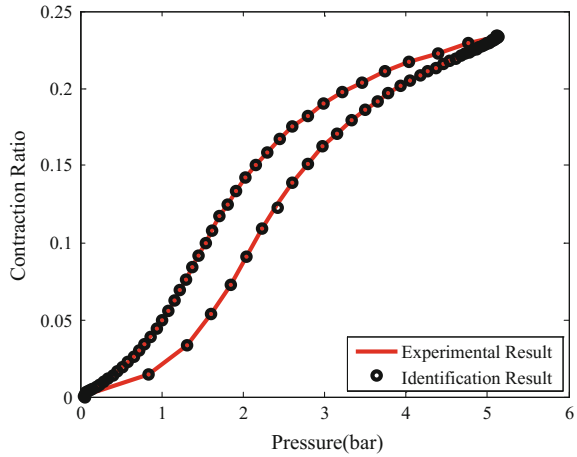
$$x'_i(k) = \max\{y(k) - r'_i, \min\{y(k) + r'_i, x'_i(k - 1)\}\} \tag{12}$$

$$x(k) = \sum_{i=1}^n \omega'_i \max\{y(k) - r'_i, \min\{y(k) + r'_i, x'_i(k - 1)\}\} \tag{13}$$

The inverse hysteresis model can then be formulated as follows.

$$x(k) = H^{-1}(y(k)) = \omega'^T \mathbf{H}'_r [y(k), \mathbf{x}_0] \tag{14}$$

Fig. 6 Comparison of the experimental result and the PI model



where \mathbf{H}'_r denotes the inverse PI operator; $\omega' = [\omega'_1, \dots, \omega'_n]^T$ is the weighting vector; $r' = [r'_1, \dots, r'_n]^T$ is the threshold vector; x_0 is the initial state. The parameters of the inverse hysteresis model can be derived as

$$\begin{cases} \omega'_1 = \frac{1}{\omega_1} \\ \omega'_i = \frac{-\omega_i}{\left(\omega_1 + \sum_{j=2}^i \omega_j\right) \left(\omega_1 + \sum_{j=2}^{i-1} \omega_j\right)} & i = 2, \dots, n \\ r'_i = \sum_{j=1}^i \omega_j (r_i - r_j) & i = 1, \dots, n \\ x'_i(0) = \sum_{j=1}^{i-1} \omega_j y_i(0) + \sum_{j=i}^n \omega_j y_j(0) & i = 1, \dots, n \end{cases} \quad (15)$$

Obviously, the weighting vector and threshold vector of PI model are used to obtain parameters of the inverse PI hysteresis model that will be used for feed-forward compensation control.

3.4 Fast Switching Valve Model

The process of air flowing through the valve port is very complex, which is often modelled as Sanville flow equations [18]. It has been shown that the influence of the change of PWM signal frequency to gas flow rate is negligible [19], when the frequency ranges are between 100 and 180 Hz. Thus, the mass flow rate can be expressed as a function of the duty cycle and the effective orifice area.

$$\dot{m} = \begin{cases} dA_m \frac{p_u}{\sqrt{T_u}} \sqrt{\frac{2k}{R(k-1)} \left[\left(\frac{p_d}{p_u}\right)^{\frac{2}{k}} - \left(\frac{p_d}{p_u}\right)^{\frac{k+1}{k}} \right]} & \frac{p_d}{p_u} > 0.528 \\ dA_m \frac{p_u}{\sqrt{T_u}} \left(\frac{2}{k+1}\right)^{\frac{1}{k-1}} \sqrt{\frac{2k}{R(k+1)}} & \frac{p_d}{p_u} \leq 0.528 \end{cases} \quad (16)$$

where \dot{m} is the air mass flow rate of fast switching valve; p_u is the upstream pressure; p_d is the downstream pressure; T_u is the upstream temperature; k is the ratio of specific heat; d is duty cycle of PWM signals; A_m is the effective orifice area of fast switching valve. In reference [20], the effective orifice area A_m of the MHE2-MS1H-3/2G-M7-K fast switching valve is $1.8194 \times 10^{-6} \text{ m}^2$.

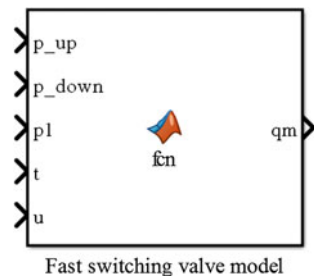
Here, the Function model in MATLAB/Simulink is used to build the simulation model of Eq. (16) for the air mass flow rate of fast switching valve. The corresponding Simulink model is given in Fig. 7, where u is the duty cycle of PWM signals, t is the temperature of air, and p_1 is the internal pressure of PMA. The simulation of the charging and discharging of PMA is carried out as follows: during the charging process, $u > 0$ and p_{up} is air source pressure, while p_{down} is the internal pressure, $p_{down} = p_1$; during the discharging process, $u < 0$ and p_{up} is the internal pressure, $p_{up} = p_1$, and p_{down} is the atmospheric pressure.

3.5 Generation of PWM

There are various methods to generate PWM signal in MATLAB/Simulink. Here, the pulse signal modulation method introduced in reference [21] is used, which has the advantage of linear relationship. The steps of generation are given as follows: first, generating a reference pulse signal sequence with 50 % duty cycle, then getting the standard triangular wave signal after bias and integral, and finally obtaining the required PWM signal after bias of the former standard triangular wave signal. Figure 8 shows the block-diagram of this method.

The pulse generator module is used for obtaining a 50 % duty cycle square wave with magnitude of 2. After bias and integration, a triangular wave modulation signal can be achieved for generating modulated PWM wave. The residual between the

Fig. 7 Simulink model of fast switching valve



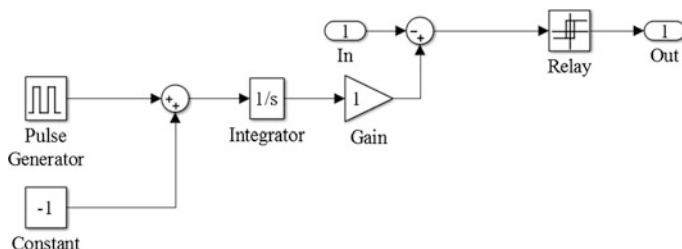


Fig. 8 Block-diagram of generation of PWM signal

input signal and the triangular wave modulation signal is inputted into the Relay module. If the input is larger than 0, the output of Relay module is 1 (simulating the inflation process); otherwise, the output is -1 (simulating the deflation process). Finally, the input signal is modulated in the PWM wave to control the fast switching valves.

4 Motion Control Method

To compensate the nonlinear hysteresis of the PMA, the input feed-forward and output feedback are combined in the motion control method. The hysteresis inverse model provides a control input, which represents the function of a desired trajectory to keep the output following the desired trajectory. It is efficient for low-frequency systems regardless of the creep and vibrations. The accuracy of the feed-forward control depends on the performance of hysteresis model. Therefore, the feedback loop is used to deal with the tracking error caused by hysteresis modeling, and the combined control method provides a high gain feedback and overcome creep and vibrations in the systems. The feedback loop is a PID controller, which is given as

$$u(t) = K_p e(t) + K_i \int_0^t e(\tau) d\tau + K_d \frac{de(t)}{dt} \quad (17)$$

where $e(t)$ is error signal; $u(t)$ is output signal; K_p is proportional gain; K_i is integral gain; K_d is derivative gain.

The control scheme is illustrated in Fig. 9. Hysteresis compensation based on inverse PI model is built into the control system through feed-forward processing. The controller of the internal pressure and contraction ratio uses a proportional-integral (PID) controller. The corresponding Simulink control scheme is shown in Fig. 10.

Figure 11 shows the simulation and experiment results of sinusoid trajectory tracking responses. It can be found that the result of simulation and experiment is very close. It indicates that the proposed position control method can achieve satisfactory accuracy.

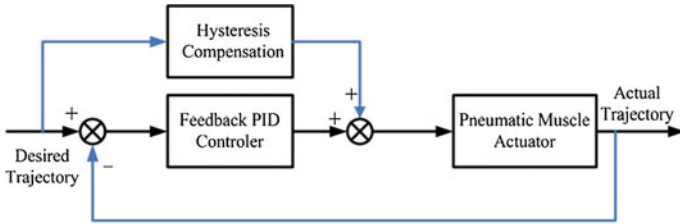


Fig. 9 Motion control scheme for pneumatic muscle actuator

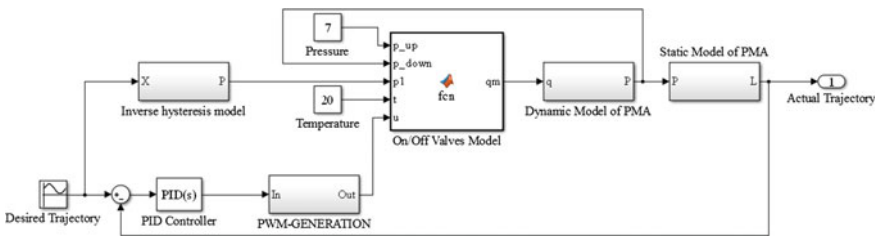


Fig. 10 Simulink control scheme for pneumatic muscle actuator

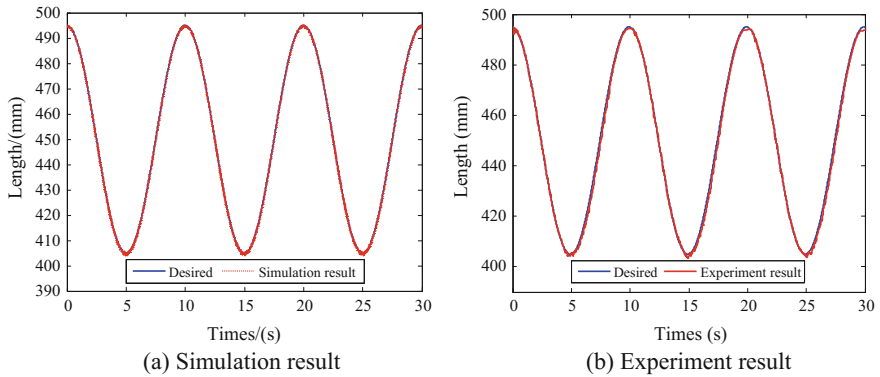


Fig. 11 Results of the motion control

5 Conclusion

This paper presents an alternative approach for accurate motion control of PMA driven by fast switching valves. The static model of the PMA is derived using a polynomial based least square fitting of the data from isometric experiment. Parameters of the PMA hysteresis model are identified using LMS by fitting the pressure-displacement hysteresis loop. Subsequently, a close-loop control scheme is

designed to achieve precise tracking control of PMA, which combined the inverse hysteresis compensation feed-forward and the feedback PID controllers. The simulation and experiment results indicate that the proposed models and control scheme are able to achieve satisfactory accuracy.

Acknowledgments Supported by National Natural Science Foundation of China (Grant No. 51405331).

References

1. Tsagarakis NG, Caldwell DG (2003) Development and control of a 'soft-actuated' exoskeleton for use in physiotherapy and training. *Auton Robots* 15(1):21–33
2. Vo-minh T, Tjahjowidodo T, Ramon H et al (2011) A new approach to modeling hysteresis in a pneumatic artificial muscle using the Maxwell-slip model. *IEEE/ASME Trans Mechatron* 16(1):177–186
3. Obiajulu SC, Roche ET, Pigula FA, et al (2013) Soft pneumatic artificial muscles with low threshold pressures for a cardiac compression device. In: ASME 2013 international design engineering technical conferences and computers and information in engineering conference. American Society of Mechanical Engineers, pp 1–8
4. Vo-minh T, Kamers B, Ramon H et al (2012) Modeling and control of a pneumatic artificial muscle manipulator joint—Part I: modeling of a pneumatic artificial muscle manipulator joint with accounting for creep effect. *Mechatronics* 22(7):923–933
5. Daerden F, Lefeber D (2002) Pneumatic artificial muscles: actuators for robotics and automation. *Eur J Mech Environ Eng* 47(1):11–21
6. Caldwell DG, Medrano-cerda G, Goodwin M (1995) Control of pneumatic muscle actuators. *IEEE Control Syst* 15(1):40–48
7. Davis S, Caldwell DG (2006) Braid effects on contractile range and friction modeling in pneumatic muscle actuators. *Int J Robot Res* 25(4):359–369
8. Taghizadeh M, Ghaffari A, Najafi F (2005) Modeling and identification of a solenoid valve for PWM control applications. *CR Mec* 337(3):131–140
9. Behrouz N, Masoud SB, Mohammad JF (2012) Modelling and controller design of electro-pneumatic actuator based on PWM. *Int J Robot Autom* 1(3):125–136
10. Kimura T, Hara S, Fujita T et al (1997) Feedback linearization for pneumatic actuator systems with static friction. *Control Eng Pract* 5(10):1385–1394
11. Repperger DW, Johnson KR, Philips CA (1999) Nonlinear feedback controller design of a pneumatic muscle actuator system. In: American control conference, vol 3, Piscataway, NJ, USA. IEEE, pp 1525–1529
12. Amato F, Colacino D, Cosentino C et al (2013) Robust and optimal tracking control for manipulator arm driven by pneumatic muscle actuators. In: 2013 IEEE international conference on mechatronics (ICM), pp 827–834
13. Zhu X, Tao G, Yao B et al (2008) Adaptive robust posture control of a parallel manipulator driven by pneumatic muscles. *Automatica* 44(9):2248–2257
14. Shen X (2010) Nonlinear model-based control of pneumatic artificial muscle servo systems. *Control Eng Pract* 18(3):311–317
15. Pujana AA, Mendizabal A, Arenas J et al (2010) Modelling in Modelica and position control of a 1-DoF set-up powered by pneumatic muscles. *Mechatronics* 20(5):535–552
16. Vo-minh T, Tjahjowidodo T, Ramon H et al (2010) Cascade position control of a single pneumatic artificial muscle–mass system with hysteresis compensation. *Mechatronics* 20(3):402–414

17. Kuhnen K, Janocha H (2001) Inverse feedforward controller for complex hysteretic nonlinearities in smart-material systems. *Control Intell Syst* 29(3):74–83
18. High A, Riche E, Hurmuzlu Y (2001) A high performance pneumatic force actuator system part 1—nonlinear mathematical model. *J Dyn Syst Meas Contr* 122(3):416–425
19. Wang X (2013) Study on key technologies of high precision motion control of a pneumatic system using high speed solenoid valves. School of Mechanical Engineering, Zhejiang University, Hangzhou
20. Meng D, Tao G, Li A et al (2015) Adaptive robust control of pneumatic cylinders using fast switching on/off solenoid valves. *J Mech Eng* 51(10):180–188 (in Chinese)
21. Ren B, Pan J, Shi G (2009) A new flight simulator driven by pneumatic artificial muscles. In: *Proceedings of the 7th international conference on fluid power conference*. Hang Zhou, China, pp 507–510

Research on SEM's Astigmatism Detection Based on Image Processing

Yihua Lu, Xianmin Zhang and Zhenya He

Abstract SEM has been commonly used in the field of micro-nano operating. The image quality of the SEM is affected by aperture, astigmatism, focus, temperature, environmental magnetic field and vibration. This paper studied the influence factors for astigmatism and their impact on imaging quality. On this basis, definition evaluation function was used in the blurred image discrimination, and an improved algorithm was developed. Experiments showed that the improved algorithm can accurately identify the astigmatism, and it has a high sensitivity, which can provide clear images of targets in the micro-nano operating process.

Keywords Image processing · Astigmatism · SEM system · Definition evaluation

1 Introduction

SEM systems generally have the following three categories of applications by providing secondary electron images: first, SEM system provides morphology functions. Through the observation of human eyes, sample microstructure such as carbon nanotubes, new type of alloy materials are studied. Second, SEM system provides morphology functions and simple analysis functions. Through image processing, particles or pores quantitative information are directly obtained, such as

Y. Lu · X. Zhang (✉) · Z. He

Guangdong Province Key Laboratory of Precision Equipment and Manufacturing Technology, South China University of Technology, Guangzhou 510640, China
e-mail: zhangxm@scut.edu.cn

Y. Lu

e-mail: 13427792055@163.com

Z. He

e-mail: mezhyhe@scut.edu.cn

Y. Lu

School of Engineering Technology, Beijing Normal University,
Zhuhai, Zhuhai 519087, China

© Springer Nature Singapore Pte Ltd. 2017

X. Zhang et al. (eds.), *Mechanism and Machine Science*,

Lecture Notes in Electrical Engineering 408,

DOI 10.1007/978-981-10-2875-5_115

rock and porosity microstructure and its 3D reconstruction [1]. Third, SEM system provides observation, analysis, identification and handling capabilities functions. By integrating micro manipulator and with the help of image processing, tools and targets are identified and track, using images for close-loop feedback, and ultimately handling, assembly, welding and other operations are achieved [2].

In the above applications, micro-nano operating demands the highest SEM imaging. And at the same time, astigmatism can also reduce the image resolution. Electron microscopy experts have the ability to completely eliminate astigmatism, but general SEM operator is difficult to eliminate astigmatism. So, if the auto-detection function of astigmatism is integrated in SEM, it can reduce the operator's requirements and avoid operator fatigue.

This paper study the blur caused by astigmatism, and definition evaluation function is used in the blurred image discrimination. An improved algorithm is developed and experiments show it can accurately identify the astigmatism, and by some astigmatism adjustment strategy, it can obtains SEM images with no astigmatism.

2 SEM's Astigmatism

Processing errors, uneven material core, or different tightness coil and other reasons, will result in asymmetry of the magnetic field, and astigmatism can be formed.

SEM equipped with astigmatism, which provides a weak field from eight directions to compensate for the asymmetry of the magnetic field in the X and Y directions and to eliminate astigmatism [3]. The astigmatism can cause image blur and decrease in resolution.

Solder ball samples are commonly used for the training of operating or as a micro-nano operating target object, and each solder ball is ideal sphere. In the focal condition, the image blur caused by astigmatism is shown in Fig. 1.

Figure 1a is a clear image; Fig. 1b–d is the blurred images caused by X direction astigmatism; Fig. 1e–g is the blurred images caused by Y direction astigmatism; Fig. 1h–j is the blurred images caused by X and Y direction astigmatism. Adjust the astigmatism knob manually and let Fig. 1b, e, h in the same amount of astigmatism, and it is set to n ; let Fig. 1c, f, i in the same amount of astigmatism, and it is set to $2n$; let Fig. 1d, g, j in the same amount of astigmatism, and it is set to $3n$.

As can be seen from Fig. 1, one direction or both directions of astigmatism led to imaging blur, the more astigmatism, the more blurred image.

Edge detection was used in a same solder ball, and the roundness e is calculated by the following formula [4]:

$$e = 4\pi \frac{S}{C^2} \quad (1)$$

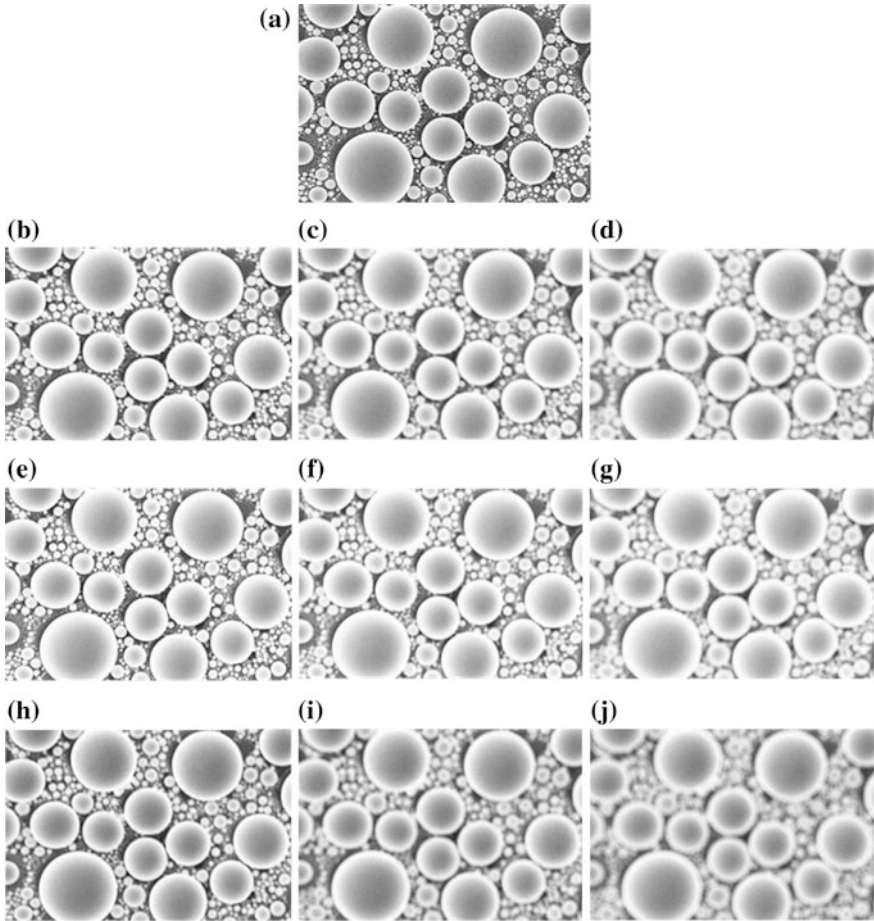


Fig. 1 Blurred images caused by astigmatism

where S is the area of the region, C is the circumference of the area. If e equal to 1, preferably a circular region.

The roundness of the same solder ball is calculated and shown in Table 1. As can be seen, the roundness changes small, it can be caused by unstable electronic imaging, edge detection error and the solder ball itself. It means, in the focal condition, astigmatism just results in blurred image, but not elongated or compressed in some direction.

Table 1 Roundness of a solder ball

Image	a	b	c	d	e
Roundness	0.981	0.969	0.961	0.987	0.963
Image	f	g	h	i	j
Roundness	0.987	0.954	0.974	0.967	0.951

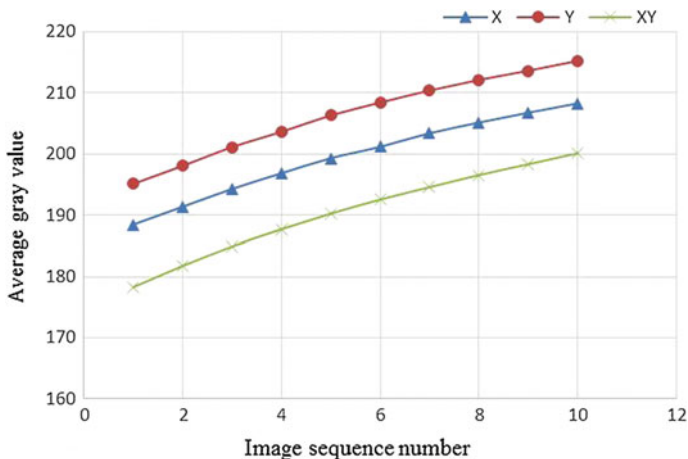


Fig. 2 Average gray value of each image

In addition, adjust the knob to gradually increase the astigmatism and get three groups of images, each group contains 10 images. Gradually increasing the X astigmatism and get the first group, gradually increasing the Y astigmatism and get the second group, gradually increasing the X and Y astigmatism and get the third group. The average gray value of each image was calculated and shown in Fig. 2. It shows that the increasing astigmatism of one direction or both directions increase the average gray value, it means the more astigmatism, the higher the average brightness of the image.

3 Definition Evaluation of SEM's Astigmatism Image

Astigmatism results in blurred image, so does defocused. In the field of auto-focus, many definition evaluation functions were constructed [5–7], such as functions based on the frequency characteristics, functions based on the statistical characteristics, etc. By focusing on the different positions of the image, definition was evaluated and the right position was found when the clearest image appeared [8]. The definition evaluation functions of auto-focus field were introduced and an improved algorithm was used to evaluate the blurred image caused by astigmatism. Definition evaluation function needs to meet the requirements of unbiasedness, unimodal and high contrast [9].

3.1 Algorithms Based on Gray Gradient

(1) **Brenner.**

Brenner is a spatial gradient evaluation algorithm, which calculate the difference pixel gray between two units [10]. A definition of $M * N$ gray image $f(x, y)$ of Brenner definition evaluation algorithm is:

$$F = \sum_x \sum_y [f(x + 2, y) - f(x, y)]^2 \tag{2}$$

where $[f(x + 2, y) - f(x, y)]^2 > \text{Threshold}$.

Brenner algorithm calculates the energy that greater than a certain threshold, and its accuracy depends on the selected threshold. An appropriate threshold is a good way to get the evaluation of the image definition.

(2) **the sum of the absolute values.**

The sum of the absolute gray values is an algorithm that calculates all pixels of its gray difference of adjacent pixels in the horizontal and vertical directions. Its formula is as follow:

$$F = \frac{1}{MN} \sum_x \sum_y [|f(x + 1, y) - f(x, y)| + |f(x, y + 1) - f(x, y)|] \tag{3}$$

(3) **square function of gradient vector.**

The formula of square function of gradient vector is as follow:

$$F = \frac{1}{MN} \sum_x \sum_y \{ [f(x + k, y) - f(x, y)]^2 + [f(x, y + k) - f(x, y)]^2 \} \tag{4}$$

(4) **evaluation of mean square error.**

The variance of average gray were evaluated by the mean square error to measure the sharpness of the image:

$$F = \frac{1}{MN} \sum_x \sum_y [f(x, y) - u_i]^2 \tag{5}$$

where u_i is the average gray value of the image, and the clearest position appears when F has a maximum value [11].

3.2 An Improved Algorithm

The algorithm firstly calculates the gray-scale difference of two adjacent pixels in the horizontal direction, and then calculates the gray-scale difference of two pixels, who's distance is two pixels in the horizontal direction, and finally calculate their absolute difference. The algorithm combines Brenner, gradient vector and the mean square error, its formula is as follow:

$$F = \left[\frac{1}{MN} \sum_x \sum_y \left| |f(x+1,y) - f(x,y)| - |f(x+2,y) - f(x,y)| \right| \right]^2 \quad (6)$$

4 Experiments

A group of 13 blurred images caused by X astigmatism were used to evaluate the definition with the above five algorithms, and the result is shown in Fig. 3. All five algorithms meet the requirements of unbiasedness, unimodal, Brenner and the improved algorithm have high sensitivity. It is worth mentioning that even if the image is very blurred, the improved algorithm still has a high sensitivity. Since it requires a long time to acquire a SEM image, the speed of the algorithm is not been considered, but considering their accuracy.

A group of 13 blurred images caused by Y astigmatism were used to evaluate the definition with the above five algorithms, and the result is shown in Fig. 4. Similar

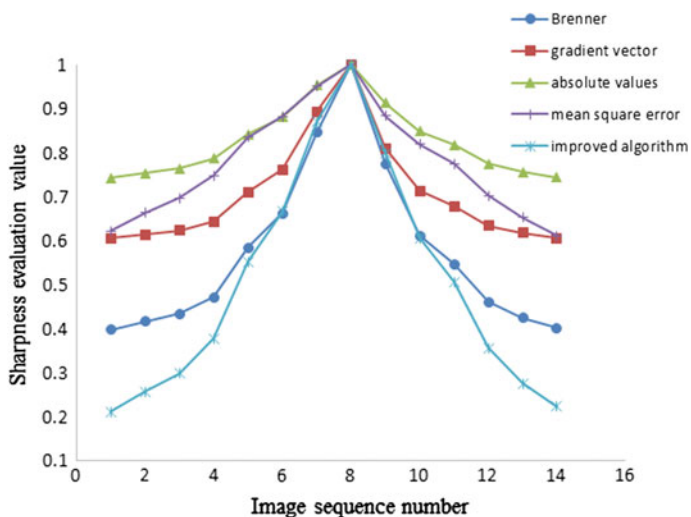


Fig. 3 Definition evaluation (caused by X astigmatism)

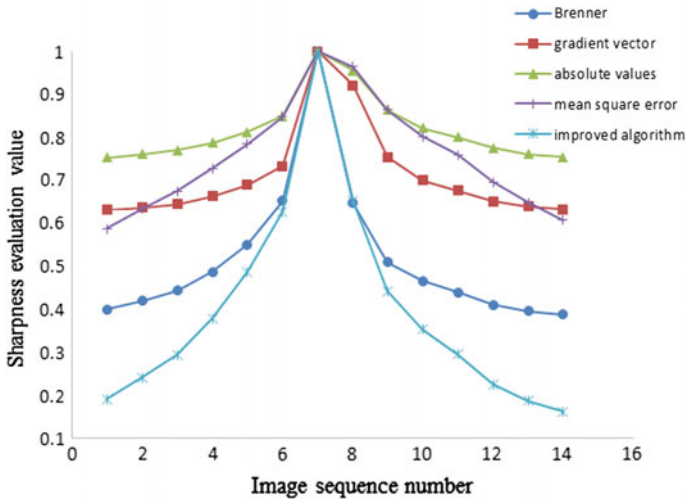


Fig. 4 Definition evaluation (caused by Y astigmatism)

with the results of X astigmatism, Brenner algorithm and the improved algorithm can stably evaluate the definition of a blurred image caused by astigmatism and the latter one has a high sensitivity when the image is very blur.

5 Conclusion

In this paper, blurred images caused by astigmatism have been studied. In the focal condition, astigmatism can results in blurred image, but not elongated or compressed in some direction. Due to the increased astigmatism, the overall brightness of the image will increase. Commonly definition evaluation functions have been introduced and an improved algorithm was developed. Experimental results show that the commonly evaluation functions also applies to the blurred images caused by astigmatism, and the improved algorithm, which can provides a more clear image when using the SEM system to study the micro-nano structures, has higher sensitivity in this type of application.

Acknowledgments This research was supported by the National Natural Science Foundation of China (U1501247), the Scientific and Technological Research Project of Guangdong Province (2015B020239001), the China Postdoctoral Science Foundation (2015M580718), and the Fundamental Research Funds for the Central Universities (2015ZM043). These supports are greatly acknowledged.

References

1. Guo H, Wen B, Xia Y, Zhu Z (2013) Three-dimensional reconstruction simulation of rock microfissure based on SEM images. *Water Resour Power* 31(11):53–56
2. Sergej F (2008) Automated nanohandling by microrobots. Springer, Germany
3. Zhang D-t (2009) Analysis technology of SEM and EDS. South China University of Technology Press, Guangzhou
4. Liu H, Xue L-q (2015) Metal cylinder detection based on digital image processing. *Softw Guide* 14(8):205–207
5. Chen G-j (2007) Study on the auto-focusing technology of digital image and realization for an auto-focusing system. Xidian University, Xi'an
6. Yu C, Wang B-x, Zheng H-q et al (2007) Improved Tennenrad function for microscopic coarse autofocusing. *Optics Precision Eng* 15(5):784–790
7. Hu F-p, Chang Y-l, Ma Y-z et al (2010) Development of video automatic focus method. *Acta Photonica Sinica* 39(10):1901–1906
8. Yang Z-h, Li Y-h, Li Q-x, Guo Yk (2005) Image definition criterion based on edge gradient feature. *Comput Eng Appl* 35–37
9. Hong Y-z, Ren G-q, Sun J (2014) Analysis and improvement on sharpness evaluation function of defocused image. *Optics Precision Eng* 22(12):3401–3408
10. Wang J, Chen H-b, Zhou G-z, An T (2012) An improved brenner algorithm for image definition criterion. *Acta Photonica Sinica* 41(7):855–858
11. Zhang Y-t, Ji S-p, Wang Q-f, Guo Z-y (2012) Definition elaluation algorithm based on regional contrast. *J Appl Optics* 33(2):293–299

A New Position and Attitude Measurement Method for Planar Parallel Mechanism

Zhicong Jian, Xianmin Zhang and Zhenya He

Abstract In order to meet the requirements of high precision, reliability and long time continuous measurement, a vision measurement system is designed by comparing several visual measurement methods, which will be the platform for reliability test on planar parallel mechanism. Measurement system uses mark point counterpoint method by one camera, and we design one kind of identifying pattern, which contains location information. By identifying the high precision pattern on a block of reference template, the camera can be easier to obtain its exact location information through the whole measurement space and then we can calculate the reliable platform position and orientation. According to this pattern, more than one image processing method is developed and compared.

Keywords Vision measurement · Image processing · Pattern for identification · Planar parallel mechanism

1 Introduction

In the field of precision engineering, fast response, high precision of the planar positioning device play an important role in lithography, precision measurement and semiconductor manufacturing equipment. The existing plane positioning device is generally used in series mechanism or parallel mechanism [1–3]. Compared with the traditional serial mechanism, the parallel mechanism has the following advantages: high rigidity, stable structure, strong carrying capacity; high precision, no

Z. Jian · X. Zhang (✉) · Z. He

Guangdong Provincial Key Laboratory of Precision Engineering and Manufacturing, Technology, South China University of Technology, Guangzhou 510640, China
e-mail: zhangxm@scut.edu.cn

Z. Jian
e-mail: 419469971@qq.com

Z. He
e-mail: mezhyhe@scut.edu.cn

error accumulation and amplification; small inertia; in position reverse solution is easily, meet the requirements of on-line calculation. So it has a wide application prospect in industrial production and other fields. Due to the error of machining and assembling, the actual parameters of the mechanism cannot be consistent with the parameters of the theoretical model that impact mechanism movement accuracy. To improve the accuracy of the parallel mechanism motion can through kinematic calibration [4] to achieve, it base on precision design [5], by the error function between the measured data and the desired output at the end effector of the structure, with identification technology modification of model parameters of the controller. Researchers have proposed different methods of kinematic calibration of planar parallel mechanism. Joubair et al. [6] put forward a simple and effective calibration program for a new type of planar parallel mechanism, using coordinate measuring machine. Meng [7–9] proposed different step by step kinematic calibration method for different 3 degree of freedom planar mechanism. He [10] thoroughly summarized the current parallel mechanism of the kinematic calibration process and methods.

Scholars pay more attention to calibration method and control strategy to realize the platform of precise positioning, and less attention to study parallel platform in the actual production process of intelligent calibration, positioning accuracy degradation process and timely warning automatic compensation. And the robot's intelligent calibration and automatic compensation system and equipment are mostly aimed at the "series" robot, such as the six axis robot arm. So to design evaluation system on parallel platform for intelligent calibration, on-line positioning error monitoring and error analysis, and even on this basis to achieve automatic compensation has the value of research and application.

Visual position measurement technique is a kind of non-contact measurement with fast detection speed, high precision, does not affect the moving target and nondestructive measurement. Compared with other expensive robot terminal full posture measurement tools, visual based measurement scheme is economical and practical.

In this article, we take 3-RRR parallel platform as measured object [11], which designed and optimized by our experimental team, and design an end effector position and orientation measurement system based on vision for planar parallel mechanism error visualization and reliability research. In chapter two, we analyze and determine measure tragedy. In the third chapter, we will discuss the hardware architecture of the measurement system and focus on the design of a reference template for a wide range of positioning. Based on the hardware system, the fourth chapter will analyze the specific positioning measurement methods and image processing methods.

2 Design of Measurement System

2.1 Determination of Measurement Strategy

This measurement system is designed to provide high precision measuring method for the reliability research of planar motion mechanism. Reliability research depends on large of experiment or production data as the support of the theoretical analysis and verification, thus requiring the measurement system is able to measure for a long time operation while maintaining high accuracy under the premise, with functions of automatic error compensation. Measurement methods adapting to industrial applications will bring more help for prolonging the equipment service life and improving the quality of the products. Therefore, it is necessary to consider the selection of suitable measurement means and concrete method combining the actual working situation of equipment. At present, most of the screen printing equipment, solar cell manufacturing equipment and electronic circuit plug-in equipment using the mark point as the work mode to ensure the processing accuracy.

The vision measurement used for positioning can be divided into single camera measurement, dual camera measurement and multi camera measurement. Among them, the multi camera measurement is used less in the planar mechanism. Monocular vision position detection system is only equipped with a camera, the structure is simple. The system uses a single two-dimensional image to get the three-dimensional information of the target. Because of the lack of depth information of the target, so it needs to add some constraints to restore the three-dimensional information of the target. Binocular vision position detection system uses two cameras to measure the target. When calculating the space position of the target, the system not only needs to calibrate the internal parameters of the camera, but also needs to calibrate the external parameters between the two cameras. Binocular system has a strong ability to restore the three-dimensional information, but the camera calibration accuracy directly affects the measurement accuracy of the system.

Combined with the equipment working scene mentioned above, there are three kinds of strategy on visual system layout as shown in Fig. 1a–c, the advantages and disadvantages of the analysis are as follows.

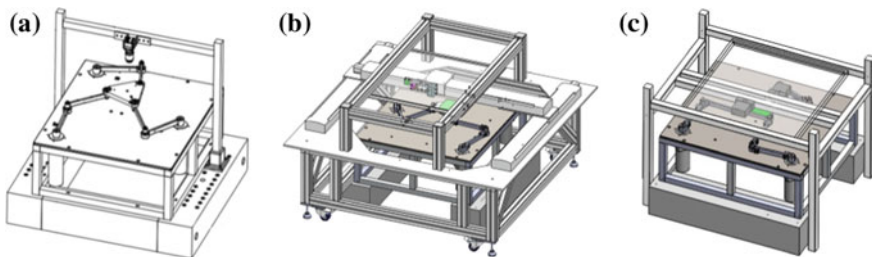


Fig. 1 Three scheme of measurement system

Figure 1a. In the strategy one, the measurement system using a single camera, and the camera is fixed. This scheme has the advantages of simple structure, easy realization and low cost. At the same time, the field can cover the entire workspace, so that the camera can continuous monitoring position and posture changes of the end effector of planar mechanism under allowable frequency. The shortage of this scheme is that the image quality is easily affected by the external illumination. At the same time, a large field of view lead to reduce pixel equivalent, and pursuit of real-time ability requires that image processing algorithms cannot be too complex, so the measurement precision with certain restrictions.

Figure 1b. In the strategy two, the measurement system using a single camera mounted in XY direction motion system with a small field of view. Through optical module of light reflection camera can takes photos for the mark points on the above and below plane. The advantage is that camera motion system can take the camera to any location in the work space of 3-RRR. Due to has its own light source and the distance between light source and photographed plane is small, the effect of ambient light is very small. Small field of view can get a more objective pixel equivalent, without the pursuit of time, the use of sub pixel image processing algorithm can achieve high precision measurement. Compared to the strategy one, in one measurement period, the camera needs to move to the next two MARK points on the diagonal of the template, so the measurement does not have real-time. In fact, most of the production equipment does not require continuous monitoring of key sports organizations, only in the processing link, the positioning accuracy of the movement mechanism is required. That means the scheme two still meets the requirements of collecting the location error of the plane mechanism.

Figure 1c. In the strategy three, the measurement system uses dual cameras. Each camera equipped the same optical module as strategy two mentioned. If the two cameras are fixed, and the position is at the top of MARK point in the lower template, the system can only measure a very small range of displacement. It is obvious that position data only from the area around the origin is obviously not persuasive if we want to study and evaluate the overall performance of the planar mechanism. If the relative position of the two cameras are fixed with distance corresponds to the mark point, and installed in XY direction motion system, the vision system will be able to measuring position of planar mechanism in the workspace with good real-time performance, but is not suitable for measurement of planar mechanism posture. The reason is that the camera field of view is small; a small angle of rotation of the plane mechanism may lead to MARK point out of the field of view. In order to measure the attitude, we need to add a rotating device, which makes the dual camera can rotate with the change of the attitude of the planar mechanism. But the introduction of the rotating device is bound to generate a new source of error, and the cost will get more.

In a word, the strategy two can realize the measurement of the position and attitude of planar parallel mechanism, and has high precision, good stability, and compatibility with the line equipment, and the cost is suitable. So we chose scheme two as the measuring method for our measurement system.

2.2 Overall Measurement System

The hardware of the measurement system is composed of a computer control system, a vision acquisition system, a camera motion system, an upper template and a lower template, as shown in Fig. 2.

Figure 2a. Computer control system is responsible for the information exchange between 3RRR planar parallel mechanism, visual acquisition system and camera motion system movement, control the three parts of the movement rhythm, monitoring abnormal situation.

Figure 2b. Image acquisition system is a key part of the measurement system. The optical component is an improved single lens optical imaging system based on the vision system of win series automatic solder paste printing machine developed by our team research group, as shown in Fig. 3. When camera is in position, light controller receives command from computer control system, and turn on the upper light source first and light on the surface of upper template. Light reflected from the upper template into spectroscopic, then the refraction beam turn to the reflector, reflect again into the telemetric lens and eventually image in the camera. By using the light shielding plate, the light entering the lower template area is blocked by the light from the upper template, and the mutual influence of the upper and the lower light path is avoided. After the upper template image is collected, lower light source turn on and collect the lower template image. Then one picture cycle of the position is complete.

Figure 2c. Camera motion system consists of Longmen frame structure motion mechanism with two degree of freedom, servo motor, motor driver and motion control card.

Figure 2d. Upper template fixed by a special fixture on the top of the visual acquisition system, is used for providing reference information for the measurement

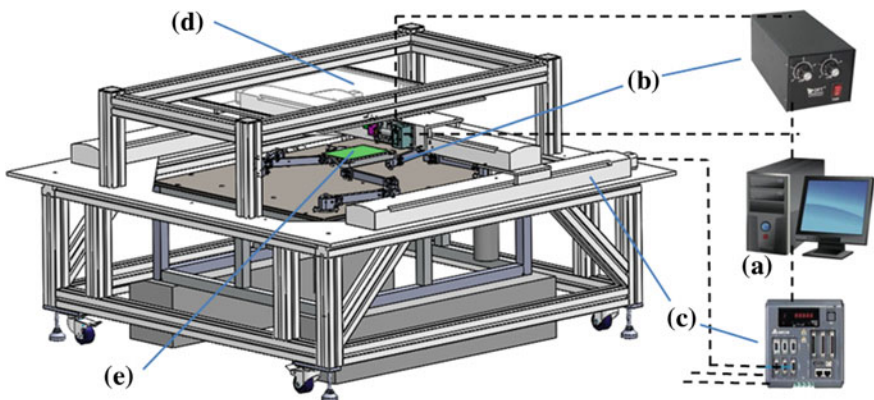


Fig. 2 Composition of the vision measurement system

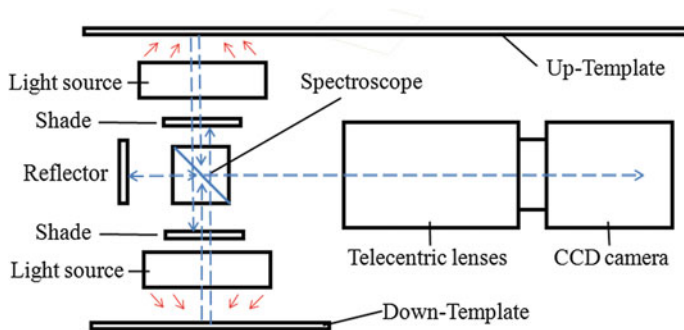


Fig. 3 Optical path in the visual system

system. Therefore, the template is made by a custom high precision calibration board with the size suiting working space of 3RRR planar parallel mechanism.

Figure 2e. Lower template is fixed by a special fixture which connected with the end effector of 3RRR planar parallel mechanism. Each of the four corners of the template contains a circular mark point. When measuring 3RRR terminal position and attitude, we only need two of them on the same diagonal.

Measurement system work flow is shown in Fig. 4: computer transmit displacement instructions to servo drives of 3RRR parallel mechanism through the motion control card and computer calculates required motion displacement for visual system, then send instructions to the camera motion system. After camera motion system reaches the position, computer send instruction respectively to light source controller and the camera to complete the image acquisition assignment.

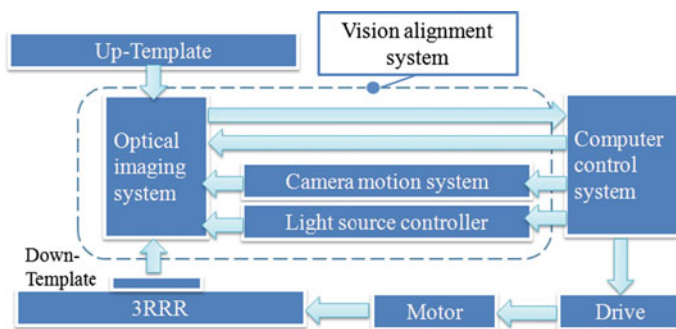


Fig. 4 Operation principle of the vision measurement system

3 Design of Pattern Recognition on Upper Template

3.1 Design Requirements Analysis

When industrial equipment is carrying out contraposition mission, the position error and attitude error are determined by calculating the distance between the MARK point position and the image center point from the upper and lower two images. For general equipment, the processing position is fixed, position error and attitude error of the parts to be machined is relatively small, so as long as the reference plane to provide two MARK points will be able to complete the positioning and rectification. If the machining position is variable and the distance is more than the field of view, at the position of the new station, at least two MARK points should be added in the corresponding position. Similarly, although our measurement system and vision measurement of screen printing equipment have similar structure, but the measurement range we need is not limited to near the center. Therefore, if a large range of positioning measurement is required, such as covering the working space of parallel mechanism, the upper template needs to provide enough reference patterns which can contain position information.

This provides a way for the design and layout of the identification pattern. It can include the location information, which means that the identification pattern can be interpreted according to a certain rule. On the one hand, the pattern should has the same characteristics, to help the computer to determine whether the image of the reference pattern is a complete information pattern. If the pattern is partly not in the image, it is possible to lose part of the location information, resulting in an inability to interpret or interpret the error information. As shown in Fig. 5a, if the model does not have a common feature for the identification of integrity, it is possible to judge the ladder and part of the triangle in the image as the same model.

On the other hand, the pattern should have their own differences, and these differences can be convenient for the computer to get the location information by simple calculation. As shown in Fig. 5b, there are differences about color or size between the reference patterns and it is very convenient to distinguish by image processing algorithms. Of course, the difference is not limited to a single geometry.

Enough number means that a picture of a captured image can cover at least two complete reference patterns and left a certain margin in the direction of the shorter length, as shown in Fig. 5c. To prevent the visual acquisition system and the

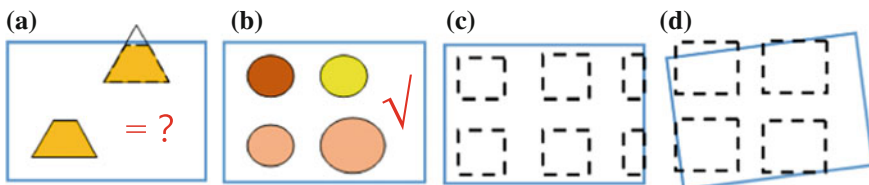


Fig. 5 Different condition when design

identification pattern due to installation errors or unexpected accidents, resulting in a small angle, resulting in the image does not have a complete pattern, as shown in Fig. 5d.

3.2 Reference Pattern Design Based on Lattice

In view of the above requirements, this paper designed a 5×5 dot array, each dot away have five row and five column with the same dot size, distance between adjacent rows or adjacent columns of two dots is equal. The distance between adjacent dot arrays is also equal. Making a rule that points in a dot array located in the position follows is fixed point: upper left corner (row 1, column 1), the lower left corner (row 5, column 1), the lower right corner (row 1, column 5), central (row 3, column 3) and below the central (rows 4, column 3)—as Fig. 6 blue dotted boxes shown, namely in all such dot array, the point located in these position must exist. On the contrary, the lower right corner of the point (row 5, column 5) does not exist, such as red dotted box shown in Fig. 6. For the convenience of making template, color of all existent dots is black. The order of the dot array is sorted by column, starting from row 1, column 1, after column 1 is full, then turn to the row 1, column 2. Through the three dots located in the upper left corner, the lower left corner and the upper right corner, we can fix the position of the lattice, and obtained the size in the image coordinate system.

By extracting the coordinate of the centre of central point in the dot array and the midpoint of line between upper right point and lower left point, we can get a more accurate central coordinate of the dot array. By using the four fixed points outside the center point, we can use the image algorithm to get the attitude of the template relative to the camera.

In addition to the above six fixed point (which one is not necessarily), we can define the presence of other dot by 0 or 1. As shown in Fig. 7b, in order to read, you can get a group containing 0/1 string with 19 places, as a binary number, on behalf of the digital $0-2^{19}$ (524, 288).

Fig. 6 Example of dot array

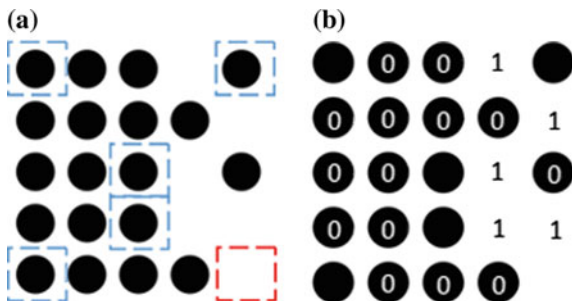
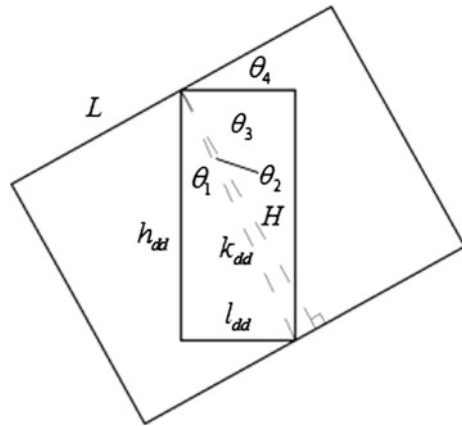


Fig. 7 Calculate the maximum corner



Taking our measuring system for example, the field of view of the camera is $L = 8 \text{ mm}$, $H = 6 \text{ mm}$, radius of every dot $r_d = 0.15 \text{ mm}$, distance of the adjacent rows or adjacent columns with a dot in one dot array is $d_d = 0.4 \text{ mm}$, distance of the central point of adjacent dot array is $D_d = 3 \text{ mm}$. According to the working space of the 3RRR plane parallel platform, the measurement range is $400 \text{ mm} * 400 \text{ mm}$, requires a scale of 133 rows and 133 columns, a total quantity of dot array is 17,689. If the visual acquisition system captured one of the complete dot array as shown in Fig. 6a, according to design rules, 0 represent having dots and 1 represent no dots, from the first non fixed point on first column, from left to right, from top to bottom records the state of each dot, we can get a binary number: 000,00000,000,10110,101, as shown in Fig. 6b, convert to decimal number is $n = 181$. And we can easily calculate that the dot array with number 181, is located in row 48, column 2. We establish a coordinate one the reference template with its origin at the centre of reference template, and x axis along row, y axis along column. We can calculate the coordinate of the dot array centre by the following formula:

$$x_{218} = (\text{column} - 67) \times 4 = -260 \text{ mm} \tag{1}$$

$$y_{218} = (67 - \text{row}) \times 4 = 76 \text{ mm} \tag{2}$$

In order to avoid the condition Sect. 3.1 mentioned that mounted camera angle error resulting in no complete pattern in the field of view, we need to check the field maximum allowable inclination: as shown in Fig. 7. Set a outer envelope rectangle outside two adjacent array in a the same column, with the size of L_{DD} and H_{DD} .

As shown in Fig. 7, the maximum rotation angle θ_4 for the camera can be determined by the geometric relationship:

$$\theta_4 = \theta_1 + \theta_2, \theta_1 = \tan^{-1}(l_{dd}/h_{dd}), \theta_2 = \cos^{-1}(H/k_{dd}) \quad (3)$$

$$k_{dd} = \sqrt{h_{dd}^2 + l_{dd}^2} \quad (4)$$

$$h_{dd} = D_d + 4 \times d_d = 4.9 \text{ mm}, l_{dd} = 2 \times r_d + 4 \times d_d = 1.9 \text{ mm} \quad (5)$$

The calculation found that $k_{dd} < H$, that means the camera can rotate in any case, and there will always be at least one complete pattern in the field of view. If in the late study, we need to upgrade the system to a dual camera program, we can also have no need to worry about that when the camera following the attitude changes by end effector of planar parallel mechanism. At the same time, as the fixed point of the three corners can be at any time for the camera to provide the direction of the template, the conversion of the coordinate system will be available.

In the actual production of processing templates, because each dot array has differences, in the face of tens of thousands of dot array, it is not possible to complete the drawing work artificially. By using secondary development in AutoCAD by Visual Basic programming software, Simply enter the lattice size parameters and measurement range, you can automatically generate the required dot array graphics.

4 Vision Based Measuring Method

4.1 Define the Coordinate System

3RRR planar parallel mechanism has three degrees of freedom: X, Y two directions of translation and rotation around the Z axis. To measure the position and attitude of the end effector M of 3RRR, the coordinate systems is established according to the law of the right hand, and the system is equivalent to the coordinate system as shown in Fig. 8a.

$R_b(O_b, x_b, y_b, z_b)$ is the base frame of the 3RRR with its origin at location hole B_1 and y axis along $B_1 B_2$. $R_m(O_m, x_m, y_m, z_m)$ is the frame of end effector of 3RRR with its origin at location hole M_1 and y axis along $M_1 M_2$. $R_p(O_p, x_p, y_p, z_p)$ is established at the centre of the lower template with y axis has the same direction of $R_m(O_m, x_m, y_m, z_m)$. $R_c(O_c, x_c, y_c, z_c)$ is the frame of camera. $R_r(O_r, x_r, y_r, z_r)$ is established at the centre of the upper template.

We can acquire position and attitude of the end effector of 3RRR relative to the world coordinate system by the hand-eye-calibration, through a series of coordinate transformation is obtained: ${}^bT_m = {}^bT_r {}^cT_r^{-1} {}^cT_p {}^pT_m$. Among them, ${}^cT_r^{-1}$ and cT_p can use the template dot array, to obtain the Z direction with distance by Zhang's calibration method [12]. pT_m can be calculated according to the installation method between lower template and end effector of 3RRR. We can use laser tracker system to measure the position of special fixture related to the base frame, then analyze the

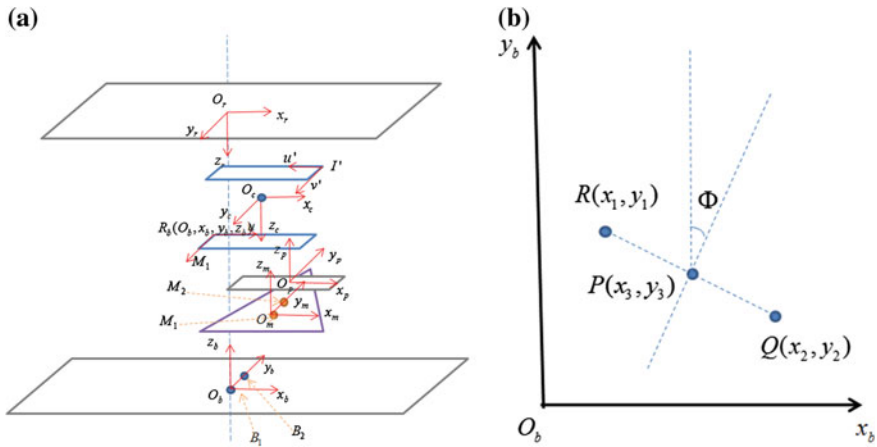


Fig. 8 a Diagram of the coordinate system, b Using two point to describe pose

position relationship between upper template and special fixture so that we can calculate the position of upper template related to base frame bT_r .

4.2 Position and Attitude Measurement

Position measurement of end effector of 3RRR is mainly equivalent to calculate the relative position between centre coordinate of reference pattern on upper template and the centre of the image1, and the relative position between centre coordinate of mark point on the lower template and the centre of the image2. Because we take photo using a common light path, the centre of image1 and image2 can be coincide. That means we can put calculate the position of mark point related to upper template coordinate system through the image centre. And then transfer to base frame. After we acquire position of both mark point P and mark point Q related to base frame, we can determine the position of end effector on 3RRR by calculate the midpoint of line between p and Q, and determine the attitude by calculate the included angle Φ between perpendicular bisector of line PQ and y axis, as shown in Fig. 8b.

4.3 Discussion on Image Processing Scheme

Dot Array Extraction

The template images obtained by visual acquisition system need two steps of image processing. The first step is a complete lattice extraction from the image after simple

pre processing, the second is to do further processing for extracted dot array, such as featuring point coordinates with high precision, and interpretation of the lattice location information (hereinafter referred to as the decoding).

The first step of the dot matrix extraction has two methods. The first method is according to the displacement command sent by computer to 3RRR. We can predict the coordinate of image centre on the upper template frame, and to find the closest dot array. Then calculate the position of the dot array centre on image frame, using this coordinate as the centre generate a rectangle ROI area which size is bigger than the dot array. As the Longman module using semi closed loop control, positioning accuracy can reach $\pm 40 \mu\text{m}$. The ROI area expand about 40 pixel is enough (pixel equivalent of camera is $5 \mu\text{m}$).

The second method is the direct use of image processing template matching method. As shown in Fig. 9a–c, we set up a model using five fixed point which are must exist. Algorithm based on the similarity between the template and scan images to determine whether to find the target. If you find a target, generate a ROI area. If the ROI region is a little too larger, you can generate a smaller new ROI region at the same place by using the same centre coordinate. It will facilitate the subsequent decoding process.

To comparison those two methods, because the first method only need to finish coordinates conversion by simple geometric calculations in the ideal case, the occupation of the program time can be nearly ignored. But considering requirement of the measurement system long time operation, during the operation of the process, if a causal factors influence camera motion system that it failed to reach the specified location timely, and the produced ROI failed to cover a complete dot array, the program receive uncertainty information and create error, the measurement system will fail to work.

The second method directly extracted dot array from the image. After calculating the dot array code, it can compare the result with the predictive code from the first method, if result is abnormal, computer can remind the participants in a timely manner, and feedback to the user interface, and even provide data support to determine the cause of failure. It seen that the second method is safer than the first one, but we still need to care about the processing time of the second method to determine whether can complete the data processing tasks within two shooting



Fig. 9 Using template matching algorithm to find dot array

Table 1 Comparison of measurement methods

Picture number	1	2	3	4	5	Average time
Time (ms)	125	176	154	162	189	161.2

cycle. Using C++ programming language to call the OpenCV computer vision library template matching algorithm for simulation experiments, the image which from the 400 mm * 400 mm calibration plate created by AutoCAD, is matched with the same model image. Table 1 shows the time for template matching.

Through the simulation, we can find that the time common template matching algorithm disposing images is not short, and the difference of time is big. To compare the images in the simulation, it will take less time when there were fewer points existing in the dot array. When there were more points existing, it takes more time. This shows that dots in the dot array may bring obvious impact to matching process as they just look like the fixed point. Maybe we will consider more about the rule of coding. Maybe 1 equal point is existent, and 0 equal point is inexistent will improve the efficiency. However, more points are good for space attitude measurement. To find a balance is necessary.

Dot Array Decoding

After obtain the ROI, through threshold segmentation, connected region analysis, sub pixel edge detection algorithm, centroid extraction and other image processing operations, you can get a higher accuracy of the dot center coordinates. Then we shall consider how to decode more easily and accurately. We also have two methods.

The first method is to analyze the deviation between the coordinate of upper left corner point and the coordinate of others. If deviation on x is 0 or smaller than a value we set, it represents that two points are in the same column, then compare with the deviation on y, we can know whether the two points are adjacent, or the number of across empty points and note down the number of 0 or 1. If the point is not in the same column with the upper left point, we should note down the deviation between upper left corner point and the point on y, as well as the deviation between upper left corner point and the previous point on y, then compare with this two deviations.

The second method ignores the coordinate we measured before, it just needs the coordinate of the upper left corner point. And then calculate the coordinate of all 19 points which contain information of 0 or 1. Then read the gray level in order. If the gray level is lower than a value, we consider there is a point here.

Both the speed of decoding in two methods is quick. So we think more about the factor of safety and reliability. In the first method, we use area as a screening condition to find out every point before extracting the coordinate. So many pre-process algorithms have reduced the influence. The value of coordinate and the analysis of deviation are credible. However, the second method is not safe. If there is a small shade located at one of the corners of the row and column, when the point here is inexistent. The second method may consider the shade as the point. So it is better to choose the first method.

5 Summary and Prospect

In this paper, a new vision measurement method for planar parallel mechanism is presented. We analyze and determine a vision measurement strategy based on using single camera fixed to camera motion system in two degrees of freedom. And we put forward A reference template which hiding location information for position and orientation and discuss the algorithm scheme on reference template image analysis by means of image processing, so that it can achieve high precision, long time safe and reliable operation that is proposed in this paper. The next step is to verify the actual effect of the proposed method and algorithm, and further analyze the factors and the influence degree of error to the measurement system.

Acknowledgments This research is supported by the National Natural Science Foundation of China (No. U1501247), the Scientific and Technological Project of Guangzhou (No. 2015090330001), the Science and Technology Planning Project of Guangdong Province (No. 2014B090917001), the China Postdoctoral Science Foundation (No. 2015M580718), and the Fundamental Research Funds for the Central Universities (No. 2015ZM043). The authors gratefully acknowledge these support agencies.

References

1. Gao W, Kim SW, Bosse H, Haitjema H, Chen YL (2015) Measurement technologies for precision positioning. *J CIRP Ann Manuf Technol* 64(2):773–796
2. Ryu JW, Gweon DG, Moon KS (1997) Optimal design of a flexure hinge based XY wafer stage. *J Precis Eng* 21(1):18–28
3. Wang H, Zhang X (2008) Input coupling analysis and optimal design of a 3-DOF compliant micro-positioning stage. *J Mech Mach Theory* 43(4):400–410
4. Besnard S, Khalil W (2001) Identifiable parameters for parallel robots kinematic calibration. In: 2001 IEEE international conference on robotics and automation, Seoul, Korea, pp 2859–2866
5. Ma L, Huang T (1999) Precision design of parallel machine tool for manufacturing. *J China Mech Eng* 10(10):1114–1117
6. Joubair A, Slamani M, Bonev IA (2012) A novel XY-theta precision table and a geometric procedure for its kinematic calibration. *J Robot Cim-Int Manuf* 28(1):57–65
7. Gao M, Li T, Tang X (2003) Calibration experiment research of parallel kinematic machine with a few degrees. *J Chin J Mech Eng* 39(9):118–122
8. Chang P, Wang J, Li T et al (2008) Step kinematic calibration of a 3-DOF planar parallel kinematic machine tool. *J Sci China Series E: Technol Sci* 51(12):2155–2167
9. Liu D, Wang L, Guan L (2010) Accuracy analysis and calibration of a special 3-DOF parallel mechanism. *J Chin J Mech Eng* 46(9):46–51
10. He X, Ding H, Fu T, Sun Houfang H (2004) Review on kinematic calibration of parallel kinematic machine. *J Mach Tool Hydraulics* 10:9–11
11. Gao MW, Zhang XM, Wu ZW (2011) Optimum design of a 3-RRR planar parallel manipulator with a singularity-free workspace. *J Appl Mech Mater* 86(08):606–610
12. Zhang Z (2005) Flexible camera calibration by viewing a plane from unknown orientations, computer vision. In: The proceedings of the seventh IEEE international conference

Research on Robot Calibration Based on Laser Tracker

Yabo HuangFu, Lubin Hang, Wushan Cheng, Liang Yu, Chengwei Shen, Jun Wang, Wei Qin and Yan Wang

Abstract With the development of intelligent manufacturing, robot absolute positioning accuracy plays an important role in advanced applications. Aiming at improving the absolute positioning accuracy of serial robot, a calibration experiment is conducted with a laser tracker, the effects of the kinematic calibration are evaluated by comparing the position errors. Firstly, the kinematic model of the robot is established according to the method of Denavit-Hartenberg parameter, and the geometric parameters of the robot to be corrected are selected. Secondly, the error function is established with measurement result of the end reflector position and calculation result by DH matrix of the corresponding position. Thirdly, the actual geometric parameters are obtained by solving the error function using LM algorithm. Finally, the kinematic model of robot system is corrected by these parameters. The result shows that the maximum/mean/root-mean-square (RMS) position errors are reduced 47.48 %/37.98 %/40.40 % after calibration.

Keywords Serial robot · Laser tracker · Robot calibration · LM algorithm

1 Introduction

With the development of robotics, robots are widely used in various industries, such as aerospace, automotive design and manufacture, medical equipment and others. At the same time positioning accuracy of the robot is becoming increasingly higher requirement. Manufacturers only provide the repeated positioning accuracy of the

Y. HuangFu · L. Hang (✉) · W. Cheng · L. Yu · C. Shen · J. Wang · W. Qin
Shanghai University of Engineering Science, Shanghai, China
e-mail: hanglb@126.com

Y. Wang
Shanghai Jiaotong University, Shanghai, China

© Springer Nature Singapore Pte Ltd. 2017
X. Zhang et al. (eds.), *Mechanism and Machine Science*,
Lecture Notes in Electrical Engineering 408,
DOI 10.1007/978-981-10-2875-5_117

1475

robot, and the accuracy can reach 0.01 mm. The absolute positioning accuracy of the robot mostly reaches 2–3 mm, and it is difficult to meet the rigid demand of intelligent manufacturing.

In order to improve the absolute positioning accuracy of the robot, the calibration method can be used to identify the accurate parameters of the robot model. Many researchers about the robot calibration technology have been done by domestic and foreign scholars. Based on quantum particle swarm optimization algorithm, Fang et al. [1] propose a kinematic calibration method that can improve position accuracy of serial robot and parallel robot. The result shows that kinematic calibration method based on quantum particle swarm optimization is more effective within the larger workspace. The main manufacturing and assembly errors are attributed to the errors of the joint parameters of robot and kinematic variables [2, 3]. Kinematic calibration is to obtain actual kinematic model. Liu et al. [4] propose two-step calibration method combined with geometric identification and parameter identification. He et al. [5, 6] use the POE formula to derive the kinematic parameters of the robot including joint angle error calibration error model, and analyze the correlation between various parameters of the robot. Verl et al. [7] introduce a method to sort the poses for the calibration, and bases on the DETMAX algorithm using the condition number of an identification matrix to predict the RMS error of the TCP of a calibrated machine depending on the number of measurement poses and the standard deviation of the measurement device.

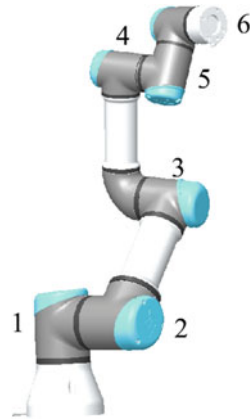
Robot calibration usually associated with measurement techniques is to improve the accuracy. Measurement tools include three coordinates measurement instrument [8], Ballbar [9], laser tracker [10, 11] and so on. Laser tracker based on IFM and ADM principles to obtain the 3D coordinates of a spatial point is an effective measurement tool. It has the advantages of high accuracy, high efficiency and real-time tracking measurement, and provides great convenience for robot calibration. Therefore, it is widely used in robot calibration. Based on laser tracker, this paper focuses on the kinematic calibration for serial 6R robot. After calibration, the experimental result shows that the absolute positioning accuracy of the robot is improved.

2 Calibration System and Experimental Platform

The serial 6R robot is considered as the research object in this paper. The robot body is compact, rated load for 3 kg, and the structure diagram is as shown in Fig. 1. The repetitive absolute positioning accuracy is 0.02 mm, but absolute positioning accuracy of the robot is poor.

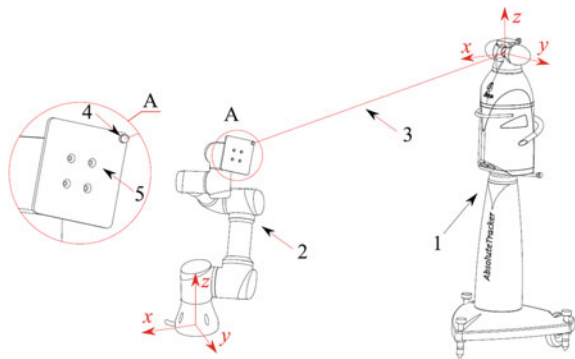
Therefore, the calibration system is built (Fig. 2), and mainly includes laser tracker, serial robot and reflector.

Fig. 1 Schematic diagram of the structure of serial robot



1-Base, 2-Shoulder, 3- Elbow, 4- Wrist 1, 5- Wrist 2, 6- Wrist 3

Fig. 2 Schematic diagram of measurement system



1-Laser tracker, 2-Serial 6R robot, 3-Laser, 4-Reflector, 5-Aluminum plate

In the calibration system, Leica AT901-MR type laser tracker is used to measure position of the reflector mounted on the end-effector based on spherical coordinate system. The measurement range is up to 50 m, and measurement accuracy is $10 \mu\text{m} + 0.5 \mu\text{m/m}$ meeting requirement of robot calibration measurement accuracy.

Figure 3 shows the installation that is used for measuring the positioning performance of a serial 6R robot with a laser tracker. Robot system includes the robot, controller and teaching apparatus; and laser tracker system includes the laser tracker, controller, weather station, reflector, computer and the power supply. The reflector is mounted on aluminum plate surface of the robot end-effector.

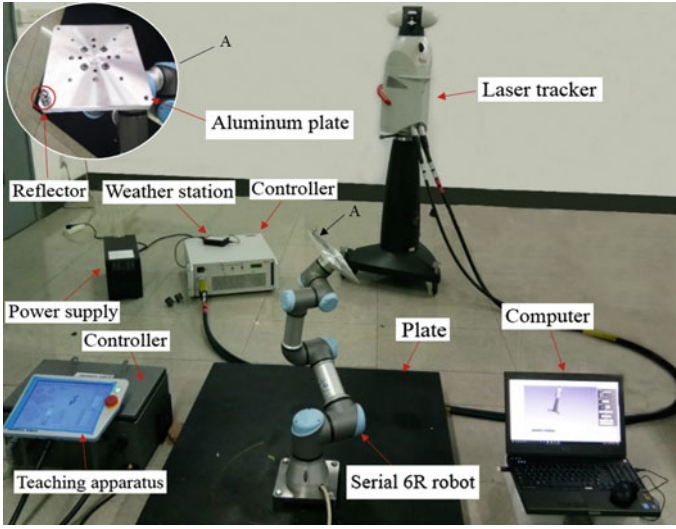


Fig. 3 Experimental setup for robot calibration

3 Geometric Parameter Identification Model

According to the DH parameter method, the kinematic model of the robot is established. The error kinematic model is derived based on the measured data and kinematic model. Finally, the geometric parameters are obtained by LM algorithm.

3.1 Kinematic Model

According to the DH parameter method, a coordinate system for each joint of the serial robot is established, as shown in Fig. 4. The motion of the mechanism is described with the link parameters, and the nominal kinematic parameters of the links are shown in Table 1.

According to the DH model in Fig. 4, the transformation matrix between the coordinate systems of two adjacent links is

$$\begin{aligned}
 {}^{i-1}T_i &= \text{trans}(z_{i-1}, d_i) \text{rot}(z_{i-1}, \theta_i) \text{trans}(x_{i-1}, a_i) \text{rot}(x_i, \alpha_i) \\
 &= \begin{bmatrix} \cos \theta_i & -\sin \theta_i \cos \alpha_i & \sin \theta_i \sin \alpha_i & -a_i \cos \theta_i \\ \sin \theta_i & \cos \theta_i \cos \alpha_i & -\cos \theta_i \sin \alpha_i & -d_i \sin \theta_i \\ 0 & \sin \alpha_i & \cos \alpha_i & d_i \\ 0 & 0 & 0 & 1 \end{bmatrix} \quad (1)
 \end{aligned}$$

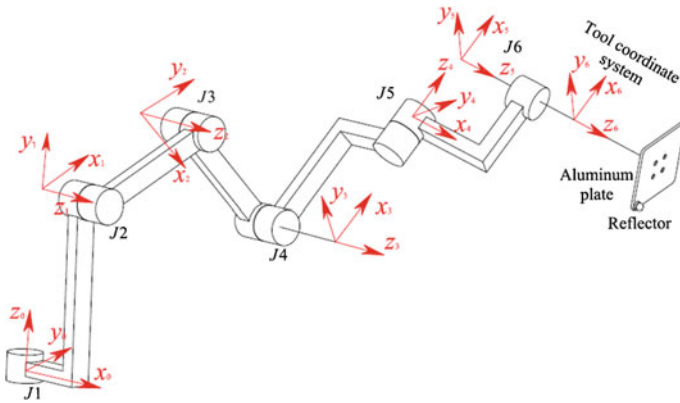


Fig. 4 DH model of serial 6R Robot

Table 1 Nominal kinematic parameters of serial 6R Robot

No.	1	2	3	4	5	6
a_{i-1} (mm)	0	243.65	213.25	0	0	0
α_{i-1} (°)	90	0	0	90	-90	0
d_i (mm)	151.9	0	0	112.35	85.35	81.9
θ_i (°)	0	-90	0	-90	0	0

Kinematic transformation matrix of the robot is

$${}^0T_7 = {}^0T_1 {}^1T_2 {}^2T_3 {}^3T_4 {}^4T_5 {}^5T_6 {}^6T_7 \tag{2}$$

where, the tool transformation matrix 6T_7 expresses as,

$${}^6T_7 = \begin{bmatrix} 1 & 0 & 0 & x \\ 0 & 1 & 0 & y \\ 0 & 0 & 1 & z \\ 0 & 0 & 0 & 1 \end{bmatrix}$$

(x, y, z)—the position of the reflector in tool coordinate system.

3.2 Error Kinematic Model

According to the kinematic robot kinematic model, corresponding homogeneous matrix is established through in each link of the robot to build the kinematics model of the robot. Substituting the kinematic DH parameters ($a_i, \alpha_i, d_i, \theta_i$) ($i = 1-6$) and the position of reflector in the tool coordinate system (a total of $4 \times 6 + 3 = 27$

parameters) into robot kinematic model can get position function P of reflector based on robot base coordinate system

$$P = f(X_0) \tag{3}$$

where, vector X_0 contains 27 elements corresponding to the geometric parameters.

$$P = [P_x, P_y, P_z]^T$$

Due to the geometric error of the mechanical structure, assembly error and transmission error, the kinematic DH parameters ($a_i, \alpha_i, d_i, \theta_i$) ($i = 1-6$) must lead to errors. In addition, the installation position of reflector with respect to the tool coordinate system contains position errors. There exists certain deviation in motion process between actual position and nominal position of the reflector. The position function of reflector P' using DH

$$P' = f(X') \tag{4}$$

where, X' —the vector of the geometric parameters

$$P = [P'_x, P'_y, P'_z]$$

The position P^* of reflector is measured using laser tracker, and position error function ΔP of the reflector

$$\Delta P_j = P_j^* - P'_j \tag{5}$$

where, ΔP_j —position error function of the j th point, $\Delta P = [\Delta P_{xj}, \Delta P_{yj}, \Delta P_{zj}]^T$

Function $e(X)$ is constructed by the position error function of the reflector

$$e(X) = [\|\Delta P_1\|^2, \|\Delta P_2\|^2, \dots, \|\Delta P_m\|^2]^T \tag{6}$$

where, m —the number of points. X —the geometric parameters.

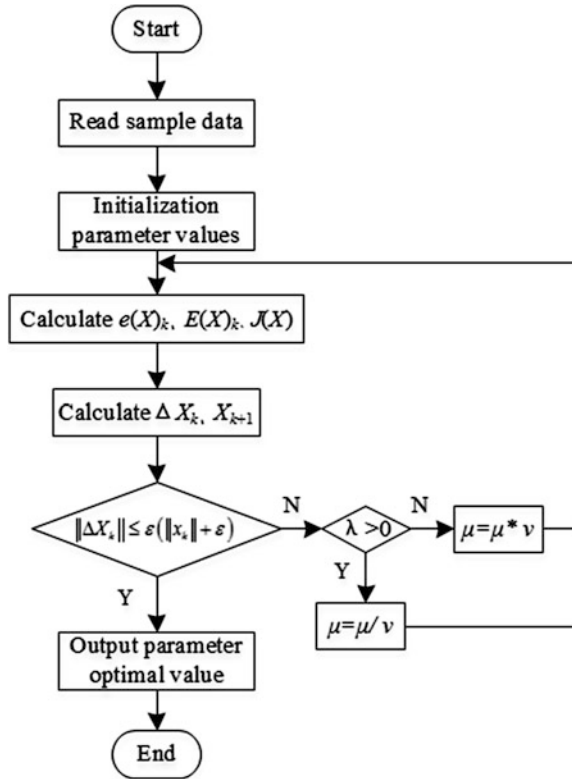
The least square objective function $E(X)$ is constructed by the function $e(X)$

$$E(X) = \min\left(\frac{1}{2}e(X)^T e(X)\right) \tag{7}$$

3.3 LM Algorithm to Solve the Objective Function

LM (Levenberg-Marquart [12]) algorithm combines gradient method with Gauss-Newton method. It has fast speed convergence of Gauss Newton method and

Fig. 5 Flow chart of geometric parameters calculation based on LM algorithm



the global characteristics of the gradient method, aiming at solving the non-positive definite problem and singular problem of Hessian matrix. It is suitable for solving nonlinear multiple objective function optimization problems [13]. Therefore, it can solve the least squares objective function $E(X)$.

Based on LM algorithm, the calculation process is used to solve the actual parameters as shown in Fig. 5. Adjusting the damping factor in the iteration process can be satisfied with the convergence rate, so as to efficiently solve the position error function.

4 Calibration Experiment Research

Combining with measurement results of laser tracker, the absolute positioning accuracy of robot is calibrated. The experiment is conducted at room temperature for 25° under the laboratory environment, constructing a good environment for laser tracker.

4.1 Experimental Procedure

Based on the kinematic calibration process of the robot, the specific steps of calibration experiment of serial 6R robot are shown in Fig. 6.

4.2 Establishment of the Robot Base Coordinate System

Based on least square circle fitting method, the robot base coordinate system is established in SA software. In order to accurately map the position and orientation of the robot base coordinate system, the reflector is mounted on the corresponding joint, and then the joint axis is fitted, and the influence of other joints is reduced.

Based on laser tracker, the robot base coordinate system is established in SA software (Fig. 7). The specific steps are as follows:

- (1) The base installation plane A is fitted out when the robot is at the zero position;
- (2) The joint No. 1 where the reflector mounted is only rotated, and the position of the reflector is measured simultaneously. The spatial position and orientation of axis l_1 of the joint No. 1 is obtained by the least square circle fitting method;
- (3) Then the joint No. 1 is moved to zero position, and the joint No. 2 has a single rotation. While the position of the reflector mounted on the joint No. 2 is measured simultaneously, and the spatial position and orientation of l_2 axis of the joint No. 2 is obtained by the least square circle fitting method;
- (4) The intersection of the l_1 axis and the plane A is the origin of the base coordinate system. At the same time, the l_1 axis and the l_2 axis are respectively considered as the z axis and the y axis.

Fig. 6 Flow chart of experimental calibration

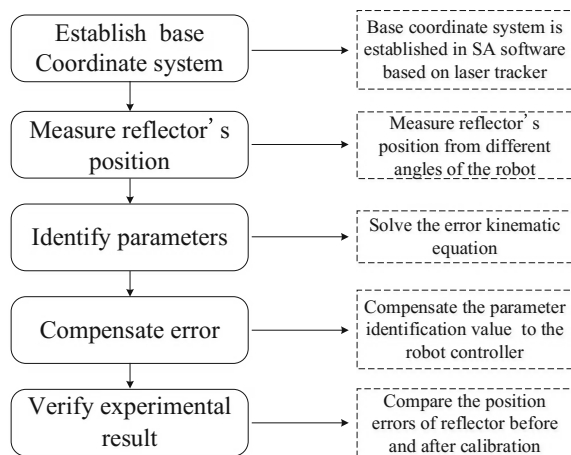
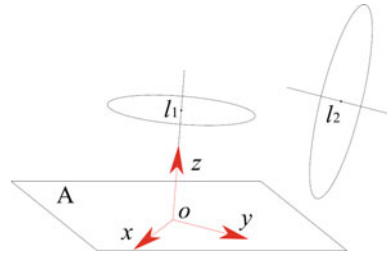


Fig. 7 Schematic diagram of the robot base coordinate system



After establishing the robot base coordinate system in SA software, laser tracker measurement coordinate system is transferred to the establishment of the base coordinate system, ensuring that subsequent measurements are based on the robot base coordinate system.

4.3 Measurement Data

The position of the reflector in tool coordinate system is (69.97 mm, -70.2 mm, 22.52 mm). TCP (Tool Center Point) of the robot transfers to the position of reflector's center. The joint angles of the robot is obtained by the robot controller, and the actual position data is measured by laser tracker.

Part of the robot workspace is selected as measurement space. The position data of 35 points (Fig. 8) is measured in the measurement space. The actual position data of points and the corresponding joint angles are as shown in Table 2, and 30 points for parameter identification, five points used to verify calibration result. It can be

Fig. 8 Spatial distribution of 35 points

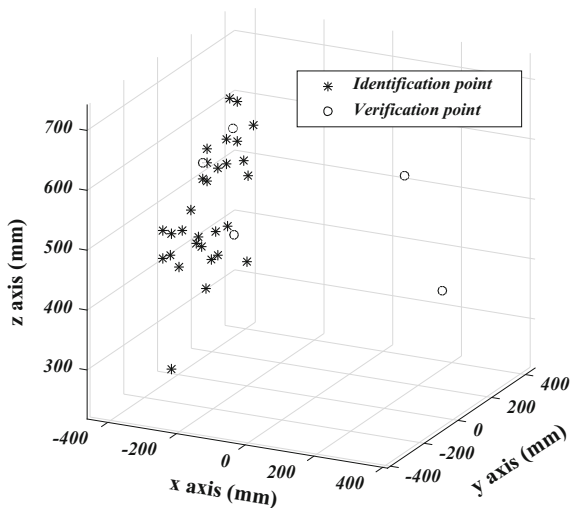


Table 2 Measurement data and the corresponding joint angles (mm or °)

No.	1	2	3	4	5	6	7
x	-149.02	-130.43	-274.68	-289.74	-341.12	-360.07	-212.08
y	-207.50	-134.57	-82.78	-80.13	-45.78	-58.46	7.79
z	742.60	600.86	599.84	571.14	506.46	473.58	591.12
θ_1	-14.69	-12.99	-11.39	-10.28	-9.82	-9.60	-29.92
θ_2	-74.76	-109.13	-72.61	-62.39	-59.85	-60.65	-60.40
θ_3	-16.64	90.55	48.77	41.27	56.55	66.77	20.25
θ_4	-57.23	-109.41	-84.41	-99.69	-101.59	-102.14	-108.52
θ_5	-18.57	28.16	43.47	44.56	57.34	50.96	58.61
θ_6	77.64	37.72	7.73	10.26	8.36	8.90	8.31
No.	8	9	10	11	12	13	14
x	-130.43	-274.68	-273.75	-97.89	-165.8	-208.33	-435.34
y	-134.57	-82.78	-137.81	-205.19	-184.63	-154.7	30.37
z	600.86	599.84	485.77	473.89	523.23	464.23	218.06
θ_1	-12.99	-11.39	-21.76	-5.11	-26.63	-36.11	-39.08
θ_2	-109.13	-72.61	-108.33	-118.56	-128.81	-124.11	-54
θ_3	90.55	48.77	113.11	123.63	111.05	99.84	88.64
θ_4	-109.41	-84.41	-118.99	-138.38	-117.25	-129.71	-125.16
θ_5	28.16	43.47	-6.41	2.29	-13.37	-42.2	-44.95
θ_6	37.72	7.73	420.75	399.71	410.57	371.94	17.87
No.	15	16	17	18	19	20	21
x	-430.76	-360.72	-372.86	-374.71	-344.58	-294.11	-293.42
y	-30.26	-116.89	-147.48	-44.55	-7.87	-74.25	-22.7
z	415.51	479.72	489.35	408.73	443.42	456.72	424.94
θ_1	-31.8	-21.2	-16.94	-29.96	-36.77	-28.54	-37.94
θ_2	-64.65	-72.16	-72.97	-66.7	-66.7	-71.88	-72.3
θ_3	69.15	63.09	54.43	54.43	54.43	59.27	65.2
θ_4	-127	-107.15	-79.92	-93.58	-116.13	-140.97	-154.13
θ_5	-29.74	-17.17	-28.54	-27.9	9.46	11.84	20.78
θ_6	31.2	15.58	21.81	-19.99	-32.48	-17.4	-24.69
No.	22	23	24	25	26	27	28
x	-278.76	-346.63	-339.92	-308.34	-286.63	-252.23	-192.94
y	-82.69	-151.8	46.65	99.09	6.73	48.17	26.68
z	388.68	451.96	591.81	559.96	571.53	612.96	649.54
θ_1	-24.12	-15.08	-48.43	-56.18	-47.63	-59.65	-72.77
θ_2	-72.31	-73.91	-86	-92.22	-92.22	-97.61	-105.14
θ_3	60.43	61	61	59.44	48.69	57.81	64.4
θ_4	-189.98	-180.62	-182.09	-165.36	-171.68	-201.57	-219.95
θ_5	50.12	22.3	2.4	-12.13	-13.32	-19.1	-23.5
θ_6	-51.78	-89	-128.05	-95	-67.86	-83.25	-105.02
No.	29	30	31	32	33	34	35

(continued)

Table 2 (continued)

No.	1	2	3	4	5	6	7
x	-243.55	-329.22	-244.75	-279.91	-202.48	389.67	158.99
y	-33.28	75.96	-171.45	80.93	-70.82	-44.23	204.8
z	631.56	448.89	620.06	625.45	483.99	440.26	563.66
θ_1	-42.53	-31.9	-23.88	-58.59	-28.69	-190.45	-144.9
θ_2	-96.82	-86.87	-89.52	-61.89	-86.58	6.77	-15.54
θ_3	49.35	94.09	56.38	36.52	77.64	-44.26	-39.55
θ_4	-193.32	-221.34	-155.11	-162.08	-131.96	-126.44	-126.59
θ_5	-23.04	-59.27	-39.03	21.63	47.38	116.46	85.76
θ_6	-79.13	-89.45	60.22	114.22	334.83	109.56	109.39

seen from Fig. 8 points for parameter identification are scattered in the measurement space and the spatial distribution of the points for verification is much more scattered. Three verification points distribute in the measurement space, two other verification points distribute outside the measurement space.

4.4 Experimental Result and Analysis

After calibration, the actual position of five verification points is measured once again using the laser tracker. The position measurement data is compared with the corresponding nominal position data before and after calibration, which is as shown in Table 3. For a more intuitive, position error curves of five verification points are as shown in Fig. 9 after processing data in Table 3.

It shows that curves are relatively stable, less volatile, and the average errors are moving closer to the zero axis after calibration in Fig. 9. The runout errors [11] in $x/y/z$ are changed form 4.35 mm/3.80 mm/1.44 mm to 2.48 mm/1.59 mm/1.45 mm after calculating the data in Table 5. The runout errors in x/y are reduced 1.87 mm/2.21 mm respectively, and the error in z remains invariability.

After calibration errors of verification point No. 1 and No. 3 are reduced, but the error of validation point No. 2 is increased, which shows that the absolute

Table 3 Position errors of five verification points before and after calibration

No.	Before calibration				After calibration			
	Δx	Δy	Δz	Δd	Δx	Δy	Δz	Δd
1	0.83	-2.71	-0.88	2.9677	-1.10	0.44	0.39	1.2473
2	-0.91	0.89	0.08	1.2754	-1.46	0.99	0.90	1.9803
3	-0.96	-0.56	-1.04	1.5221	-0.93	-0.16	-0.39	1.0211
4	3.12	-0.97	-1.28	3.5091	1.02	1.37	0.69	1.8421
5	3.39	1.09	0.16	3.5645	-0.58	1.43	1.06	1.8721

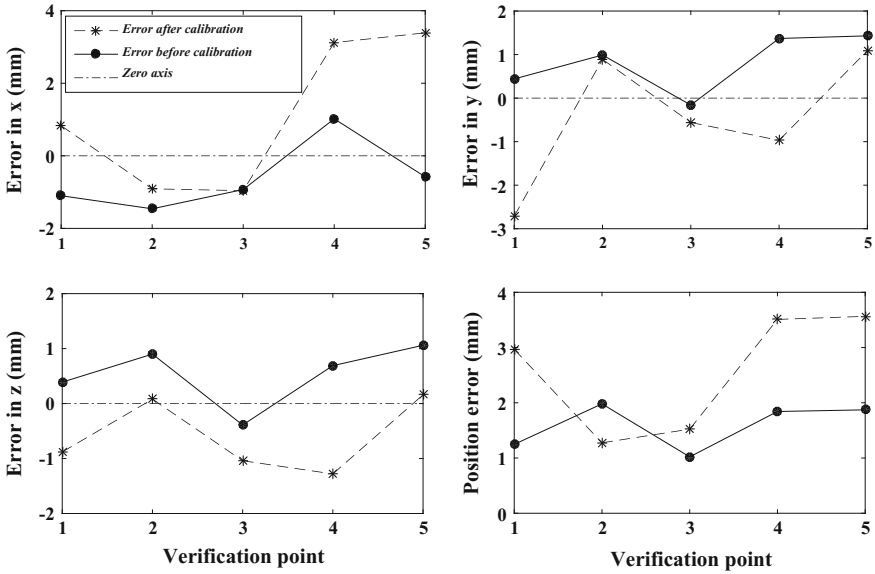


Fig. 9 Position error curves of five verification points before and after calibration

Table 4 Error statistics before and after calibration

Verification parameter	Before calibration (mm)	After calibration (mm)	Improve (%)
Maximum error	3.5645	1.8721	47.48
Average error	2.5678	1.5926	37.98
RMS error	2.7485	1.6382	40.40

positioning accuracy of reflector is relatively high when the robot joints are in certain angles before calibration, but the error of this position is increasing after calibration. Because the calibration method only guarantees the minimum of the errors of the reflector in the current 30 positions, and it cannot reach that the absolute positioning accuracy of the reflector in each position is improved.

Verification point No. 4 and No. 5 are scattered outside the measurement space, but the position errors have improved. It is concluded that absolute positioning accuracy within the range of the robot workspace is effectively improved by means of the calibration method, no matter point is inside or outside the measurement space.

The mean error and RMS error are used to evaluate the effects of the calibration method, and the formulas are respectively as follows:

$$e_{mean} = \frac{1}{m} \sum_{i=1}^m \Delta d_i \tag{8}$$

$$e_{RMS} = \sqrt{\frac{1}{m} \sum_{i=1}^m \Delta d_i^2} \quad (9)$$

where, M is the number of verification points, Δd is the position error.

Error statistics before and after calibration are as shown in Table 4 for the data in Table 6.

From Table 4, it shows that the maximum error reduces 47.48 %, the average error reduces 37.98 %, and RMS error reduces 40.40 % after calibration. Therefore, the calibration method effectively improve the absolute positioning accuracy of the serial 6R robot in whole workspace.

5 Conclusion

Aiming at improving the absolute positioning accuracy of serial robot, a calibration experiment is conducted with a laser tracker, the effects of the kinematic calibration are evaluated by comparing the position errors. The error function is established with measurement result of the end reflector position and calculation result by DH matrix of the corresponding position. The accuracy geometric parameters are obtained by solving the error function using LM algorithm. Taking five points to verify the calibration result, it is concluded that the absolute positioning accuracy within the range of the robot workspace is effectively improved by means of the calibration method, no matter point is inside or outside the measurement space. It shows that the maximum error reduces 47.48 %, the average error reduces 37.98 %, and RMS error reduces 40.40 % after calibration. Therefore, the calibration method is effective to improve the positioning accuracy of the serial 6R robot in whole workspace.

Acknowledgments This work is supported by the Shanghai Committee of Science and Technology Key Support Project (12510501100); Natural Science Foundation of China (NFS-51475050); Natural Science Foundation of Shanghai City (14ZR1422700).

References

1. Fang L, Dang P (2016) Kinematic calibration method of robots based on quantum—behaved particle swarm optimization. *J Mech Eng* 7:23–30 (in Chinese)
2. Dean-Leon E, Nair S, Knoll A (2012) User friendly Matlab-toolbox for symbolic robot dynamic modeling used for control design. In: *IEEE international conference on robotics and biomimetics (ROBIO)*. IEEE Press, New York, pp 2181–2188
3. Dasari A, Reddy NS (2012) Forward and inverse kinematics of a robotic frog. In: *4th International conference on intelligent human computer interaction (IHCI)*. IEEE Press, New York, pp 1–5

4. Liu Z, Zhao Z, Ren S, Chen K (2015) Kinematic calibration and compensation for a robot with structural deformation. *Robot* 03:376–384 (in Chinese)
5. He R, Zhao Y, Yang S, Yang S (2010) Kinematic-parameter identification for serial-robot calibration based on POE formula. *IEEE Trans Rob* 26(3):411–423
6. He R, Zhao Y, Han F, Yang S, Yang S (2011) Experimentation identifying the kinematic parameters of serial mechanism based on the product-of-exponential formula. *Robot* 01:35–39, 45 (in Chinese)
7. Verl A, Boye T, Pott A (2008) Measurement pose selection and calibration forecast for manipulators with complex kinematic structures. *CIRP Ann-Manuf Technol* 57(1):425–428
8. Ginani LS, Motta JMS (2011) Theoretical and practical aspects of robot calibration with experimental verification. *J Brazilian Soc Mech Sci Eng* 33(1):15–21
9. Slamani M, Nubiola A, Bonev I (2012) Assessment of the positioning performance of an industrial robot. *Ind Robot: Int J* 39(1):57–68
10. Nubiola A, Bonev IA (2013) Absolute calibration of an ABB IRB 1600 robot using a laser tracker. *Robot Comput-Int Manuf* 29(1):236–245
11. Ren Y, Zhu J, Yang X et al (2007) Method of robot calibration based on laser tracker. *J Mech Eng* 43(9):195–200 (2007) (in Chinese)
12. Gao H (1995) *Statistical calculation*. Peking University press, Beijing, pp 388–390 (in Chinese)
13. Al-Sharadqah A, Chernov N (2009) Error analysis for circle fitting algorithms. *Electron J Stat* 3:886–911

Calculation and Analysis on Crest Thickness of Edge Tooth of Height-Modified TA Worm

Chongfei Huai, Yaping Zhao and Yimin Zhang

Abstract As is well known, the tapering edge tooth may greatly degrade the working performance of a toroidal worm pair so checking its occurrence is always necessary in the process of the design. For this, a mathematical model is established to compute the top thickness of the edge tooth for a height-modified TA worm. Due to the geometric particularities of the height-modified TA worm, the crest thickness of its edge tooth can be obtained semi-analytically and semi-numerically. By means of the above mathematical model, the influence of the quantity of the height modification on the crest thickness of the edge tooth is investigated systematically. The results show that the tapering of the edge tooth will occur more easily when the number of worm thread is more and the transmission ratio is less. Moreover, if the cutter frame moves down, the top width of the edge tooth will decrease. From the viewpoint of avoiding the edge tooth pointing, the selection principle of the height modification amount is also recommended.

Keywords Hourglass worm drives · Crest thickness of edge tooth · TA worm · Height-modified

1 Introduction

The TA worm drive, which is known as the Hindly worm drive or the globoidal worm drive, was invented by Henry. Hindly in England for use in a dividing engine about in 1765 [1, 2]. Roughly in 1909, Samuel I. Cone, who was a draftsman of the United States, greatly improved the TA worm drive and it was named as Cone Drive by the gear community [3–5]. But in the process of using the Cone Drive, it was found that its carrying capacity would be increased after a long-time wear [6]. For this, some scholars in the Soviet Union and China studied the modification methods

C. Huai · Y. Zhao (✉) · Y. Zhang
School of Mechanical Engineering and Automation,
Northeastern University, Shenyang 110819, China
e-mail: zhy_p_neu@163.com

© Springer Nature Singapore Pte Ltd. 2017
X. Zhang et al. (eds.), *Mechanism and Machine Science*,
Lecture Notes in Electrical Engineering 408,
DOI 10.1007/978-981-10-2875-5_118

1489

to machine the worm in line with the shape of the worm helical surface after wear [7].

The tapering of the edge tooth may greatly weaken the working performance of a toroidal worm pair so checking its occurrence is always necessary during the design.

Shen et al. studied the calculation of the tooth thickness of the plane double-enveloping hourglass worm (the TP worm) [8].

Qi et al. made a systematic research on the compute of the edge tooth top width of the TP worm. Meanwhile, they suggested that the crest thickness of the edge tooth should not be less than $0.35m_t$, where m_t is the transverse module of the worm wheel [9].

Dong proposed a method to compute the crest thickness of the edge tooth of the toroidal worm, which is on the basis of solving a series of systems of nonlinear equations. This method has been applied to the TP worm and the conical surface double-enveloping toroidal worm (the TK worm). Besides, the corresponding measures to avoid the tapering of edge tooth are proposed [10].

Zhou also studied the computing of the top thickness of the edge tooth of the TP worm systematically [11].

Latterly, Zhao researched the calculation of the top width of the edge tooth of the dual-torus double-enveloping toroidal worm (the DTT worm) in detail [12, 13].

The work reported in this paper is about the crest thickness of the height-modified TA worm drive, which is attained only by changing the vertical height of the cutter frame during the machining of the worm [14]. It means that the height variation of the tool is the unique modification parameter. When the cutter frame moves downwards, this parameter is positive, whereas negative.

Generally speaking, the edge tooth tapering happens rarely in terms of the uncorrected TA worm, but for the height-corrected TA worm, it is unacknowledged. For this, a new method to compute the top thickness of its edge tooth is proposed in this paper. Due to the geometric particularities of the height-modified TA worm, the top thickness of its edge tooth can be obtained semi-analytically and semi-numerically. For the purpose of preciseness, this method is also inspected and verified by the computed results. By using the above method, the influence of the parameters on the top thickness of the edge tooth is also investigated systematically.

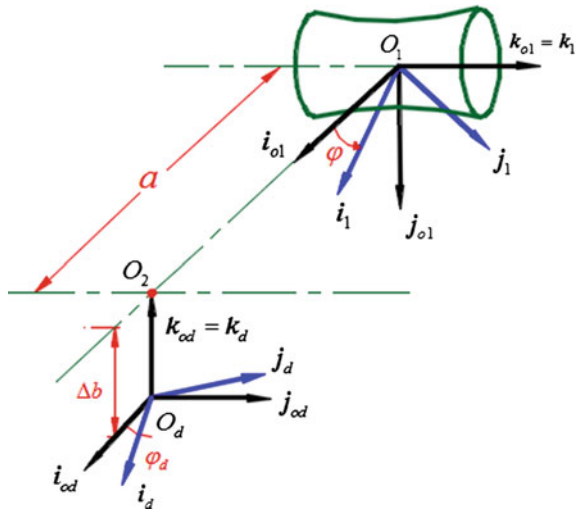
Although the computing method presented in this paper is aimed at the height-modified TA worm, it is also valid for the other modified TA worms.

2 Equations of Helical Surface and Tooth Profile of Height-Modified TA Worm

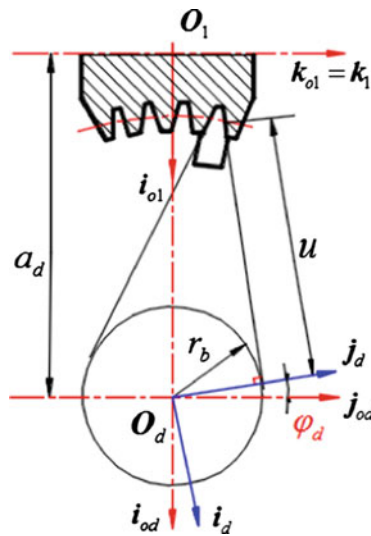
2.1 Coordinate Systems

As illustrated in Fig. 1a, two stationary coordinate systems, $\sigma_{od}\{O_{od}; \mathbf{i}_{od}, \mathbf{j}_{od}, \mathbf{k}_{od}\}$ and $\sigma_{o1}\{O_{o1}; \mathbf{i}_{o1}, \mathbf{j}_{o1}, \mathbf{k}_{o1}\}$ are used to represent the initial positions of the tool apron

Fig. 1 Drawings to expound the formation of TA worm



(a) Coordinate systems and its positional relationship



(b) Schematic diagram for machining TA worm

and the worm blank respectively, are. Therein, the two unit vectors, k_{o1} and k_{od} , are along the axes of the worm roughcast and the cutter frame severally, and they are mutually perpendicular because the discussion in this work is limited to the worm drive with orthogonal axes. The shortest distance between these two axial lines is the distance from the point O_1 to O_2 , and $|O_1O_2| = a$, where a is the center distance of the TA worm pair. The minimum distance from the point O_d to the middle plane

of the worm pair is the axial displacement of the cutter frame Δb , which is the parameter of the height modification. As shown in Fig. 1a, when the cutter frame moves down from the point O_2 , Δb is taken as positive.

Over and above that, two moveable coordinate systems, $\sigma_d\{O_d; \mathbf{i}_d, \mathbf{j}_d, \mathbf{k}_d\}$ and $\sigma_1\{O_1; \mathbf{i}_1, \mathbf{j}_1, \mathbf{k}_1\}$ are fixed with the cutter frame and the worm roughcast, respectively. During cutting a TA worm, the tool apron revolves around \mathbf{k}_{od} and the worm blank spins on \mathbf{k}_{o1} . When the rotation angle of the worm blank is φ , the corresponding rotation angle of the tool post is φ_d and $\varphi = i_{12}\varphi_d$, where i_{12} is the transmission ratio of the TA worm pair.

2.2 Vector Equation of Helical Surface of Height-Modified TA Worm

According to Fig. 1b, the vector equation of the straight cutting edge can be represented in the movable coordinate system σ_d as follows:

$$(\mathbf{r}_d)_d = -u\mathbf{i}_d + r_b\mathbf{j}_d \tag{1}$$

where r_b is the main basic circle radius of the worm gear.

Via the coordinate transformation, the locus surface of the straight cutting edge in the static coordinate system, σ_{od} , can be attained as:

$$(\mathbf{r}_d)_{od} = R[\mathbf{k}_{od}, \varphi_d](\mathbf{r}_d)_d = x_{od}\mathbf{i}_{od} + y_{od}\mathbf{j}_{od} \tag{2}$$

where $x_{od} = -u\cos\varphi_d - r_b\sin\varphi_d$, $y_{od} = -u\sin\varphi_d + r_b\cos\varphi_d$, $R[\mathbf{k}_{od}, \varphi_d]$ is the symbol of rotation transformation matrix [15] around the axis \mathbf{k}_{od} and

$$R[\mathbf{k}_{od}, \varphi_d] = \begin{bmatrix} \cos \varphi_d & -\sin \varphi_d & 0 \\ \sin \varphi_d & \cos \varphi_d & 0 \\ 0 & 0 & 1 \end{bmatrix}$$

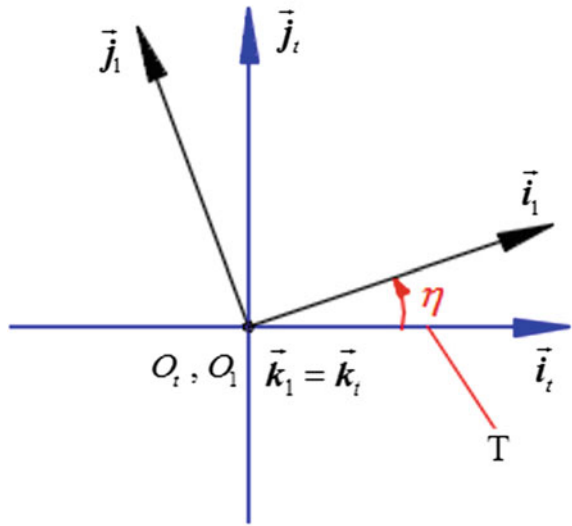
From Eq. (2) and with the relative position shown in Fig. 1a, the vector equation of the height-modified TA worm helicoidal surface in the movable coordinate system σ_1 can be expressed as:

$$(\vec{\mathbf{r}}_1)_1 = R[\mathbf{k}_1, -\varphi] \left\{ R\left[\mathbf{i}_{o1}, \frac{\pi}{2}\right](\vec{\mathbf{r}}_d)_{od} + (\vec{O}_{12})_{o1} \right\} = x_1\vec{\mathbf{i}}_1 + y_1\vec{\mathbf{j}}_1 + y_{od}\vec{\mathbf{k}}_1 \tag{3}$$

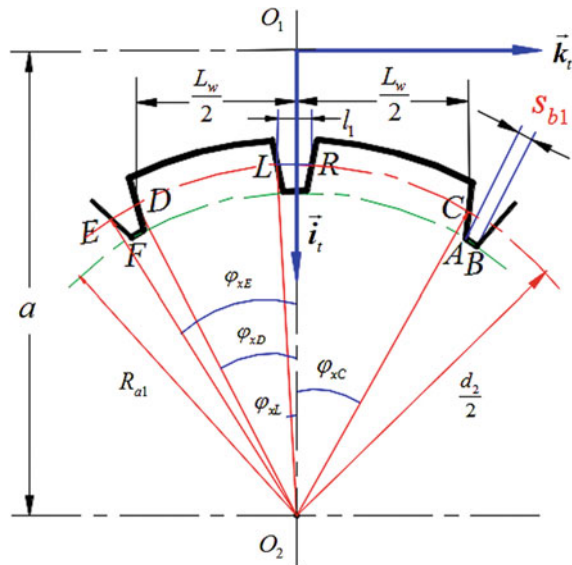
where $x_1 = (x_{od} + a)\cos\varphi + \Delta b\sin\varphi$, $y_1 = -(x_{od} + a)\sin\varphi + \Delta b\cos\varphi$, u and φ are the parameters of the height-modified TA worm helicoidal surface, and the rotation transformation matrixes in Eq. (3) are:

$$R\left[\vec{i}_{o1}, \frac{\pi}{2}\right] = \begin{bmatrix} 1 & 0 & 0 \\ 0 & 0 & -1 \\ 0 & 1 & 0 \end{bmatrix}, \quad R[\vec{k}_1, -\varphi] = \begin{bmatrix} \cos \varphi & \sin \varphi & 0 \\ -\sin \varphi & \cos \varphi & 0 \\ 0 & 0 & 1 \end{bmatrix}$$

Fig. 2 Drawings to illustrate tooth profile of height-modified TA worm



(a) Axis plane T in σ_1



(b) Tooth profile of worm in axial plane T

2.3 Vector Equation of Tooth Profile of Height-Modified TA Worm in Axial Plane T

As shown in Fig. 2, $\sigma_t\{O_t; \mathbf{i}_t, \mathbf{j}_t, \mathbf{k}_t\}$ is a moveable coordinate system. The unit vectors \mathbf{i}_t and \mathbf{k}_t are in the plane T. According to [15], the tooth profile equation of the height-modified TA worm in the plane T can be attained as:

$$\begin{cases} (\mathbf{r}_1)_t = R[\mathbf{k}_t, \eta](\mathbf{r}_1)_1 = x_t \mathbf{i}_t + y_t \mathbf{j}_t + y_{od} \mathbf{k}_t \\ y_t = 0 \end{cases} \tag{4}$$

where

$x_t = (x_{od} + a) \cos(\eta - \varphi) - \Delta b \sin(\eta - \varphi)$, $y_t = (x_{od} + a) \sin(\eta - \varphi) + \Delta b \cos(\eta - \varphi)$, and η is a directed angle from \mathbf{i}_1 to \mathbf{i}_t , which can be used to ascertain the position of T in the moveable coordinate system, σ_1 . When the value of the angle η is different, the position of T in the σ_1 is different concomitantly.

3 Computing Edge Tooth Crest Thickness of Height-Modified TA Worm

As shown in Fig. 2b, the left tooth flank of the height-modified TA worm is selected to compute the top thickness of its edge tooth. The points A, C, L, E and F are all in this tooth flank.

The point C is at the inlet portion of the TA worm and on its reference torus. Therefore, the system of nonlinear equations to determine the point C can be represented as follows, which contains the unknowns φ_{dC} , u_C and θ_C :

$$\begin{cases} (a - x_t^{(C)})^2 + (y_{od}^{(C)})^2 = \frac{1}{4}d_2^2 \\ y_{od}^{(C)} = -u_C \sin \varphi_{dC} + r_b \cos \varphi_{dC} = \frac{1}{2}L_w \\ y_t^{(C)} = 0 \end{cases} \tag{5}$$

Substituting the second equation of Eq. (5) into its first equation can yields:

$$x_t^{(C)} = a - \frac{1}{2} \sqrt{d_2^2 - L_w^2} \tag{6}$$

From the expressions of $x_t^{(C)}$ and $y_t^{(C)}$ in Eq. (4), it may have:

$$(x_t^{(C)})^2 + (y_t^{(C)})^2 = (x_{od}^{(C)} + a)^2 + \Delta b^2 = \left(a - \frac{1}{2} \sqrt{d_2^2 - L_w^2}\right)^2 \tag{7}$$

By solving Eq. (7), $x_{od}^{(C)}$ can be acquired as:

$$x_{od}^{(C)} = \sqrt{\left(a - \frac{1}{2}\sqrt{d_2^2 - L_w^2}\right)^2 - \Delta b^2} - a \tag{8}$$

From the expressions of Eq. (2), we can get the quadratic sum of $x_{od}^{(C)}$ and $y_{od}^{(C)}$ as:

$$\left(x_{od}^{(C)}\right)^2 + \left(y_{od}^{(C)}\right)^2 = u_C^2 + r_b^2 \tag{9}$$

Substituting Eq. (8) and the second equation of Eq. (5) into Eq. (9) yields:

$$u_C = \sqrt{\left[\sqrt{\left(a - \frac{1}{2}\sqrt{d_2^2 - L_w^2}\right)^2 - \Delta b^2} - a\right]^2 + \frac{1}{4}L_w^2 - r_b^2} \tag{10}$$

As well from the second equation of Eq. (5), a trigonometric equation with respect to φ_{dC} can be acquired after determining the value of u_C , and is represented as:

$$\sin(\varphi_0 - \varphi_{dC}) = \frac{L_w}{2\sqrt{u_C^2 + r_b^2}} \tag{11}$$

where φ_0 is an auxiliary angle and $\varphi_0 = \arctan(r_b/u_C)$.

Solving Eq. (11) yields:

$$\varphi_{dC} = \arctan\left(\frac{r_b}{u_C}\right) - \arcsin\left(\frac{L_w}{2\sqrt{u_C^2 + r_b^2}}\right) \tag{12}$$

From the third equation of Eq. (5), a trigonometric equation about the unknown η_C can be attained as:

$$\tan(i_{12}\varphi_{dC} - \eta_C) = \frac{\Delta b}{x_{od}^{(C)} + a} \tag{13}$$

Solving Eq. (13) leads to:

$$\eta_C = i_{1d}\varphi_{dC} - \arctan\left(\frac{\Delta b}{x_{od}^{(C)} + a}\right) \tag{14}$$

To this, this three parameters u_C , φ_{dC} and η_C are all acquired analytically.

For the point A is on the same tooth profile as the point C, $\eta_A = \eta_C$. In addition, it is also on the addendum arc of the worm. After getting the η_C , the following nonlinear equations as to the parameters u_A and φ_{dA} can be used to determine the point A:

$$\begin{cases} (a - x_t^{(A)})^2 + (y_{od}^{(A)})^2 = R_{d1}^2 \\ y_t^{(A)} = 0 \end{cases} \tag{15}$$

From the second equation of Eq. (15), the parameter u_A can be expressed by the φ_{dA} as follows:

$$u_A = \frac{a - \Delta b \cot(i_{12}\varphi_{dA} - \eta_C) - r_b \sin \varphi_{dA}}{\cos \varphi_{dA}} \tag{16}$$

Substituting Eq. (16) into the first equation of Eq. (15), a new equation can be obtained with the sole unknown φ_{dA} as follows:

$$\left([\Delta b \cot(i_{12}\varphi_{dA} - \eta_C) - a] \tan \varphi_{dA} + \frac{r_b}{\cos \varphi_{dA}} \right)^2 - R_{d1}^2 + \left(a - \frac{\Delta b}{\sin(i_{12}\varphi_{dA} - \eta_C)} \right)^2 = 0 \tag{17}$$

It is clearly that only one guess value is need for the iterative computation of Eq. (17). As shown in Fig. 1b, the values of φ_{dA} and φ_{dC} are approximately equal since they are in a same tooth profile, therefore φ_{dC} can be as a reasonable guess value to solving φ_{dA} . After determining the angle φ_{dA} , the parameter u_A can be gotten with the aid of Eq. (16). Then the coordinates of the point A in σ_t can be represented as:

$$x_t^{(A)} = (-u_A \cos \varphi_{dA} - r_b \sin \varphi_{dA} + a) \cos(\eta_C - i_{12}\varphi_{dA}) - \Delta b \sin(\eta_C - i_{12}\varphi_{dA}) \tag{18}$$

$$y_{od}^{(A)} = -u_A \sin \varphi_{dC} + r_b \cos \varphi_{dC} \tag{19}$$

As shown in Fig. 2b, the point L is at the throat of the worm and on its reference torus. Hence, the nonlinear equations about φ_{dL} , u_L and θ_L to determine the point L can be presented as follows:

$$\begin{cases} y_t^{(L)} = 0 \\ y_{od}^{(L)} = -u_L \sin \varphi_{dL} + r_b \cos \varphi_{dL} = -\frac{1}{2}l_1 \\ (a - x_t^{(L)})^2 + (y_{od}^{(L)})^2 = \frac{1}{4}d_2^2 \end{cases} \tag{20}$$

where l_1 is the chordal thickness on the worm reference torus at its throat.

By using the same calculating method as that of Eq. (5), the analytical solutions of Eq. (20) can be acquired as:

$$u_L = \sqrt{\left[\sqrt{\left(a - \frac{1}{2} \sqrt{d_2^2 - l_1^2} \right)^2 - \Delta b^2} - a \right]^2 + \frac{1}{4} l_1^2 - r_b^2} \quad (21)$$

$$\varphi_{dL} = \arctan\left(\frac{r_b}{u_L}\right) + \arcsin\left(\frac{l_1}{2\sqrt{u_L^2 + r_b^2}}\right) \quad (22)$$

$$\eta_L = i_{1d} \varphi_{dL} - \arctan\left(\frac{\Delta b}{x_{od}^{(L)} + a}\right) \quad (23)$$

As Fig. 2b shows, the point E is on the reference torus of the TA worm. But based on these existing conditions, the point E may not be determined sufficiently. So we should find out the implicit conditions from Fig. 2b. In fact, the angle φ_{dE} can be determined by the angles φ_{dL} and φ_{dC} and their relationship can be derived as follows:

According to the definition of φ_x , which is the nominal angle of the blade, the following equations can be gotten:

$$\varphi_{xC} = -\varphi_{xD} = \alpha - \varphi_{dC}; \quad \varphi_{xL} = \alpha - \varphi_{dL}; \quad \varphi_{xE} = \alpha - \varphi_{dE} \quad (24)$$

As shown in Fig. 2b, the following equation can be acquired:

$$\varphi_{xE} = \varphi_{xD} + 2\varphi_{xL} \quad (25)$$

Substituting Eq. (24) into Eq. (25) yields

$$\varphi_{dE} = 2\varphi_{dL} - \varphi_{dC} \quad (26)$$

Given the above, the nonlinear equations to determine the point E can be attained as follows:

$$\begin{cases} \left(a - x_i^{(E)} \right)^2 + \left(y_{od}^{(E)} \right)^2 = \frac{1}{4} d_2^2 \\ \varphi_{dE} = 2\varphi_{dL} - \varphi_{dC} \\ y_i^{(E)} = 0 \end{cases} \quad (27)$$

After the angle φ_{dE} is determined by Eqs. (12) and (22), the unknowns u_E and η_E also can be acquired.

Because the points F and E are on the same tooth profile, $\eta_F = \eta_E$. Besides, the point F is also on the addendum arc of the worm. Therefore, the following nonlinear equations with unknowns u_F and φ_{dF} can be expressed as follows:

$$\begin{cases} (a - x_t^{(F)})^2 + (y_{od}^{(F)})^2 = R_{d1}^2 \\ y_t^{(F)} = 0 \end{cases} \tag{28}$$

When the number of the worm thread is more and the transmitting ratio is less, it was found that the reasonable guess value of Eq. (28) is not easy to be given. Therefore, a methodology of number-shape combination to estimate the initial value is proposed in this work. The definite means are as follows:

Simplifying the second equation of Eq. (28) yields:

$$u_F = \frac{a - \Delta b \cot(i_{12}\varphi_{dF} - \eta_E) - r_b \sin \varphi_{dF}}{\cos \varphi_{dF}} \tag{29}$$

With the aid of Eq. (29), the first equation of Eq. (28) can be converted to a new nonlinear equation with respect to the sole unknown φ_{dF} and its corresponding function can be represented as follows:

$$P(\varphi_{dF}) = \left([\Delta b \cot(i_{12}\varphi_{dF} - \eta_E) - a] \tan \varphi_{dF} + \frac{r_b}{\cos \varphi_{dF}} \right)^2 + \left(a - \frac{\Delta b}{\sin(i_{12}\varphi_{dF} - \eta_E)} \right)^2 - R_{d1}^2 \tag{30}$$

Then we can draw the pattern of this function and the values of its zero can be obtained approximatively. In general, these zeros can be taken as the reasonable guess value for the iterative computation of the new nonlinear equation.

After determining the values of φ_{dF} and u_F , the coordinates of the point F in σ_t can be expressed as:

$$x_t^{(F)} = (-u_F \cos \varphi_{dF} - r_b \sin \varphi_{dF} + a) \cos(\eta_E - i_{12}\varphi_{dF}) - \Delta b \sin(\eta_E - i_{12}\varphi_{dF}) \tag{31}$$

$$y_{od}^{(F)} = -u_F \sin \varphi_{dF} + r_b \cos \varphi_{dF} \tag{32}$$

In view of the symmetry of points B and F, the crest thickness of the edge tooth of the TA worm can be represented as follow:

$$s_{b1} = |AB| = \sqrt{(x_t^{(A)} - x_t^{(F)})^2 + (y_{od}^{(A)} + y_{od}^{(F)})^2} \tag{33}$$

4 Numerical Examples and Discussion

In this section, six numerical examples are used to represent two typical cases as: less Z_1 and more i_{12} (E1, E3, E5); more Z_1 and less i_{12} (E2, E4, E6). Herein, Z_1 is the number of worm thread. The major parameters of these numerical examples are listed in Table 1, in which the value of Δb is set in the interval $[-0.35b_2, 0.35b_2]$ for considering its actual physical meaning, where b_2 is the tooth width of the worm wheel.

In order to evaluate the top thickness of the edge tooth of an hourglass worm, the coefficient of the crest thickness can be defined as $K_s = s_{b1}/m_t$. Generally speaking, the crest thickness of the edge tooth is considered to be thick enough when $K_s \geq 0.35$ [12].

For checking the correctness of the method proposed in this paper, the major calculation results of the example E1 with $\Delta b = 0.20b_2$ are listed in Table 2. As shown in Fig. 1b, the rotary angle φ_d of the cutter frame should be an acute angle during a processing cycle. As Fig. 2b shows, the value of y_{od} at the point A should be equal to the $L_w/2$ roughly, while the absolute value of y_{od} at the point F is slightly larger than $L_w/2$. Besides, the values of u at the points A and F should be nearly equal because they are both on the addendum arc of the worm. Similarly, the values of u at the points C and L should also be equal approximately. Beyond that, the values of the coefficient K_s should be less than l_1/m_t , because the value of l_1 is bigger than that of s_{b1} theoretically. Obviously, the results listed in Table 2 are in accordance with the above geometrical facts. Consequently, we have reason to believe that the method proposed in this paper is reasonable and the computed results are correct.

The relationship of k_s and Δb are shown in Fig. 3. When Z_1 is more and i_{12} is less, k_s decreases with the increase of Δb . While in the case of less Z_1 and more i_{12} , the crest thickness may be the largest when the TA worm is uncorrected, it means that the height modification may reduce the top width of its edge tooth. Besides, it

Table 1 Major parameters of numerical examples

Parameters	Examples					
	E1	E2	E3	E4	E5	E6
a (mm)	80	80	250	250	500	500
Z_1	1	10	1	10	1	10
i_{12}	60	3	60	3	60	3
b_2 (mm)	20	20	63	63	125	125
R_{a1} (mm)	62.6423	61.0361	202.1284	196.9456	411.1656	400.6229
d_2 (mm)	128.4971	128.4931	414.6223	414.6223	843.4165	843.4165
r_b (mm)	25	25	78.1250	78.1250	156.2500	156.2500
L_w (mm)	36.8176	33.9061	118.7995	109.4076	241.6595	222.5549
Δb (mm)	$-0.35b_2-0.35b_2$					

Table 2 Computed results of the example E1 with $\Delta b = 0.20b_2$

		Calculated results						
		φ_d (°)	y_{od} (mm)	u (mm)	φ_x (°)	Δb (mm)	l_1 (mt)	k_s
Points	A	6.1852	18.6211	57.8541	16.7142	4	1.2969	0.5617
	C	6.2035	18.4088	59.6415	16.6959			
	L	23.9355	-1.3887	59.7445	-1.0361			
	F	41.6547	-19.7663	57.8440	-18.7553			
	E	41.6674	-20.9575	59.6158	-18.7681			

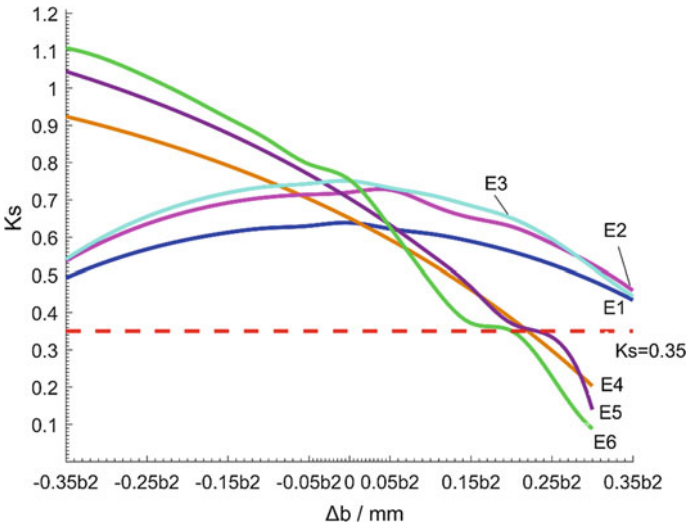


Fig. 3 Curves of $k_s - \Delta b$

can be found that the sharpening of the edge tooth may occur if the value of Δb is big enough under the condition of more Z_1 and less i_{12} , however it is scarcely happen when Z_1 is less and i_{12} is more.

5 Conclusions

For checking the tapering of the edge tooth of the height-modified TA worm, a new method, which has more universal applicability, is proposed in this work. Due to the geometric particularities of the height-modified TA worm, the crest thickness of its edge tooth can be obtained semi-analytically and semi-numerically by this method. Meanwhile, the major calculated results prove that this new method is

impeccable. By using this method, the influence of the parameters on the crest width of the edge tooth is studied systematically.

When $\Delta b < 0$, the risk of the edge tooth tapering is lower in the case of more Z_1 and less i_{12} than that of less Z_1 and more i_{12} , but it is opposite when $\Delta b > 0$. Namely, it will occur more easily when the number of worm thread is more and the transmission ratio is less.

From the viewpoint of avoiding the edge tooth pointing, the selection of the height modification quantities should be limited in a range. On the basis of the computed results in this work, we suggested $\Delta b < 0.20b_2$ under the condition of $1 < Z_1 < 10$ and $3 < i_{12} < 80$.

Acknowledgments The research work in this paper was fully supported by National Natural Science Foundation of China under Grant No. 51475083, New Century Excellent Talents Project by Education Ministry of China under Grant No. NCET-13-0116. National Key Basic Research Development Plan of China (the 973 Program) under Grant No. 2014CB046303.

References

1. Crosher WP (2002) Design and application of the worm gear. ASME press, New York
2. Litvin FL et al (2004) Gear geometry and applied theory, 2nd edn. Cambridge University Press, Cambridge
3. Dudley DW (1962) Gear handbook: the design, manufacture, and application of gears. McGraw-Hill, New York
4. Buckingham E (1988) Analytical mechanics of gears, 3rd edn. Dover Publications. INC., New York
5. Dudas I (2000) The theory and practice of worm gear drives. Penton Press, London
6. Zhao YP et al (2014) Advances in the research of hourglass worm drives. In: Proceedings of international symposium "theory and practice of gearing". Izhevsk, Russia
7. Chen YH et al (2015) Development and classification of worm drive. In: Proceedings of the 14th IFToMM world congress. Taipei, Taiwan
8. Zhao YP et al (2010) Computer aided analysis on the meshing behavior of a height-modified dual-torus double-enveloping toroidal worm drive. *Comput Aided Des* 42(12):1232–1240
9. Zhao YP et al (2010) Meshing analysis and technological parameters selection of dual tori double-enveloping toroidal worm drive. *Mech Mach Theory* 45(9):1269–1285
10. Zhao YP et al (2011) Tooth flank modification theory of dual-torus double-enveloping hourglass worm drives. *Comput Aided Des* 43(12):1535–1544
11. Shen YF (1981) Spatial meshing theory and SG-71 worm drives. Coal Industry Press, Beijing
12. Qi L et al (1987) Worm drives design. China Machine Press, Beijing
13. Dong XZ (2004) Design and modification of hourglass worm drives. Mechanical Industry Press, Beijing
14. Zhou LY (2005) Modification principle and manufacture technology for hourglass worm drives. National University of Defense Technology Press, Changsha
15. Dong XZ (1989) Meshing theory foundation of gearing. Mechanical Industry Press, Beijing

Architecture of a Hydraulic Hybrid Vehicle with Pressure Cross-Feedback Control

Zhuoqun Chen, Chaoyu Yu, Wei Wu, Chongbo Jing, Shihua Yuan and Chongfeng Di

Abstract A hydraulic hybrid vehicle equipped with the hydraulic transformer is proposed. The hybrid system features in rotary swash plate type hydraulic transformer and pressure cross-feedback control. The full numerical model has been built. Extensive simulated and tested results are given. The contributions of the hydraulic transformer dynamics to the hydraulic hybrid vehicle performance are investigated. The proposed hydraulic hybrid vehicle can achieve the ideal vehicle dynamic performance by adjusting the hydraulic transformer controlled angle. The switching between the driving and the regenerative braking of the hydraulic hybrid vehicle is realized by the pressure cross-feedback control. The propulsion mode of the hydraulic hybrid vehicle can be changed automatically. The larger hydraulic transformer controlled angle realises a higher driving pressure while the smaller one achieves a higher driving flow. Due to the small inertia of the hydraulic transformer, the hybrid system is able to satisfy the speed requirement of the driver.

Keywords Hydraulic hybrid vehicle · Hydraulic transformer · Mathematical modelling · Hydraulic transmission · Non-minimum phase system · Cross-feedback control

1 Introduction

The hybrid vehicle is an effective method for the energy saving of the automobiles [1]. Electric hybrid systems have received the most attention for the light-duty vehicle. For the heavy-duty vehicle, hydraulic hybrid systems are more cost effective [2]. Further, the hydraulic hybrid vehicle (HHV) presents the best method

Z. Chen · C. Yu · W. Wu (✉) · C. Jing · S. Yuan · C. Di
School of Mechanical Engineering, Beijing Institute of Technology,
Beijing 100081, China
e-mail: wuweijing@bit.edu.cn

Z. Chen
e-mail: chen_zhuoqun@163.com

for the regenerative braking, especially for the vehicle with a high stop-and-go frequency [3, 4]. There are three main types of the hydraulic hybrid systems: the parallel hydraulic hybrid system [5], the series hydraulic hybrid system [6] and the hydro-mechanical transmission [7]. All the hydraulic hybrid systems are composed of the hydraulic pump/motor unit [8–10]. In the driving mode, the pressure oil goes through a hydraulic pump/motor, which is connected to the power train. In the regenerative braking mode, the kinetic energy drives the hydraulic pump/motor and the pressure oils flow back into the hydraulic accumulator. With different hydraulic circuits, the control of the hydraulic pump/motor unit can be divided into the hydraulic valve controlled type and the hydraulic displacement controlled type. The hydraulic valve controlled type has a faster response and a larger throttle energy loss. The hydraulic displacement controlled type reaches a higher efficiency. However, the efficiency is still lower than the electric hybrid system.

To further increase the hydraulic system efficiency, the hydraulic transformer (HT) [11] is proposed. The HT performs both functions of a hydraulic pump and a hydraulic motor. It can transform pressure to any desired level between zero and the maximum value. In the conventional HHV, the operation of the hydraulic pump/motor unit is based on the flow conservation. However, the HT for the HHV is operated based on the torque balance of the cylinder. There is no mechanical connection between the cylinder and other rotating components. For the HHV with the HT, Acthen and co-researchers have analysed the basic configuration [12]. The comparison between the conventional vehicle and the HHV was also presented by the numerical simulation [13]. The theory of limit cycles has been applied to the analysis of the HHV [14]. The existence of limit cycle and the stability of equilibrium points in the system were discussed in detail. Further, the flow fluctuation of the HT is larger than the hydraulic pump. Chen and co-researchers have indicated that the series hydraulic accumulator is much superior to the parallel hydraulic accumulator in terms of the pulsation damping of the HT [15].

This paper presents the patented configuration and the full-cycle model of an HHV with the HT. Extensive simulated and tested results are given. The operation characteristics of the HHV are discussed. The contributions of the HT dynamics to the HHV performance are investigated. It is aimed to identify some special characteristics of the HHV in contrast with the conventional hybrid vehicle.

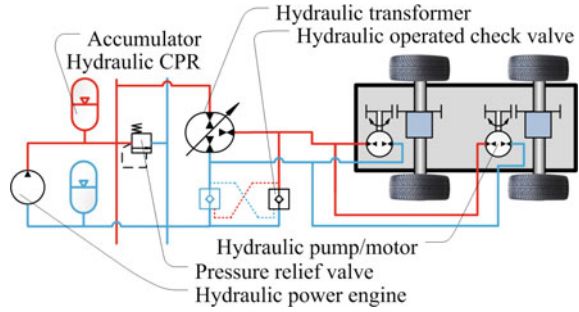
2 Mathematical Modelling

2.1 System Configuration

The HHV consists of hydraulic common pressure rail (CPR), high/low-pressure hydraulic accumulators, HT, and hydraulic pump/motor, as shown in Fig. 1.

Compared with the conventional design [12, 13], the proposed HHV has some novel features:

Fig. 1 Configuration of the hydraulic hybrid vehicle



- The HT is a patented rotary swash plate type [16]. The design features the rotary swash plate and conventional plunger pump type.
- The driving and breaking of the hydraulic motor is realized by the pressure cross-feedback control. The propulsion mode is changed automatically.

The pressure oil of the CPR is adjusted by the HT and then delivered to the hydraulic pump/motor. The vehicle speed control is achieved by changing the HT controlled angle. The HT can drive the vehicle to move backwards without the reverse gear by changing the HT controlled angle. The regenerative braking mode is also realised by changing the HT controlled angle. The HT controlled angle is adjusted by a servo-motor and a worm gear system.

The output torque-speed relation of the HHV in different operating modes is shown in Fig. 2. In the driving mode, the HT controlled angle is positive. The hydraulic operated check valve connected the port T of the HT is opened by the high-pressure of the port B of the HT, as shown in Fig. 2a. The hydraulic operated check valve connected the port B is closed at this time. The port B delivers the pressure oil to the hydraulic motor for forward propulsion. In the regenerative braking mode, the HT controlled angle is negative. The hydraulic motor performs pump function and the cylinder of the HT doesn't change the rotating direction. The pressure oil flows to the port T and opens the hydraulic operated check valve which is connected to the port B, as shown in Fig. 2b. Thus, the port B is connected the low-pressure rail. The kinetic energy of the HHV is recovered. It can be seen that the pressure cross-feedback control of the HHV can switch between the driving mode and the regenerative braking mode automatically. The only input signal is the HT controlled angle which is determined by the angular position of the swash plate. Compared with the conventional design [13], the throttle loss can be reduced and higher energy efficiency is guaranteed. It is because that the electric slid valve is replaced by a poppet valve and a larger flow area can be designed. Further, the HHV can drive the vehicle to move backwards without the reverse gear based on the hydraulic circuit.

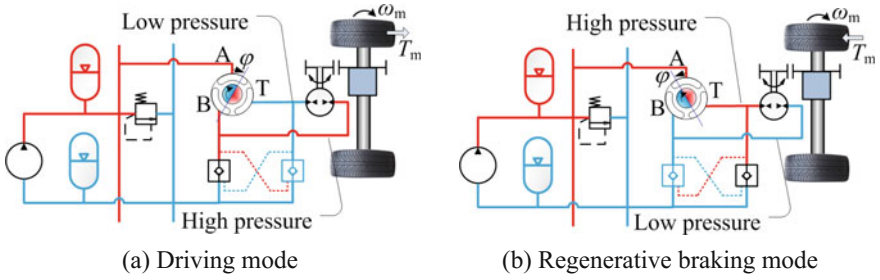


Fig. 2 Operation principle of the HHV

2.2 Key Components Model

To fully understand the vehicle operation, the governing equations of the hydraulic hybrid vehicle are obtained. The dynamic model of the integrated hydraulic energy transfer system is obtained by using the governing equations of the hydraulic circuit components. The general equations of the hydraulic circuit components are first introduced.

For axial piston pumps, both the pumping mechanism and the fluid compressibility induce flow oscillations [17]. The oscillations may cause pressure ripples and lead to vibrations and noise throughout the circuit. The same drawbacks also affect the HT performance. Thus a fluid model coupled to the model of the HT is used to predict and reduce the undesired phenomena. Vacca et al. [18] have made a comparison between four different fluid models, coupled to a swash plate axial piston pump model. It is observed that a fluid model that considers both gas and vapour cavitation, agrees with experiments over a wider range of conditions. The fluid model describes the oil phase change which occurs in a pressure range defined by a higher and a lower limit.

Due to the same working principle of the HT and the axial piston pump, the fluid model proposed has been used in the simulation. Further, the HT structure is similar to the axial piston pump/motor. However, the HT contains three ports: port A, port B and port T. Fewer pistons is allocated to each port which causes the higher pulsation of the flow. This pulsation cannot be ignored to get the detailed dynamic response of the HHV. Therefore, the HHV numerical model should be built based on the one piston dynamic model individually. The dynamics of the HT are determined by

$$J_{HT}\dot{\omega}_{HT} = \begin{cases} \sum_1^Z T_P - c\omega_{HT} - T_D & (\omega_{HT} \neq 0) \\ \sum_1^Z T_P - T_S & (\omega_{HT} = 0) \end{cases} \quad (1)$$

where J_{HT} is inertia moment of the rotate shaft-cylinder-piston assemble, ω_{HT} is HT speed, T_p is driving torque applied by each piston, c is viscous damper coefficient, T_D is dynamic friction torque, T_S is breakout friction torque and Z is piston number.

The driving torque of one piston is calculated as

$$T_p = p_p A_p R \tan \alpha \sin(\theta + \varphi) \quad (2)$$

where p_p is pressure of the piston bore, A_p is piston sectional area, R is radius of the rotating group, α is swash plate angle, θ is located angle of the piston and φ is HT controlled angle.

For the HT, a control volume is embraced by the piston bore, the cylinder barrel, the slipper, the valve plate and the swash plate. The hydraulic pressure in the piston bore is calculated by

$$\frac{dp_p}{dt} = \frac{B_H(Q - dV/dt)}{V} \quad (3)$$

where V is instantaneous volume, Q is instantaneous flow of the control volume, B_H is instantaneous bulk modulus and t is time.

The instantaneous volume can be calculated by

$$V = V_0 + A_p R \tan(\alpha) \sin(\theta + \varphi) \quad (4)$$

where V_0 is volume when the piston displacement is zero. The leakage of the piston bore is expressed as follows

$$Q_{IP} = K_P p_P \quad (5)$$

The valve plate of the H_T contains three ports: A, B and T. The ports A, B and T connect the high-pressure line of the CPR, the load and the low-pressure line of the CPR, respectively. The relationship between the piston bore and the valve plate port is described by the flow area change between the piston bore and the valve plate port. This method is extensively used in axial piston pump simulations [19].

The swash plate dynamic model is reduced to a second-order system as follows

$$X_{PV}(s) = \frac{\omega^2}{\omega^2 + 2\zeta\omega s + s^2} \quad (6)$$

where X_{PV} is transfer function for the swash plate motion, s is Laplace operator, ω is natural frequency and ζ is damping ratio.

The hydraulic motor is connected to the differential and receives the pressurised flow from the HT. The flow and torque equations are derived for the hydraulic motor using the motor governing equations. The hydraulic flow supplied to the hydraulic motor can be obtained by

$$Q_m = K_m p_m + V_m \omega_m \quad (7)$$

where Q_m is flow delivery of the hydraulic motor, K_m is leakage coefficient, V_m is displacement of the hydraulic motor, ω_m is speed of the hydraulic motor and p_m is differential pressure across the hydraulic motor.

The torque at the hydraulic motor driving shaft is obtained by

$$T_m = V_m p_m \eta_{mm} = T_{mI} + T_{mB} + T_L \quad (8)$$

where T_m is total torque in the hydraulic motor, T_{mI} is inertial torque, T_{mB} is damping friction torque T_L is load torque and η_{mm} is mechanical efficiency of the hydraulic motor.

The dynamic response of the hydraulic operated check valve affects the HHV performance during the transition of different drive modes. Thus, the dynamic modelling method is adopted which considered the dynamic response of the valve spool. The hydraulic operated check valve in the hydraulic circuit is to permit flow in one direction. The valve model is a spring-loaded check valve model with the spool dynamics considered. The dynamic model of the spool is as follows:

$$\begin{cases} m_V \frac{d^2 x_V}{dt^2} + c_{Vf} \frac{dx_V}{dt} \pm F_{Vfl} + F_{VK} + (p_{Vin} - p_{Vout}) S_V + F_C = 0 & (x_V < x_{Vmax}) \\ \frac{dx_V}{dt} = -C_{xVmax} \frac{dx_V}{dt} & (x_V = x_{Vmax}) \end{cases} \quad (9)$$

where m_V is spool mass without spring mass incorporated, x_V is spool displacement, c_{Vf} is damping coefficient, F_{Vfl} is flow force, F_{VK} is spring force, p_{Vin} is pressure at the inlet port, p_{Vout} is pressure at the outlet port, S_V is cross-section area of the spool, F_C is external spool control force, x_{Vmax} is maximum spool displacement and C_{xVmax} is spool speed coefficient.

The flow rate passing through the hydraulic operated check valve can be obtained by

$$Q_V = C_V A_V(x_V) \sqrt{\frac{2|p_{Vin} - p_{Vout}|}{\rho_O}} \quad (10)$$

where Q_V is flow rate through the valve, C_V is flow coefficient, ρ_O is hydraulic oil density and A_V is area in which fluid acts on the spool, which is determined by the spool displacement.

Pressure relief valve is used for limiting the maximum pressure in hydraulic circuit. A simplified model of the pressure relief valve in opening and closing states [20] is obtained by

$$\begin{cases} k_{RV}(p - p_{RV}) = 0 & (p > p_{RV}) \\ 0 & (p \leq p_{RV}) \end{cases} \quad (11)$$

where k_{RV} is slope coefficient of valve static characteristics, p is system pressure and p_{RV} is valve opening pressure.

The gas-charged accumulator relates the pressure at the inlet to the volume of fluid within the chamber. This element takes on two distinct states: one when the inlet pressure exceeds the precharge pressure of the gas chamber and the other is when the inlet pressure is less than or equal to the precharge pressure. The gas is assumed to be ideal. The governing equation is given below

$$V_{AC} = V_{AC0} \left(1 - \left(\frac{p_{pr}}{p} \right)^{\frac{1}{\gamma}} \right) \quad (12)$$

where V_{AC} is fluid volume within the accumulator, V_{AC0} is accumulator capacity, p_{pr} is gas precharge pressure and γ is specific heat ratio. The flow rate of the accumulator is the time derivative of V_{AC} .

The longitudinal tire force F_T acts upon the wheel shaft is described by the following equation.

$$T_T = -r_{wheel} F_T \quad (13)$$

where r_{wheel} is wheel radius and T_T is external torque. The brake torque is also applied on the rotational inertia/damper system.

The pressure of the hydraulic pipe is calculated with classical expression of a hydraulic capacitive element:

$$\frac{dp_{pipe}}{dt} = \frac{B_H}{A_{pipe}} \frac{dQ_{pipe}}{dx} \quad (14)$$

where p_{pipe} is pressure in the pipe, Q_{pipe} is flow through the pipe, A_{pipe} is cross-sectional area of the pipe and x is pipe length.

For the vehicle dynamics, a longitudinal vehicle dynamic model is used by the following equation [21].

$$F_T = fmg \cos \beta + mg \sin \beta + \frac{C_D A u^2}{21.15} + \sigma m \frac{du}{dt} \quad (15)$$

where m is vehicle mass, g is acceleration of gravity, f is rolling resistance coefficient, β is road grade, C_D is air drag coefficient, A is vehicle frontal area, u is vehicle speed and σ is mass factor of rotating components. The inertia of the rotating components has been lumped together into a single inertia element.

3 Results and Discussion

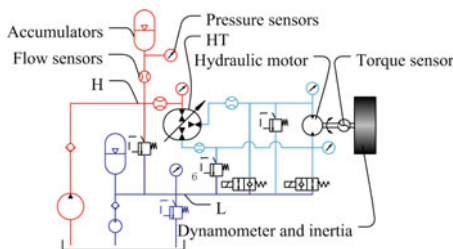
3.1 Driving Mode Performance

A HHV power train test rig, which is mainly composed of HT, hydraulic pump/motor and CPR, has been built. Figure 3 shows the hydraulic circuit and the photo of the experimental apparatus. The circuit includes the load devices which are the dynamometer and the inertia in the circuit.

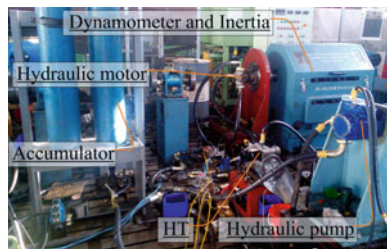
The HHV can achieve the ideal vehicle dynamic performance, as shown in Fig. 4. The constant torque output is guaranteed at a lower speed and the constant power output is realised at a higher speed. Further, the power train can output the maximum torque when the vehicle is standstill. In order to prevent the HT from speeding, the controlled angel is adjusted continuously. And the fluctuation of the controlled angel is slightly large during this time. In the constant torque stage, the drop of the hydraulic motor torque appears as the controlled angel changes, as shown in Fig. 4b. It seems that the drop mainly occurs when the controlled angel rises. The drop of the hydraulic motor torque is due to the drop of the hydraulic motor pressure. The HHV can achieve the ideal vehicle dynamic performance, as shown in Fig. 4.

The simulated and measured results about the drop are given in Fig. 5 [22]. It is seen that the drop is an inherent characteristic of the proposed HHV power train. There are three ports on the HT valve plate. When the controlled angle is larger than 30°, the port B displacement of the HT becomes small with the increasing of the controlled angle [16]. The proposed HHV power train becomes a non-minimum phase system and the negative response characteristic is the inherent characteristic of the system. To get higher control accuracy, the non-minimum phase of the system should be considered in the controller design of the HHV power train.

The HT speed has the same variation with the hydraulic motor speed, as shown in Fig. 6. Although, the variation trend between the simulation and the test are same with each other, the response of the hydraulic motor speed is much slower in the test. It is because that the efficiency of the HT prototype is low and difficult to describe accurately in the simulation model. The relationship between the hydraulic



(a) Experimental schematic diagram



(b) Experimental apparatus

Fig. 3 The HHV power train test rig

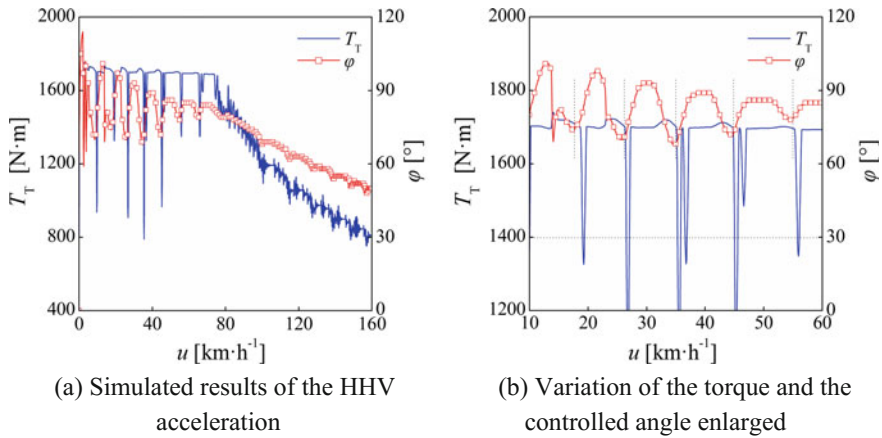


Fig. 4 The propulsion responses of the HHV power train

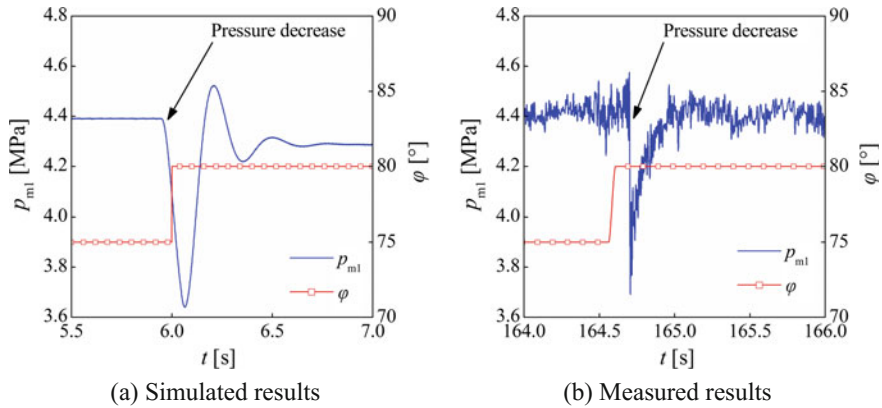


Fig. 5 The hydraulic motor pressure and controlled angle responses with a step input

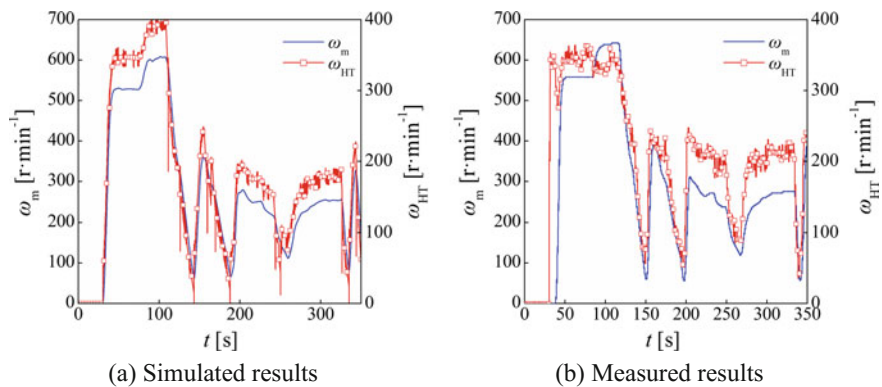


Fig. 6 Variation of the hydraulic motor speed and the HT speed

motor speed and the HT speed is nonlinear. It is because the operation of the HHV power train is based on the flow balance between the hydraulic motor and the HT. The displacement of the port on the HT changes with the controlled angel during the operation. Different from the mechanical transmission system, the rotating component speeds of the HHV power train becomes more flexible. Further, the speed has a large influence on the lifetime of the hydraulic component. Thus, the parameter matching of the hydraulic motor and the HT is important in order to prevent the hydraulic component from speeding [23].

3.2 Regenerative Braking Mode Performance

In the kinetic energy recovery operation, the rotating direction of the HT speed does not change, while the rotating direction of the controlled angle reverses. The hydraulic motor performs the pump function. The HT speed fluctuation appears during the conversion from driving to regenerative braking, as shown in Fig. 7. The conversion is usually fast for safety. The flow balance between the hydraulic motor and the HT is broken at that time. Due to the much larger inertia connected to the hydraulic motor, the fluctuation appears in the HT speed. It results in oscillations of the braking torque of the HHV in the regenerative braking mode. The inherent fluctuation is unhelpful for the service life and reliability of the HT. The tested HT speed variation is affected by the efficiency, the inertia, the friction, et al. The stability of the HT prototype at the low speed stage is also not guaranteed. All the parameters mentioned above make the differences between the simulation and the test.

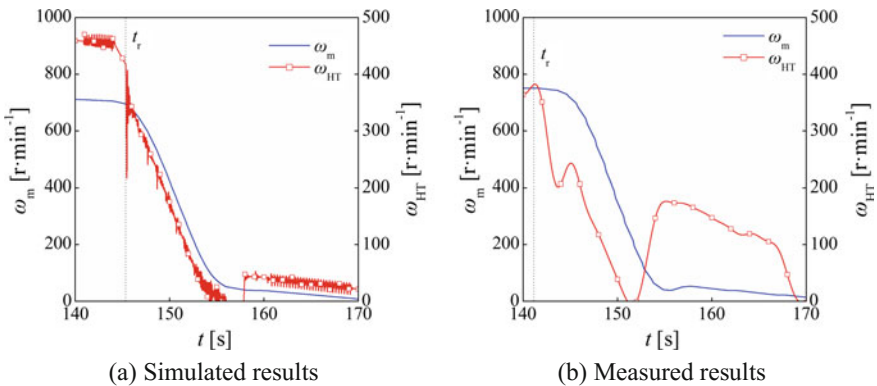


Fig. 7 The dynamic responses of the HHV power train during the regenerative braking

3.3 HT Work Points and Vehicle Performances

During the transformation of driving and braking, the high-pressure line and the low-pressure line of the hydraulic motor are interchanged by changing the controlled angel between positive and negative. To satisfy the vehicle speed requirement, the variation of the controlled angel is severe in the driving mode. In the braking mode, the controlled angel changes little and a stable deceleration is achieved.

In the urban driving cycle, the variations of the hydraulic accumulator pressure, the controlled angel and the vehicle speed are shown in Fig. 8. The hydraulic accumulator pressure boundaries are 25–30 MPa. It seems that the engine does not power on in the low-speed mode by using the energy recovered. Further, the operation time of the HHV engine t_e decreases 95 % during the whole cycle based on the on the assumption that the engine of the conventional vehicle is power on in the whole cycle. It is because that the HHV engine works at the maximum power when it powers on. This reduces the operation time of the HHV engine with a constant energy requirement. At the low-speed stage, the HHV requires a better acceleration performance and the controlled angel becomes much larger to realise a higher hydraulic motor driving pressure. With the increase of the vehicle speed, the controlled angel decreases gradually to satisfy the driving flow and the power requirements. At the regenerative braking stage, the requirement of the braking strength is low and the HT controlled angel is small. When the vehicle brakes from a certain speed to standstill in a short time at the low-speed stage, the controlled angel becomes larger to get an enough braking torque.

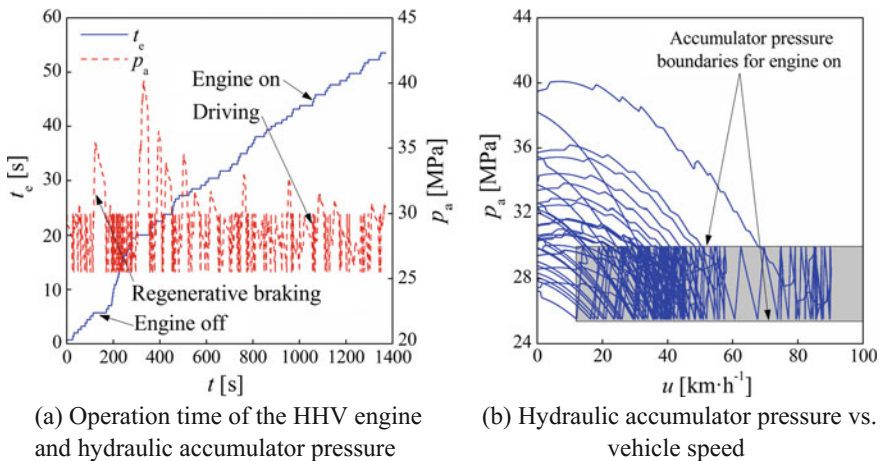


Fig. 8 Variations of the hydraulic accumulator pressure and the HT controlled angle

4 Conclusions and Future Work

The configuration and the full-cycle model of the HHV equipped with the HT were presented. The contributions of the HT dynamics to the HHV performance have been investigated. The results suggest the following. The parameter errors of the system can be estimated by simply measuring the “flatness” of a fictitious plane parallel to the x-y plane.

- (1) The proposed HHV can achieve the ideal vehicle dynamic performance by the adjustment of the controlled angle. The CPR pressure and the HT speed are used as the feedback of the control system to guarantee the fast response and reliability of the HHV power train.
- (2) The switching between the driving and the regenerative braking of the HHV is realized by the pressure cross-feedback control. The propulsion mode of the proposed HHV is changed automatically. Both the fast response and the high efficiency are guaranteed.
- (3) Due to the variation of the HT displacements determined by the HT controlled angle, the relationship between the hydraulic motor speed and the HT speed is nonlinear. The rotating component speeds of the HHV power train become more flexible.

Acknowledgments This work is supported the National Natural Science Foundation of China (Grant No. 51305034).

References

1. Wouk V (1995) Hybrids: then and now. *IEEE Spectr* 32(7):16–21
2. Kim N, Rousseau A (2013) A comparative study of hydraulic hybrid systems for class 6 trucks. In: *Proceedings of the SAE 2013 world congress and exhibition*. Detroit MI, 16–18 Apr 2013
3. Midgley WJB, Cebon D (2012) Comparison of regenerative braking technologies for heavy goods vehicles in urban environments. *P I Mech Eng D-J Aut* 226(7):957–970
4. Ji C, Zhu Y, Liang C, Liu X (2013) Simulation study on the operating characteristics of a hybrid hydraulic passenger car with a power split transmission. *Veh Syst Dyn* 51(10):1518–1532
5. Bender FA, Kaszynski M, Sawodny O (2013) Drive cycle prediction and energy management optimization for hybrid hydraulic vehicles. *IEEE Trans Veh Technol* 62(8):3581–3592
6. Ramakrishnan R, Hiremath SS, Singaperumal M (2012) Theoretical investigations on the effect of system parameters in series hydraulic hybrid system with hydrostatic regenerative braking. *J Mech Sci Technol* 26(5):1321–1331
7. Rossetti A, Macor A (2013) Multi-objective optimization of hydro-mechanical power split transmissions. *Mech Mach Theory* 62(2013):112–128
8. Zhang Z, Chen J, Wu B (2012) The control strategy of optimal brake energy recovery for a parallel hydraulic hybrid vehicle. *P I Mech Eng D-J Aut* 226(11):1445–1453
9. Molla S, Ayalew B (2011) Power management strategies for a series hydraulic hybrid drivetrain. *Int J Powertrains* 1(1):93–116

10. Wu B, Lin CC, Filipi Z, Peng H, Assanis D (2004) Optimal power management for a hydraulic hybrid delivery truck. *Veh Syst Dyn* 42(1–2):23–40
11. Achten P, Fu Z (2000) Valving land phenomena of the innas hydraulic transformer. *Int J Fluid Power* 1:39–47
12. Achten P, Brink T, Potma J, Schellekens M, Vael G (2009) A four-quadrant hydraulic transformer for hybrid vehicles. In: Proceedings of the 11th scandinavian international conference on fluid power. Jönköping, Sweden, 2–4 June 2009
13. Ibrahim MS (2011) Investigation of hydraulic transmissions for passenger cars. PhD Dissertation. RWTH Aachen University
14. Chen YL, Liu SA, Shang T, Zhang YK (2012) Characteristic analysis of hydraulic hybrid vehicle based on limit cycle. *Sci China Ser E: Technol Sci* 55(4):1031–1036
15. Chen YL, Liu SA, Jiang JH, Shang T, Zhang YK, Wei W (2013) Dynamic analysis of energy storage unit of the hydraulic hybrid vehicle. *Int J Auto Tech* 14(1):101–112
16. Jing C (2010) Research on characteristics of rotate-plate hydraulic transformer. PhD Dissertation. Beijing Institute of Technology
17. Bergadaa JM, Kumara S, Daviesb DL, Wattonb J (2012) A complete analysis of axial piston pump leakage and output flow ripples. *Appl Math Model* 36(4):1731–1751
18. Vacca A, Casoli P, Franzoni G, Berta GL (2006) Modeling of fluid properties in hydraulic positive displacement machines. *Simul Model Pract Theory* 14(8):1059–1072
19. Shu W (2010) The analysis of cavitation problems in the axial piston pump. *J Fluids Eng* 132(7):074502
20. Hamzehlouia S, Izadian A, Anwar S (2013) Modeling and control of a hybrid hydraulic-electric propulsion system. *Adv Automob Eng* 2(1)
21. Popp K, Schiehlen W (2010) Ground vehicle dynamics. Springer, Berlin
22. Wu W, Di CF, Hu JB (2015) Dynamics of a hydraulic—transformer-controlled hydraulic motor system for automobiles. *P I Mech Eng D-J Aut*
23. Wu W, Hu JB, Jing CB, Jiang ZL, Yuan SH (2014) Investigation of energy efficient hydraulic hybrid propulsion system for automobiles. *Energy* 73:497–505

The Vibration Modal Analysis of the Ball Screw About Precision Machine Tools

Nian- Cong Liu, Jin Xie and Hao- Ran Zeng

Abstract In view of low accuracy in the traditional analysis method, the slender ball screw is equivalent to the spring and the mathematical model is established by the energy method, and the accurate solution of the natural frequency is obtained. The SOLID187 element is applied to analyze the modes of the ball screw accurately on the ANSYS workbench and obtain the first four modes. The result shows that the prediction of the first 4 modes from the FEM of the ball-screw and that from the measured ones is within 5 %, therefore the method avoids the error caused by the traditional method effectively, and it is feasible to reduce the vibration of the feed system in numerical control machine and improve the machining accuracy of machine tool.

Keywords Ball screw · Modal analysis · Natural frequency

1 Introduction

Ball screw is an important transmission component for converting rotary motion into linear motion. Due to its small frictional resistance, high transmission efficiency, excellent wear resistance and high-speed characteristics and reversibility advantages, the ball screw has been adopted in the machine tool industry, industrial robots, agricultural machinery, automatic control system, and so on [1–3]. With the increasingly high demands on the high speed, and high accuracy of the ball screw, the vibration modal analysis is applied in the fault diagnosis and prediction, optimization of structural dynamic characteristics, prevention of resonance and

Nian-C. Liu (✉) · J. Xie
School of Mechanical Engineering, Southwest Jiaotong University,
Chengdu 610031, China
e-mail: ncliu@163.com

Nian-C. Liu · Hao-R. Zeng
The College of Nuclear Technology and Automation Engineering,
Chengdu University of Technology, Chengdu 610059, China

self-excitation vibration more and more, and has become one of the focus at home and abroad.

As researchers at home and abroad analyze the dynamic characteristics of ball screw, the theoretical method used in the study mainly include: (1) based on Timoshenko beam, Euler-Bernoulli beam, the dynamics model was constructed. For example, the dynamics model of machine feed system was built based on Timoshenko beam, and the coupling vibration relations of the screw in different direction were analyzed [4, 5]. Accused of neglecting the impact stiffness loss of screw thread, analytical error is bigger. (2) the finite element method (FEM). According to whether or not to ignore the characteristics of screw thread, the FEM was classified into two categories. The effects of dynamic characteristics for screw thread features were adequately considered [2, 6, 7]. The simplified model of ball screw was directly adopted [8–10]. For small pitch, deep groove ball screw, ignoring the influence of the characteristic of thread on damping, elasticity coefficient will tend to have larger error.

In this paper, a small pitch, deep groove ball screw is equivalent to the spring whose axial-stiffness is large, the lateral vibration model for screw is established by the energy method, and the accurate solution of the natural frequency is obtained. FEM (finite element method) is applied for SFU2005-800. The comparison result verifies the accuracy of the theoretical model, and provides a theoretical basis in dynamic analysis of ball screw and wide bandwidth control of feed system.

2 Mechanical Model of Ball Screw

The ball screw structure, thrust bearing one side and radial ball bearing another side, is considered the statically indeterminate structure that one end is hinged but the other is rigid connection. For the ball screw, the heterogeneity of material wasn't considered, and the centroid of cross section is a spiral line. So the slender ball screw can be regarded as the cylindrical helical spring with the great axial stiffness and tight and smooth structure on both ends, as shown in Fig. 1.

The pure bending is tend to happen under the action of moment. Assuming that the height of the spring is H , ρ is the curvature radius under bending, α is the helix

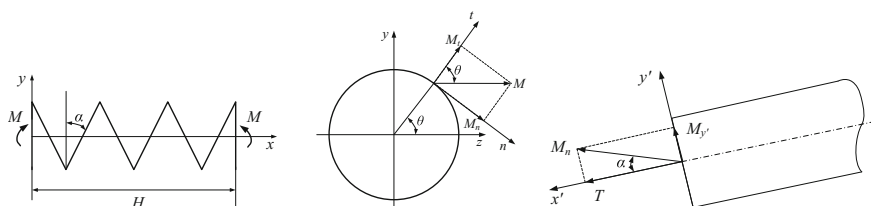


Fig. 1 Equivalent model of lead screw

angle of the spring, so The work for the moment can be represented in the following form:

$$U = \frac{1}{2} M \frac{H}{\rho} \tag{1}$$

M is the principal moment in arbitrarily section of cylindrical spring, and the radial and tangential component of M are: $M_n = M \sin \theta, M_t = M \cos \theta$. M_n can be divided into torque T and bending moment M'_y which is vertical or tangent to cross-section of spring wire.

$$\left. \begin{aligned} M'_y &= M \sin \theta \sin \alpha \\ T &= M \sin \theta \cos \alpha \end{aligned} \right\} \tag{2}$$

Synthesize M'_y and M_t , and leads to

$$M_Z = \sqrt{M^2 \sin^2 \alpha \sin^2 \theta + M^2 \cos^2 \theta} \tag{3}$$

The total deformed energy can be calculated as follows.

$$W = \int_0^{2n\pi} \left(\frac{\sin^2 \alpha \sin^2 \theta + \cos^2 \theta}{2EI_Z} + \frac{\cos^2 \alpha \sin^2 \theta}{2GI_P} \right) \frac{M^2 D}{2 \cos \alpha} d\theta \tag{4}$$

where n is number of active coils of spring, E is elastic modulus of materials, G is shear modulus of materials, I_Z is inertia moment of cross section of spring wire, I_P is polar moment of inertia of cross section of spring wire, D is middle diameter of cylindrical spring.

According to work-energy theorem $W = U$

$$\int_0^{2n\pi} \left(\frac{\sin^2 \alpha \sin^2 \theta + \cos^2 \theta}{2EI_Z} + \frac{\cos^2 \alpha \sin^2 \theta}{2GI_P} \right) \frac{MD}{\cos \alpha} d\theta = \frac{H}{\rho} \tag{5}$$

The relationship between helical pitch and helix angle is taken as

$$H = n\pi D \tan \alpha \tag{6}$$

$$\frac{1}{\rho} = \frac{M}{n\pi \sin \alpha} \int_0^{2n\pi} \left(\frac{\sin^2 \alpha \sin^2 \theta + \cos^2 \theta}{2EI_Z} + \frac{\cos^2 \alpha \sin^2 \theta}{2GI_P} \right) d\theta \tag{7}$$

The equation integrating (7) is given by

$$\frac{1}{\rho} = \frac{M}{\sin \alpha} \left(\frac{\sin^2 \alpha + 1}{2EI_Z} + \frac{\cos^2 \alpha}{2GI_P} \right) \quad (8)$$

Based on the definition of curvature

$$\frac{1}{\rho} = \frac{d^2 y}{dx^2} \quad (9)$$

So

$$\frac{d^4 y}{dx^4} = \frac{q}{\sin \alpha} \left(\frac{\sin^2 \alpha + 1}{2EI_Z} + \frac{\cos^2 \alpha}{2GI_P} \right) \quad (10)$$

where q is transverse distributed load.

When

$$q = -\frac{A\gamma l}{H} \cdot \frac{\partial^2 y}{\partial t^2} \quad (11)$$

where γ is mass per unit volume.

$$\frac{\partial^4 y}{\partial x^4} = -\frac{A\gamma l}{H} \cdot \frac{1}{\sin \alpha} \left(\frac{\sin^2 \alpha + 1}{2EI_Z} + \frac{\cos^2 \alpha}{2GI_P} \right) \frac{\partial^2 y}{\partial t^2} \quad (12)$$

Assume that

$$a^2 = \frac{H \sin \alpha}{A\gamma l \left(\frac{\sin^2 \alpha + 1}{2EI_Z} + \frac{\cos^2 \alpha}{2GI_P} \right)} \quad (13)$$

So

$$a^2 \frac{\partial^4 y}{\partial x^4} + \frac{\partial^2 y}{\partial t^2} = 0 \quad (14)$$

Equation (14) is the partial differential equation of free vibration about equivalent beam.

The separation variable method is adopted to solve it. Because the vibration mode has nothing to do with the time, the general solution is assumed as follows.

$$y(x, t) = Y(x) \cdot Z(t) \quad (15)$$

The modal can be obtained by substituting (15) into (14)

$$a^2 \frac{d^4 Y}{dx^4} \cdot \frac{1}{Y} = - \frac{d^2 Z}{dt^2} \cdot \frac{1}{Z} \tag{16}$$

The left and right ends of Eq. (14) are constant which is assumed to p^2 .

$$\frac{d^2 Z}{dt^2} + p^2 Z = 0 \tag{17}$$

$$\frac{d^4 Y}{dx^4} - k^4 Y = 0 \tag{18}$$

where $k^4 = \frac{p^2}{a^2}$.

The solution of equations for vibration is obtained by formula (17) and (18).

$$y(x, t) = (C_1 \sin kx + D_1 \cos kx + C_2 \sinh kx + D_2 \cosh kx)[A \sin \omega t + B \cos \omega t] \tag{19}$$

where A, B, C_1, C_2, D_1 and D_2 are the coefficients and determined by boundary conditions.

While $x = 0$

So

$$y = 0 \quad \frac{\partial y}{\partial x} = 0 \tag{20}$$

$$C_1 \sin kx + D_1 \cos kx + C_2 \sinh kx + D_2 \cosh kx = 0$$

While $x = H$

So

$$y = 0 \quad \frac{\partial^2 y}{\partial x^2} = 0 \tag{21}$$

So

$$D_1 = -D_2, \quad C_1 = -C_2$$

By formula (21), the equation of frequency can be derived.

$$\tan kH = \tanh kH \tag{22}$$

The solution of equation can be obtained by MATLAB.

$k_1 H = 3.9266, k_2 H = 7.0686, k_3 H = 10.2102, k_4 H = 13.3518.$

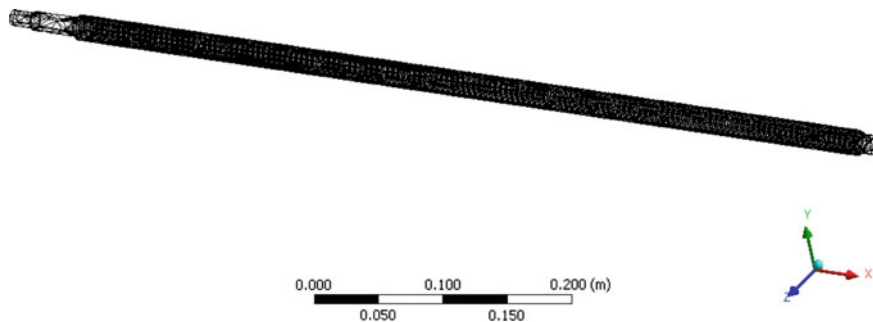


Fig. 2 Finite element model of a ball screw

The parameters of single-nut ball screw for SFU2005-800 is: the nominal diameter of 20, 5 mm lead, helix Angle of $4^{\circ} 33'$, the maximum length of 800 mm. The first four grades of natural frequency of Screw can be obtained which are 107.5614, 321.81, 640.12 and 1074.93 Hz.

3 Analysis of Speed Ball Screw Based On FEM

The entity model of single-nut ball screw for SFU2005-800 is establish and imported into ANSYS. The model material is given for GCr15. The screw is meshed by adopting the structural unit with 3D 10-node tetrahedron and smart grid meshing [11]. The meshing refinement level is 5, and 29,498 units and 54,672 nodes are obtained, as shown in Fig. 2. To simplify the analysis, the Lanczos Block method is used to solve the model under the free boundary condition. Because the

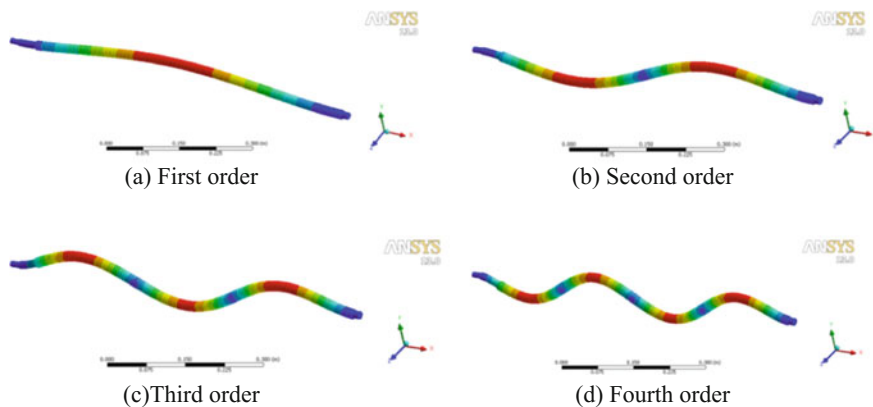


Fig. 3 Vibration mode of the ball screw

Table 1 Contrast of theoretical calculation and simulation results

Category	First order	Second order	Third order	Fourth order
Simulation mode/Hz	108.21	322.46	638.05	1058.12
Theory mode/Hz	108.21	270.8664	453.2502	634
Maximum error/%	2.98	4.86	3.07	2.71

external excitation (noise) is low frequency commonly, so the first four order vibration mode are analysed mainly, as shown in Fig. 3.

From Fig. 3, the first four modes are bending mode and the vibration type are orthogonal modes in the two mutually perpendicular planes. The maximum bending deformation is in the middle of each order bending of the ball screw. The first four grades of natural frequency of screw obtained by simulation is shown in Table 1.

Table 1 shows that compared with the calculated value of natural frequency of ball screw, the error is less than 5 % of every order mode, and proves that the calculation result is accurate and reliable.

4 Conclusions

- (1) The equivalent transformation is adopted to transform slender ball screw into the spring, and the energy method is used to establish its mathematical model, and the accurate natural frequency is obtained. The method avoids the error caused by the traditional method effectively, which lays the foundation in the analysis of the vibration of the feed system and the improvement of the machining precision.
- (2) Simulation results show that compared with FEM the error of the theoretical calculation is less than 5 %, and verifies the validity and reliability of the mechanical model, and provides an accurate modeling method for the dynamic analysis of the lead screw.

Acknowledgments Supported by the National Natural Science Foundation of China (Grant No. 51575457), and the Scientific research project of Sichuan Provincial Department of Education of China (Grant No. 16ZB0098).

References

1. Yong Z, Guoxian W, Xiaohua C (2013) A measuring and analysis method to identify torsional vibration modes of ball screw feed drives. *China Mech Eng* 24(23):3240–3244
2. Li B, Tu Z, Mao K (2013) Model test and dynamic modeling of ball screw using finite element method. *J Huazhong Univ Sci Technol (Nat Sci Ed)* 41(8):74–78
3. Mu G, Feng Y (2011) Study of the dynamic characteristic of high-speed ball screw. *J Hunan Univ (Nat Sci)* 38(12):25–29

4. Gu UC, Cheng CC (2004) Vibration analysis of a high-speed spindle under the action of a moving mass. *J Sound Vib* 4–5(278):1131–1146
5. Yang Y, Zhang W, Zhao H (2013) Dynamic characteristics of ball screw system. *J Vib Meas Diagn* 33(8):664–669
6. Dadalau A, Mottahedi M, Groh K (2010) Parametric modeling of ball screw spindles. *Prod Eng Res Dev* 4(6):625–631
7. Bertolaso R, Cheikh M, Barranger Y (2014) Experimental and numerical study of the load distribution in a ball-screw system. *J Mech Sci Technol* 28(4):1411–1420
8. Okwudire CE, Altintas Y (2009) Hybrid modeling of ball screw drives with coupled axial, torsional, and lateral dynamics. *J Mech Sci Technol* 131(7):10021–10029
9. Xu H, Li X (2013) Modal analysis of a grinding wheel carriage for a vertical glass-edge grinding machine with a long ball screw. *J Vib Shock* 32(18):189–194
10. Xia J, Hu Y, Wu B (2009) Research on thermal dynamics characteristics and modeling approach of ball screw. *Int J Adv Manuf Technol* 43(5–6):421–430
11. Lin J (2011) *The modal analysis and experiment*. Tsinghua University Press, Beijing

Author Biography

Liu Niancong (1976–), male, Associate Professor of Chengdu University of Technology, Post Doctor of Southwest Jiao Tong University. Research filed: Analysis of Mechatronic Dynamics.

The Kinematic Invariants in Testing Error Motion of Machine Tool Linear Axes

Yu Wu, Delun Wang, Zhi Wang, Huimin Dong and Shudong Yu

Abstract A discrete kinematic geometry (DKG) approach is proposed in this paper to deal with the kinematic behavior of testing a machine tool linear axis when geometry errors are taken into consideration. An apparatus is set up in connection with a newly acquired 6D high-precision measurement instrument to investigate the actual motion of a worktable (three translations and three rotations) using the proposed model and the measurement data. The invariants for the evaluation of the discrete error motions, especially the spherical image curve and the directrix (Wang and Wang in *Kinematic differential geometry and saddle synthesis of linkages*. Wiley, Singapore, 2015, 1) are analyzed and compared with the ideal curves, which produce some remarkable global invariants of the erroneous motion of the worktable like the spherical envelope circle error surface and the directrix error space. Three test cases are presented to illustrate how the DKG approach is used to evaluate the accuracy of a machine tool linear axis in a comprehensive and systematic way.

Keywords Discrete kinematic geometry · Invariant · Spherical image curve · Directrix · Error evaluation

1 Introduction

A machine tool linear axis consists of a worktable and a relative fixed frame, and is actually a prismatic joint or a slide way. A perfect linear axis, or an ideal prismatic joint, restrains five degrees of freedom (DOFs), and permits one linear displacement. If machining errors of the joint interfaces and component deformations are to

Y. Wu (✉) · D. Wang · Z. Wang · H. Dong
School of Mechanical Engineering, Dalian University of Technology,
Dalian 116024, China
e-mail: wuyu1091154038@163.com

S. Yu
Department of Mechanical and Industrial Engineering, Ryerson University, Toronto, Canada

be taken into consideration, the worktable actually moves in a three-dimensional manner and causes deviations from the ideal motion.

According to the standards ASME B5.54-2005 [2] and ISO 230-1-2012 [3, 4], the geometric accuracy of the linear axis consists of six error terms covering the linear displacement errors (including positioning accuracy) and the straightness errors (also called the roll, pitch and yaw). The measurement approaches of the linear error motion are defined in the standards above. The typical measuring instrument is the XD instrument with laser interferometer. Furthermore, many researchers proposed a number of methods for the linear error motion test. Lin [5] measured the volumetric errors by means of the laser tracker system which moved toward the space diagonal and only in need of one setup. Knapp [6], Okuyama [7], Ziegert [8] focused on the circular test for numerically controlled machine tools by CBP method and DBB method, analyzed the motion of each axis by error separation. With the multi-line method such as 9-line and 22-line method, Chen [9] and Tian [10] established the parameter identification model for geometric error assessment.

The common point above is that, the error evaluation is based on the measured function point. The result of the evaluation depends on the measurement coordinate system, and it is not the unique one. For example, the linear displacement errors can be affected by the angular displacement errors in tests, such as the Abbe error/offset and the Bryan principle [11]. Can the errors be clearly and strictly defined for a linear axis? Is there another convenient analysis method to decompose the angular and linear displacements and provide a theoretical base for evaluating accuracy of an individual linear axis of machine tools?

During testing the six error terms of an individual linear axis, the worktable occupies a series of permissible discrete positions. The points and lines on the worktable will trace the corresponding discrete trajectories whose geometric characteristics are used to evaluate the accuracy of the linear axis, which naturally is a DKG topic. In this paper, a kinematic geometry model, corresponding to a typical measuring scheme, is presented to describe and analyze the accuracy in testing a machine tool linear axis. The kinematic parameters of the worktable, three rotations and three translations, are determined using the proposed model and measured displacements. The discrete trajectories traced by the points and lines on the worktable are mapped into the directrices and the spherical image curves, whose invariants are used to evaluate the accuracy of the linear axis.

2 The Kinematic Geometry Model

2.1 Description of Testing a Machine Tool Linear Axis

A typical scheme, similar to that mentioned in ASME B5.54-2005, is used to test machine tool linear axis by the XD measuring instrument, shown in Fig. 1. A fixed

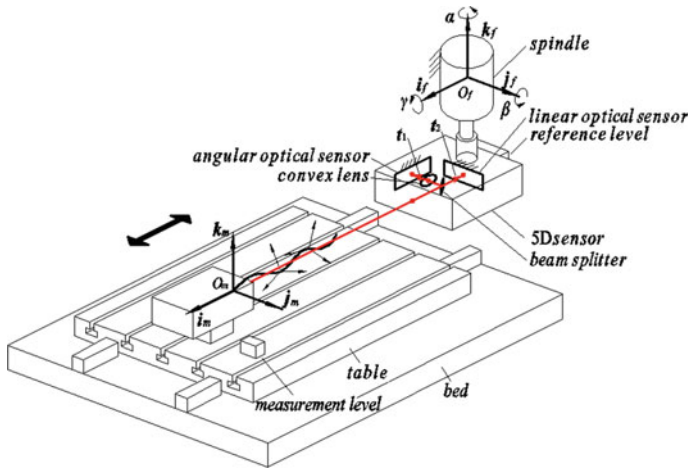


Fig. 1 Schematic of testing a machine tool linear axis

coordinate system $\{O_f; i_f; j_f; k_f\}$, attached to the frame, is chosen in such a way that its coordinate axes coincide with the axes of the machine tool. A moving coordinate system $\{O_m; i_m; j_m; k_m\}$ attached to the moving worktable, or the assembling position of the laser instrument on the work table, is chosen in way that its origin O_m coincides with the original-point of the laser, and its i_m axis coincides with the direction of the laser, its k_m and j_m axes are perpendicular to i_m . A discrete location is described in $\{O_f; i_f; j_f; k_f\}$ with superscript (i) , such as $\{O_m^{(i)}; i_m^{(i)}; j_m^{(i)}; k_m^{(i)}\}$.

The six error terms of a linear axis, both linear and angular displacements, can be measured by the XD measuring instrument for a measuring position (i) of the worktable, as shown in Fig. 1. The linear displacements $x_{om}^{(i)}$ of the worktable in the direction of the linear axis can be directly revealed by the laser interferometer; the two other linear displacements $(y_{om}^{(i)}, z_{om}^{(i)})$, or the lateral motion in the two directions orthogonal to the direction of the linear axis are measured and shown by means of the sensors in the fixed frame. The angular displacements (errors) corresponding to the yaw $\alpha^{(i)}$, pitch $\beta^{(i)}$ and, roll $\gamma^{(i)}$ can be determined by the angular optical sensors mounted on the fixed frame. Generally, five of the six error terms come from the loci of the lines of the laser beam except that the angular displacement $\gamma^{(i)}$, measured by an electric level sensor.

In the ideal case, or the worktable moves straight in the desired direction, the trajectory of any line of the worktable, including the line of the laser beam, is a plane or a line in the fixed frame. In fact, the worktable has an error motion in six-DOF, five error terms come from the line-trajectory by comparing it with that in the ideal case. Hence, different positions of the laser beam line produce different line-trajectories. Some useful cases were pointed out by Abbe and Bryan [11].

2.2 Kinematical Geometry Model in Testing a Linear Axis

Figure 2 shows a typical machine tool linear axis with erroneous slide ways and erroneous worktable interfaces.

To study the kinematic geometry of the worktable, the relationship between the moving frame $\{O_m; i_m; j_m; k_m\}$ and the fixed frame $\{O_f; i_f; j_f; k_f\}$, or the six kinematical parameters—three translations $\{x_{om}, y_{om}, z_{om}\}$ and three angles of rotation $\{\alpha, \beta, \gamma\}$ need to be established. The origin O_m of the laser beam has the coordinates $(0, 0, 0)$ in the coordinate system $\{O_m; i_m; j_m; k_m\}$ of the worktable Σ^* , and its coordinates are $\{x_{mf}, y_{mf}, z_{mf}\}$ in the fixed frame $\{O_f; i_f; j_f; k_f\}$. The rotation transformation matrix from the coordinate system $\{O_m; i_m; j_m; k_m\}$ to the coordinate system $\{O_f; i_f; j_f; k_f\}$ can be written as

$$[R_{mf}] = \begin{bmatrix} c\alpha c\beta & c\alpha s\beta s\gamma - s\alpha c\gamma & c\alpha s\beta c\gamma + s\alpha s\gamma \\ s\alpha c\beta & s\alpha s\beta s\gamma + c\alpha c\gamma & s\alpha s\beta c\gamma - c\alpha s\gamma \\ -s\beta & c\beta s\gamma & c\beta c\gamma \end{bmatrix} \tag{1}$$

A point P_m on the worktable with coordinates (x_{pm}, y_{pm}, z_{pm}) moves with the worktable and traces a trajectory Γ_P in $\{O_f; i_f; j_f; k_f\}$, whose vector equation is

$$\Gamma_P : R_{Pf} = R_{Om} + [R_{mf}]R_{Pm} \tag{2}$$

where $R_{mf} = [x_{mf}, y_{mf}, z_{mf}]^T$ is the vector of point O_m ; and $R_{Pm} = [x_{Pm}, y_{Pm}, z_{Pm}]^T$ is the vector of point P_m .

Similarly, a line L_m on the worktable Σ^* with the direction angular $(\delta_{sm}, \theta_{sm})$, passes through point P_m can be represented in the matrix form as

$$[l_{m1}, l_{m2}, l_{m3}] = [s\delta_{sm}c\theta_{sm}, s\delta_{sm}s\theta_{sm}, c\delta_{sm}] \tag{3}$$

Line L_m of the worktable moves in $\{O_f; i_f; j_f; k_f\}$, traces a line-trajectory Σ_{lf} , or a ruled surface, whose equation can be written as

Fig. 2 Sketch of a machine tool linear axis

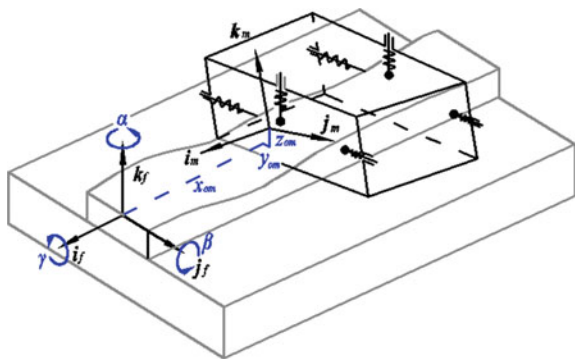
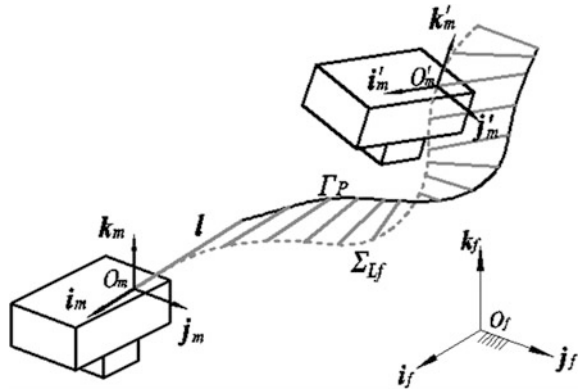


Fig. 3 Line-trajectory of laser beam in the fixed frame



$$\sum_{L_f} : \mathbf{R}_{L_f} = \mathbf{R}_{P_f} + \lambda[\mathbf{R}_{m_f}]l_m \tag{4}$$

where λ is the parameter of the generatrix; $l_m = [l_{m1}, l_{m2}, l_{m3}]$ is the unit direction vector of line L_m .

Specially, the line-trajectory \sum_{L_f} traced by the line of the laser beam i_m , shown in Fig. 3 for a series of discrete positions, can be denoted as

$$\sum_{L_f} : \mathbf{R}_{L_f} = \mathbf{R}_{m_f} + \lambda[\mathbf{R}_{m_f}]i_m \tag{5}$$

In testing a machine tool linear axis, the loci traced by points and lines of the worktable in $\{O_f, i_f, j_f, k_f\}$ can be determined from the kinematic geometry equations in connection with the measurements. It is noted that the measurements of the actual motion of the worktable relative to the fixed frame with six DOFs including the nominal linear motion, need to be taken only once. The kinematic geometry characteristics of all point-trajectories and line-trajectories can be determined and described by the kinematic invariants of the erroneous motion of the worktable.

3 The Discrete Kinematic Invariants

3.1 Kinematical Geometry Model in Testing a Linear Axis

As mentioned above, both point-trajectories and line-trajectories can be described in Eqs. (1)–(5). However, the actual motion of the worktable are expressed by a series of discrete data, acquired using an instrumentation. Hence, in this paper, we propose to use the discrete kinematic invariants of spatial motion of a rigid body to study the actual erroneous motion of a machine tool linear axis.

A ruled surface in the fixed frame $\{O_f; i_f; j_f; k_f\}$, traced by a line of the worktable, represented by Eq. (4) for continuous parameters, can be rewritten for the discrete parameters as

$$\sum_{L_f} : \mathbf{R}_{L_f}^{(i)} = \mathbf{R}_{P_f}^{(i)} + \lambda[\mathbf{R}_{m_f}^{(i)}]l_m \tag{6}$$

Corresponding to the discrete position in testing an individual linear axis $x_{om}^{(i)}$, the geometric properties of a discrete ruled surface traced by a line of the worktable can be completely calculated by Eq. (6), whose vector equation can be written in a standard form as

$$\sum_{L_f} : \mathbf{R}_{L_f} = \boldsymbol{\rho}_{L_f}^{(i)} + \lambda \mathbf{l}_f^{(i)}; \quad i = 1, \dots, n \tag{7}$$

The kinematic invariants, independent of the coordinates system used, are naturally a set of most effective parameters for studying the geometric properties of discrete ruled surfaces. The directrix and spherical image curve are the typical invariants of a ruled surface. Consequently, the DKG approach is a powerful tool to compare geometric characteristics of two discrete ruled surfaces, which is believed as a novel approach in testing an individual linear axis.

3.2 The Minimal Directrix of Error Motion

The trajectory of any point $P_m^{(i)}$ in the generator of the ruled surface, defined a directrix, could be written as following:

$$\Gamma_P^{(i)} : \mathbf{R}_{P_f}^{(i)} = \mathbf{R}_{O_m}^{(i)} + [\mathbf{R}_{m_f}^{(i)}] \mathbf{R}_{P_m} \tag{8}$$

Obviously, the directrix degenerates into a straight line without error motion. While in the actual situation, there is a minimal directrix in the fixed frame, corresponding to a point in the moving body, which has the minimal error respect to its fitting line. The mathematical model for the minimal directrix can be written as follows:

$$\begin{cases} \Delta = \min_{1 \leq i \leq n} \{f^{(i)}(\mathbf{x})\} \\ f^{(i)}(\mathbf{x}) = \sqrt{\|\mathbf{R}_p^{(i)} - \mathbf{R}_0\|^2 - ((\mathbf{R}_p^{(i)} - \mathbf{R}_0) \cdot \mathbf{l}_0)^2} \\ \mathbf{R}_0 = (x_0, y_0, 0) \\ \mathbf{x} = (x_0, y_0, \xi, \eta) \end{cases} \tag{9}$$

$$\begin{cases} \delta = \min \Delta(\mathbf{p}) \\ \mathbf{p} = (x_{pm}, y_{pm}, z_{pm}) \end{cases} \quad (10)$$

while (x_{pm}, y_{pm}, z_{pm}) is the coordinate parameters of the point in the moving body, and (x_0, y_0, ζ, η) is the parameters for the fitting line \mathbf{l}_0 . The optimization model (9) is for the saddle line fitting [12] of all the points and their corresponding errors, while (10) is to search for the point corresponding to the minimal directrix called the minimal error point. Both the minimal directrix and the minimal error point are the invariants of the error motion of the worktable.

3.3 The Spherical Image Curve of Error Motion

The directions of the generatrix of the discrete ruled surface can be mapped into a curve on a unit spherical surface, or a spherical image curve of the direction vector \mathbf{l}_f , and can be calculated from the following equation

$$\mathbf{l}_f^{(i)} = [\mathbf{R}_{mf}^{(i)}] \mathbf{l}_m; \quad i = 1, \dots, n \quad (11)$$

In the case of ideal linear motion, the discrete spherical image curve is a single point on the unit spherical surface. Similar to the directrix, there is a vector with the minimal angular error, called as the minimal error vector. The optimization model for minimal error vector can be written as:

$$\begin{cases} \Delta = \min_a \{g(\mathbf{x})\} \\ g(\mathbf{x}) = \arcsin(\mathbf{l}_0 \cdot \mathbf{l}^{(i)}) \\ \mathbf{x} = (\delta_1, \delta_2)^T \end{cases} \quad (12)$$

$$\begin{cases} \delta = \min \Delta(\mathbf{p}) \\ \mathbf{p} = (\alpha_m, \beta_m) \end{cases} \quad (13)$$

while (α_m, β_m) are the direction parameters of the vector in the moving body, and (δ_1, δ_2) are the parameters for the fitting orientation in the rigid system. All the orientations and their errors, including the minimal error orientation, can be solved.

From the viewpoint of the DKG of a rigid body, the global kinematic invariants, the directrix error space and the spherical image curve error surface can thoroughly describe the properties of the moving worktable in its erroneous motion, as discussed as follows.

4 Case Studies

4.1 Case 1: Line-Trajectory

In this test case shown in Fig. 4, the laser instrument is placed on the worktable of a machine center (DMG-DMC1035V) at approximated coordinates (150, 0, 0). The parameters of the instrument are as follows: the linear accuracy is 0.5 ppm, the straightness accuracy is $1 + 0.2$ ($\mu\text{m}/\text{meter}$ traveled), while the angular accuracy is $1.0 + 0.1$ ($\text{arcsec}/\text{meter}$ traveled). The six error terms measured are shown in Fig. 5.

The line-trajectory of the laser beam can be calculated by means of the proposed kinematic geometric model and Eqs. (1)–(9). The line-trajectory \sum_{lf} of the laser beam line and its directrix are calculated and shown in the fixed frame in Fig. 6. The discrete spherical image curve of the line-trajectory of the laser is calculated by Eq. (9) and shown in Fig. 7.

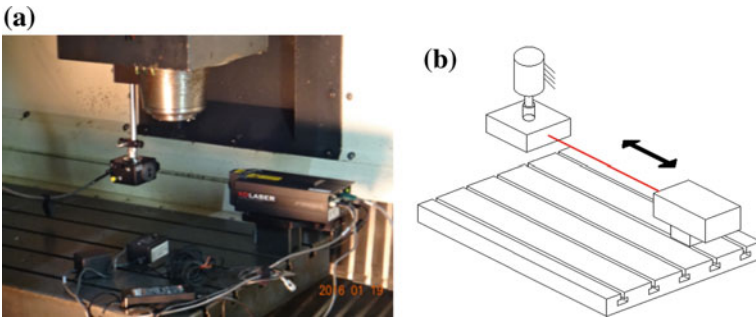


Fig. 4 Test apparatus for a linear axis (case 1)

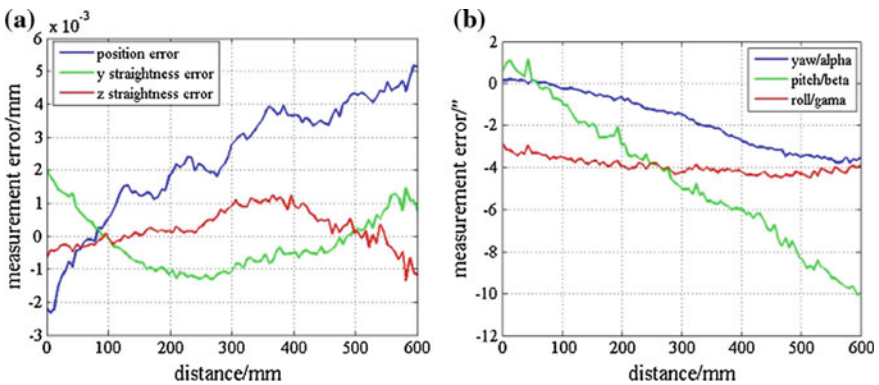


Fig. 5 Erroneous linear and angular motions of the X-axis on the worktable (case 1)

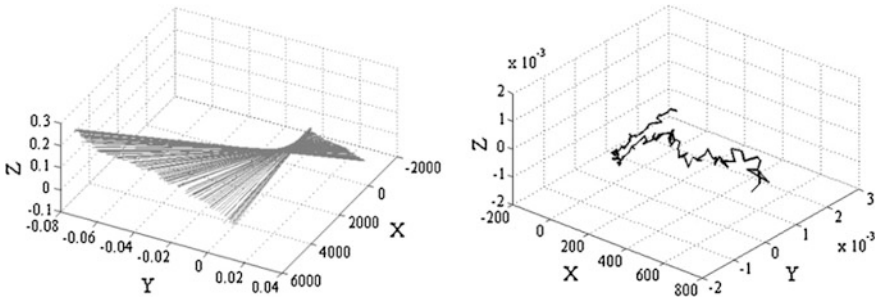


Fig. 6 The line-trajectory of laser beam and the directrix of line-trajectory of laser (case 1)

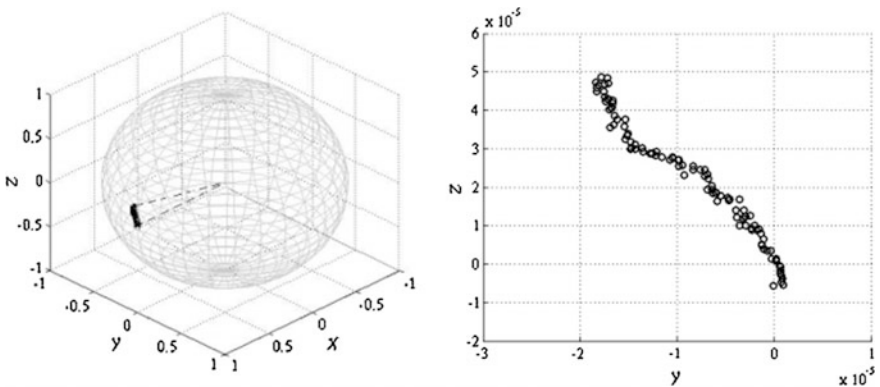


Fig. 7 Discrete spherical image curve of laser and the detail view (case 1)

The laser line in Case 1 is just one of the lines of the worktable. Does it show the linear accuracy of the linear axis? If not, measurements for a different laser line can be obtained by putting the laser instrument on the worktable with another position, but is there is a most suitable position on the work table for the laser with least error? It would certainly be the global invariants of the linear axis error motion of the work table.

4.2 Results from Three Test Cases

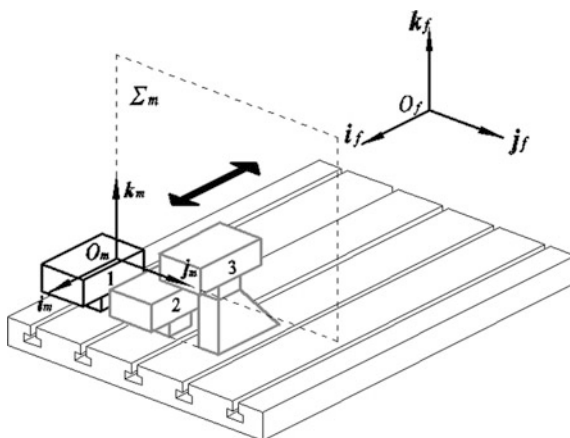
The laser instrument is placed for other two test cases. All the three cases are described in Table 1 for the laser instrument on the worktable, shown in Fig. 8. One hundred discrete positions are measured in each case.

By means of the XD measuring instrument, the measuring data was obtained corresponding to the three cases, the three linear errors are shown in Fig. 9a–c, and the angular errors are shown in Fig. 10a–c.

Table 1 Three cases for testing an individual linear axis

Cases	X-axis travel distance	Y coordinate	Z coordinate
1	150–750	0	0
2	150–750	145	0
3	150–750	245	120

Fig. 8 Three measuring cases for locations of laser instrument



Three groups of data, shown in Figs. 9 and 10, for the erroneous motion of the worktable in testing a single linear axis, indicate that the measuring results are sensitive to the positions of the laser instrument, which agrees with the Bryan principle in the ASME standard. The question is how to choose a reasonable measuring position of the laser instrument on the worktable. Is there any intrinsic relationship among different groups of measurements? This is a fundamental question faced by today’s machine tool design and manufacture engineers.

4.3 Kinematic Invariants of the Error Motion

- (1) The directrix error space and the minimal straightness error point

In case one, the directrix error space and its 3-D contour lines are depicted by Eqs. (8)–(10) in Fig. 11a, b, which show the directrix errors of all points in the moving body. Particularly, the deep blue position with the coordinate (247.72, -220.25, -67.13) corresponds to the minimal straightness error point, and the trajectory is closest to a straight line with the spatial straightness error 1.79 μm. Figure 11c shows the contour lines on plane $z = -87.13$ mm.

Similar to case one, the directrix error space and its contour lines in case two and case three can be obtained, shown in Figs. 12 and 13. The coordinates of minimal

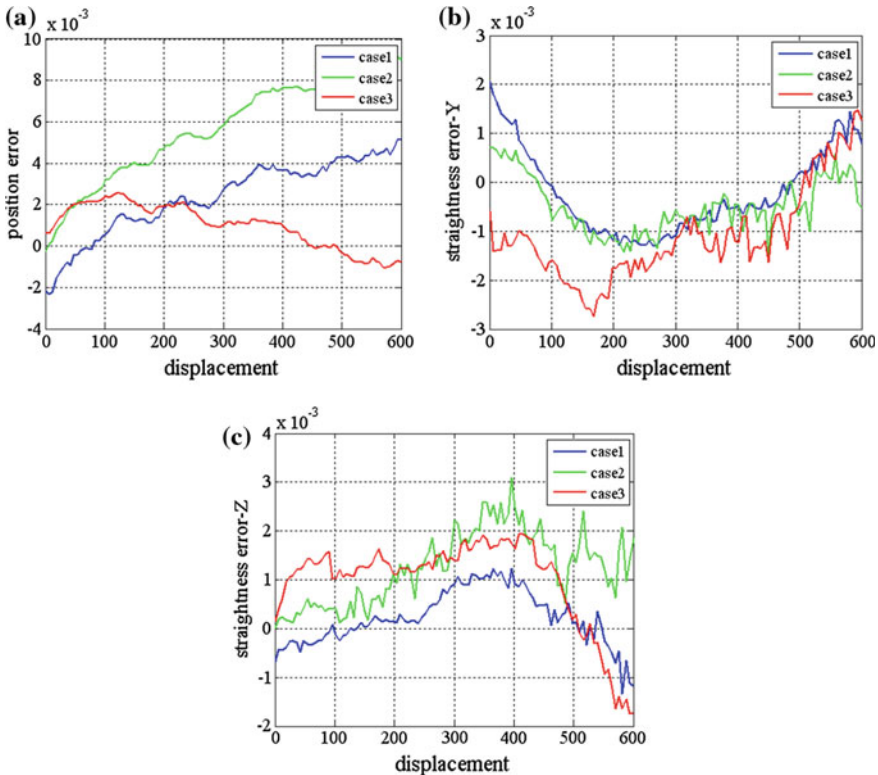


Fig. 9 Linear errors of a linear axis for three cases

straightness error points are $(256.17, -365.48, -69.62)$ and $(253.22, -425.08, -188.47)$, corresponding to the minimal error 1.71 and 1.74 μm separately.

Actually, the trajectory of each point in the moving body lies on the linear error motion itself. When the working space and the moving coordinate system are confirmed, the directrix error space is uniquely determined. Therefore, the it can be used as the global invariant and the minimal straightness error as a special one to evaluate the position accuracy of an individual linear axis integrally and objectively.

(2) The spherical envelope circle error surface, the minimal/maximal error vector

A line of the worktable will correspond to its discrete spherical image curve error and discrete directrix error. All of these errors are taken as the Z-coordinate and the direction parameters of the line of the worktable are designated as the X and Y coordinates, which form a spherical envelope circle (SEC) error surface in three dimensions in Fig. 14a and projecting plane with contour lines in Fig. 14b. There exists a minimal error vector R_{P1} on the SEC error surface, corresponding to line L_{m1} $[0.1052, 0.9306, 0.3507]$ of the worktable, and its discrete spherical image

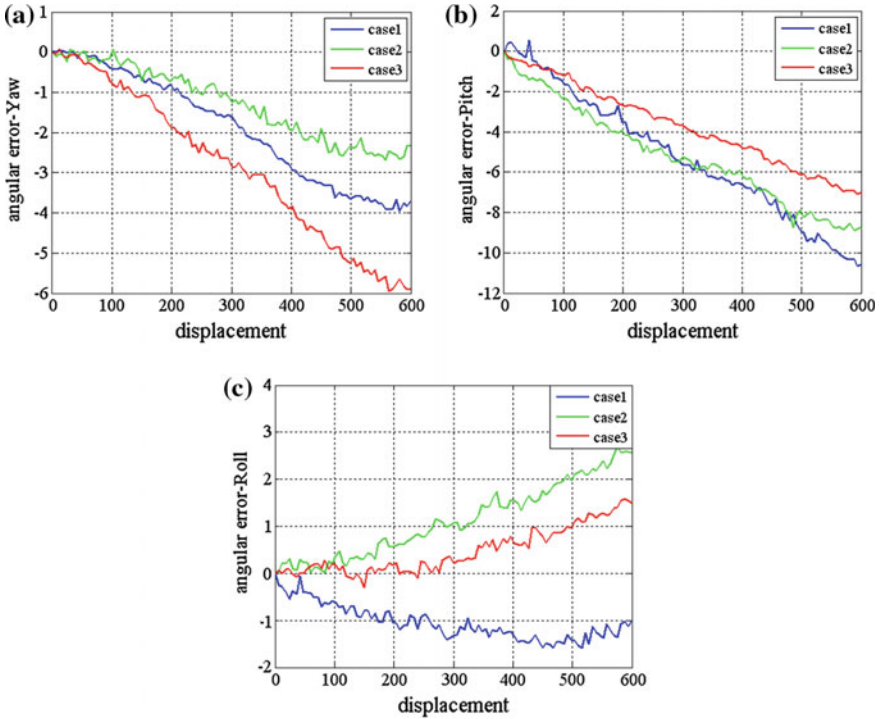


Fig. 10 Angular errors of a linear axis for three cases

curve error is $2.42e-06$ rad. There also exists maximal error vector R_{P2} corresponding to L_{m2} $[-0.0400, -0.3193, 0.9468]$, with the maximal error $2.31e-5$ rad and forms an angle 88.23° with the minimal vector. The SEC error surface reveals the kinematic geometric properties of the erroneous motion and is independent of the measuring positions. The local coordinate system $\{O; L_1; L_2; L_3\}$ of the SEC error surface can be set up to identify the position and orientations of the worktable, while $L_3 = L_1 \times L_2$.

Similarly, the SEC error surface in Case 2 can also be drawn in three dimensions in Fig. 15a, and the projecting plane with contour lines in Fig. 15b. Here line L_{m1} $[-0.2490, 0.9218, 0.2970]$ of the worktable corresponds to a minimal error value of $2.47e-06$ rad. Line L_{m2} $[0.1941, -0.2254, 0.9563]$ corresponds to a maximal error $2.33e-5$ rad forms an angle 88.43° with the minimal vector.

The local coordinate system of the SEC error surface in Case 3 can be established by the line of the worktable with the minimal SEC error value and the line with maximum error value shown in Fig. 16, which is same as that in Fig. 14 of Case 1.

In the same way, the SEC error surface in case three can be drawn in three dimensions in Fig. 16a, and the projecting plane with contour lines in Fig. 16b. Line L_{m1} $[-0.1589, 0.7343, 0.6599]$ corresponds to a minimal error value of $2.44e$

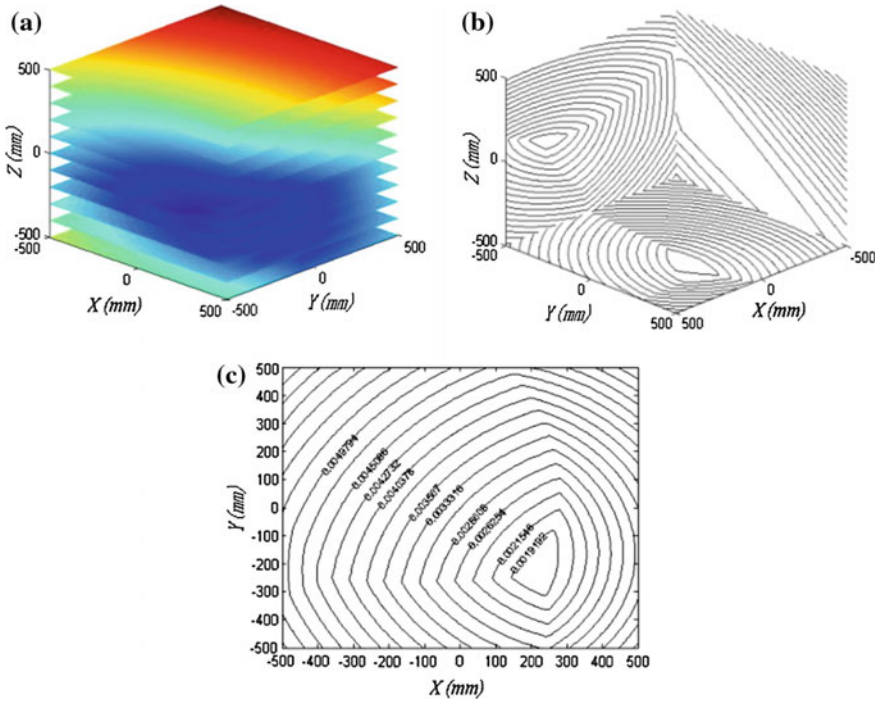


Fig. 11 The directrix error space and its contour lines in case one

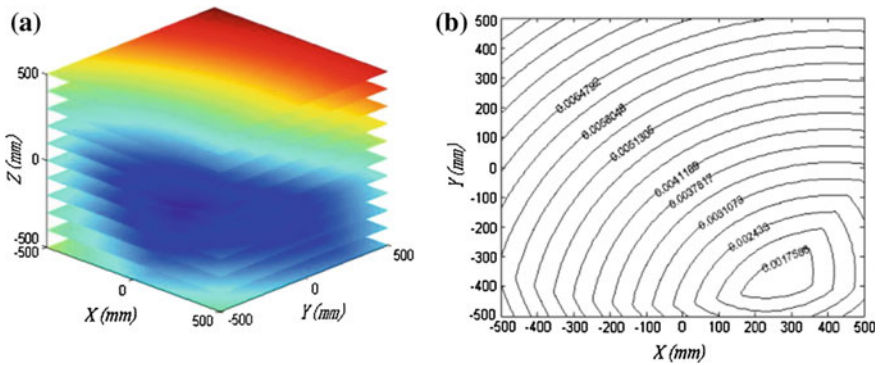


Fig. 12 The directrix error space and its contour lines in case two

-06 rad. Line L_{m2} $[-0.8954, -0.3801, 0.2316]$ corresponds to a maximal error $2.27e-5$ rad forms an angle 89.08° with the minimal vector.

The local coordinate system of the SEC error surface can be established by the line of the worktable in Fig. 16, which is similar to that in Fig. 14 of Case 1, and in Fig. 15 of Case 2. Eliminate the repeatability influence, both the line of the

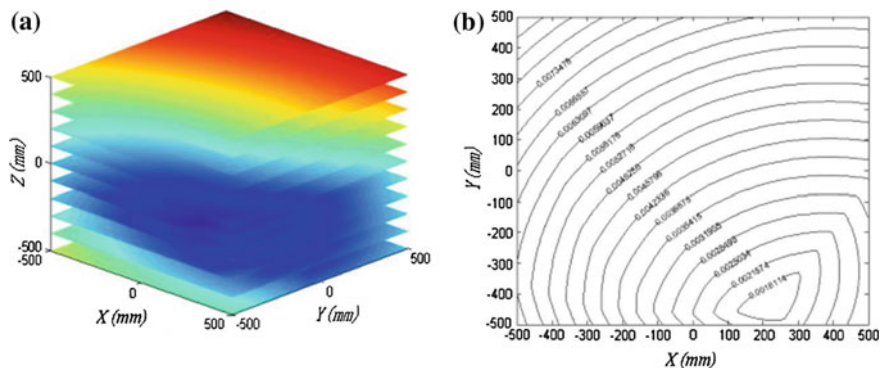


Fig. 13 The directrix error space and its contour lines in case three

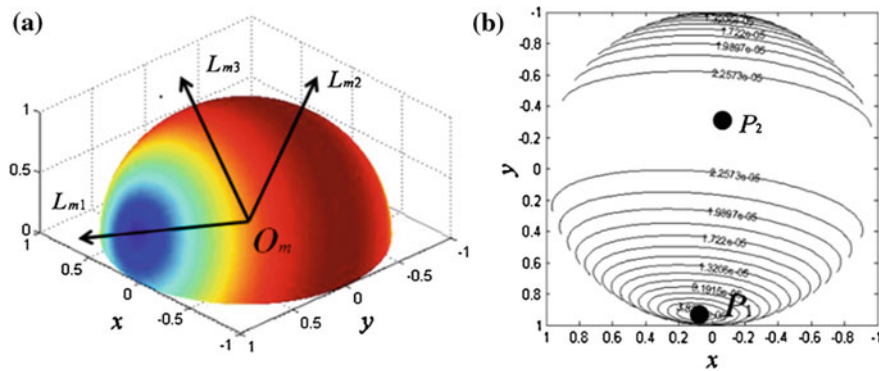


Fig. 14 The local coordinate system of SEC error surface and with contour lines in case one

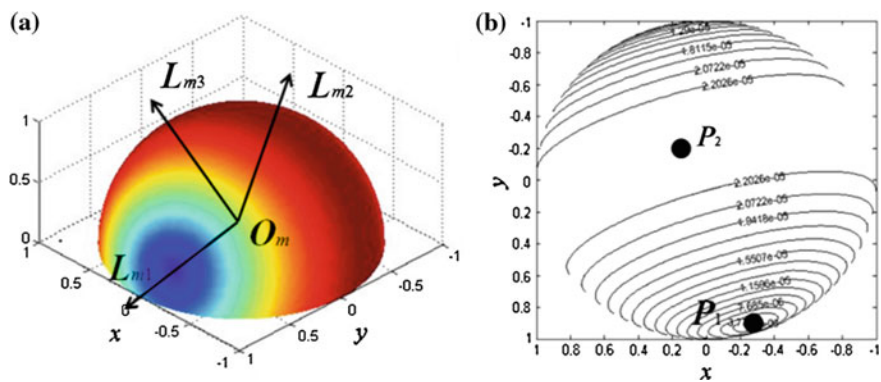


Fig. 15 The SEC error surface and with contour lines in case two

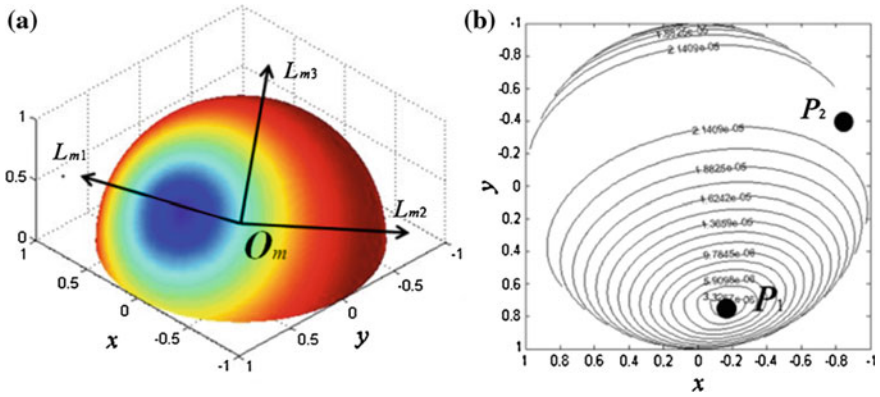


Fig. 16 The SEC error surface and with contour lines in case three

worktable with the minimal/maximal SEC error and the coordinate system of the SEC error surface are the same in all three cases since they are the invariant in testing a machine tool linear axis. This implies that one measuring position (location of laser beam on the worktable) is enough for testing to determine the line of worktable with the minimal SEC error, which is the benchmark of accuracy in testing a machine tool linear axis.

5 Conclusions

- (1) The kinematic geometric model of a typical testing device, XD measurement instrument, can completely describe the kinematic geometric properties of the actual motion of the worktable.
- (2) The discrete kinematic invariants, the spherical image curve and the directrix, of the ruled surfaces traced by lines of the worktable reveal the intrinsic geometric properties of the erroneous motion of the worktable.
- (3) The global kinematic invariants of the erroneous motion of the worktable including the directrix error space and the SEC error surface, are a new benchmark in evaluating the accuracy in testing a machine tool linear axis.

Acknowledgments This research was supported by the Technology Major Project (No. 2015ZX04014021-03).

References

1. Wang D, Wang W (2015) Kinematic differential geometry and saddle synthesis of linkages. Wiley, Singapore
2. ASME B5.54 (2005) Methods for performance evaluation of computer numerically controlled machining centers
3. ISO 230-1 (2012) Test code for machine tools—part 1: geometric accuracy of machines operating under no-load or quasi-static conditions
4. ISO 230-2 (2006) Test code for machine tools—part 2: determination of accuracy and repeatability of positioning numerically controlled axes
5. Lin CC, Her JL (2005) Calibrating the volumetric errors of a precision machine by a laser tracker system. *Int J Adv Manuf Technol* 26(11–12):1255–1267
6. Knapp W, Matthias E (1983) Test of the three-dimensional uncertainty of machine tools and measuring machines and its relation to the machine errors. *CIRP Ann Manuf Technol* 32(1):459–464
7. Okuyama S, Yano H, Watanabe S (1997) Effect of floating capacity on the measurement error of the CBP method. *J Jpn Soc Precis Eng* 63:1427–1431
8. Ziegert JC, Mize CD (1994) The laser ball bar: a new instrument for machine tool metrology. *Precis Eng* 16(4):259–267
9. Chen G, Yuan J, Ni J (2001) A displacement measurement approach for machine geometric error assessment. *Int J Mach Tools Manuf* 41(1):149–161
10. Tian W, Niu W, Chang W (2015) Research on geometric error tracing of NC machine tools. *Chin J Mech Eng*, 2015, 28(4):763–768, 2014, 50(7):128–135 (in Chinese)
11. Bryan JB (1979) The Abbé principle revisited: an updated interpretation. *Precis Eng* 1(3):129–132
12. Wu Y, Wang DL, Wang W et al (2015) Kinematic geometry for the saddle line fitting of planar discrete positions. *Chin J Mech Eng* 28(4):763–768

Research on the Principle of Six Degree-of-Freedom Laser Tracker Metrology

Liang Yu, Lubin Hang, Wushan Cheng, Yabo Huangfu, Wentao Li and Guobin Yang

Abstract Due to the demand for precise positioning and high precision trajectory of robots end-effector, laser tracker measurement functions in position and gesture of a target are studied respectively. For the position measurement of the target, laser interference (IF) measurement method based on phase difference and absolute distance (AD) measurement method based on dual frequency modulation signal are analyzed. In order to ensure position measurement accuracy, switch condition for two measuring methods and operation mode are introduced, and the measurement accuracy up to $6\ \mu\text{m/m}$. For the gesture measurement of the target, the measurement principle of the monocular camera is analyzed. Based on four non-coplanar feature points of measuring auxiliary instruments (such as Leica T-Mac) mounted on the target, the monocular camera imaging model is simplified as the pinhole imaging model, and combined with the quaternions transformation form of the rotation matrix, measurement system's single direction angle accuracy is up to $0.60''$. This paper constructs based on the position and gesture measurement system of the robot end-effector with laser tracker, setting the robot end-effector according to the predetermined linear trajectory, to move with different velocities. And the laser tracker is used to measure the position and gesture of the robot end-effector trajectory discrete points and the robot end-effector's position error and gesture error are analyzed to check the robot end-effector positioning accuracy. The laser tracker is the measurement device of the position and gesture of the robot end-effector, which can lay the foundation for robot calibration.

Keywords Laser measurement · Monocular vision · Dual frequency modulation · Phase difference interferometry

L. Yu · L. Hang (✉) · W. Cheng · Y. Huangfu · W. Li · G. Yang
College of Mechanical Engineering, Shanghai University of Engineering Science,
Shanghai 201620, China
e-mail: hanglb@126.com

© Springer Nature Singapore Pte Ltd. 2017
X. Zhang et al. (eds.), *Mechanism and Machine Science*,
Lecture Notes in Electrical Engineering 408,
DOI 10.1007/978-981-10-2875-5_122

1541

1 Introduction

Six Degree-of-Freedom (DOF) laser tracker can achieve the position and gesture measurement of a target, and it has been widely used in calibration of the space robot positioning accuracy, and trajectory planning and so on for aerospace manufacturing and assembly. Laser tracker has a variety of types, and the measurement methods include absolute distance measurement, relative distance measurement and absolute and relative distances measurement. In the position measurement of the target, In Reference [1], laser interferometer (IFM) is used to achieve the measurement. The measurement accuracy is high, but the system needs to be reinitialized after the laser beam is off. In Reference [2], the absolute distance meter (ADM) is used to measure the target position, which can ensure the system to continue to measure without initialization, but the measurement accuracy is low. In the gesture measurement of the target, [3] calculates the target's gesture by combining the position where the laser beam irradiates to optoelectronic devices with other sensors(such as angle instrument); the volume and weight of the retroreflector target are large, so its applications are limited.

The paper focuses on the demand for precise positioning and high precision trajectory of the robot end-effector, and researches on the principle of the laser tracker measurement functions in position and gesture of the robot end-effector. Through experimental measurements, by laser interferometer and absolute distance measurement principle, the position of the robot end-effector is measured and researched. By using monocular camera, the gesture of robot end-effector is measured. Combined both, the high precision measurement of the position and gesture of the robot end-effector trajectory is ultimately achieved.

2 System Composition and Measurement Principle

A laser tracker system is mainly composed of a laser tracker, retroreflector targets, an auxiliary controller, an auxiliary computer, and a gesture measurement camera. As shown in Figs. 1 and 2, a laser tracker includes a body, a lengthened sleeve, a magnetic nest and other components. The body includes a gesture measurement, a distance measurement and a tracking controller and other auxiliary components [4–6].

Based on the polar coordinate measurement principle, a retroreflector target is placed on the measurement target, and the coordinates of the center of the retroreflector can be determined by measuring the horizontal and vertical angles and the distance. Through the coordinate transformation, the target position within the Cartesian coordinate system can be calculated. As shown in Fig. 2, taking the steering mirror center as the origin o , a spherical coordinate system $o-R \alpha\beta$ can be established. Taking $P(x, y, z)$ as the target point to be measured, $A(x_a, y_a, z_a)$ as the point of the magnetic nest and L as the distance between point P to point A , the

Fig. 1 Schematic diagram of the six DOF laser tracker appearance. 1 T-Cam camera; 2 body; 3 lengthened sleeve; 4 magnetic nest



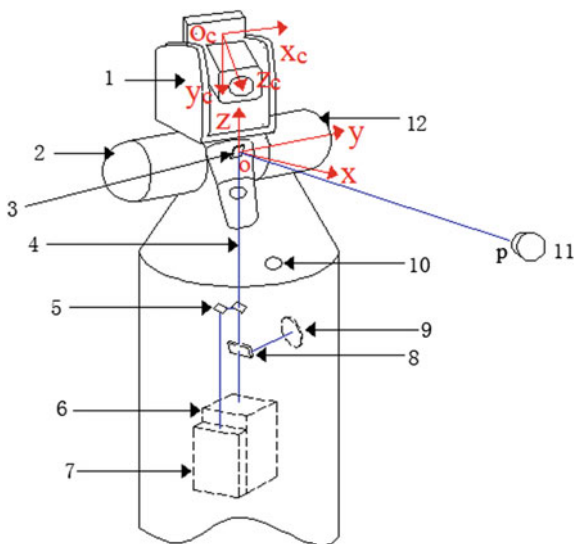
included angle between the AP and the Z axis is β , and the included angle between the projection of AP in the oxy plane and the X axis is α , so the coordinates of the point P(x, y, z) are:

$$\vec{OP} = \vec{OA} + \vec{AP} \tag{1}$$

$$\begin{cases} x = x_a + L\sin\beta\cos\alpha \\ y = y_a + L\sin\beta\sin\alpha \\ z = z_a + L\cos\beta \end{cases} \tag{2}$$

In the above formula (3), the value of β and α are measured by two angle encoders, and the value of L is obtained from the distance measurement.

Fig. 2 Schematic diagram of internal structure of the six DOF laser tracker. 1 monocular camera; 2 angle encoder; 3 steering mirror; 4 laser beam; 5 reflector; 6 IFM; 7 ADM; 8 spectroscope; 9 position detector; 10 magnetic nest; 11 retroreflector; 12 motor



3 Target Position Measurement Principle Based on Laser Tracker

3.1 IFM Measurement Principle

As the laser interferometer optical path diagram is shown in Fig. 3, the He-Ne laser beam splits into the reflected beam S1 and the transmitted beam S2 through a spectroscop. The beam S1 is took as an interference reference light, the beam S2 is took as a measurement light. When the beam S2 is reflected back through the retroreflector target, combined with the beam S1, the coherent beam is formed.

If the retroreflector target is moving at the speed of V , according to the Doppler effect, the frequency of the laser beam returned from the retroreflector target will be

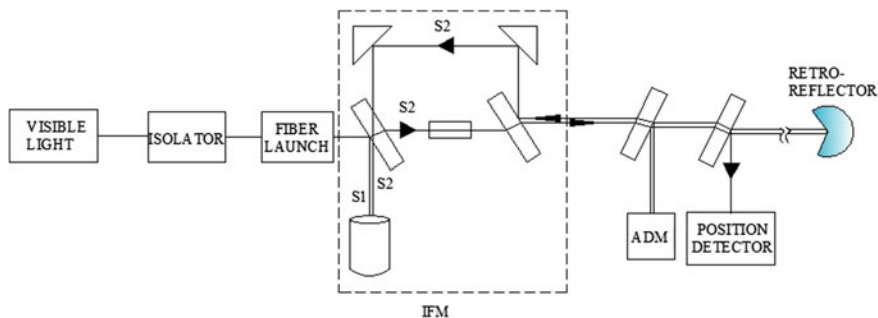


Fig. 3 IFM measurement optical path diagram

changed. If the reference light frequency is f_1 , the measurement light frequency is f_2 , the frequency change will be:

$$\Delta f = f_2 - f_1 \quad (3)$$

And the measurement beam path changes are 2 times of retroreflector target displacement, so the Doppler frequency shift can be given as:

$$\Delta f = \frac{2v}{c}f \quad (4)$$

In the above formula (4), c is the light propagation velocity in the air, v is the movement speed of the retroreflector target, f is the light wave frequency (about 10^{14-15} Hz). Accordingly, assuming $v = 10$ m/s, $c = 3 \times 10^8$ m/s, so $\Delta f = 6.7 \times 10^{6-7}$ Hz.

Setting the distance between the measurement light and the reference light or the movement distance of the retroreflector target as L , n is refractive index of air (about 1.00029), Δt is the movement time of the retroreflector target, $\Delta\varphi$ is phase difference between the measurement beam S2 with the reference beam S1, λ is the wavelengths of the light, so we can get the value of L :

$$L = \frac{c}{n} \cdot \frac{\Delta t}{2} = \frac{c}{n} \cdot \frac{\Delta\varphi}{2\Delta 2\pi f} = \frac{\Delta\varphi}{2\pi} \cdot \frac{\lambda}{2n} \quad (5)$$

By the above formula (5), if the phase difference is 2π , and because the Doppler frequency shift is small, the movement distance resolution L of the retroreflector target can be approximately equal to half a wavelength (about $0.3 \mu\text{m}$). In order to improve the measurement resolution of the laser interferometer, the frequency multiplication method, the CCD subdivision method and the microcomputer subdivision method can be used. The methods can make the measurement resolution reach nanometer level [7]. For example, the four frequency multiplication, the eight frequency multiplication method can be recorded to $1/4$, $1/8$ interference fringe movement.

3.2 ADM Measurement Principle

As the laser interferometer (IFM) is an incremental code measurement device, the interference (IF) device will stop counting when the system breaks off the light. And the entire system will need to be reinitialized. So absolute distance meter (ADM) is configured in the laser tracker. When lights are broken off, quick connection with measurement system can provide reference distance measurement data to ensure the IF device return to work.

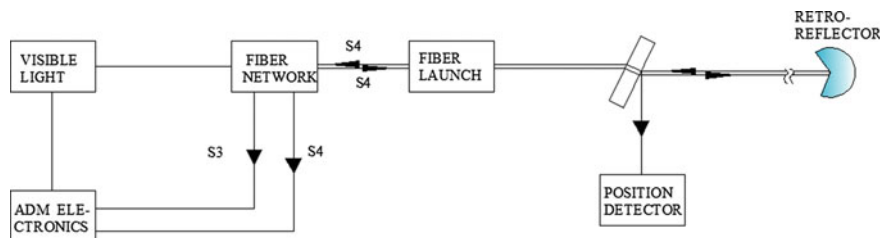


Fig. 4 ADM distance optical path diagram

As absolute distance meter optical path diagram is shown in Fig. 4, the ADM laser modulated by the ADM electronic device is divided into the reference beam S3 and the measurement beam S4 through the optical fiber coupler. The reference beam S3 and the measurement beam S4 with phase information are converted into electrical signals to be mixed with the local oscillator signal respectively, and then the phase difference heterodyne detection is performed.

When laser phase method is used to measure the absolute distance, the amplitude of the laser is modulated with the modulation frequency f , and the absolute distance d can be measured.

$$d = \frac{c}{2fn} \cdot \frac{\Delta\theta}{2\pi} \quad (6)$$

In the formula (6), $\Delta\theta$ is the phase difference between the reference beam S3 and the measurement beam S4. As $\Delta\theta$ is 2π for a period to change, and the phase difference changed as 2π for a period is unable to be determined in laser phase method, the distance d cannot be calculated. In order to solve the problem, the lower modulation frequency is used to make the measurement distance (calculated by phase difference) less than 2π . But when the phase error is constant, the modulation frequency is smaller, the measurement distance error will be larger. In order to improve the measurement precision and achieve the long distance measurement, the dual frequency modulation signal can be used to measure the distance. Low frequency signal to ensure the measurement range, and high frequency signal to ensure the measurement accuracy [8].

When the system uses high frequency signal to measure the distance, the frequency will be above 10^9 Hz. This has a very high demand to the digital instrumentation, and the distance error may be larger. So we need to introduce the mixing process, that's a method by using difference frequency to process the reference signal and the measurement signal [8, 9]. After reducing frequency, the phase difference is constant, the signal period is enlarged, the phase measurement resolution is improved, and the measurement accuracy is also improved.

According to the parameters of a laser tracker, ADM maximum distance is 25 m, ADM measurement accuracy is $10 \mu\text{m}$. We can select the launch frequency is 5 MHz and 1 GHz respectively, the vibration frequency is 5.004 MHz and

1.004 GHz, the difference frequency signal Δv is 4 kHz, the pulse signal frequency v is 300 MHz. Assuming $v_1 = 5$ MHz, $v_2 = 1$ GHz, $\Delta\theta = 2\pi$, the maximum distance can be measured.

$$d_1 = \frac{\Delta\theta}{2\pi} \cdot \frac{c}{2nv_1} = \frac{3 \times 10^8}{2 \times 1.00029 \times 5 \times 10^6} \approx 29.99(\text{m}) \quad (7)$$

$$d_2 = \frac{\Delta\theta}{2\pi} \cdot \frac{c}{2nv_2} = \frac{3 \times 10^8}{2 \times 1.00029 \times 1 \times 10^9} \approx 0.15(\text{m}) \quad (8)$$

The distance resolution of measurement phase distance is

$$\partial d_1 = \lambda_1 \cdot \frac{\Delta v}{v} = 59.98 \times \frac{4 \times 10^3}{300 \times 10^6} = 0.80(\text{mm}) \quad (9)$$

$$\partial d_2 = \lambda_2 \cdot \frac{\Delta v}{v} = 0.3 \times \frac{4 \times 10^3}{300 \times 10^6} = 4(\mu\text{m}) \quad (10)$$

The calculation results show that the above parameters can meet the requirements of the instrument measurement. After the reference beam and the measurement beam have been photoelectric converted, mixing filtered, and amplified and shaped, the absolute distance d is

$$d = 0.80 \times n_1 + 4 \times 10^{-3} \times n_2(\text{mm}) \quad (11)$$

In the formula (11), n_1 , n_2 are all integers.

4 Gesture Measurement Principle

4.1 Coordinate System Definition

The laser tracker system in the measurement involves multiple coordinate systems, including the target coordinate system and the camera coordinate system, the image plane pixel coordinate system, the image plane physical coordinate system [10]. Each coordinate system is shown in Fig. 5.

The definition of each coordinate system as follows:

Target coordinate system $o_t x_t y_t z_t$: the origin o_t of the coordinate system is located in the upper surface geometry center of the target unit; the z_t axis is vertically upward to the target unit, the x_t axis is up to parallel to the paper surface, and the y_t axis and the x_t and z_t axes form the right hand coordinate system.

Camera coordinate system $o_c x_c y_c z_c$: the origin o_c of the coordinate system is located in the optical center of the camera; the positive z_c axis goes along the optical

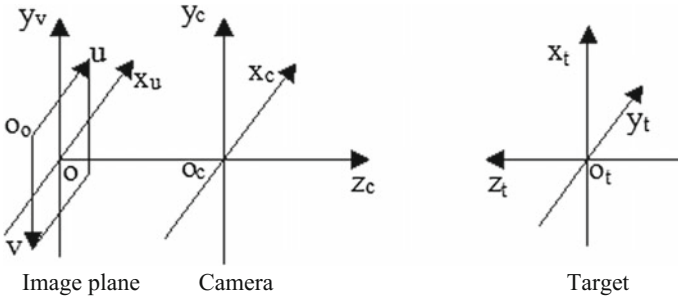


Fig. 5 The laser tracker coordinate systems

axis of the camera toward the target, the x_c axis and the y_c axis respectively parallel with the image plane U axis and V axis.

Image plane physical coordinate system $ox_u y_v$: the coordinate system is the physical coordinate system; the origin o of the coordinate system is the intersection point of the optical axis of the camera and the image plane, the x_u axis and the y_v axis are parallel to the U axis and the V axis of the image plane.

Image plane pixel coordinate system $o_o uv$: the coordinate system is the pixel coordinate system; the coordinate system origin o_o is located in the upper left corner of the image, the U axis and the V axis are parallel with the row and column of the image plane.

4.2 Monocular Camera Measurement Model

Setting any feature point p_t in space as (x_t, y_t, z_t) in the target coordinate system, as (x_c, y_c, z_c) in the camera coordinate system, as (x_u, y_v) in the image plane physical coordinate system, as (u, v) in the image plane pixel coordinate system.

If origin o in the image plane physical coordinate system $ox_u y_v$ is coordinates (u_0, v_0) in the coordinate system $o_o uv$. d_x, d_y respectively represents the physical dimensions of each pixel in the x axis and the y axis direction. So we can get the following formula.

$$\begin{bmatrix} u \\ v \\ 1 \end{bmatrix} = \begin{bmatrix} \frac{1}{d_x} & 0 & u_0 \\ 0 & \frac{1}{d_y} & v_0 \\ 0 & 0 & 1 \end{bmatrix} \begin{bmatrix} x_u \\ y_v \\ 1 \end{bmatrix} \tag{12}$$

If the laser tracker coordinate systems are set according to Fig. 5, the relationship between the camera coordinate system and the target coordinate system can be expressed by the linear combination of the rotation matrix R and the translation matrix t . Therefore, the space conversion between the two coordinate systems are as follows:

$$\begin{bmatrix} x_c \\ y_c \\ z_c \\ 1 \end{bmatrix} = \begin{bmatrix} R & t \\ 0^T & 1 \end{bmatrix} \begin{bmatrix} x_t \\ y_t \\ z_t \\ 1 \end{bmatrix} \tag{13}$$

In general, the object distance is far greater than the focal length f . By Gaussian imaging formula, we can approximately replace the camera lens imaging model with the pinhole imaging model. The feature point p_t transformation relationship between the image plane physical coordinate system and the camera coordinate system is:

$$z_c \begin{bmatrix} x_u \\ y_v \\ 1 \end{bmatrix} = \begin{bmatrix} f & 0 & 0 & 0 \\ 0 & f & 0 & 0 \\ 0 & 0 & 1 & 0 \end{bmatrix} \begin{bmatrix} x_c \\ y_c \\ z_c \\ 1 \end{bmatrix} \tag{14}$$

With the formula (12)–(14), we can know

$$z_c \begin{bmatrix} u \\ v \\ 1 \end{bmatrix} = \begin{bmatrix} f_x & 0 & u_0 & 0 \\ 0 & f_y & v_0 & 0 \\ 0 & 0 & 1 & 0 \end{bmatrix} \begin{bmatrix} R & t \\ 0^T & 1 \end{bmatrix} \begin{bmatrix} x_t \\ y_t \\ z_t \\ 1 \end{bmatrix} = M_0 \begin{bmatrix} x_t \\ y_t \\ z_t \\ 1 \end{bmatrix} \tag{15}$$

In the above formula (15), $f_x = f/d_x, f_y = f/d_y, M_0$ is the product of the projection matrix and the transformation matrix.

4.3 Monocular Camera Gesture Measurement

Quaternion method is used to represent the target’s 3D gesture parameters, combined with non-coplanar four feature points for linear solving target gesture; avoid rotation angle to be not limited and the 3D gesture parameters may be multi-valued when the Euler angle is used to represent the parameters [11]. Setting the feature point p_i in the target coordinate system as coordinates $p_{ci}(x_{ci}, y_{ci}, z_{ci})$, in the image plane physical coordinate system as coordinates $p_{ti}(x_{ti}, y_{ti})$. The coordinate mapping relation of the feature point p_i in the two coordinate system is:

$$z_c x_{ti} = x_{ci} f, \quad z_c y_{ti} = y_{ci} f \tag{16}$$

By the formula (13), the target’s gesture function:

$$p_{ci} = M_1 p_{ti} + t \tag{17}$$

In the above formula (17), M_1 is expressed with quaternion. ($q = q_0 + q_1i + q_2j + q_3k$).

$$\mathbf{M}_1 = \begin{bmatrix} q_0^2 + q_1^2 - q_2^2 - q_3^2 & 2(q_1q_2 + q_3q_0) & 2(q_1q_3 - q_2q_0) \\ 2(q_1q_2 - q_3q_0) & q_0^2 - q_1^2 + q_2^2 - q_3^2 & 2(q_2q_3 + q_1q_0) \\ 2(q_1q_3 + q_2q_0) & 2(q_2q_3 - q_1q_0) & q_0^2 - q_1^2 - q_2^2 + q_3^2 \end{bmatrix}$$

The four parameters q_0, q_1, q_2, q_3 in \mathbf{M}_1 matrix meet the unit constraints:

$$q_0^2 + q_1^2 + q_2^2 + q_3^2 = 1 \quad (18)$$

Camera focal length is set to 0.033 m, distance between the camera and the target is set to 2 m, the four feature points coordinates in the target coordinate system are $p_{t1} = [-0.15 \ 0.08 \ 0]^T$, $p_{t2} = [-0.15 \ 0.08 \ 0]^T$, $p_{t3} = [0.15 \ 0.08 \ 0]^T$, $p_{t4} = [0 \ 0 \ 0.1]^T$. According to the formula (16), we know, the target feature points coordinates in the image plane physical coordinate system are corresponding to $p_1'(-0.00198, 0.001056)$, $p_2'(0.00198, -0.001056)$, $p_3'(0.00198, 0.001056)$, $p_4'(0,0)$. The feature points coordinates in the image plane physical coordinate system and the corresponding coordinates in the target coordinate system are substituted into the formula (17), and we can get between two coordinate systems 180° around the X axis rotation angle, 0° around the y-axis rotation angle, 90° around the Z axis rotation angle, which matches with the relationship in Fig. 5.

5 Experimental Application and Analysis

Experimental equipment configuration is shown in Fig. 6. With 6R Serial Robot as the target to be measured, the laser tracker and Leica T-Mac tracking control detector are used to measure linear trajectory and position and gesture of the robot end-effector to verify accuracy.

5.1 Linear Trajectory Measurement

Experimental operation and procedure: The laser tracker sampling frequency is respectively set to 500 and 1000 Hz, and the “space scan” mode is used to real-time track the robot end-effector. The Leica T-Mac tracking control detector is fixed to the robot arm end-effector, and the robot end-effector moves at 50 mm/s, 100 mm/s speed along the same direction in a straight line, repeat operation 5 times, and the distance is 200 mm.

Figures 7 and 8 are respectively the theoretical and actual trajectories of the robot end-effector with the speed of 50, 100 mm/s in 5 times repeat motion. The dotted lines are the actual trajectories composed of the 200 mm sampling points, and the thick real line is the theoretical trajectory. Comparing the actual trajectories with the theoretical trajectory, the robot end-effector trajectory maximum error is

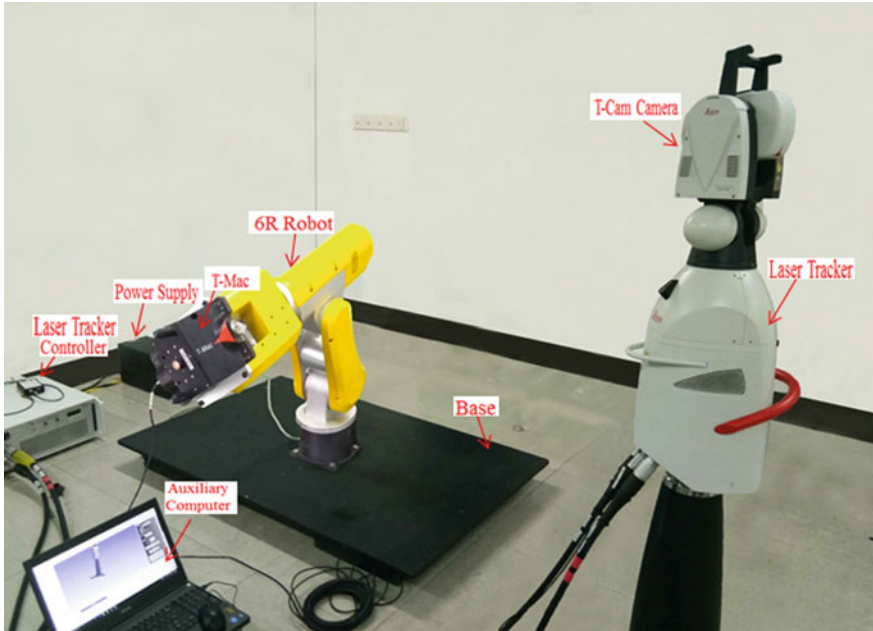


Fig. 6 Experimental measurement equipment

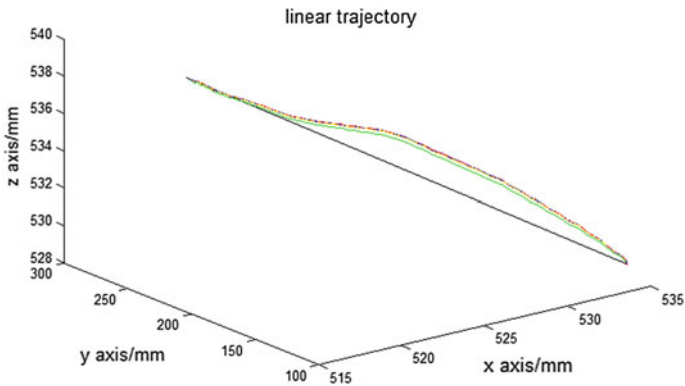


Fig. 7 The robot end-effector trajectory plot at 50 mm/s speed

4.1502 mm with the speed of 50 mm/s, speed is 100 mm/s, the robot end-effector trajectory maximum error for 4.8978 mm with the speed of 100 mm/s. Compared with the five actual trajectories sampling point position coordinates of the robot end-effector, the maximum error of the repetitive motion trajectory of the robot

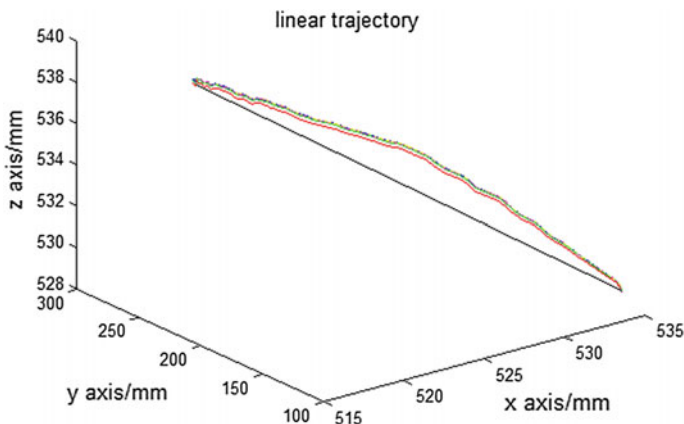


Fig. 8 The robot end-effector trajectory plot at 100 mm/s speed

end-effector of a robot at the speed of 50 mm/s is 0.0526 mm, and at the speed of 100 mm/s is 0.0817 mm.

5.2 Position and Gesture Accuracy Measurement

Experimental operation and procedure: The laser tracker sampling frequency is set to 1000 Hz, and the “6D scan” mode is used to measure the position and gesture of the robot end-effector. The Leica T-Mac tracking control detector is fixed to the robot arm end-effector, and the robot end-effector moves at 200, 500 mm/s speed along the same direction, and the distance is 200 mm. When the robot end-effector reaches a predetermined position to stop, the coordinates are set to (-181.9754, 548.0354, 216.1769), and the test repeats 30 times.

Tables 1 and 2 are respectively the position and gesture measurement statistical results of the robot end-effector moving at 200, 500 mm/s speed. From Table 1, we can see when the robot end-effector moves at the speed of 200 mm/s, the position error in the y axis direction and the gesture error around the x axis are the maximum error, respectively 0.0540 mm, 0.0049°, and the robot end-effector repeat

Table 1 The position and gesture measurement results at 200 mm/s speed

Error	Index						
	x axis position	y axis position	z axis position	Position	Angle around x axis	Angle around y axis	Angle around z axis
RMS	0.0096	0.0048	0.0059	0.0122	0.0009	0.0012	0.0006
Maximum	0.0493	0.0540	0.0307	0.0793	0.0049	0.0024	0.0020

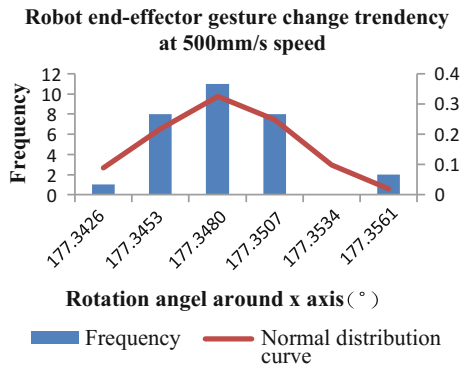
Distance units: mm, angle unit: °

Table 2 The position and gesture measurement results at 500 mm/s speed

Error	Index						
	x axis position	y axis position	z axis position	Position	Angle around x axis	Angle around y axis	Angle around z axis
RMS	0.0207	0.023	0.0088	0.0328	0.0032	0.0011	0.0014
Maximum	0.0745	0.0820	0.0342	0.1159	0.0138	0.0048	0.0045

Distance units: mm, angle unit: °

Fig. 9 x axis gesture histogram and normal distribution curve of the robot end-effector



positioning accuracy is 0.0122 mm. From Table 2, when the robot end-effector moves at the speed of 200 mm/s, the position error in the y axis direction and the gesture error around the X axis are the maximum error, respectively 0.0820 mm, 0.0138°, and the robot end-effector repeat positioning accuracy is 0.0328 mm.

Comparing Table 1 with Table 2, we know when the robot movement speed is not at the same time, the repeat positioning accuracy will change. Figures 9, 10, 11 are the frequency histogram and normal distribution of the x, y and z axis direction of the robot end-effector gesture when the speed is 500 mm/s. Setting the robot

Fig. 10 y axis gesture histogram and normal distribution curve of the robot end-effector

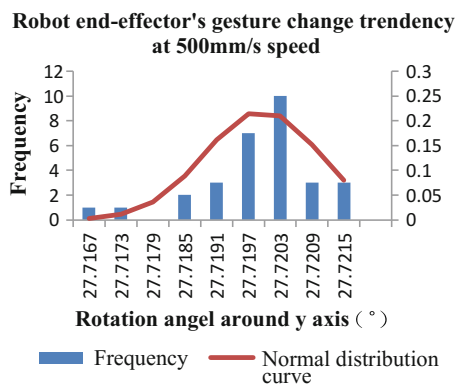
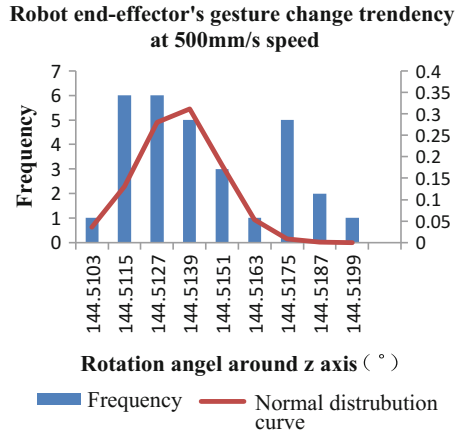


Fig. 11 z axis gesture histogram and normal distribution curve of the robot end-effector



end-effector predetermined gesture to $(177.3469^\circ, 27.7196^\circ, 144.5139^\circ)$, by normal distribution curve, the robot end-effector reaches the practical gesture with the highest probability, namely $(177.3477^\circ, 27.7203^\circ, 144.5139^\circ)$, and the gesture errors are $(0.0008^\circ, 0.0007^\circ, 0^\circ)$.

6 Conclusion

- (1) With laser interferometry, absolute distance and monocular vision technology, six DOF laser tracker can realize the high precision measurement of the robot end-effector's position and gesture.
- (2) Based on laser tracker, the position and gesture measurement system of the robot end-effector is constructed, and the coordinates involved in the measurement system are defined.
- (3) With six DOF laser tracker, the position and gesture of the robot end-effector trajectory discrete points are measured. By comparing the theoretical position and gesture, the position and gesture errors of the robot end-effector are analyzed, and the positioning accuracy of the robot end-effector are detected.
- (4) Through the analysis of six DOF laser tracker measurement principle, it cannot only provide a certain basis for the calculation of robot error calibration and error compensation, but also provide corresponding theoretical references for the research and development of the measurement equipment and application.

Acknowledgment This work is supported by the Shanghai Committee of Science and Technology Key Support Project (12510501100); Fund for Nature (NFS51475050).

References

1. Yang Z, Dong H, Hu K (2013) Design of phase difference measurement system for dual frequency laser interferometer. *Inf Technol* 2:11–14
2. Bridges RE, Hoffer JM. Absolute distance meter that measures a moving retroreflector. US: 7701559 B2.2010-04-20
3. Chen J, Tang T, Fan B (2007) Five/six degrees of freedom laser tracking measurement technology principle analysis. *Aersp Meas Technol* 27(3):58–62
4. Bridges RE. Six degree-of-freedom laser tracker that cooperates with a remote sensor. US: 2012/0265479 A1. 2012-10-18
5. Hou B (2012) The research on 6D precision laser tracking measurement technology. Xi'an Institute of Optics and Precision Mechanics in Chinese Academy of Sciences, Xi'an
6. Muralikrishnan B, Phillips S, Sawyer D (2016) Laser trackers for large-scale dimensional metrology: a review. *Precis Eng* 44:13–28
7. Chen J, Zhang Y, Zhang Y, Xie Z (2015) A comprehensive evaluation of the CCD pixel subdivision algorithm based on analytic hierarchy process. *J Opt*, 35(7)
8. Jiao Y, Yang J, Ji R (2015) Research and design on laser tracker absolute distance measurement in phase method. *Exp Technol Manage* 32(6):79–83
9. Jiao M, Feng Q, Wang M, Liu J (2014) Laser sensor and measurement. Science Press, Beijing
10. Neumayr R, Harker M, O'Leary P et al (2012) New approaches to machine vision based displacement analysis. In: 2012 IEEE international instrumentation and measurement technology conference (I2MTC). Graz, Austria, pp 979–984
11. Ye Y (2011) The method and system to realize of 3D pose measurement based on monocular vision. Harbin Institute of Technology, Harbin
12. Yang F, Fan B, Li G, Yang Z (2014) Laser tracker dynamic accuracy test. *J Metrol* 35 (6A):119–122

Kinematic Synthesis of Planar Cam Mechanism with Translating Roller Follower by Kinematic Analysis of Binary Link Chain

W.W. Zhu and Z.H. Lan

Abstract In the synthesis of planar cam mechanisms, the designer should check the pressure angle and radius of curvature of the cam profile which involve burdensome mathematical derivation and calculation. In order to simplify the mathematical derivation and calculation, the kinematic analysis of a binary link chain is carried out and the results are then used to synthesize the planar cam mechanism with translating roller follower, including the calculation of cam profile, pressure angle and radius of curvature of the cam profile. A numerical example is given to verify the effectiveness of the method.

Keywords Planar cam mechanism · Translating roller follower · Kinematic synthesis · Kinematic analysis · Binary link chain

1 Introduction

Planar cam mechanisms with translating follower are widely used to realize the expected output motion. After the output motion of the follower is determined, the designer should choose some basic kinematic dimensions of the mechanism, such as radius of prime circle and the offset. Then he or she should calculate the profile of the cam. The pressure angle and radius of curvature of the cam profile should also be calculated to check the performance of the mechanism. Many researchers have focused on the graphical solution method for determining the radius of curvature of the planar cam [1–3]. Xu [4, 5] calculated the radius of curvature of the planar cam by application of Freudenstein's third theorem to the equivalent four-bar linkage of the cam mechanism. Zhang et al. [6] discussed the effect of some cam's parameters on the minimum radius of curvature of the cam profile for the disk cam mechanism with oscillating follower and a constant base circle. Ye et al. [7] calculated the radius of curvature of the cam by differentiating the coordinates with

W.W. Zhu (✉) · Z.H. Lan

School of Mechanical Engineering and Automation, Fuzhou University, Fuzhou, China
e-mail: lgth@fzu.edu.cn

respect to the cam rotating angle. Yu et al. [8–10] proposed a method of determining the radius of curvature of a planar cam profile by spline interpolation. Xia et al. [11] calculated the radius of curvature of the cam profile by the least square method. The above methods involve burdensome mathematic derivation and calculation. In order to simplify the mathematic derivation and calculation, Lan Z.H. et al. applied the knowledge of a binary link chain to the synthesis of planar cam mechanisms with oscillating roller follower by analyzing the coordinates, velocity and acceleration of a point in the binary link chain [12]. In this paper, the above work is extended to the cam mechanisms with translating follower.

2 Kinematic Synthesis of Planar Cam Mechanism with Translating Roller Follower

2.1 Inversion Principle of the Mechanism

A planar cam mechanism with translating roller follower is shown in Fig. 1. The cam is represented by its pitch curve. The cam rotates counter-clockwise with a constant angular velocity ω . The angular acceleration ε of the cam is supposed to be 0 as usual. The follower translates back and forth along the guide way of the frame

Fig. 1 A planar cam mechanism with translating roller follower

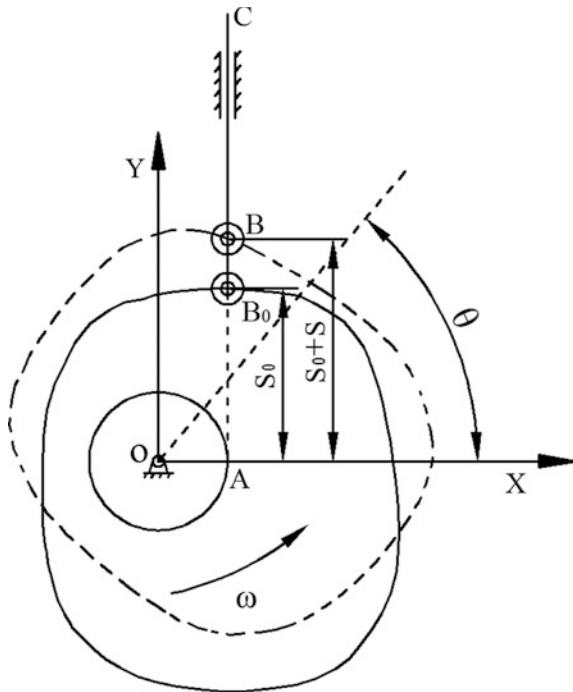
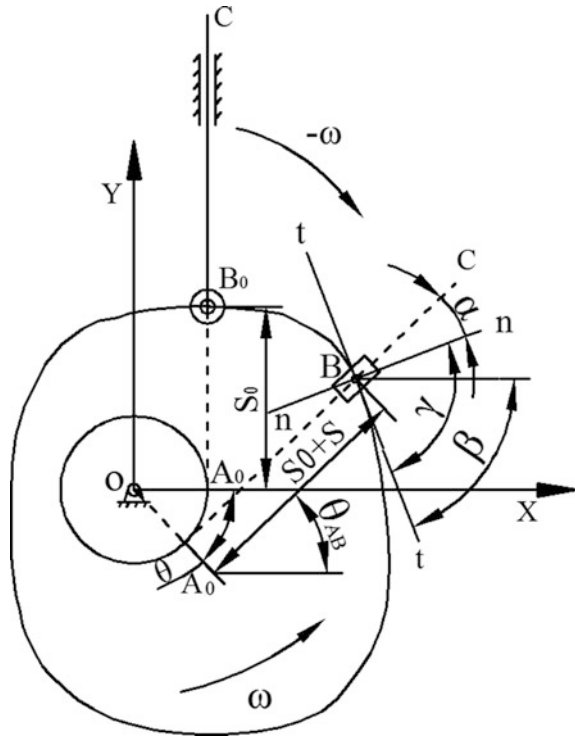


Fig. 2 The inverted mechanism of the planar cam mechanism



from the initial position B_0 with the distance S_0 . After the cam rotates through an angle θ , the follower reaches the position B with the distance $S_0 + S$, as shown in the figure.

To get the cam profile, the inversion principle of the mechanism is applied. That is adding an inverse angular velocity $-\omega$ imaginatively to the whole mechanism about the axis O of the cam while the cam rotates with an angular velocity ω . This makes the cam fixed at the initial position and the frame rotate clockwise about the axis O as shown in Fig. 2.

As distance S is the function of θ and prescribed by the motion law of the follower, the motion of the follower after the inversion is determined and the path which the center of the roller follows is the pitch curve of the cam. The cam contour which meshes with the roller can be solved as the parallel curve of the pitch curve. That is the general principle in synthesis of planar cam mechanisms with roller followers.

2.2 Kinematic Analysis of Binary Link Chain

To get the pitch curve and the cam contour of the cam, the motion of the point B (center of the roller) after the inversion of the mechanism should be solved. This

can be achieved by the kinematic analysis of binary chain OAB. Firstly, the motion of the guide-bar OAC is solved according to the inversion of the frame. Constructing coordinate system xOy in Fig. 2, the angular velocity of the guide-bar OAC is $-\omega$. Then if we know the motion law of the slider, we can easily get the coordinates of point B

$$\begin{cases} x_B = x_A + s_{BA} \cos(\theta_{AB}) \\ y_B = y_A + s_{BA} \sin(\theta_{AB}) \end{cases} \quad (1)$$

where x_A and x_B are the coordinate of A, s_{BA} is the distance between point A and point B on the slider. θ_{AB} is the orientation of the slider after the inversion with

$$\theta_{AB} = \frac{\pi}{2} - \theta \quad (2)$$

Considering all situations, we have Eq. (3)

$$\theta_{AB} = \frac{\pi}{2} - M\theta \quad (3)$$

where M is the cam rotation coefficient. M takes $+1$ when the cam rotates counter-clockwise while -1 for the clockwise rotation of the cam.

Taking the time derivative of Eq. (3) gives

$$\begin{cases} v_{xB} = v_{xA} - s_{BA}\omega_{AB} \sin(\theta_{AB}) + v_{BA} \cos(\theta_{AB}) \\ v_{yB} = v_{yA} + s_{BA}\omega_{AB} \cos(\theta_{AB}) + v_{BA} \sin(\theta_{AB}) \end{cases} \quad (4)$$

where v_{xB} and v_{yB} are the velocities of point B, v_{xA} and v_{yA} are the velocities of point A, v_{BA} is the relative velocity of slider to the guide bar, i.e. the velocity of the follower respect to the frame. ω_{AB} is the angular velocity of the guide-bar after the inversion, i.e., $\omega_{AB} = -M\omega$.

Taking the time derivative of Eq. (4) gives

$$\begin{cases} a_{xB} = a_{xA} - s_{BA}\omega_{AB}^2 \cos(\theta_{AB}) - 2v_{BA}\omega_{AB} \sin(\theta_{AB}) - s_{BA}\varepsilon_{AB} \sin(\theta_{AB}) + a_{BA} \cos(\theta_{AB}) \\ a_{yB} = a_{yA} - s_{BA}\omega_{AB}^2 \sin(\theta_{AB}) + 2v_{BA}\omega_{AB} \cos(\theta_{AB}) + s_{BA}\varepsilon_{AB} \cos(\theta_{AB}) + a_{BA} \sin(\theta_{AB}) \end{cases} \quad (5)$$

where a_{xB} and a_{yB} are the accelerations of point B, a_{xA} and a_{yA} are the accelerations of point A, ε_{AB} is the angular acceleration of the guide-bar (in the inverted mechanism $\varepsilon_{AB} = 0$), a_{BA} is the relative acceleration of slider to the guide bar, i.e. the acceleration of the follower respect to the frame.

2.3 Cam Contour and Pressure Angle

By the kinematic analysis of the follower after the inversion, the coordinates, velocity and acceleration of point B are known as x_B , y_B , v_{xB} , v_{yB} , a_{xB} , a_{yB} . x_B and y_B represent the pitch curve of the cam. v_{xB} and v_{yB} can be used to represent the tangent tt of the point B on the pitch curve with its direction angle as

$$\beta = a \tan 2(v_{yB}, v_{xB}) \quad (6)$$

where $a \tan 2$ is the inverse tangent function with the value covering 2π . The direction angle of the outer normal nn at point B to the pitch curve is then

$$\gamma = \beta + \frac{\pi}{2} \quad (7)$$

When all situations are considered, Eq. (8) is obtained

$$\gamma = \beta + M \frac{\pi}{2} \quad (8)$$

Now the cam contour can be solved as

$$\begin{cases} x_T = x_B \mp r_r \cos \gamma \\ y_T = y_B \mp r_r \sin \gamma \end{cases} \quad (9)$$

where r_r is the radius of the roller, the minus sign is for the inner cam contour and plus sign for the outer one.

The pressure angle of the cam mechanism is the angle between the normal of the pitch curve and the segment AB in Fig. 2, that is

$$\alpha = |\beta + \theta| \quad (10)$$

2.4 Radius of Curvature of the Cam Profile

It is well-known that the normal acceleration of a moving particle on a plane can be calculated as

$$a_n = \frac{v^2}{\rho} \quad (11)$$

where ρ is the radius of curvature of the path of the moving particle. As the pitch curve of the cam can be seen as the path of the roller center, the radius of the curvature of the pitch curve can be calculated through the kinematic analysis of the roller center after the inversion. First of all, the normal acceleration of the roller center is

$$a_n = -(a_{yB} \cos \beta - a_{xB} \sin \beta) \quad (12)$$

When all situations are considered, Eq. (13) is obtained

$$a_n = -M(a_{yB} \cos \beta - a_{xB} \sin \beta) \quad (13)$$

Then the radius of the curvature can be calculated as

$$\rho = \frac{1}{a_n} \left(v_{xB}^2 + v_{yB}^2 \right) \quad (14)$$

As the cam contours are parallel to the pitch curve, their radii of curvature are

$$\rho_T = \rho \mp r_r \quad (15)$$

where the minus sign is for the inner cam contour and plus sign for the outer one.

3 Numerical Example

A numerical example of a planar cam mechanism with translating roller follower as Fig. 1 is given, It's a positive offset mechanism. In this mechanism, the cam rotates counterclockwise, the radius r_p of the prime circle is 40 mm, the lift of the follower is 38 mm, the value of the offset e is 24 mm, the radius of the roller $r_r = 12$ mm. The follower rises with cosine acceleration motion curve and returns with 3-4-5 polynomial motion. In this example the cam angle for rise, the cam angle for outer dwell, the cam angle for return and the cam angle for inner dwell are 150° , 60° , 120° , and 30° , respectively.

Then the coordinates of a series of point on the cam pith curve, the inner cam contour, the outer cam contour, the pressure angle and the radius of the curvature of the inner cam contour, the radius of the curvature of the outer cam contour can be calculated. Some numerical synthesis results are shown in Figs. 3, 4 and 5. Figure 3 is the pitch curve and inner cam contour. Figure 4 is the radius of curvature of the inner cam contour, while Fig. 5 is the pressure angle of the cam mechanism.

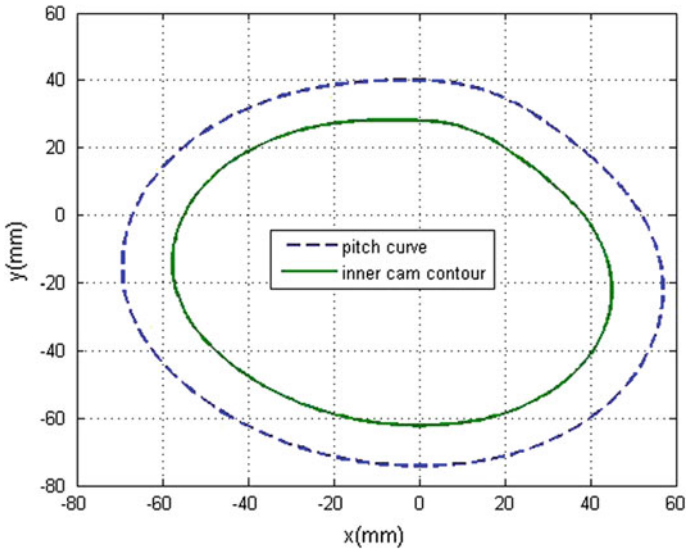


Fig. 3 The pitch curve and inner cam contour

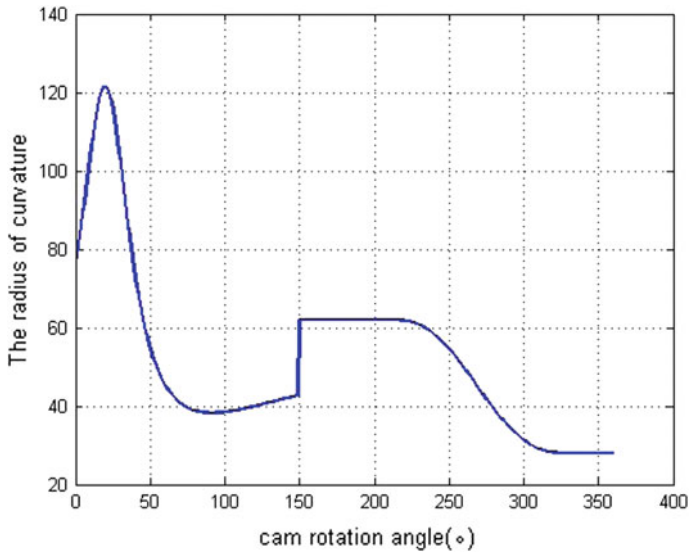


Fig. 4 The radius of curvature of the inner cam contour

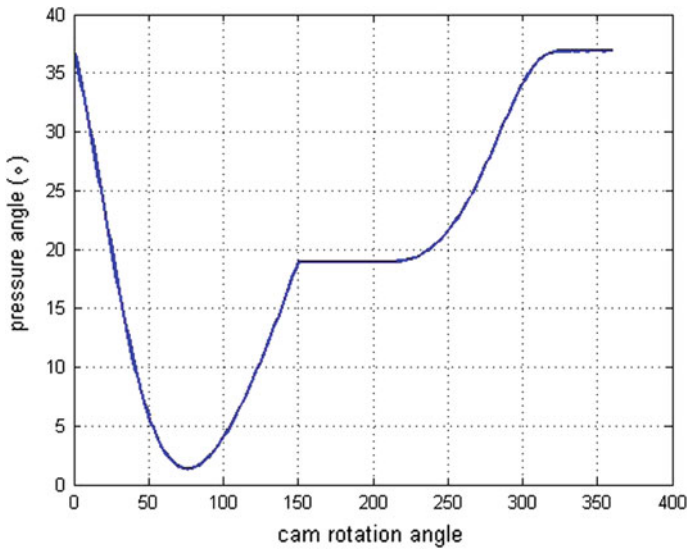


Fig. 5 The pressure angle of the mechanism

4 Conclusions

The kinematic analysis of a binary link chain is applied to synthesize the planar cam mechanism with translating roller follower, including the calculation of cam profile, pressure angle and radius of curvature of the cam profile. Burdensome mathematic derivation and calculation are not needed.

References

1. Xu GS (2001) The determination of radius of curvature of contour for disk-cams with straight moving follower. *Mach Des (Chinese)* (6):14–15
2. Xu GS (2001) A graphical method for determining the radius of curvature of disk-cam. *Mech Sci Technol (Chinese)* 20(1):64–65
3. Zhang J, Yang XP, Wu HW (2004) CAD animation method for designing profile curve and cutter center track of disk-cam with straight moving follower. *Machine (Chinese)* 31(12):48–50
4. Xu GS, Gao XD, Xu WX (2002) A new method for computing the radius of curvature of a cam profile with oscillating flat-faced follower. *Mech Sci Technol (Chinese)* 21(3):204–206
5. Xu GS, Gao XD (2004) A new method for computing the radius of curvature of cam with oscillating roller follower. *J Xi'an Univ Eng Sci Technol (Chinese)* 18(1):72–75
6. Zhang YT, Qiao YD (2000) Relationship between cam profile curvature radius and the basic parameters. *J Yanshan Univ* 24(1):24–26
7. Ye ZH, Lan ZH, Smith MR (2001) *Mechanisms and machine theory*. Higher Education Press, Beijing

8. Yu XY, Lan ZH (2008) The application of substitute equivalent linkage instead of higher pair in kinematic analysis of a planar cam mechanism with a roller translating follower. *J Fuzhou Univ (Nat Sci) (Chinese)* 36(5):709–713
9. Yu XY, Lan ZH (2008) The application of cubic spline interpolation in determining planar cam profile curvature radius. *Mech Transm (Chinese)* 32(1):50–51
10. Yu XY, Lan ZH (2012) Kinematic analysis of planar cam mechanism with translating flat-faced follower by equivalent linkage method. In: *CCMMS2012, Huangshan, China*
11. Xia HJ, Chen XM, Han QS (2014) Application of curve fitting in solving the curvature radius of cam. *Mach Res Appl (Chinese)* 27(6):105–106
12. Lan ZH, Yu XY (2015) Kinematic synthesis of planar cam mechanism with oscillating roller follower by kinematic analysis of binary link chain. In: *The 14th IFToMM world congress, Taipei, Taiwan*